The Overpotential of the Manganese Dioxide Electrode

A. M. Chreitzberg, Jr., and W. C. Vosburgh

Duke University, Durham, North Carolina

ABSTRACT

The overpotential of electrodeposited MnO_2 electrodes can be measured with fair reproducibility. Overpotential is a linear function of the logarithm of the ammonium ion concentration, at constant *p*H, but not of the logarithm of the apparent current density. It varies much less with the hydrogen ion than with the ammonium ion concentration. When ammonium ion in the electrolyte is replaced by methylammonium, dimethylammonium, or trimethylammonium ion the overpotential is increased. The change of overpotential with temperature was measured. The bearing of the results on the theory of the discharge mechanism is considered.

Experience in determining open-circuit discharge curves (1) suggested a method of measuring the overpotential of MnO_2 electrodes made by electrodeposition on graphite rods. The open-circuit discharge curve is determined by interrupting a discharge at intervals, measuring the equilibrium open-circuit potential, and plotting this against the amount of discharge in milliampere-minutes. The difference in electrode potential between the open-circuit discharge curve and the closed-circuit discharge curve at any stage in the discharge is taken as the overpotential at that stage.

Experimental

Preparation of electrodes.—Electrodes were made essentially as described previously (1–3). MnO_2 was deposited electrolytically on graphite rods of 8 cm^2 exposed area which had been pretreated by immersion in boiling water until evolution of gas ceased. The temperature of electrodeposition was 80°–85°C for some electrodes and 90°–95°C for others. All electrodes intended for a single series of experiments were made in the same way and otherwise treated the same. The current density was 3.13 ma/cm^2 or 25 ma for the electrode. The total manganese per electrode was about 0.2 millimole and the composition by analysis was about $MnO_{1.90}$. After preparation and thorough washing with water, the electrodes in groups of six were stored for one week in a solution of 2*M* NH_4Cl and 0.5*M* NH_3, *p*H 8.80. During this time the potentials decreased. Then the electrodes were stored in an electrolyte similar to that in which they were to be discharged.

Two groups of electrodes were washed with 0.1*N* H_2SO_4 instead of water, by keeping immersed in frequently changed acid solution until little more manganese(II) ion was washed out. The potentials of these electrodes before discharge were higher than those of electrodes washed with water, and the overpotentials were a little higher than the average for electrodes washed with water.

Electrodes for comparable overpotential measurements were selected to be as nearly alike as possible and with as nearly equal initial potentials as practicable. From a group of electrodes prepared at one time, those with lower potentials were used first, and, on standing in electrolyte, the others fell toward the lower potentials and were used later. If the differences in potential are ascribed to differences in composition of the oxide, and the decrease in potential on standing in electrolyte is the result of a reduction of dioxide (2), this procedure should favor uniformity of composition of the electrodes when used. A constant amount of discharge should then cover the same portion of the discharge curve for all electrodes of a series.

Measurement of overpotential.—For discharge, electrodes were mounted one at a time centrally in a glass vessel of about 250 ml capacity by means of a rubber stopper. A cylindrical silver electrode of a size to fit around the interior wall of the vessel was employed as the anode. A Luggin capillary was provided for the introduction of a calomel electrode with the tip placed at a distance two to four times its outside diameter from the central electrode. At the highest current density the *iR* drop between the MnO_2 electrode and the tip of the capillary was negligible, as shown by an experiment with a second capillary.

Solutions used as electrolytes were prepared from reagent grade chemicals by weighing and making up to volume with water, except that a 2*M* stock solution of acetic acid was used when this was to be included.

The measurement of electrode potential, against a saturated calomel electrode, was made by means of a L&N Speedomax recording potentiometer which was checked frequently by a more precise potentiometer. Current was measured also by the recording potentiometer in terms of the potential drop across known resistance.

During discharges the solution in the cell was stirred continuously at a rate such that an increase did not increase the closed-circuit potential. In some of the earlier discharges this was accomplished by a current of N which had been purified and passed through a solution similar to the electrolyte. At the highest current density this stirring was inadequate and a magnetic stirrer was employed instead. This was more satisfactory as it led to better *p*H control and better reproducibility of overpotential. It was adopted for all of the later measurements.

When a cell was ready for discharge it was placed in an air bath at 25° ± 1°C, except as otherwise noted. On attainment of approximately constant potential by the MnO_2 electrode, a current was started between this and the silver electrode and adjusted at 1.60 ma or 0.2 ma/cm^2,

except as otherwise noted. With three No. 6 dry cells and suitable resistance in the circuit the current decreased not more than 6% during a discharge. In some of the later experiments the current was maintained constant. A continuous record of both current and potential was made. The current was discontinued at about 125 ma-min and a sample of the electrolyte was taken for a *p*H measurement by means of a Beckman *p*H meter. Stirring was discontinued and the cell allowed to stand for 24 hr, after which stirring was started, and the open-circuit potential and *p*H were measured. The difference between the open-circuit potential and the last closed-circuit value was taken as the overpotential. It did not need correction to exactly 125 ma-min as such corrections were negligible. However, it was often necessary to make a small correction for change in *p*H during the 24-hr period.

One source of error was a slow decrease in electromotive force of the cell during the 24-hr period on open-circuit before the final measurement. This decrease compensated the last part of the recovery from polarization. If it were not for this, complete recovery would probably require more than 24 hr, and the allowance of this period is somewhat arbitrary.

Two causes of the decrease can be recognized: (*a*) the manganese(II) ion formed (3) should eventually return to the electrode and reduce some MnO_2; (*b*) after the completion of most of the present measurements it was shown that Ag electrodes in NH_4Cl solutions react with oxygen to give H_2O_2, which if carried to the other electrode can reduce MnO_2 (4). If the Ag electrode is covered with AgCl this self-discharge reaction is reduced in importance and can be practically prevented by a thick enough layer. In the latter part of this work the silver electrode was coated thickly with chloride by electrolysis with a current of 0.05 ma cm^2 for 12 hr in 0.1*M* KCl. In the early part it had been coated in previous discharges and not cleaned.

In 24 hr standing in NH_4Cl electrolyte an insufficiently coated silver electrode can cause reduction of a fresh MnO_2 electrode equivalent to about 10 mv (4). Inspection of an open-circuit discharge curve (1) shows that after 125 ma-min of discharge (of an electrode of 0.2 mmole of total Mn) the same amount of reduction would lower the potential 2–3 mv.

Some of the final open-circuit measurements, and hence overpotentials, might be 2–3 mv too low from this cause. This error does not affect the conclusions.

The reproducibility is shown in the upper curve of Fig. 1. It should be noted that the reproducibility is as good as indicated in Fig. 1 only when the procedure is

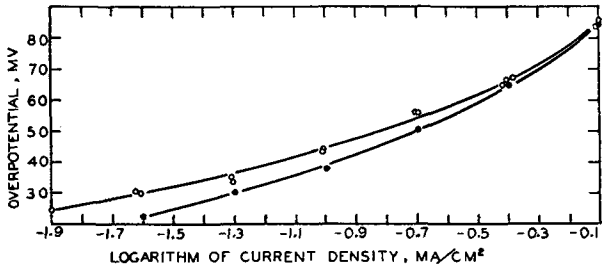

FIG. 1. Variation of overpotential with current density. Upper curve, *p*H 7; lower curve, *p*H 5.

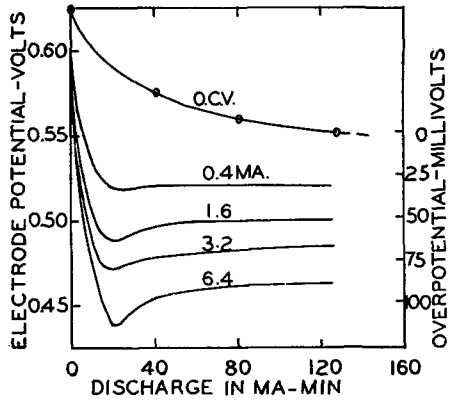

FIG. 2. Discharge curves at *p*H 5 and various currents (electrode area 8 cm^2) compared with an open-circuit discharge curve.

carefully standardized, especially in the preparation of the electrodes and the composition of the solution. Some electrodes plated at a higher temperature gave, with a current density of 0.2 ma cm^2, an overpotential of 69 mv as compared with 56 mv from Fig. 1.

Overpotential and Current Density

The overpotential at *p*H 7 increases relatively rapidly at the beginning of a discharge, then increases slowly or remains practically constant for a time, increasing greatly at the end (1). In the measurements the discharge was allowed to proceed until an approximately steady state of polarization had been established, but when possible not so long that much manganese(II) ion appeared in solution (3). At *p*H 5 the second condition was not possible. At *p*H 7 the manganese(II) ion is first detectable after about 40 ma-min. Not much is formed up to 125 ma-min, and this point was chosen for the measurements. At *p*H 5 some of the discharges had not attained a steady state until about 125 ma-min as shown in Fig. 2, so this point was appropriate for the lower pH also.

For measurements at *p*H 7 and various current densities the electrolyte was 2*M* NH_4Cl and 0.01*M* NH_3. Currents were varied from 0.1 ma to 6.4 ma for the 8 cm^2 electrodes. Results are shown in the upper curve of Fig. 1 in which overpotential is plotted against current density. When the current decreased during the discharge, the measured overpotential was considered to correspond to the value of the current when the discharge was discontinued.

A second series was made at *p*H 5. The electrolyte was 2*M* NH_4Cl, 0.068*M* potassium acetate, and 0.032*M* acetic acid, the *p*H of which was 4.72. Magnetic stirring was employed throughout this series. As shown in Fig. 1 the curves for *p*H 5 and 7 are of the same shape.

A linear relation between overpotential and the logarithm of the current density has been observed for the PbO_2 electrode discharging in acid solution (5).

Concentration polarization in the solution can account for only a small part of the curvature of Fig. 1. The concentration changing the most was that of the ammonia in the *p*H 7 series, while in the *p*H 5 series both components of the buffer might have changed appreciably. Estimation of the approximate concentration overpotential (6) for the largest current density gives 2.5 mv for *p*H 7 and 1 mv for

*p*H 5, as compared with 85 mv total overpotential. At smaller current densities, values would be smaller. If these corrections were made, the curvature of the *p*H 7 line would be reduced a little, but not eliminated.

*Overpotential and p*H

For discharges at *p*H 5 it was necessary to provide a buffer in the electrolyte if close control of *p*H was desired. An acetate buffer of potassium acetate and acetic acid (0.1*M* in total acetate) was used. For uniformity in experiments on the variation of overpotential with *p*H, 0.1*M* potassium acetate was included in the electrolytes of *p*H 7 and 8.6. All electrolytes contained 2*M* NH_4Cl. Overpotentials were measured with a current of 1.6 ma (current density 0.2 ma/cm²). Deviations from this current were so small that corrections were negligible. Corrections for *p*H changes were not more than ± 3 mv. Results are given in Table I. In Fig. 3 it is shown that variation in overpotential with hydrogen ion concentration is much smaller than its variation with ammonium ion concentration.

TABLE I. *Variation of overpotential with p*H

*p*H	4.79	4.80	7.10	7.06	8.53	8.56
Overpotential, mv	58	50	69	63	53	56

Microscopic examination of electrodes after discharges of 125 ma-min indicated a lack of uniformity in the reaction. After a discharge at *p*H 7 the surface was pitted and at occasional spots, graphite was uncovered. In electrodes discharged similarly at *p*H 8.6 the pitting was greater, but at *p*H 5 it was much less; no graphite was exposed. When the stirring was by N there was more pitting at the ends of the electrode than in the middle, whereas with magnetic stirring the attack on the electrode was much more nearly uniform. Because of the differences in the attack on the electrodes, the overpotentials at different *p*H values must be considered only roughly comparable. However, no differences in pitting were observed at different current densities or at different ammonium ion concentrations when *p*H was constant.

Overpotential and Ammonium Ion Concentration

For the investigation of the effect of ammonium ion concentration a series of electrolytes was prepared 0.1, 0.3, 1.0, and 2*M* in NH_4Cl with enough KCl in each case to give 2*M* chloride ion, an ionic strength of 2, and enough NH_3 to give a *p*H of 7.1–7.5. The two most dilute solutions in NH_4Cl were poorly buffered and for the most dilute the final *p*H values were 7.7 and 7.8 for two discharges. However, in this range the variation of overpotential with *p*H is small. Results of overpotential measurements of electrodes in these electrolytes are given in Fig. 3.

In this series of experiments, concentration polarization must have been largest in the solutions with least ammonium ion, since ammonia concentrations required were small. Calculation gave about 3 mv for both the 0.1*M* and 0.3*M* solutions and 1 mv for the 1*M*. The most dilute solution, having a higher *p*H after the discharge than the other solutions, had more ammonia in proportion to the ammonium ion, making the calculated value lower than would otherwise have been the case. If the small calculated corrections were made in Fig. 3 there would be no effect on the conclusions to be drawn. The slow rate of decay of overpotential as shown in Fig. 4 is also evidence of the absence of appreciable concentration polarization in the solution.

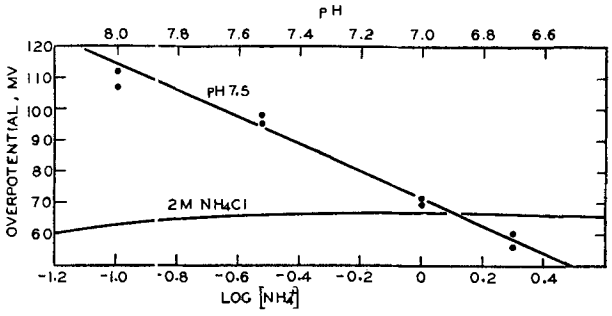

FIG. 3. Variation of overpotential with the logarithm of the ammonium ion concentration at constant *p*H (upper line and bottom abscissa scale) and with *p*H at constant ammonium ion concentration (top abscissa scale).

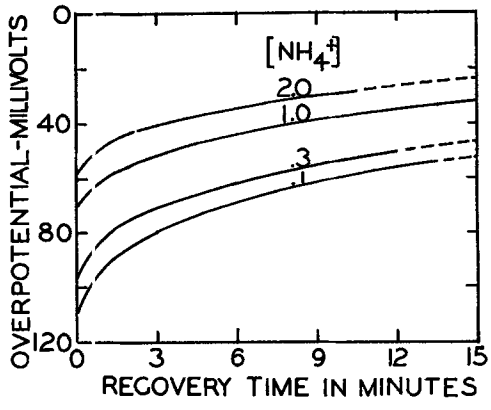

FIG. 4. Decay of overpotential after discharge of 125 ma-min in electrolytes of various ammonium ion concentrations. (See Fig. 3.)

It is of interest to compare the effect on overpotential of an NH_4Cl electrolyte with that of methyl, dimethyl and trimethylamine hydrochlorides, the amines being stronger bases than ammonia. Amine hydrochlorides of Eastman reagent grade were dried at 110°C, and 2*M* solutions were made by weight. When necessary some of the free amine was added to give a *p*H of from 7.2 to 7.4. A slight yellow color in each of the solutions was removed by stirring with decolorizing carbon. Experimental data and results are given in Table II.

TABLE II. *Overpotentials with* NH_4Cl *and amine hydrochlorides as electrolytes*

Electrolyte	*p*H* (final)	Overpotential* mv	pK_a	Concentration overpotential mv
NH_4Cl	7.33	65 ± 3	9.26	0
$CH_3 \cdot NH_3Cl$	7.59	132 ± 4	10.64	4
$(CH_3)_2NH_2Cl$	7.70	140 ± 3	10.71	3
$(CH_3)_3NHCl$	7.31	104 ± 4	9.72	1

*Each value is the mean of two.

The larger the pK (7), (Table II), the less dissociated is the ammonium or substituted ammonium ion, and the overpotentials increase in the same order.

Magnesium Chloride Electrolytes

Some overpotential measurements were made with $MgCl_2$ electrolytes buffered with excess $Mg(OH)_2$. Concentrations of $MgCl_2$ varied from 0.05 to 0.67M with enough KCl to give an ionic strength of two. Overpotentials varied irregularly from 113 to 141 mv, with an average of 126 mv. Considerable differences in the surface condition of the electrodes were observed after discharge, the electrodes showing the larger overpotentials being more heavily pitted than the others. Because of the high pH, 8.7–9.5, these experiments cannot be compared quantitatively with the others.

Overpotential and Temperature

A series of two measurements each at 25, 15, and 5°C was made. The electrolyte was 2M NH_4Cl of pH 7.3 and conditions were those described for the experiments on overpotential and current density, except that the current was held constant at 1.60 ma. The overpotential in millivolts as a function of temperature in centigrade degrees can be expressed by the equation

$$\eta = 103.86 - 1.415\,t$$

which was determined by the method of least squares. Results are shown in Table III.

Maximum Overpotential

Discharge curves at pH 5 show a peculiarity not found at pH 7. Four of the pH 5 curves are shown in Fig. 2 together with an open-circuit discharge curve for comparison. The real discharge curves all pass through a minimum at about 20 ma-min giving a maximum in the overpotential. The overpotentials measured at 20 instead of 125 ma-min are about twice those at 125 ma-min. When they are plotted against the logarithm of the current density a curve like those of Fig. 1, but with somewhat less curvature, is obtained.

Although discharge curves at pH 7 do not have a minimum, the overpotential passes through a maximum. In the experiments leading to Fig. 3, in which the ammonium ion concentration was varied, the maximum came at 30–40 ma-min and its height was larger the smaller the ammonium ion concentration.

Recovery from Polarization

It has been shown that the recovery from polarization, or decay of overpotential, is slow (1). Fig. 4 shows the first portions of the recovery curves of the electrodes of the ammonium ion series at pH 7.5 (Fig. 3). Each curve is the average for two electrodes. It is shown that the electrodes having the larger overpotentials have the more rapid recovery, but there was no sudden change on breaking the circuit. Each curve starts at the overpotential at which the circuit was broken.

TABLE III. *Variation of overpotential with temperature*

t °C	pH* (final)	Overpotential	
		Obs,* mv	Calc, mv
25	7.27	69 ± 1	68.5
15	7.29	82 ± 0	82.6
5	7.28	97 ± 3	96.8

* Each value is the mean of two.

Discussion

It has been postulated (3, 8) that the potential of a MnO_2 electrode depends on the composition of the surface of the oxide. The closed-circuit discharge curve starts at the open-circuit potential, if the iR drop included in the measurement is negligible. The closed-circuit potential decreases considerably faster than the open-circuit potential in the early part of the discharge. This can be explained as the result of the accumulation on the surface of lower oxide, which in the early part of the discharge is formed more rapidly than it is removed. The overpotential may be assumed to arise from the presence on the surface of more than the equilibrium amount of lower oxide.

That the lower oxide is removed from the surface is indicated by the slow rise in potential when the circuit is broken (Fig. 4) and by the appearance of manganese(II) ion in the solution (2, 3). In discharges at pH 7 manganese(II) ion is not formed in the early part of the discharge, but on breaking the circuit the potential rises slowly, indicating that lower oxide is being removed from the surface (1). It has been postulated that the lower oxide can become mixed effectively with the dioxide (1, 9), which also accounts for the decrease in the equilibrium open-circuit potential with discharge (10).

During the middle part of a discharge the overpotential remains constant or changes only slowly, indicating an approximately steady state in which the reaction products are being removed as fast as they are formed. An increase of current increases the rate of formation of products, which accumulate and lower the closed-circuit potential until a new steady state with a faster rate of removal is attained.

The dependence of the overpotential on the ammonium ion concentration (Fig. 3) cannot be satisfactorily explained at present. It is probably connected with the phenomenon of the maximum overpotential, as the ammonium ion concentration had considerable effect on the size of the maximum. It was observed that in the first 10 ma-min of discharge the curves for the four ammonium ion concentrations were much alike, but after this they deviated more and more as the various maximum overpotentials were approached. No explanation of the maximum overpotential and the minima in Fig. 2 can be given other than the suggestion of nucleus formation given for the similar minima in discharge curves for the PbO_2 electrode (5).

A quantitative treatment of the theory of overpotential has not been undertaken at this time because of the complexity of the problem. Experiments on discharge in acid electrolytes are being made, since in this case the removal of the reaction product seems to be a single process instead

of two. A quantitative treatment of these results seems possible.

ACKNOWLEDGMENT

This work was carried out under Contract Nonr-1016(00) with the Office of Naval Research.

Manuscript received July 27, 1955. This paper was prepared for delivery before the Boston Meeting, October 3 to 7, 1954.

Any discussion of this paper will appear in a Discussion Section to be published in the December 1957 JOURNAL.

REFERENCES

1. D. T. FERRELL, JR., AND W. C. VOSBURGH, *This Journal*, **98**, 335 (1951).
2. W. C. VOSBURGH, R. S. JOHNSON, J. S. REISER, AND D. R. ALLENSON, *ibid.*, **102**, 151 (1955).
3. A. M. CHREITZBERG, JR., D. R. ALLENSON, AND W. C. VOSBURGH, *ibid.*, **102**, 557 (1955).
4. W. C. VOSBURGH, D. R. ALLENSON, AND S. HILLS, *ibid.*, **103**, 91 (1956).
5. W. H. BECK, P. JONES, AND W. F. K. WYNNE-JONES, *Trans. Faraday Soc.*, **50**, 1249 (1954).
6. C. V. KING, *This Journal*, **102**, 193 (1955).
7. H. S. HARNED AND R. A. ROBINSON, *J. Am. Chem. Soc.*, **50**, 3174 (1928).
8. A. KOZAWA AND K. SASAKI, *J. Electrochem. Soc. Japan*, **22**, 569 (1954).
9. J. J. COLEMAN, *Trans. Electrochem. Soc.*, **90**, 545 (1946).
10. R. S. JOHNSON AND W. C. VOSBURGH, *This Journal*, **100**, 471 (1953).

The Change of Potential of Manganese Dioxide Electrodes on Standing

STANLEY HILLS[1] AND W. C. VOSBURGH

Department of Chemistry, Duke University, Durham, North Carolina

ABSTRACT

MnO_2 that has been in contact with ammonium salt solutions can be analyzed correctly if washed free of ammonium ion. Electrodes of electrodeposited MnO_2 on graphite with electrolytes of NH_4Cl, $(NH_4)_2SO_4$, buffered KCl, or $MgCl_2$ saturated with hydroxide decreased in potential 50-100 mv in 3 months at 50°C. On Au and Pt with buffered KCl electrolyte a similar decrease took place. The decrease was accompanied by a loss in available oxygen. Precipitated MnO_2 decreased more than 100 mv in 2 months under similar conditions, but lost little available oxygen.

MnO_2 electrodes of both the precipitated and electrodeposited type in NH_4Cl electrolytes decrease in potential slowly over long periods of time (1, 2). The decrease is associated with loss of available oxygen, but this could not be demonstrated by direct analysis, because the analytical method was questionable for an electrode that had been in an ammonium salt solution.

In the present investigation it is shown that the analytical method can be applied to MnO_2 that has been in ammonium salt solutions if the ammonium ion is first removed. A further investigation was made of the decrease in potential on standing in four different electrolytes. Also, for electrodeposited electrodes the effect of substitution of Au and Pt for graphite was tested.

PREPARATION OF MnO_2

Electrodes were prepared by electrodeposition of MnO_2 on graphite rods which had been prepared for spectroscopic work as previously described (3). Plating time was 30 min, and the total Mn deposited was 0.2 mmole on a surface 8 cm^2.

Precipitated MnO_2 was made by reaction of manganese (II) sulfate and $KMnO_4$ in acid solution (4). It was washed thoroughly and dried at room temperature.

[1] Present address: Reduction Research Laboratory, Reynolds Metals Co., Sheffield, Ala.

ANALYTICAL METHOD

The value of x in the formula MnO_x can be determined without weighing the sample by a combination of the H_3AsO_3 method for available oxygen and potentiometric titration in the presence of pyrophosphate for total Mn (5–7). For electrolytic electrodes on graphite rods this method gives low results if the electrode has been exposed to an NH_4Cl electrolyte, and also if an H_3AsO_3 solution much more dilute than $0.1N$ is used in dissolving the sample (2). A further study of the method was made before it was used in analyzing manganese oxides.

Electrolytic electrodes prepared as noted above and washed free from acid with water gave, on analysis, the results in the first four lines of Table I. Seven electrodes used as controls and analyzed with $0.1N$ H_3AsO_3 for the available oxygen determination gave $x = 1.90$, with an average deviation of ± 0.016. Two similar electrodes analyzed with $0.025N$ H_3AsO_3 gave $x = 1.63$, in agreement with the earlier observation (2). However, when either $0.1N$ or $0.025N$ $FeSO_4$ was substituted for the H_3AsO_3 the

value of x found was in agreement with the controls. Therefore, it is probable that analysis with 0.1*N* H_3AsO_3 gives correct results even though the value of x is considerably lower than the theoretical. The variation in the results is the sum of the analytical error and the variation in composition of the oxide on different electrodes; therefore, it should not be taken as a measure of the former alone.

When electrodes were kept in a solution 2M in NH_4Cl and 1M in NH_3 for 24 hr before analysis, the value of x found by analysis (line 5) was much lower than that of the controls. With only 1 hr of treatment instead of 24 (line 6), the value of x was still much too low. It seemed probable that the low results were to be ascribed to interference in the analysis by NH_4Cl or NH_3 and not to reduction of the MnO_2. Ammonium ion is held tightly by the oxide, probably as the result of exchange adsorption, and it is not easily removed by washing with water. Na_2SO_4 solution removes it, as shown by tests with Nessler's reagent, and after ten washings the wash solution gives only a faint test. The last two lines of Table I show that ammonium ion can be removed by washing with 1M Na_2SO_4. It is not completely removed by four washings, but fairly well by ten.

There was a fairly constant error in the results of Table I. After the available oxygen determination, and after the addition of pyrophosphate, it was necessary to neutralize much of the acid present to attain the proper *p*H for the potentiometric titration. When Fe was present, extreme care was needed in the addition of NaOH to avoid a temporary precipitate, which would lead to low results. Neutralization by NH_3 is much safer in this respect, and this was done in all of the analyses of Table I. However, analysis of several preparations of precipitated MnO_2 and a sample from the National Bureau of Standards using both methods of neutralization showed that the NH_3 method gives high results for total Mn by about 17 parts in 1000, or a negative error in x of about 8 parts in 1000. This error does not seem to affect the analysis of electrolytic electrodes as much (probably because less acid is used), but in any event the conclusions from Table II would not be affected.

TABLE I. *Effect of concentration of the reagent and exposure of the sample to* NH_4Cl *solution on the analysis of electrolytic* MnO_2 *on graphite rods*

No. of samples	Exposure to NH_4Cl*	Washing†	Solution for digestion	Results as x in MnO_x
7	None	—	0.1*N* H_3AsO_3	1.90 ± 0.016
2	None	—	0.025*N* H_3AsO_3	1.63 ± 0.1
4	None	—	0.1*N* $FeSO_4$	1.91 ± 0.005
2	None	—	0.025*N* $FeSO_4$	1.88 ± 0.01
2	24 hr	—	0.1*N* H_3AsO_3	1.59 ± 0.06
3	1 hr	—	0.1*N* H_3AsO_3	1.70 ± 0.03
3	1 hr	4 Times	0.1*N* H_3AsO_3	1.84 ± 0.02
3	1 hr	10 Times	0.1*N* H_3AsO_3	1.88 ± 0.01

* MnO_2 placed in solution 2M in NH_4Cl and 1M in NH_3 for the time indicated.

† Samples washed repeatedly with 1M Na_2SO_4 solution.

NaOH was used for neutralization in the analysis of precipitated MnO_2. It was found that protection from air by a current of N was desirable during the neutralization (as well as during the potentiometric titration) to prevent a small amount of oxidation by air.

Ammonium ion present during the available oxygen determination in the analysis of precipitated MnO_2 also caused low results, although the effect was not as large as for electrolytic oxide on graphite rods. Five analyses of a MnO_2 preparation gave $x = 1.969 \pm 0.002$. When 1 g of $(NH_4)_2SO_4$ was added to the acidified H_3AsO_3 solution used for dissolving the sample, the values of x found in two analyses were 1.90 and 1.92.

Three samples of precipitated MnO_2 were kept 24 hr in a solution 2M in NH_4Cl and 1M in NH_3, then washed ten times with 1M Na_2SO_4 solution. In each washing the precipitate was stirred with the solution mechanically for 15 min, then the solution was decanted. Finally, samples were washed with water, dried in a vacuum desiccator over P_2O_5, and analyzed. The average x value was 1.954 ± 0.0003 as compared with 1.959 ± 0.001 for the untreated oxide. The experiment was repeated, but after removal of the ammonium ion, and before analysis, one part by weight of Shawinigan black (50% compressed) was mixed with 9 parts of the sample. The mixture was digested with the acid H_3AsO_3 solution and the C removed by filtration before titration of the excess H_3AsO_3. Three samples treated in this manner gave $x = 1.953 \pm 0.0003$. For the precipitated oxide, treatment with ammonium salt and NH_3 and subsequent removal of ammonium ion gave an apparent loss of 3 parts in 1000 in the value of x. One possible source of error in the procedure is the loss of fine particles of oxide in the washing by decantation, if the fine material differs in composition from the coarser.

Treatment with ammonium salt and NH_3 and washing with Na_2SO_4 solution, with the subsequent addition of C, was tried with Standard Sample 25b from the National Bureau of Standards. The value of x was 1.984 ± 0.003 as compared with 1.982 ± 0.002 with no treatment, three samples each. The agreement with the value of x calculated from the National Bureau of Standards analysis is very satisfactory.

It was not attempted to add C to a MnO_2 sample while in an ammonium salt solution, because of the possibility of a real change in the oxide composition under these con-

TABLE II. *Change in potential of electrodeposited* MnO_2 *on graphite on standing 3 mo. in electrolyte at 50°C*

Electrolyte	*p*H	Potential,* Corr. to *p*H 7.5, 25°C		$-\Delta E$, mv	x in MnO_x
		Initial, mv	Final, mv		
NH_4Cl	7.5	444 ± 5	371 ± 13	73	1.74 ±0.01
$(NH_4)_2SO_4$	7.5	453 ± 2	402 ± 6	51	1.76 ±0.02
KCl	8.3	472 ± 5	401 ± 11	71	1.72 ±0.02†
$MgCl_2$	8.3	507 ± 5	398 ± 12	109	1.64 ±0.05

* Each value is the average for 4 electrodes.

† Average of 3.

ditions (4). There is no reason to expect an effect of the combined treatment on the analysis itself. MnO_2 contaminated with ammoniacal electrolyte and mixed with C (or oxide electrodeposited on the surface of graphite) can be analyzed well enough for the purposes of this investigation.

Change in Potential on Standing in Electrolyte

Electrodeposited MnO_2

Sixteen comparable electrodes of electrodeposited MnO_2 on graphite rods were divided into four equal groups, and each group was mounted in a rubber stopper fitting a glass container of about 120-ml capacity. A fifth hole in each stopper permitted measurement of the electrodes against a saturated calomel electrode. Four different electrolytes were used: (*a*) 2M NH_4Cl with enough NH_3 to give *p*H 7.5; (*b*) a similar 1M $(NH_4)_2SO_4$; (*c*) 2M KCl with a carbonate buffer, *p*H 8.3; (*d*) 1M $MgCl_2$ saturated with $Mg(OH)_2$, *p*H, 8.3. The first and last were chosen because of their use in Leclanche and Mg dry cells. The second does not have the chloride ion which is present in the other three, and the third contains the K cation instead of ammonium or Mg.

Measurements of electrode potential and *p*H were made at 25°, then the holes for the calomel electrode were stoppered, and the vessels placed in an oven at 50° ± 3°C. At intervals of a week or two the vessels were cooled to 25° and measured. Most of these potential measurements were not comparable with the initial and final values, because of a lag in the attainment of equilibrium which was not recognized at first. For this reason the shape of the potential-time curves was not determined.

It was later found that standing for four days at 25° after a temperature decrease assured satisfactory measurements. Changes in *p*H took place in the first three electrolytes, the change being especially large in the third, containing the carbonate buffer. For convenience all electrode potentials were corrected to a *p*H of 7.5 by the use of the coefficient 75 mv/*p*H unit (1). It is believed that the error in this correction is not large enough to affect the conclusions.

The initial and final values for a three-month period are shown in Table II, along with results of analyses of the oxide on the electrodes. Decrease in potential correlates qualitatively with the change in composition, assuming that all electrodes were of $MnO_{1.9}$ at the beginning. The correlation held for individual electrodes within a group also. A few of the glyptal seals which joined the graphite rods to the glass tubes in which they were mounted were faulty. This allowed electrolyte to come in contact with the bare graphite rod. Such electrodes were invariably lower in potential than the others of their group and were lower also in *x*-value. They were nevertheless included in the averages on the assumption that the effect of the cracked seal was merely to accelerate the change taking place, and not to introduce a new process.

However, the magnitude of the change in potential is rather large in relation to the change in the ratio of MnO_2 to lower oxide (assumed to be MnOOH). Electrodes made of mixtures of MnO_2 and MnOOH have been shown to change 73 mv with unit change in the logarithm of the oxide ratio (8). The corresponding change in the electrodes of Table II is 90–120 mv. This suggests that part of the change in potential may be the result of a change other than reduction. A suggestion as to the nature of this change is made in the discussion of changes on standing of electrodes of precipitated MnO_2.

TABLE III. *Change in potential of electrodeposited* MnO_2 *on* Pt *and* Au *on standing 4 wk in electrolyte at 50°C, p*H *7.5*

Electrode	Potential,* *p*H 7.5, 25°C		$-\Delta E$, mv	x in MnO_x
	Initial, mv	Final, mv		
Pt	520 ± 7	410 ± 2	110	1.77 ± 0.02
Au	528 ± 4	398 ± 3	130	1.77 ± 0.01

* Average for three electrodes.

It is not apparent what is oxidized when the MnO_2 is reduced. The only substances present in all four systems are water and graphite. The oxidation of chloride ion requires a higher potential than that available. The oxidation of water should be easier, though still apparently requiring too large potential. To test whether graphite was involved, Pt and Au were substituted as supports for the MnO_2. Previously (2) MnO_2 on Pt in NH_4Cl electrolyte was found to decrease in potential faster than on graphite.

MnO_2 was electrodeposited on three bright Pt and three gold-plated Pt electrodes at the same current density as used for deposition on graphite. These were placed in a single vessel containing 2M KCl electrolyte buffered with a borate buffer at *p*H 7.5. As a precaution against traces of reducing impurities a little permanganate had been added, and the solution was boiled and filtered prior to use. Potentials (relative to the saturated calomel electrode) before and after four weeks at 50°C are given in Table III, along with the composition of the oxide as found by analysis after the final potential measurements. The experiment was discontinued after four weeks because large changes in both potential and available oxygen were shown in that time. The higher initial values correspond to a higher initial available oxygen content. Analysis of four freshly prepared electrodes, two on Pt and two on Au, gave $MnO_{1.97}$ as compared with $MnO_{1.90}$ for electrodes on C.

Precipitated MnO_2

Sixteen electrodes were prepared with precipitated MnO_2. The same four electrolytes were used as for the electrodeposited electrodes, except that the 2M KCl was buffered with borate instead of carbonate, and its *p*H was 7.7. The MnO_2 to be used with the ammonium salt electrolytes was digested at room temperature with similar solutions containing 1M NH_3. Other samples were digested with the unaltered electrolytes.

The electrodes were set up in long narrow tubes with Pt

wires sealed in at the bottom (4). Two electrodes with each electrolyte were made by placing in the tubes a suspension of MnO_2 in the electrolyte and centrifuging to pack the oxide around the Pt wire. Two other electrodes with each electrolyte were made with C (Shawinigan black, 50% compressed) mixed with the oxide. The oxide and C were mixed in the form of a paste with a little of the electrolyte, and the paste was packed around the wire by centrifuging, before the main part of the electrolyte was added.

A fifth set of four similar oxide samples (two of them with C) were placed in electrode vessels with water in place of an electrolyte. These samples served as controls and were analyzed with the others at the end of the experiment, but no potential measurements were made.

The electrodes were kept at 50° ± 3°C and occasionally cooled to 25°C for measurement against a saturated calomel electrode. The potentials decreased, and in the latter part of the second month they seemed to be approaching constancy. On two occasions the potentials immediately after the reduction in temperature were roughly 200 mv below the previous values, but they rose within four days to values only a little below the previous ones. This phenomenon could not be repeated later. Decreasing *p*H values in the first two electrolytes were probably the result of loss of NH_3, in spite of tight stoppers. Before the final measurements the electrolytes in the first two sets of electrodes were changed. Table IV shows the initial and final electrode potentials all corrected to *p*H 7.5. In the last column is given the composition of the MnO_2 as found by analysis, each value being the average for two electrodes. With these are included the analyses of the samples kept under water instead of electrolyte.

Most of the final potentials were smaller than those of Table II and the decrease larger, but the loss of available oxygen was much smaller. The oxide kept under water changed from the initial $MnO_{1.959}$ to $MnO_{1.946}$. The change in the electrodes with the $MgCl_2$ electrolyte and no C was little more than this. The oxide samples in the KCl and $(NH_4)_2SO_4$ electrolytes changed to $MnO_{1.934}$ and $MnO_{1.922}$, respectively. The much larger change in the NH_4Cl electrolyte may have been the result of an undetected error. The electrodes containing C decreased more than those without C (except in the NH_4Cl electrolyte), and more available oxygen was lost.

Comparison of Tables II and IV shows that even if the change in potential in the former should be ascribed wholly to the change in oxide composition, the change in Table IV cannot be so explained. A change to a more stable physical form is not a satisfactory explanation for the decrease of potential. Maxwell and Thirsk (9) found a much smaller change of potential, sometimes even an increase, on heating a number of different preparations of MnO_2 to temperatures of 200°C or above. In their experiments the cells in which the various preparations were compared were made with electrolytes of HCl and $MnCl_2$. Kozawa and Sasaki (10) believe that the potential of a MnO_2 electrode depends mainly on the surface state of the oxide. The presence of lower oxide on the surface leads to a low electrode potential. If the lower oxide is removed by acid, the electrode potential rises. In an ammonium salt (or other) electrolyte at *p*H 7 or higher, MnOOH on the surface of MnO_2 would not be removed, and a decrease in potential could be the result of a decrease in available oxygen in the surface layer.

TABLE IV. *Change in potential of electrodes of precipitated MnO_2 on standing 2 mo. in electrolyte at 50°C*

Electrolyte	*p*H	Potential,* corr. to *p*H 7.5, 25°C		x in MnO_x
		Initial, mv	Final, mv	
NH_4Cl	7.5	485 ± 15	331 ± 10	1.875
NH_4Cl†	7.5	478 ± 17	357 ± 0	1.902
$(NH_4)_2SO_4$	7.5	496 ± 0	380 ± 5	1.922
$(NH_4)_2SO_4$†	7.5	534 ± 1	368 ± 2	1.907
KCl	7.7	516 ± 2	404 ± 1	1.934
KCl†	7.7	504 ± 0	380 ± 1	1.920
$MgCl_2$	8.3	524 ± 1	384 ± 6	1.942
$MgCl_2$†	8.3	504 ± 1	356 ± 7	1.924
Water	—	—	—	1.946
Water†	—	—	—	1.906

* Each value is the average for 2 electrodes.
† C was mixed with the MnO_2.

The effect of heating the MnO_2 in the dry state was tested by keeping samples in the oven at 50°C for 1–5 weeks. Analysis of the five-weeks sample gave $MnO_{1.919}$ and $MnO_{1.925}$, showing less available oxygen than most of the samples heated under water or electrolyte for a longer period. However, electrodes made with the heated samples were on the average only 20 mv lower than control electrodes made with unheated oxide. Both sets of electrodes decreased about 100 mv during the period of observation.

Conclusions

It is assumed that the changes at 50°C are no different in kind from similar changes at 20°–30°C. The decrease in potential of electrodes of precipitated MnO_2 indicates a self-discharge process taking place at the MnO_2 surface. This conclusion is based on the proposition that the potential is determined by the composition of the surface together with the observation that analysis showed only a small decrease in composition of the oxide as a whole. The self-discharge does not depend on any particular ion in solution, nor on the presence of any substance more easily oxidized than water.

Electrodeposited MnO_2 on graphite, Pt, or Au loses considerable available oxygen while decreasing in potential. This suggests an electrolytic effect by which the self-discharge process, occurring primarily at the surface, spreads to the interior. The effect of cracks in the electrode seals is in agreement with this suggestion.

It does not appear possible to bring MnO_2 electrodes to complete equilibrium with neutral or slightly alkaline solutions.

Acknowledgment

This work was supported in part by a fellowship from E. I. du Pont de Nemours and Company and in part by the Office of Naval Research under contract Nonr 1016(00).

Manuscript received April 9, 1956. Based in part on a

thesis submitted to the graduate faculty of Duke University in partial fulfillment of the requirements for the degree of Doctor of Philosophy by S. Hills.

Any discussion of this paper will appear in a Discussion Section to be published in the December 1957 JOURNAL.

REFERENCES

1. R. S. JOHNSON AND W. C. VOSBURGH, *This Journal*, **99**, 317 (1952).
2. W. C. VOSBURGH, R. S. JOHNSON, J. S. REISER AND D. R. ALLENSON, *ibid.*, **102**, 151 (1955).
3. D. T. FERRELL, JR. AND W. C. VOSBURGH, *ibid.*, **98**, 334 (1951).
4. C. W. JENNINGS AND W. C. VOSBURGH, *ibid.*, **99**, 309 (1952).
5. R. F. STALZER AND W. C. VOSBURGH, *Anal. Chem.*, **23**, 1880 (1951).
6. I. M. KOLTHOFF AND E. B. SANDELL, "Textbook of Quantitative Inorganic Analysis," revised ed., p. 605, Macmillan Co., New York (1943).
7. J. J. LINGANE AND R. KARPLUS, *Ind. Eng. Chem. Anal. Ed.*, **18**, 191 (1946).
8. R. S. JOHNSON AND W. C. VOSBURGH, *This Journal*, **100**, 471 (1953).
9. K. H. MAXWELL AND H. R. THIRSK, *J. Chem. Soc.*, **1955**, 4057.
10. A. KOZAWA AND K. SASAKI, *J. Electrochem. Soc., Japan*, **22**, 569 (1954).

Study of the Cathodic Reduction of Oxide Films on Iron

I. Reduction of Alpha-Fe_2O_3 Films

H. G. OSWIN[1] AND M. COHEN

Division of Applied Chemistry, National Research Council, Ottawa, Ontario

ABSTRACT

Apparatus and technique for cathodic reduction of α-Fe_2O_3 films is described. Measurements of the reduction efficiency in buffered and unbuffered electrolytes are given. Effects of *p*H of the electrolyte, dissolved oxygen current density, and film thickness are noted and discussed. Electrolytes containing "ferrous-complexing" ions have also been investigated. Methods of determining quantities of α-Fe_2O_3 in thin films are suggested and their limits of accuracy considered.

Dissolution of iron oxide films on Fe in acid media was investigated by Evans, *et al.* (1–7), and it appears to be a process of reduction and dissolution.

The reduction of α-Fe_2O_3 can be represented by:

$$Fe_2O_3 + 6H^+ + 2e \rightarrow 2Fe^{++} + 3H_2O \qquad (I)$$

When no external emf is applied, electrons can be supplied by the anodic corrosion process:

$$Fe \rightarrow Fe^{++} + 2e \qquad (II)$$

The combination of processes (I) and (II) is known as "autoreduction". However, if a cathodic potential is applied, reaction (II) should be suppressed and reaction (I) will be predominant. There will also be another cathodic process competing with (I):

$$2H^{++} + 2e \rightarrow H_2 \qquad (III)$$

The present work was carried out to investigate whether the cathodic reduction technique could yield an accurate determination of α-Fe_2O_3 on iron.

PRELIMINARY INVESTIGATIONS

Some preliminary investigations were carried out using a simple electrolytic cell similar to those used by previous workers. The quantity of Fe dissolved in the electrolyte after reduction was determined and used as a measure of the efficiency of the reduction. This was done by comparing the quantity of Fe found with that which would be expected from reaction (I) and a consideration of the number of coulombs put into the system.

Efficiencies calculated on this basis showed considerable variation when the reductions were carried out in $N/10$ NH_4Cl; efficiencies in aerated systems were particularly difficult to correlate with each other. Further, the efficiencies were generally found to be greater than 100%, especially when low current densities were used. There was much more Fe found in solution than would have been expected from the number of coulombs put into the system, assuming that all the coulombic energy was used solely for the reduction of α-Fe_2O_3. This indicated that autoreduction, i.e., a combination of reactions (I) and (II), still prevailed under these conditions. It had been thought previously that rates of autoreduction were very small in solutions of *p*H exceeding 3.0 (7). However, these experiments had been carried out in unbuffered solutions of dilute HCl, in which the *p*H in the region of the electrode might have changed during the experiment. Consequently, it was decided to investigate first the rates of autoreduction in buffered solutions.

Rates of Autoreduction

Immersion of oxidized Fe specimens in $N/10$ NH_4Cl solutions resulted in a gradual disappearance of the oxide

[1] Present address: Cities Service Research & Development Corp., New York, N. Y.

film. Measurement of the amount of Fe going into solution indicated that the autoreduction rates were still considerable—of the order of 40 $\gamma Fe/cm^2/hr$. Specimens which had been immersed in $N/10$ NH_4Cl for a while were then reduced cathodically and compared with ordinary oxidized specimens. It was observed that a much smaller reduction step was found in the case of specimens which had been previously immersed in $N/10$ NH_4Cl.

Several deaerated buffered solutions were prepared in which Fe specimens (oxidized to the blue stage) were immersed. The time taken for the film to disappear completely was noted. These times varied somewhat and the average of a number of observations was taken.

*p*H	Time (min)
5	5
6	20
6.5	30

Several buffers were tried in the *p*H range 5–7.5, and it was observed that rates of autoreduction decreased with increasing *p*H. Rates varied somewhat, depending on the buffer used. Reduction rates appeared to be lower in aerated buffers, presumably because of depolarization by oxygen of reaction (III), which is then the preferred cathodic process.

In sodium borate-HCl buffers of *p*H 7.5, rates of autoreduction were quite low: approximately 2–4 $\gamma Fe/cm^2/hr$. This is a very low rate of reaction and should be completely suppressed or minimized on application of a cathodic potential to the electrode. Hence it was decided to investigate the cathodic reduction process in electrolytes of *p*H greater than 7.5.

Experimental

Preparation of standard oxidized Fe specimens was carried out in the following manner. For most of the experimental work Armco iron sheet 0.006 in. (0–152 mm) thick was used. Specimens 7 x 1 cm were oxidized, then trimmed to a size and shape suitable for use as electrodes. The reducible area used was approximately 10 cm^2. Before oxidation the Fe was polished with 3/0 emery paper, degreased in trichlorethylene, etched 1 min in N HCl, washed with distilled water followed by dry methyl alcohol, and finally dried at room temperature. Specimens prepared for electron-diffraction examination were made from Fe of the same specification, but thickness 0.062 in. (1.57 mm). Preparation of the metal was similar to that already described above, except that it was polished with 4/0 emery paper to obtain best results.

Oxidation was carried out in a glass vessel through which there was a continuous flow of oxygen; to obtain even oxidation, specimens were suspended from a central support and were not allowed to touch the walls of the vessel. The glass vessel was contained in a furnace heated to a suitable temperature maintained at ±2°C. For most of the experimental work, except where otherwise specified, specimens were oxidized 18 hr at 250°C, which usually produced a first-order blue film. In view of the preliminary observations of the effect of oxygen, the apparatus was designed to work under anaerobic conditions. Cathodic reduction of specimens and storage of the necessary electrolytes were effected under a N_2 atmosphere. The N_2 was purified by bubbling through Fieser's solution and then passing over a column of finely dispersed Cu on kieselguhr, heated to 220°C.

Solutions were deaerated by heating to 90°–95°C in the storage vessel while pure N_2 was bubbled through for 24 hr before using. The transference of electrolyte from storage vessel to cell was effected by a system of three-way taps. It was found that solution-lubricated glass stopcocks served most satisfactorily.

The reduction cell was designed: (*a*) to permit exclusion of air; (*b*) to permit complete flushing with pure N_2 with the specimen in position; (*c*) to minimize diffusion of oxygen to the cathode by removing the anodes as far as possible; and (*d*) to facilitate accurate analysis for dissolved Fe by making the cell volume as small as possible. The cell is shown in Fig. 1, its dimensions being approximately 25 x 150 mm. The specimen was suspended on a heavy

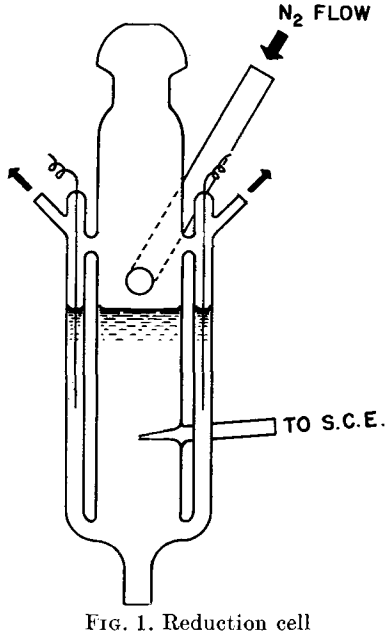

Fig. 1. Reduction cell

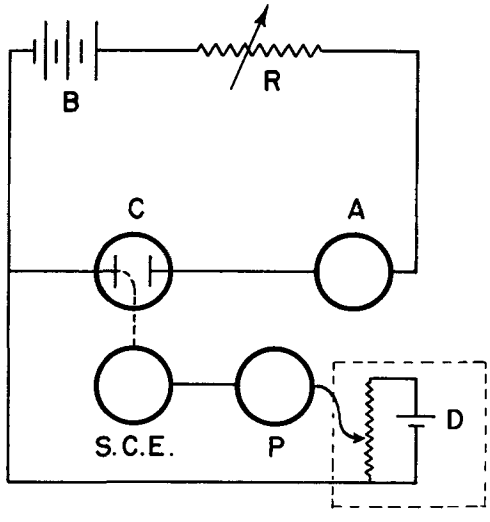

Fig. 2. Electrical circuit. A—Microammeter; B—d-c supply; C—reduction cell; D—"bucking" circuit; P—emf recorder; R—large variable resistance; S.C.E.—standard calomel electrode.

gauge-W wire sealed into a ball-joint. This allowed location of the specimen against the tubulus connecting the cell to a standard calomel electrode via a salt bridge.

Fig. 2 is a diagram of the electrical circuit used. Basically this is similar to those used by previous workers and consists of a source of d-c voltage (B) connected to the reduction cell in series with a very large resistance (R). If (R) is considerably larger than the resistance of the cell, small changes in the cell resistance will not affect the total resistance of the circuit, and a constant current can be maintained during reduction. (In some cases a small variation in current was noticed, but this did not exceed ±0.5%.) Accuracy of the microammeter used is estimated to be better than ±0.5%; hence the maximum error in measuring the current is ±1%.

The emf measurements against a standard calomel electrode were recorded on a Speedomax, range 0–1000 mv. As shown in Fig. 2 at D, a bucking potential was used to retain the measured emf's on the recorder scale.

The bucking potential used was 0.2 v, but all potentials shown and mentioned were corrected by this amount.

Briefly, the method of using the apparatus was as follows:

1. Before any experiment, the cell was first washed with N/HCl and finally washed well with distilled water.

2. Pure N_2 was then allowed to flow through the cell, and after 2 min the cell was flushed out with deaerated electrolyte, some of which was allowed to flow through the salt bridge. Thus, any aerated electrolyte was removed.

3. The cell was drained and the electrode placed in position against the tubulus. With the lower stopcock still open, pure N_2 was allowed to flush through the cell for an additional 10 min. The necessary electrical connections were then closed, and fresh electrolyte admitted via the lower, three-way stopcock, until the required liquid level in the cell was obtained. Immediately the stopcock in the salt bridge was opened, the electrical circuit main switch closed, and the recording of emf's commenced.

4. On completion of reduction, the circuit was opened, the electrode quickly removed from the cell, and excess electrolyte washed from it with distilled water. These washings plus the remaining electrolyte in the cell were collected, together with further washings of the cell with N/10 HCl and distilled water.

The total Fe content of the collected electrolyte and washings could then be estimated colorimetrically. The amount of Fe involved was usually of the order of 100 γ but at times quantities as low as 10 γ and as high as 400 γ were determined. The total volume of liquid involved was 75–100 cc.

Several colorimetric reagents were tried, and the most satisfactory for these conditions appeared to be thioglycollic acid. The technique consisted of: (*a*) evaporation to a very small bulk followed by transference of the material (washing with N/10 HCl and distilled water) to a 50 cc volumetric flask; (*b*) addition of 2 cc 10% thioglycollic acid solution neutralized with 6N NH_3; (*c*) addition of 10 cc 6N NH_3 and dilution to a total volume of 50 cc; and (*d*) measurement of optical density in silica cells at 540 mμ. For use as a blank solution for these measurements, a dummy run was made in the cell without an electrode, the electrolyte being removed and treated in the manner described. The spectrophotometer was calibrated using standard solutions of Fe in HCl added to a normal quantity of the electrolyte.

Reproducible accuracy of better than ±1.5% was obtained, but an over-all accuracy of only ±2% is claimed. The accuracy increases with quantity of Fe involved, presumably because of the reduced significance of small losses by adsorption on the glassware.

Specimens required for electron-diffraction examination or microweighings after cathodic reduction were treated as follows: after removal from the cell, the specimen was washed with distilled water repeatedly, then with dry methyl alcohol, and finally dried at room temperature.

Effect of *p*H and Current Density

In view of the autoreduction rates observed in buffered solutions, reductions were carried out in solutions of high *p*H. A series of sodium borate-HCl buffers was used (8). A series of reductions was carried out using standard specimens and a current density of 30 μa/cm^2. The emf-time curves are shown in Fig. 3.

In a buffer of *p*H 7.65, the inflection is clearly marked, less marked at *p*H 8.1, and nonexistent at *p*H 8.6. Reduction of the α-Fe_2O_3 was achieved at *p*H 8.6, but the time required to remove all the Fe_2O_3 indicated a very low over-all efficiency of reduction.

By using a buffer of twice the prescribed concentration (8), at a current density of 30 μa/cm^2, it was possible to reduce α-Fe_2O_3 slowly even at *p*H 9.1.

Fig. 4 shows the emf-time curve observed at different current densities in a borate buffer of *p*H 7.7. The inflection point becomes less distinct with increasing current density: the same effect as is produced by increasing *p*H.

The lack of an inflection, or definite potential change, must mean that processes (I) and (III) are concurrent. Although from a consideration of standard potentials, process (I) should occur at a much higher emf than process (III), it is obvious from the observed potentials that

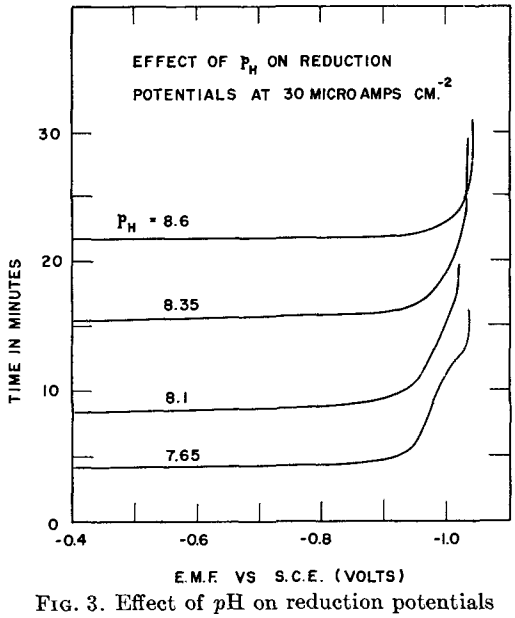

Fig. 3. Effect of *p*H on reduction potentials

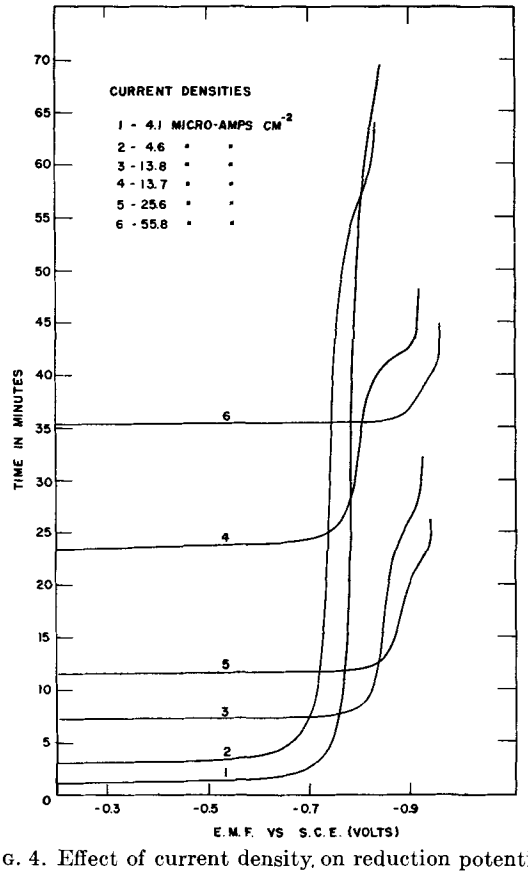

FIG. 4. Effect of current density on reduction potentials

process (I) is highly polarized and has a potential near to that of process (III).

Increasing the current density or the *p*H must cause polarization of the electrode, by a lowered H ion activity and/or formation of $Fe(OH)_2$ at the interface.

INTERPRETATION OF EMF-TIME CURVES

An electrode system of the iron-iron oxide type can provide several cathodic processes. For the present purposes, an ideal system obviously would be one in which these processes would occur consecutively. Curve 1, Fig. 5 represents reduction potentials at an ideally unpolarized electrode. In practice, the electrode is polarized because of the reduction process, and the potential is of the type

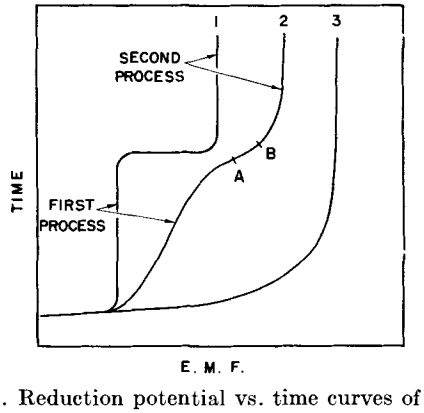

FIG. 5. Reduction potential vs. time curves of different types.

shown in curve 2, the steadily decreasing potential being caused by changes in the activities of ionic species formed during the reduction process rather than by a decrease in H ion concentration. This is indicated by the effect of Fe complexing ions which produce potential curves approximating type 1.

In the case of potential curves such as curve 3, the polarization of the first reduction process is so great that the reduction potential of the second process is reached, and the processes are then concurrent.

EFFICIENCIES OF REDUCTIVE-DISSOLUTION

The processes occurring at the electrode in the absence of oxygen consist of processes (I), (II), (III), and possibly

$$Fe^{++} + 2e \rightarrow Fe \qquad \text{(IV)}$$

Of these processes, (I), (II), and (IV) alone contribute to the quantity of ferrous ions in the electrolyte after the reduction. It does not seem likely that processes (II) and (IV) are concurrent, and the amount of dissolved Fe in the electrolyte will be dependent on a combination of either (I) and (II) or (I) and (IV).

The efficiency of process (I) was calculated as

$$\frac{\text{Quantity of Fe dissolved in electrolyte}}{\text{quantity of Fe expected if all the coulombic energy is used in process (I)}}$$

which can be written

$$\frac{\text{micrograms of Fe} \times 1.726 \times 10^5}{\text{time of reduction (sec)} \times \text{current } (\mu a)}$$

If this efficiency exceeds 100%, the amount of Fe in solution is greater than would be expected from coulombic considerations of process (I); therefore process (II) must be occurring. The excess Fe is unlikely to be mechanically removed or undermined α-Fe_2O_3, since Evans (9) has shown that α-Fe_2O_3 films isolated from the metal are stable in acid media of quite low *p*H. Efficiencies of less than 100% do not necessarily mean that process (I) does not occur, since the excess electrons could be used in process (III). This possibility is discussed later.

For efficiency determinations, standard oxidized specimens were used. Two deaerated electrolytes were used: *N*/10 NH_4Cl and sodium borate-HCl buffer of *p*H 7.65–7.72. Fig. 4 shows typical potential vs. time curves of the reduction processes in the buffered solutions at different current densities.

In order to determine whether the inflection of these curves does in fact correspond to complete reduction of the α-Fe_2O_3 layer, a series of specimens was prepared for surface examination by electron diffraction reflection. Reduction of oxidized specimens was carried out, corresponding to points A and B as shown on curve 2, Fig. 5, i.e., before and after the inflection. It was found that in both *N*/10 NH_4Cl and the buffered solution specimens reduced to stage A still showed α-Fe_2O_3 lines in the diffraction patterns. Specimens reduced to stage B usually showed Fe_3O_4 lines only, although in a few cases faint lines of α-Fe_2O_3 still appeared. This was mainly observed after reductions at high current density.

The absence of α-Fe_2O_3 lines in the diffraction patterns is presumed to indicate a complete removal of α-Fe_2O_3 from the surface layer.

The Fe_3O_4 patterns originate from the underlying magnetite layer in the duplex oxide film, which has been exposed by removal of the upper layer of α-Fe_2O_3. The Fe_3O_4 is most unlikely to have been formed by cathodic reduction of α-Fe_2O_3, and if this did occur it would be observed even in the early stages of the α-Fe_2O_3 reduction. This is not the case.

Having established that the inflection of the emf vs. time curve corresponds to complete removal of the α-Fe_2O_3, a series of current efficiency measurements were made at different current densities. Two sets of determinations were made: incomplete reductions corresponding to point A, before the inflection, and complete reductions as far as point B, beyond the inflection. The efficiencies plotted against current density are shown in Fig. 6. Values for incomplete reduction in the buffered solution seem to be fairly reproducible and exceed 100% only at very low current densities. The values for complete reduction are less reproducible, which may be explained by the following possibilities: (*a*) the inflection-point has to be determined visually, and, although it cannot be determined precisely, the limits within which it must lie have been found to be less than ±3% of the time period involved; (*b*) a change in processes occurring between points A and B which might affect the total amount of Fe found in solution after complete reduction.

Incomplete reductions in $N/10$ NH_4Cl show considerable variations in current efficiency. For this reason no attempt was made to measure the efficiencies of the complete reduction in this electrolyte. These large variations can be attributed to the low *p*H of NH_4Cl solutions, usually less than 6.0. The very high efficiencies indicate that autoreduction is an important process here even at current densities as high as 20–30 $\mu a/cm^2$. The autoreduction process is dependent on the rate of process (II) which in turn will depend on the area of exposed Fe surface; this may vary considerably from specimen to specimen.

The effect of oxygen in the electrolyte was investigated, and in the sodium borate-HCl buffers the effect was quite marked, especially at low current densities. It was decided not to carry out a series of quantitative measurements in view of the errors involved in determining oxygen content of electrolytes. However, several current efficiency determinations were made with specimens reduced in deaerated buffers of *p*H 7.7 during which no attempt was made to exclude oxygen from the cell. The average of the measurements was 60% at a current density of 15 $\mu a/cm^2$. It was observed during these runs that the potential was about 150 mv greater than the corresponding potential in the absence of oxygen.

Reduction of Thin α-Fe_2O_3 Films on Pt

In an attempt to exclude the process of autoreduction, thin films of α-Fe_2O_3 were prepared on a Pt surface. Carefully polished and clean Pt electrodes were degassed and a thin film of pure Fe evaporated onto the surface. This Fe surface was then oxidized in the same manner as the standard Fe specimens. By careful control of the quantity of Fe

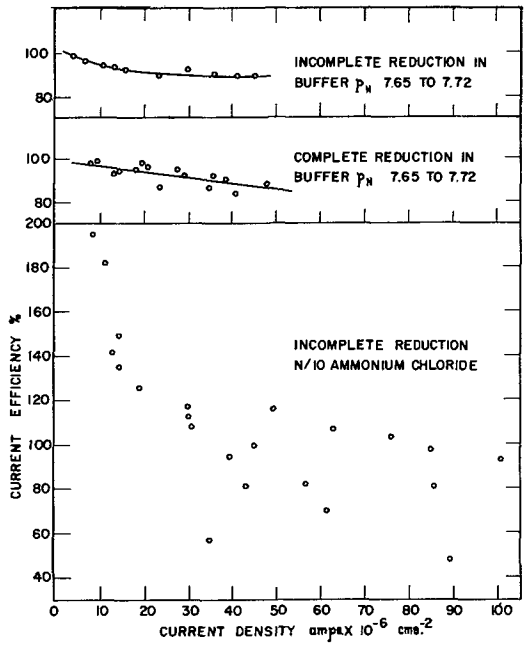

Fig. 6. Current efficiencies of reduction

evaporated, films of α-Fe_2O_3 of average thickness between 200 and 800Å were produced, the thicknesses being calculated from weight-increase measurements. The surface conditions after each stage—evaporation (Fe) and subsequent oxidation (α-Fe_2O_3)—were checked by electron diffraction examination.

The oxidized films were then cathodically reduced in sodium borate-HCl buffers and $N/10$ NH_4Cl at various current densities. In all cases, the current efficiency of reductive-dissolution was very low, and in the case of the thicker, visible films, complete reduction was attained only after several hours. Generally, it was observed that the thicker the film, the more difficult the reduction process. A similar effect was reported during the cathodic reduction of bulk α-Fe_2O_3 (7). It was found that α-Fe_2O_3 produced at high temperatures was quite difficult to reduce. It was also reported that the rate of reductive-dissolution of α-Fe_2O_3 (bulk) decreased after the initial stages. This was attributed to the low conductivity of bulk α-Fe_2O_3. It was suggested that the conductivity depended mainly on the existence of defects in the surface layers which were quickly removed during the initial stages of reductive dissolution.

The present work with oxide films on Pt seems to agree with this. The nature of these thin evaporated films is such that there is probably very poor contact between the film and the underlying Pt, thus introducing a high electrical resistance into the system. If this resistance is sufficiently high, the potential on the large exposed areas of Pt will probably be high enough to discharge H ions by process (III).

A further factor, which tends to increase the resistance of these evaporated films, is that there are likely to be less lattice-defects of the Fe-excess type in α-Fe_2O_3 layers when supported and formed on a Pt base. Unless the Pt itself is soluble in the oxide lattice, the electrical conductivity should be lower.

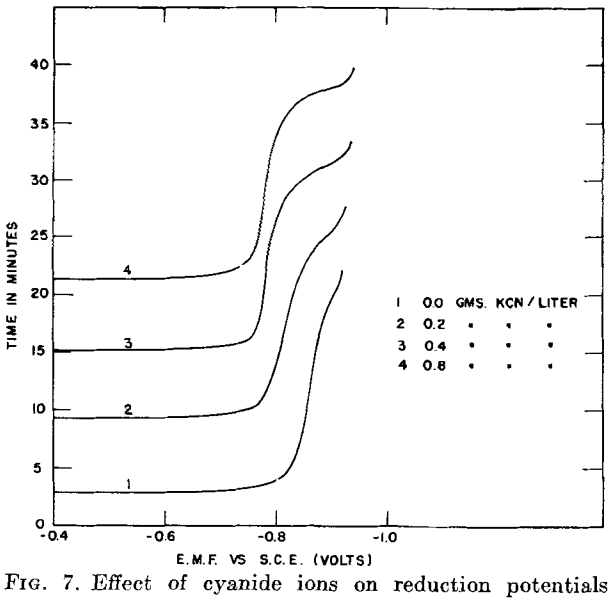

FIG. 7. *Effect* of cyanide ions on reduction potentials

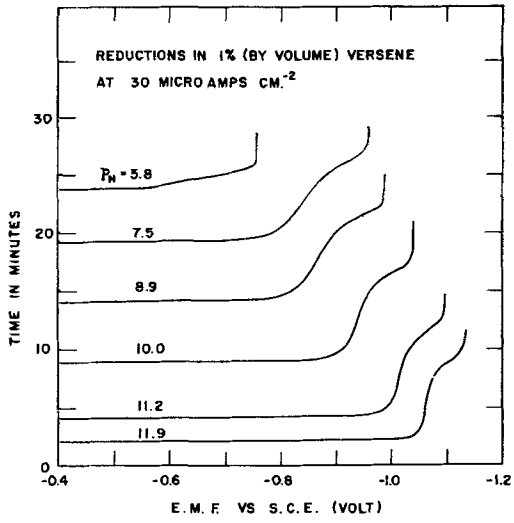

FIG. 8. Effect of varying *p*H in 1% Versene solutions

In the case of these thin films it does not seem likely that local overheating during oxidation could cause the formation of ignited oxides, since high temperatures would be attained for very short periods of time only.

EFFECT OF FE-COMPLEXING IONS

Effect of cyanide ions.—The effect of cyanide ions on reductive dissolution had been noted previously by Pryor and Evans (7) using 0.7 g KCN/1 *N*/10 NH_4Cl. An increase of the reduction potential was observed, presumably due to lower concentrations of ferrous ion at the electrode surface. This results in a greater difference between the reduction potential and the final H evolution potential, consequently a sharper inflection is observed on the emf-time curve.

In the present work, the effect of cyanide ions in sodium borate-HCl buffers was investigated. Typical reduction curves are shown in Fig. 7. A current density of 30 μa/cm^2 was used. Apparently an increase in concentration of cyanide ions results in an increase of the reduction potential. However, after reduction to a stage beyond the inflection point of the curve, specimens removed from the cell were observed to be blue-green in color and somewhat unevenly reduced. Examination of the surface of many of these specimens by electron diffraction failed to give any patterns; this may have been caused by the presence of an amorphous deposit on the surface. However, from a few specimens, lines were obtained due to the presence of α-Fe_2O_3 and Fe_3O_4, indicating that only an incomplete reduction had been achieved. The surface of one specimen which failed to give any electron diffraction patterns was carefully cleaned to remove the milky-green deposit; on further examination, α-Fe_2O_3 and Fe_3O_4 lines were observed. Two specimens gave electron diffraction patterns which appeared to match those of $Fe_4[Fe(CN)_6]_3$. The nature and formation of the surface deposit did not appear to be too definite, but obviously a deposit was formed on the surface when cyanide ions were present, which prevented complete reductive-dissolution of the α-Fe_2O_3 layer. Formation of $Fe_4[Fe(CN)_6]_3$ could have occurred on exposing the surface to air, and indeed in some cases it was observed that the specimens appeared colorless while still in the electrolyte.

It would seem that cyanide ions were not diffusing to the electrode surface at a rate sufficiently high to complex all the ferrous ions as ferrocyanide. This is perhaps not surprising in view of the fact that each ferrous ion requires 6 cyanide ions.

Since the presence of cyanide ions appears to prevent the complete reduction of α-Fe_2O_3, no current-efficiency measurements were made.

Effect of Versene, the tetrasodium salt of ethylenediamine tetra-acetic acid.—Some preliminary reductions were carried out in borate-buffered electrolyte containing 1% by volume of Versene, at *p*H 7.7. Reduction steps were found to be shorter than for similar reductions in ordinary borate buffer, probably due to depolarization of one or both of processes (I) and (II).

A further series of reductions was made in solutions of 1% by volume Versene adjusted to the required *p*H by the addition of HCl. A typical set of emf vs. time curves is shown in Fig. 8. Electron diffraction examination of the surface indicated that all the α-Fe_2O_3 was reduced even at *p*H 11.9. At *p*H 5.8 there must be considerable autoreduction.

The potentials show a marked trend to become more negative with increasing *p*H. From a consideration of process (I), this must be caused by decreasing H ion activity, or increasing ferrous ion activity, or both. The reduction potentials at *p*H 8.9 and 11.9 differ by approximately 0.18 v. Assuming the ferrous ion activity is constant over this region, and that the potential of process (I) is dependent on $(\alpha_{H^+})^6$, the potential difference should be of the order 0.5 v. Obviously these assumptions would require larger increases in polarization than are observed. It is probable, however, that the dissociation constant of the ferrous-Versene complex decreases with increasing *p*H, thus the activity of the ferrous ion will be lower at higher *p*H values. To account for the observed emf differences, the activity of ferrous ion would vary by a factor of 10^{-6} over the *p*H range 8.9–11.9. Versene is not a good buffering

ion; consequently, in a dynamic system the activity of the H ion may not agree with measured *p*H. This would reduce the change in ferrous ion activity over a given *p*H range required to satisfy observed potential changes.

Since Versene is not a good buffering ion, its main effect on reduction potentials must be due to the lowering of the ferrous ion activity. The failure to effect reductions at a reasonable current efficiency, in borate buffer above *p*H 8.5, must be due to the polarization by ferrous ions, or the precipitation of ferrous hydroxide on the reducible surface.

At *p*H 11.9, the reduction potential is −1.06 v (vs. S.C.E.); calculations of the standard potential (10) indicate that at this emf the ferrous ion activity should be 10^{-9}. In the presence of Versene, the activity of ferrous ion should be lower than this, since 10^{-9} is the approximate activity to be expected at *p*H 11.9 in the absence of Versene. If the ferrous ion activity is lower than 10^{-9}, there must be an overpotential to account for the low emf, possibly associated with the discharge of hydrogen ions:

$$H^+ + e \rightarrow H \qquad (V)$$

or the removal of iron from the Fe_2O_3 lattice as Fe^{++} or Fe^{+++}.

The curve shown in Fig. 8 at *p*H 5.8 exhibits a very indistinct inflection and a very short period of reduction. The high current efficiency means that autoreduction is taking place because of depolarization of anodic process (II). This effect restricts the usefulness of Versene in quantitative reductions.

Effect of Variations in Film Thickness

Three specimens were prepared differing only in the extent of their oxidation, and the current efficiencies of complete reductive dissolution were measured in borate buffer of *p*H 7.75. Table I lists the values. The calculated current efficiency did not appear significantly different, the differences being of the order of the experimental error.

The last two columns show, respectively, the actual weight loss of the specimens, and the weight loss (as Fe_2O_3) calculated from the Fe found in solution after reduction. In all three cases the calculated weight loss is slightly larger than that measured, which could mean that some of the Fe is not leaving the surface as reduced Fe_2O_3, but rather by the anodic process (II). However, the differences (8–9 γ) are not very significant. If this difference is real it could mean that process (II) is more important in the case of thinner oxide films where there is probably a greater area of exposed Fe.

Further measurements were made on somewhat thicker films of oxide. These were produced on B.I.S.R.A. iron (11), which after annealing in H at 350°C was oxidized at 320°C. The color of these specimens varied throughout the surface, indicating different oxidation of individual grains. Reduction of these specimens was carried to completion at approximately the same current density in a buffer solution of *p*H 7.7; the weight loss of each specimen was also determined. Results are shown in Table II.

TABLE I. *Current efficiencies on first-order films*

Oxidation time at 250°C	μa/cm² amps	γ of Fe in solution	Current efficiency %	Weight loss γ	Calculated wt loss γ
20 min	14.8	40	103	49	57
2 hr	13.0	75	106	99	107
16 hr	14.4	98	101	131	140

TABLE II. *Current efficiencies on second- and third-order films*

No.	μa/cm²	Fe in solution γ	Current efficiency %	Weight loss γ	Calculated weight loss γ	Percentage difference
1	15.2	288	82	384	411	3
2	14.6	312	80	461	446	6
3	14.8	570	86	815	814	—
4	14.9	212	97	283	303	6

With the exception of the thinnest film (No. 4), the current efficiency of these thicker films seems to be somewhat lower than in the case of the standard specimens shown in Fig. 6. This could be due to a larger ohmic resistance across the thicker films (the average thickness of these α-Fe_2O_3 films was 3–8 times greater than that of the standard specimens).

The last column in Table II shows a percentage difference between measured weight loss and the weight loss (as Fe_2O_3) calculated from the amount of Fe found in solution. The largest difference is 6% in the two thinner films, and would indicate that a very small amount of autoreduction may be occurring. In the case of the two thicker films the differences are of the same order as the experimental error.

Quantitative Estimation of α-Fe_2O_3 Films by Reductive Dissolution

There are three measurements which can be used for the determination of α-Fe_2O_3 quantities by cathodic reduction: (*a*) the coulombic energy used in the reduction process, (*b*) the amount of ferrous ion formed in solution by reductive dissolution, (*c*) the weight difference between the oxidized and reduced states. These three quantities can be used singly or together to estimate the α-Fe_2O_3, with varying degrees of accuracy.

Considering (*a*), the factors involved in calculating the coulombic energy are the current passed through the cell and the time of reduction. As previously pointed out the maximum errors in current and time measurements are, respectively, ±1%, ±3%; the maximum error in the coulombic energy will then be ±4%. To determine from the coulombic energy the amount of reductive dissolution of Fe_2O_3, it is necessary to know the current efficiency of the process and how much energy is discharged by process (III). Fig. 6 indicates that the current efficiency is dependent on current density; therefore, if the current density is known, it is possible to estimate approximately the current efficiency for each experiment. However, it seems probable that the current efficiencies are also dependent on the true surface area (as compared with the apparent surface area), the film thickness, and the conductivity of the oxide layer. Therefore, α-Fe_2O_3 quantities calculated purely from coulombic measurements cannot claim an accuracy of better than ±15%.

If the measurement (*b*) is used in the calculation of oxide quantities, then a more accurate value can be derived.

The unknown factor here is the amount of autoreduction occurring. Even when the indicated current efficiency is below 100%, the autoreduction process cannot be ignored, especially in the case of thin films. However, the rates of autoreduction in buffers quoted earlier are quite low, especially at *p*H values above 7.5; these rates will certainly be reduced further when higher current densities are applied to the electrode. Although at higher current densities the current efficiency may drop to 90% or less, the anodic process will be minimized, and the amount of Fe found in solution will be a truer measure of the quantity of Fe_2O_3 reduced. Unfortunately the emf vs. time curve inflections become less marked with increasing current density; consequently, the end of the reduction is less easily determined.

Assuming then that the current density is high enough to minimize autoreduction, the accuracy is dependent on the determination of Fe in solution (±2%) and the determination of the reduction end point (±3%). The maximum accuracy is then of the order ±5%.

Utilizing measurement (*c*), the most accurate measure of the oxide reduced can be obtained if the quantity involved is greater than 100 γ. By careful control of conditions and by check weighings, it was found that a maximum accuracy of ±2 γ could be achieved on difference-weighings. Consider now how the accuracies of measurement will affect interpretation of the results; in the case of 100 γ of Fe found in solution:

(*A*) When all Fe is from reduced Fe_2O_3, (process I)

$$100\,\gamma\ (\pm 2\%)\ \text{found} = \frac{160}{112} \times 100\,\gamma\ (\pm 2\%)\ Fe_2O_3$$
$$= 143\ (\pm 2\%)\ \gamma$$
$$\text{total weight loss} = 140\,\gamma \text{ to } 146\,\gamma \text{ (as } Fe_2O_3 \text{ only)}$$

(*B*) If 90 γ of Fe is formed by process (I), and the remainder by process (II)

$$90\gamma \text{ found} = \frac{160}{112} \times 90 = 129\,\gamma \text{ of } Fe_2O_3$$

the remaining 8–12 γ was lost as Fe, and the total weight loss = 127 γ to 131 γ (as Fe and Fe_2O_3).

Assuming a measured weight loss of 133 γ (±2 γ), it is obvious that these accuracy limits cannot differentiate between (*A*) and (*B*), and on the basis of these measurements, the amount of reduced Fe_2O_3 would be between the limits 129 γ and 145 γ or 137 γ (±6%). This accuracy will increase slowly as the quantities increase. For example, for 200 γ of Fe in solution, the accuracy would be (±4.5%).

This method then is capable of determining quantities of Fe_2O_3 without assuming that there is no autoreduction occurring. In the case of small quantities of oxide, the accuracy limits will be quite large.

Working on the previous assumption that autoreduction rates are very small, the accuracy of determination of Fe_2O_3 depends entirely on the accuracy of difference-weighings. This accuracy (±2 γ) is independent of quantities weighed. Consequently the percentage accuracy will increase with increasing weight differences.

Conclusions

1. It would seem that the autoreduction process can occur at low current densities in buffered electrolyte systems, even with *p*H's higher than 7. The weight loss and total Fe found in solution will indicate within limits whether autoreduction is taking place.

2. The current efficiency of the reduction process is quite dependent on current density and the electrolyte used. The true surface area of the specimen, the conductivity of the complete oxide layer, the *p*H, and probably the concentration of the electrolyte are important factors. Current efficiencies in a buffer of *p*H 7.6–7.7 are usually less than 100% if the current density is greater than 15 $\mu a/cm^2$.

3. Calculations of quantities of α-Fe_2O_3 from coulombic measurements alone cannot have an accuracy greater than ±15%. Accuracies of the order of ±6% can be obtained from the measurements of specimen weight loss and iron in solution, depending on the quantities involved.

4. Iron-complexing agents can be used to create sharper inflections in the emf vs. time curves, thus increasing the accuracy of measurement of the reduction period. The advantage of this, however, is outweighed by other undesirable effects such as depolarization of (and consequent increase in rate of) the corrosion reaction (II); or precipitation of material on the electrode preventing complete reduction of the oxide. Reductions in Versene solution alone indicate that electrode polarization is mainly due to a build-up of the ferrous ion concentration at the interface, or perhaps deposition of $Fe(OH)_2$.

Manuscript received November 21, 1955. This paper was prepared for delivery before the Pittsburgh Meeting, October 9 to 13, 1955.

Any discussion of this paper will appear in a Discussion Section to be published in the December 1957 Journal.

REFERENCES

1. U. R. Evans, *Proc. Roy. Soc.*, **A107,** 228, (1925).
2. U. R. Evans, *J. Chem. Soc.*, **1930,** 478.
3. U. R. Evans, *ibid.*, **1930,** 481.
4. H. A. Miley and U. R. Evans, *Nature* **139,** 283 (1937).
5. H. A. Miley and U. R. Evans, *J. Chem. Soc.*, **1937,** 1295.
6. H. A. Miley, *Carn. Schol. Mem. Iron and Steel Inst.*, **25,** 197 (1936).
7. M. J. Pryor and U. R. Evans, *J. Chem. Soc.*, **1950,** 1259.
8. W. M. Clark, "The Determination of Hydrogen Ion," p. 209, Williams & Wilkins Co., Baltimore (1928).
9. U. R. Evans, *J. Chem. Soc.*, **1927,** 1024; *Nature*, **120,** 584 (1927).
10. W. M. Latimer, "The Oxidation States of the Elements and Their Potentials in Aqueous Solutions," 2nd ed., Prentice-Hall, New York (1952).
11. E. J. Caule and M. Cohen, *Can. J. Chem.*, **31,** 237 (1953).

The Mechanism of Deposition of Titanium Coatings from Fused Salt Baths

M. E. Straumanis, S. T. Shih, and A. W. Schlechten

University of Missouri School of Mines and Metallurgy, Department of Metallurgy, Rolla, Missouri

ABSTRACT

The mechanism of the titanizing process, as described previously, consists mainly in the direct collision of Ti particles dispersed in a molten salt bath (KCl, NaCl, or both together) with the surface of the metallic or ceramic object submerged. The Ti particles stick to the surface, and, if the temperature is high enough (e.g., for Fe above 910°C) a part of the Ti deposited diffuses into the substrate forming a diffusion layer. Its thickness conforms to Rhines' diffusion equation.

By the titanizing method described not only can Fe, low carbon steel, Co, Ni, and noble metals be coated, but so can ceramic materials such as porcelain and alundum.

Coatings on Fe can also be produced in fused salts (KCl or NaCl) containing lower Ti chlorides in larger amounts but no metallic Ti. In this case the coating is produced by an exchange mechanism, e.g., $2TiCl_3 + 3Fe \rightarrow 3FeCl_2 + 2Ti$ (coating on excess Fe), or by Ti formed in the $TiCl_3$ disproportionation reaction.

The collision mechanism and the exchange mechanism may go on simultaneously with more active metals. However, not more than 4.0% of the total Ti coating is produced by the latter mechanism. The lower Ti chlorides in the fused salt baths are formed by the reaction $Ti + 3NaCl \rightarrow TiCl_3 + 3Na$; the Na evaporates partially at the working temperature of above 900°C.

In one of the previous articles (1) on titanizing metallic objects it was assumed that the coating was formed by direct collision of Ti particles, dispersed in the molten salts (NaCl or KCl), with the metal (*A*):

$$\text{Ti (powder)} + \text{Me} \rightarrow \text{TiMe alloy} \qquad \text{(I)}$$

However, another possible mechanism is an exchange reaction (*B*):

$$2TiCl_3 + 3Fe \rightarrow 3FeCl_2 + 2Ti \text{ (on excess Fe)} \qquad \text{(II)}$$

$$\text{or } TiCl_2 + Fe \rightarrow FeCl_2 + Ti \text{ (on excess Fe)} \qquad \text{(III)}$$

especially as it was noticed that some lower oxidation state Ti chlorides were always present in the salt after the coating experiments. But these could also produce a Ti coating by disproportionation (*C*) on the surface of the object at the high temperature in the salt bath (2–5):

$$2TiCl_3 \text{ (formed in the salt bath)} \rightarrow TiCl_2 + TiCl_4 \qquad \text{(IV)}$$

$$\text{or } 2TiCl_2 \text{ (formed in the salt bath)} \rightarrow Ti + TiCl_4$$

$$\text{or } 3TiCl_3 \rightarrow Ti + 2TiCl_3 \qquad \text{(V)}$$

The Ti freed may adhere to the surface and may alloy with the metal forming coatings rich in Ti according to equation (I). Therefore, the titanizing process in case (*C*) would differ from (*A*) or (*B*) only in the source of metallic Ti for the coating process.

As it is not possible to prove exactly the correctness of the direct reaction (I), the reactions (II) and (III) will be discussed first, to arrive at the most probable titanizing mechanisms.

Experimental Procedure and Results

Exchange Reaction (B)

In order to decide whether reaction (*B*) is possible, the following data were necessary: the amount of iron chlorides present in the melt after the reaction, and the amount of Ti deposited on Fe (1, 3). For more complete information the amounts of Ti present as lower chlorides in the melts were also estimated.

There was evidence enough that the titanium lower chlorides were formed in the coating experiments carried out at above 1000°C: the solutions, obtained by leaching the salt with water, showed a slight violet (or brownish) color; they decolorized dilute $KMnO_4$ solutions and always exhibited an acidic reaction,[1] which resulted from hydrolysis of the titanium chlorides.

Iron chlorides were not formed when ingot iron alone was heated in KCl or NaCl under conditions identical to those above. Thus Fe^{2+} (and a little Fe^{3+}) found in the leaching solutions could result only from reaction (*B*).

Amount of titanium chlorides in the melt.—This estimation was based on the assumption that mainly $TiCl_2$ was present in the NaCl or KCl salt melts. The easiest way for determination was to hydrolyze the Ti salt and to titrate the acid obtained. Thus, the melt was placed in water. During the leaching and decanting operations and while standing overnight exposed to air, $Ti(OH)_4$, acid and hydrogen (6) were formed:

$$2Ti^{2+} + 7H_2O + 0.5\,O_2 \rightarrow 2Ti(OH)_4 + H_2 + 4H^+ \qquad \text{(VI)}$$

[1] The acidity of the solutions excludes reactions such as $TiO_x + 2xNaCl \rightarrow xTiCl_2 + (Ti - x) + xNa_2O$ during the heating process.

TABLE I. *Mg* Ti *converted into chloride during heating (1–4 hr) of the 14 g charge containing 90 w/o* KCl *and 10 w/o* TiO_x *(x = 0.053).* He *atmosphere*

Charge KCl + TiO_x	Temp, °C	Heating time, hr			
		1 Ti mg	2 Ti mg	3 Ti mg	4 Ti mg
No Fe	850	0	0	4.7	—
With ingot Fe	850	0	0	2.9	—
No Fe	950	4.5	7.5	20.6	23.0
With ingot Fe	950	4.3	6.0	17.7	21.3
No Fe	1000	9.2	23.8	78.5	90.0
With ingot Fe	1000	6.3	19.7	57.4	67.0

The iron chlorides present hydrolyzed also, but this introduced no error since these were formed in equivalent amounts on the basis of reaction (*B*). The acid was titrated and the Ti present was calculated, as each milligram equivalent of the acid in the leaching solution corresponded to about 24 mg of Ti transformed into the chloride during the heating operation (see Table I). The clear solutions after the titration did not show any presence of Ti or Fe ions.

Table I shows that titanium chloride formation is slow at 850°C, and that the rate of reaction increases with time and temperature, the influence of the latter being much more pronounced than that of time. However, the melts obtained in the presence of a piece of ingot iron always contained smaller amounts of Ti than those without Fe. It is possible that this effect was caused by a difference in the temperature of the superimposed crucibles during the heating. Of importance is the fact that only 0.3–6.4% of the Ti present in the crucibles was converted into chlorides, depending on temperature and time. However, this represents a maximum amount, because $TiCl_2$ should be in equilibrium with $TiCl_3$. As the latter oxidizes and hydrolyzes according to the equation

$$2Ti^{3+} + 7H_2O + \tfrac{1}{2}O_2 \rightarrow 2Ti(OH)_4 + 6H^+ \quad \text{(VII)}$$

the actual amount of Ti will be less than mentioned in Table I (1 milliequivalent of acid = 16 mg of Ti instead of 24 mg). No separate determinations were made of Ti^{2+} and Ti^{3+} in the melts.

Fe in the leaching solutions.—For these determinations new melts were prepared using a 10 g charge but the same ingredients (90% KCl and 10% $TiO_{0.053}$), and always with ingot iron (~3 g) embedded in the mixture. The Fe of the leaching solutions was converted to the trivalent state and determined colorimetrically by the thiocyanate method (see Table II).

Ti in the coatings.—After treatment in the furnace, Fe samples were completely coated with Ti. Each sample was washed, dried, and cut into 4 pieces to expose the base metal. The coatings were parted from Fe by dissolving the latter in dilute HNO_3. The parted coatings then were analyzed for their Ti contents by a method similar to the one described by Rahm (7). Results are shown in Table II.

Results.—Since a known amount of Fe was present in the salt after the runs, the maximum amount of Ti which could be deposited on the Fe due to reactions (II) and (III) could be calculated. This result could be compared with that obtained by direct analysis of the sample coatings (*see* Table II).

Table II shows that the Fe-Ti exchange reaction (*B*) is favored by increasing temperature, but the time does not seem to have a marked effect on the reaction. At most only 4% of the Ti deposited on Fe can be attributed to the exchange reaction (*B*). The rest must have been deposited by other mechanisms.

A comparison of Tables I and II shows that the small amount of Ti deposited by the exchange reaction originated from a much higher concentration of titanium chloride in the salt bath, in accordance with theoretical expectations.

Decomposition Reaction (C)

As it was not definitely known whether Ti coatings on metals could be produced by disproportionation reactions such as (VIII), experiments were made using large amounts of lower titanium chlorides and iron or steel specimens. The chloride was prepared by partial reduction of $TiCl_4$ with metallic Na. The exact composition of the reaction product was not known, but preliminary tests showed the presence of NaCl, $TiCl_3$, $TiCl_2$, Ti (in small amounts), and perhaps some $NaTiCl_4$. This fused salt mixture reacted readily with water with the evolution of H; on standing, oxidation and hydrolysis occurred and a white insoluble residue, probably $Ti(OH)_4$, appeared.

Coating experiments were made using this salt mixture (~ 80%) with NaCl added, all under He at 1000°C for about 2 hr. A large increase in gas pressure was noticed during the heating, presumably due to disproportionation of $TiCl_3$ and $TiCl_2$ according to the reactions (4, 5)

$$4TiCl_3 \rightarrow Ti + 3TiCl_4 \text{ or}$$

$$2TiCl_2 \rightarrow Ti + TiCl_4 \text{ occurring at about } 475°C \text{ (2)}, \quad \text{(VIII)}$$

and as a result of evaporation of the chlorides. However, well coated samples of ingot iron plates, iron pennies,

TABLE II. *Determination of the extent of reaction (B) as a possible mechanism of* Ti *deposition on* Fe *from molten salt* (90 *w/o* KCl) *and* Ti *dispersions* (10 *w/o* $TiO_{0.053}$). *Mixture:* 10 g; *ingot* Fe ~ 3 *g*

Temp, °C	850		950		950		1000	
Time, hr	4		3		4		4	
Sample	a	b	a	b	a	b	a	b
Total Fe found in solution, mg	0.15	0.15	0.3	0.4	0.35	0.4	0.8	0.6
Mg Ti calc. from Eq. (II)	0.08	0.08	0.16	0.224	—	0.224	0.464	0.336
Mg Ti calc. from Eq. (III)	0.12	0.12	0.24	0.336	—	0.336	0.696	0.504
Total Ti found in coating, mg	6.2	3.8	11.6	15.6	—	14.0	17.5	15.1
%Ti due to exchange, Eq. (II)	1.3	2.1	1.4	1.4	—	1.6	2.6	2.2
%Ti due to exchange, Eq. (III)	1.9	3.2	2.1	2.1	—	2.4	4.0	3.3

and steel bolts were obtained, in part because of the good fluidity of the molten bath.

Thus, coatings can also be obtained by interaction of the metal with lower titanium chlorides under He. The question remains whether such coatings could be produced in salt baths containing only a small amount, e.g., 90 mg at a maximum, of Ti as lower chlorides in a charge of 14 g (0.64 w/o). These amounts accumulated only toward the end of the experiments (*see* Table I).

The proofs that under such conditions deposition due to the disproportionation reaction (*C*) could not occur to any appreciable extent are as follows:

1. Coatings on Fe could also be produced at 800°C and below, even during a time of about 1 hr, when, according to Table I, no titanium chloride at all was found in the melt (1).

2. The weight of good coatings obtained at 950° or 1000°C (Table II) in 3 hr was nearly equal to the total amount of Ti accumulated in the form of chlorides in larger charge (14 g vs. 10 g) during the whole experiment under the same conditions (Table I). To avoid excessive evaporation of the salts, He pressure was kept just above atmospheric pressure. It is improbable that a heavier coating could be produced with less of the titanium chlorides present.

3. As appreciable amounts of Ti were deposited on Fe during the experiments (Table II), $TiCl_4$ gas should have escaped from the crucibles, as in case of reaction (VIII). However, all efforts to detect $TiCl_4$ failed.

4. Any catalytic decomposition of the lower chlorides to Ti metal should also result in the development of $TiCl_4$, as the disproportionation temperature of the lower titanium chlorides is below 500°C (2).

Hence, in the experiments with fused salt and Ti powder, only very limited amounts of Ti, if any, could be plated on Fe because of reactions (IV) and (V). Reaction (II) or (III) produced in the best case only about 4% of the coating. Therefore, (I) was the only possible reaction that remained responsible for 96% of the Ti coating. This is also logical because the melts contained 10% Ti or TiO_x powder, while there was only 0.6% or less Ti in the form of lower chlorides at the end of the experiments. Of course, if the amount of lower chlorides in such melts were much higher, deposition from chlorides would be possible, as in the case of mixtures rich in $TiCl_2$ and $TiCl_3$.

Titanium Deposition Reaction (A)

Further evidence in favor of reaction (I) is the fact that metals can be titanized even though they are electrochemically more noble than Ti. It may be that in fused salt baths the potential of Ti and of Fe approach each other so that the exchange mechanism (*B*) becomes possible. However, it is difficult to assume that the potentials of Co, Ni, Cu, Au, and Pt also will be close to that of Ti in molten salt baths under He. Nevertheless, it is possible to titanize all these metals using the same technique as that used to obtain Ti deposits on Fe. In the case of Cu the weight of the sample always increased after the titanizing, and no Cu ions could be found in the leaching solutions. Thick and coherent Ti layers were obtained on Au and Pt, which could be easily removed by dipping the samples in HF.

Discussion and Conclusion

All the facts mentioned above lead to definite conclusions concerning the mechanism of titanizing. In addition, the formation of Ti dispersions (8) and the corrosion of Ti in salt baths in the presence of air must be considered.

Oxygen of air diffuses through the molten salt layer and is absorbed by the metallic Ti giving TiO_x solid solutions (14). As these have a greater volume than the pure metal and also probably different expansion coefficients, the TiO_x breaks away in small particles from the solid Ti. Particles are dispersed throughout the liquid salt melt mainly by convection currents. X-ray pictures of the TiO_x particles showed an expanded lattice but no abnormal broadening of the powder lines. This indicates that the particle size of the TiO_x alloy formed is not of colloidal dimensions. Hence, the salt melt obtained cannot be called a colloidal solution (9), but it is rather a dispersion of TiO_x particles in a fused salt bath. Of course, corrosion of the metal is very small in the absence of O_2; that which does occur may be due to some residual O_2 or to presence of oxides, e.g., SiO_2 of the crucibles.

It could not be determined whether fine particles of TiO_x are necessary for the coating process or simply fine particles of pure Ti. Oxygen-free powder in a sufficiently small grain size was not available; fines obtained by sieving Ti sponge always contained 3–5% O_2.

These experiments indicate that the coatings were formed on the direct impact of Ti particles. Evidently the metallic surface was first cleaned by action of the fused salt, and surface oxides were reduced by dispersed Ti particles. Thus, titanium particles could easily stick to the clean metallic surface. It was not determined in detail whether or not the O_2 of the Ti particles was transferred to the coating during the deposition process. But there were indications that there was more O_2 in the particles than in the coating, because the oxygen content of the remaining particles (not used up in the deposition process) increased (3).

Formation of coatings on ceramic material, such as the inside of alundum crucibles and thimbles, can be explained by the direct collision and sticking of titanium particles to the walls. Contrary to a patent description (10), no electric current and no lower chlorides are necessary to produce thick Ti layers on silica-containing ceramic material. Immersion in a fused salt bath and Ti mix suffices. The inside walls of porcelain crucibles in the present experiments were always titanized: Ti particles in the

TABLE III. *Observed and calculated thicknesses x of diffusion layers of* Ti *into ingot iron*
Bath: KCl 90%, $Ti_{95}O_5$ 10%

Coating temp, °C	Coating temp, °K	Coating time hr	Diffusion layers x in mm: obser.	Diffusion layers x in mm: calc.	Δ_{mm}
850	1123	2	0.000	0.013	−0.013
950	1223	2	0.044	0.042	+0.002
950	1223	4	0.068	0.066	+0.002
950	1223	6	0.088	0.081	+0.007
1000	1273	2	0.082	0.085	−0.003
1000	1273	4	0.135	0.120	+0.015
1000	1273	6	0.150	0.148	+0.002
1000	1273	9	0.164	0.178	−0.014

fused salt reduced the SiO_2 to Si (black in appearance), and Ti was deposited, in forming solid solutions with this Si. X-ray powder pictures of the black substance of the crucibles, from which the Ti was removed by dissolution in dilute HF, showed the presence of weak Si lines.

If deposition of Ti occurred from lower titanium chlorides in molten NaCl or KCl baths [Eq. (VIII)], the mechanism was the same, i.e., by alloying the Ti formed with the object. If deposition occurred by the displacement mechanism (*B*), the necessary lower titanium chlorides were formed in the melts because of the reaction (5):

$$Ti + 2NaCl \rightarrow TiCl_2 + 2Na \qquad (IX)$$

$$\text{or } Ti + 3NaCl \rightarrow TiCl_3 + 3Na \qquad (X)$$

At the temperatures used, Na partially evaporated and the reaction went to the right so that some amounts of Ti chlorides could accumulate in the salt. Reactions (IX) and (X) are in agreement with previous work on the Ti-fused salt-Pt cell (11) and with the experimental results of Skinner and Ruehrwein (5), which, however, were carried out at much higher temperatures (1670°–1830°C). Evidence for the presence of Na vapor was the reduced Si on the outside of the crucibles and on the inside of the mullite tubes of the furnaces. It is not very probable that the effect was produced by Ti because of its low vapor pressure as compared with that of Na. The formation of $TiCl_3$ in the leaching solutions is then explained by decomposition of water by the divalent Ti ion (6):

$$Ti^{2+} + H_2O \rightarrow Ti^{3+} + OH' + \tfrac{1}{2}H_2 \qquad (XI)$$

In fact, evolution of small gas bubbles could be observed in the leaching solutions, which were brownish at first. The trivalent titanium chloride which gave violet solutions could also be formed directly according to reaction (X). Furthermore, thin layers of a green substance were sometimes visible in the solid salt if broken out of the crucibles [see reactions (IV) and (V)]. This substance probably resulted from the reaction:

$$NaCl + TiCl_3 \rightarrow NaTiCl_4 \qquad (XII)$$

The Ti layer formed on the surface of a metallic object either by direct collision with Ti or TiO_x particles or by the exchange mechanism (*B*) was never pure (as proved by x-ray fluorescence analysis) but contained appreciable amounts of the metal of the substrate, e.g., Fe. Hence, by the method under discussion, good Ti layers will be produced only if the mutual solid solubility and the rate of diffusion of Ti in the metal of the substrate is high enough at the temperatures of the experiment. At such conditions Ti coatings can be formed with a decrease of the free energy of the system. If the concentration of pure Ti in the outer layer becomes too high, deposition stops. This explains why the Ti coatings are comparatively thin (3). However, diffusion of Ti into the depth of the substrate continues, producing the diffusion layer [Fig. 5 of Ref. (3)]. The Ti for the diffusion layer is delivered by the outer coating. The thickness x of the diffusion layer at a time t is related according to Rhines (12) with the absolute temperature T at which the diffusion occurs in the following way:

$$\log x^2/t = a - b/T \qquad (XIII)$$

where a and b are constants different from the diffusion coefficient appearing in Fick's diffusion law (13). In the previous article (3) a series of $x - t - T$ data were summarized in Table II. From this table data were drawn which were obtained at completely identical experimental conditions, and the constants a and b were calculated from the data. The following values were obtained: $a = 10.03$ and $b = 15{,}880$. Substituting these values for a and b in Eq. (XIII), the thickness x of the diffusion layer was calculated for the time t at a temperature T, and compared with the experimental values (Table III).

Table III shows clearly that the diffusion of Ti into ingot iron proceeds according to equation (XIII). However, at a temperature of 850°C no diffusion layers in Fe could be observed, although a layer of about 0.013 mm was indicated by Eq. (XIII). Hence, it is very possible that the diffusion of Ti in Fe starts with a faster rate only above the $\beta - \gamma$ transformation point of Fe, i.e., above 910°C. The thin Ti coating of 0.0044 mm obtained at 850°C is formed by Ti particles sticking to the Fe surface. Iron diffused into the layer, decreasing its free energy.

ACKNOWLEDGMENT

The authors are grateful to the Wright Air Development Center for support of this work [under Contract No. AF 33(616)-75] and for permission to publish the results obtained.

Manuscript received October 24, 1955.
Any discussion of this paper will appear in a Discussion Section to be published in the December 1957 JOURNAL.

REFERENCES

1. A. W. SCHLECHTEN, M. E. STRAUMANIS, AND C. B. GILL, *This Journal*, **102**, 81 (1955).
2. P. EHRLICH AND G. PIETZKA, *Z. anorg, Chem.* **275**, 121, 137 (1954); see also Project Rand R-131 "Titanium and Titanium-Base Alloys," p. 41. Battelle Memorial Institute, Columbus, Ohio, (1949).
3. S. T. SHIH, M. E. STRAUMANIS AND A. W. SCHLECHTEN, *This Journal*, **103**, 395 (1956).
4. M. FARBER AND A. J. DARNELL, *J. Phys. Chem.*, **59**, 156 (1955).
5. G. B. SKINNER AND R. A. RUEHRWEIN, *J. Phys. Chem.*, **59**, 113 (1955).
6. O. RUFF AND F. NEUMANN, *Z. anorg. Chem.*, **128**, 81 (1923).
7. J. A. RAHM, *Anal. Chem.* **24**, 1832 (1952).
8. C. B. GILL, M. E. STRAUMANIS AND A. W. SCHLECHTEN, *This Journal*, **102**, 42 (1955).
9. J. D. CORBETT AND S. VON WINBUSH, *J. Am. Chem. Soc.*, **77**, 3964 (1955).
10. H. F. ROSS, German Pat. No. 830,858, Feb. 7, 1952; British Pat. No. 679,419, Sept. 17, 1952.
11. M. E. STRAUMANIS AND A. W. SCHLECHTEN, *This Journal*, **102**, 131 (1955).
12. F. N. RHINES, in "Surface Treatment of Metals", p. 136, Am. Soc. of Metals, Cleveland, (1941).
13. See also D. M. DOVEY, I. JENKINS, AND K. C. RANDLE in "Properties of Metallic Surfaces", p. 219, The Institute of Metals, London (1953).
14. M. E. STRAUMANIS, C. H. CHENG, AND A. W. SCHLECHTEN, *This Journal*, **103**, 439 (1956).

Electrodeposition of Metals from Organic Solutions

III. Preparation and Electrolysis of Titanium and Zirconium Compounds in Nonaqueous Media

W. E. Reid, Jr., J. M. Bish, and Abner Brenner

National Bureau of Standards, Washington, D. C.

ABSTRACT

Numerous nonaqueous solutions of Ti and Zr compounds were electrolyzed in an attempt to electrodeposit the metals. Ether solutions containing halides, hydrides, borohydrides, and organo-metallic compounds of Ti and Zr were the most promising. A mixed type of bath containing both hydrides and borohydrides yielded Ti-Al alloys containing about 6% Ti. Similar baths containing Zr instead of Ti gave alloy deposits containing up to 45% Zr. New methods of preparation of titanium and zirconium borohydrides were developed.

Coatings of Ti would be of considerable value for protecting steel against corrosion. For this reason, methods for electrodepositing Ti have been under intensive investigation by many workers during the past few years.

Attempts to electrodeposit Ti go back over 100 years when Becquerel (1) claimed to have deposited a Ti-Fe alloy from aqueous solution. Experiments on aqueous electrolysis have continued since that date without success, despite claims to the contrary. Russell (2, 3), investigating electrode potentials, reported that Ti amalgamated with Hg to a very slight extent. He electrolyzed an acid solution of $TiCl_3$ using a water-cooled rocking Hg cathode at a high current density. He claimed a deposition rate of 0.2 g Ti/hr. A method was patented (4) for plating Ti on a base metal from strongly alkaline solutions at low current density. About 20 mg Ti were deposited by 0.1 amp-hr. Thin, black coatings of Ti on Pb, Zn, or Sn cathodes were deposited from solutions containing $Ti_2(SO_4)_3$ and Na_2SO_4 (5–7). Tartaric acid solutions were also suitable. Gratzianskii (8) obtained thin Ti films on a Cu cathode from sulfanilic acid solutions. A patent was issued (9) covering the electrolysis of salts melted in their water of crystallization; titanium sulfate trihydrate was one of the salts mentioned. Fink (10) patented a bath consisting of TiO_2, HF, HCl, and gelatine with traces of Cu to depolarize the deposition of Ti. Keys and Swann (11) reported their ability to plate Ti from aqueous solutions.

Ti contaminated with oxides has been deposited from mucous sols containing colloidal Ti, but it could not be electrodeposited from solutions of its salts (12). A very thin deposit of Ti-Zn alloy was obtained from aqueous solutions containing a peroxide and tartrate (13). Some alloy deposits containing Ti were formed from anhydrous and aqueous systems (14). Three general references on Ti are included in the bibliography (15–17).

Experiments on the electrodeposition of Zr have also failed to yield any successful metallic deposits. Bradt (18) claimed to have established optimum conditions for plating bright Zr from solutions of zirconyl sulfate on a Cu cathode. The deposits were very thin. Laubengayer (19) confirmed the findings of Bradt, but Plotnikov (20) obtained only H at the cathode. An investigation of the electrodeposition of Zr from organic plating baths was unsuccessful (21). Holt (22) investigated the electrodeposition of Zr from aqueous and organic plating baths without obtaining any successful metallic Zr deposits.

This shows that up to now no substantiated evidence has been presented for the successful electrodeposition of Ti or Zr from either aqueous or organic plating solutions. Although Ti metal can be deposited from high temperature fused salt baths (23, 24), the operational difficulties involved make the development of a plating bath capable of operation at room temperature highly desirable.

The available evidence indicates that these metals are probably too reactive to be electrodeposited from aqueous solutions. This conclusion has focused attention on the use of organic solvents as a plating medium. Although organic plating baths have been known for many years (25), it was not until the development of the hydride aluminum plating bath by Couch and Brenner (26) that the consistent deposition of good plates from an organic plating bath was demonstrated as feasible.

Solvents

In the exploratory phase of the work here (1951–52), Sherfey and Senderoff of this laboratory dissolved Ti halides in a number of solvents and electrolyzed the resulting solutions. No successful deposition of the metal resulted. However, the systems investigated are listed in Table I to indicate the diversity of solvents tried. The conclusion is that Ti halides were not the proper type of compound. Of the solvent types used, ethers were the most suitable.

Atmospheric oxidation of ethers to peroxides and other compounds occasionally caused difficulties. For example, the first additions of lithium aluminum hydride to 1,2-dimethoxyethane or tetrahydrofuran reacted very vigorously. This was caused by impurities resulting from atmospheric oxidation. Acetaldehyde was identified in the dimethoxyethane. The latter is so sensitive to oxidation that even a very brief exposure to the atmosphere resulted in formation of peroxides. Ethers should be free of oxidized

TABLE I. *Solvents in which* Ti *halides were electrolyzed*

Hydrocarbons
Benzene
Toluene + Li
Toluene + Na

Halogenated Hydrocarbons
Benzotrichloride
Bis (trifluoromethyl) benzene
Tert-butyl chloride
Tert-butyl chloride + dry HCl
Ethyl bromide
Ethylidene chloride
Ethylpyridinium bromide + aluminum chloride
1,1,1-Trichloroethane
Trichloro-fluoro-methane

Alcohols
Butyl alcohol
Tert-butyl alcohol
Carbitol
Ethanol (0°C and 25°C)
Ethanol + boron trifluoride
Ethanol + ethyl ether + HCl
Ethanol + HCl
Ethanol + HCl (aqueous)
Ethanol + Na
Ethanol + tetramethylammonium hydroxide
Ethylene glycol
Glycerine
Glycol
Methanol
Methanol + tetraethyl-lead

Ethers
Butly ether + $AlCl_3$
2-Ethoxyethanol
1,4-Dioxane
1,4-Dioxane + Li
1,4-Dioxane + Na
Ethyl ether
Ethyl ether + $AlBr_3$
Ethyl ether + $AlBr_3$ + $LiAH_4$
Ethyl ether + $AlCl_3$
Ethyl ether + $AlCl_3$ + $LiAH_4$
Ethyl ether + Li
Ethyl ether + $LiBH_4$
Ethyl ether + Na
Ethyl ether + $NaBH_4$
Tetrahydrofuran

Ketones
Acetone

Acids
Acetic acid
Acetic acid + acetic anhydride
Trifluoracetic acid anhydride

Amines
Pyridine
Pyridine + boron trifluoride
Iminodipropionitrile
Ethylenediamine
Isopropylamine

Amides
Dimethylacetamide
Dimethylformamide
Dimethylformamide + Li
Dimethylformamide + Na
N,N - dimethyltrichloroacetamide

Nitriles
Diallylcyanamide
Dimethylcyanamide
Acetonitrile
Acrylonitrile
Oxydipropionitrile

Miscellaneous
Aluminumdiethyl bromide + aluminum ethyl dibromide
Aluminumdiethyl bromide + aluminum ethyl dibromide + toluene
Benzothiazole
Methylmagnesium bromide
Methylmagnesium bromide + ether
N-methylpyridinum methyl sulfate
Methyl sulfate
Methyltrichlorosilane
3-Nitro 4-chloro benzotrifluoride
Nitromethane
Isopropyl titanate

Inorganic
PCl_3
S_2Cl_2
SO_2Cl_2
$SOCl_2$
TiI_4
Water

compounds when used as solvents for organometallic, hydride, or borohydride type compounds, such as were used in this study.

A necessary prerequisite of a plating bath is that a high concentration of complexed ions be maintained in solution. This made necessary a study of the solubilities of Ti and Zr compounds in various organic solvents. Approximate solubilities obtained at room temperature are given in Table II.

Ti and Zr Complex Hydrides

Ti (III) borohydride solutions.—The borohydrides constitute a new type of electrolyte, the electrolytic properties of which have not been previously investigated. These compounds may be divided roughly into two classes: the ionic borohydrides and the covalent borohydrides. The ionic borohydrides, such as $NaBH_4$, are quite stable even when exposed to the atmosphere. They are insoluble in the usual organic solvents. The covalent borohydrides, such as those of Be or Al are unstable and are much more reactive. They react spontaneously with the atmosphere, often with explosive violence, and must be studied in an

TABLE II. *Solubilities of* Ti *and* Zr *compounds in various organic solvents*

Solvents	Solubility (g/100 ml)
Bis-cyclopentadienyl Titanium Dibromide	
Petroleum ether	Insoluble
Ethanol	Very slight
Ethyl ether	0.17
Benzene	0.34
Chloroform	0.92
Phenetole	1.09
Acetone	1.15
Tetrahydrofuran	1.24
1,2-dimethoxyethane	1.99
Dimethylformamide	3.55
$TiCl_4$	
Benzene	Completely miscible
Acetone	Very soluble
Ethanol	Very soluble
$TiBr_4$	
Ethyl ether	4.4
Titanium Trifluoroacetate	
Ethyl ether	Slightly soluble
Anisole	Soluble
1,2-Dimethoxyethane	Soluble
Dimethylformamide	Soluble
Benzene	Insoluble
$ZrCl_4$	
Ethanol	Soluble
Ethyl ether	1.1
Methyl ether	5.4 at −23.6°C
Benzene	Very low (less than ether)
Anisole	2.7
Dimethoxyethane	6.8
Phenetole	7.1
Tetrahydrofuran	14.1
$ZrBr_4$	
P-xylene	0.2
Ethyl ether	1.2
Dimethoxyethane	50.3
Tetrahydrofuran	53.0
$TiCl_3$	
Tetrahydrofuran	2.5

inert atmosphere. The covalent borohydrides are usually very soluble in organic solvents, and this property makes them of interest as electrolytes.

Hoekstra and Katz (27) prepared titanium(III) borohydride, $Ti(BH_4)_3$, by passing $TiCl_4$ over $LiBH_4$. Titanium (III) monochloroborohydride, $TiCl(BH_4)_2$, was formed when $TiCl_4$ reacted with $Al(BH_4)_3$. $Ti(BH_4)_3$ was green and the monochloroborohydride was blue. $Ti(BH_4)_3$ was reported to be unstable at room temperature, decomposing completely within several days (27).

$Ti(BH_4)_3$ was prepared by this method, but it was unsatisfactory for preparing more than milligram quantities. $Ti(BH_4)_3$ for plating experiments was prepared by the reaction of a Ti halide with $Al(BH_4)_3$ or $LiBH_4$ in ethereal solution. All experiments were performed in a He atmosphere, and no attempt was made to isolate the resulting $Ti(BH_4)_3$. As shown in Table III, some Ti halides reacted with $Al(BH_4)_3$ to give green solutions, and some gave blue solutions. Assuming that the ether solutions had the same color as the compounds, this indicated in some cases the solutions probably contained a mixture of both types of titanium borohydrides.

Results of the electrolysis experiments with the $Ti(BH_4)_3$ solutions are included in Table III. Pure metal was not obtained. Ethereal borohydride solutions prepared from Ti halides all yielded nonmetallic, black, moisture-sensitive deposits on electrolysis. None of the solutions conducted very well. A tetrahydrofuran solution of titanium (III) borohydride tetrahydrofuranate did not conduct at all.

The black deposit obtained from electrolysis of the green solution of $TiCl_4$-$Al(BH_4)_3$ (Table III, No. 7) contained 19% Ti and may be considered typical in composition and appearance for the nonmetallic Ti deposits described in Table III. It also contained 19% Al, 33% Cl, and undetermined B. As this solution was electrolyzed, the intensity of the green color diminished and a brownish-red material which formed at the Al anode soon discolored the solution.

Ethyl ether solutions of Ti borohydride were unstable on standing for several days at room temperature, as indicated by a change in color from green to brown, a decrease in conductivity, and precipitation of a brown solid.

Addition of hydride aluminum plating bath (26) to $TiCl_4$-$Al(BH_4)_3$ solution gave a brown solution (Table III, No. 9). Electrolysis of this solution gave a good metallic deposit containing Ti, Al, and B. Maximum Ti content of an alloy deposit obtained from a bath of this type was 6.5%. A deposit obtained from this same bath four days later contained 1.6% Ti, 94.7% Al, and 2.6% B.

Uncertainty regarding composition of the borohydride compound in the solutions led to attempts to prepare pure $Ti(BH_4)_3$ by a new method satisfactory for producing large quantities. This involved the reaction of diborane with a Ti ester of the type $Ti(OR)_4$. Titanium borohydride tetrahydrofuranate, $Ti(BH_4)_3 \cdot C_4H_8O$, was formed in tetrahydrofuran. Preparation of this compound is discussed in the Appendix.

An ether solution containing titanium borohydride tetrahydrofuranate and hydride aluminum plating bath was electrolyzed. The resulting alloy deposit contained 6.3% Ti. Attempts to prepare a plating bath by direct addition of $LiAlH_4$ solution alone instead of addition of the hydride aluminum bath to $Ti(BH_4)_3$ solution at room temperature caused decomposition as indicated by a vigorous evolution of gas and the formation of a black solid which discolored the solution. This would indicate that $LiAlH_4$ reacts or complexes with $AlCl_3$ preferentially so that its reactivity with $Ti(BH_4)_3$ is decreased.

TABLE III. *Electrolysis of ethyl ether solutions of* $Ti(BH_4)_3$ *and* $Zr(BH_4)_4$

Preparation of electrolyte		Color of solution	Nature of deposit	Wt. % Ti or Zr in deposit
Ti or Zr salt present	Reagent added			
1. K_2TiF_6	$Al(BH_4)_3$	Colorless	None	—
2. $TiCl_3$	$LiBH_4$	Blue	Black, moisture sensitive	—
3. $NaTiCl_4$	$LiBH_4$	Colorless	None	—
4. TiF_3	$LiBH_4$	—	Li deposit	—
5. TiF_4	$LiBH_4$	Blue	Black, moisture sensitive	—
6. $TiCl_3$	$Al(BH_4)_3$	Blue	Black, moisture sensitive	22.4
7. $TiCl_4$	$Al(BH_4)_3$	Green	Black, moisture sensitive	19.1
8. $TiBr_3$	$LiBH_4$	Blue	Black, moisture sensitive	—
9. $TiCl_4$	$Al(BH_4)_3$ + Al plating bath	Brown	Metallic	6.5
10. $ZrCl_4$	$Al(BH_4)_3$ + Al plating bath	Brown	Metallic	22.9
11. $ZrCl_4$	$Al(BH_4)_3$	Colorless*	Black, moisture sensitive	34.2

* $Zr(BH_4)_4$ solutions are colorless.

Titanium aluminum hydride.—In the reaction of $LiAlH_4$ with $Ti(BH_4)_3$, titanium aluminum hydride, $Ti(AlH_4)_4$, may be formed first but then decomposes immediately. This seems likely because the compound has been reported in the literature (28) as being stable only at dry ice temperature or below and decomposing on warming to room temperature. The compound is insoluble in ethyl ether at its temperature of existence. Some of the compound was prepared in methyl ether at −80°C and the solution was electrolyzed as it warmed up slowly to the boiling point of this solvent. The compound did not appear to be very soluble in this ether, and conductivity was very low. No metallic deposit was obtained.

Zr-Al Alloy Baths

Type A bath ($Zr(BH_4)_4$ and $LiAlH_4$).—$Zr(BH_4)_4$ in ether did not conduct, and ether solutions of $LiAlH_4$ were only slightly conducting. When these two solutions were mixed, however, the resulting solution conducted very well, and

a sound metallic deposit containing about 8% Zr was obtained. The ratio of $LiAlH_4$ to $Zr(BH_4)_4$ necessary to obtain a metallic deposit from these ether solutions was critical. This was shown by a comparison of baths containing the following ratios: (*a*) 1.7; (*b*) 1.0; and (*c*) 0.5. Only in the case of (*b*) was a metallic deposit obtained on electrolysis. The other two solutions gave black moisture-sensitive deposits. Solution (*a*) was unstable and, after standing for several hours at room temperature, a metallic deposit was formed which coated the wall of the reaction vessel. Similar decomposition occurred with solution (*b*), but much more slowly and to a lesser degree. Solution (*c*) did not decompose, remaining unchanged even after standing several days.

Type B bath (Type A bath with $AlCl_3$*).*—The successive addition of $AlCl_3$ to Type A baths resulted first in a marked increase in the amount of Zr in the alloy deposit, and then a gradual decrease. However, even when the $AlCl_3$ content was relatively large, the Zr content of the deposit was still greater than in the alloys from Type A baths. The result suggests that $AlCl_3$ is an important component of these baths. Several baths of this type were made up with differing ratios of $Zr(BH_4)_4$ to $AlCl_3$ to determine the relation between bath composition and deposit composition. Results of this study are listed in Table IV. These data show that Zr content of the deposits does not vary regularly with Zr content of the baths.

Type C bath.—In earlier work, $Al(BH_4)_3$ and $ZrCl_4$ were used instead of pure $Zr(BH_4)_4$. The deposits obtained were similar in appearance and Zr content to the alloys from Type B baths. The deposit with the highest Zr content obtained from this type of bath contained 44.5% Zr, 53.0% Al, and 2.5% B. Due to the greater number of variables in Type C baths, they were not studied as extensively as Type B baths.

Characteristics of the Zr *Plating Bath*

These baths are similar to the aluminum hydride bath (26) in that they are subject to decomposition by the atmosphere. As Zr and Ti dissolved anodically with poor current efficiency in these solutions, Al anodes were used in all cases. Although this metal dissolved anodically with good efficiency, some decomposition still occurred at the anode. With Zr and Ti anodes, decomposition was much more rapid.

TABLE IV. *Electrodeposited* Zr-Al *Alloys from plating baths containing hydrides, borohydrides, and chloride*

Bath composition (moles/liter)					Mole ratio	Composition of deposit		
						% by weight		
$Zr(BH_4)_4$	$AlCl_3$	$LiAlH_4$	$ZrCl_4$	$Al(BH_4)_3$	Zr/$AlCl_3$	Zr	Al	B
1. 0.335	—	0.335	—	—	—	8.1	85.2	1.9
2. 0.223	0.057	0.153	—	—	4:1	11.8	90.8	2.5
3. 0.335	0.150	0.235	—	—	2:1	42.1	48.6	—
4. 0.804	0.784	0.616	—	—	1:1	9.5	—	—
5. 0.335	0.450	0.305	0.112	—	1:1	26.3	74.5	3.4
6. 0.168	0.168	0.108	—	—	1:1	14.0	82.6	2.5
7. 0.335	0.670	0.305	—	—	1:2	19.2	70.0	4.5
8. 0.335	2.01	0.305	—	—	1:6	15.1	—	—
9. —	0.653	0.720	0.287	0.440	1:2	8.9	71.5	—
10. 0.335	0.650	0.525	0.335	—	1:2	9.3	89.0	6.4

The alloy baths were unstable and gave no deposit after a few weeks use. They appeared to be stabilized by $AlCl_3$, which also improved the appearance of the deposits. Those baths which contained only a small amount of $AlCl_3$ relative to $Zr(BH_4)_4$ were so unstable that metal deposition usually ceased after the bath had stood for 24 hr. On prolonged electrolysis, the Zr content of the deposits usually decreased more than could be accounted for by depletion of the Zr content of the solution.

At a $LiAlH_4$—$Zr(BH_4)_4$ mole ratio greater than unity, spontaneous decomposition of the bath occurred, and a metallic mirror deposited on the surface of the electrolysis cell. Analysis of one such deposit gave the following results: 12.4 Zr, 78.8 Al, 9.2 B (per cent by weight).

If the complexes in these baths are similar to those of the hydride aluminum plating bath, then LiH should be as effective as $LiAlH_4$, but this was not the case. LiH did not react with an ether solution of $Zr(BH_4)_4$, and the resulting suspension did not conduct. When this experiment was repeated with equimolar quantities of $AlCl_3$, LiH, and $Zr(BH_4)_4$, the resulting solution gave no metallic deposit on electrolysis.

Ethyl ether plays a more important role than that of a mere solvent in these baths, as $LiAlH_4$ and $Zr(BH_4)_4$ do not react in its absence. In the presence of ether they reacted vigorously to form a brownish-purple solution. Since the resulting solution conducted well and gave an alloy deposit when electrolyzed, the ether apparently served both as a complexing and ionizing medium for the $LiAlH_4$.

The Zr compound responsible for deposition of the alloys is probably a zirconium borohydride-aluminum hydride complex which is formed in solution. This view is supported by the observation that $LiAlH_4$ conducts poorly in ethyl ether, and $Zr(BH_4)_4$ does not conduct at all. When the two solutions were mixed, a white solid of empirical composition $Zr(AlH_4)_4$ formed immediately. With excess $Zr(BH_4)_4$, the white solid dissolved to give a solution of good conductivity. The solubility of $Zr(AlH_4)_4$ in an excess of $Zr(BH_4)_4$, and the good conductivity of the resulting solution indicate the presence of a complex.

Preparation of the compound $Zr(AlH_4)_4$ is included in the Appendix since it has not been reported previously in the literature.

Organometallic Compounds

Organotitanium compounds.—Only within the last few years have methods become available for preparation of compounds containing Ti—C bonds (29–31). Such compounds would have greater solubility and greater stability in organic solvents than the hydride type previously used in plating solutions. Although preparation of such compounds is time-consuming, it was thought that their study would be of interest in view of the fact that other metals can be deposited from baths containing organometallic compounds (32).

Two organotitanium compounds were studied: bis-(cyclopentadienyl)titanium(IV) dibromide and phenyltitanium triisopropylate.

A quantity of bis-(cyclopentadienyl)titanium(IV) dibromide (29) was prepared, and numerous solutions of this compound in various solvents were electrolyzed. In no case was Ti deposited. Solubility of this compound in organic solvents is very low, and its solutions are weakly conducting, indicating that it does not form ionic complexes easily. Solubilities of this compound are listed in Table II.

Phenyltitanium triisopropylate was prepared as described by Herman and Nelson (30). The compound was not isolated, but its resulting ether solution was electrolyzed. Conductivity was very small and was not improved by addition of NaH or phenyllithium. Electrolysis of this solution did not give a metallic deposit.

Organozirconium compounds.—Up to the present, the only organozirconium compound described in the literature is the bis-(cyclopentadienyl)zirconium (IV) dibromide (31). In view of the lack of success with the similar Ti compound, no attempt was made to synthesize this Zr compound.

Addition of $Zr(BH_4)_4$ to an ether solution of phenyllithium turned the solution black and caused evolution of heat. A similar reaction occurred with $ZrCl_4$ and phenyllithium. In both cases the isolated reaction product gave a good Michler's ketone test for a carbon to metal bond. Although the exact composition of this compound was not determined, analyses indicated that it contained an appreciable amount of C. When the solvent was completely removed from this compound, the product was a tan powder (mp 175°–185°C) which reacted vigorously on exposure to the atmosphere. It was soluble in phenetole, benzene, and tetrahydrofuran, and sparingly soluble in ethyl ether and dimethoxyethane. Ethyl ether solutions of this compound conducted slightly, but no metallic deposit was obtained on electrolysis. Although the compound was not very soluble in ether, it dissolved readily when phenyllithium was added to a suspension in ethyl ether. A solid separated out of the benzene solution after several weeks. The precipitate was insoluble in the solvents previously mentioned and did not react with phenyllithium. This compound, discussed further in the Appendix, is probably an impure phenylzirconium derivative.

Perfluoroacid Salts

The presence of the fluorinated hydrocarbon chain in perfluoroacid salts makes these salts highly soluble in many organic solvents and suggests their use in organic plating baths. The Ni, Ag, Ti, and Zr salts of perfluoroacetic acid were prepared as described in the Appendix.

None of these salts yielded a conducting solution in ethyl ether or benzene. The Ni salt of perfluoroacetic acid dissolved in dimethylformamide to give a conducting solution from which a Ni deposit was obtained. These deposits were stressed, poorly adherent, and contained organic matter.

A Ti derivative containing chloride was prepared by direct reaction of $TiCl_4$ with trifluoroacetic acid. An attempt to prepare the Ti salt in benzene solution was unsuccessful. $TiCl_4$ reacted in benzene solutions of silver trifluoroacetate or silver perfluorobutyrate to form a white precipitate. It probably consisted of the Ti compound, which is relatively insoluble in benzene, mixed with AgCl. Conducting solutions were obtained with the titanium trifluoroacetate derivative dissolved in dimethoxyethane, anisole, or dimethylformamide. No deposit was obtained from any of these solutions on electrolysis.

Fused Organic Salt Systems

Several organic salt systems, which are molten at low temperatures, were studied. Two quaternary ammonium tetrachlorodibromotitanates which were the double salts of $TiCl_4$ with tetraethylammonium bromide and ethylpyridinium bromide (33) were prepared and investigated. These salts melt near 200°C. Electrolysis of each of these salts at 250°C gave no deposit. Addition of either of these salts to the ethylpyridinium bromide-$AlCl_3$ type of Al plating bath (34) gave a black, tarry deposit when electrolyzed. These deposits contained Ti.

When this bath was electrolyzed with a Ti anode, metallic deposits of a Ti-Al alloy were obtained, but with very low cathode efficiency. This bath yielded deposits containing up to 14% Ti. Alloys of higher Ti content could not be obtained, presumably because of electrolytic decomposition of the bath on prolonged electrolysis.

Hurley-Wier baths containing the following compounds were also electrolyzed: tetraisopropyltitanate, bis (cyclopentadienyl)titanium(IV) dibromide, and sodium titanium chloride. The anode was Al. In no case was a metallic deposit obtained.

For use in fused salt electrolysis, a series of anhydrous trivalent Ti halogen derivatives of the general formula $MTiCl_4$ was prepared. The sodium derivative was prepared by reduction of $TiCl_4$ with Na in an inert solvent at 100°C. The green salt obtained reacts with many polar organic solvents, and behaves much as $TiCl_3$. It dissolves in fused halide melts to form a solution from which Ti may be obtained on electrolysis. These compounds have been described (38) and will be the subject of a future publication.

Lower Valent Ti Compounds in Organic Solutions

Lower valent Ti compounds were prepared in various ether solutions by the reduction of $TiCl_4$ with various reducing agents (see Appendix). Electrolysis of these solutions did not yield a metallic deposit.

Preparation of $TiCl_3$

An essential part of this program was preparation of new compounds and simplification of present methods of preparation of compounds used in electrolysis studies. An improved method for preparation of $TiCl_3$ falls under the latter category.

By reaction of $TiCl_4$ with hydrogen in a bomb at 500°C and 2000 lb/in.^{2}, 12% was reduced to $TiCl_3$ in 30 hr. If allowed to proceed for a longer time this reaction may give a rather high yield of $TiCl_3$. This method has certain advantages over other procedures employing hydrogen in that a lower temperature is used, so that the possibility of contamination with $TiCl_2$ is minimized, and the reaction requires no attention while in process. Presumably, the use of higher pressures would considerably speed up the reaction. The preparation of this compound is discussed further in the appendix.

Manuscript received May 21, 1956. This paper was prepared for delivery before the Boston Meeting, October 3 to 7, 1954. The work was sponsored by the Wright Air Development Center under USAF Contract No. AF(33-616)53-11.

Any discussion of this paper will appear in a Discussion Section to be published in the December 1957 JOURNAL.

REFERENCES

1. M. BECQUEREL, *Ann. chim. phys.*, **48,** 337 (1831).
2. A. S. RUSSELL, *Nature*, **127,** 273 (1931).
3. A. S. RUSSELL, *Nature*, **142,** 210 (1938).
4. E. POKORNY, (I. G. Farbenindustrie, A. G.), German Pat. 605,551, Nov. 13, 1934.
5. M. HAISSINSKY AND H. EMMANUEL-ZAVIZZIANO, *Compt. rend.*, **204,** 759 (1937).
6. M. HAISSINSKY AND H. EMMANUEL-ZAVIZZIANO, *J. chim. phys.*, **34,** 641 (1937).
7. H. EMMANUEL-ZAVIZZIANO, *Compt. rend.*, **203,** 161 (1936).
8. N. N. GRATSIANSKII AND A. P. VOVKOGON, *Zapiski Inst. Khim. Akad. Nauk URSR*, **7,** 173 (1940).
9. N. H. M. DEKKER, U. S. Pat. 1,113,546, Oct. 13, 1914.
10. C. G. FINK, U. S. Pat. 1,885,700, Jan. 2, 1932.
11. D. B. KEYES AND S. SWANN, *Bull. Univ. Ill. Eng. Exp. Sta. No. 206* (1930).
12. Final Report, Contract No. DA-36-034-ORD-1048 (RD), Virginia Institute for Scientific Research, 1953.
13. Progress Report No. 3, Contract No. AF 33(616-75), School of Mines and Metallurgy, Univ. of Missouri, 1952.
14. Final Report, AF 33(038)50-1085, U. S. Bureau of Mines, Materials Laboratory, 1953.
15. J. BARKSDALE, "Titanium," The Ronald Press Co., New York (1949).
16. C. A. BROPHY, B. F. ARCHER, AND R. W. GIBSON, "Titanium Bibliography 1900–1951," Battelle Memorial Institute, Columbus (1952); see also 1952 Supplement by B. J. ARCHER AND R. W. GIBSON (1953).
17. GMELINS "Handbuch der anorganischen Chemie," 8th ed., Vol. 41, Verlag Chemie, GmbH, Germany (1951).
18. W. E. BRADT AND H. B. LINFORD, *This Journal*, **70,** 431 (1936).
19. A. W. LAUBENGAYER AND R. B. EATON, *J. Am. Chem. Soc.*, **62,** 2704 (1940).
20. V. A. PLOTNIKOV AND E. B. GUTMAN, *J. Appl. Chem. USSR*, **19,** 826 (1946).
21. GRAHAM, CROWLEY, AND ASSOCIATES, INC., Electrodeposition of Zirconium, 1951–53, Contract No. AT(11-1)-173.
22. M. L. HOLT, *This Journal*, **98,** 33*C* (1951).
23. A. BRENNER AND S. SENDEROFF, *ibid*, **99,** 223*C* (1952).
24. G. D. P. CORDNER AND H. W. WORNER, *Australian J. Appl. Science*, **2,** 358 (1951).
25. W. A. PLOTNIKOFF, *J. Russ. Phys. Chem. Soc.*, **4,** 466 (1902).
26. D. E. COUCH AND A. BRENNER, *This Journal*, **99,** 234 (1952).
27. H. R. HOEKSTRA AND J. J. KATZ, *J. Am. Chem. Soc.*, **71,** 2488 (1949).
28. E. WIBERG AND R. USON, *Z. Naturforsch.*, **6b,** 392, (1951).
29. G. WILKINSON, P. L. PAUSON, J. M. BIRMINGHAM, AND F. A. COTTON, *J. Am. Chem. Soc.*, **75,** 1011 (1953).
30. D. F. HERMAN AND W. K. NELSON, *J. Am. Chem. Soc.*, **74,** 2693 (1952).
31. D. F. HERMAN AND W. K. NELSON, *ibid.*, **75,** 3877 (1953).
32. D. B. KEYES, S. SWANN, JR., W. KLABUNDE, AND S. T. SCHICKTANZ, *Ind. Eng. Chem.*, **20,** 1068 (1928).
33. J. BYE AND W. HAEGI, *Compt. rend.*, **236,** 381 (1953).
34. F. H. HURLEY AND T. P. WIER, U. S. Pat. 2,446,349, Aug. 3, 1948.
35. S. Z. HAIDER, M. H. KHUNDKAR, AND MD. SIDDIQULLAH, *J. Appl. Chem. (London)*, **4,** 93 (1954).
36. D. C. BRADLEY AND W. WARDLAW, *J. Chem. Soc.* **1951,** 280.
37. V. L. HANSLEY, *Ind. Eng. Chem.*, **43,** 1759 (1951).
38. J. M. SHERFEY, Paper presented before the New York meeting of the Electrochemical Society, April, 1953.

APPENDIX

PREPARATION OF TITANIUM (III) BOROHYDRIDE FROM TETRABUTYL TITANATE, $Ti(OC_4H_9)_4$, AND DIBORANE, B_2H_6

Diborane (67.0 millimoles) was passed into a tetrahydrofuran solution containing 29.0 millimoles of tetrabutyl titanate.[1] A dark blue solution was formed and blue crystals settled out. The solution was filtered in a He atmosphere and the crystals washed with petroleum ether. Yield as $Ti(BH_4)_3$: 26.1 millimoles. The filtrate was evaporated nearly to dryness, and a high boiling (225°C) colorless liquid remained [the reported boiling point of tributyl borate is 229°–230°C (35)]. This liquid had properties similar to those of boron esters, but the amount isolated was too small to study thoroughly. With tetraisopropyl titanate, the borohydride was obtained in 90% yield.

Analysis:

Calculated for $Ti(BH_4)_3 \cdot C_4H_8O$ (%)		Found
Ti	29.2	29.1
B	19.4	14.5
H	12.2	10.3
C	29.2	33.0

The crystalline blue solid underwent partial decomposition at 135°–140°C, and on heating to a higher temperature decomposed completely with the formation of a bright metallic mirror on the walls of the container. It was insoluble in the usual organic solvents except for tetrahydrofuran but reacted readily with peroxide-contaminated ethers and active solvents, such as water.

$Ti(BH_4)_3$ apparently is stabilized by coordination with tetrahydrofuran, as indicated by the facts that large crystals of the compound react rather slowly on exposure to the atmosphere (the finely divided compound occasionally ignites spontaneously), and the compound can be stored in closed containers for long periods of time without noticeable decomposition.

REACTION OF DIBORANE WITH $TiCl_4$ AND $ZrCl_4$

When $TiCl_4$ or $ZrCl_4$ reacted with diborane in tetrahydrofuran, the borohydride was not obtained. Crystalline Ti and Zr compounds having the approximate empirical formula $MCl_{2.6}(C_4H_8O)_{2.3}$ were isolated from these solutions.

Analyses: Ti compound: %Ti = 14.5, %Cl = 28.1, %C = 37.9, %H = 6.4; Zr compound: %Zr = 24.5, %Cl = 26.1, remainder organic material. The impure compounds contained a small amount of B. The Zr and Ti compounds were white and blue, respectively.

Compounds similar to those described here were obtained by reduction of $TiCl_4$ in tetrahydrofuran with LiH.

PREPARATION OF $Zr(BH_4)_4$

Preparation of this compound from $KZrF_5$ and $Al(BH_4)_3$ has been described by Hoekstra and Katz (27). Initially,

[1] Obtained from the du Pont Co.

ether solutions of this compound were prepared *in situ* by adding to an ether solution the stoichiometric quantities of reactants, according to either of the following reactions:

$$ZrCl_4 + 2Al(BH_4)_3 = Zr(BH_4)_4 + 2AlBH_4Cl_2 \quad (I)$$

$$KZrF_5 + 2Al(BH_4)_3 = Zr(BH_4)_4 + KF + 2AlBH_4F_2 \quad (II)$$

Reaction (I) has the disadvantage that both reaction products are soluble in ether and difficult to separate.

Since $Zr(BH_4)_4$ and $Al(BH_4)_3$ are soluble, the latter contaminates the product of both reactions (I) and (II) if an excess is used. For this reason reaction (II) was carried out with a slight excess of $KZrF_5$. This K salt was used because a comparison of the relative reactivities of $NaZrF_5$, $KZrF_5$, and a product corresponding to $KF \cdot 2ZrF_4$, showed that $KZrF_5$ reacted more rapidly and completely.

When $KZrF_5$ was used in excess, the yield was much less than expected. An examination of the products showed that the reaction probably proceeded by a stepwise mechanism involving the intermediate formation of a compound such as $Zr(BH_4)_2F_2$, and for the reaction to go to completion, an excess of $Al(BH_4)_3$ must be used. Since both reactions were unsatisfactory for the preparation of an ethereal solution of $Zr(BH_4)_4$, other methods of preparing this compound were investigated.

It was found that $Zr(BH_4)_4$ could be prepared conveniently by passing diborane into an ether solution of a Zr ester of the type $Zr(OR)_4$. A product of this reaction is probably the corresponding boron ester, $B(OR)_3$, as in the similar preparation of $Ti(BH_4)_3$. This method is not satisfactory for the preparation of pure $Zr(BH_4)_4$ since the B ester and $Zr(BH_4)_4$ are both present in the resulting solution.

The preparation of pure $Zr(BH_4)_4$ was accomplished by the dry reaction of $LiBH_4$ and $ZrCl_4$ at room temperature.

$$ZrCl_4 + 4LiBH_4 = Zr(BH_4)_4 + 4LiCl \quad (III)$$

This method is convenient and rapid, and the yield is about 75% with respect to both reactants.

Reaction of $Al(BH_4)_3$ *with* $KZrF_5$

A mixture of 25.9 millimoles of $KZrF_5$ and 57.8 millimoles of $Al(BH_4)_3$ (mole ratio 1:2) in 20 ml ether was shaken for 16 hr. The solution was filtered and the resulting clear solution showed no fluoride. By means of hydride and Zr analyses, the yield of $Zr(BH_4)_4$ was calculated to be 65%. When this experiment was repeated using the Na salt, the mole ratio of $3NaZrF_5$:$4Al(BH_4)_3$, and 24 hr of shaking, the yield of $Zr(BH_4)_4$ was only 30%, indicating formation of intermediate zirconium borohydrides such as $Zr(BH_4)_2F_2$ owing to the use of insufficient $Al(BH_4)_3$

Reaction of Zirconium Tetraisopropylate with Diborane

Diborane (0.14 mole) was passed into a tetrahydrofuran solution containing 0.02 moles of tetraiospropyl zirconate (36). The resulting clear solution (34 ml) was analyzed for hydride and Zr content. It contained 0.6 millimoles of Zr and 14.7 millimoles of hydride per milliliter (determined by evolution of H). The theoretical hydride content for 0.6 millimoles of $Zr(BH_4)_4$ is about 10 millimoles. The analytical results indicate the solution contained $Zr(BH_4)_4$ and a small amount of diborane.

Preparation of $Zr(BH_4)_4$ *from* $LiBH_4$ *and* $ZrCl_4$

In an inert atmosphere chamber, 67.0 millimoles powdered $ZrCl_4$, 272 millimoles powdered $LiBH_4$, and some 0.5 cm diameter dry Ni balls (to help mixing) were swirled by hand for about 15 min at room temperature. The material in the flask became wet and heat was evolved. The flask was shaken for about 5 min more until its contents had become paste-like and the Ni balls were no longer able to produce mixing.

After cooling to room temperature the flask was placed in a vacuum system and evacuated for about 30 min. The $Zr(BH_4)_4$ was collected in a liquid N trap. The yield was 77%.

When an excess of $LiBH_4$ was used, the induction period was lessened and the yields were increased. Yields as high as 90% have been obtained by using an excess of $LiBH_4$ and/or by breaking up the LiCl and evacuating again at about 50°C. The latter procedure increased the yield by 6% in one run. Analysis of the product gave 55% Zr, 30% B, and 10% H. The theoretical values for $Zr(BH_4)_4$ are 60.6% Zr, 28.7% B, and 10.7% H. The melting point of the product was 28.7°C which is identical with the previously reported melting point of $Zr(BH_4)_4$ (27).

For a metallic derivative, the compound showed a surprising solubility in organic solvents, including ether, petroleum ether, and benzene.

Attempts to prepare $Zr(BH_4)_4$ in this manner by use of $NaBH_4$ or KBH_4 were unsuccessful.

Preparation of $Zr(AlH_4)_4$

To a dilute ether solution of $Zr(BH_4)_4$ in a sintered glass filter funnel was added an ether solution of $LiAlH_4$. The reaction was carried out in an atmosphere of He. After a sufficient amount of white solid was formed, the ether solution was removed rapidly and the solid was isolated. It was unstable at room temperature, decomposing within several hours into a pyrophoric black solid. Analysis of the white solid indicated a formula corresponding to $Zr(AlH_4)_4$.

Results of analysis: wt. sample, 41.9 mg; 62 ml H_2 at 26°C = 2.52 millimoles hydride; 13.8 mg Zr = 0.15 millimoles Zr; 17.6 mg Al = 0.63 millimoles Al. This data would indicate an empirical formula: $ZrAl_{4.2}H_{16.8}$.

Preparation of Phenylzirconium Compound

Method A: On adding 3.7 millimoles $Zr(BH_4)_4$ to an ethyl ether solution containing 13.5 millimoles phenyllithium, a black colored solution formed with evolution of heat. The solution was diluted with benzene and filtered. The filtrate was then evaporated to dryness and pumped under vacuum for 1 hr at 50°C. During the drying process a small amount of biphenyl condensed on the upper wall of the container. The resulting black solid gave a positive Michler's ketone test for a carbon to metal bond.

Method B: Phenyllithium was allowed to react with a slurry of $ZrCl_4$ in ethyl ether in a manner similar to Method A above. The solution was evaporated to a low volume, filtered, and the product (a tan powder) precipitated by addition of petroleum ether. It contained 63% of the Zr initially used, gave a positive Michler's ketone test and the melting point was 175°–185°C.

The analysis of the compound prepared by each method gave the following results:

	Method A	Method B	Theory for Zr $(C_6H_5)_3$
Zr	27.5	29.6	28.3
C	49	42	67.0
H	5.3	4.7	4.7

The compound prepared by Method A contained about 8% $Zr(BH_4)_4$ as impurity, and the product from Method B contained about 4% LiBr as impurity.

TABLE V. *Reduction of* $TiCl_4$ *in solution*

Reducing agent	Solvent	Conc. of Ti in reacted soln. in g/l	
		Total	Reduced (as trivalent Ti)
1. Na dispersion	Tetrahydrofuran	14.3	9.6
2. Na dispersion	Ether	1.8	2.2
3. Na dispersion	50% tetrahydrofuran 50% benzene	15.0	5.8
4. Na*	Tetrahydrofuran	15.4	24.1
5. Na-K†	Anisole	5.0	0.0
6. LiH	Tetrahydrofuran	10.2	8.3

* In experiment 4, metallic Na was added to a tetrahydrofuran solution of $TiCl_4$ in a steel bomb and the resulting solution was ball-milled at 100°C.

† Reduction occurred in experiment 5, but reduced Ti was found only in a black solid formed as a product of the reaction.

In two cases the reduced Ti content calculated as trivalent Ti ion was greater than the total Ti concentration. From this it would appear that a mixture of di- and trivalent Ti is formed in these reduced solutions.

Preparation of Lower Valent Ti Compounds

Use of $Ti(BH_4)_3$ in the Ti-Al alloy bath to give a deposit containing Ti suggests the use of organic baths containing di- or trivalent Ti compounds. However, the available lower valent compounds, such as the halides, are not soluble in ethers. They are soluble in more polar carbonyl and hydroxyl types of solvents which are too reactive for purposes of deposition.

Lower valent Ti compounds in ethers were prepared by reduction of $TiCl_4$ with the following reagents: sodium naphthalene (37), diborane, LiH, NaH, Na, Na-K alloy, and dispersions of Na and Li in hydrocarbons. Only LiH and Na dispersion were used for a large number of experiments.

Sodium naphthalene and $TiCl_4$ reacted in tetrahydrofuran solution. A qualitative test indicated that trivalent Ti was present. The resulting solution conducted well, but gave only a Na deposit.

Diborane reacted with $TiCl_4$ in tetrahydrofuran to form a green solution of $TiCl_3$ which did not conduct electricity. After the solution had stood for several days, a blue solid crystallized out [*cf.* preparation of $Ti(BH_4)_3$].

LiH and $TiCl_4$ did not react in a hydrocarbon solvent such as benzene, but addition of ethyl ether caused a reaction to occur with evolution of hydrogen and formation of a green color which changed to reddish-brown on further reduction. The green compound could not be isolated. The hydrogen initially present in the hydride evolved as gas, and the resulting solution, when allowed to react with water, gave no evidence of hydride. The reduced compound had properties similar to a lower valent Ti halide and was in no way like a hydride compound.

The reaction of NaH with $TiCl_4$ was similar to the reaction of LiH except that it was much slower. This was probably due to the lower solubility of NaH in ethyl ether. The reaction of Li, Na, or Na-K alloy with $TiCl_4$ in ether solutions appeared to give products similar to those obtained when LiH was used. Na and Li were used as dispersions to obtain a more rapid and complete reaction.

The reaction of $TiCl_4$ with LiH in ethyl ether resulted in the formation of two liquid layers. The denser layer was smaller in volume and richer in Ti; on electrolysis it conducted well but gave no metallic deposit. The upper layer was low in Ti and conducted poorly. In the more strongly complexing ethers, tetrahydrofuran and tetrahydropyran, a separation of the solution into layers was not observed when $TiCl_4$ reacted with lithium hydride, but an insoluble solid usually formed. Although the composition of the solid product formed in these reactions was not determined, reduced Ti was detected in it. The concentration of trivalent Ti in the resulting solution was about 8–10 g/l in both solvents. This is close to the content of trivalent Ti (7.7 g/l) in a saturated solution of $TiCl_3$ in tetrahydrofuran. These solutions yielded no metallic deposit on electrolysis although they did conduct well.

Na and Li in the form of dispersions reacted with $TiCl_4$ in various ethers to yield solutions containing lower valent Ti compounds. This is similar to the reactions of LiH as described above. Some of the reactions of Na dispersion with $TiCl_4$ in various ethers are listed in Table V. Similar results were obtained with Li dispersion. Table V is a summary of results obtained using various reducing agents and solvents. The mole ratio of $TiCl_4$ to reducing agent is unity in all cases.

$TiCl_4$ in tetrahydrofuran reacted with Na dispersion to form a blue solid. Analysis of this solid gave 12.7% Ti and 30.5% chloride, which has approximately the composition $TiCl_3 \cdot (C_4H_8O)_3$. A similar blue solid was formed when LiH reacted with $TiCl_4$ in tetrahydrofuran, but the composition of this blue solid was not determined. The reaction of diborane with $TiCl_4$ in tetrahydrofuran also formed a blue crystalline solid having the approximate composition $TiCl_{2.6}(C_4H_8O)_{2.7}$. It was probably the same compound as above.

In addition to the more active reducing agents listed above, metals such as Ni, Fe, Cu, Ag, or Mg were also effective for reduction of $TiCl_4$ to trivalent Ti, but only in solvents such as dimethylformamide, acetone, dimethoxyethane, and tetrahydrofuran.

Preparation of $TiCl_3$

In an inert atmosphere, 0.9 mole $TiCl_4$ was placed in a one liter bomb equipped with a glass liner. Four moles hydrogen were added, and the bomb was kept at 500°C for 29 hr. The pressure was maintained at about 2000 lb/in.^{2}, which required that some of the gas be vented occasionally.

At the end of the reaction the pressure was released and the bomb taken into an inert atmosphere chamber. A yield of 16.5 g $TiCl_3$ as flaky red crystals was obtained. The yield was 12% based on the amount of $TiCl_4$ initially placed in the bomb. Most of the unreacted $TiCl_4$ could have been recovered.

In the above reaction, the bomb also contained small amounts of Pd and Pt sponge in test tubes, but later observations indicated that neither of them aided the reaction.

A sample of the product was dissolved in water and found to contain 1.5% insoluble matter; the soluble portion was $TiCl_3$. The insoluble material was believed to be TiOCl. The latter had formed previously when the same reaction had been allowed to continue for about an hour at 450°C and 1650 lb/in.^{2} In this experiment a small amount of a gold colored material was formed. It was insoluble in all the usual acids and was not affected by the atmosphere. This compounds has been previously described (17).

Preparation of the Salts of Perfluoroacids
Ti and Zr Salts

Ti and Zr salts were prepared by reaction of the metal tetrachlorides with trifluoroacetic acid. The preparation of the Ti salt illustrates the method used.

To 1.9 g $TiCl_4$ was added 4.6 g trifluoroacetic acid. The

reaction mixture was heated at 65°C and evaporated to dryness. A yield of 4.5 g (90%) of white solid was obtained.

The Zr salt was prepared in a similar manner, but in a solution of ethyl ether. Both salts contained a small amount of Cl. Analysis of the salts for metal content gave: Ti, 17.6%; Zr, 25.2%.

Ni and Ag Salts: These were prepared by reaction of the metal oxides with acids in aqueous solution and subsequent evaporation of the resulting solution to dryness. The salts were then dried at 150°C for several hours.

Nickel trifluoroacetate, silver trifluoroacetate, and silver perfluorobutyrate were prepared in this manner.

The solubility of silver trifluoroacetate was found to be 17.8 g/100 ml in benzene and 47.1 g/100 ml in ethyl ether

Electrodeposition of Metals from Organic Solutions

IV. Electrodeposition of Beryllium and Beryllium Alloys

GWENDOLYN B. WOOD AND ABNER BRENNER

National Bureau of Standards, Washington, D. C.

ABSTRACT

The electrodeposition of Be from nonaqueous media was studied. Be compounds used as solutes were the hydride, aluminohydride, borohydride, halides, alkyls, and aryls. Their preparation, chemical properties, and electrochemical properties in nonaqueous media were investigated. Electrodeposits of Be (95% pure) and Be alloys, such as Be-B and Be-Al, were obtained from organic solutions. It is believed that these represent the first metallic deposits consisting essentially of Be that have been obtained from organic baths.

Be has a low density (sp. gr. 1.8^{20}), fairly high melting point (approx. 1280°C), good corrosion resistance, and relatively high strength per weight ratio, which make it potentially valuable in structural engineering. However, because of its brittleness the pure metal has had little industrial use. Be is of interest in the field of atomic energy because of its property of slowing down neutrons with little tendency for absorbing them.

The literature concerning Be and its compounds is covered in several reviews (1–4). Be is produced commercially in the form of powder, flake, compact rod, or beads by the electrolysis of fused salt baths (5–10), many of which are operated near the melting point of the metal. The production of pure Be metal by thermal dissociation of BeI_2 or $BeBr_2$ has been reported (11).

Electrolysis of Be salts in acetamide was reported to give a black amorphous deposit which gave a qualitative test for Be (12). Beryllium nitrate, sulfate, and halides were dissolved in fused alkylpyridinium halides, but no Be was deposited on electrolysis (13).

Booth and Torrey (14–16) made a comprehensive investigation of the electrodeposition of Be using anhydrous Be halides, sulfate, nitrate, acetylacetonate, beryllium basic acetate, and sodium beryllium fluoride. They used a number of nonaqueous organic and inorganic solvents and reported that a majority of the solutions conducted poorly. They reported electrodeposition of pure metallic Be only from solutions of its compounds, particularly the nitrate and chloride, in liquid NH_3 on the basis that the deposit gave a qualitative test for Be. Their deposit did not dissolve in HCl, and they ascribed its nonreactivity to its purity. Without quantitative analytical determinations, conclusions as to the purity of deposits are questionable. Several unsuccessful attempts to duplicate their work have been made in this laboratory. Thin deposits of black, nonmetallic material soluble in dilute HCl were obtained.

The purpose of this investigation was to develop methods of electrodepositing coherent coatings of pure Be or Be alloys. This involved a study of the chemistry of known Be compounds, the preparation of new Be compounds, and the investigation of the electrochemical properties of these compounds in nonaqueous solvents. A successful method of electrodepositing metallic Be from nonaqueous media other than from fused salts would have several useful applications, such as: electrowinning, improvement of the purity and mechanical properties of the metal, production of electroplated coatings for protection of other metals against corrosion, and electroforming of complicated shapes.

Since hydrogen is so much more noble than Be, it is preferentially discharged from aqueous solutions. Consequently, this investigation was limited to organic solvents and fused salt baths.

Electrolytic properties of the following types of Be compounds were investigated: the hydride, aluminohydride, borohydride, halides, alkyls, and aryls. Beryllium fluoride was not used because of its low solubility in organic solvents. The halides are covalent in nature and do not carry an electric current when fused. Other types of compounds do not lend themselves to fused salt electrolysis, since they cannot be fused without decomposition.

The apparatus used for electrolytic studies and the purification of the solvents has been discussed (17, 18). The electrolytic investigations and preparation of compounds were performed under an atmosphere of dried A or He. A compound is considered soluble if it dissolves to the extent of 0.5 g/l.

Electrolytic Studies

Be *Compounds in Liquid* NH_3

Electrodeposition of Be from liquid NH_3 solutions was reported by Booth and Torrey (16), and one of their experiments was repeated several times. Liquid NH_3 was condensed on anhydrous beryllium chloride ($BeCl_2$). Ammoniates initially formed with the $BeCl_2$, and this had some solubility in excess NH_3. At current densities of 1–8 amp/dm^2, only a small quantity of a stressed black deposit was obtained, and this was partially soluble in dilute HCl. Coherent deposits could not be built up in this bath.

Some modifications of this experiment were investigated. (*A*) Fused ammonium nitrate (NH_4NO_3) and $BeCl_2$ were dissolved in NH_3 to yield a fairly conductive solution, but no deposit was obtained on electrolysis. (*B*) $2BeBr_2 \cdot Be(NH_2)_2 \cdot 8NH_3$ was prepared by adding metallic Be to ammonium bromide (NH_4Br) dissolved in liquid NH_3 (19). Electrolysis of the resulting solution decomposed the bath giving a black residue. (*C*) A mixture of lithium amide, $BeBr_2$, and NH_4Br in liquid NH_3 on electrolysis gave only a black mossy scum on the cathode. No coherent Be deposits of high purity were obtained from liquid NH_3.

Beryllium Halides

$BeCl_2$.—Anhydrous $BeCl_2$ is one of the few Be compounds available commercially. Extensive qualitative observations of its solubility and conductivity in nonaqueous media were made. Electrolytic studies were limited to a great extent by its insolubility in most nonaqueous solvents. In some solutions the conductivity was low at room temperature but increased greatly at the boiling point of the solvent. Listed in Table I are the solvents investigated (except ethers). In no case was a metallic deposit obtained on electrolysis. The material on the electrode usually reacted with either the moisture or the oxygen of the atmosphere.

TABLE I. *Solubility studies involving anhydrous* $BeCl_2$

Solvent	Solubility	Deposit obtained on electrolysis
Acetal	R	None, tarry residue
Acetone	S	None
Acetonitrile	SS	None, viscous bath
Acrylonitrile	SS	None
Ammonia (−50°C)	S	Black, treed
Benzene	i	None
n,n-Dimethyl aniline	S	None
Dimethyl cyanamide	Rr	None
Dimethylformamide	S	None
Ethyl alcohol	S	None
Ethyl bromide	SSr	None
Pyridine	S	None
Pyrrolodine	S	Thin black film
Toluene	i	None
Triethylamine	SSr	None
Tri-n-propylamine	Sr	None

NOTE: R = Reaction at room temperature; Rr = reaction at reflux temperature; S = soluble at room temperature; SS = slightly soluble at room temperature; SSr = slightly soluble at reflux temperature; i = insoluble.

TABLE II. *Ethereal baths containing anhydrous* $BeCl_2$

Solvent	Deposit obtained on electrolysis
Anisole	Black, reactive with H_2O
Bis (2-chloroethyl) ether	Thin black film
Bis (2-ethoxyethyl) ether	Black film
n-Butyl ether	Black, H_2O soluble
1,4-Dioxane	None
Ethyl ether	Black powder
Ethylbutyl ether	Black, reacts with H_2O
Ethylene oxide	None
Isopropyl ether	None
1,2-Dimethoxyethane	Black stain
Methyl ether	Gray, oxidizes in air
Phenetole	None
Phenyl ether	None
Propyl ether	Black powder
Tetrahydrofuran	Black, brittle

Electrolysis carried out at temperatures sufficient to give homogeneous solutions and at reflux temperatures of the solutions.

Many ethers (Table II) were studied as solvents for anhydrous $BeCl_2$, with which probably all formed etherates. Deposits from the various ethereal solutions both at room temperature and at their boiling points were inferior in appearance and coherency to those obtained from ethyl ether. Consequently, only the latter bath is discussed in detail.

Anhydrous $BeCl_2$ forms two immiscible liquid layers with ethyl ether (20). Qualitative tests show the upper layer to be a weak solution of $BeCl_2$ in ether and the lower layer a solution of ethyl ether in beryllium chloride etherate, which solidifies to a crystalline mass of $BeCl_2 \cdot 2Et_2O$, mp 330°C (21). This compound apparently dissolves enough ethyl ether to liquefy, forming approximately a 2.8*M* solution in the etherate. Electrolysis at 1 amp/dm^2 required 25 v across a small cell. The deposit was a fine black powder which was 92% Be. The impurities probably arose from adsorbed constituents of the solution. The powders were difficult to wash free of beryllium chloride etherate since this has limited solubility in ethyl ether.

A beryllium chloride etherate bath operated at elevated temperatures gave improved deposits which were harder and somewhat more coherent than those obtained at room temperature. A bath operated at 200°C and at a current density of 2 amp/dm^2 required only 6 v. A similar bath operated at 150°C and at 1 amp/dm^2 required 10 v. A black powdery deposit was obtained which was found to be 90% Be.

Since in electrodeposition from aqueous solutions the coherence of deposits is improved by having the metal in solution as a complex ion and by the use of addition agents, a similar approach was tried with the $BeCl_2$ solutions. For example, $BeCl_2$ and lithium chloride (LiCl) might form a complex such as Li_2BeCl_4, as aluminum chloride ($AlCl_3$) and other metallic halides are known to do with alkali halides. The addition agents listed in Table III were investigated, but none led to improved deposits.

Although neither $BeCl_2$ nor its reaction product with various ethers is soluble in many organic liquids, $BeCl_2 \cdot 2Et_2O$ is fairly soluble. The 2.8*M* ethereal solution of the

TABLE III. *Effect of addition agents on deposit obtained from* $BeCl_2 \cdot 2Et_2O$ *in* Et_2O

Compound added	Deposit obtained on electrolysis
Aluminum chloride etherate	Flaky
Ammonia (gas)	Smoother deposit but thin
Beryllium hydride etherate	Not improved
Cesium bromide	Not improved
Cesium iodide	Gray deposit
Lithium amide	Not improved
Lithium borohydride†	Smoother but brittle
Lithium bromide†	Not improved
Lithium chloride	Not improved
Lithium hydride*	Not improved
Lithium iodide†	Not improved
Sodium†*	Not improved
Sodium borohydride	More reactive with H_2O
Sodium hydride	Not improved
Potassium cyanate	Not improved
Potassium iodide	Not improved
Potassium thiocyanate	Not improved

* Showed no solubility.
† Electrolysis run at both room temperature and 150°C.

TABLE IV. *Electrolytic studies of 2.8M* $BeCl_2 \cdot 2Et_2O$ *mixed with other solvents*

Current density 0.5 amp/dm²

Solvent	Initial voltage of bath	Solvent per cent of total volume	Bath voltage	Remarks and comparison of deposits with those obtained from 2.8M $BeCl_2 \cdot 2Et_2O$ in Et_2O
	v	%	v	
1. No solvent.	—	—	34–28	Black, powdery
2. Xylene....	34	1–33	32–11[a]	Similar
3. Acetal.....	28	1–20	39–16[a]	No deposits
4. Pyridine...	34	1–5	30–23[a]	No deposits
5. Anisole....	32	9–15	16–33[a]	Better[b]
			13–3[b]	Black to gray, smooth, stressed
6. Phenyl ether....	27	20–31	13[a]	Better[b]
			20–2[b]	Black to gray, smooth, stressed[b]

[a] Studies made at room temperature.
[b] Studies made at boiling point.

etherate was diluted with the following solvents so that the latter formed from 1 to 33% by volume of the mixture: xylene, acetal, pyridine, anisole, phenyl ether, butyl ether, bis(2-chloroethyl) ether, 1,2-dimethoxyethane, ethyl alcohol, ethyl bromide, ethyl iodide, and toluene. Some representative experiments are listed in Table IV. Some of the deposits obtained from these baths at room temperature and at the baths' boiling points were slightly better than the deposits obtained from a solution of ethyl ether and $BeCl_2$ alone. No deposit was obtained in the presence of acetal, pyridine, butyl ether, or 1,2-dimethoxyethane.

The most promising results were obtained with the baths containing anisole or phenyl ether. The resistance of each bath at room temperature was lower than that of an unmodified ethyl ether bath, but the deposits were no better. The resistance was still lower at the boiling point of the solutions, and the electrodeposits were improved. From both baths, gray, brittle deposits were obtained which were fairly smooth, nonreflective, and stressed, but more coherent than the black powders obtained from the ethyl ether solution alone.

Lithium aluminum hydride ($LiAlH_4$) was added in increasing amounts to a xylene-ethyl ether-$BeCl_2$ solution. The deposit gradually improved, appearing more like the Al deposits obtained from the hydride-aluminum bath (22) as the concentration of hydride was increased to 0.3*M*. A brittle deposit from this bath was identified spectrochemically as a Be-Al alloy.

$BeBr_2$.—Beryllium bromide ($BeBr_2$) forms an etherate with ethyl ether. Ethyl ether is only slightly soluble at room temperature in $BeBr_2 \cdot 2Et_2O$. A 3.0*M* solution was prepared and electrolyzed between 35° and 40°C and proved to be a poorer electrolyte than the corresponding chloride etherate solution. Electrolysis at 77 v and 0.34 amp/dm² gave a granular black deposit. Because of occlusion of nonmetallic constituents from the bath, the deposits reacted with the moisture of the atmosphere. The deposits were not improved by operating the baths at 55° and 120°C. Chemical analyses of these powders indicated that the deposits were less pure than those obtained from beryllium chloride etherate. The addition of lithium iodide (LiI), lithium chloride (LiCl), sodium hydride (NaH), or potassium borohydride (KBH_4) to the bath did not improve the coherency of the deposits.

BeI_2.—Beryllium iodide[1] was only slightly soluble (0.05*M*) in ethyl ether at both room temperature and at the boiling point. The solution was a nonconductor. LiH reacted with the residue from the above ethereal solution, but no deposit was obtained from the resulting solution.

Dialkylberyllium Compounds

In order to carry out a systematic study of the electrolysis of solutions of dialkylberyllium compounds, it would be necessary to prepare several hundred grams of each of these compounds. Dimethylberyllium is more easily isolated from the solvent, ethyl ether, in which it was prepared than its homologs, diethyl- and di-*n*-butylberyllium. It could be studied as a pure compound rather than as a mixture with ether. Electrolysis of ethereal solutions of dimethyl-, diethyl-, and di-*n*-butylberyllium indicated that these solutions were only slightly different in character. As a consequence, dimethylberyllium was chosen as a representative dialkylberyllium compound for investigation. Details of the "ether-vapor method" which were developed for preparing dimethylberyllium are given in the Appendix.

Dimethylberyllium is a white, polymeric solid. Both the pure dialkyl as well as its concentrated ethereal solutions are spontaneously flammable in the air and must be handled in a dry atmosphere of A or He. Dimethylberyllium was insoluble in many common solvents. High polymerization in the solid state may greatly affect its solubility. It reacted with some solvents to form insoluble products and dissolved to a clear solution in others; ethyl ether and tetrahydrofuran solutions showed conductivity. The solvents investigated are listed in Table V.

Increasing the concentration of the ethyl ether bath

[1] Compound was contaminated with a few per cent of silicon tetraiodide.

TABLE V. *Solubility of dimethylberyllium in various solvents at room temperature*

Solvent	Solubility or reactivity
Acetone	Reacts
Anisole	Insoluble
Benzene	Insoluble
Boron trichloride etherate	Reacts
n-Butylamine	Yellow ppt.
Diethylamine	Reacts
Ethyl ether*	Soluble
Nitrobenzene	Reacts
Phenetole	Insoluble
Phenyl ether	White ppt.
n-Propyl ether	White ppt.
Pyridine	Reacts
Tetrahydrofuran*	Soluble
Tetrahydropyran	White ppt.
Triethylamine	White ppt.
Toluene	Insoluble

* Solution shows conductivity.

as methyl borate, methyllithium, cesium bromide, lithium hydride, lithium chloride, etc., did not improve the electrodeposits and in most cases reacted with the bath to form precipitates.

Mixed Halide-Alkyl Baths

Electrolytic studies were made on mixed alkyl and halide type baths. Several baths were investigated which contained 3*M* dimethylberyllium and varying quantities of beryllium chloride etherate as follows: 0.3*M*, 0.6*M*, 0.9*M*, and 2.3*M* (*see* Table VI). Electroformed tubes of Be which were coherent but stressed were obtained from the mixed baths. These deposits were far more coherent and metallic in appearance than those obtained separately from the alkyl or halide type of bath, and the resistance of the baths was lower. The most reflective and metallic-appearing deposits were obtained from baths containing 3*M* dimethylberyllium and 0.9*M* to 2.3*M* $BeCl_2$. These coherent deposits were 93–95% Be, while the powders from 1.2*M* to 3*M* lowered the resistance of the bath but did not improve the deposits. They were nonreflective, dark, smooth, and brittle. The Be content of the deposits from the 1.2*M* and 3*M* solutions was 77 and 63%, respectively (*see* Table VI). A 2*M* solution of dimethylberyllium in tetrahydrofuran yielded deposits which were black and coherent and which appeared less brittle than those from the ethyl ether solution.

TABLE VI. *Electrolysis of ethyl ether solutions of* $Be(Me)_2$ *and* $Be(Me)_2$ *with* $BeCl_2$

Bath constitution	Bath voltage v	C.D. amp/dm²	Deposit	Beryllium content %
3*M* $Be(Me)_2$	9	0.09	Brittle, black, treed	63
1.2*M* $Be(Me)_2$	49	0.05	Brittle, black, treed	77
3*M* $Be(Me)_2$ + 0.3*M* $BeCl_2$	10 to 15	0.1–0.3	Dark gray, metallic, brittle	80
3*M*$Be(Me)_2$ + 0.6*M* $BeCl_2$	18	0.15	Black, brittle	—
3*M* $Be(Me)_2$ + 0.9*M* $BeCl_2$	18	0.15	Black, brittle, thin	93
3*M* $Be(Me)_2$ + 2.3*M* $BeCl_2$	18 to 25	0.1	Gray, metallic, brittle, thin ($BeCl_2 \cdot 2Et_2O$ crystallized out of solution, to leave about 1*M* $BeCl_2$ in solution)	95
2.8*M* $BeCl_2$	7	0.1	Black powder	92

A 2.4*M* solution of dimethylberyllium in ethyl ether was found to be miscible with a majority of the organic solvents which were investigated. Electrolytic studies were carried out on solutions containing 3–66% by volume of the added solvent. Cathode current densities up to 0.5 amp/dm² were obtained at applied voltages of 60–120 v, but no deposits were obtained in the presence of the following solvents: dimethylformamide, pyridine, anisole, phenetole, phenyl ether, isopropyl ether, bis-(2-chloroethyl) ether, butyl ether,[2] piperidine,[2] n-methylmorpholine,[2] benzothiazole, thiophene, acetonitrile, and 1,2-dimethoxyethane.[2] These experiments illustrate the highly specific nature of the solvent-solute combinations which are amenable to electrodeposition. Data for the solutions from which deposits were obtained are given in Table VII. None of the deposits was improved over those obtained from the ethyl ether bath. Addition agents such

[2] These solvents were not miscible with dimethylberyllium etherate.

TABLE VII. *Electrolytic studies of* $BeMe_2 \cdot$*etherate in different solvents*

Solvents	Solvent dilution %	Deposits* compared with those from 2.4*M* $BeMe_2 \cdot$etherate in ethyl ether (*see* Table VI)
Tetrahydrofuran	66	Similar
1,2-Dimethoxyethane	3–50	Similar
Pyrrolidine	3	Similar
	9, 23†, 50†	No deposit
Pyrrole	3–23	Similar
	50	No deposit
Xylene	3	Similar
	9–66	No deposit
Acetal	3	Poorer
	9	No deposit
Ethyl bromide	3	Similar
	9–23	Poorer
	50	No deposit
Triethylamine	3–23	Similar
	50	No deposit

* Cathode current densities from 0.03 to 0.5 amp/dm² at applied voltages from 60 to 120 v.
† Not miscible.

from the 2.8*M* $BeCl_2$ bath were 92% and the less stable deposits from the 3*M* dimethylberyllium were 63%.

Polarization studies were run in the bath containing 3*M* dimethylberyllium and 2.3*M* $BeCl_2$. A Cu cathode, Be anode, and a reference electrode of Al wire were em-

ployed. The reference electrode included a "Luggin-Haber capillary" in order to eliminate the *IR* drop between the reference electrode and the other electrode. The solution made contact with the Al wire through this capillary. High anode polarization was indicated.

Diphenylberyllium

Phenyl derivatives of Be were prepared by reported methods (23, 24) and also by the reaction between $BeCl_2$ and phenyllithium in ethereal solution (*see* Appendix). The phenyl derivative was reported in the literature to be diphenylberyllium, but analyses were not reported, and the compound was not clearly characterized. Some doubt exists whether the products of these various reactions are the same compound or in the same state of polymerization. The product of the reaction between Be metal and diphenylmercury dissolved in ethyl ether, benzene, toluene, and tetrahydrofuran but did not give conducting solutions. The product isolated at 100°C from the reaction between phenyllithium and $BeCl_2$ was slightly soluble in 1,2-dimethoxyethane, tetrahydrofuran, phenyllithium etherate, and benzene but was insoluble in several other solvents as shown in Table VIII. The resulting solutions, with the exception of those containing benzene, conducted the current but gave no electrodeposit.

Beryllium Borohydride

Beryllium borohydride [$Be(BH_4)_2$] a volatile, white solid, has been systematically studied as a means of depositing Be metal by electrolysis from organic solutions. It is spontaneously flammable in air and reacts very vigorously with water and oxidizing agents. It is a monomer which appears to be more covalent than ionic (25). Data on the solubility and conductivity in various solvents are given in Table IX. Like dimethylberyllium it is not soluble in many organic solvents. This contrasts with $Zr(BH_4)_4$ and $Al(BH_4)_3$, which are soluble in a variety of solvents, including paraffin hydrocarbons. Beryllium borohydride was soluble in anisole, phenyl ether, and ethyl ether; the latter solution was the best conductor. It was insoluble in the other solvents tested.

The resistance of an ethyl ether solution of beryllium borohydride was considerably reduced by increasing the solute concentration. Brittle, coherent gray deposits were obtained from 6*M* baths at room temperature. At a cathode current density of 0.62 amp/dm² the potential drop across the cell was only 2 v, a striking contrast to the higher voltages found for the dimethylberyllium solution. Several deposits 0.01 in. thick were obtained; they had an average composition of 70% Be and 30% B. These are probably the first B alloys electrodeposited at room temperature.

The voltage drop across the bath decreased with an increase in the operating temperature. At 80°C a more lustrous, smooth Be alloy deposit, which was 0.002 in. thick, was obtained. After the bath was operated for 30 hr between 85° and 90°C, the solution gradually decomposed, and the deposits became black and powdery.

Beryllium Hydride Etherate

Relatively little is known about beryllium hydride, BeH_2. Whether or not it exists in the free state is still controversial. Kassner and Stempel (26) claimed no satisfactory evidence existed for the isolation of solid BeH_2. Various methods (27–29) have been reported for

TABLE VIII. *Solubility and conductivity tests on a phenyl derivative of* Be *in various solvents*

Solvent	Solubility at R.T. (25°–30°C)	Conductivity
Benzene	SS	None
n-Butyl ether	i	None
1,2-Dimethoxyethane	SS	Yes
Isopropyl ether	i	None
Phenyl ether	i	None
Phenyllithium etherate	SS	Yes
Pyridine	i	Yes
Tetrahydrofuran	SS	Yes
Tetrahydropyran	i	None

NOTE: i = insoluble; SS = slightly soluble.

No promising deposits obtained in the above experiments.

Phenyl lithium etherate appeared to be insoluble in most of the solvents listed above.

TABLE IX. *Solubility and conductivity tests for beryllium borohydride in various solvents*

Solvent	Solubility at R.T. (25°–30°C)	Conductivity
Ethyl ether	S	Good*
Anisole	S	Poor
Phenyl ether	S	Poor
Benzene	i	None
Butyl ether	i	None
Tetrahydrofuran	i	None
Diethylene glycol dimethyl ether	i	None
Triethylene glycol dimethyl ether	i	None
Tetraethylene glycol dimethyl ether	i	None
Pyridine	S	None
Dimethylamine	i	No deposit

S = soluble; i = insoluble.

* 6 *M* solution with cell voltage of 2 amp/dm² gave a lustrous, coherent alloy containing 30% B and 70% Be.

TABLE X. *Beryllium hydride etherate in the presence of nonaqueous solvents*

Solvent	Solubility	Conductivity of beryllium hydride etherate and beryllium chloride in various solvents $\frac{Mole_{BeCl_2}}{Mole_{BeH_2}} = 1$
Acetone	S	Yes
Anisole	i	None
Benzene	i	None
Ethyl ether	i	Yes
1,2-Dimethoxyethane	i	Low
Dimethylformamide	S_t	Yes
Dioxane	S_t	None
Phenetole	S_t	None
Pyridine	i	Yes
Tetrahydrofuran	i	Low
Triethylamine	i	None

NOTE: S = soluble; i = insoluble; S_t = dissolves on standing at room temperature.

TABLE XI. *Deposition of* Be-Al *alloys from ethyl ether solutions*

Bath type	Be^{++}/AlH_4^-	Be^{++}	Composition of deposit	Appearance of deposit
	ratio	g at./l		
$Be(AlH_4)_2$*	0.5	0.5	14% Be	Powder
$Be(AlH_4)_2$ plus $BeCl_2$*	1–27	1.0–2.5	0–57% Be	In order of increasing $BeCl_2$ content of bath: white → gray → black; smooth → rough → stressed
H-Al Bath† plus $BeCl_2$	1.3–40	0.7–2.5	% Be small but increasing	In order of increasing $BeCl_2$ content of bath: white → gray → black; smooth → rough → stressed

* Al anode;† Be anode; Cu cathode; electrolysis at room temperature; cathode C.D. varied from 0.05 to 0.5 amp/dm²; voltage range from 0.6 to 4 volts; all deposits metallic and coherent.

the preparation of its etherate. This compound is more covalent than $BeCl_2$, and the corresponding alkali metal hydrides but more ionic than aluminum hydride.

BeH_2 was prepared by reaction of $LiAlH_4$ with dimethylberyllium (28). The compound was insoluble in ethyl ether, anisole, 1,2-dimethoxyethane, tetrahydrofuran, triethylamine, pyridine, or benzene. It appeared to dissolve on standing several days in dioxane or dimethylformamide (Table X), but the resulting solutions were not conductors.

The possibility of producing a BeH_2 or beryllium chlorohydride type of bath analogous to the hydride-aluminum bath (22) was investigated. BeH_2, as produced above, was added to samples of $BeCl_2$ solvated with different liquids. No increase in solubility of the hydride in the solvents listed in Table X was effected by the presence of $BeCl_2$. On electrolysis no deposit was obtained except from the ethyl ether solution, and this one was no better than that obtained from the $BeCl_2 \cdot 2Et_2O$ alone.

Be-Al Alloys

Systematic studies of hydride baths containing both Be and Al have been completed and are summarized in Table XI. The hydride baths were made by mixing ethereal hydride solutions and $BeCl_2$ in different proportions. The hydride content of the baths came either from an ethereal solution of $Be(AlH_4)_2$ (from $LiAlH_4$ and $BeCl_2$), or from the hydride-aluminum plating bath (22). Deposits obtained from the two types of solutions for a given ratio of Be^{++} to AlH_4^- were similar. The Be concentration of the baths was changed so that the Be^{++} to AlH_4^- ratio varied from 0.5 to 40. The deposits obtained when this ratio was unity contained only traces of Be. They were white-gray, crystalline, reflective, ductile, and similar to deposits from the pure hydride-aluminum bath. The deposits obtained when this ratio was 11 contained 46% by weight Be. They were gray to black in color, reflective, and stressed. As the ratio increased, the percentage of Be in the deposit increased. The deposits were not wholly metallic but were more coherent than those obtained from the beryllium chloride etherate solution alone. It is significant that they were deposited at a much lower voltage for a given current density.

In the analyses of the alloys, Al was determined as the aluminum quinolate by weighing or by bromate-bromide titration. Be was precipitated from solution as the hydroxide and ignited to the oxide.

Although BeH_2 is insoluble in ether, there is evidence that a soluble complex containing Be, Al, and hydride-hydrogen exists in the solution obtained by mixing ethereal solutions of $BeCl_2$ and $LiAlH_4$. A precipitate was formed, but the solution remaining was approximately 1*M* in Be and contained Be, Al, and H in a stoichiometric ratio of 1/1.8/9.2. This reaction was reported by Wiberg and Bauer (27), who implied that $Be(AlH_4)_2$ existed in the solution in a stoichiometric ratio of 1/2/8, but they gave no evidence to support this view. This solution did not yield a precipitate with a solution of $BeCl_2$ in ethyl ether, which indicated that the hydride ion must be tightly complexed. Ethereal solutions of $BeCl_2$ and aluminum hydride, AlH_3, were completely miscible. This indicates either that the same soluble $Be(AlH_4)_2$ complex as that obtained with $LiAlH_4$ is formed, or that the hydride ion in aluminum hydride is too tightly complexed to form the insoluble BeH_2.

Summary

Powdery deposits were obtained from halide-ethereal solutions of Be, Mg, and Al. Consequently, it seems that to obtain coherent deposits of these metals a different ionic or molecular species must be found. The alkyl baths gave very brittle coherent deposits of Be containing occluded constituents from the bath as impurities. Electrolysis of a mixed halide-alkyl bath gave gray, lustrous, coherent flakes which were much improved over the deposits obtained separately from each solution. Deposits of purity as high as 95% were obtained from this type of organic bath. A brittle, coherent alloy containing 70% Be and 30% B was obtained from the ethereal beryllium borohydride bath. Stressed coherent alloys of Be and Al were obtained from the mixed baths containing $Be(AlH_4)_2$ and $BeCl_2$. These deposits did not show much promise. This study has resulted in the first reported thick, coherent deposits consisting essentially of Be from organic baths.

Acknowledgment

The authors wish to acknowledge the contributions made by the following people who assisted in collecting exploratory data: Dwight E. Couch (Tables I, II, and III), Paul A. Krasley (Tables IV and X), Miriam S. McDonald (preparation of dialkylberyllium compounds), and Margaret A. Reid (preparation of beryllium borohydride). Work was sponsored by the A.E.C., Metallurgy and Materials Branch, Division of Research.

Manuscript received October 12, 1955. This paper was prepared for delivery before the Boston Meeting, October 3 to 7, 1954. Work was sponsored by the AEC, Metallurgy and Materials Branch, Division of Research.

Any discussion of this paper will appear in a Discussion Section to be published in the December 1957 JOURNAL.

REFERENCES

1. SIEMENS-KONZERN, "Beryllium," translated by the Chemical Catalogue Co., Inc., New York (1932).
2. G. V. RAYNOR, "Beryllium and Beryllium Alloys," The Royal Aeronautical Society, March (1946).
3. W. KROLL, U. S. Bureau of Mines, Information Circular I.C. 7326, June 1945.
4. A. R. KAUFMANN, P. GORDON, AND D. W. LILLIE, *Trans. Am. Soc. Metals*, **42**, 785 (1950).
5. C. L. MANTELL, "Industrial Electrochemistry," p. 431, McGraw-Hill Book Co., New York (1940).
6. A. STOCK, *Trans. Electrochem. Soc.*, **61**, 255 (1932).
7. A. C. VIVIAN, *Trans. Faraday Soc.*, **22**, 211 (1926).
8. Beryllium Develop. Corp., Brit. Pat. 377,858 (1932).
9, 10. C. B. SAWYER AND B. R. KJILLGREN, Can. Pat. 371, 194 (1938); U. S. Pat. 2,311,257 (1943).
11. A. E. VAN ARKEL, Metallwirtschaft, **13**, 405 (1934).
12. T. P. DIRKSE AND H. T. BRISCOE, *Metal Ind., (New York)*, **36**, 284 (1938).
13. F. H. HURLEY AND T. P. WIER, JR., *This Journal*, **98**, 203 (1951).
14. H. S. BOOTH AND G. G. TORREY, *J. Phys. Chem.*, **35**, 2464 (1931).
15. H. S. BOOTH AND G. G. TORREY, *ibid.*, **35**, 2492 (1931).
16. H. S. BOOTH AND G. G. TORREY, *ibid.*, **35**, 3111 (1931).
17. A. BRENNER, *This Journal*, **103**, 652 (1956).
18. W. E. REID, JR., J. M. BISH, AND A. BRENNER, *ibid.*, **104**, 21 (1957).
19. F. W. BERGSTROM, *J. Am. Chem. Soc.*, **50**, 657 (1928).
20. R. FRICKE AND F. RUSCHHAUPT, *Z. anorg. Chem.*, **146**, 103 (1924).
21. R. FRICKE AND F. ROBKE, *ibid.*, **170**, 25 (1928).
22. D. COUCH AND A. BRENNER, *This Journal*, **99**, 234 (1952).
23. H. GILMAN AND F. SCHULTZ, *J. Chem. Soc.*, **1927**, 2663.
24. G. WITTIG, F. J. MEYER, AND G. LANGE, *Ann. Chem.*, **571**, Heft 3, 167 (1951).
25. A. B. BURG AND H. I. SCHLESINGER, *J. Am. Chem. Soc.*, **62**, 3425 (1940).
26. G. KASSNER AND B. STEMPEL, *Z. anorg. Chem.*, **181**, 83 (1929).
27. E. WIBERG AND R. BAUER, *Z. Naturforsch.*, **6b**, 171 (1951).
28. G. D. BARBARAS, C. DILLARD, A. E. FINHOLT, T. WARTIK, K. E. WILZBACK, AND H. I. SCHLESINGER, *J. Am. Chem. Soc.*, **73**, 4589 (1951).
29. G. E. COATES AND F. GLOCKLING, *J. Chem. Soc.*, **1954**, 2526.
30. O. RAHLFS AND W. FISCHER, *Z. anorg. Chem.*, **211**, 349 (1933).
31. W. SCHLENK AND W. SCHLENK, JR., *Ber.*, **62**, 920 (1929).
32. H. GILMAN AND R. E. FOTHERGILL, *J. Am. Chem. Soc.*, **51**, 3149 (1929).
33. H. I. SCHLESINGER, H. C. BROWN, AND E. K. HYDE, *ibid.*, **75**, 209 (1953).

APPENDIX

PREPARATION OF Be COMPOUNDS

$BeCl_2$.—Anhydrous $BeCl_2$ was obtained commercially. Spectroscopic analysis showed Ni was the largest metallic impurity present. Gravimetric analysis showed 0.06% Ni. This commercial $BeCl_2$ was purified by sublimation *in vacuo* at 400°C.

$BeBr_2$.—$BeBr_2$ was not obtainable commercially. It was made readily by direct union of the elements in the apparatus shown in Fig. 1. Br_2 was vaporized in flask A by means of an infrared lamp and passed with a stream of argon over Be powder contained in a Vycor tube furnace, B, operating at 550°C. Rahlfs and Fischer reported that the compound sublimes at 473°C (30). The vapors were carried out of the heated area of the furnace by the stream of A. The cold delivery end of the Vycor tube was heated internally to 450°–500°C by a helical heating element, E, to prevent clogging. This heating element was in a Vycor tube of small diameter closed at one end. In this way the $BeBr_2$ was kept above its melting point until it emerged from the reaction tube, which projected into the cold collection chamber, C, consisting of a large glass cylinder. The apparatus was sealed from the atmosphere by means of a series of liquid bubblers, D. In a 6-hr period 0.6–0.7 lb of the bromide was produced. The anhydrous $BeBr_2$ was transferred under dry He to storage bottles.

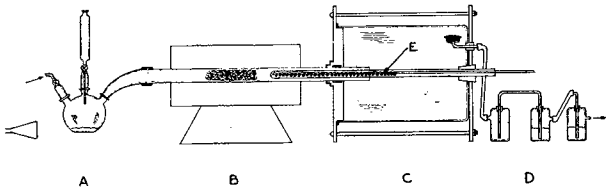

FIG. 1. Apparatus for preparing beryllium bromide: A—flask containing bromine; B—furnace; C—collection chamber; D—absorption bubblers used as measure of gas flow; E—helical heating coil.

An attempt was made to prepare $BeBr_2$ from Be metal and Br_2 in boiling CS_2, but no reaction took place.

BeI_2—BeI_2 was prepared in a manner similar to that used for the bromide. The rate of reaction between I_2 vapor and Be metal at temperatures below 800°C was very slow, and the small amount of iodide obtained was badly contaminated with I_2, proving the method unsatisfactory.

Sealed tubes containing Be metal mixed with I_2 shattered when heated to 500°C, but when the metal was placed in a separate glass container inside the sealed tube, in such a manner that only I_2 vapor came in contact with the metal, the tubes remained intact. After 65 hr at 480°C very little I_2 remained unreacted. Four grams of Be (1.8 g excess) was allowed to react with 63 g of I_2/tube.

The resulting BeI_2 was purified by distillation at 500°C. The tubes were broken in an atmosphere of dry A and placed in a C crucible surrounded by a ceramic cylinder. The entire assembly was placed in a resin reaction kettle. Induction heating was employed. An atmosphere of dry A was maintained throughout the purification. An air condenser was suspended from the top of the resin reaction kettle into the reflux area. Since BeI_2 melts rather than sublimes, an inlet stream of A was flushed through the refluxing BeI_2 in order to carry the vapor up into the cooled area where it condensed. A yield of approximately 50% (130 g) was obtained. The resulting product contained about 5% SiI_4. The light salmon color was probably caused by the impurities present. The product was stored in a dry atmosphere of A in sealed ampoules, wrapped in Al foil as a precautionary measure.

Dialkylberyllium compounds.—Dimethylberyllium was prepared in quantities up to 0.3 g-mole by Gilman and Schultz (23) by an "ether cycling method" which gave yields of 85–90%. This method consisted of reacting beryllium chloride etherate with an excess of the appropriate Grignard reagent in dry A and distilling the etherate of the dialkylberyllium compound with an excess of ether. The ether in the receiver was continuously evaporated, condensed, and

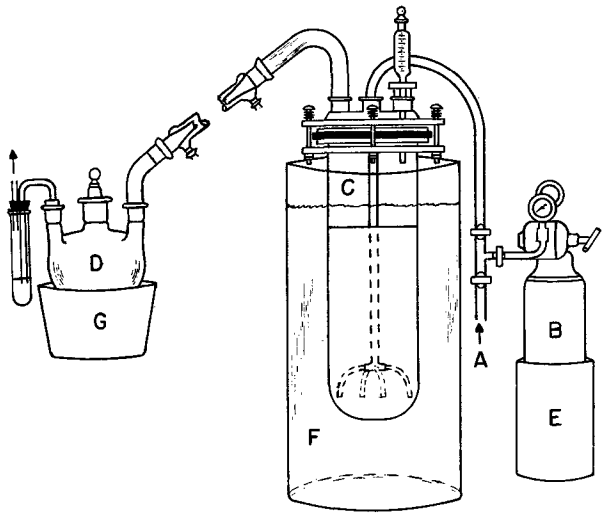

FIG. 2. Apparatus for "ether-vapor method" for preparing beryllium dialkyls: A—inert gas source; B—ether boiler; C—resin reaction kettle; D—collection flask; E and F—oil baths; G—butyl cellosolve-dry ice cooling bath.

returned to the reaction vessel. The reason for this procedure is that the etherate is more volatile than the pure alkyl and hence more readily isolated.

1. "Ether Cycling Method."—Initially this method was used with 0.5 g-mole of anhydrous $BeCl_2$ as starting material, but only a 40% yield was obtained. The efficiency of this method for preparing dimethyl- or diethylberyllium decreased as the quantity of starting material was increased. The main objection to this method was the low yield.

A study of the "ether cycling method" was made in order to improve the yield. To eliminate any variations in the reactants, stock solutions of ethylmagnesium bromide and beryllium chloride etherate, adequate for a set of experiments, were prepared. The effect of each of the following variables were studied, but no significant effect on the yield was noticed: (*a*) quantity of initial reactants, (*b*) molar ratio of initial reactants, (*c*) type of halide in Grignard reagent, (*d*) pressure of distillation, (*e*) method of heating reaction mixture, (*f*) concentration of ethyl ether in system, (*g*) elements of design of equipment, (*h*) distillation temperature, and (*i*) distillation time. Since it was not possible to produce good yields of beryllium dialkyls in quantities greater than 0.3 g-mole by the "ether cycling method", a different procedure was sought.

2. "Extraction Method."—Grignard reagents are reported to be mixtures of compounds according to the following equilibrium (31, 32):

$$2RMgX \rightleftarrows MgX_2 + R_2Mg$$

$BeCl_2 \cdot 2Et_2O$ reacts with this solution to produce BeR_2 and $MgCl_2$. The halide-containing compounds in the resulting mixture are insoluble in 1,4-dioxane whereas both dialkylmagnesium and dialkylberyllium compounds remain soluble. This difference was the basis of an attempt to separate dimethylberyllium but it was unsuccessful.

3. "Ether-Vapor Method."—The factors which were found to influence the yield most in Method 1 were (*a*) the intimate contact of the reaction mixture with ether vapor, (*b*) the speed with which the distillation of the alkyl from the reaction mixture took place while the temperature was raised to 240°C, near the decomposition temperature of the alkyl, and (*c*) the length of the distilling head between the reaction vessel and the collecting vessel. Making use of factors (*a*) and (*b*) the "ether-vapor method" was developed for the preparation of several moles of dimethylberyllium.

The apparatus used is shown in Fig. 2. He from tank A was used to keep an inert atmosphere in the entire apparatus. Tank B was filled with Na-dried ethyl ether and was used as the ether boiler. The pressure in tank B was controlled by the temperature of oil bath E. The ether boiler was connected to a resin reaction kettle, C, by means of Cu tubing which extended to within a few inches of the bottom of the kettle. The temperature of the reaction kettle was controlled by an oil bath, F. A condenser with circulating ice water connected the reaction kettle and a 2-l flask, D. The flask was sealed from the atmosphere by a mercury trap and cooled by a butyl cellosolve-dry ice mixture, G.

The required quantity of Grignard reagent was placed in the reaction kettle which had been flushed with He. The beryllium chloride etherate was added from a dropping funnel, which was replaced by a rubber stopper. The kettle was flushed by a rapid flow of He while the mixture was heated to 80–100°C by means of an oil bath, F. After most of the ether had been removed and collected, and the residue had become nearly dry, the temperature was further raised to 187°–220°C. Ether vapor from B was passed through the powdered residue under a pressure of 10–20 lb/in.^{2} at the rate of $\frac{1}{4}$–1 l/hr. This pressure was necessary to force the vapor through the dry mass. Each 2-l lot of distillate was tested to determine the rate at which the organometallic compound was being distilled. The experiment was stopped when the amount of alkyl distilled became less than 2 g/l.

During the preparation the condensates were transferred to a 3-l resin reaction kettle from which ether was distilled at 50°–100°C, leaving solid dimethylberyllium. A stock quantity of 300 g dimethylberyllium was prepared by this method. The capacity of the equipment was enlarged for

TABLE XII. *Preparation of dimethylberyllium by "ether-vapor method"*

Run	Theoretical yield	Actual yield	Temperature range	Percentage yield	Total volume of ether distillate collected
	mole	*mole*	*°C*	*%*	*liters*
I	1.4	1.1	150–220	79	8.5
II	4.1	2.6	170–200	63	8.5
III	6.8	4.4*	185–210	64*	15

Resin Reaction Kettle Capacity—I: 4-liter (6 in. diameter) II and III: 6-liter (6 in. diameter).
* Estimated.

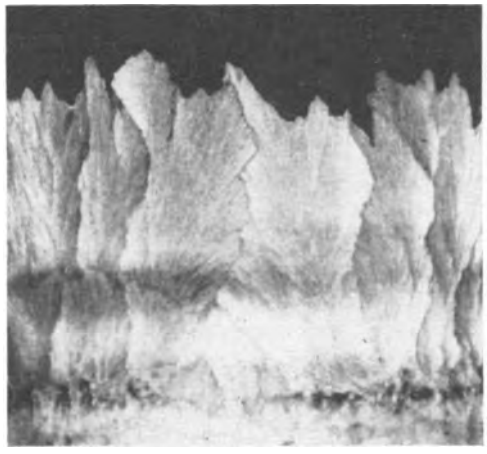

FIG. 3. Beryllium dimethyl crystals. × 0.25

each successive run, and in the last run about 4.4 moles of dimethylberyllium were prepared. Table XII summarizes the results of these experiments. The dried crystals obtained are shown in Fig. 3.

Arylberyllium compounds.—Several methods of preparing phenyl derivatives of Be were studied.

Method 1(a)—A black solid product was obtained by Gilman and Schulze (23) when Be metal, diphenylmercury, and $HgCl_2$ catalyst were heated in sealed tubes at 225°C for 6 hr. It was reported to be insoluble in benzene, toluene, and ethyl ether at their boiling temperatures, but it gave a strong positive Michler's ketone test.

A brick red crystalline solid was obtained here with this method. It also was not readily soluble in xylene or warm ether, but it dissolved in ethyl ether during several hours of refluxing. Both the resulting ethereal solution and solid remaining undissolved gave a positive Michler's ketone test.

Method 1(b)—Wittig, Meyer, and Lange (24) reported the preparation of diphenylberyllium by a similar reaction but in the presence of xylene as a solvent at 150°C and in the absence of a catalyst. These authors did not describe a method of isolation of their diphenylberyllium, but reported it to be soluble in benzene and xylene and soluble on warming in ethyl ether and tetrahydrofuran.

A similar reaction was obtained here only after the addition of $HgCl_2$ as catalyst at a temperature of 175°C while using powdered Be metal. (Flaked metal did not give a reaction under these same conditions.) Beads of mercury and a yellow-to-red solution indicated that reaction had taken place. After the xylene solution was filtered and concentrated, a straw-colored compound settled out. The sample was dried under vacuum. A temperature of 210°C produced some decomposition. The very dark residue dissolved slowly in ethyl ether during several days of refluxing to give a red-orange solution.

Method 2.—Phenyl derivatives of Be were prepared by a new method, which involved the reaction of $BeCl_2$ and phenyllithium in ethyl ether. The conversion of phenyllithium to diphenylberyllium in solution was indicated by the Michler's ketone test. Two general methods of isolating diarylberyllium compounds from the ethereal solution were investigated. The first involved precipitating LiCl with xylene followed by concentrating the solution at temperatures up to 100°C. The second method involved evaporating the ethyl ether in a vacuum at −15°C. Straw-colored crystals were isolated in both cases. The product of the first method was insoluble in ethyl ether, which was surprising since it was crystallized from this solvent. The probable reason for this insolubility may be decomposition or polymerization at the elevated temperatures of the isolation. The product of the second method was found to be still soluble in ethyl ether. Preliminary analyses indicate that the products from methods one and two contained a beryllium to phenyl ratio of 1/1 and 1/2, respectively.

Beryllium borohydride.—Beryllium borohydride was prepared from an equimolar mixture of dry $LiBH_4$ and anhydrous $BeCl_2$. The reaction took place slowly at room temperature but was rapid at elevated temperatures. The procedure used was similar to that of Schlesinger and coworkers (33), who reported an 80% yield. They heated the mixture quickly to 90°C and then to 140°C over a period of 8 hr during continuous evacuation. The authors found that when $LiBH_4$ and $BeCl_2$ were mixed in a molar ratio of 2/1 and were heated immediately to 180°C and heated continuously under a pressure of approximately 2×10^{-5} mm Hg for 5 hr, a 74% yield resulted. Other runs indicated that at pressures approaching 0.2 mm the initial mole ratio must be decreased to 1 in order to keep the yields high. Beryllium borohydride begins to decompose at temperatures as low as 123°C. The percentage yield is consequently influenced by the temperature at which the reaction is run as well as by the pressure and the speed with which the compound is sublimed. Because of the danger involved in preparing under reduced pressure and in glass equipment a spontaneously inflammable material like beryllium borohydride, larger preparations were not attempted. All-metal equipment should be considered for large-scale runs.

In an effort to prepare beryllium borohydride more cheaply and safely as well as in larger quantity, various other procedures were tried. These methods will be mentioned only briefly since none proved as successful as the method already described. (*A*) A dry mixture of $NaBH_4$ and $BeCl_2$ was heated under essentially the same conditions as above but failed to yield any beryllium borohydride. (*B*) Beryllium borohydride etherate was shown to distill under reduced pressure. An attempt to distill beryllium borohydride etherate from a mixture of $LiBH_4$ and $BeCl_2$ was unsuccessful. (*C*) The slow addition of $LiBH_4$ to a molten eutectic mixture of $BeCl_2$ and NaCl at about 250°C gave low yields. Higher yields might have been obtained if a suitable material could have been found, which, when mixed with $BeCl_2$, would have melted below 180°C. (*D*) KBH_4 and $BeCl_2$ react in *n*-butylamine, but the isolation of solvent-free products is difficult. (*E*) A dry mixture of KBH_4, LiCl, and $BeCl_2$ was heated under reduced pressure to 200°C without reaction. Reaction and decomposition occurred when the temperature was raised up to 400°C. Both beryllium borohydride and diborane were trapped at −196°C. The yield was low due to decomposition at the elevated temperature.

Beryllium hydride etherate.—The etherated beryllium hydride used in these studies was prepared by the method of Schlesinger and co-workers (28).

The reaction between LiH and $BeCl_2$ in ethereal solution was studied. Mixtures in various proportions were either ball milled or heated in a bomb at 125°C for 24 hr. Isolation of beryllium hydride was difficult since LiH, LiCl, and $BeCl_2$ are all only slightly soluble in ether. In all reactions, the concentration of Be remaining in solution was low. Evidence for the presence of beryllium hydride in the solid reaction product was obtained by thermal decomposition. The solid, when heated from 125° to 150°C, turned gray, owing to the decomposition of beryllium hydride to beryllium metal.

Beryllium aluminum hydride.—Beryllium aluminum hydride was prepared by the method of Wiberg and Bauer (27). Ethereal solutions of $BeCl_2$ and $LiAlH_4$ were mixed in a molar ratio of 1:2 in an inert atmosphere. A white precipitate formed and was filtered from the solution. Analysis of the filtrate confirmed the presence of Be, Al, and H in a ratio of 1/1.82/9.2, indicating $Be(AlH_4)_2$ in solution.

The stability of $Be(AlH_4)_2$ in ethereal solution was found to be a function of temperature. It decomposed within a few hours at the boiling point of ether but was stable for several days at temperatures between −10° and 10°C. Consequently, reactions were run and solutions stored within this temperature range. The solution was stabilized at room temperature for a period of several days by the addition of the chloride of Be or Al.

The precipitate from the above reaction contained both LiCl and beryllium aluminum hydride, since the solubility of both compounds was exceeded in the ethereal solution. Both the precipitate and solution underwent reaction with alcohol to give Al metal and Be oxide and with water to give the oxides of Al and Be.

Electrodeposition of Metals from Organic Solutions

V. Electrodeposition of Magnesium and Magnesium Alloys

JEAN H. CONNOR, WALTER E. REID, JR., AND GWENDOLYN B. WOOD

National Bureau of Standards, Washington, D. C.

ABSTRACT

The electrodeposition of Mg from ether solutions of such Mg compounds as (*a*) halides, (*b*) aluminohydrides, (*c*) borohydrides, and (*d*) Grignard reagents was investigated. White, metallic deposits containing 90% Mg and 10% B were obtained from an ether solution of $MgBr_2$ and $LiBH_4$. However, thick deposits could not be built up. An alloy (7% Mg, 93% Al) was obtained from a bath containing $MgBr_2$, $AlBr_3$, and $LiAlH_4$. Electrodeposited alloys of Zr, Ti, or Be with Mg, obtained from hydride or borohydride baths, were stressed, treed, or powdery. The preparation and solubilities of some of the solutes are given.

The electrodeposition of Mg and Mg alloys would be useful in electroforming objects of small mass. Since Mg is so much less noble than H, it cannot be deposited from aqueous solutions, and no satisfactory organic plating baths have been reported up to the present time. Overcash and Mathers (1) were unable to electrodeposit Mg from such Mg salts as the bromide, thiocyanate, perchlorate, ethylate, or methylate dissolved in pyridine, formamide, benzonitrile, acetonitrile, *o*-toluidine, aniline, ethyl bromide, dimethylaniline, or ether. Dirkse and Briscoe (2) reported no deposit of Mg was obtained from solutions of its salts in acetamide, nitrobenzene, aniline, acetone, benzoyl chloride, or glacial acetic acid. They did report a deposit of Mg from an ethanolamine solution of $Mg(NO_3)_2$, but no analysis of the deposit was given.

Deposition of Mg from Grignard reagents has been known for some time (3, 4). French and Drane (5), using various anodes in isoamylmagnesium chloride, found that Zn and Cd dissolved anodically to a slight extent, Al dissolved appreciably, and Mg did not dissolve at all. Overcash and Mathers (1) attempted to increase the stability of the Grignard baths and to improve the character of the deposits by the use of addition agents. They reported that the addition of dimethylaniline to an ether solution of ethylmagnesium bromide yielded brighter, more adherent deposits and increased the bath life. An ethylmagnesium iodide bath had a somewhat longer life than the ethylmagnesium bromide bath. The short life of the Grignard baths was due in part to the failure of the Mg anodes to dissolve.

Most of the electrolytic studies on Grignard reagents (1, 6–8) have been concerned with identifying by-products and with studying the mechanism of the reactions. Mg deposits were described as spongy and brittle. The resistance of the solutions was very high; for example, 110 v were required to pass 0.02 amp (current density, 0.23 amp/dm^2) through an ether solution of ethylmagnesium bromide containing an addition agent (1).

EXPERIMENTAL

This investigation sought to obtain deposits of both Mg and Mg alloys from organic solutions operated at room temperature. Since Al had been electrodeposited successfully in this laboratory from an ethereal hydride-type bath (9), the possibility of a hydride bath for Mg was indicated. Also, since deposits of Be, Zr, and Ti were obtained from baths containing borohydrides, aluminohydrides, and alkyls, similar Mg compounds were prepared.

The fact that most Mg salts are not readily soluble in organic liquids limits the number of compounds that may be used as solutes. $MgCl_2$ is practically insoluble in ethyl ether, but $MgBr_2$ dissolves slowly at room temperature to form magnesium bromide dietherate, $MgBr_2 \cdot 2Et_2O$. If the concentration of $MgBr_2$ in ether exceeds 3% by weight, two liquid layers are formed. The lower layer contains about 39% by weight of $MgBr_2$ (approximately 2.5M). Magnesium bromide dietherate crystallized from the lower layer at about 21°C. The low solubility of $MgBr_2$ in most common organic solvents limited the electrolytic studies to solutions of ethyl ether and tetrahydrofuran. The following solvents did not dissolve sufficient amounts of $MgBr_2$, even at the boiling point of the solutions, to be considered for plating solutions: benzene, phenyl ether, dioxane, phenetole, anisole, triethylamine, xylene, and cyclohexylamine. $MgBr_2$ reacted to form precipitates with tetrahydrofuran, pyridine, and *N*,*N*-diethylacetamide at room temperature.

The preparation and electrolysis of the plating solutions to be described were performed in an inert atmosphere. Techniques and apparatus used are described in the first paper of this series (10). The volumes of the baths studied were about 50 ml. Deposits were obtained on Cu cathodes. Anodes of Al were used instead of Mg because they dissolved more readily, and because Mg anodes decomposed the baths more rapidly than those of Al. There was no evidence to show that Al from the anode was codepositing with the Mg.

Magnesium Plating Baths

Magnesium halides.—The electrolysis of a 2.5M $MgBr_2$ solution in ether yielded dark, brittle deposits which contained 60–70% Mg (No. 1, Table I). The remainder of the deposit was probably oxide and organic matter oc-

cluded from the bath. The conductivity of the solution was low, and thick deposits were difficult to build up because of excessive treeing. The throwing power was also low. The electrolysis of $MgBr_2$ in tetrahydrofuran at the boiling point of the solution and at a current density of 1.2 amp/dm² yielded black, powdery deposits. No deposits were obtained at lower current densities.

Magnesium Borohydride.—The addition of a small amount of $LiBH_4$ to magnesium bromide dietherate considerably improved the conductivity of the solution. A smooth, dense deposit containing 90% Mg was obtained from this bath (No. 3, Table I) at 1 amp/dm². A bath containing equimolar quantities of the reactants conducted current well and yielded a sound metallic deposit (No. 4, Table I). However, treeing occurred and a thick deposit was difficult to obtain. When viewed under a microscope the deposit appeared pitted.

A similar bath containing $LiBH_4$ and $MgBr_2$ in the mole ratio of two was prepared. These compounds react to give $Mg(BH_4)_2$ (11). Electrolysis of this bath at a current density of 1 amp/dm² gave a deposit containing 90% Mg and 10% B (No. 5, Table I). The measured cathode efficiency was 91%, but because of the treeing that occurred the true efficiency was probably higher than this. The Mg content of the deposits from baths No. 3, 4, and 5 was close to 90% and appeared to be independent of the magnesium to borohydride ratio.

Ether solutions of $Mg(BH_4)_2$ were also obtained from the reaction of anhydrous $MgCl_2$ and $LiBH_4$ in ether. One such bath gave a treed deposit containing 79% Mg (No. 6, Table I). The addition of thiophene reduced somewhat the treeing of the deposit. This addition agent was objectionable in that the conductivity of the bath was lowered and the resulting solution was less stable.

In general, these baths yielded brittle, rough, metallic deposits which rapidly became coated with oxide when exposed to the atmosphere. Since these coatings contained occlusions from the baths, precise analysis of a deposit was difficult.

Attempts to prepare $Mg(BH_4)_2$ from $NaBH_4$ and $MgBr_2$ or $MgCl_2$ in ether were not successful.

Magnesium Grignard.—A few Mg deposits were obtained from Grignard reagents for the purpose of comparing them with those obtained from the hydride and borohydride baths. Although these deposits were white and metallic in appearance, they were not pure Mg and were very brittle. The treeing which occurred during electrolysis was not alleviated by rotating the cathode.

A deposit obtained from a bath having a concentration of 2.5M ethylmagnesium bromide contained 71% Mg (No. 7, Table I); the remainder of the deposit was probably organic matter. The conductivity of this solution was low; a current density of 0.3 amp/dm² required 50 v. The addition of small amounts of $LiBH_4$ to the bath improved the conductivity, but no change in the quality of the deposits was noted.

Magnesium Alloy Plating Baths

A study was made of the codeposition of Mg with Al, Be, Ti, and Zr. The electrodeposition of these metals or their Al alloys from organic solvents is described in one of the preceding papers (10).

TABLE I. *Electrolysis of ethereal solutions of Mg compounds*

Composition of bath	Mole ratio AlH_4^-/Mg^{++} or BH_4^-/Mg^{++}	Composition of deposit % by wt.		Remarks
		% Mg	% Al	
1. $MgBr_2$	—	60–70	—	Low conductivity
2. $MgBr_2$ in tetrahydrofuran	—	—	—	Black, powdery deposits
3. $MgBr_2$ + $LiBH_4$	0.25	90	—	Good, metallic deposit
4. $MgBr_2$ + $LiBH_4$	1.0	87	—	Smooth, bright deposit. Much treeing
5. $MgBr_2$ + $LiBH_4$	2.0	90	—	Smooth, bright deposit. 10% B
6. $Mg(BH_4)_2$	—	79	—	Addition of thiophene reduced treeing
7. C_2H_5MgBr (2.5M)	—	71	—	Very low conductivity
8. $MgBr_2$ + $LiAlH_4$	0.08	X*	1 to 10*	Brittle, white deposit
9. $MgBr_2$ + $LiAlH_4$	0.2	X*	1 to 10*	Fair, white deposit
10. $Mg(AlH_4)_2$	2.0	—	—	White, coherent deposit, solution unstable, finally yielding a gray powdery deposit
11. $MgBr_2$ + $LiAlH_4$ (in tetrahydrofuran)	0.7			Brittle, metallic deposit; cathode efficiency poor

* Spectrochemical analysis.
X Major constituent.

Mg-Al *Alloys.*—The simplest alloy bath studied was that formed by reacting $MgBr_2$ or $MgCl_2$ with $LiAlH_4$ in ether to form $Mg(AlH_4)_2$. The addition of small amounts of $LiAlH_4$ to ether solutions of $MgBr_2$ improved the electrodeposits (Nos. 8, 9, Table I) which by spectrochemical analysis were identified as alloys containing Mg as the main constituent and 1–10% Al.

A solution of $Mg(AlH_4)_2$ was prepared by using $LiAlH_4$ and $MgCl_2$ in the mole ratio of 2:1. Most of the LiCl precipitated. Electrolysis of a freshly prepared 1.7M ether solution of $Mg(AlH_4)_2$ yielded a white, coherent deposit. However, the solution was unstable and after being electrolyzed for a short period, yielded a dark gray powdery deposit which rapidly oxidized on exposure to the atmosphere (No. 10, Table I). In this respect these deposits were similar to those obtained from the $Mg(BH_4)_2$ baths.

The conductivity of the Grignard bath was increased by the addition of magnesium aluminum hydride etherate, and the deposits obtained were more coherent and more ductile than from the plain bath. However, these deposits were not so reflective, coherent, or metallic as those obtained from the $MgBr_2$-$LiBH_4$ bath (No. 5, Table I).

Tetrahydrofuran was investigated as a possible solvent for use in Mg alloy plating baths. The coordination compound between $MgBr_2$ and tetrahydrofuran is a solid. At room temperature it had a low solubility in a solution

TABLE II. *Electrolytic studies for the electrodeposition of Mg alloys*

Exp.	Composition of ethereal baths	Mole ratio of constituents	Remarks
1 (*a*)	$AlCl_3 + LiAlH_4 + MgBr_2$	$Mg/AlCl_3$ = 1.5 to 2.5	Very good deposit; 96% Al, Mg absent.
(*b*)	Similar	Mg/Al = 2.7	Fair, brittle deposit; 97% Al, Mg absent.
(*c*)	Similar	Mg/Al = 5.1	Very poor deposit.
2 (*a*)	$AlBr_3 + LiAlH_4 + MgBr_2$	Mg/Al = 1.5	No deposit.
(*b*)	Similar	Mg/Al = 1.05	Fair deposit, gray-white.
(*c*)	Similar	Mg/Al = 0.8	Very good, ductile deposit; 93% Al, 7% Mg.
3	$AlCl_3 + Mg(AlH_4)_2 + MgBr_2$	—	Fair deposit.*
4	$Mg(AlH_4)_2 + MgBr_2$	Mg/AlH_4^- = 3 to 1.5	Fair, white deposit, Mg and Al present.
5	$Zr(BH_4)_4 + Mg(AlH_4)_2 + AlCl_3$	—	Stressed deposit, 10% Zr, remainder Al.*
6	$Ti(BH_4)_3 \cdot C_4H_8O_2 + Mg(AlH_4)_2 + MgBr_2$	—	Poor deposit; low conductivity of solution.*
7	$Ti(BH_4)_3 \cdot C_4H_8O_2 + Mg(AlH_4)_2 + AlCl_3$	—	Fair Al deposit with trace of Ti.
8	$TiBr_4 + Mg(BH_4)_2$ in tetrahydrofuran	—	Fair deposit, Ti absent.
9	$BeCl_2 + MgBr_2$	Mg/Be = 1.0	Precipitate of $MgCl_2$, poor Be deposit.
10	$BeBr_2 + MgBr_2$	Mg/Be = 1.0	Poor, dark powdery deposit.
11	$BeBr_2 + MgBr_2 + LiAlH_4$	$Mg/Be/AlH_4^-$ = 3/3/1	Poor, brittle deposit.
12	$Be(BH_4)_2 + MgBr_2$	Mg/Be = 1.2	Treed, gray deposit; 80% Mg, 3.5% Be at 1 amp/dm^2; no deposit at 0.13 or 5 amp/dm^2.
13	$Be(BH_4)_2 + Mg(AlH_4)_2$	Mg/Be = 1.0	Treed, crystalline magnesium deposit.

* Mg anode used.

of $LiAlH_4$ in tetrahydrofuran, but dissolved completely at about 45°C. On electrolysis a smooth, reflective, metallic deposit was obtained (No. 11, Table I), but the cathode current efficiency was low. On the basis of these data and previous observations not reported herein, ethyl ether has proved to be superior to tetrahydrofuran as a solvent for plating baths.

A modified Al plating bath (9) containing $AlCl_3$ or $AlBr_3$, $LiAlH_4$, and $MgBr_2$ was investigated. The stability of the bath and the composition of the electrodeposits were dependent on the Al halide chosen and the order in which the compounds were mixed. For example, if $AlCl_3$ in ether was added to an ethereal mixture of $MgBr_2$ and $LiAlH_4$, a precipitate formed and the bath yielded poor electrodeposits. However, if $MgBr_2$ in ether was added to the hydride-aluminum plating bath, no precipitate formed and an aluminum deposit was obtained which, however, contained no Mg (No. 1, Table II). A modification of the Al bath (No. 2, Table II) containing $AlBr_3$, $MgBr_2$, and $LiAlH_4$ so as to give a Mg/Al ratio of approximately 0.8, yielded good alloy deposits on electrolysis. This bath required a short period of electrolysis before use. The hardness of this Mg-Al alloy containing 7% Mg and 93% Al was appreciably lower than that of typical electrodeposited Al. The hardness of one sample of the alloy was 21 Vickers compared with a hardness of 37–97 Vickers for 100% Al.

Alloys of Mg *with* Be, Ti, *or* Zr.—Those baths, from which the codeposition of Mg with Be, Ti, or Zr was attempted, are listed in Table II. The ethereal bath containing $Zr(BH_4)_4$ (No. 5) yielded Al alloys containing 10% Zr. The deposits were exfoliated and the bath unstable. A bath consisting of titanium (III)-borohydride tetrahydrofuranate, $Mg(AlH_4)_2$, and $MgBr_2$ had low conductivity and gave very poor deposits (No. 6). A fair deposit was obtained from a similar bath in which $AlCl_3$ was substituted for $MgBr_2$. The major constituent of the deposit was Al with traces of Ti (No. 7).

Tetrahydrofuran was used to prepare a bath containing $Mg(BH_4)_2$ and $TiBr_4$ (No. 8). The deposit obtained was comparable in appearance to that obtained from $Mg(BH_4)_2$ in ethyl ether. The deposit contained no Ti.

To prepare a plating bath for depositing Be-Mg alloys, ether solutions of beryllium chloride and magnesium bromide were mixed. A precipitate formed which was probably magnesium chloride (No. 9). However, ether solutions of beryllium bromide and magnesium bromide were miscible (No. 10). Electrolysis of the solution yielded inferior powdery deposits. The addition of $LiAlH_4$ slightly improved the deposit from this bath (No. 11).

An ethereal solution containing magnesium bromide and beryllium borohydride was a good conductor. The deposits (No. 12) obtained were treed and dull-gray. They contained 80% Mg and 3.5% Be. The remainder probably was nonmetallic matter occluded from the bath. Deposits oxidized readily in the air.

A precipitate formed when ethereal solutions of $Mg(AlH_4)_2$ and $Be(BH_4)_2$ were mixed. At a current density of 2.5 amp/dm^2 the filtered solution yielded a shiny, crystalline, treed deposit; at a current density of 1 amp/dm^2 no deposit was obtained.

None of the baths showed any promise for commercial plating of Mg alloys.

Preparation of Magnesium Compounds

Anhydrous magnesium bromide was prepared by reacting bromine vapor with molten magnesium metal at 800°C in the absence of air. The product was almost white in color and an 86% yield was obtained.

Anhydrous magnesium bromide was also prepared from magnesium metal and bromine in cooled ether according to the method of Rowley (12). The resulting magnesium bromide etherate was extracted with benzene and then the ether was removed under reduced pressure. This method was satisfactory only on a small scale (40–80 g) because of the volume of liquids involved. Yields of only 60–70% were obtained.

Wiberg and Bauer (11) reported the preparation of magnesium aluminum hydride in ether solution by the reaction of (*a*) magnesium bromide with lithium aluminum hydride or (*b*) magnesium hydride with aluminum chloride. No analysis of the product was given. The resulting solutions had a reducing power similar to lithium aluminum hydride.

Magnesium aluminum hydride was prepared according to the reaction:

$$MgCl_{2(s)} + 2LiAlH_4 \xrightarrow{Et_2O} Mg(AlH_4)_2 + \underline{2LiCl}$$

Solid magnesium chloride, which was prepared by passing hydrogen chloride through a Grignard reagent, was added to $LiAlH_4$ in ether. Lithium chloride precipitated immediately and was removed by filtering. The concentration of magnesium aluminum hydride in ether was 1.7M, as determined from hydrogen evolution upon hydrolysis. The product was left in an ether solution for convenience of use in plating baths.

Summary

1. The best magnesium deposit (approximately 90% Mg, 10% B) was obtained from a magnesium bromide-lithium borohydride ether bath. Thick deposits could not be built up.

2. Difficulties in operating a Grignard bath render it an impractical source of Mg. The addition of magnesium aluminum hydride or lithium borohydride improved the conductivity of the Grignard bath and the ductility of the Mg electrodeposits.

3. Electrodeposited alloys of Zr, Ti, or Be with Mg obtained from hydride or borohydride baths were generally stressed, treed, or powdery.

4. An alloy (7% Mg, 93% Al) was obtained from a solution containing magnesium bromide, aluminum bromide, and lithium aluminum hydride. The hardness of the deposit was appreciably lower than that of electrodeposited Al.

Manuscript received October 12, 1955. The work was sponsored by the Department of the Army, Office of the Chief of Ordnance, ORDTA.

Any discussion of this paper will appear in a Discussion Section to be published in the December 1957 JOURNAL.

REFERENCES

1. D. M. OVERCASH AND F. C. MATHERS, *Trans. Electrochem. Soc.*, **64**, 305 (1933).
2. T. P. DIRKSE AND H. T. BRISCOE, *Metal Ind. (N.Y.)*, **36**, 284 (1938).
3. P. JOLIBOIS, *Compt. rend.*, **155**, 353 (1912).
4. P. JOLIBOIS, *ibid.*, **156**, 712 (1913).
5. H. E. FRENCH AND M. DRANE, *J. Am. Chem. Soc.*, **52**, 4904 (1930).
6. N. W. KONDYREW AND D. P. MANOJEW, *Chem. Ber.*, **58**, 459, 464 (1925).
7. L. W. GADDUM AND H. E. FRENCH, *J. Am. Chem. Soc.*, **49**, 1295 (1927).
8. W. H. RODEBUSH AND J. M. PETERSON, *ibid.*, **51**, 638 (1929).
9. D. E. COUCH AND A. BRENNER, *This Journal*, **99**, 234 (1952).
10. A. BRENNER, *ibid.*, **103**, 652 (1956).
11. E. WIBERG AND R. BAUER, *Z. Naturforsch.*, **5b**, 397 (1950).
12. H. H. ROWLEY, *J. Am. Chem. Soc.*, **72**, 3305 (1950).

Effect of Crystal Disorder on the Electroluminescence of Zinc Sulfide Phosphors

A. H. MCKEAG AND E. G. STEWARD

Research Laboratories, The General Electric Company Ltd., Wembley, England

ABSTRACT

A blue electroluminescent ZnS phosphor was prepared by prefiring precipitated ZnS at a high temperature, activating with Cu, and refiring at about 700°C. The material was characterized by strong pale blue electroluminescence throughout the body of the crystal. The Cu entered most effectively at that temperature of refiring where the transformation from hexagonal to cubic structure occurred most readily. This transformation was associated with a process of one-dimensional disorder in the crystals, and it is suggested that for maximum electroluminescence brightness, fullest use must be made of the disorder process simultaneously with the entry of the activator.

The phosphors used by Destriau, in his work on electroluminescence (1), were distinguished from conventional ZnS phosphors by much higher Cu concentrations and by addition of ZnO to ZnS before firing. The effect of higher Cu concentrations in promoting electroluminescence has since been confirmed (2, 3), while the formation of "blue" or "green" emitting Cu centers has been shown to depend on the concentrations of Cu and Cl used in the prepara-

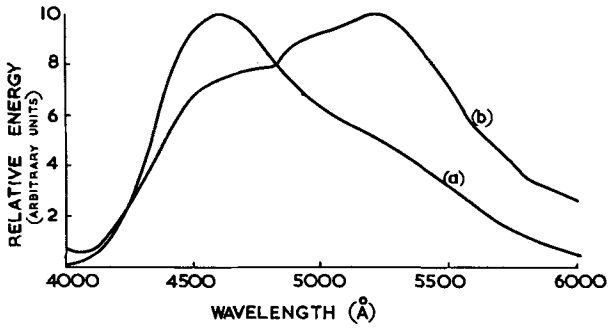

FIG. 1. Spectral energy curves of blue electroluminescent ZnS phosphor. (*a*) Electroluminescence (400 v 50 cycles); (*b*) u.v. excited (3650Å).

tion. Thus, high Cu and Cl contents favor formation of "green" rather than "blue" centers. Al may be used as a coactivator in place of Cl (3, 4) with similar effect. With still higher Cu contents, and in the absence of chloride, Froelich (5) showed that phosphors with yellow and red emission bands are obtained. While the crystal structure of the sulfides described by Homer and co-workers (2) was predominantly "cubic", those prepared by Zalm and co-workers (3) were described as "hexagonal" plates or needles.

Phosphors described in the present paper are characterized by a process which introduces, during preparation, an irregular stacking sequence of the (0001) layers of Zn-S tetrahedra in the wurtzite structure.

Both the wurtzite (hexagonal) and blende (cubic) forms of ZnS consist essentially of layers of Zn-S tetrahedra, and the two ways in which these layers can pack on top of one another lead to the two different structures. In the hexagonal structure the tetrahedral groups in each layer are rotated through 180° with respect to those in the preceding layer; this gives a 2-layer repeat unit. In the cubic structure, successive layers are simply "displaced" sideways, and the structure has a 3-layer repeat unit. Disordered stacking sequences (one-dimensional disorder) based on the above two stacking possibilities can occur, however. Where there is a specific periodicity in the disorder one has "polytypism" (6), but alternatively there can be a completely random stacking sequence (7).

The hexagonal ZnS structure is stable at high temperatures and the cubic structure is stable at low temperatures. It is known that firing temperature and cooling rate determine whether the structure of ZnS is hexagonal, cubic, or disordered (8). One-dimensional disorder is believed to be the mechanism of transformation from one structure to the other (9).

It is this disorder process which played an important role in the formation and constitution of the phosphors described in this paper.

PREPARATION

Precipitated ZnS of high purity was first prefired at 1100°–1300°C in a SiO_2 tube, closed at one end, with the open end projecting from the furnace and partially sealed with a tight glass wool plug. The plug allowed escape of volatile components present in the precipitate. NH_4Cl in the starting material acted as a flux and promoted marked crystal growth. The phosphor, which contained no Cu at this stage, and only a trace of chloride (*ca.* 0.01% by weight), showed a weak blue fluorescence under 3650Å radiation, and no electroluminescence. X-ray examination showed that this material had true hexagonal crystal structure.

$CuSO_4$ solution was added to give 0.1% (by weight) of Cu to the prefired ZnS. About 25% (by weight) of ZnO was also added, and this tended to improve the macroscopic uniformity of the product. After drying, the mixture was fired at 700°C for 15 hr in a SiO_2 tube, the open end of the tube being closed on this occasion with a Bunsen valve attachment to prevent ingress of air. The Bunsen valve maintained a static atmosphere during the long heating period and prevented air from diffusing back and causing excessive oxidation of the ZnS. In both the prefiring and refiring stages some SO_2 was probably present in the atmosphere. Such conditions, as shown by Froelich (4), would favor blue rather than red emission in the sulfides produced. The fired powder, which had a dark gray body color, was washed in dilute acetic acid followed by KCN to remove free ZnO and superficial Cu compounds, respectively. The powder then had a pale buff-gray body color, with a bluish white fluorescence under 3650Å radiation. It had a strong pale blue electroluminescence comparable in brightness to standard green electroluminescent samples prepared by conventional methods (10).

Fig. 1(*a*) shows the spectral energy distribution of the electroluminescence. There is a peak in the blue at about 4600Å. It is interesting to note that Bube (11) gave a figure of 4500Å for the peak in self-activated phosphors having hexagonal structure and 4700Å for the cubic form. The corresponding curve (*b*) for the same phosphor excited by long u.v. radiation gives evidence of a similar blue band, although the predominant emission band is now in the green region at about 5200Å.

Examination under the polarizing microscope showed that a high proportion of the material consisted of relatively weakly birefringent crystals together with a small proportion showing strong birefringence. There was no possibility of confusion arising from the presence of free ZnO, since x-ray examination confirmed that the acid treatment to remove free oxide had been effective. However, since the material appeared to consist of a mixture of two phases, attempts were made to separate these in order to study separately the properties of each. Even if one phase consisted of cubic and the other of hexagonal ZnS, densities would only differ by ½%, but it was found that by using a "panning" technique commonly employed in mineral dressing laboratories, a partial separation could be made. Strong electroluminescence was found to be associated with the relatively nonbirefringent material and weak electroluminescence with the markedly birefringent material.

The following is a simplified description of the "panning" operation used. The powder sample was placed on an inclined trough which, at short intervals, was bumped in such a way as to move the powder particles up the incline. A small flow of water in the opposite direction tended to wash down the incline the lighter particles which worked their way to the surface. In this manner, particles of only slightly differing densities could be separated.

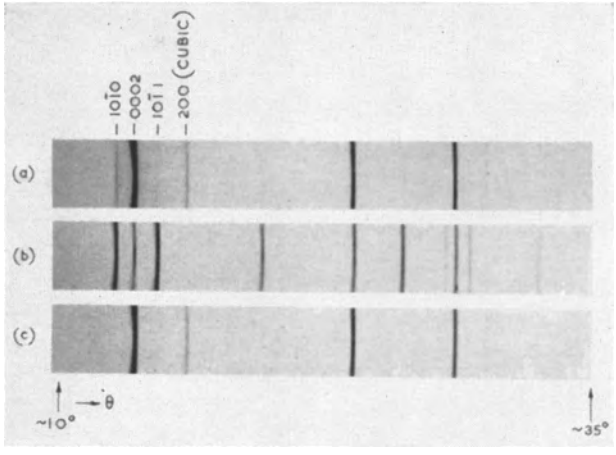

FIG. 2. X-ray powder diffraction patterns of ZnS. (*a*) Blue electroluminescent ZnS (refired at 700°C); (*b*) hexagonal ZnS; (*c*) cubic ZnS.

X-ray examination showed that the crystal structure of the more birefringent constituent was hexagonal but with considerable stacking disorder. In the relatively non-birefringent material, which was the most strongly electroluminescent, transformation to cubic structure through the mechanism of disorder was found to be more advanced.

Part of the x-ray powder diffraction pattern given by this material is shown in Fig. 2 together, for comparison purposes, with the patterns for normal hexagonal and cubic ZnS. The diffuseness and lowered intensity of, for example, the 10$\bar{1}$1 reflection compared with the 10$\bar{1}$0 reflection indicates the disordered condition of the hexagonal structure while the enhanced 0002 reflection and the presence of the cubic 200 reflection indicate the conversion of a large part of the material to cubic stacking (12).

EFFECT OF VARIABLES IN PREPARATION

Firing treatments.—The phosphors described in this paper are distinguished from more conventional electroluminescent powder phosphors by the pronounced volume as opposed to surface electroluminescence, which they exhibit (13).

The effect of different firing schedules on the electroluminescent properties was studied, and it was found that the temperature of prefiring, although not critical, should be above 1100°C. Best results were obtained at a prefiring temperature of about 1250°C and the product at this stage was essentially of true hexagonal crystal structure. The effect of different refiring temperatures (for a constant firing time of 15 hr) on the electroluminescent brightness is shown in Fig. 3(*a*). An optimum effect at about 700°C is indicated with a rapid decline in brightness at high temperatures. All samples after refiring were allowed to cool to room temperature in approximately ½ hr.

Optical and x-ray examination of the samples refired at the higher and the lower temperatures showed, as would be expected, that the crystal structure was little changed. Refiring at the intermediate temperatures (600°–900°C), however, introduced considerable one-dimensional stacking disorder into the hexagonal crystal structure with partial transformation toward cubic stacking. The constitution of a preparation refired at 700°C for 15 hr and cooled to room temperature in ½ hr has already been described. X-ray and optical examination show that this member of the series, which gives maximum brightness, showed the most advanced transformation by this disordering process toward cubic structure [cf. Hedvall effect (14)]. There are indications that disorder introduced by grinding (15) may act in a similar manner.

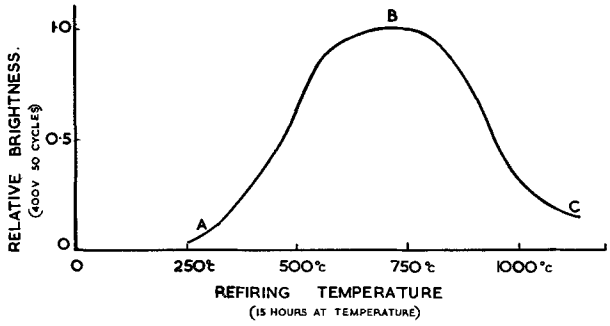

FIG. 3(*a*). Effect of refiring temperature on brightness of electroluminescence.

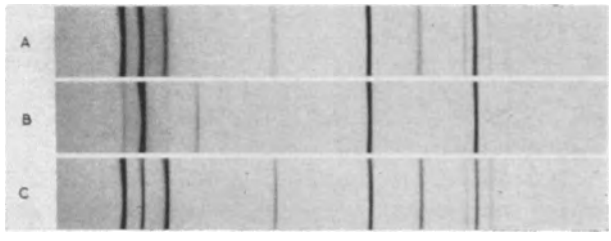

FIG. 3(*b*). X-ray diffraction patterns corresponding to points A, B, and C of Fig. 3(*a*).

In Fig. 3(*b*) parts of the x-ray diffraction patterns are shown for three members of the series corresponding to points A, B, and C on the brightness curve.

Short, Steward, and Tomlinson (16) reported that activated single crystals of ZnS showed strong electroluminescence occurring as parallel streaks in a manner similar to that reported by Diemer (17). These streaks were parallel to, and associated with, stacking disorder of the hexagonal (0001) planes (16). However, luminescence under 3650Å radiation in these crystals was uniform and diffuse, indicating as one would expect that Cu had diffused uniformly throughout the crystal during the activation heat treatment. The restriction of the electroluminescence to disorder boundaries suggested, therefore, that where activator centers are associated with disorder boundaries, conditions are most favorable for electroluminescence.

The present observations showed that actual maximum brightness of electroluminescence in the powders described, was associated with the most advanced transformation to cubic through a process of disorder.

If the preliminary high temperature prefiring treatment was omitted and phosphors were prepared in the lower temperature range (700°–900°C), the product remained in essentially a cubic form without any intermediate disordered states; predominantly surface green or blue electroluminescence was produced, depending on the relative proportions of Cu and chloride present (2, 3). With low

chloride contents, phosphors were obtained with a more saturated blue electroluminescence color than those which were prefired. The electroluminescent brightness of these phosphors, even in the blue, was appreciably lower than that produced by the "disorder" treatment, and though exhibiting bright uniform u.v. luminescence throughout the crystal, unlike the latter, they showed no appreciable volume electroluminescence.

For volume electroluminescence, therefore, it would appear that Cu necessary for electroluminescence should enter the lattice while the structure is experiencing disorder; however, u.v. fluorescence following entry of Cu throughout the body of the crystal was not dependent on this process. These results support the view (4, 18, 19) that, in addition to the electroluminescent phosphor particles containing Cu in solid solution (and this produces the normal u.v. fluorescence), Cu in some other association was also present. The function of the disorder treatment therefore may be to introduce this other special environment into the body of the crystal.

Cooling range.—To investigate the effect of temperature and cooling rate on incorporation of the activator, the following experiments were carried out:

(*A*) With a refiring temperature of 1250°C (after addition of Cu) only very weak electroluminescence resulted [see Fig. 3(*a*)].

(*B*) Cu was added to prefired ZnS (0.1% by weight), and five separate boats containing this material were heated to 1250°C. The furnace was then allowed to cool at approximately 120°C/hr to 500°C. Boats were removed successively at 1140°, 1000°, 700°, and 500°C, and were then cooled quickly; the fifth boat remained in the furnace until it reached 50°C; the total time taken for the fifth sample was 22 hr. All samples showed enhanced body color and only a very weak blue electroluminescence.

(*C*) Experiment (*B*) was repeated, but with refiring commencing at 950°C. With the same slow cooling, boats were withdrawn at 750°, 500°, and 50°C. These showed a strong pale blue electroluminescence with a slight increase in brightness with the longer cooling times.

These experiments again suggest that introduction of the activator into the lattice to provide electroluminescence centers needs the simultaneous formation of disorder in the structure.

Effect of Cu *concentration.*—Phosphors prepared by the method described, showed an optimum brightness with about 0.1% by weight of Cu added to the fired ZnS. With larger amounts, the color of electroluminescence tended to become slightly greener. As the amount was reduced the brightness fell off slowly, and with 0.01% Cu (equivalent to 1.6×10^{-4} g atoms Cu added to 1 g-mole ZnS), a moderately bright electroluminescent phosphor of a somewhat more saturated blue color was obtained. If a further reduction in Cu content to about half this quantity was made, a remarkable change in luminescent properties occurred. The color under long u.v. excitation changed from pale blue to bright green, while the afterglow changed to that of a normal Cu-activated green ZnS phosphor. However, the electroluminescence was negligible. Results of varying Cu concentration agree closely with those of Riehl and Ortmann (20) who prepared phosphors by a similar technique for u.v. excitation.

Summary and Conclusions

A new method of preparing a blue electroluminescent ZnS phosphor consists of prefiring precipitated ZnS at a high temperature, followed by activation with Cu and refiring at *ca.* 700°C. The material was characterized by strong pale blue electroluminescence throughout the body of the crystal in contrast to surface electroluminescence normally obtained (3).

Properties of these phosphors appeared to be related to the mechanism of activation. The copper necessary for electroluminescence entered most effectively at the refiring stage which was the temperature where transformation from hexagonal to cubic structure occurred most readily. This transformation was associated with the process of one-dimensional disorder, and observations reported elsewhere (16) showed the correlation between electroluminescence and disorder. For maximum electroluminescence brightness, fullest use must be made of the disorder process simultaneously with the entry of the activator. As would be expected, therefore, the optimum refiring temperature was in the region of 700°C.

Ultraviolet fluorescence following entry of the Cu throughout the body of the crystal is not, however, dependent on the disorder process. The results support the view (4, 18, 19) that in addition to the electroluminescent phosphor particles containing Cu in solid solution (and this produces the normal u.v. fluorescence), Cu in some other association is also present. Froelich (4), for example, suggested that an "oxide" phase can provide barriers "which are distributed in extreme subdivision in or on the phosphor particles and in close physical contact with them." The function of the disorder treatment may be to introduce this other special environment into the body of the crystal.

Manuscript received on March 12, 1956. This paper was prepared for delivery before the San Francisco Meeting, April 29 to May 3, 1956.

Any discussion of this paper will appear in a Discussion Section to be published in the December 1957 JOURNAL.

REFERENCES

1. G. Destriau, *Phil. Mag.*, **28,** 700, 774 (1947).
2. H. H. Homer, R. M. Rulon, and K. H. Butler, *This Journal*, **100,** 566 (1953).
3. P. Zalm, G. Diemer, and H. A. Klasens, *Philips Research Repts.*, **9,** 81 (1954).
4. H. C. Froelich, *This Journal*, **100,** 496 (1953).
5. H. C. Froelich, *ibid.*, 280.
6. L. W. Strock and V. A. Brophy, *Am. Mineralogist*, **40,** 94 (1955).
7. H. Jagodzinski, *Acta Cryst.*, **2,** 201, 208, 298 (1949).
8. A. Kremheller, *Sylvania Technologist*, **8,** 11 (1955).
9. L. W. Strock, *ibid.*, 71.
10. B. E. Hunt and A. H. McKeag, Brit. Prov. Patent Appln. 19242/53.
11. R. H. Bube, *J. Chem. Phys.*, **20,** 708 (1952).
12. M. A. Short and E. G. Steward, *Acta Cryst.*, **8,** 733 (1955).
13. T. B. Tomlinson, Private communication.

14. J. A. Hedvall, "Einführung in die Festkorperchemie," Vieweg, Brunswick (1952).
15. A. H. McKeag and E. G. Steward, Unpublished work.
16. M. A. Short, E. G. Steward, and T. B. Tomlinson, *Nature*, **177**, 240 (1956).
17. G. Diemer, *Philips Research Repts.*, **10**, 194 (1955).
18. K. H. Butler and J. F. Waymouth, *Brit. J. Appl. Phys.*, Suppl., No. 4, S33 (1955).
19. W. Lehmann, Bull. Am. Phys. Soc. Meeting, March 15, (1956).
20. N. Riehl and G. Ortmann, *Doklady Akad. Nauk S.S.S.R.*, **66**, 613 (1949).

Contact Electroluminescence

Willi Lehmann

Lamp Division, Westinghouse Electric Corporation, Bloomfield, New Jersey

ABSTRACT

Many powdered crystal phosphors which are normally nonelectroluminescent become electroluminescent if they are simply mechanically mixed with suitable powdered metals, or with some nonmetals of good electrical conductivity. The conclusion is drawn, and supported by many facts, that ordinary electroluminescence in powdered phosphors excited by an alternating electric field (Destriau effect) is also due to substances of relatively high conductivity incorporated as small segregations within the essentially insulating phosphor particles. The electric field near sharp edges of these "contact substance" particles is considerably higher than the average electric field across the phosphor crystals. Preconditions for the electroluminescent excitation process are fulfilled in these localized regions of high field strength.

Up to the present, the well-known excitation of powdered phosphors by alternating electric fields (intrinsic electroluminescence or Destriau effect) was limited to a comparatively small group of phosphors, mainly of the ZnS type. Even with these materials, a good result was possible only if the phosphor was prepared under special conditions different from those conditions which give the brightest photoluminescent phosphor. Several questions naturally arise. Why are these special preparative conditions necessary? What is the essential difference between an electroluminescent ZnS phosphor and another which is only photoluminescent? Why are not all phosphors, or at least all zinc sulfides, able to electroluminesce?

This paper gives details about a phenomenon which the author calls "contact electroluminescence." The similarity of this contact electroluminescence to ordinary electroluminescence is so clear that it is likely that ordinary electroluminescence in powdered phosphors (Destriau effect) is caused, or at least strongly favored, by the presence of a second substance in addition to the phosphor itself. Although the conclusion as to the necessity of a second substance in electroluminescent phosphors is not new, the experiment described here seems capable of throwing new light on the action between the phosphor and the second substance.

Experiments on Contact Electroluminescence

Powdered phosphors which are unable to electroluminesce under the usual conditions in a strong alternating electric field have been mixed mechanically with metal powders (ratio of phosphor to metal about 4:1 to 1:1 by weight). This mixture, with castor oil as the embedding dielectric, was placed in a normal plaque cell consisting of a front electrode of conducting glass overcoated with a thin, transparent, insulating film and a back electrode of Al (Fig. 1). When an alternating voltage was applied to this cell, the mixture of phosphor and metal was electroluminescent.

This behavior becomes most distinct in the arrangement shown in Fig. 2. Here part A of the cell area containing only metal powder in castor oil is, of course, not luminescent at all. Part B containing only phosphor powder in oil is, although photoluminescent, not electroluminescent. However, the intermediate region AB, containing both phosphor and metal, is electroluminescent.

The great variety of phosphors which are able to show this contact electroluminescence is remarkable. A qualitative survey of some results obtained with mixtures of various phosphors with metal powder is given in Table I for an applied sinusoidal voltage of 600 v rms and a frequency of 10,000 cps. The embedding dielectric material here was castor oil; similar results are obtained, however, with other organic dielectric materials or even with air as the embedding material. The emission color of some phosphors is different for photo- and for electroluminescence, indicating that the phosphors have really been excited by electroluminescence and not by u.v. radiation generated by a glow discharge in the cell. No direct correlation could be found between the nature of the phosphor and its ability to be excited by contact electroluminescence, but, in addition to the general type of the material, the crystallinity, the activator concentration (if activators are necessary), and other properties may also have an influence. No contact electroluminescence could be observed under the conditions described in CaO-U, CaF_2-U, $ZnAl_2O_4$-Mn, $CaWO_4$, ZnF_2-Mn, and some other phosphors. Cal-

cium halophosphates and magnesium fluorogermanates were somewhat erratic; some samples showed a very weak contact electroluminescence, while other samples did not.

The contact electroluminescence of a mechanical mixture of a phosphor with a metal powder in an electroluminescent cell is not uniform; emission is confined to many localized spots randomly distributed over the cell area. Observation reveals that all those phosphor particles luminesce which, either accidentally or due to electrostatic forces caused by the strong field, are in intimate contact with a metal particle. Two photographs of this distinctly nonuniform emission are shown in Fig. 3. The brightness of a single spot may be comparable with that of an ordinary electroluminescent phosphor, but the over-all emission intensity is much lower.

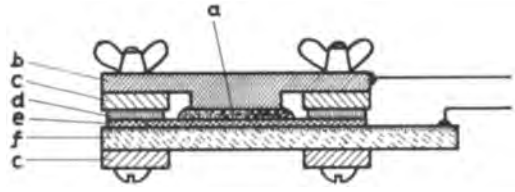

FIG. 1. Cross section of the electroluminescent cell used: a = phosphor and/or metal powder in castor oil; b = aluminum; c = Lucite; d = spacer; thickness about 100μ; e = insulating transparent film, thickness about 12μ; f = conducting glass.

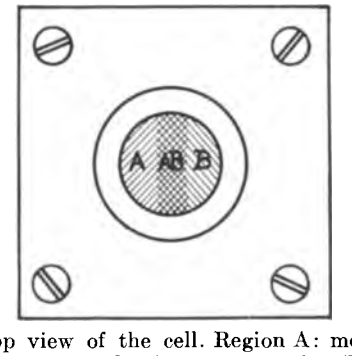

FIG. 2. Top view of the cell. Region A: metal powder alone in castor oil, no luminescence; region B: phosphor powder alone in castor oil, no electroluminescence; region AB: mixture of metal and phosphor powder in castor oil, electroluminescence.

The dependence of the over-all emission intensity (sum of emission of all individual spots) on the applied voltage and frequency is the same as for an ordinary electroluminescent phosphor. As an example, the dependence of the over-all brightness L on the applied voltage V can, for contact electroluminescence as well, be closely approximated by the equation (1)

$$L = A \exp [-B/(V + V_0)] \qquad (I)$$

with A, B, and V_0 as constants (Fig. 4). Other equations proposed to describe the dependence of ordinary electroluminescence on the voltage are also applicable.

The dependence of the brightness of a single spot on the applied voltage has been measured through a microscope and by use of a visual photometric method. In almost all cases this dependence can also be described by (I) or by any of the proposed equations for $L(V)$ of ordinary electroluminescence, although the constants in these equations [e.g., A, B, and V_0 in (I)] differ from spot to spot. In some cases, however, dependence of the spot brightness on the applied voltage could not be described by any of these equations, but here the simple equation

$$L = A \exp (-B/V) \qquad (II)$$

gave a good fit. An example is shown in Fig. 5.

During the first experiments with contact electroluminescence the most striking fact was that not all metal powders tested were effective as contact substances. Efforts to correlate this ability or nonability to other properties of the metals, e.g., to the electronic work function, were without success. However, the metal powders were examined microscopically; all with definitely rounded particle shape were not effective as contact substances, while those powders having particles with sharp edges were (Fig. 6). Different metals, e.g., Mn, Fe, Al, Cu, etc., with

TABLE I. *Photoluminescent and electroluminescent emission of various phosphors*

Phosphor	Photoluminescence		Electroluminescence	
	2537Å	3650Å	Pure phosphor	Mixed with metal powder
ZnS-Cu (0.03%)	br green	br green	—	m blue
ZnS-Cu (0.1%)	br blue green	br blue green	m blue	br blue
ZnS-Cu (0.01%)	br green	br green	—	m green
ZnS-Ag (0.03%)	br blue	br blue	—	br blue
ZnS-Mn (1%)	m yellow	br yellow	—	br yellow
(ZnCd)S-Cu	br yellow	br yellow	—	w green
(ZnCd)S-Ag	br yellow	br yellow	—	br yellowgreen
CaS-Bi	m blue	m blue	—	w blue
(CaSr)S-Bi	m blue	m blue	—	w blue
Zn_2SiO_4-Mn	br green	vw green	—	br green
Zn_3GeO_5-Mn	br green	—	—	m green
$CaWO_4$-Pb	br white	—	—	vw blue
$Cd_2B_2O_5$	br red	w red	—	vw red
Cd_2SiO_4-U-Sm	br pink	w brown	—	w green
$CaPO_4$-Tl	br white	br white	—	m white
$UO_2(NO_3)_2 \cdot 6H_2O$	br green	br green	—	w green
Anthracene	br blue	br blue	—	w blue

Intensities: br = bright, m = moderate, w = weak, vw = very weak

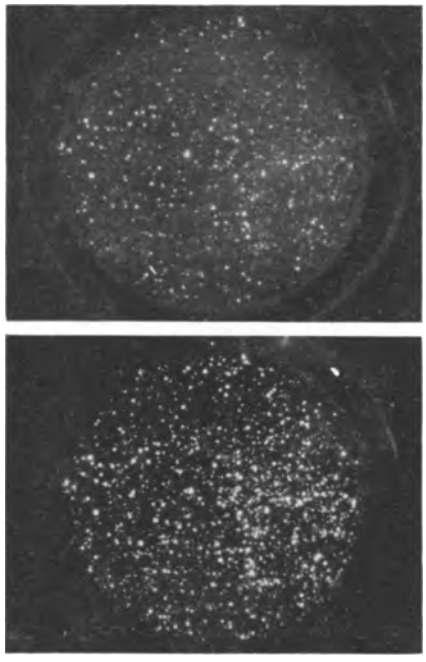

FIG. 3. Nonuniform distribution of the emission of contact electroluminescence over the cell area. Phosphor: green emitting Zn_2SiO_4-Mn (normally not electroluminescent); contact substance: Cu metal powder; frequency: 10,000 cps; voltage: above, 400 v rms; below, 600 v rms.

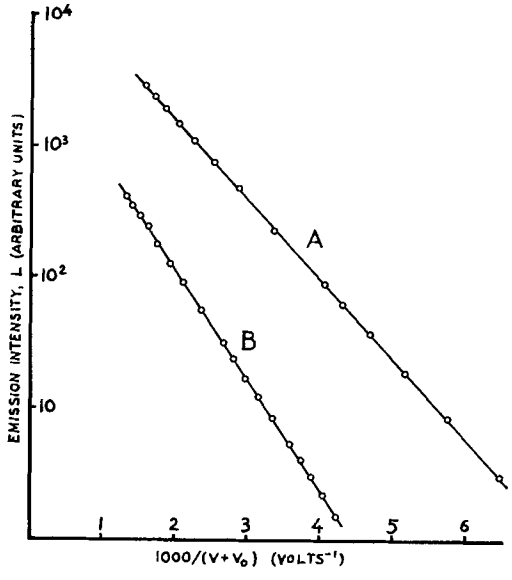

FIG. 4. Dependence of the over-all brightness, L, on the applied voltage, V. Curve A: ordinary electroluminescence of ZnS-Cu(0.3%), Cl, (V_o = 55 v); curve B: contact electroluminescence of ZnS-Mn in mixture with Mn-metal powder, (V_o = 180 v); frequency in both cases: 10,000 cps.

roughly similar particle size and shape gave about the same effect. In addition it was found that some nonmetallic powdered substances, such as Cu_2S, Ag_2S, or fired ZnO, also acted as contact substances.

These experiments gave strong evidence that the contact substance particles acted mainly by creating regions of high electric field strength in the immediate neighborhood of their sharp edges. For this purpose it was only

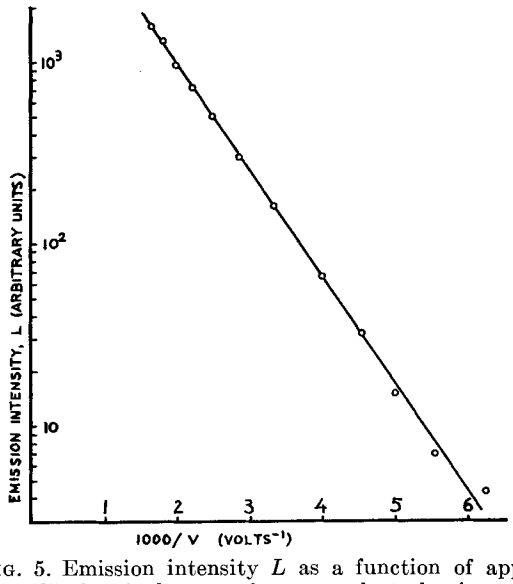

FIG. 5. Emission intensity L as a function of applied voltage V of a single spot of contact electroluminescence, following the law $L = A \exp(-B/V)$. Phosphor: green emitting Zn_2SiO_4-Mn; contact substance: CuS powder; frequency: 20,000 cps.

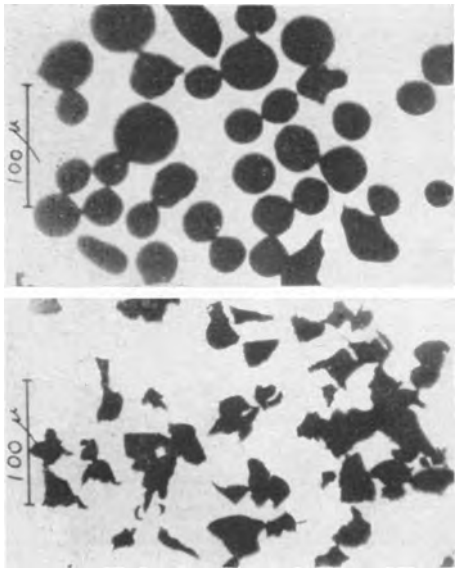

FIG. 6. Two samples of copper metal powder tested as contact substance in contact electroluminescence. Above: this Cu powder was not able to act effectively as contact substance; below: this copper powder was able to act as a good contact substance.

necessary that the particles have suitable geometrical size and shape (sharp edges) and a certain electric conductivity; all their other chemical and physical properties seem to be unimportant for this kind of electroluminescence.

CONSIDERATIONS ON THE STRUCTURE OF ELECTROLUMINESCENT ZINC SULFIDES

The close agreement of the dependence of the over-all emission intensity on voltage and frequency for contact electroluminescence and for ordinary electroluminescence suggested strongly that the emission of an ordinary electroluminescent ZnS was also caused, or at least favored, by

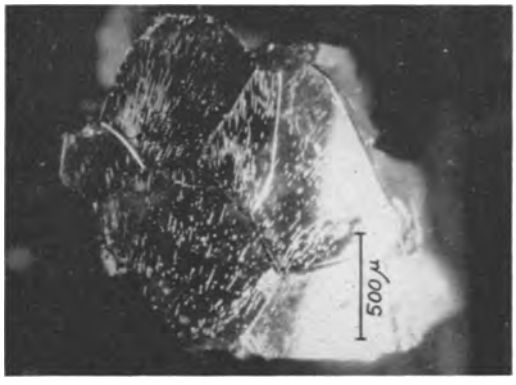

FIG. 7. Needlelike dislocations in a CdS crystallite, observed in sharply reflected light.

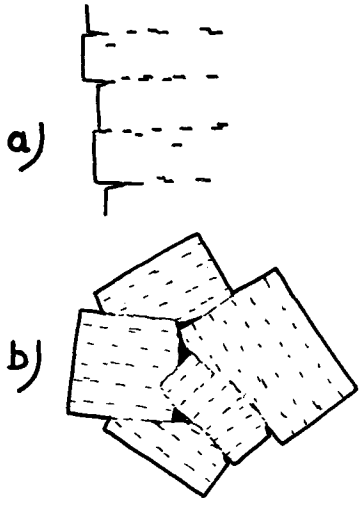

FIG. 8. Structure of a real single crystal (a) and a real polycrystal (b) containing a nonisomorphous second substance (schematic).

the presence of a suitable second substance in intimate contact with the phosphor crystals. This contact substance in electroluminescent zinc sulfides may be ZnO or Cu_2S or, in special cases, other materials. The general assumption that in an electroluminescent phosphor a second substance must be present has already been made (2–6). This assumption is supported not only by the phenomenon of contact electroluminescence described here, but also by the usual methods of preparing efficient electroluminescent zinc sulfides which have been empirically developed. A typical example, in which ZnO is the contact substance, is considered in detail.

Destriau (7) originally prepared his first efficient electroluminescent phosphors by firing a mixture of ZnS with ZnO. The activator concentration of this type of phosphor may be relatively low (about 0.01–0.1% Cu), but the amount of ZnO has to be considerably higher (up to 75% of the phosphor and even more). Later on, this preparative technique was used by others (8, 9), who used mostly about 25% ZnO. Similar phosphors are obtainable if a ZnS phosphor is fired (or refired) under oxidizing conditions, e.g., in air (6, 10); these phosphors, too, must contain high percentages of ZnO after the firing process.

The solubility of ZnO in ZnS has been examined by Kröger and Dikhoff (11). In contrast to the ZnS-ZnSe or ZnS-CdS systems, ZnS-ZnO does not form mixed crystals over the whole concentration range under the usual conditions; e.g., after firing at 1200°C ZnO is dissolved into ZnS only to the extent of about 1%. If, therefore, the complete phosphor contains more than this amount of oxide, the excess must remain undissolved.

It is know that real crystals of all substances are never free from defects. Even the best single crystal contains disorders, dislocations, and cavities, which are often geometrically arranged in parallel layered structure (12–18), for reasons still unknown. Such parallel layered, needlelike dislocations could be photographed directly by the author in a CdS crystallite using sharply reflected light (Fig. 7). It is generally assumed, and in some cases it can be stated definitely (14, 15, 17), that these small cavities (holes in the crystal structure) contain undissolved contaminations of nonisomorphous foreign substances if these are present. This situation is shown schematically in Fig. 8*a*. The geometrical dimension of a cavity containing undissolved contaminations depends on the kind of crystal and its crystallization conditions and may be very small, down to the order of 10^{-5} to 10^{-7} cm. In addition to these segregations present even in single crystallites, polycrystals have larger spaces between their individual crystallites which also may contain nonisomorphous second substances, if present (15) (Fig. 8*b*). This tendency of insoluble contaminations to segregate in dislocations and holes within the real crystal has been shown especially for ZnS crystals by Diemer (14). Each ZnS single crystal or polycrystal must contain unavoidable dislocations, holes, and cracks, and, if the crystal was prepared in the presence of oxygen, either intentionally or accidentally, these holes and cracks must contain more or less undissolved zinc oxide.

The electrical conductivities of the two substances ZnS and ZnO have considerable influence on electroluminescence. Fired ZnS is known to be a relatively poor conductor, while fired ZnO has a much higher conductivity. Thus, when so much ZnO is present that each phosphor particle is practically surrounded by ZnO, ZnS crystals are largely electrically shunted and can hardly be excited by an external electric field. It is usual, therefore, to wash these phosphors in a weak acid solution (such as acetic acid) which dissolves ZnO without attacking the ZnS crystals too much (8, 9). However, only ZnO on the surfaces of ZnS crystals can be dissolved in this way; ZnO segregated inside the ZnS crystals is retained. The conclusion must be drawn, therefore, that this type of electroluminescent ZnS, washed or unwashed, always contains small segregations of ZnO incorporated inside the larger ZnS crystals.

Another efficient type of electroluminescent ZnS can be prepared without any ZnO but by introduction of a relatively high amount of Cu (of the order of 0.5–1%) and use of such firing conditions that not all of the Cu is built into the lattice as an activator (6, 19). It must be assumed in this case that the phosphor after firing contains large amounts of copper sulfide (probably Cu_2S). Since copper sulfide is also nonisomorphous with ZnS, similar conclusions as for the case of ZnO show that this type of

electroluminescent ZnS must contain copper sulfide as contact substance segregated in dislocations, holes, and cracks inside the ZnS crystals. Other electroluminescent zinc sulfides can be prepared with other contact substances, such as PbS (20, 21), or several contact substances at once, such as ZnO and Cu_2S (22, 23). Since early preparations of electroluminescent phosphors were guided mostly by empirical intuition rather than by logical conclusions, in many cases it is not easily possible to decide which contact substance is present in a particular phosphor, because no attention has been given to this point.

Electric Field Inside Electroluminescent Phosphor Particles

The presence in the crystals of a ZnS phosphor of segregated particles of a contact substance of higher electrical conductivity and irregular shape necessarily causes a strong nonuniformity of the electric field inside the phosphor particles when these are subjected to an external field. This strong nonuniformity of the internal electric field must be present even in the case where no special potential barriers, e.g., chemical or exhaustion barriers, exist between the bulk of the ZnS crystal and the contact substance. This statement should not be taken as a conclusion that no exhaustion or other type of barriers are present in an electroluminescent phosphor. However, it is believed, and supported by the experiments of contact electroluminescence described, that these barriers are outweighed by the local field distortions which are caused by the simple presence of contact substance segregations of higher conductivity. Since in electroluminescence the phosphor is excited by the electric field, it is evident that this nonuniformity of the field must play an important role. An estimate of the nonuniformity of the field caused only by the presence of segregated, better conducting, contact substances is made below, neglecting the influence of any barriers, in order to obtain rough but quantitative data. Consideration is limited to zinc sulfides and related phosphors since the electrical and electroluminescent properties of this class of phosphors are relatively well known. However, these considerations can be extended to other groups of phosphors if they have roughly similar properties.

When an external alternating field is applied to the phosphor, internal field conditions are greatly influenced by the relaxation times of phosphor bulk and contact substance and by the applied frequency. Elementary electrodynamics gives the relaxation time of a homogenous substance as

$$\tau = \frac{1}{4\pi \times 9 \times 10^{11}} \frac{k}{\sigma} \text{ (sec)} \qquad \text{III}$$

where k is the real dielectric constant and σ the conductivity measured in $(\text{ohm-cm})^{-1}$. In general, the resulting equations for a nonhomogenous material are rather complicated even under simplifying assumptions (24, 25). The situation is simpler, however, when the relaxation time of the material considered is not of the order of the reciprocal frequency $1/f$. In the case of $\tau \ll 1/f$ any small field induced inside the substance vanishes within this very short time τ and, therefore, practically no field is possible inside an insulated particle of this substance. But if $\tau \gg 1/f$, then the influence of conductivity can be neglected and the behavior of the substance insofar as the field distribution is concerned is practically that of an insulator. These facts are well known, but they shall now be applied to electroluminescent ZnS phosphors.

Consider first the phosphor crystal itself. The real dielectric constant of ZnS is known to be roughly of the order of $k = 10$ (26). The conductivity is less exactly known and it may vary from sample to sample depending mainly on the purity of the crystals. However, in general, ZnS phosphors are known to have a relatively low conductivity and values of the order of 10^{-2} to 10^{-15} $(\text{ohm-cm})^{-1}$ have frequently been measured (14, 27, 28). Introducing these values for k and σ into (III) one obtains a relaxation time for the pure phosphor crystal itself of the order of 1–1000 sec. This is a much longer time than the reciprocal of the frequency usually applied to electroluminescent phosphors. The conclusion may be drawn, therefore, that the conductivity of the ZnS crystal itself normally has very little influence on the field condition inside the phosphor, and it is not too wrong, in a first approximation, to consider the ZnS crystal as an insulator.

The contact substance demonstrates the other extreme. Fired ZnO, as an example, has a rather high conductivity, up to the order of one $(\text{ohm-cm})^{-1}$ and more (5, 29–31). Also, black copper sulfide Cu_2S is a relatively good conductor. Exact values cannot be given since the conductivity of these typical semiconductors depends greatly on the impurity concentration, and also on the history of the material. But, since their dielectric constant in no case is very different from the order $k = 10$, Eq. (III) shows that the relaxation time of these substances is much shorter than the reciprocal frequency usually applied to electroluminescent phosphors. Under these conditions, therefore, an electric field practically cannot exist inside the relatively highly conducting contact substances and their electric behavior inside the phosphor particles is nearly that of metals.

Now consider the somewhat idealized case of a contact substance particle with infinitely good conductivity surrounded by an ideally insulating phosphor crystal. If an average electric field F_0 is applied to this system, the highest local field F_{max} appears near edges of the conducting particle, and the ratio F_{max}/F_0 is of the order of R/r, where r is the radius of curvature of the edge and R the particle diameter.

The largest possible geometrical dimension of a contact substance particle in a ZnS phosphor may be of the order of 1μ. Much larger dimensions are hardly possible, since the embedding phosphor particles themselves normally have average diameters of the order of several microns. The smallest possible radius of curvature may be considered to be of the order of magnitude of the lattice constant of the crystalline material. Assuming, roughly, $R = 3 \times 10^{-4}$ cm and $r = 3 \times 10^{-8}$ cm as the most ideal cases, one obtains.

$$F_{max} = 10^4 F_0$$

as the highest possible field strength in the phosphor particles under the best conditions. Obviously, conditions for the highest possible field strength are only very sparsely

distributed throughout the phosphor, if at all. Most edges of the conducting segregations have less favorable conditions so that here the field may be increased only by lower factors, e.g., of the order of 10 to 10^3. Furthermore, all these regions of high fields must be limited to very small spaces near the sharp edges of the contact substance segregations, i.e., to "spots" inside the phosphor crystals. The field in much the largest part of the phosphor is only of the order of F_0, the average field applied to the phosphor.

Conclusions

The evidence outlined above for the presence in electroluminescent phosphors of localized "spots" of high electric field strength due to incorporated segregations of relatively highly conducting contact substances must necessarily be of the greatest significance for the electroluminescent excitation mechanism itself. Several conclusions can be drawn from this picture.

(*A*) Due to the nonuniform electric field, the local electroluminescent excitation and emission intensity must also be nonuniformly distributed throughout the phosphor crystals. This is in good agreement with published observations (6, 32). As a result of this nonuniformity of the local emission intensity β, the over-all emission intensity L of a given amount ν of an electroluminescent phosphor cannot be described by the simple product $L = \beta\nu$, but requires an integral

$$L = \int_0^{\nu} \beta \, d\nu$$

(*B*) The emission of an electroluminescent ZnS crystal should be limited to very small spots. These spots may be so closely arranged that they cannot be resolved microscopically and, therefore, a more or less uniform emission distribution may be simulated. However, the emitting spots have actually been observed already (14, 33, 34). A microscopic observation of these spots in phosphor powders with particles of irregular shape may not be possible due to the high index of refraction of ZnS.

(*C*) Experience shows that electroluminescence of powdered phosphors requires an average electric field strength of at least some 10^3 v/cm. It is hard, of course, to assume that such low fields should be able to produce any direct excitation of the phosphor and any reasonable mechanism requires higher fields. Local regions of higher fields are a consequence of the simple presence of better conducting contact substance segregations in the phosphor, e.g., ZnO or Cu_2S in ZnS phosphors. Near the edges of these contact substance segregations, the field may be higher by a factor of 10 to 10^3 or, in extreme cases, even more. It is thus easily possible to reach localized fields of the order of 10^6 v/cm or more.

(*D*) The electric field strength at any fixed point in the phosphor crystal must be proportional to the average electric field F_0 (i.e., to the applied voltage), as long as the preconditions for these considerations are given. Deviations from this proportionality between F and V are to be expected only where either the contact substance is no longer a nearly ideal conductor, i.e., at very high applied frequencies, or where the phosphor crystal is not a nearly ideal insulator, i.e., at very low frequencies or in localized regions of extreme field strength and excitation density. The influence of such deviations are not discussed.

(*E*) The presence of a second, better conducting substance segregated in small regions inside the phosphor crystals is one condition that a crystal phosphor be able to electroluminesce under the usual conditions. The phosphor crystals should themselves be relatively poor conductors. How far this requirement can be realized in any preparation technique is a matter of search; but when it is realized, probably many more types of phosphors other than the ZnS class can be made to exhibit a good Destriau effect. This conclusion has been drawn from experimental results of contact electroluminescence described here. It appears that this electroluminescence of a simple mixture of a phosphor powder with a metal powder can serve as a valuable tool in the search for new systems of electroluminescent phosphors.

Manuscript received February 24, 1956. Some of the material in this paper was presented at the American Physical Society Meeting in Pittsburgh, March 1956.

Any discussion of this paper will appear in a Discussion Section to be published in the December 1957 Journal.

REFERENCES

1. G. Destriau and H. F. Ivey, *Proc. I. R. E.*, **43**, 1911 (1955).
2. L. Burns, *This Journal*, **100**, 572 (1953).
3. K. H. Butler and J. F. Waymouth, *Brit. J. Appl. Phys.*, Suppl. No. 4, p. 37 (1955).
4. H. C. Froelich, *This Journal*, **100**, 496 (1953).
5. H. Gobrecht, D. Hahn, and F. W. Seemann, *Zeits. f. Phys.*, **140**, 432 (1955).
6. P. Zalm, G. Diemer, and H. A. Klasens, *Philips Research Repts.*, **9**, 81 (1954).
7. G. Destriau, *Phil. Mag.*, **38**, 700 (1947).
8. British Thomson-Houston Co., Ltd., Brit. Pat. 718,804 (1954).
9. General Electric Co., Brit. Pat. 733,352 (1955).
10. H. Gobrecht, D. Hahn, and H. E. Gumlich, *Z. Physik*, **136**, 612, 632 (1954).
11. F. A. Kröger and J. A. M. Dikhoff, *This Journal*, **99**, 144 (1952).
12. C. G. Darwin, *Phil. Mag.*, **43**, 800 (1922).
13. W. S. Dekeyser, S. Amelinck, E. Votana, and G. Vandermeersche, *ibid.*, **44**, 1142 (1953).
14. G. Diemer, *Philips Research Repts.*, **10**, 194 (1955).
15. E. Justi, "Leitfähigkeit und Leitungsmechanismus fester Stoffe," p. 317 f.f. Göttingen (1948).
16. A. Smekal, *Physik. Z.*, **32**, 581 (1931).
17. M. Straumanis, *Z. anorg. Chem.*, **180**, 1 (1929).
18. F. Zwicky, *Helv. Phys. Acta*, **16**, 211 (1930).
19. H. C. Froelich, *This Journal*, **100**, 280 (1953).
20. Sylvania Electric Products Inc., Brit. Pat. 731,365 (1955).
21. Sylvania Electric Products Inc., French Pat. 1,022,100 (1953).
22. H. H. Homer, R. M. Rulon, and K. H. Butler, *This Journal*, **100**, 566 (1953).
23. General Electric Co., Brit. Pat. 716,159 (1954).
24. D. C. A. Bruggeman, *Ann. Physik*, **24**, 636,645 (1935); *ibid.*, **25**, 645 (1936).
25. H. Fricke, *Phys. Rev.*, **24**, 575 (1924).
26. P. Lenard, "Handbuch d. Exp. Phys. XXIII, Teil 1" (1928).
27. R. E. Halsted and L. R. Koller, *Phys. Rev.*, **93**, 394 (1954).
28. R. E. Freund, *ibid.*, **100**, 760 (1955).
29. A. Fischer, *Z. Naturforsch.*, **8a**, 756 (1953).
30. E. E. Hahn, *J. Appl. Phys.*, **22**, 855 (1951).
31. E. Mollwo, *Z. Physik*, **138**, 478 (1954).
32. J. F. Waymouth and F. Bitter, *Phys. Rev.*, **95**, 941 (1954).
33. E. E. Loebner and H. Freund, *ibid.*, **98**, 1545 (1955).
34. D. R. Frankl, *ibid.*, **100**, 1105 (1955).

Preparation of Zirconium and Hafnium Metals by Bomb Reduction of Their Fluorides

O. N. Carlson, F. A. Schmidt, and H. A. Wilhelm

Institute for Atomic Research and Department of Chemistry, Iowa State College, Ames, Iowa

ABSTRACT

A bomb process for preparing Zr and Hf metals with Ca by the reduction of their tetrafluorides is described. A detailed method of preparing the high purity tetrafluorides is presented, and the purity and physical properties of the metals obtained are discussed.

Experiments on the preparation of Zr by bomb reductions of ZrF_4 have been described by Walsh (1), Peterson (2), and Lambert, *et al.* (3). These workers all employed the ZrF_4 reduction with Ca, but Walsh alone employed Zn in the process. In this paper the preparation of Zr and also of Hf metal by a process similar to that of Walsh is described in detail.

Zr and Hf metals are obtained in massive form as Zn alloys by the reduction of their tetrafluorides with Ca in the presence of Zn. The reaction, which is sufficiently exothermic to yield liquid products, is carried out in a sealed bomb. The dense alloy which is immiscible with the molten slag phase separates as a homogeneous liquid. The Zn may later be removed from the solidified alloy by heating in a vacuum, yielding a sponge of the residual metal. Subsequent melting in a vacuum or inert atmosphere yields pure Zr or Hf metal in massive form. Although Hf so prepared is somewhat brittle, high quality, ductile Zr can be obtained by this method.

Because of the importance of quality of the tetrafluorides to the success of this method, a detailed description is given for their preparation. In this investigation the greater amount of the research and development work was done with Zr. It was found that Hf parallels Zr quite closely in all processing steps, so less effort was required for this development.

The main properties which have been used here to evaluate the quality of Zr obtained were its hardness and ability to be cold rolled. Generally when the metal had a hardness of less than 50 Rockwell A, or 155 Brinell (3000 kg load), it was found to be readily fabricable by cold rolling. Since the effect of oxide impurity on cold fabricability of Zr is generally detrimental, successful preparation of ductile Zr metal depends largely on exclusion of oxygen from all materials and equipment used in processing.

Preparation of High Purity ZrF_4

Williams and Weaver (4) prepared anhydrous ZrF_4, free of significant amounts of oxygen by hydrofluorination of ZrO_2 at 500°C followed by vacuum sublimation of ZrF_4 at 650°C. Hydrated ZrF_4 may be prepared by the reaction of aqueous HF and $ZrOCl_2 \cdot 8H_2O$. This tetrafluoride may then be dehydrated in a stream of HF gas at elevated temperatures to yield anhydrous ZrF_4. In the work described here the latter process was employed for preparing the tetrafluoride.

$ZrOCl_2 \cdot 8H_2O$ was prepared from $ZrCl_4$ (Hf free).[1] The chloride was dissolved in distilled H_2O, and this solution was then evaporated to a concentration of approximately 6*N* in HCl, followed by cooling. Stirring the concentrated solution during cooling resulted in a deposit of crystalline $ZrOCl_2 \cdot 8H_2O$ from which the excess liquid was easily removed by filtration. These crystals were further purified of Fe by washing in acetone.

Aqueous HF (48–70%) was added to the solid $ZrOCl_2 \cdot 8H_2O$ resulting in the initial formation of a homogeneous liquid solution from which $ZrF_4 \cdot H_2O$ was precipitated on further addition of HF in accordance with the following reaction:

$$ZrOCl_2 \cdot 8H_2O + 4HF \rightarrow ZrF_4 \cdot H_2O \text{ (ppt)} + 2HCl \qquad \text{(I)}$$

The supernatant liquid was approximately 7*N* in HCl, in which the solubility of the monohydrate was quite low. Use of more dilute HF or aqueous solutions of $ZrOCl_2$ decreased the acid concentration of the supernatant liquid, and the yield of $ZrF_4 \cdot H_2O$ crystals decreased. Addition of excess HF to the reaction mixture likewise resulted in a decrease in the yield of $ZrF_4 \cdot H_2O$, probably due to formation of the more soluble H_2ZrF_6. Consequently, it was highly desirable to add essentially a stoichiometric amount of HF. Addition of 2–3 drops of $Th(NO_3)_4$ solution to a few milliliters of the supernatant liquid determined the end point. If a slight excess of fluoride ion was present, the $Th(NO_3)_4$ formed a white precipitate of $ThF_4 \cdot 2H_2O$.

The mixture was stirred continuously during addition of the acid to help dissipate the heat evolved from the reaction and to aid in formation of a granular crystalline precipitate. After cooling to room temperature the product was filtered using plastic filtration equipment. The precipitate was dried in air at 70°C to yield a dry $ZrF_4 \cdot H_2O$ product.

Anhydrous ZrF_4 was obtained by dehydrating this monohydrate in a stream of dry HF gas. This was accomplished in a relatively short time in a heated rotating chamber. The experimental equipment consisted of a Monel tube inside of which was a Mg cylinder for containing the monohydrate. The entire assembly was slowly rotated in an automatically controlled furnace.

[1] Obtained from U. S. Bureau of Mines, Albany, Oreg.

TABLE I. *Dehydration of* $ZrF_4 \cdot H_2O$ *in* HF *Atmosphere*

Batch of ZrF_4	Initial heating at 250°C. Time, hr	Final heating of ZrF_4		Hardness of Zr metal from the batch of ZrF_4 Rockwell A
		Temp, °C	Time, hr	
1	2	400	2	48
2	3	400	5	48
3	3	450	5	51
4	1	500	7	55
5	2	550	6	70
6	2	600	6	71

A study was made of the temperature and time at which the water of hydration could be removed from 500-g batches of fluoride. Dehydration without pyrohydrolysis is essential in the drying of ZrF_4. It was shown experimentally that an initial dehydration in an HF atmosphere at 225°–300°C is desirable for good grade tetrafluoride. The treatment removes about 80% of the water of hydration in 1–3 hr. On the basis of several experiments 250°C was selected for this initial drying step. At this temperature the hydrate underwent considerable decomposition, and the rate of pyrohydrolysis of ZrF_4 was exceedingly slow.

The remaining water was readily removed by increasing the drying temperature. As shown in Table I, the hardness of the final metal is critically dependent on the final drying temperature of the fluoride employed in its preparation. The higher hardness values of metal from some batches of the fluoride is believed to be due to the presence of greater amounts of $ZrOF_2$ in the tetrafluoride. It is assumed that the rate of pyrohydrolysis to give $ZrOF_2$ is much greater at the higher drying temperatures. On laboratory scale a drying treatment of 1½ hr at 250°C followed by 2½ hr at 400°C with constant rotation of the charge gave a fluoride that could be employed to give metal of high ductility. However, for larger scale drying operations the practice was to double the times at these temperatures.

Several thousand pounds of ZrF_4 were prepared for research use. Equipment was set up for this operation with an output capacity of approximately 100 lb ZrF_4/individual batch.

$ZrCl_4$, if in lump form, was dissolved directly in distilled water. Since the solution reaction is very exothermic and HCl is evolved, it was carried out by slow addition of lumps to water in a ventilated area. In powder form, the chloride was introduced into the water by suction through a tube that extended below the surface of the water. About 50 lb of $ZrCl_4$ could be dissolved in 20 gal of water, but, if greater amounts were added, $ZrOCl_2$ began to crystallize out upon cooling. Either polyethylene-lined steel drums or glass-lined equipment may be used as solution vessels. Activated charcoal was added to the chloride solution to aid in filtering out the undissolved ZrO_2 and C present in the tetrachloride. The filtrate was then concentrated by evaporation in a glass-lined steam-heated tank to a 6*N* HCl concentration. $ZrOCl_2 \cdot 8H_2O$ crystallized out upon cooling, and this was filtered through a plastic-coated centrifugal filter.

Hydrofluorination of the $ZrOCl_2 \cdot 8H_2O$ was carried out in the equipment shown in Fig. 1. $ZrOCl_2$ crystals were

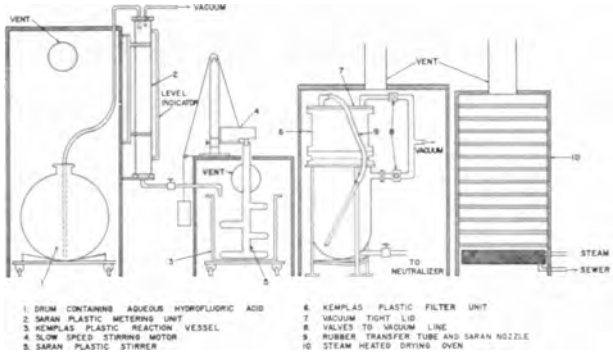

FIG. 1. Precipitation and filtration equipment used in the preparation of $ZrF_4 \cdot H_2O$.

placed in the Kemplas reaction vessel [3], and aqueous 70% HF was transferred from the storage tank [1] into the metering unit [2] by means of a suction lift. The acid was then metered into the reaction vessel until a stoichiometric quantity had been added. Vigorous stirring was necessary during reaction to assure an easily filterable product.

Transfer of the supernatant liquid and the $ZrF_4 \cdot H_2O$ precipitate from the reaction vessel to the filter unit [6] was carried out by suction. A vacuum tight lid [7] was fitted over the top section of the filter unit and a vacuum drawn on the entire unit by opening both valves [8] to a steam operated aspirator. A flexible 1½ in. diameter rubber tube with Saran nozzle [9] connected to the lid of the filter unit was submerged in the reaction vessel sucking both the precipitate and the supernatant liquid into the top of the filter unit. A Saran filter cloth placed over a perforated Kemplas filter plate at the junction of the two sections of the filter unit retained the solid and allowed the liquid to pass into the lower section of this apparatus. Filtration was speeded up by closing the top valve [8] and maintaining reduced pressure on the lower portion of the filtering unit.

The acid filtrate was discharged to the neutralizer, and the wet precipitate was transferred to the steam heated dryer [10]. After drying at 70°C for a few hours, the hydrated fluoride was transferred to the equipment shown in Fig. 2 for dehydration. Batches of about 100 lb of fluoride were placed in the Mg chamber [9] and the flange bolted in place on the iron furnace tube [8]. This assembly

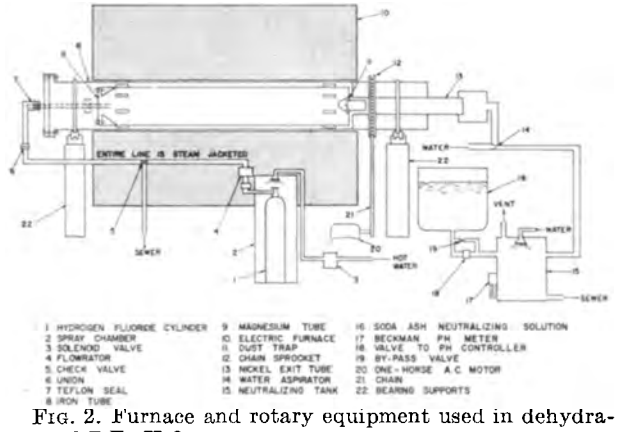

FIG. 2. Furnace and rotary equipment used in dehydration of $ZrF_4 \cdot H_2O$.

extended through the electric resistance furnace [10] which had automatic temperature control. The HF gas line was connected and the furnace tube rotated slowly (about 20 rpm) while anhydrous HF from the cylinder [1] was passed over the powder. Horizontal fins inside the Mg chamber increased agitation of the powder during rotation. A conical shaped trap [11] at the exit end of this chamber prevented excessive loss of material as dust in the exit gas stream. Dehydration of the monohydrate was carried out at 250°C for 3 hr and 400°C for 5 hr. The exit gases were scrubbed by a water spray [14] and passed into a neutralizing tank [15] where a soda ash neutralizing solution [16] was added.

Chemical analysis of a representative batch of ZrF_4 dried at 250° then at 400°C showed it to contain 54.63 w/o Zr and 45.36 w/o F, which is close to the theoretical ZrF_4. The common metallic impurities were found to be less than the following: 0.007 w/o Si, 0.003 w/o Cr, 0.002 w/o Mg, 0.004 w/o Ni, 0.002 w/o Cu, 0.002 w/o Ti, 0.025 w/o Fe, 0.002 w/o Ca, and 0.003 w/o Al. A major source of the Fe contamination is the 70% HF which is received in steel containers. Use of higher purity HF results in much lower Fe contamination.

Preparation of Zr Metal by Ca Reduction of Tetrafluoride

Lambert, Hagelston, and Hutchison (3) employed only I_2 as an additive in their preparation of Zr by bomb reduction. They reported that the metal thus obtained had a hardness of 88–90 R_B (approximately 180 Bhn), and that it could be hot forged and subsequently cold-rolled with an over-all reduction of 80%. However, in the process presented here, Zn was added to the charge in order to form a low-melting alloy during the bomb reduction. I_2 was added to form CaI_2 which raised the temperature of the products and increased the fluidity of the slag. Zn was subsequently removed almost quantitatively by heating in a vacuum up to 1500°C. This left a Zr sponge which could be arc melted or melted in graphite to a dense ingot. Metal thus obtained had a hardness of 40–45 R_A (120–135 Bhn) and was, with intermittent annealing, cold rolled to thin sheet.

The experiments described here were carried out in a steel bomb constructed from a 2½ in. diameter steel pipe. One end of a 12 in. section of the pipe was closed by a welded-in plate; the other end, referred to as the top of the bomb, was threaded for a pipe cap. A refractory liner was inserted to prevent interaction between the charge and the bomb wall. The liner either was of a formed and presintered type or was formed by jolting the refractory powder around a mandrel inside the bomb. The reaction was initiated either by placing the charged bomb in a gas furnace or by a hot wire ignition method. In the latter case a coil of suitable wire was embedded in the charge and a current passed through the wire to start reaction.

Purity of the ingredients in the bomb charge, ratios of Zn, I_2, and Ca to the ZrF_4, and the nature of the refractory liner were major factors that determined quality and yield of the final metal. The effects of these factors were studied independently in numerous experiments by varying the amount or quality of each of the materials.

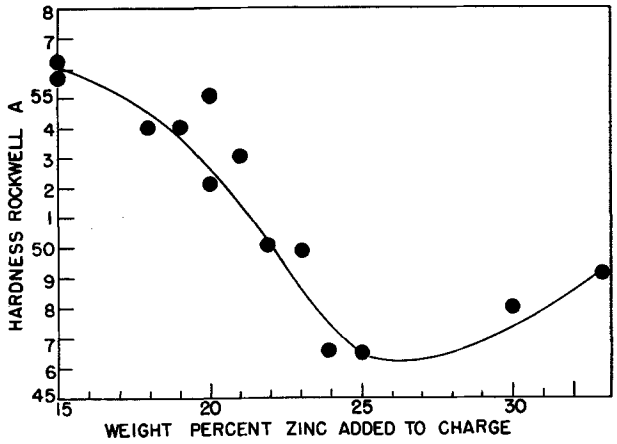

Fig. 3. Zn content of bomb charge vs. hardness of Zr after melting in graphite.

Addition of Zn to Zr lowered its melting point quite markedly, approaching a eutectic at 1000°C at approximately 33 w/o Zn. The percentage of Zn in the alloy had a pronounced effect on the quality of the final Zr metal. Fig. 3 illustrates graphically the effect of varying the amount of Zn, added as turnings to the bomb charge, on the hardness of the as-cast Zr, other factors remaining constant. As seen from the figure, addition of about 25 w/o Zn yielded Zr metal of lowest hardness. The alloy obtained with the 25% addition, actually contained, by chemical analysis, approximately 21 w/o Zn. The Zr metal obtained from the alloy showed a hardness of Rockwell A 46.

The effect of the quality of the ZrF_4 on the final metal hardness (described in a preceding section of this report) was equally pronounced.

Another factor which was recognized but not fully understood was the effect of amount and quality of the Ca reductant. A Ca excess of at least 25% over the stoichiometric amount appeared to be a prerequisite in order to obtain ductile Zr. Ca used in these experiments was prepared by vacuum redistillation of commercial Ca.[2] The Zr metal obtained with redistilled Ca was generally found to be soft, although occasionally a batch of the redistilled Ca would consistently yield a harder Zr. No correlation, however, between quality of the Ca and hardness of the resulting Zr metal was found. Chemical analysis of the major impurities of a typical "good" batch of Ca showed less than the following amounts: 0.005 w/o Fe, 0.004 w/o Mn, 0.003 w/o N, 0.001 w/o Al, 0.003 w/o C, and 0.3 w/o Mg.

Addition of a thermal booster was also essential in obtaining good yields and in producing good slag-metal separation. Although the amount of I_2 added as a booster was not as critical as that of other constituents of the charge, the minimum quantity of booster required for good yields was studied and was found to vary in a manner dependent on the size of the bomb. In a few experiments ZnF_2 was substituted for both the Zn and I_2. Good yields were observed, and metal of comparable quality was obtained when ZnF_2 was used.

[2] Obtained from the New England Lime Co.

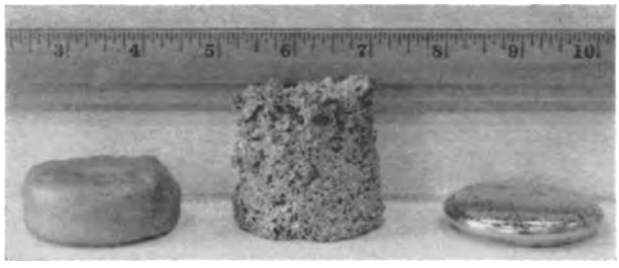

FIG. 4. (*a*) Zr-Zn alloy biscuit, as-reduced; (*b*) Zr sponge after dezincing in vacuum showing considerable volume expansion resulting from rapid heating; (*c*) arc-melted button of Zr.

The liner material was also a potential source of oxygen contamination. Early work in which a few grams of MgO, CaO, and ZrO_2 were added to individual reduction charges showed that MgO and ZrO_2 additions resulted in greatly increased hardness of the Zr, whereas the CaO addition had relatively little effect. As a result of this and other experiments, ZrO_2, MgO, and dolomitic oxide were eliminated as suitable liner materials. Ductile Zr was prepared using a liner of CaO which was prefired to 2000°C. Results, however, were quite inconsistent, with some reductions resulting in ductile metal and others in quite brittle metal. Consequently, CaF_2 was tried and found to be much more satisfactory. Acid grade fluorspar, 97% CaF_2,[3] was used successfully and resulted in metal of consistently low hardness. Chief contaminants introduced by this liner were Si, Al, and N. Pretreating CaF_2 by leaching in aqueous HF or by heating in anhydrous HF at 575°C reduced the contamination effects of these elements considerably.

A charge consisting of 350 g of ZrF_4, 221 g Ca, 64 g Zn chips, and 56 g I_2 gave ductile Zr in yields of greater than 96% when carried out under conditions pointed out above. Equally good results were obtained regardless of whether the charge was ignited by internal or external heating. Successful reductions were also carried out on a larger scale (1 kg ZrF_4) employing a reduced ratio of thermal booster.

The massive alloy obtained by reduction is referred to as a "biscuit". Fig. 4(*a*) shows a biscuit of the Zr-Zn alloy obtained in the smaller scale reduction. Zn can be removed from the alloy by heating it slowly *in vacuo*. At least 95% of the Zn is readily removed at temperatures below 1250°C; however, removal of the remaining Zn requires considerably longer time at 1250°C or higher temperatures. After being heated to 1500°–1600°C in a graphite crucible, the sponge contains less than 0.05 w/o Zn but picks up some C. By use of a liner of Zr sheet inside the graphite crucible it is possible to keep the C content of the sponge at less than 0.03 w/o. The remaining Zn is removed subsequently during the melting. Care must be taken in the dezincing procedure, since heating through the temperature range of 900°–1250°C may result in too rapid evolution of Zn vapors with splattering and excessive expansion in sponge volume, see Fig. 4(*b*). A sample of arc-melted sponge Zr is shown in Fig. 4(*c*).

[3] Obtained from Ozark-Mahoning Co.

PROPERTIES OF BOMB REDUCED ZR METAL

Several pounds of Zr metal sponge were prepared by the method described in the preceding sections. Some of the sponge was melted in a graphite crucible *in vacuo* and some arc melted under A in conventional arc-melting equipment employing a W electrode and a water-cooled Cu pot. The hardness of the metal melted by either method was found to be in the range of 40–45 R_A (120–135 Bhn with a 3000 kg load). Zr thus prepared was cold-rolled and, with intermittent annealing, fabricated into thin sheets 10 mils thick.

The lattice constants of bomb reduced, and arc-melted Zr were determined from x-ray diffraction patterns taken with a precision back-reflection camera. The values calculated by Cohen's analytical extrapolation method (5) were $a = 3.234$ and $c = 5.149$Å, which compare favorably with values of $a = 3.232$ and $c = 5.148$Å reported by Treco (6) for high-purity crystal bar Zr. The purity of Zr metal prepared by the bomb process and arc melted in an inert atmosphere was determined by chemical and spectrographic analysis. Representative amounts of the major impurities present in metal produced by this method are shown in Table II.

The microstructure of a representative specimen of

TABLE II. *Chemical purity of bomb-reduced and arc-melted* Zr *metal*

Impurity	w/o	Impurity	w/o
Al	0.01	Mg	0.002
C	0.03	Mn	0.003
Ca	0.003	N	0.005
Co	0.001	Ni	0.003
Cr	0.003	O	0.1*
Cu	0.003	Si	0.02
Fe	0.02	Ti	0.001

* The oxygen content of this metal has not been determined by vacuum fusion methods, but has been estimated as 0.10–0.15 w/o from Treco's (6) plot of hardness and lattice constants vs. oxygen content.

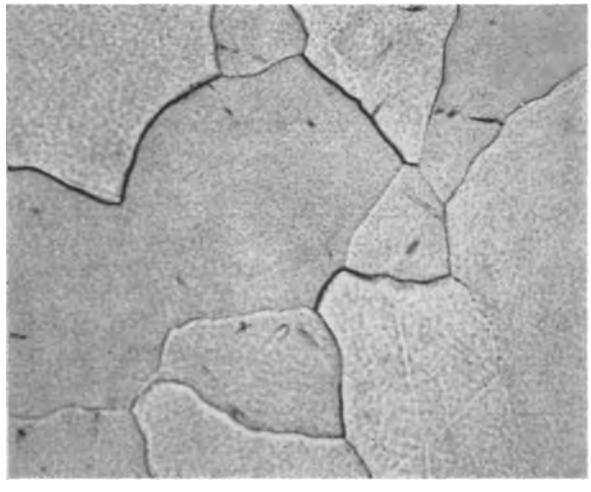

FIG. 5. Bomb-reduced Zr metal, as arc melted. Annealed at 800°C and furnace cooled. Etchant: 1% HF in HNO_3. 250×.

bomb-reduced and arc-melted Zr is shown in Fig. 5. The large equiaxed grains are a result of an annealing treatment.

PREPARATION OF HF METAL

Starting material for the Hf preparation was a Hf concentrate from a Zr purification process. This contained Zr and Hf in the ratio of approximately 1:24. Zr was separated by a liquid-liquid extraction method employing tributyl phosphate and an aqueous HNO_3 solution of their oxychlorides (7). The resulting Hf contained less than 0.010 w/o Zr. High-purity hafnium hydroxide was precipitated from the aqueous phase, the hydroxide was redissolved in HCl, and hydrated hafnium oxychloride was crystallized out of the solution. Aqueous HF (70%) was added to these crystals to form hydrated hafnium fluoride. This material was dehydrated in a stream of HF gas by the same method and temperature conditions described in the section on the preparation of ZrF_4.

The Hf reduction step was also very similar to that for Zr with slight modifications in the ratios of some of the ingredients in the charge. Zn turnings were added to the charge in an amount calculated to give a Hf alloy containing 21 w/o Zn. A representative charge for the experimental $2\frac{1}{2}$ in. diameter bomb consisted of 350 g HfF_4, 275 g I_2, 192 g Ca, and 65 g Zn. A number of reductions were also made in a 6 in. bomb in which 16 lb biscuits of Hf-Zn alloy were obtained. The Zn was removed by heating slowly in a graphite crucible under vacuum to 1800°C. An over-all yield of 97% Hf metal was obtained from the reduction and dezincing steps. The resulting sponge was analyzed chemically and spectrographically, and the principal impurities are shown in Table III. Although oxygen content of the sponge was not determined, it was undoubtedly present in considerable amounts as indicated by the extreme brittleness of the material.

TABLE III. *Chemical purity of bomb-reduced* Hf *sponge*

Element	w/o
Ca	<0.01
Fe	<0.01
Mg	<0.01
Si	<0.01
Zn	<0.002
Zr	<0.01
C	0.07
N	0.05
O	Not determined

TABLE IV. *Comparison of physical properties of sponge and iodide* Hf

	Hf sponge as arc melted	Hf crystal bar as arc melted
Melting Point, °C	2235	2150
Hardness, (R_A)	69	60
Lattice Constants (Å)		
a	3.199	3.197
c	5.072	5.057
c/a	1.585	1.582
Density (g/cc)		
Measured	13.19	13.29
Calculated from x-ray data	13.19	13.25

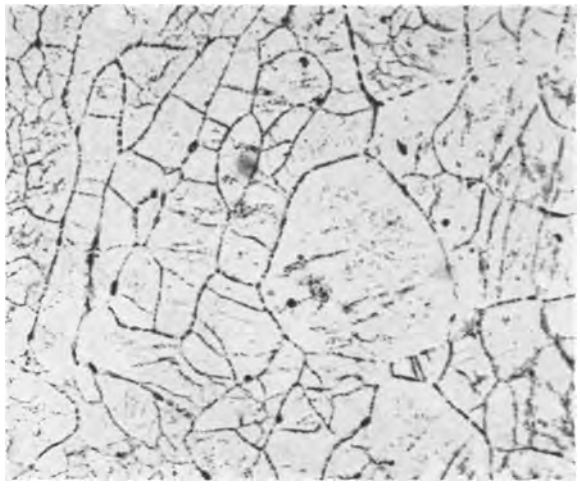

FIG. 6. Bomb-reduced Hf metal, as arc melted. Etchant: 1% HF in HNO_3. 250×.

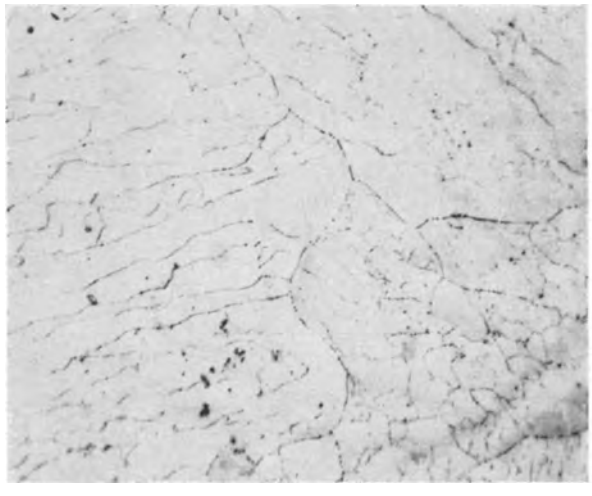

FIG. 7. Crystal bar Hf metal, as arc melted. Etchant: 1% HF in HNO_3. 250×.

Most of this sponge was sent to the Foote Mineral Co. for further purification by the iodide process. The dense crystal bar metal obtained by this processing treatment was analyzed chemically and found to have undergone significant reduction in the C (0.03 w/o) and N (0.009 w/o) content. Some of the sponge Hf was arc-melted directly, and a few of its physical properties were compared with those of the crystal bar Hf as shown in Table IV.

The microstructure of the arc melted sponge is shown in Fig. 6 and of the arc melted crystal bar in Fig. 7.

SUMMARY

A practical process was developed for the preparation of Zr and Hf metals. The method entails a bomb reduction of ZrF_4 or HfF_4 with Ca to form a massive Zn alloy. The Zn was removed by heating in vacuum to yield a sponge of Zr or Hf metal.

ZrF_4 and HfF_4 can be prepared in high purity by an

aqueous reaction to form the hydrated fluorides which are subsequently dehydrated at elevated temperatures in an atmosphere of HF gas. Extensive studies were made of the conditions for the preparation of high-purity ZrF_4, and pilot plant equipment is described which was used to prepare 100 lb batches of the fluorides.

The reduction step was investigated thoroughly, particularly for Zr, and those factors which affect metal quality and yield were determined. Reduction yields of 96% were obtained with both Zr and Hf. After arc-melting, the sponge Zr had a hardness of 40–45 Rockwell A and was readily cold-rolled into sheet. Zr metal thus prepared had a purity of about 99.8%.

Hf metal, similarly prepared, had a hardness of 69 Rockwell A and was hot-rolled but was too brittle to be easily cold worked. The Hf was low in metallic impurities, but contained considerable amounts of C, N, and oxygen.

ACKNOWLEDGMENTS

The authors are especially grateful to J. W. Starbuck for his valuable contribution in the experimental reduction studies, to B. A. LaMont and co-workers for the chemical analyses, and to C. Lentz and associates for the spectrographic analyses.

Manuscript received February 23, 1956. Contribution No. 480. Work was performed in the Ames Laboratory of the A.E.C.

Any discussion of this paper will appear in a Discussion Section to be published in the December 1957 JOURNAL.

REFERENCES

1. K. A. WALSH, U. S. A.E.C. Report No. AECD-3640, (1950).
2. D. PETERSON AND H. A. WILHELM, Unpublished work, Ames Laboratory, Iowa State College, (1950).
3. F. J. LAMBERT, P. J. HAGELSTON, AND R. O. HUTCHISON, Oak Ridge National Lab. Report No. Y-595, (1950).
4. J. L. WILLIAMS AND B. WEAVER, U. S. A.E.C. Report No. AECD-3329, (1950).
5. M. U. COHEN, *Rev. Sci. Instr.*, **6**, 68, (1936).
6. R. M. TRECO, *J. Metals*, **5**, 344, (1953).
7. R. A. FOOS AND H. A. WILHELM, U. S. A.E.C. Report ISC-693, (1956).

Electrochemical Polarization

I. A Theoretical Analysis of the Shape of Polarization Curves

M. STERN AND A. L. GEARY

Metals Research Laboratory, Electro Metallurgical Company, A Division of Union Carbide and Carbon Corporation, Niagara Falls, New York

ABSTRACT

At low overvoltage values, deviations from Tafel behavior for a noncorroding electrode are due primarily to the reverse reaction of the oxidation-reduction system, and at high overvoltages to concentration and/or resistance polarization. It is shown further that the practice of placing straight lines through a few experimental points is extremely hazardous, while the indiscriminate introduction of "breaks" is contrary to the electrode kinetics described.

Further complexities arising from a corroding electrode are described. In this instance, the forward and reverse reactions of both of the oxidation-reduction systems forming the corrosion couple must be considered. This representation of the local polarization diagram of a corroding metal is more fundamental than that used previously in the literature, and thus provides a clearer picture of the various factors which affect the corrosion rate and the shape of polarization curves.

A region of linear dependence of potential on applied current is described for a corroding electrode by treating it in a manner analogous to that for a noncorroding electrode. An equation is derived relating the slope of this linear region to the corrosion rate and Tafel slopes. This relation provides an important new experimental approach to the study of the electrochemistry of corroding metals since, in some instances, interfering reactions prevent determination of Tafel slopes at higher current densities.

Polarization measurements are an important research tool in investigations of a variety of electrochemical phenomena. Such measurements permit studies of the reaction mechanism and the kinetics of corrosion phenomena and metal deposition. In spite of their wide applicability and extensive use, considerable uncertainty in the interpretation of polarization measurements still exists. Some of the uncertainties include the proper method of plotting data and the correct interpretation of "breaks" in polarization curves. Abrupt changes in slope of overvoltage vs. log current have been given considerable significance in the past few years. Logan (1) examined various methods of plotting cathodic polarization measurements to evaluate the correspondence between current required for complete cathodic protection of a system and current flow at the potential break. He reported that the potential break

method indicated a different current requirement than that indicated by other criteria. In addition, breaks could be obtained regardless of whether the potential was plotted as a linear or logarithmic function of applied current. However, examination of the data presented indicates that there is no real experimental evidence pointing toward existence of breaks. In most cases, the plots would best have been considered smooth curves rather than a series of straight lines. Schwerdtfeger and McDorman (2) presented a theory which permitted calculation of the corrosion rate of a metal from its polarization characteristics. The calculation was based on plotting both anodic and cathodic polarization as linear functions of current and using currents at the potential "breaks" in a formula derived essentially from trigonometric considerations. Again, however, experimental evidence for the existence of breaks was not clear-cut. Still another discussion of potential "breaks" was presented recently by Johnson and Babb (3) who used irreversible thermodynamics to derive Pearson's (4) equation for the relation between the corrosion current and potential breaks. Data presented by these investigators for the corrosion of Fe in KCl solutions indicate that a great deal of imagination must be used when drawing the curves in order to obtain "breaks".

Changes in slope rather than a sharp break can be obtained in H activation overvoltage measurements as a result of the H being discharged by two different rate-determining reactions. Parsons (5) discussed a dual mechanism of H discharge and from energy considerations calculated the potential ranges where more than one rate-determining step might be expected. However, he did not imply that a "break" should be found. Bockris and Conway (6) found the cathodic overvoltage vs. log i plots for Ag in 0.1–7.0N HCl solutions showed a marked change in slope at current densities which depended on acid concentration. They attribute the change in slope to a change in symmetry of the energy barrier at the electrode interface rather than to a dual discharge mechanism. Here again a sharp break was not found, the two linear portions of the plot being connected by a curve over a short range of overvoltage values.

The purpose of this discussion is to analyze the shape of polarization curves in terms of modern concepts of electrochemistry. It is shown that many of the reported breaks in polarization curves are not real, and result either from attempts to apply activation overvoltage theory to data obtained under conditions where other types of overvoltage are included in the measurements, or from a combination of insufficient data and an erroneous assumption that a break must exist. In such a presentation, it is convenient to consider first the shapes of polarization curves for a noncorroding electrode, then to extend the analysis to include further complexities which arise from local action currents.

A Noncorroding Electrode System

Consider a substance Z in a solution containing its ions Z^+.[1] In such a system at equilibrium, the rate of oxidation

[1] This might be Cu in equilibrium with Cu^+. The same analysis also applies to an inert electrode in an oxidation-reduction system such as Pt in a ferrous-ferric solution or in a reducing acid solution saturated with H gas.

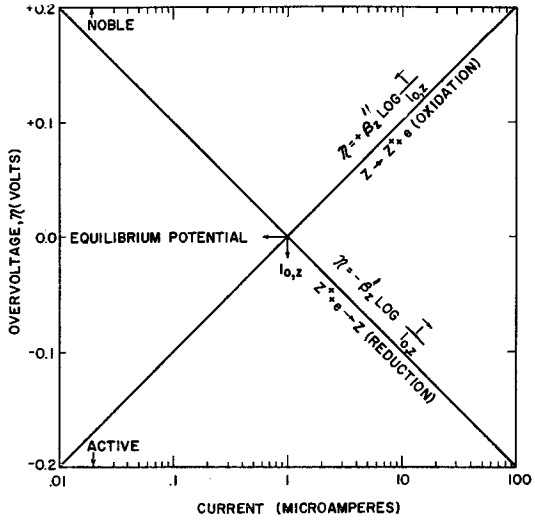

Fig. 1. Relationship between overvoltage and current for the anodic and cathodic reactions of a single electrode system.

of Z is equal to the rate of reduction of $Z^+(Z^+ + e \leftrightarrows Z)$. The reaction rate and current flow are directly related according to Faraday's Law. If $\vec{\imath}_z$ is defined as the current in the forward (reduction) direction ($Z^+ + e \rightarrow Z$) and $\overleftarrow{\imath}_z$ as the current in the reverse (oxidation) direction ($Z \rightarrow Z^+ + e$), the electrode equilibrium may be expressed in the form

$$\vec{\imath}_z = \overleftarrow{\imath}_z = i_{o,z} \tag{I}$$

where $i_{o,z}$ is commonly called the exchange current. When the reaction rate is controlled by a slow step requiring an activation energy, the dependence of current on overvoltage may be expressed as[2]

$$\vec{\imath}_z = i_{o,z} \exp\left(-\frac{\eta}{\beta'_z}\right) \tag{II}$$

$$\overleftarrow{\imath}_z = i_{o,z} \exp\left(+\frac{\eta}{\beta''_z}\right) \tag{III}$$

where the overvoltage, η, is the difference between the potential of the working electrode and the equilibrium potential of the reaction being studied, and β'_z and β''_z are constants. For a system with a symmetrical energy barrier at the electrode interface, β'_z is equal to β''_z. Therefore, Eq. (II) and (III) may be written as

$$\eta = -\beta_z \log \frac{\vec{\imath}_z}{i_{o,z}} \tag{IV}$$

$$\eta = +\beta_z \log \frac{\overleftarrow{\imath}_z}{i_{o,z}} \tag{V}$$

where $\beta_z = 2.3\,\beta'_z = 2.3\,\beta''_z$.

To aid in visualizing the relations given by Eqs. (IV) and (V), they have been plotted on Fig. 1 by arbitrarily giving β_z a value of 0.100 v and $i_{o,z}$ a value of 1.0 μa. These

[2] Other investigators have expressed these equations in more fundamental terms. They are simplified here in order not to detract from the main purpose of the discussion. Excellent literature reviews and discussions on the subject are presented by Bockris (7, 8) and Vetter (9).

are of the same order of magnitude commonly found by experiment; exchange current values generally vary from 10^{-4} to 100 μa and β values from 0.03 to 0.30 v.

Fig. 1 illustrates the relationship between the oxidation and reduction rates and the exchange current at the equilibrium potential and the effect of overvoltage on these rates. When the electrode equilibrium is disturbed by external polarization, the reaction rates change in accord with the curves in Fig. 1. Experimentally, however, the individual oxidation or reduction rates cannot be measured. The external current used for polarization actually is a measure of the difference between the two rates. For example, if the electrode under discussion (Fig. 1) is cathodically polarized from its equilibrium potential to an overvoltage of -0.1 v, the rate of reduction is equivalent to 10 μa while the rate of oxidation is 0.1 μa. The external current required to polarize to this potential is the difference between $\vec{i}_z$ and $\overleftarrow{i}_z$, or 9.9 μa. If the absolute difference between the forward and the reverse reaction currents is defined as $\vec{i}_x$ so that

$$\vec{i}_z - \overleftarrow{i}_z = \vec{i}_x \qquad \text{(VI)}$$

then $\vec{i}_x$ is the external cathodic current when the electrode is polarized to some overvoltage value, η. It is evident that $\vec{i}_x$ approaches $\vec{i}_z$ at overvoltage values sufficiently removed from the reversible potential. It is important to emphasize again that experimentally the only factors measured directly are η and $\vec{i}_x$ or $\overleftarrow{i}_x$. The individual rate of oxidation or reduction cannot be measured. Although theory shows that there is a linear (Tafel) relationship between η and log $\vec{i}_z$ or log $\overleftarrow{i}_z$, only η vs. log $\vec{i}_x$ is measured and plotted. Therefore, substituting Eq. (VI) in Eq. (IV), the theoretical relationship between overvoltage and the logarithm of the external cathodic current is obtained.

$$\eta = -\beta_z \log \frac{\vec{i}_x + \overleftarrow{i}_z}{i_{o,z}} \qquad \text{(VII)}$$

Using the same arbitrary values for the constants β_z and $i_{o,z}$ as indicated previously, and knowing the relation between η and $\overleftarrow{i}_z$ (Eq. V), a plot of the variation of η with log $\vec{i}_x$ may be constructed. This is shown in Fig. 2.[3] Note that deviation from a Tafel slope exists at the low values of applied current. Only when the reverse (oxidation) current, $\overleftarrow{i}_z$, becomes insignificant in comparison to the forward or reduction current can a true Tafel relation be expected. Further, Tafel slopes cannot be obtained until applied currents reach magnitudes of several times $i_{o,z}$. If it is assumed that experimental verification of a linear relationship between η and log $\vec{i}_x$ requires linearity over a range of about two logarithmic cycles of current, reliable estimates of the Tafel constants β_z and $i_{o,z}$[4] require measurements in the region of 1000 times $i_{o,z}$.

[3] Points shown on this figure and all subsequent figures are not experimental. They are calculated from the derived equations and are included to illustrate the need for considerable data to define accurately the shape of a polarization curve. It is quite evident, on inspection of several of the figures, that insufficient data might lead to a series of straight lines.

[4] These constants are derived experimentally from data obtained in the Tafel region. β_z is obtained by measurement of the slope of η vs. log i_x in the Tafel region, while $i_{o,z}$ is found by extrapolation of the Tafel region to the reversible potential.

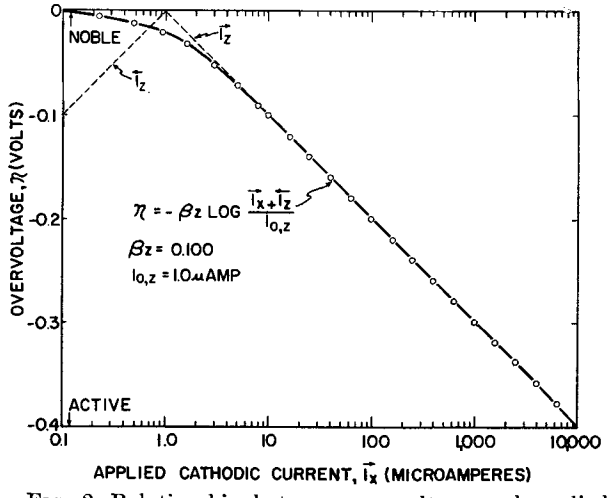

FIG. 2. Relationship between overvoltage and applied cathodic current for a single electrode system.

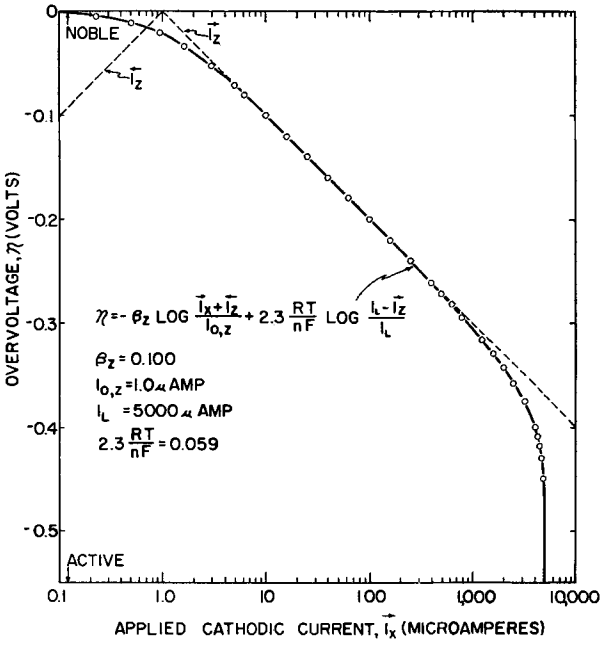

FIG. 3. Effect of concentration polarization on the relationship between overvoltage and applied cathodic current for a single electrode system.

The measurement of activation overvoltage may be complicated by two interfering phenomena—concentration polarization and resistance drop effects—when the value of the exchange current is large. Concentration polarization occurs when the reaction rate or the applied external current is so large that the species being oxidized or reduced cannot reach the surface at a sufficiently rapid rate. The solution adjacent to the electrode surface becomes depleted of the reacting ions, and the rate then is controlled by the rate at which the reacting species can diffuse to the surface. The electrode potential changes sharply in this region until a potential is reached where a new reaction proceeds. The change in potential caused by

concentration polarization may be represented in its simplest form[5] as

$$\eta_{\text{conc.}} = 2.3 \frac{RT}{n\mathbf{F}} \log \frac{i_L - \vec{i}_z}{i_L} \qquad \text{(VIII)}$$

where i_L is the limiting diffusion current for the forward reaction, R the gas constant, T the absolute temperature, and $\mathbf{F}$ Faraday's constant. When $\vec{i}_z$ approaches 0.1 i_L, concentration polarization starts to become significant experimentally. The shape of a curve, including both activation and concentration polarization, is illustrated in Fig. 3. For the purpose of this illustration, i_L has arbitrarily been selected as 5000 μa. The limiting diffusion current is a function of the concentration of the reacting species, the stirring rate of the solution, and all the other factors which influence the maximum rate at which an ion can approach a surface.[6]

Examination of Fig. 3 shows that deviation from Tafel behavior caused by concentration polarization is quite marked and illustrates the difficulties in overvoltage measurements when working near the limiting diffusion current. Note that it would be quite convenient to separate an experimental curve of this type into at least three distinct straight line regions and then to attempt to interpret the breaks theoretically. Such complicating interpretations are obviously unnecessary. Stern (13) illustrated the interference which occurs when H overvoltage measurements are conducted in the region where concentration polarization becomes significant. Both Stern (14) and King (15) criticized the recent work of Schuldiner (16), pointing out that the breaks in the reported H overvoltage curves on Pt were caused by concentration polarization effects. In addition, King pointed out that corrections for concentration polarization cannot be made quantitatively without accurate data for ion diffusion rates. Unfortunately, however, concentration polarization appears to have been overlooked again in more recent work with Pd (17). It is interesting to note that more than 25 years ago Bowden (18, 19) recognized the possibility that concentration polarization was the cause of breaks which he obtained during H overvoltage measurements on Hg.

Resistance between the reference electrode and the polarized electrode contributes still a third term to the total overvoltage measured. This is a linear function of current and can be expressed as $\eta_{\text{res}} = \vec{i}_x K_r$. If the resistance term K_r[7] is arbitrarily given a value of 10 ohms, the resulting deviation from Tafel behavior appears as illustrated in Fig. 4. Note here again that it is not only a simple matter to draw a break in this curve, but that there is considerable latitude in choice of the break position.

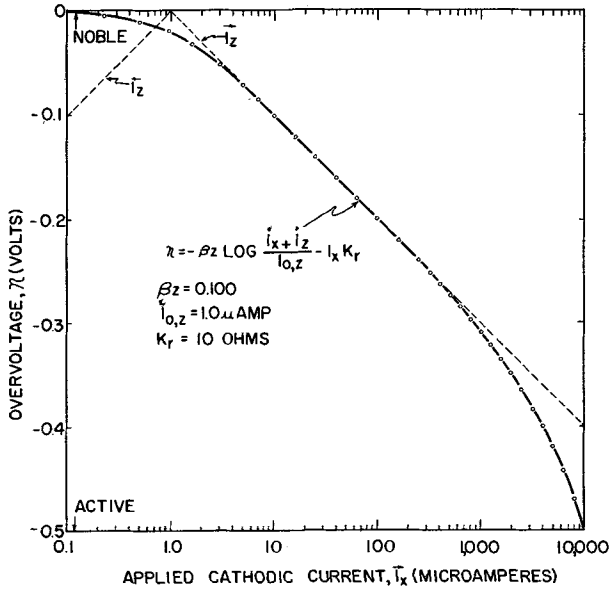

FIG. 4. Effect of resistance polarization on the relationship between overvoltage and applied cathodic current for a single electrode system.

CORRODING ELECTRODE SYSTEM

One additional factor is responsible for deviations from Tafel linearity in the low-current region: corrosion or local action current. When shifting from a noncorroding to a corroding system, many complicating factors arise. Two co-existing electrochemical reactions now appear: the previously discussed oxidation reduction system, $Z^+ + e \rightleftarrows Z$, and the oxidation reduction system of the metal, $M^+ + e \rightleftarrows M$. Each of these systems has its own exchange current and Tafel slope so that the steady-state potential of the corroding metal occurs where the total rate of oxidation equals the total rate of reduction. Thus at the steady-state corrosion potential,

$$\vec{i}_z + \vec{i}_m = \vec{i}_z + \vec{i}_m \qquad \text{(IX)}$$

where $\vec{i}_m$ is the rate of reduction of M^+ and $\vec{i}_m$ is the rate of oxidation of metal M, and $\vec{i}_z$ and $\vec{i}_z$ are the rates of reduction and oxidation of species Z, respectively. Since the corrosion rate by definition is $\vec{i}_m - \vec{i}_m$, it is evident that the rate may also be defined as $\vec{i}_z - \vec{i}_z$ at the corrosion potential. When the corrosion potential is sufficiently removed from the equilibrium potentials of the reactions, $\vec{i}_m$ and $\vec{i}_z$ become insignificant in comparison to $\vec{i}_z$ and $\vec{i}_m$. Thus the corrosion rate becomes equal to $\vec{i}_z$ or $\vec{i}_m$. This has been used directly by Stern (13) to calculate corrosion rates of Fe from H overvoltage measurements, and indirectly by Elze and Fisher (22) to determine corrosion rates in inhibited acid environments. Fig. 5 illustrates the potential-current relationships for such a mixed electrode system. The metal oxidation reduction system has been drawn assuming an $i_{o,m}$ of 0.1 μa, a β_m value of 0.060 v, and a reversible potential of -0.160 v. The Tafel constants for the Z oxidation reduction system are as previously described. Thus, equations for the various reaction

[5] Tobias, Eisenberg, and Wilke (10, 11) and Petrocelli (12) have presented extensive discussions on concentration polarization.

[6] The limiting diffusion current for H ion reduction in HCl containing an indifferent electrolyte and stirred by natural convection is approximately 100 μa/cm^2 at pH 3.1, 1000 μa/cm^2 at pH 2.1, and 10,000 μa/cm^2 at pH 1.1 (13).

[7] The resistance is a function of solution conductivity, distance between the reference electrode and the sample, and the geometry of the system. Barnartt (20) has presented an analysis of the magnitude of the IR drop expected as a function both the current density and the solution conductivity. K_r may actually be a function of applied current if the conductance of the solution adjacent to the electrode interface changes (21).

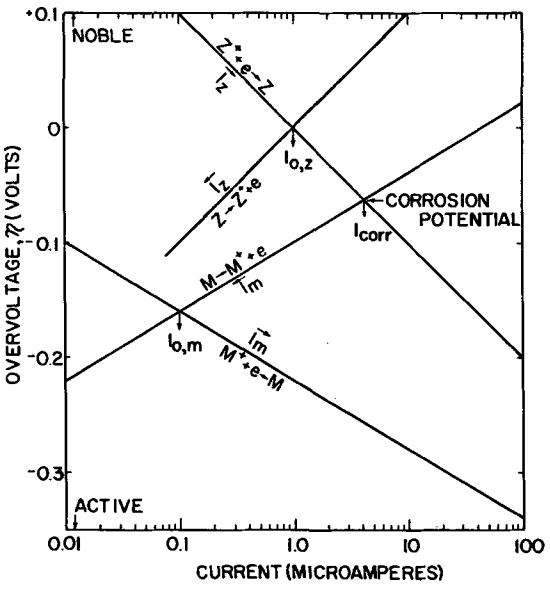

FIG. 5. Relationship between overvoltage and current for a corroding electrode system consisting of two coexisting electrochemical reactions.

rates, using the equilibrium potential of the Z species reaction as a zero reference, are as follows:

Z Reduction

$$\eta = -\beta_z \log \frac{\vec{i}_z}{i_{o,z}} = -0.100 \log \frac{\vec{i}_z}{1.0} \qquad (X)$$

Z Oxidation

$$\eta = +\beta_z \log \frac{\vec{i}_z}{i_{o,z}} = +0.100 \log \frac{\vec{i}_z}{1.0} \qquad (XI)$$

Metal Reduction

$$\eta = -0.160 - \beta_m \log \frac{\vec{i}_m}{i_{o,m}} = -0.160 - 0.060 \log \frac{\vec{i}_m}{0.1} \qquad (XII)$$

Metal Oxidation

$$\eta = -0.160 + \beta_m \log \frac{\vec{i}_m}{i_{o,m}} = -0.160 + 0.060 \log \frac{\vec{i}_m}{0.1} \qquad (XIII)$$

The constants are all arbitrary values. At any given potential, the rate of each reaction is indicated in Fig. 5. As already discussed, the corrosion potential is closely approximated by the potential at which $\vec{i}_z = \vec{i}_m$. This current is labeled i_{corr} in Fig. 5. It is quite important to note both the similarities and differences between this diagram of the electrochemistry of a corroding metal and that commonly used in the earlier literature (23, 24). Since the various oxidation reduction reactions occur at a finite rate even at the equilibrium potentials, it is apparent that the usual simplified polarization diagrams which have a linear current ordinate starting at zero are not strictly valid. Although the diagram in Fig. 5 is more in accord with modern electrochemical principles, its greatest value lies in the ease with which it permits an understanding of the shape and nature of experimental polarization curves. An expression describing the shape of the experimental cathodic polarization curve of a corroding electrode may be derived in the following manner. The external applied cathodic current, $\vec{i}_x$, is equal to the difference between the sum of the rates of all the reduction reactions and the sum of the rates of all the oxidation reactions. Thus,

$$\vec{i}_x = (\vec{i}_z + \vec{i}_m) - (\vec{i}_z + \vec{i}_m) \qquad (XIV)$$

Since the local action current during cathodic polarization may be defined as

$$i_{la} = \vec{i}_m - \vec{i}_m \qquad (XV)$$

$$\vec{i}_x = \vec{i}_z - \vec{i}_z - i_{la} \qquad (XVI)$$

but

$$\eta = -\beta_z \log \frac{\vec{i}_z}{i_{o,z}} \qquad (X)$$

therefore,

$$\eta = -\beta_z \log \frac{\vec{i}_x + \vec{i}_z + i_{la}}{i_{o,z}} \qquad (XVII)$$

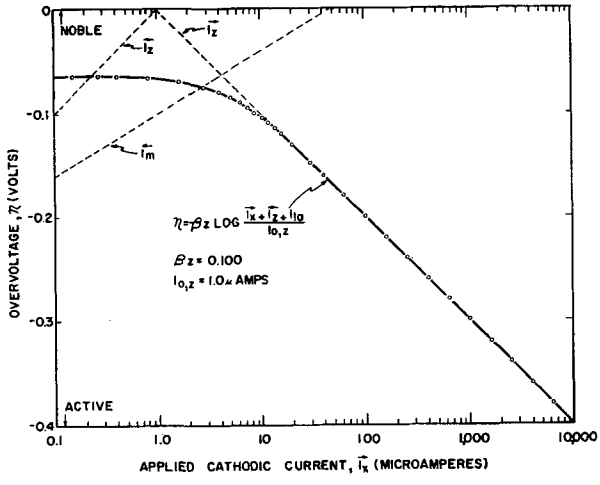

FIG. 6. Relationship between overvoltage and applied cathodic current for a corroding electrode system.

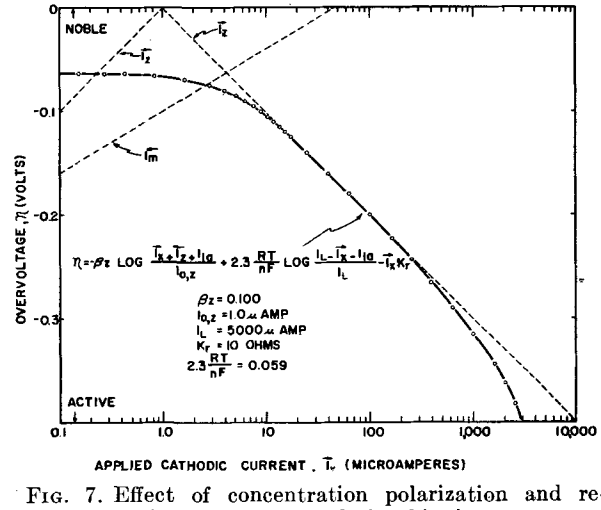

FIG. 7. Effect of concentration polarization and resistance polarization on the relationship between overvoltage and applied cathodic current for a corroding electrode system.

Since the variations of $\bar{i}_z$ and i_{la} with η are known [Eq. (XI), (XII), and (XIII)], Eq. (XVII) permits a calculation of the potential change as a function of applied cathodic current. A similar equation may be derived for anodic polarization and would be of the form:

$$\eta = -0.160 + \beta_m \log \frac{\bar{i}_x + i_{la} + \bar{i}_m}{i_{o,m}} \quad \text{(XVIII)}$$

Fig. 6 shows the expected curve for the overvoltage as a function of the applied cathodic current, ($\bar{i}_x$), for the system described above. This should be compared with Fig. 2 which shows the corresponding cathodic polarization curve for a noncorroding electrode with the same Tafel constants. Note that deviation from Tafel behavior occurs at much higher polarizing currents for the corroding electrode. True Tafel behavior is not evident until polarizing currents of the order of several times the corrosion current are applied.

If concentration polarization and resistance drop effects are included in the measurements, Eq. (XVII) becomes

$$\eta = -\beta_z \log \frac{\bar{i}_x + \bar{i}_z + i_{la}}{i_{o,z}} + 2.3 \frac{RT}{n\mathbf{F}} \log \frac{i_L - \bar{i}_x - i_{la}}{i_L} - \bar{i}_x K_r \quad \text{(XIX)}$$

For the same values of i_L and K_r used previously, Fig. 7 shows the effect of external applied cathodic current, $\bar{i}_x$, on the measured potential, η. Fig. 7 contains only a very short region which exhibits the Tafel slope, β_z. This is, of course, due to the choice of numbers used in this example. An increase in the corrosion current or in K_r and a decrease in i_L would completely eliminate any observable Tafel behavior. It is worth emphasizing here again that with a curve such as Fig. 7 a variety of straight line sections may be drawn with breaks placed at convenient positions. Obviously, such a treatment would be quite incorrect and contrary to the electrode kinetics described.

Linear vs. Tafel Polarization Behavior

In addition to the problem of polarization breaks, the question arises continually as to whether polarization should be a linear or logarithmic function of applied current. For example, Straumanis, Shih, and Schlechten (25, 26) have found Tafel behavior for H overvoltage on Ti in HCl, HBr, and H_2SO_4, but report a linear dependence of overvoltage on applied current in HF. In addition, these authors show that the linear relation is maintained if the Ti dissolves, while the Tafel relation holds if the Ti ceases to dissolve because of fluoride additions. That these results are in accord with the electrode kinetics described above is illustrated here.

A Noncorroding Electrode

Butler and Armstrong (27) have shown that the overvoltage of a reversible electrode is a linear function of applied current for values of overvoltage only slightly removed from the reversible potential. Proof of this can be found in the following derivation. Rearrangement of Eqs.

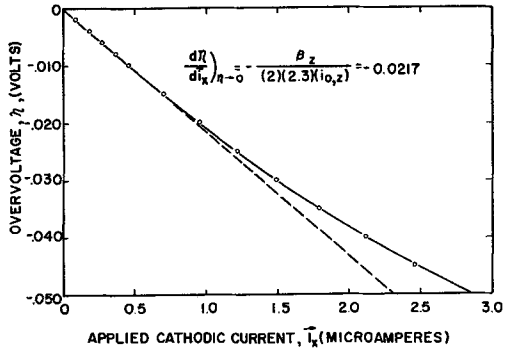

Fig. 8. Linear relationship between overvoltage and applied current for a single electrode system at overvoltage values only slightly removed from the reversible potential.

(IV) and (V) and substitution of these into Eq. (VI) yields

$$\bar{i}_x = i_{o,z}[10^{-\eta/\beta_z} - 10^{+\eta/\beta_z}] \quad \text{(XX)}$$

For small values of η/β_z where $10^{-\eta/\beta_z}$ may be approximated by $1 - \eta/\beta_z$ (2.3) and $10^{+\eta/\beta_z}$ may be approximated by $1 + \eta/\beta_z$ (2.3), Eq. (XX) reduces to

$$\bar{i}_x = -(2)(2.3)(i_{o,z})\eta/\beta_z \text{ and} \quad \text{(XXI)}$$

$$\left(\frac{d\eta}{d\bar{i}_x}\right)_{\eta\to 0} = -\frac{\beta_z}{i_{o,z}(2)(2.3)} \quad \text{(XXII)}$$

Thus, measurements of overvoltage close to the reversible potential will yield results in accord with Eq. (XXII). For the system $Z^+ + e \rightleftarrows Z$ where $\beta_z = 0.100$ and $i_{o,z} = 1.0$ μa (Fig. 1), Eq. (XXII) indicates that $\left(\frac{d\eta}{d\bar{i}_x}\right)_{\eta\to 0} = -0.0217$ v/μa. Fig. 8 is a plot of η as a function of $\bar{i}_x$ calculated from Eq. (VII) for small values of η. Note that the linear relation predicted by Eq. (XXII) applies for η values up to about 20 mv.

Corroding Electrode

The same analysis may be applied to a corroding electrode where the corrosion potential is determined by the intersection of two logarithmic polarization curves. The corrosion current in this case is analogous to the exchange current of a noncorroding electrode.
Thus[8]

$$\bar{i}_x = -2.3\, i_{\text{corr}}\, \epsilon \left(\frac{\beta_z + \beta_m}{\beta_z \beta_m}\right) \text{ and} \quad \text{(XXIII)}$$

$$\left(\frac{d\epsilon}{d\bar{i}_x}\right)_{\epsilon\to 0} = -\frac{\beta_z \beta_m}{(2.3)(i_{\text{corr}})(\beta_z + \beta_m)} \quad \text{(XXIV)}$$

For the mixed electrode system described earlier and illustrated in Fig. 5,

$$\left(\frac{d\epsilon}{d\bar{i}_x}\right)_{\epsilon\to 0} = -0.0040 \text{ v/}\mu\text{a}$$

Fig. 9 is a plot of ϵ as a function of $\bar{i}_x$ calculated from Eq. (XVII) for small values of ϵ. Here again a linear relation between electrode potential and applied current is found. It is important to note that the linear behavior extends to

[8] ϵ is the difference between the polarized potential and the corrosion potential.

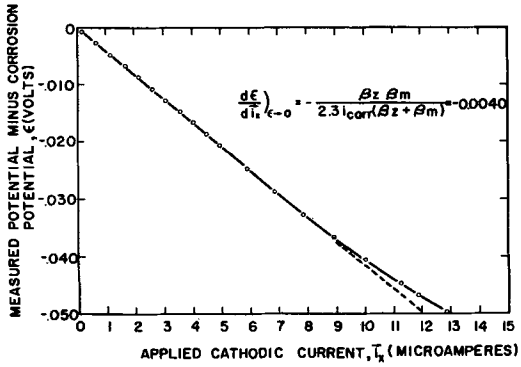

FIG. 9. Linear relationship between potential and applied current at potentials only slightly removed from the corrosion potential. ϵ is the difference between the polarized potential and the corrosion potential.

applied current values higher than the corrosion current. As stated previously, Tafel behavior would not be indicated until applied current values approximately ten times i_{corr} are reached.

In the data reported by Straumanis (25, 26) for the linear dependence of H overvoltage on applied current for Ti in HF, the region where Tafel behavior would be expected to appear had not been reached experimentally because of the high corrosion current under the conditions of test. For example, the corrosion rate of Ti in 1*N* HF has been reported as equivalent to 85 ma/cm² (28), while the overvoltage measurements were not carried farther than 50 ma/cm².

Eq. (XXIV) is valuable from both a theoretical and an experimental point of view, since it relates the corrosion rate and the Tafel slopes to polarization measurements close to the corrosion potential. Thus, low current polarization measurements combined with corrosion rate data permit a calculation of one of the Tafel slopes if the other is known. This is of great value when concentration polarization or *IR* drop effects interfere with measurements at the higher currents. In addition, measurements are made close to the corrosion potential, thus eliminating any surface changes which may result from high current polarization.

Additional Causes for Tafel Deviation

The Tafel constants for Fig. 5 have been picked conveniently to yield a single Tafel relation at the currents illustrated in Fig. 6. Inspection of Fig. 5, however, reveals that $\bar{i}_m$ becomes significant in respect to $\bar{i}_z$ at very high current values. In this current region, the Tafel slope of Fig. 6 will gradually change from β_z to β_m. When $\bar{i}_m \gg \bar{i}_z$, a new Tafel slope exists with a value of β_m. A plot of the overvoltage curve for this situation is presented in Fig. 10. Obviously, a different choice of β_z, β_m, $i_{o,z}$, and $i_{o,m}$ could create this shift in Tafel slope at lower currents and smaller values of overvoltage. It is important to note that the change in slope takes place gradually and results in a curve which is only "Tafel-like" in nature over a considerable range of current. It would be a simple matter, although incorrect, to draw several Tafel lines through this curve. Thus, it is evident that real Tafel behavior will not be observed in a potential range where two or more reduction reactions occur at similar rates.

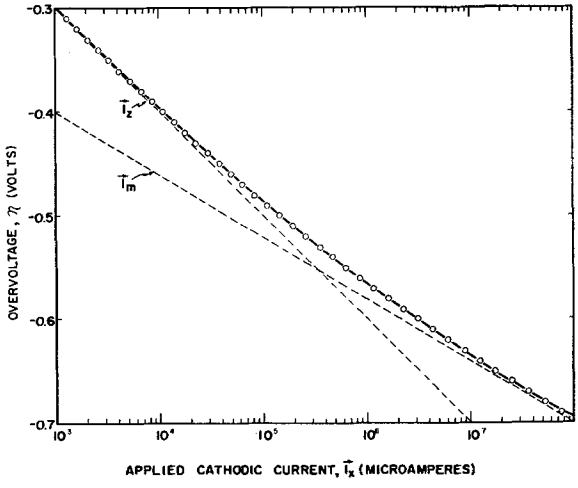

FIG. 10

A further extension of the concepts presented here shows that an improvement in the efficiency of reducing M^+ at any given potential may be achieved by increasing β_z, decreasing β_m, increasing $i_{o,m}$, decreasing $i_{o,z}$, or by reducing the difference between the reversible potentials of the two oxidation reduction systems. Thus, the analysis presented here is important in the study of metal plating efficiency as well as corrosion phenomena.

Discussion

The picture of a mixed electrode presented above could be made more extensive by including even a third oxidation reduction system.[9] It is doubtful whether a detailed discussion of such a system would be of benefit at the present, but it will be included in a future publication. It is worth noting in passing, however, that the polarization curves would be even more complex than those discussed here.

This analysis has illustrated several important concepts which are worth listing for emphasis.

1. The representation of a corroding metal by polarization diagrams should be extended to include the reverse reactions of the various oxidation reduction systems which are operative.
2. Deviations from Tafel behavior may be caused by local action currents, concentration polarization, and *IR* drop effects, and by a change in the predominant electrode reaction.
3. An experimental polarization curve may show a linear dependence of potential on applied current for small amounts of polarization.
4. An equation has been derived which relates the slope of the linear region of a polarization measurement to the corrosion rate and the Tafel slopes. This equation will prove valuable when interfering reactions prevent the determination of the Tafel constants at higher currents.
5. The shape of an experimental electrochemical polarization curve, either cathodic or anodic, can be analyzed

[9] An example of this would be Fe corroding in acid with a depolarizer such as oxygen or ferric ion.

if sufficient data are obtained to permit an accurate description of the curve. Placing straight lines through four or five experimental points is hazardous, while the indiscriminate introduction of "breaks" is contrary to modern electrochemical concepts. Sufficient information concerning the system should be available to estimate whether concentration polarization or resistance drop effects have been included in the measurements.

Although this analysis contains only calculated polarization curves, a subsequent discussion will illustrate how experimental measurements comply with the electrode kinetics described.

The picture of a corroding metal presented here is consistent with the concept or theory of mixed potentials originally treated by Wagner and Traud (29) and subsequently discussed by Petrocelli (30). The concept of discrete anodic and cathodic areas in electrochemical corrosion may be considered a special case of this theory.

Manuscript received Feb. 24, 1956.
Any discussion of this paper will appear in a Discussion Section to be published in the December 1957 JOURNAL.

LIST OF SYMBOLS USED

$\vec{i}_z$ = Cathodic or reduction current of Z oxidation reduction system.

$\vec{i}_m$ = Cathodic or reduction current of M oxidation reduction system.

$\overleftarrow{i}_z$ = Anodic or oxidation current of Z oxidation reduction system.

$\overleftarrow{i}_m$ = Anodic or oxidation current of M oxidation reduction system.

$i_{o,z}$ = The exchange current of the Z reaction. This is equal to the oxidation or reduction current at equilibrium

$i_{o,m}$ = The exchange current of the M reaction. This is equal to the oxidation or reduction current at equilibrium

β_z = The Tafel slope or $\frac{d\eta}{d \log i}$ for the Z oxidation reduction system.

β_m = The Tafel slope or $\frac{d\eta}{d \log i}$ for the M oxidation reduction system.

$\vec{i}_x$ = The external applied cathodic current.

$\overleftarrow{i}_x$ = The external applied anodic current.

η = Overvoltage or difference in potential between a polarized electrode and an electrode at equilibrium for the same reaction.

η_{conc} = Concentration overvoltage.

η_{res} = Resistance overvoltage.

i_L = Limiting diffusion current.

i_{la} = Local action current.

i_{corr} = Corrosion current or the local action current at the corrosion potential.

K_r = Resistance factor for calculating the IR drop included in polarization measurements. This factor includes the solution conductivity and the system geometry.

ϵ = The difference between the potential polarized by applied current and the corrosion potential.

$\left(\frac{d\eta}{d\vec{i}_x}\right)_{\eta \to 0}$ = The slope of the overvoltage vs. current curve for small overvoltage values.

$\left(\frac{d\epsilon}{d\vec{i}_x}\right)_{\epsilon \to 0}$ = The slope of the ϵ vs. current curve for small values of ϵ.

REFERENCES

1. K. H. LOGAN, *Corrosion*, **10**, 206 (1954).
2. W. J. SCHWERDTFEGER AND O. N. MCDORMAN, *This Journal*, **99**, 407 (1952).
3. P. A. JOHNSON AND A. L. BABB, *Ind. Eng. Chem.*, **46**, 518 (1954).
4. J. M. PEARSON, *Trans. Electrochem. Soc.*, **81**, 483 (1942).
5. R. PARSONS, *J. Chim. Phys.*, **49**, C 82 (1952).
6. J. O'M. BOCKRIS AND B. E. CONWAY, *Trans. Faraday Soc.*, **48**, 724 (1952).
7. J. O'M. BOCKRIS AND E. C. POTTER, *This Journal*, **99**, 169 (1952).
8. J. O'M. BOCKRIS, "Modern Aspects of Electrochemistry," Academic Press Inc., New York (1954).
9. K. J. VETTER, *Z. Elektrochem.*, **59**, 435 (1955).
10. C. W. TOBIAS, M. EISENBERG, AND C. R. WILKE, *This Journal*, **99**, 395C (1952).
11. C. R. WILKE, M. EISENBERG, AND C. W. TOBIAS, *ibid.*, **100**, 513 (1953).
12. J. V. PETROCELLI, *ibid.*, **98**, 187 (1951).
13. M. STERN, *ibid.*, **102**, 609, 663 (1955).
14. M. STERN, *ibid.*, **102**, 356 (1955).
15. C. V. KING, *ibid.*, **102**, 193 (1955).
16. S. SCHULDINER, *ibid.*, **101**, 426 (1954).
17. J. P. HOARE AND S. SCHULDINER, *ibid.*, **102**, 485 (1955).
18. F. P. BOWDEN, *Trans. Faraday Soc.*, **24**, 473 (1928).
19. F. P. BOWDEN, *Proc. Roy. Soc.*, **126A**, 107 (1930).
20. S. BARNARTT, *This Journal*, **99**, 549 (1952).
21. J. N. AGAR AND F. P. BOWDEN, *Proc. Roy. Soc.*, **169A**, 206 (1938).
22. J. ELZE AND H. FISHER, *This Journal*, **99**, 259 (1952)
23. U. R. EVANS, "Metallic Corrosion, Passivity, and Protection," p. 350, Longmans Green and Co., New York (1948).
24. H. H. UHLIG, ed., "Corrosion Handbook," p. 436, J. Wiley & Sons, Inc., New York (1948).
25. M. E. STRAUMANIS, S. T. SHIH, AND A. W. SCHLECHTEN, *J. Phys. Chem.*, **59**, 317 (1955).
26. M. E. STRAUMANIS, S. T. SHIH, AND A. W. SCHLECHTEN, *This Journal*, **102**, 573 (1955).
27. J. A. V. BUTLER AND G. ARMSTRONG, *J. Chem. Soc.*, **1934**, 743.
28. M. E. STRAUMANIS AND P. C. CHEN, *This Journal*, **98**, 234 (1951).
29. C. WAGNER AND W. TRAUD, *Z. Elektrochem.*, **44**, 391 (1938).
30. J. V. PETROCELLI, *This Journal*, **97**, 10 (1950).

Technical Feature

High-Temperature Material Requirements of the Air Force

R. A. JONES

Materials Branch, Equipment Division, Headquarters, Air Research and Development Command, Baltimore, Maryland

"Aircraft designers are always on the lookout for any improvement in the heat resistance of materials. They will utilize any such improvement providing availability and production requirements can be met and providing unacceptable compromises in strength/weight properties, fatigue resistance and reliability are not involved." This statement summarizes Air Force requirements for heat-resistant materials, but the subject of high temperatures is too important to be dismissed with such a statement. More detailed discussion is necessary to obtain a clearer understanding of the problem facing the aircraft industry and the Air Force materials suppliers and scientists. As background information, high temperatures have consistently worried engine designers. In fact, much of the high-temperature metallurgical research and development, which later made the turbojet engine possible, resulted from requirements of the turbo-supercharger. This reciprocating engine booster harnessed surplus energy in the hot exhaust gases and permitted the high level flight operations in which the U. S. excelled during World War II. Its success was directly dependent on materials which could stand high stresses while at temperatures of 1200°–1500°F.

Even though high temperatures do not pose an entirely new set of problems to the aeronautical engineer, two facts which have become increasingly apparent over the past few years focus increased attention on the subject. The first is the advent of aerodynamic heating as a major design and operational factor for both piloted and pilotless aircraft. The second is the realization that many of the easy-to-use materials, especially metal alloys, have been quite fully exploited and further progress toward greater heat resistance has approached a condition of diminishing returns. These factors will be discussed briefly from the standpoint of their impact on materials research, development, and engineering.

Fig. 1 indicates the nature of the "thermal thicket" posed by aerodynamic heating. Temperatures are calculated maximum values based on standard atmospheric conditions. An aircraft operating under conditions of aerodynamic heating may be considered to be immersed in a hot gas stream but free to radiate into outer space. Actual temperatures will be somewhat lower than these theoretical values and may vary appreciably over the surface due to variations in airflow and boundary layer conditions. Furthermore, as the vehicle penetrates or emerges from the "thermal thicket," there will be a certain time lag in the heating or cooling of the structure (Fig. 2).

As mentioned previously, high temperatures are nothing new to aeronautical designers and reasonably good success has been attained in coping with temperatures using present materials. Why then does this aerodynamic heating, even to the low value of 300°–400°F associated with extended Mach 2.5 flight, cause so much concern? Some of the reasons follow:

1. In the case of power plants and other heat-generating components, the excessively hot areas can be cooled, insulated, and even replaced after having received a limiting amount of stress and heat. Aerodynamic heating, however, has a more general effect since it subjects to heat those structural components customarily designed to operate at or near normal atmospheric temperatures. It also limits or eliminates the atmosphere as a low-temperature heat sink; thus, cooling becomes difficult and expensive and more heat resistance is desired from all materials. "Heat resistance" and "high temperatures" are relative terms and the problem of increasing heat toleration of rubber tires from 250° to 350°F may be as perplexing as that of developing a 2500°F turbine bucket material.

2. Since the days of wood and fabric airplanes, aluminum alloys, and to a lesser extent magnesium, have served as the primary aircraft structural materials. As shown in Fig. 3, the strength of these materials decreases so rapidly above 300°–400°F that they become of limited use for Mach 2 plus aircraft. These materials will, undoubtedly, be improved further, but a change over to more heat-resistant materials appears necessary to optimize future high performance designs. The change over will make obsolete most of the design data, know-how, and manufacturing experience which has been accumulated over the past 30 years.

3. The duration of operation under severe aerodynamic heating is comparatively short in many cases. Structural stresses must, however, be high under the conditions which produce this heating in order to avoid prohibitive overdesign for the less severe conditions which occur during most of the life of the vehicle. Material properties which control designing for these conditions are short time, high-temperature strength, and creep. Such design data are not adequately available even for existing materials, and, in many cases, the test equipment and techniques for obtaining such data are not available.

4. Aerodynamic heating often occurs under transient conditions with intense temperature gradients being established in the missile or aircraft structure. This may result in a buildup of thermal stresses which can equal or exceed aerodynamic loads. New design concepts considering thermal expansion and conductivity properties of materials and structures will be needed to cope with these

conditions. Insulation and cooling, in addition to a general increase in the heat toleration of materials and components, may be necessary to handle some of the more severe conditions.

Having recognized the fact that future aircraft and missiles will be exposed to a temperature environment which may exceed the melting point of any material, what can the designer and materials engineer do to insure successful operation? Obviously, one should not expect the problem to be completely solved by either approach. Adroit designing can and will surmount many of the difficulties but, as in the past, optimum designs result from a coordinated effort by both designers and materials engineers. It may very well be that the necessary margin of superiority of future weapon systems will stem directly from the materials engineer's ability to provide more heat-resistant materials which will simplify the design problem. In the past, aeronautical designers were faced with materials problems, but these were dwarfed by the stability, control, engine and propeller design problems. Furthermore, suitable materials have either been available or have been developed without undue delay. Today the situation is reversed and more and more often the statement is heard that "the limiting factor is suitable heat-resistant materials."

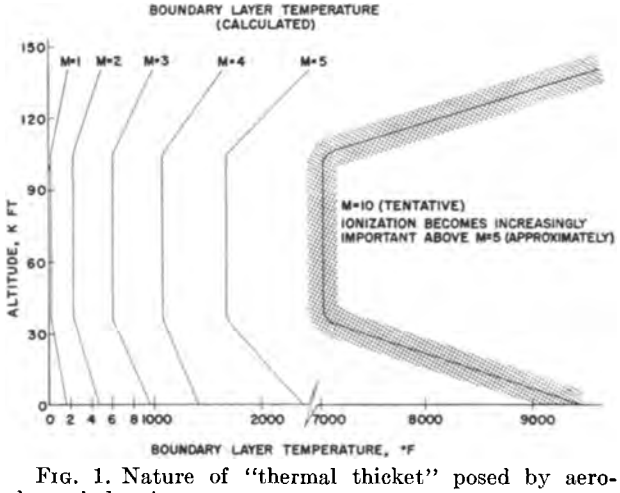

FIG. 1. Nature of "thermal thicket" posed by aerodynamic heating.

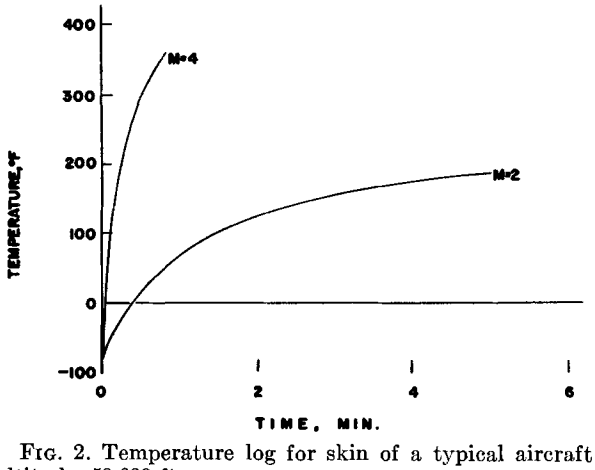

FIG. 2. Temperature log for skin of a typical aircraft; altitude, 50,000 ft.

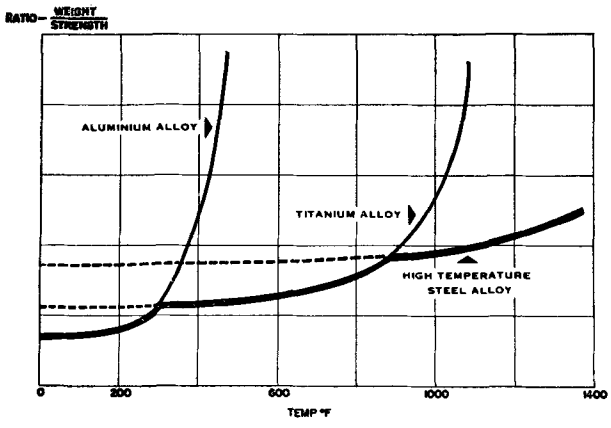

FIG. 3. Weight-strength ratio, 'short time tension'

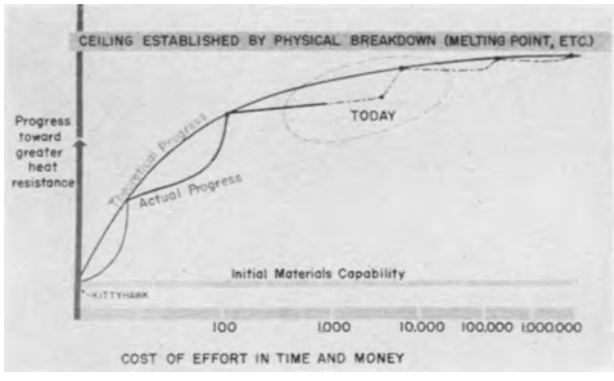

FIG. 4. Manner and limits of progress for common aeronautical materials.

Just what is the "suitable heat-resistant material?" Generally speaking, from a design and production standpoint, it is a "souped up" or improved version of some well-known, currently used material. Such a material is applicable to current design concepts and is amenable to production by existing techniques and equipment. There is, however, a limit to the progress and improvements which can be made in this direction. All materials have a structural use ceiling or plateau established by melting point, thermal decomposition or some other temperature-affected characteristic. Fig. 4 indicates the usual nature of progress toward this use ceiling. Unfortunately, the "easy" steps of progress have already been made for many conventional type of materials and further steps upward will become increasingly costly and difficult. The real promise for breaking this "diminishing returns" situation lies with the refractory but difficult to use materials which have not yet been fully exploited. In the upper temperature bracket, they include such materials as molybdenum and various ceramic and cermet compositions.

Development of the refractory metals, ceramics, and cermets to a point suitable for aircraft and missile uses poses a challenge to both the aeronautical and materials engineer. The materials man is not quite sure what is wanted and the specific requirements he receives are too often derived from design concepts based on materials currently used. The "promising" new material is then

evaluated and employed under adverse or less than ideal conditions, with unsatisfactory results familiar to all. It would be fine if the Air Force and aeronautical designers could present requirements for heat-resistant materials on which to base future designs. This is possible only on a generalized basis since engineering designs in actuality are based on the materials of construction. Until new materials are developed, evaluated, and design data determined, the designer must rely on the "old" materials and use design ingenuity to surmount their limitations. This manner of making progress, with gradual introduction of new materials, is satisfactory and even essential in industrial competition where amortization of equipment and facilities is of controlling importance.

If the Air Force is to achieve the "breakthroughs" and major spurts in progress, which are essential to retaining technical superiority, then the materials research and development people must take a leading—not a supporting—role. They cannot wait for someone to tell them exactly what is needed, but must assume a share of the responsibility for suggesting applications and carrying developments of new materials through prototype application and production without the usual long incubation period. They must work shoulder to shoulder with experimental designers in order to insure the optimum design-material combination for breaking through the thermal thicket. Since, as J. B. Macauley, Deputy Assistant Secretary of Defense for R & D, recently wrote, "... materials are in so many instances the limiting factors in progress on development of weapons," then weapon designs should be adapted to materials rather than the reverse procedure which is now too often the hardware development philosophy. This will require teamwork of the type which characterized the successful development of ceramic nozzles and combustion chamber liners for rocket thrust cylinders. The history and status of that program are well known and, according to the program, more will be heard on that subject later. Such teamwork, in which materials scientists and engineers play a leading role, will be absolutely essential if the U.S. Air Force is to maintain its position of technical superiority.

Manuscript received May 2, 1956. This paper was prepared for delivery before the San Francisco Meeting, April 29 to May 3, 1956.

Any discussion of this paper will appear in a Discussion Section to be published in the December 1957 JOURNAL.

MANUSCRIPTS AND ABSTRACTS FOR FALL MEETING

Papers are now being solicited for the Fall Meeting of the Society, to be held at the Statler Hotel in Buffalo, N. Y., October 6, 7, 8, 9, and 10, 1957. Technical Sessions will be scheduled on Batteries, Corrosion, Electrodeposition (symposium on "Metal Powders"), Electrodeposition—Corrosion (Joint Symposium on "Corrosion of Electrodeposited Metals"), Electro-Organics, and Electrothermics and Metallurgy.

To be considered for this meeting, triplicate copies of abstracts (*not to exceed 75 words in length*) must be received at Society Headquarters, 216 West 102nd St., New York 25, N. Y., *not later than June 1, 1957. Please indicate on abstract for which Division's symposium the paper is to be scheduled.* Complete manuscripts should be sent in triplicate to the Managing Editor of the JOURNAL at the same address.

* * *

The Spring 1958 Meeting will be held in New York City, April 27, 28, 29, 30, and May 1, 1958, at the Statler Hotel. Sessions will be announced in a later issue.

Instrumentation for Use in Storage Battery Studies

G. W. Work and C. P. Wales

Naval Research Laboratory, Washington, D. C.

ABSTRACT

Instrumentation for use in a wide range of storage battery studies has been evolved. This storage battery analyzer features simplicity and accuracy of control, a wide scope of variables measured, and a complete, continuous record.

A null-balance servo system controls the output of the rectified d-c power supply at any desired current or voltage by continuously regulating the a-c input. Individual plate potentials, temperature, gas concentrations, and gas volumes are continuously measured and recorded. Optional equipment permits additional types of automatic cycling or other use in varied applications. The possibilities of the use of such methods are briefly illustrated and discussed from data on some Ni-Cd cells.

While many storage battery studies have been made in the past, much of the information has been difficult to interpret, at least partly because of the limited scope or type of measurements. The cell characteristics usually measured are voltage, current, and temperature, plus scattered observations of gas evolution, and, in the case of the Pb-acid battery, specific gravity of the electrolyte. Since each of these measured functions often includes several variables, the data may fail to indicate clearly where changes are taking place. The cell voltage, for example, is made up of the potential of both the positive plate and the negative plate. Since many factors affect each of these individually, cell voltage does not necessarily reflect the true picture. Individual plate potential measurements have often been made but seldom on a continuous basis. If the individual plate potentials are correlated with the gas evolution from that plate, the data become much more useful. In addition, data taken on a 24 hr/day basis, with such variables as current and temperature accurately controlled, would not only save time but might turn up unexpected yet important features.

In an attempt to obtain a more complete picture of an operating battery, a number of methods have been developed over the course of several years at this laboratory. More recently these methods have been incorporated into a single system which can be put into use and operated like any other laboratory instrument. This storage battery analyzer is simple to understand and use, and can, for the most part, be built from commercially available parts at a reasonable cost. Although the principles involved are not necessarily new, this analyzer's uniqueness lies chiefly in the combination of simplicity and accuracy of control, the scope of the variables measured, and the complete and continuous record obtained. While the equipment described is an outgrowth of work on alkaline storage batteries, it was so designed that it may be used with any other type of battery or with related problems.

Basic Units

The instrumentation consists of three general groups of components: (*a*) the power supply, (*b*) the analyzer, and (*c*) the recorder. All components are mounted on a standard 19-in. relay rack in a single cabinet except for the large wet test meters and power units rated at 30 amp or more.

Power supply group.—The power supply group includes the main power unit, a controller unit, and a battery for a low-voltage d-c source.

The main power units are built in several sizes in the interest of efficiency. Beginning with a 60-cycle a-c supply in each case, a full-wave rectified DC with maximum ripple of 1% is obtained by means of a variable transformer, a copper oxide type of rectifier, and a filter circuit. The small to medium size units operate from a 115-v single-phase line as a matter of convenience. Three-phase AC would be preferred, if available, since it gives a better current characteristic with less filtering and has been used with all large power units. The unit also houses the appropriately sized charge-discharge current relays, shunts, current and voltage indicating meters, and terminals. The recorder shunt value is chosen so as to give an indication well up on the recorder scale and so that the recorder reading will be a simple multiple of the actual current. Control shunt sizes are chosen so that the 10-turn variable resistors are not operated at their extreme ends and may usually be selected for easy reading from the dial for presetting both charge and discharge values. Regardless of the size or rating, all power units have uniform plug-in connections to the recorder and the controller, and thus may be used interchangeably to meet the specific power need. Terminals are also provided for attaching an appropriately sized discharge resistor. This resistor is selected to give the discharge circuit a potential drop somewhat greater than the cell potential so that the power unit must add a little to drive the discharge at the desired rate. These discharge resistors range from small radio types to large water-cooled units. An unusual type in this latter group is a motor-driven variable resistor consisting of a pair of spirally wound brass tubes with graduated wall thickness. This construction gives the effect of a tapered rheostat with a resistance range which permits a 2 v battery to be discharged at rates between 50 and 1000 amp.

The heart of the controller unit is a servo-amplifier system operating on the null balance principle. From the wiring diagram, Fig. 1, it may be seen that the input sig-

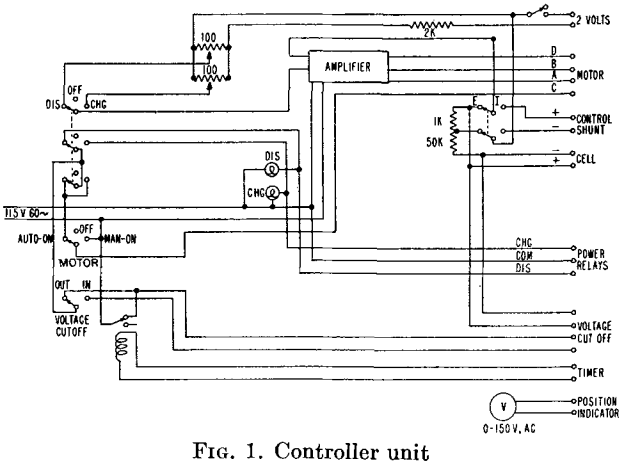

FIG. 1. Controller unit

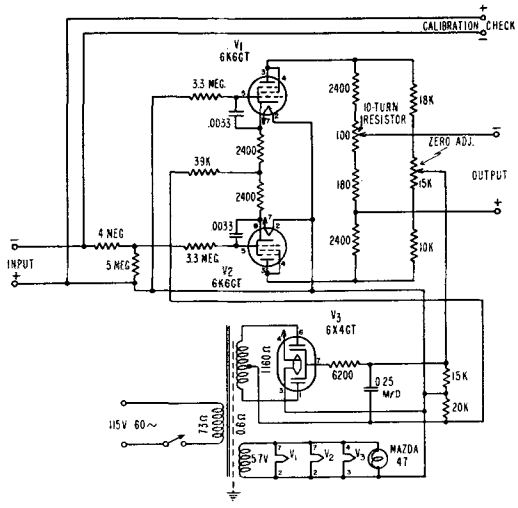

FIG. 2. Reference electrode unit

nal to the servo, taken from the control shunt (if current is to be controlled) or from a voltage divider (if voltage is to be controlled), is continuously compared with a standard millivoltage set by means of the 10-turn potentiometers, and powered by the 2 v Pb-acid cell. Any unbalance is converted to AC, amplified, and used to drive a two-phase induction motor geared to the variable transformer in the main power unit. Thus, the d-c output is continuously regulated by changing the a-c input to the rectifier. The controller unit also includes the necessary control switches, indicating lights, control knobs for setting the current or potential values for both charge and discharge, and a meter to indicate the position of the variable transformer. In addition there is space on the panel for insertion of a voltage cutoff unit. Although this controller has not been used for that purpose, there appears to be no reason why it could not regulate the output of a d-c generator, the servo motor being geared to the field rheostat.

The third part of the power supply group is a constant low-voltage d-c source, which is required to supply the bucking potential for the controller, power for the H analyzers, and, in some cases, power to the solenoid-operated gas volume marking pens. Suitable regulated electronic d-c sources are available but are expensive. A 2-v, 200-amp hr, low-discharge type of Pb-acid cell has been found quite satisfactory for the first two needs, and a small transformer-rectifier mounted on the recorder case is adequate for the recorder pens. Ideally, the H analyzers should have a constant current source, but, since the current can be recorded continuously for reference, this type of battery is adequate.

Analyzer group.—The reference-electrode unit plus an auxiliary electrode make possible continuous individual plate potential measurements. A Hg, HgO/OH^- half cell with its tip in the electrolyte just above the tops of the plates has been found quite satisfactory as a third electrode with alkaline batteries. The indication is somewhat affected by the position of the electrode tip in the lines of force about the tops of the plates during current flow through the cell being measured. If the tip is kept in the same position, however, reproducible measurements of magnitude and direction of potential change can be made.

The electronic part of the reference-electrode unit converts the potential between the half-cell and one battery terminal to a continuously recordable signal without polarizing the half-cell. This unit serves as many as three reference electrodes and is basically the pertinent parts of three high-resistance electronic voltmeters modified and mounted on a single chassis. A voltmeter is modified by simply replacing a resistor ahead of the indicating meter with a voltage divider of the same total resistance and taking the output to the recorder from part of this new voltage divider. Fig. 2 is a circuit diagram of one such modified voltmeter. Provision is also made for periodic setting or checking of the calibration by plugging a portable potentiometer into the jacks on the front panel.

The H analyzer determines the concentration of H in the gas evolved from one to three cells at a time by means of commercially available, thermal-conductivity-type measuring cells. The degree of bridge unbalance and the current passing through the cells are both recorded. The analyzer is calibrated at three current values with several concentrations so that if the current varies, the gas concentration can still be determined from the recorded cell current. Any spray is removed, and the gas is dried by passing it over solid KOH before it reaches the analyzing cells. With the water vapor thus removed, oxygen may be calculated readily from the H record.

Gas volumes are measured by the use of the proper size of wet test meter. Commercial wet test meters are available in volumes of one liter or more and need no alteration other than the addition of an electrical contact to facilitate recording the revolutions on a time recorder. In this case, the revolutions may be recorded by pens, mounted on the side of the main recorder, which mark on the edge of the chart in line with the recorder printing. A 20-ml wet test meter for use with small cells or low gas flows has been designed and built along the same general principles as the larger types. Fig. 3 shows an exploded view of the plastic rotor which is the basic measuring element in this meter. The revolutions of the rotor are counted by an optical photocell system triggered by a small mirror on the rim of the rotor. Thus, knowing the volumes of gas recorded

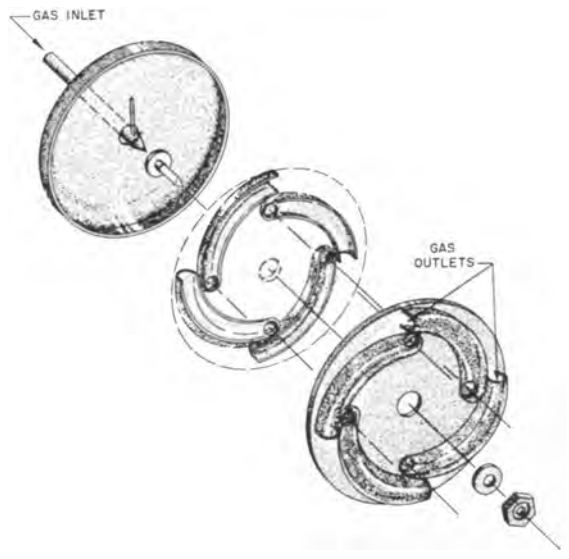

FIG. 3. Midget wet test meter rotor

against time and the gas concentration, H and oxygen gassing rates may be calculated.

Voltage dividers made from precision resistors are used to get recordable cell and/or battery voltages. Current values are obtained from appropriately sized shunts. Temperature measurements utilize the usual thermocouples. Using the measuring instruments in a temperature-controlled room simplifies gassing calculations, and another variable may be eliminated if the batteries being studied are in a temperature-controlled box.

Recorder.—Any standard, multipoint, strip chart, electronic, millivolt potentiometer which records continuously may be used to indicate and record data provided its selector switch is fully nonshorting between adjacent points. Staggering the points on the switch not only makes chart reading easier but also helps prevent trouble from high voltages between leads from opposite ends of a battery. The instrument most commonly used at this laboratory is a 16-point, 0–20 mv, self-balancing recorder with a choice of several chart speeds. It prints the sequence of points in about 2½ min, although this may be speeded up when desired. The three-pen, gas-volume marking equipment often used at the right side of the recorder paper was designed and built at this laboratory, but one or two pen units are available as part of the recorder from some manufacturers.

Optional Equipment

Voltage cutoff.—Control points are available for installation on some recorders. When so equipped, the recorder checks certain points each time they are measured, and if the value has reached an adjustable, pre-set upper or lower limit, a switch is operated automatically to open or close a circuit. If the cell voltage, for example, is connected to one of these control points, it may be used as an automatic voltage cutoff to end a charge or discharge.

For recorders not equipped with control points, a voltage cutoff unit may be added to the basic controller unit. This cutoff unit consists of a voltage-sensitive relay with built-in solenoid reset, an adjustable series resistor, and a small relay wired into the basic controller at the point indicated in Fig. 1.

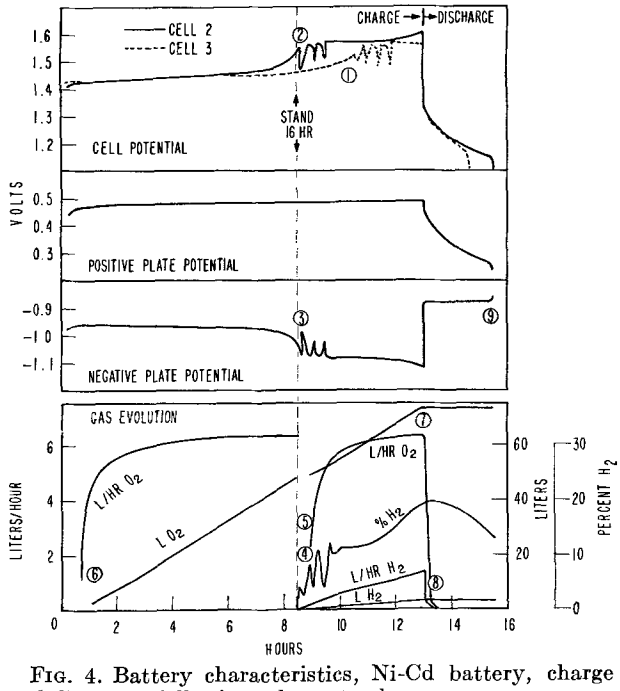

FIG. 4. Battery characteristics, Ni-Cd battery, charge and discharge following a long stand.

Cycler.—The basic controller has provision for starting, stopping, or delaying an operation by means of an external timer. Where automatic cycling is desired, the functions of the CHG-OFF-DIS switch are transferred to a pair of interlocking relays. The original CHG-OFF-DIS switch or a single-pole, double-throw, three-position switch then operates the relays during manual operation and a single-pole, double-throw timer operates them during cycling.

Another type of cycle to which the controller may be adapted is a cycle lasting a definite length of time but with both charge and discharge cutoff on voltage. Some AgO-Zn cells, for example, discharged at 10 amp to 1 v, immediately recharged at 4 amp to 2.1 v, and stood the remainder of 48 hr before automatically repeating the cycle.

A somewhat more common cycle is one where the charge is against time and the discharge is to a voltage. This is readily accomplished with the controller to which a voltage cutoff has been added with a minor wiring change to include a time-delay relay. This latter relay resets the voltage cutoff at the start of the charges.

Applications

Data from a Ni-Cd battery cycle may be used to illustrate one type of study made possible by the instrumentation and techniques described. In this cycle, cell voltage was measured on all four cells of the battery and, in addition, individual plate potential and gas evolution measurements were made on two of the cells.

In Fig. 4, data from one cell in each pair have been replotted from the recorder chart for easier reading. The voltage rise on cell 3 during the charge was slower than would be anticipated, but it appeared to be otherwise

normal until it began to fluctuate at ①. Although this fluctuation was found on two of the four cells in this cycle, it is not characteristic of a normal charge. Lacking any other information, this erratic behavior might be confused with a bad electrical connection or breakdown of a measuring component. A similar fluctuation appears at ② on cell 2, but, from the additional data taken, it is obvious that the fluctuations in the cell voltage are due to fluctuations in the negative plate potential ③, and are also reflected in the H concentration at ④. The volume of the gas meter per revolution was large enough to obscure a similar fluctuation appearing in the gassing rate at ⑤, but it was undoubtedly there.

Gas measurements ⑥ also indicate that gas evolution began early in the charge for cell 2. This suggests that the cell was either not deeply discharged or that it was not taking a charge. Calculations from the gas record ⑦ indicate that the net charge put into the positive plate of cell 2 was, however, about equal to the rated capacity of the cell. This would be the maximum, since positive plate capacity normally limits the cell capacity. In sharp contrast, the negative plate appears to have charged quite efficiently with only a limited amount of H having been evolved during the charge ⑧. When the charge was stopped, over twice the rated capacity of the cell appears to have been put into the negative plate; yet the lack of H evolution showed it was far from being fully charged. Furthermore, the negative plate potential began to drop near the end of the following discharge ⑨ in spite of the long charge. All this suggests that the self-discharge rate of the Cd plate was high under these conditions of stand and that there was a high ratio of negative plate to positive plate capacity in this battery.

More recent work on similar cells indicates that the apparent amount of charge taken by the Cd plate was not necessarily related to the true capacity. Gas measurements during stand show that the gassing rate of the Ni-Cd battery dropped off rapidly during the first few hours of stand. This lack of gas evolution does not mean that self-discharge had stopped, however, for residual discharges following stands indicate appreciably more capacity loss than could be accounted for by the evolved gas. While the cell characteristics were being observed on a 24 hr/day basis, the cell actually began to absorb oxygen from the atmosphere; this oxygen in turn oxidized the Cd plate.

Thus, it is sometimes possible to pick up and interpret unexpected characteristics from the detailed measurements on a 24 hr/day basis. A permanent record is also available for future evaluation in the light of later developments.

Manuscript received March 22, 1956.
Any discussion of this paper will appear in a Discussion Section to be published in the December 1957 JOURNAL.

Thermogalvanic Potentials and Currents at Aluminum Surfaces in Industrial Water

EDGAR C. PITZER[1]

Hanford Atomic Products Operation, General Electric Co., Richland, Washington

ABSTRACT

Potentials and galvanic currents at 2S Al surfaces in Columbia River water were studied between room temperature and 100°C. The Al potential changed by approximately 0.6 v over this interval, becoming more anodic with increase in temperature. Similar but somewhat smaller changes in potential were noted in buffer solutions.

By coupling identical Al samples, one at 100° and the other at room temperature, a maximum current density of 40 μamp/cm^2 was maintained.

During a study of the corrosion of Al in Columbia River water, an appraisal of possible thermogalvanic potentials and currents was undertaken.

In certain other systems, thermogalvanic effects of an appreciable order of magnitude have been observed. For example, Carr and Bonilla (1) found that a heated Ni electrode is anodic to its cooler counterpart. Similar results were reported by Uhlig and Noss (2) for Fe corrosion. Berry (3) found that Cu behaved in the opposite sense: a cold Cu electrode was anodic to a warmer one.

Only two references to the temperature coefficient of the Al electrode were found in the literature (4, 5). In both cases, a heated specimen of Al was anodic to a similar cooler specimen, but, as the determinations were made in fairly concentrated salt solutions, the results are not necessarily applicable to industrial water.

No quantitative predictions of thermogalvanic effects could be deduced from physical theory. The Thomson effect, a measure of the difference in potential between two areas of unequal temperature in a metal object, could not be used even qualitatively for Al, because of uncertainties in existing data (6). An analytical expression for the difference in electrical potential congruent with a difference in temperature between two points on a metal surface is afforded by the Fermi-Dirac statistics (7), but

[1] Present Address: General Electric Co., Appliance Park, Louisville, Ky.

no provision is made for possible electrolytic effects if the surface is immersed in a liquid.

An attempt by Jahn (8) to show that the Gibbs-Helmholtz equation applies to single electrode potentials is of doubtful validity, since at least two fundamental assumptions are involved: (*a*) that the temperature coefficient of a reference electrode may be determined, and (*b*) that the Nernst equation applies to the electrode under investigation. The first assumption is discussed by Lewis and Randall (9) and by Clark (10). In a more recent paper, Buffington (11) calculated that the temperature coefficient of the H electrode was −0.91 mv/°C, the minus sign indicating that the potential becomes more noble with increasing temperature. Combining this value with other thermodynamic data, Buffington computed a table of temperature coefficients for the electrode potentials of a number of metals. For Al, his estimate was −1.45 mv/°C, indicating a decrease in anodic tendency with increasing temperature. This result differs in algebraic sign from that reported in the previously cited papers (4, 5).

A specimen of Al immersed in a natural water is, of course, fundamentally different from a standard Al electrode. Not only is the water substantially free from Al ions; it is also within a range of *p*H incompatible with appreciable concentrations of Al in cationic form. Under such conditions the Nernst equation is inapplicable, either as originally derived or in the more sophisticated forms proposed by Butler (12) and by Gurney (13). In fact, the potential of an Al electrode in an aqueous solution within the *p*H range 5.5–7.5 lies near the bottom of a roughly U-shaped curve (14), and is extraordinarily sensitive to changes in acidity or alkalinity but not appreciably responsive to changes in concentration of Al ions.

An equation for the electrode potential of a metal dissolving in a solution practically free from its own ions has been derived by Glasstone, Laidler, and Eyring (15) in a form containing kinetic constants for which the temperature coefficients are not readily evaluated.

In view of these considerations, it is perhaps more realistic to abandon the concept of a reversible electrode, and to consider the metal to form not Al ions, but $Al_2O_3 \cdot 3H_2O$, which, according to Draley and Ruther (16), has been identified by x-ray diffraction methods on a corroding Al surface.

Writing the equation in terms of the observed phase:

$$2Al + 6H_2O \rightarrow Al_2O_3 \cdot 3H_2O + 3H_2$$

the standard free energy change can be calculated from the entropies of the reactants and products. From Kelley's monograph (17), the pertinent entropies at 25° are: Al, 6.77; $Al_2O_3 \cdot 3H_2O$, 33.5; H_2, 31.3; H_2O, 16.75.

The entropy change for the reaction is therefore 13.4 e.u., and the temperature coefficient, −13.4 cal/°C. The tendency for Al to react with water therefore increases with increase in temperature in the vicinity of 25°.

The course of the reaction is undoubtedly affected by the type of oxide film initially present on the Al. Samples were therefore tested with factory finish in order to evaluate the type of surface on the Al actually in use.

Experimental

Potentials in Columbia River water.[2]—Six 2S Al cans were immersed in a beaker of treated Columbia River water through which the rate of flow was 500 cc/hr. The cans were protected at the air-water interfaces by a coat of Tygon paint, leaving approximately 60 cm² of Al surface exposed to the water. Potentials of the cans were measured by comparison with a Beckman calomel electrode at room temperature at intervals during a 3-hr period in order to establish a basis of reference and to observe any variations in potential with time. Two of the cans were maintained in water at room temperature as controls during a further interval of 210 min, during which the remaining four cans were slowly heated in the beaker of flowing water. Potentials of the cans were measured throughout the experiment, as shown in Table I. Values of the electrode potentials are recalculated to the H electrode scale, correcting for the temperature coefficient of the calomel electrode. The difference in potential between hot and cold specimens was of the order of 0.6 v.

The *p*H of the exit hot water was observed to have risen from 7.4 to about 8.5 as measured at room temperature, presumably because of the decomposition of bicarbonate and expulsion of carbonic acid. The change in alkalinity was considered to be a possible contributing factor to the change in potential of the Al, hence a suitably buffered substitute for the river water was sought. Obvious requirements for a suitable solution were believed to be freedom from bicarbonates and extraneous salts, and a low enough permanent hardness to avoid precipitation of scale on Al during heating.

Potentials in simulated bicarbonate-free industrial water.—A solution containing 1 g $CaSO_4$/l was considered to be typical of a simulated bicarbonate-free natural water. Duplicate cans were heated in this solution as in the preceding experiment with two similar cans held in reserve in cold solution. A decrease in potential of 0.5 was noted, as recorded in Table II. During the experiment, potentials of the control cans changed by about 0.12 v, hence the net potential difference was approximately 0.4 v. The *p*H of the solution was 7.2 at the end of the experiment, indicating that a closer control of the *p*H does not eliminate the temperature coefficient of the electrode potential of Al observed during heating.

Potentials in 0.01M acetate buffer solution.—As a further expedient to confine the change in *p*H observed during heating within narrower limits, a series of 0.01*M* acetate solutions of initial *p*H 5.0, 5.5, 6.0, 6.5, 7.0, and 7.5 were substituted for the simulated industrial water. Admittedly, a difference in film characteristics should be obtained, but a marked change in the electrode potential of the underlying Al would not be expected as a result of the substitution of acetate for sulfate ion. Al cans were heated in the buffer solutions in the same manner as in the previous cases. Portions of the solution were removed periodically and cooled for *p*H determinations. Measured *p*H values were constant within 0.1 unit throughout all of

[2] Composition of Columbia River water (ppm): SO_4, 11; Mg, 4.2; SiO_2, 5.3; PO_4, 0.021; Mn, 0.008; Cl, 0.5; Na, 2.0; Ca, 21. Soap hardness, 69. Alkalinity: phenolphthalein, 0.5; methyl orange, 58. Specific resistance, 4,000 ohm-cm.

TABLE I. *Potentials of 2S* Al *in Columbia River water*
Flow rate, 500 cc/hr; convention: Std. H electrode scale (v)
(*a*) Room temperature

Time, min.	0	30	60	90	120	150	180
Specimen 1	−0.13	−0.13	−0.20	−0.29	−0.35	−0.36	−0.37
2	−0.13	−0.17	−0.19	−0.24	−0.29	−0.30	−0.33
3	−0.13	−0.12	−0.21	−0.29	−0.35	−0.36	−0.36
4	−0.15	−0.14	−0.19	−0.26	−0.30	−0.31	−0.33
Control 1	−0.14	−0.14	−0.14	−0.21	−0.27	−0.32	−0.36
2	−0.15	−0.15	−0.21	−0.27	−0.35	−0.39	−0.41

(*b*) Increasing temperatures

Time, min. Temp, °C	240 38	270 55	300 80	345 90	350 92	380 96	385 98	390 98
Specimen 1	−0.50	−0.52	−0.53	−0.60	−0.61	−0.67	−0.82	−0.85
2	−0.50	−0.52	−0.53	−0.61	−0.63	−0.69	−0.80	−0.85
3	−0.51	−0.52	−0.53	−0.65	−0.69	−0.70	−0.85	−0.88
4	−0.48	−0.51	−0.52	−0.64	−0.70	−0.75	−0.85	−0.93
Control 1	Maintained at room temperature							−0.19
2								−0.24

TABLE II. *Potential of 2S* Al *in* $CaSO_4$ *Solution (1 g/l)*
Voltages recalculated to standard H_2 electrode

Time (min). Temp, °C *p*H	0 6.15	15 6.13	30 6.10	45 6.09	60 Room temperature 6.09	75 6.12	90 6.15	105 6.20	210 6.21
Specimen 1	−0.06	−0.06	−0.06	−0.06	−0.06	−0.07	−0.09	−0.10	−0.12
2	−0.11	−0.11	−0.11	−0.11	−0.12	−0.12	−0.12	−0.13	−0.14
Control 1	−0.11	−0.12	−0.08	−0.09	−0.13	−0.12	−0.12	−0.12	−0.12
Control 2	−0.08	−0.08	−0.06	−0.06	−0.09	−0.08	−0.19	−0.09	−0.10

Time, Temp, °C *p*H	135 44 6.33	150 48 6.41	165 51 6.45	180 55 6.52	195 59 6.58	210 61 6.61	225 62 6.65	240 69 6.78
Specimen 1	−0.18	−0.18	−0.18	−0.18	−0.19	−0.25	−0.22	−0.21
2	−0.20	−0.22	−0.22	−0.29	−0.23	−0.24	−0.26	−0.38

Time. Temp, °C *p*H	255 70 6.86	270 73 6.95	285 82 7.10	300 85 7.22	315 91 7.25	330 95 7.32	345 97 7.30	360 97 7.20
Specimen 1	−0.42	−0.51	−0.64	−0.64	−0.66	−0.67	−0.66	−0.65
Specimen 2	−0.45	−0.56	−0.66	−0.65	−0.67	−0.67	−0.67	−0.66
Control 1	Maintained at room temperature							−0.26
Control 2								−0.26

TABLE III. *Potential of 2S* Al *in acetate buffer solutions at various temperatures*
Voltages recalculated to standard H scale at 25°C

Initial *p*H*	5.0		5.5		6.0		6.5		7.0		7.5	
Potential at room temp.	−0.15	−0.10	−0.16	−0.24	−0.26	−0.27	−0.17	−0.17	−0.06	−0.11	−0.10	−0.15
Potential at 99°C.	−0.38	−0.35	−0.83	−0.79	−0.75	−0.78	−0.72	−0.74	−0.82	−0.65	−0.70	−0.72
Potential after cooling at room temp			−0.26	−0.26	−0.25	−0.10	−0.26	−0.07				
Duration of experiment, min.	165		180		270		270		345		420	

All *p*H determinations were made on portions of solution cooled to room temperature.
* Value of *p*H constant within +0.1 unit through experiment.

TABLE IV. *Thermogalvanic currents*

Concentric cylindrical electrodes, approx. 45 cm² area.
Cold electrode at 20°.
Hot electrode temperature as noted.
Gas bubbling through cell.

None		Nitrogen		Oxygen	
Temp, °C	Current (μamp)	Temp,°C	Current (μamp)	Temp, °C	Current (μamp)
67	44	70	30	65	30
75	56	75	50	69	36
76	72	76	60	73	40
84	136	77	80	90	50
92	250	85	120	97	250
93	320	86	140	98	350
94	420	88	154	99	490
98	600	92	160	99.5	600
99	720	99.5	180	100	640
100	860	100	220		
Maximum C.D., anodic, amp/cm²					
1.9×10^{-5}		4.9×10^{-6}		1.4×10^{-5}	

the heating intervals. The Al became more anodic in all cases, as shown in Table III.

Galvanic currents between hot and cold specimens of Al *in Columbia River water.*—Potential differences reported in the preceding section were obtained by open-circuit measurements. There remained a need to determine whether a measurable current might be maintained between two similar Al surfaces at widely different temperatures when immersed in water.

An electrolytic cell was assembled, consisting of an Al can approximately 5 cm in diameter and 20 cm deep, and a sheet of Al obtained by shearing open a similar can. The upper ends of facing surfaces were painted with Tygon, leaving exposed surface areas of approximately 45 cm². The sheet of Al was bent to conform to the cylindrical can, leaving a clearance of approximately 2 mm around the intact can. The electrodes were mounted in a beaker through which Columbia River water was passed at a rate of 12 l/min. The can was provided with a rubber stopper containing a thermometer and inlet and outlet tubes, through which (*a*) hot water and (*b*) steam were passed. Temperatures up to 100° were readily maintained inside the heated electrode. The electrodes were connected through an external resistance of 1000 ohms and a microammeter.

(*A*) The galvanic current was small, of the order of only a few microamperes, until the temperature of the can reached about 60°C. From this point, the current increased rapidly with rising temperature to 860 μamp. Agitation with N served to lower the current by an appreciable amount, whereas the effect of a stream of oxygen was less marked (Table IV).

(*B*) The temperature of the can was held at 100° by a current of steam for 75 hr. The current was fairly constant at 1.8 ma throughout the experiment, corresponding to an average anodic current density of approximately 4×10^{-5} amp/cm².

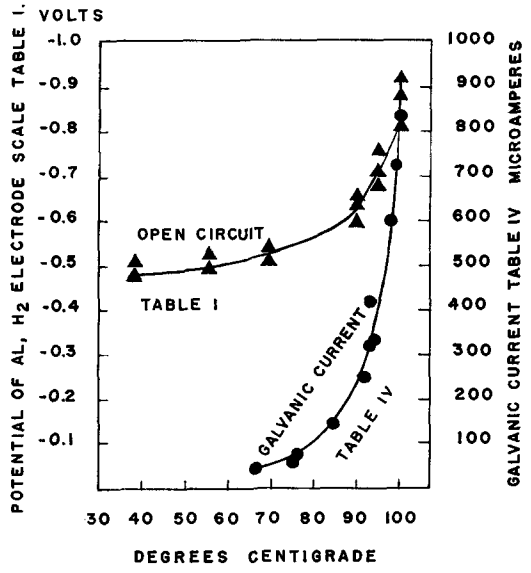

FIG. 1. Thermogalvanic potentials and currents o 99.4% 2S Al in Columbia River water.

DISCUSSION

Potentials in Columbia River Water

A comparison of potentials obtained at 100° with those of the control samples at room temperature is sufficient evidence that the differences in potential cannot be explained on the basis of time-dependency. The abrupt changes in potential indicate a mechanism unrelated to a simple temperature coefficient. It is more probable that the effects are related to film impairment.

The exact role played by the oxide film in depressing the electrode potential of Al has been the subject of much speculation and many ingenious explanations (18). Any operation that removes a portion of this film enhances the apparent "solution potential" of the metal (19). The results of Brown and Mears (20) show that the potential of Al becomes more anodic as the film is progressively scratched. A potential difference of 0.32 v was noted between the potentials of an unscratched coupon and one scratched by a standard procedure.

If the integrity of the hydrated oxide film is indeed the chief factor governing the magnitude of the observed electrode potential, the marked change above 90° might be attributed to an accelerated deterioration of this film. According to data of Draley and Ruther (16), the corrosion product undergoes a transition from β-$Al_2O_3 \cdot 3H_2O$ to α-$Al_2O_3 \cdot H_2O$ in approximately this temperature region. Accompanying the phase transition, there is undoubtedly widespread impairment of the protective film on the Al surface, so that unprotected metal is exposed as effectively as if it were scratched mechanically, as for instance by the technique of Brown and Mears.

Galvanic Currents

It was not feasible to make simultaneous measurements of open-circuit potentials and galvanic currents with the same specimens. By plotting the data of Tables I and IV on the same graph (Fig. 1), however, a significant correlation is evident. In the temperature range 40°–70°, the

open-circuit potential was fairly constant at -0.50 ± 0.02 v. Within the same range the galvanic cell measurements were very low, of the order of 1 μamp/cm^2. The gradual slope of the open-circuit potential curve over the temperature range 70°–90° is reflected in the galvanic current curve. From 90° to 100° the potential became more anodic by about 0.2 v, and the galvanic current increased from 220 to 860 μamp, corresponding to an increase from 5 to nearly 20 μamp/cm^2. For the duration of the experiment, at least, the slope of the galvanic current curve kept pace with that of the potential curve.

The 75 hr experiment demonstrated that the current was not stifled by polarization or film formation. The constant current of 1.8 ma corresponded to a current density of approximately 40 μamp/cm^2 of anode surface.

If this galvanic current is associated with a corrosion process, the rate of attack of the anodic surface under these conditions is readily calculated. One μamp is equivalent to 3.35×10^{-7} g Al attacked/hr. In the steam-heated cell, therefore, the rate of attack equivalent to the observed current was, for the duration of the experiment, 1.35×10^{-5} g/cm^{2}hr. From these data, it may be concluded that the observed galvanic current represented a serious corrosion hazard unless curbed by an inhibitor.

ACKNOWLEDGMENT

The author is grateful to the General Electric Co. and the Atomic Energy Commission for permission to publish this work, and to Y. B. Katayama and H. C. Bowen for assistance in making the electrical measurements.

Manuscript received August 22, 1955.

Any discussion of this paper will appear in a Discussion Section to be published in the December 1957 JOURNAL.

REFERENCES

1. D. S. CARR AND C. F. BONILLA, *This Journal*, **99**, 475 (1952).
2. H. H. UHLIG AND O. F. NOSS, *Corrosion*, **6**, 140 (1950).
3. N. E. BERRY, *Corrosion*, **2**, 261 (1946).
4. L. KAHLENBERG AND S. J. FRENCH, *Trans. Am. Electrochem. Soc.*, **52**, 355 (1927).
5. R. B. MEARS AND R. H. BROWN, *Ind. Eng. Chem.*, **33**, 1001 (1941).
6. GMELIN'S, "Handbuch der anorganischen Chemie," 35A, 268, Verlag Chemie, G.M.B.H., Berlin (1934).
7. J. E. MAYER AND M. G. MAYER, "Statistical Mechanics," pp. 407–414, John Wiley & Sons, Inc., New York (1940).
8. H. JAHN, *Z. physik. Chem.*, **18**, 399 (1895).
9. G. N. LEWIS AND M. RANDALL, "Thermodynamics," p. 431, McGraw-Hill and Co., New York (1923).
10. W. M. CLARK, "The Determination of Hydrogen Ions," 3rd ed., pp. 449–451, Williams and Wilkins Co., Baltimore (1928); T. W. RICHARDS, *Z. physik. Chem.*, **24**, 39 (1897).
11. R. M. BUFFINGTON, *Corrosion*, **3**, 613 (1947); N. E. BERRY, *Corrosion*, **3**, 216 (1946).
12. J. A. V. BUTLER, "Electrical Phenomena at Interfaces," p. 18, Methuen, London (1951).
13. R. W. GURNEY, *Proc. Roy. Soc.*, **136A**, 378 (1932).
14. R. MULLER AND F. HOLZL, *Z. anorg. Chem.*, **121**, 103 (1922); A. SMITS, *Z. Elektrochem.*, **30**, 431 (1924).
15. S. GLASSTONE, K. J. LAIDLER, AND H. EYRING, "The Theory of Rate Processes," p. 597, McGraw-Hill Book Co., New York (1941).
16. J. E. DRALEY AND W. E. RUTHER, ANL 5001.
17. K. K. KELLEY, "Entropies of Inorganic Substances," U. S. Bur. Mines Bull. 477.
18. W. J. MULLER, *Trans. Electrochem. Soc.*, **76**, 171 (1939).
19. L. H. CALLENDAR, *Proc. Roy. Soc.*, **115A**, 342 (1927).
20. R. H. BROWN AND R. B. MEARS, *This Journal*, **74**, 495 (1938).

Metallographic Study of Electroplated Coatings of Chromium and Nickel on Molybdenum

ROGER J. RUNCK

Battelle Memorial Institute, Columbus, Ohio

ABSTRACT

Single-layer and multiple-layer coatings of electroplated Ni and Cr on Mo were studied metallographically to determine why these coatings failed when heated in air. In single-layer coatings, Cr was less subject to bonding failure than Ni and afforded better protection against oxidation. Cracking of Cr coatings was probably a major cause of failure, but good protection by Cr was possible if a layer of Cr-Mo alloy was developed at the interface. Multiple-layer coatings of Cr and Ni in which Cr formed the initial layer may be superior to single-layer coatings, but formation of blisters between the layers of Cr and Ni was a major cause of failure of this type of coating.

Because of its outstanding mechanical properties, Mo is attractive for use in construction of parts that must function at high temperatures; however, a serious drawback to its use is its very high oxidation rate above 700°C.

Many coatings have been developed which show good promise of preventing this oxidation. Prominent among elements used for this purpose are Si, Cr, Ni, B, Al, and combinations of these elements. Some of the most protective of these coatings are brittle, and they are damaged if the coated part is deformed. Furthermore, many po-

tentially effective coatings can be applied only by heating the Mo to very high temperatures, e.g., by painting and sintering, flame spraying and sintering, vapor plating, metallizing, etc. Many of these coatings can be applied effectively only above the recrystallization temperature of cold-worked Mo (900°–1100°C) or potentially useful Mo alloys (1100°–1300°C). Since the mechanical properties of recrystallized Mo are inferior to those of the cold-worked metal, it should be coated and used below the recrystallization temperature (1, 2).

Electroplating is of interest because it is a method of applying protective coatings at low temperatures. Metals such as Cr and Ni are of interest because they are oxidation-resistant metals that can be electrodeposited readily. Cr is of particular interest because it is soluble in Mo and does not form brittle intermetallic compounds, and because it has low thermal expansion, similar to that of Mo (Table I). Ni is of interest because it has relatively good resistance to oxidation by atmospheres containing MoO_3 (3), and because it has very high ductility. Ni forms brittle intermetallic compounds with Mo, however. Ni also has relatively high thermal expansion.

Electroplated coatings of Cr and Ni on Mo were very effective in protecting Mo from oxidation; however, they did not produce consistent results. A solution to the problem of protecting Mo, therefore, appears to depend more on finding the causes of failure of the more promising coatings than on finding new or different types of coatings that may be used.

The protective value of any coating on Mo is limited to that of its poorest area. This is uncommonly true for Mo because a body of Mo can be oxidized and completely distilled at an amazingly rapid rate through even the minutest flaw in the protective coating.

It was because of this characteristic that a metallographic study of protective coatings on Mo was made. The primary purpose of this study was to determine some of the probable causes of failure. For this reason, many of the areas examined were those containing defects or those suspected of containing defects.

Procedures

Plating.—Standard plating procedures for Cr and Ni were generally effective when Mo was properly cleaned. Plating procedures similar to those used at Battelle were described by Korbelak (4).

Most of the samples included in this study were prepared for plating by etching in HF, but some were prepared by etching in alkaline ferrocyanide. This latter method now is generally preferred to the acid etch, but both methods appear to be effective.

Cr plating was done in a chromic acid bath, and both hard Cr and low contraction Cr plates were deposited and examined. Except where noted, all Cr plates were low contraction Cr.

Ni plating was from a Watts-type bath, but it was necessary to employ a Ni strike prior to plating in order to obtain a good bond. A high-chloride Ni strike bath was used.

Testing.—Most of the specimens plated and tested consisted of 5- to 6-in. lengths of 80-mil rod. Some flat specimens about $\frac{1}{2}$ in. wide and about $\frac{1}{20}$ in. thick also were tested.

TABLE I. *Coefficients of linear thermal expansion near 20°C*

Metal	Micro-Inches/°C.
Mo	4.9
Cr	6.2
Ni	13.3

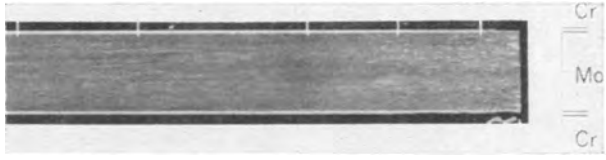

Fig. 1. Longitudinal section of 80-mil Mo rod electroplated with low-contraction Cr after 1077 hr at 900°C. Enlarged views of sections indicated are shown in Fig. 2. 10× before reduction for publication.

The coated specimens were tested in air by clamping them between water-cooled electrodes and applying sufficient electrical current to bring the temperature of the central portion up to the desired level. Most of the specimens were tested at 900°C, which was estimated to be about the maximum temperature to which cold-worked Mo could be heated without danger of recrystallization.

Temperatures were read with an optical pyrometer and were corrected for emissivity on the basis of an assumed value of 0.4.

Many of the specimens were removed before the protective coatings failed, but some of them were tested to destruction. Specimens that failed interrupted the current to an electrical timer so that testing time was automatically recorded in all cases.

Specimens tested in the above manner contained areas at all temperatures from room temperature to the maximum testing temperature. Because of this, it was possible to examine the structural changes at all intermediate temperatures for the period of time of any given test.

Metallography.—The metallographic procedures used were selected primarily for the purpose of revealing the crystalline structure of Mo. Specimens were first polished with a slurry of Al_2O_3 and chromic acid with heavy pressure on a fast wheel. A final short polish with light pressure was given with Al_2O_3 but without the chromic acid. Polished specimens were etched with Murakami's reagent. This procedure did not reveal the crystalline structure of the electroplated metal, but it did show the condition of this metal and revealed different phases in the coating.

Metallographic Structures

Fig. 1 shows a photomicrograph of a section of 80-mil rod plated with about 3 mils of low-contraction Cr. This specimen was held at 900°C for 1077 hr. The left end of the section was at room temperature, the right end at 900°C. As may be observed, recrystallization of Mo occurred in the high-temperature zone of the specimen. Enlarged views of five sections of this specimen from left

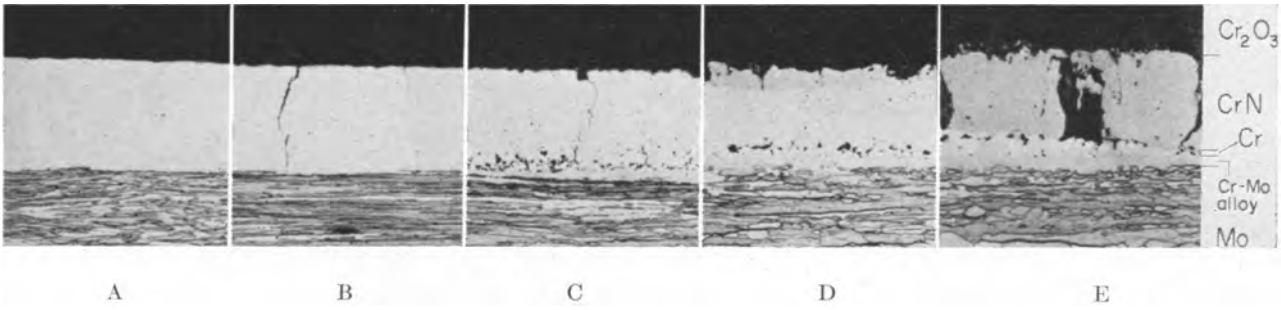

FIG. 2. Low-contraction Cr on Mo: section A, outside of heated zone; section B, inside heated zone; section C, inside heated zone; section D, inside heated zone; section E, after 1088 hr in air at 900°C. 250× before reduction for publication.

TABLE II. *Effect of different types of plate and of heat treatment in* H *on the lives of specimens of* Mo *electroplated with 3 mils of* Cr

Type of Cr plate	Life in air at 900°C, hr
Low contraction	300
Low contraction, heat treated	200
Hard	240
Hard, heat treated	50

to right, as indicated by the markers of Fig. 1, are shown in Fig. 2.

Fig. 2A, which is a section outside of the heated zone that is under the water-cooled electrode, shows the Cr plate to be nonporous, well-bonded plating. Section B shows this plating in a zone heated only to moderate temperature, well below red heat. Severe cracking is apparent. Cracking is also apparent in section C. In this zone, there is evidence of some alloying of the Cr plate and the Mo base. Under the microscope, the dark areas of section C appeared to be voids. It also may be noted that very slight recrystallization of Mo is apparent in this area. The layer of Cr-Mo alloy also is evident in section D, and it is of interest to note that it apparently is little greater in thickness than it was in the lower temperature zone shown in section C. Some chromium oxide on the outer surface of the plating is barely apparent in this section. The structure of this material, however, does not indicate that it afforded much protection to the underlying metal. Evident also is an additional phase under the chromium oxide layer which apparently is CrN. The formation of a nitride layer under the oxide layer on Cr plate heated in air was described by Snavely and Faust (5).

Section E shows the structure of the Cr plate at the zone of maximum temperature, i.e., 900°C. Of particular interest in this section is the indication that only the Cr-Mo layer would appear to afford protection to the body of Mo. This layer, which apparently is less than 1 mil in thickness, is only slightly thicker than it was in zones of lower temperature. The indication that the thickness of the Cr-Mo layer is not highly time and temperature dependent under the conditions employed in this work was further supported by the structure of Cr-plated Mo after being heated to 1500°C in air. The Cr-Mo alloy layer on one specimen heated for 45 hr at 1500°C was about the same thickness as that on another specimen heated only 12 hr at 1500°C, and both were

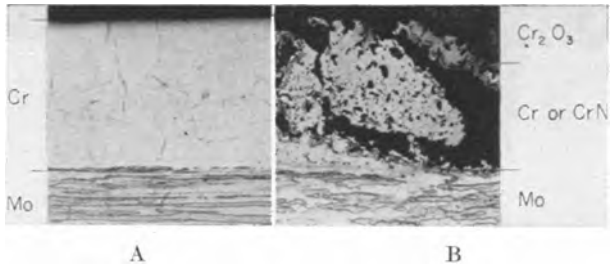

FIG. 3. Hard Cr on Mo: section A, outside heated zone; section B, after 1077 hr in air at 900°C. 250× before reduction for publication.

approximately the same as that of the specimen heated over 1000 hr at 900°C.

Because of the apparently protective nature of the layer of Cr-Mo alloy, it would appear desirable to preheat plated Mo in a nonoxidizing atmosphere, such as H, to develop the alloy layer before the specimen is heated in air. Such a procedure did not appear to improve the effectiveness of Cr plate, however, as is indicated by the results in Table II. Specimens tested were strips of Cr-plated Mo sheet $\frac{1}{2}$ in. wide by $\frac{1}{20}$ in. thick. Both low contraction and hard Cr were tested and one specimen of each type of plating was heated in H at 900°C for 72 hr prior to testing.

While flat specimens of Mo plated with Cr did not last more than a few hundred hours in air at 900°C, specimens of 80-mil rod plated with either low contraction or hard Cr were still good after 1000 hr under these conditions. The appearance of the low-contraction Cr after heating in air is shown in Fig. 1 and 2. The appearance of a similar sample plated with hard Cr is shown in Section A of Fig. 3. The porous nature of this type of plated metal is evident. The appearance of this plate after 1077 hr at 900°C is shown in Section B of Fig. 3. The Cr-Mo alloy layer, which was characteristic of the low-contraction Cr after heating, is not apparent in this figure. While this plating afforded better protection than was expected, it appears from Fig. 3 that its probable life at this temperature would be less than that of low-contraction Cr after similar treatment as was shown in Fig. 2.

Fig. 4 shows a specimen of 80-mil rod plated with about 3 mils of Ni. This specimen failed after 574 hr at 900°C. No general recrystallization of Mo is apparent in the zone of highest temperature except for a central zone which probably became very hot shortly before complete failure occurred.

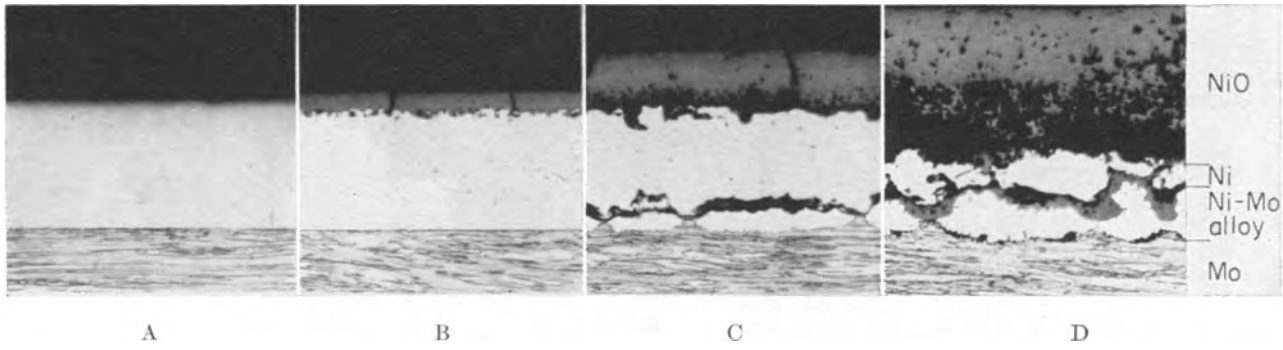

FIG. 4. Ni on Mo: section A, outside heated zone; section B, inside heated zone; section C, inside heated zone; Section D, after 574 hr in air at 900°C. 250× before reduction for publication.

FIG. 5. Longitudinal section of 80-mil Mo rod electroplated with Ni that blistered when heated in air to 900°C. 10× before reduction for publication.

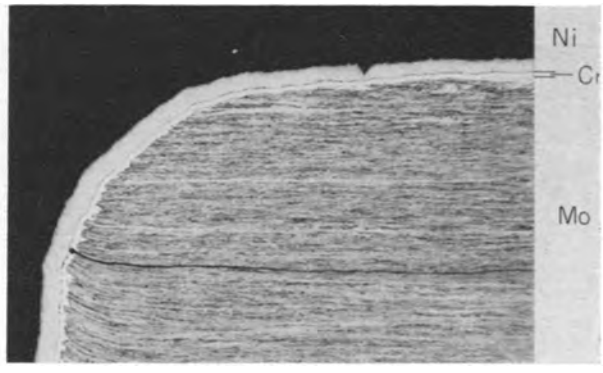

FIG. 6. Cr and Ni on laminated Mo sheet. 100× before reduction for publication.

Fig. 4A shows the Ni plate to be nonporous and to be apparently well bonded. Some porosity of the metal is apparent in a heated zone, however, as is shown in section B. A layer of NiO also is apparent in this section. Although NiO is very refractory (mp 1950°C), this oxide layer may not afford much protection to the underlying metal when it is thermally cycled because of the formation of cracks.

In section C, a zone very near that of section B, some alloying of Ni and Mo is apparent. This alloy formed only in islands, however, rather than in a continuous layer as did alloy between Cr and Mo. The formation of islands rather than a continuous layer of Mo-Ni alloy probably indicates imperfect bonding between the Mo and the electrodeposited Ni.

Section D shows a zone approximately at the maximum temperature, i.e., about 900°C. Islands of Ni-Mo alloy are connected in this zone, and this layer may well have afforded protection against oxidation in this zone.

While the Ni plating did not last as long at 900°C as a similar thickness of Cr, Ni might be serviceable as a protective coating. As was stated earlier, however, it was more difficult to obtain good adhesion of Ni than of Cr, and this characteristic of Ni probably contributed to blistering in Ni coatings.

Fig. 5 shows Ni plating on a specimen of 80-mil Mo rod, which blistered severely when heated to 900°C. A section of this plate in an unheated zone, as shown in Fig. 5, shows that it was not bonded to the base metal.

Because electroplated Cr cracked while Ni did not, it was thought desirable to cover the Cr plate with a layer of Ni. Two different types of multilayer coatings were examined, one a double-layer coating consisting of Cr and Ni, and the other a triple-layer coating consisting of Cr, Ni, and Cr. Double-layer coatings were attempted both with Cr as the initial layer and with Ni as the initial layer. Both types of coatings were successfully applied to 80-mil rods, but on flat specimens, attempts to plate Cr over Ni invariably caused the underlying Ni coating to peel from the Mo.

Of these various types of multilayer coatings, the double-layer coating in which Cr was the initial layer appeared to be the most promising.

Two outstanding features of this type of coating were: (*A*) If the layer of Cr was not too thick, the covering of Ni appeared to prevent the formation of cracks in the Cr layer. (*B*) The throwing power of Ni was better than that of Cr, and it usually covered faults or laminations in the Mo that extended through the Cr plate.

These properties of double-layer coatings of Cr and Ni are illustrated in Fig. 6 and 7 which are sections inside the heated zone of a flat test specimen.

However, blisters frequently formed inside the heated zone and often were centers of failure. Separation of metal to form a blister apparently occurred between the Ni and Cr layer, as is shown in Fig. 8. Laminations in the Mo, however, also may permit the formation of blisters, as is indicated in Fig. 9.

The tendency of Ni to buckle probably results because

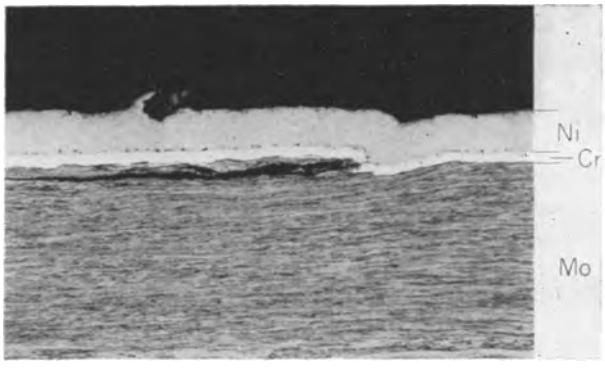

FIG. 7. Cr and Ni on laminated Mo sheet. 250× before reduction for publication.

FIG. 8. Cr and Ni on Mo sheet in a zone that blistered when heated. 100× before reduction for publication.

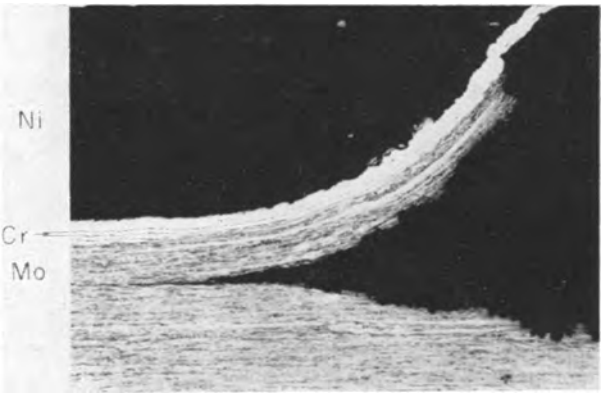

FIG. 9. Cr and Ni on Mo sheet in a zone that blistered when heated. 100× before reduction for publication.

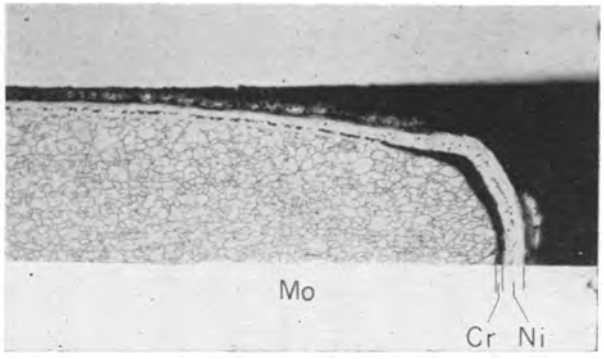

FIG. 10. Cr and Ni on edge of Mo sheet after 185 hr in air at 900°C. 100× before reduction for publication.

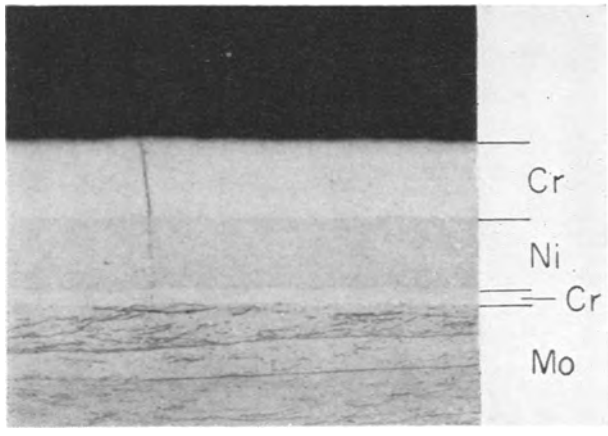

FIG. 11. Cr-Ni-Cr on Mo sheet. 250× before reduction for publication.

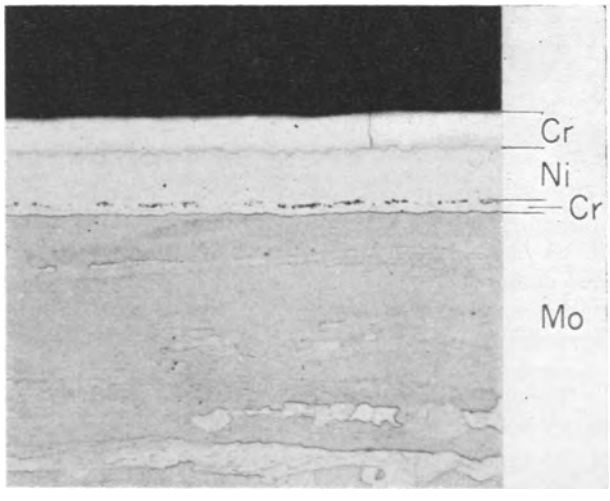

FIG. 12. Cr-Ni-Cr on Mo sheet after ½ hr in H at 1100°C. 250× before reduction for publication.

of its high thermal expansion. This explanation is supported by the separation of coating on the edges of flat specimens, as is shown in Fig. 10. In this figure, as in Fig. 8, it appears that separation occurred between the Ni and Cr layers.

An objection to the triple-layer plate consisting of Cr-Ni-Cr is the tendency of the outer layer of Cr to crack. In some cases, this crack extended through the underlying layers of Ni and Cr. Fig. 11 shows such a crack in a coating as plated. Fig. 12 shows the same type of coating with cracks only in the outer layer of Cr. This latter specimen was heated in H for the purpose of diffusing Cr into the Mo.

All of the multilayer coatings were effective in protecting Mo. Fig. 13 shows the structure of a double-layer coating of Ni over Cr on an 80-mil rod of Mo after 1000 hr at 900°C. It may be noted that the outer layer of NiO

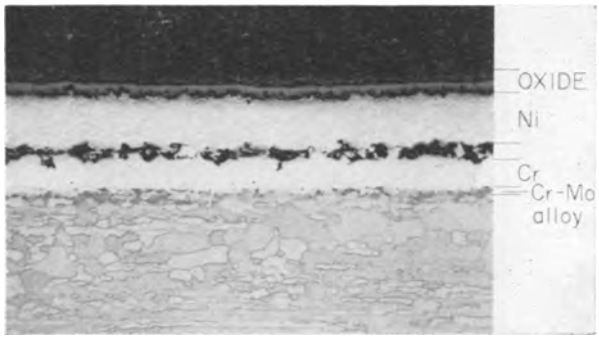

FIG. 13. Cr and Ni on 80-mil Mo rod after 1000 hr in air at 900°C. 250× before reduction for publication.

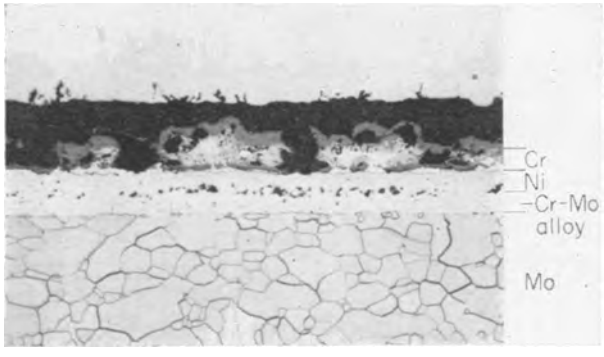

FIG. 14. Cr-Ni-Cr on Mo sheet after 185 hr in air at 900°C. 250× before reduction for publication.

is not cracked to the same extent as it was on samples of Mo coated with Ni only. Diffusion of Cr through the layer of Ni might have occurred to a sufficient extent to cause modification of the oxide layer on this specimen.

Fig. 14 shows a triple-layer coating of Cr-Ni-Cr on a flat specimen of Mo after 185 hr at 900°C. The outer layer of Cr does not appear to have afforded much protection to the underlying metal.

CONCLUSIONS

Electroplated coatings of either Cr or Ni afford considerable protection to Mo at high temperatures, but both types of coatings have shortcomings and, if used singly, are not likely to produce consistent results.

From this study, it appeared that the principal problems with electroplated Cr were its tendency to crack and its relatively poor throwing power during plating. Cr forms a good bond with Mo, however, and the interfacial alloy between these two metals appears to have good oxidation resistance and probably has good ductility. Electroplated Cr may be superior to Ni for protecting Mo. Of different types of Cr plate, low-contraction Cr probably is superior to hard Cr. Electroplated Ni, in contrast, apparently did not form cracks and it effectively bridged flaws in the base metal, but the problem of obtaining good adhesion of Ni appeared to be more formidable than that for Cr.

Undesirable features of electroplated Cr, that is cracking and poor coverage, may be overcome to some extent by covering it with a layer of Ni. The Ni layer appears to be capable of covering many of the faults that extend through the Cr plate and also preventing the Cr from cracking when heated. Ni has high thermal expansion, however, and, therefore, must be well bonded or it may buckle and form blisters when heated.

Electroplated Cr over Ni is not desirable because of the formation of cracks that not only may cause rapid deterioration of the Cr but also may extend through the Ni layer.

ACKNOWLEDGMENTS

The work described was done in 1951 and 1952 and was sponsored by the Fansteel Metallurgical Corp., whom the authors wish to thank for permission to publish this information. They wish to thank Dr. Yntema in particular for council and advice on problems associated with this work. They also wish to acknowledge the assistance of C. A. Snavely, G. M. Scanlon, and J. E. Clifford of the Battelle Electrochemical Division who did the electroplating, and R. D. Buchheit of the Battelle Metallographical Division who did the metallographical work.

Manuscript received February 13, 1956. This paper was prepared for delivery before the Pittsburgh Meeting, Oct. 9 to 13, 1955.

Any discussion of this paper will appear in a Discussion Section to be published in the December 1957 JOURNAL.

REFERENCES

1. J. H. BECHTOLD, *Trans. Am. Soc. Metals*, **46**, 1449 (1954).
2. N. L. DEUBLE, *Metal Progr.*, **68**, 105 (1955).
3. M. GLEISER, W. L. LARSEN, R. SPEISER, AND J. W. SPRETNAK, ONR Tech. Rept. 467-3, February, 1955.
4. A. KORBELAK, *Plating*, **40**, 1126 (1953).
5. C. A. SNAVELY AND C. L. FAUST, *This Journal*, **97**, 99 (1950).

Electrodeposition of Uranium at the Microgram Level

CHARLES L. RULFS, ANIL K. DE, AND PHILIP J. ELVING

Department of Chemistry and Engineering Research Institute, University of Michigan, Ann Arbor, Michigan

ABSTRACT

The recovery of microgram and submicrogram quantities of U by electroplating has been studied, using radioactive U-233 as a tracer with and without the presence of microgram quantities of natural U as carrier. Optimum results were obtained in an ammonium oxalate medium with electrolysis at 80°–85°C being performed first in acidic solution and then in alkaline solution. A small Pt disk which fitted into a flow counter was used as cathode, and a Pt spiral served as anode. With 20 μg of U carrier present and a volume of 25 ml, an average recovery, based on alpha counting, of 94 ± 3% was obtained for amounts of U-233 ranging from 0.03 to 0.13 μg.

Several methods have been described for the analytical electrodeposition of milligram quantities of U (1–6). In acetate medium, up to 4 mg U were deposited (2); results were not accurate due to variation in composition of the plates. Use of an oxalate medium at 80°–85°C gave satisfactory results with about 3 mg U (2). Up to 0.5 mg U was plated quantitatively from fluoride medium at room temperature (3–5). Micro quantities of U were deposited from oxalate medium containing potassium hydrogen phthalate buffer by electrolyzing at 80°–85°C in two stages: first on the acid side, then on the alkaline side (6). In all these cases a Pt disk was used as cathode, and the plated films were ignited to U_3O_8.

The use of an Al-Zn disk as cathode in oxalate medium at *p*H 8.0–8.5 and 80°–85°C has been reported (7). Two German patents (8) describe the deposition of metallic U onto Pt and other surfaces from an organic solvent like acetone which exerts no oxidizing action.

Recovery of microgram quantities of U from human urine by electroplating for the determination of alpha activity has been examined (9). One microgram of enriched U_3O_8 (130 α counts/min/μg) was added to 100-ml urine samples. After evaporation to dryness and ignition to destroy organic matter, the residues were dissolved; Ca was removed by double precipitation as the oxalate; and U was then electroplated at 80°C onto a Ni disk from the resulting ammonium oxalate medium of *p*H 9.6, using a current of 3 amp for 60 min. The recovery of U from 18 samples was 85 ± 4% with a precision of ±16% on a single sample.

Previous studies on the electrodeposition of U such as those cited above have generally been applicable only to the recovery of milligram amounts of U. Attempts to plate microgram quantities of U, usually present in rather small volumes of solution, resulted in U recoveries which were both low and variable. Apparently no reliable results have been reported for electrodeposition of submicrogram amounts of U. Consequently, the present study was initiated in an attempt to define conditions for more nearly quantitative recovery by electrodeposition of microgram amounts of U. In addition, an attempt was made to investigate the feasibility of electrodeposition of submicrogram amounts of U and to define the reproducibility of the procedure for microgram levels of U.

Initially, qualitative observations were made on the plates obtained from solutions containing 10^{-10} g U; such studies were deemed more significant than quantitative orientative work using much larger quantities and titrimetric or colorimetric measurement, since it was not felt that any proof of quantitative deposition at higher concentration, e.g., milligram amounts of U, would necessarily permit valid prediction of the behavior at very low concentrations. Moreover, the nature and appearance of the plate for milligram amounts of U could not be judged with any degree of reliability with respect to its suitability for radiochemical counting.

Quantitative studies were then made at microgram levels of U using a tracer technique and counting. The procedure finally developed may be applied for the recovery of 10^{-7} or 10^{-8} g of radioactive U, using 10^{-5} g of carrier natural U. At the milligram level, self-absorption phenomena become an important factor in counting. The present method uses for electrodeposition an ammonium oxalate medium, which has been found to be superior to citrate, tartrate, and phthalate media, inasmuch as the latter media introduce some difficulty in *p*H control during electrolysis.

The present procedure of recovering U by electrodeposition, and of measuring it by counting the activity of the plate, has been applied as the final separation stage and the measuring step in an analytical procedure for the determination of submicrogram quantities of U when present in admixture with large amounts of fission products (10).

EXPERIMENTAL

Apparatus.—The electroplating assembly consisted of a d-c power supply (Fisher Scientific Co. Powerhouse); a Tracer-Lab E-16 electrolysis cell containing a spiral Pt wire anode [a 10-in. (25 cm) length of 1-mm diameter wire, about 3 in. (7.5 cm) of which were wound into a flat spiral of 0.5-in. (1.25 cm) OD], a Pt disk cathode, and a motor-activated 500 rpm glass stirrer; and a simple external water bath for controlling the temperature of the electrolysis cell.

The cathode was a Pt disk or planchet, 0.15 mm thick by 25 mm diameter, obtained from the American Platinum Works. New Pt disks were pretreated by a hot HNO_3

wash, a water wash, then flaming; they were stored in a cell under water until used. For some of the runs, used Pt disks containing a U_3O_8 film were cleaned by repeated hot concentrated HNO_3 treatment and flaming. When their activity was close to the background level, the disks were considered good enough for use in another plating process. These disks were counted as blanks before plating and were stored under water until used.

A Model 952 windowless flow counter (2″ cathode) and a Model 1070 scaler (both made by the Atomic Instrument Company, Cambridge, Mass.) were used to count the alpha emission of the plated disks. The counting gas employed was Q-gas (99.05% He and 0.95% isobutane), which was dried with indicating Drierite (8-mesh), followed by Dehydrite.

Materials.—All chemicals used were of reagent grade.

The radioactive U-233 was obtained as a nitrate solution from the Oak Ridge National Laboratory; isotopic analysis gave 1.0–1.5% U-232 and 98.5–99% U-233 (α 4.82 mev; $t_{\frac{1}{2}} = 1.68 \times 10^5$ *y*). The original solution (13 μg U-233) was diluted to 100 ml which was about 0.01*N* in HNO_3; aliquots of the latter solution containing 1.3×10^{-8} g U/ml were taken for the experimental work. The activity per microgram of U-233 was determined, as subsequently described, to be 7700 ± 88 counts/min (background subtracted).

The carrier U was prepared from natural uranium nitrate (Baker and Adamson). The stock solution contained about 1 mg U/ml (0.01*N* in HNO_3), from which, after proper dilution, the solution used to furnish carrier, which contained about 10 μg U/ml (0.01*N* in HNO_3), was prepared.

Qualitative Studies on the Electrodeposition of Uranium

Three procedures were investigated to see what happened on electroplating about 10^{-10} g of U. In procedure A, based on that of Manning, Cali, and Phillips (6), the electrolysis cell solution was prepared by diluting 1 ml uranium nitrate solution (10^{-10} g U) to 25 ml and adding 5 ml saturated ammonium oxalate solution, 10 ml buffer solution (5.85 ml 0.217M potassium hydrogen phthalate and 4.20 ml 0.298M NaOH), and 2 drops methyl red indicator; the *p*H was 6.48. Electrolysis was carried out for 45 min at 80°–85°C, using an applied potential of 9 v with a resulting current flow of about 0.2 amp; the stirrer speed was about 500 rpm. Then, 1 drop (0.01%) phenolphthalein was added, followed by sufficient 6M NH_3 to turn the solution pink; the plating was continued for 10 min more with additional indicator and NH_3 being added as needed to keep the solution pink; temperature, current, etc., were the same as before.

In procedure B, 1 ml uranium nitrate solution (10^{-10} g U), 17.35 ml 0.1003M citric acid solution, 1 ml of 6M NH_3 solution, and 4 drops phenol red indicator (yellow at *p*H 6.50) solution were diluted to 25 ml. Electrolysis was performed as before at *p*H 6.50 for 45 min. NH_3 was added until the solution was red; more NH_3 and indicator were added, as necessary, to keep the solution red as the deposition was continued for 10 min more.

Procedure C was the same as procedure B, except that 21.0 ml 0.0927M tartaric acid solution was substituted for the citric acid and 0.75 ml 6M NH_3 was added.

At the end of electrolysis the current was left on as the spent electrolyte was siphoned off, and the cell and its contents were washed repeatedly with distilled water until the solution remaining in the cell was colorless. The circuit was then disconnected and the cell disassembled. The Pt cathode was rinsed with water followed by acetone, air dried, then ignited for about 10 min to U_3O_8.

The plates obtained by the three procedures were smooth, shiny, and adherent, showing bright interference colors. Procedures B and C seemed to be much simpler than A, at the same time giving deposits of better appearance. An additional advantage in the use of citrate or tartrate medium was that gas evolution at the electrode was much less than that in oxalate. Unfortunately, later quantitative studies showed that the use of citrate, tartrate, and phthalate introduced certain difficulties in the procedure; the latter were apparently due to reactions of these organic compounds which gave rise to very dark brown solutions. Consequently, an oxalate medium was used generally similar to that of procedure A except for the omission of phthalate.

Use of Al-Zn *disks.*—Attempts to use as cathode an Al disk coated with Zn were unsuccessful. In no case was the coating of Zn on Al smooth; as a result, electrodeposition was not at all satisfactory. An added disadvantage in actual use would be chemical contamination of the U sample when its recovery was desired. While Al-Zn disks are less expensive than Pt disks, the latter do permit recovery of uncontaminated U. The same considerations would be against the use of Ni or other disks.

Electrodeposition from organic solvents.—In an attempt to explore possibilities of plating U from organic solvents, the electrical resistances of various organic mixtures were examined in the electrodeposition apparatus described; results are summarized in Table I. Attention was focused on such compositions as could be achieved readily subsequent to a cupferron extraction of U(IV) which would be

TABLE I. *Qualitative studies of the conductivity of solution containing acetone, ethanol, and ethyl ether*

Run No.	Solution composition	Voltage applied, v	Current flow, ma
1	20 ml acetone (containing 0.8 g LiCl) + 10 ml ether	9	0.0
2	20 ml acetone (0.8 g LiCl) + 2 ml ether	9	0.6
3	25 ml ether (1.0 g LiCl) + 5 ml alcohol	9	0.0
4	5 ml ether (0.2 g LiCl) + 20 ml alcohol	9	1.5–2.0
5	10 ml ether + 10 ml alcohol (0.25 g LiCl) + 0.2 ml water	6	3.0
6	10 ml ether + 10 ml alcohol (0.25 g LiCl) + 0.5 ml water	6	3.1
7	10 ml ether + 10 ml alcohol (0.2 g LiCl) + 1.0 ml water	6	3.3–3.5
8	12 ml ether + 8 ml alcohol (0.2 g LiCl) + 0.5 ml water	6	2.2
9	15 ml ether + 5 ml alcohol (0.12 g LiCl) + 0.5 ml water	9	0.5

an efficient way of separating U from many other elements. The alcohol used in Nos. 3–9 was 95% ethanol. Although media of moderately good conductance were found, no electrodeposition of U from solutions of uranium(IV/III) cupferrate in such media was realized.

Quantitative Studies on Electrodeposition of Uranium at Microgram Level

Plating procedure.—The desired volume of U-233 solution was added to the electrolysis cell, followed by about 20 μg natural U carrier (uranyl nitrate solution), 5 ml saturated ammonium oxalate solution, 1 drop 6M HCl, 1 drop methyl red indicator, and 6M NH_3 until the solution was yellow. HNO_3 (6M) was then added until the indicator turned pink plus 2 or 3 drops in excess. The volume was about 20 ml. The cell was placed in a water bath, maintained at 80°–85°C, and the anode rotated at about 500 rpm. The solution was electrolyzed for approximately 30–45 min, using an applied potential of about 9 v with a resulting current flow of approximately 0.8–1.0 amp; from time to time HNO_3 and indicator were added dropwise to keep the solution pink. Then, 1 drop of phenolphthalain (0.01%) (more, as needed) and 6M NH_3 (more, as needed) were added dropwise to turn the solution pink, and the plating continued for 60–75 min more; temperature, current, etc., were almost the same as before.

The washing procedure at the end of electrolysis was the same as that previously described; the Pt disk was rinsed with water, followed by acetone, and air dried. It was then ignited for 10 min to U_3O_8, cooled to room temperature, and counted in a windowless flow counter.

Procedure for alpha counting.—With the counter set in "count" position, an initial flushing was done for 5 min with the pressure regulator gauge reading about 2 lb/in.^{2} and the gas flow being about 100 bubbles/min. Then the instrument was set in "load" position and the sample was introduced into the sample compartment. The counter was rotated to "flush" position, kept there for about 2 min, then moved to the "count" position. (The gas flow rate was then about 60 bubbles/min.)

The voltage plateau for alphas using pure U-233 was checked periodically. The operating voltage was 1550–1575 v, and discriminator setting was fixed at around 16–18. Betas are not counted under these conditions, as was noted by using a pure beta-emitting sample of Sr-90. Each U plate was counted over a sufficient period of time to give the desired statistical accuracy (±1–2% relative probable error). For calibration, a standard sample of U_3O_8 (National Bureau of Standards No. 836-5; 16.3 alpha counts/sec, assuming 50% geometry) was counted, then the unknown sample was counted. This was repeated five or six times and the average values were taken. Readings were fairly reproducible within statistical error. The background level of the instrument was 60–70 counts/min.

The calibrated activity of the plated sample was compared to the activity of the U-233 solution taken. The latter was determined by pipetting a 1-ml aliquot of the U-233 solution (1.3×10^{-8} g/ml) into a small 10-ml beaker by means of an ultramicro pipet, transferring the solution in portions by a medicine dropper with HNO_3 rinses onto a Pt planchet, evaporating under an infrared heater, igniting to U_3O_8, and counting the planchet. Five or six such samples were measured; the average activity was 7700 ± 88 counts/min/μg U-233.

Electrodeposition of U.—Results for the direct electroplating of U-233 in the presence of carrier are presented in Table II. The plates obtained were very smooth, shiny, and adherent, showing brilliant interference colors. If the first two runs are omitted because of their large error due largely to the low count, an average recovery of 94% ± 3% was obtained, after making correction for the activity of the 20 μg natural U used as carrier (15 ± 3 counts/min). Samples having 100–200 counts/minute (Nos. 1–4) were counted to give totals of 1000–2000 counts (relative probable error of ±2%), and those having 500 counts/min and higher activity were counted so as to give a total of 5000 counts (relative probable error of ±1%). Since only the percentage recovery of U-233 was required, disks containing evaporated and ignited aliquots of U-233 solution were used as a comparison for the plates obtained from electrodeposition.

Influence of carrier on electrodeposition of U-233.—Re-

TABLE II. *Electrodeposition of U-233 with 20 μg of natural U Carrier*

Sample No.	U-233 taken, g	Counts/min and standard deviation	Recovery, % (corrected for carrier activity)
1	1.3×10^{-8}	98 ± 9.9	82
2	1.3×10^{-8}	97 ± 9.9	81
3	2.6×10^{-8}	200 ± 14.1	91
4	2.6×10^{-8}	195 ± 14.0	89
5	6.5×10^{-8}	505 ± 22.5	97
6	6.5×10^{-8}	490 ± 22.1	94
7	13×10^{-8}	1004 ± 32.0	97
8	13×10^{-8}	1010 ± 32.0	98

Mean recovery (samples 3–8): 94.3%.
Standard deviation of the mean recovery: 3.0%.

TABLE III. *Effect of carrier on the recovery of U-233 by electroplating*

U-233 taken		Natural U carrier taken, μg	U-233 activity found, counts/min	Recovery, % (corrected for carrier activity)
Mass, g	Activity, counts/min			
3×10^{-8}	324 ± 17	10	284 ± 17	85.4
13×10^{-8}	1200 ± 35	0	840 ± 29	70.0
13×10^{-8}	1200 ± 35	10	1140 ± 34	94.6

TABLE IV. *Effect of carrier concentration on recovery by electroplating of 0.065 μg of U-233*

Natural U carrier taken, μg	U-233 recovery, %
50	96
20	101
10	102
5	95
2	70
1	84
0	77

coveries of 0.01–0.1 μg U-233 with no carrier present averaged about 70% (63% for 0.013 μg, 77% for 0.065 μg, and 70% for 0.13 μg). A series of runs using various amounts of carrier indicated that the presence of about 10–20 μg natural U as carrier was requisite for a satisfactory recovery of submicrogram quantities of U-233 (Tables III and IV). The figures in the last columns of Tables II, III, and IV have been corrected for carrier activity by subtracting 0.75 counts/min/μg of carrier from the observed counts/min (11).

In Table IV, the lower (apparent) recovery with 50 μg of carrier than the recovery with 10 or 20 μg, is indicative of the fact that self-absorption becomes a factor at this level.

Miscellaneous observations.—Recoveries using minimal electrolysis times of 30 min in acidic solution plus 60 min in alkaline solutions at 9 v applied were sometimes low. A safer specification is to maintain a current of 1.0 amp for 60 min on the acidic side and 90 min on the basic side.

The form in which U electrodeposits at a cathode is not definitely known, but it is thought to plate as a hydrous oxide (12, 13). In any event, the plate after ignition in air has been shown to be U_3O_8.

Attention should be called to the fact that current and time requirements for microgram level electrodeposition bear no relation to theoretically predicted requirements based on reasonable current efficiencies. Some of the quantitative studies at the milligram level have specified 10–15 min electrolyses at reasonable voltages and amperages; however, conditions such as 1 or more amp at 9 v for 1–2 hr are requisite at the microgram level. While the reasons for such a large discrepancy are not at all obvious, it is true that some precedent exists in more familiar and reversible systems. For example, a given arrangement which deposits 99.5% of a 0.5 g sample of Cu in less than 1 hr may yet require another full hour to plate out the next 0.4–0.5% (14).

ACKNOWLEDGMENT

The authors wish to thank the Air Force Cambridge Research Center, which supported the work described, and John L. Griffin and Herman Wissenberg for help with the experimental work.

Manuscript received March 2, 1956.

Any discussion of this paper will appear in a Discussion Section to be published in the December 1957 JOURNAL.

REFERENCES

1. C. J. RODDEN, "Analytical Chemistry of the Manhattan Project", in National Nuclear Energy Series VIII-I, pp. 523–535, McGraw-Hill Book Co., New York (1950).
2. B. COHEN AND D. E. HULL, Report A-1235, Part II, August 1944; cited in ref. (1).
3. M. KAHN, Special Report 24, April, 1943; cited in ref. (1).
4. R. C. LILLY, Assay Report 30, September, 1944; cited in ref. (1).
5. R. C. LILLY, Report RL-4.8.48, October, 1945; cited in ref. (1).
6. B. MANNING, J. P. CALI AND G. PHILLIPS, "Studies on the Decontamination and Determination of Uranium", Air Force Cambridge Research Center research report, June 15, 1954.
7. C. R. WILSON AND R. LANGER, *Nucleonics*, **11,** [8], 48 (1953).
8. WOLFRAM LAMPEN, A. G., German Pat. Nos. 231,657 and 237,014 (1911).
9. T. C. WHITSON AND T. KWASNOSKI, U. S. A.E.C. Report K1101, June, 1954.
10. C. L. RULFS, A. K. DE AND P. J. ELVING, *Anal. Chem.*, **28,** 1139 (1956).
11. E. H. FLEMING, JR., A. GHIORSO AND B. B. CUNNINGHAM, *Phys. Rev.*, **88,** 642 (1952).
12. H. J. S. SAND, "Electrochemistry," Vol. II, p. 84, Blackie & Son, London (1940).
13. G. E. F. LUNDELL AND J. I. HOFFMAN, "Outlines of Methods of Chemical Analysis," p. 168, John Wiley & Sons, New York (1938).
14. G. W. SLOMIN, "Rapid Quantitative Electrolytic Methods of Analysis", p. 10, E. H. Sargent & Co., Chicago (1942).

Influence of Impurities on the Photoconductance of Zinc Oxide

HAROLD A. PAPAZIAN,[1] PAUL A. FLINN,[2] AND DAN TRIVICH

Departments of Chemistry and Physics, Wayne University, Detroit, Michigan

ABSTRACT

The photoconductance of pure ZnO and ZnO with known impurities, both in powder form, has been measured using a condenser method. When irradiated by light, ZnO undergoes a "memory mechanism" which depends on the past irradiation history. It is suggested that the memory is caused by formation of traps independent of charge carrier formation. The concentration of traps is a function of impurity concentration and temperature. Consistent results in agreement with those of previous investigators could be obtained, but it is shown that this depends on predetermining the irradiation history of the samples.

The rate of excitation is given by $d\sigma/dt = kI^n$ where both k and n are sensitive to impurity concentration and temperature. The decay of photoconductance is largely the sum of two first order processes, but there can be no assignment of time constants to either hole or electron decay. A qualitative kinetic mechanism is proposed which agrees with phenomena observed in this investigation.

The photochemical formation of H_2O_2 as catalyzed by solid ZnO has received considerable attention recently (1–3). It has been shown in this laboratory that impurities in the ZnO affect this reaction rate (4). A fuller knowledge of the role of ZnO requires examining some of the details of the processes that follow light excitation; for this reason it was decided to study the photoconductance of ZnO. The relation of semiconductivity to catalysis has been pointed out (5–7), and the catalysis of nonphotochemical reactions on ZnO has been studied from this standpoint (8–10).

Previous workers have used very different samples of ZnO and, as a consequence, their results have not been comparable. Mollwo and co-workers (11–13) and Weiss (14) used thin films (0.1–0.3 μ) made by oxidizing Zn metal films evaporated onto quartz. They first presented the following equations as characteristic of photoeffects in ZnO:

$$i_L = ki_0^{2/3}I^{1/3} \quad \text{(I)}$$

$$(di/dt)_1 = k_1 i_0 I \quad \text{(II)}$$

$$(di/dt)_2 = k_2 i_L^2 i_0^{-2/3} \quad \text{(III)}$$

where i_L is the saturation or equilibrium photocurrent, i_0 is the dark current, I is the light intensity, $(di/dt)_1$ is the slope of the initial rise of the photoconductivity with time, and $(di/dt)_2$ is the slope of the initial decay of photoconductivity. It is shown later that Eqs. (I) and (II) are true only under special conditions and that under other conditions, exponents of I depart from the above values. Warschauer (15) and Melnick (16) used sintered pellets of ZnO.

In the present research photoconductance was studied on ZnO samples drawn from large prepared batches which also furnished samples for several catalytic chemical studies in this laboratory. The catalytic experiments required this material to be in powder form. The experimental method best suited for the investigation of photoconductivity of powders is the condenser method (17–19) in which the powder is put between the plates of a condenser. One plate of the condenser is transparent so that the sample can be irradiated, and the subsequent changes in the dielectric are measured.

EXPERIMENTAL

Preparation of the ZnO *powders.*—ZnO samples were prepared by starting with a $ZnSO_4$ solution[3] which had been especially purified for phosphor preparation. The solution was further treated, and Zn was precipitated as the oxalate with twice-recrystallized oxalic acid. The purified ZnC_2O_4 was decomposed to ZnO by firing in air at 410°C to constant weight. The sample without intentionally introduced impurities is called "pure" ZnO.

Impurities were introduced by adding to ZnC_2O_4 a soluble decomposable salt of the desired substance. The resulting slurry was evaporated to dryness with stirring, then fired at 410°C for 4–6 hr. Impurities were Li, Cu, Al, and Ga. The amounts were calculated to replace 0.01%, 0.1%, and 0.5% of the Zn atoms by impurity metal atoms. In the case of the Li samples it was necessary after the initial 410° firing to heat the ZnO to 600° to obtain constant weight. These samples were then cooled and held at 410° for 4 hr. [The ZnO samples containing Ga, for example, are referred to as "gallium samples" or as "ZnO-Ga (0.01%)"].

Analysis showed that the samples contained on the average about 99% of the expected Zn content for ZnO. Spectroscopic and other analysis showed the laboratory samples to be of very high purity. X-ray analysis gave the expected pattern for ZnO. Surface areas were measured (10) by a modified BET method and the samples were found to fall in the range of 10–20 m^2/g.

Since it has been shown (8) that foreign oxides affect the

[1] Present address: Research Lab., Raytheon Manufacturing Co., Pittsburgh, Pa.

[2] Present address: Research Lab., Westinghouse Electric Corp., Pittsburgh, Pa.

[3] Obtained from the Chemical Division of the General Electric Co., Cleveland, Ohio.

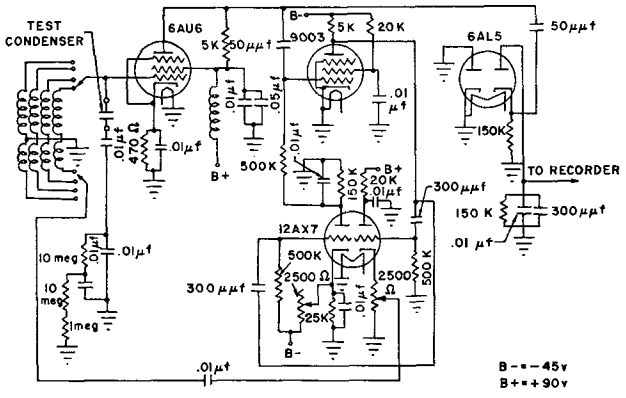

FIG. 1. Circuit for the measurement of the change in Q of the experimental condenser.

conductivity of ZnO, and presumably this is possible only when solid solutions are formed, it was assumed that the added impurities went into solid solution, as supported by the dark conductivity of the samples.

Apparatus.—In previous work with the condenser method the change in capacitance was usually measured. Because a change in Q [$Q = (X_L/R)$ = Inductive reactance/resistance] rather than a change in capacitance is more indicative of liberated photoelectrons, the measuring circuit in this research was designed with this point in mind. The oscillator always maintained itself on the resonance peak and was driven via the feedback coil with a constant driving voltage (Fig. 1). The RF signal was filtered, rectified, and recorded as millivolt changes on a Speedomax recorder which had a 1-sec full range sweep time. The circuit was calibrated by putting noninductive resistors of suitable value across the condenser, which had plain paraffin as dielectric. The resistors simulated the loss the condenser undergoes during irradiation. A calibration curve was made by plotting the change in millivolts appearing on the recorder against σ where $\sigma = 1/\text{resistance}$. Thus σ is proportional to the number of charge carriers released during irradiation and is called here the "photocurrent," or more properly the "photoconductance."

Fig. 2 shows the construction of the experimental condenser. It was machined from brass with Bakelite for insulation. The transparent electrode was electrical conducting glass.[4] A separation of 50μ was maintained between the plates of condenser. For measurements at low temperatures, the condenser was placed in a toluene thermostat.

The light source was a Hanovia Mercury Arc Sc5043. The various wave lengths were isolated with a Bausch and Lomb Grating Monochromator Type 33-86-40. The light intensity was measured with an Eppley Copper Constantan Spectrum Type Thermopile.

Procedure.—The powder was prepared for use as dielectric in the following manner: 6 g of paraffin was placed in a 20 x 70 mm vial and melted in a boiling water bath and 1.5 g ZnO was thoroughly mixed in. The mass was centrifuged to give a high density of ZnO in paraffin. It did not produce any undesired preferential packing of sample since slices from the top or bottom of the pellet gave the same results. The resulting pellet was allowed to cool and then was cut with a microtome into slices 50μ thick. The slices were kept in the dark until they were irradiated for measurement.

For measurement, a slice was placed in the condenser and the assembly completed. The condenser was placed in the thermostat and irradiated with the desired wave length. The resulting change in Q was recorded as a change in millivolts vs. time on the recorder.

Experimental Results

In general, each sample was characterized by a dark conductivity σ_D which appeared as a steady reading on the recorder. The dark conductivity was estimated by comparing the loss of the condenser using ZnO-paraffin as dielectric with the loss when the dielectric was plain paraffin. Ideally each grain is isolated from every other grain and the photoliberated electron is confined to the grain in which it originates.

When the light impinges on the sample there is a rapid increase in the number of charge carriers and this appears as a sudden change in millivolts on the recorder. After a time, a new equilibrium value of σ is reached. In many cases σ goes through a pronounced maximum and finally settles down to a new lower equilibrium or saturation value, σ_S. When the light is shut off, the photocurrent decays toward the value σ_D. Fig. 3 gives a typical curve. The value of the maximum photocurrent is σ_M; the saturation or equilibrium photocurrent is σ_S. The eventual value of the current after the light is shut off and rate of decay becomes essentially zero is $(\sigma_D)_\infty$. This value is taken as the end of the observable decay.

Preliminary experiments were made to check the applicability of equations (I), (II), and (III) to the samples and methods of this research. These were carried out on Merck Reagent ZnO Lot No. 53551. It eventually became apparent that the ZnO was undergoing a "memory mechanism" during irradiation in that when the light was shut off and the photocurrent decayed to σ_D, the samples were not the same as before irradiation. If the same experiment was repeated immediately neither σ_M nor σ_S was as large as in the first experiment. Weiss (14) was able to

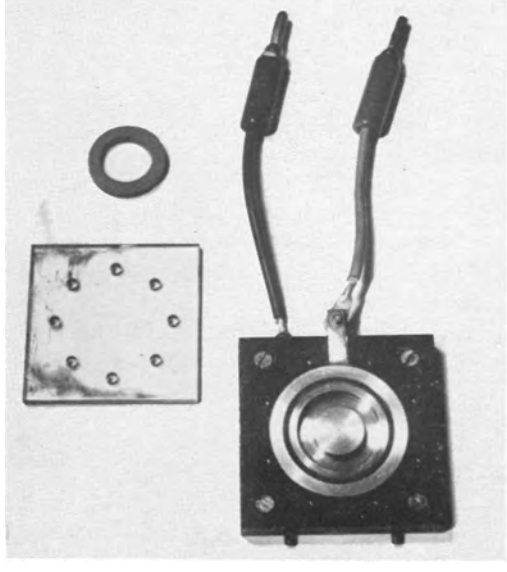

FIG. 2. Experimental condenser

[4] Obtained from the Corning Glass Works, Corning, N. Y.

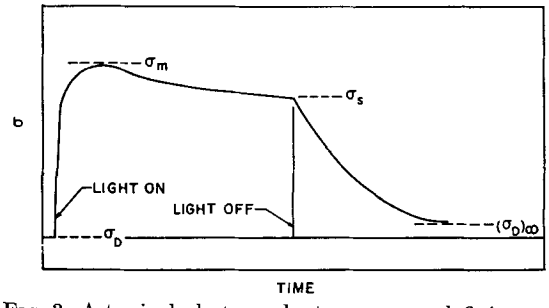

FIG. 3. A typical photoconductance curve defining terms used.

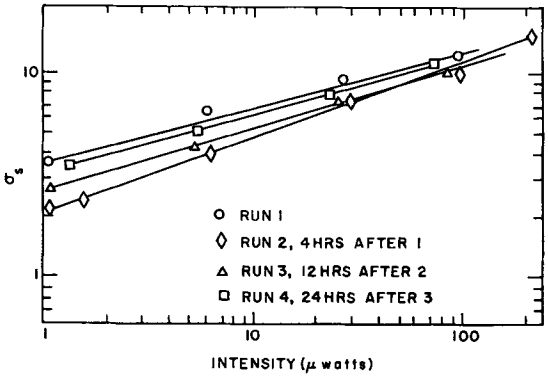

FIG. 4. Effect of various experimental time sequences, illustrating the memory effect (Merck Reagent ZnO).

reproduce equations (I), (II), and (III) only by doing his experiments in a prescribed fashion. Before each measurement he pre-irradiated his samples with light of $\lambda = 280$ mμ and then exposed them to the desired wave length.

In the present work a wide variation in the value for the exponent of I in eq. (I) was obtained depending on how the experiment was carried out. Fig. 4 shows how the exponent depends on the previous irradiation history. In Fig. 4 the exponent is given by the value of the slope of the plot of log σ vs. log I. The first point taken on each curve was the lowest intensity point; the sample was allowed to decay apparently fully and the next higher intensity point was taken immediately. Each point was taken in this manner until the curve was completed. From Fig. 4 the stages of recovery of the sample can be followed by the various time intervals between curves. Run 2 was taken 4 hr after Run 1, Run 3 was 12 hr after Run 2, and Run 4 was 24 hr after Run 3. If another sample was taken and the same sequence of measurements made, reproducible results were obtained. It is interesting to note that Run 1 in Fig. 4 has a slope of 0.32 in apparent agreement with equation (I). Values of about 0.3 could be obtained at will with new samples if the same sequence of measurements was followed, i.e., essentially the pre-irradiation treatment used by Weiss (14).

The effect of variation in sequence of measurement is further shown in Fig. 5. A curve starting with the highest intensity point taken first is compared with a curve with the lowest intensity point taken first. It can be seen that the curves do not coincide, indicating again the sensitivity of the sample to irradiation history.

Since oxygen plays a role in the photoconductivity of sintered zinc oxide samples (16), it was felt that perhaps oxygen on the surface of the ZnO was responsible for the memory by contributing a slow step to the rate processes.

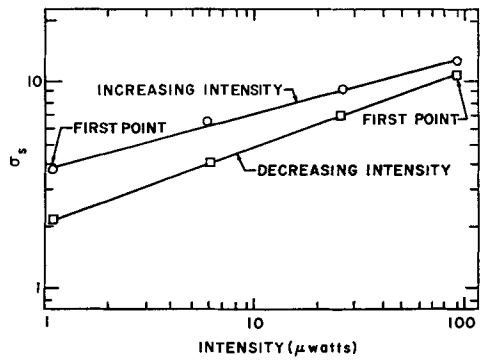

FIG. 5. Effect of irradiation history on memory (Merck Reagent ZnO).

Therefore, an experiment was carried out eliminating oxygen by mixing ZnO into paraffin under vacuum. The powdered ZnO was outgassed for several hours at 235°C, then mixed under vacuum with melted paraffin, which had also been outgassed. All subsequent steps were carried out in an oxygen-free N atmosphere. The sample had a much greater memory effect in that σ_M and σ_S were much less on the repeat measurement than on the first. It was also noted that the photoconductance curve for the oxygen-free sample exhibited a more prominent maximum. Thus it was apparent that the memory could not be removed by removing oxygen from the surface of the ZnO. These results cannot be correlated exactly with the effect of oxygen on the surface because on outgassing the ZnO became slightly colored, and this darkening has been interpreted as indicating interstitial reduced zinc (12, 22, 23). Samples used in this research were equilibrated with air and paraffin at the temperature of the boiling water bath.

Fig. 4 shows that the sample had substantially recovered after 12-24 hr, so it was decided to wait 24 hr between measurements to insure recovery, as in Fig. 6. The plot is no longer a straight line but shows curvature in contrast with the curves in Fig. 4.

The general procedure established in the preliminary experiments with the Merck sample was then applied to the other samples containing impurities. Fig. 7 shows a number of characteristic photoconductance curves for these samples. The figures are arranged in rows according to impurity type and in columns according to the experimental conditions of wavelength and temperature. All the samples are characterized by a saturation photocurrent, and many show pronounced maxima at room temperature. At 367 mμ all curves show at least a slight

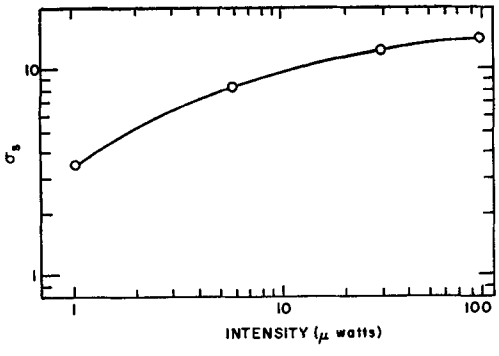

FIG. 6. Photoresponse of a sample rested between experimental points (Merck Reagent ZnO).

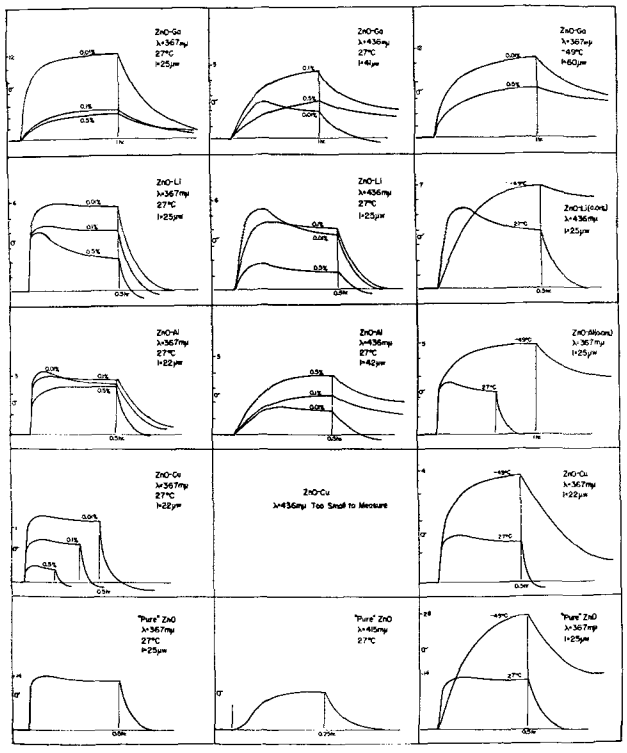

FIG. 7. Summary of a number of photoconductance vs. time curves, showing the build-up and decay. The subfigure in the third column and fourth row (Fig. 7—III—4) should be labelled ZnO-Cu (0.01%).

maximum except the samples containing Ga. In all cases but one to be discussed later, the photocurrent decreased when the light was shut off, but the current did not necessarily decay to the original dark current before illumination. The current, $(\sigma_D)_\infty$, may be either larger or smaller than σ_D, although in many cases it became equal to σ_D.

A number of measurements were made at −49°C also. The effect of temperature can be seen by comparing the curves in the third column of Fig. 7 with other appropriate curves. The saturation photocurrents are greater at −49°C than at room temperature for every case studied except Ga samples at 436 mμ. All of the maxima obtained at room temperature disappear at the lower temperature. The rise and decay are much slower, and the decay is very incomplete in all cases.

The effect of light intensity is shown for Ga in Fig. 8. All samples gave similar results in that the current values increased regularly at low intensities and decreased at very high intensities. The fact that the curve bends down at the higher intensities is taken to mean that even any one measurement is subject to error because of slow reversible changes in the sample due to illumination, i.e., the sample acquires an irradiation history even during the course of one measurement, and this memory effect is more pronounced at higher intensities.

If the values for the initial slope, $(di/dt)_1$, are plotted against light intensity on a log-log scale, good straight lines are obtained for several hundred-fold variation in intensity (Fig. 9). Thus the data can be fitted to an equation of the form $(di/dt)_1 = kI^n$. The value of the exponent, n, as determined from the slopes of the log-log plot, was found to be about 1 for all samples at room temperature at 367 mμ. However, at the lower temperature and at other wave lengths, the values of the exponent depart quite widely from unity. The fact that n can be different from 1 is indicative of a complicated process. Values of k and n are listed in Tables I and II. At very low light intensities, all samples showed a slight but definite induction period before the onset of photoconductance. The period varied from ¼ to 1½ sec. No induction was observed at lower temperatures and longer wave lengths, presumably because higher intensities were required to yield measurable photoconductance.

The decay curves could be analyzed as consisting of two first-order rate processes. Over 98% of the decay could be fitted to two first-order processes by proper choice of the asymptote for $(\sigma_D)_\infty$. The adjustment for the asymptote was no more than 1–2% of the decay. Applicability of the method is illustrated in Fig. 10 showing a typical plot of a sample containing Al impurity. The shorter time constants were of the order of ¼–2 min and the longer, about 4–20 min. Specific values are also given in Tables I and II. (It should be recalled here that there are other still slower decay processes which are responsible

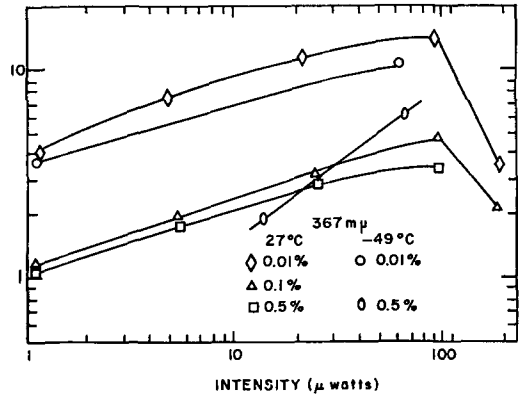

FIG. 8. Photoresponse of various ZnO-Ga samples as a function of light intensity and at two temperatures.

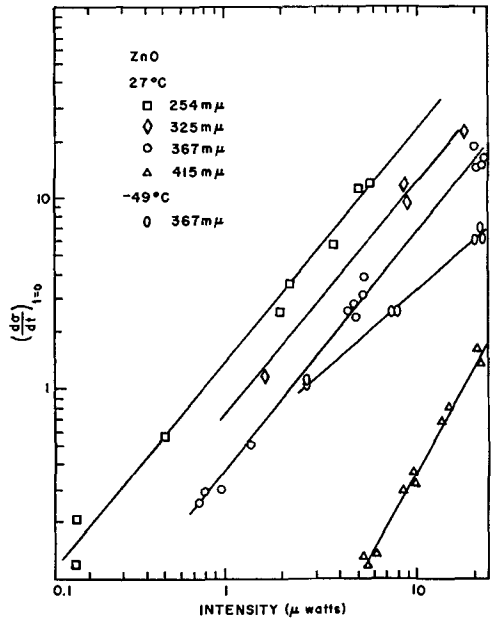

FIG. 9. Typical set of curves showing the effect of light intensity on the initial slopes of photoconductance. These plots are used to evaluate k and n in $d\sigma/dt = kI^n$.

TABLE I. *Summary of data at 367 mμ*

Sample	27°C										−49°C			
	k	n	Dark current	Low intensity	Medium intensity	High intensity	Decay constants		Max. wave length of response		k	n	Low intensity	High intensity
			σ_D	σ_S $(\sigma_D)_\infty$	σ_S $(\sigma_D)_\infty$	σ_S $(\sigma_D)_\infty$	$t_{1/2}$ min	$t_{1/2}$ min					σ_S $(\sigma_D)_\infty$	σ_S $(\sigma_D)_\infty$
ZnO				1 μw/cm²	25 μw	90 μw			cut off at				1 μw	67 μw
	0.36	1.23	2.5	0.6 0.0	6.5 0.0	12.5 0.0	¼–½	½–3	425 mμ		0.14	0.87	2.4 1.6	28 18
Cu					22 μw	80 μw							3 μw	63 μw
0.01%	0.32	1.1	5		1.2 −0.1	1.8 −0.2	¼	2	~436 mμ		0.40	0.91	2.8 0.8	4.5 0.7
0.1	0.05	1.1	4.2											
Li				1 μw	24 μw	72 μw							1 μw	65 μw
0.01%	2.2	1.0	6	2.4 0.0	5.2 0	12 0	½	2¾	~600 mμ		1.3	0.7	8 8	40 39
0.1	1.0	1.0	7		2.8 −0.1	4 −0.1	¾	3¼					3.8 μw	
0.5	1.4	1.16	5	0.8 0.0	1.5 −0.4	2.5 −0.5	¼	5			1.5	0.75	4 1.3	9.5 4.7
Ga				1 μw	25 μw	90 μw							1 μw	60 μw
0.01%	1.4	1.17	4	3.8 0.4	12 0.8	15 0		8½	~600 mμ		1.7	0.7	3.6 3.6	11 6.6
0.1	0.5	1.12	4	1.1 0.8	3.3 0.7	3.4 0.8		12					14 μw	
0.5	0.11	1.08	18	1.1 0.7	3 0.9	4.2 1.5		19			0.4	0.2	2.5 2.5	6.2 5.8
Al				1.4 μw	22 μw	80 μw							1.4 μw	25 μw
0.01%	0.28	1.1	5	1 0.1	2.2 0	2.5 0.2	¼	1½	~600 mμ		0.8	0.5	1.6 0.8	5.0 2.6
0.1	0.10	1.2	5		2.4 0.4		¼	3½						
0.5	0.30	0.68	6.5		2.1 0.3		½	3¼			0.2	0.5		14 13

TABLE II. *Summary of data at 436 mμ and 546 mμ*

	436 mμ						546 mμ	
	27°C					−49°C	27°C	
Sample	k	n	σ_S $(\sigma_D)_\infty$	$t_{1/2}$ min	$t_{1/2}$ min	σ_S $(\sigma_D)_\infty$	σ_S $(\sigma_D)_\infty$	
Cu			Too small to measure					
Li			25 μw					
0.01%	0.07	2.5	3.5 0	1	6	7.5 7	1.7	0.4
0.1	0.02	1	4.0 0	1.75	12			
0.5			0.8 −0.3	0.5	1.75			
Ga			41 μw					
0.01%	0.0002	3.2	2 −0.1	1	6	1 0.9	0.8	0
0.1			4.8 2.4		13.5		0.8	0.6
0.5			2.8 2.2		10		0.5	0.5
Al			42 μw					
0.01%	0.17	0.38	0.8 −0.1	0.25	3.5			
0.1			2.6 1.3	1	11			
0.5			3.6 2.3	1	11			

for the slow recovery of the samples over periods of 12–24 hr.) In the case of Ga samples, only a single measurable first-order process was observed, but a deviation from the first-order plot at very short times suggested the presence of an additional process with a very short time constant.

The saturation photocurrent, σ_S, usually decreased with increasing impurity concentration at 367 mμ (see Fig. 7). The only exception was the Al sample where there was some irregularity in σ_S; however, σ_M decreased regularly with increasing impurity concentration. At the lower temperature the same regularity was observed.

At wave lengths longer than 436 mμ the same sort of regularity of σ_S as a function of impurity was observed as at 367 mμ. At 436 mμ irregularities and inversions occurred. From Fig. 7 it can be seen that Ga and Li show an irregularity, where σ_S does not decrease with increasing impurity. With the Al samples there is complete inversion, that is σ_S increases with increasing impurity content.

The energy gap between valence and conduction bands in ZnO is approximately 3.2 ev, so that wave lengths longer than 385 mμ are not energetic enough to excite the width of the band. In the case of "pure" ZnO irradiated with 415 mμ light, the photoconductance shows an induction period at all intensities. A typical curve is shown in Fig. 7 in the fifth figure of column 2 (Fig. 7-II-5). In samples with 0.01% Li impurity, irradiation at 436 mμ produced a pronounced maximum in the curve where only a slight maximum was found at 367 mμ (Fig. 7-I-2 and Fig. 7-II-2). With 0.01% Ga, illumination at 436 mμ again produced a pronounced maximum, although in this case the total

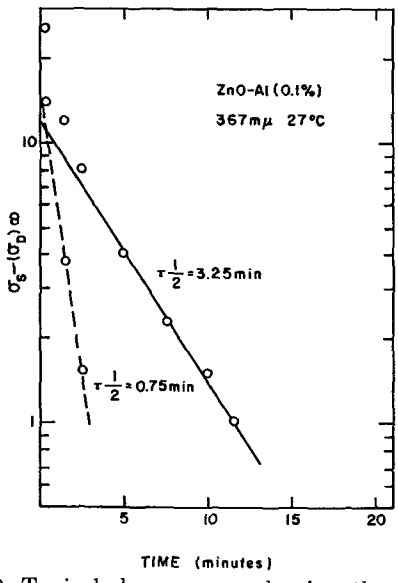

FIG. 10. Typical decay curve showing the manner of determining decay constants.

photocurrent was smaller than at 367 mμ. At still longer wave lengths these pronounced maxima disappeared again, and in both cases the photocurrents became much smaller.

The "pure" ZnO prepared in this laboratory behaved in a manner very similar to the Merck ZnO except that the Merck sample gave photoconductance to wave lengths as long as 700 mμ whereas the ZnO prepared in this laboratory cut off sharply at 425 mμ. This may be because of differences in purity of the samples since an emission spectrogram showed that the laboratory prepared ZnO was purer.

DISCUSSION

In general the shapes of all the photoconductance curves in Fig. 7 are similar, differing only in degree, e.g., at 367 mμ they all go through a maximum and then settle down to a lower final saturation photocurrent (σ_S). All samples show a decay in photoconductance which is the sum of two first-order processes, except possibly the Ga samples.

It appears that some transfer phenomenon is associated with the absorption of light and subsequent liberation of charge carriers which may be either electrons or holes or both. At 367 mμ and low light levels (~1 μwatt) there was a very definite induction period before onset of photoconductivity. As mentioned before, "pure" ZnO at 415 mμ (Fig. 7-II-5) exhibited an induction period at all light levels. If no transfer mechanism was involved, it would be expected that photoconductivity would begin immediately upon irradiation of the sample, but the fact that a finite length of time elapsed before the photocurrent began is indicative of the transfer phenomenon. Further, in the equation $(d\sigma/dt) = kI^n$, n changes with temperature. If liberation of electrons involved a direct interaction with photons, it would not be expected that n would change with temperature. Even in the simplest case of the results obtained at 367 mμ and at room temperature n is somewhat different from 1 indicating a complicated process. The wider departure of n from unity at other conditions is an even stronger indication.

Heiland (21) also postulated an energy transfer mechanism. From calculations of quantum yield during electron bombardment he concluded that the impinging energy must be absorbed in the lattice, then transferred to centers liberating charge carriers. According to Heiland, these centers are Zn^+ in interstitial positions, and from a calculation based on the energy required to split off another electron and the density of absorption centers, the capture cross section of these centers for bombarding electrons would have to be some 2×10^4 times larger than that for a lattice position, an unlikely situation.

Once the light is absorbed, the energy is transferred to electron or hole liberating centers and trap forming centers. These may be identical with each other or independent of each other. If only charge carriers were produced, a continuous regular increase of photocurrent would be expected, e.g., curve AB in Fig. 11. However, after a while the curve bends and establishes an equilibrium value. Either some saturation value in the number of charge carriers available has been reached, or as many carriers are being trapped out of their conduction bands as are being excited into them. The latter is more reasonable since the absence of traps is not likely. Curve ACD represents a saturation situation. When a maximum appears in the curve (ACE) it can be interpreted in terms of still another trapping mechanism which is photochemically induced and which becomes available after a time lag. If this trapping is not restrained by a time lag, the expected curve would be like AFE. Therefore the experimentally obtained curve ACE may be interpreted with the help of at least two trapping mechanisms, one of which has a time lag and is independent of charge carrier formation. On irradiation, charge carriers are liberated and these very soon begin to be trapped since the curve begins to bend over. After a time the delayed trapping mechanism becomes increasingly important and the photocurrent is reduced to a new lower equilibrium value (curve ACE).

Another observed phenomenon can be explained with another light-induced trap mechanism. When the irradiation is cut off on samples containing Li impurity, there is a small but definite temporary increase in photocurrent before decay sets in. A more detailed general mechanism is given below, considering the charge carriers as electrons and remembering that a similar scheme can exist for holes. According to this mechanism, the incoming photon can participate in two types of processes, leading to the production of photoelectrons and to the production of traps.

Generalized Mechanism

Photoelectron production

Excitation	$A + h\nu \rightarrow A^*$	(IV)
Transfer	$A^* + B \rightarrow A + B^*$	(V)
Photoelectron production	$B^* \rightarrow C + e$	(VI)
Trapping and immediate recovery	$C + e \rightarrow B +$ energy	(VII)
or	$X + e \rightarrow (X + e)$ and $(X + e) + C \rightarrow B +$ energy	(VIII)

Independent trap formation

Trap formation	$A^* + G \rightarrow A + H$	(IX)
Trapping	$H + e \rightarrow (H + e)$	(X)
Recovery (after trapping)	$(H + e) + C \rightarrow B + G +$ energy	(XI)
or recovery of traps	$H \rightarrow G +$ energy	(XII)

Possible subsequent trap formation

Trap formation...	$A^* + C \rightarrow A + D$	(XIII)
Trapping and recovery.....	$D + e \rightarrow B +$ energy	(XIV)
or.....	$D + e \rightarrow F \rightarrow B +$ energy	(XV)

A schematic representation of this generalized mechanism involving steps (IV) through (XII) is

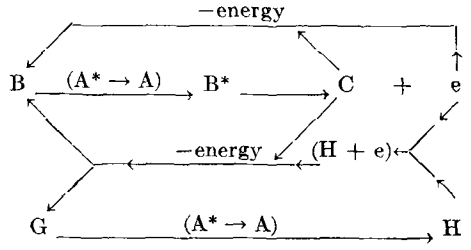

In this mechanism, H and C or D are traps for the photoelectrons.

In order to show that the generalized mechanism can be made more specific, Eqs. (XVI) through (XXVI) are given as a possibility. However, this example is only one of several possibilities, and there is not sufficient evidence at present to permit a selection of the correct mechanism from these possibilities.

Example

Photoelectron production

Excitation.....	$A + h\nu \rightarrow A^*$	(XVI)
Transfer.....	$A^* + Zn_i^+ \rightarrow (Zn_i^+)^* + A$	(XVII)
Photoelectron production...	$(Zn_i^+)^* \rightarrow Zn_i^{++} + e$	(XVIII)
Trapping and immediate recovery.....	$Zn_i^{++} + e \rightarrow Zn_i^+ +$ energy	(XIX)

Independent trap formation

Trap formation.	$A^* + Zn_i^+ \rightarrow A + Zn_L^+ + O_O^=$	(XX)
Trapping.....	$O_O^= + e \rightarrow \textcircled{e}_O^=$	(XXI)
Recovery.....	$\textcircled{e}_O^= + Zn_i^{++} \rightarrow Zn_i^+ + O_O^=$	(XXII)
	$O_O^= + Zn_L^+ \rightarrow Zn_i^+ +$ energy	(XXIII)

Subsequent trap formation

Trap formation.	$A^* + Zn_i^{++} \rightarrow A + Zn_L^{++} + O_O^=$	(XXIV)
Trapping.....	$O_O^= + e \rightarrow \textcircled{e}_O^=$	(XXV)
Recovery.....	$Zn_L^{++} + \textcircled{e}_O^= \rightarrow Zn_i^+ +$ energy	(XXVI)

where A = lattice; A^* = excited lattice; Zn_i^+ = interstitial Zn^+; Zn_L^+ = lattice Zn^+; $O_O^=$ = anion vacancy; and $\textcircled{e}_O^=$ = electron trapped in anion vacancy (F center).

The initial discussion is confined as much as possible to the generalized mechanism. According to this, the photon excites the lattice in a fast step giving A^*, which subsequently passes on its energy in a thermal step to the charge liberating center B. The excited B^* releases conduction electrons in a subsequent thermal step (VI). If B^* is a reservoir requiring buildup, the mechanism will explain the observed induction period.

The probability of trapping increases with increasing concentration of conduction electrons, and the photocurrent will rise only until the rate of production and rate of removal of charge carriers become equal. The trapping could be a simple recombination according to reaction (VII), but the first-order decay processes observed suggest that a good portion of the trapping may be by a large relatively constant concentration of traps X as in (VIII). The sequence of steps (IV) through (VIII) results in a curve of the form ACD with a steady-state photocurrent as at D.

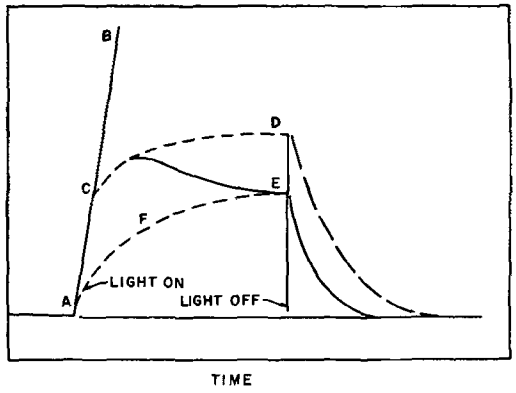

FIG. 11. Various hypothetical photoconductance curves

The fact that the photocurrent usually goes through a maximum requires a more extended interpretation. Assuming that the rate of production of photoelectrons is constant with time, then it becomes necessary to postulate a later increased rate of trapping. The fact that this lags behind the onset of illumination suggests that the traps are photochemically produced through a moderately slow thermal step. This independent formation of traps and their trapping is given in steps (IX) through (XI). Combining steps (IV)-(VIII) with steps (IX)-(XI) would result in curve of the form of ACE.

The two-trap mechanism involving one independent trap formation also helps to explain the memory of the samples. If two photocurrent curves are run consecutively, both σ_M and σ_S in the second curve are smaller, and in curves with a maximum the maximum becomes modified and $(\sigma_M - \sigma_S)$ is decreased. If only Eqs. (IV)-(VIII) were the trapping mechanism, then when e combined with C the original lattice would be reproduced. With H being formed independently, the sample can have a memory, i.e., there may be many H traps left after the initial decay of photocurrent. When the sample is irradiated the second time, these traps can contribute to trapping immediately. In a photocurrent curve with a maximum, the maximum tends to disappear since now a time lag is not required for some H traps to be available. In other cases with small maxima, the total photocurrent is reduced.

The postulated H trap formation [Eq. (XX)] requires some explanation. In ZnO, anion vacancy formation by an anion jumping into an interstitial position is unlikely; therefore, some other mechanism must be operative. It is assumed that an anion on a normal lattice site moves to the outer surface, along with its cation, by an unspecified diffusion process. The cation vacancy formed is filled by an interstitial monovalent cation, and the anion vacancy remains as such. This complicated mechanism may require an unduly long lifetime for the exciton for which no explanation can be given.

For the recovery mechanism [Eq. (XXIII)] there is surface to bulk diffusion of the ions. These involved processes are in accord with the slow buildup of traps and the memory of ZnO.

The evidence indicates that both trap formation and charge carrier formation are very temperature dependent. At −49° C the buildup of photocurrent as measured by initial slopes is very much slower than at room temperature. This indicates a strong temperature dependence for charge carrier formation. The induction period before onset of photoconductivity may also indicate an activation or thermal step.

At the low temperature in spite of the lowered rate of production of charge carriers, there is appreciable photoconductivity, in most cases larger than at room temperature, with a very small amount of decay when irradiation is cut off. This can mean either that the rate of production of traps is greatly dependent on temperature or that, instead, the rate of trapping after the traps have been formed is very dependent on temperature. If the latter part of this statement were true, then the rate of trapping should slow up but not stop until the decay of the photoconductivity is substantially complete. In fact, the trapping not only slows up but stops completely at very small values of total trapping. Hence, the trap formation mechanism must be the one which is very strongly influenced by temperature.

In the case of the Li-containing samples which exhibit a temporary slight increase in photocurrent after illumination is cut off, it becomes necessary to extend the general mechanism further. Apparently in these cases some contribution to the total trapping rate which is present in the illuminated steady state becomes inoperative in the dark. This suggests a light-induced trap formation and trapping such as that given by Eqs. (XIII)–(XV). These traps would be used almost as quickly as formed so that none would remain to contribute to the trapping in the dark during the decay. Thus the reservoir of B^* could continue to supply conduction electrons for a short time in the dark so that a temporary imbalance in production and removal of conduction electrons could exist in favor of a temporary increase in their number. Later this reverts to a decay of photoconductance as the reservoir of B^* becomes depleted and the trapping by other processes continues.

There seems to be some resonance phenomenon associated with the second trapping mechanism [Eqs. (IX)–(XI)]. Samples such as 0.01% Ga and 0.01% Li which show no maxima at 367 mμ show a very appreciable peaking when irradiated with 436 mμ. When irradiated with wave lengths longer than 436 mμ, the peaking again disappears. Since light absorption by the lattice is presumably confined to wave lengths below 385 mμ, the phenomena studied at longer wave lengths probably involve initial absorption of photons by portions of the ZnO which are dependent on the manner of preparation, such as impurities and other types of imperfections.

It is tempting to seek a model to describe the general mechanism in more detail. However, it is dangerous to ascribe any great reality to such models since the present state of knowledge on such a complicated system as ZnO is too meager for such detailed examination. Miller (23) has expressed a similar opinion. However, it is instructive to inquire into the more common models proposed by other authors to see to what extent they can serve to explain the experimental facts developed in this research and more particularly to see what discrepancies become obvious.

While it is not definitely known yet to what extent the bonds in ZnO are covalent or ionic, the convention of previous authors will be used, and the structure will be considered as ionic. The normal condition for strongly fired ZnO is that the composition of the compound departs from a stoichiometric ratio in the direction of excess Zn. The excess Zn is said to occupy interstitial positions and ionize to give excess electrons. These excess electrons are responsible for the electrical conductivity and cause the ZnO to be an *n*-type semiconductor. This may be represented by the equation

$$\mathrm{ZnO} \rightarrow \mathrm{Zn}_i^{+} + e + \tfrac{1}{2}\mathrm{O}_2 \qquad \text{(XXVII)}$$

or

$$\mathrm{ZnO} \rightarrow \mathrm{Zn}_i^{++} + 2e + \tfrac{1}{2}\mathrm{O}_2 \qquad \text{(XXVIII)}$$

It is well known that the electrical conductivity of ZnO increases with decreasing O_2 pressure. This can be easily understood with mass action concepts. An equivalent situation arises if ZnO is considered to have anion vacancies instead of excess cations in interstitial positions. This general type of model has been carried further in order to explain the probable effect of impurities on the electrical conductivity of ZnO.

If a small amount of gallium oxide is introduced as an impurity in ZnO, the process may be viewed as a replacement of a lattice Zn ion by a Ga ion. If the restriction is imposed that the oxygen ions are not disturbed and that the Ga assumes its normal valence of three, the model would predict that an additional electron would become available for conduction. Thus Ga or in general any trivalent metal oxide added as an impurity would increase the excess semiconduction of ZnO. An equivalent argument can be made by postulating that the effect of Ga is to decrease the number of interstitial Zn ions as suggested by Molinari and Parravano (9). In the case of Li and monovalent metal oxides, the model would require the replacement of two lattice Zn ions by Li and increase the interstitial Zn. Then by mass action it would be expected that the electrical conductivity would decrease.

This sort of model was used by Mollwo (12) and later by others to explain the increased conductivity which results from excitation of ZnO by light. He postulated that the interstitial Zn was in the form of Zn^{+} and the light, after being accepted into the crystal, was used to split off the second electron giving Zn^{++}.

The model requires that the electrical conductivity of ZnO should be increased by addition of trivalent metal oxides and decreased by monovalent metal oxides. In this paper the electrical conductivity is designated by σ_D (Table I). The predictions are not borne out by the present experimental data inasmuch as all of the samples containing impurities exhibit a larger σ_D than "pure" ZnO. However the samples were fired at a relatively low temperature. This choice was made in order to minimize the normal departure from stoichiometry so that the effect due to the purposely added impurities would not be

swamped by large effects due to temperature-induced imperfections. The firing temperature may have been too low to establish predicted equilibria.

With this model and assuming equilibrium, it might be expected that the final value of the photocurrent would depend on the interstitial Zn and the interstitial Zn in turn depend on the type and concentration of impurity. Detailed examination of the present data does not show the expected trends in all cases. This situation is not surprising if a closer examination is made of the data. The value of the photocurrent at any point is a resultant of the opposing processes of excitation and trapping. It can be seen from Table I that the excitation rate, as measured by the k values, not only depends on the temperature but also on the type and concentration of the impurity. The trapping also depends on temperature and impurity concentration. The photocurrent that arises from these opposing processes can have no easily predictable values.

It should also be recalled that in the case of powders, surface effects can be quite important. Adsorbed substances can also act as acceptors or donors to the bulk of the ZnO. Melnick (16) has shown the effect of adsorbed oxygen on the conductivity of sintered ZnO. In the present experiments all samples were given the same pretreatment in order to avoid further complication in the study of the effect of desired introduced impurities. Even in the case of the desired impurity, the possibility of a nonuniform distribution of the impurity on the surface and through the bulk of the samples introduces additional uncertainty in interpretation. Because of this it will be difficult to find a correlation between conductivity and catalysis with semiconductors, since conductivity is primarily a bulk phenomenon influenced to a considerable extent by the surface, while catalysis is primarily a surface phenomenon perhaps affected in part by the bulk properties of the catalyst. Correlation between photoconductivity and photocatalysis may be even more difficult to establish. In the case of samples used in this research, some correlation was found (4) between the photocatalytic efficiency for the H_2O_2 reaction and the initial rise of the photoconductivity at 367 mμ as measured by the values of k in the second column of Table I. Details of this correlation and its significance in the photocatalytic process will be reported later with the photocatalytic studies.

Summary and Conclusions

ZnO undergoes a memory mechanism when irradiated by light with a time constant of the order of 12–24 hr. The memory depends on the past irradiation history of the sample, and because of this any measurement is subject to some uncertainty. In the light of the present work, relations for the dependence of photoconductivity on the intensity of light found by Mollwo seem to be conditioned by his choice of procedure. Analysis of the curves for a possible mechanism for photoconductivity leads to the suspicion that the memory is caused by the formation of traps independent of charge carrier formation.

Concentration of traps is a function of impurity concentration and temperature. The rate of excitation, as measured by the k values, is also a function of impurity concentration and temperature. Since both excitation and trapping appear to depend on the impurity concentration in a complex manner, the matching of the two effects at σ_S can occur almost anywhere. Thus, it is dangerous to try to establish any regular progression in photoconductivity with impurity.

The decay of photoconductivity is largely the sum of two first order processes, and it is attractive to assign one decay constant to the decay of holes and the other decay constant to the decay of electrons. This cannot be done with any certainty, however, since it is not known which contributes the most to conductivity.

The results of this investigation cannot be reconciled with any existing model for ZnO. Since it is shown that the results depend on the impurity and the irradiation history, it appears that disagreement or agreement among previous workers is due to dissimilarities or similarities in their samples and procedures in these respects.

Acknowledgment

This work was made possible by grants from the C. F. Kettering Foundation.

Manuscript received May 25, 1955. Based in part on a dissertation presented to the Graduate Faculty of Wayne University by Harold A. Papazian in partial fulfillment of the requirements for the Ph.D. degree, January 1955.

Any discussion of this paper will appear in a Discussion Section to be published in the December 1957 Journal.

References

1. J. G. Calvert, K. Theurer, G. T. Rankin, and W. M. MacNevin, *J. Am. Chem. Soc.*, **76,** 2575 (1954).
2. T. R. Rubin, J. G. Calvert, G. T. Rankin, and W. M. MacNevin, *ibid.*, **75,** 2850 (1953).
3. M. C. Markham, and K. J. Laidler, *J. Phys. Chem.*, **57,** 363 (1953).
4. R. Stephens, B. Ke, and D. Trivich, Unpublished work.
5. M. Boudart, *J. Am. Chem. Soc.*, **74,** 1531 (1952).
6. D. A. Dowden, *J. Chem. Soc.*, **1950,** 242.
7. H. M. Hulburt, "Catalysis," Vol. II, Ch. 3 and 4, p. 167, Reinhold Publishing Corp., New York (1955).
8. C. Wagner, *J. Chem. Phys.*, **18,** 69 (1950).
9. E. Molinari, and G. Parravano, *J. Am. Chem. Soc.*, **75,** 5237 (1953).
10. H. Soonpaa, Ph.D. Thesis, Wayne University, January 1955.
11. E. Mollwo, and F. Stöckmann, *Ann. Physik*, (6) **3,** 223 (1948).
12. E. Mollwo, *ibid.*, (6) **3,** 230 (1948).
13. E. Mollwo, and F. Stöckmann, *ibid.*, (6) **3,** 240 (1948).
14. H. Weiss, *Z. Physik*, **132,** 335 (1952).
15. D. Warschauer, Technical Report No. 2, Contract N6-onr-24914, University of Pennsylvania (Jan. 25, 1952).
16. D. Melnick, Technical Report No. 9, Contract N6-onr-24919, University of Pennsylvania (Feb. 5, 1954).
17. L. Bergmann, *Physik Z.*, **33,** 209 (1932).
18. A. Volke, *Ann. Physik*, (5) **14,** 193 (1932).
19. E. K. Putseiko, *Izvest. Akad. Nauk S.S.S.R., Ser. Fiz.*, **13** (2), 224 (1949).
20. G. Heiland, *Z. Physik*, **132,** 367 (1952).
21. F. Stöckmann, *ibid.*, **127,** 563 (1950).
22. E. E. Hahn, *J. Appl. Phys.*, **22,** 855 (1951).
23. P. H. Miller, "Semi Conducting Materials," p. 172, Academic Press Inc., New York (1951).

Ultraviolet Fluorescence of Some Ternary Silicates Activated with Lead

H. A. KLASENS, A. H. HOEKSTRA, AND A. P. M. COX

Philips Research Laboratories, N. V. Philips' Gloeilampenfabrieken, Eindhoven, Netherlands

ABSTRACT

The fluorescence and phase diagrams of the following Pb-activated ternary systems were investigated: SrO-MgO-SiO_2; SrO-ZnO-SiO_2; BaO-MgO-SiO_2; BaO-ZnO-SiO_2. Eleven new ternary silicates were identified, some of which proved to be very good base materials for Pb-activated phosphors with peak emissions ranging from 3000 to 4000Å.

Fluorescent lamps producing radiation in the region of 3000–4000Å are important for many applications, e.g., the sunlamp, which emits in the short wave-length region near 3000Å, and which is used to produce erythema. For this, radiations of 2800–3200Å are most effective with maximum response at 2970Å (1). Sunlamps are used also for the production of vitamin D from sterols. The most effective region for synthesizing vitamin D from ergosterol is 2490–3130Å (2).

A second type of ultraviolet (u.v.) lamp, the black-light lamp, emitting in the region of 3600Å, is used in a number of applications such as laundry marking, blueprinting, instrument dial illumination, window displays, etc. For the last two applications use is made of phosphors, such as sulfides, which are excited by long wave length ultraviolet.

The number of fluorescent substances which produce u.v. radiation in the region of 3000–4000Å, when excited by the Hg resonance radiation of 2537Å, is not very large. Ce-activated phosphors often fluoresce in this region, but they are less suitable in practice because of maintenance difficulties in Hg-discharge lamps and deterioration during processing. Tl-activated phosphors are more suitable. One which is used often is $Ca_3(PO_4)_2$-Tl (3, 4), which has an emission maximum at 3250Å. A more effective erythemal phosphor can be produced by partial substitution of Zn for Ca (5) which shifts the maximum to shorter wave lengths. In black-light lamps Pb-activated $BaSi_2O_5$, having an emission maximum at 3500Å, is often used (3).

The present article describes an attempt to extend the list of suitable u.v. phosphors. Since Pb-activated phosphors often have an emission in the u.v. region, most attention was paid to this activator. Because silicates appear to be the most suitable base materials for activation with Pb, several ternary systems containing SiO_2, one oxide of the group CaO, SrO, BaO and furthermore MgO or ZnO were investigated. Many new compounds were found, some of which appeared to be excellent base materials for Pb-activated phosphors.

EXPERIMENTAL METHODS

Materials used included the carbonates of Ca, Sr and Mg, ZnO, SiO_2 of very fine grain size,[1] and a Pb compound, usually the nitrate. A thick alcoholic slurry was made of the oxides and carbonates. This slurry was ground in a small glass jar mill and mixed with the required amount of the activator, mostly $Pb(NO_3)_2$ dissolved in water. The paste was dried and sometimes milled in a small agate runner mill. The resulting powder was fired in open alundum crucibles at 1000°–1200°C for a few hours. Often the activator was added in the form of PbF_2. A few percent of the fluoride of one of the basic oxides was also added occasionally. Although very little F is found in the fired material by analysis, its presence in the raw material blend often has a marked effect on the fired product. Judging from the x-ray diffraction patterns of the fired products, the reaction is more complete in the presence of a little F. Moreover, addition of a fluoride promotes crystal growth and sometimes the transition between two crystal phases. The amount of Pb added was usually of the order of 1 mole % of the basic oxides. X-ray diagrams of the fired products were made with Co-K_α radiation, using a North American Philips Geiger counter x-ray diffractometer.

Sufficient compositions were fired and x-ray analyzed to make it possible to identify the composition of new phases and to construct the composition diagrams for the ternary systems investigated. The identification of new compounds was in many cases greatly aided by their isomorphism with known Ca,Mg- and Ca,Zn-silicates.

Binary Compounds

The following are the binary compounds which may occur and their fluorescent properties when activated with Pb:

CaO-SiO_2.—Four compounds are known: Ca_3SiO_5, Ca_2SiO_4, $Ca_3Si_2O_7$, and $CaSiO_3$. In the fired products only the last three were found. This is in agreement with the results of Carlson (6) who found that Ca_3SiO_5 is not stable below 1250°C and decomposes into CaO and Ca_2SiO_4. The α-form of the metasilicate, or pseudowollastonite, was found predominantly. The orthosilicate occurred only in the low temperature β-form.

The fluorescence of $CaSiO_3$-Pb has already been intensively studied (7–14). With 2537Å excitation, emission bands are found at 3000 and 3500Å. Fonda and Studer (9, 11, 13) attribute the 3000Å band to α-$CaSiO_3$-Pb and the 3500Å emission to β-$CaSiO_3$-Pb. This is disputed by

[1] Aerosil from Degussa.

TABLE I. *Spacings (d) and intensities (I) for x-ray patterns of* $SrSiO_3$ *and* $BaSi_2O_5$

$SrSiO_3$		α $BaSi_2O_5$				β $BaSi_2O_5$			
d(Å)	I	d(Å)	I	d(Å)	I	d(Å)	I	d(Å)	I
5.0	20	6.9	10	2.00	15	6.8	20	2.13	60
3.56	45	5.6	10	1.95	20	6.4	5	2.11	20
3.36	30	4.75	10	1.92	40	5.8	5	2.03	30
2.92	100	4.05	100	1.88	40	5.5	5	1.99	20
2.53	20	3.85	15	1.83	20	5.0	30	1.92	30
2.06	80	3.55	50	1.79	30	4.3	30	1.915	25
1.905	30	3.35	40	1.73	10	4.0	95	1.855	25
1.78	15	3.27	35	1.70	10	3.8	30	1.795	35
1.76	5	3.17	75	1.68	10	3.40	75	1.74	5
1.68	20	2.88	35	1.65	10	3.32	95	1.69	35
1.60	10	2.78	45	1.62	10	3.25	35	1.67	5
1.525	20	2.61	25	1.60	55	3.09	100	1.65	5
1.46	15	2.51	20	1.59	20	2.98	10	1.60	15
1.395	10	2.41	5	1.48	20	2.89	10	1.58	20
1.305	25	2.35	35	1.46	25	2.72	75	1.56	10
		2.26	60	1.42	15	2.58	25	1.535	5
		2.22	80	1.41	15	2.54	5	1.485	15
		2.16	25	1.395	15	2.50	5	1.47	20
		2.07	40	1.335	10	2.40	10	1.465	20
		2.04	35	1.295	25	2.32	20	1.45	10
						2.23	60	1.43	10
						2.19	25	1.415	15
						2.16	40	1.405	25

Schulman and co-workers (12, 14) who are of the opinion that both forms of $CaSiO_3$-Pb can emit a band at 3500Å depending on the Pb content.

SrO-SiO_2.—The phase diagram of this system is known (15). Only two compounds occur, the ortho- and metasilicate. Since no x-ray data for the metasilicate were found in the literature, spacings and intensities of the x-ray lines of this compound are given in Table I.

The ortho- and metasilicate show a weak fluorescence with maxima at 3600Å and 3000Å, respectively, when activated with Pb and exposed to 2537Å radiation.

BaO-SiO_2.—All four silicates occurring in this system (15) (Ba_2SiO_4, $BaSiO_3$, $Ba_2Si_3O_8$, and $BaSi_2O_5$) were identified using x-ray data from the A.S.T.M. 1950 card index. In SiO_2-rich binary and ternary mixtures, however, extra lines were found which at first could not be identified. It appeared that $BaSi_2O_5$ could occur in two modifications. After the compound was fired at 1350°C and quenched, the x-ray pattern agreed with that of the A.S.T.M. index. Both modifications were found after firing below this temperature. When a little BaF_2 was added to the firing mixture, only the low temperature- or β-modification was present. The characteristic lines of both modifications are listed in Table I.

Pb-activated Ba silicates were made by Butler (16) and by Clapp and Ginther (3). The latter used Pb contents of about 1 mole % and found a weak fluorescence with maxima at 3200Å and 3750Å in the metasilicate and mesotrisilicate, respectively. Strong fluorescence with a maximum at 3500Å was obtained with Pb-activated $BaSi_2O_5$.

Butler made reasonably efficient phosphors from the metasilicate and mesotrisilicate by using Pb contents of 10 mole % or more. When more than 0.1 mole PbO/mole BaO was added to the metasilicate, a new phase appeared. The emission of these phosphors was predominantly in the blue-green region.

MgO-SiO_2, ZnO-SiO_2.—The well-known compounds Mg_2SiO_4 (forsterite), $MgSiO_3$ (clinoenstatite), and Zn_2SiO_4 (willemite) showed no appreciable fluorescence when activated with Pb. When mixtures of MgO and SiO_2 were fired together, the orthosilicate was formed first, even with MgO:SiO_2 ratios of one or less. To obtain the metasilicate the mixture has to be fired at temperatures above those employed here. Lines belonging to the metasilicate were found only occasionally in the x-ray diagrams of ternary mixtures.

Ternary Systems

The following ternary systems were investigated: CaO-MgO-SiO_2; CaO-ZnO-SiO_2; SrO-MgO-SiO_2; SrO-ZnO-SiO_2; BaO-MgO-SiO_2; BaO-ZnO-SiO_2.

The phase diagrams of CaO-MgO-SiO_2 (17) and CaO-ZnO-SiO_2 (18) are known. The following compounds exist, all of which occur in nature as minerals: $CaMgSiO_4$, monticellite; $Ca_2MgSi_2O_7$, akermannite; $Ca_3MgSi_2O_8$, merwinite; $CaMgSi_2O_6$, diopside; $Ca_2ZnSi_2O_7$ hardystonite.

Hardystonite and akermannite are isomorphous. X-ray data for the Ca, Mg silicates are all given in the A.S.T.M. index. The spacings of hardystonite are given by Segnit (18). None of the other systems has been fully explored. Butler and Cassanos (19) made x-ray patterns of various Pb-activated BaO-MgO-SiO_2 mixtures and found a number of new complex silicates, but they did not establish their compositions. Moreover, they used such high Pb contents that compounds were formed which were not produced in the absence of lead. Their pattern "A" was similar to that of $BaMg_2Si_2O_7$ found here. The product obtained by firing a mixture of the molar composition

TABLE II. *X-ray data of the new 1-1-1 silicates*

$BaZnSiO_4$		$BaMgSiO_4$	
d(Å)	I	d(Å)	I
4.55	20	4.55	40
4.05	20	4.05	10
3.15	100	3.15	100
2.64	75	2.65	50
2.53	5	2.53	10
2.46	15	2.47	5
2.26	25	2.25	40
2.19	25	2.18	15
2.02	55	2.03	40
1.97	30	1.96	25
1.80	10	1.72	15
1.72	15	1.68	20
1.68	30	1.63	5
1.64	15	1.60	40
1.60	60	1.58	15
1.58	20	1.52	20
1.52	35	1.385	10
1.485	10	1.35	15
1.455	5	1.315	10
1.435	5	1.25	10
1.39	20		
1.35	20		
1.315	20		
1.275	20		

TABLE III. *X-ray data of the new 1-2-2 silicates*

$BaMg_2Si_2O_7$				$BaZn_2Si_2O_7$				$SrZn_2Si_2O_7$			
d(Å)	*I*	*d*(Å)	*I*	*d*(Å)	*I*	*d*(Å)	*I*	*d*(Å)	*I*	*d*(Å)	*I*
4.6	20	1.93	35	6.4	5	1.76	15	6.5	5	1.60	20
3.6	10	1.84	10	4.6	15	1.71	40	4.6	10	1.59	20
3.4	20	1.80	15	3.7	5	1.66	15	3.75	15	1.575	10
3.20	100	1.75	15	3.22	100	1.60	10	3.30	100	1.55	5
3.15	65	1.72	15	3.17	90	1.57	40	3.25	75	1.49	10
3.00	45	1.69	15	3.01	85	1.505	35	2.92	80	1.46	25
2.88	15	1.65	15	2.88	20	1.465	5	2.48	55	1.42	10
2.85	20	1.61	10	2.50	70	1.43	5	2.34	15	1.395	10
2.70	5	1.56	20	2.40	25	1.395	25	2.30	40	1.385	5
2.62	5	1.51	15	2.38	50	1.38	10	2.08	20	1.36	15
2.49	30	1.49	5	2.15	20	1.35	10	1.97	40	1.325	5
2.35	25	1.44	5	2.11	15	1.335	10	1.92	10	1.315	10
2.32	15	1.42	5	2.02	15	1.28	25	1.88	20	1.30	10
2.25	50	1.39	10	1.97	40			1.83	5		
2.14	15	1.37	10	1.94	30			1.80	15		
2.10	10	1.34	10	1.85	20			1.75	15		
2.00	15	1.285	10	1.81	30			1.64	15		
1.95	30	1.275	10					1.63	25		

$BaO:MgO:PbO:SiO_2$ = 6:4:1:6, which according to Butler and Cassanos produces pattern "C", was shown by x-ray diagrams to be a mixture of the phases $Ba_3MgSi_2O_8$ and $Ba_2MgSi_2O_7$. In patterns "B" and "D", found by Butler and Cassanos, lines occur which are found only with products containing a large amount of Pb.

Eskola (15) tried to make Ba and Sr compounds analogous to diopside and failed. Neither were such compounds found here.

Nagy and co-workers (20) activated $Ca_2ZnSi_2O_7$ with Pb and found a strong emission band with a maximum at 3450Å on excitation with 2537Å. The best phosphor was made with excess SiO_2 and with a Pb content of 0.003 mole PbO/mole BaO.

Anderson and Wells (21) investigated part of the system $BaO-ZnO-SiO_2$ using Mn as an activator. On excitation with 2537Å they found a red Mn emission at 6900Å for compositions of $BaO \cdot 2ZnO \cdot ySiO_2$, where y was between 1.7 and 7, preferably 2. With such compositions Larach (22) found a strong green band next to the red one on excitation with cathode rays, while the red band alone was found with a composition of $BaO \cdot ZnO \cdot 2SiO_2$. X-ray diffractions were reported to be complex and not readily interpretable in terms of luminescence.

After studying numerous x-ray diagrams of a large number of the fired ternary mixtures mentioned above, the following new compounds were identified: $SrZn_2Si_2O_7$, $Sr_2ZnSi_2O_7$, $Sr_2MgSi_2O_7$, $Sr_3MgSi_2O_8$, $BaZnSiO_4$, $BaZn_2Si_2O_7$, $Ba_2ZnSi_2O_7$, $BaMgSiO_4$, $BaMg_2Si_2O_7$, $Ba_2MgSi_2O_7$, $Ba_3MgSi_2O_8$.

The x-ray patterns of some of these new compounds could easily be indexed because of their isomorphism with known Ca,Mg- and Ca,Zn-silicates. All available x-ray data are collected in tables II–V. Sufficient information was collected from the x-ray analysis to make it possible to draw conjugation lines in the composition diagrams as shown in Fig. 1. These lines divide the ternary diagrams into a number of triangles. The final phases produced by the firing of compositions falling within these triangles are given by the apexes of the triangles.

Indicating the mole compositions in the order (CaO, SrO, BaO)-(MgO, ZnO)-SiO_2, it is seen that except for diopside, only the following compounds occur: 1-1-1, 1-2-2, 2-1-2, and 3-1-2.

These compounds and their fluorescence, when activated with Pb are discussed below in more detail.

1-1-1 Compounds.—Three compounds exist: $CaMgSiO_4$,

TABLE IV. *X-ray data of the new 3-1-2 silicates*

Indices, hkl	$Ca_3MgSi_2O_7$		$Sr_3MgSi_2O_7$		$Ba_3MgSi_2O_7$	
	d(Å)	*I*	*d*(Å)	*I*	*d*(Å)	*I*
020			4.75	5		
110			4.52	5		
111	3.85	5	3.93	40	4.05	70
002			3.50	5		
012			3.31	5	3.41	5
121			3.20	5	3.16	10
102	2.85	35	2.97	5	3.02	5
112; 022	2.72	50	2.81	80	2.93	95
130	2.66	100	2.74	100	2.81	100
040	2.31	15	2.40	10		
032	2.27	15	2.37	10		
013	2.21	30	2.32	40	2.43	35
221	2.16	20	2.24	45	2.31	55
113; 023	2.02	20				
231; 042; 123	1.91	45				
222	1.87	30	1.96	55	2.03	65
150	1.76	10				
310	1.73	5	1.77	25	1.84	40
241			1.74	15	1.78	25
	1.62	10	1.67	5		
	1.575	15	1.63	20	1.71	20
	1.555	15	1.59	35	1.64	50
	1.53	30	1.58	30	1.63	30
			1.545	5		
	1.43	10	1.465	5	1.53	10
	1.39	10	1.40	15	1.46	20
	1.34	15	1.365	30	1.405	30
	1.33	15				
			1.335	10	1.395	15
			1.305	5	1.35	20
			1.29	5	1.33	15
					1.295	20

TABLE V. *X-ray data of the new 2-1-2 silicates*

$Sr_2ZnSi_2O_7$			$Sr_2MgSi_2O_7$			$Ba_2ZnSi_2O_7$		$Ba_2MgSi_2O_7$	
d(Å)	I	hkl	d(Å)	I	hkl	d(Å)	I	d(Å)	I
			5.7	15	110			5.4	5
5.2	5	001	5.2	5	001	3.92	15	3.93	40
4.35	4	101				3.48	15	3.45	20
			4.0	10	220	3.16	100	3.17	100
3.85	30	111	3.80	10	111			3.02	10
3.59	5	210	3.58	5	210	2.92	30	2.92	55
3.17	55	201	3.18	30	201	2.86	10	2.86	20
2.96	100	211	2.95	100	211	2.72	40	2.72	25
2.83	15	220	2.84	5	220	2.55	15	2.54	10
2.60	15	002	2.58	10	002	2.39	20	2.39	20
2.54	35	310	2.53	25	310	2.36	10	2.36	10
2.48	10	221	2.48	10	221	2.21	10	2.21	20
2.38	5	301	2.38	10	301	2.12	15	2.12	10
2.32	2	112				2.08	15	2.08	25
			2.28	10	311	2.05	15	2.06	20
			2.18	5	202			2.02	5
2.10	30	212	2.10	30	212	1.94	55	1.94	45
2.05	2	321				1.91	25	1.91	20
2.01	5	400	2.00	10	400	1.86	10	1.85	20
1.95	15	410	1.95	20	410	1.78	15	1.79	10
1.91	10	330				1.74	20	1.74	10
1.89	10	401	1.89	25	410; 330	1.70	40	1.70	30
1.87	5	302				1.68	5		
1.82	45	312	1.82	30	312	1.645	5	1.65	10
1.80	15	420				1.585	10	1.595	5
1.78	20	331	1.78	20	331	1.555	10	1.555	15
1.73	5	003	1.72	5	003	1.505	15	1.55	5
1.69	5	103; 322	1.69	5	103; 322	1.49	20	1.495	15
1.65	5	113	1.65	5	113			1.485	10
1.59	10	203	1.59	5	203	1.46	10	1.46	10
1.55	20	213	1.56	20	213	1.435	10	1.44	5
1.53	4	332	1.53	10	332	1.405	15	1.41	10
1.505	10	511	1.505	5	511	1.35	10	1.345	5
1.475	10	223	1.475	5	223	1.315	5	1.315	5
1.43	20	521; 313	1.43	20	521; 313	1.295	30	1.295	15
1.42	5	440	1.42	5	440	1.275	15	1.28	10
1.375	5	441				1.265	15	1.27	10
1.365	5	512	1.365	5	512				
1.34	10	531	1.335	5	531				
1.31	5	403							
1.29	20	004	1.29	20	004				
1.275	10	620	1.275	10	620				

$BaZnSiO_4$, and $BaMgSiO_4$. The last two compounds are isomorphous. This was invariably the case for corresponding Mg and Zn compounds when both occur. It is noteworthy however that the corresponding Zn analogs for some Mg compounds do not occur. For example, hardystonite and akermannite are isomorphous, while there are no CaZn compounds corresponding in composition to the other CaMg compounds, merwinite, diopside, and monticellite. From a fluorescence point of view the 1-1-1 compounds are not of interest. The Ba-containing compounds emit a broad band in the visible near 4200Å when activated with lead and excited by 2537Å. Pb-activated monticellite emits a band at 3050Å. Although this band lies in the erythemal region, the efficiency of the phosphor is too low for practical application.

1-2-2 Compounds.—The similarity between x-ray diagrams for $BaZn_2Si_2O_7$ and $BaMg_2Si_2O_7$ (Table III) indicates that these substances are isomorphous. This was also confirmed by the formation of an uninterrupted series of solid solutions.

$BaZn_2Si_2O_7$ is an excellent base material for activation with Pb. With low Pb contents the emission spectrum has a peak at 3030Å (Fig. 2). With higher activator content a second peak develops at 3300Å while the over-all efficiency drops. The best phosphors were obtained by firing a mixture of $BaCO_3$, ZnO, and SiO_2 with about 1 mole % PbO added in closed quartz crucibles for a few hours at 1000°C. The amount of BaO added preferably should be lower than indicated by the stoichiometric composition. A stoichiometric ratio of the basic constituents leads to phosphors with a comparatively low output. This is further illustrated in Fig. 3 where contour lines are drawn indicating compositions having efficiencies approximately 80% and 50% of those of the best products as measured with a 1P 21 photomultiplier in combination with Schott UG 5 and WG 7 filters, transmitting u.v. radiation between 2700 and 4000Å. The position of these contour lines is not fixed. They vary with the method of preparation. When the raw materials are mixed very thoroughly, near-stoichiometric compositions may have a higher efficiency than indicated in Fig. 3.

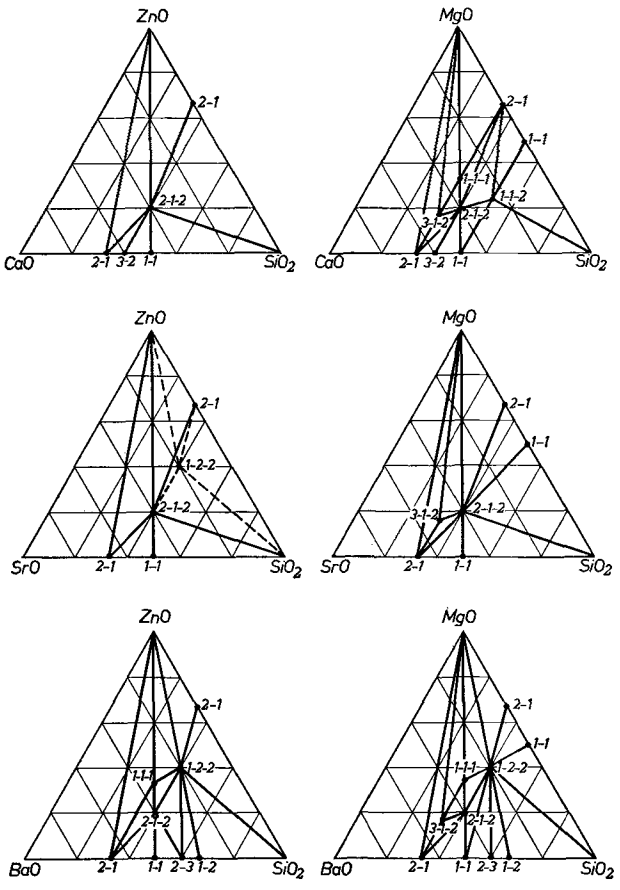

FIG. 1. Composition diagrams of the six ternary silicate ystems investigated showing conjugation lines.

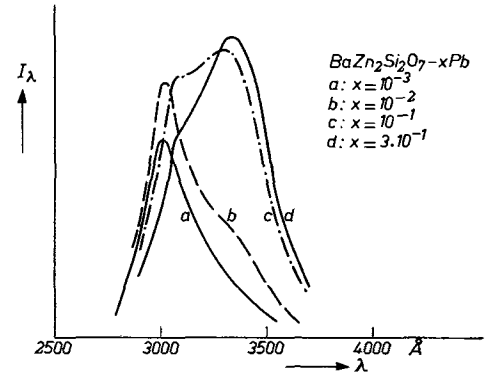

FIG. 2. Spectral distribution curves of the fluorescence of $BaZn_2Si_2O_7$-xPb fired at 1000°C and excited with 2537Å radiation.

The explanation of this effect is quite simple. When compositions near the stoichiometric point and lying in the shaded area of Fig. 3 are fired, hardly any luminescence at all is found. This shaded area is separated from the "fluorescence area" by two fairly sharply defined lines. On comparing Fig. 3 with the composition diagram of Fig. 1 it is noticed that these lines represent the boundaries between ternary mixtures containing ZnO and those without it. ZnO absorbs 2537Å very strongly, but has no appreciable fluorescence when fired with PbO under oxidizing conditions. In contrast, Zn_2SiO_4 and SiO_2 have no strong absorption for 2537Å. Therefore, their presence in the fired product is not very detrimental to the efficiency, while traces of ZnO are to be avoided. Because a solid reaction is hardly ever complete, the last remaining unreacted materials having to diffuse over increasing distances, the raw material composition must be chosen so that it is very unlikely for ZnO to remain unreacted. This is done by taking an excess of SiO_2.

This principle of taking an excess of the basic constituent which is comparatively harmless, in order to suppress the presence of deleterious reaction products or unreacted basic constituents, is quite generally applied in preparative phosphor chemistry [*see*, for example ref. (23–26)].

$BaMg_2Si_2O_7$ activated with Pb has a weaker emission than the corresponding Zn compound. The spectral distribution of the emission shows a maximum at 2900Å and a second maximum at 3700Å. In solid solutions of $BaZn_2Si_2O_7$ and $BaMg_2Si_2O_7$, emission shifts gradually from 3030Å to shorter wave lengths as the Mg:Zn ratio increases (Fig. 4). The efficiency is at first little affected, and may increase somewhat but it begins to drop when more than 20% of the Zn in $BaZn_2Si_2O_7$-Pb is replaced by Mg. At the same time the second 3700Å band begins to appear. This can be explained as follows.

The strong 3030Å emission in $BaZn_2Si_2O_7$-Pb is prob-

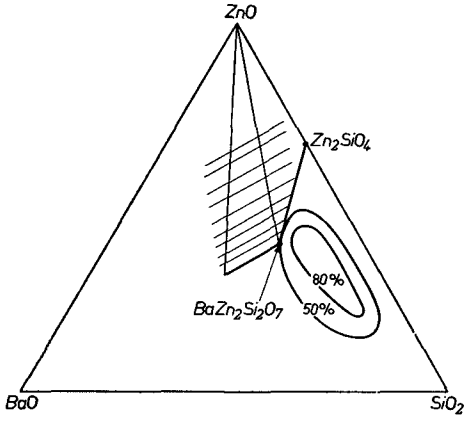

FIG. 3. Composition diagram of the BaO-ZnO-SiO_2 system showing contour lines for phosphors of equal brightness. The shaded area is practically nonfluorescent. The composition of the phosphors can be represented by xBaOyZnO$z$$SiO_2$-$r$ PbO with r: $(x + y + z) = 0.005$.

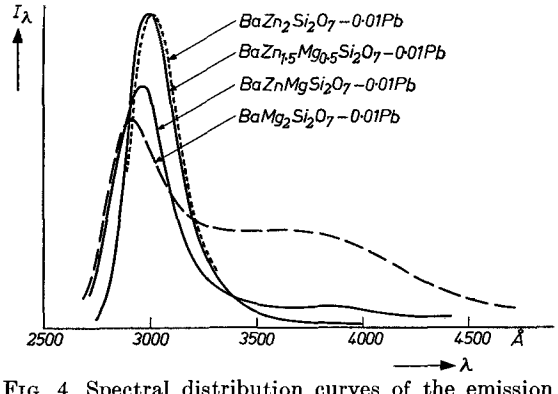

FIG. 4. Spectral distribution curves of the emission of Ba(Zn, Mg)$_2$$Si_2O_7$-Pb excited with 2537Å.

ably due to a transition from the ^3P to the ^1S ground state of the Pb^{2+} ion. If the phosphor is to be efficient for 2537Å excitation, this wave length must lie within the excitation band corresponding to the reverse transition, preferably near its maximum. This is apparently the case with $BaZn_2Si_2O_7$-Pb. But when Mg is substituted for Zn, the emission band and presumably the excitation band move to shorter wave lengths. If the maximum of the latter moves to wave lengths shorter than 2537Å, the exciting radiation is not only less strongly absorbed, but competing transitions, such as those associated with Pb-Pb pairs, come to the fore giving rise to new emission bands, while more energy is also lost to radiationless transitions. Reflection measurements confirmed that when more than 20% of the Zn was replaced by Mg, the reflection for 2537Å began to decrease noticeably. Because of its high efficiency (quantum efficiency of the order of 90%) and the suitable spectral range of its emission, $BaZn_2Si_2O_7$ should be a very good phosphor for erythemal lamps. When lamps were made with this phosphor, however, an unexpected difficulty arose when powder came off the wall of the tube during the baking process.

It became evident from thermal analysis curves that this resulted from a reversible crystallographic transition at about 270°C. Substitution of 3% Mg for Zn moved this point to 285°C, while with more than 5% Mg added, a transition point was no longer noticeable on the thermal analysis curve. No further trouble arose from bad powder adherence after 10% of the Zn had been replaced by Mg. This partial substitution has the added advantage of moving the emission peak nearer the maximum of the erythemal sensitivity curve.

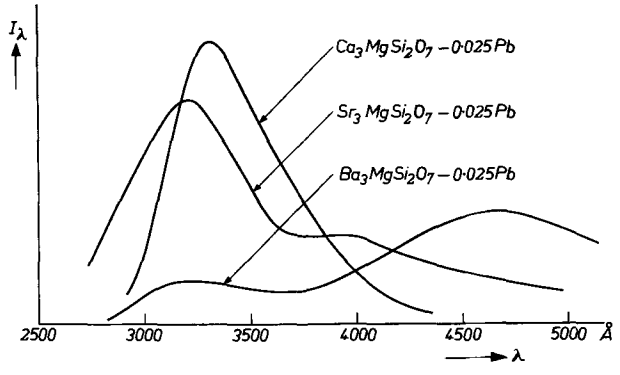

FIG. 5. Emission spectra of Pb-activated 3-1-2 compounds excited with 2537Å.

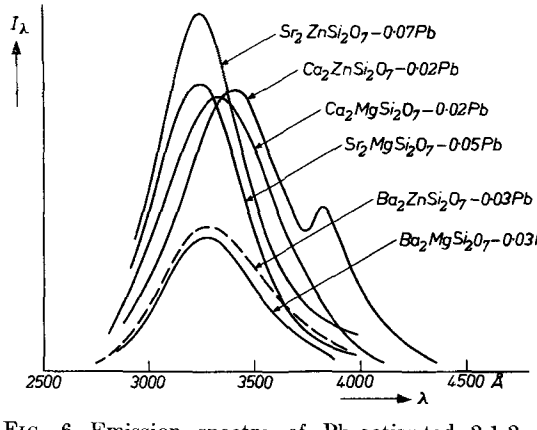

FIG. 6. Emission spectra of Pb-activated 2-1-2 compounds excited with 2537Å.

$SrZn_2Si_2O_7$ has a structure different from that of the corresponding Ba salt. The composition of this compound was at first difficult to establish mainly because the x-ray diagrams were not reproducible.

$SrZn_2Si_2O_7$ and $Sr_2ZnSi_2O_7$ were nearly always found together, even in compositions falling within the triangle formed by ZnO, SiO_2, and $SrZn_2Si_2O_7$ in the composition diagram. When some fluoride was added to the raw material blend, the characteristic lines for $SrZn_2Si_2O_7$ disappeared altogether. However, when a small percentage of Sr was replaced by Ba, the $SrZn_2Si_2O_7$ structure became stabilized. As much as 80% of the Sr can be replaced by Ba before a new phase appears. With more Ba added, lines belonging to the $BaZn_2Si_2O_7$ phase begin to show up.

The identification of $SrZn_2Si_2O_7$ was further complicated by the fact that its Pb·emission and that of $Sr_2ZnSi_2O_7$-Pb both have a maximum at 3250Å.

3-1-2 Compounds.—These compounds occur only in the complex silicates containing Mg. Judging from x-ray diagrams the compounds appear to be isomorphous (Table IV). The lines of the x-ray pattern of merwinite ($Ca_3MgSi_2O_8$) were indexed by Phemister (27) and by Bredig (28), showing this substance to be orthorhombic with the following unit cell: a_0 = 5.2Å, b_0 = 9.2Å and c_0 = 6.8Å.

By analogy, the lines of the Sr and Ba compounds could be indexed quite easily and were found to give the following unit cells: $Sr_3MgSi_2O_8$—a_0 = 5.4Å, b_0 = 9.6Å, c_0 = 7.2Å; $Ba_3MgSi_2O_8$—a_0 = 5.5Å, b_0 = 9.8Å, c_0 = 7.6Å.

An uninterrupted series of solid solutions was found to exist between $Ca_3MgSi_2O_8$ and $Sr_3MgSi_2O_8$ and between $Sr_3MgSi_2O_8$ and $Ba_3MgSi_2O_8$. However, when mixtures of $Ca_3MgSi_2O_8$ and $Ba_3MgSi_2O_8$ were fired, the final product consisted usually of two phases. From the diagram of a 1:1 mixture it was evident that the lines for the Ca-rich phase were the strongest and the cell was considerably larger than that of pure $Ca_3MgSi_2O_8$. A substantial amount of Ca can be replaced by Ba, while little Ca seems to have been taken up by $Ba_3MgSi_2O_8$.

Regarding their fluorescence, all three compounds are of little importance. Spectral distributions are shown in Fig. 5.

2-1-2 Compounds.—These compounds occur in all six ternary systems investigated. X-ray diffraction data listed in Table V show that $Sr_2ZnSi_2O_7$ and $Sr_2MgSi_2O_7$ are isomorphous with $Ca_2ZnSi_2O_7$ (hardystonite) and $Ca_2MgSi_2O_7$ (akermannite) and may be considered as new members of the melilite group of silicates. The crystals are tetragonal, and the cell dimensions of both Sr compounds are about equal with a_0 = 8.06Å and c_0 = 5.19Å.

The spectral distributions of the emission of the six compounds activated with Pb and excited by 2537Å are given in Fig. 6. The Pb-activated Ca and Sr compounds are efficient phosphors with quantum efficiencies of the order of 90%. The best phosphors are again obtained when an excess of SiO_2 is used. Fig. 7 shows contour lines

for phosphors in the system SrO-ZnO-SiO_2 with about equal efficiencies. As with the ternary system BaO-ZnO-SiO_2, the fluorescence area is separated by sharp lines from an area of little or no fluorescence (shaded in Fig. 7) which corresponds to ternary mixtures containing ZnO. In the system SrO-MgO-SiO_2 an excess of MgO is not so detrimental to the efficiency, and reasonably efficient phosphors are obtained with compositions lying to the left of the lines connecting $Sr_2MgSi_2O_7$ with Mg_2SiO_4 in the composition diagram. Too much $Sr_3MgSi_2O_7$ must, however, be avoided since this compound is only weakly fluorescent when activated with Pb.

The Ca and Sr compounds formed an uninterrupted series of solid solutions as shown by x-ray diagrams and by the Pb emission of such solutions. Pb emission, for example, shifted gradually from 3400 to 3250Å when the Ca in $Ca_2ZnSi_2O_7$ was replaced gradually by Sr.

In both $Sr_2ZnSi_2O_7$ and $Sr_2MgSi_2O_7$, 80% of the Sr was replaced by Ba before the character of the patterns began to change, showing lines belonging to $Ba_2ZnSi_2O_7$ and $Ba_2MgSi_2O_7$, respectively. The same conclusion can be drawn from the spectral distribution of the Pb emission. When Sr was replaced by increasing amounts of Ba, the peak of the emission shifted gradually from 3250Å to longer wave lengths (Fig. 8) until it reached 3600Å with 80% replacement. With further replacement of Sr by Ba,

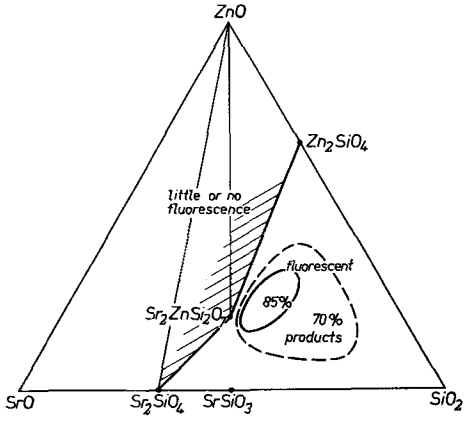

FIG. 7. Equal intensity contour lines of phosphors with composition xSrOyZnO$z$$SiO_2$-$r$ PbO with r: $(x + y + z) = 0.0025$.

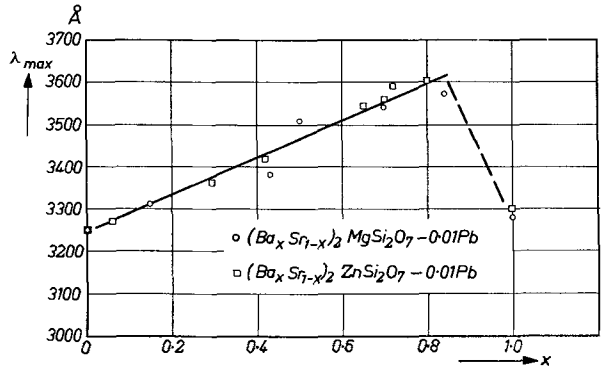

FIG. 8. Shift of the peak emission resulting from substitution of Ba for Sr in $Sr_2MgSi_2O_7$-Pb and $Sr_2ZnSi_2O_7$-Pb.

a second band belonging to $Ba_2ZnSi_2O_7$-Pb or $Ba_2MgSi_2O_7$-Pb appeared at approximately 3300Å.

All phosphors with the akermannite structure were efficient with 2537Å excitation radiation. The amount of Pb added before firing was not very critical. The optimum intensity of the 3550Å band in phosphors of the composition 10 SrO-25BaO-20ZnO-45SiO_2-xPbO, fired for 4 hr in an open crucible at 1050°C, was reached with x of about 0.6 (0.03 mole PbO added/mole base material). When the PbO content in the raw material blend was further increased, emission intensity began to drop. Part of the PbO volatilized during preparation, depending on the firing conditions. Occasionally a loss of about 50% was found.

Concluding Remarks

The investigation of Pb-activated ternary systems containing one oxide of the group CaO, SrO, BaO together with MgO or ZnO and SiO_2 led to the discovery of important phosphors with emission in the u.v. region between 3000 and 4000Å. For "sunlamps," $BaZn_{1.9}Mg_{0.1}Si_2O_7$-Pb is most useful, while for "black-light" lamps producing long wave u.v. radiation near 3600Å, $Sr_{0.6}Ba_{1.4}ZnSi_2O_7$-Pb or $Sr_{0.6}Ba_{1.4}MgSi_2O_7$-Pb are very suitable.

It is remarkable that, whereas silicates have proved to be such good base materials for the fluorescence of Pb ions, no phosphates have ever been produced with an efficient Pb emission. The reverse is true for Tl as activator. The best Tl-activated phosphors are $Ca_3(PO_4)_2$-Tl and $(CaZn)_3(PO_4)_2$-Tl. Good Tl-activated silicates have not been made so far. No explanation can be offered for this empirical rule. Many of the usual activators such as Mn, Tl, Bi, Sb, Sn, etc., were tried in the new ternary compounds. Although some of them produced a weak fluorescence, none led to phosphors of any appreciable efficiency.

Manuscript received January 18, 1956. This paper was prepared for delivery before the San Francisco Meeting, April 29 to May 3, 1956.

Any discussion of this paper will appear in a Discussion Section to be published in the December 1957 JOURNAL.

REFERENCES

1. M. LUCKIESH AND A. H. TAYLOR, *Gen. Elec. Rev.*, **42,** 274 (1939).
2. L. R. KOLLER, "Ultraviolet Radiation," p. 201, John Wiley & Sons, New York (1952).
3. R. H. CLAPP AND R. J. GINTHER, *J. Opt. Soc. Amer.*, **37,** 355 (1947).
4. H. C. FROELICH, *J. Electrochem. Soc.*, **91,** 241 (1947).
5. R. NAGY, R. W. WOLLENTIN, AND C. K. LUI, *This Journal*, **97,** 29 (1950).
6. E. T. CARLSON, *J. Research Nat. Bur. Standards*, **7,** 893 (1931).
7. H. C. FROELICH, *J. (and Trans.) Electrochem. Soc.*, **93,** 101 (1948).
8. H. C. FROELICH AND G. R. FONDA, *ibid.*, **93,** 114 (1948).
9. F. J. STUDER AND G. R. FONDA, *Phys. Rev.*, **74,** 1241 (1948).
10. J. B. MERRILL AND J. H. SCHULMAN, *J. Opt Soc. Amer.*, **38,** 471 (1948).
11. F. J. STUDER AND G. R. FONDA, *ibid.*, **39,** 655 (1949).
12. J. H. SCHULMAN, R. J. GINTHER, AND C. C. KLICK, *This Journal*, **97,** 123 (1950).
13. G. R. FONDA AND F. J. STUDER, *J. Opt. Soc. Amer.*, **42,** 360 (1953).

14. J. H. SCHULMAN, R. J. GINTHER, AND E. W. CLAFFY, *ibid.*, **43**, 318 (1953).
15. P. ESKOLA, *Am. J. Sci.*, (V) **4**, 331 (1922).
16. K. H. BUTLER, *Trans. Electrochem. Soc.*, **91**, 265 (1947).
17. *See* W. EITEL, "The Physical Chemistry of the Silicates," p. 661, Univ. of Chicago Press (1954).
18. E. R. SEGNIT, *J. Am. Ceramic Soc.*, **37**, 273 (1954).
19. K. H. BUTLER AND J. G. CASSANOS, *This Journal*, **97**, 83 (1950).
20. R. NAGY, C. K. LUI, AND R. W. WOLLENTIN, *ibid.*, **99**, 137 (1952).
21. J. T. ANDERSON AND R. S. WELLS, *ibid.*, **95**, 299 (1945).
22. S. LARACH, *ibid.*, **98**, 369 (1951).
23. J. L. OUWELTJES AND W. L. WANMAKER, *ibid.*, **103**, 160 (1956).
24. G. R. FONDA, *J. Phys. Chem.*, **48**, 303 (1944).
25. C. G. A. HILL, *Trans. Faraday Soc.*, **42**, 685 (1946).
26. M. TRAVNICEK, F. A. KRÖGER, TH. P. J. BOTDEN, AND P. ZALM, *Physica*, **18**, 33 (1952).
27. J. PHEMISTER, *Mining Mag.*, **26**, 225 (1942).
28. M. A. BREDIG, *J. Phys. Chem.*, **49**, 537 (1945).

An Improvement for the Electrolytic Preparation of Aminoguanidine

MOTOJI YAMASHITA AND KIICHIRO SUGINO

Laboratory of Organic Electrochemistry, Department of Chemical Engineering, Tokyo Institute of Technology, Tokyo, Japan

ABSTRACT

An improved method for the electrolytic preparation of aminoguanidine from nitroguanidine is described. Nitroguanidine was reduced in a suspension in 30% $(NH_4)_2SO_4$ catholyte at Pb, amalgamated Pb, Zn, spongy Zn coating Pb, and Fe at a current density of 3–10 amp/dm^2 at about 10°C. A yield above 80% aminoguanidine was constantly obtained. Among these cathodes, Pb was the most favorable one, giving above 85% yield.

Some considerations are also given to the reasons for getting a good yield.

Electrolytic preparation of aminoguanidine was first claimed in yield as high as 80% by reduction of nitroguanidine suspended in a dilute solution of H_2SO_4 using a Sn cathode (1). Lieber and Smith reported that this work has not yet been confirmed (2).[1]

Recently, the authors carried out this electrolytic reduction and obtained aminoguanidine in about 60% yield by use of a concentrated solution of nitroguanidine in 80% H_2SO_4 with cathodes such as Pb, amalgamated Pb, or Sn (3). Similar work was reported by Shreve and Carter (4). In this process, a suspension of nitroguanidine in 8–10% H_2SO_4 was reduced using a Hg cathode to give aminoguanidine in yields as high as 50–60%.

Spreter and Briner (5) also suggested a mechanism for the electrolytic reduction of nitroguanidine in dilute H_2SO_4. A yield of 75–80% was recorded for the Sn cathode. However, only about 1.00 g of the sample suspended in 230 cc 5% H_2SO_4 was used as catholyte, so these results did not seem to be applicable on an industrial scale.

As the result of these early works, it seemed that in practice the yield of aminoguanidine could not exceed 50–60% of theoretical if an acid medium such as H_2SO_4 were used as catholyte.

Sugino and Yamashita also studied the reaction mechanism (3). Nitroguanidine, on electrolytic reduction in a solution of strong H_2SO_4 at a Pb cathode, yielded aminoguanidine and guanidine as the main products. The latter compound was probably not a final reduction product, but an acid hydrolytic product of nitrosoguanidine which might be the primary reduction product. It was also found that nitroguanidine could not be reduced to aminoguanidine at Pt under the same conditions, and guanidine was the main product in this case. On the other hand, reduction potentials ($E_{\frac{1}{2}}$) of nitroguanidine and nitrosoguanidine were found to be -0.67 v and -0.56 v (vs. S.C.E., conc. 2×10^{-4} mole/l, pH 3.0), respectively, by the polarographic method as shown in Fig. 1.[2]

This led to the conclusion that both compounds must be reduced electrolytically not only at Pb or Hg cathodes, but also at Pt or Fe cathodes, regardless of the current or material yield. It seemed that the reason for not obtaining aminoguanidine at cathodes having a low H overvoltage was the superiority of the decomposition velocity of nitrosoguanidine in an acid medium over its reduction speed at these cathodes. This assumption could be verified by a careful experiment. Suspension of nitroguanidine in a dilute acetic acid solution was used as catholyte. At a Pt cathode, aminoguanidine was found in the reduction product after the theoretical amount of current was passed. By further experiments, however, even in this catholyte and at a Pb cathode, the yield of aminoguan-

[1] Later the same authors published a paper reporting 75% yield of aminoguanidine with a current efficiency of 38% using 5% H_2SO_4 and an amalgamated Pb cathode (6).

[2] This is not the reproduced polarograms from the previous paper, but those newly measured. In a previous paper (3), the reduction potentials were shown not as $E_{\frac{1}{2}}$, but as so-called decomposition potential vs. $\frac{1}{10}$ N.C.E.

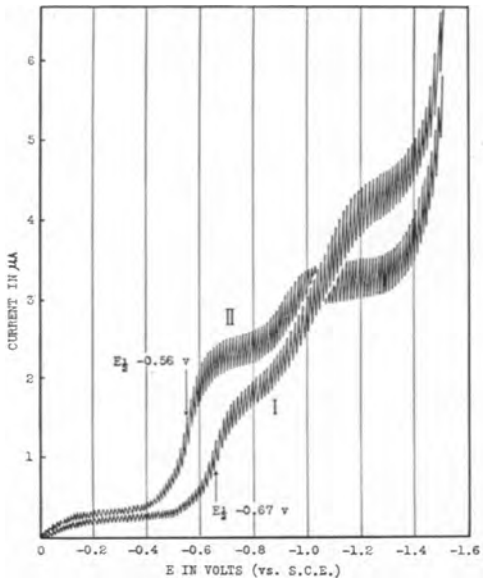

FIG. 1. Polarograms of nitroguanidine (curve I) and nitrosoguanidine (curve II) in 0.1 *N* KCl with added HCl (*p*H 3). The *m* and *t* values (h = 44 cm): *m*, 1.41 mg/sec; *t*, 3.3 sec; 22°C.

idine did not reach a satisfactory value from a practical point of view.

The problem was studied further in order to find a better catholyte which would prevent decomposition of nitrosoguanidine and facilitate its reduction to aminoguanidine; an $(NH_4)_2SO_4$ solution proved the most suitable catholyte. In a caustic alkaline medium,[3] very poor yield of aminoguanidine was obtained because of decomposition of nitroguanidine itself and other intermediate reduction products. So it seemed interesting that the reduction proceeded smoothly without side reactions in an ammoniacal solution in the presence of an acid radical.

Apparatus and Procedure

Material used.—The sample of nitroguanidine used in these reduction studies was prepared by dehydration of guanidine nitrate by the usual method. It melted with decomposition at 240°–245°C.

Catholyte.—The catholyte of this reduction consisted of a suspension of nitroguanidine in 30% $(NH_4)_2SO_4$ solution. The catholyte became ammoniacal during electrolysis, and nitroguanidine was dissolved gradually in the catholyte during electrolysis.

Apparatus.—The apparatus is shown in Fig. 2. A 200 cc beaker served as the cell. A porous cylindrical pot (unglazed earthenware) separated the anode space from the surrounding cathode chamber. The cathode consisted of a metal sheet bent into the form of a cylinder which stood in the beaker and encircled the porous pot (active area: 1 dm² except runs 13, 15, and 16). A thermometer was inserted within the cathode space. The catholyte was stirred slowly by a glass stirrer. The anode was a Pb sheet or a Pt plate.

[3] This medium was suitable to obtain nitrosoguanidine by the electrolytic reduction of nitroguanidine, as described in footnote [4].

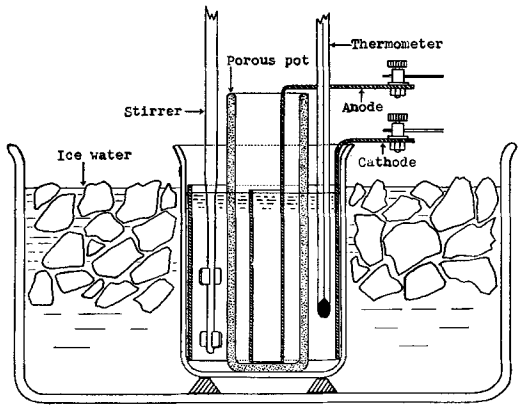

FIG. 2. Electrolytic cell

Duration of electrolysis.—All electrolyses except those in Table IV were conducted until reduction was complete, as indicated by the disappearance of suspended nitroguanidine which resulted in a clear solution. Three runs in Table IV were carried out with a constant amount of current.

Determination of the products.—After reduction, aminoguanidine was determined by Jamieson's KIO_3 method (7) which gave reliable results. This determination was thought to be influenced by the presence of nitrosoguanidine and also hydroxylamine or guanylhydroxylamine, the formation of which might be expected. But such compounds did not exist in the final reduction product, so the substance having the reducing power was aminoguanidine only. The accuracy of this method was checked by direct determination of aminoguanidine as bicarbonate by passing carbon dioxide in the reduction product. Good agreement was observed between the two methods. In a large experiment using 50 g nitroguanidine at a time, aminoguanidine was determined directly as aminoguanidine bicarbonate.

Guanidine was determined as picrate after removal of aminoguanidine as bicarbonate.

Results and Discussion

Influence of cathode materials.—Material yields and current efficiencies for the reduction of nitroguanidine at various cathode materials are shown in Table I.

It is seen that Pb was the most effective cathode mate-

TABLE I. *Reduction of nitroguanidine at various cathodes*

Anode: Pt; anolyte: 10% H_2SO_4 (60–65 cc); catholyte: 5.20 g nitroguanidine suspended in 100 cc 30% $(NH_4)_2SO_4$; amperage: 3; current density: 3 amp/dm²; temp: 8°–10°C.

Run No.	Cathode	Duration of run (hr)	Aminoguanidine (as free base) yield		Current efficiency (%)
			(g)	(%)	
1	Pb	4.5	3.14	85	51
2	Amalgamated Pb	4.0	3.11	84	56
3	Zn	4.0	2.98	80	54
4	Fe	4.5	2.98	80	48
5	Sn	4.5	2.14	58	34
6	Ni	4.5	1.79	48	29
7	Cu	4.5	0.90	24	15

TABLE II. *Effect of temperature on the yield of aminoguanidine*

Cathode: Pb; other conditions: same as in Table I.

Run No.	Temp, °C	Duration of run (hr)	Aminoguanidine yield		Current efficiency (%)
			(g)	(%)	
8	−4 to −2	5.65	3.22	87	41
9	8-9	5.0	3.17	86	46
10	14-16	4.0	2.99	81	54
11	24-26	3.5	2.81	76	58

TABLE III. *Effect of current density on yield of aminoguanidine*

Cathode: Pb; other conditions: same as in Table I; 3 amp.

Run No.	Cathodic current density (amp/dm²)	Duration of run (hr)	Aminoguanidine yield		Current efficiency (%)
			(g)	(%)	
12	3	4.3	3.22	87	54
13	10	5.5	3.20	86	42

rial, and at this cathode, the yield of aminoguanidine reached about 85%. Amalgamated Pb gave almost the same result as Pb. Zn and Fe seem to be the next best cathode materials, and an 80% yield of aminoguanidine was obtained at these cathodes. At Sn and Ni cathodes, the yield of aminoguanidine was about 60% and 50% respectively. Cu was the most inefficient cathode for preparing aminoguanidine. At these cathodes, large amounts of guanidine and NH_3 were obtained with aminoguanidine. In view of these results, all subsequent experiments were carried out with Pb cathodes.

Influence of temperature.—The influence of temperature on the yield of aminoguanidine is shown in Table II. Conditions of electrolysis were the same as in Table I.

Temperatures below 8°–10°C gave the highest aminoguanidine yields, but even at 25°C, the yield was very little less. This fact is very important from a practical point of view, because in the usual catholyte using H_2SO_4, the temperature rise showed marked unfavorable effect on the aminoguanidine yield.

Influence of current density on aminoguanidine yield.—In an attempt to compare the influence of current density on the yield of aminoguanidine, two runs were made at current density of 3 amp/dm² and 10 amp/dm². Results are shown in Table III.

The same yield of aminoguanidine was obtained at 10 amp/dm² as at 3 amp/dm².

Influence of current density on current efficiency.—Current efficiencies for the reduction at several current densities are shown in Table IV. All electrolyses in Table IV were made with the same amount of current (1.5 amp-hr).

There is a decrease of current efficiency as current density changes from 3 to 20 amp/dm². Since the increase of current density minimizes the duration of electrolysis for the same cathode area with the same yield of aminoguanidine as described above, it should be possible, in practice, to determine the current density which will give the maximum economical efficiency.

TABLE IV. *Effect of current density on current efficiency*

Cathode: Pb; other conditions: same as in Table III; duration of run, 1.5 hr.

Run No.	Cathodic current density (amp/dm²)	Aminoguanidine yield		Current efficiency (%)
		(g)	(%)	
14	3	1.12	30	54
15	10	0.97	26	47
16	20	0.78	21	38

TABLE V. *Large scale experiments*

Anode: Pb; anolyte: 200 cc 10% H_2SO_4; catholyte: 52.0 g nitroguanidine suspended in 450 cc 30% $(NH_4)_2SO_4$ solution.

Run No.	Cathode	Amperage (amp)	Current density (amp/dm²)	Voltage (v)	Temp, °C	Time (hr)
1′	Pb	10	4	4.8–4.9	10	12
2′	Fe	10	3.7	4.6	10–12	12
3′	Pb (base)–Zn (surface)	15	15	6.5–6.6	11–13	8.4

Run No.	Yield of aminoguanidine bicarbonate					Current efficiency (%)
	crystal		in solution (g)	total		
	(g)	purity		(g)	(%)	
1′	56.3	99.0	2.5	58.2	86	57
2′	52.8	97.8	2.1	53.7	79	53
3′	54.3	97.7	2.2	55.2	81	52

Result of a large experiment using 50 g nitroguanidine.—With reference to the results obtained by the above runs, a set of experiments was performed using 50 g nitroguanidine at once in order to confirm the applicability of this method to the practical electrolysis.

The apparatus used in this experiment was similar to that described above, but had somewhat larger dimensions (1 l beaker, active area of cathode: Run 1 and 2, 2.5 dm², Run 3, 1 dm²).

When reduction was complete the *p*H of the catholyte was adjusted to 8 by passing CO_2, and the catholyte was allowed to stand overnight. The precipitate of aminoguanidine bicarbonate was filtered, washed, dried below 50°C, and weighed. By this procedure, 96–97% of aminoguanidine in the catholyte was crystallized out as bicarbonate. Results are shown in Table V.

At Pb cathodes, the yield was 86% of theoretical with the current efficiency of 57% which was almost the same as those obtained in the small experiment. Also at Fe cathodes, the yield was about 80% with 53% current efficiency, but the resulting aminoguanidine was somewhat colored. Use of spongy Zn-coated Pb[4] as cathode seemed to be favorable because of the application of high current density which reduced the time required, but little decrease of current and material yield resulted.

Formation of guanidine.—It was shown in Table I that at cathodes such as Ni and Cu the yield of aminoguan-

[4] This cathode was first applied to the electrolytic reduction of nitrobenzene to hydrazobenzene in alkali emulsion by K. Sugino and T. Sekine. The detail was described in that paper to be published.

idine was only 48 and 24% of theoretical, respectively. In these cases, guanidine and NH_3 were the main products. Table VI shows comparative yields of aminoguanidine and guanidine at Pb and Cu cathodes.

The formation of guanidine is seen to result from direct reduction of nitrosoguanidine and not from hydrolysis of it as in acidic medium, accounting for the observations described below. Cu seems to accelerate this reaction especially.

Some considerations about reasons for obtaining aminoguanidine in good yield in ammonium sulfate catholyte.—In order to clarify the reasons for the above results, the following experiments were carried out.

Isolation of nitrosoguanidine—the intermediate product.—It is seen that nitrosoguanidine is the primary product in this reduction, because the catholyte becomes yellow in the earlier stage of the electrolysis. Indeed, it could be detected when the reduction was carried out at 45°C. An example follows:

Anode, Pt; anolyte, 30% $(NH_4)_2SO_4$; catholyte, 5.2 g nitroguanidine suspended in 100 cc 30% $(NH_4)_2SO_4$; cathode, lead; amp, 7; current density, 7 amp/dm²; temp, 45 ± 2°C; duration of run, 35 min.

After reduction, unconverted nitroguanidine was separated out by cooling the deep yellow catholyte at 5°C. After removal of nitroguanidine by filtration, the filtrate was allowed to stand for 2 hr at 5°–10°C. Yellow powder of nitrosoguanidine was then separated out slowly from the filtrate. It was filtered and dissolved in 10 cc 3% HCl, to remove nitroguanidine. A small amount of undissolved matter was removed by filtration, and the resulting solution was neutralized with NH_3. Pure nitrosoguanidine was precipitated out. It was filtered, washed with water, methanol, and ether, air-dried, yield 0.10 g. Calc'd for CH_4N_4O: N, 63.6%. Found: N, 63.3%.

Identity was further confirmed by the precipitation of a brown Cu complex salt by adding an ammoniacal solution of $CuSO_4$ to an aqueous solution of nitrosoguanidine thus obtained.

Hydrolysis of nitrosoguanidine.—This compound was found not to hydrolyze to guanidine in ammoniacal catholyte at low temperature under the same conditions as in the electrolysis.

Sample: 4.40 g of nitrosoguanidine[5] suspended in a solution prepared from 10 g $(NH_4)_2SO_4$, 10 cc 28% NH_3, and 90 cc water. For 4 hr stirring at 10°C no guanidine was obtained; at 30°–33°C, only 7% guanidine was formed. Copper or copper ion was proved to have no effect on hydrolysis of nitrosoguanidine.

It is well known that, in acidic medium, nitrosoguanidine is hydrolyzed very rapidly to guanidine and other products (9).

Nitroguanidine and aminoguanidine did not hydrolyze to guanidine under the same conditions.

Reduction of nitrosoguanidine.—Then, nitrosoguanidine was reduced at a Pb cathode, the results of which are shown in Table VII.

[5] The sample of notrosoguanidine was prepared in yield as high as 45–50% by the electrolytic reduction of nitroguanidine in a caustic alkaline catholyte. The details will be published in a separate paper (8).

TABLE VI. *Reduction of nitroguanidine at* Pb *and* Cu *cathodes*

Catholyte: 10.4 g (Pb) and 5.2 g (Cu) nitroguanidine suspended in 100 cc 30% $(NH_4)_2SO_4$ solution; other conditions: same as in Table I.

Run No.	Cathode	Duration of run (hr.)	Aminoguanidine yield		Guanidine picrate yield	
			(g)	(%)	(g)	(%)
17	Pb	8.5	6.27	85	2.18	7.6
18	Cu	4.5	0.78	21	9.40	65

TABLE VII. *Reduction of nitrosoguanidine at* Pb *cathode*

Catholyte: 4.40 g (Run 19), 8.80 g (Run 20) nitrosoguanidine suspended in 100 cc 30% $(NH_4)_2SO_4$; other conditions: same as in Table I.

Run No.	Duration of run (hr)	Aminoguanidine yield		Guanidine picrate yield	
		(g)	(%)	(g)	(%)
19	3.0	2.94	79	0.61	4.2
20	5.5	5.82	79	1.59	5.5

These results almost agreed with those of the reduction of nitroguanidine at Pb in Table VI.

The reduction of nitrosoguanidine at a Cu cathode under the same conditions gave a considerable amount (40 ~ 50%) of guanidine with aminoguanidine just the same as the reduction of nitroguanidine at the same cathode.

Behavior of aminoguanidine toward reduction in $(NH_4)_2SO_4$ *catholyte.*—Aminoguanidine itself was found not to be further reduced electrolytically to guanidine and NH_3 at Pb or Cu cathode under the same conditions.

From these observations, it seems that the relative stability of nitrosoguanidine toward hydrolysis in ammoniacal catholyte is one of the reasons for obtaining aminoguanidine in good yield at Pb or other suitable cathodes. Another reason may be the existence of sulfate in the catholyte. This combines with aminoguanidine to stabilize it, because aminoguanidine is a stronger base than ammonia. This assumption was supported by the fact that this process was not applicable to the electrolytic reduction of nitrourea to semicarbazide or to the reduction of nitroguanylurea to aminoguanylurea (10). In the latter cases, the products are a weaker base than NH_3, so that sulfate cannot combine and stabilize them during electrolysis.

Conclusions

1. A greater than 80% yield of aminoguanidine was constantly obtained in $(NH_4)_2SO_4$ catholyte at Pb, amalgamated Pb, Zn, spongy Zn coated Pb and Fe. Among these cathodes, Pb is the most favorable one, giving above 85% yield.

2. Cu is the most inefficient cathode for the preparation of aminoguanidine in this catholyte. At this cathode, guanidine and NH_3 were the main products of the reduction.

3. The reduction of nitroguanidine in $(NH_4)_2SO_4$ catholyte seems to be the true electrochemical reaction accounting for the polarographic wave and not the chemical reaction with soluble electrode as suggested by Briner and co-worker in H_2SO_4 catholyte.

ACKNOWLEDGMENT

This investigation was promoted by a grant for fundamental scientific research from the Ministry of Education of Japan and also a grant from Nippon (Japan) Carbide Industries Inc., for which the authors wish to express their deep appreciation.

Manuscript received November 2, 1955. This paper was prepared for delivery before the Pittsburgh Meeting, October 9–12, 1955.

Any discussion of this paper will appear in a Discussion Section to be published in the December 1957 JOURNAL.

REFERENCES

1. C. F. BOEHRINGER AND SOHNE, Ger. pat. 167637 (1904).
2. E. LIEBER AND G. B. L. SMITH, *Chem. Rev.*, **25**, 216 (1939).
3. K. SUGINO AND M. YAMASHITA, *J. Chem. Soc. Japan*, Pure Chem. Sect., **70**, 71 (1949); M. YAMASHITA, *ibid.*, **70**, 73 (1949).
4. R. N. SHREVE AND R. P. CARTER, *Ind. Eng. Chem.*, **36**, 423 (1944).
5. V. C. SPRETER AND E. BRINER, *Helv. Chim. Acta*, **32**, 215 (1949).
6. G. B. L. SMITH, P. B. Report No. 31096, Scientific and Industrial Reports, U. S. Chamber of Commerce, Washington.
7. G. S. SMITH, *J. Chem. Soc.*, **1937**, 1325.
8. K. SUGINO AND M. YAMASHITA, Unpublished results.
9. J. THIELE, *Ann.*, **273**, 133 (1893); M. YAMASHITA, *J. Chem. Soc. Japan*, Pure Chem. Sect., **70**, 73 (1949).
10. M. YAMASHITA, Unpublished result.

Structure of Chemically Deposited Nickel

A. W. GOLDENSTEIN, W. ROSTOKER, AND F. SCHOSSBERGER

Armour Research Foundation of Illinois Institute of Technology, Chicago, Illinois

AND

G. GUTZEIT

General American Transportation Corporation, Chicago, Illinois

ABSTRACT

An analysis was made of the structure of the Ni deposit produced by the catalytic Ni reduction process. X-ray and electron diffraction revealed that the Ni deposit was an amorphous solid. The structure appeared to be unrelated to and independent of the nature of the substrate and thickness of the deposit.

Metallographic examination revealed a dense material, free of voids, and perfect conformity to the substrate surface profile. Etching produced a lamellar structure, the variation in etching intensity being interpreted as variations in dissolved P. In platings, the lamellae lay parallel to the plane of the substrate. Growth faults were observed traversing the thickness dimension from substrate surface irregularities. The amorphous structure reverted to a crystalline phase mixture of Ni and Ni_3P at low temperatures with a large heat evolution.

Basic reactions of chemical Ni *coating processes.*—The Kanigen[1] Ni plating process is based on catalytic reduction of Ni ions in the presence of hypophospite ions.

The hypophosphite anion in aqueous medium is oxidized to the phosphite ion with evolution of H, the rate being a function of temperature and hypophosphite concentration. This oxidation takes place spontaneously (homogeneous reaction) in alkaline solution at elevated temperature, while, under neutral or moderately acid conditions, the presence of a catalytic metal belonging to Group VIII of the periodic system, particularly Pd or Ni, is required (catalytic heterogeneous reaction). Wieland and Winkler (1) assumed, on the basis of organic analogies, a catalytic de-hydrogenation of the hypophosphite molecule according to the equation:

$$\underset{\text{Hypophosphorous acid}}{H(H_2PO_2)} \xrightarrow[\text{Catalyst}]{-2H} \underset{\text{Metaphosphorous acid}}{HPO_2} + H_2O \longrightarrow \underset{\text{Orthophosphorous acid}}{H_2(HPO_3)} \quad (I)$$

In a study of the mechanism of catalytic hypophosphite oxidation, Franke and Moench (2), using D as a tracer in lieu of H atoms, confirmed Wieland's hypothesis, and demonstrated that hypophosphite did not actually "decompose" the water molecule.

If the aqueous alkaline hypophosphite solution is relatively concentrated and contains cations of heavy metals which can be reduced, such as Ni, Co, Cu, Bi, Ag, Pd, Rh, Au, etc., a dark spongy or lustrous precipitate forms

[1] Kanigen is a trade name used by General American Transportation Corp. and its licenses to identify the Ni deposit or coating which is the product of a catalytic Ni reduction process.

when the solution is heated. In the case of Ni and Co, solid metal-phosphorus alloys are formed.

Furthermore, if the metal cation present in the neutral or slightly acid hypophosphite solution is that of a catalytic metal such as Ni, and a catalytic solid surface is immersed simultaneously, deposition will be limited to said surface and will continue until the solution is depleted of hypophosphite ion or of the metallic cation. The gross equation was written by Brenner and Riddell (3):

$$NiCl_2 + NaH_2PO_2 + H_2O \xrightarrow{\text{Catalyst}} Ni + NaH_2PO_3 + 2HCl \quad \text{(II)}$$

The reduction of Ni ions appears to be caused by atomic (nascent) H adsorbed as a condensed layer on the catalytic surface. Concurrently, there is a secondary reaction among the hypophosphite (and probably the phosphite) ions, atomic H, and Ni cations, resulting in the formation of Ni phosphide (possibly with a phosphonium salt as intermediate compound).

The basic reactions can be expressed tentatively by the following:

$$n(H_2PO_2)^- \xrightarrow[\text{Catalyst}]{-2nH} n(PO_2)^- \quad \text{(III)}$$

$$2H^+ \rightarrow H_2 \quad \text{(IV)}$$

$$(PO_2)^- + H_2O \rightarrow H(HPO_3)^- \quad \text{(V)}$$

$$Ni^{++} + 2H \xrightarrow[\text{Catalyst}]{} Ni^\circ + 2H^+ \quad \text{(VI)}$$

$$(H_2PO_2)^- + 3Ni^{++} + 7H \xrightarrow[\text{Catalyst}]{} Ni_3P + 5H^+ + 2H_2O \quad \text{(VII)}$$

From the catalytic surface of the solid, a stream of H bubbles escapes, and deposition of a high Ni-low P alloy takes place. This alloy is itself a catalyst, so that the coating thickness will grow constantly for a certain time period, which is limited by the *p*H decrease and instantaneous ion concentration. As can be seen from Eq. (VI) and (VII), the *p*H of the bath will drop as the reaction proceeds.

General American processes.—The character of the basic reaction and the drawbacks of the Bureau of Standards method, including published modifications thereof, indicated the direction research and development work should take for industrial production.

The principal disadvantages of the original Bureau of Standards process (3) are: slow rate of deposition, lack of stability of the bath in continuous operation, dull and even rough plating when the bath is used for longer periods, nonhomogenous deposits in the vertical direction, and relatively high cost (mainly because of a short useful life of the coating solution).

Study of a simple acid bath containing Ni and hypophosphite ions and a buffer such as sodium acetate revealed that in order to obtain both maximum deposition rates and optimum plating quality, reagent concentrations, ion ratios, and initial *p*H are critical (4).

It was discovered that the addition of short-chain aliphatic dicarboxylic acids and/or soluble fluorides ("exaltants") will substantially raise the coating rate (5, 6).

If a chemical coating bath is to be used in a production plant, it is very important to increase the span of its useful life. The limit of phosphite concentration, at which nickel phosphite precipitates, can be raised from 0.07 to about 1.0 mole/l by judicious addition of certain Ni chelating compounds, provided an "exaltant" is present to keep the deposition rate at a practical level.

The problem of bath stability is among the most serious in an industrial plant. The first visible result of excessive bath lability is the appearance of foam (due to excess H) and finely dispersed "black precipitate" (Ni-P alloy), which, because of its enormous area, acts as a very large catalytic surface. It was found that certain inhibitors, if used in properly adjusted amounts, act selectively (mainly because of geometric factors) on the suspensoids (active nuclei) making them noncatalytic, while they reduce only very slightly the rate of Ni-P deposition on the solid body to be coated.

In addition to the above improvements in bath composition, which are essential for industrial production, new principles were established relating to continuous operation and plant design, based on the requirements of catalytic reduction (7), as follows: (*A*) Because the plating rate is an exponential function of temperature, the highest possible operating temperature (below the boiling point of the solution) is desirable in order to obtain maximum speed of deposition. (*B*) It is necessary to feed continuously the consumable reagents (Ni, hypophosphite, hydroxyl ions, and stabilizer) in order to maintain maximum coating rate, optimum quality, and have the coating composition constant in a direction perpendicular to the catalytic surface. The regeneration chemicals can be added as concentrated solutions or powdered solids (to avoid bath dilution) if the bath is first cooled to a relatively low temperature (8, 9) (to prevent bath decomposition). (*C*) It is possible to meter the regeneration chemicals controlled by *p*H measurements because the various reactions in the bath are interrelated [see Eq. (III)–(VI)], and there is a fixed proportionality between the quantity of hydroxyl ions required to keep the *p*H constant, the weight of Ni-P deposited, and the amount of hypophosphite consumed.

The requirements stated above have been incorporated into the industrial Kanigen coating system, which can be described schematically as follows (7, 8, 10). The bath is prepared and kept at a relatively low temperature of about 130°F. It flows into the coating tank through a heat exchanger, which raises its temperature to 208°–210°F. From the coating tank, it is pumped into a regeneration vessel where reagents are added in controlled amounts to bring the solution's components back to their original concentration. The liquor then flows through a filter and circulates back through the heater to the coating tank.

The plant is designed in such a manner that most of the handling (pumping, filtration, etc.) of the bath is done in the "cold" section.

In many cases, when the interior of a large vessel is to be coated, the part itself becomes the plating tank.

The bath can be used until such time as the concentration of phosphite ions builds up to the point where nickel phosphite begins to precipitate. A procedure has been developed (patent pending), with several improvements

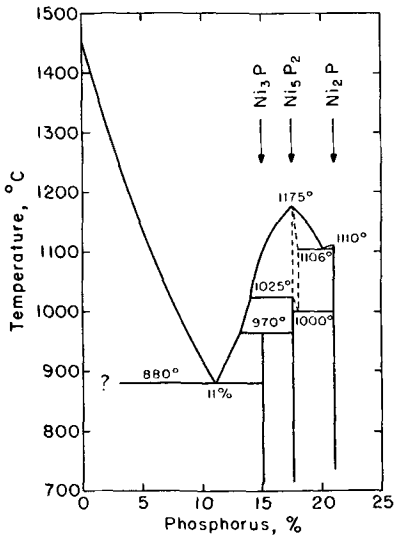

FIG. 1. Constitution of the system Ni-P

under study, which allows removal of phosphites and reclamation of the used bath without introducing any foreign ions.

Pretreatment of parts for coating by chemical reduction is essentially the same as for electrolytic plating. Because no electrical equipment is needed in a chemical coating plant, soak-cleaning procedures are preferred. Some special techniques had to be developed or adapted for deposition of Ni on certain noncatalytic metals, alloys, and nonmetals.

COMPOSITION AND CONSTITUTION

The chemically reduced metal coating was primarily metallic Ni containing 7–10 w/o P. Analyses were conducted for both metallic and nonmetallic impurities. The material used for this purpose was a quantity of deposited foil about 10 mils thick which had been stripped from panels specially treated to permit easy stripping. The foil was bright, smooth, and apparently free of surface imperfections.

Spectrographic analysis for heavier elements showed only trace amounts of Al, Ca, Fe, Mg, Pb, and Si. The term "trace" is a qualitative definition for less than 0.1% and probably less than 0.01%. Analyses for what are normally considered interstitial elements yielded the following results: C, 0.04%; O, 0.0023%, N, 0.0005%, H, 0.0016%.

The form of the phase diagram was originally mapped out by Konstantinov (11) in 1908; no work has been reported since. His version of the diagram is shown in Fig. 1. There is no information on the solid solubility of P in Ni, although from considerations of size factor and relative electro-negativity, it might be expected to be of the order of 5 w/o.

The low melting eutectic is a phase mixture of Ni solid solution and Ni_3P. The structure of the Ni_3P phase was reported by Nowotny and Henglein (12) as tetragonal: $a = 8.93_4$Å; $c = 4.39_8$Å; $c/a = 0.49$.

X-RAY STUDIES ON THE NI COATING

Investigations on the structure of the Ni deposit were carried out by Debye-Scherrer photographs of surface scrapings, Geiger counter tracings of surface reflections of the platings, transmission photographs of stripped films, and low-angle-scattering photographs of ground chips.

The Ni coatings showed the structure of an amorphous solid substance with "liquid-like" disorder of the atoms. Different base materials (such as Al, brass, steel, and Bakelite) and different pretreatments of Al base plates had no appreciable influence on the structure of the platings. The deposition of different thicknesses (1–10 mils) on these base materials had no influence on the amorphous structure of the coating.

The unique character of this physical state justifies a short discussion of amorphous solids and the experimental evidence for describing chemically reduced Ni plating as a liquid-like amorphous solid. The term "amorphous" is often used to describe structural forms for which more specific terms can now be given. In some deposits and dehydration products, a chaotic state of aggregation can be detected (13), e.g., small molecular groups loosely bound together in a quite irregular way show a high percentage of free space. The diffracted x-ray intensity of this gas-type, chaotic state extends continuously from the direct beam as in the case of diffraction of gases. The intensity of the scattered radiation in the vicinity of the central beam depends on the difference in scattering power or electron density between the two phases of the porous system. Other examples which show gas-type scattering are amorphous SiO_2, amorphous Al_2O_3, and highly dispersed carbon black (14).

With colloidal crystallites, the somewhat broadened central beam and the broadened diffraction lines are separated by distinct minima in the intensity of the scattered radiation. When the amorphous or crystallized particles are squeezed close together, the interstices are small compared with the particle size; the resultant intensity of the low-angle scattering is considerably decreased. All dense systems produce a weak, low-angle scattering, and this phenomenon can be used for analysis of the internal structure of the amorphous Ni.

A low-angle scattering x-ray photograph of ground chemically reduced Ni showed the very small scattering effect of a dense substance. This was probably not caused by pores between the amorphous aggregates but by the microlayer structure shown in the section on metallography and representing pseudo variations in P content.

In ordinary liquids, a clear intensity minimum separates the direct beam which is not broadened from the first diffraction band, i.e., the liquid halo. The x-ray patterns are characterized by a few wide bands, generally less than three (15). Distances which frequently occur between the atoms or molecules of the amorphous solid correspond to each halo on the diffraction pattern.

The x-ray powder patterns of chemically reduced Ni and the Geiger counter tracings of plated surfaces showed only one diffuse ring with a "d" spacing of 2.01Å. The occurrence of only one ring together with the extremely

small low-angle scattering characterize chemically reduced Ni deposits as liquid-like, dense, amorphous solids.

In the x-ray diagrams of liquids and liquid-like substances, the position of the peak intensity of the first halo corresponds approximately to the first strong line of the crystallized modification of the same substance. Closer investigation of the peaks of the x-ray patterns have shown, however, that in some cases the peaks do not coincide with the position of the strongest reflection of the crystallized compound. X-ray diagrams of vitreous silica, amorphous Se (obtained by quenching from a melt), and amorphous explosive Sb are examples of liquid-like amorphous solids with shifts in the positions of the halo (14, 16).

A visual inspection of the x-ray diagrams of amorphous and crystallized (heat treated at 430°C) Ni seemed to indicate that a similar shift of the position of the halo occurred with amorphous Ni. The sharp line of (111) reflections from crystalline Ni lay on the inner side of the halo. Because of the breadth of the halo and its diffuseness, a quantitative estimate of the shift was difficult.

Ring or line broadening could also have been caused by a very small crystalline particle size, but the broadening would have been symmetrical about the sharp line position. Furthermore, use of an approximate estimate of the halo breadth and the Scherrer formula for line broadening yielded the ridiculous answer of a mean particle size of a few atomic distance dimension. Electron diffraction patterns of 15 different chemically reduced Ni deposits plated under a wide variety of different conditions and in different thicknesses confirmed the amorphous character of at least the surface layers.

The density of amorphous Ni was determined in a pycnometer at 20°C and found to be $D_{20°} = 7.85$ g/cc.

The powder pattern of amorphous Ni heated in N for 1½ hr at 430°C showed a sharp line sequence of two structures. The Ni lines were easily distinguished. The remaining lines indexed provisionally on a tetragonal lattice of parameters $a = 9.01$Å and $c = 4.42$Å which is reasonably similar to the structure of Ni_3P proposed by Nowotny and Henglein (2).

A Metallographic Study of Chemically Reduced Ni

Preparation of specimens for optical metallography.—The first important phase of preparation was cutting and mounting specimens. The as-deposited coating was brittle, and simple cutting of a plated specimen with a hack saw tended to crack and flake off the deposit. It was convenient to electroplate the specimen with a heavy deposit of Ni to provide some support for the coating. The choice of Ni as a backing material was based on mechanical properties and final etching characteristics. Probably Cr would be too brittle to provide suitable support, and Cu would induce undesirable staining during etching. There was no difficulty in distinguishing the electroplated Ni from the chemically reduced Ni in polished and etched specimens.

Metallographic specimens are normally mounted in a thermosetting Bakelite under several thousand psi pressure. This method tended to promote formation of cracks in the plate, the so-called "dikes" observed by others

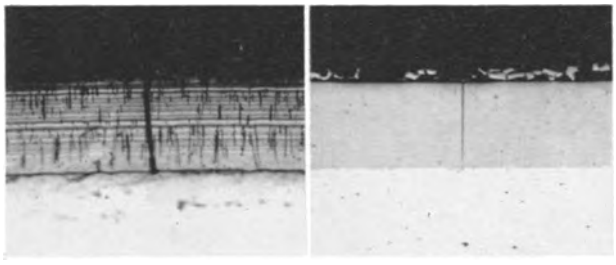

Fig. 2. (*Left*) Microstructure of 10 mil chemically reduced Ni on steel (etched). Fig. 3. (*Right*) Microstructure of 10 mil chemically reduced Ni on steel (unetched).

(Fig. 2 and 3). The etched structure revealed dark bands traversing the deposit from the substrate interface to the surface. On removal of the etch by repolishing, the dark band was more clearly resolved as a true crack.

It was possible to avoid the occurrence of cracks (which are artifacts) by mounting specimens in a room-temperature-setting compound, Epon, manufactured by the Shell Oil Company. This medium was mixed prior to casting with 8–10% by weight of triethylene tetramine which acts as a polymerizer. During curing the temperature remained below 50°C and no pressure was applied. The specimen was placed inside a polyethylene ring, approximately ½ in. high, 1 in. OD, and $\frac{1}{16}$ in. thick, which rested on a thin sheet of polyethylene film. The mixed resin was poured into the mold thus formed and allowed to solidify. Mounts thus prepared were ready for polishing in 3 hr.

Specimens for microexamination were processed as follows: (*a*) rough grind on a belt sander to create a flat surface, (*b*) rough lap on a cast iron lapping wheel with oil-suspended Carborundum abrasive. (*c*) rough polish (kerosene suspension of diamond powder), and (*d*) fine polish (water suspension of Linde "B" sapphire powder).

Routine etching reagents recommended for Ni alloys were unsuitable for revealing the structure of as-deposited chemically reduced Ni. An electrolytic etch was developed in which an electrolyte of 10% chromic acid in water was used. A cell potential of 2 v applied for about 5 sec was usually sufficient. Both cast chemically reduced Ni and heat-treated metal reacted satisfactorily to the standard $FeCl_3$-HCl etchant used for Ni alloys.

Analysis of the structure of chemically reduced Ni *coatings by optical metallography.*—Most of the studies were conducted on 10 mil plates on steel panels. On occasion it was easier to reveal the detail of basic structures on lump specimens of tank deposits.

In the unetched condition, platings at 1000 magnification were completely sound and showed no porosity, channels, or other types of voids. The plate followed the fine contour of the substrate surface in amazing detail. A number of the photomicrographs show burrs and other asperities with re-entrant angles. In all instances, the Ni deposited so completely that there were no observable voids between plating and substrate.

Fig. 4 and 5 illustrate some of the essential structural characteristics of chemically reduced Ni coatings. The structures reveal a peculiar array of parallel or concentric

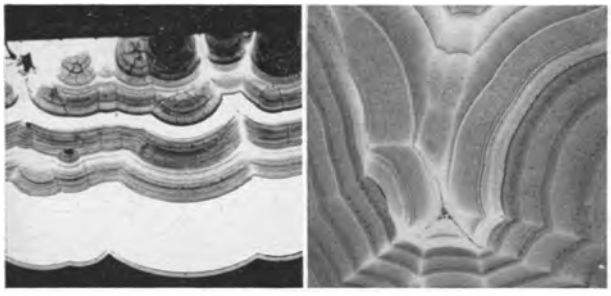

FIG. 4. (*Left*) Microstructure of tank deposited chemically reduced Ni in cross section. FIG. 5. (*Right*) Microstructure of tank deposited chemically reduced Ni in cross section.

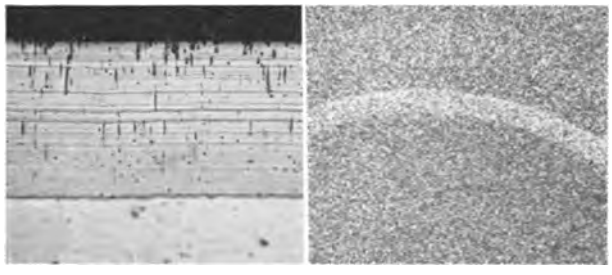

FIG. 6. (*Left*) Microstructure of 10 mil chemically reduced Ni on steel (as deposited). FIG. 7. (*Right*) Microstructure of a piece of tank deposited chemically reduced Ni after heat treatment at 700°C for 1 hr.

striations. These striations are characteristic of periodic variations of composition (presumably P) rather than alternate lamellae of different phases. Growth appears to originate at point centers or nuclei and develops at an equal rate in all directions, hence, the concentric circle pattern. When the two growth colonies meet, they generate a matching interface or fault. There is no evidence optically that the match at the fault is less than complete. If it were not true that x-ray diffraction patterns indicate an amorphous structure, these faults would come under the normal designation of grain boundaries. But since a grain boundary connotes an interface between two unique adjoining crystallographic orientations, the term cannot be properly used in this instance. It does appear, however, that the atomic disregistry at the fault is of the same degree as is thought to exist at a grain boundary, although this must be regarded only as reasonable conjecture.

On thin platings of the order of 10 mils and less, the population of surface nuclei is apparently so high that the spherical growth fronts join as a common "wave" front almost immediately, and the resultant structure shows the laminations as parallel (Fig. 6).

Evidence that the striations in the as-deposited chemically reduced Ni reflect variations in P content may be observed in microstructures of heat-treated deposits. By heat treatment the metastable as-deposited state reverts to the equilibrium phase mixture of Ni solid solution (containing very little P) and the intermetallic compound Ni_3P. The population of Ni_3P particles may be used as an indication of the original P content. Fig. 7 shows the appearance of one of the original striations after heat

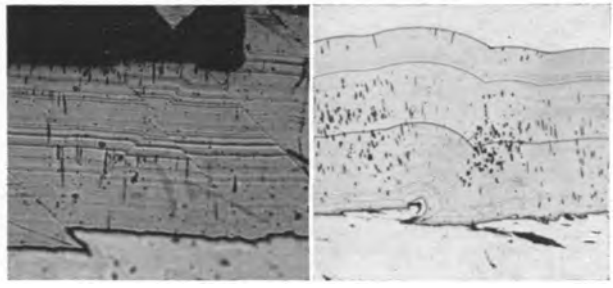

FIG. 8. (*Left*) Microstructure of 10 mil chemically reduced Ni on steel illustrating the effect of surface irregularities on the occurrence of growth faults in the deposit. FIG. 9. (*Right*) Microstructure of 10 mil chemically reduced Ni on steel illustrating the effect of surface irregularities on

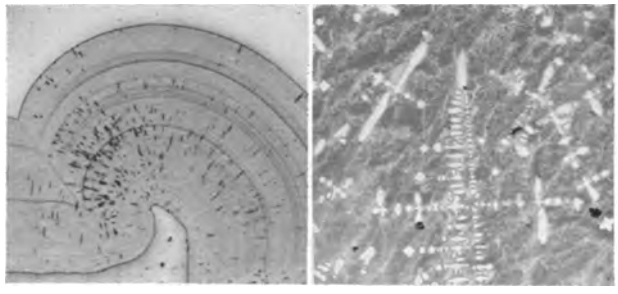

FIG. 10. (*Left*) Microstructure of 10 mil chemically reduced Ni on steel illustrating the growth of chemically reduced Ni around the burr of a sheared edge. FIG. 11. (*Right*) Structure of as-cast chemically reduced Ni—primary dendrites of Ni in a eutectic of Ni and Ni_3P.

treatment, and it can be seen that the number of Ni_3P particles within the striation is less than on either side of it.

All the as-deposited coatings (Fig. 4 and 6) showed a series of secondary striations radiating from individual nucleus points or the surface. These secondary striations were discontinuous in pattern, and appeared only on etching. Therefore, they reflected some variation in chemical content. There was no vestige of them after heat treatment. Their nature could not be deduced from studies so far pursued.

Three microstructures are presented to illustrate the influence of surface imperfections on the structure of deposits on steel panels. Fig. 8 and 9 show the occurrence of burrs left on the steel by machining. In each instance growth faults originate from the surface irregularities. A particularly detailed picture of structures and growth faulting is illustrated in Fig. 10 at a sheared edge of a steel panel.

Fig. 8 is particularly important to the general theory of the deposition process. In the first set of parallel striations in the deposit, the displacement in adjoining growth areas is the same as the original displacement of the two surface levels on the steel. This indicates that growth rates are identical everywhere in the immediate vicinity, and that modifications in the reaction kinetics which develop different P content deposits occur at the same time over the surface, irrespective of their projection into the solution.

Transformation Characteristics of Chemically Deposited Ni

Nature of transformations.—Since it was concluded that the as-deposited Ni may be interpreted as a liquid-like structure in which the primary alloy element, P, is randomly distributed on an atomic scale, the structure is metastable, both with respect to crystallinity and with respect to an equilibrium phase mixture of Ni solid solution and a Ni-P intermetallic phase, Ni_3P.

The ultimate equilibrium state was easily developed by melting a lump of chemically reduced Ni originally deposited on tank walls. The microstructure illustrated in Fig. 11 shows primary dendrites of Ni solid solution and a fine but resolvable eutectic of Ni and an intermetallic compound. The actual configuration seen in Fig. 11 is characteristic of the solidification process, but the products of crystallization are identical to what must ultimately derive from heat treatment of chemically reduced Ni below its melting point. X-ray diffraction powder patterns of the cast material gave a sharp pattern from which lines of the Ni structure could be easily distinguished from those of the intermetallic compound.

Metallography of heat treated chemically reduced Ni.—Fig. 12 and 13 illustrate structural configurations developed at two temperatures of heat treatment. In each case the transformation proceeded to equilibrium as revealed by x-ray diffraction patterns. The transformation to equilibrium produced a dispersion of Ni_3P in a Ni matrix. Clearly, the size of the Ni_3P particles was temperature dependent, i.e., the lower the heat treatment temperature, the finer the dispersion. The structure of a specimen annealed for 1 hr at 400°C was so fine that the particles cannot be individually resolved.

Generally, it may be inferred from such a sequence of microstructures that the finer the dispersion, the harder the structure. This is shown by hardness tests which show a progressive decline in the hardnesses of structures annealed at 400°, 500°, 600°, 700°, and 800°C. Hardnesses for these temperatures (1 hr anneal) were 1195, 980, 739, 665, and 544 VHN, respectively. Furthermore, it may be inferred that if some ductility can be induced in this material, it will be by annealing at 800°C or as close to the melting point as possible.

Kinetics of transformation.—It was found by experiment that hardness can serve as a tool for following time dependence of the state of transformation. Coupons were cut from a steel panel plated with a 10 mil deposit of chemically reduced Ni. The coupons were then annealed for specific times at 200°, 300°, or 400°C. Vickers hardness measurements were taken of the heat-treated Ni in the plane of cross section after cold mounting and polishing. A microhardness tester is mandatory for this type of work. In this instance, a Leitz instrument with a 100 g load was used. Reported hardnesses are averages of 5–10 measurements.

Trends of hardness vs. time for three temperatures are shown in Fig. 14. At 400°C a hardness peak is reached in about 10 min. Actually, in x-ray diffraction patterns the amorphous halo disappears after only 1 min at temperature and only the sharp lines of Ni and Ni_3P appear. There is a question then of why hardness continues to increase after 1 min. It may be that transformation proceeds by two successive processes: a reversion from undercooled liquid solution to a supersaturated crystalline solution, then a rejection of Ni_3P from the crystalline supersaturated solid solution. There are differences in relative intensities of lines and in the occurrence of certain lines in patterns taken after 1 min and after 60 min of heat treatment. Whatever the processes involved, the times are so brief that control short of complete transformation would be impractical.

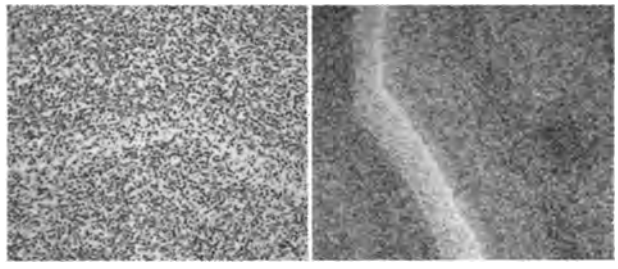

Fig. 12. (*Left*) Structure of chemically reduced Ni after heat treatment for 1 hr at 800°; dispersions of Ni_3P in a matrix of Ni. Fig. 13. (*Right*) Structure of chemically reduced Ni after heat treatment for 1 hr at 600°C; dispersions of Ni_3P in a matrix of Ni.

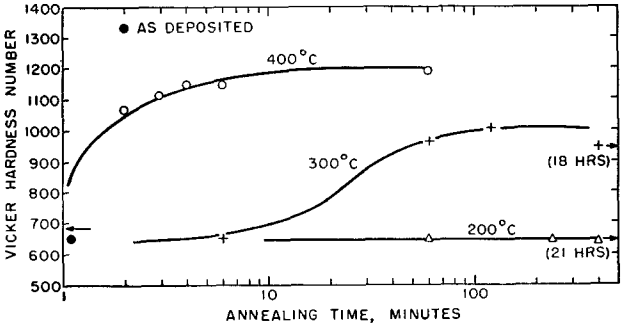

Fig. 14. Hardness of chemically reduced Ni vs. time and temperature of heat treatment.

At 200°C, even after 21 hr of heat treatment, there was no measurable change in hardness. X-ray patterns also showed the same amorphous halo observed in the as-deposited state. Accordingly, it may be concluded that no transformations occur at 200°C, at least none within 21 hr.

The 300°C anneal, as expected, followed a trend of slow transformation. Hardness continuously increased over a 2-hr period. As at 400°C, the amorphous structure, although it persisted for at least 5 min at temperature, disappeared long before the hardness reached a peak value.

Thermal evolution during heat treatment of chemically reduced Ni.—One of the main questions regarding the nature of the as-deposited metal is whether the structure is that of an undercooled liquid or of a submicroscopically fine-grained supersaturated solid solution. If the particle size of crystalline aggregates is small enough, the line broadening conceivably could approach the magnitude customarily found with undercooled liquids. One of the methods for distinguishing between these alternatives is through a study of x-ray low-angle-scattering and x-ray diffraction characteristics which are discussed in another section of this paper.

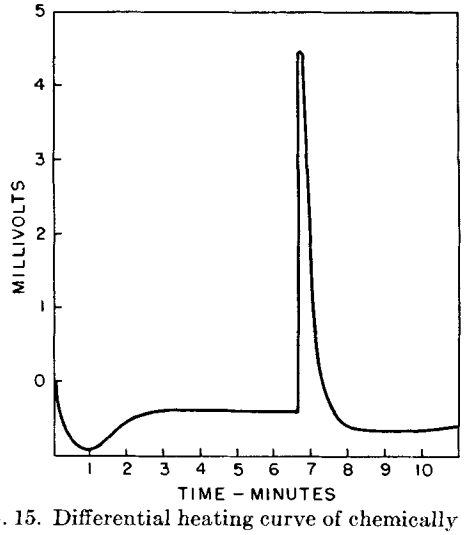

FIG. 15. Differential heating curve of chemically reduced Ni.

A second method which can give a qualitative indication is some measure of the magnitude of thermal evolution accompanying the transformation of the as-deposited metal to the equilibrium phase mixture of Ni and Ni_3P. Invariably, latent heats of fusion are substantially larger than latent heats of crystalline state transformations. For instance, the latent heat of fusion of Fe is 3700 cal/g-mole, whereas the heat of transition from $\alpha \rightarrow \gamma$ Fe is only 210 cal/g-mole; under adiabatic conditions these would correspond to temperature rises of 330° and 21°C, respectively. A survey of available data on latent heats of transformation indicates that they are all less than 1000 cal/g-atom and usually much less. Such thermal evolutions should then incur ideal temperature rises of less than 100°C, but since an ideal adiabatic system is very difficult to attain, the temperature rises should actually be considerably less.

A simple experiment was devised to study thermal evolution effects in chemically reduced Ni. Two pieces of Ni tank deposit in the form of plates about 0.020 in. thick and 1 cm^2 area were chipped to size. One piece was heat treated in advance so that no further transformations would occur. A fine wire chromel-alumel thermocouple was spot welded to each of the pieces and connected in opposition to a Speedomax high-speed recording potentiometer. Each of the pieces of chemically reduced Ni was set in a test tube for convenience of handling, and the assembly was immersed in a lead bath.

Since both pieces were heated at about the same rate, differential potential remained about zero. At 400°C, as recorded by an auxiliary thermocouple, there was a sharp rise in differential potential which lasted for about 1½ min and then disappeared. A reproduction of this portion of the record is shown in Fig. 15. The burst of differential potential verified that the chemically reduced Ni liberated a substantial amount of heat on transformation to its equilibrium state. Furthermore, it is obvious that the transformation rate at 400°C is extremely rapid.

The maximum differential potential was 5 mv, which corresponds to a temperature rise during transformation of 122°C. Since the conditions of testing were far from adiabatic, this corresponded to a thermal evolution of considerably more than 1000 cal/g-mole. These results lend support to the hypothesis that as-deposited chemically reduced Ni is an undercooled liquid.

SUMMARY

The Ni deposit containing 7–10 w/o P produced by the catalytic Ni deposition process has been found to possess a dense, amorphous, liquid-like structure. It is probably the first occurrence of an amorphous metallic solid in massive form. The structure is unrelated to the nature of the substrate, manner of preparation, and thickness. The deposits were shown to conform, within microscopic resolution, exactly to the surface contour of the substrate. The deposit itself showed no porosity but in the etched state revealed striations in etching intensity and growth faults originating from asperities in the substrate surface. These striations in etching intensity were interpreted as banded variations in P content.

The as-deposited state of chemically reduced Ni is highly metastable and at 300°C or above reverts rapidly to the equilibrium condition of a phase mixture of crystalline Ni and crystalline Ni_3P. The dispersion of Ni_3P in Ni can be used as a means for promoting and controlling hardness of heat treated chemically reduced Ni.

ACKNOWLEDGMENTS

This work represents part of a program sponsored by the General American Transportation Corporation at the Armour Research Foundation, and their permission to publish is gratefully acknowledged. Some of the x-ray diffraction studies were conducted by Miss Irene Corvin. Mr. E. Klimek was responsible for the metallography. Useful discussion was contributed by Dr. R. J. Spraul and Mr. W. J. Crehan of the sponsoring company.

Manuscript received March 14, 1956. This paper was prepared for delivery before the San Francisco Meeting, April 29–May 3, 1956.

Any discussion of this paper will appear in a Discussion Section to be published in the December 1957 JOURNAL.

REFERENCES

1. H. WIELAND AND A. WINKLER, *Ann. Chem.*, **34,** 198 (1923).
2. W. FRANKE AND J. MOENCH, *Ann. Chem.*, **550,** 1 (1942).
3. A. BRENNER AND G. RIDDELL, *J. Research Nat. Bur. Standards*, **39,** 385 (1947).
4. G. GUTZEIT AND A. KRIEG, U. S. Pat. 2,658,841, Nov. 10, 1953.
5. G. GUTZEIT AND E. RAMIREZ, U. S. Pat. 2,658,842, Nov. 10, 1953.
6. G. GUTZEIT, U. S. Pat. 2,694,019, Nov. 9, 1954.
7. G. GUTZEIT AND R. W. LANDON, *Plating*, **41,** 14 (1954).
8. P. TALMEY AND W. J. CREHAN, U. S. Pat. 2,658,839, Nov. 10, 1953.
9. P. TALMEY AND W. J. CREHAN, U. S. Pat. 2,717,218, Sept. 6, 1955.
10. G. GUTZEIT, *Metal Progress*, **65,** 113 (1954).
11. N. KONSTANTINOW, *Z. anorg. Chem.*, **60,** 405 (1908).
12. H. NOWOTNY AND E. HENGLEIN, *Z. phys. Chem.*, **B40,** 281 (1938).
13. J. BOWMAN, "X-Ray Crystallography," 191, Interscience Publishers, Inc., New York (1951); J. A. PRINS, *Z. Naturforsch.*, **6a,** 276 (1951).
14. R. GLOCKER, "Materialprüfung mit Röntgenstrahlen," Springer Verl., Berlin (1949).
15. A. GUINER, "X-Ray Crystallographic Technology," Hilger and Watts, London (1952).
16. B. E. WARREN, *J. Appl. Phys.*, **8,** 654 (1937).

Electrochemical Properties of a Cation-Transfer Membrane

N. W. Rosenberg, J. H. B. George,[1] and W. D. Potter[2]

Ionics, Inc., Cambridge, Massachusetts

ABSTRACT

The electrochemical behavior of a cation-transfer membrane with respect to cations of various charge was investigated. Measurements were made of capacity, water content, Donnan sorption, conductance, water transfer, and transport numbers. Results suggest that ionic mobilities are lower in the membrane than in free solution, indicating a high degree of association between the cations and the charge centers of the membrane.

Previous measurements of electrochemical properties of ion-exchange membranes have been confined almost exclusively to their behavior with univalent ions. In this paper comparative data are presented for a single cation-permeable membrane equilibrated with aqueous solutions of K, Ba, La, and $ThCl_4$, as representative of uni-, di-, tri-, and tetravalent cations. At a series of solution concentrations, measurements were made of the Donnan sorption equilibria, membrane conductance, cation transport numbers from membrane potentials, cation transport numbers from Hittorf-type measurements, and water transfer. The membrane[3] studied was a sulfonated, cross-linked, polystyrene-type, cation-exchange resin, cast as a homogeneous film, prepared as described in (1), and with properties as reported below. Experimental measurements, made at laboratory temperature, were not designed for a high order of accuracy, but to establish general membrane behavior. Results are discussed in terms of existing theories and possible structural concepts.

Theoretical

A sheet of ion-exchange resin forms a permselective ion-transfer membrane, with fixed electrochemical properties determined by the solution with which it is equilibrated (2). In equilibrating solutions of high ionic strength, Donnan sorption of equilibrating electrolyte MX into the resin phase MR increases the concentration of M but also introduces an equivalent quantity of X into the resin phase (3). Thus the cation transport number in the membrane decreases (from unity at low ionic strength of equilibrating electrolyte, when the only mobile species is M) to a value determined by the concentrations and mobilities of the sorbed species, and the membrane conductivity rises from similar considerations (4).

Donnan sorption.—When an ion-exchange membrane is immersed in a salt solution, the structure is penetrated by both positive and negative ions of the salt until the position of thermodynamic equilibrium is obtained where the partial molal free energy of the salt is equal in the membrane and solution phases. Assuming the same standard state for the ions in the membrane as in solution, expression of this Donnan equilibrium for a salt such as KCl leads to the relation $\gamma_{\pm s}^2\ (K^+)_s\ (Cl^-)_s = \gamma_{\pm m}^2\ (K^+)_m\ (Cl^-)_m$ where $\gamma_\pm$ represents mean activity coefficients, the quantities in parentheses represent concentrations, and subscripts s and m refer to the solution phase and membrane phase, respectively. Little is known of activity coefficients of ions in the membrane phase, so this relation cannot be verified independently. As has been pointed out (3–6), Donnan sorption in ion-exchange resins is significant, but is not explained from classical theory without assuming enormous variations in activity coefficients in the resin phase at low concentrations of equilibrating electrolyte.

In this paper, observed Donnan sorptions in the range 0.1–1.0N equilibrating solutions are reported and used in conjunction with transport numbers and conductance values to compute apparent ion mobilities.

Membrane conductivity and ionic mobilities.—The specific conductivity of a membrane (L) can be determined in an appropriate conductivity cell (7). From the conductivity and transport number measurements, individual ionic conductivities L_M and L_X and equivalent ionic conductivities λ_M and λ_X in the resin phase may be defined as: $L_M \equiv LT_+$; $L_X \equiv L(1 - T_+)$; $\lambda_M \equiv 1000\ L_M/(M) = 1000L\ T_+/(A) + (R)$; $\lambda_X \equiv 1000\ L_X/(X) = L(1 - T_+)/(A)$ where L represents the conductivity of the membrane (mho/cm), L_M cationic conductivity; L_X anionic conductivity; T_+—true cation transport number; λ_M—cation equivalent conductivity; λ_X—anion equivalent conductivity; (M)—concentration of cations, millieq./wet resin; (X)—concentration of sorbed anions, millieq./wet g resin; (A)—concentration of sorbed ions, millieq./wet g resin; (R)—concentration of ionized exchange sites, millieq./wet g resin.

Transport numbers and water transfer from Hittorf measurements.—The true transport number (T_+) of a cation across the membrane and the accompanying water transfer can be determined in a Hittorf cell. In such a cell the electrical transfer of ions through a membrane is accompanied by a flow of water, and the high hydraulic resistance of the membrane enables the extent of this water transfer to be measured.

When current is passed through a chloride solution contained in a cell bounded by a membrane and an electrode reversible to chloride, the transport number is given

[1] Present address: Arthur D. Little, Inc., Cambridge, Mass.

[2] Present address: Tracerlab, Inc., Boston, Mass.

[3] NEPTON CR-61.

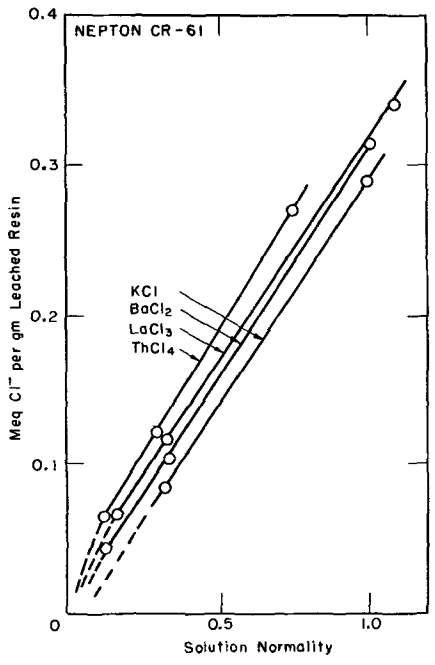

FIG. 1. Donnan sorption of salts in the membrane[3]

by $d(NV)d\mathbf{F} = NdV/d\mathbf{F} + VdN/d\mathbf{F}$ where N and V are the normality and volume (in liters) of the solution, and $\mathbf{F}$ represents the Faradays of electricity passed.

The electrical transfer of ions through a membrane is accompanied by water transfer, which can be expressed as $V^* = dV/d\mathbf{F}$ liters transferred per Faraday passed. It can be measured unambiguously in a Hittorf-type cell without a knowledge of whether the source of the transfer is endosmosis or ion hydration, or a combination of the two. Corrections must be made for the change in volume due to the electrode processes and volume of salt transferred. These corrections are small and have been calculated from published values of the partial molal volumes of the salts (8) and the densities of Ag and AgCl.

The transferred water, however, may carry with it salt from one electrode chamber to the other, and the concentration of this "water-transported" salt has a value N' between zero and N. It contributes $N'dV/V$ to dN so that the true transport number of T_+ is given by

$$T_+ = V(dN/d\mathbf{F} - N'dV/Vd\mathbf{F}) + NdV/d\mathbf{F}$$
$$= VdN/d\mathbf{F} + (N - N')dV/d\mathbf{F}$$

Since there is no means of determining N', its value is set arbitrarily at zero, and the values of T_+ so obtained set an upper limit for the value of the transport number, the lower limit of which is set by $VdN/d\mathbf{F}$.

Transport numbers from cell potentials (9, 10).—Cation transport numbers across a membrane can also be determined from emf measurements. The emf developed between Ag-AgCl electrodes immersed in two chloride solutions of different concentration separated by a membrane is given by $E = t_+(RT/n\mathbf{F}) \ln [(m_\pm\gamma_\pm)_2/(m_\pm\gamma_\pm)_1]$ where $m_{\pm 2}$, $m_{\pm 1}$, $\gamma_{\pm 2}$, and $\gamma_{\pm 1}$ are the mean molarities and stoichiometric activity coefficients of the electrolytes, and t_+ is the apparent cation transport number in the membrane uncorrected for water transfer. This corresponds to $VdN/d\mathbf{F}$ in the expression above, and values from the two methods of measurements have been compared.

EXPERIMENTAL

Capacity, water content, and density.—The membrane[3] as purchased was a sheet-form ion-exchange resin supported on a glass fiber backing. In the specimens employed in the present work (10 x 3 x 0.08 cm), the fiber constituted 24% by weight of the total membrane.

Water content was determined by drying at 110°C to constant weight. The water content of the backed material was 44% corresponding to 58% for the unbacked resin.

The capacity of the membranes was determined by converting a sample of known weight to the H form by equilibrating with 1N HCl, followed by leaching with water and subsequent exchange with 1N NaCl solution. The liberated H ion was titrated with standard alkali. The capacity (expressed as eq./1000 g water-equilibrated resin) was 0.87, corresponding to 1.15 for the unbacked wet resin. The capacity (expressed as eq./1000 g dry resin) was 2.75 on the unbacked dry resin.

The density of the membrane in the leached Na form was determined by measuring the dimensions of a rectangular specimen of known weight. The density (expressed as g/cc) was 1.27, corresponding to 1.09 for the unbacked resin.

Donnan sorption.—Data were obtained for the Donnan sorption of KCl, $BaCl_2$, $LaCl_3$, and $ThCl_4$ in the membrane.[3] Samples of the membrane of known weight were immersed in solutions of each salt at various concentrations. After equilibrium had been attained, the supernatant solution was withdrawn and analyzed; the membrane sample surface was dried, then leached with water until free of chloride. A chloride analysis of the leach water was made, from which the equilibrium concentration of chloride in the membrane and solution phases was determined. It is recognized that this technique yields only "leachable" chloride, i.e., sorbed chloride capable of desorbing into water. The experimental procedure allowed errors of ±5% in 1N solutions, increasing to ±15% in 0.1N solutions, in the data which are presented as Fig. 1.

Membrane conductivity.—A cell for determining the conductance of membrane strips has been described (7). Strips with dimensions 10 x 3 x 0.08 cm were equilibrated with salt solutions of various normalities, withdrawn from the solution, and surface-dried with fiber. Specific conductivities (mmho/cm) of these strips were then determined. Results are presented graphically in Fig. 2. The experimental procedure allowed probable errors of ±5% in conductivity values. Equivalent conductance values are based on the total volume of the leached membrane and are therefore relative values. The ambiguity of the term "solvent" in a solid phase containing 50% organics and 50% water prevents the use of a molal basis for conductance values.

Transport numbers and water transfer from Hittorf measurements.—Hittorf transport numbers were measured in a four-compartment cell consisting of a Ag disk, a membrane disk, a Ag disk, a membrane disk, and a Ag disk,

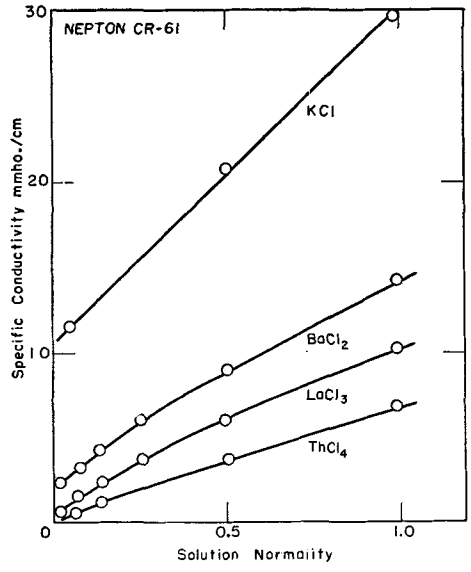

FIG. 2. Membrane conductance in salt solution

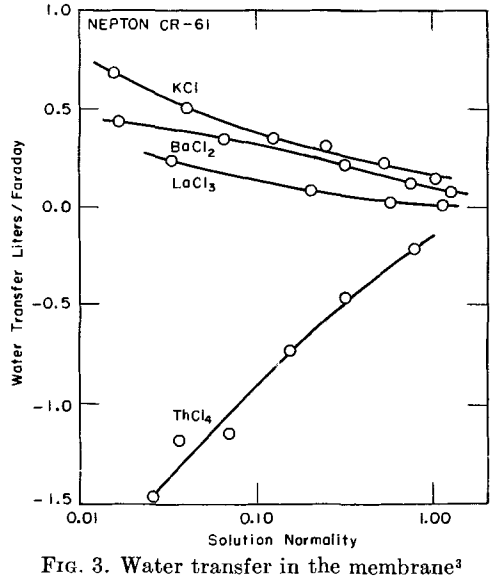

FIG. 3. Water transfer in the membrane[3]

separated from each other by plastic washers 1 cm thick with an OD of 10 cm and an ID of 5 cm. The centers of the washer disks formed the solution compartments, each of which was therefore bounded by a membrane and a Ag electrode. Each washer contained two tubes for filling and draining, and for connecting a graduated pipet on which volume changes were read. The Ag disks were given chloride coats sufficient to allow them to function as reversible electrodes for passage of up to 0.005 Faraday of electricity.

In an experimental run each compartment was filled initially with aliquots of a given solution and a voltage imposed across the two end Ag electrodes. With this arrangement it was possible to make quadruplicate determinations of concentration changes and volume changes simultaneously. Current was passed for a time sufficient to cause a concentration change of about 20%. Measurements were made of current, time, initial and final solution normality, and initial and final solution volume. From the

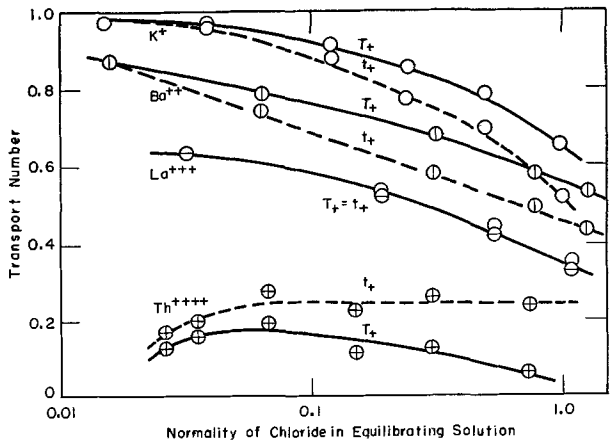

FIG. 4. Hittorf transport numbers with and without water correction.

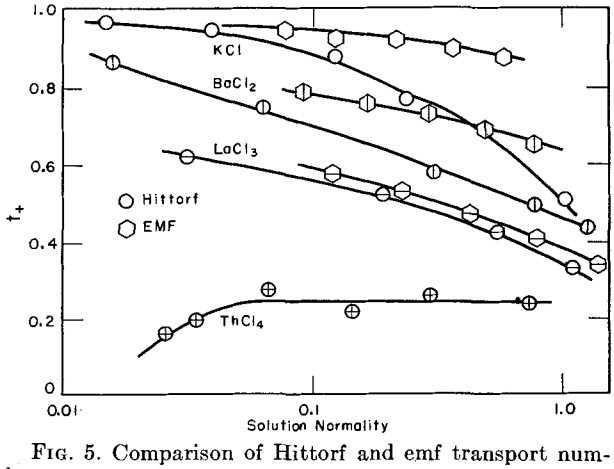

FIG. 5. Comparison of Hittorf and emf transport numbers.

data, the values of water transport (Fig. 3) and transport number (Fig. 4) were computed, corrections being made for the volumes of transported salt and the changes in volume at the electrodes. Probable errors in V^* are about 3%, and in the transport numbers about 0.03.

Transport numbers from cell potentials.—In the determination of transport numbers from cell potentials, solutions were passed through two compartments of a Lucite cell separated by a membrane. In each experiment the salt concentration of the solution in one compartment was approximately twice the concentration of the other. The potential between Ag-AgCl electrodes immersed in the two solutions was measured on a potentiometer. From the observed potential, the concentrations, and activity coefficients, an apparent transport number was computed. The equilibrating solution concentration was taken as the geometrical mean of the two concentrations. Experimental techniques and uncertainties in activity coefficients result in a probable error of ±0.03 in the transport number values. Potentials in the $ThCl_4$ system were erratic and not reproducible, and transport numbers from emf measurements were not computed or reported for this ion. Transport numbers, t_+ (uncorrected for water transfer), as determined by emf and Hittorf methods, are compared in Fig. 5.

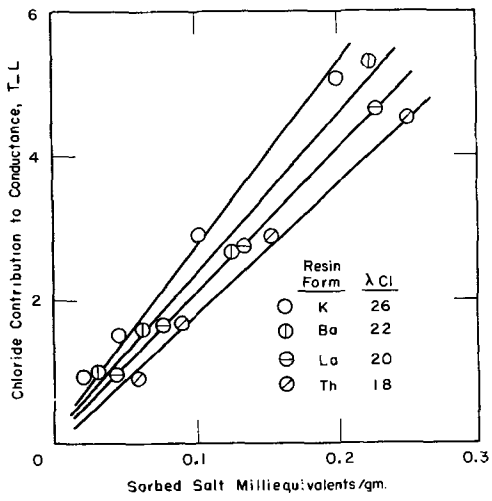

FIG. 6. Chloride contribution to conductance

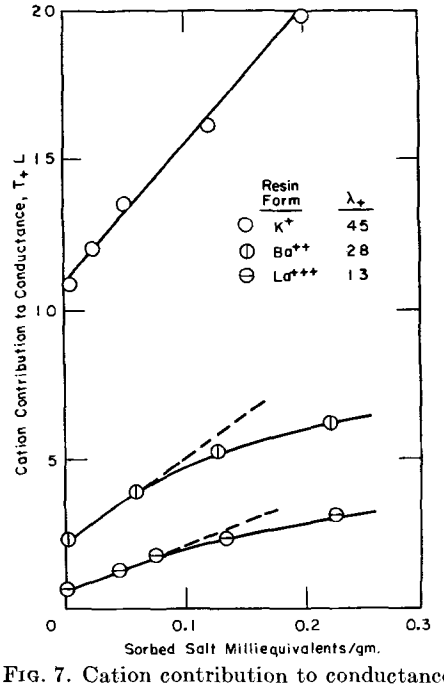

FIG. 7. Cation contribution to conductance

DISCUSSION

Donnan sorption.—Fig. 1 shows an almost linear relationship between chloride concentration in the resin and chloride concentration in the equilibrating solution. This indicates that the exchange centers within the membrane are much less effective in excluding equilibrating electrolyte than would be predicted from capacity values. This discrepancy has been found to some degree in other ion-exchange work (3–6).

One possible explanation is that the cations are associated to a large extent with the exchange sites and thus are not effective in screening. An alternative description of the same physical situation is that, in the molecular pores of the membranes, the exchange cations are not distributed uniformly but are relatively concentrated at the walls of the pores and therefore ineffective in screening the center of these pores. The assumption of such association and estimates as to its extent based on observed conductivities are made below.

Transport number.—It can be seen from Fig. 5 that the agreement between the transport numbers, t_+, as determined by emf measurements and by Hittorf cell measurements, is not good in the K system, but is better in the Ba and La systems. Because of erratic emf measurements in the Th system, only Hittorf cell measurements are reported for this ion.

Trends discernible from Fig. 5 are of considerable interest. At the same concentration of sorbed chloride ion, the membrane shows greatest selectivity in the univalent system, while in the quadrivalent system the membrane appears to be anion selective at all concentrations. This view is supported by the water transfer data but cannot be finally confirmed because of the absence of transport number measurements for $ThCl_4$ in free solution. Some published work (11), however, shows that a major fraction of Th in chloride solution exists as Th^{+4} and $ThCl^{+3}$, indicating anion transport numbers in free solution much lower than the value of 0.9 found in the membrane.

A possible explanation for the lower selectivity of the membrane to multivalent cations is that there is increased association of the cations with the charge centers of the membrane. If it is assumed that the exchange sites in the membrane cannot be deformed to allow association of more than one site with a cation, then the existence of positively charged centers in the membrane is possible. This would account for the lower transport numbers for multivalent cations and for the water transfer data and membrane conductance data discussed below.

Water transfer.—The passage of ions across a membrane is accompanied by the transfer of water, either as water of hydration of the transferred ions, as electro-osmotic water, or as a combination of the two. It is difficult to picture any experiments which would distinguish unambiguously the relative contributions of the two phenomena. In a cation-permeable membrane both processes would transfer water in the same direction as the ion transfer, and the magnitude of hydration of an ion crossing a membrane cannot be assumed to be that of the same ion in free solution. As seen from Fig. 3, water transfer values decrease with increasing concentration of sorbed salt and with increasing valence. They become highly negative in the Th system, offering some indication of the anionic character of the membrane in this form.

Conductance data.—Fig. 2 shows that the mobilities of the cations in the leached membranes differ much more markedly relative to each other than in free solution. This is in agreement with work of Boyd and Soldano (12) who found a similar strong dependence of self-diffusion coefficients on the ionic charge of the exchange ion.

Ionic mobilities.—It is possible to combine the experimental data on conductance, Donnan sorption, and transport numbers to calculate the relative mobilities of the various ionic species in the membrane. This has been done for the K^+, Ba^{++}, and La^{+++} systems, the concentration units being expressed as millieq/g leached resin in the salt form under consideration.

The contribution of cations, including both exchange cations and Donnan-sorbed cations, to the membrane con-

ductance L is given by LT_+, and the contribution of anions, which are present solely due to Donnan sorption, is given by $L(1 - T_+)$.

If LT_+ and $L(1 - T_+)$ are plotted as a function of Donnan sorption, it is found that the anion contribution is proportional to Donnan sorption. The computation of a nominal equivalent anionic conductance can be made from the ratio LT_+ to concentration. In Fig. 6 the equivalent conductance of the sorbed chloride varies from 18–26, depending on the exchange cation. This very small variation is striking in view of the large conductance variation in the leached resins in different ionic form. The equivalent conductance compares with a value of about 60 in aqueous NaCl of the same concentration.

The cation contribution is given by LT_+ (Fig. 7). Here the conductance is not zero at zero Donnan sorption because of the conductance due to exchange cations present.

There are two bases on which equivalent cationic conductances can be calculated. One estimate can be made by taking the increase in conductance as Donnan-sorbed salt concentrations increase, and represents the equivalent cationic conductance of the nonexchange cations. These estimates, from Fig. 7, indicate values of 45, 28, and 13 for K^+, Ba^{++}, and La^{+++}, respectively, and are not radically different from aqueous values. The other basis is to take the ratio of leached membrane conductance to exchange site concentration, which represents an equivalent cationic conductance of the exchange cations. These estimates, from Fig. 7, indicate values of 12.5, 2.7, and 0.7. In other words, the apparent mobilities of the exchange ions are much lower than those of the nonexchange ions. As pointed out by previous workers (4, 13), this can best be explained by assuming only partial dissociation of the resin salt. On this assumption the degrees of dissociation are 28%, 9.6%, and 5.4% for the salts KR, BaR_2, and LaR_3.

ACKNOWLEDGMENT

The authors wish to express their thanks to Dr. Walter Juda, who suggested the study, and to Miss P. A. LaFortune for assistance with the experimental work.

Manuscript received December 5, 1955.
Any discussion of this paper will appear in a Discussion Section to be published in the December 1957 JOURNAL.

REFERENCES

1. J. T. CLARKE, U. S. Pat. 2,731,411 (1956).
2. W. JUDA AND W. A. MCRAE, *J. Am. Chem. Soc.*, **72,** 1044 (1950); M. R. J. WYLLIE AND H. W. PATNODE, *J. Phys. & Colloid Chem.*, **54,** 204 (1950); T. R. E. KRESSMAN, *Nature*, **165,** 568 (1950).
3. W. C. BAUMAN AND J. EICHORN, *J. Am. Chem. Soc.*, **69,** 2830 (1947).
4. W. JUDA, J. A. MARINSKY, N. W. ROSENBERG, AND A. A. KASPER, *ibid.*, **74,** 3736 (1952).
5. G. F. BOYD AND Q. V. LARSON, A.C.S. Symposium on Polyelectrolytes, Ithaca, N. Y., June 18, 1951.
6. G. E. MOORE AND K. A. KRAUS, *J. Am. Chem. Soc.*, **75,** 1475 (1953).
7. J. T. CLARKE, J. A. MARINSKY, W. JUDA, N. W. ROSENBERG, AND S. A. ALEXANDER, *J. Phys. Chem.*, **56,** 100 (1952).
8. H. S. HARNED AND B. B. OWEN, "Physical Chemistry of Electrolytic Solutions," 2nd ed., p. 253, Reinhold Publishing Co., New York (1950).
9. K. SOLLNER AND H. P. GREGOR, *J. Phys. & Colloid Chem.*, **54,** 325 (1950).
10. G. SCATCHARD, *J. Am. Chem., Soc.*, **75,** 2883 (1953).
11. W. C. WAGGENER AND R. W. STOUGHTON, *J. Phys. Chem.*, **56,** 1 (1952).
12. G. E. BOYD AND B. A. SOLDANO, *J. Am. Chem. Soc.*, **75,** 6091 (1953).
13. B. A. SOLDANO AND G. E. BOYD, *ibid.*, **75,** 6099 (1953).

Kinetics of Metal Deposition

Polarography Using Stationary Microelectrodes

T. PAVLOPOULOS AND J. D. H. STRICKLAND[1]

Chemistry Division, British Columbia Research Council, Vancouver, B. C., Canada

ABSTRACT

Current-voltage curves arising from metal deposition were determined using a variety of stationary microelectrodes, mostly vertical wires, and the concentration polarization approximated that expected from convective diffusion. The Nernst diffusion equation is not valid, and current densities I, in amp/cm^2, for systems containing excess inert electrolyte are given by the equation:

$$I = 1.4nFD^{0.8}(C - C_e)^{1.2}\left(\frac{1}{2r} + \frac{1}{\delta}\right)$$

This can be used to calculate limiting current densities during alloy formation and to characterize deposition processes as reversible or irreversible. Graphical methods can be used to determine transfer coefficients and rate constants, for a markedly irreversible process

The kinetics of diffusion to and reduction at a dropping mercury electrode has been studied extensively by means of current-voltage curves, but comparatively little work of a similar nature has been reported for metal deposition on solid microelectrodes. This is true despite the fact that such a technique could provide a simple method for evaluating rate constants and transfer coefficients of irreversible processes if the purely transport behavior could be adequately represented mathematically.

Following Wilson and Youtz (1), Glasstone (2) suggested that the simple Nernst theory of diffusion could be used to predict maximum current densities in plating baths. This approach, although an oversimplification, does predict the kinetics of many heterogeneous transport-controlled reactions with reasonable precision (3).

By far the largest proportion of recent work with solid micro-electrodes has been undertaken using an electrode moving relative to the solution, and the direct proportionality of current and concentration of reducible species is fully established. Use of stationary electrodes has much to recommend it on the grounds of simplicity and ease of reproducibility of experimental conditions. The approach has been used by Laitinen and Kolthoff (4) who reported that diffusion currents with a stationary Pt wire electrode were represented to a fair approximation by a Nernst type equation. The resulting direct proportionality of current and concentration has found analytical applications (5–8).

However, Levich (9) and Agar (10) deduced from theoretical grounds that for vertical macro plate electrodes convective processes should operate and limiting current densities be proportional to concentration raised to a power of five-fourths. This has been confirmed theoretically and experimentally for macro systems (11–16).

Despite this work, micro wire electrodes have been tacitly assumed to be some sort of exception. In the present work, a Nernst type of relationship with these electrodes was not confirmed, and current densities were reproduced with much greater precision and ease than generally assumed possible. The behavior of these systems is quite close to that to be expected if convective diffusion were operative. The purpose of this work is to establish a general equation applicable to polarography with these electrodes and to demonstrate the applicability of the equation to a study of electrode kinetics.

EXPERIMENTAL PROCEDURE

Chemicals and apparatus.—Metal perchlorates were prepared by evaporating nitrate solutions with excess $HClO_4$, fuming off the bulk of the acid, and neutralizing the remainder with NaOH. $NaClO_4$ was recrystallized and stored over neutral chromatographic activated Al_2O_3, and other salts were of analytical reagent quality. The metal content of all stock solutions (0.1M) was checked by standard chemical procedures. The final solutions of metals and inert electrolyte were adjusted to a *p*H just below the hydroxide precipitation values to minimize possible errors from H ion reduction.

The cell used in most experiments is shown in Fig. 1. The electrode was placed in the center compartment of the cell and the sheath, [5], passed over the cell. On placing the assembly in a water bath, thermostatically controlled to about ±0.1°C, a water seal was formed, and on passing electrolytic H through tube [1] to deoxygenate the solution, the residual H was held in [5] and formed a protective layer against the ingress of atmospheric oxygen. The two salt bridges, [2], were built onto the center compartment and curved round to dip into two half-cells, [4], the bridge ends being closed by sintered glass discs, [3].

The electrodes were prepared from Pt wire polished with fine emery, rinsed with aqua regia and then distilled water,

[1] Present address: Pacific Oceanographic Group, Fisheries Research Board of Canada, Nanaimo, B. C., Canada.

and finally annealed. The disc electrode was in the form of a small circle cut from Pt sheet and sealed flush with the end of glass tubing of equal external diameter. The disc was held in a vertical plane, only one face being exposed to the electrolyte. To prevent the formation of "trees" of deposited metal on the sharp edges of the cut ends of the wire electrodes, the ends were covered by a bead of fused glass. The apparent surface area of the electrodes was measured to better than 1–2% by means of a cathetometer.

Currents were measured with a Sargent No. 21 polarograph and potentials to better than 1 mv by a Rubicon potentiometer. The precision and linearity of the polarograph was checked at all sensitivity settings by measuring the voltage drop across reference standard resistors and was found always correct to better than 1%.

Procedure.—Saturated calomel half-cells were prepared by the method of Hills and Ives (17) and the salt bridges filled with saturated NH_4NO_3. The center compartment was flushed and filled with the solution under study and the electrode inserted into the cell with the whole assembly in a constant temperature bath. H was passed for at least 30 min to remove dissolved oxygen. One half-cell was made the working anode and attached to the polarograph. The other half-cell was connected to the potentiometer and used to measure the potential of the microelectrode, giving values substantially free from *iR* drop and liquid junction errors.

To prevent roughening and tree formation resulting from prolonged plating, the electrodes were stripped of metal between each reading. This was accomplished by lowering the applied potential to about 0.2 v more positive than the deposition potential of the metal (too great a positive potential sometimes led to electrode poisoning) and turning on a stream of H bubbles to stir the electrolyte. The stripping process, as judged by a negative current returning to a zero value, took only a few minutes. The only exception to this process was observed with the most dilute solutions or at very low potentials, when plating was so slow that several minutes were required to cover the electrode with deposit.

The blank currents from the base electrolyte, when determined without added metal ions, were negligible, provided that deoxygenation was adequate. However, in the presence of metal ions, in particular Tl, blank currents were sometimes obtained at voltages too low for metal deposition. The cause of this remains obscure, but what may be a similar type of behavior has previously been noted (18). If the electrodes were alternately plated and stripped several times these blank currents were nearly always entirely eliminated. Temperature control to within a few tenths of a degree was adequate, and current values did not seem to be unduly affected by normal laboratory vibrations, although precautions to minimize disturbances during measurements were observed. The sudden rise of current due to tree formation, particularly bad during alloy deposition, was quite characteristic, and, once recognized, could be eliminated as a source of error. However, without the blob of glass at the end of the wire electrodes, the onset of tree formation was often so rapid that reliable measurements could not be made. Some form of end covering was essential for accurate work at high current densities.

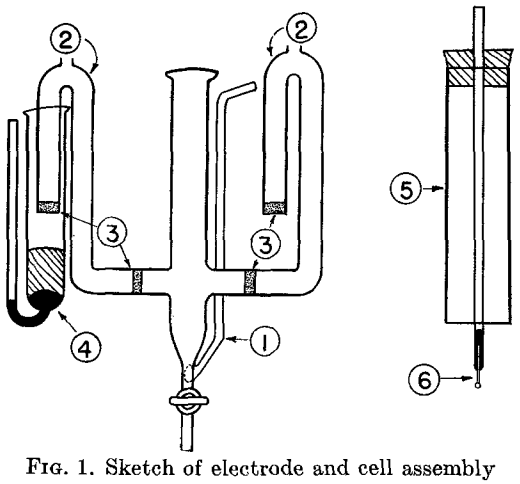

FIG. 1. Sketch of electrode and cell assembly

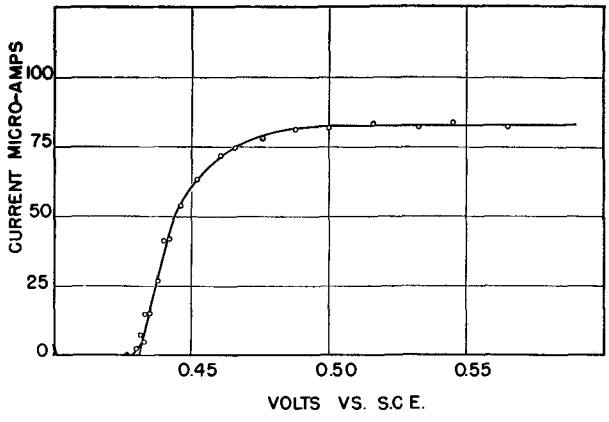

FIG. 2. Current-voltage curve for the reduction of 5.0 $\times 10^{-3}$ M Pb^{2+} in 1M $NaClO_4$ at 25.0°C, using wire electrode of length 0.45 cm and radius 0.064 cm.

Diffusion coefficients, *D*, were determined polarographically. The best modification of the Ilkovic equation is still in doubt, but mainly as a result of the work of Wang (19) the Strehlow and von Stackelberg version (20) was used.

RESULTS

The experimental data consisted essentially of current voltage curves such as that in Fig. 2. Limiting current densities were calculated from geometrical areas, and the mean value of at least four points was taken to determine a plateau such as that shown in Fig. 2. Reversible voltages were obtained by extrapolation to zero current.

The steady current value at each voltage was recorded as the mean of results taken every minute, after allowing 3 min for values to stabilize. As seen in Fig. 3, the initial high value for the current decreased during the first minute or so in a manner reminiscent of the behavior with linear diffusion, then rapidly became steadier, fluctuating slowly about a mean value which changed very little during a further 5 min or even longer. When eventually gross roughening or tree formations caused a marked rise in current the onset was nearly always obvious. In all cases fluctuations around a mean current never exceeded about ±5%,

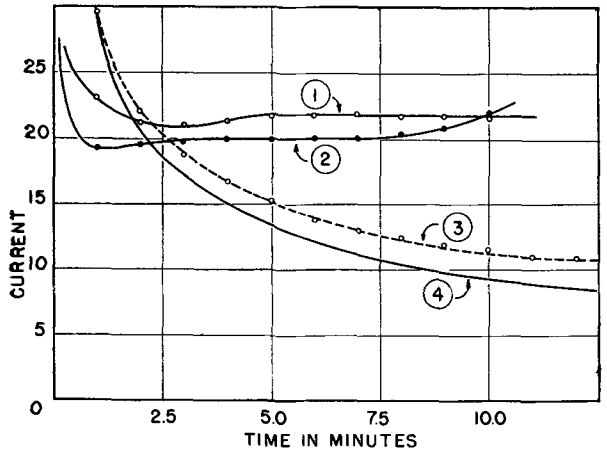

FIG. 3. Some representative current-time curves at constant potential. 1—Ferric → ferrous reduction; 2—Pb^{2+} → lead metal deposition; 3—ferric → ferrous reduction at a sheltered horizontal disc electrode; 4—theoretical curve for linear diffusion.

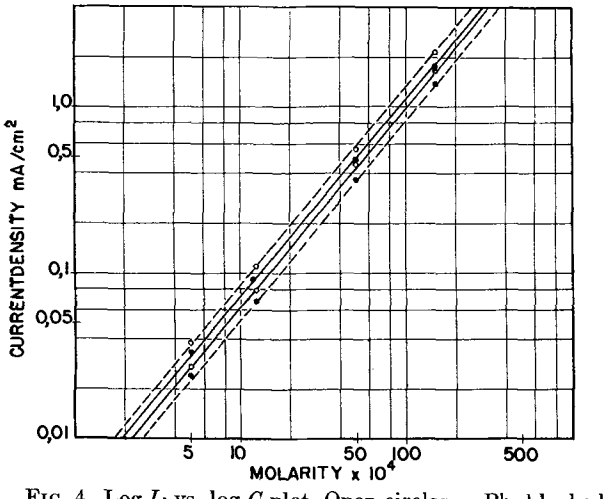

FIG. 4. Log I_d vs. log C plot. Open circles = Pb, blocked circles = Tl. Dotted lines = 2.45×10^{-2} cm radius of wire. Full lines = 6.4×10^{-2} cm radius wire.

TABLE I. *Exponent p under various conditions*

Electrode. l = 0.423 cm r = 0.0245 cm except where indicated.

Ion	Concentration M × 10^4	Conditions of experiment	I_d μamp/cm²	p
Pb^{2+}	2.0	25°C 0.099M KCl	12.2	1.19
	20.0		189.5	
Pb^{2+}	5.0	25°C 0.275M KCl	35.4	1.21
	50.0		575	
Ag^{+}	15	25°C 0.5M KNO_3	92.4	1.21
	100		915	
Fe^{3+}	50	25°C 1.5M $NaClO_4$	91.0	1.23
	250		660	
Pb^{2+}	12.5	25°C No supporting	120	1.23
	50.0	electrolyte	660	
Pb^{2+}	12.5	4°C 1.0M $NaClO_4$	57.5	1.17
	50.0		290	
Pb^{2+}	12.5	25°C Disc electrode	80.4	1.22
	50.0	(0.427 cm diameter) 1.0M $NaClO_4$	438	
Tl^{+}	12.5	25°C Disc electrode 1.0M	63.1	1.19
	50.0	$NaClO_4$	328	

and final limiting current plateau values could be obtained to better than ±2–3%.

Contrary to reports in the literature, limiting current density values were not proportional to the concentration of reducible ion but were proportional to this concentration raised to a power of near 1.2. This is seen in the logarithmic plot in Fig. 4 where an exponent of 1.20 ± 0.02 applies over a concentration range of 5.10^{-4}M–1.25×10^{-2}M for Tl and Pb in 1M perchlorate. Table I gives values for the exponent taken with a variety of reductions, including the redox system ferric-ferrous perchlorate, and the exponent is in the range 1.17–1.23 over a concentration range of about 2.10^{-4}M–2.5×10^{-2}M. The same behavior was found even when no inert electrolyte was present and when reduction took place at 4°C.

The current density for a wire electrode depended on the length and radius of the wire. For a given length it was proportional to a term $(1/2r + 1/\delta)$ where r is the radius in cm of the wire and δ a parameter which (*see* below) should be a measure of the transport layer thickness. Fig. 5 shows data for the graphical evaluation of δ with the reduction of thallium and lead perchlorates at wire elecarodes, values being given in Tables II and III. The lines the drawn through the two means of four experiments with the wire electrodes of radius 0.064 and 0.025 cm, as these are the most precise values, but values for the other wire electrodes fall on the same line within reasonable experimental error. If $1/r$ is used for the small disc electrode values are again near the lines. A mean value of 3.3×10^{-2} cm for δ was found.

Finally, current densities were found to be a function of the diffusion coefficients D of the reducing salts in the base electrolyte employed. If the full current relationship is given by:

$$I_d = KnFD^qC^{1.2}(1/2r + 1/\delta) \qquad (I)$$

where I_d is the limiting current density in amp/cm², n the number of electrons involved in the reduction, F = Faraday, D the diffusion coefficient in cm²/sec, and C the concentration in moles/cm³. K and q can be evaluated graphically by plotting log D against log X, where

$$X = I_d/nFC^{1.2}(1/2r + 1/\delta) \qquad (II)$$

This plot is shown in Fig. 6 from data given in Table IV. The method does not determine the value of K and q unambiguously, but 1.4 and 0.80, respectively, give the best line for a wide range of diffusion coefficients. Considering the approximations involved in assuming a constant value for δ and the exponent of C with such a wide variety of reducing and inert electrolytes, the fit may be considered good. Eq. (IA) predicts

$$I_d = 1.4nFD^{0.8}C^{1.2}(1/2r + 1/\delta) \qquad (IA)$$

to about 5% the limiting current density to be expected with stationary wire microelectrodes of length 0.4–0.5 cm when used for solid metal deposition at 25°C.

Discussion

With moving micro wire electrodes, the thickness of the transport layer adjacent to the electrode may be assumed to be negligible in comparison with the radius of the wire

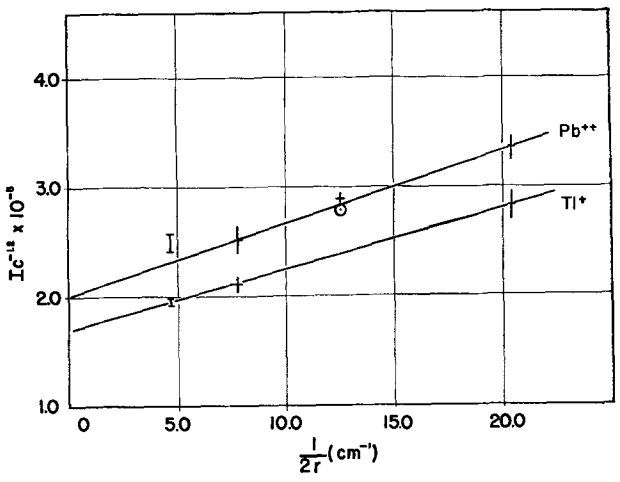

FIG. 5. Plot of $I_d \times C^{-1.2}$ against $1/2r$ for Pb and Tl plated onto various electrodes.

(say 0.5 cm), but with stationary electrodes this is not the case. A correction must be made to allow for the fact that when mass transfer takes place at a curved surface, the flux at the outer side of the transfer layer is greater than would be the case if transfer took place through a parallel sided segment. This is illustrated by Fig. 7*a*. Following the reasoning suggested by Strehlow (20), it can be assumed that the current density predicted for a plane electrode must be corrected by a factor greater than unity to allow for the increase of flux brought in by a curved layer. If the transfer layer is of definite fixed thickness with an approximately linear concentration gradient throughout, this factor should be roughly equal to the ratio of the volume of the actual layer to the volume of the layer adjacent to a plane electrode of the same area. In the case of a long cylindrical wire of radius r, the correction factor (Fig.7*b*) is $(\delta/2r + 1)$. Even for a disc electrode an appreciable correction may be necessary for transport around the elec-

TABLE II. *δ values. Thallous thallium in* $NaClO_4$ *at 25°C*

Graphical value for $\delta = 3.30 \times 10^{2}$ cm

Electrode length, cm	Radius, cm × 10^2	Concentration M × 10^4	Area, cm^2	I_d μamp/cm^2	$I_d C^{-1.2} \times 10^{-5}$	$\frac{1}{2r}$	Calculated $\delta \times 10^2$ cm
Wire 0.45	6.4	5.0	0.184	23.9	2.17	7.8	3.2
		12.5		67.5	2.05		3.45
		50.0		364	2.14		3.3
		150.0		1390	2.16		3.25
							Mean 3.30
Wire 0.423	2.45	5.0	0.065	32.9	2.98	20.4	3.05
		12.5		92.5	2.80		3.4
		50.0		485	2.85		3.3
		150		1740	2.70		3.53
							Mean 3.33
						$\left(\frac{1}{r}\right)$	
Disc	21.4	12.5	0.144	63.1	1.90	4.7	3.4
		50.0		328	1.95		3.35

TABLE III. *δ values.* Pb *in 1M* $NaClO_4$ *at 25°C*

Graphical value for $\delta = 3.28 \times 10^{-2}$ cm

Electrode length, cm	Radius, cm × 10^2	Concentration M × 10^4	Area, cm^2	I_d μamp/cm^2	$I C^{-1.2} \times 10^{-5}$	$\frac{1}{2r}$	Calculated $\delta \times 10^2$ cm
Wire 0.45	6.4	5.0	0.184	27.2	2.50	7.8	3.35
		12.5		79.0	2.40		3.5
		50.0		451	2.65		3.1
		150		1640	2.55		3.25
							Mean 3.30
Wire 0.33	4.0	50.0	0.083	531	3.12	12.5	2.9
Wire 0.648	4.0	50.0	0.162	495	2.91	12.5	3.15
Wire 0.423	2.45	5.0	0.065	38.0	3.45	20.4	3.15
		12.5		111	3.35		3.35
		50.0		553	3.25		3.5
		150		2155	3.33		3.4
							Mean 3.35
						$\left(\frac{1}{r}\right)$	
Disc	21.4	12.5	0.144	80.4	2.43	4.7	3.15
		50.0		438	2.58		2.95

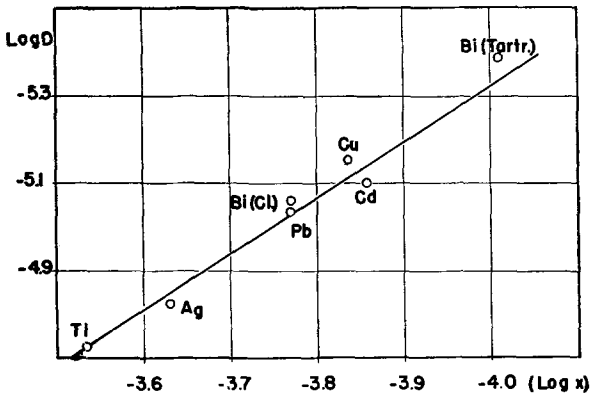

FIG. 6. Plot of log D against log X where:

$$X = \frac{I_d}{nFC^{1.2}\left(\frac{1}{2r} + \frac{1}{\delta}\right)}$$

TABLE IV. *Data for the evaluation of q and k in eq. (I)*

Metal ion	Electrolyte	$D \times 10^5$	$X \times 10^4$
Tl	1M $NaClO_4$	1.88	2.32
Ag	0.5M KNO_3	1.50	1.85
Pb	1M $NaClO_4$	0.92	1.35
Bi	1M KCl 0.1M HCl	0.87	1.37
Cd	1M KCl	0.80	1.10
Cu	1M $NaClO_4$	0.68	1.16
Bi	1M $HClO_4$	0.60	1.17
Bi	1M Tartaric acid	0.41	0.775

$$X = \frac{I_d}{nFC^{1.2}\left(\frac{1}{2r} + \frac{1}{\delta}\right)}$$

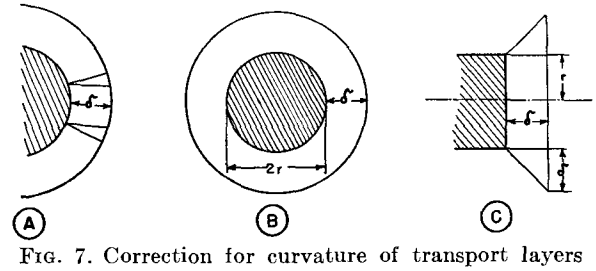

FIG. 7. Correction for curvature of transport layers

trode edge. Provided the radius of the disc exceeds about 0.1 cm, this correction factor (Fig. 7*c*) is roughly $(\delta/r + 1)$.

The hydrodynamic treatments of the problem of heat or mass transfer to a vertical plate (infinitely wide) all lead to an equation of the type:

$$(\text{Nusselt's number})^{\frac{1}{4}} = J(\text{Grashoff's number})^{\frac{1}{4}} \times (\text{Prandtl's number})^{\frac{1}{4}} \quad \text{(III)}$$

The factor J is open to some doubt, but when using an average flux value over an electrode in aqueous electrolyte solutions, a value of 0.68 is probably best (13). This leads to the theoretical relationship that

$$\text{flux}_{\text{wire}} = \text{flux}_{\text{plane}} \times (\delta/2r + 1) \quad \text{(IV)}$$

$$\text{flux}_{\text{plane}} = \frac{D^{0.75} \times (C - C_e)^{1.25}}{Z} \quad \text{(V)}$$

where D is the diffusion coefficient of the reducing ion and $C - C_e$ the difference in its concentration between the bulk of the solution and the electrode surface. Z is given by the relation.

$$Z = 1.5\left(\frac{l\gamma}{g\alpha}\right)^{0.25} \quad \text{(VI)}$$

where l is the vertical height of the electrode, g is the acceleration due to gravity, γ the kinematic viscosity of the electrolyte solution, and α a constant relating the relative density change between the bulk solution and solution at the electrode surface with the corresponding concentration gradient $(C - C_e)$.

Expressing flux in terms of current density and combining the above equations lead to:

$$I = \frac{\delta}{Z} nFD^{0.75}(C - C_e)^{1.25}\left(\frac{1}{2r} + \frac{1}{\delta}\right) \quad \text{(VII)}$$

Eq. (I) resembles the limiting form of this equation where $C_e \rightarrow 0$ and K has the value δ/Z. The experimentally determined exponents for C and D of 1.20 and 0.80 are at variance with theory over the range of conditions used. The trouble may be due to the assumption that density differences are exactly proportional to concentration differences (21). An approximate value for Z can be calculated from eq. (VI). If l is taken as 0.45 cm, γ as 0.9×10^{-2} cm^2/sec, and α as 50 $cm^3/mole$, Z evaluates to about 2.5×10^{-2} $cm^{\frac{1}{2}}$ $sec^{\frac{1}{2}}$ which gives a value for K of around 1.3. As the current density is proportional to $l^{-0.25}$ the value of K changes significantly if l varies substantially from 0.45 cm. This was noted with the 0.33 mm electrode (Table III), and suitable correction was made when plotting data in Fig. 5 and 6. With wires exceeding about 0.75 cm in length, current values were found to be erratic and data were not precise enough to be useful.

The assumption that δ is sharply defined and constant under all conditions is not theoretically justified, but a mean value for a wire can be shown to change comparatively little under most conditions likely to be used in this type of polarography. Although the errors resulting from neglecting a correction for wire curvature may be serious, the errors in the correction itself are probably within the general experimental precision of the method. The value for δ measured optically by Ibl and co-workers for a small plate (15) were in agreement with the theoretical value given by Keulegan (12) and were near to 3.3×10^{-2} cm at the current density values used in the present investigation.

As the exact value of I is a critical function of the value of K and the exponent of D, it is best to determine the constant B equal to $\frac{\delta}{z} nFD^q(1/2r + 1/\delta)$ experimentally for any given reduction at a given wire electrode when the relation:

$$I = B(C - C_e)^{1.2} \quad \text{(VIII)}$$

should apply with considerable precision.

The behavior when two ions are transported and discharged simultaneously is shown in Fig. 8. Tl and Pb were chosen because they show complete mutual solubility in

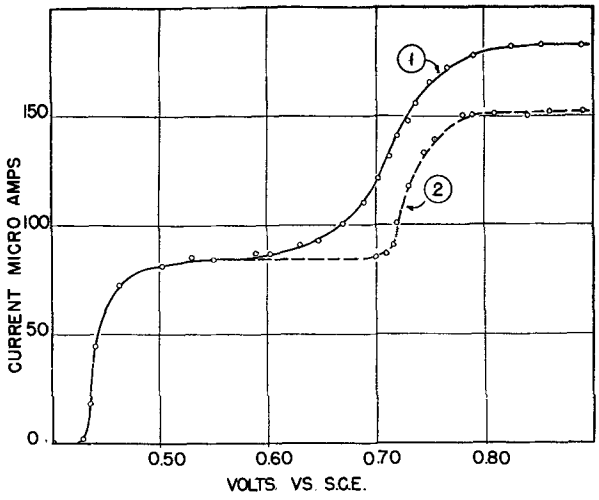

FIG. 8. Deposition of Pb and Tl separately and together with both ions at 5.0×10^{-3} at 25.0°C in 1M $NaClO_4$. 1—Experimental; 2—curves to be expected if transport and deposition processes free from mutual interaction.

TABLE V. *Simultaneous diffusion of* Pb *and* Tl
1M $NaClO_4$ at 25°C
Limiting current densities

Concentrations $\times 10^4$ M		$I_{Pb} + I_{Tl}$	I_{total} found	I_{total} calculated
Pb	Tl			
50.0	50.0	815	990	990
50.0	12.5	517	595	595
12.5	50.0	444	520	540

the solid state and the diffusion coefficients of the ions differed by about 100%. The curve for Pb in the presence of Tl is identical with that for Pb alone. However, the subsequent deposition of Tl not only occurs at a lower potential, due to the free energy of solution of Tl in a Tl-Pb alloy assisting the reduction, but the limiting current for Tl appears to be enhanced some 40%. This enhancement is found for other ratios of Tl and Pb (Table V) and can be predicted with precision if it is assumed that the flux of ions depends on $C_T^{1.2}$, where C_T is the total molarity of reducible ions, and a weighed mean of the $D^{0.8}$ values for each species. As the current equals the flux times the mean charge per particle, if C_1 and C_2 are the two concentrations of ions having charge, n_1 and n_2 and diffusion coefficients D_1 and D_2 respectively:

$$I_d(\text{Total}) = K\left(\frac{n_1C_1 + n_2C_2}{C_T}\right)\left(\frac{C_1D_1^{0.8} + C_2D_2^{0.8}}{C_T}\right) \cdot FC_T^{1.2}\left(\frac{1}{2r} + \frac{1}{\delta}\right) \quad \text{(IX)}$$

Values of I_d obtained using this equation are given in the last column of Table V.

Eq. (VIII) can be used to test the reversibility of electrodeposition at a stationary electrode. Substituting for C_e in the Nernst equation:

$$\text{Overvoltage} = \text{Constant} - \frac{2.3RT}{nF}\log\left(I_d^{0.83} - I^{0.83}\right) \quad \text{(X)}$$

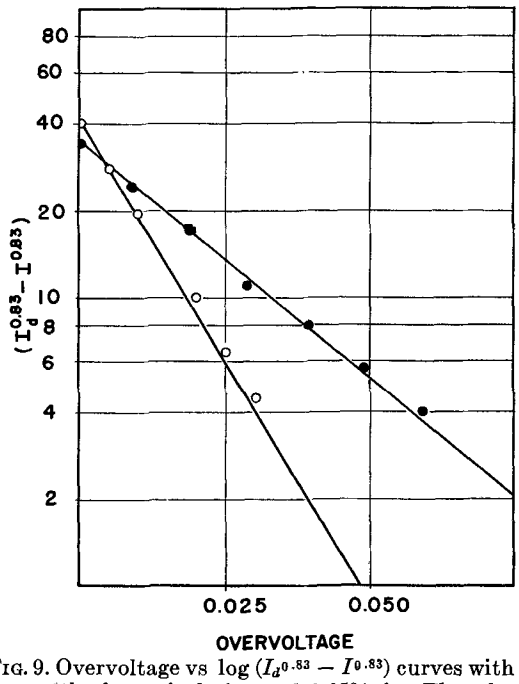

FIG. 9. Overvoltage vs $\log (I_d^{0.83} - I^{0.83})$ curves with lines drawn with theoretical slope of 0.0591 for Tl and 0.0296 for Pb.

and a plot of the data for Tl and Pb deposition from perchlorate gave points lying on lines of the theoretical slope as shown in Fig. 9. However, with most depositions a marked irreversibility is found, although eq. (VIII) can again be used. Values for a heterogeneous constant and transfer coefficient α can be obtained from polarograms, but the writing is tedious. At values $0.1/n$ v cathodic to the zero current potential, however, the rate of the back reaction (metal dissolution) can be neglected and the current can be written in the form:

$$i = nFA^1k_f^0\,C_e \exp\left(\frac{\alpha nF}{RT}E\right) \quad \text{(XI)}$$

where E is on the H scale with Lewis-Randall sign convention, C_e in moles/cc, and A^1 is the area of the reactive surface of the metal. This may well be considerably greater than the geometrical area affecting the transport process. If k_f^a is defined as equal to βk_f^0, where $\beta = \frac{A^1}{A}$, then on substituting for C_e from equation (VIII)

$$E = \frac{2.3RT}{\alpha nF}\log\left(\frac{I}{I_d^{0.83} - I^{0.83}}\right) - \frac{2.3RT}{\alpha nF} \cdot \log\left(\frac{nFk_f^a}{B^{0.83}}\right) \quad \text{(XII)}$$

where I is in amp/cm² and $B^{0.83}$ is given by the relation

$$B^{0.83} = \frac{I_d^{0.83}}{C} \quad \text{(XIII)}$$

Plots of E against $\log\left(\frac{i}{i_d^{0.83} - i^{0.83}}\right)$ are shown for Cu and Bi in Fig. 10. Where the back reaction can be neglected, points fall on a straight line the slope of which gives

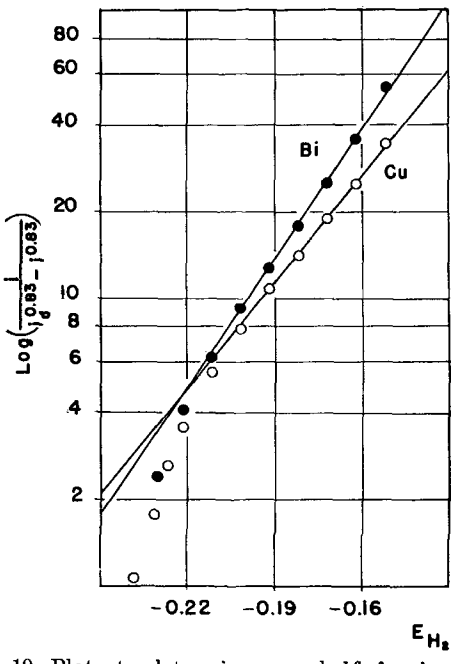

FIG. 10. Plots to determine α and k_f^a for irreversible depositions. 4.0 × 10^{-3}M copper perchlorate in 1M $NaClO_4$ and 4.0 × 10^{-3}M bismuthyl perchlorate in 1M $HClO_4$.

where E_r is the reversible potential in the given solution of concentration C. Data for k^1 and I_0 are also shown in Table VI with limiting values (assuming α equal to 0.5) given for Pb, Tl, and Ag where the reaction is too rapid to be measured directly. These data are only approximate and are reported here to illustrate the method. More precise studies with this technique and the comparison of k^1 and I_0 values obtained by this and other methods will form the basis of further communications.

The true value for k_f^0 and the exchange current density is unknown unless the value of β is known, but ignorance of this number is common to a greater or lesser extent to all studies on solid metal electrodes. The apparent "reversibility" of a reaction depends on both the conditions of transport (diffusion, stationary convective diffusion, convection in stirred solution, etc.), the value for k_f^0, and the value for β. The statement that a deposition is or is not "reversible," therefore, cannot be generalized without reference to the technique employed. The present method relates, at least approximately, to normal electroplating practice.

ACKNOWLEDGMENTS

This work was undertaken with funds from a consolidated grant from the National Research Council of Canada. The authors would like to thank Dr. G. M. Shrum, Director of the British Columbia Research Council, for his encouragement.

TABLE VI. *Summary of kinetic data*

Metal ion	Concentration 10^3M	Base electrolyte	Zero current potential (H scale)	Alpha	k_f^a cm/sec	k^1 cm/sec	I_0 amp/cm²
Thallous	5.0	1M $NaClO_4$	+0.47	—	$>10^{-5}$ Reversible	>0.1	>0.5
Pb	5.0	1M $NaClO_4$	+0.19	—	$>10^{-5}$ Reversible	$>10^{-2}$	>0.01
Ag	4.0	0.5M KNO_3	−0.63	—	>1000 Reversible	$>2.10^{-2}$	>0.01
Bi	5.0	1M KCl; 0.1M HCl	−0.12	0.55	1.5	7.10^{-4}	10^{-3}
Cupric	4.0	1M $NaClO_4$	−0.25	0.35	0.65	7.10^{-4}	5.5×10^{-4}
Bi	4.0	1M $HClO_4$	−0.25	0.3	2	3.10^{-4}	3.5×10^{-4}

α, and the intercept enables k_f^a to be calculated. A few values are shown in Table VI. The method is approximate, and apart from effects of impurities on the value of α, the precision of the determination of α depends on the exact shape of the current-voltage curve near the top of the curve and the exact value of I_d. By taking sufficient points in this region, however, α values should be obtainable to about 10–15% and rough values for k_f^a calculated. The method has the great advantage that these kinetic parameters are obtained under actual conditions of metal deposition when the entire surface is being refurnished with atoms several times a second, and many of the complications of using methods studying the reaction at the reversible potential with an a-c bridge (22) are avoided. A constancy of α with applied potential must be assumed but if this is the case:

$$I_0 = nFk^1C$$

where I_0 is the apparent exchange current density at concentration C and k^1 is given by the expression:

$$k^1 = k_f^0\beta \exp\left(\frac{\alpha nFE_r}{RT}\right)$$

Manuscript received December 12, 1955.
This paper was prepared for delivery before the San Francisco Meeting, April 29 to May 3, 1956.
Any discussion of this paper will appear in a Discussion Section to be published in the December 1957 JOURNAL.

REFERENCES

1. R. E. WILSON AND M. A. YOUTZ, *Ind. Eng. Chem.*, **15**, 603 (1923).
2. S. GLASSTONE, *Trans. Electrochem. Soc.*, **59**, 277 (1931).
3. L. L. BIRCUMSHAW AND A. C. RIDDIFORD, *Quart. Rev. London*, **6**, 157 (1952).
4. H. A. LAITINEN AND I. M. KOLTHOFF, *J. Phys. Chem.*, **45**, 1061 (1945).
5. L. B. ROGERS, H. H. MILLER, R. B. GOODRICH, AND A. F. STEHNEY, *Anal. Chem.*, **21**, 777 (1949).
6. E. M. SKOBETS, P. P. TUROV, AND V. D. RYABOKON, *Zavodskaya Lab.*, **14**, 131 (1948); C.A. **43**, 8946, (1949); *ibid.*, **14**, 772, (1948); *ibid.*, **44**, 5729 (1950).
7. D. B. JULIAN AND W. R. RUBY, *J. Am. Chem. Soc.*, **72**, 4719 (1950).
8. T. L. MARPLE AND L. B. ROGERS, *Anal. Chem.*, **25**, 1351 (1953).

9. B. LEVICH, *Acta Physicochim. U.R.S.S.*, **19**, 117 (1944).
10. J. N. AGAR, *Disc. Faraday Soc.*, **1**, 26 (1947).
11. C. WAGNER, *J. (and Trans.) Electrochem. Soc.*, **95**, 161 (1949).
12. G. H. KEULEGAN, *J. Research Nat. Bur. Standards*, **47**, 156 (1951).
13. C. R. WILKE, M. EISENBERG, AND C. W. TOBIAS, *This Journal*, **100**, 513 (1953).
14. N. IBL, W. RUEGG, AND G. TRUMPLER, *Helv. Chim. Acta*, **36**, 1624 (1953).
15. N. IBL, Y. BARRADA, AND G. TRUMPLER, *ibid.*, **37**, 583 (1954).
16. N. IBL, K. BUOB, AND G. TRUMPLER, *ibid.*, **37**, 2251 (1954).
17. G. J. HILLS AND D. J. G. IVES, *J. Chem. Soc.*, **1951**, 311.
18. D. J. FERRETT AND C. S. G. PHILLIPS, *Trans. Faraday Soc.*, **51**, 390 (1955).
19. J. H. WANG, *J. Am. Chem. Soc.*, **76**, 1528, 1584 (1954).
20. H. STREHLOW AND M. VON STACKELBERG, *Z. Elektrochem.*, **54**, 51 (1950); M. VON STACKELBERG, *ibid.*, **57**, 388 (1953).
21. C. W. TOBIAS AND M. EISENBERG, Private communication.
22. P. J. HILLSON, *Trans. Faraday Soc.*, **50**, 385 (1954).

Preparation and Reproducibility of the Thermal-Electrolytic Silver-Silver Chloride Electrode

HARRY TANIGUCHI AND GEORGE J. JANZ

Rensselaer Polytechnic Institute, Troy, New York

ABSTRACT

Preparation of the thermal-electrolytic Ag-AgCl electrode for precision use is described. A reproducibility of the electrode of ±0.1 mv can be achieved readily by this procedure. Freshly prepared electrodes are evaluated relative to equilibrated Ag-AgCl electrodes selected as reference standards. With care, reference standards corresponding to an electrode in the ground energy state, and of constant potential (±0.005 mv) for periods of several months can be attained. It is suggested that the difference in the values of the standard potential of this electrode may be attributed in part to the limited reproducibility of these electrodes. The importance of the porosity, amount of AgCl, and color, relative to the attainment of stable electrodes that equilibrate rapidly, is considered.

The widespread use of Ag-AgCl electrodes as secondary reference electrodes of the second kind in emf measurements has been reviewed (1). The thermal-electrolytic electrode probably has been used more extensively than any other form in recent work. The procedure (2, 3) of preparation may be conveniently itemized as follows: (*a*) preparation of the electrode base, (*b*) precipitation and purification of Ag_2O, (*c*) application of the Ag_2O paste, (*d*) thermal reduction of the oxide to Ag, (*e*) purification of the chloride to be used for anodizing, (*f*) chloridizing the Ag, and finally, (*g*) aging and bias potential tests prior to use. These points are covered here in sufficient detail to emphasize factors important in the preparation of reproducible and stable electrodes of precision quality. Concepts of the bias potential and aging tests are reexamined briefly as criteria in evaluating the quality of the Ag-AgCl electrode.

When identical kinds of electrodes are immersed in a solution so that the activity of the electrolyte to which the electrodes are reversible is the same at each electrode, there is no difference in potential, providing each electrode is in equilibrium with the solution in the ground energy state. In practice, differences in potential are often observed. The term "bias potential" is used here to denote this difference of potential.

The reproducibility of three types of Ag-AgCl electrodes was shown by Smith and Taylor (4) to be of the order of ±0.02 mv. It was stressed that intra-agreement in a set of electrodes at a given time is no criterion that their potential has come to equilibrium since an aging effect may be present. It was found that Ag-AgCl electrodes freshly chloridized were positive with respect to electrodes in equilibrium with a test solution. The origin of this was traced to concentration polarization. When the electrodes of the electrolytic and thermal-electrolytic types are chloridized, the solution within the pores of the AgCl coating becomes more dilute than the surrounding solution. The magnitude of the change in concentration can be estimated from the bias potential assuming the system approximates a concentration cell (4):

$$\text{Ag-AgCl} \mid \text{MCl}(C) \mid \text{MCl}(C - \delta) \mid \text{AgCl-Ag},$$

where δ is the effective decrease in the concentration of the electrolyte within the pores. The emf of this cell is given by

$$E = 2t_{M^+} RT/\mathbf{F} \ln C/(C - \delta)$$

(where E is the emf, t_{M^+} the transference number of the cation, C and $C - \delta$ are the concentrations of the solutions about each electrode, respectively, and R, T, and $\mathbf{F}$ are the gas law constant, temperature, and Faraday, respectively) if the variation in ionic mobilities between the two concentrations is negligible, and if the activity ratio is equal to the concentration ratio. Substituting the bias potentials observed, typical concentration changes, δ, are obtained for KCl and HCl as electrolytes:

E (mv)	10	1	0.1	0.025
δ(KCl)	$0.33C$	$0.04C$	$0.004C$	$0.001C$
δ(HCl)	$0.21C$	$0.023C$	$0.0023C$	$0.0005C$

A freshly prepared electrode in the bias solution is thus positive relative to the aged reference electrode since C is greater than $C - \delta$. The time required to attain equilibrium depends on the porosity, the concentration, and the stirring of the solution. In some cases it is as long as 20 days (4).

Even when care is exercised in preparation, equilibrated electrodes may still exhibit a constant, but finite, bias potential. Assuming that the aging process has proceeded to completion, as shown by a constant bias, a difference in energy states of the AgCl must exist. Thus, for two Ag-AgCl electrodes, A and B, in equilibrium with the common electrolyte, if A is negative in potential to B, then the cell reactions are:

Electrode	Polarity	Reaction
A	Negative	Oxidation: $Ag + Cl^- \rightarrow AgCl_A + e$
B	Positive	Reduction: $AgCl_B + e \rightarrow Ag + Cl^-$

Net cell reaction: $AgCl_B \rightarrow AgCl_A$.

Thus, the spontaneous reaction is the formation of more AgCl at electrode A at the expense of the silver chloride electrode B. Accordingly, the negative electrode, A, is in the lower energy state. The magnitude of energies corresponding to these bias potentials is as follows:

E(mv)	ΔF (cal)
1	23.07
0.1	2.31
0.02	0.46

Thus, a bias potential of 0.02 mv introduces an error of 0.46 cal in the free energy.

Experimental

Electrode base.—The electrode base was a spiral (1 mm diameter) of 2–3 turns of 24–26 gauge Pt wire. This was sealed into a 4–6 mm diameter glass tube, or a ground glass extension joint, so as to leave the end of the wire protruding inside the tube for a mercury contact. Soft glass was preferable to Pyrex glass since it permits a neater, stronger seal. No observable differences in ultimate bias potentials were found to be attributable to the glass used. Soft glass was used in the present bias studies.

Precipitation and purification of Ag_2O.—Ag_2O was precipitated from a vigorously stirred solution of $AgNO_3$ ($\frac{1}{2}$ equiv. of C.P. $AgNO_3$ in 750 ml of de-ionized water) by dropwise addition of $\frac{1}{2}$ equiv. NaOH in 100 ml of water. Vigorous stirring was continued until homogeneity and complete precipitation were ensured. An important precaution was thorough washing of the resulting precipitate to remove all water-soluble impurities. Bates (3) found that a number of washings was required to reduce the conductivity of the wash water to 3×10^{-6} ohm^{-1}/cm. In the present work, with vigorous mechanical shaking, the conductivity was 4×10^{-5} ohm^{-1}/cm for several washes. Calculations from solubility considerations predict 3×10^{-5} ohm^{-1}/cm.

On washing to the above criterion (30 washes), Ag_2O was recovered in a sintered glass filter. Subsequent use of this material as an aqueous paste necessitated only a superficial drying by a short continuation of the suction. Both the filter and the storage weighing bottle were cleaned in a standard fashion (hot chromic acid followed by repeated rinses with distilled water, and final cleaning with hot water) the filter by passing near-boiling water through it, and the bottle by boiling in water for $\frac{1}{2}$–1 hr.

Application of Ag_2O *Paste.*—Ag_2O, when mixed with water, forms a paste such that it can be applied easily to the Pt spirals with a small spatula. With the inside of the spiral completely filled and the wire totally covered (except for a few mm between glass and spiral), a sphere of 3–4 mm diameter was obtained. Prior to application of the paste, the Pt spirals were cleaned by boiling briefly in concentrated HNO_3 followed by repeated flushings with distilled water and boiling in de-ionized water.

In the application of a second coat, a much thinner consistency was used, so that the paste almost yielded to gravity when held on a spatula or when suspended from the sphere of silver.

Thermal reduction of Ag_2O *to* Ag.—Electrodes for thermal reduction were suspended in the central portion of the furnace well (Hoskins, type FD14) by means of a simple support fashioned from two parallel squares of heat-resistant asbestos board separated by 1.5 in. spacers. Rubber bands held the electrode in place in vertically coincidental holes. A centrally located hole admitted a thermocouple.

In order to preclude the possibility of "sputtering" by the rapid formation of steam, the electrodes were maintained in the furnace at just below 100°C for $\frac{1}{2}$–1 hr to permit superficial drying. The temperature was then raised at a uniform rate to 450°C. The latter temperature was held for $\frac{1}{2}$ hr further to complete the reduction to porous Ag. The electrodes were permitted to cool within the furnace to avoid thermal shock.

Reduction of the second coat of AgO proceeded in a completely analogous manner. The electrodes were finally stored in a desiccator for protection until required for the chloridizing.

Purification of chloridizing electrolyte.—The need for purification of the chloride for anodizing was clearly demonstrated (5). For example, the potential increased by 0.1–0.2 mv for each 0.01 mole % bromide in solution. Removal of trace impurities of bromide, therefore, is an important aspect in the purification of the electrolyte to be

TABLE I. *Description of thermal-electrolytic* Ag-AgCl *electrodes*

Electrode set	K	A	B	C	D
No. of Ag coats	2	1	2	1	2
Wt. Ag (g)	0.0702	0.1214	0.0822	0.1481	0.1087
AgCl (%)	10.5	5.5	8.2	4.5	16.2
Current (ma)	10	1	1	10	10
Chloridized in	0.05*N* KCl	1*N* HCl	1*N* HCl	1*N* HCl	1*N* HCl
Aged in	0.05*N* KCl	0.1*N* HCl	0.1*N* HCl	0.1*N* HCl	0.1*N* HCl
Equilibrium (hr)	10	8	4	20	6
Surface area (m^2/g)	0.3	3.4	0.3	3.4	0.3

used for chloridizing and subsequent potential measurements. In the present work, KCl was purified by the Pinching-Bates method (5).

Concentrated HCl for subsequent dilution was prepared by azeotropic distillation (6). HCl (C.P.), diluted with de-ionized water to the recommended density of 1.10 g/ml, was used as the starting material. The condenser and fittings were quartz. The final distillate was stored in a quartz flask.

Chloridizing the Ag.—The Ag electrode was chloridized by making it the anode in a simple U-tube cell. The electrode chambers were 8 cm long and 2 cm in diameter. The central portion was constricted to 1 cm while fashioning the U-bend. Pt spirals, similar to those used for the preparation of Ag electrodes, served as cathodes. A current of 10 ma was passed through an assembly consisting of 6–12 cells in series. Generally, about 10–20% of the Ag was converted to AgCl, assuming 100% current efficiency.

Two solutions were used for chloridizing, 0.05 *N* KCl and 1*N* HCl, both electrolytes being readily obtained in a high degree of purity. The freshly prepared electrodes varied in color from almost white to dark brown.

Aging and bias potential tests.—The cell use for intra-comparison consisted of a 1-l flask modified to take the set of electrodes in a circle of short necks concentric to the neck of the flask. A slow stream of oxygen-free N_2 was introduced through the latter to agitate the bias solution. After chloridizing, the electrodes were removed from the U-tube cells, rinsed in de-ionized water, and transferred to the bias cell. All tests were carried out under a N_2 atmosphere in oxygen-free solutions.

To observe the time required for the potential to attain its equilibrium value, i.e., aging of the set of electrodes, the procedure of Smith and Taylor (4) was adopted. The new electrodes were measured relative to a set of two or more electrodes that had been aged for at least one week before use. Selection of the electrodes for the aged reference standards was arbitrary, guided only by the constancy (±0.005 mv) of the bias potential which was taken as a criterion of the stability of the equilibrated state.

Experimental data on the aging tests are summarized in Table I and illustrated in Fig. 1 and 2. Data in each case represent average values of at least three electrodes. The mass of thermal Ag was weighed to estimate quantitatively the AgCl formed in the next step.

The effect of increasing amounts of AgCl on the aging and stability of the electrodes was investigated. Since a constant current was used, each electrode had to be chloridized for a different length of time. This was accomplished by placing all the electrodes as before in the U-cells, but leading the current initially only through the

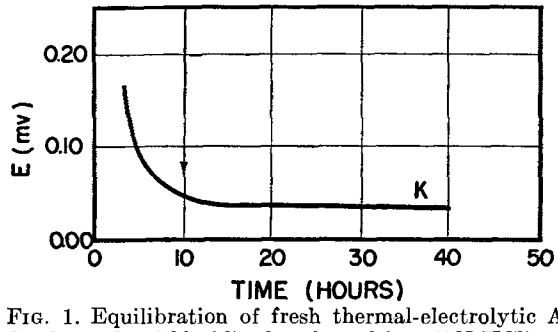

FIG. 1. Equilibration of fresh thermal-electrolytic Ag-AgCl electrodes (chloridized and aged in 0.05*N* KCl).

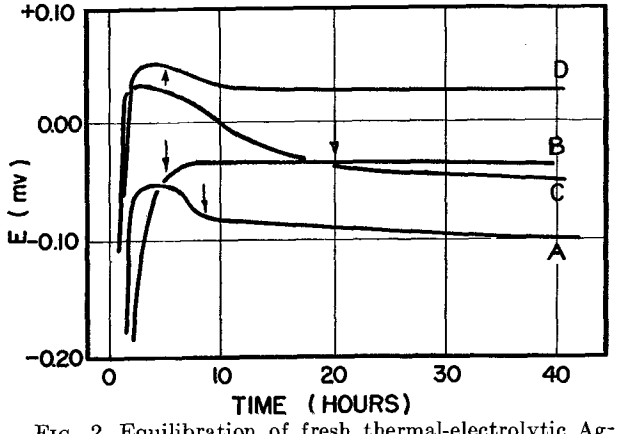

FIG. 2. Equilibration of fresh thermal-electrolytic Ag-AgCl electrodes (chloridized and aged in 1 and 0.1M HCl, respectively).

electrodes to be most highly chloridized. At proper time intervals, the current was lead through additional electrodes until the desired range of chloridizing had been achieved. In this manner, all the electrodes were in contact with the electrolyte for the same length of time and could be removed together so that the aging tests could be initiated on the set simultaneously. Results are summarized in Table II and illustrated in Fig. 3.

Surface area measurements.—Some measurements were undertaken to determine the porosity of the Ag in relation to its mass and the method of formation. As a first approximation, it was assumed that the surface area as determined by N_2 adsorption would be in direct proportion to the porosity of the surface. A B.E.T. adsorption apparatus of standard design (7) was used. Samples of thermal Ag were prepared on Pt spirals simultaneously with the electrodes selected for chloridizing by severing the beads from the glass electrode holder. Ag was deposited both in one and in two applications. The weight of Ag sphere for the single and double coats and the total weight of Ag

TABLE II. *Effect of increasing* AgCl *on equilibration of fresh electrodes*

Electrodes	α	β	γ	δ	ε
	(Double Coats of Silver)				
Wt of Ag (g)	0.1214	0.3645	0.1810	0.1737	0.1165
AgCl (%)	16.2	20	30	50	90
Equilibrium Time (hr)	8	10	8	18	21

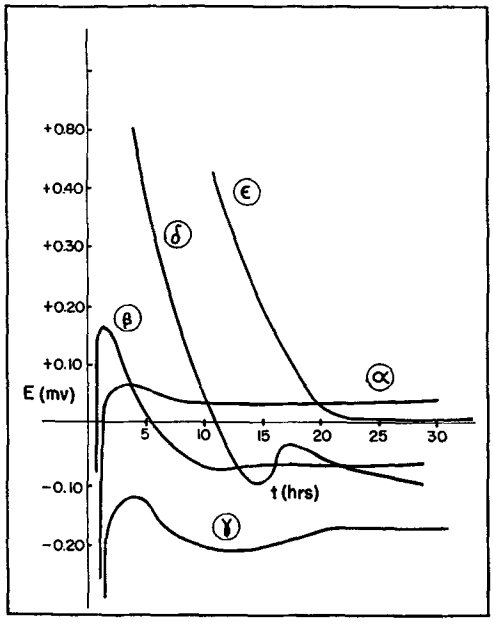

FIG. 3. Effect of increasing AgCl on equilibration of fresh electrodes.

TABLE III. *The B.E.T. surface area of thermal* Ag

Sample	Wt (g) of Ag/electrode			Total wt (g) of sample	Surface area (m^2/g)	Equilibrium Time (hr)
	First coat (avg)	Second coat (avg)	Sum			
1	0.0406	None	0.0406	0.4464	3.4	15
2	0.0321	None	0.0321	0.1925	39	150
3*	0.1422	None	0.1422	1.1378	1.2	8
4	0.0441	0.0151	0.0592	2.7805	0.3	6

* This sample was degassed at 400°C for 17 hr. All others were degassed at 120°–150°C for periods up to 18 hr.

taken for each experiment is summarized in Table III together with the results of the measurements. The equilibration times refer to aging periods for electrodes prepared from thermal Ag of the surface areas listed.

Degassing of samples prior to determination of the adsorption isotherm was carried out by heating for 90 min under a high vacuum when 4×10^{-5} mm Hg was attained (that of the system alone). Because of the heating at 450°C. during preparation, this was sufficient. Owing to the relatively small surface areas, the initial dose of N_2 to the sys- had to be restricted to 8–10 mm pressure for successful measurements.

Discussion

The recommendations of Smith and Taylor (4) and Bates (3) for preparation of the thermal-electrolytic Ag-AgCl electrode for precision use have been independently checked and confirmed. Electrodes are readily obtained equilibrating to constant values within a period of 10–24 hr and showing an agreement of ±0.02 mv within a set prepared at a given time.

The aging histories show that when the chloridizing and aging solutions were of the same strength (Fig. 1), freshly prepared electrodes were positive in potential to the aged reference standards as predicted by the theory of concentration-polarization (4). Data for the experiments in which the chloridizing was continued until approximately 90% of the Ag was AgCl are informative (Fig. 3, Table II). In this work, the chloridizing solution (1*N* HCl) was ten times more concentrated than the bias test solution. Freshly prepared electrodes with greater than 30% AgCl were positive to the reference standards, in accord with a depletion of the electrolyte concentration to a strength less than that of the bias solution. The electrodes with less than 30% AgCl were initially negative. It follows that with shorter periods of electrolysis, depletion of electrolyte within the porous Ag is not sufficient to attain a concentration less than that of the bias test solution.

Minima and maxima have been observed in the aging history during the initial approach to equilibrium. Since the adjustment of the electrolyte concentration within the pores is a rate process, some fluctuations about the equilibrium value are not unexpected.

Results of the investigation of the dependence of equilibration time on electrode porosity are summarized in Table III. Electrodes with relatively high surface area (39 m^2/g) aged in 120–160 hr in contrast to low surface area electrodes (0.3–3.4 m^2/g) for which the period was as short as 6 hr. Application of the Ag in two coats effected this decrease.

When the initial application yielded a relatively nonporous thermal Ag (e.g., 3.4 m^2/g), the aging period was quite short (8–20 hr). Application of a second coat of Ag to this surface to obtain a still less porous surface (0.29 m^2/g) decreased the aging period only by a slight amount.

Results of these measurements leave little doubt that the role of the second coat of thermal Ag, as recommended by Bates (3), is to yield a less porous surface for chloridizing, leading to electrodes that equilibrate rapidly.

Surface areas and aging periods for single coats decreased markedly as the mass of thermal Ag was increased above 30 mg. If significant, this suggests that rapidly equilibrating electrodes can be achieved in one application of Ag_2O if the electrode is made sufficiently massive. Bates (5) suggests that about 150–200 mg Ag be used.

Aging tests with increasing AgCl content (Fig. 3) showed that the best Ag-AgCl electrodes were obtained when electrolysis was controlled to change about 10–20% of the Ag to AgCl (assuming a current efficiency of 100%). Electrodes having less AgCl (5%, Fig. 2), and somewhat more (30%, Fig. 3) were still quite satisfactory from the viewpoint of rapid equilibration and sensitivity. Increasing AgCl much above this limit of 20% (e.g., 50 and 90%) re-

sulted in a thick coat of AgCl which added little to stability and tended to make the electrode more sluggish. A current of 10 ma was recommended (3) for the electrolysis, but lower currents (1 ma) were just as effective if the total time of electrolysis was increased accordingly. Use of currents greater than 10 ma was not investigated in the present work.

It was observed that, with 1*N* HCl as the chloridizing electrolyte, the electrodes were occasionally brown or plum colored, although utmost care was given in each step of the procedure as described. Normally, the electrodes were dirty white to light brown. Bates reported (8) that with repeated use of this chloridizing solution, light gray and even white, rather than brown, electrodes were obtained and recommends that the initial chloridizing solution be used repeatedly until the conductance is too low for the operation. The highly colored electrodes, while showing good intra-agreement in a set, tended to equilibrate at somewhat larger values (0.1–0.3 mv) relative to the aged reference standards. It may well be that pre-electrolysis of the chloridizing solution was beneficial in achieving conditions for the best electrodes. Work described elsewhere (4) showed that the electrode potential was not affected by light. Dark electrodes were also obtained in recent studies when more than 20% of the Ag was chloridized. In this case, the color may indicate that the chloride layer is heavier than desirable for good performance. It is of interest to note that the color of the best electrodes of the totally electrolytic type is, by contrast, a rose or plum shade rather than light gray or white (1). Factors affecting color are least understood.

An observation of the present work is that the new electrodes equilibrated at potentials both positive and negative to the reference standard at values significantly different (−0.08–+0.05 mv). This difference was not due to changes in the reference standard itself since two or more of the latter were observed to maintain a constant potential (±0.005 mv) for periods of several months. The explanation for these differences in equilibrated potentials is not obvious, but may be attributed in part to states of strain in the thermal Ag. The choice of the reference standard is made less arbitrary if electrodes having the lowest potential after equilibration are selected, corresponding to the lowest thermodynamic energy state.

Thus, while equilibrated electrodes showing intra-agreement of ±0.02 mv in a set are readily gained, the limits of reproducibility in equilibrated potential appear to be greater. In many measurements of concentration cells, this effect may be partially compensated for by using opposing electrodes from the same set and by interchanging electrodes. However, it may be of considerable significance in measurements where the standard potential of Ag-AgCl is involved.

Constancy of the equilibrated bias potential enables a correction to be applied to refer all emf values to a common energy level. The experimental scatter observed in measurements with this electrode may thus be partially reduced.

It is significant that the careful determination of the standard potential of the Ag-AgCl electrode in aqueous solutions by Harned and Ehlers (9) and more recently by Bates and Bower (10) differs by a small, but finite, value, 0.18 mv, at 25°C. The same type of electrode—the thermal-electrolytic—and a similar technique were employed. Activities of the HCl in these solutions were in agreement with each other as well as with other independent determinations (10). In the light of the present results, the reported difference in values for the standard potential may be partially attributed to the thermal-electrolytic type of Ag-AgCl electrode.

ACKNOWLEDGMENT

The authors wish to thank S. C. Wait, Jr., M. DeCrescente, and F. Peper of this laboratory for assistance with measurements, and Dr. Roger G. Bates for continued interest and helpful discussions in all phases of this research. The work was made possible by support extended by the Office of Scientific Research, Air Research and Development Command under Contract No. AF 18 (600)-333.

Manuscript received January 24, 1956.
Any discussion of this paper will appear in a Discussion Section to be published in the December 1957 JOURNAL.

REFERENCES

1. G. J. JANZ AND H. TANIGUCHI, *Chem. Rev.*, **53,** 397 (1953).
2. H. S. HARNED, *J. Am. Chem. Soc.*, **51,** 416 (1929).
3. R. G. BATES, "Electrometric *p*H Determinations," p. 200, John Wiley & Sons, Inc., New York (1954).
4. E. R. SMITH AND J. K. TAYLOR, *J. Research Nat. Bur. Standards*, **20,** 837 (1938).
5. G. D. PINCHING AND R. G. BATES, *ibid.*, **37,** 311 (1946).
6. C. W. FOULK AND M. HOLLINGSWORTH, *J. Am. Chem. Soc.*, **45,** 1220 (1923).
7. W. E. BARR AND V. J. ANHORN, "Scientific and Industrial Glass Blowing and Laboratory Techniques," Instruments Publishing Company, Pittsburgh (1949).
8. R. G. BATES, Private communication.
9. H. S. HARNED AND R. W. EHLERS, *J. Am. Chem. Soc.*, **54,** 1350, 2179 (1932).
10. R. G. BATES AND V. E. BOWER, *J. Research Nat. Bur. Standards*, **53,** 283 (1954).

Degree of Dissociation from the Onsager Equation

FRED H. BROCK

Department of Chemistry, Pennsylvania State University, University Park, Pennsylvania

ABSTRACT

A new, analytical method is presented for calculating the degree of dissociation of weak, uni-univalent electrolytes from the Onsager equation. Also, the error involved in this procedure is discussed.

Various procedures have been published for the determination of the dissociation of weak, uni-univalent electrolytes from conductance data (1–5). In this paper, a noniterative method using the Onsager equation is derived.

The Onsager equation for a uni-univalent electrolyte is written as

$$\Lambda = \alpha(\Lambda_0 - (A + B\Lambda_0)\sqrt{\alpha c}) \qquad \text{(I)}$$

where Λ = equivalent conductance, Λ_0 = equivalent conductance at infinite dilution, A, B = constants, c = concentration, α = degree of dissociation.

After rearranging, eq. (I) becomes

$$f(\alpha) = \alpha^{\frac{3}{2}}c^{\frac{1}{2}}k - \alpha\Lambda_0 + \Lambda = 0 \qquad \text{(II)}$$

where $k = (A + B\Lambda_0)$. If α_1 is the first approximation of α, so that $\alpha = \alpha_1 + h$, where h is a constant, then expanding $f(\alpha)$ in a Taylor's series about α_1 yields

$$f(\alpha) = f(\alpha_1) + hf'(\alpha_1) + h^2f''(\alpha_1)/2 + \qquad \text{(III)}$$

Assuming that the third term is small and may be neglected,

$$h_1 = -f(\alpha_1)/f'(\alpha_1) \qquad \text{(IV)}$$

so that the second approximation of α becomes

$$\alpha_2 = \alpha_1 - f(\alpha_1)/f'(\alpha_1) \qquad \text{(V)}$$

Eq. (V) is the same expression as that used in the Newton-Ralphson method.

Eq. (II) is now substituted in equation (V) and the value of α_1 is taken as the conductance ratio, Λ/Λ_0 to give

$$\alpha_2 = \frac{\Lambda}{\Lambda_0} - \frac{(\Lambda/\Lambda_0)^{\frac{3}{2}}\, c^{\frac{1}{2}}\, k}{\frac{3}{2}(\Lambda/\Lambda_0)^{\frac{1}{2}}\, c^{\frac{1}{2}}\, k - \Lambda_0} \qquad \text{(VI)}$$

Although several rearrangements of the above equation are possible, the above form is very convenient for computation purposes.

It now becomes of interest to determine the error, E, in α. The neglected terms of equation (III) form an alternating, convergent series. Consider the third term only. Obviously,

$$E = h - h_1 < f''(\alpha_1)h^2/2f'(\alpha_1) \qquad \text{(VII)}$$

It can be shown (6) that to a good approximation h can be replaced by h_1 on the right side of eq. (VII). This conclusion also follows from the fact that the neglected terms are small.

In order to evaluate a useful expression for E, values of the derivatives are now substituted in eq. (VII), and it is assumed that $f'(\alpha) = -\Lambda_0$. Hence,

$$E < \frac{3c^{\frac{1}{2}}k}{8(\Lambda/\Lambda_0)^{\frac{1}{2}}\Lambda_0} \cdot h_1^2 \qquad \text{(VIII)}$$

Considering experimental conditions, the coefficient of h_1^2 is not greater than 1. Consequently,

$$E < h_1^2 \qquad \text{(IX)}$$

Thus, the number of significant figures in h_1 may be taken as the number of zeros between the decimal point and the first significant figure in the value of h_1.

It is also of interest to determine the dependence on c of the ratios of h_1/α_1 and of E/α_2, i.e., the relative correction and the relative error.

The approximation is now introduced that

$$\alpha_1^2 = K/c \qquad \text{(X)}$$

where K = the dissociation constant of the electrolyte. By use of the value of h_1 in equation (VI), modified by the above simplification of $f'(\alpha_1)$ and with the aid of equation (X), it is found that

$$h_1/\alpha_1 \cong -(kK^{\frac{1}{4}}/\Lambda_0)c^{\frac{1}{4}} \qquad \text{(XI)}$$

The relative error, calculated by suitable combination of the value of h_1, eq. (VIII), (X), and (XI) is given by

$$E/\alpha_2 < \frac{3k^3K^3}{8\Lambda_0^3(1 + kK^{\frac{1}{4}}\, c^{\frac{1}{4}}\, \Lambda_0)} \cdot c^3 \qquad \text{(XII)}$$

where the term in parentheses is the ratio α_2/α_1.

From eq. (XII), it follows that the relative error is negligibly small at all practical values of c.

As a typical example, the conductance data of MacInnes and Shedlovsky (3) at low, intermediate, and high concentrations of acetic acid in water at 25°C are used to demonstrate the adaptability of eq. (VI). Since $A = 60.20$, $B = 0.229$, and $\Lambda_0 = 390.59$, it follows that $k = 149.65$. The necessary data are listed in Table I. Considering the rule stated above for the magnitude of the error, it will be observed that the formula for α_2 holds over all the concentra-

TABLE I. *Conductance data of aqueous acetic acid solution.*

c	Λ	α_1	$-h_1$	α_2 (eq. VI)	α_2 (Ref. 3)
0.000028014	210.32	0.53847	0.0008031	0 53927	0 53925
0.0010283	48.133	0.12323	0.0005348	0.12376	0.12375
0.100000	5.200	0.013313	0.0001901	0.01350	0.01350
0.230785	3.391	0.0086817	0.0001528	0.008834	0.008827

tion range. At high concentrations, the formula will not be expected to give results agreeing with published values, since the simple Onsager equation will not be valid due to dimerization of the acid (7, 8).

Manuscript received February 23, 1956.
Any discussion of this paper will appear in a Discussion Section to be published in the December 1957 JOURNAL.

REFERENCES

1. C. W. DAVIES, "The Conductivity of Solutions," p. 87, John Wiley & Sons, Inc., New York (1930).
2. W. H. BANKS, *J. Chem. Soc.*, **1931**, 3341.
3. D. A. MACINNES AND T. SHEDLOVSKY, *J. Am. Chem. Soc.*, **54**, 1429 (1932).
4. R. M. FUOSS AND C. A. KRAUSS, *ibid.*, **55**, 476 (1933).
5. R. M. FUOSS, *ibid.*, **57**, 488 (1935).
6. J. B. SCARBOROUGH, "Numerical Mathematical Analysis," pp. 182–184, The Johns Hopkins Press, Baltimore (1930).
7. A. KATCHALSKY, H. EISENBERG, AND S. LIFSON, *J. Am. Chem. Soc.*, **73**, 5889 (1951).
8. D. R. CARTWRIGHT AND C. B. MONK, *J. Chem. Soc.*, **1955**, 2500.

Current Distribution in Galvanic Cells Involving Natural Convection

CARL WAGNER

Department of Metallurgy, Massachusetts Institute of Technology, Cambridge, Massachusetts

ABSTRACT

From equations for mass transfer due to natural convection in a laminar boundary layer, it is derived that, in electrolytic cells used for the refining of metals such as Cu, the current density is virtually constant, although concentration polarization at both the cathode and the anode varies from bottom to top.

When a metal is deposited at a cathode, the steady-state concentration of cations in the solution next to the cathode is lower than in the bulk solution. Conversely, the steady-state concentration of cations in the solution next to the anode is higher than in the bulk solution. The resulting density difference between boundary layer and bulk solution brings about an upward or downward flow of the solution next to the electrode, analogous to natural convection for heat transfer. The effective thickness of the boundary layer is zero at the leading edge of the electrode where the flow of the solution originates, and increases with increasing distance from the leading edge.

Solutions of the boundary layer equations are available for the following conditions.

1. If an appropriate potential is applied to a cell containing a $CuSO_4$ solution, all Cu ions arriving at the cathode are readily discharged, but no other electrode reaction, such as evolution of H_2, may take place. Under these conditions, cation concentration at the electrode is virtually equal to zero, and the current reaches a limiting value I_{max}. Approximate solutions of the differential equations for the concentration and the velocity distribution in the boundary layer have been obtained by using solutions for the analogous heat transfer problem (1–7). For a laminar boundary layer, the local limiting current density is proportional to the fourth root of the distance from the leading edge of the electrode in accord with experimental results (3, 5–7).

2. If the applied current is lower than the aforementioned limiting current, concentration of cations discharged at the electrode is finite. The following limiting cases may be considered.

(*A*) The single electrode potential of the cathode and the anode may be assumed to be constant. Thus, if only concentration polarization occurs, the cation concentration at each electrode is constant, and the solution worked out for case 1 may be used with a slight modification. Accordingly, the local current density would be inversely proportional to the fourth root of the distance from the leading edge of the electrode.

(*B*) The current density may be essentially constant. This implies that the local concentration gradient at the surface of the electrode is constant, whereas the cation concentration at the electrode varies with the distance from the leading edge. In this case, the concentration difference between the bulk solution and the surface of the electrode is proportional to the fifth root of the distance from the leading edge of the electrode as follows from the analogy between heat and mass transfer (8) .

In cells involving Cu electrodes and a solution of $CuSO_4$ as electrolyte, Wagner (3) and Ibl, Ruegg, and Trümpler (6) found experimentally that current density is virtually constant if the applied current is less than $\frac{1}{3}$ the limiting current for exclusive cathodic deposition of Cu. In what follows it is shown theoretically that this is expected to be true under most conditions.

As a special case of practical importance, a galvanic cell used for the refining of Cu is considered. Electrodes of height h at a distance s from each other are supposed to fill the cross section of the trough completely so that no edge effects occur and the primary current density would be constant.

It is assumed tentatively that the current density is virtually uniform, and conditions under which this assump-

tion is valid are investigated below. For a uniform current density J, the conventional form of Ohm's law may be used. If the potential-current density curve for the cathode and the anode are approximately linear,

$$\Delta\phi = E - J \mid dE_c/dJ \mid - J \mid dE_a/dJ \mid = Js/\sigma \quad \text{(I)}$$

where $\Delta\phi$ is the potential difference within the solution between cathode and anode, E is the voltage applied to the cell, i.e., the potential difference measured between metallic terminals connected with the electrodes, σ is the electrical conductivity of the electrolyte, s/σ is the resistance of the electrolyte for a cross section of 1 cm², and $\mid dE_c/dJ \mid$ and $\mid dE_a/dJ \mid$ are the absolute values of the slopes of the potential-current density curves for the cathode and the anode, respectively.

Solving Eq. (I) for J,

$$J = \frac{E}{s/\sigma + \mid dE_c/dJ \mid + \mid dE_a/dJ \mid} \quad \text{(II)}$$

From Eq. (II), it follows that the current density will be essentially constant if the variation of the sum of the two terms

$$\mid dE_c/dJ \mid + \mid dE_a/dJ \mid$$

with distance x from the lower edge of the electrodes is small in comparison to the total value of the denominator in Eq. (II). In what follows it is shown that this is the case under conditions which are most likely to be encountered in industrial cells.

Considering only concentration polarization and disregarding the difference between activities and concentrations, the following is obtained from Nernst's formula

$$\left|\frac{dE_c}{dJ}\right| = \frac{RT}{2\mathbf{F}}\left|\frac{d\ln c}{dJ}\right| = \frac{RT}{2\mathbf{F}}\frac{1}{c_0}\left|\frac{d\Delta c}{dJ}\right| \text{ if } \mid \Delta c \mid \ll c_0 \quad \text{(III)}$$

where c is the concentration of Cu ions at the cathode, c_0 is the bulk concentration, and Δc is the concentration difference between the bulk solution and the surface of the electrode.

Using the analogy between heat and mass transfer problems, the value of Δc may be calculated in the same way as the temperature difference between a wall and an ambient fluid for a uniform heat flow per unit area has been calculated (8). Hence the value of Δc at distance x from the leading edge of the electrode is found to be

$$\mid \Delta c \mid = 1.62 \frac{jx}{D} \frac{0.8 + Sc}{Sc^2\, Gr_x^*} \quad \text{(IV)}$$

where j denotes the rate of mass transfer of Cu ions in mole/unit area/unit time due to diffusion, which is related to the current density by

$$j = J(1 - t)/2\mathbf{F} \quad \text{(V)}$$

where $\mathbf{F}$ is the Faraday constant and t is the transference number of Cu ions. Moreover, D is the diffusion coefficient, and Sc is the Schmidt number defined as the ratio of the kinematic viscosity ν to D. The modified Grashoff number Gr_x^* is defined as

$$Gr_x^* = g\beta' j x^4/D\nu^2 \quad \text{(VI)}$$

TABLE I. *Numerical values in Eq. (II) and (VIII)*

$\frac{x}{h}$	$\left\|\frac{dE_c}{dJ}\right\| + \left\|\frac{dE_a}{dJ}\right\|$ (ohm cm²)	$\frac{s}{\sigma} + \left\|\frac{dE_c}{dJ}\right\| + \left\|\frac{dE_a}{dJ}\right\|$ (ohm cm²)
0 or 1	0.24	67.74
0.01 or 0.99	0.34	67.84
0.05 or 0.95	0.37	67.87
0.1 or 0.9	0.39	67.89
0.2 or 0.8	0.40	67.90
0.5	0.42	67.92

where g is gravitational acceleration and β' is the rate of change in the natural logarithm of the density of the solution with the concentration of $CuSO_4$.

Since the Schmidt number $Sc = \nu/D$ in aqueous electrolytes is of the order of 10^3, the approximation $0.8 + Sc \cong Sc = \nu/D$ may be used in Eq. (IV). On substituting Eq. (IV)–(VI) in Eq. (III), it follows that

$$\frac{dE_c}{dJ} = 1.62\,\frac{4}{5}\,\frac{RT}{2\mathbf{F}}\,\frac{(1-t)^{\frac{1}{3}}\,x^{\frac{1}{3}}}{2\mathbf{F}Dc_0}\left(\frac{2\mathbf{F}\nu D^2}{gJ\beta'}\right)^{\frac{1}{3}} \quad \text{(VII)}$$

An analogous equation with $x' = h - x$ as the distance from the upper end of the electrode holds for the anode. Hence,

$$\left|\frac{dE_c}{dJ}\right| + \left|\frac{dE_a}{dJ}\right| = 1.62\,\frac{4}{5}\,\frac{RT}{2\mathbf{F}}\,\frac{(1-t)^{\frac{1}{3}}\,h^{\frac{1}{3}}}{2\mathbf{F}Dc_0} \cdot \left(\frac{2\mathbf{F}\nu D^2}{gJ\beta'}\right)^{\frac{1}{3}}\left[\left(\frac{x}{h}\right)^{\frac{1}{3}} + \left(\frac{h-x}{h}\right)^{\frac{1}{3}}\right] \quad \text{(VIII)}$$

Table I lists the results of a numerical evaluation of Eq. (VIII) for selected values of x and the following values corresponding to experimental conditions used in an experiment by Ibl, Ruegg, and Trümpler (6) with 1.0M $CuSO_4$ as electrolyte: $R = 8.31$ joule/mole/degree; $T = 298°K$; $\mathbf{F} = 96{,}500$ coulombs/equivalent; $\sigma = 0.04$ ohm^{-1}/cm; $s = 2.7$ cm; $t = 0.3$; $J = 0.003$ amp/cm²; $D = 5 \cdot 10^{-6}$ cm²/sec; $g = 981$ cm/sec²; $\beta' = 150$ (mole/cm³)$^{-1}$; $h = 20$ cm; $\nu = 10^{-2}$ cm²/sec; $c_0 = 10^{-3}$ mole/cm³.

Table I shows that values of the denominator in Eq. (II) vary only slightly with distance x since the first term $s/\sigma = 67.5$ ohm cm² exceeds by far the following terms accounting for polarization. Thus, the current density is found to be virtually uniform in accord with experimental results reported by Ibl, Ruegg, and Trümpler (6).

This result deduced for special conditions may be generalized. The following deviations from the foregoing presuppositions are to be considered.

1. If a supporting electrolyte, e.g., H_2SO_4 in addition to $CuSO_4$ is present, the density of the boundary layer is also affected by changes in the supporting electrolyte (3, 5). Thus, modifications of the foregoing equations are required, but the value of the right-hand member of Eq. (VIII) is not changed significantly. In addition, presence of a supporting electrolyte yields a higher conductivity corresponding to a smaller value of s/σ. Even for a ten times greater conductivity, however, values of the denominator in Eq. (II) at different heights differ by not more than 2½%.

2. In Eq. (VIII), activation polarization is disregarded. If activation polarization is considered, constant terms

on the right side of Eq. (VIII) have to be added. Thus, variation of the current density would be even smaller than has been estimated above.

3. Since the height h of the cell occurs in Eq. (VIII) only as the fifth root, values other than $h = 10$ cm give essentially the same result.

4. The current density J also occurs in Eq. (VIII) as the fifth root; therefore, different values of J give qualitatively the same results. The condition of a nearly linear potential-current density curve, however, requires that $|\Delta c| \ll c_0$ according to Eq. (III). For the foregoing qualitative considerations, $|\Delta c| = \frac{1}{2} c_0$ may be used as an upper limit. In view of Eq. (IV) for $x = h$, $Sc \gg 0.8$, and the auxiliary Eq. (V) and (VI) the condition

$$J \leqq 0.55 \frac{\mathbf{F} D c_0^{\frac{5}{4}}}{1 - t} \left(\frac{g\beta'}{2\nu D h} \right)^{\frac{1}{4}} \qquad \text{(IX)}$$

is obtained for the validity of the foregoing considerations. It is obvious that, on increasing the current in a $CuSO_4$ cell, the solution at the cathode eventually becomes exceedingly depleted with respect to $CuSO_4$, and the limiting value of the current I_{max} for exclusive cathodic deposition of Cu is approached. Under these conditions, Eq. (VIII) is not valid. Instead, the current density at the cathode is proportional to the fourth root of the distance from the lower edge as mentioned above.

5. The local current density would vary to a somewhat greater extent in a cell with a smaller width s, but such conditions are far from normal experimental conditions.

6. A large variability of the current density is expected in solutions involving a much lower value of c_0 than 1 mole/liter if the solutions contain a high concentration of supporting electrolyte which provides the same order of magnitude of the electrical conductivity assumed above. These conditions may be realized in a laboratory experiment (9), but do not occur in cells used for industrial refining of metals.

Consequently, as far as cells for industrial refining of metals are concerned, the current density is expected to vary only slightly from bottom to top of a cell, regardless of changes in the aforementioned parameters, provided the applied current is only a fraction of the limiting current for exclusive cathodic deposition of metal, i.e., the current density is lower than the value calculated in Eq. (IX).

Manuscript received May 28, 1956.
Any discussion of this paper will appear in a Discussion Section to be published in the December 1957 JOURNAL.

REFERENCES

1. B. LEVICH, *Acta Physicochim. U.R.S.S.*, **19**, 117 (1944).
2. J. N. AGAR, *Disc. Faraday Soc.*, **1**, 26 (1947).
3. C. WAGNER, *This Journal*, **95**, 161 (1949).
4. G. H. KEULEGAN, *J. Research Nat. Bur. Standards*, **47**, 156 (1951).
5. C. R. WILKE, M. EISENBERG, AND C. W. TOBIAS, *This Journal*, **100**, 511 (1953).
6. N. IBL, W. RUEGG, AND G. TRÜMPLER, *Helv. Chim. Acta*, **36**, 1624 (1953).
7. N. IBL, K. BUOB, AND G. TRÜMPLER, *ibid.*, **37**, 2251 (1954).
8. E. M. SPARROW, NACA Technical Note 3508 (1955); *Trans. ASME*, **78**, 435 (1956).
9. J. N. AGAR, *This Journal*, **95**, 361 (1949).

Supercooling, Preferred Orientation, and Inverse Segregation in Lead-Antimony Alloys

A. C. Simon and E. L. Jones

Naval Research Laboratory, Washington, D. C.

ABSTRACT

Experiments are described which confirm the previously reported inverse segregation of Sb in the Pb-Sb alloy castings. Supercooling of Sb at eutectic temperatures and a preferred orientation and growth direction for the Sb crystals are responsible for the excessively large coverage by Sb in the surface of the cast alloy. Interdendritic flow, previously claimed as a principal factor in this inverse segregation, is now found to be unnecessary. Preferred orientation with the [111] direction perpendicular to the surface and preferred directions of growth parallel to the (111) plane are shown to be caused by the strong covalent linkages within the (111) pairs of planes. This, plus a number of factors such as temperature gradient, surface tension, and Sb concentration in the surface film, favors the growth of those nuclei that originate with their (111) planes parallel to the surface. This preferred orientation of Sb can influence the tensile strength and ductility of hypereutectic Pb-Sb alloys.

An unusual concentration of Sb is found at the surface of hypoeutectic (below 11% Sb) Pb-Sb castings (1). The crystal form of this Sb indicates that it has solidified prior to the eutectic, contrary to the equilibrium phase diagram of the system.

The primary crystallization of Sb at the surface in excessive concentration was previously explained as being caused by an interdendritic flow of molten metal from the interior of the casting into the gap left between the semi-solid crust and the mold face during the solidification contraction. This satisfactorily explained the observed phenomena, but required the assumption of an unusual degree of supercooling to explain the large amount of Sb that froze as primary crystals.

Additional work and a reappraisal of the original observations have shown that supercooling of Sb takes place not only at the surface but throughout the interdendritic melt. In addition, excessive concentrations of Sb were also found at the surface of hypereutectic (above 11% Sb) alloy castings. A modification of the original explanation appears necessary. The following discussion shows that there is a preferred orientation of Sb at the surface with the [111] direction perpendicular to the surface, and that there is a preferred growth direction parallel to the surface. These factors influence not only the surface appearance of the as-cast Pb-Sb alloy series but the physical properties as well.

Experimental Procedure

The method of casting against polished mold walls in order to obtain a surface suitable for metallographic examination has been described (1) and criticized (2). Interpretation of the results, however, had been carefully verified by comparison with conventionally prepared metallographic cross sections for each of the alloys studied and by comparison with commercially prepared castings obtained from various sources. In addition, the presence of this Sb surface layer had been confirmed by x-ray analysis and chemical tests and additionally, as herein reported, by crystallographic measurement and identification of the actual crystals formed, so that the authors do not feel that such criticism is justified.

Alloy series were prepared in a concentration range of 3–21% Sb in increments of 2% under five casting conditions. The reasons for these conditions are brought out in the subsequent discussion.

1. Additional series of castings were made under the conditions reported previously (1).

2. Castings were made between highly polished parallel Al plates separated by 0.005-in. shim stock that acted as the narrow sides of the mold so that a 3 x 4 x 0.005-in. foil resulted. The mold was heavily insulated and suspended so that the parallel plates were vertical, with the width (3-in. dimension) and thickness (0.005-in. dimension) parallel to the base and with the height (4-in. dimension) vertical to the base. Heating was from the base, and controlled reduction of temperature began at the base. Cooling took place from the small, uninsulated top surface. The freezing therefore proceeded from top to bottom, and the cooling rate was approximately 5°/min.

3. Cast foils were made under the above conditions except that the top was heavily insulated immediately after casting, the source of heat was removed from the bottom, and a water-cooled Al plate was substituted. Freezing began at the bottom and cooling was at approximately the same rate as above. Series 2 and 3 were cast with the mold temperature initially slightly above the freezing point of the alloy since this was the only way in which such thin foils could be prepared.

4. Series 2 and 3 were duplicated except that the foil was made 0.125-in. thick.

5. Castings were made in a mold in which was suspended an Al sheet with both sides polished. This sheet was supported in the center of the mold by pointed Transite blocks so that heat transfer was at a minimum. The polished plate was 1-in.^{2} and 0.125-in. thick and was

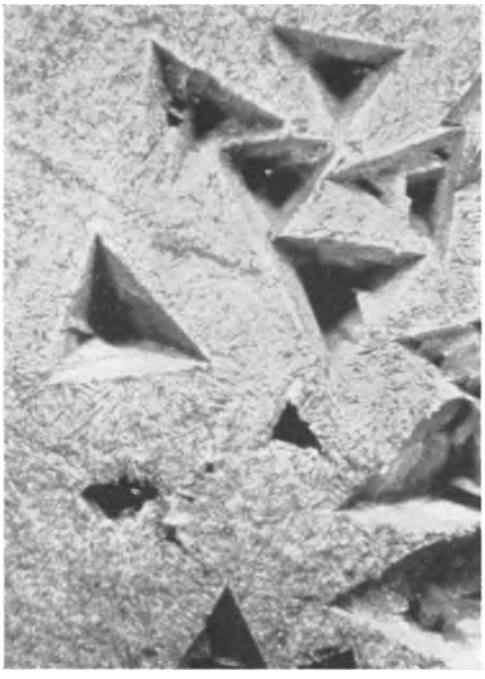

FIG. 1. Etch pits left in Pb-Sb alloy surface by removal of primary Sb crystals; from the as-cast surface of a hypereutectic alloy containing 13% Sb. 500×.

surrounded on all sides by a 1-in. thick casting section. The mold was originally at a temperature above the melting point of the alloy and was held at this temperature a sufficient length of time after casting so that the interior plate reached the melt temperature before cooling began. By milling the edges of the resulting casting, the two halves of the casting could be separated at the interior Al surface.

To determine crystal orientation and habit, the following procedure was used: When a Pb-Sb alloy is corroded anodically in a H_2SO_4 solution, visible formation of lead oxides does not take place until the Sb present in the surface of the casting has been leached out (3). Specimens of the various castings that contained suitable Sb crystals were given this treatment, using a very low current density. Removal of Sb resulted in a negative replica of the crystal in the surrounding Pb (Fig. 1). Surface dimensions and angles of this depression, its depth, and the position of the deepest portion with relation to the surface outline were measured with various microscope accessories. With this information, the shape of the crystal was reconstructed, the angles that the sides made with one another calculated, and the crystal habit and the preferred directions of dendritic growth determined. Preferred directions of dendritic growth were then used to determine the orientation of the thin platelets which were not suitable for the above method of determination.

OBSERVATIONS AND CONCLUSIONS

Hypoeutectic Alloys

1. Primary crystallization of Sb and excessive amounts of Sb in the as-cast surface occur under all casting conditions for the hypoeutectic alloys. Whether the casting was large or small (relatively speaking, since the largest casting examined was only 5 in. long by 3 in. in diameter), rapidly or slowly cooled, or subjected to differential cooling, the surface always showed segregation of excess Sb and primary crystallization. As reported previously, the degree to which segregation occurred depended on the cooling rate and the amount of Sb in the alloy, but it was always present to some extent. This was true even at the internal surface formed by suspending a plate in the center of the mold. Repetition of the experiments reported previously led to the same conclusions as formerly. Castings made against Al, Fe, glass, Cr, Pb, and Transite and against Al and Fe surfaces under silicone oil all exhibited this same excessive Sb segregation at the surface.

2. The appearance of primary Sb crystals and excessive proportions of Sb at the casting surface of the hypoeutectic alloys is evidence of a larger than eutectic concentration of Sb and of supercooling. The eutectic concentration of Sb is reported to be about 11% by weight, and on that basis the eutectic structure would be expected to contain an Sb-to-Pb ratio of approximately 1:8 by weight or 1:5 by volume. Conditions that reverse this ratio in the surface cannot be explained by previous theories of inverse segregation.

A layer of eutectic composition and structure has been observed at the surface of many alloys. This has been proved to be caused by the natural enrichment of the remaining melt in solute as primary crystals of solvent precipitate. This melt, enriched to eutectic composition, may be extruded as a surface layer (4), or may only appear to be in excess at the surface because the roughly spherical or cylindrical primary crystals have a minimum area in the surface layer (5).

The term primary crystallization is used herein to mean the formation of an extensive dendritic crystal or a regular crystal of recognized form and habit, of a much larger size than would be associated with eutectic structure, and which has been precipitated prior to the eutectic in its immediate vicinity. For the hypoeutectic alloys, the real primary crystals are, of course, the Pb crystals that form the bulk of the solid. The primary crystallization of Sb in the surface layer of such an alloy depends on the melt in the immediate vicinity having some hypereutectic composition. The process of interdendritic flow, whereby molten metal flowing to the surface to compensate for shrinkage is enriched in Sb by the deposition of Pb on the colder walls of the interdendritic channels, cannot produce an Sb concentration greater than eutectic. The only process that suggests itself as a way out of this difficulty is that in which Sb supercools in the presence of Pb when the eutectic composition is reached. Just as one metal may supercool in a crucible made of another, so may Sb supercool in the interdendritic channels and at the surface of the primary Pb structure. But Pb can continue to precipitate, and so the remaining melt becomes enriched in Sb to a point where extensive primary crystallization of Sb occurs. The reasons that such supercooling is possible have been discussed previously (1).

3. The formation of a solid crust or extensive interdendritic flow is not necessary to produce the surface film of Sb. The possibility of a solid crust being formed and subsequently being partially remelted by heat from the interior as the heat transfer becomes interrupted by shrinkage from

the mold (4) was not considered likely from the evidence previously obtained, but such a possibility was advanced as a criticism (2) of the previous report.

Formation of a solid crust, made possible by normal eutectic freezing, not only would be evidence that supercooling of Sb did not occur but would leave no explanation of how Sb could occur in greater than eutectic amounts at the surface. For, if a solid crust is first formed and then remelted, the first portion to remelt would be of eutectic composition (lowest melting point), and any further remelting would cause enrichment of the melt in Pb. Enlargement of the surface pores by hotter material from the interior would aggravate this condition, so that the extruded material could not contain more than the eutectic amount of Sb and would probably contain less.

Thin alloy foils of 0.005 in. thickness cast as described were frozen so that the primary Pb dendritic crystals grew in one direction only, parallel to the mold faces. The thickness of the foil equaled the average diameter of one dendritic arm, and by proper control of cooling a row of parallel dendritic branches could be produced which were parallel to and between the foil surfaces. In other words, a foil was produced in which freezing had begun either at the upper or lower end and not from either foil surface. The resulting foil was not a single crystal, but the individual grains were large and their thickness equaled that of a single dendritic branch. The individual dendritic branches of each grain were parallel to the foil faces and roughly parallel to the long dimension of the foil which was also the vertical axis of the mold. This was checked by the preparation of chemical replicas (6), and by alternately etching and stripping the surface film with pressure-sensitive tape until the underlying dendritic structure was revealed.

In all of the foils, whether growth of the primary Pb dendritic crystals started from the bottom of the mold or from the top, the surface film of the casting showed excessive concentration and primary crystallization of Sb. The diameter of the individual dendritic branches was nearly the same as the thickness of the foil, and their length was many times their diameter. These crystals, the first solid to form in a given section, evidently had been able to grow to their final diameter in a medium that was still unfrozen.

In these circumstances there could be no formation of a solid crust with liquid center, nor any buildup of a higher concentration of Sb toward the center. Gravitational flow of still-molten metal through the interdendritic channels along the length of the foil maintained a liquid layer in contact with the mold surfaces during the shrinkage contraction so that the castings conformed closely to mold dimensions. For a mold of these dimensions, however, contraction of the solidifying metal would be small and movement of molten metal past any given point in the interdendritic channels would be small, far too small to cause any appreciable increase in concentration or the introduction of Sb-rich material at the surface in considerable quantity.

The argument might be made that a given section of the foil had been completely solid and, as shrinkage occurred, feeding had taken place from other regions through the gap between the metal and mold. That this is not true is attested to by the fact that the surface film of Sb was present regardless of whether freezing of the foil began at the bottom (which would favor gravitational flow) or from the top (which would preclude gravitational flow if the melt in a given section became completely solid).

Additional proof that there is no necessity for the formation of a solid crust or extensive interdendritic flow is given by the experiment wherein an Al plate was suspended in the interior of the mold. This plate, being well insulated from the exterior surfaces, centrally located, and at the temperature of the melt, would approximate conditions at the center of a casting that was being cooled through the exterior mold surfaces. The area around this plate then represents the last portion to freeze and cannot be supplied with liquid metal from any other region. Although the surface was always marred by many shrinkage cavities, freezing at this interior surface nevertheless took place with the formation of a surface layer of high-Sb concentration and primary crystallization, just as at the exterior surfaces.

The conclusion is reached, therefore, that this is a process that occurs in situ and does not depend on interdendritic flow. A completely solid crust was evidently not present at the time the surface film formed, but the main function of interdendritic flow is to maintain the liquid layer in contact with the mold face during solidification contraction.

4. For both hypoeutectic and hypereutectic Pb-Sb alloys there is a preferred orientation of Sb with the [111] direction perpendicular to the casting surface. Examination of the surface of castings made from hypoeutectic alloys revealed a host of elementary growth forms (Fig. 2), all of the same type, which on investigation were revealed as dendritic Sb crystals. In the most elementary form, these consisted of three needlelike or acicular dendritic branches parallel to the surface and meeting at a common center at angles of 120° to one another. As the concentration of Sb was increased or rate of cooling decreased, the dendritic crystals began to exhibit a center of regular crystal structure with the dendritic branches radiating from the corners (Fig. 3). This center was normally in the form of an equilateral triangle, although other forms appeared occasionally. These equilateral crystals were found to have

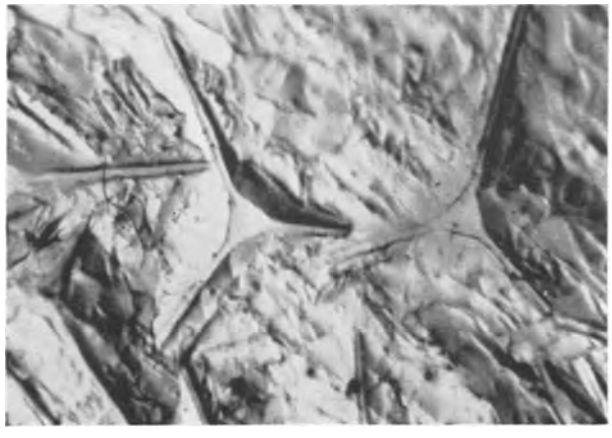

FIG. 2. Primary Sb crystals of primitive dendritic form, crystallized in the as-cast surface layer of a Pb-Sb alloy containing 9% Sb. 800×.

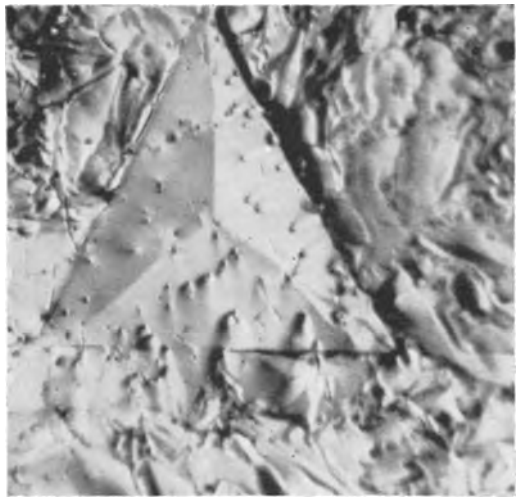

FIG. 3. Primary Sb crystals of regular form but with dendritic corner extensions, crystallized in the as-cast surface layer of a Pb-Sb alloy containing 11% Sb. 800×.

their (111) planes parallel to the surface. Cross sections revealed that for the hypoeutectic alloys these crystals had developed the (111) planes at the expense of all others, so that a very thin platy crystal was formed. For the hypereutectic alloys the equilateral triangle at the surface had developed into a tetrahedron with the (111) plane at the surface and the apex beneath the surface. The sides of this tetrahedron were made up of (110) planes. The tetrahedral crystals formed in the hypereutectic alloys did not exhibit dendritic growth from their corners or edges for reasons to be explained in a later section.

The hypoeutectic alloys showed a decided tendency toward dendritic growth from the corners of the equilateral triangles in the [11$\bar{1}$] and equivalent directions. As the cooling rate increased, these crystals began to exhibit

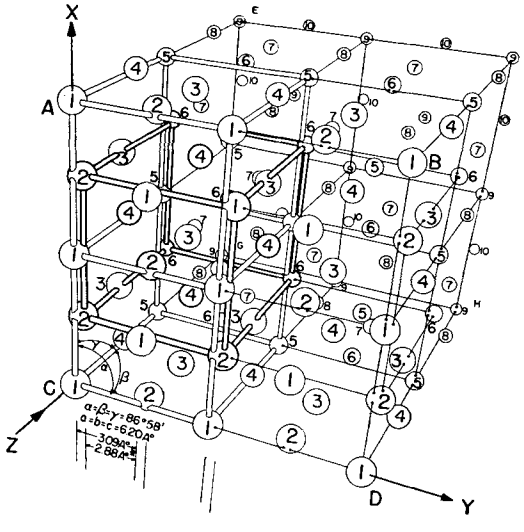

FIG. 4. Schematic representation of the interpenetrating lattice configuration of Sb. Similar numbers identify lattice points on the same plane, successively increasing numbers refer to planes at increasing depth behind plane ABCD. Note that the configuration forms a very slightly askew face-centered lattice.

additional directions of dendritic growth. While the dendritic growth usually originated at the corners of the triangle, and while dendrites at 120° to one another were the directions of principal growth, numerous other dendritic growths appeared at lesser angles, radiating from the corners like a diverging bundle of rays.

The occurrence of crystals with the (111) planes approximately parallel to the surface was estimated at about 95% of all the orientations that appeared. The crystals show a decided preferred orientation with the [111] direction at right angles to the surface, but the individual crystals appear to have no preferred orientation with respect to one another other than sharing a common axis in the [111] direction.

5. Preferential growth occurs at right angles to the direction of preferred orientation and causes a surface layer of Sb without the need for excessive supersaturation. In examining cross sections of the foils, the Sb particles in the matrix surrounding the primary dendritic branches of the Pb crystals were observed to have random orientation except at the as-cast surface, where they were almost invariably aligned with their long axis parallel to the surface. In addition, those crystals formed in the surface layer, when viewed from above the surface, showed extensive and continuous dendritic structure and even large crystals of regular structure but, when viewed in the cross section, were found to have grown very little in any direction away from the surface. This refusal of Sb crystals to grow into the interior, even when there was plenty of room to do so, was taken as evidence of a preferred direction of growth in the plane of the surface. Preferential growth direction is also indicated by the internal structure of Sb.

The lattice of Sb has been determined to have orthorhombic symmetry. As originally pictured (7), Sb atoms lie in two interpenetrating face-centered rhombohedral lattices (Fig. 4), and the unit rhombohedral cell is pictured as face-centered. The early literature reports the lattice constants on this basis, and some reports on crystal form and cleavage planes have been based on this notation.

But a primitive rhombohedron of the same height, but one-quarter of the volume of the original, can be outlined in the face-centered unit cell (Fig. 5), and it is the lattice constants of this cell that are reported in the recent literature. Since this change in cell also causes a transformation of axes and face indices, care is necessary in comparing reports on the habit, structure, orientation, and cleavage characteristics of Sb. Axes and face indices mentioned in the present report are based on the primitive cell of Fig. 5 and on the Miller system which employs three axes of reference.

Reported lattice constants (7–12) are in good agreement, but the exact positions of the atoms (the relative displacement of the two interpenetrating lattices) are still in doubt (7, 8).

The lattice structure of Sb is unusual, but this alone does not furnish the clue to the odd behavior of the surface film in alloy castings. As was shown for Ge (13), the preferred growth parallel to the metal surface is caused by its method of atom bonding. The (111) planes of the Sb lattice are arranged in double layers, with the two layers spaced at approximately 1.50Å apart and repeated at intervals of

about 2.25Å. The fourth layer is vertically over the first. In this arrangement, each atom has three close neighbors in the other plane of its double layer and three others at a somewhat greater distance in the next double layer (Fig. 6). Of the four covalent bonds associated with each atom, three appear to be bound with the three closest neighbors in the other half of the same double layer at a distance equivalent to the closest atom spacing. The remaining covalent bond could be considered to act through the next adjoining double layer on an atom at twice the above distance. Actually, each double layer might be regarded as a huge molecule held together by simple covalent bonds, while the layers themselves may be considered as held together by Van der Waals' forces or something like metallic bonds.

Atoms within a given double layer, therefore, attract each other strongly, being held together by the mutual attractions of three of their covalent linkages, while the attraction for atoms in other layers is much weaker. A strong tendency for approaching atoms to be drawn into an existing double layer rather than to begin another layer in the [111] direction would be expected to occur, and this effect would be strongest for the conditions favorable for dendritic growth. The evidence indicates that this is actually what does occur. The perfect cleavage parallel to the (111) planes is also explained by the bonding of the crystals.

Since the crystals show a preferred orientation with the [111] direction perpendicular to the surface and a preferred direction of growth parallel to the surface, there results an excessive coverage by Sb in the surface layer which appears to be caused by a large excess of Sb but, in reality, is the result of preferential growth of a comparatively small excess.

The cause of the preferred orientation is not obvious. In the case of those crystals which consist largely of the three dendritic arms meeting at 120° to one another, it appears that the nucleus itself must have been formed with this orientation or acquired it shortly after birth. The effect cannot be attributed to a thermal gradient extending into the interior because the same effect was observed at interior surfaces where the temperature differential was reversed. The effect does not appear to be caused by nucleation from the mold because, as was mentioned previously, various mold surfaces and air and silicone oil contact surfaces produce the same effect.

The phenomenon might be attributed to surface tension since it appears at all interfaces. The energy associated with the surface layer may have an influence on the formation of the nucleus or may influence the nucleus after its formation, since the effect of surface tension acting on an object becomes more and more important compared with its weight as the object becomes smaller.

As Gibbs has shown, if a substance lowers the surface tension of a liquid when dissolved in it, the concentration of the substance is greater in the surface film than in the bulk of the liquid. If this is true, the concentration of Sb in the interface will be higher than elsewhere. To be sure, the layer concerned may be only one or several atoms thick, but consideration is here being given only to the formation of a nucleus.

The supersaturated surface layer of the semisolid alloy may therefore be pictured as having an interface of high Sb concentration, a greater than eutectic concentration of Sb in the layer, a temperature gradient that produces the greatest supercooling at the interior mold surface or at the liquid-mold interface, and conditions that are ideal for

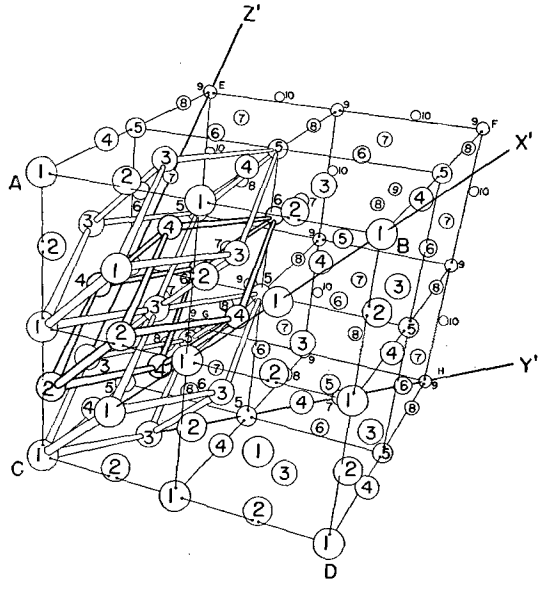

FIG. 5. Lattice configuration of Sb when a more primitive cell is used, same spatial distribution as before. For clearness only a portion of the new lattice has been drawn in. Note that an interpenetrating body-centered rhombohedral structure is produced. Observe also that the indices X', Y', Z' are differently located than X, Y, Z of Fig. 4.

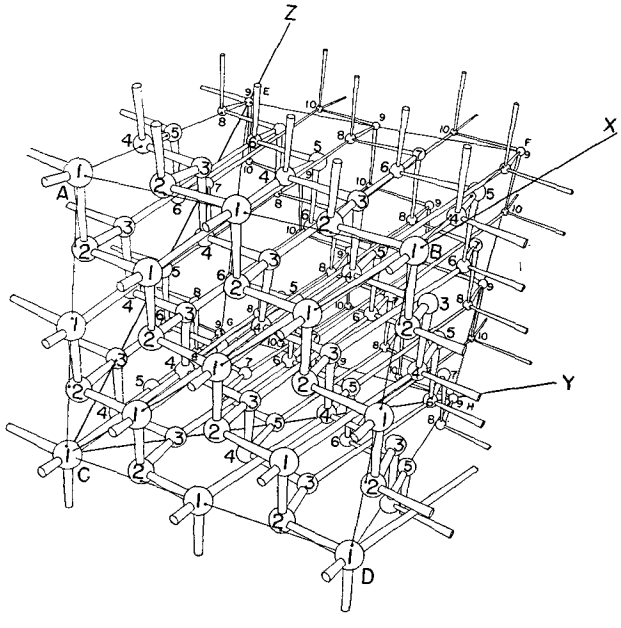

FIG. 6. Bonding configuration of Sb, same spatial arrangement as before. Covalent bonding forces are pictured as rigid bonds with maximum interaction shown in the closely grouped pair of (111) planes. Observe that the bonds operating within the closely grouped pairs are more numerous and act over shorter distances than those operating between paired planes.

dendritic-type crystal growth. Nucleation should logically occur at the interface with orientation as described. In addition, the heat associated with crystallization is radiated in all directions but is most readily transferred by the solid mold rather than by the liquid melt. Thus there exists briefly a more favorable condition along the mold face than into the molten material beneath the surface. Nuclei with an unfavorable orientation that causes them to grow away from the surface should be overwhelmed by those more favorably located with their (111) planes parallel to the surface. If this evaluation of the cause of preferred orientation is correct, the decease of the unfavorably located crystals must occur while they are yet very small, since very few crystals of other than the preferred orientation were found in the surface layer.

The surface of Pb-Sb alloys is not the only place where this preferred orientation of Sb occurs. A similar phenomenon has been reported for thin films of Sb, vacuum-evaporated upon a suitable support (14–16). These films are condensed as an amorphous layer and then spontaneously crystallize with the (111) planes parallel to the film surface. In one of these reports (15), the optical appearance is described in detail and photographs of the structure are included. The description and illustrations of the crystals obtained from the evaporated film apply equally well to the crystals obtained here in the surface film of the alloy, indicating a marked similarity in growth habit.

Another interesting observation has been reported concerning the orientation texture present at the cast surface of pure Cd and Zn (17). These metals, of hexagonal structure, had the basal (0001) planes oriented parallel to the surface, and this same texture was observed whether cast against air, Transite, Fe, or molten Pb.

FIG. 7. Cross section through thin Pb-Sb foil. Primary tetrahedral Sb crystal (bright triangle at right edge) is surrounded by an area in which Pb predominates. This dark area isolates the primary crystal and also outlines the shape of the dendritic Pb crystal. Remainder of Sb in picture represents "eutectic" structure formed upon relief of supercooling. 500×.

While the structure of Sb cannot be compared with that of Cd and Zn, the planes of maximum density are parallel to the surface in each case. This indicates that surface tension might be the largest single factor in determining orientation, whereas the solid-state conversion of an amorphous solid into an oriented crystal structure might require a different conclusion. In deposits condensed from the vapor, however, only materials having a high atomic mobility like Zn, Cd, Sb, Bi, and NaCl show a densely populated plane parallel to the surface (16).

Hypereutectic Alloys

The conclusions and observations pertaining to the hypereutectic alloys cover only that part of the alloy series containing between 11 and 21 % Sb, a small segment of the total series. In general, observations and conclusions are the same for the hypoeutectic range. There is the same excessive surface Sb, preferred orientation, and preferred growth direction as previously mentioned but there are also the following additional observations:

1. Since primary crystals of Sb precipitate first and at the surface, excess Sb at the surface cannot be explained by the usual explanation of inverse segregation. This must be considered as a special type of "normal" segregation.

2. In the hypereutectic alloys, the surface is made up of two kinds of crystals. Individual tetrahedra appear with preferred orientation with the [111] direction perpendicular to the surface, the basal (111) plane at the surface, and the apex beneath the surface. The remainder of the surface is covered with a thin, continuous, platy film of Sb in which neither dendritic structure nor individual crystals could be detected by the methods being used. For the reasons already given, this film was assumed to have the same preferred orientation with the [111] direction perpendicular to the surface. This was confirmed by x-ray analysis of a 15% Sb alloy foil which also verified the excessive amount of Sb in the surface layer (18).

3. Supercooling of Sb and preferred growth direction is responsible for the surface layer in the hypereutectic alloys just as in the hypoeutectic. When the amount of Sb in the alloy is increased beyond the eutectic composition, the surface is still covered with an Sb film, but the regular crystals of Sb in this film no longer have dendritic extensions from the edges or corners, and they are no longer platy but have become regular tetrahedra with the base at the surface.

The cross section of a thin Pb-Sb foil (Fig. 7) shows that each regular Sb crystal is surrounded by a region rich in Pb and in which there are no detectable particles of Sb. Beyond this lead envelope the so-called eutectic structure occurs. Examination shows that this Pb envelope around the regular Sb crystal sometimes is extended for considerable distances into the eutectic as dendritic prolongations. Although an effort was made to promote freezing of these alloys in a direction parallel to the foil faces as was done for the hypoeutectic alloys, the cross sections showed that all regular Sb crystals were formed at the foil surface (mold face) and grew inward. Dendritic Pb crystals had

completely random growth directions. If one mold face was intentionally made less well insulated, all the Sb crystals were found to have originated at this cooler mold face.

The evidence indicates that initial freezing of the melt occurs without supercooling. Under these conditions relatively few nuclei are formed, and the growth conditions favor regular rather than dendritic crystal growth. The crystals that do form naturally do so at the mold face and grow to a fairly large size in the tetrahedral form already described.

The Pb-rich area surrounding each crystal, in which no Sb appears, indicates that growth proceeds faster than diffusion can keep pace. The crystal thus becomes surrounded by a Pb-rich region which effectively prevents further growth and in which conditions are suitable for solidification of Pb. This permanently seals off the original Sb crystal and prevents it from nucleating any further precipitation of Sb. With all the original nuclei sealed off in this manner, the regular crystal growth of Sb crystals becomes a self-extinguishing process. The remainder of the Sb now supercools, for its most effective nucleation agents have been removed. Conditions are now the same as in the hypoeutectic alloys. The metal at the surface contains a greater than eutectic amount of Sb and is in a supercooled condition. Dendritic crystallization of Sb occurs with preferential growth in the surface plane. This is followed by eutectic-type crystallization throughout the remainder of the melt.

The relatively few regular crystals and their concentration at the surface suggests the possibility of heterogeneous nucleation. Their preferred orientation, however, indicates that the same combination of factors previously outlined is also responsible for this type of crystal. The thickness of the Pb envelope and the dendritic growth of Pb from it suggest that Pb also may have supercooled in the region surrounding each primary regular Sb crystal.

Under the conditions that encourage dendritic growth, such as supercooling, the crystallization of Sb does not become a self-extinguishing process because the rapid extension of dendritic filaments of relatively small cross section requires such a small removal of Sb from a given area that formation of a Pb-rich envelope does not occur until the tip of the growing dendrite has passed into an area as yet undepleted.

Effect of Preferred Orientation on Physical Properties

The preferred orientation of Sb and its excessive concentration in the surface film would be expected to exert some influence on the physical properties of the alloy concerned. Sb is an anisotropic material, and its physical properties vary with direction in the crystal. A preferred orientation at the surface of the crystal produces a maximum or minimum effect, depending on the property concerned.

One effect that was investigated was cleavage. Sections of the foil were bent at right angles and the result investigated. When hypoeutectic alloys were employed, no noticeable effect was obtained. When hypereutectic alloys were investigated, a significant difference was noted. When the bend occurred over the site of a regular tetrahedral Sb crystal, cleavage of the crystal occurred if the crystal was in the surface under tension (Fig. 8). Crystals in the surface under compression did not cleave. Cleavage of the crystal resulted in an open crack extending from the surface down through the crystal and well into the underlying lead. The brittle crystal, with its apex pointed at the center of the foil, was evidently acting much like a mechanical notch and causing failure in the underlying structure. This effect was either absent in the dendritic crystals or resulted in twinning, and no visible failure occurred through this type of crystal.

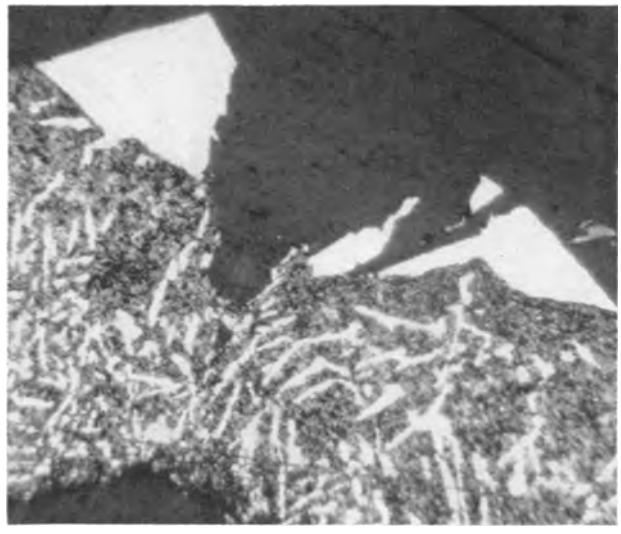

FIG. 8. Cross section of foil with 90° bend. Primary crystal of Sb has split, and crack has spread to eutectic portion of section. This effect is highly localized under site of crystal and does not represent an extensive crack across the foil. 500×.

As-cast Pb-Sb alloys show a sudden decrease in tensile strength near the eutectic concentration of Sb (19, 20); extruded and annealed specimens show no such decrease (21). Tetrahedral Sb crystals first make their appearance at this same point, and their demonstrated failure under tension would indicate that their presence is responsible for the sudden decrease of tensile strength at above eutectic concentrations.

Manuscript received July 17, 1956. This paper was prepared for delivery before the Cleveland Meeting, September 29 to October 3, 1956.

Any discussion of this paper will appear in a Discussion Section to be published in the December 1957 JOURNAL.

REFERENCES

1. A. C. SIMON AND E. L. JONES, *This Journal*, **101**, 536 (1954).
2. ANON., *Metal Ind. (London)*, **85**, 539 (1954).
3. J. B. BURBANK AND A. C. SIMON, *This Journal*, **100**, 11 (1953).
4. D. E. ADAMS, *J. Inst. Metals*, **75**, 809 (1949).
5. K. DETERT, *Z. Metallkunde*, **45**, 550 (1954).
6. J. BURBANK, *J. Metals*, **5**, 55 (1953).
7. R. W. JAMES, *Phil. Mag.*, **40**, 233 (1920).
8. A. OGG, *Phil. Mag.*, **42**, 163 (1921).
9. E. ROSA, *Nuovo cimento*, **12**, 448 (1935).
10. E. R. JETTE AND F. FOOTE, *J. Chem. Phys.*, **3**, 605 (1935).

11. J. E. Dorn and G. Glockler, *J. Phys. Chem.*, **41**, 499 (1937).
12. S. S. Lu and Y. L. Chang, *Proc. Phys. Soc (London)*, **53**, 517 (1941).
13. E. Billig, *Proc. Roy. Soc. (London)*, **A229**, 346 (1955).
14. J. E. Ruedy, *Phys. Rev.*, **59**, 926 (1941).
15. W. Lotmar, *Helv. Phys. Acta*, **18**, 232 (1945).
16. D. M. Evans and H. Wilman, *Acta Cryst.*, **5**, 731 (1952).
17. G. Edmunds, *Trans. Am. Inst. Mining and Met. Engrs.*, **161**, 114 (1945).
18. J. Burbank, Unpublished work.
19. A. M. Fairlee, *Metal Ind. (N. Y.)*, **9**, 24 (1911).
20. L. J. Gurevich and J. S. Hromatko, *Chem. & Met. Eng.*, **25**, 62 (1921).
21. R. S. Dean, L. Zickrick, and F. C. Nix, *Trans. Am. Inst. Mining and Met. Engrs.*, **73**, 505 (1926).

The Question of Space Charge in Anodic Ta_2O_5 Films

D. A. Vermilyea

Research Laboratory, General Electric Company, Schenectady, New York

Dewald (1) has extended the oxidation theory of Cabrera and Mott (2) to include the effect of an ionic space charge in the oxide film. Such a space charge will develop if, for example, the time required for an excess interstitial ion to move from one side of the film to the other is not very much smaller than the time required for the ion to cross the interface. Space charges do not develop in all types of film formation, since a mechanism involving the creation of pairs of defects within the film, rather than of single defects at an interface, leaves the film electrically neutral at all times. In a previous publication (3) an attempt was made to detect the presence of space charge in anodic Ta_2O_5 films. It was concluded that such space charges must be quite small. Recently Young (4) suggested that an ionic space charge would explain his measurements of the frequency and time dependence of the capacitance of niobium oxide films, and stated that behavior similar to that of niobium oxide is shown by Ta_2O_5 films "under certain conditions". In this paper the results of measurements of the capacitances of Ta_2O_5 films of various thicknesses are discussed. Measurements indicate there may be a charge in the film of such a density that the variation of electric field across a film 5000Å thick is about 1%.

Experimental

Oxide films were formed on chemically polished Ta sheet,[1] using a solution of 0.05% Na_2SO_4 in water as the electrolyte. The metal specimens were 2 in. x $\frac{1}{4}$ in. x 0.005 in. and had a tab $\frac{1}{2}$ in. x $\frac{1}{32}$ in. on one corner. They were cut from Ta sheet with a die and then chemically polished, so that the edges cut by the die and the rolled surfaces were smoothed and cleaned. It is known that chemical polishing leaves a film of unknown composition at the oxide-metal interface, and it is conceivable that such a film might have an effect on the results. However, the same results were obtained whether this film was kept in place or removed prior to formation by dipping the specimen in HF. It was necessary to have a very well-defined area on each specimen so that the current density of formation at all voltages would be constant and so that the capacitance would be measured on the same area. This was accomplished by applying a heavy coating of "Cello-Seal" (a semifluid substance which does not creep along the metal surface) to the specimen at the point where the tab joined the main part of the specimen, anodizing the tab up to the coating, and then removing the Cello-Seal. It was possible in this way to prevent the oxide film from creeping above the water line; a very sharp boundary between the anodized and clean part was produced.

Voltages applied to the specimens were measured by means of a voltage divider and a L&N type K potentiometer to a precision of 0.1%. The potential in the electrolyte near the Ta electrode was also measured with a calomel reference electrode so that changes in the cathode-solution potential could be compensated for.

The procedure employed was to apply a constant voltage across the forming cell and to allow the current to fall to 1.0 ma. The specimen was then removed from the bath, cleaned in H_2SO_4-$K_2Cr_2O_7$ cleaning solution, and placed in a cell containing 2% HNO_3 and a platinized-Pt electrode of 100 cm². The capacitance was measured using a General Radio impedance bridge which had been calibrated so that the capacitance could be measured with a precision of 0.5%.

It is known that a plot of oxide film thickness vs. voltage extrapolates to zero thickness at a voltage which is about 1 v negative. The value of the intercept cannot be calculated precisely, and hence some extrapolation method must be used to find it. For this purpose a plot of the measured capacitance times the measured voltage against the voltage was made for large voltages and extrapolated to zero voltage. Then, values of voltages required to make the results at small thicknesses fall on the extrapolated line were determined and compared to the measured voltages. It was found that a small constant voltage (about 0.9 v) added to all of the voltages would result in a smooth curve of C·V vs. film thickness. The constant to be added can be obtained by plotting the reciprocal of the capacitance against the voltage and extrapolating to zero voltage, but the accuracy is not as great. For an extrapolation of either type to be valid, it is necessary that there be no rapid change in either the density or the sign of any space charge in the film at very small distances from either electrode. Earlier measurements (5) at negative

[1] Obtained from Fansteel Metallurgical Corp.

applied voltages and film thicknesses down to a few angstrom units showed that a plot of reciprocal capacitance against voltage was still linear and was a continuation of the line obtained with positive voltages and larger thicknesses. Therefore, it appears that there is no sudden change of field in the oxide film close to either interface; hence the extrapolation used is valid.

Results and Discussion

Fig. 1 and 2 show plots of C(V + k) against film thickness, where k is a small constant as shown. There is a slight decrease of this product with increasing film thickness for specimens held either at 19°C and a field of 0.067 v/Å or at 86°C and a field of 0.056 v/Å. Three specimens anodized under each set of conditions gave nearly identical results. For the 29°C specimens the decrease of the product C(V + k) averaged 1.1%, while for the 86°C specimens the decrease averaged 1.4%.

There is a possible source of a decrease in C(V + k) with thickness which makes the interpretation of these results difficult, that is that the area of the film could decrease as the film grew thicker. This might occur in two ways. First, a very thin film would follow the very small scale contours of the surface, while the outer surface of a thicker film would undoubtedly tend to be smoother and hence have a smaller area. Second, the metal surface itself would tend to become smoother as the film grew. An experiment was performed to see whether there was any permanent change of specimen area after formation by dissolving all but about 100Å of a film in HF and then repeating the measurement of capacitance vs. voltage. The second set of measurements shown in Fig. 1 was made in this way and it may be seen that the two sets of measurements agree very well. Thus there appears to be no permanent change in area, but it cannot be concluded that an effect of this type is entirely absent.

Therefore, it seems that there is some justification for interpreting these measurements as indicating that there is a small decrease in the average field across an oxide film during formation as the film thickness increases. If it is assumed that the space charge density is uniform, it can be shown that a density of 10^{16} electron charges/cm^3 would result in a change of the average field in the film by 1%. It may be that a slightly higher field is required near one of the interfaces of the film to make the rates of ion transport in the film and at the interface equal. Because the effect is so small, however, it appears about equally justifiable to say that the field is essentially constant and that the small apparent decrease is the result of a change of effective area with film thickness or some other similar effect.

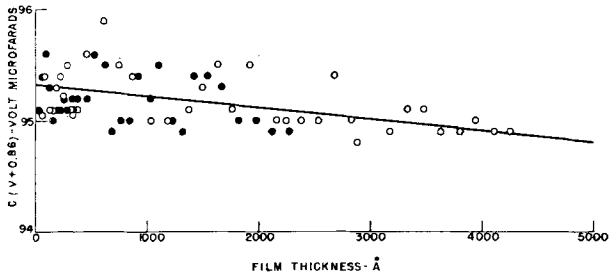

Fig. 1. Plot of C(V + k) vs. film thickness for a specimen formed at 19°C. Closed circles represent the first run to about 150 v. All but about 100Å of the oxide film was then dissolved in HF and the second run (open circles) was made.

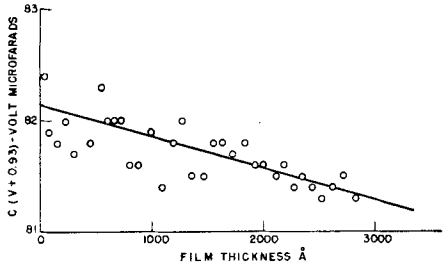

Fig. 2. Plot of C(V + k) vs. film thickness for a specimen formed at 86°C.

Manuscript received March 23, 1956.
Any discussion of this paper will appear in a Discussion Section to be published in the December 1957 Journal.

REFERENCES

1. J. F. Dewald, *This Journal*, **102**, 1 (1955).
2. N. Cabrera and N. F. Mott, *Rep. Prog. Phys.*, **12**, 163 (1948-1949).
3. D. A. Vermilyea, *This Journal*, **102**, 655 (1955).
4. L. Young, *Trans. Faraday Soc.*, **51**, 1250 (1955).
5. D. A. Vermilyea, *This Journal*, **101**, 189 (1954).

Low-Pressure Solubility and Diffusion of Hydrogen in Zirconium

M. W. Mallett and W. M. Albrecht

Battelle Memorial Institute, Columbus, Ohio

ABSTRACT

Low-pressure solubilities were determined for H in α- and β-Zr and in two Zr-O alloys at 700°-1000°C and pressures of 0.1–4 μ Hg. The data followed Sieverts' law for each phase, and H solubility decreased with increasing temperature at a given pressure. Also, there was a slight increase in H solubility in α-Zr with increasing oxygen content. Diffusion coefficients for H in α-Zr were obtained in the range 300°–600°C by analysis of prepared concentration gradients. In the range 600°–800°C, degassing coefficients were determined from rate of H evolution from Zr cylinders. Degassing coefficients were much lower than expected from diffusion theory, and it was concluded that the degassing was not a pure diffusion phenomenon. Terminal solubilities obtained from the gradient analysis were in good agreement with those found by previous investigators.

It has been established that the presence of H has a deleterious effect on the mechanical properties of Zr, particularly those related to impact, creep, and fatigue (1–3).

H concentrations as low as 10 ppm can embrittle the metal, depending on previous heat treatment. Because arc-melted sponge Zr normally contains 25–100 ppm H, it must be vacuum annealed to 10 ppm or less H to eliminate brittleness.

Knowledge of optimum conditions for removal of H from Zr is commercially important. Therefore, determinations were made of low-pressure equilibrium solubilities and the diffusion coefficients of H in Zr. The resulting data indicate the effects of time, temperature, degree of vacuum, and section thickness on degassing of Zr.

Literature.—Early work (4) showed an abrupt change in H solubility at the allotropic transition of Zr. Later, a thorough investigation was made of the Zr-H system at pressures of 1–760 mm Hg from room temperature to 1050°C (5). Extrapolation of the data to low pressures, along with other solubilities calculated from diffusion studies in the range 400°–500°C, were reported in a discussion of the properties of Zr-H alloys (1). Gulbransen and Andrew (6) studied rather extensively the equilibrium and terminal solubilities of H in α-Zr in the range 425°–600°C at pressures of about 0.001–0.1 mm Hg. More recently Edwards, Levesque, and Cubicciotti (7) determined the solid-solution equilibria in the Zr-H system and presented a partial phase diagram of the system. H solubilities were determined at H pressures of 1–760 mm Hg in the range 600°–900°C. A phase diagram based on results of high temperature x-ray diffraction studies and solubilities established by Schwartz and Mallett (1) was published by Vaughan and Bridge (8).

Several investigators have given theoretical interpretations of the solubility of H in Zr. Martin and Rees (9) applied a statistical-mechanical theory of two-component interstitial solid solutions. They also accounted for the saturation (terminal) solubility of H in Zr-O solutions by observing that apparently oxygen atoms in solution at octahedral sites block neighboring tetrahedral sites normally available to H atoms. A similar explanation was suggested earlier (10). This would explain the decrease in H solubility with increase in oxygen content.

Considerable experimental data on the solid solution equilibria in the Zr-O-H system were reported by Edwards and Levesque (11). Their work was carried out in the range 600°–900°C at H pressures of 1–760 mm Hg.

Very little work has been reported on the diffusion of H in Zr. Schwartz and Mallett (1) determined diffusion coefficients at 400°, 500°, and 600°C. Gulbransen and Andrew (12), in investigating the mechanism of the reaction of pure H with Zr, determined diffusion coefficients for the diffusion of H and D through a hydride film. Their data cannot be compared with those of the present study since they were for a hydride phase rather than the metallic phase.

An important feature of all these investigations is that the Zr in each case contained 1 w/o or more of Hf. It is not known what effect the Hf may have had on the properties of the Zr-H system. Therefore, the present investigation was made with low-Hf (<0.02 w/o) Zr.

Experimental Work and Results

For the present study, the low-pressure solubility of H in Zr was determined in the range 700°–1000°C at pressures of 0.1–4 μ Hg. The effect of oxygen in solution on the H solubility at the low pressures was also investigated.

The rate of diffusion of H in Zr was studied in the range 300°–800°C.

Materials.—Zr used in this work was iodide metal, arc-melted, and cold rolled to $\frac{3}{8}$ in. and $\frac{3}{16}$ in. diameter rods. This material was analyzed by spectrographic, chemical, and vacuum-fusion techniques. Results are given in Table I.

Zr-O alloys were prepared from the above mentioned Zr stock by reacting known quantities of pure oxygen with the metal. The alloys were then double arc-melted and cold rolled to $\frac{3}{16}$ in. diameter rods. Alloys so prepared

TABLE I. *Analysis of arc-melted iodide Zr*

Element	Amount present, w/o
Fe	0.12
Cu	0.006
Al	0.005
Mg	0.005
Ca	0.003
Cr	0.003
Ni	0.002
Ti	0.002
Si	0.001
Hf	<0.02
Pb	<0.005
Mn	<0.001
N_2	0.003
O_2	0.032
H_2	0.0046

contained 0.14 and 0.43 w/o oxygen as determined by vacuum-fusion analysis.

Pure H for the study was obtained from thermal decomposition of uranium hydride. This hydride had been prepared by allowing dried commercial H to react with clean U turnings.

Low-pressure solubility of H *in* Zr—*Method.*—Studies of the low-pressure H solubility were made in an apparatus (13) consisting of three main sections: a pure H source, a heated specimen chamber, and a vacuum pumping system. H from the decomposition of uranium hydride was diffused into the apparatus through a Pd tube. The flow of H through the apparatus at the desired pressure level was controlled by proper manipulation of the temperatures of the uranium hydride and Pd tube. An ionization gauge was used for continual pressure indication. However, a McLeod gauge was used for periodic measuring of the absolute H pressure.

The H pressure in the apparatus could be regulated to any desired value in the range 0.1–4 μ Hg (range of this work) and maintained within $\pm$ 5% of that value for several hours.

The specimen chamber was heated with a wire-wound furnace. Temperatures were measured with a Pt-Pt + 10% Rh thermocouple in contact with the specimen. Temperatures of the specimens were controlled to $\pm$ 5°C.

Specimens, $\frac{1}{8}$ in. in diameter by $\frac{1}{2}$ in. long, were dry abraded with 240-grit SiC paper, washed in A. C. S. reagent grade acetone, and placed in the furnace tube of the apparatus.

All experiments were carried out for a period of 6 hr at constant temperature and pressure. The equilibrium solubility was obtained within this time, as shown by the fact that a few specimens heated for 12 hr did not show significantly different results. At the end of an experiment the furnace tube containing the specimen was quenched with cold water. The specimen was then analyzed for its H content by the vacuum-fusion method. Usually a duplicate specimen was prepared for metallographic examination to determine the structure of the metal under equilibrium solubility conditions.

Results and discussion.—Solubility limits were determined for H in massive Zr, and Zr-O alloys from 700° to 1000°C at 50°C intervals, and at pressures of 0.1-4 μ Hg. These solubility data are given in Table II. For the iodide Zr H solubility was determined in the α-phase at 700°–800°C and in the β-phase at 850°C–1000°C. In both phases H solubility decreased with increasing temperature for a given pressure. This was also the case for the Zr-O alloys. For the Zr + 0.14 w/o oxygen alloy, the solubility was determined in the α-phase at 700°–800°C, and in the β-phase at 900°–1000°C. At 850°C the alloy had an α-β structure. The Zr + 0.43 w/o oxygen was investigated in the α range 700°–850°C. Above 850°C the alloy had an α-β structure, and no reliable solubility measurements could be made. Even after this alloy had been heated for 12 hr in an effort to reach equilibrium, results were very erratic. Metallographic examination of these specimens indicated that a β-to-α transformation was occurring during equilibration. Apparently very long times in this temperature range would be necessary to reach equilibrium.

All solubility data for iodide Zr and Zr-O alloys follow Sieverts' Law, which states that the solubility of a diatomic gas in a metal is proportional to the square root of the gas pressure: $S = k \cdot p^{\frac{1}{2}}$. In this equation k is Sieverts' constant with units of $S/p^{\frac{1}{2}}$, S is H solubility in ppm H by weight, and p is pressure in microns of Hg. Fig. 1 and 2 show H solubility plotted against pressure according to Sieverts' Law, for α and β iodide Zr, respectively. All plots are drawn through the origin since there is no solubility at zero H pressure. Slopes of these lines are the Sieverts constants at the various temperatures. Similar plots (not shown) can be drawn for Zr-0.14 w/o oxygen and Zr-0.43 w/o oxygen alloys.

For an exothermic solution of H in metals, solubility can be related to pressure and absolute temperature by the general equation, $\log S/p^{\frac{1}{2}} = A/T + B$, where $S/p^{\frac{1}{2}}$ is Sieverts' constant, T is the absolute temperature, and A and B are constants. Plots of Sieverts' constant against reciprocal temperature for iodide Zr and the Zr-O alloys are given in Fig. 3. It is seen that at a given temperature and pressure, H solubility in α-Zr increases with oxygen content. This is evident because the Sieverts' constant, $S/p^{\frac{1}{2}}$ increases in a similar manner. Apparently, the oxygen in solution expands the α-Zr lattice to make more interstitial sites available for H. However, this is true only at low H pressures, since it has been shown (5, 14)

TABLE II. *Solubility of H in Zr and Zr-O alloys*

Material	Pressure, μ Hg	H solubility at temperature indicated, ppm						
		700°C	750°C	800°C	850°C	900°C	950°C	1000°C
Iodide Zr	0.10	—	—	—	—	5.0	—	—
(0.03 w/o	0.15	—	—	5.2	6.8	6.1	—	—
oxygen)	0.50	13	—	10	—	13	—	12
	1.0	—	—	13	—	18	—	—
	1.5	25	21	—	23	—	—	—
	2.0	—	—	19	—	26	—	24
	4.0	40	32	27	38	34	—	33
Zr + 0.14	0.50	16	12	10	—	11	8.9	6.7
w/o oxy-	1.5	26	21	17	21	18	16	12
gen	4.0	42	31	29	33	31	24	20
Zr + 0.43	0.50	18	13	9.3	8.0	—	—	—
w/o oxy-	1.5	30	22	18	14	—	—	—
gen	4.0	46	36	30	24	—	—	—

that terminal H solubility in the α-phase decreases with increasing oxygen content. Here the total number of interstitial sites available for H is decreased by the addition of oxygen.

Equations for the best straight lines through the points in Fig. 3 were determined by the method of least squares. Values of the constants A and B in the above equation are given in Table III. Heats of solution for H in Zr and Zr-O alloys are also given in Table III. It is seen that the heat of solution increases with increasing oxygen content. For each increase of 0.1 w/o in the oxygen content of α-Zr the heat of solution of H increases by about 500 cal/g-atom. This indicates that there is some interaction between the oxygen and H atoms within the Zr lattice in the concentration range of this work. At higher concentrations of both oxygen and H, Edwards and Levesque (11) found that the heat of solution did not change with oxygen concentration.

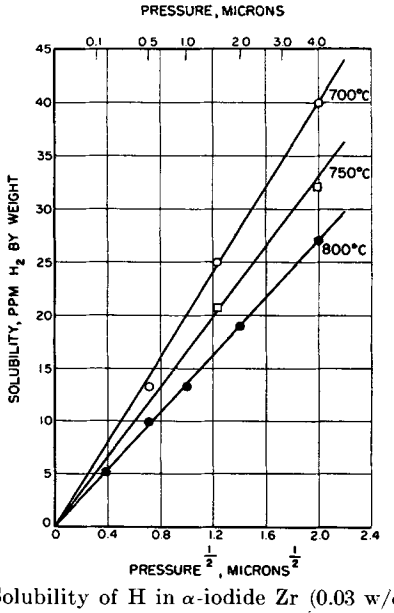

FIG. 1. Solubility of H in α-iodide Zr (0.03 w/o oxygen)

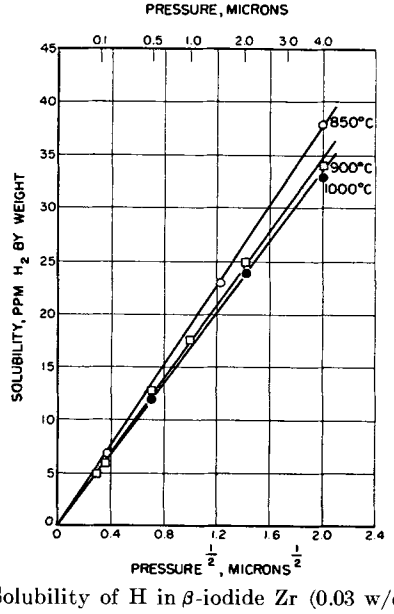

FIG. 2. Solubility of H in β-iodide Zr (0.03 w/o oxygen)

Diffusion of H *in* Zr—*Method.*—The technique used to determine diffusion of H in Zr has been described in the literature (14, 15). Essentially, the method consists of analyzing a H concentration gradient produced in a Zr cylinder by reaction for a predetermined length of time. For this work, Zr cylinders about $\frac{1}{2}$ in. in diameter and $1\frac{1}{2}$ in. long were degassed in a vacuum for 20 hr at 900°C. After this treatment, the residual H content in the metal was 2–3 ppm H by weight. A degassed cylinder was then dry abraded with 240-grit SiC paper. After physical measurements of the specimen were taken, a beaded junction of a Pt-Pt 10% Rh thermocouple was spot welded to one end of the Zr cylinder. The cylinder was then placed in the reaction tube of a modified Sieverts apparatus and heated with a resistance-wound furnace at 800°C for 1 hr in a vacuum of the order of 1×10^{-5} mm Hg. This heat treatment dissolved any superficial oxygen into the metal, leaving a clean active surface. The temperature was then lowered to the temperature of the run and maintained within $\pm$ 5°C of the desired value for the entire experiment. Pure H was then added to the reaction tube at about $\frac{1}{2}$ atm of pressure. At this pressure a thin hydride film could be maintained on the surface. At higher pressures the rate of surface reaction was so rapid that a very thick hydride film was formed.

A specimen was heated in H for a predetermined length of time to prepare a suitable H concentration gradient. At the end of the experiment the furnace was removed and the furnace tube containing the specimen was immediately quenched with a cold water bath.

Lengths equal to the radius of the cylindrical specimen were cut from the ends and discarded. The rest of the sample was machined radially into layers of equal weight. These layers were then analyzed for their H content by the vacuum-fusion method. The outer layers containing the hydride film and β-phase were thin enough to be ignored in calculations (14) of the rate of diffusion. Only the remaining inner layers, containing H that had diffused in the α-phase, were considered. Diffusion coefficients

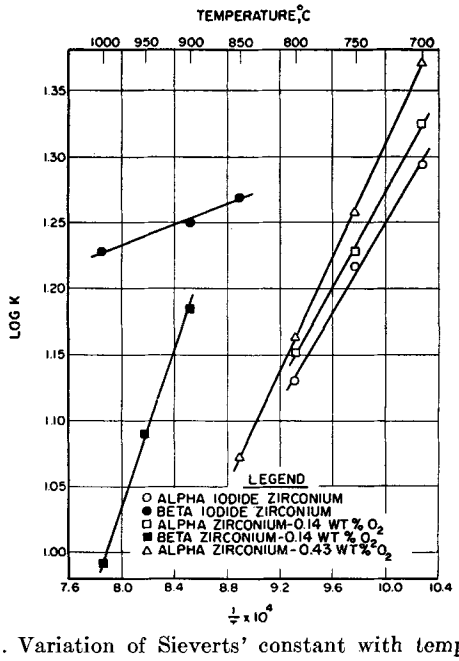

FIG. 3. Variation of Sieverts' constant with temperature

TABLE 3. *Summary of the constants in the equation log* $S_{ppm}/(p_{micron})^{\frac{1}{2}} = A/T + B$

Material	α-Phase			β-Phase		
	A	*B*	H, cal/g-atom	*A*	*B*	H, cal/g-atom
Iodide Zr	1710	0.463	−7830 ± 400	390	0.921	−1780 ± 130
Zr − 0.14 w/o oxygen	1820	0.545	−8320 ± 270	2960	1.33	−13,540 ± 480
Zr − 0.43 w/o oxygen	2170	0.858	−9920 ± 90	—	—	—

TABLE IV. *Diffusion coefficients for H in α-Zr (gradient technique)*

Time, min	Temp, °C	C_0,* ppm	$D \times 10^6$ cm²/sec
75	305	86	1.7
50	350	140	2.0
35	410	270	3.7
13	446	340	5.2
10	486	530	6.9
10	567	470	9.7
6	610	430	13

* C_0, terminal solubility.

TABLE V. *Degassing coefficients of H in α-Zr*

Temp, °C	$D \times 10^6$ cm²/sec
635	2.9
690	7.4
717	9.8
745	10
780	21

were determined by the graphical method (14) using the average H concentrations of each layer, the average radii of the layers, and the time of diffusion.

An alternative method based on degassing rates (16) was used to determine rates of diffusion in iodide Zr. The technique and apparatus were the same as those described previously (13). The rate of H evolution from $\frac{3}{8}$ in. diameter Zr cylinders initially containing 46 ppm H by weight was measured. The diffusion (degassing) coefficient was calculated from the rates of evolution of H into a vacuum of 10^{-5}–10^{-6} mm Hg at various temperatures.

Results and discussion.—The diffusion of H in α-Zr was investigated in the range 305°–610°C by the gradient technique. The diffusion coefficients that were obtained are given in Table IV. Values of C_0 are also given. As defined previously (14), C_0 is the saturation concentration maintained at the surface of the α diffusion layer during preparation of the gradient. At higher temperatures, data were not obtained because of the rapidity of diffusion. The time needed to quench the specimen adequately was too long for preparation of a suitable diffusion gradient (which takes less than 5 min). At temperatures below 300°C, prepared gradients showed erratic behavior and could not be fitted to the diffusion theory.

Table V gives the degassing coefficients obtained in the range 635°–780°C. No data could be obtained at lower temperatures since very little or no H was evolved from a specimen. At higher temperatures, above 780°C, diffusion was too rapid to permit use of the degassing technique.

Variation of the diffusion coefficient with temperature

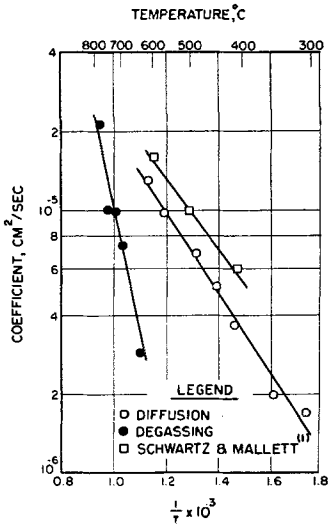

FIG. 4. Temperature variation of diffusion and degassing coefficients for H in Zr.

can be evaluated by the equation, $D = D_0 \exp(-Q/RT)$. Fig. 4 is a plot of logarithms of the diffusion coefficient against reciprocal temperature for the data obtained by the gradient technique. Results are compared with the coefficients reported by Schwartz and Mallett (1).

Degassing coefficients are also plotted in Fig. 4. It is seen that the gradient and degassing data give separate curves having quite different slopes. This indicates that the two sets of data represent different rate-controlling processes. Although the experimental temperature ranges do not overlap, the metal is single-phase α-Zr throughout. Therefore, if the controlling processes were diffusion in the metal (true diffusion mechanism), both sets of data should have the same slope and form a continuous curve for all temperatures.

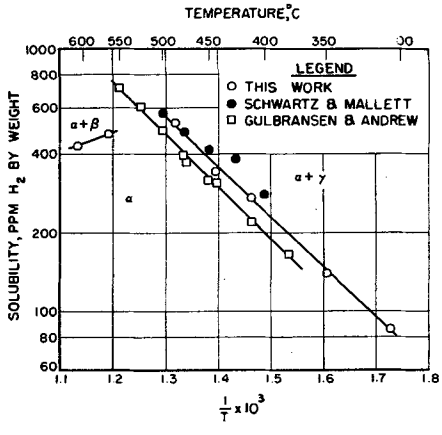

FIG. 5. Temperature variation of terminal solubility of H in α-Zr.

It is believed that the gradient method, which is based on direct analysis, gives the more nearly true diffusion coefficient. In the degassing technique, it is quite possible that surface effects are important in the determination of degassing rates. The rate of desorption of H from the metal surface may be the controlling process and not diffusion in the metal. Some such surface effect is evidenced by the fact that little or no H could be evolved from a Zr cylinder below 630°C at about 10^{-5} mm Hg, while it is known that H can diffuse in the metal at lower temperatures, as shown by the gradient method. It is evident that one should be wary of considering degassing as a pure diffusion phenomenon. Studies of the diffusion of H in Fe summarized by Johnson and Hill (17) showed in that case the controlling step in degassing to be a function of diameter. Degassing of cylinders with diameters less than $\frac{3}{8}$ in. was dependent on processes occurring at the surface, while for larger diameters the degassing rate was dependent on a true diffusion process. For the present work with Zr, the effect of specimen dimensions on the degassing rate was not determined.

In Fig. 4, equations for the best straight lines through the various sets of points were determined by the method of least squares. The experimental energy of activation for diffusion in the range 305°–610°C is 7060 ± 260 cal/mole, and the diffusion coefficient in cm²/sec is $7.00 \times 10^{-4} \exp -7060/RT$. This is in fair agreement with the 5700 cal/mole calculated from the work of Schwartz and Mallett (1), whose studies were made with high-Hf Zr. The experimental energy of activation for the degassing of Zr in the range 635°–780°C is 22,000 ± 3,000 cal/mole, and the degassing coefficient in cm²/sec is 0.59 exp $-22{,}000/RT$.

Terminal solubility of H *in* α-Zr.—In previous studies (1, 14) it was pointed out that the terminal solubility (solubility limit) of H in α-Zr is the concentration in the α-phase at the α-β interface. Therefore, the calculated values of C_0 obtained in the gradient study are the approximate terminal solubilities of H in α-Zr. These values are given in Table IV and plotted along with data of other investigators in Fig. 5. At the lower temperatures (300°–500°C) there appears to be good agreement between the present work and that of Schwartz and Mallett, who also obtained solubilities from diffusion studies. Less close agreement was obtained with the data of Gulbransen and Andrew (6), who used Sieverts plots and pressure-temperature plots to determine the terminal solubilities. Solubilities at the lower temperatures represent the boundary between α and α + γ phases in the Zr-H system (8).

It is also seen in Fig. 5 that at higher temperatures (571° and 610°C) the solubility decreases with increasing temperature. These terminal solubilities represent the boundary between the α- and the α + β-phases. However, these limited data do not permit prediction of the temperature of the isotherm where the α, β, and γ phases are in equilibrium. Vaughan and Bridge (8) show this temperature to be 560° ± 10°C.

The best equation expressing variation of terminal solubility with temperature in the range 305°–486°C is

$$\log C_0 \text{ (ppm } H_2 \text{ by weight)} = -1880/T + 5.18$$

The heat of solution for H in α-Zr obtained from this equation is 8600 ± 200 cal/g-atom. This is in very good agreement with the 8616 cal/g-atom obtained by Gulbransen and Andrew.

ACKNOWLEDGMENTS

This work was performed under AEC Contract W-7405-eng-92. The authors gratefully acknowledge the assistance of Mr. B. G. Koehl in making the experimental diffusion gradients. Special thanks are given to Mr. W. R. Hansen for obtaining the experimental degassing data.

Manuscript received April 2, 1956.
Any discussion of this paper will appear in a Discussion Section to be published in the December 1957 JOURNAL.

REFERENCES

1. C. M. SCHWARTZ AND M. W. MALLETT, *Trans. Am. Soc. Metals*, **41**, 306 (1945).
2. W. L. MUDGE, JR. in "Zirconium and Zirconium Alloys", p. 146, American Society for Metals, Cleveland (1953).
3. A. D. SCHWOPE, *ibid.*, 292.
4. J. H. DEBOER AND J. D. FAST, *Rec. trav. chim.*, **55**, 350 (1936).
5. M. N. A. HALL, S. L. H. MARTIN, AND A. L. G. REES, *Trans. Faraday Soc.*, **41**, 306 (1945).
6. E. A. GULBRANSEN AND K. F. ANDREW, *Trans. Am. Inst. Mining Met. Engrs.*, **203**, 136 (1955).
7. R. K. EDWARDS, P. LEVESQUE, AND D. CUBICCIOTTI, *J. Am. Chem. Soc.*, **77**, 1307 (1955).
8. D. A. VAUGHAN AND J. R. BRIDGE, *Trans. Am. Inst. Mining Met. Engrs.*, **206**, 528 (1956).
9. S. L. H. MARTIN AND A. L. G. REES, *Trans. Faraday Soc.*, **50**, 343 (1954).
10. C. F. BEVINGTON, S. L. MARTIN, AND D. H. MATHEWS, *Proc. Intern. Congr. Pure and Appl. Chem. 11th Congr. London 1947*, **1**, 3 (1950).
11. R. K. EDWARDS AND P. LEVESQUE, *J. Am. Chem. Soc.*, **77**, 1312 (1955).
12. E. A. GULBRANSEN AND K. F. ANDREW, *This Journal*, **101**, 560 (1954).
13. C. B. GRIFFITH AND M. W. MALLETT in "Vacuum Metallurgy", p. 147, The Electrochemical Society, Inc., New York (1955).
14. M. W. MALLETT, E. M. BARRODY, H. R. NELSON, AND C. A. PAPP, *This Journal*, **100**, 103 (1953).
15. M. W. MALLETT, J. BELLE, AND B. B. CLELAND, *ibid.*, **101**, 1 (1954).
16. A. DEMAREZ, A. G. HOCK, AND F. A. MEUNIER, *Acta Metallurgica*, **2** (2), 214 (1954).
17. E. W. JOHNSON AND M. L. HILL, *ibid.*, **3**, 99 (1955).

Mechanisms of Aqueous Corrosion of Aluminum at 100°C

K. M. CARLSEN[1]

Joint Establishment for Nuclear Energy Research, Lillestrøm, Norway

ABSTRACT

Various alloys of Al, as well as superpurity Al material, have been tested in aqueous solutions at 100°C. Samples have been polarized cathodically and anodically to study the effect of cathodic and anodic reactions, respectively, on the corrosion behavior. Results are interpreted as showing that the alkalinity produced at the cathodes facilitates film breakdown in these places. Consequently, alloys containing cathodic constituents were attacked where these constituents were situated, while polycrystalline superpurity material was attacked in the grain boundaries. The influence of bulk *p*H and inhibitors is discussed in some detail.

There is general agreement (1–3) that at higher temperatures the aqueous corrosion resistance of Al is smaller the greater the purity. Draley and Ruther (2) have drawn attention to the importance of providing cathodic sites, and in this way greatly clarified the difference in behavior between pure and impure material.

As for the influence of the composition of the aqueous phase, it is known that additions of H_2SO_4 and certain inhibitors produce beneficial effects, but it is not known for certain exactly how these additions influence corrosion behavior. However, it is clear that the idea of H_2– as the chief offender is not sufficient to explain all the observations satisfactorily.

Thus, there seems to be a need for a closer study of the corrosion mechanisms of various grades of materials in liquids of varying compositions, and it was with this in mind that the present investigation was started. Since the difference between pure and impure material is very pronounced at 100°C (4), it was hoped that results obtained at this temperature could be used to predict the behavior at higher temperatures.

There are obvious advantages in working at 100°C; no autoclaves are necessary, and corrosion reactions are so slow that they can be studied in detail by means of the microscope.

EXPERIMENTAL

The materials used were sheet of superpurity Al (99.99% purity, from British Aluminium, Ltd.) and Al alloys. Alloys were made from ingots of 99.99% purity Al (supplied by A/S Vigelands Brug), and high conductivity Cu, electrolytic Ni (99.98%), electrolytic Fe (British Drug House), and silicon powder (99.5% purity, from A/S Bjölvefossen), respectively. The alloys had the following compositions: 1.04% Ni, balance Al; 1.95% Cu, balance Al; 0.93% Fe, balance Al; 1.02% Si, balance Al, hereafter referred to as Al—1% Ni, Al—2% Cu, Al—1% Fe, Al—1% Si alloys, respectively.

Alloys were cast in graphite moulds and rolled to a thickness of approximately 1 mm. All test samples were given an anneal at 450°C for 1 hr and allowed to cool in the furnace, except in cases where cold-worked material was desired.

Some single crystals of superpurity Al were kindly supplied by R. W. K. Honeycombe, University of Sheffield.

All samples were carefully electropolished in a bath containing 100 ml perchloric acid (sp gr 1.54) and 900 ml ethyl alcohol.

In tests at 100°C, samples were suspended in Pyrex flasks fitted with reflux condensers. In some cases the samples were externally polarized making them anode and cathode, respectively, by means of a d-c potential, keeping the current density constant during the experiment.

After exposure, the samples were examined by means of a metallographic microscope.

RESULTS

Superpurity Metal

On polycrystalline material immersed in distilled water at 100°C there develops during the first hours a pattern of spots, together with a delineation of grain boundaries. Fig. 1 and 2 show two samples during the first stages of development. After the pattern has formed, the matrix corrosion apparently slows down, while the attack on the grain boundaries continues (Fig. 3 and 4). After periods as long as 130 hr the grain boundary attack seems to fall off somewhat, while a blurring of the pattern suggests that the matrix has started corroding in a more uniform way.

These observations at 100°C are in agreement with those of other workers obtained at higher temperatures, as far as the grain boundary attack is concerned.

At temperatures as high as 230°C, single crystals of high-purity material are attacked very seriously, showing that grain boundary attack is not necessary for disintegration to occur.

Some samples were deformed to see if slip lines were preferentially attacked, but this was not found to be the case.

When polycrystalline material is cathodically polarized at a current density of approximately 0.1 ma/cm², grain boundaries are preferentially attacked as shown in Fig. 5. Besides a pattern of lines is found, nearly all of them joining each other at an angle of 90°. Because of this angular relationship, it is believed that they result from the relief of two-dimensional stresses.

[1] Present address: Pigments Dept., E. I. du Pont de Nemours & Co., Wilmington, Del.

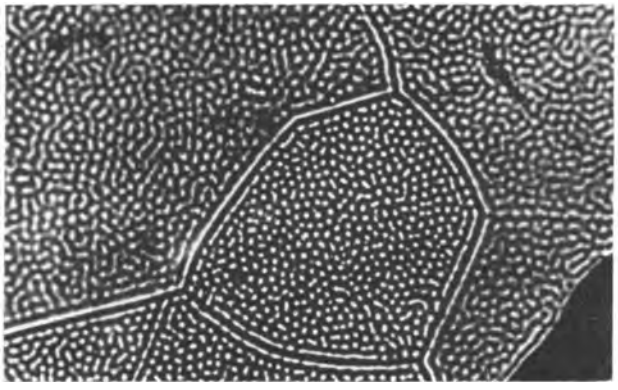

FIG. 1. Superpurity sample 3 hr at 100°C in distilled H_2O. 405×.

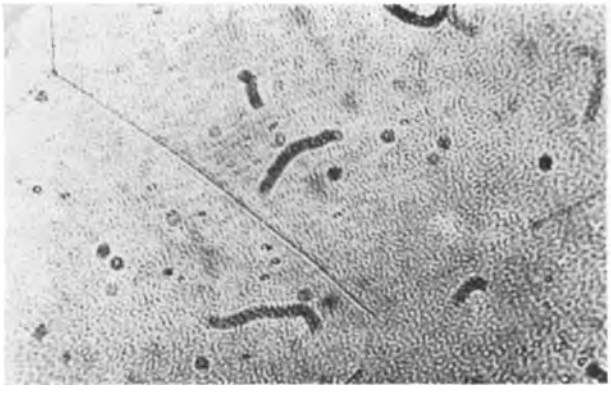

FIG. 2. Superpurity sample 10 min at 100°C in distilled H_2O. 765×.

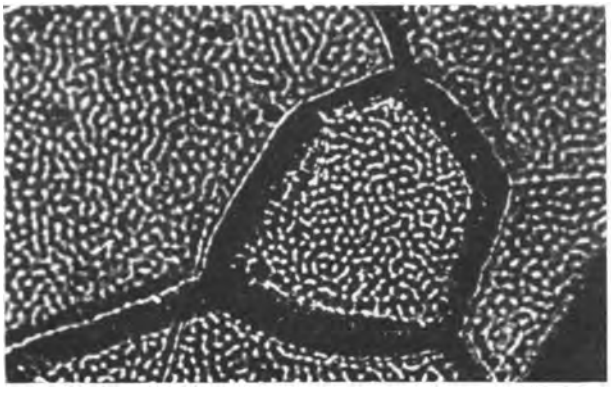

FIG. 3. Same sample as Fig. 1, but after 68½ hr at 100°C in distilled H_2O. 405×.

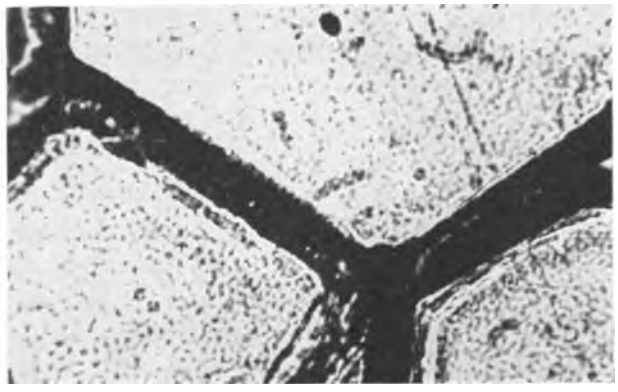

FIG. 4. Same sample as Fig. 2, but after 48½ hr at 100°C in distilled H_2O. 765×.

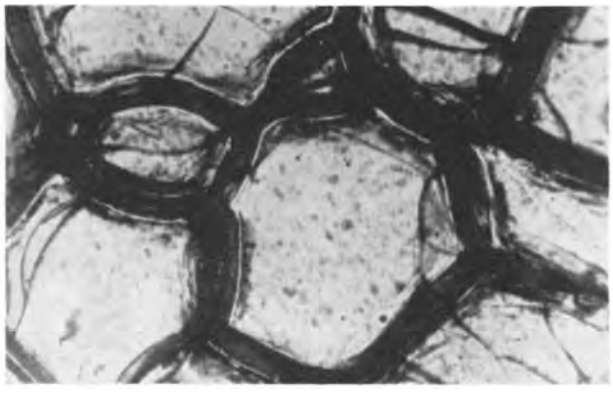

FIG. 5. Superpurity material, cathode for 48 hr at 100°C in distilled H_2O. 135×.

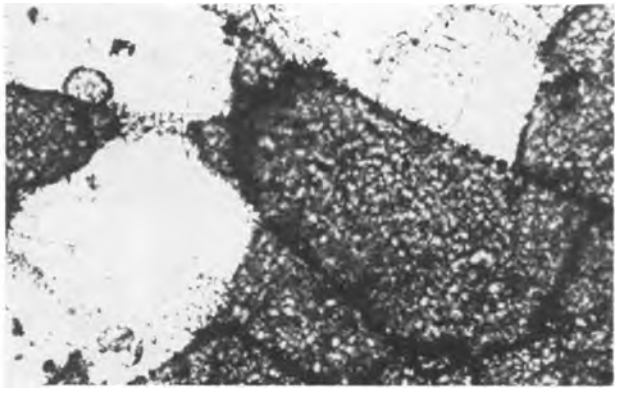

FIG. 6. Single-crystal superpurity material cathodically polarized in H_2O at 100°C. 135×.

When a single crystal was polarized cathodically at a current density of 0.16 ma/cm², much the same pattern of lines was found again. After 24 hr, a fairly thick layer of corrosion products had formed, but this layer was not adherent, and could be brushed off without difficulty. Fig. 6 shows the surface where part of the oxide layer has been removed, and part of it remains, showing up as dark bits. The layer is fragmented by lines very similar to the cracks found on ceramic objects. A notable feature was that the attack on the cathode was orientation dependent, being stronger on two of the crystal faces than on the remaining two faces (the single crystal was in shape of a square rod).

Polycrystals and single crystals show identical behavior when anodically polarized at 0.16 ma/cm²; in both cases pits, or rather heaps of oxide covering the pits, develop (Fig. 7). With time the number of pits increases somewhat; they also grow in size. Although the corrosion products obviously do not protect completely the underlying metal, as shown by the continued growth of the heaps, there is

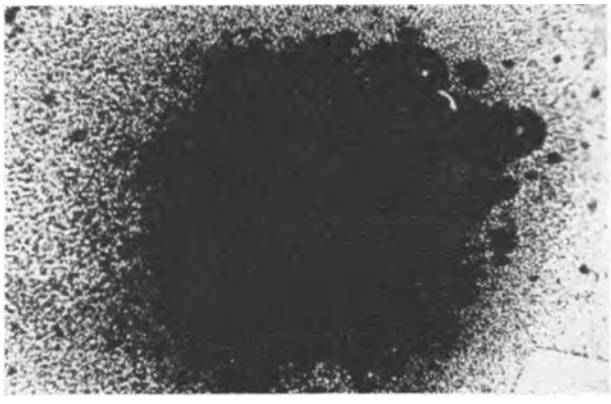

FIG. 7. Superpurity material, anode for 6 hr at 100°C in distilled H_2O. 285×.

some adherence to the metal, and they cannot be brushed off in the same way as are the cathodic corrosion products.

Alloy Materials

Rolled alloys with Ni and Fe additions show similar microstructures, viz., eutectics of $NiAl_3$ and Fe_2Al_7, respectively, with Al, embedded in a matrix of pure Al. The structure of an uncorroded Al-1% Ni sample is shown in Fig. 8. When such alloys are exposed to water at 100°C, the material in the eutectics is preferentially attacked both on cold worked and annealed specimens and the matrix is only very slightly attacked, as shown in Fig. 9. At 230°C, the eutectic regions are again attacked, but the matrix also starts to corrode in a more general manner; indeed, on some specimens the matrix seems to have suffered more attack than the eutectic regions. When Al-1% Ni samples were made cathodes at 0.1 ma/cm² they were severely attacked in the eutectic regions and anodic samples developed pittings.

The Al-Cu alloys show a microstructure different from that of Al-Ni and Al-Fe alloys. In the water-quenched condition no second phases can be seen; correspondingly, the attack on quenched specimen is fairly uniform to start with. At 100°C, the attack in the initial stages gives rise to beautiful interference colors when viewed in the microscope. After some time pits develop. These pits are not covered with corrosion products, nor does it seem that the

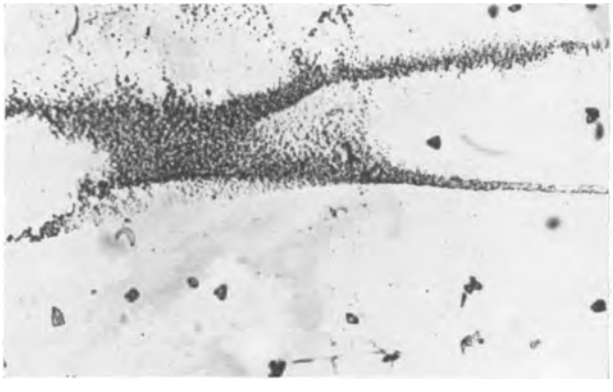

FIG. 8. Al-1% Ni-alloy, uncorroded. 285×

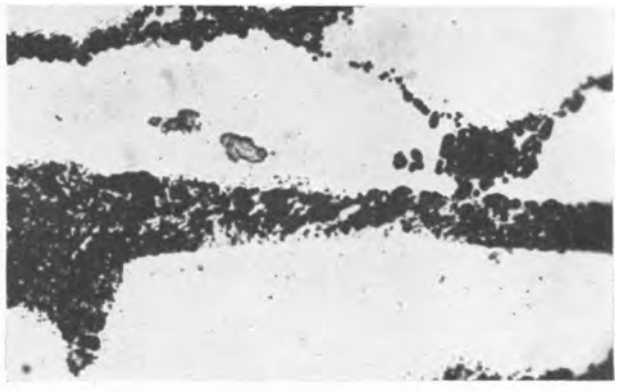

FIG. 9. Al-1% Ni-alloy, 21 hr in H_2O at 100°C. 285×

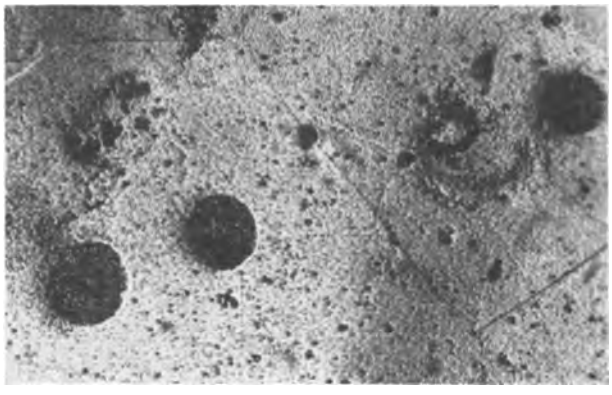

FIG. 10. Al-2% Cu-alloy (water-quenched) 45½ hr at 100°C in H_2O. 285×.

corrosion products have collected around the pits. Fig. 10 shows some big pits and numerous small ones. By using oblique light in the microscope one gets a very clear impression of the shape of the pits; unfortunately, it is difficult to get good photomicrographs with this type of illumination.

On specimens which had been furnace cooled (and consequently were overaged), pits developed very quickly. In addition an etching effect as shown in Fig. 11 was found,

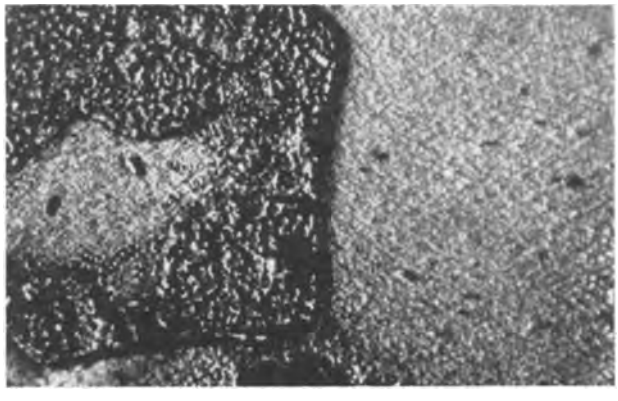

FIG. 11. Al-2% Cu-alloy (furnace-cooled) 21 hr at 100°C in H_2O. 765×.

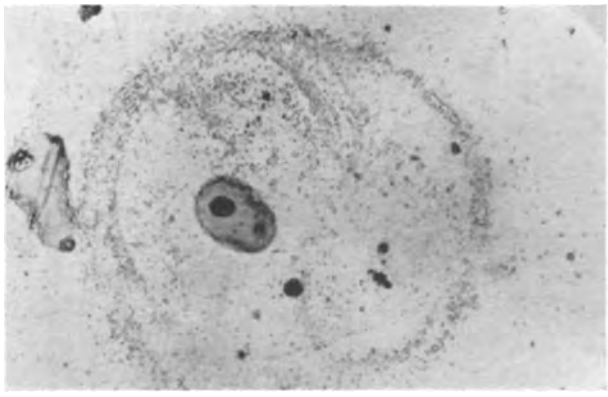

FIG. 12. Same sample as Fig. 10, 45½ hr at 100°C in H_2O. 285×.

where some regions were much more attacked than the neighboring matrix.

One might think that the development of pits was cathodically stimulated, because of precipitates acting as cathodes; this would serve to some extent as an explanation of the absence of corrosion products. Results on externally polarized specimens might seem to confirm this view. On the cathodic sample, the same type of pits are found as on unpolarized samples. Admittedly, such pits are also found on the anodically polarized sample, but here one finds in addition large pits covered with corrosion products, of the same shape as the pits found on anodic samples of pure material.

Fig. 12 shows a ring-like type of attack very frequently found on Al-Cu alloy samples (and occasionally on cast Al-Ni alloys). Sometimes the rings are not full, having the shape of a crescent.

At temperatures higher than 200°C, there is considerable aggregation of corrosion products on the surface, making it difficult to obtain a clear idea of the structural details of the attack.

When rolled Al-1% Si alloy samples are tested in overaged condition, the attack appears to be concentrated in the regions around the Si particles, although attack is also found elsewhere. The attack is probably of a type giving rise to very small pits, which at low magnifications gives the impression of a more or less general attack.

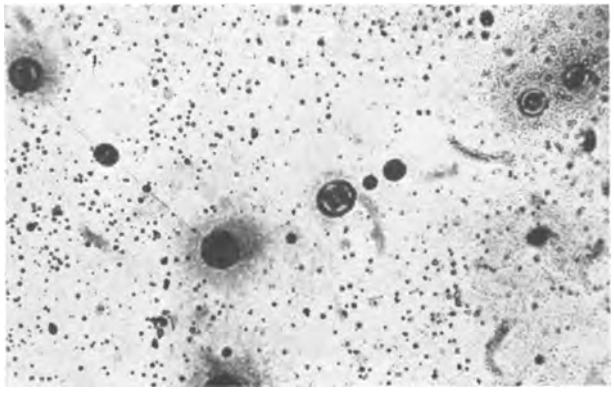

FIG. 13. Al-1% Si-alloy, 69 hr in H_2O at 100°C. 285×

In one case larger pits are observed, namely, after fairly long exposures of solution-treated and water-quenched specimens. Fig. 13 shows these pits, which are found on the grain boundaries and give an impression of grain boundary attack when viewed with the unaided eye. In some way these pits may be tied up with precipitation of Si in the grain boundaries. The structure of aged samples shows precipitate in the grain boundaries, with a denuded zone running along the boundaries.

When solution-treated and water-quenched specimens are cathodically polarized at a current density of approximately 0.16 ma/cm², the same type of intergranular attack is found as is observed on superpurity material. When furnace-cooled specimens are used the cathodic grain boundary attack is not so pronounced; instead, the matrix in the grains suffers corrosion.

Anodically polarized samples develop pits covered with corrosion products in the same manner as found for all the other materials.

Effect of Liquid Composition

As stated earlier, superpurity material suffers intergranular attack in distilled water at 100°C. When the *p*H is lowered to 4 by addition of H_2SO_4, this intergranular attack is suppressed to a great extent, while the matrix corrosion within the grains probably increases somewhat. Fig. 14 shows that the grains are attacked at different rates.

At *p*H 3, beautiful interference colors are produced in the grains, and grain boundary attack is slight.

At *p*H 2, there is considerable attack both in grain boundaries and in the grains. However, the grain boundary attack is of a type different from that met with in neutral water. Fig. 15 and 16 serve to emphasize the difference between the two types of grain boundary attack. It is believed that in the case of neutral water cathodic properties are responsible for the attack; anodic properties are responsible in the acid case.

Polarization experiments were carried out at various *p*H's and at a current density of 0.16 ma/cm². At *p*H 4, results on both cathodes and anodes are similar to results in distilled water, although the grain boundary attack on the cathode is less severe than in distilled water. At *p*H 3, the cathodic attack has not changed much, but on the

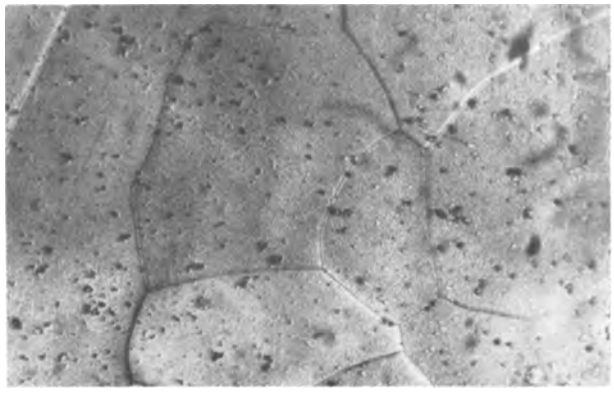

FIG. 14. Superpurity material, 48 hr at 100°C in H_2SO_4 solution with *p*H 4. 285×

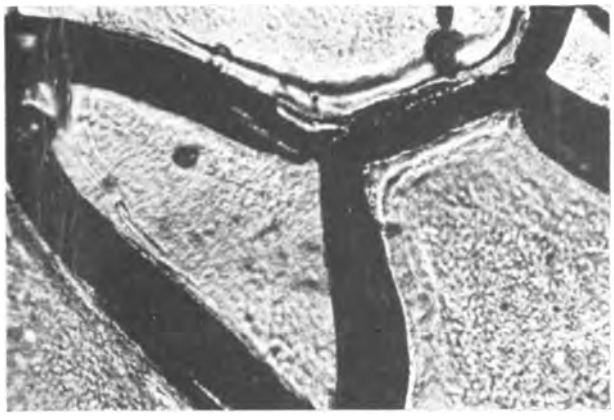

FIG. 15. Superpurity material 138 hr in H_2O at 100°C. 765×.

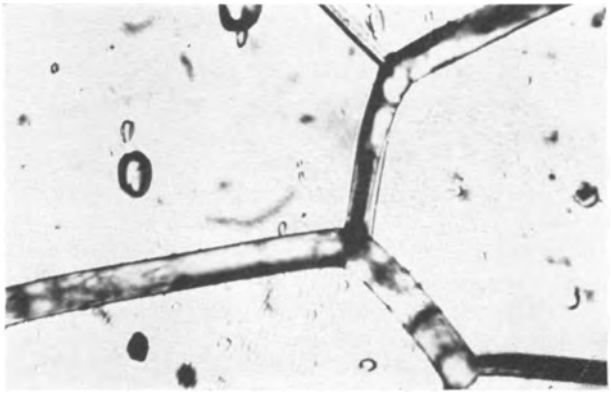

FIG. 16. Superpurity material 7 hr at 100°C in HCl solution with *p*H 2. 764×.

anode there are no longer pit-like breakdowns; instead interference colors can be seen in the microscope. At *p*H 2, there is general attack on both cathode and anode; no differences between the electrodes can be detected.

In NaOH solution (*p*H 10.7) the cathode is attacked apparently much more than the anode. When polarization experiments were carried out in 0.1% NaCl solution and in 1% Na_2SO_4 solution, respectively, grain boundary attack was observed on the cathodes, but to a smaller extent than in distilled water. On the anode in the sulfate-solution there was no breakdown of the type usually found on the anodes.

As reported elsewhere (3), it has been found that a 0.5% $K_2Cr_2O_7$ + 0.5% sodium silicate solution is a good inhibitor. Polarization experiments in this solution show quite strong general matrix attack on the cathode, but no attack whatsoever could be detected on the anode. Fig. 17 shows the cathode after 4 hr at 100°C; it is evident that the grains corrode at different rates. Microscopical examination at earlier stages show that attack starts in the form of numerous pits.

The same features are found in 1% $K_2Cr_2O_7$ solution, strongly indicating that the effects are due to the chromate.

Still another interesting effect was found in these solutions. As stated above, anodes from the solutions showed no attack, but when these anodes were exposed subsequently to boiling distilled water, strong general matrix attack similar to the cathodic attack was found, much stronger than and different from that found on samples which had not been treated anodically in advance.

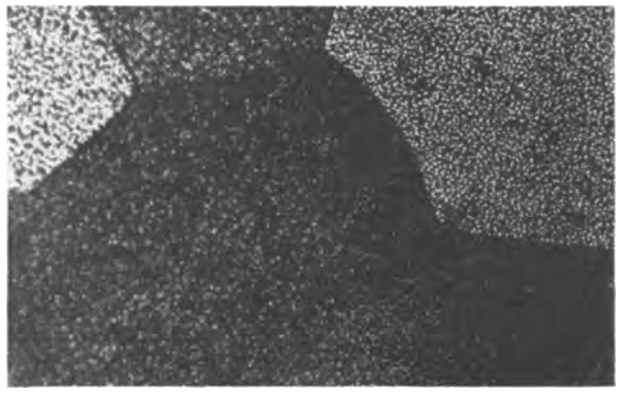

FIG. 17. Superpurity material, cathode for 4 hr in 0.5% $K_2Cr_2O_7$-0.5% sodium silicate solution. 285×.

When 1% $K_2Cr_2O_7$ solution is made acidic (*p*H 2.4) by adding H_2SO_4, both anodes and cathodes suffered very little attack. However, when the chromate solution is made alkaline (*p*H 10.5) by adding NaOH, the cathode suffers strong grain boundary attack, while the anode suffers general attack.

Results from experiments in a solution of CrO_3 (*p*H 1.1) were very similar to those from the acid $K_2Cr_2O_7$ solution.

Experiments in 1% sodium silicate solution with *p*H 10.8 show that the anode is protected to some extent by the silicate addition. Some parts of the anode were virtually unattacked after 20 hr at 100°C at a current density of 0.1 ma/cm². It is not quite certain that an attack on the cathode is similarly reduced; it is probably correct to say that the general rate of attack on the cathode is reduced, while the grain boundary attack is still very pronounced.

DISCUSSION

Role of Film Breakdown

Since it has been found that O_2 plays no significant role in high temperature corrosion, and since it has been reported from various sources (1, 2) that the corrosion product at high temperature is boohmite, the reaction can be written as

$$Al + 2H_2O \rightarrow AlO\cdot OH + \tfrac{3}{2} H_2$$

with the corresponding anodic and cathodic reactions

$$Al + 2H_2O \rightarrow AlO\cdot OH + 3H^+ + 3e \text{ and}$$

$$3H^+ + 3e \rightarrow \tfrac{3}{2}H_2$$

The experimental results quoted in the previous section nearly all have one thing in common; the attack is never uniformly and homogeneously distributed over the surface on a microscopical scale, nor, in most cases, on a macroscopical scale. Thus, in places where the attack is appreciable, corrosion has proceeded in some other way than by the continuous building up of a film. Let this attack be

called film breakdown, indicating that in some way or another the ordinary film growth has been interrupted.

In the previous section it was found that the film breakdown on cathodic samples differed from that on anodic ones. Let these phenomena be called cathodically stimulated breakdown and anodically stimulated breakdown, respectively.

Anodically stimulated breakdown.—The microscopical appearance is usually as seen in Fig. 7. On superpurity material it seems to have no relation to the grain boundaries, and experiments on single crystals indicate that crystal orientation does not have any effect on the occurrence of the breakdown. In the alloys containing Ni, Cu, or Fe, the breakdown seems to lie near the cathodic constituents, but this cannot be the only reason for breakdown, since the regions around the cathodic constituents are always attacked somewhat, without the attack developing into the large type of breakdown as exemplified by Fig. 7.

To some extent, the anodically stimulated breakdown can be looked on as caused by the inability of the solution to deliver ions for the building up of a protective oxide layer. In neutral solutions of tartaric and boric acid and in chromate solutions, such breakdowns are not observed, apparently because of the ability of these solutions to provide O^{--} ions for the formation of Al_2O_3 films, an explanation suggested by Huddle (5).

It is felt that pit formation cannot be explained satisfactorily without assuming that some autocatalytic process is involved. Edeleanu and Evans (10) and Huddle (5) point out that local acidity may be produced at the anode, and this acidity may, indeed, be the autocatalytic effect responsible for the pit formation.

Cathodically stimulated breakdown.—This type of attack occurs on samples which have been polarized cathodically in neutral solutions. On superpurity material it manifests itself as grain boundary attack, on Al alloys containing cathodic constituents as attack around these constituents, and as general attack on single crystals.

Having thus established that the attack is concentrated around the cathodes, one may look for an explanation of this behavior. One such explanation has been furnished by Draley and Ruther (2), who assume that the H produced is responsible for the stimulation of attack. A second explanation is that the increased OH^- concentration resulting from the removal of protons is the responsible factor, as suggested by a number of investigators, e.g., Groot (11).

It is believed that (*a*) the cathodic attack on single crystals, (*b*) the shape of attacked grain boundaries in polycrystalline pure material, (*c*) the fact that cathodic attack is reduced by lowering the *p*H, and (*d*) the attack around the cathodic constituents in Al alloys, all point away from H as the main factor in causing the cathodically stimulated attack observed in these experiments.

It is assumed, therefore, that the factor responsible for the attack is the increased concentration of OH^- in the immediate vicinity of the cathodes. The detrimental effect of OH^- ions on the corrosion of Al is well known, and experiments show that deviations from neutrality on the alkaline side are far more serious for the corrosion resistance than deviations on the acid side.

When protons are removed at the cathode, more water molecules dissociate to keep the ionic product constant, resulting in a more alkaline solution. At the same time, there will be an excess of negatively charged ions in the liquid next to the cathode, and the field set up by these ions will attract positively charged ions from the rest of the liquid. It is seen that a stationary state is reached, with a field in the liquid just strong enough to produce a current of positive ions toward the cathode, equivalent to the removal of protons at the cathode. Everything being equal, it is expected that the higher the purity of the water, and, correspondingly, the lower the conductivity, the stronger will be the field needed to force the necessary number of positive ions toward the cathode. Since the field is set up by OH^- ions, this means that the higher the purity of the water, the higher the local OH^- concentration to be expected. This may explain in part the aggressiveness of distilled water relative to pure Al.

Disintegration of superpurity material.—As seen from the micrographs, there is great similarity between corrosion of unpolarized specimens and attack on cathodically polarized samples. No such similarity exists between the behavior of unpolarized and anodically polarized specimens. For this and other reasons, it is justifiable to assume that the rapid corrosion of superpurity material in high temperature water is due to cathodically stimulated attack.

In polycrystalline material, the disintegration starts at the grain boundaries which, as pointed out earlier, are sites for the cathodic reaction. As the attack penetrates into the metal in a notch-like fashion, the tip of the notch will be the cathode, producing alkalinity where it is most dangerous. Corrosion products have greater volume than the metal from which they are formed, and tend to break up the metal, as evidenced by the deformation of the metal along the grain boundaries, seen on the photographs. It is not known whether the primary factor in the penetration of attack is the action of OH^- ions at the tip of the notch or the expansive action of the corrosion products. The fact that single crystals also disintegrate would seem to be in favor of the first hypothesis.

Lavigne (7) has pointed out that there is some resemblance between grain boundary attack on superpurity material in acid and in distilled water. In the author's opinion this resemblance is purely superficial. In acid, the grain boundaries are very evenly attacked, the metal dissolving away to yield a smooth, possibly U-shaped groove, the reason for attack probably lying in the smaller anodic polarization of the boundaries as compared to the matrix. In distilled water, on the other hand, the metal is broken up by the corrosion products, and the relevant factors in this case are thought to be the cathodic properties of the grain boundaries, as discussed above.

*Effect of Bulk p*H

As is well known, Al hydrates are soluble both in acid and alkaline solutions. The mechanisms of the solution of Al hydrate in acid cannot be said to be understood fully, and the concept of a solubility product of $Al(OH)_3$ will un-

doubtedly be found unsatisfactory as a description of the phenomena taking place. However, since little is known about the matter, the solubility product is used as a starting point for this discussion.

Assuming ideal conditions, the concentration of OH^- enters the product in 3rd power, thus showing that small decreases in OH^- concentration appreciably increase the concentration of Al^{+++}. Also, the solubility in acid is not due to the presence of H_3O^+ but to the absence of OH^-. Thus, if one could conceive of an acid with a low *p*H, but in which the *p*OH could be kept at 7, a protective layer of Al hydrate should be formed, which would prevent corrosion. Such an acid is impossible of course, but when an acid solution is heated to higher temperatures, the result is in fact somewhat similar to this unrealistic acid. The *p*H remains practically constant, if the acid is a strongly dissociating one, while the *p*OH decreases with increasing temperature. Consequently for Al, an acid should be less dangerous from a corrosion point of view the higher the temperature, provided the solubility product of $Al(OH)_3$ remained constant as a function of temperature.

For solutions on the alkaline side, there would be no corresponding effect, except perhaps for solutions very close to neutrality.

In distilled water, the *p*OH decreases markedly with temperature, and this may bring about serious corrosion, since it is known from low temperature work that deviations from *p*H 7 on the alkaline side is much more dangerous than deviations on the acid side. The reason for this behavior is not quite clear. Apparently it is connected with the greater rate of dissolution of the hydroxide in alkalies than in acids: in other words, it is more a question of dissolution kinetics than of equilibrium solubilities.

Thus, with increasing temperature of exposure the range in which the Al hydrate is able to protect the metal is displaced toward more acid solutions. It has been found by Draley and Ruther (8) that the *p*H of minimum corrosion is displaced toward lower values as the temperature is increased.

Apart from the effect of increasing OH^- concentration as a function of temperature, it is possible that a low *p*H is desirable also for another reason, viz., because of the alkalinity produced in the cathodic reaction. Indeed, there is evidence that even at temperatures as low as 100°C, a low *p*H arrests the damaging intergranular attack on superpurity metal met with in distilled water. Although the general rate of corrosion may be greater when the solution is made acidic, the total damage may nevertheless be smaller because of its more uniform nature. It appears, for instance, that superpurity metal suffers less dangerous attack in HCl with *p*H 2 at 100°C than in distilled water.

There is strong evidence that the anion of the acid plays an important role in corrosion, for instance if the anion can act as a carrier for O^{--} ions, as suggested by Huddle (5), but it is also to be expected that the anion influences corrosion by determining the nucleation conditions near the surface.

Effect of Inhibitors

The compounds which inhibit corrosion are to some extent those which can be used for building up anodically oxide films on Al. The action of such anions as SO_4^{--} or CrO_4^{--} may very well be tied up with their ability to donate O^{--} ions to the oxide lattice, as suggested by Huddle (5).

It is found that chromate additions do not protect annealed superpurity Al at 230°C, and it is also found that, when Al is made cathodic in chromate solutions at 100°C, the metal is attacked. These facts seem to suggest that when chromate is present where the cathodic reaction takes place on the Al surface, no protection, in fact the opposite action, is found. Possibly this is connected with the difference in potential needed to liberate H from Al and cathodic impurities, respectively; when no cathodic impurities are present, the potential may be negative enough to reduce hexavalent Cr to trivalent, producing alkalinity as a result of liberation of four O^{--} ions. (The green color found on superpurity specimens which had disintegrated in chromate solutions indeed points to the presence of trivalent Cr.) This would mean then that, in order to act in a protective way, there must be present sufficient amounts of cathodic impurities with a low H overpotential to give a compromise potential which is relatively positive.

When the chromate solution is made acid, there is no attack on samples made cathodic by external polarization, indicating that OH^{--} ions produced may indeed be the factor responsible for the breakdown. It is not clear whether Cr ions as such are incorporated in the protective layer. In any case, the experiments mentioned above where chromate treated samples were found to corrode faster than nontreated samples would indicate that the chromate plays a more active role than merely being an oxygen donator.

Silicate as an inhibitor presumably acts in a way different from chromate. Work is being carried out at present to clarify the matter, and the results hitherto obtained suggest that SiO_2 is incorporated in the surface layer (9).

Effect of Alloying Additions

In the light both of the observations described above on the effect of cathodic polarization on corrosion of superpurity Al, and of the reported success of Al-Fe, Al-Ni, and Al-Cu alloys, there seems to be no doubt that these alloying elements protect the metal by providing sites for the cathodic reaction.

Silicon can to some extent increase the corrosion resistance of superpurity metal toward water. Most probably it does not act as a cathodic impurity, but its effect on corrosion cannot be said to be understood.

Acknowledgment

The author wishes to acknowledge with thanks the valuable help given by J. L. H. Grinn and T. O. Wulff in carrying out the experiments. The author would also like to thank Mr. Grinn for fruitful discussions.

Manuscript received March 20, 1956. This paper was prepared for delivery before the Cleveland Meeting, September 30 to October 4, 1956.

Any discussion of this paper will appear in a Discussion Section to be published in the December 1957 JOURNAL.

REFERENCES

1. R. A. U. Huddle and N. J. M. Wilkins, M/R 1669, Atomic Energy Research Establishment, Harwell, Berkshire, England.
2. J. E. Draley and W. E. Ruther, Geneva Conference on the Peaceful Uses of Atomic Energy, P/535. Vol. 9, p. 391 (1955).
3. K. Carlsen, *ibid.*, P/880, Vol. 9, p. 397 (1955).
4. J. M. Bryan, *J. Soc. Chem. Ind.*, **69**, 169 (1950).
5. R. A. U. Huddle, Geneva Conference on the Peaceful Uses of Atomic Energy, P/411, Vol. **9**, p. 403 (1955).
6. K. Carlsen, Unpublished work.
7. M. J. Lavigne, *Met. Prog.*, **64** (3), 84 (1953).
8. J. E. Draley and W. E. Ruther, ANL-5001, Argonne National Laboratory, Lemont, Illinois.
9. J. Markali, Unpublished work.
10. C. Edeleanu and U. R. Evans, *Trans. Faraday Soc.*, **47**, 1121 (1951).
11. C. Groot, HW-33881, Hanford Atomic Products Operation, General Electric Co., Richland, Wash. (1955).

Rates of Oxidation of Germanium

J. T. Law and P. S. Meigs

Bell Telephone Laboratories, Murray Hill, New Jersey

ABSTRACT

Oxidation rates of the (110), (111), and (100) faces of a Ge crystal have been measured between 450° and 700°C and at various oxygen pressures. For all three faces, oxidation rates were inversely dependent on oxygen pressure at and above 550°C, and no differences in behavior between faces were observed. At 500°C only the (110) face oxidized appreciably. A theory has been developed to explain the effect of oxygen pressure on the oxidation rate and calculated values found to be in fair agreement with experiment.

Recent measurements of the electrical properties of a Ge surface (1) have shown that the thickness of the oxide film present has a marked effect on the magnitude of these quantities. Therefore, it would be of interest to be able to change the film thickness in a controlled way. One way of doing this is to preoxidize at some elevated temperature.

The only previous measurements on the high temperature oxidation of Ge were reported by Bernstein and Cubicciotti (2) who investigated an abraded surface between 575° and 700°C. As the roughness factor for this type of surface is uncertain it seemed worthwhile to repeat the work using definite crystal faces of known area.

Here oxidation rates from 450° to 700°C on the (100), (110), and (111) faces were measured as a function of oxygen pressure.

Experimental

The two principal means of following oxidation rates are (*a*) pressure change in a closed system, and (*b*) weight change of the sample as determined with a microbalance. Since any loss of Ge due to evaporation of GeO would make weight measurements very difficult to interpret, the former was used.

A modified form of Campbell and Thomas's apparatus (3) was used. It is essentially a constant volume differential pressure system with the two halves connected through an oil manometer. The silica bulbs containing the sample and the blank were placed in a furnace whose temperature was controlled by a potentiometer controller. As a check, the temperature was recorded on a millivoltmeter and found to be constant within ±2°C at all temperature settings. To prevent thermal fluctuations the two halves of the system were wrapped together with asbestos tape.

After location of the desired crystal face, slices 5.5 x 0.8 x 0.15 cm were cut and a small hole drilled near one end. These were then polished and etched in a mixture of equal volumes of HNO_3 and HF after which they were attached to a Pt wire winding device so that they could be lowered in vacuum into the furnace and degassed. The oxygen was prepared from $KMnO_4$ and purified by passage through a dry ice-acetone bath. After each run the sample was removed, lightly abraded with 600 mesh carborundum powder, and re-etched.

If the volumes of the various parts of the system are known, it is possible to calculate from the change in pressure how many oxygen molecules have been removed from the gas phase. Assuming a linear temperature gradient between the furnace and the system, no thermomolecular flow, and ignoring virial coefficients, equation (I) is obtained.

$$\Delta n = \frac{P_2}{R}\left(\frac{V_9 \Delta l}{T_1}\right) + \frac{\Delta P}{R}\left(\frac{V_1}{T_1} + \frac{V_5}{T_2} + \frac{V_7}{T_2 - T_1} \ln \frac{T_2}{T_1} - \frac{V_9 \Delta l}{2T_1}\right) \quad [1]$$

where P_2 is the final pressure in the system in mm Hg, ΔP is the change in pressure in mm Hg, Δl is the change in pressure in mm of oil, T_2 is furnace temperature, T_1 is the temperature of the remainder of the system, V_1 is the volume at temperature T_1, i.e., all the system outside the

furnace and temperature gradient, V_7 is the volume in the temperature gradient, V_5 is the volume in the furnace, V_9 is the volume/mm of the manometer tubing, and Δn is the number of oxygen molecules removed from the gas phase.

All the data were calculated by means of this equation. To obtain Δn in terms of molecules/cm^2 it is necessary to assume a roughness factor. Previous work (4) on the adsorption of gases on Ge gave a roughness factor of 1.3 ± 0.1 for a CP-4 etched surface which was found to be identical with ones prepared by the present technique; this value has been used in the present work. The size of the sample was measured immediately after each run.

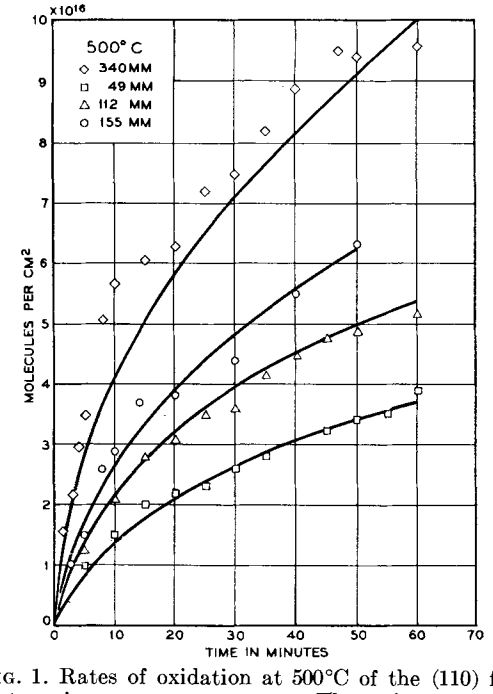

FIG. 1. Rates of oxidation at 500°C of the (110) face of Ge at various oxygen pressures. The points are experimental and the curves calculated from Eq. [24].

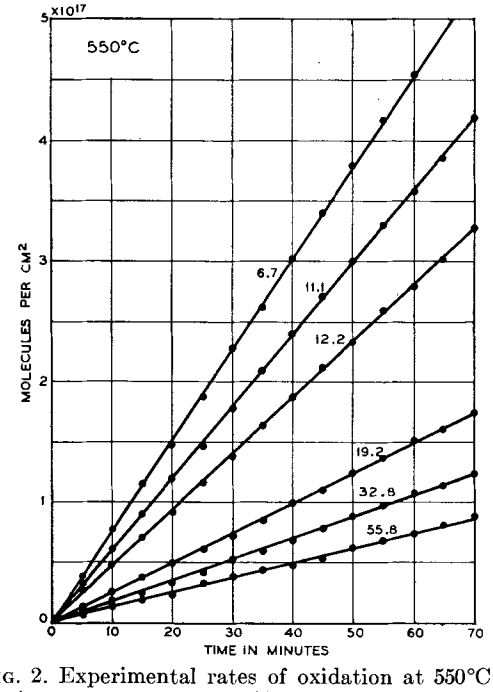

FIG. 2. Experimental rates of oxidation at 550°C of Ge at various oxygen pressures. Numbers indicate the oxygen pressure in mm.

RESULTS

No measurable uptake of oxygen was observed during 2 hr at 450°C for oxygen pressures between 5 and 350 mm. This does not imply that a clean Ge surface will not take up oxygen at 450°C. The surface under discussion, by its

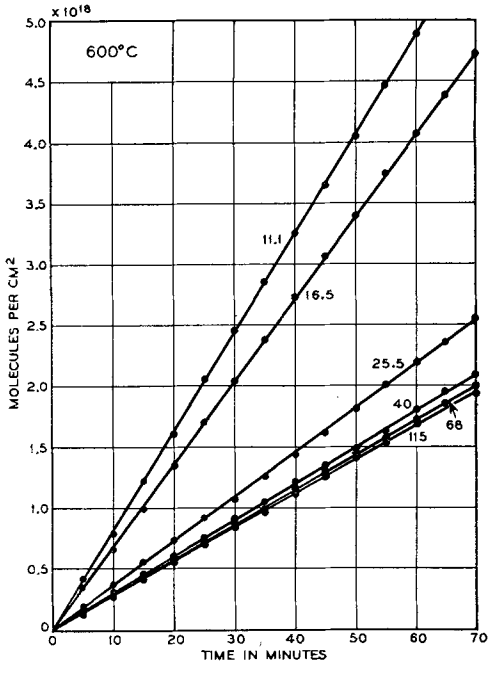

FIG. 3. Experimental rates of oxidation at 600°C. Numbers indicate the oxygen pressure in mm Hg.

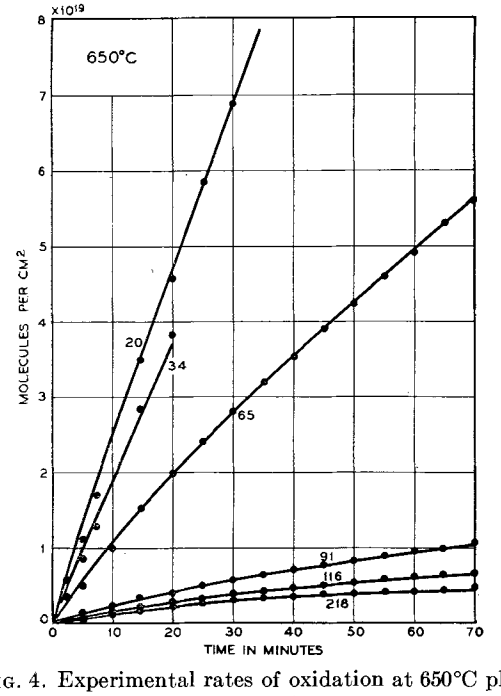

FIG. 4. Experimental rates of oxidation at 650°C plotted with oxygen pressure as parameter.

method of preparation, was almost certainly covered by one or more layers of oxygen before any measurements could be made.

Measured rates of oxidation of the (110) face at 500–700°C are shown in Fig. 1–5. The number of oxygen molecules removed from the gas phase is plotted as a function of time (in minutes) with the oxygen pressure as parameter. At and above 550°C the measured rates were found to be identical for the three faces studied. This is shown in Fig. 6 where the slopes of the rate curves at 550°C for the various faces are plotted as a function of oxygen pressure. A single curve describes the results adequately. At 500°C oxidation occurred only on the (110) plane.

In Fig. 2 through 5 smooth curves are used to represent the experimental data. The maximum deviation of the experimentally determined points from these curves was

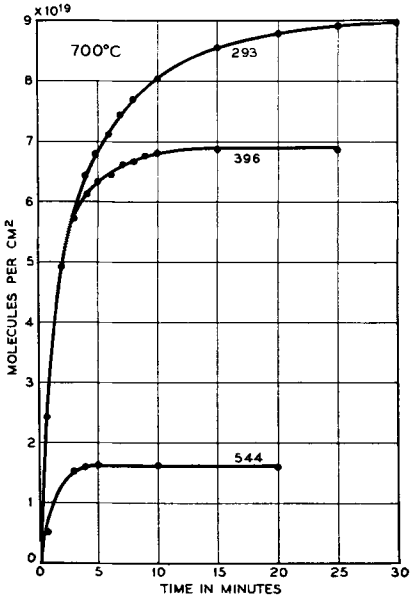

FIG. 5. Experimental rates of oxidation of Ge at 700°C. Numbers indicate the total oxygen pressure.

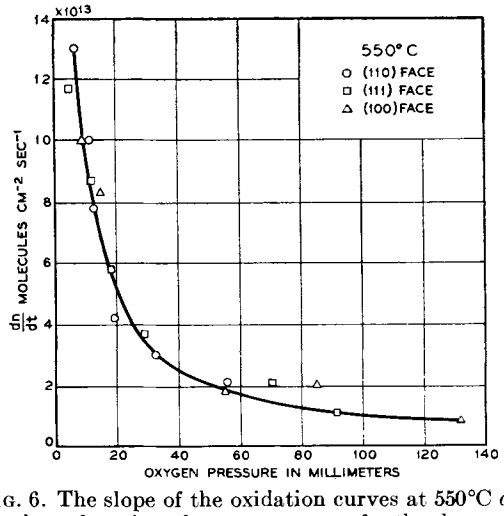

FIG. 6. The slope of the oxidation curves at 550°C dn/dt, plotted as a function of oxygen pressure for the three crystal faces.

1%. The reproducibility of duplicate runs at a given temperature and pressure was also within 1%.

The most interesting feature of the results is the strong inverse dependence of oxidation rate on oxygen pressure at 550°C and above. For most metals, oxidation rates at oxygen pressures above 1 mm are either independent of pressure or increase with increasing pressure. This effect was found only with Ge at 500°C as shown in Fig. 1. This was also the only temperature at which the oxidation rate was dependent on crystal orientation.

Discussion

Oxidation rates from 550° to 700°C showed no dependence on crystal orientation and were inversely proportional to the oxygen pressure. The main difference between Ge and other metals for which oxidation rates have been measured lies in the existence of a volatile Ge monoxide. Although this material may be unstable in the solid form at all temperatures, there is strong evidence for its existence in the gas phase. The vapor pressure of GeO over mixtures of Ge and GeO_2 corresponding to the reaction

$$Ge + GeO_2 \rightleftarrows 2\,GeO(g)$$

is available (5, 6). At temperatures above 550°C the vapor pressure is at least 10^{-3} mm Hg so that transport of this material through the gas phase could have a marked effect on the measured rates of oxidation. At the oxygen pressures used, transport through the gas is by diffusion so that one can explain the increase of oxidation rate as the pressure is lowered as being due to the increase in the interdiffusion coefficient. If this is true and a mixture of oxygen and an inert gas is used, the oxidation rate measured will be dependent on the total pressure and not on the partial pressure of oxygen. Mixtures of oxygen and nitrogen were used at 550°C and it was found that the rate is indeed determined by the total pressure. From these experiments one has confidence in proposing an evaporation mechanism to explain the $1/p$ dependence of oxidation rate.

An evaporation process of this type would obviously cause the Ge specimen to lose weight. Such a loss in weight was reported by Bernstein and Cubicciotti (2), and both these workers and the authors have observed the formation of a deposit on the walls of the tubing above the specimen after an oxidation run.

Consider the possible reactions

$$Ge_i \rightarrow Ge^\sigma \qquad \text{(I)}$$

$$Ge^\sigma + O_2 \rightarrow GeO_2{}^\sigma \qquad \text{(II)}$$

$$Ge^\sigma + GeO_2{}^\sigma \rightarrow 2GeO^\sigma \qquad \text{(III)}$$

$$GeO^\sigma \rightarrow GeO_{(g)} \qquad \text{(IV)}$$

$$GeO_{(g)} + \tfrac{1}{2}\,O_2 \rightarrow GeO_{2(\text{wall})} \qquad \text{(V)}$$

where the superscript σ refers to material at the solid-gas interface and the subscript i to material at the Ge-GeO_2 interface.

An equation for formation of GeO^σ from Ge^σ and oxygen at the surface could be included, but this only complicates matters without changing the form of the rate equation. Reaction (III) could also occur at the Ge-GeO_2 interface,

but any GeO produced there would have to reach the solid-gas interface before it could evaporate and be detected by the authors' measurements. Since the diffusion of a GeO species through the GeO_2 layer is unlikely, only (III) is considered as a source of GeO at the solid-gas interface.

Let c_1 be the concentration of Ge^σ in molecules cm^{-2}, c_2 be the concentration of GeO^σ in molecules cm^{-2}, and α be the number of molecular layers of GeO_2^σ. Then assuming that the rate of arrival of Ge at the surface is diffusion controlled,

$$\frac{dc_1}{dt} = \frac{K}{\alpha} - k_2 c_1 p^m - k_3 c_1 \qquad [2]$$

or at the steady state

$$\frac{K}{\alpha} = k_2 c_1 p^m + k_3 c_1 \qquad [3]$$

The rate of growth of the GeO_2 film is given by

$$\frac{d\alpha}{dt} = k_2 c_1 p^m - k_3 c_1 \qquad [4]$$

From Eqs. [3] and [4] c_1 can be determined and therefore so can the rate of formation of GeO_2^σ by reaction (II). The latter is equal to $k_2 c_1 p^m$ or

$$k_2 c_1 p^m = \left[\frac{K(k_2 p^m)^2}{2[(k_2 p^m)^2 - k_3^2]}\right]^{1/2} \frac{1}{t^{1/2}} \qquad [5]$$

Hence, Eq. [5] also describes the rate of oxygen removal by the formation of GeO_2^σ; but, oxygen is also removed by reaction (V) so that the total rate of removal is given by

$$-\frac{dn}{dt} = \frac{d[GeO_2^\sigma]}{dt} + 1/2\,\frac{dc_2}{dt} \qquad [6]$$

the second term accounts for oxygen removal via reaction (V). It is assumed that the rate of this reaction is governed by the rate of arrival of $GeO_{(g)}$ and since two molecules of GeO are required for the removal of one oxygen molecule the rate is given by $\frac{1}{2}\, dc_2/dt$. GeO^σ evaporates at a rate

$$-\frac{dc_2}{dt} = \frac{\gamma'}{p} \qquad [7]$$

where γ' includes the concentration gradient and pressure independent part of the interdiffusion coefficient or taking into account the limit for vacuum evaporation

$$-\frac{dc_2}{dt} = \frac{\gamma'}{\beta p + 1} \qquad [8]$$

Eqs. [7] and [8] assume the evaporation process is diffusion controlled. The inverse dependence on pressure arises from the variation of the diffusion constant D with pressure. It was also assumed that the equilibrium vapor pressure of GeO is always attained at the surface so that the evaporation rate is independent of c_2. If this assumption is not made, the final equation gives a rate that is independent of oxygen pressure, for as the pressure is increased, D decreases, but the concentration gradient increases and the product is nearly constant.

Adding the two terms for removal of oxygen from the gas phase

$$-\frac{dn}{dt} = \left[\frac{K(k_2 p^m)^2}{2[(k_2 p^m)^2 - k_3^2]}\right]^{1/2} \frac{1}{t^{1/2}} + \frac{\gamma''}{\beta p + 1} \qquad [9]$$

where $\gamma'' = \gamma'/2$ (because 2 molecules of GeO are oxidized by one molecule of oxygen).

Let

$$\left[\frac{K(k_2 p^m)^2}{2[(k_2 p^m)^2 - k_3^2]}\right]^{1/2} = B \qquad [10]$$

Then

$$\Delta n = 2B\, t^{1/2} + \frac{\gamma''}{\beta p + 1}\, t \qquad [11]$$

The assumption that the rate of evaporation of GeO^σ is independent of the concentration breaks down when c_2 becomes very small. It must go to zero when $c_2 = 0$. This is accounted for by including an extra term for the variation of the second term in [11] with c_2 when c_2 is very small. Let c_2' be the value of c_2 below which the equilibrium vapor pressure is no longer maintained. Then

$$\Delta n = 2B\, t^{1/2} + \frac{\gamma''}{\beta p + 1}\,(1 - e^{-c_2/c_2'})\, t \qquad [12]$$

When $c_2 \gg c_2'$ the term in the final brackets equals unity and the vapor pressure is constant; below this value of c_2 the term decreases to zero with c_2.

This equation has the correct form to explain the experimental results. If the second term predominates with $c_2 \gg c_2'$, a linear rate is obtained. If the first term is important, a parabolic or sum of parabolic and linear rates is obtained. With very thick GeO_2^σ films both terms should approach zero and a protective film should be formed. In Eq. [12] the first term describes the formation of an oxide film on the surface (parabolic), while the second refers to the oxidation of GeO which has evaporated to the walls of the apparatus.

It now remains to fit this equation to the experimental data and see if the values of the constants required are reasonable.

The values of the constants in the term for evaporation can be calculated. Following the treatment of Fuchs (7), suppose that the concentration of vapor at a distance Δ from the surface is c^* and that the equilibrium concentration at the surface is c_0 molecules cm^{-3}.

If the accommodation coefficient is λ, the rate of evaporation into a vacuum is $\Gamma\lambda\, c_0$ molecules cm^{-2} sec^{-1}, where $\Gamma = (kT/2\pi M)^{1/2}$, k is Boltzman's constant, and M the mass of the evaporating GeO molecule. Hence the rate at which molecules arrive at the plane, distant Δ from the surface is $\Gamma\lambda\,(c_0 - c^*)$. This may be equated to the rate at which molecules leave by diffusion or

$$\Gamma\lambda(c_0 - c^*) = -D\frac{\partial c^*}{\partial x} \qquad [13]$$

Assume a linear concentration gradient

$$c = Ux + W \qquad [14]$$

TABLE I. *Calculated quantities for the diffusion of* GeO *through oxygen*

Temp, °K	P_{MM}	Γ	$c_0\Gamma$	ΓL	D
773	4.0×10^{-4}	1.08×10^{4}	5.3×10^{16}	5.4×10^{3}	0.68
823	3.2×10^{-3}	1.12×10^{4}	4.1×10^{17}	5.6×10^{3}	0.76
873	2.0×10^{-2}	1.15×10^{4}	2.5×10^{18}	5.75×10^{3}	0.84
923	1.3×10^{-1}	1.18×10^{4}	1.6×10^{19}	5.9×10^{3}	0.92
973	6.3×10^{-1}	1.22×10^{4}	7.5×10^{19}	6.1×10^{3}	1.01

But at the wall, i.e., distant L from the surface, $c = 0$. Therefore

$$UL + W = 0 \qquad [15]$$

Then

$$\lambda(c_0 - c^*) = -\frac{DU}{\Gamma} \qquad [16]$$

Assume that the accommodation coefficient is unity and substitute for c^*

$$c_0 = U\left[(\Delta - L) - \frac{D}{\Gamma}\right] \qquad [17]$$

The rate of evaporation is equal to $-DU$ so on substituting for U

$$-\frac{dc_2}{dt} = \frac{-Dc_0}{\Delta - L - \frac{D}{\Gamma}} = \frac{Dc_0}{L - \Delta + \frac{D}{\Gamma}} \qquad [18]$$

Let

$$D = \frac{D_0 \times 760}{p}$$

Then

$$-\frac{dc_2}{dt} = \frac{c_0}{\frac{(L-\Delta)}{D_0 760}p + \frac{1}{\Gamma}} = \frac{c_0\Gamma}{\frac{\Gamma Lp}{D_0 760} + 1} \qquad [19]$$

assuming that Δ, the mean free path of the molecule, is small compared to the distance to the wall at all the pressures investigated. As $p \geq 5$ mm Hg this is a good approximation. Hence comparing coefficients of [8] and [19]

$$\gamma' = c_0\Gamma \qquad [20]$$

and

$$\beta = \frac{\Gamma L}{D_0 760} \qquad [21]$$

All the quantities in Eq. [19] can be calculated or estimated so that the rates of evaporation of GeO^{σ} may be obtained and therefore the rates of uptake of oxygen due to its subsequent oxidation.

No data are available in the literature for the diffusion constant of GeO in oxygen. However, it is approximately true that $D = K/M^{1/2}$, where M is the mass of the diffusing species. Using data for the diffusion of H_2, CO_2, and O_2 in oxygen K was found to be unity, and D for GeO equal to 0.106 at 273°K and 760 mm. On the basis of a simple theory D should vary as $T^{2/2}$, but Lonius (8) has found that the exponent is nearer 1.75. Using $D = D_0\ (T/273)^{1.73}(760/p)$ the values of D at 760 mm and various temperatures have been calculated and listed in Table I. The average velocity (Γ) of GeO molecules leaving the surface was obtained from $\Gamma = (kT/2\pi M)^{1/2}$ and the product $c_0\Gamma$ from

$$c_0\Gamma = 3.95 \times 10^{20} P_{mm}\left(\frac{M}{T}\right)^{1/2} \text{ molecules cm}^{-2}\,\text{sec}^{-1} \qquad [22]$$

where P_{mm} is the vapor pressure of GeO.

The value of the vapor pressure of GeO over a mixture of GeO_2 and Ge is not well established but the data of Jolly and Latimer (6) have been used in the present calculations. Inaccuracies in the vapor pressure data make the calculated values of the oxidation rate equally uncertain, but give values correct at least within an order of magnitude. In the derivation of Eq. [19], the accommodation coefficient λ was assumed to be unity. If it is included in the final equation

$$-\frac{dc_2}{dt} = \frac{\lambda c_0\Gamma}{\frac{\lambda\Gamma Lp}{D_0 760} + 1} \qquad [23]$$

TABLE II. *Calculated and experimental values of dn/dt in molecules cm^{-2} sec^{-1}*

Oxygen pressure	*dn/dt* (Calculated)	*dn/dt* (Experimental)
t = 550°C		
6.7	2.6×10^{15}	1.3×10^{14}
11.1	1.7×10^{15}	1.0×10^{14}
12.2	1.6×10^{15}	7.8×10^{13}
19.2	1.0×10^{15}	4.2×10^{13}
32.8	6.0×10^{14}	3.0×10^{13}
55.8	3.6×10^{14}	2.1×10^{13}
t = 600°C		
11.1	1.2×10^{16}	1.3×10^{15}
16.6	8.4×10^{15}	1.1×10^{15}
40.0	5.5×10^{15}	6.1×10^{14}
68.0	2.0×10^{15}	4.9×10^{14}
115.0	1.2×10^{15}	4.7×10^{14}

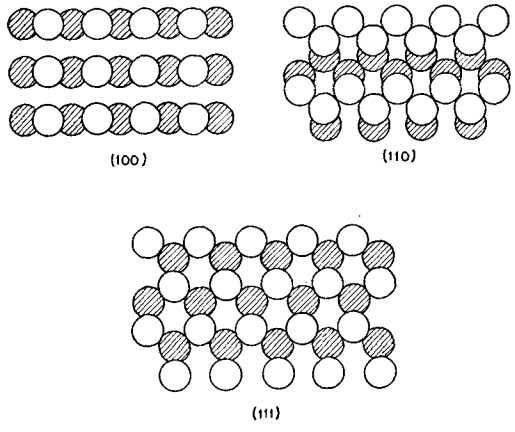

FIG. 7. The arrangement of atoms on the (110), (100), and (111) faces of a Ge crystal showing the different type of bonding.

In general, λ will be less than unity and probably between 1 and 10^{-3}.

From the values listed in Table I it is possible to calculate dc_2/dt from 773° to 973°K and at any pressure. From these results the second term in Eq. [6] can be evaluated and hence the linear parts of the rate curves predicted. Unfortunately it is impossible to carry out an independent calculation of the first term which includes several rate constants.

Oxidation rates at 550° and 600°C are shown in Fig. 2 and 3 as linear curves. However, at very short time intervals $\leq$ 3 min they were practically parabolic. Because of the difficulty of obtaining accurate data at the beginning of the run only the linear portions were plotted by moving the zero of time to +3 min. It is believed that this initial region describes the growth of an oxide film. This film grows until its growth rate is just equal to the rate of evaporation of GeO. It then remains at a constant thickness and the oxidation curve becomes linear with respect to time.

This theory predicts that the linear part of the rate curves describes the diffusion of GeO through the oxygen atmosphere. In Table II the experimental and calculated (from Eq. [6] and [23]) values of dn/dt in molecules cm^{-2} sec^{-1} at 550° and 600°C are given as a function of oxygen pressure. Calculated values are all higher than experimental ones, although the agreement is satisfactory. The difference could be due to either inaccurate vapor pressure data for GeO or to the use of unity for the accommodation coefficient (λ). In general λ is less than one and therefore reduces the calculated value of dn/dt.

At temperatures above 600°C no comparison of theory and experiment is possible since the oxidation curves are no longer linear. That evaporation of GeO is still important is shown by the inverse dependence of rate on oxygen pressure, but this process is reduced and finally (at 700°C) prevented by the growth of a protective film of GeO_2. Once a stable GeO_2 film has been formed at 700°C no further oxidation is observed even if the oxygen pressure is lowered. The difference between the uptakes at the various pressures is due to the amount of GeO that can evaporate before a complete GeO_2 film is formed. This is certainly greater at the low pressures.

The data at 500°C shown in Fig. 1 differ from all the others in that the oxidation rate increases with increasing oxygen pressure. The term due to diffusion of GeO away from the surface is found to be quite small, being approximately 5×10^{12} molecules cm^{-2} sec^{-1} at a pressure of 50 mm. The linear term in Eq. [11] is therefore unimportant and there is left

$$\Delta n = 2Bt^{1/2} \qquad [24]$$

where B is a function of oxygen pressure. In other words, the oxidation rate under these conditions is controlled by the thickness of the oxide film and a parabolic law results. It is not possible to calculate a value for B, which contains a number of rate constants. However Eq. [24] may be written as $\Delta n = c\, p^m\, t^{1/2}$ and values of c and m may be calculated from two runs and used to compare the rest of the data. The solid lines in Fig. 1 were all calculated from $\Delta n = 9.10^{13} p^{1/2} t^{1/2}$; agreement between them and experiment is good at all pressures.

Effect of Crystal Orientation on Oxidation Rate

The lack of dependence of rate on crystal orientation at 550°C is to be expected if the oxidation process is indeed diffusion controlled. The slopes of the rate curves at 550°C for the three faces are shown in Fig. 6 as a function of oxygen pressure. A single curve describes all the results.

At 500°C no removal of oxygen from the gas phase by the (100) and (111) faces could be detected over a period of 2 hr at oxygen pressures between 50 and 700 mm. This was in contrast to the (110) face where appreciable oxidation occurred, as shown in Fig. 1. At this temperature the results show that diffusion through the gas phase is unimportant, so the rate-determining step must be either the removal of a Ge ion from the lattice or its transport across the oxide film. For any difference between crystal faces to be important the former of these must be operative. In Fig. 7 the arrangement of Ge atoms on the (100), (111), and (110) faces is shown. On the (100) face each surface atom is bonded to two atoms in the layer below, while on the (111) face each surface atom is bound to three in the next lowest layer. These numbers remain constant even when the surface layer is partially depleted. On the (110) face, however, each surface atom is bound to two neighboring surface atoms but to only one atom in the underlying layer. Thus, if one atom is removed from the surface, the bonding of the two neighboring atoms is weakened and one can get progressive removal along the chain. Therefore, from the crystal structure it does not seem unreasonable that the (110) plane is more reactive than either the (100) or the (111). Further measurements at temperatures below 500°C are needed for confirmation.

Conclusions

At and above 550°C the oxidation process is controlled by the diffusion of GeO away from the surface and no effect of crystalline orientation is found.

Between room temperature and 550°C little data are available but these results suggest that in this region the (110) plane oxidizes more readily than either the (100) or the (111) and that the rate of oxidation is controlled by either the removal of a Ge ion from the lattice and/or its transport across the oxide film.

Manuscript received April 24, 1956. This paper was prepared for delivery before the San Francisco Meeting, April 29 to May 3, 1956.

Any discussion of this paper will appear in a Discussion Section to be published in the December 1957 Journal.

REFERENCES

1. W. H. Brattain and J. Bardeen, *Bell System Tech. J.*, **32,** 1 (1953).
2. R. B. Bernstein and D. Cubicciotti, *J. Am. Chem. Soc.*, **73,** 4112 (1951).
3. W. E. Campbell and U. B. Thomas, *Trans. Electrochem. Soc.*, **91,** 623 (1947).
4. J. T. Law, *J. Phys. Chem.*, **59,** 543 (1955).
5. W. Bues and H. V. Wartenberg, *Z. anorg. u. allgem. Chem.*, **266,** 281 (1951).
6. W. L. Jolly and W. M. Latimer, *J. Am. Chem. Soc.*, **74,** 5757 (1952).
7. N. Fuchs, *Phys. Z. Sowetunion*, **6,** 224 (1934).
8. A. Lonius, *Ann. Physik*, **29,** 664 (1909).

Electrolytic Reduction of Cyanamide

KEIJIRO ODO AND KIICHIRO SUGINO

Laboratory of Organic Electrochemistry, Department of Chemical Engineering, Tokyo Institute of Technology, Tokyo, Japan

ABSTRACT

The electrolytic reduction of cyanamide was investigated in order to confirm each product and thus to clarify the reduction mechanism.

Ten per cent aqueous cyanamide solution was reduced electrolytically in 8% $(NH_4)_2SO_4$ catholyte at *p*H range 3–7 at a spongy Sn cathode. Final products were NH_3 and methylamine as previously reported. In addition, a considerable amount of formamidine was isolated in the form of picrate. Formic acid was also obtained as a product of the reduction. No proof was obtained for the existence of hydrocyanic acid in the catholyte during electrolysis. On these bases, the intermediate compound of the cyanamide reduction to NH_3 and methylamine is not hydrocyanic acid, but formamidine, contrary to the results of earlier workers. The main side reaction is hydrolysis of formamidine to NH_3 and formic acid.

Drechsel (1) first observed that cyanamide could be reduced to give methylamine and NH_3 by prolonged treatment with Zn and HCl. He supposed that cyanamide was first reduced to NH_3 and hydrocyanic acid, the latter compound being further reduced to methylamine.

$$NH_2CN + 2H \rightarrow NH_3 + HCN \quad (I)$$

$$HCN + 4H \rightarrow CH_3NH_2 \quad (II)$$

Kameyama (2) later carried out this reduction by an electrolytic method. He used a 1.3–6.7% aqueous solution of cyanamide prepared by extracting commercial calcium cyanamide as catholyte, and Cd, Zn, Pb, Hg, etc., as cathode. By combining the measurement of H absorption at the cathode and simple identification of the product, he concluded, as did Drechsel, that cyanamide was reduced to give methylamine and NH_3. He also supposed the mechanism to be the same as Eqs. (I) and (II).

Nothing further has been reported, and it appears that a complete separation and identification of cyanamide reduction products had not been made before the present work. Therefore, an investigation was made in order to confirm each reduction product and thus to clarify the reduction mechanism.

In this paper, the detection of formamidine as an intermediate product and the proposed mechanism based on this discovery are reported. Experiments were carried out mainly at a spongy Sn cathode and in a catholyte containing $(NH_4)_2SO_4$ at *p*H 3–7. Work on the quantitative study of the effect of cathode materials and other electrolytic conditions on the yield of each product is in progress.

EXPERIMENTAL, RESULTS, AND DISCUSSION

Apparatus.—Apparatus used was similar to that described earlier (3). Area of the cathode was 80 cm^2. The catholyte was thoroughly agitated by a magnetic stirrer to maintain the *p*H of the catholyte as constant as possible.

Material used.—Crystalline cyanamide was freshly prepared from commercial calcium cyanamide by a previously reported procedure (4), and its purity was determined by the usual method (as silver cyanamide) before use.

Formation of methylamine and ammonia.—Several runs were made using various cathodic materials such as Pb, Hg, Sn, Zn, Cu, etc. The reduction of cyanamide was found to occur with all cathodes, but spongy Sn gave the most favorable results (Table I).

Cyanamide converted was calculated by subtracting the amount of remaining cyanamide in the catholyte from that in the starting catholyte. Remaining cyanamide was determined by the usual method (as silver cyanamide).

Methylamine and ammonia were isolated by the following procedure.

Ammonia.—After reduction, the catholyte (102 cc) was neutralized with H_2SO_4, and 20 cc was pipetted into the beaker; 100 cc methanol was added to it and the mixture was allowed to stand for several hours. Precipitated $(NH_4)_2SO_4$ was filtered, washed with 20 cc methanol, and weighed. Solubility correction was applied (0.47 g/20 cc). Then, NH_3 formed by the reduction was calculated by subtracting the amount of NH_3 in the starting catholyte.

Methylamine.—Each 40–60 cc of catholyte was pipetted into the beaker, and five times that amount of methanol was added to it. The precipitated $(NH_4)_2SO_4$ was filtered off and washed with 40 cc methanol. The filtrate was combined with washing solution and concentrated under diminished pressure. The residue was diluted to 150 cc with water, poured into a Kjeldahl flask, and heated with 60 g 50% NaOH solution. Methylamine was distilled into HCl, and the resulting solution was evaporated to dryness. The residue was extracted with 40 cc then 10 cc hot butanol to separate NH_4Cl; the extract was again evaporated to dryness to give crude methylamine hydrochloride, which was weighed. The analytical sample was recrystallized from butanol.

It was confirmed that the reduction of cyanamide gave NH_3 and methylamine as final products in fair yield under suitable conditions. But the amount of methylamine was relatively small as compared with the amount of NH_3 expected from:

$$NH_2CN + 6H \rightarrow NH_3 + CH_3NH_2 \quad (III)$$

It may be that part of the NH_3 was formed not by direct reduction, but by decomposition of some intermediate

product. So, further experiments were carried out to seek the intermediate product of the reduction of cyanamide.

Isolation of formamidine, the intermediate product.—By careful observations, it was found that formamidine existed in the reduction product. Isolation of this compound was difficult and incomplete quantitatively; it could be caught as picrate by the following procedure.

Ten grams cyanamide (purity 97.5%, 9.75 g as pure cyanamide) was reduced at a spongy Sn cathode with 40 amp-hr of current. Other conditions were the same as in Table I; 5.17 g of cyanamide was converted.

After the reduction, 25 cc of the catholyte (total 110 cc) was pipetted into the beaker. To it, a suitable amount of picric acid was added either as solid, aqueous solution, or methanolic solution. Formamidine picrate (solubility about 0.2 g/100 cc) could be precipitated together with ammonium picrate.[1] The quantitative separation of formamidine picrate from this mixture was very difficult,[2] but after adding a hot methanolic solution of picric acid (1.5 g/5 cc) very cautiously, 1.57 g crude formamidine picrate was obtained (mp 232°–234°C). Recrystallization from 30 cc hot water gave 0.91 g of pure compound. Yield 12.0%, mp 242°–244°C. Calc'd for $C_7H_7N_5O_7$: N, 25.64%; found: N, 25.95%.

A mixed melting point with the product[3] prepared from thiourea showed no depression.

Identity was further confirmed by converting the picrate into the hydrochloride. Pure formamidine picrate (2.15 g, mp 242°–244°C) obtained by the reduction was converted to hydrochloride (0.51 g, mp 66°–70°C). Calc'd for CH_5N_2Cl: N, 34.78%; found: N, 35.05%.

Isolation of formic acid.—Since formamidine was found to be the intermediate product, hydrolysis of this compound to ammonia and formic acid may be expected as follows:

$$NH_2\cdot CH = NH \xrightarrow{H_2O} NH_3 + HCONH_2 \xrightarrow{H_2O} 2NH_3 + HCOOH \qquad (IV)$$

The existence or formation of this compound in the reduction product was verified by the following procedure.

Ten grams cyanamide (purity 96%, 9.60 g as pure cyanamide) was reduced at a spongy Sn cathode with 35.8 amp-hr of current. Other conditions were the same as in Table I, and 4.37 g cyanamide was converted. After the reduction, 30 cc of the catholyte (total, 105 cc) was pipetted into the beaker; 30 cc 20% H_2SO_4 was added to it, and the mixture was distilled in a Kjeldahl flask to give 50 cc of distillate. Formic acid content in the distillate was determined by titration with 0.1*N* NaOH solution. Yield: 0.35 g (total, 1.21 g), sodium formate obtained from the distillate had mp 250°–255°C (decomposition), and the mixed melting point with the known sample showed no depression.

Existence of formaldehyde.—The existence of small amounts of formaldehyde in the distillate of the run described above was proved. The distillate had a very indistinct odor of formaldehyde and gave a very weak silver mirror reaction. Moreover, it gave a little precipitate when treated with dimedon.

Existence of hydrocyanic acid.—Careful observation was also made in order to determine the existence of hydrocyanic acid in catholyte during the electrolysis. This test was made by prussian blue formation. Two or three cubic centimeters of the catholyte was pipetted into the test tube and made alkaline with a drop of NaOH. To it, a piece of crystalline ferrous sulfate was added, and the solution was boiled for 30 min. The resulting solution was acidified with HCl, and a solution of $FeCl_3$ was added. Color change to blue could not be observed throughout the experiments.

Side reactions other than reduction.—Cyanamide is expected to dimerize to dicyandiamide at *p*H 8–12. But during the reduction, under the conditions described above, an appreciable amount of dicyandiamide was not

TABLE I. *Reduction of cyanamide at* Sn

Catholyte:* 10 g cyanamide in 100 cc 8% $(NH_4)_2SO_4$. *p*H range adjusted at 3–7 by adding small amount of H_2SO_4 during the electrolysis.
Current: 34.4 amp-hr (5 Faradays).
Current density: 5 amp/dm²
Temp: Kept at 15°C by cooling catholyte with ice water.
Results: Cyanamide used: 10.00 g (purity 97.6%, 9.76 g as pure cyanamide)
Cyanamide converted: 3.96 g
$(NH_4)_2SO_4$ obtained: 3.12 g
Methylamine hydrochloride obtained: 1.87 g, mp 196°–200°C (recrystallized); Calc'd for CH_6NCl: N, 20.74%; found: N, 21.40%.

* Acidic catholyte is also applicable to this reduction. For example: 10 g cyanamide in 100 cc 5% H_2SO_4. Concentration of H_2SO_4 is controlled so as to be 5–2% during electrolysis.

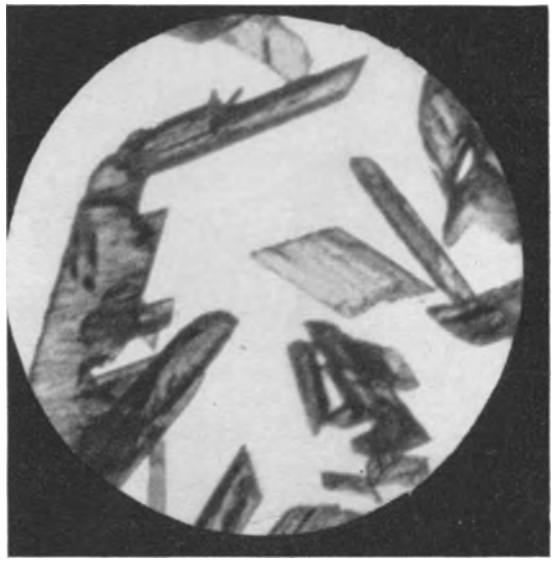

FIG. 1. Formamidine picrate

[1] When the amount of formamidine in the catholyte was small, the speed of crystallization of the picrate was relatively slow, so that it might have been better to let the mixture stand for a few days. Formamidine picrate could be recognized easily by the characteristic form.

[2] Indeed, in another run, separation of formamidine picrate from the mixture was even more difficult, and it could be accomplished only by the careful technique of picking out characteristic picrate crystals from the mixture.

[3] Prepared from thiourea by the procedure of D. J. Brown (5), mp 246°C.

detected. Also, any conversion of cyanamide to urea by hydration in the presence of acid is unlikely to occur during the reduction.

Conclusion

It is interesting to note that a fairly large amount of formamidine was obtained in the reduction product of cyanamide. Formation of this compound was completely missed by earlier workers. Since hydrocyanic acid was absent, the reduction of cyanamide is best represented by the following succession of reactions:

$$NH_2CN \xrightarrow{2H} NH_2 \cdot CH = NH \xrightarrow{2H} [NH_2 \cdot CH_2NH_2] \xrightarrow{2H} NH_3 + CH_3NH_2 \quad (V)$$

Main side reaction is the hydrolysis of formamidine to give NH_3 and formic acid.

$$NH_2 \cdot CH = NH \xrightarrow{H_2O} [NH_3 + HCONH_2] \xrightarrow{H_2O} 2NH_3 + HCOOH \quad (VI)$$

The mechanism proposed by Drechsel (1) and adopted by Kameyama (2) for the electrolytic reduction is disproved by this experiment.

Acknowledgment

This investigation was promoted by a grant for fundamental scientific research from the Ministry of Education of Japan and also a grant from Nippon (Japan) Carbide Industries Inc., for which the authors wish to express their deep appreciation.

They are also indebted to Mr. E. Ichikawa and H. Kawada for their generous assistance in carrying out the experiment.

Manuscript received November 2, 1955. This paper was prepared for delivery before the Pittsburgh Meeting, October 9 to 12, 1955.

Any discussion of this paper will appear in a Discussion Section which will be published in the December 1957 Journal.

References

1. E. Drechsel, *J. prakt. Chem.*, **11**, 319 (1875).
2. N. Kameyama, *J. Fac. Eng. Tokyo Imp. Univ.*, **13**, 271 (1924).
3. M. Yamashita and K. Sugino, *This Journal*, **104**, 100 (1957).
4. K. Sugino, Y. Takenouchi, Y. Aiya, and H. Usui, Japanese Pat. 179,981 (Aug. 19, 1949).
5. D. J. Brown, *J. Appl. Chem. (London)*, **2**, 202 (1952).

The Voltage of Sodium Chlorate Cells

Vivion de Valera

Department of Chemistry, University College, Dublin, Ireland

ABSTRACT

The cell voltage of technical chlorate cells with carbon anodes and rod iron cathodes is correlated with reported overvoltage values. At working current densities the cell voltage is expressible as the sum of a constant, the overvoltages, and an ohmic term. Results are found to be consistent with the theory that the anode potential is conditioned by hydroxyl discharge. Back emf measurements are discussed.

To calculate the energy efficiency of a chlorate cell a value for the theoretical cell voltage must be assumed but, owing to the complexity of the reactions involved, the value to be taken is not obvious. Knibbs (1) quotes 1.43 v as being the theoretical voltage required according to Luther for producing chlorate from chloride, but he further points out that the voltage corresponding to the thermal absorbtion in the change:

$$NaCl\ (aq.) + 3H_2O\ (liq.) = NaClO_3\ (Aq.) + 3H_2\ (Gas) - 224\ (Cal.)$$

is 1.62 v. In subsequent literature this value has been adopted (2). On the other hand, Koehler (3) states that the decomposition potential of NaCl solutions may be taken as 2.3 v and uses this factor for calculating the efficiency of chlorine-caustic cells. Generally, it is not easy to interpret voltage measurements recorded in the literature and a systematic correlation of cell voltages with current densities is needed. This prompted the present investigation.

Although it is difficult to get reproducible values, current voltage curves for chloride electrolysis are always more or less definite in form. Apart from the peculiarities at low current densities, especially at the commencement of electrolysis, they have the usual approximately logarithmic shape (4). In the case of simpler electrolytes, such curves are usually resolvable as the superposition of a linear ohmic increase of potential with current on a logarithmic overpotential. This suggests that chlorate cell voltages might also be separable approximately into the sum of the electrode overvoltages, the electrolyte resistance, and a constant, provided other variables are suitably controlled and that values for the overvoltages are known.

An analysis of data relating to the operation of chlorate cells both on the semitechnical and technical scales confirmed that the curves obtained by plotting current against voltage were of the type expected. The results of Pfleiderer (5) and others (4) then indicated correlation with H and oxygen overvoltages obtained by the direct method. As the values of Knobel, *et al.* (6) (assembled in the International

Critical Tables) seemed the most appropriate, these were used.

Analysis of Routine Factory Data

During the operation of an experimental installation, results heretofore unpublished of routine observations over a period of nearly two years became available. These were extracted from the log sheets and analyzed. The data related to concrete cells fitted with electrode assemblies of the rod cathode type similar to those described by McLaren and co-workers (7). The anodes consisted of 2 in. diameter graphite rods with an effective length of 20 in. Each anode was surrounded by 20 steel rods, $\frac{3}{16}$ in. diameter, forming its cathode. Cells were operated on a batch basis and current, voltage, and other readings were taken hourly throughout a run. Cell temperatures ranged from 23° to 31°C. One lb of $K_2Cr_2O_7$ was added to the electrolyte at the beginning of each run and the *p*H was maintained between the limits 6.2–6.9 by addition of HCl. A large number of readings were available corresponding to ten runs. Results shown in Table I relate to two runs with cells of approximately 470-l capacity fitted with 30 electrode units per cell. Cell conditions were practically the same during both these runs, and the figures given here are representative of the results for other runs. In one of the runs in question 8 cells were operated in series. Observations were made each hour on one master cell and one other observed cell. Throughout the run, cell conditions and performance were almost the same for the 8 cells. In the second run, 32 similar cells were operated in series. The figures taken were hourly observations made on two master cells. Cell conditions and performance for the two master cells were closely parallel, but some of the remaining 30 cells showed wider variations than those noticed in the 8-cell run. As far as current-voltage relations were concerned these variations seemed to be explainable in terms of varying cell resistances. These runs were selected because they afforded the largest number of comparable readings at various current values. Great accuracy cannot be claimed for these measurements.

Figures given in Table I refer to early portions of these runs after the cells had settled down but before the chloride concentration had fallen below 200 g/l. Cell resistance can be taken as approximately constant in this interval although it rises toward the end of a run. In the present case, cell resistance, R, was estimated at 4×10^{-4} ohms. The voltages E_{obs} are mean values obtained by plotting observed voltages against the corresponding current. Overvoltages V_a and V_c were taken from the graphs obtained by plotting the values given in the International Critical Tables[1] for the oxygen overvoltages on graphite and the H overvoltages on Fe, against current density. The seventh column of the table gives the sum of the anode and cathode overvoltages together with the ohmic term RI, corresponding to the current values in the first column, while the last column gives the difference of the observed voltages, E_{obs}, and this sum. The difference so obtained is practically constant over a wide current

[1] International Critical Tables, vol. VI, pp. 339, 340.

TABLE I. *Current-voltage: average from plant log sheets*

I (amp)	C.D. anode (amp/cm²)	V_a (v)	C.D. cathode (amp/cm²)	V_c (v)	RI (R = 0.0004) (v)	$V_a + V_c + RI$	E_{obs} (v)	Difference (v)
30	0.0012	0.55	0.0006	0.36	0.01	0.92	1.92	1.00
300	0.012	0.91	0.006	0.53	0.12	1.56	2.60	1.04
400	0.016	0.94	0.008	0.55	0.16	1.65	2.71	1.06
500	0.020	0.96	0.010	0.56	0.20	1.72	2.82	1.10
600	0.024	0.98	0.012	0.57	0.24	1.79	2.92	1.13
700	0.028	0.99	0.014	0.58	0.28	1.85	2.98	1.13
850	0.034	1.00	0.017	0.59	0.34	1.93	3.06	1.13
900	0.036	1.01	0.018	0.60	0.36	1.97	3.08	1.11
1000	0.040	1.01	0.020	0.61	0.40	2.02	3.14	1.12
1100	0.044	1.02	0.022	0.62	0.44	2.08	3.18	1.10
1200	0.048	1.02	0.024	0.62	0.48	2.12	3.22	1.10
1300	0.052	1.03	0.026	0.63	0.52	2.18	3.29	1.11

Note: I is cell current; V_a is oxygen overvoltage on anode; V_c is hydrogen overvoltage on cathode; R is cell resistance; and E_{obs} is observed cell voltage.

range, the average value being 1.09 v. In fact, the result for the runs in question may be written in the form:

$$E_{obs} = 1.09 + (V_a + V_c) + RI \qquad (I)$$

Correlation with Reported Values

The value 1.09 v is very close to the value found experimentally for the "reversible" oxygen electrode with reference to a reversible H electrode in the same aqueous solution. Taken in conjunction with the fact that the overvoltages concerned are those of H and oxygen, this coincidence seemed to be of some significance. It was therefore of interest to inquire how far the above result could be fitted to the cell data published by other workers.

It is unfortunate that the information given in the literature usually omits to specify the cell resistance, R, so that the extent to which the above equation can be tested on the figures given is very limited. However, Pitman and co-workers (8) describe the operation of two cells for which they give the necessary data (Cells Nos. 2 and 4). Taking the voltages and current densities experimentally determined for these cells in conjunction with the overvoltages V_a and V_c obtained in the same way as before, the following result was obtained:

Cell No.	C.D. anode (amp/cm²)	C.D. cathode (amp/cm²)	V_a (v)	V_c (v)	RI (v)	E_{calc} (v)	E_{obs} (v)
2	0.019	0.011	0.96	0.56	0.22	2.83	2.81
4	0.022	0.012	0.97	0.57	0.22	2.85	2.91

McLaren and associates (7) measured the components of the over-all cell voltage of small chlorate cells with rod cathodes. They determined anode and cathode potentials with a saturated calomel reference cell. They state that the voltage measured depended on many cell conditions but give "representative values." Table II gives their values in relation to the overvoltages V_a and V_c.

Notice that the difference between the measured anode potential and the corresponding oxygen overvoltage is almost constant, the average value of this difference being about 0.26 v. The figures indicate a similar constancy for the cathode relations, but values of V_c taken are those corresponding to the anode current densities given. In the

TABLE II. *Electrode potentials and overvoltages*

Anode C.D. (amp/cm²)	Anode potential (v)	V_a (v)	Diff. $E_a - V_a$ (v)	Cathode potential (v)	V_c (v)	Diff. $E_c - V_c$ (v)
0.01	1.17	0.90	0.27	1.27	0.56	0.71
0.02	1.22	0.96	0.26	1.42	0.61	0.81
0.04	1.28	1.01	0.27	1.46	0.67	0.79
0.06	1.30	1.04	0.26	1.49	0.73	0.76
0.09	1.33	1.07	0.26	1.52	0.79	0.73
0.12	1.34	1.10	0.24	1.55	0.85	0.70
0.16	1.37	1.12	0.25	1.58	0.91	0.67

TABLE III. *Voltages calculated from results of McLaren, et al. (7)*

NaCl (g/l)	I (amp)	C.D. anode (amp/cm²)	V_a (v)	C.D. cathode (amp/cm²)	V_c (v)	R (ohms)	RI (v)	E_{calc} (v)	E_{obs} (v)
250	200	0.04	1.01	0.03	0.64	0.0006	0.12	2.86	2.80
100	200	0.04	1.01	0.03	0.64	0.0011	0.22	2.96	2.95
50	200	0.04	1.01	0.03	0.64	0.0012	0.24	2.98	3.00
250	400	0.09	1.07	0.06	0.73	0.0006	0.24	3.13	3.25
100	400	0.09	1.07	0.06	0.73	0.0011	0.44	3.33	3.40
50	400	0.09	1.07	0.06	0.73	0.0012	0.48	3.37	3.55
250	600	0.12	1.10	0.09	0.79	0.0006	0.36	3.34	3.35
100	600	0.12	1.10	0.09	0.79	0.0011	0.66	3.64	3.66
75	600	0.12	1.10	0.09	0.79	0.0012	0.72	3.70	3.70
250	800	0.16	1.12	0.12	0.85	0.0006	0.48	3.54	3.6
100	800	0.16	1.12	0.12	0.85	0.0011	0.88	3.94	3.9
75	800	0.16	1.12	0.12	0.85	0.0012	0.96	4.02	4.0
250	185	0.08	1.06	0.06	0.73	0.0020	0.37	—	3.25
250	110	0.16	1.12	0.09	0.79	—	—	—	3.9

paper referred to, the authors omit cathode current densities and hence the anode values are taken in default. It is almost certain that the correct cathode current densities were less than the corresponding anode values and a correction in this direction would tend to make the sum of the two differences more nearly approach the value 1.09 v.

In the same paper the authors tabulate data relating to the operation of cells at various current loads and salt concentrations (7). They do not give the values of their cell resistances but, if the cell voltages are calculated by means of the equation under test on the assumption that the values of R were: 6×10^{-4} ohms at a chloride concentration of 250 g/l, 11×10^{-4} ohms at 100 g/l, and 12×10^{-4} ohms at 50–75 g/l, the resulting voltages accord with the observed values. Table III shows that agreement is good except in the case of the 400-amp run. The authors, however, point out that the data for this run were obtained after the anodes had worn from 2 in. diameter to 1¾ in. diameter. Data for the 185-amp run were also obtained with worn anodes. Thus, an increased cell resistance is to be expected in the case of both of these runs. Table III, then, affords a circumstantial check on Eq. (I).

Direct Experimental Test

The matter was then submitted to a direct test with the 32-cell installation already mentioned. The cells were charged with fresh brine from the one mixing and 1 lb dichromate was added to each cell. The initial *p*H of the electrolyte was 9.4 and the initial cell temperature was 9°–10°C for all cells. Care was taken to insure that starting conditions were the same for all cells. The current was switched in at a low value, and, after some preliminary measurements, it was raised to the vicinity of 1000 amp. Cell temperatures were allowed to rise to 25°C and thereafter maintained at this value. A standard glass electrode *p*H meter was used to control the *p*H of the cell liquors and HCl was added to each cell in regulated quantities to reduce the *p*H of the electrolyte slowly and uniformly for all cells. The cells were then run for 20 hr under these conditions before the observations discussed below were taken.

It is necessary to make a slight digression at this point to refer briefly to the resistances of chlorate cells. These do not remain constant but increase with time, manifesting themselves as a rise in cell voltage. This increase is due to two distinct causes: (*a*) the specific resistance of the electrolyte increases with rising chlorate concentration from about 4 to 6 ohms/cm³ at chloride concentrations above 100 g/l (1); (*b*) resistances of electrodes and electrode connections tend to increase with time because of corrosion, rusting, or anode wear (7). It is also conceivable that local emf's may develop at connections if these are faulty and exposed to damp spray from the cells. The first factor made it necessary to take all readings within a relatively narrow chlorate and chloride concentration range. The second factor is noticeable in cells fitted with graphite anodes and iron rod cathodes after about four successive batch runs. The age and history of an assembly of this type must be taken into consideration when estimating its resistance. In the present case, the age and history of the electrode assemblies in the 32 cells was practically the same and the performance and characteristics of the individual cells were sufficiently uniform to warrant the consideration of average values taken over all the cells (±0.15 v at 1000 amp, maximum deviation from average).

It was decided to take current and voltage readings before the chloride concentration had fallen below 250 g/l but after a reasonable time had been allowed for the cells to settle down. On the basis of cell dimensions and the specific resistance of the electrolyte, taken as 4.7 ohms/cm³, it was estimated that the corresponding resistance of the electrolyte would be 1.5×10^{-4} ohms/cell. The resistance of the graphite anodes was estimated at 0.5×10^{-4} ohms/cell. Voltage drops over the anode and cathode connections and the voltage drops in the leads had been measured in detail with current passing, by means of an accurate millivoltmeter toward the end of a previous run very shortly before the present run commenced. On the basis of these measurements and check measurements made during the present run, the resistance of the anode and cathode connections combined was taken as 2×10^{-4} ohms/cell. The total resistance was thus estimated at 4×10^{-4} ohms/cell. This should approximate to the actual value for new cells; data available indicated that this was so. However, examination of the increase in voltage at specified current values during successive previous runs indicated that the internal cell resistance had increased with age to the average extent of $1.0–1.5 \times 10^{-4}$ ohms/cell. Accordingly, it was expected that the average resistance during the present run should be about $5.0–5.5 \times 10^{-4}$ ohms/cell for the period selected.

Current flowing through the cells was measured by an

ammeter of standard type. The total voltage drop over the 32 cells was measured by means of a voltmeter of suitable range and from the readings so taken, together with the known corrections for the potential drops in the leads, average cell voltages corresponding to observed current values were determined. In addition, one cell was selected for individual observation, the voltage for this cell being measured by means of a separate instrument of suitable range. Before the voltage readings were taken for any selected amperage the cells were run at this value for some time. Presumably because of polarization effects, when the cell current is altered the cell voltage does not adjust itself to the new equilibrium value at once. With the installation in question it took approximately 30 min for the cell voltage to settle down for current changes of 100–200 amp at current values above 200 amp. Below 200 amp a longer time was required. In the present experiment, two series of observations were made. In each series, observations were commenced at high current values. The current was then reduced by stages, one hour at least being allowed to elapse between the current change and voltage readings for the new value. Values so obtained were then checked by restoring the current to its original high value, again by stages with suitable intervals. Invariably under these conditions, readings corresponding to a particular amperage were effectively the same whether the approach was from a higher or a lower value. The first series of observations were made while the *p*H of the cell liquors was slightly on the alkaline side, the initial and final average *p*H values for this series being 7.4 and 7.1, respectively. The second series were taken on the acid side, the corresponding average *p*H values being 6.9 to 6.8, respectively. At the beginning of the first series the chlorate concentration was 39 g/l and the chloride concentration was 260 g/l. At the end of the second series the chlorate concentration was 67 g/l and the chloride concentration was 251 g/l. Cell temperatures were maintained at the desired value by a suitable control of the cooling water to each cell until all measurements were completed.

Results of this experiment for the observed cell are given in Table IV. The figures for one series only are given since those for the other series were almost identical. Average values for the 32 cells are given in Tables V and VI.

Tables V and VI show that the average cell voltages observed in this experiment agree well with the values calculated from Eq. (I) when the cell resistance R is taken as 5.5×10^{-4} ohms. The cell voltage for the observed cell, however, was consistently lower than the corresponding average value for all the cells. Assuming that the differences in voltage between individual cells is attributable to differences in cell resistance, results indicate that the resistance of the observed cell was about 4.8×10^{-4} ohms. E_{calc} in Table IV is derived on this basis.

TABLE IV. *Current-voltage: values for 1 cell*

Temp, 25°C *p*H 6.8–6.9

I (amp)	E_{calc} (v)	E_{obs} (v)	I (amp)	E_{calc} (v)	E_{obs} (v)
50	2.07	2.12	795	3.06	3.03
150	2.40	2.44	900	3.13	3.12
200	2.50	2.52	925	3.14	3.13
260	2.61	2.58	1000	3.19	3.20
300	2.66	2.65	1100	3.26	3.26
325	2.70	2.66	1150	3.28	3.30
665	2.97	2.94	1250	3.35	3.35

TABLE V. *Current-voltage: averages for 32 cells*

Temp, 25°C *p*H 7.4–7.1

I (amp)	Anode C.D. (amp/cm²)	V_a (v)	Cathode C.D. (amp/cm²)	V_c (v)	RI (ohms)	E_{calc} (v)	E_{obs} (v)
50	0.002	0.56	0.001	0.40	0.03	2.08	2.26
100	0.004	0.67	0.002	0.45	0.06	2.27	2.35
200	0.008	0.82	0.004	0.49	0.11	2.51	2.49
300	0.012	0.91	0.006	0.52	0.17	2.69	2.63
500	0.020	0.96	0.010	0.56	0.27	2.88	2.87
650	0.026	0.98	0.013	0.58	0.36	3.01	3.00
810	0.032	1.00	0.016	0.59	0.45	3.13	3.11
955	0.038	1.01	0.019	0.60	0.53	3.23	3.25
1000	0.040	1.01	0.020	0.61	0.55	3.26	3.27
1100	0.044	1.02	0.022	0.62	0.61	3.34	3.34
1250	0.050	1.03	0.025	0.63	0.69	3.44	3.44

TABLE VI. *Current-voltage: averages for 32 cells*

Temp, 25°C *p*H 6.9–6.8

I (amp)	Anode C.D. (amp/cm²)	V_a (v)	Cathode C.D. (amp/cm²)	V_c (v)	RI (ohms)	E_{calc} (v)	E_{obs} (v)
50	0.002	0.56	0.001	0.40	0.03	2.08	2.13
150	0.006	0.76	0.003	0.48	0.08	2.41	2.46
200	0.008	0.82	0.004	0.49	0.11	2.51	2.52
260	0.010	0.90	0.005	0.50	0.14	2.63	2.65
300	0.012	0.91	0.006	0.52	0.17	2.69	2.67
325	0.013	0.93	0.006	0.52	0.18	2.72	2.70
665	0.027	0.98	0.013	0.58	0.37	3.02	3.02
795	0.032	1.00	0.016	0.59	0.44	3.12	3.10
900	0.036	1.01	0.018	0.60	0.50	3.20	3.20
925	0.037	1.01	0.018	0.60	0.51	3.21	3.22
1000	0.040	1.01	0.020	0.61	0.55	3.26	3.27
1100	0.044	1.02	0.022	0.62	0.61	3.34	3.36
1150	0.046	1.02	0.023	0.62	0.63	3.36	3.41
1250	0.050	1.03	0.025	0.63	0.69	3.44	3.46

Back EMF Measurements

In earlier runs with the cells mentioned above it was noticed that the back emf of these cells when freshly filled, and before electrolysis was started, was in the neighborhood of 1.6 v. At the commencement of the experimental run already described, before any current was passed, it was found to be 1.60 v for the observed cell and the average cell back emf for the 32 cells was found to be 1.59 v. Corresponding initial cell temperatures were 10° and 9.5°C, respectively. The current was then switched in at a very low amperage and gradually increased to 40 amp. Simultaneously, voltage readings were taken and it was found that cell voltage increased nearly linearly with current over this range. The circuit was then broken and the back emf was again measured. This was now found to be 1.75 for the observed cell and 1.85 (avg) for the remainder. It showed no tendency to fall below this value on being left standing for 30 min. The current was again switched in after this interval and again increased by stages. It was now found that the voltage increased regularly with the current, the shape of the current-voltage curve being generally similar to those obtained by plotting data given in Tables IV, V, and VI.

There was no evidence of a definite decomposition voltage at any stage.

After the cells had settled down, some measurements were made to determine the back emf of the cells at various current values. The method adopted was simply to open the main switches of the cell circuit at the current values selected and observe changes in cell voltage. These measurements could not be very precise under the conditions of the experiment, but they definitely indicated a back emf corresponding to each current value which was reproducible. On cutting out the cells it was observed that the voltage dropped suddenly to a certain value and then decreased very slowly thereafter. It was found that the back emf decreased slightly as the corresponding current was decreased. The decrease appeared to be fairly regular. In the vicinity of 1000 amp the recorded back emf was 2.37 v; in the vicinity of 500 amp it was 2.32; in the vicinity of 200 amp it was 2.30 v. On reducing the current to zero slowly and then isolating the cells it was found to be approximately 2.10 v but this value seemed to depend on the rate at which the current was reduced before isolating the cells. On leaving the cells standing on open circuit the emf fell to 1.85 v in 1 hr. These measurements were made at 25°C.

It was noticed in the course of the foregoing experiments that the needle of the voltmeter frequently paused momentarily at a somewhat higher value than that at which it steadied and which was taken as the back emf. For instance, at 670 amp when the cells were quickly isolated, the voltage dropped rapidly, paused at about 2.4 v, and then quickly dropped to the value 2.34 v. Although successive readings were not very concordant, there is an indication that this happens at all parts of the current range investigated. It might have been, however, an inductive effect.

Discussion and Conclusion

Variation in cell voltage at 25°C with electrode current densities appears to be accounted for adequately by Eq. (I) for anode current densities above 0.005 amp/cm². At lower anode current densities, calculated values deviate from those observed. Indeed, the closeness of the agreement between observed and calculated voltages above this value is rather surprising since one would expect greater irregularities in measurements involving electrode overvoltages which were not made under very carefully controlled laboratory conditions. Fluctuations of at least 0.05 v would be expected and variations in the condition of the electrode surfaces should be reflected in variations in overvoltage values.

A laboratory investigation confirmed the results reported above (9). The experimental cells used were fitted with graphite anodes and iron cathodes. A linear equation in the form of (I) was found in all cases to apply above 0.015 amp/cm², the value for the constant at 25°C being always close to 1.1 v., and the reproducibility of the measurements was sufficient to justify the conclusion.

The most obvious interpretation is that above a certain anode current density the reaction system adjusts itself to constitute a cell having a reversible potential of 1.09 v. This in turn suggests that the anode of a chlorate cell is essentially an oxygen electrode rather than a chlorine electrode. On the other hand, at very low current densities, the anode probably behaves as a chlorine electrode and this conclusion would appear to accord with the results of Foerster, Müller, Luther, and others (4). It may be said in passing that the behavior of the cell voltage at low current densities noticed in the present experiments was generally what would be expected from the results of these workers.

It would be interesting to repeat calculations using chlorine overvoltages instead of the oxygen values. However, comparable values for chlorine overvoltages on graphite at 25°C are not available for current densities below 0.04 amp/cm², that is, for a great part of the range considered above. Nevertheless, if the values given by Knobel and co-workers (6) are plotted against current density as was done in the case of the oxygen overvoltages, the chlorine overvoltage curve so obtained is parallel to the corresponding oxygen curve in the range 0.04–0.20 amp/cm². In fact for this range, $V_o \simeq V_{Cl} + 0.84$ v. Assuming that this parallelism continued down to low values for the anode current densities, experimental results would be equally well expressed by the equation:

$$E_{obs} = 1.93 + (V_{Cl} + V_c) + RI \qquad \text{(II)}$$

Considering the cell back emf, at about 800 amp, this was approximately the same as that noted by Knibbs and Palfreeman (1) for a cell which had a Pt anode. However, they found that the back emf was independent of current density over a fairly wide range, whereas the present experiments indicated a decrease with current density. It is to be noted that they attempted to correlate their results with Newbery's overvoltage values, but were unable to account for the cell voltage on this basis. Why this was so is now clear. Newbery's overvoltages were obtained by the original commutator method which only measures a part of the total electrode polarization when the current is flowing. In addition, the back emf does not measure the quantity represented above as $1.09 + V_a + V_c$, the discrepancy between this quantity, (2.71 v at 1000 amp in the foregoing experiments), and the back emf corresponding (2.37 v) apparently arising in the same way as the similar discrepancies noticed between overvoltages measured by the direct and commutator method. Hence, the precise significance to be attached to back emf measurements in the present case is not clear but it may possibly be worth noticing that the values obtained by Newbery (10) for a laboratory cell with carbon electrodes and H_2SO_4 bear a close resemblance to the values noted above.

Over-all, the results appear to be in harmony with the idea that both hydroxyl and chlorine ions are discharged at the anode. This conclusion would seem consistent likewise with the results of Pfleiderer (5) and earlier workers. It is also supported by the work of Glasstone and Hickling (11) and accords with the theory of the process recently given (12). Hydroxyl discharge and the associated oxygen overpotential perhaps may be the principal factors determining the anode potential at appreciable current densi-

ties. In any case, the results furnish a basis for assessing the energy efficiency of a chlorate cell at specific current densities.

ACKNOWLEDGMENT

The author must thank Professor T. S. Wheeler for his interest and the many facilities he made available during the course of the work.

Manuscript received April 27, 1956.
Any discussion of this paper will appear in a Discussion Section to be published in the December 1957 issue of the JOURNAL.

REFERENCES

1. N. V. S. KNIBBS AND H. PALFREEMAN, *Trans. Faraday Soc.*, **16**, 402 (1920).
2. P. H. GROGGINS, A. L. PITMAN, AND F. H. DAVIS, *Chem. & Met. Eng.*, 468 (1940); Rogers "Industrial Chemistry," 1942, I, 458.
3. H. J. CREIGHTON AND W. A. KOEHLER, "Electrochemistry," Vol. II, p. 280 (1935).
4. F. FOERSTER, "Elektrochemie Wässeriger Lösungen," Chap. 14, Leipzig, 1923; R. LUTHER AND F. J. BRISLEE, *Z. Phys. Chem.*, **45**, 216 (1903); and ref. (5) below.
5. G. PFLEIDERER, *Z. Phys. Chem.*, **68**, 49 (1909).
6. M. KNOBEL, P. CAPLAN, AND M. EISEMAN, *Trans. Am. Electrochem. Soc.*, **43**, 55 (1923).
7. J. MCLAREN, J. TURER, F. H. DAVIS, A. L. PITMAN, AND P. H. GROGGINS, *ibid.*, **79**, 93 (1941).
8. A. L. PITMAN, J. MCLAREN, F. H. DAVIS, AND P. H. GROGGINS, *Chem. & Met. Eng.*, **45**, 692 (1938).
9. V. DE VALERA, Dissertation, National University of Ireland (1955).
10. E. NEWBERY, *Trans. Faraday Soc.*, **15**, 126 (1919).
11. S. GLASSTONE AND A. HICKLING, *J. Chem. Soc.*, **1932**, 2345, 2800; **1933**, 829; **1934**, 10.
12. V. DE VALERA, *Trans. Faraday Soc.*, **62**, 250 (1956); *ibid.*, **49**, 1338 (1953).

Influence of Impurities in the Electrolyte in Chlorine-Caustic Electrolysis by the Mercury Cell Process

VI. Investigation of the Influence of Graphite Particles on Amalgam Decomposition and Cathodic Current Efficiency

GÖSTA ANGEL, ROLF BRÄNNLAND, AND STIG DAHLERUS

Division of Applied Electrochemistry, Royal Institute of Technology, Stockholm, Sweden

ABSTRACT

The influence of graphite particles on the Hg cell process for the production of chlorine and caustic soda has been investigated using the technique described in a series of earlier papers, *viz.*, partly by shaking sodium amalgam with buffered solutions of NaCl and measuring the decomposition rate, and partly by studying the cathodic current efficiency of a Hg cell for laboratory use.

The experiments show that the effect of moderate quantities of graphite (< 3 g/l) is small in pure brine but that, in the presence of Mg or Al, the loss of current efficiency is appreciable. The simultaneous presence of graphite and either Fe, Ca, or small quantities of V (< 0.1 mg/l) does not affect the electrolysis process. Silicates and stannates inhibit the action of the graphite particles.

Besides the metallic impurities earlier investigated (1-5), graphite is usually present in technical brines, viz., in the form of a suspension. Opinions are very much divided about the influence of the graphite; considering the action of graphite in the amalgam decomposer, a strong decrease of the cathodic current efficiency may be expected in the presence of graphite particles in the brine. On the other hand, it has been shown practically that it is possible to run a Hg cell with an extremely graphite-rich brine without any noticeable influence on the current efficiency.

In order to elucidate the effect of the graphite, a series of experiments with graphite-contaminated brines was performed. The investigation was carried out partly as amalgam decomposition experiments and partly as electrolysis experiments in a laboratory cell. Varying particle size and concentration of the graphite as well as the simultaneous presence of Mg, Al, Fe, and V were investigated. In all cases, the graphite powder was obtained by crushing and screening fresh anode pieces of various origins.

AMALGAM DECOMPOSITION EXPERIMENTS

Complete agreement could not be expected between amalgam decomposition and electrolysis experiments since the reaction conditions are quite different in the two cases. In the latter, a well-defined cathode film is formed over a quiet Hg surface (6) and the graphite particles are affected mainly by convection forces caused by the gases

formed at the cathode. In the former, the contact surface between brine and Hg is continuously regenerated and simultaneously a relatively high concentration of buffering substances contributes to a breakdown of the alkaline film at the Hg surface. Furthermore, the graphite particles come into very close contact with the Hg phase when, due to shaking, thin layers of the brine are forced toward the walls of the reaction vessel by the Hg. Deviations in results of the two types of experiments, however, make it possible to draw important conclusions concerning the mechanism of the reactions investigated.

Amalgam decomposition experiments were carried out in exactly the same manner as those described earlier (1–3) except that a certain quantity of graphite powder, after careful washing and classification with respect to particle size, was added to the buffered brine. The decomposition rate of the amalgam was studied by measuring the volume of H formed per minute.

Influence of particle size.—The following particle sizes were investigated: G_0 < 0.30 mm; G_1 0.30 – 0.43 mm; G_2 0.55 – 1.00 mm.

The experiments showed that the large particles were crushed in a few minutes to smaller dimensions. Some representative results are shown in Fig. 1. These curves indicate that larger particles would have only a small effect but, due to crushing, form a finer and more active powder. For unknown reasons, the finest grains on the other hand seem to be gradually de-activated.

Influence of graphite concentration.—A series of experiments was performed with the smallest particle size (<0.3 mm) in which the graphite concentration was varied. These experiments demonstrate, Fig. 2, that the reaction rate increases with increasing graphite concentration only to a certain extent. However, for higher graphite concentrations, the reaction rate falls off gradually, possibly due to an agglomeration of the graphite particles to larger aggregates.

Influence of graphite in the presence of metal ions.—In the presence of 250 mg/l of the finest graphite fraction, the effect of a number of cations, viz., Fe, Mg, and Al, was studied. Their concentrations in the brine were 25 mg/l in the case of Fe and Mg and 5 mg/l in the case of Al. In all experiments no increased H evolution beyond that of the pure graphite effect could be observed.

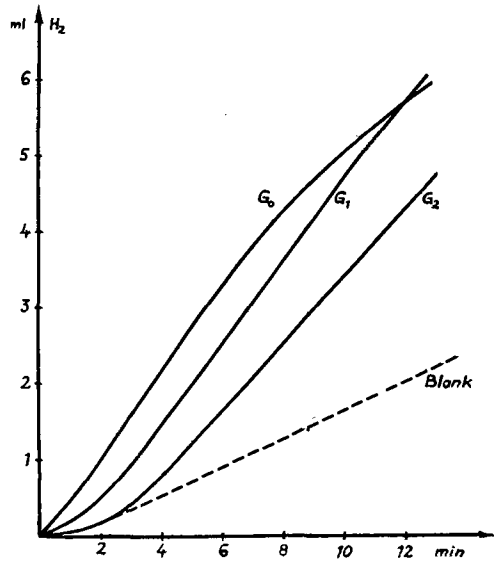

FIG. 1. Amalgam decomposition rate vs. particle size (500 mg/l graphite).

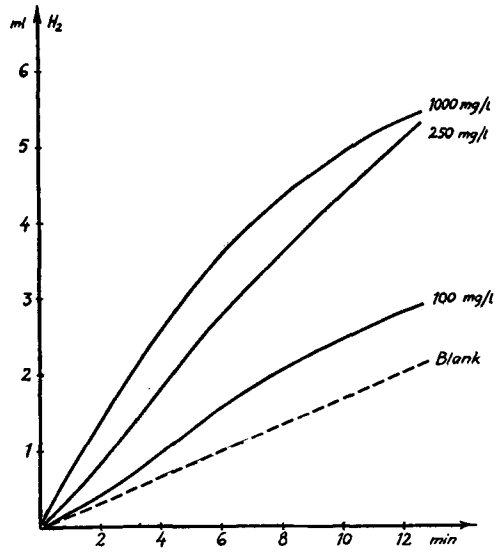

FIG. 2. Amalgam decomposition rate vs. graphite concentration (particles <0.30 mm).

ELECTROLYSIS EXPERIMENTS

Experiments were performed in the apparatus previously described (4, 5). In order to facilitate the reaction in the amalgam decomposer, an electric preheater for the water was supplied. A temperature of 40°–60°C in the secondary cell was thereby obtained and the electrolyzer could be run without difficulty with a cathodic current efficiency of 99.6–99.9%. The brine feeding rate was 0.40–0.45 l/h, the current density 25 amp/dm^2, and the Hg circulation rate about 10.4 ml/min, corresponding to a Na concentration of 0.1% in the amalgam. Current efficiency was determined either by analysis of the departing Hg or by determination of the H content in the chlorine gas.

Since it was impossible to maintain a uniform graphite content in the feeding brine, graphite was added directly to the electrolysis cell. When other impurities were investigated, the cell was fed with brine containing the actual metal salt, while the graphite was added directly to the cell.

Influence of particle size.—For electrolysis experiments with pure brine, a weighed quantity of graphite (0.1 g) dispersed in saturated brine, was added to the cell.

No influence on the electrolysis process could be observed with particle sizes > 0.3 mm. Graphite particles did not seem to come into contact with the cathode, were gradually broken up into smaller pieces, and were conveyed out of the cell together with the departing brine.

With particle sizes < 0.3 mm, a slight H evolution was observed (0.5–1.5%) immediately after the graphite addition, but the electrolysis then proceeded undisturbed and the graphite was gradually removed with the brine. H evolution was mainly concentrated at the Hg seal and, to a very slight extent, at the boundary between Hg and

glass wall. Graphite entered the cell as a thick suspension and part of it was immediately conveyed by the Hg to the seal where, owing to the vigorous streaming of the Hg, it came into contact with the amalgam, the decay of which was thereby promoted. After the graphite had become more uniformly dispersed in the cell, H evolution ceased.

Influence of graphite concentration.—Graphite was added in quantities up to 0.4 g, corresponding to about 3 g/l in the cell. No measurable increase in the activity in this concentration range and also no differences between graphite samples of various origins could be observed. Thus, graphite particles in otherwise pure brines do not interfere with the electrolysis process.

If very large graphite particles fall on to the cathode, they may come into direct contact with the Hg and, owing to the low overvoltage of H on graphite, H gas is formed at the graphite surface. Since such pieces generally have a small area compared with the whole of the cathode, the resultant H evolution seems to be of no practical importance.

Influence of graphite and Mg *when present simultaneously.*—On electrolyzing Mg-containing brine, it was found that the addition of graphite may have a disastrous influence on the current efficiency. It has already been reported (5) that, with high Mg concentrations, the cathode is covered with a layer approximately 1 mm thick, probably consisting of a mixture of hydroxide and amalgam.

If graphite is present in the brine, it will stick in the hydroxide film and thereby come into firm electrical contact with the Hg. Owing to the low H overvoltage on graphite and the large surface of the graphite particles, a very considerable decrease in the cathodic current efficiency is caused. Fig. 3 shows a typical current efficiency curve from an experiment with 5 mg/l Mg and 0.1 g graphite. Only the first part of the curve (corresponding to 10-min electrolysis) could be reproduced exactly since the hydroxide film caused a very irregular streaming of the Hg and, hence, considerable error in the analyses.

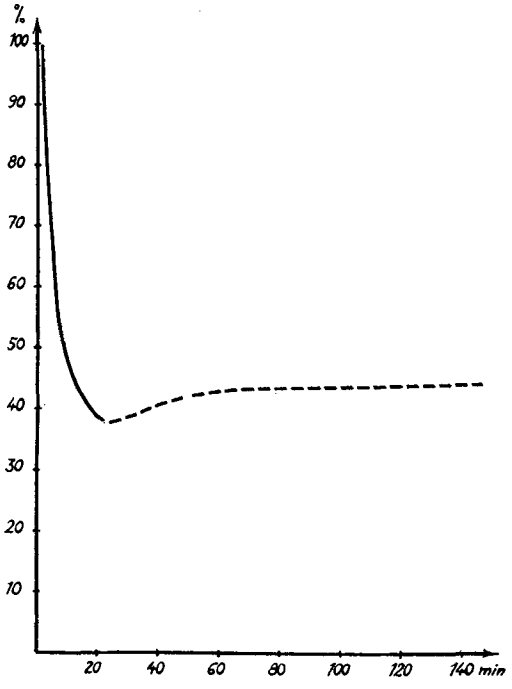

FIG. 3. Cathodic current efficiency vs. time (5 mg/l Mg + 100 mg/l graphite, particles <0.30 mm).

The reaction seemed to be practically independent of the quantity of graphite added; experiments were performed with graphite additions down to 0.01 g with a current efficiency of about 40%. Brines containing 1.0 and 2.5 mg/l Mg were also investigated, but in these cases no decrease in the current efficiency could be observed.

Thus the experiments show that Mg in concentrations above 5 mg/l and in the presence of graphite particles affect the cathodic current efficiency disastrously. However, owing to the special streaming conditions of Hg, the electrolysis cell used for these experiments is considerably more sensitive to impurities of this kind than are technical Hg cells.

Influence of Al *and graphite when present simultaneously.*—In experiments with Al as a brine contaminant (5), it was found that this also forms a thin cover on the Hg. If graphite particles were present simultaneously, they stuck in the layer and, with 5 mg/l Al, a reaction analogous to that of Mg-containing brine was obtained, cf. Fig. 3. Current efficiency thus decreased to about 40%. Experiments with 1.0 and 2.5 mg/l Al caused no decrease in current efficiency.

Influence of graphite and either V, Fe, or Ca *when present simultaneously.*—Addition of graphite to a solution containing either V (100 γ/l), Fe (10 mg/l), or Ca (25 mg/l) had no influence on current efficiency.

De-activation of Graphite by Addition of Sodium Silicate or Stannate

In a special series of experiments it was shown that it is possible to de-activate the interfering graphite particles by addition of sodium silicate or sodium stannate (10–50 mg/l Si or Sn). Both of these substances were very efficient inhibitors of graphite and the blank values for H evolution, i.e., values obtained with pure brine, were obtained in amalgam decomposition experiments with 250 mg/l graphite. This de-activation of the graphite particles may depend possibly on a covering of the electrochemically active centers on the particles with inhibitor molecules which are deposited on the graphite when the *p*H is lowered. This is also indicated by the fact that the sedimentation rate of the graphite particles is considerably increased on addition of both these inhibitors.

However, it should be observed that the colloidal silicic and stannic acids may be transported to the cathode in the electrolysis cell, thus hindering the diffusion of the Na ions and causing H evolution. Consequently, it would appear necessary to allow the inhibitors to flocculate and then to separate the precipitate from the brine before it is added to the cell.

Summary

The experiments have shown that graphite particles have a negligible influence on the cathodic current efficiency in Hg cells when the brine is pure. In the presence of Mg and Al in concentrations sufficient to form a hydroxide layer on the cathode, graphite particles cause an additional H evolution which decreases the current

efficiency to about 40%. Silicates and stannates inhibit the action of graphite particles.

These results explain why, in the chlorine-caustic field, one is generally anxious to avoid graphite in the brine whereas, on the other hand, examples are known of technical brines with high graphite contents which were regularly used without disturbances. Evidently these brines must have been very pure with respect to interfering metal salts.

ACKNOWLEDGMENTS

This investigation was promoted by a grant from Elektrokemiska AB, Bohus; Mo och Domsjö AB, Örnsköldsvik; Svenska Cellulosa AB, Sundsvall; and Uddeholms AB, Skoghall, for which the authors wish to express their deep appreciation.

Manuscript received July 16, 1956.

Any discussion of this paper will appear in a Discussion Section to be published in the December 1957 JOURNAL.

REFERENCES

1. G. ANGEL AND T. LUNDÉN, *This Journal*, **99**, 435 (1952).
2. G. ANGEL AND R. BRÄNNLAND, *ibid.*, **99**, 442 (1952).
3. G. ANGEL, T. LUNDÉN, AND R. BRÄNNLAND, *ibid.*, **100**, 39 (1953).
4. G. ANGEL, T. LUNDÉN, R. BRÄNNLAND, AND S. DAHLERUS, *ibid.*, **102**, 124 (1955).
5. G. ANGEL, T. LUNDÉN, R. BRÄNNLAND, AND S. DAHLERUS, *ibid.*, **102**, 246 (1955).
6. L. BARR, *ibid.*, **101**, 497 (1954).

Streaming Potential in Spherical-Grain Sands

WILLIAM SCHRIEVER AND CARL E. BLEIL

Department of Physics, University of Oklahoma, Norman, Oklahoma

ABSTRACT

Streaming potentials in very uniform spherical-grain sands were measured with doubly distilled atmosphere-saturated water and with NaCl, NaI, Na_2SO_4, $MgSO_4$, and $MgCl_2$ solutions. A vacuum tube electrometer was used to measure the potential differences.

The streaming potential, V, was directly proportional to the pressure difference, P, in every case, and V/P was independent of changes in configuration of the sand matrix as well as changes in its porosity and its length. A variation of V/P with grain diameter was only partially accounted for by surface conductance alone. Also neither Wood's equation nor Ghosh, Rakshit, and Chattoraj's equation fit the data well.

The data fit the empirical equation:

$$V/P = (V/P)_a(1 + k/d + k^2/d^2) \exp(-k/d)$$

where $(V/P)_a$ is the value approached in sands having large grains. For water $k = 535 \times 10^2\ \mu$ and $(V/P) = 51.2$ mv/cm-of-water. k is characteristic of spherical-grain sands since it was the same for all solutions, and $(V/P)_a$ is a function of solution composition at constant temperature. The ζ potential of a water-glass interface has a positive temperature coefficient whose approximate value is 0.039/°C, and the streaming potential has a positive temperature coefficient of 0.0535/°C.

It has long been known that the streaming potential for a liquid flowing through circular capillary tubes, all of one kind of glass, is proportional to the pressure difference and is independent of the length and radius of the tube. One might infer from this that the streaming potential per unit of pressure difference for a column of sand should be independent of the length of the column and of the diameter of the sand grains if the flow is laminar. In fact, the Helmholtz-Smoluchowski (1) theory predicts that the streaming potential is independent of the size and shape of the pore through which the liquid flows. A development given by Kruyt (2) leads to the same result. However, Bull and Gortner (3) reported a dependence of streaming potential on grain size for sand columns composed of sieved crushed quartz grains; for the smaller sizes the streaming potential decreased with the grain size. Their attempts (4) to explain these results by using the measured conductance of the liquid-filled matrix, instead of the conductance of the bulk liquid, were not completely successful.

Later Bull and Moyer (5) attempted to account for Bull and Gortner's results by taking into account the influence of the surface conductance, the electrical backpressure due to the electro-osmotic effect, and the change in viscosity of water with the capillary size. Their conclusion was: "The peculiar results obtained by Bull and Gortner with quartz particles . . . are still unexplained and are apparently inexplicable on the basis of any of the above calculations".

Rutgers (6) studied the variation of the ζ potential with the radius of the capillary. By taking into account surface conduction he arrived at the "true zeta potential" from the measured values computed by the use of the Helmholtz-Smoluchowski equation. His expression for the true ζ potential is:

$$\zeta = \zeta_0(1 + 2\lambda_s/r\lambda) \qquad (I)$$

where ζ_0 is the measured value, λ_s is the surface conductivity, λ is the conductivity of the solution, and r is the radius of the capillary.

Wood (7) arrived at a Helmholtz-Smoluchowski type equation in which the conductivity term λ_t is the effective conductivity of the tube of solution; thus surface conduct-

ance is taken into account. By making certain assumptions he arrived at an expression for the streaming potential in a column of sand, namely:

$$\eta V\lambda_t/P = M - A/d \qquad \text{(II)}$$

where η is the coefficient of viscosity, V is the streaming potential for a pressure difference P, d is the diameter of the sand grains, and M and A are empirical constants. He found that a proper choice of M and A made this equation a good fit to Bull and Gortner's data for quartz sands.

It is interesting to note that Rutger's equation can lead to an equation similar to Wood's if Wood's assumption, that the effective diameter of the pore space between the sand grains is directly proportional to the diameter of the grains, is made. When this is done one can write:

$$P/\eta V\lambda = N + B/d \qquad \text{(III)}$$

where λ is the conductivity of the solution, and N and B are adjustable constants.

Ghosh, Rakshit, and Chattoraj (8) arrived at a relation for the ζ potential, determined in a sand, that is exactly of the same form as Eq. (I). Therefore, their equation leads directly to Eq. (III). They tested their equation with the data of Bull and Gortner and found it satisfactory.

It may be observed that if A/d in Eq. (II) is very small compared to M, the reciprocal of $(M - A/d)$ is approximately equal to $(M + A/d)$, and that therefore Eq. (II) can be put in the exact form of Eq. (III). Both of these equations are empirical equations even though the capillary tube theory was used as a background in setting them up. They differ in that Eq. (II) takes surface conductance into account in λ_t and any other effect of grain diameter in the terms M and A/d, whereas Eq. (III) takes account of both of these effects in the two terms N and B/d.

In order to make certain practical applications of streaming potential it is important to know how the streaming potential in a sand column depends on the size of the sand grains. In the study of this problem it was deemed advisable to use the most nearly ideal sands that could be provided, namely, sands each composed of spherical glass grains of very uniform size.

The purpose of this research was to establish the effect of grain-size on streaming potential in spherical-grain sands and to determine the effect of temperature and solution composition on such streaming potentials.

Experimental

Apparatus

Flow-tubes.—Two flow-tubes were used. The first was constructed of a rod of Lucite by boring an accurate hole 2 cm in diameter throughout its entire length. Two accurately machined Lucite pistons were arranged so that the distance between them was adjustable over a range of 11 cm. Holes were drilled in each piston to allow liquid to pass freely through it, and a 150-mesh (58 mesh/cm) Pt screen, forming the face of the piston, served both as a potential probe and to prevent the sand from passing through the holes. A port-hole provided with a plug and covered by a cap was made in the side of the tube; this permitted additions of sand to be made without completely disassembling the apparatus.

This flow-tube was mounted in a metal box which was partially submerged in a thermostatically controlled water bath. It was found necessary to use a stirrer driven with an induction motor since arcing at the brushes was observed to disturb seriously the potential measuring electrometer.

The pressure on the solution was supplied by compressed air acting on top of a glass piston in a large vertical glass tube which served as a reservoir. The liquid was heated to the desired temperature by an electric preheater. The line from the reservoir to the flow-tube was Pyrex glass. Very short lengths of Saran tubing were used for connectors. The pressure difference across the sand column was measured with a suitable mercury and water manometer. The volume rate of flow of the solution was determined with a calibrated flow-meter which consisted of an inclined open-end manometer for indicating the pressure difference across a short length of small-bore tubing.

The entire system was electrically shielded with sheet metal, and shielded leads connected the electrodes in the flow-tube to the shielded electrometer. All metal shielding was grounded to a water pipe.

Preliminary experiments with this plastic flow-tube revealed a variation of streaming potential per unit of pressure difference, V/P, with the diameter of the sand grains. Although different batches of the distilled water used for these experiments were as nearly identical as could be produced by a careful double distillation, one could not be certain that at least a part of the observed change of V/P with grain diameter was not due to slight variations in the distilled water. Therefore, a second flow-tube was constructed in such a manner that exactly the same liquid flowed through each of the different sands.

This second flow-tube was made of a 1.5 cm. diameter Pyrex glass tube. Five 1 cm-long No. 28 B&S gauge Pt wire probes were sealed through the wall of the tube at 3.5 cm intervals. Directly above each electrode an open manometer tube was sealed to the flow-tube. Two additional Pt electrodes were sealed through the glass near each end of the flow-tube; these were used to send an electric current through the sand columns during the resistance measurements. Each of the four 3.5-cm intervals was filled with a sand having a different grain diameter. The ends of this flow-tube were equipped with ground joints so that the flow of the solution could be reversed easily through the contiguous sand columns. The solution was supplied at the desired constant pressure from a Mariotte's bottle which was mounted on a vertically continuously adjustable platform. A plug of glass wool prevented the sand from entering the lower end of each manometer. The volume rate of flow was calculated from the mass of the solution caught in an observed time interval. This entire system was mounted in a wire screen cage and shielded leads were used to connect the probes to the electrometer.

Spherical grain sands.—The sands were composed of spheres of soft glass.[1] They were sorted very carefully by

[1] Obtained from the Cataphote Corp., Toledo, Ohio.

retaining only those spheres which stuck in the meshes of the appropriate Tyler sieves. Four sizes were prepared: 50, 80, 90, and 100-mesh (0.300, 0.175, 0.153, 0.147 mm). After sorting, beads of each size were washed in water containing a detergent, rinsed several times, and dried. The beads next were washed in concentrated nitric acid for 24 hr, and then at least 12 times in doubly distilled water until the *p*H of the water was the same before and after rinsing. Finally the beads were dried in an electric oven at 400°C.

Liquids.—The water was distilled first in a tin-lined still and then in an all-Pyrex glass system. It was allowed to stand in contact with the atmosphere with periodic stirring for 2–4 days, after which it was found that the Beckman *p*H meter indicated a constant *p*H in the range 5.48–5.65.

NaCl solutions in concentrations of 10^{-6}, 10^{-5}, 10^{-4}, and 10^{-3} mole/kg of water, and solutions of concentrations 10^{-5}, 10^{-4}, and 10^{-3} mole/kg of each of the salts $MgCl_2$, $MgSO_4$, Na_2SO_4, and NaI, were prepared with the distilled water described above, and with AR grade salts.

Electrometer.—A vacuum-tube electrometer having a Victoreen 5803 electrometer tube, was used to make all potential difference measurements. The circuit included a multiple contact key which, when depressed connected a highly insulated 0.001 mf condenser to the two probes whose potential difference was desired; when the key was released it connected the charged condenser to the grid and filament of the tube. The resulting change in plate current was indicated by the steady deflection of a critically damped galvanometer containing the magnet and coil of a L&N type 2420 instrument, but having a 50 cm scale distance. The electrometer contained its own calibrating circuit. It was found that the scale deflection was directly proportional to the potential difference of the condenser for steady deflections both to the right and to the left of zero. The two sensitivities used were 3.63 mv/mm and 10.06 mv/mm.

The rate at which charge was delivered by the streaming through a sand column was found to be so small that it required nearly 5 sec to charge the 0.001 mf condenser to a potential difference of the order of 0.1 v. Therefore the key was depressed for 5 sec for each potential measurement; this gave duplicable results.

It was found necessary to have all elements of the grid-probe circuit, including switches and the multiple-contact key, provided with polystyrene insulation. The shielded leads to the probes had polyethylene insulation.

Microammeter.—A two-megohm potential divider connected across a 45-v dry-cell battery was used to send a current through a sand column for resistance measurements. This current was measured with a Rubicon galvanometer shunted with a critical-damping resistor of 12,000 ohms. This current meter had a sensitivity of 2.28×10^{-8} amp/mm.

Experimental Procedure

The procedure for obtaining data showing streaming potential as a function of pressure difference was essentially the same for both flow-tubes. The sand was placed in the flow-tube in the presence of water to insure the removal of all the air. The tube was jarred gently with a rubber mallet, and mechanical pressure was applied to pack it securely in place. In the case of the plastic tube, pressure was applied by tightening the plastic screw above one of the pistons.

The sand column was then flushed out by running the desired liquid through it for an hour. Next, the liquid-filled column was allowed to stand for 24 hr after which it was thoroughly flushed out again. In addition, just before streaming potential measurements were made the liquid was allowed to flow through the system for about an hour, the flow was stopped, and the potential difference of the probes was measured; hereafter, this is designated the self-potential of that pair of probes.

The flow was started again and, after the system reached dynamic equilibrium as indicated by the manometer, the potential difference of the probes was measured again. Such potential differences were then measured for various pressure differences. After the series of measurements at different pressures was completed the self-potential was measured again. This self-potential was subtracted from the potential difference observed during the streaming of the liquid; this difference was the observed "streaming potential". These observed streaming potentials turned out to be zero for zero pressure difference, to within the reproducibility of the measurements. For each pressure difference the volume rate of flow was measured.

At the end of each set of measurements at various pressures the electrical resistance of the liquid-filled sand column was measured. This was achieved by measuring the fall of potential across the sand column for a measured direct current through the column. In the plastic flow-tube the current was introduced at the screens; it was always less than 3×10^{-7} amp. In the Pyrex flow-tube the current was introduced at the two end-electrodes and the potential differences of the different pairs of probes were measured; again the currents were kept below 3×10^{-7} amp.

Results

Streaming potential as a function of pressure difference.—A typical set of curves depicting streaming potential, V, as a function of pressure difference, P, for four sizes of spherical-grain sands, is shown in Fig. 1. These curves were obtained with the Pyrex flow-tube.

Similar sets of curves were obtained for the doubly distilled atmosphere-saturated water and for each of the solutions listed earlier. In every case V was found to be directly proportional to P. Usually the pressure differences ranged from 1 to 10 cm-of-water for the 100-mesh beads and from 1 to 3 cm-of-water for the 50-mesh beads. For the water V/P varied regularly from 42.5 mv/cm-of-water for the 50-mesh beads to 13.4 mv/cm-of-water for the 100-mesh beads. The value of V/P decreased with increasing concentration of solution.

Streaming potentials in several sand columns were measured up to pressure differences of 1 atm. Here again V was found to be directly proportional to P.

The resistances of the water-filled sand columns in the Pyrex tube varied from 3.2×10^5 ohms for the 50-mesh to 1.7×10^5 ohms for the 100-mesh beads. Resistances of

the salt-solution-filled sand columns were less than those for water, and they decreased with increasing concentration for each salt.

In every case the volume rate of flow through a sand column was proportional to the pressure difference. Rates of flow varied from 0.01 cm³/sec at the lowest pressure used up to 0.12 cm³/sec for the highest pressure differences. For any one set of curves the temperature was held constant in the neighborhood of 27°C.

The data described above were used for making calculations concerning the variation of V/P with grain size.

Effect of configuration and porosity of the sand matrix on V/P.—The 90-mesh glass beads in the plastic flow-tube were used in these experiments. A fixed mass of the beads was packed to a fixed length of column several different times; between packings the beads were thoroughly shaken up. With water as the liquid it was found that the values of V/P obtained for the different packings agreed well within the reproducibility of the measurements. These data showed that V/P did not vary with the configuration of the matrix.

A column of the beads approximately 17 cm long was packed successively to porosities of 0.432, 0.411, and 0.392. It was found that V/P was constant within the reproducibility of the measurements for these three packings. As would be expected the volume rate of flow decreased regularly as the porosity decreased. These results show that V/P does not vary measurably with experimentally obtainable porosities.

Effect of length of sand column on V/P.—Three different columns of the 90-mesh beads, having lengths of 4.05, 13.23, and 17.02 cm, were packed successively to the same porosity in the plastic flow-tube. It was found that V/P was the same for all three columns to within the reproducibility of the measurements. These results demonstrated that V/P is independent of the length of column of a spherical grain sand.

Effect of grain diameter on V/P.—As was explained earlier the Pyrex tube with its four contiguous sand columns was designed especially for this study. Although exactly the same liquid passed through each column there was the possibility that modification of the liquid occurred during its passage through the successive sands. Two separate checks showed that such a change did not take place. First the *p*H's of the incoming and outgoing liquid were measured, the latter being made after the liquid had been standing in the sands for 48 hr and then as a function of time thereafter. It was found after about an hour of flow that the two *p*H's were the same. The second check was accomplished by reversing the flow through the entire system and observing V/P for each direction. It was observed that V/P for each of the four sand columns was the same for both directions of flow. If appreciable modification of the liquid had occurred during its passage through the four contiguous columns, this result would not have been observed. Thus it is clear that the change of V/P with grain diameter, as shown by Fig. 1, was not due to change in the constitution of the liquid.

Exactly the same four sand columns were used in obtaining all the data for all the solutions. It should be added that, before using the sands for the solutions of a new salt,

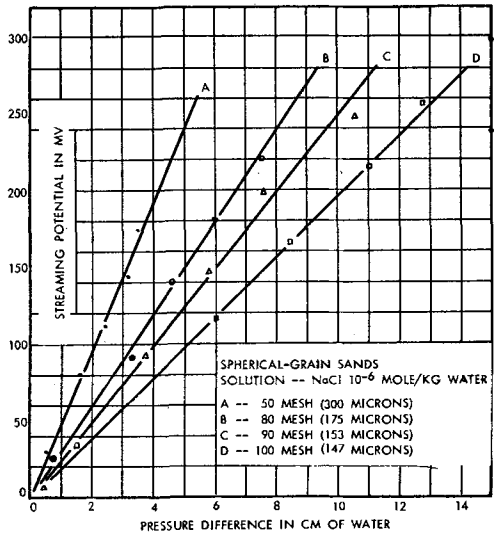

FIG. 1. Streaming potential as a function of pressure difference for four sizes of spherical-grain sands.

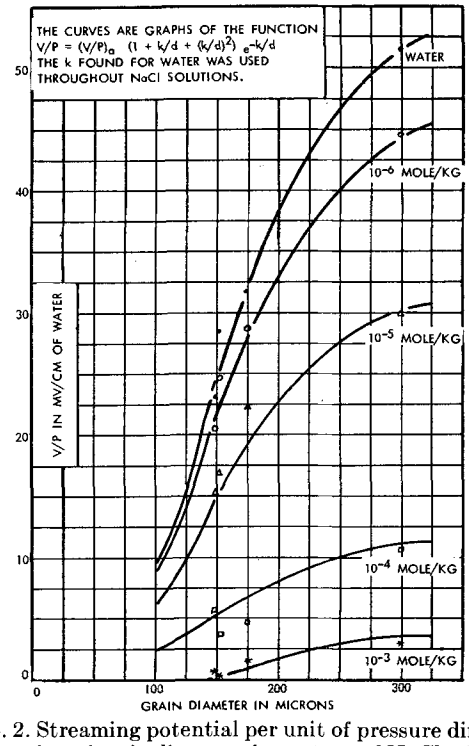

FIG. 2. Streaming potential per unit of pressure difference as a function of grain diameter for water and NaCl solutions.

the sands were washed with the doubly distilled water until the V/P for each sand had returned to the original value obtained with water.

Variation of V/P with grain diameter for water and for the four concentrations of NaCl are shown in Fig. 2. Similar curves for NaI, Na_2SO_4, $MgSO_4$, and $MgCl_2$ are shown in Fig. 3. Each of the 15 different liquids exhibited a V/P that decreased with decrease in diameter of the spherical sand grains, and that for any one salt the magnitude of the decrease became less as the concentration of the salt became greater.

Resistance of a liquid-filled sand column.—It has been suggested that the variation of the streaming potential

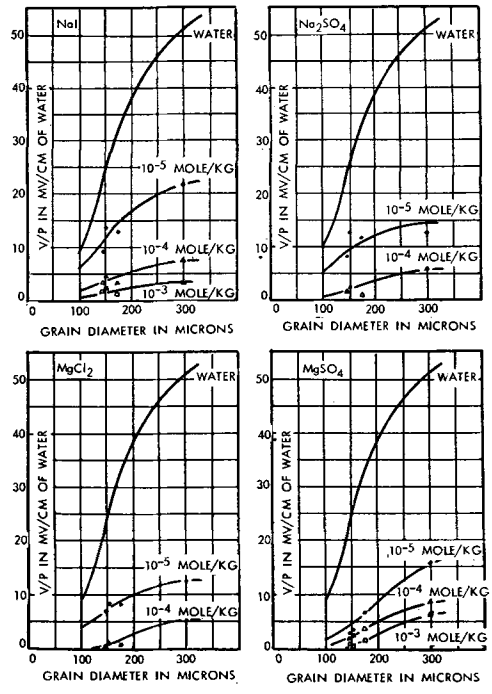

FIG. 3. Streaming potential per unit of pressure difference as a function of grain diameter for various concentrations of four different salts.

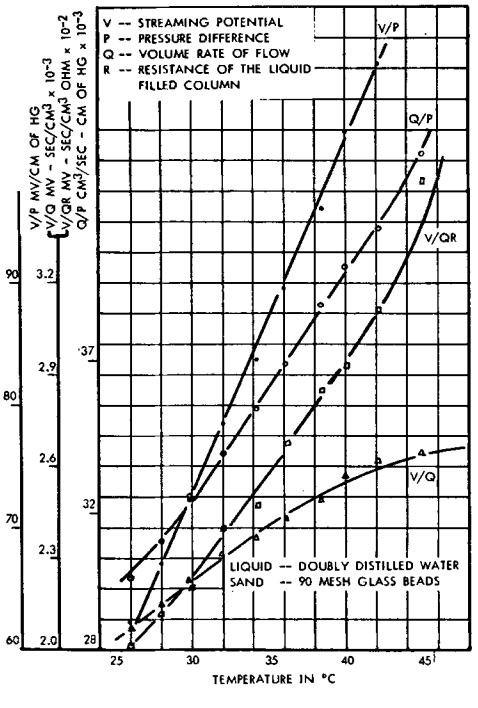

FIG. 4. Effect of temperature on streaming potential

with diameter of sand grain might be explained by the change in the fraction of the conductance of the liquid-filled sand column that is due to the conductance of the liquid-glass interface. For this reason the resistance of each liquid-filled sand column was measured by sending a measured current of less than 3×10^{-7} amp from a battery through the four contiguous columns in the Pyrex flow-tube, and then observing the potential drop between each pair or probes with the electrometer. The self-potential was subtracted from each of the observed potential differences. It was difficult to obtain satisfactory results. Fortunately, with four columns in series the resistance of two or more columns in series could be checked against the sum of the resistances of the separate columns. These resistance determinations were made with the liquid at rest in the sand but after the liquid had flowed through the sand for at least an hour.

If the observed curves of the streaming potential as a function of grain diameter are to be explained solely by the increase in the surface conductance of the liquid-glass interfacial layer, then V/PR (R is resistance of column) should be independent of the diameter of the sand grain. Dividing the values of V/P in Fig. 2 by the appropriate resistances did bring the curves much closer together, but each curve still showed that V/PR decreased regularly with decrease in grain diameter, and to an extent that was much greater than the variability of the measurements. With water V/PR for the 300 μ sand was twice as large as it was for the 147 μ sand.

Thus it must be concluded that the change in V/P with grain diameter for a uniform spherical-grain sand cannot be accounted for by surface conductance alone.

Effect of temperature on V/P.—The volume rate of flow per unit pressure difference, Q/P, and the streaming potential per unit pressure difference, V/P, were measured as functions of the temperature, θ, with the plastic flow-tube apparatus. Doubly distilled water was the liquid and 90-mesh glass beads formed the sand. These results are shown by two of the curves in Fig. 4. The data show that V/P was a linear function of the temperature between 25° and 45°C.

The fact that $\eta Q/P$ for any one sand was observed to be constant in accord with Darcy's law, (η is the coefficient of viscosity of water) showed that the flow was laminar. If the temperature coefficient of V/P were due almost entirely to viscosity changes, then $\eta V/P$ should be a constant for all values of θ. Since $\eta Q/P$ is a constant, $(\eta V/P)(\eta Q/P) = V/Q$ should be constant for all temperatures. The graph of V/Q as a function of θ is shown in Fig. 4. Since the value of V/Q increases about 25% in the temperature range 25°–45°C, the temperature coefficient of V/P cannot be due to changes in viscosity alone.

The fact that V/QR changes even more rapidly with temperature than does V/Q (*see* curves Fig. 4) demonstrates that the change in conductance of the sand column with temperature is also an important factor in determining the temperature coefficient of V/P. Other factors are treated later.

Effect of concentration of solution on V/P.—Data obtained with the NaCl solutions are presented in another form in Fig. 5 which shows V/P as a function of log $1/c$, where c is the concentration of the solution, for each of the four sizes of spherical-grain sands. Similar sets of curves were obtained for each of the other salts used. These curves are roughly of the form already reported by others (2, 9). They show that the effect of concentration on V/P diminishes with the diameter of the sand grain and that V/P is small for NaCl solutions even as dilute as 10^{-3} mole/kg.

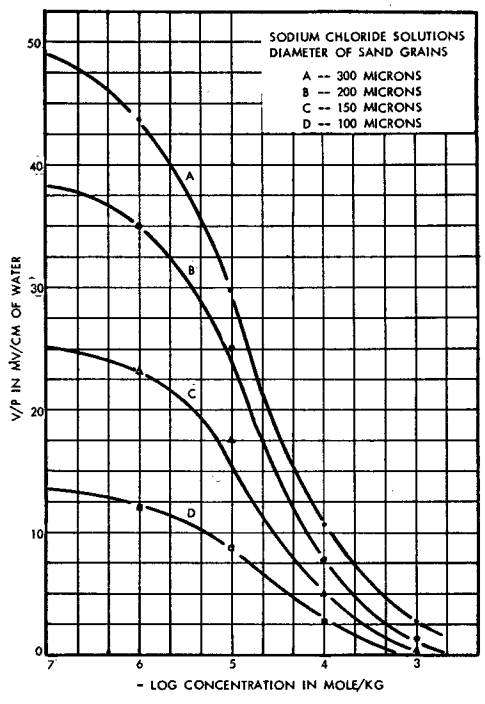

FIG. 5. Effect of concentration of the solution on streaming potential per unit of pressure difference for four sizes of spherical-grain sands.

DISCUSSION OF RESULTS AND EMPIRICAL EQUATIONS

Effect of grain diameter on V/P.—Marked variations of V/P with diameter of the spherical sand grains were obtained for all concentrations of all the solutions (Fig. 2 and 3). Since V/PR decreases with grain diameter, surface conductance alone does not account for all the variation of V/P with grain diameter.

Data shown along the curves of Fig. 2 were used to test both Eq. (II) and (III). Data for a fifth sand ($d = 127\ \mu$) were available; they were included.

For any one solution η, M, and A of Eq. (II) are constants. Therefore $\lambda_t V/P$ should be a linear function of $1/d$ if this equation represents the data. The plot was not a straight line. In fact the negative slope of the curve decreased as the value of $1/d$ increased, which suggests that $\lambda_t V/P$ was approaching a limiting value for very small sand grains.

In Eq. (III) η, λ, N, and B are constants for any one solution. Thus, a plot of P/V as a function of $1/d$ should be a straight line if this equation represents the data. Again the plot was not a straight line. In fact the positive slope of the curve decreased as $1/d$ decreased, which suggests that P/V was approaching a limiting value for very large grains.

The following empirical equation was devised.

$$V/P = (V/P)_a(1 + k/d + k^2/d^2) \exp(-k/d) \quad \text{(IV)}$$

where $(V/P)_a$ is the value of V/P for grains of large size, and k is a constant. In the constant $(V/P)_a$ is included the factor $\zeta\epsilon/\eta$ where ϵ is the dielectric constant of the solution.

Data given for water in Fig. 2 were used to determine the constants $(V/P)_a$ and k in the equation; the method of least squares as described by Scarborough (10) was employed, and the datum for the largest size grain was given extra weight. With d expressed in microns the value of k was found to be $5.35 \times 10^2\ \mu$ and that of $(V/P)_a$ to be 51.2 mv/cm-of-water. In Fig. 2 the curve for water represents this empirical curve; observed data are shown also.

The other four curves of Fig. 2 are also plots of this empirical equation for the four concentrations of NaCl. For all these curves the value of k was that determined from the data for water, namely $5.35 \times 10^2\ \mu$. Each value of $(V/P)_a$ was determined by the method of least squares from the observed data; again the datum for the largest grain diameter was given extra weight. The fact that these empirical curves fit the data fairly well indicates that the constant k is the same for all concentrations of all the solutions and therefore is a characteristic of spherical-grain sands, and that $(V/P)_a$ is a function of the kind and concentration of the electrolyte. It is reasonable that V/P should be zero for $d = 0$, but V/P might become zero for d slightly greater than zero. It also appears reasonable that V/P should approach a limiting value (or perhaps a maximum) as d increases.

These experimental results demonstrate beyond reasonable doubt that V/P varies greatly with the diameter of the grain for uniform spherical-grain sands. Bull and Gortner (4) observed much smaller variations of V/P with size of grain. However, their sands were made of sharp crushed quartz and they undoubtedly were sorted much less carefully than were the spherical glass grains used here.

Effect of temperature.—In Fig. 4 the curve showing V/P as a function of temperature may be represented by an equation of the form:

$$V/P = (V/P)_{25}[1 + \beta(\theta - 25)] \quad \text{(V)}$$

where $(V/P)_{25}$ is the value of V/P at 25°C, θ is the temperature in degrees, and β is a constant. The value of β was found by the method of least squares to be 5.35×10^{-2}/°C.

The equation for streaming potential derived from fairly simple theory (11) is:

$$V = \epsilon\zeta P/4\pi\eta\lambda \quad \text{(VI)}$$

where ϵ is the dielectric constant of the liquid, η is the coefficient of viscosity of the liquid, λ is the electrical conductivity of the liquid, and ζ is the ζ potential. This has been reported (6, 12) to hold well for capillary tubes of circular section, especially if the effective conductivity is calculated from the measured resistance of the liquid-filled tube and the dimensions of the tube. Thus it appears reasonable to suppose that the streaming potential in a spherical-grain sand may be expressed as:

$$V/P = K\epsilon\zeta f(d)/\eta\lambda \quad \text{(VII)}$$

where $f(d)$ is some function of the diameter of the sand grain, and K is a constant.

It has already been shown in connection with Fig. 4 that the effect of temperature on η and λ together does not account for all the effect of temperature on V/P, namely, V/QR varies with temperature. This variation (Fig. 4) may be expressed by an equation of the form:

$$V/QR = (V/QR)_0(1 + a\theta + b\theta^2) \quad \text{(VIII)}$$

where $(V/QR)_0$ is the value of V/QR at 0°C, θ is the temperature in degrees, and a and b are constants.

By Darcy's law for laminar flow $Q = SAP/\eta L$, where S is the permeability of the sand matrix, L is its length, and A is its sectional area. Also the effective conductivity, $\lambda = L/RA$. From these relations Eq. (VII) can be written:

$$V/QR = K\zeta\epsilon f(d)/S \qquad \text{(IX)}$$

The term $Kf(d)/S$ is essentially constant for all temperatures. The dielectric constant of water varies with the temperature (13) according to the equation:

$$\epsilon = \epsilon_0(1 - \gamma\theta) \qquad \text{(X)}$$

where $\epsilon_0 = 88$ and $\gamma = 4.55 \times 10^{-3}$/°C. Since the ζ potential [Eq. (IX)] for a spherical-grain sand may be expressed as:

$$\zeta = SV/KQR\epsilon f(d) \qquad \text{(XI)}$$

its variation with temperature may be written, in view of Eqs. (VIII) and (X):

$$\zeta = \frac{S}{Kf(d)}\left(\frac{V}{QR}\right)_0 \frac{1}{\epsilon_0}\left(\frac{1 + a\theta + b\theta^2}{1 - \gamma\theta}\right) \qquad \text{(XII)}$$

The approximate magnitude of the temperature coefficient of the ζ potential may be calculated. Eq. (XII) may be written in the form:

$$\zeta = \zeta_0[1 + (a + \gamma)\theta + (a\gamma + \gamma^2 + b)\theta^2] \qquad \text{(XIII)}$$

From the slope of the greater portion of the V/QR curve of Fig. 4 the approximate value of the temperature coefficient of V/QR was found to be $a = 3.4 \times 10^{-2}$/°C. Since $\gamma = 4.55 \times 10^{-3}$/°C the temperature coefficient of ζ for the water glass interface was approximately $(a + \gamma) = 3.9 \times 10^{-2}$/°C.

Thus it appears that each of the four factors η, λ, ζ, and ϵ has a temperature coefficient and that the temperature coefficient of V/P is caused by the combined effect of the temperature coefficients of these four factors.

Manuscript received May 16, 1955. This paper was submitted by C. E. Bleil to the University of Oklahoma in partial fulfillment of the requirements for the Ph.D. degree.

Any discussion of this paper will appear in a Discussion Section to appear in the December 1957 JOURNAL.

REFERENCES

1. M. VON SMOLUCHOWSKI, "Graetz Handbuch der Elektrizitat und des Magnetismus," II, p. 379, Leipzig (1921).
2. H. R. KRUYT, Editor, "Colloid Science," Vol. I, p. 202, Elsevier Co., New York (1952).
3. H. B. BULL AND R. A. GORTNER, *J. Phys. Chem.*, **36,** 111 (1932).
4. H. B. BULL AND R. A. GORTNER, *ibid.*, **39,** 577 (1935).
5. H. B. BULL AND L. S. MOYER, *ibid.*, **40,** 9 (1936).
6. A. J. RUTGERS, *Trans. Faraday Soc.*, **36,** 67 (1940).
7. L. A. WOOD, *J. Am. Chem. Soc.*, **68,** 432 (1946).
8. B. N. GHOSH, S. C. RAKSHIT, AND D. K. CHATTORAJ, *J. Indian Chem. Soc.*, **30,** 601 (1953).
9. J. A. V. BUTLER, Editor, "Electrical Phenomena at Interfaces," p. 75, Methuen & Co., London (1951).
10. J. B. SCARBOROUGH, "Numerical Mathematical Analysis," p. 375, Johns Hopkins Press, Baltimore (1930).
11. D. A. MACINNES, "The Principles of Electrochemistry," p. 439, Reinhold Publishing Co., New York (1939).
12. D. A. MACINNES, *loc. cit.*, p. 440.
13. N. E. DORSEY, "Properties of Ordinary Water Substance," p. 363, Reinhold Publishing Co., New York (1940).

The Galvani Electrode Potential

PAUL RÜETSCHI

Research Department, The Electric Storage Battery Company, Philadelphia, Pennsylvania

ABSTRACT

The surface potential of Hg can be evaluated by comparing the real potential α_i (negative work function) of different impurity ions, dissolved in Hg. The real potential of an ion is the sum of a chemical term, corresponding to the interaction energy with the Hg in the bulk of the phase (depending on the ionic radius), and a constant electrical term corresponding to the surface potential of Hg (independent of the ionic radius).

An electrostatic model is developed to calculate the chemical term of the real potential. This chemical component becomes negligible for very large ionic radii, and the surface potential χ_{Hg} of Hg can be determined by extrapolation. A value of $0 < \chi_{Hg} \leqslant +0.5$ v is obtained. The fact that χ_{Hg} is positive indicates that the surface dipoles of Hg are oriented with their negative poles against the vacuum.

Using the free energies of hydration given by Latimer, a value of $0.44 < \Delta\phi \leqslant 0.94$ v is calculated for the Galvani electrode potential of a N-calomel electrode This result compares with the value of 0.5 v quoted by Latimer, Pitzer, and Slansky. The latter authors neglected the surface potential of Hg.

The object of the present paper is to compute approximately the surface potential of Hg and the Galvani potential of the N-calomel electrode. It has recently been pointed out (1) that this can be achieved by use of a thermodynamic cycle involving a dilute amalgam and a non-thermodynamic calculation of the interaction energies of impurity ions with the Hg in the dilute amalgam. In the following discussion a more accurate and detailed calculation is presented.

Guggenheim (2) considered the theory of electric poten-

tial differences between dissimilar media, based on the work of Gibbs (3). He claimed that such potential differences have no physical meaning and cannot even be defined, whereas Gibbs stated only that such potential differences are not accessible to measurements and are thermodynamically not defined. In more recent work, however, it was realized by theoretical electrochemists (4) including Guggenheim (5) that such differences of potential could be calculated in principle. However, Guggenheim's older point of view has been taken by Grahame (6) in a recent review on the electrical double layer and it has been stated that a definition of an absolute potential difference is unnecessary, since it is possible to describe all the actual experimental observations in terms of potential differences of the types already known. This is true for purely thermodynamic considerations. In studies on the kinetics of electrode reactions, however, and in all the cases where the electric fields at the interfaces are investigated, electric potential differences between the phases are important. The reality and importance of such potential differences can hardly be denied in view of the fact that in all the overvoltage studies the changes of these potentials are observed and it is hard to see why a quantity whose changes can indeed be measured experimentally should not have a definite physical meaning.

In fact, it is possible to calculate theoretically such electric potential differences on the basis of an exact knowledge of the interaction energies between the particles in the bulk of the phases or on the basis of a precise picture of the free surfaces and especially the surface dipoles (surface double layer) of the phases against vacuum. The definition of the Galvani-potential given by Lange (7–9) has made it possible to discuss the subject of electrical potential differences between dissimilar media without ambiguity. The terms "absolute," "single," or "true" electrode potentials should not be used in future discussions. It must be stressed, however, that the Galvani potential discussed below corresponds precisely to the meaning of such "absolute," "single," or "true" electrode potentials which were considered to have no physical meaning by Guggenheim (2) and Grahame (6).

In this discussion the Galvani, Volta, and surface potentials as introduced by Lange (7–9) are used.

The electrochemical potential $\bar{\mu}_i$ of a particle i in the bulk of a material phase can be written as the sum of three terms:

$$\bar{\mu}_i = Z_i e_0 \psi + Z_i e_0 \chi + \mu_i \qquad \text{(I)}$$

$Z_i e_0$ is the charge of the particle i; ψ is the Volta potential (outer potential); and $Z_i e_0 \psi$ the electric energy involved in bringing a unit positive charge from a point at charge-free infinity to a point just outside the phase, where the influence of the image force is negligible, i.e., at 10^{-4} cm from the surface of the phase. χ is the surface potential and $Z_i e_0 \chi$ the electric energy required to transfer a unit positive charge from a point just outside of the phase, across the surface dipole layer, into the phase. μ_i is the chemical potential or the energy corresponding to the interaction of the particle i with the other particles of the phase in which it has been transferred. The name "chemical potential" is misleading because all forces between atoms and ions are fundamentally electric in nature. μ_i can include terms of simple electrostatic interactions, polarization interactions, dispersion interactions, etc., according to the nature of the material.

The sum of the Volta potential ψ and the surface potential χ is defined as the Galvani potential ϕ

$$\phi = \psi + \chi \qquad \text{(II)}$$

When a phase has no net charge, its Volta potential is zero. In this case it is convenient to define another potential, viz., the real potential α_i,

$$\alpha_i = \mu_i + Z_i e_0 \chi \qquad \text{(III)}$$

which is the negative work function of the ion i. The difference between the Volta potentials of two phases may be determined experimentally (8, 9, 11), but the Galvani potential difference cannot be measured by any means.

Chemical and Surface Potentials of Aqueous Solutions

The real potential α_i is a quantity which is determinable experimentally. The chemical potential μ_i and the surface potential χ are not measurable and can be calculated only on a theoretical basis, somewhat like the activity coefficients in the Debye-Hückel theory.

According to Eq. (III) a calculation of the real potential α_i of an ion in a condensed phase consists of two parts: (*a*) the calculation of the chemical potential μ_i, and (*b*) the calculation of the surface potential χ. The apriori evaluation of the surface potentials is usually more difficult than the evaluation of the chemical potential. Therefore, most workers have calculated only μ_i and have estimated the surface potential by comparison with the measured real potential α_i [Eq. (III)].

By this semiempirical method the surface potential χ_s of diluted aqueous solutions has been determined (4, 12, 13). The index s designates a liquid phase (solution). χ_s is, of course, the surface potential of this liquid phase against vacuum. χ is essentially independent of the electrolyte (8), if no electrocapillary active substances are present, and if the solutions are not too concentrated. The surface potential results primarily from the orientation of water multipoles, mainly dipoles, in the surface. The validity of the results for χ_s depends on the reliability of the calculated values for the chemical potentials μ_i. Using the values for the free energy of hydration given by Latimer (14, 15), the surface potential of diluted aqueous solutions becomes (4, 12, 13, 16):

$$\chi_s = -0.33 \text{ v} \qquad \text{(IV)}$$

Latimer, Pitzer, and Slansky obtained the free energy of hydration for single ions by separating the experimental energy of hydration for salts according to the Born equation (17). In order to fit this equation, 0.85Å was added to the crystal ionic radii of the positive ions, and 0.10Å to the crystal ionic radii of the negative ions.

Many objections could be made against the values for the free energies of hydration quoted by Latimer and coworkers:

1. The model of Born, who regarded the ion as a rigid sphere of radius r_i and charge $Z_i e_0$ in a continuous dielectric medium, is an oversimplification.

TABLE I. *Free energy of hydration*

Metal	Kcal/mole
Li^+	−114
Na^+	−91
K^+	−74
Rb^+	−68
Cs^+	−61
Be^{++}	−565
Mg^{++}	−434
Ca^{++}	−363
Sr^{++}	−334
Ba^{++}	−304
Zn^{++}	−466
Cd^{++}	−413
Al^{+++}	−1090
In^{+++}	−965
Tl^{+++}	−962

2. The ion-dipole interaction in the primary hydration sheath is neglected.

3. The repulsion between the ion and the water molecules is not taken into account.

The theoretical values for the single ion free energies of hydration by Eley and Evans (18) are, according to Conway (19), based on a more correct model; however, a discrepancy of 20–30 kcal/mole exists between added values given by Eley and Evans for cations and anions, and experimental values given by Latimer for the salts.

At the present time the assignment of values to the individual ions is still highly questionable. Values quoted by Latimer are used tentatively in this study.

This assignment seems to be consistent with the absolute entropies of the single ions (15).

Table I gives the free energy of hydration for some ions according to Latimer (14, 15).

It must be pointed out that the use of enlarged radii ("effective Born radii") in the theory by Latimer does not correspond strictly to the idea of dielectric saturation in the vicinity of the ion. The two models have been incorrectly identified in the past. Fig. 1a illustrates the model used by Born (enlarged radii) and Fig. 1b the model with dielectric saturation in the vicinity of the ion. The electric energy of the system 1a is given by:

$$E = \frac{(Z_i e_0)^2}{8\pi\epsilon_0} \cdot \frac{1}{\epsilon r_e} \qquad (V)$$

but the electric energy of the system in Fig. 1b is given by:

$$E = \frac{(Z_i e_0)^2}{8\pi\epsilon_0} \cdot \left\{\frac{1}{r_i} - \frac{1}{r_e} + \frac{1}{\epsilon r_e}\right\} \qquad (VI)$$

where e_0 is the unit charge (1.6 10^{-19} coulomb) Zi the valence of the ion i, ϵ_0 the dielectric constant for vacuum (8.854 10^{-12} amp sec volt^{-1}. m^{-1}), ϵ the relative dielectric constant (vacuum = 1), r_i the crystal ionic radius (in meters) and r_e the cavity radius (in meters). E is the electric energy in wattseconds (Joule).

If the ion in the initial state (at charge free infinity) has the enlarged radius r_e in case 1a, but the correct crystal ionic radius r_i in case 1b, then the free energy of hydration (for one particle) is the same for both instances, viz.;

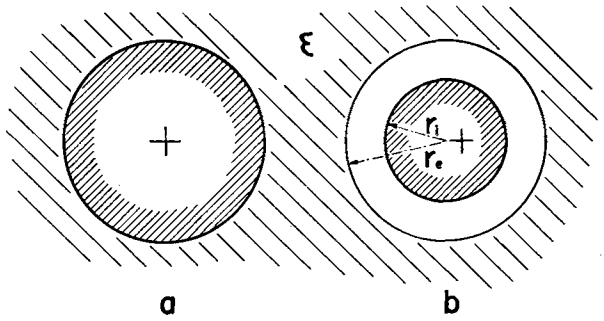

FIG. 1. Models of hydrated ions (a) enlarged radii, (b) dielectric saturation.

$$\mu_{i_s} = -\frac{(Z_i e_0)^2}{8\pi\epsilon_0} \cdot \frac{1}{r_e}\left\{1 - \frac{1}{\epsilon}\right\} \qquad (VII)$$

which is the Born equation.

If model of Fig. 1a is correct, the addition to the radii should be independent of the solvent and the free ions in a gas would have larger radii than in the crystals. Enlarged radii for ions in a dissolved state have been proposed by Eucken (20, 21), but are unlikely in view of modern work on the electronic structure of atoms and ions.

Both models are based on the use of a uniform dielectric constant in atomic dimensions, and are subject to the objections mentioned above.

Surface Potentials of Metals

Theoretical calculation of surface potentials of metals has been attempted several times (22–24). Table II illustrates some results.[1]

Values in Table II have been obtained from the difference between the real potential α_e (negative work function) and the chemical potential μ_e of an electron in the metal. Calculations for μ_e, based on the simple electron gas theory, are valid only for the alkali metals. The surface potentials listed for Cu, Mg, Ca, Be are highly questionable.

Recently it has been shown that there is still another way to evaluate the surface potentials of the metals (1). Summarizing shortly, this method makes use of a thermodynamic cycle involving an alloy system whereby only a trace of a foreign metal M′ is alloyed with a pure metal phase M. The following cycle is then applied: One mole of the added metal M′ is removed from the alloy. The removed metal M′ is thereafter vaporized, ionized in the gas phase, the ions and electrons are added separately to the alloy, and finally recombined in the bulk of the alloy to the initial state. From this cycle the real potential α_i of the impurity ions can be obtained.

$$-\alpha_i = -A + S + J - \theta - J^* \qquad (VIII)$$

where A = free energy of alloying (free energy of mixing); S = free energy of sublimation of the metal M′; J =

[1] Parsons (10) gives a complete table of calculated surface potentials. Although the absolute values of the surface potentials are cited correctly by this author, the signs in his table are in error. The surface potentials of the metals must be given positive signs.

TABLE II. *Surface potentials of metals*

Metal	Surface potential χ_M in volts	
	Herring (22)	Seitz (26)
Li	0.7	0.1
Na	0.3	0.1
K	0.2	0.4
Cu	0.8	
Ca	1.3	
Mg	2.5	
Be	5.1	

ionization energy for the first electron of M′; θ = electronic work function of the alloy (identical with the electronic work function of the metal M); and J^* = ionization energy of M′ in the alloy for the first electron (energy to lift an electron of the impurity center from its energy level to the conduction band of the alloy).

The term J^* is in many cases small and can be neglected. Sometimes J^* can be determined separately (i.e., ionization energy of impurity centers in semiconductors). In the following treatment it is assumed that the impurity atoms are completely ionized and J^* is therefore zero. It should be noted that the terms in Eq. (VIII) correspond to free energies, and α_i depends, therefore, on the concentration.

The real potential α_i of impurity ions can be calculated with Eq. (VIII) from experimental data. According to Eq. (III) the real potential α_i is the sum of the surface potential term $Z_i e_0 \chi$ and the chemical potential μ_i, the surface potential χ now being constant for different impurity ions and identical with the surface potential of the "solvent" metal M.

Difference in the real potentials from one impurity ion to another must correspond to difference in the chemical potentials. The differences may be obtained from experimental data, and can be correlated to the radii and to the electronic configuration of the ions.

Equations for the interaction energies between the impurity ions and the excess metal can be derived on a quantum-mechanical basis (25, 26). These calculations are difficult, especially for metals other than those of the alkali group, and show that the main interaction terms are inversely proportional to the ionic radii or to the square of the ionic radii. In the following, a simple electrostatic model is used to estimate the interaction energy of ions dissolved in Hg.

The dissolved ions are treated as small charged spheres with the crystal radii r_i. They will be surrounded by a cloud of electrons in the Hg.

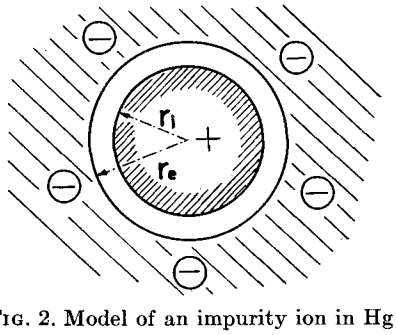

FIG. 2. Model of an impurity ion in Hg

With this model the dissolved ion can be described as a very small spherical condenser, as it is shown in Fig. 2. The capacity of this spherical condenser is given by:

$$c = 4\pi\epsilon_0 \cdot \epsilon \cdot \frac{r_i r_e}{r_e - r_i} \qquad \text{(IX)}$$

where r_i is the crystal radius of the ion, r_e the cavity radius and ϵ the relative dielectric constant in the gap.

The electric energy of this system equals

$$E_1 = \frac{(Z_i e_0)^2}{2c} = \frac{(Z_i e_0)^2}{8\pi\epsilon_0 \epsilon} \cdot \frac{\delta}{r_i^2 + r_i \delta} \qquad \text{(X)}$$

whereby:

$$\delta = r_e - r_i$$

Since the electric energy of the free ion in vacuum is given by

$$E_2 = \frac{(Z_i e_0)^2}{8\pi\epsilon_0} \cdot \frac{1}{r_i} \qquad \text{(XI)}$$

the energy of amalgamation equals

$$\mu_{iM} = \Delta E = -\frac{(Zie_0)^2}{8\pi\epsilon_0} \cdot \frac{1}{r_i}\left\{1 - \frac{\delta}{(r_i + \delta)\epsilon}\right\} \qquad \text{(XII)}$$

The free energy of amalgamation, μ_{iM}, varies inversely with the ionic radii r_i. According to Eq. (III) the real potential then becomes:

$$\alpha_i = -\frac{(Z_i e_0)^2}{8\pi\epsilon_0 r_i} \cdot \left\{1 - \frac{\delta}{(r_i + \delta)\epsilon}\right\} + Zie_0\chi \qquad \text{(XIII)}$$

The term in the brackets becomes approximately 1 if one inserts reasonable values for δ and ϵ. (δ is probably in the order of $\frac{1}{10} r_i$ and ϵ in the order of 10.) With these approximations one obtains:

$$\alpha_i = -\frac{C}{r_i} + Z_i e_0 \chi \qquad \text{(XIV)}$$

where c is a constant. A plot of the experimental values of the real potentials α_i against $1/r_i$ should therefore be a straight line. The intersection of this straight line with the ordinate at $1/r_i = 0$ corresponds to the surface potential χ.

It should be pointed out that an identical type of relation between the chemical potential μ_i and the ionic radii r_i could be derived on a quantum-mechanical basis (25, 26) which shows that the simple condenser model gives a reasonable result. In the less rigorous treatment given recently (1) it was assumed that the leading term of the chemical potentials of the impurity ions is inversely proportional to the square of the ionic radii. A relation of this type can be derived on a theoretical basis using the free electron theory and the theorem of Clausius, according to which the total energy of an electron equals the negative kinetic energy of the electron. The interaction energy between the impurity ions and the Hg is then essentially determined by the Fermi-energy of the electrons (25). It should be noted that under this assumption the ionic radii should not be identified with the crystal ionic radii (given by Pauling) and that it is reasonable to assume them to be larger than the crystal ionic radii. This fact was, indeed, confirmed in the cited paper (1).

TABLE III. *Data on real potentials of impurity ions in Hg**

Metal	A	S	J	θ_{Hg}	α_i	r_i[Å]
Li^+	−0.942	1.266	5.363	4.530	−3.041	0.68
Na^+	−0.854	0.810	5.120	4.530	−2.254	0.95
K^+	−1.040	0.634	4.318	4.530	−1.462	1.33
Rb^+	−1.052	0.579	4.159	4.530	−1.260	1.48
Cs^+	−1.070	0.531	3.870	4.530	−0.941	1.69

* Pauling's values for the ion radii r_i have been used with the exception of Li. For the latter metal the value quoted by Pauling (0.60Å) is probably too small [*see* Strehlow (4), Latimer (15)]. The free energies of amalgamation A of the alkali metals have been taken from a recent polarographic study (27). The free energies of sublimation S are taken from "Selected Values of Thermodynamic Properties," National Bureau of Standards, Washington, D. C., Series 1, Tables 91-1 to 95-1 (1950). The ionization energies and the electronic work function θ_{Hg} of Hg correspond to the values given in "Handbook of Chemistry and Physics," 33rd ed., pp. 2125-2126 and p. 2129, Chemical Rubber Publishing Co., Cleveland (1951/1952).

Table III shows the data used to calculate the real potentials α_i of alkali ions dissolved in mercury (energy terms in ev).

The free energies of amalgamation A of the alkali metals are, of course, dependent on the concentration of the amalgams. The influence of the concentration is, however, rather small since a factor of 10 in the concentration changes the value of A only in the order of 100 mv, which is less than the error limits for α_i. The values of A listed in Table III correspond to polarographic concentrations (in the order of 10^{-3} mole/liter). The values for S given in Table III are free energies of sublimation. It should be noted that in the earlier treatment (1) the heats of sublimation were used (in lack of proper references) which caused the real potential to become too large by an amount of 0.3 ev, and the upper limit for the surface potential χ_{Hg} to become too small by the same amount. If the correct values for the free energies of sublimation S are inserted in the earlier treatment, the value of the surface potential becomes identical with the value computed below. This fact is particularly interesting and shows that the described "trace method" seems to be not very sensitive to the model used as long as this model is a reasonable approximation. It must also be mentioned that in the earlier paper (1) α_i designated the work function of the ions. Here it is used for the real potential of the ions (which is the negative work function) according to the nomenclature given by Lange (7–9).

Fig. 3 shows a plot of the real potentials α_i against $1/r_i$. The slope of the straight line does not correspond exactly to the value predicted by Eq. (XIII), but is somewhat smaller. An exact agreement cannot be expected.

The condenser model has merely been used to derive the $1/r_i$ relation, which takes in account the Coulambic interaction. The value of χ can therefore be obtained by extrapolation without a theoretical evaluation of the other factors in the $1/r_i$ term, if these other factors can be assumed to be constant for a series of similar ions. This point shows the main advantage of the "trace method". The chemical potentials (or the slope on the plot $\mu_i \longrightarrow 1/r_i$) need no longer be calculated apriori in detail. It is sufficient to know the type of relation between μ_i and r_i. This relation can, indeed, be studied experimentally.

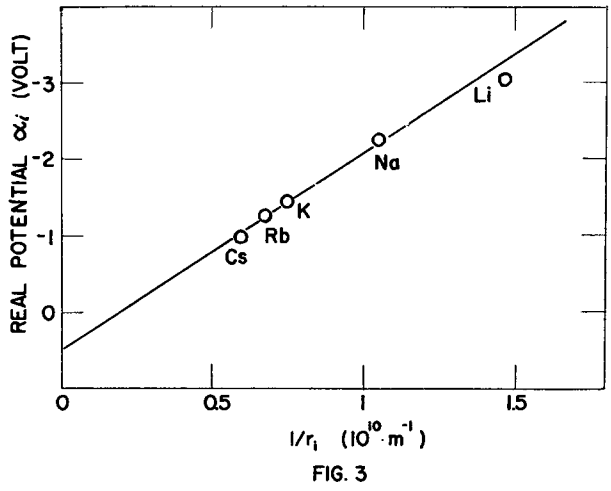

FIG. 3

FIG. 3. Real potentials of impurity ions in Hg plotted against reciprocal ionic radii.

From the plot of α_i against $1/r_i$ it is concluded that the surface potential of Hg amounts to

$$0 < \chi_{Hg} \leqslant 0.5 \text{ v} \qquad \text{(XV)}$$

The value of 0.5 v gives the upper limit rather than an average for χ_{Hg}, because of the fact that the repulsion terms of μ_i have been neglected.

The positive value of the surface potential indicates that the surface dipoles are oriented with their negative pole toward the gas phase. This is reasonable since one would expect the electrons to overlap into the vacuum beyond the positive cores.

The free energies of amalgamation can now be obtained with Eq. (III):

$$\mu_{iM} = \alpha_i - Z_i e_0 \chi_M$$

From Eq. (I) and (II) one deduces that the difference in Galvani potentials $\phi_I - \phi_{II}$ between two phases I and II in equilibrium ($\bar{\mu}_{i_I} = \bar{\mu}_{i_{II}}$) is given by $\phi_I - \phi_{II} = \phi_{Hg} - \phi_s = \dfrac{\mu_{i_s} - \mu_{i_{Hg}}}{Z_i e_0}$.

Using the free energies of amalgamation of the ions obtained in this study and the free energies of hydration of

TABLE IV. *Data on Galvani potentials of amalgam electrodes and the N-calomel electrode*

Electrode	μ_{i_S}	$\mu_{i_{Hg}}$	$\Delta\phi_{amalgam}$	E	$\Delta\phi_{N\text{-calomel}}$
Li (Hg)/Li^+...	−4.95	−3.54	−1.41	−2.38	0.97
Na (Hg)/Na^+.	−3.95	−2.75	−1.20	−2.14	0.94
K (Hg)/K^+....	−3.21	−1.96	−1.25	−2.17	0.92
Rb (Hg)/Rb^+.	−2.95	−1.76	−1.19	−2.15	0.96
Cs (Hg)/Cs^+..	−2.65	−1.44	−1.21	−2.14	0.93

μ_{i_S} = free energy of hydration according to Latimer of the ion i. $\mu_{i_{Hg}}$ = free energy of amalgamation according to this work of the ion i. $\Delta\phi_{amalgam}$ = Galvani electrode potential of the amalgam electrode. E = electrode potential of the amalgam electrode measured against a N-calomel electrode. $\Delta\phi_{N\text{-calomel}}$ = Galvani electrode potential of the N-calomel electrode.

the ions given by Latimer, the Galvani potential difference $\phi_{Hg} - \phi_s = \Delta\phi_{amalgam}$ of the diluted amalgam electrodes may be obtained. In Table IV Galvani potential differences are listed together with the experimental electrode potentials of the amalgam electrodes against a N-calomel electrode (27). The difference between these two potentials should be constant and should be equal to the Galvani potential of a N-calomel electrode. Table IV shows that this is indeed the case. The latter fact of course does not provide any measure for the degrees of correctness and accuracy of the presented method, although it does present further evidence that relation (XIV) is adequate.

Experimental values for the free energies of hydration listed in Table IV correspond to equal concentrations of the ions in the gas phase and in the liquid phase; ion (gas) = ion (aq) = 0.041M, that is with no change in volume (14, 15). Values listed for E correspond to somewhat smaller concentrations, but the error introduced by this fact can again be neglected in view of the approximate nature of all the calculations at the present stage of refinement of the described "trace method".

Therefore, it can be concluded that the Galvani potential of a N-calomel electrode $\Delta\phi_{N\text{-calomel}} = \phi_{Hg} - \phi_{sN\text{-calomel}}$ has a value of $\Delta\phi_{N\text{-calomel}} \simeq 0.94$ v, which is again the upper limit for the Galvani potential.

If the surface potential of mercury were zero, a value of 0.44 v, would be obtained. Therefore,

$$0.44 < \Delta\phi_{N\text{-calomel}} \leqslant 0.94 \text{ v} \qquad \text{(XVI)}$$

Latimer, Pitzer, and Slansky (14), neglecting the surface potential of Hg, have calculated a value of $\Delta\phi_{N\text{-calomel}} = 0.495$ v. As has been noted (4, 16, 28–31) the surface potential of Hg must be added to the calculated value of 0.495 v in order to obtain the correct Galvani potential of the N-calomel electrode:

$$\Delta\phi_{N\text{-calomel}} = +0.495 \text{ v} + \chi_{Hg}$$

[*see* Eq. 5, reference (16).]

The value of the surface potential of Hg is of particular interest in the theory of zero charge electrodes (16). It should also be noted that the outlined theory can be applied to an apriori calculation of polarographic half-wave potentials of metal ions.

Finally, it must be stressed that the present treatment is only a first approximation, although the principle of the "trace method" is quite fundamental and will be applied in the future for more rigorous evaluations of the Galvani potentials on the basis of more accurate experimental data for work functions and real potentials and on the basis of more accurate quantum mechanical calculations for the interaction energies in condensed phases.

Manuscript received January 16, 1956. This paper was prepared for delivery before the San Francisco Meeting, April 29 to May 3, 1956.

Any discussion of this paper will appear in a Discussion Section to be published in the December 1957 JOURNAL.

REFERENCES

1. P. RÜETSCHI, *Z. Elektrochem.*, **60,** 29 (1956).
2. E. A. GUGGENHEIM, *J. Phys. Chem.*, **33,** 842 (1929); **34,** 1758 (1930).
3. W. GIBBS, "Collected Works," Vol. I, p. 429, Longmans and Green, New York (1928).
4. H. STREHLOW, *Z. Elektrochem.*, **56,** 119 (1952).
5. R. FOWLER AND E. A. GUGGENHEIM, "Statistical Thermodynamics," p. 488, Cambridge Univ. Press (1952).
6. D. C. GRAHAME, *Chem. Rev.*, **41,** 441 (1947).
7. E. LANGE, "Handbuch der Experimentalphysik," Vol. 12, Pt. 2, p. 267 ff, Akademische Verlagsgesellschaft, Leipzig (1933).
8. O. KLEIN AND E. LANGE, *Z. Elektrochem.*, **43,** 570 (1937).
9. E. LANGE, *ibid.*, **55,** 76 (1951); **56,** 94 (1952).
10. An excellent discussion by R. PARSONS in J. O'M. BOCKRIS, "Modern Aspects of Electrochemistry," Academic Press, Inc., New York (1954).
11. K. MÖHRING, *Z. Elektrochem.*, **59,** 102 (1955).
12. E. VERWEY, *Rec. Trav. Chim.*, **61,** 564 (1942).
13. R. HUSH, *Aust. J. Sci. Res.*, **A1,** 482 (1948).
14. W. M. LATIMER, K. S. PITZER, AND C. M. SLANSKY, *J. Chem. Phys.*, **7,** 108 (1939).
15. W. M. LATIMER, *J. Chem. Phys.*, **23,** 90 (1955).
16. P. RÜETSCHI AND P. DELAHAY, *ibid.*, **23,** 697 (1955).
17. M. BORN, *Z. Physik.*, **1,** 45 (1920).
18. D. D. ELEY AND M. G. EVANS, *Trans. Faraday Soc.*, **34,** 1093 (1938).
19. B. E. CONWAY AND J. O'M. BOCKRIS, "Modern Aspects of Electrochemistry," p. 47, Academic Press Inc., New York (1954).
20. A. EUCKEN, "Lehrbuch der Chemischen Physik," II, 2, p. 992, Geest and Portig, Leipzig (1949).
21. G. PASSOTH, *Z. Phys. Chem.*, **203,** 275 (1954).
22. C. HERRING, "Metal Interfaces," American Society of Metals, Cleveland (1952).
23. C. HERRING AND M. NICHOLS, *Rev. Mod. Phys.*, **21,** 185 (1949).
24. A. HUANG AND E. WYLLIE, *Proc. Phys. Soc.*, **62A,** 180 (1949).
25. H. FRÖHLICH, "Elektronentheorie der Metalle," pp. 256–285, Springer, Berlin (1936).
26. F. SEITZ, "The Modern Theory of Solids," McGraw-Hill Book Co., New York (1940).
27. A. VLCEK, *Coll. Czech. Chem. Commun.*, **20,** 400 (1955).
28. P. VAN RYSSELBERGHE, *J. Chem. Phys.*, **21,** 1550 (1953).
29. A. FRUMKIN, *ibid.*, **7,** 552 (1939).
30. W. C. BURGERS, *Chem. Weekblad*, **39,** No. 16–17, 1, (1942).
31. R. PIONTELLI, Int. Committee Electrochem. Therm. Kin. Proc. 2nd Meeting, pp. 344–369, Milan (1951).

Hydrogen Evolution Reaction on Copper, Gold, Molybdenum, Palladium, Rhodium, and Iron

Mechanism and Measurement Technique under High Purity Conditions

N. PENTLAND

Technical College, Brighton, England

J. O'M. BOCKRIS

University of Pennsylvania, Philadelphia, Pennsylvania

E. SHELDON

Technical College, Acton, London, England

ABSTRACT

Various aspects of technique in measurements of electrode kinetics under conditions where competing reactions due to the presence of trace impurities in the solution are important are examined.

The kinetics of the hydrogen evolution reaction in acid and alkaline solutions on several transition metals has been examined with special reference to the low current density region. Inferences concerning the rate-determining step in the reactive $2H^+ + 2e_0^- \rightarrow H_2$ are thus drawn. In general, there is a tendency for the metals examined in acid solution to have a rate-controlling electrochemical desorption reaction and for those in alkaline solution to have a rate-determining discharge step.

During the past five years, a number of experimental and theoretical techniques have been devised whereby the attack on the mechanism of electrode reactions need no longer be prosecuted by qualitative inference but by the evaluation of diagnostic criteria which allow unambiguous decisions between mechanisms to be made (1). Two different modifications of these approaches have been made, the first depending on d-c measurement of the rate of the reaction as a function of the overpotential, and the second depending on the evaluation of the impedance of the reaction as a function of frequency (2). Roughly, these two approaches have maximum applicability for slow electrode reactions (exchange current density $<10^{-3}$ amp cm^{-2}) and fast reaction (exchange current density $>10^{-3}$ amp cm^{-2}), respectively. The hydrogen evolution reaction has relatively low rate constants on all metals. Detailed studies of the mechanism of this reaction on several metals have been published (1). In this paper, the determination of the most important relevant parameters used for the evaluation of diagnostic criteria for the hydrogen evolution reaction have been applied to Cu, Au, Mo, Pd, Rh, and Fe cathodes. The necessary details of the technique of measuring currents at electrodes under ultra-high-purity conditions for electrode reactions which are easily vitiated by the presence of trace impurities are also here published for the first time.

EXPERIMENTAL METHODS

Electrolytic Cell

The cell used (Fig. 1) was fundamentally that of Bockris and Pentland (3) with the following modifications: (*a*) provision of a water-cooled, water-sealed tap (Fig. 2); (*b*) provision of a trident shaped graphite anode, for use with pre-electrolysis at high current density (Fig. 3). The cathode compartment of the cell was of As-free glass ("Hysil"). Gases entering the cell escaped through water-sealed non-return valves; all joints, caps, and valves were sealed with equilibrium water to avoid use of tap grease. The cell was attached to a paxolin base and positioned inside a polythene tray to ensure electrical insulation.

The H reference electrode was constructed by pinch sealing Pt to glass, spot welding being avoided in order to reduce contamination by foreign metals. After platinization (without use of lead acetate), the electrode was washed in equilibrium water, then in conductivity water, and its potential checked against that of a calomel electrode. The electrode was stored in conductivity water for 30 hr before use and checked frequently. When not in use it was kept in equilibrium water. The same electrode maintained potential to 0.2 mv for more than 14 months.

The cathode compartment contained the electrode-bulb breaker F, which entered the cell obliquely through a ground glass sleeve which allowed the plunger to be withdrawn from the catholyte without exposing the latter to the air. The cathode cap (Fig. 4) carried five parallel ground glass sleeves, thus enabling the electrodes to be rotated and moved vertically without subjecting the solution to contact with the air. Each syringe tube carried a cup at its upper end for sealing with solvent against atmospheric contamination.

For alkaline work, concentrated pure NaOH solution entered through H and for acid preparation HCl gas was admitted via J. Conductance water distilled in H_2 was led

through H and pure H_2 through the capillary K. Concentration of the electrolyte was determined by measurement of conductance between fixed Pt electrodes L, the cell constant of which had been previously established. The arrangement of L high in the anode compartment limited the time of contact of a solution to the short period of adjustment of solution concentration. After the solution had attained concentration and was shared with the cathode compartment, its level was below that of L.

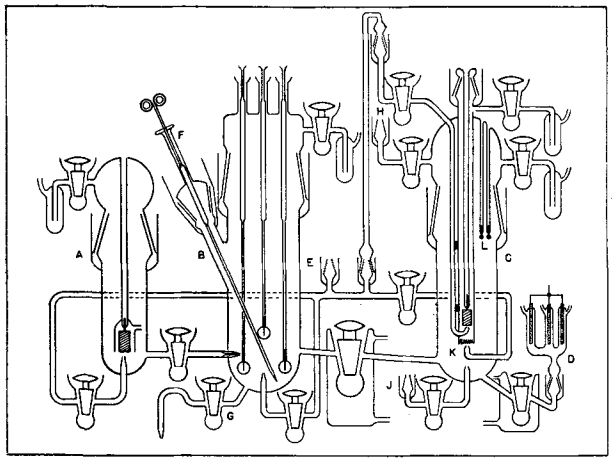

FIG. 1. Cell for measurement of hydrogen evolution under pure conditions at low current densities. A = reference hydrogen electrode; B = cathode compartment; C = anode compartment and solution preparation vessel; D = supplementary anode; D = trident shaped anode; E = H_2 inlet; F = plunger for breaking electrode bulbs; G = tap for removal of washing; H = inlet to anode compartment; J = inlet for HCl gas; K = inlet for H_2 gas; L = conductivity points for establishing concentration.

The anode cap (Fig. 1 and 5) consisted of an additional central tube sealed at the lower end by a sintered glass disc, porosity 3, inside which was a Pt foil, over which H_2 (discarded via a water-sealed bubbler at the top of the cap) swept to carry off anodically produced gases. During long pre-electrolysis, the solution level sometimes fell below the Pt, so that a supplementary anode was also employed and in work at the highest c.d.'s the trident shaped anode (Fig. 3) was utilized. The latter consisted of rods, 6.5 mm diameter graphite, 10 cm long, sealed into Hysil tubes (Fig. 6). A hole 1 mm diameter and 2 cm long was drilled in the top of the graphite and a side hole for escape of liberated Cl_2 was attached below the seal.

Cathode preparations.—Each metal used was of spectroscopic purity. Each cathode material, except Mo, was attached to a short length of 28 S.W.G. Pt wire so that a good metal-glass seal could be obtained (Table I). Mechanical attachment was performed by flattening one end of the electrode, using cleaned stainless steel pliers, and a $\frac{1}{64}$-in. hole was drilled. Pt was secured in the hole by pinching. This procedure was employed for Cu. For Au and Pd cathodes, fusion to Pt in an oxygen flame was used. Rh and Fe were spot welded to Pt. The metal under investigation was cut with cleaned Cr plated cutters and handled only with Pt tipped tweezers or filter paper.

Mo electrodes contained traces of surface oxide and carbide, introduced in drawing-down, which were difficult to remove except as follows: 30 cm lengths of wire were clamped in a bell jar of a high vacuum coating unit. Pressure was reduced to 10^{-5} mm Hg and 28 amp was passed through the wire for 10 min, the temperature being about 2200°C. The wire was cooled and air admitted to raise the pressure to 10^{-2} mm Hg. Mo was heated to red heat for

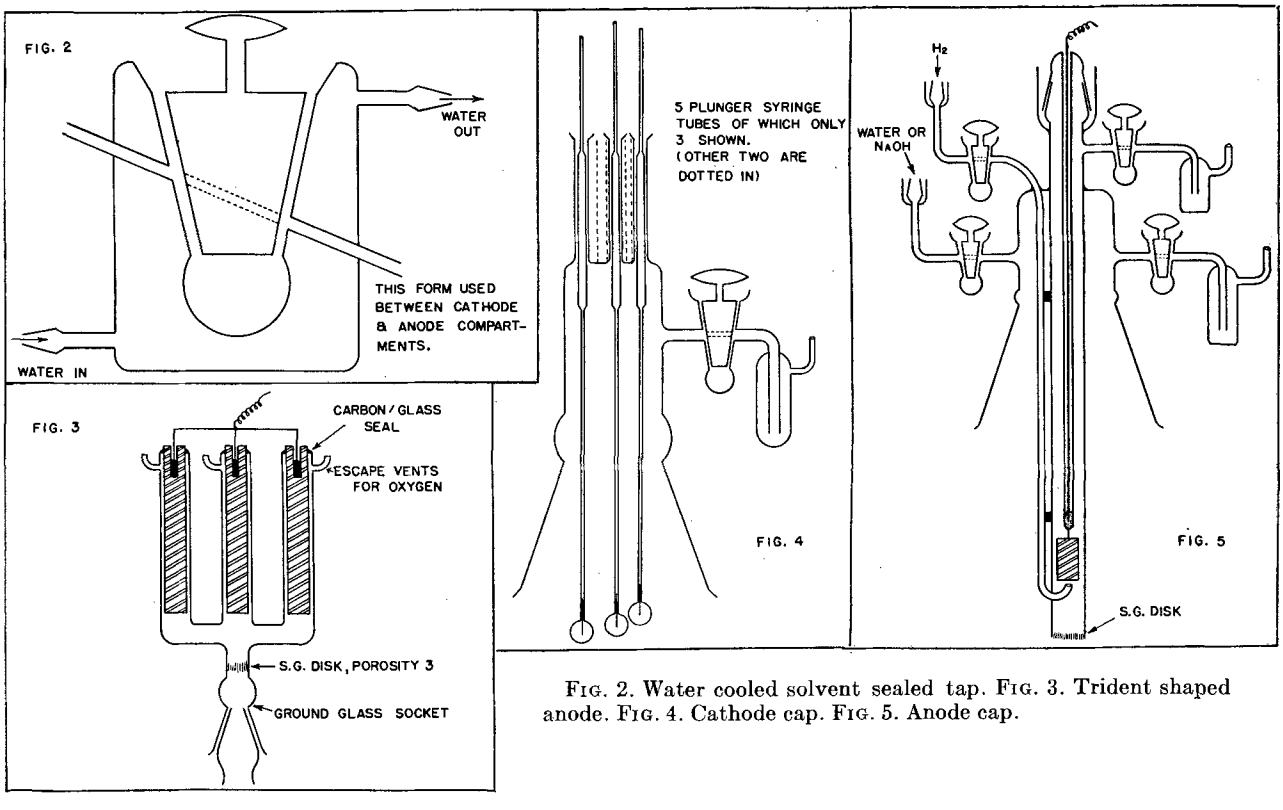

FIG. 2. Water cooled solvent sealed tap. FIG. 3. Trident shaped anode. FIG. 4. Cathode cap. FIG. 5. Anode cap.

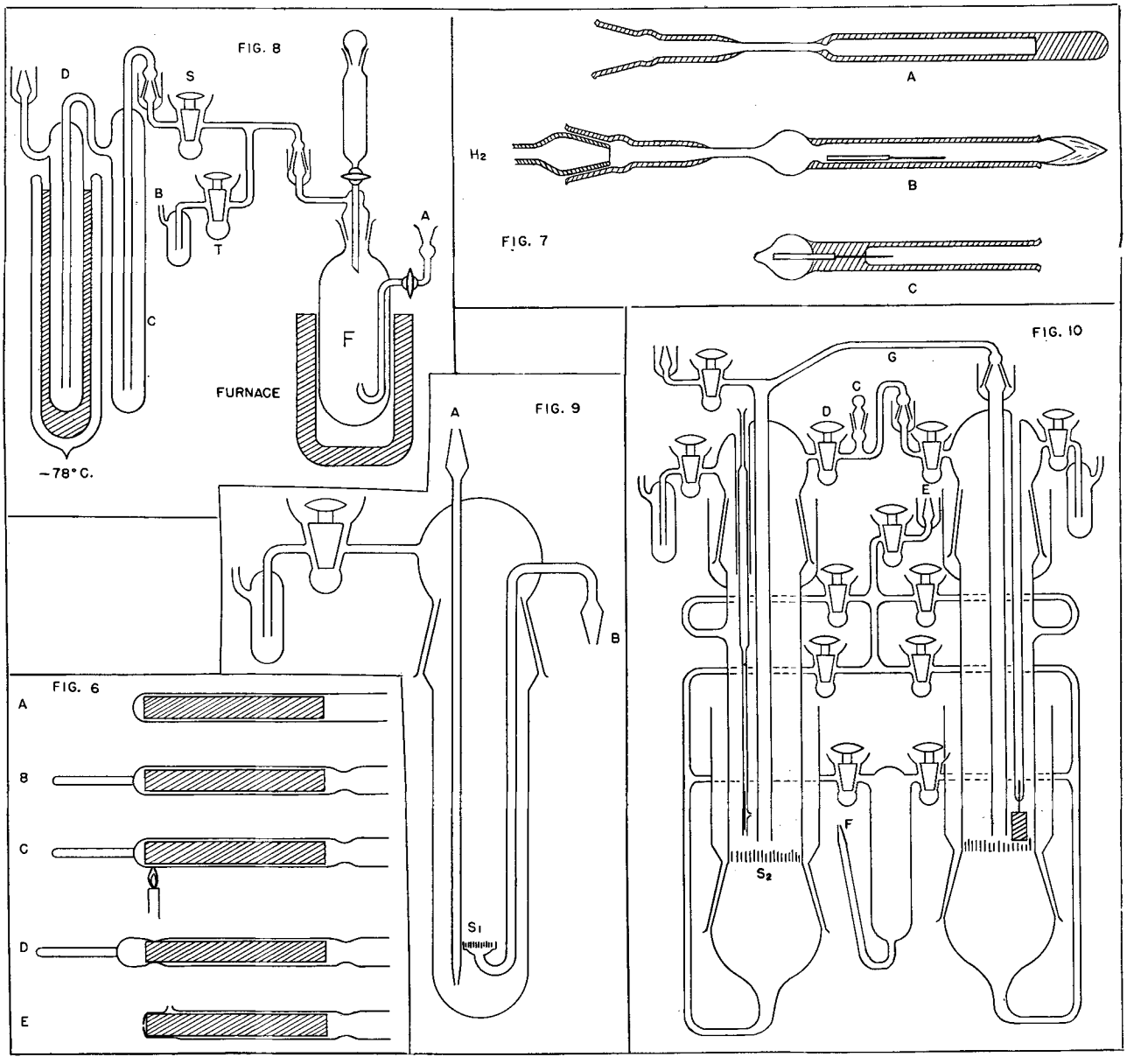

FIG. 6. Sealing of graphite rods into glass for use as anodes: A, initial position; B, constriction made to hold graphite in place, and holder fused on end; C, heating; D, glass pulled rapidly over graphite surface and annealed; E, top portion drawn off and vent blown at top near seal. FIG. 7. Preparation of cathode, sealed into bulb containing H_2. A, socket attached to tube of arsenic-free glass; B, wire of cathode material in position for heating with H_2 passing over it and burnt out at end; C, cathode sealed into bulb. FIG. 8. Apparatus for preparation of pure HCl solutions. A = inlet for H_2; B = sealed trap for escape of gas; C = preliminary trap; D = trap in solid CO_2 freezing mixture; F = vessel containing recrystallized KCl onto which drops Analar H_2SO_4. FIG. 9. Preliminary alkaline preparation vessel (for annotation, *see* text). FIG. 10. Main alkaline purification vessel (for annotation, *see* text).

2–5 min, until a perceptible oxide film was formed (C and CO_2 now removed). The pressure was reduced to 10^{-6} mm Hg, the wire heated to 2200°, and the oxide film removed, the surface becoming lustrous and light gray. When cool, the wire was removed and treated with H_2 (see below).

Electrode sealing in H_2.—As-free glass tubes were cleaned for 5 days in strong chromic acid. They were then washed in tap water, followed by equilibrium water, and stored therein. One such tube was withdrawn using Pt-tipped, cleaned tweezers, dried, and attached at one end to a piece of Hysil tubing by which it could be manipulated. [The rest of the procedure was similar to that of Bockris and Conway (4) except in the following way.] A cleaned socket was fused to the other end and a constriction made 2.5 cm from it. The tubing before the constriction was drawn into a thin walled section (c) 5 cm long and 2 mm diameter (Fig. 7A). A minute intense oxy-gas flame was used to blow a fragile bulb near the constriction, the subsidiary holding tube was withdrawn, and simultaneously the end of the electrode tube was blown open, its form being as in Fig. 7B. (In all glass blowing operations, the pressure is transmitted from the mouth through cotton wool pads and silica gel to

TABLE I. *Dimensions and preparation of metal electrodes*

Metal	Diameter (cm)	Approximate length (cm)	Method of attachment to Pt
Cu	0.0914	1.0	Mechanical
Au	0.0914	1.0	Mechanical and fusion
Mo	0.100	4.5	—
Pd	0.100	1.0	Fusion
Rh	0.150	0.7	Spot welding
	and 0.050	1.3	
Fe	0.0914	1.0	Spot welding

remove contaminants from the breath.) The electrode tube was then plugged to a cone from which issued H_2, led from a distribution head by means of cleaned glass tubing, containing only water-sealed joints, and passed through an empty trap, a trap at liquid air temperatures and a T piece, its entire limb leading to the atmosphere via a tap and bubbler, sealed with equilibrium water. H_2 was led to the cone by a very short length of polyethylene tubing, necessary to give flexibility.[1] The electrode was inserted into the tube and the H_2 issuing from the end was ignited, whereupon the composite electrode was heated to red heat before being tapped forward into the bulb. A seal was made over the metal-Pt junction and continued for 1.5 cm along the Pt, the surplus H_2 being allowed to escape via the T piece bubbler. After allowing the glass-metal seal to cool, the bulb was closed and simultaneously drawn away from the thin walled section by momentary application of an intense flame beyond the bulb. The electrode appeared as in Fig. 7C. This was then attached to a plunger of the ground glass tubes of the cathode cap, and washed with equilibrium water. Mo electrodes would not seal to Hysil and Chance GSC glass was used.

This method has the following advantages compared with its predecessor (4): (*a*) volatile impurities cannot condense on the bulb walls; (*b*) an improved seal over a considerable length of Pt can be achieved; (*c*) cooling of this seal before sealing bulb caused the H_2 pressure inside the bulb to remain uniform (otherwise implosion is frequent).

Vacuum heating and sealing of electrodes.—This was used mainly for Mo cathodes which, in method (*a*), had to be exposed to air between heating in high vacuo and introducing into H_2-filled bulbs. A 12 cm length of As-free Chance GSC glass tubing, 4 mm ID and 5 mm OD was cleaned as for the Hysil glass above. Two thickened constrictions were made, one at the end of the tube, and a fragile bulb was blown at this end. A 5 cm spectroscopically pure Mo wire, 0.1 cm diameter, previously vacuum heated in an Edwards unit, was introduced and arranged so that 1 cm projected into the bulb without touching the sides. The other end of the Mo was attached lightly to the glass by heating the second constriction sufficiently just to melt the glass and allow the wire to sink into it. The electrode tube was then fused horizontally to a Pyrex glass pump head, Chance GSC glass forming an intermediate seal, and was evacuated to 10^{-5} mm (until no discharge could be observed), the electrode holder being isolated from the pump by a liquid air trap. The electrode tube was thereupon surrounded by the coil of a radio frequency electronic heater and 2000°C induced in the Mo by 85 amp in about 2 sec. The temperature was maintained for 1 min. A seal over the Mo wire was made by heating the constriction near the bulb with an oxy-gas flame. The Mo-glass seal was 2–3 cm long; about 1 cm of light gray, lustrous Mo projected into the bulb. The electrode tube was withdrawn from the GSC/GSD glass joint at the end remote from the bulb and sealed to preserve a high vacuum inside the tube. This was then immersed in 1:1 HNO_3-H_2SO_4 mixture for 1 hr and washed with distilled, equilibrium, and conductivity water. The closed end away from the bulb was opened, and the tube mounted in the cell. Tubes were handled only by tweezers or filter paper.

[1] Caution must be taken in choice of the polyethylene tubing. Certain varieties show slight change of color after passage of H_2 for many hours and hence must be avoided.

Materials

Purification of hydrogen.—The "oxygen free" H_2 in cylinders contained 0.001% O_2, 0.001% CO, and 0.05% hydrocarbons. It passed through a few inches of polyethylene tubing to a two-way T trap through which the whole of the purification train could be evacuated, through a trap (5) and pressure indicator, SiO_2 gel, hopcalite (removes CO in absence of moisture), and soda lime. H_2 was then passed through palladised asbestos (5%) at 550° and further tubes of SiO_2 gel to remove water produced in the Pd tube. Four glass traps followed, the central two containing activated charcoal and the extreme ones empty. The first three traps were immersed in liquid N_2, the level of which was always maintained above that of the charcoal. The fourth trap served to retain water spray which sometimes arises during evacuation of the H_2 purification train. Traps were flamed out and charcoal reactivated after each run and then evacuated and flushed with H_2 for 1 hr before any was allowed to enter the cell.

H_2 was also purified by passage through a heated Pd tube but the maximum convenient yield was only 7 l/hr and the method was not extensively used.

Purification of water.—Distilled water from an electric still from which all rubber connections had been removed was redistilled from alkaline $KMnO_4$ and fractionally condensed in a block tin condenser. About 60% of the distillate was used. Its specific conductance was 1×10^{-6} mhos cm^{-1}. This water was transferred by pure H_2 pressure to a Hysil flask, refluxed in pure H_2 for 15 hr, and distilled into the cell when it had a conductance of 1×10^{-7} mhos cm^{-1}. The water purification apparatus was periodically cleaned with nitric-sulfuric acid, distilled and equilibrium water.

Preparation of acid solutions.—The apparatus is shown in Fig. 8. KCl of analytical reagent grade was placed in reaction vessel F and air swept out by H_2 entering at A and escaping by a valve. The vessel was heated at 500° for 3–4 hr. Capillary active impurities were thus removed. H_2 was still passed until the salt was cooled, and the H-passage allowed to occur through S into the anode compartment through a vigorously cleaned glass bridge. Trap D was then cooled to −78°C and H_2SO_4 dropped upon the KCl. Trap C caught acid spray (which otherwise blocks D). D condenses H_2S, etc.

After use the apparatus was always washed with nitric-

sulfuric mixtures for 24 hr, and rinsed many times with distilled and equilibrium water, being finally dried in an oven at 150°C.

Preparation of pure alkaline solutions.—The method used closely resembled that of Bockris and Potter (6), but its description has not been published previously. Pickering (7) showed that large amounts of solid separates from concentrated NaOH solution in ranges −22° to −2° and 20°–52°. The former range was chosen because of lessened attack on the glass.

The purification cell is shown in Fig. 9 and 10. A concentrated solution of A.R. NaOH pellets in conductance water was prepared in the vessel of Fig. 9, and transferred to the main vessel. (Both preliminary and main vessel were washed several times with conductance water before use.) 70 g of NaOH were introduced into the preliminary vessel, and first H_2, and then conductance water, were introduced from the conductance still while the lower part of the vessel was cooled in ice. The vessel was then disconnected from the still, sealed from air, and dissolution in H_2 proceeded. After sweeping out all air from bridges and connecting tubes, the solution in the preliminary vessel was transferred to the left hand limb of the main vessel (Fig. 10) by connecting joint B to joint C of the main vessel by applying pressure at A. Solid impurities were trapped by the sintered glass disc S1, porosity 1; after transfer of solution, tap D of the main vessel was closed, and H_2 bubbled through the solution via E and the sintered glass disc S2, porosity 3. Into the glass jacket surrounding the left limb (Fig. 10) was now introduced a CO_2 alcohol mixture. Solid CO_2 is added very gradually, until crystallization just commences. Supernatant liquor is drawn off through S2 from the crystals which were left dry, by applying a vacuum line at F. The crystals were liquified. The concentrated solution was transferred to the right-hand limb via tube G and again recrystallized, the left-hand limb meanwhile being washed with conductance water. After three or four recrystallizations in alternate limbs, the remaining highly concentrated solution was diluted by distilling in conductance water. The solution was shared between the two limbs, and electrolysis commenced by lowering the cathode (on a syringe plunger) into the solution. The current was $5–7 \times 10^{-2}$ amp. Wire, not foil, was used to increase current density and thus impurity removal. Pre-electrolysis was continued for a minimum of 30 hr and indefinitely during storage of the NaOH solution, H_2 always being passed through the solution. Termination of pre-electrolysis was carried out by raising the Pt cathode by means of its ground glass syringe (it is important to allow cessation of current to be brought about by the electrode removal).

When required, a few milliliters of concentrated purified solution were transferred by H_2 pressure to the anode compartment of the cell of Fig. 1 and diluted to required concentration. Solutions prepared in this way were subject to further pre-electrolysis in the cell.

Suitable glass.—The rate of the hydrogen evolution reaction is noticeably altered by 10^{-10} moles l^{-1} of As_2O_3 which diffuses out of glass containing it (8). Pyrex glass contained 0.6% AS_2O_3 until recently; at present it contains 0.01–0.02%. It is important not to let solution come into contact with As-containing glass; in particular, electrode preparation tubes must be As-free. Hysil, containing no AS_2O_3, was the glass generally used. A number of other As-free glasses, particularly that of Chance GSC, were also used.

Nitric-sulfuric mixtures are to be preferred for cleaning; rinsing with tap water lasted several hours, followed by washing with equilibrium and conductance water. (The advisability of rinsing with tap water depends on its local quality; if sufficiently bad, it is better to omit entirely and use only distilled water.)

Electrical Apparatus

This was as previously described. A powerpack giving 1,500 v was used for pre-electrolysis in dilute solutions. All leads were coaxial screened types, the screens being earthed. A Doran electrometer tube potentiometer was used to measure potentials to 0.5 mv and drew off balance currents of less than 10^{-11} amp. On Rh, potentials were measured to 0.01 mv by means of a Pye d-c potentiometer. Numerous continuous recording devices for current and potential were also used for preliminary and rough work.

Preparation of Experiment

Each piece of apparatus was left overnight in HNO_3-H_2SO_4, exposed joints being closed by ground glass caps. Washing with various stages of water of increasing purity followed, taps and joints were sealed with equilibrium water, and the air swept out by pure H_2, passing through rigorously cleaned glass tubing. The cell was then washed further with conductance water and the five electrodes in the ground glass syringe units introduced with the cathode cap, air expelled from the cell which is again washed with conductance water, this now washing also the bulbs of the electrodes and the breaker. Washing with further portions of hydrogen-saturated conductance water was carried out until the conductance water from the washings had a specific conductance of less than 5×10^{-7} mhos cm^{-1}. Fresh conductance water was distilled into the anode compartment and then, for acid solutions, HCl led in. Allowance must be made for diminution in strength of the solution during pre-electrolysis.

After sharing the solution thus prepared with the cathode compartment, each electrode bulb was lowered into the catholyte and tested to insure insulation. The bulb of one electrode was then broken and pre-electrolysis commenced under appropriate conditions (see below), H_2 bubbling in the catholyte, and with the breaker and all insulated electrode bulbs immersed in solution, so that impurities upon their outsides might be removed during pre-electrolysis This was ceased by raising the auxiliary cathode clear of the solution while still polarizing.

Polarization on a first test electrode was prepared for by making electrical connections to this electrode and setting controls such that on subsequent breaking of the protective glass bulb the current density would be a few $\mu amp\ cm^{-2}$. The electrode was lowered into the solution, the bulb broken, and polarization commenced. The current density was reduced to zero and it was confirmed that the electrode potential attained the value of a reversible hydrogen electrode. (This attainment is itself evidence of high

purification.) Hydrogen bubbling was now stopped to decrease diffusion of remaining impurities up to the electrode surface. The current density was now gradually increased from zero, about 30 current densities being established while the overpotential increased from 0 to 30 mv. (On Mo and Fe electrodes, some time variation was still observable even after pre-electrolysis; the 30 values at low current densities were therefore taken very rapidly.) For overpotential of greater than 30 mv, values were recorded at current density intervals of about 0.2 decade. The Tafel line was then remeasured in descending and ascending order of current densities.

The used electrode was raised above the solution during polarization, electrical connection made to another, this one lowered into solution, the bulb broken, and so on.

Photomicrographs

Photomicrographs of the electrode surfaces were taken through an optical microscope, having a 16 mm objective, with a six times or ten times eye piece. The electrode was illuminated by a Pointolite arc lamp. Front, side, and oblique illumination was used to highlight the surface characteristics. The net magnification upon enlargement was about 150.

Pre-electrolysis Conditions

Those used for each cathode after preliminary investigations of the variations of parameters with degree of pre-electrolysis are shown in Table II.

Miscellaneous

The most important factor in the technique of obtaining results unvitiated by side reactions is certainly pre-electrolysis. However, pre-electrolytic purification is certainly a method for removing trace impurities, i.e., those with concentrations of, say, less than 10^{-6} moles l^{-1}. If the preliminary purification of reagents, etc., is not thorough, pre-electrolysis is ineffective in any practical time. Some 20% of experiments still fail, even with the use of pre-electrolysis, presumably because of undetected contamination before the commencement of pre-electrolysis.

Glass blowing operations on the cell usually necessitate a particularly long period of cleaning. There is some evidence that this difficulty is removed by using pure N_2 pressure.

Grease traces are difficult to eliminate, even with procedures described here. They depend greatly on the original water supply. They can always be observed on the glass walls of the cell by the adherence of drops. Experiments in the presence of such adsorbed water drops are generally vitiated.[2]

The extreme sensitivity to trace impurities exhibited by the hydrogen evolution reaction at low current densities is not likely to be an isolated instance in electrode kinetics. A similar sensitivity to impurities (successfully removed by pre-electrolysis) has also been established for the oxygen evolution reaction, for a number of redox reactions and for certain technological deposition reactions. It is unlikely that electrode kinetic measurements carried out without attention to the extreme purities needed refer to clean electrode surfaces.[3]

[2] Traces of fats in conductance water can be eliminated by distillation through a column containing glass chips at 400°–500°C (9).

TABLE II. *Preëlectrolysis conditions*

Metal	Solution	Current density (μamp cm^{-2})	Duration (hr)	Quantity (coulombs)
Cu	0.001*N* HCl	550	36	24
	0.01*N* HCl	330	17	8
	0.1*N* HCl	900–75,000	43–37	60–3,000
	0.01*N* NaOH	360	14	6
	0.1*N* NaOH	450	13	7
Au	0.001*N* HCl	600	13	12
	0.01*N* HCl	5,000	16	100
	0.1*N* HCl	27,000	42	1,400
	0.001*N* NaOH	2,400	63	124
	0.01*N* NaOH	12,000	22	550
	0.1*N* NaOH	180,000	43	7,000
Mo	0.001*N* HCl	600	36	24
	0.01*N* HCl	8,500	58	530
	0.1*N* HCl	75,000	37	3,000
	0.001*N* NaOH	3,000	37	89
	0.01*N* NaOH	30,000	42	1,800
	0.1*N* NaOH	240,000	71	14,000
Pd	0.01*N* HCl	35,000	36	1,000
	0.1*N* HCl	240,000	13	1,600
	0.001*N* NaOH	1,200	24	63
	0.01*N* NaOH	21,000	40	800
	0.1*N* NaOH	120,000	38	4,500
Rh	0.1*N* HCl	50,000	34	1,700
	0.01*N* NaOH	6,000	20	250
Fe	0.001*N* HCl	1,400	16	14
	0.01*N* HCl	18,000	36	500
	0.01*N* NaOH	15,000	35	260
	0.1*N* NaOH	25,000	35	3,600

Experimental Results

Variation of overpotential with time at constant current density.—It has been shown that the variation of overpotential with time is largely an impurity-dependent phenomenon and is removed or very greatly reduced by pre-electrolytic purification (8). This result was confirmed in the present work on all cathode materials except Mo, in acid and alkaline solutions, and Fe, in alkaline solutions. If the bulb surrounding these electrodes were broken under the solution without application of external potential, these electrodes would indicate the reversible hydrogen electrode potential as expected, but upon passage of a constant current density, an upward drift of overpotential occurred for some 10 min before constancy was attained. If the $\eta - i_c$ relation at low c.d.'s were plotted using the η values attained at the end of this variation, anomalous values of η were obtained. If the values were those taken very soon (3 sec) after the setting up of a certain c.d., rational values of η were obtained.

Gross contamination effects.—In certain cases the seal on Mo electrodes cracked and the solution became contaminated. Such contamination was not removed by pre-electrolysis. All Tafel lines measured in the solution (on electrodes the bulbs of which were broken after the contamination) showed deviations at low c.d.'s from theoretical behaviors expected for one reaction.

[3] The analogy with the situation in the kinetics of reactions at the solid-gas interface is clear.

TABLE III. *Statistically computed values of exchange current density and transfer coefficient as a function of metal and concentration*

Metal	Solution	$\bar{n}$	$-\bar{a}$ (v)	$\bar{b}$ (v)	$\overline{-\log i_o}$	conf $\bar{b}$	$\frac{\text{conf}}{\log i_o}$	Range of $-\log i_c$
Cu	0.001*N* HCl	7	0.822	0.109	7.56	0.007	0.58	5.75–4.05
	0.01*N* HCl	5	0.844	0.116	7.25	0.010	0.29	5.23–3.98
	0.1*N* HCl	6	0.778	0.114	6.84	0.008	0.05	4.51–3.47
	0.01*N* NaOH	11	0.714	0.117	6.09	0.006	0.12	5.19–3.75
Au	0.001*N* HCl	17	0.524	0.072	7.32	0.005	0.20	6.33–4.62
	0.01*N* HCl	15	0.558	0.084	6.63	0.010	0.24	5.26–3.93
	0.1*N* HCl (1st)	19	0.468	0.071	4.59	0.006	0.23	5.63–4.02
	0.1*N* HCl (2nd)	13	0.548	0.097	5.64	0.010	0.23	3.67–2.41
	0.001*N* NaOH	13	0.548	0.097	5.64	0.010	0.23	3.67–2.41
	0.01*N* NaOH	17	0.832	0.118	7.05	0.006	0.15	5.90–4.54
	0.1*N* NaOH	12	0.836	0.119	7.04	0.007	0.24	5.92–3.68
Mo	0.001*N* HCl	5	0.577	0.081	7.12	0.016	0.41	5.56–4.19
	0.01*N* HCl	15	0.543	0.076	7.19	0.003	0.27	5.23–3.72
	0.1*N* HCl (1st)	21	0.586	0.080	7.30	0.004	0.21	5.52–3.48
	0.1*N* HCl (2nd)	23	0.671	0.104	6.45	0.004	0.21	3.34–1.80
	0.001*N* NaOH	4	0.667	0.092	7.27	0.010	0.46	5.87–4.42
	0.01*N* NaOH	11	0.664	0.103	6.42	0.010	0.52	4.89–3.59
	0.1*N* NaOH (1st)	15	0.641	0.087	7.35	0.003	0.21	4.74–3.72
	0.1*N* NaOH (2nd)	10	0.739	0.116	6.37	0.008	0.34	3.58–2.10
Pd	0.01*N* HCl	19	0.447	0.107	4.18	0.006	0.45	3.87–3.13
	0.1*N* HCl	15	0.321	0.099	3.25	0.003	0.11	2.89–1.41
	0.001*N* NaOH	5	0.589	0.100	5.88	0.015	0.61	5.04–3.92
	0.01*N* NaOH	23	0.610	0.110	5.56	0.004	0.48	5.35–3.98
	0.1*N* NaOH	4	0.637	0.125	5.01	0.002	0.33	4.14–3.08
Rh	0.01*N* HCl	30	0.209	0.055	3.80	0.003	0.09	3.38–3.08
	0.01*N* NaOH	25	0.579	0.119	4.85	0.003	0.21	4.18–3.51
Fe	0.001*N* HCl	6	0.787	0.127	6.19	0.008	0.23	4.02–3.76
	0.01*N* HCl	5	0.741	0.118	6.29	0.015	0.32	4.06–3.19
	0.01*N* NaOH	6	0.776	0.117	6.62	0.007	0.47	4.52–3.82
	0.1*N* NaOH	29	0.726	0.120	6.06	0.002	0.08	4.09–2.16

In acid solutions when high pre-electrolysis currents were employed, the original graphite anode, having a small area, tended to disintegrate. Subsequent transport of carbon to the catholyte turned the solution yellow brown. The Tafel line became strikingly anomalous, the b value rising to 0.8 v.

The micrographs[4] were taken under numerous states of oxidation and contamination, as well as for the pure surface before and after a run. Contamination and oxidation caused by a few seconds' contact with the atmosphere were clearly visible. No alteration of the appearance of the electrode before and after a run was visible.

Statistically computed Tafel parameters.—Tafel parameters from the "first up," "second up," and subsequent lines coincided well. Reproducibility between "up" and "down" lines was excellent; at low c.d.'s it declined and the $i_c - \eta$ line was sometimes slightly displaced although $\left(\frac{\partial \eta}{\partial i_c}\right)_{\eta=0}$ from up and down runs retained excellent concordant values. In instances of significant discrepancy between up and down lines, up lines were preferred, the electrode not having attained highly negative potentials, which encourage impurity depositions.

Tafel lines observed could be divided into three classes: (*a*) those showing the form in the $\eta - i_c$ relation expected if the hydrogen evolution reaction is not interferred with by competitive reactions with trace impurities; (*b*) slightly imperfect lines, i.e., form and slope indicate lack of impurity effects except at the lowest current densities where slight deviations occurred; (*c*) lines showing a large scatter of points, and distinct deformities from the theoretically expected relation, particularly at low current densities.

Only class (*a*) results have been considered in the statistical evaluation for Fe, Cu, Rh, Au, and Pd. For Mo, the remaining time variation made it necessary to accept some results of class (*b*).

The statistical terms used in the next section have their usual significance. Values of exchange current densities

[4] Some 25 photomicrographs are available (10).

TABLE IV. *Statistically computed values of exchange current density and transfer coefficient summarized for each metal*

Metal	Solution	$\overline{\overline{n}}_T$	$\overline{\overline{b}}$	$\overline{\overline{-\log i_o}}$	$\overline{\overline{-a}}$	conf $\bar{b}$	$\frac{\text{conf}}{\log i_o}$
Cu	HCl	18	0.113	7.23	0.814	0.033	0.31
	NaOH	11	0.117	6.09	0.714	0.006	0.12
Au	HCl-1st	37	0.073	6.83	0.496	0.003	0.16
	-2nd	13	0.097	5.64	0.548	0.010	0.23
	NaOH	52	0.120	7.00	0.844	0.003	0.03
Mo	HCl-1st	41	0.079	7.24	0.569	0.003	0.14
	-2nd	23	0.104	6.45	0.671	0.004	0.21
	NaOH-1st	30	0.094	7.00	0.656	0.005	0.26
	-2nd	10	0.116	6.37	0.739	0.008	0.34
Pd	HCl	34	0.103	3.77	0.389	0.004	0.30
	NaOH	42	0.110	5.54	0.811	0.004	0.35
Rh	HCl	30	0.055	3.80	0.209	0.003	0.09
	NaOH	25	0.119	4.85	0.579	0.003	0.21
Fe	HCl	11	0.123	6.24	0.766	0.007	0.15
	NaOH	35	0.119	6.16	0.735	0.002	0.12

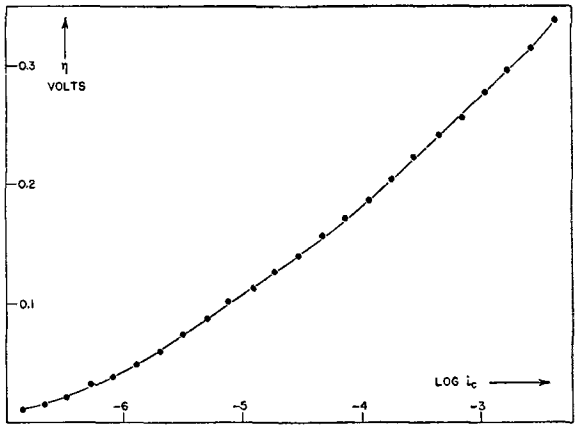

FIG. 11. Typical Tafel line on Au in 0.1N HCl solutions

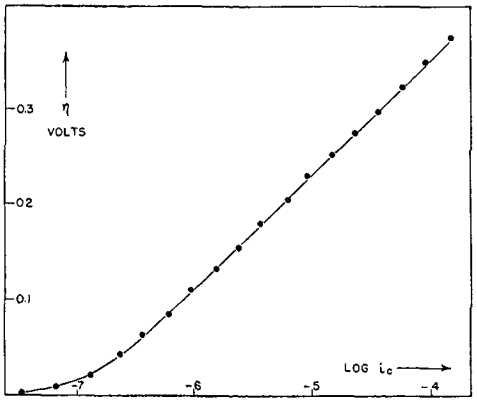

FIG. 12. Typical Tafel line on Au in 0.01N NaOH solutions.

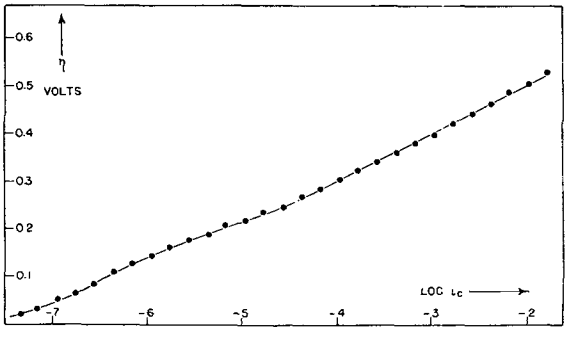

FIG. 13. The anomalous type of Tafel line observed on Mo in 0.1N HCl.

were calculated by the extrapolation of the linear sections of Tafel lines to zero overpotential. Stoichiometric numbers were calculated from

$$\nu = -2i_0 \frac{F}{RT}\left(\frac{\partial \eta}{\partial i_c}\right)_{\eta \to 0}$$

The term $\bar{n}$ represents the number of Tafel lines used in the statistical analysis; $\bar{a}$ represents the mean value of a in the Tafel equation, and $\bar{b}$ the same for b in this equation. The term i_c represents the net cathodic current at an electrode and "Range of η − log i_c" means the range of values

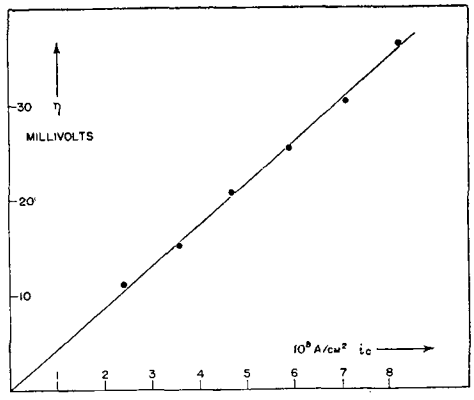

FIG. 14. The current density-overpotential relation at current densities in the neighborhood of the reversible potential on Mo in 0.1N HCl.

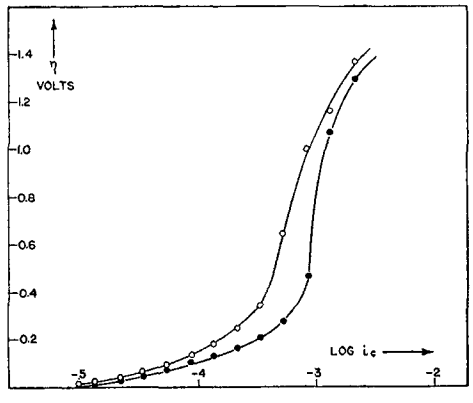

FIG. 15. Effect of carbon contamination in the catholyte on the Tafel lines at Pd electrodes in 0.01N HCl. (—— ● —— = first up;——⊙—— = first down).

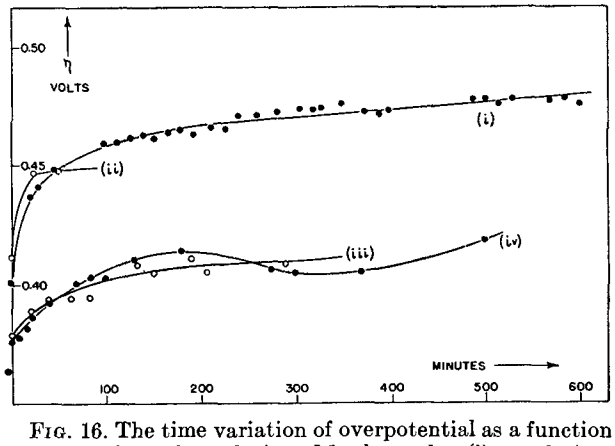

FIG. 16. The time variation of overpotential as a function of degree of pre-electrolysis on Mo electrodes: (i) = polarization at 7.10^{-4} amp/cm^{-2} after pre-electrolysis of 50 hr at 1.10^{-3} amp/cm^{-2}; (ii) = polarization at 1.10^{-3} amp/cm^{-2} after p.e. of 36 hr at 1.10^{-3} amp/cm^{-2}; (iii) = polarization at 9.10^{-4} amp/cm^{-2} after p.e. of 20 hr at 1.10^{-3} amp/cm^{-2}; (iv) = polarization at 6.10^{-4} amp/cm^{-2} after 36 hr p.e. at 1.10^{-3} amp/cm^{-2}.

of log i_c during which the η − log i_c relation was observed and linear. The term conf. means "95% confidence limits."

Concentration effects on the parameters are not significant. If values are grouped together for each metal, irre-

spective of concentration, and meaned, one obtains Table IV ("first" and "second" refer to the appropriate reactions of the Tafel line when twin linearity was observed).

Analogous Tables to III and IV follow for the stoichiometric number.

The graphical representation of most of the Tafel lines indicates expected theoretical behavior. Fig. 11 and 12 represent typical behaviors, e.g., on Au. Fig. 13 shows the anomalous behavior of Mo, while Fig. 14 shows that although the Tafel line is anomalous, the corresponding $\eta - i_c$ graph has theoretical shape. Fig. 15 shows the behavior of Au electrodes contaminated with carbon.

The time variation on Mo electrodes in alkaline solution (cf. "Variation of Overpotential with Time . . .") is represented in Fig. 16 as a function of pre-electrolysis. The result is qualitatively similar to observations of the effect of pre-electrolysis on the time variation at Ni cathodes in acid solution (8).

Discussion

Reproducibility

The measure of reproducibility of the determination of the kinetic parameters used here is the 95% confidence limit of the mean value of log i_0. In Fig. 17, BC is "conf. log i_0," where CD is the most probable Tafel line (and its extrapolation). AC may then be suggested as a measure of the reproducibility in overpotential units, and AC = $\bar{b}$ conf. $\overline{\log i_0}$. Hence:

$$\overline{\Delta\eta} = \bar{b} \text{ conf. } \overline{\log i_0}$$

and $\overline{\Delta\eta}$ is the meaned probable error of the overpotential measurements for 95% confidence limits. Table VII shows these values for the present work.

The over-all mean reproducibility for overpotential expressed on this basis is 19 mv. More reproducible values on solid metals have not been published previously, except the values of Bockris and Potter (6) on Ni in acid solutions where the reproducibility on the same basis is 15 mv. (On Hg electrodes in acid solutions, the reproducibility is about 5 mv.)

Ohmic and Concentration Components

For a cylindrical electrode, the approximate correction equations for ohmic overpotential have been discussed elsewhere (1); they yield only values of the correct order

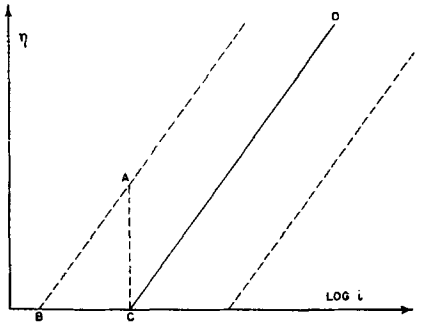

Fig. 17. Expression of reproducibility in overpotential measurements.

TABLE V. *Statistically computed values of the stoichiometric number as a function of metal and concentration*

Metal	Solution	$\bar{n}$	$\bar{v}$	conf $\bar{v}$
Au	0.001*N* HCl	8	1.02	0.16
	0.01*N* HCl	5	1.07	0.35
	0.1*N* HCl	9	0.99	0.20
	0.001*N* NaOH	7	1.93	0.30
	0.01*N* NaOH	9	2.10	0.14
	0.1*N* NaOH	11	0.88	0.16
Mo	0.001*N* HCl	4	1.09	0.11
	0.01*N* HCl	7	0.95	0.18
	0.1*N* HCl	6	0.97	0.21
	0.001*N* NaOH	3	0.76	0.24
	0.01*N* NaOH	7	0.86	0.18
	0.1*N* NaOH	7	1.13	0.22
Pd	0.01*N* HCl	13	1.88	0.19
	0.1*N* HCl	10	2.12	0.20
	0.001*N* NaOH	5	1.97	0.55
	0.01*N* NaOH	10	2.01	0.17
Rh	0.01*N* HCl	30	0.96	0.06
	0.01*N* NaOH	13	1.86	0.10
Fe	0.01*N* NaOH	2	1.36	—
	0.1*N* NaOH	16	1.01	0.10

TABLE VI. *Statistically computed values of the stoichiometric number summarized for each metal*

Metal	Solution	$\bar{\bar{b}}$	$\overline{\overline{-\log i_0}}$	$\bar{\bar{v}}$	conf $\bar{\bar{v}}$	$\bar{\bar{n}}$
Au	HCl	0.076	6.85	1.02	0.10	22
	0.001*N* NaOH	0.118	7.05	2.03	0.14	16
	0.01*N* NaOH					
	0.1*N* NaOH	0.123	6.96	0.88	0.16	11
Mo	HCl	0.078	7.20	0.99	0.09	17
	NaOH	0.094	7.01	0.95	0.14	17
Pd	HCl	0.104	3.72	1.98	0.14	23
	NaOH	0.112	5.45	1.99	0.17	15
Rh	HCl	0.055	3.80	0.96	0.06	30
	NaOH	0.119	4.85	1.85	0.10	13
Fe	NaOH	0.118	6.34	1.05	0.11	18

TABLE VII. *Mean probable error (95% confidence limits) in overpotential for various metals*

Metal	Solution	Reproducibility	Metal	Solution	Reproducibility
Cu	HCl	35 mv	Pd	HCl	31 mv
	NaOH	14		NaOH	38
Au	HCl	12	Rh	HCl	5
	NaOH	4		NaOH	25
Mo	HCl	11	Fe	HCl	18
	NaOH	24		NaOH	14

because of various factors not taken into account, e.g., bubbles near the electrode surface.

The equation for η_0 can be applied to the present results in instances where the Tafel line indicated positive deviations from linearity at high overpotential, e.g., for Rh (Fig. 18). If the deviations are plotted against current density, a linear relation should exist if they are due to ohmic errors. No linear relation was found. Application of an ohmic correction formula to the Rh results, with values of 0.1 cm or greater for the distance between the Luggin capillary tip and the electrode (the intended value in the experiments was always apparently less than this), gave

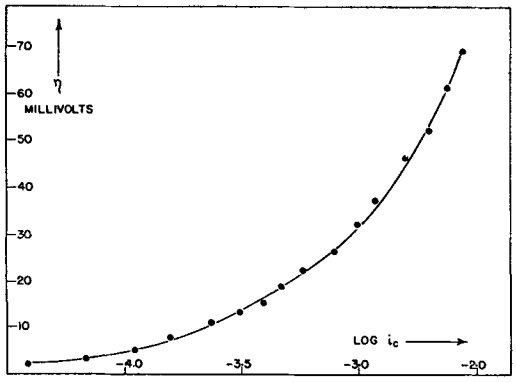

FIG. 18. Positive deviations at high current densities for Rh electrodes in 0.01N acid solutions.

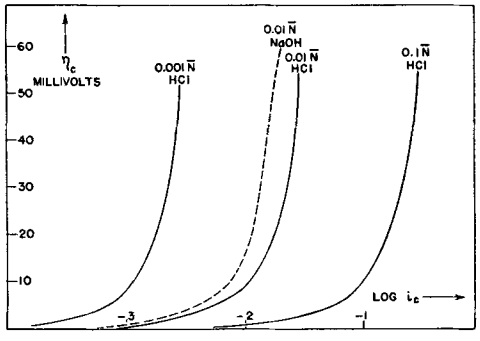

FIG. 19. Concentration overpotential (calculated for a diffusion layer thickness of 0.005 cm and $t_+ = 0.82$) in acid solutions of various strengths and in 0.01N NaOH solutions.

poorly defined "corrected" Tafel lines with no linear portions. Therefore, no ohmic errors affect the Rh results.

Similar results were found for Pd, which also indicated slight positive deviations at current densities of 10^{-1} amp cm^{-2} in 0.1N HCl.

The limits of the concentration overpotential can be calculated from well-known equations (1) in which the only adjustable term is the thickness of the diffusion layer. For the present conditions, in which stirring is almost entirely by means of hydrogen evolved at the electrodes, the appropriate value is approximately 0.005 cm. Values are shown in Fig. 19. The concentration component in the overpotential can therefore be considered negligible for 0.001N solution of HCl or NaOH below 10^{-3} amp cm^{-2}; for 0.01N solution below 10^{-2} amp cm^{-2}, and for 0.1N solution below 10^{-1} amp cm^{-2}. The statistical computation of Tafel lines were carried out only for current densities lower than these limits.

Variations with Time

An essential improvement in measurements brought about by the technique of pre-electrolytic purification is a considerable reduction in the total amount of time variation and an elimination of the irregular time variation (*see* Fig. 16) which formerly made comparison of overpotential measurements carried out by two different authors of little significance. The absence of time variation on Cu, Au, Pd, and Rh reported here makes the regular variation on Mo and Fe in alkaline solutions of particular interest. Possible interpretations would be: (*a*) presence of impurities after pre-electrolysis. If this were the cause of time variation, or of the imperfect Tafel lines on Mo, the drift should be augmented by increasing the rate of transport of impurities to the electrode, i.e., by stirring. This effect was absent. Further, the impurity will only compete with the hydrogen evolution reaction if its concentration is sufficient to give it a sufficiently high limiting current density.[5] Calculation shows that, to cause the deviation observed in the Tafel lines on Mo (Fig. 13), the impurity concentration would have to be 10^{-6} moles l^{-1}, which is improbably high after the pre-electrolysis detailed in Table II [cf. calculations of the rate of "clean up" of a solution during pre-electrolysis (1)]. (*b*) Oxide film dissolution. Reduction of an oxide film would cause a decrease of overpotential with time at constant current density (11). In the present work, an increase was observed at low current densities. (*c*) Hydrogen diffusion into the interior. No time variations were observed on Pd, where diffusion would be greater than on Mo. Change of the Mo wire thickness did not alter the observed time variation, as would be expected if diffusion were rate determining. (*d*) Change of "activity." Progressive deactivation of the electrode surface may be invoked to explain the increase of overpotential with time at a given current density, but only with great caution, because many systems where this explanation has been applied have been proved later to exhibit no time variation in the absence of impurities. Deactivation would lead to a steady increase of overpotential with time and probably to a linear relation between η and log time;[6] neither of these behaviors were observed on Mo or Fe. Therefore, none of these explanations appears applicable to the time variations observed on Mo electrodes

Results of the present work confirm previous work that there is no variation of the stoichiometric number with time, even on Mo electrodes.

Rate-Determining First Order Combination of Hydrogen Atoms

The rate-determining combination reaction between two hydrogen atoms both adsorbed on a metal surface gives rise to a Tafel line for which $b = 2.303 \frac{RT}{2F} = 0.029$ at 25°C. The model in which one H atom is adsorbed and the other is not has not yet been formulated [but cf. Bockris (12)]. Consider

$$H_3O^+ + e_0^- \underset{V_{-1}}{\overset{V_1}{\rightleftharpoons}} MH \qquad (I)$$

Let it be supposed that a negligible rate of combination occurs between the H on the surface and that the formation of H_2 is by reaction between one adsorbed H and one nonadsorbed H atom, as is the mechanism of formation

[5] For details of this calculation, see (8).

[6] Cf. Bockris and Huq (9), where such a view has been worked out in some detail.

of H_2 at a catalytic surface in the gas phase, i.e.,

$$MH \underset{V_{-2}}{\overset{V_2}{\rightleftharpoons}} H_{(g)} + M \qquad \text{(II)}$$

$$MH + H_{(g)} \underset{V_{-3}}{\overset{V_3}{\rightleftharpoons}} H_2 \qquad \text{(III)}$$

Then,

$$v_1 = k_1 e^{-\Delta\phi F/2RT}(1 - k^1 c_H)c_{H\cdot} \qquad \text{(IV)}$$

where $\Delta\phi$ is the Galvani p.d. between metal and solution; c_H is the concentration of H on the surface, $(1 - k^1 c_H)$ is the fraction of the surface free, and $c_{H\cdot}$ is the hydroxonium ion concentration in the Helmholtz double layer.

$$v_{-1} = k_{-1} c_H e^{\Delta\phi F/2RT} \qquad \text{(V)}$$

$$v_2 = k_2 c_H \qquad \text{(VI)}$$

$$v_{-2} = k_{-2} c_{H,g}(1 - k^1 c_H) \qquad \text{(VII)}$$

$$v_3 = k_3 c_{H,g} c_H \qquad \text{(VIII)}$$

from which the Christiansen coefficients (13) follow as

$$w_1 = k_1 c_{H\cdot} \qquad \text{(IX)}$$

$$w_{-1} = k_1 k^1 e^{-\Delta\phi F/2RT} c_{H\cdot} - k_{-1} e^{\Delta\phi F/2RT} \qquad \text{(X)}$$

$$w_2 = k_2 + k_{-2} k^1 c_{H,g} \qquad \text{(XI)}$$

$$w_{-2} = k_{-2} \qquad \text{(XII)}$$

$$w_3 = k_3 c_H \qquad \text{(XIII)}$$

where c_H is the concentration of adsorbed H and $c_{H,g}$ is the nonadsorbed H atom concentration.

It follows that the current density for this path is

$$i_c = 2F\left[\frac{k_1 c_{H\cdot} e^{-\Delta\phi F/2RT}(k_2 + k_{-2}k^1 c_{H,g})k_3 c_H}{k_1 e^{-\Delta\phi F/2RT} c_{H\cdot}(k_2 + k_{-2}k^1 c_{H,g}) + k_1 e^{-\Delta\phi F/2RT} k^1 c_{H\cdot} + (k_1 k^1 e^{-\Delta\phi/2RT} - k_{-1})k_{-2}}\right]$$

whence, with $k_3 \to 0$ and at high negative potentials, i.e., reaction (III) is rate determining,

$$i_c = 2F\left[\frac{(k_2 + k_{-2}k^1 c_{H,g})k_3 c_H}{(k_2 + k_{-2}k^1 c_{H,g}) + k_{-2}k^1}\right] \qquad \text{(XIV)}$$

Therefore, if $k_{-2}k^1 \ll (k_2 + k_{-2}k^1 c_{H,g})$, then,

$$i_c = 2Fk_3 c_H = 2Fk_3 \frac{k_1}{k_{-1}} c_{H\cdot} e^{-\Delta\phi/RT} \qquad \text{(XV)}$$

or:

$$\frac{\partial\eta}{\partial \log i_c} = 2{\cdot}303\frac{RT}{F} \qquad \text{(XVI)}$$

Eq. (XVI) is the result formally obtained if one calculates the reaction on the basis of a first order hydrogen atom combination, and the Tafel line to be expected for such a condition has been mentioned by Knorr (14), although without formulation. However, it does not seem a likely mechanism because (XV) results from the assumption that the coverage of the surface with adsorbed H is small, so that $c_H = c_{H\cdot} Ke^{-\Delta\phi F/RT}$. If this is so, the value of $c_{H,g}$ is small and hence it is less probable that the condition quoted for the simplification (XIV) – (XV) will occur. As the surface becomes saturated, and the condition for (XV) becomes no longer true, c_H becomes independent of $\Delta\phi$ and a limiting current density is set up.

TABLE VIII. *Diagnostic criteria and rate in the hydrogen evolution reaction* (1)

Tafel slope	Stoichiometric no.	Consistent rate-determining step	Remarks
0.116	2	$H_3O\cdot + e_0^- \to MH$ (Followed by combination)	Implies low coverage of electrode with adsorbed H
0.116	1	$H_3O\cdot + MH + e_0 \to H_2$	Implies that coverage with adsorbed H is near to complete
0.058	1	$(MH)_1(MH)_2$	Slow diffusion
0.058	1	$MH + H_g H_2$	Physically improbable
0.038	1	$H_3O\cdot + MH + e_0^- \to H_2$	Implies low coverage of electrode with adsorbed H
0.029	1	$MH + MH \to H_2$	Could show limiting current at sufficiently high current density.

Deduction of Detailed Mechanism at Various Cathodes

Summary of connection between parameters and mechanisms.[7] At the present time, the connections between observed diagnostic parameters and the mechanism they indicate is as shown in Table VIII.

Copper (3).—The absence of a stoichiometric number value for Cu in acid solution (not determinable owing to its dissolution) leaves the distinction between a rate-determining proton discharge and electrochemical desorption to be made on secondary grounds, i.e., the invariance of the capacity with frequency. This indicates a small coverage of the metal surface with H in the steady state and hence favors a rate-determining proton discharge mechanism in acid solution.

For alkaline solutions, the values of $\nu = 2$ and $b = 0.116$ indicate a rate-determining proton discharge, probably from a water molecule.

Gold.—In acid solutions, the relevant values are $b = 0.076$ at low current densities and $b = 0.097$ at higher current densities, while $\nu = 1$. Had the lower slope been near to 0.058, then, with $\nu = 1$ it would have seemed probable that under these conditions a rate-determining diffusion mechanism was taking place. A value of $b = 0.076$ does not refer, however, to any characteristic parameter of a given rate-determining step, and the fact that the Tafel line remains linear for some two decades of current density precludes the possibility of the contribution of two mechanisms to the reaction. The slope is in fact one between 0.116 and 0.058 which was recently shown (15) to follow for an electrode in the vicinity of the electrocapillary maximum if the slope fundamentally associated with the mechanism was 0.116, as is confirmed by the fact that the slope becomes 0.097 at potentials sufficiently far from the electrocapillary maximum. On grounds of the Tafel slope, the mechanism could be the discharge of protons or the slow electrochemical desorp-

[7] These mechanisms are not complete, cf., e.g., the development of a new mechanism involving H_2 (10).

tion, and these are distinguished by the value of unity for the stoichiometric number. Therefore, these results indicate a rate-determining electrochemical desorption on Au in acid solutions.

The results for Au in alkaline solutions are $b = 0.116$ but $\nu = 2$ for solutions of concentration < 0.1 and 1 at $0.1N$. For the results in the solutions at lower concentrations, Table VIII indicates that the rate-determining mechanism must be proton discharge. [The parameters would also be consistent with the combination of H_2O and Na atoms as the rate-determining reaction but it can be shown that the rate of deposition of Na on Au in alkaline solution is negligibly small (10).]

In $0.1N$ NaOH, with $b = 0.123$, and $\nu = 1$, the two possibilities are rate-determining proton discharge from water molecules, followed by a fast electrochemical desorption step, or, proton discharge from water, followed by a slow electrochemical desorption. No evidence is available, e.g., on coverage of the surface with adsorbed H in the steady state, to indicate which of these two mechanisms is preferable. It may be supposed, however, that as the slow discharge step has been established as slow in the more dilute solutions (where the value of $\nu = 2$, combined with $b = 0.116$, indicated slow proton discharge, followed by rapid atomic combination), it will remain relatively sluggish in $0.1N$ NaOH.

Molybdenum.—In acid solutions, the values of $b = 0.078$ and $\nu = 1$ at low current densities, together with a higher value of b (0.104) at more negative potentials, suggest the same type of explanation as for Au in acid solution (cf. "Gold"). The mechanism is therefore a rate-determining electrochemical desorption mechanism.

In alkaline solutions, the values are $b = 0.094$ and $\nu = 1$ at low current densities with a value of $b = 0.116$ at higher current densities. Two possibilities would be consistent with these parameters. Assuming that the Tafel slope unaffected by the $\frac{\partial \phi_2}{\partial \Delta \phi}$ term (where ϕ_2 is the potential of the Gouy-Helmholtz layer), which becomes important near the electrocapillary maximum (15), is 0.116, then the rate-determining step may be proton discharge from a water molecule, followed by the electrochemical desorption step, or a rate-determining electrochemical reaction. The latter seems probable by analogy to the unambiguous result in acid solutions.

Palladium.—The values of $b = 0.103$ and $\nu = 2$ and the mechanism is therefore a rate-determining discharge of a proton from a hydroxonium ion, followed by rapid combination of H atoms.

These conclusions for Pd differ from those of Frumkin and Aladjalowa (16) and also of Bockris and Azzam (17), both of these workers recording a Tafel slope of 0.03 in acid solution. These earlier results were obtained under sufficiently rigorous conditions of solution preparation, but the method of preparing the electrode involved heating in air, while here the electrodes were prepared by the method of sealing in hydrogen. There was absence of time variation in the present results, whereas the former workers found considerable variations with time (in their purified solutions) indicating the effect of H diffusion into the electrode was important. Owing to the mode of electrode preparation used here, H diffusion would doubtless have already occurred into the Pd before electrolysis. This would mean that the d levels of the Pd lattice would be already filled with the electrons of diffused H at the commencement of the electrolysis so that the disappearance of electrons from the atoms from the discharge step into the d holes would be improbable. The discharged H would therefore behave like free H atoms on a holeless metal and hence combine rapidly, making the discharge step rate-determining.

It may be observed that on Pt, where the Tafel slope in pure solution is 0.03 and the stoichiometric number is 1 [cf. Pd as measured by Bockris and Azzam (17)], it is possible to induce a slope about 0.12 (cf. Pd as measured by Pentland, Bockris, and Sheldon), by poisoning the solution. However, it is improbable that the present results on Pd are due to poisoning because of the very high degree of pre-electrolytic purification which was carried out [considerably higher, for example, than that used by Frumkin and Aladjalowa (16)]. The difference in observed slopes provides an example of mechansim change caused by change of the electronic character of the electrode by the presence of H.

In alkaline solutions, $b = 0.112$ and $\nu = 2$ indicates that the mechanism is the rate-determining discharge of protons from water, followed by the fast atomic combination. (As with Au, it can be shown that the discharge step of Na onto Pd is very slow compared with that of H_2O, so that the possibility of a rate-determining reaction between H_2O and Na, also consistent with the observed parameters, is to be rejected.)

Rhodium.—In an acid solution the parameters of $b = 0.056$ and $\nu = 1$ would be consistent with a rate-determining slow diffusion reaction, or with the first order atomic combination. No direct distinction between these mechanisms is possible. The parameters could be consistent with a rate-determining electrochemical desorption mechanism if the section of slope 0.056 were in the vicinity of the electrocapillary maximum potential. However, there is no twin linearity with the upper slope of about 0.1 as would be expected if this were the mechanism, the behavior being similar to that observed for a Pt electrode prepared in air (15).

In alkaline solution, $b = 0.119$ and $\nu = 2$, indicating that the rate-determining step is the discharge of protons from water molecules, followed by the rapid atomic combination. Na^+ discharge is too slow to be of consequence, as with Au and Mo.

Iron.—No stoichiometric number for acid solutions is available, owing to the dissolution which occurs near to the reversible potential. The slope of 0.122 would be consistent with a rate-determining electrochemical or slow discharge reaction.

In alkaline solution, the value of $b = 0.118$ and $\nu = 1$ are consistent with either a rate-determining proton discharge reaction from water molecules or a proton discharge from water, followed by a rate-determining electrochemical desorption reaction.

There is only qualitative evidence to distinguish the two steps here. Fischer and Heiling (18) have shown that on Fe, overpotential is easily "transferred" from the

"polarization side" to the "diffusion side" of an electrode. It follows that there is a large concentration of H on the polarization side in the steady state and this is in favor of a rate-determining electrochemical mechanism, which demands a well covered surface, compared with a rate-determining slow proton discharge reaction, which requires low coverage of the electrode with H atoms in the steady state.

ACKNOWLEDGMENTS

The authors wish to acknowledge the facilities afforded by the Governing Body of Acton Technical College, where the experimental work was carried out; one of them (E.S.) wishes to acknowledge a grant given him by the Middlesex Education Committee.

Manuscript received April 25, 1956.
Any discussion of this paper will appear in a Discussion Section to be published in the December 1957 JOURNAL.

REFERENCES

1. J. O'M. BOCKRIS, "Modern Aspects of Electrochemistry," Chap. IV, Academic Press, New York (1954).
2. D. C. GRAHAME, *Ann. Rev. Phys. Chem.*, **6**, 337 (1955).
3. J. O'M. BOCKRIS AND N. PENTLAND, *Trans. Faraday Soc.*, **48**, 833 (1952).
4. J. O'M. BOCKRIS AND B. E. CONWAY, *J. Sci. Inst.*, **25**, 283 (1948).
5. A. M. AZZAM, J. O'M. BOCKRIS, B. E. CONWAY, AND H. ROSENBERG, *Trans. Faraday Soc.*, **46**, 918 (1950).
6. J. O'M BOCKRIS AND E. C. POTTER, *J. Chem. Phys.*, **20**, 614 (1952).
7. S. U. PICKERING, *J. Chem. Soc.*, **63**, 890 (1893).
8. J. O'M. BOCKRIS AND B. E. CONWAY, *Trans. Faraday Soc.*, **45**, 989 (1949).
9. J. O'M. BOCKRIS AND A. K. M. S. HUQ, *Proc. Roy. Soc.*, **237A**, 277 (1956).
10. E. SHELDON, Thesis, London (1955).
11. R. PARSONS, Thesis, London (1948).
12. J. O'M. BOCKRIS, *J. Chem. Phys.*, **24**, 817 (1956).
13. A. CHRISTIANSEN, *Z. physik. Chem.*, **33B**, 145 (1936).
14. C. A. KNORR, *Z. Elektrochem.*, **57**, 599 (1953).
15. J. O'M. BOCKRIS, I. A. AMMAR, AND A. K. M. S. HUQ, *J. Phys. Chem.*, In press.
16. A. FRUMKIN AND A. ALADJALOWA, *Acta Physicochim.*, **19**, 1 (1944).
17. J. O'M. BOCKRIS AND A. M. AZZAM, *Trans. Faraday Soc.*, **48**, 145 (1952).
18. H. FISCHER AND A. HEILING, *Z. Elektrochem.*, **54**, 184 (1950).

Kinetics of Silver–Silver Ion Exchange

CECIL V. KING AND ANN-MARI SIMONSEN

Department of Chemistry, New York University, New York, New York

ABSTRACT

Silver is known to exchange rapidly with its own ions on initial immersion in solution, with much slower exchange continuing through a sluggish layer of adsorbed salt. In the present work Ag coupons were immersed repeatedly in radioactive $AgNO_3$ of four concentrations, with hot water washing to remove adsorbed salt between immersions. Followed in this way, the exchange was found to be kinetically of first order, with one immersion as the time unit. The "rate constant" is nearly independent of concentration, and the calculated maximum exchange corresponds to the Ag in 35–50 atomic layers, based on measured area. Four-day measurement of the slow exchange which follows initial immersion indicated an equilibrium exchange current of about 4×10^{-9} amp/cm^2 in 0.5N $AgNO_3$.

Radioactive tracers make it possible to measure the amount of adsorption of metal salts on metal specimens of small surface area, and to study the nature, extent, and kinetics of metal ion exchange. Such studies give useful information concerning the nature of the metal and especially of its surface layers, and assist in explaining its behavior as an electrode. To study adsorption it is necessary to use radioactive anions, which cannot exchange with the metal. In the study of exchange, the amount of adsorption can be neglected usually since it is comparatively small; however, adsorption does have profound influence on the kinetics of exchange, at least in the case of Ag.

The Ag-Ag ion exchange has been studied from several viewpoints (1–4). It is apparent that three stages need to be considered: (*a*) rapid initial exchange, quickly blocked by a slow adsorption-desorption process; (*b*) slow exchange through the adsorbed layer and extending through several atomic layers of the metal; and (*c*) final equilibration throughout the metal, negligibly slow at room temperature.

King and Levy (3) studied the effect of repeated brief immersion of Ag coupons in $AgNO_3$ solutions with Ag^{110} as tracer, with long washing between immersions to remove adsorbed salt. The present experiments are an extension of that work, with a study of the effect of washing in hot and cold water, of the role of solution concentration on the kinetics and amount of exchange, and of other matters of interest.

EXPERIMENTAL

Inch-square coupons of commercial rolled silver sheet were cleaned and treated as described before (3). They

TABLE I. *Amount of exchange on 30-sec immersions in active $AgNO_3$ of the concentrations given, followed by 5-min washing*

No. of immersions	Equivalents/cm², × 10^{10}				
	0.025*N*	0.1*N**	0.1*N*	0.25*N*	0.5*N*
2	80	91	67	148	123
4	109	115	114	214	167
6	150	109	163	242	225
8	164	114	185	273	287
10	223	120	235	310	335
12	236	128	262	320	367
14	275	131	274	346	407
16	290	154	321	360	435
18	317	161	354	378	470
20	330	165	374	410	491
22	361	169	412	437	531
24	375	179	437	452	552
26	409	190	447	465	562
28	430	210	467	486	584
30	—	217	479	—	596
32	470	226	504	—	611
34	479	244	513	—	670
36	—	262	532	—	688
38	520	270	552	—	704
40	—	274	561	—	720
42	529	288	570	—	748
44	525	316	580	—	773
46	—	340	598	—	780
48	537	347	602	—	781
50	539	—	605	—	782

* Washed in stirred water at room temperature; all others in boiling water.

were kept in 0.1*N* inactive $AgNO_3$ until needed (at least one week). The conversion of counts per minute to equivalents exchanged was made as before. Immersions were at room temperature, 25°–30°C, in 100 ml of solution, and numerical values are the averages from two coupons, which seldom differed more than 10% except in the first series as noted below. The solutions contained enough radioactivity to insure at least 100 cpm above background, after one immersion.

Removal of activity by washing.—Coupons were immersed in 0.1*N* active $AgNO_3$, blotted dry with tissue, and counted; then washed for 1-min periods, or longer, by suspending in 400 ml of distilled water at room temperature, with a motor stirrer. After a 30-sec immersion, the activity remaining after three 1-min washes was not reduced by further washing up to 60 min. However, if the coupons remained in the active solution 24 hr, washing up to a total of 40 min was necessary to reduce activity to a minimum.

Boiling water removed more activity than cold water. In one experiment cold water reduced activity to 465 cpm, further washing in hot water decreased it to 425 cpm. The drop in activity is not great, but since it is due to removal of firmly adsorbed salt it is important in the exchange kinetics as shown below.

Exchange on repeated immersion.—Coupons were given 30-sec immersions, followed by 5-min washes in cold or hot water, with results as shown in Table I. Since in the first runs (0.1*N* $AgNO_3$) it became obvious that hot water washing was much more effective in promoting further exchange, it was used in further experiments. In the first experiments the coupons were counted after every washing; later, to save time, after every second washing. Only every second immersion is reported in Table I.

The series done in 0.1*N* $AgNO_3$ with cold washing shows irregularities near the start and near the end, and the two coupons eventually differed in count by 30%. The experiments were done over a 3-week period, and the coupons acquired a slight visible tarnish. They were now cleaned by a 5-min immersion in 0.1M KCN solution, which was deaerated (30 min in advance) with N (passed over hot Cu and through $CrCl_2$ solution). The activity remaining corresponded to the fourth previous immersion. On the first new immersion it jumped to the 15th previous value, and thereafter for 22 immersions, carried out within three days, exchange proceeded at a "rate" 25% greater than in the original series. It is concluded that the Ag area was probably increased by the cyanide treatment.

Kinetics of the exchange.—With hot water washing the exchange per immersion decreases steadily, and this suggests an upper limit far short of equilibrium distribution of the activity. Plots of the reciprocal of the amount exchanged ($1/x$) vs. the reciprocal of the number of immersions ($1/n$) are nearly linear if the first several points are disregarded. They all extrapolate at $1/n = 0$ to points corresponding to end-values near 1000×10^{-10} equiv/cm² of exchange. With two coupons (25 cm²) in 100 ml of 0.025*N* solution, 0.1% of the active Ag ion would finally enter the metal; equilibrium through all the Ag would require that 90% of the activity be found in the metal.

Data were compared with the first-order rate equation in the form

$$kn = \ln a - \ln (a - x) \qquad \text{(I)}$$

With a, the maximum exchange, taken as 1000×10^{-10} equiv/cm², plots of log $(a - x)$ vs. n are nearly straight lines. From the slopes the constant k can be determined.

Since the above extrapolation is somewhat uncertain, k was evaluated by the Guggenheim method (5), which does not require prior knowledge of a in a first-order process. The equation used in the present case is

$$kn = \text{constant} - \ln (X_2 - X_1) \qquad \text{(II)}$$

where X_2 and X_1 represent exchange values a constant number of immersions apart. By plotting log $(x_{26} - x_2)$, log $(x_{28} - x_4)$, etc., vs. n (either subscript), straight lines are obtained, and k is found from the slopes. From the equation

$$n_{\frac{1}{2}} = 0.693/k \qquad \text{(III)}$$

the number of immersions for half-complete exchange is determined, and $X_{\frac{1}{2}}$ read from the data of Table I. The value of a was actually obtained by starting from the second immersion and adding its value to $2\ X_{\frac{1}{2}}$ later.

TABLE II. *"Rate constants" for* Ag-Ag *ion exchange*

C_{AgNO_3}	k	a, eq/cm² × 10^{10}
0.025	0.029	740
0.10*	(0.007)	—
0.10	0.034	760
0.25	0.032	760
0.50	0.028	1010

* Washed in cold water.

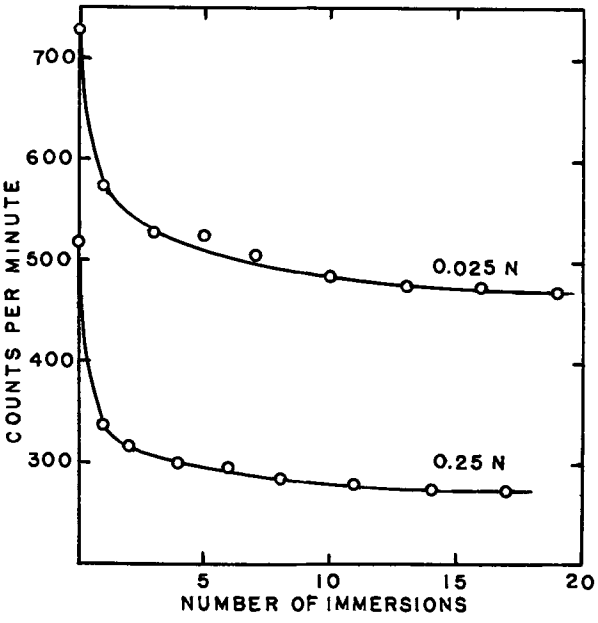

FIG. 1. Loss of activity in inactive solution

Values of a and k determined in this way are given in Table II. More exchange measurements in 0.25N $AgNO_3$ would have been helpful. The method could not be applied to the series with cold washing and k as given is an approximation from the first method described above.

Reversibility of exchange.—After the experiments of Table I with 0.025N and 0.25N $AgNO_3$, immersions were continued in inactive solutions of the same concentrations, with hot water washing as before. Fig. 1 indicates that continued treatment would not be effective in removing all activity. This is similar to the results found by other experimenters (1, 2, 4), who did not, however, wash with hot water between immersions.

Exchange current.—To obtain information about the exchange current, i_0, after adsorption equilibrium has been reached, it is necessary to immerse coupons for longer periods of time, and subtract the immediate exchange from the total. The following experiments were carried out: (*A*) two coupons were given four 30-sec immersions in 0.5N $AgNO_3$, with 5-min hot water washing, all within 2 hr; (*B*) two coupons were immersed for 30 sec each day for 4 days; (*C*) two coupons were immersed and removed each day for a 1-hr wash in hot water and counting. The amount of exchange is given in Table III.

Exposure to laboratory air or simply the 24-hr time lapse may be responsible for the greater exchange in (*B*) than in (*A*), and the same factor may account for some of the irregularities in Table I. In any case, if the values of column (*A*) are subtracted from those of (*C*), the indicated exchange current density is about 4×10^{-9} amp/cm². Actually, the rate of slow activity pickup should be extrapolated to zero time to calculate i_0 properly. Similar values are estimated from previous work (2, 3, 7).

TABLE III. *Exchange under various conditions, equiv/cm² × 10¹⁰*

Immersion	*A*	*B*	*C*
1	56	63	69
2	80	100	165
3	97	133	212
4	120	150	236

DISCUSSION

The ordinarily close agreement of exchange with two coupons treated identically, and the general agreement of "rate constants" and maximum exchange values (Table II), indicate that the experimental method used here was satisfactory. The lack of detailed reproducibility shows that small, perhaps uncontrollable variations in technique may lead to large variations in the results obtained. The true surface area is easily changed by slight corrosion or etching. Unknown amounts of sulfide were picked up from the laboratory air. Adsorbed oxygen may be present but it is doubtful if any oxide is formed at room temperature; it has been reported that no oxide is formed on polishing Ag in air (6).

Gerischer and Tischer (2) found that the rate of activity pickup is essentially the same on single crystals as on polycrystalline silver, and that deaeration of the solutions has little effect.

Tingley, Henderson, and Coffin (4) showed that the method of preparing Ag specimens makes a large difference in the rate and extent of exchange. Annealed, etched samples exchanged to a maximum of about 10 atomic layers in 10 hr, while unannealed, polished samples exchanged about 100 layers in 40 hr of constant immersion. This compares with the authors' values on commercial rolled sheet of 35–50 layers, only 25% of which was reached in 4 days of immersion (Table III). Tingley, *et al.*, also found that the apparent depth of exchange increased with solution concentration, which agrees with the results of Table II.

It is clear that the initial exchange is quickly blocked by adsorption of the Ag salt, not hampered by slow diffusion within the metal or by deposition of impurities from the solution, since the type of washing is more important than other factors. Both initial adsorption and initial exchange rates are no doubt proportional to solution concentration; this accounts for an activity pickup per immersion which is not highly dependent on concentration.

Baerg and Winkler (1) introduced a technique which could be used to remove adsorbed salt more quickly and certainly than washing alone. After brief immersion and rinsing the Ag specimen, they discharged adsorbed Ag ions cathodically. On reimmersion the activity pickup was similar to that shown in Table I. Baerg and Winkler thought this due entirely to chemisorption, and repeated the procedure only 5 times. If continued, results similar to those reported here should be obtained, the discharged ions adding a small amount to the activity. No surface compounds such as sulfide would accumulate.

Gerischer postulated that a concentration gradient of radioactive ions is set up at the Ag surface, in dilute solutions. Data of Table I support this view, since there was more apparent initial exchange from the more concentrated solutions. For complete exchange in only one atomic layer (20×10^{-10} equiv/cm²), the equivalent of all the Ag ions in a layer of 0.1N solution 2×10^{-5} cm thick must enter the metal. The concentration of active ions is about 10^{-11} equiv/cm³, and they could be replaced by

diffusion across a definite layer of the above thickness at a rate of about 5×10^{-12} equiv/cm²/sec. Each immersion must result in some surface deficiency of active ions, so that the measured exchange is always less than the true exchange. The effect is minimized in more concentrated solutions or when the exchange is slow.

Stirring has little or no effect on the amount of activity pickup per immersion (3). This is understandable even though diffusion is involved, since even extremely vigorous stirring has little effect on liquid less than 10^{-4} cm from the surface.

The irreversible part of the exchange is not due appreciably to interior diffusion. Extrapolation of self-diffusion coefficients in Ag from temperatures at which they can be measured to 25° or even 100°C gives negligible values (7), and interior diffusion would be incompatible with definite end-values of exchange. The present experiments with hot water washing show that it is not merely a question of low rate because of adsorbed salt. Gerischer and Tischer report that the amount of immobilized Ag depends on the time and temperature of storage. Tingley, Henderson, and Coffin found similar results; certain samples of active Ag which were stored for 220 days did not lose activity at all to an inactive solution, although they acquired more activity in an active solution.

Gerischer and Tischer showed that a fresh Ag surface, prepared by cathodic reduction of a layer of AgCl, becomes smoother in contact with $AgNO_3$ solution. Different faces of Cu single crystals show a difference in potential for a long time (8), and less stable faces rearrange to expose more stable planes (9). Long pre-equilibration in inactive solution should minimize local cell action, but autoradiographs have shown that Ag acquires more activity at scratches and edges than elsewhere, even after 5 months of pre-equilibration (7).

Local cell electrolysis no doubt buries some of the acquired activity, but can take place only when the metal is immersed. Additional trapping of activity may be explained in the following way: (*a*) It is assumed that most of the exchange takes place at comparatively few active centers, which are too close and uniformly spaced to be detected by autoradiographs. These centers may be due to a high surface concentration of lattice vacancies, to surface dislocations, or to imperfections or irregularities in the distorted layer of polished or cold-worked surfaces. (*b*) Rapid diffusion can occur around and under these centers, perhaps to a few thousand Å in depth, depending on the surface preparation. (*c*) In the course of time most or all of these active centers are obliterated, while new ones are formed, by vacancy migration, surface diffusion, etc. It is known that surface and grain boundary diffusion are much faster in Ag than lattice diffusion (10), but it is not known to what depth the faster diffusion takes place.

Exchange current.—This term is defined as the rate of exchange at the equilibrium potential, but values are usually estimated from measurements in which the electrode is not at equilibrium with the solution, as from the relation of double layer capacity to overvoltage, or from the constants of the Tafel equation (11). Gerischer and Tischer calculated i_0 from the initial Ag-Ag+ exchange rates; in one series of experiments they attempted to dissolve Ag anodically at a rate just sufficient to prevent activity pickup. Under these conditions i_0 is about 10^{-3} amp/cm².

Vielstich and Gerischer used a potentiostatic method to measure i_0 for Ag in cyanide and ammonia solutions (12). The current at constant potential, extrapolated to zero time, was plotted vs. overvoltage in both cathodic and anodic directions. From the slope at equilibrium potential ($\eta = 0$) i_0 was estimated, the values being near 10^{-3} amp/cm² in both types of solution. Measurements were also made without complexing agents but not published, since the authors felt that metal lattice formation was partially rate-controlling, and thus a complicating factor (13). The exchange current was estimated as about 2×10^{-3} amp/cm².

Exchange current as measured at an active electrode is greatly influenced by inhibitors and even by minute traces of firmly adsorbed impurities. In the present case adsorption of the Ag salt evidently reduces i_0 to a low value, and anything from 10^{-3} to 10^{-9} amp/cm² might be obtained, depending on how much the experimental method disturbs the adsorbed layer. The exchange current at adsorption equilibrium is evidently large enough to allow potential measurements without undue difficulty, or perhaps the adsorbed layer has always been disturbed in making such measurements. As explained by Akimov (14), if i_0 is less than 10^{-10} amp/cm² the potential becomes unstable; even very small forced currents polarize the electrode so much that equilibrium is not restored in a reasonable time, and usually other reactions will take over. The effects of impurities and competing reactions have been summarized and discussed by Bockris (15).

Manuscript received January 23, 1956. This paper was prepared for delivery before the San Francisco Meeting, April 29 to May 3, 1956, and is taken from a Master's Thesis submitted by Ann-Mari Simonsen to the Graduate School Faculty of New York University.

Any discussion of this paper will appear in a Discussion Section to be published in the December 1957 JOURNAL.

REFERENCES

1. A. BAERG AND C. A. WINKLER, *Can. J. Chem.*, **31,** 319, 521 (1953).
2. H. GERISCHER AND W. VIELSTICH, *Z. Elektrochem.*, **56,** 380 (1952); H. GERISCHER AND R. P. TISCHER, *ibid.*, **58,** 819 (1954).
3. C. V. KING AND B. LEVY, *J. Phys. Chem.*, **59,** 910 (1955).
4. I. I. TINGLEY, I. H. S. HENDERSON, AND C. C. COFFIN, *Can. J. Chem.*, **34,** 14 (1956).
5. E. A. GUGGENHEIM, *Phil. Mag.*, (7) **2,** 538 (1926).
6. S. DOBINSKI, *ibid.*, **23,** 397 (1937).
7. C. V. KING, *Ann. N. Y. Acad. Sci.*, **58,** 910 (1954).
8. H. LEIDHEISER AND A. T. GWATHMEY, *Trans. Electrochem. Soc.*, **91,** 97 (1947).
9. W. E. TRAGERT AND W. D. ROBERTSON, *This Journal*, **102,** 86 (1955).
10. W. C. WINEGARD AND B. CHALMERS, *Can. J. Phys.*, **30,** 422 (1952).
11. G. KORTÜM AND J. O'M. BOCKRIS, "Textbook of Electrochemistry", p. 441, Elsevier Publishing Co., Houston (1951).
12. W. VIELSTICH AND H. GERISCHER, *Z. Physik. Chem.*, **4,** 10 (1955).
13. W. VIELSTICH, Private communication.
14. G. W. AKIMOV, *Corrosion*, **11,** 477t, 515t (1955); a translation prepared by R. B. Mears and J. D. Gat.
15. J. O'M. BOCKRIS, "Modern Aspects of Electrochemistry", Chap. IV, Academic Press, Inc., New York (1954).

The Gassing of Dry Cells

Earl M. Otto and Woodward G. Eicke, Jr.

National Bureau of Standards, Washington, D. C.

ABSTRACT

A satisfactory method and suitable apparatus for determining the rate of gassing of dry cells are described. Gassing rates for undischarged D-size cells were found to range between 0.02 ml/day as the minimum at +21°C and 8 ml/day as the maximum at +55°C. Rates were independent of the age of the cells. Initial capacity of dry cells is not a function of gassing rate. Retention of capacity also is not a function of gassing rate, but is a function of the total volume of gas evolved before cell discharge.

Although considerable work has been done to prevent gas evolution from the Leclanché type of dry cell, little has been published on the measurement of the actual rate of gassing. Hamer and associates (1) investigated gassing at +130°F while studying packaging methods for cells and batteries for high temperature storage, and Boyer (2) measured gas evolution while studying methods of preventing explosions in closed battery containers. There are references (3, 4) to the study of gas evolution from Zn strips immersed in dry-cell electrolytes, but the paste wall, the bobbin or method of construction of the dry cell might well affect the corrosion of Zn in dry cells. Therefore, it was deemed advisable to develop an accurate method for measuring the gassing rate of completely assembled dry cells.

The chemical reaction which is responsible for the production of useful current does not include the formation of gaseous end products except when the cell is on heavy discharge and ammonia is produced. Likewise, the consumption of oxygen does not enter into the main cell action. The production of H_2 has been accounted for by a reaction of the anodic material resulting in the self-discharge of the dry cell (5)

$$Zn + 2NH_4Cl \rightarrow ZnCl_2 \cdot 2NH_3 + H_2$$

Oxygen may be consumed in the reaction (1)

$$\tfrac{1}{2} O_2 + Zn + H_2O \rightarrow Zn(OH)_2$$

Jennings and Vosburgh (6) have offered an explanation of one self-discharge process by proposing the mechanism of oxygen be liberated from the MnO_2 and deposited on C, with subsequent desorption of the oxygen and reaction with Zn.

Since dry-cell reactions involving evolution of H_2 and the consumption of atmospheric oxygen promote self-discharge of the dry cell, it is assumed that cells with less tendency to evolve or to consume gas should have longer shelf life. Hence, the gas study method should be a useful tool for evaluating dry cells. More specifically, a comparison of gassing rates of cells of different ages or states of discharge might afford a nondestructive way of evaluating these cells and estimating the remaining life in cells which have been in storage or partly discharged. The present investigation is directed toward the measurement of gases evolved under different conditions and the determination of the composition of representative gas samples.

Two methods of measuring the amount of gas evolved by the dry cell were considered, one involving a determination of the change in pressure of the constant volume of the atmosphere confining the cell, and the other involving a determination of the change in volume at a constant pressure. The latter method was finally adopted as the one having the lesser difficulties. Under the conditions of the experiment, gas evolved into a fixed volume, but measurement was accomplished by reducing the pressure to its original value.

Experimental

A sketch of the apparatus is given in Fig. 1. The gasometer consists of four main parts: cell container [5], Hg reservoir [6], manometer [4], and the reference reservoir [11]. In operation the reser-

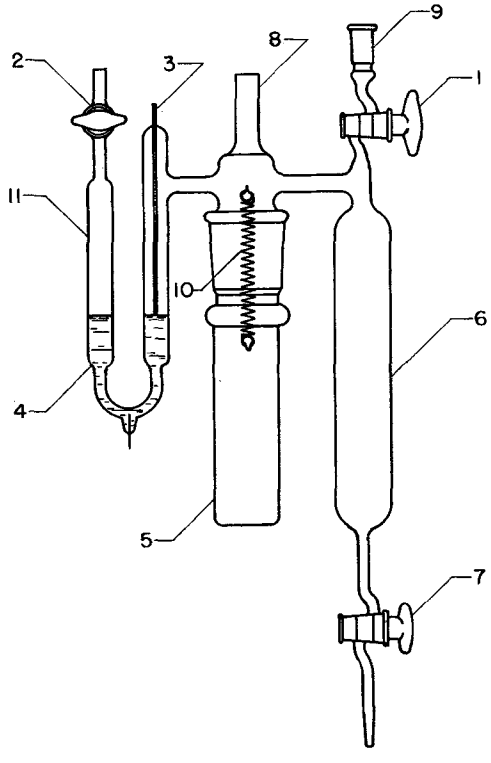

Fig. 1. Diagrammatic sketch of gasometer. Principal parts are cell container [5], Hg reservoir [6], the manometer [4], and reference reservoir [11].

voir [6] is nearly filled with Hg and Hg is injected by hypodermic syringe into the manometer at stopcock [2] until it just touches the Pt-tipped W lead-in wire [3]. The cell being studied is placed in the cell cup [5], which is held to the gasometer proper by means of springs. All ground-glass joints are lubricated and sealed with Apiezon T grease. When an atmosphere other than air is used, a vacuum pump is attached to positions [2] and [9] and, after evacuation, the desired gas is admitted. (In preliminary work, air was used, but for the most part an inert atmosphere of N has been used.) The gasometer is then brought to thermal equilibrium at a selected temperature in an oven.

In order to have a reference volume of gas at known pressure, stopcock [2] is opened. If the Hg in the right arm of the manometer is far below the Pt tip, gas is allowed to escape at [9] until the gap is less than ¼ in. If the Hg is already touching the Pt, more gas is added at [1] or Hg at [7]. After thermal equilibrium is re-established, Hg is removed at [7] until electrical contact is just established between the Pt tip and the Hg of the manometer. This is observed by means of a neon bulb in series with a source of current and the two lead-in wires. As soon as this balance is established, stopcock [2] is closed, thereby trapping a reference quantity of gas at the constant temperature of the oven and at the barometric pressure prevailing at the time of the closure. The gasometer is allowed to stand at the constant temperature until the Pt tip and Hg are separated by about ¼ in. Hg is withdrawn at [7] until electrical contact is re-established. In most cases this contact-making is sensitive to as little change in pressure as 0.01 ml of Hg. From the weight of Hg withdrawn the volume of evolved gas is readily calculated.

Runs were made at +21°, +35°, +45°, and +55°C because these temperatures were used in shelf-life studies of dry cells. The cell cup used at the two lower temperatures was long enough to accommodate two cells.

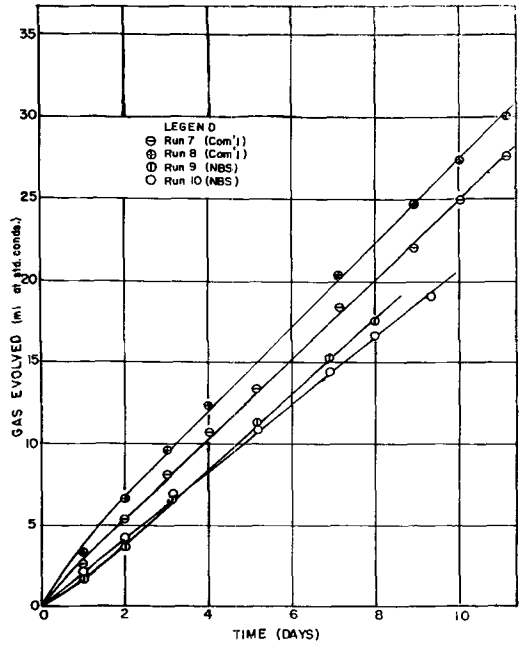

Fig. 2. Evolution of gas from four dry cells stored in an atmosphere of N at +45°C.

Table I. Composition of gas at completion of run*

Component	Oxygen atmosphere	Nitrogen atmosphere
	mole %	mole %
H_2	44	45.5
O_2	14	0.04
CO_2	39	12.1
A	0.17	0.01
N_2	2.0	42
CO	0.6	0.2
Net vol. gas produced	47.9 ml	59.9 ml

* Both runs were made at +55°C for 8.9 days before the gas samples were taken. Analysis by mass spectrometry.

Results

Fig. 2 shows typical gassing curves. Straight lines are obtained after the first day, when an inert gas, such as N_2, is the surrounding atmosphere. With air a straight line is not obtained in less than about 15 days. When the oxygen of the air within the gasometer has been exhausted, the volume increases at a constant rate.

Analysis of the residual gases after a run in oxygen and one in N_2 are shown in Table I. Approximately equal volumes of H_2 and high percentages of CO_2 were obtained regardless of the atmosphere initially surrounding the cells. Based on earlier investigations that MnO_2 oxidizes cornstarch (7) and that dry cells evolve CO_2 (1) the following calculations were made from data on the gasometer which initially contained pure oxygen.

	ml
Volume of O_2 initially in gasometer	40
Volume of gas in gasometer after 8.9 days	87.9
Oxygen content of final volume	12.3
Hence oxygen consumed by cell	27.7
Volume of CO_2 produced by MnO_2 on paste*	12.1
Volume of CO produced by MnO_2 on paste*	0.2
Volume of CO_2 assumed produced by oxygen gas	22.2
Volume of CO assumed produced by oxygen gas	0.4
Volume of O_2 required to produce CO_2 and CO	22.4
Oxygen unaccounted for†	5.3

* This figure is taken from results of run in N_2 atmosphere. It is assumed that MnO_2 acts the same in O_2 as in N_2.
† This oxygen probably may be accounted for in accord with Ref. (1).

Fig. 3 shows the gassing rates of four commercial brands of dry cells at different temperatures. These show the large temperature effect on gassing rates of dry cells.

Fig. 4 gives a plot of performance on the BA-30 test[1] against the calculated volume of gas evolved prior to the discharge. (For convenience the square root of the volume was used as the abscissa.) In each case the loss in performance is less for a given volume of gas liberated at higher temperatures than at lower. Of course, a much longer time is required at low temperatures to evolve the same volume of gas. Also the slopes steepen, and after the cells lose a certain capacity, independent of temperature but

[1] This test, specification MIL-B-18, consists in discharging a cell through 6.67 ohms resistance 4 min/half hour, 10 hr/day, 5 days/week. Results are given as the number of minutes on discharge to an end voltage of 0.93 v.

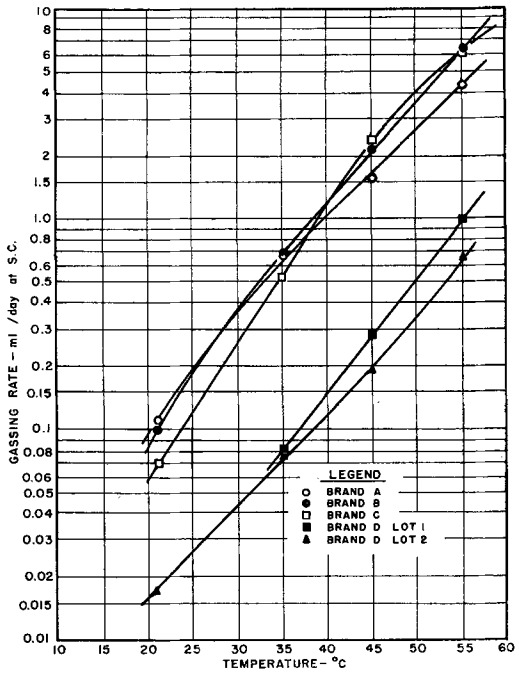

Fig. 3. Effect of temperature on the gassing rates of several brands of dry cells.

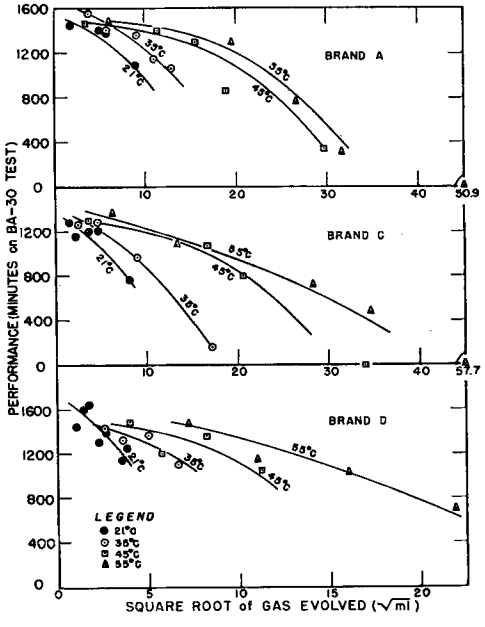

Fig. 4. Effect of gassing during storage at different temperatures on subsequent performance on the BA-30 test.

dependent on type, deterioration progresses at a more rapid rate. Hence, gas producing reactions are not solely responsible for lowering the cell capacity.

Cells on Closed Circuit

Some of the cell cups were modified so that lead wires could pass from the cell in the gasometer to a resistor outside the cell cup. Thus it was possible to determine the gassing rate of a cell on open circuit and then during discharge of the cell. Since five or more days are required to insure that a steady gassing rate has been obtained and since an intermittent type of cell action is not desired, an 83 1/3-ohm continuous discharge test was selected. (This is the BA-8 test adapted to a single cell basis.) On this test two weeks of service were expected, to the end voltage of 1.133 v. To secure appreciable gassing during this period of discharge the temperature was maintained at +55°C.

The predischarge gassing rates on the three cells were determined in five days as described above. Without disturbing the gasometers or the oven, the circuits were closed and the gassing rate determinations continued. Within 0.3 day the first measurements were made, and the gassing rates were found to be less than the predischarge rates; they continued to be less until the voltage of the cell reached about 0.5 v, which is considerably below the usual end voltage, 1.133 v, of the BA-8 test. From 0.5 v to about 0.1 v the gassing rate exceeded the predischarge rate by about 50% (see Fig. 5). Below 0.1 v the gassing rate became much less than the predischarge rate, and it continued at that rate (0.4 ml/day) until the test was stopped on the 173rd day of discharge. Fig. 5 presents graphically the results obtained on one of the three cells, the predischarge gassing rate for this particular cell being 3.5 ml/day at 55°C, which is below the average value found at 55°C.

The curve for gassing during discharge shown in Fig. 5 has three distinct parts: (*a*) that prior to the usual end voltage and down to 0.5 v covering about 23 days, (*b*) that at closed circuit voltages between 0.5 and 0.1 v extending for the next 17 days, and (*c*) that at extremely low voltages or below 0.1 v. The rates found in (*a*) are lower than predischarge rates because the Zn is being used in electrochemical rather than in corrosion reactions. The rates found in (*b*) are higher than predischarge rates probably because the partially reduced MnO_2 is being polarized to the extent that H_2 can readily be discharged from the cathode. The rates found in (*c*) are less than predischarge rates probably because the surface of the Zn is largely covered with corrosion products.

Due to the long duration of this experiment and the limited volume of the reservoir (6), the gas evolved had to be released three times and the Hg replenished. While the gas was being removed the third time, a gas sample was taken from each gasometer for analysis. The analyses showed the gas to

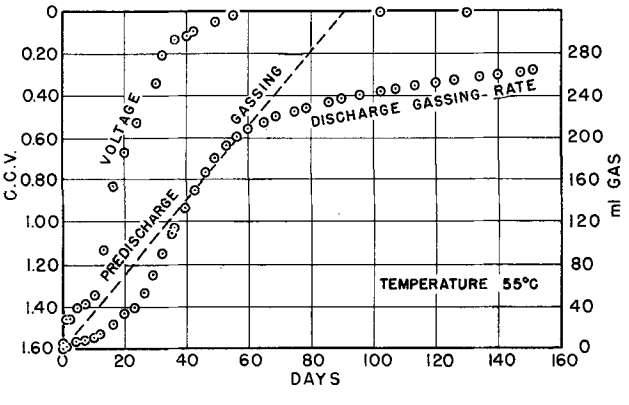

Fig. 5. Effect of 83-1/3-ohm continuous discharge on gassing of cell. Gassing rate is obtained by determining the slope at any desired point on the curve.

Table II. Rates of gassing of intimate mixtures of various thickening agents and MnO_2 in electrolyte*

Temperature	Thickening agent		Kind of MnO_2	Rate of gassing		Length of period
	Kind	Wt		Initial	Avg over period	
°C		g		ml/day	ml/day	days
+45	Wheat flour	1	African	2.68	2.30	13
+45	Cornstarch	2	African	3.97	3.54	13
+45	Wheat flour Cornstarch	1 2	African	3.97	3.12	13
+45	Vulca-60	2	African	2.31	1.82	8
+45	Potato starch	2	African	3.46	2.00	17
+45	Locust bean gum	2	African	4.45	2.91	8
+55	Wheat flour	1	African	4.17	3.34	20
+55	Cornstarch	2	African	4.76	3.57	20
+55	Vulca-60	2	African	5.3	3.28	20
+55	Locust bean gum	2	African	7.7	3.34	20
+55	Wheat flour Cornstarch	1 2	African	6.9	5.3	11
+45	Wheat flour	1	Electrolytic	34.4†	28.6†	2
+45	Cornstarch	2	Electrolytic	45.8†	41.8†	2
+45	Wheat flour Cornstarch	1 2	Electrolytic	39.8†	34.3†	2
+45	Cornstarch	1	Electrolytic	83	52	1.2
+45	Cornstarch	2	Electrolytic	130	91	0.8
+45	Cornstarch	4	Electrolytic	153	132	0.4
+45	Methocel	2	Electrolytic	—	0.61	38
+45	Amylose	2	Electrolytic	97	—	0.3
+45	Amylopectin	2	Electrolytic	83	—	0.3
+55	Separator paper (Coated)	0.48	Electrolytic	0.71	0.51	30

* See footnote to Table III for composition of electrolyte. The weight of MnO_2 used each time was 32 g.
† These values are only relative since the rate was so high and assembled gasometers had been stored over night.

be about 90% H_2 and the balance N_2 with its normal trace of A. Thus it seems that CO and CO_2, if produced at all during discharge, were evolved only in the early stage and then completely flushed out. Further experimental work would be required to furnish evidence as to whether or not oxides of carbon are formed during discharge of a cell.

Cell Components

Gassing studies conducted on dry-cell components (excluding Zn) yielded interesting results. Various thickening agents intimately mixed with MnO_2 and electrolyte were gelatinized in the cup of the gasometer and gassing rates determined at +55° and +45°C. The data are shown in Table II. One sample of gas was analyzed, the gas having resulted from the digestion at +45°C of a mixture of natural African MnO_2, ordinary cornstarch and electrolytic solution in an atmosphere of N_2. After 34 days, during which time the equivalent of 65 ml of gas at standard conditions was produced, a sample of gas was taken. The mole-percentage composition was 1.2% H_2, 3.0% CO, 48.3% N_2, 0.03% O_2, 0.04% A, and 47.4% CO_2.

Locust bean gum appeared to be the most reactive. Vulca 60 (a National Starch Co. product) was the least active of the grain products at +45°C, but at +55° its initial gassing rate was in an intermediate position. The gassing rates of wheat flour-corn starch mixtures do not equal the sums of those of the separate components, but come nearer to their averages. It is quite likely that the MnO_2 is the limiting factor. It was observed that increasing the quantity of corn starch from 1 to 2 and 4 g caused an increase in the gassing rate, but not in proportion to the quantity of starch. Amylose would seem to be more active than amylopectin, but the difference is small. Hence, little would be gained by separating cornstarch into its two components. The ratio of gassing rates obtained on cornstarch with natural African and electrolytic manganese dioxides is about 1-25. At +21°C and lower this would not be of much consequence, but it is evident that cells produced for storage and use at high temperature should not contain starch and such an active MnO_2.

Methocellulose and battery paper are included in Table II because they may be used as separator materials. The gassing rates are about equal, and less than 1% of the rates for starch. In both of these materials glucopyranose units are joined by beta-glucosidic linkages. Starches, however, have alpha glucosidic linkages. Since methyl substitutions in cellulose and starch have little effect, if any, on the gassing rates, it would appear that the two linkages must account for the difference in performance.

Data obtained on the use of bobbins of depolarizer imbedded in paste are given in Table III. Table IV presents data on mixtures which have been assumed to be inactive. It was expected that some would serve as blanks in gassing rate determinations. It is noteworthy that oxygen gas did not oxidize flour or starch when wet with NH_4Cl and $ZnCl_2$ solution, and maintained at +55°C. Natural African MnO_2 apparently oxidized acetylene black, but at a low rate. This rate of 0.43 ml/day was steady over a period of 24 days, during which time ten gassing-rate determinations were made. (The resulting gas was not analyzed, but it was assumed to be CO_2.)

Table III. Rates of gassing of D-size bobbins imbedded in paste*

Temp	Thickening agent: Kind	Thickening agent: Wt	Kind of MnO_2	Rate of gassing: Initial	Rate of gassing: Avg over period	Length of period
°C		g		ml/day	ml/day	days
+45	Wheat flour Cornstarch	1 2	African	1.6	1.6	3.5
+45	Wheat flour Cornstarch	1 2	Electrolytic	9.3	10.2	4.8
+55	Wheat flour Cornstarch	1 2	Electrolytic	42	33	3.7

* The wet mix for the bobbins was made by adding sufficient electrolyte to a mixture of 78.1% African MnO_2, 9.8% acetylene black, and 21.1% NH_4Cl. The electrolyte was composed of 24.4% NH_4Cl, 14.6% $ZnCl_2$, and 61.0% H_2O. The composition of the paste was 22.7% $NHCl_2$, 6.1% $ZnCl_2$, 7.2% wheat flour, 14.4% cornstarch, and 49.6% H_2O.

Table IV. Rates of gassing of supposedly inert mixtures of dry cell components

Temp	Atmosphere	Components of mixture*	Rate of gassing
°C			ml/day
+55	N_2	African MnO_2, electrolyte	0.00
+55	N_2	Acetylene black, water	0.00
+55	N_2	African MnO_2, acetylene black, water	0.43
+55	O_2	Wheat flour, cornstarch, electrolyte	0.00

* The quantity of MnO_2 was 32 g and that of acetylene black was 3.9 g. The composition of the electrolyte is given as a footnote to Table III.

Conclusions

A precise method has been developed for determining the rate of gassing of dry cells. Rates of gassing are greatly affected by temperature, approximately logarithmically. The initial rates of gassing in D-size cells are about 0.1, 0.6, 2.0, and 6.0 ml/day for +21°, +35°, +45°, and +55°C, respectively.

No correlation exists between the rate of gassing and the initial capacity on a BA-30 test. It can be concluded that, prior to discharge on the BA-30 test, evolution of a certain volume of gas during storage of a cell at a high temperature is less detrimental than at a low temperature. However, the time required to produce a given volume at higher temperatures is far less than at lower temperatures. For each temperature and each type of dry cell it is indicated that there is a critical volume of gas a cell may evolve before there is substantial loss in capacity. Once the critical volume has been evolved the cell deteriorates more rapidly. Cells which have lowest gassing rates appear to have best capacity after storage at high temperatures. It appears that, for each brand of a given cell type, a relation exists between the volume of gas evolved during storage at a given temperature and the loss in capacity.

In the early stage of the discharge of a cell gassing continues at a reduced rate. The rate is not constant, but shows trends similar to that shown by the decrease in closed-circuit voltage. Gassing continues long after the cell has no useful life.

Gassing studies conducted with dry cell components have shown that cereal products are definitely oxidized by MnO_2, electrolytic MnO_2 being a much stronger oxidizing agent than natural African MnO_2. Cellulose products such as paper and Methocel are relatively inactive to MnO_2.

Acknowledgments

The authors express their thanks to the Department of the Navy, Bureau of Ships, for granting permission to publish this material. They are indebted to Dr. Walter J. Hamer, who has had such a keen interest in the project and under whose direction the experimental work was performed. Dr. Wm. J. Youden, of the Applied Mathematics Division of the National Bureau of Standards, graciously assisted the authors in the analysis of data and in preparation of graphs.

Manuscript received July 25, 1956. This paper was prepared for delivery before the Boston Meeting, Oct. 3-7, 1954.

Any discussion of this paper will appear in a Discussion Section to be published in the December 1957 issue of the JOURNAL.

REFERENCES

1. W. J. Hamer, J. P. Schrodt, and G. W. Vinal, *Trans. Electrochem. Soc.*, **90**, 449 (1946).
2. M. H. Boyer, Naval Research Laboratory Report P-2315 (1944).
3. C. Drucker, *Z. Elektrochem.*, **29**, 412 (1923).
4. C. K. Morehouse, W. J. Hamer and G. W. Vinal, *J. Research Nat Bur. Standards*, **40**, 151 (1948), RP 1863.
5. N. C. Cahoon, *Trans. Electrochem. Soc.*, **92**, 159 (1947).
6. C. W. Jennings and W. C. Vosburgh, *This Journal*, **99**, 309 (1952).
7. E. M. Otto, C. K. Morehouse, and G. W. Vinal, *Trans. Electrochem. Soc.*, **90**, 419 (1946); unpublished work of E. M. Otto, E. H. Ostrander, and W. G. Eicke, Jr.

Lead Storage Battery Oxides with Metallic Additions

B. Agruss, E. H. Herrmann, and F. B. Finan

Research Laboratories, National Lead Company, Brooklyn, New York

ABSTRACT

Oxides were produced from lead containing various added metals. The concentrations more than covered the range of impurities ordinarily present in primary lead used in manufacturing battery oxides. The influence of these metals, both singly and combined, on battery performance has been studied. Battery capacity and life are unaffected by any of the added metals. Shelf life is unaffected by Bi, Ag, and Cu and is shortened by Ni, Sb, and Te. With the exception of Bi, each of these elements depressed the initial end-of-charge voltage, Te being particularly effective. The effect on end-of-charge voltage is more than additive when several added metals are present.

Data on the effects of impurities on storage battery performance are limited. Gillette (1) has studied the effects of a number of elements while Vinal (2) has carried out tests under rather special conditions. Willihnganz (3) recently evaluated the effects of Fe.

In all of these studies the impurity was added to the electrolyte. Sb which is present in grid metal is anodically corroded and deposits on the negative active material. In the latter state, it may be considered as an impurity and its effects are well understood. Zachlin (4) along with others has shown the part played by the concentration of Sb in the grid metal on the self-discharge rate.

No data are available showing the effects of impurities when present in the Pb from which the oxides are made. Such information is required for a better understanding of the lead-acid battery and this is the reason for the present investigation.

Experimental

This study was confined to the more common elements associated with Pb, viz., Bi, Ag, Cu, Ni, Sb, and Te. Impurities were introduced in concentration ranges which would more than cover the percentages usually found in Pb used for storage battery oxides. With the exception of Te, alloys were made by adding the proper amount of each element to U.S.S. electrolytic Pb. Metals were added singly or in combination with others as required. The alloys were then converted to high metallic litharges in a small size Barton pot. Each oxide was analyzed spectrographically for the added elements. Results were close to the anticipated concentrations.

The oxides containing Te as a single added impurity were prepared by blending TeO_2 with pure oxide made from the electrolytic metal. Oxides were also prepared from alloys consisting of corroding Pb and added Te. Because of the mode of preparation, the results obtained with the Te-bearing oxides are not strictly comparable with results corresponding to the other oxides. However, this does not obviate the validity of the conclusions. Te has been investigated because of its presence in corrosion-resistant grid metal.

Oxides were processed into batteries of the standard height, 100 amp-hr, 15 plate, 6 v automobile type. Both the positive and negative plates in any one battery were made from the same oxide sample. The negative plates contained carbon black, blanc fixe, and a ligneous material as is customary.

TABLE I. Composition of grid and post alloys

Metal	Per cent Grid	Post
Sb	8.4	4.4
Cu	0.028	0.05
As	0.023	0.017
Sn	0.38	0.33
Ag	0.0034	0.0033
Bi	0.017	0.017
Fe	<0.001	—
Ni	<0.001	<0.001
Cd	<0.0005	<0.001
Zn	<0.001	—

All grids were cast from one lot of 8% antimonial lead. The post straps were cast from a single lot of 4% antimonial lead. The composition of these alloys is shown in Table I. Analyses were made spectrographically. Cedar separators were used throughout and these were screened and shuffled.

Three batteries were made from each sample of oxide. This entailed a total of 12 batteries for each element studied since four concentrations were made for each added metal. All 12 batteries were prepared and tested in series and at the same time.

Formations were carried out by the group container method using H_2SO_4 of 1.100 specific gravity as the electrolyte, a rate of 12.5 amp and an input of 290 amp-hr. The conditioning charge input was about 100 amp-hr. Final electrolyte specific gravities were approximately 1.280.

Elements were examined at the end of the forming period. Since all of the plates were substantially cleared of visible lead sulfate, it was concluded that over the concentration ranges studied none of the added impurities had any appreciable retarding action on formation. With regard to the copper series, when concentrations of 0.01 and 0.06% were used a deposit of this metal was distinctly visible on both the negative plates and post straps. When oxides containing 0.005% Cu were used, the deposit was barely visible.

Cell voltages and negative plate to cadmium voltages were determined at the 10 amp rate just prior to termination of the conditioning charge. Since cell voltage variations are entirely attributable to variations in the negative plate voltages, no further mention of the former will be made.

Shortly after completing the conditioning charge, one battery representing each sample of oxide was placed in a constant temperature room operating at 90°F (32°C) for a 28-day shelf test. The drop in the electrolyte specific gravity during this period was determined for each cell and recorded in terms of number of points, one point being equal to 0.001 sp gr. Shelf life is an indirect function of the drop in the specific gravity. Stated another way, the self-discharge rate is a direct function of the specific gravity drop.

At the conclusion of the shelf test, the batteries were fully charged and then tested for capacity and deep cycle life according to S.A.E. specifications (5). Results were averaged with those obtained from S.A.E. capacity and cycle life tests made on two sets of batteries placed on test shortly after the conditioning charge. Over the concentration ranges investigated, neither capacity nor cycle life was affected by any of the elements studied.

Single Elements

The negative plate to cadmium voltage taken toward the end of the conditioning charge is shown in Table II for each oxide tested. This table shows that Bi has no effect in concentrations of up to 0.25% while Ag, Cu, Ni, Sb, and Te serve to decrease the voltage. Of these, Ni and Te are particularly effective.

The change in electrolyte specific gravity during a 28-day open circuit period at 90°F is shown in Table III for each of the oxides tested. These data show that, within the concentration limits studied, shelf life is unaffected by Bi, Ag, and Cu. Ni, Sb, and Te serve to shorten the shelf life.

Combinations of Elements

In the preliminary work with combinations of elements, the desired compositions were obtained by intimately blending oxides containing the individual elements. Later work has shown that the results corresponding to such blends are misleading. The effects are much less pronounced than when the additions are made to the base Pb. For this reason, work reported here is confined to oxides prepared from metal containing the added elements.

TABLE II. Negative plate to cadmium voltages on conditioning charge at 10 amp

%	Bi	Ag	Cu	Ni	Sb	Te
0.0000	—0.24	—0.24	—0.23	—0.23	—0.27	—0.24
0.0001	—	—	—	—	—	—0.24
0.0005	—	—	—	—	—	—0.21
0.0010	—	—	—	—0.15	—	—0.20
0.0050	—0.24	—0.24	—0.23	—0.05	—0.27	—0.13
0.0100	—	—	—0.20	—	—	—
0.0350	—	—	—	—	—	—
0.0500	—0.25	—0.20	—	—0.02	—0.24	—
0.0600	—	—	—0.15	—	—	—
0.1000	—	—	—	—	—0.11	—
0.2500	—0.26	—0.12	—	—	—	—

TABLE III. Drop in electrolyte specific gravity 28-day open circuit period

%	Points Drop Bi	Ag	Cu	Ni	Sb	Te
0.0000	24	31	28	28	27	28
0.0010				27		
0.0050	27	31	27	36	28	40
0.0350				53		
0.0500	25	34			32	
0.0600			26			
0.1000					44	
0.2500	27	30	27			

TABLE IV. Impurities combined negative cadmium voltages drop in electrolyte specific gravity

No.	Per cent Ag	Cu	Bi	Sb	Ni	Te
1	no added impurity					
2	0.01	0.009	0.27	0.05	0.0004	—
3	0.0034	0.0036	0.04	—	0.0038	—
4	<0.0006	<0.0008	0.016	<0.001	—	0.0002
5	<0.0006	<0.0008	0.016	<0.001	—	0.0003
6	<0.0006	<0.0008	0.016	<0.001	—	0.0004

No.	Negative to cadmium Volts Computed	Actual	Electrolyte sp gr Points Drop Computed	Actual
1	—	—0.24	—	29
2	—0.17	—0.10	32	47
3	—0.18	—0.09	27	26
4	—	—0.09	—	34
5	—	—0.09	—	—
6	—	—0.10	—	36

Data covering oxides containing more than one added element are shown in Table IV. Computed negative plate charge voltages as well as computed electrolyte specific gravity drops represent summations of the effects of the individual added metals. These effects were picked off from curves representing the data shown in Tables II and III. Comparisons are made with the results of actual determinations.

Based on the data for single elements, one would expect the negative plate voltage corresponding to oxide 2 to be influenced primarily by Ni with Sb also making a small contribution. The computed voltage is —0.17. Since the actual voltage is —0.10, it is obvious that with this particular combination the effects on voltage are considerably more than additive. The same situation applies to oxide 3 which contains no added Sb.

Reference to the last two columns of Table IV shows that the elements present in sample 2 serve to increase the open circuit electrolyte specific gravity drop to a marked degree. The actual drop was 47 points as compared to a computed drop of 32 points. The impurities in oxide 3 have no effect on the specific gravity drop and this is to be expected from computations. The only essential difference in the composition of the two oxides is the presence of antimony in oxide 2. From this, it follows that Sb exerts a synergistic effect on shelf life.

Te in concentrations of 0.0002, 0.0003, and 0.0004% is represented by samples 4, 5, and 6, respectively. All of these samples contain 0.016% Bi and only very small concentrations of other elements. Te is

the only impurity present which would be expected to have any effects. No computed values are shown since there are no data at hand covering the effects produced by Te when present as a single impurity added to the Pb used in producing oxide. Nevertheless, its depressing action on the negative plate voltage is obvious. Table IV shows a voltage of about —0.10 corresponding to the three Te-bearing oxides as compared to a voltage of —0.24 when no impurity is present. Similarly, the impurities in these oxides bring about a moderate increase in the open-circuit electrolyte specific gravity drop.

Discussion

Bi, Ag, Cu, Ni, Sb, and Te have been added to the base Pb from which both positive and negative battery oxides have been produced. The metals were added singly and in combination. The oxides have been processed into batteries and tested.

None of the added metals affects battery capacity or life, nor is the positive plate voltage affected.

When added as single elements, Bi, Ag, and Cu have no effect on shelf life. Ni, Sb, and Te serve to shorten shelf life. When present with other metals, Sb has a synergistic action on the self-discharge rate.

With the exception of Bi, each of the elements studied depresses the end of charge voltage, the most outstanding effect being produced by Te. As little as 0.0002% of this element introduced by way of corroding Pb depresses the voltage to a marked degree. When a number of added metals is present in an oxide, the effect on the end of charge voltage is more than additive.

Since the grid metal used in this work contained Sb in the concentration commonly present in automotive batteries, it is felt that conclusions based on the findings of this report are generally applicable to this type of battery. Batteries such as the L.D. type and those made from calcium-lead grids may not be affected in the same manner.

The findings justify the conclusion that no change should be made for the present in the long established practice of using only high purity Pb for making storage battery oxide.

Acknowledgment

The authors take pleasure in acknowledging the direction, suggestions and assistance of Dr. J. A. Orsino during the course of the work and in the preparation of this paper. They express their thanks also to the management of the National Lead Company for permission to publish this paper.

Manuscript received July 7, 1955. This paper was prepared for delivery before the Boston Meeting, Oct. 3-7, 1954.

Any discussion of this paper will appear in a Discussion Section to be published in the December 1957 JOURNAL.

REFERENCES

1. H. Gillette, *Trans. Am. Electrochem. Soc.*, **41**, 217 (1922).
2. G. W. Vinal, "Storage Batteries," p. 135, John Wiley & Sons, Inc., New York (1940).
3. E. Willihnganz, *This Journal*, **100**, 527 (1953).
4. A. C. Zachlin, *ibid.*, **92**, 259 (1947).
5. Hand Book, Society of Automotive Engineers, 29 West 39th St., New York, N. Y. (1952).

A Reproducible and Stable Silver-Silver Oxide Electrode

Walter J. Hamer and D. Norman Craig

National Bureau of Standards, Washington, D. C.

ABSTRACT

A method is described for the preparation of silver-silver oxide electrodes which are stable and reproducible. When used in cells of the type Hg(l), HgO(s) | NaOH, aq. | Ag_2O(s), Ag(s) the silver-silver oxide electrodes give stable potentials over periods of 38 days. No evidence was found that Ag, Ag_2O electrodes evolve oxygen, that Ag_2O exists in different forms in aqueous solutions at normal temperatures, that Ag_2O reverts to a lower oxide, or that imperfections exist in the Ag_2O crystal. The free energy and entropy changes for the reaction in the above cell are —11254 cal. and —9.12 e.u., respectively, at 25°C. These values are reasonably consistent with the best available thermodynamic data. The standard electrode potential of the Ag, Ag_2O electrode is found to be —0.342 v at 25°C.

The literature states that silver-silver oxide (Ag_2O) electrodes cannot be prepared in a reproducible or stable condition. Luther and Pokorny (1) and Buehrer [reported by Lewis and Randall (2)] investigated the cell:

$$Pt, H_2(g) \mid KOH, aq. \mid Ag_2O(s), Ag(s) \quad [A]$$

and reported that the emf decreased with time. The former concluded that the decrease was due to the formation of Ag_4O; the latter also attributed the decrease to the formation of a lower oxide of silver but did not speculate on its composition. Furthermore both obtained emf's which differed by many millivolts from the one calculated from thermodynamic data.

Fried (3) also found variable and uncertain results at 0°, 23.5°, and 58°C for the cell:

$$Hg(l), HgO(s) \mid NaOH, aq. \mid Ag_2O(s), Ag(s) \quad [B]$$

Reasoning that the fall of emf was caused by the re-

lease of oxygen from the Ag_2O, he subjected his silver oxide to prolonged heating at 200°C. Even so, his heated oxides gave potentials that first increased with time and attained a fairly constant value only for a short time. Also, two different samples of his oxide gave free energy changes for the reaction of cell [*B*] which were lower by about 10 and 14%, respectively, than from the best thermodynamic data (4). Furthermore, he obtained +0.000182 v/°C and +0.000195 v/°C for the emf-temperature coefficient. A positive emf-temperature coefficient, however, corresponds to a positive entropy change for the cell reaction whereas the best thermodynamic data (4) give a negative value of −0.00020 v/°C.

Rördan (5) believed that he found evidence for two forms of Ag_2O having free energies of formation of −2420 and −3980 cal mole, but Kelley and Anderson (6) stated that there is no real proof of the existence at room temperature of two forms. Also, Pitzer and Smith (7) in their heat-capacity measurements of Ag_2O found no evidence of two forms, although they did find anomalies in the heat capacity from 15° to 50°K. Kobayashi (8) found that the heat capacity of Ag_2O depended on the treatment given the oxide. He concluded that Ag_2O undergoes a change in physical structure when heated between 100° and 200°C, this change not being one of lattice transition, as Fried also considered unlikely, but rather one associated with the melting of the "freezing in" of the imperfections in the crystal produced by the dehydration of Ag_2O precipitated below 100°C. This fact may account in part for the "hump" observed by Pitzer and Smith in their capacity curve as their sample of oxide was heated only to 110°C.

Kobayashi found that the heat change for the transformation

$$Ag_2O \text{ (precipitated below 100°C)} = Ag_2O \text{ (heated above 100°C)}$$

was −315 cal/mole, which would correspond to 6.8 mv assuming an entropy change of zero. (This instability would manifest itself as a decrease in the potential of Ag, Ag_2O electrodes.) Kobayashi further believed that the instability of the Ag, Ag_2O electrode could cause emf variations greater than 6.8 mv owing to the nature of the Ag_2O surface.

In view of the above inconsistencies, especially the difference in sign for the entropy change between the best thermodynamic data and Fried's results, it was deemed advisable to reinvestigate the behavior of Ag, Ag_2O electrodes. This paper gives some results of such a reinvestigation. The most significant result pertains to a method of preparing stable and reproducible Ag, Ag_2O electrodes whose potentials are reasonably consistent with most recent thermodynamic data.

Experimental

In this study of Ag, Ag_2O electrodes, cells of type [*B*] were used. Although there is some uncertainty in the standard potential of Hg, HgO electrodes, they were used nevertheless as reference electrodes so that the potentials of the Ag, Ag_2O electrodes could be measured conveniently over long periods of time. The uncertainty in the potentials of the Hg, HgO electrodes has been attributed to a difference in the particle size and solubility of the red and yellow forms of HgO. The potential difference between the red and yellow forms has been reported to be only 0.685 mv at 25°C (9) and to decrease with time, the decrease being about 0.3 mv in 15 days (10). The uncertainties in the potential Hg, HgO electrodes were, however, of little moment in these initial studies, consequently a sample of HgO designated as red was used. It is recognized, however, that this is not an adequate description of HgO and ultimately H_2 electrodes should be employed to establish the most accurate value of the standard potential of Ag, Ag_2O electrodes.

The Ag_2O and HgO used in making the electrodes were of certified reagent grade. Both were digested for prolonged periods in distilled water on a steam bath and the water was frequently poured off and replaced with a fresh portion. Simple H-type Pyrex glass containers were used in assembling the cells. The legs were 1 in. in diameter and 5 in. long and were connected near the top by a cross tube 2 in. long and 0.5 in. in diameter. One leg contained two Ag, Ag_2O electrodes and the other leg two Hg, HgO electrodes. One of the Hg, HgO electrodes, made in the usual way, was at the bottom of the respective leg and the other was in a glass cup suspended in the same leg by a glass tube which was sealed to the cup and protruded through a rubber stopper at the top of the leg. The electrode at the bottom of the leg is referred to as electrode No. 1 and the suspended or upper electrode is referred to as electrode No. 2. Purified Hg was used in preparing these electrodes and the HgO was well washed with successive portions of the NaOH solution to be used in filling the cells. The silver oxide electrodes were prepared by two methods.

Method No. 1.—The first Ag, Ag_2O electrodes were prepared as follows: Ag_2O was washed repeatedly with the NaOH solution to be used in filling the cell and was then placed in one leg of the cell. In this slurry were placed two small Pt helices completely covered with Ag and sealed in the end of soft glass tubes. These tubes were supported in the leg of the cell by a rubber stopper. The Pt helices were covered with Ag by a process similar to that used in preparing silver for Ag-AgCl electrodes of the Harned (11) type. Ag thus prepared is considered to be superior to the electrolytic Ag because the removal of the electrolyzing solution from the interstices of the electrolytic Ag is known to be most difficult, if not impossible. The cell was then carefully filled with NaOH solution.

Method No. 2.—These Ag, Ag_2O electrodes consisted of pieces of Pt gauze 1.5 cm x 1.5 cm welded to Pt wires 2.5 cm long sealed into a soft glass tube. The lower portion of the Pt gauze was folded up thereby making a small v-shaped trough suitable for holding Ag_2O. The platinum trough was filled with moist Ag_2O, slowly dried over a hot plate, and repeatedly pasted until the Pt was totally incased in dry Ag_2O. The electrodes were then mounted in a glass reduction tube and the Ag_2O partially reduced at 60°C to Ag by passing H_2 through the tube. It is

necessary to avoid too rapid a rate of reduction otherwise the heat liberated by the reaction

$$H_2(g) + Ag_2O(s) \rightarrow 2\ Ag(s) + H_2O(g) \qquad (I)$$

will flash the electrodes and the reaction will go to completion. When the Ag_2O was sufficiently reduced as judged by the gray color of the electrodes, the reduction tube was cooled to room temperature and the electrodes were transferred quickly to an H-cell containing two Hg, HgO electrodes and the requisite amount of NaOH solution. Ag, Ag_2O electrodes can be prepared by this method without the necessity of repeatedly washing them to free them of objectionable electrolytic impurities. Furthermore, the Ag should be free from occluded or adsorbed oxygen and be intimately mixed and in close contact with the Ag_2O.

Results

Cells Containing Ag, Ag_2O *Electrodes Prepared by Method No. 1*

Results obtained with electrodes prepared by method No. 1 confirmed results of Luther and Pokorny (1), Buehrer (2), and Fried (3) in that the potentials decreased with time as shown in Fig. 1 for a 15% NaOH solution. Similar results were also obtained for 5-40% NaOH solutions. During these measurements no evidence of O_2 evolution was obtained and all attempts by x-ray analysis failed to indicate lower oxides of Ag. However, two phenomena were observed, not reported by the above authors, namely: (*a*) the decline in emf, approximating 0.01 v in 17 days, was accompanied by a decrease in the reproducibility of the electrodes and the sensitivity of the measurements, and (*b*) if the Ag were removed from the Ag_2O slurry, after 17 days, and replaced by new Ag the emf's returned to their original high values and again exhibited high sensitivity, after which the potential and sensitivity of the electrodes again declined (*see* Fig. 1). These facts proved conclusively that the abnormal behavior observed by the authors cannot be attributed to changes in Ag_2O.

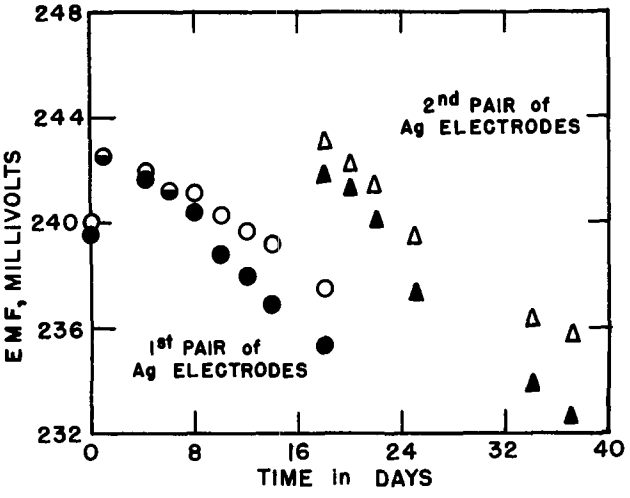

Fig. 1. Emf at 25°C of a Hg, HgO/NaOH (15% solution)/Ag_2O, Ag cell containing two Ag, Ag_2O electrodes prepared by Method No. 1 and two Hg, HgO electrodes. Each indicated value is an average value for each Ag, Ag_2O electrode against the two Hg, HgO electrodes.

It was also observed that the decline in potential and sensitivity was more rapid when small Ag foils were used instead of the Ag-covered helices. This suggested that the abnormal behavior of the electrodes is caused by a surface phenomena which is a function of the relative amounts of free oxygen in the cell and the surface area of the Ag. This is supported by the fact that the temperature coefficient of the emf of the cells when first assembled is about −0.2 mv/°C which leads to an entropy change for the cell reaction which approximates the thermodynamic value.

One might postulate that the exposed Pt of the electrodes caused the observed abnormalities, but exposed Pt does not cause Ag, AgCl electrodes to behave abnormally; data presented later in this paper do not support such a postulation. One might suspect that oxygen adsorbed on the Ag or Ag_2O or dissolved in the electrolyte might give rise to the high initial values and as it was dissipated the potential of the electrodes would fall and the higher potentials would again be observed when new Ag electrodes were placed in the cell. Two facts tend to contradict such an explanation, viz., (*a*) it does not explain the decrease in the sensitivity or reproducibility of the measurements with respect to the age of the electrodes, (*b*) the lower emf values do not agree within a few 0.01 of a volt with those calculated from thermodynamic data for the cell reaction. Benton and Drake (12) have reported that oxygen reacts with Ag at room temperature to form chemabsorbed films of nonstoichiometric composition. Conceivably such films could be of a passive nature and their effectiveness and rate of formation could be a function of the available oxygen and the area of the Ag surface thereby accounting for the more pronounced abnormalities observed with the small Ag foil electrodes. Such considerations prompted the authors to make cells with Ag, Ag_2O electrodes prepared by method No. 2.

Cells Containing Ag, Ag_2O *Electrodes Prepared by Method No. 2*

Results obtained with cells containing Ag, Ag_2O electrodes prepared by method No. 2 are given in Table I.[1] These cells are definitely superior and with respect to time are relatively free of the difficulties encountered in the earlier experiments discussed above. It is evident from Table I that the electrodes attained equilibrium in about ½ day and that Ag, Ag_2O electrodes prepared by method No. 2 do give steady and reproducible potentials to within a millivolt for periods of 14-38 days.

The emf's of Table I show a slight concentration dependence. Although, theoretically, the emf should be independent of alkali concentration, the observed dependence may be real and of the type found in Ni-Fe alkaline batteries. Until such is established, a total average value (averaging all values) are taken which is 0.2440 ± 0.0005 v for cell [*B*] at 25°C. Using

[1] An extended version of Table I has been deposited as Document 5109 with the ADI Auxiliary Publications Project Photoduplication Service, Library of Congress, Washington 5, D. C. A copy may be secured by citing the Document number and by remitting $1.25 for a photoprint or for a 35-mm microfilm. Advance payment is required. Make check payable to: Chief, Photoduplication Service, Library of Congress.

TABLE I. Electromotive forces at 25°C of the cell Hg, HgO | NaOH (aq.) | Ag_2O, Ag

	Weight % NaOH										
	30		20		15		10		5		
Time	HgO(1)*	HgO(2)*	HgO(1)	HgO(2)	HgO(1)	HgO(2)	HgO(1)	HgO(2)	HgO(1)	HgO(2)	Avg
(days)	(v)	(v)	(v)	(v)	(v)	(v)	(v)	(v)	(v)	(v)	(v)
0.5	0.2445	0.2444	0.2442	0.2444	0.2439	0.2438	0.2438	0.2440	0.2429	0.2429	0.2439
1	0.2446	0.2445	0.2445	0.2444	0.2438	0.2438	0.2431	0.2438	0.2430	0.2430	0.2439
5	0.2450	0.2449	0.2438	0.2445	0.2434	0.2437	0.2431	0.2439	0.2430	0.2426	0.2438
10	0.2451	0.2451	0.2436	0.2445	0.2435	0.2437	0.2434	0.2442	0.2434	0.2432	0.2440
14	0.2450	0.2451	0.2439	0.2444	0.2434	0.2437	0.2439	0.2442	0.2435	0.2431	0.2440
35			0.2436	0.2444	0.2427	0.2433					
38			0.2435	0.2439	0.2426	0.2432					

* Electrode (1) means lower Hg, HgO electrode; electrode (2) means upper Hg, HgO electrode.

TABLE II. Electromotive forces of the cell Hg, HgO | NaOH (aq.) | Ag_2O, Ag at various temperatures in the order of observation

Wt % NaOH							
30		20		10		5	
t°C	E (v)	t°C	E (v)	t°C	E (v)	t°C	E (v)
22.70	0.24556	22.90	0.24452	22.60	0.24429	22.80	0.24382
0.00	0.24963	0.00	0.24899	12.30	0.24641	0.00	0.24770
23.90	0.24528	23.10	0.24459	0.00	0.24870	23.10	0.24372
24.80	0.24506	51.75	0.23863	12.05	0.24654	51.75	0.23733
46.90	0.24018	46.75	0.23975	36.80	0.24122	46.85	0.23834
41.85	0.24124	75.45	0.23420	21.70	0.24468	23.90	0.24347
25.00	0.24463	69.20	0.23539	54.50	0.23771	75.70	0.23282
11.15	0.24745	25.10	0.24421	70.55	0.23466	69.15	0.23402
13.86	0.24698			69.55	0.23495	24.10	0.24186
25.10	0.24469			55.10	0.23791		
				22.40	0.24495		
				90.50	0.23061		
25.00*	0.24487	25.00*	0.24410	25.00*	0.24388	25.00*	0.24278
(dE/dT) 25°C	−0.0002035		−0.0001951		−0.0001958		−0.0001967

* Calculated.

23,060.5 cal/abs. volt g-equiv. (4) for F, the free energy change for the reaction of cell [*B*] is −11,254 ± 24 cal at 25°C.

The effect of temperature on the emf of the cell is given in Table II. Observations for each cell covered a period of from 3 to 6 days and no appreciable emf temperature hysteresis was noted. The emf-temperature coefficients at 25°C obtained from the emf at the various temperatures by the method of least squares are listed in the last row of the table. The noteworthy fact observed in these studies is that the temperature coefficient is negative and not positive as reported by Fried. The authors have no explanation for the positive temperature coefficient observed by Fried (3), except that he probably either was not dealing with Ag_2O or was working in the range of electrode insensitivity. The average value for the coefficient at 25°C is −0.0001978 ± 0.0000029 which gives −9.12 ± 0.14 e.u. for ΔS at 25°C, since $\Delta S = nF\ (dE/dT)$. Then ΔH, the heat of the reaction is −13.973 ± 69 cal at 25°C since $\Delta H = \Delta F + T\Delta S$.

It remains to be seen if the above values for ΔF and ΔS are reasonably consistent with the thermodynamic data reported in the literature for Ag_2O.

Thermodynamic Considerations

The free energy change of the reaction for cell [*B*] is equal to the difference between the free energies of formation of HgO and Ag_2O. The former may be calculated from the free energy of formation of liquid water, which value (−56,690 cal) is well known (4) and the free energy change for the reaction:

$$H_2\ (g) + HgO\ (s) = Hg\ (1) + H_2O\ (1) \quad (II)$$

given by the cell:

$$Pt, H_2(g)\ |\ NaOH \text{ or } KOH, aq.\ |\ HgO\ (s), Hg\ (l)\ [C]$$

The emf of this cell has been measured at 25°C by Brönsted (13), Chow (14), Miyamoto (15), Fried (3), Ishikawa and Kimura (10), Shibata and Murata (16), Shibata, Kobahashi, and Furukawa (17), and Kobayashi and Wang (18). Their results are brought together in Table III. Using only those values corrected to infinite dilution, and assuming all experimenters used the correct international volt, −13,977 cal is the free energy of formation of HgO. When this value is combined with that found for the free energy of the cell reaction, −2723 cal is the free energy of formation of Ag_2O.

TABLE III. Entropy and free energy changes for the reaction $H_2(g) + HgO(s) = Hg(l) + H_2O(l)$

Experimenter	Emf (25°C)	(dE/dT) 25°C	$\Delta F°$ (25°C) cell reaction	$\Delta S°$ (25°C) cell reaction	$\Delta F°$ (25°C) formation HgO	$S°$ HgO
	(v) [b]	(v) [b]/deg	cal	e.u.	cal	e.u.
Brönsted*	0.9261[a]	—0.0002791	—42727	—12.88	—13963	16.89
Chow	0.9264	—	—42741	—	—13949	—
Mujamoto	0.9268	—	—42759	—	—13931	—
Fried	0.92598[a]	—0.0002918	—42721	—13.46	—13979	17.47
Ishikawa and Kimura	0.92565[a]	—0.0002949	—42706	—13.61	—13984	17.62
Shibata and Murata	0.92558	—0.000284	—42703	—13.10	—13987	17.11
Shibata, Kobayashi, and Furukawa	0.92445	—0.000281	—42697	—12.96	—13993	16.97
Kobayashi and Wang	0.925495[a]	—0.0002854	—42699	—13.17	—13991	17.18
Avg.	0.92593	0.0002860	—42719	—13.19	—13971	17.21
Avg†	0.92581	0.0002878	—42713	—13.27	—13977	17.29

* At the time of his measurements Brönsted used an international volt which was 0.03% too high; the above value includes a correction for this.
[a] Corrected to infinite dilution.
[b] International volt.
† Average of only those corrected to infinite dilution.

Pitzer and Smith (7) obtained the free energy of formation of Ag_2O at 25°C from heat capacity measurements from 12.9 to 285.3°K and the free energies of dissociation of Ag_2O as calculated from the equilibrium data of Lewis (19), Keyes and Hara (20), and Benton and Drake (12) for the temperature range 446.1-773.1°K, and an assumed heat capacity curve for Ag_2O from 285.3 to 773.1°K. [Kobayashi's subsequent heat capacity measurements at high temperatures (8) showed their assumed curve to be reliable.] By this procedure, Pitzer and Smith (7) calculated a value of —2585 cal for the formation of Ag_2O at 25°C. This value is 135 cal lower than that found in this investigation.

However, Pitzer and Smith in their determinations of the heat capacity of Ag_2O observed an anomalous "hump" in their curve of C_p against log T at 15-50°K which amounted to 0.48 e.u. in the entropy, to 14.2 cal in $H° - H°_0$, and to 0.44 cal in $(H°_0 - F°)/T$ for Ag_2O at 25°C. If this "hump" were ignored, the free energy of formation of Ag_2O becomes —2654 cal, which agrees within 69 cal of that found herein.

It is also interesting, as was shown by Pitzer and Smith (7), that a value of —2649 cal is obtained by the sum of the equations:

$$2Ag + 2H^+ + 2Cl^- = 2AgCl + H_2 \; ; \quad \Delta F' = 10{,}259 \text{ cal (21)} \qquad \text{(III)}$$

$$2AgCl + 2\,OH^- = Ag_2O + H_2O \; ; \quad \Delta F° = 5{,}596 \text{ cal (22)} \qquad \text{(IV)}$$

$$2H_2O = 2H^+ + 2\,OH^- \; ; \quad \Delta F° = 38{,}186 \text{ cal (23)} \qquad \text{(V)}$$

$$H_2 + \tfrac{1}{2}\,O_2 = H_2O \; ; \quad \Delta F° = -56{,}690 \text{ cal (4)} \qquad \text{(VI)}$$

which agrees remarkably well, perhaps fortuitously, with that of Pitzer and Smith if their "hump" is ignored.

In spite of this agreement, the values of —2654 and —2649 may be low. Pitzer and Smith's evaluation of the heat content and entropy involves an extrapolation to absolute zero. They made this extrapolation with the aid of the Debye theoretical heat capacity equation. Inspection of their data at low temperatures suggests that their $H°_{15} - H°_0$ and $S°_{15} - S°_0$ values may be high by as much as 1.0 cal and 0.11 e.u., respectively.[2] Also, the low-temperature heat capacities of Ag_2O do not follow the simple or extended Debye equations. For the simple case, a straight line should be obtained if C_p/T were plotted against T^2 whereas a curve is obtained. For the extended case, constant values of θ, the characteristic temperature, should be found; actually values of θ decrease rapidly as the temperature becomes high.

Assuming that Pitzer and Smith's values are high by the above amount, —2683 cal is obtained for the free energy of formation of Ag_2O which agrees within 40 cal of that found herein. This agreement is considered good especially since the correction for the "hump" in the Pitzer and Smith data may have been arbitrarily chosen by the author of this paper as smaller than it actually is. Also, some uncertainty exists concerning the second of the 4 equations added above. Randall and Halford (22) used the equilibrium data of Noyes and Kohr (24) and Newton (25) in evaluating $\Delta F°$. They plotted the concentration equilibrium constants as obtained by these authors against the square root of the ionic strength and extrapolated to zero concentration whereby they obtained $-\log K = 2.050 \pm 0.003$ at 25°C from which $\Delta F° = 2798$. However, using the procedure of Lewis and Randall (26) and the same data 2779 is obtained for $\Delta F°$. Furthermore, Böttger (27) by conductivity measurements found the solubility product of Ag_2O in water at 25°C to be 1.96×10^{-8} which was confirmed by Johnston, Cuta, and Garrett (9). From the potentiometric data of Owen (28) and the conductometric data of Gledhill and Malan (29) a value of 1.778×10^{-10} is obtained for the solubility product of AgCl in water at 25°C. These two values lead to $\Delta F° = 2786$. Therefore, if this value is averaged with the Lewis and Randall value and used in the second of the 4 equations above, —2679 cal is obtained for the free energy of formation of Ag_2O which agrees

[2] These maximum uncertainties were arrived at as follows. A smooth curve was placed through the low-temperature heat capacities of Pitzer and Smith for their Series I and II, ignoring the "hump". The best curve was obtained by the method of least squares. The value at 15°K was then calculated from the least square equation and used in the Debye equation, $C_p = 464\,(T^3/\theta^3) = aT^3$ to obtain values of C_p down to absolute zero. By this procedure 9.7 cal is obtained for $H°_{15} - H°_0$ and 0.86 e.u. for $S°_{15} - S°_0$ whereas Pitzer and Smith gave 10.7 cal and 0.97 e.u., respectively.

quite well with the Pitzer and Smith maximum value given above, and is within 44 cal of that found herein.

Further insight into the thermodynamic consistency may be seen from a consideration of the entropy of Ag_2O. The entropy change for cell [*B*] is given by

$$\Delta S_{reaction} = 2S_{Ag} + S_{HgO} - S_{Hg} - S_{Ag_2O} \qquad \text{(VIII)}$$

or S_{Ag_2O} by

$$S_{Ag_2O} = 2S_{Ag} + S_{HgO} - S_{Hg} - \Delta S_{reaction} \qquad \text{(IX)}$$

The values for S_{Ag} and S_{Hg} are, respectively, 10.206 and 18.5 e.u. (4). The value for S_{HgO} is 17.29 e.u. (*see* Table III). The value for $\Delta S_{reaction}$ has been shown to be −9.12 cal. Therefore, the entropy of Ag_2O, as found herein, is 28.32 e.u. Pitzer and Smith (7) gave 29.09 ± 0.2 e.u. However, if the "hump" were ignored in their heat capacity curve, their value would be 28.61 ± 0.2 e.u. which agrees quite well with the value found in the present investigation. Also, their value could well be high due to uncertainty in their extrapolation to absolute zero. This agreement in entropy is comparable to that usually found between calorimetric and emf data (30).

From the present investigation a value of −0.342 v[3] is obtained for the standard potential of the Ag, Ag_2O electrode. This value is arrived at from the measurements of cell [*B*], the data of Table III, and the standard potential 0.8282 v (31) of the H electrode at unit activity of OH^- ion. This value is 0.002 v lower than that given by Latimer (32) who based his value on the data of Pitzer and Smith.

In conclusion, it has been shown how stable and reproducible Ag, Ag_2O electrodes may be prepared which give potentials reasonably consistent with thermodynamic data. The comparison of thermodynamic data involves low-temperature heat capacity measurements, high-temperature dissociation measurements, and free energy functions for Ag and O_2 on the one hand, as compared with combined emf measurements of Ag, Ag_2O and Hg, HgO electrodes and free energy functions of H_2O, Ag, Hg, and HgO on the other hand. A more direct comparison could be realized by comparing Ag, Ag_2O, and H_2 electrodes. Such measurements are contemplated, although they would be involved owing to the high solubility of Ag_2O in alkali.

Manuscript received July 2, 1956. This paper was prepared for delivery before the Cleveland Meeting, Sept. 30 to Oct. 4, 1956.

[3] According to the Stockholm IUPAC convention the sign here would be + with the half-cell reaction written as a reduction of Ag_2O.

Any discussion of this paper will appear in a Discussion Section to be published in the December 1957 JOURNAL.

REFERENCES

1. R. Luther and F. Pokorny, *Z. anorg. u. allgem. Chem.*, **57**, 290 (1908).
2. G. N. Lewis and M. Randall, "Thermodynamics and the Free Energy of Chemical Substances," p. 483, McGraw-Hill Book Co., New York (1923).
3. F. Fried, *Z. physik. Chem.*, **123**, 406 (1926).
4. "Selected Values of Chemical Thermodynamic Properties," National Bureau of Standards Circular 500 (1952).
5. H. N. K. Rördan, *Kgl. Danske Videnskab. Selskab, Mat-fys. Medd.*, **3**, No. 7 (1920).
6. K. K. Kelley and C. T. Anderson, *U. S. Bur. Mines Bull. 384* (1935).
7. K. S. Pitzer and W. V. Smith, *J. Am. Chem. Soc.*, **59**, 2633 (1937).
8. K. Kobayashi, *Science Repts. Tôkoku Univ.*, Ser. I, **35**, 173 (1951).
9. E. Cohen, *Z. physik. Chem.*, **34**, 69 (1900).
10. F. Ishikawa and G. Kimura, Sexagint, Y. Osaka, *Chem. Inst. Dept. Science Kyoto Imp. Univ.*, 255 1927.
11. H. S. Harned, *J. Am. Chem. Soc.*, **51**, 416 (1929).
12. A. F. Benton and L. C. Drake, *ibid.*, **54**, 2186 (1932).
13. J. N. Brönsted, *Z. physik. Chem.*, **65**, 84 (1908).
14. M. Chow, *J. Am. Chem. Soc.*, **42**, 488 (1920).
15. S. Mujamoto, *Sci. Papers, Inst. Phys. Chem. Res. Tokyo*, No. 4, **1**, 31 (1922).
16. F. L. E. Shibata and F. Murata, *J. Chem. Soc. (Japan)*, **52**, 399 (1931).
17. F. L. E. Shibata, Y. Kobayashi, and S. Furukawa, *ibid.*, **52**, 404 (1931).
18. Y. Kobayashi and S. Furukawa, *J. Sci. Hiroshima Univ.*, **5A**, 71 (1934).
19. G. N. Lewis, *J. Am. Chem. Soc.*, **28**, 139 (1906).
20. F. G. Keyes and H. Hara, *ibid.*, **44**, 479 (1922).
21. H. S. Harned and R. W. Ehlers, *ibid.*, **55**, 2179 (1933).
22. M. Randall and J. O. Halford, *ibid.*, **52**, 178 (1930).
23. H. S. Harned and G. E. Mannweiler, *ibid.*, **57**, 1873 (1935).
24. A. A. Noyes and D. A. Kohr, *Z. physik. Chem.*, **42**, 336 (1902).
25. R. F. Newton, *J. Am. Chem. Soc.*, **50**, 3258 (1928).
26. Ref. (2), p. 482.
27. W. Böttger, *Z. Physik. Chem.*, **46**, 521 (1903).
28. B. B. Owen, *J. Am. Chem. Soc.*, **60**, 2229 (1938).
29. J. A. Gledhill and G. McP. Malan, *Trans. Faraday Soc.*, **48**, 258 (1952).
30. D. A. MacInnes, "The Principles of Electrochemistry," p. 123, Reinhold Publishing Corp., New York (1939).
31. Ref. (32) p. 253.
32. W. M. Latimer, "The Oxidation States of the Elements and Their Potentials in Aqueous Solutions," 2nd ed., Prentice-Hall, Inc., New York (1952).

Effect of Ultraviolet Irradiation on the Growth of Anodic Ta_2O_5 Films

D. A. Vermilyea

Research Laboratory, General Electric Company, Schenectady, New York

ABSTRACT

Ultraviolet irradiation during the growth of amorphous Ta_2O_5 films in aqueous solutions results in the transformation of the outer portion of the film from Ta_2O_5 to a material which dissolves more rapidly than Ta_2O_5 in HF. If the formation field is high, the transformed region has a very high resistance and both Ta and oxygen are mobile in the region. When the formation field is low, the region has a lower resistance, contains water which can be removed partially by heating the film in air, and only oxygen is mobile. It is suggested that the transformation of the outer portion of the film occurs after an increased field, necessary to maintain the flow of electrons into the oxide from the solution by tunneling, is produced by a positive space charge in the outer portion of the film. Under the influence of this high field Ta ions migrate out of the outer part of the film, leaving defects. As the defect concentration increases, oxygen probably also starts to move in the film, and the film becomes either hydrated or porous depending on the applied field strength. Ultraviolet irradiation during growth also results in a similar transformation of the outer portion of crystalline anodic Ta_2O_5 films.

A recent note (1) reported that anodic Ta_2O_5 films grown while irradiated with u.v. light consisted of two layers, the one nearer the metal being a normal anodic Ta_2O_5 film and the outer one being less resistant to corrosion in HF and having a higher conductivity. This paper presents the results of a more extensive study of the nature and growth of the outer layer. It is suggested that this outer layer is formed by transformation of the original Ta_2O_5 film when a space charge produced by irradiation has caused a considerable increase in the electrical field strength at the oxide-solution interface.

Experimental

The Ta used in these experiments was 0.005 in. sheet,[1] and was stated to be 99.9% pure. The specimens had a surface area of about 6.4 cm^2. Only dilute aqueous electrolytic solutions (usually 1% Na_2SO_4) were used and identical results were obtained in all solutions (such as 0.1% KOH, 1% H_2SO_4) which did not adsorb the light and reduce the photo effect. The u.v. light source was a 4-w Hg vapor lamp.[2, 3] The source was placed outside a quartz beaker containing the specimen and the solution, and was about ½ in. from and parallel to the specimen. The maximum photocurrent obtained was about 1 ma/cm^2.

Two methods were used to obtain an estimate of the oxide film thickness. The first was a comparison with the interference color step gauge described previously (2). This method has the advantage that it gives a rough indication of the total thickness of the film, including both layers. The values obtained are accurate only for the dense amorphous Ta_2O_5 film, and the absolute value of the thickness measured when both layers are present might be considerably in error. The second method was a measurement of the electrical capacitance of a cell consisting of the specimen, a 2% HNO_3 solution, and a platinized Pt electrode of 100 cm^2 area. The series capacitance and series resistance of the cell were measured at 1000 cps. This second method has the advantage that a conducting layer in the oxide film behaves approximately like a resistance, and the capacitance is thus determined primarily by the dense inner Ta_2O_5 film. The actual equivalent electrical circuit of the oxide film is much more complex than a simple series resistance and capacitance and a determination of the true thicknesses of both films could only be made by making much more extensive measurements.

Results

Growth at High Current Density

Consider first the results of u.v. irradiation at an applied electric field of such a magnitude that the film would be growing at a fairly high rate, say about 0.1-10Å/sec, in the absence of light. It is found (Fig. 1) that as the film grows the optical thickness and capacitance are both smaller on the irradiated side. The capacitance of the irradiated side is found by calculating the capacitance of the dark side from the observed optical thickness and the dielectric constant, and subtracting the result from the total measured capacitance. At these high growth rates the series resistance of the condenser formed by the oxide film remains constant and equal to the resistance of the electrolyte. When the film is dissolved in HF the rates of decrease of the optical thickness and reciprocal capacitance (Fig. 2) indicate that the outer portion of the film on the illuminated side is not the ordinary Ta_2O_5 film found on the dark side. The fact that the series resistance is unchanged shows that this transformed material is highly insulating like the normal Ta_2O_5 film. It should be noted that the inner layer which comprises most of the film is apparently normal Ta_2O_5,

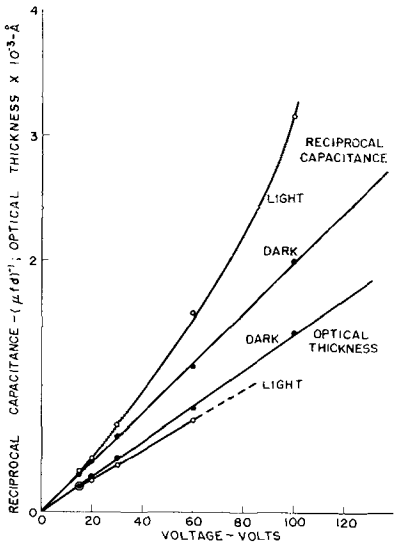

Fig. 1. Growth in thickness of a film formed at 3 ma/cm² in 1% Na_2SO_4 at room temperature with and without irradiation with u.v. light.

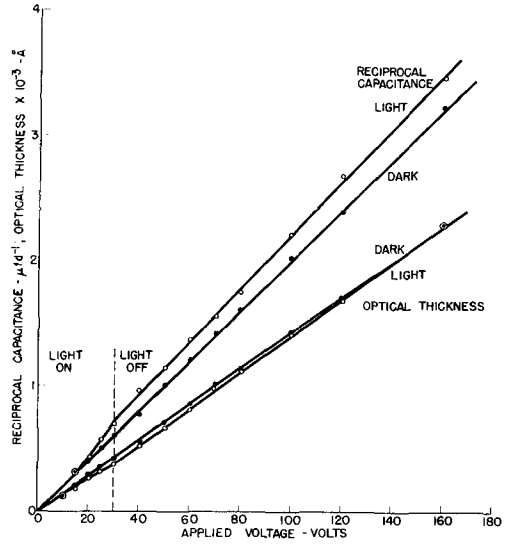

Fig. 3. Growth in thickness of a film formed at 1.5 ma/cm² in 1% Na_2SO_4 at room temperature, with one side irradiated for the first 30 v.

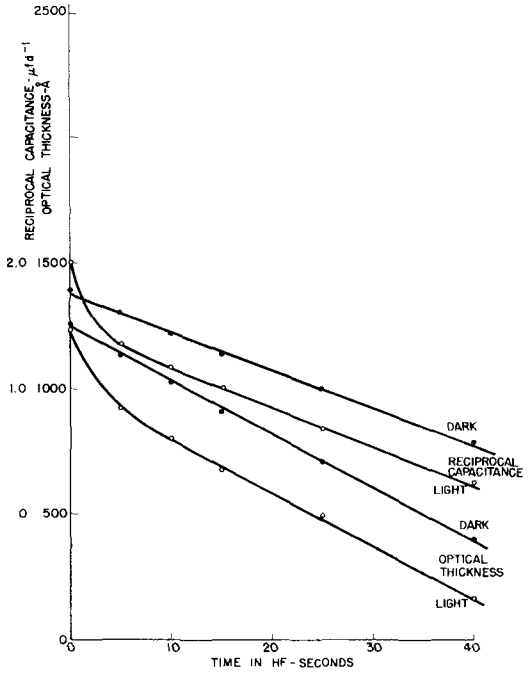

Fig. 2. Thickness decrease on solution in 48% HF of a film formed in a manner similar to that of Fig. 1.

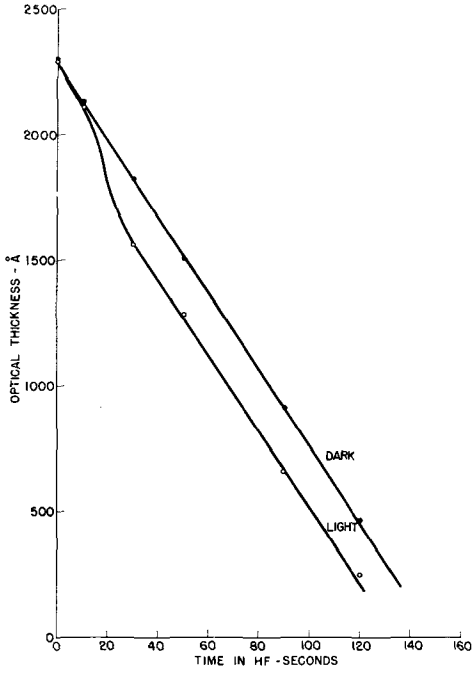

Fig. 4. Thickness decrease on solution in 48% HF of the film formed in Fig. 3.

since it has the same corrosion rate as the film on the dark side.

If the u.v. light is applied until the thickness has increased to about 400Å and then turned off while the formation is continued, the thickness and reciprocal capacitance increase as shown in Fig. 3. It may be seen that the change produced by the irradiation is permanent, the optical thickness and capacitance remaining smaller on the originally illuminated side. When the resulting film is dissolved in HF, it is found (Fig. 4) that the altered, rapidly dissolving film remains near the outer surface, but some normal Ta_2O_5 has been formed over the altered layer. It appears, therefore, that both oxygen and Ta are mobile in this altered layer [only Ta is mobile in normal Ta_2O_5 (3)]. Films formed under u.v. irradiation at these high growth rates behave in a manner which is very similar to that observed when anodic films are formed on Ta in solutions which are largely nonaqueous (3). Both types of formation produce films which have a layer of normal Ta_2O_5 next to the metal and a layer with different properties near the solution; both types of altered film become buried upon subsequent formation in simple dilute aqueous solutions.

Growth at Low Field Strength

Ultraviolet irradiation will cause the growth of Ta_2O_5 films held at such low field that no measurable growth would occur in the period of an experiment if the light was not present (4, 5). Fig. 5 shows plots of the values of series resistance, reci-

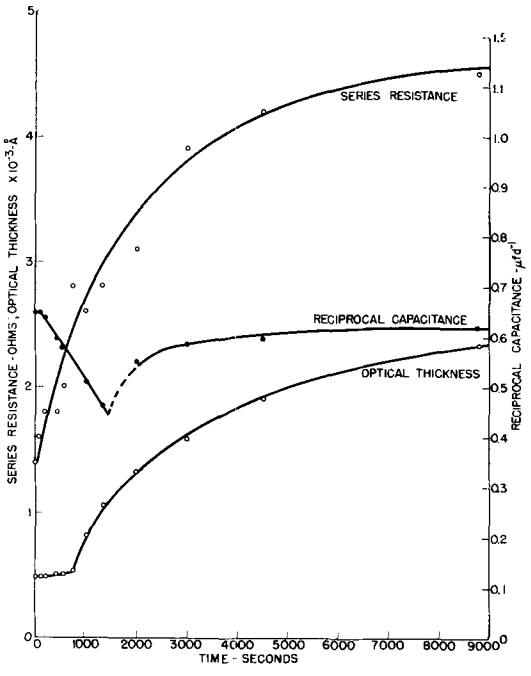

Fig. 5. Changes in thickness, reciprocal capacitance, and series resistance in the capacitance test on irradiation with u.v. light of a film initially 477Å thick with an initial applied field of 0.04 v/Å. The values plotted are for the light side; the thickness of the dark side remained unchanged.

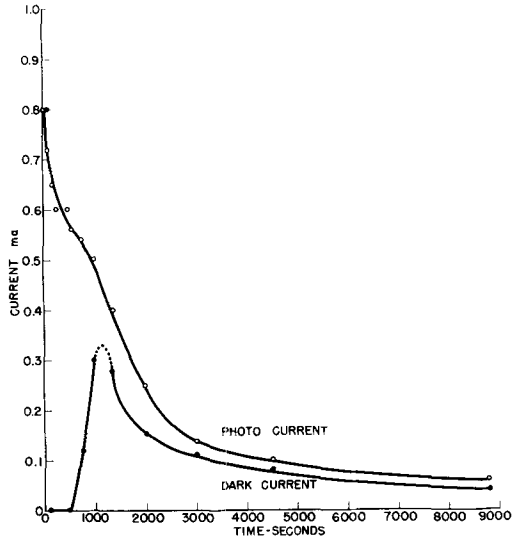

Fig. 6. Change of current with time for the experiment of Fig. 5. The current on the dark side was a negligible fraction of these currents.

procal capacitance, and optical thickness for a film formed in the dark to a thickness of 477Å and then held at a field of 0.04 v/Å with the u.v. light on. The series resistance and capacitance started to increase as soon as irradiation was started. The series resistance increased continuously at a decreasing rate during the entire run, while the capacitance first increased and then at about 1500 sec began to decrease again. The optical thickness began to increase very slowly at first, but at 750 sec the rate of increase suddenly became very great and the thickness increase then continued at a decreasing rate. Fig. 6 shows the values of photocurrent[4] and dark current during the experiment. The dark current was very low initially but became comparable with the photocurrent when the optical thickness began to increase very rapidly. The photocurrent decreased continuously during the experiment.

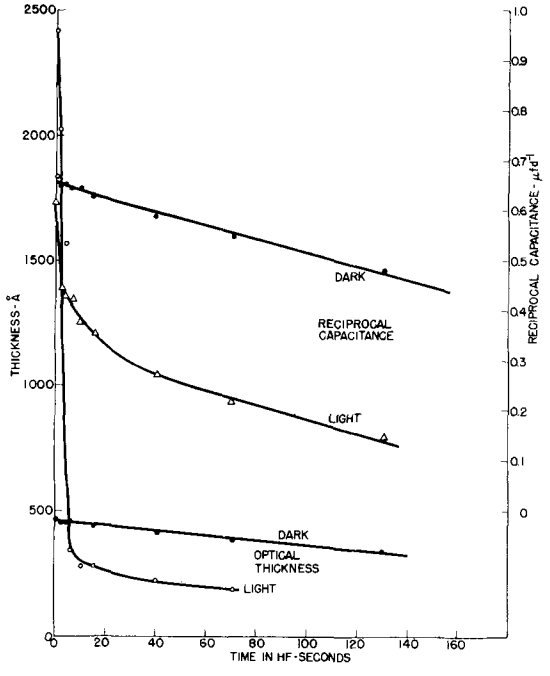

Fig. 7. Decrease in thickness on solution of the film of Fig. 5 in 24% HF.

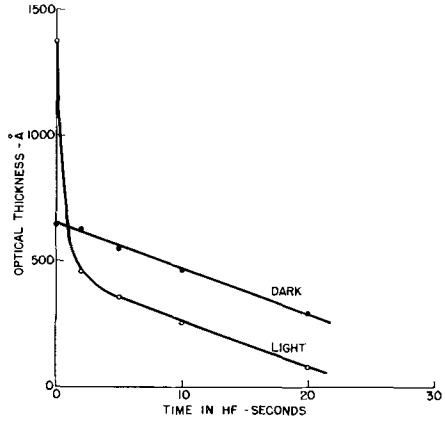

Fig. 8. Decrease in thickness on solution in 48% HF of a film grown in a manner similar to that of Fig. 5 until the optical thickness was 1050Å on the light side, and then formed at 1 ma/cm² to an optical thickness of 1380Å.

When a film formed with a low initial field was dissolved in HF the optical thickness and reciprocal capacitance decreased as shown in Fig. 7. There was a rapid initial decrease of both values for the film on the light side. After the rapidly dissolving part of the film was removed the rates of decrease of optical thickness and reciprocal capacitance became equal on both sides; hence it is likely that the remaining film on the light side was normal Ta_2O_5.

When a film was irradiated with u.v. light with a low initial applied field so that growth occurred as described above, and was then subsequently grown in the absence of u.v. light, it was found that the altered portion of the film remained at the oxide-solution interface. Fig. 8 shows the decrease of the values of reciprocal capacitance and optical thick-

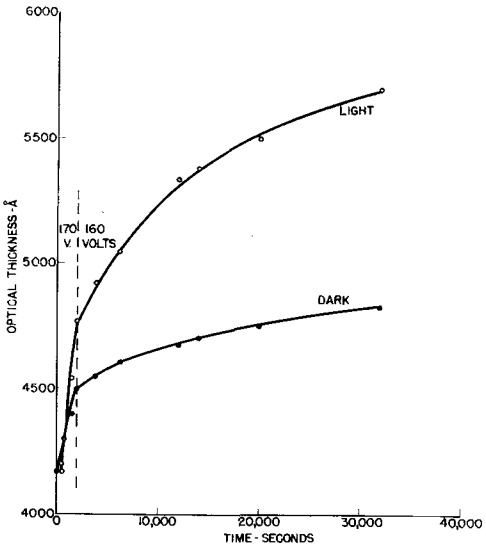

Fig. 9. Growth of a crystalline film illuminated with u.v. light on one side.

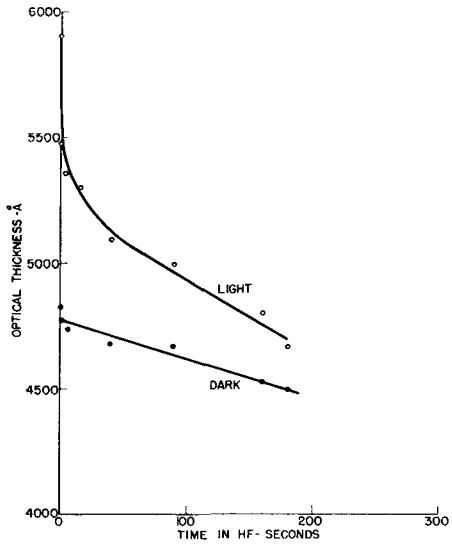

Fig. 10. Decrease in thickness on solution in 48% HF of the film of Fig. 9.

ness when such a film was dissolved in HF. The rapidly dissolving portion of the film was still on the outside of the film; thus, it appears that only oxygen is mobile in this portion of the film.

The transformed portion of the films formed with an initially low field strength is different from that of films formed at higher fields in several respects. In the first place, the conductivity of the altered layer of a low field film is much higher than that of a high field film, as shown by the fact that the altered low field film behaves approximately like a series resistance in the capacitance tests, while the high field film behaves like a pure capacitance. In the second place the dissolution rate in HF is much greater for the low field films (compare Fig. 2 and 7). Another difference is that the high field films are mostly Ta_2O_5 and have only a thin outer layer of transformed material. The low field films, on the other hand, are mainly transformed material with only a thin inner Ta_2O_5 film.

The final difference is that the low field film contains water which can be removed easily. For example, when a specimen formed at an initially low field to an optical thickness of 3580Å was heated to 500°C in air for 30 min, the optical thickness decreased to 3180Å. This change could be partly reversed; soaking the film in water resulted in an increase of the optical thickness to 3230Å after 15 min and to 3280Å after 16 hr. The optical thickness of another specimen heated to 200°C for 1 hr decreased from 3400Å to 3100Å, while on soaking in water for 1 hr the optical thickness increased to 3280Å. Holding at room temperature in a vacuum of 10^{-5} mm Hg changed the optical thickness of a third specimen from 3580Å to 3450Å, and this change could be reversed completely by soaking in water for 1 min. It appears, therefore, that there is some water present in the low field film which can be removed by evacuating or by heating. The high conductivity which short circuits the capacitance of the outer portion of the film is associated with the presence of this water, since after heating at 200°C for 1 hr the electrical capacitance of a specimen decreased from 2.52 mfd to 1.37 mfd, while after soaking in water for 3 hr the capacitance increased again to 2.33 mfd. The capacitance calculated from the optical thickness assuming a Ta_2O_5 film was 1.31 mfd, which is nearly identical with the 1.37 mfd observed after heating. For films formed at high fields, on the other hand, no change in optical thickness occurred on heating at temperatures up to 500°C, and the capacitance increased about 6% instead of decreasing. Such an increase is expected from other data obtained for normal Ta_2O_5 films (6). For high field films, therefore, any water present is bound so strongly that it is not removed by heating at 500°C.

Growth of a Crystalline Ta_2O_5 Film During U. V. Irradiation

U.V. irradiation also produces more rapid growth of a crystalline Ta_2O_5 film. Crystalline films can be formed by anodizing Ta specimens at 90 v in 2% HNO_3 at 100°C for about 15 hr (7). The response of these films to u.v. light was about the same in wave length dependence[5] and the magnitude of the photocurrent for a given light intensity as that of an amorphous Ta_2O_5 film. Upon irradiation of a crystalline film 4170Å thick with 170 v applied for the first 2000 sec and 160 v thereafter the optical thickness increased as shown in Fig. 9. There was a greater rate of growth on the irradiated side, and the outer portion of the film on the irradiated side subsequently dissolved at a more rapid rate in HF as shown in Fig. 10. There was an increase of about 2 ohms in the series resistance of the capacitor formed from the film, and the value of capacitance was about the same as would have been obtained for a film consisting entirely of crystalline Ta_2O_5 of the thickness of the dark side. The photocurrent decreased from 0.5 ma/cm² to 0.05 ma/cm² during the course of the experiment. The behavior is very similar to that observed with amorphous films.

Discussion

The two layer films produced by u.v. irradiation might be formed in the following manner. When a

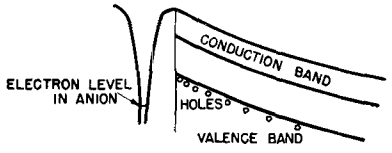

Fig. 11. Schematic drawing of the electronic levels in the oxide film and on anions in the solution during the passage of photocurrent.

Ta_2O_5 film is irradiated with u.v. light, electrons are excited into the conduction band, leaving holes in the valence band. Some of the electrons reach the metal, lowering its potential, as found by Young (4). If a field is applied across the film, a current flows, the electrons traveling via the conduction band to the Ta and the holes in the reverse direction. There would probably be little barrier for the passage of electrons from the oxide to the metal, but it would be difficult for electrons to tunnel from the solution to the full band of the oxide in order to fill the positive holes. A positive space charge would therefore develop near the oxide-solution interface, and the field at the interface would increase until the tunneling process was able to supply electrons from the solution rapidly enough to maintain the current. It is expected that a very large field would be required to bring the level of holes in the full band down to the level of electrons on ions in the solution (*see* Fig. 11). The Fermi energy of the anodic Ta_2O_5 film is not known, and hence an accurate estimate of the field required cannot be made. However, the electronic levels in the solution are many[6] volts below the vacuum and probably lie well below the top of the full band of the oxide. If the top of the full band is 1 v above the level of the electrons in the ions, a field in excess of 10^7 v/cm would be required to make the tunneling distance short enough so that a large current could be carried across the interface. The time required to develop a field of this magnitude at the observed photocurrent, assuming that all of the light is absorbed in the outer 400Å of the film, can be shown to be of the order of a few seconds.

If it is accepted that a positive space charge develops in the oxide film, then the observations made during the growth of the film at high fields can be explained as follows. While the film is very thin, most of the light would be absorbed in the metal rather than in the oxide, little space charge would develop, and the optical thickness and capacitance would be the same whether the film was illuminated or not. After the film had grown to a thickness of a few hundred Angstrom units, nearly all the light would be absorbed in the film (4, 9), an appreciable space charge would have developed and the field near the oxide-solution interface on the irradiated side would be very great. Now in addition to maintaining the photocurrent the increased field at the oxide-solution interface would increase the Ta ion current locally. Ta ions would move out of the outer layers of the oxide more rapidly than they came in from underneath, leaving behind a number of vacancies which could not be filled because of the smaller ionic current in the rest of the film. The resulting negative space charge would cancel part of the positive space charge, but the photo effect would again increase the field at the interface in order to maintain the flow of electronic current.

It is clear that this situation could not exist indefinitely because *soon* all the Ta ions in the outer portion of the film would be exhausted. Probably as soon as the defect concentration becomes sufficiently large, oxygen ions start to move inward. It would then be possible to reach a steady state with a large defect concentration of both ions in the outer layers and an increased field near the surface, both ions being mobile. Since the change produced in the film by the u.v. light is permanent during further formation in the absence of u.v. light, it is likely that some chemical change in the outer layer occurs in addition to the production of large numbers of ionic defects. By analogy with the films obtained upon formation in nonaqueous solutions which behave similarly and are solvated, it may be that the outer portion of the film becomes hydrated. There is a decrease in the photocurrent by about a factor of two when this altered film is present, perhaps because some of the charge carriers can recombine in the outer layers with its high concentration of ionic defects.

When a film is formed to a certain thickness and then irradiated with a low applied field, a similar transformation occurs as follows. Shortly after irradiation is started, the field at the outer interface is greatly increased in order to maintain the photocurrent. A defect structure is then produced as at a high field strength, and a transformed layer results. However, the experiments showed that the altered portion of the low field film has a different structure from that of the high field film, containing loosely bound water. It is suggested that this film is porous rather than simply hydrated. The explanation for the difference in the structure of the two types of transformed film can be attributed to the fact that some ionic motion occurs in the underlying Ta_2O_5 film when the initial field is high. The influx of ions into the transforming layer from underneath causes some repair of the defect structure, and hence a less drastic change from the original Ta_2O_5.

The curves shown in Fig. 6 and 7 for low field films can be explained in terms of the proposed mechanism in the following manner. Shortly after irradiation is started, the transformation of the outer layers begins. The series resistance and capacitance increase because the outer portion of the Ta_2O_5 is now a poor conductor instead of an insulator. The optical thickness increases slowly during this initial period as Ta leaves the outer portion of the film under the influence of the high field and forms new oxide at the oxide-solution interface. As the transformation proceeds the applied voltage is concentrated across the untransformed portion of the film, since the transformed layer has a low resistance, and the field in this portion therefore increases as transformation proceeds. Finally the field becomes great enough for ionic motion in the inner layer, and rapid growth begins. At this time the dark current, which is now ionic rather than electronic, increases very markedly and becomes comparable in magnitude with the photocurrent. As growth pro-

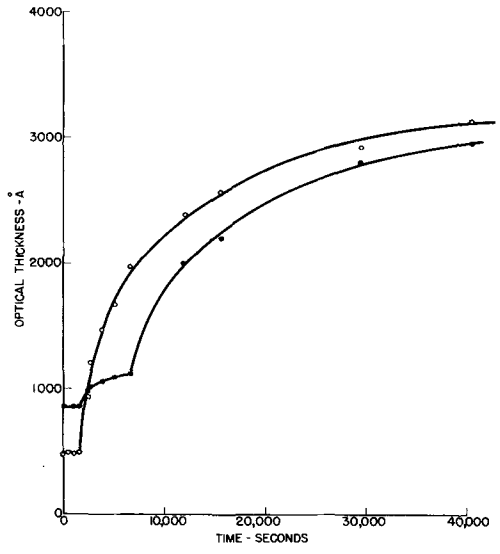

Fig. 12. Growth during illumination of two films initially 485Å and 860Å thick. Both films were held simultaneously at 20 v in 1% Na_2SO_4 solution at room temperature.

ceeds the new oxide formed underneath the transformed region is itself transformed, so that the inner Ta_2O_5 layer remains approximately constant in thickness and the field in it remains high. As the outer porous film becomes very thick, the capacitance decreases again since the porous film does contribute some capacitive reactance.

In order for this explanation to be possible it is necessary for the absorption of some u.v. light to occur in the inner Ta_2O_5 layer. The oxygen necessary for new growth under the porous layer comes from water in the pores. The decrease in photocurrent with time is caused presumably by absorption of some of the light in the porous layer of the film.

According to the proposed mechanism of formation of the highly conducting film, if the initial field was less but the applied constant voltage the same in a low field experiment, it should take longer for the rapid growth to start, since more of the original oxide would have to be transformed to conducting oxide in order to concentrate the voltage in the same small thickness of dense Ta_2O_5. In order to test this prediction, two films of different thickness (485Å and 860Å) were held simultaneously at 20 v in 1% Na_2SO_4 solution at room temperature while being irradiated. Fig. 12 shows that the thicker film required 7000 sec before rapid growth started as compared to 2000 sec for the thinner film.

Summary

1. When Ta_2O_5 films are irradiated with u.v. light while a strong electric field is present in the film, the outer layers of the film are transformed to a material of different composition which dissolves more rapidly in HF than does the Ta_2O_5 film. If the applied field is large enough to cause rapid film growth in the absence of irradiation, the transformed region is still a good insulator and is stable at temperatures up to at least 500°C. If the initially applied field is so low that no growth of the film would occur in the absence of irradiation, the transformed region becomes a poor conductor instead of an insulator, and contains water that can be removed partially by evacuation at room temperature. The low field film is probably porous, and may also be hydrated, while the high field film is probably simply hydrated.

2. When the initially applied field is very low, the production of the transformed layer of low resistance concentrates the applied voltage across the untransformed region of the film. As the transformation proceeds, the field in the untransformed layer rises until eventually ionic motion starts and rapid film growth occurs. The newly formed oxide is itself transformed so that the field in the inner layer remains high and growth continues.

3. Irradiation causes a similar transformation of a crystalline Ta_2O_5 anodic film.

4. It is suggested that the transformation occurs when an increased electric field is produced at the oxide-solution interface by the irradiation. A defect structure is produced as the Ta ion current is increased locally in this increased field, and eventually structural and chemical changes occur as well. The differences observed in the high and low field films are attributed to the partial repair of the defect structure at high applied field by the Ta ion current entering the transforming region from underneath.

Manuscript received May 16, 1956.

Any discussion of this paper will appear in a Discussion Section to be published in the December 1957 JOURNAL.

[1] From Fansteel Metallurgical Co.
[2] G. E. "Germicidal".
[3] Percentage of lamp watts in various spectral ranges as follows: below 2800Å 13%, 2800-3200Å 0.25%, 3200-3800Å 0.25%, 3800-5000Å 1%, 5000-7000Å 0.52%.
[4] The photocurrent is equal to the total current minus the dark current.
[5] Determined by the use of filters which cut off at approximately 2200Å, 2600Å, 2800Å, 3000Å, 3400Å (Corning numbers 2910, 9700, 7740, 0160, and 7380, respectively).
[6] The electronic levels of even the simple halogen anions are about 6-8 v below the vacuum, and other anions have still lower electronic levels (8).

REFERENCES

1. D. A. Vermilyea, *J. Appl. Phys.*, **26**, 489 (1955).
2. D. A. Vermilyea, *Acta Met.*, **1**, 282 (1953).
3. D. A. Vermilyea, *ibid.*, **2**, 482 (1954).
4. L. Young, *Trans. Faraday Soc.*, **50**, 153 (1954).
5. W. Bar, *Z. Physik*, **115**, 658 (1940).
6. D. A. Vermilyea, Submitted to *Acta Metallurgica*.
7. D. A. Vermilyea, *This Journal*, **102**, 207 (1955).
8. R. W. Gurney, "Ions in Solution," Cambridge (1936).
9. L. Apker and E. A. Taft, *Phys. Rev.*, **88**, 58 (1952).

Oxidation of 50 Weight Per Cent Uranium-Zirconium Alloy

Sidney Barnartt, Robert G. Charles, and Earl A. Gulbransen

Research Laboratories, Westinghouse Electric Corporation, Pittsburgh, Pennsylvania

ABSTRACT

The reaction of 50% uranium-zirconium with oxygen at 1 atm pressure was studied over the range 200°-500°C. Two forms of the alloy, the stable ϵ-phase and the quenched γ-phase, were reacted to an oxide-scale thickness of 0.1 mm at the higher temperatures. In general, the weight gain increased linearly with time, although in many cases the oxidation curve showed a bend and could be represented by two straight lines. At 400°C and above, the stable ϵ-phase reacted considerably faster than the γ-phase. The thick oxide scales were porous and showed uranium enrichment. During the formation of thin oxide films at 200° and 250°C the reaction followed the parabolic rate law approximately. The alloy oxidizes somewhat more rapidly than pure Zr, but very much more slowly than U.

Uranium tarnishes rapidly at room temperature. At elevated temperatures the reaction with pure oxygen is very rapid, and even bulk specimens become inflammable above 360°C (1,2). Plots of weight gain (w) vs. time (t) are approximately linear above 200°C, the linear oxidation curve being associated with a cracked, nonprotective oxide.

Zr, on the other hand, is moderately resistant to oxidation and forms a protective layer of ZrO_2 on the surface (3-5). The cubic rate law, $w^3 = k_c t$, is reported to be applicable to the reaction with oxygen over the temperature range 300°-950°C (5), although the parabolic rate law, $w^2 = k_p t$, shows better agreement in some cases (4, 6). It would be anticipated that the addition of U to Zr would decrease the oxidation resistance of the latter. If considerable U could be added, while maintaining high resistance to oxidation and corrosion at elevated temperatures, such alloys would be useful as reactor fuels.

This study concerns the reaction of oxygen with the 50% by weight U-Zr alloy (72 at. % Zr) at temperatures of 200°-500°C. The phase diagram of the uranium-zirconium system (7) indicates that this composition would be a two-phase alloy below 600°C. More detailed studies have shown that a stable ϵ-phase exists at and near the 50% composition (8-11).[1] Above about 650°C this material enters the γ-phase.

Two forms of the alloy were used in these studies. The first,[2] designated "as-rolled," was material that was heated to produce the γ-phase, then quenched rapidly in water and cold-rolled to sheet 0.63 mm (25 mils) thick. This should consist mainly of the γ-phase. The second form, designated "annealed," was prepared from the as-rolled sheet by heating for 24 hr at 800°C *in vacuo* (10^{-5} mm Hg) and then cooling slowly, in order to obtain the ϵ-phase. X-ray diffraction patterns confirmed these structures, although photomicrographs and x-ray data showed that each form of the alloy contained small amounts of a second phase, which was found to be α-Zr in the as-rolled alloy but was not identified in the annealed alloy.

[1] Note that ref. (8) uses an earlier system of naming the phases. The nomenclature used in this report is the one in general use now.
[2] Material supplied by Westinghouse Atomic Power Division.

Experimental

Oxidation Procedure

The rate of oxidation of the alloy in dry oxygen at 1 atm pressure was measured over the temperature range 200°-500°C. Test specimens were heated in a furnace in a slow stream of oxygen; periodically they were cooled and weighed on a microbalance. In this procedure, oxidized specimens were subjected to cyclic thermal stresses, so that the results may not be strictly applicable to conditions of uninterrupted heating.

The oxidizing furnace, shown schematically in Fig. 1, was simply a tube of Pyrex glass, 54 mm ID, with a heater wound over a 30-cm length at the constricted end. In an attempt to achieve a region of uniform temperature at the center of the furnace, the hot zone was surrounded by reflecting Al surfaces. A layer of Al foil covered the glass surface under the heater and around the constricted end of the tube. A perforated Al disk served as reflector at the other end of the furnace. The heating element was a Nichrome ribbon wound over a layer of asbestos and covered with asbestos tape. A stabilized voltage, which could be set at any desired value up to 130 v, provided a constant heat input to the heater. With this arrangement, a given setting of the applied voltage yielded constant furnace tempera-

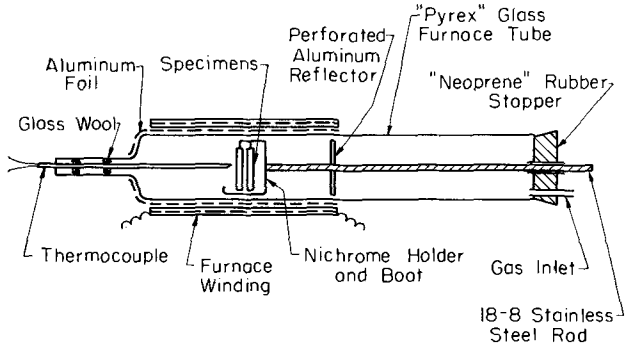

Fig. 1. Schematic diagram of oxidizing furnace

ture to ±3°C, and no change of setting was required for many hours. A Chromel-Alumel thermocouple, situated near the center of the furnace and attached to a recorder, provided continuous temperature-time records.

Test specimens of the alloy sheet were 3 cm x 2 cm in size. To each was attached a Pt hook for handling. Four such specimens, two of as-rolled material and two of annealed, were generally used for each run. They were hung from a Nichrome rod over a Nichrome boat designed to catch any oxide that spalled off during oxidation. (Actually no spalling was ever observed.) When this assembly was pushed into the hot zone, the four specimens were symmetrically situated around the center of the furnace. The temperature variation over the region occupied by the specimens was found to be approximately ±1°C.

The following procedure was used for each period of oxidation. The flow of oxygen through the furnace tube was maintained constant at 0.5 liter/min. Specimens were placed in the cold zone until the hot zone was at a predetermined temperature (10°-15° lower than the desired value). After the specimens were moved into the hot zone, the temperature as indicated by the thermocouple rose to within 3°C of the nominal value in 5 min and to the nominal value within another 10 min. The oxidation period was computed from the moment that the specimens were placed in the hot zone, although an unmeasured interval of time is required to bring the test specimens up to temperature. After the desired oxidation time, the reaction was quenched by moving the specimens to the cold zone and quickly switching the gas flow from oxygen to argon at 2 liters/min.

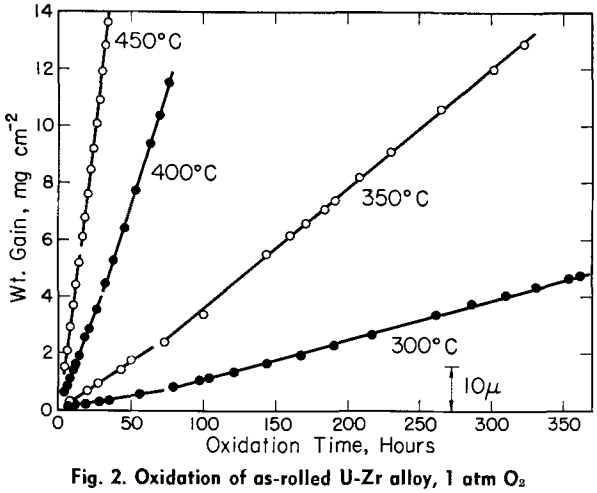

Fig. 2. Oxidation of as-rolled U-Zr alloy, 1 atm O_2

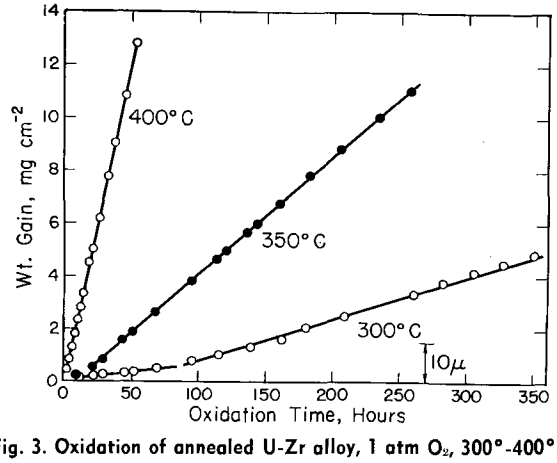

Fig. 3. Oxidation of annealed U-Zr alloy, 1 atm O_2, 300°-400°C

Materials

The alloy analyzed 49.7 ± 0.2% U and 50.1 ± 0.3% Zr. The oxygen content was 0.07%, as determined by the vacuum-fusion method using a Pt bath. The Hf content was estimated to be less than 0.005%, based on analyses of constituent metals. Spectrographic analysis indicated the presence of the following impurities (%):

$$Si < 0.07,\ Mn < 0.03,\ Fe < 0.01.$$

Forty-five other elements specifically sought were not detected spectrographically.

Test specimens were polished to a 4/0 finish using polishing paper wet with purified kerosene, then wiped with petroleum ether, and washed in redistilled acetone. The effects of variations in surface preparation were not studied, since oxidation rates after the formation of relatively thick oxide layers were the primary concern of this study.

The oxygen used was commercial 99.5+% grade, which was dried by passage through a column of $Mg(ClO_4)_2$.

Results and Discussion

Oxidation Rates

Fig. 2-5 show oxidation data obtained over the temperature range 300°-500°C. Each point on the

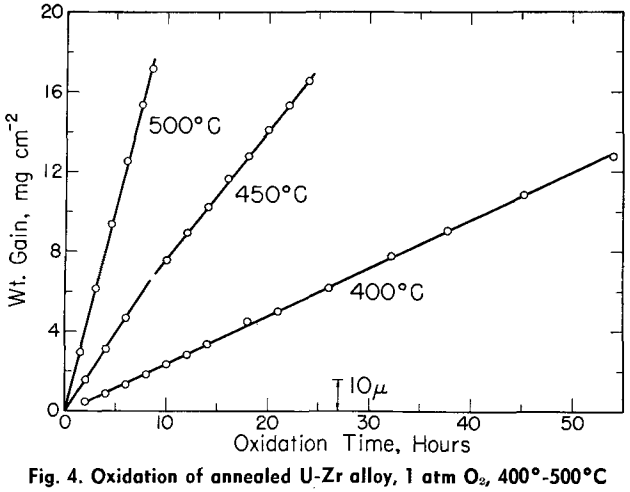

Fig. 4. Oxidation of annealed U-Zr alloy, 1 atm O_2, 400°-500°C

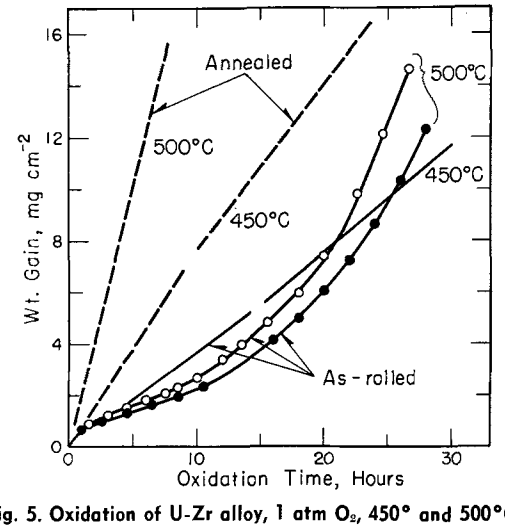

Fig. 5. Oxidation of U-Zr alloy, 1 atm O_2, 450° and 500°C

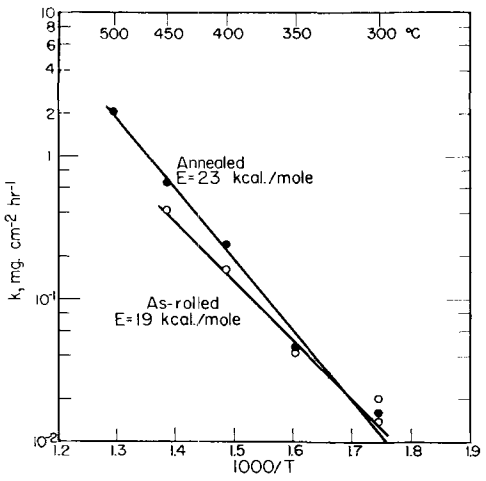

Fig. 6. Oxidation of U-Zr alloy; variation of linear rate constant k with temperature.

curves represents the average weight gain of duplicate specimens oxidized simultaneously. Duplicate specimens always yielded the same general shape of curve, but the individual weight gain varied from the average value by as much as 15%.

In general the 50% alloy, whether as-rolled or annealed, oxidized according to the linear rate law, $w = kt$ + constant. However, a change in the rate constant k, particularly with the as-rolled material (Fig. 2), sometimes occurred after the oxide had grown to an appreciable thickness. Where such a change was found, the linear portions of the curve were drawn with a break near the intersection, merely to accentuate the change in slope. Sharp discontinuities apparently did not occur. The bend in the oxidation curve was toward higher rates in all cases except one (annealed alloy at 450°C, Fig. 4).

The annealed material followed the linear law over the entire temperature range 300°-500°C (Fig. 3 and 4). The as-rolled material oxidized linearly between 300° and 450°C, but not at 500°C. Fig. 5 shows two curves obtained at 500°C in separate runs. Each curve represents average measurements on duplicate specimens oxidized simultaneously. The two curves are far from coincident, but have the same general shape. It is noteworthy that the as-rolled alloy at 500°C oxidized initially more slowly than it did at 450°C. At 400°C and above the annealed alloy reacted considerably faster than the as-rolled.

Linear rate constants, obtained from the final straight-line portions of the oxidation curves, are listed in Table I. They are plotted as log k vs. $1/T$ in Fig. 6. Each plot appears to be linear, although

TABLE I. Linear rate constant, k, as a function of temperature

Temp, °C		k, mg cm^{-2} hr^{-1} As-rolled	Annealed
300	(a)	0.014*	0.016
	(b)	0.020*	
350		0.042	0.046
400		0.16	0.24
450		0.42	0.64
500		—	2.05
E, kcal/mole		19.	23.

* Two separate runs. Each value of k is the average for duplicate specimens. Only run (a) is shown in Fig. 2.

the values of k at 300°C tend to be relatively high and less reproducible. The activation energy E for the oxidation reaction, calculated from the Arrhenius, equation is 23 kcal/mole for the stable ϵ-phase (annealed), and 4 kcal/mole lower for the supposedly unstable γ-phase (as-rolled). Transformation of the latter to epsilon would be expected to occur at an appreciable rate at 500°C, and this may have been a contributing factor in the nonlinear oxidation curve exhibited by the as-rolled material at 500°C.

Oxidation runs on the as-rolled alloy were made also at 200° and 250°C, for periods of 192 and 274 hr, respectively, but these were of a preliminary nature only. The procedure differed from that later standardized (described above) only in the use of an ordinary analytical balance for weighing; hence weight gains were less accurately determined. Nevertheless the oxidation curves obtained were roughly parabolic. Rate constants k_p are compared below with parabolic constants reported for Zr at these temperatures (3):

	k_p, (mg cm^{-2})^2 hr^{-1} 200°C	250°C
50% U-Zr, as-rolled	$3. \times 10^{-5}$	$18. \times 10^{-5}$
Zr	0.38×10^{-5}	3.0×10^{-5} (258°C)

Thus the alloy reacts with oxygen somewhat more rapidly than does Zr at these temperatures. In comparison with U, however, it reacts much more slowly (1, 2).

Oxide Layer

The chemical composition of the surface oxide[3] produced during the oxidation runs was found to be practically independent of the material oxidized (annealed or as-rolled) and of the temperature of oxidation. All analyses were within the range:

U — 40.8 ± 0.8% by wt
Zr — 37.6 ± 0.4 by wt
O — 21.6 by wt (by difference)

The U/Zr weight ratio in the oxide, 1.08, was greater than that in the alloy, 0.99, hence some preferential migration of U into the oxide layer had occurred.

The density of the oxide at 30°C, as measured pycnometrically by water displacement, was found to be 7.6 g/cc. The thickness of the oxide layer corresponding to a given oxygen uptake can be calculated from the density and composition of the oxide. The thickness scale shown in Fig. 2-4 was obtained in this way. It was found, however, that thickness values measured from metallographic cross sections averaged about 20% greater than those calculated, indicating a porous oxide.

The density of the original alloy, measured pycnometrically, was found to be 9.8 g/cc. From the chemical composition and density of the alloy and its oxide, the volume ratio (low temperature) was calculated to be:

[3] In the analytical procedure used, the oxide layer was separated mechanically and fused with potassium bisulfate. The fused material was dissolved in acid, and Zr precipitated as the phosphate. The latter was fused with sodium carbonate, dissolved in acid, precipitated with ammonia, ignited, and weighed as ZrO_2. U in the first filtrate was precipitated as the phosphate on neutralizing, then ignited and weighed as uranyl pyrophosphate, $(UO_2)_2P_2O_7$.

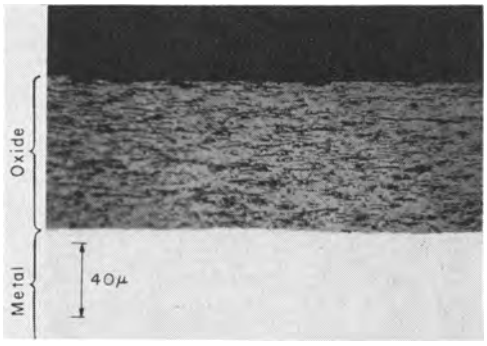

Fig. 7. Cross section of oxide layer produced on as-rolled 50% U-Zr alloy after 76.5 hr at 400°C in oxygen at 1 atm pressure.

$$\frac{\text{volume of oxide produced}}{\text{volume of metal reacted}} = 1.6$$

This ratio is much greater than unity; therefore, according to Pilling and Bedworth (12, 13), shrinkage of the oxide during its formation to yield a cracked layer would not be expected.

A polished cross section of the oxidized alloy is shown in Fig. 7. The oxide is seen to contain relatively large voids. The thick oxides produced over the temperature range 300°-500°C, whether on the as-rolled or the annealed alloy, all exhibited the same type of voids. The latter are elongated in a direction parallel to the oxide-metal interface, indicating periodic formation of blisters at the interface during the growth of the oxide (14). In no case was any transition layer observed at the oxide-metal interface.

As discussed in detail by Evans (14), blistering which forms voids large enough to admit oxygen leads to a linear oxidation curve. On this basis, the bending of a linear curve toward a higher rate of reaction, as was obtained in several cases above, can be explained qualitatively as resulting from an increase in the rate of blistering. Similarly, a decrease in rate constant, which was observed in one case, indicates a slowing down of the blistering process. Some variation in the average size and concentration of voids in the oxide was observed from specimen to specimen, but no correlation was apparent either with temperature or with the initial state of the alloy.

The annealed alloy oxidized to a uniform surface, whereas the as-rolled material exhibited small white spots on the oxidized surface. The white spots began to appear while the oxide layer was still relatively thin, and were grouped along rolling lines. They were similar in appearance to the white particles of ZrO_2 which have been observed in this laboratory on oxidized Zr.

Examination of the bulk oxide scale from the alloy specimens by x-ray diffraction, however, did not reveal the presence of ZrO_2. Diffraction patterns of all oxides produced over range 300°-500°C, with one exception, showed essentially the same lines, and hence indicated the same structure. The lines were too diffuse, however, to permit accurate indexing. Only the oxide produced on the as-rolled material at 500°C gave a different x-ray pattern, and the latter was also too diffuse to permit elucidation of the structure.

Acknowledgment

Data and advice from Dr. R. J. Ruka (x-ray diffraction), J. F. Reed (chemical analysis), and R. L. Anderson (metallography), aided materially in the interpretation of this work.

Manuscript received July 9, 1956. This paper was prepared for delivery before the Cleveland Meeting, Sept. 30 to Oct. 4, 1956.

Any discussion of this paper will appear in a Discussion Section to be published in the December 1957 JOURNAL.

REFERENCES

1. J. Loriers, *Compt. rend.*, **234**, 91 (1952).
2. D. Cubicciotti, *J. Am. Chem. Soc.*, **74**, 1079 (1952).
3. E. A. Gulbransen and K. F. Andrew, *J. Metals*, **185**, 515 (1949).
4. D. Cubicciotti, *J. Am. Chem. Soc.*, **72**, 4138 (1950).
5. J. Belle and M. W. Mallett, *This Journal*, **101**, 339 (1954).
6. E. A. Gulbransen and K. F. Andrew, "Oxidation of Zirconium between 400° and 800°C," paper submitted to *J. Metals*.
7. D. Summers-Smith, *J. Inst. Metals*, **83**, 277 (1955).
8. B. Lustman and F. Kerze, Jr., editors, "The Metallurgy of Zirconium," p. 477, McGraw-Hill Book Co., Inc., New York (1955).
9. A. G. Knapton, Discussion in *J. Inst. Metals*, **83**, 598 (1955).
10. A. N. Holden and W. E. Seymour, Preprint #101, A.I.M.M.E., Nuclear Engineering and Science Congress, Cleveland, Dec. 1955.
11. R. P. Larsen, *et al.*, Argonne Natl. Lab. Report ANL-5135, July 1954.
12. N. B. Pilling and R. E. Bedworth, *J. Inst. Metals*, **29**, 529 (1923).
13. O. Kubaschewski and B. E. Hopkins, "Oxidation of Metals and Alloys," p. 14, Academic Press Inc., New York (1953).
14. U. R. Evans, *Trans. Electrochem. Soc.*, **91**, 547 (1947).

Silicon Diffused Junction "Avalanche" Diodes

H. S. Veloric and K. D. Smith

Bell Telephone Laboratories, Inc., Murray Hill, New Jersey

ABSTRACT

Silicon N+, P, P+ diffused junction diodes have been made by diffusion of B and P into p-type Si. Units have been fabricated with breakdown voltages from 6 to greater than 200 v, with areas from 5×10^{-3} cm^2 to 5 cm^2. Design problems associated with high and low voltage diodes are discussed.

Reverse saturation currents at half the breakdown voltage are often in the order of 10^{-6} amp/cm^2. Impedance after breakdown is shown to be a function of the breakdown voltage and the magnitude of the avalanche current. The cut-off frequency is in the order of one megacycle, and is shown to increase with decreasing transition region capacitance. Some units with areas of 5×10^{-2} cm^2 have been operated at power levels of 10 w, with special provision for heat dissipation.

The diffusion technique for introducing impurities into semiconductors (1) has been shown to be a feasible method of producing large area p-n junctions or ohmic contacts in Si. This technology has been used to develop a family of diodes for various applications. A series of "avalanche" or voltage limiting diodes are considered in this paper. These diodes are characterized by rather high surge capability, low impedance in the breakdown region, and moderately low saturation currents.

Representative diffusion and fabrication techniques are described in the first sections of the paper; this material is followed by discussion of device characteristics. Of particular interest are the impedance before and after breakdown, temperature coefficient of voltage in the breakdown region, surge capability, and barrier capacitance. Reliability of these devices under various environmental conditions is being studied.

Diffusion of Phosphorus and Boron

If the diffusant is deposited, and serves as an infinite source, then the resulting added impurity distribution in the Si is given by

$$C = C_o \operatorname{erfc} \frac{x}{\sqrt{4Dt}} \qquad \text{(I)}$$

where C is the concentration at distance x below the surface, C_o is the surface concentration, D is the diffusion constant, and t is the time of diffusion. The indication is that, if elements in the third or fifth column of the periodic table are considered as diffusants for Si, then the surface concentration and diffusion constant decrease with increasing atomic weight (2). The high surface concentrations of B and P result in degenerate surfaces which facilitate low resistance ohmic contacts to the diode. High surface concentration is also necessary to convert low resistivity material.

For an error function impurity distribution, at some depth x_j the concentration of added donors equals the original acceptor concentration. Here the Si changes conductivity type, resulting in a p-n junction. The concentration gradient, a, at the junction is

$$a = \left.\frac{dc}{dx}\right|_{x=x_j} = \frac{-C_o}{\sqrt{\pi Dt}} \exp \frac{-x_j^2}{4Dt} \qquad \text{(II)}$$

The breakdown voltage (3), V_b, in a diffused junction may be increased by increasing the diffusion depth (4), thereby decreasing the impurity gradient. For a given diffusant

$$\frac{V_b}{V_{bo}} = \left(\frac{Dt}{D_o t_o}\right)^{1/4}_{\rho=k} = \left(\frac{x_j}{x_{jo}}\right)^{1/2}_{\rho=k} \qquad \text{(III)}$$

where ρ is the resistivity of the starting material, and the subscript o refers to a reference diffusion. For the devices reported here, P is used for the rectifying junction and B for the ohmic contact for diffusion into p-type silicon.

Fabrication

The preparation requires a number of sequential steps which are not inherently difficult. The most critical operations may be carried out on a number of Si slices at one time; each such slice may be used for the fabrication of a large number of device elements. The required Si raw material characteristics depend on the device performance objectives established. A particular breakdown voltage is feasible with a certain range of Si resistivity and diffusion program. Other fabrication details may remain essentially the same for a number of related device designs.

As an example, suppose it is desired to prepare single junction voltage reference diodes, having breakdown voltage near 20 v, using single-crystal p-type Si as the raw material. As noted in Fig. 1 the net acceptor concentration in the Si must be such as to make the resistivity lie in the general range 0.02-0.15 ohm-cm if a reasonable diffusion program is to be used. Thus, the first step in the preparation is to secure sufficient usable material, slice and lap it into 10 mil slices, and to measure the resistivity of these slices in order that the diffusion program may be determined.

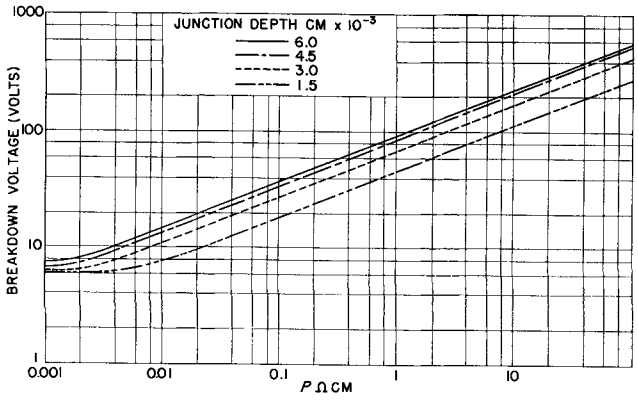

Fig. 1. Breakdown voltage for P diffused *p*-type Si as a function of resistivity and junction depth.

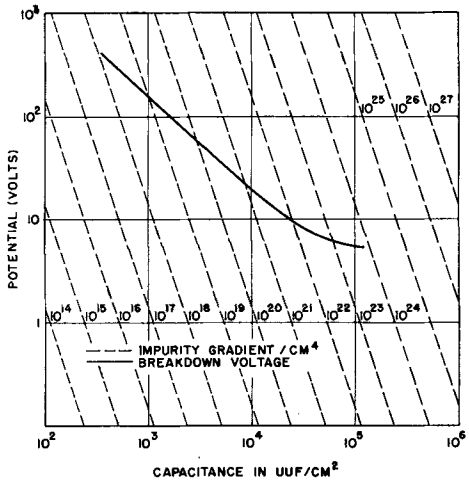

Fig. 2. Relationship for a Si *P-N* junction between impurity gradient, capacitance, and potential.

Diffusion operations are carried out in a quartz tube, in the temperature range 1100°-1350°C. Si slices are exposed to a gaseous environment by standing them on edge in small slots in a quartz boat which is placed in the hot zone of the globar furnace. The diffusant source, in the first case P_2O_5, is located in the quartz furnace tube on the inlet side, at a temperature of about 200°C. Dry N gas is flowed over the P_2O_5 and the Si during the run; this carries sufficient P_2O_5 vapor into the diffusion zone to provide P atoms in high concentration at the Si surface. A high surface concentration of the diffusant is necessary for diode devices, to permit very low resistance electrical contacts to be made. The above procedure results in P surface concentrations in the range 10^{21}-10^{22} at./cm^3, thus the surface is degenerate.

After the P diffusion the *p*-type Si slices have a thin *n*-layer all over their exposed surfaces. To prepare single junction reference diodes, the *n*-layer is lapped off one side of each slice, which is then treated at the diffusion temperature in an atmosphere containing a small concentration of BCl_3 gas. BCl_3 reacts with the exposed Si, depositing B. This second diffusion step may be carried out at a lower temperature or for a shorter time than the initial diffusion, since only a thin *p*-layer is required to obtain low contact resistance to the Si body. Contact resistances of 10^{-3} ohm are achieved for areas of 1 cm^2, by application of an electroless nickel plating (5). The plating is subsequently fired for a few minutes in a N atmosphere at a temperature in the 800°-900°C range. After this firing or sintering operation, a second electroless Ni plating is given to facilitate later soldering operations.

Up to this stage in the fabrication, operations are carried out on a group of whole Si slices, of any convenient size or shape. These slices must now be cut into smaller elements before assembly into devices. The sub-assembly is then mounted in a suitable package, which is flushed with an inert gas, and hermetically sealed.

Where appreciable power is to be dissipated, care must be exercised in the design to keep the thermal impedance between the *p-n* junction and external heat sink low. With an element area of 5×10^{-2} cm^2, mounted directly to a Cu stud, it is not difficult to keep the internal temperature rise below 2°C/w dissipated. The means for external cooling depend on the particular installation.

Design Considerations

Fig. 1 indicates that it is possible to predict the breakdown voltage of a diffused junction in the range from 5 to 1000 v. Fig. 2 shows[1] that for one junction impurity gradient there is one breakdown voltage. The error in predicting the breakdown voltage is the error in predicting the impurity gradient from the measured impurity concentration in the Si and the selected diffusion parameters. Previous work (4) shows that in the range of 10-100 v the mean value of the breakdown voltage of a large group of units can be predicted to within 2%.

Certain design problems are encountered with units intended for voltage limiting applications below 9 v. In this range the ionization rate of electron-hole pairs (3) increases slowly as the field in the barrier region increases. Fig. 2 shows that in this low voltage range the field at breakdown increases rapidly with decreasing breakdown voltage. The maximum field in a diode which breaks down at 4 v has been calculated to be greater than 10^6 v/cm. At these high fields mechanisms other than avalanche also play a role in the breakdown process (6). In Fig. 1 the breakdown voltage levels off in the range near 5 v. The picture is further complicated by the "soft" breakdown characteristics obtained in these low voltage diodes.

In Fig. 3 a plot of the I-V characteristics is given for several typical diffused junction diodes with cross-sectional area in the order of 10^{-2} cm^2. Two low voltage diodes are shown which have impurity gradients[2] in the order of 10^{24} and 5×10^{23}, respectively. Diffused junction diodes which pass 100 ma at less than 8 v reverse bias are characterized by the "S" shaped curve observed in Fig. 3. It may be noted from Fig. 2 that the breakdown voltage in this range is not very sensitive to variation in the impurity gradient.

The units with breakdown voltages above 10 v have saturation currents less than 10^{-6}Å at low volt-

[1] The relation between "avalanche" breakdown, impurity gradient, and breakdown voltage was calculated from unpublished data supplied by K. G. McKay.

[2] These values were calculated with C. S. Fuller's data (2).

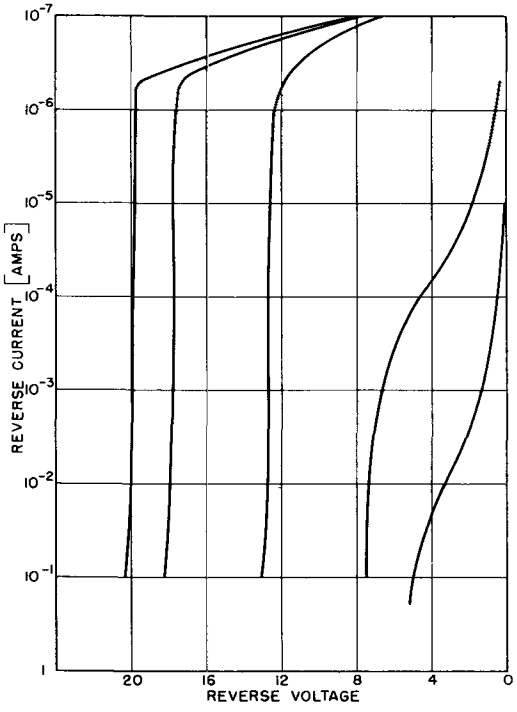

Fig. 3. Current-voltage characteristics of some typical diodes

age and at avalanche breakdown the voltage changes less than 0.5 v for a current change of several decades. In the current range of 10^{-1} to 10^{-2}Å series resistance and thermal effects cause a somewhat larger voltage change.

The prediction of breakdown voltage above 100 v is a more difficult problem. In the derivation of Eq. (III) the diffused impurity gradient at the junction was assumed to be linear over the width of the space charge (4) region. In a p-n junction where the depletion layer extends beyond the graded region, the electrical characteristics will approach those of a "step" junction rather than a linear graded one.

Some information on conditions in the space charge region can be obtained by measurements of barrier capacitance at different barrier bias potentials. In plotting log $(V_A + V_i)$ vs. log C, a relation $VC^{n=k}$ would be obtained, where V_A is the applied voltage, V_i is the internal or "built in" barrier voltage, C is the capacitance, and n is a constant. For a linear graded junction, $n = 3$; a step junction, $n = 2$. In Fig. 4, log-log plots of V vs. C are given for several diodes with junction depths in the order of 2.5×10^{-3} cm. It is noted that n is in the range from 2.8 to 3.0 for diodes with V_b less than 60 v. For the 150-v units $n \doteq 2.7$ at low bias, but decreases as the applied voltage is increased. For higher breakdown voltage, barrier conditions approximate those for a step junction at high reverse bias, and the observed value (7) of n is as low as 2.2. The extrapolation to 500 v in Fig. 1 is therefore not strictly justified.

Attempts to use Fig. 1 to predict breakdown voltage for diodes in the range 150-200 v, or higher, gave erratic results. Departures in the order 15% from the predicted values were observed. Further experimentation showed that if Si containing the order of 10^{15} acceptors/cm^3 was heated in the range 1200°-1300°C, relatively large changes in resistivity

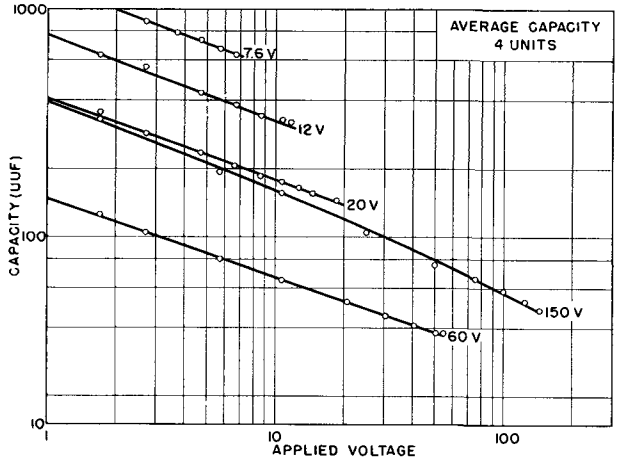

Fig. 4. Depletion layer capacitance of diffused junction diodes

resulted. These changes were unpredictable, and the amount of change varied from crystal to crystal.

In Table I some of the observed resistivity changes are listed. It is interesting to note that use of resistivity values after heat treatment for prediction of breakdown voltage gives better correlation than if the initial resistivities are used. The largest resistivity changes are observed for resistivities above 15 ohm-cm.

Electrical Characteristics

The diffused junction Si avalanche diodes show promise of extensive application as voltage control and surge protection devices. Of particular interest are the low effective impedance in the breakdown condition, and the power handling capabilities. Some other characteristics which have been evaluated are the temperature coefficient of the breakdown voltage, frequency limitations, and some preliminary aging data.

The current-voltage characteristics of a diffused junction diode depend on the internal atomic structure, surface conditions, and the junction area. P-N junction theory (8) predicts reverse saturation current at room temperature in the order of 10^{11} amp/cm^2. This value should be independent of applied reverse bias until the field becomes sufficient to result in avalanche multiplication. In a typical diode

TABLE I. Some thermally induced resistivity variations

	Crystal #	Starting ρ (Ω cm)	(1) After heat treatment ρ (Ω cm)	V_b (Observed) v	(2) V_b (Calculated)
# 1	A–380	11.5	11.5	190	200
	A–320	10.6	8.8	185	185
	314	10.	15.	215	230
	314	7.8	8.1	195	175
	Si IV–378	8.7	8.4	180	180
	Si IV–378	8.7	13.1	185–195	210
# 6	Si A–102	6.2	8.8	135–140	160
	Si A–102	6.2	9.1	145	160
	Si A–102	6.1	7.3		
	Si V–1392	6.6	46.2	180–190	300
	Si V–1392	6.4	35.1	180	290
	Si V–1392	6.9	21.7		

(1) Si was heated in N_2 at 1200° for 16 hr.
(2) The breakdown voltage was calculated from the heat treated resistivity using Fig. 1. P_2O_5 was diffused at 1225° for 16 hr in lot 1 and at 1200° for 16 hr in lot 6.

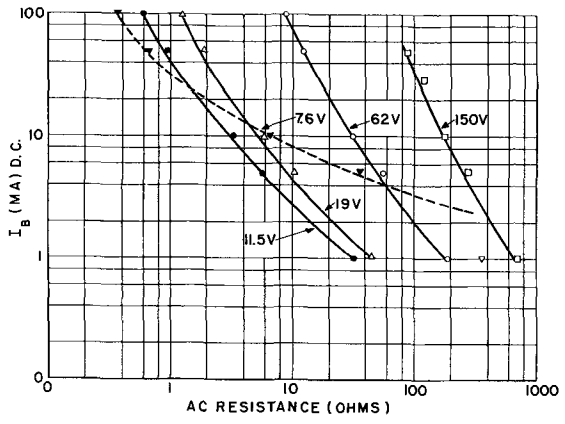

Fig. 5. Impedance in the breakdown region as a function of current

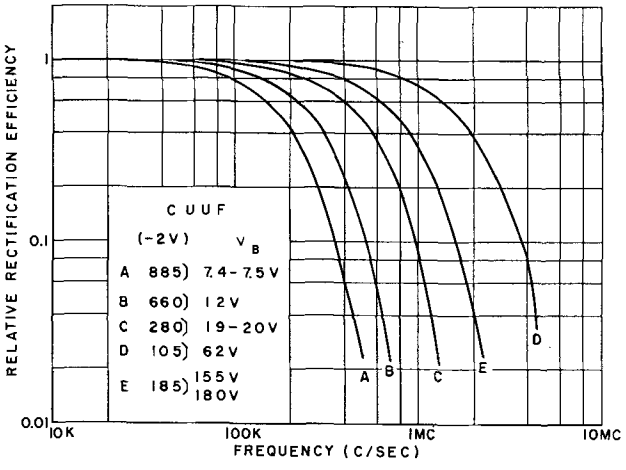

Fig. 6. Frequency response of diffused diodes as low voltage rectifiers.

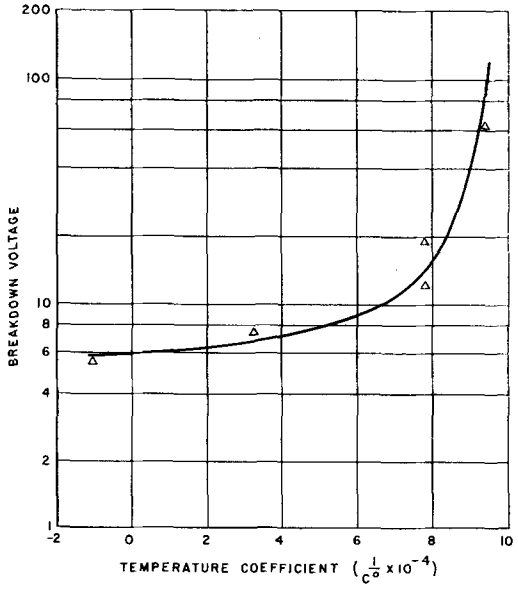

Fig. 7. Temperature coefficient of breakdown voltage vs. voltage

the observed reverse current is many orders of magnitude greater than the predicted saturation current and increases slightly with increasing bias. Diodes with breakdown voltages less than about 7 v exhibit large reverse currents which increase rapidly as the breakdown voltage is approached. This characteristic varies considerably from diode to diode. For all breakdown voltages the transition from high impedance before breakdown to low impedance in the breakdown region is more gradual than predicted by multiplication theory (9) from the low voltage saturation current. Typical current-voltage curves for several diodes are shown in Fig. 3. The forward characteristics of the diodes are as would be expected for a Si p-n junction device, if the body resistance is included in the calculation. The body resistance term becomes small for the lower voltage diodes made of very low resistivity material; forward currents in the order of 1 amp at 1 v forward bias are commonly observed for diodes with breakdown in the 10-20 v range.

The impedance in the breakdown region is a function of the diode structure and the avalanche breakdown current. Impedance at the onset of breakdown is very large; at very high current densities this reduces to a value approaching the body resistance. McKay's breakdown mechanism (10) describes the current as being transmitted by 50-80 μa pulse increments carried in a small spot in the junction. This mechanism would predict a high impedance for a small number of pulses; the impedance should decrease as additional pulses are turned on. For extremely high current densities, such as a pulse of 10^4 amp/cm^2, essentially the entire diode is turned on and only the body resistance is observed. Fig. 5 is a plot of the low frequency a-c resistance in the breakdown region for various breakdown voltages as a function of reverse current. The resistance values were obtained by superimposing a small a-c signal on an adjustable d-c bias current, and measuring the a-c potential across the diode.

The high barrier capacitance associated with large area low voltage breakdown diodes restricts their application to some extent. In Fig. 6 a plot of the rectified a-c current as a function of frequency for several diffused junction diodes, the frequency cutoffs (output D.C. down 3 DB) are observed to be proportional to the transition region capacitance. Curves A, B, C, and D in Fig. 6 are for a series of diodes of approximately 10^{-2} cm^2 area; curve E is for a power diode of about 5×10^{-2} cm^2 area. The location of the response curves along the frequency axis in a plot such as Fig. 6 depends on the load resistance, each curve shifts to a higher frequency if the load resistance is reduced.

Pearson and Sawyer (11) have shown that for certain Si step junctions the breakdown voltage varies linearly with temperature between —196° and 25°C, or

$$V_{B(T)} = V_{B(T_0)} [1 + \beta (T - T_0)] \qquad \text{(IV)}$$

where $V_{B(T_0)}$ is the breakdown voltage at a reference temperature, and $V_{B(T)}$ is the breakdown voltage at any temperature T. The equation for the temperature dependence of breakdown voltage in a diffused junction has been observed (6) to have the same linear variation. An analysis for diodes of various breakdown voltages in the range —90°-150°C is in qualitative agreement with this picture. Fig. 7 is a plot of the temperature coefficient vs. breakdown voltage. Diodes having substantially zero temperature coefficient of breakdown may be fabricated in the 6 v region.

At this stage in the development it is not possible to make accurate estimates of reliability or life expectancy for the diffused junction avalanche diodes. On the basis of information obtained so far, the following summary statements appear reasonable: *(a)* with present technology, reliable high performance Si junction devices must be hermetically sealed; *(b)* a long life is to be expected if a sufficient heat sink is provided to keep the junction temperature at a reasonable value. Several of the units of element size 5×10^{-2} cm^2 have been operating continuously for more than a year without significant deterioration, at a power dissipation of 10 w. These units were provided with a heat dissipation fin to hold the junction temperature below 100°C.

Conclusion

The gaseous diffusion technique has been used to fabricate a family of avalanche Si diodes with a wide range of breakdown voltage and of junction areas. These diodes have application as voltage regulation or control devices, as voltage reference elements, or in signal circuits as surge protective elements. The impedance of these devices is lower, and the power capability higher, than have been available previously.

Several design and fabrication problems are simplified by use of the diffusion technology: the junction depth may be controlled within 3×10^{-4} cm; the breakdown voltage for a particular Si resistivity can be controlled over a moderate range, by adjustment of the diffusion program; the same fabrication techniques may be used for a wide range of junction areas and device properties; the more critical operations may be carried out on large slices of Si, which are later cut as desired into small elements for device fabrication.

Acknowledgments

It is evident that this work has been made possible only through the cooperative efforts of a number of individuals. In addition to the specific footnote acknowledgments the authors wish to thank T. J. Vasko who obtained all the data on device characteristics, D. W. Bodle for his unpublished data on surge properties of diodes, S. L. Miller, A. Uhlir, and M. B. Prince for many stimulating discussions concerning the theory. The method of presenting the data in Fig. 2 was suggested by C. H. Knowles.

Manuscript received June 13, 1956. This paper was prepared for delivery before the San Francisco Meeting, April 29 to May 3, 1956.

Any discussion of this paper will appear in a Discussion Section to be published in the December 1957 JOURNAL.

REFERENCES

1. G. L. Pearson and C. S. Fuller, *Proc. I.R.E.*, **42**, 760 (1954).
2. C. S. Fuller and M. Tannenbaum, I.R.E. Semiconductor Device Conference, Philadelphia, June 1955.
3. K. G. McKay, *Phys. Rev.*, **94**, 877 (1954).
4. H. S. Veloric, M. B. Prince, M. J. Eder, *J. Applied Phys.*, **27**, 895 (1956).
5. M. V. Sullivan, *This Journal*, **104**, 226 (1957).
6. K. G. McKay and K. B. McAfee, *Phys. Rev.*, **91**, 1079 (1953).
7. M. B. Prince, *Bell System Tech. J.*, **35**, 661 (1956).
8. W. Shockley, *ibid.*, **28**, 435 (1949).
9. S. L. Miller and J. J. Ebers, *ibid.*, **34**, 883 (1955).
10. K. G. McKay, *Phys. Rev.*, **94**, 877 (1954).
11. G. L. Pearson and B. Sawyer, *Proc. I.R.E.*, **40**, 1348 (1952).

Electroless Nickel Plating for Making Ohmic Contacts to Silicon

Miles V. Sullivan and John H. Eigler

Bell Telephone Laboratories, Inc., Murray Hill, New Jersey

ABSTRACT

A technique is described whereby an adherent plate of nickel may be deposited on silicon for use as an electrical contact. The contact may be used on either *n*- or *p*-type silicon.

The use of Si in semiconductor devices is growing very rapidly and each device requires at least two electrical connections to the Si. It has not been possible to make simple reliable soft-solder connections directly to Si as was done in the case of Ge. As a result quite a number of different types of contacts have been devised for use on Si each having certain advantages and certain disadvantages. No one contact, however, has been entirely satisfactory, and the final choice by the device engineer has been a compromise.

Some of the most successful contacts to Si depend on alloying the contact metal with the Si. Some of the metals used for this alloying are Ag, Ni, Al, and Au. All of these are sufficiently soluble in Si to alloy quite deeply. This solubility is a disadvantage when one desires to control closely the depth of penetration of the surface contact metal. Also the resulting alloys are rather brittle and the over-all mechanical properties of the contacts may not be as good as desired. The use of Pb at alloying temperatures under 1000°C avoids both of these difficulties.

Because of its limited solubility in Si the depth of alloying is quite shallow (1), and because of the soft nature of unalloyed Pb there is a minimum of mechanical difficulties.

Although alloy-type contacts are extremely useful, they usually involve high fabricating temperatures which in turn generally result in a loss of the minority charge carrier lifetime of the Si. For some applications this degradation of lifetime is undesirable. Of the various methods studied for making contact at low temperature, an electroless nickel plating appears to be outstanding from both a mechanical and an electrical standpoint.

The method of applying electroless Ni is based on a technique developed by Brenner (2, 3). It involves the catalytic reduction of Ni in a system which is also liberating H. A number of companies have made limited commercial applications of this plating process. The scope of some of these applications and an evaluation of the electroless process has also been reported (4-6). It is believed that the present application to Si is new.

Plating

The reaction is catalytically controlled, and since one product of the reaction, namely, the Ni, catalyzes the reaction, the plate continues to build up indefinitely as long as the temperature, and the supply of appropriate ions are maintained. This is in contrast to a displacement type plating which stops as soon as the base metal is covered by the plate.

Detailed discussion of the various plating bath compositions and general operating features may be obtained from Brenner's articles (2-4). The composition of the plating bath which was used in the present work was as follows:

Nickel chloride ($NiCl_2$ $6H_2O$)	30 g/l
Sodium hypophosphite (NaH_2PO_2 H_2O)	10 g/l
Ammonium citrate [$(NH_4)_2HC_6H_5O_7$]	65 g/l
Ammonium chloride (NH_4Cl)	50 g/l

Solution was filtered

Ammonium hydroxide (NH_4OH) was added until the solution turned from green to blue (*p*H 8-10).

This solution keeps indefinitely at room or elevated temperatures. When used for plating, the solution becomes depleted in Ni, hypophosphite, and hydroxyl ions. The only addition recommended for laboratory work, however, is that of ammonium hydroxide in sufficient quantity to maintain the blue color. This addition is more necessary in systems like an open beaker where ammonia is lost to the atmosphere.

The hot (90°-100°C) alkaline plating bath with a rapid evolution of H exhibits an excellent cleaning power, and in many cases no special cleaning of the Si is necessary to obtain an adherent Ni plate. In order to make all of the data consistent and reproducible, however, Si was cleaned in the following manner. Surfaces reported as "polished" were mechanically polished with various grades of abrasives ending with 0.1 μ Al_2O_3, and were given a chemical etch (HNO_3, 44%; HF, 18%; H_2O, 38%). Specimens were stored in this condition. Immediately prior to plating the specimens were given a 10-sec dip in HF (48%) and a thorough rinsing in water. Specimens reported as "lapped" were lapped with 600 mesh Carborundum and scrubbed clean with detergent (sodium hexametaphosphate) and water. Immediately prior to plating these specimens were dipped for 3-5 min in boiling NaOH (5%) and rinsed thoroughly with water. A few experiments were performed in which room temperature HF (48%) was substituted for the hot NaOH with no apparent difference in results.

At a temperature of 95°±2°C the Ni plate thickness as a function of plating time was determined and is shown in Fig. 1. (Plating rate increases at higher temperatures and decreases at lower temperatures.) A fresh plating bath containing about 35 cc of plating solution for each square centimeter of Si surface was used for each sample. The initial rate appears to be about 0.02 mm Ni/hr but after about one-half hour the rate drops to about 0.005 mm/hr. This is in reasonably good agreement with the value of 0.008 mm/hr reported by Brenner. Data were taken on lapped Si surfaces; the rate appears to be almost identical, however, on polished surfaces.

The high initial deposition rate has not been explained. Although Ni would be expected to displacement plate on the Si, the high initial deposition rate cannot be attributed entirely to displacement, since other base metals, including Ni itself, cause a high initial deposition rate. Since the high initial rate is observed when plating on any one of several base metals, one immediately considers the bath and its composition as a function of plating time. It is known that a certain ratio of Ni to hypophosphite ion is most efficient (7) and it is possible that in use the bath is departing from this optimum ratio.

Results

A semi-quantitative evaluation of the adhesion of the electroless Ni to Si was made by measuring the

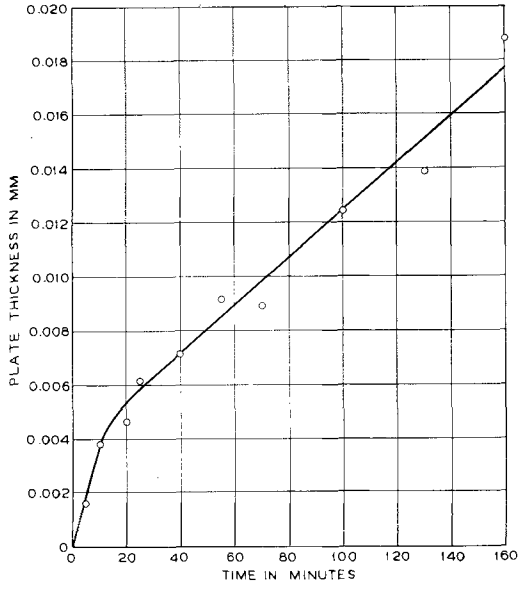

Fig. 1. Thickness of electroless Ni deposits as a function of plating time. The plating rate is about 0.005 mm/hr after the first ½ hr. Each point is one sample. Bath temperature is 95°±2°C.

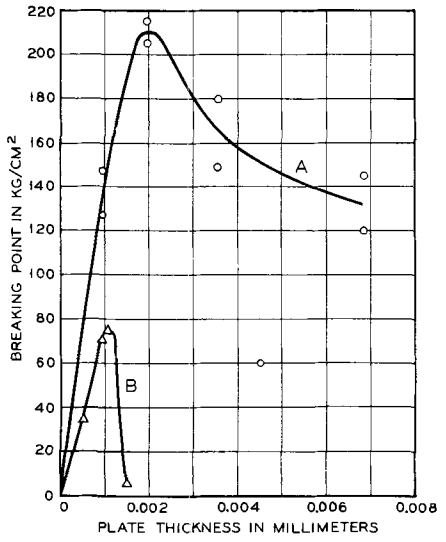

Fig. 2. Adhesion of electroless Ni as a function of plate thickness. Curve A is for a surface which had been lapped with 600 mesh Carborundum and Curve B for a chemically polished surface. Each point is one sample.

force required to pull from the surface a Cu wire that had been soldered to the Ni in the following manner. Tinned copper wire A.W.G. No. 20 was stretched to provide straight sections and was ground flat on one end perpendicular to the axis of the wire. This flat end was butt soldered to the large face of a slice of Ni-plated Si about 0.75 mm thick. A small amount (0.5 mg) of tin-lead solder (50-50) was used so that little or no fillet would be formed and the cross-sectional areas of the bonds would be uniform. Rosin-in-alcohol flux was used.

No heat treatment was given these samples except for the heat involved in the soldering. The force required to pull the wire from the surface was measured with a simple spring-type gauge; the breaking point was then calculated. Fig. 2 shows how this breaking point varied with the thickness of Ni plate. The corresponding deposition times varied from 1 to 30 min. The upper curve is for a surface lapped with 600 mesh Carborundum and the lower curve for a surface which was first mechanically polished (ending with 0.1 μ Al_2O_3) and then chemically polished (HNO_3, 44%; HF, 18%; H_2O, 38%). On lapped surfaces the break was always in the Si. On polished surfaces the separation was predominantly at the Si-Ni interface although small sections of Si were often pulled out. The average area of the break was 1.05 mm² with an average deviation of 15%.

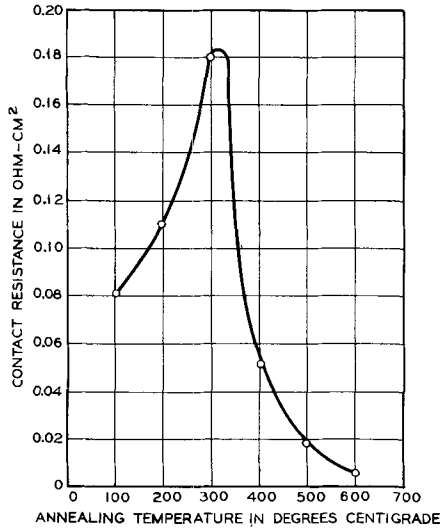

Fig. 3. Contact resistance of electroless Ni on 0.05 ohm-cm *n*-type Si as a function of annealing temperature. Total of 18 samples, 3 for each point.

For these surfaces the optimum adherence was observed for a plate thickness of about 0.002 mm on the lapped surface and 0.001 mm on the polished surface. The increased height of the curve for the lapped surface compared to the height for the polished surface is probably due mainly to the keying action of the surface with the Ni, but it may be due in part to the larger actual surface area involved. The loss of adhesion for thick films is probably due to the increase of internal stress in the Ni with increasing thickness.

The electrical measurements were made by soldering leads to opposite faces of Ni-plated slices of Si about 0.5 mm thick and about 1 cm². The Ni plate was removed from all edges by grinding. The resistance, that is, the d-c voltage divided by the d-c current, was then measured on this specimen. The resistance attributable to the Si itself was calculated from the Si resistivity and subtracted from the measured resistance. The remainder is what is called here the contact resistance and is reported as the number of ohms for a 1 cm² contact.

In view of the fact that the deposited Ni contains phosphorus, one might anticipate doping under some conditions. This means that one might expect to obtain a good ohmic contact to *n*-type Si but a poor, or possibly a rectifying contact, to *p*-type Si if the conditions are such that the phosphorus can diffuse or alloy into the Si.

Contact resistance on 0.05-ohm-cm *n*-type Si is plotted in Fig. 3 as a function of annealing temperature. The samples were annealed for a period of about 1 hr. A second Ni plate was then applied in order to facilitate making the measurements and the contact resistance was measured at room temperature. No significant changes occurred in the Si resistivity. As expected, the contact resistance goes down as a result of high temperature annealing, but the rise in resistance after treatment at intermediate temperatures was not anticipated. The cause of this rise is not known, but it is interesting to note that the peak in the contact-resistance curve occurs in the same range of temperatures that is effective in modifying the hardness of the Ni. As deposited the Ni is quite hard compared to electroplated Ni. On heating at temperatures near 400°C the hardness at first increases, but on heating for longer times or higher temperatures the hardness decreases and the Ni may even become somewhat ductile (4).

With 1-ohm-cm *n*-type Si a similar result is obtained as shown in Curve A of Fig. 4, except that the contact resistance is higher in this case than it was for 0.05-ohm-cm material. In diode fabrication a common technique which is used for improving such a contact is the introduction of a thin layer of highly doped Si between the Ni and the main body of Si. The resistance between a metal and heavily

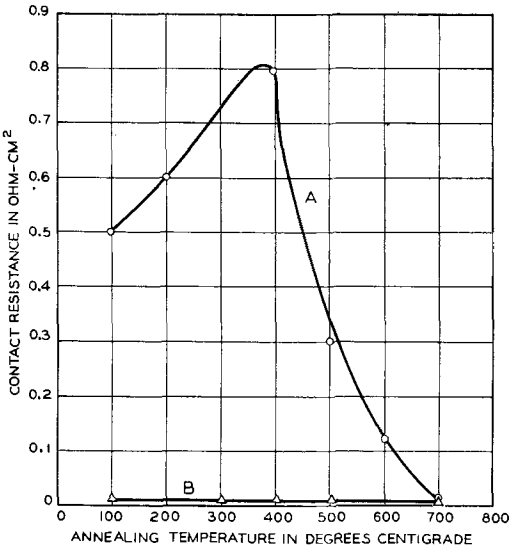

Fig. 4. Curve A, contact resistance of electroless Ni on 1.0 ohm-cm *n*-type Si as a function of annealing temperature. Curve B, similar to Curve A but on material with a diffused *n* layer about 1 mil deep on the 1.0 ohm-cm Si. Total of 22 samples, 2 for each point.

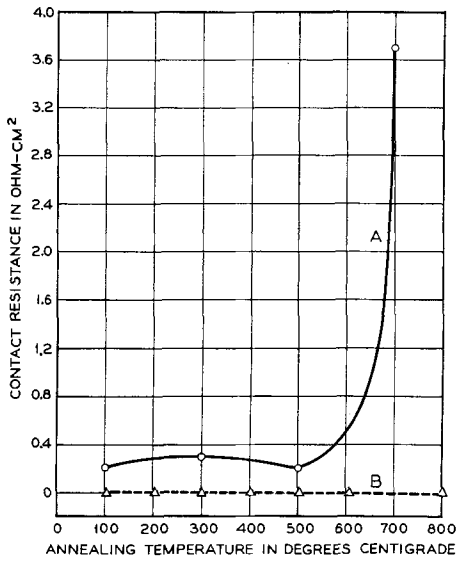

Fig. 6. Curve A, contact resistance of electroless Ni on 1.5 ohm-cm *p*-type Si as a function of annealing temperature. Curve B, similar to Curve A but on material with a diffused *p*-layer about 1 mil on the 1.5 ohm-cm Si. Each point is one sample.

doped (degenerate) *p*- or *n*-type Si is known to be quite low. Such a layer may be formed by diffusing phosphorus from the gaseous phase into the 1-ohm-cm Si to a depth of about 0.01 mm[8]. Curve B shows the resistivity of an electroless Ni contact on such a surface. No peak occurs in the curve.

On *p*-type Si, on the other hand, high temperature annealing causes the contact resistance to become very great and rectification may be observed. Contact resistance on 0.04 ohm-cm *p*-type Si is shown in Fig. 5. It should be noted that for normal temperatures encountered in use, that is 100°-300°C, low contact resistance is obtained. Some simple diodes have been kept on test at 150°C for almost a year with no apparent degradation of the contact.

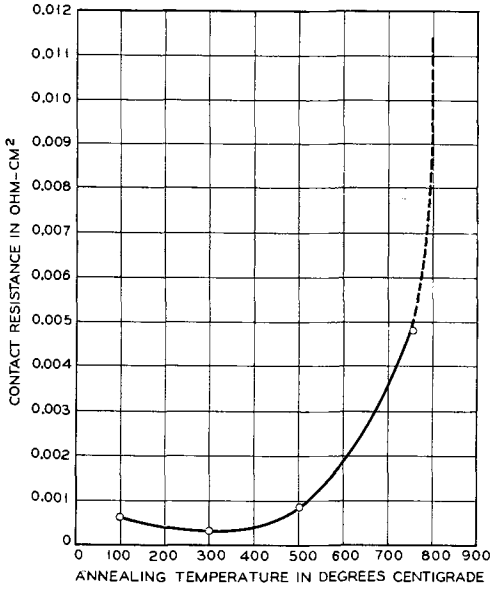

Fig. 5. Contact resistance of electroless Ni on 0.04 ohm-cm p-type Si as a function of annealing temperature. Total of 16 samples, 4 for each point.

On the 1.5 ohm-cm *p*-type Si the resistance was appreciably higher as shown in Curve A of Fig. 6. However, just as in the case of the *n*-type Si in Fig. 4, the contact resistance can be reduced considerably by introducing a thin highly doped layer on the surface of the Si. Curve B shows the resistivity of an electroless Ni contact on such a surface. In this case the doping was obtained by diffusing B into the Si (8).

Some of the properties of electroless Ni have already been mentioned, namely, the hardness of the Ni as deposited, the changes which occur on heat treating, the solderability, and the presence of phosphorus in the Ni. Several other properties are also of interest in connection with the present application. The deposit is fine-grained laminar, bright in appearance and relatively nonporous. Deposition occurs quite uniformly over the exposed semiconductor surfaces, thus eliminating excessive build-up on points and thin deposits on recesses. The magnetic permeability is lower than for pure Ni. This is presumably due to the presence of the phosphorus. It is reported that if the deposit contains as much as 11% phosphorus it is no longer ferromagnetic (7). Electroless Ni may also be used in a similar manner on Ge.

Manuscript received May 9, 1956. This paper was prepared for delivery before the Pittsburgh Meeting, Oct. 9-13, 1955.

Any discussion of this paper will appear in a Discussion Section to be published in the December 1957 JOURNAL.

REFERENCES

1. M. V. Sullivan and J. H. Eigler, *This Journal*, **103**, 218 (1956).
2. A. Brenner and Riddell, Grace, E. J., *Proc. Am. Electroplaters' Soc.*, **33**, 16 (1946).
3. A. Brenner, and Riddell, Grace, E. J., *ibid.*, **34**, 156 (1947).
4. A. Brenner, *Metal Finishing*, **52**, No. 11, 68 (1954).
5. A. Brenner, *ibid.*, **52**, No. 12, 61 (1954).

6. Joseph Haas, *Am. Machinist*, **99**, No. 6, 158 (1955).
7. W. A. Wesley, *Plating*, **37**, No. 7, 732 (1950).
8. C. S. Fuller and J. A. Ditzenberger, *J. Appl. Phys.*, **27**, 544 (1956).
9. P. Baeyens, *Nat. Bur. Standards Circ.* 529, p. 25, May 22, 1953.
10. P. H. Eisenberg, *Plating*, **42**, 1268 (1955).
11. L. Pessel, (RCA) U. S. Pat. 2,430,581.

Anodic Formation of Oxide Films on Silicon

P. F. Schmidt and W. Michel

Research Division, Philco Corporation, Philadelphia, Pennsylvania

ABSTRACT

Dense oxide films have been formed anodically on *p*- and *n*-type single-crystal Si in connection with the electrical properties of Si surfaces. Concentrated HNO_3 or H_3PO_4 permit forming, but the highest voltage obtainable is less than 200 v. A solution of KNO_3 in *N*-methylacetamide permits forming to 560 v, and is also preferable in other respects.

The field during forming is of the order 2.6×10^7 v/cm corresponding to a thickness increment of about 3.8Å/v. The ratio has been found as well from interference colors and direct weighing, as by capacitance measurements. Above an oxide thickness of 400Å the rate-limiting step for film growth is inside the oxide.

The ionic current efficiency of film growth is very low. In methylacetamide it can be increased by addition, for example, of chloride ions or more so by fluoride ions. The oxide is an electrolytic rectifier and behaves similar to an oxide on Al or Ta. The direction of easy flow for electrons is from the Si to the electrolyte.

Anodic formation of dense oxide films and the manufacture of electrolytic rectifiers is well known. The classical work on Al was done by Guenterschulze and Betz (1); in recent years, Van Geel (2-5) and Decker (6), Charlesby (7-11), Young (12), Vermilyea (13-16), Adams, Maraghini, and Van Rysselberghe (17), and Misch and Fisher (18) have published on the anodization of Al, Zr, Ta, and U. An extension of the theory of Mott and Cabrera (19) to include the case of thick oxide films was offered by Dewald (20), who also reported work on indium antimonide (21).

There seems to be only one reference to the formation of dense oxide films on Si, given by Guenterschulze and Betz (1), who mention that incomplete forming[1] can be accomplished in concentrated H_2SO_4.

Experimental

Production of dense oxide films on Si was first tried using concentrated acids and some of the electrolytes commonly used for Al (i.e., borate solutions). Formation in concentrated acids (HNO_3) or (H_3PO_4) proved possible but, as already found (1), forming cannot be continued to high voltages in strong acids because of the large concentration of the acid anion. In ammonium borate a dense oxide of comparatively low resistance was formed; porous oxides were formed in oxalic acid or chromate solutions.

Most of the work reported here has been carried out in *N*-methylacetamide,[2] the *N*-methylacetamide being used without further purification. This solvent was used because of its high dielectric constant, 179. The forming was done in an 0.04*N* solution of potassium nitrate in methylacetamide, the bath being kept at room temperature. *N*-methylformamide also permits forming of Si but not nearly so well as methylacetamide. No particular efforts were made to thermostat the system for reasons made obvious below. Addition of a salt like KNO_3 is necessary in order to increase the conductivity of the electrolyte and in order to supply the oxygen for the anodic reaction. Si will not form in *N*-methylacetamide containing only NaCl; forming starts when nitrate or sulfate ions are added.

The Si used, both *n*- and *p*-type, was of resistivity 2-5 ohm cm, single crystalline, 111 oriented,[3] and had lifetime for minority carriers in the order of 10-20 μ sec. Prior to forming, the Si was etched in a 2:1 HF—HNO_3 mixture and then dried in air.

The method of introduction of the Si sample into the electrolyte must be such as to prevent creep of the electrolyte. One way to accomplish this is first to form the Si to a higher voltage than is reached during the actual experiment, then dissolve the oxide at the part of the wafer farther removed from the base tab, and to use the remaining oxide as a protection for the base tab region. Another method is to immerse the wafer in the electrolyte to the desired depth and to blow a slow stream of air at

[1] *Incomplete forming* means that formation in a given electrolyte cannot be carried to the same voltage, which the concentration of the anion in the solution would permit (e.g., if Ta were to be formed in the same solution), but which the solubility of the oxide does not permit to reach. The true maximum forming voltage depends only on the concentration of the anion, provided that the anion does not contain a heavy metal ion like, e.g. $KMnO_4$, compare (1).

[2] Supplied by Distillation Products, Rochester, N. Y.

[3] No effect of crystal orientation was noticed using a 511 plane instead. We are indebted to Dr. Charles Sutcliffe of our metallurgy group for preparation of the samples.

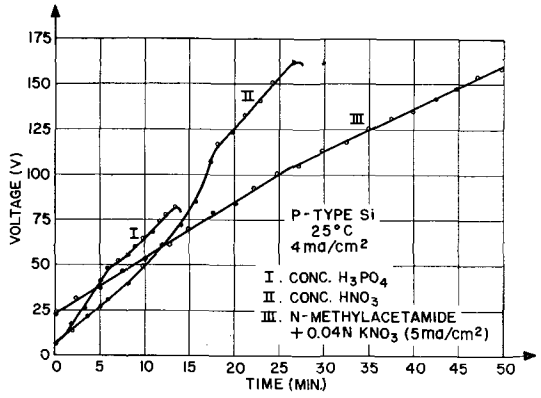

Fig. 1. Forming of p-type Si in different electrolytes

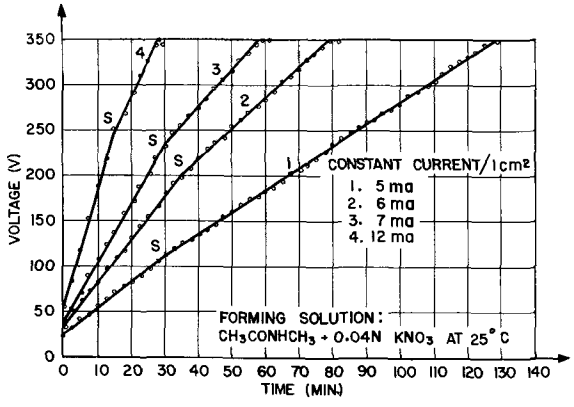

Fig. 2. Forming of p-type Si at different constant current densities

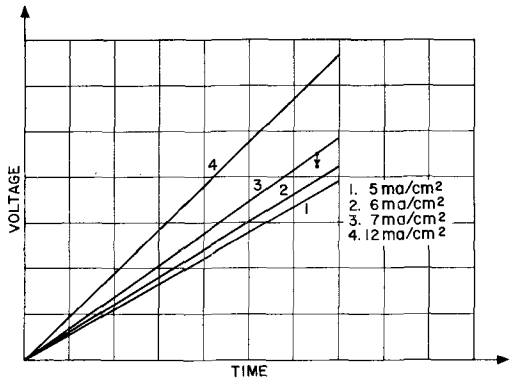

Fig. 3. Replotting curves of Fig. 2 employing a normalized voltage scale.

the rest of the wafer. This method is quite effective against creep of the electrolyte and gives a rather sharply defined area of oxidation. Stop-offs cannot be used at higher voltages because of the very high electrostatic field, which forces the electrolyte underneath the insulation.

Results

Anodic Formation of Oxide Films on p-Silicon

Fig. 1 shows voltage-time curves at constant current density on p-type silicon, formed in concentrated HNO_3, concentrated H_3PO_4, and in *N*-methylacetamide.[4] It is evident that the true maximum forming voltage is not reached in the concentrated acids and that also the voltage-time curve is not nearly so linear as in M.A.

Fig. 2 shows oxidation runs on p-silicon at different current densities. Several points deserve mentioning.

1. The current density is very high compared to the current density usually employed in the investigation of oxide formation on other metals. The reason is that under the given conditions of forming the ionic current efficiency is only about 0.8%, i.e., of a nominal current density of 7 ma/cm², only 54μa are used for oxide growth, the rest is electronic current due to discharge of ions in the electrolyte. Proof of this assertion is offered in the section on oxide thickness determination.

2. Each curve shows a point, marked "S", at which the slope decreases abruptly. This change in slope is well known in the oxidation of other metals, where it is associated with the onset of the so-called "metal sparks". On Si, no sparks were seen at point "S" or in the branch of the curve above it. This may be due to the very low ionic current efficiency or possibly that the light emission occurs only in the ultraviolet. The curves have been idealized in that small oscillations which always occur, particularly above point "S", are not shown. They are caused by the "metal sparks" and become appreciable when the true maximum forming voltage is approached.

3. If anodization at constant current density is continued after the voltage has risen to 350 v, the oxide breaks down; the voltage starts to oscillate without rising any further, while severe damage to the oxide results. This breakdown phenomenon is not shown in the graph.

4. The higher the current density, the steeper the slope of the curve. In Fig. 3 the same curves up to point "S" are plotted again. The value of V_0 (voltage at time = 0) has been subtracted so that all curves start from the origin, and all current densities have been normalized to unity by dividing the ordinate for each curve by the original value of the current density for the given curve. The curve corresponding to the highest current density has the steepest slope. This must mean that the resistance of the oxide deposited at the higher current densities is larger. This larger resistance could be due either to a thicker oxide layer, i.e., a higher current efficiency, or to a higher resistivity of the oxide.

Even after normalizing the voltage ordinate, the curves are, strictly speaking, not yet comparable because it takes a slightly larger voltage to drive a larger current through the same oxide thickness (log I ≈ field).

On curve No. 3 of this figure is shown the reduction in voltage necessary to drop the current from (its actual value of) 7 ma/cm² to 5 ma/cm². This point was obtained experimentally. This factor is not sufficient to make the 7 ma/cm² curve coincide with the 5 ma/cm² curve.

Samples were always prepared in the same manner, i.e., after a cleanup etch in the HNO_3-HF mixture they were carefully washed under running distilled water, dried in warm air, and inserted in the M.A. bath. However, in view of the large effect of

[4] This solvent is hereafter symbolized by M.A.

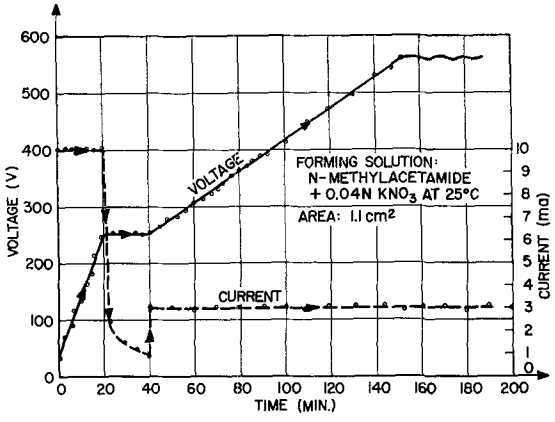

Fig. 4. Forming of *p*-type Si to a maximum voltage of 560 v

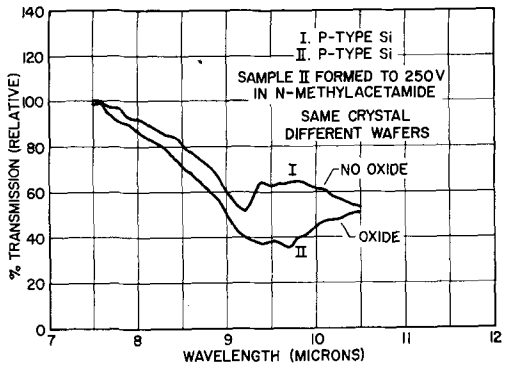

Fig. 5. Infrared absorption of SiO_2 film

fluoride ions on ionic current efficiency, (*see* section on factors influencing the ionic current efficiency) there is a possibility that the rates could be influenced by traces of fluoride having remained on the Si surface. The trend of the curves should not be affected by this.

Measurement of the increases in weight or the changes in interference colors would in principle permit to differentiate between an increase in current efficiency or a change in the nature of the film. On Si, neither of these methods is very sensitive (compare section on oxide thickness determination). However, it is likely that a combination of both effects is involved: on metals like Ta and Al an increase of current efficiency with increasing current density has been reported [*see* e.g. (1) and (8)] and on Zr and Hf formation of low resistance films at very low current densities has also been reported (18).

If a Si sample is held at a constant voltage of 300 v for some time, forming thereafter can be continued up to 560 v. At 560 v bright sparks appear in the solution, the true maximum forming voltage having been reached (*see* Fig. 4).

The slope of the curve after forming at constant voltage is considerably steeper than before, i.e., the ionic current efficiency is higher. For a given increase in forming voltage the increase in thickness is considerably greater than it was before forming at constant voltage as shown by the interference colors. It is likely that forming at constant voltage induces a structural change of the oxide. Vermilyea (16) has reported similar phenomena on Ta.

Determinations of the Oxide Thickness

Thicknesses of oxide films *in situ* can be measured by direct weighing of the sample, by optical methods, and by capacitance measurements.

Weighing.—Direct weighing of *p*-silicon sample before and after anodization gave an average value of about 9 μg of weight increase/cm^2 for each 100 v increase in forming voltage (forming done at a current density of 6.2 ma/cm^2 and the sample then kept at constant voltage for 10 min). This indicates a thickness increment of about 4Å of SiO_2 for 1 v rise in forming voltage. The determination presumes that no SiO_2 is lost by solution in the electrolyte. In view of the fact that only electrolytes with an extremely low dissolving power for the oxide permit obtaining the true maximum forming voltage (as is possible with Si in M.A., although only after forming at constant voltage) this assumption is probably not much in error.

Optical methods—Interference colors and also infrared absorption have been tried to determine the oxide thickness. Fig. 5 gives infrared measurements. In view of the high noise level encountered in these measurements, it has not been attempted to utilize this method for oxide thickness determinations, although this could probably be done.

Interference colors on Si are rather faint; however, by evaporation of a thin Au film (20Å) they can be made to appear quite brilliant. Thickness determinations from interference colors require a knowledge of the refractive index of the film. In order to obtain the refractive index of the film *in situ*, the method indicated by Charlesby (8) has been applied. On Si, the first order blue extends up to 300 v. Above 350 v the thickness voltage relationship valid up to 350 v is lost; consequently, only different shades of blue and a silver-green film (350 v) are available for the determination. Determination of the refractive index in white light gave a value of about 1.5 which is a reasonable value for silica.

For the blue wave lengths a value of $n = 1.55$ was adopted with some degree of arbritrariness for the calculation of the oxide thickness. Using $n = 1.55$ the voltage-thickness relationship as given in Fig. 6 was calculated. The straight line relationship is very gratifying, in view of the many inaccuracies involved. A small negative phase shift can be noted in Fig. 6. Such a negative phase shift of a similar

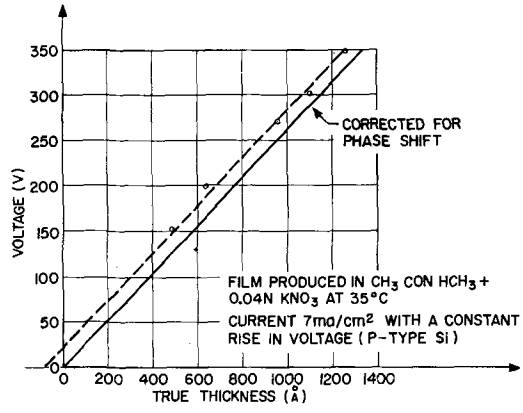

Fig. 6. Voltage vs. thickness plot for SiO_2 assuming $N = 1.55$

magnitude is also observed on Al (1). The thickness-voltage increment from Fig. 6 is 3.8Å/v and checks with the increment found by direct weighing of the sample.

If the charge required for deposition of an oxide film of a given thickness is compared to the total charge passed during anodization (compare Fig. 2) it can be seen that at a current density of 7 ma/cm^2 the ionic current efficiency is only about 0.8%.

Capacitance measurements.—Assuming a surface roughness factor of about 1.5, capacitance measurements of the Si-oxide system yielded the same voltage-thickness increment as obtained from interference colors. Capacitance measurements, however, are not a convenient way of measuring the oxide thickness on a semiconductor like Si, since the capacitance includes also the space charge inside the Si. Capacitance measurements are being made at present with the purpose of investigating the behavior of the barrier inside the Si as a function of oxide thickness, and of investigating space charges inside the oxide according to the methods developed by Van Geel (4, 5).

An exact measurement of oxide thickness would permit establishing the dependence of the ionic current on the electric field strength; present data are not good enough for this purpose. From the ratio of 3.8Å/v it can only be said that fields of the order of 2.6×10^7 v/cm are involved, which is not surprising in view of the great stability of the SiO_2 lattice. It is obvious that a more accurate determination of the thickness-voltage increment could be made either gravimetrically, or by interferometry using monochromatic light, or by use of the polarimetric method developed by Vasicek (22); such was not attempted, however, because other measurements appeared more urgent.

Factors Influencing Ionic Current Efficiency

Addition of small amounts of water to the M.A.-KNO_3 solution increases the forming rate by a factor of about two without apparently effecting the thickness-voltage relationship. The best forming is at 2.5 vol % H_2O. However, the deviation in rate, i.e., the divergence of the voltage-time curves, becomes apparent only after a certain anodization time, e.g., after 2 min at a current density of 10 ma/cm^2. On the other hand, drying of the M.A. with calcined K_2CO_3 does not change the slope of the voltage-time curve.

Fig. 7 shows anodization runs in M.A. + KNO_3 in the presence of chloride ions. A very great increase in ionic current efficiency can be seen, but again it becomes apparent only after a certain time has elapsed. The curves show a slope increasing with time, which can probably be ascribed to a continuous increase in temperature of the oxide layer.

Recent experiments using fluoride ions instead of chloride ions (e.g., a solution of 40 mg KNO_3 and 5 mg NH_4F in 10 cc of M.A.) showed the same effect even more pronounced. The ionic current efficiency increases to above 50%; at the same time the film thickness (for a given forming voltage reached at constant current operation) is reduced to about half of its value in the absence of fluoride ions. It was observed, furthermore, that at constant voltage the film thickness increases quite rapidly.

Tentatively the authors attribute the phenomenon to the incorporation of fluoride ions into the oxide film.

Anodic Oxidation of N-Type Si

The anodic current is in the reverse direction for a barrier on *n*-type Si, consequently, the rate of the anodic oxide growth is limited by the supply of minority carriers, holes, to the Si-oxide interface. Therefore, it is to be expected that the rate of forming is sensitive to minority carrier generation, and that the voltage-time curves on *n*-Si have different shapes in the dark than under illumination. Fig. 8 shows that this is indeed the case. Several peculiarities deserve discussion.

In the dark, the voltage necessary to drive a current of 7 ma/cm^2 is initially about 200 v but drops rapidly to about 100 v, becoming more or less stable at this value until the voltage after about 6 min of anodization again begins to rise linearly with time.

The initial drop from 200 to 100 v cannot be attributed only to excessive power dissipation across

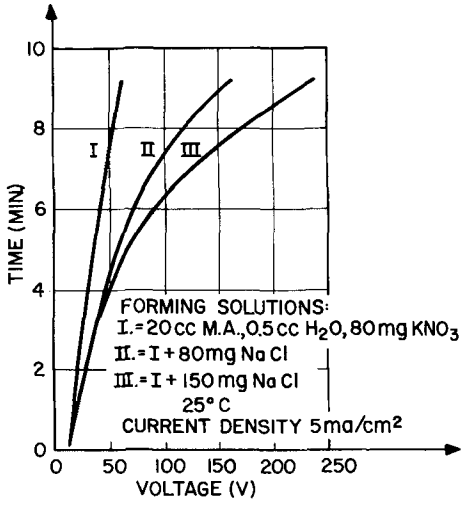

Fig. 7. Forming of *p*-type Si in the presence of chloride ions

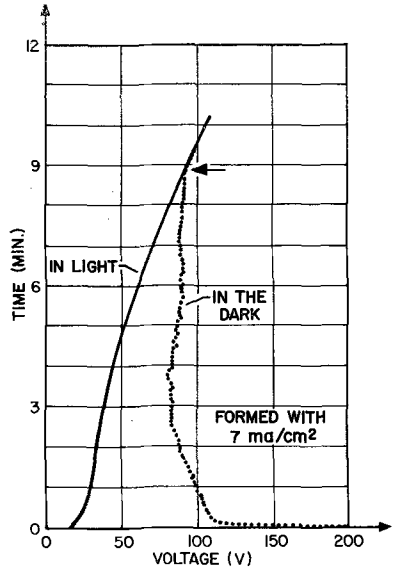

Fig. 8. Forming of *n*-type Si at a constant current density in darkness or under illumination.

the reversely biased n-Si barrier, as can be seen from the following simple experiment. After the voltage has dropped to 100 v forming is discontinued for several minutes; if forming is then resumed at the same current density, the voltage shows no tendency to go much beyond the value at which forming was discontinued.

It would appear that the first layers of oxide deposited decrease the height of the barrier inside the n-type Si.

The curve taken under illumination of the wafer is similar to that on p-Si but is slightly convex to the ordinate. The illumination was rather weak; in strong light the curve would probably straighten out completely.

The following method was used to measure the heat generated by power dissipation across the barrier in the Si. An Al alloyed diode was formed on the reverse side of a wafer to be anodized. The alloyed region was at a distance of 3 mils from the front surface of the wafer. The reverse saturation current of the diode as a function of temperature was measured in a separate run. Monitoring the magnitude of the reverse saturation current of the diode was then used as a measure of the temperature inside the Si during anodization. Only the front surface of the wafer was accessible to the electrolyte, the rest was embedded in plastic.

This measurement indicated that the temperature at a distance of 3 mils from the front surface rose to approximately 65°C within 30 sec of anodization at a current density of 6 ma/cm^2, the bath temperature being 25°C.

Fig. 8 shows that the curves in light and in the dark merge at about 100 v, corresponding on p-Si to an oxide thickness of about 380Å. Above this point anodic oxide growth on n-Si is no longer sensitive to hole injection by light or other means. The oxide thickness on n-Si, when formed under illumination is also about 380Å, as shown by the interference colors. The oxide thickness on a sample anodized in the dark is somewhat larger, because this oxide grew at a higher temperature because of the large power dissipation.

If light is shone onto an n-type Si wafer, anodized in the dark, or, conversely, if illumination of an n-type Si wafer is cut off, the voltage necessary to drive a given current will change sharply. This photosensitivity is lost at an oxide thickness of about 400Å. From there on, the voltage-time curve is a straight line. A thickness of 400Å is reached somewhat sooner in the dark than under illumination, due to the above mentioned heating effect. The dark curve, therefore, becomes linear earlier than the curve taken under illumination. If an n-Si sample is anodized at a constant voltage of less than 100 v (actually 45 v were chosen for this particular experiment), photosensitivity of the anodic current disappears also after some time. Forming under constant voltage should lead to a more ordered structure of the oxide, and thus increase the mean free path of electrons in the oxide. It seems plausible that the loss of photosensitivity is due to collision ionization in the Si by electrons coming out of the oxide at high speeds.

Loss of photosensitivity has a twofold meaning in that it indicates that above about 400Å the rate-determining step for oxide growth occurs inside the oxide, and that the field at the oxide-Si interface (or perhaps the energy dissipation there) is large enough to satisfy the supply of minority carriers for the growth of the oxide.

This assertion can be proved better if anodization is done at constant voltage instead of at constant current. At constant voltage, the current decays to a small value. In the dark, part of the voltage is dropped across the oxide, part across the reversely biased n-Si barrier. If light is now allowed to shine onto the wafer, more of the voltage will be dropped across the oxide; simultaneously, positive ions become available at the oxide-Si interface. A larger current can now flow, which results in an increase in the oxide thickness. When the oxide has reached the thickness corresponding to the given voltage drop the current again decays to a small value. This process is repeatable with successively higher voltages, provided the sample is not kept under constant voltage for any greater length of time, (compare above), but only up to a limiting oxide thickness of about 400Å. Above this thickness the magnitude of the forming current at constant voltage does not depend on illumination or hole injection by other means.

These measurements could mean that above an oxide thickness of about 380Å the barrier inside the n-Si disappears. Fig. 9 shows that this is not the case. The sample was formed to 150 v under illumination, then, without forming at constant voltage, the bias over a period of 80 sec was reduced to zero. During the same time chopped light fell onto the wafer (duration of the light and dark pulse 1.66 sec each). There is a voltage range in which the resistance of the system is photosensitive. The capacitance behaves in the same manner. The higher the voltage, to which the sample had been formed, the narrower the region of photosensitivity (Fig. 10).

Electrolytic Rectification by the Oxide Film

Fig. 11 shows the voltage necessary to drive the same current either anodically or cathodically as a function of time of anodization or oxide thickness. The cathodic curve for p-Si is shown both in the dark and under illumination, as is the anodic curve for n-Si. Since the current densities on Si, Al, and

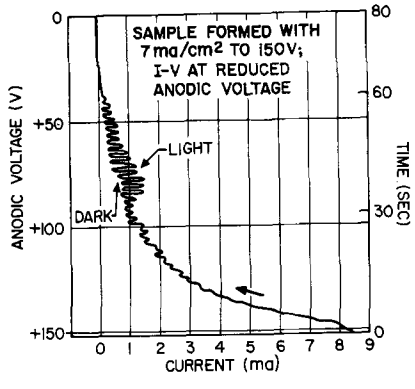

Fig. 9. Photosensitivity of anodic current on n-type Si at reduced voltage. Sample formed to 150 v.

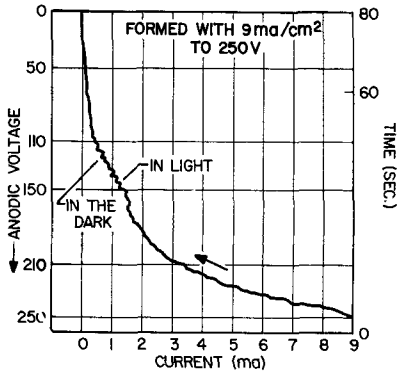

Fig. 10. Photosensitivity of anodic current on *n*-type Si at reduced voltage. Sample formed to 250 v.

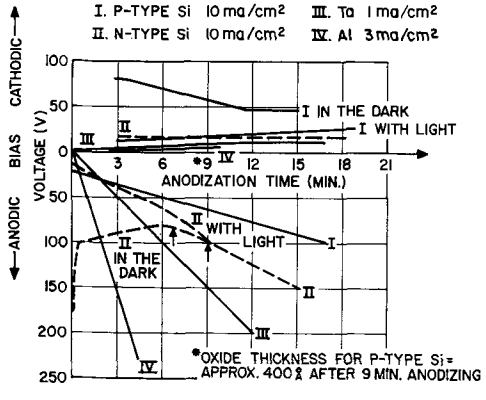

Fig. 11. Rectification by anodically formed oxide films on Si, Ta, and Al.

Ta are different, the anodic curves for the three metals have greatly different slopes.

As can be seen *n*-Si behaves cathodically like Al or Ta. The cathodic curve has hardly any slope at all.

P-type Si under illumination behaves cathodically in the same manner as *n*-Si. In the dark, the cathodic curve shows a peculiar behavior which, as yet, has not been investigated closely. At greater oxide thicknesses the cathodic voltage on *p*-Si is definitely much smaller than the anodic voltage for the same current density.

If a formed *n*-Si wafer is cathodized above a certain critical voltage, about 12-15 v, the current suddenly increases in magnitude. If cathodizing is continued, the oxide is "deformed"; and on switching the current in the anodic direction, the voltage necessary to drive a given current is much smaller than before cathodizing, however, returning to its old value within about 30 sec. Exactly the same phenomenon was reported by Van Geel and Bouma (3) for Al.

Electronic Current Through the Oxide in the Direction of Difficult Flow

Fig. 12 shows the current in the anodic direction on the same *p*-type Si sample, formed to 300 v and then kept at 300 v for 1 hr, 5 hr, 23 hr, and 35 hr. There is, of course, a strong decrease in current during forming at constant voltage.

Vermilyea (14) has reanalyzed Charlesby's (9) data concerning the electronic current through thin

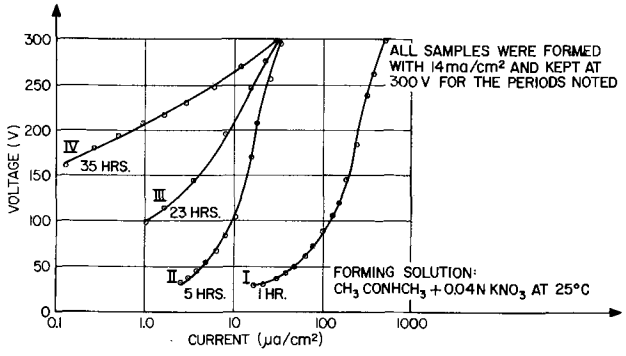

Fig. 12. Electronic current through SiO_2 film on *p*-type Si in the anodic direction after differing forming times.

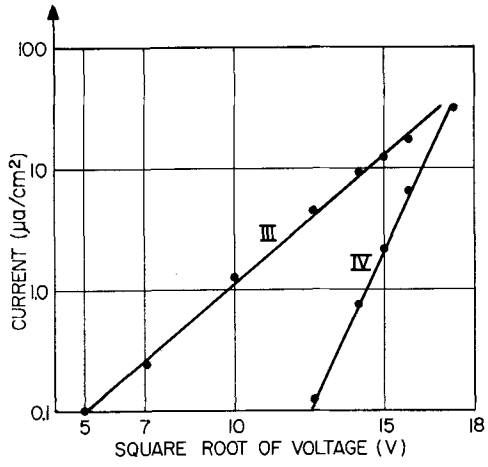

Fig. 13. Replotting of curves III and IV from Fig. 12 according to Vermilyea.

layers of ZrO_2. He suggests a mechanism which yields a linear relationship on plotting log I vs. square root of the voltage. If the same method of plotting current vs. voltage is used for a well-formed *p*-type Si sample, e.g., the ones formed for 23 and 35 hr, a linear relationship results in the voltage range 250-25 v, as shown in Fig. 13.

The longer the time the sample is kept under constant voltage, the larger the range in which the linear relationship holds, and the steeper the slope of the straight line. According to Vermilyea it should be possible to calculate the dielectric constant of the oxide from this slope. There is a strong tendency for the slope to go toward the expected value with increasing time of forming at constant voltage; however, the value for ϵ for the sample formed for 35 hr at 300 v is still too large by a factor of 2.20, assuming $\epsilon = 3.78$ for fused quartz. After forming for 35 hr, part of the oxide became opaque indicating a structural change in the oxide and probably also a change in dielectric constant. Therefore, the experiment was discontinued at this point. Vermilyea's theory does not explain the existence of rectification by the oxide. On the other hand, Schottky (23) has recently considered the possibility of electron tunneling occurring through the whole oxide layer under the influence of the very high electric field in the oxide. This assumption, in conjunction with Vermilyea's derivation, could perhaps explain the I-V characteristic, as well as the existence of rectification. No high barrier would

exist for electrons entering the oxide from the metal side (or the conduction band of the n-Si).

During the 35-hr run it was also observed that the thickness of the oxide had increased by about 30% (this increase in thickness was taken into account when calculating ϵ). This behavior is in sharp contrast to that of oxides on Al or Ta which do not continue to grow under constant voltage. It is surmised that this phenomenon might be connected with the wide spacing of the SiO_2 lattice and with vacancies in the anion lattice which could permit growth of the oxide by outward diffusion of oxygen vacancies.

Rectification of Metal Contacts on Si

The fact that the SiO_2 film is an n-type semiconductor, at least at the oxide-Si interface, raises the question whether or not in the case of metal contacts made to the surface of the semiconductor (24, 25) the very thin oxide film present around and underneath the Si to metal contact influences the rectification behavior.

As was reported by Bornemann (26), low work function metals rectify on p-Si, high work function metals rectify on n-Si, and metals with intermediate work functions rectify on both p- and n-type Si, although to a lesser degree.

The work function picture alone, however, does not suffice for a quantitative explanation. Among other things, the highest barriers on p-Si are higher than the highest barriers on n-Si. It is quite likely that the oxide film has something to do with this behavior.

Gold electrodes have been evaporated onto formed n- and p-type Si, and n-type rectification was found on n-Si, and p-type rectification on p-Si. Normally, as already stated, gold is ohmic on p-Si.

Comparison of Forming in Aqueous Solution and in M.A.

Vermilyea (15) reported that forming of Ta in ethylene glycol solution resulted in the deposition of two different oxide layers, one on top of the other. Except for a greater brilliance of the interference colors obtained in aqueous solution, there appeared to be no difference between Si samples formed to the same voltage in M.A. and in concentrated HNO_3. However, in view of the extreme thinness of the SiO_2 film, small differences in interference colors might be difficult to detect.

In order to check the influence of the M.A. on the oxide film with a more sensitive indicator, Ta was formed both in aqueous KNO_3 solution and in M.A. Except for a greater brilliance of the colors obtained in aqueous solution, no difference in thickness was observable. The thickness of the tantalum oxide film as determined from interference colors agreed with the thickness determination from capacitance measurements.

Forming of Ge *in M.A.*

Both p- and n-type Ge can be formed in M.A. in much the same manner as Si. These measurements are now in progress.

Acknowledgments

The authors wish to acknowledge the helpful discussions and criticisms extended by Dr. E. H. Borneman and Mr. J. F. Walsh. The work described in this paper was supported in part by the Department of Navy, Bureau of Ships, under Contract No. NObsr-64760, Index No. NE-110458-Subtask 3. The authors are grateful to Bureau of Ships for permission to publish.

Manuscript received May 1, 1956. This paper was prepared for delivery before the San Francisco Meeting, April 29 to May 3, 1956.

Any discussion of this paper will appear in a Discussion Section to be published in the December 1957 JOURNAL.

REFERENCES

1. A. Guentherschulze and H. Betz, "Elektrolytkondensatoren," M. Krayn, Berlin (1937).
2. W. Ch. van Geel, *Philips Research Repts.*, **6**, 54 (1951).
3. W. Ch. van Geel and B. C. Bouma, *ibid.*, **6**, 401 (1951).
4. W. Ch. van Geel, *ibid.*, **8**, 47 (1953).
5. W. Ch. van Geel, *Halbleiterprobleme*, **1**, 299 (1954).
6. A. J. Decker, *J. Applied Phys.*, **21**, 708 (1950).
7. A. Charlesby, *Proc. Phys. Soc. (London)*, **66B**, 317 (1953).
8. A. Charlesby, *Acta Metallurgica*, **1**, 340 (1953).
9. A. Charlesby, *ibid.*, **1**, 348 (1953).
10. A. Charlesby, *ibid.*, **2**, 314 (1954).
11. A. Charlesby, *ibid.*, **2**, 668 (1954); **2**, 698 (1954).
12. L. Young, *Trans. Faraday Soc.*, **50**, 153 (1954); **51**, 1250 (1955).
13. D. A. Vermilyea, *Acta Metallurgica*, **1**, 282 (1953).
14. D. A. Vermilyea, *ibid.*, **2**, 346 (1954).
15. D. A. Vermilyea, *ibid.*, **2**, 482 (1954).
16. D. A. Vermilyea, *This Journal*, **102**, 207 (1955).
17. B. Adams, Jr., M. Maraghini, and P. Van Ryssel-berghe, *ibid.*, **102**, 502 (1955).
18. R. D. Misch and E. S. Fisher, *ibid.*, **103**, 153 (1956).
19. N. Cabrera and N. F. Mott, *Repts. Prog. Phys.*, **12**, 163 (1948-9).
20. J. F. Dewald, *This Journal*, **102**, 1 (1955).
21. J. F. Dewald, *ibid.*, **104**, 244 (1957).
22. A. Vasicek, *Czechoslovak J. Physics*, **4**, 204 (1954).
23. W. Schottky, *Halbleiterprobleme*, **2**, 233 (1955).
24. W. E. Bradley, J. Tiley, R. E. Williams, R. Kansas, R. F. Schwarz, J. Walsh, and J. Angell, *Proc. IRE*, **41**, 1702 (1953).
25. E. Bornemann, R. Schwarz, and J. Stickler, *J. Applied Phys.*, **26**, 1021 (1955).
26. E. Bornemann, to be published.

Semiconducting Properties of Some Vanadate Glasses

P. L. Baynton, H. Rawson, and J. E. Stanworth

Research Laboratory, British Thomson-Houston Co. Ltd., Rugby, England

ABSTRACT

Glasses have been made in the systems BaO-V_2O_5-P_2O_5 and Na_2O-BaO-V_2O_5-P_2O_5 with V_2O_5 contents ranging between 50 and 87 mole %. The glasses were found to be semiconductors, those with the highest V_2O_5 contents having a specific conductivity of the order of 10^{-5} ohm^{-1} cm^{-1} at room temperature. The relationship between the specific conductivity, σ, and the temperature was determined, and it was found that the slope of the log $\sigma - 1/T$ plots was equivalent to an activation energy in the range 0.35-0.40 ev for all the glasses. The value of log σ at 25°C plotted against the mole per cent V_2O_5 gave a straight line relationship for each series of glasses. Conductivity values obtained could be easily reproduced and were not sensitive to variations in melting conditions.

The preparation and properties of a number of glasses based on vanadium pentoxide were described in a previous publication (1). It was shown that glasses could be made from certain binary oxide mixtures of V_2O_5 with the oxides P_2O_5, As_2O_3, GeO_2, TeO_2, BaO, and PbO. The V_2O_5 contents of these glasses were quite high; thus, in the V_2O_5-P_2O_5 system, glasses containing as much as 90% of V_2O_5 could be made easily. Measurements of the electrical properties of some of the glasses showed that they were semiconductors; the sign of the thermo-emf was observed for a few of the glasses and it was found that the hot junction was positive for each glass tested, indicating that the glasses are *n*-type semiconductors.

This paper deals with the electrical properties of some of the glasses in more detail.

Preparation of the Glasses

A number of glasses was melted in the system BaO-V_2O_5-P_2O_5 and the compositions, calculated from the compositions of the raw material mixtures and expressed in mole per cent, are shown in Table I. A similar series of glasses in the system Na_2O-BaO-V_2O_5-P_2O_5 was also melted and their compositions are shown in Table II. The glasses of Table I were melted from mixtures of $BaCO_3$, V_2O_5, and P_2O_5; those in Table II were melted from $BaCO_3$, V_2O_5, and commercial meta phosphoric acid which was shown by chemical analysis to contain 17.0% Na_2O.

The glasses were melted in silica crucibles in a nichrome wound furnace at 950°C on a scale sufficient to yield about 20 g of glass. In general, the melts were quite fluid at this temperature and the crucible was agitated frequently during the melting period, so that after about 15 min the melt appeared to be quite homogeneous and free from bubbles. It was then poured into carbon molds to produce cylindrical rods of glass about 1 cm long and 1 cm in diameter.

TABLE I. Composition of the glasses melted in the system BaO-V_2O_5-P_2O_5

Glass No.	Mole percentage composition		
	V_2O_5	P_2O_5	BaO
1	87.5	12.5	—
2	80.0	20.0	—
3	75.0	20.0	5.0
4	70.0	20.0	10.0
5	69.5	22.5	8.0
6	65.0	20.0	15.0
7	62.5	25.0	12.5
8	60.0	20.0	20.0
9	55.0	30.0	15.0

TABLE II. Composition of the glasses melted in the system Na_2O-BaO-V_2O_5-P_2O_5

Glass No.	Mole percentage composition			
	V_2O_5	P_2O_5	BaO	Na_2O
10	83.0	10.0	—	6.5
11	75.2	16.5	—	8.2
12	72.6	17.4	2.3	7.7
13	70.6	16.5	4.7	8.2
14	65.8	16.5	9.4	8.2
15	61.2	16.5	14.1	8.2
16	58.0	20.3	11.6	10.2
17	50.8	24.4	13.9	10.8

As soon as possible after pouring, the molds containing the glass were placed in a muffle furnace and the glass annealed at a temperature in the range 250°-300°, depending on the composition. (Measurements of the thermal expansion of the glasses indicated that their annealing temperatures were within this range of temperature.)

Little volatilization of P_2O_5 occurred during melting, less than 1% in each case tested by analysis. No attack on the silica crucibles could be detected after melting the glasses.

All the glasses were very intensely colored, and appeared black in any thickness other than that of very thin films, the color of these films being dark green.

Several of the glasses were examined by x-ray diffraction methods to test for the presence of crystalline material but none was found.

Techniques Used for Determining the Specific Conductivity of the Glasses

The ends of the cast glass cylinders were ground plane and parallel, and gold contacts were evaporated on to the ground surfaces. The resistance be-

tween the contacts was then measured, using a commercial d-c bridge resistance measuring set.[1] This instrument measures resistances up to 5×10^9 ohm, and the applied voltage varies up to a maximum of 25 v depending on which resistance range is being used. The use of different test voltages raised the question of whether or not the resistance varies with the test voltage. This point was checked by a-c measurements on a very thin sheet (0.020 in. thick) of one of the glasses, the test voltage being applied parallel to the plane of the sheet. An oscilloscope was used to observe the form of the voltage-current curve and no departure from ohmic behavior was observed with fields up to 1500 v/cm.

To reduce surface leakage caused by adsorbed moisture films on the glass surface, samples were maintained at 140°C for 3 hr, after which they were allowed to cool in a desiccator before resistance measurements were made. As the resistances of the glasses were always less than 10^7 ohms, it was considered that the effect of surface leakage on the resistance values obtained would be negligible.

The resistance of the glasses did not appear to be very sensitive to differences in heat treatment and the resistivities of different samples cast from the same melt did not differ by more than 10%, provided that no devitrification had occurred. In cases where devitrification had occurred, the resistance decreased by a factor of ~100.

When measuring the resistances of a few of the specimens, a very slight change of resistance with time was observed. The resistance soon settled down to a steady value, however, which rarely differed by more than 10% from the original value.

Measurements were made at room temperature and various temperatures up to 150°C. The specimen was mounted in a simple holder which provided pressure contacts on to the gold contact films; this was immersed in clean liquid paraffin in a liter beaker. This was slowly heated and the resistance of the samples measured at intervals of approximately 15° during the heating period. A further set of measurements was made on cooling. Values obtained on heating usually were a little higher than those obtained on cooling, but the difference was never more than 10%; in plotting results, average values were used.

Results and Discussion

Crystalline vanadium pentoxide is a semiconducting oxide of the excess metal type. Arsenev and Kurchatov (2) showed that for the particular sample of vanadium pentoxide which they investigated there was a deficiency of oxygen of about 0.1 at. %.

Boros (3) investigated the electrical properties of single crystals of the material and showed that the conductivity was *n*-type. The conductivity varied according to the direction in the crystal in which it was measured, the average value at 20°C being approximately 10^{-3} ohm^{-1} cm^{-1}.

It is clear from the experimental work described in this paper that the vanadate glasses are also semiconductors. This is not a surprising result since Yurkov (4) has already shown that molten V_2O_5 is semiconducting and semiconductivity has also been observed in molten materials by other workers (5-7). Furthermore, both liquid and amorphous selenium are well known for their semiconductor behavior. Thus, it is not necessary for a material to have a regular crystalline structure for it to show semiconductivity.

Fig. 1 shows the relationship between the logarithm of the conductivity (σ) and the reciprocal of the absolute temperature T for a number of glasses in the BaO-V_2O_5-P_2O_5 system. On the same figure is plotted the relationship obtained from measurements on a rod sample of crystalline V_2O_5 produced by pouring the molten material into a carbon mold. It is seen that the slope of the lines is greater for the glasses than it is for the crystalline material. Fig. 2 shows the curves for the Na_2O-BaO-V_2O_5-P_2O_5 glasses.

The equation for plots of this type is usually expressed in the form

$$\sigma = \sigma_0 e^{-E/kT}$$

where σ_0 is a constant for the material, k is Boltzmann's constant, and E is a term having the dimen-

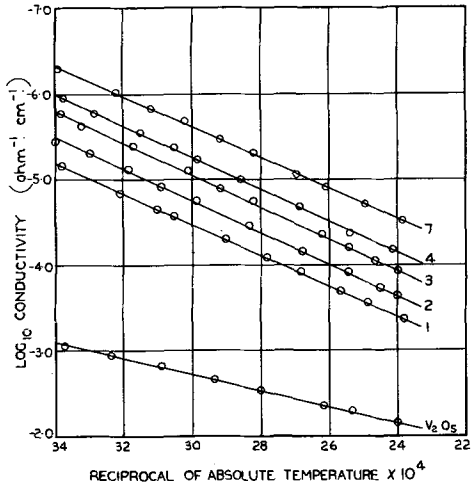

Fig. 1. Relationship between conductivity and temperature for polycrystalline V_2O_5 and glasses in the system BaO-V_2O_5-P_2O_5. (See Table I for compositions).

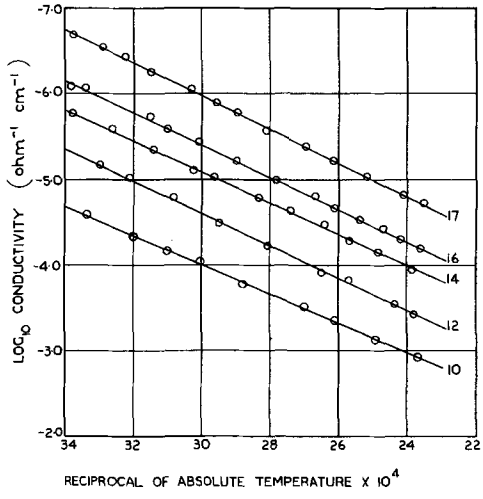

Fig. 2. Relationship between conductivity and temperature for glasses in the system Na_2O-BaO-V_2O_5-P_2O_5. (See Table II for compositions).

[1] A Baldwin "Logohm" meter. Tests had previously been made to assess the magnitude of the contact resistances. They were made on a rod sample onto which gold current and voltage contacts were evaporated. These tests indicated that the contact resistance could be neglected.

TABLE III. Values of E in expression $\sigma = \sigma_0 e^{-E/KT}$ derived from Fig. 1 for BaO-V_2O_5-P_2O_5 glasses

Glass No.	Mole % V_2O_5	E (e.v.)
1	87.5	0.36
2	80.0	0.37
3	75.0	0.37
4	70.0	0.36
7	62.5	0.36

TABLE IV. Values of E in expression $\sigma = \sigma_0 e^{-E/KT}$ derived from Fig. 2 for Na_2O-BaO-V_2O_5-P_2O_5 glasses

Glass No.	Mole % V_2O_5	E (e.v.)
10	83.0	0.34
12	72.6	0.37
13	70.6	0.35
14	65.8	0.35
15	61.2	0.37
16	58.0	0.37
17	50.8	0.39

sions of energy which in semiconductor theory is related to the energy e, necessary to raise an electron from the donor levels to the conduction band. In fact E is equal to e or $e/2$ depending on the proportion of electrons which have been activated to the conduction band (8).

It seems unlikely that in a random structure such as that which exists in a glass there would be a single value of e since each donor center has slightly different surroundings from the rest. The fact that a straight line is obtained when $\log_{10} \sigma$ is plotted against $1/T$ does not necessarily imply that there is a single value of e or that the range of values of e is small. The straight line relationship may still hold over a limited temperature range even when the range of values of e is appreciable, because of the peculiar properties of the e^{-x} function. It appears, however, that the average value of the energy necessary to raise the electrons into the conduction band in the glasses is greater than in crystalline vanadium pentoxide.

Tables III and IV show that the value of E, derived from the slope of the lines in Fig. 1 and 2, remains constant at about 0.36 e.v. over the range of composition studied in both series of glasses. There is evidence that similar barium phosphate glasses containing smaller percentages of V_2O_5 (5-20%) show much smaller conductivities but have greater values of E. Any interpretation of these results can only be conjectural in the absence of knowledge of the structure of vanadate glasses.

Fig. 3 shows that, when the logarithm of the conductivity σ_{25} at 25°C is plotted against the molecular percentage of V_2O_5 in either series of glasses, a straight line is obtained with very little scatter of the experimental points. The general trend of increasing conductivity with increasing V_2O_5 content is of course easy to understand, but the low scatter of the points about the lines is quite remarkable, particularly when one remembers that the BaO/P_2O_5 ratio is not constant throughout the series. This indicates that the conductivity of these glasses is not strongly influenced by factors other than the V_2O_5 content. Conductivity values for a glass of given composition are also easily reproducible, showing that small variations in melting conditions do not greatly influence the conductivity. Even melting under strongly reducing conditions has very little effect. Thus a glass of the composition V_2O_5 87.5%, P_2O_5 12.5% was melted in air at 900°C from a mixture of vanadium pentoxide and red phosphorus. When the melt had become homogeneous it was cast to form rods. The conductivity of these rods was $10^{-4.2}$ ohm^{-1} cm^{-1}. On melting the glass for longer periods of time, the value slowly decreased to $10^{-4.5}$ ohm^{-1} cm^{-1}, only slightly higher than that normally obtained for a glass melted from V_2O_5 and P_2O_5.

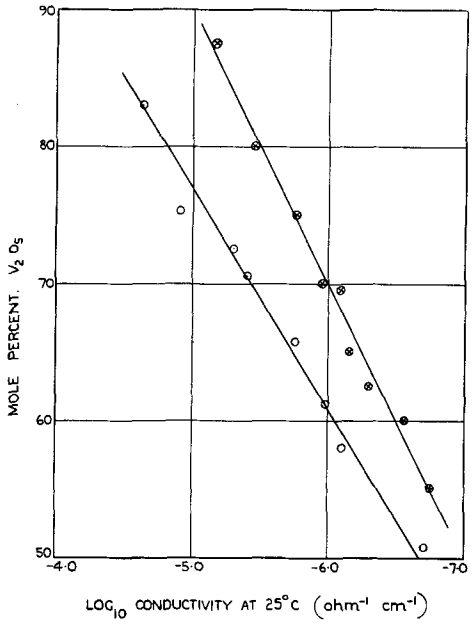

Fig. 3. Relationship between the conductivity and composition of glasses. Cross in open circle—refers to glasses in the system BaO-V_2O_5-P_2O_5; open circle—refers to glasses in the system Na_2O-BaO-V_2O_5-P_2O_5.

Fig. 3 shows that the conductivity of glasses in the system Na_2O-BaO-V_2O_5-P_2O_5 is greater than the conductivity of those in the system BaO-V_2O_5-P_2O_5. This effect of soda of increasing the conductivity is not easy to understand. It is considered most improbable that the effect is due to the transport of Na^+ ions. If this were so, then polarization effects would certainly be apparent during the resistance measurements, but no polarization was observed. Also the magnitude of the difference in conductivity between the two series of glasses is not proportional to the percentage of Na_2O which they contain. It would seem more probable that the introduction of soda into the glass disturbs the balance of the $V^{5+} \rightleftarrows V^{4+}$ equilibrium to an extent which is dependent on the percentage of V_2O_5 present.

Manuscript received June 20, 1955.

Any discussion of this paper will appear in a Discussion Section to be published in the December 1957 JOURNAL.

REFERENCES

1. E. P. Denton, H. Rawson, and J. E. Stanworth, *Nature*, **173**, 1030 (1954).
2. A. Arsenev and B. Kurchatov, *Zhur. Eksptl. Teoret. Fiz.*, Ser. A, **4**, 576 (1934).
3. J. Boros, Z. *Physik*, **126**, 721 (1949).
4. V. Yurkov, *Zhur. Eksptl. Teoret. Fiz.*, **22/2**, 223 (1952).

5. A. Joffe, Jubilee Collection, No. 1, 305, Izv.A.N. M-L (1947).
6. A. Blum, N. Mokrovsky, and A. Regel, *Izvest. Akad. Serja Fiz.*, **16** (2), 139 (1952).
7. N. Mokrovsky and A. Regel, *Zhur. Tekh. Fiz.*, **22**, 1281 (1952).
8. N. F. Mott and R. W. Gurney, "Electronic Processes in Ionic Crystals," p. 156-160, Oxford (1940).

Zone Melting of Uranium

C. I. Whitman, V. Compton, and R. B. Holden

Atomic Energy Division, Sylvania Electric Products Inc., Bayside, New York

ABSTRACT

A study was made of the possible application of the zone melting technique to the separation of uranium from fission products and other impurities. Bar specimens of U having various alloying elements were zone purified in thoria-coated alumina boats. Uranium bars previously irradiated in the Brookhaven pile were also zone melted. Zone melting has potential application in the removal of such impurities as B, Fe, Si, Ni, and Co from ordinary U. In the reprocessing of irradiated U, zone melting offers a method for removing such fission products as Zr, Nb, Ru. However, as employed here, it shows little promise as a method for complete decontamination of irradiated U from fission products, primarily because of concurrent slagging effects.

Zone melting is a purification technique which has been used to prepare very pure Ge metal in which the quantity of impurities present is of the order of parts per billion. The success of this technique with Ge suggested an investigation of its possible application to the purification of U from fission products and other impurities. This report presents the results of such an investigation.

In the zone melting process a narrow molten zone, produced by induction or resistance heating, is made to traverse the solid metal by movement either of the heater or of the metal, as shown in Fig. 1. Since the solubility of an impurity is generally different for solid and liquid, segregation occurs as the solid refreezes at the rear solid-liquid interface. Impurities which are more soluble in the liquid phase tend to concentrate in the molten zone and are carried to one end of the bar. Impurities which are more soluble in the solid phase tend to move to the opposite end, and thus the center portion of the bar is purified. Additional passes in the same direction produce further purification, although eventually an "ultimate distribution" is reached after which additional passes have no effect.

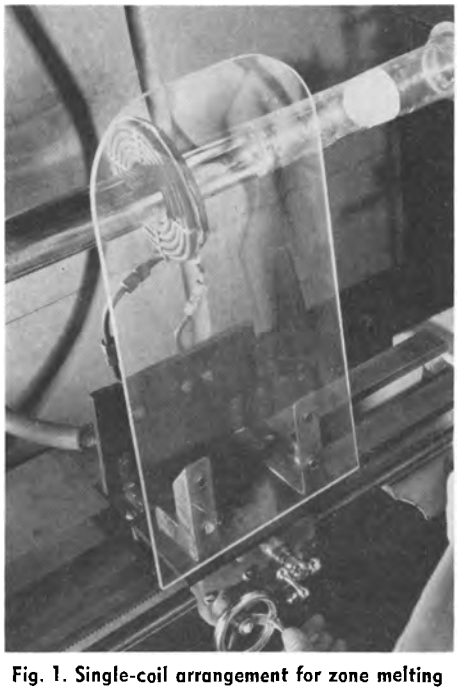

Fig. 1. Single-coil arrangement for zone melting

A measure of the tendency of the impurity to migrate is given by the distribution coefficient k, which is defined as the ratio of the solute concentration in the solid to that in the liquid at equilibrium. The greater the factor by which k differs from unity, the more readily impurities migrate.

A simple theory of zone melting has been developed by Pfann (1), in which it is assumed that solute diffusion in the liquid is sufficiently rapid that the impurity concentration is uniform in the molten zone while diffusion in the solid phase is negligible. From this theory it is possible to calculate the effect of repeated zone passes if the distribution coefficient is known. In practice, one expects less migration than that calculated, because the assumptions of complete equilibrium on which the calculation is based are not strictly true. In any case, the purification attained depends on the number of passes, the ratio of molten zone length to bar length, the equilibrium distribution coefficient k, and the rate of zone travel.

In Table I are given k values for some metals in U, estimated from the particular uranium-metal phase diagrams (2). It should be noted that these k values are at best approximate since generally the phase diagrams have not been accurately determined in the region of low impurity concentration. The theoretical ratio of impurity concentration at the low concentration end of the bar before and after

TABLE I. Distribution coefficients for some metals in uranium

Element	k*	Theoretical concentration ratio† for seven zone passes: [Impurity concentration in purified end after zone melting / Initial impurity concentration]
Fe	0.1	$\sim 10^{-5}$
Mo	1.0	1
Ni	0.03	$<10^{-5}$
Nb	5.0	$<10^{-5}$
Si	0.2	$\sim 10^{-4}$
Sn	1.0	1
Zr	2.0	$\sim 10^{-3}$

* Estimated from available phase diagrams.
† Taken from calculations by I. G. Dillon, kindly furnished by L. Burris and I. G. Dillon of Argonne National Laboratory.

seven zone passes (zone-length to bar-length ratio of 1:10) is also given.

Experimentation

Apparatus

Two types of apparatus were employed in the study; one, used for the most part, in which the coil moved relative to the bar, and one in which the bar was moved.

In the single-coil arrangement shown in Fig. 1, the induction coil was mounted on the travelling carriage of a small lathe bed. The coil was advanced by means of a gear reduced motor connected to a "Zero-Max" adjustable ratio torque converter, which in turn was used to drive the lead screw of the lathe. In this way, rates of molten zone travel of 0-12 in./hr could be obtained. The U was contained in a boat placed within a Vycor tube, approximately 2 in. in diameter, closed at one end. The other end of the tube was connected by means of a 75/50 semi-ball connection to a high vacuum system consisting of a three-stage oil diffusion pump and a mechanical pump. If desired, the zone melting could also be carried out in an inert atmosphere.

The multi-coil apparatus shown in Fig. 2 utilized stationary coils surrounding a Vycor tube. The boat containing the sample was pulled through the coils by means of a Zr wire attached to the rod of a National Research Corp. rotary, push-pull vacuum seal at one end of the Vycor tube. The wire was wound on the rod at an adjustable rate controlled by a variable ratio "Zero-Max" torque converter in a manner similar to the simple coil arrangement discussed previously. The vacuum seal was connected to the glass vacuum system through a metal male ground joint. The other end of the tube was attached by means of a 75/50 semi-ball connection to a high vacuum system similar to the one described previously. This arrangement operated satisfactorily but was developed late in the program and used for only a few runs.

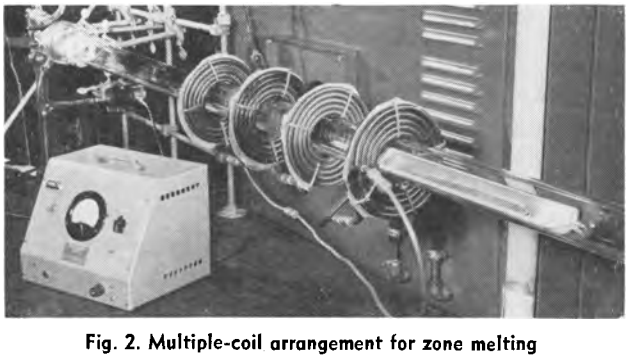

Fig. 2. Multiple-coil arrangement for zone melting

A double pancake-type coil (2¼ in. ID) with a total of ten turns (five for each pancake) of ⅜ in. diameter Cu tubing was used in these studies. Power for the single-coil apparatus was supplied from a Sylvania induction heater with an operating frequency of 400 kc and an output rating of 10 kw. The multi-coil apparatus used a Ther-Monic Generator with a 10 kw output and an operating frequency of 400 kc. Both induction heating units were of the vacuum tube type.

Container Materials for U.—The development of a suitable container material for U proved to be the principal experimental problem encountered. Graphite boats, which were used early in the program, reacted excessively with the U. Stabilized zirconia boats were used next. Although these were sufficiently inert with respect to U attack, they had extremely poor thermal shock resistance under the conditions of zone melting, and as a result cracked frequently in use. Alumina (Norton Co. mixture RA 98) was found to be more resistant to thermal shock and was used subsequently in preference to zirconia.

Alumina boats used to contain the uranium were obtained by cutting furnace tubes (12 in. long, ¾ in. bore) in half length-wise and plugging the ends with alumina disks. A thoria wash, consisting of ThO_2 powder suspended in a nitrocellulose, lacquer (Raffi and Swanson No. 2695) diluted 5-to-1 with *n*-butyl acetate, was applied to the inner surface of the boat and to the end plugs. This served to reduce any attack of alumina by U. Three such coats were usually applied, with drying under an infrared lamp between coats. The boats were then fired at 900°-1000°C to form a loosely adhering protective coating of thoria. The use of higher firing temperatures resulted in a decrease in the thermal shock resistance of the alumina. Boats made in this manner have been used for as many as 20 zone passes without breakage. If this treatment were omitted, the principal effect would be Al pickup by the U.

Prior to use, the alumina boats were outgassed to a vacuum of <0.02 μ by heating a bar of Zr within the boat to approximately 1300°C. The boat containing the U was placed in an outer boat which would prevent U from flowing onto the Vycor tube in case of failure of the inner boat.

Atmosphere.—The uranium alloys used in the study were prepared by powder metallurgy hot-pressing techniques (3). This material contained far more residual gas than the usual vacuum-cast U.

Upon melting of the alloys under vacuum, considerable outgassing occurred, which was sometimes violent enough to spatter U over the interior surface of the Vycor tube. This was avoided by melting under a static atmosphere of 200-300 mm of A.

Zone melting of vacuum-cast U was conducted under a continuous vacuum of $\leqq 0.01$ μ. The resulting bar had a smooth, steel-gray surface (presum-

TABLE II. Representative results

Alloy	Nominal comp. Wt %	No Passes	Speed in./hr	Analysis First to freeze	Analysis Last to freeze	Concentration ratio* Theo.	Concentration ratio* Obs'd
Nb	0.5	7	1	0.59	0.30	10^{-3}	0.6
Zr	0.5	3	2	0.44	0.16†	10^{-2}	0.3
Ru	0.5	8	1	0.5	0.9		
Ni	0.1	4	1	0.065	0.19	10^{-4}	0.65
Fe	0.2	1	2	0.13	0.26	10^{-1}	0.65
Si	0.2	2	4, 2	0.17	0.24	10^{-1}	0.85
Sn	0.5	6	1	0.5	0.6	1.0	1.0

* As defined in Table I.
† Anomalous concentration peak observed.

ably UO) which remained virtually unchanged for weeks.

Zone length.—The boats used varied in length from 6 to 12 in. and in width from ¾ to 1½ in. The boundaries of the molten zone were distinguished by a slight jarring of the apparatus. Experiments in which boats cracked demonstrated that the zone was molten all the way through. Generally, the desired zone length was 1/10 the bar length, but experimentally this was difficult to maintain. Most of the runs were conducted at a constant power input in which the zone length for 10 in. bars varied from ¾ in. in the center portion to 2 in. at the ends of the bar.

In spite of this increased zone length at the ends, it is believed that this procedure is preferable because the frequent manual power adjustment required in attempts to maintain a constant zone length cause a back and forth motion of the liquid-solid interface. This rapid melting and solidifying is not conducive to establishment of the equilibrium impurity distribution between the liquid and the solid.

The increase in zone length at the ends is attributed to heat transfer from the molten zone through the uranium bar in only one direction; whereas in the center portion heat transfer occurs in two directions. In some experiments variation in zone length was corrected by appropriate adjustment of the power input, resulting in a uniform zone length of ¾-1 in.

Results

Zone melting was applied to: binary uranium alloys; vacuum-cast uranium; irradiated uranium, in that order. Suitable experimental procedures were developed simultaneously as the investigation progressed. A rate of zone travel of 1-2 in./hr was eventually adopted as the best for these reasons: *(a)* at faster zone travel rates, separation was poorer; *(b)* while slower rates may have increased separation because of a closer approach to equilibrium conditions, any practical application of zone melting would require a reasonable rate of zone travel for economic reasons; and *(c)* with this rate it was not necessary to allow experiments to run unattended overnight.

Uranium Alloys

The early experimental work was performed with binary uranium alloys using graphite and stabilized zirconia boats. Little migration was observed until the zone travel rate was reduced to 2 in./hr. Representative results are summarized in Table II. Samples about 0.1 in. thick were cut from each end of the bar.

Where comparison is possible with Table I, it is seen that the actually observed differences are, at best, only factors of two or three whereas factors of 10 to 100 and more would be expected from theory. There experiments were the earliest and suffered from experimental difficulties with container materials and outgassing as noted previously. In addition, the zirconia boats available were 6 in. in length and zone lengths at the beginning and end of the runs were as much as 2 in. Problems also arose in the manufacture and analyses of the alloys and were incompletely resolved prior to proceeding to work on vacuum cast uranium. This is especially noticeable in the discrepancies in Table II between the nominal composition and analysis on Zr, Ru, and Sn alloys. For this reason, absolute significance should not be attached to the observed concentration ratios although it is believed they are sufficiently accurate to justify the comparison that has been made with theory. If these experiments were to be repeated, improved results would be expected because of subsequent improvements in container materials, boat length, etc., although it is unlikely that anything resembling the theoretical migration would be attained except with impractically slow rates of zone travel.

Vacuum Cast Uranium

The results of two representative experiments on migration of impurity elements in vacuum cast U are summarized in Table III. In Run 27, seven samples, approximately 0.1 in. in length, were cut from each end of the bar and at approximately 2 in. equally spaced interval along the bar, sample 1 being the first portion to freeze and sample 7 the last. The same applies to Run 34, except that a total of only six samples were taken. The zone travel rate was 2 in./hr in Run 27 and 1 in./hr in Run 34. In this latter run additional metallic impurities[1] were deliberately added to the uranium. The influence of zone travel rate on the extent of migration shows clearly in the comparison of the two runs since greatly enhanced migration is evident for B, Co, Fe, Ni, and Si at the slower zone travel rate of Run 34. Of the remaining elements that were detectable spectrographically, V showed some segregation. Al,

[1] Ag, Al, Co, Cu, Mn, Mo, Ni, Pb, Si, Sn, V, were added.

TABLE III. Effect of zone travel rate on impurity migration.
Run 27 (9 zone passes) @ 2 in./hr

	First to freeze	Direction of zone travel →					Last to freeze
Sample Impurity	1	2	3	4	5	6	7
B	<0.2	<0.2	<0.2	<0.2	0.20	0.22	0.22
Co	—	—	2	5	5	5	7
Cu*	<1	<1	<1	<1	<1	<1	<1
Fe	28	21	29	48	50	63	68
Ni	20	15	20	30	40	40	60
Si	20	20	20	30	20	30	30

All concentrations given in ppm.
* The concentration of Cu prior to zone melting was 10 ppm. The anomalous zone melting behavior may be due to volatility of the Cu during zone melting.

Run 34 (9 zone passes) @ 1 in./hr

	First to freeze	Direction of zone travel →				Last to freeze
Sample Impurity	1	2	3	4	5	6
Al	200	200	200	200	200	200
B	—	—	—	<0.2	0.20	0.41
Co	10	10	30	50	70	150
Cu	1	2	5	5	5	5
Fe	15	15	30	45	70	200
Mg	<5	<5	<5	<5	<5	<5
Mn	5	5	5	5	5	5
Mo	100	100	100	100	100	100
Ni	20	20	30	50	100	200
Si	20	20	50	50	70	200
Sn	50	50	50	50	50	50
V	30	30	30	50	50	50

All concentrations given in ppm.

Mo, and Sn did not segregate and Mg and Mn evidently volatilized in the course of zone melting. While still far less than that expected on the basis of the equilibrium k derived from the phase diagram, migration is sufficiently extensive to suggest the possibility of using zone melting as a method of producing high purity U.

Irradiated Uranium

A bar of U metal, irradiated in the Brookhaven pile at a flux of 10^{13}nv for 55 min followed by approximately 60 days cooling, was subjected to 10 zone passes (ZM-36); the single-coil arrangement was used in these experiments. Autoradiographs were taken and the total radiation level along the length of the bar was measured.

The individual behavior of fission products was not observed but the autoradiographs and counting experiments indicated a definite migration of activity to each end of the bar. Considerable radioactivity concentrated in the surface layer of the U where it could be removed by pickling and a substantial amount also diffused into the alumina boat.

A possible explanation for these qualitative observations is as follows: The activity concentration noted at one end was probably due to Zr and Nb, and that at the other due to Ru since these migrate in opposite directions. The conditions under which the zone melting was carried out are exactly those for a combined oxide slagging and volatilization. As has been determined experimentally (4), the major portion of the fission products, comprising the rare earth, alkali and alkaline earth metals either enter a slag layer, volatilize, or diffuse into the oxide container. The remaining important fission products Zr, Nb, Ru, and Mo are incompletely removed by this oxide slagging and volatilization. Of this group only Mo does not migrate. This suggests that zone melting has potential application for removal of Zr, Nb, and Ru in conjunction with oxide slagging pyroprocessing methods currently being considered for application to certain types of reactor fuels (4) where a high degree of decontamination of the fuel is not required. It should be noted that slagging was not a factor in the experiments reported earlier since only metals more active with regard to oxide formation will enter a slag layer and none of the impurities observed in these experiments were in that classification.

It would be extremely difficult to eliminate slagging completely in zone melting of irradiated U since oxide slag can be formed through interaction with oxygen in the container material, with oxygen traces in the atmosphere and from oxygen originally present in the metal itself.

A high-vacuum floating zone technique (5) using oxygen-free U is a possible approach which might prevent the formation of an oxide skin. It would be interesting to compare the results of floating zone experiments with those in which a ceramic container is used for the U. However, it appears rather unlikely that the floating zone technique is adaptable to processing commercial quantities of U.

When slagging occurs concurrently with zone melting important limitations on the use of zone melting as a reprocessing technique are imposed. A fission product present in a slag skin is in equilibrium with the fission product concentration in the melt and hence acts as a source, resupplying fission product to the melt as rapidly as zone melting might move it away. This fact plus the relatively slow rate of travel of impurities makes it doubtful that zone melting by the techniques developed here could ever effect the degree of decontamination required for direct handling of recovered material.

A report (6) on the zone melting of U appeared when this paper was in review. It is noted that the results obtained in these two entirely independent investigations are quite consistent and in at least qualitative agreement, although a direct comparison is difficult because of substantial differences in the experimental arrangement, concentration ranges studied, and methods of analysis.

Summary and Conclusions

1. Satisfactory apparatus for the zone melting of U has been developed. An alumina boat, coated with a loosely adhering layer of thoria, was the most satisfactory container found for U from the standpoint of inertness and resistance to thermal shock.

2. Migration of B, Fe, Ni, Co, Si, Cu, Zr, Nb, and Ru was observed. No migration was detected for Al, Mg, Mn, Mo, and Sn. It was found that a slow zone

travel rate (~1 in./hr) improved the extent of migration appreciably, presumably because of a closer approach to equilibrium conditions.

3. An autoradiograph of irradiated U subjected to zone melting showed that migration had occurred to each end of the bar. This was attributed to Zr, Nb, and Ru. A considerable amount of activity was found to concentrate in the surface of the bar.

4. Zone melting shows promise as a means of purification of U from traces of such elements as B, Fe, Ni, Co, Si, and Cu, although under the conditions employed the extent of migration was not as extensive as would be expected on the basis of simple zone melting theory.

5. The removal of such elements as Zr, Nb, and Ru is a potential application for zone melting in conjunction with oxide slagging pyroprocessing methods currently under consideration for use with certain types of reactor fuels. However, zone melting, as employed here, shows little promise as a method for complete decontamination of irradiated U from fission products, primarily because of concurrent slagging effects.

Acknowledgment

The assistance of H. R. Mullin of the Atomic Energy Commission, New Brunswick Laboratory, in providing spectrographic analyses is gratefully acknowledged.

Manuscript received June 29, 1956. The work on this paper was supported by A.E.C.

Any discussion of this paper will appear in a Discussion Section to be published in the December 1957 JOURNAL.

REFERENCES

1. W. G. Pfann, *Trans. Am. Inst. Mining Met. Engrs.* **194**, 747 (1952).
2. H. A. Saller and F. A. Rough, BMI 1000, June 1, 1955 "Compilation of U.S. and U.K. Uranium and Thorium Constitutional Diagrams."
3. H. H. Hausner and J. L. Zambrow, *Nuclear Science and Engineering*, **1**, 92 (1956).
4. H. M. Feder, "Pyrometallurgical Processing of Nuclear Materials" Geneva Conference, paper 544 (1955).
5. P. H. Keck, W. Van Horn, J. Soled, and A. MacDonald, *Rev. Sci. Insts.*, **25**, 331 (1954).
6. J. E. Antill, *Nuclear Power*, **1**, 155 (1956).

The Kinetics and Mechanism of Formation of Anode Films on Single-Crystal InSb

J. F. Dewald

Bell Telephone Laboratories, Inc., Murray Hill, New Jersey

ABSTRACT

Studies of the kinetics-of-formation and composition of anode films on several crystal faces of indium antimonide are reported. A marked dependence of oxidation rate on crystal face is observed at low fields, the (111) and (332) faces oxidizing at more than ten times the rate of the (110) and ($\bar{1}$11) and ($\bar{3}$32) faces. At high fields all faces oxidize at the same rate. Data are interpreted in terms of the detailed structure of InSb and the theories of Cabrera and Mott and of Dewald. With one major exception, the composition effects, the data may be qualitatively understood in terms of these theories.

In the past few years a sizable effort has been made by many workers to achieve a detailed understanding of the mechanism of formation of anode films generally. Experimental work has been concerned largely with simple metal systems, in particular the Ta, Al, and Zr systems (1-5).

The present study was undertaken to illuminate some of the ambiguities which have arisen in the theoretical interpretation of experimental data on simple metal systems. The intermetallic compound, InSb, was chosen as the electrode for study because its crystal structure and its binary nature uniquely highlighted the effects being studied.

The theory of the high-field formation process was first put in quantitative form by Cabrera and Mott (6). It has recently been extended by Dewald (7). Two major uncertainties are implicit in both of these developments, (*a*) the nature of the mobile species, and (*b*) the location of the rate-determining step. Cabrera and Mott assumed that cations move through the film interstitially and that the rate-determining step is located at the metal/oxide interface. Dewald also assumed ionic transport by interstitial cations, but allowed for the existence of space charge effects in the event that passage through the film was the rate-determining step.

Charlesby and co-workers (3) attempted to resolve the second of these uncertainties by studying the rate of formation on different crystal faces of Al. If entrance into the film were the difficult step, one might expect differences in kinetics depending on the crystallographic orientation of the surface being oxidized. Charlesby's apparently negative result implies either that the potential energy parameters of the faces studied [(100) and (110)] do not differ greatly or that the rate-determining step is located elsewhere than at the metal/oxide interface. It is difficult to choose between these alternatives since

the structure of Al (f.c.c.) is not one likely to exhibit large differences in bonding energy between the (100) and the (110) face. A surface atom makes 8 bonds to the crystal on the (100) face and 7 bonds to the crystal on the (110) face. Since each bond is rather weak, and breaking the surface bonds is only a part of the total activation process, it would not be at all surprising if the difference in activation energy between the (110) and (100) faces were as small as 5%, the experimental uncertainty in Charlesby's experiments. Differences in activation energy on different faces of InSb were expected to be many times as great as on Al (*see* below).

The data of Young (5) and Vermilyea (2) on Ta_2O_5 films also offer an uncertainty as to the location of the rate-determining step in the formation process. The formation rate appears to be a simple exponential function of electric field over the entire range of fields studied, suggesting that a single activation process is operative over this range of fields. An anomalous temperature independence of Tafel slope $\left[\left(\frac{\partial \bar{E}}{\partial \log i}\right)_T\right]$ was observed, however, which has been taken by Dewald (7) to indicate the existence of two rate-determining processes, one operative at high fields, the other at low fields. He identified the two steps as passage into and passage through the film, but could not identify uniquely which was the high- and which the low-field process.

The validity of some sort of a duplex process in the Ta_2O_5 system has now been confirmed by new data of Vermilyea (8). Using a technique of measurement especially designed to minimize the effects of heating at high current density, Vermilyea now finds that the formation rate is not a simple exponential function of the field but rather that there are two exponential regions, at high and at low fields, with different slopes and a smooth transition in between.

To the extent that one believes the hypothesis of Cabrera and Mott and of Dewald, that interstitial ions move through a perfect lattice and are the only mobile species, one is strongly led to the conclusion that the two processes correspond to entrance into and passage through the oxide film. However, if this is the case, a significant space charge should arise in the film. Such a space charge would be expected to give rise to a small dependence of formation rate on film thickness, the field being kept constant. Vermilyea has looked for such a thickness dependence with negative result (9). This suggests that a reconsideration of the nature of the mobile species may be necessary or that lattice imperfections may play a significant role. The experiments described below on the composition of the films formed on InSb give additional insight into this problem.

Experimental Methods

Crystal and Surface Preparation

The indium antimonide single crystals employed in this study were grown from zone-refined material and were pulled in the (100) direction. The impurity content, as estimated from Hall effect and conductivity measurements at liquid nitrogen temperature, was approximately 5×10^{15} at./cc, (corresponding to 1 part in 10^7). This value would include any departures from stoichiometry. The crystals were oriented with an x-ray goniometer and then cut abrasively to any desired orientation.

Perhaps the most subtle and at the same time most troubling problem encountered in the course of this work was in the preparation and identification of the precise nature of the surface condition of the crystals.

First, there is the problem of locating the positive direction of the crystal. InSb has the ZnS structure. In this structure the (100) axis is not a fourfold axis but rather a fourfold inversion axis and thus, although standard x-ray diffraction techniques cannot distinguish the dissymetry involved, the face (h k l) does not in general have the same properties as the face ($\bar{h}$ k l). The simplest set of faces on which one may see the differences is the [111, $\bar{1}$11] set. On one of these faces (what label it is given is completely arbitrary) any surface antimony atom makes three bonds to the crystal, any surface indium atom makes just one bond to the crystal. On the other face just the reverse is the case, every surface indium is three-bonded, every surface antimony is one-bonded. The similar orientation problem has been solved for ZnS using the absorption edge technique (10); however, since the atomic numbers of In and Sb differ by only two, this is not possible in the present case. Index (111) has been assigned arbitrarily to the face which forms the thicker oxide films under the same formation conditions.[1]

An even greater ambiguity arises from the distinction that must be made between the macroscopic, the microscopic, and the atomic nature of the surface. Depending on the method of surface preparation and the particular face in question, these three ways of defining the orientation may or may not be the same. Four general methods of surface preparation have been used; cleavage, crystallographic etches, and chemical and electropolishes. Three crystal faces have been studied in some detail, the (110), the (332), and the ($\bar{3}$32). These faces were chosen primarily because they are the cleavage planes of the crystal, and cleavage should yield surfaces in a much less ambiguous condition than can be achieved by any other technique. The (110) face is the primary cleavage plane while the (332) and ($\bar{3}$32) planes appear to be the secondary cleavage planes.[2]

Much of the data for the (110) face have been obtained on freshly cleaved surfaces. Using a simple razor-blade guillotine, mirror bright (110) surfaces as large as 1 cm^2 have been obtained. These generally show several steps, but apart from these, the

[1] It is shown below that the kinetic data can be understood only if the (111) face (as defined above) is the face with 3-bonded antimony atoms and 1-bonded indiums.

[2] G. Wolff (11) has reported secondary cleavage on the (111) plane. In a few cases fragmentary cleavage has been observed on faces which are approximately in the (111) direction. However, goniometric measurements on two such cleavages showed the optical surface to be much closer to the (332) than to the (111) plane. Since the (111) plane is not electrically neutral, i.e., contains either all indium or all antimony atoms, cleavage was not expected to occur on the (111) plane.

macroscopic, microscopic, and atomic planes should be identical. The crystals were immersed in the electrolyte within a few seconds after cleavage. The fragmentary cleavages which have been obtained on the (332) and ($\bar{3}$32) faces have been used for the colorimetric determination of the effect of crystal orientation; however, the inability to produce these surfaces at will and in large area has required dependence primarily on other techniques of surface preparation for the study of the effects of temperature and electric field, on the (332) and ($\bar{3}$32) faces. The efficacy of these other methods of surface preparation was checked by colorimetric comparison with the films formed on the fragmentary ($\bar{3}$32) and ($\bar{3}$32) cleaved surfaces.

Data on the ($\bar{3}$32) face have been obtained largely on faces prepared using a crystallographic etch of the composition: 48% HF, 4 pts; Conc. HNO_3, 5 pts; H_2O, ~12 pts. This etch develops microscopic faces which, regardless of the macroscopic orientation, are most closely identified as ($\bar{3}$32). As in the case of the cleaved faces, goniometric data show deviations as large as one or two degrees from the theoretical angles. The indexing as ($\bar{3}$32) is made as a relatively simple indexing of what is probably a considerably "stepped" atomic configuration.

A crystallographic etch to develop (332) surfaces could not be found and therefore it was necessary to use nonselective methods of surface preparation on this face. Crystals were oriented by the combination of x-ray and kinetic techniques discussed above and then were mechanically lapped and polished to the (332) face. Just prior to the formation of the anode films, they were either chemically or electrochemically polished to remove the mechanically disturbed surface layer. The chemical polish had the composition; HNO_3, 40 pts., 48% HF, 24 pts., acetic acid, 24 pts. Polishing times ranged from 5-30 sec. The electropolish had the composition: $HClO_4$, 10 pts; acetic anhydride, 40 pts; H_2O, 2 pts. It was employed at ~5°C at a current density of ~50 ma/cm^2 and yielded a solid black film of oxidation product which was readily stripped off under a stream of water leaving a mirror bright surface.

Various techniques were employed for masking the faces of the crystal other than the face under study. A coat of polystyrene, applied in a toluene solution to a lapped-but-not-polished surface, seemed to give completely adequate protection. The coating was generally applied over the edges of the face under study in an attempt to minimize edge effects; however, since there were almost certainly edges or steps present in the initial surface proper, this was probably a futile effort.

The electrolyte employed in all the experiments reported here has been 0.1*N* KOH. This electrolyte dissolves the pure antimony oxides, as antimonites and antimonates, but does not dissolve In_2O_3.

Chemical Analysis of Films

Chemical analyses of the oxide films for their In and Sb content were made by microtechniques closely similar to those devised by Moeller (12) for In and by Luke and Campbell (13) for Sb.

Films were formed on large area crystals which showed (110) faces primarily. Crystals were chemically polished just prior to anodic treatment. The films, ranging in thickness from 200 to 1000Å, were dissolved in tartaric acid. They dissolve slowly and, judged by the perfectly uniform interference colors, at a uniform rate, thus allowing a layer-by-layer analysis of their composition. The sensitivities of the analytical methods (0.1 μg for Sb and 1 μg for In) were sufficient to allow determination of the In/Sb ratio with a precision of about 5% on layers as thin as 20Å.

Kinetic Measurements

The determination of the kinetics of anode film formation resolves itself into the measurement, for any given crystal face and temperature, of the instantaneous electric field and the rate of film growth. Different workers have used many different methods of determining these quantities.[3] The evaluation of the precise absolute value of the electric field, involving as it does the measurement of film thicknesses in the range from 100Å to perhaps 5000Å, is difficult. Fortunately, one does not need to know the precise absolute value of the electric field in order to understand the main features of the kinetic mechanism. Any uncertainty in the absolute field will reflect itself only in an uncertainty about the "jump" distance parameter [cf. (6, 7)]. Since the jump distance is at present only an incompletely defined quantity, only cursory coulombic measurements of the absolute fields have been made in this investigation.

Two techniques were employed to obtain the relative fields; a colorimetric method and a new method described below. These methods are both based on the fact that the ratio of the fields acting across two films of the same thickness is simply the ratio of the voltage drops across the films. The methods differ only in the manner of obtaining films of the same thickness: *(a)* films were formed, under identical conditions of surface preparation, temperature and formation rate, to the same voltage; *(b)* films were formed to the same interference color. Method *(a)* was used to obtain the dependence of formation rate on temperature and electric field on each of the crystal faces studied. Method *(b)* was used to determine the dependence of formation rate on crystal face.

Colorimetric methods such as *(b)* have been used by a number of workers in the past. Vermilyea (8) for example has made particularly effective use of the technique in the study of the Ta_2O_5 system. As in the previous work, an optical step-gauge proved to be quite a simple method of comparison of film thickness. The gauge was constructed using a series of cleaved (110) surfaces, these being formed at 25°C and at a rate of 0.1 v/sec, to various voltages in the range from 10 to 30 v. Comparison of a film of unknown thickness with the step gauge allowed the determination of the relative thickness within perhaps one half of a volt in the most sensitive

[3] See, for example, references (1), (2), (5), and (8). See also, A. Vasicek, Czech. Jl. Phys. 4, 204-19, (1954).

region of the spectrum. The first order colors are very intense.[4]

Method *(a)* is a novel and particularly sensitive one for studying the kinetics of these processes and should be of general applicability. The procedure is illustrated in Fig. 1, and described in some detail below.

A particular crystal face, a convenient temperature (T_0), and a convenient formation rate (S_0) are selected. Under these conditions a number of films are formed to the same voltage, V_0; these films are then all of the same thickness. The formation rate, or the temperature, or both, are then changed to a different value on each film and the change of voltage with time is measured under the second conditions. The voltage rises, rapidly at first, passes through a maximum, then a minimum, and finally rises again, now linearly with time, at a rate closely proportional to the external current density. The final linear rise in voltage with time corresponds to the steady-state behavior for which the various theories have been derived.

The transient effects shown in Fig. 1 have been separated from the steady-state effects by extrapolation of the linear voltage rise portion of the formation curve back to the time when the current was reapplied. This is shown by the dotted line in Fig. 1. The ratio of the extrapolated voltage (V_1) to the initial voltage (V_0) gives the relative field (referred to the initial field) under the final conditions of formation rate and temperature. The validity of the extrapolation procedure has been checked by experiments in which the final formation rate and temperature were made the same as the initial values. The extrapolated voltages (V_1) under these conditions were found to be identical (within ~0.1%) to the voltages (V_0) to which the films had been formed.[5]

Voltages were measured against a Hg-HgO reference electrode which was separated from the solution by a 0.1*N* KOH salt bridge. The tip of the bridge was placed approximately 1 mm away from the InSb electrode. The voltages in the data reported below have been referred to the InSb electrode, which in 0.1*N* KOH is ~0.7 v[6] more active than the Hg-HgO electrode, by adding 0.7 v to the measured voltage; thus the voltages below represent the voltage drops across the oxide film itself.

Formation rates have been determined from the rate of voltage rise with time. Since, at a given formation rate, the electric field is, to a very good approximation, independent of the film thickness, the formation rate is taken to be given by the rate of change of voltage with time divided by the electric field at that formation rate. The data below were obtained on films formed initially at T_0 = 25°C, $S_0 \approx 0.1$ v/sec to V_0 = 5, 10, and 15 v. Owing to variations in surface area and formation efficiency, the initial formation rate could not be controlled precisely to 0.1 v/sec and therefore the rate of change of voltage with time under the initial conditions was determined experimentally and corrections applied for the departure from 0.1 v/sec.

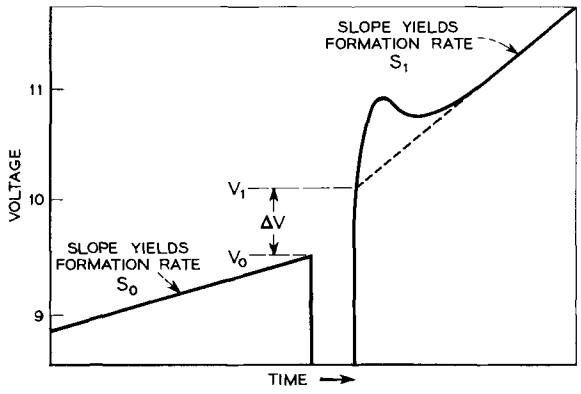

Fig. 1. Typical voltage vs. time curves for the formation of anode films on InSb. Note the initial transient and the extrapolation used to eliminate its effects.

Most of the experiments were performed allowing just enough time between the initial formation process and the final formation process to get the film to the new temperature. However, identical results were observed when the films were allowed to stand in contact with the electrolyte for as long as 70 hr between the initial and final formations. The films apparently do not dissolve on prolonged contact with KOH.

Voltage-time curves similar to Fig. 1 were obtained using a Sanborn Model 127 recorder in conjunction with a Sanborn Model 126 amplifier (10 meg input impedance) and a calibrated voltage-zero-suppressor. The recorder has a response time of about 0.01 sec for full scale deflection. Data presented here on the InSb system show a precision of the order of one half a percent in relative field, on films as thin as 100Å; similar data on somewhat thicker Ta_2O_5 films have been obtained with a precision approaching 0.1%.

For want of a better name, this technique might be called an isopachic (for equal thickness) method.[7]

Results and Discussion

Composition of the Films

The composition of the anode films formed in 0.1*N* KOH has been determined as a function of both the position in the film and the rate of formation of the film. Fig. 2 shows a typical result of the layer by layer chemical analyses. The Sb to In ratio is very low close to the electrolyte interface; however, it rises sharply as one goes into the bulk of the film, approaching the value 1 at a distance about 100Å into the film and remaining essentially constant all the way from there to the metal/oxide interface. This behavior is difficult to rationalize with the interstitial transport of positive ions. One would

[4] Unfortunately the second order colors in the InSb system are quite faint, and, toward the "blue" end of the second order, the films appear gun-metal to black in color. The restriction to the first order makes the colorimetric method less attractive in the InSb system than it has been in other systems.

[5] The transients observed in these measurements constitute an interesting problem in themselves. Almost identical effects have been observed on Ta_2O_5, SiO_2, and Nb_2O_5 films [*see* ref. (15)].

[6] J. F. Dewald, unpublished data.

[7] Adams and co-workers (14) have used a technique somewhat similar to this.

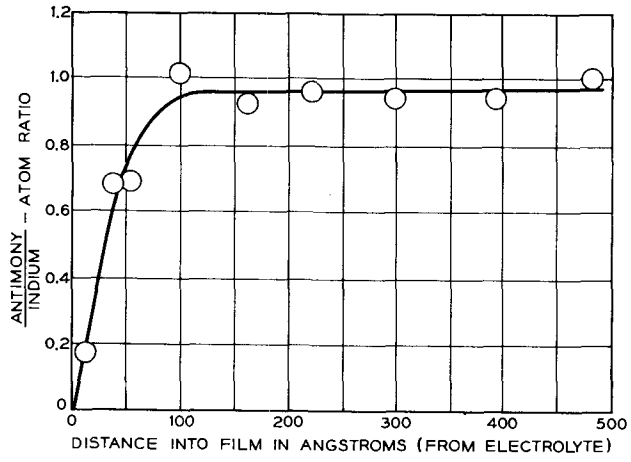

Fig. 2. Typical dependence of anode film composition on position in the film. Close to the electrolyte (KOH) the Sb content is very nearly zero while at depths greater than about 100Å, the composition is practically that of the base material.

expect, in view of the large and fairly rapid solubility of antimony oxides in KOH, that any Sb ion arriving at the electrolyte interface would dissolve. A part of the Sb does dissolve, but the largest fraction of it remains in the film.

Such behavior might be accounted for if the dissolution rate of antimony oxide were slow and the antimony ions arriving at the electrolyte interface were covered up by subsequent In ions before they could dissolve. This explanation is contradicted by the experimental data shown in Fig. 3. Within experimental error, the composition of the films is independent of the formation rate. Coupling this fact with the observation that, even at current densities appreciably higher than those of Fig. 3, an Sb electrode dissolves anodically in KOH without film formation, it is concluded that most of the Sb ions never come in contact with the electrolyte and that thus the use of the interstitial mechanism of film formation is probably an oversimplification.

Kinetic Data on the (110), (332), and ($\bar{3}32$) Faces

The kinetic data which have been obtained are illustrated in Fig. 4 and 5, and are summarized in Table I. Fig. 4 shows typical Tafel plots of field vs. the logarithm of formation rate for the (110), (332) and ($\bar{3}32$) faces. These data were obtained at 25°C, on films formed initially to 10 v. Fields are expressed relative to the field on the (110) face at a formation rate of 0.1 v/sec, and formation rates are expressed in volts/sec at this field.

A number of features of the data in Fig. 4 should be noted. First, the electric field is not a simple logarithmic function of formation rate on any of the faces studied. In the extremes of both high and low formation rate, the field on each of the faces may be adequately represented as a simple logarithmic function of the formation rate. This behavior seems to imply a duplex process, similar to that observed in the study of Ta_2O_5 films, with the rate-determining step shifting from one site at low fields to a different site at high fields.

The respective locations of the two rate-determining sites may be inferred from the data in Fig.

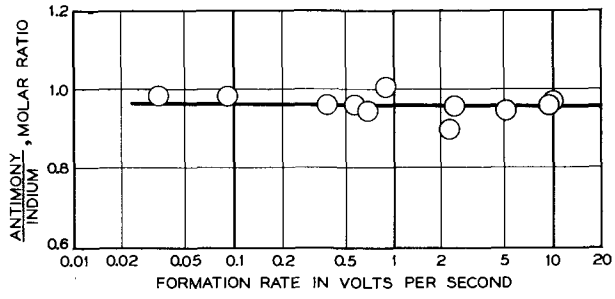

Fig. 3. The Sb/In ratio deep in the film plotted as a function of the rate of formation on the film.

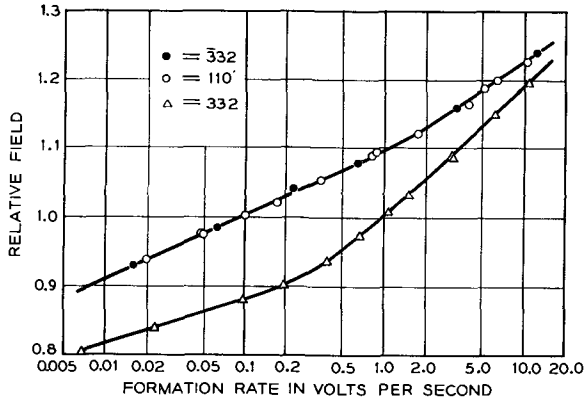

Fig. 4. Tafel plots, showing the dependence of electric field on formation rate, for the (110), (332), and ($\bar{3}32$) faces of InSb at 25°C.

4. At low and intermediate fields a large effect of crystal orientation is observed, the (332) face oxidizing more than 10 times as rapidly, at the same field, as do the other two faces. At high fields, on the other hand, the three faces oxidize at nearly the same rate. Thus the low field process must be associated with the metal/film interface, and it seems reasonable to suppose that the rate-determining step in the high field process is located elsewhere.

Another rather interesting feature of the data in Fig. 4 is that the ($\bar{3}32$) and (110) faces show almost identical formation rates over the entire range of fields studied at this temperature. This should not be taken to mean that the various kinetic parameters are identical on the two faces, for at temperatures other than 25°C the formation rates on the two faces are not identical.

Data given in Fig. 4 show a small inconsistency between the two methods which have been used to determine the relative field. As mentioned in the experimental section above, the colorimetric method was employed to determine the relative field [referred to the (110) face] on the (332) and ($\bar{3}32$) faces, this comparison being made (arbitrarily) at a formation rate of 0.1 v/sec. The curves in Fig. 4 were then drawn from the isopachic data which covered the entire range of formation rates. Now films formed at high formation rates (greater than about 5.0 v/sec) show no crystallographic effect on colorimetric comparison. Thus, if the two methods of determining the electric field were completely consistent, the curves of Fig. 4 should all superimpose at formation rates above about 5.0 v/sec. As can be seen the two curves seem to be approaching

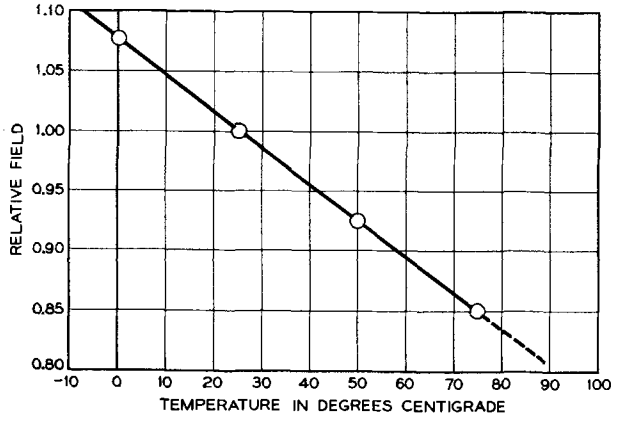

Fig. 5. Temperature dependence of field at constant formation rate on the (110) face.

one another but, even at the highest formation rates, they differ by about 4% in field. This difference is roughly twice the estimated uncertainty in the colorimetric method in the first order range of colors and seems to be a real effect. It may be that the index of refraction of the film depends on the face on which it is formed, or that the optical properties of the base "metal" vary from face to face [such a variation would be unlikely to occur between the (332) and ($\bar{3}32$) faces]. In any case, the discrepancy is a relatively small one and should not affect the qualitative conclusions presented.

The data in Fig. 5 show the temperature dependence of the electric field for 10-v films formed on the (110) face at 0.1 v/sec. Both the Mott-Cabrera and the Dewald models of the system predict an essentially linear dependence of field on the temperature at any given formation rate. The dependence shown in Fig. 5 is in accord with these predictions, over the range from 0° to 75°C. Similar linear dependences of field on temperature have been observed on the (332) and ($\bar{3}32$) faces both at low and at high fields.

Since the functional dependences of field on formation rate and on temperature are fairly simple in the extremes of high and low field, and the transition from the low to the high field behavior is moderately sharp, the experimental data may be summarized in the form of three coefficients (one of each for the high- and one for the low-field region), $\bar{E}$, $(\partial\bar{E})/(\partial \log i)_T$, and $(\partial\bar{E})/(\partial T)_i$. The values of these coefficients vary from face to face in the low field region but show only small, if any, orientation

TABLE I. Summary of experimental data

Formation rate	Crystal face	$\bar{E}/E_0$	$\frac{1}{E_0}\frac{\partial\bar{E}}{\partial \log i}$	$\frac{1}{E_0}\frac{\partial\bar{E}}{\partial T}$
Low (0.1 v/sec)	110	1.00*	0.092	—0.00306
	$\bar{3}32$	1.00	0.092	—0.00380
	332	0.85	0.060	—0.0020
High (10 v/sec)	110 & $\bar{3}32$	1.22	0.17	—0.0036
	332	1.17	0.18	—0.0035

* By definition of E_0.
E_0 = the field on the 110 face at 25°C and a formation rate of 0.1 v/sec

TABLE II. Parameters derived from data in Table I using equation of Cabrera and Mott

	Face	bq* (Å)	q (assumed)	b (Å)	ϕ (e.v.)	i_0 (A/sec)
Low field						
	110	12.8	3	4.3	1.22	$10^{10.1}$
	$\bar{3}32$	12.8	3	4.3	1.37	$10^{12.7}$
	332	20.0	5	4.0	1.4	$10^{10.3}$
High field						
	Any	7.0	3	2.3	0.8	10^{8}

* bq values calculated using $E_0 = 5\text{x}10^6$ v/cm.

effects at high fields. They are summarized in Table I.

Table II shows the data from Table I re-expressed in the form of the kinetic parameters of the interstitial transport model. At either low or high fields the theory of this model predicts dependences essentially of the form

$$i = i_0 \exp\,(Ebq - \phi)/kT \qquad (I)$$

Regardless of the validity of the model, the data may be fitted empirically to an equation of the form of (I) in either the high- or low-field regions of formation. Values of the parameters ϕ, bq, and i_0 depend on which region, as well as which crystal face, is being considered. As mentioned above, values of i_0 and the activation energy are determined unambiguously by the data in Table I, independent of the measurement of the absolute electric field. The absolute values of bq depend, however, on the measurements of the absolute field. Values of bq given in Table II were calculated using the value $E_0 = 5\text{x}10^6$ v/cm. This value is derived from coulometric data on the (110) face and represents a minimum value for E_0 which may have to be revised upward when accurate measurements of the absolute field become available. The relative values of the bq product should be unaffected by more accurate evaluation of E_0.

The interpretation of the kinetic parameters which have been derived from the experimental data is difficult, since the detailed mathematical theory of the oxidation process in binary systems such as InSb has not yet been developed. Several novel features of mechanism are introduced by the binary nature of the system and others arise because of the strongly directional character of the surface bonding of the atoms; thus, the use of the Cabrera-Mott equation, (I), or even the complete equations of the space charge model, can hardly have more than qualitative validity. Nevertheless some interesting conclusions may be drawn.

Consider first the values of the bq product obtained from the low-field kinetic data. From Table II these are seen to vary appreciably from face to face, the (332) face exhibiting a value nearly 5/3 as large as the value observed on the other two faces. The variation of the (bq) product can hardly be ascribed to variations in the jump distance (b) since the geometry of the faces is so very similar and, as shown below, the "jump distances" so very large. Thus the variation of the bq product almost

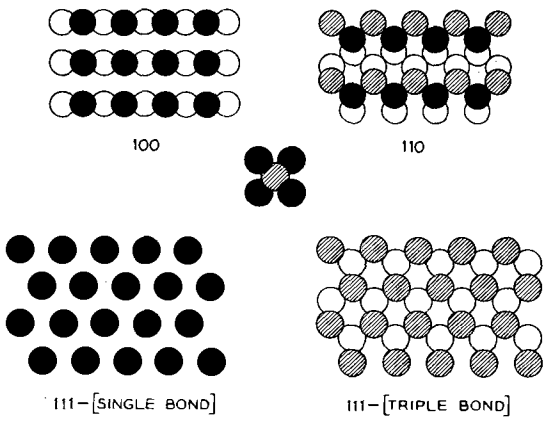

Fig. 6. Surface bonding on the (110), (100), and (111) faces of InSb. Black atoms are surface In, shaded atoms are Sb, unshaded atoms are below the surface atoms. The ($\bar{1}11$) face differs from the (111) only in the identity of the atoms.

certainly results from variations, from face to face, of the effective charge q.

The fact that the ratio of the bq products turns out to be very close to 5/3 implies that on the (332) face the removal of the Sb (+5) ions is rate-determining, while on the ($\bar{3}32$) and (110) faces, removal of the In (+3) ions is the slow step in the oxidation.

Since diffusion in the InSb lattice is very slow at room temperature, the oxidation of any face of an InSb crystal must, of course, involve the removal of both kinds of atoms. To say that, on a particular face, removal of the In ions is rate-determining simply means that at any given instant most of the surface atoms are indiums, the relative numbers of the two kinds of atoms being inversely proportional to their specific rates of removal.

At first glance it might seem strange that one face allows ready removal of one kind of atom while another face allows ready removal of the other kind of atom. Inspection of the type of surface bonding in zinc-blend structures makes this behavior quite clear. Fig. 6 shows the surface bonding of the (100), (110), and (111) faces. [The reasoning may be greatly simplified, with little loss in accuracy, by thinking of the (332) and ($\bar{3}32$) faces, respectively, as "stepped" (111) and ($\bar{1}11$) faces.] The antimony atoms on a (110) face are bonded to the crystal in exactly the same way as the In atoms; by virtue of their larger charge they will be acted on more strongly by the field and therefore the rate-limiting step from this face will presumably be the removal of In atoms.

On the ($\bar{1}11$) face two factors operate to make the In atoms the more tightly bound. There is the same effect of the field as on the (110) face, and in addition a surface In atom on the ($\bar{1}11$) face makes three bonds to the crystal while a surface Sb atom makes only one bond. On both counts the In atoms should be less easily removed than the Sb atoms.

A different behavior is expected on the (111) face; here the chemical and electrical effects act in opposite directions, a surface Sb atom being held to the crystal by three bonds, a surface In atom only by one bond. Thus, in spite of its smaller charge, the In atoms might well be less strongly held to this face than the antimonys and so, except perhaps at very high fields, the removal of antimonys could well be the rate-limiting step in oxidation.

The discussion above makes possible the evaluation of the jump distances themselves, from the bq products and the assumed values of q. These jump distances are shown in Table II. The values obtained (4.0-4.3Å) are roughly equal on the three faces as would be expected, and are quite comparable to those previously obtained on Al (3.5Å) (6) and on Ta at low fields (4.8Å) (8). These values are all surprisingly large, it being remembered that they are supposed to represent the distance from the potential energy minimum to the maximum.

The value of the bq product obtained at high fields is very much less than those obtained at low fields; the calculation of the value of b itself again depends on the value assumed for the effective charge. This has been taken as +3, the assumption being made that motion of the In ions through the film would, by virtue of its smaller charge and larger size, surely be the slower moving ion. Using this value of charge, the value 2.3Å for the jump distance at high fields was obtained. Again there is a surprising concordance with the results obtained on Ta; Vermilyea (8) finds a value of 2.4Å for the jump distance in Ta_2O_5 films at high fields. (He assumes +5 for the charge of the Ta ion.)

The activation energies (ϕ) and frequency factors (i_0) which have been calculated from the data show a definite dependence on crystal face at low fields. Differences are not very large, and the interpretation must therefore be largely speculative. Now the activation-energy-for-diffusion (ϕ) of a surface atom is determined by a whole complex of forces. The two largest factors would be presumably, *(a)* the chemical bonds which would hold the atoms to the crystal regardless of whether a film is present or not, and (*b*) the repulsive forces incident to squeezing past the first oxide ions in the film. Presumably the second of these factors will not vary significantly from one face to another if the activation process involves the same kind of ion on the faces considered. This is the case if the ($\bar{1}11$) and (110) faces are compared; thus the differences observed on the two faces probably arise from the nature of the bonding.

Fig. 6 shows that the In atoms make three bonds to the crystal on both the (110) and ($\bar{1}11$) faces. One might conclude from this that the bonding contribution to the activation energy would be the same on the two faces. This reasoning might be valid if one had a perfect crystal face with no edges or steps. However, it would not be true for any real crystal, since the (110) face has a structure which would "transmit" the edge or imperfection effects over the entire crystal face while the (111) does not. This can be seen quite simply by removing just one atom from each of the "perfect" planes of Fig. 6. On the (110) face the two neighboring atoms would then each be converted from a three-bonded to a two-bonded state. If these two-bonded atoms were in turn removed, the two adjacent atoms would be left

in a two-bonded state. Since two-bonded atoms would be expected to come off more readily, i.e., with lower activation energy, than three-bonded atoms, the (110) face would be expected to oxidize by a chain process of this sort. A similar chain process would not be anticipated on either the (111) or $(\bar{1}11)$ faces, for on these faces the surface atoms are not bonded to one another; thus the removal of one surface atom does not change the bonding of the neighboring surface atoms.

This argument explains in a qualitative way the differences in activation energy observed between the (110) and $(\bar{3}32)$ faces. It also explains the smaller i_0 value on the (110) face, for only a small fraction of the atoms on such a face are, at any given instant, subject to activation. In the simple Cabrera-Mott approximation, the frequency factor is given by

$$i_0 = m_s \nu \cdot V \qquad \text{(II)}$$

where m_s is the surface density of atoms susceptible to activation, ν is of the order of typical vibration frequencies ($\nu \sim 10^{12}$ sec^{-1}), and V is the atomic volume of the mixed oxide. Values of m_s calculated from the experimental data using (II) indicate that essentially all atoms on the $(\bar{3}32)$ face are at all times subject to activation while only about 1 in 400 is subject to activation, at any given instant, on the (110) face. These values seem eminently reasonable, both in a relative and an absolute sense.

Summary

The kinetics of formation of anode films on InSb have been studied on three crystallographic faces and the composition of the resulting films has been determined as a function of the position in the film and the rate of formation. The kinetic data, both transient and steady-state, show striking similarities to those observed previously on the Ta_2O_5 system. The steady-state data may be understood, at least in qualitative fashion, in terms of the theories of Cabrera and Mott, and of Dewald. The pronounced crystallographic effects observed at low fields and the absence of such effects at high fields establish the location of the rate-limiting processes; at low fields, passage into the film is the difficult step; at high fields, passage through the film is the difficult step. Attempts are made to account for the various crystallographic effects in terms of the structure of InSb.

Films formed on InSb in 0.1*N* KOH are found to contain nearly equal quantities of In and Sb in spite of the fact that antimony oxide is strongly and readily soluble in the electrolyte. This result is taken to throw considerable doubt on the assumption of a simple interstitial-ion transport mechanism.

Manuscript received June 25, 1956. This paper was prepared for delivery before the Cincinnati Meeting, May 1-5, 1955.

Any discussion of this paper will appear in a Discussion Section to be published in the December 1957 JOURNAL.

REFERENCES

1. A. Gunterschultze and H. Betz, *Z. Phys.*, **92**, 367 (1934).
2. D. A. Vermilyea, *Acta Met.*, **1**, 282 (1953).
3. S. J. Basinka, J. J. Polling, and A. Charlesby, *ibid.*, **2**, 312 (1954).
4. D. A. Vermilyea, *This Journal*, **102**, 207 (1955).
5. L. Young, *Trans. Faraday Soc.*, **50**, 153 (1954).
6. N. Cabrera and N. F. Mott, *Repts. Progr. in Phys.*, **12**, 163 (1948-49).
7. J. F. Dewald, *This Journal*, **102**, 1, (1955).
8. D. A. Vermilyea, *ibid.*, **103**, 655 (1956).
9. D. A. Vermilyea, *Acta Met.*, **3**, 106 (1955).
10. Coster, Knolls, and Prins, *Z. Physik*, **63**, 345 (1930).
11. G. Wolff, paper delivered at the Chicago Meeting of the ECS, May (1954).
12. T. Moeller, *Ind. Eng. Chem. Anal. Ed.*, **15**, 272 (1943).
13. C. L. Luke and M. E. Campbell, *Anal. Chem.*, **25**, 1588 (1953).
14. G. B. Adams, Jr., Pierre Van Rysselberghe, and Mario Maraghini, *This Journal*, **102**, 502 (1955).
15. J. F. Dewald, *J. Phys. Chem. Solids*, In press.

Density and Electrical Conductance in the System KCl-$ZnCl_2$

Frederick R. Duke and Richard A. Fleming

Institute for Atomic Research and Department of Chemistry, Iowa State College, Ames, Iowa

ABSTRACT

The phase diagram of the system KCl-$ZnCl_2$ indicates the presence of the solid-state 2KCl·$ZnCl_2$. Density vs. composition isotherms in the range 475°-650°C are approximately linear. Isotherms of equivalent conductivity deviate negatively from additivity when plotted against composition, the maximum negative deviation being found near $X_{KCl} = 0.71$. The heat of activation for ionic migration falls rapidly from that of $ZnCl_2$ until X_{KCl} has reached 0.30, then slowly falls to the limiting value for pure KCl.

A knowledge of the electrical properties of fused salt systems has been found to be a powerful tool aiding the understanding of the physical nature of the systems. The work of Bloom and Heymann (1) in 1946 pointed out a possible relationship between the physical nature of the solid state and the electrical properties of the fused state. Their results indicated that isotherms of equivalent conductivity would be expected to exhibit moderate negative deviations from additivity in systems showing no

evidence of intermediate compound formation in the solid state. Strong negative deviations would be found to be associated with systems whose phase diagrams indicated the presence of congruently melting compounds, and could be explained on the basis of persistence to some extent in the liquid state of the complex known to be present in the solid state. Experimental heat of activation isotherms for ionic migration calculated on the basis of the Arrhenius equation would exhibit maxima near compositions corresponding to unstable liquid state complexes.

Data were found indicating the existence of the compound $2KCl \cdot ZnCl_2$ (2). A study of this system was undertaken to see whether or not the electrical properties would agree with the above generalizations. The information required included the phase diagram of the system and isotherms of specific conductivity and density at various concentrations.

Preparation and Analysis of Sample

"Bakers' Analyzed broken lump" $ZnCl_2$, meeting ACS specifications, was fused in a Pyrex test tube in the furnace at a temperature of about 400°C. The test tube was then transferred to an oven maintained at 110°C and the contents were allowed to solidify. A predetermined amount of Baker and Adamson reagent grade crystalline KCl was added and the mixture returned to the furnace. At this time hydrogen chloride gas was passed through the melt if any yellow ZnO was observed to be present, following which, in the case of conductivity measurements, the mixture was poured into a preheated cell. The cell was placed in the furnace and when the desired temperature was approached hydrogen chloride gas was passed through the cell, thus completing the preparation of the sample.

Bunker Hill brand electrolytic Zn with a minimum purity of 99.99% was dissolved in Baker and Adamson HCl (maximum heavy metal impurity of 0.0008%). The pure $ZnCl_2$ produced was used to standardize 1, 2-diaminocyclohexanetetraacetic acid from the Alrose Chemical Co. For analysis, some of the molten mixture was drawn up into a 5 mm diameter glass tube in which it was allowed to solidify. The mixture was quite hygroscopic, but by breaking the ends off the tube and quickly weighing the sample plus tube, the dry weight was determined. The solid sample was then dissolved from the tube and analyzed for Zn^{++} by the method of Loomis (3) following which the empty tube was reweighed. Knowing the weight of the sample and the weight of the $ZnCl_2$, the weight of the KCl was found by difference and the composition then calculated.

Apparatus

All the Pyrex conductivity cells used (Fig. 1) had cell constants in the range 400 ± 100 cm^{-1}. In the presence of water, $ZnCl_2$ may hydrolyze and form the oxide which is yellow at high temperatures. If the oxide is treated with hydrogen chloride gas, it is reconverted to the chloride and water vapor, and agitation will expell the latter from the melt. The long arm of the cell extended out of the furnace so that gas could be passed through it. The bulb on the short arm served two purposes. It prevented expulsion of the melt from the cell during passage of hydrogen chloride gas, and also allowed the use of larger samples, thus making chemical analysis of the composition of the melt easier and more accurate. The bubbling of the gas prior to a run also insured the homogeneity of the melt. Preliminary experiments indicated that the electrical conductivity of pure samples was unchanged following the passage of hydrogen chloride gas.

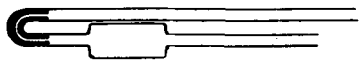

Fig. 1. Typical conductivity cell

The conductivity bridge was basically a L&N Wheatstone Bridge (Type S Test Set No. 5300). An audio-frequency vacuum tube oscillator served as the power source. No appreciable variation of resistance with frequency was noted and all measurements were made at 1000 cps. The waveform delivered by the oscillator was excellent as viewed on an oscilloscope. A variable condenser was used to balance capacity in the bridge. A cathode ray oscilloscope was used as a visual, null-point indicator [*see* ref. (4) for example]. All connecting leads were shielded and grounded.

The electrodes were open cylinders of Pt with a length of 3/8 in. and a diameter 3/16 in. They were connected to 10-in. Pt leads. The electrodes were kept well platinized.

The resistance furnace was operated by a Brown Indicating Controller operating through a proportioning motor. The chromel-alumel measuring thermocouple was connected to a L&N No. 8662 potentiometer with a reference junction compensator. The measuring thermocouple was calibrated at the melting points of Zn, Sb, and Al (5).

A slight modification of the method of Peake and Bothwell (6) was used in determining densities by the sinker method. The sinker was of Pt and weighed 16.815 g in air. Its volume at various temperatures was calculated from literature values of the density and the coefficient of expansion of platinum (7-9).

The phase diagram was constructed by the standard method of thermal analysis of cooling curve data. It was necessary to locate the position of the liquidus curve closely, since in the region on the temperature-composition diagram below this line, the composition in the melt is not the same as the over-all composition of the system.

Results

The phase diagram (Fig. 2) of the system indicates the formation of a solid phase compound corresponding to the composition $2KCl \cdot ZnCl_2$. Eutectics are found at about 433°C (mole fraction KCl of 0.69) and 230°C (mole fraction KCl of 0.51). The solid state compound has a melting point of about 450°C.

Density data were taken at five temperatures for each of eight compositions (Table I). Data at intermediate temperatures for each composition were determined graphically from the linear density-temperature graph. Densities at intermediate com-

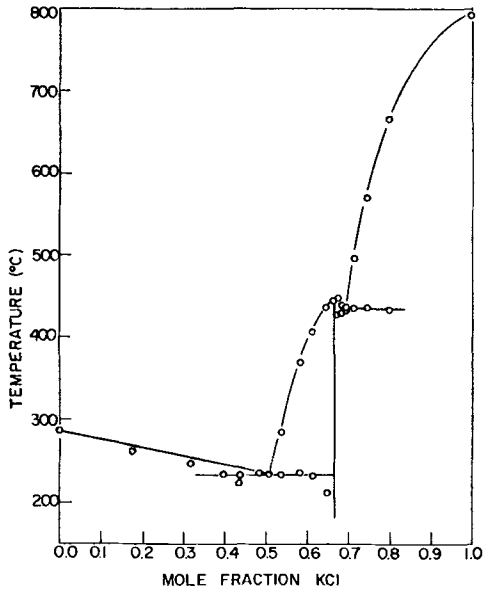

Fig. 2. Phase diagram of the system KCl-$ZnCl_2$

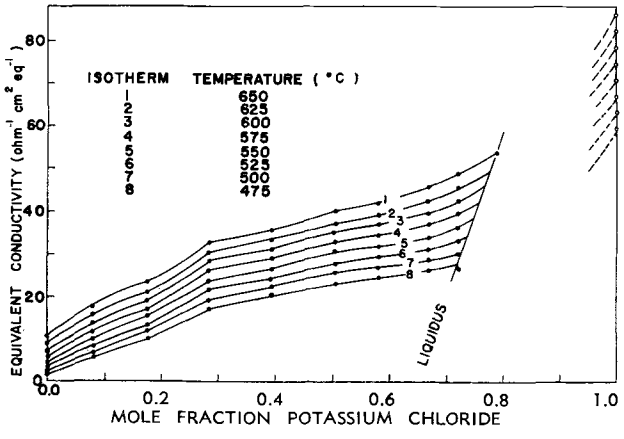

Fig. 3. Equivalent conductivity in the system KCl-$ZnCl_2$

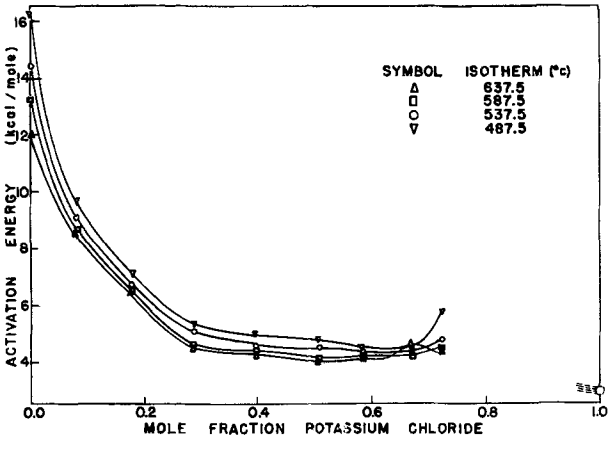

Fig. 4. Experimental heats of activation in the system KCl-$ZnCl_2$

positions were determined by interpolation on the graph of density vs. composition at constant temperature. The isotherms are somewhat "S" shaped. They deviate slightly from additivity in a positive direction at low KCl concentrations and have the suggestion of a negative deviation at low $ZnCl_2$ concentrations. The maximum relative error for the densities is $\pm 6 \times 10^{-4}$.

TABLE I. Density in the system KCl-$ZnCl_2$

X_{KCl}	t (°C)	d (g/cm³)	X_{KCl}	t (°C)	d (g/cm³)
0.000	450	2.457	0.452	453	2.150
	503	2.434		494	2.120
	555	2.405		540	2.094
	593	2.390		591	2.058
	637	2.360		645	2.022
0.094	462	2.399	0.639	442	2.007
	506	2.377		498	1.974
	548	2.351		554	1.939
	602	2.323		612	1.906
	674	2.283		658	1.876
0.158	454	2.369	0.698	447	1.950
	462	2.367		500	1.917
	486	2.349		547	1.888
	504	2.334		596	1.857
	554	2.304		649	1.830
	598	2.276			
	646	2.249	0.811	688	1.687
	660	2.242		715	1.672
0.313	451	2.261			
	500	2.228			
	548	2.201			
	603	2.170			
	661	2.131			

TABLE II. Equivalent conductivity in the system KCl-$ZnCl_2$ equivalent conductivity at different temperatures (°C)

X_{KCl}	650°	625°	600°	575°	550°	525°	500°	475°
0.000	10.55	8.80	7.23	5.78	4.51	3.43	2.50	1.76
0.080	17.81	15.66	13.58	11.73	10.00	8.41	6.90	5.60
0.176	23.26	21.08	19.06	17.06	15.08	13.25	11.67	10.01
0.284	32.52	30.29	28.24	26.13	23.81	21.61	19.39	17.28
0.395	35.58	33.33	31.13	28.87	26.61	24.38	22.39	20.11
0.506	39.97	37.61	35.13	32.75	30.33	27.83	25.41	22.88
0.582	41.77	39.08	36.71	34.18	31.64	29.15	26.69	24.19
0.670	45.51	42.43	39.52	36.82	33.95	31.22	28.57	25.97
0.722	48.64	45.45	42.40	39.33	36.16	33.00	29.87	26.36
0.790	53.60	*	*	*	*	*	*	*

* This temperature is below the liquidus on a temperature-composition diagram.

Isotherms of equivalent conductivity (Table II and Fig. 3) consequently look much like those of specific conductivity. Negative deviations become noticeable at a KCl mole fraction of about 0.30 and reach a maximum at about 0.71, corresponding closely to the composition $2KCl \cdot ZnCl_2$. The maximum relative error is $\pm$ 0.0054.

Experimental heats of activation for ionic migration computed from the Arrhenius equation, $\Omega = A \cdot \exp(-\Delta H^{\ddagger}/RT)$, change only slightly in the range of KCl mole fraction from 1.0 to 0.3, and do so in an approximately linear manner (Fig. 4). At the latter concentration, the activation energy begins a rapid rise to the limiting value for pure $ZnCl_2$. The maximum relative error is $\pm$0.025.

The large negative deviation from additivity exhibited by isotherms of equivalent conductivity and the maximum negative deviation occurring in the neighborhood of the composition corresponding to $2KCl \cdot ZnCl_2$ are both in agreement with the pro-

posals of Bloom and Heymann. Recent work by Duke and Laity (10) assigns ionic transport numbers t_+ and t_- of 0.25 and 0.75, respectively, in lead (II) chloride at 565°C. These results lend experimental support to earlier predictions of a number of authors that alkali halides are predominantly cationic conductors, while in the alkaline earth halides, the anions carry a larger share of the current. In the system KCl-$ZnCl_2$, K^+ dominates the equivalent conductivity and activation energy for pure KCl while Cl^- does the same for pure $ZnCl_2$. An interesting proposal is that K^+ dominates for the mixture in the KCl mole fraction range between 0.3 and 1.0, while Cl^- begins to become important at mole fraction 0.3, increasingly dominating these properties of the mixture from mole fraction 0.3 to 0.0. This proposal must be regarded as pure speculation, however, since a requisite for attempting any further significant discussion of the activation energy isotherms is the availability of data on the transport numbers of the ions at different compositions.

Manuscript received July 2, 1956. Contribution No. 502. Work was performed in the Ames Lab. of the A.E.C.

Any discussion of this paper will appear in a Discussion Section to be published in the December 1957 JOURNAL.

REFERENCES

1. H. Bloom and E. Heymann, *Proc. Roy. Soc. (London)*, **A188**, 392 (1946).
2. J. W. Mellor, "A Comprehensive Treatise on Inorganic and Theoretical Chemistry," Vol. 4, p. 551, Longmans, Green and Co., London (1947).
3. T. C. Loomis, Ph.D. Thesis, Iowa State College Library, Ames, Iowa (1953).
4. R. N. Haszeldine and A. A. Woolf, *Chemistry & Industry*, **1950**, 544.
5. H. F. Stimson, *J. Research Natl. Bur. Standards*, **42**, 209 (1949).
6. J. S. Peake and M. R. Bothwell, *J. Am. Chem. Soc.*, **76**, 2653 (1954).
7. R. Kieffer and W. Hotop, *Kolloid Z.*, **104**, 208 (1943).
8. J. Austin, *Physics*, **3**, 240 (1932).
9. L. Holborn and A. L. Day, *Ann. Physik*, **4**, 104 (1901), (original not seen). Referred to by R. F. Vines, "The Platinum Metals and their Alloys," The International Nickel Co., Inc., New York (1941).
10. F. R. Duke and R. W. Laity, *J. Phys. Chem.*, **59**, 549 (1955).

Technical Feature

The Potential of an Electrode of a Voltaic Cell; A New Definition with Justification for the Use of Two Sign Conventions

J. B. Ramsey

Department of Chemistry, University of California, Los Angeles, California

ABSTRACT

For orientation purposes a brief review of the meaning of the potential of an electrode, first proposed by Lewis and adopted by most American physical chemists, is given. A definition of the potential of an electrode, basically different from those of Lewis and of Gibbs, is developed on the basis of the thermodynamic analysis of conditions existing in an electrode system (half-cell) at equilibrium. It is shown that the partial molal free energy (chemical potential) of the electrons in the electrode of an electrode system at equilibrium provides a meaningful definition of the potential of an electrode. It is suggested that the potential of an electrode, so defined, be designated as the "electron chemical potential" of the electrode, in volts. The value of the electron chemical potential of an electrode, so defined, is shown (*a*) to be invariant in sign as is that of the Gibbs potential, and (*b*) to be equal in magnitude and opposite in sign to that of the Gibbs potential. A justification for the use of both of these definitions of an electrode potential, and therefore of two sign conventions, is presented.

It is well known that, at present, there is a lack of uniformity among chemists in the sign convention used in the designation of the values of the potentials of electrodes. Also the term "potential," as applied to electrodes, has, in general, been used somewhat indefinitely and with different meanings by different authors, and in some cases by the same author, in treating this subject. Even the terminology used, especially by American physical chemists, is quite varied. Reference to the most recent editions of American textbooks which treat this subject will substantiate this statement (1).

The new definition of the potential of an electrode developed in this paper, along with the derivation of its relation to the potential of an electrode (the Gibbs potential) as defined and used by electrochemists, most European chemists and many American biological and analytical chemists, may, it is hoped, be helpful in removing some of the confusion now existing among chemists regarding this subject. The basic thermodynamic and electrostatic principles involved are known, the latter less well than the former.

The meaning of electrode potentials as defined and used by Lewis and Randall (2) (referred to as the Lewis potential).—The definition of an "electrode potential," as given by these authors, is the one adopted and used by most American physical chemists. This usage has been more firmly established by its adoption in the well-known book by Latimer (3). The meaning of an "electrode potential" according to Lewis and Randall (to be symbolized by E) is given in the following quotation: "Thus if we are considering the junction at an electrode, we may represent this junction by the expression: electrode, electrolyte. We then say that the single potential measures the tendency for negative electricity to pass from right to left, that is from the electrolyte to the electrode. On the other hand, we may express the junction as: electrolyte, electrode. Here again the potential measures the tendency of the negative current to pass from right to left. It has the same magnitude as before, but the opposite sign."

The authors' interpretation of this statement (quoted above) may be most clearly given by a simple illustration. Consider the junction, Zn; solution containing Zn^{++}. The passage of negative electricity from right to left involves the change of Zn to Zn^{++}. The change in state (per faraday), which Lewis and Randall correlate with this junction, is formulated

$$\tfrac{1}{2}\,Zn \rightarrow \tfrac{1}{2}\,Zn^{++} + e^{-} \qquad (I)$$

It is understood that the thermodynamic state of the Zn is that of pure solid Zn and that of Zn^{++} is that determined by the composition of the solution. The state of the electron substance is that of the electrons in the electrode of the defined standard hydrogen electrode system at equilibrium. That this is

the state of electrons in all such formulations of half-reactions is a consequence of the fact that the authors assign arbitrarily the value, zero, for the ΔF (change in free energy) accompanying the change

$$\tfrac{1}{2}\ H_2\ (ss) \rightarrow H^+\ (ss) + e^-\ (\text{in the electrode at equilibrium}) \qquad (II)$$

where (ss) denotes the hypothetical standard state. The E of the Zn, Zn^{++} junction is then defined by the relation

$$E = -\Delta F/\mathbf{F} \qquad (III)$$

where ΔF is the change in free energy accompanying the change formulated in reaction (I) above and $\mathbf{F}$ represents the faraday. It should be noted that this ΔF is not the ΔF accompanying the change

$$\tfrac{1}{2}\ Zn \rightarrow \tfrac{1}{2}\ Zn^{++} + e^-\ (\text{in the Zn electrode after contact with the solution, i.e., at equilibrium}) \qquad (IV)$$

for the value of this latter ΔF would obviously be zero.

Now if the junction is written in the reverse direction, viz., solution containing Zn^{++}; Zn, the passage of negative electricity from right to left is correlated with a change in state which is the reverse of that of reaction (I). The E ascribed to this junction would therefore be equal in absolute value but opposite in sign to that of the junction, Zn; solution containing Zn^{++}.

According to the convention regarding the emf of a voltaic cell [first adopted by Lewis and Randall (1) and universally accepted] it follows that the value of E for the junction, Zn; solution containing Zn^{++}, is related to the ΔF accompanying the isothermal change

$$\tfrac{1}{2}\ Zn + H^+\ (ss) \rightarrow \tfrac{1}{2}\ Zn^{++}\ (\text{in the solution}) + \tfrac{1}{2}\ H_2\ (ss) \qquad (V)$$

by the equation

$$E = -\Delta F/\mathbf{F} \qquad (III)$$

The standard E-value of this junction, symbolized $E°$, refers to the E-value when the Zn and the Zn^{++} are also in their standard states and is equal to +0.76 v. The $E°$-values, tabulated by Lewis and Randall (2) and by Latimer (3) are given the sign corresponding to the junction: electrode, electrolyte.

The electromotive force of any voltaic cell, as formulated, is then equal to $E_{left} + E_{right}$, where E_{left} is that of the junction (electrode, electrolyte)$_{left}$, and E_{right} is that of the junction (electrolyte, electrode)$_{right}$.

Use of the term "junction" by these authors may be misleading since changes in state considered in defining E may be misinterpreted to pertain to those changes when all the substances in the half-reactions (including the electrons) are in the states existing after contact (junction) between the electrode and electrolyte is made, i.e., after equilibrium exists in the electrode system. This interpretation is obviously not correct. The E of Lewis and Randall (2) has been more fully discussed by de Béthune (4). He designates E as the "half-cell E.M.F.," a name which is generally well-accepted.

Use of the term "potential."—It seems probable that some of the confusion now existing regarding the potentials of electrodes arises from the fact that the term "potential" has been used ambiguously quite often in the treatment of this subject. It may be noted that Lewis and Randall (2) (*see* p. 402) consider "potential" to be synonymous with the "electromotive force," E, as they define it. This does not conform with the well-accepted use of these terms. For the term "potential" to have precise meaning it must apply to some definite point or phase, not to a junction between two phases. This is true whether it is defined in an electrostatic sense or in a thermodynamic sense.

Thermodynamic basis for a new definition of the potential of an electrode and its relation to the Gibbs electrode potential (4b).—According to generally accepted views, when two different uncharged media (phases), containing charged species, ions, and/or electrons, are brought into contact, a practically instantaneous flow (through the interface) of those charged species, which the two media have in common, will occur in the establishment of equilibrium between the two media. The resultant quantity of positive charge transferred in one direction (or of negative charge in the other) can be shown to be infinitesimal (5); so infinitesimal that the change in the composition of each of the two media due to this transfer is entirely negligible. As an illustration, consider a piece of uncharged Cu and one of uncharged Zn (both at the same temperature and pressure) each conceived to consist of uncharged metal atoms, positive ions, and electrons. On contact a spontaneous and practically instantaneous flow of electrons from the Zn to the Cu will occur in the attainment of equilibrium between the two metals. Thermodynamically it follows that the chemical potential, μ_{e^-}, or more specifically in this case, the partial molal free energy, $\overline{F}_{e^-}$, of the electrons [called the electrochemical potential of the electrons by Guggenheim (6), and the electron potential by Eastman and Rollefson (7)] is greater in the uncharged Zn than in the uncharged Cu. These two partial molal free energies become equal after contact, i.e., after equilibrium is attained. Briefly $(\overline{F}_{e^-})_{Zn} > (\overline{F}_{e^-})_{Cu}$ prior to contact and $(\overline{F}_{e^-})_{Zn} = (\overline{F}_{e^-})_{Cu}$ after contact. Restated in the terminology of Lewis (*see* Ref. 2, Chapter XVI) this means that the escaping tendency of electrons from uncharged Zn is greater than the escaping tendency of electrons from uncharged Cu, each at the same temperature and pressure.

In describing the equilibrium condition existing between Cu and Zn after contact, it is often said that the electrostatic potential of the Zn is greater than that of Cu, meaning by this statement that the electrostatic potential at any point within the Zn is greater than it is at any point within the Cu. [It should be noted that this potential difference should not be identified with the "Volta" or "contact potential difference" (*see* Ref. (5a), p. 336).] That this description has no physical significance has not been generally realized. A principal of electrostatics enunciated in 1899 by Gibbs (8) justifies this con-

clusion. He wrote, "Again, the consideration of the electrical potential in the electrolyte, and especially the consideration of the difference of potential in electrolyte and electrode, involve the consideration of quantities of which we have no apparent means of physical measurement, while the difference of potential in 'pieces of metal of the same kind attached to the electrodes' is exactly one of the things which we can and do measure." In 1929 Guggenheim (6) rediscovered this principle and brought it to the attention of physical scientists. He reformulated the principle as follows: "The electric potential-difference between two points in different media can never be measured and has not yet been defined in terms of physical realities. It is therefore a conception which has no physical significance." There is no doubt that the abandonment of the use of such a conception in discussing electrode systems and voltaic cells is imperative if confusion and misleading terminology are to be avoided. If one considers that one piece of the metal M (to be used in connecting the electrodes of a voltaic cell), is connected with one of the electrodes and another piece of M with the other, then it is physically meaningful to refer to the electrostatic potential difference between these two pieces of M. (The nature of M is immaterial.) This then is the only meaning that "the electrostatic difference in potential between two electrodes" can have.

Example of the two general types of electrode systems may now be analyzed. First, consider a piece of Zn and a solution containing a Zn salt. On dipping Zn into the solution, equilibrium is established between the Zn and the solution, and also within the metallic Zn. The following thermodynamic relations will then apply:

$$(\bar{F}_{Zn^{++}})_{\text{in the Zn}} = (\bar{F}_{Zn^{++}})_{\text{in the solution}} \qquad \text{(VI)}$$

and within the Zn

$$(\tilde{F}_{Zn}) = \bar{F}_{Zn^{++}})_{\text{in the Zn}} + 2(\bar{F}_{e^-})_{\text{in the Zn}} \qquad \text{(VII)}$$

where $\tilde{F}_{Zn}$ represents the molal free energy of pure Zn.

Since at a given temperature and pressure the value of the molal free energy of Zn, $\tilde{F}_{Zn}$, is fixed, and since the value of $\bar{F}_{Zn^{++}}$ in the metal is determined by (and equal to) the value of $\bar{F}_{Zn^{++}}$ in the solution, it follows that the value of $\bar{F}_{e^-}$ in the Zn is determined by the composition of the solution of the Zn salt.

It should be noted that even though the description of the equilibrium conditions has been given in terms of the fictitious electrochemical potentials, $\bar{F}_{Zn^{++}}$ and $\bar{F}_{e^-}$, nevertheless only linear combinations of these, which appear in the treatment of voltaic cells, are definable in terms of physical realities.

A second general type of electrode system is one in which the metallic electrode is not one of the chemical reactants or products of the half-reaction involved. The hydrogen electrode system is an example of this type. Another, more simply analyzable, is the ferrous-ferric electrode system. Consider a piece of Pt (or other suitable noble metal) dipping into a solution containing ferrous and ferric salts. In this case the equilibrium condition is described by the relation

$$(\bar{F}_{Fe^{++}}) = (\bar{F}_{Fe^{+++}}) + (\bar{F}_{e^-})_{\text{in the electrode}} \qquad \text{(VIII)}$$

It is seen that the electrochemical potential of the electrons, $\bar{F}_{e^-}$, in the metal electrode is determined by the composition of the solution, i.e., by the values of $F_{Fe^{+++}}$ and of $F_{Fe^{++}}$ in the solution.

It follows that, in general, the value of the partial molal free energy of the electrons, $\bar{F}_{e^-}$, in the electrode of any electrode system at equilibrium is determined by the tendency of the substances constituting the reduced state to change to the substances, constituting the oxidized state, and to electrons in the state in which they exist in the hydrogen electrode in the standard hydrogen electrode system at equilibrium. The greater the tendency for this change to occur, that is the greater the decrease in free energy ($-\Delta F$) accompanying this change, the greater will be the value of $\bar{F}_{e^-}$ in the metal electrode of that electrode system at equilibrium. In terms commonly used, it may be said that the greater the strength of the reduced state, as a reducing agent, the greater will be the value of $\bar{F}_{e^-}$ in the electrode.

In order to give a value to the $\bar{F}_{e^-}$ in the electrode of any electrode system at equilibrium, it is necessary to assign arbitrarily the value zero to the $\bar{F}_{e^-}$ in the electrode of a specified electrode system at equilibrium. This is necessary since only differences in $\bar{F}_{e^-}$-values are physically measurable. It has been universally agreed to assign zero-value to the $\bar{F}_{e^-}$ of the electrons in the metal electrode (Pt generally used) when it is in equilibrium with hydrogen gas and hydrogen ion, each in their defined standard states, the latter in aqueous solution. This means that, according to the Lewis terminology, the fugacity of electrons in this electrode is taken as unity.

A voltaic cell in which the only significant changes in free energy accompanying the reversible isothermal flow of electricity through the cell are those occurring within the two electrode systems may be formulated

Electrode system (l), Electrode system (r) *(A)*

where l and r designate the system on the left and the one on the right, respectively. When referring to the potential (electrostatic) difference between the two electrodes, it is recalled that, to have meaning, this must refer to the potential difference between the two pieces of metal, M (usually Cu), which are considered to be attached to the two electrodes, respectively.

Consider a reversible transfer of electrons through M from the left electrode to the one on the right. This may or may not be the direction in which the transfer of electrons will occur spontaneously. Such a transfer will be accompanied by oxidation in the system on the left and reduction in the one on the right.

The resultant (total) chemical change in the cell per faraday passed is given by the general expression

$$Rd_l + Ox_r \rightarrow Rd_r + Ox_l \qquad (I)$$

where each of the four symbols represents one equivalent of each of the substances involved in the reduced and oxidized states of the respective electrode systems at equilibrium. This change in state is the resultant of the following three simultaneous changes in state:

(a) $Rd_l \rightarrow Ox_l + e^-$ (in left electrode)
$\Delta F_a = 0$

(b) e^- (in left electrode) $\rightarrow e^-$ (in right electrode)
$\Delta F_b = (\overline{F}_{e^-})_r - (\overline{F}_{e^-})_l$

(c) e^- (in right electrode) $+ Ox_r \rightarrow Rd_r$
$\Delta F_c = 0$

It is seen that $\Delta F_a + \Delta F_b + \Delta F_c$ is equal to the ΔF of the above resultant change in state, Eq. (I), which is thus given by

$$\Delta F = (\overline{F}_{e^-})_r - (\overline{F}_{e^-})_l \qquad (II)$$

Now the limiting (reversible) available work, $W'_{rev.}$, produced during this isothermal transfer of electrons from the piece of metal, M, connected with the left electrode, to the piece of metal, M, connected with the right electrode, is equal to that produced during the isothermal transfer of an equivalent quantity of positive electricity in the opposite direction, viz., from right to left through the external circuit. This quantity of work, in joules per faraday passed, is thus equal to $\mathbf{F}\,(V_r - V_l)$, where $\mathbf{F}$ is 96,491 coulombs and $V_r - V_l$ is expressed in volts. V_r and V_l are the electrostatic potentials of the pieces of metal, M, connected to the right and left electrodes, respectively. Therefore, the decrease in free energy accompanying the reaction, Eq. (I), is given by

$$-\Delta F = W'_{rev.} = \mathbf{F}\,(V_r - V_l) \qquad (III)$$

and, from the relation, Eq. (II)

$$-\Delta F = (\overline{F}_{e^-})_l - (\overline{F}_{e^-})_r = \mathbf{F}\,(V_r - V_l) \qquad (IV)$$

It is seen that if the process considered (electrons transferred from left to right through the external circuit) will occur spontaneously, i.e., $-\Delta F > 0$, then $(\overline{F}_{e^-})_l$ is greater than $(\overline{F}_{e^-})_r$ and V_r is greater than V_l. The electrostatic potential difference, $V_r - V_l$, the quantity directly measured experimentally, is equal in magnitude and sign to the electromotive force of Cell A. It should be noted, however, that $V_r - V_l$ is the difference in electrostatic potential existing between the two pieces of the metal, M, attached to the two electrodes, respectively, and not that between the two electrodes. The latter has no physical meaning.

The direct relation between the emf of any Cell A (symbolized by $E_{\text{Cell A}}$) and the value of ΔF accompanying the reaction, represented by Eq. (I), $[=(\overline{F}_{e^-})_r - (\overline{F}_{e^-})_l]$ is of primary interest to many chemists. This relation is obtained by rearranging Eq. (IV) to give

$$E_{\text{Cell A}} = -(V_l - V_r) = \frac{(\overline{F}_{e^-})_l}{\mathbf{F}} - \frac{(\overline{F}_{e^-})_r}{\mathbf{F}} = \frac{-\Delta F}{\mathbf{F}} \qquad (V)$$

From this relation, it is apparent that the quantity $\overline{F}_{e^-}/\mathbf{F}$ represents, for each electrode, an intensive-thermodynamic property, whose value is determined, as shown above, by the electrochemical equilibrium of the substances constituting the oxidized state, those constituting the reduced state, and the electrons in the electrode. Differences between the values of this thermodynamic property for different electrode systems determine the electromotive forces of cells made by combining any two electrode systems, as shown in Eq. (V). This thermodynamic property is a potential, in volts, and should be designated by an appropriate name and symbol. The symbol adopted here is the script capital $\mathcal{E}$, and it is suggested that the quantity $\mathcal{E}_i$, to be defined by the equation

$$\mathcal{E}_i = (\overline{F}_{e^-})_i/\mathbf{F} \qquad (VI)$$

should be designated as the "electron chemical potential" of the *ith* electrode (in volts). This designation seems meaningful and unambiguous.

The electron chemical potential $\mathcal{E}$ coincides in sign (and magnitude) with a quantity to which MacDougall (1c) gave the name, "electrode E.M.F." However, in definition, the two quantities are fundamentally different, since nothing is said in the definition of $\mathcal{E}$ about the "potential difference between two phases" [Ref. (1c), page 580], and the latter phrase has been shown above to be devoid of physical significance. On the other hand, the designations "electrode emf" and "half-cell emf" have been much more commonly applied to the E of Lewis and Randall (2), a quantity which (as shown above) changes its sign when the half-cell diagram and half-cell reaction are reversed, viz., from electrode, electrolyte to electrolyte, electrode. Thus there is justification for the new name "electron chemical potential" and for the new symbol $\mathcal{E}$ for the potential defined here.

The emf of Cell A is then given by

$$E_{\text{Cell A}} = \mathcal{E}_l - \mathcal{E}_r = -(V_l - V_r) \qquad (VII)$$

It may be noted that the sign of the value of $E_{\text{Cell A}}$ thus obtained conforms to the convention regarding the sign to be given to the emf of a cell which has been recommended by the Commission on Physico-Chemical Symbols and Terminology and the Commission on Electrochemistry of the International Union of Pure and Applied Chemistry (9) meeting in Stockholm in 1953. As previously mentioned this convention was originally adopted by Lewis [*see* Ref. (2), p. 390]. de Béthune (4*b*) has given a thorough discussion of the recommendations of these Commissions, and a valuable synthesis of the electrochemical thermodynamic conventions of Nernst, Lewis and Randall, together with those of the Stockholm Commissions, and with the thermodynamic treatment of Gibbs. Also certain important historical facts pertinent to the development of this subject are to be found in this paper.

The electron chemical potential of the electrode of any electrode system at equilibrium may now be defined by the relation

Electron chemical potential of the *ith* electrode

$$= \mathcal{E}_i - \mathcal{E}^\circ_{H_2} \qquad \text{(VIII)}$$

where $\mathcal{E}^\circ_{H_2}$ refers to the electron chemical potential of the electrode (Pt) in equilibrium with $H_2(g)$ and $H^+ \cdot Aq$, each in their defined standard states. The Gibbs electrode potential, V, is defined by the relation

Gibbs electrode potential of the *ith* electrode

$$= V_i - V^\circ_{H_2} \qquad \text{(IX)}$$

where the V's represent the electrostatic potentials of the two pieces of the metal, M (to be used in connecting the electrodes), attached to each of the two metal electrodes of the two electrode systems at equilibrium.

If now the electrode system on the left in the Cell A (formulated above) is considered to be any electrode system and the one on the right to be the standard hydrogen electrode system, it follows from Eq. (VII) that

$$E_{cell} = \mathcal{E}_i - \mathcal{E}^\circ_{H_2} = -(V_i - V^\circ_{H_2}) \qquad \text{(X)}$$

Since $\mathcal{E}^\circ_{H_2}$ is arbitrarily taken as zero, as is also $V^\circ_{H_2}$, it follows that

$$\mathcal{E}_i = -V_i \qquad \text{(XI)}$$

It is therefore evident that when the potential of an electrode is given its $\mathcal{E}$-value, the word, "potential," is used in a thermodynamic sense in that it refers to the electron chemical potential of the electrode. When given its V-value, "potential" is defined in its electrostatic sense and refers to the piece of connecting metal, M, attached to the electrode. It is the latter which is referred to by de Béthune (4*b*) as "the Gibbs electrode potential." For example, $\mathcal{E}^\circ(Zn, Zn^{++}) = +0.76$ and $V^\circ(Zn, Zn^{++}) = -0.76$.

It should be noted that the sign of the value of $\mathcal{E}_i$, as defined above, is independent of the direction of the reversible flow of electrons (through the connecting wire), as is also the sign of V_i. In other words, its sign (and value) is the same whether the reversible process considered makes the electrode in question the cathode or the anode, that is the sign of $\mathcal{E}$ is invariant. Thus $\mathcal{E}$ differs fundamentally from the E as defined by Lewis and Randall and as used by most American physical chemists. The sign of E is bivariant. Both $\mathcal{E}_i$ and V_i may be properly considered to be intensive properties of any electrode system, *i*, at equilibrium at a certain temperature and pressure, and their signs and values are consequently independent of the direction of the reversible process under consideration. The V-values (the Gibbs electrode potentials) of electrodes are used by electrochemists, most European chemists, and many biological and analytical chemists. It is important to note that the "potential" of an electrode as defined by its $\mathcal{E}$-value is fundamentally different from "potential" as defined by its V-value even though the two values are very simply related ($\mathcal{E}_i = -V_i$). The value of $\mathcal{E}_i$, that is of $\mathcal{E}_i - \mathcal{E}^\circ_{H_2}$, is correctly described as a measure of the difference between the escaping tendency of the electrons in the electrode of the *ith* electrode system at equilibrium and that of the electrons in the electrode of the standard hydrogen electrode system at equilibrium. The escaping tendency of the electrons in an electrode, as defined here, is measured by the partial free energy per coulomb of the electrons in that electrode.

Justification for the use of two sign conventions.— Valid reasons can be given for the designation of the potentials of electrodes by their V-values as is done by electrochemists, most European chemists, and many biological and analytical chemists. The V-values have the practical advantage, namely, that the electrode of a voltaic cell which has the larger V-value, that is, the larger electrostatic potential of the piece of connecting metal attached to it, is designated "the positive pole." The relative polarity of the two electrodes of a cell follows directly from the relative V-values of the two pieces of the same metal connected with the two electrodes. Also, it is the difference, $V_r - V_l$, which is experimentally measured in determining the emf of a cell, that is $(emf)_{cell} = V_r - V_l$.

Those chemists who, along with the author, choose to designate the potentials of electrodes by their $\mathcal{E}$-values (as defined in this paper and named "electron chemical potentials") can find justification for their choice in the fact that the emf of a cell follows in a more direct thermodynamic way from the two $\mathcal{E}$-values. The $\mathcal{E}$-value of an electrode is directly proportional (proportionality constant = $1/\mathbf{F}$) to the value of the partial molal free energy (chemical potential) of the electrons in the electrode of the electrode system at equilibrium. It is the difference between the two $\overline{F}_{e^-}$-values which gives directly the value of ΔF (per faraday) accompanying the isothermal change in state in the cell. The basis for these statements is shown by the following relations applicable to any voltaic cell, as symbolized by Cell A, per faraday of electrons passed reversibly through the outer circuit from the left-hand electrode to the right-hand electrode.

$$(emf)_{cell} = \frac{(\overline{F}_{e^-})_l}{\mathbf{F}} - \frac{(\overline{F}_{e^-})_r}{\mathbf{F}} = \mathcal{E}_l - \mathcal{E}_r$$

and

$$\Delta F \text{ (per faraday passed)} = (\overline{F}_{e^-})_r - (\overline{F}_{e^-})_l = \mathbf{F}(\mathcal{E}_r - \mathcal{E}_l) = -\mathbf{F}(\mathcal{E}_l - \mathcal{E}_r) = -\mathbf{F}(emf)_{cell}$$

It may be recalled that the value of the so-called "potential," E, as defined by Lewis and Randall (2), is such that the emf of a voltaic cell, as formulated, is given by the relation

$$(emf)_{cell} = E_l + E_r = E(\text{electrode, electrolyte}) + E(\text{electrolyte, electrode})$$

The value of the emf of a voltaic cell in terms of V, $\mathcal{E}$, and E is thus given by

$$(emf)_{cell} = V_r - V_l = E_l + E_r = \mathcal{E}_l - \mathcal{E}_r$$

where the meaning of the Lewis and Randall expression, $E_l + E_r$, is that given above.

Continued use by some chemists of the V-values for the potentials of electrodes (with one sign con-

vention) and of the $\mathcal{E}$-values by other chemists (with the opposite sign convention) seems completely justifiable.

In phraseology commonly used in the discussion of half-cells, it may be of value to reiterate that in any electrode system the greater the tendency of the substances in the reduced state to change to the substances in the oxidized state, and to electrons, in the thermodynamic state in which they exist in the electrode of the standard hydrogen electrode system at equilibrium, the greater will be the value of $\mathcal{E}$ (as defined in this paper) and the less will be the value of V, both on an algebraic scale.

Acknowledgment

The author wishes to thank Professor André J. de Béthune for his generous assistance in the clarification and organization of this presentation.

Manuscript received Jan. 3, 1956.

Any discussion of this paper will appear in a Discussion Section to be published in the December 1957 JOURNAL.

REFERENCES

1. As examples, *see* (*a*) F. Daniels and R. A. Alberty, "Physical Chemistry," pp. 422-431, John Wiley & Sons, Inc., New York (1955); (*b*) Linus Pauling, "General Chemistry," 2nd ed., pp. 652-654, W. H. Freeman and Co., San Francisco (1953); (*c*) F. H. MacDougall, "Physical Chemistry," 3rd ed., pp. 609-610, The Macmillan Co., New York (1952); (*d*) C. F. Prutton and S. H. Maron, "Fundamental Principles of Physical Chemistry," Revised Ed., p. 531, The Macmillan Co., New York; (*e*) A. A. Noyes and M. S. Sherrill, "A Course of Study in Chemical Principles," 2nd ed., pp. 366-370, The Macmillan Co., New York (1938).
2. G. N. Lewis and M. Randall, "Thermodynamics and the Free Energy of Chemical Substances," pp. 402-404, McGraw-Hill Book Co., Inc., New York (1923).
3. W. M. Latimer, "Oxidation Potentials," 2nd ed., Prentice-Hall, Inc., New York (1952); *see* also Latimer, *J. Am. Chem. Soc.*, **76**, 1200 (1954).
4. A. J. de Béthune, (*a*) *This Journal*, **101**, 252C (1954); (*b*) *ibid.*, **102**, 288C (1955).
5. (*a*) E. A. Guggenheim, "Thermodynamics," Chap. X, p. 331, Interscience Publishers, Inc., New York (1949); (*b*) A. A. Noyes and M. S. Sherrill, "Chemical Principles," 1st ed., p. 255, The Macmillan Co., New York (1929).
6. E. A. Guggenheim, *J. Phys. Chem.*, **33**, 842 (1929); also E. A. Guggenheim, ref. (5*a*), pp. 331-332.
7. E. D. Eastman and G. K. Rollefson, "Physical Chemistry," pp. 438-440, McGraw-Hill Book Co., Inc., New York (1947).
8. "The Collected Works of J. Willard Gibbs," Vol. 1, p. 429, Longmans, Green and Co., New York (1928).
9. J. A. Christiansen and M. Pourbaix, *Compt. rend. XVII Conf. Inter. Union Pure and Appl. Chem.*, held in Stockholm in 1953, pp. 82-84, Maison de la Chimie, Paris (1954).

Effect of Pre-Oxidation in Oxygen on the Steam Corrosion Behavior of Zircaloy-2

D. E. Thomas and S. Kass

Atomic Power Division, Westinghouse Electric Corporation, Pittsburgh, Pennsylvania

ABSTRACT

The effect of pre-oxidation in dry oxygen gas on the corrosion behavior of Zircaloy-2 and unalloyed zirconium in steam was investigated. In the case of Zircaloy-2, pre-oxidation has no effect on corrosion behavior, the kinetics being the same whether all or part of the total exposure is in oxygen. A transition in kinetics from quasi-cubic to linear occurs in the corrosion of Zircaloy-2 in either medium, indicating that the transition is not associated with corrosion product hydrogen. On the other hand, unalloyed Zr shows neither transition nor breakaway (spalling) when exposed to oxygen, and exhibits breakaway on exposure to steam whether pre-oxidized or not, suggesting that breakaway is associated with corrosion product hydrogen. The phenomena of breakaway and transition are shown to be distinctly different.

The corrosion properties of Zircaloy-2 sponge Zr base with 1.5% Sn, 0.12% Fe, 0.10% Cr, and 0.05% Ni have been studied as a function of temperature and time (1, 2). The corrosion behavior in 750°F (400°C) steam at 1500 psi, Fig. 1, exhibits a change in slope ("transition") at a weight gain of 40 mg/dm^2 after 40 days (3). It has been shown that Zr and Zircaloy-2 pick up H during exposure to high temperature water or steam, and it has been suggested that the transition normally results when the pick-up of H during corrosion causes hydride to form at the metal/oxide interface or at some other site in the reaction zone.

If hydride formation is a factor in causing transition, specimens which have been exposed to dry oxygen for various periods of time and subsequently transferred to steam should show transition at total weight gains and total times greater than those for specimens not previously oxidized in dry oxygen. Furthermore, specimens which have been exposed only to dry oxygen should not show transition. The purpose of the work described here was to determine the effect of pre-oxidation in oxygen on the transition during subsequent exposure to steam at the same temperature, and thereby test the hypothesis.

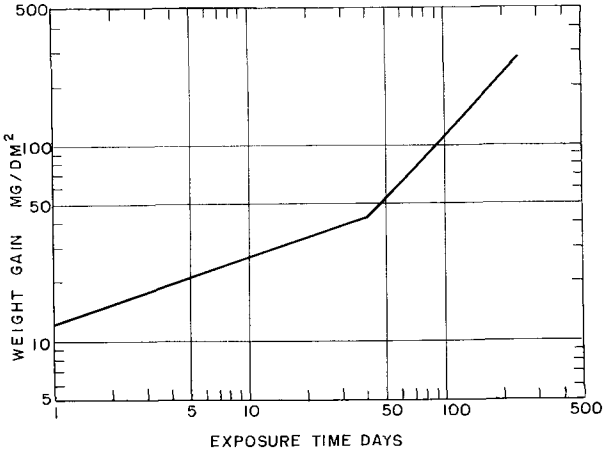

Fig. 1. Corrosion of Zircaloy-2 in steam at 750°F (400°C) and 1500 psi.

In the case of unalloyed, arc-melted sponge or crystal bar Zr, corrosion in high temperature water and oxygen is characterized by the formation of thin, adherent corrosion product which results in a protective or passive type of rate law relating weight gain and exposure time. After a time a new and more rapid corrosion rate sets in, coincident with the appearance of a nonadherent white corrosion product on the surface of the metal. This behavior has been called "breakaway". Specimens of crystal bar Zr were included in this study to provide a point of comparison with Zircaloy-2.

Experimental Procedure

Approximately forty specimens each of arc-melted crystal bar Zr and Zircaloy-2, measuring 1.0 in. x 0.5 in. x 0.1 in., were vacuum annealed for 1 hr at 775°C and furnace cooled. Specimens were bright etched in 38% HNO_3-5% HF-57% H_2O and were placed in the oxidation furnace. After a vacuum of 10^{-6} mm Hg was obtained, the entire system was flushed two or three times with tank oxygen dried by passing through "Drierite". After each addition of oxygen, the system was evacuated to 10^{-6} mm Hg. Finally, oxygen was added to the furnace until a pressure of 30-40 cm Hg was reached and heat was applied.

The temperature of 400° ±3°C was maintained by a thermocouple placed adjacent to the test specimens. This temperature was chosen since considerable data are available for comparison on the corrosion of Zircaloy-2 in 750°F (400°C) steam.

Three specimens each of crystal bar Zr and Zircaloy-2 were removed from the furnace after 1, 3, 7, 14, 28, 56, 84, and 112 days and subsequently transferred to steam at 750°F (400°C) and 1500 psi.

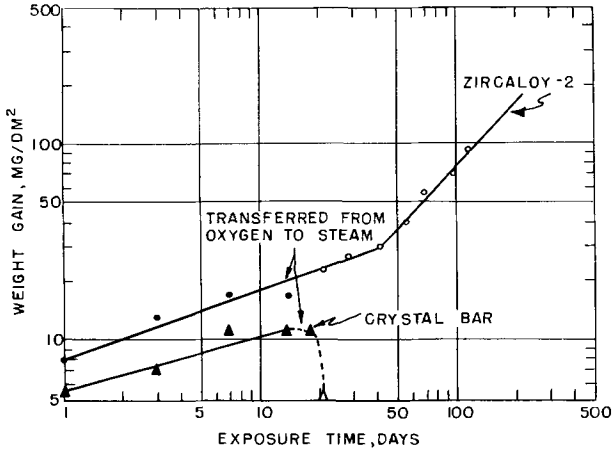

Fig. 2. Weight gain-time curves for exposure of crystal bar Zr and Zircaloy-2 at 750°F (400°C) for 14 days in oxygen followed by exposure to steam. Crystal bar Zr begins to lose weight on transfer. Solid circle, solid triangle = oxygen; open circle, open triangle = steam.

The evacuation and flushing technique outlined above was followed each time samples were returned to the furnace.

Weight gains were determined periodically during initial and final exposures. The corrosion product was not removed when samples were transferred.

Results

Results are represented graphically in Fig. 2, 3, 4, and 5.

Zircaloy-2.—The kinetics of the reaction of Zircaloy-2 with oxygen, shown in Fig. 4, are identical to those for reaction with steam shown in Fig. 1. Results shown in Fig. 2 and 3 are typical of those experiments in which the exposure was first in oxygen then in steam. It is seen that corrosion proceeds after transfer as though the entire exposure had been in steam. The interchangeability of exposure in the two media is exhibited in Fig. 5 in which data points for exposure to steam alone, oxygen alone, and to first oxygen then steam are combined. A single curve results within experimental error.

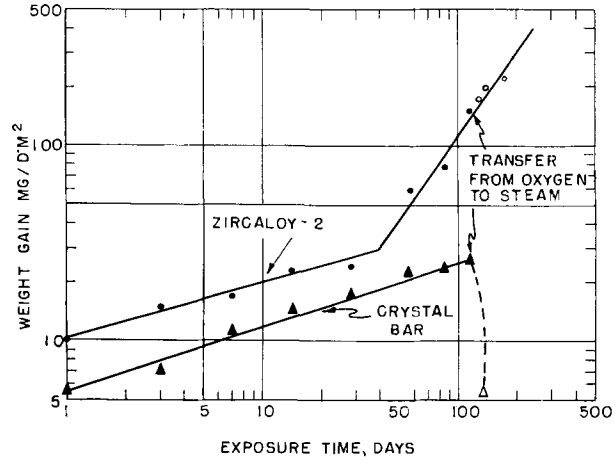

Fig. 3. Weight gain-time curves for exposure of crystal bar Zr and Zircaloy-2 at 750°F (400°C) for 112 days in oxygen followed by exposure to steam. Crystal bar Zr begins to lose weight on transfer. Solid circle, solid triangle = oxygen; open circle, open triangle = steam.

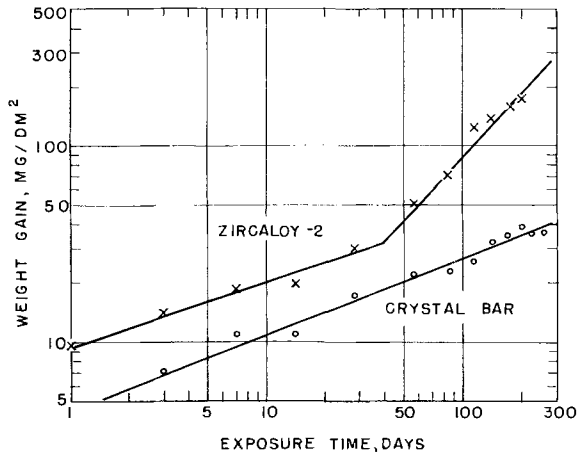

Fig. 4. Weight gain-time curve for corrosion of crystal bar Zr and Zircaloy-2 in oxygen at 750°F (400°C).

Crystal bar zirconium.—The kinetics of reaction of crystal bar Zr with oxygen are shown in Fig. 4. It is seen that the curve is quite different from that for Zircaloy-2. Significantly, transition is not apparent. This is not characteristic of the behavior of crystal bar Zr or sponge Zr in high temperature water or steam. No curves are shown for the attack of crystal bar Zr by 750°F (400°C) steam because "breakaway" and loss of oxide occur within the shortest exposure period investigated (1 day). Typical of the experiments in which crystal bar Zr was first exposed to oxygen then to steam are the results shown in Fig. 2 and 3. Upon transfer from oxygen to steam the specimens begin immediately to lose weight by spalling.

It should be noted here that the crystal bar Zr employed was of high purity. Isolated instances in which crystal bar Zr has shown higher resistance to attack by 750°F steam have been associated with the presence of somewhat greater than normal Fe, Ni, or Cr content.

Discussion

The observation that part of the H evolved by the reaction of Zr or Zircaloy-2 with water or steam is found in the unreacted metal has been thought to be

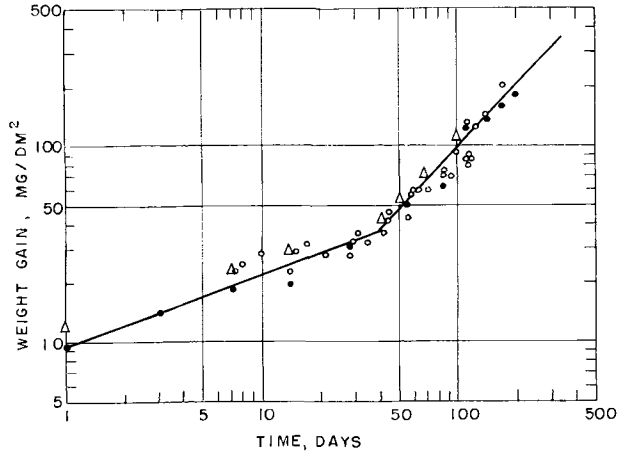

Fig. 5. Combined plot for the corrosion of Zircaloy-2 in oxygen, steam, and in oxygen followed by steam at 750°F (400°C). Solid circle = oxygen; open triangle = steam; open circle = oxygen and steam.

of considerable significance (1, 2, 4, 5). It has been suggested that the H content of the underlying metal may build up sufficiently to cause the precipitation of a zirconium hydride at the metal/oxide interface which could destroy coherency between metal and oxide, and result in more rapid corrosion locally, or possibly complete loosening of the oxide (1, 2). It was suggested that this would explain the phenomena of "breakaway" in the case of Zr and "transition" in the case of Zircaloy-2. In view of the fact that transition is observed for Zircaloy-2 whether the exposure is in oxygen or steam or both removes H from consideration.

On the other hand, the fact that crystal bar Zr does not exhibit transition or breakaway on exposure to oxygen suggests that H is in some way related to breakaway. Specimens of crystal bar Zr which had been exposed to steam for one day and which had begun to lose oxide were examined in cross section under the light microscope. No evidence for hydride was found. Thus, the circumstantial evidence points to H being associated with the breakaway phenomena, but it is evident that further work is necessary to secure direct evidence.

The results of these experiments suggest that a distinction is to be made between two terms which have been used to denote the point at which a change in kinetics occurs, namely breakaway and transition. Transition appears to be an abrupt change from protective-type kinetics (quasi-cubic) to linear corrosion kinetics, the newer corrosion rate being somewhat greater than that prevailing immediately prior to the change. The corrosion product remains adherent. It is not associated with the pickup of corrosion-product H, but is presumably associated with some as yet undetermined physical change in the oxide film. On the other hand, breakaway, while it refers to a change of kinetics in that a new corrosion rate sets in, is characterized by the loss of oxide at a relatively rapid rate, and is presumably associated in some way with the pickup of H. Since crystal bar Zr does not show transition or breakaway when exposed to oxygen, but does exhibit breakaway when exposed to steam, and since Zircaloy-2 exhibits transition but not breakaway in both oxygen and steam, it is apparent that the addition of Sn in combination with Fe, Ni, and Cr in Zircaloy-2 prevents the occurrence of breakaway. The elimination of breakaway by the addition of these elements may be associated with a change in the behavior of the material toward H in some way which is not apparent at present. Furthermore, it is not yet understood why Zircaloy-2 shows transition while crystal bar Zr does not.

Conclusion

1. Zircaloy-2 exhibits the same behavior in oxygen and steam at 750°F (400°C). Transition is not associated with the pickup of H.
2. Crystal bar Zr exhibits breakaway when exposed to steam. It exhibits neither breakaway nor transition when exposed to oxygen.
3. A distinction between "transition" and "breakaway" is made. Transition is not associated with H pickup during corrosion. Breakaway is presumably associated with H pickup.
4. The addition of some alloying elements to crystal bar Zr prevents the occurrence of breakaway, but promotes the occurrence of transition.

Acknowledgment

This work was performed under AEC Contract AT-11-1-GEN-14.

Manuscript received September 4, 1956.

Any discussion of this paper will appear in a Discussion Section to be published in the December 1957 JOURNAL.

REFERENCES

1. B. Lustman and F. Kerze, Editors, "Metallurgy of Zirconium," Vol. 4, Div. VII, Chap. II, McGraw Hill Book Co., New York (1955).
2. D. E. Thomas, "Aqueous Corrosion of Zirconium and its Alloys at Elevated Temperature", U.S. Paper No. 537, Geneva Conference (1955).
3. D. E. Thomas and S. Kass, *This Journal*, **103**, 478 (1956).
4. K. M. Goldman and D. E. Thomas, "Hydrogen Pickup during Corrosion Testing of Zirconium," unpublished work.
5. S. Kass, Work in progress.

A Hydrogen Effusion Method for the Determination of Corrosion Rates in Aqueous Systems at Elevated Temperature and Pressure

M. C. Bloom and M. Krulfeld

Metallurgy Division, Naval Research Laboratory, Washington, D. C.

ABSTRACT

This paper analyzes the limitations of weight change techniques at elevated temperature and pressure, and presents a description of a new technique based on the measurement of the hydrogen generated by the corrosion reaction. This H, which diffuses through the walls of a test specimen containing the aqueous solution, is collected and measured in a vacuum system of known volume which surrounds the test specimen; the corrosion rate is calculated from the hydrogen effusion rate. Results obtained with the technique show good reproducibility and compare well with results obtained by an independent method.

Corrosion rates of metals in aqueous solutions at elevated temperature and pressure have been obtained almost exclusively by weight gain or weight loss measurement of specimens subjected to corrosion in autoclaves of various types (1-4). Such measurements are inherently difficult. Loss of corrosion products by spalling or dissolution introduces serious errors into weight gain data. Weight loss data are reliable only if complete removal of corrosion products without attack on the uncorroded metal beneath can be obtained. Galvanic effects between autoclave and specimens may affect the results obtained if the two differ in composition or treatment history prior to the test. One of the most serious limitations is that from a single specimen only a single value of total corrosion can be obtained from which only an "average" corrosion rate over the period of exposure can be calculated. In the usual case, however, where corrosion resistance depends on the type of protection provided by corrosion product films, such average rates are misleading. The information needed in such cases is the differential corrosion rate. Using weight gain and weight loss methods, differential rates can be obtained only by corroding a large number of samples under the given conditions for varying times, the rates being obtained by differences between the gains or losses of the specimens at the different time intervals. Since reproducibility from sample to sample determines the accuracy of any rates calculated by difference, and since reproducibility using these techniques is usually not good, a large number of samples must be run simultaneously to obtain dependable average values for such calculations. These limitations of weight gain and weight loss methods are particularly serious when the corrosion rates are low.

To overcome the difficulties enumerated, a method was developed in which there is no error due to loss of oxide or of metal in the measuring process, the sample constitutes its own autoclave, samples need not be destroyed in the process of measurement, and observation can be continuous on a single sample so that a differential corrosion rate can be determined using only one specimen.

Theoretical Considerations

Examination of the reaction

$$\text{Metal} + H_2O \rightarrow \text{Metal Oxide} + H_2 \qquad \text{(I)}$$

indicates four possible methods of measuring corrosion rate, i.e., measurement of *(a)* metal consumed, *(b)* water consumed, (c) metal oxide formed, and *(d)* hydrogen formed. Methods *(a)* and *(c)* entail the difficulties outlined above, and method *(b)* involves analogous difficulties, so attention was turned to method *(d)*. Since H_2 diffuses rather readily through metals at elevated temperatures, the possibility of correlating effused H_2 with the corrosion reaction was investigated.

In a container of the metal under test, nearly filled with water or an aqueous solution, and heated to an elevated temperature, H_2 is generated by the corrosion reaction. It is generated initially as atomic H at the interface between liquid and container. It may pass through the container wall in this form to emerge on the other side and there combine to form molecular H_2, or it may recombine to form molecular H_2 within the container. In the latter case, the H_2 gas initially distributes itself between the liquid and the available vapor space but, as it builds up pressure, some of this H_2 also diffuses through the container wall. Thus, there are two sources of H_2 passing through the container wall. H_2 from the latter source permeates the wall at a rate governed by the equation

$$dQ/dt = S_T\, A\, (\sqrt{P_1} - \sqrt{P_2})/d \qquad \text{(II)}$$

where dQ/dt is the amount effused per unit time, S_T is a constant determined by the nature of the metal and the temperature, A is the area of the metal, d is the thickness, P_1 is H_2 pressure on the high-pressure

side, and P_2 the H_2 pressure on the low-pressure side. If P_2 is maintained at a negligible value the equation reduces to

$$dQ/dt = S_T A \sqrt{P}/d \qquad \text{(III)}$$

where P is H_2 pressure within the container. As the corrosion reaction proceeds the pressure inside the container increases until *(a)* the rate of effusion from both sources becomes equal to the corrosion rate, or *(b)* the pressure inside the container continues to increase until the equilibrium pressure of the reaction is reached or the container is shattered. In the case of ferrous metals, the latter would be expected.

The data on S_T for mild steel (5, 6) indicate it is approximately 10^{-2} at 300°C when dQ/dt is in cc H_2 (STP)/hr, A is in cm^2, d is in mm, and P in atmospheres. Assuming a mild steel container with a wall 0.5 mm in thickness and an internal H_2 pressure of 1 atm, rates of H_2 effusion equivalent to a corrosion rate of 2700 mg/dm^2-mo are obtained based on the reaction $3Fe + 4H_2O \rightarrow Fe_3O_4 + 4H_2$. This is a much greater rate than would be anticipated for the corrosion of mild steel under these conditions (1) and indicates that a low H_2 pressure should be sufficient to obtain the required steady-state effusion rate.

In order to reach the steady state rapidly a maximum area to volume ratio, a minimum thickness of wall, and a minimum of vapor space are desirable. For a maximum A/V in a cylinder, where

$$A/V = \frac{2\pi r^2 + 2\pi rh}{\pi r^2 h} = \frac{2}{h} + \frac{2}{r} \qquad \text{(IV)}$$

the smallest dimensions feasible should be used. To avoid vapor space the capsule should be filled so that it develops a hydraulic pressure slightly in excess of the vapor pressure of the fluid at the temperature of test. This can be achieved by flattening a cylindrical container prior to complete filling and sealing. Upon heating, the flattened cylinder will react to the hydraulic pressure by expanding partially toward its original dimensions, developing an internal pressure which will depend on the amount of flattening and the thickness and character of the metal.

Based on the above considerations a technique was developed for the measurement of corrosion at elevated temperature and pressure employing a small, thin-walled, flattened capsule of the metal under test, heated within a vacuum system which was provided with means for measuring the amount of effused H_2.

Experimental Apparatus and Procedures

Metal tubing carefully fabricated to develop a smooth uniform interior surface free of foreign matter (preferably made in one lot from a single ingot) is used to encapsulate a small quantity of corroding fluid. A fluid-filled capsule, attached to a counterweight of magnetic material so that it can be moved up and down by an external magnet, is then inserted in the experimental apparatus shown in Fig. 1. After the capsule is dropped into the oven, H_2 is generated by corrosion and effuses through the capsule walls to build up a pressure in the surrounding

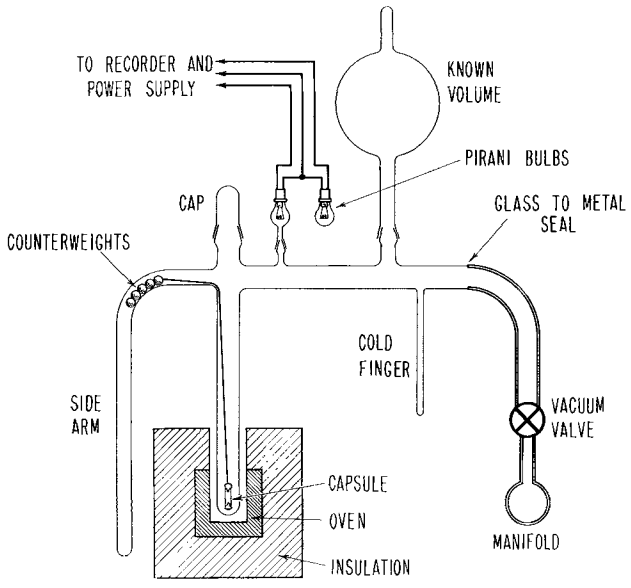

Fig. 1. Single system for hydrogen effusion measurement

glass envelope. This pressure is continuously recorded by the Pirani gauge circuit.

In actual operation a number of such systems are connected in parallel to a common furnace, pumping system, and associated apparatus. The furnace is a cast block of Al 8 ft long and 5 in. square drilled with 15 holes 1¼ in. in diameter and 3½ in. deep. The furnace is insulated with 2 in. of glass wool housed in an asbestos sheet duct 9 in. square and 3/16 in. thick. It is heated by means of cartridge heaters maintained at temperature by a thermocouple-actuated control circuit which maintains the temperature within ±2°C.

Fabrication of Capsules

The following description is based on operations with low-carbon steel, with which the work thus far has been mostly concerned. Procedures for other materials differ only in minor details.

One-foot lengths of seamless low-carbon steel tubing 0.25 in. in external diameter and 0.020 in. thick are washed in a hot detergent solution, degreased in hot trichloroethylene, and dried. They are then given a H_2 anneal, usually followed by a vacuum anneal, prior to fabrication in order to obtain clean oxide-free reproducible metal. The H_2 anneal is for 1 hr at 875°C, followed by cooling in the H_2 atmosphere to about 90°C in a water-cooled chamber. If a vacuum anneal is given, the tubing is placed in a vacuum furnace maintained at a pressure of less than 10^{-5} mm Hg, heated at 875°C for a minimum of 1 hr, and furnace cooled to room temperature.

In the fabrication procedure the annealed tubing is subjected first to a flattening operation with a hydraulically operated die. A second die with equally spaced flat teeth then outlines the capsule form. In this form the tubing, held vertically, is completely filled, by aspiration, with the fluid to be used as the corroding medium. Another die then closes the bottom flat section under a pressure of several tons per square inch. The die is moved upward to seal the ends of each filled capsule section successively. The

capsules are then separated by cutting across the centers of the flat sealed sections and are made pressure tight by spot welding across the flat ends. The over-all length of the finished capsule is 4 cm, of which the completely flattened, welded ends constitute 1 cm and the fluid-filled capsule section constitutes 3 cm. The over-all width of the capsule perpendicular to the flat sides is 0.28 cm.

Operation of Apparatus

Each capsule is connected by means of thin, flexible Pt-clad Mo wire to Ni-plated steel counterweights, and the capsule and counterweights are inserted in the vacuum system (Fig. 1). The capsules are maintained in the room temperature section of the apparatus by manipulation of external magnets. The system is sealed and then outgassed by opening the vacuum valve to the manifold. After overnight outgassing, a run is started by closing the vacuum valve to the manifold and raising the counterweights until the capsule drops into the furnace zone which is maintained at the desired temperature. The capsule heats rapidly as evidenced by a sudden, very rapid increase in the pressure within the system. The pressure rise, due to the corrosion-generated H_2 effusing through the capsule wall and collecting in the system, is measured by means of the Pirani bulb, connected in a calibrated bridge circuit whose output is recorded. To insure accuracy, the pressure measuring system is calibrated with pure dry H_2 gas and a McLeod gauge before each run.

When the pressure within the system reaches a value of about 50 μ, a pressure sufficiently low to make Eq. (III) valid, the system is pumped down to a pressure of less than 0.1 μ by opening the valve to the manifold and pumping system. After pumpdown the valve is again closed until the system pressure builds up again; the process is repeated as frequently as necessary.

The rate of pressure buildup for mild steel varies over a wide range. At the beginning of a run, a buildup of 50 μ in 3 min is not uncommon. After several months, when the formation of a protective film has reduced the corrosion rate, a buildup of the order of 2 μ a day is observed. Fluid leakage can readily be identified by chilling the cold finger shown in Fig. 1. If the presence of gases other than H_2 is suspected in the system, a rough check can be made by connecting an absolute gauge, such as a McLeod gauge, to the manifold. Unlike an absolute gauge, the Alphatron vacuum gauge shown connected to the manifold is sensitive to the nature of the gas being measured. If the Alphatron gauge, using the calibration curve for H_2, gives a pressure reading different from that indicated by the McLeod gauge after the unit has been opened to the manifold, the presence of gases other than H_2 is indicated. If it can be assumed that the foreign gas is air or water, the above readings also permit a rough calculation of the amount of foreign gas present. If more accurate analyses are desired, gas from any of the systems can be transferred to a gas analysis system.

A slight pressure rise not attributable to effusing H_2 has been encountered in gas-tight systems, varying from less than 0.01 μ/hr to a rise as high as 0.15 μ/hr, with average values of about 0.05 μ/hr being found most frequently. A pressure buildup of 0.05 μ/hr corresponds to a corrosion rate of approximately 4 mg/dm^2-mo under the conditions of operation. The exact nature of the residual pressure is not yet known, but it can probably be attributed to gas adsorbed on the walls and parts of the system which slowly desorbs at the low pressures normally used in making these measurements.

While the apparent corrosion rates due to causes other than corrosion within the capsules are low and do not affect significantly values obtained during early portions of a run when the corrosion rates are high, they become significant when the corrosion rate has diminished. They must, therefore, be evaluated and subtracted from the measured rates in order to obtain corrected corrosion rates. These "blank rates" for the individual system are obtained readily by raising the corroding capsule out of the hot zone of the system during the course of a run. The capsule then cools rapidly to room temperature, the corrosion rate dropping substantially to zero. The capsule is maintained in this position until sufficient pressure rise has been obtained for an accurate determination of the blank rate. Normally the rate is so low that at least five days of pressure buildup is required. The capsule is then returned to the hot zone of the system, with no disturbance other than the temporary change in temperature. Ordinarily the corrosion rate measured after the determination of the blank rate is approximately the same as that measured before the thermal shock imposed by the blank-rate measurement (Fig. 2). In a few cases some change in the corrosion rate has been encountered.

Determination of System Constants

The volume of a system is measured by expanding gas from a reservoir of known volume into the system. Pressures in the system and reservoir are measured before and after expansion and the system volume is calculated from these pressures using the gas laws. The arithmetic mean of several such

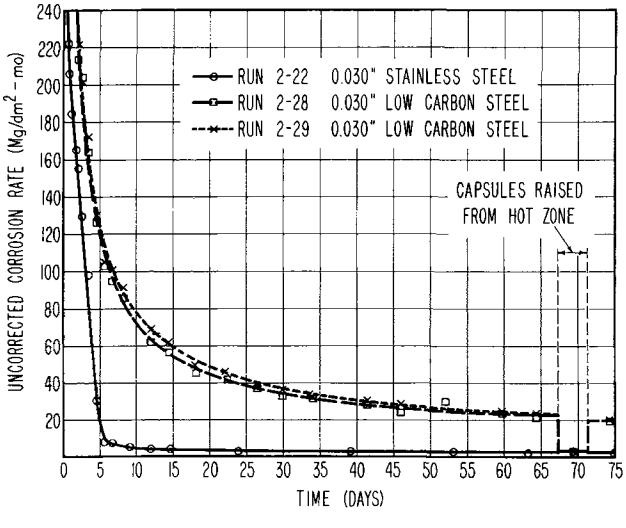

Fig. 2. Corrosion at 316°C of capsules containing NH_4OH (pH = 10.6 at room temperature).

measurements is taken to be the system volume. By this method the system volume is determined with an estimated accuracy of ±1.5%. These systems normally have a volume of about 2700 cc. If a more rapid rate of pressure buildup is desired, the system volume may be reduced by removing the bulb of known volume (approximately 2 liters) (Fig. 1), and replacing it with a cap.

The mean temperature of the gas in the system is taken to be the temperature of the room in which the apparatus is situated (maintained constant within ±1°C), modified by correcting for the higher temperature of that small part of the system which is in the heated zone. Data for this correction are obtained by thermocouple measurements of the temperature distribution within this heated zone. In this manner the mean temperature of the gas is determined with an estimated accuracy of ±1%.

Assuming that the surface area of a length of tubing undergoes negligible change in the flattening processes used in capsule fabrication, the inside surface area of a capsule is calculated from the length of tubing between the seals and the known dimensions of the tubing. The roughness factor was estimated as 1.2 from microscopic examination. Measurements on a large number of capsules indicate that variables in the fabrication process produce capsules which vary in length from 2.9 to 3.3 cm, the average length being 3.1 cm. There is a corresponding variation of inside surface area, the average surface area being 5.2 cm^2.

Determination of Pressure Rise

Pressures in the system are measured by means of a Pirani vacuum gauge that is a modification of that described by Schwartz and Lavender (7). The output of the Pirani circuit is recorded continuously to give a record of the pressure buildup within the system. At the beginning of each run the Pirani gauge is calibrated by determining the relationship between the Pirani output and the H_2 pressure in the system. The linear portion of this relation (pressures up to 60 μ) is then used for pressure determination. Although indications are that the errors involved are minor, certain gauge characteristics give rise to possible errors not yet evaluated. The Pirani gauge tends to exhibit some drift with time, which introduces uncertainty into the accuracy with which the pressure measurements can be made. It is clear that large errors could be introduced if the slope of the calibration curve changed markedly as a result of the drift. However, exploratory studies have indicated that this drift does not affect the slope of the linear portion of the curve appreciably. Another error which could be introduced is that resulting from drift in the interval between successive pressure measurements. Such errors are minimized by making successive pressure-rise measurements over the shortest time intervals practical and by the apparent fact that the drift is usually gradual. Due to the factors mentioned, it is not possible to make definite estimates of the probable errors in pressure-rise measurements. However, studies are contemplated to determine the errors more accurately and to improve stability in the pressure-measuring system.

Table I. Corrosion rate of low-carbon steel at 316°C after 40 days

Sample			Corrosion rate (mg/dm^2-mo)		
Run	Vacuum Annealed	Fluid	Uncorrected	Blank	Corrected
3–1	Yes	H_2O	35	6	29
3–2	Yes	H_2O	44	11	33
3–6	No	H_2O	30	14	16
3–7	No	H_2O	22	4	18
2–24	No	NaOH*	19	1	18
2–26	No	NaOH*	18	3	15
2–27	No	NaOH*	22	3	19
2–28	No	NH_4OH*	29	3	26
2–29	No	NH_4OH*	31	3	28

* Solution pH = 10.6 at room temperature.

Calculation of Corrosion Rates

The rate of corrosion of a sealed capsule is calculated from the rate of pressure rise corrected for system outgassing as explained above. From this rate of pressure rise, with the volume and temperature known, the gas laws are used to calculate the rate of H_2 increase within the system. This is equal to the rate of H_2 effusion from the corroding capsule. This rate of H_2 effusion is converted to corrosion rate per unit area by use of the internal surface area of the capsule combined with stoichiometric calculations from the equation $3Fe + 4H_2O \rightarrow Fe_3O_4 + 4H_2$.

Typical Results

The reproducibility obtained using the apparatus and procedures described is shown in Table I, which also illustrates the improvement obtained by blank rate correction.

The reproducibility obtainable during the course of a run on like samples is also indicated in Fig. 2, which shows the data on some typical runs including uncorrected corrosion rate and blank-rate data.

Discussion

One source of possible error in these measurements must be considered. High apparent rates may be indicated at the beginning of a run due to material adsorbed on the outside surface of the capsule which desorbs when the capsule is heated. Correction might be made for such errors by using blank capsules put through precisely the same treatment as the capsules under consideration but which contain dry air, inert gas, or a vacuum instead of the corroding fluid. Subtraction of the average values given by such blanks from the measured rates of corroding capsules would be expected to give more accurate corrosion data at the beginning of a run. Preliminary work in this direction indicates that such blanks may vary in magnitude. The indications are that the error from this source is normally negligible after the first few days of a run, but a few blank samples have shown significant outgassing for periods as long as several weeks. This matter is receiving further attention.

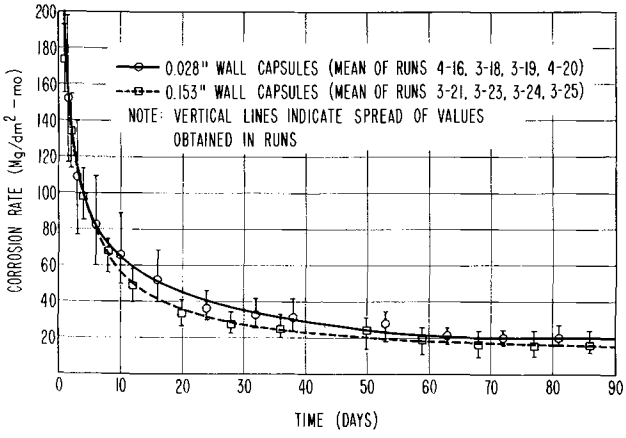

Fig. 3. Effect of wall thickness on apparent corrosion rates at 316°C.

Careful standardization of annealing operations prior to capsule fabrication is necessary. Table I indicates that vacuum annealing has an effect on the corrosion rate of low-carbon steel. Thus, standardization of conditions during the annealing operation is a prerequisite for the determination of the effect of other variables upon corrosion rates.

It is clear from Table I and Fig. 2 that fairly reproducible H_2 effusion rate data are obtained by employing the apparatus and techniques described. The question of the relationship between these hydrogen effusion rates and corrosion rates depends on how soon a steady state is reached. A categorical answer is not yet available, but there is evidence that, for mild steel treated as described above, it is achieved fairly rapidly.

The first piece of evidence deals with the effect of wall thickness on rates of H_2 effusion from corroding capsules. Fig. 3 exhibits data obtained from a series of experiments in which capsules of different wall thickness (0.153 in. vs. 0.028 in.) but otherwise identical in dimensions and machined from the same low-carbon steel rod were subjected to corrosion by distilled, deionized water at 316°C. Because the heavier-walled capsules could not be sealed readily by the usual welding technique, closure of all capsules in this series was effected by means of a threaded cap seating a 59-degree cone into a 60-degree conical opening. The capsules, after H_2 and vacuum annealing, were filled with the water to a level just sufficient to allow for heating to 316°C without exerting hydraulic pressure on the capsule walls. Results were not as reproducible from sample to sample as those obtained using the standard technique of sample preparation, but they suffice to demonstrate that the difference in H_2 effusion rates and corresponding calculated corrosion rates is small. If the diffusion rate through the metal wall were controlling the rate of effusion of H_2, such a fivefold increase in wall thickness would produce a much greater change in H_2 effusion rate than was observed. The data clearly indicate that diffusion through the metal wall of the capsule is not the controlling factor in H_2 effusion under the stated conditions. At least, this is true after the first few day of a run, and perhaps earlier.

A second piece of evidence confirms the rapid attainment of the steady-state rate. More important,

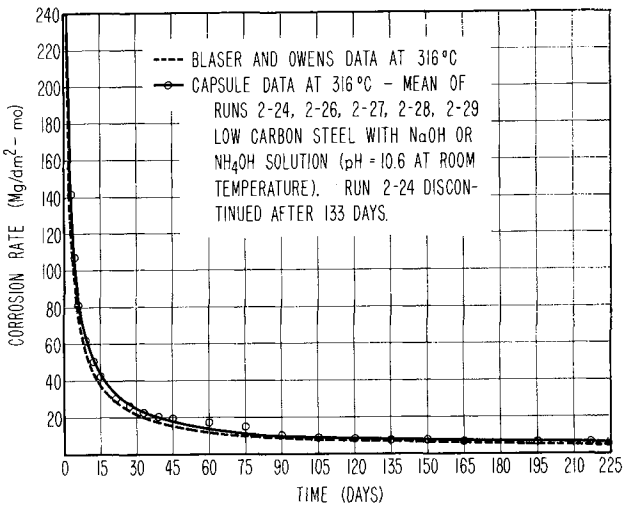

Fig. 4. Comparison of corrosion rates obtained by the H_2 effusion method with those obtained by the descaling method using multiple samples.

it demonstrates that the corrosion rates determined by the H_2 effusion method agree well with rates found on similar material by conventional methods. Fig. 4 exhibits a comparison of results obtained by the H_2 effusion method and those obtained by Blaser and Owens (8) in static systems (autoclaves) and semistatic systems (where the flow of fluid across the specimens was 1 ft/min or less) by means of descaled weight-loss measurements on a large number of samples. During their work, despite considerable variation from sample to sample, consistent average corrosion rates were obtained on low-carbon steel exposed to 315°C high purity water brought up to a *p*H (cold) of 11 with NH_4OH or LiOH. Within the limit of accuracy of the method, corrosion rates appear to be independent of the material used to produce the alkalinity. In Fig. 4 the average results obtained by Blaser and Owens are compared with the average results of five long-time runs in similar low-carbon steel capsules (not vacuum annealed) filled with air-saturated distilled water brought to a *p*H (cold) of 10.6, in two runs with NH_4OH and in the remaining three runs with NaOH. Agreement with the results of Blaser and Owens is excellent.

Douglas and Zyzes (9) measured corrosion rates of autoclaved specimens in high temperature water by mass spectrometric analyses of H_2 evolved. Their corrosion rates on Armco and high purity iron in water at 316°C are of the same order of magnitude as the measured corrosion rates of low carbon steel in 316°C water presented above.

These results indicate that, within the limitations herein stated, the H_2 effusion technique is capable of giving reliable corrosion data in aqueous systems at elevated temperature and pressure. The technique avoids the inherent experimental difficulties encountered in weight-gain or weight-loss methods and allows differential corrosion rates to be determined on a single specimen.

Acknowledgments

Particular thanks are due to W. A. Fraser, G. N. Newport, I. M. Patterson, P. N. Vlannes, and F. O.

Westfall, who operated the apparatus and made the measurements reported here and to G. M. Dinnick and D. I. Walter whose suggestions were especially helpful during the design stages.

Manuscript received April 16, 1956. This paper was prepared for delivery before the Pittsburgh Meeting, Oct. 9-13, 1955.

Any discussion of this paper will appear in a Discussion Section to be published in the December 1957 JOURNAL.

REFERENCES

1. C. R. Breden, S. Greenberg, R. M. Robinson, A. H. Roebuck, V. F. Saitta, and C. C. Scott, Argonne National Laboratory Rpt. ANL-4519, July 15, 1951.
2. S. C. Datsko, Argonne National Laboratory Rpt. ANL-5354, Oct. 4, 1954.
3. H. L. Solberg, G. A. Hawkins, A. A. Potter, and J. T. Agnew, *Trans. Am. Soc. Mech. Engrs.*, **59**, 725 (1937); **64**, 303 (1942); **65**, 47, 301 (1943); **66**, 291 (1944).
4. I. A. Rohrig, R. M. Van Duzer, Jr., and C. H. Fellows, *Trans Am. Soc. Mech. Engrs.*, **66**, 277 (1944).
5. W. Baukloh and W. Wenzel, *Arch. Eisenhüttenw.*, **11**, 273 (1937).
6. P. S. Flint, Knolls Atomic Power Lab. Rpt. KAPL-659, Dec. 14, 1951.
7. C. M. Schwartz and R. Lavender, *Rev. Sci. Inst.*, **19**, 814 (1948).
8. R. U. Blaser and J. J. Owens, Symposium on High-Purity Water Corrosion, ASTM Special Technical Publication No. 179, 1956.
9. D. L. Douglas and F. C. Zyzes, Knolls Atomic Power Lab. Rpt. KAPL-1376, Nov. 1, 1955.

Galvanic Corrosion

I. Current Flow and Polarization Characteristics of the Aluminum-Steel and Zinc-Steel Couples in Sodium Chloride Solution

M. J. Pryor and D. S. Keir

Kaiser Aluminum & Chemical Corporation, Spokane, Washington

ABSTRACT

Current flow, weight loss, and polarization measurements have been carried out on the aluminum-mild steel and zinc-mild steel couples in normal NaCl solution at 25°C. Under a wide variety of experimental conditions both aluminum and zinc are anodic to mild steel and completely protect it against corrosion. In both galvanic couples the current flow and weight losses of the anodes are proportional to the area of the steel cathode and are much less dependent on the anode area. Galvanic corrosion rates of both couples appear to be controlled by oxygen depolarization and are thus markedly increased by stirring. At high stirring rates, the aluminum-steel couple delivers a much higher galvanic current than the zinc-steel couple.

Zinc (1) and aluminum (2-4) are anodic to steel in many aqueous solutions and often corrode sacrificially to impart partial or complete protection to steel. This tendency of Zn and Al to protect steel cathodically has been reflected in the good corrosion resistance of galvanized and aluminized steel (5), particularly in marine environments (6, 7). Although cases are reported when Zn (8-10) and Al (3, 11, 12) reverse their polarity with respect to steel, it is generally true, at least for the zinc-steel couple, that the chance of a polarity reversal is much decreased in the presence of chloride.

Despite a large volume of research on galvanic corrosion, there has been little effort directed toward measuring the actual galvanic current flow in the aluminum-steel couple particularly at zero external resistance. Hoxeng and Prutton (10) carried out potential and current flow measurements on the zinc-steel couple during an extensive study of the effects of different anions in solution. However, many of their measurements refer to cases where the steel was anodic to Zn and are thus not directly comparable to results in NaCl when Zn functions as the anode. Akimov and his co-workers (12), using Cu cathodes coupled to a wide variety of dissimilar metal anodes in NaCl solution, demonstrated that the current flow was proportional to the area of the Cu cathode and was essentially independent of the area of dissimilar metal anode. This was a direct confirmation of the earlier work of Whitman and Russell (13) on the copper-steel couple. Later work by Evans (2) indicated that the additional corrosion produced by contact with a dissimilar metal cathode was approximately proportional to the area of the cathode only when the solution resistance was fairly low.

Because of the lack of quantitative information on the aluminum-mild steel couple in chloride solutions, the investigation described below was carried out. In this phase of the over-all investigation, currents flowing between Al and steel electrodes and between Zn and steel electrodes in normal NaCl were measured, together with weight losses of the electrodes. Polarization curves were determined for the two galvanic couples, and the effect of relative areas of anode and cathode on current flow, weight

loss, and electrode polarization examined. The effect of agitation of the solution on current flow and corrosion rate was also determined for both galvanic couples.

Experimental

Materials

The Al, Zn, and mild steel used in this investigation were in the form of cold rolled sheet 0.088 cm thick. Their compositions are: aluminum—Si 0.001%, Fe 0.001%, Cu 0.002%, balance Al; zinc—Si 0.08%, Fe 0.001%, Cu 0.009%, Pb 0.002%, balance Zn; mild steel—C 0.07%, Si 0.02%, Mn 0.45%, P 0.010%, S 0.005%, Cu 0.06%, Ni 0.08%, Mo 0.005%, Co 0.03%, balance Fe.

All solutions were made from C. P. chemicals and distilled water and were thoroughly shaken to insure saturation with dissolved air.

Steel samples were degreased in benzene, pickled in inhibited HCl, rinsed in distilled water, dried, rinsed again in benzene, and stored in dry air for 24 hr before use. Initial experiments were carried out in which Al specimens were etched in either HF or NaOH, rinsed, dried, and stored in dry air for 24 hr before use. The anodic weight loss, polarization data, and number of coulombs passing in the aluminum-steel couple in 96 hr were found to be insensitive to the surface preparation of the anodic metal. Consequently, Al and Zn specimens used in subsequent experiments received no surface pretreatment other than thorough degreasing in benzene.

Experimental Method

Current flow and weight loss determinations.—Two parallel dissimilar metal electrodes were held in position in a Lucite cell by means of micarta frames lined with neoprene gaskets. The backs of the specimens were masked with waterproofed Scotch pressure-sensitive tape to protect against seepage of the solutions. The masking and gasketing confined the area of each specimen in contact with the solution to 100 cm^2 unless smaller electrode areas were specifically desired.

The space between the electrodes was filled to a constant level with approximately 1600 ml of normal NaCl solution saturated with dissolved air. Evaporation was prevented largely by loosely covering the cell with Saran tissue. The cell was contained in a water bath thermostatted at 25° ±0.05°C.

Dissimilar metal electrodes were short-circuited for the test period of 96 hr. Current readings were taken periodically by introducing a zero resistance microammeter into the circuit. Potential measurements[1] of each electrode against a saturated calomel electrode showed that the closed circuit potentials of the anode and cathode were virtually the same and independent, to within 1 mv, of the position of the calomel electrode in the solution. Evidently any significant potential changes in the couple are limited almost entirely to the electrode-solution interfaces and do not occur gradually across the entire solution path as pictured by Akimov (19). These potential changes at the electrode surfaces may be regarded as energy barriers which alone control the rate of galvanic corrosion when the resistances of the external circuit and of the solution are very low. Measurements of both pH and conductivity of the solution were carried out before and after the experiment. After 96 hr, each test was discontinued and corrosion products removed chemically so that the weight loss of the electrodes could be determined. Steel specimens were cleaned by immersion for 2 min in 1:1 HCl inhibited with 3% Rodine 41; Al specimens were cleaned by immersion for 10 min in a solution containing 2% chromic acid and 5% syrupy H_3PO_4 at 80°C. Zn specimens were cleaned in 10% NH_4Cl solution followed by immersion in a boiling chromic acid/silver nitrate solution (14). Blank weight losses were determined for the cleaning procedures on uncorroded panels and were used in calculating corrected weight loss values of the corroded specimens. The total number of coulombs flowing in each experiment was calculated from the current/time curve. By also knowing the weight loss of the uncoupled specimens in normal NaCl solution, both the decrease in weight loss of the cathodic member of the couple and the efficiency of dissolution of the anodic member of the couple could be calculated.

Polarization studies.—The variation in potential of the anodes and cathodes with current was determined by short-circuiting the galvanic couple through a low variable series resistance and permitting both the current and potential to reach steady values at different arbitrary values of external resistance. It has been pointed out previously (15) that this method of measuring polarization curves is more truly comparable with conditions existing during galvanic corrosion, since in both cases the potential and galvanic current may vary together in achieving steady-state conditions.

Results

Potential measurements.—Potential/time curves in normal NaCl solution at 25°C for uncoupled specimens (100 cm^2) of Zn, Al, and mild steel are shown in Fig. 1. Whereas the potentials of Zn and mild steel are fairly steady after a short time, the potential of the Al shows considerable variation. The steady potential of the Zn is near the Nernst potential (16) corrected for Zn ion activity.

Effect of relative area of dissimilar metal electrodes on current flow and weight loss.—Triplicate experiments were carried out for 96 hr on the Zn-steel and Al-steel couples in normal NaCl solution

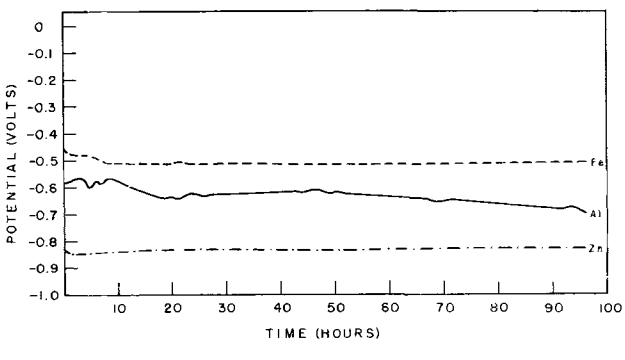

Fig. 1. Potential/time curves for Al, Zn, and mild steel in *N* NaCl solution at 25°C. Equal areas (100 cm^2) of uncoupled metals.

[1] All potentials in this paper are expressed on the Standard Hydrogen Scale.

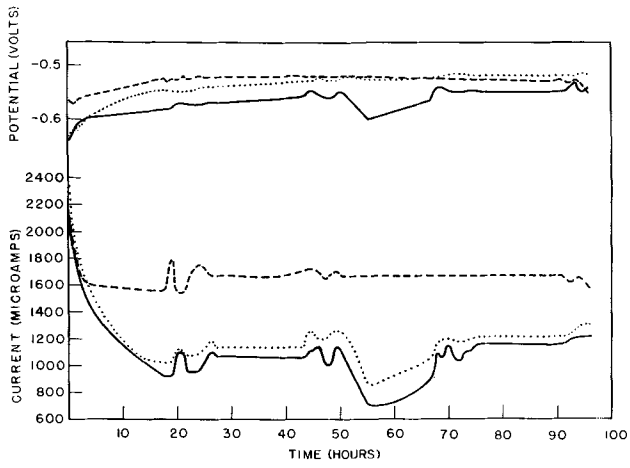

Fig. 2. Triplicate curves relating current flow and potential to time for the Al-mild steel couple in *N* NaCl solution at 25°C. Equal areas (100 cm²) of dissimilar metals.

at 25°C. Equal areas of dissimilar metals (100 cm²) were situated 15 cm apart in these experiments and were short-circuited through zero external resistance. The values of current flow at different times were not highly reproducible in replicate experiments, the degree of scatter between the current/time curves being shown for the Al-steel couple in Fig. 2 and for the Zn-steel couple in Fig. 3. During these experiments the pH of the solution increased from about 5.2 to 7.2 and the conductivity remained unchanged.

Similar experiments were carried out in which the distance of separation of the electrodes was held constant at 15 cm but in which the electrode areas were varied between 2 and 100 cm². Effect of cathode area on the weight losses of the Zn and Al anodes and on the total number of coulombs flowing in 96 hr is shown in Fig. 4. The effect of anodic area on anodic weight loss is shown in Fig. 5 and 6. These figures also contain the weight loss figures for the experiments with equal areas of Al, Zn, and steel. The experiments in which the area of the Al anode was varied (Fig. 5) gave less reproducible results than those in which the area of the steel cathode was varied.

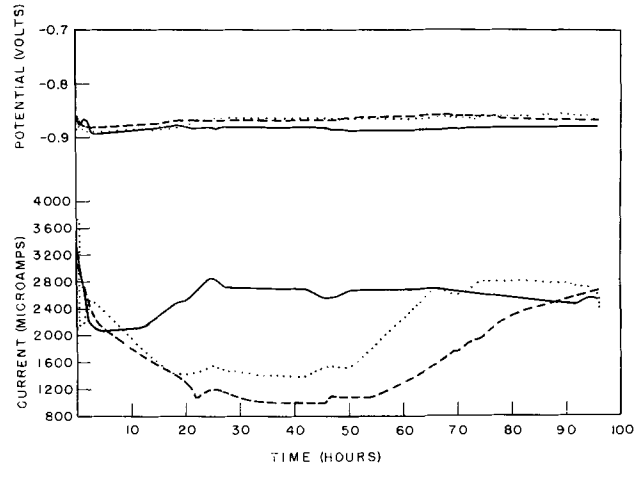

Fig. 3. Triplicate curves relating current flow and potential to time for the Zn-mild steel couple in *N* NaCl solution at 25°C. Equal areas (100 cm²) of dissimilar metals.

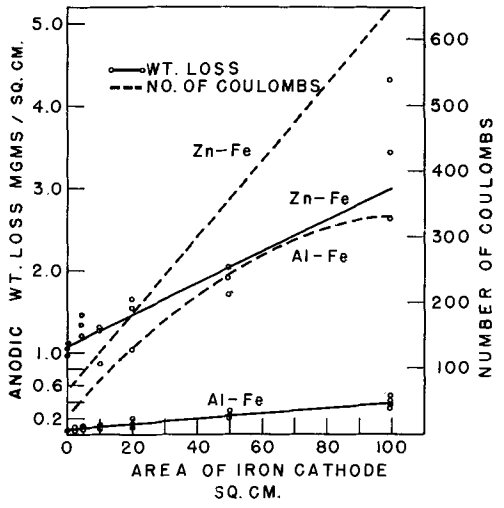

Fig. 4. Effect of area of mild steel cathode on the weight loss of Al and Zn anodes (of area 100 cm²) and on the number of coulombs flowing in the Al-mild steel and Zn-mild steel couples over a 96-hr period in 1*N* NaCl solution at 25°C.

In all experiments described in this paper the steel specimens were strongly cathodic to either Al or Zn and were, within the limits of experimental error, i.e., <0.01 mg/cm² completely protected against corrosion by coupling to either of these anodes. The weight losses of the Zn and Al specimens were, of course, markedly increased by coupling to the mild steel cathodes. In static solutions both the Al and Zn anodes were galvanically corroded in a uniform manner. From calculation of the number of coulombs flowing, it was apparent that the weight losses of the anodes were appreciably in excess of those calculated from the current flow data, particularly in the case of Zn. These additional losses in weight will be referred to as the "weight losses due to local action". Since the current was only measured on an intermittent basis, the estimation of the number of coulombs flowing is

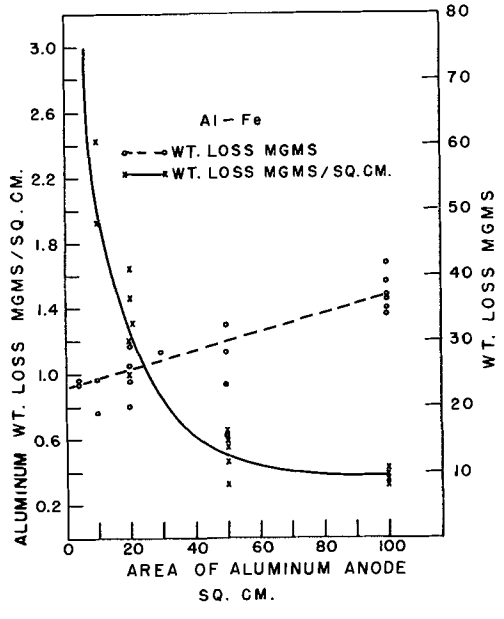

Fig. 5. Effect of area of Al anode on the total corrosion and on the intensity of corrosion of Al coupled to mild steel (100 cm² mild steel) over a 96-hr period in *N* NaCl at 25°C.

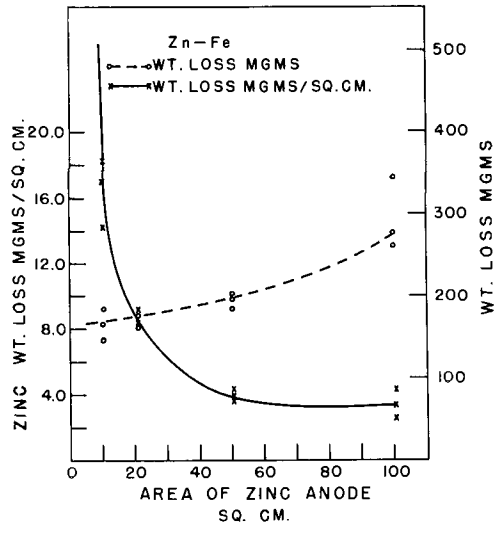

Fig. 6. Effect of Zn anode area on the total corrosion and on the intensity of corrosion of Zn coupled to mild steel (100 cm² mild steel) over a 96-hr period in *N* NaCl at 25°C.

less accurate than the measurements of weight loss. Consequently, the accuracy of the weight losses due to local action, which were calculated by difference, is not high, particularly for Al anodes where the total weight loss is relatively low. The variation in local action weight losses of Zn and Al with dissimilar metal electrode area is shown in Fig. 7.

Distance of separation of the electrodes.—Experiments were next carried out to determine the effect, if any, of distance of separation of the electrodes on the rate of galvanic corrosion of the Al-steel couple. In these experiments, weight losses alone were determined. The results (Fig. 8) show that the weight loss on Al anodes in experiments of 96 hr duration decreased somewhat as the electrodes approached each other closely. It must also be realized that, as the distance of separation decreased, the total volume of solution also became smaller. However, when the electrodes were 15 cm apart, the effect of small variations in distance of separation was insignificant.

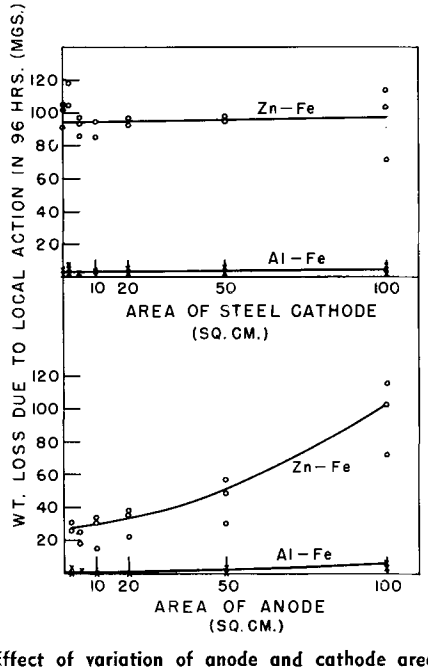

Fig. 7. Effect of variation of anode and cathode areas on the anodic weight losses due to local action in the Al-mild steel and Zn-mild steel couples in *N* NaCl solution at 25°C. When anodic area is variable the cathode area is constant at 100 cm²; when cathode area is variable the anodic area is constant at 100 cm².

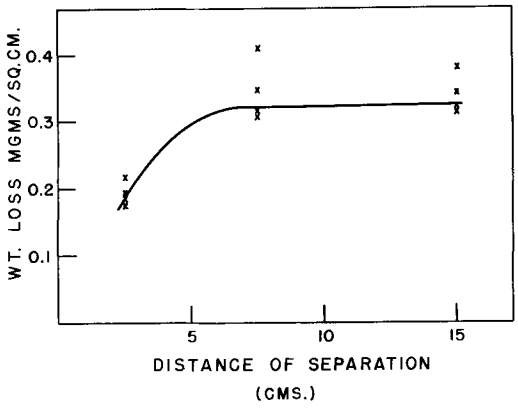

Fig. 8. Effect of distance of separation of Al and mild steel electrodes on the weight loss of Al anodes in *N* NaCl at 25°C. Equal areas (100 cm²) of dissimilar metals.

Polarization measurements.—Anodic and cathodic polarization curves were determined for both galvanic couples in the manner described above.

Variation of anodic and cathodic polarization curves as a function of cathode area was determined for both galvanic couples by employing a 15 cm electrode separation after a fixed time of 24 hr. Results are contained in Fig. 9 and 10 and may be used to assist in explaining the weight loss results shown in Fig. 4. Variation of the anode area had no significant effect on polarization curves determined in a similar manner.

Effects of stirring.—Experiments were carried out in which dissimilar metal electrodes having equal areas (20 cm²) were clamped 5 cm apart by means of a Lucite holder in a 400 ml beaker. A constant volume (320 ml) of normal NaCl at 25°C was used in these tests. The solution in the beaker was stirred by a variable speed stirrer located centrally in a

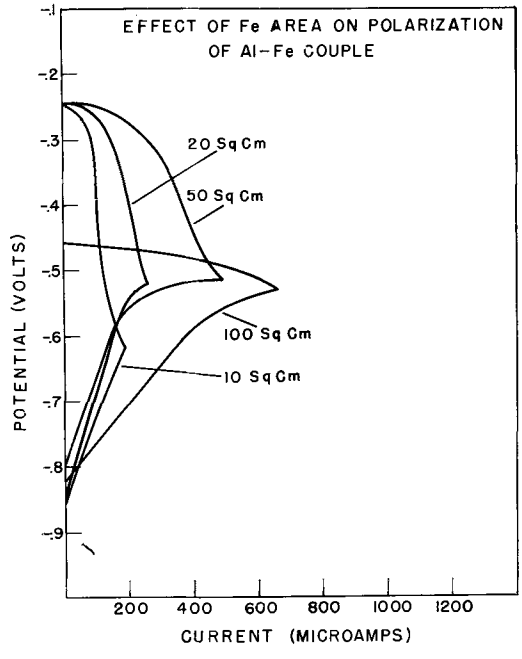

Fig. 9. Effect of area of steel cathode on the polarization curves for the Al-mild steel couple in *N* NaCl at 25°C using 100 cm² of Al.

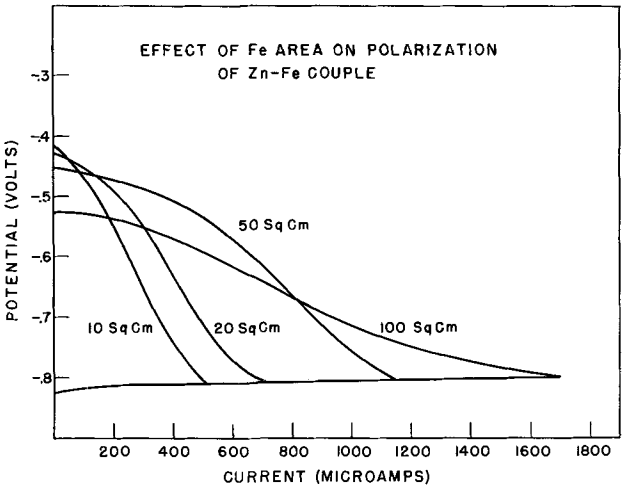

Fig. 10. Effect of area of steel cathode on the polarization curves for the Zn-mild steel couple in *N* NaCl at 25°C using 100 cm² of Zn.

fixed position between the electrodes. Experiments on the effects of stirring were carried out for a period of 24 hr on account of the greatly increased rate of galvanic corrosion. Weight loss, current flow, and potential measurements were made as described previously. The effect of stirring on weight loss and current flow in the Al-steel couple is shown in Fig. 11. In unstirred solutions, the Zn-steel couple delivered a higher galvanic current than the Al-steel couple. At 150 ppm both couples delivered the same galvanic current. At 300-500 rpm, the Zn-steel couple gave low and highly erratic current. For instance, at a stirring rate of 500 rpm the total number of coulombs flowing in six experiments on the Zn-steel couple varied between 105 and 202. In view of the highly irreproducible nature of the results on the Zn-steel couple at the higher stirring rates, a representative curve cannot be included in Fig. 11.

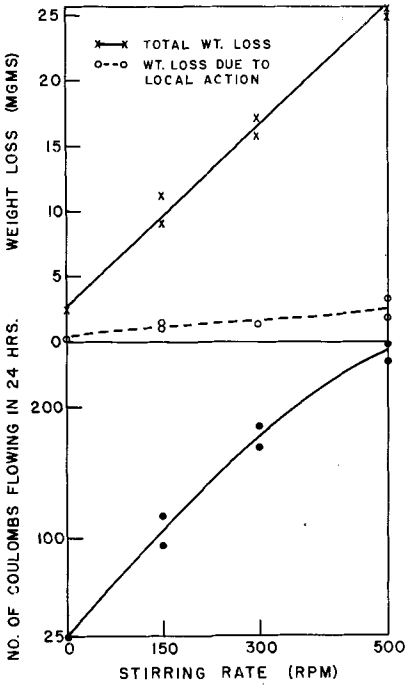

Fig. 11. Effect of stirring rate on the total Al weight loss, Al weight loss due to local action, and number of coulombs flowing (in 24 hr) in the Al-mild steel couple in *N* NaCl at 25°C. Equal areas (20 cm²) of Al and steel.

Discussion

It should be pointed out first that the results described in this paper are concerned primarily with the initial stages of galvanic corrosion. Such factors as the slow formation of protective films over long periods of time, which can markedly affect galvanic current flow, have not been investigated in this work.

The results of this investigation demonstrate that, in normal NaCl under a wide variety of experimental conditions, both Al and Zn are anodic to mild steel and completely protect it against corrosion, at least for periods up to 96 hr. Fig. 2, 3, and 4 demonstrate that the current flow under similar experimental conditions is somewhat greater in the Zn-steel couple than in the Al-steel couple except at rates of stirring in excess of 150 rpm. The current/time curves for both couples are quite erratic (Fig. 2 and 3) and show no evidence of settling down to really steady values. Whereas the potential of the Zn-steel couple is quite uniform at around −0.88 v (Fig. 3), irrespective of variations in current flow, the potential of the Al-steel couple shows much more variation (Fig. 2).

Fig. 10 shows that the galvanic corrosion of the Zn-steel couple is under cathodic control and that increasing currents may be drawn from a Zn anode with practically no change in potential. Indeed, as pointed out previously, the potential taken up by the Zn in NaCl solution containing dissolved air appears to be approximately the Nernst potential corrected for Zn ion activity. Consequently, variations in current flow must be tolerated without greatly altering the potential of the couple. From the form of the cathodic polarization curves for the Zn-steel couple (Fig. 10), it appears that the variations in current flow are due to the relative rates of consumption and replacement of dissolved oxygen at the cathode/solution interface.

Polarization curves for the Al-steel couple (Fig. 9) at first sight indicate that corrosion should be under mixed control. Furthermore, comparison with Fig. 1 shows that, as the Al is corroded galvanically, its open-circuit potential shifts substantially in the more anodic direction. Consequently, although the potential/time curves (Fig. 1) would indicate an open-circuit potential difference of around 150 mv for the Al-steel couple (and around 330 mv for the Zn-steel couple), Fig. 9 shows that, on coupling to 100 cm² of steel, there is actually an open-circuit potential difference of around 370 mv for the Al-mild steel couple. This is somewhat greater than that for the Zn-steel couple under similar conditions (Fig. 10). Since the potential of Al in NaCl is so far displaced from the Nernst potential (16), probably due to the formation of protective oxide films, factors increasing its corrosion rate and assisting in the breakdown of these protective films will displace its potential in the less noble direction. Evidently for metals such as Al, which behave in a highly irreversible manner, differences in corrosion or solution potential are a very unreliable guide to the true magnitude of open-circuit emf of galvanic corrosion. However, the magnitude of the galvanic

corrosion current will be controlled usually by the polarization characteristics of the electrode reactions.

Fig. 9 also shows that the anodic polarization curve for Al is not flat as is that for Zn. Therefore, changes in oxygen concentration due to relative rates of consumption and replacement of oxygen at the steel cathode will affect not only the current flow but also the potential of the Al-steel couple. That the more rapid decreases in current usually coincide with corresponding shifts in potential in the less noble direction (Fig. 2) supports the contention that the corrosion rate of the Al-steel couple is also controlled by oxygen depolarization. This is subsequently confirmed by the stirring experiments in Fig. 11.

In local-cell corrosion it is quite difficult to check the validity of polarization curves due to the experimental difficulty of separating anodic and cathodic areas. However, in studies of galvanic corrosion this difficulty does not exist to the same extent. Consequently, experiments with different relative areas of Al, Zn, and steel were carried out as described. Polarization curves for the Zn-steel couple (Fig. 10) indicate that the galvanic corrosion is under cathodic control. Therefore, the current flow and weight loss of the Zn should be proportional to the area of the steel cathode and should be less dependent on the area of the Zn anode. Experiments with partial areas of steel and Zn (Fig. 4 and 6) demonstrate that this is so, thereby affording a direct confirmation of the "Catchment Principle" (17). Furthermore it is evident that, since the weight loss of a Zn anode is only slightly affected by decreasing its area, the intensity of corrosion on the Zn must markedly increase with decreasing area (Fig. 6).

The polarization curves for the Al-steel couple with equal electrode areas are characterized by steeply sloping anodic polarization curves and relatively flat cathodic polarization curves (Fig. 9). Despite this, experiment shows that, as in the case of the Zn-steel couple, current flow and weight losses of the Al are almost directly proportional to the area of the steel cathode (Fig. 4) and are less dependent on the area of the Al anode, even though the results with variable areas of Al show much scatter (Fig. 5). Actually, these results and the polarization curves are not as mutually inconsistent as appears at first sight. Examination of the cathodic polarization curves for steel (Fig. 9) shows that the cathodic reaction (the reduction of dissolved oxygen) becomes diffusion controlled[2] at a current density of around 10-12 μamp/cm^2 under these experimental conditions. Whereas in the Zn-steel couple some gaseous H_2 can probably be evolved from the steel cathode, it is probable that when a steel cathode is coupled to Al in a NaCl solution containing dissolved oxygen, its potential cannot be depressed far enough to evolve significant quantities of H_2.[3] Consequently, the cathodic reaction in the Al-steel couple should be dependent primarily on oxygen depolarization. Thus, if the cathodic area is reduced, the current density at the cathode can only achieve a certain maximum value which depends on the rate at which oxygen diffuses from the bulk of the solution to the cathode. Further reductions in cathode area, therefore, should result in a proportional reduction in both galvanic current flow and weight loss of the Al. This effect is shown in the polarization curves in Fig. 9 and by the weight loss and current flow results in Fig. 4. However, the relative insensitivity of the current flow and corrosion rate to variations in the area of the Al is less easy to understand. It appears from Fig. 9 that the potential of Al in NaCl solution has to be ennobled to around 0.5 v before Al ions will migrate rapidly through the oxide film on the Al. Once this potential is achieved, the rate of migration of Al ions through the oxide film may be varied widely with little change in potential. This assists in explaining the very small effect of Al anode area on galvanic corrosion of the Al-steel couple.

The experiments in which the distance of separation of Al and steel electrodes was varied (Fig. 8) demonstrated that the rate of galvanic corrosion decreased as the electrodes approached each other more closely. Since the over-all volume of solution decreases as the distance of separation decreases, these experimental conditions favor the development of higher bulk pH values in the solution and, consequently, an increased absorption of CO_2 from the atmosphere. Separate experiments to be reported later have shown that, as with Zn (10), increasing concentrations of sodium bicarbonate progressively ennoble the potential of Al and thus decrease the open-circuit emf of the Al-steel couple. Alternatively, the change in geometry of the cell with decreasing distance of electrode separation certainly tends to reduce diffusion of dissolved oxygen from the surface of the solution to the lower portions of the steel cathode. This should reduce the area of steel acting as an effective cathode and, consequently, should proportionately reduce current flow and the weight loss on the Al anode. However, it should be pointed out that this effect is probably confined to solutions of very low resistance since, with higher resistance solutions, the effect of reducing the resistance of the solution path would tend to mask the effect shown in Fig. 8.

Experiments involving stirring (Fig. 11) further support the contention that the galvanic corrosion rate of the Al-steel couple in NaCl solutions is largely controlled by oxygen depolarization at the steel cathode. Although the Zn-steel couple delivers more current than the Al-steel couple in static NaCl solutions, the situation is reversed at stirring rates of 300 and 500 rpm. Very deep pitting of the Zn

[2] The cathodic reaction is said to be diffusion controlled with respect to oxygen when the rate-controlling step is the note at which oxygen diffuses from the bulk of the solution to the solution-cathode interface.

[3] This view is supported by the fact that the potential of steel coupled to Al is not depressed far enough to cathodically reduce the air-formed oxide film on the iron cathode (18). Thus, with small areas of steel cathode the air-formed oxide film is probably reinforced due to contact with an alkaline, oxygen-containing solution. Consequently, as shown in Fig. 9, the open-circuit potential of the steel cathode can be markedly ennobled during galvanic corrosion due to a reduction in the ratio of film-free to oxide film-covered areas. However, during galvanic corrosion of the Zn-steel couple, the potential of the steel is shifted far enough in the active direction to reduce the air-formed oxide film on the steel cathodically. Therefore, as marked a shift in the open-circuit potential of the steel cathode in the noble direction is not observed (Fig. 10) since the cathode is free from oxide during the experiments.

anodes is observed at these stirring rates accompanied by low and erratic currents and high weight losses due to local action. On the other hand, the Al is uniformly attacked even at stirring rates of 500 rpm and weight loss due to local action increases only slightly over that in static solutions (Fig. 11). The potentials of both couples become ennobled with increasing stirring rate, but the shift in potential of the Al-steel couple is only about half of that of the Zn-steel couple (100 mv) under similar conditions. This suggests that the anodic polarization curve of Al is flatter than that of Zn within the current density range of 10-100 μamp/cm^2 as has been suggested previously.

Fig. 7 shows the weight losses (in 96 hr) due to local action on Zn and Al anodes of different areas coupled to various areas of mild steel. It may be seen that the local action weight loss on Zn is always very much greater than that on Al. This is probably due to the relative shapes of the anodic polarization curves of Al and Zn (Fig. 9 and 10). These indicate that the local cathodes on an Al anode should be suppressed more effectively by a relatively large shift in potential of around 300 mv in the noble direction during galvanic corrosion (Fig. 9) as compared with a shift of only around 20 mv (Fig. 10) in the case of Zn. Furthermore, this effect would be heightened by the fact, pointed out previously (20), that the cathodes on Al in NaCl solution containing oxygen are very small and comprise only about 5% of the total specimen area.

Acknowledgment

The authors wish to thank Dr. H. G. Oswin for his helpful comments and for his criticism of the paper.

Manuscript received May 3, 1956. This paper was prepared for delivery before the Pittsburgh Meeting, Oct. 9-13, 1955.

Any discussion of this paper will appear in a Discussion Section to be published in the December 1957 JOURNAL.

REFERENCES

1. R. M. Burns and A. E. Schuh "Protective Coatings for Metals," Reinhold Publishing Corp., New York (1939).
2. U. R. Evans, *J. Soc. Chem. Ind.*, **47**, 73T (1928).
3. G. D. Bengough and O. F. Hudson, *J. Inst. Metals*, **21**, 37 (1919).
4. J. D. Edwards and C. S. Taylor, *Trans. Electrochem. Soc.*, **56**, 27 (1929).
5. F. Fancutt and J. C. Hudson, *J. Oil & Colour Chemists Assoc.*, **35**, 396 (1952).
6. S. G. Clarke and W. N. Bradshaw, *J. Appl. Chem.*, London, **3**, 147 (1953).
7. M. L. Hughes and D. P. Moses, *Metallurgia*, p. 105, Sept. 1953.
8. G. Schikorr, *Trans. Electrochem. Soc.*, **76**, 247 (1939).
9. L. Kenworthy and M. D. Smith, *J. Inst. Metals*, **70**, 463 (1944).
10. R. B. Hoxeng and C. F. Prutton, *Corrosion*, **5**, 330 (1949).
11. M. R. Whitmore and J. Teres, *Ind. Eng. Chem.*, **31**, 608 (1939).
12. G. W. Akimov, S. A. Wruzewitsch, and G. B. Clark, *Korrosion u. Metallschutz*, **11**, 145 (1935).
13. W. G. Whitman and R. P. Russell, *Ind. Eng. Chem.*, **16**, 276 (1924).
14. H. H. Uhlig, Editor, "Corrosion Handbook," p. 1082, John Wiley & Sons, Inc., New York (1948).
15. M. J. Pryor, *This Journal*, **102**, 694 (1955).
16. W. M. Latimer, "Oxidation Potentials," p. 155, Prentice Hall, New York (1938).
17. U. R. Evans, "Metallic Corrosion, Passivity and Protection," p. 513, Edward Arnold and Co., London (1938).
18. M. J. Pryor and U. R. Evans, *J. Chem. Soc.*, **1950**, 1259.
19. G. V. Akimov, *Corrosion*, **11**, 515, (1955).
20. M. J. Pryor and D. S. Keir, *This Journal*, **102**, 605, (1955).

Inclusion of Fuchsin in Bright Nickel Deposits

Kedzie Chemical Laboratory, Michigan State University, East Lansing, Michigan

J. L. Dye and O. J. Klingenmaier

ABSTRACT

Fuchsin, a brightener used in nickel plating, was recovered from nickel deposits by dissolving the deposits in HCl. The amount of fuchsin recovered per gram of Ni was roughly linear in fuchsin concentration and decreased with increasing current density. Some pertinent properties of fuchsin were studied. The amount of fuchsin included and its brightening effect are correlated with a model which assumes preferential adsorption at grain corners and edges.

This investigation was carried out to determine whether an organic brightener of the second class (1) is included in Ni deposits without complete decomposition. When this was found to be the case, a study was made of the effect of brighter concentration and current density on the amount included in the deposit.

During plating, a gradual decrease occurs in the concentration of the brightening agent or agents. While decomposition products undoubtedly account for some of this loss, it seems reasonable to assume that some of the brightening agent or its decomposition products are included in the deposit.

The presence of carbonaceous matter in electrodeposited metals of the iron group has been reported by a number of investigators, and recently, Brenner and co-workers (2), found the carbon and sulfur contents of electrodeposited bright Ni to

range from 0.02 to 0.08%. A search of the literature failed to disclose any successful investigations of the identity of these inclusions.

A common brightener of the second class used in Ni plating is the organic dye, fuchsin, also known as rosaniline hydrochloride. Its molecular formula is: $C_{20}H_{20}N_3Cl$.

Fuchsin was chosen for study primarily because its intense color permitted the spectrophotometric determination of as little as 50 μg/l. A sensitive method of analysis was necessary in this investigation since the brightening agent is used in amounts as low as 1 mg/l. Accordingly, it was felt that only a small amount would be included in the Ni deposit. One of the drawbacks involved in the choice of fuchsin for study is that some decomposition could be expected because of its complex nature.

Experimental

The nickel stock solution used in the experimental work was a typical Watts-type bath of the following composition: $NiSO_4 \cdot 7H_2O$, 240 g/l; $NiCl_2 \cdot 6H_2O$, 45 g/l; boric acid, 30 g/l. The solution was purified by the method of Ewing (3). Bright baths were made by adding to the above solution (4): sodium naphthalene disulfonate, 4.5 g/l; sodium lauryl sulfonate, 0.1 g/l; fuchsin, 0.5-3.0 mg/l.

The fuchsin[1] was purified by two recrystallizations from water. The other chemicals used were analytical reagent grade and were used without further purification except that mentioned above.

Brass sheet stock 0.020 in. thick was electrocleaned and plated with dull Ni in the usual fashion. The surface was then buffed and passivated electrolytically. To accomplish this, the panel was alternately electrocleaned (anodically) and dipped in HCl 4 or 5 times. Plating was carried out in a one liter electrolysis jar at 55° ± 1°C. Agitation of the solution was provided by a low-pitch, glass stirring rod, rotating at 200 rpm. Anode bags were not used for these depositions because of the great tendency for fuchsin to adsorb on cloth. A current density of 0.02 amp/cm^2 was used, and all deposits were mirror bright. Fuchsin reduced with Ni and HCl was used in the first experiments. Because of the difficulty of preparing standard solutions of reduced fuchsin, as described later, plating was done with nonreduced fuchsin. The appearance of the deposits was identical to that obtained with reduced fuchsin.

A number of bright Ni deposits were also prepared from separate 250 ml amounts of bright Ni solution in a Hull cell (5). The deposits were then cut and combined to give five current density ranges for study.

In the course of this research, it was necessary to determine fuchsin quantitatively, both in the plating baths, and in the solutions obtained by dissolving the deposits. The procedure adopted was as follows: a 25 ml sample of the solution was heated with 1 g of nickel formate to 90°-95°C. The solution was cooled and transferred to a 125 ml separatory funnel. Successive small portions of methyl ethyl ketone were shaken with the solution to extract the dye. Whenever the fuchsin concentration was less than 2.5 mg/l, a total of 25 ml of extractant was used; otherwise, 50 ml was necessary. The absorbancy of the methyl ethyl ketone extraction at a wave length of 548 mμ (corresponding to the maximum absorbance) was determined with a Beckman Model DU Spectrophotometer using 1 cm cells. When working with solutions obtained by dissolving the deposits or with reduced fuchsin solutions, the absorbancy increased somewhat over a period of a few hours to a constant value.

Several methods of dissolving deposits containing fuchsin were attempted, including anodic dissolution, and the use of Classen's reagent (6). The only method which led to recovery of fuchsin was dissolution of the deposits in HCl solution. Ni foil, weighing about 1.2 g, was cut into small pieces and dissolved in 15 ml of 36% HCl. The process required 2-3 weeks at room temperatures, but only 4 hr at 70°-80°C. Both methods were used with about the same degree of success. The pH value of the solution was raised to the range of 2 to 3 with sodium carbonate, followed by the treatment with nickel formate as described previously.

Polarographic studies were made with a Sargent Model XXI Polarograph and infrared studies with a Perkin-Elmer Model 21 Recording Spectrophotometer.

Results

While fuchsin has many advantages in a study of this type, its principal disadvantage is the tendency to undergo complex reactions. Some of the reactions involving fuchsin are illustrated in Fig. 1*a* and 1*b*.

The reactions of fuchsin important in plating are its electrolytic reduction and oxidation. One liter of a solution containing 2.0 mg fuchsin and 10 g H_3BO_3, pH 3.2, was electrolyzed between graphite electrodes at a current of 0.1 amp for about 4 hr. Periodic sampling showed that the fuchsin content decreased roughly linearly with time at a rate of 0.4 millimoles/Faraday of electricity. A repeat experiment with a porous cup to separate the anode and cathode compartments showed that the loss of color was oc-

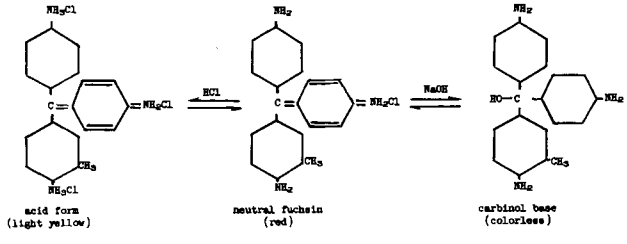

Fig. 1*a*. Acid-base behavior of fuchsin

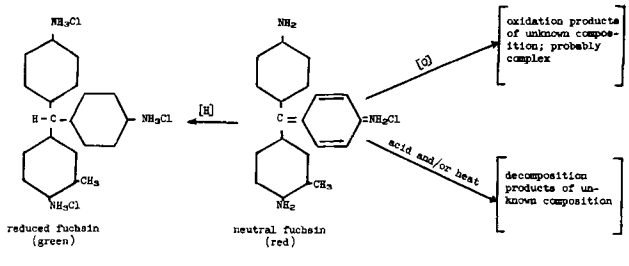

Fig. 1*b*. Oxidation-reduction and decomposition behavior of fuchsin

[1] A certified biological stain distributed by Eastman Kodak Co.

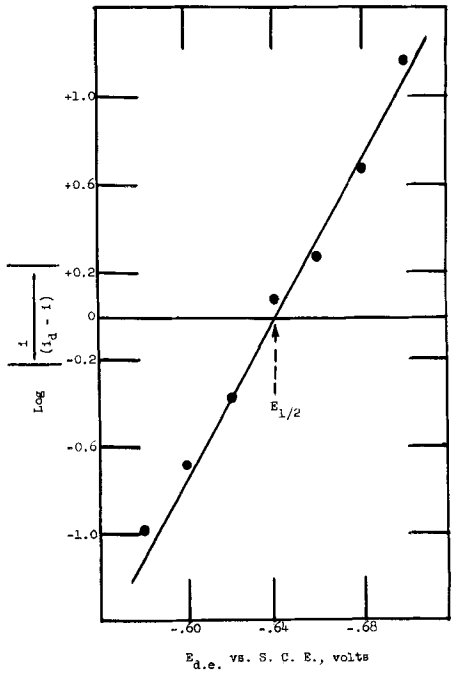

Fig. 2. Determination of the number of electrons involved in the primary reduction step for fuchsin from polarographic data.

curring in the anode compartment. This could not be made quantitative because of the strong adsorption of the dye into the porous cup. Attempts were made to analyze the oxidation products without success. The oxidation products appeared to be a complex mixture rather than a single pure substance.

Because reduced fuchsin is recommended as a brightening agent for Ni, the first deposits were made from a bath containing the reduced dye. This was made by heating fuchsin with Ni and HCl. This invariably resulted in the loss of 20-40% of the fuchsin. Since plates of excellent quality could be obtained with nonreduced fuchsin, use of the reduced material was abandoned.

Some polarographic studies of fuchsin were made to gain further insight into its electrolytic properties. It was found that excellent reduction waves could be obtained at the dropping mercury electrode. Fig. 2 shows a graph of $\log \frac{i}{i_d - i}$ vs. the dropping electrode potential relative to the saturated calomel electrode. The least-squares slope gives a value of 1.06 for n, the number of electrons involved in the reduction. While quantitative polarographic studies of the reduction were made at only two concentrations, it appears that the initial step in the reduction is the formation of a free radical. A corresponding oxidation wave could not be found with reduced fuchsin solutions. A rather poorly defined oxidation wave was obtained with fuchsin solutions at +0.28 v vs. the saturated calomel electrode when a rotating Pt electrode was used.

Fuchsin was recovered from the deposits by dissolving the deposits in HCl. A study was made of the effect of acid strength, temperature, and time of heating, on the decomposition of fuchsin. Thirty-one runs were made under various conditions. Results are given in Table I. They may be summarized by stating that high temperatures, high acid strengths, and long times of standing or heating resulted in the loss of fuchsin.

The absorption spectrum of solutions of fuchsin in water and in methyl ethyl ketone were determined at a number of concentrations. The molar extinction coefficients were found to be 65,000 in water at 545 mμ, and 91,000 in methyl ethyl ketone at 548 mμ. These wave lengths correspond to the absorption maxima in the two solvents.

Beer's Law was obeyed in both solvents within the experimental error. These calibration curves were used to evaluate the concentrations of the unknown samples.

A total of 19 depositions from solutions containing fuchsin were made, and both the fuchsin recovered from the plate and the fuchsin remaining in the bath were determined spectrophotometrically. Results are represented graphically in Fig. 3.

The effect of current density on the amount of fuchsin included in the Ni deposits was determined with a Hull cell (5). The 250 ml portions of bright Ni solution used in these experiments each contained 470 μg of fuchsin so that the concentration was 1880 μg/liter. Ni deposits were excellent in appearance. Table II gives results obtained in analyses of fuchsin from deposits covering five ranges of current density. There is a notable decrease in the

Table I. Recovery of fuchsin from HCl solutions subjected to different conditions of time and temperature

Fuchsin content (μg)	Amount of conc. acid (ml)	Temp, (°C)	Time (hr)	% Recovered
80	3*	95	0.1	94
40	5*	95	0.1	87
40	3*	70–90	0.1	94
40	3*	70–90	0.1	94
40	3*	70–90	0.5	77
40	3*	70–90	1.0	63
40	3*	25	0.2	100
40	5	25	0.2	100
40	15	90–95	4	58
40	15	90–95	4	58
41	15	60–70	4	64
41	15	60–70	4	65
42	15	50–55	1	64
42	15	50–55	2	66
42	15	50–55	3	58
42	15	50–55	4	60
84	15	50–55	6	72
40	5	25	24	86
40	10	25	24	84
40	15	25	24	84
40	10	25	72	60
40	15	25	168	57
40†	15	80–85	1	72
40†	15	80–85	4	46
40†	15	70–80	4	64
40†	15	60–70	4	60
40†	15	50–55	4	63
40†	15	50–55	4	60
40†	15	25	48	58
40†	15	25	168	58
40†	15	25	168	66

* Plus 25 ml of water.
† 1.2 g of pure Ni foil added to the acid solution.

Table II. Distribution of fuchsin in Hull cell deposits

Current density (amp/ft²)	Amount of Ni dissolved (g)	Fuchsin recovered (μg)	
		Per deposit	Per g of Ni
0–15	0.125	14	112
15–40	0.405	26	62
40–80	0.576	30	52
80–120	0.334	8	24
>120	0.409	12	29
	1.849*	90†	

* Total Ni deposited was 1.995 g.
† This value was 28% of the total decrease of fuchsin in the plating solutions.

amount of fuchsin recovered per gram of Ni as the current density is increased.

Conclusions

Even though conditions other than concentration were made as identical as possible during the various depositions, a considerable scatter of points resulted. This may be due to at least two important factors.

1. Unequal solution agitation at the electrode surface would certainly have a pronounced effect on the amount of fuchsin included in the deposit. It would be expected that too vigorous stirring would increase the amount of fuchsin destroyed by oxidation as well as the amount included in the plate. The data seem to indicate that this effect is operating.

2. Fuchsin is slowly destroyed in HCl solution, and by heat, as is shown in Table I. Lack of reproducibility of the results could well be due to this loss of fuchsin.

In spite of the difficulties encountered in obtaining quantitative data, several conclusions can be drawn from this study.

1. Fuchsin, when used as a brightener of the second class in Ni plating, is included in the deposits without being completely destroyed. About 30% of the total decrease of fuchsin in the plating bath could be recovered from the deposit. Probably much of the rest of the decrease resulted from the anodic oxidation of fuchsin.

2. The amount of fuchsin recovered from the deposits increased with the concentration of fuchsin in the bath from about 18 μg/g Ni at a bath concentration of 500 μg/liter, to about 90 μg/g Ni at 2500 μg/liter. These values are low because of losses of fuchsin, and it is believed that the values should be revised upward by 30-40% to obtain a better value of the fuchsin content in the Ni. Even if all of the decrease of fuchsin in the bath were due to its codeposition with Ni, the concentration of fuchsin in Ni could not exceed 500 μg/g Ni in this range of concentration.

3. The amount of fuchsin recovered from the deposits per gram of Ni decreases with an increase in current density. This is to be expected on a macro scale because of local depletion of the organic molecules at regions of high current density.

Since the percentage of fuchsin found in the deposits was very low (about 0.01%), it is possible that the brightening action occurs because of a preferential adsorption of fuchsin at points of high current density, such as grain corners and edges. Deposition of Ni would then be interrupted at these points and accentuated at low current density areas. Such action would tend to smooth out the deposit and produce randomly oriented small grains leading to a bright plate. To check the plausibility of this argument, the ratio of fuchsin molecules to Ni grains was calculated.

The amount of fuchsin recovered from 1 g Ni, plated from a bath containing 1800 μg of fuchsin/liter, was used as the basis for the calculation. Reference to Fig. 3 indicates that 65 μg fuchsin was recovered per gram of Ni. Assuming 35% loss of fuchsin in the process of solution of the deposit, a value of 100 μg, or 3×10^{-7} gram-moles of fuchsin/g Ni was chosen. This figure corresponds to 1.8×10^{17} molecules/g Ni. Using a density of 8.9 g/cc for Ni and the information that the grain size of bright Ni deposits is less than 10^{-4} mm (7), the number of fuchsin molecules per grain of Ni would vary from 1600 at a grain size of 10^{-4} mm to 1.6 at a grain size of 10^{-5} mm. Table III shows that, depending on the grain size produced, it would be possible for the included fuchsin molecules to cover the edges of each grain, or merely the corners.

Attachment of organic molecules at the grain corners and edges during deposition could restrict grain growth. A higher fuchsin concentration in the

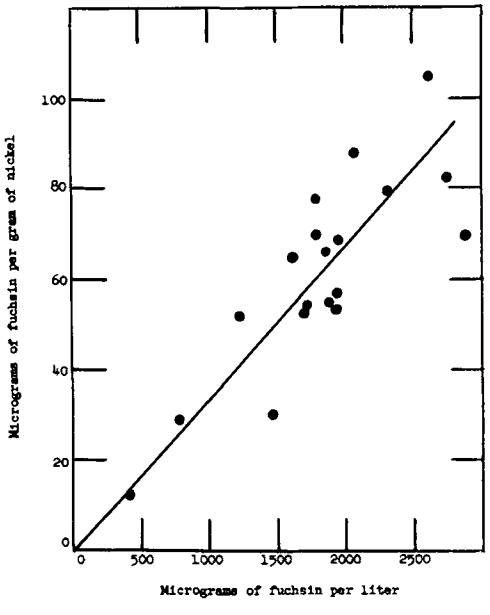

Fig. 3. Effect of fuchsin concentration in the bath on the amount recovered from Ni deposits.

Table III. Distribution of 100 μg of fuchsin in 1 g Ni

Grain size (mm)	Fuchsin molecules per grain	Length of grain edge per fuchsin molecule (A)
1×10^{-4}	1600	1.9
5×10^{-5}	200	7.5
4×10^{-5}	100	12.0
3×10^{-5}	43	21.0
2×10^{-5}	13	47.0
1×10^{-5}	1.6	—
9×10^{-6}	1.2	—
8×10^{-6}	0.8	—

solution would then increase this effect by making a larger number of molecules available at the surface. The concentration of brightener could thus play an important role in determining the grain size, with more brightener producing smaller grains, but at the same time more brittle deposits.

Acknowledgments

The authors wish to acknowledge the helpful advice of Dr. A. Timnick, who aided in the polarographic studies reported in this paper. Credit is also due to Mr. P. O. Sawyer for his discussions of the mechanism of plating with one of the authors.

Manuscript received August 6, 1956. This paper was prepared for delivery before the Cleveland Meeting, Sept. 30 to Oct. 4, 1956, and work on it was performed by O. J. Klingenmaier in partial fulfillment of the requirements for the M. Sc. degree from Michigan State University.

Any discussion of this paper will appear in a Discussion Section to be published in the December 1957 JOURNAL.

REFERENCES

1. A. G. Gray, Editor, "Modern Electroplating," Chap. 13 on Nickel by W. L. Pinner, G. Soderberg, and W. A. Wesley, pp. 311-317, John Wiley & Sons, Inc., New York (1953).
2. A. Brenner, V. Zentner, and C. W. Jennings, *Plating*, **39**, 865 (1952).
3. D. T. Ewing, R. J. Rominski, and W. M. King, *ibid.*, **36**, 1137 (1949).
4. R. Lind, W. J. Harshaw, and K. E. Long (to Harshaw Chemical Co.) U. S. Pat. 2,198,267, April 23, 1940.
5. R. O. Hull, *Monthly Rev. Am. Electroplaters' Soc.*, **26**, 753 (1939).
6. P. K. Froelich, *Trans. Electrochem. Soc.*, **46**, 87 (1924).
7. W. L. Pinner, G. Soderberg, and E. M. Baker, *ibid.*, **80**, 539 (1941).

Throwing Index

A New Graphical Method for Expressing Results of Throwing-Power Measurements

Robert V. Jelinek and Hero F. David[1]

Department of Chemical and Metallurgical Engineering, Syracuse University, Syracuse, New York

ABSTRACT

A new direct method is proposed for expressing the results of throwing-power measurements made on plating solutions in a conventional rectangular throwing-power box with plane parallel electrodes. The metal distribution ratio (M) is plotted vs. the linear ratio (P) on arithmetic coordinates. The reciprocal of the slope of this plot is called "Throwing Index" and represents a direct measure of bath throwing-power. Experimental data on several solutions are presented and advantages of this method are discussed.

Of prime importance in establishing the practical value of a commercial electroplating solution is "throwing-power," the capacity for producing uniform coatings on both accessible and inaccessible cathode areas. This paper presents a new graphical method for analyzing directly the results of throwing-power measurements in terms of "Throwing Index".

Haring and Blum (1) introduced the rectangular cell with plane parallel electrodes as a device for measuring throwing-power. They proposed the definition,

$$\text{Throwing power} = (P - M)/P \qquad \text{(I)}$$

where P = linear (or primary) ratio and M = metal distribution ratio between the two equi-potential plane parallel cathodes placed at different distances from the anode.

Two modified equations are (2-4):

$$\text{Throwing Efficiency} = (P - M)/(P - 1) \qquad \text{(II)}$$

$$\text{Throwing power (BSI)} = (P - M)/(P + M - 2) \qquad \text{(III)}$$

[1] Present address: Solvay Process Div., Allied Chemical & Dye Corp., Syracuse, N. Y.

These reduce the effect of P on the numerical results.

Valid objections have been raised to the throwing-power box. Chief among these are that it is an empirical device with an electrode arrangement dissimilar to many actual configurations, that numerical values obtained from it are dependent on cell dimensions, and that results may even be misleading for small differences in throwing-power. However, the fact remains that it is a simple and useful test apparatus which permits direct and rapid comparison of different plating solutions or operating conditions with sufficient precision for most practical purposes.

Throwing Index

In a recent study of the electrodeposition of alloys (5), the throwing-power of several solutions was compared under varied operating conditions. Measurements were made in a cell of the Haring-Blum type, 1 in. wide x 6 in. long, with 2 in. solution depth.

Table I presents the results of a typical group of runs, showing measured values of M and P, together with throwing-power calculated by means of each of the three equations above. None expresses

Table I. Throwing-Power measurements*

Linear ratio (P)	Metal ratio (M)	Throwing Power [Eq. (I)]	Throwing efficiency [Eq. (II)]	Throwing Power-BSI [Eq. (III)]
Tin-zinc cyanide bath:				
(150°F, 30 amp/ft²)		%	%	%
2.17	1.49	31.4	58.1	41.0
5.40	2.25	58.4	71.5	47.4
9.50	3.05	67.9	76.0	61.1
(75°F, 30 amp/ft²)				
2.02	1.18	41.5	82.4	70.0
3.80	1.25	67.1	91.0	83.5
5.70	1.42	75.0	91.2	83.5
Lead-tin fluoborate bath:				
(80°F, 40 amp/ft²)				
2.30	2.22	3.5	6.2	3.2
4.50	3.84	14.7	18.9	10.4
9.50	7.63	19.7	22.0	12.3
(80°F, 30 amp/ft²)				
2.08	1.95	6.3	12.0	6.4
4.85	3.88	20.0	25.2	14.4
9.50	7.02	26.1	29.2	17.1
Cadmium cyanide bath:				
(80°F, 15 amp/ft²)				
2.11	1.26	40.4	76.5	62.0
4.30	1.70	60.5	78.8	65.0
9.00	2.23	75.1	84.5	73.5
Acid zinc sulfate bath:				
(80°F, 15 amp/ft²)				
1.25	1.25	0	0	0
1.85	1.87	−1.1	−2.4	−1.2
4.76	5.27	−10.7	−13.6	−6.3
6.00	6.94	−15.7	−18.8	−8.6

* Haring-Blum type throwing-power box, 1 in. x 6 in., 2 in. solution depth. Thin polished-steel cathodes.

throwing power satisfactorily in terms of a fairly constant value over a range of linear ratios for one bath at constant plating conditions. Such a value would be useful for expressing variations in throwing-power with changes in current density, temperature, etc.

Accordingly, the simple procedure of plotting metal ratio vs. linear ratio on arithmetic coordinates was tried for a group of runs. The result was a linear relationship for each bath over the full range of the data. Fig. 1 shows such a plot for the data in Table I. Table II identifies the plating baths tested.

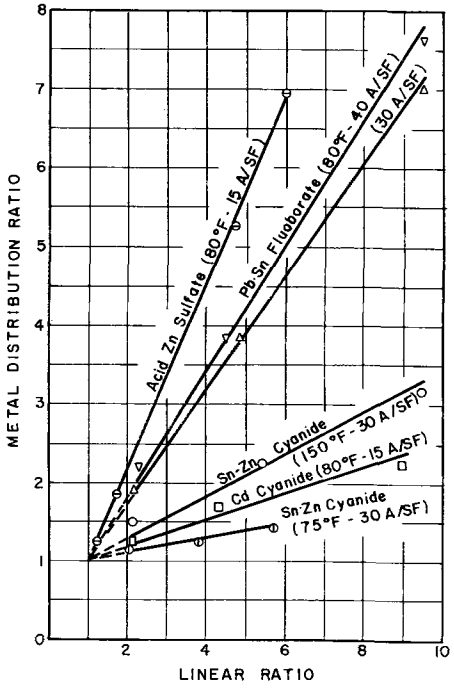

Fig. 1. Throwing Index plot

Table II. Solution composition

Tin-zinc cyanide:	
Sodium stannate	16.0 oz/gal
Zinc cyanide	1.2
Potassium cyanide	2.8
Potassium hydroxide	0.87
Lead-tin fluoborate:	
Lead	11.8 oz/gal
Total tin	0.98
Stannous tin	0.80
Free fluoboric acid	5.4
Free boric acid	3.4
Acid zinc sulfate:	
pH	3.3
Zinc	5.7 oz/gal
Cadmium cyanide:	
Cadmium	2.10 oz/gal
Total cyanide (as NaCN)	1.74
Alkalinity (as NaOH)	0.17

At first it was thought the result might be fortuitous for the particular throwing-box and solutions used in this work. To test the method, data were taken from the papers of Pan (3) and Gardam (6) and plotted in the same way. Pan used a Haring-Blum box measuring 10 x 10 x 60 cm; Gardam's data are from two cells, one 10 x 10 x 60 cm, and the other 2 x 2 x 12 cm. These data are shown in Fig. 2 and 3.

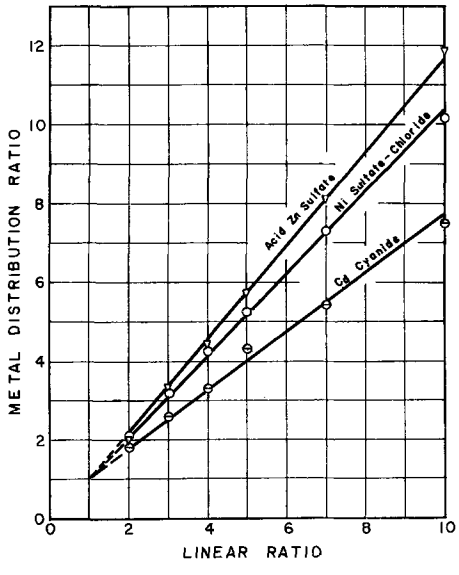

Fig. 2. Throwing Index plot, data of Pan (3)

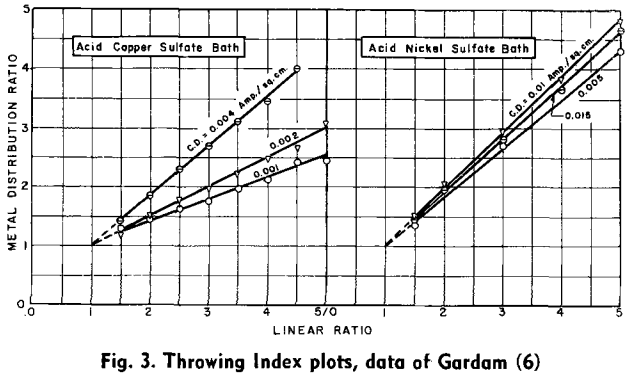

Fig. 3. Throwing Index plots, data of Gardam (6)

Table III. Values of Throwing Index

Bath	Temp (°F)	Current density (amp/ft²)	Throwing Index
Authors' Data:			
Sn-Zn cyanide	75	30	10.0
	150	30	3.68
Pb-Sn fluoborate	80	30	1.38
	80	40	1.24
Cd cyanide	80	15	5.75
Acid Zn sulfate	80	15	1.19
Data of Pan (3):			
Cd cyanide	68	15	1.34
Acid Zn sulfate	77	15	0.83
Ni sulfate-chloride	80	28	0.96
Data of Gardam (6)			
Acid Cu sulfate	75	0.92	2.58
	75	1.85	1.98
	75	3.70	1.18
Acid Ni sulfate	75	4.63	1.19
	75	9.25	1.04
	75	13.9	1.10

The point $M = 1$, $P = 1$ should be common to all of the curves, and so each of the lines on Fig. 1, 2, and 3 was extended to include this point. A solution with ideal throwing characteristics would produce a horizontal line at $M = 1$, and one with poor throwing-power would show a very steep line on this type of plot. Thus it was reasoned that the slope of the line could be used as an indication of throwing-power. In order to have larger values associated with better throwing-power, the reciprocal of the slope was used. The designation "Throwing Index" is suggested for this number, in order to distinguish it from Throwing Power and Throwing Efficiency used in the literature.

Values of Throwing Index obtained from Fig. 1, 2, and 3 are listed in Table III. Fig 4 presents the relation between Throwing Index and current density for two solutions, as shown by Gardam's data (6).

Discussion

There are several advantages associated with the new Throwing Index method:

1. Experimental data from the familiar Haring-Blum cell are used directly and conveniently. No formulas are required, and there is no question as to which equation was used when the results are reported.

2. A single number is obtained, characteristic of a range of linear ratios. This makes it convenient to follow experimentally the effects of temperature, current density, bath concentration, and other plating variables.

3. Throwing Index is obtained from several experimental points, minimizing errors in measurement at any one point. The three formulas in use at present all require individual throwing-power calculations at each point; relatively small errors in one or two points can then produce an anomalous throwing-power curve when the data are graphed.

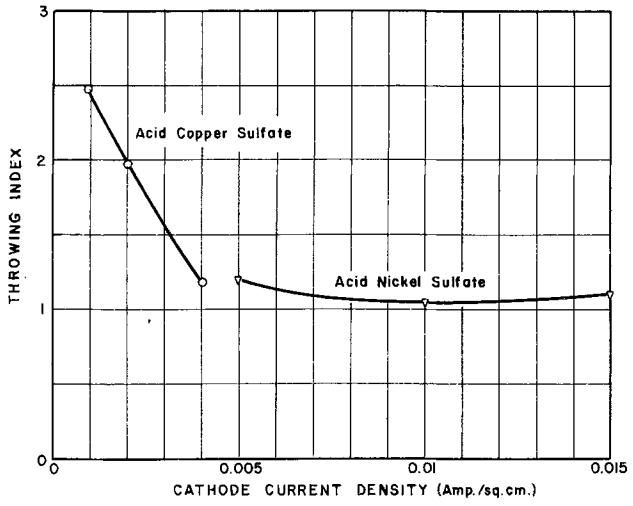

Fig. 4. Throwing Index vs. current density, data of Gardam (6)

The method does not present any new theoretical approach to the throwing-power problem. It is subject to the same limitations that have already been pointed out for the Haring-Blum cell (7-9). Throwing Index is offered principally as a useful empirical tool, convenient for practical electroplating studies, operating specifications, and production control tests.

Acknowledgment

The authors wish to express their appreciation to the Crouse-Hinds Co. for support of this work through a contract with the Syracuse University Research Institute. Thanks are also due to Walter Beck and C. S. Grove, Jr., for their advice and encouragement and to Ardeshir Aidun for analytical assistance.

Manuscript received August 6, 1956. This paper was prepared for delivery before the Cleveland Meeting, Sept. 30 to Oct. 4, 1956.

Any discussion of this paper will appear in a Discussion Section to be published in the December 1957 JOURNAL.

REFERENCES

1. H. E. Haring and W. Blum, *Trans. Electrochem. Soc.*, **44**, 313 (1923).
2. A. H. Heatley, *ibid.*, **44**, 283 (1923).
3. L. C. Pan, *ibid.*, **58**, 423, (1930).
4. S. Field, *J. Electrodep. Tech. Soc.*, **9**, 144 (1934).
5. H. F. David, "Electroplating of Tin-Zinc and Lead-Tin Alloys," M.Ch.E. Thesis, Syracuse University, May 1956.
6. G. E. Gardam, *Trans. Faraday Soc.*, **34**, 698 (1938).
7. T. P. Hoar and J. N. Agar, *Disc. Faraday Soc.*, No. 1, 162 (1947).
8. C. Kasper, *Trans Electrochem. Soc.*, **77**, 353, 365 (1940); **78**, 131 (1940).
9. M. Schlotter and J. Korpiun, *ibid.*, **62**, 129 (1932).

Tin Plating from the Pyrophosphate Bath

J. Vaid and T. L. Rama Char

Department of General Chemistry, Indian Institute of Science, Bangalore, India

ABSTRACT

The complex $Sn_2P_2O_7$ bath was found satisfactory for the electroplating of Sn since it gave good quality deposits over a wide range of experimental conditions. Addition agents like dextrin-gelatin increased the brightness of the deposits. This bath has several advantages over the stannate bath.

Acid sulfate and alkali stannate baths are widely used for industrial plating of Sn. In the literature, use of pyrophosphate baths is mentioned only by Roseleur (1-3) and Marino (4). Recently, Safranek and Faust (5) used the $Sn_2P_2O_7$-copper cyanide bath for deposition of Sn-Cu alloys.

The principal advantages of using pyrophosphate solutions for electroplating relate to high solubility, nonpoisonous nature, stability, and low metal ion concentration due to complex formation. Detailed investigations on the electrodeposition of various metals and alloys from this bath were undertaken to study the electrochemistry of metal pyrophosphate solutions, optimum operating conditions for satisfactory deposition, and to compare its performance with that of well-established baths. Electrodeposition of Sn, Zn, Cu-Sn alloy and Ni from the pyrophosphate bath has been reported briefly in preliminary notes from this laboratory (6-9). This paper presents in detail the work on the deposition of Sn.

Experimental

Plating solutions were prepared by dissolving $Sn_2P_2O_7$ in $Na_4P_2O_7$ solution, resulting in formation of a complex: $Sn_2P_2O_7 + Na_4P_2O_7 \rightarrow 2Na_2[Sn(P_2O_7)]$. Potentiometric and conductimetric titrations showed that the ratio of pyrophosphate to Sn in the complex is 1:1. The Sn ion concentration in the solution as found from potential measurements was of the order of 10^{-14} g-ion/l (10). The pyrophosphate content of the bath was always in excess of that required for complex formation. $Sn_2P_2O_7$ was prepared by adding $Na_4P_2O_7$ solution to a solution of $SnCl_2$ in HCl. The precipitate formed was washed thoroughly, dried, and kept for use. Stannous pyrophosphate was analyzed for Sn by the cupferron method, and for pyrophosphate by decomposition to orthophosphate and then volumetric estimation by the ammonium molybdate method. Composition (by weight) was: Sn, 54.0, pyrophosphate 39.5, and water 6.5%.

It was possible to maintain a fairly high Sn content in the plating bath because of the high solubility of $Na_4P_2O_7$ in water. Keeping in view the cost, drag out losses, and necessity for the presence of a high free pyrophosphate content (and consequently the tendency of the bath to crystallize at low temperatures), it was not advisable to go beyond a Sn content of 33 g/l. The $Na_4P_2O_7$ concentration in the range 80-480 g/l was found suitable for the metal concentrations used, the ratio (by weight) of $Na_4P_2O_7$ to $Sn_2P_2O_7$ being from 4:1 to 8:1. The free pyrophosphate improved anode corrosion, conductivity, and throwing power. Nine bath compositions were studied, the $Sn_2P_2O_7$ content being 20, 40, and 60 g/l, and the ratio of $Na_4P_2O_7$ to $Sn_2P_2O_7$ being 4:1, 6:1, and 8:1.

Chemicals employed for the plating bath were of C.P. quality, $SnCl_2$ being "Bakers Analyzed" and sodium pyrophosphate British Drug Houses brand. Fresh solutions were run for each experiment. Canning and Co. Sn anodes (3 x 1 x ⅛ in.) and Cu sheet cathodes (3 x 1 x 1/32 in.) were used, the inter-electrode distance being 1 in., immersed area of each electrode 2 in.^{2}, and plating time 20-30 min. Experimental details concerning cleaning electrodes, plating equipment, current efficiencies (on the basis of divalent Sn), temperature, agitation (speed 500 rpm approximately), pH, and resistivity were the same as described previously (11, 12). The pH was varied by the addition of H_3PO_4 or NaOH.

Cathode and anode potentials during deposition were determined as follows. The electrode whose potential was to be measured was coupled with a saturated calomel electrode and the emf of the combination determined by using a Tinsley potentiometer. The connection to the electrode was made by an agar-agar bridge whose tip, drawn into a capillary of approximately 1 mm diameter, pressed lightly against the electrode, minimizing thereby the error due to potential drop through the electrolyte. A thick layer of Sn was deposited on the cathode before taking measurements. Then, commencing from the static potential, emf readings were taken at various current densities. Sufficient time, approximately 2-3 min, was allowed for each measurement to enable the potential to reach a steady value. Plating conditions were carefully controlled to obtain results of the accuracy of ±0.001 v, as far as possible. Potential values refer throughout to the H scale.

The limiting C.D. was found from (*a*) C.D.-cathode potential curves, there being a sudden change in the form of the curve at the limiting C.D., and (*b*) current efficiency-C.D. data. Both methods gave practically the same values. The throwing power was calculated from the equations of Schlotter-Korpiun (13) as well as those of Gardam (14). In the latter case, the equation for a linear relationship between cathode potential and log C.D. was used, and as approximation, the inter-electrode distance was substituted for l_2 of the equation.

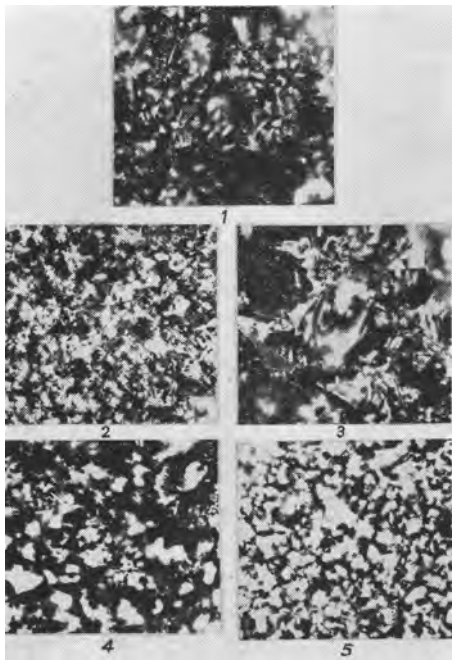

Fig. 1. Photomicrographs of deposits from $Sn_2P_2O_7$ 60, $Na_4P_2O_7$ 360 g/l, Cu cathode. Magnification 1 x 500 before reduction for publication. *Plate 1.* Fine-grained, bright deposit at 80°C and 1.6 amp/dm², from stannate bath (composition, Table II); *Plate 2,* fine-grained, semibright deposit at 50°C and 0.54 amp/dm², from pyrophosphate bath; *Plate 3,* coarse-grained, semibright deposit at 80°C and 0.54 amp/dm²; *Plate 4,* fine-grained, bright deposit at 80°C and 1.6 amp/dm²; *Plate 5,* fine-grained and brighter deposit with same conditions as Plate 4 and with 10 g/l dextrin and 1 g/l gelatin.

To study the structure, a thick coating of Sn was deposited under various conditions on polished cathode plates, and photomicrographs were taken with a Vicker's projection microscope at 500 magnification, using Kodak B20 process plates.

Results

A detailed study of the effect of important variables on deposition was made, and results are presented graphically in Fig. 1-11 and Tables I and II. Results obtained for all concentrations studied have not been covered graphically to avoid overlapping; for the same reason points corresponding to 100% efficiencies or static potentials have not been marked. The data correspond to good quality deposits. The decomposition potential for the plating solution was 2.5-2.6 v and the bath voltage 0.30-1.00 v. The standard stannate bath composition was modified to bring the Sn content on a par with that of the pyrophosphate bath.

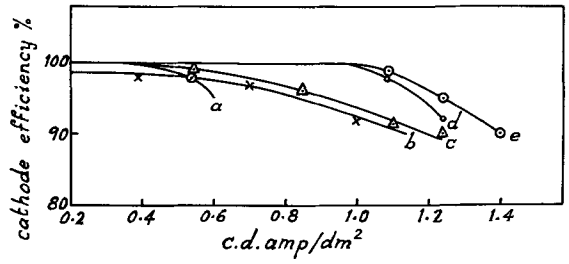

Fig. 2. (a) $Sn_2P_2O_7$ 20 g/l, ratio 6; (b) $Sn_2P_2O_7$ 40 g/l, ratio 6; (c) $Sn_2P_2O_7$ 60 g/l, ratio 4; (d) $Sn_2P_2O_7$ 60 g/l, ratio 6; (e) $Sn_2P_2O_7$ 60 g/l, ratio 8; temp, 60°C.

Table I. Effect of addition agents on current efficiency and quality of deposit

$Sn_2P_2O_7$ 60 g/l, $Na_4P_2O_7$ 360 g/l, temperature 60°C, pH 9.0, cathode Cu, anode Sn, still plating. Quality of deposit: A—marked improvement, B—slight improvement, C—no effect, D—deterioration.

No.	Addition agent	Amount added g/l	C.D. amp/dm²	Current efficiency % Cathode	Current efficiency % Anode	Brightness of deposit
1.	Nil	—	0.85	100	103	—
			1.01	100	103	—
			1.24	92	104	—
2.	Sodium nitrate	15.0	0.85	99	106	C
			1.01	98	104	C
			1.16	97	106	C
3.	Ammonium citrate	15.0	0.85	93	107	B
			1.01	93	105	B
			1.16	95	101	B
4.	Sodium oleate	5.0	0.85	97	103	D
			1.01	92	97	D
5.	Sodium tartrate	15.0	1.01	100	106	A
			1.16	96	105	B
			1.32	95	103	C
6.	Sodium acetate	15.0	1.16	98	105	C
			1.32	90	104	C
7.	Resorcinol	20.0	0.85	100	98	D
			1.16	92	103	D
8.	Dextrin	5.0	1.01	100	105	A
			1.16	99	104	A
			1.32	95	103	B
9.	Dextrin	10.0	1.32	100	105	A
			1.47	100	105	A
			1.63	96	104	A
10.	Gelatin	0.5	1.32	93	105	C
			1.47	90	100	C
11.	Gelatin	1.0	1.01	100	105	B
			1.32	94	106	B
			1.63	95	101	C
			1.94	95	100	D
12.	β-naphthol	1.0	1.16	96	104	A
			1.32	92	100	B
13.	Dextrin + Gelatin	10.0 + 1.0	1.32	94	105	A
			1.63	94	102	A
			1.94	90	100	A
			2.25	91	99	A
			2.71	88	99	C

Nature of deposit.—The bath gave matte, white, smooth, and adherent deposits of Sn on Cu (steel or brass) cathodes over a wide range of plating conditions: metal content, ratio of $Na_4P_2O_7$ to metal pyrophosphate, pH (8.0, 9.0, and 9.5). Increase in C.D. gave finer-grained deposits and increase in temperature or agitation gave coarser grained ones. The addition of dextrin or dextrin-gelatin combination, tartrate, and β-naphthol in optimum concentrations increased brightness. The dextrin-gelatin combination was the best and gave deposits com-

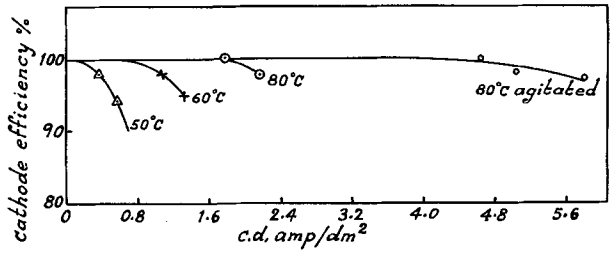

Fig. 3. Concentration (d) of Fig. 2.

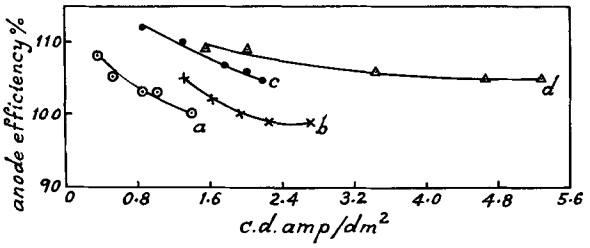

Fig. 4. (a) $Sn_2P_2O_7$ 60 g/l, ratio 6, temp, 60°C; (b) $Sn_2P_2O_7$ 60 g/l, ratio 6, temp, 60°C + (gelatin 1, dextrin 10 g/l); (c) $Sn_2P_2O_7$ 60 g/l, ratio 6, temp, 80°C; (d) $Sn_2P_2O_7$ 60 g/l, ratio 6, temp, 80°C (agitated).

parable with those obtained from the stannate bath (Fig. 1, plates 1-5). The effect of various addition agents on quality of the deposit and current efficiency is recorded in Table I.

Current efficiencies.—In the working C.D. range, cathode efficiency was nearly 100%, anode efficiency was a bit higher, 100-110%, although the anode did not dissolve chemically in the plating solution. Current efficiencies remained practically unaffected by changes in concentration, temperature, agitation, pH (not recorded), or use of addition agents (Fig. 2-4 and Table I).

Current density.—The C.D. range and limiting C.D. increased with increase in metal content, the ratio of $Na_4P_2O_7$ to metal pyrophosphate (to a small extent), rise in temperature, agitation, and the addition of few substances like dextrin, gelatin or their combination. pH variation had little effect. It

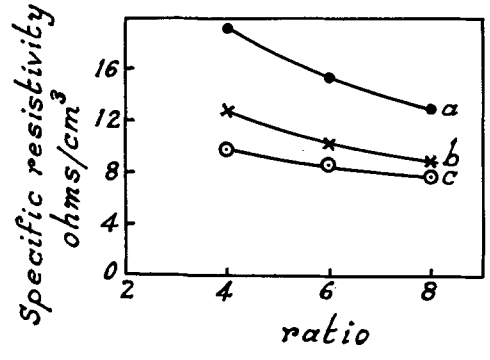

Fig. 5. (a) $Sn_2P_2O_7$ 20 g/l; (b) $Sn_2P_2O_7$ 40 g/l; (c) $Sn_2P_2O_7$ 60 g/l; temp, 60°C.

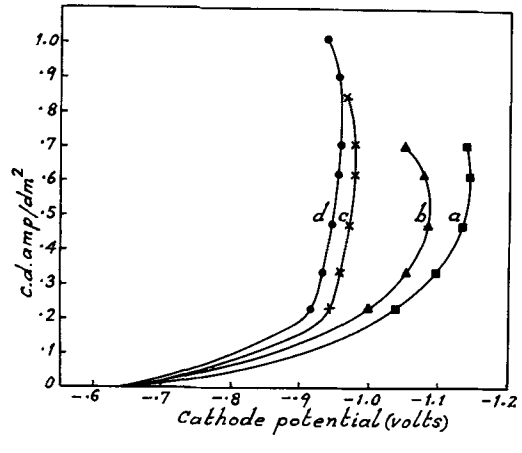

Fig. 6. (a) $Sn_2P_2O_7$ 20 g/l, ratio 4; (b) $Sn_2P_2O_7$ 20 g/l, ratio 8; (c) $Sn_2P_2O_7$ 60 g/l, ratio 4; (d) $Sn_2P_2O_7$ 60 g/l, ratio 8; temp, 60°C.

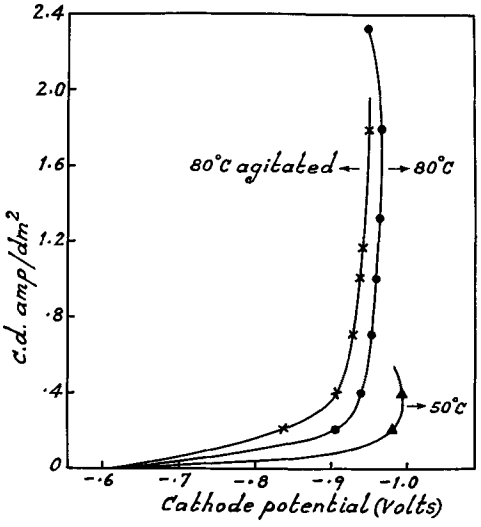

Fig. 7. $Sn_2P_2O_7$ 60 g/l, ratio 6

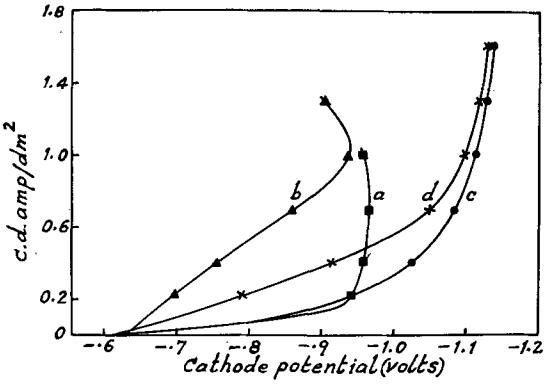

Fig. 8. Concentration as in Fig. 7, temp, 60°C: (a) addition nil; (b) addition ammonium citrate 15 g/l; (c) addition gelatin 1 g/l; (d) addition gelatin 1, dextrin 10 g/l (dextrin only also).

was possible to go up to 5 amp/dm². There was no interference with anode dissolution due to film formation, etc., even at high C.D. (Fig. 2-4 and Table I).

Specific resistivity.—Increase in metal content, ratio of $Na_4P_2O_7$ to metal pyrophosphate, or temperature (not shown) and decrease of pH (slightly) lowered the resistivity (Fig. 5). The addition of dextrin-gelatin combination had no effect.

Polarization.—Cathode polarization decreased with increase of metal content (keeping the ratio same), ratio, temperature, agitation, and pH (not recorded). Addition of dextrin, gelatin, or dextrin-gelatin combination had the general effect of increasing polarization; at low C.D., however, a lowering was observed. Ammonium citrate decreased polarization. In all cases it increased with rise in C.D. up to the limiting C.D. only. After this stage, a decrease was observed from the available data. Current efficiency then decreased, H evolution commenced, and the deposit was not good (Fig. 6-8). C.D.-potential curves for stannate bath are also recorded in Fig. 9.

The effect of variables on anode polarization was similar to that on cathode polarization. No limiting value for the anode C.D. was found in the C.D. range studied. Dextrin-gelatin decreased polarization (Fig. 10).

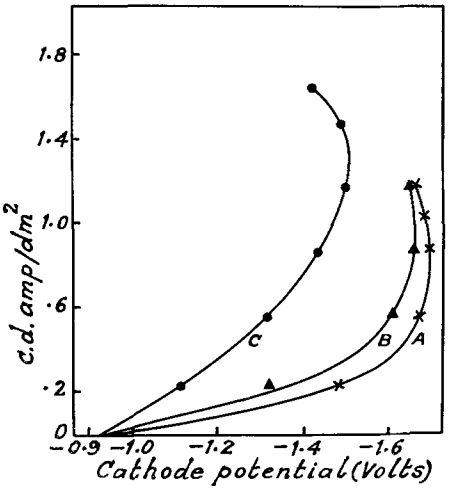

Fig. 9. Concentration Table II: (A) temp, 50°C; (B) temp, 60°C; (C) temp, 70°C.

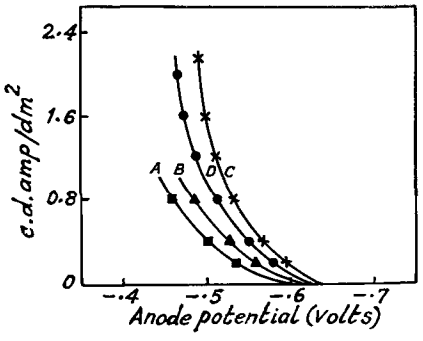

Fig. 10. $Sn_2P_2O_7$ 60 g/l: (A) ratio 4, temp, 60°C; (B) ratio 6, temp, 60°C; (C) ratio 6, temp, 80°C; (D) ratio 6, temp, 60°C + (gelatin 1, 10 dextrin g/l).

Throwing power.—The plating solution possessed good throwing power. Calculations on the basis of the Schlotter-Korpiun equation showed that the throwing power increased with rise in metal content and temperature, and with the use of dextrin, gelatin, or their combination, while it decreased with increasing C.D., and to a small extent with rise in pH and agitation. The Schlotter-Korpiun throwing power values were in the range 5.7-10.8 for the pyrophosphate, and 9.8-16.4 for the stannate baths. For the optimum pyrophosphate bath, the Gardam value was 59% as against 64% for the stannate (Fig. 11, curves A and D, Table II).

Control and maintenance of bath.—The bath was quite stable and did not decompose with high temperatures. Composition did not change appreciably after electrolysis, since current efficiencies were high and practically balanced, and there were no difficulties due to anode corrosion. In a typical case with a solution containing 60 g/l of $Sn_2P_2O_7$ and 360 g/l of $Na_4P_2O_7$, changes before and after electrolysis for 40 min at 0.7 amp/dm², 60°C, were: metal content, 32.4-32.6 g/l; total pyrophosphate (P_2O_7), 164.2-164.3 g/l; pH, 9.0-9.2; specific resistivity, 8.65-8.66 ohms/cm³. The solutions did not contain orthophosphate before and after electrolysis as estimated by the method of Kolthoff and Stenger (15). A freshly prepared solution could be used for 4-5 runs without any deterioration in its performance (quality of deposit, C.D. range, current efficiencies, etc.). A solution which was aged for about two months was equally satisfactory.

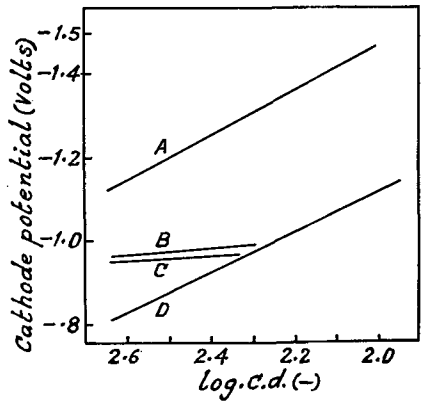

Fig. 11. (A) $Na_2Sn(OH)_6$ bath concentration Table II, temp, 70°C; (B) $Sn_2P_2O_7$ 40 g/l, ratio 6, temp, 60°C; (C) $Sn_2P_2O_7$ 60 g/l, ratio 6, temp, 60°C; (D) $Sn_2P_2O_7$ 60 g/l, ratio 6, temp 60°C + (gelatin 1, dextrin 10 g/l).

Testing of deposits.—Coatings of any desired thickness of 0.0005 in. or above (calculated from area and weight) could be obtained by varying the plating time. Adherence of deposits to the base metal as determined by bending and breaking tests was good. Ferricyanide (steel base) and hot water tests showed that they were free from porosity. Corrosion resistance was good in the laboratory atmosphere (4-6 mo). Sn content of the deposits was above 99.8%.

Optimum plating conditions.—A study of experimental results led to the following optimum bath composition and operating conditions for the best performance of the $Sn_2P_2O_7$ bath. Bath composition: $Sn_2P_2O_7$ 60 (tin content 32.4), $Na_4P_2O_7$ 360, dextrin 10, gelatin 1 g/l. Operating conditions: Cathode C.D.: 0.2-2.3 amp/dm² (still, 60°C), up to 5.0 amp/dm² (agitated, 80°C, without addition agents); pH 9.0, temperature: 60-80°C; time to deposit 0.001 in. thickness at 2.2 amp/dm², 80°C: 25 min.

Comparison of pyrophosphate and stannate baths.—Table II gives an idea of the relative performance of the pyrophosphate and stannate baths for Sn plating. Data recorded for stannate bath were obtained experimentally as well as from literature (1, 16, 17).

The $Sn_2P_2O_7$ bath is superior to the stannate bath in the following respects: *(a)* current efficiencies up to the limiting cathode C.D., *(b)* bath voltage, *(c)* stability, *(d)* wide range of anode C.D., and *(e)* absence of critical anode C.D. which facilitates bath control. It compares well with the stannate bath in throwing power, quality of deposit, and cost of plating solution. In view of these considerations, it can be stated that the pyrophosphate bath compares favorably with the commercial stannate bath and is suitable for Sn plating.

Discussion

The $Sn_2P_2O_7$ bath gives satisfactory deposits of Sn on steel, Cu, or brass over a wide range of operating conditions and has many advantages over the conventional stannate bath. Roseleur (2) used a

Table II. Comparison between pyrophosphate and stannate baths

No.		Pyrophosphate	Stannate	
			Experimental	Literature
1.	Composition g/l	$Sn_2P_2O_7$ 60 $Na_4P_2O_7$ 360	$Na_2Sn(OH)_6$ 74 NaOH 7.5 Sodium acetate 11 30% H_2O_2 3 drops	$Na_2Sn(OH)_6$ 90 NaOH 7.5 Sodium acetate 15.0 H_2O_2 (100 vol) 0.5 ml
2.	Tin g/l	32.4	32.4	40.0
	Free pyrophosphate (P_2O_7) g/l	116.4	—	—
3.	Addition agents g/l	Dextrin 10.0 Gelatin 1.0	— —	—
4.	*pH*	9	12	—
5.	Temp, °C	60-80	60-70	60-80
6.	Bath voltage, v, 80°C	0.3-1.0 (0.6-2.3 amp/dm²)	4.5 (0.4-2.3 amp/dm²)	3.0-4.5 (1.1-2.7 amp/dm²)
7.	Specific resistivity 60°C, ohms/cm³	8.65	8.56	—
8.	Cathode C.D. (max) amp/dm²	5.0	1.6	1.1-2.7
9.	Anode C.D. (max) amp/dm²	5.0	1.6	1.1-4.3
10.	Cathode current efficiency, %	91-100	70-83	60-90
11.	Anode current efficiency, %	99-112	80-98	60-90
12.	Cathode polarization 60°C, v	0.28-0.60 (0.4-2.3 amp/dm²)	0.40-0.73 (0.23-1.60 amp/dm²)	—
13.	Throwing power, 60°C, Schlotter-Korpiun (0.54 amp/dm²)	10.8	16.3	—
	Gardam % (0.39 amp/dm²)	59	64 (70°C)	68-74
14.	Stability of bath	Good	Fair	Fair
15.	Quality of deposit	Good	Good	Good
16.	Time in min to deposit 0.001 in. at 1.6 amp/dm² 80°C	34	—	70
17.	Cost of bath, dollars per liter (approx)	0.76	—	1.00

solution of the composition: fused $SnCl_2$ 1.0-1.5, $Na_4P_2O_7$ 10.0-12.5 g/l. However, no mention was made of the plating conditions except that this bath was unable to give heavy deposits. Another Roseleur solution (3) was made up of $SnCl_2$ 9.4, $Na_4P_2O_7$ 75.0, dextrin 6.25 g/l; operating conditions: 60°C and C.D. of 5 amp/ft². Solutions used in the present investigation were simpler in composition, addition agents being used only to obtain some beneficial effects. The metal content was high, and it was possible to work the bath at current densities up to 5 amp/dm².

Organic brighteners like dextrin, gelatin, and β-naphthol in the pyrophosphate bath were also used in the acid Sn bath. Henricks (18) attributed the brightening action to their acid pickling inhibiting tendency. Tartrate had some brightening effect, as in the deposition of Cu from the pyrophosphate bath; it is perhaps due to complex formation. The grain size became finer and the cathode polarization increased with addition of dextrin-gelatin.

Cathode polarization was fairly high, although slightly less than that of stannate bath. The relationship between cathode potential and log C.D. is linear for the pyrophosphate as well as the stannate bath (Fig. 11) and both of them give fine-grained deposits (Fig. 1). Gardam (19) suggested that the logarithmic type, i.e., $\Delta E \propto \log I$, indicates frequent formation of new grain nuclei, viz., production of fine-grained deposits. Experimental results are in accordance with the Gardam theory. However, it should be stated that exhaustive polarization measurements were not made for the stannate bath. The anode potential measurements showed that no limiting C.D. was found for anode dissolution. This is one of the important advantages of the pyrophosphate bath against the stannate, where there is a limit to the anode C.D. The throwing power of the bath, Schlotter-Korpiun as well as Gardam, was of the same order as that of stannate bath. The latter is among the best of the plating baths, so far as this property is concerned.

In the electrodeposition of Sn from the complex pyrophosphate bath, the metal ion concentration was low; smooth, fine-grained, and bright deposits were obtained at electrode efficiencies close to 100%. The cathode polarization was high, and the throwing power of the bath was very good. The performance of the bath was in accordance with the general expectations for a complex salt plating bath. The present work indicates that this bath shows promise and is suitable for further investigation on a commercial scale.

Acknowledgment

The authors are thankful to Professor K. R. Krishnaswami, Head of the Department of General Chemistry, for his keen interest in the work.

Manuscript received November 14, 1955. This paper is based in part on a thesis presented by J. V. to the graduate faculty of Punjab University in partial fulfillment of the requirements for the degree of Master of Science.

Any discussion of this paper will appear in a Discussion Section to be published in the December 1957 JOURNAL.

REFERENCES

1. F. F. Oplinger and F. Bauch, *Trans. Electrochem. Soc.*, **80**, 617 (1941).
2. E. F. Kern, *ibid.*, **23**, 193 (1913).
3. S. Field and A. D. Weill, "Electroplating", Ch. 21, p. 428, Sir Isaac Pitman and Sons, London (1951).
4. P. Marino, Brit. Pat. 10,133, July 12, 1915; *Chem. Abstr.*, **11**, 121 (1917).
5. W. H. Safranek and C. L. Faust, *Plating*, **41**, 1159 (1954).
6. J. Vaid and T. L. Rama Char, *Current Sci. India*, **21**, 310 (1952).
7. J. Vaid and T. L. Rama Char, *J. Sci. Ind. Research, India*, **11B**, 503 (1952).
8. J. Vaid and T. L. Rama Char, *Current Sci. India*, **22**, 170 (1953).
9. S. K. Panikkar and T. L. Rama Char, *J. Sci. Ind. Research India*, **14B**, 603 (1955).
10. J. Vaid and T. L. Rama Char, *Current Sci. India*, **22**, 170 (1953); *Chem Abstr.*, **48**, 4353 (1954).
11. T. L. Rama Char and N. B. Shivaraman, *This Journal*, **100**, 227 (1953).
12. T. L. Rama Char and R. Sadagopachari, *J. Indian Inst. Sci.*, **35A**, 298 (1953).
13. M. Schlotter and J. Korpiun, *Trans. Electrochem. Soc.*, **62**, 129 (1932).
14. G. E. Gardam, *Trans. Faraday Soc.*, **34**, 698 (1938).
15. I. M. Kolthoff and V. A. Stenger, "Volumetric Analysis," Vol. II, p. 140, Interscience Publishers, New York (1947).
16. P. R. Pine, *Trans. Electrochem. Soc.*, **80**, 631 (1941).
17. "Instructions for Electrodepositing Tin," p. 9, Tin Research Institute, England (1946).
18. J. A. Henricks, *Trans. Electrochem. Soc.*, **82**, 113 (1942).
19. G. E. Gardam, *Disc. Faraday Soc.*, **1**, 182 (1947).

A Simplified Procedure and Apparatus for Measuring Surface Area of Fine Powders By Gas Adsorption

F. M. Starkweather and D. T. Palumbo[1]

Chemistry Laboratory, Sylvania Electric Products Inc., Flushing, New York

ABSTRACT

A modification of the standard Brunauer-Emmett-Teller (BET) gas adsorption technique for the determination of surface areas of fine powders is presented. Data show that values usually within 10% of those by the standard method are obtained for Ba, Sr, Ca carbonates, ZnS, CdS, and Zn_2SiO_4. A simplified design of the conventional gas adsorption apparatus is described. It is simple to operate, less subject to accidental damage, and can be set up with simpler accessories than are required for the standard BET system.

In the investigation of the preparation of triple carbonates for use in oxide cathode studies, a reliable measure of the particle size is required. Past practice has been to measure the surface area by the BET gas adsorption method (described below) and to calculate the mean particle diameter (MPD) assuming spherical particles. Ordinary gravitational sedimentation methods are not suitable for these materials as the mean particle diameters are in the range 0.07-1 μ. The Fisher Sub-Sieve Sizer (FSSS), which has been used for control of commercial preparation of carbonates, was also unsuitable. Here, the size values obtained depended, in part, on the degree of agglomeration of the precipitate. For particles of rough external or with large internal surface, the air permeation method (FSSS) would not be expected to give values comparable to the gas adsorption method. However, large internal surface can result from the agglomeration of individual particles with smooth surface. In these cases, the air permeation method would not indicate whether the agglomerate size, crystallite size, or both have changed.

The major drawback of the BET procedure is the time required for a determination. Unless overnight outgassing is used, at least two days' elapsed time per sample are required for the measurement. Actual operational time required is approximately 6 hr. The result is that any experimental program which depends on BET measurements is slowed down correspondingly.

In preliminary experiments, such as those where various procedures for preparation of carbonates are surveyed, a surface area value within 25% of the true area is usually sufficient for meaningful results. A simplification of the BET method to reduce the time per determination to about 1 hr with a negative error usually no greater than 10% of the standard BET value is discussed below. The magnitude of the error is a function of sample composition and surface area. In general the error increases with samples of larger surface area. The design and construction of a simplified unit, particularly suited for rapid measurements, is described.

The major saving in the time of a determination results from the use of a single point surface area determination, elimination of the dead space determination, and a short outgassing schedule. Other workers have proposed and employed these modifications. Emmett (1), for example, points out that the slope of an adsorption curve using a zero inter-

[1] Present address: Sylvania Electric Products Inc., Towanda, Pa.

cept and one measured point is usually within 5% of the slope determined by three or four points. Bugge and Kerlogue (2) have shown that shorter outgassing time and avoidance of the dead space determination gave results only slightly lower (ca. 3%) than values obtained by the standard method. Amron and Starkweather (3) have shown that <2% error is introduced by using two or three points for determining the curve rather than five or more and had considered the feasibility of a single point adsorption run. The modifications described below represent the natural extension and integration of these ideas into a unit simple to construct and operate and a method which permits determinations of surface area in a minimum of time.

Experimental

Standard BET adsorption method.—The apparatus used for the determination of surface area is of standard design (4). A complete run entails the following steps: sealing a weighed sample in an adsorption bulb onto the system; outgassing at elevated temperature to remove adsorbed water and gases; calibration of the adsorption bulb for volume, using helium; measurement of nitrogen taken up by the sample as a function of pressure at constant temperature; calculation of the surface area from the adsorption isotherm (1).

The time for a run is determined by the outgassing procedure and the number of experimental points measured on the adsorption curve.

Simplified BET procedure.—The apparatus used for the simplified procedure may be the same as for the standard method, with the sample tube position fitted with a ground glass joint. This eliminates a glass sealing operation. Further simplifications are possible, including elimination of the diffusion pump, McLeod gauge, and mercury reservoirs. The simplified method incorporates the following features: *(a)* outgassing at room temperature 10-20 min to a pressure of 1 μ or less; *(b)* sample tube calibrated for volume with ground glass connection to the system; *(c)* a one-point run at about 15 cm pressure and assumption of zero intercept.

With samples of known density and a calibrated sample tube volume, the helium run can be omitted.

The accuracy of the proposed method was checked by determining the surface area of samples of interest (phosphors and triple carbonates) by both procedures.

A Simplified Gas Adsorption Apparatus

A simplified BET apparatus is shown in Fig. 1a, b, c. The major points of difference are the substitution of a variable volume manometer for the fixed volume manometer and a fixed "calibrated" volume for the "variable" calibrated volume of the standard apparatus. These modifications eliminate the mercury reservoir and eliminate adjustment of the mercury levels. The elimination of the need for mercury level adjustment represents a considerable simplification in the procedure. Other modifications include the use of: *(a)* restricted capillaries in the helium and nitrogen entrance lines to reduce the possibility of pressure surges damaging the apparatus; *(b)* ground glass joints for attaching sample tubes, helium and nitrogen reservoirs to the system; (c) a sample tube volume which can be isolated from the calibrated volume, gas inlets, and manometer.

Direct pumping on the sample tube volume is possible without disturbing the gas metering portion of the system. Entrained powder, resulting from too rapid an evacuation, is prevented from depositing in the calibrated volume (requiring a cleaning of the system and recalibration). A two-way stopcock in the sample tube line also permits initial outgassing of the sample through a restricted capillary, further reducing the possibility of powder entrainment into the system.

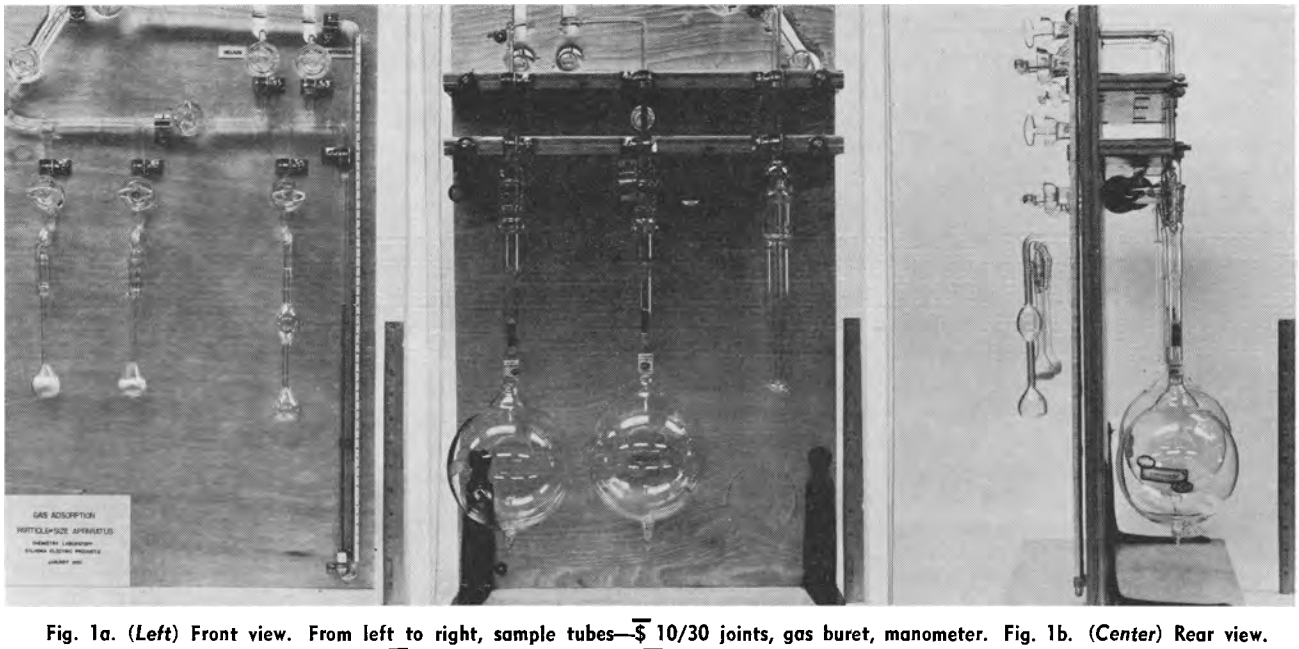

Fig. 1a. (*Left*) Front view. From left to right, sample tubes—$\overline{\$}$ 10/30 joints, gas buret, manometer. Fig. 1b. (*Center*) Rear view. From left to right, N_2 and He supply—$\overline{\$}$ 19/38 joints, cold trap—$\overline{\$}$ 29/42 joint. Fig. 1c (*Right*) Side view.

Table I. Comparison of standard and simplified BET systems (simplified gas adsorption method)

Sample	Standard system m^2/g	Standard system MPD	Simplified system m^2/g	Simplified system MPD
Cadmium sulfide	19.0	0.0656	17.8	0.070
	19.1	0.0653	18.3	0.068
Triple carbonate #2	2.20	0.713	2.20	0.713
	2.23	0.705	2.10	0.745
Zinc sulfide #1	20.3	0.072	18.8	0.078

Table II. Reproducibility of gas volume measurement for simplified gas adsorption system

Sample tubes	Volume, cc	Avg dev, %
#1	10.55	0.48
	10.45	
#2	6.14	0.13
	6.12	
	6.12	
#3	4.00	0.13
	3.99	

The manometer, made from precision bore tubing, and gas buret of the system are calibrated for volume (with mercury) before the system is assembled. The tubing volume, i.e., from the zero level of the manometer to stopcocks of calibrated volume, gas bottles, and sample tube, is then determined by introducing He into the evacuated system at known pressure and temperature, then measuring the change in pressure when the calibrated volume is thermostated with liquid N_2.

The validity of this method of calibration was checked by determining the volume of the buret with He at liquid N_2 temperature and comparing this value to the calibration made with mercury. In the calculation for determining the tubing volume it is assumed that there is no temperature transition zone from the section at liquid N_2 temperature to that at room temperature. The buret was attached to the conventional BET system for the volume measurement. Mercury and helium calibrations agreed to within 0.1%. A comparison of runs on typical powders made with the standard and simplified systems using the rapid procedure (short outgassing time and one point adsorption) are given in Table I. In general, there is close agreement in the values for surface area obtained on the two systems.

To indicate the inherent accuracy of the simplified system, Table II gives results of volume measurements with the simplified system. In all cases the average deviation of duplicate determinations was less than 0.5%. Where conventional runs were made on both systems (powder outgassed at 140°C for 4 hr, three adsorption points) the surface area values agreed within experimental error. For example, a CdS powder gave a value of 20.9 m^2/g on the conventional system and 21.3 m^2/g on the simplified system.

Comparison of the Methods

Reproducibility of each method.—For the standard procedure, Table III gives the areas of samples

Table III. Reproducibility of standard BET determinations* (samples re-run without removal from system)

$BaCO_3$ m^2/g	$BaCO_3$ MPD, μ	$CaTiO_3$ unmilled m^2/g	$CaTiO_3$ unmilled MPD, μ	$CaTiO_3$ milled 65 hr m^2/g	$CaTiO_3$ milled 65 hr MPD, μ
4.88	0.277	4.21	0.348	9.79	0.149
4.88	0.277	4.14	0.353	9.58	0.153
4.96	0.274	4.21	0.348	10.01	0.146
4.96	0.274	4.22	0.347	10.06	0.145
4.79	0.283				
5.27	0.257				
5.14	0.263				
5.40	0.251				
5.03±0.17		4.19±0.04		9.86±0.18	

* Mean particle diameters computed from surface area values by the relation MPD = 6/surface area x density.

Table IV. Reproducibility of standard BET determinations of surface area and mean particle diameter

(Different samples of same materials used for runs 1 and 2)

Sample	Area m^2/g	MPD, μ	Avg dev, %
Triple carbonate #1	5.76	0.273	0.17
	5.74	0.274	
Triple carbonate #2	2.45	0.642	0.00
	2.45	0.642	
Triple carbonate #3	9.31	0.169	1.67
	9.00	0.175	
$CaTiO_3$	4.33	0.338	0.12
	4.22	0.339	

that were remeasured without being removed from the system. The average deviation was found to vary from 0.95 to 3.3%. In cases where duplicate samples were run (Table IV) the average deviation was 0 to 1.8%. With duplicate samples using the simplified method the average deviation was 0.26 to 1.5% (Table V).

Agreement of surface area values between the two methods.—In most cases it was found that the simplified BET method gave values that varied less than 10% from the standard BET value (Table VI). Only in the case of a ZnS with a large surface area was the simplified method appreciably in error (about 27% low). Also, reported values are always on the low side of the standard BET value. It should be pointed out that although in this case the simplified method gives a value of 0.072 μ MPD compared to 0.052 μ MPD by the conventional method, the Fisher Sub-Sieve Sizer and optical microscope examination would give values of 6 μ.

Discussion of Results

In determining the reproducibility of surface area measurements a distinction must be made between the system accuracy and the sample stability. The former is a function of the physical design (i.e., accuracy of volume and pressure measurement) of the system, the latter a function of composition and previous history of the sample.

For a standard BET determination a minimum of four pressure readings are required for a single adsorption point, namely, two readings each for a he-

Table V. Reproducibility of simplified BET determinations of surface area and mean particle diameter

(Different samples of same material used for runs 1, 2, and 3)

Sample	Area m^2/g	MPD, μ	Avg dev, %
Zinc sulfide #1	20.5	0.0715	0.78
	20.3	0.0722	
	20.6	0.0711	
Zinc sulfide #2	0.277	5.28	1.25
	0.284	5.16	
Triple carbonate #1	5.18	0.303	0.38
	5.22	0.301	
Triple carbonate #2	2.20	0.713	0.68
	2.23	0.705	
Cadmium sulfide	19.0	0.0656	0.26
	19.1	0.0653	

Table VI. Comparison of standard and simplified BET surface area determinations

Material	Standard BET m^2/g	Standard Value MPD	Simplified BET m^2/g	Simplified Value MPD	Error, % standard value for surface area
ZnS (Fired)	0.30	4.9	0.28	5.2	— 6.1
ZnS (Unfired)	27.9	0.0524	20.4	0.0722	—26.9
Zn_2SiO_4	0.90	1.7	0.84	1.8	— 5.9
CdS	20.9	0.0596	19.1	0.0653	— 3.9
Triple carbonate	2.45	0.642	2.21	0.711	— 9.8
Triple carbonate	5.74	0.279	5.20	0.302	— 9.4

lium and a nitrogen run. With the standard BET system, pressure readings are accurate to ±0.02 cm, or 0.1% for a 20 cm height. In the worst case, the error expected would be 0.4%. In general, duplicate determinations show deviations of this order of magnitude (Tables IV and V). Larger deviations may be the result of incomplete outgassing of the samples or actual changes in the surface area.[2] From Table III (Col. 1 and 5) there is noted a trend to a larger surface area when the same sample is measured repeatedly on the system. Here it is possible that the apparent increase in surface area is a result of more complete outgassing.

In evaluating this method it was pointed out that the surface area values obtained were, in general, lower than those given by the standard procedure. That this is attributed to the shortened outgassing procedure is shown in Table VII. Outgassing efficiency (for fixed time and temperature) should increase with decreased surface area and degree of agglomeration of the powder. However, there appears to be little difference in outgassing efficiency over a wide range of pumping conditions (Table VIII). For example, outgassing for 15 min at liquid N_2 temperature (77.4°K) gave a surface area only 6% lower than for outgassing at 300°K.

In the calculation of the surface area of powders using a single point adsorption measurement the assumption was made that the curve had a zero intercept. The data of Table IX show that if the value of

[2] Changes in surface area as a result of the preparation history of triple carbonates is currently under investigation. This work will be described in a future report.

Table VII. Effect of time and temperature of outgassing on surface area. Outgassing schedule

Time, min	Temp, °C	Simplified BET m^2/g	Simplified Value MPD	Error, % of standard value
10	25	20.3	0.0722	—26.9
30	110	24.2	0.0605	—13.4
90	140	25.6	0.0511	— 9.4
360	140	27.9*	0.0524	0

* Standard method—outgas 2 hr at room temperature, 6 hr at 140°C.

the intercept is assumed greater than zero (usually the case in an actual run) the simplified BET value approaches the standard value more closely.

The accuracy of the simplified procedure is much better than the data imply. Although the simplified procedure gives values that are 3-27% lower than the standard run for a variety of materials, for a particular material in a given size range the surface area values by both procedures differ by a relatively constant factor. For example, for triple carbonates with surface areas of 2.45 and 5.76 m^2/g the modified value was from 9.0 to 10.2% lower than the standard value. Based on these data, it is possible to predict the surface area that would be obtained by a standard run within 2% of the actual value obtained by measurement. The accuracy of this procedure was demonstrated in a batch precipitation of triple carbonate. It was required that a 2-lb sample be prepared having a mean particle diameter of close to 0.64 μ.

There being no previous background in precipitations with the particular reagents used, trial preparations were measured by the one point adsorption method. Based on a difference of 11% between the standard and one point adsorption run on a typical sample, the trial runs were designed to give a sample 11% lower in area when measured by the simplified procedure. The 2-lb batch was then prepared based on data from the trials. When measured by

Table VIII. Effect of outgassing samples with varied pumping procedures. Outgassed 15 min

Method of outgassing	Temp, °C	Pressure μ	Surface area m^2/g
Welch duo seal pump	25	~4	18.3
Two stage oil diffusion pump	25	<2	18.3
Two stage oil diffusion pump	—195.8*	<2	18.3

* Liquid nitrogen temperature.

Table IX. Effect of assumed values of intercept on surface area of triple carbonate

Run No.	Intercept	Surface area	MPD, μ	Error, % of standard value for surface area
1	0.000	5.22	0.301	—9.3
	0.003	5.31	0.296	—8.0
	0.015	5.71	0.275	—1.2
2	0.000	5.18	0.303	—9.8
	0.003	5.25	0.299	—8.5
	0.007	5.36	0.293	—6.6

the conventional procedure, it had a mean particle diameter of 0.63 μ compared to the desired size of 0.64 μ.

Manuscript received July 13, 1955. This paper was prepared for delivery before the Cincinnati Meeting.

Any discussion of this paper will appear in a Discussion Section to be published in the December 1957 JOURNAL.

REFERENCES

1. P. H. Emmett, "Advances in Colloid Science," Vol. I, Chap. I, Interscience Publishers Inc., New York (1942).
2. P. E. Bugge and R. H. Kerlogue, *J. Soc. Chem. Ind., London*, **66**, 377 (1947).
3. I. Amron and F. M. Starkweather, Unpublished data.
4. P. H. Emmett, *ibid.*

Temperature Dependence of Electroluminescence

C. H. Haake

Lamp Division, Westinghouse Electric Corporation, Bloomfield, New Jersey

ABSTRACT

Electroluminescent brightness measurements were carried out on several zinc sulfide phosphors over wide ranges of temperature and frequency. From the temperature dependence of photoluminescence a thermal extinction factor was derived which, when introduced in the electroluminescent brightness values, led to an ideal electroluminescent brightness unaffected by thermal quenching. In general, this ideal brightness was found to increase or tend to saturation with increasing temperature, but did not decrease. The temperature sensitivity of the ideal electroluminescence is explained on the basis of a two-step mechanism: the excitation process and the return process. Luminescence is assumed to occur only during the latter process. On the phosphors studied the temperature dependence of the ideal electroluminescent brightness seems to be due mainly to the thermal behavior of traps during the return process, since the electron return is impeded by traps.

This work constitutes an attempt to obtain the temperature dependence of electroluminescence of some zinc sulfide phosphors detached from thermal quenching of luminescence and to arrive at conclusions as to which mechanism is mainly responsible for the temperature sensitivity of electroluminescence in these phosphors. Electroluminescence of powdered samples was measured between −180° to +150°C at various frequencies and voltages of operation. Measurements of photoluminescence were carried out on the same phosphor samples over the same temperature range. By combining photoluminescence and electroluminescence at any given temperature in a proper manner, an ideal electroluminescence was derived which is that expected if no thermal quenching were effective. Thus it was possible to consider the temperature dependence of electroluminescence due to thermal quenching and that due to an intrinsic temperature sensitivity of the ideal electroluminescent brightness separately.

The mechanism which leads to electroluminescence is believed to occur in two steps which are separated in time and space. The excitation process provides a number of electrons liberated from centers in a high field zone by field ionization and inelastic collisions. These electrons are rapidly swept out into low field zones where they become trapped. Only when the electrons return to empty luminescence centers upon field reversal (return process) does luminescence occur.

Experimental Arrangement

The phosphor powders investigated were inserted into a condenser-type cell. The phosphor was embedded in air which excluded any brightness variations due to thermal changes of the dielectric properties of the embedding medium. Premature electrical breakdown was avoided by a thin transparent film (Mylar). The thickness of this film was about 5 μ compared to ~85 μ thickness of the phosphor layer. Hence, thermal changes of the dielectric properties in the film affected the field across the phosphor particles only to a minor degree. The cell parts were made of aluminum and Teflon.

The unit in which the cell could be subjected to temperatures from −180° to +150°C is shown in Fig. 1. The cell was inserted into a copper chamber

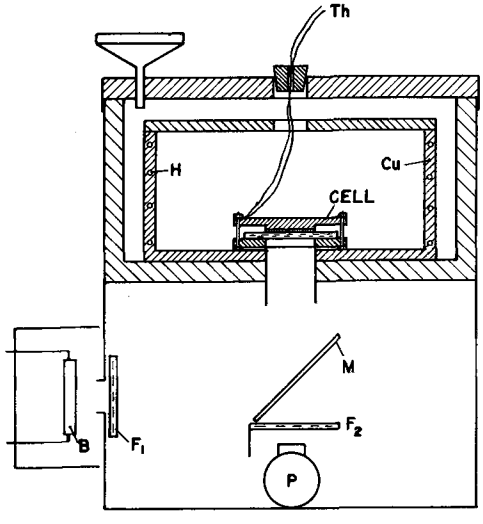

Fig. 1. Apparatus for measuring the temperature dependence of electroluminescence.

(Cu). It could be cooled by liquid N_2 or warmed by heating elements (H) in the walls. The heating current was controlled by a Variac. The phosphor in the cell was excited to luminescence either electrically or by u.v. light from a high pressure mercury lamp (B) over a semi-transparent mirror (M). An audiofrequency generator connected to a power amplifier served as a voltage source to operate the cell. The voltage applied to the u.v. lamp (B) was stabilized electronically. The u.v. intensity could be varied by varying the distance of (B) to the inlet. The light emitted from the phosphor was measured by a photomultiplier (P) (1P21) operated on a regulated power supply.

The time averaged photocurrent was measured by a Keithley vacuum tube electrometer. The temperature of the phosphor was obtained by means of a copper-constantan thermocouple (Th) screwed onto the metal back electrode of the cell. The thermo-voltage was measured by a L&N precision potentiometer. The filter F_1 transmitted only u.v. radiation in the neighborhood of 3500Å (Corning 5860). The filter F_2 cut off u.v. light and thus prevented it from falling onto the cathode of the photomultiplier. F_2 transmitted mainly between 4600-7000Å (yellowish Schott-filter). Since no vacuum was applied, care had to be taken to avoid condensation of water vapor on the glass parts of the temperature system at low temperatures. This was accomplished by inserting vessels in the cell chamber and around the photomultiplier which contained an efficient drying agent.

Elimination of Thermal Quenching

It is assumed that thermal quenching as observed with photoluminescence also occurs with electroluminescence such that the brightness tends to decrease with increasing temperature (1). One may then define the electroluminescent brightness (I_{el}) actually measured as equal to an ideal electroluminescent brightness (I_{el_0}) modified by the probability of thermal quenching of luminescence ($p_f = I_{el}/I_{el_0}$). This probability is assumed to be the same as that for photoluminescent brightness (I_f) at any temperature T. Hence

$$p_f(T) = \frac{I_{el}(T)}{I_{el_0}(T)} = \frac{I_f(T)}{I_{f_0}} \qquad \text{(I)}$$

where I_{f_0} stands for the photoluminescent brightness which is unaffected by thermal quenching and thus usually occurs only at low temperatures. Here I_{el_0} is a function of temperature because of the temperature sensitivity of pure electroluminescence but not of quenching.

Thus with Eq. (I)

$$I_{el}(T) = I_{el_0}(T) \cdot \frac{I_f(T)}{I_{f_0}} \qquad \text{(II)}$$

If the luminescence probability $I_f(T)/I_{f_0}$ were dependent only on temperature, one plot of I_f over the whole temperature range of interest would be sufficient, since $I_{el}(T)$ need be divided simply by $p_f(T)$ in order to obtain $I_{el_0}(T)$. However, p_f is also dependent on the intensity of the exciting radiation (2). This may lead to an increase of photoluminescent brightness faster than linear with increasing excitation intensity (3). More specifically, at a given temperature the effect of thermal quenching may be less pronounced at higher brightnesses I_f. This phenomenon must also be expected with electroluminescence. In order to account for this effect, not only must the ratios of Eq. (I) be considered equal but also either numerator and denominator. Hence, Eq. (II) can be written

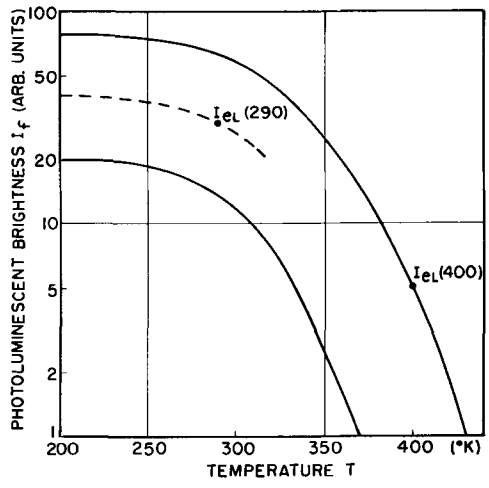

Fig. 2. Schematic procedure for finding I_{el_0} from $I_f(T)$ plots

$$I_{el}(T) = I_{el_0}(T) \frac{I_{el}(T)}{I_{f_0}}$$

or simply

$$I_{f_0} = I_{el_0}(T) \qquad \text{(III)}$$

This means that there must be a known I_f-value equal to each I_{el}-value measured at any temperature T. Consequently a series of plots of $I_f(T)$ must be taken with different exciting u.v. intensities in order to cover the whole range of the I_{el}-values at any temperature.

The principle of the procedure to determine $I_{el_0}(T)$ is illustrated in Fig. 2. For example, let an electroluminescent brightness of $I_{el} = 5$ units be measured at 400°K. Among the number of various plots of photoluminescent brightness $I_f(T)$ there must be one plot which also shows a brightness of 5 units at 400°K. The maximum brightness of this particular plot of photoluminescence then is the appropriate value of I_{f_0} (here about 80 units) according to Eq. (III). If at $T = 290$°K an electroluminescent brightness $I_{el} = 30$ units is measured and none of the $I_f(T)$-plots previously obtained goes through this I_{el}-value, the $I_f(T)$-plots must be sufficiently close to each other so that interpolation is possible. In this particular case I_{f_0} is found to be about 40 units. From these examples it becomes obvious that I_{f_0} in Eq. (III) is a function of I_{el} and one should therefore write

$$I_{f_0}(I_{el}) = I_{el_0}(T) \qquad \text{(IIIa)}$$

With this procedure a spectral emission shift with temperature which would cause a falsified response of the photomultiplier is excluded from the I_{el_0} values, since both I_{el} and I_f show about the same emission color at any given temperature (4). This, however, is true only if the frequency of the alternating field applied to the phosphor has no effect on

the emission color. Fortunately there are some single-band phosphors for which the shift of the emission color is negligible from 15 to 10,000 cps. Only those phosphors were studied here.

This procedure is based on the assumption that both electroluminescence and photoluminescence are uniformly emitted throughout the phosphor crystals. However, it has been observed (5, 6) that electroluminescence occurs preferentially in a number of single spots. Hence, the electroluminescent spot brightness is higher than the photoluminescent brightness when the electrometer connected to the photocell reads the same photocurrent. The I_{el_0}-values obtained can, therefore, be taken only as first approximations.

Experimental Results

The temperature dependence of electroluminescence was measured on a number of powdered single-band zinc sulfide phosphors containing Cu, Cu-Pb, oxygen and Cl impurities (heating rate about 3°/min). Two of these phosphors were chosen at random and subjected to a more intensive study: WL77 (ZnS.ZnO activated with Cu and Pb, coactivated with Cl, fired in air) and WL702 (ZnS activated with Cu, coactivated with Cl, fired under special conditions).[1] At room temperature both phosphors emitted in the green nearly independent of frequency up to 10 kc. Fig 3*a* and *b* show the averaged electroluminescent brightnesses I_{el} as functions of temperature on WL77 and WL702 at an average field strength of about 5 x 10^4 v/cm (corresponding to 400 v rms across the cell) with 15, 100, 1000, and 10,000 cps (gas discharge and breakdown did not occur below 6-7.10^4 v/cm). After the phosphors were kept at about +50°C for 1 hr, during which time the above field alternating with about 500 cps was applied, the curves proved reproducible in shape, regardless of the direction of the temperature change.

Fig 3*a* and *b* clearly illustrate the shift of the brightness curves to higher temperatures with increasing frequency. This phenomenon has been observed before by several workers (7-10). Brightness curves are less sensitive to changes of the electric field strength. In general, the brightness peaks shift but slightly to lower temperatures with increasing field strength and usually some minor changes occur on the low temperature side of the peaks.

Employing the method described above the electroluminescent brightness, I_{el}, was converted to the ideal electroluminescent brightness, I_{el_0}, which would exist without interference from thermal quenching of luminescence. For this purpose a set of photoluminescent brightness plots as functions of temperature was measured such that the whole scope of the brightnesses I_{el} at any temperature was covered or at least easily accessible to extrapolation. The conversion of the I_{el}-values to corresponding I_{f_0}-values as demonstrated in Fig. 2 was carried out in a more convenient way by plotting log (I_{f_0}) as a function of log (I_f) with the temperature T as parameter (Fig. 4). As can be seen in Fig. 4 the phosphor has acquired a linear emission at about −80°C. Below this temperature photoluminescence is constant and only upon further decrease of temperature begins to decrease slightly, which is due to changes of the u.v. absorption characteristics (2). However, this has no bearing on the present considerations of electroluminescence. Thus, I_{f_0} is assumed constant for all $T < -80°$.

The general result is consistent with both phosphors. I_{el_0} increases steadily with increasing temperature or exhibits a tendency to saturation, but it does not decrease. Fig. 5 shows such a step-curve. Similar curves have been reported by Alfrey and Taylor (7) in temperature ranges where thermal quenching is not yet predominant. The shape of the

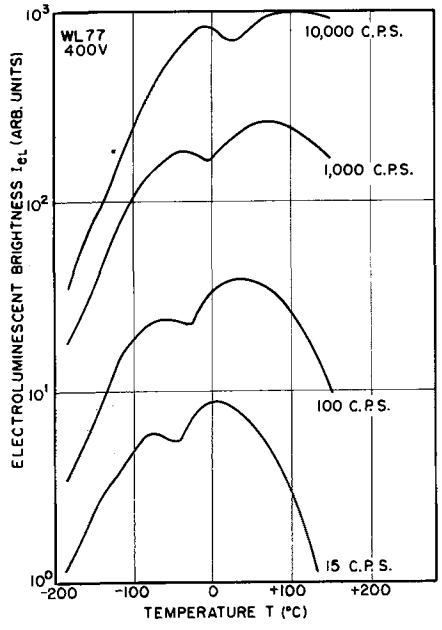

Fig. 3*a*. Electroluminescent brightness as function of temperature at 400 v rms and various frequencies. WL77.

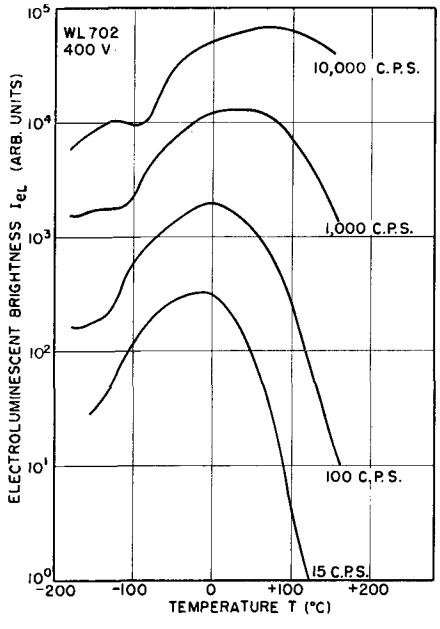

Fig. 3*b*. Electroluminescent brightness as a function of temperature at 400 v rms and various frequencies. WL702.

* Both phosphors were prepared by W. Lehmann in this laboratory.

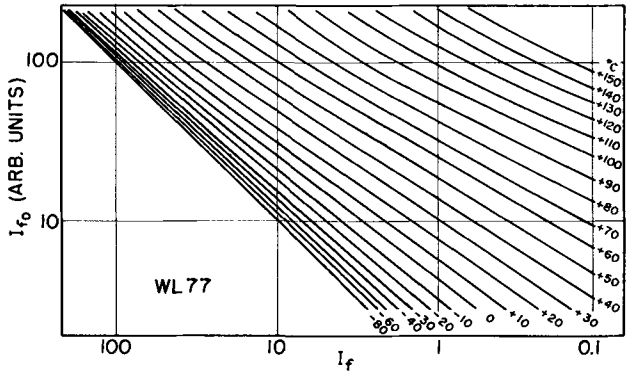

Fig. 4. Practical chart for finding I_{el_0} from plots of I_{f_0} as function of I_f with the temperature as parameter (WL77).

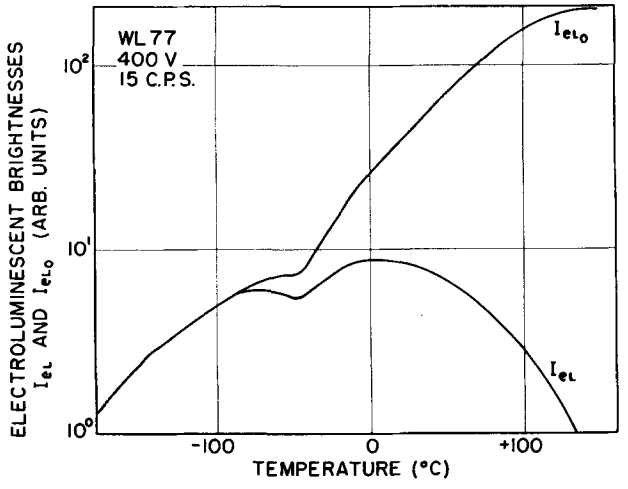

Fig. 5. Real brightness, I_{el}, and ideal brightness I_{el_0}, as function of temperature at 400 v rms and 15 cps (WL77).

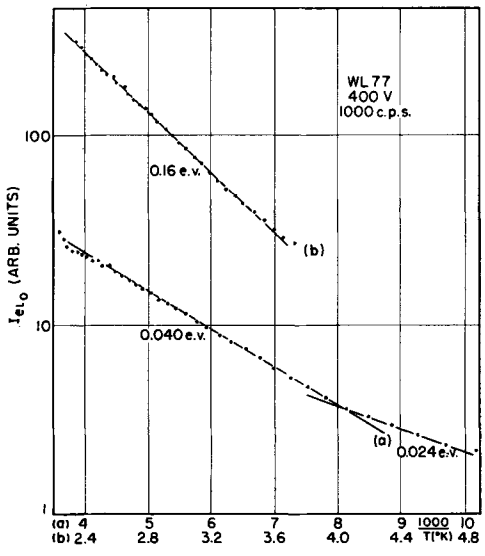

Fig. 6. Plot of log (I_{el_0}) as function of 1000/T for 400 v rms and 1000 cps (WL77).

$I_{el_0}(T)$-plots leads one to expect some kind of thermal activation energies which should become revealed when log (I_{el_0}) is plotted over 1000/T (°K). [A first attempt in this direction has already been made by Mattler (11) who plotted log I_{el} as a function of 1000/T.] Indeed, a series of straight lines was found with average slopes which correspond to about 0.02; 0.05; and 0.16 e.v. with WL77, and 0.006; 0.08; 0.13; and 0.24 e.v. with WL702 (Fig. 6). Sometimes the slopes ceased to be straight lines at the high temperature side of the straight lines and log I_{el_0} became only weakly dependent on 1000/T. An indication of this behavior is found in Fig. 6 near 1000/T = 4. The activation energies are dependent on frequency such that increasing frequency tends to increase the activation energies. Also, decreasing voltage shows a pronounced increase of the activation energies, and the straight lines of log (I_{el_0}) vs. 1000/T sometimes appear broken so that effectively the number of activation energies found between −180° and + 150°C seems to increase. Table I shows results obtained on both phosphors for various frequencies and voltages across the cell.

In order to compare the activation energies with the trap depths, glow curves were taken for both phosphors (*see* Fig. 7). Trap depths were calculated according to a method described by Curie and Curie (12) [heating rate ~ 2.5°/min (WL77), and ~ 3°/min (WL702), s = 5 x 10^8 sec^{-1}]. Results are given in Table II. (The values in brackets are derived from unresolved glow peaks.)

Table III shows a correlation of the temperatures T_{max} and T_{min} at which electroluminescent brightness extrema occur, the activation energies, and the temperature ranges in which these activation energies are observed as straight lines from the plots of log I_{el_0} as a function of 1000/T for various frequencies and a voltage of 400 v rms across the cell. It will be noted that the temperature ranges in which the activation energies occur exhibit the same tendency to shift to higher temperatures with increasing fre-

Table I. Activation energies at various frequencies and voltages

WL77 Frequency (cps)	Voltage (v)	Activation energies (e. v.)			
15	400	0.024	0.035		0.15
100	400	0.022	0.038		0.17
	250	0.032	0.049		0.23
1000	400	0.024	0.040		0.16
	250	0.028	0.056		0.23
10000	400	0.025	0.055		0.16
	250	0.043	0.06; 0.105		0.25
	150	0.06	0.10; 0.12; 0.15; 0.18		0.32

WL702 Frequency (cps)	Voltage (v)	Activation energies (e. v.)			
15	400	—	0.077	0.099	0.14
100	400	0.006	0.076	0.096	0.18
	200	0.018	0.11	0.13	0.21
1000	400	0.006	0.084	0.13	0.26
	200	0.014	0.132	0.17; 0.23	0.33
10000	400	0.0095	0.094	0.27(?)	0.36(?)

Table II. Trap depths of WL77 and WL702

Phosphor	Trap Depths (e. v.)			
WL77	(~0.2)	0.25	(~0.3)	0.38
WL702	—	(~0.26)	0.30	(?)

Table III. Survey of experimental results with respect to temperature and frequency

Frequency (cps)	EL. brightness T_{max} (°C) T_{min}	Activation energy (e.v.)	Temp. range of act. energy (°C)
WL77:			
15		0.02	−168 to −131
	−75	0.04	−120 to − 76
	−45		
	+ 6	0.15	− 37 to +124
100		0.02	−172 to −151
	−65	0.04	−137 to −65
	−30		
	+37	0.17	− 18 to +120
1000		0.02	−168 to −150
	−38	0.04	−142 to −13
	− 5		
	+70	0.16	+6 to +150
10000		0.03	−176 to −142
	− 9	0.06	−120 to −8
	+25		
	+100	0.16	+30 to +144
WL702:			
15		?	?
		0.08	−127 to −56
	−10	0.10	−43 to +9
		0.14	+22 to +80
100		0.006	−174 to −144
		0.08	−120 to −40
	0	0.10	−28 to +30
		0.18	+36 to +108
1000		0.006	−174 to −122
		0.08	−104 to −44
	+31	0.13	−30 to +20
		0.26	+36 to +148
10000	−123	0.01	−180 to −120
	−97		
		0.09	−84 to +12
	+72	0.27(?)	+20 to +84
		0.36(?)	+86 to +150

quencies as the extrema of the electroluminescent brightness.

Discussion and Interpretation

Ideal Brightness

If one relates the exponential factor of I_{el_0} which leads to the observation of activation energies to a thermal release process of electrons from certain centers, the activation energies appear as energy "depths" E^*. The probability p of electron escape from such centers is facilitated in the presence of an electric field (13):

$$p \propto \exp - E^*/kT = \exp - [E - f(F)]/kT \quad \text{(IV)}$$

[E, depth of center in the absence of a field; F, field strength; $f(F)$, function of field strength such that $f(F)$ increases with increasing F]. The influence of frequency on E^* is most likely due to capacitive effects. Combinations of high field regions and low field regions as exist inside the phosphor crystals form some sort of microcapacitors across which the potential drop decreases with increasing frequency. Hence increasing frequency reduces the effective field and E^* increases as observed. If now the values of Table II are compared with those of Table III, one finds that with low voltages and high frequencies the high values of E^* approach those of the trap depths

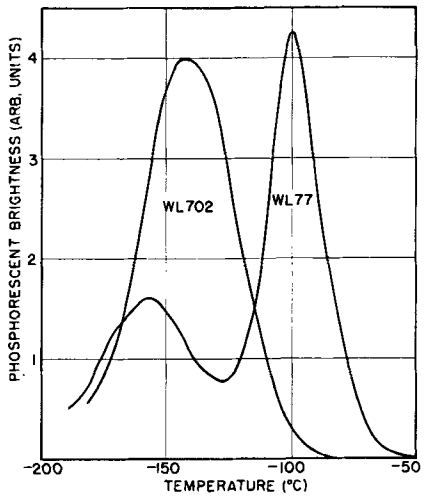

Fig. 7. Glow curves on WL77 and WL702

as determined from glow curves. Therefore, it seems justifiable to identify E in relation (IV) with a trap depth. Then the low values of E^* observed at low temperatures would correspond to traps which are too shallow to be detectable by glow curves.

The temperature behavior of electroluminescence can now be considered in a simplified model based on the action of electron traps. There is ample evidence that the essential processes of electroluminescence are confined to certain high field regions and adjacent low field regions. The high field regions may occur either in potential barriers (14) or near sharp points or edges of conducting segregations in the host crystal (e.g., Cu_2S) (15). In these regions electrons field-ionized from donors or injected electrons are accelerated and thus become able to collision-ionize luminescence centers. The electrons, quickly increasing in number, are swept out into the low field regions where the energy gain by field action is lower than the energy loss by impact. Thus the electrons become trapped to an extent determined by temperature and frequency. During this part of the process (excitation process) hardly any emission occurs, since the transit time of electrons through the high field region is extremely small (*see* Appendix). Particularly in the case of conducting segregations in the host crystals, the high field region reverses its sign with the next half-cycle of the applied voltage and conduction electrons are attracted from the low field region to the high field region where they recombine with empty luminescence centers. It is this part of the process (return process) which gives the major contribution to light emission. Experimental proof for the time-separation of excitation and return process was obtained when the buildup of electroluminescence on previously quenched phosphors was studied (16). No light emission could be observed during the first half-cycle of the voltage applied, in agreement with Waymouth and Bitter (6).

Both processes are functions of field, frequency, and temperature. The production and behavior of conduction electrons in the high field zone during the excitation process, however, probably is determined mainly by the comparatively high field and

its frequency and only to a lesser degree by temperature.

Let m be the number of traps occupied by electrons at the time t. Disregarding retrapping, the time dependence of trap emptying can then be described by

$$dm/dt = -pm$$

where p is the probability of electron escape from traps in the low field region, as given by Eq. (IV). $f(F)$ in p not only depends on time but also in an unknown fashion on spatial coordinates. However, as a first approximation, $f(F)$ is set proportional to an averaged field strength $\overline{F}$ which renders p independent of time and space. Thus

$$m = m_0 \exp(-pt)$$

where m_0 is the number of traps at the beginning of the return process and depends mainly on the excitation process, i.e., on field and frequency.

If it is assumed that each electron ejected from a trap is quickly carried away to luminescence centers in the high field zone during the time the return process is in effect, dm/dt is a measure of the momentary light emitted so that the mean emission during one half-cycle is

$$I_{el_0} \propto -2fp \int_0^{1/2f} m\, dt = 2f\, m_0(f)\,[1-\exp(-p/2f)] \quad (V)$$

$I_{el_0}(T)$ increases steadily with temperature as long as $p << 2f$, i.e.,

$$I_{el_0} \alpha\, m_0(f)p = m_0(f)s \exp - [E - \text{const}\,\overline{F}]/kT \quad (Va)$$

A straight line appears on plotting log (I_{el_0}) as a function of $1/T$. As the temperature is further increased, $p > 2f$ and I_{el_0} tends to saturation as actually observed. The temperature range in which this tendency prevails occurs at higher temperatures for higher frequencies. This agrees very well with experiment where, however, more than one activation energy appears. This is because trapping levels of different depths have different p-functions. Whenever $p_1 >> 2f$ prevails with one group of traps, the next deeper traps with $p_2 << 2f$ may begin to show in I_{el_0}.

A quantitative expression of the shift of the brightness curves to higher temperatures along the temperature scale can be derived by defining a normalized ideal brightness which is the ratio of I_{el_0} to I_{el_0} at $p >> 2f$

$$W_{T,f} = \frac{2f\, m_0(f)\,[1-\exp(-p/2f)]}{2f\, m_0(f)} = 1 - \exp(-p/2f)$$

Fig. 8 shows a schematic diagram of two plots of the normalized ideal brightness for two different frequencies. The relative brightness found at a temperature T_1 with a frequency f_1 can only be reproduced at a higher frequency f_2, if the temperature T_1 is increased to T_2 which is derived from the equality condition

$$W_{T_1,\, f_1} = W_{T_2,\, f_2}$$

or

$$1 - \exp(-p_1/2f_1) = 1 - \exp(-p_2/2f_2)$$

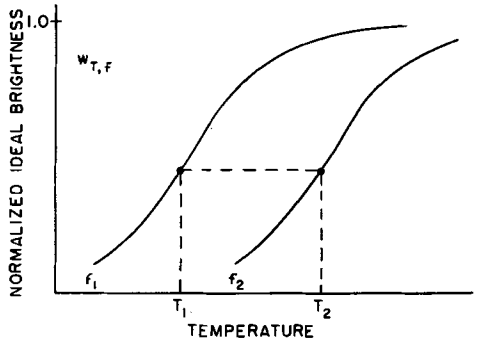

Fig. 8. Shift of the normalized electroluminescent brightness to higher temperatures with increasing frequency.

or

$$p_1/2f_1 = p_2/2f_2$$

Hence $p/2f$ is constant for corresponding points of the normalized brightness curves, so that

$$f = \text{const} \exp -E^*/kT_c \quad (VI)$$

where T_c denotes the temperatures at corresponding points. This expression was first postulated by Alfrey and Taylor and should always appear when trap emptying is time restricted by the frequency of operation. However, it is hard to find such corresponding points in the unnormalized $I_{el_0}(T)$-curves.

Real Brightness I_{el}

It is now easy to see what determines the shape of an $I_{el}(T)$-curve. In the temperature range where thermal quenching has not yet become effective, I_{el} is equal to I_{el_0}. The brightness measured will increase with increasing temperature or tend to saturation as the lifetime p_1^{-1} of electrons in a certain group of traps decreases to $p_1^{-1} << 1/2f$. Then the next deeper group of trapping levels begins to eject electrons discernibly so that I_{el} again increases. At this point let thermal quenching become effective. At first, quenching will be weak and I_{el} still increases although with a slightly lower rate. On approaching the condition $p_2^{-1} << 1/2f$, thermal quenching, however weak it may be, causes I_{el} to decrease and a brightness maximum is observed. If this last group of traps were the deepest one in the phosphor, I_{el} would decrease continuously with increasing temperature as determined by quenching. However, if a deeper trapping group exists, I_{el} can rise again, because thermal trap emptying may temporarily overcompensate thermal quenching. Therefore, a minimum of I_{el} occurs. With further temperature increase, thermal quenching gains more and more importance so that a maximum of I_{el} is observed, and then I_{el} decreases again. These conditions are illustrated in Fig. 5.

However, the life time p^{-1} not only decreases with increasing temperature but also with increasing field strength. Following this reasoning, a maximum of I_{el} should be found at a lower temperature on increasing the voltage. This could be confirmed by experiment, although with the relatively small range of voltage used the temperature shift of the brightness maxima never exceeded 10°. A good example of these conditions, however, has been given

by Mattler (4) who varied the voltage applied to his ZnS.Cu phosphors up to a factor of 6.

It was stated earlier that it is hard to find corresponding points in the unnormalized I_{el_0}-curves which relate the frequency of operation to T_c according to Eq. (VI). Exact normalization from experimental plots is difficult, especially on phosphors with several trapping groups. Therefore, one may attempt to find these corresponding points from the I_{el}-curves actually measured. The only outstanding, easily localized points are the extrema of the I_{el}-curves. However, it is not quite correct to regard these as corresponding points. As has been shown above, brightness maxima (or minima) arise from a competition process of trap emptying and thermal quenching. If, e.g., a maximum occurs at a temperature T_1 for a frequency f_1, the maximum will be shifted to $T_2>T_1$ for a frequency $f_2>f_1$. However, at the temperature T_2 thermal quenching is much more effective than at the lower temperature T_1. Hence, this increased effect of quenching gives a maximum occurring at the temperature T_2, which is lower than that expected from Eq. (VI). Upon plotting the maxima positions logarithmically according to Eq. (VI) one would find more or less distorted straight lines and the E-values derived from their slopes are higher than those which one would obtain from plots of exactly corresponding points.

The two maxima in WL77, and the single maximum in WL702 were treated as approximately corresponding points and plotted according to Eq. (VI). As expected, the values of E obtained are higher than the thermal activation energies of I_{el_0} and even higher than the trap depths derived from the glow curves, as can be seen in Table IV.

Summary and Conclusions

Measurements of electroluminescence and photoluminescence carried out on several zinc sulfide phosphors over a wide temperature range permitted determination of an ideal electroluminescent brightness which is unaffected by temperature quenching of luminescence. The thermal behavior of this ideal brightness seems to imply that trap emptying is the major effect of temperature on electroluminescence apart from thermal quenching. Various authors have realized the significance of electron traps [*see*, e.g., references (9, 17-21)]. However, there is still some controversy as to whether the traps in the high field region or those in the low field region are predominantly responsible for the thermal behavior of electroluminescence. The present study indicates the importance of traps in the low field region. This conclusion is based on the assumption that electroluminescence occurs in a coupled two-step process. During excitation electrons are freed in the high field zone and caught in traps in the low field zone. The number of electrons returning for luminescent recombinations is mainly determined by the rate of thermal and field release of electrons from traps. A simple model can explain the general trend of electroluminescent brightness with varying temperature and frequency.

These conclusions lead to the practical consequence that, beside other qualities, a good electroluminescent phosphor should have only a few shallow traps and no deep traps. The temperature at which thermal quenching sets in should be high. Unfortunately, the latter can be accomplished only by compromising with another essentiality. Experiment shows that good electroluminescent phosphors need a high copper concentration, but that thermal quenching sets in at a temperature which decreases with increasing copper concentration (22).

As a final comment it should be emphasized that the above explanation of trap action on electroluminescence is not all-embracing. It predicts extrema in electroluminescence-temperature curves only in temperature regions where thermal quenching is already effective. However, Johnson, Piper, and Williams (9) have shown that a ZnS.Al.Cu phosphor exhibited extrema in a temperature range far below the onset of thermal quenching. Some measurements were carried out on the same phosphor in these laboratories. This effect must be accounted for as a temporary super-position of a different temperature action on the one outlined above. Fig. 9 shows a plot of log (I_{el_0}) as a function of $1000/T$ obtained from this phosphor. It can be seen that with this phosphor straight lines (activation energies) also occur, except in the comparatively small temperature range between 150°-220°K.

Table IV. Activation energies derived from Eq. (VI) with T_c as temperatures of brightness maxima

	WL77	WL702
E_1 (e.v.)	~0.57	~0.55
E_2 (e.v.)	~0.7	

Acknowledgment

The author is indebted to Dr. H. F. Ivey, Dr. B. Rosenberg, and Mr. W. Lehmann for helpful discussions, and to Dr. P. D. Johnson (General Electric Co.) for kindly supplying one of his phosphor samples.

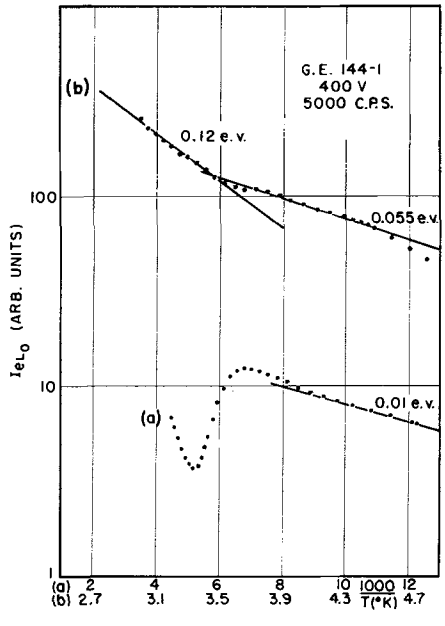

Fig. 9. Plot of log (I_{el_0}) as function of $1000/T$ at 400 v rms and 5000 cps (G.E. 114-1).

APPENDIX

Recombination Probability in High-Field Regions

If it is agreed that, because of inelastic scattering with lattice atoms, on the average, conduction electrons cannot exceed a kinetic energy higher than that of the band-to-band gap (23), the following energy balance is valid in ZnS

$$e\bar{F}\,\lambda_0 \sim 3.5 \text{ e.v.}$$

(e, electron charge; $\bar{F}$ average electric field; λ_0, mean electron path between two exciting collisions). With $\bar{F} \sim 10^6$ v/cm

$$\lambda_0 \sim 3.5 \cdot 10^{-6} \text{ cm}$$

With m^* as effective electron mass, x as distance an electron has traveled in the field-direction, and dx/dt as drift-velocity

$$\frac{m^*}{2}\left(\frac{dx}{dt}\right)^2 = e\bar{F}x$$

Integration results in

$$\tau_0 = \sqrt{\frac{2m^*\lambda_0}{e\bar{F}}} = 7.10^{-14} \text{ sec}$$

as the time required for an electron to drift the distance $\lambda_0 \cdot (m^* \sim m)$. If the width of a high field region is assumed to be of the order of 10^{-3} to 10^{-5} cm which is about 300 to 3 times λ_0, the transit time of an electron through this region is of the order of $\tau = 10^{-11}$ to 10^{-13} sec.

If n conduction electrons are created per cm^3 of the high field region per second, the total number of possible recombinations is n. The capture volume of one empty center available for recombinations per second is βcm^3/sec so that the total number of capture volumes per second is βn. Then the favorable number of recombinations is determined by βn, by the number of available electrons, n, and by the time τ actually available for these transitions. Hence the probability of radiative return per electron is

$$\frac{(\beta n)\, n\tau}{n} = \beta n\tau$$

With n being of the order of 10^{18} cm^{-3} or less, and $\beta = 10^{-14}$ cm^3 sec (24) this probability becomes 10^{-7} to 10^{-9} or less which indeed is negligible. [This value is in accord with findings of Zalm (24).] Consequently there should be virtually no electroluminescence during the excitation process.

Manuscript received July 12, 1956.

Any discussion of this paper will appear in a Discussion Section to be published in the December 1957 JOURNAL.

REFERENCES

1. D. Curie, *J. Phys. Radium*, **14**, 672 (1953).
2. G. F. J. Garlick, "Luminescent Materials," Oxford University Press, Oxford (1949).
3. F. Urbach, A. Urbach, and M. Schwarz, *J. Opt. Soc. Amer.*, **37**, 122 (1947).
4. J. Mattler, *J. Phys. Radium*, **17**, 42 (1956).
5. E. E. Loebner and H. Freund, *Phys. Rev.*, **98**, 1545 (1955); G. Diemer, *Philips Research Rpts.*, **10**, 194 (1955).
6. J. F. Waymouth and F. Bitter, *Phys. Rev.*, **95**, 941 (1954).
7. G. F. Alfrey and B. Taylor, *Brit. J. Appl. Phys.*, Suppl. #4, p. S44 (1955).
8. C. H. Haake, *Phys. Rev.*, **98**, 1544 (1955).
9. P. D. Johnson, W. W. Piper, and F. E. Williams, *This Journal*, **103**, 221 (1956).
10. R. E. Halsted and L. R. Koller, *Phys. Rev.*, **93**, 349 (1954).
11. J. Mattler, Private Communication.
12. G. Curie and D. Curie, *J. Phys. Radium*, **16**, 199 (1955).
13. N. F. Mott and R. W. Gurney, "Electronic Processes in Ionic Crystals," p. 42, Oxford University Press, Oxford (1948).
14. W. W. Piper and F. E. Williams, *Brit. J. Appl. Phys.*, Suppl. #4, p. S39 (1955).
15. W. Lehmann, *Bull. Am. Phys. Soc.*, II/1, 113 (1956).
16. C. H. Haake, *ibid.*, II/1, 113 (1956).
17. D. Curie, *J. Phys. Radium*, **13**, 317 (1952).
18. A. Fischer, *Physik. Verhandl.*, **5**, 64 (1954).
19. C. H. Haake, Symposium on Electroluminescence and Photoconduction in Inorganic Phosphors, Brooklyn (1955).
20. W. A. Thornton, *Phys. Rev.*, **102**, 38 (1956).
21. G. F. Neumark, *ibid.*, **103**, 41 (1956).
22. G. F. Alfrey, *Phys. Radium*, **17**, 719 (1956).
23. G. Diemer, H. A. Klasens, and J. G. Van Santen, *Philips Research Rpts.*, **10**, 401 (1955).
24. P. Zalm, *J. Phys. Radium*, **17**, 777 (1956).

Transport Numbers and Structures in Fused $AgNO_3$-$NaNO_3$ Mixtures

Frederick R. Duke, R. W. Laity,[1] and Boone Owens

Institute for Atomic Research and Department of Chemistry, Iowa State College, Ames, Iowa

ABSTRACT

The transport numbers of the ions in $NaNO_3$-$AgNO_3$ mixtures are very closely proportional to the mole fractions. The transport number of the nitrate ion remains essentially constant. It is thus concluded that there are no complex species in $NaNO_3$ or $AgNO_3$ and that all cations present are structurally in identical positions. This argues strongly against any concept except complete dissociation in this nitrate system.

A complete transport number-composition curve for a binary fused salt mixture has not been obtained previously. Such data are of much interest because transport numbers should be sensitive probes to changes in structure of salt mixtures with composition. For such a binary mixture two types of data are needed to yield a complete determination of transport numbers: Hittorf cell data concerning changes in relative composition of salt near the electrodes, and volume-change data, to determine total change in equivalents of salt in each electrode compartment. In principle, both types of data could be obtained in a single experiment of proper design, but in practice it was found simpler to perform separate experiments.

The fundamental equations relating to the Hittorf experiments were developed by Wetmore and Aziz (1) who performed some experiments on the $AgNO_3$-$NaNO_3$ mixture.

Experimental

Hittorf type of transport data was obtained by using a cell made from 4 mm ID Pyrex tubing bent into the shape of a very broad U tube. This tube was placed in a muffle furnace maintained at 305° ±5°C and was filled by pouring the molten salt into one end. Silver electrodes were inserted into the ends of the tube and about 30 coulombs of electricity passed. An alternating current of about 100 ma (five times the direct current) was superimposed to help prevent trees from growing out from the cathode. The tubes were carefully removed and cooled and cut into three parts, an anode section, a cathode section, and a short center section. These sections were analyzed by titrating the Ag^+ (Volhard) and determining the net weight of salt in each section. Only those tubes with center sections closely corresponding to the original mixture (approximately 10% of the runs) were used. Total equivalents of current were measured by using a silver coulometer.

An alternative procedure was to place an ultrafine, sintered glass membrane in the center of the U, the membrane thus corresponding to Hittorf center compartment. The two portions obtained after electrolysis and after breaking the cell at the membrane were analyzed. The use of this type of cell eliminates the overlap of the anode and cathode compartments due to convection which is found in a majority of the cells not containing the membrane.

The volume change in the electrode compartments was determined by using a modified cell similar to that described by Duke and Laity (2). The modification consisted of omitting the capillary with the bubble and measuring directly by changes in height the volume change in the electrode compartments. The moving bubble could not be used because it responds to density as well as to volume changes. The electrodes were Ag plated from aqueous cyanide onto tungsten. The level was measured in a capillary (two 1-mm capillaries were sealed to the top of each electrode compartment to facilitate filling) which constituted the upper part of each cell compartment. It was found that differences in head across the ultrafine membrane produced a slight leakage (about 0.06 cm^3/hr/cm head). This leakage was calibrated and taken into account for each run. A d-c current of about 50 ma was used, and from 5 to 10 measurements were taken over periods of 2000 sec on a given mixture. In case of pure $NaNO_3$, Ag-$AgNO_3$ electrodes were used.

Results and Discussion

Consider first the Hittorf type of experiment. For the anode compartment, $n_1 - n_{o1} = Z - t_1Z$, and

$$n_2 - n_{o2} = -t_2Z$$

where n_1 and n_2 are the final numbers of equivalents of $AgNO_3$ and $NaNO_3$, respectively, in the anode compartment after Z equivalents of current have been passed, n_{o1} and n_{o2} are the original number of equivalents of these salts in the anode compartment, and t_1 and t_2 are the transport numbers of Ag^+ and Na^+, respectively. A silver anode is used. Combining these equations with the following,

$$t_1 + t_2 + t_3 = 1 \qquad \text{(I)}$$

$$\frac{n_{o1}}{n_{o1} + n_{o2}} = N_{o1}, \text{ and}$$

[1] Present address, Frick Chemical Lab., Princeton University, Princeton, N. J.

Table I. Variation of ϕ with composition

N_{o_2}	ϕ
0.91	0.94
0.70	0.69
0.50	0.50
0.29	0.30

$N_{o_1} + N_{o_2} = 1$, where t_3 is the transport number of the nitrate ion and N_{o_1} and N_{o_2} are the original equivalent fractions of $AgNO_3$ and $NaNO_3$, respectively, Eq. (II) is obtained

$$\phi \equiv \frac{N_{o_2} n_1 - N_{o_1} n_2}{Z} = 1 - t_1 - N_{o_1} t_3 \qquad \text{(II)}$$

where ϕ combines all of the experimental values as a function of the transport number and can be seen to be t_2 if the reference point is the nitrate ion ($t_3 = 0$). This equation was first derived by Wetmore and Aziz (1). Notice that the reference point is not fixed by this equation which contains one degree of freedom. Values of ϕ are shown in Table I. The authors cannot account for the reasons for the discrepancy between these results and those of Wetmore and Aziz (1) on the same system.

The volume change equations for the anode are:

$$V_a = (1 - t_1)\, Z\, \overline{V}_{AgNO_3} - t_2 Z\, \overline{V}_{NaNO_3} - Z\, V_{Ag} \qquad \text{(III)}$$

where the $\overline{V}$'s are the partial molal volumes in the mixture, and V_{Ag} is the equivalent volume of silver. Then Eqs. (I), (II), and (III) may be solved for the transport numbers t_1, t_2, and t_3, if n_1, n_2, Z, V_a, $\overline{V}_{AgNO_3}$ and $\overline{V}_{NaNO_3}$ and the original compositions are known. Eq. (III) combined with (I) and (II) fixes the reference point as being the porous disk; this point is a fixed point in the liquid providing the liquid is not allowed to leak past the disk due to pressures caused by gravitational head and momentum changes at the disk. Any leakage must be properly calibrated and taken into account. Another possibility is that the disk affects the transport numbers by preferential adsorption of an appreciable fraction of one of the ions; this seems unlikely in view of the small surface to volume ratio inside the disk, and in this work it is assumed that the disk has no preferential effect. The volume changes observed are listed in Table II.

Table II. Volume changes in the anode compartment of the cell using mixtures of $AgNO_3$ and $NaNO_3$

N_{O_2}	$V_a \times 10^{+3}$ (cc)	$Z \times 10^3$ (Equivalents)
1.00	2.0 ± 2.0	1.00 ± 0.03
0.73	−1.0 ± 3.0	0.52 ± 0.03
0.50	0.7 ± 0.3	0.52 ± 0.03
0.30	+0.6 ± 0.6	0.52 ± 0.03
0.00	+1.0 ± 3.0	0.52 ± 0.03

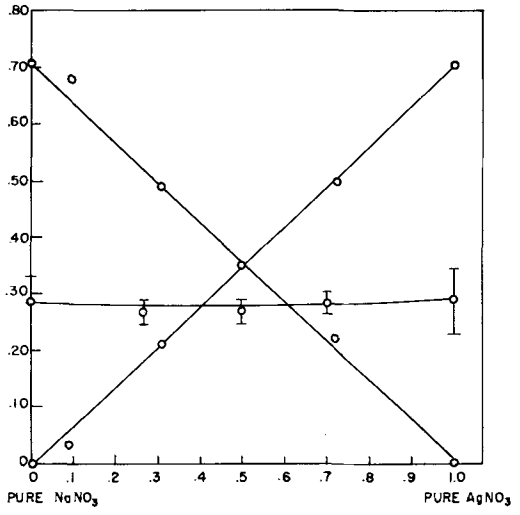

Fig. 1. Transport numbers vs. composition in $AgNO_3$-$NaNO_3$ mixtures.

The results of Byrne, Fleming, and Wetmore (3) on densities and total conductivities show that the molal volumes are essentially identical to the molar volumes ($V_1 = 43.86$ cc and $V_2 = 44.43$ cc), and, combined with the authors' results, show that the mobilities of the ions are constant (total conductivity being linear and almost constant with composition). The final results are shown in Fig 1. The lack of dependence of mobility on composition, mobility being t/X where X is the ion fraction, shows that there is no systematic change in the character of either salt when diluted with the other. If complex ions or incomplete dissociation were present, one would expect a change in mobility at low concentrations due to a change in degree of dissociation under these conditions. Thus it has been shown by nonthermodynamic considerations that these fused nitrates essentially are completely dissociated in mutual mixtures and the pure salts.

Manuscript received August 16, 1956. This paper was prepared for delivery before the San Francisco Meeting, April 29-May 3, 1956. This is Contribution No. 482; the work was performed in the Ames Lab. of the U. S. Atomic Energy Commission.

Any discussion of this paper will appear in a Discussion Section to be published in the December 1957 JOURNAL.

REFERENCES

1. P. M. Aziz and F. W. Wetmore, *Can. J. Chem.*, **30**, 779 (1952).
2. F. R. Duke and R. W. Laity, *J. Phys. Chem.*, **59**, 549 (1955).
3. J. Bryne, H. Fleming, and F. W. Wetmore, *Can. J. Chem.*, **30**, 922 (1952).

The Mechanism of Titanium Production by Electrolysis of Fused Halide Baths Containing Titanium Salts

J. G. Wurm, Lucien Gravel, and Roger J. A. Potvin

Laval University, Quebec, Quebec, Canada

ABSTRACT

Titanium was produced by electrolyzing a molten bath of a sodium and potassium chloride mixture containing potassium fluotitanate, K_2TiF_6, and sodium fluotitanate, Na_2TiF_6. The formation of trivalent titanium double fluorides of sodium and potassium always preceded the production of metallic titanium during the electrolysis. These new trivalent titanium compounds were positively identified as K_2NaTiF_6, K_3TiF_6, and Na_3TiF_6. Free metallic sodium was deposited at the same time as titanium when using a cooled cathode. This fact together with the measured polarization voltage and the presence of trivalent titanium compounds indicate that production of metallic titanium proceeds by secondary reactions in two steps: first, tetravalent titanium is reduced to the trivalent state; second, trivalent titanium is finally reduced to metallic titanium.

Metallic titanium may be produced by electrolysis of potassium fluotitanate, K_2TiF_6, or sodium fluotitanate, Na_2TiF_6, in fused halide baths under argon cover. However, due to lack of protective atmosphere during the electrolysis, several experimenters (1, 2) failed to produce Ti by this method. For similar reasons (3) the formation of some titanium oxyfluoride compounds was observed while conducting electrolysis in open tubes.

Recently, positive results were obtained (4) on the production of Ti metal by electrolyzing, under an argon atmosphere, potassium fluotitanate K_2TiF_6 dissolved in NaCl; the outstanding industrial possibilities of this process have been shown.

The present authors (5) reported some of their results on the production of Ti by electrolysis of sodium and potassium fluotitanates in a mixture of fused sodium and potassium chlorides conducted in an argon atmosphere, and they have shown that this electrolysis lent itself very well to the study of the mechanism of the reaction involved in the production of metallic Ti.

In the present work, special attention has been paid to the determination of polarization voltages and of intermediary compounds appearing during electrolysis in order to find out more definitely by which steps the production of Ti occurred and also to verify if Ti was produced directly by electrolysis as a primary product or if it was the result of a secondary reaction between Ti compounds and Na formed as a primary deposit.

Experimental

Electrolysis was studied in graphite cells with ordinary or water cooled cathodes and also in U-shaped fused quartz cells using either a normal cathode or a rotating cathode with a dry salt injection system. Polarization voltage considered as the back emf of the over-all reaction was measured by the interruptor-commutator method using an electronic voltmeter.

Gases were analyzed in a mass spectrometer for chlorine and fluorine. The cathode products and the residual melt were submitted to a combined chemical, spectrographic, and x-ray analysis.

The electrolytic cell.—Fig. 1 represents a section through the furnace and the electrolytic graphite cell. The furnace has chromel wire heating elements with automatic temperature control. The graphite cell is the anode and is located in a closed gas-tight stainless steel cylinder. The central cathode is interchangeable. Argon gas is introduced through the top by means of an Inconel tube down to the crucible.

Fig. 2 shows a U-shaped tube used as a second cell; it is made of transparent fused quartz in order to follow the color change during the melt and the electrolysis. The electrodes are removable and both compartments of the U tube are flushed with a continuous flow of argon. Fig. 3 gives a detailed view of a similar cell with a rotating cathode and a dry salt injection system under argon atmosphere. In Fig. 4, more details are shown of the rotating cathode and the mercury seal and contact.

Results

The first experiments dealt with two series of electrolyses in which the fused bath mixtures consisted essentially of NaCl and KCl but differed by the addition either of potassium fluotitanate or sodium fluotitanate in the proportion of 20-30% as indicated in Tables I and II. These experiments were conducted in a graphite crucible maintained at 650°C or 700°C using a Mo cathode except in a few cases where it was replaced by a stainless steel water-cooled cathode.

In Series F, the voltage applied on the cell was between 3.80 and 4.5 v and the current between 9 and 15 amp. The polarization voltage measured between 2.60 and 2.80 v. The gas evolved was mainly chlorine containing but a trace of fluorine.

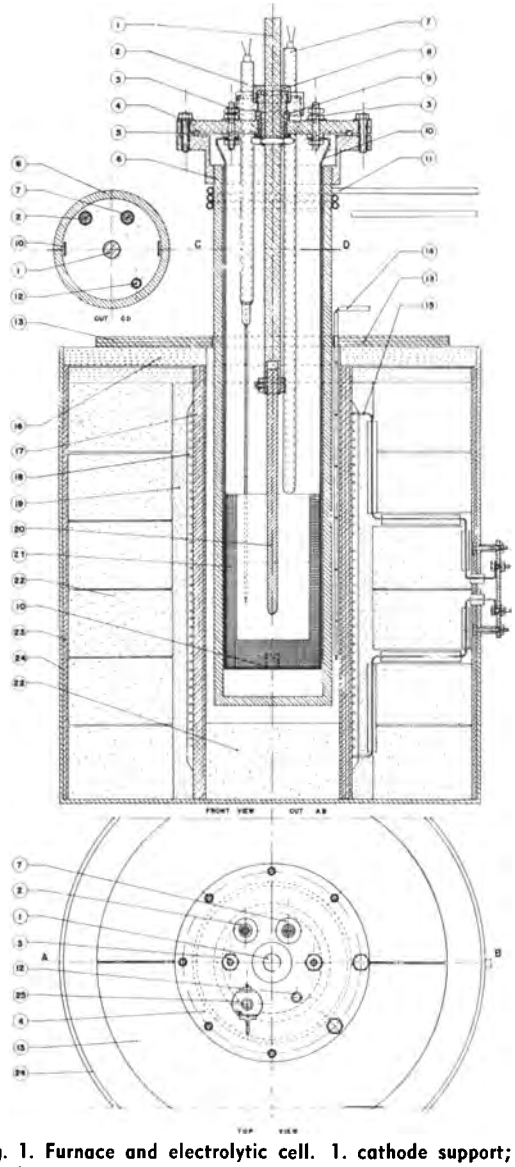

Fig. 1. Furnace and electrolytic cell. 1. cathode support; 2. Pt-PtRh thermocouple; 3. anode connections; 4. bolted lid (brass); 5. rubber seal; 6. stainless steel cylinder; 7. chromel-alumel thermocouple; 8. adjusting nut for electrode; 9. asbestos insulation; 10. stainless steel crucible support; 11. cooling spiral; 12. Argon inlet (stainless steel); 13. asbestos cover; 14. thermocouple for furnace control; 15. heating element (chromel); 16. alundum cement; 17. fused alumina tube; 18. refractory cement; 19. Sil-O-Cel; 20. stainless steel cathode; 21. graphite crucible; 22. refractory bricks; 23. asbestos; 24. furnace shell; 25. Argon outlet control valve.

In the second series, Series N, the applied voltage on the cell varied from 4.5 to 5.2 v with a current of 15-20 amp; polarization voltage was somewhat lower than in the first series, but it increased to 3.05 v when a water-cooled electrode was used. The gas evolved contained chlorine and appreciable amounts of fluorine in comparison with Series F.

Electrolytic Products

After cooling the melt, it was separated from the crucible as a cylindrical solid mass surrounding the cathode. When cut in half, it showed a section comprising two well-defined zones: (*a*) a spherical "nut" or ball around the cathode where metallic Ti crystals were embedded in a deep violet salt, and (*b*) a residual frozen melt of white salt with a light violet shade.

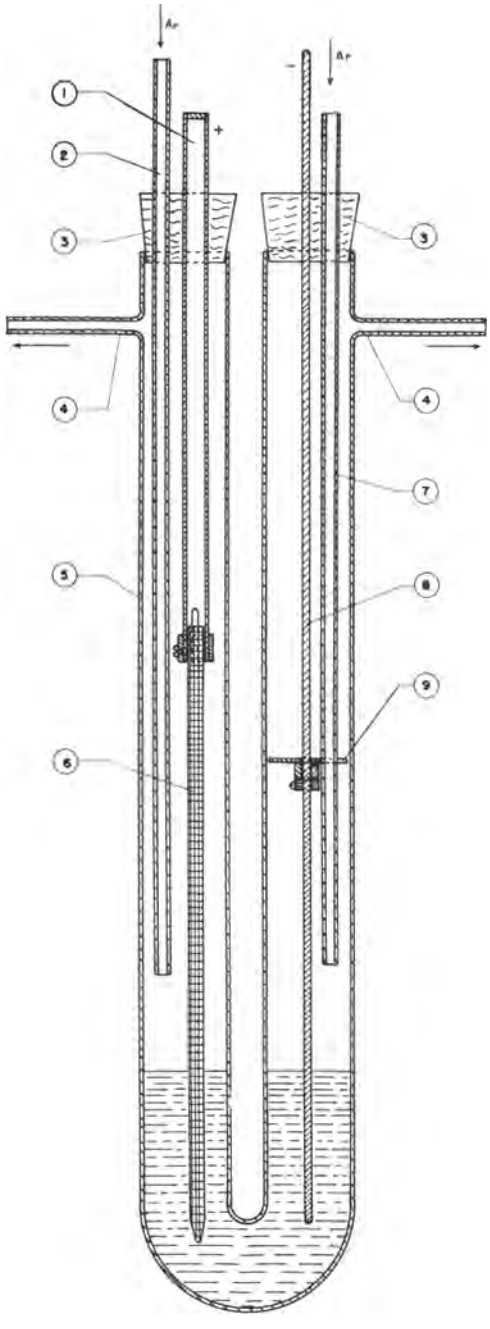

Fig. 2. U-tube cell with normal electrodes. 1. anode holder; 2. Argon inlet; 3. rubber stopper; 4. Argon outlet; 5. quartz U-shaped tube; 6. graphite anode; 7. Pyrex tube; 8. stainless steel cathode; 9. cathode guide.

After separating these two zones mechanically they were analyzed by physical and chemical methods.

The cathode "nut" proved to be Ti metal interlocked with a titanium fluoride compound which had never been described before in the literature. This deep violet compound was present invariably in all electrolyses mentioned above as it was established by x-ray diffraction.[1] It was isolated and analyzed spectrographically and chemically. Its formula was found to be K_2NaTiF_5 (compound A). K_2NaTiF_6 may

[1] Tracings have been deposited as Document 5134 with the ADI Auxiliary Publications Project, Photoduplication Service, Library of Congress, Washington 5, D. C. A copy may be secured by citing the Document number and by remitting $1.25 for a photoprint or for a 35-mm microfilm. Advance payment is required. Make check payable to: Chief, Photoduplication Service, Library of Congress.

Table I. Typical electrolyses of Series F

N°	Bath composition, g	Volts:cell	Amps:cell	Volts: polarization	Temp, °C	Amp-hr	Gas evolved	Analyses: Cathode* products	Analyses: Residual† melt
	Graphite crucible as anode, Mo wire as cathode								
F3	NaCl —35.2 KCl —44.8 K_2TiF_6—20	3.75	8	2.82	660	10	Cl F (minor)	Ti K_2NaTiF_6	NaCl-KCl (major) NaF (minor) K_2NaTiF_6 (minor)
F14	NaCl —35.2 KCl —44.8 K_2TiF_6—20	4.40	15	2.85	690	17.5	Cl F (minor)	Ti K_2NaTiF_6	NaCl-KCl (major) NaF (minor) K_2NaTiF_6 (minor)

* NaCl-KCl and some NaF leached out with H_2O.
† No KCl or K_2TiF_6 and also no free TiF_3 or divalent titanium compounds could be detected.

be written 2KF, NaF, TiF_3 to indicate better that the K and Na contents are constantly in the ratio 2:1 and that the Ti is trivalent.

Compound A was also identified in the residual melt where it was present in smaller amounts, together with an excess of KCl, NaCl, and some NaF. It should be emphasized that no KF, nor TiF_3, nor divalent compounds could be detected; neither could any of the potassium and sodium fluotitanates added at the start of the electrolysis be detected.

Based on the spectrographic and chemical data alone, compound A could well have been a mixture of two other trivalent fluoride compounds, K_3TiF_6 (compound B) and Na_3TiF_6 (compound C), in the ratio 2:1.

Since compounds B and C are not described in the literature, it was necessary to synthesize them by electrolyzing two different melts which contained the tetravalent titanium fluoride compounds in the chloride salts and in which either solely sodium ions or solely potassium ions were present. The compositions of these melts are shown in Table III including also the conditions of the electrolysis of both types of melts. Although chlorine was evolved abundantly during the process, no fluorine could be detected with the mass spectrometer. Furthermore, in these two series of experiments, Ti was produced at the cathode interlocked with a dark violet salt. In the sodium bearing melt, this salt was identified by x-ray, spectrographic and chemical analysis as Na_3TiF_6 (compound C). In the potassium bearing melt it was identified as K_3TiF_6 (compound B).

Some important physical characteristics of the three new compounds A, B, and C are given in Table IV. From x-ray diagram tracings, it was found that compound A has a well-defined face-centered cubic lattice with a 8.374Å parameter and compounds B and C have a close to cubic structure distinctly different from compound A.[2]

Electrolysis with Water-Cooled Cathode

Another series of electrolysis was conducted in the graphite crucible using a water-cooled cathode. Operating conditions (Table V) were approximately the same as in the two series, mentioned previously, except for the total ampere-hours. Use of the cooled cathode produced a temperature gradient and made it possible to freeze out Na which was deposited as a primary product even at the very start of the electrolysis.

As expected with a cooled cathode, polarization voltage was higher than in the first series. Also, there was an excess of titanium salts in all the residual melts, indicating that Na was not formed at the end of the electrolysis on account of the exhaustion of titanium bearing raw materials in the electrolytic bath. If this had been the case, the polarization voltage would have shown a large increase and would have corresponded to the polarization voltage of NaCl which, for this low temperature, may be estimated at approximately 3.8 v.

As a blank run, a bath of the same composition as the above electrolytic melts was submitted to simple fusion without electrolysis and kept at 700°C for 5 hr. Traces of chlorine were evolved and appreciable amounts of K_2NaTiF_6 could be detected in the

[2] More details on the characteristics of these compounds will be published in a paper by Norman F. H. Bright, J. F. Rowland, and J. G. Wurm.

Table II. Typical electrolyses of Series N

N°	Bath composition, g	Volt: cell	Amp: cell	Volt: polarization	Temp, °C	Amp-hr	Gas evolved	Analyses: Cathode* products	Analyses: Residual† melt	Cathode
	Graphite crucible as anode									
N2	NaCl — 87.75 KCl —111.9 Na_3TiF_6— 49.5	4.2	16.0	2.30	675	24	Cl F	Ti K_2NaTiF_6 unidentified minor	NaCl-KCl (major) NaF (minor) K_2NaTiF_6 (minor)	Mo wire
N7	NaCl — 87.75 KCl —111.90 Na_3TiF_6— 49.50	5.2	20.0	3.05 3.01	670	30	Cl F	Ti K_2NaTiF_6 unidentified minor (Na)	NaCl-KCl (major) NaF (minor) K_2NaTiF_6 (minor)	Stainless steel water-cooled

* NaCl; KCl; NaF; leached out with H_2O.
† No KF or Na_3TiF_6 also no free TiF_3 or divalent titanium compounds could be detected.

Table III. Typical electrolyses of Series S

N°	Bath composition, g	Graphite crucible as anode, stainless steel cathode Volt:cell	Amp:cell	Volt: polarization	Temp, °C	Amp-hr	Gas evolved	Analyses: Cathode products	Analyses: Residual melt
S1	NaCl —200 Na_2TiF_6— 50	4.3	20	2.60	820	20	Cl	Ti Na_3TiF_6 no Na_2TiF_6	NaCl (major) Na_3TiF_6 NaF (small minor)
S4	NaCl —200 K_2TiF_6— 50	5	25	2.87	780	25	Cl	Ti K_3TiF_6 K_2TiF_6 (minor)	KCl (major) K_3TiF_6 K_2TiF_6 (minor) KF (small minor)

melt. This proves that the reduction of the tetravalent titanium to the trivalent titanium in the complex fluoride starts as a chemical reduction by simple heating.

Fig. 5 is a photograph and matched drawing of a typical section through a spherical cathode nut; concentric zones are clearly visible showing compound A around the cathode with a well-defined zone of small Ti crystals and of larger crystals and also an external layer of compound A. At lower current density (5 amp/cm^2), the Ti crystals were of compact form as shown in Fig. 6, while at higher current density (10 amp/cm^2), they had a dendritic form (Fig. 7).

Current efficiency.—Typical current efficiencies obtained during electrolysis of K_2TiF_6 and Na_2TiF_6 in fused KCl-NaCl baths are given in Table VI.

Electrolysis in U-Shaped Tubes

With a U-shaped tube, it is possible to prevent recombination of cathode and anode products and to obtain more precise measurements of the polarization voltage.

In Tables VII and VIII are given the operating conditions used during the electrolysis in U-tubes. In the first series of electrolyses, bath composition and general conditions were approximately the same as in graphite cells with ordinary cathodes.

However, in the second of these series, only sodium and potassium chlorides were present at the start. This made is possible to measure polarization voltage when Na was produced under a given set of conditions and, also, to follow the polarization voltage when potassium fluotitanate K_2TiF_6 was injected subsequently in the cathode compartment already containing the electrodeposited metallic Na. The effect of rotating the cathode during these measurements was also ascertained.

Fig. 8 records the voltage applied in the cell and the corresponding amperage before and after injection of K_2TiF_6. The first curve shows that the current could not exceed 3 amp before injection due to the anode effect and to metallic sodium entering the melt; the resulting unstable condition was aggravated on attempting to raise the applied voltage

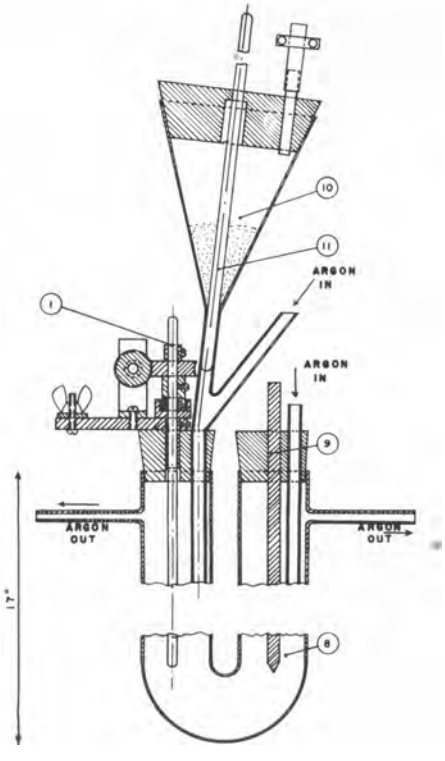

Fig. 3. Dry salt injection system

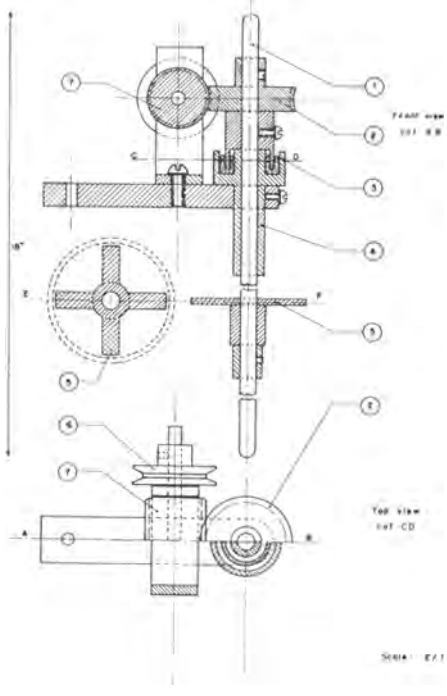

Fig. 4. Details of rotating electrode and mercury seal. 1. rotating electrode (stainless steel); 2. gear; 3. mercury container; 4. brass support; 5. cathode guide; 6. pulley; 7. worm gear; 8. U-shaped quartz tube; 9. graphite anode; 10. feeder (Pyrex); 11. glass stopper.

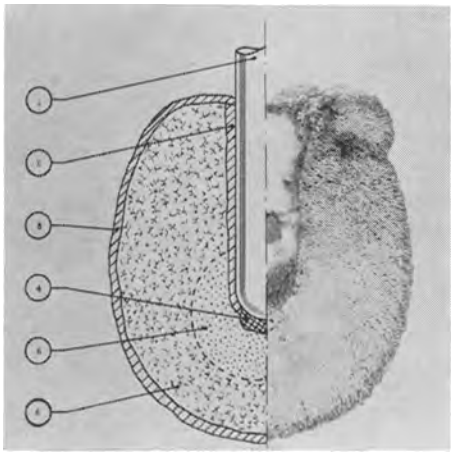

Fig. 5. Section through a cathode ball. 1. Water cooled stainless steel cathode; 2. and 3. layers of violet salt rich in K_2NaTiF_6 with some minor amounts of residual melt; 4. metallic Na embedded in residual melt; 5. fine Ti crystals with some K_2NaTiF_6 and residual melt; 6. large Ti crystals with small amounts of K_2NaTiF_6 and residual melt.

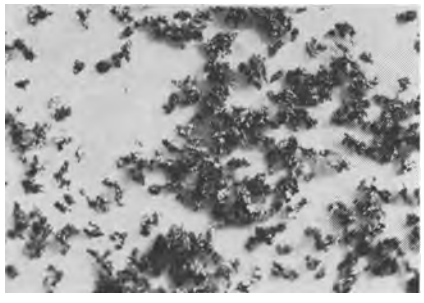

Fig. 6. Compact Ti crystals obtained with a current density at the cathode of 5 amp/cm^2.

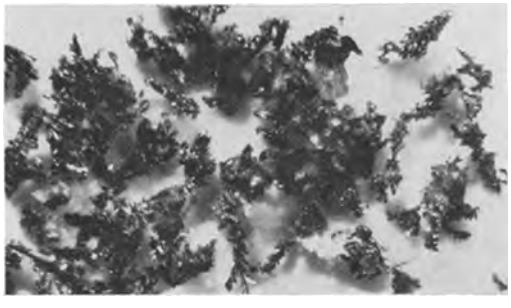

Fig. 7. Dendritic Ti crystals obtained with a current density at the cathode of 10 amp/cm^2.

whence the amperage dropped to a very low value. Immediately after injecting K_2TiF_6, the stability of the bath was improved considerably and the applied voltage and the corresponding current could be raised. At the same time, there was a sharp drop in the polarization voltage due to a secondary reaction between the Na present and the injected Ti bearing

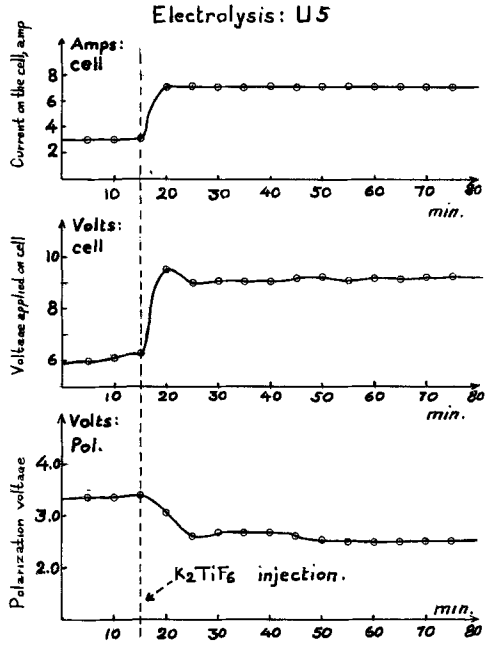

Fig. 8. Amperage and applied voltage on the cell and the corresponding polarization voltage before and after injection of K_2TiF_6 in a fused KCl-NaCl bath.

salts to produce metallic Ti as may be inferred from the constant value of 2.35 v which was reached by the polarization voltage. This voltage is close to the theoretical value calculated from the free energy change of the simplified reaction:

$$TiF_3 + 3NaCl \rightarrow Ti + 3NaF + 3/2\ Cl_2$$

which is 2.26 v at 680°C.

It should be emphasized that the melt turned violet immediately after the injection, indicating the formation of the trivalent fluoride compound at the very start much before the polarization voltage attained a constant value.

Interpretation of Results

Reaction in the Melt and Dissociation

The foregoing results show that in the early stage of melting and during electrolysis the following reaction takes place:

$$K_2TiF_6 + NaCl \overset{a}{\rightleftharpoons} K_2NaTiF_6 + 1/2\ Cl_2 \qquad (I)$$

The marked stability of the compound K_2NaTiF_6 points to a high heat of formation which favors reaction (I) in direction "a". Furthermore it may be seen in this reaction that the potassium fluotitanate must necessarily undergo ionization, that the radical (TiF_6) is carried along in the products and,

Table IV. Some physical characteristics of new compounds A,B,C

	Compound	Structure	Refractive indices	Cell-edge	Solubility in H_2O
A	K_2NaTiF_6	Face-centered cubic	1.408	8.374Å	Little soluble
B	K_3TiF_6	Close to cubic	(ω) 1.406 (e) < 1.406	—	More soluble in hot water with hydrolysis
C	Na_3TiF_6	Close to cubic	(ω) 1.387 (e) 1.382	—	Slightly soluble in hot water

Table V. Typical electrolyses of Series F

N°	Bath composition, g	With water cooled, stainless steel as cathode, graphite crucible as anode Volt:cell	Amp:cell	Volt: polarization	Temp, °C	Amp-hr	Gas evolved	Cathode* products	Analyses Residual† melt
F16	NaCl — 88 KCl —122 K_2TiF_6— 50	5.0	20	3.10	675	20	Cl F (minor)	Ti K_2NaTiF_6 (Na)	NaCl-KCl (major) NaF (minor) K_2NaTiF_6 (minor)
F17	NaCl — 88 KCl —122 K_2TiF_6— 50	6.0	30	3.15 3.40 (end)	660	30	Cl F (minor)	Ti K_2NaTiF_6 (Na)	NaCl-KCl (major) NaF (minor) K_2NaTiF_6 (minor)
F18	NaCl — 88 KCl —122 K_2TiF_6— 50	5.5	25	3.10	670	9	Cl F (minor)	Ti K_2NaTiF_6 (Na)	NaCl-KCl (major) NaF (minor) K_2NaTiF_6 (minor)
F19	NaCl — 88 KCl —122 K_2TiF_6— 50	Blank melt, fused at 700°C not electrolyzed					Cl No F	—	NaCl-KCl (major) K_2TiF_6 K_2NaTiF_6 (minor)

* NaCl-KCl, some NaF and Na leached out.
† No KF or K_2TiF_6, no free TiF_3 or divalent Ti compounds could be detected.

finally, that the tetravalent titanium is reduced to the trivalent state. However, from the data presented in Table V (Experiment F-19) and also in Table VII (Experiment U-3), it becomes evident that reaction (I) is slight in direction "a" when it is taking place by simple melting, but it will be greatly accelerated and rapidly completed by the passage of the current according to the equation:

$$K_2TiF_6 + NaCl \xrightarrow{e} K_2NaTiF_6 + 1/2\ Cl_2 \qquad (Ia)$$

It follows that K_2TiF_6 in the melt is not dissociated according to the equation:

$$K_2TiF_6 \rightleftharpoons 2K^+ + 2F^+ + TiF_4$$

since TiF_4, due to its high vapor pressure, would have showed up in the gaseous products. Apparently, this compound does not follow the same type of dissociation as cryolite (Na^+, F^-, and AlF_3). It follows therefore that the potassium fluotitanate dissociates as follows:

Table VI. Current efficiency

Electrolyses of NaCl—KCl—K_2TiF_6 (50 g)
Graphite crucible anode, stainless steel cathode

No.	Volt: cell	Amp: cell	Temp, °C	Cathode current densities, amp/cm²	Amp-hr	Current efficiency, %
F21	4.9	25	710	5.3	22.9	48.5
F22	5.1	30	680	6.3	27.5	41.3
F23	4.8	20	710	4.2	20	43.6
F24	4.85	25	700	5.3	22.9	47.2

Theoretical yield: 0.44 g Ti/amp-hr

Table VII. Typical electrolyses in U-shaped quartz tubes

Bath composition: NaCl—KCl—K_2TiF_6 (20%)
Cathode: stainless steel; anode: graphite

No.	Volt:cell	Amp:cell	Temp, °C	Polarization voltage
U3	7.0	7.0	680	2.40 2.50

Important observations before electrolysis: (a) color change of the melt: to violet; (b) significant amounts of chlorine evolved.

$$K_2TiF_6 \rightleftharpoons (TiF_6)^{--} + 2K^+ \qquad (II)$$
$$\downarrow\uparrow e$$
$$(TiF_6)^{---}$$

The dissociation of sodium fluotitanate Na_2TiF_6 follows a similar pattern as may be inferred from the products found after the electrolysis.

By analogy with K_2TiF_6 and Na_2TiF_6, dissociations of the trivalent titanium compounds may be written:

$$K_3TiF_6 \rightleftharpoons (TiF_6)^{---} + 3K^+ \qquad (III)$$

$$Na_3TiF_6 \rightleftharpoons (TiF_6)^{---} + 3Na^+ \qquad (IV)$$

$$K_2NaTiF_6 \rightleftharpoons (TiF_6)^{---} + Na^+ + 2K^+ \qquad (V)$$

That the possible alternative dissociation

$$M_3TiF_6 \rightleftharpoons TiF_3 + 3M^+ + 3F^-$$

does not take place is also confirmed by the absence of TiF_3 in the melt or in the gas evolved.

Mechanism of Electrolysis

First step.—Reduction of tetravalent to trivalent titanium.

(*A*) K_2TiF_6 in NaCl-KCl

Since metallic Na was found from the very start of the electrolysis it appears evident that the primary electrolytic reaction may be written

$$NaCl \rightarrow Na + 1/2\ Cl_2 \text{ (primary electrolytic reaction)} \qquad (VI)$$

followed by the secondary reaction

$$Na + K_2TiF_6 \rightarrow K_2NaTiF_6 \qquad (VII)$$

Table VIII. Typical electrolyses in U-shaped quartz tubes

Bath composition: NaCl—KCl, initial K_2TiF_6 injected after 15 min adding up to 20% of the total bath
Cathode: stainless steel; anode: graphite

No.	Cathode	Volt: cell	Amp: cell	Temp, °C	Polarization volt. before injection v	Polarization volt. after injection v
U2	Rotating	7.5	7	680	3.40	1.95-2.0
U3	No rotation	9.2	7	682	3.40	2.35

the latter is contributory to increasing the K_2NaTiF_6 formed by reaction (I) and predominantly (I*a*) and is the first step in the reduction of Ti.

The main features of the spherical cathode nut as illustrated in Fig. 5 may now find a logical explanation which at the same time brings further proof that the reactions written in (I), (I*a*) and (VII) actually take place at the same time. In fact, the outer concentric zone of the K_2NaTiF_6 violet salt is a visual proof that there is an advancing front of the trivalent compound formed to a large extent by reaction (I) and (I*a*) while, in the immediate vicinity of the cathode where Na tends to deposit before flowing down toward the end of the electrode, the K_2NaTiF_6 violet salt is formed nearly exclusively by way of reaction (VII).

(*B*) Na_2TiF_6 in NaCl-KCl

It should be noted that when Na_2TiF_6 instead of K_2TiF_6 is added to a NaCl-KCl bath the observed compound K_2NaTiF_6 formed during the electrolysis may possibly find its origin from the two different processes illustrated below.

First possibility

$$Na_2TiF_6 + 2KCl \overset{a}{\rightleftharpoons} K_2TiF_6 + NaCl \qquad \text{(VIII)}$$

b) $\downarrow\uparrow + NaCl$

$K_2NaTiF_6 + 1/2\ Cl_2$

[as in (I) and also as in (VII)]

Although on thermodynamic basis, reaction (VIII) should be slight in direction (a), it is increased considerably by the formation (b) of the very stable compound K_2NaTiF_6.

Second possibility

The primary cell reaction (VI) $NaCl \rightarrow Na + 1/2\ Cl_2$ followed by the secondary reaction

$$Na_2TiF_6 + Na \rightarrow Na_3TiF_6 \qquad \text{(IX)}$$

However, this Na_3TiF_6 found as a free compound in the absence of potassium ions, as for instance in the electrolysis S_1, could not be detected in the presence of KCl. This indicates how strongly the following reaction takes place

$$Na_3TiF_6 + 2KCl \rightarrow K_2NaTiF_6 + 2NaCl \qquad \text{(X)}$$

(*C*) Na_2TiF_6 in NaCl and K_2TiF_6 in KCl

In the series S_1 of bath composition Na_2TiF_6 — NaCl the intermediary product Na_3TiF_6 was formed during the electrolysis by a reaction similar to (IX).

Furthermore, in series S_4 made by electrolyzing a bath of K_2TiF_6 in KCl, the intermediary product K_3TiF_6 similarly may be explained by a reaction of the same type as (IX).

$$K + K_2TiF_6 \rightarrow K_3TiF_6 \qquad \text{(XI)}$$

where K is the primary product of electrolysis in the absence of Na ions.

Second step.—Reduction of trivalent titanium to the metallic state.

The second step proceeds directly from the trivalent state to metallic Ti and may be explained by a series of two boundary mechanisms according to the following equations

$$3NaCl \overset{3e}{\rightarrow} 3Na + 3/2\ Cl_2 \qquad \text{(VI}a\text{)}$$

$$K_2NaTiF_6 + 3NaCl \overset{3e}{\rightarrow} Ti + 4NaF + 2KF \qquad \text{(XII)}$$

which may be written as an over-all electrolysis reaction as follows

$$K_2NaTiF_6 + 3NaCl \overset{3e}{\rightarrow} Ti + 4NaF + 2KF + 3/2\ Cl_2 \qquad \text{(XII}a\text{)}$$

Reaction (VI*a*) is the initial primary electrolytic reaction. In presence of the compound K_2NaTiF_6, it is immediately followed by the depolarization reaction (XII). This phenomenon in fact has been noticed and measured in particular in the U-tube cell with a delayed injection of K_2TiF_6. The use of a cooled cathode actually introduced a delay between reactions (VI*a*) and (XII) so that some metallic Na remained unreacted on the cathode after electrolysis.

In zone 5 of Fig. 5 Na diffuses more slowly in the partially cooled molten mass in the vicinity of the cathode and thus gives rise to finer Ti crystals according to reaction (XII). In zone 6 on the contrary, formation of dendritic crystals would result predominantly from the over-all electrolytic reaction (XII*a*). This difference between the size of the deposited Ti crystals was less marked when ordinary uncooled cathodes were used; in this latter case it appears that Ti was produced mostly under dendritic form by the over-all electrolytic reaction (XII*a*).

Another plausible intermediary step involving the reaction of trivalent into divalent titanium was discarded as of major occurrence since it would not be in agreement with the measured polarization voltages and, furthermore, would have given rise to divalent titanium compounds which could not be detected in the products.

Since appreciable quantities of KF were not found in the reaction products, it follows that the KF formed by equation (XII) reacts readily with the NaCl present in the bath as follows

$$KF + NaCl \rightarrow NaF + KCl \qquad \text{(XV)}$$

Hence the over-all cell reaction of this second step may be summarized by the following equation

$$2KF \cdot NaF \cdot TiF_3 + 5NaCl \overset{3e}{\rightarrow} Ti + 6NaF + 2KCl + 3/2Cl_2 \qquad \text{(XVI)}$$

The small amounts of fluorine detected in some of the experiments may be explained by traces of NaF participating in the primary reduction ($NaF \rightarrow Na + 1/2\ F_2$).

Conclusions

From the foregoing discussion, it may be concluded that the potassium and sodium trivalent titanium fluoride compound K_2NaTiF_6 or its parent compounds of the type M_3TiF_6 are always formed in the first stage of metallic Ti production upon electrolysis of fluotitanates in fused halide baths. The knowledge of the important part played by these trivalent fluoride compounds during electrolysis will lead to a better insight and a better control of the conditions

of Ti production and may possibly open the field to direct plating of Ti from baths containing these compounds, to refining and recovery processes using soluble impure Ti anodes.

Acknowledgment

The authors wish to express their indebtedness to the Defense Research Board of Canada for financial assistance. They also wish to thank Dr. J. Convey, Director, Dr. K. W. Downes and Dr. T. R. Ingraham, of the Bureau of Mines and Technical Surveys, Ottawa, for their continued interest and support. In addition appreciation is expressed to Dr. N. H. Bright from the above Bureau of Mines for his able collaboration in the crystal analysis of the new compounds.

REFERENCES

1. J. De Bussy, *Compt. rend.*, **36**, 540 (1853).
2. S. I. Sklyarenko and J. Lipkes, *Zhur. Priklad. Khim.*, **13**, 51 (1940).
3. P. Drossbach, *Z. Elektrochem.*, **57**, 548 (1953); **58**, 686 (1954); **59**, 512 (1955).
4. M. A. Steinberg, S. S. Carlton, M. E. Sibert, and E. Wainer, *This Journal*, **102**, 333 (1955).
5. Annual Reports of 1954 and 1955 to the Defense Research Board of Canada.

Manuscript received May 1, 1956. This paper was prepared for delivery before the San Francisco Meeting, April 29 to May 3, 1956 and is based on experimental work done by J. G. Wurm toward a Ph.D. degree at the Graduate School, Laval University.

Any discussion of this paper will appear in a Discussion Section to be published in the December 1957 JOURNAL.

Galvanic Cells for the Determination of the Standard Molar Free Energy of Formation of Metal Halides, Oxides, and Sulfides at Elevated Temperatures

Kalevi Kiukkola[1] and Carl Wagner

Department of Metallurgy, Massachusetts Institute of Technology, Cambridge, Massachusetts

ABSTRACT

The use of electromotive force measurements on galvanic cells for the determination of standard molar free energies of formation of halides, oxides, sulfides, and other compounds at elevated temperatures is surveyed. New potentialities and inherent limitations are shown. Formulas for the estimate of errors resulting from electronic conduction and from transference of the components of electrolytes between different activity levels are derived.

The standard free energy of formation of metal-nonmetal compounds may be obtained from: (*a*) standard heats of formation and standard molar entropies; (*b*) dissociation equilibria, e.g., $PdO(s) = Pd(s) + \frac{1}{2} O_2(g)$; (*c*) reduction equilibria, e.g., $PbS(s) + H_2(g) = Pb(l) + H_2S(g)$; and (*d*) emf measurements of galvanic cells.

The third method was widely used during the first three decades of this century. Nowadays the first method is favored by many authors after the precision of the determination of heats of formation has been increased, reliable standard entropy values at 25°C have become available, and the accuracy of the measurement of specific heats and heat contents at higher temperatures has been steadily improved. The first method is generally applicable. In contrast, the second method applies to very few compounds since in most cases dissociation pressures are much too low for reliable direct measurements. Likewise, the third method is confined to compounds for which the equilibrium ratio of the constituent molecules in the gas phase is not too extreme.

The fourth method has also been used for many years. Pertinent results have been obtained at room temperature and elevated temperatures as well. Although this method is not generally applicable, its usefulness seems to be underestimated. In what follows an attempt is made to show the potentialities of this method at elevated temperatures and some inherent limitations. For a comparison, cells involving aqueous electrolytes for measurements at room temperature are also considered but not discussed in detail.

Determination of standard molar free energies of formation at elevated temperatures is especially important in conjunction with metallurgical problems. Data deduced from emf data may supplement data obtained from reduction equilibria and other gas equilibria, e.g., $Cu_2S(s) + 2Cu_2O(s) = 6Cu(s) + SO_2(g)$.

The free energy change ΔF of a reaction is obtained from the emf E of a galvanic cell as

$$\Delta F = -nEF \qquad [1]$$

where n denotes the number of faradays to be passed across the cell in order to effect the reaction under consideration and F is the Faraday constant.

From Eq. [1] it follows that an uncertainty of 0.001 v = 1 mv in the emf corresponds to an uncertainty of 23 n cal in ΔF, i.e., 46 cal if $n = 2$. On the other hand, if the standard free energy change of a chemical reaction is obtained from gas equilibrium

[1] Present address: Ratakatu 5 B 18, Helsinki, Finland.

measurements by using the formula $\Delta F^\circ = -RT \ln K$, an uncertainty in the equilibrium constant of 1% corresponds to an uncertainty of 20 cal in ΔF° at 1000°K. In view of these figures an accuracy of the order of 1 mv in emf measurements may be considered as desirable and also as satisfactory in order to obtain significant data which supplement data deduced from gas equilibrium measurements, or may be used in order to predict gas equilibria.

Cells for the Determination of the Free Energy of Formation of Halides, Oxides, and Sulfides

Cells without Auxiliary Electrolyte

The standard free energy of formation of a compound A(X) may be obtained most directly from the emf of the cell

$$\text{A} \mid \text{A(X)} \mid \text{Pt, X} \qquad \text{(I)}$$

if the compound A(X) is a purely ionic conductor and if metal A, compound A(X), and nonmetal X are present as virtually pure phases at atmospheric pressure, i.e., in their standard states.

For convenience, the nonmetallic constituent may not be present in its standard state, e.g.,

$$\text{Ag(s)} \mid \text{AgI (s)} \mid \text{Pt, I}_2\ (p_{I_2} = 0.01\ \text{atm}), \text{N}_2\text{(g)} \qquad \text{(II)}$$

Then Eq. [1] gives the free energy of formation ΔF of AgI from silver and iodine vapor of partial pressure p_{I_2}. Therefrom the standard free energy of formation ΔF° is obtained by adding $\frac{1}{2} RT \ln p_{I_2}$.

From the emf of cells of type (I), standard free energies of formation at elevated temperatures have been obtained for silver halides (1-10), lead halides (1-3, 7-13), $CdCl_2$ (1, 9, 10), $ZnCl_2$ (1, 9, 11), and $MgCl_2$ (10, 14) in both the solid and the liquid state.

Solid compounds may exhibit electronic rather than ionic conduction. Therefore, the standard free energy of formation of compounds such as Cu_2O or Ag_2S cannot be obtained from emf measurements on cells of type (I). Even in the case of typical ionic conductors such as solid AgBr or AgI, electron hole conduction becomes appreciable at higher halogen partial pressures (15, 16), and therefore the relation between emf and ΔF stated in Eq. [1] is to be replaced by a more elaborate relation. If the compound A(X) exhibits only slight deviations from the ideal stoichiometric ratio, it has been derived that (17)

$$E = \frac{1}{z_X F}\int_{\bar{F}_X'}^{\bar{F}_X''} (t_A + t_X)\, d\bar{F}_X = \frac{1}{z_X F}\int_{\bar{F}_X'}^{\bar{F}_X''} (1 - t_e)\, d\bar{F}_X \qquad [2]$$

where t_A,t_X and t_e, respectively, are the transference numbers of metal A, nonmetal X, and electrons in compound A(X), z_X is the absolute value of the valence of nonmetal X and $\bar{F}_X'$ and $\bar{F}_X''$, respectively, are the partial molar free energies of nonmetal X on the left-hand and on the right-hand side of cell (I).

The free energy change $\Delta F_{A(X)}$ for the formation of compound A(X) in cell (I) for one mole of metal A of valence z_A is

$$\Delta F_{A(X)} = F_{A(X)}^\circ - F_A^\circ - (z_A/z_X)\bar{F}_X'' \qquad [3]$$

where $F_{A(X)}^\circ$ and F_A° are the standard molar free energies of compound A(X) and metal A, respectively.

The value of $\bar{F}_X'$ is given by the equilibrium condition between A, X, and A(X) on the left-hand side of cell (I),

$$F_A^\circ + (z_A/z_X)\bar{F}_X' = F_{A(X)}^\circ \qquad [4]$$

Upon combining Eqs. [3] and [4], it follows that

$$\bar{F}_X' = \bar{F}_X'' + (z_X/z_A)\Delta F_{A(X)} \qquad [5]$$

In view of Eq. [5], it follows from Eq. [2] that

$$\Delta F_{A(X)} = -z_A E F - \frac{z_A}{z_X}\int_{\bar{F}_X'}^{\bar{F}_X''} t_e\, d\bar{F}_X \qquad [6]$$

where the second term on the right-hand side is a correction term if the compound A(X) is mostly an ionic conductor, i.e., t_e is much smaller than unity.

In order to determine the value of t_e, the following methods may be considered.

(*A*) A significant contribution of electronic conduction is revealed by deviations from Faraday's law when an electrolysis is conducted. It is difficult, however, to determine small deviations from Faraday's law especially if the partial molar free energy of metal A or nonmetal X is to be varied.

(*B*) Another possibility is to measure the total conductivity of compound A(X) as a function of the partial pressure of metal A or nonmetal X (15, 18). If ionic conduction prevails, it is justifiable to assume that variations in the total conductivity are essentially due to *n*-type or *p*-type semiconduction since the mobilities of excess electrons or electron holes are much greater than the mobilities of ionic defects.

(*C*) Polarization measurements are especially profitable in order to determine very small contributions of electronic conduction (19, 20) and to ensure that the last term in Eq. [6] is negligible.

(*D*) For silver chloride the value of t_e has been calculated indirectly from the rate of the reaction between silver and chlorine (15). Therefrom the value of the integral in Eq. [6] for a cell involving the formation of silver chloride from chlorine of atmospheric pressure has been calculated to be 140 cal at 300°C. Since electron hole conduction in AgCl increases with increasing chlorine partial pressure, the error due to appreciable electron hole conduction may be minimized by applying a low halogen partial pressure. Eventually, free chlorine may be replaced by a mixture of hydrogen halide and hydrogen.

In the design of cells of type (I), care has to be exercised to minimize diffusion of nonmetal X to the left-hand electrode because otherwise there results a "mixed potential" (21-23) rather than an equilibrium potential due to cathodic reduction of nonmetal X and anodic dissolution of metal A at the left-hand electrode. In cells of type (I) involving solid A(X), the solid electrolyte must form a gas-tight seal between the two electrodes. Even under these conditions, continuous dissolution of metal A takes place by virtue of migration of ions and electrons in the solid compound as is known from in-

vestigations on reactions of metals with oxygen, sulfur, or halogen at elevated temperatures (17). A significant shift of the emf seems likely only if the distance between the two electrodes in cells of type (I) is less than 0.1 cm. If cells involving different thicknesses of the solid compound A(X) corresponding to different rates of the aforementioned side reaction show essentially the same emf, the effect of this side reaction can be regarded to be negligible.

In the case of a liquid compound A(X), separate electrode compartments warranting a minimum of convective mass transfer between the two compartments are needed. To prevent any transfer of nonmetal to the left-hand electrode in cell (I), Grube and Rau (7) have used glass as a solid intermediate electrolyte, e.g.,

$$Ag(s)\,|AgCl(l)\,|glass|AgCl(l)\,|graphite, Cl_2(g) \quad (III)$$

The potential difference between liquid AgCl and glass on the left-hand side is supposed to cancel against that on the right-hand side. However, since silver chloride and glass have neither a cation nor an anion in common, the potential difference between liquid AgCl and glass is thermodynamically not well defined. Therefore, asymmetry potentials may occur. This may explain inconsistencies of the order of 0.01 v reported by Grube and Rau (7). The absence of asymmetry potentials may be checked by measuring the emf of symmetrical cells involving silver electrodes on both sides.

Cells Involving Aqueous Electrolytes

At room temperature the conductivity of most salts is inconveniently low. Therefore, cells involving aqueous electrolytes are used. If the compound A(X) is sufficiently soluble, an auxiliary electrolyte is, in principle, not needed. In general, however, an auxiliary electrolyte is used. The auxiliary electrolyte may have the anion in common with compound A(X). For instance, the cell

$$Ag|AgCl\ (s), HCl\ (aq)\,|HCl\ (aq)\,|Pt, Cl_2\ (g) \quad (IV)$$

may be used to determine the standard free energy of formation of silver chloride (24). Under conditions where the composition of the electrolyte is virtually constant throughout cell (IV), the cell reaction for passing one faraday may be written as

$$Ag\ (s) + 1/2\ Cl_2(g) = AgCl\ (s) \qquad [7]$$

In addition, the amount of HCl in the left-hand compartment of cell (IV) decreases, and the amount of HCl in the right-hand compartment increases. Transfer of HCl from the left-hand to the right-hand compartment is immaterial for the free energy balance if the transfer takes place between solutions involving virtually equal activities.

If chlorine of atmospheric pressure is used, the activity of HCl on the right-hand side of cell (IV) is lowered by the formation of Cl_3^- ions and is increased by the hydrolysis of Cl_2. Thus, on passing current across cell (IV), not only silver chloride is formed according to Eq. [7] but also HCl is transferred between different activity levels. The difference in the HCl activity may be minimized by using low chlorine partial pressures (21) and extrapolating results to zero chlorine partial pressure. In this way, all uncertainties usually ascribed to liquid junction potentials may be eliminated.

This procedure becomes impractical in the case of iodides since the complex I_3^- is formed more readily than the complex Cl_3^-. Therefore, it is expedient to use an auxiliary electrolyte which has the cation in common with the compound whose free energy of formation is to be determined. As an example the cell (25)

$$Pb\left|\begin{matrix}Pb(ClO_4)_2,\\ HClO_4\ (aq)\end{matrix}\right|\left|\begin{matrix}Pb(ClO_4)_2, HClO_4\ (aq),\\ PbI_2(s), I_2\ (s)\end{matrix}\right|Pt \qquad (V)$$

is cited.

On passing two faradays, the cell reaction is

$$Pb(s) + I_2\ (s) = PbI_2\ (s) \qquad [8]$$

since the solubilities of solid PbI_2 and I_2 in the electrolyte are sufficiently low so that there is no significant difference in composition between the left-hand and the right-hand electrolyte.

In cells of type (IV) involving an auxiliary electrolyte with the anion in common with compound A(X), formation of A(X) on passing current takes place at the left-hand electrode. Therefore, compound A(X) must be present in the left-hand compartment of cells of type (IV). If compound A(X) is only slightly soluble, presence of solid A(X) in the right-hand compartment is immaterial. If, however, the solubility of compound A(X) is appreciable, compound A(X) should be present in both compartments in order to ensure equal activities of the auxiliary electrolyte.

Conversely, in cells of type (V) involving an auxiliary electrolyte with the cation in common with compound A(X), formation of A(X) on passing current takes place at the right-hand electrode. Therefore, the electrolyte in the right-hand compartment of cells of type (V) must be saturated with compound A(X). Saturation of the left-hand compartment is immaterial if the solubility is low, but is necessary if the solubility is appreciable.

Cells with Auxiliary Electrolytes at Elevated Temperatures

If an auxiliary electrolyte is used as in cells (IV) and (V), not only the magnitude but also the nature of the conductivity of the compound A(X) is immaterial for the cell reaction. Therefore, cells involving auxiliary electrolytes are also profitable in order to determine the free energy of formation of halides, oxides, and sulfides at elevated temperatures. As an analogue to cell (IV), the cell

$$Al(s)\left|\begin{matrix}KCl, NaCl\ (l),\\ AlCl_3\ (s)\end{matrix}\right|\left|\begin{matrix}KCl, NaCl\ (l),\\ AlCl_3\ (s)\end{matrix}\right|Pt, Cl_2(g) \qquad (VI)$$

has been investigated by Treadwell and Terebesi (26) between about 100° and 200°C. The cell reaction on passing three faradays is

$$Al(s) + 1.5\ Cl_2\ (g) = AlCl_3(s) \qquad [9]$$

Thus the emf of cell (VI) gives the free energy of formation of aluminum chloride.

In contradistinction to cell (IV), the electrolyte in cell (VI) must be saturated with solid $AlCl_3$ on both

sides in order to have a constant activity of the electrolyte because the solubility of $AlCl_3$ in the liquid electrolyte is substantial.

Hill and Porter (27) have investigated cells of type

$$Ni|NiO(s), \text{salt melt with } CaO|\text{salt melt with } CaO|Pt, O_2(g) \quad (VII)$$

Spurious results may have been caused by diffusion of oxygen to the left-hand electrode.

The compound A(X) whose free energy of formation is to be determined may not be stable in the presence of nonmetal of atmospheric pressure. This is true for FeO, CoO, and Cu_2O. In this case, the electrolyte in the right-hand compartment of cell (VII) cannot be saturated with compound A(X). If only the electrolyte in the left-hand compartment is saturated, there is necessarily a difference in the activity of the components of the electrolyte between the left-hand and the right-hand compartment. Thus the cell reaction involves not only formation of compound A(X) but also transfer of electrolyte between different activity levels. A simple evaluation of emf measurements is possible only if the solubility of compound A(X) in the electrolyte is sufficiently low, and therefore, the activity difference between the electrolyte with and without saturation with compound A(X) is negligible. To overcome this restriction, Treadwell (28) has used porcelain as an intermediate solid electrolyte in determining the standard free energy of formation of Cu_2O, CoO, NiO, and other oxides. As an example, we quote the cell

$$Cu(s)|Cu_2O(s), \text{borate melt}|\text{porcelain}|Ag(l), O_2(g) \quad (VIII)$$

which involves the cell reaction

$$2Cu(s) + 1/2\,O_2(g) = Cu_2O(s) \quad [10]$$

on passing two faradays if oxygen ions alone carry the current in porcelain used as an intermediate electrolyte.

To ensure a low solubility of compound A(X), use of a solid auxiliary electrolyte may be considered, e.g.,

$$Cu(s), Cu_2O(s)|(ZrO_2 + CaO)|Pt, O_2(g) \quad (IX)$$

Since the current in a solid solution of CaO in ZrO_2 is carried essentially by oxygen ions (18), the virtual cell reaction on passing two faradays is that in Eq. [10].

Cell (IX) has not been investigated so far. Oxygen must be prevented from diffusing to the left-hand electrode since otherwise a mixed potential rather than an equilibrium potential would prevail. To this end, gas-tight crucibles consisting of the solid electrolyte are needed. Since such crucibles are not easy to make, measurements on cell (IX) do not seem recommendable. Instead, cell (XXI) has been investigated (*see* below).

As an example for a cell where the compound A(X) and the electrolyte have the cation in common, the cell

$$Mg(l)\left|\begin{matrix}MgF_2(s),\\MgO(s)\end{matrix}\right|\left|\begin{matrix}MgF_2(s),\\MgO(s)\end{matrix}\right|Pt, O_2(g) \quad (X)$$

is cited. Cell (X) has been investigated by Treadwell, Ammann, and Zürrer (14) between 637° and 727°C. Regardless of the nature of the migrating ions in solid MgF_2, the cell reaction on passing two faradays is

$$Mg(l) + 1/2\,O_2(g) = MgO(s) \quad [11]$$

Thus the emf of cell (X) gives the standard free energy of formation of solid MgO.

Another example is the cell

$$Ag(s)|AgI(s)|Ag_2S(s), S(l), Pt \quad (XI)$$

with solid AgI as electrolyte involving migration of silver ions. The virtual cell reaction on passing two faradays is

$$2Ag(s) + S(l) = Ag_2S(s) \quad [12]$$

The emf of cell (XI) has been measured by Reinhold (29) and by Kiukkola and Wagner (18). Therefrom the standard molar free energy of formation of Ag_2S has been deduced. Analogous investigations have been made with Ag_2Se (18, 29).

In cells involving liquid electrolytes, diffusion of nonmetal to the metal electrode must be prevented. To this end, an intermediate solid electrolyte analogous to that in cell (III) may be used. In order to obtain the standard free energy of formation of Al_2O_3, Treadwell and Terebesi (30) have investigated the cell

$$Al(l)\left|\begin{matrix}Na_3AlF_6(l),\\Al_2O_3(s)\end{matrix}\right|\text{porcelain}\left|\begin{matrix}Na_3AlF_6(l),\\Al_2O_3(s)\end{matrix}\right|Pt, O_2(g) \quad (XII)$$

Cells for Determination of the Standard Free Energy Change of Displacement Reactions

The foregoing measurements may be supplemented by investigations on cells involving metal displacement reactions,

$$(1/z_A)\,A + (1/z_B)\,B(X) = (1/z_A)A(X) + (1/z_B)\,B \quad [13]$$

where z_A and z_B, respectively, denote the valences of metals A and B in the compounds A(X) and B(X). The standard free energy change of reaction [13] formulated for one equivalent is equal to the difference of the standard free energies of formation of the metal compounds A(X) and B(X) per equivalent. Consequently, if one of the latter values is known, the other value may be calculated readily from the difference which in turn may be obtained from the emf value of an appropriate cell.

Cells without Auxiliary Electrolyte

In some cases, it is possible to design cells without any auxiliary electrolyte, e.g. (2, 3, 31-33)

$$Pb(s)|PbCl_2(s)|AgCl(s)|Ag(s) \quad (XIII)$$

Since chlorine ions migrate in $PbCl_2$ and silver ions in AgCl, the virtual cell reaction on passing two faradays across cell (XIII) is

$$Pb(s) + 2AgCl(s) = 2Ag(s) + PbCl_2(s) \quad [14]$$

Cell (XIII) is a so-called Daniell-type cell. In general, investigations on such cells have been made with molten salts, e.g. (1, 7, 10, 32, 34-39)

$$\mathrm{Pb(l)\,|PbCl_2(l)\,|AgCl(l)\,|Ag(s)} \qquad \text{(XIV)}$$

In view of the liquid junction, the virtual cell reaction also involves transfer of $PbCl_2$ and AgCl between different activity levels. Thus the emf of cell (XIV) does not give directly the standard free energy change of displacement reaction [14].

To derive a general formula, consider the cell

$$\mathrm{A|A(X)\,|B(X)\,|B} \qquad \text{(XV)}$$

in which the composition of the salt melt is supposed to be a continuous single-valued function of distance x from the left-hand electrode at $x = 0$ up to $x = L$ at the right-hand electrode. The transference numbers of the cations, t_A and t_B, may be defined by assigning a value of zero to the transference number of the anion. Thus the value of t_A in pure A(X) is equal to unity by definition, and the same is true for t_B in pure B(X).

On passing electrical current across cell (XV), A-ions enter the melt of pure A(X), A-ions and B-ions are transferred in the salt melt in the x-direction, and B-ions are discharged at the right-hand electrode. Then it follows from the free energy balance for one faraday that

$$\begin{aligned}&(1/z_A)\,[\overline{F}_{A\text{-ion}}\ (x = 0) - F_A^\circ]\\ &+ (1/z_A)\int_0^L t_A\ (\partial\overline{F}_{A\text{-ion}}/\partial x)\,dx\\ &+ (1/z_B)\int_0^L t_B\ (\partial\overline{F}_{B\text{-ion}}/\partial x)\,dx\\ &+ (1/z_B)\,[-\overline{F}_{B\text{-ion}}\ (x = L) + F_B^\circ] = -EF\end{aligned} \qquad [15]$$

Using the general relations

$$(1/z_A)\overline{F}_{A\text{-ion}} + (1/z_X)\overline{F}_{X\text{-ion}} = (1/z_A)\overline{F}_{A(X)} \qquad [16]$$

$$(1/z_B)\overline{F}_{B\text{-ion}} + (1/z_X)\overline{F}_{X\text{-ion}} = (1/z_B)\overline{F}_{B(X)} \qquad [17]$$

one may eliminate the partial molar free energies of the ions from Eq. [15] and obtains

$$\begin{aligned}&[(1/z_A)\ (F_{A(X)}^\circ - F_A^\circ) - (1/z_B)\ (F_{B(X)}^\circ - F_B^\circ)]\\ &+ \int_0^L (t_A/z_A)\,(\partial\overline{F}_{A(X)}/\partial x)\,dx\\ &+ \int_0^L (t_B/z_B)\,(\partial\overline{F}_{B(X)}/\partial x)\,dx = -EF\end{aligned} \qquad [18]$$

where the expression in brackets is equal to the standard free energy change ΔF° of the displacement reaction formulated in Eq. [13].

The derivatives of $\overline{F}_{A(X)}$ and $\overline{F}_{B(X)}$ are interrelated by the Gibbs-Duhem equation

$$N_{A(X)}\,d\overline{F}_{A(X)} + N_{B(X)}\,d\overline{F}_{B(X)} = 0 \qquad [19]$$

where $N_{A(X)}$ and $N_{B(X)}$ are the mole fractions of A(X) and B(X), respectively. Substituting Eq. [19] and transposing integrals to the right-hand side of Eq. [18],

$$\Delta F^\circ = -EF - \int_0^L \left[\frac{t_B}{z_B N_{B(X)}} - \frac{t_A}{z_A N_{A(X)}}\right] N_{B(X)}\,\frac{\partial F_{B(X)}}{\partial x}\,dx \qquad [20]$$

Finally, the relation

$$F_{B(X)} = F_{B(X)}^\circ + RT \ln N_{B(X)}\,\gamma_{B(X)} \qquad [21]$$

may be introduced where $\gamma_{B(X)}$ is the activity coefficient of B(X) in the binary melt A(X)—B(X). Substitution of Eq. [21] in Eq. [20] yields

$$\Delta F^\circ = -EF + \Delta F^* \qquad [22]$$

where

$$\Delta F^* = -RT\int_0^L \left[\frac{t_B}{z_B N_{B(X)}} - \frac{t_A}{z_A N_{A(X)}}\right]\left(1 + \frac{\partial \ln \gamma_{B(X)}}{\partial \ln N_{B(X)}}\right) dN_{B(X)} \qquad [23]$$

If the mobilities of A-ions and B-ions are equal and independent of the composition of the salt melt, the expression in brackets under the integral vanishes and thus the emf of cell (XV) gives directly ΔF°. In general, equal mobilities of A-ions and B-ions cannot be expected and, therefore, the integral in Eq. [23] does not vanish. If the mobilities of the ions in the melt A(X)-B(X) are of the same order of magnitude, deviations from Raoult's law are not excessive, and $z_A = z_B$, then the absolute value of ΔF^* is of the order of or less than RT/z_A, i.e., 1000 cal at 1000°K for $z_A = z_B = 2$.

The value of ΔF° for the displacement reaction in Eq. [13] can be obtained rigorously as the product of the Faraday constant and the difference E' of the emf values of cells of type (I) involving the formation of compounds A(X) and B(X) as virtual cell reactions. Upon substituting $\Delta F^\circ = -E'F$ in Eq. [22], it follows that

$$(E - E')F = \Delta F^* \qquad [24]$$

As far as experimental values are available (7, 10, 34-39), it has been found that the absolute value of the difference $E - E'$ is, in general, of the order of or less than 0.03 v and, therefore, ΔF^* is of the order of or less than 700 cal in accord with the above estimate based on Eq. [23]. If this result is generalized, the error may be estimated when the emf of a cell of type (XV) has been measured and the value ΔF° of the displacement reaction in Eq. [13] is calculated approximately from Eq. [22] under neglect of the term ΔF^*. Greater discrepancies reported by Lorenz and Velde (10) for cells involving magnesium seem to be due to errors resulting from mixed potentials in view of the high reactivity of magnesium.

As a rule, measurements on Daniell-type cells are not recommended for a thermodynamic evaluation since reliable transference numbers are not available. Schwarz (40) has pointed out that it may be more appropriate to calculate transference numbers from emf measurements rather than to measure these values directly with the aid of the Hittorf method.

In cell (XIII) both compounds A(X) and B(X) show predominantly ionic conduction. This is not a necessary condition. The virtual cell reaction is also represented by Eq. [13] if only the compound of the less noble metal is an ionic conductor. A hypothetical cell is

$$\mathrm{Zr|ZrO_2\,(+\,CaO)\,|Ni,\,NiO} \qquad \text{(XVI)}$$

where solid ZrO_2 is doped with CaO in order to ensure ionic conduction and the right-hand electrode is a tablet consisting of an intimate mixture of nickel and nickel oxide. Thus the virtual cell reaction on passing four faradays would be

$$Zr\ (s) + 2NiO\ (s) = ZrO_2\ (s) + 2Ni\ (s) \quad [25]$$

It is doubtful, however, whether zirconia doped with CaO is still an ionic conductor under highly reducing conditions corresponding to the coexistence of zirconium metal and zirconia.

Cells Involving Aqueous Electrolytes

If the compound of the less noble metal of the pair A-B is considerably more soluble than the compound of the more noble metal, a cell without auxiliary electrolyte may be investigated, e.g.,

$$Pb|PbCl_2(s), aq|PbCl_2(s), AgCl(s), aq|Ag \quad (XVII)$$

with reaction [14] as the virtual cell reaction.

In order to minimize the difference in composition of the electrolyte, an auxiliary electrolyte which has the anion in common with compounds A(X) and B(X) may be used, e.g.,

$$Pb|0.1M\ KCl, PbCl_2(s)|\ 0.1M\ KCl, PbCl_2(s), AgCl(s)|Ag \quad (XVIII)$$

It is also possible to use a soluble salt of the less noble metal of the pair A-B as auxiliary electrolyte, e.g.,

$$Pb\left|\begin{matrix}0.1M\ Pb(ClO_4)_2,\\ PbCl_2(s)\end{matrix}\right.\left|\begin{matrix}0.1M\ Pb(ClO_4)_2,\\ PbCl_2(s), AgCl(s)\end{matrix}\right|Ag \quad (XIX)$$

Instead of displacement reaction [13] involving two metals A and B and their compounds, also consider displacement reactions involving hydrogen instead of metal A, e.g.,

$$1/2\ H_2(g) + AgCl(s) = HCl(aq) + Ag(s) \quad [26]$$

for which the free energy change may be obtained from the emf of the cell

$$Pt, H_2(g)|0.1M\ HCl|0.1M\ HCl, AgCl(s)|Ag \quad (XX)$$

In the presence of water, most halides are not stable as anhydrous salts. Therefore, pertinent results have been obtained for AgCl, HgCl, and $PbCl_2$ but not for other chlorides such as $CdCl_2$ or $ZnCl_2$. For the latter salts, however, values are obtainable from emf measurements on cells of type (I) at elevated temperatures without presence of water as has been reported above.

Similarly, reactions involving metal oxides and sulfides have been investigated (41-46). For various reasons, however, the applicability of emf measurements is limited. Reasons for lack of accuracy in some cases needs further clarification.

Cells Involving Auxiliary Electrolytes at Elevated Temperatures

If both compounds A(X) and B(X) exhibit electronic conduction, cells of type (XV) or (XVI) must be replaced by cells involving an auxiliary electrolyte. In the first place, an auxiliary electrolyte may be used which has the anion in common with compounds A(X) and B(X), e.g.,

$$Fe, FeO|ZrO_2\ (+ CaO)|Cu, Cu_2O \quad (XXI)$$

with a solid solution of CaO in ZrO_2 involving anionic conduction. Measurements on cells of types (XXI) have been used in order to calculate the standard molar free energy of formation of Cu_2O, NiO, and CoO between about 800° and 1100°C (18).

A liquid electrolyte may also be used, e.g.,

$$Cu(s)|Cu_2S(s), Na_2S(l)|Na_2S(l)|\ Na_2S(l), Ag_2S(s)|Ag(s) \quad (XXII)$$

where the left-hand compartment contains a Na_2S melt saturated with solid Cu_2S and the right-hand compartment contains liquid Na_2S saturated with solid Ag_2S. If the solubilities of Cu_2S and Ag_2S in molten Na_2S are sufficiently low, the virtual cell reaction on passing two faradays may be formulated as

$$2Cu(s) + Ag_2S(s) = 2Ag(s) + Cu_2S(s) \quad [27]$$

under neglect of transfer of Na_2S between different compartments of cell (XXII).

Under conditions involving an appreciable solubility of Cu_2S and Ag_2S in molten Na_2S, the virtual cell reaction also involves transfer of Na_2S between different activity levels and, therefore, the emf of cell (XXII) does not give directly the standard free energy change of displacement reaction [27].

To derive a general formula, consider the cell

$$A|A(X), C(X)|C(X)|C(X), B(X)|B \quad (XXIII)$$

where the auxiliary electrolyte is liquid C(X). The left-hand compartment and the right-hand compartment of cell (XXIII) are supposed to be saturated with solid A(X) and B(X), respectively. The composition of the liquid phase is assumed to be a single-valued function of distance x from the left-hand electrode at $x = 0$.

In essence, cell (XXIII) consists of two half cells, one extending from $x = 0$ to $x = L_1$ and the other one extending from $x = L_1$ to $x = L_2$ where L_1 is the coordinate of a plane within the middle compartment containing pure C(X), and L_2 is the coordinate of the right-hand electrode.

On passing current across cell (XXIII), A-ions are formed at the left-hand electrode, and A-ions and C-ions are transferred in the x direction. On the right-hand side of cell (XXIII), B-ions and C-ions are transferred in the x-direction, and B-ions are reduced to metal B.

From the free energy balance for one faraday it follows that

$$(1/z_A)[\bar{F}_{A\text{-ion}}\ (x = 0) - F_A^\circ] + (1/z_A)\int_0^{L_1} t_A\ (\partial \bar{F}_{A\text{-ion}}/\partial x)\ dx + (1/z_C)\int_0^{L_1} t_C\ (\partial \bar{F}_{C\text{-ion}}/\partial x)\ dx + (1/z_B)\int_{L_1}^{L_2} t_B\ (\partial \bar{F}_{B\text{-ion}}/\partial x)\ dx$$

$$+ (1/z_C) \int_{L_1}^{L_2} t_C \, (\partial \bar{F}_{C\text{-ion}}/\partial x) \, dx$$

$$+ (1/z_B) \, [\bar{F}_{B\text{-ion}} \, (x = L_2) + F_B^\circ] = -EF \qquad [28]$$

Using Eqs. [16] and [17] and an analogous equation for C(X), one may eliminate the partial molar free energies of the ions from Eq. [28] and obtains

$$[(1/z_A) \, (F_{A(X)}^\circ - F_A^\circ - (1/z_B) \, (F_{B(X)}^\circ - F_B^\circ)]$$

$$+ \int_0^{L_1} (t_A/z_A) \, (\partial \bar{F}_{A(X)}/\partial x) \, dx$$

$$+ \int_0^{L_1} (t_C/z_C) \, (\partial \bar{F}_{C(X)}/\partial x) \, dx$$

$$+ \int_{L_1}^{L_2} (t_B/z_B) \, (\partial \bar{F}_{B(X)}/\partial x) \, dx$$

$$+ \int_{L_1}^{L_2} (t_C/z_C) \, (\partial \bar{F}_{C(X)}/\partial x) \, dx = -EF \qquad [29]$$

For the two binary systems A(X)—C(X) and B(X)—C(X) the Gibbs-Duhem equations read

$$N_{A(X)} \, d\bar{F}_{A(X)} + N_{C(X)} \, d\bar{F}_{C(X)} = 0 \qquad [30]$$

$$N_{B(X)} \, d\bar{F}_{B(X)} + N_{C(X)} \, d\bar{F}_{C(X)} = 0 \qquad [31]$$

Substituting Eqs. [30] and [31] in Eq. [29] and recalling that the expression in brackets in Eq. [29] is equal to the standard free energy change ΔF° of the displacement reaction formulated in Eq. [13], one obtains

$$\Delta F^\circ = EF$$

$$- \int_0^{L_1} \left[\frac{t_A}{z_A N_{A(X)}} - \frac{t_C}{z_C N_{C(X)}} \right] N_{A(X)} \frac{\partial \bar{F}_{A(X)}}{\partial x} \, dx$$

$$- \int_{L_1}^{L_2} \left[\frac{t_B}{z_B N_{B(X)}} - \frac{t_C}{z_C N_{C(X)}} \right] N_{B(X)} \frac{\partial \bar{F}_{B(X)}}{\partial x} \, dx \qquad [32]$$

For solubilities of A(X) and B(X) lower than 10 mole %, the relations for dilute solutions

$$d\bar{F}_{A(X)} = RT \, d \ln N_{A(X)} \qquad [33a]$$

$$d\bar{F}_{B(X)} = RT \, d \ln N_{B(X)} \qquad [33b]$$

may be used as fair approximations.

Writing Eq. [32] for ΔF° in the general form in Eq. [22], one finds from Eqs. [32], [33a], and [33b] that the additional term ΔF^* resulting from the contribution of transference effects is

$$\Delta F^* = - RT \int_0^{N_{A(X),\,sat}} \left[\frac{t_C}{z_C N_{C(X)}} - \frac{t_A}{z_A N_{A(X)}} \right] dN_{A(X)}$$

$$+ RT \int_0^{N_{B(X),\,sat}} \left[\frac{t_C}{z_C N_{C(X)}} - \frac{t_B}{z_B N_{B(X)}} \right] dN_{B(X)} \qquad [34]$$

where $N_{A(X),\,sat}$ and $N_{B(X),\,sat}$ are the mole fractions of A(X) and B(X) in the auxiliary liquid electrolyte saturated with solid A(X) and B(X), respectively.

For a numerical evaluation, we assume equal valences of the cations

$$z_A = z_B = z_C \qquad [35]$$

Moreover, for an estimate of the order of magnitude, we assume a negligible mobility of the anions and denote the ratio of the mobility of cations A and B to that of C by f_A and f_B. Thus

$$u_A = f_A u_C; \; u_B = f_B u_C; \; u_X = 0 \qquad [36]$$

Hence in mixtures of the binary system A(X)-C(X)

$$t_A = \frac{f_A \, N_{A(X)}}{1 + (f_A - 1) N_{A(X)}} \qquad [37]$$

$$t_C = \frac{1 - N_{A(X)}}{1 + (f_A - 1) N_{A(X)}} \qquad [38]$$

and in mixtures of the binary systems B(X)-C(X)

$$t_B = \frac{f_B \, N_{B(X)}}{1 + (f_B - 1) N_{B(X)}} \qquad [39]$$

$$t_C = \frac{1 - N_{B(X)}}{1 + (f_B - 1) N_{B(X)}} \qquad [40]$$

Upon substitution of Eqs. [35] to [40] in Eq. [34], it follows that

$$\Delta F^* = (RT/z_A) \ln[1 + (f_A - 1) N_{A(X),\,sat}] - (RT/z_A) \ln[1 + (f_B - 1) N_{B(X),\,sat}] \qquad [41]$$

or approximately,

$$\Delta F^* \cong (RT/z_A) \, (f_A - 1) N_{A(X),\,sat} - (RT/z_A) \, (f_B - 1) N_{B(X),\,sat}$$
$$\text{if } z_A = z_B = z_C, \; N_{A(X)} << 1, \; N_{B(X)} << 1 \qquad [42]$$

According to Eq. [42] the value of ΔF^* is determined by two terms which are proportional to the solubilities of compounds A(X) and B(X) in the auxiliary electrolyte C(X) and moreover proportional to the difference between the mobilities of ions A and C and ions B and C, respectively.

As an illustrative example, it is assumed that $z_A = z_B = z_C = 1$, $f_A = 2$, $f_B = 1$, $N_{A(X),\,sat} = 0.01$, and $T = 1000°K$ whereupon ΔF^* is found to be equal to 20 cal. For most purposes, such a low value is negligible but the term ΔF^* may be significant if one of the compounds A(X) or B(X) has a higher solubility in the auxiliary electrolyte C(X).

The foregoing considerations also apply to galvanic cells involving solid electrolytes. Cell (XXI) represents a particularly simple case, since the auxiliary electrolyte (ZrO_2 + CaO) is essentially an anion conductor due to the presence of anion vacancies (47, 48). If none of the cations Zr^{4+}, Ca^{2+}, Ni^{2+}, and Cu^+ has a mobility comparable to that of oxygen ions, passage of current does not result in transfer of one of the oxide components between different activity levels in the electrolyte. Thus the virtual cell reaction is given by the general Eq. [13] regardless of the magnitude of the solubility of the oxides at the electrodes in the auxiliary electrolyte (ZrO_2 + CaO).

Another cell involving a liquid auxiliary electrolyte is the cell

$$\mathrm{Ni(s)}\ \left|\begin{matrix}\text{borate melt,}\\ \mathrm{NiO(s)}\end{matrix}\right|\ \left|\begin{matrix}\text{borate}\\ \text{melt}\end{matrix}\right|\ \left|\begin{matrix}\text{borate melt,}\\ \mathrm{Cu_2O(s)}\end{matrix}\right|\ \mathrm{Cu(s)} \qquad \text{(XXIV)}$$

The virtual cell reaction on passing two faradays is

$$2\mathrm{Ni(s)} + \mathrm{Cu_2O(s)} = 2\mathrm{Cu(s)} + \mathrm{NiO(s)} \quad [43]$$

if the solubilities of NiO and Cu_2O in the borate melt are sufficiently low so that the difference in composition of the electrolyte on the left-hand and the right-hand side of the cell can be disregarded.

A calculation of the term ΔF^* accounting for transference effects in the general Eq. [22] is more involved than for cell (XXIII) since the auxiliary electrolyte involves two components, Na_2O and B_2O_3. On the left-hand side of cell (XXIV) there is, therefore, a liquid junction potential for the ternary system $NiO\text{-}Na_2O\text{-}B_2O_3$. Thus the emf of cell (XXIV) is not completely defined by the composition of the terminal solutions next to the electrodes but also depends on the trajectory in the Gibbs triangle $NiO\text{-}Na_2O\text{-}B_2O_3$ for the transition from the electrolyte next to the left-hand electrode to the electrolyte in the middle compartment, and likewise on the trajectory in the Gibbs triangle $Cu_2O\text{-}Na_2O\text{-}B_2O_3$ for the transition from the electrolyte in the middle compartment to the electrolyte next to the right-hand electrode. This is essentially the same situation found in ternary aqueous solutions where a liquid junction potential may correspond to the Planck formula, to the Henderson formula, or other formulas, depending on the experimental conditions provided for establishing a liquid junction (49).

In addition, one may consider auxiliary electrolytes which have the cation in common with the compound of the less noble metal of the pair A-B, e.g., (18)

$$\mathrm{Pb(s)}\,|\,\mathrm{PbCl_2(s)}\,|\,\mathrm{PbS(s), Ag_2S(s), Ag(s)} \qquad \text{(XXV)}$$

where $PbCl_2$ shows predominantly ionic conduction and the right-hand electrode is an intimate mixture of PbS, Ag_2S, and Ag. Thus the virtual cell reaction on passing two faradays is

$$\mathrm{Pb(s)} + \mathrm{Ag_2S(s)} = 2\mathrm{Ag(s)} + \mathrm{PbS(s)} \quad [44]$$

Treadwell, Ammann, and Zürrer (14) have investigated cells analogous to cell (XXV) in order to determine the free energy change of the reaction

$$3\mathrm{MgO} + 2\mathrm{Al} = \mathrm{Al_2O_3} + 3\mathrm{Mg} \quad [45]$$

but the formation of the spinel phase $MgAl_2O_4$ may interfere with the main reaction.

Similarly, displacement reactions between compounds of metal A with different nonmetals may be investigated, e.g.,

$$\mathrm{PbI_2(s)} + \mathrm{Cl_2(g)} = \mathrm{PbCl_2(s)} + \mathrm{I_2(g)} \quad [46]$$

Appropriate cells may be devised by using the same principles as for metal displacement reactions. In general, cells of this type do not seem recommendable since use of gas electrodes is inconvenient.

Conclusions

In the foregoing sections, different types of galvanic cells have been listed. A careful selection of the most promising type is necessary because the relation between emf and ΔF stated in Eq. [1] never holds rigorously, but is an approximation. The most important deviations are due to the following reasons.

1. Electronic conduction may occur in addition to ionic conduction. A more elaborate relation between E and ΔF has been stated in Eq. [6] for cells of type (I). Similar equations may be derived for other types of cells. By and large, interference due to electronic conduction is more serious with solid than with liquid electrolytes.

2. In view of mutual solubility, reactants and reaction products may not be present in their standard states. If the solubilities are known, correction terms may be estimated in order to obtain standard free energy changes. Reference is made to recent calculations for Cu_2S (50).

3. If the solubility of reactants and reaction products in solid or liquid electrolytes is not negligible, the virtual cell reaction also involves transfer of the components of the electrolyte between different activity levels which have to be considered in the thermodynamic evaluation, e.g., Eq. [22]. A rigorous evaluation requires numerical values of the transference numbers as a function of the composition of the electrolyte. Unfortunately, these values are difficult to obtain.

As a rule, solubilities in solid electrolytes are lower than in liquid electrolytes. Cells involving solid electrolytes have, therefore, some merits in comparison to cells involving liquid electrolytes, but it must be ascertained that the error resulting from electronic conduction is sufficiently low when a solid electrolyte is used.

This survey has been used as a basis for the selection of cells which were considered to be particularly promising for the determination of standard molar free energies of formation of metallurgically important compounds at elevated temperatures.

In a separate paper (18) results of emf measurements on galvanic cells involving solid electrolytes are presented. Therefrom the standard molar free energies of formation of CoO, NiO, Cu_2O, Ag_2S, Ag_2Se, PbS, and several phases of the system Ag-Te have been deduced. Experimental investigations have been made exclusively with solid electrolytes in order to show new potential uses, but further investigations on cells involving liquid electrolytes are likewise desirable. To obtain reliable results, it will be necessary to determine solubilities of the reactants and reaction products in liquid electrolytes for an estimate of the contribution of transference effects with the help of formulas derived above.

Emf measurements may be considered especially for the investigation of compounds which are difficult to reduce by means of hydrogen or carbon monoxide and, therefore, do not lend themselves readily for gas equilibrium investigations. Treadwell and his associates (14, 26, 30) have shown the usefulness of emf measurements in the case of magnesium

oxide, aluminum oxide, and aluminum chloride. Adaption of emf measurements to thermodynamic investigations on titanium and zirconium compounds may be possible. Use of emf measurements for thermodynamic investigations on the system uranium-oxygen has been discussed in a separate report (51).

Manuscript received August 9, 1956. The paper is based on a thesis submitted by Kalevi Kiukkola in partial fulfillment of the requirements for the D.Sc. degree, Massachusetts Institute of Technology. Work was done under Contract AT(30-1)-1002 with the U.S.A.E.C.

Any discussion of this paper will appear in a Discussion Section to be published in the December 1957 JOURNAL.

REFERENCES

1. R. Lorenz, Die Elektrolyse geschmolzener Salze, Vol. 3, Knapp, Halle (1906).
2. M. Katayama, *Z. physik. Chem.*, **61**, 566 (1908).
3. H. Reinhold, *Z. anorg. u. allgem. Chem.*, **171**, 181 (1928).
4. E. J. Salstrom and J. H. Hildebrand, *J. Am. Chem. Soc.*, **52**, 4650 (1930).
5. E. J. Salstrom, *ibid.*, **55**, 4426 (1936).
6. E. J. Salstrom, *ibid.*, **56**, 1272 (1934); E. J. Salstrom, T. J. Kew, and T. M. Powell, *ibid.*, **58**, 1848 (1936).
7. G. Grube and E. A. Rau, *Z. Elektrochem.*, **40**, 352 (1934).
8. U. Croatto and C. Bruno, *Ricerca Sci.*, **17**, 1998 (1947).
9. R. Lorenz and M. G. Fox, *Z. physik. Chem.*, **63**, 109, 121 (1908).
10. R. Lorenz and H. Velde, *Z. anorg. u. allgem. Chem.*, **183**, 81 (1929).
11. J. H. Hildebrand and A. Wachter, *J. Am. Chem. Soc.*, **52**, 4655 (1930).
12. J. H. Hildebrand and G. C. Ruhle, *ibid.*, **49**, 722 (1927).
13. E. J. Salstrom and J. H. Hildebrand, *ibid.*, **52**, 4641, 4650 (1930).
14. W. D. Treadwell, A. Ammann, and Th. Zürrer, *Helv. Chim. Acta*, **19**, 1255 (1936).
15. C. Wagner, *Z. physik. Chem.*, **B32**, 447 (1936).
16. W. Jost and K. Weiss, *Z. physik. Chem. N. F.*, **2**, 112 (1954).
17. C. Wagner, *Z. physik. Chem.*, **B21**, 25 (1933).
18. K. Kiukkola and C. Wagner, *J. Electrochem. Soc.*, to be published.
19. C. Wagner, *Z. Elektrochem.*, **60**, 4 (1956); Proc. Internat. Committee of Electrochemical Thermodynamics and Kinetics, 1956.
20. J. B. Wagner and C. Wagner, *J. Chem. Phys.*, June 1957.
21. C. Wagner and W. Traud, *Z. Elektrochem.*, **44**, 391 (1938).
22. K. Nagel, *ibid.*, **44**, 637 (1938); E. Lange and K. Nagel, *ibid.*, **44**, 792, 856 (1938).
23. I. M. Kolthoff and C. S. Miller, *J. Am. Chem. Soc.*, **62**, 2171 (1940).
24. L. Wolff, *Z. Elektrochem.*, **20**, 19 (1914).
25. R. H. Gerke, *J. Am. Chem. Soc.*, **44**, 1684 (1922).
26. W. D. Treadwell and L. Terebesi, *Helv. Chim. Acta*, **18**, 103 (1935).
27. D. G. Hill and R. Porter, AEC Report Contract AT-(40-1)-1526, Sept. 15, 1953.
28. W. D. Treadwell, *Z. Elektrochem.*, **22**, 414 (1916).
29. H. Reinhold, *ibid.*, **40**, 361 (1934).
30. W. D. Treadwell and L. Terebesi, *Helv. Chim. Acta*, **16**, 922 (1933).
31. F. Haber and S. Tolloczko, *Z. anorg. Chem.*, **41**, 407 (1904).
32. B. A. Rose, G. J. Davis, and H. J. T. Ellingham, *Disc. Faraday Soc.*, **4**, 154 (1948).
33. A. Sator, *Compt. rend.*, **234**, 2283 (1952).
34. R. Suchy, *Z. anorg. Chem.*, **27**, 152 (1901).
35. G. Tammann, *Z. anorg. u. allgem. Chem.*, **133**, 267 (1924).
36. L. Holub, F. Neubert, and F. Sauerwald, *Z. physik. Chem.*, **A174**, 161 (1935).
37. R. Lorenz, *ibid.*, **130**, 39 (1927).
38. R. Lorenz and F. Michael, *ibid.*, **A137**, 1 (1928).
39. F. Oppenheimer, *Z. anorg. u. allgem. Chem.*, **189**, 297 (1930).
40. K. E. Schwarz, *Z. Elektrochem.*, **45**, 740 (1939); **47**, 144 (1941).
41. D. F. Smith and H. K. Woods, *J. Am. Chem. Soc.*, **45**, 2632 (1923).
42. C. G. Maier, G. S. Parks, and C. T. Anderson, *ibid.*, **48**, 2564 (1926).
43. C. G. Maier, *ibid.*, **51**, 194 (1929).
44. A. A. Noyes and E. S. Freed, *ibid.*, **42**, 476 (1920).
45. I. A. Makolkin, *Zhur. Fiz. Khim.*, **16**, 13, 18 (1942).
46. J. R. Coates, A. G. Cole, E. L. Gray, and N. D. Faux, *J. Am. Chem. Soc.*, **73**, 707 (1951).
47. C. Wagner, *Naturwissenschaften*, **31**, 265 (1943).
48. F. Hund, *Z. physik. Chem.*, **199**, 142 (1952).
49. D. A. MacInnes, The Principles of Electrochemistry, pp. 226 ff., Reinhold Publishing Corp., New York (1939).
50. J. B. Wagner and C. Wagner, *This Journal*, 1957.
51. C. Wagner, "Thermodynamics of the System Uranium-Oxygen", AEC Report WAPD-144, July 23, 1955.

Growth of Silicon Crystals by a Vapor Phase Pyrolytic Deposition Method

R. C. Sangster,[1] E. F. Maverick, and M. L. Croutch

Research and Development Department, Semiconductor Division,

Hughes Aircraft Company, Culver City, California

A study has been made of the feasibility of growing Si crystals by the reaction of gaseous $SiBr_4$ with H_2 at the surfaces of hot Si seed filaments (1). The immediate objective has been to produce deposits of a purity and a crystal perfection sufficient for semiconductor device purposes. An ultimate objective has been the deposition of arbitrary, complex, *p-n* junction structures by control of the types and amounts of impurities deliberately introduced into the process gas stream. This is a partial report covering the more interesting observations and results.

$SiBr_4$ has been produced by reaction of Br_2 with hot Si (2) and has been purified by fractional distillation and chromatographic adsorption techniques. The product normally used was spectrographically pure according to Harvey's semiquantitative method (3).

The deposition reaction has been assumed to be

$$2H_2(g) + SiBr_4(g) = Si(s) + 4HBr(g)$$

Computations based on data in the literature (4) give for this reaction $\Delta H^\circ = 50.4 \pm 1.2$ kcal/mole in the range 0°-1500°C, and indicate that ΔF° is favorable above about 1000°C. This reaction has been studied in the apparatus shown in Fig. 1.

Description of Apparatus

Purified H_2 and He—clean, dry and oxygen-free—are supplied to the deposition apparatus of Fig. 1 from other equipment not shown. He is used to flush the apparatus before and after the runs. During the runs, part of the purified H_2 is bubbled through the boiling $SiBr_4$ in the "pot." The resulting H_2-$SiBr_4$ mixture is stripped down to a known concentration in the thermostated "stripping condenser." The remaining, make-up H_2 is added to the gas emerging from the condenser to produce the desired reaction mixture. This mixture passes through a glass tube system, heated to prevent condensation, into the reaction tube. The gas passes first over a hot (1100°-1300°C) Ta impurity-scavenging filament and then over the Si filament. The effluent gases then enter more apparatus not shown here and are disposed of.

The Si filaments are 0.02-0.06 in. (0.5-1.5 mm) thick, 0.05-0.10 in. (1.25-2.5 mm) wide, and 1.5-2.5 in. (3.7-6.2 mm) long. They are mounted on the power leads by Ni and Ta wire loops anchored to the ends of the filaments by bundles of tightly wound, fine Ta wire. Glass-to-metal seals are used for the two central power leads. The two end power leads consist of heavy tungsten wires sliding in close-fitting capillary tubes. Bits of "Tackiwax" provide a flexible seal between the wires and the capillaries. Spring tension applied to the tungsten leads keeps the filaments taut. The filament power supplies each consist of a Variac, a rheostat, and an ammeter, in series. The rheostat is necessary in the case of the Si filaments because of the negative resistance characteristics of Si. The useful filament temperature range is 1100°-1350°C. Below 1100°C the reaction yield drops off rapidly. Above 1350°C difficulties due to the alloying of Si and Ta are encountered.

The filament temperatures can be measured optically with a precision of ±10°-20°C. The precision of setting and determining the H_2 flow rates is ±2.5%, and the $SiBr_4$ concentration ±10%.

Semi-Empirical Analysis of the Deposition Process

Basic phenomena.—The basic phenomena determining the physical nature of the deposit seem to be

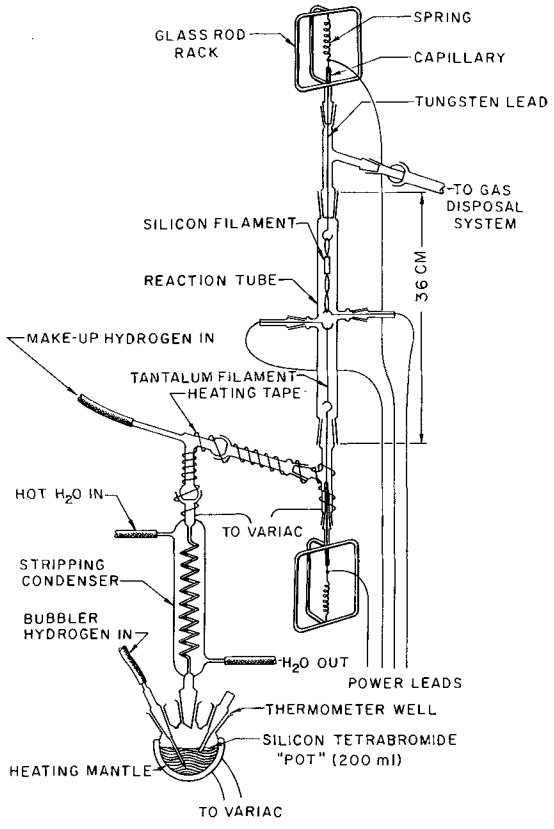

Fig. 1. Deposition apparatus

[1] Present address: Texas Instruments Incorporated, 6000 Lemmon Avenue, Dallas, Texas.

the following: (*a*) competitive nucleation rates for oriented and disoriented growth; (*b*) mobility of the atoms on the surface of the deposit; (*c*) rate of deposition of the Si; and (*d*) turbulence and inhomogeneity of the process gas at the surface of the filament.

Nucleation for disoriented growth obviously must be suppressed when monocrystalline deposits are desired. The mobility of the atoms on the surface of the deposit should be such that an atom can get to a normal surface lattice site before the next layer of atoms is deposited, but not so high that many can be attracted to regions of incipient disoriented or dendritic growth. The deposition rate should be such that atoms are supplied as rapidly as the growing crystal can accept them, but not so fast that nucleation for polycrystalline growth is favored, or so slow that the atoms have a chance to migrate very far before the next layer is put down. The turbulence of the process gas must be high enough to insure reasonably thorough contact with the filament surfaces, but not so high as to lead to pronounced inhomogeneity near the surfaces; such inhomogeneity can produce local areas of either high or low deposition rate and can otherwise favor disoriented or nonuniform growth.

Effects of process variables.—Proper pretreatment of the Si seed surface is necessary if oriented growth is to be obtained. Chemical etching is desirable for producing a superficially clean surface, but all such techniques apparently leave an oxide film which must be destroyed before deposition is begun. For this purpose the only successful technique that has been found is preheating in a stream of pure H_2 for 30-60 min at 1275°C.

The purity of the $SiBr_4$ affects directly the chemical purity and therefore the electrical properties of the deposit; equally important, however, is the fact that some impurities can make it impossible to obtain monocrystalline deposits. Moreover, even when clean, dry, oxygen-free H_2 and highly purified $SiBr_4$ are used, it is still necessary to use a hot Ta scavenging filament for further purification of the gas.

The thermodynamic effects of the filament temperature are, of course, basic to the entire process. In addition, temperature affects the physical nature of the deposit through its influence on the rates of nucleation and on the mobility of the atoms on the surface of the deposit. Nucleation for disoriented growth is favored by the higher temperatures; the mobility of the atoms is increased.

The effects of changes in the $SiBr_4$ concentration are caused primarily by changes in the rate at which the Si is deposited. The accompanying variation in the total amount of Si which happens to be deposited in a given run is important only secondarily. In general, dendrite formation is suppressed and deposit uniformity favored by the higher $SiBr_4$ concentrations.

Longer running times lead to the deposition of more material, other conditions being equal. Whenever the total amount of the deposit increases, characteristic changes occur. The deposits become thicker; dendrites, if present, grow larger; the smaller dendrites are crowded out by the larger; and there are more opportunities in general for disoriented growth.

The most important effects of the process gas flow rate are due to the turbulence and inhomogeneity of the gas phase. The higher the flow rate, the greater the turbulence, and the more dendritic the deposit. However, with the composition of the gas phase held constant, the higher flow rates also involve higher Si deposition rates, and this tends to counteract some of the effects of the increased turbulence.

In the case of the reaction chamber diameter, turbulence is again the important factor. The larger diameters lead to greater effective turbulence at the filament surface. This is in direct contrast to the normal expectation that a constant volume flow rate and a larger diameter will yield a less turbulent flow. The thermal convection effects existing in the deposition chamber complicate much of the reasoning about turbulence.

With regard to position on the filament, the deposits on the lower portions of the filaments are cooler, thicker, and usually more impure than those higher up.

Results

Deposits of Si on Si seed filaments have been produced with properties adequate for experimental device purposes (*see* Fig. 2 and 3). Both metallographic sectioning and x-ray diffraction techniques show that the best deposits have the same orientation as the base filaments. There are only faint indications of the junctions between the seeds and the deposits, and there is relatively little indication of lineage structure. The deposited Si is normally *n*-type, with a resistivity in the range 1-100 ohm-cm, as computed from the results of two-point probe measurements on the filament before and after deposition. The existence of *p-n* junctions between *n*-type deposits and *p*-type seeds makes it possible to apply Gudmundsen's (1) micro-optical probe technique to measure the minority carrier lifetimes. The

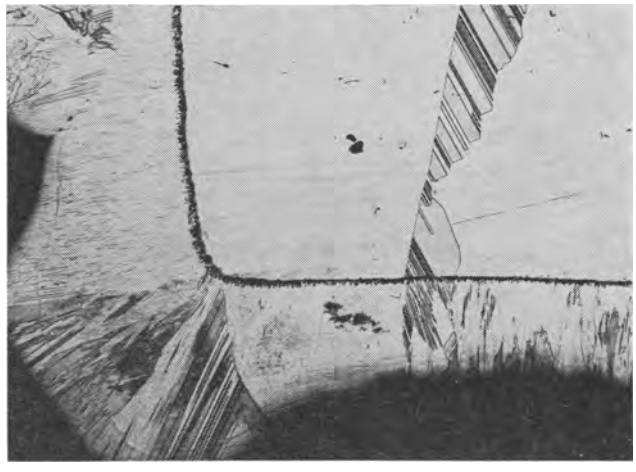

Fig. 2. Part of a metallographic cross section of the first filament produced with a reasonably uniform, oriented deposit. The deposit is about 0.010 in. (0.25 mm) thick at the lower right. The area toward the upper right represents part of the original seed. Several characteristic structures are present: a layer of inclusions at the seed-deposit interface, propagation of seed structures into the deposit, and lineage and polycrystalline regions in the deposit proper.

Fig. 3. Part of a metallographic section of a very good filament. The seed is at the left, the deposit at the right. The total width of the picture corresponds to about 0.003 in. (0.075 mm). Most of the apparent imperfections are surface scratches and grain.

lifetimes found for the deposits range from 0.1 to 1 μsec.

Optimum conditions for the formation of these deposits involve $SiBr_4$ concentrations in the range 0.6-1.0 mole %, total H_2 flow rates of about 1.5 l/min, and filament temperatures in the range 1100°-1200°C, when a reaction chamber with a 25 mm inner diameter is used. Under these conditions 0.005-0.010 in. (0.125-0.25 mm) of Si/hr is deposited.

Deposits can also be obtained on both Si and Ta filaments in the form of dendrites which have large, well-formed, pyramidal endcaps, with face edges 0.01-0.02 in. (0.25-0.5 mm) long. Individual dendrites of this sort might be useful in some point-contact devices. Optimum reaction conditions for the formation of this type of deposit are a $SiBr_4$ concentration of about 0.3 mole %, a total H_2 flow rate of 1-1.5 l/min, and a filament temperature of 1275°C, with a reaction tube having a 25 mm inner diameter.

Above approximately 1100°C, about 40% of the input $SiBr_4$ reacts to deposit Si, with no apparent dependence on the temperature and with relatively little on the other reaction conditions, within the ranges covered. There appears to be a maximum in the rate of deposition vs. concentration curve at about 0.6-0.7 mole % $SiBr_4$.

Acknowledgments

The authors wish to acknowledge the aid of the many individuals in these laboratories who helped with the different specialized phases of this work. This project was part of Contracts No. DA-36-039 SC-42574 and DA-36-039 SC-56755 with the United States Army Signal Corps. The authors are grateful to the Signal Corps for permission to publish.

Manuscript received May 2, 1956.

Any discussion of this paper will appear in a Discussion Section to be published in the December 1957 JOURNAL.

REFERENCES

1. Final Report No. SC-14A-F, "Silicon Transistor," Signal Corps Contract No. DA-36-039 SC-42574, Hughes Aircraft Co., Culver City, California (October, 1953); Final Report No. SC-14-F, "Silicon Transistor," Signal Corps Contract No. DA-36-039 SC-56755, Hughes Aircraft Co., Culver City, California (December, 1954).
2. J. W. Mellor, "A Comprehensive Treatise on Inorganic and Theoretical Chemistry," Vol. VI., pp. 977-978, Longmans, Green and Co., New York (1925).
3. C. E. Harvey, "A Method of Semi-Quantitative Spectrographic Analysis," Applied Research Laboratories, Glendale, Calif. (1947).
4. F. D. Rossini, D. D. Wagman, W. H. Evans, S. Levine, and I. Jaffe, *U. S. Natl. Bur. Standards Circ. 500* (1952); K. K. Kelley, *U. S. Bur. Mines Bull.*, **476**, 241 (1949); *ibid.*, **477**, 147 (1950); O. Kubaschewski and E. Ll. Evans, "Metallurgical Thermochemistry," Butterworth-Springfield, London (1951); L. L. Quill, Editor, "The Chemistry and Metallurgy of Miscellaneous Materials," NNES IV-19B, McGraw-Hill Book Co., Inc., New York (1950).

Notes on Hydrogen Overvoltage

I. Maximum Concentration of Atomic Hydrogen on the Surface of a Working Cathode

Hugh W. Salzberg

College of the City of New York, New York, New York

and

Sigmund Schuldiner

Naval Research Laboratory, Washington, D. C.

Several recent papers (1-3) have expressed the idea that the rate of direct combination of hydrogen atoms on a cathode surface is too slow to support currents of more than 10^{-1} amp/cm^2. In consequence, removal of atomic hydrogen from the surface would have to occur by an alternative mechanism, specifically the electrochemical combination of an adsorbed atom and a hydronium ion. However, calculations indicate that the rate of direct atomic combination is great enough to support extremely high current densities. These calculations and some conclusions drawn from them appear below.

The rate of combination of hydrogen atoms on a surface may be expressed as follows

$$r = K\,(kT/h)\,H^2\,(f^*/F^2_H)\,\exp -\Delta H_0/RT \qquad (I)$$

where r is the number of combinations/cm^2/sec, (kT/h) is the Eyring frequency factor, H is the number of hydrogen atoms/cm^2 of surface, f^* is the partition function of the activated complex, f_H is the partition function of the hydrogen atom, ΔH_0 is the heat of activation at 0°K, and K is the transmission coefficient. The dimensions of $f^*/f^2_H \exp -\Delta H_0/RT$ are cm^2-molecule/atom^2 and the term is equal to $\exp - G^*/RT = K = H^*/H^2$, where G^* is the free energy of activation and H^* refers to the activated complex.

Values for the partition function depend on the mobility of the atoms, i.e., for immobile atoms there are no rotational or translational contributions. Since vibrational partition functions are of the order of unity at room temperature, the ratio of partition functions in this case is approximately unity.

For mobile hydrogen atoms, as in a two-dimensional monatomic gas, the partition functions include translational terms only since these mobile hydrogen atoms have 2 degrees of translation freedom and no modes of rotational or vibrational freedom. Therefore (5)

$$f_H = 2\,\pi\,mkt/h^2$$

where m is the mass of a hydrogen atom.

The activated complex has two degrees of translational freedom and only one mode of rotation, since the other rotational mode of this linear molecule would be normal to the surface. The normal mode of vibrational freedom of this diatomic molecule is replaced by translation in the coordinate of decomposition. Therefore

$$f^* = (4\,\pi\,mkt/h^2)\,(4\,\pi^2\,kt\,\sigma^2\,m/h^2)^{1/2}$$

σ is the distance between centers of the atoms in the activated state, here taken as 0.74×10^{-8} cm. Therefore, in the case of a mobile atom the ratio of partition functions is equal to $2\sigma h/(mkt)^{1/2}$. The over-all equations can then be expressed as

$$r_{\text{mobile}} = (kT/h)\,\sigma\,H^2\,[h/(mkt)^{1/2}] \exp -\Delta H_0/\text{RT}$$
$$= H^2\,\sigma\,(kT/m)^{1/2} \exp -\Delta H_0/RT \qquad (IIa)$$

The term $H^2\,\sigma\,(kT/h)^{1/2}$ is equal to the collision number, as it should be.

$$r_{\text{immobile}} = (kT/h)\,H^2\,(S/2L) \exp -\Delta H_0/RT \qquad (IIb)$$

where S is the number of adjacent sites per atom (either 2 or 4), and L is the number of sites/cm^2 (about 10^{15}). The factor $(S/2L)$ is necessary since only adjacent atoms can combine.

Inserting the correct numerical values into the first terms on the right hand sides of (IIa) and (IIb) gives

$$r_{\text{mobile}} = 1 \times 10^{-3}\,H^2 \exp -\Delta H_0/RT$$
$$r_{\text{immobile}} = 3 \times 10^{-3}\,H^2 \exp -\Delta H_0/RT$$

Surprisingly enough it seems to make little difference in the numerical calculation whether the hydrogens are considered mobile or immobile. However, since immobility seems more probable, it is assumed that the rate is $3 \times 10^{-3}\,H^2 \exp -\Delta H_0/RT$.

To obtain the values of ΔH_0, it is assumed that this will be equal to ΔH, the experimental activation energy. ΔH_0 is less than ΔH by only 300 cal in the case of a mobile layer and 600 cal in the case of an immobile layer.

ΔH has been determined only for Pt, since for cathodes at which combination is not rate-determining there is no obvious way of determining the activation energy for a nonrate-determining step. It was found to be about 2 kcal/mole (3). Estimates have been made (1-4) to the effect that on other metals the activation energy for combination should be even less than 2 kcal/mole. These estimates are based on the ideas that: (*a*) the combination rate is essentially a surface radical reaction and should be very rapid; (*b*) the more tightly the atom is held to the surface the lower the energy of the initial state and therefore the higher the energy of activation should be. Pt has a very high heat of adsorption of H. For other metals with lower heats of adsorption, the energy of activation for combination should be less than that on Pt.

Also, on a theoretical basis [(5) p. 214], the specific rate constant for the homogeneous gas phase combination of hydrogen atoms has been estimated to be given by the expression

$$k = k' \times 2.98 \times 10^{14} \text{ cc mole}^{-1} \text{ sec}^{-1}$$

where k' is the transfer coefficient. The free energy of activation calculated from this is less than 1 kcal/mole. The entropy of activation at a standard state of 1 mole/cc is estimated by the same source to be 5.3 e.u. The energy of activation would therefore be about 2½ kcal/mole or less for the gas phase reaction. Normally the heterogeneous reaction would be expected to have a lower activation energy, or at the most only a slightly higher value. Therefore the value of ΔH is taken as being about 3 kcal or less with an upper limit of 6 kcal. This is three times that determined for Pt and more than twice the estimated value for the gas phase reaction.

Numerical Calculations

This provides all the information needed to calculate the rate at any surface coverage and the surface coverage at any given combination rate. Expressing the specific rate in terms of current density by multiplying by $2F/N$, i.e., two electrons per combination, gives

$$i_{\text{comb.}} = 6 \times 10^{-21}\,H^2 \exp -\Delta H_0/RT \qquad (III)$$

If the surface is saturated with hydrogen atoms, H is 10^{15}. The following combination currents result for indicated values of ΔH:

i (amp/cm^2)	ΔH (kcal/mole)
10^9	0
6×10^6	3
2×10^4	6
50	10

Even with the extremely high value of activation energy of 10 kcal/mole, the calculated combination rate is 50 amp when the surface is saturated.

To determine the surface concentration at any particular current density, it is necessary to relate

the rate of direct combination to the over-all current density.

If the rate-determining step is direct combination, the over-all rate is the combination rate. However, if the electrochemical mechanism is the rate-determining step, it must be at least 100 times as fast as the direct combination. Consequently, direct combination is at most one one-hundredth of the observed current density and the maximum concentration of atomic hydrogen is that which supports this fraction of the over-all current density. If the discharge is the rate-determining step, maximum coverage may be obtained by assuming a minimum rate of removal which will equal the current.

From these considerations, for the various rate-determining mechanisms the combination rate at any observed over-all current can be calculated, and from this a maximum value of the surface concentration of hydrogen can be obtained using Eq. (III). Table I shows values of hydrogen atom concentration, expressed as the fraction of the total surface covered, at a current density of 1 amp/cm^2.

From Table I it can be seen that only 2% of the surface would be covered at a current density of 1 amp/cm^2 even if the activation energy were 10 kcal, which is five times that of the observed value for combination on Pt.

Table I

Rate-determining step	ΔH = 3 Kcal	6 Kcal	10 Kcal
Slow combination	$10^{-6.8}$	$10^{-4.6}$	$10^{-1.7}$
Slow discharge	$10^{-6.8}$	$10^{-4.6}$	$10^{-1.7}$
Electrochemical combination	$10^{-7.8}$	$10^{-5.6}$	$10^{-2.7}$

Conclusions

In the case of the combination of hydrogen atoms on a cathode surface, the frequency factor is independent of the mobility of the adsorbed hydrogen.

The surface of a working cathode is only sparsely covered with hydrogen atoms even at high current densities.

The electrochemical mechanism may be rate determining but not because the combination rate is too slow to support the current.

Reduction of cations at a cathode would not seem to be due to the action of adsorbed hydrogen atoms but would take place at the metal surface, i.e., such reduction is electrochemical, not chemical.

The action of depolarizers, such as KNO_2 in the study of dissolution of metals in acids (6), seems to be something other than removal of hydrogen atoms from the surface.

Manuscript received March 12, 1956.

Any discussion of this paper will appear in a Discussion Section to be published in the December 1957 JOURNAL.

REFERENCES

1. P. Parsons and J. O'M. Bockris, *Trans. Faraday Soc.*, **47**, 920 (1951).
2. J. O'M. Bockris and A. M. Azzam, *ibid.*, **48**, 145 (1952).
3. J. O'M. Bockris and E. C. Potter, *This Journal*, **99**, 169 (1952).
4. K. J. Laidler, Private communication.
5. S. T. Glasstone, K. J. Laidler, and H. Eyring, "Theory of Rate Processes", McGraw-Hill Book Co., Inc., New York (1950).
6. M. B. Abramson and C. V. King, *J. Am. Chem. Soc.*, **61**, 2290 (1939).

Electrical Conduction in Silicon Carbide

G. H. Fetterley

Norton Company, Chippawa, Ontario, Canada

ABSTRACT

Commercial SiC is a semiconductor that can be prepared as predominantly *n*- or *p*-type at will. The body conductivity is linear and determines the behavior of SiC heating elements, which are usually made from *n*-type. The interfacial conductivity is much lower, nonlinear, and is exploited in lightning arresters, which are made from *p*-type. While the electrical behavior of this material is poorly understood in detail, the broad outlines are summarized in terms of semiconductor theory.

SiC is manufactured and used on a large scale as an abrasive and refractory, and is a familiar material to workers in the electrothermic industries. More interesting from a theoretical point of view and of more recent development are its applications as an electrical conductor. In the following, the two basic types of electrical application are described, followed by a discussion of the attempts to explain the observed phenomena. The objective is to present a survey for the nonspecialist and a guide to the widely scattered literature on this subject.

Crystal Structure

When SiC is formed at a temperature of 2000°C or lower, it has a cubic structure. This modification has been designated beta silicon carbide. It has been prepared only in very small crystals, and the bulk properties have not been reported to any extent in the literature. Attempts to hot press or sinter the crystals to form a coherent body cause a transformation to the alpha form, which is the ordinary SiC of commerce.

Alpha silicon carbide occurs in a number of hexagonal and rhombohedral crystal types, which have been investigated extensively by Thibault (1), Ramsdell (2), and Lundqvist (3). A review of the literature on crystal structure has been compiled by Harman and Mixer (4).

Since it has been impossible to isolate specimens of the various types of alpha silicon carbide the relationship, if any, between crystal form and electrical properties has not been clarified. Therefore, this approach is not considered further here. The remainder of the text deals for the most part with the usual alpha type, and essentially without consideration of the various crystal habits described by Thibault, Ramsdell, and Lundqvist.

Commercial Silicon Carbide

Transparent crystals of SiC, colorless or pale yellow to greenish, occur as occasional isolated pockets in commercial ingots. This material is of no importance commercially. In spite of the attractive appearance of the crystals, chemical analysis shows that impurities are still present to the extent of possibly 0.3%.

Green SiC is available commercially in moderate quantities, and is used in the manufacture of certain grades of grinding wheels and in heating elements. It has been shown to conduct electricity principally by flow of electrons, and is classed as an *n*-type or electron excess semiconductor.

So-called gray SiC is the standard abrasive and refractory material, and is the type usually encountered under the name silicon carbide and various trade names. The color of individual crystals varies widely through dark green, blue, various shades of dark gray, and black. Electrical properties are quite variable, but charge is transferred principally by flow of holes, and this material is classed rather loosely as a *p*-type or electron defect semiconductor.

Gray SiC may be called black if it is unusually dark in color. However, this designation usually means a material to which alumina has been added to produce strong electron defect conduction. This material is used to make nonlinear resistors of various kinds, ranging in size from automatic volume controls the size of a dime to large lightning arresters several feet high.

While the nomenclature described above has grown up with the industry and is serviceable within its limitations, it has been shown by Kendall (5) that the color and mechanism of conduction can be made independent of each other to a considerable degree by special techniques of preparation. In general, Kendall's light colored crystals were *n*-type, but black ones could be made either *n*-or *p*-type at will. The above classification should therefore be regarded only as a useful guide to currently available commercial products.

Table I. Chemical analysis of commercial silicon carbides, in per cent

	Colorless	Green	Gray	Black
SiC	99.7	99.0	98.7	98.7
Free C	0.11	0.30	0.20	0.20
Free SiO_2	0.02	0.00	0.75	0.71
Al	<0.05	0.05	0.20	0.30
Fe	<0.05	<0.05	<0.05	<0.05
Ca	<0.03	<0.03	0.03	0.03
Mg	<0.05	<0.05	<0.05	<0.05

The various types of commercial SiC do not differ very much in chemical analysis. The most obvious difference is in the aluminum content. The colorless material is purer but still far short of the purity required for basic research on electrical conduction. Table I shows typical analyses for samples of SiC that have undergone a severe acid treatment to remove surface contamination.

Silicon Carbide Heating Elements

When granular SiC is pressed or rammed with a temporary bond and subsequently fired at 2000°-2500°C, the individual grains sinter together to form a strong, refractory and somewhat porous body. When suitably processed, this body is a fairly good electrical conductor, having a specific resistance of about 0.1 ohm-cm at 1000°C and not more than about 0.2 ohm-cm at room temperature. It can be exposed to oxidizing conditions at temperatures as high as 1400°C for several thousand hours without serious loss in strength or change in electrical resistance. Since the individual grains are welded together at points of contact, the electrical properties are determined by the body conductivity of the crystals. Current is proportional to voltage, and conduction is linear by definition. Simple, rugged heating elements made of sintered SiC have been available for many years, both in Europe and North America, under various trade names.

While heating elements can be made from any of the commercially available types of SiC, the green n-type is used ordinarily. The electrical characteristics are more uniform than those of the black type, the change in resistance with temperature is smaller, and the temperature coefficient of resistance is positive in the usual operating range.

The commercial development of SiC heating elements in this country during the last thirty years has involved two complementary and concurrent mechanisms: (*a*) a steady improvement in physical properties, both in mechanical ruggedness and resistance to deterioration in service, and (*b*) a gradual education of industrial consumers to the advantages of this method of heating, and the development of practical electric kilns.

An important feature of the modern SiC heating element is the so-called "cold end". Integral end sections of the elements are impregnated with silicon on other materials to make them highly conducting. Since the end sections are strong mechanically and the same diameter as the central heating section, the element is easily mounted and replaced, and little electrical energy is wasted outside the heating zone of the kiln.

SiC heating elements were originally used only in laboratory furnaces and in small kilns for high grade ceramic ware, but are now being used in many industries such as the currently booming ceramic dielectric industry. At least two large abrasive plants in the United States use electric kilns for firing grinding wheels.

Mann (6) recently published a discussion of SiC heating elements as used in Europe, largely from the point of view of operating economics. The art of making such heating elements has received little attention in the scientific and industrial literature, and is best studied from patents. It has been impossible to prepare a list of patents for inclusion in the bibliography of this review.

Silicon Carbide Nonlinear Resistors

SiC nonlinear resistors operate by entirely different mechanism from heating elements and are prepared in a different way. For this purpose black (p-type) SiC is used to form a column of discrete grains, which is made into a monolith by adding a ceramic bond and firing in a kiln. The temperature must be high enough to mature the bond, but much too low to sinter the grains together. Contacts are added to the ends with a metal spray. A body made in this way has the following characteristics: (*A*) It can conduct at very high current densities for short periods of time without damage. As much as 3000 amp/in.^{2} can be carried for a few microseconds. (*B*) Most of the voltage drop across the resistor occurs at the interfaces between the grains. Ohm's law becomes completely invalid and an approximate empirical relationship is used

$$V = KI^n \qquad (I)$$

where V is the voltage drop, K is a constant depending on the geometry of the body and the manufacturing process, I is current, and n is an empirically determined exponent. For small resistors that are used at current densities measured in milliamperes per square inch, n ranges between 0.20 and 0.35. At current densities of hundreds of amperes per square inch, as found in lightning arrester applications, n may be as low as 0.1.

SiC nonlinear resistors lend themselves readily to use in lightning arresters, since the current passed increases very rapidly with increasing voltage. They have a pronounced valving action and do not allow high voltages to be built up across them. In a typical installation, a SiC nonlinear resistor and a series of air gaps are connected in series from the line to ground. A sudden increase in voltage, such as is caused by a lightning discharge, breaks down the gap and a large current flows to ground, limiting the peak voltage on the line to a safe value. As soon as the line voltage returns to normal, the resistor reduces the current to such a low value that the arc across the gaps goes out.

Such lightning arresters were first used about 1908, when two patents were issued. Since that time development has been continuous and there are now at least five large manufacturers of SiC lightning arresters in this country. Recently, small nonlinear

SiC resistors, down to a watt or two in rating, have become increasingly available for use as surge suppressors, automatic volume controls, and for many applications in electronic equipment.

An outstanding paper on SiC nonlinear resistors was published in 1946 by Ashworth, Needham, and Sillars (7). This review is recommended as a basic text on the subject. Teszner *et al.* (8) have made an extensive investigation of the effect of the bond on the properties of lightning arrester blocks. An excellent article on lightning arresters was published by Roth (9) in 1954. Thien-Chi and Vergnolle (10) and Zückler (11) have published papers of general interest recently. The literature noted above is essentially practical in outlook. More theoretical papers are listed below.

Pure Silicon Carbide

The past ten years have seen tremendous advances in the basic theory of semiconductors. Such advances are possible only when a large commercial demand, either actual or potential, is coupled with adequate materials and facilities for research. The need for microwave rectifiers, followed by the discovery of transistor action, and the pressure for miniaturization of electronic components provided the impetus. In addition the most promising materials, Ge and Si, melt at readily attainable temperatures and can be prepared in extremely high purity. While SiC might potentially be equally useful as a semiconductor as Ge and Si, work on this material has been greatly hampered by the lack of specimens of high or even accurately known purity. SiC cannot be melted, sublimes with partial decomposition at about 2600°C, and its formation temperature under the usual conditions of manufacture is well above 2000°C. Under such handicaps it is not remarkable that this compound has not yet been made to the purity levels (impurities measured in parts per 10^9) required for basic research on semiconductors. In spite of these difficulties, three research groups have succeeded in recent years in preparing SiC of purity greatly exceeding that of the commercial material.

In 1931 Moers (12) reported the preparation of pure SiC by passing a gaseous mixture of hydrogen, silicon tetrachloride, and toluene over a filament heated to a temperature of at least 2200°C. Small, transparent yellow crystals grew on the filament. They were found by x-ray analysis to be of the cubic or beta modification, and were reported to be nonconducting, although no very serious attempt seems to have been made to measure their conductivity.

In 1947 Kendall and Yeo (13) described a development of the same process, and in 1953 Kendall (14) reported a further refinement of the technique. Using a carbon filament at 2100°-2200°C, and the mixture of gases noted above, he was successful in producing small, transparent yellow crystals of beta silicon carbide. Kendall and Yeo reported a readily measurable conductivity for all of their specimens, and noted that the deposited crystals conducted better than commercially prepared crystals. This may have resulted from the fact that their crystals were the beta modification, while the commercial crystals were almost certainly the alpha type. The few observations that have been made indicate that beta silicon carbide is probably a better conductor than the alpha type. Data available are not sufficient to show whether this apparent difference in conductivity is consistent.

Kendall determined the sign of the thermoelectric coefficient at room temperature and concluded that all yellow crystals were n-type. Black crystals could be made at temperatures below 2000°C and were usually found to be n-type, although commercial black SiC is p-type.

In 1955 Lely (15) reported a new approach to the problem of making the pure compound. By heating a SiC crucible from the outside to a temperature of 2500°-2600°C, he produced sublimed crystals for which he claimed a content of total impurities as low as 10^{-5} at. %. This figure represents a long step toward the purity required for research on semiconductors and probably exceeds anything done previously. The crystals were hexagonal, as would be expected in this temperature range, and the best ones were colorless and transparent. While Lely did not report conductivity figures, he apparently calculated the purity of 10^{-5} at. % from such measurements. If so, he must have obtained some crystals that were very low in conductivity.

Since atomic bonding in SiC is almost purely covalent, and since intrinsic conduction does not become significant below 1600°-1700°C, it is reasonable to expect that the pure compound is colorless, transparent, and substantially nonconducting at all ordinary temperatures. All the reported work supports this conclusion, in that the above array of properties is approached more and more closely as the purity increases. Therefore, it is assumed that the general nature of the pure compound is established, and that any explanation of the observed electrical properties of the commercial material must be based on the effects of various impurities that it contains.

Mechanism of Linear Conduction

The bare fact of electrical conduction by SiC is readily explained by the presence of impurities, especially those trivalent and pentavalent atoms that can occupy normal lattice sites. In general, a trivalent atom provides at its lattice site one less valence electron than is necessary to produce the four covalent bonds of the perfect SiC lattice. The missing electron acts as a hole that conducts very much as a positive electron would, with possibly a lower mobility. The only trivalent atom used commercially for this purpose is that of Al. Lundqvist (3) reported that the presence of Al favors the formation of the so-called type III modification of the hexagonal structure, but the resulting correlation between electrical properties and crystal type is probably coincidental.

A pentavalent atom provides at a lattice site one more than the number of electrons required for the normal covalent bonds. The excess electron is loosely bound and is easily raised to an energy level at which it can migrate through the lattice under

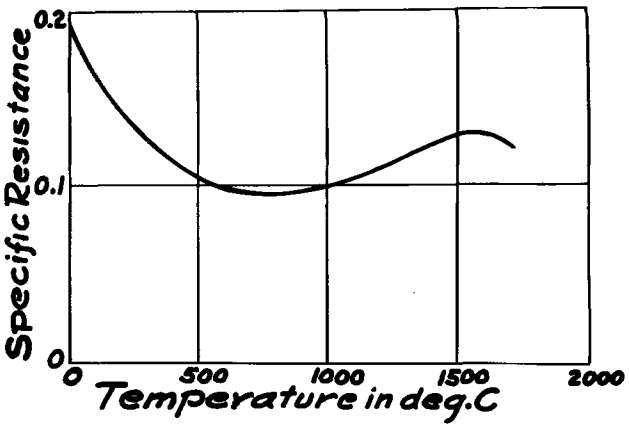

Fig. 1. Specific resistance in ohm-cm as a function of temperature for a typical SiC heating element.

the influence of an applied field. This phenomenon constitutes n-type conduction by definition.

It is instructive to examine a typical curve of specific resistance vs. temperature for a commercial SiC heating element (Fig. 1). The temperature scale has been divided rather arbitrarily into low, medium, and high ranges, respectively. In the low temperature region, the density of conducting electrons increases progressively with rising temperature as more and more electrons are released by thermal excitation from imperfect covalent bonds. These imperfect bonds occur at lattice sites occupied by atoms other than Si and C, or possibly where there is a local deficiency of C. The resistivity falls with increasing temperature, as is usually the case with semiconductors. In the medium temperature range, most of the available bonds have been broken and the number of conducting electrons changes little with temperature. In this range the thermal vibration of the lattice plays the leading role. Since this vibration interferes with the migration of conduction electrons, resistivity rises with increasing temperature. The conduction is essentially metallic, except for the low density of electrons as compared with typical metals. At about 1600°-1700°C, intrinsic conduction becomes significant as electrons are released from the normal covalent bonds, and the resistivity falls steeply with increasing temperature.

The "metallic" conduction range is of the greatest importance commercially, since the positive temperature coefficient of resistance confers a large degree of temperature stability on an electrically heated kiln. Heating elements made from gray SiC tend to have a higher initial resistance than those made from green SiC, and the range of negative temperature coefficient tends to extend over the metallic range and frequently to obscure it completely. This is probably the principal reason for the choice of green SiC as the raw material for commercial heating elements.

Theoretically it is possible for SiC containing nothing but Si and C to act as an impurity semiconductor as long as there are points in the crystal where the compound is at least locally nonstoichiometric. The existence of nonstoichiometric SiC has often been conjectured but never proved. The departure from stoichiometric proportions that would be necessary to explain the observed electrical effects is very much less than can be detected by chemical analysis, and there seems little likelihood that the question will ever be settled in this way. Lely (15) states rather positively that there is no evidence of any kind for the existence of nonstoichiometric SiC. He attributes the green color and conductivity to the presence of 0.0001-0.001% of pentavalent nitrogen, which would produce n-type conductivity as observed. Lely used a furnace with a protective atmosphere, and added various volatile halides to the gas to control the composition of the product. He found that Al and B additions promote p-type conductivity and that N and P cause n-type.

Kendall (14) produced SiC by deposition from the gas phase as noted earlier. By changing the Si/C ratio in the gases entering the furnace he was able to produce n- or p-type material at will, from which he concluded that he was obtaining a slight departure from stoichiometric proportions. If his starting materials were pure, his conclusion seems inescapable.

Summarizing the data, it seems likely that nonstoichiometric but otherwise pure SiC can be prepared under special conditions. The commercially important green variety seems to be an n-type semiconductor containing pentavalent nitrogen atoms on normal lattice sites. The ordinary gray SiC contains so many impurities that it may never be possible to explain its properties except in a qualitative way. As might be expected, it is quite variable electrically, and this variability extends down to individual crystals, where p-n junctions are not uncommon although the material is predominantly p-type. While black electrical grade SiC is also a comparatively impure product, the deliberate addition of Al swamps out the effect of the other impurities and results in stable and consistent p-type conductivity.

Mechanism of Nonlinear Conduction

In nonlinear SiC resistors the bulk resistivity of the crystals has no significant influence, since practically the entire voltage drop occurs at the interfaces between grains. Eq. (I) is sufficiently accurate for most purposes, but closer examination shows that n changes with current density if the latter is allowed to vary over a sufficiently large range.

In 1944 Kendall (16) reported measurements of voltage vs. current for single contacts between metal and SiC and between crystals of SiC. In the experiment most pertinent to the present discussion, he worked with a single contact between a green crystal and a black one. The range of current was from 10^{-10} to about 10^{-4} amp. Log-log voltage-current plots were approximately linear (n constant) over a current range of several powers of ten, but were far from linear when considered in their entirety. One of Kendall's curves is reproduced in Fig. 2. This example illustrates the fact that current flow between grains of SiC is a complicated phenomenon, and different mechanisms may be expected to play the leading role at different current densities.

Since the theory is controversial, it is well to examine first the empirical observations. To this end it

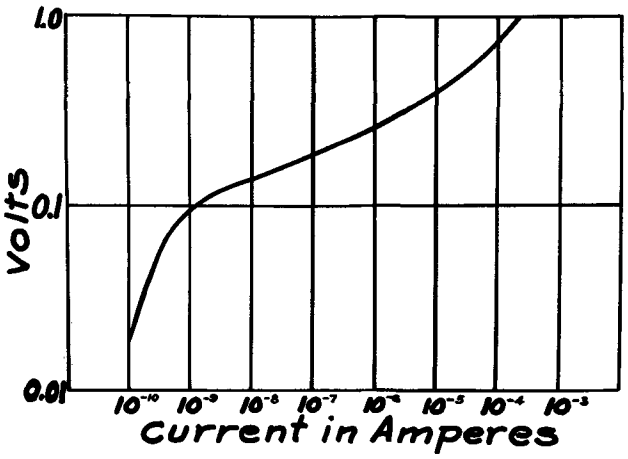

Fig. 2. Volt-ampere characteristic curve for a single contact between grains of SiC.

is convenient to speak of low, medium, and high current ranges.

In the low current range, current is proportional to voltage. Both Braun and Busch (17) and Kendall (16) made measurements in this range, and Kendall showed that for his particular crystals it extended up to a current density of about 10^{-9} amp/contact. The conclusion is clear that grain contacts conduct linearly at sufficiently low current densities.

The medium current range extends to 10^{-4}-10^{-3} amp/contact. In this range n of Eq. (I) is constant. The value of n is different for different specimens of SiC, but is within the range 0.20-0.35. The medium range of current densities is characterized by the fact that conduction is clearly nonlinear, and independent of secondary thermal effects caused by the dissipation of electrical energy at the contacts.

The high current range extends up to a current density at which the contacts suffer permanent damage from excessive heating, of the order of 0.1-1.0 amp/contact. This range is characterized by strong thermal effects, as shown by the appearance of a hysteresis loop in the voltage vs. current plot. Because of the thermal effects, it becomes difficult to attach a clear meaning to n, but the apparent value decreases to about 0.1. This low value of n is advantageous in lightning arrester applications, since it means that the nonlinear resistor has a pronounced "safety valve" action, and strongly resists any influence that tends to build up a high voltage across it.

With the above facts in mind, an attempt will be made to set up a model by which the various phenomena can be understood. Experience in this field has shown that a statement made today is likely to be proved wrong tomorrow. With this reservation in mind, it is still possible to trace some sort of logical path through the maze of experiment and argument that has grown up about this subject.

The basic fact to be explained is that the resistance of a single contact is much too high to arise from the known fairly low resistivity of the bulk material. This is true even if the true area of contact is a small fraction of the apparent area, leading to a so-called constriction resistance. Further, this contact resistance is nonlinear, the current changing much more rapidly than the impressed voltage. It is clear that a voltage-sensitive barrier to current flow exists at each grain to grain contact, and controversy has centered essentially about the nature of this barrier.

For a long time it was considered that the barrier was a solid mechanical one, made up predominantly of silica or siliceous materials. This theory received its strongest support from Braun and Busch (17). The assumption was reasonable, since the presence of such films on SiC crystals can be shown by electron diffraction. Also, some manufacturers obtain increased voltage drop and nonlinearity in their resistors by making them from SiC grain that has been calcined in air to form a silica layer on the surface. In addition, bonded lightning arrester blocks have a high initial resistance and must be "formed" by subjecting them to repeated high current surges. Forming greatly reduces and also stabilizes the resistance. There is little doubt that forming breaks down films of siliceous bond that infiltrate between the grains in the manufacturing process.

However, in 1949, Jones, Scott, and Sillars (18) and Mitchell and Sillars (19) showed clearly that the high and nonlinear contact resistance remained undiminished when all surface films were very carefully and completely removed. Surfaces for which the residual film, if any, was certainly less than 3Å thick were almost indistinguishable electrically from ones on which silica had been evaporated to a thickness of 90Å.

Since the barrier is a fairly good insulator at low field strengths, it can be made to act as the dielectric in a capacitor by firing a thin layer of silver on the surface. This experiment was carried out at the Norton Co. and capacitance was found to increase with increasing voltage. Assuming an effective dielectric constant of 10 for the barrier, its apparent thickness remained constant at 500Å up to 0.5 v, but decreased rapidly with increasing voltage and reached a value of 40Å at 2.0 v. A much more elaborate experiment of the same general type was reported by Mitchell and Sillars (19).

Since it has been shown that a mechanical film is not necessary to produce the observed effects, and that the apparent barrier thickness can be changed over a range of ten to one by changes in field strength, the mechanical film theory has become untenable. Meanwhile, research on transistors has provided plausible models of charge distribution that predict, at least qualitatively, the observed effects. The present consensus is that the barrier results from the distribution of space charge in the SiC lattice within a few angstroms of the surface. Further discussion of this phenomenon would exceed the scope of this article. Williams (20) has written a theoretical survey of the problem, and it can be followed in detail in the excellent series of papers by the research staff of Metropolitan-Vickers in England (5, 7, 13, 14, 16, 18, 19, 21).

Conclusions

While electrical uses of SiC have assumed industrial importance in recent years, the art has greatly exceeded the science. Research on SiC has been

hampered by an almost total lack of specimens of high or even known purity. Two methods have been developed to make the pure compound, and this problem is no longer insurmountable. The linear body resistance, and especially the nonlinear contact resistance, are both exploited commercially, but still present unsolved problems to the theoretician. Much excellent experimentation has been reported, especially in England, and a theoretical solution is probably attainable by the use of quantum mechanics. An attempt has been made to list the principal papers that should be read by those who would like to become conversant with the work that has been done in this field.

Manuscript received October 29, 1956. This paper was prepared for delivery before the Cleveland Meeting, Sept. 30 to Oct. 4, 1956.

Any discussion of this paper will appear in a Discussion Section to be published in the December 1957 JOURNAL.

REFERENCES

1. N. W. Thibault, *Am. Mineralogist*, **29**, 249 (1944); **29**, 327 (1944); **31**, 512 (1946); **33**, 588 (1948).
2. L. S. Ramsdell, *ibid.*, **32**, 64 (1947).
3. Dick Lundqvist, *Acta Chem. Scand.*, **2**, 177 (1948).
4. C. G. Harman and W. G. Mixer, Jr., U. S. A.E.C. Rpt. BMI 748, June 3, 1952.
5. J. T. Kendall, *J. Chem. Phys.*, **21**, 821 (1953).
6. F. J. Mann, *Elektrizitätswirtschaft*, **54**, 871 (1955).
7. F. Ashworth, W. Needham, and R. W. Sillars, *J. Inst. Elect. Engrs. (London)*, **93**, Part 1, 385 (1946).
8. S. Teszner, P. Seguin, and J. Millet, *Annales des Télécommunications*, **8**, 271 (1953).
9. A. W. Roth, *Elektrotech. u. Maschinenbau*, **71**, 107 (1954).
10. N. Thien-Chi and J. Vergnolle, *L'Onde Électrique*, **35**, 336, 222 (1955).
11. K. Zückler, *Z. angew. Phys.*, **8**, 34 (1956).
12. K. Moers, *Z. anorg. u. allgem. Chem.*, **198**, 243 (1931).
13. J. T. Kendall and D. Yeo, *Proc. Intern. Congr. Pure & Appl. Chem.*, **11**, 167 (1947).
14. J. T. Kendall, *J. Chem. Phys.*, **21**, 821 (1953).
15. J. A. Lely, *Ber. deut. keram. Ges.*, **32**, 229 (1955).
16. J. T. Kendall, *Proc. Phys. Soc. London*, **56**, 123 (1944).
17. A. Braun and G. Busch, *Helv. Phys. Acta*, **15**, 571 (1942).
18. T. K. Jones, R. A. Scott, and R. W. Sillars, *Proc. Phys. Soc. London*, **62**, 333 (1949).
19. E. W. J. Mitchell and R. W. Sillars, *ibid.*, **62**, 509 (1949).
20. M. O. Williams, *Automatic Telephone and Electric J., British*, **10**, 144 (1954).
21. R. Stratton, *Proc. Phys. Soc., London*, **68**, 746 (1955).

Some Unusual Effects of Hydrogen in Corrosion Reactions

J. E. Draley and W. E. Ruther

Argonne National Laboratory, Lemont, Illinois

ABSTRACT

Consideration of corrosion in the presence of water has led to the postulation of damage by hydrogen produced in the reaction. For cases where the metal surface is covered with a protective layer, it is considered that some hydrogen ions diffuse through the layer and form hydrogen atoms beneath it. The consequence of the production of hydrogen in this location is to decrease corrosion resistance. Three types of harmful effects are illustrated.

Existing theory has left a number of inconsistencies and anomalies in its explanation of corrosion phenomena. The following has been developed in an effort to provide reasonable explanation for some of these cases. This theory has evolved largely as a consequence of studies of the behavior of Al, U, and their alloys. Much of its development during investigation of high temperature aqueous corrosion of Al and its alloys has been reported (1). This paper presents the theory in a more generalized form, and an effort is made to show instances in which it applies. In addition, its applicability is suggested in some cases where the theory might be valuable but for which there is little or no evidence to indicate its validity. It is suspected that the phenomenon (acceleration of corrosion damage by H produced) is more widespread than has hitherto been believed, and it is hoped that the present work will promote more active consideration of its possibility.

The description of the processes is given for corrosion reactions which proceed through a thin continuous protective film on the metal, which is called a "barrier film." Probably the most common type of barrier film is that which is formed as a consequence of the corrosion reaction, most frequently being an oxide. There might be cases in which films with similar properties can be formed prior to the corrosion exposure.

One of the most interesting properties of such films is their adherence to the base metal. At this time the nature of the bonding between the film and the metal is not believed to be well understood. There does seem to be indication that the protective properties of the film and probably its very existence (as a film) require attachment to and support by the metal beneath.

It is not unusual for the barrier film to be covered over with a thicker corrosion product layer. In some cases this thicker layer appears to be a considerably more porous material. It is likely that it is formed by some sort of transformation process from the thinner barrier layer. The nature of this transformation process probably changes from case to case. In some instances the compositions are different and the transformation might consist of an oxidation or a hydration process. In some cases it appears not to be one of these and perhaps represents only a cracking or fragmentation into discrete crystals (the barrier layer is probably under a considerable stress). This type of situation would be expected to lead to a diminishing rate of reaction for an initial period, followed by a constant oxidation or corrosion rate, as the rates of destruction and formation of the protective barrier film became equal. The concept of double layered corrosion product for Al has been developed by Dekker and Urquart (2) and Hunter and Fowle (3), among others.

The present theory will be developed in terms of barrier films but no restriction is intended against other cases such as adsorbed layers. With minor modifications the theory can be adapted to fit these cases.

Description of Corrosion Process

Oxidation probably proceeds through barrier films by ionic migration. For the case of corrosion in environments containing water the important processes are represented in Fig. 1. Migrations are represented as occurring through the bulk of a continuous oxide film. If some of these actually occur by diffusion through breaks or cracks in barrier films it will not alter the general argument. The barrier film is represented as consisting of oxide because this is the most general case. Only small changes in wording would be necessary to allow application of the description to films of other con-

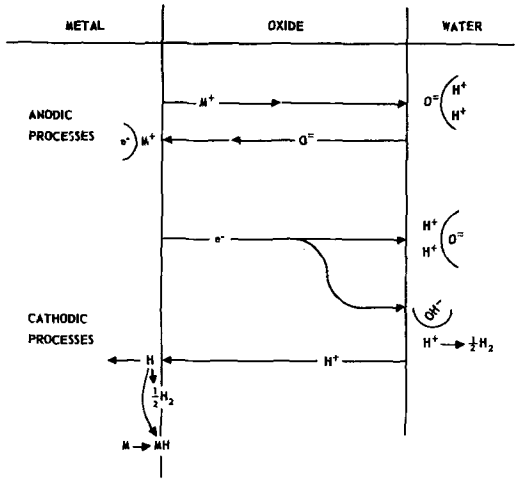

Fig. 1. Schematic representation of corrosion processes

stitution. In those cases where there is a porous solid on the outside of the barrier layer of oxide the water indicated in Fig. 1 should be imagined as being absorbed in the porous layer.

The anodic process can proceed by cation diffusion outward through the oxide or by anion diffusion inward. Both encourage the oxidation of the metal and the formation of new oxide, and this is the reason they are classed as anodic. Also, two types of diffusion are shown for the cathodic process: diffusion of electrons out through the oxide and, the new feature proposed here, inward migration of H ions. Some of the possible reactions forming oxide ion, hydroxide ions, and hydrogen ions from water are shown at the oxide interface. Other possible surface reactions perhaps should have been illustrated, such as the reduction of oxygen and the reduction of cations to form metal.

Probably the H ions in the oxide are combined with oxide ions and diffusion, or migration, proceeds by a series of transfers. They could also be interstitial, of course, with no instantaneous attachment to any particular oxide ion. The so-called hydrated oxides contain hydroxide ions and it is suspected that at least some of the diffusing protons were originally incorporated into the oxide in this form. The driving forces for the diffusion of protons are presumably the potential gradient and a proton concentration gradient through the oxide. It is believed that H is formed beneath the oxide largely as a result of cathodic proton migration rather than anodic hydroxide ion migration. The basic evidence is that the accumulation of corrosion product H in the metal is decreased by anodic polarization and increased by cathodic polarization. The metals for which this is known to have been demonstrated include steels, aluminum, and uranium alloys.

One could also propose that the H is transported through the oxide in the form of atoms rather than ions. There is no known positive refutation of this hypothesis, but it is considered unlikely. First, the H atoms would be considerably larger than the ions; this would make migration through the oxide lattice much more difficult. Second, it appears unlikely that such a neutral atom could exist for very long in an environment such as an oxide, with its very high local electric fields. Third, the driving force for the migration would be considerably lower than for the migration of protons. The potential gradient would not be influential, and the only known driving force leading to a net transfer would be a concentration gradient set up by removal of the H atoms at the metal-oxide interface. In many cases such removal does not occur without a hydrogen (atomic?) pressure to increase the rate.[1] If the diffusion of H atoms occurred through the oxide, no greater pressure of this sort could develop beneath the oxide than existed above it.

The cathodic reduction of H ions produces H atoms at the most active cathode spots, that is, where the electrons are most available. It is not necessarily possible to describe such cathode points in terms of their potential, although the reactions should alter the potential gradients in the oxide and adjacent solution.

Three types of disposal of the hydrogen atoms thus produced beneath the barrier film are illustrated:

(*A*) *Diffusion into the metal.*—It is notable that the same metallurgical factors which characteristically increase local cathodic activity usually also increase permeability to H diffusion. Included among such factors are the presence of inclusions (usually cathodic), porosity, and structural defects. As will be illustrated, the resultant diffusion into the metal can lead to quite harmful effects.

(*B*) *Formation of gaseous* H.—Such gas can rupture the barrier film as its pressure becomes sufficient to do so. This rupturing action would result in increased corrosion, probably localized at any one time. The actual rate of corrosion might be determined by the rate of rupturing. This appears likely if the unbroken film is quite protective and the anodic reaction can take place only very slowly by diffusion or migration through it.

(*C*) *Formation of metal hydride in cases where this reaction is possible.*—The hydride produced would be expected to interfere with the bond between the barrier film and the supporting metal. In this way the barrier film stability would be destroyed, the oxide perhaps recrystallizing, and its highly protective nature would disappear.

The total reaction can be summarized as two sets of competing processes in series. The anodic current will be carried by anion and cation migration, in inverse proportion to the "resistances" of the competing total anode processes. The cathodic current will be carried by electron and proton migrations, in inverse proportion to the "resistances" of these respective total processes. Such processes include the acquisition and incorporation of the diffusing species into the oxide, diffusion, cathodic reduction, and liberation and disposal of the products. Control of the corrosion reaction can be considered to be the sum of the anodic and cathodic resistances (each of which is the parallel sum of two complex "resistances").

Disposal of those H atoms which are produced beneath the oxide will be divided among the three competing processes. All can be expected to reduce corrosion resistance.

Preventing their damaging effects can be accomplished by making the "resistance" of the electron migration process very low compared to that for the proton migration process. Note that the substitution of a more favorable cathodic reaction on the surface of the oxide can be a case of this type, since chemical reduction becomes easier. However, if the electronic resistance of the oxide is high, no diminution in damage by H would be expected to occur as a result of the addition of a typical "cathodic depolarizer" such as oxygen (unless the incorporation of H into the oxide is simultaneously reduced).

Certain otherwise anomalous results can be explained in these terms. In particular, some cases of anodic protection or partial protection and cathodic acceleration of corrosion are logical, as far as is known, for the first time.

[1] Hydrogen overvoltage to liberate gaseous hydrogen or to cause rapid embrittlement.

Illustrations of Effects of Liberated H on Corrosion Behavior

In many of the cases given, proof that it is the H which causes the objectionable acceleration of corrosion damage will appear inconclusive. In some instances good correlation will be demonstrated between behavior and H found in the metal after corrosion (or metal hydride found after corrosion). For the liberation of gas beneath the film, however, no such direct evidence can be obtained and less direct indications must be used.

Diffusion into the metal.—Al alloys form blisters at elevated temperatures in moist air. These are believed to be caused by H_2 accumulating in cavities and rifts in the metal structure to produce the pressure which causes swelling. The phenomenon is observed to increase in intensity as metallurgical factors are added which tend to cause less sound surface structures. Thus surface defects caused by incorporated second phases and from severe working cause more blistering by the opening of the surface texture to allow more rapid diffusion of H into the metal. Such surface blistering can be prevented by dissolving off the surface oxide prior to heating. One effective method of accomplishing this is by immersing Al in brazing flux.

This is perhaps evidence that the barrier film prevents the escape of H formed beneath it. This restriction of its free escape appears to be necessary to cause the H to penetrate a material with a low H diffusion rate. Smith (4) reports the difficulty of diffusing H outward through surface films.

In water at temperatures much above 200°C most common Al alloys suffer rapid corrosive deterioration. The samples in Fig. 2 show appearance typical of the beginning of damaging attack of 1100 Al after about 2 weeks in distilled water at 275°C. At a temperature of 350°C this material is entirely disintegrated and corroded to oxide in a few hours. Analysis has shown a considerable increase in H content of the surface layers of corroding 1100 Al prior to damaging attack. The phenomenon can be prevented up to about 350°C by forming active cathode sites for H combination on the metal surface. Metals of low H overvoltage can be deposited from solution or incorporated into the Al by alloying. It has not been determined whether this method owes most of its effectiveness to its ability to cause combination of the H atoms (beneath the oxide) before they can diffuse into the metal, or whether at such points the cathodic metal protrudes through and above the barrier film of oxide, providing active liberation sites for the H on the outside. The latter possibility can be considered to be a case where the total process involving movement of electrons outward through such places in the oxide is made quite easy. For the purpose of preventing H_2 penetration into Al, Ni is the most effective metal which has received much attention. An alloy, made by the addition of 1% nickel to 1100 Al, shows no measurable increase in H content during corrosion in water at temperatures as high as 350°C, and no corrosion damage other than normal surface attack. This development has been described by Draley and Ruther (1).

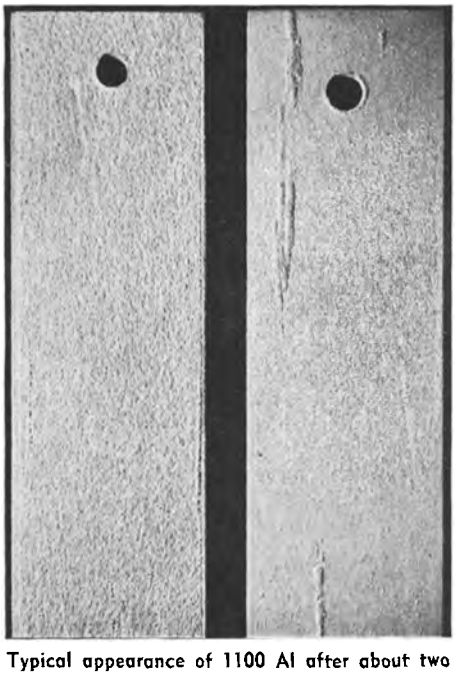

Fig. 2. Typical appearance of 1100 Al after about two weeks in distilled water at 275°C.

Metallic U corrodes quite rapidly in water at elevated temperatures. A barrier film oxide can be stabilized by alloying to produce materials of low corrosion rate in the same environment. These alloys are generally observed to fail by cracking or crumbling after prolonged corrosion testing. Such failure has been shown to occur after an accumulation of more than a critical concentration of H in the corrosion sample. In some cases (U-Mo alloys), a second phase has been observed to form at about the same time, dispersed within the metallic matrix (5). This is believed to be a hydride. It is considered that the increase in volume in the formation of the new phase creates quite high local stresses. In another class of U alloys, typically containing small amounts of Nb and Zr, no such second phase has been discovered in normal corroded specimens, although some H accumulation in the metal and mechanical failure occur. It is clear that high local stresses are produced. For both types of alloy, corrosion "lifetime" can be increased materially by adding a Ni salt to the water. As has been shown to occur on Al, this should result in Ni deposits, providing good H liberation sites.

During its corrosion in distilled water at elevated temperatures, Zr produces a thin protective layer of corrosion product. By determining the H content of the metal, Thomas (6) has shown that a significant fraction of the total H produced in the corrosion reaction is absorbed in the metal, some of which ultimately forms zirconium hydride crystals at the surface, and growing into the metal (7). At about the same time the corrosion rate increases, with the formation of crystalline corrosion product (less protective). It has not been determined experimentally whether a critical H concentration in the surface layers of the metal influences the transition in corrosion behavior, so that the evidence to support the present thesis is not conclusive.

The absorption of H in steels during corrosion and especially during pickling or electroplating has been

well known for many years. The most serious result is sometimes severe embrittlement of the steel. Damage of this type is generally postulated to occur in the same fashion as has earlier been mentioned for Al: by the formation of molecular H in pores or open places in the metal structure and the resultant high local stresses produced. This kind of embrittlement of Fe can occur in dry H although it is accelerated by the presence of moisture [shown by Stanley (8)]. Several reviews of the damage of steel by H have been written, for example, Buzzard and Cleaves (9).

The initial presence of H in some U alloys (10) and in Zr (6) accelerates the rate of further H pickup during aqueous corrosion, in the former case leading to higher corrosion rates and early "failure." There have also been a number of instances in which the presence of H in other metals has caused increased corrosion. For example, Berger and Tull (11) observed correlation between the amount of blistering of pure (99.8%) Al in air at 600°C and the formation of deep pits in electrolytic etching. Iwamura and co-authors (12) observed that Al alloys containing H corroded faster in 10% NaOH solution than those which contained little or no H. Smith and Derge (13) have shown that the susceptibility of Pd to attack by etching agents varies in parallel with the avidity with which the metal takes up H_2 from the gas phase. The rate of H_2 uptake was shown to be related to the presence of fissures in the metals.

When metal structures have somewhat borderline H diffusion rates, that is, when a small change in metal structure might be expected to increase the acquisition of H by the metal to an extent which would then be discernible, such metal might be expected to be susceptible to "stress corrosion." In this instance, applying tension should produce a small amount of opening in the metal lattice, resulting in diffusion of H inward at the most susceptible places. The reasoning is supported by the fact that the amount of internal hydride formed during cathodic charging of a U alloy is increased by tension and decreased by compression (5). It is perhaps significant that in nearly all cases of "stress corrosion cracking" it is only the effect of tension which increases corrosion susceptibility (14). This type of reasoning does not seem to explain all stress corrosion cracking, however, because some metals which show the phenomenon (e.g., Al alloys at ordinary temperatures) would not be expected to have "borderline hydrogen diffusion rates." It is not clear whether such reasoning should apply to corrosion fatigue. Experimentally it was shown by Evans and Simnad (15) that small cathodic currents decreased the fatigue life of mild steel (although greater cathodic polarization increased fatigue life).

Formation of gaseous hydrogen.—As previously remarked, there is no known unequivocal evidence as to whether H_2 liberated in the corrosion reaction influences corrosion rates by rupturing protective films. The following discussion on Al can be considered useful only where barrier films will form and determine corrosion rates. This probably restricts attention to cases where corrosion is quite slow and uniform on a gross scale, i.e., where significant local attack does not occur.

Corrosion of Al alloys in distilled water at ordinary temperatures is characterized by the formation of tiny shallow pits. It is proposed that these are the places where H_2 is formed beneath the film and ruptures it. At such areas the corrosion reaction then takes place rapidly for a short but significant period (during which time the areas are, of course, anodes), with the ultimate result of reforming the film there. Note that the "etch pits" are proposed to form at what were originally active cathode sites rather than at sites which differed from the rest of the surface by being intrinsically more reactive anodically. In environments where pitting is observed, the same reasoning might be applicable as providing one kind of pit initiation. That is, pits might start at or about what were originally cathodes. It is clear that once pits are formed and continue to grow, the laws that govern the progress of the corrosion reaction must be different, since barrier films do not form at the pits.

This theory predicts that corrosion rates should be increased by mild cathodic polarization, and decreased by mild anodic polarization. In oxygen-saturated KOH solution (*p*H 10.5), the corrosion of 1100 Al follows this pattern exactly. As much as 90% reduction in rate was caused by anodic polarization. Unfortunately, the corrosion rate is strongly dependent on *p*H in this solution, and there is no way of knowing how much of the observed changes were caused by the local *p*H changes resulting from the induced cathodic and anodic reactions.

Much more valuable evidence would be provided by accurately determining the effects of polarizing current (of both polarities) on the corrosion rate of this metal in distilled water. Published data show that the corrosion rate is minimum in this *p*H range (at 50°C) (16), so that changing the *p*H by polarization (in either direction) would be expected to increase the corrosion rate slightly. This work has been started, but it will be a long job because of the requirement of accurate determination of extremely low rates.

In some cases striking increase in metal oxidation rate in gases (such as oxygen, air, carbon dioxide, sulfur, and sulfur-containing gases) is caused by the addition of a little water vapor (17). It is reasonable to propose that this is the result of the formation of H_2 beneath the oxide layer. Only a small amount of H_2 might be sufficient to cause a considerable amount of more rapid oxidation by oxide rupturing.

Formation of metal hydride.—U corrodes in hot distilled water at a rapid rate (300-500 mdd at 100°C), which is constant after a short initial period of slower reaction. The corrosion product is usually a fine granular powder of UO_2. After corrosion test, the corrosion product has been observed to contain UH_3 as well as the oxide, UO_2. Since water converts hydride to the oxide, it is inferred that the hydride is formed on the metal surface. This disrupts an initial film of oxide and prevents its subsequent formation. It is believed that during

continuing corrosion, uranium hydride forms under the oxide and prevents the formation of a barrier film.

At lower temperatures, thin protective oxide films form on the same U, only when there is oxygen in the water. This oxide is also UO_2, although it limits corrosion to quite small rates. Here it is perhaps true that the reduction of oxygen occurs in preference to the formation of H_2 so that there is little hydride formed beneath the barrier film. However, it appears that a small amount of H_2 is produced, for, after protracted testing, oxide breakdown occurs at local spots which then spread and the corrosion becomes much more rapid. Careful diffraction work by Waber (18) has shown the existence of UH_3 in such cases.

Conclusion

It is clear that justified application of the theory of increased corrosion caused by H_2 formation beneath the protective film is not universal. However, it appears to be valuable as an addition to existing theory, in affording understanding of some corrosion phenomena, and in a few cases it has predicted successful means of providing better corrosion resistance.

Manuscript received January 20, 1956. This paper was prepared for delivery before the Pittsburgh Meeting, Oct. 9-13, 1955. Work was performed under the auspices of the Atomic Energy Commission.

Any discussion of this paper will appear in a Discussion Section to be published in the December 1957 JOURNAL.

REFERENCES

1. J. E. Draley and W. E. Ruther, *Proc. Intern. Conf. on Peaceful Uses of Atomic Energy* (Geneva, August 1955); **9**, 391; also J. E. Draley and W. E. Ruther, *Corrosion*, **12**, 480t (1956).
2. A. J. Dekker and H. M. A. Urquart, *Can. J. Research*, **28**, 541 (1950).
3. M. S. Hunter and P. Fowle, *This Journal*, **101**, 481 (1954).
4. D. P. Smith, "Hydrogen in Metals," pp. 192 and 285, University of Chicago Press, Chicago (1948).
5. B. Lustman and D. E. Thomas, Private communication.
6. D. E. Thomas, "Metallurgy of Zirconium," edited by B. Lustman and F. Kerze, p. 621, McGraw-Hill Book Co., New York (1955).
7. C. M. Schwartz, D. A. Vaughan, and G. G. Cocks, BMI-793, "Identification and Growth of Oxide Films on Zirconium in High Temperature Water," Battelle Memorial Institute, Columbus, Ohio.
8. J. K. Stanley, Am. Soc. Metals preprint No. 15W, 10 pp. (1952).
9. R. W. Buzzard and H. E. Cleaves, *National Bureau of Standards Circular 511*, Sept. 24, 1951.
10. S. Greenberg and J. E. Draley, To be published.
11. F. J. Berger and V. F. G. Tull, *Nature*, **172**, 729 (1953).
12. H. Iwamura, T. Chihaya, and M. Suzuki, *J. Japan. Inst. Metals*, **14B**, 22 (1950).
13. D. P. Smith and G. J. Derge, *Trans. Electrochem. Soc.*, **66**, 253 (1934).
14. H. H. Uhlig (Editor), "Corrosion Handbook," p. 569, John Wiley & Sons, Inc., New York (1948).
15. U. R. Evans and M. T. Simnad, *Proc. Roy. Soc.*, **A188**, 372 (1947).
16. J. E. Draley and W. E. Ruther, *Corrosion*, **12**, 441t (1956).
17. O. Kubaschewski and B. E. Hopkins, "Oxidation of Metals and Alloys," pp. 205, 208, 210, 211, Academic Press, New York (1953).
18. J. T. Waber, Private communication.

Kinetics of the Oxidation of Chromium

Earl A. Gulbransen and Kenneth F. Andrew

Research Laboratories, Westinghouse Electric Corporation, Churchill Borough, Pittsburgh, Pennsylvania

ABSTRACT

The oxidation of high purity chromium was studied over the temperature range 700°-1100°C using the vacuum microbalance method. Below 900°C conventional oxidation curves were obtained which can be fitted to the parabolic rate law. Above 900°C and for a film thickness of approximately 4800Å, the rate of oxidation increased in an unusual manner. This increase in the rate of oxidation disappeared on further oxidation. At temperatures of 1050°C and higher a large increase occurred in the rate of oxidation, suggesting that the oxide film was no longer protective for film thicknesses greater than 42,000Å.

A logarithmic plot of the parabolic rate law constant vs. $1/T$ shows two straight lines separated by a transformation region. This gives 37,500 cal/mole and —15.3 entropy units for heat of activation and entropy of activation between 700° and 900°C and 59,400 cal/mole and +6.2 entropy units for 1000°-1100°C.

The rate of evaporation and the rate of oxidation of Cr are equal at about 950°C. This corresponds to the transformation region between the two mechanisms of oxidation. It is concluded that the failure of Cr in oxidation is closely related to the high vapor pressure of Cr above 900°C.

A preliminary study was made of the oxidation of Cr and the data could be fitted to the parabolic rate law. The heat of activation was reported to be 66,300 cal/mole (1). This paper presents a more complete study of the kinetics of the oxidation of a pure grade of Cr over the temperature range 700°-1100°C and for reaction times of 6 hr.

Since Cr is an important component of oxidation resistant high temperature alloys, one of the objectives of this work was to study the conditions under which Cr fails in oxidation. This failure occurs when a rapid reaction develops in which diffusion processes are no longer rate controlling. Poor adhesion of the oxide to the metal is observed for these conditions. For some metals, this breakdown of the protective oxide film is termed "break-away" corrosion.

Two oxides form on Cr, Cr_2O_3 and CrO_3, the latter under strong oxidizing conditions. Cr_2O_3 exists in more than one phase (2,3). Rhombohedral Cr_2O_3 is formed on oxidizing Cr (4). The resistance to oxidation of alloys containing Cr has been attributed to the formation of Cr_2O_3 or to spinels containing Cr_2O_3 (5-7).

Experimental

The vacuum microbalance method has been described (8-10). In this study a new type of microbalance of low sensitivity for the high temperature reaction range was used. The sensitivity is 0.22 divisions per microgram and one division equals 0.001 cm. The weight change could be estimated to 1.2 μg.

The furnace tube containing the specimen was constructed of mullite (11). This tube was sealed direct to the all-Pyrex glass vacuum system.

To avoid evaporation of Cr at 900°C and higher the specimen and reaction tube were heated rapidly to the reaction temperature in a vacuum of less than 10^{-6} mm Hg. Purified oxygen (8) was added as soon as thermal equilibrium was established.

The reproducibility of the oxidation experiments was about 5-10% above 950°C and 10-20% below 950°C.

Samples.—Table I shows the analyses of the Bureau of Mines grade of Cr used in this study. Strips of 10 mil sheet were sawed to specimens 1 cm wide and 1.6 cm long. Samples had surface areas of 3.5 cm^2 and weighed 0.50 g. Specimens were abraded and cleaned following the procedures used previously (1).

Results and Discussion

The rate curves are shown in Fig. 1 and 2. The weight gain is in $\mu g/cm^2$ and is converted to thickness in Å by multiplying by 60. This is calculated on the basis of the oxide Cr_2O_3 (4) and a surface roughness ratio of unity.

Table I. Analyses of chromium metal (Bureau of Mines)

Metal	Analyses Wt % or ppm	Method
Al	0.01 — 0.1%	Spectroscopic
Si	0.05%	Spectroscopic
Fe	0.001 — 0.01%	Spectroscopic
Cu	0.001 — 0.01%	Spectroscopic
Mg	Less than 0.001%	Spectroscopic
O*	150 ppm	Vacuum fusion
H*	5 ppm	
N*	Less than 10 ppm	
C	0.0032%	

* Ingot material.

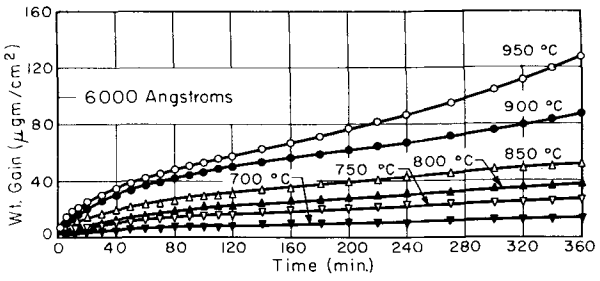

Fig. 1. Oxidation of Cr, 700°-950°C, 7.6 cm Hg of O_2, abraded 1-4/0.

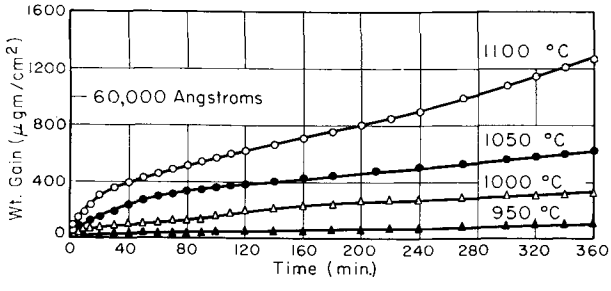

Fig. 2. Oxidation of Cr, 950°-1100°C, 7.6 cm Hg of O_2, abraded 1-4/0.

Time and Temperature

Fig. 1 shows conventional oxidation curves for temperatures of 700°-950°C. A rapid initial rate of oxidation is found, with the rate decreasing as the film thickens. A new phenomenon appears in the 950°C experiment. Here, the rate of oxidation does not decrease continually with time. Instead, at a film thickness of 80 $\mu g/cm^2$ or 4800Å, the rate of oxidation increases. A similar phenomena occurs in oxidation experiments in Fig. 2 at 975°, 1000°, 1025°, and 1050°C for similar film thicknesses. However, for these temperatures, the increase is only temporary and the course of the oxidation again appears to follow a normal behavior.

For oxidation experiments above 1050°C the oxidation curves show a second type of breakdown phenomenon with the rate of oxidation increasing for thicknesses above 700 $\mu g/cm^2$ or 42,000Å. Due to the limitations of the balance it has not been possible to study the end result of this type of breakaway oxidation.

A comparison of the results of this study with that of the older work (1) shows lower oxidation rates. The lower oxidation rates are attributed to the greater purity of the present Cr samples.

Parabolic Rate Law Correlation

The parabolic rate law is of value in studying the mechanism of oxidation, even though deviations may occur, since the law is based on fundamental physical theory. Deviations from the rate law suggest that physical and chemical changes do occur in the oxide film as a function of time, film thickness, and temperature.

The parabolic rate law states that

$$W^2 = At + C$$

Here W is the weight gain, t is the time, and A and C are constants. The constant A includes the diffusion coefficient of the diffusing specie, the number of defects in the lattice, and has an exponential temperature dependence (12).

Fig. 3 to 6 show parabolic rate law plots for the 700°, 900°, 1000°, and 1100°C oxidation experiments. At 700°C the parabolic rate law fitted except for the initial stage of the reaction (Fig. 3). A deviation from the parabolic rate law occurred after 240 min of reaction at 900°C (Fig. 4). Deviation from the parabolic rate law is noted at B (Fig. 5) for the 1000°C oxidation. This was at approximately the same film thickness as found in the 900°C ex-

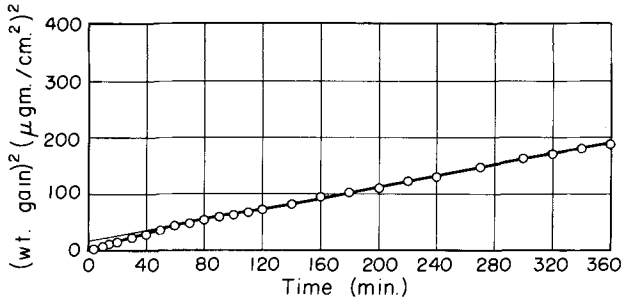

Fig. 3. Oxidation of Cr, 700°C, 7.6 cm Hg of O_2, abraded 1-4/0, parabolic plot A = 8.22 × 10^{-15} $(g/cm^2)^2/sec$.

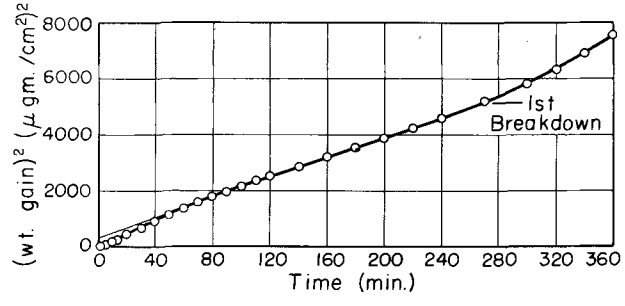

Fig. 4. Oxidation of Cr, 900°C, 7.6 cm Hg of O_2, abraded 1-4/0, parabolic plot A = 2.92 × 10^{-13} $(g/cm^2)^2/sec$.

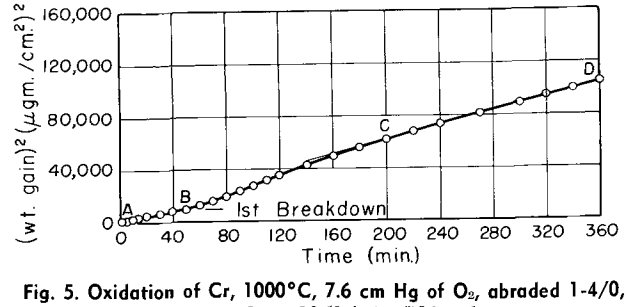

Fig. 5. Oxidation of Cr, 1000°C, 7.6 cm Hg of O_2, abraded 1-4/0, parabolic plot A_{C-D} = 4.51 × 10^{-12} $(g/cm^2)^2/sec^{-1}$.

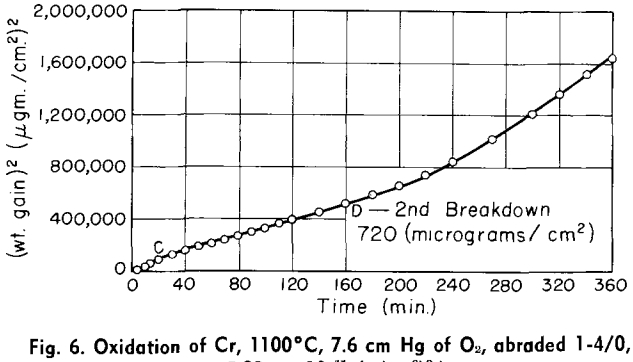

Fig. 6. Oxidation of Cr, 1100°C, 7.6 cm Hg of O_2, abraded 1-4/0, parabolic plot A_{C-D} = 5.28 × 10^{-11} $(g/cm^2)^2/sec$.

Table II. Properties of oxide films on Cr

Temp, °C	Thickness* μgm/cm²	A°	Color	Stability of film to cracking on cooling	Rate law
700	13.7	822	Straw	Stable	Parabolic
750	26.9	1614	Green	Stable	Parabolic
800	38.1	2286	Green	Stable	Parabolic
850	52.5	3150	Green	Stable	Parabolic
900	87	5220	Green	Stable	Parabolic
950	127	7620	Green	Stable	Parabolic
975	228	13680	Gray-green	Stable	Parabolic
1000	324	19440	Gray-green	Stable	Parabolic
1000	346	20760	Gray-green	Stable	Parabolic
1025	516	30960	Gray-green	Stable	Parabolic
1050	640	38400	Dark gray	Stable	Some acceleration of reaction
1075	960	57600	Dark gray	Unstable	Accelerating reaction
1100	1280	76800	Dark gray	Unstable	Accelerating reaction

* 6-hr experiments.

periment. At C the film appears to regain its protective properties. However, the slope C-D is greater than the slope A-B. Deviation from the parabolic rate law is only temporary in nature. Due to the rapid reaction at 1100°C the temporary deviation noted at lower temperatures is not easily observed (Fig. 6). At D for a film thickness of 720 μg/cm² the rate of oxidation deviates in a positive sense from both the parabolic rate law and the linear rate law. On cooling the specimen, the oxide film flaked off from the metal.

Table II gives a summary of the experimentally observed properties of oxide films on Cr. The thickness of the oxide film formed after 6 hr of reaction is tabulated, together with the color of the oxide, its stability to flaking off of the metal on cooling, and the type of rate law correlation.

Comparison with Nickel

Fig. 7 shows a comparison of the oxidation curve of Cr at 1050°C with that for Ni at 1050°C. Cr oxidizes at an appreciably slower rate than Ni (13). In the Ni oxidation experiment the oxide film flaked away from the metal on cooling, while the oxide

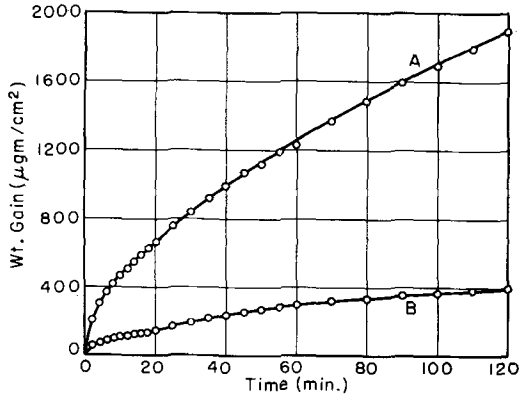

Fig. 7. Oxidation of Ni (curve A) and Cr (curve B), 1050°C, 7.6 cm Hg of O_2, abraded 1-4/0.

Table III. Summary of parabolic rate law constants

Temp, °C	A (g/cm²)² sec⁻¹
700	8.22×10^{-15}
750	3.14×10^{-14}
800	6.95×10^{-14}
850	1.18×10^{-13}
900	3.02×10^{-13}
950	5.50×10^{-13}
975	1.20×10^{-12}
1000	4.51×10^{-12}
1000	4.93×10^{-12}
1025	1.15×10^{-11}
1050	1.81×10^{-11}
1075	3.08×10^{-11}
1100	5.28×10^{-11}

film formed on Cr was near to the unstable condition.

Temperature Dependence

Table III summarizes the parabolic rate law constants over the temperature range. For experiments below 950°C, parabolic rate law constants are calculated for thicknesses below that for the first deviation of the rate law correlation. Above 950°C, parabolic rate law constants are calculated for conditions above the first deviation and below the second deviation noticed at temperatures above 1050°C.

Fig. 8 shows a log A vs. $1/T$ plot. Two straight lines are found to describe the temperature dependence of the parabolic rate law constants. Between the two straight line portions of the plot a transformation region exists. The heat of activation is 37,500 cal/mole between 700° and 950°C and 59,400 cal/mole between 1000° and 1100°C. The existence of this transformation zone suggests that a major change is occurring within the oxide-metal system.

It is concluded that Cr fails in oxidation above 1000°C. The rapid increase in the parabolic rate law

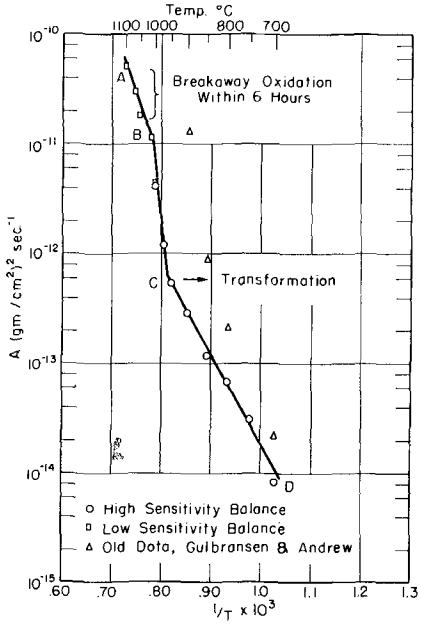

Fig. 8. Oxidation of Bureau of Mines Cr, abraded 4/0, log A vs. $1/T$, 700°-950°C, ΔH_{C-D} = 37,500 cal/mole, 1000°-1100°C, ΔH_{A-B} = 59,420 cal/mole.

constants at 950°-1000°C suggests that this increase is a preliminary symptom of breakdown.

Comparison of Rate of Oxidation with Rate of Evaporation

One property of Cr which plays an important role in oxidation at high temperature is the high vapor pressure of the metal above 900°C (1). To discuss the role of vapor pressure in oxidation, it is essential to review briefly the fundamental principles of oxidation and to indicate that the oxide film formed on metals consists of many small crystallites of variable size.

In the usual oxidation process, only the oxide very close to the metal interface is in equilibrium with the metal. Metal ions are transferred from the metal to the oxide only at locations where the oxide and metal are in intimate contact. The energy barrier for this transport process is usually less than the sublimation energy of the metal. Due to this fact, concentration gradients of Cr occur across the oxide crystallites and oxide film, and diffusion of metal follows. The vapor pressure of the metal for these conditions plays no direct role in the rate-controlling process.

Consider a higher temperature where the rate of evaporation of metal from a free surface approaches that of the rate of metal diffusing through the oxide during oxidation. For these conditions, metal atoms or ions can be transferred to the oxide crystals from the vapor phase as well as at the metal oxide interface, since the oxide film is not continuous, but composed of many oxide crystals. Thus, metal vapor can penetrate through portions of the film and short circuit the normal diffusion processes.

It is of interest therefore to compare for Cr the rate of evaporation with the rate at which metal atoms diffuse through the oxide and react with oxygen. The rate of evaporation data come from an earlier paper (1), while the rate at which Cr atoms diffuse through the oxide is calculated from the 1- to 2-hr oxidation period. Fig. 9 shows a log rate vs. $1/T$ plot of the data.

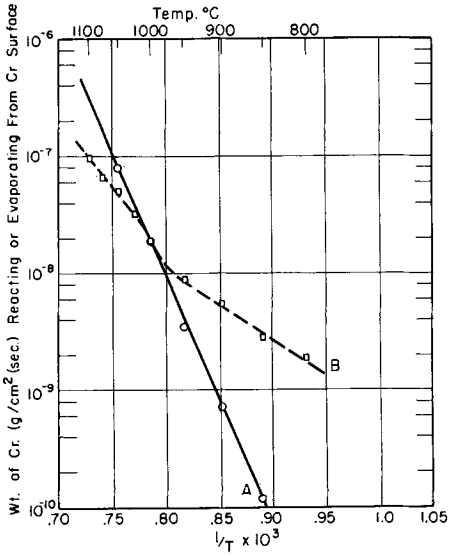

Fig. 9. Comparison rate of evaporation of Cr from clean surface (curve A) with rate of oxidation of Cr (curve B), rate (log scale) vs. 1/T.

The transformation point (C-B in Fig. 8) corresponds to the condition in Fig. 9 at which the rate of evaporation is equal to the rate of Cr diffusion. Above 1000°C the rate of evaporation is greater than the rate of Cr diffusion. For these conditions (1000°C and higher), the oxide film appears to lose its protective properties after a definite thickness of oxide has formed. The reaction rate increases rapidly with time and the adhesion of the oxide to the metal is very poor.

Thus the high vapor pressure of Cr short circuits the normal diffusion processes and for these conditions a greatly increased rate of reaction results.

Theoretical

The transition rate-theory (1) and the classical expression (12) for the diffusion coefficient as expressed by Zener (14) have been used to interpret the parabolic rate law. Following this treatment, the following equation for the parabolic rate law constant can be derived, assuming a mechanism based on cation vacancy diffusion.

$$A = 2\gamma\nu\, a^2 e^{\left(\frac{\Delta S^\circ}{8/3} + \Delta S^*\right)/R}\, e^{-\left(\frac{\Delta H^\circ}{8/3} + \Delta H^*\right)/RT}$$

Here $\frac{\Delta S^\circ}{8/3}$ and $\frac{\Delta H^\circ}{8/3}$ are the entropy and heat of formation of the vacancies, while ΔS^* and ΔH^* are the entropy and heat of activation of diffusion, a is the interatomic distance between diffusion sites, ν is the frequency of vibration along the direction across the saddle configuration, R is the gas constant, T is the temperature, and γ a coefficient determined by the geometry of the atomic jumps. A has the units of $cm^2\ sec^{-1}$.

To evaluate ν and γ it was necessary to assume a particular oxide and a mechanism for diffusion. According to the work of Gulbransen and Hickman (4), rhombohedral Cr_2O_3 is formed on oxidizing Cr.

Details of the application of this equation to Cr_2O_3 have already been discussed (15). From the temperature coefficient of the reaction and the value of A at a given temperature, the value of the heat and entropy terms can be evaluated. These terms have been called heat and entropy of activation, since a rate process is involved.

Table IV shows a summary of the experimental heats, entropies, and free energies of activation for the oxidation of Cr (12). Below 950°C an entropy of activation of -15.3 ± 0.4 cal/mole/°C was calculated from the equation. Above 1025°C an entropy of activation of 6.2 ± 0.3 cal/mole/°C was calculated.

The experimental entropy of activation is made up of two terms (12): (*a*) entropy of formation of vacancies, and (*b*) entropy of activation of diffusion. Zener (14) has shown for the case of metals that the entropy of activation of diffusion should be positive. This has been verified by Gulbransen and Andrew (13) for the oxidation of pure Ni. However, other oxidation reactions have shown negative values for the entropy of activation of diffusion.

The entropy associated with the formation of a lattice vacancy for the Cr_2O_3 lattice is approximately

Table IV. Parabolic rate law constants, entropies, heats, and free energies of activation for the oxidation reaction

t °C	A cm^2/sec	ΔH^* cal/mole	ΔS^* cal/mole/°C	$-T\Delta S^*$ cal/mole	ΔF^* cal/mole	Comments
700	3.06×10^{-15}	37,500	—15.7	15,300	52,800	
750	1.17×10^{-14}	37,500	—15.0	15,300	52,800	Oxide film adherent, rate of evaporation lower than rate of oxidation.
800	2.59×10^{-14}	37,500	—15.1	16,200	53,700	
850	4.39×10^{-14}	37,500	—15.6	17,500	55,000	
900	1.12×10^{-13}	37,500	—15.2	17,800	55,300	
950	2.05×10^{-13}	37,500	—15.3	18,700	56,200	
1025	4.28×10^{-12}	59,400	5.9	—7700	51,700	Oxide film flakes off on cooling, rate of evaporation higher than rate of oxidation.
1050	6.73×10^{-12}	59,400	5.9	—7800	51,600	
1075	1.15×10^{-11}	59,400	6.2	—8400	51,000	
1100	1.96×10^{-11}	59,400	6.4	—8800	50,600	

—7.5 cal/mole/°C. From this the entropy of activation of diffusion is —8 cal/mole/°C for the temperature range 700°-950°C. Above 1025°C a value of +13.7 cal/mole/°C is calculated.

The positive value of the entropy of activation found for the high temperature range is in agreement with Zener's diffusion picture (14). However, the value appears high when it is compared to the value of +2 found for the oxidation of Ni (13).

The negative value of —7.5 cal/mole/°C for the temperature range 700°-950°C is unexplained, although similar negative values of the entropy of activation are found for a number of metals. The different heat and entropy of activation values found for the two temperature regions suggest that a different reaction mechanism is rate controlling.

Failure of Cr in Oxidation

An analyses of the kinetic data show several interesting facts. (*A*) Cr begins to fail in oxidation at a temperature where the rate of evaporation of Cr from a clean surface is equal to the rate of reaction. This suggests that the distribution of defects in the Cr_2O_3 lattice may change greatly at this temperature. (*B*) For oxidation above 1000°C the adhesion of the oxide to the metal depends on the oxide film thickness. This may be related to the fact that at a certain thickness the rate of evaporation approaches or becomes equal to the rate of oxidation. (*C*) The heat and entropy of activation change drastically for oxidation conditions where the metal will ultimately fail at thicker film thicknesses.

Thus, the failure of Cr in oxidation is clearly related to its high vapor pressure at 900°C and higher.

Manuscript received July 9, 1956. This paper was prepared for delivery before the Cleveland Meeting, Sept. 29 to Oct. 3, 1956.

Any discussion of this paper will appear in a Discussion Section to be published in the December 1957 JOURNAL.

REFERENCES

1. E. A. Gulbransen and K. F. Andrew, *This Journal*, **99**, 402 (1952).
2. C. T. Anderson, *J. Am. Chem. Soc.*, **59**, 488 (1937).
3. L. Blanc and G. Chaudron, *Compt. rend.*, **182**, 386 (1926).
4. E. A. Gulbransen and J. W. Hickman, *Trans. Am. Inst. Mining Met. Engrs.*, **171**, 306 (1947).
5. E. Scheil and K. Kiwit, *Arch. Eissenhuttenw.*, **9**, 405 (1936).
6. J. W. Hickman and E. A. Gulbransen, *Trans. Am. Inst. Mining Met. Engrs.*, **180**, 519 (1949).
7. E. A. Gulbransen and W. R. McMillan, *Ind. and Eng. Chem.*, **45**, 1734 (1953).
8. E. A. Gulbransen, *Trans. Electrochem. Soc.*, **81**, 187 (1942).
9. E. A. Gulbransen, *Rev. Sci. Instruments*, **15**, 201 (1944).
10. E. A. Gulbransen, "Advances in Catalysis," Vol. V, p. 119-175, Academic Press, Inc., New York (1953).
11. E. A. Gulbransen and K. F. Andrew, *Ind. Eng. Chem.*, **41**, 2762 (1949).
12. E. A. Gulbransen, *Anals. N. Y. Acad. Sciences*, **58**, 830 (1954).
13. E. A. Gulbransen and K. F. Andrew, *This Journal*, **101**, 128 (1954).
14. C. Zener, *J. Appl. Phys.*, **22**, 372 (1951).
15. E. A. Gulbransen and K. F. Andrew, *This Journal*, **101**, 163 (1954).

Anodic Oxidation of Aluminum, Chromium, Hafnium, Niobium, Tantalum, Titanium, Vanadium, and Zirconium at Very Low Current Densities

Herman A. Johansen,[1] George B. Adams, Jr., and Pierre Van Rysselberghe[2]

Department of Chemistry, University of Oregon, Eugene, Oregon

ABSTRACT

Some aspects of the mode of formation of anodic oxidation films in the potential region below oxygen evolution were examined for a number of metals under as nearly constant experimental conditions as possible. The metals selected were Al, Ti, Hf, V, Nb, Ta, and Cr. Results for Zr were reported in earlier publications. Electrolytic parameters and formation fields were evaluated from the unitary formation rates. Local currents were estimated using the method described previously.

The mode of formation of anodic oxide films on metals is of increasing technical and scientific interest. The technical applications of anodization are well known, and further interest in the subject has derived from its importance from the point of view of the mechanism of electrode processes in general.

The purpose of the present work was to examine the formation of anodic oxide films on certain metals below the potential of oxygen evolution under experimental conditions sufficiently constant to permit comparisons. The metals selected for study were Al, Ti, Hf, V, Nb, Ta, and Cr. Zr had been studied previously (1, 2).

The pioneer work of Güntherschulze and of Güntherschulze and Betz initiated much of the present day interest in oxide film formation, many of the theoretical discussions having been based on their empirical results. The formation of anodic oxide films on Ta was reported by Güntherschulze and Betz (3), and formation of films on the additional metals W, Zr, and Al was discussed (4). Güntherschulze and Keller (5) reported that electrolytically formed oxides had high densities and high dielectric constants corresponding to the properties of fired oxides. Studies of the formation of these films led Güntherschulze and Betz (6) to the conclusion that the ion current forming the films followed an exponential relationship with the electric field. The work of Güntherschulze and Betz has been published in a book on electrolytic capacitors (7).

The general literature on anodization was found to be too extensive for detailed comment; however, references (8) through (33) have been selected as being of interest in connection with anodization of the particular metals examined in this work.

Experimental

The apparatus used consisted of a constant temperature bath containing the anode, cathode, and reference electrode compartments; the potential measuring circuit with potentiometer, galvanometer, and millivoltmeter; the current measuring circuit with sensitive galvanometer (null type) and potentiometer; and the current regulator.

For most of the experiments the galvanometer for the current measuring circuit was an A. C. Brown Electronik null indicator with a sensitivity of 10^{-3} μ amp/mm. For the 1 μ amp current density runs a L&N reflecting-type galvanometer with a sensitivity of 3.7×10^{-4} μ amp/mm was used.

Grounding of the cathode through a large condenser was found to be necessary to avoid fluctuations in millivoltmeter readings due to stray currents. Likewise, all motor and metal parts were systematically grounded, as was the a-c galvanometer.

Test specimens were mounted as follows: The metal specimen was first turned to accurate diameter (usually 1.595 cm, equivalent to 2 cm^2 on the face), bored, tapped, and mounted in plastic, using a standard metallographic plastic mounting powder, heated die, and press technique. The plastic cylinder was then drilled and tapped to take a threaded tube through which a brass rod could be inserted to thread into the backside of the metal specimen, thus establishing a firm electrical connection. This method showed special advantages of speed of preparation and reproducibility of apparent surface area, and provided a convenient holder for abrasion of the metal.

Experimental Procedure

Many experiments were carried out to devise a standard method which would minimize the variations due to the experimental conditions. The tests were all run at 25°C and in the same electrolyte (*see* below). Air was bubbled constantly through the electrolyte to maintain air saturation, and to provide stirring. The same reference electrode,

[1] Present address: Research Labs., Westinghouse Electric Corp., Pittsburgh, Pa.

[2] Present address: Dept. of Chemistry, Stanford University, Stanford, Calif.

saturated mercurous sulfate, was used in all experiments, and all potentials given here are referred to this electrode.

The specimens were abraded dry on either metallographic paper or emery cloth immediately before each test. For Ti, Cr, Ta, V, Nb, and Hf, the abrasion consisted of 100 parallel strokes on 3/0 emery cloth. This was sufficient to remove all visible right angle scratches and yet it was believed not to produce an unduly cold-worked surface. Reproducibility between runs was good. With Al, separate studies were made using 3/0 emery cloth in one case, and 400 metallographic paper in the other. With Al, the formation rate (rate of change of potential with time ($\Delta E/\Delta t$) was found to vary considerably with the degree of abrasion (particularly noticeable on the coarser grits), 25 strokes on 400 paper being found sufficient to expose a new surface and give reproducible results. The 3/0 abrasion produced lower initial and lower constant formation rates, as would be expected on the basis of the greater surface area and consequent lower current density in the case of this coarser abrasion.

After abrasion the specimen was connected to the current regulator and the millivoltmeter and immersed with current switched on. Times from final abrasion to first reading were of the order of 6-10 sec and, depending on the applied current, measurements were carried out over a period of up to 8 hr.

The range of current densities was 0-100 μ amp/cm^2 and the apparent surface area of all specimens was about 2 cm^2.

Each metal was anodized at several current densities up to 100 μ amp. At least three check runs were made at each current density except 0 and 1 μ amp where usually only two runs were made in each case.

Materials

The electrolyte used throughout these experiments was a boric acid-ammonia solution. This electrolyte was selected because of its use by many previous investigators for the anodization of Al, Ta, and Zr. The solution was conveniently made by saturating distilled water with reagent grade boric acid at 25°C, then bubbling in gaseous ammonia to a *p*H of 8.

The present availability of various rare metals in high purity was one of the reasons for initiating the present work on anodic polarization. Further than the availability of the pure metals, a form suitable for experiment was required. Developments in arc-melting and metal-forming techniques permitted the testing of dense metal, whereas earlier investigators frequently had to work with powders or lumps of relatively impure materials.

The Al was obtained as Hoopes pig, recast to bar, and rotary swaged to approximate size.

The iodide titanium was arc-melted from the crystal bar to the arc-cast button, which was then turned to specimen size. Kroll process Ti was obtained as swaged rod and specimens turned from this rod.

The iodide hafnium was arc-melted from the crystal bar to the arc-cast button, which was then turned to specimen size.

Table I. Experimental metals

Metal	Type	% Metal	Chief impurities %
Al	Hoopes	99.99	Fe, Cu, Si traces
Ti	Kroll	99.6	Fe = 0.2, O = 0.05, Mg = 0.1, N, C, Mn traces
Ti	Iodide	99.9	Fe = 0.02, Al, Mn, C traces
V	Calcium bomb	99.9	O = 0.05, N, C traces
Nb	Fansteel	99.9	Labeled research grade by Fansteel
Ta	Electrolytic	99.9	Fe, C, O traces
Hf	Iodide	96.1	Zr = 3.8, Fe, Si, Al traces
Cr	Ductile	99.95	O = 0.04, Fe, Si traces
Zr	Kroll (not annealed)	99.6	O = 0.16, Fe = 0.06, C = 0.037, Sn = 0.05, Hf = 0.03

Va was obtained as lumps from the Ca bomb reduction process and arc-melted to a button which was turned to specimen size.

Nb was obtained as rolled sheet, cut up, and arc-melted to a button, which was turned to specimen size.

Ta and Cr were obtained as swaged rod.

Zr (Kroll process) was tested in sheet form as reported previously (1, 2).

Table I lists the metals with approximate total metal contents and chief impurities.

The arc-melted buttons were used in the as-cast condition directly without further annealing. The swaged rod materials were annealed by sealing in evacuated Vycor ampoules and heating to 950°C for Cr, Ta, and Ti, and to 500°C for Al.

Experimental Results

Experimental results for the different metals were recorded in the following manner: potential vs. time curves, representing the primary data, were obtained for each metal; from the potential-time data a second series of curves was constructed which show the relationship log ($\Delta E/\Delta t$) vs. log time and also the relationship of the log of the constant rate vs. log current density. Such plots show, for the film formers, how the limiting constant formation rate ($\Delta E/\Delta t$) at constant current density increases with this current density. From the log rate vs. log time and vs. log I plots the local currents were calculated, according to the method developed earlier (1).

If the values for the constant rate of change of potential at a given current density be divided by that current (in microamperes per cm^2) a new value is obtained which has been called the unitary formation rate, $1/I$ ($\Delta E/\Delta t$), or R_I. From the plots of the unitary formation rate vs. log current density, a third series of curves was obtained showing the linear dependence of the unitary rate on the logarithm of the current density. This result is predicted from the empirical law of anodic film growth $I = A_+e^{B_+F}$ where I is the total anodic current, A_+ and B_+ are the electrolytic parameters, and F is the field across the oxide film.

Aluminum.—Fig. 1 shows the potential vs. time curve for annealed Al abraded on 400 paper. The log

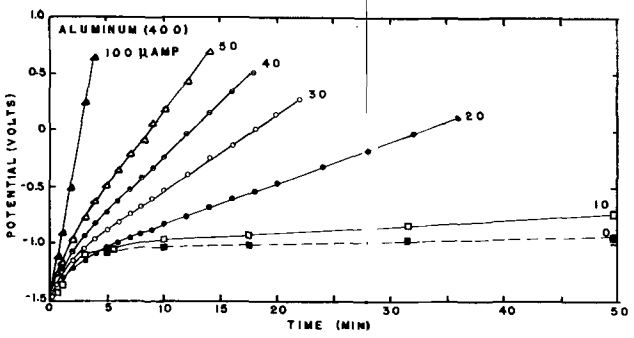

Fig. 1. Potential vs. time for Al abraded on 400 grit paper. Anodized in air-saturated ammonium borate solution at 25°C.

rate vs. log time and log current density curves for Al abraded on 3/0 and 400 are similar in form to that shown for Ta in Fig. 2. Fig. 3 shows the plots of unitary rates vs. log current density. The 400 test as seen from the dotted line shows deviation from linearity. However, for purposes of calculation a straight line was drawn through the intermediate points.

Experimental runs in the region below 10 μ amp were found to give unreproducible results. Indeed, the formation rate at 10 μ amp is seen to be scarcely more than that at zero applied current. Although Al is considered here to be a genuine film former under the conditions of these experiments, the abnormally low film formation rate, which may be due to partial dissolution of the film, did prevent ready discrimination of the results at the lowest current densities, i.e., below 10 μ amp. Reproducibility on the 3/0 emery cloth with Al was found to be very poor. This was attributed to the virtual impossibility of duplicating the degree of abrasion between runs. High purity Al is extremely soft, and consequently very small changes in pressure during abrasion would be expected to cause large variations in the degree of abrasion and, hence, in the real surface area. The increased formation rate of the 400 grit over the 3/0 grit quite probably reflects this difference.

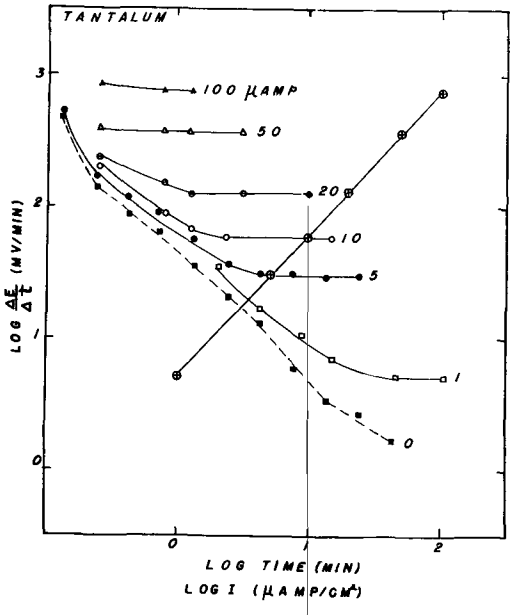

Fig. 2. Log rate of change of potential vs. log time and vs. log current density of Ta in air-saturated ammonium borate solution at 25°C.

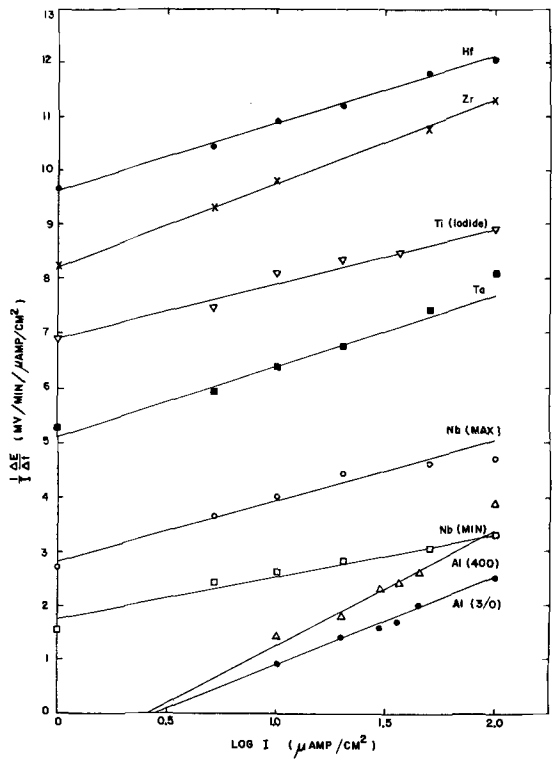

Fig. 3. Comparison of the unitary formation rate vs. the log of the current density for Hf, Zr, iodide titanium, Ta, Nb, and Al. Air-saturated ammonium borate at 25°C.

Since 3/0 was found to be unsuitable, 400 grit paper was used and reproducibility found to be more satisfactory. Despite the improvement noted using 400 grit paper, other variables continued to influence the formation rate. In particular, it was found that the age of the ammonium borate electrolyte had a pronounced effect on the results. A fresh, i.e., previously unused, solution produced formation rate values about 30% lower than those obtained in solutions which had been used repeatedly (a possible indication of solubility of the film in the electrolyte or of discharge of certain anions in the solution, such as chloride).

Attempts to study the effect of cold work on the formation rate for Al were abandoned because of these irregularities.

Titanium.—Ti received the most detailed examination of the metals tested in the present investigation. Iodide titanium was tested because of its relatively higher purity compared with the commercial Kroll process metal.

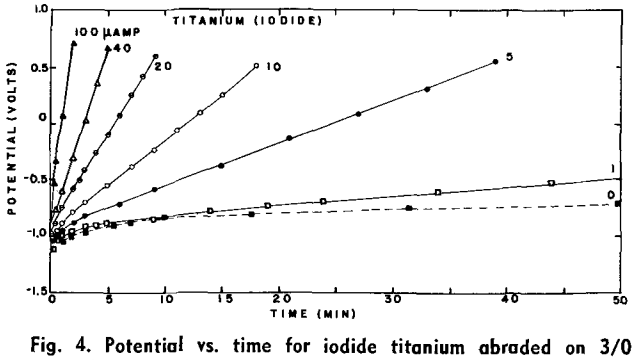

Fig. 4. Potential vs. time for iodide titanium abraded on 3/0 emery. Anodized in air-saturated ammonium borate solution at 25°C.

In addition to iodide and Kroll process Ti (corresponding to two different purities), three series of runs were made using Kroll process Ti which had been given different degrees of cold work. Three cylinders of Kroll process Ti of about ⅝ in. diameter and ½, ½, and ¾ in. in height, respectively, were vacuum annealed at 800°C, then cold pressed axially to reductions of 11%, 24%, and 34% each. The specimen reduced 34% slipped in shear on the diagonal of the pressed cylinder and the slipped plane was made the face of the specimen for anodic testing. The 11% and 24% cold-worked specimens were tested on the original circular faces.

The specimen reduced 11% was found to give values of the formation rate virtually unchanged from annealed material. The specimen reduced 24% gave slightly higher values than the annealed, but of such slight differences as not to be clearly conclusive. The specimen reduced 34%, however, showed quite positive increase. Fig. 4 shows the potential-time curve for iodide Ti. Curves for Kroll process Ti and the 34% cold work were indentical in form but with greater slopes in each case, the cold-worked having greater slope than the Kroll Ti, and the latter more than iodide. It should be noted that the zero applied current curve was nearly identical for the three cases. Fig. 5 shows the log rate vs. log time and log current density for iodide Ti. Fig. 6 shows the dependence of the unitary rate on the log current density for the three types of Ti specimens. Kroll process and the cold-worked specimens gave curves displaced upward from the iodide curves.

Other metals.—Results for iodide Hf are shown in Fig. 7. The log rate vs. log time and log current

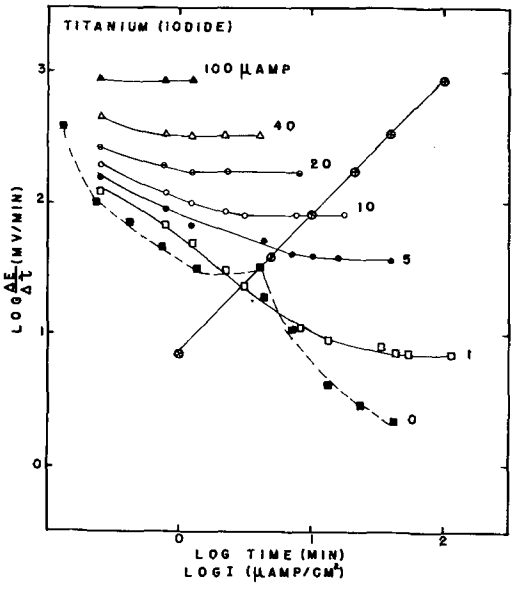

Fig. 5. Log rate of change of potential vs. log time and vs. log current density for iodide titanium in air-saturated ammonium borate solution at 25°C.

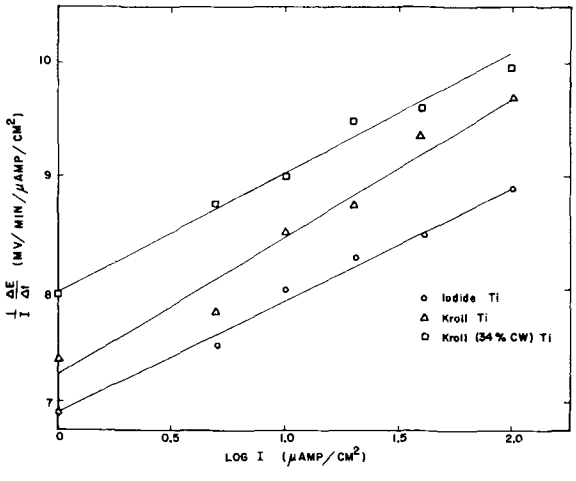

Fig. 6. Unitary formation rate vs. log current density for iodide titanium, Kroll process Ti, and Kroll process, 34% cold-worked Ti. Air-saturated ammonium borate solution at 25°C.

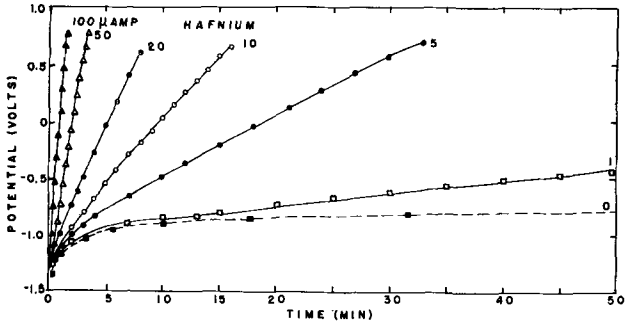

Fig. 7. Potential vs. time for Hf abraded on 3/0 emery. Anodized in air-saturated ammonium borate solution at 25°C.

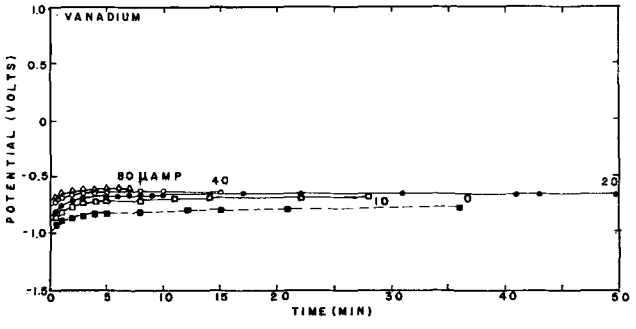

Fig. 8. Potential vs. time for V abraded on 3/0 emery. Anodized in air-saturated ammonium borate solution at 25°C.

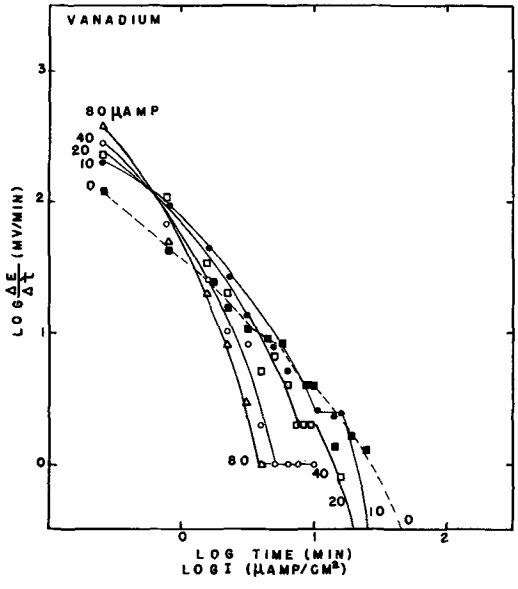

Fig. 9. Log rate of change of potential vs. log time and vs. log current density of V in air-saturated ammonium borate solution at 25°C.

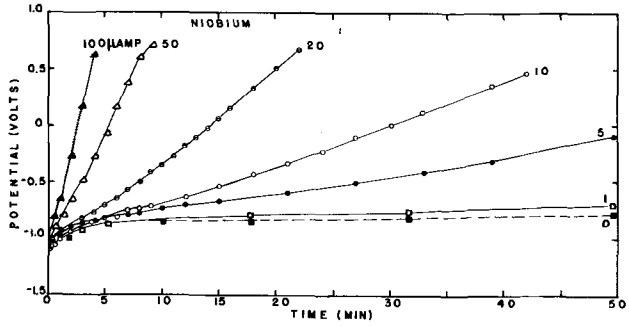

Fig. 10. Potential vs. time for Nb abraded on 3/0 emery. Anodized in air-saturated ammonium borate at 25°C.

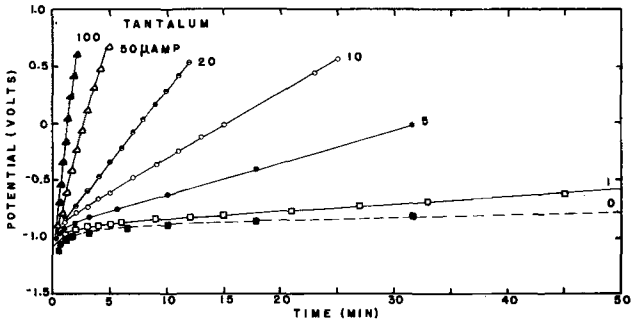

Fig. 12. Potential vs. time for Ta abraded on 3/0 emery. Anodized in air-saturated ammonium borate solution at 25°C.

density curve is again of the same type as shown by Ta, Fig. 2.

Results for V are shown in Fig. 8 and 9.

Results for Nb are shown in Fig. 3, 10, and 11.

Potential vs. time curves for Ta are shown in Fig. 2, 3, and 12.

Results for Cr are shown in Fig. 13. The log rate vs. log time curves are of the same type as shown by V, Fig. 9. Anodization of Cr at high current densities gave a distinctly green dissolution product.

Discussion

Metal Types

The results show that the metals tested under the conditions of these experiments fall roughly into three categories: (*a*) the non film-formers Cr and V; (*b*) the film-formers Al, Ti, Hf, Ta, and Zr; (*c*) an intermediate class containing Nb as a single member.

Examination of the potential-time curves for representative metals of these groups, for example, V, Ta, and Nb, show certain differences. The V potential time curves (Fig. 8) rise rapidly to a nearly constant common value of about minus 0.6 v. This potential is far below that of oxygen evolution. Ta, on the other hand, shows (Fig. 2) a family of curves typical of a film former. Each curve has an initial sharp rise followed by a distinctly linear portion which persists up to the oxygen evolution potential, where the rate falls off suddenly. Increasing current density does not change this characteristic behavior; only the slope of the linear portion of the curve is increased, and the time to reach oxygen evolution potentials is decreased.

Nb (Fig. 10) shows another set of curves. While superficially resembling the performance of the film formers, the behavior is somewhat different. In the potential time plots the expected "linear" portion is not linear, as may be determined by sighting along the curves in the plane of the page.

The differences among the three types are more apparent, however, when the logarithm of the rate of change of potential log ($\Delta E/\Delta t$) is plotted vs. the logarithm of the time. The data for V (Fig. 9), Ta (Fig. 3), and Nb (Fig. 11) may be compared. The non film-former V is seen to give an initial negative slope which rapidly becomes steeper. With the exception of several unexplained arrests at the higher current densities (for both V and Cr), the curves appear to go downward steadily. This type of curve can be explained possibly on the basis of film dissolution, or else on the basis of an extremely porous film structure. In the case of Cr and V the only effect of increasing current density was merely to accelerate the rapid rise of potential to a constant value.

For the typical film-former Ta (Fig. 2) the curves are seen to decrease more or less rapidly to horizontal lines corresponding to the linear region of constant slope of the potential-time plot.

For Nb (Fig. 11), an initial decrease to a minimum followed by a distinct rise to a maximum is observed. This suggests a combination of the non-

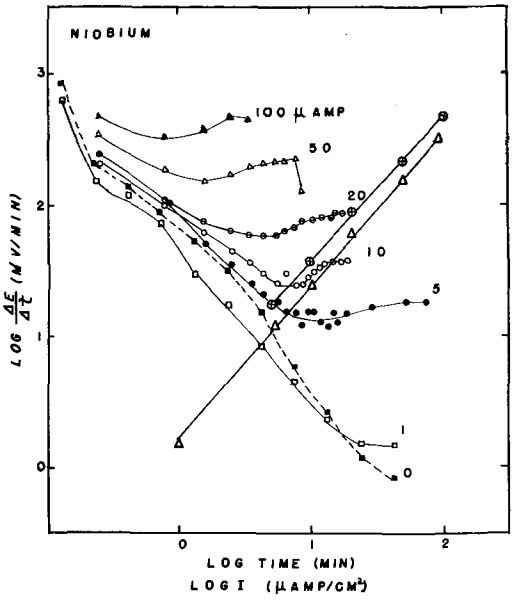

Fig. 11. Log rate of change of potential vs. log time and vs. log current density for Nb in air-saturated ammonium borate solution at 25°C.

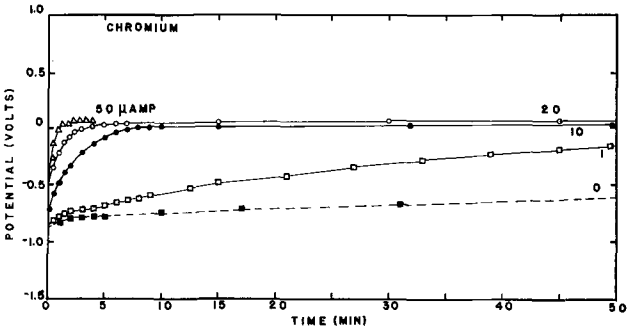

Fig. 13. Potential vs. time for Cr abraded on 3/0 emery. Anodized in air-saturated ammonium borate solution at 25°C.

Table II. Local currents (electrolyte: saturated ammonium borate)

Metal	A mv/min	B slope	(μamp/cm^2) at time Current (min) 0.5	1	5	10	50
Al 3/0	0.355	1.45	36.3	30.2	17.4	9.33	0.925
Al 400	0.447	1.5	67.6	53.7	11.8	5.01	0.977
Ti (iodide)	7.08	1.05	7.94	4.63	2.69	0.895	0.282
Ti (Kroll)	6.61	1.12	7.84	5.41	3.66	0.815	0.38
Ti (Kroll CW)	7.94	1.07	6.50	4.72	1.61	0.65	0.18
Hf (iodide)	10.5	1.03	10.12	8.91	2.09	0.855	0.007
Nb (Max)	3.16	1.06	32.4	17.4	3.31	1.24	0.141
(Min)	1.78	1.12	44.7	25.1	5.19	2.05	0.263
Ta	5.25	1.08	12.3	7.25	1.90	0.899	0.330

film-former and film-former types and hence Nb was considered as belonging to an intermediate type.

Since no distinct horizontal portion of the curve was obtained on the log rate vs. log time plot, the customary plot of log constant rate vs. log current density could not be obtained. However, by assuming either the maxima or minima of the curves to be constant rate portions, a linear relationship was again obtained in both cases. The two straight lines are shown in Fig. 11.

The fact that the potential changes with time, even at zero applied current, has been interpreted as due to a film building process resulting from the passage of local currents between microscopic anodes and cathodes in the surface of the electrode. A method for estimating these local currents at a given time has been developed (1). The rate of change of applied potential with time necessary to maintain a constant current has been found to fit the relationship

$$\Delta E/\Delta t = AI^B \qquad (I)$$

or

$$\log \Delta E/\Delta t = \log A + B \log I \qquad (II)$$

where E is the potential, I the current density, and A is the formation rate at unit current density.

Constants A and B are determined from the log rate vs. log I plot and the value of log formation rate at a given time read from the zero applied current curve. From this the local current I at the given time may be calculated. Table II lists the local currents for the various metals at 0.5, 1, 5, 10, and 50 min, respectively, together with the constants A and B. Except for Al, the value of B is seen to be remarkably constant, even among the different metals. The constant A, however, shows a large variation among the metals. Two sets of values for Nb are included, reflecting the fact that the local currents are calculated from the maximum or minimum values of the log rate vs. log I plots.

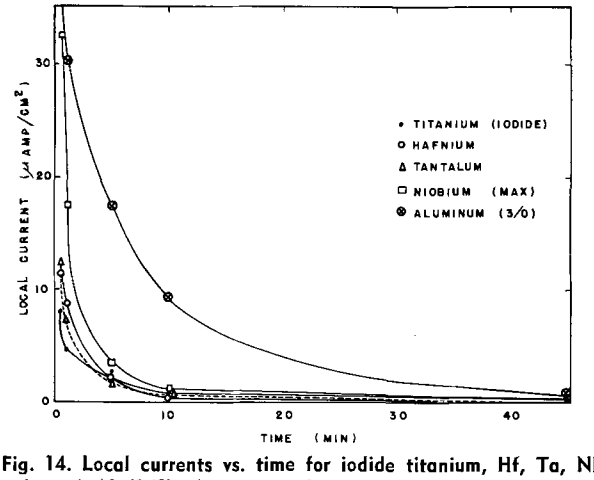

Fig. 14. Local currents vs. time for iodide titanium, Hf, Ta, Nb (max), and Al (3/0). Air-saturated ammonium borate solution at 25°C.

Table III. Unitary formation rates (mv/min/μ amp/cm^2)

Metal	Current Density 1	5	10	20	30	40	50	100
Ti (iodide ann)	6.9	7.4	8.1	8.3		8.4		8.9
Ti (Kroll ann)	7.4	7.8	8.5	8.9		9.35		9.5
Ti (Kroll 34%)	7.95	8.75	9.0	9.5		9.6		9.95
Zr (Kroll ann)	8.2	9.3	9.8				10.8	11.3
Hf (iodide ann)	9.7	10.45	10.9	11.2			11.8	12.05
V				No stable film				
Nb (Max)	2.7	3.6	4.0	4.4			4.6	4.7
(Min)	1.55	2.4	2.6	2.8			3.05	3.3
Ta	5.25	5.95	6.35	6.75			7.4	8.1
Cr				No stable film				
Al (3/0)			0.9	1.4	1.6	1.7	2.0	2.5
Al (400)			1.4	1.8	2.3	2.4	2.6	3.9

The local current values for Ti, Hf, and Ta are of the same order as those calculated for Zr (1) both in ammonium borate and other electrolytes, i.e., about 10 μ amp/cm^2 at about 0.5 min. For Nb, however, a value between 32 and 44 μ amp/cm^2 was obtained, and for Al, abraded on 400 grit paper, the very large value of 67.6 μ amp/cm^2 was obtained. At 50 min it had diminished to only 1 μ amp/cm^2. Fig. 14 shows a plot of the local currents vs. time for the film-formers. Only Al appears to diverge from the pattern of the other metals.

Unitary Formation Rates

The unitary formation rate, $1/I$ $(\Delta E/\Delta t)$, or R_I, affords some comparison of the behavior of the different metals. Table III gives the values for the metals examined in the present work, plus Zr from other work for comparison.

Table III shows that R_I increases with current density for a given metal. The R_I value is found to increase also with impurity content in Ti and to increase with cold work.

Further, if the metals are arranged according to their places in the periodic table as in Table IV, the R_I values for all current densities show an increase in going from top to bottom and from right to left as shown by the path of the arrows. Values of R_I for 100 μ amp/cm^2 are arranged in Table IV for illustration.

The position of Al is somewhat uncertain, but the very low unitary formation rate does show that it probably belongs to the right in the table.

Electrolytic Parameters

Plots of the unitary formation rate vs. log current density gave linear relationships as predicted from the empirical law of anodic film growth

$$I = A_+ e^{B_+ F} \qquad (III)$$

where I is the total anodic current, A_+ and B_+ are electrolytic parameters, and F is the field across the

Table IV. Trends of R_I with the Periodic Table

Al (2.5) 3/0
(3.9) 400

Ti (8.9)	V (0)	Cr (0)
Zr (11.3)	Nb (4.7) max	
	(3.3) min	
↓ Hf (12.05)	↓ Ta (8.1)	

←

Table V. Electrolytic parameters

Metal	Slope	Intercept $\frac{mv}{min}$ $\frac{cm^2}{\mu amp}$	σA_+ $\mu amp/cm^2$	σB_+ cm/v	$F_{100/\sigma}$ v/cm	$B_+ F_{100}$
Ti (iodide)	1.0	6.9	1.23×10^{-7}	6.75×10^{-6}	3.04×10^{6}	20.5
Ti (Kroll)	1.2	7.25	8.91×10^{-7}	5.63×10^{-6}	3.30×10^{6}	18.6
Ti (Kroll 34%)	1.1	8.0	5.37×10^{-8}	6.14×10^{-6}	3.48×10^{6}	21.4
Zr ref. (36)	1.69	7.68	2.9×10^{-5}	4.6×10^{-6}	3.26×10^{6}	15
Hf	1.25	9.6	2.09×10^{-8}	6.2×10^{-6}	3.60×10^{6}	22.3
Nb Max	1.15	2.7	4.47×10^{-3}	7.35×10^{-6}	1.36×10^{6}	10.0
Nb Min	0.75	1.8	3.98×10^{-3}	11.3×10^{-6}	0.89×10^{6}	10.1
Ta	1.28	5.07	1.05×10^{-4}	5.8×10^{-6}	2.38×10^{6}	13.8
Al (3/0)	1.6	−0.7	2.74	3.8×10^{-6}	0.95×10^{6}	3.6
Al (400)	2.12	−0.7	2.14	2.86×10^{-6}	1.34×10^{6}	3.84

oxide film. The Cabrera-Mott theory leads to an equation of the above type (29).

It is possible (2) to calculate A_+ and B_+ using the slope and intercept of the unitary rate vs. log I plot. The values of σA_+ and σB_+ (where σ is the roughness factor), with the slopes and intercepts they are calculated from, are shown in Table V. The dimensionless constant B_+F_{100} for each metal is also shown (where F_{100} is the formation field for a current of 100 μ amp/cm^2).

In addition to the results reported in Table V for Ta, low potential runs were made on the same specimen in 0.1% Na_2SO_4 solution at 48°C, using both mechanically polished and bright-etched surfaces. The average unitary formation rate obtained for 25 different runs was 19.0 $\frac{mv \quad cm^2}{min \ \mu amp}$. This corresponds to $F_{100/\sigma} = 6.3 \times 10^6$ v/cm using 8.74 g/cc for the density of tantalum oxide. Formation rates on the polished surfaces were not constant. The time required for the potential to increase by 200 mv was measured over the pre-oxygen evolution potential range. Eighty-three of these measurements were taken in the 25 different runs and averaged to obtain the final average unitary formation rate.

Ta was studied in the high potential range by Vermilyea (14) and by Young (25). Vermilyea obtained a value of $F_{100/\sigma}$ for anodic Ta_2O_5 films on bright-etched Ta of 6.13×10^6 v/cm. These measurements were made at 48°C in 0.1% Na_2SO_4 solution. Young obtained 6.17×10^6 v/cm (interpolated to 48°C) for Ta_2O_5 formed on mechanically polished Ta in 0.5M Na_2SO_4.

The product B_+F_{100} may be used as an estimate of the amount the activation barrier must be lowered by the field in order that a constant current density of 100 μ amp/cm^2 may pass through the oxide film. The higher the zero-field barrier height, the higher the product B_+F_{100} should be for a given metal. (The parameter A_+ should also be a measure of this barrier height; an increase in barrier height would decrease A_+.)

It would also be expected that the local current would decay at increasing rate for increasing barrier height for a given metal.

The foregoing treatment permits an analysis, up to a point, of the kinetics of the film building process. An alternative treatment, more directly based on the methods of electrochemical kinetics, has been developed and will be the object of another communication.

Acknowledgments

The receipt by one of the authors (H.A.J.) of a fellowship from the Alcoa Research Foundation is gratefully acknowledged. The kind assistance received from the personnel of the U. S. Bureau of Mines Station at Albany, Ore., in the preparation and analysis of several specimens, is acknowledged with thanks. The work on Zr, referred to here for comparison, was carried out under contract AT(45-1)-535 between the University of Oregon and the U.S. Atomic Energy Commission.

Manuscript received July 17, 1956. This paper was prepared for delivery at the San Francisco Meeting, April 29 to May 3, 1956. It was taken from the thesis submitted by H. A. Johansen in partial fulfillment of the requirements for the Ph.D. degree.

Any discussion of this paper will appear in a Discussion Section to be published in the December 1957 JOURNAL.

REFERENCES

1. M. Maraghini, G. B. Adams, Jr., and P. Van Rysselberghe, *This Journal*, **101**, 400 (1954).
2. G. B. Adams, Jr., P. Van Rysselberghe, and M. Maraghini, *ibid.*, **102**, 502 (1955).
3. A. Güntherschulze and H. Betz, *Z. Physik*, **68**, 145 (1931).
4. A. Güntherschulze and H. Betz, *Z. Elektrochem.*, **37**, 726 (1931).
5. A. Güntherschulze and F. Keller, *Z. Physik*, **75**, 78 (1932).
6. A. Güntherschulze and H. Betz, *ibid.*, **92**, 367 (1934).
7. A. Güntherschulze and H. Betz, "Elektrolyt-Kondensatoren," M. Krayn, Berlin (1937).
8. R. H. Brown and R. B. Mears, *Trans. Electrochem. Soc.*, **74**, 495 (1938).
9. R. B. Mears, *J. (and Trans.) Electrochem. Soc.*, **95**, 1 (1949).
10. R. B. Mears and R. H. Brown, *This Journal*, **97**, 75 (1950).
11. R. H. Brown, G. C. English, and R. D. Williams, *Corrosion*, **6**, 186 (1950).
12. W. G. Burgers, A. Claasen, and I. Zernike, *Z. Physik*, **74**, 593 (1932).
13. A. Charlesby, *Acta Met.*, **1**, 340 (1953).
14. D. A. Vermilyea, *ibid.*, **1**, 282 (1953).
15. R. B. Mason and C. J. Slunder, *Ind. Eng. Chem.*, **39**, 1602 (1947).

16. A. Charlesby, *Proc. Phys. Soc. (London)*, **B66**, 317 (1953).
17. M. S. Hunter and P. Fowle, *This Journal*, **101**, 481 (1954).
18. C. D. Hall, Jr., and N. Hackerman, *J. Phys. Chem.*, **57**, 262 (1953).
19. R. D. Misch and E. S. Fisher, *This Journal*, **103**, 153 (1956).
20. R. K. McKechnie and A. U. Seybolt, *ibid.*, **97**, 311 (1950).
21. E. Deltombe, N. de Zoubov, and M. Pourbaix, Report 29, "Electrochemical Behavior of Vanadium," *Centre Belge d'Etude de la Corrosion*, Brussels, January (1956).
22. U. Sborgi, *Gazz. chim. ital.*, **42**, II, 331 (1912).
23. G. Schulze, *Ann. Physik*, **25**, 775 (1908).
24. L. Young, *Trans. Faraday Soc.*, **51**, 1250 (1955).
25. L. Young, *ibid.*, **50**, 153 (1954).
26. H. E. Haring, *This Journal*, **99**, 30 (1952).
27. D. A. Vermilyea, *Acta Met.*, **2**, 476 (1954).
28. J. F. Dewald, *ibid.*, **102**, 1 (1955).
29. N. Cabrera and N. Mott, *Rep. Prog. Phy.*, **12**, 163 (1948).
30. R. H. Roberts and W. J. Shutt, *Trans. Faraday Soc.*, **34**, 1455 (1938).
31. I. Issa, I. Ammar, and H. Khalifa, *J. Phys. Chem.*, **59**, 492 (1955).
32. A. Charlesby, Atomic Energy Research Establishment M/R 714, Harwell, Berks, England, May 1951.
33. R. D. Misch and W. E. Ruther, *This Journal*, **100**, 531 (1953).

Metal-Water Reactions

IV. Kinetics of the Reaction between Calcium and Water Vapor

Harry J. Svec and Charles Apel

Institute for Atomic Research and Department of Chemistry, Iowa State College, Ames, Iowa

ABSTRACT

Calcium metal was reacted with water vapor in the temperature range 20°-70°C and at water vapor pressures of 18-93 mm Hg. The experiments indicated that the only products were $Ca(OH)_2$ and H_2 and that the reaction proceeded according to the equation

$$Ca + 2H_2O \rightarrow Ca(OH)_2 + H_2$$

A manometric study of the reaction showed that it followed the logarithmic rate law. The rate constant was observed to be linearly dependent on water vapor pressure below 70°C and to decrease with increasing temperature in the range 20°-50°C. At 70°C the rate constant was observed to be independent of water vapor pressure. The activation energy was found to be —7.52 kcal/mole in the pressure dependent range.

The kinetics of gas-metal reactions involving N_2, O_2, and H_2 have been widely studied and numerous references are available (1). Recently there has been interest in the reactions between metals and water vapor. Svec and Deal have shown that Li (2) and Th (3) both follow the logarithm law when reacted with water vapor.

A study of the rate at which reaction takes place between Ca and water vapor was undertaken in order to compare the reactivity of Ca with that of Li and the other alkaline earth metals. An examination of reaction products showed that the reaction takes place according to the equation

$$Ca + 2H_2O \rightarrow Ca(OH)_2 + H_2 \qquad (I)$$

Because of the nature of the reaction, the rate was followed by observing the evolution of H_2 as a function of time. Conditions of temperature and water vapor pressure were regulated carefully in order to determine their effect on the rate of the reaction.

Experimental

One pound cylinders of cast, redistilled Ca metal were obtained from the Metallurgical Division of the Ames Laboratory. Spectrographic analysis showed that the impurities totalled approximately 0.5%, occurring as a mixture of Al, Ba, Cr, Fe, Mg, Mn, Si, Sr, Y, and Zr. Some of these elements, notably Y and Zr, were probably introduced in trace amounts during the machining of the sample specimens. Rough cylinders, approximately ½ in. in diameter and 2 in. in length, were cut and turned under Na-dried turbine oil on a lathe in the machine shop. They were then finished by machining on a lathe mounted in a controlled atmosphere box containing He. The final machining conditions were carefully duplicated for each cylinder to insure uniform metal surfaces for the entire group of specimens used in this study. Before use, freshly prepared cylindrical specimens were stored under Na-dried turbine oil through which purified He had been bubbled.

Immediately preceding use, dimensions of each cylinder were measured with machinists' calipers. Following this, a stainless steel hook was fastened to the top of the cylinder in order to hang the cylinder in the reaction vessel. The oil in which the Ca had been stored was removed by means of rinses in Na-dried, low boiling petroleum ether, followed by one rinse in Na-dried diethyl ether.

The reactions occurred in apparatus slightly different from the one described in a paper to be published.[1]

During the study, water vapor pressures of 18, 32, 55, 72, and 93 mm Hg were used at reaction temperatures of 20°, 25°, 30°, 35°, 40°, 45°, 50°, 55°, 60°, and 70°C. Water was introduced into the apparatus through the Hg covered serum bottle stopper by means of a hypodermic syringe. As the reaction between water vapor and Ca proceeded, the pressure of the H_2 evolved was continuously followed by means of a recording Hg manometer (4).

Values for the amount of water vapor undergoing reaction per unit area of metal were obtained from H pressures by determining the total volume of the reaction apparatus and the volume and surface areas of the Ca cylinder. The H_2 pressures were obtained by subtracting the water vapor pressure employed in a particular run from the total gas pressures throughout the run. It was assumed that the Ca surface areas obtained from the cylinder dimensions and used in these calculations were minimum areas, but that they were proportional to the true areas by a constant factor. The reproducibility of the experimental results supported this assumption.

Results

Inasmuch as the reaction of Ca with water vapor proceeds with the formation of a surface film, the reaction data are expected to fit one of the gas-solid reaction rate laws. A comparison of the most common of these laws (5,6) is presented in Fig. 1. It is evident that a straight line is followed by the logarithmic treatment of the data, while the linear, parabolic, and cubic plots are curved. Plots of data from water vapor-Ca reactions at other temperatures and pressures corroborate this conclusion.

The value of the constant in the logarithmic equation was set equal to 0.4 by Brodsky and Cubicciotti (7) in silicon-oxygen reaction rate studies. Svec and Deal observed that a value of 0.45 for a fit the data when water vapor was reacted with Li (2) and Th (3). The value 0.45 also fit the data in the present study.

Logarithmic plots were made for each reaction and values of the logarithmic rate constant K were obtained from the slopes of the first 100 min of the curves. Several typical plots are shown (Fig. 2) for reaction data obtained at various temperatures and a water vapor pressure of 32 mm Hg. On extending the data presented in Fig. 2 over longer periods of time, definite changes or breaks were observed in the slopes of the curves. After each of these breaks, the reaction rate became unpredictable.

The temperature dependence of the rate constant K was determined by plotting the values of K obtained at constant water vapor pressure against temperature, as shown in Fig. 3. The rates were found to decrease with increasing temperature until attaining a minimum between 50° and 70°C. The rate then increased with temperature up to 70°C, which was the highest temperature employed in this study. With the exception of the runs at 18 mm Hg, all isobars converge to a K value of about 12 at 70°C.

[1] This Journal, July 1957 issue.

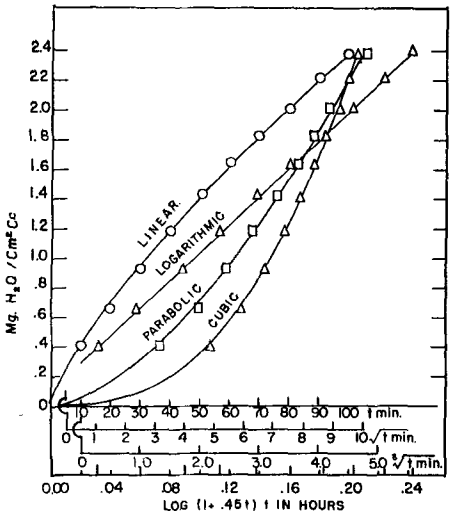

Fig. 1. Comparison of four rate laws for gas-metal reactions using Ca-water vapor data. Temperature, 36°C; water vapor pressure, 32 mm Hg.

Arrhenius plots were made for each isobar over the temperature range in which the reaction rate decreased with increasing temperature, and activation energies were obtained from the slopes of the lines. These were positive (Fig. 4) and were linear within experimental error, indicating negative energies of activation. At the temperatures employed the activation energy appeared to be independent of water vapor pressure and had an average value of −7.52 ± 0.28 kcal/mole.

The dependence of the rate constant on water vapor pressure was determined by plotting the values of K at constant temperature against water vapor pressure. Each isothermal plot was linear and most of them indicated a value of zero for K at a vapor pressure of about 10 mm Hg.

On the basis of the pressure dependence of the rate constant and the activation energy −7.52 ± 0.28 kcal/mole, an empirical equation was derived relating the rate constant K to temperature and water vapor pressure. This equation states that

$$K = A(P - 10)e^{3785/T} \text{ mg } H_2O/cm^2 \text{ Ca surface-log hr} \qquad \text{(II)}$$

where A is a constant, P is the water vapor in mm Hg, and T is the absolute temperature. The value 3,785 is the $-Q/R$ of the Arrhenius equation which states that K is proportional to e^{-Q}/RT. The constant −10 was taken from the value for P when $K = 0$ from the plots of the rate constant vs. water vapor pressure.[2] This equation applies to the temperature range 20° −60°C in which the minimum values of the rate constant occur as indicated in Fig. 3. In this range the constant A was found to have a value of $(2.57 \pm 0.31) \times 10^{-6}$ mm H_2O/cm^2 Ca mm Hg log hr. Using this value leads to the rate expression

$$W = 2.57 \times 10^{-6} (P - 10)e^{3785/T} \log (1 + 0.45t) \qquad \text{(III)}$$

where W is the number of milligrams of water consumed per square centimeter of Ca surface, P is the water vapor pressure in millimeters of mercury,

[2] The authors believe that a different rate law is followed at pressures below 10 mm. No experimental data were obtained, however, due to the limitations of the present method. $K = 0$ only applies here where the logarithmic law holds.

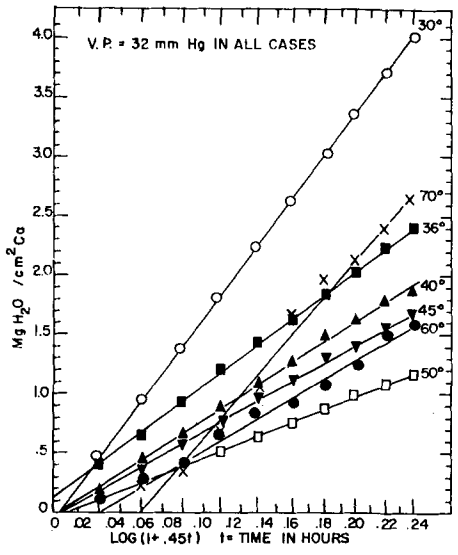

Fig. 2. Logarithmic plot of Ca-water vapor data at 32 mm Hg water vapor pressure and varying temperatures.

T is the absolute temperature, and t is the time in hours. Values of K determined from Eq. (II) compare favorably with the experimental values of K obtained in the water vapor pressure dependent ranges.

The ratio of the molecular volume of $Ca(OH)_2$ to that of Ca metal is 1.20. According to Evans (8) such a ratio should lead to blistering and flaking as the coat thickens. This was found to be true, especially for runs of more than 100-min duration, after which the reaction rate often changed abruptly and fragments of the $Ca(OH)_2$ coat were observed at the bottom of the reaction vessel. Under such conditions, $Ca(OH)_2$ does not form a truly protective coating, but is crazed with minute cracks giving rise to many possible diffusion paths.

Discussion of Results

Inasmuch as a reaction product film separates the two species undergoing reaction, a diffusion process must occur before reaction can take place. Either water molecules must be absorbed and diffuse inward or Ca ions must diffuse outward. It is possible that a combination of both occurs. The first order dependence of the rate constant on water vapor pressure indicates that, in the temperature range 20°-50°C, the inward diffusion of water molecules through the crazed reaction product coat is probably the rate-controlling step. Further evidence in support of this concept is the decrease of the reaction rate with increasing temperature in this range. To explain this dependence of the reaction rate on temperature and water vapor pressure (9), it should be considered that the number of water molecules striking the $Ca(OH)_2$ surface is directly proportional to the water vapor pressure at a given temperature. Of these, a certain fraction adhere and diffuse inward through the $Ca(OH)_2$ layer. However, as the temperature of the system increases, some of the adhered water molecules attain enough thermal energy to break away from the surface of the specimen and return to the gas phase. This process decreases the number of molecules which can diffuse through the $Ca(OH)_2$ coat and become available for reaction with the Ca, and leads to a reduction in the value of the rate constant. A negative activation energy as a heat of desorption results. At 70°C, the reaction rate becomes independent of the water vapor pressure, probably because of another mechanism becoming dominant, such as the outward diffusion of Ca ions through a coating in which crazing is at a minimum or is absent due to healing of the crystal discontinuities.[3] In this case the Ca ions and electrons reach the $Ca(OH)_2$ gas interface and undergo reaction with all available water molecules before the water molecules receive sufficient thermal energy to escape from the surface. The number of Ca ions diffusing outward then becomes the rate-controlling factor. When this process becomes rate-controlling, the reaction rate should increase with temperature because the rate at which Ca ions diffuse outward increases with increasing temperature. This was found to be true (Fig. 3) inasmuch as

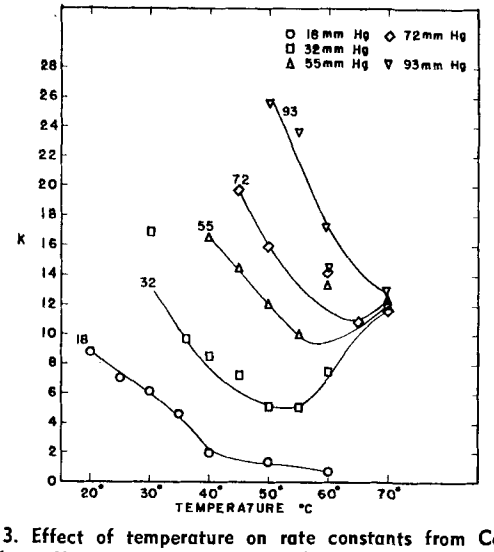

Fig. 3. Effect of temperature on rate constants from Ca-water vapor data. Units of K are mg H_2O/cm^2 Ca.

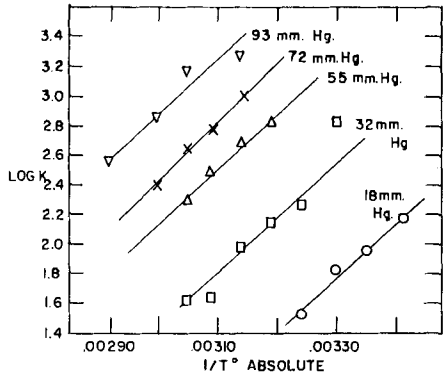

Fig. 4. Log K vs. $1/T$ at different water vapor pressures from Ca-water vapor data. Units of K are mg H_2O/cm^2 Ca. (Naperian logarithms are plotted in this figure.)

[3] That this is reasonable is indicated by some work in which samples of both $Ca(OH)_2$ and $Ca(OD)_2$ were prepared by the metal-water vapor reaction at room temperature. X-ray data on this materials as it was first prepared were very poor, appearing as extremely diffuse or even spotty powder diagrams. Annealing the material at about 100°C in the presence of water vapor completely eliminated this difficulty, indicating considerable crystal growth by a kind of coalescing of very small crystallites. X-ray diagrams of the $Ca(OH)_2$ coating from reactions at 70°C show considerably sharper lines than do those from material produced at lower temperatures.

the reaction rate was observed to increase with temperature as soon as the pressure dependence disappeared.

The work in this study was limited to the temperature range 20°-70°C. The inward diffusion of water molecules through the $Ca(OH)_2$ coat is primarily responsible for the observed phenomena. Further studies at higher temperatures are complicated by the formation of new or different reaction products. The work of Svec and Gibbs (10) certainly supports this contention. A detailed study at temperatures above 70°C is under way. The results of this new study differ from those reported here and will be reported separately.

Manuscript received August 6, 1956. Work was performed in the Ames Laboratory of the A.E.C. Contribution No. 000.

Any discussion of this paper will appear in a Discussion Section to be published in the December 1957 JOURNAL.

REFERENCES

1. O. Kubaschewski and B. E. Hopkins, "Oxidation of Metals and Alloys," Academic Press Inc., New York (1953).
2. H. J. Svec and B. E. Deal, *J. Am. Chem. Soc.*, **75**, 6173 (1953).
3. B. E. Deal, Ph.D. Thesis, Iowa State College Library, Ames, Iowa (1955).
4. H. J. Svec and D. S. Gibbs, *Rev. Sci. Instr.*, **24**, 202 (1953).
5. N. F. Mott, *Trans. Faraday Soc.*, **36**, 472 (1940).
6. N. B. Pilling and R. E. Bedworth, *J. Inst. Metals*, **29**, 529 (1923).
7. M. Brodsky and D. Cubicciotti, *J. Am. Chem. Soc.*, **73**, 3497 (1951).
8. U. R. Evans, *Trans. Electrochem. Soc.*, **91**, 547 (1947).
9. S. Glasstone, "Textbook of Physical Chemistry," 2nd ed., p. 1118-9, D. Van Nostrand Co., Inc., New York (1946).
10. H. J. Svec and D. S. Gibbs, *J. Am. Chem. Soc.*, **75**, 6052 (1953).

Reaction of Zirconium with Water Vapor at Subatmospheric Pressures

M. W. Mallett, W. M. Albrecht, and R. E. Bennett

Battelle Memorial Institute, Columbus, Ohio

ABSTRACT

The reaction of iodide zirconium with water vapor at 33 mm Hg pressure was investigated in the range 300°-600°C. The rates follow a cubic law. The cubic rate constant in $(\mu g/cm^2)^3/sec$ is $k = 6.71 \times 10^8 \exp(-29{,}700/RT)$ where $29{,}700 \pm 700$ cal/mole is the activation energy. Reaction films of monoclinic ZrO_2 are *N*-type semiconductors. Therefore, it is concluded that the mechanism of film formation is the same as that for the zirconium-oxygen reaction.

The performance of Zr in high-temperature water is of great interest in nuclear reactor technology. Therefore, considerable work has been carried out on this subject. Work on the corrosion of Zr in water at high temperature and pressure has been reviewed (1). No specific rate law was reported for the corrosion reaction, but one could infer from the published data that the cubic law might have been followed.

In the usual corrosion testing it is customary to cool the samples from the experimental temperature periodically, remove them from the pressure vessel, and weigh them at room temperature in order to determine corrosion rates. It is not known what effect this periodic temperature cycling may have on the reaction kinetics. Because of the insensitivity of the technique the initial stage of reaction is often indiscernible and the means by which later rate-controlling conditions are established in the surface film cannot be determined. Therefore, the present study of the reaction of Zr with water vapor was made in a system in which continuous measurement of weight gain data could be obtained. Subatmospheric pressure (33 mm Hg) water vapor was used in order to slow the reaction so that the kinetics during the initial period of reaction could be determined. Also, tests were made to determine some of the mechanisms of formation of the reaction products.

Experimental

Material.—Cylindrical test specimens, 1 cm in diameter by 1 cm long, were machined from arc-melted iodide-zirconium rod. For low temperature runs, some of this rod was fabricated into foil, 0.03 cm thick. Results of spectrographic, chemical, and vacuum-fusion analyses are given in Table I. An accelerated corrosion test of this material in 400°C steam gave a weight gain of 360 mg/dm^2 after 90 hr.

Apparatus.—A Sartorious Electrona Microbalance was used to measure the weight gain of the specimen. Essentially this balance is an electronically controlled null-type instrument. The amount of current necessary to maintain balance is measured on a microammeter which is calibrated directly in micrograms.

The balance was evacuated by a three-stage Hg-diffusion pump, backed by a mechanical vacuum pump. A liquid-N cold trap was placed between the pumping system and the microbalance to prevent

Table I. Analysis of arc-melted iodide zirconium

Element	Amount present, wt %
Fe	0.060
Hf	0.030
Cr	0.010
Al	0.010
Ni	0.005
Si	0.003
Mg	0.002
Pb	0.002
Cu	0.002
Ca	0.002
Mn	<0.001
Sn	<0.001
Ti	<0.001
H_2	0.0004*
N_2	0.003
O_2	0.042

* After degassing.

back diffusion of Hg into the balance section. An ionization gauge between the cold trap and balance was used to measure pressures in the system.

The sample was spot welded to a Pt wire 0.005 in. in diameter and 24 in. long, which suspended the sample from the beam of the balance into the reaction tube. A resistance wound furnace was used to heat the specimen. Temperatures were controlled to ±5°C.

Water vapor was supplied to the specimen through a stainless steel bellows-type vacuum valve from a glass storage bulb, containing deaerated distilled water. This water was previously boiled for 5 min at atmospheric pressure. After it was placed in the storage bulb, the bulb was evacuated to 10 mm Hg and held there for ½ hr to remove any dissolved gases that might have remained in the water.

Method.—Rates of reaction of Zr with water vapor were determined by measuring the rates of weight gain of the specimens. Prior to the rate determinations, the specimens were degassed for 4 hr at 800°C. Then they were abraded with dry 240-, 400-, and 600-grit SiC paper. The specimen was suspended in the reaction tube and heated to temperature in a vacuum of 0.01 μ Hg pressure by a resistance-wound furnace. The reaction was started by adding water vapor at a pressure of 33 ± 2 mm Hg to the furnace section. Rate data were not taken until 1 min after the reaction was started to allow for adsorption of water vapor by the Pt suspension wire and balance beam of the microbalance. Preliminary experiments showed this time to be sufficient to establish equilibrium with the apparatus. Weight gain measurements were made at 2-20 min intervals for 6-24 hr. The original geometric dimensions of the specimens were used to calculate the weight gain per unit surface area.

Approximations based on weight gain of samples indicated that the maximum amount of H_2 that was formed in the reactions was 3 ml STP. For most of the reactions the amount of H_2 produced was much less than this. The partial pressure of H_2O in the system remains constant. Because of mass differences the H_2 product does not noticeably effect the diffusion of water vapor from the reservoir to the specimen. Calculations show that the minimum mole ratio of water vapor to H_2 in the reaction chamber was about 3-1.

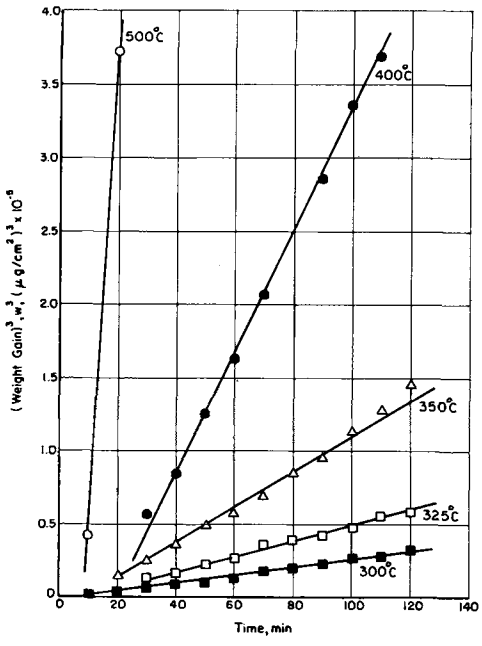

Fig. 1. Reaction of Zr with water vapor at 33 mm Hg pressure

Results

Kinetic data.—Reaction rates of arc-melted iodide zirconium with water vapor at a pressure of 33 mm Hg were measured from 300° to 600°C. The data followed the cubic rate law, $w^3 = kt$, where w is the weight gain in micrograms per square centimeter, t is the time, and k is the cubic rate constant. In Fig. 1, w^3 is plotted against t for several representative experiments. It is seen that the data fall on a straight line. Accordingly a plot of log w vs. log t should give a straight line with a slope of 0.33 if the cubic law is followed exactly. Values of the cubic rate constants, computed from the various plots, and the slopes of the log-log plots are given in Table II. Although the slopes vary somewhat, they agree more closely to the slope for the cubic law than to that for any other simple rate law.

A plot of the cubic rate constants against the reciprocal of the absolute temperature is shown in Fig. 2. The equation for the best straight line through the set of points was calculated by the method of least squares. The Arrhenius equation was used to calculate the energy of activation and frequency factor. In the range 300°-600°C the cu-

Table II. Rate constants for the reaction of arc-melted iodide zirconium with water vapor

Temp, °C	Rate constant, k, in $(\mu g/cm^2)^3/sec$	Slope of log-log plot
300	1.7	0.39
325	9.1	0.35
350	2.8×10	0.41
400	1.2×10^2	0.40
475	1.2×10^3	0.27
500	2.3×10^3	0.39
570	6.7×10^3	0.35
600	2.2×10^4	0.35

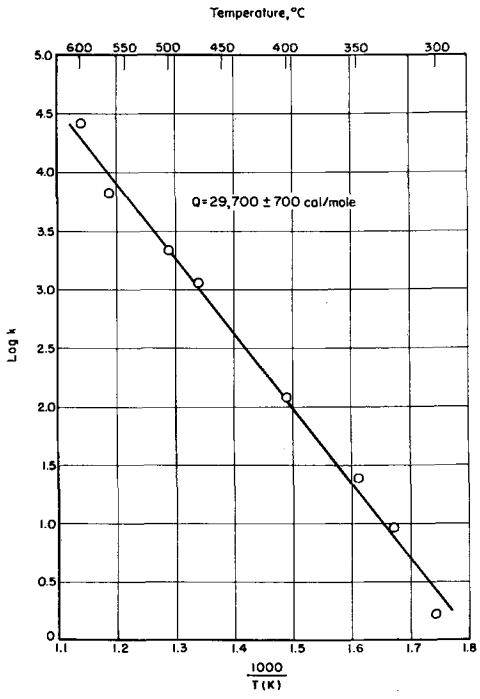

Fig. 2. Temperature dependence of cubic rate constant for reaction of Zr with water vapor.

bic rate constant in $(\mu g/cm^2)^3/sec$ is $k = 6.71 \times 10^8 \exp(-29{,}700/RT)$ where 29,700 ± 700 cal/mole is the activation energy and the probable error in a calculated k is approximately 2.7%.

Films.—At the end of reaction rate runs, specimens were cooled to room temperature and examined. In all cases, a gray-black film covered the reacted specimens. This film adhered very strongly to the base metal. Metallographic examination showed that the film was a dense single-phased material. A photomicrograph of a film produced on a specimen reacted with water vapor at 400°C for 24 hr is shown in Fig. 3. The film is very thin (about 0.0001 cm) and x-ray analysis showed it to be monoclinic ZrO_2.

Mechanisms.—Experiments were made to determine the mechanisms of the reaction as discussed in a previous study on the oxidation of Zr (2).

A marker experiment was made to determine the diffusing species in the reaction film. The marker was a thin layer of Cr_2O_3 powder (in water) painted on a sheet specimen. The specimen was then reacted with water vapor at 400°C for 1400 hr. At the end of the reaction the Cr_2O_3 marker remained entirely at the film-gas interface indicating that the oxygen ion is diffusing through the film and the ZrO_2 is being produced at the metal-film interface.

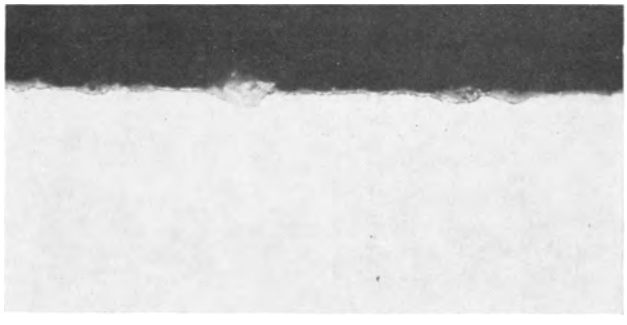

Fig. 3. Zr reacted with water vapor at 400°C for 24 hr. Note thin (0.0001 cm) gray-black film of ZrO_2. Magnification, 1200X.

Thermoelectric power measurements were made to determine the type of electronic conduction through the films. A measurement was made using a hot (700°C) tungsten probe on an oxide film produced on a specimen at 400°C. The sign of the thermoelectric power was found to be negative. Electronic conduction in the films is through excess electrons. Therefore the films are *N*-type semiconductors. Apparently the mechanism of film formation in the reaction of water vapor with Zr is similar to that for the reaction of oxygen with Zr (2).

Specific resistivity measurements made at room temperature on reaction films produced at 400°C gave a value of 4×10^7 ohm-cm. This is considerably lower than the specific resistivity (6×10^{18} ohm-cm) of the films produced in the zirconium-oxygen reaction. This difference in specific resistivity may be caused by H in some form in the film. Vacuum-fusion analysis of an entire reacted specimen (24 hr at 400°C) for H gave 6 ppm by weight. This agrees within the precision of the analysis with 4 ppm obtained on the analysis of the Zr before reaction with water vapor. Therefore, if there is an effect of H on the properties of the film, it is at lower concentrations than could be detected.

Discussion and Conclusions

It was found that in the temperature range 300°-600°C the reaction of Zr with water vapor at 33 mm Hg pressure follows the cubic rate law with an activation energy of 29,700 cal/mole. Thomas (1) in reviewing the various works on the corrosion of Zr in water at high temperature (250°-360°C) and pressure showed that the slope of the plot of log of weight gain against log of time was of the order of 0.3. This indicates that the cubic law was being followed. Thomas reports an activation energy of 11,400 cal/mole which is considerably lower than that from the present study.

The cubic rate law had been found to hold for the reaction of oxygen at 1 atm pressure with Zr (activation energy, 47,200 cal/mole) (3) and with a Zr-1.5 wt % tin alloy (activation energy, 38,400 cal/mole) (2) in the temperature range 500°-900°C. Gulbransen and Andrew (4) in investigating the reaction of Zr with oxygen at low pressures (0.076 to 7.6 cm Hg) in the range 200°-425°C indicated that the reaction may be parabolic. However, their data were replotted (3) and excellent agreement with the cubic law was found for the reaction for which the activation energy is 26,200 cal/mole. This is in fair agreement with the 29,700 cal/mole obtained in the present study. The over-all mechanism of film formation is the same in both cases. This indicates that the controlling steps in reactions of Zr with water vapor and oxygen at low pressures are very similar.

Acknowledgment

The authors wish to acknowledge the assistance of R. K. Willardson who performed the thermoelectric

power and resistivity measurements of the oxide films.

Manuscript received September 14, 1956. Work performed under AEC Contract W-7405-Eng-92.

Any discussion of this paper will appear in a Discussion Section to be published in the December 1957 JOURNAL.

REFERENCES

1. D. E. Thomas, *Nuclear Engineering*, **50**, 16 (1954).
2. M. W. Mallett and W. M. Albrecht, *This Journal*, **102**, 407 (1955).
3. J. Belle and M. W. Mallett, *ibid.*, **101**, 339 (1954).
4. E. A. Gulbransen and K. F. Andrew, *Trans. Am. Inst. Mining Met. Engrs.*, **185**, 515 (1949).

A New Commercial Process for Electrowinning Manganese

M. C. Carosella and R. M. Fowler

Electro Metallurgical Company, A Division of Union Carbide Corporation, Niagara Falls, New York

ABSTRACT

The development of a novel process for the electrowinning of manganese from aqueous solutions is described with emphasis on the raw materials used and the advantages gained thereby. A commercial plant based on this process was built and a description of the methods of quality control, chemical analyses, and characteristics of the metal so produced is given.

Allmand and Campbell (1) reported that they had prepared pure Mn in a coherent form from a Mn $SO_4 \cdot (NH_4)_2 SO_4$ electrolyte in a diaphragm cell, but after a small amount deposited the deposits became loose and scaled off. Shelton (2) and co-workers (3,4) made a number of improvements and developed the first continuous process for producing Mn by electrolysis. The results of these investigations were sufficiently encouraging to justify in 1939 the construction of a commercial plant (5). While this plant started operations in 1941, some process changes had to be introduced so that by 1949 the rather complex process using selected high grade ores was stated to be under close control (6).

Investigation of the process for electrowinning Mn as developed by Shelton, *et al.*, started here in 1938. Also other methods for producing a pure grade of Mn were being investigated with some success. Numerous sources of Mn, including ferromanganese, ores, and slags, were investigated. As a result of these studies, a pilot plant was built to develop a process for electrowinning Mn.

Pilot Plant

The pilot plant was designed to be quite flexible so that it would be suitable for handling various types of starting materials and methods of solution purification.

Processes, based on ferromanganese and several different types of ores, were developed and studied from an economic viewpoint. Some difficulties were experienced in the electrolytic step because the level of impurities in electrolytes derived from some of these source materials was above tolerable limits. Methods of purification as reported by the U. S. Bureau of Mines were not always successful in eliminating all of the deleterious impurities.

After the ore and ferromanganese processes had been demonstrated to be technically feasible, an economic evaluation showed that the cost of Mn in these materials was the largest single factor in the total cost of producing electrolytic Mn. In addition, the methods used to produce an electrolyte of sufficient purity were complex and costly. As a result of these studies, various types of slag, which were available from Mn ore smelting operations, were investigated as source materials for Mn. During these studies it was discovered that the Mn in some of these slags could be extracted with dilute acid solutions, and that the extract liquors were easily purified.

Concurrently an investigation to develop suitable electrolytic cells for this process had been under way. The staff of the Bureau of Mines at Boulder City, Nev., (7) had done considerable experimentation on various types of cells. Their work indicated that a false-bottom-type cell was the best. Although their cell had many inherent advantages, it had the disadvantage of complex design and was difficult to disassemble and clean. Further experimentation here led to the development of a cell (8) which is

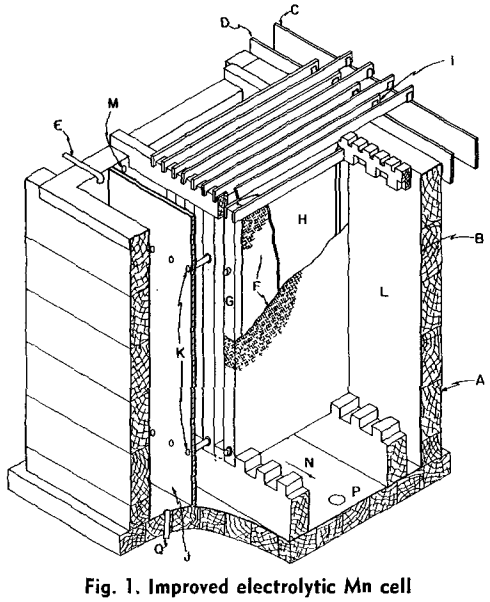

Fig. 1. Improved electrolytic Mn cell

simple in design. Fig. 1 shows the main features of the new cell. Basically, it is a rectangular wooden tank, A, with lead lining, B; C and D are the cathode and anode busbars connected to the Hastelloy alloy cathodes H (9) and 99% lead, 1% silver (10) anodes, I, respectively. Feed is introduced at E into the catholyte header, J, which supplies the individual frames, G, which are covered with canvas or synthetic fiber diaphragms, F. Two outlets, K, are provided on each cathode frame for circulating catholyte to the common header. Hydrogen generated at the cathodes, H, acts as a gas-lift to cause the catholyte to circulate freely, thus resulting in a uniform Mn concentration and pH in all catholyte compartments. The solution passes through the diaphragms, F, into the anolyte compartment, L. The spent anolyte overflows from the cell at M. The anode sludge formed during electrolysis falls freely into the bottom of the anolyte chamber. The bottom of this chamber, N, is sloped to permit flushing the sludge through a valve at P without disassembling the cell. The catholyte header can be readily flushed out, when required, through Q.

Since cathodes for deposition of Mn must be chemically inert, with a surface of such a nature that the electrodeposit adheres but can be easily stripped by flexing or hammering, many corrosion-resistant alloys were tried as cathode materials in the pilot plant. Cathodes made from the Hastelloy alloys performed better than those made from stainless steels because they were more corrosion resistant and required infrequent polishing. In addition any metal which did not strip from the Hastelloy alloy cathodes could be dissolved in anolyte without destroying the polished surface. Stainless steel cathodes had to be polished after each stripping to prevent the next deposit from adhering so tightly that removal was difficult.

Commercial Plant

When an economic analysis of the pilot plant operation showed that the slag process was favorable, a commercial plant was designed and built. In the new process (11), Mn ore was smelted in a submerged arc furnace with coke and a flux, when necessary, to produce standard ferromanganese and a high-manganese slag. As shown in Table I, the slag contains only small amounts of metals which cause trouble in the electrowinning step.

The general flowsheet of the new process is as follows. The manganese silicate slag, milled to −200 mesh in a dry grinding unit, is leached to a pH of 4.4 with anolyte and make-up H_2SO_4. The resulting slurry is next treated with gaseous ammonia to a pH of 6.6 to precipitate most of the impurities. The neutralized slurry is filtered and the residue washed with water to recover the soluble Mn. The filtrate and wash water are treated with a small amount of H_2O_2 to oxidize and precipitate the residual iron. The precipitate is filtered from the solution which is pumped to a cell feed storage tank. SO_2 is added to this solution before it enters the cell circuit. Anolyte produced in the cells is returned to the leaching circuit.

Provisions have been made in the plant to remove Mg from the circuit when necessary. Anolyte is cooled in a continuous vacuum crystallizer and a complex Mg, Mn, $(NH_4)_2SO_4$ crystallized. After removing the salt, the solution is returned to the leaching circuit.

This process is quite different and has less processing steps than either the processes described by Bennett (6) or that developed by the investigators at the Bureau of Mines (7). Typical analyses of the cell feed and anolyte are shown in Table II.

Hastelloy alloy C cathodes, 42- by 24-in. by 16-gauge, are regularly removed from the cells on a 72-hr schedule. They are first dipped in a dilute solution of sodium bichromate to prevent the metal surface from darkening, then washed with water to remove soluble salts, and dried. The brittle cathode deposits are stripped with the aid of a rubber mallet. The cathodes are then soaked in anolyte to dissolve any residual Mn metal. After this treatment, followed by washing with a detergent solution and rinsing with water, they are ready to return to the cells.

The plant is equipped with a buffing machine to restore the polished surface when needed. Under normal operating conditions, cathodes are usually polished aproximately twice each year.

The stripped metal is either packed in drums for shipment or loaded in stainless steel cans which are placed in an electrically heated furnace to remove H.

Quality Control of Electrolytic Mn

One of the major problems in any research program leading to a new product is the development of procedures for determining the quality of the product. Direct estimation of Mn is not a sufficient measure of purity of the product because there is no highly precise method for estimating Mn. The standard bismuthate method (12) in the hands of its developers was not better than one part in a thousand or 0.10% Mn. With improvements that have been incorporated, results still tend to be on the low side because oxidation is never quite complete. The Volhard method is even more empirical and is likewise unsuitable. There is no highly precise gravimetric method for Mn. The classical determination of Mn as $Mn_2P_2O_7$ (13) leaves much to be desired in the way of the composition of precipitate, other elements precipitated, etc., so in all this work the percentage

Table I. Typical analyses of deleterious impurities in slag

	%
Iron	0.14
Molybdenum	0.006
Copper	0.003
Nickel	<0.001
Cobalt	<0.0001

Table II. Analyses of cell solutions, g/l

	Feed	Anolyte
Mn	32 – 34	10 – 12
$(NH_4)_2SO_4$	120 – 140	120 – 140
SO_2	0.30 – 0.50	–
H_2SO_4	–	36 – 44

Table III. Analysis of electrolytic Mn, content in ppm

<10 if present	<10	10-20
Al, B, Cr, Ti, V, Zr	Fe, Cu, Ag, Co, Ni	Pb, Si, Ca, Mg

of Mn was obtained by subtracting the sum of the other elements from 100.

Determination of other metals.—The most satisfactory method for estimating residual metallic elements in electrolytic Mn is by emission spectroscopy. For low concentrations, it is both rapid and precise. Table III lists the results of a quantitative examination of typical electrolytic Mn samples. In the case of the results in this table, excellent agreement was obtained between spectrographic and wet chemical laboratories, and the spectrographic laboratory of an independent research institution to whom samples were submitted. Some of the metals, such as Cu and Pb, can be determined readily with spectrophotometric procedures but for others, for example, Ca, there are no wet procedures with satisfactory sensitivity in the presence of such a preponderance of Mn.

Determination of metalloids.—P, S, and C are of interest to the user of electrolytic Mn. In fact, one advantage of the electrolytic over the electrothermic material is the very low P content of the former. The spectrophotometric method for P (14) is sufficiently sensitive. Using this method, the plant material is consistently below 5 ppm.

Since Mn is deposited from an $(NH_4)_2SO_4$ bath, there is opportunity for S to contaminate the metal. The exact mode of occurrence of S in the metal is not known, although it is probable that under certain conditions some of the complex S compounds in the electrolyte are reduced to sulfides at the active cathode surface. Likewise, any electrolyte trapped in the deposit would contribute to the S present. Initially, it was the practice to determine both sulfide and sulfate sulfur, but it was found that there was no correlation even in successive portions of the same analytical sample. The indications were that it was possible by variations in the rate of solution of a particular sample to alter the percentage of the two forms present. Similar difficulties encountered in the analysis of material containing ferric iron and sulfides (15) can be eliminated by the addition of stannous chloride. Similar tests on electrolytic Mn, while better than without stannous chloride, were not too satisfactory, so it appears that the evolution method has limited utility for the determination of S.

S present in any form would be recovered in the metal when the Mn is used for alloying. Since it is not the form but the amount of S that is important for metallurgical uses, only a determination of total S, by the combustion method that is standard in the steel industry, is now made. A sample is also treated with water to get an estimate of the completeness of the washing of the cathodes for process control. The washer is so operated that no test is obtained for soluble sulfates.

The S content of the Mn has dropped as the process operated and more control was exercised over various factors. At the present time the S is less than 0.030%.

The amount of C present is so small that it is not of importance. The carbon level in the metal has been consistently below 0.005%.

Determination of gaseous elements.—For many metallurgical uses, the content of gaseous elements in electrolytic Mn is important. Since it is deposited from a solution containing large amounts of ammonium ion, N could be present. Fortunately, N can be determined very precisely by the standard method used for steels (17). All the analyses that have been made indicate that the N content is less than 50 ppm although 100-300 ppm may be picked up in the dehydrogenation process. For special purposes, a nitrided grade with about 6% N is produced.

Oxygen is important because it may be an undesirable addition, as for example in Mn-Ti alloys. Also if the Mn is to be determined by difference, a substantial error is introduced in the result for Mn if oxygen is ignored. The only suitable method for oxygen is by vacuum fusion. An apparatus similar to that described by Hamner and Fowler (18) with the sample enclosed in a tin capsule has been found satisfactory. The cells are operated to keep the oxygen content below 0.15%. However, it must always be kept in mind that Mn is a readily oxidizable metal and the oxygen content can be increased by improper handling.

For some purposes, the H content is of interest, and since significant amounts are codeposited, it must be removed by subsequent treatment if low-hydrogen material is desired. As deposited, the Mn metal contains about 0.02% H. Much of this can be removed by treatment at 500°C as was pointed out by Potter, *et al.* (19). Unfortunately they did not start with hydrogen-free material nor did they ever determine the amount of H remaining after their treatments.

Sieverts and Moritz (20) also studied the solubility of H in Mn. Their material was vacuum-distilled on a small scale and equilibrated with H. They measured the changes in H content of the metal by means of the gas evolved and showed that at 400°-600°C there was about 9 ml of H/100 g or 8 ppm in solution. Potter, *et al.* (19) report that about 7 cc of gas/100 g of metal is reabsorbed below 600°C. Sieverts and Moritz found about 35 ml was reabsorbed on cooling in H at 760 mm pressure. Since neither of these investigators analyzed the Mn for H, the results are the differences of two rather large numbers containing considerable variation. It is not possible to decide precisely from their work how much H would remain on heating electrolytic Mn to 500°C and on cooling to room temperature. The indication is that there may be at least 16 ml/100 g or 14 ppm remaining in material so treated.

Since primary interest lies in the total amount of H present and not in checking whether additional H can be driven off, the apparatus described by Potter, *et al.*, is not suitable for the determination of total H in dehydrogenated metal; the only satisfactory procedure is by vacuum fusion. A 100-g

Table IV. Hydrogen in dehydrogenated electrolytic Mn

Sample	Hydrogen obtained in successive treatments			
	600°C ppm	1000°C ppm	1700°C ppm	Total ppm
No. 1	2	–	9	11
	–	3	11, 12	14, 15
	–	–	11, 12	11, 12
No. 2	3	–	18	21
	–	4	11	15
	–	–	13, 15, 20	13, 15, 20

sample was heated to 600°C in an apparatus, similar to that described by Potter, *et al.*, for 30 min at a pressure of 10^{-5} mm Hg and the H collected. The sample was cooled, dry argon admitted, and 20 g removed. The sample was then reheated *in vacuo* to 1000°C for 30 min and the evolved H collected. After cooling, as before, the remainder was then analyzed by the vacuum-fusion procedure (*see* Table IV). Samples of the original material were also analyzed directly by vacuum fusion. The results are in good agreement and show clearly that all the H cannot be removed at 600°C *in vacuo* in a reasonable time. To see if this was a property peculiar to the electrolytic Mn produced by the present process, samples produced and dehydrogenated in other places were analyzed; similar results were obtained. All the evidence points to the necessity of stating the conditions used to obtain the H content. In other words, a specification that the H content of electrolytic Mn is less than a given figure is meaningless unless the analytical method used to obtain that figure is described. If dehydrogenated at 510°C (950°F), all the evidence obtained here indicates that there is about 10-15 ppm remaining. Table V shows the precision that can be obtained by the vacuum fusion procedure. For this test, samples were chosen sized 16 by 48 mesh. Each sample was divided into three portions. The samples were mixed, dried in air at 110°C for 1 hr, then stored in a dessicator. Before they were sent to the laboratory, they were assigned random numbers so that they were analyzed in random fashion by two different chemists. From a statistical study of these data, it was concluded that the precision of the H determination, using vacuum fusion, is of the order of 5 ppm. Factors such as drying and the size of sample used are important.

Sampling electrolytic Mn.—In any quality control program, it is essential that the sample examined in the laboratory represent adequately the lot of material from which it was drawn. The plant procedure for sampling follows.

The material is combined in 42,000-lb lots. When a lot is packed in drums, 500 lb to the drum, 5 lb are taken from each drum by periodically cutting the stream as the drum is filled. Thus a 400-lb gross sample is accumulated. This is broken into small pieces ¼ x ⅛ in., and a sample riffled out for gas analysis. A second portion is rolled to 20 mesh, riffled to 1 lb, and crushed to 100 mesh for the analytical sample.

Table V. Precision of the determination of H in electrolytic Mn

Sample No.	Sample not dried	Dried 110°C for 1 hr, ppm
1	220	192, 204, 195
2	21	13, 15, 21
3	15	10, 11, 13
4	13	10, 11, 14
5	13	10, 10, 10

Table VI. Effect of crushing on oxygen content

Sample preparation	Oxygen, %
Coarse	0.13, 0.14
Coarse (pickled 3% HNO_3)	0.13, 0.14
8 × D	0.15, 0.16
8 × D (dried 1 hr at 110°C)	0.18, 0.18
35 × D	0.17, 0.18
35 × D (dried 1 hr at 110°C)	0.23, 0.23

Since Mn is readily oxidized, the reduction of the gross sample presents problems. Table VI shows some results obtained by crushing to fine sizes. They indicate that substantial oxidation may take place if the metal is reduced from ¼ x ⅛ in. to pass a 35-mesh sieve. The minus 35-mesh material, or even minus 100-mesh material, is much more desirable as a sample. If one is not interested in oxygen, the sample can be reduced to a suitable size by the standard tools used in the ferroalloy industry (21). If the iron content is of interest, it is essential to use only alloy-steel equipment and aliquot a large sample rather than crush to fine sizes, since considerable amounts of adventitious iron can be obtained from ordinary cast iron equipment.

Summary

A plant based on the slag process has been shown to have a simple flowsheet, yet gives a very pure solution amenable to easy electrolysis. Plating difficulties which may be caused by impurities in the solution have never been encountered in the cell room.

The metal produced has been consistently of high quality. The new type of cell has proved to be easy to operate and simple to control. The Hastelloy alloy C cathodes, while higher in initial cost than stainless steel, have been very satisfactory and have justified their higher cost in savings in maintenance and ease of stripping the deposited metal.

With the new process it is possible to smelt a Mn ore to ferromanganese and a slag, then recover the Mn in the slag as electrolytic Mn. In this way nearly all the Mn in an ore is converted into forms suitable for the metallurgical industry, thus conserving Mn resources. This program has made available for the metal industries additional supplies of high-purity Mn metal for the production of better alloys.

Acknowledgments

Any development such as has been described is the work of many minds and hands. Among Electro Metallurgical Co. groups who contributed to this project are the Metals Research Laboratories, the General Engineering Department, the Product and Process Development Department, and the Operating Department. The authors wish to thank the management of Electro Metallurgical Co. for supporting this development and for the opportunity of publishing the results of the work.

Manuscript received July 26, 1956. This paper was prepared for delivery before the San Francisco Meeting, April 29 to May 3, 1956.

Any discussion of this paper will appear in a Discussion Section to be published in the December 1957 JOURNAL.

REFERENCES

1. A. J. Allmand and A. N. Campbell, *Trans. Faraday Soc.*, **19**, 559 (1924).
2. S. M. Shelton, *U. S. Bur. Mines R.I. 3322*, 29 (1936).
3. S. M. Shelton, M. B. Royer, and A. P. Towne, *U. S. Bur. Mines R.I. 3406*, 3 (1938).
4. R. S. Dean, *U. S. Bur. Mines R.I. 3580* (1941).
5. W. L. Hammerquist, *Steel*, **105**, 42 (1939).
6. R. H. Bennett, *Eng. and Mining J.*, **150**, 80 (1949).
7. J. H. Jacobs and Co-workers, U. S. Bur. Mines Bull. 463.
8. M. C. Carosella, (to Union Carbide & Carbon Corp.), U. S. Pat. No. 2,739,116, Mar. 20, 1956.
9. G. D. Bagley and M. C. Carosella (to Union Carbide & Carbon Corp.), U. S. Pat. No. 2,755,241, July 17, 1956.
10. M. C. Carosella (to Union Carbide & Carbon Corp.), U. S. Pat. No. 2,766,198, Oct. 9, 1956.
11. M. C. Carosella (to Union Carbide & Carbon Corp.), U. S. Pat. No. 2,766,197, Oct. 9, 1956.
12. T. R. Cunningham and R. W. Coltman, *Ind. Eng. Chem.*, **16**, 58 (1924).
13. W. F. Hillibrand and G. E. F. Lundell, "Applied Inorganic Analysis," 2nd ed., p. 499, John Wiley & Sons, Inc., New York (1953).
14. *Ibid.*, p. 710.
15. H. A. Bright, *J. Research Nat. Bur. Standards*, **18**, 137 (1937).
16. E. L. Bennet, J. H. Harley, and R. M. Fowler, *Anal. Chem.*, **22**, 445 (1950).
17. ASTM Methods Chemical Analysis Metals, p. 131 (1950).
18. H. L. Hamner and R. M. Fowler, *J. Metals*, **4**, 1313 (1952).
19. E. V. Potter, E. T. Hayes, and H. C. Lukens, *Metals Tech.*, **12**, [4], TP 1809, (June 1945).
20. A. Sieverts and H. Moritz, *Z. physik. Chem.*, **180** (4), 249 (1938).
21. Ref. (17), p. 63.

Effects of Various Polyvalent Metal Anion Additions to an Alkaline Magnesium Anodizing Bath

W. McNeill and R. Wick

Pitman-Dunn Laboratories, Frankford Arsenal, Philadelphia, Pennsylvania

ABSTRACT

The effects of some polyvalent metal anions in magnesium anodizing were compared. Coated panels were exposed to salt spray to determine their corrosion resistance. Hardness and dielectric strength tests were also carried out. Coatings from chromate, stannate, vanadate, tungstate, and manganate baths were compared with those from a bath containing no polyvalent metal anion. Differences in corrosion resistance were noted, with vanadate baths producing the best results. Differences in color were noted also.

Anodic coatings available for magnesium are of two types, those coatings formed at low voltage (under 10 v) and those formed at high voltages (60-320 v).

The low voltage coatings are thin and have low surface roughness in comparison with those coatings formed at high voltages. Low voltage coating formation is probably a simple process, involving only the electrochemical reaction of Mg with the anions in the bath to form an oxide or hydroxide coating. On the other hand, high voltage coatings are formed by a complex process. Sparking, which occurs on the Mg surface during anodizing, results in the formation of very hard deposits which resemble sintered ceramic materials. The chemical reactions which occur in the spark zone are not known, but it is clear that reduction products occur in the coating even when formation is carried out using direct current. The process cannot be electrochemical since oxidation only can occur at an anode. It is more likely, then, that the high voltage anodic coatings are formed by a thermal process which is brought about by electrochemical means. An interesting feature of the baths used for high voltage anodizing is that they usually contain anions such as dichromate or manganate which are reduced, the reduction products appearing in the coating. The use of anions of this type in Mg finishing has been known for many years (1-5), but their value in high voltage anodic baths has been a subject of considerable speculation.

The development of the HAE process (4) afforded an opportunity to investigate the effect of a variety of polyvalent metal anions in alkaline anodizing baths for magnesiums. It was possible to carry out such a study with the HAE bath because anions such as chromate, stannate, etc., could be substituted for manganate and these substitutions were found to have no significant effect on operating conditions necessary for coating formation. With the Cr-22 bath (6), for example, no substitute for chromate has been found which does not adversely affect coating formation.

Early work on substitutes for manganate in the HAE anodic bath gave inconclusive results because

two important variables were not recognized. The first of these was "aging" of the anodic coating. The corrosion resistance of coated panels increased if exposed to the laboratory atmosphere, at ambient temperatures, for several weeks during seasons of high humidity. The same effect could be obtained by placing coated panels in air of approximately 100% relative humidity at about 180°F for several hours. Several acidic post dips were tried also. One of these, an aqueous bifluoride dichromate dip, when combined with humid aging, was found capable of increasing the corrosion resistance of HAE coated panels by several hundred per cent (7).

The second important variable was in the Mg alloy itself. Panels from different production lots gave test differences which were significant and attributable to the alloy stock. These differences appeared repeatedly even after as much as 0.010 in. of surface was removed by acid pickling.

To control variations in the post treatment, all of the panels in a given test are dipped for the same length of time and aged simultaneously. To control the effect of variations in the alloy, stock panels are all cut from the same production lot and randomized before being coated. This procedure gives a measure of control over tests on anodic coatings on Mg which was not obtained formerly. It was necessary, in view of the importance of the above variables, to reinvestigate the role of polyvalent metal anions in Mg coating baths.

Experimental

Mg panels, 4 in. x 6 in. x 0.051 in., were cut from a single lot of FS1 alloy sheet. The Mg was received from the manufacturer with a producer's dichromate pickle and stencilled ink identification marks on one side of each sheet, i.e., the inked side; the opposite side is called here the clear side. The panels were deburred and then numbered on the inked side; they were degreased in acetone prior to anodizing, but were not cleaned otherwise.

A 200-liter stock solution was prepared containing 150g/l USP grade KOH, 30 g/l USP grade (dried gel) Al $(OH)_3$, 35 g/l purified anhydrous KF, 35 g/l technical grade $Na_3PO_4 \cdot 12\ H_2O$, and tap water to make the required volume.

From this solution, five 30-liter baths were prepared, respectively containing chromate, tungstate, vanadate, stannate, and manganate (HAE bath). Each was made 0.086M in the additive. A sixth bath, containing no additive, was used as control.

Anodizing was carried out in a steel tank equipped with a Cu cooling coil. Bath temperature during anodizing varied somewhat, but generally remained within four degrees of 24°C.

Power was supplied to the bath by a 60-cycle, 45-amp unit which maintained bath current constant by automatically varying the voltage as resistance changed. Panels were coated in batches of six at a current density of 15 amp/ft^2, and a treatment time of 90 min. Voltages at the completion of treatment were between 80 and 90 v. After anodizing, the panels were rinsed in cold running water and allowed to stand until dry. After drying the panels were stored in a desiccator over anhydrous magnesium perchlorate to prevent natural aging.

Panels were selected from each bath and two groups of 36 panels each were assembled. One group remained in storage in the desiccator while the other group was dipped and aged. The post treatment consisted of a 45 sec immersion in an aqueous solution consisting of 10% NH_4HF_2 and 2% $Na_2Cr_2O_7 \cdot 2H_2O$.

The dipped panels were allowed to dry without rinsing and were then placed in air of approximately 100% relative humidity for 4 hr at a temperature of from 175° to 180°F. After aging they were removed, wrapped in contact with each other, and stored in the laboratory. Five days later all 72 panels were exposed to the salt spray in accordance with ASTM B-117-44T. The clear side of each panel was exposed with the rack mark down. Observations were made after 48, 120, and 312 hr.

The panels were removed from the salt spray and flushed with tap water (prevailing temperature, 67°F). No brushing was given. The panels were allowed to dry and the number of pits counted. Pits originating on panel edges were not counted. After each observation the panels were replaced in the salt spray cabinet in different order.

Dielectric strength measurements were made in accordance with ASTM test B-110-45, on duplicate samples from each of the six baths. The object of this test was merely to determine whether large differences due to bath composition existed, and no attempt was made to determine the nature of the relationship between bath composition and dielectric properties.

Coating hardness was tested by rubbing a bar of steel of Rockwell C63 hardness over the panels. This test was used only to determine whether any of the coatings were notably deficient in this respect.

Results and Discussion

Appearance.—The appearance of the various coatings was strongly dependent on bath compositions. Texture was not much affected, but, as would be expected, coatings of different colors were obtained. The HAE coated panels were medium brown, while those coated in the chromate and vanadate baths were light green and slate gray, respectively. Panels from the other three baths were all off-white, although those from the stannate bath might be described as light gray. All the coatings had the same type of partly sintered ceramic appearance, when examined under a magnification of 75X. They were all of about the same texture, with the exception of those treated in the no-additive bath. These had a few small white nodules distributed over the surface. It was found that, by adding suitable quantities of chromate and manganate to the no-additive bath, olive drab coatings could be produced which matched the lusterless green No. 3412 (olive drab) of Federal Specification TT-C-595, Jan. 12, 1950.

Whether such a bath could be regulated well enough to be practical was not investigated because it would have required experimental effort beyond the scope of the work reported.

Hardness.—The hardness of all six types of coatings was tested as described in the preceding sec-

Table I. Results of dielectric strength test

Bath type	Mean breakdown voltage	Standard deviation
Stannate	566	48.2
Vanadate	610	50.6
Manganate	581	43.7
Chromate	591	48.0
Tungstate	638	54.0
No-additive	600	51.8

tion. In each case, the coating abraded the steel. There was no noticeable difference between the hardness of the various coatings.

Dielectric strength.—The dielectric strengths of the coatings were measured and the means and standard deviations are shown in Table I.

None of the groups of panels was different from the no-additive group at the 0.95 level of significance.

Corrosion resistance.—In the salt spray tests, each bath composition was represented by two groups of six panels each. One group was post-treated, and the other was not. A summary of the corrosion data in pits per panel is given in Table II.

Nearly all the panels in both groups showed some corrosion, even at 48 hr and this was surprising in view of past experience with some of the coatings in the test. This was believed to be due to the FS1 alloy stock from which the panels were obtained, and does not reflect the maximum corrosion resistance that can be obtained with such coatings. In the case of the post-treated specimens, moreover, further improvement could have been obtained by repeating the post-dipping and aging steps several times, or by increasing the aging time. In an earlier experiment, 16 panels, cut from a different lot of FS1 alloy, were coated in a no-additive bath, dipped in the dichromate-bifluoride solution, aged 22 hr, and exposed to salt spray. After 400 hr exposure the panels averaged 3.6 pits per 4 in. x 6 in. panel, and the standard deviation was 2.3 pits per panel.

With the type of panels included in this test, corrosion usually begins between 48- and 120-hr exposure. In this test corrosion was well underway after 48-hr exposure. Corrosion results for the group of panels coated in the no-additive bath were compared with those for the other coatings. The data were tested for significance using Student's t-test; results are given in Table III.

Table II. Summary of corrosion data

	Bath type	Not post treated 48 hr	120 hr	312 hr	Post treated 48 hr	120 hr	312 hr
	Stannate						
Mean		17.8	22.2	23.2	6.5	12.8	14.8
Std dev		8.9	7.4	8.1	5.8	5.3	6.1
	Vanadate						
Mean		8.5	13.0	15.5	2.0	6.3	7.7
Std dev		2.7	3.5	3.8	1.7	2.9	3.3
	Manganate						
Mean		26.2	56.5	59.0	1.7	12.3	13.5
Std dev		7.1	6.5	7.5	1.9	3.8	3.3
	Chromate						
Mean		36.0	52.2	52.3	6.7	10.8	13.7
Std dev		4.0	11.4	12.2	6.9	6.6	7.3
	Tungstate						
Mean		48.5	58.5	58.3	8.7	17.0	20.3
Std dev		24.8	16.9	12.4	3.9	7.2	6.0
	No-additive						
Mean		46.7	57.7	57.7	3.7	10.3	12.7
Std dev		13.2	11.8	10.1	2.3	2.2	2.2

Table III. Results of significance test

Bath type	Not post treated 48 hr	120 hr	312 hr	Post treated 48 hr	120 hr	312 hr
Stannate	+3	+3	+3	0	0	0
Vanadate	+3	+3	+3	0	+1	+1
Manganate	+3	0	0	+1	0	0
Chromate	+3	0	0	0	0	0
Tungstate	0	0	0	−1	0	−1

Positive values indicate significantly greater, and negative values indicate significantly less, corrosion resistance than that of the corresponding group of no-additive panels. Numerical values indicate the highest levels at which the differences were significant, and are as follows: 1—0.95 level; 2—0.99 level; 3—0.995 level. Zero values indicate no significant difference at the 0.95 level.

Differences between coatings are much larger at 48-hr exposure than at other exposure times. This is probably because the corrosion at the earlier time was not fully developed at all the potential points of failure. It would appear that the 120-hr exposure was sufficient to produce pits at nearly all of these points since increases in corrosion, from 120 to 312 hr, were small. Probably, then, more reliable conclusions can be drawn from the 120- and 312-hr data. In some cases, fewer pits were counted at 312 hr than at 120 hr. This was not necessarily due to erroneous counting, but occurred when neighboring pits grew so large that they merged. However, no pits over 1/16 in. in diameter were observed on any of the panels. While it is true that this exposes a weakness in pit counting as a method of estimating salt spray corrosion, other methods that might be used have greater shortcomings. An example would be that of estimating the per cent of the area of the panel that was corroded. Here the total area of corrosion per panel is quite small and estimates frequently fail to show differences. The reversals that did occur had little effect on the results of the test, and it was not worthwhile to attempt to refine the technique.

The data show clearly that the post treatment causes a tremendous increase in the corrosion resistance of all the panels. With the exception of vanadate, the effects of bath additives are relatively minor. The non-post-treated vanadate specimens showed almost as much corrosion resistance as most of the post-treated groups, and far more corrosion resistance than any of the other non-post-treated groups.

Conclusions

Protective coatings on FS1 Mg alloy can be obtained by anodizing a bath prepared from potassium hydroxide, aluminum hydroxide, trisodium phosphate, and potassium fluoride. The addition of stannate, vanadate, manganate, chromate, or tung-

state to this bath makes it possible to produce coatings which differ with respect to color and corrosion resistance. The corrosion resistance of all these coatings is greatly improved by a post treatment consisting of immersion in a bifluoride-dichromate solution followed by aging in a hot, humid atmosphere.

The addition of vanadate increases the corrosion resistance of the coating.

All the coatings studied are hard enough to abrade Rockwell C63 steel.

Acknowledgment

This paper describes experimental work supported by the Ordnance Corps and conducted at Frankford Arsenal under Project TB4-302B-5. The authors wish to express their appreciation to the Ordnance Corps for permission to publish this paper.

Manuscript received April 12, 1956. This paper was prepared for delivery before the Cleveland Meeting, Sept. 29 to Oct. 4, 1956.

Any discussion of this paper will appear in a Discussion Section to be published in the December 1957 JOURNAL.

REFERENCES

1. Siemens & Halske, Aktiengesellschaft, British Pat. 459,017, Dec. 31, 1936.
2. L. Renault, French Pat. 815,115, July 7, 1937.
3. R. W. Buzzard, U. S. Pat. 2,314,341, March 23, 1943.
4. H. A. Evangelides, "The HAE Process for Magnesium, I. Introductory Report," Frankford Arsenal Report R-1000, Jan. 1951.
5. H. A. Evangelides, U. S. Pat. 2,723,952, Nov. 1955.
6. W. McNeill, *Metal Finishing*, **53**, 57, December (1955).
7. H. A. Evangelides, *Product Finishing*, (British) p. 54, October (1954).

Electric Moments of Certain Partially Fluorinated Esters

J. B. Romans and T. D. Callinan[1]

U. S. Naval Research Laboratory, Washington, D. C.

ABSTRACT

The electric moments of six partially fluorinated esters have been determined. The materials studied were liquids at room temperature and were known to be chemically inert and thermally stable. All six esters were found to be highly polar compounds exhibiting marked tendencies to associate molecularly; they possessed dipole moments of the order of 2.8 to 3.8 $\times 10^{-18}$ esu-cm. From the experimentally determined permanent electric moments, the most probable molecular configurations were calculated for each of the esters. The predominating structure includes one cis-type configuration. It is evident that the molecules exist, for the most part, in a nonplanar form.

The electrical properties of some partially fluorinated esters have been determined for the purpose of elucidating their molecular configurations. The fluoresters studied (Tables I and Ia) were synthesized by the esterification of partially fluorinated alcohols with unfluorinated acids (1). The straight chain primary alcohols employed were:

1H, 1H, 5H-octafluoropentanol-1 .....
$H(CF_2)_4CH_2OH$ ... ψ'-amyl alcohol
1H, 1H, 7H-dodecafluoroheptanol-1 ...
$H(CF_2)_6CH_2OH$ ... ψ'-heptyl alcohol
1H, 1H, 9H-hexadecafluorononanol-1 ..
$H(CF_2)_8CH_2OH$ ... ψ'-nonyl alcohol

The acids used were 2-ethyl hexanoic acid, glutaric acid, 3-methylglutaric acid, tricarballylic acid, and phthalic acid. In the case of the polybasic acids, only the totally esterified derivatives were prepared. All the materials studied were liquids at room temperature and were known to be chemically inert and thermally stable (1). The density, index of refraction, and molecular weight determined previously (1) are given because they are essential to the calculation of the molar polarization.

The dipole moments of the six partially fluorinated esters were obtained by determining the molar polarization of the material when dissolved in a nonpolar solvent (2), and then calculating the extrapolated value of polarization at infinite dilution. The experimental values obtained and the results of calculations performed are presented in Table II. Solutions of the partially fluorinated esters were prepared in ACS grade benzene. The densities were measured at 20°C with a modified Sprengel-type pycnometer in a constant temperature bath. The dielectric constant data at 1 Mc were obtained at 20°C with a Q meter and cell described previously (3) except that in order to obtain greater precision with this type of apparatus, the main tuning condenser of the Q meter was provided with a detent stop and all tuning was done by means of the vernier condenser. With this arrangement, the dielectric constants of the benzene solutions were determined within ± 0.001.

In determining the molar polarization of the substance at infinite dilution, $P\infty$ graphs were prepared and the required linear extrapolation performed. The dipole moments were then calculated from the values of the polarization at infinite dilution. As shown in Table III, bis(ψ'-amyl) phthalate was found to have the highest dipole moment of the six esters studied (3.8D), while ψ'-nonyl 2-ethylhexanoate had the lowest (2.8D); all are higher than

[1] Present address: International Business Machines Corp., Poughkeepsie, N. Y.

Table I. Formulas and abbreviations (I) of certain partially fluorinated esters

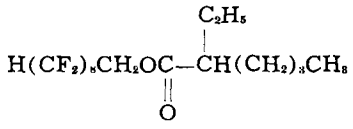

I

ψ'-Nonyl 2-ethylhexanoate
1H,1H,9H-Hexadecafluorononyl
2-ethylhexanoate

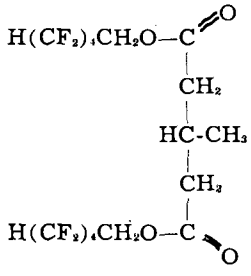

III

Bis(ψ'-amyl) 3-methylglutarate
Bis(1H,1H,5H-octafluoropentyl)
3-methylglutarate

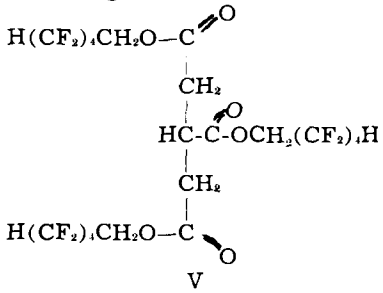

V

Tris(ψ'-amyl) tricarballylate
Tris(1H,1H,5H-octafluoropentyl
tricarballylate

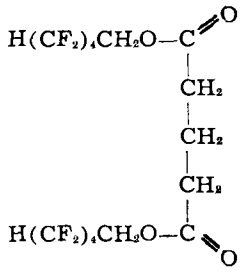

II

Bis(ψ'-amyl) glutarate
Bis(1H,1H,5H-octafluoropentyl)
glutarate

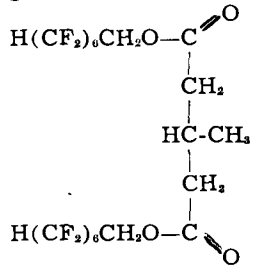

IV

Bis(ψ'-heptyl) 3-methylglutarate
Bis(1H,1H,7H-dodecafluoroheptyl)
3-methylglutarate

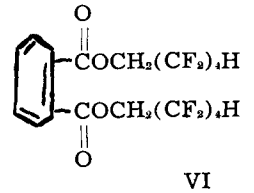

VI

Bis(ψ'-amyl) phthalate
Bis(1H,1H,5H-octafluoropentyl)
phthalate

Table Ia. Physical constants of partially fluorinated esters studied

Substance	Molecular wt (theory)	Density at 20°C (g/cc)	Index of refraction $N_{D}20$	Viscosity (cs) 68°F†	Viscosity (cs) 210°F	Flash point (°F)	Freezing* point (°F)
I	558.31	1.4384	1.3555	12	1.44	—	0
II	560.25	1.5980	1.3560	29	2.65	380	—17
III	574.27	1.5570	1.3595	33	2.79	375	—75**
IV	774.31	1.6484	1.3505	66	3.70	440	—30
V	818.32	1.6800	1.3588	240	6.74	—	—30**
VI	594.26	1.6237	1.3990	160	4.80	400	39

† Values interpolated from data.
* The esters supercool readily and are difficult to crystallize.
** Pour point.

water (1.87D), the common alcohols (1.7D) and the esters (1.6D). The effect of introducing the side chain into the acid sector of the ester is to reduce the dipole moment slightly, while the introduction of each CF_2 group in the alcohol chain increases the dipole moment slightly. The high dielectric constants observed arise from the permanent electric moments of these molecules. Values would be higher were it not for molecular association, the arrangement of the molecules being such that the moments cancel each other appreciably.

By determining the polarization of these esters in dilute benzene solution and vectorially adding the polar moments of constituted atomic groups, it is possible to obtain information on the configuration of the molecules. In order to do this the following steps were taken:

1. The dipole moments of the three partially fluorinated alcohols employed in synthesizing the esters were determined.

2. From these dipole moments, the group moments of the $H(CF_2)_4CH_2$-, $H(CF_2)_6CH_2$-, and $H(CF_2)_8CH_2$- radicals were calculated on the assumption that the alcohols were similar in structure to normal aliphatic alcohols and might be considered to have an electric moment arising from the vector addition of two group moments, $\overleftarrow{H(CF_2)CH_2O}$- and $\overrightarrow{HO}$- operating at an angle of 110° (4a).

3. From the group moments thus established, the structures of the partially fluorinated esters which

Table II. Polarization of partially fluorinated esters in benzene at 20°C

Mole fraction	Density (g/cc)	Dielectric constant at 1Mc	Polarization (cc)
	ψ'-Nonyl 2-ethylhexanoate		
0.0022	0.8827	2.301	240
0.0045	0.8878	2.317	232
0.0092	0.8981	2.349	227
1.0000	1.4384	4.66	213
	Bis(ψ'-amyl) glutarate		
0.0045	0.8897	2.340	294
0.0092	0.9015	2.397	291
0.0291	0.9512	2.641	288
1.0000	1.5980	7.48	240
	Bis(ψ'-amyl) 3-methylglutarate		
0.0045	0.8895	2.337	290
0.0092	0.9014	2.399	299
0.0293	0.9493	2.645	283
1.0000	1.5570	7.44	252
	Bis(ψ'-heptyl) 3-methylglutarate		
0.0045	0.8947	2.339	329
0.0093	0.9118	2.399	332
0.0303	0.9811	2.638	325
1.0000	1.6484	5.94	292
	Tris(ψ'-amyl) tricarballylate		
0.0045	0.8962	2.358	394
0.0093	0.9148	2.433	390
0.0304	0.9919	2.787	395
1.0000	1.6800	7.81	340
	Bis(ψ'-amyl) phthalate		
0.0045	0.8907	2.366	381
0.0092	0.9037	2.447	372
0.0292	0.9564	2.804	366
1.0000	1.6237	8.67	263
	Benzene		
1.0000	0.8776	2.283	26.66

were theoretically possible according to known data of stereochemistry were constructed and their dipole moments calculated.

4. The experimentally determined dipole moments were then compared with those theoretically possible.

The dipole moments of the three partially fluorinated alcohols studied were determined by the benzene solution technique outlined previously, the results of which are given in Tables IV and V. Upon dilution with benzene the polarization of all three alcohols increased; the highest values obtained ranged from 198 to 237 cc. The dipole moments of the partially fluorinated alcohols are high (2.88-3.06D) being approximately 90% greater than the dipole moments of the corresponding unsubstituted alcohols. In the liquid state the molecules are highly associated as shown by the relatively low polarization values of the pure compounds.

Table III. Dipole moments of six partially fluorinated esters

$$\mu = 0.219 \sqrt{P - R} \times 10^{-18} \text{ esu-cm}$$

Substance	Extrapolated polarization P(cc)	Molar refraction R	Dipole moment* (esu-cm) (±0.04)
ψ' Nonyl 2-ethylhexanoate	248	84.70	2.80D
Bis(ψ-amyl) glutarate	297	76.60	3.25D
Bis(ψ'-amyl) 3-methylglutarate	281	81.30	3.09D
Bis(ψ'-heptyl) 3-methylglutarate	326	101.2	3.28D
Tris(ψ'-amyl) tricarballylate	398	107.2	3.73D
Bis(ψ'-amyl) phthalate	390	88.53	3.80D

* $D = 1 \times 10^{-18}$ esu-cm.

Table IV. Polarization of partially fluorinated alcohols in benzene at 20°C

Mole fraction	Density (g/cc)	Dielectric constant at 1Mc	Polarization (cc)
	ψ'-Amyl Alcohol		
0.0045	0.8827	2.331	198
0.0180	0.8979	2.471	192
1.0000	1.6647	16.93	117
	ψ'-Heptyl Alcohol		
0.0045	0.8852	2.331	216
0.0182	0.9084	2.468	206
1.0000	1.7532	11.69	148
	ψ'-Nonyl Alcohol		
0.0045	0.8877	2.332	237
0.0185	0.9185	2.466	221

Since the hydroxyl group moment has a known value (4a) of 1.51D and the experimentally determined value of ψ'-amyl alcohol is 2.88D, using the modification of the Law of Cosines for determining the concurrent diagonal,

$$\mu^2_{2.88D} = \mu^2_{1.51D} + \mu^2_x - 2\mu_{1.51D}\,\mu_x \cos 110°$$

the value of the group moment $\overleftarrow{H(CF_2)_4CH_2O}$- was found to be 1.98D and taking 0.74D (4a) as the $\overrightarrow{-C-O-}$ value, the group moment $\overleftarrow{H(CF_2)_4CH_2}$- has a value of 2.72D. By similar reasoning the value of $\overleftarrow{H(CF_2)_6CH_2}$- is 2.81D and that of $\overleftarrow{H(CF_2)_8CH_2}$-, 2.93D.

ψ'-Nonyl 2-ethylhexanoate.—The dipole moments of the planar forms of the aliphatic esters such as amyl, heptyl and nonyl 2-ethylhexanoate were calculated according to the usual methods and found to possess values slightly higher than those of 2-ethylhexanoic acid. The direction of the moment within the ester molecule is, of course, different from that in the acid (4b). Nonyl 2-ethylhexanoate has a value of 1.6D in the cis configuration while the acid has a value of 1.4D in the corresponding planar form. The nonplanar structures calculated on the basis of a 30° tilt (4c) at the C-O-C linkage have dipole moment values of 1.8D for the ester and 1.7D for the acid. A calculated value of 4.4D is obtained for the planar cis form of the ψ'-nonyl 2-ethylhexanoate,

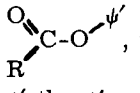

, where R is the 2-ethylhexyl radical and ψ' the ψ'-nonyl radical. For the nonplanar cis form in which the plane of the ψ'O chain is at an angle of 30° with the plane of the 2-ethylhexanoate group, the calculated dipole moment is 3.8D. This differs from the experimentally determined value of 2.8D. On the other hand, the planar trans form of the 2-

Table V. Dipole moments of the partially fluorinated alcohols

Substance	Extrapolated polarization P(cc)	Molar refraction R	Dipole moment* (esu-cm) (±0.04)
ψ'-Amyl alcohol	200	27.48	2.88D
ψ'-Heptyl alcohol	219	37.34	2.95D
ψ'-Nonyl alcohol	243	47.20	3.06D

* $D = 1 \times 10^{-18}$ esu-cm.

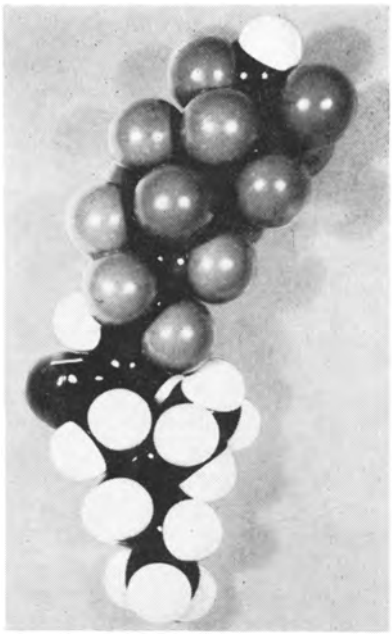

Fig. 1. Probable structure of ψ'-nonyl 2-ethylhexanoate (nonplanar cis form).

ethylhexanoic acid has a calculated dipole moment of 3.9D and the value for the planar trans form of the corresponding nonyl ester 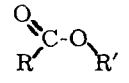 is 3.5D. The calculated value of the dipole moment of the ψ'-nonyl 2-ethylhexanoate in the planar trans form is 0.4D, a value one-seventh that observed experimentally. For these reasons it is probable that the structure of the ψ'-nonyl 2-ethylhexanoate shown in Fig. 1, corresponding to the nonplanar cis form, predominates.

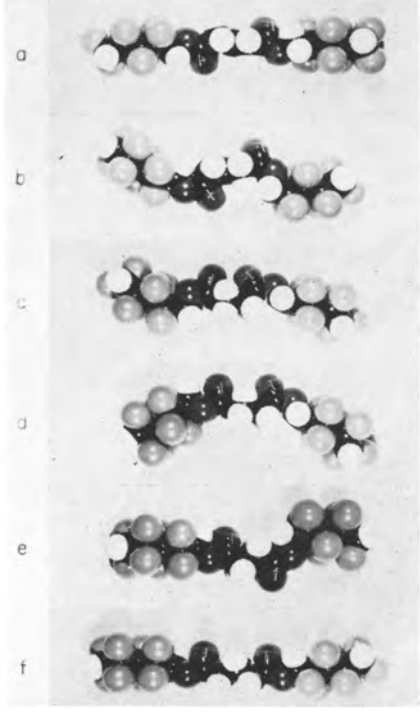

Fig. 2. Planar molecular structure of bis (ψ'-amyl) glutarate: (a) Cis-cis form with carbonyl oxygens opposed; (b) Trans-trans form with carbonyl oxygens opposed; (c) Trans-trans form with carbonyl oxygens adjacent; (d) Cis-trans form with carbonyl oxygens adjacent; (e) Cis-trans form with carbonyl oxygens opposed; (f) Cis-cis form with carbonyl oxygens adjacent.

Bis(ψ'-amyl) glutarate.—Bis(ψ'-amyl) glutarate may be considered for the purposes of structural analysis to be composed of eight electric vectors which give rise to six planar structures, the dipole moments of which can be calculated from the group moments previously established. Two of these structures arise from the cis-cis configurations of the two ester groups, two from the trans-trans configurations and two from combined cis-trans configurations (Fig. 2). Two of the electrically symmetrical planar structures ($\mu=0$), one consisting of a cis-cis form (Fig. 2a) and the other of a trans-trans form (Fig. 2b) are coupled oppositely through the glutaric acid chain; neither of these configurations are thought to be present in the actual material since the latter has an observed dipole moment of 3.2D. By coupling two trans configurations in a plane through the glutaric acid carbon chain and having the carbonyl oxygens on the same side of the molecule (Fig. 2c), an electrically unsymmetrical molecule having a calculated dipole moment of 0.1D results. This value differs appreciably from that observed experimentally and could be present in the material only in very small quantities. Another possible electrically unsymmetrical structure consists of a coupled array of one cis and one trans configuration with both carbonyl oxygens on the same side of the molecule (Fig. 2d). Such a structure has a calculated dipole moment of 3.7D, a value 0.5D greater than that observed experimentally. When either the cis or the trans configuration is rotated through 180°, an unsymmetrical molecule is obtained (Fig. 2e) which has a dipole moment of 3.7D also. Finally by coupling two cis configurations in a plane through the glutaric acid chain, and arranging the carbonyl groups on the same side of the molecule as shown in Fig. 2f, a structure having a calculated dipole moment of 2.6D is obtained.

The observed electric moment of 3.2D, which is intermediate between the two cis-trans configurations (Fig. 2d and 2e) and the cis-cis oxygens adjacent configuration (Fig. 2f), suggests that if the material is planar, it consists of a mixture of all three structures, possibly in the proportions of 50% cis-cis oxygens adjacent, 25% cis-trans oxygens adjacent, and 25% oxygens opposed.

If it is assumed that the molecule is not planar, but rather that the C-O-C atoms form an angle of 30° with the plane of the glutaric acid chain (4c), then it is possible to derive configurations in space having an electric moment approaching 3.2D and structures possessing some of the characteristics of all three planar configurations. As an example, consider the effect of rotating each of the ψ'-O groups in the cis-cis oxygens adjacent configuration (Fig. 2f) (the most abundant planar form) in such a way that each is incident to the same side of the glutaric acid plane at an angle of 30°; the theoretical electric moment is 3.3D. Such a configuration is shown in Fig. 3. No change in the dipole moment would have occurred if the rotation of the ψ'-O groups had been such that both made 30° angles with the glutaric acid chain from opposite sides.

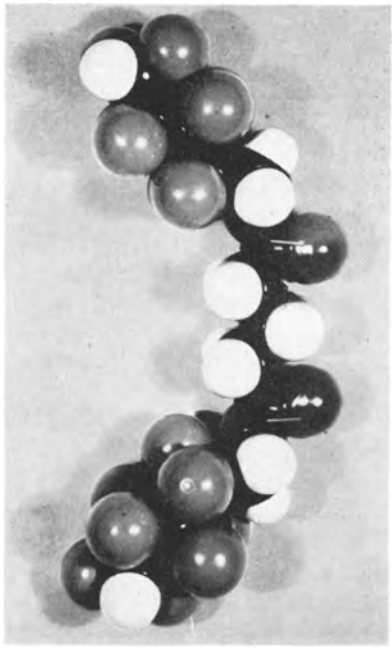

Fig. 3. Probable structure of bis (ψ'-amyl) glutarate (nonplanar cis-cis form with carbonyl oxygens adjacent).

Bis(ψ'-amyl) 3-methylglutarate.—The electrical fields in bis(ψ-amyl) 3-methylglutarate resemble those in bis(ψ'-amyl) glutarate and may be considered to arise from nine electric vectors, four associated with the carbonyl groups, four with the partially fluorinated alkoxy groups, and a small one arising from the 3-methyl group. The latter group causes the slight but measurable difference in the dipole moment of the bis(ψ'-amyl) 3-methylglutarate from that of the bis(ψ'-amyl) glutarate. While the introduction of the 3-methyl group in a planar structure might be thought at first to raise the number of possible structures to twelve, studies made using Stuart-Briegleb atom models indicate that because of steric hindrance only eight structures are likely.

Two cis configurations of ester chains, or two trans configurations coupled oppositely through the 3-methylglutaric acid chain result in structures having dipole moments of 0.4D. A cis configuration coupled to a trans structure with the carbonyl oxygens on the same side of the molecule gives rise to a dipole moment of 3.9D when the 3-methyl group is near the trans carboxyl group and 3.6D when it is near the cis carboxyl group. Two trans configurations with the 3-methyl group on the same side as the adjacent carbonyl oxygens result in a calculated dipole moment of 0.5D, while rotation of the 3-methyl group 180° around the glutaric acid chain results in a calculated value of 0.3D; these values are much lower than that observed experimentally (3.1D). Two cis configurations with the 3-methyl on the same side as the adjacent carbonyl oxygens give rise in a planar structure to a dipole moment of 2.2D. Rotating the 3-methyl group through 180° raises the calculated moment to 3.0D. If the bis(ψ'-amyl) 3-methylglutarate is thus considered to exist in the planar form, the cis-cis configuration with carbonyl oxygens adjacent would seem to predominate. If it is assumed that the molecule is not planar but rather

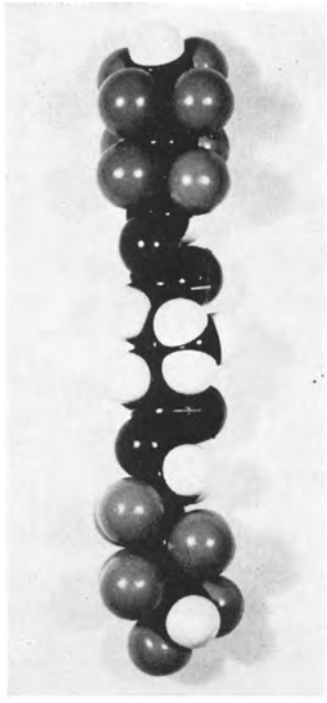

Fig. 4. Probable structure of bis (ψ'-amyl) 3-methylglutarate (nonplanar cis-cis form with carbonyl oxygens adjacent).

that each ψ'-O group is tilted 30° from the same side of the plane of the 3-methylglutaric acid chain, the dipole moment would approach the value determined experimentally. Such a configuration is shown in Fig. 4.

Bis(ψ'-heptyl) 3-methylglutarate.—Bis(ψ'-heptyl) 3-methylglutarate (3.3D) differs from bis(ψ'-amyl) 3-methylglutarate in that the value of the electric moment associated with the partially fluorinated heptyl group (2.8D) is higher than that associated with the corresponding amyl group (2.7D). The effect of adding vectorially the increment of 0.1D to each of the possible structures results in only small changes in the calculated values from those previously discussed. Thus two cis configurations of ester chains or two trans configurations coupled oppositely through the 3-methyl glutaric acid chain result in structures having dipole moments of 0.4D. A trans-trans configuration with the carbonyl oxygens adjacent and with the 3-methyl group on the same side has a calculated dipole moment of 0.6D, while rotation of the 3-methyl group through 180° around the glutaric acid chain results in a calculated value of 0.2D; these values are much lower than that observed.

A cis-trans configuration with carbonyl oxygens adjacent gives rise to a dipole moment of 3.7D when the 3-methyl group lies near the adjacent oxygens. When it is rotated through 180°, the moment rises to 4.0D. A similar configuration but with the carbonyl oxygens opposed gives rise to a dipole moment of 3.8-4.0D depending on the position of the 3-methyl group. A cis-cis configuration with the 3-methyl group on the same side of the molecule as the carbonyl oxygens gives rise to a dipole moment of 2.2D, while rotating the 3-methyl group through 180° raises the calculated moment to 3.0D.

If it is assumed that the bis(ψ'-heptyl) 3-methylglutarate molecule is not planar but that the ψ'-O

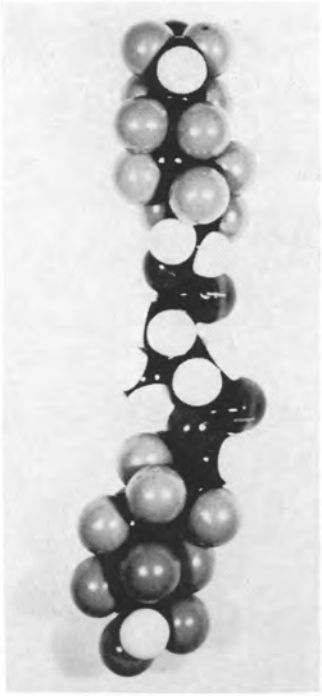

Fig. 5. Probable structure of bis (ψ'-heptyl) 3-methylglutarate (nonplanar cis-cis form with carbonyl oxygens adjacent).

groups are tilted from the same side of the plane of the 3-methylglutaric acid chain, the dipole moment would approach the observed value of 3.3D. Such a structure is shown in Fig. 5.

Tris(ψ'-amyl) tricarballylate.—The tris(ψ'-amyl) tricarballylate molecule (3.7D) may be thought of as being a bis(ψ'-amyl) 3-methylglutarate molecule in which a -C(O)Oψ' group has been substituted for the 3-methyl group. This suggests the possibility of molecular configurations in the form of a T. If the groups are aligned in this way in a plane, there are five combinations of cis and trans configurations possible which lead to electrically unsymmetrical models having permanent moments in the range 0.2-4.7D. Thus the model consisting of two trans groups in the cross-bar of the T and one cis group as the center post (trans-cis-trans) has a calculated moment of 4.0D, while a cis-trans-cis configuration has a moment of 2.4D. Furthermore, a cis-cis-cis configuration has a calculated moment of 4.7D and a trans-trans-trans configuration a moment of 0.2D. Finally, the cis-trans-trans configuration has a calculated moment of 3.6D. All the foregoing are theoretical planar structures; when assembled from Stuart-Briegleb atom models, however, none appear likely because of steric hindrance. Rather, it appears more likely that the actual configuration is nonplanar. One such structure which appears likely is that shown in Fig. 6; the center post of the T is a cis configuration having its vector in the plane perpendicular to the paper; the cross-bar consists of two cis configurations which have been tilted down out of the plane of the paper. The calculated moment of such a molecule is 3.7D when the angle between the cross-bar vector and the center-post vector is 114°.

Bis(ψ'-amyl) phthalate.—The observed electric moment of bis(ψ'-amyl) phthalate is 3.8D, the highest value of the esters studied. In establishing the structure of the ortho-substituted benzene derivatives, the assumption is made that the benzene ring is planar and that the groups exert electric forces at an angle of 80° (5). Assuming this, a trans-trans oxygens adjacent configuration

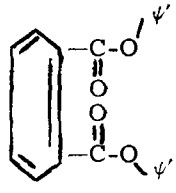

results in a calculated value of 0.3D, while a value of 0.3D is also obtained from a trans-trans oxygens opposed configuration

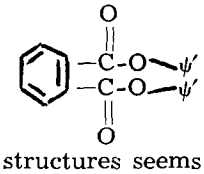

Neither of these structures seems likely. A configuration having cis-trans oxygens opposed has a value of 3.9D while, cis-trans oxygens adjacent results in a value of 4.0D. Both of these values are close to that observed experimentally. Finally, a cis-cis oxygens opposed structure has a calculated moment of 3.9D, while the cis-cis oxygens adjacent structure has a value of 7.3D. From results obtained, it thus appears that one of three planar structures is possible; from Stuart-Briegleb atom models, however, none seems probable; actually, a number of nonplanar configurations containing at least one cis structure possess dipole moments in the range of 3.9D, but due to the limitations of the dipole analysis technique, the exact nonplanar structure is not deducible.

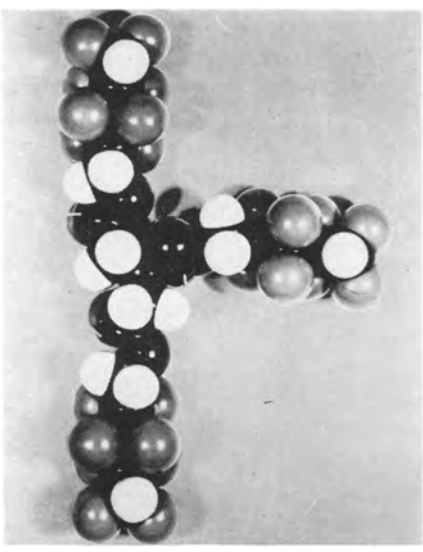

Fig. 6. Probable structure of tris (ψ'-amyl) tricarballylate (tri-cis form).

Conclusions

The dipole moments of the partially fluorinated esters were found to be higher than that of water, the common alcohols, and unhalogenated esters. The introduction of a side chain into the acid sector of the ester tends to reduce the dipole moment slightly. The introduction of each CF_2 group increases the dipole moment slightly. The high dielectric constants of the esters arise from the permanent mo-

ments and would be even higher were it not for molecular association.

A study of the molecular structure of the esters has indicated that several possible structures may exist for each compound, but experimental data limits these possible structures to ones which contain a cis form. It is also concluded that the molecules exist for the most part in a nonplanar form.

Acknowledgments

The authors wish to thank W. A. Zisman for suggesting this investigation and P. D. Faurote, C. M. Murphy, and J. G. O'Rear for making available the samples of partially fluorinated alcohols and esters used in these studies.

Manuscript received November 5, 1956. This paper was prepared for delivery before the Washington Meeting, May 12-16, 1957.

Any discussion of this paper will appear in a Discussion Section to be published in the December 1957 JOURNAL.

REFERENCES

1. P. D. Faurote, C. M. Henderson, C. M. Murphy, J. G. O'Rear, and H. Ravner, *Ind. Eng. Chem.*, **48**, 445 (1956).
2. C. P. Smyth, "Determination of Dipole Moments" in "Physical Methods of Organic Chemistry—II," A. Weissberger, Editor, p. 994, Interscience Publishing Co., New York (1946).
3. T. D. Callinan, J. B. Romans, and R. M. Roe, U. S. Naval Research Laboratory Report 4488, Feb. 17, 1955.
4. C. P. Smyth, "Dielectric Behavior and Structure," (*a*) p. 301, (*b*) p. 306, (*c*) p. 307, McGraw-Hill Book Co., New York (1955).
5. R. J. W. LeFevre, "Dipole Moments," 2nd ed., p. 66, Methuen & Co., Ltd., London (1948).

The Thermoluminescence of CaF_2:Mn

Robert J. Ginther and Russell D. Kirk

United States Naval Research Laboratory, Washington, D. C.

ABSTRACT

The thermoluminescence of manganese-activated calcium fluoride has been found to be dependent on both its manganese content and the presence of other foreign ions. Sodium and oxygen promote high temperature glow peaks, whereas the addition of trivalent cations causes the thermoluminescence of oxygen-containing material to occur at lower temperatures. Thermoluminescence may be excited by x-rays, by mechanical handling, or by irradiation with blue light. Glow peak positions are independent of the method of excitation.

In a current investigation of the application of thermoluminescence to the dosimetry of high energy radiation, one of the most efficient materials found was CaF_2:Mn. The preparation of this phosphor and its sensitization by Ce have been described previously (1). In the present paper, the dependence of the thermoluminescence of this phosphor on both its Mn content and on the effect of substituents are presented. Its application as a thermoluminescent dosimeter will be described elsewhere.

Among the most important characteristics required of a thermoluminescent dosimeter material is freedom from low temperature glow peaks which would enable thermal radiation to free trapped electrons at low temperatures and erase the effect of the high energy radiation (2). It is therefore the search for materials having only high temperature thermoluminescence and the study of the effect of compositional variation on glow peak position which were the principal subjects of the investigation. Consequently, only thermoluminescence above room temperature was of interest.

Consideration of calcium fluoride as a possible dosimeter material was occasioned by the observation of an intense thermally stimulated emission following the x-irradiation of a mineral sample from Franklin, N. J. Wick (3) has studied the thermoluminescence of both synthetic and natural fluorite containing manganese. In her work, glow curves were not obtained, and some low temperature (<100°C) thermoluminescence was observed with every sample.

Experimental

Synthetic samples of Mn-activated calcium fluoride were prepared by the technique described earlier (1).

For the thermoluminescence measurements, ½ in. diameter powder plaques were pressed into the recess of either a brass or Al holder. After irradiation, samples were heated at a rate of 10°C/min in a light-tight container. The light output of the phosphor was detected by a 1P21 photomultiplier tube, and amplified by a sensitive d-c amplifier. The phosphor temperature was detected by a thermocouple. The phototube and thermocouple signals were simultaneously recorded with an X-Y recorder yielding a direct plot of thermoluminescence vs. temperature.

A Corning No. 9780 filter was employed in the phototube housing to minimize the signal contributed by black body radiation at high temperatures. In the case of weak thermoluminescent emissions, the red light emitted by the hot sample and surroundings can exceed the thermoluminescence signal and limit the sensitivity of measurement. Use of

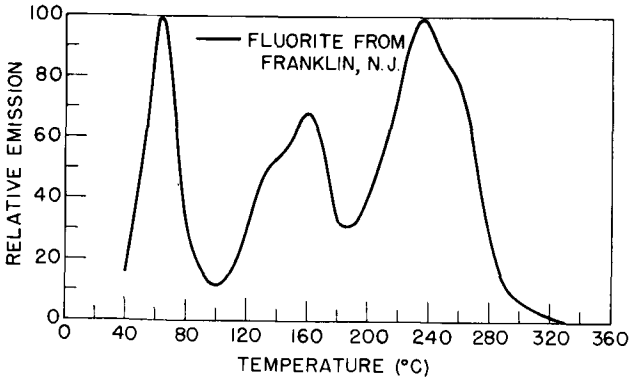

Fig. 1. Thermoluminescence of natural fluorite

the 9780 filter which transmits the green emission of the phosphor, but absorbs in large measure the red thermal radiation, permits the employment of the amplifier at its full sensitivity (0.001 μa for full scale meter deflection). At this high sensitivity the signal from the thermal radiation is evident from an increasing phototube signal beginning at a temperature of about 340°C. Since the thermoluminescence of CaF_2:Mn is almost completely exhausted at this temperature, an increasing signal at 340°C does not interfere with the measurement.

For the measurement of very low thermoluminescent emission a second apparatus employing a 5819 phototube was constructed. This apparatus was designed to employ powder plaques 1½ in. in diameter rather than the ½ in. diameter plaques used in the earlier model. The larger plaques together with the greater cathode area of the 5819 compared to that of the 1P21 tube gave a sensitivity increase of about a factor of five. The new unit employed the same circuitry and did not differ in principle from the earlier apparatus.

For the determination of the effect of composition on the glow spectrum or on relative sensitivity, samples were exposed to 40 KVP x-rays from a Bucky Therapy Unit[1] employing a Machlett tungsten target, Be window tube.

Thermoluminescence as a Function of Composition

The glow curve for the sample of fluorite from Franklin, N. J., is shown in Fig. 1. This material has a large proportion of its emission at temperatures below 200°C. The mineral has a high temperature peak at 235°C, however; its thermoluminescent yield to the given x-ray exposure placed it among the most sensitive materials the authors have observed. Its green emission suggested the presence of a Mn activator, and it therefore seemed of interest to determine the thermoluminescent properties of Mn-activated CaF_2.

The first series of synthetic samples measured were those containing from 0.10 to 7.50 mole % Mn. Their thermoluminescence following equal exposure to 40 KVP x-rays is shown in Fig. 2. With the two lowest Mn concentrations strong low temperature thermoluminescence is obtained. There is evidence of low temperature peaks at about 90° and 140°C in the glow curve for the 1.0% Mn sample, but

[1] X-ray Manufacturing Corp.

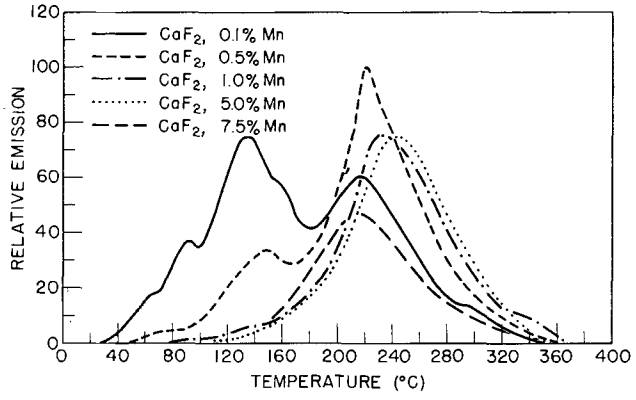

Fig. 2. Thermoluminescence of synthetic CaF_2:Mn as a function of Mn content.

samples of 5.0% and 7.5% have but a single glow peak. Apparently 7.5% of Mn exceeds the optimum activator content with respect to both the thermoluminescent yield and the position of the glow peak.

Samples having Mn contents of 2, 3, and 4% were then prepared. Their glow curves are shown in Fig. 3 along with those of the 1.0 and 5.0% samples for comparison. The optimum Mn content appears to be 3.0%. Of the samples containing no vestiges of the low temperature glow peaks it is the most efficient, and its peak is at the highest temperature, 255°C. However, since a number of samples containing 5.0% of Mn together with additions of other foreign ions were already available, this higher concentration was used for further investigation of the thermoluminescence of the system.

It was known that the emission spectrum of calcium fluoride varied with its Mn content, and a correlation of the glow peak position with Mn concentration at first appeared plausible. However, it will be shown that freedom from low temperature thermoluminescence is a function of more than simply the Mn content, so that a correlation of the glow curves with the emission spectra is not warranted.

The above samples had been prepared from calcium fluoride precipitated from $CaCO_3$ with dilute HF. This precipitation technique yielded a coarse grained product which is resistant to hydrolysis on drying and believed to contain a minimum of hydrolyzed products such as $Ca(OH)_2$. Use of commercially available CaF_2 known to contain either Ca $(OH)_2$ or $CaCO_3$ yielded phosphors with very inefficient thermoluminescence. It was therefore of interest to determine the effect of employing a CaF_2

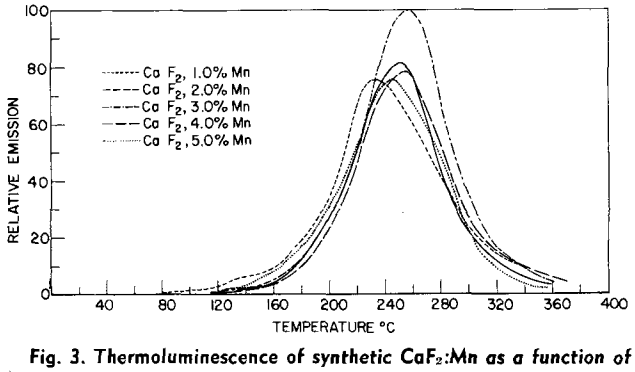

Fig. 3. Thermoluminescence of synthetic CaF_2:Mn as a function of Mn content.

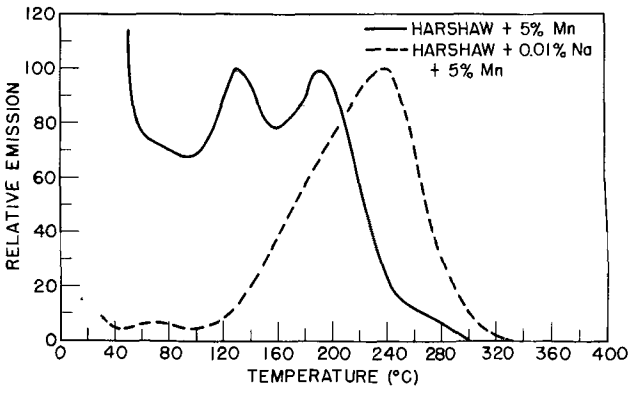

Fig. 4. Thermoluminescence of CaF_2:Mn prepared from Harshaw CaF_2.

raw material with the lowest available oxygen content. Such a source presumably is optical quality crystals, either synthetic or natural. Accordingly samples were prepared from both Harshaw and Optovac synthetic calcium fluoride, as well as from a clear, colorless mineral sample. The glow curve of a CaF_2, 5% Mn sample prepared from Harshaw calcium fluoride is shown in Fig. 4. There is a large proportion of the thermoluminescence below 100°C, and none of the predominant glow peaks are at temperatures above 200°C. Phosphors made from Optovac and natural fluorite gave similar, but not perfectly identical glow curves. Minor variations in the height of the glow peaks were obtained depending on the raw material source, but in every case the glow curve consisted of three approximately equal peaks at 190°, 130°, and in the neighborhood of 40°-60°C. With none of these raw material sources was a strong glow peak above 200°C observed. Spectrographic analysis of the single crystal sources of calcium fluoride indicated that they were all relatively pure. Traces of only B, Mg, and Sr were found in the synthetic crystals. The natural crystal contained in addition faint traces (ca 0.0001%) of Fe and Na.

Addition of 0.01% Na to this formulation by incorporating ground single crystal NaF in the batch composition did produce a phosphor having a glow curve showing mainly high temperature thermoluminescence, but the glow peak obtained was much broader than that of samples prepared from precipitated calcium fluoride with the same Mn concentration. Moreover, as shown in Fig. 4, with 0.01% Na there is still evidence of low temperature peaks. Spectrographic analysis of the precipitated CaF_2 revealed much less than 0.01% of any alkali ion, so the high temperature characteristic associated with use of precipitated CaF_2 is not due to alkali impurity. Inclusion of Na in samples prepared with precipitated CaF_2 did not influence the glow peak position, but produced a loss of efficiency.

It was found that the incorporation of oxygen in Harshaw CaF_2 produced CaF_2:Mn phosphors with a high temperature thermoluminescence similar to that of samples made with precipitated CaF_2. Oxygen may be effectively incorporated by preheating the CaF_2 in a moist atmosphere or by refiring finished phosphors in a dry atmosphere with $CaCO_3$. Experiments performed to date do not distinguish

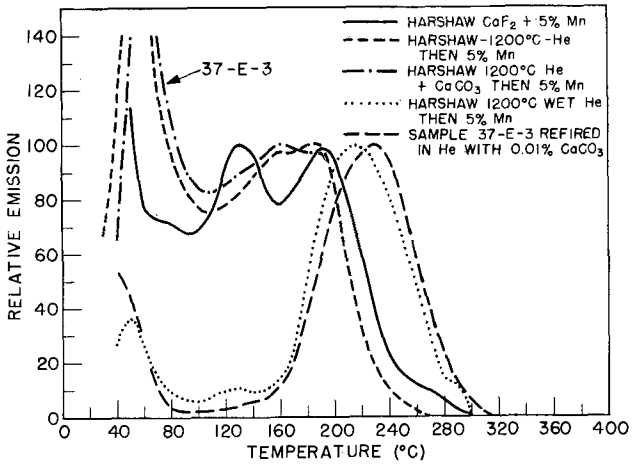

Fig. 5. Effect of oxygen upon thermoluminescence of CaF_2:Mn prepared from Harshaw CaF_2.

whether the oxygen is combined as O^{2-} or OH^- ion.

In Fig. 5 are reproduced the glow curves of some samples prepared with oxygen additions to Harshaw CaF_2. Included in this figure for comparison is the glow curve of the 5% Mn sample with no oxygen addition. When Harshaw CaF_2 was first fired at 1200°C in wet He, and then this partially hydrolyzed material was employed in the synthesis of a 5.0% Mn phosphor, a glow curve having its main peak at 215°C was obtained. Presumably the wet He firing effected the incorporation of oxide or hydroxide ion. Insofar as the authors are aware, neither the existence of a calcium oxyfluoride nor the solubility of O^{2-} or OH^- ions in CaF_2 have been reported, so the mechanism of oxygen incorporation is unclear.

An attempt was made to clarify this situation by preparing a sample from Harshaw CaF_2 in which O^{2-} ion was introduced in a dry atmosphere by prefiring the fluoride with $CaCO_3$ in dry He. As shown in Fig. 5 the variation of the glow curve produced by this synthesis procedure is very different from that obtained by hydrolysis. Moreover, the variation observed is in no way connected with the addition of oxygen as shown by the glow curve of a sample prepared in the same way except that $CaCO_3$ was omitted in the dry He firing. However, if any of the three phosphors shown to have low temperature thermoluminescence in Fig. 5 is refired with 0.10% $CaCO_3$, a phosphor with high temperature thermoluminescence is obtained.

From the above experiments it is observed that the order in which the oxygen and the Mn are incorporated in CaF_2 is important. For the hydrolysis procedure, the CaF_2 must first be fired in wet He and then refired with the source of Mn in a dry atmosphere to produce the phosphor. Experiments in which Mn-containing fluorite was fired in wet He led to oxidation of Mn and a dark brown, weakly luminescent product. The required order in which oxygen and Mn must be introduced when $CaCO_3$ is the source of oxygen is more difficult to understand. In this case the oxygen must be incorporated after the Mn has been combined in the calcium fluoride. From these experiments it has been concluded that the impurity responsible for the thermoluminescence

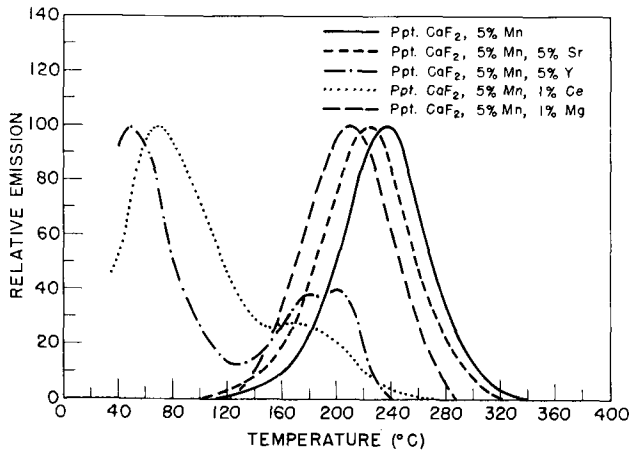

Fig. 6. Effect of substituents on the thermoluminescence of CaF_2: Mn.

characteristics of phosphors prepared from precipitated CaF_2 is oxygen. While some low temperature emission was observed from samples prepared from Harshaw calcium fluoride with oxygen additions, the high temperature glow peak of these materials is similar in breadth to that of phosphors made with precipitated CaF_2.

In a further attempt to confirm that oxygen is the impurity responsible for the thermoluminescence characteristic of phosphors prepared from precipitated calcium fluoride, attempts were made to process the precipitated material in order to remove the contained oxygen and to demonstrate that phosphors prepared from such material have low temperature thermoluminescence. To date such attempts have been unsuccessful. Firing phosphor samples with either ammonium fluoride or bifluoride had no effect upon their glow curves. Incorporation of PbF_2 in the formula, a technique employed by Stockbarger and Blanchard (4) to deoxidize fluoride melts, shifted the glow peak only about ten degrees to lower temperature. Apparently the ammonium fluoride volatilizes before reaction can occur and PbF_2 is ineffective at 1200°C. The minor shift produced by PbF_2 is probably associated with the presence of Pb^{++} ion rather than the removal of oxygen.

Low temperature thermoluminescence may be obtained by incorporating certain foreign ions in Mn-activated calcium fluoride prepared from precipitated material. Fig. 6 illustrates the glow curves obtained with some of these additives. Sr and Mg are shown to provide rather minor shifts of the glow peaks to lower temperature. Ce and Y suppress the high temperature thermoluminescence and produce strong low temperature peaks. No addition was found which would either intensify the high temperature glow peak of phosphors made with precipitated CaF_2 or shift this peak to even higher temperatures.

The above observations were obtained with x-ray excitation of the phosphor. The material may also be excited by γ-rays, by visible light, and by mechanical treatment to produce the same glow peaks. Observation of thermoluminescence following the grinding of glass and of fluorite was made by Nyswander and Cohn (5) who named the phenomenon tribothermoluminescence. Wick observed tribothermoluminescence in Mn-activated fluorite. The 5.0% Mn samples employed in the current investigation exhibited this property. The extreme sensitivity of this material to mechanical handling is illustrated by the following sequence of experiments. Instead of pressing the sample into a plaque, the phosphor was cemented in with sodium silicate and a glow curve measurement was made. A thermoluminescence excited by the grinding of the fired sample cake was observed. Without disturbing the apparatus in any way, the glow curve measurement was repeated. No thermoluminescence was recorded, indicating that the heating of the previous run had exhausted the phosphor. The sample holder was then removed from the apparatus and replaced in complete darkness, and a third glow curve was measured. Approximately one-half of the original thermoluminescence was recorded. The same results were obtained regardless of whether the glow curves were obtained by heating the samples in air, in He, or in vacuum.

The thermoluminescence excited by visible light is very weak, and is best observed only after the mechanically stimulated emission is removed. If a sample is not removed from the apparatus after a thermoluminescence measurement, but is irradiated with white light, a glow curve is obtained upon reheating the sample. Some irradiations made with filters showed that blue light produced the effect but that red light did not. Blue light is absorbed in a 4000Å Mn absorption band. This absorption band was first detected by excitation measurements on powdered samples (1). Garlick (6) has recently confirmed its existence by absorption measurements on clear crystals.

Conclusions

The high temperature glow peak of CaF_2:Mn has been shown to be a function of both its Mn content and the presence of either alkali or oxygen impurity. The simplest explanation of the effect of alkali or oxygen in producing a distinct glow peak is that these ions produce local deficiencies of positive charge (7) which are compensated by the production of either negative ion vacancies or interstitial positive ions. The compensating defects provide deep electron traps resulting in high temperature thermoluminescence. Addition of trivalent ions to oxygen-bearing fluorite suppresses the positive charge deficiency and diminishes the high temperature thermoluminescence.

Results obtained by blue light excitation are not easily accounted for by the above explanation. Blue light is absorbed in a discrete Mn absorption band and would not be expected to produce free electrons. In the light of this observation the influence of the impurity must be attributed to a direct effect upon the Mn activator.

Acknowledgment

The authors wish to thank Phillip Pizzolato who assembled the apparatus and made many of the thermoluminescence measurements.

Manuscript received November 1, 1956. This paper was prepared for delivery before the San Francisco Meeting, April 29 to May 3, 1956.

Any discussion of this paper will appear in a Discussion Section to be published in the December 1957 JOURNAL.

REFERENCES

1. R. J. Ginther, *This Journal*, **101**, 248 (1954).
2. F. Daniels and W. P. Reiman, University of Wisconsin, Final Report "The Thermoluminescence Dosimeter," Chemical Procurement Agency, Contract No. DA-18-108-CML3069, Feb. 16, 1954.
3. F. Wick, *J. Opt. Soc. Amer.* **27**, 275 (1937).
4. D. C. Stockbarger and A. A. Blanchard, U. S. Pat. 2,498,186, Feb. 21, 1950.
5. R. E. Nyswander and B. E. Cohn, *Phys. Rev.*, **36**, 1257 (1930).
6. G. F. J. Garlick, Private communication.
7. J. H. Schulman, R. J. Ginther, and R. D. Kirk, *J. Chem. Phys.*, **20**, 1966 (1952).

Defect Structure and the Temperature Dependence of Hardness of an Intermetallic Compound

J. H. Westbrook

Research Laboratory, General Electric Company, Schenectady, New York

ABSTRACT

The temperature dependence of hardness of the intermetallic compound AgMg was studied from —190°C to the solidus temperature over the entire homogeneity range. The effect of structure on hardness at high homologous temperatures differs radically from that at low temperatures. These results, over virtually the full homologous temperature range, appear to rationalize previously contradictory studies of the effect of defect structure on the room temperature strength of intermetallic compounds.

Numerous studies have confirmed the importance of defect structure in determining mechanical properties of intermetallic and interstitial compounds. Experimental results are contradictory, however, some plots of strength vs. composition showing minima, others maxima. Kornilov (1) has suggested that time and temperature might also affect mechanical properties of a compound. Moreover, it was found recently (2) that iron group aluminides containing either vacancy or substitutional defects were considerably harder than the corresponding defect-free stoichiometric compositions, although the magnitude of this effect diminished with increasing temperature. Since in that study the effect of defect structure could not be examined at temperatures higher than about 0.6 of the melting point, the experiments were repeated using AgMg, a stable compound which melts congruently at a substantially lower temperature (820°C) and which exists over a broad homogeneity range. It has the ordered BCC or CsCl structure, as did the previously studied aluminides. This compound permitted testing of the suggestion arising from the earlier work that, at sufficiently high homologous temperatures, lattice defects have a softening effect even with short times of loading.

The Silver-Magnesium System

Although the Ag-Mg system has been investigated many times, no single investigator has done a thorough job over the whole range of the diagram. The main features of the diagram were first delineated by Zemczuzny (3) and later refined and supplemented by other investigators (4-12). The early findings of Saeftel and Sachs (13) are by now completely discredited. Fig. 1 is a composite of what appear to be the most accurate portions of the previously cited works.

Solubility limits of the compound AgMg or β phase are deserving of special mention, not only because of their importance to the present investigation, but also because this is one of the most serious areas of disagreement among investigators. Zemczuzny (3) on the basis of his thermal analyses set the maximum solubility limits at 37.4 and 65.43 A/o Mg. Smirnov and Kurnakov (4), working with specimens annealed at 400°C, claimed confirmation of Zemczuzny's figures, but their actual hardness and resistivity data would seem to indicate limits at 400°C more like 40.0 and 58.2 A/o Mg. X-ray and metallographic studies by Ageev and Kuznetzov (7) on specimens annealed at and quenched from a series of temperatures show somewhat narrower

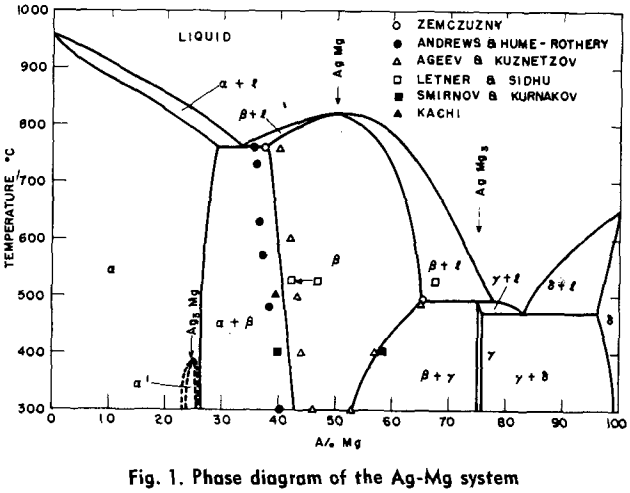

Fig. 1. Phase diagram of the Ag-Mg system

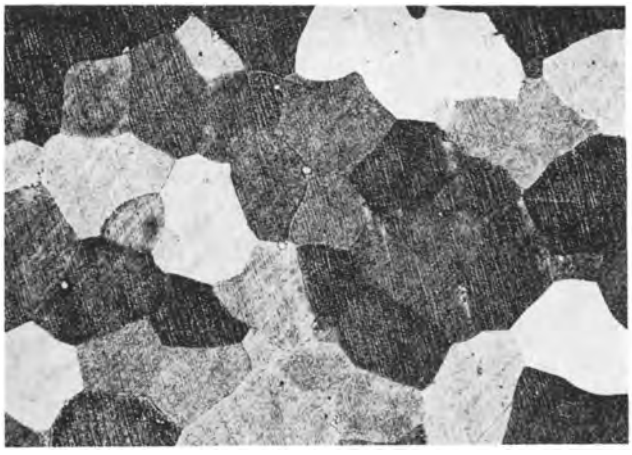

Fig. 2. Photomicrograph of AgMg, etchant H_2SO_4, CrO_3 + H_2O. 100X.

Fig. 3. Photomicrograph of AgMg + α-Ag solid solution, etchant H_2SO_4, CrO_3, + H_2O. 100X.

solubility limits on both sides, as well as a significant temperature dependence of solubility. Andrews and Hume-Rothery (9) determined the limit only on the Ag-rich side. Their results agree only approximately with those of Zemczuzny (3) and Smirnov and Kurnakov (4). Letner and Sidhu (10) claimed the limits at 525°C to be 47.0 and 67.5 A/o Mg, but their lattice parameter data indicate that 42.0 A/o Mg is more likely for the Ag-rich limit. The emf data of Kachi (12) at 500°C define the same limit as just under 40 A/o Mg. Consideration of all these results, as well as the findings of the present study,[1] indicate that the probable boundaries of the β phase lie as shown in Fig. 1.

Experimental

Preparation of samples.—Approximately 500 g heats of several different β phase alloys were induction melted in a graphite crucible and cast into a 1 in. diameter split graphite mold. The Mg [2] and Ag [3] used were both 99.99% pure. Cl gas was bubbled through the melt continuously and maintained as a cover during pouring to protect the metal from oxidation. The ingots were then homogenized 8 hr at a temperature 50°-100° below the supposed melting point. Early in the program, laboratory dry H was used for the heat treating atmosphere. However, variations in dew point at times resulted in serious oxidation of samples. Therefore, most of the heat treatments were carried out in Vycor tubes filled with dry A at approximately 0.5 atm; Ti chips separated from the sample by a plug of quartz wool were used as a getter. This technique was successful even with Mg-rich samples.

Metallographic preparation of the samples was impeded by a pronounced tendency for the material to flow badly during polishing, resulting in the production of structural artifacts. Satisfactory surface preparation was achieved only with extreme care and repeated polishing and etching. Representative

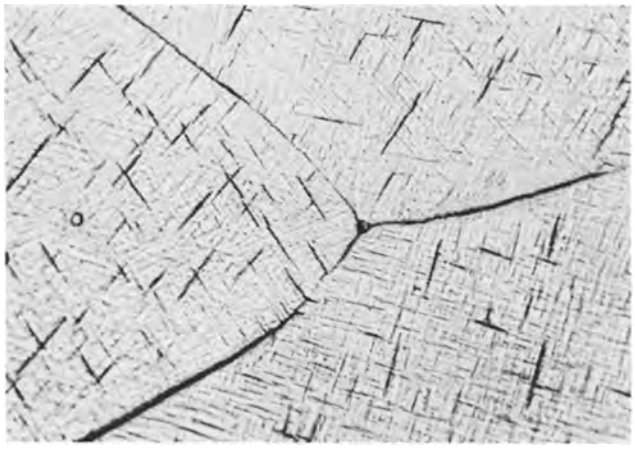

Fig. 4. Photomicrograph of AgMg + γ-$AgMg_3$, etchant HNO_3, Hac + H_2O. 250X.

photomicrographs of structures obtained are shown in Fig. 2-4. Fig. 2 is typical of those alloys near the middle of the homogeneity range, i.e., a simple, single phase of equi-axed grain structure. Fig. 3 and 4 are typical of alloys, single phase at high temperature, which have precipitated Ag and $AgMg_3$, respectively, on cooling due to decreasing solubility, as shown in Fig. 1. The homogeneity of each ingot was checked metallographically, following which a hardness test specimen approximately ½ in. high and 1 in. in diameter was cut from the ingot. Drilled chips were then removed from an immediately adjacent portion of the ingot for chemical analysis. These fine particles oxidized quite rapidly so that it was necessary to weigh the sample immediately after obtaining it. Ag was determined by electrodeposition from alkaline cyanide solution. In most cases, the balance of the ingot was remelted to make other compositions. Analysis confirmed that usually a small but significant amount of Mg was lost on melting. Therefore, all compositions noted herein are analyzed rather than intended values.

Hardness tests.—Indentation hardness measurements were made on all samples[4] with a Vickers diamond indenter and a 200 g load. From room tem-

[1] A 38.8 A/o Mg alloy was found to be two phase at 700°C and below. A 65.8 A/o Mg alloy showed no evidence for peritectic formation of γ phase when quenched from 475° or 500°C but only a characteristic Widmanstatten precipitate of γ from solid solution. The same alloy quenched from 525°C showed evidence of liquid phase formation. The inability to retain the solid solution condition at least for the 500°C quench must be attributed to insufficient rapidity of quench. This could perhaps have been circumvented had a vacuum quenching furnace been available.

[2] Dow Chemical Co.

[3] Handy and Harman.

[4] The 38.8 A/o Mg alloy was tested even though a very small amount of second phase was present. It is believed that the occurrence of this second phase in the amount and distribution present did not significantly affect the results. However, fine precipitate present in the 65.8 A/o Mg sample as in Fig. 4 did affect the results; consequently, data for this composition were excluded from further consideration.

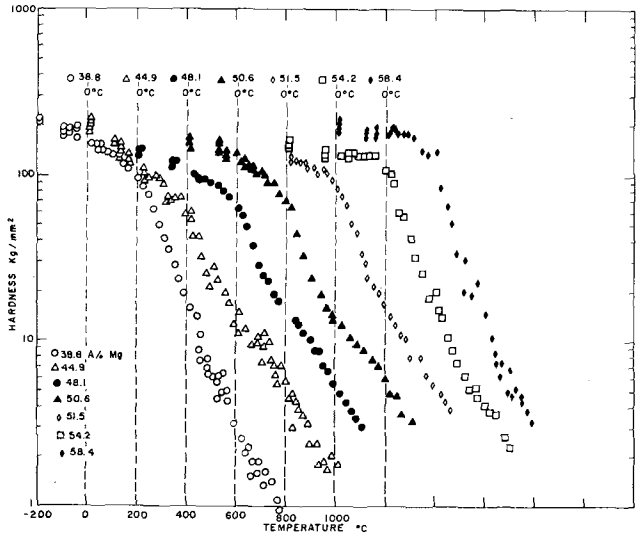

Fig. 5. Temperature dependence of hardness of several AgMg compositions.

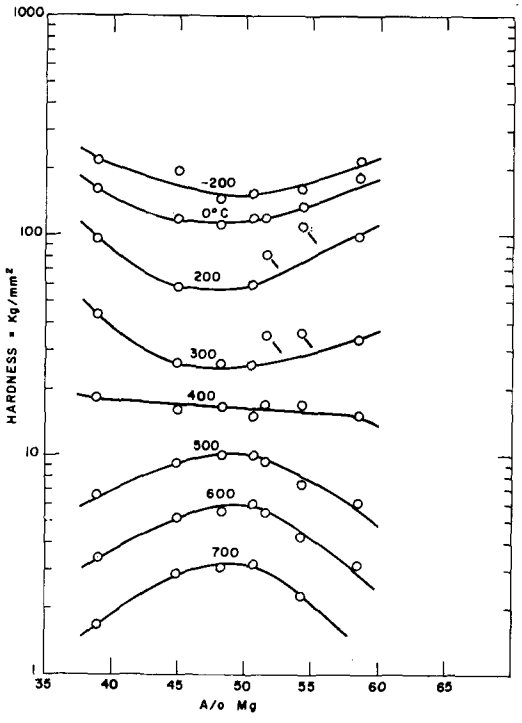

Fig. 6. Hardness-composition isotherms for a series of AgMg alloys

perature to the melting point a micro hot hardness tester of modified Bergh design was used (14). The instrument and testing procedure were identical to those previously employed (2), except that a positive pressure of argon was used as an atmosphere rather than vacuum in order to minimize volatilization of Mg at high temperatures. Argon was purified before introduction into the testing chamber by passage over hot Mg chips (500°C). For tests below room temperature, a Tukon micro hardness tester was used together with cooling baths of liquid N, Freon-12, or dry ice-acetone. Room temperature points determined with both instruments were found to agree satisfactorily. Hardness-temperature curves were run at least twice on each sample to insure that surface work hardening effects had been eliminated (2). The reduced data were finally plotted for convenience on a semi-logarithmic scale (14,15). All of

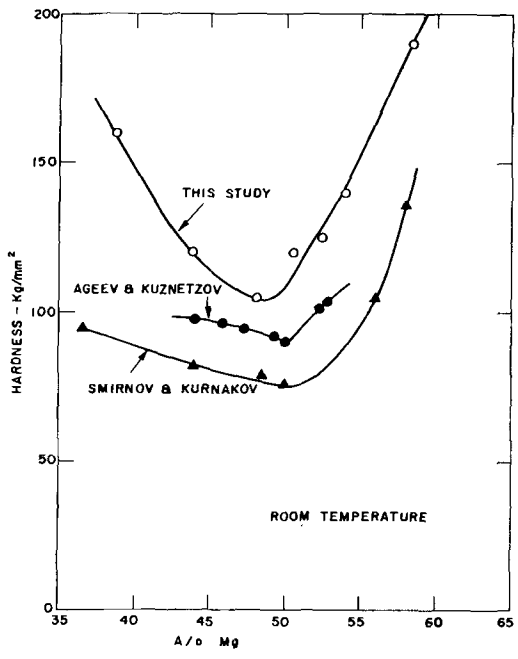

Fig. 7. Comparison of the effect of composition on room temperature hardness of AgMg according to different investigators.

these data are given in Fig. 5. The origins for compositions of successively higher Mg content have each been shifted 200°C higher than the previous curve, to prevent confusion of points.

Discussion

The curves of Fig. 5 are similar in their general features to those previously observed (2,14,15) in that on these semi-logarithmic coordinates the curves are comprised of two approximately linear segments which cross at about 0.5 of the melting point. In this case, however, certain regular and reproducible deviations from true linearity were observed in the high temperature segment of all curves except that for the most Ag-rich alloy. Careful consideration of and testing for possible sources of this anomaly have thus far failed to disclose any unequivocal explanation for this behavior (16).

The effects of defect structure on hardness are most readily perceived from hardness-composition isotherms. The data of Fig. 5 have been cross plotted in this manner in Fig. 6. Here it will be observed that hardness minima are located near the stoichiometric composition at low temperatures. As the temperature increases, these minima flatten and ultimately reverse to become maxima at very high temperatures. The room temperature hardness data by Smirnov and Kurnakov (4) and by Ageev and Kuznetzov (7) are compared with the results of the present study in Fig. 7.[5,6] In view of the differences in testing technique (Smirnov and Kurnahov-Brinell 5.6 mm ball, 50 kg load; Ageev and Kuznetzov unknown), agreement is considered satisfactory. The x-ray studies of Ageev and Kuznetzov (7) and of Letner and Sidhu (10) and the thermodynamic

[5] Ageev and Kuznetzov present their data normalized to a value of 1.00 at 50.0 A/o Mg. Therefore, it was necessary to choose some real hardness for this composition for purposes of comparison. A value of 90 kg/mm² was assumed.

[6] The minimum in the curve as drawn deviates slightly from the stoichiometric value of 50 A/o. It is believed that the data are inadequate for this to be significant.

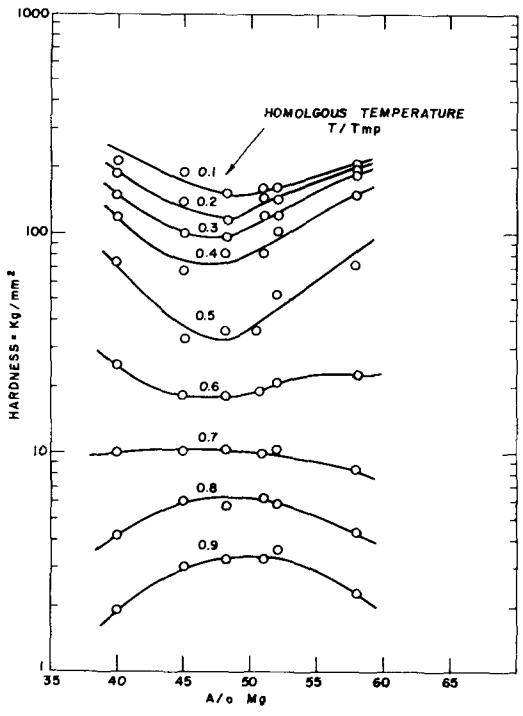

Fig. 8. Hardness-composition isohomologs for a series of AgMg alloys

investigations of Kachi (12) show that AgMg is most perfectly ordered at the stoichiometric composition and has a substitutional defect structure on both sides of stoichiometry. The hardness minima found at low temperatures are therefore in agreement with the previously established effects of defect structure (2).

In rationalizing the high temperature behavior of AgMg, one might wonder whether the lower hardness of compositions near the solubility limits is a result of closer approach to the melting point as has been discussed for other systems by Westbrook and Nisbet (17). To assess this possibility, experimental data are plotted in Fig. 8 as isohomologous temperature curves, i.e., the hardness values on any one curve represent data for different actual temperatures, but for the same ratio of test temperature and solidus temperature. This method of plotting has only altered the shapes of the curves slightly as compared to Fig. 6; the curves become flat at about 0.6 of the melting point and definite maxima still exist above a homologous temperature of about 0.8. This result indicates that the apparent softening is truly an effect of defect structure and not of variations in melting point.

The need for consideration of possible effects of a temperature dependent defect concentration has been obviated by the thermodynamic studies of Kachi (12). Kachi deduced from emf measurements that the degree of disorder of AgMg in the neighborhood of 500°C is 10^{-4}, a value about 100 times as small as that usually experienced for 3/2 electron compounds.[7] These data also permit calculation of a hypothetical disordering temperature of 1500°K, far above the actual melting point of the compound, a result which is indicative of the high stability of AgMg.

[7] A similar study by Trzebiatowski and Terpilowski (35) published since the completion of this manuscript shows a disorder value of 0.03. Their data are believed by the present author to be less accurate than those of Kachi (12).

On the basis of the foregoing results a tentative general postulate can be advanced that, at low temperatures, lattice defects—substitutional or vacancy—are strengthening factors, while at temperatures substantially above 0.5 of the melting point, lattice defects are weakening factors. Of those cases reported in the literature, Cu_3Au (18), CuAu (18), MgCd (19), and PbTl (20,21) all show minima at stoichiometry and all were tested at temperatures below about 0.6 T_{mp}.[8] Two cases have been reported which show maxima near the stoichiometric composition Bi_5Tl_3 (22) and TiO (23). In the former instance, room temperature (the only temperature studied) is slightly above 0.6 T_{mp} and the duration of loading is long (30 min). The observed behavior thus conforms with that postulated for high (homologous) temperatures. TiO is a particularly interesting case since Ehrlich (24) found that, contrary to the usual case, the maximum number of defects is located at the stoichiometric composition and that each sub-lattice becomes more perfect as the composition becomes enriched in its particular component.[9] The low (homologous) temperature hardness results on TiO, although superficially similar to the high temperature behavior of AgMg and Bi_5Tl_3, actually are consistent with the observed low temperature behavior of all compounds of variable composition.

All the observed behaviors of compounds of variable composition are consistent with the above postulate. The physical basis for the observed high temperature behavior is also apparent, at least in a crude sense. If high temperature deformation is diffusion-controlled as is supposed (26-28), then any factor tending to increase the diffusion coefficients will tend to increase the amount of deformation for a given load and time. Both substitutional and vacancy defects have been shown (29) to enhance diffusion coefficients in an isomorphous compound at high temperatures.

Similar effects of lattice defects may explain some long puzzling anomalies. For example, it has been found that certain Al-Zn alloys have an abnormally high plasticity, greater even than either of the two pure components, at both room and elevated temperatures (30-32). The nature of the solidus curve is such that the behavior cannot be accounted for by a "melting point effect" (17). However, Ellwood (33) has shown that the Al-Zn solid solution has a surprisingly high concentration of lattice vacancies and room temperature for this system is about 0.5 T_{mp}.

The effects of radiation on the creep strength of metals have been apparently conflicting. Radiation has been found to raise, to lower, and to have no effect on the resistance to creep (34). Since the principal effect of radiation is to produce a higher than normal concentration of defects in the lattice, one might expect from the present results that radiation would increase creep strength at low (homologous) temperatures, decrease it at high (homologous) temperatures, and have no significant effect at inter-

[8] T_{mp} = temperature of melting.

[9] Rostoker (25) has shown how this peculiar structural behavior may be rationalized from the viewpoint of preserving a critical electron concentration per unit cell.

mediate temperatures. Such consideration would seem to rationalize the observations of the effect of radiation on creep.

Summary

Hardness-temperature studies of six alloys in the compound AgMg or β phase show that lattice defects are a strengthening factor at low homologous temperatures ($<0.5\ T_{mp}$) and a weakening factor at high homologous temperatures ($>0.7\ T_{mp}$). The effects at high homologous temperatures are thought to be a result of the effect of defect structure on diffusion rates. These results appear to rationalize previous studies of the effects of defect structure on the room temperature strength of intermetallic compounds.

Acknowledgment

The author is pleased to acknowledge the many substantial contributions of A. J. Peat to the experimental work. J. E. Burke and R. C. DeVries read and criticized the manuscript.

Manuscript received June 26, 1956. This paper was prepared for delivery before the San Francisco Meeting, April 29 to May 3, 1956.

Any discussion of this paper will appear in a Discussion Section to be published in the December 1957 JOURNAL.

REFERENCES

1. I. I. Kornilov, *Doklady Akad. Nauk S.S.S.R.*, **86**, 721 (1952).
2. J. H. Westbrook, *This Journal*, **103**, 54 (1956).
3. S. F. Zemczuzny, *Z. anorg. u. allgem. chem.*, **49**, 400 (1906).
4. W. Smirnov and N. Kurnakov, *ibid.*, **72**, 31 (1911).
5. R. J. M. Payne and J. L. Haughton, *J. Inst. Metals*, **60**, 351 (1937).
6. W. Hume-Rothery and E. Butchers, *ibid.*, **60**, 345 (1937).
7. N. V. Ageev and V. G. Kuznetsov, *Bull. acad. sci., U.R.S.S.*, **1937**, 289.
8. H. H. George, Master's Thesis, University of Pittsburgh (1939).
9. K. W. Andrews and W. Hume-Rothery, *J. Inst. Metals*, **69**, 485 (1943).
10. H. R. Letner and S. S. Sidhu, *J. Appl. Phys.*, **18**, 833 (1947).
11. L. M. Clarebrough and J. F. Nichols, *Australian J. Sci. Research*, **3A**, 284 (1950).
12. S. Kachi, *Science Repts. Research Insts. Tohoku Univ., Ser. A*, **1**, 351 (1955).
13. F. Saeftel and G. Sachs, *Z. Metallkunde*, **17**, 258 (1925).
14. J. H. Westbrook, *Proc. ASTM*, To be published.
15. J. H. Westbrook, *Trans. Am. Soc. Metals*, **45**, 221 (1953).
16. A. J. Peat and J. H. Westbrook, Unpublished data.
17. J. H. Westbrook and J. D. Nisbet, G. E. Research Lab. Rpt. RL 687, June (1952).
18. N. Kurnakov, S. Zemczuzny, and M. Zasedatelev, *J. Inst. Metals*, **40**, 305 (1916).
19. G. G. Urasov, *Z. anorg. Chem.*, **73**, 31 (1912).
20. N. Kurnakov and S. Zemczuzny, *Z. anorg. u. allgem. Chem.*, **64**, 149 (1909).
21. V. P. Shishokin and V. A. Ageev, *Tsvetnye Metal.*, **1932**, 119.
22. N. Kurnakov, S. Zemczuzny, and V. Takarin, *Z. anorg. u. allgem. Chem.*, **83**, 200 (1913).
23. W. J. Kramers, *et al.*, Atomic Weapons Research Establishment Aldermaston, Berks., Rpt. #0-15/55, May (1955).
24. P. Erhlich, *Z. Elektrochem.*, **45**, 362 (1939).
25. W. Rostoker, *J. Metals*, **4**, 981 (1952).
26. I. Dekhtar, *Doklady Akad. Nauk S.S.S.R.*, **73**, 303 (1950).
27. N. F. Mott, *Proc. Phys. Soc.*, **64B**, 729 (1951).
28. O. D. Sherby, *et. al., Trans. Am. Inst. Mining Met. Engrs.*, **200**, 71 (1954).
29. A. E. Berkowitz, F. E. Jaumot, and F. C. Nix, American Physical Society Meeting paper, March (1954).
30. A. A. Bochvar and Z. A. Sviderskaya, *Bull. acad. sci. U.R.S.S.*, Classe sci. tech., **1945**, 821.
31. A. A. Bochvar, *ibid.*, **1946**, 743.
32. A. A. Bochvar and Z. A. Sviderskaya, *ibid.*, **1946**, 1001.
33. E. C. Ellwood, *J. Inst. Metals*, **80**, 217 (1951-2).
34. S. Glasstone, "Principles of Nuclear Reactor Engineering," p. 477, D. Van Nostrand Co., Inc., New York (1955).
35. W. Trzebiatowski and J. Terpilowski, *Bull. acad. polon. sci.*, Classe III, **3**, 391 (1955).

Preparation of Thorium Bismuth Dispersions from Electrolytic Thorium

M. E. Sibert and M. A. Steinberg
Metallurgical Department, Horizons Incorporated, Cleveland, Ohio

and

R. J. Teitel
Dow Chemical Company, Midland, Michigan

ABSTRACT

The preparation of Th_3Bi_5 dispersions in liquid Bi utilizing electrolytic Th has been investigated by three techniques. These materials are potentially useful as fuels for liquid metal reactors. Dispersions have been prepared successfully in desired concentration, particle size, and shape by addition of crushed Th cathode deposits to Bi, addition of as-deposited cathode to Bi in the cell, and by electrolysis of $ThCl_4$ using a liquid Bi cathode. Procedures, conditions, and results are fully described.

In recent years a variety of reactor types have been proposed as potential nuclear power production systems. Among the more interesting of these reactors is the liquid metal fuel reactor (LMFR).

The basic principle behind such reactors is that they employ low melting alloys for transport of fissionable material in and out of the reactor in place of the usual solid fuel elements. This concept has been extended to include the breeding of fissionable material in the same or secondary liquid metal circuit.

All designs of liquid metal fuel reactors (1,2,4) require a blanket to breed fissile fuel from Th. Since the solubility of Th in low melting alloys is low, the use of dispersions has been considered. One proposed dispersion is that of a thorium bismuthide in Bi. This paper is concerned with the preparation of that particular dispersion.

A liquid metal fuel dispersion such as Th_3Bi_5 in Bi must meet certain requirements to be a satisfactory material. The particle size and shape of the Th_3Bi_5 are of prime importance. If particles are too large or not equiaxed, clogging of pumps, filters, and lines could occur. Large particles would also tend to promote excessive settling of the dispersion. Some pertinent properties are shown in Table I and the liquid Bi solubilities of Th and U in Fig. 1.

It is seen that density and melting point of the dispersion are no particular problem. The main considerations taken into account in preparation of the material are particle size and shape. Small particles ($<50\mu$) of equiaxed shape are desired.

These dispersions may be prepared in at least three ways:

1. Precipitation of Th_3Bi_5 from solution by cooling from 1200°C where the Th would be dissolved. However, large platelets form, so this is not a useful procedure.
2. Exfoliation of Th chips or powder in the Bi melt. Use of powder may give added control over ultimate Th_3Bi_5 particle size. Powder can be produced by: (*a*) hydriding of Th followed by decomposition, and (*b*) fusion electrolysis.
3. Direct electrodeposition of Th from a fused salt bath into liquid Bi cathode.

Th precipitated from solution (method 1) forms undesirable, large platelets. Other methods have

Table I. Properties involved in Th_3Bi_5 system

Material	mp, °C	d(s) g/cc	d(l) g/cc	Solubility in Bi(l)	Neutron absorbtion cross section Barns/atom
Bi	271.3	10.00	9.80	—	0.032
Th	1690±10	11.7	—	0.006%-350°C	7.0
Th_3Bi_5	—	~10.4	—	0.006%-350°C	—

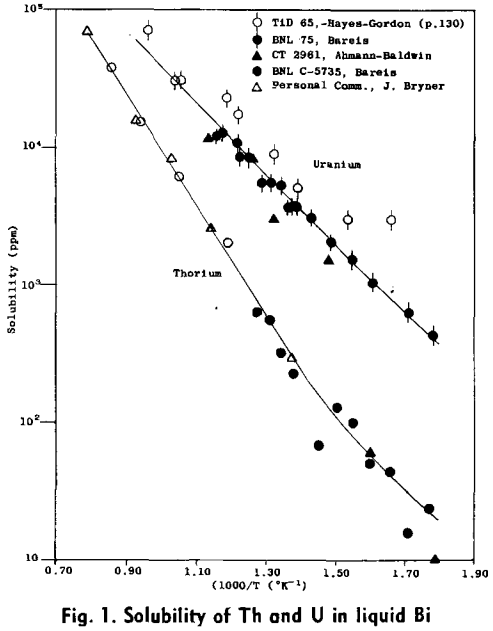

Fig. 1. Solubility of Th and U in liquid Bi

Fig. 2. Typical Th cathode deposit prepared by electrolysis of $ThCl_4$-NaCl system.

an advantage in that stable equiaxed particles are produced by the exfoliation of the compound from Th metal at low temperatures.

This work is concerned primarily with the methods utilizing electrolytic Th powder. It is thought that electrolytic methods could be carried out more economically as a result of the basic economy of electrolytic methods and also because the Th would not have to be recovered as metal prior to formation of the alloy.

Numerous examples of alloy and intermetallic preparation by fused salt electrolysis exist in the literature. At least 3 general methods are used:

1. Deposition of one metal in a liquid metal cathode (5-9).
2. Codeposition of 2 or more metal powders.
3. Deposition of one metal on a solid metal (cathode) to form a liquid alloy eutectic.

The third process type has been carried out here. Intermetallics of Zr-Ni, Ti-Fe, etc., have been prepared by deposition of Zr, Ti, etc., from fused fluoride-chloride melts on a solid base metal cathode. A eutectic forms, drips off, and collects in a pool on the cell bottom.

The basic Th metal powder preparation employed in this work has been described (10); $ThCl_4$ in NaCl or similar halide melt is electrolyzed in an inert atmosphere graphite lined cell. The cathode deposit particle size may be varied by changes in electrolysis conditions.

A typical Th deposit containing 40-50% metal is shown in Fig. 2.

The work described below involves the use of this technique and also the direct electrodeposition of Th in a molten Bi cathode.

Experimental

The experimental program included a systematic investigation of all possible methods involving the electrolytic cell. It has been demonstrated (11) that powder produced by electrolytic methods can be used to produce dispersions with desirable properties. The first set of experiments omitted the aqueous leaching steps and the crushed comminuted deposit was added directly to molten Bi. In the second group, the cathode removal and crushing steps were eliminated and the Th deposit simply mixed into a molten Bi bath on the bottom of the cell. In the last series, Th was deposited directly into a molten Bi cathode.

In all cases the goal of the work was the application of suitable conditions to yield a dispersion of fine particle size ($<50\mu$) containing equiaxed particles and 5-10% by weight Th (12.5-25% Th_3Bi_5). Th content and particle size were determined metallographically.

Mechanical Dispersion Preparation

Initially prepared dispersions of Th_3Bi_5 in Bi were made by the addition of comminuted, screened as-produced (not leached) electrolytic Th deposits to liquid Bi. Conditions of time, temperature, and agitation were controlled.

The following factors were briefly studied in this phase of the work: dispersion time; temperature; effect of deposit mesh size; effect of salt addition to cathode mix (e.g., $MgCl_2$).

This work indicated that unleached cathode deposits could not be used to form the dispersions and was thus abandoned in favor of the more direct methods described below.

Mechanical Preparation within the Cell

The second approach involved the omission of cathode removal and comminution steps as well as the leaching operation. The Th electrodeposit was first prepared by electrolysis of $ThCl_4$ and then dropped into a pool of molten Bi contained within the cell.

Equipment used for this procedure has been described previously (10). All internal parts are of graphite including the crucible. The crucible is supported on a graphite topped Ni post which also serves as the anode connection. Cathode entry is through the port in the removable head. Steel-tipped Ni rods were used as cathodes. The cell is heated by a machined graphite resistance element. Lampblack is employed as an insulating material. The Bi was contained in a porcelain cup on the crucible bottom.

The heating current was supplied by a 7.5 kva transformer coupled with a powerstat. The d-c source was a 200 amp Se rectifier.

Conditions of the electrolysis were adjusted to give a fine particle size deposit, i.e., high current density, lower temperature, and relatively high Th concentration in the melt.

When the melt had been exhausted essentially of Th content, the cell was shut down and the cathode support rod tapped so that the deposit slipped off into the Bi. The mixture was then vigorously stirred 1-1½ hr. Proper stirring is essential in achieving complete reaction and obtaining a homogeneous dispersion.

Data from several runs of this type are summarized in Table II. This was the most consistently successful procedure of the three approaches tried.

Table II. Mechanical dispersion preparation in cell

Melt wt. %	Temp, °C	C.D. amp/dm²	% Th_3Bi_5 in Bi	Th_3Bi_5 character, particle size—μ
37.7 $NaCl \cdot ThCl_4$ 33.5 NaCl 28.8 KCl	650	250	20	Fine grained equiaxed, 9-35 μ
19.0 $NaCl \cdot ThCl_4$ 44.5 NaCl 36.5 KCl	650	250	50	Equiaxed, 42 μ
Like (406-12)	635	250	50	Equiaxed, 42 μ
26.4 $NaCl \cdot ThCl_4$ 16.8 NaCl 56.8 $CaCl_2$	540	250	60	Equiaxed, fine

Note: All melts—5-10% Th by wt, 500 g, Bi pool; all melts agitated using motor-driven stirrer with graphite or stainless steel paddle after deposit dropped.

Dispersions containing up to 60% Th_3Bi_5 were prepared.

The following conditions are important to the successful use of this procedure:

1. The electrolysis of $ThCl_4$ must be carried out under conditions to yield a fine particle size Th powder; temperature, 550°-650°C; Th concentrations 5-10 w/o; ccd, 200-300 amp/dm².
2. Efficient mechanical agitation must be carried out during addition of the deposit to the Bi and for a period of time afterward.
3. Longer stirring periods tend to reduce particle size of the Th_3Bi_5.

Direct Electrodeposition

Direct electrodeposition of Th from a fused $ThCl_4$-MCl_x system using a liquid Bi cathode was carried out in cells, whose design is essentially a closed Ni-lined stainless steel tube heated externally by nichrome wound resistors. The head is a gasketed, water-cooled Ni-lined steel plate with openings for cathode, anode, and stirrer. The melt container was a porcelain beaker inserted in a graphite crucible as a safety measure in case of breakage. Electrolysis was carried out in an A atmosphere using a graphite anode. A graphite tipped Ni rod served as a contact to the molten Bi cathode in the bottom of the porcelain crucible.The cathode contact was insulated from the melt by a quartz sleeve. In earlier runs, stirring was attempted by bubbling A gas through the cathode contact. Later mechanical stirring was used, with a graphite paddle immersed in the cathode; this was more successful. Crucibles, electrodes, and stirrer are illustrated in Fig. 3. The cell was operated through a West controller using a thermocouple in the crucible wall. Temperature was controlled to ±10°C. A 100-amp Se rectifier acted as a d-c source for the unit.

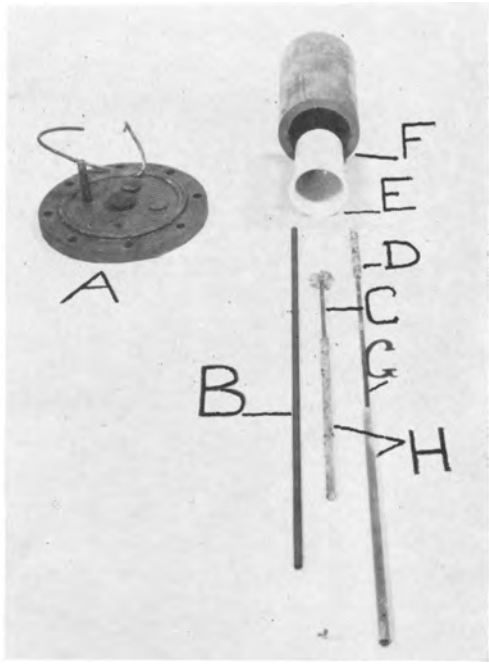

Fig. 3. Component parts of cell used in liquid Bi cathode electrolysis. A, Ni lined steel, water-cooled cell head; B, graphite anode; C, steel stirrer; D, graphite tip, cathode contact; E, porcelain crucible; F, graphite outer crucible; G, Ni shaft of cathode contact; H, quartz sleeves.

The $ThCl_4$ used was prepared in this laboratory from $ThOCO_3$ by procedures previously described (10). Other salts were of reagent grade and care was taken to exclude air, moisture, and other contaminants from the system. In many runs, the melt was first sparged with HCl for further purification.

Electrolysis was generally carried out for a sufficient number of ampere hours to yield a Th_3Bi_5-Bi ingot containing 25% Th_3Bi_5 (10% Th) based on a 50% current efficiency.

Table III. Electrodeposition of Th in liquid Bi

Run	Melt	Temp, °C	% Th melt	Wt Bi g	C.D. amp/dm²	Agitation	% Th_3Bi_5 in Bi	Th_3Bi_5 character; avg. particle size
368-5	NaCl-KCl (1:1)	730	5	150	22	None	2	Small—at grain boundaries 9 μ
368-11	NaCl-KCl(1:1)	755	10	100	140	None	16	Large, long rectang. plates—630 x 42 μ
368-6	NaCl-KCl(1:1)	725	25	150	18	None	11	Massive clusters—10 μ
368-14	NaCl-$CaCl_2$	625	10	150	28	None	0.8	Small amt.—top of ingot—40 μ
368-22	NaCl-$CaCl_2$	625	21	150	160	None	1	Small amt. equiaxed—particles—7 μ
368-25	LiCl-KCl	425	10	150	18	Bubble	2.5	Massive needle like—12 μ
368-24	LiCl-KCl	405	25	150	18	Bubble	1.5	Small amt. large—26 μ
368-34	$MgCl_2$-NaCl-KCl	405	12	150	50	Mech.	5	Small amt. equiaxed—14 μ
368-36	$MgCl_2$-NaCl-KCl	600	12	150	50	Mech.	20	Equiaxed—39 μ
368-38	$MgCl_2$-NaCl-KCl	600	17	500	100	Mech.	30	Equiaxed, some plates

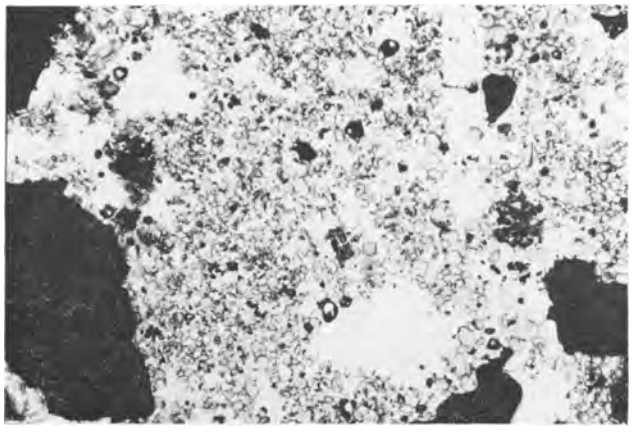

Fig. 4. Button obtained by dropping technique. Middle of specimen. Magnification, 150X before reduction for publication.

Melts were allowed to cool within the cell. The ingot was easily separated from the salt and then sectioned for examination.

Initial runs were of a survey nature in order to establish conditions required to deposit Th in a liquid Bi cathode. Variations were effected in temperature, current density, Th concentration in the melt, and agitation at the cathode.

In order to investigate a range of temperatures from 400°-700°C various alkali and alkaline earth chloride eutectics were employed as melts. Current density variation was from 20-160 amp/dm^2, and melt Th concentration from 5-25% by weight.

Data from several electrolytic runs are summarized in Table III. The following general observations were gained from this work.

1. Runs employing no agitation or bubble agitation generally gave low concentration dispersions with a large amount of residual unreacted Th powder in the vicinity of the cathode.
2. Mechanical agitation of the cathode produced completely reacted dispersions of maximum concentration and more uniform particle size and homogeneity.
3. Bath concentrations of around 10% by weight Th gave the best results from the standpoint of uniform equiaxed particles.
4. Low current densities (<50 amp/dm^2) generally produced inferior results.
5. Bath composition other than Th content has little if any effect on the resulting dispersion.

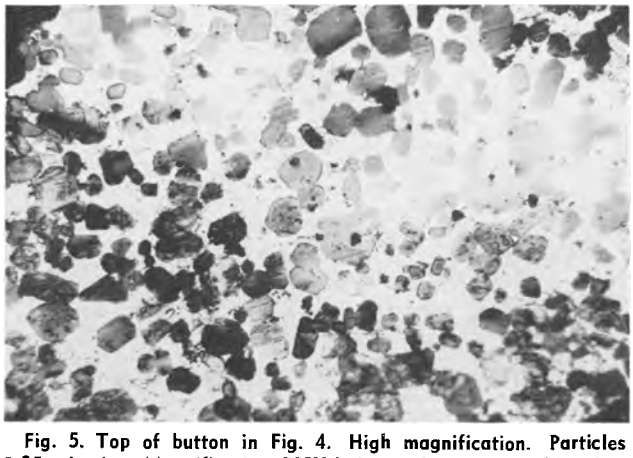

Fig. 5. Top of button in Fig. 4. High magnification. Particles 9-35 μ in size. Magnification, 500X before reduction for publication.

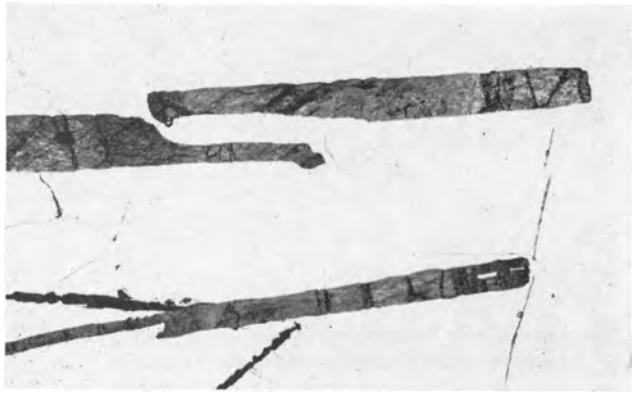

Fig. 6. Electrolytic Th deposited in Bi. Large rectangular plates of Th_3Bi_5. 630 × 42 μ. Magnification, 75X before reduction for publication.

6. Better mixing was obtained using 500 g cathodes as opposed to 100-150 g (in 350-g melts).
7. Stirring is effective in breaking up and/or hindering formation of clusters and large plates of Th_3Bi_5.
8. Temperatures of 600°-700°C are preferred to 400°-500°C from a resulting particle size standpoint.

Evaluation

Metallographic techniques were employed both for particle size analysis and for estimating Th_3Bi_5 content of the dispersion ingots prepared.

All ingots were first washed to remove any surface salts. This produced some surface oxidation, since Th_3Bi_5 reacts readily with moisture. The samples were sectioned for examination, so this did not interfere. All cutting and polishing operations were done under CCl_4 to prevent tarnishing of the specimen surfaces. Bakelite mountings were employed. Plane surfaces were obtained in a grinding belt, and polishing was done on a slow lapping wheel with either 1 μ diamond powder or Linde levigated alumina (B 5125). Specimens were stored under CCl_4.

Particle size determinations were made by use of a Filer eye piece, taking the average of 6 or more readings. Concentrations of the dispersion was estimated by surface area of Th_3Bi_5 particles.

Several specimens produced by the electrolytic methods employed are shown in Fig. 4-7.

The ingots in Fig. 4 and 5 were prepared by the *in situ* addition method. Fig. 4 is a typical middle

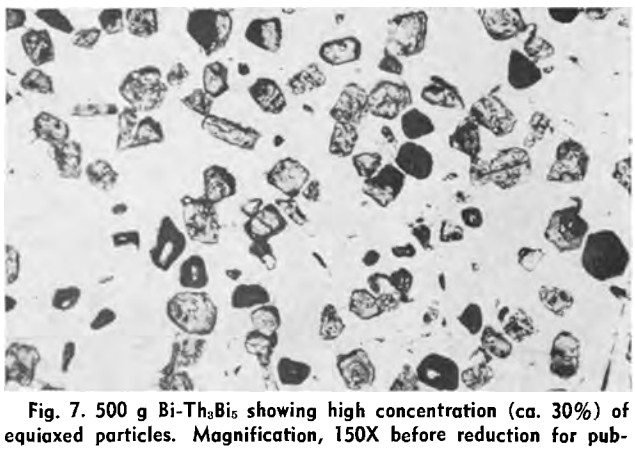

Fig. 7. 500 g Bi-Th_3Bi_5 showing high concentration (ca. 30%) of equiaxed particles. Magnification, 150X before reduction for publication.

section of such an ingot, and Fig. 5 is a specimen containing about 50% Th_3Bi_5 with an average particle size of 42 μ.

Fig. 6 and 7 were prepared by the direct electrodeposition technique. Fig. 6 illustrates the large platelet formation which can occur where stirring is not used or is ineffective. Fig. 7 is the desired type of equiaxed particle in about 30% concentration.

Conclusions

Three approaches to the preparation of Th_3Bi_5 dispersions in liquid Bi have been investigated. These three methods have amounted to a progressive elimination of steps in the recovery of Th metal powder from fusion electrolysis cathode deposits. Dispersions satisfactory in both particle size and shape characteristics have been prepared using comminuted deposits, as-deposited cathodes, and also by direct electrodeposition in Bi.

The particular method suitable for a given practical use would depend largely on the economics involved with respect to the required quantity of dispersion. For laboratory quantities, the use of Th powder or comminuted deposit would be simpler. For small scale commercial amounts, the *in situ* preparation would seem desirable. If large quantities were required, the direct electrolytic procedure would probably offer the most economical preparation. Use of a flowing Bi cathode would enable preparation of the dispersion on a continuous basis.

The more important considerations pertinent to successful preparation of a dispersion suitable for use as a liquid reactor fuel as indicated by this investigation, are summarized below:

1. Th metal powder utilized should be of fine particle size and as uniform as possible. Conditions of high current density, minimum temperature, and high Th melt concentration should be used whether Th is directly deposited in Bi or Th deposit is prepared first.
2. Vigorous mechanical stirring is required during and following mixing of Th with Bi regardless of procedure used. This promotes formation of Th_3Bi_5 and also serves to reduce final particle size and platelet formation.
3. Particle size of Th_3Bi_5 in general decreases with increased temperature, although in the direct electrolysis the tendency of increased temperature to produce larger Th particles minimized the effect somewhat.
4. Th_3Bi_5 particle size tends to decrease with an increase of dispersion or stirring time.
5. Other salts have little effect either as constituents of an electrolytic melt or added to a mechanical mixture.
6. Dispersions may be prepared containing up to 50% Th_3Bi_5 depending on conditions employed. Particle size may range from 5-1000 μ dependent on the Th metal used and on dispersion conditions. Th_3Bi_5 may be prepared as platelets or as equiaxed particles.

This initial investigation has demonstrated adequately the feasibility of preparing liquid metal fuel dispersions, and in particular, Th_3Bi_5-Bi, using electrolytic Th. It is not necessary to remove Th from its salt matrix prior to reaction with the Bi. It also may be directly deposited in an agitated Bi cathode to form the desired dispersion.

Acknowledgment

Acknowledgment is given to the Brookhaven National Laboratory for their sponsorship of this work and permission to publish these results. The assistance of the following staff members of Horizons Incorporated in carrying out this work is also acknowledged: R. Baskey, K. P. Chatham, A. L. Cunningham, and T. S. Liu.

Manuscript received August 13, 1956. This paper was prepared for delivery before the San Francisco Meeting, April 29 to May 3, 1956.

Any discussion of this paper will appear in a Discussion Section to be published in the December 1957 JOURNAL.

REFERENCES

1. R. J. Teitel, D. H. Gurinsky, and J. S. Bryner, *Chem. Engr. Progr. Symposium Ser.*, **50** [13], 11 (1954).
2. C. Williams and F. T. Miles, *Nucleonics*, **12** [7], 11 (1954); R. J. Teitel, D. H. Gurinsky, and J. S. Bryner, *ibid.*, **12** [7], 14 (1954).
3. R. J. Teitel, Reprint No. 34, Nuclear Eng. and Sci. Congress, Cleveland (1955).
4. O. E. Dwyer, D. H. Gurinsky, and R. J. Weeks, Preprint No. 50, Nuclear Eng. and Sci. Congress, Cleveland (1955).
5. H. Fischer and K. Dorsch, German Pat. 615,951, March 18, 1933.
6. J. Smolinski, J. C. Hannan, and A. L. Leach, Report Met. 80, Oct. 1954, Royal Aircraft Estab., Farnsborough, Hauts, England.
7. N. N. Gratsianskii and A. P. Vovkogon, *Zapiski Inst. Khim. Akad. Nauk U.R.S.R.*, **7**, 174 (1940).
8. S. C. Pyk, U. S. Pat. 2,558,627, June 26, 1951.
9. V. A. Plotnikov and E. T. Kirichenko, *Mem. Inst. Chem. Acad. Sci. Ukr. S.S.R.*, **6** [1], 3 (1939).
10. B. C. Raynes, J. C. Bleiweiss, M. E. Sibert, and M. A. Steinberg, To be published.
11. R. J. Teitel, Private communication.

Measurements on Galvanic Cells Involving Solid Electrolytes

Kalevi Kiukkola[1] and Carl Wagner

Department of Metallurgy, Massachusetts Institute of Technology, Cambridge, Massachusetts

ABSTRACT

Electromotive force measurements on galvanic cells involving solid electrolytes have been made in order to obtain the standard molar free energy of formation of CoO, NiO, Cu_2O, Ag_2S, Ag_2Se, PbS, and several phases of the system Ag-Te at elevated temperatures.

Haber and Tolloczko (1), Katayama (2), Reinhold (3, 4), Treadwell, Ammann, and Zürrer (5), Croatto and Bruno (6), Rose, Davis, and Ellingham (7), Sator (8), and others have shown that emf measurements on galvanic cells involving solid electrolytes may yield valuable thermodynamic data. The following investigations have been made in order to show new potentialities of emf measurements on galvanic cells involving solid electrolytes for the determination of the standard molar free energy of formation of oxides, sulfides, selenides, and tellurides at elevated temperatures.

Oxide Cells

General

In order to obtain the standard molar free energy of formation of CoO, NiO, and Cu_2O, cells of type

$$\text{A, A(O)} \mid \text{electrolyte} \mid \text{B, B(O)} \qquad \text{(I)}$$

involving oxides A(O) and B(O) of metals A and B have been investigated. The electrolyte was a solid solution of ZrO_2 and CaO involving oxygen ion vacancies according to Hund (9). Electrical conduction due to migration of oxygen ions via vacancies has been ascertained by tests described below. Analogous solid oxide solutions were tested but found to be less satisfactory.

For predominant ionic conduction due to migration of oxygen ions in the electrolyte, the virtual cell reaction may be expressed in terms of oxygen transfer from the right-hand to the left-hand electrode. Hence the emf E of cell (I) is

$$E = \left[(\bar{F}_{O_2}'' - F_{O_2}^\circ) - (\bar{F}_{O_2}' - F_{O_2}^\circ) \right] / 4F \qquad [1]$$

where $\bar{F}_{O_2}'$ and $\bar{F}_{O_2}''$, respectively, are the partial molar free energies of oxygen on the left-hand and the right-hand side of cell (I), $F_{O_2}^\circ$ is the standard molar free energy of oxygen, and F is the Faraday constant.

In most experiments reported below, a mixture of iron and wüstite was used on the left-hand side of cell (I). Upon combining values of the CO_2/CO ratio over iron and wüstite according to Darken and Gurry (10) and standard molar free energies of formation for CO and CO_2 according to Coughlin (11), values for the relative partial molar free energy $\bar{F}_{O_2} - F_{O_2}^\circ$ over iron and wüstite have been calculated and are listed in Table I. Upon substituting these values and experimental values of E in Eq. [1], values of $\bar{F}_{O_2} - F_{O_2}^\circ$ over metal B and oxide B(O) and the standard molar free energy of formation of oxide B(O) have been calculated for B = Co, Ni, Cu.

Table I. Free energy values for the system iron-oxygen from gas equilibrium measurements

Temp, °C	Iron + Wüstite p_{CO_2}/p_{CO}	Iron + Wüstite $\bar{F}_{O_2} - F_{O_2}^\circ$ kcal	Wüstite + Magnetite p_{CO_2}/p_{CO}	Wüstite + Magnetite $\bar{F}_{O_2} - F_{O_2}^\circ$ kcal
800	0.532	−93.00	2.56	−86.30
900	0.460	−89.76	3.47	−80.34
1000	0.396	−86.68	4.62	−74.26
1100	0.355	−82.52	6.12	——

In some runs, a mixture of wüstite and magnetite was used on the left-hand side of the cell in order to define the oxygen potential. For the evaluation of these experiments, values of $\bar{F}_{O_2} - F_{O_2}^\circ$ over wüstite and magnetite have been calculated and are also listed in Table I.

Preparation of the Electrolytes

The following solid solutions were prepared according to Hund (9, 12),

A: 0.85 ThO_2 + 0.15 $LaO_{1.5}$
B: 0.75 ThO_2 + 0.25 $LaO_{1.5}$
C: 0.85 ThO_2 + 0.15 CaO
D: 0.85 ZrO_2 + 0.15 CaO
E: 0.60 ZrO_2 + 0.40 CaO

To prepare electrolytes A and B, a solution of $Th(NO_3)_4$ and La_2O_3 in dilute nitric acid was precipitated with ammonia. The coprecipitated hydroxides were converted into oxides as is described below for ZrO_2-CaO. Electrolyte C was prepared by evaporating a solution of $Th(NO_3)_4$ and $CaCO_3$ in dilute nitric acid. Similarly, to prepare electrolytes D and E, zirconyl nitrate was dissolved in boiling concentrated nitric acid and calcium carbonate was dissolved in dilute nitric acid. A mixture of these solutions was evaporated in a porcelain dish to dryness on a water bath. The remaining solid material was dried overnight at 120°C, ground in an agate mortar, decomposed at about 500°C, and fired 12 hr at

[1] Present address: Ratakatu 5 B 18, Helsinki, Finland.

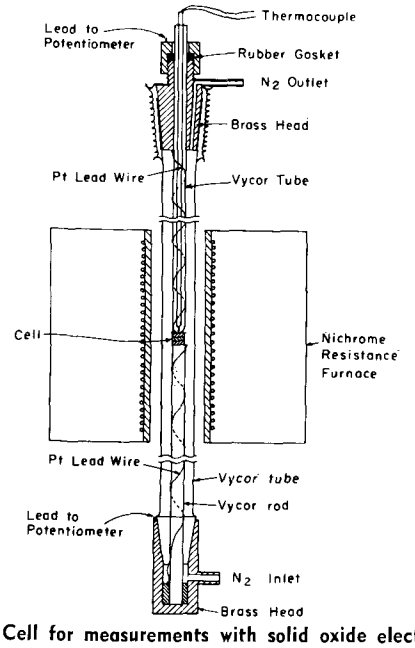

Fig. 1. Cell for measurements with solid oxide electrolyte

1000°C and 12 hr at 1250°C in a Pt boat with grinding after each firing. The powder was pressed into tablets 0.5 cm in diameter and about 0.2 cm thick at a pressure of about 10 tons/cm^2. The tablets were finally sintered overnight in a Pt boat under air at 1400°-1450°C.

When the powder was fired at a temperature below 1250°C, it was too voluminous and not suitable for pressing tablets. On the other hand, when the powder was fired at higher temperatures, it was not sufficiently reactive to yield dense tablets during the final sintering.

Arrangement of the Cell

A cell of type (I) consists of a tablet of a mixture of metal A and its oxide, a tablet of the electrolyte, and a tablet of a mixture of metal B and its oxide between Pt disks connected with Pt leads. The cell assembly is shown in Fig. 1. Since one lead goes to the top and the other lead to the bottom of the furnace, the external resistance between the leads in parallel to the cell is determined by the resistivity of the structural components of the cell assembly which are at room temperature with a negligible leakage current. The small distance between the electrodes minimizes local temperature differences within the cell and therefrom eventually resulting thermoelectric forces. The temperature of the cell can be measured with the help of a thermocouple next to the top electrode of the cell.

To assemble the cell, the bottom brass head with the vycor rod was lowered until the top of the vycor rod was outside the furnace. After assembling the cell on top of the vycor rod, the outer vycor tube was brought in position and the remaining parts of the cell assembly were installed so that the cell was under light pressure. Finally the whole cell assembly was raised so that the cell was in the middle of the resistance-heated furnace.

Use of an outer transparent vycor tube facilitated assembling of the cell but limited the maximum operating temperature to about 1150°C.

All measurements were made in purified nitrogen or argon. The gas was purified by passing over ascarite, anhydrous magnesium perchlorate, active copper at 200°C (13), and finally once more over ascarite and anhydrous magnesium perchlorate. The upper part of the copper tower was oxidized in order to remove hydrogen or hydrocarbons possibly present in the tank gas.

Conductivity Measurements

At elevated temperatures, concentrations of excess electrons and electron holes in the solid oxide electrolytes are presumably determined by the oxygen partial pressure of the surrounding atmosphere by virtue of the reactions

$$O_2(g) + 4 \text{ excess electrons} + 2 \text{ anion vacancies} = 2\,O^{2-} \quad [2]$$

$$O_2(g) + 4 \text{ valence electrons} + 2 \text{ anion vacancies} = 2\,O^{2-} + 4 \text{ electron holes} \quad [3]$$

In view of the low total conductivity, concentrations of excess electrons and electron holes are much smaller than the concentration of anion vacancies. Thus, concentrations of anion vacancies and valence electrons are virtually independent of the external oxygen partial pressure. Hence, on applying the ideal law of mass action to Eqs. [2] and [3], it follows that

$$c_- = K_1(p_{O_2})^{-1/4} \quad [4]$$

$$c_+ = K_2(p_{O_2})^{1/4} \quad [5]$$

where c_- and c_+, respectively, are the concentrations of excess electrons and electron holes, and K_1 and K_2 are constants.

In view of Eqs. [4] and [5], an appreciable contribution of excess electrons or electron holes is indicated by a rise of the total conductivity with decreasing or increasing oxygen partial pressure, respectively.

In order to test the dependence of the total conductivity on oxygen partial pressure, the electrical resistance of electrolyte tablets was measured between Pt electrodes with alternating current at 870°C. In order to minimize contact resistance, the tablets were provided either with thin Au layers applied by vacuum vaporization, or with thin Pt films obtained by cathodic sputtering.

The following atmospheres were used.

1. Oxygen of atmospheric pressure, $p_{O_2} = 1$ atm,
2. Air of atmospheric pressure, $p_{O_2} = 0.21$ atm,
3. Nitrogen of atmospheric pressure, $p_{O_2} \sim 10^{-5}$ to 10^{-3} atm,
4. Argon saturated with water vapor at room temperature with an addition of electrolytic hydrogen corresponding to a H_2O/H_2 ratio of the order of unity, $p_{O_2} \sim 10^{-17}$ atm,
5. Hydrogen of atmospheric pressure saturated with water vapor at 25°C, $p_{O_2} \sim 10^{-20}$ atm,
6. Hydrogen of atmospheric pressure saturated with water vapor at 0°C, $p_{O_2} \sim 4 \times 10^{-22}$ atm.

The electrical conductivity of electrolyte D (0.85 ZrO_2 + 0.15 CaO) at 870°C was found to be virtually constant (about 1.6×10^{-4} ohm^{-1}cm^{-1}) when the oxygen

partial pressure was varied within the aforementioned wide limits. In contrast, the conductivity of ThO_2-La_2O_3 solid solutions varied up to 50% whereby an objectionable magnitude of electronic conduction is indicated. Even greater variations have been observed with electrolyte C (ThO_2 + CaO). For this reason, the following measurements have been made with solid ZrO_2-CaO solutions.

Electronic conduction in ThO_2-La_2O_3 and ThO_2-CaO samples may have been caused by the presence of impurities. Further investigations are needed in order to clarify the nature of electronic conduction in such solid oxide solutions.

In order to determine small contributions of electronic conduction in ionic conductors, polarization measurements are profitable as has been shown recently (14). Measurements on the cell

$$\text{Fe, wüstite} \mid (ZrO_2 + CaO) \mid \text{Au} \qquad \text{(II)}$$

confirmed that electronic conduction yields only a minor contribution to the total conductivity. These measurements, however, were not carried sufficiently far in order to make possible a comprehensive quantitative evaluation.

Measurements on Cells Involving Iron Oxides

To verify the presupposition of predominant ionic conduction in ZrO_2-CaO solid solutions, there was investigated the cell

$$\text{Fe, } Fe_xO \mid (ZrO_2 + CaO) \mid Fe_yO, Fe_3O_4 \qquad \text{(III)}$$

where Fe_xO and Fe_yO denote wüstite coexisting with metallic iron and with magnetite, respectively.

Two-phase mixtures Fe, Fe_xO and Fe_yO, Fe_3O_4 with Fe/O ratios of 2 and 0.875, respectively, were made by pressing well mixed hydrogen-reduced iron powder (−200 mesh, Mallinckrodt A.R.) and magnetite powder (−200 mesh, prepared from C.P. Fe_2O_3) into tablets at a pressure of 10 tons/cm^2.

In each run, the emf of the cell was measured at rising and falling temperature. In general, steady potentials were attained more rapidly at higher temperatures than at lower temperatures. A single run lasted one or two days, or even longer. Observed emf values were plotted vs. temperature. Runs were considered to be satisfactory when values for ascending and descending temperatures agreed within 1 or 2 mv. Values for even temperatures read from these plots are listed in Table II.

In some runs, potentials were found to be ill-defined. In these runs, the electrolyte was not sufficiently dense as was indicated by penetration of the constituents of the electrodes toward the interior of the electrolyte tablet, possibly because of capillary suction by virtue of plastic flow, or surface diffusion. Other runs failed probably because of harmful impurities in the oxides used for the preparation of the electrolyte.

Table II. Electromotive force *E* of cell (III) Fe, Fe_xO | electrolyte | Fe_yO, Fe_3O_4

Temp, °C	Electrolyte 0.85 ZrO_2 + 0.15 CaO *E* (mv)		Electrolyte 0.6 ZrO_2 + 0.4 CaO *E* (mv)				Calc. from Eq. [6] *E* (mv)
800	72	73	71	71	71	70	72.5
900	103	103	103	103	102	101	102.1
1000	134	133	136	134	132	134	134.8
1100	166	165	—	166	—	166	168.5

Table III. Electromotive force *E* of cell (IV) Fe, wüstite | (0.85 ZrO_2 + 0.15 CaO) | Co, CoO and standard free energy change $\Delta F°$ of the reaction Co(s) + ½ O_2(g) = CoO(s) from emf measurements and calculations by Coughlin (11)

Temp, °C	No. of runs	*E* mv	$\Delta F°$ (kcal) cell (IV)	$\Delta F°$ (kcal) Coughlin
900	1	186	−36.30	−35.65
950	4	188 ± 2	−35.49	−34.75
1000	4	189 ± 2	−34.62	−33.80
1050	4	191 ± 2	−33.74	−32.90
1100	4	192 ± 2	−32.88	−31.95

The observed emf values may be compared with the results of gas equilibrium investigations. To this end, one may rewrite Eq. [1] as

$$E = \frac{RT}{2F} \ln \frac{(p_{CO_2}/p_{CO})_{II}}{(p_{CO_2}/p_{CO})_{I}} \qquad [6]$$

where the subscripts I and II, respectively, refer to the left-hand and the right-hand electrode of cell (I). Numerical values of these ratios according to Darken and Gurry (10) are listed in Table I. Emf values calculated from Eq. [6], which are listed in the last column of Table II, agree very satisfactorily with observed emf values.

Standard Molar Free Energy of Formation of Cobalt Oxide

Results for the cell

$$\text{Fe, } Fe_xO \mid (0.85\ ZrO_2 + 0.15\ CaO) \mid \text{Co, CoO} \qquad \text{(IV)}$$

and the standard molar free energy of formation $\Delta F°$ of cobalt oxide are shown in Table III. Reliable values were obtained only above 900°C. The reproducibility of the emf values is ±0.002 v or better corresponding to an uncertainty in $\Delta F°$ of ±0.1 kcal.

Upon substituting observed emf values and CO_2/CO ratios over iron and wüstite in Eq. [6], CO_2/CO ratios over cobalt and cobalt oxide and the standard free energy change of the reaction

$$CoO(s) + CO(g) = Co(s) + CO_2(g) \qquad [7]$$

have been calculated. Fig. 2 shows these values together with values deduced from gas equilibrium measurements by Emmett and Shultz (15), Watanabe (16), and Schenck and Wesselkock (17) as a

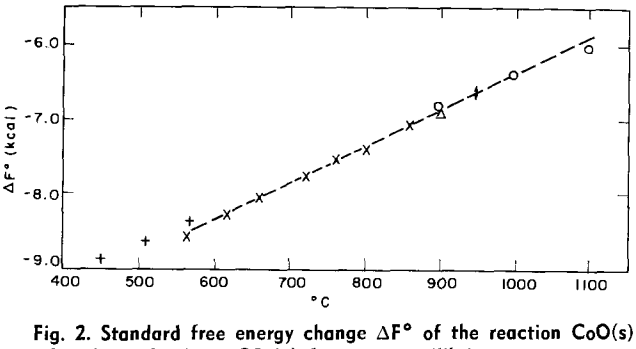

Fig. 2. Standard free energy change $\Delta F°$ of the reaction CoO(s) + CO(g) = Co(s) + CO_2(g) from gas equilibrium measurements [+ Emmett and Shultz (15), × Watanabe (16), Δ Schenck and Wesselkock (17)] and emf measurements (o). The uncertainty in the latter value is indicated by the length of the arrow.

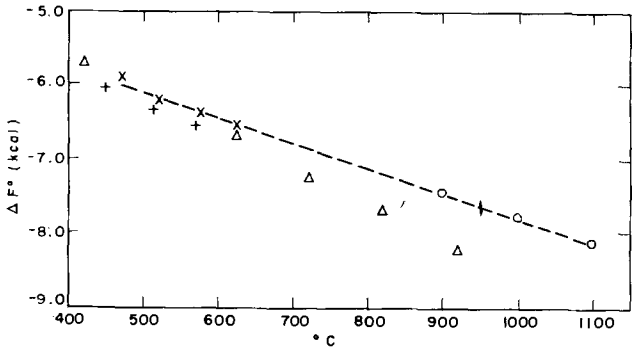

Fig. 3. Standard free energy change ΔF° of the reaction CoO(s) + H_2(g) = Co(s) + H_2O(g) from gas equilibrium measurements [+ Emmett and Shultz (18), × Kleppa (19), Δ Shibata and Mori (20)] and emf measurements (o).

function of temperature. Both sets of data supplement each other and may be represented by a smooth curve.

Upon combining ΔF° values for reaction [7] and the water gas equilibrium calculated from data compiled by Coughlin (11), the standard free energy change for the reaction

$$CoO(s) + H_2(g) = Co(s) + H_2O(g) \qquad [8]$$

has been calculated. Fig 3 shows that these data agree with values calculated from determinations of the H_2O/H_2 ratio over cobalt and cobalt oxide according to Emmett and Shultz (18) and Kleppa (19) but differ from those reported by Shibata and Mori (20), possibly because of their neglect of thermal diffusion.

Standard Molar Free Energy of Formation of Nickel Oxide

Results of the cell

Fe, Fe_xO | 0.85 ZrO_2 + 0.15 CaO) | Ni, NiO (V)

are shown in Table IV. The reproducibility of the emf values is 0.002 v or better, corresponding to an uncertainty in ΔF° of ±0.1 kcal. Results were compared with results of gas equilibrium measurements in the same way as for cobalt, *see* Fig. 4 and 5. ΔF° values deduced from emf values for the reduction of NiO by means of CO lie between values calculated from CO_2/CO ratios according to Schenck and Wesselkock (17), Watanabe (21), and Fricke and Weitbrecht (22). Since the CO_2/CO ratios over nickel and nickel oxide are fairly large (63 to 454), errors

Table IV. Electromotive force E of the cell (V)
Fe, wüstite | (0.85 ZrO_2 + 0.15 CaO) | Ni, NiO
and standard free energy change ΔF° of the reaction
Ni(s) + ½ O_2(g) = NiO(s)
from emf measurements and calculations by Coughlin (11)

Temp, °C	No. of runs	E mv	ΔF° (kcal) cell (V)	Coughlin
750	2	261 ± 2	−35.20	−34.58
800	2	266 ± 1	−34.23	−33.49
850	3	271 ± 1	−33.29	−32.40
900	6	276 ± 1	−32.15	−31.31
950	6	281 ± 1	−31.19	−30.22
1000	6	286 ± 2	−30.15	−29.14
1050	5	291 ± 2	−29.12	−28.07
1100	5	296 ± 2	−28.11	−26.92
1140	2	300 ± 1	−27.22	−26.13

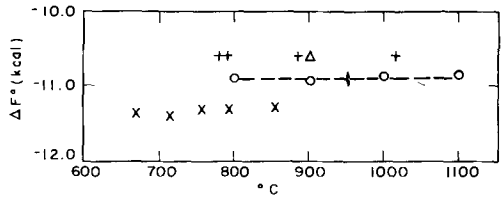

Fig. 4. Standard free energy change ΔF° of the reaction NiO(s) + CO(g) = Ni(s) + CO_2(g) from gas equilibrium measurements [Δ Schenck and Wesselkock (17), × Watanabe (21), + Fricke and Weitbrecht (22)] and emf measurements (o).

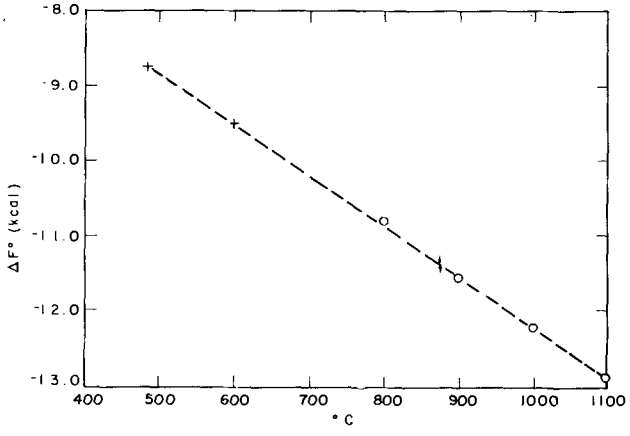

Fig. 5. Standard free energy change of the reaction NiO(s) + H_2(g) = Ni(s) + H_2O(g) from gas equilibrium measurements [+ Pease and Cook (23)] and emf measurements (o).

are probably greater than for the analogous equilibria in the systems Fe-O and Co-O. ΔF° values for the reduction of NiO by means of H_2 according to Pease and Cook (23) are in accord with ΔF° values calculated from emf values at higher temperatures as is shown in Fig. 5.

For a comparison, Table IV lists standard molar free energies of the formation of nickel oxide recommended by Coughlin (11). These values are about 1 kcal more positive than values calculated from emf measurements. No explanation for this divergence can be given.

Standard Molar Free Energy of Formation of Cuprous Oxide

Emf values of the cells

Fe, Fe_xO | electrolyte | Cu, Cu_2O (VI)

Fe_yO, Fe_3O_4 | electrolyte | Cu, Cu_2O (VII)

with the electrolytes (0.85 ZrO_2 + 0.15 CaO) and (0.6 ZrO_2 + 0.4 CaO) are shown in Table V. Values

Table V. Electromotive force E of the cells
Fe, Fe_xO | electrolyte | Cu, Cu_2O (VI)
Fe_yO, Fe_3O_4 | electrolyte | Cu, Cu_2O (VII)

Temp, °C	E (mv) of cell (VI) 0.85 ZrO_2 + 0.15 CaO	0.6 ZrO_2 + 0.4 CaO	E (mv) of cell (VII) 0.85 ZrO_2 + 0.15 CaO	0.6 ZrO_2 + 0.4 CaO
800	532	532	456	461
850	536	537	448	448
900	539	540	436	436
950	541	542	424	423
1000	543	543	412	409
1035	544	544	402	398
1050	545	545	398	—

Table VI. Standard free energy change $\Delta F°$ of the reaction $2\,Cu(s) + \frac{1}{2}\,O_2(g) = Cu_2O(s)$ calculated from emf values of cells (VI) and (VII), emf measurements of Treadwell (24) (Tr) corrected for thermoelectric effects (25), and calculations by Coughlin (Co) (11).

Temp, °C	$\Delta F°$ (kcal) from cell (VI)	cell (VII)	Tr	Co
800	−21.96	−21.98	−21.17	−22.2
900	−19.97	−20.06	−19.70	−20.7
1000	−18.29	−18.17	−18.08	−19.1
1050	−17.42	−17.20	——	−18.4

for the standard molar free energy of formation of cuprous oxide are listed in Table VI. These values agree fairly well with results deduced from emf measurements made by Treadwell (24) with a correction for thermoelectric effects (25). Treadwell investigated the cell

$$Cu(s)\,|\,Cu_2O(s),\text{ borate melt}\,|\,\text{porcelain}\,|\,Ag(l),\,O_2(g) \qquad \text{(VIII)}$$

which involves the reaction $2Cu + \frac{1}{2}\,O_2 = Cu_2O$ on passing two faradays if oxygen ions alone carry the current in porcelain as an intermediate solid electrolyte.

The reproducibility of the emf values is ±0.002 v or better, corresponding to an uncertainty in $\Delta F°$ of ±0.1 kcal. For a comparison, Table VI also lists values of $\Delta F°$ calculated from various sources by Coughlin (11) with an estimated uncertainty of ±1.5 kcal. These values are about 1 kcal more negative than values from emf measurements.

No CO_2/CO and H_2O/H_2 equilibrium ratios over Cu and Cu_2O have been determined since these ratios are inconveniently high.

Roberts and Smyth (26) have determined oxygen partial pressures over liquid copper and solid Cu_2O between 1119° and 1184°C. Therefrom values between −14,100 and −14,250 cal for the standard molar free energy of formation of Cu_2O are calculated. These values are considerably more positive than the values listed in Table VI. In view of inherent difficulties discussed in the paper by Roberts and Smyth, it seems probable that the effect of side reactions has not been sufficiently eliminated in their measurements of oxygen partial pressures.

Standard Molar Free Energy of Formation of Silver Sulfide

Reinhold (4) has already determined the emf of the cell

$$Ag(s)\,|\,AgI(s)\,|\,Ag_2S(s),\,S(l),\,C \qquad \text{(IX)}$$

involving the virtual cell reaction

$$2Ag(s) + S(l) = Ag_2S(s) \qquad [9]$$

Additional measurements were made in order to obtain a higher accuracy. The setup of the cell is shown in Fig. 6. To assemble the cell, silver iodide was melted in the Pyrex tube, and the graphite electrode B, the glass tube A, and the thermocouple shield were immersed. Then the cell was transferred to another furnace whose temperature was below the melting point of AgI but above its transformation point at 146°C. After the AgI had solidified,

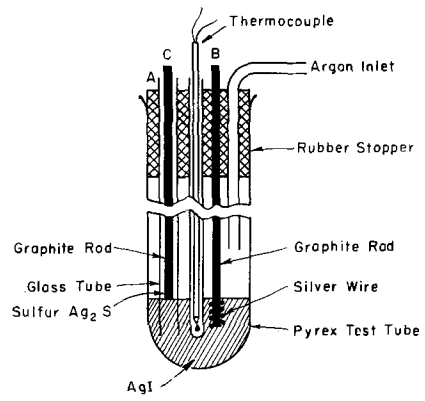

Fig. 6. Cell Ag(s) | AgI(s) | Ag_2S(s), S(l), C

sulfur was introduced into glass tube A, and the graphite electrode C was brought in contact with the AgI. To start a run, silver sulfide was formed electrolytically at graphite rod C by passing a current of 5 to 20 ma for about half an hour with graphite rod B as anode. In some runs, more silver sulfide was formed after the first emf measurements had been made. In other runs, graphite rod C was wrapped with silver wire which transformed to silver sulfide. The emf values were found to be independent of the procedure of preparation of silver sulfide and its amount.

Observed emf values are shown in Table VII. They agree with Reinhold's values within 0.01 v, which is the limit of accuracy of the latter values. In addition, Table VII lists values for the free energy of formation of silver sulfide computed from emf values with the aid of the formula

$$\Delta F° = -2EF \qquad [10]$$

The reproducibility of the emf values is ±0.001 v, corresponding to an uncertainty in $\Delta F°$ of ±0.05 kcal.

The equilibrium of the reaction

$$Ag_2S(s) + H_2(g) = 2Ag(s) + H_2S(g) \qquad [11]$$

has been investigated by various authors, most recently by Rosenqvist (27) between 490° and 900°C. $\Delta F°$ values for reaction [11] extrapolated to 200°-400°C from Rosenqvist's data agree within ±0.2 kcal with values calculated from standard molar free energies of formation of Ag_2S according to Table VII and values for H_2S recommended by Rossini, *et al.* (28) and Kelley (29).

Table VII. Electromotive force E of cell (IX) Ag(s) | AgI(s) | Ag_2S(s), S(l), C and standard free energy change $\Delta F°$ of the reaction $2\,Ag(s) + S(l) = Ag_2S(s)$

Temp, °C	No. of runs	E mv	$\Delta F°$ kcal
150	3	220 ± 1	−10.15
178	3	224 ± 1	−10.35
200	3	228 ± 1	−10.52
250	3	236 ± 1	−10.89
300	5	244 ± 1	−11.24
350	5	252 ± 1	−11.62
400	5	260 ± 1	−11.99
425	3	264 ± 1	−12.18

Standard Molar Free Energy of Formation of Silver Selenide

Similarly, the emf of the cell

$$Ag(s) \mid AgI(s) \mid Ag_2Se(s), Se(s,l), C \quad (X)$$

has been determined. Results are shown in Table VIII.

The emf of cell (X) was found to be well reproducible below 380°C. In some runs, higher, unsteady potentials were observed above 380°C, presumably because Ag_2Se dissolved in liquid selenium (30) and its amount was insufficient for saturation. Only if excess silver selenide is present, the chemical potentials of silver and selenium are well defined. Even under these conditions, a correction for the calculation of the standard free energy of silver selenide is needed because selenium as a reactant is not present in its standard state. This correction is supposedly not significant below 400°C because the solubility of Ag_2Se in liquid selenium is small (31)

Solid-state coulometric titrations analogous to those made with Ag_2S (32) indicate variations of the Ag/Se ratio as low as 0.004 to 0.005 between 200°-300°C. Therefore, deviations from the ideal composition of silver selenide in cell (X) are insignificant.

Cell (X) has previously been investigated by Reinhold (4). These values show considerable scatter and differ up to 0.1 v from values shown in Table VIII for unknown reasons.

From the temperature dependence of the standard free energy of formation of Ag_2Se it follows that

$$2Ag(s) + Se(l) = Ag_2Se(s)$$
$$\Delta F^\circ = -13.46 - 0.0074 \times (T - 500) \text{ kcal};$$
$$\Delta H^\circ = -9.76 \text{ kcal}; \Delta S^\circ = 7.4 \text{ e.u. at } T > 500^\circ K \quad [12]$$

Upon using enthalpy and entropy increments of Ag, Se, and Ag_2Se between 298° and 500°K as compiled by Kelley (29), the values of ΔH° and ΔS° at 298°K are obtained. Therefrom $\Delta F^\circ = \Delta H^\circ - T\Delta S^\circ$ at 298°K may be calculated. Thus,

$$2Ag(s) + Se(s) = Ag_2Se(s)$$
$$\Delta F^\circ = -11.94 \text{ kcal}; \Delta H^\circ = -11.38 \text{ kcal};$$
$$\Delta S^\circ = 5.24 \text{ e.u. at } 298^\circ K \quad [13]$$

The value $\Delta H^\circ = -11.38$ kcal seems to be more consistent than the value of −2.9 kcal, which was obtained by Fabre (33) on combining the values for several reactions which were investigated calorimetrically.

The standard molar entropy of Ag_2Se at 298°K is obtained as

$$S^\circ_{Ag_2Se} = \Delta S^\circ + 2S^\circ_{Ag} + S^\circ_{Se}$$
$$= 5.24 + 2 \times 10.206 + 10.0 = 35.65 \text{ e.u. at } 298^\circ K \quad [14]$$

with standard entropy values for Ag and Se recommended by Rossini, *et al.* (28).

Table VIII. Electromotive force E of the cell (X)
Ag(s) | AgI(s) | Ag_2Se(s), Se(s,l), C
and standard free energy change ΔF° of the reaction
2 Ag(s) + Se(s,l) = Ag_2Se(s)

Temp, °C	No. of runs	E mv	ΔF° kcal
160	2	281.0 ± 0.6	−12.96
170	3	282.5 ± 0.5	−13.03
200	3	287.4 ± 0.6	−13.26
250	3	295.4 ± 0.5	−13.63
300	3	303.5 ± 0.6	−14.00
350	3	311.6 ± 0.7	−14.37
370	3	314.8 ± 0.7	−14.52

Standard Molar Free Energy of Formation of Lead Sulfide

Solid lead chloride, pure or doped with KCl, is known to be an anionic conductor (34-36). Thus, the standard free energy of formation of lead sulfide should be obtainable from a cell analogous to cell (IX),

$$Pb(s) \mid PbCl_2(s) \mid PbS(s), S(l), C \quad (XI)$$

The emf of cell (XI) was found to be not well reproducible, presumably for the following reason. In view of the shrinkage during the solidification of $PbCl_2$ and lack of plasticity, no tight seal of lead chloride between the two electrodes was obtained and, therefore, sulfur vapor could diffuse to the lead electrode so that a mixed potential rather than an equilibrium potential prevailed.

Therefore, a cell involving a Ag-Ag_2S electrode instead of a sulfur electrode was investigated,

$$Pb(s,l) \mid PbCl_2(+KCl) \mid PbS(s), Ag_2S(s), Ag(s) \quad (XII)$$

with the virtual cell reaction

$$Pb(s,l) + Ag_2S(s) = PbS(s) + 2Ag(s) \quad [15]$$

Preliminary investigations have shown that the solubility of Ag_2S in PbS is less than 1 mole % below 400°C. Similarly, a low solubility of PbS in Ag_2S is assumed. Ag_2S and PbS are, therefore, considered to be present virtually in their standard states.

The electrolyte was solid lead chloride containing 0.5 w/o KCl in order to increase the conductivity, presumably due to a higher anion vacancy concentration (37). To prepare the electrolyte, $PbCl_2$ and KCl were melted under a stream of argon containing a small amount of chlorine. The solidified melt was crushed to powder.

In order to extend measurements above the melting point of lead at 327°C, a crucible of lead chloride filled with liquid lead was used. Fig. 7 shows the assembled cell which was placed in the furnace shown in Fig. 1.

Crucibles of lead chloride were pressed in the tool shown in Fig. 8. A nearly uniform density was obtained by applying pressure from top and bottom punches and by providing nearly equal compression ratios of the powder at the bottom and in the walls

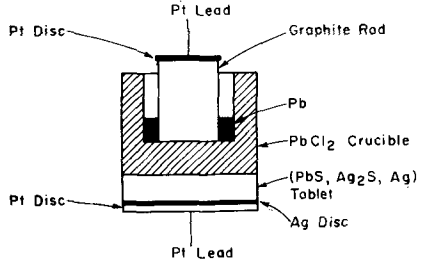

Fig. 7. Cell Pb(s, l) | $PbCl_2$(+KCl) | PbS(s), Ag_2S(s), Ag(s)

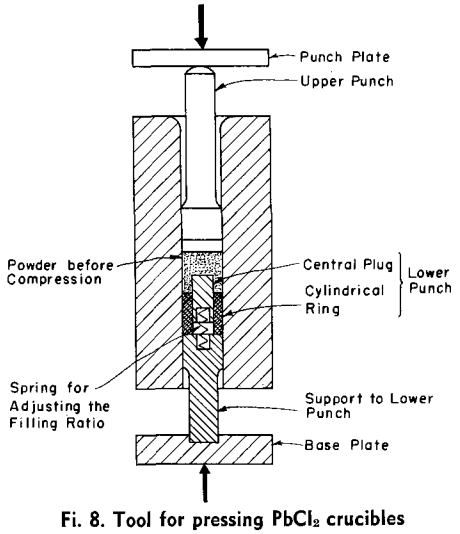

Fi. 8. Tool for pressing $PbCl_2$ crucibles

of the crucible. The pressed crucibles were ejected through the upper end of the die, which was slightly tapered. The crucibles were used either as such, or after sintering under argon at about 400°C. Different procedures did not result in systematic differences in the measured emf.

On replacing the lower punch by a short steel rod, cylindrical tablets of a mixture of Ag, Ag_2S, and PbS for the right-hand electrode in cell (XII) could be made.

Results of emf measurements are listed in Table IX.

Upon combining $\Delta F°$ values for reactions [9] and [15], values for the standard free energy of formation of PbS are obtained. These values are also shown in Table IX.

The equilibrium

$$PbS(s) + H_2(g) = Pb(l) + H_2S(g) \quad [16]$$

has been investigated by Jellinek and Zakowski (38), Jellinek and Deubel (39), and Sudo (40). $\Delta F°$ values for reaction [16] calculated from standard free energies of formation of PbS listed in Table IX and values for H_2S recommended by Rossini, *et al.* (28) and Kelley (29) are consistent with Sudo's measurements (40) but diverge from earlier measurements by Jellinek and his associates (38, 39).

The System Silver-Tellurium

The phase diagram of the system silver-tellurium has been investigated by Pélabon (41), Pellini and Quercigh (42), Chikashige and Saito (43), Koern (44), and Kracek and Ksanda (45). In addition to the compound Ag_2Te, which has a congruent melting point at about 958°C, there is at least one other intermediate phase involving a smaller Ag/Te ratio with an incongruent melting point, for which the formulas

$$AgTe\,(42),\ Ag_7Te_4 = Ag_{1.75}Te\,(43),\ Ag_{12}Te_7 = Ag_{1.71}Te\,(44),\ \text{and}\ Ag_{1.50}Te\,(45)$$

have been suggested.

Table IX. Electromotive force E of the cell (XII) Pb(s,l) | $PbCl_2$ (+KCl) | PbS(s), Ag_2S(s), Ag(s) and standard free energy change $\Delta F°$ of the reaction Pb(s,l) + S(l) = PbS(s)

Temp, °C	No. of runs	E mv	$\Delta F°$ kcal
250	7	254 ± 3	−22.60
300	7	240 ± 3	−22.33
327	7	232 ± 3	−22.14
350	6	226 ± 3	−22.05
400	6	211 ± 2	−21.73
427	2	203 ± 1	−21.54

To clarify, the activity a_{Ag} of silver in Ag-Te "alloys" has been determined as a function of the Ag/Te ratio by measuring the emf of the cell

$$Ag(s) \mid AgI(s) \mid (Ag, Te) \qquad (XIII)$$

Since silver iodide is an ionic conductor, the emf E of the cell (XIII) is

$$E = -(RT/F) \ln a_{Ag} = -F^M_{Ag} \quad [17]$$

where F^M_{Ag} is the partial molar free energy of mixing of silver for pure solid silver as reference state.

Upon passing current across cell (XIII) from right to left, a definite amount of silver can be transferred from the alloy to the left-hand electrode consisting of pure silver. Thus, cell (XIII) permits a solid-state titration analogous to that used for silver sulfide (32). The change in the Ag/Te ratio, Δr, is in view of Faraday's law

$$\Delta r = it/n_{Te}F \quad [18]$$

where i is the current applied during time t, n_{Te} is the number of moles of tellurium, and F is the Faraday constant.

At the beginning of a titration, the Ag-Te alloy was equilibrated with metallic silver by short-circuiting cell (XIII). Subsequently, silver was removed. In contradistinction to measurements of the analogous cell for the system Ag-S, a steady potential was attained not immediately but only after about half an hour.

Results for 250° and 300°C are shown in Fig. 9 and 10. Points indicated by solid squares were obtained from measurements of cells with predetermined constant composition of the Ag-Te alloy. There are three regions involving a variable potential E corresponding to three different phases designated as α, γ, and ϵ. The one-phase regions are

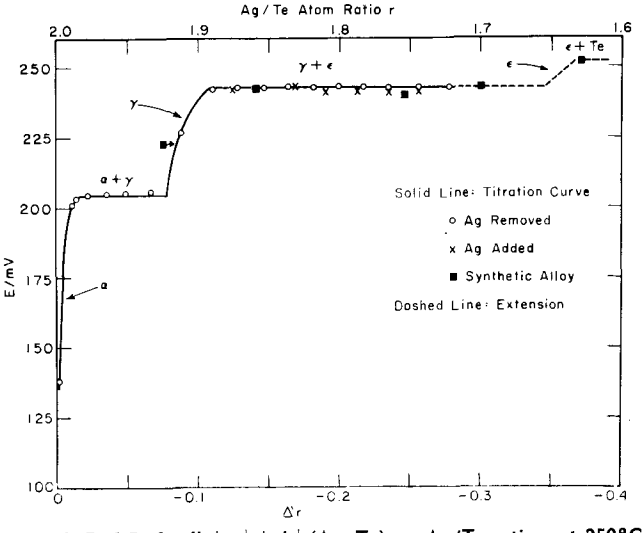

Fig. 9. Emf E of cell Ag | AgI | (Ag, Te) vs. Ag/Te ratio r at 250°C

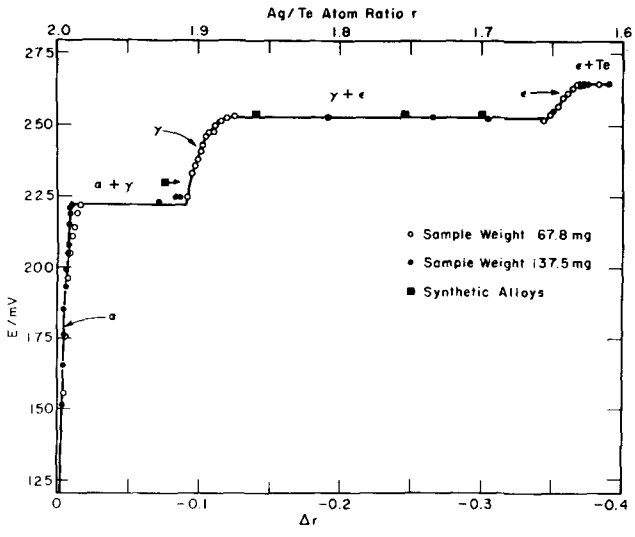

Fig. 10. Emf E of cell Ag | AgI | (Ag, Te) vs. Ag/Te ratio r at 300°C

separated by two-phase regions indicated by plateaus in the E vs. Δr plots.

Since the homogeneity range of the alpha phase is rather narrow, it may be assumed without considerable error that the phase equilibrated with metallic silver has nearly the formula Ag_2Te whereupon the Ag/Te ratio shown on top of Fig. 9 and 10 may be calculated as

$$r = 2 - \Delta r \qquad [19]$$

At 300°C, the Ag/Te ratio ranges from 1.99 to 2.00 for the α phase, from 1.88 to 1.91 for the γ phase, and from 1.63 to 1.66 for the ϵ phase.

From the values shown in Fig. 9 and 10, the free energy of formation of a one-phase or two-phase alloy involving N_{Ag} g-atom Ag and $(1-N_{Ag})$ g-atom Te may be calculated as (46)

$$F^M = (1-N_{Ag})\int_0^{N_{Ag}} \frac{F^M{}_{Ag}}{(1-N_{Ag})^2}\, dN_{Ag} \qquad [20]$$

Upon dividing F^M by $N_{Te} = (1 - N_{Ag})$, the standard molar free energies of formation $\Delta F°$ of the silver tellurides having the formulas Ag_2Te, $Ag_{1.90}Te$, and $Ag_{1.64}Te$ have been calculated. These values are listed in Table X.

The emf of the cell

$$Ag \mid AgNO_3(aq) \mid (Ag,Te) \qquad (XIV)$$

has been determined at room temperature by Puschin (47). A plot of emf vs. the Ag/Te ratio does not indicate another compound in addition to Ag_2Te. It is possible, however, that the scatter in Puschin's plot of E vs. composition obscures small steps corresponding to different compounds. Moreover, complete electrochemical equilibrium may not have been reached at room temperature as has been found, e.g., for the system Cu-Zn by Sauerwald (48).

Manuscript received August 9, 1956. The paper is based on a thesis submitted by K. Kiukkola in partial fulfillment of requirements for the degree of D.Sc. in metallurgy, Massachusetts Institute of Technology, Cambridge, Mass. Work was done under Contract AT(30-1)-1002 with the U.S.A.E.C.

Any discussion of this paper will appear in a Discussion Section to be published in the December 1957 JOURNAL.

Table X. Thermodynamic values for the system silver-tellurium

	250°C	300°C
$\Delta F°$ ($2Ag + Te = Ag_2Te$)	−11.4	−12.0 kcal
$\Delta F°$ ($1.90Ag + Te = Ag_{1.90}Te$)	−11.0	−11.5 kcal
$\Delta F°$ ($1.64Ag + Te = Ag_{1.64}Te$)	−9.5	−10.0 kcal

REFERENCES

1. F. Haber and S. Tolloczko, *Z. anorg. Chem.*, **41**, 407 (1904).
2. M. Katayama, *Z. physik. Chem.*, **61**, 566 (1908).
3. H. Reinhold, *Z. anorg. u. allgem. Chem.*, **171**, 181 (1928).
4. H. Reinhold, *Z. Elektrochem.*, **40**, 361 (1934).
5. W. D. Treadwell, H. Ammann, and Th. Zürrer, *Helv. Chim. Acta*, **19**, 1255 (1936).
6. U. Croatto and C. Bruno, *Ricerca Sci.*, **17**, 1998 (1947).
7. B. A. Rose, G. J. Davis, and H. J. T. Ellingham, *Disc. Faraday Soc.*, **4**, 154 (1948).
8. A. Sator, *Compt. rend.*, **234**, 2283 (1952).
9. F. Hund, *Z. physik. Chem.*, **199**, 142 (1952).
10. L. S. Darken and R. W. Gurry, *J. Am. Chem. Soc.*, **67**, 1398 (1945).
11. J. P. Coughlin, *U. S. Bur. Mines Bull. 542* (1954).
12. F. Hund and W. Dürrwächter, *Z. anorg. u. allgem. Chem.*, **265**, 67 (1951).
13. F. Meyer and G. Ronge, *Angew. Chem.*, **52**, 637 (1939).
14. C. Wagner, *Z. Elektrochem.*, **60**, 4 (1956); *Proc. C.I.T.C.E.*, in press. J. B. Wagner and C. Wagner, *J. Chem. Phys.*, June 1957.
15. P. H. Emmett and J. F. Shultz, *J. Am. Chem. Soc.*, **52**, 1782 (1930).
16. M. Watanabe, *Sci. Repts. Tohoku Imp. Univ. I*, **22**, 892 (1933).
17. R. Schenck and H. Wesselkock, *Z. anorg. u. allgem. Chem.*, **184**, 39 (1929).
18. P. H. Emmett and J. F. Shultz, *J. Am. Chem. Soc.*, **51**, 3249 (1929).
19. O. J. Kleppa, *Svensk Kem. Tidskr.*, **55**, 18 (1943).
20. Z. Shibata and I. Mori, *Z. anorg. u. allgem. Chem.*, **212**, 305 (1933).
21. M. Watanabe, *Sci. Repts. Imp. Tohoku Univ. I.*, **22**, 436 (1933).
22. R. Fricke and G. Weitbrecht, *Z. Elektrochem.*, **48**, 87 (1942).
23. R. N. Pease and R. S. Cook, *J. Am. Chem. Soc.*, **48**, 1199 (1926).
24. W. D. Treadwell, *Z. Elektrochem.*, **22**, 414 (1916).
25. J. Gundermann, K. Hauffe, and C. Wagner, *Z. physik. Chem. B.*, **37**, 148 (1937).
26. F. H. Smyth and H. S. Roberts, *J. Am. Chem. Soc.*, **43**, 1061 (1921).
27. T. Rosenqvist, *Trans. Am. Inst. Mining Met. Engrs.*, **185**, 451 (1949).
28. F. D. Rossini, D. D. Wagman, W. H. Evans, S. Levine, and I. Jaffe, *Nat. Bur. Standards Circ. 500*, U. S. Government Printing Office, Washington (1952).
29. K. K. Kelley, *Bureau of Mines Bull. 476*, U. S. Government Printing Office, Washington (1949).
30. C. Tubandt, H. Reinhold, and A. Neumann, *Z. Elektrochem.*, **39**, 227 (1933).
31. M. Hansen, "Der Aufbau der Zweistofflegierungen," p. 59, Springer, Berlin (1936).
32. C. Wagner, *J. Chem. Phys.*, **21**, 1819 (1953).
33. C. Fabre, *Ann. chim. phys.*, **14**, 110 (1888).
34. C. Tubandt and S. Eggert, *Z. anorg. u. allgem. Chem.*, **110**, 196 (1920); C. Tubandt, *ibid.*, **115**, 105 (1921).

35. C. Tubandt and H. Reinhold, *Z. Elektrochem.*, **29**, 313 (1923).
36. J. B. Wagner and C. Wagner, *This Journal*, To be published.
37. E. Koch and C. Wagner, *Z. physik. Chem. B*, **38**, 295 (1937).
38. K. Jellinek and K. Zakowski, *Z. anorg. u. allgem. Chem.*, **142**, 1 (1925).
39. K. Jellinek and A. Deubel, *Z. Elektrochem.*, **35**, 451 (1929).
40. K. Sudo, *Sci. Repts. Res. Inst. Tohoku Univ. A*, **2**, 325 (1950).
41. H. Pélabon, *Compt. rend.*, **143**, 295 (1906).
42. G. Pellini and E. Quercigh, *Atti R. Accad. dei Lincei Roma*, (5) **19**, *II*, 415 (1910).
43. M. Chikashige and I. Saito, *Mem. Coll. Sci. Kyoto Imp. Univ.*, **1**, 361 (1916).
44. V. Koern, *Naturwissenschaften*, **27**, 432 (1939).
45. F. C. Kracek and C. J. Ksanda, *Tran. Am. Geophys. Union*, **21**, 363 (1940).
46. C. Wagner, "Thermodynamics of Alloys," p. 14, Addison-Wesley Press, Cambridge, Mass. (1952).
47. N. Puschin, *Z. anorg. u. allgem. Chem.*, **56**, 1 (1908).
48. F. Sauerwald, *ibid.*, **111**, 243 (1920).

Technical Notes

Measurement of Ion and Water Transport across Membranes

J. G. McKelvey, Jr., K. S. Spiegler, and M. R. J. Wyllie

Gulf Research & Development Company, Pittsburgh, Pennsylvania

Electrical migration of ions and solvent (electroösmosis) plays an important part in the study of membrane transport processes. The different transport processes, such as diffusion, conductance, and hydraulic permeation, are related to each other by a system of equations based on the thermodynamics of the steady state (1,2). In order to comply with the definitions used in this system and thus obtain maximum accuracy, the transport should be measured when the solutions separated by the membrane are of equal concentration and without changing this condition during the experiment. This restriction limits the applicability of the conventional methods for the measurement of electrical ion and water transport.

Transport numbers of ions across membranes can be computed from membrane potentials ("emf method") or may be determined directly by electrolysis ("dynamic" method). The emf method is dependent on a concentration gradient, and, therefore, only an average transport number with respect to solution concentration can be calculated. Also, the potential depends not merely on the ion transport number, but on a combination of ion and solvent transport (3,4).

In the dynamic method, electric current is passed through the system:

Electrode 1 - Solution 1 - Membrane - Solution 2 - Electrode 2

Transport numbers are then calculated from concentration changes caused by the electrolysis. When Pt electrodes are used, the electrode reactions produce hydrogen and/or hydroxyl ions, both of which have high membrane mobilities and may interfere. However, the dynamic method allows separate determination of ion migration and electroösmotic water transport.

In order to overcome the difficulties inherent in the dynamic method, Murakoshi (5) used a K amalgam anode and Hg cathode in his study of systems of KCl solutions and cation-exchange membranes. Ag-AgCl electrodes have frequently been employed (2,6-8). Their effective use is restricted to chloride systems and, in the case of cation-exchange membranes, they do not eliminate the creation of a concentration difference across the membrane.

For these reasons a new method was devised here using radioactive tracers, which allows ion and water transport to be measured at a constant concentration, without interference from electrode reactions, and with a high degree of precision. In this method the solution concentration is kept constant by adding small amounts of ion-exchange resins, which act as buffers, to each electrode compartment. While the solution concentration remains constant, the specific radioactivity of at least one solution changes. The ion transport is then determined from this change in the specific activity of the solution after electrolysis.

This method overcomes limitations imposed on conventional transport measurements which need special electrodes (e.g., Ag-AgCl electrodes for measurements in chloride solutions) and which almost always cause concentration changes. For instance, even Ag-AgCl electrodes cause enrichment of NaCl in the cathode compartment in transport measurements across cation-exchange membranes. The present method should be applicable to solutions of other salts also, e.g., sulfates, perchlorates, phosphates, etc., for which no suitable electrodes are available.

The cell (Fig. 1) consists of two "Lucite" compartments, each equipped with a calibrated buret, thermometer, Pt electrode, and a plug for removing samples. Each half-cell holds about 260 ml of solution and measures about 7.5 cm on the outside edges. The membrane is mounted between the two half-

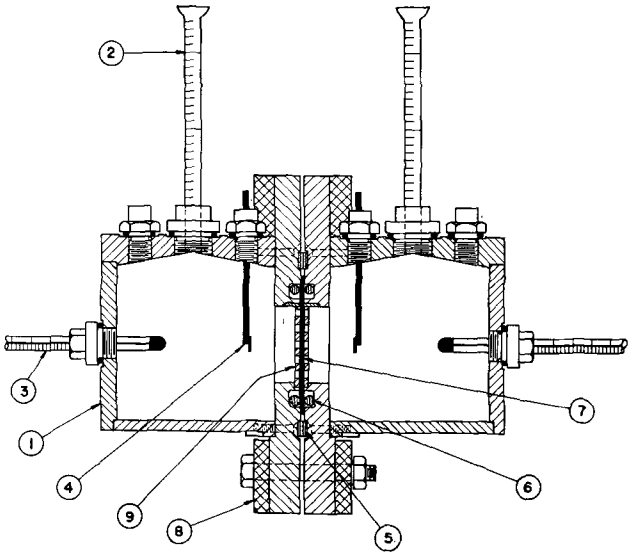

Fig. 1. Sectional view of transport cell: 1, cell body; 2, calibrated buret; 3, thermometer; 4, Pt electrode; 5, rubber dam gasket; 6, "O" ring gasket; 7, membrane; 8, Al support plate; 9, perforated "Lucite" disk. Cell material : "Lucite"; fittings: "Teflon" except thermometer fitting which is "Nylon"; gaskets: "O" rings (except No. 5). Plugs on the extreme left and right close holes which have been provided for future insertion of other probes.

cells and held securely in place by two "O" rings. Two perforated "Lucite" disks are mounted, one on each side of the membrane, to prevent bulging caused by unequal liquid levels in the two burettes. Stirring is accomplished by a small (⅞ x ¼ in.) "Kel-F" coated magnetic stirring bar in each compartment. The stirrer is driven by a commercial magnetic stirring device slightly modified to fit the limited space. Small tubes filled with "Drierite" are mounted on top of each buret to determine minor losses due to evaporation and spray. A silver coulometer was used to measure the amount of charge passed. [A photographic reproduction of the cell in actual operation may be found in (10).]

In operation, each half-cell is filled with a salt solution, and current is passed between the two Pt electrodes. Drastic concentration changes and contamination by electrode reactions during the passage of current are overcome by adding a few grams of a weakly acid carboxylic cation-exchange resin[1] to each half-cell. In transport measurements across a cation-exchange membrane, the resin in the cathode compartment is in the hydrogen form; that in the anode compartment, in the appropriate metal form. The presence of these resins buffers the concentrations of sodium ions, which migrate through the membrane to a much greater extent than the chloride ions. The transport experiment can be represented schematically for NaCl and a cation-exchange membrane in the following manner:

		Membrane	
Pt anode	Na*Cl solution	NaCl solution	Pt anode
+	+ Na*R	+ HR	−
Anode compartment		Cathode compartment	

where R represents the ion-exchange resin radical. The asterisk signifies that the Na ion in the anode compartment is traced with 2.6 y Na^{22}. The specific activity of Na in the anode solution and on the granular resin is the same. As current is passed between the two electrodes, the following reactions take place in the cathode compartment:

$$H_2O + e^- \rightarrow OH^- + \tfrac{1}{2} H_2\ (g) \qquad [1]$$

$$Na^+ + OH^- + HR \rightarrow NaR + H_2O \qquad [2]$$

where e^- represent the electron. The net cathode reaction is, therefore:

$$Na^+ + e^- + HR \rightarrow NaR + \tfrac{1}{2} H_2\ (g) \qquad [3]$$

Thus the transported cation is removed without introducing extraneous ions or water. Anode compartment reactions are based on the high affinity of the resin for hydrogen ions:

$$Cl^- - e^- \rightarrow \tfrac{1}{2} Cl_2\ (g) \qquad [4]$$

or

$$\tfrac{1}{2} H_2O - e^- \rightarrow \tfrac{1}{4} O_2\ (g) + H^+ \qquad [5]$$

In the latter case, hydrogen ions are removed from the solution by the granular resin:

$$H^+ + NaR \rightarrow HR + Na^+ \qquad [6]$$

When reaction [5] predominates over [4], as is the case in dilute chloride solutions, the concentration on both sides of the membrane remains about constant. At any rate, no new types of ions are introduced into the solution phase. In more concentrated solutions, where reaction [4] becomes appreciable, the percentage change of chloride concentration for a given amount of current transferred can always be kept low, because of the high concentration of the solutions.

In the region of imperfect membrane selectivity, the electrode reactions do not even compensate approximately for the ion transport across the membrane. In fact, if less than half of the current is carried by cations, concentration changes in the electrode compartments are greater than in a cell with Ag-AgCl electrodes. In this case it may be possible to substitute a weakly basic granular anion exchange resin in both compartments. An analogous series of reactions may be expected to those described above for the weakly acid cation exchange resin.[2] Use of the weakly basic resin should prove particularly useful in the study of anion exchange membranes.

In a typical experiment it was verified by analysis of the resin grains and the solutions that the reactions do indeed take place as cited above. The pH of the solutions was determined after each experiment using "Alkacid" test paper, and in all cases was found to be neutral. In order to verify that solutions remained neutral at all times during the experiment, methyl red was added to the anode compartment and phenolphthalein to the cathode compartment. Under these conditions, current densities of 2.5 ma/cm² or lower did not produce any color change. When smaller resin grains are used and stirring is more vigorous, higher current densities are permissible.

[1] Amberlite IRC-50, Rohm & Haas, Philadelphia, Pa., >#12 U.S. mesh.

[2] The authors are indebted to Dr. N. W. Rosenberg, of Ionics, Inc., Cambridge, Mass., for this suggestion.

Table I. Ion and water transport across "Permaplex C-1" membrane (product of the Permutit Co., London)
Water content: 37.5%. Capacity: 1.75 meq. per g wet membrane or 0.146 meq. cm^{-2}. Thickness: 0.077 cm.

			Ion transport data				
Experiment			1	2	3	4	5
Normality of NaCl solutions	Cathode compartment	before	0.1013	0.1023	0.1014	0.3044	0.3002
		after	0.1019	0.1017	0.1004	0.3054	0.3021
	Anode compartment	before	0.1013	0.1085	0.1014	0.3104	0.3017
		after	0.1002	0.1024	0.1009	0.3043	0.2945
Charge passed (millifaradays)			9.22	13.38	7.38	11.28	11.28
Transport number, t_{Na^+}							
From radiotracer transfer			—	0.97	—	1.02	1.03
From chloride-ion concentration change in cathode compartment			—	0.976	—	0.985	1.009
Avg			—	0.973±.03	—	1.00±.03	1.02±.03
			Water transport data				
Anode buret loss (ml)			1.11	—	0.91	—	1.33
Cathode buret gain (ml)			1.04	1.57	1.00	—	1.40
Average water transport (ml)			1.08	1.57	0.96	—	1.36
Water transport (moles $faraday^{-1}$)			6.4±0.3	6.5±0.3	7.2±0.4	—	6.7±0.3

The transport number of the anion is calculated from the change in chloride concentration of the cathode compartment. With appropriate minor corrections for water transport and swelling and exclusion of sorbed salt by the resin when changing from the hydrogen to sodium form, the anion transport number can be determined within at least ±0.03.

The transport number of the cation is determined independently by tagging the solution and resin in the anode compartment, as well as the membrane, with a radioactive isotope of the cation under consideration and observing the change in specific activity in both compartments with passage of current. Thus, the transport number of the cation can be determined within ±0.03 transport units. The specific activity of Na in the solution and resin in the anode compartment and on the membrane is the same at the start and throughout the whole experiment. It is important to remove the solution from the cathode compartment as soon as possible after the stoppage of the current and the reading of the liquid level in the burets. If this solution is kept in contact with the membrane for more than about 10 min, an appreciable error may result from the increase of the specific activity of the solutions by exchange of ions with the membrane.

On the other hand, exchange with the granular resin in the compartments is much faster than with the membrane and therefore the specific activity on the granular resin is not appreciably smaller than in the solution. This was verified by the authors in one experiment. However, for precision measurements they recommend that the specific activity in the granular resin, on the membrane and in the solution, be determined at the end of the experiment, thus verifying the equality of the specific activities of anolyte and membrane, on the one hand, and catholyte and granular resin in the cathode compartment on the other hand. Corrections can then be made for minor deviations from the expected specific activities.

The activity of the solutions was determined by evaporating a sample to dryness and counting, using a thin end-window G.M. tube connected to a Model 1070 "Multiscaler".[3] Sufficient activity was incorporated in the anode compartment so that, at the end of the experiment, the activity in the cathode compartment was at least 10% of that in the anode compartment. The counting rate varied between 200 to 3000 counts/min in different samples (background: about 28 counts/min). At least four different samples of each solution were prepared and about 10,000 counts were accumulated for each sample. Counting rates were corrected for background and nonlinearity. Under these conditions, the activities of the solutions could be determined within ±1%.

Since the sum of the electrical transport numbers is unity, the above two methods, used in conjunction, provide useful checks on the individual procedures as well as an increase in over-all accuracy. Table I lists ion and water transport data taken from several representative experiments.

It is seen that, within the estimated error of 3%, the transport number of sodium, t_{Na^+}, in "Permaplex C—1" was found to be unity in solutions about 0.1 and 0.3*N* with respect to NaCl. There is little in the literature with which to compare this result. Kressman and Tye (9) reported $t_{Na^+} = 0.98$ for 0.1*N* NaCl. The authors' result is not inconsistent with theirs. It is important that calculations of the transport number (*a*) from the radiotracer transfer and (*b*) from the chloride ion concentration change in the cathode compartment lead to the same result, within experimental error, although these determinations are essentially independent of each other.

Water transport is determined directly from the buret readings after correction for temperature changes, electrolytic decomposition (reaction [5]), evaporation, and spray. All gas bubbles which are evolved at the electrodes must be removed carefully before the final reading of the buret level. This was accomplished in this cell by designing the inside surface of the roof of each compartment in the shape of a dome and by carefully polishing it so that the gas bubbles escaped speedily through the

[3] Atomic Instrument Co., Cambridge, Mass.

burets. It was found that a trace of a commercial nonionic detergent was very helpful in removing gas bubbles continuously. The type of detergent to be used depends on the salt under investigation, solution concentration, and current density. In the case of NaCl solutions, the authors added a 1:9 mixture of "Pluronic" L-61 and L-72[4] in the cathode compartment, and "Triton" X-45[5] in the anode compartment. When used in the cathode compartment, however, Triton X-45 produced excess foam, while the Pluronics appeared ineffective in the presence of chlorine when used in the anode compartment. The effective detergent concentration for 1*N* solutions is about 0.075 ml of the commercial detergent per liter. In experiments with $CaCl_2$ solutions, Fisher Aerosol[6] was used in both compartments.

Water transport is calculated as the average of the volume decrease in the anode compartment and the volume increase in the cathode compartment. It is, of course, necessary to expel all gas bubbles before reading the burets. It is estimated that the values so obtained are accurate within 5%.

The magnetic stirrers used generate considerable heat, even when operated from rheostats located some distance from the cell. Large changes in temperature, however, were overcome by blowing compressed air through the motor housings.

[4] Wyandotte Chemical Corp., Wyandotte, Mich.

[5] Rohm & Haas Co., Philadelphia, Pa.

[6] Fisher Scientific Co., Pittsburgh, Pa.

The same cell may be used for the measurement of membrane potentials and diffusion across membranes. In the latter cases it is advisable to use more vigorous stirrers or circulation systems for the solutions.

Manuscript received July 24, 1956. The method used in these studies was presented at the A.A.A.S. Gordon Conference on Ion Exchange in 1954.

Any discussion of this paper will appear in a Discussion Section to be published in the December 1957 JOURNAL.

REFERENCES

1. A. J. Staverman, *Trans. Faraday Soc.*, **48**, 176 (1952).
2. J. W. Lorimer, E. I. Boterenbrod, and J. J. Hermans, *Disc. Faraday Soc.*, **21**, 141 (1956).
3. G. Scatchard, *J. Am. Chem. Soc.*, **75**, 2883 (1953).
4. M. R. J. Wyllie, *J. Phys. Chem.*, **58**, 67 (1954).
5. M. Murakoshi, Paper presented at Ion Exchange Symposium (Japan) June 19, 1954; *see* also Y. Kosaka, *J. Electrochem. Soc. Japan*, **23**, 659 (1955).
6. W. Juda, J. A. Marinsky, and N. W. Rosenberg, *Ann. Rev. Phys. Chem.*, **4**, 373 (1953).
7. N. W. Rosenberg, J. H. B. George, and W. D. Potter, *This Journal*, **104**, 111 (1957).
8. A. G. Winger, R. Ferguson, and R. Kunin, *J. Phys. Chem.*, **60**, 556 (1956).
9. T. R. E. Kressman and F. L. Tye, *Disc. Faraday Soc.*, **21**, 185 (1956).
10. F. C. Nachod and J. Schubert, Editors, "Ion Exchange Technology," p. 137, Academic Press, New York (1956).

Anodic Behavior of Iron in Acid Solutions

Milton Stern and Richard M. Roth[1]

Metals Research Laboratories, Electro Metallurgical Company,

A Division of Union Carbide Corporation, Niagara Falls, New York

The electrochemical behavior of iron has been the subject of extensive research within the last few years. Stern (1) has described the relationships which exist betweeen the corrosion potential, the corrosion rate, and the hydrogen activation overvoltage of pure Fe in acid NaCl solutions. Anodic polarization measurements were not reproducible and showed marked hysteresis. Thus, a quantitative description of the local anodic polarization curve for the material could not be presented. However, since the corrosion rate and the hydrogen activation overvoltage parameters, i_o and β, were constant over the *p*H range 1-4 and the corrosion potential varied by 0.056 v for each unit *p*H change, it was concluded that the local anodic polarization curve for Fe at currents corresponding to the corrosion current is extremely steep.

On the other hand, another explanation is possible if one considers that the anodic formation of ferrous ions from iron is *p*H dependent. In particular, for this mechanism to explain the data properly, anodic polarization must show an RT/F dependence on *p*H. The former explanation was selected because no obvious process could be devised which gave the anodic reaction the proper *p*H dependence.

Bonhoeffer (2) described the work of Heusler and Kaesche, two of his associates at the Max-Planck-Institut. These investigators also found a hysteresis effect during anodic polarization but reported that in $HClO_4$ solutions the local anodic polarization behavior of Fe does indeed show the *p*H dependence required to support the second explanation described above. However, anodic measurements in $HClO_4$ cannot be considered typical of behavior in acid NaCl solutions, particularly for a situation where ferrous ion complexing may be important.

These results, however, required that anodic behavior in acid NaCl be examined critically to determine which of the possible proposals is correct.

The question can be summarized simply. Does the Tafel slope for dissolution of Fe ($Fe \rightarrow Fe^{++} + 2e$) have a normal value of about 0.1 v, or is the slope an order of magnitude greater?

Procedure

Two new experimental approaches are possible, either of which can supply the answer to this question. Both have been described by Stern and Geary

[1] Present address: Lehigh University, Bethlehem, Pa.

(3). The techniques have been applied to the Fe problem, and thus are discussed here briefly. The methods make use of accurate low-current polarization measurements close to the corrosion potential and thus have the advantage of eliminating changes in surface composition and structure which may occur at higher currents.

Equipment and experimental techniques have been described elsewhere (1).

Method I.—If the corrosion potential and current are determined by the intersection of anodic and cathodic Tafel-type polarization curves, it can be shown that

$$\left(\frac{d\mathcal{E}}{di_{app}}\right)_{\substack{\mathcal{E}\to O \\ i_{app}\to O}} = \frac{\beta_C \beta_A}{(2.3)\ (i_{corr})\ (\beta_C + \beta_A)} \qquad (I)$$

where β_C is the cathodic Tafel slope, β_A is the anodic Tafel slope, and $\mathcal{E}$ is the difference between the polarized potential and the corrosion potential. Thus, a linear plot of potential as a function of applied current yields a straight line for sufficiently small values of applied anodic or cathodic current. The slope of this straight line section is $d\mathcal{E}/di$. Simultaneous measurement of the corrosion rate and hydrogen overvoltage yields values of i_{corr} and β_C. Thus, sufficient information is available to calculate the slope of the anodic polarization curve using Eq. (I).

Such measurements have been conducted in 4% NaCl acidified with HCl to a *p*H value of 1.5. The analysis of the Fe used was different from that reported previously (1), the S content being 0.01%. The material thus exhibited different values for the hydrogen activation overvoltage parameters. The exchange current, i_o, was found to be 0.041 μ amp/cm^2, while β_C was determined as 0.083 v. The corrosion rate in this case is equivalent to 26.2 μ amp/cm^2. Fig. 1 is a plot of the cathodic polarization data in the low-current region where the potential is a linear function of applied cathodic current. The value of $d\mathcal{E}/di$ is $6.7(10^{-4})$ v/μamp/cm^2. Using the above data in Eq. (I) produces a calculated value of β_A of 0.078 v.

It is interesting to note that the factor $\left(\frac{d\mathcal{E}}{di}\right)_{\mathcal{E}\to O}$ is exactly the term which Bonhoeffer (4) prefers to call "polarization resistance." In Eq. (I), which expresses this term, the corrosion current is in the denominator. This explains the increase in polarization resistance which is found with decreasing corrosion rates. Actually, $\left(\frac{d\mathcal{E}}{di}\right)_{\mathcal{E}\to O}$ is neither a resistance in the usual sense of the term nor a fundamental electrochemical parameter which controls corrosion rate. The linear dependence of potential on current only exists because the difference between two logarithmic functions of current approximates a linear function when the logarithmic functions are of the same order of magnitude (3).

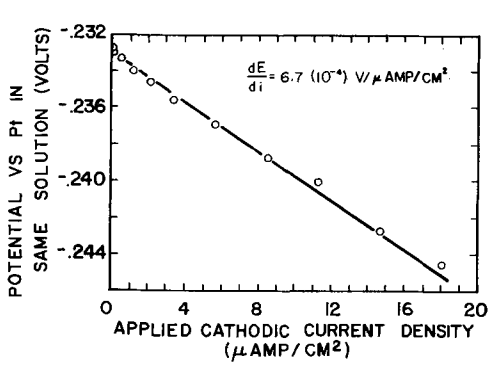

Fig. 1. Linear relation between potential and applied cathodic current.

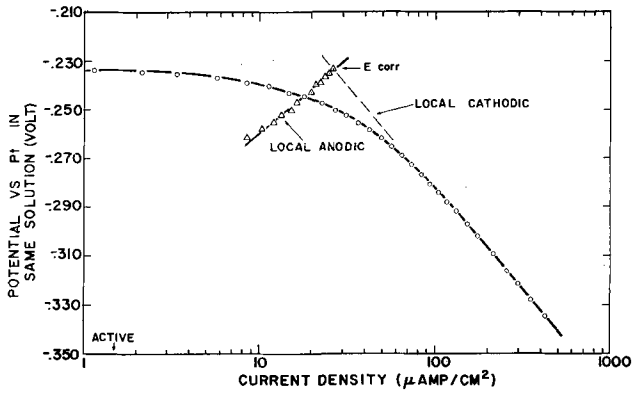

Fig. 2. Potential as a function of applied cathodic current

Method II.—For a system in which the corrosion potential and corrosion rate are determined by the intersection of two Tafel lines, where the intersection is sufficiently removed from the equilibrium potentials of the oxidation and reduction reactions involved, it has been shown (3) that the experimental cathodic polarization curve is described by the following equation:

$$\mathcal{E} = -\beta_C \log \frac{i_{app} + i_A}{i_{corr}} \qquad (II)$$

where i_{app} is the applied cathodic current and i_A is the total anodic current. Hydrogen activation polarization measurements in the Tafel region supply a value for β_C.

Thus, using Eq. (II), the local anodic current may be calculated as a function of potential during cathodic polarization.

Fig. 2 is a plot of potential as a function of applied cathodic current. Calculated values of i_A are included and trace the shape of the local anodic polarization curve. It is quite apparent here again that the local anodic polarization curve is not steep, the measured value being 0.068 v. Thus, it has been established that anodic behavior in HCl is similar to that reported by Bonhoeffer in $HClO_4$.

Discussion

It is necessary to explain the particular *p*H dependence of anodic polarization which produces the potential and corrosion rate dependence already reported by several investigators. In the *p*H range 1-4, it is difficult to accept the fact that the equilibrium potential of the Fe solution reaction is *p*H sensitive. Thus, one possible alternative explanation resides in a reduction of the exchange current density for the reaction $Fe \rightleftarrows Fe^{++} + 2e$ as the hydrogen

ion activity increases. This is not the only possibility, however. It has already been shown that during corrosion of Fe in acids, the major portion of the surface appears to function as the cathode. If one considers that the cathodic area increases as the hydrogen ion activity increases, possibly caused by greater hydrogen adsorption, then a decrease in the real area of the anode results. The anodic and cathodic polarization curves in Fig. 2 are based on a current-density calculation which uses the entire geometric sample surface area. Essentially, this is a plot of the polarization curves on a current basis rather than a current-density basis so that the curves intersect at the corrosion potential and the corrosion current. Thus, even though the equilibrium potential, β_A, and i_o for the solution of Fe are completely independent of pH, a decrease in the anode area will shift a plot of potential vs. anodic current to the left and produce a decrease in the exchange current even though the exchange current density is constant. Therefore, the pH dependence of the corrosion rate and corrosion potential of Fe may also be explained as a decrease in anodic area with an increase in hydrogen ion activity.

It is interesting to note that Hillson (5) reported that a Cu/Cu^{++} electrode showed a decrease in active area as a function of concentration of surface active agent. This produced a decrease in the exchange current. However, the exchange current density remained constant.

There is no obvious experiment which can distinguish between a shift in the real exchange current density and a change in the anode area of Fe. However, without any apparent reason for considering the reaction $Fe \rightleftarrows Fe^{++} + 2e$ to be pH dependent, it appears that the better of the two explanations is that based on a decreasing anode area as the pH is decreased.

Manuscript received July 24, 1956.

Any discussion of this paper will appear in a Discussion Section to be published in the December 1957 JOURNAL.

REFERENCES

1. M. Stern, *This Journal*, **102**, 609 (1955).
2. K. F. Bonhoeffer, Paper presented at ECS Meeting, San Francisco, April 30, 1956.
3. M. Stern and A. L. Geary, *This Journal*, **104**, 56 (1957).
4. K. Bonhoeffer and W. Jena, *Z. Elektrochem.*, **59**, 151 (1951).
5. P. J. Hillson, *Trans. Faraday Soc.*, **50**, 385 (1954).

Discussion Section

Anodic Transients of Copper in Hydrochloric Acid

Ralph S. Cooper (pp. 307-315, Vol. 103)

James H. Bartlett[1]: (*A*) If the anode be horizontal and shielded, and if the current has decreased to zero, what is the nature of the break transient and what factors govern its duration?

(*B*) During a break transient, is the main process dissolution of the anode layer or is it diminution of the amount of $CuCl^-_2$ in the pores, with the attendant consequences?

Ralph S. Cooper: (*A*) For horizontal shielded anodes the current decreases monotonically, approaching zero as the layer resistance increases with time but never actually becoming zero. Upon breaking the circuit, the anode voltage will change by the amount of the *IR* drop across the layer, and will immediately assume the open circuit electrode potential. No extensive experiments of this type have been performed, but it may be expected that the break transients observed will be similar to those for unshielded anodes with three differences. First, for $V_a \leq -0.05$, an appreciable layer resistance is to be expected. Secondly, the duration of the —0.05 v voltage decay plateau may possibly be longer because of the lower rate of solubility of the layer. Finally, the electrode potential will not drop below —0.27 v as the anolyte will remain saturated with CuCl.

(*B*) There are, in general, two processes associated with the break transient. The first is the opening of the pores in the CuCl layer, which results in decay of the layer resistance. The completion of the resistance decay is coincident with the end of the —0.05 v voltage decay plateau. Only 1% of the CuCl layer need dissolve in order for its resistance to become small compared to the solution resistance. The second process is the removal of the bulk of the CuCl layer. This occurs only for unshielded electrodes where convection can act to remove the $CuCl^-_2$ ion complex at an appreciable rate. This process requires of the order of 10 sec for completion, during which the anode potential remains at —0.27 v. Upon completion the solution becomes unsaturated with respect to CuCl and the potential falls below —0.27 v, ending the second voltage decay plateau.

The Nature of the Film Formed on Copper during Electropolishing

E. C. Williams and Marjorie A. Barrett (pp. 363-366, Vol. 103)

I. Epelboin and M. Froment[2]: The study, by electron diffraction, of metals polished electrolytically gives contradictory results. Thus, Bouillon, Bouillon-Nyssen, and Delplancke[3] have reported that it is possible to obtain, by electrolytic polishing, copper surfaces free of all foreign layers. This conclusion is in disagreement with the results of Williams and Barrett, although in both cases the copper was polished in phosphoric acid.

We think that it is difficult to draw conclusions from an examination carried out after the specimen has been removed from the solution. This is why we study the polishing during the course of the electrolysis, by superimposing a low-amplitude alternating current on the continuous current. The study of variations of the components of impedance as a function of frequency enables one to obtain information about the structure of the anode layer, and it has been established[4] that the phenomena are more complex in phosphoric acid than in solutions based on ClO_4^- ions.

Assuming that it is possible to polish small copper surfaces in magnesium perchlorate-ethyl alcohol mixtures, it would be interesting to examine such surfaces by electron diffraction.

E. C. Williams and Marjorie A. Barrett: Our observations are not necessarily in disagreement with those of Bouillon, Bouillon-Nyssen, and Delplancke. They confirm the previous results of Hoar and Farthing concerning the existence of a film during polishing and we have furthermore emphasized that the film is formed, and remains on the surface, under the current-density conditions for polishing but that it dissolves in the acid when the circuit is opened. It is therefore possible to obtain a surface substantially free of a nonmetallic layer by withdrawing the specimen from the electrolyte some time after the cessation of current. Whether or not it is then completely free of all adsorbed radicals is doubtful, but we think that Messieurs Epelboin and Froment probably do not have in mind contamination of a molecular order of magnitude.

We agree that it is difficult to draw conclusions from an examination carried out after the specimen has been removed from solution. On the other hand our conclusions, which we arrived at after taking due precautions, do not in any way offend electrochemical principles and they appear to complete a fairly satisfactory picture of the polishing process based on Elmore's theory. The superimposed alternating current technique is no doubt promising as a means of providing information on the structure of the anode layer, but in our opinion it is a very indirect method and difficult to interpret.

Pitting Corrosion of 18Cr-8Ni Stainless Steel

M. A. Streicher (pp. 375-390, Vol. 103)

N. D. Greene, Jr.[5]: In his paper the author states that pitting may be divided into two distinct steps:

This Discussion Section includes discussion of papers appearing in the JOURNAL of The Electrochemical Society, 103, No. 6-12 (June-December 1956). Discussion not available for this issue will appear in the Discussion Section of the December 1957 JOURNAL.

[1] Dept. of Physics, University of Illinois, Urbana, Ill.

[2] Lab. de Physique Enseignement de la Faculté des Sciences de Paris, 1 rue Victor Cousin, Paris, France.

[3] F. Bouillon, Y. Bouillon-Nyssen, and A. Delplancke, *Bull. soc. chim. Belges*, 65, 245 (1956).

[4] I. Epelboin, *J. chim. phys.*, 49, C214 (1952); *Métaux (Corrosion-Inds.)*, [376], 31, 475 (1956).

[5] Corrosion Research Lab., Ohio State University, Columbus 10, Ohio.

pit initiation and pit growth. Pit initiation is a most curious technical term. To my knowledge, it has never been defined. True, a pit does start at some point; however, this fact surely does not constitute a definition of an initiation step.

If pitting involves two distinct steps it must be possible to characterize and separate each of these steps. Likewise, it should be possible to state the point at which the initiation step ceases and the growth step begins or assumes major importance. I would appreciate having the author's definition of the pit initiation step and his comments on the above points.

How does the author separate the initiation and growth steps in the test he describes? If pitting is a two-step process, as proposed, wouldn't the number of pits which appear during the test represent the cumulative action of initiation and growth under conditions of impressed current?

A test similar to the author's test in 0.1*N* sodium chloride was performed in this laboratory. Microscopic examination of the specimen showed numerous extremely small pits in addition to those visible to the naked eye. Many of these fine pits were clustered around the larger macroscopic pits. Probing indicated that they were definitely pit depressions and not the result of "roof collapse" of the larger pit cavities. Fig. 11 in the author's paper illustrates this phenomenon. Close examination of this photograph indicates the presence of approximately six tiny pits. Were these numerous microscopic pits included in the total pit counts?

M. A. Streicher: The division of pitting into pit initiation (surface break-down) and pit growth is a convenient method for separating various factors involved in each of these two steps, and follows naturally from the fact that one large, deep pit may be of much greater importance than many shallow pits. The factors in the metal or the environment which lead to surface break-down are not necessarily the same as those which promote excessive growth. These concepts of pit initiation and pit growth (propagation) have been found useful by other investigators.[6]

The break-down of the surface may be detected in several ways, by changes in electrode potential (*see* Ref. 25 of the discussed paper) or by the appearance of a pit. In my investigation, electrolytic methods were used to break down the passive surface. The number of pits formed in this way was used as a measure of the pitting resistance of the steel. The actual size of the pit was largely a function of the number of pits formed and the amount of current passing through the cell. Therefore, this method was not suitable for the study of pit growth and was not used for this purpose. Pits were grown only to reveal the number of points of break-down in the surface.

In order to observe pits in their relationship to the metallurgical structure the growth process must be stopped while they are still very small. Also, for metallographic studies a very large number of pits must be formed in order to obtain pits within the minute area under observation in the microscope. The current densities required to form these large numbers of pits are much greater than those used in the standard test described in the paper; i.e., a gradual increase of anodic current from zero to 3 ma/cm^2 in about 15 min.

For metallographic observation of pit formation a large current was applied for a short period, which resulted in many pits, a few of which grew to the cavity stage before the current was stopped. This phenomenon was also shown by time-lapse motion pictures taken during the extended application of an anodic current. Pits grew irregularly. After some growth a few pits stopped growing, while others continued, and then suddenly grew again.

Microscopic examination of specimens which had been subjected to the standard pitting test, as described in the paper, did not reveal any pits which were not readily visible to the unaided eye.

[6] P. M. Aziz, *Corrosion*, 9, 85 (1953); R. May, *J. Inst. Metals*, 32, 65 (1953).

Natural and Thermally Formed Oxide Films on Aluminum

M. S. Hunter and P. Fowle (pp. 482-485, Vol. 103)

D. A. Vermilyea[7]: This paper is extremely interesting and does much to clarify the phenomena occurring during the gaseous oxidation of Al. One of the most interesting results of the study is the fact that the barrier layer thickness is a linear function of the temperature of oxidation. According to the theory of Mott and Cabrera[8] a plot of the reciprocal of the thickness against temperature should be linear. The experiments of Rhodin[9] on Cu agree well with the Mott-Cabrera theory, but the present results on Al do not. To my knowledge there is at present no theory which predicts the observed dependence of barrier thickness on temperature, and a further study of this system might prove very enlightening.

M. S. Hunter and P. Fowle: The linear relationship between barrier thickness and temperature is an observed fact which has not yet been explained by theory. Work is continuing in an attempt to evolve such an explanation. A possible key to this behavior may be the fact that the thickness of anodically formed barrier oxide films is a linear function of voltage, which suggests that the thermal forces which create natural barriers may be analogous to voltage which creates anodic barriers.

Preparation of High Purity Rhenium

D. M. Rosenbaum, R. J. Runck, and I. E. Campbell (pp. 518-521, Vol. 103)

Alan Seybolt[10]: Would it be possible to reduce the $ReCl_5$ to metal directly by hydrogen, instead of going through the ReO_2 step?

D. M. Rosenbaum, R. J. Runck, and I. E. Campbell: We have prepared rhenium metal by hydrogen reduction of the chloride, but the "hydrolyzed method" gave a purer product, that was in a form

[7] Research Lab., General Electric Co., Schenectady, N. Y.

[8] N. Cabrera and N. F. Mott, *Repts. Progr. Phys.*, 12, 163 (1948-49).

[9] T. N. Rhodin, *J. Am. Chem. Soc.*, 72, 5102 (1950); *ibid.*, 73, 3143 (1951).

[10] Research Lab., General Electric Co., Schenectady, N. Y.

more suitable for the intended processing by powder-metallurgy techniques.

A Mechanism for the Anodic Dissolution of Magnesium

J. H. Greenblatt (pp. 539-543, Vol. 103)

I. Epelboin and M. Froment[11]: (*A*) The work of J. H. Greenblatt is very interesting, because for certain problems it is important to know the proportion between the quantity of magnesium retained in the anodic corrosion products and those rendered soluble in the 3% NaCl solution. On the other hand, it appears to us that for the understanding of the mechanism of the irregular dissolution of different metals, it is preferable to avoid the formation of an insoluble layer, and it is for this reason that we use electrolytic polishing. The latter applies actually to all the metals and it permits[12-15] us to distinguish, by the application of Faraday's law, two modes of anodic dissolution. The first is characterized by the dissolution of the metal in the form of such stable ions as: Ag^{+}, Au^{3+}, Hg^{+}, Ni^{2+}, Co^{2+}, Cu^{2+}, Zn^{2+}, Cd^{2+}, Ge^{4+}, Si^{4+}, Fe^{2+}, Mn^{2+}, Ga^{2+}, Mo^{6+}, W^{6+}, Zn^{2+}, Mg^{2+}, U^{6+}, V^{4+}, Al^{3+}, Be^{2+}. The other mode of dissolution becomes evident with ions as: Au^{+}, Cu^{+}, Ge^{2+}, Si^{2+}, Ga^{+}, W^{4+}, Zn^{+}, Mg^{+}, U^{+}, V^{2+}, Al^{+}, Be^{+}, La^{+}, Ce^{+}, Ti^{+}, Li^{+}, and it takes place in the presence of a compact adsorption of certain anions on the surface of the metal, notably with ClO^{-}_{4} ions. The majority of the metals which we have mentioned are polished in the presence of these anions and we have proved, by gravimetric determination of Cl^{-}, that unstable ions such as Mg^{+}, Zn^{+}, V^{2+}, Al^{+}, Be^{+}, La^{+}, Ti^{+}, reduce the ClO^{-}_{4} anions. The perfect agreement between the coulometric data and the gravimetric determination of Cl^{-}, which persists in a large range of current density, as well as other experimental work (*see* footnotes 14 and 15), seems to remove certain hypotheses such as: chemical attack of the anode, formation of complexes, presence of simultaneous reactions at the electrode, etc.

(*B*) We do not understand how the comparison between the amount of Mg equivalent to the liberated hydrogen and the distribution of Mg after its dissolution is capable of informing us of the eventuality of reactions I and IV shown on page 542 of the paper. It is a pity that for the discussion of these reactions Mr. Greenblatt has not sufficiently utilized his own data indicated, for example, in Table I, p. 541. In effect, if one supposes that the ions Mg^{+} eventually reduce water, the agreement between the coulometric data (column 5) and the total quantity of liberated hydrogen (column 4) is excellent. One deduces by the two methods, with the exception of the measurements made at very low current densities (0.0196 amp/cm^2), that the initial average valence is equal to 1.3. This figure permits the deduction, according to Eq. I and IV, that the dissolution of one gram atom of Mg involves 70% ions of the Mg^{+} state and 30% of the Mg^{2+} state. By creating a more compact adsorption of certain anions on the surface of the metal, one can increase the percentage of Mg^{+} ions. For example, with the polishing baths with a base of magnesium perchlorate we have found that 80% of the Mg ions are in the monovalent state. This result, published three years ago,[13] confirms that the mechanism of the irregular anodic dissolution of Mg, like that of other metals, must be connected with the constitution of the electrochemical double layer.[16]

J. H. Greenblatt: The comments of I. Epelboin and M. Froment have been noted and the author finds no disgreement with them. The author became aware of the work of Epelboin and co-workers late in 1955 after the paper under discussion had been submitted for publication and has followed their work with interest since that time.

The author has attempted to explain the solution of Mg under what might be called "normal" conditions of use for Mg anodes when insoluble products do form. To do this, of course, it is necessary to establish the amounts of dissolved material found in the various reaction products. The distribution of products and their ratios is a consequence of the relative occurrence of reactions (I) and (IV), since insoluble Mg can only result if reaction (I) is occurring and there is no self-corrosion. When self-corrosion did occur, the excess weight loss always appeared as insoluble product, and this reaction path could be thus accounted for. If no self-corrosion occurred, efficiencies of roughly 50% were obtained and the insoluble and soluble Mg were in roughly 1:1 ratio. This product distribution could only occur through the predominance of 1. What is said in effect is that Mg^{+} reacts close to the surface with H_2O and the amount of reaction can be deduced from the amount of MgO produced. This is an exactly analogous procedure to that of Epelboin and Froment who determine the amount of Mg^{+} present by determining the amount of reaction product between Mg^{+} and ClO^{-}_{4}, i.e., Cl^{-}.

The author did not utilize the data of Table I, p. 541, in the manner suggested by Epelboin and Froment because he felt that it was sufficiently accurate to draw only the broader and more general conclusions about the kinetic mechanism proposed. The quantities of hydrogen collected were thought to suffer from the maximum experimental error because of the method of conducting the experiments. Small variations in this quantity would lead to reasonably large variations in apparent valence which the author felt might not reflect the true situation.

More accurate analyses of the distribution of reaction products have been obtained since the above mentioned work, and they can be used to distinguish between reactions (I) and (IV) as follows:

$$Mg \rightarrow Mg^{+} + e \qquad (I)$$

$$2Mg^{+} + H_2O \rightarrow Mg^{++} + MgO + H_2 \qquad (II)$$

$$Mg \rightarrow Mg^{++} + 2e \qquad (IV)$$

[11] Lab. de Physique Enseignement de la Faculté des Sciences de Paris, 1 rue Victor Cousin, Paris, France.

[12] I. Epelboin and M. Froment, *Compt. rend.*, 238, 2416 (1954).

[13] Ph. Brouillet, I. Epelboin, and M. Froment, *Compt. rend.*, 239, 1795 (1954).

[14] Ph. Brouillet, Thesis, Paris (1955); *Métaux (Corrosion-Inds.)*, 30, 141 (1955).

[15] I. Epelboin, 54° Réunion de la Bunsen-Gesellschaft, Goslar, May 1955; *Z. Elektrochem.*, 59, 689 (1955).

[16] I. Epelboin and M. Froment, 73° Colloque International de la Centre National de la Recherche Scientifique, Paris, October 1956.

Table I. Electrolysis data for pure Mg anodes at room temperature 22°C

Current density (amp/cm²)	Wt loss (mg)	Calculated wt loss $Q/F \cdot 12$ (mg)	Soluble Mg (mg)	Insoluble Mg (mg)	α
0.027	259	136	136	117	0.86
0.027	260	136	136	124	0.91
0.036	262	134	133	133	1.00
0.036	265	134	139	130	0.97
0.044	254	131	133	120	0.92
0.044	248	131	131	121	0.93
0.052	250	136	139	116	0.85
0.052	246	136	139	123	0.91
0.056	248	136	138	122	0.90
0.056	234	136	141	110	0.81
0.056	257	136	136	133	0.98
0.064	230	131	139	115	0.88
0.064	231	131	136	114	0.87
0.064	227	131	135	102	0.77

Suppose α is the fraction of (I) occurring and $(1-\alpha)$ the fraction (IV). Then for the passage of Q coulombs, $\alpha(Q/F) \cdot 24$ g of Mg will dissolve according to (I), of which, if (II) holds true, $Q\alpha \cdot 24/2F$ will be soluble and $\alpha Q \cdot 24/2F$ will be insoluble. The amount dissolving by (IV) is $(1-\alpha)\ Q/F \cdot 12$, all of which is soluble.

Total soluble Mg^{++} is then $Q/F \cdot 12$. The insoluble magnesium is $\alpha Q/F \cdot 12$. According to this, the soluble reaction product should always be constant at $Q/F \cdot 12$ while the insoluble material and total weight loss should decrease if (IV) occurs. The data above obtained over a range of current densities indicate that this is essentially true.

Values of α or the fraction of (I) occurring are seen to average about 0.9. At higher current densities it can be seen that the totals of columns 4 and 5 are greater than the total weight loss. This strengthens the author's contention that such data should be used in a general way and that the conclusion to be drawn from the above table is that, under the conditions of electrolysis as carried out in the author's work, reaction (I) predominates almost exclusively and that (IV) is relatively unimportant.

Depth of Surface Damage Due to Abrasion on Germanium

T. M. Buck and F. S. McKim (pp. 593-597, Vol. 103)

B. A. Irving[17]: The figures for depths of surface damage on abraded Ge reported by Buck and McKim represent average depths over the area of their measurement (about 2 cm²). In the course of work in this laboratory on the etching of Ge it has been shown that damage caused by a scratch can reach considerably greater depths.

A (100) surface on a single-crystal Ge specimen was ground on 320 mesh Carborundum paper and then on progressively finer abrasive down to one micron diamond dust, to give a metallographically polished surface. A distincitve array of scratches was observed during the initial stages of grinding with the 320 mesh Carborundum paper. It is estimated that at least 20 μ of material were removed during grinding and polishing. The specimen was

Fig. 1. Etched Ge surface, showing facetted etch-marks. 5X before reduction for publication.

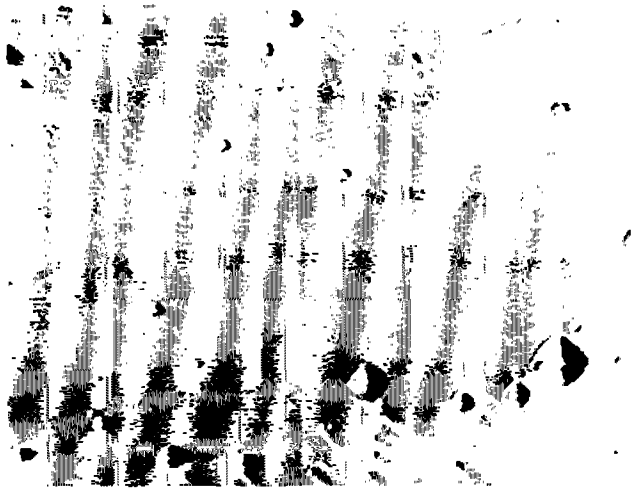

Fig. 2. Single facet enlarged to show etch pits. 2,000X before reduction for publication.

then etched in hypochlorous acid until a further layer, 40 μ thick, had been removed. The distinctive scratches, noticed during grinding, were reproduced with others as an array of facetted etch-marks (Fig. 1). Small etch pits occurred distributed over the surface but concentrated along the etch-marks (Fig. 2). The density and distribution of the pits (other than those on the etch-marks) were similar to that obtained for the same specimen etched in CP-4 which is known to produce pits at dislocations.[18] It is suggested that dislocations are responsible for the persistence of the scratches as etch-marks.

Abrasion can, therefore, cause local damage at depths greater than 40 μ taking the form of rows of dislocations.

T. M. Buck and F. S. McKim: Our data showed principally that, by etching to depths approximately equal to the particle size of the abrasive used in lapping or polishing, the average recombination velocity over the surface area used was reduced to low levels ($\sim$ 100 cm/sec) where no further significant change could be detected in the PME method.

[17] Research Lab., Associated Electrical Industries Ltd., Aldermaston Court, Aldermaston, Berkshire, England.

[18] F. L. Vogel, W. G. Pfann, H. E. Corey, and E. E. Thomas, *Phys. Rev.*, 90, 489 (1953).

We have, in our paper, recognized the possibility of deeper local damage, in view of Uhlir's[19] studies of reverse characteristics of electrolyte-Ge barriers. Mr. Irving's data furnish useful information regarding the nature of such local damage. The scratches he observes are probably deeper than any we have encountered since he used 320 mesh abrasive (maximum particle diameter 50-60 μ) as the initial lapping treatment. However, we have observed that the recombination velocity does not drop as sharply, with etching, for a fine-polished surface on which numerous scratches are visible owing to insufficient polishing or foreign particles in the polishing compound.

Kinetics of Formation of Porous or Partially Detached Scales

C. Ernest Birchenall (pp. 619-624, Vol. 103)

U. R. Evans[20]: The effect of vacancies developing at the base of a growing oxide film on the growth law is of great interest today, and Professor Birchenall's detailed treatment should be welcomed.

In a slightly different way, it has been possible[21] to arrive at an equation which seems to fit such facts as are known to us. Any vacancy arising from the passage of an atom (as cation) into the film may either (*a*) move into the oxide or metallic phase—possibly, in the latter case, becoming extinguished on arrival at a dislocation or (*b*) settle at the oxide-film interface, not necessarily at the original point of formation.

The second of these occurrences must help to cut down the area over which movement of ions across the film can occur. Presumably the chance of it happening will be proportional to the number of sites still available. The assumption led me a few years ago to an expression for the weight change (W) at time (t)

$$W = k_1 \log (t^{1/2} + k_2) + k_3$$

when k_1, k_2, and k_3 are constants. Somewhat later Mills,[22] studying the oxidation of Cu, experimentally found this equation to be obeyed under circumstances where neither the parabolic nor the ordinary logarithmic equation was obeyed.

Of course, in other cases the conditions on which this equation is based may not be fulfilled, and then those developed by Professor Birchenall, starting from different premises, may have useful application.

L. Seigle[23]: We have found Dr. Birchenall's paper interesting because of the similarity of the phenomenon he is considering to that of void formation in metals during diffusion. Studies of the latter process[24] indicate that the formation of voids is sometimes catalyzed by oxides in the solid metal, suggesting that the oxide-metal interface can be a favored site for vacancy condensation. If void formation by this mechanism is looked upon as a nucleation and growth process, the nucleation frequency is seen to be dependent upon the relative interfacial energy of the oxide-metal interface, and the degree of vacancy supersaturation attained at this interface.

The same ideas might be applied to the nucleation of voids at the oxide-metal interface during scale formation. For example, if it is assumed that vacancies pass across an initially coherent interface into the base metal, the vacancy concentration at the interface will tend to build up until a quasi-steady state is reached in which the rate of arrival of vacancies through the oxide is equal to the rate of removal through the metal. The excess vacancy concentration in the metal at the interface, N_i, can then be obtained by solving the equation (*see* footnote 24):

$$I_v = D_v \frac{\partial^2 N_v}{\partial x^2} - \frac{N_v}{\tau} = 0$$

with the boundary conditions $N_v = 0$ for $x = \infty$ and $-D_v(dN_v/dx) = (D_o \Delta X_o/l)$ for $x = 0$.

The solution is

$$N_v = \frac{D_o X_o}{l} \sqrt{\frac{\tau}{D_v}} \exp\left(-\frac{x}{\sqrt{D_v \tau}}\right)$$

$$\text{and } N_i = N_v\,(x = o) = \frac{D_o \Delta X_o}{l} \sqrt{\frac{\tau}{D_v}}$$

In the above equations N_v, D_v, and τ are the excess concentration, diffusion coefficient, and lifetime of vacancies in the metal, respectively, ΔX_o and D_o are the concentration differential and diffusion coefficient of cations in the oxide, and l is the thickness of the scale. The quantity τ/D_v can be written in terms of density of dislocations, N_d, jogs on dislocations, j, equilibrium vacancy concentration, N_e, and self-diffusion coefficient, D_m, in the metal, and expressions obtained for the relative excess concentration of vacancies at the oxide-metal interface:

$$\frac{N_i}{N_e} = \frac{D_o \Delta X_o}{D_m\, l\, N_d^{1/2}} \text{ (low temperatures)}$$

$$\frac{N_i}{N_e} = \frac{D_o \Delta X_o}{D_m\, l (N_d\, ja)^{1/2}} \text{ (high temperatures)}$$

In the above a is the atom spacing in the metal and ΔX_o must be expressed as atom fraction. Making appropriate assumptions about N_d and j, a value of N_i/N_e can be calculated which might indicate the probability of nucleation at the interface. No attempt has been made to apply these equations, but they are offered as a possible approach.

It is also possible that the oxide-metal interface acts as a source and sink for vacancies in the way that grain boundaries in metals seem to.[25] If this is true, the vacancy flow would not cross the interface, but be eliminated at it by a mechanism whose details are not yet understood.

C. E. Birchenall: The author appreciates the additional remarks furnished by Doctors Evans and Seigle. Since I am in general agreement with

[19] A. Uhlir, *Bell System Tech. J.*, 35, 333 (1956).

[20] 19 Manor Court, Grange Rd., Cambridge, England.

[21] U. R. Evans, *Reviews of Pure and Applied Chemistry (Melbourne)*, 5, 1 (1955).

[22] T. Mills and U. R. Evans, *J. Chem. Soc.*, 1956, 2182.

[23] Metallurgy Labs., Sylvania Electric Products Inc., Bayside, N. Y.

[24] R. Resnick and L. Seigle, *J. Metals*, 9, 87 (1957).

[25] R. Balluffi and L. Seigle, *Acta Met.*, 3, 170 (1955).

these observations, I should like to take the opportunity to make several comments which may be somewhat repetitious but seem to me to be important, if only as points requiring further experimental or theoretical study.

I, as well as others, have looked for porosity developing within a metal while an oxide grows upon it. Such porosity has not been found when the substrate is a pure metal, only when it is an alloy. In the latter case the porosity is probably Kirkendall porosity arising from metallic interdiffusion as the oxidation preferentially removes one component.

Porosity does occur frequently within the oxide layer. Its extent and distribution seems to be very sensitive to specimen geometry, indicating that inclusions or impurities are not all-important, although they be major factors in determining where pores start in any given geometry.

In an ionic crystal it appears that annihilation of vacancies of one charge requires a deformation of the lattice of ions of the other charge. For this reason it becomes important to learn more of the behavior of the immobile ions in order to construct a more complete picture of the oxidation process.

It is evident that the critical region is at the metal-oxide interface. The region is liable to modification by the accumulation of inclusions and slowly diffusing impurities. It is also difficult to prepare for metallographic examination. In the long run, new techniques must be refined to give explicit answers about the exact state of the interfacial region.

Rectifying Semiconductor Contacts

H. K. Henisch (pp. 637-643, Vol. 103)

R. E. Burgess[26]: In discussing the number of impurities in the barrier layer, the appropriate quantity would seem to be the number in a cube of edge equal to the barrier thickness and not the total number present.

[26] Dept. of Physics, University of British Columbia, Vancouver, B. C., Canada.

H. K. Henisch: In order to make a quantitative assessment, it is convenient to assume that the impurities are distributed in the form of a regular superlattice. The parameter which concerns us then is the distance between neighboring impurities in relation to the thickness which the barrier would have if the space charge were continuous. In practice, the impurity distribution would, of course, be random or at any rate nonperiodic in some other way. An approximate treatment of this case has been given by Wiles.[27]

New Method of Studying Corrosion Inhibition of Iron with Sodium Silicate

E. F. Duffek and D. S. McKinney (pp. 645-648, Vol. 103)

L. Lehrman and H. L. Shuldener[28]: The authors assume that the protective action is due to an invisible film on the metal. If this is true, then it is conceivable that this film is a combination of the initial corrosion products with silica.

It would be interesting to know if any silica was removed from the test solutions. Our work clearly indicated that, when sodium silicate acts as a corrosion inhibitor, corrosion products at the surface of the metal combine with silica to form a protective deposit.

The experimental technique used is very interesting. It might also be used for determining the effect of silica occurring naturally in water vs. that added as sodium silicate. Sodium silicate could be added to a low silica water and caustic soda added to a high silica water, both of the same *p*H and final silica content, and the passifying effects of both solutions observed.

We agree with the emphasis put on visual examination as against weight loss in experimental work of this type.

[27] G. G. Wiles, *Phil. Mag.*, 46, 363 (1955).

[28] Water Service Labs., Inc., 423 West 126th St., New York 27, N. Y.

December 1957 Discussion Section

A Discussion Section, covering papers published in the January—June 1957 JOURNALS, is scheduled for publication in the December 1957 issue. Any discussion which did not reach the Editor in time for inclusion in the June 1957 Discussion Section will be included in the December 1957 issue.

Those who plan to contribute remarks for this Discussion Section should submit their comments or questions in triplicate to the Managing Editor of the JOURNAL, 216 W. 102 St., New York 25, N. Y., *not later than September 1, 1957.* All discussion will be forwarded to the author, or authors, for reply before being printed in the JOURNAL.

The Overpotential of the Manganese Dioxide Electrode

II. Acid Electrolytes

Shiro Yoshizawa[1] **and W. C. Vosburgh**

Duke University, Durham, North Carolina

ABSTRACT

The overpotential of electrodes prepared by electrodeposition on graphite was measured in solutions of sulfuric acid and manganese(II) and sodium sulfates as a function of acidity, current density, and temperature. The relation of overpotential to current density and the shapes of the growth and decay curves can be explained quantitatively, on the assumption that the primary reduction product is MnOOH on the MnO_2 surface and the electrode potential is dependent on the ratio of MnOOH to MnO_2 on the surface.

The overpotential of the MnO_2 electrode in NH_4Cl electrolyte at *p*H 5 and *p*H 7 was measured by Chreitzberg and Vosburgh (1). The overpotential was defined as the difference between the open-circuit potential in the steady state attained after a discharge and the closed-circuit potential at the end of the discharge. The outstanding features observed in this and previous work (2) were (*a*) the overpotential increases slowly at the beginning of a discharge, (*b*) the decay after breaking the circuit is slow, (*c*) the relation between overpotential and the logarithm of the current density is not linear, and (*d*) the overpotential is a linear function of the logarithm of the ammonium ion concentration at constant ionic strength. These facts seemed best explained qualitatively on the basis of two assumptions: (*a*) the potential of a MnO_2 electrode depends on the composition of the oxide at the surface exposed to the solution (3, 4); (*b*) during or after discharge the lower oxide formed at the surface can diffuse into the higher oxide below, perhaps by a process involving the movement of only protons and electrons (2, 5). In addition, when enough of a suitable electrolyte is present it is known that considerable managanese(II) ion goes into solution during a discharge, and this reaction continues for a time after the circuit is broken (4, 6). In solutions of high *p*H the manganese(II) ion in solution should eventually react with any MnO_2 remaining on the electrode to bring the system to complete equilibrium.

The slow growth of the overpotential is considered to result from the reduction of MnO_2 at the surface exposed to the solution at a rate faster than that at which the lower oxide produced is removed. In the steady state of polarization these two rates become equal, with more lower oxide on the surface than at open-circuit equilibrium. After breaking the circuit the excess lower oxide continues to be removed from the surface by the two processes, inward diffusion and reaction with the electrolyte to give manganese(II) ion. The effect of the ammonium ion concentration is explained as an effect on the rate of reaction of ammonium ion with the lower oxide.

With two independent processes for the removal of lower oxide from the surface, the discharge is more complicated than desirable for a quantitative explanation. By changing the conditions, one or the other of the processes can be reduced in importance or eliminated. In a sufficiently acid solution containing considerable manganese(II) ion the MnO_2 electrode potential after a discharge returns to a value equal to that before discharge (7). This indicates that all of the lower oxide produced has reacted with the acid.

Discharges in several acid solutions have been carried out. The overpotentials have been measured and the discharge and recovery curves observed. It has been possible to develop equations for the variation of the overpotential with current density and for the growth and decay of the overpotential.

Experimental Methods

The preparation of MnO_2 electrodes by electrodeposition on graphite rods and the preparation of cells were as previously described (1, 8). The electrodes were made of cylindrical graphite rods with 8 cm^2 of exposed area on which was electrodeposited 0.2 mmole of MnO_2. The cells consisted of a centrally located MnO_2 electrode in a vessel holding about 190 ml of electrolyte with a cylindrical Pb electrode lining the wall of the vessel. A Luggin capillary was provided for a reference electrode which was of Hg and Hg_2SO_4 with an electrolyte the same as, or similar to, that of the cell.

Constant current for discharges was provided by four dry cells in series, with hand regulation of the resistance in the circuit. Both current and the potential difference between the MnO_2 and Hg_2SO_4 electrodes were measured by a recording potentiometer sensitive to about 1 mv. The cells were maintained at 25° ± 0.5°C in an air bath during measure-

[1] Present address: Department of Industrial Chemistry, Kyoto University, Kyoto, Japan.

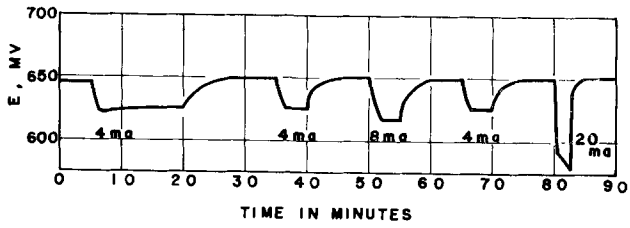

Fig. 1. Open- and closed-circuit potentials of a single electrode in electrolyte 1. The equilibrium open-circuit potential was 650 mv, while the closed-circuit potential depended on the current as shown. The curve was redrawn from a recording potentiometer graph.

ments and the electrolyte was stirred during measurements by a magnetic stirrer.

Overpotential Measurements

The cells were allowed to stand over-night before measurements were begun. After 15 min or more on open circuit a current was passed until constancy was attained. With an electrolyte 1M in H_2SO_4 and 0.1M in $MnSO_4$ constancy of closed-circuit potential was ordinarily attained within 2 min, except in the first discharge, as shown in Fig. 1. On breaking the circuit, constancy of open-circuit potential was usually attained in about 6 min. The difference between the constant closed-circuit potential and the constant open-circuit potential after the discharge was taken as the overpotential. Several successive measurements were possible with a single electrode as illustrated in Fig. 1, which was copied from part of a recorder graph.

Overpotentials at the same current density either on a single electrode or on different electrodes seldom differed by more than 1 mv. In the first discharge of a fresh electrode the potential usually passed through a pronounced minimum before becoming constant as shown in Fig. 1. In subsequent discharges made soon after the first a minimum was detected only when a more sensitive recording potentiometer was used, in which case there was a faint minimum in each discharge curve. When the first discharge was at very small current density there was usually only a small minimum, but a larger one appeared later when a sufficiently large current was passed. When an excessively large current was passed the closed-circuit potential did not become constant, as illustrated in the 20-ma discharge at 83 min in Fig. 1. Such a discharge always damaged the electrode so that overpotentials measured afterward at lower current densities were too large. With lower acid concentration the attainment of equilibrium was a little slower and the reproducibility not quite so good, but the overpotential was larger and the relative error about the same. When the electrolyte contained 0.01M H_2SO_4, 0.99M Na_2SO_4 and 0.10M $MnSO_4$, closed-circuit potentials became constant in 3-4 min and, after a discharge, 30-45 min was required for constancy of the open-circuit potential.

Overpotential measurements were made at several current densities and with five electrolytes containing H_2SO_4, the compositions of which are given in Table I. In column 4 of Table II the observed overpotentials are given. An approximate calculation of the concentration overpotential showed that only at the highest current densities was this appreciable. When the calculated value was over 0.5 mv a correction was made, but no corrections were over 1 mv. The iR drop included in the measurements was a little larger. This was calculated in two parts, that along the graphite rod, and that through the solution; the two were of approximately equal magnitude. The larger part of the difference between the observed and corrected values in Table II is this correction. The last column was calculated by Eq. (XXVI).

Table I. Composition of acid electrolytes

No.	Composition, M H_2SO_4	Na_2SO_4	$MnSO_4$	pH
1	1.00	—	0.10	0.12[a]
2	0.50	0.50	0.10	0.55[a]
3	0.10	0.90	0.10	1.55[a]
4	0.05	0.95	0.10	2.12[a]
5	0.01	0.99	0.10	2.59[a]
6	b	0.33	—	4.0[a]
SH1	0.04	—	0.01	1.39[c]
SH2	0.0125	0.015[d]	0.01	1.94[c]

[a] Measured with a glass electrode. [b] Acetic acid, 0.1M, and 0.01M sodium acetate. [c] Calculated. [d] K_2SO_4.

Table II. Variation of overpotential with current density and acidity. 25°C.

No. of electrodes	No. of measurements	Current density ma/electrode	Overpotential, mv Obs.	Corr.	Calc.
		Part 1. Electrolyte No. 1.			
1	1	0.40	8	8	8
1	1	0.50	10	10	10
1	2	1.00	16	16	15
3	4	2.0	20	20	21
3	5	4.0	25	24	29
1	1	8.0	32	31	37
1	1	16.0	46	44	45
1	1	24.0	54	51	50
		Part 2. Electrolyte No. 2			
2	2	1.00	14	14	11
2	2	2.0	18	18	17
2	2	4.0	22	21	23
2	2	8.0	30	29	31
2	2	16.0	42	40	40
2	2	32.0	51	47	49
		Part 3. Electrolyte No. 3			
1	1	0.50	10	10	10
1	1	1.00	14	14	17
1	1	2.0	21	21	23
1	3	4.0	29	28	31
1	1	6.0	39	38	36
1	1	8.0	42	40	40
1	1	10.0	45	43	43
1	1	12.0	53	51	46
		Part 4. Electrolyte No. 4			
1	3	1.00	22	—	—
1	1	2.0	28	—	—
1	1	4.0	33	—	—
		Part 5. Electrolyte No. 5			
2	2	0.70	19	19	19
3	5	1.00	21	21	22
3	4	2.0	28	27	31
3	4	4.0	39	37	41
1	1	6.0	50	47	47
1	1	8.0	56	53	52

Table III. Variation of overpotential with current density in an electrolyte of 0.33M Na_2SO_4, 0.1M acetic acid, and 0.01M sodium acetate, pH 4.0, 25°C

Current ma	Obs. overpotential, mv, at 100 ma-min	200 ma-min	300 ma-min
0.4	30	33	39
0.5	38	39	40
1.0	52	52	—
2.0	68	68	68
3.0	(57)	78	78
5.0	90	92	95
1.0*	44	50	56
2.0*	64	67	69

* Ammonium sulfate instead of sodium sulfate in the electrolyte.

In Table III are shown some overpotentials in an electrolyte of 0.33M Na_2SO_4, 0.1M acetic acid, and 0.01M sodium acetate (electrolyte 6). The establishment of a steady state of polarization was slower in this electrolyte, and measurements were made on each electrode after 100, 200, and 300 ma-min of discharge at a single current density. At the lowest current density the overpotential increased appreciably as the discharge proceeded, but usually the increase was small up to 300 ma-min of discharge. In two discharges ammonium sulfate was substituted for the sodium sulfate, with only a small effect in the direction of less overpotential.

With electrolyte 6, trouble was experienced in getting constant initial open-circuit potentials, and it was suspected that peroxide formation was responsible (9). Exclusion of oxygen by a current of nitrogen led to satisfactory constancy.

Overpotential and Acidity

The relation of overpotential to the acidity of the electrolyte is shown in Table IV. In the second column are given the total H_2SO_4 concentrations of all but two of the electrolytes. The acid must have been ionized mostly to H_3O^+ and HSO_4^-. The *p*H values of electrolytes 1-6 and the C and V electrolyte were measured by means of a glass electrode. Those of SH1 and SH2 were calculated, these electrolytes having an ionic strength of only 0.1.

The overpotentials in the fifth column were calculated by the empirical equation $\Delta E_e = 17 + 7$ *p*H. This expresses the results well for electrolytes 2-5 and C and V, but fails for the others. The assumption that the overpotential is determined by the nature and concentration of the source of protons for the electrode reaction leads to a better equation. It is sufficient for present purposes to assume that the H_3O^+ and HSO_4^- ions are equivalent and to relate the overpotential to twice the total H_2SO_4 concentration. This gives the equation $\Delta E_e = 22 - 9\log 2c$ in which c is the concentration. The last column of Table IV shows that this equation gives good calculated values for all of the electrolytes containing H_2SO_4 except electrolytes 1 and SH1, for which the calculated values are 5 and 3 mv too low, respectively. These two solutions were the only ones that contained no cations other than H_3O^+ and Mn^{++}.

Table IV. Variation of overpotential with acidity; current density 4 ma/8 cm^2; 25°C

Electrolyte[a]	H_2SO_4 M	pH	Overpotential, mv Corr.[b]	Calc'd (1)	Calc'd (2)
1	1.00	0.1	24	18	19
2	0.50	0.6	21	21	22
3	0.10	1.6	28	28	28
4	0.05	2.1	32	32	31
5	0.01	2.6	37	35	37
SH1	0.04	1.3	35	26	32
SH2	0.0125	1.9	36	30	36
C and V	c	7	70	66	—
6	d	4.0	85	45	—

[a] *See* Table I for composition of electrolytes.
[b] Corrections for *IR* drop and concentration polarization not exceeding a total of 2 mv have been applied.
[c] The source of protons for the reaction was 2M NH_4Cl (1).
[d] The source of protons was 0.1M acetic acid.

Growth and Decay of Polarization

For the investigation of the shapes of the growth and decay curves a recording potentiometer with a chart speed of about 5 cm/min and a sensitivity of about 0.01 mv was used. This instrument had a range of only 0-10 mv, so most of the electromotive force was balanced by a hand-operated potentiometer.

The curves showed evidence of a small *iR* drop in agreement with the calculated values and negligible for these experiments. Some curves are shown in connection with their discussion below.

The discharge curves all showed minima like that in the first discharge in Fig. 1. The minima in second and subsequent discharges made soon after the first were too small to have been recognized in the measurements of Fig. 1.

Evidence for the Presence of Lower Oxide on the Electrode Surface

If polarization is the result of the accumulation of lower oxide on the surface it should be possible to demonstrate its presence. An electrode was discharged in electrolyte 1 to a steady state of polarization at a current of 1 ma/8 cm^2. It was then quickly removed from the electrolyte, washed, and placed in a test tube containing 1M H_2SO_4 without added manganese sulfate. After 5 min it was transferred to a second portion of the same solution, and after increasing periods of time to a third, fourth, and fifth portion. Mn was determined colorimetrically in each portion of the solution. The electrode was replaced in the cell with electrolyte 1 and the experiment repeated with a discharge at 4 ma. Two more experiments were made with 4-ma discharges of another electrode. Blank experiments were made by bringing the two electrodes to open-circuit equilibrium with electrolyte 1 and then transferring to the successive portions of 1M H_2SO_4. Results are shown in the three upper curves of Fig. 2.

All three curves show that manganese(II) ion is extracted continuously for more than 80 min both after a discharge and in the blanks. The curves for the discharged electrodes lie above those for the blanks as the result of the extraction of more manganese(II) ion in the first 5 min. After 5 min all are approximately parallel. The experiment was repeated with electrolyte 5 with similar results. It may be concluded that there is an excess of lower

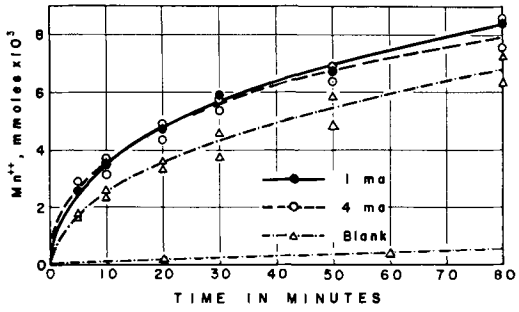

Fig. 2. Manganese(II) ion dissolved from partially discharged and undischarged electrodes. In the experiments represented by the three upper curves the electrodes were transferred from a solution containing 0.1M $MnSO_4$ and 1M H_2SO_4 to one of 1M H_2SO_4. The lowest curve represents an electrode at constant potential in 1M H_2SO_4 transferred to 1M H_2SO_4.

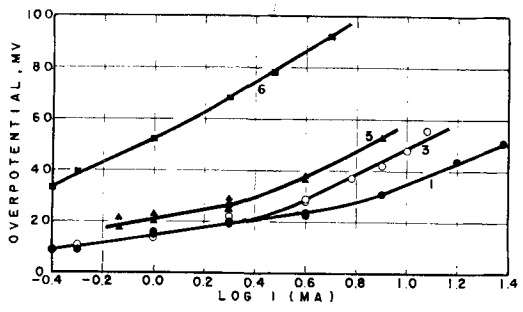

Fig. 3. Relation between overpotential and the logarithm of the current density (ma/8 cm^2). The numbers indicate the electrolytes, compositions of which are given in Table I.

oxide on the surface of a freshly discharged electrode.

The continuous extraction of manganese(II) ion from the electrodes is largely the result of the transfer of the electrode from a solution containing 0.1M $MnSO_4$ to one free from Mn. In the first solution the electrode takes up manganese(II) ion and in the second solution releases it slowly. A corresponding slow change in electrode potential takes place when the electrode is transferred from one solution to the other.

When an electrode was kept in 1M H_2SO_4 free from Mn, with occasional change of solution, until there was no further change of potential, it released only a little manganese(II) ion to fresh 1M H_2SO_4. The record of such an experiment is given in the lower blank curve of Fig. 2. A sample at 180 min confirmed the linear relationship shown. This may be a true self-discharge and is equivalent to a current density of 0.02 ma/8 cm^2.

Effect of Temperature

Measurements similar to those in Table II were made at different temperatures. Some of the results are shown in Fig. 8, below, in connection with their discussion. The 15°-values are in poor agreement with the others. Similar measurements were made with electrolyte 5.

The effect of temperature can be compared with that at *p*H 7. The ratio of the overpotential at 5°C to that at 25°C is 1.4 at *p*H 7 (1) with a current density of 1.6 ma/electrode, while with electrolyte 1 the corresponding ratio is 2.2 for 1 ma/electrode and 2.7 for 2 ma/electrode. For electrolyte 5 the ratios for 15° and 25°C are 1.7 and 1.9 as compared with 1.2 for *p*H 7. The ratios increase with acidity. Electrolytes 1 and 5 can be compared at temperatures 25° and 50°C; the ratio for a current of 2 ma/electrode is 2.3 for electrolyte 1 and 1.4 for electrolyte 5.

Effect of Thickness of MnO_2

A few electrodes were made with thinner and thicker deposits of MnO_2 by plating for 15 min or 2 hr instead of the usual 30 min at 25 ma/electrode. The overpotential for a 4-ma discharge was 29 mv for a 15-min electrode, 24 mv for a 30-min electrode, and 11 mv for a 2-hr electrode. Comparison of the discharge curves for a 1-ma discharge of a 30-min and a 2-hr electrode shows that the minimum value comes considerably later for the 2-hr electrode, at 12 min after the beginning of the discharge instead of 5 min. The minimum usually comes at about the same stage of discharge as measured in ma-min (1). This suggests that the true current density may be smaller for the 2-hr electrode, because of larger surface area. A smaller current density should give a smaller overpotential in qualitative agreement with experiment. However, ratios of surface area estimated from the minima and from the overpotentials did not agree.

Discussion

The Tafel Equation.—In Fig. 3 the relation between the overpotential and the logarithm of the current density for electrolytes 1, 3, 5, and 6 is shown. The curves for the more acid solutions might be considered to consist of two interesting straight lines. All resemble the relation in NH_4Cl electrolyte at *p*H 7 except that the overpotential decreases considerably with the large increase in acidity (1). The slope of the low-current portion for electrolytes 1 and 3 is 15 mv/log *I*. At lower acidity the slope is larger but approaches this value as the current decreases. For the lead dioxide electrode the corresponding slope is about 18 mv/log *I* (10).

A theory of the overpotential similar to that for the hydrogen evolution reaction (11) does not account for the slow growth and decay of polarization and predicts too high a slope for the Tafel equation. An alternative theory has been developed that accounts for the slow decay of polarization and is also in accord with the observed relation of current and overpotential.

Decay of Polarization.—The postulates adopted are as follows. (*A*) The potential of a MnO_2 electrode is determined in part by the composition of the surface exposed to the electrolyte (3, 4). (*B*) Overpotential results from an excess of the reaction product on the surface. (*C*) In a steady state of discharge in sufficiently acid electrolytes the reaction product is removed by reaction with the acid as fast as it is formed. (*D*) The primary reaction product is MnOOH, which reacts with the acid of the electrolyte according to the equation:

$$2MnOOH + 2H^+ \rightleftarrows MnO_2 + Mn^{++} + 2H_2O \qquad (A)$$

Consider the concentrations of hydrogen and manganese(II) ions and the ionic strength constant,

which was approximately true in the experiments. Let L be the mole fraction of MnOOH in the electrode surface and $(1-L)$ the mole fraction of MnO_2. The rate at which MnOOH is removed from the surface in accordance with Eq. (A) can be expressed by

$$-\frac{dL}{dt} = k_1 L^2 - k_2(1-L) \qquad \text{(I)}$$

in which k_1 and k_2 are the velocity constants of the forward and reverse reactions. These constants include the constant hydrogen and manganese ion concentrations. If the postulates are correct, Eq. (I) should apply to the reaction of excess lower oxide on the electrode surface with acid, on open circuit, that is, to the decay of polarization. At equilibrium, $-dL/dt$ is zero and L becomes L_e, the mole fraction of lower oxide in the surface at equilibrium on open circuit. It will be assumed that L_e is small with acid electrolytes. Then, at equilibrium

$$\frac{k_1}{k_2} = \frac{1-L_e}{L_e^2} \cong \frac{1}{L_e^2} \qquad \text{(II)}$$

Integration of (I) and simplification using (II) and assuming L_e^2 negligible compared with L, gives

$$\ln\frac{L+L_e}{L-L_e} = t\sqrt{(k_2)^2 + 4k_1k_2} + C \qquad \text{(III)}$$

in which C is the integration constant. Taking L_e as negligible when added to or subtracted from unity, (III) can be arranged to give

$$\ln\frac{\frac{1}{L_e}+\frac{1-L}{L}}{\frac{1}{L_e}-\frac{1-L}{L}} = kt + C \qquad \text{(IV)}$$

in which $k = \sqrt{(k_2)^2 + 4k_1k_2}$

It is assumed, in agreement with postulate (A), that the electrode potential E is determined by L and $1-L$ in accordance with the equation

$$E = E^\circ - \frac{RT}{F}\ln\frac{L}{1-L} \qquad \text{(V)}$$

In the steady state of polarization $L = L_p$ and $E = E_p$, and at open-circuit equilibrium $L = L_e$ and $E = E_e$. The increase of potential at any time after opening the circuit is $E - E_p = \Delta E$ and the overpotential is $E_e - E_p = \Delta E_e$. It follows that

$$\Delta E = \frac{RT}{F}\ln\frac{1-L}{L}\cdot\frac{L_p}{1-L_p} \qquad \text{(VI)}$$

$$\Delta E_e = \frac{RT}{F}\ln\frac{1-L_e}{L_e}\cdot\frac{L_p}{1-L_p} \cong \frac{RT}{F}\ln\frac{L_p}{L_e(1-L_p)} \qquad \text{(VII)}$$

Combining (IV), (VI), and (VII)

$$\ln\frac{\exp[(\Delta E_e)F/RT] + \exp[(\Delta E)F/RT]}{\exp[(\Delta E_e)F/RT] - \exp[(\Delta E)F/RT]} = kt + C \qquad \text{(VIII)}$$

Since $\Delta E = 0$ when the circuit is opened at $t = 0$,

$$C = \ln\frac{\exp(\Delta E_e)F/RT + 1}{\exp(\Delta E_e)F/RT - 1} \qquad \text{(IX)}$$

Eqs. (VIII) and (IX) give the change in ΔE with time when the polarized electrode is allowed to stand in the electrolyte on open circuit.

Decay curves were determined as described above. From the initial and final values of the electrode potential ΔE_e was calculated, and k was evaluated from one value of ΔE after 2-5 min. It was then possible to calculate the curves. If the left-hand term of Eq. (VIII) is plotted against the time, a straight line is obtained, with a few of the early points and some of the last ones deviating from the line. Since errors in the later observations are magnified in this plot, it is more satisfactory to plot ΔE against time, as in Fig. 4 and 5. The equation holds well for electrolyte 1, except near the beginning, and less well for electrolyte 5. The considerably smaller acid concentration in electrolyte 5 and slower rate of dissolving of the lower oxide may make possible an appreciable amount of diffusion of lower oxide into the interior of the MnO_2 thus complicating the decay of polarization.

Growth of polarization.—One may now proceed on the assumption that the overpotential is determined by a balance between the formation of lower oxide and its dissolution by the electrolyte. In the

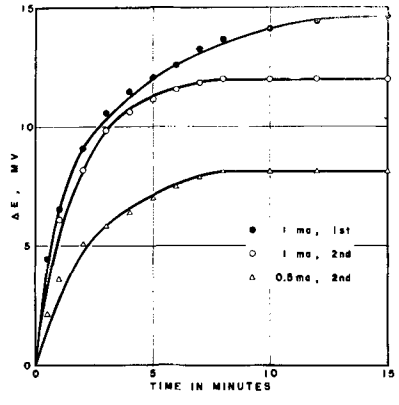

Fig. 4. Decay of polarization, electrolyte 1; the increase in potential after opening the circuit, ΔE, plotted against time. The lines were calculated by means of Eqs. (VIII) and (IX) and the points were taken from the recorded decay curves. The topmost curve followed the first discharge of an electrode, while the other two followed second discharges.

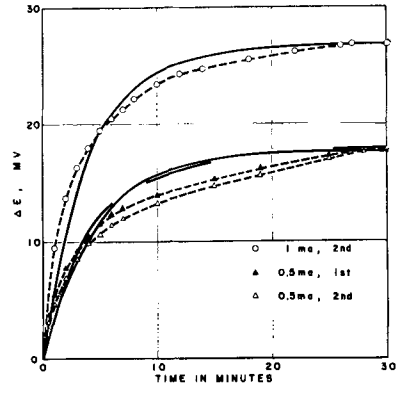

Fig. 5. Decay of polarization, electrolyte 5. The solid curves were calculated by means of Eqs. 8 and 9 and the dashed curves are drawn to pass through the experimental points. First and second refer to first and second discharges of a particular electrode. The discontinuous line is the theoretical curve for the second discharge at 0.5 ma.

early part of a discharge the rate of increase, dL/dt, of the lower oxide concentration on the electrode surface is equal to the difference between the rate of production of lower oxide by the electrochemical reaction, which may be represented by $k' I$, and the rate of dissolution, which is given by Eq. (I).

$$\frac{dL}{dt} = k' I - k_1 L^2 + k_2(1 - L) \qquad (X)$$

Eq. (X) becomes Eq. (I) when $I = 0$. In the steady state of polarization at constant current $dL/dt = 0$, and $L = L_p$. Substituting in (X) and rearranging

$$k' I = k_1 L_p^2 + k_2 L_p - k_2 \qquad (XI)$$

Combining (X) and (XI)

$$\frac{dL}{dt} = k_1\left(L_p - L\right)\left(L_p + L + \frac{k_2}{k_1}\right) \qquad (XII)$$

Integrating (XII),

$$\frac{1}{2L_p + k_2/k_1} \ln \frac{L_p + L + k_2/k_1}{L_p - L} = k_1 t + C \qquad (XIII)$$

In a sufficiently acid solution k_2/k_1 should be small, while L_p should be fairly large. Neglecting k_2/k_1 and noting that $L = L_i$ when $t = 0$

$$\ln \frac{L_p + L}{L_p - L} - \ln \frac{L_p + L_i}{L_p - L_i} = 2k_1 L_p t \qquad (XIX)$$

Combining with (V) and defining E_i as the electrode potential at $t = 0$, $\Delta E_i = E_i - E$, and $\Delta E_p = E_i - E_p$

$$\ln \frac{2L_i(1 - L_i) + e^{-x} + e^{-a}}{e^{-x} - e^{-a}} = 2k_1 L_p t + \ln \frac{L_p + L_i}{L_p - L_i} \qquad (XX)$$

in which $x = (\Delta E_i)F/RT$ and $a = (\Delta E_p)F/RT$. If $2L_i/(1 - L_i)$ can be neglected, which will be shown later to be justified when ΔE_i is small,

$$\frac{e^{-x} + e^{-a}}{e^{-x} - e^{-a}} = 2k_1 L_p t + \ln \frac{L_p + L_i}{L_p - L_i} \qquad (XXI)$$

The left-hand term can be changed to the form of the corresponding term of Eq. (VIII), but the meanings of x and a are slightly different.

Eq. (XXI) is in approximate agreement with discharge curves that do not pass through the pronounced minimum of a first discharge, which is illustrated in Fig. 1. It does not predict the small minima found by the more accurate measurements in the later discharges. However, a simple empirical correction can be applied for the unknown process causing the minimum, and this leads to excellent agreement of calculated and observed values. A calculated curve and some experimental points taken from the recorded discharge curves of two electrodes are shown in Fig. 6.

The first step in the empirical correction was to extrapolate the portion of the experimental curve at the right of the minimum back to zero time, giving a curve like that ending at 16.5 mv in Fig. 6. This intercept was arbitrarily assumed to be ΔE_p, the value of ΔE_i at the steady state of polarization

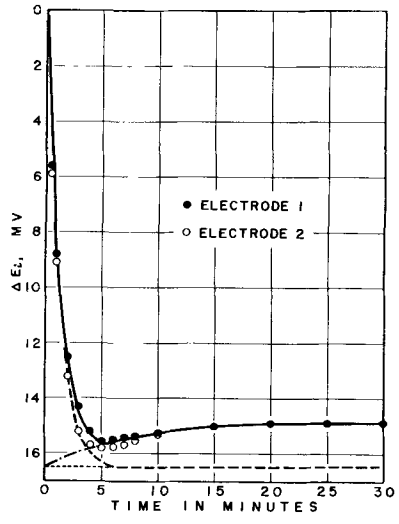

Fig. 6. Growth of polarization. The dashed curve is the theoretical curve for a discharge with no minimum. The solid curve is the theoretical curve corrected empirically to include the minimum.

if the process leading to the minimum had not taken place. The process leading to the minimum is assumed to start at $t = 0$ and its effect on ΔE_i at any time to be given by the difference between 16.5 mv and the appropriate point on either the extrapolated or the real portion of the discharge curve. Addition of these differences to the corresponding averages of the two sets of experimental values gives the dashed curve, which is the hypothetical discharge curve uncomplicated by the second process. This should be in accord with Eq. (XXI). The graphical method gave only a first aproximation to the correction shown in Fig. 6. From the first approximation the left-hand term in Eq. (XXI) was calculated and plotted against the time. This should give a straight line, but the plot was very sensitive to small differences in ΔE_p and only one value gave a satisfactory line, 16.5 mv in Fig. 6. From this value and the slope and intercept of the straight line the final dashed curve was calculated. When from this final curve the proper differences were subtracted the solid curve was obtained, agreeing with both sets of experimental points well within a millivolt for the most part, or as well as the two experimental curves agree.

This shows that it is possible to explain the discharge curves with the smaller minima as a combination of the curve predicted by the above theory and another process. This other process might be a change of physical form of the lower oxide (10).

The same treatment was applied to some discharges in electrolyte 5. Here, the corrections were much larger than for electrolyte 1; in one case the estimated theoretical ΔE_p was 45 mv while the actual steady-state value was 25 mv. However, the corrected curve was in good agreement with the observed values, better than would be expected on the basis of the decay of polarization in electrolyte 5. The approximations in the derivation of Eq. (XXI) are somewhat questionable here, and there is the possible complication of the inward diffusion of lower oxide. The empirical correction seems to correct for both of these.

Overpotential and current density.—At the steady state of polarization $dL/dt = 0$ in Eq. (X) and

$$I = K_1 L_p^2 - K_2(1 - L_p) \qquad \text{(XXII)}$$

in which K_1 and K_2 are equal to $k_1 k'$ and $k_2 k'$, respectively. Solving Eq. (VII) for L_p

$$L_p = \frac{1}{1 + [(1 - L_e)/L_e]e^{-y}} \qquad \text{(XXIII)}$$

in which $y = (\Delta E_e)F/RT$, and combining (XXII) and (XXIII)

$$I = \frac{K_1}{\{1 + [(1 - L_e)/L_e]e^{-y}\}^2} - \frac{K_2[(1 - L_e)/L_e]e^{-y}}{1 + [(1 - L_e)/L_e]e^{-y}} \qquad \text{(XXIV)}$$

Constant K_1 can be eliminated, since at open-circuit equilibrium

$$\frac{k_1}{k_2} = \frac{K_1}{K_2} = \frac{1 - L_e}{L_e^2} \qquad \text{(XXV)}$$

Combining (XXIV) and (XXV) and simplifying gives

$$I = \frac{K_2(1 - L_e)}{[L_e + (1 - L_e)\,e^{-y}]^2} - \frac{K_2(1 - L_e)\,e^{-y}}{L_e + (1 - L_e)\,e^{-y}} \qquad \text{(XXVI)}$$

When the acid concentration is large and ΔE_e is small, $L_e/(1 - L_e) << e^{-y}$ and (XXVI) can be simplified to

$$I = \frac{K_2}{1 - L_e} \exp\left[\frac{2(\Delta E_e)F}{RT}\right] - K_2 \qquad \text{(XXVII)}$$

The applicability of Eq. (XXVII) is shown in Fig. 7 and 8, in which exp $[2(\Delta E_e)F/RT]$ is plotted against I. In Fig. 8 the lines are drawn to fit the

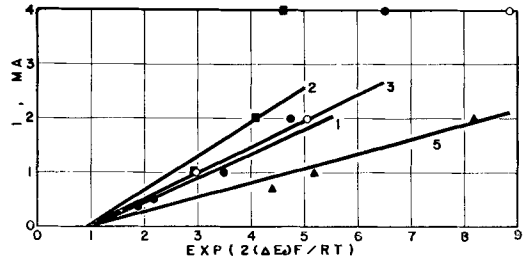

Fig. 7. Test of Eq. (XXVII) for the relation of overpotential (ΔE_e) and current density; exp $[2(\Delta E_e)F/RT]$ plotted against the current/8 cm² of electrode surface. The lines were drawn after finding the best values for the slopes and intercepts by use of Eq. (XXVI).

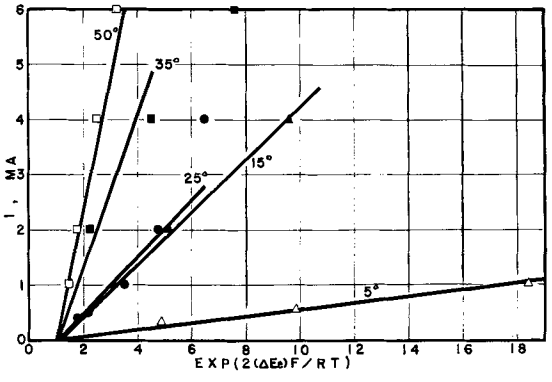

Fig. 8. Application of Eq. (XXVII) to overpotentials at various temperatures (°C).

Table V. Values of K_2 and $1 - L_e$ in Eq. (XXVI) at 25°C

Electrolyte No.	1	2	3	5
K_2	0.46	0.78	0.46	0.25
$1\text{-}L_e$	1.00	0.99	0.97	0.95

points, with most weight given to small values of ΔE_e. In a preliminary drawing of Fig. 7 values of K_2 and $(1 - L_e)$ were determined from the slopes and intercepts. Using the values so obtained as first approximations it was found by repeated trial in Eq. (XXVI) which values gave the best agreement with experiment. The values adopted are given in Table V and were used in drawing the lines in Fig. 7. The values of ΔE_e calculated by Eq. (XXVI) are given in the last column of Table II.

Calculated and experimental values of ΔE_e agree quite well except at 4 and 8 ma for electrolyte 1. There are smaller deviations in the same direction for the other electrolytes at these currents, or at 2 and 4 ma, while the agreement at the smallest and largest currents is generally better. It is possible that the approximations in the theory are responsible.

It is worthy of note that electrolyte 1 seems to be out of place in Fig. 7 and its value for K_2 does not fit in with the series of values for the other electrolytes. It will be recalled that electrolyte 1 also did not agree well with the others in the relation of overpotential to acidity.

Variation with temperature.—In Fig. 8 Eq. (XXVII) is applied to the data for the overpotential in electrolyte 1 at the temperatures 5°, 15°, 25°, 35°, and 50°C. The values of K_2 found graphically are 0.064, 0.41, 0.46, 1.25, and 2.60. When log K_2 is plotted against $1/T$ in accordance with the Arrhenius equation a straight line is obtained, with the 15° value deviating more than expected. The value of the Arrhenius constant derived from the slope of the line is 14.6 kcal. This is in the range for chemical reactions rather than diffusion processes.

For electrolyte 5 the values of K_2 found from a plot similar to Fig. 8 were 0.17, 0.25, 0.46, and 0.82 for temperatures 15°, 25°, 35°, and 50°C. From these the value 9.5 kcal was obtained for the Arrhenius constant.

Acknowledgment

The authors are indebted to Dr. Stanley Hills for some preliminary experiments and two of the values in Table IV. This work was supported in part by Contract Nonr-1016 (00) with the Office of Naval Research and in part by a research grant from Duke University.

Manuscript received August 22, 1956. This paper was prepared for delivery before the Cleveland Meeting, Sept. 29 to Oct. 4, 1956.

Any discussion of this paper will appear in a Discussion Section to be published in the June 1958 JOURNAL.

REFERENCES

1. A. M. Chreitzberg, Jr., and W. C. Vosburgh, *This Journal*, **104**, 1 (1957).
2. D. T. Ferrell, Jr., and W. C. Vosburgh, *This Journal*, **98**, 334 (1951).

3. A. Kozawa and K. Sasaki, *J. Electrochem. Soc., Japan*, **22**, 569 (1954).
4. A. M. Chreitzberg, Jr., D. R. Allenson, and W. C. Vosburgh, *This Journal*, **102**, 557 (1955).
5. J. J. Coleman, *Trans. Electrochem. Soc.*, **90**, 545 (1946).
6. N. C. Cahoon, *This Journal*, **99**, 343 (1952).
7. S. Hills, Ph.D. Thesis, Duke University (1955).
8. W. C. Vosburgh, R. S. Johnson, John S. Reiser, and D. R. Allenson, *This Journal*, **102**, 151 (1955).
9. W. C. Vosburgh, D. R. Allenson, and Stanley Hills, *ibid.*, **103**, 91 (1956).
10. W. H. Beck, P. Jones, and W. F. K. Wynne-Jones, *Trans. Faraday Soc.*, **50**, 1249 (1954).
11. H. Eyring, S. Glasstone, and K. J. Laidler, *J. Chem. Phys.*, **7**, 1053 (1939).

Anodic Corrosion and Hydrogen and Oxygen Overvoltage on Lead and Lead Antimony Alloys

P. Rüetschi and B. D. Cahan

Research Department, The Electric Storage Battery Company, Philadelphia, Pennsylvania

ABSTRACT

Constant current techniques permit rapid evaluation of the anodic corrosion of lead and lead antimony alloys. The amount of PbO_2 formed during anodization can be evaluated by measuring the length of the potential plateau of the $PbO_2/PbSO_4$ couple produced during discharge. The rate of self-discharge and the degree of utilization of the lead dioxide must be taken into account in order to obtain correct corrosion figures. Methods for evaluating the self-discharge and degree of utilization of the PbO_2 are described.

X-ray diffraction patterns were taken of the anodized Pb and Pb-Sb alloy samples. Patterns of $PbSO_4$, Pb, α-PbO_2, and β-PbO_2 were observed, but there was no indication that PbO was formed on any sample. The principal anodization product was α-PbO_2, a new crystalline modification of PbO_2. Hydrogen and oxygen overvoltages were measured on various alloys of the Pb-Sb system, using interrupter techniques. Overvoltage and anodic corrosion of single crystal faces of Pb were also investigated.

The anodic corrosion of Pb and Pb-Sb alloys is of fundamental importance to the lead-acid battery industry. Positive grid corrosion is one of the principal reasons why lead-acid batteries wear out in service. The standard method in the battery industry for evaluating positive grid corrosion is the SAE overcharge test. This is essentially a constant current experiment performed in the region of oxygen evolution.

In this study constant current techniques were used to study the anodic behavior of Pb and Pb-Sb alloys under precisely defined conditions.

Lander (1,2) and Wolf and Bonilla (3) investigated corrosion by constant potential techniques. The former finds tetragonal β-PbO_2 is formed by the reaction of H_2O and Pb but this PbO_2 is unstable on electrochemical grounds and goes to PbO and $PbSO_4$.

Formation of PbO as a product of anodic corrosion in H_2SO_4 has also been reported by Burbank (4). These findings are in contrast with the views of Wynne-Jones and co-workers (5) who find that PbO_2 and $PbSO_4$ are the only possible reaction products. Kabanov, *et.al.* (6) determined the rate of anodic corrosion by measuring the capacity of the PbO_2 layer formed. A similar technique was used in this study. It has been shown that the hydrogen overvoltage of metals can be correlated to the strength of the intermetallic bond (7), and, therefore, to anodic corrosion. According to this theory the hydrogen overvoltage decreases with increasing bond strength. The oxygen overvoltage also depends in a similar way on the characteristics of the electrode material so that it decreases with increasing strength of the bond M-O between the metal and oxygen (8). In the present investigation on anodic corrosion, hydrogen and oxygen overvoltage studies were therefore included.

Experimental

Pb alloys used for the experiments were cast into strips using identical casting conditions for all alloys. The strips measured 2 cm x 2 cm x 2 mm with an 8 cm x 1 cm x 2 mm tab for handling and electrical connection. One flat surface of the strips was cut with a highly polished carbon steel microtome blade. To minimize cold-working and surface oxidation effects, five additional cuts of 2 μ depth were taken less than 5 min prior to insertion into the experimental cell. Measurements showed the final depth of roughness to be smaller than 1/10μ. Table I lists the alloys used and their analyses.

Table I. Analyses of alloys used (%)

Alloy #	Sb	As	Sn	Cu	Bi	Ag	Fe	Ni
1	0.0001	—	0.0001	0.0001	0.0005	0.0001	—	0.0001
2	1.08	—	0.0001	0.003	0.05	0.003	0.0005	0.0003
3	2.16	0.008	0.0001	0.003	0.01	0.004	0.0005	0.0003
4	3.48	0.03	0.0001	0.003	0.018	0.005	0.0005	0.0003
5	5.76	0.025	0.0002	0.01	0.015	0.004	0.0005	0.0003
6	7.26	0.015	0.0001	0.008	0.008	0.005	0.0005	0.0008
7	8.76	0.015	0.0001	0.01	0.003	0.004	0.0005	0.001
8	10.98	0.015	0.0001	0.005	0.008	0.002	0.0005	0.001

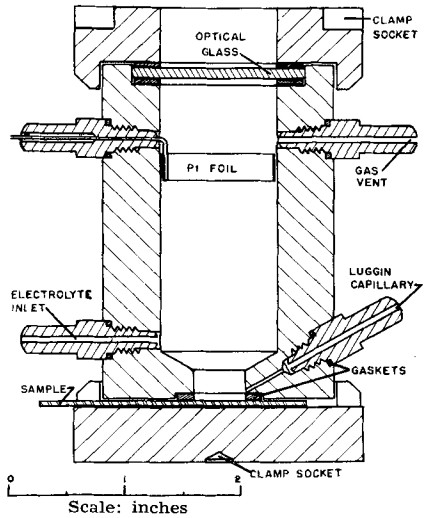

Fig. 1. Electrolytic cell

Large single crystals of Pb were prepared using differential cooling (9) and cut with the (100), (110), and (111) faces parallel to the surface. Orientations of the planes were determined by etch-pit analysis (10) and checked with x-ray back reflection. The planes were oriented with an accuracy of 1-2%.

Fig. 1 is a sectional view of the special electrolytic cell designed for rapid mounting of specimens. The cell exposes a defined electrode area of 0.95 cm^2 to the electrolyte. The Luggin capillary intersects the cylindrical anode compartment at the specimen surface and thus causes a minimal distortion of the uniform electric field in the electrolyte.

Fig. 2 is the schematic diagram of the circuit used to provide interrupted current studies of the *IR* drop during overvoltage measurements. A standard power supply (V_1 and V_2) supplied + 325 v D.C. and +200 v D.C., respectively. V_3 is a thyratron oscillator adjustable by means of R_{10} and C_{6-12} to a frequency range of 5 cps to 50 kc. The resultant sawtooth wave is differentiated by C_{18} and R_{15}, producing a sharp negative pulse which triggers the monostable multivibrator V_{4a} and V_{4b}. A positive and a negative pulse are produced across the coil L_1 in the plate circuit of V_{4b}. These pulses are amplified and inverted by V_{5a} and fed to the cathode follower V_{5b}. The first of the two pulses triggers the sweep of an oscilloscope, and the second is fed to the pulse shaper V_{6a}. This produces a sharp negative pulse which passes through the gate diode V_{7a} and triggers the output multivibrator V_{6b}, V_8, and V_9. This multivibrator is arranged so that V_8 is normally conducting. The cell to be investigated is placed in the plate circuit of V_8. The screen voltage of the output tubes is held constant by the VR tubes V_{10} and V_{11}. In this way the output current is held at a constant value, except when the multivibrator is triggered. The diode V_{12} serves to couple the cathodes of the multivibrator, and increases the cutoff speed by rapidly turning V_{6b} on and off at a given cathode voltage of V_8. Constant or interrupted currents variable from 15 to 100 ma were produced with the apparatus just described, with an accuracy of ±0.5%.

Currents below 15 ma were produced by the dual control heptode V_{15}, whose screen grids are held at

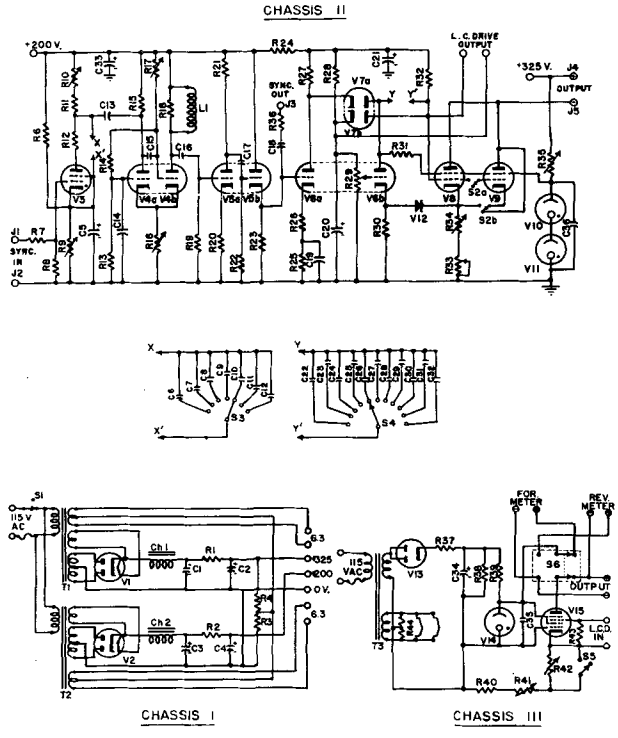

Fig. 2. Schematic diagram of the electronic interrupter. Power supply (Chassis I), oscillator and interrupter (Chassis II), low current output (Chassis III).

R1, 2, 12 — 100 2w
R3 — 39k ½w
R4 — .22M ½w
R6 — .18M ½w
R7) — Determined by ampli-
R8) — tude of sync pulses
R9, 41 — 5K pot 2w
R10 — 2M pot 2w
R11, 25, 30 — .27M ½w
R13 — 27K ½w
R14, 36, 38 — .1M ½w
R15 — 4.7K 1w
R16 — 10K pot 2w
R17 — .25M pot 2w
R18 — 470 1w
R19, 22 — 1.2M ½w
R20, 24 — 1K 1w
R21 — 3900 1w
R23 — 5600 1w
R26, 40 — 100 ½w
R27, 31 — 4.7K ½w
R28, 32 — .39M ½w
R29 — 50K pot 2w
R33 — 1K pot 10w
R34 — 100 10w adj.
R35 — 5K pot 4w
R37 — 100 2w
R39 — 390 2w
R42 — 5M pot ½w
R43 — .47M ½w
R44 — 100 pot ½w
C1, 2, 3, 4-40-40 mfd 475V elec
C5 — 50 mfd 25V
C6 — .25 mfd 400 V
C7 — .15 mfd 400 V
C8, 25 — .05 mfd 400 V
C9 — .015 mfd ceramic
C10 — .005 mfd ceramic
C11, 28 — .002 mfd ceramic
C12 — .008 mfd ceramic
C13 — 50 mfd ceramic
C14, 18, 19, 26 — .01 mfd ceramic
C15 — 200 mmfd ceramic
C16, 17 — .001 mfd ceramic
C20 — 4 mfd 150V elec
C21 — 10 mfd 350 V
C22 — 1 mfd 200 V
C23 — .5 mfd 200 V
C24 — .1 mfd 200 V
C27 — .006 mfd ceramic
C29 — 680 mmfd ceramic
C30 — 300 mmfd ceramic
C31 — 82 mmfd ceramic
C32 — 10 mmfd ceramic
C33 — 20 mfd 300 V elec
C34 — 40 mfd 350 V elec
C35, 36 — .02 mfd ceramic
S1, 5 — SPST Toggle Switch
S2 — DPDT Toggle Switch
S3 — 7 pos. switch
S4 — 11 pos. switch
S6 — DPDT Switch with off position
Ch 1, 2 — 4Hy @ 120 mA choke
T_1 — 750CT @ 150mA, 5V
@ 3A 6.3CT @ 4.5A
T_2 — 500CT @ 70mA, 5V
@ 3A, 6.3CT @ 4.5A
T_3 — 117 @ 70 mA, 6.3 @ 2A
L_1 — 2mH coil
V1, 2 — 5V4G
V3 — 2D21
V4, 6 — GL6463
V5 — 12AU7
V7 — 6AL5
V8, 9 — 6CM6
V10, 11, 14 — OC3
V12 — CK742 Hi Current Diode
V13 — 6X4
V15 — 5915A or 6CB6

105 v by an OC3 voltage regulator tube. The currents were constant to ±0.5%. The tube V_{15} acts as a constant current device until a negative pulse is impressed on its second control grid. This shuts off the tube until the pulse is removed. The driving pulse is produced across the diode V_{7b}. Off times as short as 0.5 μ sec with cutoff times of 0.2 μ sec were produced by this apparatus.

All experiments were made in a constant temperature bath at 30° ±0.02°C. The H_2SO_4 used in the cell had a specific gravity of 1.225 (at 20°C corresponding to 308g H_2SO_4/1000g of solution) prepared from C. P. H_2SO_4 and triple distilled water with a

specific resistance greater than $2x10^6$ ohm-cm. Potentials were measured with either a hydrogen electrode or a mercury-mercurous sulfate electrode calibrated at 0.607 v to hydrogen. Potentials were recorded by a #42200-F Model S Micromax recorder operated together with a high input impedance (10^{14} ohm) electrometer amplifier circuit from a L & N Electrochemograph Unit No. 7673. A voltage divider of 60 megohms impedance was built to change the range of the instrument. A bias-adjuster consisting of a 100,000 ohm ten-turn precision Helipot and a constant voltage source was placed in series with the voltage divider. Transient and high speed phenomena were recorded by a Minneapolis-Honeywell ½ second recorder, Model Y153X(19)V-X-156, operated in conjunction with a General Radio Electrometer Voltmeter amplifier type 1230-A.

X-ray diffraction patterns were taken with a GE XRD-3 Geiger Diffractometer. Anodized Pb samples were removed from the electrolytic cell, washed, and dried with acetone within 3 sec of the interruption of current. Readable patterns could be obtained within 5 min of removal from the cell, although no change was observed after a 2 week stand in the dry state.

Samples of α-PbO_2 and β-PbO_2 were prepared for x-ray analysis and potential measurements by several methods. The α-PbO_2 was prepared in the following ways:

1. Electrolysis on Pt foil, in a concentrated solution of NaOH, saturated with $Pb(OH)_2$, at a current density of 1-10 ma/cm^2. The adhering film sample was ground, washed with hot ammonium acetate solution and with conductivity water. Further purification was obtained by treating the washed product with 2% HNO_3 and H_2O_2 until violent reaction ceased. The material was then washed with water, hot ammonium acetate, and again with water.

2. Electrolysis of a strongly ammoniacal solution of concentrated ammonium acetate (50%) saturated with lead acetate with current densities of 0.1-10 ma/cm^2.

3. Precipitation at 15°C from an ammoniacal solution of lead acetate (200-300 g/l) in 50% ammonium acetate by ammonium persulfate solution (50 g/l).

4. Conversion from β-PbO_2 at a pressure of 125,000 psi.

β-PbO_2 was produced by the following methods:

1. Electrolysis of a saturated solution of lead nitrate containing excess HNO_3 at a current density of 0.1-10 ma/cm^2.

2. Baker C.P. PbO_2, washed with hot saturated ammonium acetate and water.

Samples of α- or β-PbO_2 used for potential measurements were further treated by digestion with 1.225 sp gr H_2SO_4 on a steam bath for 1 week, according to the procedure described by Hamer (11).

Current for anodization runs was obtained from the interrupter, with the oscillator disconnected. Samples were anodized for 1, 2, 3, 4, and 20 hr with a current density of 3 ma/cm^2. The formed PbO_2 layers were then discharged with currents of 100 μa, 500μa, or 2.5 ma, or left on open circuit where they underwent self-discharge.

Samples were removed from the cell immediately after formation and also after discharge to determine the quantity of PbO_2 present. The PbO_2 layers were treated with KI in sodium acetate containing acetic acid. The liberated iodine was titrated with standardized sodium thiosulfate, using semi-micro techniques.

Results

In this paper all current values are given for a specimen area of 0.95 cm^2. Alloy samples were anodized with a current of 3 ma for various time periods and were then discharged with varying currents. Before the anodization period was started, the sample was usually cathodized for 30-60 min with a current of 3 ma. During this cathodization period hydrogen overvoltage measurements were taken.

Fig. 3 shows the initial potential transients after reversing the current for a specimen of pure Pb (alloy No. 1). The plateau at the $Pb/PbSO_4$ potential has a length of about 8 sec. There is also a very slight break visible slightly above the theoretical potential of the Pb/PbO_2 couple as indicated by the arrow in Fig. 3 The cell reaction for this couple is

$$PbO_2 + 4H^+ + 4e \rightleftarrows 2H_2O + Pb \qquad (1)$$

corresponding to a reversible potential of +0.665 v. Therefore, it is theoretically possible that PbO_2 can be formed at potentials far below the $PbSO_4/PbO_2$ potential. The latter has a value of +1.685 v (11, 12). It will be shown later that the α-crystal modification of PbO_2 is probably formed by reaction (I), whereas β-PbO_2 is formed by oxidation of $PbSO_4$. The overshoot of the potential transient above the potential for oxygen evolution is approximately 360 mv. Since a current of 3 ma was used the resistance of the passivating sulfate layer was estimated to be 120 ohms. From the length of the $Pb/PbSO_4$ plateau (8 sec) one can calculate that approximately 1.25×10^{-7} moles $PbSO_4$ were formed, corresponding to a thickness of 640Å if a density of 6.2 g/cm^3 is assumed for the sulfate layer. The "mean specific re-

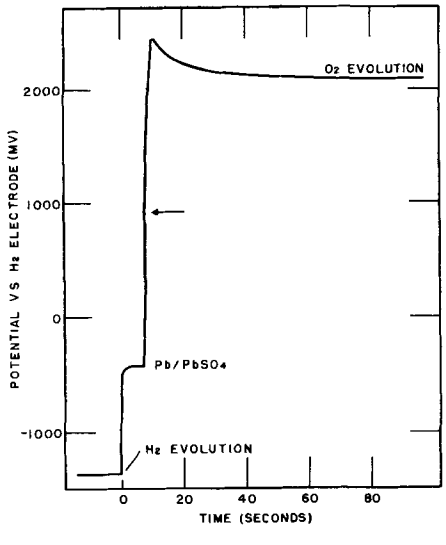

Fig. 3. Initial voltage transients for a specimen of pure Pb (alloy No. 1) anodized at 3 ma.

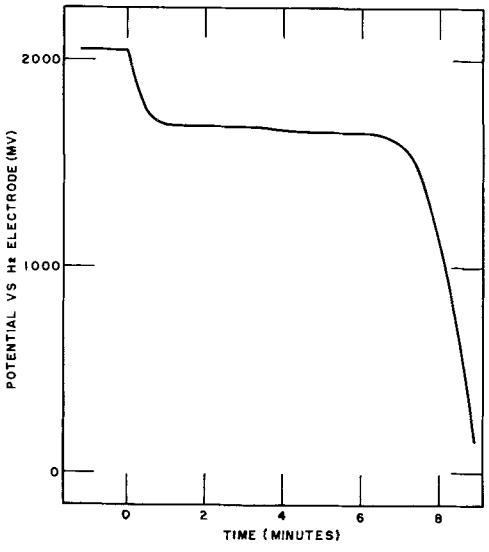

Fig. 4. Discharge curve of a sample with 1% Sb (alloy No. 2) after 20 hr of anodization at 3 ma; discharge current 500 ma.

sistance" of the sulfate was calculated to be 10^9 ohm-cm and the electric field in the sulfate layer at the breakdown point 5 x 10^4 v/cm. These very approximate calculations are valid only for a uniform surface. The potential of the positive electrode, after the initial peak, passed through a slight minimum and maximum and then decreased slowly with time. This behavior has previously been described by Wynne-Jones and co-workers (13). After anodization for 1, 2, 3, 4, or 20 hr, the extent of anodic corrosion was determined by discharging the PbO_2 formed on the electrode.

A typical discharge curve is shown in Fig. 4. This curve was obtained after anodization of a sample of 1% Sb (alloy No. 2) for 20 hr with a current of 3 ma in H_2SO_4 sp gr 1.225 and at a temperature of 30°C. The discharge current was 500 μa. A small drop in potential of 20 to 30 mv is visible approximately in the middle of the discharge curve. This small change in potential was observed in all discharge runs. Its position varied with the Sb concentration in the alloy. For pure Pb the change occurred near the end of the total discharge curve, whereas for alloys with Sb concentrations above 3% it was near the beginning of the curve. While the two plateaus might be explained possibly as a passivation phenomenon, it is more probable that they correspond to the two crystalline modifications α and β-PbO_2.

The formation and breakdown of the passivating sulfate layer produced initially upon anodization using a constant current was shown in Fig. 3. A similar study was made using an interrupted current of 3 ma and a repetition rate of about 1000 times/sec, whereby the length of current interruption was about 1/10 of the length of the current pulse. These current pulses were directed initially in the cathodic direction during which time the build up and decay of hydrogen overvoltage were studied. Voltage transients were observed on the screen of an oscilloscope and the ohmic component of the overvoltage was determined. Additional work

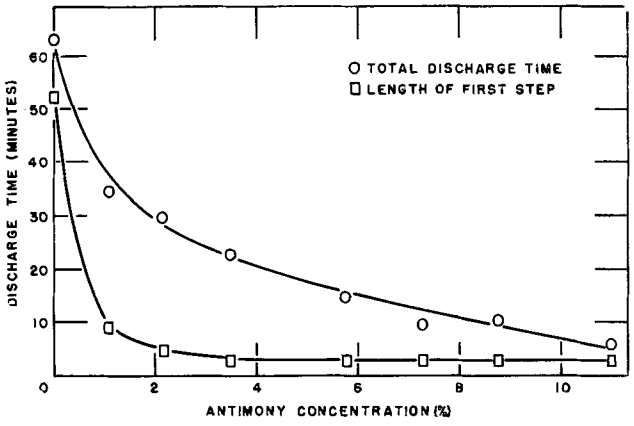

Fig. 5. Total discharge time and the length of the first step after 20 hr of anodization at 3 ma as a function of the antimony concentration; discharge current 100 μ a.

is planned using this new technique for the study of passivation phenomena.

A large number of discharge runs similar to those in Fig. 4 were made; anodization was for 20 hr at 3 ma, while the discharge current was 100 μa. Results are shown in Fig. 5 to 8. Fig. 5 shows the length of the total discharge step (sum of the two plateaus) after anodization of samples containing various Sb concentrations. The length of the first plateau is also given, and this length is constant for all alloys with an Sb concentration higher than 3%. The value of 2.94% represents the limit of solid solubility of Sb in Pb at 257°C (14).

In Fig. 6 the length of the total discharge step after anodization for 4 hr at 3 ma has been plotted. The curve of the squares was obtained by measuring the potential decay on open circuit (self-discharge). The curve of the circles represents the length of the discharge steps applying discharge current of 100 μa. For any Sb concentration the length of the self-discharge step is of the same order of magnitude as the length of the 100 μa discharge step. Therefore, the total length of the discharge step is a fair measure of the extent of anodic corrosion only if the rate of self-discharge is properly taken into account.

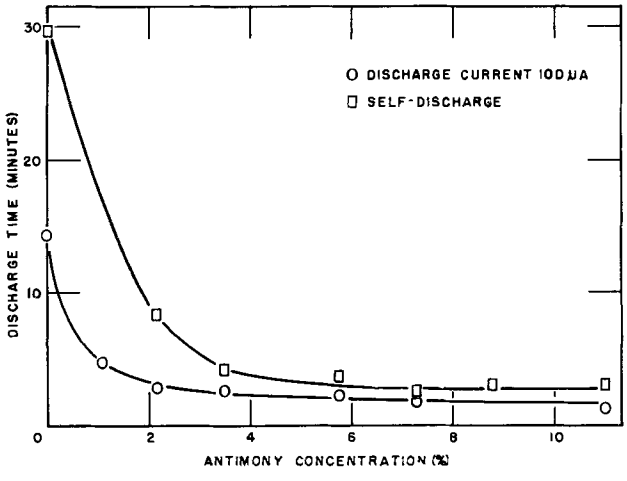

Fig. 6. Total discharge time and self-discharge time after 4 hr of anodization at 3 ma as a function of Sb concentration.

In order to determine the loss of capacity (amp sec) due to self-discharge of the PbO_2 layers the following experiments were made. A series of pure Pb specimens (alloy No. 1) which had previously been anodized with a current of 3 ma for a period of 20 hr were discharged at various rates. Fig. 7 shows a plot of the product $i \times t$ where i is the discharge current in amperes and t is the discharge time in seconds, against the discharge time in seconds. Even if the same amount of the PbO_2 remained in the corrosion layer at the end of the potential plateau, i.e. independent of discharge current or discharge time, this plot should not yield a horizontal straight line because the layer suffers different amounts of self-discharge for different discharge times. It can be seen that the available capacity thus increases with decreasing discharge time. By microtitration, it was found that the amount of PbO_2 left in the layer at the end of discharge was, indeed, practically independent of the discharge rate. A titration of the absolute amount of PbO_2 in a freshly formed oxide layer was inconclusive because self-discharge effects interfered during dissolution of the PbO_2 in the solution to be titrated. A much smaller error might be anticipated when discharged layers were titrated.

One can now assume that an extrapolation of the curve in Fig. 7 to zero discharge time yields the maximum obtainable capacity because self-discharge is now eliminated. The total amount of corrosion is obtained by adding to this limiting capacity value, the capacities corresponding to the amount of PbO_2 left in the layers as found by microtitration. Capacity values obtained by this procedure are marked with circles in Fig. 7 and correspond to the total amount of PbO_2 formed on the sample surface during the 20-hr anodization. This amount should, of course, be the same for the different discharge runs. An investigation as illustrated for pure Pb in Fig. 7 would essentially be necessary for each alloy studied in order to determine exactly the total amount of corrosion. This is anticipated for future work.

Fig. 8 shows the discharge time after various periods of anodization for pure Pb samples. The discharge current was 100 μa. Values for self-discharge

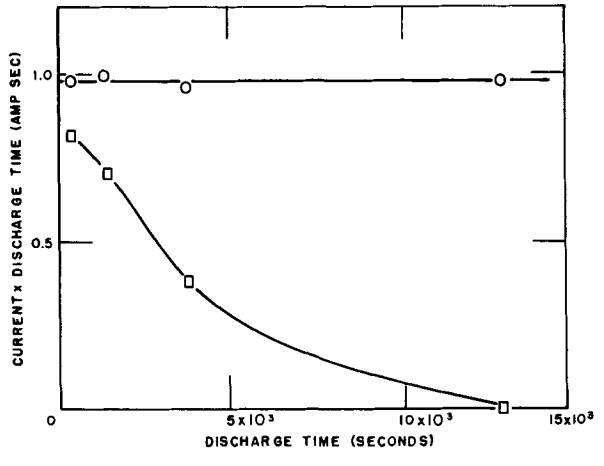

Fig. 7. Evaluation of the total amount of corrosion for a specimen of pure Pb (alloy No. 1). The available capacity as a function of discharge is shown by the squares; the circles indicate the amount of total corrosion.

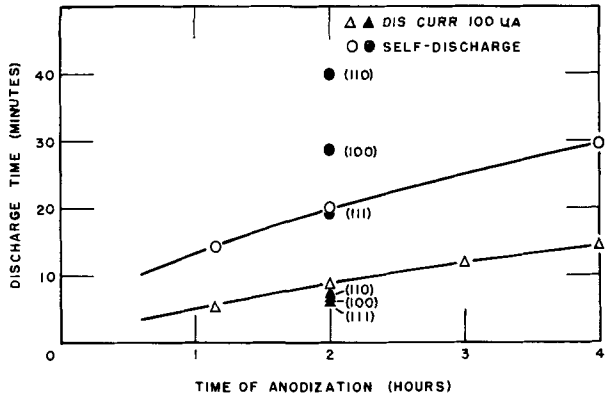

Fig. 8. Total discharge time and time for self-discharge as a function of time of anodization at 3 ma. Solid symbols show data obtained on single crystal faces.

are given. Data on single crystal faces (solid symbols) are also shown on Fig. 8. The extent of self-discharge varied significantly for different crystal faces, whereas only slight differences were observed with the 100 μa discharge.

It must be kept in mind that the actual corrosion values obtained by the procedure outlined above and illustrated in Fig. 7 give the amount of PbO_2 formed. The depth of attack can be calculated from these values using the specific gravities of the alloys. Specific gravities and conversion factors are given in Table II.

X-ray diffraction patterns were taken of a series of Pb-Sb alloys which had been anodized for varying time periods and of specimens which had been discharged to the end of the first potential plateau. The only patterns observable on any sample were those of $PbSO_4$, Pb, α-PbO_2, and β-PbO_2. The α-PbO_2 pattern was usually dominant. Also, after discharge of the samples to the end of the first potential plateau, the α-PbO_2 pattern was still quite strong, even though partially obscured by the $PbSO_4$ pattern. Fig. 9 shows a typical pattern of a sample (alloy No. 8) which had been anodized for 18 hr with a current of 3 ma in 1.225 sp gr H_2SO_4 at 30°C. Also shown are the pattern of electrolytically produced (*see* Experimental Procedure 1) α-PbO_2, Baker's C. P. β-PbO_2, and, for purposes of comparison, tetragonal PbO produced by the oxidation of lead ground in a ball mill.

Hydrogen overvoltage measurements were not very reproducible, due to apparent changes in the surface of the alloys. After polarization with currents larger than 5-10 ma/cm², the overvoltage usually decreased with time because the surface was

Table II. Specific gravities of Pb-Sb alloys

% Sb	Sp gr (g/cm³)	cm³ / g Pb	cm³ / g Pb in % of pure Pb
0	11.35	0.0882	100
4	11.02	0.0945	107.1
6	10.89	0.0978	110.8
8	10.75	0.1011	114.7
9	10.67	0.1031	116.9
11	10.52	0.1068	121.0
12	10.44	0.1088	123.3

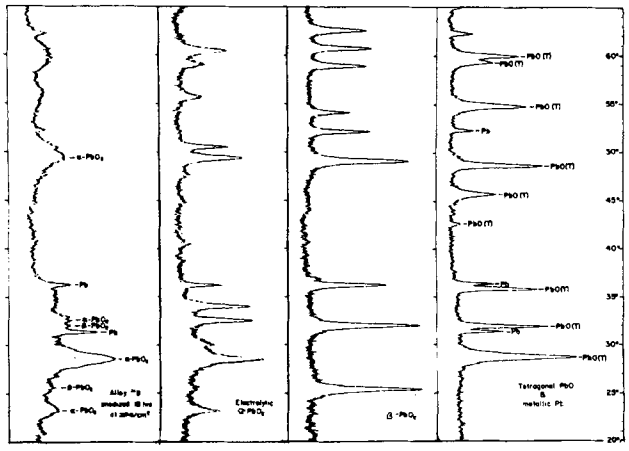

Fig. 9. X-ray diffraction patterns of PbO + Pb, β-PbO_2, α-PbO_2 and of alloy No. 8 after anodization with 3 ma for a period of 18 hr. The patterns were taken with G.E. XRD-3 diffraction unit.

increased by cathodic corrosion (15, 16). There was probably a slight simultaneous production of stibine. At current densities below 0.5-1 ma/cm^2 the hydrogen overvoltage decreased due to adsorption of anions (17). The Tafel-slopes were nearly the same (0.120) for all the alloys, in the current density range between 1 and 10 ma/cm^2. In order to compare the various surfaces, the overvoltage was measured as soon as possible after immersion of the sample, starting with currents of 3 ma/cm^2 and increasing to 10 ma/cm^2. Experiments with the interrupter showed that the ohmic resistance contributed less than 2 mv (at a current of 3 ma) to the total overvoltage in the cell described in Fig. 1. Experiments with single crystal faces of pure Pb showed that the differences in hydrogen overvoltage between the three planes investigated, namely (100), (111), and (110), were very small. Slopes of the Tafel lines were close to 0.120 on all three faces. The hydrogen overvoltage on the (111) face was only about 20 mv higher than on the (100) face at a current of 1 ma/cm^2. The hydrogen overvoltage on the (110) plane showed an unstable behavior and fluctuated periodically with time between the values for the (111) and (100) plane.

Hydrogen overvoltage decreased with increasing Sb concentration. However, this decrease was smaller than expected. It is conceivable that Sb in solid solution does not lower the hydrogen overvoltage as effectively as free Sb. Some results are given in Table III where i_o denotes the exchange current in amperes, α the transfer coefficient, and b the slope of the Tafel line, together with literature values [*see* also (18-22)] for pure Pb and pure Sb taken from the recent review by Bockris (23).

Table III. Hydrogen overvoltage on Pb-Sb alloys

Alloy	% Sb	i_0	α	b
1	0	1.8×10^{-13}	0.50	0.120
2	1.08	7.5×10^{-13}	0.46	0.130
3	2.16	1.4×10^{-12}	0.45	0.133
5	5.76	4.5×10^{-12}	0.44	0.136
Pb(23)	0	2×10^{-13}	0.48	
Sb(23)	100	10^{-9}	0.58	

Table IV. Oxygen overvoltage on Pb-Sb alloys

Alloy	% Sb	i_0	α	b
1	0	1.4×10^{-10}	0.55	0.110
2	1.08	8.9×10^{-11}	0.55	0.110
3	2.16	2.1×10^{-10}	0.55	0.110
5	5.76	4.4×10^{-10}	0.55	0.110

The oxygen overvoltage decreased with time. The decrease amounted usually to about 60 mv in 20 hr. This decrease has been previously described (13), and is due possibly to increased surface area. One would also expect different oxygen overvoltages for α-PbO_2 and β-PbO_2 and therefore a change of oxygen overvoltage with time as the relative amount of the two oxides on the surface changes with time. The ohmic component of the overvoltage was only about 1 mv (at 3 ma) as determined by the current interrupter technique.

The reversible potential of the oxygen electrode ($O_2 + 4H^+ + 4e \rightarrow 2H_2O$) is +1.260 v (for H_2SO_4 sp gr 1.225) as calculated from data given in references (12), (24), and (25). Overvoltage values are given relative to this potential. Table IV summarizes some results on oxygen overvoltage measurements using the same symbols as were used in Table III. These measurements have been taken after 20 hr anodization with 3 ma.

After 2 hr of anodization at 3 ma, the oxygen overvoltage of pure Pb was 0.840 v. The difference in oxygen overvoltage on the single crystal faces (100), (111), and (110) of the pure Pb specimen were less than 5 mv. The Tafel slope was the same for the three planes, namely 0.110.

Discussion

During x-ray diffraction analysis of formed positive lead acid battery plates, several diffraction peaks were noted that did not correspond to any known compounds of Pb. Further experimentation has positively identified this material as a new crystalline modification of lead dioxide, found independently by Cahan in this laboratory and Zaslavsky, *el al.* (26), called α-PbO_2 for the purpose of differentiating it from the more common tetragonal or rutile form, herein called β-PbO_2. The α-PbO_2 has an orthorhombic spatial group of Pbcn (or D_{2h}^{14}) with the axes $a = 4.938$Å, $b = 5.939$Å, $c = 5.486$Å (26).

Alpha-PbO_2 has been prepared by several means, as indicated in the experimental section. Noteworthy among these methods of preparation was the conversion of β-PbO_2 to α-PbO_2 at a pressure of 125,000 psi.

The pattern for α-PbO_2 also appears on x-ray diffraction studies of anodized Pb alloy surfaces. A study of Pb strips anodized for varying periods of time with current densities between 100 ma/cm^2 and 1 ma/cm^2 shows first the production of an intense pattern for $PbSO_4$, a gradual replacement of the $PbSO_4$ pattern by β-PbO_2, and the appearance of the α-PbO_2 pattern along with the gradual disappearance of the β-PbO_2 pattern. At higher current densities, the pattern of α-PbO_2 becomes more and more pronounced. Results of this study indicate that

anodic oxidation of $PbSO_4$ produces the β-form of PbO_2, while the α-form is produced by the direct oxidation of Pb metal to PbO_2. Since α-PbO_2 forms directly from the Pb metal, it can be produced at potentials between the reversible $PbSO_4$-PbO_2 potential (1.685 v) and the Pb-PbO_2 potential (0.67 v). Large hard black nodules consisting primarily of α-PbO_2 have been found in the examination of positive grids from lead-acid batteries after removal from service. This condition has been noticed by other investigators (1, 4, 27) but has been interpreted as formation of tetragonal PbO.

The major peak of the powder pattern of α-PbO_2 coincides with the major peak of tetragonal PbO (*see* Fig. 9). The thin films produced on anodization of Pb give very diffuse patterns, and in many instances the major peak is the only one clearly visible. It is, therefore, easy to misinterpret the pattern of α-PbO_2 on these films as belonging to tetragonal PbO.

Lander (1, 2, 27) and Burbank (4) have postulated the formation of tetragonal PbO as the result of a solid-state reaction between Pb and the PbO_2 formed on anodization. The existence of PbO in a strong H_2SO_4 solution is difficult to picture thermodynamically or kinetically and in no case has any tetragonal PbO been detected in this laboratory by x-ray diffraction of Pb corroded in H_2SO_4. Samples of Pb anodized for various periods of time have been removed from the electrolyte, dried, and x-rayed within 5 min. In all cases, the only products were α-PbO_2, β-PbO_2, $PbSO_4$, and no PbO. No change in these patterns was detected even after 2 or more weeks in the dry state. Liberation of iodine from KI solutions by these films even after several weeks of storage in the dry state indicate PbO_2 to be present. Discharge of these films showed voltage steps corresponding to the PbO_2-$PbSO_4$ potential. Even samples which showed no β-PbO_2 pattern after anodization liberated iodine from KI solutions and showed the PbO_2-$PbSO_4$ potentials during discharge.

The following mechanism is proposed for anodic corrosion. In the initial stages of anodization (Fig. 3) $PbSO_4$ is first formed from the Pb at the Pb/$PbSO_4$ potential. As this film is completed, the potential rises to the oxygen overvoltage value, where two reactions occur. $PbSO_4$ is converted to β-PbO_2, and the underlying grid metal, due to the high potential, is converted directly to α-PbO_2 according to a Cabrera-Mott type film formation. As the anodization progresses, the $PbSO_4$ is used up in the production of β-PbO_2.

Referring to Fig. 5 and 6, the total discharge time cannot give a correct measure of the anodic corrosion without taking into account the self-discharge. The results demonstrate that additions of Sb up to 3% strongly decrease anodic corrosion, whereas practically nothing is gained by further addition of Sb up to 11%. This behavior can be explained plausibly by keeping in mind that the solid solubility of Sb in Pb is 3%. For concentrations above 3% Sb all the alloys in the range studied have the same basic grain structure, the only difference being the relative proportion of free Sb in the interstices (28). It has been reported elsewhere that self-discharge increases with increasing Sb concentration (29). Therefore, by correcting the upper curve of Fig. 5 for self-discharge according to the procedure described in Fig. 7, one would obtain a leveling out of the corrosion curve. Indeed, such a correction could change the shape of the curve remarkably.

The corrosion results described above do not agree with those of Kabanov, *et al.* (6). This might be due to the fact that the latter authors used surfaces as-cast rather than microtomed and surface film effects might have interfered. These authors also neglected self-discharge and inefficiency of discharge.

The equilibrium value for the solubility of Sb in Pb is only 0.24% at 25°C (14). During the cooling and aging period, Sb crystals are precipitated from the 3% phase. The structure of the Pb grains, and hence the rate of corrosion, is the same for all the alloys with Sb concentration above 3% if the cooling rates are the same. Using conventional cooling rates, a major amount of Sb remains initially in solid solution and the lattice constants substantially decrease (14). According to the laws of electrochemical kinetics, the anodic corrosion in constant current experiments should increase with increasing potential (if passivation is not interfering) and with decreasing strength of the metallic bond. The addition of Sb causes a deformation of the Pb lattice and probably high bond strength.

It has been shown that the hydrogen overvoltage decreases with increasing strength of the bond between the metal atoms (7) while lower overvoltage values could be associated on this basis with higher corrosion resistance. One also must keep in mind that free Sb metal has a lower hydrogen overvoltage than Pb [Table III (23)].

Oxygen overvoltage can also be correlated to the rate of corrosion. According to the rate equation for electrochemical anodic attack the corrosion current depends exponentially on the electrode potential if no passivating effects interfere. Alloys with low oxygen overvoltage, therefore, should be more resistant to anodic corrosion during constant current experiments. Calculations from data on single crystals presented in Fig. 9 show that the (100) and (111) faces have practically the same corrosion resistance while the (110) face is more corrodible. McGivern, working with cylindrical single crystals has also concluded that the (110) face is least resistant to corrosion (30).

Acknowledgments

The authors are indebted to J. F. McGivern, H. Stoertz, and A. Pippel, of the Metallurgy Division, for their assistance in preparing single crystals of Pb and the microtomed samples used in this study. They would also like to thank G. S. Hartman, Administrative Assistant, for editorial help and C. G. Grimes, Director of Research of the Electric Storage Battery Co., for permission to publish this paper.

Manuscript received Nov. 29, 1956. This paper was prepared for delivery before the Cleveland Meeting, Sept. 29 to Oct. 3, 1956.

Any discussion of this paper will appear in a Discussion Section to be published in the June 1958 JOURNAL.

REFERENCES

1. J. J. Lander, *This Journal*, **98**, 213 (1951).
2. J. J. Lander, *ibid.*, **103**, 1 (1956).
3. E. Wolf and C. Bonilla, *Trans. Electrochem. Soc.*, **79**, 307 (1941).
4. J. Burbank, *This Journal*, **103**, 87 (1956).
5. W. W. Beck, R. Lind, and W. F. K. Wynne-Jones, *Trans. Faraday Soc.*, **50**, 147 (1954).
6. E. V. Krivolapova and B. N. Kabanov, *Trudy Sov. Elektrokhimii. Akad. Nauk. SSSR*, **1950**, 539 (1953).
7. P. Rüetschi and P. Delahay, *J. Chem. Phys.*, **23**, 195 (1955).
8. P. Rüetschi and P. Delahay, *ibid.*, **23**, 556 (1955).
9. W. P. Davey, "A Study of Crystal Structure and Its Applications," p. 369, McGraw Hill Book Co., New York (1934).
10. C. S. Barrett, "Structure of Metals," p. 175, McGraw Hill Book Co., New York (1943).
11. W. J. Hamer, *J. Am. Chem. Soc.*, **57**, 9 (1935).
12. W. M. Latimer, "Oxidation Potentials," p. 155, Prentice Hall Inc., New York (1953).
13. P. Jones, R. Lind, and W. F. K. Wynne-Jones, *Trans. Faraday Soc.*, **50**, 972 (1954).
14. W. Hofman, "Blei und Bleilegierungen," p. 15, Springer, Berlin (1941).
15. E. Kure, E. Yeager, and F. Hovorka, Enlarged Abstracts of Papers Presented at the Sessions of The Theoretical Division, The Electrochemical Society, San Francisco Meeting (1956).
16. J. Van Muydler and M. Pourbaix, "Proceedings of the 6th meeting of the International Committee for Electrochemical Thermodynamics and Kinetics," p. 342, Poitiers (1954).
17. Y. M. Kolotyrkin and N. Y. Bune, *Zhur. fiz. Khim.*, **29**, 435 (1955).
18. B. Kabanov and Z. Iofa, *Acta Physicochim. USSR.*, **10**, 617 (1939).
19. H. Hunt, J. Chittum, and H. W. Ritchey, *Trans. Electrochem. Soc.*, **73**, 299 (1938).
20. A. Hickling and F. Salt, *Trans. Faraday Soc.*, **36**, 1226 (1940).
21. J. O'M. Bockris, *ibid.*, **43**, 417 (1947).
22. Y. Kolotyrkin and L. Medredera, *Zhur. fiz. Khim.*, **25**, 1355 (1951).
23. J. O'M. Bockris, "Modern Aspects of Electrochemistry," p. 199, Academic Press Inc., New York (1954).
24. P. Delahay, M. Pourbaix, and P. Van Rysselberghe, *This Journal*, **98**, 57 (1951).
25. H. S. Harned and W. J. Hamer, *J. Am. Chem. Soc.*, **57**, 27 (1935).
26. A. I. Zaslavsky, Y. D. Kondrashov, and S. S. Tolkachev, *Doklady Akad. Nauk. SSSR.*, **75**, 559 (1950).
27. J. J. Lander, *This Journal*, **98**, 220 (1951).
28. A. C. Simon and E. L. Jones, Enlarged Abstracts of Papers Presented at The Electrochemical Society Fall Meeting, Cleveland (1956).
29. P. Rüetschi and R. T. Angstadt, Abstracts of Papers Presented at a Joint Symposium of the Battery and Theoretical Divisions of the ECS, Cleveland Meeting (1956).
30. J. F. McGivern, Private communication.

Oxidation of Iron-Nickel Alloys

II. Electron Diffraction at High Temperature

R. T. Foley, C. J. Guare, and H. R. Schmidt

General Engineering Laboratory, General Electric Company, Schenectady, New York

ABSTRACT

The oxidation of iron-nickel alloys of 30%, 41%, and 78% Ni content has been studied at temperatures of 600°, 700°, 800°, and 900°C by the electron diffraction technique. A special furnace was developed for the electron diffraction instrument for these experiments.

Usually more than one oxide was present on the alloy at these elevated temperatures. Unlike the conclusion drawn from exclusively room temperature observations, the predominant oxide on the 30% and 41% Ni alloys was the ferrite (Fe_3O_4 or $NiFe_2O_4$) rather than alpha-Fe_2O_3. At 700° and 900° both NiO and MoO_3 exist on the 78% alloy. (This alloy contains 3.8% Mo.) The presence of MoO_3 above its melting point and where it exerts considerable vapor pressure is difficult to explain.

In some cases the lattice spacings of the alloy structure are carried over into the first formed oxide film. With subsequent growth the spacings achieve the normal (x-ray) values for the oxide.

Iron and nickel form a continuous series of solid solution alloys, both components of which are oxidizable. Such alloys, often with the addition of other elements, provide materials of considerable engineering usefulness because of their magnetic characteristics, thermal expansion coefficients, ability to form glass-to-metal seals, or general corrosion resistance. The study of the oxidation of Fe-Ni alloys is thus of practical as well as theoretical interest.

The examination of oxide films by the electron diffraction technique is of particular value in oxidation work because the electron beam penetrates to a depth of less than 50Å. As has been pointed out before (1, 2) maximum information is obtained when the measurement is made at the temperature

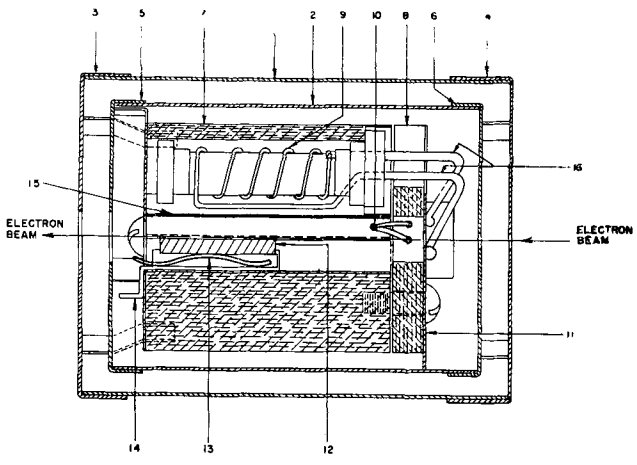

Fig. 1. High temperature electron diffraction furnace; 1, outer radiation shield—stainless steel; 2, inner radiation shield—Pt; 3-4, outer radiation shield end caps with apertures—stainless steel; 5-6, inner radiation shield end caps with apertures—Pt; 7, furnace body—ceramic; 8, insulator—ceramic; 9, heater solenoid wound on ceramic spool—Pt; 10, thermocouple—chromel—alumel; 11, locator and shield—Pt; 12, sample; 13, spring for positioning sample—stainless steel; 14, sample tray—Pt; 15, screen—Pt; 16, leads—Pt.

of reaction. The transformations and decompositions that take place upon cooling from the reaction temperature to room temperature may mislead one in the interpretation of the reaction mechanism.

This paper reports an electron diffraction study of the oxidation of three commercial Fe-Ni alloys at 600°, 700°, 800°, and 900°C. The purpose of the study was to achieve a better understanding of the structure of the oxide films formed on these alloys to add to the over-all knowledge of the mechanism of the oxidation of alloys.

Experimental

Electron diffraction equipment.—For the oxidation studies, a furnace originally designed for use in vacuum up to 1000°C was modified. W and Ta parts were replaced by Pt in regions of highest temperature and by stainless steel in the cooler areas to insure resistance to oxidation. This unit has produced a sample temperature of 900°C for a number of hours and 1000°C for a short time with no evidence of deterioration. The furnace construction is shown in Fig. 1.

Alloys.—The Fe-Ni alloys were nominally 30, 41, and 78% Ni in composition. Since they all contained more than 29% Ni, they were assumed to be austenitic. All three alloys are manufactured commercially and used because of their special physical properties. They were obtained in the form of cold-rolled sheet stock, thickness 0.051 cm (0.020 in.) for the 30 and 78% Ni alloys, and 0.080 cm (0.031 in.) for the 41% Ni alloy. Small sections, 0.80 x 1.60 cm (5/16 x 5/8 in.), were sheared from the stock for oxidation in the furnace. Careful shearing was necessary to insure flatness of the samples, and all edges were deburred to prevent obstruction of the electron beam by edge particles.

After shearing, samples were heat treated for 2-3 hr in H_2, dew point 30°F, at 1100°-1125°C. They were then cooled in H_2 to room temperature.

Surface preparation.—The chemically cleaned surface was prepared by pickling at 80°-90°C for 2 min in a bath of nine parts water and one part each of concentrated H_2SO_4, HNO_3, and HCl. This was followed by a water rinse and a bright dip in a solution of two parts concentrated H_2SO_4 and one part HNO_3. A second rinse was followed by immersion in NaCN solution (5 g/100 ml) for about 1 hr. Samples were then washed in running water, dried, and stored in dry acetone or benzene. At this point, the surface possessed a matte appearance. Composition of the alloys in the chemically cleaned condition is shown in Table I.

Electron diffraction studies.—Patterns were first taken at room temperature and a pressure of 0.01 -0.1 μ Hg. The sample was brought up to 600°C and a pattern obtained before oxidation. The alloy was then oxidized at 600°C by introducing air to bring the system to atmospheric pressure and maintaining at temperature and pressure for 2 min. The system was then evacuated and a pattern obtained. This was repeated to effect oxidations for additional 10- and 20-min periods, patterns being recorded for each time interval. (Total oxidation time at the end of each period was 2, 12, and 32 min.) The sample was then allowed to cool in vacuum and a pattern obtained when room temperature was reached. A similar procedure was used for studies at 700°, 800°, and 900°C.

The approximate times for the various operations in the electron diffraction unit were: 25 min to bring the sample to temperature in vacuum, 5 min to evacuate from atmospheric pressure after an oxidation period to obtain a pattern and 4 hr to cool the sample to room temperature in vacuum after oxidation. Heating and cooling periods varied somewhat depending on the temperatures.

Results

Oxides Found on 30% Ni-Fe Alloy

Observations made on oxide films developed during the oxidation of the 30% Ni alloy are given schematically in Table II. The "before oxidation" column refers to the situation wherein the sample was heated to temperature in the vacuum of the instrument, and any oxidation at this stage was not deliberate but occurred as the result of oxygen pressure in the vacuum. The "first formed oxide" refers to the 2-min oxidation only. Usually the 12- and 32-min diffraction patterns supplemented each other, and the "thicker oxide" column in the table then was based on the composite data for these two

Table I. Composition of alloys studied

Alloy	A	B	C
Nominal Ni content	30%	41%	78%
Ni	29.6	40.9	78.0
Fe	balance	balance	17.4
Mn	0.57	0.49	0.73
C	0.010	0.012	0.010
Mo	—	—	3.80
S	0.012	—	0.009
Si	0.17	0.14	0.13
P	0.02	0.02	0.02

Table II. Patterns found on 30% Ni-Fe alloy

Temp, °C	Before oxidation	First formed oxide	Estimated* thickness, Å	Thicker oxide	Estimated thickness, Å
600	Alloy pattern —Fe_2O_3 or Fe_3O_4	Distorted Fe_3O_4 or Fe_2O_3	Less than 500	Fe_3O_4 and Fe_2O_3	1000
700	Distorted alloy pattern	Distorted Fe_2O_3	1000	Distorted Fe_3O_4	2000-3000
800	Alloy pattern (trace Fe_2O_3 or Fe_3O_4)	Fe_2O_3 (possibly Fe_3O_4)	2000	Fe_3O_4	4000-8000
900	Alloy pattern (trace Fe_3O_4)	Fe_3O_4	5000	Fe_3O_4 (possibly Fe_2O_3)	10,000-20,000

* This was based on the kinetic equation developed in a parallel investigation.

time periods. On a few occasions, however, one or the other of these two time periods produced a very poor pattern, and in those cases "thicker oxide" refers to the good pattern only.

When the alloy was heated to 600°C, the diffraction pattern was that of the alloy plus a few lines corresponding to Fe_2O_3 or Fe_3O_4. (In this paper, Fe_2O_3 refers to the alpha form only.) The pattern obtained after the 2-min oxidation was quite distorted and could be assigned to Fe_2O_3 or Fe_3O_4. As used here, "distorted" means the spacings of the lines were shifted from those found in the corresponding x-ray pattern probably because of altered lattice parameters. Upon oxidation for longer times, a very good pattern for Fe_2O_3 developed, and there was strong evidence for Fe_3O_4.

All patterns at 700°C were distorted although distortion lessened with increasing thickness. The best pattern fit for the thicker films was Fe_3O_4. This film showed Fe_2O_3 as well as Fe_3O_4 at room temperature. Generally patterns were not obtained at room temperature.

At 800°C the alloy pattern and a few oxide lines were apparent. After 2-min oxidation, the preferred oxide was Fe_2O_3. The thicker film was Fe_3O_4.

At 900°C the preferred oxide was Fe_3O_4. The alloy pattern was observable at temperature "before oxidation." The presence of Fe_2O_3 was also indicated.

41% Ni-Fe *Alloy*

When this alloy was heated to 600°C in the instrument vacuum, the alloy pattern as well as a few lines for Fe_2O_3 were obtained as shown in Table III. With continued oxidation, both oxides $NiFe_2O_4$ and Fe_2O_3 appeared. From the electron diffraction patterns it was not possible to distinguish between Fe_3O_4 and $NiFe_2O_4$. However, previous investigation (3) had shown that the composition of the ferrite was $NiFe_2O_4$. Both Fe_2O_3 and the ferrite existed even in the first formed oxide films.

A pattern was obtained on the alloy before heating to 700°C. In addition to the alloy pattern, oxide lines were seen. It was interesting to note that heating to 700°C caused a distortion of the spacings. At 700°C the predominant oxide was the ferrite. In several incidents, the lines for the ferrite were distorted. As the oxidation progressed, a given spacing was seen to increase or decrease to approximate more closely the spacing reported from x-ray data.

At 800°C both oxides $NiFe_2O_4$, and Fe_2O_3 were in evidence.

When the sample was heated to 900°C in the instrument vacuum the alloy structure was covered by $NiFe_2O_4$. The ferrite was produced first at low oxygen pressure. Certain strong lines observed in the first formed films were carried through on oxidation and continually distorted. In the thicker films both $NiFe_2O_4$ and Fe_2O_3 were present as shown by "unique" lines.

A general observation appears to be that both oxides, $NiFe_2O_4$ and Fe_2O_3, grow on the 41% Ni-Fe when oxidized at these temperatures.

78% Ni-Fe *Alloy*

In addition to Ni and Fe, this alloy contained 3.8% Mo which entered into the reaction. Electron diffraction results are listed in Table IV.

A very good pattern for the alloy was obtained when the strip was examined at 600°C before oxidation. As oxidation proceeded, the alloy pattern distorted toward that of Fe_3O_4 and additional lines began to fill in the pattern. The distortion and addition of lines continued until the pattern from the thickest film gave excellent agreement with Fe_3O_4. This Fe_3O_4 probably contained considerable Ni.

Table III. Patterns found on 41% Ni-Fe alloy

Temp, °C	Before oxidation	First formed film	Estimated thickness, Å	Thicker film	Estimated thickness, Å
600	Alloy pattern (Fe_2O_3)	$NiFe_2O_4$, Fe_2O_3	Less than 500	$NiFe_2O_4$, Fe_2O_3	Less than 1000
700	Alloy pattern (Fe_2O_3)	$NiFe_2O_4$, (Fe_2O_3)	Less than 1000	$NiFe_2O_4$	1000-2000
800	Alloy pattern (Fe_2O_3, $NiFe_2O_4$)	$NiFe_2O_4$, Fe_2O_3	1500	$NiFe_2O_4$, Fe_2O_3	3000-6000
900	$NiFe_2O_4$	$NiFe_2O_4$, Fe_2O_3	4000	$NiFe_2O_4$, Fe_2O_3	10,000-20,000

Table IV. Patterns found on 78% Ni-Fe alloy

Temp, °C	Before oxidation	First formed film	Estimated thickness, Å	Thicker film	Estimated thickness, Å
600	Alloy pattern	Distorted alloy pattern	Less than 500	Fe_3O_4	Less than 500
700	Distorted alloy pattern, MoO_3	Distorted NiO, (MoO_3)	Less than 500	NiO, MoO_3	1000-2000
900	Alloy pattern, MoO_3	MoO_3, (NiO)	1000-2000	NiO, (MoO_3)	3000-10,000

At 700°C before oxidation, the pattern showed lines from the alloy and from MoO_3. In the first formed film a distorted NiO was observed along with lines for MoO_3. There was good evidence that the $NiFe_2O_4$ characteristic of oxidation on the 41% Ni alloy was also present. The thicker film appeared to be a mixture of MoO_3 and NiO, the lattices of which were distorted.

At 900°C "before oxidation" the lines for the alloy were observed. The alloy appeared to be covered with a thin layer of MoO_3 which was distorted. In the first formed film a very good pattern for MoO_3 was obtained. Upon further oxidation NiO predominated. The thickest film appeared to be composed of NiO with a trace of MoO_3.

Discussion of Results

Generally the electron diffraction patterns were of fair quality with respect to number and intensity of lines. Agreement with ASTM x-ray standards was almost always within 2-3% which is good considering the possibility of compounded deviations resulting from the inherent inaccuracy of the electron diffraction technique, the elevated temperatures, and distortion of oxide layers by substrates. The best patterns were obtained at 600° and 700°C, the room temperature, 800° and 900°C, patterns being less definite. There were no unidentified lines. Because of the shallow penetration of the electron beam, these patterns identified the surface structure only.

The ASTM x-ray standards used for comparison were those for Ni, NiO, $NiFe_2O_4$, Fe, FeO, α-Fe_2O_3, γ-Fe_2O_3, Fe_3O_4, MoO_2, MoO_3, and $NiMoO_4$. Alloy pattern standards were obtained from an examination of the alloys with a G-E XRD-3 unit and a SPG-2 spectrogoniometer head.

The studies demonstrated quite well that at these elevated temperatures more than one oxide layer was present even on fairly simple binary alloys. Unlike the conclusion to be drawn from exclusively room temperature observations (3), the predominant oxide on the 30% and 41% Ni alloy was not the α-Fe_2O_3 species, but rather the ferrite structure. Other chemical analyses (3) have shown the ferrite on the 41% Ni alloy to be $NiFe_2O_4$ rather than Fe_3O_4, and it might be inferred that the oxide produced on the 30% Ni alloy contained appreciable Ni.

The oxide layer produced on the 78% Ni alloy was complex. At 600°C the growth of the thin film was influenced by the structure of the alloy and the thick film by the ferrite structure. The ferrite probably contained considerable Ni. At 700°C there was evidence for MoO_3 along with NiO. Thus, the mechanism of oxidation must certainly change between 600°C and 700°C. More surprising, excellent agreement with the MoO_3 pattern was found for thin films at 900°C. The melting point of MoO_3 is 795°C and present thought (4) suggests that the formation of MoO_3 at temperatures above its melting point should lead to catastrophic oxidation of alloys containing Mo, whereas a stable compound such as $NiMoO_4$ must be produced to prevent catastrophic attack (5). In our case the nickel molybdate was definitely absent, but the 78% Ni alloy was the most resistant to oxidation of the three alloys studied as shown by kinetic data. The thick film showed less positive evidence for MoO_3 so the volatile oxide was eliminated as oxidation continued. This elimination could result by evaporation of MoO_3 from the surface followed by more rapid diffusion of Fe or Ni through the remaining oxide layer to give an oxide containing one or both of those atoms rather than Mo.

Although agreement of some electron diffraction patterns of the 78% Ni alloy was excellent with respect to MoO_3, almost equally good agreement was obtained for those same patterns with γ-Fe_2O_3. However, γ-Fe_2O_3 is not stable at 500°C or higher (6, 7).

It is encouraging that the pattern for the basis metal was obtained at these elevated temperatures in the oxygen pressure characteristic of the instrument. While less than 0.1 μ, this pressure would be termed high in terms of oxidizing potential (7). Even so, usually good patterns for the alloy itself were obtained. In many cases a few lines of an oxide were obtained in addition. It is possible that some reduction of the oxides by the carbon in the alloy was taking place (8).

Many patterns were distorted. This distortion could be accounted for in different ways. In at least one instance the distortion was produced by heating the sample from room temperature to 700°C. Very often the "d" spacings for the alloy were carried over to influence the "d" spacings of the oxide and a trend in distortion occurred. The termination of this trend in spacings was the x-ray spacing for the oxide. An excellent example is shown in Fig. 2 for the 78% alloy at 600°C.

The evidence in Fig. 2 indicates that in the growth of an oxide film, there is formed on the surface a series of structures with continuously varying parameters which change from those of the alloy when the film is thin to those of the oxide when the film is thick. Apparently this transformation can be completed at a thickness less than 500Å, and the intermediate values of parameters would cause an error in the estimated values of film thickness based on the assumption that the film was entirely oxide of normal density. As the film increases in thickness,

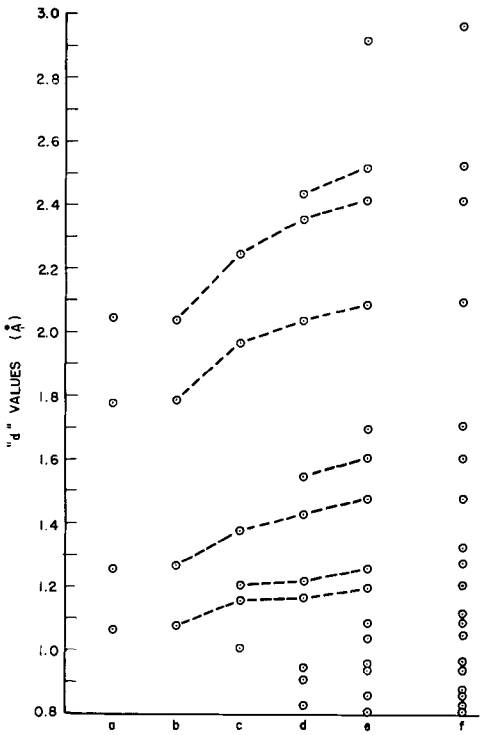

Fig. 2. Change in surface structure with oxidation on 78% Ni-Fe alloy at 600°C; (a) x-ray diffraction, alloy, chemically clean, 25°C; (b) electron diffraction, alloy, chemically clean, 600°C; (c) electron diffraction, alloy, 2 min in air, 600°C; (d) electron diffraction, alloy, 12 min in air, 600°C; (e) electron diffraction, alloy, 32 min in air, 600°C; (f) x-ray diffraction, Fe_3O_4, 25°C.

these intermediate parameter values are probably retained by that portion of the film near the alloy-oxide interface.

It would be of interest to know what alloy spacings were being distorted to the new oxide spacings. In a majority of the cases the trend in distortion could not be followed over the entire range because of multiple oxides or incomplete patterns. In the case of Fig. 2, the alloy planes 111, 200, 220, and 311, respectively, went to oxide planes 222, 400, 440, and 444 if the dotted lines are correct. Further work on orientation influences will be carried out in this laboratory.

In these studies it was difficult to distinguish between Fe_2O_3 and $NiFe_2O_4$ (or Fe_3O_4). Certain characteristic or "unique" lines were used to establish the presence of one or the other of these compounds. These lines were usually quite strong and were not ambiguous. For the nickel ferrite, a spacing at about 1.95 was significant. For Fe_2O_3, a "d" spacing at 1.84 was used. These varied from sample to sample; for example, the characteristic "d" spacing for the $NiFe_2O_4$ compound occurred at 1.97, 1.96, 1.91, 1.92, and 1.93 in various samples.

Observations reported at the present time are being used along with kinetic studies to establish the mechanism of oxidation of these alloys.

Acknowledgment

The authors would like to acknowledge the considerable contribution made by M.J. Columbe in the construction of the furnace and operation of the electron diffraction apparatus.

Manuscript received August 3, 1956. Some of the material in this paper was given at the American Chemical Society Meeting at Dallas, Texas, April 8-13, 1956.

Any discussion of this paper will appear in a Discussion Section to be published in the June 1958 JOURNAL.

REFERENCES

1. E. A. Gulbransen, *J. Appl. Phys.*, **16**, 718 (1945).
2. R. Jackson and A. G. Quarrell, *Proc. Phys. Soc., London*, **51**, 237 (1939).
3. R. T. Foley, J. U. Druck, and R. E. Fryxell, *This Journal*, **102**, 440 (1955).
4. O. Kubachewski and B. E. Hopkins, "Oxidation of Metals and Alloys," p. 3, 13, 88, Butterworths Scientific Publications, London (1953).
5. S. S. Brenner, *This Journal*, **102**, 7 (1955).
6. Z. G. Pinsker, "Electron Diffraction," p. 257, Butterworths Scientific Publications, London (1953).
7. E. A. Gulbransen and J. W. Hickman, *Trans Am. Inst. Mining Met. Engrs.*, **171**, 306 (1947).
8. Private communication.

Dissolution of Iron in Acidified Chromic Chloride Solutions

Robert Skomoroski and Cecil V. King

Department of Chemistry, New York University, New York, New York

ABSTRACT

The rate of dissolution of iron from rotating cylinders was studied in 4M HCl containing purple and green $CrCl_3$, also $AlCl_3$ and NaCl up to 0.2M. These salts affect the rate of dissolution somewhat, but chromic ion does not undergo reduction. While the standard potentials predict that reduction is possible, the actual potential of iron in acid solutions is not sufficiently negative. Cathodic polarization did not accomplish direct or indirect reduction of chromic ion, but only cathodic protection of the iron. It was also shown that metallic iron catalyzes the oxidation of chromous ion by hydrogen ion.

The dissolution of Fe in HCl-$CrCl_3$ solutions was studied in order to compare the reaction with that of Zn and Cd under similar conditions (1,2). From the published "standard" potentials, the equilibrium constant of the reaction

$$Fe + 2Cr^{+++} \rightleftharpoons Fe^{++} + 2Cr^{++} \qquad (I)$$

is found to be about 10, indicating nearly complete reduction of chromic ion by Fe to be thermodynamically possible. However, the actual potential

of Fe in acid solutions is always polarized cathodically by the H_2 evolution reaction, and is insensitive to ferrous ion. Reaction (I) then cannot take place unless the measured potential is not a determining factor, or the chromic ion acts as a depolarizer.

Chromous ion is thermodynamically unstable in acid solutions, the potential of the reaction

$$Cr^{++} + H^+ \rightleftharpoons Cr^{+++} + \tfrac{1}{2} H_2 \qquad (II)$$

being given in volts at 25°C by the equation

$$E = 0.40 - 0.059\ pH - 0.059 \log (a_{Cr^{+++}}/a_{Cr^{++}}) \qquad (III)$$

At $pH < 6$, essentially no chromous ion is present at equilibrium ($E = 0$). Reaction (II) is slow or negligible in many solutions and is not catalyzed by Zn or Cd, so that it may be neglected in studies with these metals (1,2). It is catalyzed by some metals, especially Pt (3,4), and, as shown below, by Fe. Nevertheless, if reactions (I) and (II) were to take place in succession, rates of Fe dissolution and H_2 evolution would be greater than in the absence of chromic ion. This research was designed to clarify the actual behavior of the system.

Experimental

Cylinders of high-purity Fe (SVEA Metal), about 1.9 x 2.5 cm in dimensions and 15 cm^2 in area, were rotated in 100 ml of acid solution, deaerated with N, as described before (2). The reaction cell was thermostatted at 25°C. A small saturated KCl-calomel cell was inserted for potential measurements, *IR* drop between the Fe cylinder and calomel cell being negligible in all cases. The experiments were done in 4M HCl to avoid *p*H changes or surface oxide complications. The Fe was polished lightly with No. 600 SiC paper before each third or fourth run since this gave the best reproducibility. Weight loss was determined after 1-hr immersions; it is linear with time in similar experiments with HCl alone (5).

Reproducibility was tested by repeating runs 6 or 7 times in some of the solutions. The average deviation from the mean varied from 4 to 9%, with a maximum single deviation of 17%. Results in other solutions are the average of 2 or 3 determinations. The rates and the average deviations are similar to results reported by Makrides, Komodromos, and Hackerman for Fe in HCl (5).

Table I gives the weight loss in deaerated 4M HCl solutions containing green and purple forms of $CrCl_3$, also $AlCl_3$ and NaCl for comparison.

Several solutions were tested for reduction of Cr^{+++} by introducing excess deaerated $K_2Cr_2O_7$ solution into the reaction cell at the end of the runs.

Table I. Average weight loss of iron cylinders, mg/cm^2/hr; peripheral speed 15,000 cm/min; 4M HCl; 25°C

C_{salt}, M	$CrCl_3$ Purple	$CrCl_3$ Green	$AlCl_3$	NaCl
0	4.3	4.3	4.3	4.3
0.05	4.3	3.6	4.6	4.8
0.10	4.6	3.6	4.4	4.6
0.15	4.7	3.1	4.7	4.8
0.20	5.1	2.9	5.0	4.5

The excess dichromate was then titrated with standard ferrous solution with diphenylamine sulfonic acid as indicator. The reducing power of the solutions averaged 2.9% less than calculated from the weight losses (40-50 mg), indicating that only Fe^{++} and no Cr^{++} had been formed.

To test the effect of $CrCl_3$ on H_2 evolution directly, strips of Fe sheet of 70 cm^2 area were rolled into spirals and inserted into a reaction flask which was connected to a manometer through a flexible glass capillary. The solution was introduced, the apparatus evacuated with shaking, and, after sealing from the pump, the pressure rise was followed. Initial rates were erratic, but after several periods of reading and re-evacuating, reasonably reproducible values were obtained. Averages were as follows:

4M HCl alone	5.55 cm Hg/5 min
+ 0.2M $CrCl_3$ (green)	4.35
+ 0.2M $CrCl_3$ (purple)	5.70

While these experiments cannot be compared directly with those of Table I, the green $CrCl_3$ evidently decreases H_2 evolution as well as weight loss; the effect of purple $CrCl_3$ is within the experimental error.

Potentials and polarization.—The potential of the rotating Fe cylinder was measured in deaerated solutions much as described by Makrides, Komodromos, and Hackerman (5). It drifted with time as these authors describe, in 4M HCl alone and with 0.2M $CrCl_3$, $AlCl_3$, or NaCl present. After 1 hr the value was −0.38 to −0.40 v vs. the SCE in all cases.

Since a more negative potential should be required to reduce Cr^{+++}, potential and weight loss studies were made with the Fe polarized cathodically. A vessel containing 1M KCl and a sheet Ag anode was connected to the reaction cell through an agar bridge (large enough to avoid overheating), and current was supplied from dry cells. Since the potentials did not change rapidly after 5 min, readings were taken after holding the current constant for that time. Polarization curves are shown in Fig. 1.

Weight losses were determined at small increments of polarizing current, over 1-hr periods as be-

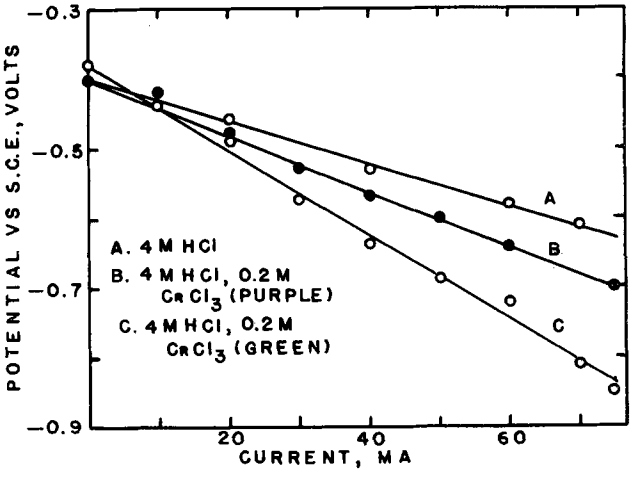

Fig. 1. Change in potential for rotating Fe cylinder with polarizing current.

fore. The Fe is protected in HCl alone and with both forms of $CrCl_3$ at 0.2M with any current from 10 to 75 ma (on 15 cm^2), weight losses falling to the order of 0.01-0.1 mg/cm^2/hr. Runs up to 8 hr at 75 ma showed no visual change in color of the solutions.

Other experiments.—To test the catalytic effect of Fe on reaction (II), 50 ml of 0.2M $CrCl_2$, prepared by reduction of $CrCl_3$ with amalgamated Zn and containing about 2M HCl, was brought into contact with an Fe cylinder in a Jones reductor tube, and stirred with purified N. In 30 min the bright blue color had changed to dark green, indicating oxidation to Cr^{+++}. An Fe cylinder was also rotated in 100 ml of 0.2M $CrCl_2$ containing about 4M HCl, in the reaction cell, the Fe being polarized cathodically with a current of 75 ma. The blue color changed to green in the course of 20 min.

Since the polarographic reduction of Cr^{+++} in 4M HCl has not been reported, polarization curves were run with 0.002M green and purple forms in 4M HCl at 25°C.[1] The green ion showed a rather poor wave starting at about —0.55 v (vs. SCE), with no clearly defined reduction plateau or half-wave potential. The purple form showed some reduction starting at about —1.0 v. Apparently reduction of both forms at the Hg surface is slow and the purple form shows considerable overvoltage.

Discussion

Since Fe catalyzes reaction (II) one cannot expect permanent reduction of Cr^{+++} unless the potential is in the region of stability of Cr^{++} according to Eq. (III). Alternate reduction by unpolarized Fe, reoxidation by H^+ does not take place. Cathodic reduction followed by reoxidation cannot be tested directly, since the amount of H_2 evolved depends only on the number of coulombs passed.

The potential of the chromic-chromous couple is somewhat uncertain, and the values of —0.40 to —0.41 given in the literature (6,7) are not strictly standard potentials, since activity coefficients in the solutions used are not reliably known. If Eq. (III) is correct, then in 4M HCl ($pH = -0.9$) a mixture of Cr^{+++} and Cr^{++} at equal activities should be stable at —0.71 v vs. the SCE.

The best work on polarographic reduction of Cr^{+++}, for comparison in the present connection, appears to have been done by Hamm and Shull (8). This was with very dilute $CrCl_3$ in 0.1-0.4M KCl and dilute HCl. With freshly prepared green solutions, a half-wave potential was found at —0.61 v vs. SCE. This wave disappeared with time, while another appeared at —0.89 v in the aged solutions (the hexaaquo ion). The violet ion thus displays an overvoltage on Hg even in dilute HCl. Some investigators have noted another wave at —1.06 v in purple solutions (9).

[1] Experiments by John Gorman, whom the authors wish to thank.

No plateaus appear in the curves of Fig. 1, which indicates that even in the region of supposed stability of Cr^{++} the reduction overvoltage on Fe is greater than any overpotential which was imposed. However, the oxidation of Cr^{++} at the Fe surface, even with 75 ma of current and a potential near —0.85 v, indicates that Cr^{++} is not stable at this potential under the given conditions.

It is significant that while $AlCl_3$ and purple $CrCl_3$ increase the dissolution rate somewhat, green $CrCl_3$ decreases it up to 30%. This probably indicates that the green ion is strongly adsorbed on Fe, decreasing the number of sites at which H^+ can be reduced (polarization of cathodes). While both forms of $CrCl_3$ react with Cd in HCl solution, the rate of H_2 evolution is diminished (2). Also, while ferric ion is reduced by Fe in H_2SO_4, H_2 evolution is decreased during this reaction (10). This has been ascribed by Gatos to competition for adsorption sites (10). Both the dichlorochromic ion and the sulfatoferric ion should be more strongly adsorbed than the symmetrical hexaaquo ions.

This view is supported at least partly by the polarization curves of Fig. 1. The green ion increases the H_2 overvoltage more than twice as much as the purple ion does. The question is raised, how can the purple ion be adsorbed to some extent, increase the H_2 overvoltage, and still increase the dissolution rate? Probably the purple ion is not adsorbed with no applied potential, and the green is adsorbed to a greater extent when the Fe is polarized.

It should be possible to investigate the adsorption of both chromic ions on Fe by classical or radiotracer methods. It has been shown that chromate and dichromate ions are retained on a steel surface (11), with the possibility that reduction to Cr^{+++} is involved.

Manuscript received September 18, 1956. This paper was prepared for presentation before the Cleveland Meeting, Sept. 29 to Oct. 3, 1956.

Any discussion of this paper will appear in a Discussion Section to be published in the June 1958 JOURNAL.

REFERENCES

1. C. V. King and N. Mayer, *This Journal*, **100**, 473 (1953).
2. C. V. King and E. Hillner, *ibid.*, **103**, 261 (1956).
3. K. Jablczynski, *Z. physik. Chem.*, **64**, 748 (1908).
4. A. Asmanov, *Z. anorg. u. allgem. Chem.*, **160**, 209 (1927).
5. A. C. Makrides, N. M. Komodromos, and N. Hackerman, *This Journal*, **102**, 363 (1955).
6. G. S. Forbes and H. W. Richter, *J. Am. Chem Soc.*, **39**, 1140 (1917).
7. G. Grube and L. Schlecht, *Z. Elektrochem.*, **32**, 178 (1926).
8. R. E. Hamm and C. M. Shull, *J. Am. Chem. Soc.*, **73**, 1240 (1951).
9. G. F. Reynolds, H. I. Shalgosky, and T. J. Webber, *Anal. Chim. Acta*, **8**, 564 (1953).
10. H. C. Gatos, *This Journal*, **103**, 286 (1956).
11. R. A. Powers and N. Hackerman, *ibid.*, **100**, 314 (1953).

The Activation and Passivation of Stainless Steel in Aerated Sulfuric Acid

G. H. Cartledge

Chemistry Division, Oak Ridge National Laboratory, Oak Ridge, Tennessee

ABSTRACT

Potential-time curves have been determined at 85°C for a niobium-stabilized stainless steel during its transition to the state that is essentially stable in aerated 0.1*N* sulfuric acid. Experiments were conducted both with pre-oxidized specimens and with others that were previously saturated with hydrogen by electrolysis. It was found that the potential passes through characteristic inflections, and an attempt was made to relate these to the processes with which they are associated. In particular, it was found that, for the conditions used, there is a "critical recovery potential" above which spontaneous passivation occurs, and this potential was shown to be approximately equal to the hydrogen potential for the same conditions. The corrosion rate was shown to be characteristically related to the changes in potential.

When certain types of stainless steel are superficially oxidized by exposure to hot air and then placed in aerated H_2SO_4 under suitable conditions, the initially noble system may first become active and subsequently return to an essentially stable passive state (1). Bonhoeffer and Vetter (2), who have studied the analogous phenomenon manifested by carbon steel in HNO_3, found that radical and characteristic changes in potential occur over an interval of about 0.5 sec. Berwick and Evans (3) studied the ennobling of the electrode potential of 18-8 stainless steel in aerated H_2SO_4 at 25°C and showed that a certain minimum amount of oxygen was required to produce passivity. Copper(II) ions and iron(III) ions also raise the potential of stainless steel and modify corrosion rates (4). The present work was undertaken as an introduction to an investigation of the mechanism of the action of a variety of substances on the electrochemical behavior of stainless steel in acidic solutions. To understand the possible effects of ions or molecules on the potential of a composite surface like that of a real metal, it was desirable to study in detail the processes involved in the transition between noble and active states of the system in the absence of ions other than corrosion products. Preliminary experiments disclosed conditions under which the activation and subsequent passivation by oxygen could be followed over much longer time intervals than were involved in the carbon-steel HNO_3 system, thus permitting a more thorough investigation of the several processes involved. It was found that the potential-time curves obtained by continuous recording showed smooth transitions or inflections that were very similar to the familiar titration curves of analytical chemistry. The problem, therefore, was to correlate these potential changes with the chemical processes with which they are associated.

Experimental Procedure

The metal used in most of the experiments was a Nb-stabilized stainless steel (type 347) having the following analysis: C, 0.05; Ni, 9.75; Cr, 18.10; Mn, 0.71; Si, 0.59; Nb, 0.57. The metal was in the form of cold-rolled, annealed, and pickled sheet 0.010 in. thick. In some cases the surface was the original mill finish; in others it was either abraded with 2/0 emery or else electropolished in a mixture of H_2SO_4, H_3PO_4, and water. The electrodes were, in most cases, 1 cm square and had an integral lead which was insulated by a coat of glyptal varnish dried at 110°C. In preliminary experiments at temperatures between 25° and 95°C, it was found that when such electrodes were placed in 0.1*N* H_2SO_4 the time required for a stable potential to be attained diminished with rising temperature. The potential became less noble with rise of temperature in the aerated acid and became progressively more noble when the electrode was repeatedly heated and cooled in the acid. The temperature of 85°C was selected for most of the experiments as a matter of convenience, since this is near the temperature of maximum corrosion rate in dilute H_2SO_4 exposed to the air and is far enough below the boiling point so that excessive evaporation is avoided. At this temperature the potentials were reestablished quickly after any displacement by polarization.

In those experiments in which an oxide film was artificially produced, the electrodes were heated in a muffle furnace for times varying between 15 min and 40 hr, and at temperatures between 300° and 450°C. For most of the experiments, the standard heating procedure was 2 hr at 445°C. This treatment produced a brown film on specimens having the mill finish, and pure, brilliant gold on electropolished specimens. Evidence that the results obtained were not influenced by any possible altera-

tion of the metal structure by the oxidation was found in the fact that similar results were obtained in the ultimate spontaneous passivation of specimens which received no prior oxidation, although the behavior at the beginning of an experiment was, of course, different.

The well-lacquered electrode stems passed through rubber stoppers into 150 ml of H_2SO_4 contained in a 250-ml, round-bottom flask having three or four necks. Through the central neck a glass stirrer was passed which operated at approximately 600 rpm. The stirring rate was just insufficient to draw bubbles of air into the solution. A bridge containing 0.1*N* H_2SO_4 made connection to a reference electrode of $Ag\text{-}Ag_2SO_4$ in 0.1*N* H_2SO_4 maintained at room temperature. This half-cell was frequently calibrated against a saturated calomel electrode (S.C.E.). Potentials were measured and continuously recorded by use of a vibrating-reed electrometer and Brown recorder. Pt electrodes (smooth or platinized for different purposes) were also inserted in the H_2SO_4. It was shown by tests that there was insufficient leakage between electrodes to give detectable polarization. Because of the experimental arrangement employed, all potentials given include a small but unknown potential due to the temperature gradient in the bridge. When desired, dissolved Fe was determined spectrophotometrically by use of thioglycolic acid (5).

All potentials are expressed by reference to the saturated calomel electrode. Nobility therefore is indicated by potentials that are positive to this electrode by 100 mv or more. Ennobling and debasing are frequently referred to as opposite processes, since the meaning of these terms is clear without regard to conventions as to signs. Under the conditions of these experiments the system may be reasonably stable only in the noble, or passive, region (more positive than +100 mv S.C.E.) or in the base, or active, region (more negative than —300 mv S.C.E.). In the intervening region of potentials rapid transitions of state are occurring.

General Results

The different types of potential-time curves obtained in aerated solutions are summarized in Fig. 1. Curve 1 represents the behavior of an electropolished and oxidized specimen which passed from the air-stable state to the acid-stable state with only a slight dip in its electrode potential and with only a minimum amount of corrosion. Curve 2 represents the other extreme, in which the initially noble electrode after a time underwent an abrupt activation to a potential at which H_2 was liberated, and after a slight rise in potential continued at an active potential with rapid corrosion. After some time, passivation was artificially induced in this experiment by passing a stream of O_2 through the flask. Curve 3 represents a case in which the dE/dt value in the base region was slightly positive until an abrupt ennobling began which was followed by ultimate passivation. Curve 4 represents the behavior of an electrode which was connected to a platinized electrode in the same solution throughout most of the experiment. In this case the potential

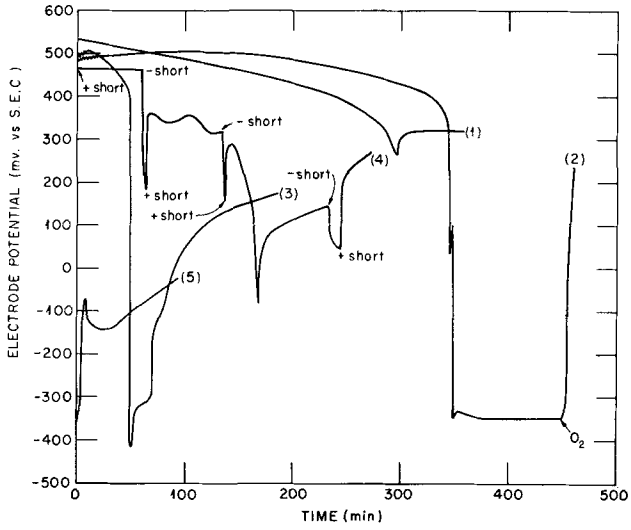

Fig. 1. Types of potential-time curves at 85°C, referred to the saturated calomel half-cell.

never reached the region of active potentials and there was only a small amount of corrosion. Finally, curve 5 shows the behavior of an electrode which was saturated with H_2 by cathodic treatment in very dilute NaOH before being inserted into the aerated H_2SO_4 solution. Here there was rapid ennobling from the initially active potential, with very little corrosion.

Potential-Time Curve for Initially Oxidized Electrodes

As indicated in Fig. 1, curves 2 and 3 represent the contrast between conditions which resulted in continuous corrosion, in the one case, and in spontaneous recovery with essentially complete stability in the other case. Which of the two curves was followed proved to be highly dependent on temperature, acidity, concentration of oxygen, and specific corrosion resistance of the metallic specimen. Thus,

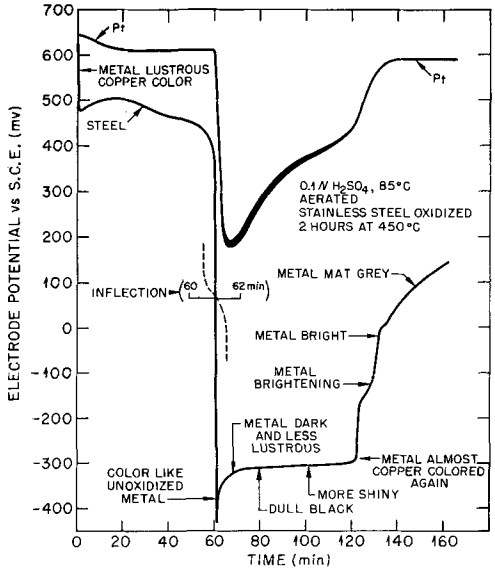

Fig. 2. Potential-time curves for oxidized stainless steel and smooth Pt in aerated 0.1*N* H_2SO_4 at 85°C. The brief inflection recorded on the chart at 61 min is indicated on an expanded time scale by the dashed curve.

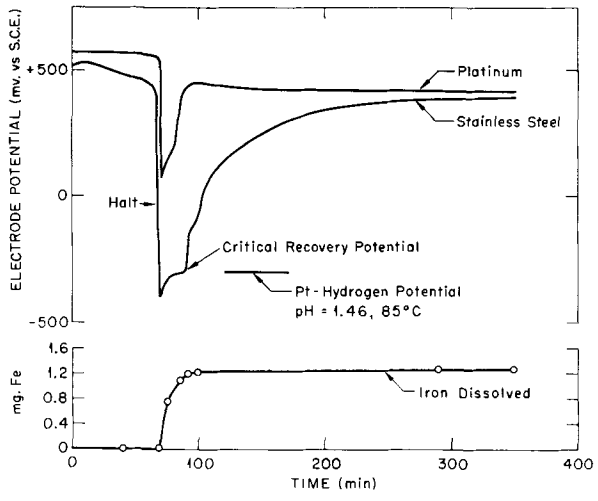

Fig. 3. Potential-time and corrosion curves at pH 1.46, 85°C, aerated.

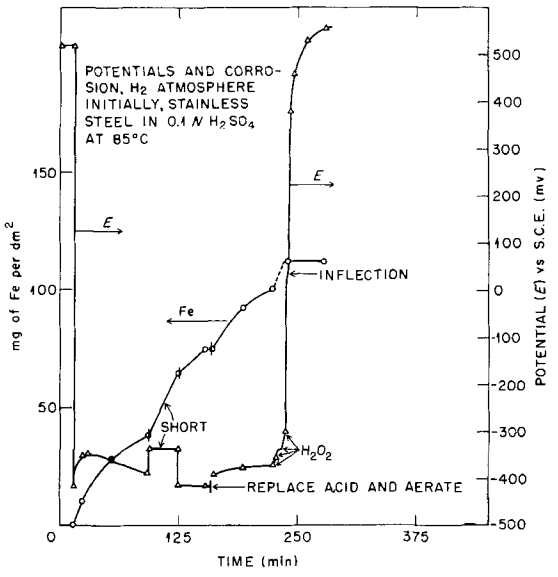

Fig. 4. Potential-time and corrosion curves in a hydrogen atmosphere initially: pre-oxidized electrode.

when the temperature was 85°C and the electrolyte was 0.1*N* H_2SO_4, one specimen of stainless steel (type 347) almost invariably followed curve 3, whereas electrodes cut from a different batch of metal having approximately the same analysis invariably followed curve 2 under the same conditions. It was found that the dE/dt slope in the active region could be changed from zero or negative to positive, as a rule, by lowering the temperature by 5-10 degrees, or by raising the pH by a few tenths of a unit. Other means of producing the ennobling artificially are discussed later.

Fig. 2 shows the potential-time curve of a specimen which was abraded with 2/0 emery, oxidized for 2 hr at 450°C, and then placed in 0.1*N* H_2SO_4 at 85°C, together with a smooth Pt electrode. The behavior shown is typical of numerous experiments made under these conditions. The figure indicates also the consistently observed visual changes. The disappearance of film coloration, particularly on specimens that were not abraded, was often spectacularly abrupt when the brief halt around 0 mv was passed. In the numerous experiments of this type, the fairly sudden change from a slow to a very rapid ennobling of the potential occurred uniformly when the rising potential reached −295 ±5 mv. This characteristic potential is called here the "critical recovery potential". It was observed to vary slightly with changes in pH and temperature.

Variations in the potential of the Pt electrode are also shown in Fig. 2. During the noble period of the stainless steel electrode the Pt remained nearly constant after a few minutes. Its potential fell sharply with the activation of the stainless steel electrode and underwent subsequent changes that were clearly correlated with the processes occurring at the surface of the stainless steel.

Fig. 3 shows the results of an experiment of similar character except that the electrolyte was a mixture of 0.1*N* H_2SO_4 with 0.1*N* sodium sulfate in such proportions (3:1) that the mixture had a pH of 1.46. In this case careful spectrophotometric determinations were made on the Fe which passed into solution during the experiment. As long as the potential remained noble, the dissolved Fe was barely detectable. The break in potential was accompanied by the onset of an extremely high rate of corrosion and the subsequent diminution in corrosion rate coincided precisely with the passage through the critical recovery potential. Chromium and Ni were determined in only a few instances, since it is known (6) that stainless steel dissolves essentially in the proportions present in the metal. The relation between the drop in potential and increase in corrosion rate is similar to that observed by Schwartz (7) in the activation of passive iron.

In Fig. 4, which is considered more fully later, an experiment is shown which was conducted in a current of purified H_2 with an electrode that was initially oxidized. The curve shows that the stainless steel held its noble potential with no immediate response whatever to the molecular H_2. After 15 min, the electrode was activated by momentarily short circuiting it to a platinized electrode in the same solution. This electrode was about 800 mv negative to the stainless steel and the treatment instantaneously destroyed the nobility. Thereafter, corrosion proceeded rapidly.

Experiments in an Atmosphere of H_2

When the oxide film on the stainless steel electrode broke down, the potential fell to a sufficiently low value for H_2 to be liberated. It was suspected that the inflections or halts observed in the recovery of nobility were somehow associated with the presence of hydrogen in the metal and with processes connected with its displacement by oxygen. For this reason experiments were conducted to determine the electromotive behavior of electrodes which were initially saturated with hydrogen. Such electrodes were measured in an atmosphere of purified H_2, in a stream of an inert gas, and also when the solution was stirred in contact with air according to the standard procedure.

Cylinder H_2 was purified by passage through a catalytic oxygen remover followed by a solution of

Table I. Empirical potential of the hydrogen electrode, 85°C

Electrolyte	pH	E (mv vs. S.C.E.)
0.1N H_2SO_4	1.25	−284
0.1N H_2SO_4 + 0.1N Na_2SO_4 (2:1)	1.50	−303

chromous chloride in HCl. Abraded electrodes of stainless steel type 347 of 2.0 cm^2 area were used. The electrodes were made cathodes in very dilute NaOH solution in a porous cup. A Pt anode was used outside the cup and current of approximately 10 ma/cm^2 was passed for various periods of time from 15 min to 48 hr. For the potential measurements, the electrode was quickly transferred to the solution of H_2SO_4 or sulfate mixture which had already been brought to temperature and equilibrated with the appropriate gas.

For comparative purposes the potential of a platinized coil was measured simultaneously to obtain an empirical reversible hydrogen potential appropriate to the experimental conditions. Table I gives the values obtained, the potential being referred to a saturated calomel half-cell dipping into the specified acid solution at 25°C. It is to be understood that hydrogen bubbled over the Pt electrode in the acid solution at 85°C and escaped at a barometric pressure of approximately 740 mm, and that the potential difference was measured between this hydrogen half-cell and a reference half-cell of Ag-Ag_2SO_4 in 0.1N H_2SO_4 at 25°C. The Ag half-cell was then measured against a calomel half-cell which dipped into a 0.1N sulfate solution of the indicated pH value. Over the narrow range of acidities involved, the variation of potential with pH corresponds to that calculated from the Nernst equation within 1 mv, although pH was measured at 25°C.

Fig. 4 and 5 show results that are typical of experiments done in an atmosphere of hydrogen with subsequent aeration, Fig. 4 referring to a preoxidized electrode and Fig. 5 to one that was first treated cathodically to saturate it with hydrogen. For these experiments the apparatus was equipped

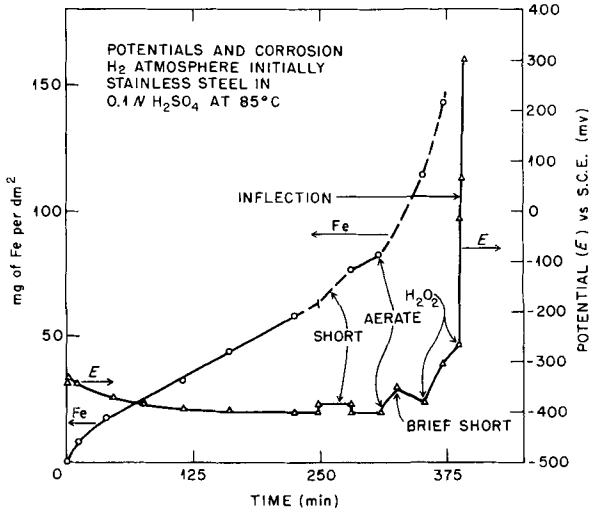

Fig. 5. Potential-time and corrosion curves in a hydrogen atmosphere initially: cathodized electrode.

with a sampling device for transferring electrolyte to or from the flask without admission of air. The significant observations in these experiments were as follows. (*A*) The initially oxidized electrode remained noble until it was momentarily short-circuited to the platinized hydrogen electrode. (*B*) On being activated, the preoxidized electrode went to a more negative potential than that initially exhibited by the cathodized electrode. (*C*) The potentials of the stainless steel electrodes were negative to the platinized electrode and became essentially constant during the period of active corrosion in hydrogen. (*D*) The corrosion rate of the oxidized electrode immediately after its activation exceeded that of the cathodized electrode. (*E*) The corrosion rate increased during periods when the stainless steel was short-circuited to the platinized electrode; the rate decreased when the circuit was opened. (*F*) The current passing between the stainless steel and Pt electrodes was measured by a microammeter in one experiment. This current accounted for 75-82% of the total corrosion occurring during the short. [The calculation was based on the analysis for Fe and on the assumption that the metallic constituents of the alloy dissolved in the proportions in which they were present to give Fe(II), Ni(II), and Mn(II) ions. The two percentages shown are for the alternative assumptions that Cr(III) and Cr(II), respectively, were the immediate products of the electrode reaction.] (*G*) The corrosion rate increased temporarily when air displaced the hydrogen atmosphere or when very small amounts of H_2O_2 were added. (*H*) The corrosion rate fell nearly to zero after the potential ennobled past the critical recovery potential (Fig. 4). (*I*) The potentials showed the characteristic brief halts during the ennobling process in air. (*J*) When a cathodized electrode was transferred directly to aerated electrolyte, ennobling began at once and was quite rapid (curve 5 of Fig. 1). (*K*) In one experiment, after the electrode had reached a nearly constant active potential in hydrogen, the hydrogen was replaced by an indifferent gas that was freed of oxygen.[1] The potential of the stainless steel electrode continued its slow drift to more negative potentials.

Experiments with Composite Electrodes

When pre-oxidized electrodes were first introduced into aerated 0.1N H_2SO_4 at 85°C, the potential was unsteady, irregular fluctuations of 50 mv or so being generally observed for a time. This behavior would be expected if the film were heterogeneous, so that currents could flow between local cathodes and anodes. It was consistently observed that specimens that were electropolished prior to oxidation had potentials 50-150 mv more noble than specimens that were not so treated before formation of the oxide film. This observation made it possible to separate anodic and cathodic processes to a very considerable degree by studying the potential of a composite electrode made by connecting an electro-

[1] The gas is believed to have been N_2 but owing to the erroneous labeling of a cylinder that was discovered after completion of the experiment it is possible that the gas was A.

polished electrode through a microammeter to a specimen having the mill finish, both electrodes having been oxidized 2 hr at 445°C. The electrodes were of 3.74 cm^2 area each.

Because the actual extent of the functioning areas is unknown, the polarizations measured can have no quantitative significance. It was found, however, that, when the potentials of the separate components were measured while both were in the noble region, the mixed potential of the composite electrode was almost that of the unpolished component. The polarization of the cathodic process therefore greatly exceeds that of the anodic process, even though the effective anodic area was doubtless very much smaller than the cathodic film of the electropolished member.

A composite pair was observed through the fall to an active potential, both the potential and the interelectrode current being measured. It was observed that the current increased rapidly when the potential of the anode began to fall, then dropped to zero as the electropolished component debased, and briefly reversed its direction when the activation approached completion. Correspondingly, the electropolished component, although normally the more stable, lost its golden color while some brown film was still visible on the unpolished member. It is clear that the loss of nobility is associated with a "reductive-dissolution" of the oxide, as demonstrated by Pryor and Evans (8) for the case of carbon-steel films. As shown by repeated analysis, however, a barely detectable amount of Fe passed into solution until activation was complete (Fig. 3 and 4).

Experiments on the Ennobling Process

One of the most striking results of the experiments was the abrupt ennobling that occurred whenever the potential reached the critical recovery potential. The complexity of the ensuing processes is indicated by the two inflections that were generally observed before the ultimate passive potential was reached. The relation of hydrogen to the persistence of active potentials is clearly indicated by the approximate coincidence of the empirical hydrogen potential with the critical recovery potential in the same environment. For these reasons, further experiments were devoted to an attempt to explore the factors operative in the ennobling process.

As indicated previously, not all samples of type 347 stainless steel ennobled spontaneously after debasing into the region of active potentials. The selected experimental conditions of temperature, acidity, and oxygen concentration were definitely marginal in this regard for specimens of the alloy employed. Thus, in the experiment illustrated in curve 2 of Fig. 1, the corrosion potential was essentially constant at −350 mv, a steady state of some kind having been reached. Upon replacing the air with a stream of O_2, immediate passivation was induced. Addition of small amounts of other oxidizing agents acted in like manner; thus, less than 1 mg of Fe^{3+} or of Cu^{2+} in 150 ml was found to cause immediate recovery. Addition of 1 mg of Cr^{3+} as sulfate had no influence on the potential. When the potential of a specimen persisted in the active region, passivation could also be induced by lowering the temperature 5 or 10 degrees, raising the pH value from 1.25 to perhaps 1.50, or, usually, by shorting the stainless steel to a platinized electrode in the same aerated solution. It is clear that all these ennobling procedures affected the relative polarizations of the cathodic and anodic processes in such a way that the mixed potential became more noble.

In many experiments a smooth Pt wire was used to serve as a ferric-ferrous indicator electrode after an appreciable concentration of Fe had built up. As may be seen in Fig. 3, such an electrode ennobled rapidly once the stainless steel electrode passed the critical recovery potential and hydrogen ceased to be evolved. The Pt soon reached a maximum positive potential and then slowly debased until the two electrode potentials in time became essentially equal. The declining Pt potential indicated that the Fe^{3+}/Fe^{2+} ratio was decreasing as ennobling of the stainless steel proceeded, hence the following experiment was done with radioactive Fe to determine whether dissolved Fe ions and the passivating film were interacting.[2]

The electrolyte was aerated 0.1*N* H_2SO_4 and the temperature 85°C. In one experiment four abraded electrodes of 2 cm^2 area each were placed in the acid together with a smooth Pt electrode. All four electrodes were cathodized directly in the solution from an external source of current, using the Pt as anode. The four electrodes had potentials in the neighborhood of −310 mv when the current was stopped. One pair of electrodes was then held at −324 mv by continuing the passage of 0.6-0.8 ma; the other pair was allowed to begin the ennobling process while stirring of the solution in contact with air was maintained. At this point radioactive Fe (Fe^{55}, Fe^{59}) in 0.1*N* H_2SO_4 was added. This Fe had been electrolytically reduced to Fe(II) before addition. After the addition (1 mg Fe), the two electrodes which were not being cathodized ennobled by about 600 mv in the next 10 min, while the first pair of electrodes was held at the base potential. Fifteen minutes after addition of the radioactive Fe all four electrodes were removed, thoroughly washed in water and acetone, and counted on a beta proportional counter. As may be seen in Table II, electrodes 77a, b had a small count; a considerably greater count was obtained on the specimens which had been allowed to ennoble (77c, d).

Table II gives also the results of a second experiment which was done in similar manner except that electrodes 77e, f were kept at the base potential only 6 min before addition of 1 mg of Fe containing radioactive tracer. An additional electrode, 77g, was first ennobled by heating it in 0.1*N* H_2SO_4 containing 1.68 mg of ordinary Fe(III) until its potential had passed +350 mv. It was then quickly transferred to the acid containing the radioactive Fe and held for 15 min at 85°C to determine whether the

[2] The assistance of Dr. Franz A. Posey in this experiment is gladly acknowledged.

Table II. Exchange of $Fe^{55,59}$ between film and solution

Specimen	Condition	Total cpm
77-a	—324 mv	91
77-b	—324 mv	100
77-c	Ennobled	415
77-d	Ennobled	270
77-e	—320 mv	61
77-f	Ennobled	314
77-g	Pre-ennobled	304
77-g	Overnight	466*
77-g	—330 mv, 48 min	82†

* Kept overnight in $Fe^{55, 59}$ at 60°C, then 1 hr at 85°C.
† Same electrode cathodically reduced in radioactive solution.

surface state of the already ennobled metal was in dynamic exchange with the Fe in solution. As seen from the table, this electrode also gained radioactive Fe amounting to 304 cpm (counts per minute). This activity was increased to 466 cpm after the sample had stood overnight in the same radioactive Fe solution at about 60°C.

The following experiment demonstrated that the radioactive Fe measured in these experiments is associated with the noble potential. The same specimen, 77g, was returned to the radioactive Fe solution and current of about 1 ma was passed between it and the Pt electrode, the stainless steel being the cathode. Meanwhile, the solution was stirred in contact with air in the usual manner. After the potential had been maintained at about —330 mv for 48 min the sample was withdrawn, washed, and again counted. The activity had reduced to 82 cpm, showing that about 83% of the activity previously present had gone back into solution. Measurement of the potential of a smooth Pt electrode in the same solution showed that the Fe was still approximately 85% in the form of Fe(III).

The counts of the radioactivity deposited on the electrodes cannot be considered precise, but a count on the H_2SO_4 solution at the time specimens a-d were removed, coupled with an Fe analysis at the same time, indicated that the total amount of Fe associated with the radioactivity on the metal surface was of the order of $2\text{-}4 \times 10^{18}$ at./cm^2, which would represent only a small fraction of a monatomic layer.

Experiments with numerous other ions such as Cu^{2+} and $Cr_2O_7^{2-}$ showed that many of them also enter into the ennobling process by a reaction that deposits some form of the added species almost irreversibly in the oxide film. These results will be reported in a subsequent paper.

Discussion

As shown in Fig. 3, the initial potential of abraded and oxidized electrodes was almost as noble as that of smooth Pt. This potential very generally became less noble for a time until its value was in the neighborhood of +350 mv, when the rate of debasing increased greatly. During this rapid fall of potential a brief, but definite, halt or inflection was usually observable, its mid-point averaging 0 mv in 33 experiments in which it was measurable (Fig. 2). During this halt the last traces of film coloration disappeared. The visual effect was most noticeable with specimens having the original mill finish when oxidized, since the irregular disappearance of the film left spots of color which flashed off abruptly at the end of the halt. One of the inflections observed during the subsequent reennobling occurred at approximately the same potential (cf. Fig. 2, 4, and 5). This behavior closely resembles that observed by Flade (9) and by Bonhoeffer and Vetter (2) in connection with the activation and passivation of Fe. With electropolished electrodes, in most instances the golden color gradually faded into the bright, silvery appearance of the unoxidized metal without activation and, hence, with very little corrosion (curve 1, Fig. 1). As previously indicated, the activation process is doubtless to be ascribed to reductive-dissolution of the film by local action.

While the metal was actively corroding at around —330 mv the corrosion rate was shown to be limited by the hydrogen polarization, since the rate increased when the stainless steel was short-circuited to Pt or when oxygen or other oxidizing agent was added. The fact that the corrosion rate was highest just after activation and higher for the preoxidized specimen than for a cathodized specimen (Fig. 4 and 5) can be accounted for by two considerations. Immediately after activation the H polarization has not built up; in this condition the electrode was shown to have a much higher anodic polarization resistance (dE/di) than it had later when fully charged with hydrogen. Secondly, it has been shown that oxidation of stainless steels causes Cr (10) and Si and Nb (11) to pass into the film in considerable excess over the proportions in which they are present in the metal. The outer metallic layer is therefore depleted of these stabilizing elements and of higher chemical activity than normal metal. This enhanced activity was observed also by Vernon, Wormwell, and Nurse (10).

The corrosion rate decreased as the most active metal was dissolved (Fig. 3 and 4) and the potential slowly became less negative under conditions of aeration (Fig. 3). During this period, hydrogen was being removed from the surface (*a*) by reaction with oxygen; (*b*) by reduction of ferric ions present in only minute concentration; or (c) by formation of molecular H_2. (At more positive potentials the hydrogen may also pass back into solution by ionization.) Since ultimate passivation is accomplished by reduction of oxygen (3), it is obvious that spontaneous passivation depends on the relative rates of the two chief cathodic processes, namely, reduction of oxygen and reduction of hydrogen ions. The experimental results indicate that, for the present conditions, the oxygen reaction becomes preponderant at the critical recovery potential of —295 mv, or just slightly below the reversible hydrogen potential.

For passivation to result, it is necessary that the metal be polarized above this potential for a sufficient time to remove the hydrogen. The extremely rapid ennobling that results when the critical recovery potential is reached is believed to be associated with reaction of oxygen with the active hydrogen on or in the metal to form a peroxy com-

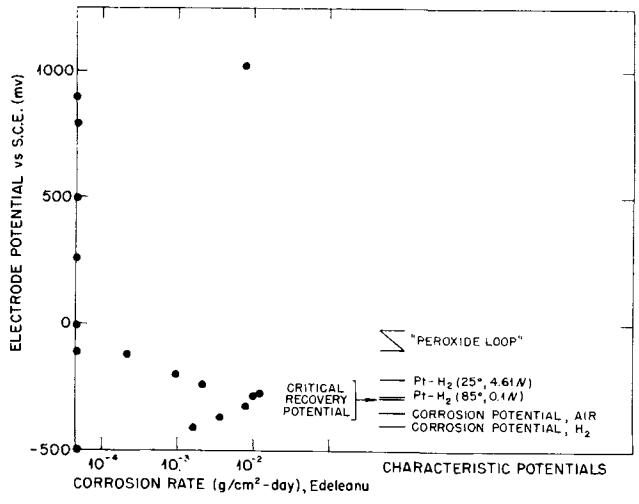

Fig. 6. Corrosion rate at fixed potentials (Edeleanu) in relation to characteristic potentials observed in the present work.

pound. The formation of H_2O_2 by reduction of oxygen at the cathode in electrolysis of dilute H_2SO_4 is well established, the yield being very high when the current density is low, as it is in the corrosion process (12, 13). Such an effect was seen in the present experiments in the following way: a Pt electrode in aerated H_2SO_4 was at a stable potential a few hundred millivolts more noble than a corroding stainless steel electrode in the same solution. When the electrodes were connected, the Pt was the cathode of the cell so formed and its potential became less noble. When the circuit was opened, the potential of the Pt rose at once to a more noble value than it had before being short-circuited, and in a few minutes returned to the initial stable value.[3] On the basis of this interpretation, the first halt observed after the rapid ennobling above the critical recovery potential most probably represents the time required for the residual hydrogen to diffuse from the interior of the metal. The second halt usually observed is most likely associated with the building of the acid-stable film, in which Fe(III) ions were shown to be involved.

There would seem to be no qualitative or fundamental difference between stainless steel and Fe with respect to the essential condition for passivation to occur. As has been pointed out elsewhere (14), the passivation of Fe can be achieved by atmospheric oxygen provided an efficient inhibitor such as the XO_4^{n-} ions or molecules is present. It was suggested (15, 16) that these particles are adsorbed and exert electrostatic forces at the interface such as to diminish the chemical activity of the electrons in the metal sufficiently to prevent the reduction of hydrogen ions.[4] The difference between Fe and stainless steel, therefore, is a quantitative one, in that stainless steel may be raised above the hydrogen potential by oxygen without benefit of a cathodic inhibitor, as if its electrons already had a somewhat diminished chemical activity. To this extent there is merit in the electron theory of passivity developed by Uhlig and Wulff (17) and by Uhlig (18). That the difference is not very large, however, is shown by the fact that electrolytic Fe corroded under the conditions of these experiments at a potential only about 200 mv below that of stainless steel.

The present experiments shed light on the results of Edeleanu (19), who studied the corrosion rate of an 18-8 stainless steel held at constant potentials in 20% H_2SO_4 (4.61*N*) at 25°C. For comparison with his results, the empirical hydrogen potential under his conditions was determined and found to be −217 mv. The corrosion rates of Edeleanu are shown by the points at the left of Fig. 6. The characteristic potentials found in the present work are indicated at the right. It is clear that the maximum corrosion rate occurred just slightly below the empirical hydrogen potential for 4.61*N* acid at 25°C. As was shown previously, the corroding metal in 0.1*N* acid at 85°C has a potential somewhat more negative than the hydrogen potential for the same conditions. A potential just under the hydrogen potential would then represent the highest anodic polarization that could be applied to the metal without going to the potential for passivation.

Manuscript received August 13, 1956. The work on this paper was done for the A.E.C. under contract with the Union Carbide Nuclear Co.

Any discussion of this paper will appear in a Discussion Section to be published in the June 1958 JOURNAL.

[3] Similar activation of oxygen by hydrogen in Pt was observed in the slower conversion of cathodically deposited TcO_2 into $HTcO_4$ by aerated water when the hydrogen was removed from the electrode before exposure to oxygen. H_2O_2 rapidly effects the oxidation.

[4] It is to be noted that, in the kinetics of irreversible electrode processes, the cathodic consumption of electrons as a reactant may be affected by factors that do not appear in the chemical equation expressing the electrode process. Such effects may conceivably alter the pre-exponential factor as they surely change the activation energy in the exponential term. It is in this sense that the term "activity" of electrons is used, without assuming any specific mechanism for the effects in question.

REFERENCES

1. G. H. Cartledge, *Nature*, **177**, 181 (1956).
2. K. F. Bonhoeffer and K. J. Vetter, *Z. physik. Chem.*, **196**, 127 (1950).
3. I. D. G. Berwick and U. R. Evans, *J. Applied Chem., London*, **2**, 576 (1952).
4. *See*, for example, H. H. Uhlig and A. Geary, *This Journal*, **101**, 215 (1954).
5. H. W. Swank and M. G. Mellon, *Ind. Eng. Chem., Anal. Ed.*, **10**, 7 (1938).
6. S. A. Burke, *Trans. Faraday Soc.*, **33**, 309 (1937).
7. W. Schwartz, *Z. Elektrochem.*, **55**, 170 (1951).
8. M. J. Pryor and U. R. Evans, *J. Chem. Soc.*, **1950** 1259.
9. F. Flade, *Z. physik. Chem.*, **76**, 513 (1911).
10. W. H. J. Vernon, F. Wormwell, and T. J. Nurse, *J. Iron and Steel Inst.*, **150**, 81P (1944).
11. T. N. Rhodin, *Corrosion*, **12**, 123t (1956).
12. M. Traube, *Ber. König. Akad. Wiss. Berlin*, 1041 (1887).
13. F. Fischer and O. Priess, *Ber.*, **46**, 698 (1913).
14. R. F. Sympson and G. H. Cartledge, *J. Phys. Chem.*, **60**, 1037 (1956).
15. G. H. Cartledge, *ibid.*, **60**, 32 (1956).
16. G. H. Cartledge, *ibid.*, **60**, 1571 (1956).
17. H. H. Uhlig and J. Wulff, *Am. Inst. Mining Met. Engrs.*, **135**, 494 (1939).
18. H. H. Uhlig, *Trans. Electrochem. Soc.*, **85**, 307 (1944).
19. C. Edeleanu, *Nature*, **173**, 739 (1954).

Ionic Conductivity of Anodic Films at High Field Strengths: Transient Behavior

D. A. Vermilyea

Research Laboratory, General Electric Company, Schenectady, New York

ABSTRACT

Studies of the changes in ionic conductivity of anodic Ta_2O_5 films following rapid changes of applied voltage or following a heat treatment of the film have shown that the activation energy and activation distance for ionic motion vary with changes in electric field and temperature. A consideration of these results along with other information obtained from the corrosion behavior of the films and from x-ray diffraction by the films shows that a mechanism proposed earlier to account for ionic conduction in these films requires modification. It is suggested that a change of the applied field changes not only the number of conducting ions, as proposed earlier, but also changes the average local configuration in the glass-like film and, hence, changes the mobility of the ions as well. Transient behavior similar to that shown by the Ta_2O_5 films is also shown by anodic films of Al_2O_3 and Nb_2O_5, but not by anodic ZrO_2.

According to a recent theory (1) of high field ionic conduction in Ta_2O_5, the current is carried by interstitial Ta ions which are created when a Ta ion leaves its normal position. The Ta ion vacancies left behind act as traps for interstitials, and an equilibrium is established when the rates of formation and capture of interstitials become equal. The equilibrium interstitial Ta ion concentration is field dependent. If the field in the Ta_2O_5 is suddenly changed, a transient current should be observed because of the finite time required to establish the new equilibrium. If, for example, the field was suddenly increased, the initial current would be lower than the steady value corresponding to the new field, and there would be a measurable increase in the current while the new equilibrium was being established. Such transients have been known to exist for many years (2); this paper is a report of a study of these transients. The data obtained considered together with results of x-ray diffraction and corrosion studies (3) make it appear unlikely that the proposed theory is adequate for the description of ionic conduction in Ta_2O_5 films, and a modification which takes account of the glass-like structure of the films is discussed. Preliminary experiments using other anodic films are also discussed briefly.

Theory

Two types of experiments can provide useful information. In one type transient currents are observed at constant voltage and in the other voltage transients are observed at constant current. The theory for the voltage transient at constant current is discussed first.

Transients at constant current.—According to the theory of high field ionic conduction (1), the rate of creation of interstitials is given by

$$\frac{dn_+}{dt} = (N - n)\ \exp\ \nu\ [-(Q_i - q\lambda_i E)/kT] \qquad (I)$$

where n is the concentration of interstitials, N is the concentration of Ta ions in the film, ν is a frequency, Q_i is the activation energy for creation of an interstitial, q is the charge on the ion, λ_i is the distance from the normal position of the ion to the top of the activation barrier, and E is the magnitude of the electric field. Q_i and λ_i have different values in different ranges of field strengths. The rate of capture of interstitials is

$$\frac{dn_-}{dt} = \frac{n^2}{N}\nu \exp\ [-(Q - q\lambda E)kT] \qquad (II)$$

where Q is the activation energy for migration of an interstitial far from a vacancy and λ is the corresponding activation distance. The equilibrium concentration can be found by equating Eqs. (I) and (II) and solving for n.

Now consider an anodic Ta_2O_5 film through which a current is passing so that there are n_0 interstitial Ta ions per cubic centimeter. If the field is interrupted and the specimen is held at a temperature T_a these ions will move about in the film by diffusion and eventually will all recombine with vacancies. The rate of recombination will be given by an equation similar to Eq. (II) with $E = 0$. For zero field, however, the capture cross section should be considerably larger than for high fields. This can be allowed for formally by multiplying the right hand side of Eq. (II) by b, where $b >> 1$. The number of ions left at any time t, n_t, is found by integration to be

$$n_t = \frac{n_0}{1 + n_0 \gamma t} \qquad (III)$$

where $\gamma = b\nu/N \exp(-Q/kT_a)$. If a constant ion currently density, j, is now passed through the film the initial field, E_i, can be found from

$$j = 2\lambda\nu\, n_i \exp -(Q - q\lambda E_i)/kT \qquad \text{(IV)}$$

where T is the temperature at which the transient is observed. Solving for E_i gives

$$E_i = \frac{kT}{q\lambda}\left[\ln\frac{j}{2\lambda\,\nu\,n_0} + \frac{Q}{kT} + \ln(1 + n_0\gamma t)\right] \qquad \text{(V)}$$

which shows that when $n_0\gamma t >> 1$ a plot of the initial field required to give a particular current vs. the logarithm of the annealing time should give a straight line of slope $kT/q\lambda$. If the temperature at which the transients are observed is constant and the annealing temperature variable, a plot of the logarithm of the annealing time required to cause a given initial field vs. the reciprocal of the absolute temperature should give a straight line of slope Q/k. It should therefore be possible to determine both the activation energy Q and activation distance λ for the diffusion of Ta ions when they are far from any vacancies. From the data on the kinetics of growth of the film (4), it would then be possible to determine the activation energy Q_i and activation distance λ_i for the creation of interstitial ions and hence their number at any particular field strength.

It is not easy to obtain an expression for the voltage as a function of time during a constant current transient. However, the order of magnitude of the duration of the transient can be estimated in the following manner. Upon application of a constant current to an annealed Ta_2O_5 film the voltage increases rapidly to a maximum and then decreases as new interstitial Ta ions are formed. The time required for the complete disappearance of the transient depends primarily on the steady field in the oxide when the transient has disappeared. The time for the voltage transient to disappear at a constant current is therefore the same as the corresponding time for a current transient at the final steady field. Rewriting Eqs. (I) and (II) for a constant field experiment and assuming $n << N$ gives

$$\frac{dn_+}{dt} = \alpha \qquad \text{(I')}$$

$$\frac{dn_-}{dt} = \beta n^2 \qquad \text{(II')}$$

where α and β are constants. Adding Eqs. (I') and (II') to obtain dn/dt and integrating gives

$$\frac{\alpha - n\sqrt{\alpha\beta}}{\alpha + n\sqrt{\alpha\beta}} = \frac{\alpha - n_0\sqrt{\alpha\beta}}{\alpha + n_0\sqrt{\alpha\beta}} \exp(-2t\sqrt{\alpha\beta}) \qquad \text{(VI)}$$

where n_0 is the number of interstitial ions present initially and t is the time. Eq. (VI) shows that the transient will have disappeared almost completely when

$$t \cong \frac{3}{\sqrt{\alpha\beta}} \qquad \text{(VII)}$$

at which time $n = \sqrt{\alpha\beta}$. From Eqs. (I), (I'), (II), and (II')

$$\sqrt{\alpha\beta} = \nu \exp\{-[Q_i + Q - q(\lambda_i + \lambda)E]/kT\} \qquad \text{(VIII)}$$

where E is the steady field after the disappearance of the transient. With Eq. 6 of Ref. (1) Eq. (VIII) becomes

$$\sqrt{\alpha\beta} = 2\lambda N j \qquad \text{(VIII')}$$

Transients at constant voltage.—Analysis of data from constant voltage experiments is much simpler than with that of the constant current experiments. Consider an anodic Ta_2O_5 film which is held at a constant voltage. If a current j_1 is passing through the film, a sudden change of voltage will cause a sudden change of current to j_2. The value of $q\lambda$ is now found from Eq. (IV) to be

$$q\lambda = \frac{kT}{E_1 - E_2}\ln\frac{j_1}{j_2} \qquad \text{(IX)}$$

where E_1 and E_2 are the initial and final field strengths.

Once the value of $q\lambda$ has been determined from Eq. (IX), the activation energy Q can be determined by taking several specimens all in the same initial condition and recording the initial current upon sudden application of a convenient field strength. The currents at the same field strength at several temperatures can then be determined with the use of Eq. (IV), and the activation energy determined from a plot of log current vs. $1/T$.

Experimental Methods

Anodic Ta_2O_5 films were formed on chemically polished Ta sheet obtained from Fansteel Metallurgical Company. This material was the same type as that used previously (5). All of the films used in the constant current experiments were formed at 1.56 ma/cm^2 (specimen area 6.4 cm^2) to 120 v at 29°C using 2% Na_2SO_4 solution in water, and were 1760Å thick.[1] As soon as the required thickness was reached the cell was short circuited to eliminate any changes in the film due to a slow discharge of the applied potential. After formation the films were annealed at various temperatures using heating baths of water or silicone oil depending on the annealing temperature. After the anneal a current of 0.1 ma/cm^2 was impressed on the specimen again using 2% Na_2SO_4 solution at 29°C, and the voltage recorded as a function of time on a Brush Recording Oscillograph. The zero point of the recorder was suppressed so that only about 40 v appeared on the scale, and the voltage could be read with an estimated uncertainty of ±0.4 v.

Constant voltage experiments were conducted using the same material and electrolytic solution. Sudden changes in the applied voltage were made with the apparatus shown in Fig. 1. By operating switch S the voltage set on the potentiometer could be added to or subtracted from that of the constant voltage supply.

Results

Experiments using constant current.—Fig. 2 shows typical voltage-time traces at constant current. Each horizontal division represents 0.2 sec, and each

[1] Thickness measured by comparison with optical step gauge (5).

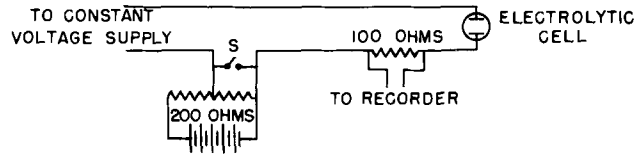

Fig. 1. Apparatus used for producing sudden changes in the voltage applied across a specimen.

small vertical division is 1.0 v. The voltage rises fairly rapidly, reaches a maximum, and then decreases. The voltage rises slowly because of the necessity for charging the condenser formed by the system Ta-Ta_2O_5-solution which has a capacitance of 0.8 mfd and requires 0.15 sec to reach 120 v at 0.64 ma. As the voltage approaches the maximum some conduction in the film occurs, so that the voltage rises more slowly and the maximum is reached in all cases at about 0.35 sec. As the conductivity of the film increases due to the process responsible for the transient the voltage falls, reaches a minimum in about 10 sec, and then increases slowly as the film continues to grow at a steady rate. The increase in film thickness during the transient is only about 5Å, so no appreciable error is made in calculating the field if it is assumed that the thickness is constant.

The duration of the voltage transients at constant current, 10 sec, was the same for all specimens as it should be according to the theory. With $\lambda \approx 2 \times 10^{-8}$, $N = 2.3 \times 10^{22}$, Eq. (VIII′) gives $t \sim 8$ sec, in very good agreement with the experimental value.

Fig. 3 shows the maximum field reached during the transient at constant current against the logarithm of the time. An approximation to the initial field [Eq. (V)] can be obtained by extrapolating the voltage time curve back until it meets the voltage time curve for charging the condenser. Data obtained in this way are shown in Fig. 4, and linear field vs. log time plots are obtained. This extrapolation method is probably fairly good when the maximum field is small so that the voltage changes slowly with time, but is very inaccurate when the maximum field is large.

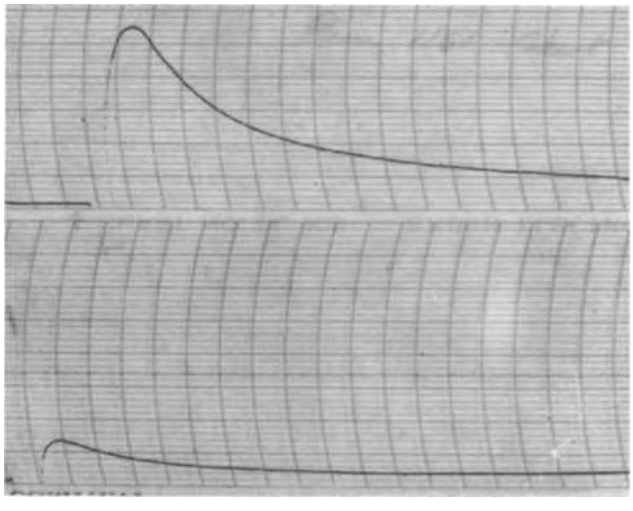

Fig. 2. Voltage vs. time at constant current. Upper curve, specimen annealed 1.5 x 10^5 sec at 100°C; lower curve, specimen annealed 4 sec at 100°C. Each small division in the vertical direction is 1.0 v, and each division in the horizontal direction is 0.2 sec.

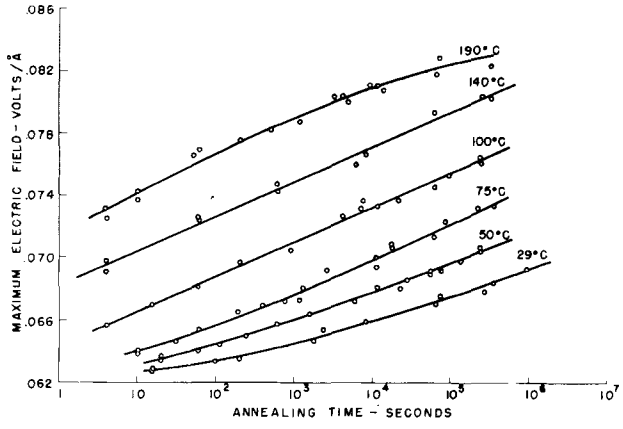

Fig. 3. Maximum field reached during formation of films at constant current after annealing for various times at different temperatures.

Fig. 5 shows the logarithm of the annealing time required to reach a given maximum field against the reciprocal of the absolute annealing temperature. Since all of the curves which have a given maximum field also have approximately the same shape, each maximum field corresponds to a given initial field and hence a given state of the oxide. The slopes of the curves of Fig. 5 thus are equal to Q/k, and activation energies calculated from the slopes are plotted vs. maximum field in Fig. 6. It may be seen that the activation energy increases with increasing extent of annealing from about 0.8 ev to 1.35 ev.

The activation distance λ times the charge q can be estimated from the slopes of the curves of Fig. 4 using Eq. (V). Values of $q\lambda$ thus obtained increase from 12 at 190°C to 21 at 29°C, in units of electron charges times angstrom units. While these values are clearly of the right order of magnitude, they are probably considerably too large because of the fact that the activation energy increases as annealing progresses.

Dependence of transient on the history of the film. —Several experiments were performed using the constant current method to determine whether the

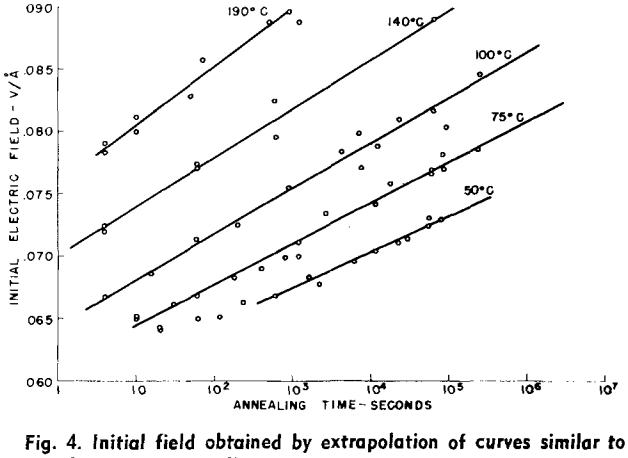

Fig. 4. Initial field obtained by extrapolation of curves similar to those of Fig. 2 vs. annealing time.

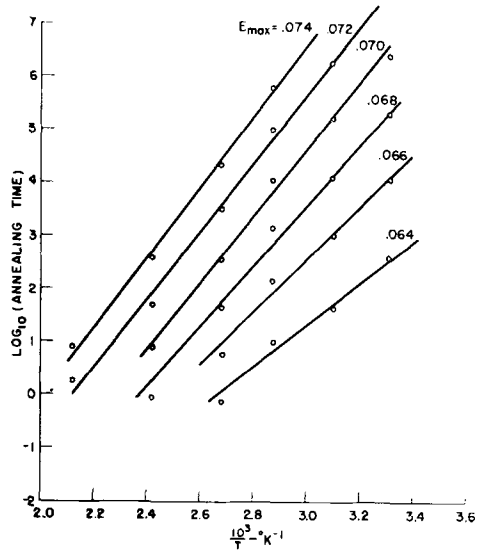

Fig. 5. Logarithm of the annealing time required to reach a given value of maximum field (see Fig. 3) vs. $1/T$.

curve of E_{max} vs. time was sensitive to the previous history of the film. Fig. 7 shows typical results. Curve 1 is the curve for 140°C from Fig. 3. Curve 2 is for specimens first held at 190°C for 10 sec to give an E_{max} of 0736. Since this E_{max} would have been produced in 250 sec at 140°C, E_{max} was plotted against log (time + 250). There is some indication of a more rapid initial rate and a slower final rate. When the specimens were first held at 80°C until the current was 0.5 ma (curve 3) the value of E_{max} was about the same (0.0734) corresponding to 200 sec at 140°C. Upon annealing these specimens at 140°C, however, there is a marked deviation from the previous results. Thus, a given value of E_{max} is not associated only with a certain number of interstitials and vacancies, since the behavior of the film on subsequent annealing is a function of the manner in which the given E_{max} was achieved. The presence of history effects makes it possible that the activation energies shown in Fig. 6 might be in error.

Experiments at constant voltage.—Fig. 8 shows typical current transients at constant voltage. Each hoizontal division is 0.04 sec, and each small vertical

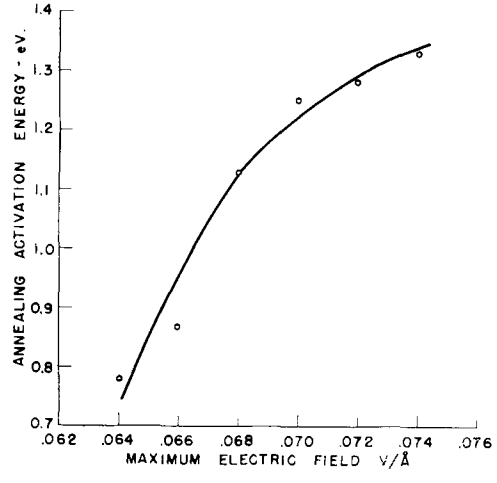

Fig. 6. Activation energy obtained from Fig. 5 vs. maximum field

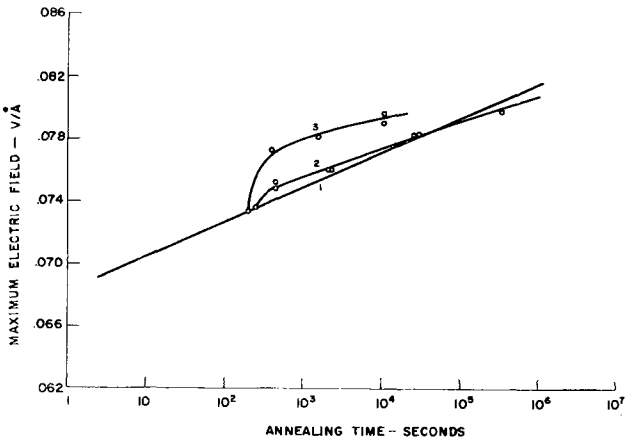

Fig. 7. History effects. Annealing at 140°C alone (curve 1) and after annealing 10 sec at 190°C (curve 2) or forming at 0.5 ma, 80°C (curve 3).

division 0.05 ma on the upper trace, 0.4 ma on the lower trace. There is some oscillation of the oscillograph pen after the sudden voltage change, but the oscillation is damped out in about 0.02 sec and causes no difficulty in determining the current immediately after the voltage change. The major advantage of the constant voltage method is that the time required to charge the condenser is now only about 10^{-4} sec.

Values of $q\lambda$ were obtained for many different ratios of initial and final currents using different temperatures. At any one temperature the value of $q\lambda$ was approximately constant, independent of the field or film thickness, although there was some indication that $q\lambda$ was larger when the field before the voltage change was smaller. Increasing the temperature caused an increase in $q\lambda$ from 4.5 e.Å at 19°C to 6.1 e.Å at 100°C as shown in Fig. 9. Other experiments designed to detect a dependence on specimen history used specimens formed at 29°C, 10 ma to 1750Å, then annealed at 100°C for 5 and 15 min. Values of $q\lambda$ observed initially in these history

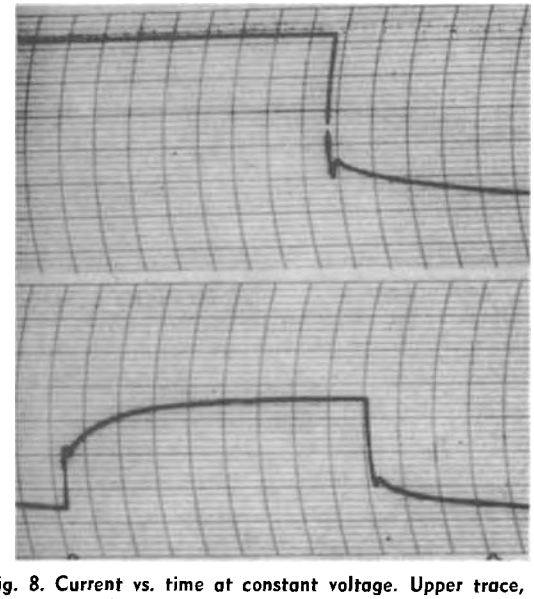

Fig. 8. Current vs. time at constant voltage. Upper trace, 91°C, small vertical division = 0.05 ma, field changed from 0.056 to 0.0515 v/Å. Lower trace, 81°C, small vertical division = 0.4 ma, field changed from 0.062 to 0.0575 v/Å. Both curves, one horizontal division = 0.04 sec.

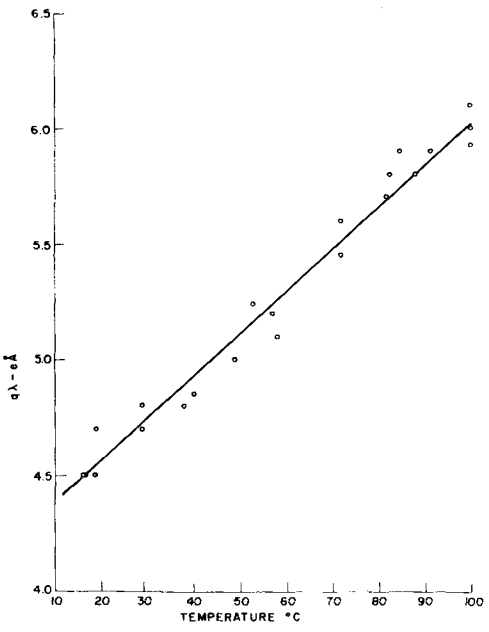

Fig. 9. Variation of $q\lambda$ with temperature

experiments were 6.3 and 6.5, respectively. As current flowed, however, the values of $q\lambda$ decreased to 4.7. Thus the value of $q\lambda$ is not a single valued function of the temperature but depends on the previous history of the specimen.

To determine the activation energy for ionic conduction several specimens were formed at 1.56 ma/cm^2 to 1759Å at 29°C in 2% Na_2SO_4, annealed at 100°C in boiling water for 5 min, and the initial current measured when a suitable field was applied at different temperatures. Currents which would be produced by a field of 0.058 v/Å were then calculated using Eq. (IV) with $q\lambda = 6.3$ as obtained above for specimens annealed in this manner. The slope of a plot of the logarithm of the current at $E = 0.058$ v/Å vs. $1/T$ (Fig. 10) gives an activation energy for ionic conduction of 0.7 ev. The zero field activation energy would be $0.7 + 0.058 \times 6.3 = 1.06$ ev. Annealing for 5 min at 100°C would result in an E_{max} of about 0.07 v/Å (Fig. 3), and from Fig. 6 the activation energy would be about 1.2 ev. Thus, considering the uncertainty in the annealing activation energies caused by history effects, activation energies for annealing and for ion conduction appear to be the same. The activation energy for ion conduction is therefore probably variable, and the value of 1.06 ev would be found only for specimens treated in exactly the same manner as those used above.

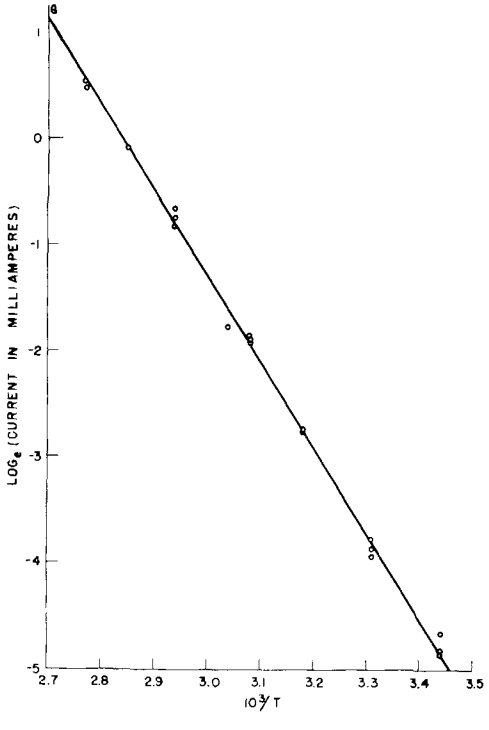

Fig. 10. Logarithm of the current produced by a field of 0.058 v/Å on specimens annealed 5 min at 100°C vs. $1/T$.

Transient studies using other metals.—It might be expected that the kinds of changes which occur in anodic Ta_2O_5 films might also occur in other amorphous anodic films such as Al_2O_3, Nb_2O_5, and ZrO_2. The constant voltage method has been used to determine the values of $q\lambda$ for films formed on chemically polished Zr, Nb, and Al. For these tests a solution of 5% $NH_4HB_4O_7 \cdot 3H_2O$ in water, with sufficient H_3BO_3 to give a *p*H of 7, was used; all tests were conducted at room temperature (26°C). The thickness of the ZrO_2 and Al_2O_3 films was estimated from capacitance measurements using values for the dielectric constant of 20 and 10,[2] respectively, and are fairly reliable. The thicknesses of the Nb_2O_5 films were estimated by comparison with the optical step gauge for Ta_2O_5 films, and may be in error because of differences in the refractive indices for the two materials. Results are given in Table I, along with the results obtained for Ta. The "effective $q\lambda$" in the table is found by allowing the transient to decay completely, using the ratio of initial to final current in Eq. (IX). Values of effective $q\lambda$ agree fairly well with those reported earlier by various authors as shown in the table.

The results show that Nb_2O_5 behaves in a manner similar to that of Ta_2O_5, having a small value of $q\lambda$ which does not vary with the current density. Al and Zr show somewhat different behavior, the values of $q\lambda$ increasing with decreasing current density. For Zr this increase is probably the result of the increasing electronic component of the current at small currents; probably only the results at high currents are reliable. For Al, on the other hand, the current is almost all ionic at all of the current densities used (12), and the change in $q\lambda$ may be a result of an actual change of structure with changing current.

The most interesting part of these data is the difference between Zr and the other metals. There is almost no transient with Zr, the current immediately after the change of voltage being nearly the steady value. Attempts to increase any possible transient by intermediate annealing were not successful. Also, the value of $q\lambda$ found for Zr is much larger than that for the other metals. It may be that

[2] This value for the dielectric constant of anodic aluminum oxide was chosen so that the thickness for formation at room temperature, 3 ma/cm^2, would be about 13.5Å/v, in agreement with the results of Hass (7).

Table I. Results of transient studies using several metals

Material	Oxide film thickness, Å	Current density range, ma/cm²	Initial qλ e.Å	Effective qλ e.Å	Values of effective qλ from the literature
ZrO_2	1500	0.007-0.003	4.0	——	
		0.3-0.15	5.0	——	
		1.5-1.0	10.8	11.3	11.2 Charlesby (8)
Al_2O_3	1200	3.0-1.5	3.3	10.6	
		0.3-0.15	4.1	——	7.5 Charlesby (9)
		0.03-0.015	4.5	12.1	10.5 Guntherschulze and Betz (10)
Nb_2O_5	1800	0.5-0.2	5.8	12.2	
		0.005-0.02	5.8	——	
Ta_2O_5	1600	3-1.5	4.6	12.1	11.7 Vermilyea (4)
		0.5-0.2	4.6		12.5 Young (11)
		0.1-0.05	4.8		

the ionic current in the ZrO_2 film is controlled at an interface rather than in the bulk of the material.

Except for Zr, however, results show that slow changes in the film follow changes in the applied field, as for tantalum oxide films. Values of $q\lambda$ for all except ZrO_2 are all very reasonable, giving values of λ ranging from 1 to 1.5Å if the full ionic charges are assumed. In view of the lack of transients in ZrO_2 films and the very large value of $q\lambda$ it would be interesting to make a more thorough study of ionic conduction in these films.

Discussion

Results obtained from constant current and constant voltage tests are summarized in Table II.

Values of $q\lambda$ obtained in constant voltage experiments are believed to be more reliable.

The points of agreement between the results and theory are that transients which are qualitatively of the type predicted are observed, and that the duration of the transients agrees with the predicted value. There are, however, several serious points of disagreement. In the first place, $q\lambda$ varies with the temperatures at which it is measured and also with the history of the film. Second, the constant current transients also depend on the history of the film. Third, the activation energy for annealing depends on the extent of annealing, while, if the only process occurring were the recombination of defects, it should be constant. Finally, the numbers of defects, calculated with the values given in Table I and using Eq. (5) of Ref. (1), approach the number of lattice ions in some ranges of field and temperature. The theory should apply only to very low concentrations of defects, of the order of 10^{-4} or less of the number of lattice ions.

Further evidence which appears to contradict the theory has been obtained in tests to determine the solution rate of the films in HF (3). It was found that the solution rate decreased linearly with log time at annealing temperatures from room temperature to 330°C. Since the theory predicts that the change which is occurring is simply a decrease in the number of defects, and that the number of defects is inversely proportional to the time, these results imply that the corrosion rate is proportional to the logarithm of the defect concentration. It would be expected that for small defect concentrations the solution rate would be proportional to the number of defects rather than to the logarithm of the number, and it is therefore difficult to account for this behavior unless it is postulated that changes in solution rate and rate of ion transport are completely unrelated. However, the magnitudes of the activation energies for the process responsible for the change in corrosion rate are the same as those for the change in the constant current transient, which indicates that the processes are probably the same.

Table II. Summary of activation energies and values of qλ

Method	Activation energy ev	q-e.Å
Constant current	0.8-1.35	12-21
Constant voltage	1.06	4.5-6.5

In addition to the changes in solution rate which occur upon annealing the films, it was also found (3) that x-ray diffraction patterns from the film become somewhat less diffuse upon annealing at temperatures between 200° and 600°C. A decrease in the diffuseness of the pattern might conceivably occur if the concentration of interstitial Ta ions decreased as predicted by the theory. It is probable, however, that such a change would have to involve defect concentrations of about a tenth of a percent or more, that is, a concentration so high that the theory would not apply.

All the evidence suggests, therefore, that some change other than that of the concentration of defects alone must be occurring. A modification of the theory which can explain qualitatively all of the observed results follows. The anodic oxide film on Ta is amorphous, and appears to be glass like. It is assumed that the passage of a current through the film produces a change in the local ionic configuration and that the change is of such a nature that conduction is made easier. For example, the current flow might change an originally uniform Ta ion concentration to one in which the spacing between ions varied slightly from place to place in the film, with the result that some ions would be located so that jumps to a neighboring position would require relatively less energy. An increase in the current density would be expected to change both the number and the activation energy for motion of these favorably located ions, the total effect being to increase the conductivity. This mechanism bears a strong resemblance to that originally proposed, since

here there are a field dependent number of mobile ions which correspond to the "interstitial ions" of the earlier theory. The differences are, first, that all ions are now supposed to be lattice ions, some of which are in favorable configurations for motion and, second, that both the number and the activation energy for motion of these ions changes with the passage of current instead of just the number as previously assumed. Support for the reasonableness of changes in local configuration is found in the fact that changes in local configuration in ordinary glasses accompany heat treatments such as rapid cooling from high temperature or annealing in the transition range of temperatures (6), and the changes are believed to be responsible for the observed variations in density, refractive index, conductivity, and other properties.

No quantitative predictions are attempted, but qualitatively the explanations of the experimental results are as follows. First, consider a constant voltage transient experiment such as those described above. When the field is suddenly changed there is an instantaneous change in current because the effect of the smaller field on the activation barrier is less. Following the instantaneous change there is a slow change in both the number of conducting ions and in the barriers to their motion which makes ionic motion more difficult. The net result is that the field has produced a much larger effect than that due solely to changing the field on the barrier which existed before the voltage change. In other words, the effective value of $q\lambda$, defined by an equation similar to Eq. (IX) but measuring the final current after the decay of the transient, is much larger than the ionic charge times half the distance between successive minima in the energy of an ion. The change of $q\lambda$ with temperature and the history dependence of $q\lambda$ are, according to this mechanism, a result of an actual change of activation distance with changes in local configuration. The range of values of $q\lambda$, 4.5 — 6.5 e.Å, is reasonable, particularly since it is possible that the ionic charge would be less than five. The value of the pre-exponential factor calculated from the data shown in Fig. 10 is about 2×10^{24}, while the value of $2\lambda\nu N$ is about 4×10^{27} if $\nu = 5.10^{12}$. Thus it appears that for Ta_2O_5 films treated in this one particular manner only about one Ta ion in a thousand is in a favorable local configuration for motion. The values of preexponential factors found in the earlier work (0.2×10^{27} to 2×10^{27}) are difficult to interpret since they represent the intercepts of log rate vs. $1/T$ plots for specimens with different local configurations held at the same electric field.

When a film is annealed the structure would tend to change toward a more stable configuration, so that upon re-application of a field the current would be smaller. The activation energy for annealing is that observed above, 0.8-1.35 ev, and increases as annealing progresses. Annealing and conduction may both involve the same sort of atomic movements, since the activation energies are similar. The effect of the history of the film on the annealing process is the result of the fact that different methods of reaching a state measured by the transient behavior result in different local configurations, and hence films brought to such a state by different methods behave differently on subsequent annealing by the same method.

In addition to producing changes in the rate of ionic transport, such changes of local configuration would be expected to change the x-ray scattering by the film and also the chemical properties of the film. Furthermore, there is no reason to suppose that such changes would be restricted to annealing in any particular small range of temperatures. The results of measurements of the solution rate in HF and of x-ray scattering by the films are thus in good qualitative agreement with this mechanism, since it would be expected that the most stable state would be one of minimum lattice distortion and would show greater chemical stability and give less diffuse x-ray patterns.

If it is accepted that changes in local configuration do occur, it is clear that the only experiments which can supply easily interpreted information about the values of activation distance and activation energy are those in which measurements are made on specimens having the same history and in a time short enough so that no changes in local configuration can occur. Measurements such as those reported earlier (4) for Ta_2O_5 are very difficult to interpret in terms of the activation energies and distance actually existing at any instant in the film.

Acknowledgement

Discussions with C. P. Bean were of great value in arriving at an interpretation of these experimental results. Helpful criticisms of the manuscript by D. Turnbull are gratefully acknowledged.

Manuscript received October 2, 1956.

Any discussion of this paper will appear in a Discussion Section to be published in the June 1958 JOURNAL.

REFERENCES

1. C. P. Bean, J. C. Fisher, and D. A. Vermilyea, *Phys. Rev.*, **101**, 551 (1956).
2. A. Guntherschulze and H. Betz, "Elektrolytkondensatoren," p. 69, Berlin (1937).
3. D. A. Vermilyea, *This Journal*, to be published.
4. D. A. Vermilyea, *ibid.*, **102**, 655 (1955).
5. D. A. Vermilyea, *Acta Met.*, **1**, 282 (1953).
6. R. O. Davies and G. O. Jones, *Adv. in Physics*, **2**, 370 (1953).
7. G. Hass, *J. Opt. Soc. Amer.*, **39**, 532 (1949).
8. A. Charlesby, *Acta Met.*, **1**, 340 (1955).
9. A. Charlesby, *Proc. Phys. Soc.*, **66B**, 317 (1953).
10. A. Guntherschulze and H. Betz, *Z. Phys.*, **92**, 367 (1934).
11. L Young, *Trans. Faraday Soc.*, **50**, 153 (1954).
12. A. Charlesby, *Proc. Phys. Soc.*, **66B**, 533 (1953).

Metal-Water Reactions

V. Kinetics of the Reaction between Magnesium and Water Vapor

Harry J. Svec and Dale S. Gibbs

Institute for Atomic Research and Department of Chemistry, Iowa State College, Ames, Iowa

ABSTRACT

The rate of reaction between magnesium and water vapor was studied in the temperature range between 425° and 575°C and in the water vapor pressure range between 31 and 208 mm Hg. The reaction took place according to the linear rate law. Rate constants were found to be linearly dependent on the water vapor pressure. The activation energy for the reaction was found to vary with both temperature and water vapor pressure, increasing as the temperature was increased and the water vapor pressure was decreased. This type of variation is explained on the basis of a change from a surface to a vapor phase reaction due to the very large increase in the vapor pressure of Mg metal in the temperature range between 500° and 600°C.

The kinetics of the oxidation of Mg metal by oxygen gas have been studied by many workers (1-5). The effect of the presence of water vapor on the rate of reaction was also examined in some of these researches. The work reported here includes the study of the surface oxidation of Mg metal by water vapor in the absence of other gases. Reaction temperature and water vapor pressure are varied independently to determine their influence on the rate of reaction. The results of these studies are correlated with the results of the oxidation of Mg by oxygen and other metal-gas reactions.

In the temperature range covered by this work, the products of the reaction between Mg and water vapor are MgO and H_2, according to the equation

$$Mg + H_2O \rightarrow MgO + H_2$$

Because of the nature of this stoichiometry, the rate was followed by measuring the pressure increases due to H evolution in a closed system.

Experimental

Apparatus

The apparatus for the study of the reaction of water vapor and Mg is depicted diagrammatically in Fig. 1. The vacuum apparatus was built around a 25 mm OD, Pyrex glass tube (A) which was suspended vertically in the center of a 12 gal, controlled-temperature water bath. A 10 mm, high-vacuum grade stopcock (S_1) at the top of the tube and at the water line of the bath isolated the thermostatted part of the apparatus from the outer vacuum pumping system. Apiezon T grease was used to lubricate this stopcock, and it was found to hold satisfactorily at all bath temperatures up to 72°C. The lower portion of the tube (A) was connected to an opening through the bottom of the bath by means of a kovar seal (B) and a stainless steel ball joint (C). The port was fitted with a thin disk which was sealed to the glass water bath jar with Apiezon W wax to give a water-tight seal. A 35/20 ball joint (T_1) was an integral part of the stainless steel port. The reaction tube (D) was constructed of 24 mm OD Vycor tubing and the socket was also made of Vycor. The metal sample (F) was suspended in the reaction tube by means of nichrome wire, A.W.G. 34. The sample was insulated from the nichrome wire by a small alumina tube placed in a hole drilled across one end of the specimen.

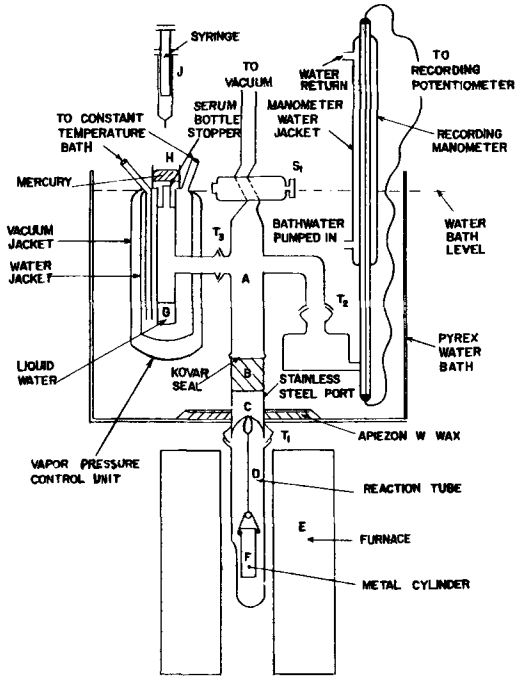

Fig. 1. Manometric apparatus for the study of the kinetics of the reaction of Mg and water vapor.

The reaction tube was heated by an electric furnace (E), the core of which consisted of an Inconel tube 18 in. long, with an ID of 1.0 in. The linear temperature variation was ±0.1°C for a section 4.0 in. long in the middle of the tube. The furnace had a Chromel A heating winding and a Pt temperature-sensing winding. An electronic proportioning furnace controller (6) was used, and the temperature in the region of the sample was controlled to better than ±0.05°C in the temperature range between 400° and 600°C.

A recording mercurial manometer (7) was connected to the vacuum apparatus through a 35/20 ball joint (T_2) using Apiezon W wax. At high bath temperatures, breaks occurred in the calibration curves when the Hg in the manometer emerged above the water line of the bath. A glass jacket through which bath water was circulated was placed over the manometer tube as shown in Fig. 1. The calibration curves were then linear at all bath temperatures up to 72°C, the highest employed in this work.

A water vapor pressure control unit, following the design of Apel (8), was connected to the vacuum apparatus through a 35/20 ball joint at (T_3). Water was pumped from a second controlled temperature bath through the jacket enclosing the tube containing liquid water (G), thus controlling the temperature of the liquid water and, therefore, the water vapor pressure. An evacuated jacket was placed around the water jacket to insulate the water jacket from the surrounding bath. The surrounding bath and the reaction tube were always maintained at sufficiently high temperatures to prevent condensation of water in areas outside the vapor pressure control unit. Only the ball joint (T_1) was in an unthermostatted region, but convection of heat upward from the furnace was sufficient to prevent condensation in this area. The top of the vapor pressure control unit was fitted with a rubber serum bottle stopper (H) and covered with Hg to give a vacuum tight seal. Water was introduced into the vapor pressure control unit through the stopper, using a hypodermic syringe (J). The water vapor pressure control unit was calibrated for several temperatures of the second controlled temperature bath. The vapor pressures were reproducible to within ±1.5 mm for successive runs at all temperatures employed in this work. The limiting water vapor pressure for this apparatus was approximately 250 mm Hg. The greases and waxes used in assembling the apparatus and the pumps used for circulating the water would not withstand the temperatures necessary to produce higher water vapor pressures. Also, the increment of change of water vapor pressure for small temperature changes became increasingly large at higher temperatures, to the extent that above 70°C close control with the present apparatus was virtually impossible.

Procedure

Mg metal, in the form of blocks with the approximate dimensions 1 x 1 x 8 in., was obtained from the Dow Chemical Company, Midland, Mich. Spectrographic analysis for impurities, furnished with the metal, was as follows: Al, 0.0047%; Ca, 0.01%; Cu, 0.009%; Fe, 0.031%; Mn, 0.058%; Ni, 0.003%; Pb, 0.005%; Si, 0.001%; Sn, 0.001%; Zn, 0.001%. The blocks of Mg were cut lengthwise into four pieces and turned into rods. The rods were cut into cylinders approximately 4.5 cm long. These specimens were then finished on a lathe under carefully controlled and duplicated machining conditions. After this treatment the cylinders averaged 4.1 cm in length and 1.1 cm in diameter. They were washed in dry, thiophene-free benzene to remove traces of surface oil, and were allowed to stand in air until needed for an experiment.

In preparation for a run, the dimensions of the cylinders were measured with machinist's calipers, and a ⅛ in. hole was drilled across one end of the sample to accommodate an alumina tube. The cylinders were handled with polyethylene covered forceps to eliminate finger prints on the surface. They were etched for 5 min in a solution containing 2% HNO_3 in absolute ethanol, followed by two rinses of dry, 1:1 acetone-methanol; then the cylinders were placed in a beaker of dry, thiophene-free benzene. The alumina tube was positioned in the hole in the end of the cylinders, and a nichrome hook, connected to the nichrome suspension wire, was positioned into the ends of the tube. Samples were protected from the atmosphere in the benzene bath during these operations.

After the etching and rinsing procedure had been completed, the ball joint on the stainless steel port (T_1) (*see* Fig. 1) was heated and de Khotinsky-hard cement was applied. After the socket on the reaction tube had been heated, the sample was taken out of the benzene rinse and suspended on a nichrome wire clip inside the ball joint (C). The reaction tube was placed over the sample and sealed to the apparatus immediately. After being evacuated for about 1 min with an auxiliary pump, and with a cold trap to catch the benzene, the apparatus was opened to a high vacuum pumping system. Pumping was continued for 5 min at 200°C in order to outgas the system. Then the system was brought to the reaction temperature (425° to 575°C) by sliding the furnace up over the reaction tube. By continuing the pumping for 5 min more, the pressure was reduced to less than 10^{-4} mm Hg. The apparatus was isolated from the vacuum pumps by closing stopcock (S_1) (*see* Fig. 1) and 1 ml of degassed water was introduced into the vapor pressure control unit. The water vapor pressure corresponding to the temperature of the vapor pressure control unit was attained in less than 3 min, even at the highest water vapor pressures. The reactions were generally allowed to proceed for 10 hr or longer. At the lowest reaction temperatures, the induction periods approached 8 hr, and it was necessary to increase the length of a run to get suitable rate data. At the end of each run, the water vapor, the excess liquid water, and the H_2 were pumped out of the apparatus by the auxiliary pumping system. The samples were cooled to room temperature in a vacuum, air was admitted to the apparatus, and the specimens and products were stored under argon

gas for x-ray analysis. The reaction was studied at 31, 55, 92, 153, and 208 mm water vapor pressures and 425°, 450°, 475°, 500°, 525°, 550°, and 575°C.

At the beginning of each reaction there was an induction period. The length of the induction periods was a function of the reaction temperature and ranged from approximately 8 hr at 425°C to 15 min at 575°C. During this time the increases in pressure were so small that the apparatus was not sensitive enough to furnish data for the determination of the rate law. Toward the end of the induction periods, the rate increased sharply and then became constant with time.

At the end of each run, as the cylinders cooled to room temperature, the reaction product on the surface of the metal broke away from the cylinders spontaneously, exposing etched metal surfaces. The coatings were identified by x-ray powder photographs for the highest and lowest water vapor pressures at each reaction temperature. In every case the only product was MgO. The gas evolved during the reaction was analyzed mass spectrometrically, and only H_2 and water vapor appeared in the samples.

Reactions of Mg and water vapor of different character than described above occurred under conditions of high temperature and low water vapor pressure. These reactions began with the usual induction period, followed by a sharp increase in the rate and the leveling off to a constant rate. However, after proceeding normally for periods of 1-4 hr, depending on the temperature, a second sharp rise in the reaction rate was observed. MgO was deposited on the walls of the reaction tube following each reaction of this type. When the Mg cylinders were cooled, most of the oxide coating peeled off spontaneously, leaving a sheath surrounding the metal cylinders. The metal cylinders could be easily lifted out of these sheaths, and the insides of the sheaths were found to be lined with Mg crystals. The reaction rate always decreased after recrystallization of Mg began. Due to limitations of the apparatus and method used in this work, it was not possible to determine the rate law governing the vapor phase reactions. Rate law determinations in this work were limited to reactions in which the oxide product was confined to the metal surface.

Because of the formation of the MgO coating on the metal surface, the reaction of Mg and water vapor was expected to follow one of the four principle rate laws (4, 9, 10) governing gas-solid reactions. A plot comparing these laws for the data of a typical run is shown in Fig. 2. Water vapor-weight values were obtained readily from the knowledge of the H_2 pressure, the volume of the apparatus, the area of the Mg cylinders, and the stoichiometry of the reaction. It was assumed that the measured areas of the cylinders were minimum values and that these values were proportional to the true surface areas by a fairly constant factor. Reproducibility of the data corroborated this assumption.

For each run the amount of water vapor reacted per cm^2 was plotted against the time in hours. Examples of these plots for each reaction temperature of this study, at a constant water vapor pressure of 208 mm Hg, are shown in Fig. 3. Rate constants were calculated from the slopes of these curves. Three or more reactions were carried out for each set of reaction conditions. Rate constants for each run are listed in Table I with average rates for each temperature and water vapor pressure indicated. It may be noted that the rate constants at 31 mm water vapor were greater than for 55 mm water vapor at both 525° and 550°C. This was attributed to the vapor phase character of these reactions which is explained in the discussion which follows. Above 500°C, the lower limiting water vapor pressures for this work were determined by the appearance of the vapor phase type of reaction. The lower

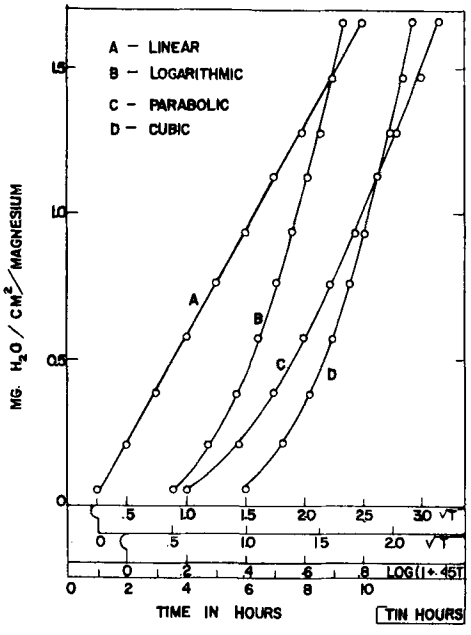

Fig. 2. Rate data for the reaction of Mg and water vapor at 525°C and 55 mm water vapor are plotted according to four rate laws.

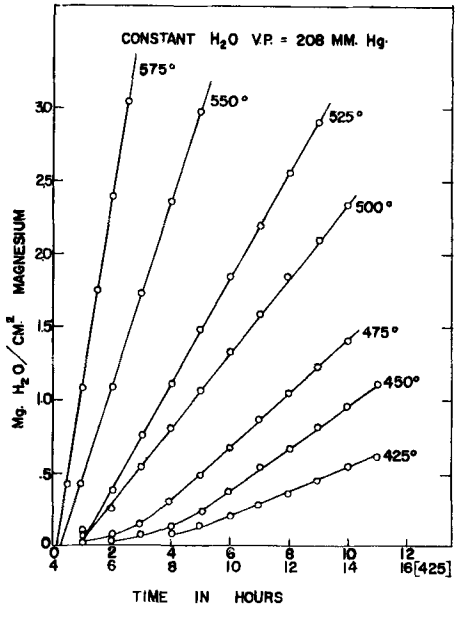

Fig. 3. Examples of the plots of mg water vapor reacted per cm^2 Mg surface against time for each reaction temperature of this study. Rate constants were calculated from the slopes of these curves.

Table I. Results of rate studies of the reaction of Mg and water vapor in the temperature range between 425° and 575°C in the water vapor pressure range between 31 and 208 mm Hg

Reaction temp, °C	Water vapor Press, mm Hg	Rate constants Runs 1	2	3	Mean	Avg. dev.
425	153	0.075	0.097	0.084	0.082	0.007
425	208	0.067	0.078	0.101	0.085	0.013
450	153	0.103	0.103	0.086	0.097	0.008
450	208	0.131	0.141	0.153	0.141	0.007
475	31	0.041	0.039	0.039	0.039	0.002
475	55	0.055	0.055	0.050	0.053	0.002
475	92	0.095	0.097	0.086	0.092	0.004
475	153	0.141	0.138	0.143	0.140	0.002
475	208	0.182	0.187	0.189	0.186	0.002
500	31	0.068	0.067	0.066	0.067	0.001
500	55	0.100	0.080	0.109	0.096	0.011
500	92	0.128	0.125	0.133	0.128	0.002
500	153	0.197	0.190	0.190	0.192	0.003
500	208	0.261	0.253	0.253	0.255	0.003
525	31	0.225	0.174	0.122	0.174	0.034
525	55	0.168	0.165	0.157	0.163	0.004
525	92	0.212	0.205	0.211	0.209	0.003
525	153	0.277	0.284	0.283	0.281	0.002
525	208	0.350	0.365	0.362	0.359	0.006
550	31	0.337	0.400	0.400	0.379	0.028
550	55	0.288	0.316	0.337	0.313	0.017
550	92	0.394	0.390	0.408	0.397	0.007
550	153	0.507	0.480	0.514	0.500	0.013
550	208	0.612	0.623	0.620	0.618	0.004
575	208	1.273	1.200	1.323	1.265	0.058

limit was 55 mm water vapor at 525° and 550°C and was 208 mm at 575°C. Because the apparatus was not capable of attaining higher water vapor pressures, only one water vapor pressure was examined at 575°C. Plots of rate constant against water vapor pressure show a linear dependence in the temperature range covered.

Plots of log k against $1/T$ for water vapor pressures of 55, 92, 153, and 208 mm Hg are shown in Fig. 4. Two straight lines were obtained for each water vapor pressure. One of the straight lines covers the temperature range between 425° and 500°C, and the other covers the range between 525° and 575°C. Activation energies at the various water vapor pressures for the two temperature ranges are shown in Table II.

Activation energies for the water vapor pressures below 208 mm were not calculated for the temperature range between 525° and 575°C because only two points were available for these curves. There was a gradual decrease in activation energy with increase in water vapor pressure in the lower temperature range, and there was a sharp increase in

Table II. Activation energies for the reaction of Mg with water vapor

Water vapor pressure, mm Hg	Activation energy, kcal/mole 425°-500°C	525°-575°C
55	31.7 ± 7.6	—
92	21.8 ± 3.9	—
153	15.2 ± 2.7	—
208	11.1 ± 2.7	33.7 ± 1.5

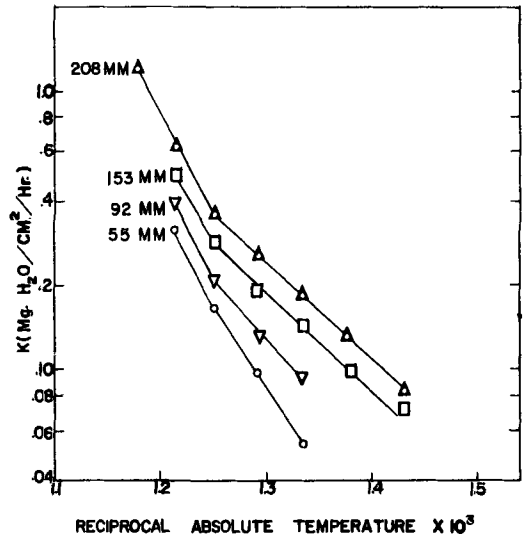

Fig. 4. Log k is plotted against the reciprocal of the absolute temperature for four water vapor pressures to demonstrate the variation of the rate constants with temperature in the Arrhenius equation.

activation energy above 500°C at all water vapor pressures investigated. The trend of all plots in Fig. 4 indicates that all activation energies above 500°C are the same.

In the early part of this work, difficulty was encountered in the development of a method of preparation and handling Mg so that the reaction with water vapor would take place. The Mg cylinders were etched for 2 min in a solution of 2% HCl in ethanol, washed in two baths of acetone-methanol, and rinsed in dry, thiophene-free benzene. The cylinders were supported in the bottom of the reaction tube by a small, U-shaped, stainless-steel clip. Screws at each end of the clip were used to hold the cylinders in place. The cylinders were insulated from the clip by ceramic tips on the ends of the screws, and the clip served to support the cylinders concentrically in the reaction tube. Even with this preparation and with the temperature at 525°C for periods as long as 20 hr there was no visible evidence of reaction in over 80% of the trials. In some instances the reaction took place only at isolated spots on the Mg surface. The metal around the spots appeared bright and shiny. Each variable in the procedure of preparing for a run was changed independently in an effort to determine the important factors involved. None of the variables investigated made significant differences as to whether or not the reaction took place. When the use of the nichrome wire method of suspension of the sample was adopted and the HNO_3 etch was used to replace the HCl etch, only about 5% of the specimens failed to undergo reaction. This phase of the surface oxidation of Mg by water vapor warrants further investigation. The apparent passivation of the metal under certain conditions offers an opportunity for future study.

Discussion

The oxidation of Mg by water vapor in the temperature range between 425° and 575°C and the water vapor pressure range between 31 and 208 mm

Hg can be explained by three different mechanisms, all of which are related to the vapor pressure of the Mg metal.

1. In the temperature range between 425° and 500°C and over the entire range of water vapor pressures, the reaction is confined to or takes place very near the metal surface. Water vapor diffuses readily through the loose oxide structure and reacts at the metal-oxide interface. As the water vapor pressure is reduced, some Mg atoms actually leave the surface of the metal before encountering water vapor molecules, and the reaction takes place either in the vapor phase within the porous oxide structure or on the internal surface of the oxide sheath. This concept is supported by the occurrence of a gradual increase in the activation energy which is observed as the water vapor pressure is reduced in this temperature range.

2. In the temperature range between 500° and 575°C and at water vapor pressures sufficiently high to confine the MgO product to the surface of the metal cylinders, the reaction takes place interstitially in the loose oxide coat. The rate of vaporization of the Mg atoms is so great that few water vapor molecules ever reach the solid metal surface before reaction takes place, and a large water vapor concentration gradient exists between the metal-oxide and the gas-oxide interfaces. The reaction takes place either on the internal surfaces of the oxide sheath or in the vapor phase within the loose oxide structure. This mechanism explains the sharp increase in the activation energy at all water vapor pressures above 525°C.

3. When the water vapor pressure is reduced below 55 mm at 525° and 550°C and below 208 mm at 575°C, there is no longer sufficient water vapor within the oxide coat to react with all of the vaporized Mg atoms, and these atoms escape from the oxide coat. MgO is deposited on the walls of the reaction tube, and the reaction takes place either in the vapor phase or on the walls of the reaction tube. Leontis and Rhines (2) observed a vapor phase reaction above 575°C in the oxidation of Mg by oxygen.

The most important factor affecting the reaction mechanism in the temperature range of this work is the vapor pressure of the Mg metal. The rapid rise in the vapor pressure between 500° and 600°C is shown by the values given in Table III (11).

It was interesting to observe that the amount of vaporization in these experiments increased after the oxidation had taken place for some time. This increase in the amount of vaporization was due presumably to an increase in the surface area of the metal during the oxidation process. The surface of the metal under the oxide coat was always roughly etched. Gulbransen (1), by using a vacuum microbalance technique, clearly showed a similar increase in the amount of vaporization, after a period of oxidation.

Table III. Vapor pressure of Mg

Temp, °C	Vapor pressure of Mg, mm Hg
500	0.053
550	0.190
600	0.684

The concept of increase in vaporization with reaction on the metal surface serves to explain the steps leading to the vapor phase reactions. In these reactions the normal induction period is always observed and the reaction starts off at a constant rate. However, as the reaction proceeds, the amount of vaporization increases as the surface becomes etched by the oxidation process and there is no longer sufficient water vapor traversing the oxide coat to confine the reaction to the surface of the metal. When this occurs another sharp rise in reaction rate is observed. As recrystallization of Mg on the inside of the oxide sheath takes place, the rate of reaction decreases, presumably because the Mg-lined sheath is less permeable to Mg vapor than is the oxide coat.

These conclusions are corroborated by correlation of the activation energy data as determined in this study with other thermodynamic data. Reactions occurring at high temperatures and/or low water vapor pressures have been explained on the basis of the high vapor pressure of Mg. Activation energies obtained for these reactions in this work are 31.7-33.7 k/cal. These results agree well with the heat of sublimation of Mg, which is 34.4 kcal (12). At lower temperatures and at the highest water vapor pressure used in this study, the activation energy was found to be 11.1 kcal. This value compares favorably with energies determined in other water vapor-metal studies (8, 13, 14) in which adsorption on or diffusion of some species through the solid product coating was the rate-controlling step. Inasmuch as activation energies intermediate to these values have been found for some reaction conditions, the conclusion is tenable that a combination of both vaporization and diffusion through the coating determines the over-all reaction rate.

Manuscript received August 6, 1956. Contribution No. 529. Work on this paper was performed in the Ames Laboratory of A.E.C.

Any discussion of this paper will appear in a Discussion Section to be published in the June 1958 JOURNAL.

REFERENCES

1. E. A. Gulbransen, *Trans. Electrochem. Soc.*, **87**, 589 (1945).
2. T. E. Leontis and F. N. Rhines, *Metals Technol.*, **13** (4), 1 (1946).
3. I. A. Makolkin, *J. Appl. Chem. (USSR)*, **24**, 505 (1951).
4. N. B. Pilling and R. E. Bedworth, *J. Inst. Metals*, **29**, 529 (1923).
5. H. N. Terem, *Compt. rend.*, **226**, 905 (1948).
6. H. J. Svec, A. A. Read, and D. Hilker, Atomic Energy Commission A.E.C. Rept. ISC-585, 1955.
7. H. J. Svec and D. S. Gibbs, *Rev. Sci. Instr.*, **24**, 202 (1953).
8. C. T. Apel, Unpublished M. S. Thesis, Iowa State College Library, Ames, Iowa (1956).
9. U. R. Evans, *Trans. Electrochem. Soc.*, **83**, 335 (1943).
10. O. Kubaschewski and B. E. Hopkins, "Oxidation of Metals and Alloys," p. 37, Academic Press, New York (1953).

11. American Society for Metals, "Metals Handbook," p. 28 (1948).
12. F. F. Coleman and E. Egerton, *Trans. Roy Soc. London*, **234A**, 177 (1935).
13. B. E. Deal, Unpublished Ph.D. Thesis, Iowa State College Library, Ames, Iowa (1955).
14. B. E. Deal and H. J. Svec, *J. Am. Chem. Soc.*, **75**, 6173 (1953).

Enhanced Surface Reactions

Manfred J. D. Low and H. Austin Taylor

Nichols Laboratory, New York University, New York, New York

ABSTRACT

The influence of an electrodeless gaseous discharge on the rates of adsorption of hydrogen on $Pd \cdot Al_2O_3$, ZnO and Ni-kieselguhr and of carbon monoxide on ZnO was investigated. Enhanced adsorption rates and extent were found. A mechanism for the observed effect has been suggested which should have general applicability in chemisorption, oxidation of metals, and other similar phenomena.

An interesting experiment on the influence of a high-frequency induced gaseous discharge on the rate of chemisorption of oxygen on NiO has been reported by Engell and Hauffe (1). The application of a Tesla coil to the system after 150 min when adsorption had almost ceased caused a marked increase in adsorption, the amount adsorbed almost doubling in 30 min. Lack of an explanation for this large effect caused by such a minor discharge prompted a repetition of the experiment.

Experimental

A Tesla coil of the type frequently used for leak detection was applied to a standard constant volume adsorption system so that a discharge could be caused and maintained in a region 40 cm from the adsorbent chamber in an 8 mm O.D. tube leading from the chamber to the adsorption measuring apparatus. A plug of Pyrex-glass wool was located in this tube, 20 cm from the point of discharge and between the latter and the adsorbent. The coil was adjusted to give a continuous discharge which was barely visible in a darkened room. Preliminary experiments under the conditions prevailing in actual runs but in the absence of the adsorbent showed that the discharge had no noticeable effect on the pressure in the system.

Experiments using three different adsorbents are described: (*a*) 15.53 g of a commercial Pd hydrogenation catalyst made by Baker and Co. of 0.5% Pd on 1/16 in. extruded Al_2O_3 pellets; (*b*) 18.76 g ZnO from oxalate, prepared according to the method of Taylor and Sickman (2); (*c*) 10 g Ni-kieselguhr containing 11.5% Ni (3).

Gases used were H_2 and CO. Pure H_2 was prepared by diffusion of tank H through heated Pd thimbles. CO was obtained from the reaction of CH_2O_2 and H_2SO_4 and was purified by suitable washing and drying.

Results and Discussion

The statement made earlier that the discharge was without effect unless adsorbent was present is illustrated by the data of two such runs at different gas pressures shown in Table I. Pressures were measured on a dibutyl phthalate (DBP) manometer.

The small pressure changes in run II are attributable to the changes in room temperature and, as seen from run I, when this is constant, so also is the pressure before, during, and after the discharge. Pressure changes observed during discharge when adsorbent is present are exemplified by Table II showing the pressure readings for the enhanced adsorption of H_2 on ZnO shown later in Fig. 4.

It may be seen that the rate of pressure change, just before the discharge was applied, fell to about 3 mm DBP in 25 min. During the first 5 min of discharge the pressure fell 5 mm and more than 20 mm during the half hour the discharge was applied. It is seen, therefore, that the effect of the discharge is real; it is far from being a small, delicate effect and is comparable with the normal adsorption rates on the same adsorbent. It is the more startling, since this enhanced adsorption occurs on surfaces, which, from the classical point of view, are almost fully saturated at the prevailing pressure.

Fig. 1 is a plot of the data of a typical experiment on the adsorption of H_2 on $Pd \cdot Al_2O_3$ at 257°C. The

Table I. Effect of discharge in absence of adsorbent

Time, min	Run I Room temp, °C	Press. H_2 cm DBP	Time, min	Run II Room temp, °C	Press. H_2 cm DBP
5	26.4	68.20	5	27.0	30.09
10	26.4	68.20	10	27.0	30.09
15	26.4	68.20	15	27.0	30.09
20	26.4	68.20	20	27.0	30.09
	Discharge on			Discharge on	
25	26.4	68.20	25	27.0	30.09
30	26.4	68.20	30	27.0	30.09
40	26.4	68.20	35	27.0	30.09
50	26.4	68.20	40	27.1	30.8
	Discharge off		42	27.1	30.10
55	26.4	68.20	45	27.1	30.10
60	26.4	68.20	50	27.2	30.13
70	26.4	68.20	60	27.3	30.20
			65	27.0	30.05

Table II. Enhanced adsorption of H_2 on ZnO at 100°C. P_0 = 66.9 cm DBP

Time, min	Room temp	Press. cm DBP
975	30.6	27.32
1115	32.2	26.98
1190	31.2	26.65
	Discharge on	
1195	31.2	26.10
1200	31.2	25.58
1205	31.2	25.08
1215	31.2	24.38
1220	31.2	24.10
1225	31.4	23.88
1230	31.4	23.76

run having continued for 3 hr and the pressure of the H_2 having fallen from 77.23 to 56.75 cm DBP, the Tesla coil was turned on. The rate of disappearance of the gas is markedly increased under the influence of the discharge. After 70 min the Tesla coil was turned off. The rate of gas uptake is seen to decline rapidly, although the enhancing effect of the discharge is still apparent 10 min later. The insert in Fig. 1 is an Elovich plot (4) of the data and shows the return of the rate to its initial value after cessation of the discharge by the constancy of slope of the first and third parts of the curve. A similar continuation of the enhancement after the discharge is to be found in the experiment by Engell and Hauffe.

In Fig. 2 the effect of a discharge on the rate of CO adsorption on ZnO at 257°C and 55 cm DBP is shown. Again the rate of gas uptake is markedly enhanced by the discharge but decreases again when the discharge ceases, falling almost to the same rate as that before the discharge was applied.

A similar effect was observed in the influence of the discharge on the rate of adsorption of H_2 at an initial pressure of 71.3 cm DBP on a Ni-kieselguhr catalyst at 322°C as shown in Fig. 3.

The most pronounced effect was found on studying the adsorption of H_2 on ZnO. Fig. 4 and 5 again show the marked enhancement of the adsorption caused by the discharge. The enhancement is apparent not only during the course of a run while

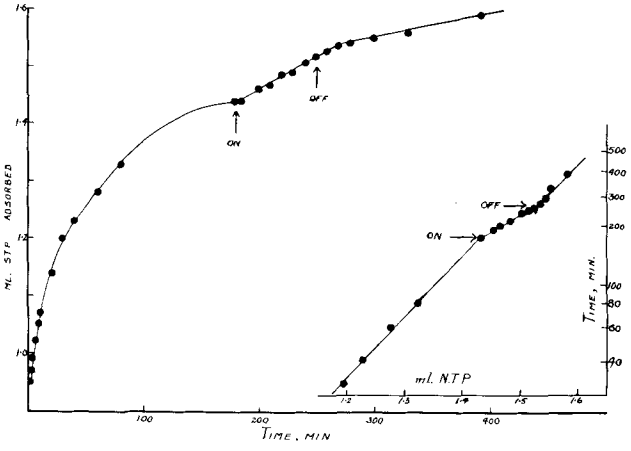

Fig. 1. Rate of adsorption of H_2 on Pd. Al_2O_3 before, during, and after application of discharge. Insert is a plot of amount adsorbed against the logarithm of time. Temp, 257°C; P_0 = 77.23 cm DBP.

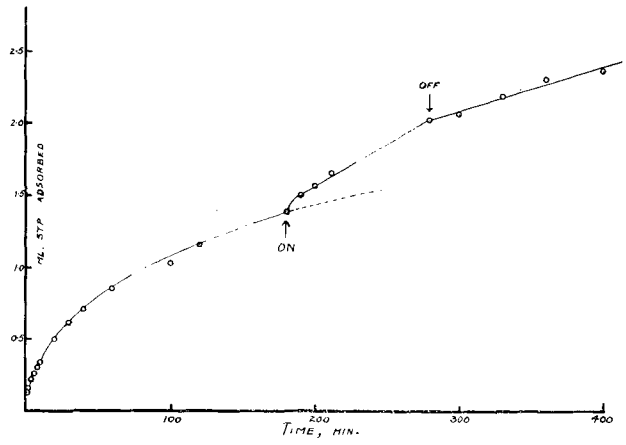

Fig. 2. Effect of discharge on adsorption of CO on ZnO. Temp, 257°C; P_0 = 55.0 cm DBP.

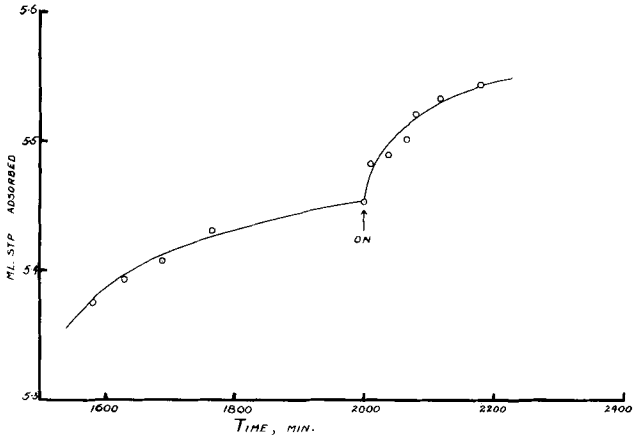

Fig. 3. Effect of discharge on adsorption of H_2 on Ni-kieselguhr. Temp, 322°C; P_0 = 71.3 cm DBP.

spontaneous gas uptake is occurring (Fig. 4) but also the adsorbent, seemingly saturated after seven days' exposure, may be made to take up more gas (Fig. 5).

As pointed out by Engell and Hauffe the increase in adsorption shown in their experiment, and in these many experiments, cannot be related to a saturation of adsorbent surface by adsorbate, since in such a case a discharge would be ineffectual. It is also unlikely that, in the case of H_2 adsorption, the effect is due to a direct and massive production of H atoms, since, in the first place, the conditions of the Tesla coil discharge are so feeble in comparison with those necessary for effective atom production in a Wood's discharge tube and, in the second place, experience shows how effective is a plug of dry glass wool, such as used here as a protection for the catalyst, in causing atom recombination. The similarity of the enhancement of adsorption of CO indicates that the effect of the discharge can at best be but a feeble excitation or activation of molecules. The concentration of such species, atoms, or molecules reaching the catalyst surface must be extremely small and the marked increase in adsorption would suggest some form of a chain process. Engell and Hauffe have attempted to explain the effect in terms of their Barrier Layer theory, suggesting that the observed increase in gas uptake is due to an increased electron-affinity of the oxygen. Gray and

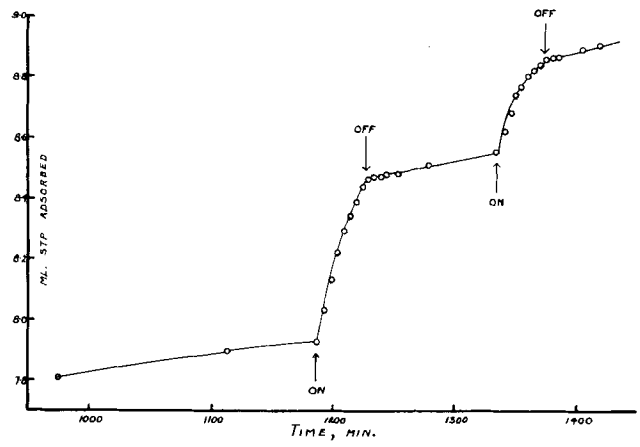

Fig. 4. Effect of discharge on adsorption of H_2 on ZnO before saturation of the surface. Temp, 100°C; P_0 = 66.9 cm DBP.

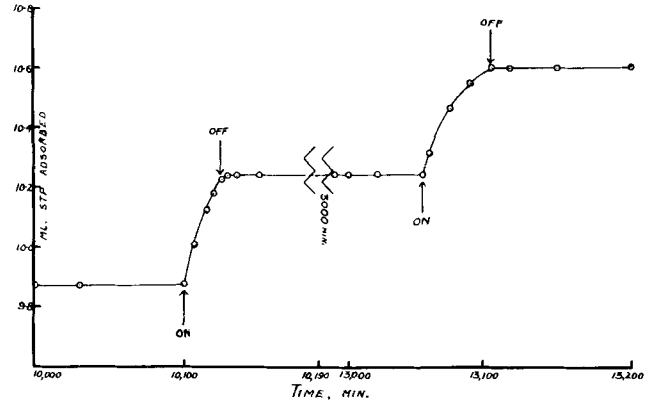

Fig. 5. Effect of discharge on adsorption of H_2 on ZnO after saturation during 7 and 9 days. Temp, 100°C; P_0 = 64.6 cm DBP.

Darby (5) suggest that the effect, in the case of oxygen on NiO, may be due to oxygen being built into the lattice of the adsorbent.

An alternative, more attractive, and more general theory, not applicable alone to semiconductor surfaces, may be deduced from the theory of Taylor and Thon (4) which Taylor (6,7) has extended. It has been amply demonstrated in the vast majority of such studies to which the Elovich equation is applicable that the rate of slow chemisorption is independent of the changing pressure in the gas phase. Therefore, the observed deceleration can be attributed only to the other reactant, the surface. Taylor and Thon (4) suggested that this effect can result from a spontaneous bimolecular disappearance of sites which are created initially through the contact of the gas and the surface. It has been shown (6,7) that this site creation can occur by a branching chain mechanism initiated by the reaction of an active particle, G, with a surface atom, S, causing a "dissociation" of the atom into two adsorption sites, V. The over-all reaction for the branched chain may be represented:

$$G + nS \rightarrow GV + (2n - 1)V$$

The remaining $(2n - 1)$ sites can be active for adsorption, or alternatively, suffer bimolecular recombination and decay. It is therefore suggested that during the discharge, a new site creation process is induced and sites are produced to an extent which is enormous in comparison with the number of exciting particles. Chemisorption of normal molecules then proceeds on the newly created sites resulting in an enhanced rate of adsorption.

Confirmation of the proposed mechanism is to be found in the continuation of the enhanced adsorption even after cessation of the discharge. Gray and Darby (5) measured the adsorption of oxygen on a NiO film by a conductimetric method and found that an R.F. discharge, momentarily applied, yielded immeasurably high values for the conductivity and that the conductivity decreased only gradually to the normal value after the cessation of the discharge. Gray and Darby offer no explanation for this observation. In terms of the above mechanism, the gradual change on cessation of the discharge is to be attributed to spontaneous site decay accompanied by site disappearance through occupancy, processes in their experiments extending over some 20 min. After the surface has returned to the "normal" state, that is, its state immediately before the discharge was applied, adsorption also continues at the "normal" rate, although somewhat decreased because of the larger concentration of material now on the surface. Gray and Darby observe this "permanent" alteration in the value of the surface conductivity.

When the discharge is applied over an extended period rather than momentarily, site production can be a continuing process. Site decay as a bimolecular process must eventually equal or exceed site production. The former leads to a constant site density, with adsorption linear in time. This was observed by Engell and Hauffe and appears in Fig. 1. Other data of the authors confirm the second case.

Confirmation of the proposed mechanism should be available also in all processes which involve any form of surface energizing. The oxidation of metals under the influence of a gaseous discharge has been studied by Dravnieks (8). In this study, although perhaps less conclusively because electrodes were used, enhanced oxidation was occasionally detected. A more precise study by Fryburg (9) on the oxidation of Pt showed that oxygen atoms are at least 400 times more effective than oxygen molecules. The proposal made here offers a mechanism for this enhancement as a branched chain length of around 400.

In like manner, photo-excited adsorptions observed by Kobayashi and Kawaji (10) of oxygen on ZnS under the influence of 3650Å radiation similarly point to site creation induced by the absorbed energy. Similar effects have found their way into the patent literature. It has been claimed (11) that the coal consumption of a vertical lime kiln was decreased from 180 to 126 kg/ton of limestone by the application of a silent electrical discharge to the kiln.

The above and other examples of abnormal reaction have the common criteria that they are (*a*) heterogeneous and (*b*) show enhancement of rate, or of extent of reaction, or both, by the application of a relatively minute stimulus. The amount of en-

ergy supplied to the system is extremely small yet its effects are large. This is precisely the situation which originally prompted the suggestion of a chain mechanism for homogeneous chemical reactions. The absence of a chain mechanism in current proposals suggested to account for heterogeneous reaction, including chemisorption, infers that none is able to account for the peculiarities described in this work. The general applicability of the site-creation mechanism to chemisorption (4), heterogeneous chemical reactions (7, 12), and to the enhancements described herein would infer a high degree of plausibility. Further quantitative data are required for its confirmation.

Manuscript received Nov. 1, 1956. It was abstracted from a dissertation by M. J. D. Law submitted to the faculty of the Graduate School of Arts and Science, New York University in partial fulfillment of the requirements for the Ph.D. degree, June 1956.

Any discussion of this paper will appear in a Discussion Section to be published in the June 1958 JOURNAL.

REFERENCES

1. H. J. Engell and K. Hauffe, *Z. Elektrochem.*, **57**, 762 (1953).
2. H. S. Taylor and D. V. Sickman, *J. Am. Chem. Soc.*, **54**, 602 (1932).
3. L. Leibowitz, Thesis, New York University (1956).
4. H. A. Taylor and N. Thon, *J. Am. Chem. Soc.*, **74**, 4169 (1952).
5. T. J. Gray and P. W. Darby, *J. Phys. Chem.*, **60**, 209 (1956).
6. H. A. Taylor, Ann. N.Y. Acad. Sci., **58**, 798 (1954).
7. H. A. Taylor, Peter C. Reilly Lectures, Notre Dame University (in press).
8. A. Dravnieks, *J. Am. Chem. Soc.*, **72**, 3761 (1951).
9. G. C. Fryburg, *J. Chem. Phys.*, **24**, 175 (1956).
10. A. Kobayashi and S. Kawagi, *ibid.*, **24**, 907 (1956).
11. British Pat. 691, 476 May 1953; *C. A.* **47**, 9069 (1953).
12. N. Thon and H. A. Taylor, *J. Am. Chem. Soc.*, **75**, 2747 (1953).

Luminescence of Modified Tin-Activated Strontium Orthophosphate

H. Koelmans and A. P. M. Cox

Philips Research Laboratories, N. V. Philips' Gloeilampenfabrieken, Eindhoven, The Netherlands

ABSTRACT

The introduction of Al, Zn, Mg, Ca, or Cd in $Sr_3(PO_4)_2$ produces a new crystal phase which is probably isomorphous with $\beta Ca_3(PO_4)_2$. Activated with tin this Sr-orthophosphate gives a strong luminescence with a maximum at about 6300Å under excitation with 2537Å.

In the systems studied so far, Sn must be present in the lattice as Sn^{2+} in order to be an effective activator. Since Sn^{2+} is easily reduced to Sn metal and, on the other hand, is also readily oxidized to Sn^{4+}, a carefully controlled atmosphere is required in preparing efficient Sn-activated phosphors. Recently, Butler (1) prepared Sn-activated alkaline earth orthophosphates. He found that a firing atmosphere of N_2 containing a small percentage of H_2 is very effective in keeping Sn in the divalent state.

$\beta Ca_3(PO_4)_2$—Sn, whose emission has a maximum at 6300Å and a secondary maximum at 4950Å, proved to be an excellent phosphor. $Sr_3(PO_4)_2$—Sn has an emission at 3700Å. On introducing Al, Zn, Mg, Ca, or Cd into the Sr-orthophosphate lattice the rather weak u.v. emission of the pure Sn-activated Sr-orthophosphate is replaced by a strong emission at 6300-6500Å.

Preparation

The raw materials used were reagent grade $SrCO_3$, $(NH_4)_2HPO_4$, SnO, $Al(NO_3)_3 \cdot 9H_2O$, ZnO, $MgCO_3$, $CaCO_3$, and $CdCO_3$. The required amounts of dry base materials were mixed in a runner mill for 10 min. The blends were preheated at 500°-600°C for 1 hr in order to eliminate NH_3, H_2O, and occasionally NO_2 in preparations containing Al. After this the mixture was milled again for 20 min.

In order to form the matrix, the powders were then heated in air for 2 hr at temperatures ranging from 1000°-1100°C. After this firing the powders are white and nonluminescent. Following Butler (1), the final firing was done in N_2 containing some H_2.

In the authors' experiments, samples were fired for 30 min at 1000°-1100°C in N_2 with 0.5-1% H_2 in alundum crucibles. The furnace tube was sintered alundum (5 cm diameter) and in all preparations the gas flow was 5 l/min. Samples were allowed to cool to about 400°C in the same reducing atmosphere by moving the crucibles from the hot zone to a cooler portion of the alundum tube.

Structure

X-ray diagrams showed that the strong luminescence at about 6300Å occurring when part of the Sr in $Sr_3(PO_4)_2$—Sn is substituted by Al, Mg, Zn, Ca, or Cd is associated with a change in crystal structure. This new crystal structure is the same, irrespective of which of the elements mentioned above is substituted for Sr. The modified $Sr_3(PO_4)_2$ is probably isomorphous with $\beta Ca_3(PO_4)_2$ as shown in Fig. 1. It appears from this figure that, starting with $\beta Ca_3(PO_4)_2$, a gradual replacement of Ca by Sr, apart from other minor differences, results in a widening of the $\beta Ca_3(PO_4)_2$ lattice until a Ca/Sr ratio of about 0.2 is reached. With more Sr added there is a rather sharp transition to the normal Sr-orthophosphate structure. This transition is accompanied by a change in emission from 6200 to

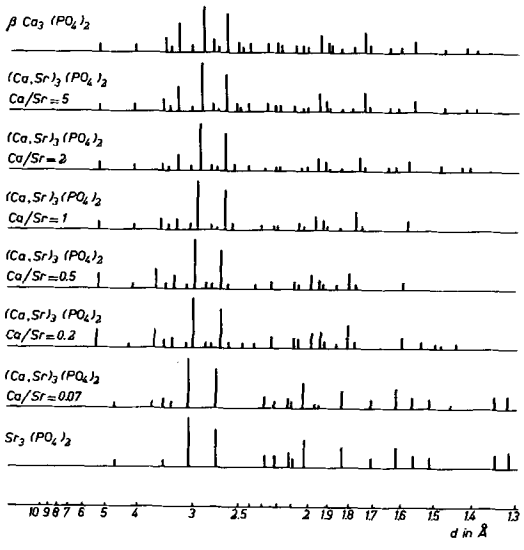

Fig. 1. X-ray diagrams of Ca,Sr-orthophosphates

3700Å. This result is different from that of Butler (1), who states that at a Ca/Sr ratio of 2.3 a new crystal phase appears without a marked change in emission and also that samples with a high Sr content, which show the long wave-length fluorescence, may have the normal Sr-orthophosphate structure.

The $\beta Ca_3(PO_4)_2$ structure as a single phase is retained between much narrower limits in the case of substitution of Sr by Mg, Zn, Cd, or Al (*see* section on Composition). With increasing substitution of Sr by Mg, Zn, or Cd there are strong indications that a new crystal phase appears of the composition $SrX_2(PO_4)_2$, where X = Mg, Zn, or Cd, with a weak greenish-bluish Sn emission. The substitution of Sr by Al is discussed later. The metal ions which produce the phase transition in $Sr_3(PO_4)_2$ are smaller than the Sr ion which they replace, so it is not surprising that their introduction results in a change to a structure like that of $\beta Ca_3(PO_4)_2$ with a smaller spacing of the metal ions. Moreover, x-ray work of Mackay (2) has shown that the structure of $\beta Ca_3(PO_4)_2$ is rather closely related to that of $Sr_3(PO_4)_2$ (3).

In agreement with this view, it was found that the smaller the metal ion substituting for the Sr ion, the less of it is required to cause the transition to the $\beta Ca_3(PO_4)_2$ structure. The minimum ratios of the cations at which the $\beta Ca_3(PO_4)_2$ structure strongly dominates, arranged in the order of increasing ionic radius of the substituting ion, are: Al/Sr = 0.08; Mg/Sr = 0.03; Zn/Sr = 0.07; Ca/Sr = 0.13; and Cd/Sr = 0.13. It is seen that Al does not fit into the series; this point is discussed later. The fact that partial substitution of the larger Ba ion for Sr does not produce the $\beta Ca_3(PO_4)_2$ structure is also consistent with the above theory.

Attempts to convert the modified Sr-orthophosphate into the normal one by varying firing conditions were quite unsuccessful. Firing at temperatures not much below the melting point resulted in highly distorted structures, x-ray diagrams showing no resemblance to either of the Sr-orthophosphate modifications. X-ray diagrams of powders fired at high temperatures and containing rather large amounts of Al showed in these structures the presence of Al_2O_3 as a second phase.

Composition

In all preparations except those containing Al an excess of 2 mole % phosphate was used. An excess of the alkaline constituents gave brownish or grayish products on firing in the reducing atmosphere due to insufficient incorporation of the Sn. Optimum ratios of the molar concentrations of the cations are: Al/Sr = 0.1 — 1; Mg/Sr = 0.07 — 0.4; Cd/Sr = 0.2; Zn/Sr = 0.1 — 0.15; Ca/Sr = ∞.

Kröger (4) suggested that the great solubility of Al_2O_3 in the Sr-orthophosphate matrix might be explained by assuming a distribution of Al over Ca and P sites in a proportion of 2 to 1, thus maintaining compensation of charge. The compositions $Sr_{6-2x}Al_{2x}P_{4-x}Al_xO_{16}$, corresponding to such a distribution of Al, are represented by the dotted line in the ternary diagram of Fig. 2a. Thus in the extreme case (x = 3) the hypothetical compound $9Al_2O_3 \cdot 1P_2O_5$ (point P in Fig. 2a) might have an orthophosphate structure without vacancies.

$$9Al_2O_3 \cdot 1P_2O_5 = 2Al_6(Al_3P)O_{16} \sim 2Sr_6P_4O_{16} = 4Sr_3(PO_4)_2$$

Since substitution of Sr ions by the smaller Al ions is accompanied by a substitution of P ions by the larger Al ions, it is clear that Al need not fit into the series (*see* section on Structure).

The symbols placed underneath each point in Fig. 2a denote the phases occurring in the phosphors in decreasing order of concentration, as found by x-ray analysis. It is seen from Fig 2a that samples with a composition corresponding to points above the dotted line (Sr + Al > 6 + x) all show the normal Sr-orthophosphate structure. Possibly more Al ions than indicated in the above formula may be incorporated at P sites; some Sr sites must then be vacant to maintain charge compensation.

Fig. 2b gives the quantum efficiency of the Al-containing phosphors as a function of their composition.

Efficient phosphors containing Cd are somewhat difficult to prepare since part of the Cd is volatilized

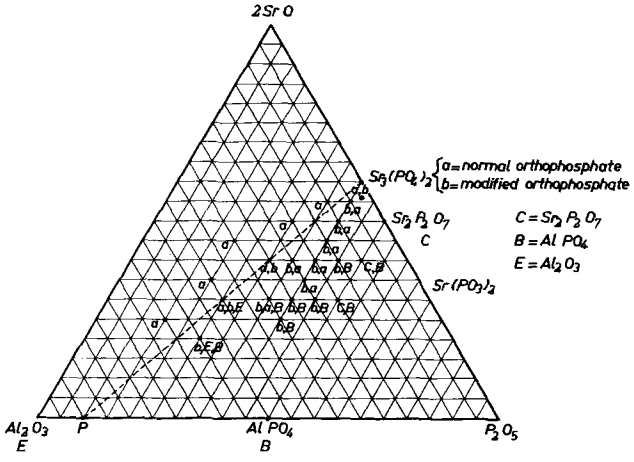

Fig. 2a. Partial composition phase diagram of the system SrO-Al_2O_3-P_2O_5. The symbols underneath each point give the various phases present in the order of their concentration.

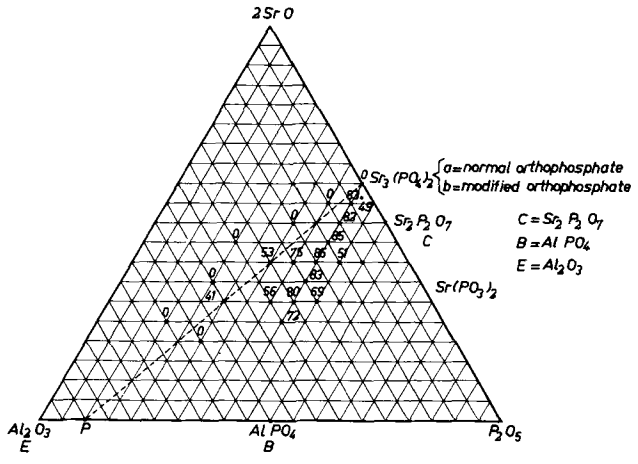

Fig. 2b. Partial composition phase diagram of the system SrO-Al_2O_3-P_2O_5. The figures give the quantum efficiency of the luminescence.

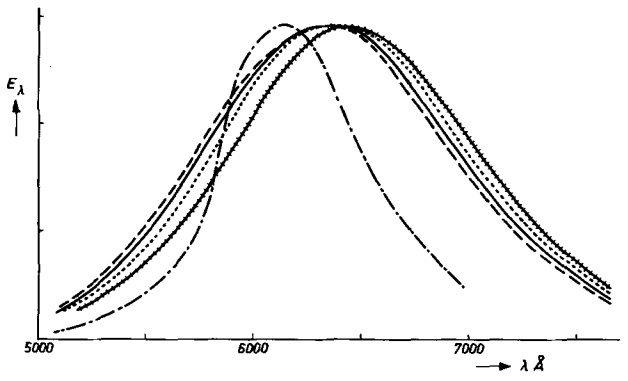

Fig. 3. Emmission of Sn- and Sn,Mn-activated Sr-orthophosphates modified with Al, Zn, Mg, or Cd. Excitation 2537Å. Sn concentration 0.4 mole %, Mn concentration 0.8 mole %. — — —$(Sr,Mg)_3(PO_4)_2$-Sn; Mg/Sr = 0.16; . . . . . $(Sr,Zn)_3(PO_4)_2$-Sn; Zn/Sr = 0.16; |-|-|-|-|-|-|-|-|-|-$(Sr,Cd)_3(PO_4)_2$-Sn; Cd/Sr = 0.16; ——— $(Sr,Al)_3(PO_4)_2$-Sn; Al/Sr = 0.33; -.-.-.-.-.-.-$(Sr,Al)_3(PO_4)_2$-Sn,Mn; Al/Sr = 0.33.

during firing in the final reducing atmosphere. Good results can be obtained by making the H_2 content of the final atmosphere as low as possible and by firing for short times.

The activator concentration can be varied between 0.1 and 1 mole % without much change in efficiency. In the authors' preparations, the Sn content was 0.4 mole %.

Emission Spectra

The emission of the modified Sn-activated Sr-orthophosphate, when excited with 2537Å, consists of a broad band at 6300-6500Å and a weak band at 4000Å. The emission energy in the blue band is about 5% of the total emission energy. The relative energies in the short wave and long wave emission bands do not change sensibly with activator concentration or the nature and amount of the substituents. The position of the main band depends slightly on the metal which is substituted for Sr, as shown in Fig. 3. In Fig. 3 all curves are normalized to the same maximum height. The emission spectra obtained when Ca is substituted for Sr are in accord with Butler's (1) results. The position of the maximum is not influenced by the Sn concentration nor by the amounts of Al, Zn, Mg, or Cd. With Mn as a second activator, the peak becomes sharper and shifts to 6100Å (Fig. 3).

Quantum Efficiency

The optimum efficiency at room temperature of a number of powders, as measured by Bril (5), are given in Table I, together with $\beta Ca_3(PO_4)_2$-Sn.

Table I. Quantum efficiency of Sn-activated orthophosphate phosphors; excitation 2537Å; activator concentration 0.4 mole %. x = Al, Zn, Mg, Ca, Cd

Phosphor	x/Sr	Q.E., %
$\beta Ca_3(PO_4)_2$		81
$(Sr,Al)_3(PO_4)_2$	0.33	85
$(Sr,Zn)_3(PO_4)_2$	0.16	87
$(Sr,Mg)_3(PO_4)_2$	0.12	87
$(Sr,Ca)_3(PO_4)_2$	0.16	75
$(Sr,Cd)_3(PO_4)_2$	0.20	70

It is seen from Table I that the quantum efficiency of the Sn-activated Sr,Al- the Sr,Zn-, and the Sr, Mg-orthophosphate is at least as good as that of $\beta Ca_3(PO_4)_2$-Sn. As the modified Sr-orthophosphates do not show the sub-band at 4950Å of $\beta Ca_3(PO_4)_2$-Sn and as the band at 4000Å corresponds to only about 5% of the total emission energy, this means that these phosphors give more light in the long wave emission band. The latter may be an advantage for applications in fluorescent lamps.

Resistance toward Oxidation

In fluorescent lamp manufacture the tubes are heated in air at about 540°C in order to remove the binder used in applying the coating. This heat treatment causes a reduction in light output of about 15% for $\beta Ca_3(PO_4)_2$-Sn due to partial oxidation of the Sn^{2+}. This decrease in light output is far less in the Sr,Mg-, Sr,Zn-, Sr,Cd-, and Sr,Al-orthophosphate phosphors as shown in Table II. The Sr,Ca-orthophosphate phosphor does not show a better resistance than the pure $\beta Ca_3(PO_4)_2$-Sn.

When samples are heated in air for longer periods, the light output decreases slowly but continuously until it is practically zero after 100 hr of heating in air at 700°C. Thus, it appears that the introduction of Mg, Zn, Al, or Cd does not affect the equilibrium between Sn^{2+} and Sn^{4+} in the lattice, but only the rate at which the equilibrium is reached.

The melting point of the Mg-, Zn-, Al-, or Cd-containing phosphors is much lower than that of Ca- or Ca,Sr-orthophosphate; therefore, they are prob-

Table II. Percentage reduction in light output on heating 200 mg samples in air for 15 min; firing 2 hr 1100° in air and ½ hr 1050° in N_2 — 0.4% H_2. Ratios of the cations are the same as in Table I. Sn concentration 0.4 mole %.

T, °C	500°	600°	700°
$\beta Ca_3(PO_4)_2$	5	27	92
$(Sr,Ca)_3(PO_4)_2$	6	39	90
$(Sr,Mg)_3(PO_4)_2$	0	0	8
$(Sr,Zn)_3(PO_4)_2$	3	10	12
$(Sr,Al)_3(PO_4)_2$	1	4	16
$(Sr,Cd)_3(PO_4)_2$	0	0	0

ably less reactive because they are better crystallized. This view is confirmed by the fact that, on lowering the firing temperature, the improved resistance toward oxidation on heating in air is gradually lost.

Manuscript received Oct. 10, 1956. This paper was prepared for delivery before the Washington Meeting, May 12-16, 1957.

Any discussion of this paper will appear in a Discussion Section to be published in the June 1958 JOURNAL.

REFERENCES

1. K. H. Butler, *This Journal*, **100**, 250 (1953).
2. A. L. Mackay, Thesis, University of London (1952).
3. W. H. Zachariasen, *Acta Cryst.*, **1**, 263 (1948).
4. F. A. Kröger, Unpublished work.
5. A. Bril, Unpublished work.

Energy Transport by Cascade and Resonance Processes in Doubly Activated Phosphors

Esther W. Claffy and Clifford C. Klick

U. S. Naval Research Laboratory, Washington, D. C.

ABSTRACT

A method, using quantum efficiency measurements, is described for obtaining the efficiency of energy transfer from sensitizer to activator centers in doubly activated phosphors when both centers have allowed transitions. From these measurements and applying the theory of resonant transfer it is concluded that, for NaCl: Ag, Cu, both cascade and resonant transfer mechanisms are important and that the resonant transfer process increases more rapidly with concentration than does the cascade process.

Processes by which energy is transferred from one activator to another in a phosphor have been of interest for a long time. Part of this interest stems from the widespread commercial use of doubly activated phosphors and part stems from interest in the mechanisms themselves. Materials such as the sulfides in which photoconductivity plays an important role are not considered here, but only materials where energy transport occurs without an accompanying transport of charge.

In inorganic phosphors a long series of experimental investigations (1-15) has shown that energy may be absorbed in one center, called the sensitizer, and transferred to another type of center, called the activator, which then emits. These investigations have been concerned with cases in which the sensitizer has allowed optical transitions, while those in the activator are largely forbidden. For this type of transfer the range of interaction between sensitizer and activator has also been determined (10, 13, 14).

In organic phosphors the field of interest has been primarily in the absorption of energy in the solvent molecules, followed by transfer from solvent molecule to solvent molecule until the energy reaches a solute molecule (16). Here the energy is transferred between identical centers with allowed transitions.

A quantum theory of resonant transfer between like molecules has been developed by Kallman and London (17), Perrin (18), and Förster (19) and applied to problems of organic phosphors. This theory has been adapted by Dexter (20) to the case of inorganic phosphors where the sensitizer and activator are different centers; the theory has also been extended to cover cases where the activator suffers forbidden transitions of various types.

In addition to a resonant type of transfer of energy from sensitizer to activator, another process may occur which is called the cascade process. This process occurs when the sensitizer actually emits light which is reabsorbed by the activator before the light has a chance to escape from the phosphor sample. For most sensitized inorganic materials previously investigated, the activator has forbidden transitions so that the direct absorption of light by the cascade process is negligibly small. However, this is not the case for phosphors where the activator has allowed transitions.

It is the purpose of this paper to describe methods for determining the efficiency of transfer of energy by resonance and cascade processes, and to investigate the relative importance of these processes in an inorganic phosphor having allowed transitions in both the sensitizer and activator. To achieve this end use is made of results both from experiment and from theory.

Determination of Transport Efficiencies

The method used here for the determination of transport efficiencies rests on measurements of quantum efficiencies. A detailed description of the experimental and mathematical techniques involved in such a measurement will be described elsewhere. The quantum efficiency for luminescence from the sensitizer in a doubly activated phosphor may be determined from the relation

$$S_D = \frac{\alpha_{sens}}{\alpha_{total}} (1 - \eta) S_S \qquad (I)$$

where (S_D) is the quantum efficiency for sensitizer emission in the doubly activated phosphor, and (S_S) is the quantum efficiency of the same phosphor with no activator present. The subscripts refer to singly or doubly activated phosphors. (α_{sens}) and (α_{total}) are, respectively, the absorption coefficients for the sensitizer centers alone and for the whole phosphor at the exciting wave length, and (η) is the efficiency of transfer from sensitizer to activator. Thus (η) may be determined from Eq. (I) if the absorption coefficients are known. For materials which can be prepared as transparent solids, coefficients of absorption may be obtained from transmission measurements; for materials obtainable only as powders the absorption coefficient may be obtained from reflection measurements (21).

In a similar way the quantum efficiency of the activator emission may be obtained. There are two contributions to the emission. One arises from the direct absorption of exciting light in the activator and the other arises from transfer of energy from sensitizer to activator. The total efficiency is given by

$$A_D = \frac{\alpha_{act}}{\alpha_{total}} Q + \frac{\alpha_{sens}}{\alpha_{total}} \eta A_S \qquad \text{(II)}$$

Here (A_D) is the observed efficiency of activator emission on irradiation in the sensitizer. Q is the efficiency of luminescence of the activator in the same phosphor sample with no sensitizer, but excited with light corresponding to the sensitizer's absorption band. A_S is the activator efficiency when excited in its main absorption band which must overlap the emission of the sensitizer for efficient transfer to occur. In many cases the first term on the right hand side of Eq. (II) may be neglected either because the absorption of the activator is small at the exciting wave length or because its efficiency is negligible. If this is the case, Eq. (II) simplifies and the ratio of Eqs. (I) and (II) becomes

$$\frac{S_D A_S}{S_S A_D} = \frac{1}{\eta} - 1 \qquad \text{(III)}$$

It should be noted that, where Eq. (III) can be used, the transfer efficiency may be obtained from quantum efficiency measurements alone without the necessity of determining absorption coefficients.

Once the total transfer efficiency has been obtained from experiment, it is necessary to separate it into its resonant transfer and cascade components. This is accomplished by the use of the results of theory. First, review the computation of resonant transfer for cases where the activator has an allowed transition. Dexter uses a reduced concentration, y, to relate experimental parameters to the resonance transfer efficiency; y is given by

$$y = 7.96 \times 10^{-10} X_a C^+ \frac{Q_a^{1/2}}{n^2} \left(\frac{\epsilon}{K^{1/2}\epsilon_c}\right)^2 \left[\int \frac{f_s(E) F_a(E)}{E^4} dE\right]^{1/2} \qquad \text{(IV)}$$

In this expression X_a is the concentration of activator centers given as a mole fraction; C^+ is the number of sites per cubic centimeter that can accommodate an activator center; n is the index of refraction. Dexter takes the term in round brackets to be unity; this is equivalent to assuming that the electric field at a center is the same as the average electric field in the medium. Q_a is the cross section of the activator for absorption of light and is defined by

$$Q_a = \int \frac{\alpha_{act}\, dE}{X_a C^+} \qquad \text{(V)}$$

where E is in units of electron volts. $f_s(E)$ is the emission spectrum of the sensitizer in terms of the relative number of emitted photons as a function of the energy in electron volts. The curve is normalized so that

$$\int f_s(E)\, dE = 1 \qquad \text{(VI)}$$

Similarly $F_a(E)$ is the absorption spectrum of the activator normalized so that

$$\int F_a(E)\, dE = 1 \qquad \text{(VII)}$$

The reduced concentration, y, is related to the quantum yield for resonant transfer by Eq. (18) of Dexter's paper which is plotted there as Fig. 1. For y much less than unity this yield varies as

$$\eta = y(\pi/2 + y \ln y - 0.4228y)$$

For y much larger than unity the yield approaches unity; it is ½ for $y = 0.65$. With these equations, then, it is possible to calculate the resonance transfer efficiency.

An attempt has been made to calculate the efficiency of transfer by cascade processes in powders. The method developed by Johnson (21) for the reflectivity of powders was extended to this case which is complicated by the fact that the exciting light arises in the powder itself. Here, however, the approximations involved became increasingly troublesome so that this technique, which is also quite cumbersome, was discarded. Instead, the quantum yield for transfer by cascade is obtained by subtracting the calculated resonant transfer yield from the total transfer yield obtained from experiment.

Measurements on NaCl:Ag, Cu

The NaCl:Ag, Cu system was chosen for study because many of its optical properties are known and because it can be prepared as a single crystal for transmission measurements. The strong absorption bands introduced in NaCl by Ag and Cu indicate that optical transitions in these centers are not strongly forbidden.

Special precautions were necessary to prepare samples which were free of luminescent impurities and gave reproducible results. Reagent grade NaCl was specially purified with dithizone to remove traces of such heavy metal impurities as Pb, Tl, Cu, and Ag. Special high purity AgCl and reagent grade $CuCl_2$ were used (the cupric salt being converted to cuprous at the temperature needed for crystal growth). Single crystals were grown from the melt by the Kyropoulos method; just before measurement the samples were pulverized and sieved to a particle size of 179-149 μ diameter (No. 80-100 mesh fraction). The final grinding and sieving were

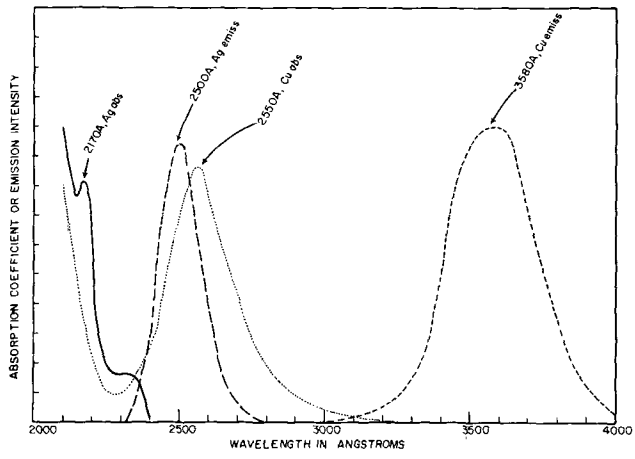

Fig. 1. Absorption and emission spectra of both Ag and Cu in NaCl plotted to arbitrary scales. The emission spectrum of Ag and the absorption spectrum of Cu overlap, giving rise to energy transfer from the Ag to Cu centers both by resonance transfer and by cascade processes.

done in a room with low humidity. Attempts to use polycrystalline melts were unsuccessful; these preparations had quantum efficiencies which were lower than the single-crystal preparations.

An attempt was made to keep the concentration of Ag constant at about 10^{-4} mole fraction while varying the Cu concentration. Analysis for Cu was made colorimetrically, for Ag, nephelometrically.

The absorption and emission spectra of both Ag and Cu luminescent centers in NaCl are shown in Fig. 1. In each case the scale of the ordinate is chosen arbitrarily. It is apparent from the figure that there is strong overlapping of the emission spectrum of Ag and the absorption spectrum of Cu. For measurements of the quantum efficiency of transfer from Ag to Cu, the exciting wave length was chosen as 2180Å which is at the peak of the Ag absorption band. At this wave length the quantum efficiency of a NaCl:Cu phosphor was measured to be only 4%. This indicates that the emission from the Cu centers due to direct absorption in the centers may be neglected although there is another Cu absorption band present which extends into the region of the exciting wave length.

It is interesting to note that both Ag and Cu alone in NaCl give rise to efficient phosphors with a measured quantum efficiency of 80%. It is apparent, then, that radiationless transitions are not an important complication in this problem.

Results of these measurements and computations are given in Table I. The transfer yield, η, is computed using Eq. (III); computations using the more exact expressions (I) and (II) indicated that the error introduced using Eq. (III) was less than the error of measurement. In all cases the resonant transfer yield is less than that due to cascade, but it increases with Cu concentration so that for sample 4 the two processes are roughly comparable. It was not possible to follow the processes to higher activator concentrations in this case because of the apparent onset of precipitation of Cu in the crystals.

Conclusions

From the measurements of this paper it may be expected that both resonant transfer and cascade processes are important in doubly activated inorganic phosphors with allowed transitions. While both processes increase with activator concentration, the resonant transfer process increases more rapidly in the case investigated here.

Acknowledgments

The authors wish to express their appreciation to Owen Gates for the silver analyses of these materials and to Robert J. Ginther and James H. Schulman for frequent discussions of this work.

Manuscript received December 26, 1956. This paper was prepared for delivery before the Cincinnati Meeting, May 1-5, 1955.

Any discussion of this paper will appear in a Discussion Section to be published in the June 1958 JOURNAL.

REFERENCES

1. S. Rothschild, *Physik. Z.*, **35**, 557 (1934); **37**, 757 (1936).
2. J. H. Schulman, L. W. Evans, R. J. Ginther, and K. J. Murata, *J. Appl. Phys.*, **18**, 732 (1947).
3. J. B. Merrill and J. H. Schulman, *J. Opt. Soc. Amer.*, **38**, 471 (1948).
4. H. C. Froelich, *This Journal*, **93**, 101 (1948).
5. F. A. Kröger, "Some Aspects of the Luminescence of Solids," Elsevier Publishing Co. Inc., Houston (1948).
6. Th. P. J. Botden and F. A. Kröger, *Physica*, **14**, 553 (1948).
7. F. A. Kröger, *ibid.*, **15**, 801 (1949).
8. H. G. Jenkins, A. H. McKeag, and P. W. Ranby, *This Journal*, **96**, 1 (1949).
9. R. Nagy, R. W. Wollentin, and C. K. Lui, *ibid.*, **96**, 183 (1949).
10. J. H. Schulman, R. J. Ginther, and C. C. Klick, *ibid.*, **97**, 123 (1950).
11. Th. P. J. Botden, *Philips Research Repts.*, **6**, 425 (1951).
12. R. J. Ginther, *This Journal*, **98**, 874 (1951).
13. Th. P. J. Botden, *Philips Research Repts.*, **7**, 197 (1952).
14. R. J. Ginther, *This Journal*, **101**, 248 (1954).
15. R. W. Wollentin, *ibid.*, **103**, 17 (1956).
16. For an introduction to this field *see* Th. Förster, "Fluoreszenz organischer Verbindungen," Vandenhoeck and Ruprecht, Göttingen (1951).
17. H. Kallman and F. London, *Z. physik. Chem.*, **B2**, 207 (1929).
18. F. Perrin, *J. Phys. et radium*, **7**, 1 (1936).
19. Th. Förster, *Ann. Physik*, **2**, 55 (1948).
20. D. L. Dexter, *J. Chem. Phys.*, **21**, 836 (1953).
21. P. D. Johnson, *J. Opt. Soc. Amer.*, **42**, 978 (1952).

Table I. Transfer efficiency values for NaCl:Ag,Cu

Sample	X_{Ag}	X_{Cu}	S_D	S_S	A_D	A_S	η	Efficiency of resonant transfer	Efficiency of cascade transfer
1	11×10^{-5}	3×10^{-6}	0.52	0.81	0.028	0.80	0.052	0.004	0.048
2	6×10^{-5}	6×10^{-5}	0.56	0.81	0.23	0.80	0.29	0.070	0.22
3	7×10^{-5}	8×10^{-5}	0.39	0.81	0.26	0.80	0.40	0.090	0.31
4	12×10^{-5}	16×10^{-5}	0.21	0.81	0.19	0.80	0.48	0.17	0.31

Electrolytic Production of Bromates

Takasi Osuga

Sanwa Pure Chemicals Co., Ltd., Tokyo, Japan

and

Kiichiro Sugino

Department of Chemical Engineering, Tokyo Institute of Technology, Tokyo, Japan

ABSTRACT

An electrolytic process for the production of potassium or sodium bromate using a pure lead peroxide anode has been operated successfully. A concentrated bromate solution was electrolyzed continuously at a cathode of stainless steel with an anodic current density of 20 amp/dm² at 70°C; current efficiency, about 90%; anode consumption about 50-60 mg/K amp-hr. Pure crystalline bromate could be obtained by cooling the cell effluent at room temperature.

Among alkali metal halogenates, only chlorates have been produced commercially in Japan by the electrolytic process. New uses for bromate brought about its electrolytic production, although in much smaller amounts than chlorate. A new electrolytic process using a lead peroxide anode is described here.

Anode for Electrolytic Production of Bromate

Electrolytic production of bromate is usually carried out at a graphite anode. However, the use of graphite has unfavorable effects. It spalls during electrolysis, forming a mud which makes continuous operation difficult. Also, the final product becomes slightly yellow[1] and can be decolorized only with difficulty. These two facts are the main reasons for the search for a better material.

A brief investigation showed that the lead peroxide electrode manufactured by a process reported earlier (2) was the most practical choice for an anode material.

A compact lead peroxide layer is deposited electrolytically from neutral lead nitrate solution upon the inner surface of an iron cylinder which acts as an anode. An example of the operating conditions is shown in Table I. Apparatus used is shown in Fig. 1.

During electrolysis, the acidity of the electrolyte gradually increased and the concentration of Pb^{++} decreased according to the following reaction.

$$2Pb(NO_3)_2 + 2H_2O \rightarrow PbO_2 + Pb + 4HNO_3$$

The change of these two was found to give a brittle deposit of lead peroxide which could not be cut for finishing or not used for an anode of the electrolysis. Moreover, sudden change of *p*H due to direct neutralization of acid in the electrolytic bath gave a deposit consisting of heterogeneous layers which was also brittle. Therefore, the *p*H and the concentration of Pb^{++} should be maintained as constant as possible during electrolysis. This was accomplished by flowing the electrolyte at constant rate and neutralizing the increasing acidity with $Pb(OH)_2$ by using the apparatus shown in Fig. 1.

The electrolysis was conducted until the thickness of the deposit reached about 8 mm. Each end of the mother cylinder 75 mm in length was cut off; then by cutting the iron part of the cylinder lengthwise, a lead peroxide cylinder of suitable strength and compactness as well as of a smooth outer surface was

Table I. Operating conditions

Electrolyte:	21-22% lead nitrate solution.
Anode:	iron cylinder with surface polished inside; length 500 mm, ID 204 mm, thickness 8 mm, weight 20.6 kg, available surface area 32 dm².
Cathode:	copper rod (diameter 25 mm)
Current:	172 amp
Current density, anodic:	5.4 amp/dm²
Voltage:	7.4 v
Temp:	50°C
Flow rate of electrolyte:	4 to 5 l/min
Time:	66 hr

[1] This coloration has been considered hitherto to be due to the presence of chromate added to the cell (1). By the use of a lead peroxide anode instead of graphite, colorless crystals were obtained as shown here.

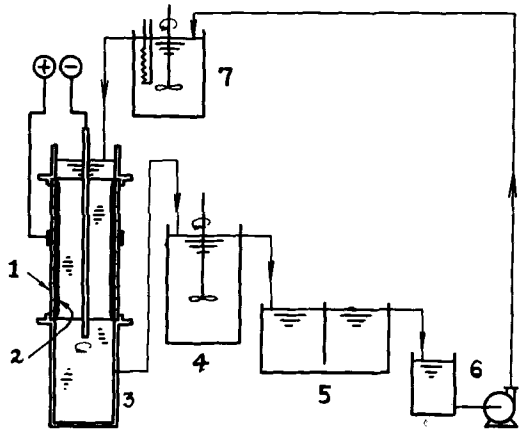

Fig. 1. Apparatus for electrodepositing lead peroxide layer. 1, Iron cylinder; 2, lead peroxide layer deposited; 3, electrolytic bath; 4, neutralization tank; 5, settling tank; 6, pump for recycling electrolyte; 7, preheating tank.

obtained (diameter, 200 mm; length, 350 mm). The lead peroxide cylinder was separated into twelve parts by cutting it again lengthwise. Each part of the lead peroxide thus obtained has the shape of a rectangular piece shown in Fig. 2. Its dimensions are as follows: length, 350 mm; width, 50 mm; thickness, 7-9 mm.

Important Factors in Electrochemical Formation of Bromate

Anodic reactions in bromate formation may be represented as follows.

$$2Br^- - 2e \rightarrow Br_2 \quad (I)$$

$$Br_2 + OH^- \rightarrow HBrO + Br^- \quad (II)$$

$$Br_2 + 2OH^- \rightarrow BrO^- + Br^- + H_2O \quad (III)$$

$$2HBrO + BrO^- \rightarrow BrO_3^- + 2HBr \quad (IV)$$

These reactions are similar to those in chlorate formation, but some differences are seen between the two cases. Reaction (IV) is about 100 times faster than that in chlorate formation according to Kretzschmar (3). On the other hand, reactions (II) and (III) seems to occur imperfectly as compared with those in chlorate formation by comparing the hydrolysis constant of Br with that of Cl_2 (4).[2] Therefore, in the case of bromate, it may be preferable to maintain the *p*H of the electrolyte slightly alkaline in order to favor these reactions and thus obtain high current efficiency. This condition can be attained easily by using a neutral or slightly alkaline solution of bromide at the start of the electrolysis. Efforts to keep the *p*H in the desirable range is not necessary except to avoid discharge of hydroxyl ion.

Reactions (II) and (III) may also be accelerated by high temperature, which has a favorable effect on current efficiency. When reactions (II) and (III) are still slow and imperfect as compared with reaction (I), the current concentration and current density may have a marked influence on the current efficiency. Preliminary experiments showed that high current concentration and also high current density [for example, 50 amp/l to 100 amp/l (13-28 amp/dm²)] had no unfavorable effect on the current efficiency. This facilitates design of the cell and also the determination of the operating conditions.

[2] This was confirmed by the fact that bromine separated at the bottom of the cell when the initial *p*H of the electrolyte was less than 8 and the circulation of the electrolyte was inefficient.

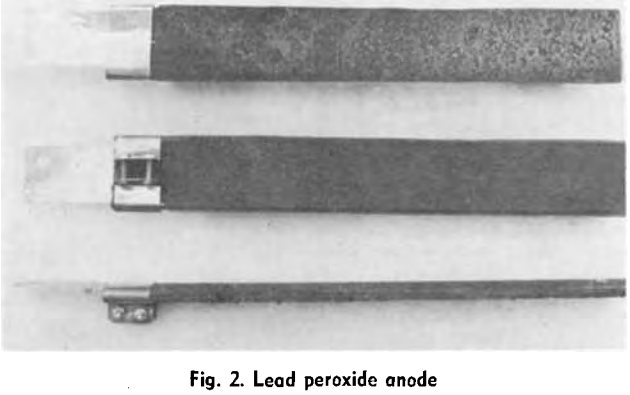

Fig. 2. Lead peroxide anode

Cell Design

The cell design depends on the use of vertical lead peroxide anodes of rectangular shape and stainless steel cathodes. A diagram of the bromate cell construction is shown in Fig. 3.

The cell body is constructed of a sheet iron rectangular tank 900 mm long x 500 mm wide x 400 mm high. All inside surfaces of the body are lined with concrete. Cell volume was determined so as to keep the cell temperature as constant as possible by balancing the internal heating with natural cooling. Three sheets of hard vinyl chloride polymer rested side by side on top of the cell and covered it entirely. The central cover supported 10 anodes and 20 cathodes. These were arranged in 6 rows running the length of the cover. Down the middle were two rows of 5 anodes, and on either side was a row of 5 cathodes. In each cell all anodes and all cathodes were in parallel.

The lead peroxide anodes were 50 mm wide, 7-8 mm thick, and 350 mm long, and extend about 55 mm above the cover. The stainless steel cathodes (Avesta 832-SV) were 35 mm wide, 2.5 mm thick, and 400 mm long. The distance from an anode to the nearest cathode was about 13 mm.

Hydrogen discharged at the cathodes caused sufficient circulation of the cell liquor. It was vented through the roof from each cell.

Batch Experiments

The cell was operated batchwise with 90-95 l of potassium bromide solution. To decrease anode loss, the temperature was kept as constant as possible. The *p*H was not controlled and reached a maximum of about 10 when a slightly alkaline solution (less than *p*H 9) of bromide was used at the start of the

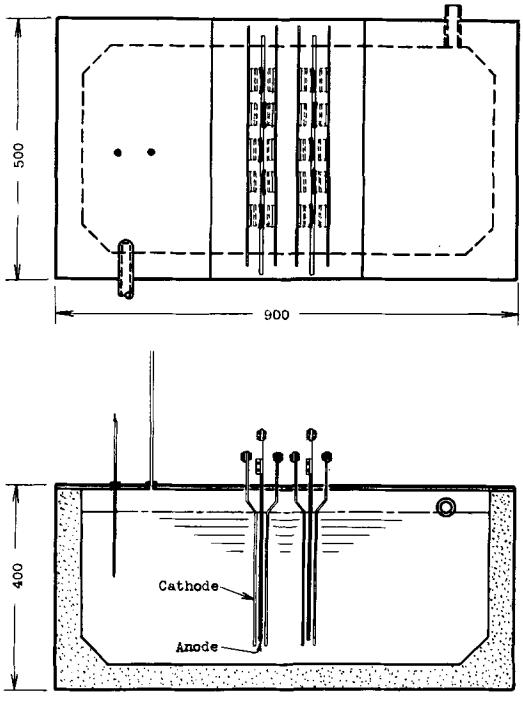

Fig. 3. Sanwa bromate cell. Dimension: length, 900 mm; width, 500 mm; height, 400 mm. Anode: lead peroxide bar; length, 350 mm; width, 50 mm; thickness, 7-9 mm. Cathode: stainless steel bar; length, 400 mm; width, 35 mm; thickness, 2.5 mm. Capacity: 95 l.

Table II. Operating conditions

Run No.	Starting electrolyte: KBr g/l	Starting electrolyte: $KBrO_3$ g/l	Starting electrolyte: Vol, l	Initial pH	Current, amp	Cell voltage, v	Temp, °C	Time, hr min	Amount of current, 1000 amp-hr
1	186	4	95	8.3	494	4.0	69	47 10	23.2_8
2	173	6	90	8.9	506	3.9*	66	44 00	22.2_7
3	229	9	95	6.9	500	3.8	67	56 40	28.3_2
4	232	9	95	8.9	500	3.7	66	56 40	28.3_2
5	233	9	95	9.2	500	4.0	70	56 40	28.3_2

* Voltage reached about 4.6 v at the end of the electrolysis.

Results

Run No.	$KBrO_3$ produced: Crystal obtained, kg	$KBrO_3$ produced: In solution, kg	Total kg	KBr unconverted, kg	Conversion of bromide to bromate, %	Current efficiency, %
1	17.3	5.6	22.9	1.0	94.2	94.6
2	15.7	5.4	21.1	0.4	97.4	91.3
3	22.7	3.9	26.6	2.7	87.4	90.5
4	22.7	4.4	27.1	2.4	88.9	92.2
5	24.0	3.1	27.1	3.0	86.7	92.2

electrolysis. All electrolyses were conducted at an anodic current density of 20 amp/dm². Operating conditions and results are given in Table II.

Two runs were made to determine what losses the anode might sustain (Table III).

Lead peroxide losses averaged 53-56 mg/1000 amp-hr and also 57-60 g/ton of product. It indicated that the loss amounted to about 2.2-2.6% of the original weight after the anode has been used for one year. Lead could not be detected in the product, the electrolyte, or in a black deposit which developed on the cathode. Lead was found in the slight amount of mud on the bottom of the cell.

An Example of Commercial Production

On a commercial scale, 24 cells were connected in series to make a circuit of 90 v and 500 amp. The cell system was divided into two solution series of 12 cells each. Electrolyte was introduced into the cell by means of a glass tube through the cover at one end and was discharged by the same means through the cover at the opposite end. The flow maintained good circulation.

A potassium bromide solution (pH 8-9), containing approximately 210-220 g/l KBr, 19-24 g/l $KBrO_3$, and 2 g/l $K_2Cr_2O_7$, was fed from a constant head tank into the cells. The concentration of bromide was adjusted so as to prevent crystallization of bromate during electrolysis. In a single pass through the cell, about 140 g/l of bromide was converted to bromate. The composition of cell effluent was approximately 270 g/l $KBrO_3$ and 90 g/l KBr. Results obtained are summarized in Table IV.

Cell effluent was a very clear solution due to the insolubility of the anode, and filtration was not necessary. After electrolysis, the electrolyte was cooled to 20°-25°C with circulating water. About 87% potassium bromate crystallized out. Almost all of the remaining potassium bromate in the mother liquor can be crystallized by adding a suitable amount of potassium bromide to return the electrolyte to the original concentration for a new cycle in the bromate cells. By this method, 97% of the bromate produced can be crystallized out without evaporation.

Potassium bromate crystal thus produced has excellent purity without recrystallization. Following

Table III. Operating conditions

Electrolyte: 180-220 g/l KBr, 15-25 g/l $KBrO_3$, 2 g/l $K_2Cr_2O_7$, pH 9-10 (during electrolysis)
Temp, 70°-85°C

Run No.	Current, amp	Amperage per one anode	Anodic current density, amp/dm²	Time, hr	Amount of current per one anode, 1000 amp-hr
Cell 1 (10 anodes)	600	60	30	2970	178
Cell 2 (15 anodes)	750	50	20	6170	308

Results

Run No.	Weight of anode*: before electrolysis, g	Weight of anode*: after electrolysis, g	Loss, g	Loss: per 1000 amp-hr mg	Loss: per ton $KBrO_3$ g
Cell 1	1146.5	1136.5	10.0	56.2	60
Cell 2	1043.6	1027.2	16.4	53.3	57

* Cell 1, mean value of 4 anodes; cell 2, mean value of 10 anodes.

Table IV. Characteristics of bromate production

Current: 510-550 amp
Voltage: 1st cell 3.8 v, 2nd cell 3.7 v, other cells 3.5 v in 12 cells
Current density, anodic: 20-22 amp/dm²
Temperature: 65°-72°C (1st to 4th cells, less than 60°C)
pH: alkaline, less than about 10
Rate of flow: 32 l/hr
Current efficiency: 90-92%
Energy consumption: 3.84 kwhr (d.c.)/kg $KBrO_3$
Cell feed: 210-220 g/l KBr, 19-24 g/l $KBrO_3$
Cell effluent: 260-280 g/l $KBrO_3$, 80-100 g/l KBr

are the chemical specifications of the final product currently being produced: colorless crystal, $KBrO_3$ assay, 99.2-99.5%; bromide as KBr, 0.05-0.1%; free acid, 0.35 cc 1/50*N* NaOH/5 g $KBrO_3$, max; total nitrogen, 0.002% max; sulfate, 0.005% max; heavy metals, 0.0005% max; iron, 0.0025% max.

Manuscript received April 30, 1956. This paper was prepared for delivery before the San Francisco Meeting, April 29 to May 3, 1956.

Any discussion of this paper will appear in a Discussion Section to be published in the June 1958 JOURNAL.

REFERENCES

1. For example: C. H. Martin and E. C. Hardy (Morton Salt Co.), U. S. Pat. 2191574 (1940).
2. K. Sugino, *Bull. Chem. Soc. Japan*, **23**, 115 (1950). [Method (I)].
3. H. Kretzschmar, *Z. Elektrochem.*, **10**, 789 (1904).
4. W. C. Bray, *J. Am. Chem. Soc.*, **32**, 932 (1910); **33**, 1485 (1911).

High Temperature Oxidation of High Purity Nickel between 750° and 1050°C

Earl A. Gulbransen and Kenneth F. Andrew

Research Laboratories, Westinghouse Electric Corporation, Pittsburgh, Pennsylvania

ABSTRACT

Kinetic studies on the oxidation of nickel using the vacuum microbalance method have been extended to 1050°C in order to determine the conditions and mechanisms of breakdown of the metal in oxidation. Below 900°C Ni oxidizes in the normal manner and the rate data fit in well with experimental rate relationship already established. At 900°C and higher, parabolic rate law plots of the data show increasing values of the constant with time. At 1000°C and higher, the oxide cracks away from the metal. It is suggested that Ni fails in protective oxidation due to a loss of adhesion at the oxide metal interface.

A number of studies have been reported on the oxidation of pure Ni. These studies were reviewed in an earlier paper (1). In recent years precise data have been obtained on the kinetics of the oxidation of pure Ni at temperatures up to 900°C. Moore (2), using a volumetric method, studied the reaction over the temperature range 400°-900°C while Gulbransen and Andrew (1), using a sensitive weight gain method, studied the reaction over the temperature range 400°-750°C. Considering the differences in method and metal, good agreement was found. In both studies the parabolic rate law was used to correlate the experimental data. Using the classical rate theory of oxidation, Gulbransen and Andrew (1) proposed a mechanism of reaction based on the diffusion of Ni ions through cation vacancies.

This paper extends the earlier work to 1050°C. Two objectives were of particular interest. First, to compare oxidation rate data with tracer studies (3) on the diffusion of Ni ions through nickel oxide and, second, to determine the conditions for transition in the mechanism of oxidation. Studies on several other metals (4) have shown that at some oxide thickness transition occurs from a slow protective oxide formation to a more rapid nonprotective type of oxide formation. If this transition phenomena is found to occur for all metals and alloys, we are dealing with a question of great technical importance.

Failure of metals in protective oxidation.—The use of metals and alloys at high temperature in many applications depends on the fact that the oxide film limits to a certain extent the rate of oxidation. In the protective range of reaction the rate of oxidation decreases as the oxide film thickens. However, at some temperature, time, and oxygen pressure, or film thickness, the rate of oxidation undergoes a transition to a more rapid reaction in which the rate of reaction does not depend on the oxide thickness. This phenomena has been termed "catastrophic reaction," "breakaway corrosion," "transition reaction," etc., depending on the degree of change in the reaction kinetics. The change in kinetics is referred to here as "failure in protective oxidation"; the film or scale is no longer rate controlling. The following physical and chemical factors have been related to the onset of transition in the kinetics of the reaction: (*a*) volatilization of the oxide; (*b*) volatilization of the metal; (*c*) phase transformations in the oxide; (*d*) phase transformations in the metal; (*e*) melting of the oxide; (*f*) loss of adhesion of the oxide to the metal; (*g*) combustion.

Apparatus and Method

Kinetic measurements were made using a vacuum microbalance method which has been described (5). However, to extend the range of the method, a low sensitivity balance was used as well as specimens of smaller area. In this way film thicknesses of 2000 μ g/cm^2 weight gain could be measured. In terms of film thickness for NiO, this weight gain is of the order of 126,000Å. The microbalance had a sensitivity of 4.75/division of 0.001 cm.

Samples were prepared from high purity nickel strip purchased from Johnson, Mathey and Company, London, and had no metallic impurities in excess of 0.0005%. Specimens were abraded through

are the chemical specifications of the final product currently being produced: colorless crystal, $KBrO_3$ assay, 99.2-99.5%; bromide as KBr, 0.05-0.1%; free acid, 0.35 cc 1/50*N* NaOH/5 g $KBrO_3$, max; total nitrogen, 0.002% max; sulfate, 0.005% max; heavy metals, 0.0005% max; iron, 0.0025% max.

Manuscript received April 30, 1956. This paper was prepared for delivery before the San Francisco Meeting, April 29 to May 3, 1956.

Any discussion of this paper will appear in a Discussion Section to be published in the June 1958 JOURNAL.

REFERENCES

1. For example: C. H. Martin and E. C. Hardy (Morton Salt Co.), U. S. Pat. 2191574 (1940).
2. K. Sugino, *Bull. Chem. Soc. Japan*, **23**, 115 (1950). [Method (I)].
3. H. Kretzschmar, *Z. Elektrochem.*, **10**, 789 (1904).
4. W. C. Bray, *J. Am. Chem. Soc.*, **32**, 932 (1910); **33**, 1485 (1911).

High Temperature Oxidation of High Purity Nickel between 750° and 1050°C

Earl A. Gulbransen and Kenneth F. Andrew

Research Laboratories, Westinghouse Electric Corporation, Pittsburgh, Pennsylvania

ABSTRACT

Kinetic studies on the oxidation of nickel using the vacuum microbalance method have been extended to 1050°C in order to determine the conditions and mechanisms of breakdown of the metal in oxidation. Below 900°C Ni oxidizes in the normal manner and the rate data fit in well with experimental rate relationship already established. At 900°C and higher, parabolic rate law plots of the data show increasing values of the constant with time. At 1000°C and higher, the oxide cracks away from the metal. It is suggested that Ni fails in protective oxidation due to a loss of adhesion at the oxide metal interface.

A number of studies have been reported on the oxidation of pure Ni. These studies were reviewed in an earlier paper (1). In recent years precise data have been obtained on the kinetics of the oxidation of pure Ni at temperatures up to 900°C. Moore (2), using a volumetric method, studied the reaction over the temperature range 400°-900°C while Gulbransen and Andrew (1), using a sensitive weight gain method, studied the reaction over the temperature range 400°-750°C. Considering the differences in method and metal, good agreement was found. In both studies the parabolic rate law was used to correlate the experimental data. Using the classical rate theory of oxidation, Gulbransen and Andrew (1) proposed a mechanism of reaction based on the diffusion of Ni ions through cation vacancies.

This paper extends the earlier work to 1050°C. Two objectives were of particular interest. First, to compare oxidation rate data with tracer studies (3) on the diffusion of Ni ions through nickel oxide and, second, to determine the conditions for transition in the mechanism of oxidation. Studies on several other metals (4) have shown that at some oxide thickness transition occurs from a slow protective oxide formation to a more rapid nonprotective type of oxide formation. If this transition phenomena is found to occur for all metals and alloys, we are dealing with a question of great technical importance.

Failure of metals in protective oxidation.—The use of metals and alloys at high temperature in many applications depends on the fact that the oxide film limits to a certain extent the rate of oxidation. In the protective range of reaction the rate of oxidation decreases as the oxide film thickens. However, at some temperature, time, and oxygen pressure, or film thickness, the rate of oxidation undergoes a transition to a more rapid reaction in which the rate of reaction does not depend on the oxide thickness. This phenomena has been termed "catastrophic reaction," "breakaway corrosion," "transition reaction," etc., depending on the degree of change in the reaction kinetics. The change in kinetics is referred to here as "failure in protective oxidation"; the film or scale is no longer rate controlling. The following physical and chemical factors have been related to the onset of transition in the kinetics of the reaction: (*a*) volatilization of the oxide; (*b*) volatilization of the metal; (*c*) phase transformations in the oxide; (*d*) phase transformations in the metal; (*e*) melting of the oxide; (*f*) loss of adhesion of the oxide to the metal; (*g*) combustion.

Apparatus and Method

Kinetic measurements were made using a vacuum microbalance method which has been described (5). However, to extend the range of the method, a low sensitivity balance was used as well as specimens of smaller area. In this way film thicknesses of 2000 μ g/cm^2 weight gain could be measured. In terms of film thickness for NiO, this weight gain is of the order of 126,000Å. The microbalance had a sensitivity of 4.75/division of 0.001 cm.

Samples were prepared from high purity nickel strip purchased from Johnson, Mathey and Company, London, and had no metallic impurities in excess of 0.0005%. Specimens were abraded through

4/0 polishing paper in a manner described previously (6).

Specimens had surface areas of 2.9 cm^2 and weighed about 0.1890 g.

Results and Discussion

The rate of oxidation of high purity Ni was studied as a function of time and temperature from 750° to 1050°C. Weight changes were calculated in units μ g/cm^2 and converted to Å of film thickness (1).

To interpret the beginning of a transition in the kinetics of the reaction, careful observations were made on the color of the oxide and adherence of the oxide to the metal. Since these observations can be made only at room temperature after reaction has stopped, certain precautions were taken to assure the best experimental conditions. Thus, if the color of the oxide is used as a criteria of loss of contact between the oxide and metal, it is necessary to equilibrate the metal and the oxide when it is in good contact. The following procedure was adopted. After oxidation and before cooling, the oxygen atmosphere was removed and the system evacuated to a pressure of less than 10^{-6} mm Hg. Specimens were held at temperature for at least 15 min to assure equilibrium between the metal and that part of the oxide film in contact with the metal.

Fig. 1 shows oxidation curves for the temperature range of 750°-1050°C for 2 hr of reaction time and an oxygen pressure of 7.6 cm Hg of oxygen. Curves were reproducible at the higher temperatures to ±5%. Table I shows the thickness of the oxide film after 2 hr of reaction, the color of the oxide film formed, and visual evidence on the loss of adhesion of the oxide film as a result of cooling.

The color of the oxide film was gray for temperatures up to 850°C, while above 900°C the oxide film was green. The color of the oxide was determined by the conditions under which it was formed. Thus green colored oxide films were formed under strong oxidizing conditions as shown by the studies of Bénard (7) and Bogatskii (8) and were probably not formed when the oxide was in equilibrium with the metal phase. Since all oxide films were equilibrated with the metal, this is interpreted to mean that the green colored oxide films are caused by a lack of contact of the oxide with the metal phase.

Table I. Oxide film thickness vs. oxide color

Temp, °C	Thickness μg/cm^2	Thickness Å*	Color	Stability
750	102.5	6,450	Gray	Adherent
800	160.0	10,060	Gray	Adherent
850	224.0	14,090	Gray	Adherent
900	385.0	24,220	Dark green	Adherent
950	653.0	41,070	Green	Adherent
1000	1220.0	76,740	Green	Nonadherent
1050	1890.0	118,900	Green	Nonadherent

* Surface roughness ratio = 1.

If the metal and oxide lose contact over a large area, the oxide film can crack away from the metal and the oxide becomes nonadherent. Stresses developed between the metal and oxide as a result of cooling aid the process of cracking the oxide loose from the metal.

Table I suggests a definite relationship between the color and the loss of adherence of the oxide as a result of cooling. The 950°C experiment was an intermediate case.

The parabolic rate law was used to interpret the oxidation data. The equation states that $W^2 = At + C$. Here W is the weight gain, t is the time, and A and C are constants. Some of the oxidation experiments could be fitted to the cubic rate law. Since the cubic rate law has not been derived from accepted physical principles, this rate law has not been used here in interpretation of the mechanism of the reaction (1) or of the transition phenomenon.

To test the agreement of the data with the parabolic rate law, plots were made of the square of the weight gain as a function of time. Fig. 2 shows the plot for the 750°C experiment. Here the value of the slope or rate law constant A decreases with time as oxidation proceeds. For this experiment the cubic rate law gives a better empirical correlation. At 750°C, the oxide film increases in its protective properties with increasing thickness faster than that predicted by normal diffusion processes. After 2 hr of reaction the change in rate law constant with increasing amounts of oxidation becomes a smaller factor.

Fig. 3 shows a parabolic rate law plot for the 900°C experiment. A detailed analysis of the plot

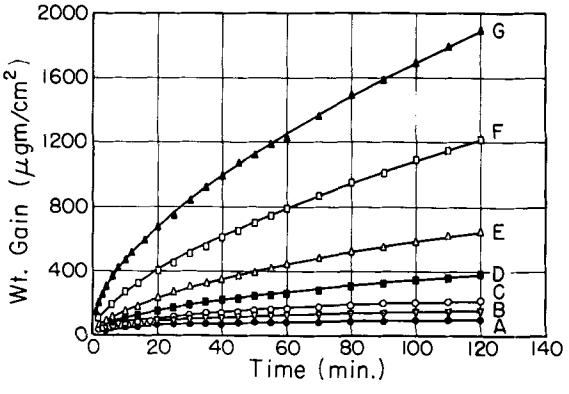

Fig. 1. Effect of temperature on oxidation of nickel, 7.6 cm Hg of O_2. A, 750°C; B, 800°C; C, 850°C; D, 900°C; E, 950°C; F, 1000°C; G, 1050°C.

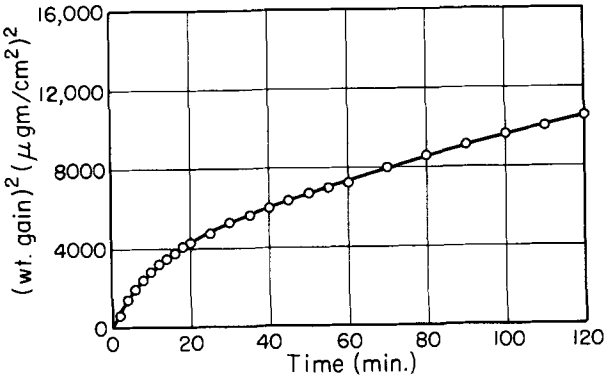

Fig. 2. Oxidation Ni, 750°C, 7.6 cm Hg of O_2, parabolic plot. Abraded through 4/0. $A = 9.03 \times 10^{-18}$ (g/cm^2)^2/sec.

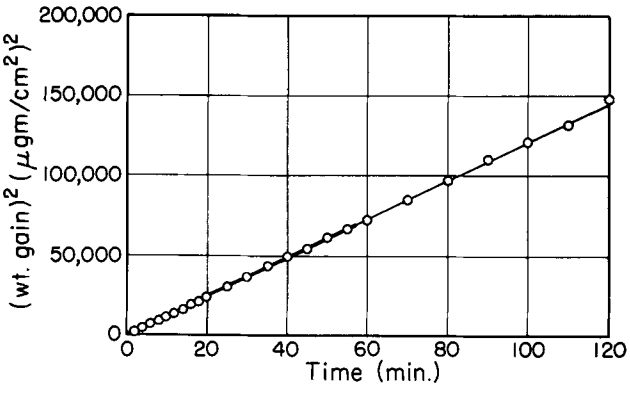

Fig. 3. Oxidation Ni, 900°C, 7.6 cm Hg of O_2, parabolic plot. Abraded through 4/0. $A_{initial}$ = 1.875 x 10^{-11} $(g/cm^2)^2/sec$; $A_{1-2\,hr}$ = 2.01 x 10^{-11} $(g/cm^2)^2/sec$.

shows a slightly increasing value of A as reaction proceeds.

Fig. 4 shows a parabolic rate law plot for the 1050°C experiment. Here, the slope A increases with the amount of oxidation. The increasing value of the slope A is taken as evidence for localized cracking of the oxide film and repair by oxidation. In the experiment the oxide was green and cracked away from the metal on cooling.

Table II shows a summary of the parabolic rate law constants taken from parabolic rate law plots. For temperatures of 850°C and higher, the initial and 1-2 hr values of the constants were tabulated. The initial slopes were determined during the first 10 min of reaction. Although the limiting slopes at times close to zero would be of theoretical interest, it was impossible to measure the reaction rate for these conditions. The very early stage of the reaction in addition was complicated by surface area and trace impurity effects.

Fig. 5 shows a plot of the parabolic rate law constants A on a log A vs. $1/T$ plot. The results of the earlier work at 550°-700°C as well as a recent measurement of Zima (9) were plotted together with the results of the present work. The data show the initial slope to be higher than the 1-2 hr slope. This was shown also earlier (1). However, above 900°C the initial slope was less than the final slope. The initial slopes above 900°C lie between the extrapolated values for the results below 900°C and

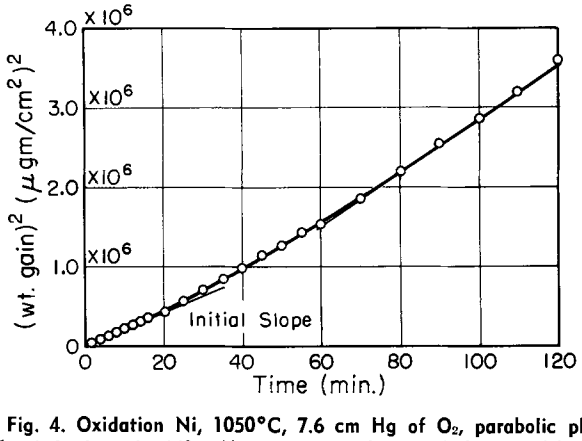

Fig. 4. Oxidation Ni, 1050°C, 7.6 cm Hg of O_2, parabolic plot. Abraded through 4/0. $A'_{initial}$ = 4.08 x 10^{-10} $(g/cm^2)^2/sec$; $A_{1-2\,hr}$ = 5.56 x 10^{-10} $(g/cm^2)^2/sec$.

Table II. Parabolic rate law constants, $(g/cm^2)^2/sec$

Temp, °C	Initial value	1-2 Hr value
750		9.03×10^{-13}
800		2.46×10^{-12}
850	7.67×10^{-12}	5.84×10^{-12}
900	1.875×10^{-11}	2.01×10^{-11}
950	3.75×10^{-11}	6.34×10^{-11}
1000	1.11×10^{-10}	2.41×10^{-10}
1050	4.083×10^{-10}	5.55×10^{-10}

the 1-2 hr slopes. If the initial values could be determined, it was suggested that these values would fall on an extrapolated line of BC in Fig. 5.

The data below 900°C fit in well with the earlier work, using a heat of activation of 41,200 cal/mole. Above 900°C, the data may be falling on a second line having a slope which yields a heat of activation of about 68,300 cal/mole. However, if the oxide loses contact with the metal, the slope of this line has little meaning.

The experimental heat of activation of 41,200 cal/mole was in agreement with some preliminary observations of Moore (3) on the heat of activation involved in the diffusion of nickel in nickel oxide at temperatures greater than 1000°C using a radioactive tracer method. Using the same grade of nickel as that used in this study, Moore (3) obtained a value of 44,200 cal/mole for the heat of activation of the diffusion process. These values can be compared since the experimental heat of activation for both the oxidation experiments and the diffusion experiments contains the same two heat terms. These were: the heat of formation of defects for diffusion and the heat of activation of diffusion. Since the parabolic rate law constant involves both the heat of formation of defects and the heat of activation of diffusion as exponential terms, the defect concentration at the oxide-metal and oxide-gas interface changes with the temperature.

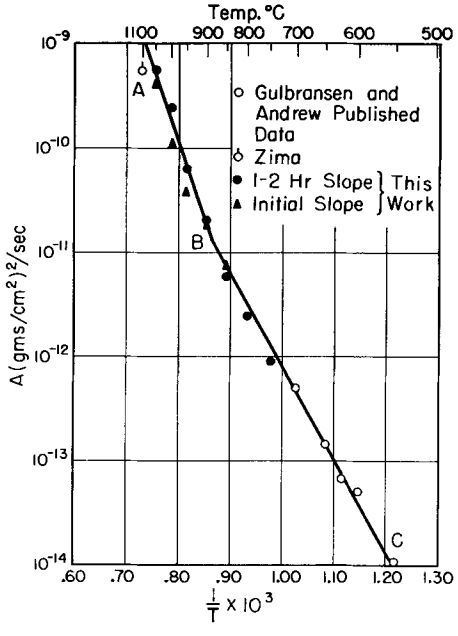

Fig. 5. Oxidation high purity nickel. Log A vs. $1/T$, 600°-875°C, ΔH_{BC} = 41,200 cal/mole; 875°-1050°C, ΔH_{AB} = 68,300 cal/mole.

This agreement of oxidation data obtained below 900°C and the diffusion data of Moore obtained above 1000°C suggests that deviations observed at 950°C and higher are due to a transition in the kinetics of the oxidation reaction. The transition in the kinetics was probably due to local loss of adhesion at the metal-oxide interface with a subsequent interruption of normal diffusion processes.

Conclusions

From experimental observations on (*a*) the color of the oxide film, (*b*) the cracking of the oxides on cooling, and (*c*) the deviations from the parabolic rate law it is concluded that the failure of nickel oxide in high temperature protective oxidation is due to a localized loss of adhesion at the interface between the oxide and metal. This failure occurs for this grade of nickel at about 900°C, at which temperature the parabolic rate law constant has a value of 1.88×10^{-11} $(g/cm^2)^2/sec$ and a film thickness value of 400-600 μ g/cm^2.

The failure of the oxide-metal adhesion may be related to one of several factors. (*A*) Stress may exist at the interface due to a mismatching of the nickel and nickel oxide lattice, which leads to failure as the oxide grows to a thick film. (*B*) Oxygen may dissolve in the nickel. This process could lead to small changes in the physical and chemical properties of the oxide-metal interface which could cause failure. (*C*) Since oxidation results from a diffusion of nickel through the oxide, the oxide must continuously collapse onto the metal as nickel diffuses from the oxide-metal interface. This process will not occur uniformly due to the different reaction rates on the several crystal orientations of the metal grains. Thus, cohesion between the oxide crystals and cohesion between the alloy and oxide would be diminished.

Manuscript received December 5, 1956. This paper was prepared for delivery before the Washington Meeting, May 12-16, 1957.

Any discussion of this paper will appear in a Discussion Section to be published in the June 1958 JOURNAL.

REFERENCES

1. E. A. Gulbransen and K. F. Andrew, *This Journal*, **101**, 128 (1954).
2. W. J. Moore, *J. Chem. Phys.*, **19**, 255 (1951).
3. M. T. Shim and W. J. Moore, *J. Chem. Phys.*, In press.
4. E. A. Gulbransen and K. F. Andrew, To be published.
5. E. A. Gulbransen, *Trans. Electrochem. Soc.*, **81**, 187 (1942).
6. E. A. Gulbransen and K. F. Andrew, *Trans. Am. Inst. Mining Met. Engrs.*, **185**, 515 (1949).
7. J. Bénard, *Ind. Chim. Belge*, **17**, 553 (1952).
8. D. P. Bogatskii, *Zhur. Olishchei Khim (J. Gen. Chem.)*, **21**, 3 (1951).
9. G. Zima, Private communication.

Impedance at Polarized Platinum Electrodes in Various Electrolytes

James N. Sarmousakis and Manfred J. Prager

William H. Nichols Chemical Laboratory, New York University, New York, New York

ABSTRACT

The results of alternating current bridge measurements of the impedances of bright Pt in contact with 1*N* aqueous solutions of KCl, KBr, and KI as functions of polarizing voltage and alternating current frequency are presented. The data may be interpreted in a manner similar to that for experiments with acid solutions. Various factors are discussed which may determine the dependence of the impedance on frequency for the electric double layer at rough surfaces.

The alternating current impedance of a polarized electrode immersed in an electrolyte can give much information (1-4) concerning conditions existing and processes occurring at or near the metal-electrolyte interface. Recent studies of this electrical property for bright Pt have been carried out by Ershler and his co-workers (5, 6) and by Schuldiner (7, 8) primarily from the kinetic point of view, while the work of Robertson (9), Wilburn (10), and Kheifets and Krasikov (11) on the same subject has been concerned mainly with the states of metal-solution systems at equilibrium. However, no systematic, comparative investigation has been reported as yet having to deal with bright Pt dipped in aqueous solutions of a number of halides of the same alkali metal. Accordingly the authors, employing an impedance bridge method, have determined the impedances of bright Pt in contact with 1*N* aqueous solutions of KCl, KBr, and KI to small alternating currents passing through the metal polarized at various direct potentials, as a function of the polarizing voltage and the frequency of the alternating current.

Experimental

The apparatus and procedures used for the measurements were essentially those of Robertson (9) with some modifications.

The glass assembly, Fig. 1, consisted of a Pyrex cell *A* attached to an evacuating assembly, *J* and *M*,

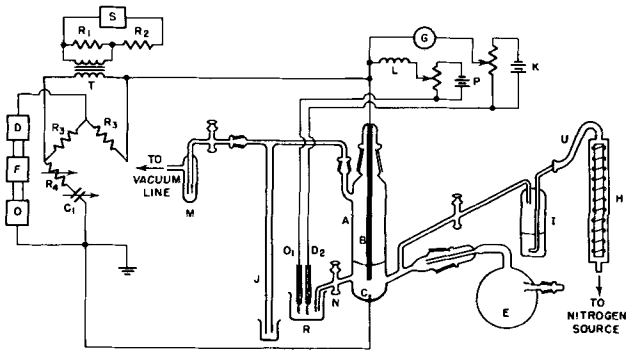

Fig. 1. Diagram of an apparatus for the determination of the impedance of a Pt microelectrode at fixed polarizing voltage. S, oscillator; D, amplifier; F, filters; O, oscilloscope; T, bridge transformer; R_1, 10 ohms; R_2, 10,000 ohms; R_3, 1000 ohms; G, galvanometer; R_4, 11111.1 ohms in steps of 0.01 ohm; C_1, 1.111 μf in steps of 0.0001 μf; A, cell; B, microelectrode; C, counterelectrode; D_1, D_2, reference electrodes; E, 500 ml flask; H, copper furnace; I gas wash bottle; J, mercury manometer; M, dry ice-acetone trap; N, ungreased stopcock; R, 50 ml beaker; U, Tygon connection; L, 62 Henry inductance; K, type K-2 potentiometer; P, Student's potentiometer.

and to a storage flask E in which the electrolyte could be degassed and then saturated with nitrogen entering from a train made up of a hot-copper furnace H and a saturator I. The electrolyte could then be transferred from flask E to cell A by a simple rotation, without coming into contact with grease. Contact between the electrolyte in the cell and the electrode vessel R was made through the closed ungreased stopcock N. Only the stopcocks leading to the dry-ice trap M and from the saturator I and the ground-glass joint from flask E to cell A were greased, the lubricant being Apiezon M grease.

There were two electrodes in cell A, the microelectrode B and the counter electrode C. The microelectrode B was made by sealing a length of Pt wire into a soft glass capillary tube so that only a cross section of the wire was exposed at the end of the capillary. The exposed end of the wire was then polished with successively finer grades of emery paper down to grade 0000 and finally on a metallurgist's wheel with a microcloth using first fine alumina and then Linde Air Products Type B-5125 Fine Abrasive. Measurement of a photomicrograph, made with a metallurgical microscope, gave the apparent area of the polished cross section of the Pt.

The counter electrode C was of much larger area than that of B so that its impedance compared with that of B was negligible. It was prepared by coating the bottom of the Pyrex cell, into which a Pt wire lead had been loosely sealed, with Liquid Bright Platinum No. 05.[1] After having been fired with a Tirrill burner flame, the mirror formed was plated (12) with a layer of Pt black. The seal through which the wire lead passed was made tight by the Pt deposited.

D_1 and D_2 in Fig. 1 were normal silver-silver halide reference electrodes. Ag-AgCl and Ag-AgBr electrodes were prepared according to the method of Harned (13), Ag-Ag I electrodes by the method of Owen (14). These electrodes were constantly checked, the chloride electrodes against calomel electrodes (15), the bromide and iodide electrodes by intercomparison of three electrodes of each type with each other.

The polarizing potential was applied across electrodes B and D_1 by means of a L&N Student's potentiometer P and measured across B and D_2 by means of a L&N Type K-2 potentiometer through a sensitive galvanometer G.

Electrodes B and C of cell A formed the unknown arm of a series-resistance bridge with equal ratio arms. The bridge was of the completely shielded type, cell A being the only component unshielded. The equal ratio arms were constructed as a Campbell-Shackleton unit (16). On measurement of L&N Type 106 mica capacitors in series with various values of resistance, it was found that the accuracy of the bridge was better than 1% and was independent of frequency.

The bridge was activated at a level of 2 mv by an oscillator S through a potential divider and an isolation transformer T with shield ungrounded. The detector circuit consisted of a high gain amplifier D tuned by means of a Wien bridge feedback circuit, of bridged-T line frequency filters F, and of an oscilloscope O.

The Pt was by report 99.5% pure.[2] All salts were reagent grade at least once recrystallized. Solutions were prepared from water obtained as a middle fraction on distillation of a solution of $KMnO_4$ in distilled water after long refluxing. N_2 was passed over Cu at 450°-500°C to remove oxygen.

An experiment began with the cleaning of the apparatus. The cell A and flask E, kept in concentrated HNO_3, were rinsed with water and then steamed for at least 1 hr over alkaline permanganate solution. The microelectrode, kept in distilled water, was immersed in warm concentrated HNO_3 for 5 min and then washed with water. The apparatus was assembled after the appropriate solution was poured into flask E. The system was then flushed with N_2 for ½ hr and evacuated for 2 hr with an oil pump to remove dissolved gases. N_2 was reintroduced to bring the system to atmospheric pressure. Solution was then transferred to the measuring cell from the flask. The reference electrodes were assembled to the apparatus and checked.

To remove trace impurities from the surface of the Pt electrode the procedure described by Robertson (9) was used. The Pt electrodes in contact with the KCl, KBr, and KI solutions were polarized repeatedly over the voltage ranges −0.6 to 1.0, −0.4 to 0.85, and −0.2 to 0.55, and back, respectively, the voltages given being referred to the corresponding silver-silver halide electrodes. This process was terminated when the capacity of the electrode, measured at a given desired potential, reached a permanent maximum value.

After the potential of the electrode was set at a given value, readings on the bridge were made every five min. The capacity generally decreased with time, at first rapidly, and then more slowly. A final reading was taken when its value was different

[1] Made by the Hanovia Chemical and Manufacturing Co., 100 Chestnut St., Newark, N. J.

[2] Supplied by the American Platinum Works, 231 New Jersey Railroad Ave., Newark, N. J.

by less than one-half of one per cent from the previous reading. This usually meant a change of no more than 0.0001 μf in capacity in 5 min. These values of capacity and those corresponding of resistance are discussed in the next sections.

The experiments were carried out at room temperature which varied from 24° to 31°C during the period of the investigation.

Experimental Results

When the equal-arm impedance bridge was brought to balance, the capacity and resistance in series in the standard arm were electrically equivalent to the microelectrode as a circuit component at the given frequency and polarizing voltage.

Capacity as a function of polarizing voltage.—In Fig. 2 are represented all the experimental values of the capacities, measured at a frequency of 980 cps, for a single microelectrode immersed in 1*N* KBr and in 1*N* KI solutions as a function of polarizing potential. The polarizing potentials are referred to the normal Ag-AgCl electrode as standard. In calculating these values of potential it was assumed, on the basis of computations employing the Lewis and Sargent equation (17), that the liquid junction potentials between the potassium halides were negligible (less than 0.01 v). The capacities are given in microfarads per square centimeter as calculated from the bridge readings and the area[3,4] of the electrode, 1.42 x 10^{-3} cm^2.

The curves are similar in form to those of Dolin and Ershler[5] for 1*N* solutions of HCl and H_2SO_4, and for 0.03*N* and 0.2*N* solutions of HCl 1*N* in KBr. In particular, the curves in Fig. 2 show a maximum at cathodic potentials near that for the reversible evolution of H_2 at unit activity. This maximum is followed by a decrease to a flat minimum at intermediate potentials. The minimum is followed by a sharp rise in capacity in the anodic region at potentials not far away from those at which the halogens would be evolved reversibly at unit activity. The sharp rise in capacity at highly anodic potentials has been followed in detail by Robertson (9) for 1*N* HCl. The minimum capacity for both salts appears to be about 18 μ f/cm^2 to be compared with 19 μ f/cm^2 for 1*N* HCl as found by Robertson (9).

Capacity as a function of frequency.—In Fig. 3 are represented the capactities in microfarads per square centimeter of the microelectrode as a function of the reciprocal of the square root of the frequency of the alternating current used in the measurement, at various polarizing voltages as indicated.

[3] Measurements of the capacity of this microelectrode, with KI as electrolyte, at the beginning and end of the work, had a maximum dispersion of 5%, indicating no change in effective area of the electrode surface within experimental error.

[4] Values of capacity per unit area were measured at nine different polarizing potentials for this electrode and for another of area, 2.05 x 10^{-3} cm^2 immersed in 1*N* KCl. The average of the various ratios of difference in capacity of the two electrodes to average capacity was approximately 7%. The data are not given in detail since the capacities were varying with time at a rate greater than one half of one per cent per five minutes.

[5] The bridge used by Dolin and Ershler in measuring impedance had a standard arm containing a capacitor and resistance in parallel. The values of capacity and resistance in series as used in this investigation may be converted by calculation with standard formulas to values in a parallel combination like that of Dolin and Ershler. The magnitudes of capacity in series and that in parallel differ from about 5% to about 12%. The shape of the curve in Fig. 2 would not be changed significantly by the transformation.

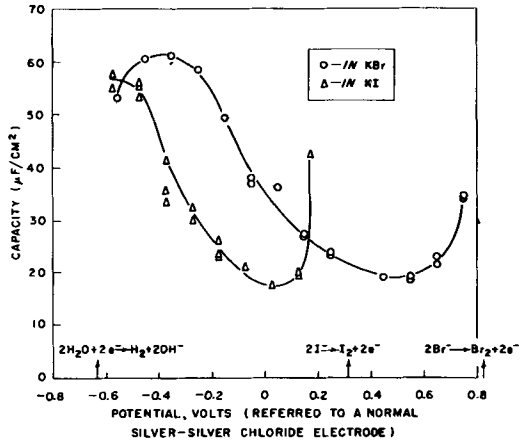

Fig. 2. Dependence on the polarizing potential, referred to a 1*N* Ag-AgCl electrode, of the capacity, measured at 980 cps, of a Pt electrode immersed in 1*N* KBr and 1*N* KI solutions.

At least 60% of the points at each potential represent averages of at least two independent measurements. However most of the points referring to KBr and polarizing potential, —0.55 v, and to KI and polarizing potential, 0.03 v, refer to the results of single measurements.

The reproducibility of the data used for Fig. 3 was no worse than that indicated by the scatter of the points in Fig. 2. It may then be presumed that the absorption of trace impurities does not play a very significant role in determining the frequency dependences as shown by the graphs. Inspection of the curves makes it appear possible that there is a

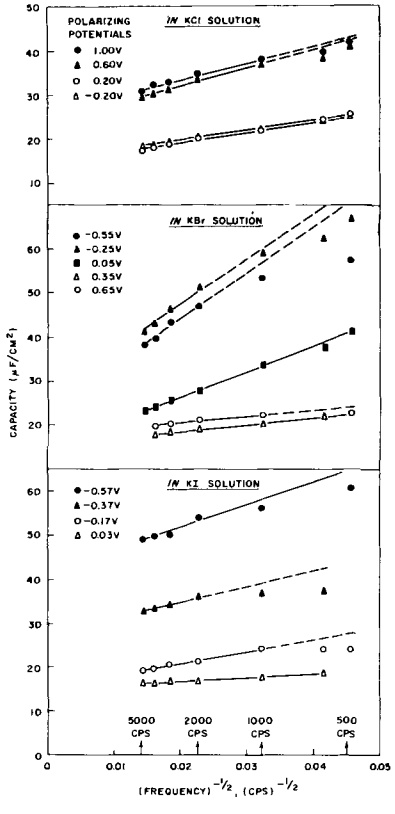

Fig. 3. Dependence on the frequency of the measuring alternating current, of the capacity of a Pt electrode immersed in aqueous 1*N* KCl, KBr, and KI solutions at various polarizing potentials referred to a 1*N* Ag-AgCl electrode.

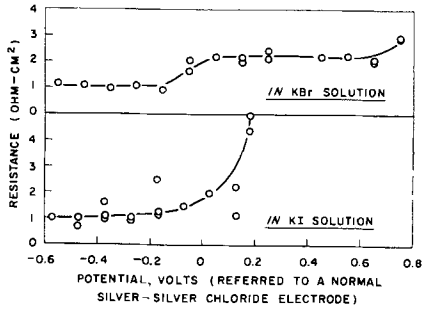

Fig. 4. Dependence on the polarizing voltage referred to a 1*N* Ag-AgCl electrode, of the resistance, measured at 980 cps, of a Pt electrode immersed in 1*N* KBr and KI solutions.

linear dependence of capacities on the reciprocal of the square root of the frequency at higher frequencies. At lower frequencies there is a tendency for the points to fall below the lines drawn through the points at higher frequencies. This trend, if continued, would lead to the maxima of capacity at lower frequencies found by Robertson (9).

Increase of frequency by a factor of ten from 480 cps produces an increase of about 35-45% for 1*N* KCl and of about 15-25% for 1*N* KI. The percentage increases for each of the two salt solutions are the same, within the experimental scatter, at all polarizing potentials studied. For 1*N* KBr, the corresponding increases are approximately 20% for the two most positive polarizing potentials and about 60-80% for the other potentials. This variation of the fractional increases in capacity, as potential varies, lies outside the experimental scatter of the measurements, and gives rise to an apparent anomaly in the results for the bromide solution for which no explanation can at present be offered.

Resistance.—Resistance measurements by the procedure described are highly irreproducible. The extent to which this statement is true may be seen in Fig. 4 in which are shown the apparent series resistances plotted as functions of the potential of

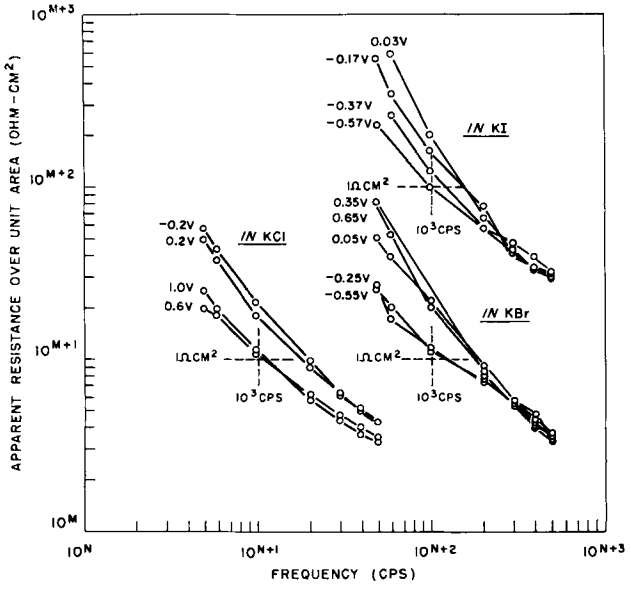

Fig. 5. Dependence on frequency of the apparent resistance of a Pt electrode immersed in 1*N* KCl, KBr, and KI solutions and for various polarizing potentials referred to a 1*N* Ag-AgCl electrode.

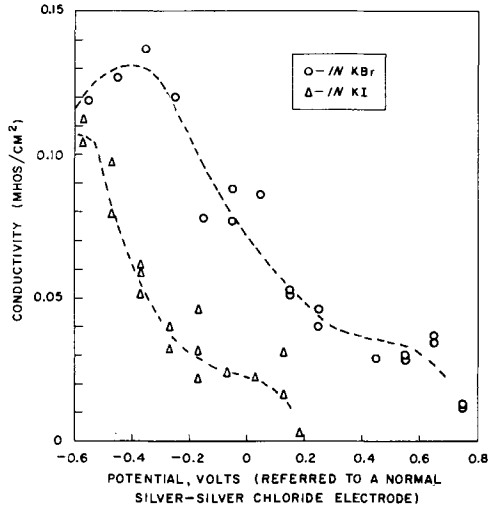

Fig. 6. Dependence on the polarizing potential referred to a 1*N* Ag-AgCl electrode, of the conductivity, in parallel with capacity, of a Pt electrode immersed in 1*N* KBr and 1*N* KI solutions. Measurements at 980 cps.

the microelectrode. These resistances in series with the capacities of Fig. 2 are equivalent to the microelectrode as electric circuit elements. Resistances are low at cathodic potentials and high at anodic potentials.

As already pointed out by Dolin and Ershler (6), Robertson (9), and Grahame (2) for systems involving solid electrodes which they studied, the series resistance is large at low frequencies and decreases very rapidly with increase of frequency for all the salts and at all potentials. Broken line graphs are drawn on a logarithmic scale in Fig. 5 to represent the resistance-area products in ohm cm² corresponding to the capacities shown in Fig. 3. The crossed dashed lines serve to indicate the values of the powers of ten, M and N, for the groups of curves closest to them, each of which corresponds to a different electrolyte as shown. The apparent resistance appears to be roughly inversely proportional to the first power of the frequency, the power being greater than one at low frequencies and less than one at higher frequencies.

The similarity in behavior, illustrated in Fig. 2, of the series capacity, as the polarizing potential changes, to that of the parallel capacity determined by Dolin and Ershler for their systems has already been noted. When the data for series capacity and resistance are used to calculate the equivalent combination of capacity and resistance in parallel and the reciprocal of resistance (conductivity) obtained therefrom, it is found that the resulting values of conductivity also change with polarizing potential in much the same way as do the corresponding quantities determined by Dolin and Ershler (*see* Fig. 6).

Discussion

The variables which may be considered to determine the combination of capacity and resistance equivalent to the microelectrode as an electrical circuit component are (*a*) type of electrolyte, (*b*) polarizing potential, (*c*) frequency, (*d*) roughness and nonhomogeneity of the electrode surface, (*e*)

shape of the electrode and its symmetry, and (*f*) presence of trace impurities at the surface.

The shape factor may be considered as not important on the presumption that the Pt electrode used in this work behaved much like those of Robertson (9) whose results indicate a similar behavior of plane and spherical electrodes with similar dependence of capacity on frequency at a given potential in 1*N* HCl. Further, considering the degree of reproducibility of the values of the capacity as shown in Fig. 2, the adsorption of trace impurities is probably not a significant factor.

As has already been pointed out for Fig. 2 and 4 the capacities and conductivities vary with polarizing potential in much the same manner as has been reported by Dolin and Ershler (6) with maxima at cathodic potentials and minima at intermediate potentials. In addition there is the sharp increase in capacity at anodic potentials which appeared in one experiment by Dolin and Ershler (6) and was followed in detail by Robertson (9) for 1*N* HCl at polarizing potentials close to that for the reversible evolution of Cl_2 at unit activity. There appears no reason to interpret the data in a way other than that of Dolin and Ershler. At cathodic potentials the discharge of hydrogen ion and reduction of water and adsorption of hydrogen together with production of hydroxyl ion give rise to a high capacity. At intermediate potentials where no reaction should be occurring, the electric double layer at the metal-solution interface should be the most important determining factor. At anodic potentials the sharp rise in capacity may be associated with a "pseudo-capacity" such as that described by Grahame (18) as occurring at the reversible potential of an electrode reaction. In this case the reversible potential should be that of the discharge of iodide and bromide ions.

The values of the potentials of the minima in capacity for the KBr and KI solutions are probably determined mainly by the rise in capacity due to reversible reaction commencing, so that they cannot be expected to have significance with respect to the structure of the double layer.

For the clean, smooth, and symmetrical surfaces presented by freshly formed mercury drops, there is no dependence on frequency of the measured capacities and resistances, which last are made up only of the bulk-electrolyte and lead resistances as components (19). It has further been shown experimentally that the variation of capacity with frequency for Tl, Cd, and Pb electrodes is much decreased by melting the electrode to form a smooth surface (20). If shape effects and the adsorption of trace impurities are to be assumed as not important in determining the variation with frequency of the capacity of the Pt electrode in contact with alkali halide solutions at potentials where no reaction can be occurring, then it may be presumed, as has already been emphasized by Grahame (1,2), that roughness is still an important factor even with the type of polishing previously described.

Any theory which is formulated to relate roughness to the frequency dependence of the measured impedance must be capable of explaining both the relatively small dispersion of the capacity and the much larger dispersion of series resistance of the electrode. For example, one might consider that, as the electric potential alternates during a measurement, the surface concentrations of ions in the hollows of the rough surface would oscillate, causing the hollows to become sources and sinks of ions moving out to and in from the bulk of the solution. The ease with which transfer by diffusion and migration would remove and supply these ions would then be frequency dependent. However, it would require an extensive mathematical procedure to determine whether this explanation would account for the differences in dispersion of the capacities and resistances just mentioned. Experimental work on surfaces of known roughness is desirable, together with theoretical analysis, before circuit components equivalent to the electrode can be set up unambiguously.

As has been pointed out by Grahame (1), double layer capacities for solid surfaces can be obtained by measurements at very high frequencies. The linear dependence of capacity on the square root of frequency which seems to be exhibited by the graphs of Fig. 3, especially for those curves involving small capacities, and corresponding to polarizing potentials in the double layer region, if continued to higher frequencies, may provide a means for carrying out extrapolations to infinite frequency.

Acknowledgment

The authors wish to express their appreciation to the College Relations Department of the Western Electric Co. for donating equipment and arranging the provision of the facilities of the Bell Telephone Laboratories, Murray Hill, N. J., to calibrate the standard condenser. Acknowledgment is also made to Dr. Remsen T. Schenck for providing the design of the tuned amplifier, and to Dr. John Nielsen, of the Department of Metallurgical Engineering of New York University, for providing facilities for the polishing of the electrodes.

Manuscript received May 31, 1956. This paper was prepared for delivery before the Washington Meeting, May 12-16, 1957.

Any discussion of this paper will appear in a Discussion Section to be published in the June 1958 JOURNAL.

REFERENCES

1. D. C. Grahame, *This Journal*, **99**, 370C (1952).
2. D. C. Grahame, *Ann. Rev. Phys. Chem.*, **6**, 337 (1955).
3. J. O'M. Bockris, "Modern Aspects of Electrochemistry," pp. 103 to 276, Academic Press, Inc., New York (1954).
4. H. Gerischer, *Z. Elektrochem.*, **59**, 604 (1955).
5. B. Ershler, *Acta Physicochim. U.R.S.S.*, **7**, 327 (1937).
6. P. Dolin and B. Ershler, *ibid.*, **13**, 747 (1940).
7. S. Schuldiner, *This Journal*, **99**, 488 (1952).
8. S. Schuldiner, *ibid.*, **101**, 426 (1954).
9. W. D. Robertson, *ibid.*, **100**, 194 (1953).
10. R. L. Wilburn, *Univ. Microfilms, Publ. No.* 10,019; *Dissertation Abstr.*, **14**, 1943 (1954).
11. V. L. Kheifets and B. S. Krasikov, *Doklady Akad. Nauk. S.S.S.R.*, **94**, 101 (1954).
12. A. Weissberger, "Physical Methods of Organic Chemistry," 2nd ed., Vol. I, Part II, p. 1722, Interscience Publishers, New York (1949).
13. H. S. Harned, *J. Am. Chem. Soc.*, **51**, 416 (1929).
14. B. B. Owen, *ibid.*, **57**, 526 (1935).

15. I. M. Kolthoff and N. H. Furman, "Potentiometric Titrations," 2nd ed., p. 79, John Wiley & Sons, Inc., New York (1931).
16. L. Behr and A. Williams, *Proc. Inst. Radio Engrs.*, **20**, 969 (1932); T. Shedlovsky, *J. Am. Chem. Soc.*, **52**, 1793 (1930).
17. G. N. Lewis and L. W. Sargent, *J. Am. Chem. Soc.*, **31**, 363 (1909).
18. D. C. Grahame, *Chem. Rev.*, **41**, 441 (1947).
19. D. C. Grahame, *J. Am. Chem. Soc.*, **68**, 301 (1946).
20. T. Borisova and B. Ershler, *Zhur. Fiz. Chim.*, **24**, 337 (1950).

Technical Note

Electrodeposition of Lead from the Pyrophosphate Bath

J. Vaid and T. L. Rama Char

Department of General Chemistry, Indian Institute of Science, Bangalore, India

Lead is commonly plated from the fluosilicate, fluoborate, and sulfamate baths. Belyaer (1) used an alkaline bath containing lead acetate, sodium hydroxide, rochelle salt, rosin, and gelatin. Ferguson and Hovey (2) state that a solution containing sodium pyrophosphate, copper acetate, and lead acetate showed little promise for Cu-Pb alloy plating. This laboratory has undertaken a detailed investigation on the electrodeposition of various metals and alloys from the pyrophosphate bath. The plating of Pb was studied mainly in connection with work on Pb-Sn alloy deposition.

Experimental

Plating solutions were prepared by addition of sodium pyrophosphate to lead nitrate, a complex, $Na_2[Pb(P_2O_7)]$, being formed. Potentiometric and conductometric titrations showed that the ratio of pyrophosphate to Pb in the complex is 1:1. The Pb ion concentration in the solution and the instability constant K of the complex as found from potential measurements were of the order of 10^{-12} g ion/l and 10^{-12}, respectively (3). Rogers and Reynolds (4) reported a value of the same order for K of the 1:1 complex, whereas Halder (5) has stated that there are two complexes corresponding to 1:1 and 2:1 ratios, K for the latter being 10^{-6}. The pyrophosphate content of the bath was always in excess of that required for complex formation. The bath control did not present any difficulties.

Cylindrical Cu-plated Pt cathodes (diameter 5/8 in., length 1½ in.) and Pb anodes (diameter 1⅝ in., length 1 in.) were used, the immersed anode area being four times the cathode area (3 in.^{2}). Plating time was 20-30 min; volume of solution used was 175 cc. The rest of the experimental procedure was the same as described before (6). Cathode potentials (hydrogen scale) were reproducible to ±5 mv. Photomicrographs of a thick coating of Pb on Cu plate were taken with a Vicker's projection microscope. X-ray powder patterns of the deposits were obtained from a Siemans Baujahr 1950 model unit, with a 57.3 mm diameter camera.

Experimental Results

Table I gives the effect of variation of electrolyte concentration and current density on the cathode efficiency and potential. Data recorded correspond to good quality deposits. The decomposition potential for the plating solution was 1.6-1.7 v.

Cathode efficiency was 90-100% throughout. Gelatin decreased the efficiency as well as the limiting current density (48-29 amp/ft^2). A solution containing 0.05M $Pb(NO_3)_2$ could be regarded as optimum. The specific resistivity and cathode polarization decreased with increase in metal ion concentration. The increase in polarization with the addition of gelatin has also been observed in Sn deposition from the pyrophosphate bath (6). The throwing power of the solution was quite good, the

Table I. 1200 rpm cathode, 60°C, 0.2-1.1 v, pH 9.5, anode efficiency, close to 100%. For each concentration the first figure under current density gives the efficiency per cent and the second the cathode potential (— sign) in volts on H scale. Static potential, —0.45 v; reference electrode, saturated calomel

	Concentration, g/l		Sp. resistivity, ohm/cm^3	Current density amp/ft^2					
	Lead	Pyrophosphate		5	10	19	29	38	48
1.	2.1	7.0	55.1	93	94	89	88	—	—
				0.70	0.70	1.24	—	—	—
2.	5.2	17.5	29.2	92	95	97	92	90	—
				0.59	0.68	0.93	—	—	—
3.	10.4	35.0	15.9	95	96	99	98	94	93
				0.57	0.59	0.71	1.10	1.20	—
	10.4	35.0							
	(+ gelatin 0.5 g/l)		15.9	87	87	80	59	—	—
				0.59	1.37	1.64	1.74	—	—
4.	15.5	52.0	11.8	95	96	100	100	100	96
				0.56	0.57	0.66	0.74	1.03	—
5.	20.7	70.0	9.5	95	99	100	100	100	96
				0.54	0.57	0.65	0.73	0.93	1.06

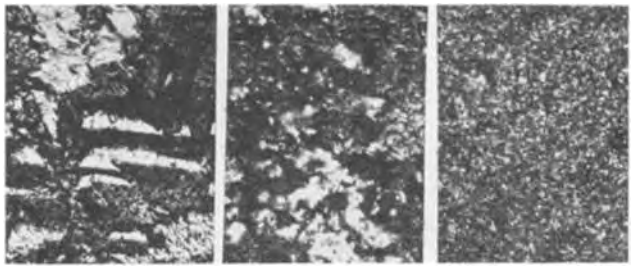

Fig. 1. (Left) Cu base; (center) Pb deposit under conditions of Table I-3, 19 amp/ft^2; (right) same with gelatin. Magnification, 500X before reduction for publication.

Schlotter-Korpiun value (7) being in the range 1.7-4.7.

The bath gave adherent and grayish-white deposits on Cu (steel or brass) cathodes. The deposit became finer grained and bright (matte) by adding gelatin (Fig. 1). It has a face centered cubic structure, with a = 4.93Å. The deposits (0.001 in.) were nonporous as indicated by the ferroxyl test (steel base), and the corrosion resistance was good in the laboratory atmosphere (0.001 in., 4 months). The time required to deposit 0.001 in. thickness at 25 amp/ft^2 was 18 min.

The performance of the pyrophosphate bath for Pb plating appears to be satisfactory. The deposition of Pb-Sn alloys from this bath will be reported later.

Acknowledgment

The author's thanks are due to K. R. Krishnaswami, Head of the Department, for his keen interest in the work. One of the authors (J. Vaid) is grateful to the Government of India for the award of a Senior Research Scholarship during the period of this investigation.

Manuscript received August 6, 1956.

Any discussion of this paper will appear in a Discussion Section to be published in the June 1958 JOURNAL.

REFERENCES

1. P. Belyaer, *Chem. Abs.*, **36**, 4031 (1942); *Korroziya i Borba s Nei*, **6**, [2], 15 (1940).
2. A. L. Ferguson and N. W. Hovey, *This Journal*, **98**, 146, (1951).
3. J. Vaid and T. L. Rama Char, *Proc. 41st Indian Science Congress*, Part 3, 86 (1954).
4. L. B. Rogers and C. A. Reynolds, *J. Am. Chem. Soc.*, **71**, 2081 (1949).
5. B. C. Halder, *Current Science*, **19**, 244 (1950).
6. J. Vaid and T. L. Rama Char, *This Journal*, 104,282 (1957).
7. M. Schlötter and J. Korpiun, *Trans. Electrochem. Soc.*, **62**, 129 (1932).

Technical Review

A Review of Patents on Silicon Carbide Furnacing

J. C. McMullen

Research and Development Division, The Carborundum Company, Niagara Falls, New York

The value of a good abrasive was brought to Edward Goodrich Achesons's attention by one of the members of Tiffany and Company. Remembering one of his early experiments in which clay, when heated in a gas-fired furnace, was converted to a hard, carbon-impregnated substance he decided to subject clay and carbon to the influence of electric heat. A small iron bowl was attached to one lead from a dynamo and filled with a mixture of clay and powdered coke. A carbon rod attached to the other lead was inserted. Current was passed through the mixture until the center was heated to a very high temperature. An examination of the cold mass revealed a few bright specks on the end of the carbon rod. When drawn across a pane of glass the rod tip cut like a diamond. The new material, he thought, was composed of carbon and corundum.

Acheson soon modified the furnace by constructing a horizontal one with firebrick walls. Between two electrodes he placed a conducting core of loose graphite surrounded by a mixture of clay, carbon, and salt. The first patent relating to SiC was issued to him in 1893 (1). It details the method of manufacture and correctly describes the product as SiC. While there have been improvements in furnacing and in mix proportions, the principles as developed by Acheson are still in use today in the commercial production of SiC.

To keep this review within bounds, only those United States patents which show marked changes over the original patent, at least in the writer's opinion, will be discussed. A complete list, comprising 59 of the subject patents reviewed, is given in the appendix. An attempt is made to arrange the subject matter in groups rather than chronologically.

Resistance Furnaces

In the original patent, a mix composed of 50% pure carbon, 25% clay, and 25% common salt was used. The salt was deemed necessary to act as a flux which on melting brought the particles of clay and carbon in intimate contact. The use of salt is mentioned frequently throughout the patent literature on SiC. Kirchner (48) described the action of salt as follows: "The salt tends to reduce the impurities in the resultant product, since it reacts at high temperatures with impurities containing iron and some other elements to form volatile chlorides."

In Acheson's second patent (2) issued in 1896, the clay is replaced by silica. Carbon is used in stoichiometric proportions rather than in excess as stated in the original patent. A generous amount of salt, 9%, is still added as a flux. Also 4% of sawdust was added to promote permeability to the mix.

F. J. Tone was issued 17 patents from 1902 to 1913. Two patents (9, 11) describe a furnace with movable sidewalls. These walls were made in sections composed of iron frames lined with firebrick. This eliminated repeated handling of individual bricks used in assembling the SiC furnace.

According to the accepted equation for the formation of silicon carbide ($SiO_2 + 3C = SiC + 2CO$), 1.4 tons of CO gas is generated for each ton of SiC produced. The heat value, on combustion, of this CO is equivalent to 3560 kwhr and, since 8000-12,000 kwhr is required to produce a ton of SiC in commercial furnaces, the recovery of the waste gas offers one method of reducing manufacturing costs.

Tone's patent (13) in 1908 described a furnace heated by a combination of electric power and combustion of gases generated during the operation. However, during one experiment an explosion occurred and further work on this method was abandoned.

Tone was granted two patents (16, 24) disclosing the use of a solid carbon core, which would be more consistent in physical properties than a loose core. However, the resistance of a solid rod is so low that either its length has to be greatly increased or its cross section reduced. Tone increased the length by the use of a zig-zag pattern. Since a loose graphite core, surrounded by the conventional sand-coke-sawdust mix, is used today, it indicates that a solid rod is not practical with this type of furnace loading.

In 1909 Tone patented (15) a pot-type furnace for producing SiC. As furnacing proceeds, mix is added, and vertically depending electrodes raised until a complete ingot is formed.

Ridgeway was an important contributor to the art. His patents (45, 47) disclose a radical departure from the conventional furnace method. He reasoned that SiC, since it becomes an excellent electrical conductor when heated, could be used as a core. A jointed graphite rod of small cross section is used to preheat the core composed of SiC-containing furnace by-products. A low voltage is used until the

graphite rod is consumed, and the remainder of the heat is made with increased voltage. It is claimed that the efficiency is improved by making use of the SiC by-products. The entire furnace charge tends to be heated electrically rather than by thermal radiation from a large central core.

Ridgeway also developed a closeable furnace (52, 55) for making abrasive metal carbides. The object here was to minimize losses by oxidation of the product and by volatilization. While the method is advantageous in making boron carbide, it is not particularly applicable for making SiC as losses, except for CO, are negligible.

Improved Product

According to Acheson's patent (22) of 1912, a new product different in appearance and having a toughness and hardness at least equal and perhaps greater than the normal product is formed when 5% boron oxide is incorporated in the furnace mix. Since the resultant SiC was found to be essentially boron-free, he postulated that the unusual properties are due to the modifying influence of the boron during the reaction. This suggests that other additives be tried to determine the effect on the crystal habit of SiC.

Tone's patents (17, 23) in 1910 and 1912 deal with making clear crystals of SiC using pure raw materials. Such crystals, it is claimed, possess double refraction and are of great value as gems, for they can be cut with regular facets and polished.

Hutchins in 1933 (44) described a method of producing a dense SiC, by adding 3% excess carbon to the mix and furnacing with a 30% increase in power rate over that normally used. Lumps of the new material, it is claimed, have an apparent density of 2.6 or greater while the ordinary variety is usually less than 1.8 g/cc. SiC made by the process is said to consist of densely compacted masses having a structure very similar to that of a material solidified from a molten state. It is also claimed that the dense material has a more uniform and also a lower electrical resistance than that of normally furnaced crystalline material.

Furnace Mix

A patent by Hutchins (34) in 1920 pertains to the more uniform production of SiC. During furnace operations the highly heated vapors of silicon and silica tend to rise through the charge. This results in a concentration of siliceous compounds in the upper part of the furnace, and a deficiency of these compounds in the lower part. In Hutchins' preferred method the bottom of the furnace is loaded with mix having a SiO_2/C ratio of 1.94 while mix with a 1.70 ratio is used in the top. Since both of these are in excess of the theoretical ratio of 1.67, it indicates that some Si leaves the reaction zone and is either condensed in the outer by-product material or is lost to the atmosphere.

A patent by Kirchner (48) in 1935 is the only one dealing with the pore forming material used to promote permeability in the raw mix. He advocates the use of buckwheat or other seed hulls to replace sawdust, since they are more consistent physically and chemically and allow better control of the furnace mix.

Use of Silicon Compounds

Four patents cover the use of materials other than free silica or silicon, with carbon, to form SiC.

Dorseman (5) in 1902 heated $ZnSiO_3$ and C in a closed arc furnace to produce metallic Zn and SiC. Zn vapors are condensed to a liquid and the CO is vented. The removal of the SiC from the closed furnace is not clearly described but it appears that this would present quite a problem.

Weber (8) in 1903 described a process for the manufacture of alumina and SiC from kaolin. Calcined clay and coke, both finely ground, are heated electrically forming a mixture of Al_4C_3 and SiC. In water, the former hydrolyzes and the inert SiC crystals settle out.

Thoms (25) in 1912 found a method of making a SiC in filament form as follows ". . . . admitting to an evacuating flashing jar a predetermined amount of the vapors of silicon tetrachloride, then a predetermined amount of a mixture of hydrogen and ethylene gases and then in flashing a carbon core in such atmosphere."

Peacock (30, 31) in 1915 heated feldspar and C to 2500°C in a N atmosphere to form carbo-nitrides of Al and K. After these gaseous products are collected, the temperature is raised to a purported 3500°C to form SiC.

Shaped Articles

Twelve patents relate to furnacing of definitely shaped articles of SiC. In most cases, the resistance-type furnace was used as a medium for heat-forming articles of SiC from preshaped carbon, wood, fine silicon carbide, or mixtures of silicon or various silicon compounds with C (4, 10, 14, 19, 20, 21, 27, and 28). In two patents (26, 46) articles are converted to SiC by an arc. In one case (42) the reaction is carried out in an induction furnace.

Geiger (58) in 1947 was successful in forming SiC at relatively low temperatures from an intimate mixture of finely divided C and Si previously molded to a desired shape. By maintaining non-oxidizing conditions the reaction was completed between 1200° and 1500°C in a fuel-fired furnace.

Continuous Furnaces

There have been numerous attempts to produce SiC continuously. The advantages of such a process might include a saving in labor and power through recuperation of waste heat, collection and use of the CO gas, as well as a saving in operating space required. However, there are many difficulties to be overcome due to the high temperatures involved, the lack of free flow of the materials and product, and the abrasive action of the moving materials.

Roberts (3) in 1897 patented a process using a modified arc furnace. A horizontal column of mix is fed by a mechanical conveyor between carbon electrodes. The electrodes are first positioned so as to strike an arc, then gradually separated as the SiC is formed and becomes the conductor. A ribbon of product emerges and there remains the problem of separating the SiC and the unconverted mix.

Tone (18) in 1910 illustrates two methods of making SiC continuously. In the first case granular core material is supplied at and around an upper electrode and is surrounded by the mix of carbon and siliceous material. The containing walls move downward, carrying with them the charge and core, at a rate governed by the ingot diameter representing most economical production. The lower electrode is tapered so that the core material and finished product move outward and may be removed readily from the furnace.

In Tone's alternate scheme, the mix, supported on cars, is moved continuously under two stationary vertically depending electrodes. After the charge passes the second electrode, the products are removed. The principal objection is again the difficulty of separating the SiC from the core and the unused mix.

Cox (49, 50) in 1937 patented an up-fed furnace. A screw arrangement pushes mix up through an inverted truncated cone-shaped furnace lined with refractory. Power is supplied through carbon electrodes projecting into the sides of the furnace.

Benner, Melton, and Boyer (56) in 1939 employed an electrically heated tunnel through which refractory trays, loaded with loose or briquetted mix, are passed. The tunnel may consist of a hollow carbonaceous conductor to act as a resistance heater, or may be heated by induction.

Van der Pyl (59) was issued a patent in 1956 covering a process to synthesize SiC. Claim #1 aptly describes the method as follows: "Process for the synthesis of silicon carbide comprising charging a mixture of carbon and silica into a plurality of open ended containers which are of a size and shape to be detachable joined at the open ends, mating a plurality of said containers and introducing them into a tube furnace having the shape of a long tube thereby forming a tube within the tube furnace which tube thereby formed constitutes a single compartment, advancing the containers through the tube furnace and removing the containers which have been advanced all the way through the tube furnace, said tube furnace being at a median location thereof heated to a temperature of at least 1800°C."

The SiC produced in Van der Pyl's furnace consists of discrete crystals which require only classification for use as abrasive grain, thus eliminating crushing operations. Costs are further reduced by the utilization of the waste gases.

Summary

In summary, the art of furnacing SiC has not departed radically from the method originated by Acheson. Today's furnaces are much larger but they still use his principle of heating from within, with the charge acting as a refractory container as well as a thermal insulator for the ingot being formed. Improvements in furnace design have facilitated loading and unloading operations. Large scale collection and utilization of waste gases have not yet been achieved. Changes in core composition and geometry have resulted in a moderate improvement in the over-all efficiency of the operation. Better physical and chemical properties of the product have been attained by controlling mix composition and power input. Several starts have been made toward a continuous commercial process for making SiC.

Manuscript received January 18, 1957. This paper was prepared for delivery before the Cleveland Meeting, Sept. 30 to Oct. 4, 1956.

Any discussion of this paper will appear in a Discussion Section to be published in the June 1958 JOURNAL.

REFERENCES

1. E. G. Acheson, U. S. Pat. 492,767, Feb. 28, 1893. Title: Production of artificial crystalline carbonaceous materials; content: substitute for diamonds.
2. E. G. Acheson, U. S. Pat. 560,291, May 19, 1896. Title: electrical furnace; content: improvement in design of furnace.
3. I. L. Roberts, U. S. Pat. 587,138, July 27, 1897. Title: process of and apparatus for manufacturing metallic carbides; content: continuous furnace.
4. F. J. Tone, U. S. Pat. 709,808, Sept. 23, 1902. Title: Carborundum® articles and process of making same; content: crystallized shapes.
5. A. Dorsemagen, U. S. Pat. 716,008, Dec. 16, 1902. Title: working zinc and substances containing silicic acid in electric furnaces; content: use of zinc silicate as raw material.
6. E. G. Acheson, U. S. Pat. 722,792, March 17, 1903. Title: method of producing compounds containing silicon, oxygen and carbon.
7. E. G. Acheson, U. S. Pat. 723,631, March 24, 1903. Title: method of heating material; content: multiple cores.
8. F. C. Weber, U. S. Pat. 728,528, May 19, 1903. Title: process of treating kaolin for the production of Carborundum® and alumina; content: Al_4C_3 and SiC from clay.
9. F. J. Tone, U. S. Pat. 800,515, Sept. 26, 1905. Title: incandescent electrical furnace; content: furnace with movable sides.
10. F. Bolling, U. S. Pat. 801,296, Oct. 10, 1905. Title: process for the production of molded blocks of SiC; content: SiC shapes made from C.
11. F. J. Tone, U. S. Pat. 834,948, Nov. 6, 1906. Title: electrical furnace; content: movable sidewalls and air-cooled base.
12. H. N. Potter, U. S. Pat. 875,673, Dec. 31, 1907. Title: method of making SiC; content: SiC from SiO and C.
13. F. J. Tone, U. S. Pat. 908,357, Dec. 29, 1908. Title: method of producing SiC; content: use of waste gases.
14. F. J. Tone, U. S. Pat. 913,324, Feb. 23, 1909. Title: manufacture of SiC; content: dense SiC.
15. F. J. Tone, U. S. Pat. 937,119, Oct. 19, 1909. Title: process of producing SiC; content: arc furnacing SiC.
16. F. J. Tone, U. S. Pat. 941,339, Nov. 23, 1909. Title: process of producing SiC; content: zig-zag core.
17. F. J. Tone, U. S. Pat. 949,386, Feb. 15, 1910. Title: method for the production of SiC; content: pure SiC.
18. F. J. Tone, U. S. Pat. 965,142, July 19, 1910. Title: method of making SiC; content: continuous furnace process.
19. F. J. Tone, U. S. Pat. 992,698, May 16, 1911. Title: method for the production of dense compacted SiC; content: dense SiC shapes.
20. F. J. Tone, U. S. Pat. 1,013,700, Jan. 2, 1912. Title: SiC; content: dense SiC shapes.
21. F. J. Tone, U. S. Pat. 1,013,701, Jan. 2, 1912. Title: manufacture of SiC; content: dense SiC shapes.
22. E. G. Acheson, U. S. Pat. 1,014,199, Jan. 9, 1912. Title: refractory body and process of making same content: B_2O_3 in furnace mix.
23. F. J. Tone, U. S. Pat. 1,015,598, Jan. 23, 1912. Title: light refracting material; content: pure SiC.
24. F. J. Tone, U. S. Pat. 1,044,295, Nov. 12, 1912. Title: process for producing SiC; content: zig-zag core.
25. F. C. Thoms, U. S. Pat. 1,048,231, Dec. 24, 1912. Title: method of manufacturing Carborundum® filaments; content: use of $SiCl_4$.

26. F. J. Tone and T. B. Allen, U. S. Pat. 1,054,372, Feb. 25, 1913. Title: process of silicidizing; content: SiC shapes in arc furnace.
27. F. J. Tone, U. S. Pat. 1,054,373, Feb. 25, 1913. Title: method of silicidizing articles containing C; content: SiC shapes in resistance furnace.
28. E. S. Smith and F. J. Tone, U. S. Pat. 1,058,800, April 15, 1913. Title: SiC article and method of making the same; content: porous article from blocks of wood.
29. G. Egly, U. S. Pat. 1,075,634, Oct. 14, 1913. Title: process for production of refractory, electrically conducting molded bodies; content: refractory shape.
30. S. Peacock, U. S. Pat. 1,129,506, Feb. 23, 1915. Title: process of making silicon compounds and by-products; content: use of feldspar.
31. S. Peacock, U. S. Pat. 1,134,081, March 30, 1915. Title: process for producing carbide of silicon and by-products; content: use of feldspar.
32. W. K. Booth, U. S. Pat. 1,299,110, April 1, 1919. Title: electric furnace; content: SiC lining formed *in situ*.
33. F. Jacoviello, U. S. Pat. 1,324,156, Dec. 9, 1919. Title: electric furnace; content: resistance furnace.
34. O. Hutchins, U. S. Pat. 1,331,435, Feb. 17, 1920. Title: manufacture of SiC; content: SiO_2/C ratio in mix.
35. H. E. Schabacker, U. S. 1,381,346, June 14, 1921. Title: SiC and method of making same; content: use of high purity coke.
36. M. O. Sem and E. Lund, U. S. Pat. 1,442,033, Jan. 9, 1923. Title: method of operating electric furnaces; content: self-baking electrode.
37. J. H. Reid, U. S. Pat. 1,445,645, Feb. 20, 1923. Title: process of and material for production of metal hydrate and gas; content: feldspar and bituminous coal.
38. L. Burgess, U. S. Pat. 1,512,271, Oct. 21, 1924. Title: reduction of oxides; content: furnace under pressure.
39. H. E. White, U. S. Pat. 1,660,144, Feb. 21, 1928. Title: process for production of SiC and CaC_2; content: tapping furnace CaC_2 and SiC.
40. T. F. Baily, U. S. Pat. 1,675,744, July 3, 1928. Title: shaft-type electric furnace; content, shaft furnace.
41. H. E. White, U. S. Pat. 1,684,611, Sept. 18, 1928. Title: electric furnace for producing SiC; content: concrete sidewalls and ends for SiC furnace.
42. M. J. Marcin, U. S. Pat. 1,804,361, May 5, 1931. Title: process of treating carbonaceous articles; content: coating articles with SiC.
43. H. E. White, U. S. Pat. 1,859,856, May 24, 1932. Title: process for production of SiC and CaC_2; content: tapping furnace for CaC_2 and SiC.
44. O. Hutchins, U. S. Pat. 1,937,060, Nov. 28, 1933. Title: SiC and the manufacture thereof; content: dense SiC ingot.
45. R. R. Ridgeway, U. S. Pat. 1,979,052, Oct. 30, 1934. Title: electric resistance furnace; content: solid rod.
46. A. L. Mingard, U. S. Pat. 1,982,012, Nov. 27, 1934; Title: process for manufacture of hard objects in silicidized carbon or other similar substances; content: SiC shapes.
47. R. R. Ridgeway, U. S. Pat. 2,005,956, June 25, 1935. Title: method of making abrasive metal carbides and an apparatus therefor; content: solid rod.
48. H. P. Kirchner, U. S. Pat. 2,018,133, Oct. 22, 1935. Title: manufacture of SiC; content: hulls as pore formers.
49. G. C. Cox, U. S. Pat. 2,068,447, Jan. 19, 1937. Title: continuous high temperature electrothermal furnace; content: upfed continuous furnace.
50. G. C. Cox, U. S. Pat. 2,068,448, Jan. 19, 1937. Title: continuous high temperature electrothermal furnace; content: upfed continuous furnace.
51. L. E. Ward, U. S. Pat. 2,122,446, July 5, 1938. Title: manufacture of calcium metal; content: making Ca metal.
52. R. R. Ridgeway, U. S. Pat. 2,123,158, July 5, 1938. Title: electric furnace structure for making abrasive metal carbides; content: closeable furnace.
53. M. Frankl, U. S. Pat. 2,131,102, Sept. 27, 1938. Title: process for operation of smelting and reducing furnaces; content: fuel fired furnace.
54. M. Frankl, U. S. Pat. 2,136,430, Nov. 15, 1938. Title: process for smelting and reduction of minerals; content: fuel fired furnace.
55. R. R. Ridgeway, U. S. Pat. 2,155,682, April 25, 1939. Title: method of making abrasive metal carbides; content: closeable furnace.
56. R. C. Benner, R. L. Melton, and J. A. Boyer, U. S. Pat. 2,178,773, Nov. 7, 1939. Title: SiC and manufacture thereof; content: continuous furnace.
57. R. R. Ridgeway, U. S. Pat. 2,285,837, June 9, 1942. Title: method of producing the abrasive metal carbides; content: deep furnace—arc type.
58. C. F. Geiger, U. S. Pat. 2,431,327, Nov. 25, 1947. Title: refractory and method of making same; content: low temperature, SiC shapes.
59. E. Van der Pyl, U. S. Pat. 2,729,542, Jan. 3, 1956. Title: synthesis of SiC; content: continuous tube furnace.

N-Halogen Organic Compounds as Cathode Materials for Primary Batteries

C. K. Morehouse and R. Glicksman

RCA Laboratories, Radio Corporation of America, Princeton, New Jersey

ABSTRACT

The electrochemical characteristics of a number of N-halogen organic compounds were studied in various electrolytes. Many of these compounds have greater theoretical ampere-minute capacity per unit of weight than the corresponding halogens, or the inorganic cathode materials used at present in primary cells. Of the compounds studied, cyclic ureides and melamine derivatives have the most promising characteristics for use as cathode materials in primary cells. Electrodes composed of these materials operate during current flow at potentials approximating the halogen-halide couple, and give in an $AlCl_3$ electrolyte ampere-minute per gram capacities corresponding to a two-electron change per "positive" halogen in the molecule.

Experimental N, N'dichlorodimethylhydantoin-magnesium reserve-type cells have been constructed and shown to operate over a wide range of current densities at potentials above 2.0 v, giving capacities over 45 whr/lb.

The desirable electrochemical properties of a cathode material for a primary cell are: (*a*) a high, reversible electrode potential, (*b*) low polarization during current flow, and (*c*) a high ampere-minute capacity per unit of weight and volume. The reversible electrode potential can be determined by the change in free energy of the cathodic half-cell reaction, while the ampere-minute capacity is directly proportional to the number of Faradays per mole involved in the reduction, and inversely to the molecular weight of the cathode material.

In addition, ce tain physical and chemical properties of a cathode material such as solubility, stability, and physical form are important in determining its use in a particular type of primary cell. For example, materials which have a high solubility, or low stability in the electrolyte, would be unsuitable for use in dry cells, but might find application in reserve cells of the type which are stored dry and activated just prior to use by adding the electrolyte or water.

The halogens are attractive materials for use as cathodes in batteries, because of their high electrode potential during current flow, and high ampere-hour capacity per unit of weight and volume. The disadvantages to the use of these materials are obvious. Fluorine and chlorine are highly toxic and corrosive gases, bromine a volatile liquid, and iodine a solid with a high vapor pressure. Many attempts (1-9) have been made to utilize these materials in electrochemical batteries, but to date the difficulties associated with their handling have not been overcome to enable the design of a practical battery.

The hypohalous acids and their salts have higher reversible electrode potentials and ampere-minute capacities per unit of weight than their corresponding halogens. However, because of their low stability, or high solubility, they are unsuitable for primary cells.

The N-halogen organic compounds have been found to have similar electrochemical properties to those of the hypohalous acids and their salts. These organic compounds can be considered as substituted ammonia analogues of hypohalous acid. Many of them are considerably more stable than their corresponding inorganic hypohalites and, therefore, are more attractive for use as cathode materials in primary cells.

Arsem (10) described dry cells containing a few N-halogen organic compounds as cathodes coupled with a Zn anode. No other reference has been found in the literature referring to the application of these compounds to electrochemical power supplies.

In this paper a survey of the electrochemical properties of various types of N-halogen organic compounds is presented, along with data obtained on experimental reserve cells containing one of the more promising materials as a cathode coupled with a Mg anode.

Electrochemical Characteristics

A typical example of a N-halogen organic compound and the manner in which the halogen is held in the molecule is shown by the equation:

$$R{:}\dot{\underset{\cdot\cdot}{N}}{:}H + Cl^+Cl^- \rightarrow R{:}\dot{\underset{\cdot\cdot}{N}}{:}H + H^+ + Cl^- \qquad (I)$$

The chlorine atom attached to the N is described as a "positive" halogen and resembles that attached to oxygen as in hypochlorous acid, since on hydrolysis it combines with the negative hydroxide ion to form hypochlorous acid.[1] It is reasoned that reactions taking place at an electrode containing a N-halogen organic compound could proceed through the hydrolysis stage, followed by subsequent re-

[1] A test for a "positive" halogen organic compound is to dissolve the compound in an aqueous solution of acetic acid and an iodide and titrate the iodine liberated. Two iodine atoms are liberated for every "positive" halogen.

duction of the hypohalite ion. There is also some experimental evidence which indicates that the electrode mechanism might be through the direct reduction of the N-halogen compound. Equations and reversible electrode potentials given by Latimer (11) for possible reactions of a N-halogen organic electrode in halide electrolytes are given below, using two mechanisms.

Hydrolysis:

$$RNHX + HOH = RNH_2 + HOX \quad (II)$$

Basic solutions:

$$ClO^- + H_2O + 2e^- = 2OH^- + Cl^- \quad E^\circ_B = 0.89 \quad (III)$$

$$BrO^- + H_2O + 2e^- = 2OH^- + Br^- \quad E^\circ_B = 0.76 \quad (IV)$$

Acidic solutions:

$$HClO + Cl^- + H^+ = Cl_2 + H_2O \quad (V)$$

$$Cl_2 + 2e^- = 2Cl^- \quad E^\circ = 1.36 \quad (VI)$$

$$HClO + 2Br^- + H^+ = Br_2 + H_2O + Cl^-$$
$$HBrO + Br^- + H^+ = Br_2 + H_2O$$
$$Br_2 + 2e^- = 2Br^- \quad E^\circ = 1.09 \quad (VII)$$

Direct Reduction:

$$RNHX + H_2O + 2e^- = OH^- + X^- + RNH_2 \quad (VIII)$$

$$RNHX + H^+ + 2e^- = RNH_2 + X^- \quad (IX)$$

$$RNHX + X^- + H^+ = RNH_2 + X_2$$
$$X_2 + 2e^- = 2X^- \quad (XI)$$

Experimental Results

Most electrode reactions do not function at their reversible electrode potentials because of the irreversible nature of the reaction and polarization effects encountered when operating an electrode at a relatively high current density. Since many inorganic and organic reactions are known to be irreversible and their electrode potentials during cur-

Table I. Capacity data for various N-halogen organic cathode materials

Cathode material	Source (see foot notes)	% "Active" halogen Actual	% "Active" halogen Theoretical	Amp-min/g capacity Theoretical*	Amp-min/g capacity Obtained†	Efficiency‡ %
Chlorine	—	50	50	45.4	—	
Bromine	—	50	50	20.1	—	
	N-halogen organic compounds					
Amides						
(a) *Carboxylic acid*						
N-bromoacetamide	1	57	57	23.3	3.0	12.9
N-bromobenzamide	1	39.3	39.9	13.6	6.3	47.0
N, N'dibromoterephthalamide	1	43.7	49.7	19.8	6.6	38.0
N, N'dibromooxamide	1	60.5	65.2	26.1	0.6	2.5
N, N'dibromosuccinamide	1	57.5	58.3	23.5	2.4	10.3
N, N'dibromoadipamide	1	51.3	53.1	21.3	7.3	35.7
(b) *Sulfonic acid*						
N-chloro-p-toluenesulfonamide, sodium salt	2	—	12.8	11.4	0.2	1.7
N, N dichloro-p-toluenesulfonamide	2	—	29.6	26.8	14.1	52.6
N, N dibromo-p-toluenesulfonamide	1	46.1	48.5	19.7	6.0	31.9
N, N dichloro-p-benzenesulfonamide	1	31.5	31.3	28.3	11.7	40.9
N, N dichloro-p-carboxylic acid benzenesulfonamide	3	—	26.3	23.8	5.7	23.9
Imides derived from dibasic acids						
N-chlorosuccinimide	2	—	26.6	24.1	11.7	48.5
N-bromosuccinimide	4	—	45.9	23.3	9.0	38.6
N-bromophthalimide	1	33.2	35.3	14.2	4.7	35.1
Amides of carbonic acid (urea)						
(a) *Straight chain*						
N, N'dichlorobiuret	1	—	41.3	37.4	~15.0	~40.1
(b) *Cyclic*						
Trichloroisocyanuric acid	5	44.7	45.8	41.5	10.2	25.3
3 Bromo,5,5 dimethylhydantoin	1	38.5	38.6	15.5	7.5	48.4
N, N'dibromodimethylhydantoin	1	55.	55.9	22.3	10.9	49.9
N, N'dichlorodimethylhydantoin	6	33.	33.	32.6	15.0	46.0
N, N'dichlorodiphenylhydantoin	6	16.	22.1	20.1	6.3	43.1
N, N'dibromodiphenylhydantoin	1	38.	39.0	15.6	7.5	49.5
N, N'dibromobarbituric acid	1	—	55.9	22.5	3.6	16.0
Amidines of carbonic acid (guanidine)						
N-chlorodicyandiamide	5	15.	30.3	27.1	~0.1	0.8
Trichloromelamine	7	44.5	46.4	42.2	~18	43.9
Tribromomelamine	7	65.3	66.7	26.6	10.9	41.8
Hexachloromelamine	7	—	64.0	58.0	~19.5	33.6

† Computed from half-cell data in Fig. 1-6 incl. using 0.20 v as an arbitrary end point.
* Theoretical capacity computed from theoretical "active" halogen content.
‡ Efficiency computed on basis of actual "active" halogen content of compound.
[1] Arapahoe Chemicals, Inc.
[2] Matheson, Coleman & Bell.
[3] Abbott Laboratories.
[4] Fisher Scientific Co.
[5] American Cyanamid Co.
[6] Wyandotte Chemicals Corp.
[7] Wallace & Tiernan, Inc.

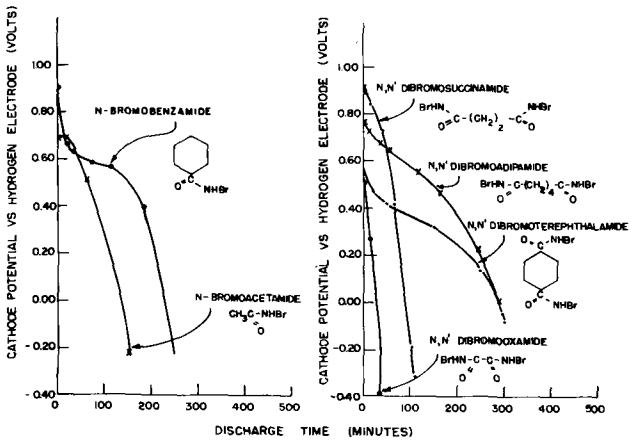

Fig. 1. Cathode potential-time relationship of various mono and dibasic carboxylic acid amide N-bromo derivatives discharged in 250 g/l $MgBr_2 \cdot 6H_2O$ electrolyte at a rate of 0.030 amp/g.

rent flow cannot be predicted by thermodynamic calculations, other methods have to be used to evaluate new materials. A technique, previously described (12), was used to study the electrochemical properties of a number of N-halogen organic compounds. This consists in discharging at a constant current drain, in a large volume of electrolyte, a 0.5-g sample of the cathode material mixed with carbon. The potential of the cathode was measured against a saturated calomel reference electrode with a L&N Type K potentiometer.

Half-Cell Discharge Data for Various N-Halogen Organic Compounds in a $MgBr_2$ Electrolyte

Half-cell data obtained on various N-halogen organic compounds discharged continuously at a 0.030 amp/g rate[2] in a $MgBr_2 \cdot 6H_2O$(250 g/l) electrolyte are shown in Fig. 1-6 inclusive. The data given include an *IR* drop amounting to 0.08 v due to the resistance of electrolyte and apparatus. No correction was made for temperature variation of the saturated calomel electrode which would amount to no more than ±0.01 v.

The capacity obtained to an arbitrary 0.20 v cut off potential (vs. S.H.E.) under current drain along with their electrode efficiencies is presented in Table I together with the theoretical capacities of these materials expressed in ampere-minutes per gram.

[2] The current flow was expressed in this manner because of the difficulty associated with determining the true surface area taking part in the electrochemical reaction, which value is necessary in order to express the current density in amperes per unit area.

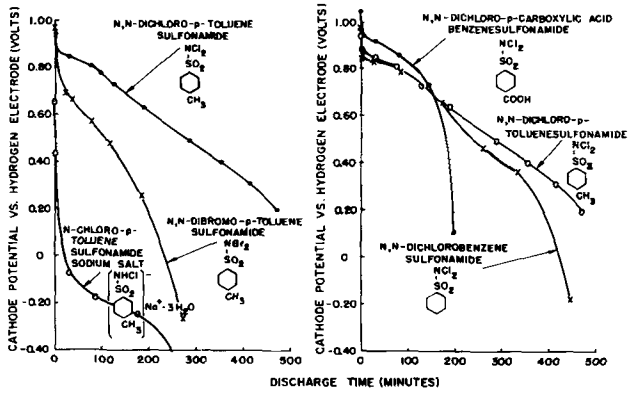

Fig. 2. Cathode potential time relationship of various N-halogen derivatives of sulfonic acid amides discharged in 250 g/l $MgBr_2 \cdot 6H_2O$ electrolyte at a rate of 0.030 amp/g.

Acid amides of the type RCOHNX.—Table I shows that four of the six listed N-bromo carboxylic acid amides have theoretical capacities greater than that of elemental bromine. However, the actual capacities obtained from these compounds are considerably lower than theoretical, ranging from 0.6-7.3 amp-min/g, with efficiencies ranging from 2.5 to 47%. Also, the efficiencies of the N-bromo aromatic carboxylic acid compounds are greater than those of the alkyl carboxylic acid compounds. This is probably due to the greater stability and lower solubility of the aromatic compounds in the electrolyte. This relationship is even more evident when one considers the capacities and efficiencies of the homologous series of alkyl N, N′ dibromo dibasic acids. Under conditions of discharge, the cathode efficiency of these compounds increases as the chain length of the dibasic acid increases, while there is a corresponding decrease in solubility as one goes from N, N′ dibromooxamide to N, N′ dibromoadipamide.

The half-cell discharge curves in Fig. 1 show that the potentials of these electrodes range from 0.60-0.90 v initially, but decrease rapidly under current drain.

Sulfonic acid amides of the type RSO_2NHX.—Discounting the data for the soluble sodium salt of N-chloro-p-toluenesulfonamide (Chloramine T), it is seen in Table I that capacities ranging for 5.7 to 14.1 amp-min/g were obtained from compounds of this class, with corresponding efficiencies of 23.9-52.6%, respectively. Because of their higher capacities and efficiencies, this class of N-halogen compounds has greater promise as cathode materials for primary cells than the previously discussed carboxylic acid amides, the best of these materials being N, N dichloro-p-toluenesulfonamide (Dichloramine T).

Half-cell data obtained on various N-halogen derivatives of sulfonic acid amides are presented in Fig. 2. As expected, the N-chloro derivatives operate at a higher potential and give a greater ampere-minute per gram capacity than the corresponding N-bromo compounds, as evidenced by the half-cell discharge data obtained on N, N dichloro-p-toluenesulfonamide and N, N dibromo-p-toluenesulfonamide. The poor performance of the sodium salt of N-chloro-p-toluenesulfonamide as a cathode material is probably due to the high solubility of this compound in the $MgBr_2$-H_2O electrolyte.

Also shown are half-cell data obtained on N, N dichlorobenzenesulfonamide, N, N dichloro-p-carboxylic acid benzenesulfonamide, and N, N dichloro-p-toluenesulfonamide, these compounds differing from one another only in the type of para substituted group. It is seen that the carboxylic acid compound has a higher potential initially, probably as a result of the effect of the acidic group on its potential.

Imides of the type $(RCO)_2NHX$.—Diacyl derivatives of ammonia, $(RCO)_2NH$, known as imides, also have a hydrogen attached to the nitrogen atom,

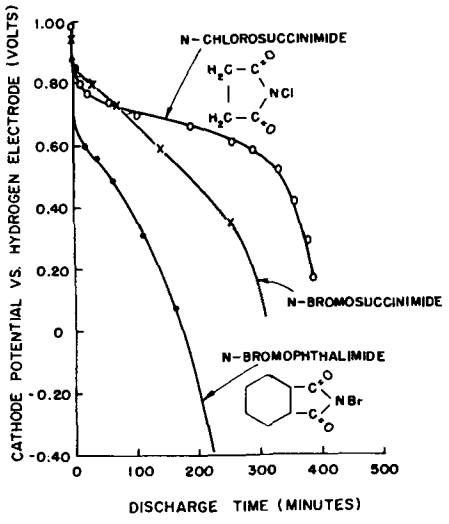

Fig. 3. Cathode potential-time relationship of various N-halogen imide derivatives discharged in 250 g/l $MgBr_2 \cdot 6H_2O$ electrolyte at a rate of 0.030 amp/g.

which is replaceable by a halogen atom to form the N-halogen derivative. Typical examples of this class are the N-chloro-, and N-bromosuccinimide, and phthalimide compounds. Capacity data for these materials are tabulated in Table I and half-cell discharge data shown in Fig. 3. These compounds had discharge characteristics similar to the previously discussed N-halogen acid amides. Of the three imides tested, N-chlorosuccinimide had the most favorable discharge characteristics.

Amides of carbonic acid (urea derivatives).— There are many urea derivatives which also have a replaceable hydrogen attached to the nitrogen atom, and thus are capable of forming N-halogen compounds. N, N′ dichlorobiuret is an example of a straight chain compound of this class, whereas trichloroisocyanuric acid, N, N′ dichlorodimethylhydantoin, and N, N′ dibromobarbituric acid are examples of cylic derivatives. All of these compounds have the characteristic property of the other N-halogen compounds cited, in that they are strong oxidizing agents.

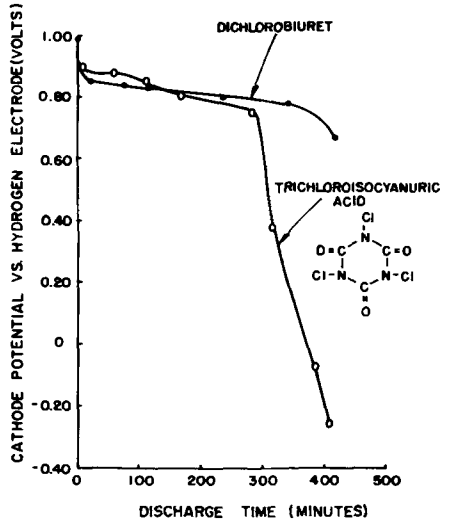

Fig. 4. Cathode potential-time relationship of various N-halogen urea derivatives discharged in 250 g/l $MgBr_2 \cdot 6H_2O$ electrolyte at a rate of 0.030 amp/g.

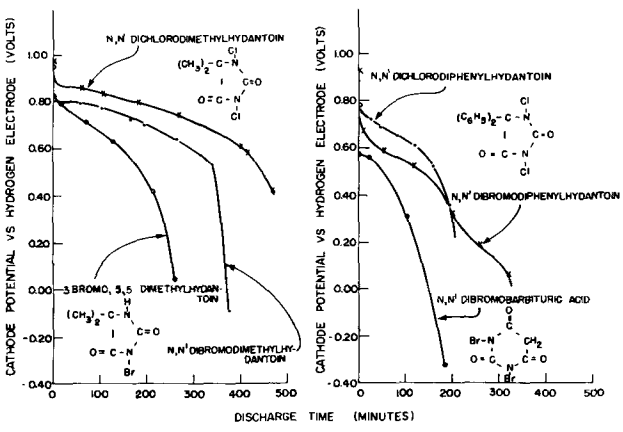

Fig. 5. Cathode potential-time relationship of various N-halogen cyclic urea derivatives discharged in 250 g/l $MgBr_2 \cdot 6H_2O$ electrolyte at a rate of 0.030 amp/g.

Among the cyclic urea derivatives tested, the hydantoin compounds are of particular interest because of their relatively high electrode efficiencies in the $MgBr_2$-H_2O electrolyte as shown in Table I. These compounds, measured at the 0.030 amp/g rate, had efficiencies ranging from 43-50%, which values are greater than those obtained for the other two cyclic urea derivatives tested. An efficiency of 40% was also obtained from the straight chain dichlorobiuret compound, which along with N, N′ dichlorodimethylhydantoin are the most promising compounds of this group because of their high flat voltage vs. time discharge curves (Fig. 4 and 5) and high theoretical and experimentally obtained ampere-minute per gram capacities.

Discharge curves for the various N-halogen hydantoin derivatives are shown in Fig. 5, and as expected the chloro compounds operate at higher potentials during current flow than the corresponding bromo compounds, while the monobromo compound has a potential lower than its corresponding dibromo compound.

Amidines of carbonic acid (guanidine derivatives).—Four compounds of this class, trichloro- and tribromomelamine, hexachloromelamine, and N-chlorodicyandiamide, all of which are solids at ordinary temperatures, have been evaluated, data being presented in Fig. 6 and Table I. N-chlorodicyandiamide performed poorly as a cathode material, probably because of low stability under the conditions of evaluation. As with other N-halogen compounds, trichloromelamine operated at a higher potential than its corresponding bromo compound, while the more highly halogenated hexachloromelamine operated during current flow in a $MgBr_2$-H_2O electrolyte at a higher electrode potential than the trichloromelamine.

From Table I it is seen that trichloromelamine and hexachloromelamine gave ampere-minute per gram capacities of approximately 18 and 19.5, respectively, which values are the highest obtained on any of the N-halogen compounds tested in this investigation. It is also significant to note that these two melamines have the highest theoretical capacity of all the N-halogen compounds considered, the capacity of hexachloromelamine being 28% greater

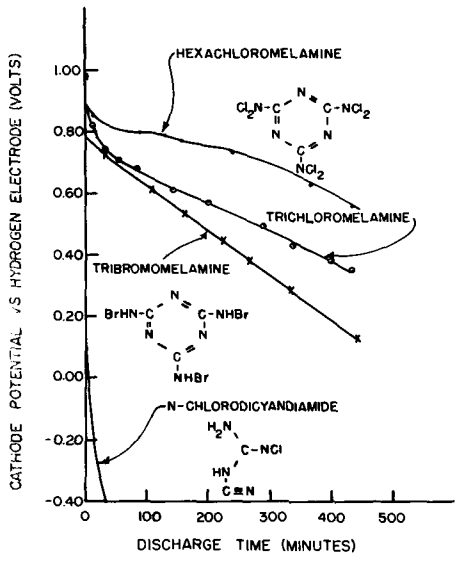

Fig. 6. Cathode potential-time relationship of various N-halogen guanidine derivatives discharged in 250 g/l $MgBr_2 \cdot 6H_2O$ electrolyte at a rate of 0.030 amp/g.

than the theoretical ampere-minute per gram capacity of chlorine.

Half-Cell Discharge Data of Three N-Halogen Organic Compounds in Various Electrolytes

It is seen from the data in Table I that in a 250 g/l $MgBr_2$ $6H_2O$ electrolyte, and at a 0.030 amp/g rate of discharge, the cathode efficiency of all the organic N-halogen compounds, except N, N dichloro-p-toluenesulfonamide, was less than 50%, indicating that not all the chlorine atoms are taking part in the electrode reaction.

Analytical data obtained by dissolving weighed samples of trichloromelamine in glacial acetic acid and in water, adding an excess of potassium iodide and titrating the iodine liberated in each solution showed that in the glacial acetic acid solution the "active" halogen content in the molecule was 44.5%, which corresponded to a two electron change per chlorine atom, whereas in a water solution the liberated iodine corresponded to only 24.3% of the "active" chlorine. In neutral or water solution a fading end point was observed in the titration of the iodine, indicating that the slow hydrolysis of trichloromelamine was the cause of the low value for the "active" chlorine content in the molecule.

Since the electrode efficiencies of most cathodes depend on the current density and electrolyte composition, half-cell data were obtained on N, N'dichlorodimethylhydantoin, trichloromelamine, and hexachloromelamine when discharged at 0.005 amp/g rate in various electrolytes. The half-cell discharge curves are presented in Fig. 7.

Data in Fig. 7 show that the potentials during current flow of all three cathode materials increase as the acidity of the electrolyte is increased, as might be expected from an examination of the electrode reactions previously cited. In addition, the ampere-minute per gram capacities of the three cathode materials increase with increasing electrolyte acidity which is in accord with the analytical data previously discussed. In a NaOH electrolyte, the three N-halogen electrodes polarized rapidly, and operated at low electrode efficiencies. This low efficiency is believed due to the poor stability of these compounds in a strongly alkaline solution.

The coulombic capacities obtained from the discharge data in a $MgBr_2$ electrolyte (allowing an 0.8 v drop in potential from initial) correspond approximately to the reduction of one halogen in the N, N'dichlorodimethylhydantoin, and two in trichloromelamine and hexachloromelamine, assuming a two electron change per halogen atom in the molecule. Discharging the N, N'dichlorodimethylhydantoin and hexachloromelamine in the more acidic (480 g/l $AlCl_3 \cdot 6H_2O$) electrolyte resulted in a 40% increase in electrode efficiency. On the other hand, no increase in electrode efficiency was obtained from the trichloromelamine electrode, although a more favorable type of discharge curve was obtained in the $AlCl_3$ electrolyte.

The two step discharge curve of the N, N'dichlorodimethylhydantoin accounts for its large increase in efficiency in the $AlCl_3$ electrolyte, since both active halogen atoms are now being utilized, whereas in the $MgBr_2$ electrolyte apparently only one halogen atom took part in the reduction. From the chemical structure of this compound, one would expect the chlorine on the nitrogen atom adjacent to the two carbonyl groups to be more easily reduced than the other "active" halogen in the molecule, thereby accounting for the two step reduction.

Cathode efficiencies computed for the discharge of trichloromelamine and hexachloromelamine in the $AlCl_3$ electrolyte indicate a reduction of 2 and 5 halogen atoms, respectively; apparently the last halogen on the melamine molecule is extremely difficult to reduce.

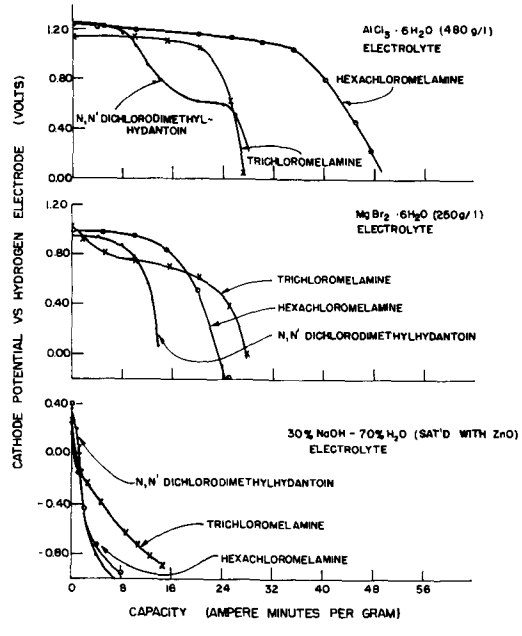

Fig. 7. Cathode potential-capacity relationship of three N-halogen organic compounds discharged in various electrolytes at a rate of 0.005 amp/g.

Comparison with Conventional Cathode Materials

Half-cell discharge data obtained at a 0.005 amp/g rate for two of the more promising N-halo-

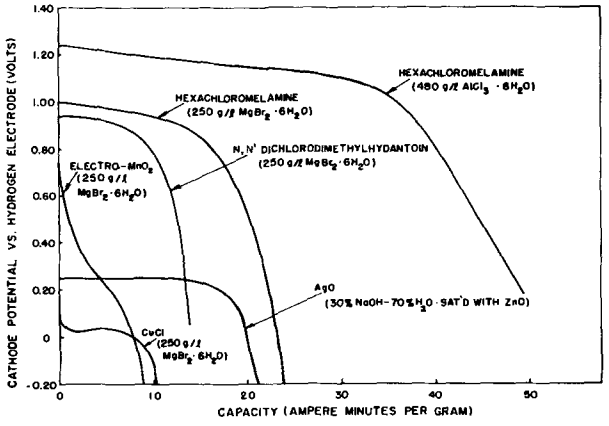

Fig. 8. Comparison of cathode potential-capacity relationship of various N-halogen organic and conventional inorganic cathode materials discharged at a rate of 0.005 amp/g in compatible electrolytes.

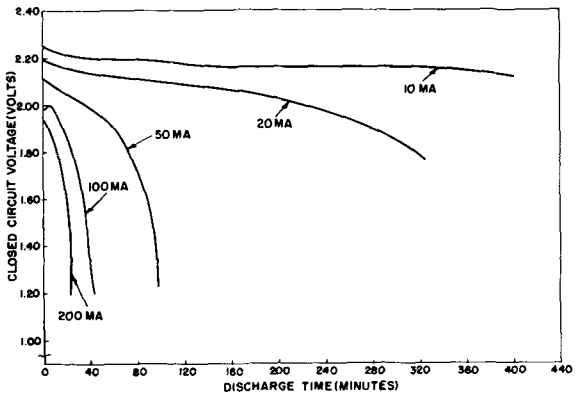

Fig. 9. Constant current discharge curves for N, N'dichlorodimethylhydantoin-magnesium reserve cells (cast type). [Approx. vol. 4 cm^3, wt 5.0 g (wet).]

gen compounds compared with three cathode materials now used in commercial primary cells are shown in Fig. 8. These data show that the hexachloromelamine and N, N'dichlorodimethylhydantoin in both a $MgBr_2$ and an $AlCl_3$ electrolyte operate at considerably higher potentials than electrolytic manganese dioxide, cuprous chloride, or silver (II) oxide cathodes when tested in their compatible electrolytes under comparable conditions of discharge. Calculations, based on a 0.2 v drop in half-cell discharge potential show that hexachloromelamine, which theoretically has 123% and 258% greater ampere-minute per gram capacity than silver (II) oxide and cuprous chloride, respectively, gave in an $AlCl_3$ electrolyte 74% and 226% greater ampere-minute capacity per unit of weight than these cathodes discharged in their compatible electrolytes. Further improvement in the performance of the hexachloromelamine cathode should be possible as it operated under these conditions of discharge at only 58.6% efficiency.

It would be expected, from the half-cell discharge data in Fig. 8, that coupling N-halogen organic cathodes with magnesium or aluminum anodes would result in primary cells with operating potentials of 2.2 and 1.8 v, respectively.

Primary Cell Data

While it has been shown that many of the N-halogen organic compounds have attractive electrochemical characteristics, they do hydrolyze in aqueous solutions forming the soluble hypohalite. The latter property limits their use as cathodes in primary batteries assembled with an aqueous electrolyte, since the shelf life of the battery would be limited. The problem of hydrolysis during storage is not encountered in reserve cells of the type which are stored dry or in an inactive condition and activated prior to use by adding the electrolyte.

N, N' dichlorodimethylhydantoin, a stable solid which can be sublimed at 130°C without decomposition, and has a low solubility in aqueous solutions (0.21 g/100 g H_2O at 25°C) was selected for trial in reserve batteries. Cathodes were constructed by taking an intimate mixture of 2 parts by weight of the material and 1 part by weight of graphite and heating to the melting point of the N, N'dichlorodimethylhydantoin. The resulting viscous mixture was poured into a paper-lined can (I. D. 0.395 in., height 1.824 in.), a carbon rod (O. D. 0.100 in., height 1.824 in.) inserted, and the mass allowed to solidify. The formed electrode was removed from the can, wrapped first with a piece of absorbent nonwoven fabric (Kendall-Mills) material, then with 0.010 in. thick magnesium sheet. The cell was held together by binding with wire. The approximate dimensions of the completed cell were: height, 1¼ in.; diameter, ½ in ; volume, 4 cm^3 (0.25 $in.^3$); weight of cathode, graphite, and carbon rod, 2.0 g; weight of cathode material, 0.7 g; weight of cell (dry), 4.0 g; weight of cell (wet), 5.0 g.

The above cells were activated by immersing them in an aqueous solution of $MgBr_2 \cdot 6H_2O$ (250 g/l) and $Na_2Cr_2O_7$ (1.0 g/l). The discharge data obtained on cells of this construction are shown in Fig. 9. The data show that these N, N'dichlorodimethylhydantoin-magnesium reserve cells operate above 2.0 v over a wide range of current drains, and give capacities of 1.1-3.2 w-min/cm^3 and 0.9-2.6 w-min/g, based on a 1.80 v cut off.

Flat cells were also constructed by pasting 3.8-4.5 g of the following cathode mix on both sides of a graphite plate (1¼ in. long x 1 in. wide x 1/16 in. thick, weight 2.0 g).

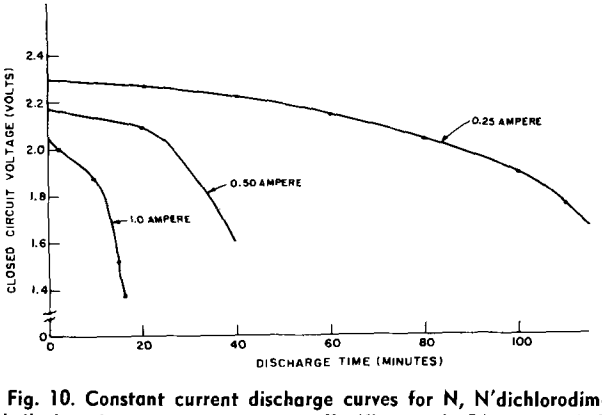

Fig. 10. Constant current discharge curves for N, N'dichlorodimethylhydantoin-magnesium reserve cells (flat type). [Approx. vol. 5 cm^3, wt 10 g (wet).]

N, N'Dichlorodimethylhydantoin, 0.96-1.13 g
Shawinigan acetylene black, 0.56-0.48 g
$MgBr_2 \cdot 6H_2O$ (500 g/l) +
$Li_2CrO_4 \cdot 2H_2O$ (1.0 g/l) electrolyte, 2.4 -2.8 g

The above cathode was wrapped with a piece of absorbent Kraft paper and then with magnesium sheet (3 in. long x 1 in. wide x 0.010 in. thick, weight 1.0 g). The approximate weight of the cell after activating with magnesium bromide electrolyte was 10 g and occupied a volume of approximately 5.1 cm^3(0.311 $in.^3$). Discharge characteristics of cells of this design are shown in Fig. 10. Capacities of 5.3-12.1 w-min/cm^3 and 2.7-6.2 w-min/g were obtained from these cells at current drains ranging from 1.0-0.250 amp.

Cells made by the two constructions described above represent laboratory samples and performance characteristics which can be expected from reserve cells using N-halogen organic compounds as cathode materials. These data, while not representing a completed development, point to the possibility of developing batteries utilizing relatively inexpensive materials which will give performance characteristics superior to existing reserve-type batteries.

Acknowledgment

The authors wish to express their appreciation to Dr. G. S. Lozier for assisting in gathering some of the cell data and his many helpful comments made during this study.

Manuscript received Jan. 2, 1957. This paper was prepared for delivery before the Cleveland Meeting, Sept. 30 to Oct. 4, 1956.

Any discussion of this paper will appear in a Discussion Section to be published in the June 1958 JOURNAL.

REFERENCES

1. D. Tommasi, "Traite des Piles Electriques," p. 298, Georges Carre, Paris (1889).
2. K. W. Zenger, German Pat. 26,819, April 2, 1884.
3. F. Foerster *Z. Elektrochem.*, **29**, 64 (1923).
4. A. Schmid, *Helv. Chim. Acta*, **7**, 370 (1924).
5. E. Baur and J. Tobler, *Z. Elektrochem.*, **39**, 169 (1933).
6. A. Schmid and P. Vogele, *Helv. Chim. Acta*, **16**, 366 (1933).
7. G. W. Heise, *Trans. Electrochem. Soc.*, **75**, 155 (1939).
8. G. W. Heise, E. A. Schumacher, and N. C. Cahoon, *J. (and Trans.) Electrochem. Soc.*, **94**, 99 (1948).
9. P. L. Howard, *This Journal*, **99**, 206C (1952).
10. W. C. Arsem, U. S. Pat. 2,306,927, Dec. 29, 1942.
11. W. M. Latimer, "Oxidation Potentials," 2nd ed., Prentice-Hall, Inc., New York (1952).
12. C. K. Morehouse and R. Glicksman *This Journal*, **103**, 94 (1956).

The Corrosion of Single Crystals and Recrystallized Single Crystals of Iron and Steel in Citric Acid[1]

W. Roger Buck, III, and Henry Leidheiser, Jr.

Virginia Institute for Scientific Research, Richmond, Virginia

ABSTRACT

Corrosion studies, largely in 0.2M citric acid at 20°C and the boiling point, were made on polycrystalline disks and monocrystalline spheres and disks of Armco iron and type L steel. Preliminary experiments indicated that the (100) face corroded at the slowest rate and the minor faces, of which the (321) is an example, corroded at the most rapid rate. Quantitative measurements were confined to these two crystal faces. The (100) face was cathodic to the (321) face as shown by potential measurements in 0.2M citric acid in the presence and absence of air. The rate of corrosion of the (321) face was approximately twice that of the (100) face on specimens which were chemically polished, electrolytically polished, machined with a sharp lathe tool, or polished with emery paper. The rates of corrosion of the polycrystalline starting material from which the single crystals were prepared were several times greater than those of the single crystals. Conversion of the single crystals to polycrystalline material by heating through the transformation temperature resulted in a considerably increased corrosion rate. In the presence of 40-45 ppm of Sn(II) the rates of corrosion of the single crystals in 0.2M citric acid at the boiling point were reduced greatly and no significant difference between the (100) and (321) faces was observed.

It is generally recognized by metallurgists that different crystal faces of a metal corrode at different rates. The differentiation of grains by etching, the varying interference colors formed on the grains of polycrystalline metals during the heating in air, and the different optical properties of the oxide film formed on the various grains of polycrystalline aluminum are but three examples from this general fund of knowledge. The importance of crystal face in controlling rates of chemical reactions has been demonstrated in a large number of recent investigations using spherical and flat single crystals (2-6); only a few of those with which the authors are more intimately concerned are mentioned here. The majority of such investigations have been qualitative in nature and only very limited quantitative information is available on the relative rates of corrosion of different crystal faces in liquid corrosion media. The only paper which is directly related to the present work and which gives quantitative information on the rates of solution of different crystal faces of iron is that of Engell (7). He studied the current-voltage curves during anodic dissolution in acid and found that ". . . the rate of corrosion, as shown by the current density-voltage curve during dissolution of iron, in all cases investigated is independent of the orientation of the crystal surfaces at low current densities. At higher densities, on the other hand, the (111) and (110) surfaces are more greatly attacked than the cube faces by a factor of 2. The other orientations lie in their properties between these extremes."

The purposes of the present investigation were (*a*) to determine the order of magnitude of the differences between the rates of corrosion of the crystal faces of iron in a fruit acid, (*b*) to determine the factors which control the rate of corrosion, and (*c*) to compare the rates of corrosion of single crystal with polycrystalline material of the same composition.

Experimental

Single crystals of Armco iron, ⅜ in. in diameter and up to 3½ in. in length, were prepared by the anneal-strain-anneal method. Rods, ⅜ in. in diameter and 4 in. long, were etched in aqua regia and were annealed at a pressure of 30-100 μ of air for 24 hr at 850°C. After cooling, the rods were reduced 3.25% in length by compression, which was carried out in a hardened-steel cylinder to prevent bending. The rods were then heated at 890°-900°C at a pressure of 30-100 μ of air for 5-10 days. Certain mill runs had a high tendency to form crystals that covered the entire cross section; the largest crystals were obtained from these rods. The Armco crystals were prepared from stock which had a ladle analysis of: C 0.02%, Mn 0.03%, P 0.009%, and S 0.016%.

Type L[2] single crystals were grown in the rim section of cross-sectional pieces, 2½ in. x 1¼ in. x ½ in. to ¾ in. thick, of a rimmed steel having a composition within the range of specifications of L

[1] The results of a few of the experiments reported herein have been described previously (1). Because of the brevity of that communication and for the sake of completeness, those results are also included in this report.

[2] Type L steel is that specified by manufacturers for containers with the maximum corrosion resistance.

steel. The mill ladle analysis of this material was C 0.08%, Cu 0.02%, Mn 0.30%, Ni 0.01%, P 0.012%, Cr 0.01%, S 0.05%, Mo 0.00%, and Si 0.008%. A wet analysis[3] of the rim area in which the crystals grew yielded: C 0.038%, P 0.011%, Mn 0.25%, and S 0.024%. Large crystals were formed in cross-sectional pieces cut from the billet by heating them at a pressure of 30-100 μ and 850°C for 5-14 days. A photograph of a typical growth experiment is given in Fig. 1.

Corrosion measurements made at 20°C were carried out in 20 ml of acid deaerated by the freeze-thaw method of Pryor and Cohen (8). The acid solution was frozen and the system was pumped down to a low pressure with a Hg diffusion pump and thawed five times. The Fe sample was inserted into the system after the fifth freeze. Pressure measurements were made with a McLeod gauge which was separated by a stop cock and dry ice trap from the acid solution. Measurements at the boiling point were made in an assembly consisting of a 250 ml Erlenmeyer flask and a reflux condenser. After the solution (100 ml) had been boiling for several hours, the cylindrical Fe single crystal, held in a short length of Tygon tubing in order to protect the sides and edges from the action of the acid, was inserted in the Erlenmeyer flask. The crystal was held by means of a permanent magnet so that the flat surfaces were perpendicular to the bottom of the flask. This precaution was necessary in order to keep the ends of the disk freely exposed to the solution. The rate of corrosion as a function of time was determined by withdrawing small samples at intervals and making colorimetric determinations using thioglycollic acid. Weight losses at the end of the experiment served as a check on the colorimetric determinations.

Single crystal spheres, 0.9 cm in diameter, with a small shaft were machined from both the Armco rods and the L-steel slabs. Disks, 0.8 cm in diameter and 0.4-0.5 cm in thickness, whose surfaces were parallel to the (100) or (321) planes were cut from the long single-crystal rod of Armco Fe. Disks parallel to (100) and (321) planes were cut from a single grain of L-steel. Other disks parallel to the (100) and (321) planes were cut from neighboring crystals in the same piece of steel. The accuracy of the cuts was determined by back reflection x-ray analysis immediately after machining and near the conclusion of the experiments. The orientation of the flat faces was within 2° of that desired in both cases. After machining, the crystals were deeply etched and were then heated for 6-16 hr at 475°-500°C in He or in a vacuum, in order to release residual strains from the machining operation. The crystals were polished with metallographic emery paper followed by chemical polishing in Mirro-Fe[4] or in the early experiments, electrolytic polishing in the perchloric acid-acetic anhydride bath of Jacquet and Rocquet (9).

[3] The authors are indebted to the American Can Company for carrying out these analyses.

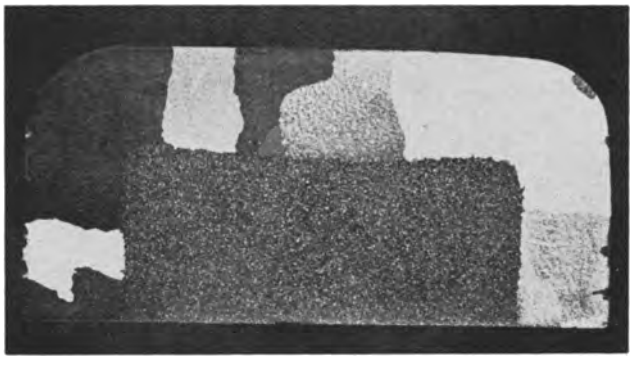

Fig. 1. Typical large grains formed in the rim area of half of a cross-sectional piece cut from a billet of L-steel.

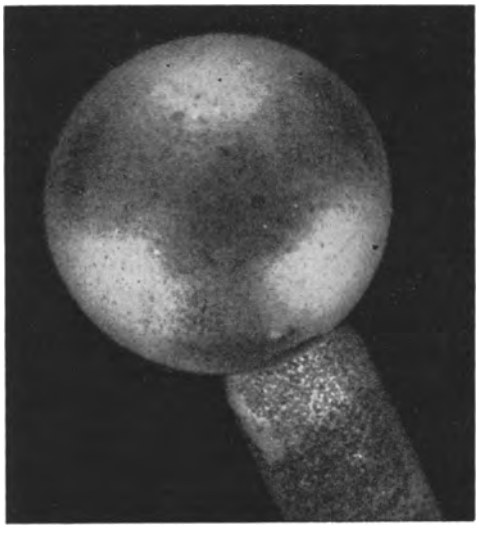

Fig. 2. Typical etch pattern on an Fe single-crystal sphere immersed in citric acid.

Preliminary Experimental Results

Results with spheres.—In order to choose experimental conditions and crystal faces for the quantitative study, single-crystal spheres were immersed for observation in citric acid solutions ranging from 0.002M to saturation, at temperatures from 25° to 85°C, and with and without stirring. The relative behavior of the different faces was the same under all conditions. The general behavior in 0.2M citric acid at room temperature was as follows: Soon after immersion of the sphere, hydrogen bubbles began to form. After 15-30 min, an etch pattern could be seen, which increased in contrast for 12-24 hr and eventually became obscured by general corrosion. First, the large areas surrounding the (111) faces lost their original high luster. The (100) faces and a small square-shaped area around them retained the high luster for as long as 70 hr. Facets developed parallel to (100) planes only. A typical etch pattern is shown in Fig. 2. Microscopic views of the (100) face and of the area adjacent to the (111) face are shown in Fig. 3 and 4.

Spherical crystals exposed to 3M acetic acid, 3M hydrochloric acid, 1M sulfuric acid, 5% nitric acid in alcohol (nital), 3M phosphoric acid, 0.2M tartaric acid, and 0.2M oxalic acid yielded results essentially the same as those obtained in citric acid. Areas surrounding the (111) faces were the first to etch and become roughened and the (100) faces showed the slowest rate of etching. There were

[4] Obtained from MacDermid, Inc., Waterbury, Conn.

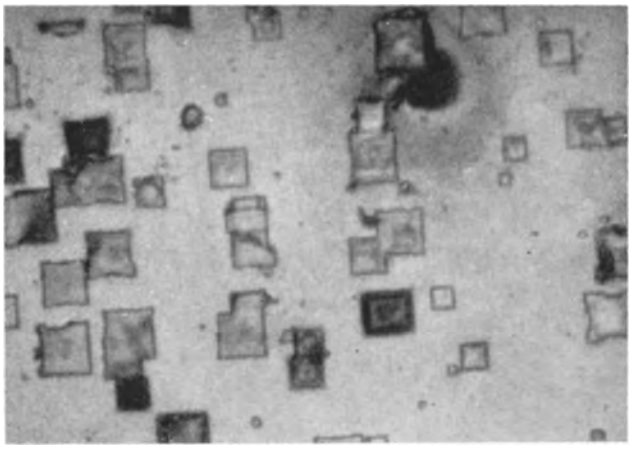

Fig. 3. Typical surface formed on (100) face of Fe when corroded in 0.2M citric acid. Magnification, 1000X.

minor differences in the details of the etch patterns with the various acids, but the great difference between the (111) and (100) areas was noted in all cases.

Previous experiments in this laboratory and at the University of Virginia offered direct proof that the rate of roughening of an electrolytically polished surface was a measure of the rate of etching. However, it was of interest to check again this conclusion. Two types of experiments bear on this problem. First, the results described in a following section on the potential measurements confirm conclusions drawn from the experiments with the spheres. Second, an experiment carried out in nital offered convincing evidence that the (100) face which roughened at the slowest rate also etched at the slowest rate. An electrolytically polished crystal sphere was immersed in nital for a total of 16 hr at room temperature. The crystal was transferred frequently to fresh solutions of nital in order to increase the rate of the reaction. At the end of the experiment the six (100) faces were raised appreciably above the surface. This result could only have been obtained if the (100) faces corroded at a slower rate than any other face.

Results observed on the various faces of the sphere were also observed on polycrystalline samples of L-steel. Grains which remained smooth during corrosion also etched at the slowest rate as shown by the fact that neighboring rough grains were at a lower level. These smooth and slow-corroding grains were identified as (100) faces from the fact that minute square pits were developed on their surfaces.

Confirmation of the general conclusion that the rate of corrosion of the minor faces making small angles with the (111) plane was greater than the (100) face was obtained in the following experiment. A flat face parallel to a (100) plane was cut on a sphere of Armco Fe and a flat face parallel to a (321) plane was cut on a second sphere. After electrolytic polishing, the spheres were wound with Sn wire and both were connected to a Sn bar. All of the surfaces except the (100) and (321) faces of Fe and a small section of the Sn bar were coated with a waterproof lacquer. The assembly was then inserted in a gel containing 7 g commercial gelatin in 300 ml of 0.02M citric acid containing just sufficient potassium ferricyanide to give a slight color. As the Fe corroded, the products diffused through the gel and formed a blue color due to ferrous ferricyanide as shown in the photograph in Fig. 5. It will be noted in the figure that the diffusion zone around the (321) face on the right is much thicker than the diffusion zone around the (100) face on the left.

Potential Measurements

Four different types of potential measurements were made at room temperature in 0.2M citric acid. The results may be summarized in the following statements:

1. The potential difference between (100) and (321) faces of Armco Fe in solutions exposed to air ranged from 7 to 17 mv after immersion for 7-72 hr, the (100) face always being cathodic.

2. The potential difference between the (100) and (321) faces of Armco Fe in solutions deaerated by freeze-thaw cycling ranged from 3 to 8 mv after immersion for 23-92 hr, the (100) face always being cathodic.

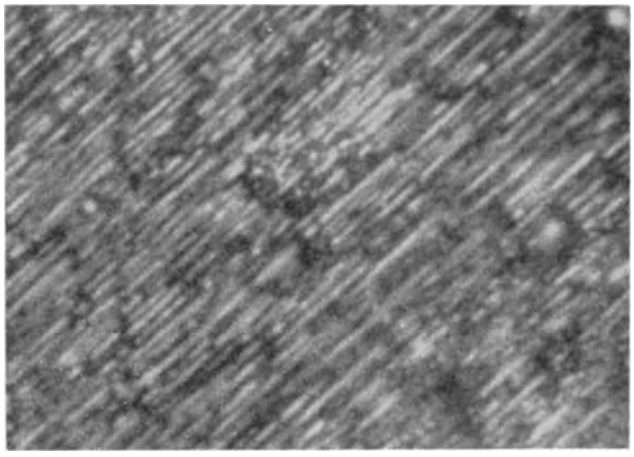

Fig. 4. Typical surface formed on (321) face of Fe when corroded in 0.2M citric acid. Magnification, 1500X.

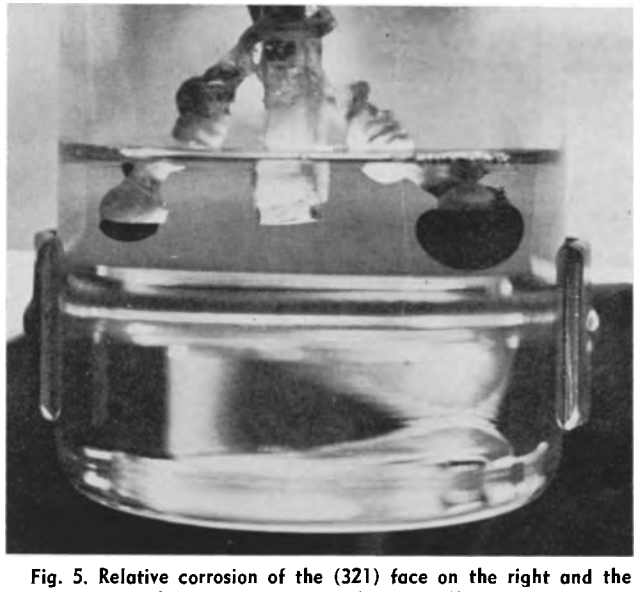

Fig. 5. Relative corrosion of the (321) face on the right and the (100) face on the left as indicated by the diffusion zone formed around the faces when connected to Sn and immersed in a citric acid gel containing potassium ferricyanide.

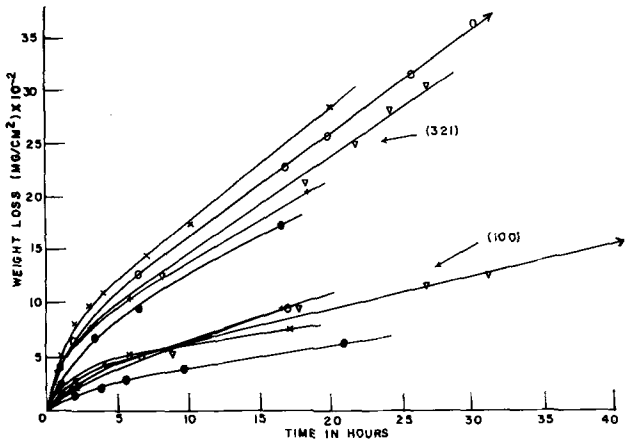

Fig. 6. Results obtained with single crystals of Armco Fe in experiments carried out at 20°C in 0.2M solutions of citric acid which had been deaerated by freeze-thaw cycling.

3. Both the (100) and (321) faces were cathodic to polycrystalline Sn in solutions deaerated by freeze-thaw cycling.

4. A potential difference existed between the (100) and (321) faces when all the exposed Fe except the flat crystal faces was coated with electrodeposited Sn and measurements were carried out in deaerated solutions. The (100)-Sn assembly was cathodic by 5-20 mv in exposures lasting up to 69 hr.

Quantitative Corrosion Measurements

Armco single crystals in deaerated 0.2M citric acid at 20°C.—Preliminary measurements were carried out on single crystals containing inclusions of one or two smaller crystals of unknown orientation. Results with these specimens were not reproducible and microscopic examination indicated that the irreproducibility could be attributed to the behavior of the grain boundary. In general, the boundary was attacked very rapidly both in the polishing operation before the start of a run and also during corrosion. The bond between neighboring crystals of Armco Fe, grown by the method described previously, is very weak as shown by the fact that often a ⅜ in. bar having two grains which cover the entire cross section can be readily broken by hand pressure.

Using crystals containing no inclusions, the results shown in Fig. 6 were obtained. For the linear portion of the curves the corrosion rate of the (100) face ranged from 0.0019 to 0.0044 mg/cm²/hr and averaged for the 5 runs, 0.0034 mg/cm²/hr. For the (321) face the rate ranged from 0.0078 to 0.0107 mg/cm²/hr and averaged 0.0091 mg/cm²/hr. Since the rates could be decreased slightly by additional freeze-thaw cycling there is reason to believe that the lack of better reproducibility was due to the presence of small amounts of air which were left after the 5 freeze-thaw operations.

Armco single crystals in deaerated 0.3N sulfuric acid at 20°C.—Three measurements were made in 0.3*N* H_2SO_4. The (100) face corroded at an average rate of 0.0091 mg/cm²/hr and the (321) corroded at 0.0168 mg/cm²/hr. These results are of minor significance since only a few measurements were performed, but they do show that the rate of corrosion of the (321) face is faster than that of the (100) face in H_2SO_4 as well as citric acid.

Table I. Rates of corrosion of the (100) and (321) faces of type L steel in boiling, refluxing 0.2M citric acid

Face	No. of measurements	Corrosion rate in mg/cm²/hr Range	Average
	First Set		
(100)	4	0.7-1.3	1.0
(321)	7	3.1-6.0	4.8
	Second Set		
(100)	5	1.3-1.8	1.5
(321)	4	2.9-4.0	3.6
	Third Set		
(100)	3	1.8-2.1	2.0
(321)	3	3.7-4.2	4.0

Armco single crystals in boiling, refluxing 0.2M citric acid.—The average corrosion rate for the (100) face was 1.4 mg/cm²/hr and of the (321) face 3.0 mg/cm²/hr. (100) facets only were developed and a great deal of the corrosion of the (100) faces occurred by pitting. These pits (Fig. 3) had a square cross section and are confirming evidence that the corrosion of the (100) face occurred at the slowest rate.

Type L steel single crystals in boiling, refluxing 0.2M citric acid.—Three sets of specimens were used in these experiments. In the first set, disks exposing (100) and (321) faces were cut from a single large grain and in the two other sets the faces were cut from neighboring grains in a second slab. The results obtained with these specimens are summarized in Table I.

Corrosion of polycrystalline Armco iron in 0.2M citric acid at the boiling point.—The rate of corrosion of the original Armco Fe rods from which the single crystals were prepared ranged from 4.8 to 7.7 mg/cm²/hr with an average rate of 6.0 mg/cm²/hr. The grain size of this material was 560 grains/mm².

Corrosion of polycrystalline Armco Fe in 0.2M citric acid at the boiling point.—The 2½ in. x 2½ in. billets of L steel used to grow single crystals showed two distinctive regions when etched in HCl, a rim and a core section having a sharp boundary between them (*see* Fig. 1). A wet analysis of the rim and core millings yielded the following:[3]

	% C	% P	% Mn	% S
Core	0.089	0.018	0.29	0.059
Rim	0.038	0.011	0.25	0.024

Additional qualitative analyses confirmed that the concentrations of C, Mn, and S were higher in the core than in the rim section.

Corrosion rates of unannealed polycrystalline rim and core specimens were determined for comparison with one another and with single-crystal rates. The rim and core samples were machined in the shape of cylinders having their axes parallel to the rolling direction in the billet. A typical run is shown in Fig. 7 where results for single-crystal specimens are also given for comparison. In a series of experiments the rate of corrosion, as determined from the

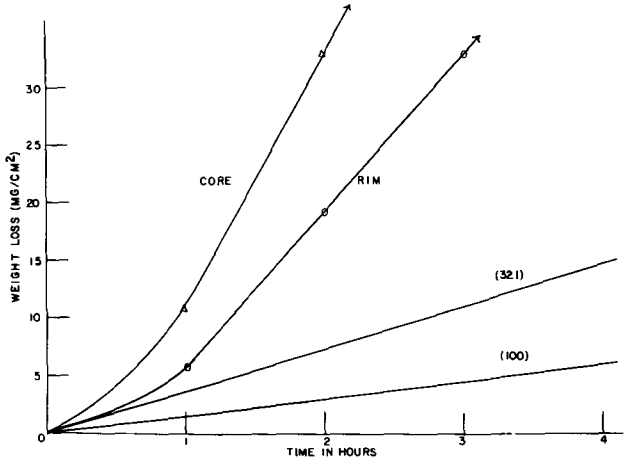

Fig. 7. Corrosion in 0.2M citric acid at the boiling point of polycrystalline samples cut from rim and core sections of the as-received billet. Rates of corrosion of single crystals prepared in the rim area are given for comparison.

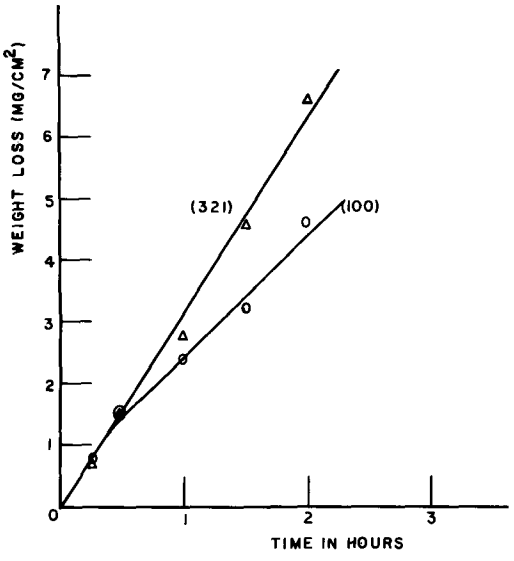

Fig. 8. Corrosion in 0.2M citric acid at the boiling point of single crystals of Armco Fe in the as-machined condition.

linear portion of the curve, ranged from 13.3 to 19.2 mg/cm²/hr for the rim and from 15.4 to 36 mg/cm²/hr for the core. The average values were 15.6 mg/cm²/hr for the rim and 26.6 mg/cm²/hr for the core.

A few experiments were also carried out on polycrystalline core specimens which were cut after the steel sample had been heated for 100 hr at an average pressure of approximately 50μ. The rates of corrosion of these specimens were in the same range as specimens which had not been subjected to any heat treatment.

Recrystallized Armco crystals in 0.2M citric acid at the boiling point.—In the first experiments, a disk exposing (100) faces and a disk exposing (321) faces were machined with a sharp lathe tool. The resulting surfaces yielded back-reflection x-ray patterns using Fe radiation indicative of fine-grained, polycrystalline iron. A typical corrosion experiment is shown in Fig. 8. The outstanding feature of this experiment is that the rate of corrosion of the machined (100) face was high at the start of the experiment and apparently was approximately the same as that of the machined (321) face. As the corrosion continued the rates diverged and assumed values of 1.7-1.9 mg/cm²/hr for the (100) face and 2.5-3.1 mg/cm²/hr for the (321) face. These values should be compared with values of the corrosion of the strain-free surfaces of 1.4 mg/cm²/hr for the (100) face and 3.0 mg/cm²/hr for the (321) face in experiments carried out immediately prior to the experiments in which the crystals were machined.

After 2 hr of corrosion, the surface of the (100) face had an appearance such as that shown in Fig. 9. When the crystal was examined with a flashlight, reflections were obtained only from one quadrant at a time. The photograph in Fig. 9 was taken with two light beams so that the 4 quadrants on the surface would be visible. Such a pattern on the surface presumably reflects the fourfold symmetry of the distortion of the crystal as it was cut in the lathe. The fact that only one quadrant at a time reflected light from the flashlight suggests that at the completion of the experiment the (100) planes in the surface layers were not parallel to the surface. Some distortion still existed in the surface layers.

Recrystallization of a disk exposing (100) faces and a disk exposing (321) faces was carried out by heating the disks in vacuum to 1000°C and cooling slowly. The phase change from the low temperature body-centered cubic structure to the high temperature face-centered cubic structure on heating and the reverse change on cooling resulted in recrystallization. The grain size obtained after slow cooling to room temperature was 42 grains/mm² on both specimens. Metallographic examination showed a striking substructure within many of the grains.

The average rate of corrosion of the recrystallized (100) disk was 4.4 mg/cm²/hr and of the recrystallized (321) disk was 4.1 mg/cm²/hr on samples polished in Mirro-Fe. In one experiment carried out on specimens which had been surfaced by machining with a sharp lathe tool, the rates of corrosion were 4.8 and 4.6 mg/cm²/hr for the recrystallized (100) and (321) disks, respectively.

Recrystallized type L steel crystals in 0.2M citric acid at the boiling point.—A disk exposing (100) faces and a disk exposing (321) faces were recrys-

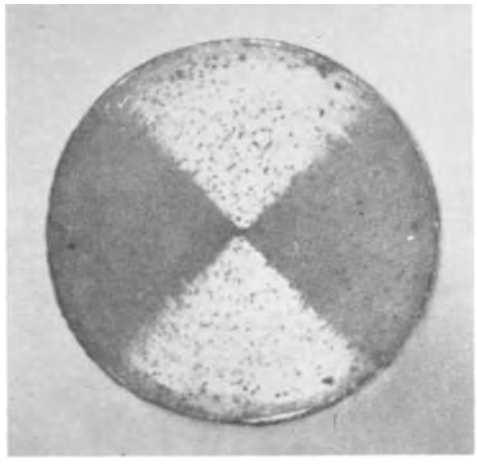

Fig. 9. Pattern on the surface of a machined (100) disk after corrosion for 2 hr in 0.2M citric acid at the boiling point.

tallized in the same manner as the Armco crystals by heating them to 1000°C in vacuum and cooling slowly to room temperature. A grain size of 48 grains/mm^2 resulted. The average rate of corrosion of the recrystallized (100) disk was 5.3 mg/cm^2/hr and of the recrystallized (321) disk was 5.5 mg/cm^2/hr.

In a second series of experiments, the recrystallized (100) was strained by compressing it so that the thickness was decreased to 75% of its former value. The average rate of corrosion of this recrystallized and strained disk was 3.5 mg/cm^2/hr.

In order to obtain preliminary information useful in a future thorough study of the effect of grain size on corrosion rate, the following experiments were performed. The recrystallized and strained (100) disk resulting from the experiments with the compressed specimen and the recrystallized (321) disk were converted to fine-grained specimens by heating them to 1000° and quenching them in cold water. Grain sizes in these specimens were 1550 and 1600 grains/mm^2. The rates of corrosion of these specimens ranged from 7.1 to 8.5 and averaged 7.9 mg/cm^2/hr.

Corrosion in the presence of dissolved Sn(II) *ions.*—Preliminary experiments were carried out in an attempt to determine the relative amounts of Sn and single-crystal Fe which corroded when the two materials were in good contact and equal areas of both metals were exposed to the solution. These experiments indicated that the presence of Sn decreased greatly the corrosion of the steel. The purpose of the next experiments was to attempt to separate effects due to galvanic action from effects due to inhibition by dissolved Sn(II) ions.

In order to avoid the introduction of other ions into the solution, the Sn(II) was added to the citric acid solutions by corroding a piece of Sn wire in the acid. The Sn wire corroded in the boiling, refluxing 0.2M citric acid at a rate of 0.0071 mg/cm^2/hr and an accuracy of 1 part in 40 could be obtained by corroding a Sn wire of known surface area for a known period of time. The results of the experiments can be summarized in the following three statements:

1. There was no difference in behavior of the (100) and (321) faces.

2. In the presence of 40 ppm of Sn(II) the average rate of corrosion at the boiling point was 0.04 mg/cm^2/hr for exposure times up to 11 hr.

3. In the presence of 43 ppm of Sn(II) the average rate of corrosion in deaerated solutions at 20°C was 0.001 mg/cm^2/hr for exposure times up to 2160 hr.

In the earliest experiments Sn(II) was introduced by dissolving SnO in the citric acid solution. In these experiments the average rate of corrosion of the (100) face was 2.1 mg/cm^2/hr and the average rate of corrosion of the (321) face was 2.5 mg/cm^2/hr. The rate of corrosion of the (100) face was apparently unaffected by the addition of Sn(II) ions, whereas the rate of corrosion of the (321) face was appreciably reduced. The concentration of Sn(II) in solution in these experiments was unknown because of incomplete solutions of the SnO, but was less than 11.5 ppm.

Discussion

Seven different types of experiments reported herein indicate that in the acids studied the (100) face corrodes at a slower rate than the minor faces of which the (321) face is an example. These seven types are: (*a*) reaction patterns on the spheres; (*b*) experiments in the citric acid gel; (*c*) potential measurements; (*d*) rates of hydrogen evolution from crystals exposed to deaerated citric and sulfuric acids; (*e*) corrosion in boiling 0.2M citric acid; (*f*) observations of the individual grains in polycrystalline steel; and (*g*) formation of facets and etch pits exposing (100) faces during corrosion in 0.2M citric acid.

On the basis of these observations there can be no doubt that the (100) corrodes at a slower rate and the (321) at a much more rapid rate in 0.2M citric acid. The question that still remains to be answered is why does this difference exist. Since (100) facets are developed on both the (100) face and the (321) face during corrosion there is the possibility that the relative rates may be correlated with the relative amounts of (100) surface exposed on the two faces. On the other hand, Fe atoms exposed at the joining edge of a (100) and (010) facet, for example, would be expected to be more vulnerable to attack by the acid. The relative rates of corrosion might be correlated with the relative amount of edge area exposed on the (100) and (321) faces. With the experimental data available at present it is not desired to express a preference for either of these or other possible explanations of the results. Regardless of the explanation of the results, the very fact that (100) facets are formed indicates that the (100) and (321) faces have different inherent rates of corrosion.

The possibility that the method of surface preparation controls the relative rates of reaction is ruled out by the fact that similar relative rates were obtained on (100) and (321) surfaces that were: (*a*) chemically polished in Mirro-Fe, (*b*) electrolytically polished, (*c*) machined, and (*d*) polished with emery paper. Of course in the latter two cases, the rates only approached the rates of the strain-free specimens, when the heavily strained outer layers had been removed in the corrosion process.

Potential measurements show that the (100) face is cathodic to the (321) face in citric acid. Potential measurements and rate measurements thus support one another. The cathodic nature of a grain exposing a (100) face relative to a neighboring grain exposing another type of face was observed many times in microscopic observations of polycrystalline aggregates. These observations confirm the view that some types of corrosion may have their origin in the potential difference between the crystal faces on the grains exposed at the surface.

The etch pattern obtained in the acids and shown in Fig. 2 indicated, on the basis of the rate of roughening, that the rates of corrosion of the minor faces surrounding the (111) pole position were much

Table II. Summary of important results on the corrosion rates in 0.2M citric acid at the boiling point

	Armco		Type L	
	(100)	(321)	(100)	(321)
	(all values in mg/cm²/hr)			
Starting material from which single crystals were prepared	4.8-7.1		13.3-19.2 (rim) 15.4-36 (core)	
Chemically polished single crystal	1.4	3.0	1.0-2.0	3.6-4.8
Machined crystal (start of corrosion)	2.2-3.0	2.8	——	——
(after reaching linear rate)	1.7-1.9	2.5-3.1	——	——
Recrystallized to 42-48 grains/mm² (chemically polished)	4.4	4.1	5.3	5.5
Recrystallized to 42 grains/mm² (machined surface)	4.8	4.6	——	——
Recrystallized to 1550-1600 grains/mm² by quenching from 1000°	——	——	7.1-8.5	
In the presence of 40-45 ppm [Sn(II)] (chemically polished)	——	——	0.03-0.1	0.02-0.07

more rapid than the (100) and the minor faces surrounding this plane. This type of surface pattern on electrolytically polished cubic single crystals is often observed and such patterns have been described for the formation of carbonaceous deposits on Cu single crystals immersed in aviation oil (10), the etching of Cu crystals in a $CuSO_4$-H_2SO_4 electrolyte (11), the deposition of C from the decomposition of CO on single crystals of Ni and Co (4), and the formation of free Ag during the photographic development of single crystals of AgCl (3). This same type of pattern has been observed many other times in unpublished experiments. This commonly observed pattern is confirming evidence for the view that the crystal planes making small angles with the (111) plane are unstable.

The corrosion studies which were carried out in 0.2M citric acid at the boiling point are summarized in Table II. Several of the important results are now discussed.

In the case of both the Armco and L-steel single crystals, the corrosion rate was apparently less than that of the starting material from which the single crystals were prepared. Significant reduction in C concentration only took place during the growth of the single crystals of L-steel as shown by the following analyses of single crystals of steel prepared from a different billet than was used in the corrosion studies.[3]

The reduced rate of corrosion of the single crystals may be accounted for in part by the reduction in C concentration, since C is known to increase the rates of corrosion of steels by fruit acids (12). That this purification is not the complete explanation is shown by the results obtained with the recrystallized single crystals. In the case of single crystals recrystallized to yield a grain size of 42-48 grains/mm² the corrosion rate of the (100) face was increased greatly and the rate of the (321) was increased appreciably, but much less than the (100). When these same crystals were recrystallized by heat treatment to a grain size of 1550-1600 grains/mm², the rate increased to an average rate of 7.9 mg/cm²/hr. Although this latter grain size is much smaller than the as-received material, the rate of corrosion is appreciably less, emphasizing the importance of both purity and grain size.

These results all point to the conclusion that the presence of grain boundaries results in a higher corrosion rate. Judging from the square pits formed on the surface of some of the grains, there was an appreciable concentration of grains whose (100) planes were oriented approximately parallel to the surface. It would be expected then, in the absence of grain boundary effects or the effect of one grain on another, that the corrosion rate of polycrystalline iron or steel would be between the low rate of the (100) face and the high rate of the (321) face.

It is generally recognized that Sn(II) ions decrease the rate of corrosion of steel in deaerated fruit acids (13-15), but the discovery made in this research is that the Sn ions had the ability to make the corrosion rate of the (100) and (321) faces the same. The apparent uniform activity of the faces was dramatically illustrated in experiments with spheres. When a single crystal sphere was immersed for two weeks in boiling, refluxing 0.2M citric acid containing 50 ppm of Sn(II), no corrosion

	Si	Mn	Mo	Cr	Cu	Ni	C	P	S
Starting material (rim)	0.005	0.36	<0.002	<0.012	0.024	0.013	0.035	0.016	0.025
Starting material (core)	0.005	0.35	<0.002	<0.012	0.020	0.018	0.042	0.028	0.022
#1 Crystal (rim)	0.005	0.29	<0.002	<0.012	0.023	0.012	0.017	0.016	——
#2 Crystal (rim)	0.012	0.36	<0.002	<0.012	0.038	0.012	0.020	0.022	——
#2 Crystal (core)	0.009	0.32	<0.003	<0.012	0.024	0.011	0.014	0.032	——
#3 Crystal (rim)									0.027
#3 Crystal (core)									0.047
#4 Crystal (rim)							0.006		
#4 Crystal (core)							0.014		

Crystals bearing the same number occupied both the rim and the core. Before analysis they were cut along the boundary between the rim and the core.

pattern formed on the sphere. In another experiment terminated at the end of 8 hr in 0.2M citric acid containing 10 ppm Sn(II), no pattern was observed. In these experiments with the spheres there was some localized pitting which did not appear to be related to crystal orientation, but the highly polished surface was retained until the end of the experiment.

In experiments carried out with single crystals at the boiling point in 0.2M citric acid containing approximately 40 ppm of Sn(II) no Sn or Sn compounds could be detected on the surface by either electron diffraction examination or by visual observation. The electron diffraction patterns showed lines due to iron oxide as would be expected. In runs with polycrystalline steel specimens and carried out for 96 hr, visible signs of Sn were detected on the surface. This experiment indicates that there is a tendency for stannous ions to be converted to metallic tin on a steel surface under the conditions used.

Acknowledgment

This work is supported by a grant from the American Can Co. Grateful acknowledgment is given for this support. The authors are also grateful to H. -J. Engell for sending them his manuscript in advance of publication and for a personal discussion of his work.

Manuscript received Oct. 3, 1956. This paper was prepared for delivery before the Cleveland Meeting, Sept. 30 to Oct. 4, 1956.

Any discussion of this paper will appear in a Discussion Section to be published in the June 1958 JOURNAL.

REFERENCES

1. W. R. Buck, III, and H. Leidheiser, Jr., *Z. Elektrochem.*, **59**, 748 (1955).
2. F. W. Young, Jr., J. V. Cathcart, and A. T. Gwathmey, *Acta Met.*, **4**, 145 (1956).
3. F. H. Cook and H. Leidheiser, Jr., *J. Am. Chem. Soc.*, **76**, 617 (1954).
4. V. J. Kehrer, Jr., and H. Leidheiser, Jr. *J. Phys. Chem.* **58**, 550 (1954).
5. A. T. Gwathmey, *Record Chem. Progr.*, **14**, 117 (1953).
6. H. Leidheiser, Jr., and R. Meelheim, *J. Am. Chem. Soc.*, **71**, 1122 (1949).
7. H.-J. Engell, *Arch. Eisenhüttenw.*, **26**, 393 (1955).
8. M. J. Pryor and M. Cohen, *This Journal*, **98**, 263 (1951); **100**, 203 (1953).
9. P. Jacquet and R. Rocquet, *Comp. rend.*, **208**, 1012 (1939).
10. A. T. Gwathmey, H. Leidheiser, Jr., and G. P. Smith, Natl. Advisory Comm. Aeronaut. Tech. Note No. 982, 52 pp. (1945).
11. H. Leidheiser, Jr., and A. T. Gwathmey, *Trans. Electrochem. Soc.*, **91**, 97 (1947).
12. M. Stern, *This Journal*, **102**, 663 (1955).
13. R. M. Lueck and H. T. Blair, *Trans. Electrochem. Soc.*, **54**, 257 (1928).
14. E. F. Kohman and N. H. Sanborn, *Ind. Eng. Chem.*, **20**, 1373 (1928).
15. T. P. Hoar, *Trans. Faraday Soc.*, **30**, 472 (1934).

Kinetic Studies on Formation of Black-Oxide Coatings on Mild Steel in Alkaline Nitrite Solutions

Ray M. Hurd and Norman Hackerman

Defense Research Laboratory and Department of Chemistry, The University of Texas, Austin, Texas

ABSTRACT

The formation of black-oxide (magnetite) coatings on mild steel in hot concentrated solutions of sodium hydroxide and sodium nitrite was studied over the temperature range 130°-150°C. The following mechanism is proposed for the over-all reaction:

$$Fe \xrightarrow[OH^-]{NO_2^-} Fe(OH)_2 \qquad [1]$$

$$Fe(OH)_2 \xrightarrow[OH^-]{NO_2^-} Fe(OH)_3 \rightleftarrows FeO_2^- \qquad [2]$$

$$Fe(OH)_2 \rightleftarrows Fe^{++} + 2\,OH^- \qquad [2a]$$

$$Fe^{++} + 2\,FeO_2^- \rightarrow Fe(FeO_2)_2 \qquad [3]$$

Of the total iron dissolved in step [1], only about 30% was converted to black oxide on the surface. Values of the rate constant for step [1] were obtained from plots of total iron dissolved vs. time. Plots of the initial rates (oxide-free surface) vs. $1/T$ were linear, with an energy term of 41 kcal/mole. As the oxide coating built up, the rates dropped to a fraction of the initial rate and the energy term increased sharply. For thicker films the rates are apparently controlled by diffusion of the reactants through the film.

Alkaline oxidizing baths are used in the metal finishing industry to form black-oxide coatings on ferrous metals, particularly mild steels. All of the proprietary baths generally use the same process conditions and salt compositions. The principal ingredients are a strong alkali, usually NaOH, and an oxidizing agent, $NaNO_2$ or $NaNO_3$, or a mixture of these two. Proportions vary somewhat from bath to bath, and some contain small amounts of addition agents, although the effectiveness of these agents has not been clearly demonstrated.

The advantages and limitations of the black-oxide coatings have been described previously (1). Briefly, they provide some additional resistance to atmospheric corrosion, but fail rapidly in salt spray tests and at high humidities. Oxide-coated pieces are usually given additional protection by use of a supplemental oil film, formed by immersion in a hot soluble oil bath (2). This treatment not only imparts a considerable increase in corrosion resistance, but also enhances the decorative value of the oxide coat.

It is believed that the low resistance of the oxide-coated steel without the supplemental oil film is due to the slight porosity and to the thinness (in the order of a micron) of the coatings. The purpose of the research described in this paper was to study the chemical processes and mechanisms involved in the oxide formation.

Experimental

The salts used in all experiments were furnished by the Eltex Chemical Corporation of Providence, Rhode Island, and were of the usual commercial grade. The composition of the salts was about 66% NaOH and 33% $NaNO_2$. The baths were prepared by adding 1000 g of the salt mixture to sufficient water to adjust the boiling point of the solution to any desired operating temperature in the range 130°-150°C. The bath temperature was controlled by operating the bath at the boiling point and adding make-up water at a rate equivalent to that lost by evaporation. The baths were contained in a large Pyrex beaker, which resulted in the accumulation of small quantities of silicates in the solution. However, the effect of silicates, if any, was minimized by preparing a fresh bath for each run, and by repeating the initial point after the completion of each run.

Coupons were cut to approximately one inch square from 0.010 in. mild steel (SAE 1045) shim stock, and were finished by sanding lightly with 3/0 emery paper. The coupons were immersed in the bath for periods ranging from 0.5 to 15 min, after which they were removed and immediately quenched in cold water. After the weight loss, of the order of a few milligrams, was obtained, the oxide coating was removed by immersing the coupons for a few seconds in 20% HCl, and again recording the weight loss. From these two weight losses, it was determined that only about 30% of the total iron dissolved appeared in the oxide coat, the remainder being lost to the solution.

Each point in the figures represents an average of data taken on three coupons, except for the run at 134°C. For some reason, considerable difficulty

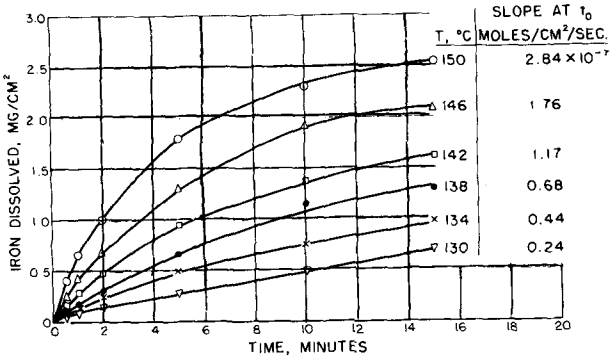

Fig. 1. Total iron dissolved at various temperatures

was encountered in obtaining reproducible weight losses at this particular temperature; the points shown were obtained by averaging data from nine coupons at each time. At the other temperatures, weight losses generally were reproducible to within less than 2.0%.

Results

The total iron dissolved by the oxidizing bath was obtained by adding the two weight losses obtained as described above. These data are shown plotted against time in the bath in Fig. 1 and 2. Fig. 1 shows that the iron dissolution reaction rate decreases markedly as the oxide film builds up. At the lower temperatures, where the film forms more slowly, the decrease is less than at the higher temperatures. As a matter of fact, the slopes of all of these curves after 15 min in the bath are approximately equal at all temperatures, while the initial rates vary over an order of magnitude. Fig. 2 shows that a log-log plot gives a family of straight lines of approximately equal slopes. The values of $d(\mathrm{Fe})/dt$ for Fig. 3 and 5 were obtained by replotting these straight lines on an expanded linear scale through the time interval desired.

In removing the oxide film, it was noted that dissolution occurred first at the corners and edges of the coupon, and then progressed very rapidly toward the center. Also there was no tendency for the steel itself to be attacked by the acid until some 2 or 3 min after the black-oxide had disappeared. This suggests that a very thin (passivating?) film remains on the surface during this period. No detectable weight loss was observed during the interval after the film was removed and before the metal was visibly attacked.

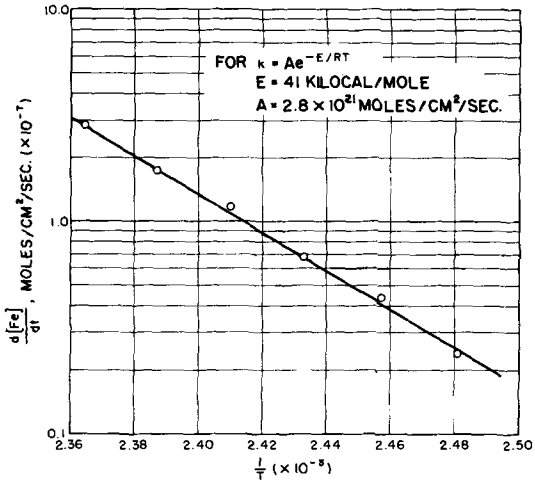

Fig. 3. Arrhenius plot of initial rate constants

In Fig. 3 the initial slopes of the curves of Fig. 1 are plotted against the reciprocal of absolute temperature. It is assumed that in the initial stage of the reaction, the rate of iron dissolution is described by:

$$\frac{d(\mathrm{Fe})}{dt} = k(X) \qquad (I)$$

where X is the fraction of the total surface available for the reaction. For Fig. 3, the slopes are taken at $t = 0$, where $X = 1.0$. A typical Arrhenius plot is obtained, with an energy of activation of 41 kcal/mole and a frequency factor of 2.8 x 10^{21} moles/cm²/sec.

The thickness of the oxide film was estimated by dividing the weight of film per square centimeter by the bulk density of magnetite, $Fe(FeO_2)_2$. While there is no evidence to show that the black-oxide is 100% magnetite, portions of the film removed intact exhibit ferromagnetism. It should be pointed out that, at temperatures only slightly above 150°C, the film contains visible amounts of reddish-yellow oxide, and is presumably a mixture of magnetite and ferric oxide. While it is possible that small amounts of ferric oxide (not visible) may be present at 150°, or even 146°, they are not likely to be significant, and the estimates of film thicknesses as

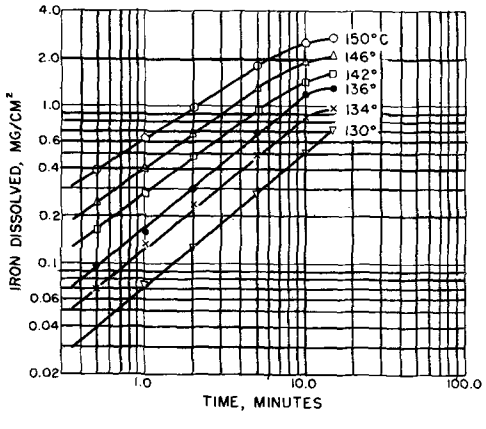

Fig. 2. Log-log plot of data of Fig. 1

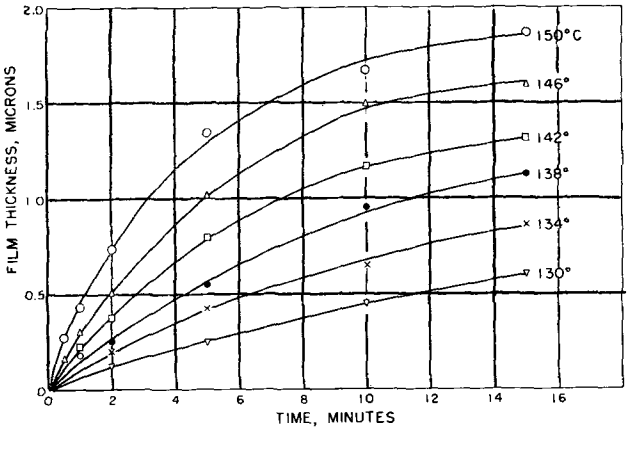

Fig. 4. Growth of film thickness

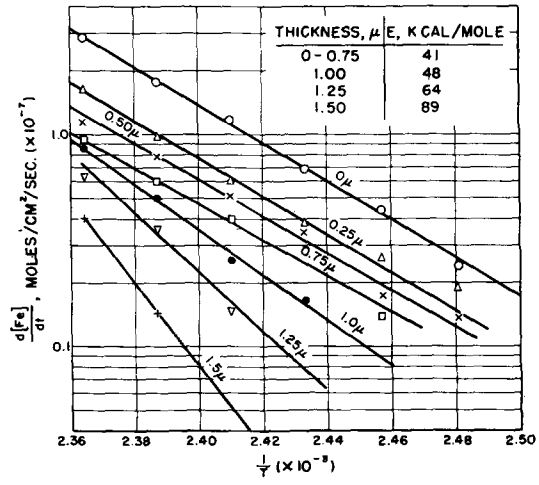

Fig. 5. Arrhenius plot of rate constants at different film thicknesses

plotted in Fig. 4 are reasonably accurate. The thickest film obtained after 15-min immersion at 150° was 1.85μ. It is interesting to note that, since only some 30% of the total iron dissolved goes into the film, there is actually a very slight decrease in the dimensions of steel pieces when treated in these baths, although the changes are so small as to be negligible in most cases.

For each temperature, the times at which the films build up to a given thickness can be read from Fig. 4. By taking the slopes of the curves in Fig. 1 at these times, the curves of Fig. 5 were obtained. Although the data do not fall on such well-defined straight lines as those of Fig. 3, it is clear that no significant change in the energy term for the iron dissolution reaction occurs until the film has built up to a thickness of at least 0.75μ. As the film thickens beyond this point, the energy term increases sharply.

Mechanism and Reactions

The determination of the exact oxidation reactions which occur in these baths is complicated by the fact that the standard oxidation-reduction potentials for the possible half-cell reactions are not known at these temperatures. Furthermore, the numerous reactions possible with the oxides of nitrogen, the nitrates and nitrites, and the equilibria between them are additional complicating factors. The possible half-reactions for a system containing iron and nitrites in alkali are given in Table I, with

Table I.

Possible half-reactions	E_0, volts
$Fe(OH)_2 + 2e \rightarrow Fe + 2OH^-$	−0.877
$2H_2O + 2e \rightarrow H_2 + 2OH^-$	−0.828
$Fe(OH)_3 + 1e \rightarrow Fe(OH)_2 + OH^-$	−0.56
$NO_2^- + H_2O + e \rightarrow NO + 2OH^-$	−0.46
$Fe^{++} + 2e \rightarrow Fe$	−0.441
$NO_3^- + H_2O + 2e \rightarrow NO_2^- + 2\,OH^-$	+0.01
$2NO_2^- + 3H_2O + 4e \rightarrow N_2O + 6\,OH^-$	+0.15
$2NO + H_2O + 2e \rightarrow N_2O + 2\,OH^-$	+0.76
$FeO_4^= + 4H_2O + 3e \rightarrow Fe(OH)_3 + 5OH^-$	+0.90

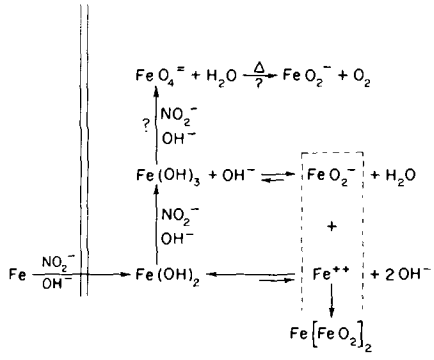

Fig. 6. Proposed mechanisms of black-oxide formation

their standard reduction potentials at 25°C, as given by Latimer and Hildebrand (3). If it is assumed that the reactions maintain approximately the same relative positions as the temperature is raised into the 130°-150°C range, then the probable net oxidation reactions are:

$$2Fe + 2NO_2^- + 3H_2O \rightarrow 2Fe(OH)_2 + 2OH^- + N_2O \quad \text{(II)}$$

$$4Fe(OH)_2 + 2NO_2^- + 3H_2O \rightarrow 4Fe(OH)_3 + N_2O + 2OH^- \quad \text{(III)}$$

According to these reactions, the gas evolved when steel is immersed in the baths should be predominantly N_2O. An effort was made to collect and analyze some of the gas, but because of the difficulties involved in carrying out such an experiment on these hot caustic solutions, it was abandoned with inconclusive results.

The last half-reaction given in Table I, the oxidation of $Fe(OH)_3$ to ferrate, is presented because there is some evidence that small amounts of ferrates are formed at the higher temperatures. The characteristic purplish-red color of the ferrates was observed momentarily in the layer of solution on the steel surface after quenching. Also, if the coupon is made sufficiently anodic (by an electrical circuit) in these solutions, a heavy purple-red streaming occurs which dissipates slowly, apparently due to the decomposition of the unstable ferrate into the colorless ferrite. A standard method of making alkali ferrates is by fusion of nitrite with $Fe(OH)_3$ (4), so that it is not unreasonable to assume that small amounts of ferrates are formed in these solutions near 150°C.

The probable over-all mechanism for the formation of the black-oxide is given in Fig. 6. The double line at the left of the figure indicates that, after the film has started to form, the reaction must be preceded by diffusion of the reactants through the oxide. The $Fe(OH)_2$ formed in the initial step must then yield the ferrous ion by dissociation and the $Fe(OH)_3$ by further oxidation. The equilibrium between $Fe(OH)_3$ and FeO_2^- in strongly alkaline solutions is well known. The loss to the solution of a considerable portion of the total iron dissolved is probably accounted for by the small amount of ferrous ion available at the surface for precipitation of $Fe(FeO_2)_2$. The low ferrous ion concentration can be accounted for either by a low solubility of $Fe(OH)_2$, or by a very rapid oxidation to

$Fe(OH)_3$. Apparently, as only 30% of the total iron appears as $Fe(FeO_2)_2$, of which only one-third is Fe^{++}, about 90% of the $Fe(OH)_2$ is oxidized to $Fe(OH)_3$.

The formation and subsequent decomposition of the ferrates are indicated in the figure, but with a question mark to indicate the uncertainty.

The kinetics of the over-all mechanism are almost certainly controlled by the initial reaction. It is suggested that for film thicknesses up to about 0.75 μ, this reaction is controlled by Eq. (I), where $k = Ae^{-41,000/RT}$ and $X = 1.0$ at thickness 0 μ, $X = 0.55$ at thickness 0.25 μ, $X = 0.42$ at thickness 0.50 μ, $X = 0.30$ at thickness 0.75 μ.

As the thickness increases beyond 0.75 μ, the change in the energy term reflects the increasing importance of diffusion through the layer in controlling the rate. This means essentially that the film is porous, but that the porosity decreases as the film thickens. Presumably, if thick enough films could be produced, the process would be entirely diffusion-controlled, and the energy term in Eq. (I) would become constant again at some value greater than 89 kcal/mole.

Acknowledgment

The authors wish to acknowledge the financial support of the Eltex Chemical Corp., Providence, R. I. They are also indebted to Mr. Mark Weisberg, President of Eltex, for many helpful discussions about the black-oxide process.

Manuscript received Nov. 17, 1956. This paper was prepared for delivery before the Cleveland Meeting, Sept. 30-Oct. 4, 1956.

Any discussion of this paper will appear in a Discussion Section to be published in the June 1958 JOURNAL.

REFERENCES

1. M. Weisberg and E. A. Parker, *Product Eng.*, **14**, 294 (1943).
2. M. Weisberg and E. A. Parker, *Steel*, **114**, 109 (1944).
3. W. L. Latimer and J. H. Hildebrand, "Reference Book of Inorganic Chemistry," p. 528, MacMillan Co., New York (1951).
4. N. V. Sedgwick, "Chemical Elements and their Compounds," Vol. II, p. 1368, Oxford University Press, London (1950).

Annealing Anodic Ta_2O_5 Films

Changes in Dissolution Behavior and X-Ray Scattering

D. A. Vermilyea

Research Laboratory, General Electric Company, Schenectady, New York

ABSTRACT

Upon annealing anodic Ta_2O_5 films the rate of solution of the film in HF decreases and the x-ray diffraction pattern from the film becomes sharper. The activation energy for the process responsible for changes in solution rate is approximately the same as those observed for changes in ionic conduction upon annealing and for ionic conduction itself. It is believed that changes in local ionic configuration are the cause of these property changes. The rate at which these changes occur appears to be controlled by the rate of tantalum ion motion.

Annealing anodic Ta_2O_5 films results in a decrease in their ionic conductivity. This decrease has been interpreted (1) in terms of a mechanism involving changes in the local ionic configuration, perhaps similar to the changes which are known to occur in glasses upon annealing. In this paper the changes in the rate of solution of the film in HF and the changes in scattering of x-rays which accompany annealing are discussed. A comparison of the activation energies involved indicates that ionic conductivity and changes in ionic conductivity and dissolution behavior may all be controlled by the same process, which is probably Ta ion migration.

Experimental

X-Ray Diffraction Studies

It was found by Hillig (2) that oxide films formed on chemically polished[1] Ta specimens could easily be stripped intact from the metal by the following procedure. A layer of nitrocellulose was applied to the surface of the oxide film from a solution of 10% nitrocellulose in amyl acetate. The edges of the coupon (¼ in. x 2 in.) were scraped with a razor blade to prevent continuity of the oxide and the nitrocellulose film around the edge. The nitrocellulose film was then carefully lifted off the specimen; the oxide film came with it.

X-ray diffraction specimens consisted of several layers of films about 3000Å thick formed in 0.2% Na_2SO_4 at room temperature using a current density of about 2 ma/cm^2. Films were stripped as described above, cut into ¼ in. squares, and placed nitrocellulose side up on a small Pt holder having a ⅛ in. hole in the center. This holder was placed in a spot plate containing ethyl acetate to dissolve the nitrocellulose. After at least four separate rinsings of the film in ethyl acetate another square was placed on top and the nitrocellulose dissolved away. This process was repeated until there were six thicknesses of oxide film (about 2μ) on the holder.

[1] Polishing solution: 55% H_2SO_4 (96%), 25% HNO_3 (70%), and 20% HF (48%) by volume.

Diffraction patterns of films heated 2 min at various temperatures were taken using Cr Kα radiation in a cylindrical camera of 10 cm diameter using a He atmosphere to reduce low angle scattering by air. The radiation was not made truly monochromatic by diffraction from a crystal because the small sample thickness would have required very long exposure times. A L&N microphotometer was used to obtain a curve of intensity vs. distance on the film. Crystalline Ta_2O_5 gives a diffraction pattern with two strong lines at $d = 2.44$ and $d = 3.14$ and a somewhat weaker one at $d = 3.9$; in the amorphous material these three lines contribute to one broad halo. The main contribution, however, is from the stronger lines at $d = 2.44$ and 3.14. In order to separate the lines it was necessary to find three symmetrical Gaussian curves which when added together gave the observed pattern (corrected for background). The breadths of the two highest Gaussian curves were then measured at half height and the result used as a measure of the diffuseness of the pattern. A pattern was also taken for a 0.001 cm flake of fused quartz for comparison with the Ta_2O_5 patterns.

Dissolution Studies

If a Ta_2O_5 film on the Ta electrode on which it was formed is dipped into 48% HF it will dissolve slowly and uniformly (3), so that changes in thickness can be measured by comparison with an optical step gauge (4). However, HF changes strength rather rapidly on standing and in use, so that some method of calibrating the dissolving power of the solution was required. The method used was to dissolve a series of films in which every third film was one formed in a standard manner, the others having been annealed. A plot of the rate of solution of the standard film vs. the test number was used to find by interpolation the solution rate of a standard film at any test. The solution rate of the standard film was taken arbitrarily as 20Å/sec, and all test results on annealed films were multiplied by the ratio of 20Å/sec to the interpolated solution rate of the standard specimen for that test. The solution rate obtained for the annealed specimen was thus the rate of solution relative to that of the standard film.

All of the films were formed by anodization at 1.56 ma/cm^2, 29°C, to 120 v using a 1% Na_2SO_4 electrolytic solution. The film thickness produced was 1759Å ± 10Å. After formation the films were annealed on the Ta electrode at different temperatures using baths of water, silicone oil, molten lead-bismuth-tin alloy, molten KCl-LiCl mixture, or air depending on the time and temperature. Results were the same regardless of the method of heating at temperatures up to 330°C. The standard films were formed in exactly the same manner but were not annealed.

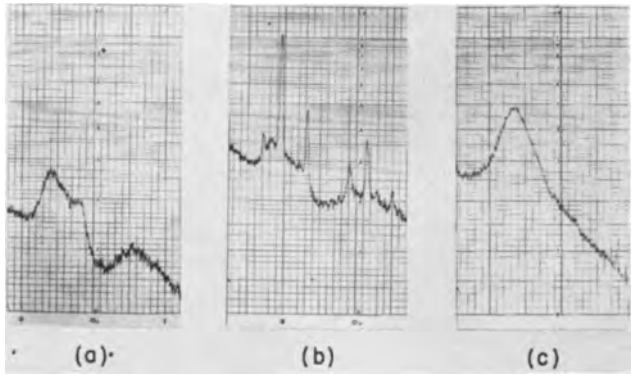

Fig. 1. Diffraction intensity vs. diffraction angle: (*a*) an anodic Ta_2O_5 film heated 2 min at 555°C; (*b*) same at 750°C; (*c*) for vitreous silica.

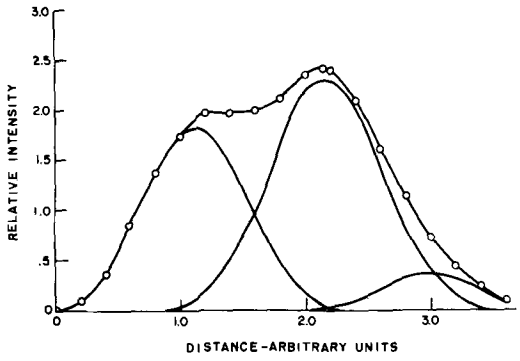

Fig. 2. Diffraction intensity (corrected for background) vs. diffraction angle, showing the resolution of the broad diffraction maximum into its three component maxima.

Experimental Results

X-Ray Diffraction Studies

Fig. 1 shows microphotometer traces of an amorphous Ta_2O_5 film, crystalline Ta_2O_5 film, and quartz, respectively. The patterns for quartz and amorphous oxide are qualitatively similar, showing very broad halos and considerable small angle scattering [the small angle scattering is probably a result of the technique used, since Warren (5) found little small angle scattering from quartz]. It seems not unreasonable, therefore, that the anodic films have a glassy structure. The peaks in the pattern for crystalline Ta_2O_5 appear at about the same position as do the maxima in the amorphous pattern.

Fig. 2 is a replot of the data from one of the microphotometer traces from which the background has been subtracted, and shows how the three Gaussian curves have been added to give the observed curve. The values of line breadths from experiments using two separate specimens are given in Table I. The time of annealing at each temperature was 5 min.

There is a definite decrease in line breadths for both films; the decrease is greater for film No. 1. The two

Table I. Values of line breadths

Film No.	Annealing temp, °C	Line breadth at half height arbitrary units
1	As formed	1.03
	210	0.93
	375	0.90
	555	0.83
2	As formed	0.92
	108	0.91
	210	0.89
	338	0.84
	505	0.83
	620	0.82

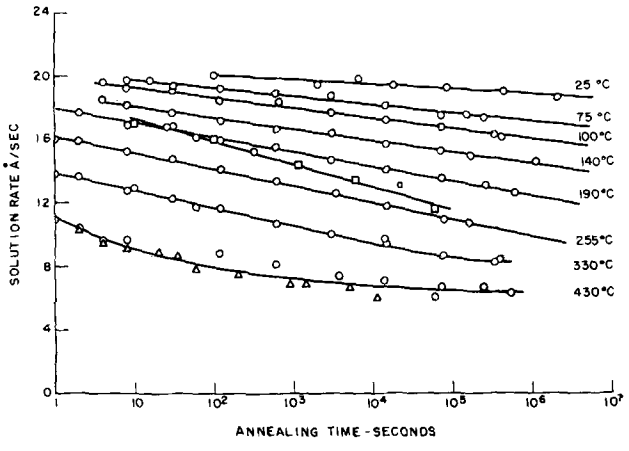

Fig. 3. Change of relative solution rate with time of annealing at various temperatures. For the 430°C anneal the circles denote that the films were heated in air while the triangles denote films heated in molten KCl-LiCl mixture. The squares are used for the data obtained when films were held at 140°C with an applied electric field of 0.029 v/Å (curve a).

films were made at the same time and in exactly the same way, so they should have been identical. However, about a month elapsed between the two sets of experiments, and the fact that the original pattern for film No. 2 was less diffuse may be the result of annealing for one month at room temperature.

No attempt was made to determine the exact structure of these films from the x-ray data. A very rough indication of the extent of local order can be obtained from the particle size which would be necessary to cause such line broadening. This does not imply that such particles exist but, if the diffuse pattern were the result of a very small particle size, the order of magnitude of the mean particle diameter would be about 10Å. Because of the qualitative similarity between the patterns for the Ta_2O_5 films and those obtained from vitreous quartz, the simplest interpretation of the x-ray data is that the anodic films have a glass-like structure, and that changes in the local configuration on annealing the film result in a sharper x-ray pattern.

Dissolution Studies

The rate of solution of annealed oxide films decreases nearly linearly with the logarithm of the

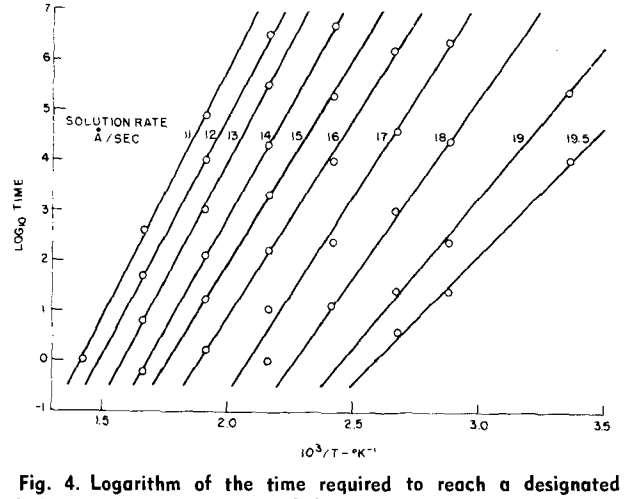

Fig. 4. Logarithm of the time required to reach a designated solution rate vs. the reciprocal of the temperature.

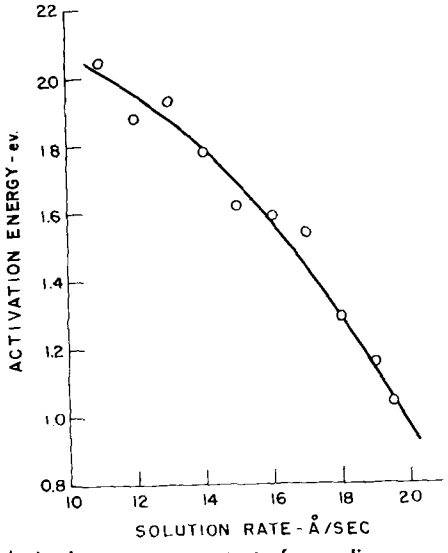

Fig. 5. Activation energy vs. extent of annealing as measured by solution rate.

time of annealing at temperatures from room temperature to 330°C (Fig. 3). At 430°C the solution rate appears to be approaching a minimum after about 10^5 sec, and the results are slightly different depending on whether the specimens were heated in air or in molten KCl-LiCl mixture. The results of transient studies on films heated at high temperatures (6) indicate that oxygen mobility in the oxide becomes appreciable above about 350°C, and that some solution of oxygen in the Ta occurs, particularly at grain boundaries. The different behavior at 430° and the dependence on atmosphere are probably associated with this increased oxygen mobility.

A plot of the logarithm of the annealing time required to reach a particular solution rate vs. $1/T$ is shown in Fig. 4, and the activation energy determined from the slopes of these curves vs. solution rate is shown in Fig. 5. The activation energy increases from about 1 ev to 2 ev as the solution rate decreases from 20 to 11.

The dependence of the solution rate on time of annealing at 140°C is shown in Fig. 6 for films having three different histories. The solution rate is plotted against log (time at 140°C plus 3700 sec) in curve 2 since the initial solution rate for these films (16.2Å/sec) would have been produced in 3700 sec at 140°C, and against log (time at 140°C plus

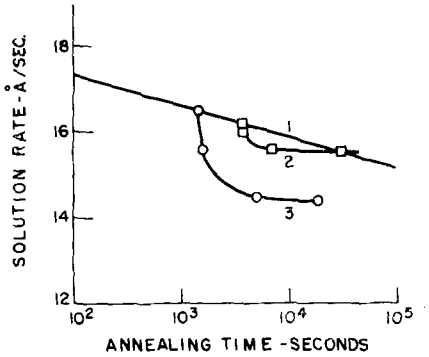

Fig. 6. History effect in annealing. Curve 1 is the same as that for 140°C from Fig. 3. Curves 2 and 3 are for films heated at 140°C after holding for 100 sec at 190°C, and at 80°C with an applied field of 0.055 v/Å, respectively.

1400 sec in curve 3. These results show clearly that a given solution rate does not completely describe the state of the film, since the behavior upon annealing at 140°C depends on film history.

It should be noted that the same solution rate is produced by holding a film at 140°C for 1400 sec or at 80°C with a field of 0.055 v/Å. Thus, annealing with an applied field results in a more rapid change in the solution rate. This is also shown very clearly in Fig. 3, curve a, which was obtained for films held at 140°C with an applied field of 0.029 v/Å. Solution rates are roughly comparable to those obtained upon annealing at 190°C with no field applied.

In addition to changes in the solution rate produced by annealing the film with or without an applied field, changes in the solution rate also occur if the rate of film formation is changed at one temperature. At room temperature, for example, the solution rates were 19.3Å/sec, 20Å/sec, and 20.3Å/sec, after formation at rates of 0.4Å/sec, 8Å/sec, and 40Å/sec, respectively. While these changes are small and probably would make observation of any change in x-ray scattering extremely difficult, it seems reasonable to expect that such changes do occur, and that the same kind of change in film structure which occurs on annealing also occurs on changing the rate of film growth.

Discussion

According to the mechanism proposed previously[1], the passage of a large ionic current through a Ta_2O_5 film results in changes in local configuration which facilitate conduction. Upon annealing, or upon formation at a lower electric field, the structure changes toward a new configuration. X-ray data clearly indicate that some kind of change in the direction of increased order does occur upon annealing. The dissolution data show an increased chemical stability of the film, which would be expected on intuitive grounds if the structural order increased. It is interesting that the crystalline anodic Ta_2O_5 film (7) is almost entirely resistant to HF. Upon attempting to dissolve a crystalline film no change in film thickness occurs, but the HF penetrates under the crystallites and separates them from the metal by dissolving away the metal.

The activation energy for the process responsible for the change in solution rate is about 1.25 ev after mild annealing.[2] The value found for the process which causes a decrease in conductivity on annealing (1) is about 1.2 ev,[2] and for ion conduction itself is 1.06 ev.[2] These values are all quite similar and in view of the history effects with attendant uncertainty in the activation energies for annealing and for changes in conductivity, it may be that all three processes involve the migration of Ta ions as the rate-determining step. Support for this idea is found in the fact that annealing proceeds more rapidly if an electric field is present in the material.

Acknowledgment

It is a pleasure to acknowledge the benefit of discussions of the x-ray diffraction results with B. W. Roberts and of the dissolution studies with C. P. Bean.

Manuscript received August 16, 1956.

Any discussion of this paper will appear in a Discussion Section to be published in the June 1958 JOURNAL.

REFERENCES

1. D. A. Vermilyea, *This Journal*, **104**, 427 (1957).
2. W. B. Hillig, Private communication.
3. D. A. Vermilyea, *Acta Met.*, **2**, 482 (1954).
4. D. A. Vermilyea, *ibid.*, **1**, 283 (1953).
5. B. F. Warren, *J. Appl. Phys.*, **8**, 645 (1937).
6. D. A. Vermilyea, *Acta Met.*, **5**, 113 (1957).
7. D. A. Vermilyea, *This Journal*, **102**, 207 (1955).

[2] These energies are for specimens annealed 5 min at 100°C, so that the corrosion rate would be 18.2 Å/sec.

A Study of Cathode Potentials in Aqueous Tungstate Solutions

D. R. Markwell[1] and M. L. Holt

Chemistry Department, University of Wisconsin, Madison, Wisconsin

ABSTRACT

Cathode potential measurements were used as a means of obtaining information about the cathode process that results in the electrodeposition of tungsten alloys. A special cell designed to apply the Luggin-Haber backside capillary technique was used for making potential measurements during electrolysis. Changes in the observed cathode potential values resulting from varying the cathode current density and the electrolysis solution were recorded. A hypothesis to explain some of the peculiarities of the cathodic reduction of aqueous tungstate solutions is offered.

Pure tungsten has not been electrodeposited in weighable amounts from aqueous tungstate solutions; however, it is known that tungsten readily codeposits with certain other metals, notably Fe, Ni, and Co. Most of the literature reports on W electrodeposition have been concerned with the development of various types of alloy plating baths and the properties of the alloy deposits obtained. There has been very little experimental work reported directed primarily at finding an explanation for the cathodic behavior of tungstate ion in the presence of metal cations, although a catalytic reduction theory

[1] Present address: Captain D. R. Markwell, 503 Edgebrook Lane, San Antonio 1, Texas.

has been proposed (1) and the mechanism of the tungsten alloys plating process has been studied (2). Solov'eva and Vagramyan (3) measured the potential of deposition of Fe-W alloys and suggested that their results did not agree with the catalytic reduction theory. Hoar and Bucklow (4) compared hydrogen overpotentials on cathodes of Co, W, and Co-W, while Pecherskaya and Stender (5) compared cathodes of Fe and Ni-W. The purpose of the work reported here was to use cathode potential measurements as a means of explaining why it is possible to electrodeposit W alloys but not pure W from aqueous tungstate solutions.

Fink and Jones reported (6, 7) an aqueous carbonate-tungstate plating bath for the electrodeposition of W. Later, it was shown in this laboratory (8) that no metallic cathode deposit was obtained from a carbonate-tungstate type of bath which had been carefully purified to remove traces of Fe. It was also found that a purified carbonate-tungstate bath gave a W-Fe alloy deposit when it was electrolyzed after the addition of small amounts of iron(III) chloride. It was also reported (9) that Fe must be added to the plating solution as simple Fe(III) or Fe(II) cations and that hexacyanoferrate(III) and hexacyanoferrate(II) ions were not effective.

There are numerous published reports of the electrodeposition of W-Fe, W-Ni, and W-Co alloys from various types of plating solutions, but much of the recent work has made use of an ammoniacal citrate type of bath. Since the ammoniacal citrate bath was to be used in this work, a preliminary survey of bath operation was made with the Hull cell (10). It was found, as expected, that Fe, Co and Ni codeposit with W to give alloy deposits on the cathode, and that Cd, Cu, Mn, Ag, and Zn do not codeposit with W from this type of bath at the conditions used. It seemed reasonable to assume that a study of cathode potentials in ammoniacal citrate solutions could lead to an explanation of why W codeposits from these solutions with certain metals but not with others.

Experimental Techniques

The cathode potentials reported in this work were obtained by the direct method using a saturated calomel electrode and the backside capillary reference electrode technique (11-13). This method produces a minimum of distortion of current density distribution by the reference electrode and salt bridge because there is no obstruction between the cathode and the anode of the electrolysis cell. The current density is a little higher around the edge of the hole in the cathode than it is on the surface of the cathode; however, this effect is small if the area of the hole in the cathode is small in comparison to the surface area of the cathode.

The test cell shown in Fig. 1, and called here the cathode potential cell, was machined from a block of Lucite 16.5 cm long, 7.6 cm wide, and 15.2 cm high which was made by glueing together 2.54 cm thick Lucite sheets. The cathode compartment drilled in the block was about 6.4 cm in diameter and 14 cm deep and was centered about 7 cm from one end of the block. The side of this compartment

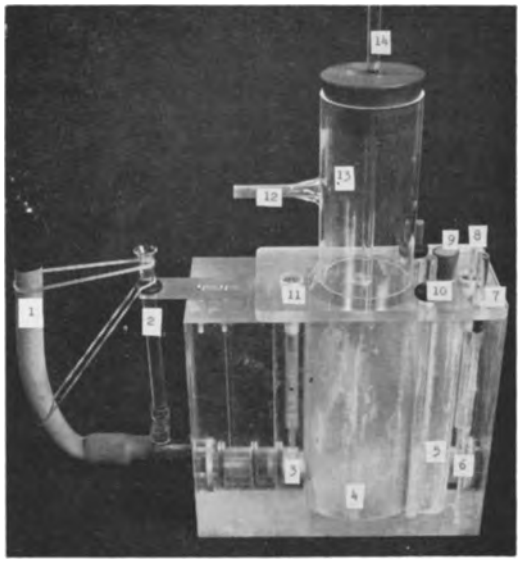

Fig. 1. Cathode potential cell. 1, lead from reference electrode through tubing; 2, side arm extension of calomel electrode; 3, cathode plug, with Pt cathode, fitted into cathode compartment wall; 4, cathode compartment; 5, anode compartment; 6, anode plug, with Pt anode, fitted into anode compartment wall; 7, gas inlet; 8, Pt wire to anode; 9, opening for solution samples; 10, one of two holders for removing diaphragm which separates anode and cathode compartments; 11, Pt wire to cathode; 12, to aspirator; 13, vapor trap; 14, stirrer.

nearest the end was opened and expanded to form the smaller rectangular anode compartment having the same depth as the cathode compartment. A removable Vinyon diaphragm was used to separate the compartments. Both the cathode and the anode were made of Pt and were imbedded in Lucite with the use of a Buehler specimen mounting mold to form electrode plugs which fit into horizontal borings opening into each compartment about 1 cm from the bottom. Each electrode plug was held firmly in position by a stainless steel cover which was fastened to the end surface of the cell by machine screws. This arrangement made it possible to remove the electrodes for inspection and cleaning. Electrical connection to each electrode was made with a Pt wire which rose vertically through the Lucite block and was spring loaded to provide rigid contact with the electrode. A Beckman saturated calomel electrode was used as the combined reference electrode and salt bridge. This electrode approached the cathode from the rear, passed through a 0.3 cm diameter hole in the cathode, and was flush with the surface of the cathode. The effective cathode surface area was 1.20 cm^2. Rubber gaskets and "O" rings provided watertight seals around the reference electrode and the working electrodes. Provision was made for gassing and stirring the solution.

There are two distinctly different electrical circuits in operation when cathode potentials are measured by the method reported here. One circuit consists of the cathode, the anode, and the source of direct current, while the other is made up of the cathode, the calomel reference electrode, and the potential measuring instrument. Practically no current flows in the latter circuit. A 12 v lead storage battery with a suitable control panel supplied

direct current to the cell and a L&N Model 7664, line operated pH (millivolt) meter was used to measure cathode potentials. The control panel was placed between the battery and the cell and consisted of six, linear taper, wirewound, continuously variable rheostats in series, and one in shunt. This allowed the potential applied to the working electrodes to be adjusted from zero to 12 v. A Simpson, Model 373, milliammeter was connected in series in the control panel to indicate the cell current. Although cathode potentials slowly and continuously increased with time with any given voltage applied to the cell they eventually become constant. The time between the application of a given power setting and the leveling off of the cathode potential varied from about 2 hr at very low current densities to about 2 min at high current densities. The signal from the pH (millivolt) meter was fed into a Speedomax recorder. The steady-state cathode potential, as indicated by a vertical trace on the recorder, is the value recorded in the data. The temperature of the cell was maintained at 30° ± 0.5°C by immersing the cell to approximately three quarters of its height in a water bath. The several pieces of apparatus were grounded to a common terminal on a cold water pipe.

Helium was used to sweep oxygen out of the cathode potential cell during each run. It was found that the rate of gas flow, within wide limits, had no effect on the cathode potential or the cell current. The same rate of flow, about two bubbles per second, was used in every run. Since the elimination of convection effects in moderately concentrated solutions being electrolyzed at current densities of from 1 to 15 amp/dm^2 is not possible, the solutions were stirred vigorously during all experiments. Stirring does not eliminate diffusion and migration effects, but it does make them unimportant as compared to convection effects, and therefore the electrolysis proceeds under convection controlled current (14). A glass stirring rod, placed midway between the cathode and anode, was rotated at 1440 rpm. The cathode potential and cell current were not visibly affected by wide variations in stirring speed. The bath pH of 9.6 ± 0.1 was maintained throughout every run by controlled gassing of the cell with anhydrous ammonia vapor.

Twenty-four different types of solutions (Table I) were used for cathode potential measurements. Hereafter, these various solutions are referred to by the symbol indicated under "Bath designation" in Table I. One liter of each of these solutions, except the "W" solution, was prepared from reagent or C.P. chemicals. Two liters of the "W" solution were prepared and one liter of this solution, called "Impure W", was used in making cathode potential runs without further treatment. The second liter of "W" solution was electrolyzed at 10 amp/dm^2 for 30 min between large Pt electrodes to remove, by electrodeposition, traces of other metals. This solution is called "Pure W". Each solution was adjusted to pH 9.6 with NH_4OH before an electrolysis run. Two hundred ml of each solution was placed in the cell for each cathode potential run.

In every solution (Table I) which contains metal ions, the total concentration of all nonalkali metal ions, regardless of species, was 0.3 m/l. Every solution, except the "W" and "NH_3 blanks," contained 0.75 m/l of citrate ion. The high concentration of citrate ions was used to provide an excess above that required for the formation of any possible complexes with metal ions. Furthermore, the large quantity of ammonium hydroxide and ammonium ion were sufficient to form all possible ammine complexes with metal ions and still have available free ammonia. No precipitation of iron(III) hydroxide was observed in the "Fe baths" except on prolonged standing.

Concentration control of the solutions was partially maintained with the use of a Lucite cover over the cell. In no case was more than 50 mg (usually much less) of metal plated on the cathode. Since each fresh 200 ml aliquot used in a run contain approximately 10 g or more of metal, the decrease in metal ion concentration of a solution, due to electrodeposition, was less than 1%. Evaporation losses were too small to be apparent to the eye and such losses were approximately the same in every solution; therefore, increase in concentration due to evaporation introduced only a small and consistent error.

Other experiments had indicated that the use of Fe(III) or Fe(II) as the codepositing metal in the electrodeposition of W alloys made little difference

Table I. Composition of the solutions used in making cathode potential measurements; concentrated NH_4OH was added to every solution to pH 9.6

Bath designation	Bath components	Formula wt	Conc, m/l	Wt, g/l
"W"	$(NH_4)_2HC_6H_5O_7$	226	0.750	170
	$Na_2WO_4 \cdot 2H_2O$	330	0.300	99.0
"Ni"	$(NH_4)_2HC_6H_5O_7$	226	0.750	170
	$NiSO_4 \cdot 6H_2O$	263	0.300	78.9
"W-Ni"	$(NH_4)_2HC_6H_5O_7$	226	0.750	170
	$Na_2WO_4 \cdot 2H_2O$	330	0.150	49.5
	$NiSO_4 \cdot 6H_2O$	263	0.150	39.4
"Cu"	$(NH_4)_2HC_6H_5O_7$	226	0.750	170
	$CuSO_4 \cdot 5H_2O$	250	0.300	74.9
"W-Cu"	$(NH_4)_2HC_6H_5O_7$	226	0.750	170
	$Na_2WO_4 \cdot 2H_2O$	330	0.150	49.5
	$CuSO_4 \cdot 5H_2O$	250	0.150	37.5
"Citrate blank"	$(NH_4)_2HC_6H_5O_7$	226	0.750	170
"Fe(III)"	$(NH_4)_2HC_6H_5O_7$	226	0.750	170
	$Fe_2(SO_4)_3 ca.6H_2O$	ca.508	0.150	76.2
"W-Fe(III)"	$(NH_4)_2HC_6H_5O_7$	226	0.750	170
	$Na_2WO_4 \cdot 2H_2O$	330	0.150	49.5
	$Fe_2(SO_4)_3 ca.6H_2O$	ca.508	0.075	38.1
"Fe(II)"	$(NH_4)HC_6H_5O_7$	226	0.750	170
	$FeSO_4 \cdot 7H_2O$	278	0.300	83.4
"W-Rich Fe(III)"	$(NH_4)_2HC_6H_5O_7$	226	0.750	170
	$Na_2WO_4 \cdot 2H_2O$	330	0.010	3.30
	$Fe_2(SO_4)_3 ca.6H_2O$	ca.508	0.145	73.7
"Rich W-Fe(III)"	$(NH_4)_2HC_6H_5O_7$	226	0.750	170
	$Na_2WO_4 \cdot 2H_2O$	330	0.290	95.7
	$Fe_2(SO_4)_3 ca.6H_2O$	ca.508	0.005	2.54
"Mo"	$(NH_4)_2HC_6H_5O_7$	226	0.750	170
	$Na_2MoO_4 \cdot 2H_2O$	242	0.300	72.6
"Cr"	$(NH_4)_2HC_6H_5O_7$	226	0.750	170
	$Na_2CrO_4 \cdot 4H_2O$	234	0.300	70.2
"W-blank"	$Na_2WO_4 \cdot 2H_2O$	330	0.300	99.0
"NH_3 blank"	A few drops of conc. NH_4OH added to H_2O to pH 9.6			
"Cd"	$(NH_4)_2HC_6H_5O_7$	226	0.750	170
	$CdSO_4 \cdot 8/3H_2O$	257	0.300	76.9
"W-Cd"	$(NH_4)_2HC_6H_5O_7$	226	0.750	170
	$Na_2WO_4 \cdot 2H_2O$	330	0.150	49.5
	$CdSO_4 \cdot 8/3H_2O$	257	0.150	38.5
"Ag"	$(NH_4)_2HC_6H_5O_7$	226	0.750	170
	Ag_2SO_4	312	0.150	46.8
"W-Ag"	$(NH_4)_2HC_6H_5O_7$	226	0.750	170
	$Na_2WO_4 \cdot 2H_2O$	330	0.150	49.5
	Ag_2SO_4	312	0.075	23.4
"Zn"	$(NH_4)_2HC_6H_5O_7$	226	0.750	170
	$ZnSO_4 \cdot 7H_2O$	288	0.300	86.3
"W-Zn"	$(NH_4)_2HC_6H_5O_7$	226	0.750	170
	$Na_2WO_4 \cdot 2H_2O$	330	0.150	49.5
	$ZnSO_4 \cdot 7H_2O$	288	0.150	43.1
"Mn"	$(NH_4)_2HC_6H_5O_7$	226	0.750	170
	$MnSO_4 \cdot H_2O$	169	0.300	50.7
"W-Mn"	$(NH_4)_2HC_6H_5O_7$	226	0.750	170
	$Na_2WO_4 \cdot 2H_2O$	330	0.150	49.5
	$MnSO_4 \cdot H_2O$	169	0.150	25.4

in the appearance or nature of the deposit. As can be seen in the graphical presentation of the data, there is little difference in the cathode potentials in Fe(III) and Fe(II) solutions in the higher current density (plating) ranges. Although Mo and Cr do not codeposit with W, the cathode potentials in their solutions were observed so that they could be compared with the W solution.

The Pt cathode was prepared for each run by soaking it overnight in concentrated HCl to dissolve the electrodeposit from the Pt and provide a fairly uniform surface. In those cases where Cu or Ag was deposited on the cathode, it was first placed in dilute HNO_3 to dissolve the plate and then rinsed and treated as above. The cathode was polished gently on fine metallographic paper only when absolutely necessary. Before placing it in the cell, the cathode was thoroughly rinsed, brushed with a moderately stiff bristle brush which had been dipped in concentrated HCl, and again rinsed with water. The anode was treated in a similar manner. In spite of these preparations the starting condition of the cathode surface was not exactly the same at the beginning of every run; this is no doubt one of the reasons for the lack of reproducibility of cathode potentials at low current densities.

No difficulty was encountered with the maintenance of the calomel reference electrode. It was allowed to stand between experiments in a saturated solution of KCl. The electrode was checked before each run to be certain it and the side arm extension were full of solution, and to be sure that there was undissolved KCl in the column. No contamination of this electrode by the highly colored electrolysis solutions was observed.

Experimental Results

The solutions used (Table I) are conveniently divided into four classes, according to the type of cathode reaction, as follows: Class 1, solutions from which an alloy deposit containing W was obtained upon electrolysis, i.e., the "W-Ni", "W-Fe(III)", "W-Rich Fe(III)", and "Rich W-Fe(III)"; Class 2, solutions from which a deposit containing no W was obtained upon electrolysis, i.e., the "Cu", "W-Cu", "Zn", "W-Zn", "Fe(II)", "Fe(III)", "Cd", "W-Cd", "Ag", "W-Ag", and "Ni" baths; Class 3, solutions from which no deposit was obtained on electrolysis, i.e., the "Impure W", "Pure W", "Mn", "W-Mn", "Mo", and "Cr" baths; and Class 4, blank solutions, i.e., the "W blank", "NH_3 blank", and "Citrate blank" baths.

The cathode potential data obtained in the various solutions are presented in Fig. 2-5. In Fig. 4 parts of the curves for the "W-Mn" and "Cr" baths and all of the curve for the "Mo" bath are not shown because they lie within a region crowded with curves from other baths and the missing parts of the curves follow the trends shown in the crowded part of the graph. Cathode potentials for values of the cell current below 0.10 ma were not reproducible and are not shown. The potential data are for average values of the cathode potentials for multiple runs with a given solution at any given current. The values of "I" are for the total cell currents of

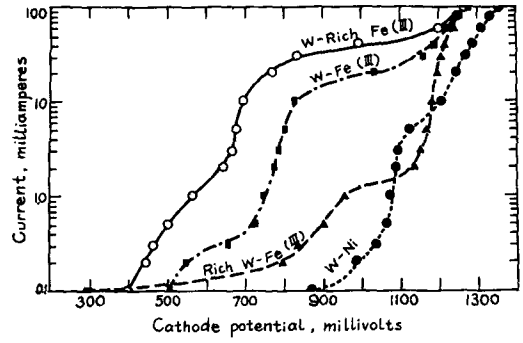

Fig. 2. Class 1 solutions (see Table I for all compositions) give alloy deposits containing W.

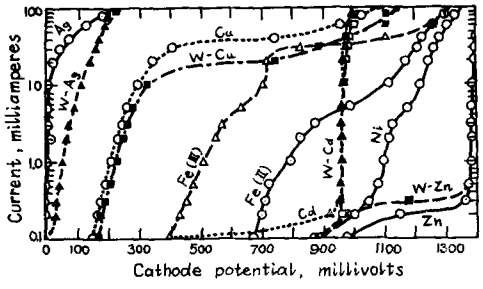

Fig. 3. Class 2 solutions give metal deposits containing no W

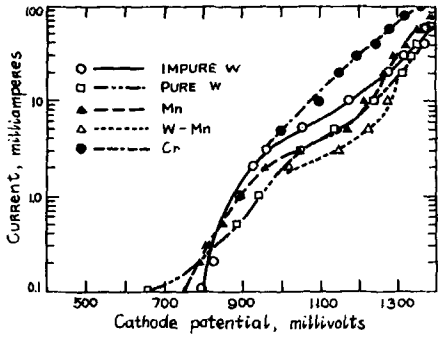

Fig. 4. Class 3 solutions—no deposit forms

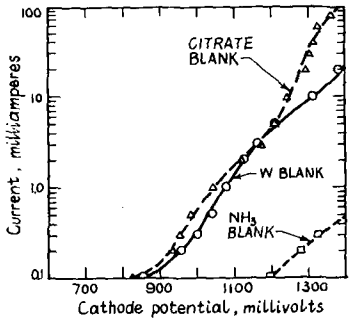

Fig. 5. Class 4 solutions—blank solutions

the electrolysis cell and may be converted to current density in amp/dm^2 by dividing any value of "I" by twelve.

Shown in Table II are the average maximum deviations of the cathode potentials from the average cathode potential (average of the several runs for a given current density and solution) for each of the 24 types of baths. The greatest deviations of the cathode potential from the average for each type of bath are also shown. The data for this table were compiled from the experimental data tables which are not included here. The average of average maximum deviations is 11 mv, and the average of the greatest deviations is 27 mv. Therefore, the average

Table II. Table of maximum deviations of cathode potentials

Bath designation	Class	Avg of maximum deviations from avg cathode potential	Greatest deviation from avg cathode potential
"W-Ni"	1	9	18
"W-Fe(III)"	1	12	26
"W-Rich Fe(III)"	1	19	26
"Rich W-Fe(III)"	1	12	49
"Cu"	2	14	297*
"W-Cu"	2	14	59
"Zn"	2	5	19
"W-Zn"	2	2	8
"Fe(II)"	2	16	37
"Fe(III)"	2	14	22
"Cd"	2	8	125*
"W-Cd"	2	5	8
"Ag"	2	6	23
"W-Ag"	2	8	16
"Ni"	2	11	36
"Impure W"	3	22	44
"Pure W"	3	27	55
"Mn"	3	10	24
"W-Mn"	3	13	29
"Mo"	3	7	16
"Cr"	3	12	28
"W Blank"	4	6	26
"NH_3 blank"	4	6	8
"Citrate blank"	4	3	8
		11	Avg. 27

* Not included in calculation.

reproducibility of the cathode potentials in all the solutions will be referred to as plus or minus 20 mv from the cathode potential indicated at any particular current density for any given solution. In averaging the greatest maximum deviations of the cathode potentials, two values, 297 mv for the "Cu" bath and 125 mv for the "Cd" bath were deleted before computation. The 297 mv deviation for the "Cu" bath is not due to poor data, but is a cathode potential taken at a very nearly horizontal portion of the "Cu" bath curve (*see* Fig. 3). A horizontal portion of such a curve, i.e., rapidly changing cathode potential at constant "I", is a region where no reaction is occurring at the cathode. In measurements of this type, it is rarely possible to get reproducible results on a flat portion of a curve, and a large deviation is not considered poor reproducibility. The 125 mv deviation for the "Cd" bath is not explained and must be considered experimental error. In general, reproducibility of cathode potentials is better in the intermediate current range, from 0.5 ma to 50 ma, than at very low or high currents probably because there is no reversible electrode reaction to stabilize the cathode potential at very low currents and there are fast irreversible electrode reactions that cause severe oscillation of the cathode potential at high currents. Storage of some solutions for several weeks between the first and duplicate runs also probably affected reproducibility of the results. Certainly with the various baths containing Fe, the relative amounts of Fe(III) and Fe(II) would change on prolonged standing. The Vinyon diaphragm allowed comparatively free passage of the solution, and it, plus the gassing with He, minimized contamination of the cathode by anodic oxygen but could not completely eliminate it. Oxygen arriving at the cathode would, of course, alter the cathode potential. A reaction is occurring at the cathode on rising portions of a log "I" vs. cathode potential curve. The greater the slope, the better is the reproducibility perhaps because a moderately fast series of cathode reactions stabilize the cathode potentials.

It is seen in the curves for the "Cu" and "W-Cu" baths (Fig. 3) that there is a large initial rise in the cell current which indicates a reaction at the cathode, probably the reduction of Cu(II) to Cu(I). This was verified by inspection which showed there was no hydrogen evolution and no deposition occurring for the condition corresponding to the first steep rise of these curves. Similarly, the initial rise in the curves for the several "Fe" baths (Fig. 3) is due to the reduction of Fe(III) to Fe(II).

In Fig. 4 all of the curves are close together. This represents the data for Class 3 solutions, i.e., those baths from which no deposit was obtained upon electrolysis. This figure also shows that the curves for the more active metals are on the right side of the graphs as would be expected. In comparing the curves for the various alloy baths with the baths containing only one metal, it is indicated that, although the presence of the tungstate ion always shifts the codepositing metal ion curve toward the "W" bath curve, the alloy curve is more nearly similar to its pure codepositing metal curve. This influence varies with the relative concentrations of tungsten to codepositing metal as seen with the "W-Rich Fe(III)" and "Rich W-Fe(III)" baths (Fig. 2); nevertheless, the codepositing metal influences the position of the curve more strongly than does the W. It is possible that the shift of the various "W-Fe(III)" bath curves toward the "W" bath curve could be due to a weakly associated complex between Fe(III) and/or (II) ions, tungstate ion, and citrate ion; however, the data do not strongly support the suggestion of such a complex.

The three blank solutions were studied so that their curves could be compared to those for the "W" baths. Fig. 5 shows that the curves for the "W blank" and the "Citrate blank" are similar to the curves for the "Pure W" and "Impure W" baths. This simply indicates that neither tungstate ion nor citrate ion have any special effect on the cathode potential. The curves obtained are due primarily to cathodic hydrogen released from buffered solutions of *p*H 9.6.

Additional experiments were made with the "Pure W", "W-Cu", "Ni", "Citrate blank", and "Fe(III)" baths to determine when hydrogen evolution began. This was accomplished by careful inspection of the solutions during electrolysis with the aid of a strong light which illuminated the cathode. It was necessary to stop stirring and gassing when making these observations and it was then possible to see the first traces of hydrogen bubble formation. In every case it was observed that hydrogen evolution began at a cathode potential of approximately 900 mv. These data do not support the suggestion that the presence of the tungstate ion in a solution

lowers the overvoltage of hydrogen on the cathode and therefore makes hydrogen evolution easier than tungsten deposition. The lowering of hydrogen overvoltage is not considered a good explanation of why pure tungsten has not been electrodeposited from aqueous solutions.

Latimer (15) gives the following values, in kcal/mole, for the free energy of formation of several aqueous anions: —220 for $WO_4^=$, —218.8 for MoO_4^-, —176.1 for $CrO_4^=$ and —107.4 for MnO_4^-. These values indicate very high thermodynamic stability of the aqueous tungstate, molybdate, and chromate ions in comparison to the permanganate ion. It is seen from the data that large energies are necessary to free W, Mo, or Cr from aqueous solutions of their ions and it would be predicted that the electrodeposition of W and Mo from aqueous solutions would be accomplished with difficulty, if at all. It is probable that there is an activation energy barrier, in addition to the free energy of formation, which must be overcome in the reduction of the aqueous tungstate, molybdate, and chromate ions to their respective metals. Cr is electrodeposited only with difficulty and with average cathode current efficiencies of approximately 15%, while pure W and Mo apparently have not been electrodeposited from aqueous solution.

Conclusions

In the plating region, i.e., 24 ma (2 amp/dm^2) and above, the cathode potentials in the various solutions are as follows: "Impure" and "Pure W" baths 1330-1375 mv, "W-Ni" bath 1250-1355 mv, "W-Fe(III)" bath 1100-1275 mv, "W-Rich Fe(III)" bath 780-1265 mv, "Rich W-Fe(III)" bath 1200-1270 mv (Fig. 4 and 2). These data show that the cathode potentials of the four alloy baths come to within 85 mv of the average cathode potential in the "W" baths. Fig. 3 shows that cathode potentials in baths other than those containing Fe or Ni are considerably more than 85 mv from the average cathode potential in the "W" baths. It is emphasized that only comparative values of the cathode potentials shown in these data are considered significant. Similar experiments would show the same relative positions of the cathode potentials of various baths compared with one another as are reported here, but would probably show different absolute values.

The following hypothesis is offered as the explanation of why pure metallic W has not been electrodeposited from aqueous tungstate ion solutions and why W codeposits with certain other metals: (*a*) aqueous tungstate ion has a very high thermodynamic stability which must be overcome to permit deposition of metallic W; (*b*) in the reactions involved in the over-all mechanism of the reduction of the aqueous tungstate ion to metallic W there is probably, in addition to the free energy of formation, an activation energy barrier which must be overcome; and (*c*) the electrostatic repulsion which exists between the negatively charged aqueous tungstate ion and the negatively charged cathode probably prevents the ion from coming sufficiently close to a cathode to allow transfer of the quantity of energy from cathode to ion necessary to overcome the free energy of formation of the ion and the activation energy barrier which probably exists in the reduction process.

Tungsten codeposits with certain metals such as Ni, Co, and Fe from aqueous tungstate ion, metal ion solutions because a freshly deposited surface of the codepositing metal has the catalytic effect of reducing the magnitude of the activation energy barrier which probably exists in the mechanism of reduction of the aqueous tungstate ion to metallic W. In order for a metal to codeposit with W from aqueous tungstate ion, metal ion solutions it must have the following properties: (*a*) the codepositing metal must electrodeposit from the solution under consideration; (*b*) the codepositing metal must be added to the solution as a simple cation; (*c*) the cathode potential in an aqueous solution of the codepositing metal, both with and without tungstate ion present in the solution, must be within 85 mv of the cathode potential in a similar solution containing tungstate ion but no codepositing metal ion while the solutions are being electrolyzed at a current density of 2 amp/dm^2 or higher; and (*d*) the codepositing metal must have catalytic properties, i. e., it will probably be a transition element.

Acknowledgment

Appreciation is expressed to the United States Army for its sponsorship of the junior author and to R.W. Schmelzer for assistance in construction of apparatus.

Manuscript received July 9, 1956. This paper was prepared for delivery before the Cleveland Meeting, Sept. 30 to Oct. 4, 1956, and was abstracted from the thesis of D. R. Markwell submitted in partial fulfillment of the requirements for the Ph.D. degree at the University of Wisconsin.

Any discussion of this paper will appear in a Discussion Section to be published in the June 1958 JOURNAL.

REFERENCES

1. M. L. Holt and L. E. Vaaler, *J. (and Trans.) Electrochem. Soc.*, **94**, 50 (1948).
2. W. E. Clark and M. H. Lietzke, *This Journal*, **99**, 245 (1952).
3. Z. A. Solov'eva and A. T. Vagramyan, *Invest. Akad. Nauk, otdel Khim. Nauk.*, 230 (1954); *C. A.*, **48**, 13487 (1954).
4. T. P. Hoar and I. A. Bucklow, *Chemistry & Industry*, **1955** 1061.
5. A. G. Pecherskaya and V. V. Stender, *Doklady Akad. Nauk S. S. S. R.*, **75**, 831 (1950); *C. A.*, **45**, 3261 (1951).
6. C. G. Fink and F. L. Jones, *Trans. Electrochem. Soc.*, **59**, 461 (1931).
7. C. G. Fink, U. S. Pat. 1,885,700; 1,885,701; 1,885,702, Nov. 1, 1932.
8. M. L. Holt, *Trans. Electrochem. Soc.*, **66**, 453 (1934).
9. M. L. Holt, *ibid.*, **71**, 301 (1937).
10. R. O. Hull, U. S. Pat. 2,149,344, March 7, 1939.
11. F. Haber, *Z. physik. Chem.*, **32**, 193 (1900).
12. R. Piontelli, *Z. Elektrochem.*, **55**, 128 (1951).
13. M. Eisenberg, C. W. Tobias, and C. R. Wilke, *This Journal*, **102**, 415 (1955).
14. I. M. Kolthoff and J. Jordan, *J. Am. Chem. Soc.*, **76**, 3843 (1954).
15. W. M. Latimer, "The Oxidation States of the Elements and Their Potentials in Aqueous Solutions," 2nd ed., Prentice-Hall, Inc., New York (1952).

Investigations on the Structure of the Color Compound in Caustic

S. Wawzonek and D. S. P. Eftax

Department of Chemistry, State University of Iowa, Iowa City, Iowa

ABSTRACT

The material isolated by Heller from stubs of graphite anodes used in chlorine-caustic soda cells and shown by him to give the color in concentrated caustic soda has been reinvestigated. An extract from the stubs after treatment with nitric acid was found to consist of mellitic acid, pentacarboxychlorobenzene, a tetracarboxychlorobenzene of unknown configuration, and material of unknown structure which is the source of the color. The acids were formed during the treatment with nitric acid. The color forming material seems to be of high molecular weight and structurally more complex than proposed by Heller.

The organic nature of the material giving the familiar color (1) to the evaporated effluent from diaphragm chlorine-caustic soda cells was first established by Heller (2) who proposed for it a pyromellitic acid-chloroquinol structure (I). Since dienones in which a hydrogen is involved are unknown because of their facile rearrangement to the corresponding phenols, a further study of the material was suggested.

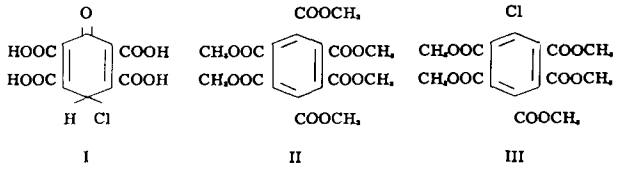

Results

The procedure for the investigation is summarized in the flow sheet (below).

By methylation of the yellow material with diazomethane an oil was obtained from which hexamethyl mellitate (II), pentamethyl chlorobenzenepentacarboxylate (III), and a tetramethyl dichlorobenzenetetracarboxylate were recovered by sublimation, distillation under reduced pressure, fractional crystallization, or chromatographic separation on alumina. The structure of pentamethylchlorobenzenepentacarboxylate (III) was demonstrated by comparison with a sample synthesized from pentamethylchlorobenzene (4). The tetramethyl dichlorobenzenetetracarboxylate was not obtained in sufficient quantities to be characterized. These three compounds did not give a color in 50% caustic.

The red residual oil obtained after removal of these compounds could not be distilled, sublimed, or crystallized and upon treatment with alkali dissolved slowly and gave a reddish purple color. This oil after treatment with HBr gave a solid which was water soluble and gave the reddish purple color with alkali.

An aqueous solution when passed through a cation exchange resin (IR-120H) gave an eluate which, on removal of the solvent, yielded a red amorphous powder. This product could not be purified further by recrystallization and was obtained in insufficient amounts to characterize further.

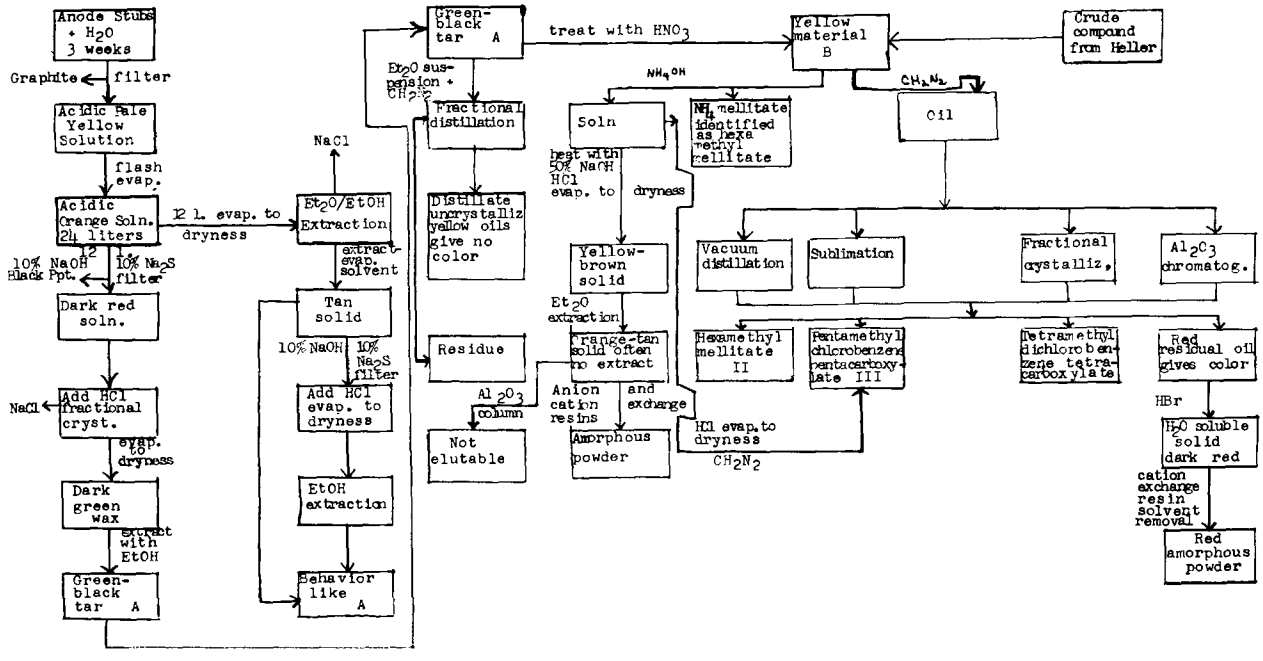

The mellitic acid could also be isolated from the yellow solid as the ammonium salt hexahydrate by treatment with concentrated ammonium hydroxide. The structure of this salt was demonstrated by acidification and conversion to the methyl ester. The mother liquor from the ammonium mellitate after acidification and methylation gave pentamethyl chlorobenzenepentacarboxylate.

The presence of mellitic acid in the yellow solid raised the question whether this acid was produced from the graphite anodes directly during the formation of the caustic or was formed in the isolation by the recrystallization step using concentrated HNO_3. Following the isolation procedure of Heller but omitting the recrystallization from HNO_3 gave a dark green tar which produced a dark purple color when boiled with 50% caustic. Methylation of an ether suspension of the tar followed by fractional distillation under reduced pressure gave yellow oils which refused to crystallize even when seeded with the esters mentioned. The oils gave no color with 50% alkali. The dark green tar when treated with HNO_3 gave an orange solid which showed similar properties to those of Heller's material. These results indicated that the recrystallization from HNO_3 degraded the more complex compounds formed from the anode during cell operation into the simpler acids. The dark green tar did not contain any suspended carbon so that the latter could be ruled out as the source of the mellitic acid.

This degradation of the complex mixture obtained from the anodes by HNO_3 into simpler compounds suggested a direct study of the compound which formed the purplish-blue color in 50% caustic. The filtrate from the precipitation of the mellitic acid as the ammonium salt was heated with 50% caustic until the bluish-purple color developed. Acidification with HCl followed by evaporation to dryness gave a yellow-brown solid. This material occasionally would give, upon ether extraction in a Soxhlet extractor, a small amount of orange-tan material which produced the bluish-purple color immediately in cold 50% caustic. This behavior was not consistent and, in the majority of the attempts, the extraction did not give any ether soluble solids. Further chromatography was not successful due to the strong adsorption on the column.

Purification of the material by passing through cation and anion exchange resins gave an amorphous powder which resisted crystallization and further purification.

The results obtained with Heller's compound indicated that at least 70% of his material consisted of mellitic acid, pentacarboxychlorobenzene, and tetracarboxydichlorobenzene. The physical data reported for the pyromellitic acid chloroquinol (I) approximate very closely the values for pentacarboxychlorobenzene (IV) as shown below,

	I	IV
%C	39.7	39.7
%H	1.68	1.51
%Cl	11-12	10.66
Neutral equiv.	75	66.5
Mol. wt.	305	337.5

and are in agreement with such a formulation.

The properties of the residue obtained after separating the simpler acids indicate that the compound or compounds responsible for the color in caustic have a higher molecular weight and are more complicated than the compound proposed by Heller.

Experimental[1]

1. *Methylation of Heller's compound.*—An ether solution of 3 g (0.07 mole) of diazomethane was added slowly, with constant swirling, to 2 g (0.006 mole based on mellitic acid) of Heller's material dissolved in 40 ml of methanol or suspended in 40 ml of ether. After the initial liberation of nitrogen, the dark solution was heated at 100° overnight and gave approximately 2.7 g of a dark viscous oil.

2. *Pentamethyl chlorobenzenepentacarboxylate (III) and hexamethyl mellitate (II):*

(*a*) *Chromatography.*—A solution of the oil in benzene was subjected to chromatography on an alumina column followed by elution with benzene and ether. By fractional crystallization of the first benzene eluate 0.6 of crude or 0.15 g of pure III was obtained and from the subsequent eluates 1 g of crude or 0.3 g of pure II.

(*b*) *Sublimation.*—By sublimation under 1 mm Hg pressure in a bath at 135°C there was obtained 1.2 g of crude or 0.65 of pure III. The temperature of the bath was then raised. At approximately 200°C 0.8 g of crude or 0.3 g of pure II sublimed.

(*c*) *Crystallization.*—Fractional crystallization from a mixture of benzene and petroleum ether (bp 60°-70°C) gave 0.6 g of crude II or 0.15 g of pure compound.

(*d*) *Distillation.*—Distillation at reduced pressure (1 mm Hg) gave a fraction boiling between 180° and 200°C which weighed 1 g and contained mostly III. The fraction boiling at 200°-220° gave 0.5 g of crude II or 0.35 g of pure III.

The pure hexamethyl mellitate (II) was obtained from the crude material separated by several recrystallizations from a mixture of benzene and petroleum ether (bp 60°-70°C) and melted at 185°-186.5°C. In some instances decolorizing carbon was used to eliminate traces of red impurities. A mixture with an authentic sample (3) melted at the same point.

The pure pentamethylchlorobenzenepentacarboxylate (III) formed colorless needles after several recrystallizations of the crude ester from a mixture of ether-petroleum ether (bp 60°-70°) and melted at 129°-130°C.

Anal. Calcd. for $C_{16}H_{15}O_{10}Cl$: C, 47.71; H, 3.75; OCH_3, 38.50; mol. wt., 403.

Found: C, 48.12; H, 3.57; OCH_3, 38.70; mol. wt., 418.

This ester was synthesized from pentamethylchlorobenzene (4) in the following manner.

Pentamethylchlorobenzene (2 g) was heated with $KMnO_4$ (30 g) in 500 ml of water containing 5 ml of 10% NaOH at 100° until all the organic material had disappeared. This process required two weeks. The resulting mixture was decolorized with sodium

[1] Melting points and boiling points are not corrected.

bisulfite, acidified, and filtered. The crude acid (1 g) was recovered from the extraction of the filtrate in a liquid-liquid ether extractor as a brown solid. This acid was not purified further but was suspended in 20 ml of methanol and treated with an excess of diazomethane in ether. Recrystallization of the resulting solid several times from a mixture of ether-petroleum ether (bp 60°-70°C) followed by a sublimation at reduced pressure (1 mm Hg) gave long colorless needles (0.25 g) melting at 130°. A mixture with a sample isolated from the caustic color compound melted at the same point.

3. *Tetramethyl dichlorobenzenetetracarboxylate.*—The mother liquors from the recrystallization of pentamethyl chlorobenzenepentacarboxylate were evaporated to dryness and the residue was sublimed at 90°C under reduced pressure (1 mm Hg). The resulting oil after several recrystallizations from a mixture of ether-petroleum ether (bp 60°-70°C) gave small colorless needles melting at 80°-85°C.

Anal. Calcd. for $C_{14}H_{12}O_8Cl_2$: C, 44.34; H, 3.19; OCH_3, 32.74; mol. wt., 379.

Found: C, 44.04; H, 3.28; OCH_3, 32.17; mol. wt., 363, 324.

4. *Ammonium mellitate hexahydrate.*—A solution of 2 g (0.006 mole based on mellitic acid) of Heller's crude caustic color in 10 ml of 95% ethanol containing a few drops of acetic acid, was treated with a small excess of concentrated ammonium hydroxide. The crystals that precipitated on standing were filtered and recrystallized three times from ethanol-water mixtures and gave 0.55 g (16%) of colorless needles that melted with decomposition in the vicinity of 100°C. A sample of caustic color weighing 3.35 g, which had been recrystallized once from 60% HNO_3, gave 1.25 g (22%) of pure ammonium salt. The yield of the ammonium salt ranged from 10-40% depending on the purity of the sample.

Anal. Calcd. for $C_{12}H_{36}O_{18}N_6$: C, 26.09; H, 6.57; N, 15.21.

Found: C, 26.03; H, 6.42; N, 15.31.

By treatment with hot HNO_3 the salt was converted to mellitic acid which melted at 275° with decomposition in an open capillary tube. This acid is reported to melt at 288° in a sealed one (5). A sample of hexamethyl mellitate obtained by reaction of the acid with diazomethane melted at 184.5°-186°C.

The mother liquor after recrystallization of the ammonium mellitate was acidified with dilute HCl and allowed to evaporate to dryness. The tan to brownish-red solids thus obtained were suspended in ether (2 g), and treated with 1.5 g (0.035 mole) of an ether solution of diazomethane at 0°C for 2 hr. The ether was decanted and evaporated. On sublimation at 135°-145°C at 1 mm Hg, the resulting red wax (1 g) obtained gave 0.6 g of a crude product. Recrystallization of the sublimate from an ether-ligroin (bp 60°-70°C) mixture after decolorization with Norit gave colorless needles melting at 129°-130°C. A mixture with a synthetic sample of pentacarbomethoxychlorobenzene showed no depression in melting point.

5. *Isolation of caustic color.*—Used graphite anodes (100 kg) were placed in a wooden barrel containing about 110 l of water and allowed to soak for three weeks. The liquid was filtered from traces of graphite and gave approximately 95 l of an acidic pale yellow solution. This solution was concentrated to 24 l of an orange colored solution using a flash evaporator and was treated in the following two ways:

(*a*) The orange solution (12 l) was made basic with 10% aqueous NaOH and metallic salts were removed by adding a 10% solution of sodium sulfide until precipitation ceased. The resulting mixture was centrifuged from the black precipitate and gave a dark red solution. Acidification with concentrated HCl was followed by repeated fractional crystallization to remove the salt and then evaporation to dryness. The dark green wax obtained was extracted in a Soxhlet extractor with absolute ethanol. Removal of the solvent gave 25 g of a green-black tar which produced a dark purple color when boiled with 50% caustic. Methylation of an ether suspension of this tar with diazomethane followed by distillation at reduced pressure (1 mm Hg) gave only small amounts of a yellow oil which did not crystallize and did not give a color upon heating with alkali. Treatment of the tar with concentrated HNO_3 followed by diazomethane gave hexamethyl mellitate and pentamethyl chlorobenzenepentacarboxylate.

(*b*) The orange solution (12 l) was allowed to evaporate to dryness. By extraction of the resulting dark yellow solid with absolute ether in a Soxhlet apparatus, 9 g of a tan material was recovered. An additional 6 g was obtained by extracting the salts with absolute ethanol. Methylation of these solids with diazomethane, as mentioned above (*a*), with or without the sodium sulfide treatment gave similar oils to those mentioned in (*a*).

Studies on the Isolation of the Caustic Color Compound

Acid hydrolysis.—The residue remaining after removal of the mellitic acid and the chloropentacarboxybenzene as the methyl esters was hydrolyzed with HBr for 10 hr. Evaporation of the solution gave a dark red powder which was separated from inorganic salts by passing an aqueous solution through a cation exchange resin (IR-120H). Removal of the solvent from the eluate gave a red amorphous powder which produced a dark purple color on standing in 50% caustic. This powder gave no ash on prolonged heating and could not be purified further by recrystallization. Aqueous solutions were found to absorb strongly at 2230Å and weakly at 2800Å in the ultraviolet region. The powder contained chlorine and was obtained in insufficient amounts to characterize further.

Basic hydrolysis.—The aqueous solution remaining from the precipitation of the mellitic acid as the ammonium salt was heated with 50% NaOH until a bluish-purple color developed. Acidification with concentrated HCl followed by evaporation to dryness gave a yellow-brown solid. Extraction of this solid in a Soxhlet extractor with absolute ether

gave a very small amount of orange-tan material which produced the bluish-purple color with cold 50% caustic immediately. The material melted in the vicinity of 170°C with decomposition and gave no color with aqueous ferric chloride.

The compound when added in ether to an alumina column could not be eluted with ether, ethyl acetate, methanol, or water. Treatment of the alumina with alkali followed by acidification gave salts from which the orange-tan material could be again extracted with ether. This material contained chlorine and gave broad absorption bands in the 5.9 μ and 8 μ infrared region. The first band is in the carbonyl region and, due to its broadness, is considered to represent several of these groups. The band at 8 μ is in agreement with such a structure.

The production of the ether soluble compound with alkali was difficult to repeat consistently and prevented the accumulation of enough material to carry out further studies. In most cases ether extraction of the material gave no product.

The yellow-brown material dissolved in water was passed through a cation exchange resin (IR-120H) and then through an anion exchange resin (IR-4B). The red eluate upon removal of the water gave a dark material which turned purple when exposed to light. This purple powder gave absorption peaks in the ultraviolet region at 2245Å and 2230Å and a broad band at 5200Å in the visible region.

Acknowledgment

The authors wish to thank Harold H. Heller of the Kimberly-Clark Corporation, Neenah, Wis., for the original sample of caustic color compound, subsequent supplies of used graphite anodes, and the procedure for the isolation of the caustic color compound. They also wish to thank Milton Janes, who reviewed the manuscript, for suggesting and making the flow sheet presented in this paper.

Manuscript received June 18, 1956. This paper was abstracted from the Thesis of D. S. P. Eftax submitted to the State University of Iowa in partial fulfillment of the requirements for the Ph.D. degree, June 1956.

Any discussion of this paper will appear in a Discussion Section to be published in the June 1958 JOURNAL.

REFERENCES

1. M. Janes, N. J. Johnson, and E. B. Pilcher, *This Journal*, **102**, 474 (1955).
2. H. H. Heller, *Trans. Electrochem. Soc.*, **87**, 501 (1945).
3. O. Diels and K. Alder, *Ann.*, **498**, 16 (1932).
4. P. S. D de La Mare and P. W. Robertson, *J. Chem. Soc.*, **1943**, 279.
5. L. F. Fieser and M. Fieser, "Organic Chemistry," p. 677, D. C. Heath and Co., Boston (1944).

Electrolytic Reduction of Nitrobenzene to Hydrazobenzene

Kiichiro Sugino and Taro Sekine

Laboratory of Organic Electrochemistry, Department of Chemical Engineering,

Tokyo Institute of Technology, Tokyo, Japan

ABSTRACT

In small scale experiments on the electrolytic preparation of hydrazobenzene from nitrobenzene in alkaline emulsion it was found that cathodes of zinc, tin, cadmium, and lead with more than 0.07 mole of spongy layer per square decimeter of the surface were most suitable for the reduction. As base materials for the spongy layers, common metals such as Pb, Fe, and others were found to be useful. At these cathodes, almost quantitative yields of hydrazobenzene were obtained at relatively high current densities with suitable agitation. The mechanism is believed to consist of true electrochemical reduction of nitrobenzene to azoxy- or azobenzene, followed by further chemical reduction of the azobenzene by sponge metal. The mechanism gains support from results of polarographic measurements which show that, while nitrobenzene is an active depolarizer with or without organic solvent in the catholyte, azobenzene is active only when a solvent such as alcohol is present.

In the interest of developing a practical electrochemical preparation of hydrazobenzene, preliminary runs have been made in a larger cell using 1.5 kg of nitrobenzene; material yields of hydrazobenzene up to 90% and current efficiencies of 80% at 17 amp/dm^2 have been obtained, compared with yields of 95% and efficiencies as high as 88% at 30 amp/dm^2 obtained with the small cell.

Interest in the electrolytic preparation of hydrazobenzene originally was based on the commercial importance of this product as an intermediate for acid rearrangement to benzidine. In Japan (1) hydrazobenzene has been produced by reduction of nitrobenzene with finely divided Zn. The cost of this reducing agent makes a practical electrochemical method attractive.

The first electrochemical reduction of nitrobenzene was carried out by Elbs and Kopp (2) at a Ni cathode in aqueous-alcoholic sodium acetate without stirring. The alcohol was added to keep the

Table I. Results of preliminary experiments

Run No.	Catholyte		Cathode	Cathodic current density, amp/dm²	Amount of current, amp-hr	Temp, °C	Yield (%) Hydrazobenzene	Yield (%) Azobenzene	Current efficiency of hydrazobenzene formation (%)
1	$C_6H_5NO_2$:	9.8 g	Fe, smooth	3.0-1.5	11.8	75-78	9	46†	8
	NaOH:	5 g							
	H_2O:	90 cc							
2	H_2O		Ni, gauze	3.0-1.5	10.8	75-78	0	97	0
3	$C_6H_5NO_2$:	9.8 g	Ni, gauze	3.0-1.5	11.1	75-78	53	35	52
	NaOH:	5 g							
	H_2O:	45 cc							
	Alcohol:	45 cc							
4	$C_6H_5NO_2$:	9.8 g	Zn, smooth	3-2	10.9	75-78	84	—	84
	NaOH (5-9%):	100 cc							
5	$C_6H_5NO_2$:	6.2 g	Zn, spongy, on Zn	7.2-4.8	8.5	80-85	92	4.5	72
	NaOH (10%):	60 cc							
6*	$C_6H_5NO_2$:	12.3 g	Zn, spongy, on Zn	12-7.2	16.0	70-80	93	0.6	77
	NaOH (10%):	60 cc							
7	$C_6H_5NO_2$:	12.3 g	Zn, spongy, on Fe gauze	12	17.5	70-80	23	32	17
	NaOH (10%):	60 cc							
8*	$C_6H_5NO_2$:	12.3 g	Pb, spongy, on Pb	12	16.0	70-80	90	3.3	75
	NaOH (10%):	60 cc							

* Toluene added to catholyte when conversion of nitrobenzene to azobenzene was approximately complete.
† Some azoxybenzene included. Runs No. 1-4, area of cathode, 80 cm², unglazed earthenware diaphragm; Runs No. 5-8, area of cathode, 42 cm², asbestos diaphragm.

azoxy compound in solution so that it could be reduced to hydrazo, which could then be oxidized to the azo by any remaining nitrobenzene or nitrosobenzene, according to the scheme of Haber (3). To obtain good current efficiency, Elbs and Kopp found it necessary to reduce the current density to about one fourth of the initial value in the final reduction of azo to hydrazo. McKee and Gerapostolou (4) using concentrated solutions of aromatic sulfonates to keep the depolarizers in solution, reduced nitrobenzene to hydrazobenzene at several cathodes, including Pb, Sn, and Zn, and with the addition of various salts. Their results were complicated by the formation of considerable amounts of aniline in the presence of copper sulfate or at bronze cathodes; they noted solubility of Pb and Zn cathodes in the alkaline electrolyte, as well as the beneficial effect of stirring, in increasing the rate of reduction of azobenzene.

Reduction of the nitro compound to the hydrazo without the use of a blending agent is described chiefly in early patent literature (5). In this work nitrobenzene, suspended by agitation in NaOH electrolyte of concentration up to 5%, was reduced at various cathodes including Fe, Ni, and Pb. Although conditions of electrolysis are inadequately described and identification of products often is insufficient, it was in this work that the importance of agitation as well as the effectiveness of addition of metals such as Zn, Sn, and Pb in promoting reduction beyond the azo level was first recognized. Some of this early work has been cited as showing that control of potential can determine the identity of the product obtained. Other patent literature of somewhat later date (6) describes the reduction of suspended nitrobenzene at about 90°C to hydrazobenzene at current densities up to 0.1 amp/cm² when Pb was added to the electrolyte. The use of hydrocarbons such as benzene as a solvent to keep the cathode surface free of adherent deposits was also introduced in some of this early work.

Most recently Dey, Govindachari, and Rajagopalan (7) reduced nitrobenzene to hydrazobenzene on a 1000 g scale in 10% NaOH at an Fe cathode with PbO added. They noted the deposition of spongy Pb on the cathode, but failed to confirm the effectiveness of some addition agents, including tin and zinc oxides, in promoting the formation of hydrazobenzene.

It was the purpose of the present research to clarify some of the points raised in the early literature, to investigate possible mechanisms whereby the electrolytic reduction of nitrobenzene can be directed to hydrazobenzene, and if possible to devise a practical electrochemical method superior to the usual zinc powder-alkali reduction.

Apparatus and Recovery of Products

The cell used for the preliminary experiments of Tables I and II consisted of a cylindrical glass container, 7 cm in height and 6.5 cm in diameter, centrally located within which was a porous pot diaphragm[1] to isolate the anode. A Ni plate within the porous pot served as anode, and the cathode was a sheet of any desired metal bent into the form of a cylinder approximately 3 cm high and resting against the wall of the cell vessel. In the catholyte space, which held approximately 60-100 cc of electrolyte, was a thermometer and a glass stirrer rotating at 1000-2000 rpm. For all small scale runs except those of Tables I and II an improved cell was used.

It consisted of a cylindrical glass beaker 8 cm in height and 9 cm in diameter on the bottom of which rested a Pt or Ni plate serving as anode. Supported above the anode and centrally located within the cell vessel was a glass cylinder 11 cm in height and 6 cm in diameter. The bottom of this cylinder was

[1] Made of unglazed earthenware or common asbestos cloth in three layers.

Table II. Effect of repeated electrolysis with a smooth and a spongy zinc cathode

Run No.	Catholyte	Cathode	Cathodic current density, amp/dm²	Amount of current, amp-hr	Material yield of hydrazobenzene (%)	Temp, °C	Current efficiency, %
1-a	$C_6H_5NO_2$: 9.8 g. NaOH (5-10%) : 100 cc.	Zn, smooth	2-3	10.9	84	92°-96°	84
1-b	(a)		2-3	12.0	81	92°-96°	73
1-c	(a)		2-3	12.0	86	92°-96°	78
1-d	(a)		2-3	12.0	85	92°-96°	77
2-a	$C_6H_5NO_2$: 12.3 g. NaOH (5%) : 60 cc.	Zn, spongy	12	17.5	77*	70°-80°	60
2-b	(b)		12	15.0	92	70°-80°	82
2-c	(b)		12	16.3	89	70°-80°	73
2-d	(b)		12	15.0	91	70°-80°	81

Run No. 1—Area of cathode 80 cm², unglazed earthenware diaphragm.
Run No. 2—Area of cathode 42 cm², asbestos diaphragm; toluene added.
* A low yield resulted from the inclusion of a part of the product in the diaphragm newly used.
(a) The restored catholyte of the same composition as in 1-a using the catholyte from the former run.
(b) The restored catholyte of the same composition as in 2-a using the catholyte from the former run.

closed with a diaphragm made of one layer of common asbestos cloth, as used for water electrolysis, which was treated with cement to adjust the porosity. Inside the cathode chamber formed by the glass cylinder, a horizontal metal disk 5 cm in diameter was connected to a vertical rod, stirring being accomplished by moving the rod and cathode disk up and down with an amplitude of 3 cm at 100 times/min (100 oscillations/min). The cell was provided with cover with reflux. After a reduction, the cooled catholyte separated into crude hydrazobenzene crystals along with an oily layer and an aqueous solution. The crystals were separated by filtration and dissolved in benzene to remove metallic contaminants. The benzene solution was combined with the oily layer which had been separated from the aqueous solution. After the benzene had been removed under diminished pressure, the solid residue was washed with 2% acetic acid to remove aniline, then with water, dried at 65°C, and weighed. It was then converted into benzidine by treating with 170 cc of 3.5% HCl at 55°-60°C for 4 hr. The undissolved residue, consisting mainly of azobenzene, was dried and weighed. The amount of hydrazobenzene was calculated by difference. The aqueous filtrate was steam distilled to remove aniline and the distillate acidified with acetic acid and combined with the 2% acetic acid wash solution described above. The amount of aniline in the combined distillate and wash was determined as tribromoaniline.

Results and Discussion

Results of preliminary experiments are summarized in Table I. In general, these confirm results of previous investigations reported in the literature. For example, runs 1, 2, and 3 show that with insoluble cathodes such as Fe and Ni, a substantial yield of hydrazobenzene can be obtained only if a solvent is added, as in run 3, to keep the azobenzene in solution. The higher efficiencies possible with Zn as cathode material are confirmed by results of run 4, *et. seq.*, of Table I. Note that the use of soluble Zn, even in the form of a smooth sheet, gives material yield and current efficiency of a higher order than the insoluble Fe and Ni, while the use of spongy Zn or Pb permits an increase of two to fourfold in current density without much sacrifice of current efficiency. The spongy metals were obtained by preliminary electrolysis in NaOH electrolyte, to which metal salt had been added, until the surface of the cathode appeared to be completely covered with electrodeposited sponge. Inferior results obtained with the Zn sponge when deposited on Fe gauze are attributed to incomplete coverage.

Toluene was added to remove coatings of azobenzene and other intermediate products which accumulate on the cathode and interfere with the electrolysis. It was added in runs 6 and 8 at about the time the nitrobenzene had been completely converted to the azo level. In these small scale experiments, the addition of the hydrocarbon did not affect the results very much when the catholyte was thoroughly agitated. However, on a manufacturing scale, it was found that smooth continuous operation seemed to be impossible without the addition of these hydrocarbons.

The results of two series of repeated electrolyses, one with smooth Zn and the other with a spongy Zn electrode are shown in Table II. In these experi-

Table III. Effect of alkali strength on formation of hydrazobenzene from nitrobenzene

Catholyte	Cathodic current density, amp/dm²	Amount of current, amp-hr	Yield (%) Hydrazobenzene	Azobenzene	Aniline
$C_6H_5NO_2$: 9.8 g NaOH (10%) : 100 cc	15	12.0	88	6	0.4
$C_6H_5NO_2$: 9.8 g NaOH (3%) : 100 cc	11	12.3	83	12	1.4

Cathode, spongy Zn on Zn; anode, Pt; anolyte, 100 cc 10% aqueous NaOH; temp, 75°-90°C.

Table IV. Reduction of nitrobenzene at spongy cathodes

Cathode	Cathodic current density, amp/dm²	Amount of current, amp-hr	Yield Hydrazobenzene, g	%	Azobenzene, g	%	Aniline, g	%
Pb	30	18.0	7.0	96	0	0	0.2	3
Cd	30	15.6	7.0	96	0	0	0.3	4
Zn	30	13.5	7.0	96	0	0	0.2	3
Sn	30	12.7	7.1	97	0	0	0.1	1

Anode, Pt; anolyte, 100 cc 10% aqueous NaOH; catholyte, 9.8 g nitrobenzene, 90 cc 10% aqueous NaOH, 10 cc benzene; 5.9 amp; temp, 57°-60°C.

Table V. Efficiency of different cathodes in reduction of nitrobenzene

Cathode	Cathodic current density, amp/dm²	Yield of hydrazobenzene g	Yield of hydrazobenzene %	Current efficiency %
Pb	30	4.7	65	65
Cd	31	4.8	66	66
Zn	29	6.0	82	82
Sn	36	6.4	88	88

Amount of current, 10.9 amp-hr; temp, 75°-80°C; other conditions as in Table IV.

ments the cathode and the catholyte were used in four successive runs. In both series the efficiency was maintained, although at different levels, depending on the cathode. Evidently no substance which would inhibit the reaction had accumulated.

From the preliminary work it was concluded that the electrolytic preparation of hydrazobenzene by reduction of emulsions of nitrobenzene in dilute alkali, without organic solvents, was a practical objective, and that the use of spongy forms of alkali soluble metals as cathode surfaces held promise of high current densities and relatively pure products. Accordingly, with the improved cell described above a more rigorous investigation of critical conditions was undertaken. For the preparation of the spongy cathodes the deposition of 0.07 mole of spongy metal/dm² of cathode surface was adopted as standard. This amount is relatively large compared with the coverage used in other investigations (4, 7), i.e., 0.019 and 0.004 mole/dm². Benzene was added to the catholyte to keep the cathode clean.

Table III compares 3% and 10% NaOH as catholyte under otherwise similar conditions of electrolysis. Since the stronger alkali gave higher yield of hydrazobenzene at considerably higher current density, 10% NaOH was used as catholyte in all subsequent experiments.

Four runs were carried out using Pb, Cd, Zn, and Sn as the cathode surface. The electrodes were prepared by depositing the spongy metal from catholyte initially containing, respectively, 3.0 g PbO, 3.7 g $CdSO_4$; $8/3H_2O$, 4.1 g $ZnS_4O \cdot 7H_2O$, and 3.2 g $SnCl_2 \cdot 2H_2O$. Each surface metal, except Sn, was deposited on the same metal in massive form as base. Spongy Sn was deposited on Pb base. In these runs electrolysis was continued until azobenzene was completely reduced. The completion of the reduction was determined by the disappearance of the red color of azobenzene. Under the conditions of Table IV, it is seen, all four metals were about equally suitable for the formation of hydrazobenzene, giving almost quantitative yields. However, to determine which electrode of the four was the most efficient, electrolyses were carried out using in each case only the theoretical current.

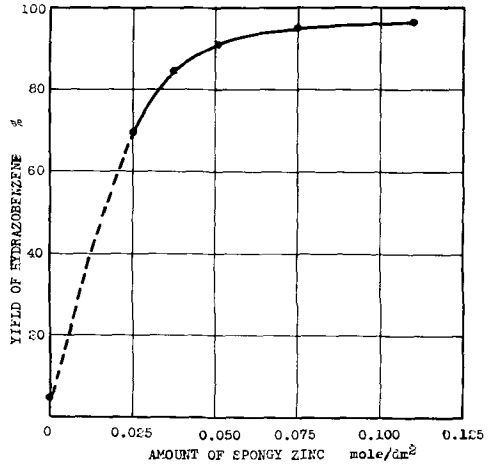

Fig. 1. Effect of amount of deposited spongy Zn on reduction of nitrobenzene at an Fe cathode.

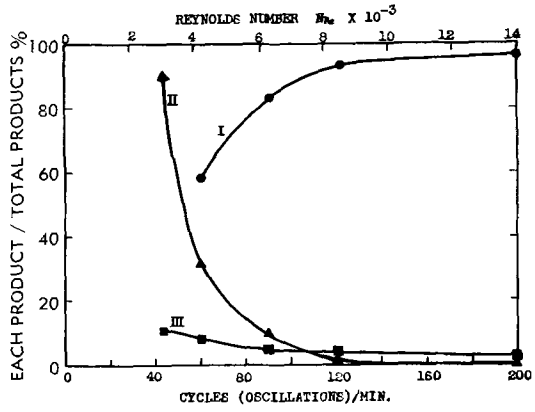

Fig. 2. Effect of agitation on yield of products. Curve I, hydrazobenzene; curve II, azobenzene; curve III, aniline.

In view of the rate of reduction Zn and Sn showed their superiority over Cd and Pb. Table V, and with them current density could be raised to about 30 amp/dm² without loss of current efficiency.

Since alkali soluble metals were observed to be corroded during the electrolysis, they seemed to be of limited usefulness in practice as base material of cathodes even if a large amount of spongy surface metal were used. Alkali insoluble metals, therefore, should be preferable, but of course would have to be covered thoroughly with surface metal. A high

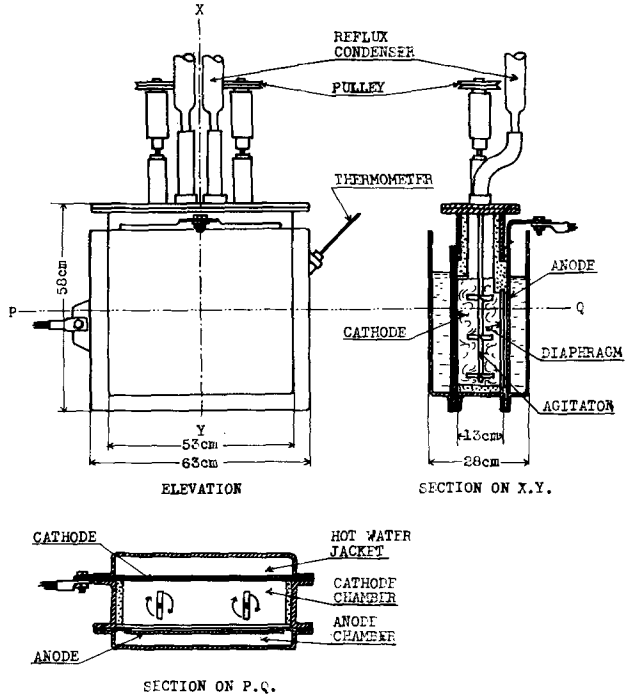

Fig. 3. Details of large scale cell

Table VI. Effect of base metal on reduction at a spongy Zn cathode

Cathode base metal	Cathodic current density, amp/dm²	Amount of current, amp-hr	Yield of hydrazobenzene g	%	Current efficiency, %
Zn	24.5	12.9	7.0	96	82
Pb	24.1	12.5	6.8	93	81
Fe	23.9	12.6	6.9	94	81

Anode, Pt; anolyte, 100 cc 10% aqueous NaOH; catholyte, 9.8 g nitrobenzene, 100 cc 10% aqueous NaOH, 10 cc benzene; temp, 60°-70°C.

overvoltage metal, such as Pb, would appear to be the best choice as the base.

Pb is less active as a surface metal as described above, so when covered with a large amount of preferred surface metal such as Zn, Pb was found to be resistant to corrosion when used as base metal. Fe was similarly useful, provided that it was well covered with active sponge. Table VI shows the results of two cathodes made by depositing the standard amount of Zn sponge on Pb and Fe, a catholyte containing 4.1 g $ZnSO_4 \cdot 7H_2O$ being used in each case for the formation of the sponge, compared with the spongy Zn cathode used in former runs.

It is clear from the table that, with thorough coverage, high conversion and current efficiency can be obtained with any of the two base metals as well as zinc base. However, when Fe, a low overvoltage metal, is used practically as the base, the amount of spongy Zn gave a marked influence upon the yield of hydrazobenzene. Fig. 1 shows that if the amount of Zn sponge is below about 0.05 mole/dm² the yield of hydrazobenzene is greatly decreased. It is believed that the amount of Zn used by Dey, *et al.*, (7) was too small for good results.

Rate of agitation also has been shown to be a critical factor in obtaining high conversion to hydrazobenzene. The oscillation was varied up to a rate of about 200 cpm in a series of experiments, results of which are shown in Fig. 2. Above about 100 oscillations/min uniformly high conversion to hydrazobenzene was obtained, and the amount of azobenzene and aniline[2] in the product fell to a minimum. Below this rate, corresponding to a Reynolds number of about 7000, the yield of hydrazobenzene fell off rapidly, while the proportion of other reduction products rose. The curves of Fig. 2 indicate that the yield of desired hydrazobenzene is influenced by the particle size of the emulsion, and that with any cell design the agitation must be at least sufficient to give particles small enough to produce the desired result.

Preliminary Large Scale Runs

The work with the small experimental cell identified the principal conditions necessary to obtain consistently high conversion of nitrobenzene to hydrazobenzene at high current efficiency and practical current density. A cell capable of using at least 1.5 kg of nitrobenzene per run was constructed and three runs were carried out in it.

The cell is a rectangular sheet iron vessel 63 x 28 x 58 cm high, provided with a rubber-lined iron cover with openings for gas vent, reflux, and two stirrers (diameter, 8 cm) for agitation of the catholyte. The vessel is partitioned as shown in Fig. 3 to provide a hot water jacket and a cell spacing of 15 cm.* Ni plated Fe with an active area 44 cm x 34 cm is used as anode. The cathode, in direct contact with the partition built into the vessel, is a lead sheet covered with spongy Zn with apparent area 48 cm x 31 cm. A sheet diaphragm (48 x 23 cm) near the anode is the product of Nippon Tokushu Togyo Company, Nagoya, Japan. It has a composition of 90% Al_2O_3 and 5%-6% SiO_2, and porosity of 35.6%. Inner surfaces of the cell vessel are lined with cement.

[2] The formation of aniline seems to be due to the incomplete conversion of phenylhydroxylamine to azoxybenzene.

* The distance from the anode to the cathode.

Table VII. Separation of reduction products (Run No. 1)

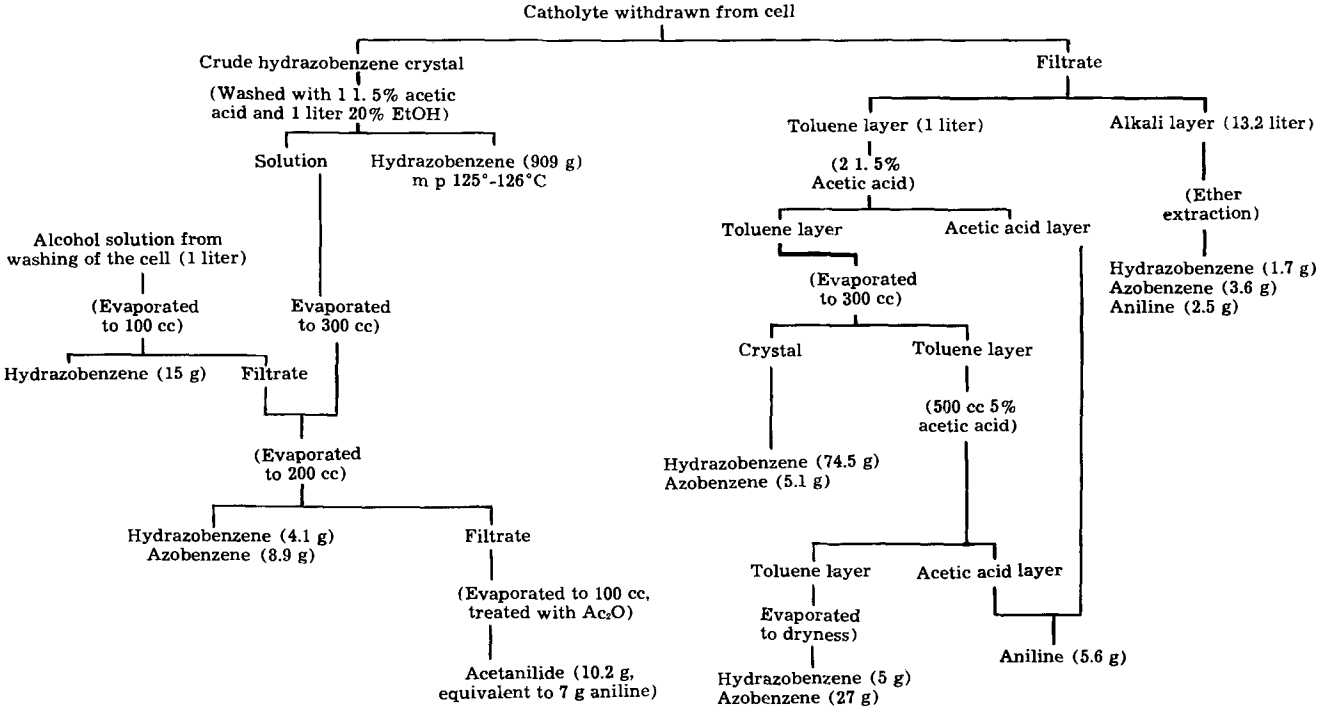

Table VIII. Three large scale experiments

	Run No. 1	Run No. 2	Run No. 3
Catholyte, $C_6H_5NO_2$:	1.5 kg	1.5 kg	1.5 kg
Water:	14 l	13 l	[a]
NaOH:	1.5 kg	1.5 kg	[a]
Toluene:	1.5 l	1.5 l	[a]
Temperature[b]	90°C	90°C	90°C
Amperage:	220-280	235-270	250-280
Mean cathodic current density (amp/dm²):	16.7	17.2	17.6
Voltage[c]:	8.8-9.8	9.6-10.2	8.6-9.7
Amount of current,			
Ampere hours:	1888	1830	1701
Per cent of theoretical:	116	113	104
Rate of agitation (rpm):	300	300	300
Material yield (%),			
Hydrazobenzene:	90.1	89.5[d,a]	
Azobenzene:	4.0	4.4	
Aniline:	1.3	2.3	
Current efficiency hydrazobenzene (%):	78	83[a]	

[a] Run 3 was a continuation of Run 2. After removal of crude hydrazobenzene by cooling the catholyte from Run 2, 1.5 kg nitrobenzene and sufficient water and toluene to restore the original proportions were added; the restored catholyte was used as starting catholyte for Run 3. Material yields and current efficiency are for combined Runs 2 and 3.

[b] This is about maximum when toluene was used.

[c] Large ohmic drop through the diaphragm. It can be reduced to a suitable value by decreasing the amperage so as to give the maximum economical efficiency.

[d] Of the total yield from Runs 2 and 3, 2004.4 g hydrazobenzene, 902 g was obtained as crude crystal by cooling the catholyte from Run 2; 1030 g was obtained similarly at the end of Run 3, and 72.4 g was obtained by further processing the catholyte in accordance with the scheme of Table VII. 97.7 g azobenzene and 52.6 g aniline were also recovered from the final catholyte.

The procedure for recovery of products from the large cell follows closely that used in the small scale experimental work and is given in Table VII.

Details of the three runs made are given in Table VIII. The cathode was prepared by electrolysis in catholyte initially containing 145 g of Zn dust until 0.11 mole of spongy metal had been deposited per dm² of surface of the Pb base. The anolyte in each run was 10 liter of 20% NaOH.

Polarographic Measurements

In the literature, theories of the mechanism of reduction of nitrobenzene have, on the one hand, recognized the effectiveness of organic solvents in promoting conversion to hydrazobenzene. On the other, there has appeared the suggestion that the reaction is voltage-controlled, and is favored by the use of a high overvoltage cathode or of the oxide of a high overvoltage metal as addition agent to the catholyte (7, 9). The early experiments were only qualitative, and if a high overvoltage cathode were really desirable, then mercury might be expected to be the best choice.

In an effort to explain the difficulty with the reduction of azobenzene or azoxybenzene to hydrazobenzene at a Ni or Fe cathode in alkaline emulsion, polarographic measurements were carried out with nitrobenzene, azobenzene, and azoxybenzene, in aqueous alkaline emulsion[3] and in aqueous-alcoholic solution. An improved Heyrovsky-Shikata polarograph made by Yanagimoto Company, Kyoto, Japan, (Type PS, Model 52) was used in connection with a galvanometer having sensitivity of 3.29 x 10^{-9} amp/mm. The sensitivities used were 1.65 x 10^{-8} and 1.65 x 10^{-7} amp/mm. The usual cell, not H type, employing a saturated calomel reference electrode, was used. As cathode, both the usual dropping mercury electrode and a micro rotating metal electrode were used. The t value of the dropping mercury cathode, 30 cm high, was 1.0-1.5 sec. The rotating cathode consisted of a section of wire, 0.2 mm in diameter with available area of 0.03 mm², sealed in a glass tube. The stem of the cathode was rotated at 1000 rpm.

[3] Polarograms in alkaline emulsion were not of the true emulsifying state with agitation, but saturated solution of azoxy and azo after allowing the emulsion to stand for 1 hr. Work on the effect of agitation on the polarograms at an emulsifying state was later made using azoxybenzene emulsion. The results showed that the wave height grew linearly with the rate of agitation.

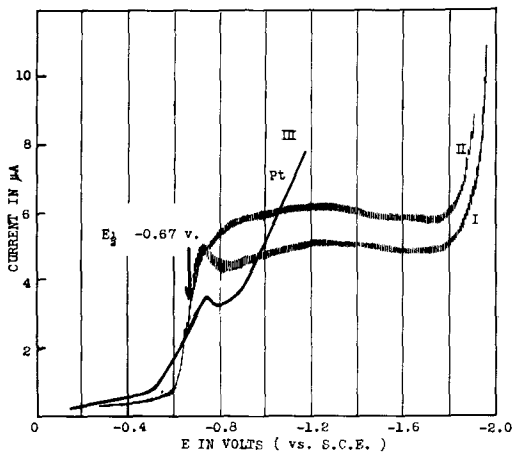

Fig. 4. Polarograms for nitrobenzene. Curve I, 1 x 10^{-3} m/l nitrobenzene in 5% aqueous NaOH at a dropping Hg electrode, 20°C; curve II, 1 x 10^{-3} m/l nitrobenzene in 40% aqueous alcoholic solution (pH 12.1) at dropping Hg electrode, 20°C; curve III, 1 x 10^{-3} m/l nitrobenzene in 5% aqueous NaOH at Pt microcathode, 20°C.

Polarograms for nitrobenzene are shown in Fig. 4. In both aqueous emulsion and in aqueous-alcoholic solution with the Hg cathode, and with both Pt and Hg cathodes in the aqueous emulsion, they show the typical wave with E ½ at about −0.67 v, which is very near the value found by Shikata (10) about thirty years ago.

It is fairly certain that these waves correspond to the reduction of nitrobenzene to nitrosobenzene and phenylhydroxylamine, which in alkaline medium react to form azoxybenzene.

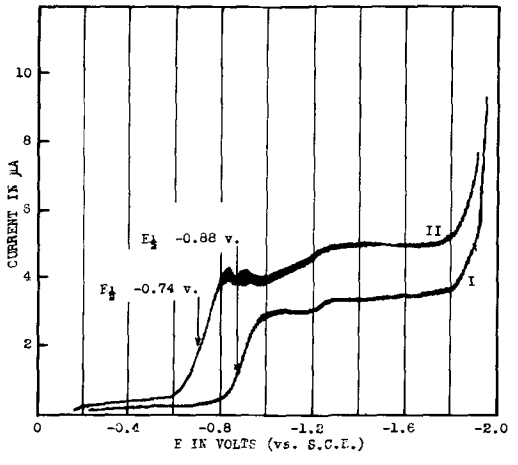

Fig. 5. Polarograms for azobenzene and azoxybenzene in 40% aqueous alcoholic solution (pH 12.1). Curve I, 2 x 10^{-3} m/l azobenzene, 20°C; curve II, 2 x 10^{-3} m/l azoxybenzene, 20°C.

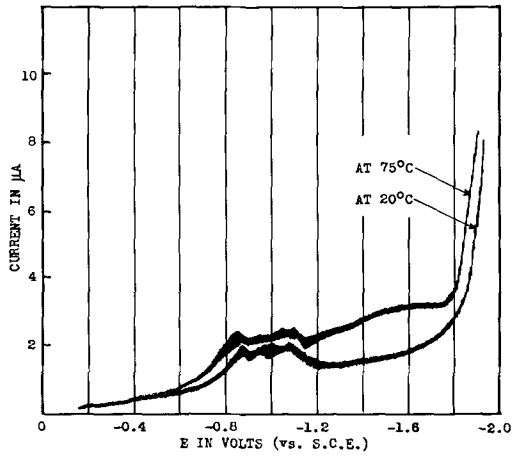

Fig. 6. Polarograms for saturated solution of azoxybenzene in 10% aqueous NaOH at 20° and 75°C.

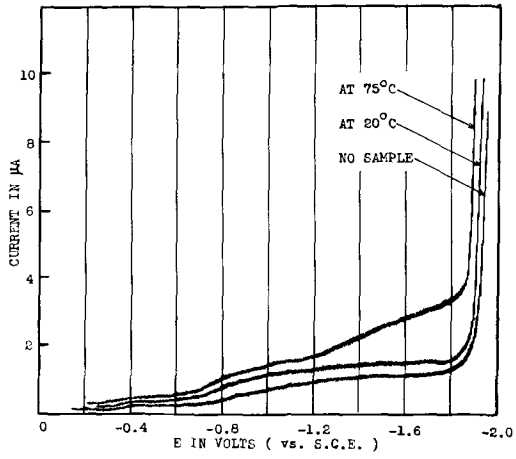

Fig. 7. Polarograms for saturated solution of azobenzene in 10% aqueous NaOH at 20° and 75°C.

Polarograms for azoxy- and azobenzene are shown in Fig. 5-7. In 40% aqueous-alcoholic solution at pH 12.1 (in $Na_2B_4O_7$-NaOH buffer), each of these compounds gave one wave of typical shape with $E\frac{1}{2}$ at −0.74 v for the azoxy and −0.88 v for the azo compound. These potentials are appreciably lower than that of hydrogen evolution at a nickel microcathode.

In contrast, the polarograms of the azoxy- and azobenzene in aqueous alkaline emulsion show little evidence of reduction even at elevated temperature. For azoxybenzene the graphs of Fig. 6 show a small wave at about −0.8 v, about the same value as observed for $E\frac{1}{2}$ in aqueous-alcoholic solution. However, the polarograms for azobenzene in Fig. 7 show no distinct wave prior to the hydrogen discharge.

The polarographic study has shown that nitrobenzene can act as a depolarizer in either aqueous emulsion or aqueous-alcoholic solution. However, of the intermediate reduction products between nitro- and hydrazobenzene, azoxybenzene is highly resistant and azobenzene almost completely resistant to further reduction in aqueous emulsion. Since azobenzene is almost completely insoluble in aqueous alkali, and since it becomes an active depolarizer under conditions when its solubility is increased by addition of organic solvent, it is believed that the difficulty in carrying the reduction of nitrobenzene to the hydrazo level is explained, not by any inadequacy of the overvoltage of the cathode, but by the insolubility of the intermediate azobenzene.

If this view is correct, it must follow that the effectiveness of certain metals in promoting formation of hydrazobenzene in the absence of organic solvents is explained on a basis other than electrochemical reaction. It is suggested that the effectiveness of these metals is explained by chemical reduction of the azo compound at the cathode. In this view the reductant would be the metal, and the function of electrode reaction would be to restore the oxidized or ionic form of the metal to the metallic condition for further reduction of azobenzene. The metal thus would function as a hydrogen carrier as already proposed (8) for the reduction of 2-amino-4-chloropyrimidine and its methyl compound to corresponding 2-aminopyrimidines at Cd and Zn cathodes. And it may be that, if cathodes of alkali soluble spongy metal and high current density have been used from the commencement of the reduction of nitrobenzene as in this work, the over-all reductions would mainly be the chemical reaction at the cathode, rather than the electrochemical one.

Conclusions

1. With the help of polarographic measurements it has been shown that the difficult step in the formation of hydrazobenzene from nitrobenzene in alkaline emulsion is reduction of azoxybenzene and, especially azobenzene.
2. The reduction of azoxybenzene and azobenzene is helped by the presence of organic solvents which keeps these compounds in solution.
3. In the absence of an organic solvent, operation with an alkali emulsion of nitrobenzene can give good results if a cathode carrying a suitable amount of a spongy layer of Zn, Sn, Cd, or Pb is used. Under these conditions yields and efficiencies are very high at a relatively high current density. High temperature is preferable and the catholyte must be well stirred.
4. The process is applicable to large scale work.

Acknowledgment

The authors wish to express their appreciation to Sherlock Swann, Jr., and C. L. Wilson for their valuable comments, and to N. M. Winslow who assisted in the revision of the manuscript, and to acknowledge the collaboration given by other members of this laboratory, especially K. Shirai, in carrying out the large scale experiments. The aid of a grant for fundamental and developmental scientific research given by the Ministry of Education of Japan also is gratefully acknowledged.

Manuscript received July 31, 1953. This paper was prepared for delivery before the New York Meeting, April 12-16, 1953.

Any discussion of this paper will appear in a Discussion Section to be published in the June 1958 JOURNAL.

REFERENCES

1. T. Sekine and K. Sugino, *J. Electrochem. Soc. Japan*, **21**, 383 (No. 8) (1953).
2. K. Elbs and O. Kopp, *Z. Elektrochem.*, **5**, 108 (1898).

3. F. Haber, *ibid.*, **4**, 506 (1898).
4. R. H. McKee and B. G. Gerastopolou, *Trans. Electrochem. Soc.*, **68**, 329 (1935).
5. Farbenfabriken F. Bayer and Co., German Pats. 121,899, Nov. 24, 1899 and 121,900, Dec. 1, 1899; W. Löb and R. Moore, *Z. physik. Chem.*, **47**, 418 (1904); O. Dieffenbach, U. S. Pat. 833,513, Oct. 16, 1906; also F. Darmstädter, British Pat. 6924 (1906); German Pats. 181,166, Mar. 15, 1903 and 189,312 (1907); Austrian Pat. 31,841 (1908).
6. A. Piguet, U. S. Pat. 1,225,052, May 8, 1917; also Soc. Chem. Ind. Basel, British Pat. 15,750 (1915); Swiss Pat. 73,098 (1916); German Pat. 297,019 (1917); E. Brunner, Swiss Pat. 85,228 (1920) and British Pat. 147,541, May 17, 1920.
7. B. B. Dey, T. R. Govindachari, and S. C. Rajagopalan, *J. Soc. Ind. Research (India)*, **4**, 559 (1946).
8. K. Sugino, K. Odo, and K. Shirai, *J. Chem. Soc. Japan*, **71**, 396 (1950); K. Shirai, *J. Electrochem. Soc. Japan*, **21**, 387 No. 8 (1953).
9. S. Glasstone and A. Hickling, "Electrolytic Oxidation and Reduction," p. 206, Chapman and Hall, Ltd., London (1935).
10. M. Shikata, *Trans. Faraday, Soc.*, **21**, 42 (1925).

The Equilibrium between Titanium Metal, $TiCl_2$, and $TiCl_3$ in NaCl-KCl Melts

Warren C. Kreye and Herbert H. Kellogg

School of Mines, Columbia University, New York, New York

ABSTRACT

The equilibrium between solid titanium metal, di-, and trivalent titanium chlorides dissolved in an NaCl-KCl melt was measured under carefully controlled experimental conditions. Divalent titanium was found to be the predominant valence state in the melt, for temperatures of 700°-800°C. The "apparent" equilibrium constant (mole fractions replacing activities) for the reaction

$$TiCl_3\ (NaCl\text{-}KCl\ melt) + 1/2\ Ti^\circ(c) = 3/2\ TiCl_2\ (NaCl\text{-}KCl\ melt)$$

was calculated and found to be a function of the total titanium concentration in the melt. Limited data indicated that the equilibrium is exothermic in agreement with expectation.

Procedures for making pure Ti metal, either on a laboratory or production scale, involve, almost without exception, reduction of titanium halides. In many of these procedures (electrowinning, Kroll process, sodium reduction process) the reduction is accomplished in the presence of a salt melt composed of alkali or alkaline earth chlorides. In the presence of this solution phase, titanium tetrachloride undergoes stepwise reduction to the trivalent, divalent and, finally, zerovalent state depending on the amount and strength of the reducing agent employed. In electrowinning of Ti, the molten salt will contain various proportions of di- and trivalent Ti [tetravalent Ti is only slightly soluble in salt melts (1)] depending on whether it is in the strongly reducing zone near the cathode, or in the oxidizing zone near the anode.

The present state of knowledge of the equilibrium relations between the Ti halides in salt melts is meager; probably the only work known to date is that of Mellgren and Opie (2) on the equilibrium between $TiCl_2$, $TiCl_3$, and Ti° in the presence of an $SrCl_2$-NaCl melt. They measured the equilibrium concentration of $TiCl_2$ and $TiCl_3$ for the reaction:

$$2TiCl_3(melt) + Ti^\circ(C) = 3TiCl_2(melt)$$

as a function of total Ti concentration, the ratio $NaCl/SrCl_2$, and temperature.

The present study is similar to that of Mellgren and Opie except that the salt melt was the equimolar mixture of NaCl and KCl. It is hoped that by studies of this kind the complex chemistry of titanium halide reduction may be better understood and more economically controlled in commercial practice.

Experimental

The desired equilibrium between Ti metal and dissolved titanium chlorides was established by addition of $TiCl_4$ to the NaCl-KCl melt in contact with excess metallic Ti. In this way, $TiCl_2$ and $TiCl_3$ were formed *in situ* by the reaction between $TiCl_4$ and Ti°, with the result that the problem of preparing pure $TiCl_2$ and $TiCl_3$ to use as melt constituents was obviated.

In essence, the method may be described as follows. The NaCl-KCl melt, containing excess solid Ti, was held in a Vycor tube under a purified argon atmosphere. An argon-$TiCl_4$ gas mixture was then bubbled through the melt briefly in order to introduce titanium chlorides to the melt. After each addition of $TiCl_4$, the melt was sampled at successive time intervals. The samples of solidified melt were then analyzed for the content of Ti^{2+}, Ti^{3+}, and Ti^{4+}.

Materials.—Titanium metal, prepared by decomposition of TiI_4, was obtained from the Foote Mineral Co. It was used in the form of rods (0.8 cm diameter, 3.8 cm length).

The salt mixture was made from equimolar amounts of reagent grade NaCl and KCl. Prior to placing the salts in the cell, they were oven dried at 110°C. Further dehydration of the salts was accom-

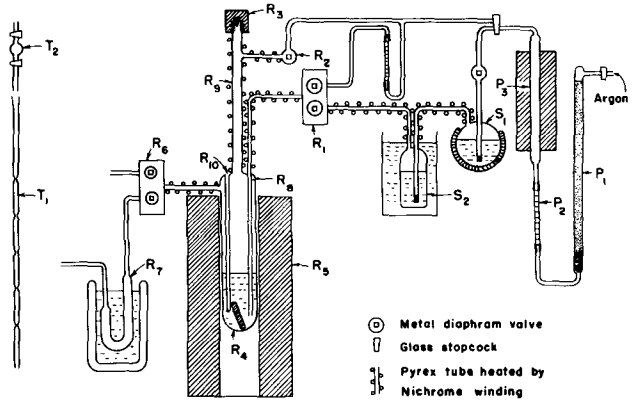

Fig. 1. Simplified schematic diagram of equilibration apparatus

plished by vacuum treatment after they were placed in the cell (*see* below). The $TiCl_4$ was a special purity product (99.99% $TiCl_4$) obtained from the National Bureau of Standards.

Apparatus.—A simplified diagram of the equilibration apparatus is given in Fig. 1; it consists of four principal sections as follows: P, the gas purification train; S, the $TiCl_4$ saturation device; R, the reactor for equilibration of the melt; and T, the sampling device.

With the exception of certain valves noted below, the entire apparatus was constructed of Pyrex and Vycor. Vycor was used for those parts heated above 450°C. Graded seals were used to connect Pyrex and Vycor parts. For those parts of the gas train which were not required to handle $TiCl_4$ vapors, standard vacuum stopcocks and joints, lubricated with silicone grease, were used. No grease was found, however, that would withstand the solvent action of hot $TiCl_4$ vapor. Therefore, in those parts of the apparatus which contain $TiCl_4$, diaphragm-type, high-vacuum valves (Hoke, 411 Series) were used. These valves, which have a Teflon gasket, gave excellent service, and no corrosion of any of the parts was observed. Kovar-to-glass seals were used to connect the Pyrex lines to the diaphragm valves.

To prevent condensation of $TiCl_4$ asbestos-covered Nichrome wire was wound on the glass tubing carrying these vapors. The temperature of the windings was controlled by Variac transformers. For the same reason, valves which must handle $TiCl_4$ vapors must be maintained hot. This was accomplished by enclosing the valves in transite boxes which were heated by Nichrome windings. The valves were operated by extensions of their stems which passed through the face of the heated boxes.

P-Gas purification.—Tank argon was passed through two $Mg(ClO_4)_2$ drying towers, P_1; then through an all-glass, float-type flowmeter, P_2; and finally through a getter consisting of sponge Ti held in a Vycor tube, P_3. The getter was heated by a furnace to 850°C.

S-$TiCl_4$ saturation.—Purified argon was first passed into a presaturator, S_1, containing liquid $TiCl_4$. The $TiCl_4$ was maintained at the approximate temperature desired by a heating mantle. The partly saturated gas stream then passed to the final saturator, S_2, which consisted of a glass chamber partly filled with liquid $TiCl_4$. Fritted-Pyrex disks were used in both saturators to disperse the gas stream. The final saturator was immersed in an oil-bath thermostat, controlled to ±0.1°C.

R-Reactor section.—The Vycor equilibration cell, R_4, was 4.6 cm O.D. and 40 cm in length. A gas inlet tube, R_8, was sealed into the top of the equilibration cell. Either pure A or an A-$TiCl_4$ mixture could be bubbled into the melt through this tube. The diaphragm valves in box R_1 were used to change from pure A to the A-$TiCl_4$ mixture. The cell also contained a Vycor thermocouple well, R_{10}. The melt temperature was determined with a calibrated Pt-Pt 13% Rh thermocouple and a L&N precision thermocouple potentiometer.

Sealed into the top of the cell was a glass sampling-chimney, R_9, 40 cm long and 13 mm O.D. At the top of the chimney was a Teflon tube which had been force-fitted to the Vycor. The top end of the Teflon tube was closed by means of a Teflon cap, carrying a female thread, which screwed to a male thread on the Teflon tube. To ensure a tight seal, a small Teflon cone was fitted into the beveled top of the Teflon tube, and was held tightly in place by the pressure of the screwed-down cap.

Exit gases from the equilibration cell passed through valve box, R_6, and a dry ice-acetone trap, R_7, which collected any unreacted $TiCl_4$. By means of one valve in box R_6, the entire assembly could be connected to a vacuum pump and evacuated to dehydrate the salts.

The equilibration cell, R_4, was heated by a Nichrome-wound furnace, R_5, which had two independent windings. When the current through these windings was properly adjusted the temperature was constant to within ±1°C for a vertical length of 10 cm. The temperature of the melt was controlled to ±1°C by a Brown Electronik Controller, activated by a chromel-alumel thermocouple located close to the main furnace winding.

T-Sampling device.—The sampling pipet, T_1, was made of Vycor tubing, 85 cm long and 8 mm O.D. Constrictions in the pipet were made at intervals of 12 cm to enable small samples to be broken off and analyzed separately. An evacuated bulb, T_2, contained between two stopcocks, fitted to the top of the sample pipet by means of a ground taper joint, and was used to suck up a predetermined amount of melt into the sample tube.

Procedure

Loading of cell and dehydration of salt.—The Ti metal and the oven dried salts were placed in the clean cell before it was sealed to the remainder of the system. The cell was then sealed to the various connecting tubes, and the system evacuated. The cell was heated in intervals of 100°C, to 450°C, with sufficient time allowed at each temperature for the system to be pumped down to 1 μ (Hg) pressure. In this way, the optimum dehydration of the salt was achieved with the least possibility of hydrolysis (3).

When the temperature of the salt reached 450°C, and the system pressure was less than 1 μ (Hg), pure A was admitted to the system through R_8 until the pressure was 1 atm. A steady flow of A at the

rate of 10-15 ml/min was maintained through R_8 throughout the experiment. The temperature was next raised to 700°C and the salt melted.

Admission of $TiCl_4$.—The presaturator, S_1, and the final saturator, S_2, were heated to the desired saturation temperature (110°C). The valves were then switched so that the A-$TiCl_4$ mixture was bubbled through the melt in place of pure A.

Since the rate of A flow and the partial pressure of $TiCl_4$ in the A stream were known,[1] the rate at which $TiCl_4$ entered the cell could be calculated. Since no $TiCl_4$ was detected in the dry ice trap, R_7, in any of these experiments, it could be assumed that it was quantitatively absorbed by the melt. When the desired amount of $TiCl_4$ was added to the melt, the valves were again changed and pure A was allowed to bubble slowly through the melt throughout the equilibration period. Continual flushing with A was necessary to prevent plugging of the tubes with vapor-deposited salts, and also to provide mixing within the melt.

Sampling the melt.—At appropriate time intervals after the introduction of $TiCl_4$ to the melt, a sample was taken for analysis. Valve R_2 was first adjusted so that a rapid flow of A was passing through the chimney, R_9. The Teflon cap on the chimney was then removed, and the sampling pipet slowly inserted into the chimney. The pipet was lowered in slowly so that the A flow would flush the air and desorbed moisture from the pipet. When the tip of the pipet reached the melt level, the evacuated bulb, T_2, was connected to the top of the sampling tube and the lower stopcock of this bulb was opened slowly. The pipet was then withdrawn, the Teflon cap replaced, and the valve R_2 was closed. The pipet was separated from the ground joint by flame-sealing the tube at the top constriction. It was then stored in a dry box to await analysis.

Analysis.—Details of the analytical method are given in (1). Only the sequence of the steps and the broad outline of the methods are given in this paper.

Each sample pipet contained four segments filled with solidified salt. The contents of two or more of the segments were analyzed separately and the average of the results reported as the analysis of the sample. To prepare a sample for analysis the segment was broken inside an argon-filled dry box and the solidified salt (about 3 g) transferred to a special flask. On solidification the melt shrinks away from the walls of the sampling pipet so that a clean and complete transfer of solid salt from each segment was made.

The analytical sequence consisted of three main steps, as follows:

1. The solid salt was reacted with HCl, under an A atmosphere, and the volume of evolved H_2 was measured. The reaction is:

$$Ti^{2+} + H^+ \rightarrow Ti^{3+} + \tfrac{1}{2}H_2(g)$$

This determined the amount of Ti^{2+} in the sample.

2. After oxidation of Ti^{2+} to Ti^{3+}, the total concentration of Ti^{3+} was determined by titration of an aliquot of the acidified solution with standard dichromate solution. The original content of Ti^{3+} in the sample was obtained by subtracting the amount of Ti^{2+} from the total amount of Ti^{3+} in the acidified solution.

3. The total Ti content of an aliquot of the acidified solution was next determined by a volumetric method. The content of Ti^{4+} in the original sample was found by difference between the total Ti content and the sum of the Ti^{2+} and Ti^{3+} contents.

[1] The partial pressure of $TiCl_4$ was calculated from the temperature of the saturator and the vapor pressure data of Arii (4).

Table I. Equilibration of $TiCl_4$ with Ti° in NaCl-KCl (1:1M) melts. Summary of experimental results

Test No.	Equilibration Time, hr†	Equilibration Temp, °C	Melt analysis:* mole/g of melt x 10^4 Total Ti ± 1%	Ti^{2+} ± 1%	Ti^{3+} ± 20%	Ti^{4+} ± 100%
A-1	24	700	3.61	3.14	0.44	0.03
A-2	130	700	3.63	3.25	0.35	0.03
A-3	270	700	3.82	3.45	0.32	0.05
B-1	96	700	5.00	4.36	0.61	0.03
B-2	300	700	5.13	4.68	0.41	0.03
C-1	2	700	4.98	4.36	0.47	0.15
C-2	47	700	5.04	4.54	0.38	0.12
D-1	1	700	8.98	7.94	1.08	0.0
D-2	289	700	9.15	8.34	0.74	0.07
D-3	625	700	9.19	8.37	0.82	0.0
E-1	1/2	700	17.17	14.96	2.11	0.10
E-2	25	700	17.28	15.12	2.08	0.08
E-3	284	700	17.82	15.86	1.84	0.12
F-1	69	780	5.24	4.39	0.85	—
F-2	189	780	5.24	4.62	0.62	—

* Analytical results are the average of two or three samples from one pipet, except for B-2 and F-1, for which only one sample was analyzed.
† Time elapsed after the last addition of $TiCl_4$ to the melt.

Results and Discussion

The results obtained for the equilibration of $TiCl_4$ and Ti°, in the presence of an equimolar mixture of NaCl and KCl, are given in Table I. The data include tests at five different levels of Ti content in the molten salt, two different temperatures, and equilibration times from ½ hr to 625 hr.

The most significant feature of these data is the predominance of divalent Ti in all of the melts. Ti^{2+} constitutes 87-91% of the total Ti dissolved in the molten salt. Most of the remainder of the Ti is present as Ti^{3+}; Ti^{4+} accounts for less than 1% of the total Ti in most cases. These results are in qualitative agreement with those of Mellgren and Opie (2) for the same equilibrium in the presence of a salt melt of NaCl and $SrCl_2$. They found that divalent Ti accounted for 78-93% of the dissolved Ti. They did not report the presence of Ti^{4+}.

Ti^{4+} *content.*—In assessing the significance of the reported values for Ti^{4+}, it should be noted that these were calculated from the difference between two large analytical values, the value for total dissolved Ti less the value for total Ti^{3+} (after oxidation of Ti^{2+} to Ti^{3+}). The average deviation of each of these analytical values, for independent analyses of the same samples, was about 1%. Hence, the results for Ti^{4+} are subject to an uncertainty of 2% of the total Ti content. This uncertainty is in most cases larger than the calculated content of Ti^{4+}. The fact, however, that the calculated content of Ti^{4+} is a positive quantity in 11 cases out of 13 suggests that the samples did contain a small amount of Ti^{4+}.

The authors prefer the explanation that the small content of Ti^{4+} originated from unavoidable oxidation of the sample by air during the analytical procedure, rather than from the equilibrium in the melt. Great care was exercised to minimize sample oxidation during handling and analysis [*see* Reference (1)], but a minor amount of oxidation was probably unavoidable. In support of this hypothesis are the following observations:

1. Analyses of samples in series A and B, (Table I) were made after a modification in analytical procedure designed to further minimize the possibility of sample oxidation. These samples contained the smallest quantity of Ti^{4+}.

2. There is no consistent trend of Ti^{4+} content with total Ti content.

3. $TiCl_4$ is a volatile component in NaCl-KCl melts (1). If there were an appreciable content of $TiCl_4$ in the melt, it should be continually swept out of the melt by the stream of A and be detected in the exit gases. Despite efforts to detect $TiCl_4$ in the exit gas from the apparatus by a variety of methods, in no case was the test positive. Further, there was no reduction in total Ti content of the melt, even after 625 hr. It is concluded that the concentration of Ti^{4+} in equilibrium with Ti° in NaCl-KCl melts is very small, and that the values reported in Table I are undoubtedly too high because of slight oxidation of the samples during handling and analysis. It can be concluded further that reduction of $TiCl_4$ to $TiCl_3$ and/or $TiCl_2$ is very rapid at 700°C, since a ½ hr equilibration period (test E-1, Table I) is sufficient to reduce Ti^{4+} content of the melt to a value below the precision of the analytical method.

Ti^{2+} and Ti^{3+} content.—The analyses for Ti^{2+} on independent samples were reproducible to 1% of the reported values. The values for Ti^{3+}, however, were calculated by difference of two large analytical values, the value for total Ti^{3+} (after oxidation of Ti^{2+} to Ti^{3+}), less the value for Ti^{2+}, each of which is subject to about 1% error. The results for Ti^{3+} are therefore in doubt by ±2% of the total Ti content of the samples. Since values reported for Ti^{3+} amount to only 8-12% of the total Ti content, the uncertainty of the values for Ti^{3+} reported in Table I is about ±20%. This uncertainty should be kept in mind as the significance of the equilibrium data is discussed.

Time of equilibration.—Values reported in Table I show significant changes in concentrations for equilibration times up to 280 hr. The one test carried beyond 280 hr (D-3) failed to show a significant change in concentration when the time of equilibration was extended to 625 hr. In all cases, increases in equilibration time resulted in small increases in total Ti and Ti^{2+}, and small decreases in Ti^{3+}. These changes are consistent with progress of the reaction,

$$Ti^{3+} + \tfrac{1}{2}Ti^\circ = 3/2Ti^{2+}$$

from left to right. Since this is the equilibrium that must obtain in the melt, it can be concluded that true equilibrium conditions were not reached for times much less than 280 hr at 700°C.

Table II. "Equilibrium" concentration of $TiCl_2$ and $TiCl_3$

Test No.	Temp, °C	Total Ti content wt %	Mole fractions* $N_{TiCl_2} \times 10^2$	Mole fractions* $N_{TiCl_3} \times 10^2$	$K_x = \frac{N_{TiCl_2}^{3/2}}{N_{TiCl_3}}$
A-3	700	1.83	2.34	0.217	1.65
B-2	700	2.46	3.20	0.281	2.04
D-3	700	4.40	5.87	0.575	2.47
E-3	700	8.54	11.71	1.36	2.95
F-2	780	2.51	3.17	0.425	1.33

* Based on the constituents $TiCl_2$, $TiCl_3$, NaCl, and KCl. The small content of $TiCl_4$ is neglected.

The unusual length of time required to reach equilibrium may be due to an inherently slow rate of reaction at 700°C. It is possible, however, that slow diffusion of Ti^{3+} to the surface of the Ti metal was rate controlling. The surface area of Ti metal was small (the metal was used in the form of rods), and the amount of agitation was slight (the slow bubbling of A, 10-15 ml/min, was the only source of agitation during the equilibration period).

In the discussion which follows, the composition of the melt at the maximum equilibration time (250-300 hr in most cases) is considered as the equilibrium composition. Proof that a state of equilibrium was reached, by experiments designed to approach the equilibrium from the other direction, could not be obtained with the experimental method employed. Since $TiCl_4$ was the source of $TiCl_2$ and $TiCl_3$ in these experiments, the equilibrium was always approached from the high oxidation state side. It would be necessary to add almost pure $TiCl_2$ to the melt in order to approach the equilibrium from the low oxidation state side.

Equilibrium constant.—Melt compositions at maximum equilibration time (presumed equilibrium condition) are converted to mole fractions and reported in Table II. Also reported in Table II are values for the apparent equilibrium constant, K_x, of the reaction:

$$TiCl_3(\text{NaCl-KCl melt}) + \tfrac{1}{2}Ti^\circ(c) = 3/2TiCl_2(\text{NaCl-KCl melt}) \qquad (I)$$

$$K_x = N_{TiCl_2}^{3/2} / N_{TiCl_3}$$

N_i = mole fraction of (i), based on the constituents:

$TiCl_2$, $TiCl_3$, NaCl, KCl

(apparent content of $TiCl_4$ neglected)

Fig. 2 shows the variation of K_x with total Ti concentration. For comparison, Fig. 2 also shows the

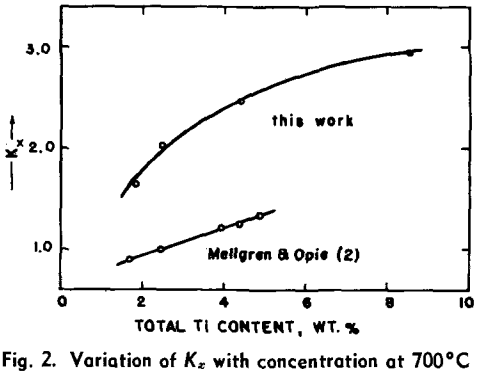

Fig. 2. Variation of K_x with concentration at 700°C

data of Mellgren and Opie (2) who determined K_x for this equilibrium in an NaCl-$SrCl_2$ melt.

The value of K_x does depend on total Ti concentration, both for the results of this investigation and for those of Mellgren and Opie. K_x should be constant if the activity coefficients of $TiCl_2$ and $TiCl_3$ are constant, i.e., if the solutions obey Henry's law over the range of concentrations studied. Since the mole fraction of $TiCl_2$ varies from 0.023 to 0.117 in these experiments, the failure to obey Henry's law is not surprising.

Other interpretations of the equilibrium results were attempted in an effort to explain the trend of K_x with concentration. Mellgren and Opie (2) point out that the assumption that divalent and trivalent Ti are associated into $(TiCl_2)_3$ and $(TiCl_3)_2$ leads to constant K values for the reaction

$$(TiCl_3)_2 + Ti^\circ = (TiCl_2)_3 \qquad (II)$$

This assumption would also lead to relatively constant K values for the results of this investigation. In the absence of more direct proof of association, however, the authors prefer to report K_x for the simpler reaction.

Temkin's rule (5) for the ideal behavior of ionic melts (both in the form of molar ionic-fractions and equivalent ionic-fractions) was applied to the equilibrium results. Values of K for the reactions

$$Ti^{3+} + \tfrac{1}{2}Ti^\circ = 3/2Ti^{2+} \qquad (III)$$

$$TiCl_4^- + \tfrac{1}{2}Ti^\circ = 3/2Ti^{2+} + 4Cl^- \qquad (IV)$$

$$TiCl_6^{3-} + \tfrac{1}{2}Ti^\circ = 3/2Ti^{2+} + 6Cl^- \qquad (V)$$

were calculated in this way. The "constants" so calculated, however, still showed the same trend with concentration displayed by K_x. It must be concluded that insufficient information is available to make a more complete explanation of the equilibrium results.

It is unfortunate that there was time for only one test at a temperature other than 700°C. This one test at 780°C (series F, Table I) did show a significantly larger value for the concentration of Ti^{3+}, and a smaller value of K_x, than test B with the same total Ti content at 700°C. This indicates that reaction (I) is exothermic. The thermodynamic data of Skinner and Ruehrwein (6) and of Sanderson and MacWood (7) show that the reaction

$$TiCl_3(s) + \tfrac{1}{2}Ti^\circ(s) = 3/2TiCl_2(s) \qquad (VI)$$

is also exothermic. Quantitative comparison of ΔH for reactions (I) and (VI) is not possible because the heats of fusion of $TiCl_2$ and $TiCl_3$ are unknown. Mellgren and Opie (2) report no change in K_x with temperature (650°-850°C) for this system, within the accuracy of their analytical method (±5%).

Conclusions

1. The equilibrium of titanium chlorides with titanium metal, in the presence of an NaCl-KCl (1:1M) melt at 700°-780°C is such that divalent Ti is the predominant species (87-91% of the total dissolved Ti).

2. The apparent equilibrium constant, K_x, for the reaction $TiCl_3$(NaCl-KCl melt) + $\tfrac{1}{2}Ti^\circ(c)$ = $3/2TiCl_2$(NaCl-KCl melt) has been determined as a function of concentration (1.8-8.5 wt % total dissolved Ti).

3. Based on limited data, the reaction equilibrium was shown to be exothermic.

4. The content of Ti^{4+} in melts equilibrated with Ti metal was proven to be less than 1% of the total dissolved Ti, and is probably much less.

Acknowledgment

The authors wish to express their appreciation to the Office of Naval Research for financial support of this work and permission to publish the results. Dr. C. J. B. Fincham constructed much of the apparatus used and Messrs. L. Nanis and M. Jaworsky aided in the experimental work. The authors' appreciation of their services is gratefully acknowledged.

Manuscript received Oct. 30, 1956. This paper was prepared for delivery before the Cleveland Meeting, Sept. 30 to Oct. 4, 1956.

Any discussion of this paper will appear in a Discussion Section to be published in the June 1958 JOURNAL.

REFERENCES

1. W. C. Kreye, C. J. B. Fincham, L. Nanis, M. Jaworsky, H. Kellogg, Final Report, Nonr 266(24), Columbia University, June, 1956.
2. S. Mellgren and W. Opie, *J. Metals*, **9**, [2], 266 (1957).
3. H. J. Gardner, C. T. Brown, and G. J. Janz, *J. Phys. Chem.*, **60**, 1458 (1956).
4. K. Arii, *Bull. Inst. Phys. Chem. Res. (Tokyo)*, **8**, 714 (1929).
5. H. Flood, T. Forland, and K. K. Grjotheim, "The Physical Chemistry of Melts," pp. 46-62, Institution of Mining & Metallurgy (London) (1953).
6. G. B. Skinner and R. A. Ruehrwein, *J. Phys. Chem.*, **59**, 113 (1955).
7. B. S. Sanderson and G. E. MacWood, Tech. Rept. 4, Nonr 495 (06), Ohio State Univ., March 1955.

Determination of the Standard Free Energy of Formation of Cuprous Sulfide at 300°C

J. Bruce Wagner[1] and Carl Wagner

Department of Metallurgy, Massachusetts Institute of Technology, Cambridge, Massachusetts

ABSTRACT

The free energy change of the displacement reaction

$$2\,Cu(s) + PbS(s) = Cu_2S(s) + Pb(s, l)$$

has been deduced from emf measurements on the cell

$$Cu \mid CuBr \mid Cu_{1.98}S \mid (Cu_{1.98}S, PbS) \mid (PbCl_2 + 1\%\ KCl) \mid Pb$$

between 250° and 350°C. Therefrom a value of −22,607 cal for the standard free energy of formation of Cu_2S at 300°C has been calculated.

To supplement available data, the standard free energy of formation of Cu_2S has been determined with the aid of electrochemical measurements. In order to obtain the free energy of formation of Ag_2S, the cell

$$Ag \mid AgI \mid Ag_2S,\ S(l),\ graphite \qquad (I)$$

has been found to be helpful (1, 2). The analogous cell for Cu_2S cannot be used because Cu_2S reacts with excess sulfur to form CuS and moreover CuI exhibits excessive electronic conduction under oxidizing conditions such as prevail in the presence of liquid sulfur (3-6). To overcome these difficulties, cells involving displacement reactions seem profitable. Since the standard free energy of formation of PbS has been determined recently (2), it seemed expedient to measure the free energy change of the reaction

$$2Cu + PbS = Pb + Cu_2S \qquad [1]$$

In accord with a general survey of the potential use of galvanic cells for such purposes, the cell

$$Cu \mid CuBr \mid Cu_2S,\ PbS,\ Pb \qquad (II)$$

may be used under conditions where the three-phase system Pb-PbS-Cu_2S is stable. Preliminary calculations indicated that the standard free energy change of reaction [1] is positive below about 300°C but negative at higher temperatures and, therefore, the three-phase system Pb-PbS-Cu_2S is stable only above about 300°C. At lower temperatures, the three-phase system Cu-Cu_2S-PbS is stable. Thus, the free energy change of reaction [1] in the reverse direction would be obtainable from the cell

$$Pb \mid PbCl_2 \mid PbS,\ Cu_2S,\ Cu \qquad (III)$$

Since it seemed desirable to determine directly the temperature at which the standard free energy of reaction [1] changes its sign, an unconventional cell, viz.,

$$Cu \mid CuBr \mid Cu_xS \mid (Cu_xS,\ PbS) \mid (PbCl_2 + 1\%\ KCl) \mid Pb \qquad (IV)$$

was investigated where Cu_xS denotes cuprous sulfide involving a deficit of copper within the homogeneity range of this phase (7). For reasons discussed below, a copper-to-sulfur ratio $x = 1.98$ was used. In view of the finite copper deficit, cuprous sulfide in cell (IV) is not in its standard state.

Cell (IV) may be considered as a double cell involving the individual cells

$$Cu \mid CuBr \mid Cu_xS \mid graphite \qquad (IVa)$$

and

$$graphite \mid (Cu_xS, PbS) \mid (PbCl_2 + 1\%\ KCl) \mid Pb \qquad (IVb)$$

where the partial molar free energy of sulfur at the graphite electrodes is determined by the copper-to-sulfur ratio x.

Under conditions involving predominantly ionic conduction in CuBr and $PbCl_2$ + 1% KCl, the virtual cell reactions in cells (IV*a*) and (IV*b*) on passing two faradays are

$$2Cu + (2/x)\underline{S}\ (\text{in } Cu_xS) = (2/x)Cu_xS \qquad [2]$$

and

$$PbS = Pb + \underline{S}\ (\text{in } Cu_xS) \qquad [3]$$

Thus, the over-all reaction for cell (IV) is

$$PbS + 2Cu + [(2-x)/x]\,\underline{S}\ (\text{in } Cu_xS) = Pb + (2/x)\,\overline{Cu_xS} \qquad [4]$$

and the free energy change ΔF of reaction [4] is

$$\Delta F = -2EF \qquad [5]$$

where E is the emf of cell (IV), and F is the Faraday constant.

Letting

$$\overline{F}_{Cu_xS} = x\,\overline{F}_{Cu} + \overline{F}_S \qquad [6]$$

one obtains for the free energy change of reaction [4] for a given value of x

$$\Delta F = F_{Pb}^\circ + 2\overline{F}_{Cu}(x) + (2/x)\,\overline{F}_S(x) - [(2-x)/x]\,\overline{F}_S(x) - 2F_{Cu}^\circ - F_{PbS}^\circ \qquad [7]$$

and for the standard free energy change ΔF° of reaction [4] as the limiting case for $x = 2$,

$$\Delta F^\circ = F_{Pb}^\circ + 2\overline{F}_{Cu}(x=2) + \overline{F}_S(x=2) - 2F_{Cu}^\circ - F_{PbS}^\circ \qquad [8]$$

[1] Present address: Department of Metallurgy, Pennsylvania State University, University Park, Pa.

Upon subtracting corresponding sides of Eqs. [7] and [8], it follows that

$$\Delta F - \Delta F^\circ = 2\,[\bar{F}_{Cu}(x) - \bar{F}_{Cu}(x=2)] + [\bar{F}_S(x) - \bar{F}_S(x=2)] \quad [9]$$

The Gibbs-Duhem equation reads

$$x\,d[\bar{F}_{Cu}(x) - \bar{F}_{Cu}(x=2)] + d[\bar{F}_S(x) - \bar{F}_S(x=2)] = 0 \quad [10]$$

Substitution of Eq. [10] in Eq. [9] yields

$$\Delta F - \Delta F^\circ = \int_0 (2-x)\,d\,[\bar{F}_{Cu}(x) - \bar{F}_{Cu}(x=2)] \quad [11]$$

Under the conditions of the following experiments, the copper deficit δ^* in cuprous sulfide may be represented by (7)

$$\delta^* = 2 - x = 2x_\oplus^\circ \; sinh \{-[\bar{F}_{Cu}(x) - \bar{F}_{Cu}(x=2)]/RT\} \quad [12]$$

where $x_\oplus^\circ$ denotes the ratio of electron holes to sulfur atoms in cuprous sulfide of ideal composition.

Upon substitution of Eq. [12] in Eq. [11], it follows that

$$\Delta F - \Delta F^\circ = -2x_\oplus^\circ\,RT \left\{\left[1 + \sinh^2 \frac{\bar{F}_{Cu}(x) - \bar{F}_{Cu}(x=2)}{RT}\right]^{1/2} - 1\right\}$$
$$= -2x_\oplus^\circ\,RT\,\{[1 + (\delta^*/2x_\oplus^\circ)^2]^{1/2} - 1\} \quad [13]$$

whence

$$\Delta F^\circ = \Delta F + \delta^*\,RT \text{ if } \delta^* >> 2x_\oplus^\circ \quad [14]$$

PbS also exhibits deviations from the ideal stoichiometric ratio. An estimate using the most recent data of Bloem and Kröger (8) indicates that under the conditions of the present experiments the contribution to the free energy of reaction [4] due to the nonstoichiometry of PbS is negligible.

Experimental

Predominantly ionic conduction in CuBr at moderately oxidizing conditions has been ascertained with the help of polarization measurements (6). A similar technique has been used in order to investigate $PbCl_2$ and $PbBr_2$, pure and doped with alkali halide.

It is known that $PbBr_2$ and $PbCl_2$ are predominantly anion conductors (9) presumably via anion vacancies (10) when the conductivity is measured under reducing conditions. This is also true for samples doped with alkali halide (11) whereby the concentration of anion vacancies and thus the ionic conductivity is increased.

The total conductivity was determined with the aid of a conventional a-c method. In addition, the magnitude of electronic conductivity has been estimated by determining current-potential curves for cells of type

$$Pb \mid PbCl_2 \mid graphite \quad (V)$$

On applying a voltage below the decomposition potential of $PbCl_2$ with the positive pole on the right-hand side, both chlorine ions and electrons migrate initially toward the graphite electrode. Since chlorine ions are not discharged at the graphite electrode, the chlorine-to-lead ratio at this electrode is slightly increased. Finally, under steady-state conditions, migration of Cl^- ions due to the electrical field is balanced by diffusion due to the concentration gradient, and the current is carried exclusively by electrons moving either as excess electrons or via electron holes.

One batch of $PbBr_2$ was prepared by synthesis from the elements and a second batch was prepared by passing the decomposition products of NH_4Br in a stream of argon over molten commercial $PbBr_2$. Both preparations gave essentially the same results. $PbCl_2$ was prepared by passing the decomposition products of NH_4Cl in a stream of argon over molten commercial $PbCl_2$.

The total electrical conductivity of undoped $PbCl_2$ at 300°C was found to be $1.2 \times 10^{-4}\,\Omega^{-1}\,cm^{-1}$ which is of the same order of magnitude as that reported by Seith (12). The total conductivity at 300°C of $PbCl_2$ + 1% KCl was found to be $1.2 \times 10^{-8}\,\Omega^{-1}\,cm^{-1}$, and that of $PbBr_2$ + 1% KBr, $1.5 \times 10^{-3}\,\Omega^{-1}\,cm^{-1}$.

Plots of the logarithm of the electronic current measured with cell (V) vs. the applied voltage gave essentially straight lines (*see* Fig. 1). This behavior is similar to that reported for cuprous halides (6), but is not amenable to a theoretical analysis because the experimental slopes in Fig. 1 are about four times smaller than suggested by theory.

Since the electronic conductivity in $PbCl_2$ + 1% KCl was found to be lower than that in $PbBr_2$ + 1% KBr, the former electrolyte was chosen for the following measurements. For a voltage of 0.2 v corresponding to the conditions of the following experiments, the ratio of the electronic current to the total current prevailing between reversible electrodes is found to be 10^{-4} for $PbCl_2$ + 1% KCl. Thus predominantly ionic conduction has been ensured.

Cu_2S and CuBr were prepared by synthesis from the elements as described elsewhere (6, 7) and the PbS was a commercial material with a listed purity of 99.67%. The sulfides and the CuBr were pressed into cylindrical pellets, 6.35 mm in diameter by 1-4 mm thick, in a die under about 4000 psi. The copper pellet was 99.999% pure and the lead pellet was of silver-free lead 99.89% pure.

In order to obtain meaningful results, the value of x in Cu_xS must be constant throughout the two Cu_xS pellets in cell (IV). To ensure this condition, the half-cell

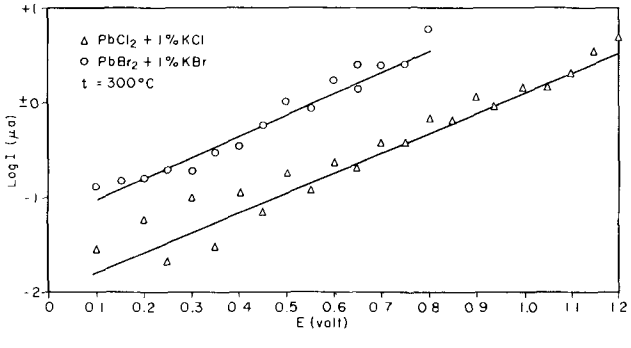

Fig. 1. Electronic current *I* as a function of potential *E* for doped lead bromide of 0.242 cm thickness and 0.316 cm² area and for doped lead chloride of 0.326 cm thickness and 0.316 cm² area.

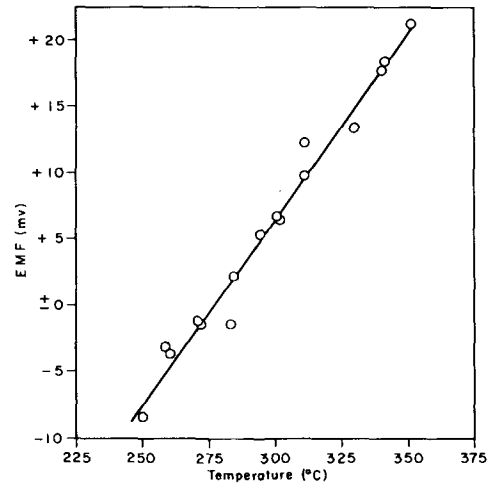

Fig. 2. Emf E of the cell $Cu|CuBr|Cu_{1.98}S|(Cu_{1.98}S, PbS)|(PbCl_2 + 1\%\ KCl)|Pb$ as a function of temperature.

$$Cu \mid CuBr \mid Cu_xS \mid (Cu_xS, PbS) \mid graphite \quad (VI)$$

was assembled and placed inside a Pyrex vessel as described by Kiukkola and Wagner (2). A positive potential of 0.2 v was applied to the graphite electrode and the cell was then heated to 300°C for 8 hr under an atmosphere of argon to fix the copper-to-sulfur ratio. The potential of 0.2 v was chosen in view of the following compromise. The higher the potential, the lower is the rate of change of the partial molar free energy of copper in the sample with x and, therefore, the more stable is the state "Cu_xS" against perturbations (7). On the other hand, the lower the potential, the lower is the fraction of electronic conduction in both CuBr and $PbCl_2 + 1\%$ KCl.

At the end of the "conditioning process" the connection with the potentiometer was interrupted, cell (VI) was cooled, and cell (IV) was assembled. The doped $PbCl_2$ was pressed into the form of a crucible (2), 10 mm in diameter by 8 mm high, in order to contain molten lead above 323°C.

Cell (IV) was then heated between 250° and 350°C under an atmosphere of argon and the emf was measured.

Fig. 2 shows a plot of a typical run. The results of the measurements on cell (IV) in the temperature range of 250° and 350°C may be expressed by the following equation

$$E(\text{volt}) = (6.5 \pm 1) \times 10^{-3} + 0.3 \times 10^{-3}\ (t - 300) \quad [15]$$

Discussion

From Eq. [15], the free energy change ΔF of reaction [4] is found to be equal to -300 ± 46 cal at 300°C.

The copper deficit in Cu_2S subjected to an oxidizing potential of 0.2 volt (7) is $\delta^* = 0.02$. Thus it follows from Eq. [14] that

$$\Delta F^\circ = -277 \pm 46 \text{ cal} \quad [16]$$

Moreover, in view of the temperature dependence of the emf of cell (IV) according to Eq. [15], it follows that $\Delta F^\circ = 0$ at $279° \pm 4$°C. Thus the three phase system Cu-Cu_2S-PbS is stable below $279° \pm 4$°C, whereas the three-phase system Pb-PbS-Cu_2S is stable above $279° \pm 4$°C.

The standard free energy of formation of lead sulfide has been deduced recently from emf measurements (2),

$$Pb + S = PbS;\ \Delta F^\circ(573°K) = -22{,}330 \text{ cal} \quad [17]$$

Upon combining Eqs. [16] and [17], the standard free energy of formation of cuprous sulfide is obtained as

$$2Cu + S = Cu_2S;\ \Delta F^\circ(573°K) = -22{,}607 \text{ cal} \quad [18]$$

On the other hand, one may extrapolate data for the H_2S/H_2 ratio over Cu and Cu_2S determined by Brooks (13) between 342° and 1037°C and by Richardson and Antill (14) between 527° and 1152°C which yield

$$2Cu + H_2S = Cu_2S + H_2;\ \Delta F^\circ(573°K) = -12{,}620 \text{ cal} \quad [19]$$

Combining the latter value with the standard free energy of formation of H_2S,

$$H_2 + S = H_2S;\ \Delta F^\circ(573°K) = -10{,}039 \text{ cal} \quad [20]$$

calculated from standard heats of formation and entropy values at 298°K (15) and from enthalpy and entropy increments between 298° and 573°K (16), one obtains

$$2Cu + S = Cu_2S;\ \Delta F^\circ(573°K) = -22{,}659 \text{ cal} \quad [21]$$

which is in practical agreement with the value obtained in Eq. [18]. This shows the consistency of the various values involved.

Acknowledgment

This work was sponsored by Office of Ordnance Research, U.S. Army under Contracts Nos. DA-19-020-ORD-2244 and DA-19-020-ORD-3661.

Manuscript received September 21, 1956.

Any discussion of this paper will appear in a Discussion Section to be published in the June 1958 JOURNAL.

REFERENCES

1. H. Reinhold, *Z. Elektrochem.*, **40**, 361 (1934).
2. K. Kiukkola and C. Wagner, *This Journal*, **104**, 379 (1957).
3. K. Nagel and C. Wagner, *Z. physik Chem.*, **B25**, 71 (1934).
4. R. J. Maurer, *J. Chem. Phys.*, **13**, 321 (1945).
5. B. H. Vine and R. J. Maurer, *Z. physik Chem.*, **198**, 147 (1951).
6. J. B. Wagner and C. Wagner, *J. Chem Phys.*, June 1957.
7. J. B. Wagner and C. Wagner, *J. Chem Phys.*, June 1957.
8. J. Bloem and F. A. Kröger, *Z. physik Chem. (N.F.)*, **7**, 1, 15 (1956).
9. C. Tubandt and S. Eggert, *Z. anorg. u. allgem. Chem.*, **110**, 96 (1920); C. Tubandt, *ibid.*, **115**, 105 (1921); C. Tubandt, H. Reinhold, and G. Liebold, *ibid.*, **197**, 225 (1931).
10. E. Koch and C. Wagner, *Z. physik Chem.*, **B38**, 295 (1937).
11. C. Tubandt and H. Reinhold, *Z. Elektrochem.*, **29**, 313 (1923).
12. W. Seith, *Z. physik.*, **56**, 802 (1929); *ibid.*, **57**, 869 (1929).
13. A. A. Brooks *J. Am. Chem. Soc.*, **75**, 2464 (1953).
14. F. D. Richardson and J. E. Antill, *Trans. Faraday Soc.*, **51**, 22 (1955).
15. Circular of the National Bureau of Standards 500 (1952).
16. K. K. Kelly, U. S. Bureau of Mines Bull. 476 (1949).

Zinc Standard Potential in Water-Organic Mixtures

Gerald Corsaro and Howard L. Stephens

Knight Hall Chemistry Laboratories, University of Akron, Akron, Ohio

ABSTRACT

The measurement of cell potentials provides one method for testing the predictions of the Debye-Hückel theoretical equations for activity coefficients of electrolytes. The emf of cells: Zn-Hg; $ZnCl_2$(m) (*S*) (Y) AgCl(*S*); Ag are investigated to verify the effect of varying dielectric constant in solutions of a 2-1 electrolyte, $ZnCl_2$. (*S*) represents percentages by weight of MeOH, EtOH, and 1,4-Dioxane with water (*Y*). The simple Hitchcock procedure is used to obtain standard cell potentials by graphical extrapolation. Confirmation of theoretical predictions is illustrated by the data obtained. The value for the standard electrode potential of zinc in water is evaluated by direct measurement and confirmed by cell emf data with mixed solvents.

Measurement of reversible cell potentials provides one experimental procedure to test the predictions of the Debye-Hückel equations for activity coefficients of strong electrolytes. Temperature, concentration, ionic charges, and dielectric constant are experimentally controllable factors which affect the values of the coefficients. Whereas considerable data are available for 1-1 electrolytes in mixed solvents (1-3), that for 2-1 and other class electrolytes is much more limited. Moreover, there is some doubt concerning the best value of the standard electrode potential for Zn in water. Harned and Owen (4) accept the value reported by Robinson and Stokes (5) at 0.7634 Int. Volt. Although this is at least 2 mv higher than the average of three previously recorded results at 0.7612 Int. Volt.

The present paper is concerned with evidence which supports the lower value for the Zn standard electrode potential. EMF measurements of cells with mixed solvents demonstrate that only the simplest extrapolation procedure is necessary to obtain standard cell potentials. Further, it may be shown that these are linear with the reciprocal of the dielectric constant of the solvent as given by the Debye-Hückel theoretical equations. Activity coefficients calculated from observed emf data are in good agreement with those calculated from the Debye-Hückel equations.

The standard electrode potential of Zn at 25°C has been determined with cells of the type:

Zn-Hg(2-phase); Zn^{++} X^-(m), MX(s); M

Ag-AgCl (6), Pb-$PbSO_4$ (7), and calomel electrodes (8) have been used as reference electrodes. If the value reported by Robinson and Stokes is omitted, the average of the remaining three results for the zinc standard potential at 25° is 0.7612 Int. Volt. None of the three results deviated from this average by more than ±0.2 mv.

Robinson and Stokes used an extrapolation procedure suggested by Bates (9) which requires the use of the Debye-Hückel extended equation for activity coefficient. They utilized two separate ion size parameters at 3.8 and 5.0Å for $ZnCl_2$ in order to extend the linearity of their extrapolation plots through a wide range of salt concentrations.

The same cell type has been used in the present work:

Zn-Hg(2-phase); $ZnCl_2$(m), (*S*), (Y), AgCl(*s*); Ag

where *S* is the percent by weight of organic solvent, Y, that of water, and m is the molality of $ZnCl_2$ in the mixed solvents. MeOH, EtOH, and 1,4-Dioxane were the organic solvents employed in the mixtures so that a range of dielectric constants from 51.9 to 78.4 was available, and conc. to 0.1*M* $ZnCl_2$.

The simple Hitchcock (10) procedure was employed to obtain the standard cell potentials. Particular emphasis was put on measurements with the more dilute solutions so that linear plots could be drawn through a sufficient number of points to assure proper extrapolation in the dilute range below 0.01*M*.

Experimental Procedure

An electrolytic cell was constructed by joining three 1 x 4 in. Pyrex tubes with 6 mm tubing in such manner as to give a top "V" view. The middle tube has sealed at the bottom a reservoir of approximately 1 cc. A Pt wire sealed in this reservoir provides communication to the external measuring circuit.

Two-phase Zn amalgams were deposited electrolytically in this cell by using pure Zn stick anodes, and $ZnSO_4$ solutions. About 1 hr at 1 amp was usually required to produce a firm Zn amalgam, when ½ cc purified Hg is used as the cathode. This procedure makes it simple to prepare amalgams prior to each individual experiment. The cell is washed readily with water and experimental solution before an emf measurement with a particular solution mixture. A zero potential difference between the amalgam and Zn or Hg has been found experimentally (11). The reference Ag-AgCl electrodes were mounted on neoprene stoppers so that they could be inserted in sections of the cell not holding the amalgam. The Ag-AgCl electrodes were prepared by a procedure essentially that recommended

by Brown (12). Number 24 Pt wire is sealed into 4 mm soft glass tubing, and Hg added in the tubing for contact with the external circuit. The wire is silver plated at low current density from a 1% solution of twice recrystallized $KAg(CN)_2$. A cell like that described is used for this purpose, thus separating anode and cathode compartments to prevent free cyanide ion contamination in the Ag. After thorough washing, the Ag is anodized in 0.1*N* HCl. The electrodes were then washed in water and NH_4OH, and reanodized, then again washed in dilute NH_4OH and water. A period of aging is required before these electrodes check against each other with a potential difference of less than ±0.05 mv.

A concentrated $ZnCl_2$ solution was prepared by dissolving a Khabaum grade Zn of 99.966% Zn in redistilled constant boiling HCl solution. With excess Zn present, the final solution had a *p*H value of near 6.0, but further acid was added to reduce the *p*H value to 4.4 to prevent hydrolysis in the very dilute solutions.

Methyl and ethyl alcohols were purified in the usual manner, but no attempt was made to collect and store absolute alcohol. Instead, the alcohols were diluted with water, and the alcohol content obtained from density measurements. The 1,4-Dioxane was obtained from Carbide and Chemicals Corp. The liquid was partially frozen, and the melted solid diluted to about 80% Dioxane, and distilled from bright Cu turnings. A constant boiling mixture of known composition is obtained in this way (13), and the distillation could be carried out prior to preparing experimental solutions in order to minimize peroxide contamination.

Each experimental solution was prepared by weighing the concentrated $ZnCl_2$ solution on the analytical balance. Water was added by weight, and the amount of organic solvent to be added could then be calculated to give the desired percent by weight.

Concentrated $ZnCl_2$ was analyzed after preparation by precipitation and weighing of zinc ammonium phosphate and silver chloride. The molality calculated from duplicate set of determinations usually checked to better than 0.0007*M* with a total concentration of 1.4*M* or better.

A conventional potentiometer circuit with a type K L&N potentiometer, a galvanometer with a sensitivity of 0.04 μa/mm division, and a standard Eppley cell with certified Bureau of Standards calibration, were used to measure emfs at 25° ±0.02°C. Readings were sensitive to 0.01 mv. A new amalgam was prepared for each run. After the cell was filled wtih the experimental solution, a flow of purified hydrogen was maintained over the amalgam during all emf measurements. A period of 24 hr was required with dilute solutions to obtain steady readings, but less time with more concentrated solutions. Concentration of $ZnCl_2$ less than 0.004*M* gave erratic results. Two Ag-AgCl electrodes in the cell made it possible to obtain duplicate results. Often, but not at all times, two runs or four separate results were obtained. Since a period of more than 4 years was necessary to obtain all the data recorded here, AgCl electrodes were prepared periodically, but always checked against older electrodes available.

Calculation and Tabulation of Results

Measured emf values of the cells are recorded in Int. Volts.

For 2-1 electrolyte:

$$E = E^\circ - \frac{RT}{n\mathbf{F}} \ln 4m^3V^3 \qquad \text{(I)}$$

in which $V\pm$ is the mean activity coefficient, E the measured emf, E° the standard cell potential, and m the molality.

Rearrangement and expansion gives:

$$E = E^\circ - \frac{3R'T}{n\mathbf{F}} \log 4^{1/3} - \frac{3R'T}{n\mathbf{F}} \log m - \frac{3R'T}{n\mathbf{F}} \log V\pm \qquad \text{(II)}$$

To introduce $f\pm$, the activity coefficient given by the Debye-Hückel equations, the expression:

$$\log V\pm = \log f\pm - \log [1 - .001\ v\ Mxy \cdot m] \qquad \text{(III)}$$

is required. Mxy is the average molecular weight of the mixed solvent, and v the number of ions produced by the electrolyte, and,

$$Mxy = \frac{100}{\frac{S}{Mx} + \frac{Y}{My}} \qquad \text{(IV)}$$

where $R' = 2.303R$; $R = 8.3142$ Int. Joules; $\mathbf{F} = 96{,}500$ coulombs.

For extrapolation of measured emf data to infinite dilution, the Hitchcock method (10) was employed. The Debye-Hückel limiting expression with an added linear team,

$$-\log f\pm = 2A(u)^{1/2} - C'u \qquad \text{(V)}$$

is substituted in (II) after first introducing (III) in (II). Expression (V) is now substituted and on rearrangement and expansion one obtains:

$$E^\circ = E - 0.08873 \times 2A(u)^{1/2} + 0.08873\ C'u - 0.08873 \log [1 - 0.003\ Mxy \cdot m] + 0.08873 \log m + 0.01781 \qquad \text{(VI)}$$

The value of A is derived from the Debye-Hückel theoretical expression:

$$A = \frac{1.824 \times 10^6}{(DT)^{3/2}} \qquad \text{(VII)}$$

Calculations are facilitated by letting $E^{\circ\prime}$ equal

$$E + 0.08873\ [\log m - \log (1 - 0.003\ Mxy \cdot m)] + 0.01781 - 0.08873 \times 2A(u)^{1/2} \qquad \text{(VIII)}$$

and,

$$E^{\circ\prime} = E^\circ - 0.08873\ C'u \qquad \text{(IX)}$$

The last expression provides the linear function by which extrapolation to $u = 0$ may be made.

Calculation is further simplified by defining:

$$E^{\circ\prime\prime} = E + 0.08873\ [\log m - \log(1 - 0.003\ Mxy \cdot m)] + 0.01781. \qquad \text{(X)}$$

and

$$E^{\circ\prime} = E^{\circ\prime\prime} - 0.08873 \times 2A(u)^{1/2} \qquad \text{(XI)}$$

The data are tabulated in Tables I through XIII.[1] These also give the dielectric constant, the Debye-Hückel constant A, the average molecular weight of the solvent, Mxy, and the Debye-Hückel constant B, defined by:

$$B = \frac{5.029 \times 10^{9}}{(DT)^{1/2}} \qquad \text{(XII)}$$

The dielectric constants were those reported by Åkerlof (14) or calculated for empirical expressions suggested by him.

The observed activity listed is that obtained from the extrapolated standard cell potential and cell emf values with different m values; the calculated value is that calculated from the equation:

$$-\log f\pm = \frac{2A(u)^{1/2}}{1 + Ba(u)^{1/2}} \qquad \text{(XIII)}$$

Discussion of Results

Data in Tables I through XIII show extrapolated values for E° which are the standard cell potentials. To obtain these values, the recorded $E^{\circ\prime}$ data were plotted against u. Large 24 in. x 30 in. graph paper made it possible to plot individual points with an uncertainty of ±0.05 mv. The linear graphing fitted most of the points in the dilute range with a precision of better than ±0.1 mv. The extrapolated standard potentials were therefore expected to be read off the plots with this precision. Graphical extrapolations are summarized in Fig. 1-4.

Fig. 1 shows the calculated $E^{\circ\prime}$ values taken some ten years apart. The smooth straight line drawn through these two sets of points indicates the excellent reproducibility attained by the electrode systems, and the simple Hitchcock extrapolation in the dilute range.

Fig. 5 depicts the plots of the standard cell potentials obtained with the three different solvent systems, against 1/D. The data for Fig. 5 are summarized in Table XIV. Linearity is retained through the lowest dielectric constant value with a precision of better than ±0.1 mv. Moreover, each separate plot extrapolates through the same single value, that for the standard cell potential with water and identical with the value for this potential obtained by measurement. This experimental evidence, together with the fact that calculated and observed activity coefficients in all solvents show an average deviation of less than ±0.01 units, supports the value of the standard potential for Zn in water at 0.7610 ±0.0002 Int. Volt.

Harned and Owen (4) report values for the standard electrode potential of the Ag-AgCl electrode in water at −0.2224 Int. Volt, and also give values for this potential in most of the solvent mixtures used in this work, so that the value for the electrode potential for Zn in these solvents could be calculated.

[1] These tables have been deposited as Document 5192 with the ADI Auxiliary Publications Project, Photoduplication Service, Library of Congress, Washington 5, D. C. A copy may be secured by citing the Document number and by remitting $1.25 for a photoprint or for a 35-mm microfilm. Advance payment is required. Make check payable to: Chief, Photoduplication Service, Library of Congress.

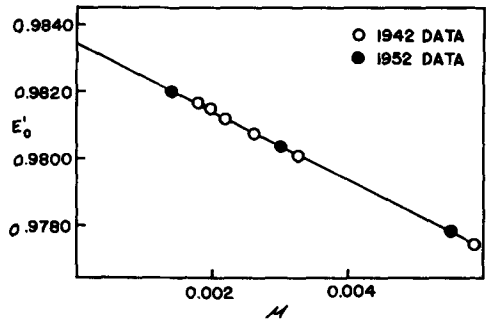

Fig. 1. $E^{\circ\prime}$ values for the cell with water as the solvent, and extrapolation to zero ionic strength.

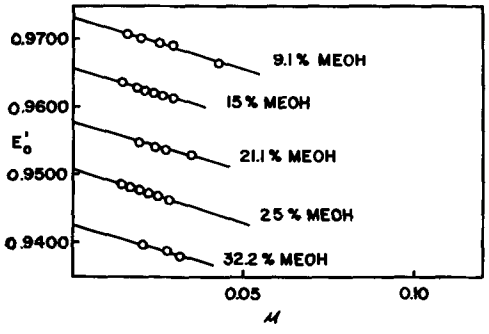

Fig. 2. $E^{\circ\prime}$ values for the cell with MeOH-water solvents, and extrapolation to zero ionic strength.

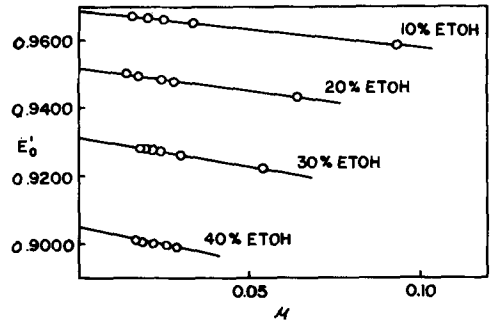

Fig. 3. $E^{\circ\prime}$ values for the cell with EtOH-water mixtures, and extrapolation to zero ionic strength.

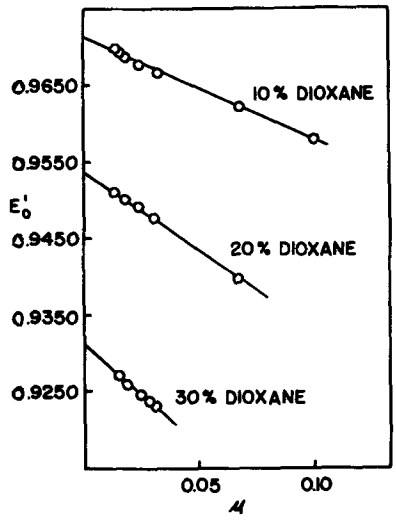

Fig. 4. $E^{\circ\prime}$ for the cell with 1,4-Dioxane-water mixture, and extrapolation to zero ionic strength.

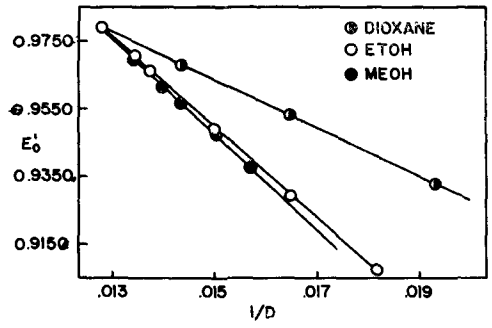

Fig. 5. Standard cell potentials for cells with MeOH, EtOH, 1,4-Dioxane, -water mixtures plotted as a function of 1/D.

A plot of

$$\frac{2A(u)^{1/2}}{\log f\pm \text{ (obs.)}} vs\ (u)^{1/2}$$

should give a slope of $1 + Ba$. From the data given here, it can be shown that such a plot with all solvent systems results in a value for a of 4.8 $\pm$0.2Å and hence justifies the choice of a single ion size chosen in these calculations.

Conclusions and Summary

The cells:

Zn-Hg(2-phase); $ZnCl_2(m)(S)(Y)$, $AgCl(s)$; Ag

have been investigated, with (S) representing mixtures of MeOH, EtOH, and 1,4-Dioxane at different percentages by weight with water, Y per cent. The cell potential with pure water gives a value for $E°$, (Zn/Zn^{+}), 25°C equal to +0.7610 Int. Volt. This is 2.4 mv lower than the result accepted by Harned and Owens, but appears to be adequately supported by the experimental data presented. The activity coefficients from the observed data are in good agreement with those predicted by the Debye-Hückel equations in solvent media of different dielectric constant. The linear variation of the standard cell potential with $1/D$ as given by theory is well confirmed by experimental data, although no simple relationship exists which gives a single linear function with different solvent mixtures of the same dielectric constant.

Manuscript received July 30, 1956. This paper was prepared for delivery before the Washington Meeting, May 12-16, 1957.

Any discussion of this paper will appear in a Discussion Section to be published in the June 1958 JOURNAL.

REFERENCES

1. H. S. Harned and H. C. Thomas, *J. Am. Chem. Soc.*, **57**, 1666 (1935).
2. H. S. Harned, F. Walker, C. Calmon, *ibid.*, **61**, 49 (1939).
3. H. S. Harned and R. W. Ehlers, *ibid.*, **54**, 1350 (1932).
4. H. S. Harned and B. B. Owens, "The Physical Chemistry of Electrolytic Solutions," Vol. 1, Rhinehold Publishing Corp., New York (1943).
5. R. A. Robinson and R. H. Stokes, *Trans. Faraday Soc.*, **36**, 740 (1940).
6. G. Scatchard and R. F. Tefft, *J. Am. Chem. Soc.*, 52, 2272 (1930).
7. I. A. Copperwaite and V. R. LaMer, *ibid.*, **53**, 4333 (1931).
8. F. H. Getman, *J. Phys. Chem.*, **35**, 2749 (1931).
9. R. A. Robinson and R. H. Stokes, *Trans. Faraday Soc.*, **36**, 740 (1940).
10. D. E. Hitchcock, *J. Am. Chem. Soc.*, **50**, 2076 (1928).
11. W. J. Clayton and W. C. Vosburgh, *ibid.*, **58**, 2093 (1936).
12. A. S. Brown, *ibid.*, **56**, 646 (1934).
13. F. Hovorka, R. A. Schaefer, and D. Dreisbach, *ibid.*, **58**, 2264 (1936).
14. G. Åkerlof, *ibid.*, **54**, 4125 (1932).

Preparation of Pure Fused Lithium Chloride-Potassium Chloride Eutectic Solvent

H. A. Laitinen

Department of Chemistry and Chemical Engineering, University of Illinois, Urbana, Illinois

W. S. Ferguson

Research Department, The Ohio Oil Company, Littleton, Colorado

and

R. A. Osteryoung

Department of Chemistry, Rensselaer Polytechnic Institute, Troy, New York

ABSTRACT

Hydrolytic decomposition occurs during the fusion of a eutectic mixture of lithium chloride-potassium chloride containing traces of moisture if the fusion conditions are not controlled. The resultant contamination by hydroxyl ion greatly lowers the utility of this mixture as a fused salt solvent. The effectiveness of various procedures used for preparation of the fused salt solvent was followed by observation of the characteristic polarographic residual current using a platinum microelectrode. A preparative method is described which involves drying the mixture under moderate vacuum, fusion under anhydrous hydrogen chloride, and removal of the hydrogen chloride from the melt.

For the initial work of a long-term general investigation in fused salt electrochemistry, a eutectic mixture of LiCl-KCl was selected as the fused salt solvent. Advantageous characteristics of this solvent are good thermal stability, wide span of electrolytic decomposition potential, absence of strongly acidic or basic properties, high conductivity and fluidity, and commercial availability of its components as the reagent grade salts. Further, the melting point is low enough and its chemical reactivity is such that Pyrex glass can be utilized as a material of construction. The properties of the solvent thus permit, in theory, a study of the electrochemistry of a wide variety of solutes with a minimum of interference from solvent effects and with only moderate experimental difficulty as high temperature work goes.

In practice, the potentiality of these desirable solvent properties, particularly the wide decomposition potential span, is limited by the purity of the fused solvent which can be prepared. The most troublesome aspect of preparing a pure LiCl-KCl eutectic fusion arises from the highly deliquescent property of the LiCl. Unless special precautions are taken, hydrolytic decomposition occurs as the temperature is raised and HCl is lost from the system. Concurrently, the melt becomes contaminated with alkaline products.

Various methods have been proposed and used to prevent hydrolytic decomposition during the preparation of anhydrous chlorides. The heating of hydrated rare earth chlorides with gross amounts of NH_4Cl is one classic method. For the preparation of fused LiCl-KCl mixtures containing potassium hexachloromolybdate, the method of heating the salt mixture to fusion in a stream of dry, inert gas followed by an electrolysis of the melt for removal of oxygen as molybdenum oxides at the cathode and by volatilization of molybdenum oxychlorides has been used (1). Another procedure involves drying the LiCl and the KCl separately by first slowly heating the salts to between 480° and 500°C under high vacuum (10^{-4} to less than 10^{-6} mm Hg), then mixing the dried salts together under a controlled atmosphere in a dry box, and finally fusing the dry mixture under high vacuum (2, 3). The method to be described here involves drying the eutectic mixture under moderate vacuum, fusing the mixture under anhydrous HCl at atmospheric pressure, and then removing the excess HCl from the fused solvent.

Experimental Procedure

The apparatus used in this work includes the following:

Furnace: Cenco-Cooley No. 13627, 115 V, 700 W, Central Scientific Company, Chicago. A separate heating circuit equivalent to 25% of the original furnace heating capacity was installed in the bottom of the furnace cavity. Only this auxiliary circuit was operated by the furnace controller.

Controller: Wheelco Indicating Controller Model 241-P, Barber-Coleman Company, Rockford, Illinois.

Vacuum Pump: Cenco "Pressovac," Central Scientific Company, Chicago.

Chemicals: Tank gases of the Matheson Company,

Joliet, Ill., were used. The argon was passed over hot Cu to remove traces of oxygen. Both argon and HCl were dried over $Mg(ClO_4)_2$. Reagent grade LiCl and KCl were used to prepare the solvent.

Electrodes: A Pt foil in equilibrium with a dilute solution of Pt (II) in the fused salt solvent was used as the reference electrode. This system has been shown to determine a stable, nonpolarizable reference potential and has been described in various modifications (4-6). The microelectrodes used consisted of 26 gauge Pt wire sealed into Corning 0120 glass with about 1 mm of the wire projecting (total electrode area of 1.4 mm^2) or 18 gauge tungsten wire sealed into Pyrex glass with the wire ground flush to the glass (total electrode area of 0.8 mm^2).

Polarograph: The polarograms reported were observed as automatically recorded curves by using an "Electrochemograph," Type E, Leeds and Northrup, Philadelphia.

Fused salt cell: The cell used is described below.

The cell in which the solvent preparation procedure is completed has been found very useful in performing both chemical and electrochemical experiments. As it is a general tool for fused salt research (6), it is described in greater detail than is necessary merely for use as the solvent preparation vessel.

Fig. 1 is an illustration of the various cell components. The cell as shown is only partially assembled and all of the various components shown are not necessarily to be in use at one time. An explanation of the function of these components serves to indicate which combination is needed for a particular purpose. All of the glass parts are Pyrex (Corning 774) except as otherwise noted.

The side arm tube A is the fused salt container. It is 33 cm long by 6 cm OD and indicates the scale of the illustration. In use, the tube contains fused salt to a depth of about 4½ cm and protrudes from the furnace above the level L-L which is 12 cm from the bottom, but in more recent work has been increased to 15 cm. The melt inside tube A can be divided into several portions by the compartments B which are closed at the bottom by medium porosity fritted glass disks. These portions of melt are then in electrolytic contact with one another but cross-contamination of the compartment contents is prevented. A number 13 rubber stopper C serves to close the tube A and to support within the tube A the inert-gas delivery tube D, the thermocouple sheath E, and various electrodes. Those holes in stopper C which are not in use are closed by glass plugs F.

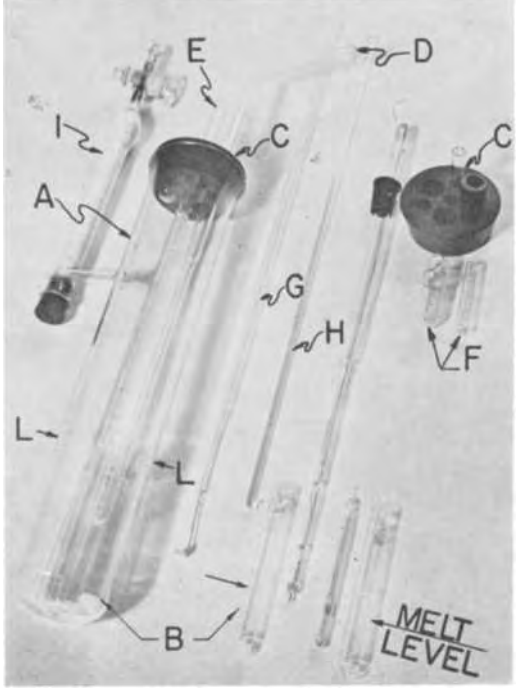

Fig. 1. Components of the fused salt cell

The large holes in stopper C permit easy manipulative access to the interior of tube A. During the experiment, for example, individual compartments can be removed from the system, using hook H, or known amounts of a solute can be added to any one of the compartments within the tube, using platinum spoon G. The entry of air into the system is prevented by an argon atmosphere which blankets the fused salt.

The seven holes in the stopper must have parallel axes and must fit their respective glass parts (10 mm and 16 mm in this case) very snugly but without binding. It has been found advantageous to bore the holes with a drill press, using a regular twist drill. The stopper is first frozen in a dry ice-"Cellosolve" mixture.

A principal advantage of this cell is that several different solution compositions can be maintained at one time in separate compartments in the tube. Thus, a new bath of fused salt solvent need not be prepared for each change of experimental condition. The precise course of an experiment need not be predetermined, since it is a simple matter to alter the composition of a compartment at any time without affecting the composition of the rest of the compartments. This is an extremely valuable advantage in fused salt research.

The fritted barriers of the compartments are very effective for preventing diffusion of a solute out of its compartment. Electrically, the barriers are efficient in that the resistance is but 20 to 50 ohms between two Pt wires immersed in the eutectic solvent of two different compartments.

Preparation of the eutectic solvent is carried out as follows. Reagent grade LiCl and KCl are taken in the proportion 0.59 mole to 0.41 mole and mixed together. The mixture is placed in a suitable vessel and exposed to a vacuum (0.1 to 0.2 mm Hg) for 6 hr to remove excessive moisture so that the material will not cake during the next step. All transfers of the material from this point on must be made as rapidly as possible to avoid excessive pickup of atmospheric moisture. The vacuum-dried mixture is ball-milled to a fine free-flowing powder in a clean, tightly closed jar, using porcelain balls which have previously been leached with 6*N* HCl, rinsed with pure water, and oven-dried. The ground mixture is stored in 1-lb screw-cap jars until needed. It has been kept as long as 1 year without caking, provided that the ground mixture is vacuum-dried

at room temperature for a few hours immediately after being transferred into the 1-lb containers.

A large desiccator having an appropriately drilled Lucite plate serves to sieve the balls from the mixture without undue exposure to atmospheric moisture.

The solvent preparation for an experiment, working from the vacuum-dried, ground mixture, is completed in tube A, referring to Fig. 1. Tube A is fitted with a stopper C carrying a gas delivery tube D and a thermocouple sheath E. All unused holes in the stopper are closed by plugs F. The spherical joint of tube D is connected to a stopcock at which either argon or anhydrous HCl is available at a pressure of 4-5 cm Hg in excess of atmospheric pressure. The sidearm of tube A is fitted with its protective drying tube I, which is in turn connected to a vacuum manifold. With the stopcock of the gas delivery system closed, the system is evacuated to check for the presence of leaks. The system is considered free of leaks if the pressure reading is 0.2 mm Hg or lower. Air is then admitted to atmospheric pressure through the drying tube I.

The charge of ground eutectic mixture is then loaded into the cell through one of the large holes. It should be emphasized that tube A does not contain the compartments B at this point and that the gas delivery tube D is within 1 cm of the bottom of tube A. After loading the charge of eutectic mixture into tube A, the system is maintained evacuated at room temperature for a period of 3 days. The system is next gradually brought to a temperature of 300°C during an 8-hr period by appropriate adjustment of the furnace controls, vacuum being maintained all the while.

Fusion of the charge is effected under the following conditions. Anhydrous HCl is slowly admitted to the evacuated cell through gas delivery tube D until, when the pressure exceeds atmospheric, HCl can be discharged from the cell through the sidearm drying tube I into a disposal sump. A convenient disposal sump for the HCl is the interior of a filter flask which is connected to a running water aspirator, the filter flask being also vented to the atmosphere. A slow flow of HCl is maintained through the salt mixture while the temperature is raised to 500°C, fusion occurring at 352°C.

After fusion, the melt is saturated with HCl which must be removed. Most of the HCl can be removed by evacuating the system for a few minutes with the water aspirator and then using argon to bring the system back to atmospheric pressure. Evacuation of the system with the water aspirator and the refilling with argon is repeated once more.

At this point it is convenient to add the compartments B to the system, if they are to be used in an experiment. Their previous treatment consists of having been thoroughly cleaned, rinsed, and vacuum-dried at 400°C. They are added to the system one by one, while hot, through the large holes in stopper C, using the hook H to make the transfer. The compartments fill by gravity during the final step of the melt preparation.

As a final step, the system is evacuated on the vacuum manifold for 3 hr. The pump is protected from HCl vapors by a 24-in. column filled with an Ascarite-$Mg(ClO_4)_2$ mixture. The system is brought back to atmospheric pressure with argon at the completion of the evacuation period and an inert atmosphere is maintained over the melt for the balance of an experiment by a continuous slow flow of argon. Argon is delivered by tube D to a level just above the surface of the melt.

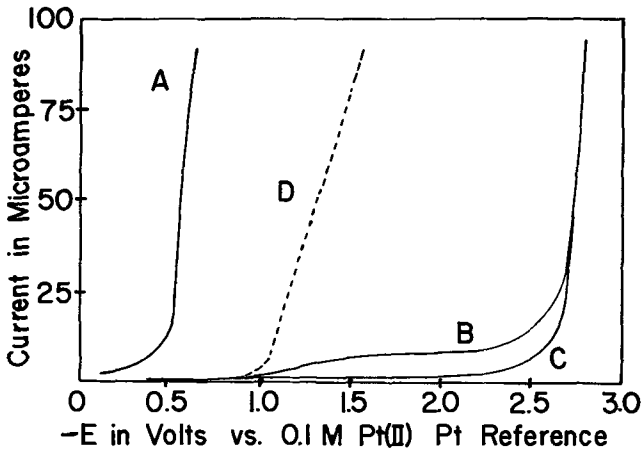

Fig. 2. Polarograms for the eutectic solvent at 450°C. A, solvent still saturated with HCl after fusion; B, after evacuation for 2 hr, most of HCl removed; C, after evacuation for 3 hr, HCl virtually absent; D, typical curve for solvent fused without precaution to prevent hydrolysis.

Results and Discussion

The polarographic method, using solid microcathodes, was found to be an excellent way of detecting the presence of electroactive impurities in the solvent preparations. Curve D of Fig. 2 is a typical polarogram of those observed for the solvents which were prepared by fusion without precaution to prevent hydrolytic decomposition or which were prepared by fusion under moderate vacuum. Evidence of solvent contamination is shown by the rapidly increasing current at −0.9 v. The cathode process giving rise to this current is accompanied by the formation of visible gas bubbles at the microcathode surface, indicating the process not to be solvent decomposition. Another experimental fact suggesting contamination is that the Pyrex container of a solvent so prepared is deeply etched within 1 or 2 hr exposure to the solvent.

The procedure of solvent preparation given here is designed, by provision of an excess of HCl, to shift the hydrolytic equilibrium

$$H_2O + Cl^- \rightleftharpoons OH^- + HCl \uparrow \qquad (I)$$

to the left. Under these conditions the moisture volatilizes from the system without the formation of hydroxyl ion. Alkaline contamination is undesirable because its corrosive attack on the Pyrex cell leads to further contamination of the solvent and because the electrode reaction

$$OH^- + e^- \rightarrow \tfrac{1}{2} H_2 + O^= \qquad (II)$$

interferes with a study of other electrode processes which occur between approximately −1 and −2.5 v vs. the Pt-Pt (II) reference system.

The effectiveness of the preparative procedure given can be judged from curve C of Fig. 2, which

is a polarogram typical of the eutectic solvent prepared as specified. For curve C the residual current preceding the terminal process of lithium metal deposition is less than 3 μa at a microcathode of 0.8 mm^2 area. The inherently wide decomposition potential span of the LiCl-KCl eutectic mixture is thus accessible for the electrochemical study of such solutes as $CrCl_2$, $FeCl_2$, CuCl, $ZnCl_2$, and $MgCl_2$. None of these solutes can be studied at low solute concentrations in the contaminated solvent because reaction (II) is competitive with most of the electrode reactions of interest. Furthermore, the alkaline environment of a contaminated solvent results in precipitation of some of the solutes as insoluble species. The freedom from alkalinity of the solvent when prepared as described is attested by the fact that the above solutes remain in solution and the fact that the Pyrex glassware is only slightly etched after days of contact with the fused salt solvent.

Although reaction (I) is written as an equilibrium, the reaction is not shifted readily to the left once it has proceeded extensively to the right. Fusion of the eutectic mixture without precaution to prevent hydrolytic decomposition yields a solvent the condition of which cannot be made satisfactory by the passage of HCl. The corrective treatment does not serve in place of the preventive treatment.

Data which illustrate the slow release of moisture by the ground eutectic mixture are shown in Table I. These data were obtained by determining the volatile material collected in a trap, cooled with a dry ice-"Cellosolve" mixture, which escaped a 195.4 g sample of the ground eutectic mixture under the conditions indicated. It was concluded that at room temperature and 0.1-0.2 mm Hg pressure the major portion of the moisture is removed from the ground eutectic mixture in 3 days. The numerical values of Gardner, Brown, and Janz (2, 3), reported on an extended study of weight changes as a function of time and temperature of alkali chlorides maintained at 10^{-4} to 10^{-6} mm Hg, cannot be compared to the data of Table I because of the differences in temperature and pressure conditions. Both sets of data yield the same general conclusion, namely, that moisture is tenaciously held by LiCl, even at low pressures.

A summary of observations, based on the results of altering the experimental conditions given above for the preparation of the fused salt solvent, indicates the conditions prescribed to be optimal for the production of a high quality solvent with a minimum of preparative effort for the amounts of solvent required in electrochemical studies.

Table I. Moisture collected from 195.4 g of eutectic mixture

Evacuation* period, hr	Temperature condition	Moisture collected in trap, g	Cumulative moisture collection, g
0-24	Room temp	0.65	0.65
24-60	Room temp	1.00	1.65
60-74	Room temp	0.10	1.75
74-84	Room temp	0.00±0.05	1.75
84-94	Slowly incr. to 245°C	0.15	1.90

* Pressure maintained at 0.1-0.2 mm Hg.

The quality of the solvent preparation, as measured by the polarographic curve, is lowered if the time of the "room temperature" evacuation of the ground eutectic mixture is less than 2 days. During this period the preparative operation requires no operator attention and little in the manner of equipment. Shortening the period is therefore not particularly to be desired. Shortening the period during which the mixture is heated, under vacuum, from room temperature to 300°C is deleterious to the solvent quality. Substitution of the vacuum condition during this step by 1 atm of HCl pressure is also deleterious. Experience shows that the fusion step must be performed under HCl in order to prevent excessive hydrolysis because the vacuum conditions prescribed are insufficient for complete removal of the moisture prior to fusion. Fusion of the mixture at low pressure of HCl is without beneficial effect on the solvent quality. The time required for removal of the HCl from the melt is not appreciably shortened by interrupting the evacuation with frequent flushes of the system with argon.

Several attempts using other means to remove moisture and hydroxyl ion from the melt proved to be unsuccessful. The chemical reaction of either $SOCl_2$ or $SiCl_4$, introduced as the vapor carried by a stream of dry N, constituted the most nearly successful elimination of moisture and hydroxyl ion. The hydrolytic reactions were slow and incomplete under the conditions of the experiments. Use of acidic metal chlorides in the same capacity was ruled out because of the cation contamination thereby introduced into the solvent. Prolonged electrolysis of the melt between graphite electrodes failed to produce a pure solvent, as judged by the polarographic criterion, probably because this method does not eliminate oxide contamination. No noticeable improvement in the residual current characteristic was produced by the scavenging effect of cathodically deposited Li. Melts prepared in contact with Vycor and Alundum containers had the same residual current characteristic as those prepared in Pyrex, indicating the container material to be of little apparent significance.

Acknowledgment

The authors take this opportunity to express their appreciation to the Diamond Ordnance Fuze Laboratory, Department of Defense, for financial sponsorship of assistantships held by two of them (R.A.O. and W.S.F.) during execution of the research.

Manuscript received Sept. 28, 1956. This paper was prepared for delivery before the Cincinnati Meeting, May 1-5, 1955.

Any discussion of this paper will appear in a Discussion Section to be published in the June 1958 JOURNAL.

REFERENCES

1. S. Senderoff and A. Brenner, *This Journal*, **101**, 16 (1954).
2. H. J. Gardner, C. J. Brown, and G. J. Janz, "The Preparation of Dry Alkali Chlorides for Conduc-

tance Studies in Aqueous Media and Molten Salts," Technical Status Report on Contract No. Nonr-591(06), supported by the U. S. Office of Naval Research.
3. C. J. Brown, J. J. Gardner, and G. J. Janz, "Electrochemistry of Molten Alkali and Alkaline Earth Halides Containing Halides of Titanium," Annual Report, March, 1956, on Contract No. Nonr-591(06).
4. R. A. Osteryoung, Ph.D. thesis, University of Illinois, 1954.
5. W. S. Ferguson, Ph.D. thesis, University of Illinois, 1956.
6. H. A. Laitinen and W. S. Ferguson, *Anal. Chem.*, **29**, 4 (1957).

Technical Note

Crystal Structures of Transition Metal Silicides

Carol H. Dauben

Radiation Laboratory and Department of Chemistry and Chemical Engineering,

University of California, Berkeley, California

Recently there has been a great interest in the compounds of silicon with the transition metals. Many new compounds have been prepared and their properties studied. In some cases, where the ideal composition was unknown, the phases were given incorrect names, and there has been some confusion as to which phases were meant.

In the following tables an attempt has been made to list the phases which have been reported in each system, their ideal structure type, lattice constants, parameters of one of the type, and adequate references. Compositions given are the ideal compositions, but in many cases actual compositions can deviate widely. For some compounds there are wide homogeneity ranges with varying lattice constants. In this table no attempt has been made to give the range of lattice parameters, for often this is not accurately known. Instead, lattice constants are given for a typical composition. For the case where compounds had been reported with the incorrect ideal composition, a note has been added in square brackets, stating the true ideal composition. All early data which had been given in *kX* units have been converted to Angstroms. The space group notation and positions of the atoms are listed as given in the International Tables (1).

Early work in this field and properties of these compounds have been cited by Schwarzkopf and Kieffer (2), and more recent work by Nowotny and Parthé (3).

Acknowledgment

The author wishes to thank Professors L. Brewer and D. H. Templeton for their assistance in the preparation of this paper. This work was done under the auspices of the U. S. Atomic Energy Commission.

Manuscript received January 18, 1957.

Any discussion of this paper will appear in a Discussion Section to be published in the June 1958 JOURNAL.

REFERENCES

1. "International Tables for X-ray Crystallography," Vol. I, Kynoch Press, Birmingham (1952).
2. P. Schwarzkopf and R. Kieffer, "Refractory Hard Metals," MacMillan Co., New York (1953).
3. H. Nowotny and E. Parthé, *Planseeberichte fur pulvermetallurgie*, **2**, 34 (1954).
4. F. Laves and H. J. Wallbaum, *Z. Krist.*, **101**, 89 (1939).
5. M. Hansen, H. D. Kessler, and D. J. McPherson, *Trans. Am. Soc. Metals*, **44**, 518 (1951).
6. P. Pietrowsky and P. Duwez, *J. Metals*, **3**, 772 (1951).
7. H. Schachner, H. Nowotny, and H. Kudielka, *Monats. Chem.*, **85**, 1140 (1954).
8. P. A. Vaughan and A. Bracuti, abstract of a paper presented at meeting of the American Crystallographic Association, June 27, 1955, Pasadena, Calif.
9. C. E. Lundin, D. J. McPherson, and M. Hansen, *Trans. Am. Soc. Metals*, **45**, 901 (1953).

Table I. Structure types of transition metal silicides

Nominal composition	Ti	Zr	V	Nb	Ta	Cr	Mo	W
MSi_2	Orth.-$TiSi_2$(4)*	Orth.-$ZrSi_2$(7,8)	Hex.-$CrSi_2$(14)	Hex.-$CrSi_2$(14)	Hex.-$CrSi_2$(14)	Hex.-$CrSi_2$(14,26)	Tetr.-CaC_2(29)	Tetr.-CaC_2(29)
MSi	Structure unknown (5)	Orth.-FeB(7)				Cubic-FeSi (26)		
M_5Si_3		Structure unknown (9); not found by ref.(7); may be part of ZrSi phase region (10).						
M_5Si_2		tetr.-U_5Si_2(11) called Zr_5Si_3 by ref. (9).		[Nb_5Si_3 reported in ref.(21) is Nb_5Si_4 = Cr_5Si_3 type.]		[Cr_5Si_2 reported in ref. (21) and (27) is Cr_5Si_3.]	[Mo_5Si_2 reported in ref. (21) is Mo_5Si_3.]	[W_5Si_2 reported in ref. (21) is W_5Si_3.]
M_5Si_3	Hex.-Mn_5Si_3(6)	Hex.-Mn_5Si_3(12) called Zr_5Si_4 by ref.(9).	[Hex.-Mn_5Si_3 type reported in ref. (15) is ternary compound requiring C or B(16).]	[Hex.-Mn_5Si_3 type reported in ref. (12) is ternary compound requiring C or B(16).]	[Hex.-Mn_5Si_3 type reported in ref. (24) is ternary compound requiring C, B, or N (16).]		[Hex.-Mn_5Si_3 type reported in ref. (30) is ternary compound requiring C (12,16).]	
M_3Si_2			Tetr.-Cr_3Si_2(17,18)	Tetr.-Cr_3Si_2(17,18)	Tetr.-Cr_3Si_2(18)	Tetr.-Cr_3Si_2(17,22,28)	Tetr.-Cr_3Si_2(17,22, 28,31)	Tetr.-Cr_3Si_2(17,22, 28,31)
M_3Si				Tetr.-Cr_3B_2(22)	Tetr.-Cr_3B_2(22)			
M_2Si		Tetr.-$CuAl_2$(11)	[V_2Si reported in earlier work does not exist (19).]	[αNb_2Si reported in (23) is Cr_3B_2 type. βNb_2Si reported in (23) is Mn_5Si_3 type.]	Tetr.-$CuAl_2$(24)	[Cr_2Si reported in ref. (26,27) is undoubtedly Cr_5Si_3]		
M_5Si			Cubic-"β W" (20)			Cubic - "β W" (26)	Cubic - "β W" (32)	
M_5Si-M_2Si		Probably more than 2 phases near this composition (12). One form is isostructural with $TaSi_{0.2}$(13).		Structure unknown; isostructural with $TaSi_{0.2}$(13). Not found by ref. (9).	Hex.-$Ta_{1-x}Si$ ideal Ni_2Sn type (24). $TaSi_{0.2}$ structure unknown (25). Different from $Ta_{1.2}Si$.			

* Another structure has been reported for $TiSi_2$—orthorhombic $ZrSi_2$ form (34).

Table II. Structural data for transition metal silicides (in Angstroms)

$TiSi_2$ — orthorhombic (4) — D_{2h}^{24} — $Fddd$			$Z = 8$		
a = 8.252				8Ti in (a)	
b = 4.782				16Si in (c)	$x = 1/3$
c = 8.540					
$ZrSi_2$ type — orthorhombic — D_{2h}^{17} — $Cmcm$			$Z = 4$		
$ZrSi_2$ a = 3.721 (8)				4Zr in (c)	$y = 0.109$ (7)
b = 14.68				$4Si_I$ in (c)	$y = 0.449$
c = 3.683				$4Si_{II}$ in (c)	$y = 0.750$
$TiSi_2$ a = 3.62 (34)					
b = 13.76					
c = 3.60					
$CrSi_2$ type—hexagonal — D_3^1 — $P\,6_222$			$Z = 3$		
$CrSi_2$ a = 4.431 (26)				3Cr in (d)	
c = 6.364				6Si in (j)	$x = 1/6$
VSi_2 a = 4.571 (14)					
c = 6.371					
$NbSi_2$ a = 4.794 (14)					
c = 6.589					
$TaSi_2$ a = 4.782 (14)					
c = 6.565					
CaC_2 type — tetragonal — D_{4h}^{17} — $I\,4/mmm$			$Z = 2$		
$MoSi_2$ a = 3.206 (29)				2M in (a)	
c = 7.877				4Si in (e)	$z = 0.333$
WSi_2 a = 3.218					
c = 7.896					
FeB type — orthorhombic — D_{2h}^{16} — $Pnma$			$Z = 4$		
ZiSi a = 6.98_2 (7)				4Zr in (c)	$x = 0.17_8$ $z = 0.125_8$
b = 3.78_0				4Si in (c)	$x = 0.03_2$ $z = 0.61_1$
c = 5.30_1					
FeSi type — cubic — T^4 — $P\,2_13$			$Z = 4$		
CrSi a = 4.629 (26)				4M in (a)	$x_{Fe} = 0.139$
				4Si in (a)	$x_{Si} = 0.845$
U_3Si_2 type — tetragonal — D_{4h}^5 — $P4/mbm$			$Z = 2$		
Zr_3Si_2 a = 7.081 (33)				2Zr in (a)	
c = 3.701				4Zr in (h)	$x = 0.17$ (11)
				4Si in (g)	$x = 0.37$
Mn_5Si_3 type — hexagonal — D_{6h}^3 — $P\,6_3/mcm$			$Z = 2$		
Ti_5Si_3 a = 7.465 (6)				$4M_I$ in (d)	
c = 5.162				$4M_{II}$ in (g)	$x_{Mn} = 0.23$
				4Si in (g)	$x_{Si} = 0.60$
Zr_5Si_3 a = 7.958 (33)					
c = 5.564					
Cr_5Si_3 type — tetragonal — D_{4h}^{18} — $I\,4/mcm$			$Z = 4$		
V_5Si_3 a = 9.42_6 (18)				$4M_I$ in (b)	
c = 4.75_6				$16M_{II}$ in (k)	$x_{Cr} = 0.075$
Nb_5Si_3 a = 10.01_8 (18)					$y_{Cr} = 0.224$
c = 5.07_2				4Si in (a)	
Ta_5Si_3 a = 9.8_6 (18)				8Si in (h)	$x_{Si} = 0.165$
c = 5.0_5					
Cr_5Si_3 a = 9.170 (28)					
c = 4.636					
Mo_5Si_3 a = 9.642 (28)	9.617 (31)	9.66 (21)			
c = 4.905	4.899	4.99			
W_5Si_3 a = 9.605 (28)	9.645 (31)	9.56 (21)			
c = 4.964	4.969	4.94			
C_5B_3 type — tetragonal — D_{4h}^{18} — $I4/mcm$			$Z = 4$		
Nb_5Si_3 a = 6.57_6 (22)				4M in (c)	
c = 11.88_2				16M in (l)	$x_{Nb} = 0.166$ $z_{Nb} = 0.15$
				4Si in (a)	
Ta_5Si_3 a = 6.51_5 (22)				8Si in (h)	$x = 0.37_5$
c = 11.87_2					
$CuAl_2$ type — tetragonal — D_{4h}^{18} — $I4/mcm$			$Z = 4$		
Zr_2Si a = 6.599 (11)				8M in (h)	$x_{Ta} = 1/6$
c = 5.298				4Si in (a)	
Ta_2Si a = 6.157 (24)					
c = 5.03_9					
"β-W" type — (W_3O) cubic — O_h^3 — $Pm3n$			$Z = 2$		
V_3Si a = 4.721 (20)				6M in (c)	
				2Si in (a)	
Cr_3Si a = 4.564 (26)					
Mo_3Si a = 4.890 (32)					
$Ta_{1.5}Si$ — hexagonal, ideal Ni_3Sn type. $Ta_3(Ta_{0.28}Si_{0.72})$ (24)					
a = 6.10_5 for Ni_3Sn type — D_{6h}^4 — $P\,6_3/mmc$			$Z = 2$		
c = 4.91_8				2Sn in (c)	
				6Ni in (h)	$x_{Ta} = 0.826$

10. D. A. Robins and I. Jenkins, *Acta Met.*, **3**, 598 (1955).
11. P. Pietrowsky, Private communication.
12. O. Krikorian and L. Brewer, *This Journal*, **103**, 38 (1956).
13. G. A. Geach and A. G. Knapton, Private communication.
14. H. J. Wallbaum, *Z. Metallkunde*, **33**, 378 (1941).
15. H. Schachner, E. Cerwenka, and H. Nowotny, *Monats. Chem.*, **85**, 245 (1954).
16. H. Nowotny, B. Lux, and H. Kudielka, *ibid.*, **87**, 447 (1956).
17. A. G. Knapton, *Nature*, **175**, 730 (1955).
18. E. Parthé, H. Nowotny, and H. Schmid, *Monats. Chem.*, **86**, 385 (1955).
19. R. Kieffer, F. Benesovsky, and H. Schmid, *Z. Metallkunde*, **47**, 247 (1956).
20. H. J. Wallbaum, *ibid.*, **31**, 362 (1939).
21. E. Parthé, H. Schachner, and H. Nowotny, *Monats. Chem.*, **86**, 182 (1955).
22. E. Parthé, B. Lux, and H. Nowotny, *ibid.*, **86**, 859 (1955).
23. G. Brauer and W. Scheele, "Anorg. Chemie," edited by W. Klemm, Vol. 24, Part II, Dietrich Verlangsbuchdlg., Wiesbaden (1948).
24. H. Nowotny, H. Schachner, R. Kieffer, and R. Benesovsky, *Monats. Chem.*, **84**, 1 (1953).
25. L. Brewer, A. W. Searcy, D. H. Templeton, and C. H. Dauben, *J. Am. Ceram. Soc.*, **33**, 291 (1950).
26. B. Boren, *Arkiv Kemi, Mineral., Geol.*, **11A**, No. 10 (1933).
27. N. Kurnakov, *Compt. rend. acad. sci., U.R.S.S.*, **34**, 110 (1942).
28. C. H. Dauben, D. H. Templeton, and C. E. Myers, *J. Phys. Chem.*, **60**, 443 (1956).
29. W. H. Zachariasen, *Z. Physik. Chem.*, **128B**, 39 (1927).
30. H. Nowotny, E. Parthe, R. Kieffer, and F. Benesovsky, *Monats. Chem.*, **85**, 225 (1954).
31. B. Aronsson, *Acta Chem. Scand.*, **9**, 1107 (1955).
32. D. H. Templeton and C. H. Dauben, *Acta Cryst.*, **3**, 261 (1950).
33. McPherson's sample (5) measured at this laboratory.
34. P. G. Cotter, J. A. Kohn, and R. A. Potter, *J. Am. Ceram. Soc.*, **39**, 11 (1956).

Chemical and Electrochemical Properties of $FeSn_2$

Roger A. Covert and Herbert H. Uhlig

Corrosion Laboratory, Department of Metallurgy,

Massachusetts Institute of Technology, Cambridge, Massachusetts

ABSTRACT

Microhardness numbers of iron, tin, and $FeSn_2$ layers formed when iron is exposed to molten tin at 465°C show that the $FeSn_2$ layer is by far the hardest phase. It is also the most noble phase in acidified NaCl or dilute citric acid, both deaerated, as shown by micropotential measurements of the phases *in situ* or by measurements of bulk electrodes. Corrosion rates of $FeSn_2$ in the same media are too low to be easily measurable. Hydrogen overvoltage values for $FeSn_2$ at low current densities are intermediate between values for iron and tin. These properties are related to the predicted corrosion behavior of tin plate.

Although much attention has been paid to the corrosion behavior of commercial tinplate, very little work has been concentrated on corrosion properties of the alloy layer existing between the steel base and the tin surface. This alloy layer is reported to be composed essentially of $FeSn_2$ (1, 3). The present investigation was undertaken to study some of the properties of this phase and its possible role in the corrosion of tin-plated steel.

Some of the known properties of $FeSn_2$ include its density (7.743 g/cm³) (1); a rectangular acicular habit of the individual grains in the alloy layer (1); extreme brittleness in comparison to Sn or Fe (2); and porosity of the compound in the alloy layer (2). Several investigators (2, 3) have reported the relative inertness of $FeSn_2$ to attack by normal etching reagents, dilute aqua regia, and dilute nitric acid compared to the corrosion behavior of both Sn and Fe. However, experiments of Kohman and Sanborn (4) led to the conclusion that presence of the alloy layer was not helpful, and very possibly detrimental to the corrosion of tin plate. An explanation was not proposed.

In this investigation measurements of hydrogen overvoltage, corrosion potential, and corrosion rates in two aqueous media are reported. The interpretation of these data bear directly on the expected corrosion behavior of the alloy layer.

Experimental Procedure

Preparation of $FeSn_2$.—Attempts to prepare $FeSn_2$ by mixing the pure components in their correct stoichiometric proportions and melting in a He atmosphere were unsuccessful. Failure resulted from the fact that when a melt containing 80.95% Sn and 19.05% Fe is solidified there are several solid-liquid transformations which take place before 496°C (the temperature below which $FeSn_2$ is formed) is reached (5). These reactions result in the formation of various solid phases of the Fe-Sn binary system. Prolonged annealing at 470° ±10°C for 21 days did not homogenize the structure to single phase $FeSn_2$; therefore another approach had to be used.

According to Jones and Hoare (6), when a chemically clean surface of Fe is immersed for a time in liquid Sn below 496°C it is found to be coated with Sn and a layer of $FeSn_2$ between the Sn coating and the Fe surface. It would appear from the phase diagram that FeSn (68.0% Sn) and a primary solid solution of Sn in Fe would also be present. However, the rate of formation of FeSn and the diffusion rates of Sn into Fe below 496°C appear to be so slow compared to the rate of formation of $FeSn_2$ that the latter phase alone has been found.

By taking advantage of this situation, samples of $FeSn_2$ for metallographic examination, microhardness measurements and micropotential measurements were prepared by immersing cylinders of high purity Fe (>99.95% Fe) ¼ in. in diameter by ½ in. long in a bath of liquid Sn (>99.9% Sn) controlled to 465° ±10°C for periods of 50-100 hr. The high purity Fe and high purity Sn used here, and in all other phases of this work, were obtained from the Vacuum Metals Corporation and the Vulcan Detinning Company, respectively.

The Fe cylinders were prepared by abrading the surfaces through 4-0 metallographic polishing paper, degreasing in boiling benzene, pickling in concentrated HCl to remove the cold worked and contaminated surface, washing in distilled water, and drying in boiling acetone. The cylinders were dropped into the Sn bath immediately after drying in acetone, and a stream of He, which was purified by passing the gas over Cu chips at 500°C and through a liquid N_2 drying trap, was maintained continuously over the surface of the liquid Sn. After the cylinders were removed from the Sn bath, they were mounted in Bakelite perpendicular to their long axis and polished metallographically. A layer of $FeSn_2$ 0.001 in. to 0.005 in. thick was observed between the Fe and Sn phases.

For corrosion potential, hydrogen overvoltage, and corrosion rate measurements, $FeSn_2$ was prepared in a similar manner using a differently shaped specimen. Small rectangular plates ⅜ in. x ⅝ in. x ⅛ in. were abraded and degreased as before. Specimens were then placed in a Vycor transfer tube and heated to red heat in a stream of hydrogen, which was purified by passing the gas over Cu chips at 500°C and through a liquid N_2 drying trap, in

order to reduce any surface oxides. Specimens were then dropped with the aid of a magnet into a liquid Sn bath maintained continuously at 488° ±5°C without removing them from the hydrogen atmosphere and allowed to remain for 7-9 days. The edges of the plates were then ground away exposing the Fe base, which, along with the Sn surface, was dissolved in a 50 volume % solution of concentrated HNO_3. Two small plates of $FeSn_2$ remained, and electrodes and corrosion rate samples were prepared from these.

$FeSn_2$ prepared by the latter method was analyzed chemically and found to contain 19.9% Fe and 79.1% Sn compared to the theoretical values of 19.05% Fe and 80.95% Sn. A Debye-Scherrer x-ray powder diffraction pattern revealed that the major phase present was $FeSn_2$. However some faint lines of Sn and of some unidentified lattices were also present. The calculated *d* values for $FeSn_2$ compared favorably with the data of Nial (7). Considering the results of these two types of analyses, it was felt that the $FeSn_2$ samples contained more than 95% $FeSn_2$ with the remainder being Sn and FeSn.

Microhardness measurements.—The microhardness values of Fe, Sn, and $FeSn_2$ in the cylindrical samples were measured with a Tukon hardness testing instrument using a Knoop diamond indentor. Etching of the surface was not necessary, since the three phases were quite distinct. A typical photomicrograph is shown in Fig. 1.

Micropotential measurements.—Micropotential measurements of Fe, Sn, and $FeSn_2$ in deaerated 4% NaCl and HCl solution of *p*H 2.0 were made using essentially the same method as developed by Pingel (8). This procedure consists of washing the metallographically polished sample with distilled water and then acetone, and coating the entire surface with a transparent plastic composed of 10 parts by weight of ethyl cellulose, 20 parts petroleum ether, 60 parts toluene, and 20 parts ethyl alcohol. The coating dries readily in about 10 min and can be removed easily with benzene. Electrical contact with the mounted specimen was obtained by drilling through the side of the Bakelite mounting until contact was made with the metal sample. A 4 mm Pyrex tube was inserted into the drill hole and sealed in place of a 50% beeswax-50% resin wax. When cool, the wax was also covered with a plastic coating. A drop of Hg and a Cu wire were inserted into the Pyrex tube, the Hg making contact with the sample and the wire with the Hg. Indentations through the plastic coating to the specimen surface were made in the desired location with the Tukon hardness testing instrument using a Vickers diamond indentor. Indentor loads of either 25 or 50 g were used, depending on the thickness of the plastic coating.

Commercial pre-purified N_2 further purified by passing over Cu chips at 500°C was bubbled through the solution for at least 4 hr before measurements were made, in order to deaerate the solution. The *p*H was measured using a glass electrode.

The test solution was contained in a 250 ml Pyrex bottle fitted with a rubber stopper which had openings for the electrode, a salt bridge containing the same NaCl solution, the gas bubbler, and a gas exit tube. The salt bridge was in contact with a standard Ag-AgCl, 0.1*N* KCl electrode. For emf measurements a portable potentiometer was used in combination with an electronic *p*H meter employed as a high input resistance galvanometer.

After deaeration was complete, the electrode was inserted into the solution and measurements were taken every 3-5 min until such time as the plastic coating absorbed water and the potentials were no longer representative of the phase being investigated. This critical time was usually 45-60 min.

All measurements were made in an air thermostat maintained at 25° ±1°C.

Hydrogen overvoltage measurements.—Corrosion potential and hydrogen overvoltage characteristics for $FeSn_2$ and pure Sn were measured in deaerated 4% NaCl + HCl at *p*H 2.0 and dearated 0.1*M* citric acid solutions.

Tin electrodes ⅜ in. in diameter by ¾ in. long were prepared from the same high purity Sn that was used for the preparation of $FeSn_2$. The electrode design is shown in Fig. 2. Electrical contact with the sample was achieved by soft soldering a 1/16 in. drill rod to a 1/16 in. stem machined on the Sn sample. The drill rod was isolated from the solution by an 8 mm Pyrex tube fitted tightly in contact with the Teflon gasket, and which was held firmly in place by a machine screw with nut and washer silver

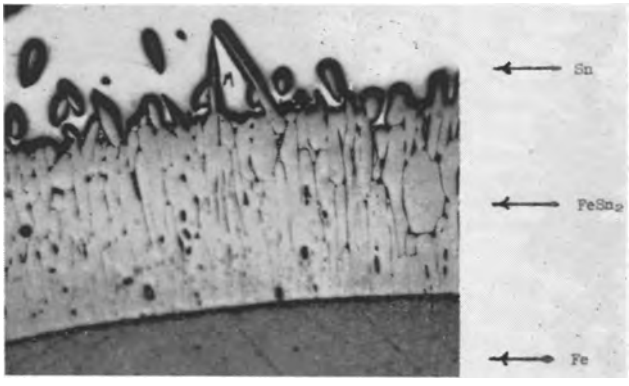

Fig. 1. Photomicrograph of $FeSn_2$ layer. 200X before reduction for publication.

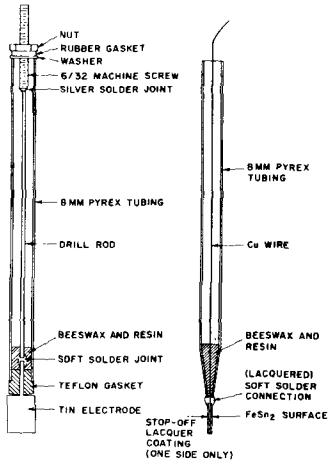

Fig. 2. Tin and $FeSn_2$ electrodes for corrosion potential and hydrogen overvoltage measurements.

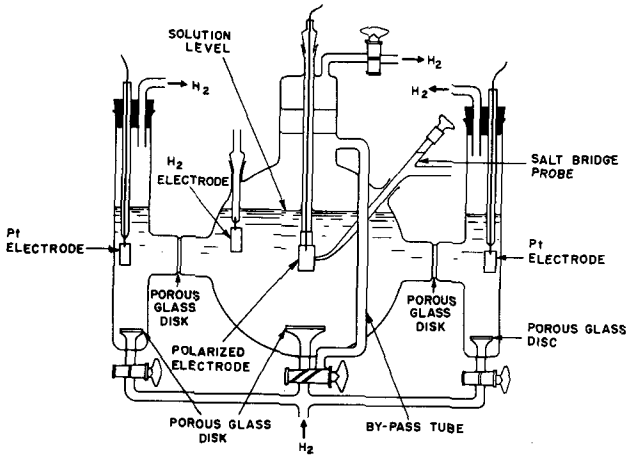

Fig. 3. Three compartment cell for hydrogen overvoltage measurements.

soldered to the other end of the drill rod. Only Sn, Teflon, and glass made contact with the solution.

$FeSn_2$ electrodes were made from plates of $FeSn_2$ described earlier. A fine Cu wire was soft soldered to one end of the plate and fitted into an 8 mm Pyrex tube with a capillary tip. The wire was sealed in place with 50% beeswax—50% resin wax. The capillary tip, soft solder connection, and one side of the specimen were coated with vinyl stop-off lacquer. This coating served not only to isolate the solder and Cu wire from the solution but also to protect the sample, which was extremely brittle and fragile.

The 3-compartment cell shown in Fig. 3 was used for all measurements. The center cathode compartment had a volume of 2200 ml and was separated from the 200 ml anode compartments by fine sintered glass disks. Since deaeration was accomplished by purified H_2, a platinized Pt electrode was inserted into the center compartment to be used as a reference electrode and for measuring *p*H.

The H_2 used for deaeration was purified by passing the gas over Cu chips at 500°C, a ruthenium catalyst at 300°C, and a palladium catalyst at room temperature. The NaCl solution was the same as was used for measuring micropotentials except for H_2 saturation instead of N_2 saturation. The citric acid solution was prepared from distilled water and reagent-grade citric acid.

Immediately prior to placing the specimen electrodes in the solution, the Sn electrode was abraded through 4-0 polishing paper, degreased in boiling benzene, pickled in concentrated HCl, and washed with distilled water. The $FeSn_2$ electrode was degreased with boiling benzene, pickled in concentrated HCl, and washed with distilled water.

In making a run, the solution was first deaerated for a minimum of 4 hr, then a smooth Pt electrode was inserted in place of the hydrogen electrode and the solution was cathodically pre-electrolyzed at a current density of 1 ma/cm² for 3 hr while deaeration continued. Then the specimen electrode, a salt bridge containing the same solution as in the cell, and the platinized-Pt electrode were inserted into the solution. The tip of the salt bridge was brought near to the electrode surface. Upon insertion of the electrodes, the potential of the sample was measured vs. the hydrogen electrode until a steady state was reached and maintained for at least 12 hr.

Hydrogen overvoltage was then measured at current densities of 0.1-1000 microamp/cm² by starting at the highest current density and reducing the current in steps of 1-min intervals to the minimum current density and then retracing the curve to the maximum again. Current was not shut off at any time during the run. Potentials in this case were measured against a saturated calomel electrode via the salt bridge using the same potentiometer circuit described earlier. During these runs H_2 was passed over the top of the solution via the by-pass tube shown in Fig. 3, and hence the solution was not stirred during measurements. A slight positive pressure of H_2 was maintained in the cell at all times.

Corrosion rate measurements.—Measurement of the corrosion rate of $FeSn_2$ was attempted in deaerated 4% NaCl + HCl, *p*H 2.0, and in deaerated 0.1*M* citric acid solutions without stirring. The electrolyte was placed in a 1500 ml spherical flask and was deaerated by bubbling purified H_2 through it for at least 4 hr before insertion of the specimens. Afterward H_2 was passed over the solution surface instead of bubbling through it.

The thin plates of $FeSn_2$, degreased with benzene and pickled in concentrated HCl as before, were placed immediately in small glass holders and immersed in the solution for periods of about five days. Because of the brittle, granular structure of $FeSn_2$, weight loss methods for measuring corrosion rates could not be used. There was always some mechanical breakage in handling the specimens. Therefore, since the corrosion products of Fe and Sn are both soluble in the solutions used, and both metals probably go into solution in the same proportion as in the metallic phase, the solutions were analyzed quantitatively for Fe alone by the orthophenanthroline colorimetric method (9). The amount of corroded metal vs. time was determined by analyzing 10 ml samples of solution twice daily.

Experimental Results

Microhardness measurements.—The maximum, minimum, and average Knoop hardness numbers for Fe, Sn, and $FeSn_2$ resulting from measurements made on four different samples are given in Table I.

A typical Knoop hardness number vs. distance plot for a tin-plate sample is shown in Fig. 4.

These results indicate, as expected, that $FeSn_2$ in the alloy layer is considerably harder than either Fe or Sn, thus supporting the contention that $FeSn_2$ is a hard, brittle phase that tends to break and crack during fabrication of tin plate. However, it

Table I. Hardness of Fe, Sn, and $FeSn_2$ phases found on Fe exposed to molten Sn

Phase	Number of readings	Knoop hardness number (100 g load) Minimum	Maximum	Average
Fe	14	76	127	96
Sn	5	7.7	10.5	9.4
$FeSn_2$	15	104	274	202

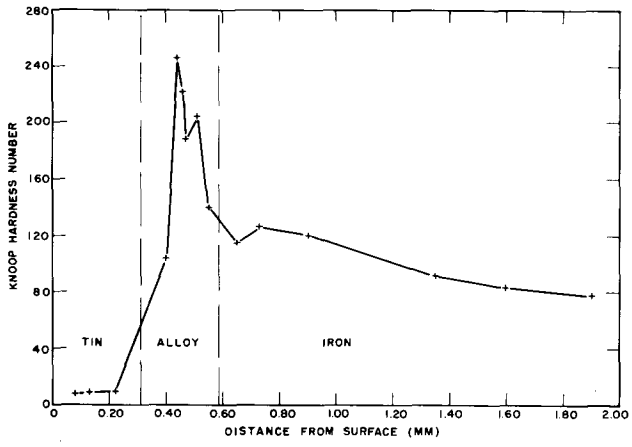

Fig. 4. Knoop hardness vs. distance for a tin-plated sample (100 g load).

should be remembered that the cold-rolled steel sheet used for making commercial tin plate is considerably harder than the soft high purity Fe used in these experiments and that consequently the magnitude of the difference between the hardness numbers of steel sheet and $FeSn_2$ is less.

The decreasing hardness of the Fe base as distance from the alloy layer increases seems to indicate that some Sn actually diffuses into the Fe lattice, thus increasing the hardness by alloying. This feature which is noticeable in Fig. 4 was characteristic of all specimens investigated. Decreased hardness of the compound at the phase boundaries probably results from diminished support at the edges, and is not real.

Potential measurements.—The micro-corrosion potentials *in situ* of Fe, Sn, and $FeSn_2$ and the corresponding corrosion potentials for separate Sn and $FeSn_2$ electrodes are given in Table II. The corrosion potentials for pure Fe, which were measured by Stern (10) in the same two media, are also listed.

The micro-corrosion potential and ordinary corrosion potential data for Sn and Fe were reproducible to ±3 mv while the data for $FeSn_2$ were reproducible to ±8 mv.

The relative potentials of Fe and Sn agree with previously reported data (1) indicating Sn to be more active than Fe in acid, oxygen-free environments. The data also indicate that $FeSn_2$ is the most noble of the three phases in these two media.

The importance of these potential relationships is discussed later.

Cathodic polarization.—If hydrogen is not removed by reaction with a depolarizer, hydrogen

Table II. Potentials of Fe, Sn, and $FeSn_2$ *in situ* on surface of Fe previously exposed to molten Sn, and comparative potentials of separate electrodes. All vs. standard H_2 electrode

Phase	Micro-corrosion potential *in situ* 4% NaCl + HCl, pH 2.0 v	Corrosion potentials of bulk electrodes 4% NaCl + HCl, pH 2.0 v	Corrosion potentials of bulk electrodes 0.1*M* citric acid v
Fe	0.328	0.319 (Stern)	0.294 (Stern)
Sn	0.354*	0.351	0.361
$FeSn_2$	0.255*	0.287	0.271

* N_2-saturated solutions, others H_2-saturated.

Table III. Hydrogen overvoltage of Fe, Sn, and $FeSn_2$ in deaerated 4% NaCl + HCl, pH 2, and in deaerated 0.1*M* citric acid (average of 2 or 3 determinations)

Phases	4% NaCl + HCl, pH 2.0 a (v)	b (v)	i_0 (amp/cm²)	0.1 *M* citric acid a (v)	b (v)	i_0 (amp/cm²)
Fe (Stern)	0.90	0.100	1.1×10^{-7}	0.590	0.084	9.3×10^{-8}
Sn	1.10	0.14	1.4×10^{-8}	0.94	0.11	2.8×10^{-9}
$FeSn_2$	0.76	0.10	2.5×10^{-8}	0.96	0.14	1.4×10^{-7}

overvoltage η can be expressed by the Tafel equation (11):

$$\eta = a + b \log i, \text{ or}$$
$$= -b \log i_0 + b \log i$$

where: a,b = constants, i_0 = exchange current density (12), and i = applied current density. Using this notation, the averaged data for Fe [from Stern (10)], Sn, and $FeSn_2$ are given in Table III.

Typical overvoltage curves for Sn and $FeSn_2$ are given in Fig. 5 to 8. Values of the slope b for Sn were reproducible to ±0.015 v. The increase in slope of these curves near 0.1 ma/cm² is probably due to the approach of applied current to the limiting diffusion current for hydrogen ion discharge. This limiting current density was determined by Stern (13) to be between 1-5 ma/cm² for solutions of *p*H 2.

In general, measurements for Sn were the same whether current values were increased or decreased. For $FeSn_2$, however, the values on return to progressively higher current densities were higher than the values obtained in the initial measurements starting with high current density. This effect may be caused by organic impurities introduced by the wax sealant and the stop-off lacquer used to coat one side of the $FeSn_2$ electrode. These impurities were not present in the case of Fe or Sn.

Corrosion rate measurements.—No measurable amount of Fe was found in either the NaCl or the citric acid solution after $FeSn_2$ specimens had been exposed to these environments for 5 days. This would indicate that the corrosion rate of $FeSn_2$ is less than 3 mdd in these environments based on a minimum amount of iron of 0.02 μg/ml detectable by the electrophotometer and a total specimen area of 0.05 dm².

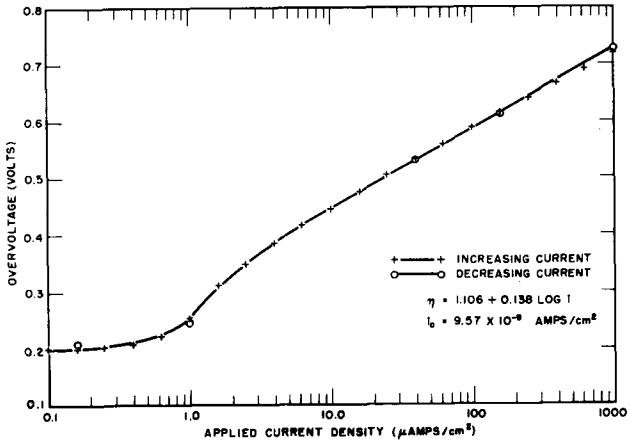

Fig. 5. Hydrogen overvoltage of Sn in deaerated 4% NaCl, pH 2.0.

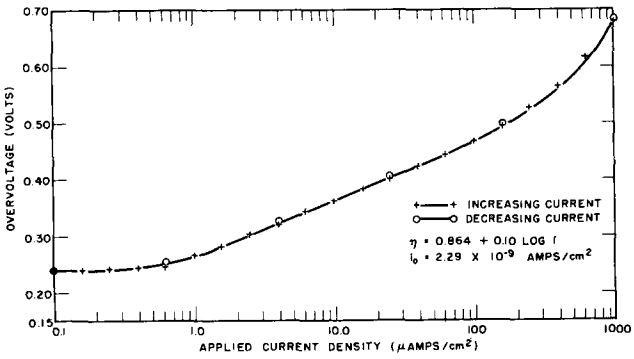

Fig. 6. Hydrogen overvoltage of Sn in deaerated 0.1M citric acid, pH 2.1.

A negative qualitative determination for Sn by the dithiol method (9) showed that Sn also did not go into solution to an extent detectable by this method.

Calculation of the corrosion rate of $FeSn_2$ from the hydrogen overvoltage and corrosion potential data by the method of Stern (10) gives values of 5.2 mdd and 6.6 mdd for $FeSn_2$ in the NaCl and citric acid solutions, respectively, provided $FeSn_2$ is assumed to corrode by the following reaction:

$$FeSn_2 \rightarrow Fe^{++} + 2Sn^{++} + 6e$$

This discrepancy between calculated and observed values is probably explained by the fact that the cathode surface of $FeSn_2$ is less than 100% of the surface as is assumed in the calculation.[1] How one can measure independently the actual cathode surface is not clear at present.

Since $FeSn_2$ is noble with respect to both Fe and Sn in the two media used here, an attempt was made to measure the anodic polarization characteristics of these two metals. However, the data were not reproducible and hence did not permit any definite conclusions.

Discussion

Certain qualitative conclusions are possible from the potential measurements. Since $FeSn_2$ is noble with respect to both Fe and Sn (Table II), it will act as the cathodic member when coupled with either of these two metals. Therefore, it becomes an undesirable substrate because it not only does not offer cathodic protection to Fe as does Sn, but it also ties up Sn which is thereafter not available to protect the Fe.

The hydrogen overvoltage of $FeSn_2$ in 0.1*M* citric acid at 10^{-5} amp/cm², for example, is 0.26 v compared with 0.39 v for Sn and 0.17 v for Fe. Hence the compound when coupled to Sn accounts for consumption of Sn at a lower rate than when an equal area of Fe is coupled to it. When the Sn is all consumed, the compound still exerts no accelerating effect on the hydrogen evolution reaction, because its overvoltage is higher than that of Fe. Therefore, the compound does not seem to be electrochemically deleterious to tin plate behavior for the described conditions of corrosion. The situation may differ, of course, when cathodic depolarizers are present, as is usually true with various foodstuffs. Behavior of the compound under depolarizing conditions requires further study.

[1] Hydrogen-overvoltage measurements are conducted typically at cathode current densities far above local-action current densities, and hence at values that polarize all the electrode surface. On the surface of a corroding metal, however, only part is cathode, the remainder being anode. For Fe in deaerated solutions, practically all the surface is cathode so that calculated and measured corrosion rates as carried out by Stern are in good agreement. Were the anode area larger, the cathode area of the corroding surface would polarize more than is assumed for 100% cathodic area; hence for this situation the measured corrosion rate is less than the calculated value.

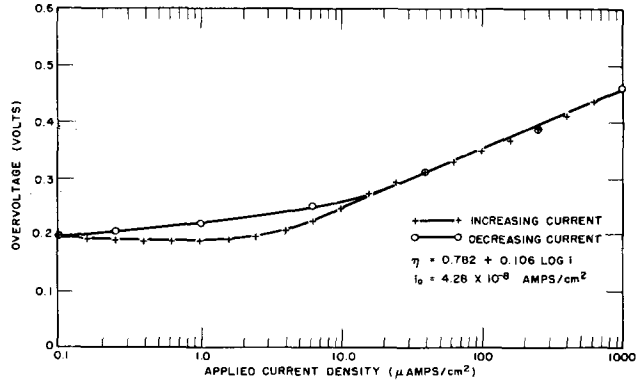

Fig. 7. Hydrogen overvoltage of $FeSn_2$ in deaerated 4% NaCl, pH 2.0.

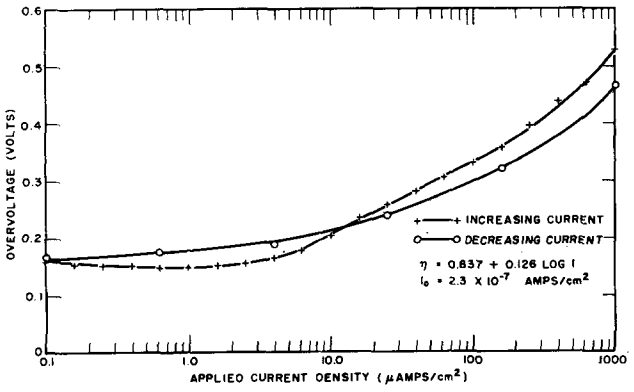

Fig. 8. Hydrogen overvoltage of $FeSn_2$ in deaerated 0.1M citric acid.

Acknowledgment

Support of this research by the Weirton Steel Company is gratefully acknowledged.

Manuscript received Dec. 17, 1956. This paper was prepared for delivery before the Cleveland Meeting, Sept. 30 to Oct. 4, 1956.

Any discussion of this paper will appear in a Discussion Section to be published in the June 1958 JOURNAL.

REFERENCES

1. W. E. Hoare and E. S. Hedges, "Tin Plate," Edward Arnold and Co., London (1945).
2. A. W. Hothersall and V. C. Prytherch, *J. Iron Steel Inst., London,* **133**, 205 (1936).
3. W. E. Hoare, *ibid.*, **129**, 253 (1934).
4. E. F. Kohman and N. H. Sanborn, *Ind. Eng. Chem.*, **19**, 514 (1927).
5. "Metals Handbook", p. 1217, *American Society for Metals,* Cleveland, Ohio (1948).
6. W. D. Jones and W. E. Hoare, *J. Iron Steel Inst., London,* **129**, 273 (1934).
7. Olaf Nial, *Arkiv Kemi, Mineral. Geol.*, **B17**, No. 11 (1943).
8. J. V. Pingel, Cornell Aeronautical Laboratory Report, No. KA-496-M-2 (1948).
9. E. B. Sandell, "Colorimetric Determination of Traces of Metals," p. 375, Interscience Publishers Inc., New York (1950).

10. M. Stern, *This Journal*, **102**, 663 (1955).
11. S. Glasstone, "An Introduction to Electrochemistry," p. 464, D. Van Nostrand Co., Inc., New York (1942).
12. J. O'M. Bockris, "Electrical Phenomena at Interfaces," edited by J. Butler, p. 167, Methuen and Co. Ltd., London (1951).
13. M. Stern, *This Journal*, **102**, 609 (1955).

Nucleation of Crystalline Ta_2O_5 During Field Crystallization

D. A. Vermilyea

Research Laboratory, General Electric Company, Schenectady, New York

ABSTRACT

Nucleation during field crystallization of amorphous Ta_2O_5 films occurs at heterogeneities on the metal surface. The time between the application of the field and the appearance of the first crystals corresponds to growth to critical size of a crystal on one of the nucleation sites. The logarithm of the incubation period increases linearly with decreasing electric field at constant temperature. Possible mechanisms for the nucleation of crystals under these conditions are discussed.

Crystallization of amorphous anodic Ta_2O_5 films may be accomplished at temperatures in the vicinity of room temperature provided that a strong electric field is present in the film (1). This process results in roughly circular crystalline areas consisting of wedge-shaped polycrystalline segments, each area being surrounded by coiled cylinders of the replaced amorphous film. Recent observations of crystalline regions of similar appearance have been made on aluminum oxide anodic films (2), on hafnium oxide anodic films (3), on corrosion films on copper (4), and on chromium oxide (5) formed in oxygen. In addition, it has been observed here that an anodic Ta_2O_5 film crystallizes in a similar manner if heated to 590°C for about 20 min.

According to the mechanism proposed earlier (1) the crystalline areas grow radially by pushing aside the amorphous film present initially. The factors influencing the radial growth rate have already been discussed, and it is felt that such growth is qualitatively fairly well understood. It is the purpose of this paper to discuss some experiments which have been performed in order to determine the cause of the long incubation period before the first crystalline areas are observed.

Nucleation Sites

The fact that the time at which the first crystals are observed depends on the surface preparation (1) makes it appear likely that heterogeneities on the surface are nucleation sites. Further experiments of two types have confirmed this idea.

In one, an anodic film was held at one voltage until crystallization was about 50% complete, and the voltage was then raised rapidly to a somewhat higher voltage to allow further crystallization. It was found that if the rate of growth of the amorphous oxide film during the voltage increase was sufficiently rapid (greater than 40 Å/sec) most of the crystals formed at the lower voltage would not continue to grow at the higher voltage. The incidence of crystallization on the remaining area was observed as a function of time at the higher voltage, and a comparison was made between the number of new nuclei on this area and on a fresh specimen with no crystals present initially. It was found that far fewer crystals formed on the specimen which had first been partially crystallized at the lower voltage. For example, a specimen was held at 99°C, 100 v[1] until 50% of the area was crystalline. The voltage was then raised rapidly to 140 v and held for 550 sec, after which about 45 new crystals were observed in the total area under the microscope at a magnification of 100 diameters. Most of these new crystals occurred adjacent to crystals already present, and only a few, perhaps 5 or 10, formed at sites clearly removed from the original crystals. A specimen held 550 sec at 140 v without previous low voltage crystallization had 800 crystals in the area visible at 100 X, or about 400 crystals in an area equal to the noncrystalline area of the other specimen. The total number of crystals formed at both 100 v and 140 v on the first specimen was about 750 in the total area visible at 100 X.

It appears that there were a certain number of crystallization sites with a range of potencies available on the surface of each specimen. For the first specimen the most active of these sites were used up at 100 v and most of the resulting crystals made inactive for further crystallization by the rapid voltage increase to 140 v. Nucleation at 140 v on the remaining area was thus greatly retarded compared to nucleation on the second specimen which still contained all the most active sites.

The second type of experiment consisted of photographing a selected area before any oxide film was formed on the specimen and again after partial crystallization to see whether visible defects existed on the original surface at sites where crystals later occurred. Fig. 1 and 2 show such "before-and-after" pictures of an area of a specimen for which the crystallization treatment was 100 v, 99°C, 600

[1] The electrolyte used in all tests described in this paper was 2% HNO_3.

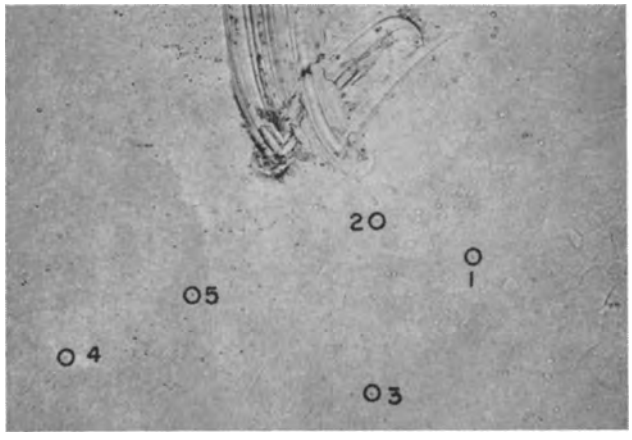

Fig. 1. Photomicrograph of Ta surface as chemically polished. 100X before reduction for publication.

sec. A total of 31 crystals were counted excluding those which occurred at the scratch introduced as a reference mark. Spots were observed on the original metal surface at all but three of the sites at which these crystals appeared. A few of these sites are indicated on both photomicrographs.

These experiments indicate that surface heterogeneities act as nucleation sites for field crystallization. Since there was no tendency for nucleation to occur at grain boundaries it is probable that the nucleation sites are inclusions of high impurity content. Crystallization of anodic films formed on evaporated Ta provides evidence that impurities are important. Tantalum films about 2000Å thick were evaporated on one side of Ta strips of the type used for the other experiments. Crystallization of the resulting specimens showed that nucleation was far slower on the evaporated side. At 99°C, 100 v crystals were observed on the nonevaporated side after 300 sec, while none was observed on the evaporated side until 1000 sec. After 6500 sec the side without evaporated Ta was 90% crystalline, while only 1 or 2% of the evaporated side was crystalline. Fig. 3 shows a photomicrograph on an area part of which was shielded during evaporation. Very few crystals appear in the evaporated region, while the shielded region is almost completely crystalline. Only part of this change in crystallization rate can be attributed to decreased nucleation rate, since the growth rate

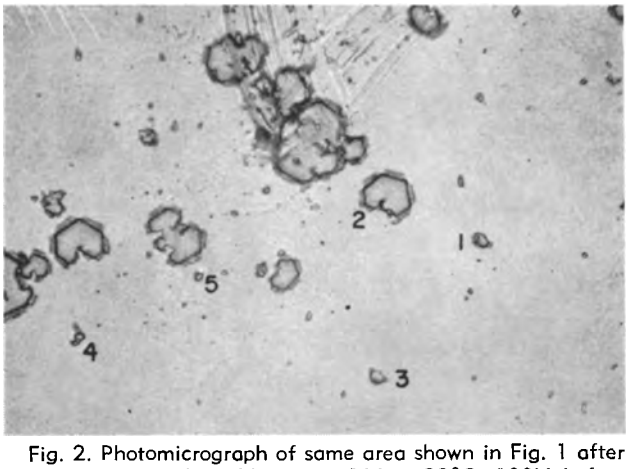

Fig. 2. Photomicrograph of same area shown in Fig. 1 after anodic oxidation for 600 sec at 100 v 99°C. 100X before reduction for publication.

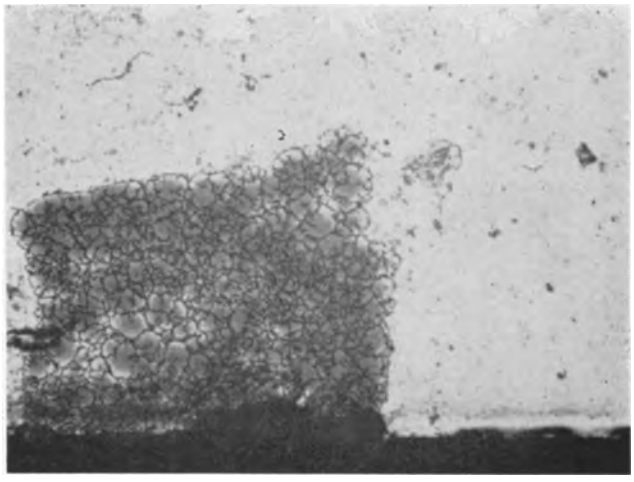

Fig. 3. Comparison of crystallization on evaporated Ta (white area) and on rolled chemically polished Ta sheet (lower left).

of the crystalline areas was also less on the evaporated side.

Effect of Voltage and Temperature on Incubation Time

Earlier data had indicated that there was a thickness dependent critical electric field for a given voltage and temperature above which crystallization did not occur (1). These data were obtained in experiments in which a constant voltage was applied to a specimen held at 99°C in 2% HNO_3 until crystallization occurred. It was found that crystallization did not occur until the thickness had grown sufficiently so that the field reached a certain value. An experiment to test the critical field hypothesis would be to form a film at a low temperature (where crystallization is extremely slow) to such a thickness that the critical field would be reached immediately at the start of the test at the higher temperature and desired voltage. When such experiments were performed, it was found that there was an even longer delay time before the start of new crystals than there had been previously. During this incubation period the field fell to values far below the field at which crystals were observed in earlier tests. In other words, there was no critical field for nucleation.

From a series of such tests at different voltages, however, it was found that the quantity of electricity passed through the cell from the start of the experiment to the time at which the first crystals were observed was approximately constant. Table I shows the number of coulombs passed through the cell from the start to the incubation time[2] for various voltages and temperatures, along with the observed nucleation times. It may be seen that the number of coulombs is roughly constant for all voltages at 99°C, and that there is an indication of an increase in the number of coulombs as the temperature is lowered. The apparent critical field was the result of the fact that the passage of a given quantity of electricity results in a greater percentage change in thickness for a thinner initial film. There was thus a greater decrease in the field at which

[2] The author defines incubation time to be that time at which the first crystals are observed.

Table I.

Experimental conditions	Nucleation time, sec	Total coulombs passed through cell
99°C, 50 v	5500	0.40
99°C, 70 v	600	0.39
99°C, 100 v	250	0.41
99°C, 140 v	130	0.44
99°C, 170 v	45	0.39
81°C, 100 v	750	0.44
47°C, 100 v	3500	0.55

crystals were first observed for specimens held at low voltages.

Experiments at Constant Field

Interpretation of the experiments described above is complicated by the fact that the amorphous oxide film grows continuously while the experiment is being performed, so that the electric field in the oxide is not constant. To eliminate this difficulty a series of experiments were performed in which specimens were held at constant field and constant temperature until crystallization occurred. All of the experiments were conducted using 2% HNO_3 as electrolyte, the temperature varying from 50° to 100° C and at 80-140 v. Each specimen was formed at the test temperature to a thickness sufficient to give the desired electric field strength at a convenient voltage. This voltage was then applied and the specimen was examined from time to time to determine when crystallization had just started. It was found that crystallization occurred in the same time at the same field regardless of film thickness or applied voltage.

Fig. 4 shows the results of these tests. It is clear that both lower temperature and lower electric field retard crystallization. At any one temperature the logarithm of the incubation time increases approximately linearly with decreasing applied field.

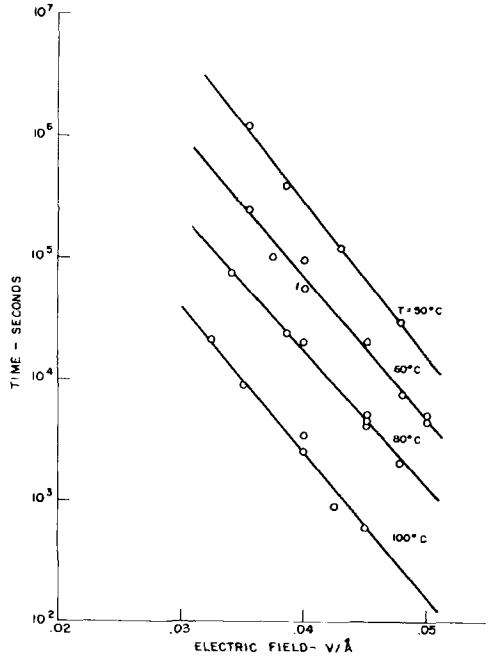

Fig. 4. Time required for the formation of the first visible crystals vs. applied electric field.

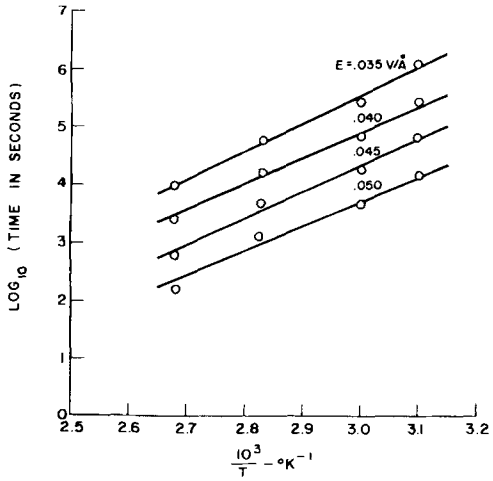

Fig. 5. Arrhenius plots of the data of Fig. 4

There is a considerable amount of scatter among the data, which is due to the difficulty of finding the very first crystals to form.

From these data the times at which crystallization started at various field strengths were obtained, and the logarithm of this incubation time was plotted against $1/T$ to obtain the activation energy (Fig. 5). The results of least square analysis of the data are shown in Table II.

It may be seen that there is a small decrease in activation energy with increasing electric field, and that the pre-exponential factor is approximately constant. The uncertainties in values given in Table II are rather large. The least square analysis shows that 50% of the measurements of activation energy would lie within an interval of about 2000 cal/mole on either side of the value given. Thus, the change of activation energy with field is not greater than the experimental error. The 50% confidence interval on the pre-exponential factor is about two orders of magnitude, so that the small variations reported are without significance.

Discussion

From the results of an electron microscope study reported earlier (1), it appears that a crystalline area begins rapid radial growth after a crack has been produced in the amorphous oxide film. Fig. 6 shows an electron micrograph of an area of a specimen on which crystallization had just started. The circular region in which a jagged crack in the amorphous oxide film is visible is apparently the first stage of crystallization, no smaller or less well developed regions having been observed. The cracks in the amorphous film are similar in appearance to those which can be produced by forcing a blunt object (such as the end of a pen-holder) through a sheet of paper. It is reasonable to assume that the

Table II.

Electric field v/Å	Activation energy, kcal/mole	Pre-exponential factor $(sec)^{-1}$
0.050	20.6	$1.6 \cdot 10^{-10}$
0.045	21.6	$1.4 \cdot 10^{-10}$
0.040	21.8	$4.5 \cdot 10^{-10}$
0.035	23.1	$2.5 \cdot 10^{-10}$

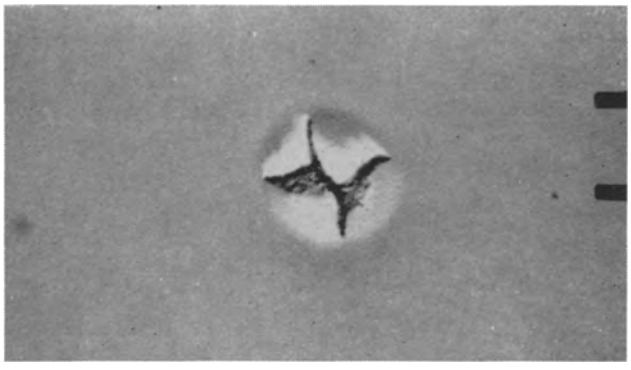

Fig. 6. Initial stage of recrystallization. 30,000X before reduction for publication.

cracks are produced by a crystal of Ta_2O_5 growing on one of the nucleation sites at the metal-oxide interface.

Two possible mechanisms are considered here for the initial growth of a crystal at a nucleation site, one in which crystallization of the already existing amorphous film occurs and the other in which completely new crystalline material forms underneath the amorphous film. Growth of new crystalline material underneath the amorphous film implies access of water to the metal under the film, presumably through pores in the amorphous oxide. The voltage drop in a pore of length 2000Å and of any diameter filled with electrolyte having a specific resistance of 100 ohm-cm in which the current density is 1 amp/cm^2 is $2 \times 10^{-5} \times 100 = 2.10^{-3}$ v. Hence, nearly all of the cell voltage (of the order of 100 v) would appear across the crystal growing at the base of the pore. Consequently a pore would be filled up almost immediately by extremely rapid growth of the crystalline or amorphous phase, and could have only a transient existence. This mechanism thus implies that there is a continuous formation and destruction of pores in a particular region or else that the pores are kept open by some process such as a vigorous gas evolution (which is not observed). It is difficult to see why there should be an incubation period which depends on field and temperature in the observed manner if pore formation is really the mechanism responsible for the initial crystal growth.

Crystal growth by transformation of the existing amorphous phase at a nucleation site seems far more likely. Stresses produced by a slight density difference in the two materials could eventually lead to a crack in the amorphous film. Once a crack was produced the solution would have access to the growing crystal which would then thicken rapidly and cause further cracking of the type observed. It is assumed that the incubation time for the formation of rapidly growing crystalline areas is the time required for a crystal growing on a nucleation site to reach the critical size necessary to cause a crack in the amorphous film. This incubation time is not a nucleation time in the ordinary sense of the term, since it is assumed that a stable crystal exists on the nucleation site at the start of the experiment. The nucleation time is the time required for this stable crystal to reach the critical size necessary to produce a crack. Presumably there would be a different critical size for each nucleation site depending on its size and configuration, but in these experiments the critical size is the same for all specimens since the first crystals observed would form on the most active type of site.

The rate of growth of the crystal is determined by the rate at which ions in the amorphous film can cross a potential barrier and assume lattice positions in the crystal. There exist strong electric fields in the two phases which can act to assist the ions in surmounting the potential barrier to their motion. The electric field at the position of the rate-determining step near a growing crystal may not be equal to the externally applied field because of differences in dielectric constant for the crystalline and amorphous phases or because of space charges which may result from unequal ionic mobilities in the two phases. For simplicity it is assumed that the field at the rate-determining barrier is proportional to the applied field.

The rate of growth of a crystal can now be calculated in terms of certain parameters suitable for comparison with experiment. The rate of motion of ions across a potential barrier in the presence of an electric field of such strength that jumps are overwhelmingly in the direction of the field is

$$R = A \exp -\left(\frac{Q - q\lambda E}{RT}\right) \qquad \text{(I)}$$

where A is a constant, Q the activation energy at zero field, q the charge on the ion, λ the distance from the equilibrium position to the top of the potential barrier, and E the electric field component in the direction of motion. To take account of the fact that field at the barrier may not be equal to the applied field it is necessary to use a proportionality constant defined by

$$E = f \cdot E_a \qquad \text{(II)}$$

where E_a is the component of the applied field in the jump direction. The rate of crystal growth is now

$$\frac{\Delta l}{\Delta t} = A \exp -\left(\frac{Q - q\lambda f E_a}{RT}\right) \qquad \text{(III)}$$

or since Δl is constant and equal to the critical size,

$$-\log \Delta t = \log A' - \frac{Q - q\lambda f E_a}{RT} \qquad \text{(IV)}$$

According to Eq. (IV) a plot of activation energy vs. electric field should give a straight line of slope $q\lambda f$. Fig. 7 shows such a plot, which has a slope of 7.2 in units of electronic charges times angstrom units. In view of the large uncertainty in the values of activation energy the value obtained for $q\lambda f$ could be in error by as much as a factor of two. A more accurate value may be obtained from the slopes of the curves shown in Fig. 2, using Eq. (IV). The values so obtained are 8.8, 7.8, 7.8, and 8.2 at temperatures of 100°, 80°, 60°, and 50°C, respectively. Taking $q\lambda f$ to be 8.2 the zero field activation energy, Q, is about 30 kcal/mole.

There are at least two ways in which the growth of a crystal nucleus could occur. In the first place

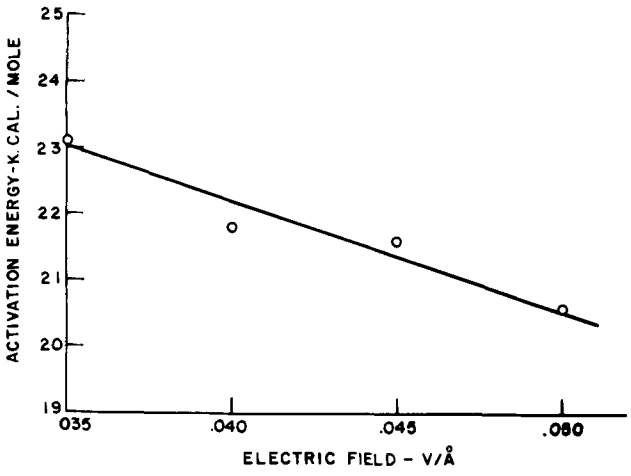

Fig. 7. Activation energy vs. electric field

oxygen and Ta ions could be transferred from the amorphous film to the crystal across the interface. Such a mechanism would require that the Ta ions move against the field, which is very unlikely at these fields and temperatures. A second possibility is that oxygen ions from the amorphous film are added to the crystal at the interface and that Ta diffuses out from the metal to the growing surface of the crystal. The Ta ions from the amorphous film would then be free to migrate through the film to the electrolyte interface and form more oxide. Such a mechanism would not have to proceed very long before a crack formed since such growth of the film at an isolated point would make it difficult to maintain contact at the oxide-metal interface without severe distortion of the oxide.

Assuming this mechanism to operate, the rate of crystal growth might be controlled by Ta ion migration in the growing crystal or in the amorphous oxide, or by oxygen ion migration across the crystal-amorphous interface. The zero field activation energy for ionic motion in the amorphous film at these fields is about 50 kcal/mole, which is considerably higher than the experimental value for nucleation. If $f = 1$, $q = 2$ (for oxygen ion migration) $2\lambda = 8.2$Å, which seems to be considerably too large. However, the values of Q and q (assuming $f = 1$) are reasonable for ionic conduction in crystalline Ta_2O_5. Gulbransen and Andrew (6) reported an activation energy of 27.4 kcal/mole for oxidation of Ta at temperatures where crystalline oxide is formed. If $q = 5$, $\lambda = 1.6$ so that the distance between equilibrium positions would be 3.2Å, a very reasonable value. A planned study of the kinetics of formation of crystalline tantalum oxide films should make it possible to tell whether ionic migration in the crystal is really the rate-determining step in crystal nucleation under these conditions.

Conclusions

1. Field crystallization occurs only at certain preferred nucleation sites at the metal-oxide interface. These sites may be inclusions of high impurity content in the metal.

2. The incubation period for the appearance of crystalline areas corresponds to the time required for a crystal growing underneath the amorphous oxide film to reach a critical size.

3. The logarithm of the incubation period increases linearly with decreasing electric field at constant temperature.

4. An incubation period consistent with experiment would result from control of the growth of the crystal by field assisted ionic motion. There is a possibility that the rate-determining step is Ta ion migration in the crystal.

Manuscript received November 21, 1956. This paper was prepared for delivery before the Buffalo Meeting, Oct. 6-10, 1957.

Any discussion of this paper will appear in a Discussion Section to be published in the June 1958 JOURNAL.

REFERENCES

1. D. A. Vermilyea, *This Journal*, **102**, 207 (1955).
2. R. C. Spooner, Private communication.
3. R. D. Misch, Private communication.
4. W. D. Robertson, Private communication.
5. M. J. Fraser, Private communication.
6. E. A. Gulbransen and K. F. Andrew, *This Journal*, **96**, 364 (1949).

Surface Protection and Selective Masking during Diffusion in Silicon

C. J. Frosch and L. Derick

Bell Telephone Laboratories, Inc., Murray Hill, New Jersey

ABSTRACT

An apparatus is described for the vapor-solid diffusion of donors and acceptors into silicon at atmospheric pressure. It consists essentially of a fused silica tube extending through one or more controlled temperature zones. A gas such as nitrogen carries the vapors from the heated impurity element or one of its compounds past the heated silicon.

At temperatures above about 1000°C, gases such as helium or nitrogen are shown to cause serious pitting or erosion of the silicon surfaces. A thin vitreous silicon dioxide envelope enclosing the silicon during the high temperature heating operation is shown to provide complete protection of the underlying surface against damage. Methods of obtaining surface passivation are described.

In addition to surface protection, a silicon dioxide surface layer also is shown to provide a selective mask against the diffusion into silicon of some donors and acceptors at elevated temperatures. Data are presented showing the masking effectiveness of the silicon dioxide layer against the diffusion of several donors and acceptors into silicon.

The application of the masking technique to produce precise surface patterns of both *n*- and *p*-type is described. An example of its feasibility in device considerations is illustrated by the construction of a transistor by double diffusion. This transistor is unique in that both the emitter and base contacts are made at the surface in adjacent areas.

Finally a new predeposition technique is described for controlling the impurity levels in diffused layers over wide ranges. Data are presented to illustrate this technique.

The vapor-solid diffusion technique has become of considerable interest recently for the introduction of selected conductivity type determining impurities into semiconductors. The application of this technique in the design of Si semiconductor devices is illustrated by the solar battery (1), power rectifiers (2), and high frequency transistors (3). The feasibility of producing such structures by vapor-solid diffusion resulted largely from the investigations of Fuller and his co-workers (4, 5). Their investigations provided the necessary information on the high temperature diffusion parameters required for controlling the impurity concentrations and depths of the diffused layers.

This paper describes: (*a*) a new apparatus for vapor-solid diffusion at atmospheric pressure, (*b*) some experiments illustrating surface protection of Si at high temperatures by oxidation, and (c) some experiments illustrating selective masking by SiO_2 surface layers against the diffusion of some impurities into Si at high temperatures. Methods for determining the electrical characteristics, surface concentrations, and diffusion depths are essentially the same as those described elsewhere (5) and are only identified in this paper.

Apparatus and Procedure

The apparatus for vapor-solid diffusion at atmospheric pressure is shown schematically in Fig. 1. It consists essentially of a fused silica tube extending through two controlled temperature zones. The first temperature zone serves to regulate the volatility of an impurity placed therein. The second temperature zone is the location of the Si samples. A rising temperature gradient between the two zones avoids the redeposition of the impurity vapor before reaching the Si samples. The temperatures are regulated to ±2°C by means of Pt-Pt 10% Rh thermocouples and automatic controllers.

The vapor from an impurity heated in the first temperature zone is carried past the Si heated in the second zone by carrier gases such as H_2, N_2, O_2, and CO_2 or mixtures thereof with or without the addition of water vapor. Flowmeters attached to one end of the furnace tube regulate the flow of the carrier gases. In this investigation flow rates of 1500 cc/min of the carrier gas were employed in furnace tubes of 2.5 cm ID. A temperature-controlled water bubbler is inserted between the flowmeters and the furnace tube when water vapor is being added to the carrier gas. Carrier gases were not saturated with water vapor under these flow conditions, but particular experimental conditions were found to be reproducible. The exit or open end of the furnace tube is inserted into a hood. This effectively removes the carrier gases which now probably contain residual amounts of 3rd and 5th column elements or their compounds. These in many cases are harmful poisons.

The Si samples are held vertically in a slotted fused silica plate as shown in Fig. 1. This assures a uniform contact of the carrier gas with both Si sur-

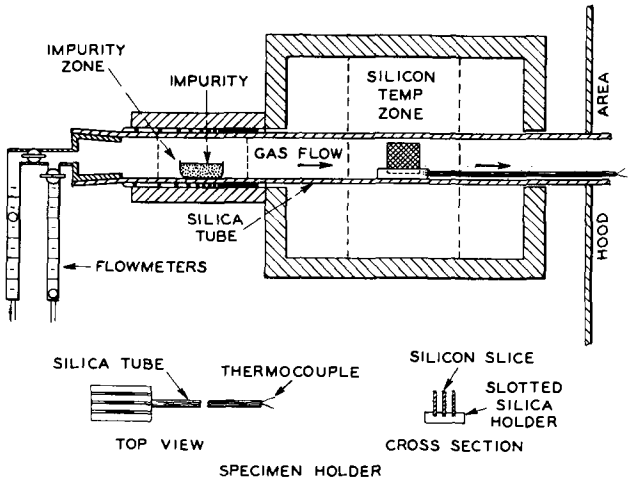

Fig. 1. Apparatus for vapor-solid diffusion at atmospheric pressure.

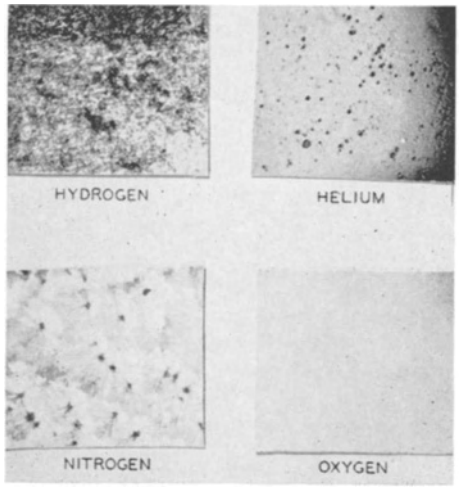

Fig. 2. Surface appearance of Si after heating for 1 hr at 1350°C in different carrier gases.

faces. A small silica tube fused to the sample holder is used to insert and remove the Si from the furnace. A Pt-Pt 10% Rh thermocouple inserted in the pusher tube is employed to measure the work temperature throughout the run.

Before the Si samples are inserted for diffusion or oxidation, the flow of carrier gas is started and allowed to continue for several minutes to establish a steady-state condition. The samples then are introduced at a reproducible rate into the desired temperature zone. At the end of the heating operation the samples generally are withdrawn at the insertion rate. In these experiments the samples were inserted and withdrawn in about 1 min.

Samples

The Si samples were cut from approximately 5 ohm cm *n*-type (arsenic doped) or *p*-type (boron doped) single crystal ingots grown in the [111] direction. The ingots were sawed perpendicular to the growth direction into slices approximately 10^{-1} cm thick. These were machine lapped on both surfaces with No. 1800 emery powder to a thickness of about 7×10^{-2} cm. After cutting into squares of 0.75 x 0.75 cm, the samples were etched for 4-5 min in a mixture of 5 parts of concentrated HNO_3 to 1 part of concentrated HF to produce a mirror finish. This resulted in final sample thicknesses of about 5×10^{-2} cm. Reproducible surfaces of excellent appearance were obtained by maintaining the etchant temperature at about 20°C and employing mechanical agitation during etching.

Surface Protection

When Si is heated in the previously described diffusion apparatus above about 1000°C for relatively short times in commercial grades of nonoxidizing gases such as H_2 or He, serious erosion or pitting of the surface occurs. A significant loss in weight also takes place. On the other hand, Si surfaces are essentially unchanged after long heating periods well above 1000°C in oxidizing gases such as O_2 and CO_2 or nonoxidizing gases containing sufficient concentrations of oxygen or water vapor.

The surface appearance of Si samples after heating in H_2, He, N_2, or O_2 gases is illustrated in Fig. 2. The surfaces were washed in concentrated HF after the heating operation to remove any surface layers such as SiO_2 which forms in the pure oxygen atmosphere. Note the damage on the Si surfaces after heating in H_2 and He. On the other hand after heating in oxygen the excellent surface appearance is essentially the same as that of the original etched surface. The crystalline surface appearance after heating in N_2 may be due to the formation of a Si_3N_4.

The effect of varying the water vapor content in a hydrogen carrier gas during heating on the surface appearance is illustrated in Fig. 3. The temperatures under the photographs represent the temperatures of the water bubbler. Note the decrease in the size of the surface pits as the water vapor content of the carrier gas is increased. Actually in this series of heating experiments at 1350°C, water bubbler temperatures between 30°-80°C resulted in excellent surfaces. However, a further increase in the water content of the carrier gas resulted in a large number of very small surface pits. The reappearance of surface pits might be explained by the failure to form a completely coherent oxide layer in the presence of high water vapor contents at this temperature. Silicon dioxide is known to be quite soluble in water at high temperatures.

Other examples of surface protection by oxidation might be given. For example, Si can be heated

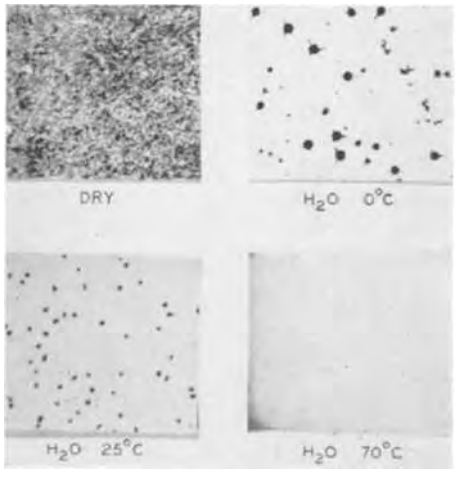

Fig. 3. Surface appearance of Si after heating for 1 hr at 1350°C in hydrogen containing different concentrations of water vapor.

in CO_2 or in various mixtures of N_2 and O_2 including air without apparent surface damage. The latter suggests many process simplifications for producing diffused junction layers. However, the oxidizing potential of the carrier gas must be sufficient so that the thermodynamic equilibrium favors the formation of SiO_2 at each processing condition. On the other hand optimum surface appearance does not necessarily result from maximum oxidizing conditions. Generally it is preferable to establish optimum conditions experimentally for each processing condition.

Surface protection of Si in oxidizing atmospheres is due to the formation of a continuous protective envelope of nonvolatile SiO_2. This prevents not only the evaporation of the underlying Si but also its complete oxidation. The oxide layer is easily removed by washing in HF. In this work the SiO_2 layers generally varied in thickness between about 1500 to 3000Å depending on the temperature, time and carrier gas composition. The layers exhibit brilliant interference colors. The constant thickness of the oxide layer on a particular Si surface is indicated by the uniformity of these interference colors.

Selective Masking

In addition to surface protection, a SiO_2 surface layer provides a selective mask at high temperatures against the diffusion of some donors and acceptors into Si. Only a few typical examples of selective masking will be given.

Masking is studied most effectively by preoxidizing etched Si slices and removing the oxide layer from one surface with HF. This provides an oxidized and unoxidized surface on the same sample for electrical, diffusion depth, and other measurements. In the examples reported here the preoxidation was done by heating at 1200°C for 1 hr in N_2 bubbled through water at 30°C. This gives an oxide layer about 2500Å thick.

Fig. 4 illustrates the masking of As by a SiO_2 layer at three diffusion temperatures. The first figure is a cross-sectional view of a p-type Si slice with an oxide layer on one surface. The next figure shows that arsenic trioxide is heated at 235°C and the carrier gas is N_2 bubbled through water at 30°C for each processing condition. In the next column the diffusion times and temperatures are given for each of the four processing conditions. The fifth column shows a cross-sectional view of the processed samples after a wash in HF which removes only the oxide envelope. The cross-hatching illustrates the relative thickness of the n-type conversion layer. The average sheet resistance values (ρ_s) and the diffusion depths (a) were measured by the four point probe and the 5 degree angle lapping-staining technique, respectively. These measuring techniques are described in some detail elsewhere (5). From the ρ_s and (a) values the surface concentrations (C_0) of the impurities given in the last column were calculated by assuming an error function distribution of the impurities through the diffused layers.

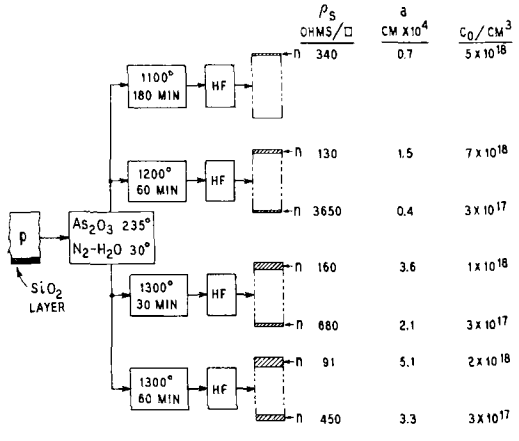

Fig. 4. Masking by an oxide layer against the diffusion of As at different diffusion temperatures.

Note the absence of a conversion layer on the oxidized surface after the 1100°C diffusion shown in Fig. 4. This indicates that the surface concentration of the As on this surface is less than 3×10^{15} cm^{-3}, the background p-type doping in the original crystal. At the two higher diffusion temperatures a conversion layer is formed on the oxidized surface. However, the C_0 values remain relatively constant and well below those for the unoxidized surfaces. The effect of the SiO_2 surface layer and the diffusion temperature on surface concentration and hence diffusion depth is clearly evident from the data.

Fig. 5 illustrates the effect of carrier gas type on the diffusion of boron. The representations have the same significance as those described previously. Because of its very low volatility, the boron trioxide source is heated at the same temperature as the Si. Note the absence of a conversion layer on the oxidized surface and the highly doped conversion layer on the unoxidized surface after heating in oxygen. An appreciable masking effect by the oxide layer also is evident after heating in the nitrogen-water carrier gas. On the other hand no masking by the preoxidized surface is evident after heating in the hydrogen-water carrier gas. The doping level also is appreciably higher for the wet hydrogen than for the unoxidized surfaces in the other two carrier gases. The reason for this effect of carrier gas type and composition on the masking by SiO_2 surface layers is not known. However, it does suggest some difference in the molecular specie of the diffusant vapor in the various carrier gases which alters its reactivity with, diffusion through, or solubility in a SiO_2 layer. A complete study of the effect of carrier gas composition on the masking of a SiO_2 surface layer against the diffusion of donors and acceptors

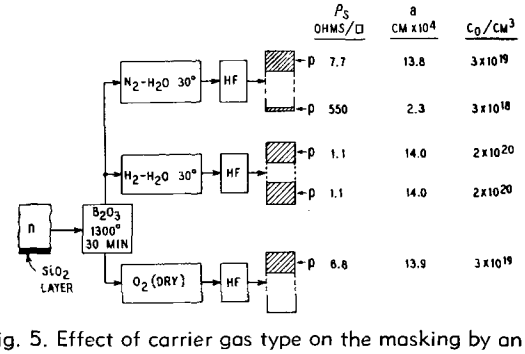

Fig. 5. Effect of carrier gas type on the masking by an oxide layer against the diffusion of B.

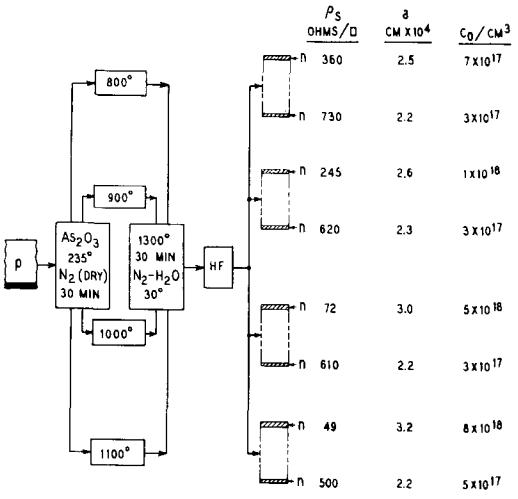

Fig. 6. Effect of predeposition temperature on masking and surface concentration.

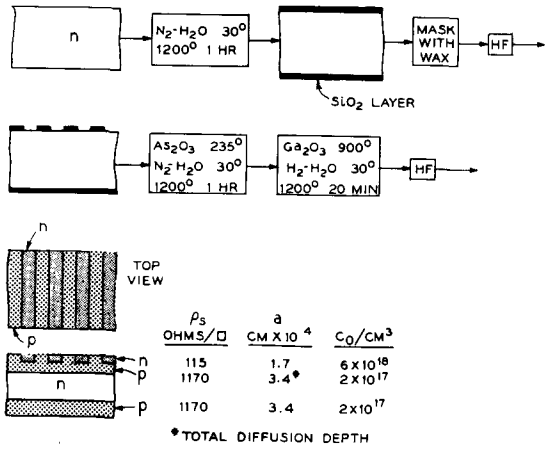

Fig. 7. Simultaneous production of single and double diffused layers of controlled structure by selective masking.

into Si at high temperatures should be very useful in the design of semiconductor devices. A few experimental results for wet hydrogen and nitrogen as well as oxygen are summarized in Table I.

Predeposition of Impurities

When a SiO_2 layer masks against the diffusion of an impurity, the simultaneous oxidation and addition of such an impurity may cause a partial masking effect on the unoxidized surface. Fig. 6 illustrates a technique for avoiding oxidation effects during the addition of the impurity. It consists essentially of predepositing the impurity in nonoxidizing gases such as N_2, He, or H_2 at low temperatures and for very short times. Under these processing conditions surface erosion is not appreciable. The diffusion of the impurity into the Si then may be carried out at higher temperatures and for longer times in oxidizing carrier gases.

In Fig. 6 As_2O_3 was predeposited for 30 min in dry nitrogen at 800°, 900°, 1000°, and 1100°C, respectively. The samples then were diffused for 30 min at 1300°C in N_2 bubbled through water at 30°C. The samples usually were washed in HF after the predeposition to remove any soluble deposits of the diffusant on the unoxidized surface and the preoxidized layer which now may contain some of the diffusant. This washing procedure was found to give more reproducible results.

As shown by the data in Fig. 6 the SiO_2 layer masks against the diffusion of As in the case of all four predeposition temperatures. The degree of masking, which is defined as the ratio of the surface concentration of the unoxidized surface to that of the oxidized surface, increases with predeposition temperature over the range studied. The data for the unoxidized surfaces also illustrate the usefulness of the predeposition technique for controlling the surface concentration over wide limits. The applica-

Table I. Masking by oxide surface layers against the diffusion of some donors and acceptors*

Diffusant Type	Diffusant Temp, °C	Diffusion Time, min	Diffusion Temp, °C	Surface type O	Surface type U	ρ_s (ohms/□) O	ρ_s (ohms/□) U	a (cm × 10⁴) O	a (cm × 10⁴) U	C_0/cm³ O	C_0/cm³ U
					N_2-H_2O-30°C Carrier gas						
As_2O_3	235	180	1100	*P*	*N*	—	340	—	0.7	—	5×10^{15}
As_2O_3	235	60	1200	*N*	*N*	3650	130	0.4	1.5	3×10^{17}	7×10^{15}
As_2O_3	235	30	1300	*N*	*N*	680	160	2.1	3.6	3×10^{17}	1×10^{18}
B_2O_3	1250	30	1250	*N*	*P*	—	76	—	5.1	—	7×10^{18}
B_2O_3	1300	30	1300	*P*	*P*	550	7.7	2.3	13.8	3×10^{18}	3×10^{18}
P(Red)	220	180	1100	*N*	*N*	2560	195	0.5	2.4	4×10^{17}	1×10^{18}
P(Red)	220	30	1300	*N*	*N*	885	170	3.6	7.4	8×10^{16}	4×10^{17}
Sb_2O_4	900	30	1300	*N*	*N*	1370	140	1.0	4.9	3×10^{17}	6×10^{17}
					H_2-H_2O-30°C Carrier gas						
As_2O_3	235	60	1200	*P-N*	*N*	—	330	—	1.3	—	1×10^{18}
As_2O_3	235	30	1300	*N*	*N*	680	86	2.1	3.7	3×10^{17}	2×10^{18}
B_2O_3	1300	30	1300	*P*	*P*	1.1	1.1	14.0	14.0	2×10^{20}	2×10^{20}
P(Red)	220	30	1300	*N*	*N*	745	150	3.6	5.6	1×10^{17}	4×10^{17}
Ga_2O_3	900	40	1200	*P*	*P*	1890	1835	5.8	5.8	6×10^{16}	6×10^{16}
Ga_2O_3	900	30	1300	*P*	*P*	675	675	9.1	9.1	1×10^{17}	1×10^{17}
Sb_2O_4	900	30	1300	*P*	*N*	—	160	—	5.6	—	4×10^{17}
					Dry O_2 carrier gas						
As_2O_3	235	30	1300	*N*	*N*	545	235	2.0	3.1	3×10^{17}	5×10^{17}
B_2O_3	1300	30	1300	*N*	*P*	—	6.8	—	13.9	—	3×10^{19}
P_2O_5	220	180	1100	*N*	*N*	1390	25	0.9	3.8	3×10^{17}	7×10^{19}
P_2O_5	220	30	1300	*N*	*N*	0.45	0.44	19.1	20.1	3×10^{20}	3×10^{20}

* Original samples about 5 ohm cm, preoxidized 1 hr at 1200°C in N_2-H_2O-30°C, U-oxide layer removed from this surface with HF before diffusions. O-oxide layer on this surface before diffusions.

tion of this technique for producing both *np* and *pn* double diffused layers from the same donor and acceptor impurity will be described later.

Multiple Layer Structures

A more interesting example of selective masking by a SiO_2 layer is illustrated in Fig. 7. After the preoxidation of an *n*-type Si sample in wet nitrogen at 1200°C, the oxide layer is removed from one surface to give alternate oxidized and unoxidized bands. This is done by applying alternate bands of wax, washing in concentrated HF, and then removing the wax with a solvent. An As diffusion followed by a Ga diffusion and an HF wash results in the structure illustrated by the top and cross-section views shown in the bottom left of Fig. 7. Note the alternate *p*- and *n*-type surfaces as well as the alternate single and double diffused layers. These correspond to the alternate oxidized and unoxidized bands, respectively, on the top face before the diffusion operations. The bottom surface, which is completely covered with an oxide layer before the diffusion treatments, is entirely *p*-type with a single diffused layer. A similar structure results if Sb_2O_4 heated at 900°C is substituted for the arsenic trioxide.

It is not necessary to remove the oxide layer after the As diffusion since Ga is not masked by the SiO_2 layer under these processing conditions (see Table I). Actually the oxide layers covering the *n*- and *p*-type surfaces before the final HF wash are distinctly different in color. The color difference probably is due to a thickness difference between the two oxide layers. This is indicated since the same colors are observed when the identical heating sequence is employed without the addition of the As and Ga. The color difference of the oxide layers covering the *n*- and *p*-type Si surface areas is useful in device fabrication as an aid in locating these regions after diffusion.

A transistor (6) has been made by these techniques which had an alpha of 0.91 at a collector voltage of 10 v and an emitter current of 1 ma. The unique feature of this transistor structure was the ability to make a direct contact on the same surface to both the diffused base layer and the diffused emitter layer. In previously described double diffused transistors (3), the base contact was made by alloying Al through the emitter layer. The direct contact to the base layer described in this paper also should allow a higher surface concentration in the emitter than is permissible in the Al alloy base contact structure.

The structure obtained in Fig. 7 can best be explained by referring to Fig. 8. This illustrates the appreciably lower surface concentration of As in the oxidized surface as compared to the unoxidized surface. Since the Ga is not masked by the SiO_2 layer under these processing conditions, its surface concentration is equivalent for both surfaces. Thus the As overdopes the Ga on the unoxidized surface, while the reverse is true on the oxidized surface. In other words a *np* diffused structure is produced in the unoxidized surface and a single *p* diffused layer is produced in the preoxidized surface. The surface concentration of the diffused As layer in the oxidized

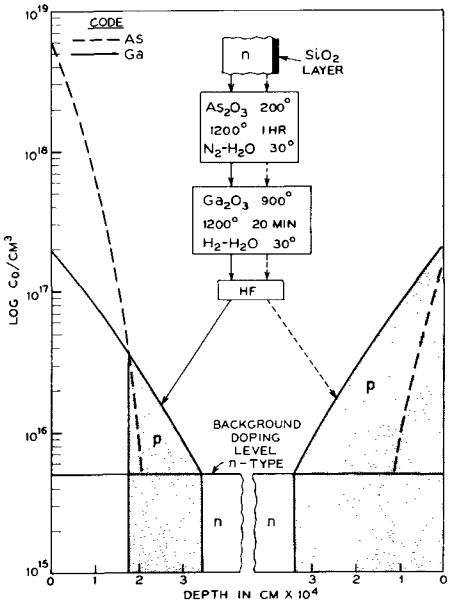

Fig. 8. Plot to illustrate the formation of single and double diffused layers by selective masking.

surface was not determined in this experiment and is drawn merely for illustration.

Fig. 9 shows a photograph of an actual diffused structure which was produced by the selective masking technique just described. The diffused layers on one surface were exposed by lapping at a 5 degree angle (5) perpendicular to alternate *p*- and *n*-type surface bands similar to those illustrated in Fig. 7. The *p* region was darkened by the HF-HNO_3 staining technique (5). Note the single *p* diffused layer in the center region with double *np* diffused layers on either side. While not evident from the photograph, the dark surface or *p* region indexes very closely with the original preoxidized surface.

Controlled structures with either *n*- or *p*-type single diffused layers and either *np*- or *pn*-type double diffused layers have been produced by the selective masking procedure when the proper diffusants and processing conditions are employed. Moreover, both structural types have been produced with B and P by employing the predeposition technique. This combination of impurities also can be employed for producing low resistance surface layers for collector contacts in transistor construction. The essential processing steps for producing either an *np*-

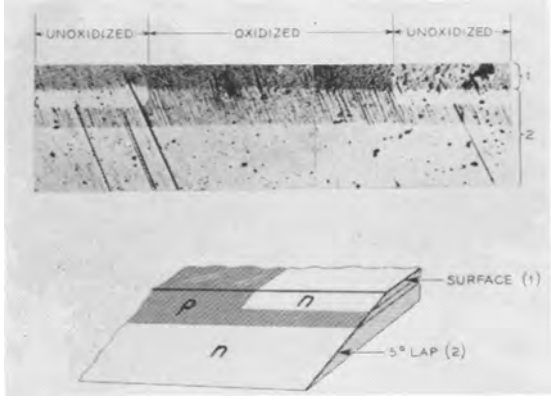

Fig. 9. Photograph of single and double diffused layers produced by selective masking.

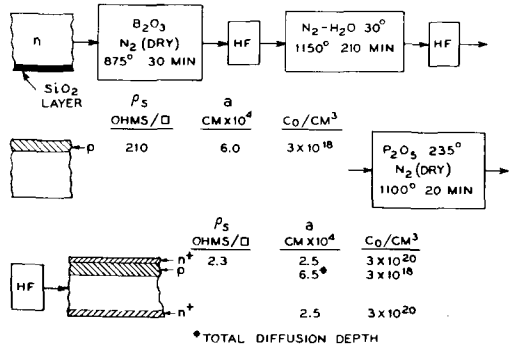

Fig. 10. Production of a p^+pnn^+ transistor structure by predisposition and selective masking.

or pn-type transistor structure of this type with B and P are shown in Fig. 10 and 11.

In the np structure illustrated in Fig. 10, the predeposition of the B_2O_3 at 875°C in dry N_2 gives a surface concentration (C_0) on the unoxidized surface which is well below that eventually reached by the P. The processing conditions are chosen to give the desired final diffusion depth of the p-layer into the originally unoxidized surface. Because of the masking effect of the oxide layer during the predeposition of the boron trioxide, the C_0 of the oxidized surface is reduced to well below that of the unoxidized surface. Actually no B conversion layer is formed in the oxidized surface under these processing conditions. Thus the structure illustrated by the last cross section in Fig. 10 results after the final phosphorus diffusion.

The pn structure illustrated in Fig. 11 is produced in a similar manner except that the P is masked and its surface concentration is reduced by predeposition below that eventually reached by the B. In this case a conversion layer is formed in the oxidized surface by the P. However, the partial masking by the oxide layer is sufficient to reduce the diffusion depth below that finally attained by the B layer. Because of this only a p^+ layer is formed on the original oxidized surface as shown in Fig. 11. At these low doping levels, red P as a source of P vapor gives more reproducible results than P_2O_5. Red P also generally results in lower surface concentrations than the phosphorus oxide for otherwise similar processing conditions.

In addition to the structural possibilities of masking, it also can be applied in conjunction with the predeposition technique to provide a wide range of controlled impurity levels in diffused layers. For example, by modifying the processing conditions illustrated in Fig. 10 and 11, the doping levels of the base and emitter layers can be varied over wide limits.

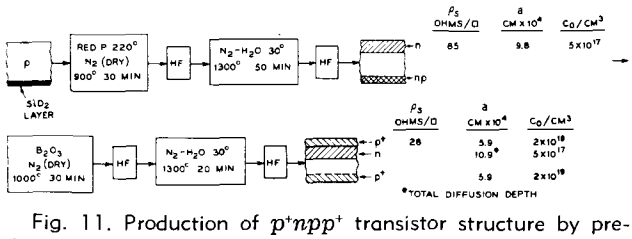

Fig. 11. Production of p^+npp^+ transistor structure by predeposition and selective masking.

It is evident from the few examples of selective masking described that a large variety of structures can be produced by the proper choice of processing conditions. It is hoped that the examples given illustrate the essential procedures for producing such structures.

Summary

The use of oxidizing atmospheres has been shown to provide surface protection of Si surfaces during high temperature heating operations. The protection results from the enclosure of the Si in a SiO_2 envelope. The latter also provides a means for masking against the diffusion of some impurities into Si at high temperatures. The masking effectiveness of the oxide layer is determined by several process parameters such as time, temperature, carrier gas composition, impurity type, impurity compound, and preoxidizing conditions. Thus far, processing parameters have been established for masking B, As, Sb, and P. Precise surface structures of both n- and p-type as well as the simultaneous production of single and multidiffused junction layers are possible by this masking technique. Finally, a wide range of controlled impurity levels in diffused layers can be obtained by means of a new predeposition technique.

Acknowledgment

The authors wish to thank several people for their contribution to this investigation. In particular, the authors are grateful to C. S. Fuller, M. Tanenbaum, J. L. Moll, and F. M. Smits for their helpful discussions; to G. Backenstoss for the calculations of the surface concentration values; and to H. E. Bridgers for supplying the crystal ingots. Thanks also are due to R. M. LeBach for some of the measurements.

Manuscript received Nov. 29, 1956. Portions of this material were presented at the Semiconductor Conference of the I.R.E. in June 1956 and portions at the Cleveland Meeting of the ECS, Sept. 30 to Oct. 4, 1956.

Any discussion of this paper will appear in a Discussion Section to be published in the June 1958 JOURNAL.

REFERENCES

1. D. M. Chapin, C. S. Fuller, and G. L. Pearson, *J. Appl. Phys.*, **25**, 676 (1954).
2. G. L. Pearson and C. S. Fuller, *Proc. Inst. Radio Engrs.*, **42** (April 1954).
3. M. Tanenbaum and D. E. Thomas, *Bell System Tech. J.*, **34**, 105 (1955).
4. C. S. Fuller and J. A. Ditzenberger, *J. Appl. Phys.*, **25**, 1439 (1954).
5. C. S. Fuller and J. A. Ditzenberger, *ibid.*, **27**, 544 (1956).
6. M. Tanenbaum, Private communication.

Density and Viscosity of Titanium Tetrabromide

John M. Blocher, Jr., Robert F. Rolsten,[1] and I. E. Campbell

Battelle Memorial Institute, Columbus, Ohio

ABSTRACT

Measurements were made of the density and viscosity of liquid $TiBr_4$. Measurements of the vapor density at the boiling point indicate that $TiBr_4$ is monomolecular.

Because of widespread interest in Ti as a strong, light-weight, corrosion-resistant construction material, many and formidable research efforts are being directed toward the development of low-cost processes for production of the metal from its relatively abundant ores. However, since the literature on the compounds of Ti is incomplete, progress would be enhanced by determination of reliable values for some of the physical and thermodynamic properties of Ti halides. These compounds represent potential intermediates in the extractive metallurgy of Ti.

The present work is part of an effort directed toward establishing the physical and thermodynamic properties of titanium bromides. The vapor pressure and thermal properties of $TiBr_4$ are the subject of another paper to be published soon.

Preparation of $TiBr_4$

$TiBr_4$ was prepared by direct synthesis from "iodide" Ti [2] and distilled Br.[3] In a typical preparation, 1 lb Br was placed in a 500 ml Pyrex flask provided with a water-cooled reflux condenser and a 9 mm sealed side arm for later use in transferring the product. After the Br had been heated with a mantle to 58°C, degreased HF-washed and dried turnings of Ti were added through the condenser under a blanket of argon which had been purified by passing through Ti chips at 1000°C. The turnings ignited spontaneously on contact with the liquid Br. A 3 in. diameter ring of Vycor extending above the Br surface acted as a fence to prevent burning pieces of Ti from contacting and cracking the Pyrex reaction flask. The burning Ti had no apparent effect on the Vycor.

The rate of addition of Ti chips was governed by the rate at which the heat of reaction could be dissipated. After approximately ¾ of the stoichiometric quantity of Ti had been added, some of the turnings settled to the bottom without reacting. The rate of reaction tapered off until it was finally necessary to supply heat to boil the liquid. Invariably some free Br remained.

One of two techniques, atmospheric and vacuum distillation, was used to purify the crude bromide.

[1] Present address: E. I. du Pont de Nemours & Company, Wilmington, Del.

[2] Prepared at Battelle by the thermal decomposition of titanium tetraiodide (1).

[3] Mallinckrodt Chemical Works, St. Louis, Mo.

Table I. Analysis of $TiBr_4$

Sample	% Ti		% Br	
	Found	Formula	Found	Formula
A	13.1	13.03	—	86.97
B	13.2	13.03	86.8	86.97
C	—	13.03	87.0	86.97

Spectrographic Analysis of the Hydrolysis Product of Sample C

	%		%
Ti	Major		
Si	<0.002	Sn	<0.0005
Fe	<0.001	Ni	<0.0003
Al	<0.001	Mo	<0.0005
Mn	0.003	V	<0.002
Mg	<0.001	Cd	<0.001
W	<0.010	Zn	<0.0015
Ba	<0.001	Zr	<0.001
As	<0.0025	Co	<0.0002
B	0.0008	Ca	<0.0005
Sb	<0.0005	Cr	<0.001
Pb	<0.0005		

Table I gives analyses of the $TiBr_4$ purified by distillation in a 30 plate column at atmospheric pressure. Ti was determined as TiO_2 and Br by the standard Volhard method.

Although the analyses given in Table I deviate from the formula values to a greater extent than would be desired, it is thought that this reflects limitations in the analytical technique, rather than variable purity.

Further evidence of the purity of the $TiBr_4$ used in this work is the reproducibility of vapor-pressure data taken with intermediate resublimation of samples in place. Freezing-point measurements indicate that the liquid-soluble, solid-insoluble impurity content is something less than 0.00008 mole fraction, which is negligible for the present purposes.

To avoid contamination, transfer of the $TiBr_4$ was accomplished through the use of Pyrex break seals either under vacuum or an atmosphere of purified argon.

Vapor Density

The vapor density of $TiBr_4$ was measured by the Dumas technique (2) suitably modified to avoid con-

Table II. Vapor Density of $TiBr_4$

Experiment	Bath temp, °C	Pressure, atm	Vol of flask, ml	Wt of $TiBr_4$, g	Mol wt
1	243.7	0.9783	250.5	2.1837	377.9
2	246.9	0.9794	246.8	2.0698	365.5
3	245.9	0.9793	253.7	2.1548	369.5
4	237.1	0.9746	250.7	2.0970	359.4
5	242.5	0.9776	253.4	2.1336	364.5

Avg. 367.3 ± 6.2

tact of the $TiBr_4$ with air. Results are summarized in Table II.

Comparison of the average result, 367.3 ± 6.2, with the formula weight, 367.56, shows that $TiBr_4$ vapor is monomeric and undissociated at the boiling point.

Liquid Density

The density of liquid $TiBr_4$ was determined with a Mohr-Westphal balance (3). The displacement method was chosen over direct pycnometric measurement, since the technique of making measurements on the volatile, reactive $TiBr_4$ at elevated temperatures was greatly simplified. However, some sacrifice in accuracy resulted.

The $TiBr_4$ was contained in a cell continuously purged with dry He through the tube which enclosed the plummet suspension. The purge effectively prevented contamination of the sample resulting from the diffusion of air down the tube.[4] The reading of the balance was independent of the purge-gas flow rate over a wide range, indicating that the drag on the suspension wire was insignificant. It was necessary, however, to correct for the effect of surface tension on the suspension wire.

The volume of the plummet was determined by displacement in distilled water, C.P. CCl_4, and C.P. C_6H_6 at measured temperatures near room temperature. Density data for these liquids were taken from the International Critical Tables and checked with a pycnometer. After all corrections were made, the volume of the plummet as determined in the individual liquids differed from the average by ±0.3%, placing that much uncertainty on subsequent measurements of the density of $TiBr_4$.

Results given in Table III were obtained with two preparations of $TiBr_4$, as indicated. Temperature measurements were made with a calibrated Chromel-Alumel thermocouple and a semiprecision potentiometer. The temperature of the oil bath containing the cell was controlled to ±0.1°C.

It will be noted that the data may be expressed by the equation

$$d = 2.953 - 0.00225\ (t - 40) \qquad (I)$$

to within ±0.03%. This deviation would encompass temperature errors of up to ±0.5°C because of the low temperature coefficient. However, since the values are dependent on the uncertain calibration mentioned above, the over-all uncertainty is ±0.3%.

[4] After standing in the apparatus for three days, one sample became visibly contaminated with hydrolysis products, resulting in an apparent decrease in density of 0.2%.

Table III. Density of Liquid $TiBr_4$

Sample	Temp, t, °C	d, g/cc, obs.	d, g/cc, calc.[a]	d, calc.-obs.
A	42.4	2.947	2.948	+0.001
A	48.8	2.933	2.933	0.000
A	55.2	2.919	2.919	0.000
A	64.1	2.899	2.899	0.000
A	71.4	2.882	2.882	0.000
A	80.0	2.863	2.863	0.000
A	86.5	2.849	2.848	−0.001
A	91.9	2.837	2.836	−0.001
B	80.1	2.864	2.863	−0.001
B	87.6	2.846	2.846	0.000
B	98.1	2.822	2.822	0.000
B	105.6	2.805	2.805	0.000
B	113.2	2.788	2.788	0.000
B	118.6	2.776	2.776	0.000
B	122.2	2.769	2.768	−0.001

[a] Calculated from the equation, $d = 2.953 - 0.00225\ (t - 40)$.

Liquid Viscosity

The viscosity of liquid $TiBr_4$, prepared and purified as described earlier, was measured by means of an Ostwald viscometer (4) into which the sample was sealed under its own vapor pressure. The viscometer, contained in an oil bath with ±0.1° temperature control, was calibrated with ethyl alcohol and CCl_4. Viscosity and density values for the reference liquids were taken from the International Critical Tables. The density of $TiBr_4$ was taken from the preceding work. The standard deviation in the values obtained for the viscometer constant was ±1.2%.

A single sample of $TiBr_4$ was used to obtain the data given in Table IV and Fig. 1 which may be expressed to ±0.36% in η by the equation

$$\mathrm{Log}_{10}\eta = 102{,}310/T^2 - 177.12/T - 0.1947 \qquad (T \text{ in } °K) \qquad (II)$$

The ±0.3% scatter in the data would encompass temperature errors in the middle of the range of as much as ±0.5°C, which is outside the estimated

Table IV. Viscosity of Liquid $TiBr_4$[a]

Temp, °C	η obs., centipoise
42.2	1.880
51.9	1.702
62.1	1.551
79.4	1.341
87.9	1.254
95.0	1.198
99.3	1.170
118.0	1.052
127.1	1.001
112.4	1.086
102.9	1.138
92.5	1.217
82.0	1.313
74.0	1.392
65.0	1.502
54.1	1.657
52.8	1.672
43.4	1.836
59.6	1.567
68.2	1.457
68.6	1.457
99.7	1.161

[a] Data listed in the order taken.

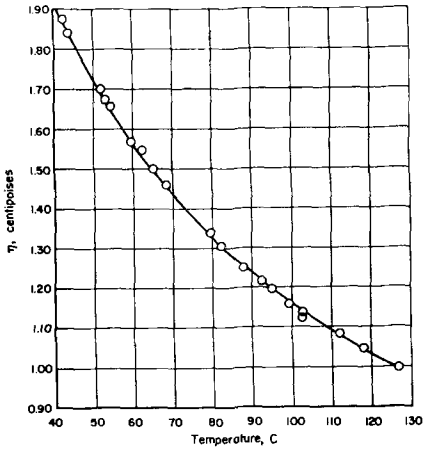

Fig. 1. Viscosity of liquid $TiBr_4$

error (±0.2°C) of the temperature measurements. The 0.3% uncertainty in the density measurements is of the same order as the above scatter. Therefore, the limiting factor in the validity of the viscosity results is the 1.2% uncertainty in the calibration of the viscometer.

Acknowledgment

This paper describes part of the research supported by the Office of Naval Research under Contract No. Nonr-1120 (00). Their permission to publish this paper is gratefully acknowledged.

Manuscript received May 17, 1956.

Any discussion of this paper will appear in a Discussion Section to be published in the June 1958 JOURNAL.

REFERENCES

1. I. E. Campbell, R. I. Jaffee, J. M. Blocher, Jr., J. Gurland, and B. W. Gonser, *J. (and Trans.) Electrochem. Soc.*, **93**, 271 (1948).
2. J. Reilly and W. N. Rae, "Physico Chemical Methods," 5th ed., Vol. II, p. 64, D. Van Nostrand Co., Inc., New York (1953).
3. *Ibid.*, Vol. I, p. 618.
4. *Ibid.*, Vol. I, p. 674.

Electrolytic Preparation of Titanium from Fused Salts

I. Preliminary Electrolytic Studies with Diaphragmed Cells

Marshall B. Alpert, Frank J. Schultz, and William F. Sullivan

Titanium Division, Research Laboratories, National Lead Company, Sayreville, New Jersey

ABSTRACT

Reduced titanium chlorides dissolved in fused alkali and alkaline earth chlorides may be electrolyzed in diaphragmed cells under an inert gas atmosphere to yield ductile titanium as adherent, crystalline deposits. The reduced titanium chlorides are prepared *in situ* by adding $TiCl_4$ through a hollow cathode at a controlled feed to current ratio.

Interest has been centered in recent years on the development of an electrolytic Ti metal process in order to avoid the difficult and batchwise operations of present commercial processes based on the reaction of $TiCl_4$ with an active reducing metal, such as Mg or Na.

The electrolysis of reduced titanium chlorides in fused salt baths has recently been described by others (1-7). In addition, a number of patents (8-13) have been issued. Review articles (5, 14) on the electrodeposition of Ti metal have been published.

In this paper experiments on the fused salt electrolytic reduction of $TiCl_4$ to the lower chlorides, $TiCl_3$ and $TiCl_2$, and further reduction to Ti metal are described. This information has served as a basis for further development in three directions, a stepwise reduction of $TiCl_4$ to Ti metal, a one step reduction of $TiCl_4$ to metal, and an electrorefining process.

At the inception of this program very little information was available on such properties of the reduced titanium chlorides as their solubility in fused salt systems, their stability, and their position in the electrochemical series. It appeared reasonable from the known ability of Mg to reduce $TiCl_4$ directly to metal that either Mg or any cations which required higher deposition potentials would be compatible with Ti deposition, but other common cations could be expected to deposit with or prior to Ti. Data here on deposition of Ti and recent free energy data (15) support these limitations. Since Ti is highly reactive with oxygen-containing compounds, the melts were also limited to anions not containing oxygen; the chlorides were most convenient. The ease of oxidation of the reduced titanium chlorides required that the melts containing them be maintained under an inert atmosphere. In addition, contact of the reduced titanium chlorides with an oxidizing anode, specifically an anode producing Cl_2, had to be avoided if a substantial portion of the dissolved Ti were not to be reoxidized and ultimately lost from the system as $TiCl_4$. This required the use of a porous diaphragm. A gas barrier was desirable to prevent Cl_2 produced at the anode from contacting the reduced titanium chloride melts and also any metal cell parts.

Experimental

Equipment.—A number of laboratory cells were designed ranging in size from 0.4 to 10 l melt capacity. A typical cell of approximately 10 l capacity is shown in Fig. 1. The cell itself was of fused silica

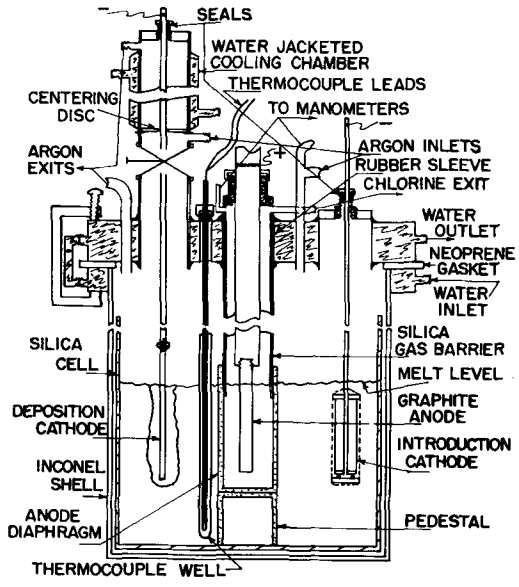

Fig. 1. Schematic drawing of electrolytic cell for Ti deposition.

contained within an Inconel outer shell and externally heated in a Globar furnace. The use of a water cooled flange and cell top permitted the cell to be tightly sealed. The diaphragm was a porous alumina cylinder (Norton Co., Alundum, grades RA98 or RA1139) resting on an alumina pedestal and loosely fitted with an internal fused silica sleeve that served as a gas barrier. Cathodes were of Ni and the anodes were graphite. The cell was carefully pressure checked after assembly and also at intervals throughout a run to insure that it was leaktight. Argon for the cell atmosphere was high purity commercial material further gettered by passage over Ti metal chips at 800°C. A cell such as that illustrated had a continuous, useful life in excess of three months.

Preparation of reduced titanium chloride containing melts.—For initial electrodeposition experiments a $TiCl_3$-LiCl mixture was prepared by reacting stoichiometric amounts of $TiCl_4$ with molten Li dispersed in mineral oil. The resulting product was washed free of mineral oil with CCl_4, and dried. Although the material did not react too rapidly with air, the electrodeposited metal was badly contaminated with oxides. The electrowinning of Ti metal through the use of such a reduced titanium chloride preparation might be considered as only three-quarters electrolytic, because of the reduction of $TiCl_4$ to $TiCl_3$ by chemical means.

For these reasons consideration was given to the preparation of reduced titanium chlorides directly in the catholyte. A suitable procedure was found to be the introduction of $TiCl_4$ underneath the surface of the melt in juxtaposition to a cathode which was passing current at the rate of from one to about two faradays per mole of $TiCl_4$. Under these conditions practically all the $TiCl_4$ was solubilized as $TiCl_3$ or $TiCl_2$, respectively. It was convenient to use a hollow tubular cathode through which the $TiCl_4$ was introduced as vapor or directly as liquid which vaporized as it approached the melt level. A stream of inert carrier gas was used with low $TiCl_4$ flow rates to keep salt melt from being drawn up the tubular cathode and freezing.

It appears that the $TiCl_4$ is solubilized chemically. During most of the introduction stage the reaction is

$$TiCl_4(\text{gas}) + TiCl_2(\text{solution in melt}) \rightarrow 2TiCl_3(\text{solution in melt})$$

with the cathode reaction being largely the reduction of trivalent Ti to divalent Ti. Supporting this viewpoint is evidence showing $TiCl_4$ to be soluble in Ti^{2+}-containing melts. The measured cathode potentials, generally 1.8-2.0 v vs. a Cl_2 electrode, are consistent with the proposed cathode reaction.

It has also been possible to prepare reduced titanium chlorides in the catholyte by reacting $TiCl_4$ with a bed of Ti metal, either scrap or metal dropped from a cathode. In cells for the electrorefining of Ti metal the hollow cathode device has been combined with the use of a scrap Ti anode, so that a portion of the reduced titanium chlorides of the bath derives from the $TiCl_4$ introduced through the hollow cathode and the remainder from the scrap Ti anode (16).

Experimental Procedure

For several of the salt systems studied the salt bath was obtained simply by fusing the reagent grade, predried components in the cell under an argon atmosphere. In some cases, particularly LiCl- or $MgCl_2$-containing systems, the fused salts were found to contain considerable quantities of moisture; it was necessary to getter the melt by reacting with Ti metal chips and then filtering under argon through a porous alumina filter directly into the cell. In the case of readily hydrolyzable salts, particularly $CaCl_2$- and $MgCl_2$-containing melts, NH_4Cl was added during fusion to prevent hydrolysis and oxide formation.

In a typical run, after the salt was fused, $TiCl_4$ was added through the hollow cathode at a rate of one mole for two faradays, the rate being maintained by a flowmeter and buret system. The cathode current density was approximately 0.2 amp/cm^2, or 50 amp in the cell of Fig. 1. After the Ti concentration had been brought to the desired level, a slow reduction period at about 0.1 amp/cm^2, total current 25 amp, could be interposed to improve the degree of reduction of the melt. This was not generally required for the cell illustrated. The deposition cathode was placed in the closed withdrawal chamber, flushed with argon for 15 min and then lowered into the cell. A 100 amp-hr deposit was taken at 1.0 amp/cm^2, or a total current of 50 amp. Successive deposits were taken until the Ti concentration of the melt was below about 0.1*M* as marked by a fairly sharp increase in cell emf. The $TiCl_4$ charging cycle was then resumed. Deposits adhered to the cathode quite well as long as the melts were free of water and other contaminants. A typical deposit is shown in Fig. 2. The metal, after being leached with 1% HCl to dissolve the occluded salts, was easily removed from the cathode, washed further with water, and dried at 110°C. The Cl_2 produced at the anode was measured and vented to the air. Over-all cath-

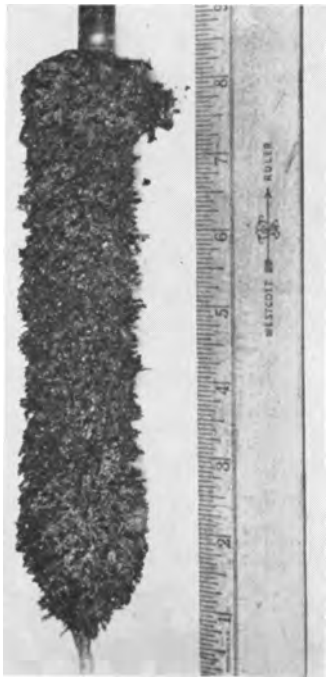

Fig. 2. Electrolytic deposit of Ti

ode and anode current efficiencies were generally in the range of 80-90%.

Samples of the melt were obtained either by drawing the liquid up thin glass tubes where freezing occurred rapidly or by introducing a small silica sampling tube fastened to a cathode. Melts were analyzed for total Ti (expressed on a molal basis, that is moles of Ti/kg of diluent salt) by a volumetric ferric ammonium sulfate titration and for degree of reduction either by titrating the acid liberated on oxidation and hydrolysis of the sample or by measuring the volume of hydrogen liberated on dissolving the divalent Ti-containing samples in dilute acid. The degree of reduction was expressed by an N value, representing the apparent valence of the Ti in the melt, viz., the subscript in the empirical formula $TiCl_N$ for the titanium chlorides present. Thus N would be 2 if the Ti were entirely divalent, 3 if the Ti were entirely trivalent.

Fig. 3. Photomicrograph of Ti metal

Parameters in Metal Deposition

Degree of melt reduction.—Experimentally it was found that one of the most important factors affecting the nature and quality of the deposits was the degree of reduction of the melt. Generally, as the N value decreased toward the equilibrium value set by the reaction

$$Ti + 2TiCl_3 \rightleftharpoons 3TiCl_2$$

the crystal size and purity of the metal showed a marked increase. The equilibrium N value was found to be 2.0 for LiCl-KCl melts at 400°-500°C, and 2.15 for NaCl or $SrCl_2$-NaCl melts at 700°-900°C for concentrations of the order of 1M. If serious air leakage occurred during $TiCl_4$ introduction, the N value was above 2.5. Deposits obtained from these melts were finely crystalline, most of the metal being less than 100 mesh and including as much as 90% by weight of fused salt. In this case the melt was further reduced by passing current at 0.1-0.2 amp/cm^2. Under these circumstances the dominant reaction was the reduction of trivalent to divalent Ti. Higher current densities polarized the trivalent to divalent Ti reaction and resulted in the formation of metal deposits. When the N value was reduced to approximately 2.3, the metal obtained was coarsely crystalline and mostly greater than 100 mesh in size. Occluded salts ranged from 10 to 50% based on total deposit weight. A photomicrograph of the product is shown in Fig. 3. This product could be handled readily after leaching either by pressing and hot sintering or by fusion in a water-cooled copper arc furnace.

While the reason for this increase in crystal size is not certain, it is suggested that, as melt reduction is improved, the melt becomes less contaminated with soluble impurities that could interfere with crystal growth. For example, a melt reduced to the equilibrium condition could not contain, in principle, any soluble impurities capable of reacting with Ti metal itself to form an insoluble phase. Removal of these impurities permits the growth of larger crystals and results in improved purity for the crystal grown.

Melt composition.—Deposition of adherent, coarsely crystalline metal has been accomplished successfully in various melts containing all the alkali and alkaline earth cations including Mg. Certain melts are less desirable because of hygroscopicity, excessive tendency toward hydrolysis or oxidation, or higher melting point. The $SrCl_2$-NaCl eutectic system, containing 73% $SrCl_2$, mp 565°C (17), was found to be particularly suitable. Typical operating temperatures were in the range 650°-750°C. It appears that the presence of Sr ion allows some improvement in metal crystal size. Thus, a product containing less than 1% minus 100 mesh was readily prepared. Coarsely crystalline deposits were also prepared in bromide and iodide baths containing the corresponding reduced titanium halides, but these baths offered no advantage over the chloride baths.

Cell sealing.—One of the most important factors in electrolytic cell operation was found to be the degree to which sealing of the equipment had been

accomplished. Oxygen and nitrogen contamination of the cell atmosphere interfered with extended operation by forming a sludge layer which ultimately short-circuited the cell, by oxidizing the soluble Ti in the melt making it difficult to obtain well reduced melts, by seriously decreasing yields, and finally by directly causing some reduction in deposit purity. In well sealed cells, metal with a hardness less than 110 Bhn was obtained consistently.

Temperature.—The effect of temperature on the product was less important. Temperatures of 400°-500°C with the LiCl-KCl bath resulted in finer crystals with the crystal faces somewhat rounded. Increased temperature resulted in larger crystal size. The change in phase of Ti at 885°C, as observed in a NaCl bath, was reflected in a change in the shape of the individual crystals, but the generally dendritic nature of the deposits was retained. Deposits were obtained at temperatures in excess of 1000°C, but no advantage was gained by operation at this temperature and cell life was shortened.

Melt agitation.—Stirring during metal deposition by use of a rotating cathode or by bubbling argon through the melt was found to reduce markedly the crystal size of the metal being deposited. In addition, agitation could disturb any oxygen containing sludge resting on the cell bottom and further contaminate the deposit.

Soluble titanium concentration.—Electrolysis was usually performed at Ti concentrations between 0.1 an 1*M*, although deposits were also obtained beyond this range. Below 0.2 *M* at about 1 amp/cm^2 for the $SrCl_2$-NaCl melt at 700°C and below 0.1*M* for the NaCl melt at 850°C, metal deposits became spongy adjacent to the cathode, apparently representing the effects of polarization. Aside from this, the effects of Ti concentration were very minor in the range covered. From a practical point of view it is preferable to operate at lower concentration to minimize losses of soluble Ti by salt dragout and diffusion through the diaphragm. For example, it was found difficult to bring the catholyte concentration above 4*M* because of increasing losses through the diaphragm.

Cell electromotive forces.—Difficulty was experienced in measuring accurately the emf's of diaphragmed cells because of the tendency of reduced Ti melts to lay down conductive layers of reduced Ti compounds (18) or sludge, thereby introducing a spurious bipolar emf at the diaphragm that became more pronounced as a cell became older. At low operating currents, reduced titanium chlorides which diffused through the diaphragm depolarized the Cl_2 electrode. This was partly overcome by providing a separate chlorine measuring electrode fabricated from a porous carbon plug. The potential for the cathodic reduction of trivalent to divalent Ti was particularly difficult to measure because the reaction was apparently polarized up to the potential for the deposition of Ti at relatively low current densities. Also the metals used for the measuring electrode became titanized (19). Therefore their inertness is open to question. A value of 1.85 v is representative of the reaction

$$TiCl_3 \rightarrow TiCl_2 + \tfrac{1}{2}\, Cl_2(gas)$$

when both reduced salts are at a concentration of 0.5*M* in a $SrCl_2$-NaCl bath at 700°C. The cell emf for the reduction to metal and Cl_2 of a 1*M* reduced titanium chloride bath, close to the equilibrium value (*N* value of 2.15) is 2.05 v. As the total Ti concentration approached zero, the value of the cell emf rose sharply to 3.3 v which is the expected value for the deposition of alkali metal and chlorine (15).

Cathode current density.—The nature of the deposit has not proved to be a marked function of cathode current density under normal deposition conditions. At very low current densities most of the current is used to reduce trivalent to divalent Ti, unless the bath is substantially in equilibrium with Ti metal. Under normal operating conditions, therefore, little or no metal is deposited at the cathode. In general, for baths of moderate Ti concentrations, crystal size increased slightly with increasing current density; 1 amp/cm^2 was usually near optimum.

Anode current density.—Difficulties with excessive anode current densities usually have been due to secondary effects, such as plugging anode gas outlets with salt spray. In cells having a very low Ti concentration a sudden rise in resistance between anode and melt, usually characterized as an anode effect, was observed with the $BaCl_2$-NaCl eutectic bath at anode current densities above 1 amp/cm^2 and other baths at somewhat higher current densities. However, once charging of the bath has been started, the evolution of a small amount of $TiCl_4$ from the anode seems to avoid the effect at practical anode current densities.

Ionic migration effects.—Since considerable quantities of charge were being carried through these cells, ionic mobility effects could be expected. With the porosity and pore size of alumina employed for diaphragms in this work the effect was substantially undetectable, although measurements of the catholyte and anolyte melt depth have indicated that the latter stood a little lower during cell operation. With finer porosity diaphragms, for example Norton Alundum grade RA360, the effect was more marked and, in extreme cases, the anolyte melt level lowered to such an extent that contact with the anode was broken. These findings indicate that a very large fraction of the current is carried by the cations. Experiments in which the cathode was surrounded by a second diaphragm indicated that most of the current was carried not by the Ti but by the other cations of the bath, at least for melts of Ti concentration less than 1*M*.

Summary

A process has been developed for the electrolytic conversion of $TiCl_4$ to metal and chlorine which involves the reduction of $TiCl_4$ to a reduced titanium chloride in solution in an alkali or alkaline earth chloride mixture for which the over-all reaction is formally

$$TiCl_4 \xrightarrow{4\text{-}N \text{ faradays}} TiCl_N + \frac{4\text{-}N}{2}\, Cl_2$$

The resulting reduced titanium chlorides were then reduced further to Ti metal

$$TiCl_N \xrightarrow{N \text{ faradays}} Ti + \frac{N}{2} Cl_2$$

By controlling the melts for the deposition of metal so that most of the dissolved Ti was in the divalent condition and by protecting the reduced titanium chloride-containing melts with an inert atmosphere it was possible to obtain Ti metal as a coarsely crystalline dendritic material, sufficiently adherent to the cathode to permit its removal from the cell. The deposits after being leached with dilute HCl were readily fabricated into ductile Ti metal pieces either by arc melting or powder metallurgical means. Since the melt after the completion of a cycle of electrolysis was substantially the same as the initial melt, the process has the elements necessary for continuous or semi-continuous operation on a larger scale.

Data have been obtained against a chlorine electrode for the emf's corresponding to the two major cathode reactions being carried out in the cell, viz., the reduction of trivalent to divalent Ti and the reduction of an equilibrium mixture of divalent and trivalent Ti to Ti metal.

Information has also been presented on the other parameters of the electrolysis such as the influence of temperature, current density, and melt composition.

Acknowledgment

The aid and encouragement of A. E. Jacobsen in this work is gratefully acknowledged.

Manuscript received Jan. 28, 1957.

Any discussion of this paper will appear in a Discussion Section to be published in the June 1958 JOURNAL.

REFERENCES

1. G. D. P. Cordner and H. W. Worner, *Australian J. Appl. Sci.*, **2**, 358 (1951).
2. K. H. Worner, G. M. Willis, and H. W. Worner, *This Journal*, **100**, 18C (1953).
3. A. Brenner and S. Senderoff, *ibid.*, **99**, 2230 (1952).
4. J. M. Sherfey and A. Brenner, Quarterly Progress Report for July 1-Sept. 30, 1953, NBS-2816 (Oct. 1, 1953); *Nucl. Sci. Abs.*, **5**, No. 3, 96 (1954).
5. A. Brenner, *Record Chem. Prog.* (Kresge-Hooker Sci. Lib.), **16**, 240 (1955).
6. S. Okada, M. Kawane, and M. Takahashi, *Bull. Eng. Research Inst., Kyoto Univ.*, **6**, 57 (1954).
7. R. M. Creamer, D. H. Chambers, and C. E. White, U. S. Bur. Mines, Rept. Invest. 5093 (1954).
8. M. B. Alpert, F. J. Schultz, and W. F. Sullivan (to Titan Co., Inc.), Swedish Pat. 142,488, Oct. 13, 1953.
9. Titan Co., Inc., Brit. Pat. 734,094, July 27, 1955.
10. Titan Co., Inc., Brit. Pat. 735,372, Aug. 17, 1955.
11. M. B. Alpert and R. L. Powell (to National Lead Co.), U. S. Pat. 2,741,588, April 10, 1956.
12. F. J. Schultz and T. M. Buck (to National Lead Co.), U. S. Pat. 2,734,856, Feb. 14, 1956.
13. Imperial Chemical Industries, Ltd., (J. C. Smart), Brit. Pat. 698,151, Oct. 7, 1953.
14. M. E. Sibert and M. A. Steinberg, *J. Metals*, **8**, 1162 (1956).
15. W. J. Hamer, M. S. Malmberg, and B. Rubin, *This Journal*, **103**, 8 (1956).
16. M. B. Alpert and T. M. Buck (to National Lead Co), U. S. Pat. 2,734,855, Feb. 14, 1956.
17. International Critical Tables, Vol. 4, p. 65, McGraw-Hill Book Co., New York (1928).
18. Battelle Development Corp., Brit. Pat. 679,419, Sept. 17, 1952.
19. M. B. Alpert (to National Lead Co.), U. S. Pat. 2,734,003, Feb. 7, 1956.

Electrochemical Polarization

II. Ferrous-Ferric Electrode Kinetics on Stainless Steel

Milton Stern

Metals Research Laboratories, Electro Metallurgical Company, Division of Union Carbide Corporation, Niagara Falls, New York

ABSTRACT

The oxidation-reduction kinetics of the ferrous-ferric sulfate system have been measured on a stainless steel surface. The data completely support theoretical equations which describe the potential-current relationships for such a system. The analysis applies to reversible electrodes and to corroding electrodes where the potential is determined by two intersecting activation overvoltage functions. Also, the analysis permits calculation of a number of electrochemical constants with a minimum number of experimental observations. The possibility of determining anode-to-cathode area ratios for corroding metals is discussed.

One of the most important trends in recent studies of electrochemical kinetics consists of the development of equations which describe the potential current relationships of an electrode (1). Bockris (2) has described these relationships in great detail, primarily for electrodes which exhibit the reversible potential. Stern and Geary (3) have extended these concepts to include electrodes at which more than one oxidation-reduction system is operative. An understanding of the nature and shape of polarization curves is important in practical studies of corrosion phenomena, electrodeposition, and battery performance.

The equations illustrated by Bockris are derived entirely from kinetic theory. Although different investigations support various phases of the theory, no

one study has been conducted which attempts to verify directly the entire concept. The equations should permit calculation of the Tafel constants for anodic polarization from cathodic measurements alone. Also, low current measurements are related to the anodic and cathodic Tafel constants.

This discussion considers experimental observations of the electrode kinetics of the ferrous-ferric oxidation-reduction systems in the light of this theory.

Apparatus and Procedures

The cell used for polarization measurements was similar to that described elsewhere (4) except that a Luggin capillary probe was not necessary because of the extremely low currents entailed in the measurements. Platinized Pt was used as a reference electrode and as auxiliary electrodes during anodic and cathodic measurements. Linde prepurified nitrogen gas was bubbled through the cell at all times.

Solutions were prepared from reagent-grade chemicals and distilled water. The material studied was commercial Type 304 stainless steel, annealed at 1050°C for 1 hr and water-quenched. The steel contained 18.36% Cr, 9.06% Ni, 0.94% Mn, and 0.05% C. The surface was degreased in boiling acetone and benzene, immersed in concentrated HCl until hydrogen evolution was observed, thoroughly rinsed in distilled water, washed in concentrated HNO_3, rinsed again, and immersed directly into the cell.

Potential measurements were made using a L&N *p*H meter as a high-impedance galvanometer in series with a precision Rubicon potentiometer. This system permits potential measurement to ±0.2 mv. The sensitivity was increased where necessary by feeding the output signal from the *p*H meter into a 0- to 1-mv recorder which was then used as the null detecting device. Applied current values below 10^{-7} amp were measured with an electrometer and a precision 10-megohm resistance. Values between 10^{-7} amp and 10^{-5} amp were measured by determining the *IR* drop across 0.1 and 0.01 megohm standard resistances. Higher current values were determined directly with a precision Weston microammeter.

Results

One of the more serious problems in activation polarization measurements arises from interference due to resistance and concentration polarization. This usually occurs because the exchange current, i_0, for most practical reversible electrodes is so high that considerable current must be applied in order to polarize the surface. Thus, the use of a Pt surface to study ferric-ferrous oxidation-reduction kinetics creates difficult experimental problems. An ideal surface for use in comparing experimental observations of electrochemical polarization with theory requires a material which does not corrode[1] and which exhibits a low exchange current. Stainless steel in a solution of ferric and ferrous sulfate is a suitable system for such a study.

[1] Actually the surface may react with the environment slightly, as long as the corrosion current is several orders of magnitude lower than the exchange current. Under these conditions, the electrode will still exhibit the equilibrium potential and will behave ideally.

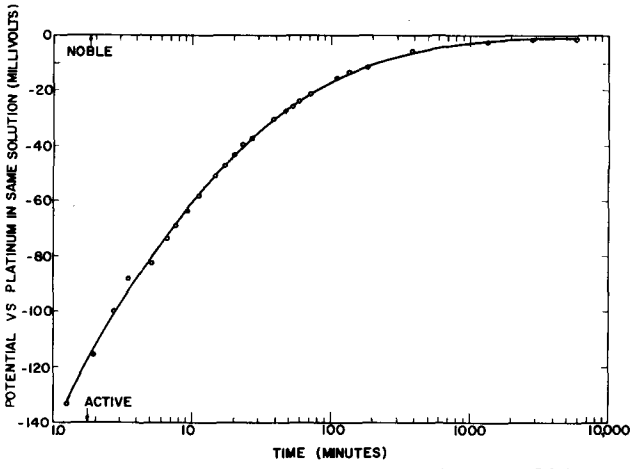

Fig. 1. Potential as a function of time for Type 304 stainless steel immersed in ferric-ferrous sulfate.

The solution was prepared by adding 100 g of $(Fe)_2(SO_4)_3 \cdot 9H_2O$ and 0.7 g of $FeSO_4 \cdot 7H_2O$ to 1 liter of water. The equilibrium ferric-ferrous potential of a solution prepared in this manner and measured with a platinized Pt electrode is approximately 0.770 v on the standard hydrogen scale. The equilibrium potential of such a solution is not exactly reproducible from batch to batch because the ferrous salt contains varying amounts of ferric contamination.

Potential-Time Behavior

When an electrode is prepared as described above, the initial potential is active to Pt in the same solution but slowly approaches the ferrous-ferric potential on Pt. A steady-state value of 1 mv more active than the reversible ferric-ferrous potential is achieved after about 100 hr. Fig. 1 illustrates this initial time dependence.

Polarization

Theory.—For an electrode at equilibrium, the rate of oxidation of ferrous ions is equal to the rate of reduction of ferric ions. This reaction rate is equivalent to the exchange current.

Thus:

$$\overleftarrow{i}_{Fe^{++}} = \overrightarrow{i}_{Fe^{+++}} = i_0 \qquad (I)$$

where $\overleftarrow{i}_{Fe^{++}}$ = current density equivalent to the rate of oxidation of ferrous ions; $\overrightarrow{i}_{Fe^{+++}}$ = current density equivalent to the rate of reduction of ferric ions; and i_0 = exchange current density.

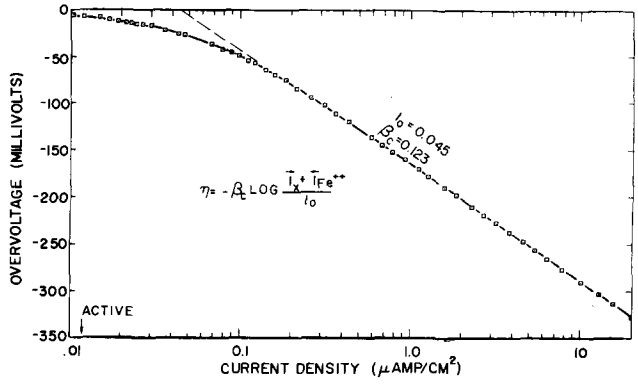

Fig. 2. Cathodic activation overvoltage for reduction of ferric ions on Type 304 stainless steel

The rate of oxidation or reduction as a function of potential is described by Eqs. (II) and (III).

$$\eta = \beta_A \log \overleftarrow{i}_{Fe^{++}}/i_0 \qquad \text{(II)}$$

$$\eta = -\beta_C \log \overrightarrow{i}_{Fe^{+++}}/i_0 \qquad \text{(III)}$$

where β_A is the Tafel slope for the oxidation reaction and β_C is the Tafel slope for the reduction reaction. Neither of these relations is observed experimentally at potentials close to the equilibrium potential because the reverse reaction is significant. That is, during low current cathodic polarization, the rate of oxidation of ferrous ions is of the same order of magnitude as the rate of reduction of ferric ions. The equations that describe experimental observations for anodic and cathodic polarization are

$$\eta = \beta_A \log \frac{\overleftarrow{i}_x + \overrightarrow{i}_{Fe^{+++}}}{i_0} \qquad \text{(IV)}$$

$$\eta = -\beta_C \log \frac{\overrightarrow{i}_x + \overleftarrow{i}_{Fe^{++}}}{i_0} \qquad \text{(V)}$$

where $\overleftarrow{i}_x$ and $\overrightarrow{i}_x$ are the applied anodic and cathodic current densities, respectively.

Cathodic polarization.—Fig. 2 is a plot of overvoltage as a function of applied cathodic current density. Deviation from Tafel behavior occurs at low values of applied current as expected from Eq. (V). At current densities greater than 20 μa/cm^2, an *IR* drop error was introduced. These data are not included. It is important to note the similarity between the shape of this experimental curve and shape derived from theory (3). The experimental values for β_C and i_0 are 0.123 v and 0.045 μa/cm^2.

Anodic polarization.—Anodic polarization for the same system is shown in Fig. 3. In this case, deviation from Tafel behavior occurs both at low currents and at high currents. The experimental data up to 3 μa/cm^2 follow the relation described by Eq. (IV). The values of β_A and i_0 are 0.102 v and 0.045 μa/cm^2. The deviation from Tafel behavior at currents greater than 3 μa/cm^2 is due to the fact that a potential region is reached where an additional oxidation reaction occurs at a rate of the same order of magnitude as the rate of oxidation of ferrous ions.[2] For the system described here, the most logical choice of this additional oxidation reaction is oxidation of water to produce oxygen, since deviation occurs in the potential range more noble than the estimated reversible potential for the reaction $2H_2O = O_2 + 4H^+ + 4e$ in the experimental environment. As illustrated previously (3), if two activation controlled reactions occur at comparable rates, the polarization curve obtained is the sum of the individual Tafel slopes. In this region, the rate of oxidation of ferrous ions plus the rate of oxidation of water are equivalent to the total applied anodic current at any given overvoltage value.

$$\overleftarrow{i}_x - \overleftarrow{i}_{Fe^{++}} = \overleftarrow{i}_w \qquad \text{(VI)}$$

where $\overleftarrow{i}_w$ is the current density equivalent to the rate of oxidation of water. Thus $\overleftarrow{i}_w$ may be calculated as a function of η. These data are shown in Fig. 3. Since the reversible potential for this reaction is unknown, a value for the exchange current cannot be calculated. β_w is 0.042 v.

[2] This same behavior was observed on a variety of passive surfaces and will be illustrated later.

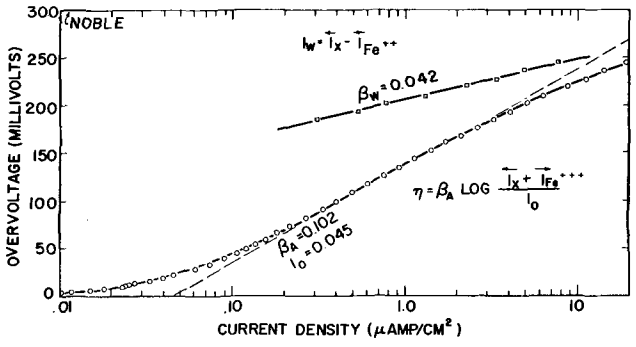

Fig. 3. Anodic activation overvoltage for oxidation of ferrous ions and water on Type 304 stainless steel.

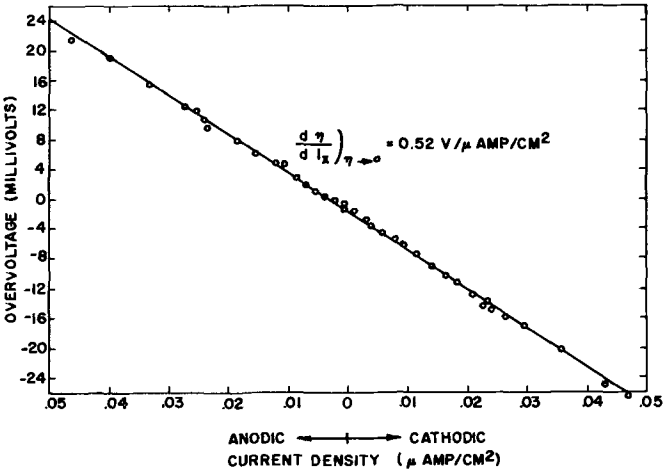

Fig. 4. Linear dependence of overvoltage on applied anodic and cathodic current density for oxidation and reduction of ferrous and ferric ions on Type 304 stainless steel.

Analysis of Low Current Data

Linear relation between overvoltage and applied current.—For overvoltage values close to the reversible potential, it can be shown[3] that

$$\left(\frac{d\eta}{d\overleftarrow{i}_x}\right)_{\eta\to 0} = -\left(\frac{d\eta}{d\overrightarrow{i}_x}\right)_{\eta\to 0} = \frac{\beta_A \beta_C}{(2.3)(i_0)(\beta_A+\beta_C)} \qquad \text{(VII)}$$

A linear plot of low current anodic and cathodic data is shown in Fig. 4. The experimental value of $\left(\frac{d\eta}{d i_x}\right)_{\eta\to 0}$ is 0.52 v/μa/cm^2. The value calculated from Eq. (VII) is 0.54 v/μa/cm^2. This agreement and the discussion which follows on stoichiometric number establish the validity of Eq. (VII).

Eq. (VII) proves quite valuable because it can be used to calculate one of the β values if concentration polarization, or an interfering reaction limits an experimental determination at high currents. Thus, a cathodic polarization measurement, which yields $\left(\frac{d\eta}{d\overrightarrow{i}_x}\right)_{\eta\to 0}$, i_0, and β_C, may be used to calculate the slope of the anodic curve.

[3] *See* Appendix.

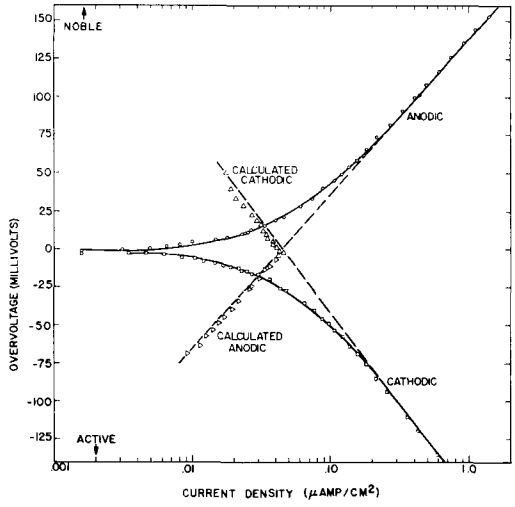

Fig. 5. Comparison of calculated and measured activation overvoltage for oxidation and reduction of ferrous and ferric ions on Type 304 stainless steel.

The stoichiometric number.—The stoichiometric number, ν, is equal to the number of times the rate-determining reaction occurs when the over-all reaction occurs once. It may be calculated from the equation (2):

$$\nu = \frac{nF\, i_0}{RT}\left(\frac{d\,\eta}{d\,i_x}\right)_{\eta\to 0} \qquad \text{(VIII)}$$

Combining this with Eq. (VII) yields

$$\nu = \frac{nF\,\beta_A\,\beta_C}{2.3\,RT(\beta_A+\beta_C)} \qquad \text{(IX)}$$

Thus, ν may be determined exclusively from high current polarization measurements or from a knowledge of i_0 and low current data. The stoichiometric number calculated from Eq. (VIII) is 0.92. Eq. (IX) yields a value of 0.95. The equations thus yield consistent results.

Direct calculation of reverse reaction rates.—In addition to using Eq. (VII) to calculate the β value of the reverse reaction, Eqs. (IV) and (V) permit the direct calculation of the reverse reaction current as a function of potential. Thus, one may calculate the rate of reduction of ferric ions, $\vec{i}_{Fe^{+++}}$, as a function of η during anodic polarization or the rate of oxidation of ferrous ions, $\overleftarrow{i}_{Fe^{++}}$, during cathodic polarization. This yields the extrapolation of the cathodic activation polarization curve on the noble side of the equilibrium potential and the extrapolation of the anodic activation polarization curve on the active side of the equilibrium potential.

Fig. 5 shows an expanded view close to the reversible potential of the experimental curves presented in Fig. 2 and 3. The calculated values of $\overleftarrow{i}_{Fe^{++}}$ and $\vec{i}_{Fe^{+++}}$ fall very close to the extrapolation of the high current activation polarization curves. Thus, for any electrode whose potential is determined by the intersection of two activation polarization curves, the local anodic polarization curve can be calculated from precise measurements of cathodic polarization. The converse is also true.

If three electrode reactions are occurring at comparable rates, the Tafel constants of two of the reactions must be known in order to calculate the third. An example of this situation will be illustrated in a future discussion.

Effect of Nitrate Additions

Measurements of the type illustrated here for Type 304 stainless steel in ferric and ferrous sulfate solutions have been conducted on a variety of passive surfaces in ferric chloride in connection with studies of the pitting mechanism. Sodium nitrate was added to several of the systems studied to inhibit the pitting process and allow an evaluation of the effect of alloy type on ferric ion reduction kinetics. In order to determine whether nitrate affects the reduction kinetics of ferric ions as well as the oxidation (pitting) of the metal, nitrate was added to the ferric-ferrous sulfate solution, where pitting does not occur, and the overvoltage behavior of Type 304 stainless steel measured. The experiment is a duplicate of that described above with the exception that the solution also contained 0.4*N* $NaNO_3$. It was found that nitrate additions to solutions of ferric-ferrous sulfate or chloride do not affect the equilibrium potential as measured with a platinized Pt electrode. The data obtained were similar to those illustrated in Fig. 1-5 and are presented in tabular form for conservation of space.

Table I compares the various electrochemical constants obtained with and without nitrate. The data show that nitrate ions do not affect the activation overvoltage values to any great extent. The exchange current and β_A are decreased while β_C is unaffected. Part of the decrease in i_0 may be attributed to the fact that the reversible ferric-ferrous potential for the two experiments differs by about 10 mv. It will be shown later that the exchange current decreases with a shift in the equilibrium potential in the noble direction caused by a decrease in ferrous ion concentration.

Discussion

The agreement between experimental observations and theoretical equations has been amply demonstrated. Application of the equations to a limited

Table I. Electrochemical constants for activation overvoltage of ferric and ferrous ions in sulfate solutions on Type 304 stainless steel

Nitrate content	$Fe^{+++}-Fe^{++}$ (I) potential (v)	η corr. (II) (v)	β_C (v)	β_A (v)	β_w (v)	i_0 (μa/cm²)	$\left(\frac{d\,\eta}{d\,i_x}\right)_{\eta\to 0}$ (III)	ν (IV)	ν (V)
None	0.7695	0.001	0.123	0.102	0.042	0.045	0.52	0.92	0.95
0.4*N*	0.7805	0.001	0.123	0.089	0.045	0.026	0.84	0.86	0.87

(I) Standard H_2 scale; (II) Potential 304 vs. Pt in same solution; (III) V/μa/cm²; (IV) Calculated from Eq. (VIII); (V) Calculated from Eq. (IX).

amount of experimental work provides a means for calculating many of the electrochemical constants. Thus, the amount of experimental work required for a complete analysis is greatly simplified. The equations also supply a method for the determination of electrochemical constants when experimental difficulties such as concentration polarization are encountered.

More important from a practical viewpoint is the fact that the analysis also applies to a corroding electrode whose potential is determined by two intersecting activation overvoltage functions. The low current analysis should be particularly helpful here because measurements are conducted with currents of the same magnitude as the corrosion current. This minimizes the possibility of surface changes caused by high values of applied currents.

Another of the more interesting aspects of this analysis from the corrosion standpoint arises from consideration of area effects. Current density data presented above were calculated on the basis of the measured geometric area. The same exchange current density was found for anodic and cathodic polarization. This is best explained by considering the surface sites for oxidation of ferrous ions as equivalent to the sites for reduction of ferric ions. Thus, at any one instant, half of the available sites function as anode while the other half serve as cathode. This concept is supported by observation that low current measurements, where area changes should be minimized, conform with high current measurements when the data are used in equations such as (VII), (VIII), and (IX).

This situation need not apply for corroding systems where different ratios of anode-to-cathode area may be encountered. When the analysis considered here for a reversible electrode is applied to a corroding system, the exchange current in the equations becomes the corrosion current. Thus, it may be possible to calculate area ratios by comparing corrosion currents determined both from anodic and cathodic high current measurements. Also, comparison of low current data with high current data may indicate area changes during polarization. Such a treatment, if proved experimentally, may provide the first useful device for determining anode-cathode area ratios so important in corrosion studies.

APPENDIX

Derivation of Eq. (VII)

Consider an electrochemical system the potential of which is determined by two intersecting activation polarization curves whose slopes are β_A and β_C. If current from an external source is applied to such a system, then the following well-known relation applies.

$$\vec{i}_x = i_0\left[10^{-\frac{\eta}{\beta_C}} - 10^{+\frac{\eta}{\beta_A}}\right] \qquad (X)$$

For small values of overvoltage, where $10^{-\frac{\eta}{\beta_C}}$ may be approximated by $1-\frac{\eta}{\beta_C}$ (2.3) and $10^{+\frac{\eta}{\beta_C}}$ may be approximated by $1+\frac{\eta}{\beta_A}$ (2.3), Eq. (X) reduces to

$$\vec{i}_x = i_0\left(1-2.3\frac{\eta}{\beta_C}-1-2.3\frac{\eta}{\beta_A}\right) \qquad (XI)$$

Rearranging produces

$$i_x = 2.3\, i_0\, \eta\left(\frac{\beta_C+\beta_A}{\beta_C\,\beta_A}\right) \qquad (XII)$$

Differentiation of overvoltage in respect to applied current results in Eq. (VII). For a corroding system, the exchange current in Eq. (X) would be replaced by the corrosion current.

Manuscript received Sept. 4, 1956. This paper was prepared for delivery before the Washington Meeting, May 12-16, 1957.

Any discussion of this paper will appear in a Discussion Section to be published in the June 1958 JOURNAL.

REFERENCES

1. J. O'M. Bockris, "Annual Review of Physical Chemistry," p. 477, Annual Reviews, Inc., Stanford, Calif. (1954).
2. J. O'M. Bockris, "Modern Aspects of Electrochemistry," Academic Press, Inc., New York (1954).
3. M. Stern and A. L. Geary, *This Journal*, **104**, 56 (1957).
4. M. Stern, *ibid.*, **102**, 609 (1955).

Mechanisms of Hydrogen Producing Reactions on Palladium

IV. Electrochemical Kinetics of the α-Palladium-Hydrogen System in Acid Solutions

James P. Hoare and Sigmund Schuldiner

U. S. Naval Research Laboratory, Washington, D. C.

ABSTRACT

An experimental investigation of the electrochemical kinetics of the α-palladium-hydrogen system was made by means of a palladium bi-electrode. The *p*H effect on the anodic and cathodic polarization behavior was determined and related to bi-electrode mechanisms. Thickness of the bi-electrode had no significant effect. It was found that catalytic activity for the hydrogen-producing reactions on α-Pd was definitely less than that on β-Pd. The fraction of the total current carried by proton flow in the bi-electrode was determined.

Studies of the mechanisms of hydrogen-producing reactions on Pd reported in earlier papers from this laboratory (1-3) were all concerned with the β-palladium-hydrogen system. The present paper is concerned with the anodic and cathodic behavior of an α-Pd-H system. Let it be defined that β-Pd is the phase in which the Pd d-bands are completely filled with electrons from H atoms (H/Pd~0.6). The alpha phase is the one in which there are positive holes in the d-bands.

Upon cathodic polarization, a Pd electrode absorbs H and tends toward the β-phase. In order to maintain a reproducible α-phase electrode, it is necessary to prevent the accumulation of H in the interior of the metal. This can be readily done experimentally by means of a Pd bi-electrode. A diagrammatic sketch of the electrode arrangement for such an experiment is shown in Fig. 1. The electrolytic cell using a bi-electrode is in fact a series arrangement of two cells, for which one side of the Pd diaphragm serves as the cathode in the first cell and the other side serves as the anode in the second cell. Since by such an arrangement there is an equivalent amount of reduction reaction on the cathode side as there is oxidation reaction on the anode side of the bi-electrode, and since H under these conditions is transported rapidly through the Pd as protons (4), there will be no tendency for the H to accumulate in the interior of the Pd. Hence by such an experimental device the Pd can be maintained at the maximum α-phase H concentration (atom ratio H/Pd = 0.03) (5) and its anodic and cathodic polarization behavior can be determined readily.

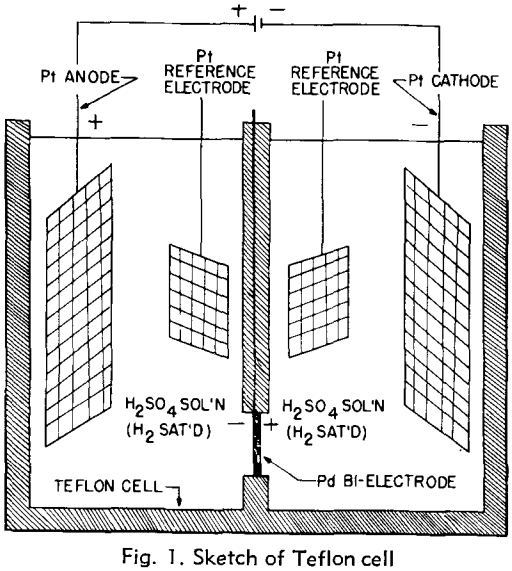

Fig. 1. Sketch of Teflon cell

An interesting aspect of the Pd bi-electrode is the fact that it is a metal membrane which is simultaneously a good electron and proton conductor. Because of this, the bi-electrode behaves as two self-depolarizing electrodes.

Experimental

The experimental technique was essentially the same as that reported in previous papers (1-3). The electrolytic cell was the same as that used in references (2, 3) except that the electrical connections were those shown in Fig. 1. The same solution was added to both compartments and the solution in both sides was stirred with H. Measurements were made with $2N$ H_2SO_4 ($pH = 0$); $0.3N$ $H_2SO_4 + 0.7N$ Na_2SO_4 ($pH = 0.9$); $0.1N$ $H_2SO_4 + 1N$ Na_2SO_4 ($pH = 1.7$). The *p*H values were determined at the conclusion of a run. Thicknesses of the Pd foil used as bi-electrodes were 0.001, 0.002, 0.003, and 0.004 in.

The solution resistance between the reference electrodes in both compartments and each side of the Pd bi-electrode was determined by interrupter measurements before each run.

The temperature was maintained at 31° ± 2°C. The exposed area of the Pd was 0.14 cm^2. All of the bi-electrode foils were made of annealed, hole-free metals.

All electrode potential measurements were made with respect to a Pt/H_2 electrode in the same solution. These potentials are termed overvoltages, η. This definition of overvoltage resulted in an open-circuit, steady-state, reversible potential of the α-Pd-H electrode of 0.0495 ± 0.0005 v.[1] The fact

[1] An explanation of the thermodynamics of this electrode system is presented in a paper entitled "Electrochemical behavior of the palladium-hydrogen system. I. Potential-determining mechanisms" by S. Schuldiner, G. W. Castellan, and J. P. Hoare, submitted to the "Journal of Chemical Physics."

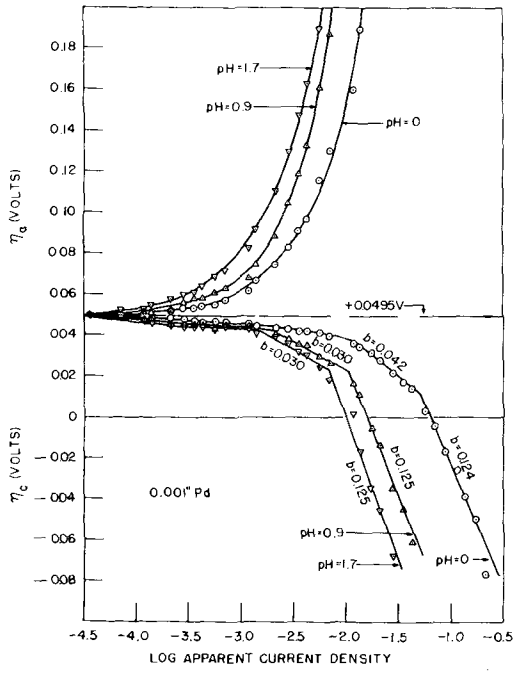

Fig. 2. Effect of pH on the hydrogen overvoltage of a Pd bi-electrode.

that this Pd had the maximum α-phase H concentration was confirmed by resistance and coulometric measurements and also by analytically determining the H content of the Pd (5).

Before the beginning of a run it was necessary to anodize (10 ma for about 45 min) both sides of the bi-electrode and then after opening the circuit to let each side of the bi-electrode reach its reversible potential (0.0495 v) in the H-saturated solution. This may require 2-3 hr. It was observed that initially the successive applications of current cause significant changes in the true area of the Pd-electrode surfaces. With repeated application of current in both an increasing and a decreasing stepwise

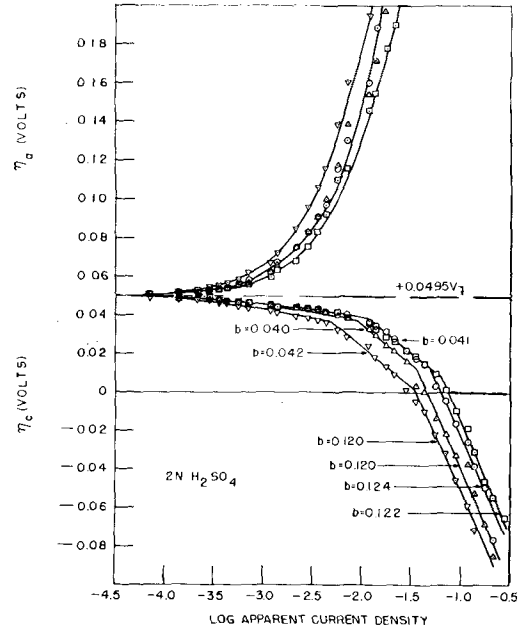

Fig. 3. Hydrogen overvoltages of Pb bi-electrodes of different thicknesses. Open circle, 0.001 in.; open triangle, 0.002 in.; inverted triangle, 0.003 in.; open square, 0.004 in.

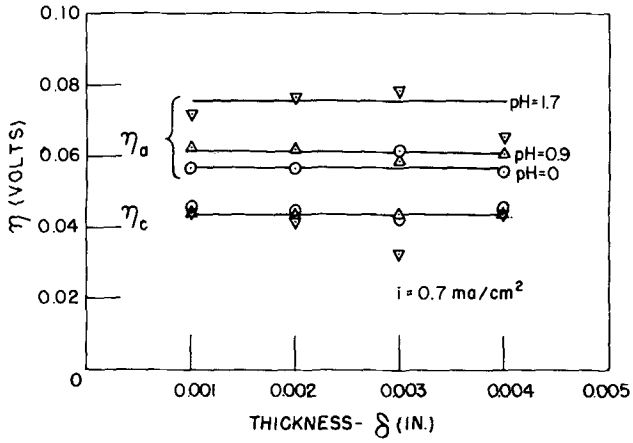

Fig. 4. Plot showing lack of thickness effect on η of Pd bi-electrodes.

fashion the area became effectively constant and reproducible time-independent measurements were possible (±2 mv). Steady-state potentials were reached within seconds after the current density was changed. The experimental results for the cathodic measurements given in this paper are the average values for each point of three separate runs in which the current was increased and decreased three times over the entire current range for each run. Those for the anodic polarization represent only the values for increasing current, because of the extremely long time required for the anodic potentials to come to steady state for decreasing currents. During a run it must be noted that coming down the current scale to open circuit conditions it was necessary that the reversible potentials on both sides of the bi-electrode be reached before obtaining measurements again at increasing currents.

Results

The overvoltage vs. log current density relationships for both the anodic polarization (η_a) and the cathodic polarization (η_c) on the Pd bi-electrode are shown in Fig. 2 and 3. Fig. 2 shows the pH effect and Fig. 3 shows the effects of bi-electrode thickness. Actually the thickness effect can be considered as negligible. This is shown in Fig. 4 where a low current density comparison is made. It is believed that the separation of the curves at higher current densities as shown in Fig. 3 is due to the differences in true areas of the electrodes. This area effect of the electrodes would be most apparent in the η vs. log i regions of higher slope.

Fig. 5 shows the effect of pH on the linear portion of η_a and η_c vs. current density curves. The fact that these curves are straight lines all passing through the 0.0495 voltage axis at zero current shows that the α-Pd-hydrogen electrode is a reversible electrode with a value of 0.0495 ± 0.0005 v vs. Pt/H_2 in the same solution.

The reciprocals of the slopes of the η vs. i curves in Fig. 5 are numerically equal to the rate constants for the over-all hydrogen producing reactions at low current densities (1, 6). A plot of these rate constants against pH yields the equation given below for α-Pd. A comparison of the rate constants ($di/d\eta$) in acid solutions (pH = 0 to ~ 3) for β-Pd, Pt, and

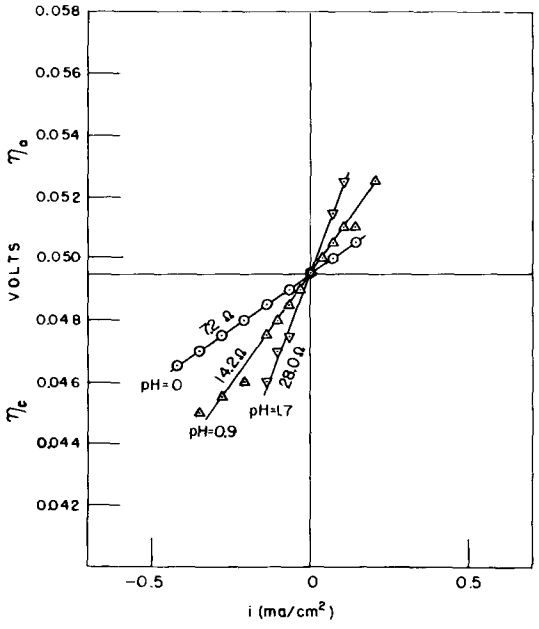

Fig. 5. The pH effect on the linear portion of η vs. i curves.

α-Pd, where in all cases the apparent current density was used in the calculation, is:

$$\beta\text{-Pd:} \quad -(di/d\eta) = 4.07 - 1.96 \ \text{pH}$$
$$\text{Pt:} \quad -(di/d\eta) = 0.356 - 0.104 \ \text{pH}$$
$$\alpha\text{-Pd:} \quad -(di/d\eta) = 0.134 - 0.061 \ \text{pH}$$

These results show that the catalytic activity of α-Pd is definitely lower than the catalytic activity for the hydrogen producing reactions of β-Pd. Since the roughness factor of Pd compared to Pt is significantly greater, a comparison of rate constants of these electrode systems using the apparent current density in the calculation is only qualitative.

Results similar to Fig. 2, 3, and 5 were obtained for all four thicknesses of bi-electrodes in the three solutions of different pH.

Discussion

Fig. 2 and 3 show three distinct η_c vs. log i regions. The first is a non-Tafel region; the second region shows a Tafel slope of either 0.03 or 0.04 depending on the pH of the solution; and the third region shows a Tafel slope of 0.12. From an analysis of the kinetics of electrode processes (1, 7) the 0.03 slope represents an atomic combination controlled mechanism, whereas 0.04 represents a mechanism which is controlled by the electrochemical desorption step.

The first of three diagrams, Fig. 6a, represents the postulated primary mechanisms for the first region (non-Tafel). On the cathode side, the reduction is hydronium ions to hydrogen atoms at the electrode surface. The hydrogen atoms move to the interior where they lose their electrons to the d-bands of palladium atoms. The protons migrate to the anode side where they regain their electrons and move to the anode surface as hydrogen atoms. At the anode surface the atoms lose their electrons and are removed from the surface as hydronium ions. The major over-all reaction in this region is the transfer of hydrogen ions from one cell to the other.

Fig. 6b indicates the principal electrode mechanisms postulated for the Tafel region for b slopes of

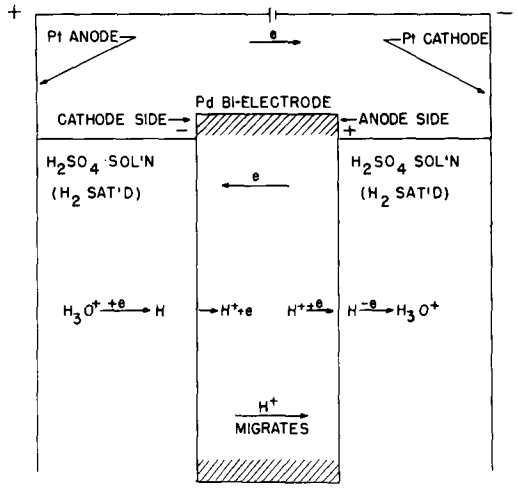

Fig. 6a. Principle electrode mechanisms of the Pb bi-electrode: a, in non-Tafel region; b, in region where Tafel slope is either 0.03 or 0.04; c, in region where Tafel slope is 0.12.

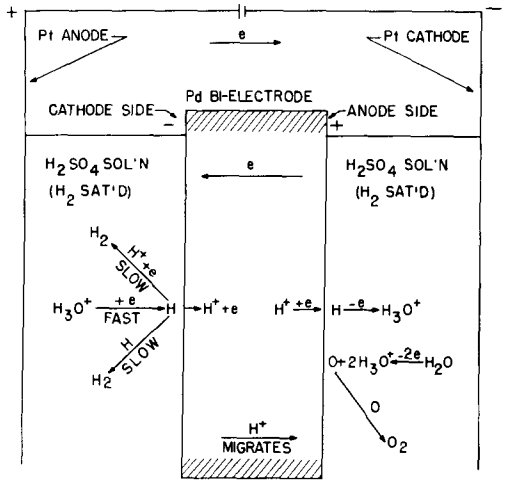

Fig. 6b

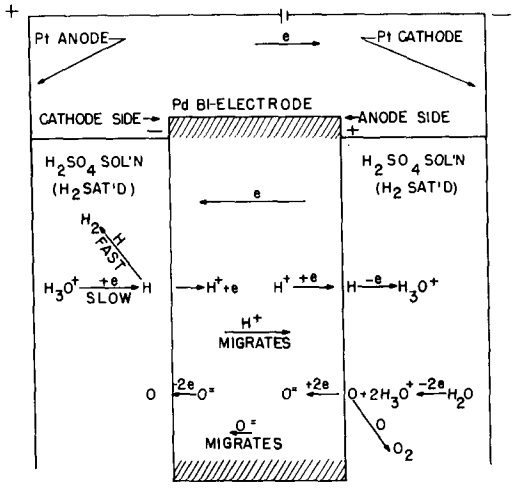

Fig. 6c

0.03 or 0.04. Here the same over-all mechanism of proton transfer from one cell to the other still occurs; however, only a fraction of the current is used in this mechanism. On the anode side, most of the oxidizing current goes into the production of oxygen and an equal portion of the reducing current on the cathode side goes into a molecular hydrogen-produc-

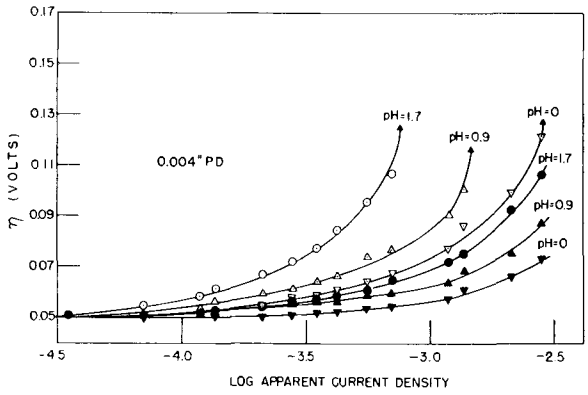

Fig. 7. Comparison of the anodic polarization of the anodic side of a Pd bi-electrode and of a simple Pd anode in solutions of various pH values. Open symbols refer to the simple anode and filled-in symbols refer to the bi-electrode.

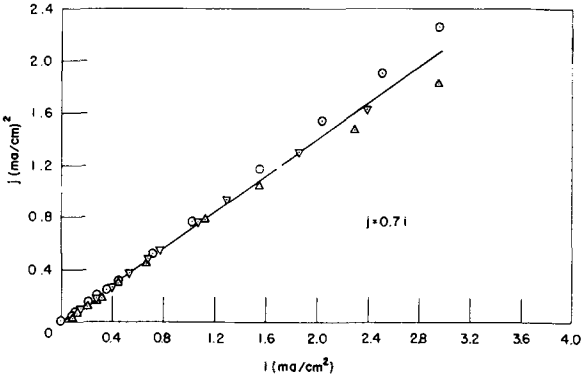

Fig. 8. Proton flow through Pd bi-electrode as a function of current density. Open circle, pH = 1.7; open triangle, pH = 0.9; inverted triangle, pH = 0.

ing reaction controlled either by the slow atomic combination step ($b = 0.03$) or by the slow electrochemical desorption step ($b = 0.04$), depending on pH.

Fig. 6c shows the postulated mechanisms for the Tafel range with a b slope of 0.12. Under these current conditions only a small portion of the current is used in transferring protons across the bi-electrode. Most of the current goes into the production of oxygen on the anode side and the production of hydrogen on the cathode side. Because of the rapid formation of oxygen on the anode side, the concentration of atomic oxygen is high enough so that a significant amount of oxygen could be dissolved in the Pd in the ionic form (8,9). The oxygen ions migrate to the cathode side, where they form atomic oxygen and subsequently exist as an oxygen or oxide particle on the surface. This oxygen can be removed by reaction with hydrogen on the surface, but Ubbelhode and Egerton (10) have shown that the removal of oxygen from the surface of Pd is a slow process. The oxygen on the surface effectively poisons the catalytic activity of the surface for the hydrogen-producing reaction. The experimental data in Fig. 2 and 3 indicate that at high current densities the poisoning of the surface with oxygen slows the hydronium discharge step more than the hydrogen combination step. This results in a change to a Tafel slope of 0.12.

Fig. 7 compares the anodic polarization on a Pd bi-electrode in various pH solutions with the anodic polarization of a simple Pd anode with the same surface. The curves for the bi-electrodes were determined in the manner described in the experimental section of this paper. The curves for the simple anodes were determined by covering the cathode sides of the same bi-electrodes with polyethylene and thus isolating that side of the electrode from the solution in that compartment. The Pd was then connected to the current source as an anode and its overvoltage, η, was determined. By comparing the two sets of curves for a given pH (simple anode vs. anode side of bi-electrode) at a definite value of η, the difference in the two current values obtained is defined as j. This j represents the amount of proton current density which is necessary to reduce the overvoltage of a simple anode to the same value as that found on the anodic side of the bi-electrode. This assumes that the same relationship between η and i exists for both electrode systems. This assumption is probably not quite correct; however, since the rate of change of overvoltage with current is small for the major portion of the current density range given in Fig. 7, any discrepancies due to variation in the η vs. log i relationship would be negligible. A plot of the relationship between j and i is given in Fig. 8. This represents the proton flow through the Pd bi-electrode as a function of current density, i. As can be seen, there is a linear relationship between j and i which is independent of pH and, as shown by Fig. 4, of thickness. The equation for this relationship is:

$$j = 0.7\, i$$

The constant 0.7 is independent of solution pH and current density as is shown in Fig. 8. It is interesting to note that, of the current carried by the Pd metal conductor between the cathode and the anode surfaces of the bi-electrode, 70% is proton current and 30% is electron current. In terms of the Pd bi-electrode as shown in Fig. 6, this means that at the low current density range 70% of the applied current goes into the transfer of hydrogen ions from the first cell to the second and 30% goes into the production of the products of the reduction reaction on the cathode side and the oxidation reaction on the anode side. The reason could be that on the cathode side of the bi-electrode the transfer of adsorbed hydrogen atoms on the Pd surface through the skin of the metal to protons in the interior of the metal is slow enough so that some surface desorption of atomic hydrogen takes place. Similar conditions exist on the anodic side of the bi-electrode. This postulate is supported by the absence of a thickness effect of the bi-electrode.

In another series of experiments, one side of the Pd membrane was made an anode without blocking off the other side with polyethylene so that this side of the metal was in contact with a hydrogen-stirred H_2SO_4 solution. In these experiments the Pd was a simple anode as in the experiment above, with the exception that in this case the back side of the Pd anode was in contact with the hydrogen-saturated solution. The anodic overvoltage curves obtained for this system at low current densities were in all

cases not significantly different from the overvoltage curves obtained for the anodic side of the bi-electrode for solutions of the same pH. Deviations occurred at the higher current densities. These results indicate that at low current densities hydrogen ion transfer took place with equal ease from the first cell to the second cell whether the Pd was used as a bi-electrode or as a simple anode.

Acknowledgments

The authors are indebted to Dr. J. C. White for his suggestion of a study of the Pd bi-electrode system and for his advice during the course of the work.

Manuscript received June 4, 1956. This paper was prepared for delivery before the Washington Meeting, May 12-16, 1957.

Any discussion of this paper will appear in a Discussion Section to be published in the June 1958 JOURNAL.

REFERENCES

1. J. P. Hoare and S. Schuldiner, *This Journal*, **102**, 485 (1955).
2. S. Schuldiner and J. P. Hoare, *ibid.*, **103**, 178 (1956).
3. J. P. Hoare and S. Schuldiner, *ibid.*, **103**, 237 (1956).
4. C. Wagner and G. Heller, *Z. Physik. Chem.*, **B46**, 242 (1940).
5. J. P. Hoare and S. Schuldiner, *J. Phys. Chem.*, **61**, 399 (1957).
6. S. Schuldiner, *This Journal*, **101**, 426 (1954).
7. R. Parsons, *Trans. Faraday Soc.*, **47**, 1332 (1951).
8. D. P. Smith, *Z. Physik*, **78**, 815 (1932).
9. J. H. DeBoer and J. D. Fast, *Rec. Trav. Chim. Pays-Bas*, **59**, 161 (1940).
10. A. R. Ubbelhode and A. Egerton, *Trans. Faraday Soc.*, **28**, 284 (1932).

Kinetics of Metal Deposition

Significance of Experimental Data and Some Results Using Voltammetry at Constant Current

T. Pavlopoulos and J. D. H. Strickland[1]

Chemistry Division, British Columbia Research Council, Vancouver, British Columbia, Canada

ABSTRACT

The discharge characteristics of the deposition of lead, thallium, silver, bismuth, copper, tin, and antimony ions onto the solid metals, using constant current voltammetry, are reported and discussed.

At least two parameters are needed to describe deposition onto solid surfaces that are not required when working with mercury electrodes. These are (*a*) a roughening factor, *f*, which may be defined as the ratio to the geometrical area of the surface area effective for the transport of discharging molecules, and (*b*) a reactivity factor, β, which is the ratio to the geometrical area of the area reactive to the discharge process.

A direct comparison of kinetic data for solid metal deposition obtained by different methods is not valid unless these measurements are made while the metals are being continuously deposited at comparable current densities and from identical solutions.

In the past decade, new methods for studying electrode kinetics, in particular the use of superimposed alternating voltage and electrolysis at constant current, have been used with a mercury electrode. However, with a few exceptions, these new techniques for kinetic study have not been employed with electrodeposits of solid metals, workers having naturally preferred to use a mercury surface where the geometrical surface area of the metal can be assumed to be identical with the area governing the transport of molecules and their subsequent discharge. With any attempt to study the discharge at a solid metal surface formidable experimental difficulties arise. A discussion of the significance of experimental data in this field and a summary of the parameters that can be obtained by modern methods are given here since most of the published formulas relate either to oxidation-reduction processes, in which both species are in solution, or to the depositions of metals into mercury to form amalgams.

General Kinetic Equations

It is common practice to write the equations for the rate of deposition processes in terms of an exchange current and Tafel slope although, as electrode kinetics are a particular case of heterogeneous chemical processes, assisted, or otherwise, by an applied potential, it would appear more logical to express reactions in terms of a heterogeneous kinetic constant of dimensions LT^{-1} and a parameter α, the transfer coefficient, showing what fraction of the applied potential assists the discharge process. It is general to write a basic equation in the form:

$$i = i_f - i_b = nFA_r \left[k_f C_e e^{\frac{\alpha nF}{RT}E} - k_b e^{-(1-\alpha)\frac{nF}{RT}E} \right] \quad \text{(I)}$$

In this equation, i is the cathodic current in amperes and C_e is the concentration of the discharging species at the electrode surface at an applied potential of E, which is here taken as the electrode potential on the hydrogen scale using the Lewis-Randall sign convention. Alpha is the fraction of the potential drop at the electrode surface, assumed to vary linearly with distance over the metal-solution interface, which assists the discharging species to surmount any energy barrier between its initial and discharged

[1] Present address: Pacific Oceanographic Group, Fisheries Research Board of Canada, Nanaimo, B. C., Canada.

states. A_r is the area of electrodes which is reactive to the discharge process, F is the Faraday, and n the number of electrons involved in the rate-determining step. This step is not necessarily the same as the complete discharge reaction when multivalent changes take place but will probably be so for the more simple ionic discharge reactions. This type of discharge kinetics gives rise to what Vetter (1) describes as a "penetration" overvoltage and is the only kinetic step considered in this discussion.

The constant k_f in Eq. (I) has the dimensions LT^{-1} of a first order heterogeneous reaction constant, but k_b, unlike the back-reaction constant for a redox reaction, has the dimensions $L^{-2}T^{-1}$. Both constants contain a voltage term, as E in Eq. (I) is measured from an arbitrary potential level. It may be argued that a reaction constant, k^0_f, should really be used, this constant applying when the potential between the metal surface and discharging species, centered some few Angstrom units from the metal-solution interface, is truly zero. Approximations to this potential could be used, such as the electrocapillary zero or the potential at which the χ potential is zero (2) or, following Mattsson (3), a potential where the difference between the galvani potential and a potential taken from infinity in the solution phase to the outside of the Helmholtz layer is zero. However, the value of such a potential is unknown, and probably unknowable, and the constants k_f and k_b, as defined by Eq. (I), are at present the only practicable parameters.

Values of k_f for discharge of a metal ion into an alloy (the most common instance is in forming an amalgam) cannot be compared directly with the k_f values found when the same ion discharges into the lattice of a pure metal, as the zero interface potential will probably be markedly different in the two cases. It is unlikely, however, that differences in k_f of much more than about one or two orders of magnitude result from this cause.

On defining a fraction:

$$\beta = A_r/A$$

where A is the geometrical area of the electrode, Eq. (I) becomes

$$I = I_f - I_b = nF\beta\left[k_f C_e e^{\frac{\alpha nF}{RT}E} - k_b e^{-(1-\alpha)\frac{nF}{RT}E}\right] \quad \text{(II)}$$

where I is the apparent current density on the solid metal, which can be directly measured, and concentrations are expressed as moles/cc.

If E_r is the reversible (zero current) potential of the electrode in a solution containing a bulk and surface concentration of C moles/cc; as $I_f = I_b$ when E equals E_r:

$$E_r = \frac{RT}{nF}\ln\frac{k_b}{k_f} - \frac{RT}{nF}\ln C$$

Comparing this with the Nernst equation:

$$E_r = E^\circ - \frac{RT}{nF}\ln \text{ (activity of discharging species)}$$

shows that the standard potential E° is given by:

$$E^\circ = \frac{RT}{nF}\ln\frac{k_b}{k_f}y$$

where y is a factor, related to the mean activity coefficient of the discharging species, which has the dimensions L^3.

Hence:

$$k_b = \frac{k_f}{y}e^{\frac{nF}{RT}E^\circ}$$

and Eq. (II) can be written:

$$I = nF\beta k^\circ\left[C_e e^{\frac{\alpha nF}{RT}(E-E^\circ)} - \frac{1}{y}e^{-(1-\alpha)\frac{nF}{RT}(E-E^\circ)}\right] \quad \text{(III)}$$

where:

$$k^\circ = k_f e^{\frac{\alpha nF}{RT}E^\circ} = k_b y e^{-(1-\alpha)\frac{nF}{RT}E^\circ} \quad \text{(IV)}$$

The constant k° is related to the constant k_{sh} used by Delahay (4). The use of such a constant has the advantage that it is more characteristic of a reaction than is k_f or k_b because it no longer depends in magnitude on the value of E which is measured on an arbitrary potential scale. However, E° is not known for many metal depositions reactions, unlike the corresponding value for a redox reaction which is comparatively easy to evaluate.

The apparent exchange current density, $I_{o(s)}$, is equal to $I_{f(s)}$ or $I_{b(s)}$ at the reversible potential $E_{r(s)}$, hence from Eq. (II):

$$I_{o(s)} = nF\beta k_f C e^{\frac{\alpha nF}{RT}E_{r(s)}} \quad \text{(V)}$$

From Eqs. (IV) and (V) and the Nernst equation, it follows that one can also write:

$$I_{o(s)} = nF\beta k^\circ y^{-\alpha} C^{1-\alpha} \quad \text{(VI)}$$

With a redox system, or where a metal is deposited into mercury, provided that the activities of oxidized and reduced forms are about equal, the equivalent equations to (V) and (VI) are:

$$I_{o(l)} = nF k_f C e^{\frac{\alpha nF}{RT}E_{r(l)}} \quad \text{(Va)}$$

and:

$$I_{o(l)} = nF k_{sh} C \quad \text{(VIa)}$$

The parentheses (s) and (l) in the above equations are used to denote a reaction taking place at a solid metal surface or at a mercury or amalgam surface. Eq. (II) is often written in terms of $I_{o(s)}$ and the overvoltage $\eta = (E_r - E)$ as:

$$I_{(s)} = I_{o(s)} e^{\frac{-\alpha nF}{RT}\eta}\left[1 - e^{\frac{nF}{RT}\eta}\right] \quad \text{(VII)}$$

or as:

$$I_{(s)} = I_{o(s)}\left[\frac{C_e}{C}e^{\frac{-\alpha nF}{RT}\eta} - e^{\frac{(1-\alpha)nF}{RT}\eta}\right] \quad \text{(VIII)}$$

where C is the bulk concentration of the discharge species. These equations can be used to determine I_o and α from experimental data by taking the extreme cases where either y is so small that an expansion of the exponentials, ignoring higher terms, is valid or y is sufficiently large for the back reaction to be negligible. In all cases, however, a determination of the $I_{o(s)}$ value for a deposition reaction onto a solid metal [Eqs. (V) and (VI)] does not

enable a velocity constant to be obtained as is the case with Eqs. (Va) and (VIa). The term ($\beta k^\circ y^{-a}$) is determined. y^{-a} can be eliminated if E_r and E° are known or (βk_f) found from Eq. (V) if E_r alone is known.

The constants β and k° or k_f cannot be determined separately by any known method and the best approximation at present is to assume that the constants k° or k_f for a given discharge reaction are the same when the metal is deposited into mercury as when it is deposited out on a solid metal surface. This assumption may, as mentioned earlier, be subject to error and the only obvious alternative is to work with single crystal faces in highly purified solutions and assume that β is near to unity.

If the rate constants and α values for liquid and solid surfaces are assumed to be approximately equal, β can be evaluated by taking the ratio of the apparent exchange current densities $I_{o(l)}$ and $I_{o(s)}$ at the same C values. From Eqs. (V) and (Va):

$$\frac{I_{o(s)}}{I_{o(l)}} = \beta\, e^{\frac{anF}{RT}(E_{r(s)} - E_{r(l)})} \qquad \text{(IX)}$$

or from (VI) and (VIa)

$$\frac{I_{o(s)}}{I_{o(l)}} = \beta\, C^{-a}\, y^{-a} = \beta\, e^{\frac{anF}{RT}(E_{r(s)} - E^\circ_{(l)})} \qquad \text{(X)}$$

these equations being practically equivalent, as with equal activtities of oxidized and reduced forms, $E_{r(l)} \doteq E^\circ_{(l)}$

In all experimental techniques used at present for the determination of k_f and α values some concentration polarization is encountered and must be eliminated by a suitable mathematical treatment, generally involving a solution of Fick's equation. When working with mercury the assumption is made that surface area effective for the transport process, A_t, is identical with the geometrical area A. This may well not be the case with a solid metal and a diffusion roughness factor, f, can be defined from:

$$f = At/A$$

This factor is not the same as β or as a true surface factor measured by gas adsorption, capacity measurements, or similar techniques. The factor f depends on the relative size of surface irregularities and on the thickness of the transport layer at the surface, which may or may not follow the surface contours. f may be related to β but this is not necessarily so and no generalizations can be made.

Techniques Employed

Steady-state current-voltage measurements.—Steady-state polarization curves have been used extensively to study electrodeposition on solid electrodes, but comparatively little work has been reported where transport polarization has been completely eliminated or accurately allowed for in calculations of kinetic data (5-7). The techniques and approximations are too numerous to summarize but generally I_o and α values are reported based on the solution of equations such as (VII) or (VIII). The present authors (8) have described a polarographic technique where transport by convective diffusion is allowed for and which enables α and (βk_f) to be determined for moderately slow discharge reactions. None of these methods is satisfactory for studying really fast discharge processes.

Impedance measurements with a periodically changing potential.—Work with solid electrodes in aqueous solutions has been reported by Hillson (9) in the case of Cu. The difficulties encountered when using this method arise from the fact that the behavior is not that to be expected from a uniform reactive surface. Continuous deposition does not take place to renew the metal surface during measurements. Rather, ions are leaving and entering the metal surface in equal numbers, a process which does not insure maintenance of a continuously active surface and remove impurities from solution in the vicinity of the metal. Fixed discharge centers form which are prone to poisoning; β tends to be less than the value found by methods involving continuous plating. β is critically dependent on surface preparation and is likely to change during the course of a single experiment. Other experimental complications center round the variation of double layer capacity with frequency encountered with solid surfaces (10, 11). There is doubt whether the technique shows much promise with solid electrodes despite its importance in studying discharge processes at mercury surfaces (12-17).

Ideally the method should give values for α, f and ($\beta k^\circ y^{-a}$) if the diffusion coefficient D of the discharging species is known or (βk_f) if E_r is also measured. The values for f and β will be quite different than those operative during a continuous plating process and will have little fundamental significance. If R_r and R_d are the reactive and diffusive resistance of an electrode, calculated from the complex impedance by making correction for the double layer capacity;

$$R = R_r + R_d = \frac{RT}{n^2 F^2 C A}\left[\frac{1}{k^\circ y^{-a} C^{-a} \beta} + \frac{1}{f(2Dw)^{1/2}}\right]$$

where $R_d = \frac{1}{w C_d}$, C_d being the diffusive capacity, whence $R_r = \frac{RT}{n F I_{o(s)} A}$ can be calculated as R and C_d are measurable quantities.

The corresponding equations for the same discharge reaction on a mercury surface, where the metal dissolves and has equal activity in both phases, are:

$$R = R_r + R_d = \frac{RT}{n^2 F^2 C A}\left[\frac{1}{k_{sh}} + \left(\frac{2}{wD}\right)^{1/2}\right]$$

whence again $R_r = \frac{RT}{n F I_{o(l)} A}$ and $I_{o(l)}$ can be calculated.

The factor f depends on the frequency $w/2\pi$ used and will be greater than unity, if the surface is uniformly reactive, unless the surface irregularities have a radius less than about 10^{-5} cm. The surface is probably far from uniform in activity, however, and Vetter (18) has considered the case where reactive centers are present on an uneven surface.

Studies at constant current.—The use of constant current voltammetry has been revived recently and applied to kinetic studies (19-24). For a rapid dis-

charge process the equation for a "reversible" deposition process at a solid electrode is:

$$E = E^\circ - \frac{RT}{nF}\ln\left(y\frac{C}{\tau^{1/2}}\right) - \frac{RT}{nF}\ln\left(\tau^{1/2} - t^{1/2}\right) \qquad \text{(XI)}$$

where E is the voltage at time t seconds and τ is the "transition time", the time taken from first applying a current of apparent density $I_{(s)}$ until the voltage abruptly tends to infinity. As $\tau^{1/2}$ is related to the current density, being inversely proportional, a plot of E against log $(\tau^{1/2} - t^{1/2})$ will give a separate line for each value of $I_{(s)}$, but all lines will have the ideal Nernst slope of $0.0591/n$ at 25°C.

For a slow discharge process the equation:

$$E = \frac{RT}{\alpha nF}\ln\left[\frac{I_{(s)}\tau^{1/2}}{nFCf\beta k_f}\right] - \frac{RT}{nF}\ln\left(\tau^{1/2} - t^{1/2}\right) \qquad \text{(XII)}$$

applies at voltages in excess of about $0.1/n$ v from the reversible potential. As $(I_{(s)}\tau^{1/2})$ is a constant, at least over a limited range of $I_{(s)}$ values, a plot of E against log $(\tau^{1/2} - t^{1/2})$ should give only one straight line irrespective of the value of $I_{(s)}$ and the slope will be a measure of α. f can be determined independently from the equation:

$$f = \frac{2I_{(s)}\tau^{1/2}}{\pi^{1/2}nFD^{1/2}C} \qquad \text{(XIII)}$$

if D is known. From Eqs. (XII) and (XIII) (βk_f) can be evaluated. $I_{o(s)}$ follows [Eq. (V)] if E_r is measured before applying the current. Gerischer (25) has used an extrapolation technique to give the E value at zero t from which $I_{o(s)}$ and α can be found. A different but elegant method of extracting data from measurements by this technique is described by Gierst (26).

Transition times of the order of 10-100 sec are obtained using $I_{(s)}$ values of the order of 10^{-4} amp/cm^2. The use of short current bursts and the oscillographic measurements of potential over short time intervals (generally very much less than τ) has been described (27-29) and ideally very large k_f values could be measured by such a method, but accurate compensation is necessary for capacitive effects at the electrode surface and this is likely to give trouble with solid electrodes.

Present Investigation

The use of continuously applied constant current (in contrast to square wave current impulses) has received little attention with electrodeposition on solid electrodes. No kinetic parameters resulted from the work of Turner and Winkler (30) or from the few experiments made by Reilley and co-workers (31) in their evaluation of the constant current technique as an analytical tool. Fianda and Nagel (23) studied the deposition of Ag and found it reversible, but a correction for roughness (24) was needed and there was sometimes evidence of the presence of a highly active surface to the initial metal until deposition of a fresh surface took place. In the present work the deposition of a large number of comparatively "uncomplexed" ions, mainly perchlorates, was studied, the factor f found and reductions classified as irreversible or reversible. In the latter case, the reactions were too rapid for kinetic analysis by constant current voltammetry at $I_{(s)}$ values around 5.10^{-4} amp/cm^2 (or about half an amp/ft^2). Values for α and (βk_f) for Bi and Cu depositions have been determined and the results compared with results obtained by other techniques.

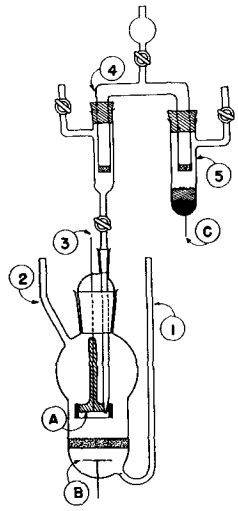

Fig. 1. Diagram of cell

Experimental Procedure

The circuit used was practically identical with that described by Delahay and Mattax (21). The cell used, however, was designed specifically for this investigation and is shown in Fig. 1. A polished Pt disk, A, acted as cathode (after plating with the metal concerned) and was fixed in a polyethylene holder and cemented into place with a mixture of Picien and paraffin wax which insulated the back of the disk and the wire lead, 3, and prevented any creep back of electrolyte. The cathode, with about ½ cm of edge shielding, was held symmetrically several cm above a Pt disk anode, B, of the same area (2.24 cm^2), being separated from it by a coarse glass sinter. The cell was filled with electrolyte and deoxygenated by passing electrolytic hydrogen through tube 1 and out of tube 2 while the whole equipment was immersed in a water bath thermostatically controlled at 25° ±0.1°C. The capillary probe for measuring the working potential was less than 0.5 mm diameter at the tip and projected less than 1 mm from the back of the cathode. Although this is not perhaps the ideal arrangement (4) it seemed about the most practical and was thought to give a representative potential for the cathode surface to within 1 or 2 mv. The probe was filled with the working electrolyte and connected via a saturated ammonium nitrate salt bridge, 4, to the calomel half-cell, 5. A constant current, varying between about 0.1 and 0.4 ma in magnitude, could be passed between A and B and the potential between A and C measured against time with a L&N Speedomox recording potentiometer of about 2 seconds response time. Transition times, between about 10 and 200 sec, were recorded and the constancy of the product $(I_{(s)}\tau^{1/2})$ and $(I_{(s)}C^{-1})$ checked for a three- to fourfold variation of $I_{(s)}$ and C before voltage-time curves were taken. These products were always constant to within 1-2%. The Pt cathode was com-

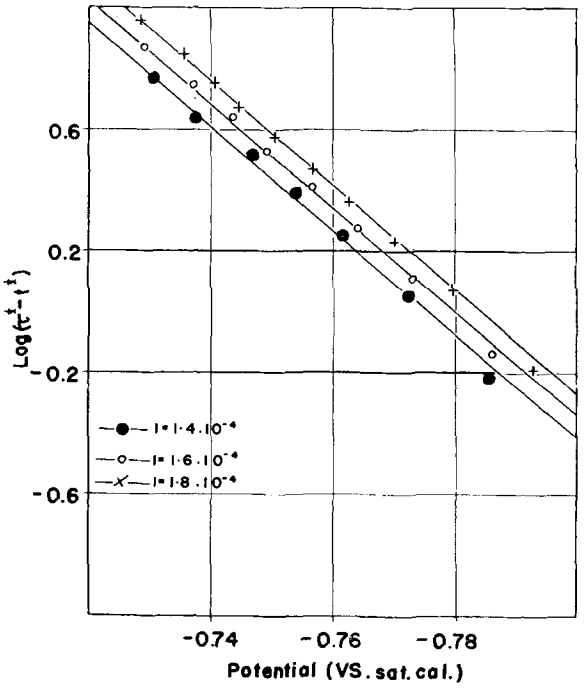

Fig. 2. Reversible reduction, 4.10^{-3}M Tl^{+} in 1M $NaClO_4$

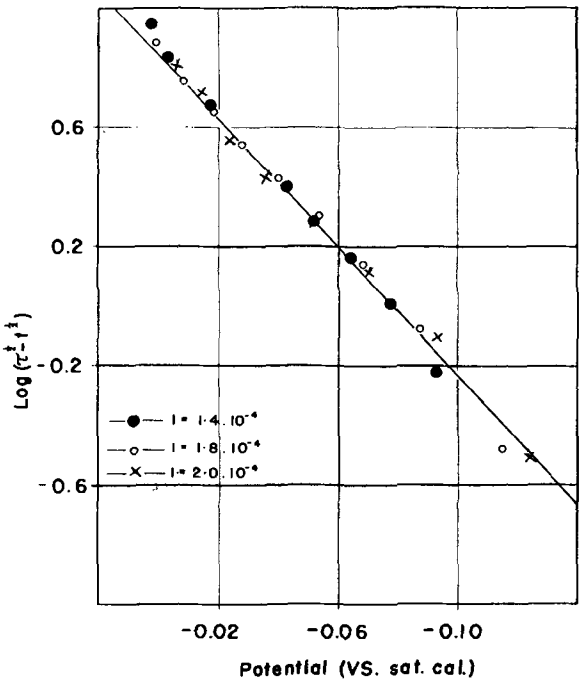

Fig. 3. Irreversible reduction, 4.10^{-3}M Cu^{2+} in 1M $NaClO_4$

pletely covered by the metal under study, after which voltage-time curves were highly reproducible from experiment to experiment.

Solutions were prepared from analytical quality reagents and the base electrolytes purified by shaking with neutral activated alumina. Diffusion coefficients and stationary electrode polarograms were determined as described previously (8). The metal salts had the same anion as the base electrolyte.

Results

The depositions studied were either reversible or markedly irreversible. An example of the former is shown in Fig. 2 for 4.10^{-3}M Tl in 1M $NaClO_4$. The slope is exactly theoretical and the separation of lines is marked even when the current density changes by only about 10%. The irreversible deposition of 4.10^{-3}M Cu in 1M $NaClO_4$ is shown in Fig. 3 where a straight line is found with potentials more cathodic than about 0.04 v. In this and other irreversible reductions all points fell on the same line, even with current density changes of 50-100%.

The quantitative results of this investigation are shown in Table I. All voltage-time curves were obtained using 4.10^{-3}M solutions in the base electrolytes shown, with apparent current densities of about $2\text{-}5.10^{-3}$ amp/cm^2, i.e., about the lowest densities used in commercial electroplating. f values were calculated from Eq. (XIII), using polarographic D values, and (βk_f) values were obtained from the plot of Eq. (XII) and thence $I_{o(s)}$ using Eq. (V). The values for (βk°) are estimates based on values for E° in Latimer (32). Data by constant current, denoted C.C., are compared with the data obtained by solid electrode polarography (8), denoted S.E.P., using the same solution for both experiments.

In addition to the experiments shown in Table I, others were made which may be reported briefly. Stannous Sn in a concentration which was undeter-

Table I. Quantitative results

Metal ion	Base electrolyte	Method	$D \times 10^5$	f	Slope	E_r	α	(βk_f)	$(\beta k^0) \times 10^5$	$I_{o(s)} \times 10^4$ amp/cm^2
Tl	1M $NaClO_4$	C.C.	1.88	1.04	0.059	+0.47		Reversible		
		S.E.P.		1.0	0.060	+0.47		Reversible		
Ag	0.5M KNO_3	C.C.	1.50	1.06	0.058	−0.63		Reversible		
		S.E.P.		1.0	0.060	−0.63		Reversible		
Pb	1M $NaClO_4$	C.C.	0.92	1.00	0.031	+0.19		Reversible		
		S.E.P.		1.0	0.0305	+0.19		Reversible		
Bi	1M Tartaric acid	C.C.	0.41	0.98	0.0208	−0.18		Reversible		
		S.E.P.		1.0	——	−0.18		Two or more reducing species Reversible reduction for major component.		
Cu	1M $NaClO_4$	C.C.	0.68	1.00	0.092	−0.27	0.32	0.14	4.1	1.7
		S.E.P.		1.0	0.080	−0.255	0.37	0.68	5.6	4.5
Bi	1M $HClO_4$	C.C.	0.60	1.12	0.0354	−0.24	0.56	960	0.17	2.9
		S.E.P.		1.0	0.056	−0.245	0.35	10	3.25	7.4
Bi	1.0M KCl 0.1M HCl	C.C.	0.87	1.17	0.0333	−0.12	0.59	0.9	2.3	3.6
		S.E.P.		1.0	0.0345	−0.125	0.57	1.3	4.6	5.2

mined but near to 4.10^{-3}M gave reversible behavior, the slope being 0.0302 compared with the theoretical 0.0296. The plots obtained with Sb in alkali and acid were poor, indicating consecutive reductions from a solution containing more than one species of ion. This effect was least marked in acid where the mean slope was near to that expected from a reversible 3 valent reduction.

Satisfactory plots were not obtainable from data for Cd in sulfate solution or for Ni and Zn solutions in either acid or alkali. Either no transition time was obtained or it was too poorly defined to be of quantitative value.

Discussion

The constant current method, using current densities giving transition times between about 10 and 200 sec, can be used for kinetic measurements with solid electrodes, but many discharge processes of the softer metals are too rapid for measurement and are recorded as "reversible". The reversible or irreversible behavior depends on β as well as the value of k°. The discharge of Cu from perchlorate and Bi from chloride, which is reversible polarographically on Hg, presumably appears irreversible here at a solid electrode because β is much less than unity. Comparison of the $I_{o(s)}$ value obtained in this work for Cu with the $I_{o(l)}$ value calculated from the data of Randles and Sommerton (17) suggests that β is only a few per cent. A similar calculation for Bi in perchlorate gives β as nearly 100% for this softer metal, indicating that the discharge process itself is slow, as would be expected from an ion such as $(Bi\ O)^+$.

Values for f are never much greater than unity, in agreement with the microscopic appearance of the plated metals.

Data obtained by Hillson (9) on solid Cu electrodes, using the a-c bridge method, have been recalculated but show no agreement with the present work. Hillson's value for f is very small, about 2%, indicating that large areas of the electrode are inactive, and yet the apparent exchange current density is nearly one hundred times as great as found in the present work and his value for α is nearly twice as great. It appears to be of little value to compare data obtained by different methods unless the nature of these methods is such that the surface condition of the metal is reproducible and this can be ensured only by having continuous deposition of fresh metal at comparable current densities from identical solutions in both procedures. In view of this, a value of 0.43 for α and 5.10^{-4} amp/cm^2 for $I_{o(s)}$ obtained by Shreir and Smith (7) with an acid copper sulfate solution and current densities 50-100 times greater than used here, may be considered to be in general agreement. The agreement between α and k° values, obtained by constant current and by solid electrode polarography on the same solutions, is very good in the case of Cu from perchlorate and Bi from chloride. The agreement is not satisfactory with the Bi reduction from perchlorate and the reason is not at once obvious as repeat experiments by both methods gave results agreeing to within a few per cent. The polarographic result may be misleading, however, as low values for α can be obtained by this method if two or more reducible forms of the metal are present in solution. The solid electrode polarograms of Sb in tartrate, Bi in tartrate and other solutions did not give smooth curves, but what appeared to be curves arising from the reversible reduction of the metal, present in one state of combination, followed by the irreversible reduction of a minor amount of the metal combined in a less easily reducible form. Such behavior, by the nature of the method used, can give misleading information by the polarographic method, but with the constant current procedure may not give results that differ greatly from those to be expected from the predominant species alone.

The unsatisfactory behavior of Ni and Zn solutions, even in alkaline media, can be attributed to water reduction (33) and the reduction of hydrogen ions, or water, prevented repetition of the published work on cadmium sulfate. Using identical conditions to those described by Lorenz (27) it was not possible to record a transition time because of the formation of hydrogen.

Acknowledgments

This work was undertaken with funds from a consolidated grant from the National Research Council of Canada. The authors would like to thank Dr. G. M. Shrum, Director of the British Columbia Research Council, for his encouragement and Dr. L. Young of these laboratories for helpful discussion.

Manuscript received Aug. 31, 1956.
Any discussion of this paper will appear in a Discussion Section to be published in the June 1958 JOURNAL.

REFERENCES

1. K. J. Vetter, *Z. Elektrochem.*, **59**, 596 (1955).
2. E. Lange and K. Nagel, *ibid.*, **42**, 50 (1936).
3. E. Mattsson, *Trans. Roy. Inst. Tech. Stockholm*, No. 96 (1955).
4. P. Delahay, "New Instrumental Methods in Electrochemistry," Interscience Publishers, New York (1954).
5. E. Lange and K. Nagel, *Z. Elektrochem.*, **53**, 21 (1949).
6. H. Gerisher, *ibid.*, **54**, 362 (1950); ibid., **54**, 366 (1950).
7. L. L. Shreir and J. W. Smith, *This Journal*, **99**, 64 (1952).
8. T. Pavlopoulos and J. D. H. Strickland, *ibid.*, **104**, 116 (1957).
9. P. J. Hillson, *Trans. Faraday Soc.*, **50**, 385 (1954).
10. D. C. Grahame, *et. al.*, Tech. Rept. 22, Office of Naval Research, Project N.R. 051-150, Amherst College, Mass.
11. J. O'M. Bockris, W. Mehl, B. E. Conway, and L. Young, *J. Chem. Phys.*, In press.
12. J. E. B. Randles, *Disc. Faraday Soc.*, **1**, 12 (1947).
13. B. Ershler, *Zhur. Fiz. Khim.*, **22**, 683 (1948).
14. H. Gerisher, *Z. physik. Chem.*, **198**, 286 (1951).
15. K. J. Vetter, *ibid.*, **199**, 285 (1952).
16. J. E. B. Randles and K. W. Sommerton, *Trans. Faraday Soc.*, **48**, 937 (1952).
17. J. E. B. Randles and K. W. Sommerton, *ibid.*, **48**, 951 (1952).
18. K. J. Vetter, *Z. physik. Chem.*, **199**, 300 (1952).
19. K. Nagel, *Z. Elektrochem.*, **57**, 908 (1953).
20. P. Delahay and T. Berzins, *J. Am., Chem. Soc.*, **75**, 2486 (1953).
21. P. Delahay and C. C. Mattax, *ibid.*, **76**, 874 (1954); *ibid.*, **76**, 5314 (1954).

22. P. Delahay and G. Mamantov, *Anal. Chem.*, **27**, 478 (1955).
23. F. Fianda and K. Nagel, *Z. Elektrochem.*, **57**, 913 (1953).
24. W. Lorenz, *ibid.*, **59**, 730 (1955).
25. H. Gerisher, *ibid.*, **59**, 604 (1955).
26. L. E. Gierst, *ibid.*, **59**, 784 (1955).
27. W. Lorenz, *ibid.*, **58**, 912 (1954).
28. T. Berzins and P. Delahay, *Z. Elektrochem.*, **59**, 792 (1955).
29. T. Berzins and P. Delahay, *J. Am. Chem. Soc.*, **77**, 6448 (1955).
30. R. C. Turner and C. A. Winkler, *This Journal*, **99**, 78 (1952).
31. C. N. Reilley, *et. al.*, *Anal. Chem.*, **27**, 483 (1955).
32. W. M. Latimer, "The Oxidation States of the Elements and their Potentials in Aqueous Solutions," 2nd ed., Prentice Hall, New York (1952).
33. P. Delahay, *J. Am. Chem. Soc.*, **74**, 3497 (1952).

Hydroelectric Power Resources of British Columbia and the Yukon

R. M. Bibbs

British Columbia Electric Company, Ltd., Vancouver, British Columbia, Canada

The hydro resources of British Columbia and the Yukon are discussed. To acquire perspective at the outset, a comparison is made between these resources and the hydro resources of the other provinces of Canada. Table I, column 2, shows the present developed horsepower in Canada, with Quebec in the lead, with nearly 8 million hp, followed by Ontario, 5.3 million hp, and British Columbia in third place with 2.2 million hp. Table I, column 1, shows the undeveloped hydro potential remaining in the various provinces, again with Quebec in the lead, with some 20½ million hp, and British Columbia in second place with 11 million hp.

These figures are taken from a publication of the Department of Northern Affairs and National Resources, March 1956, and represent the best information available to the Department at the time they were compiled.

To illustrate how the picture changes as more is learned of the resources, in place of the approximately 11 million hp figure for British Columbia, use the estimate made by the Water Rights Branch of the Provincial Government in November 1955 (Table I, column 1, figure in parentheses). On the basis of the provincial figure, the undeveloped hydro potential in British Columbia is very close to that of Quebec, standing at some 23 million hp. It is not suggested that British Columbia has more undeveloped hydro potential than Quebec, since undoubtedly extension of surveys in Quebec itself will prove up still further potential.

Table I. Available water power and developed water power in Canada at the end of 1955

	Available 24-hr power at 80% efficiency, ordinary 6 months flow hp	Installed hp
Quebec	20,445,000	7,975,657
Ontario	7,261,000	5,367,866
British Columbia	10,998,000 (22,913,000) *	2,271,460
Manitoba	5,562,000	796,900
Newfoundland	2,754,000	329,150
Alberta	1,258,000	284,010
Nova Scotia	156,000	177,018
New Brunswick	334,000	164,130
Saskatchewan	1,120,000	109,835
Yukon and N. W. T.	814,000	33,240
Prince Edward Island	3,000	1,882
Canada	50,705,000	17,511,148

Source: Dept. of Northern Affairs and National Resources, March 1956.
* Water Rights Branch, Province of British Columbia, November 1955.

Still dealing in general terms, something of the characteristic features of hydro power in British Columbia and how it may be developed are discussed briefly. This will serve as a background for reviewing the resources and will illustrate why there is such a wide discrepancy between the estimates of the potential power in the province as given by the Federal Department of Northern Affairs and National Resources and as given by the Provincial Government of British Columbia.

Geographically, British Columbia is a series of mountain ranges running north and south, with rather narrow valleys and little land for cultivation, arable land totalling not more than 6% of the area of the province; the two exceptions are the Peace River area, which is an extension of the northern prairies and is the site of oil and natural gas discoveries, and the Fraser River delta, which is the industrial and population center of the province. "A sea of mountains" is a phrase which has been used to describe the topography of British Columbia. Generally speaking, the moisture bearing Westerly winds sweeping in from the Pacific deposit their waters on the slopes and valleys of the mountain ranges as snow or seasonal rain; this gives rise to a great problem in utilizing the water since the rivers and streams are subject to sharp flooding in the spring and decline to comparatively meager flows in the winter months.

On large rivers in British Columbia, the ratio of high to low flows is of the order of 40 to 1 and as much as 2000 to 1 on smaller streams. By comparison, the St. Lawrence River at Lachine Rapids has a ratio of high to low water of only 2.2 to 1. Table II gives further detail on this.

In order to develop power economically in British Columbia, some artificial means is required to reduce flood flows and to increase the low winter flows. The usual means is the construction of dams to catch the spring flows and store the water until required the following winter.

The necessity for such storage obviously gives rise to rather high costs in hydro power engineering development, but as mentioned below, has directed engineering thinking along lines which will be

Table II. Ratio of maximum to minimum flow

River	Location	Ratio max min flow
	British Columbia Rivers	
Bridge	near Bridge River	158/1
Cheakamus	Garibaldi	146/1
Lillooett	near Pemberton	141/1
Nass	Aiyansh	135/1
Kootenay	Wardner	112/1
Campbell	near Campbell River	108/1
Columbia	Revelstoke	95/1
Kootenay	Glade	42/1
Columbia	Birchbank	35/1
Fraser	Hope	33/1
Thompson	Spence's Bridge	33/1
Chilliwack	near Veddar Crossing	31/1
Fraser	Quesnel	28/1
Tahtsa	near Ootsa Lake	27/1
Ootsa	Ootsa Lake	26/1
Stuart	near Fort St. James	19/1
Nechako	near Fort Fraser	13/1
	Eastern Rivers	
St. Maurice	Bergeron's	12.2/1
Ottawa	near Temiskaming	9.3/1
Nipigon	below Vugin Falls	8.5/1
Winnipeg	above Boundary Falls	6.2/1
St. Lawrence	Lachine Rapids	2.2/1

Source: Dominion Water & Power Bureau, 1945.

highly profitable in the future in improving the hydro potential of the province.

The estimate of hydro potential so far used by the Department of Northern Affairs and National Resources is derived from studies made over a number of years, taking into account the volume of water flowing at various times in the year and assuming that hydro plants would be installed in the various river channels where conditions appear favorable. The estimates did not include the very large developments which could be realized by diversion of several rivers into entirely different watersheds.

As well as being a land of mountains, British Columbia is a land of sharp valleys gouged by the passage of glaciers in ages past. Recent techniques for water power development have centered on making use of the differing elevations of valleys on either side of a mountain range to provide head for power generation. The various combinations of storage water, free stream flow, and diversion from one watershed to another are well illustrated by Fig. 1 which is an artist's sketch of the Bridge River power plant system of the B.C. Electric Company Ltd. At the top of the diagram is shown the La Joie reservoir which impounds 570,000 acre-feet of water. The dam contains 3¾ million ft³ of material and is 282 ft high, providing head for a 30,000 hp turbine to be installed in 1957. At present a dam diverts the water released from the La Joie reservoir into a tunnel passing through Mission Mountain to fall 1100 ft to the generating station on Seton Lake; eventually a new dam will impound water to form Lake Carpenter. The present capacity of this station is 248,000 hp and is being increased to an ultimate 600,000 hp capacity. Finally, at the outlet of Seton Creek, a 58,500 hp unit uses the water a second time as it is released from the Seton Lake generating plant and is essentially a run-of-the-river type of plant.

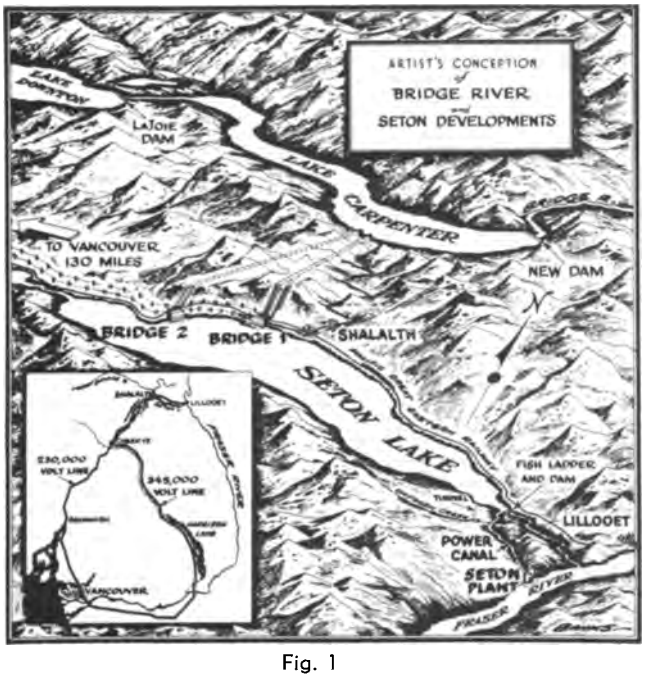

Fig. 1

This technique of diverting water from one watershed to another will permit some spectacular developments in various parts of the province, including the Yukon-Taku, estimated at 4.7 million hp and the Stikine-Liard, estimated at 6-10 million hp, both of these apparently not taken into account in the estimates of the Department of Northern Affairs and National Resources.

The present hydro development in British Columbia totals some 2¾ million hp, concentrated mainly in the south and along the coast.

The undeveloped potential of the various areas in British Columbia is widely dispersed. In general, the province is amply endowed with sites for future hydro development, with only two exceptions—Vancouver Island is rapidly reaching its full development and the Lower Fraser coastal area includes the potential of the Lower Fraser which is a major salmon migratory route. The development of the Lower Fraser presents problems which have not yet been resolved although progress is being made. If the Fraser River is excluded, one must consider this Lower Fraser coastal area as rapidly approaching its full hydro development.

There are four additional areas especially worth comment. The first is the Kitimat-Kemano project of the Aluminum Company of Canada. By damming the Nechako River near the head of the Grand Canyon, a storage reservoir is created impounding the run-off of the Eutsuk-Tetachuck-Euchu and Tahtsa-Whitesail-Ootsa-Netalkuz drainage system, permitting the flow to be reversed through a power tunnel piercing the Coast Range. The area of this watershed is some 5500 square miles.

With the water available and flows approaching 7000 ft³/sec, an estimated 1,718,000 hp can be generated, the installed capacity being 2,214,000 hp in 16 units in the complete development.

The Kenney Dam across the Grand Canyon of the Nechako River is the largest man-made structure in

Canada, some 4 million ft³ of rockfill constituting the dam and supporting on the upstream slope an impervious section of rolled earth enclosed between suitable filter layers. The crest width of the dam is 40 ft, crest length about 1500 ft, and over-all height above bedrock about 320 ft.

The powerhouse is underground. When finally completed it will have installed 16 vertical runners, 4 nozzle impulse turbines, each rated 140-150 thousand hp. Space requirements necessitate a chamber over 1000 ft long, 80 ft wide, and 135 ft high.

The second area especially worth noting is that in the far north of the province on the Yukon boundary, in which is located the complex of lakes and rivers known as the Yukon-Taku power scheme. This project has been surveyed by the Northwest Power Industries project, sponsored by Frobishers Ltd., a subsidiary of Ventures Ltd. Indications were that an early start would be made on phase 1 of the project; then early in 1956, the project was deferred to the future in favor of an earlier start on a 500,000 hp project on the Nass River. The first phase would involve a tunnel four miles above Whitehorse, on the Yukon River; in conjunction with this a one mile tunnel would drain the reservoir into Siliko Lake while a 10 mile tunnel from this lake would drain the water again into a powerhouse on Nakonake River. This development would produce some 660,000 kw. The ultimate development would harness the water power of the Yukon River's intricate system of inland waterways and could be made to generate some 3¼ million kw of electricity or better than 4½ million hp. The scheme is contemplated in conjunction with extensive exploitation of northern British Columbia's mineral resources and the establishment of a large smelting industry, just as the Kitimat project for Al production is based on the hydroelectric energy of the Nechako River.

The third area is the Lower Fraser Coastal. In the western part of southern British Columbia, in that area which is known as the Lower Mainland, the hydro potentials of a number of coastal streams totalling about 1½ milion hp have been largely developed or will be developed within the next five years, principally by the B. C. Electric Company Ltd. Outside of the Fraser River, there remains no water power of a first order in this area to be exploited. The Fraser River could yield 7½ million hp. On the Lower Fraser River some 3 million hp could be developed, in addition to the 1¼ to 1½ million which could be developed at one site alone, known as the Moran Dam site. This Moran Dam would be a dramatic development, rising 720 ft above the present water level and forming a lake 165 miles long; it would be a tremendous asset to the area lying within 150 miles of the bulk of the industries and population of the province. The Fraser River is, however, the principal migratory salmon route in the province and the annual salmon catch originating in the Fraser River and its tributaries is valued at several million dollars. Development of the Moran site might require provision for passing up to ¾ million adult salmon upstream, in a 24 hr period, as well as facilities for the safe passage of migrating fingerlings downstream. In addition to the Moran site there are four sites on the Lower Fraser where low level dams of approximately 100 ft could be built and there are a further six sites on the North Thompson River which flows into the Fraser where low level dams could be built. Again, a fish problem is involved requiring assessment of the possible detrimental effect of a series of dams placed in the path of migrating salmon and requiring solution to the problems which may be involved, although indications are a single low level dam might well be feasible.

The B. C. Electric estimates on the basis of present load growth that the Fraser River or the Columbia, or both, at least in part, will have to be developed within the next 20 years to serve the growing power needs of the area in which it provides service and which today comprises 65% of the population of the province. B. C. Electric is hopeful that techniques can be developed which will allow British Columbia to have the benefit of both fish and power and which will permit hydro development on the Fraser River while at the same time giving the needed protection to the fisheries.

In line with its convictions, on January 4, 1956, the parent company of B. C. Electric, the B. C. Power Corporation, formed a new subsidiary, Western Development and Power Ltd., with two principal functions: (*a*) to develop hydro electric power on the Fraser River to the extent that the maintenance of salmon spawning will allow and on the Columbia River where there is no fish problem, and (*b*) to study industrial opportunities in the areas which can be served with this power and to bring in new industries to use it.

Also in line with its convictions, the directors of B. C. Power Corporation donated $50,000 to the University of British Columbia to make an impartial study of the problem of fish and power on the Fraser River.

The fourth area is the Columbia River. The Columbia River is one of the great drainage basins of this continent, occupying part of British Columbia in Canada, as well as sections of Washington, Idaho, Montana, and Oregon in the United States. The river drains a total of 259,000 square miles of which 40,000 square miles are in British Columbia. However, the water originating in British Columbia accounts for 44% of the average flow of the river and ½ of the 2600 ft drop throughout its 1200 mile length occurs in British Columbia. In the United States 1000 ft of head has been developed to produce some 8 million kw. It is apparent that, although no power has yet been developed in British Columbia, a very large potential does exist.

The river rises in British Columbia in Columbia Lake, then flows northwesterly to the junction of the Rocky Mountain Trench and Selkirk Valley, at which junction, called the Big Bend, the river turns abruptly and flows almost due south. The Mica Creek Dam site is in the vicinity of the Big Bend. This is the principal power site on the Columbia and is only 350 miles from Vancouver, a distance which is within economic transmission of Vancouver at

high voltages in the order of the 345,000 v pressure which B. C. Electric has already pioneered in connection with its Bridge River and Wahleach generating stations.

In addition to the 1½ milion hp from Mica Dam, a further 1 1/3 million hp could be developed at sites at Little Dalles and Priest Rapids and a further ½ million hp on the Lower Columbia River, with sites at the outlet of Arrow Lakes or at the Murphy Creek site further downstream.

Development of the Columbia River sites in Canada hinges on a fair settlement with the United States. It is estimated that the 10 million acre-feet of water which would be stored by the Mica Dam alone would improve the capability of the existing American plants on the Columbia River by some 1.1 million kw. It is quite possible, however, that this water could be used profitably in Canada by diversion to the Fraser and North Thompson Rivers, and engineering studies on the feasibility and economics of such diversion are now nearing completion by the Department of Northern Affairs and National Resources.

In conclusion, mention should be made of the present use of Canadian hydro resources and the prospects for their use in the future. A projection to 1975 made by the Provincial Government indicates a utilization of 12½ million hp, about half the potential of the province. This forecast is certainly a conservative one and anticipates a rate of growth about one-half of that experienced in recent years. A utilization in the order of 16-18 million hp by 1975 may be as likely a figure as 12½ million hp. Nearly one-half of the present turbine capacity of the province is dedicated to the mining industry and it seems reasonable to expect that in future hydro electric development somewhat the same proportion will prevail. The vast northern power resources of the province and of the Yukon are poorly located for general commerce and manufacturing but are ideally located with respect to mineral properties.

Manuscript received Oct. 2, 1956. This paper was prepared for delivery before the Ontario-Quebec Section of the Society, May 11, 1956.

Any discussion of this paper will appear in a Discussion Section to be published in the June 1958 JOURNAL.

Trends of Electric Power Demands and the Development of Power Resources in Midwest Canada and in Ontario

Walter S. Preston

The Hydro-Electric Power Commission of Ontario, Toronto, Ontario, Canada

This paper gives a general review of the growth in power requirements in midwest Canada and in Ontario and the development of power resources to meet such requirements. Particular reference is made to the area served by The Hydro-Electric Power Commission of Ontario. It is hoped that this paper may give a broader concept of the growth of the power-producing industry and of the steps being taken to assure adequate supplies of electric power as a foundation for the basic economy of these areas.

Planning Power Supply Facilities

The growth and development of electric power has been of fascinating proportions, far greater than was contemplated in the early days when salesmen were employed to go from door to door to convince people that electric lights were superior to gas lights and that electric motors were more effective than steam engines. The main concern of the power supplier in recent years has been to keep abreast of the rapidly increasing need for power by industrial and commercial establishments and by homes and farms.

It is generally recognized that a supplier should have a reasonable reserve of power in order to provide adequate customer service. Reserve power provides for contingencies such as the removal of equipment from service for maintenance purposes, carrying of load in emergencies caused by failure of equipment, etc., and meeting of loads greater than those expected. It is necessary, therefore, that forecasts of service requirements be reviewed continually.

The extension of any organization or enterprise is always based on some estimate of future requirements. The requirements of electrical utilities are almost continuously changing and over a period of years large sums of money are expended in the construction of power plants, transmission lines, transformer stations, and other facilities. It is essential to know that such additions are required and to know when they are needed so that power is available on demand and too early use of capital is avoided. When these two items have been decided, it becomes necessary to determine where such additions should be made, their extent, and character.

Planning is not done on a national scale but rather by electrical utilities and by areas. It is obvious that power demands govern the activities of these utilities. The demand levels in the several categories of load, as well as the rates of growth, vary widely by areas and periods of time. Therefore, an accurate knowledge of past and existing load demands and their characteristics is required. The utility must have not only a good appraisal of its own service area, but a good knowledge of provincial, national, and world economic conditions in order to make a dependable forecast of future growth.

Some of the important factors that must be taken into account when planning the development of power supply facilities, are considered.

First, the electric supply business is a long-range one. There is no development on the horizon—not even atomic energy—that is relegating electric service into obsolescene. The facilities used are inher-

ently long-lived and should be planned, installed, and operated to perform their functions at minimum over-all costs for periods of their useful lives.

Next, the seasonal maxima of power requirements usually determine the amount of peak capacity (kilowatts) required, but it is also necessary to provide for the requisite energy (kilowatt-hours) capacity. Power systems based primarily on hydroelectric generation require a careful consideration of the seasonal variations in the quantity of water available. Likewise, with predominantly fuel-electric systems, careful consideration is given to the availability of types of fuel.

Next is the customer—the most important element in the electric supply picture, since the only reason for having electric systems is to supply customers. The only reason why the business has grown to present proportions is that utilities can convert energy from its raw state—coal, gas, oil, and falling water—into electricity and deliver it in more convenient form, and sell it, with few exceptions, at lower prices than could be attained by the individual customers if they were to undertake providing the service themselves.

Planning, therefore, usually begins with customers. Individually they have distributing systems on their properties and electric operated equipment, the sum total of which measured in kilowatts of absorbing capacity is greater than the productive capacity of the serving utility. The customer, too, is a long-range planner and is either installing, providing for, or changing over to the most modern and useful devices for his business, convenience, or pleasure. To foresee what the future may hold in the greater use of electricity by all classes of customer is the crux in forecasting the demands for power and the physical plant required between the customer and raw energy sources.

To jump from the customer and his requirements to raw energy sources may seem a little out of order, but a finished product cannot be produced without raw material. Alberta, Saskatchewan, Manitoba, and Ontario have in combination large quantities of raw energy resources in the form of coal, oil, gas, water, and the newcomer to the field—uranium. Unfortunately, these resources are not in the backyards of every major center of population. Transportation of large blocks of energy is necessary by some means, in either the raw state or by electric transmission.

Between the customers and raw energy sources comes the power system with its distribution and transmission lines, substations, and power plants. Co-ordinated planning from one end to the other, not the planning of each component separately, is necessary if optimum over-all investments, fixed charges, operating expenses, and service adequacy are to be secured. The task is to search for incremental long-range economies all along the line.

Trends of Power Demands and Development of Power Resources

In June 1955 the Dominion Bureau of Statistics released the first report in a new annual series of statistics relating to the electric power industry in Canada. It contained current and projected data of capability and load for the years 1950-1958 inclusive. The second report in this series, which is now in the process of preparation, will be extended to include the year 1959. The results contained in these reports are compiled from returns filed by 82 producers of electricity, including all of the major privately and publicly operated electrical utilities, and private industries producing substantial quantities of electric power, part of which is usually for sale to the public. The surveys are organized and carried out in cooperation with the Canadian Electrical Association, committees of which are set up to assist in the planning, development, and conduct of these and future surveys.

The results of the second survey are not available at this time. They would be most interesting because

Table I. Gross capability and total demand as of March 1955

		Thousands of kw		
		1950	1954	1958
	Alberta			
1.	Net generating capability			
	(*a*) Hydro	83	202	220
	(*b*) Thermal	108	193	393
2.	Firm purchases from outside the province	—	4	—
3.	Gross capability (1+2)	191	399	613
4.	Total demand	179	310	512
5.	Difference or indicated reserve (3-4)	12	89	101
6.	Indicated reserve expressed as a percentage of total demand	6.7	28.7	19.7
	Saskatchewan			
1.	Net generating capability			
	(*a*) Hydro	85	85	85
	(*b*) Thermal	125	239	422
2.	Firm purchases from outside the province	—	—	—
3.	Gross capability (1+2)	210	324	507
4.	Total demand	175	267	369
5.	Difference or indicated reserve (3-4)	35	57	138
6.	Indicated reserve expressed as a percentage of total demand	20.0	21.3	37.4
	Manitoba			
1.	Net generating capability			
	(*a*) Hydro	421	526	561
	(*b*) Thermal	11	51	136
2.	Firm purchases from outside the province	68	80	83
3.	Gross capability (1+2)	500	657	780
4.	Total demand	432	551	679
5.	Difference or indicated reserve (3-4)	68	106	101
6.	Indicated reserve expressed as a percentage of total demand	15.7	19.2	14.9
	Ontario			
1.	Net generating capability			
	(*a*) Hydro	2349	3463	4062
	(*b*) Thermal	127	524	735
2.	Firm purchases from outside the province	720	707	666
3.	Gross capability (1+2)	3217	4719	5504
4.	Total demand	3287	4246	5278
5.	Difference or indicated reserve (3-4)	—70	473	226
6.	Indicated reserve expressed as a percentage of total demand	—2.1	11.1	4.3

the majority of producers in Alberta, Saskatchewan, Manitoba, and Ontario have raised their sights considerably during the past year in forecasting future power requirements. The results shown in Table I do, however, indicate the manner in which resources are developed to meet load requirements.

Hydro Resources

In the March 1956 release on Water Power Resources of Canada by the Water Resources Branch of the Department of Northern Affairs and National Resources, it was found that:

In Alberta, the larger hydroelectric developments, from which a large part of the southern portion of the province is served, are located on the Bow River and its tributaries. The greater part of water resources is located in the northern half of the province, rather remote from present centers of population.

In Saskatchewan, water power developments are confined principally to mining uses in the northern areas in which water power resources are abundant. The transmission network serving more settled areas is supplied exclusively by fuel-electric plants. Large reserves of coal, oil, and natural gas are located in both Saskatchewan and Alberta; these fuels provide the more economic sources of power in many parts of both provinces, particularly in southern Saskatchewan.

Of the Prairie Provinces, Manitoba has the largest water power resources, there being great potential power on the Saskatchewan, Nelson, and Churchill Rivers. The larger present developments are located on the Winnipeg River and serve Winnipeg, adjacent municipalities, and the transmission network of the Manitoba Power Commission.

Ontario has large water power resources, being exceeded in this respect only by Quebec and British Columbia. It has developed about 57% of its potential water power and ranks second in power generation among the provinces.

With the completion of the St. Lawrence Power project in the International Rapids Section of the St. Lawrence River, the last major hydroelectric site in the southern half of the province of Ontario will have been developed.

In Ontario, about 90% of the total primary energy supplied by central electric stations for consumption in the province is provided by The Hydro-Electric Power Commission of Ontario.

Hydro-Electric Power Commission of Ontario

The Commission, now generally known as Ontario Hydro, was created by the Ontario Legislature following recommendations by advisory commissions appointed in response to public demand that the water power resources of the Province should be conserved and developed for the benefit of all the people of Ontario. In May 1956 it completed its fiftieth year.

The undertaking initially proposed to purchase a block of power from the Ontario Power Company, a private corporation which had promoted and developed the largest single plant on the Canadian side of the Niagara River at Niagara Falls during the period 1902-05, and to transmit this block of power to the municipalities which had signed contracts to take power at cost.

In 1909 the task of constructing a transmission system was begun and by the end of 1910 power was being supplied to several municipalities. At about the same time, a short transmission line and a substation was built to serve a community at the head of Lake Superior, with power purchased from a producer in the vicinity. Today, that part of the Province south of the east-west line drawn through North Bay forms one integrated power network called the Southern Ontario System, while the system west of a north-south line through Sault Ste. Marie is called the Northwestern Division and serves northwestern Ontario.

During the 1930's, Ontario Hydro undertook to operate in trust for the Ontario Government a group of isolated systems serving mainly the mining and pulp and paper industries in northern Ontario. One of these systems was integrated in the Northwestern Division while those remaining were integrated to form the Northeastern Division which since 1950 is interconnected with the Southern Ontario System.

There is no electrical connection at present between the Commission's properties in northwestern and northeastern Ontario.

The tremendous increase in power requirements, together with the fairly recent developments in the field of large-scale power generation and high voltage transmission has advanced considerably the potential value of large capacity regional networks.

Table II. Future primary power requirements, all systems combined, 1956-1980 inclusive

The Hydro-Electric Power Commission of Ontario

Kilowatts

December	(A) Higher estimate	(B) Lower estimate
	Application of 1950-1955 equivalent rate of growth (8.21% per annum)	By Commission's Advisory Committee on Load and Capacity (equivalent rate of growth—5.50% per annum)
1956	4,492,000	4,407,000
1957	4,861,000	4,692,000
1958	5,260,000	4,954,000
1959	5,691,000	5,166,000
1960	6,159,000	5,425,000
	Application to above estimates of 1922-55 equivalent long-term rate of growth (6.56%) per annum)	
1961	6,563,000	5,781,000
1962	6,993,000	6,160,000
1963	7,452,000	6,564,000
1964	7,941,000	6,995,000
1965	8,462,000	7,454,000
1966	9,017,000	7,943,000
1967	9,608,000	8,464,000
1968	10,239,000	9,019,000
1969	10,910,000	9,611,000
1970	11,626,000	10,241,000
1971	12,389,000	10,913,000
1972	13,201,000	11,629,000
1973	14,067,000	12,392,000
1974	14,990,000	13,204,000
1975	15,974,000	14,071,000
1976	17,021,000	14,994,000
1977	18,138,000	15,977,000
1978	19,328,000	17,025,000
1979	20,596,000	18,142,000
1980	21,947,000	19,332,000

Ontario Hydro's long-range studies envisage the interconnection of power resources in northwestern section of the province with those of the northeastern section when the power and economic demands require this final link. This interconnection will tie Ontario Hydro's generating plants into one integrated unit, extending from Quebec on the east to Manitoba on the west, a distance of about 1000 miles. At present the Provinces of Ontario and Quebec and the States of New York and Michigan are interconnected, so it is possible that in the future a vast network of electric power facilities could extend from within the Province of Manitoba in the west into Quebec in the east and from James Bay southward into New York and Michigan.

Customers in the two pioneer systems required in total about 4000 kw in 1910. In 1955 the more than 1-½ million ultimate customers served required more than 4.2 million kw. The requirements were met from 65 hydroelectric and two major fuel-electric generating stations, supplemented by power purchased from other producers.

But what of the future? The Royal Commission, under the chairmanship of Mr. Walter Gordon, which is looking into Canada's economic prospects, has focussed public attention on the future. The many submissions to the Commission from provincial, industrial, and various other bodies have all suggested striking industrial and social developments across the country. Briefs presented by the Ontario Government and by Ontario Hydro's Chairman, Dr. R. L. Hearn, have suggested that, if certain conditions prevail within the province, Ontario Hydro may be faced with loads of the order of 20 million kw by 1980 as compared with just over 4.2 million in 1955.

The two studies which take us to the year 1980 were purely statistical and the figures in Table II are all derived from a projection of past trends. Over the period from 1922 to 1955 the rate of growth for the three operating systems combined has been equivalent to 6.56% per annum and this rate has been applied to two alternative estimates of load in 1960 to give the two projections marked (*A*) and (*B*).

The two estimates for 1960 are 5.4 million or 6.2 million kw. The lower figure has been estimated by the Commission's Advisory Committee on Load and Capacity, a committee charged with the responsibility of preparing five-year forecasts of loads, while the high figure is the load which will have to be met if requirements increase as rapidly as in the period 1950-1955, a rate equivalent to 8.2% per annum. By applying the long-term rate of growth of 6.56% per annum to these 1960 figures, the following kilowatt estimates for the years ahead are reached: 1965, 7.5 or 8.5 million; 1970, 10.2 or 11.6 million; 1975, 14.1 or 16.0 million; and 1980, 19.3 or 21.9 million kw.

The resources required to meet both estimates of load have, of course, been considered, but this discussion is limited to the resources for the higher esti-

Table III. Dependable peak capacity, all systems combined, 1956-1980 inclusive
The Hydro-Electric Power Commission of Ontario

Capacity required to meet higher estimate of future primary power requirements (designated *A*) and provide a margin of reserve of about 7%

Kilowatts

December	Commission's generating stations			Power purchased	Total resources
	Hydroelectric	Fuel-electric			
		Conventional	Nuclear		
1956	3,258,000	637,000	—	645,000	4,540,000
1957	3,683,000	637,000	—	645,000	4,965,000
1958	4,209,000	826,000	18,000	623,000	5,676,000
1959	4,481,000	1,026,000	18,000	608,000	6,133,000
1960	4,622,000	1,426,000	18,000	608,000	6,674,000
1961	4,717,000	1,726,000	18,000	601,000	7,062,000
1962	4,848,000	2,026,000	18,000	601,000	7,493,000
1963	5,040,000	2,326,000	18,000	601,000	7,985,000
1964	5,052,000	3,039,000	18,000	601,000	8,710,000
1965	5,110,000	3,039,000	418,000	601,000	9,168,000
1966	5,217,000	3,039,000	931,000	601,000	9,788,000
1967	5,250,000	3,339,000	1,131,000	601,000	10,321,000
1968	5,270,000	3,339,000	1,844,000	601,000	11,054,000
1969	5,290,000	3,639,000	2,244,000	601,000	11,774,000
1970	5,333,000	4,239,000	2,644,000	269,000	12,485,000
1971	5,353,000	4,952,000	2,844,000	187,000	13,336,000
1972	5,412,000	5,252,000	3,444,000	187,000	14,295,000
1973	5,442,000	5,852,000	3,757,000	187,000	15,238,000
1974	5,485,000	6,452,000	3,957,000	187,000	16,081,000
1975	5,485,000	7,052,000	4,470,000	187,000	17,194,000
1976	5,485,000	7,765,000	5,070,000	0	18,320,000
1977	5,485,000	8,365,000	5,783,000	0	19,633,000
1978	5,485,000	8,965,000	6,183,000	0	20,633,000
1979	5,485,000	9,565,000	7,096,000	0	22,146,000
1980	5,485,000	10,578,000	7,496,000	0	23,559,000

NOTE: Nuclear resources are based on the assumption that by 1965 nuclear fuel-electric stations will be economical for base load operation.

mates so as to avoid confusion. In 1955 power resources available to the Commission had a dependable peak capacity of more than 4.5 million kw. Table III shows that the capacity required to meet requirements and provide a margin of reserve of about 7% is about 6.7 million kw in 1960; 9.2 million in 1965; 12.5 million in 1970; 17.2 million in 1975; and 23.6 million kw in 1980.

Table III also indicates that between 1956 and 1974 there remain some 2.2 million kw in hydro sites which can be developed economically. Of this amount, more than 1.2 million kw has been authorized for construction and will be in service before 1960. Of the nearly forty economic sites remaining, only six exceed 50,000 kw each. This indicates the main limitation of hydro power in Ontario—there isn't too much left.

One of the more interesting aspects of the study of required capacity is the fact that within a comparatively short period of time Ontario Hydro will start to change over from a predominantly hydroelectric utility to one in which fuel-electric power plays an important part. The rapid developments that are taking place in nuclear studies suggest that after 1965 a large part of the required capacity will be provided by nuclear resources. Nuclear energy will be used to produce steam which in turn will generate electricity in a conventional steam-electric station. Although the 20,000 kw demonstration plant now being constructed near the Des Joachims station on the Ottawa River may not be competitive with conventional fuel stations, it is expected that its operation will provide valuable data for the design, construction, and operation of larger installations. In estimating resources after 1965, it has been assumed that nuclear stations will be economical for base load operation.

Manuscript received October 2, 1956. This paper was prepared for delivery before the Ontario-Quebec Section of the Society, May 11, 1956.

Any discussion of this paper will appear in a Discussion Section to be published in the June 1958 JOURNAL.

Power from Other Energy Sources

C. E. Baltzer

Fuels and Power Section, Fuels Division, Mines Branch, Department of Mines and Technical Surveys, Ottawa, Ontario, Canada

Brief comment on thermally produced power obtained from the burning of natural mineral fuels, coal, oil, and gas, is given. Currently, the energy of these fuels is the only accepted alternative to hydro energy for producing commercial electricity in quantity, and, by and large, the bulk of electric power produced in the world, with a few nations excepted, is produced by the combustion of these fuels in steam plants of more or less conventional design.

Power from Nuclear Energy

It is now recognized that nuclear energy released through the fission process is an impending source of high-level controlled heat. As such it becomes a fourth fuel which, if proven economic to produce, safe to handle, and reliable in operation, not only has strategic advantages, but is a much larger resource on a world basis than the combined reserves of our conventional fuels.

Admittedly, if heat is generated, power can be produced in the same way as from conventional fuels, but many obstacles have yet to be overcome before competitive atomic power is a reality. Its commercial development, other than in the prototype and proving stages, is not likely in Canada for a decade or more.

The elementary concept being developed concedes that the only part of the electrical process affected is the means for producing steam; conventional boiler steam is replaced by steam produced by an atomic reactor. The turbine and generator, with ancillaries on both the prime mover and electrical sides, remain relatively the same. However, initially, there are two fundamental differences worthy of note. First, the atomic reactor costs more than the boiler it replaces. Second, atomic steam will be of relatively low pressure and temperature in comparison with the best steam cycles serving conventional steam-electric plants. Consequently, the efficiency of the conversion will be lower and the corresponding heat rate higher. Badly needed metallurgical improvement in components to withstand higher heat, pressure, and rotative forces would benefit both the atomic and conventional steam cycles. In fact, the eventual competitive success of the atomic power cycles may well depend on such improvements being made.

It would appear that the main benefit to accrue from the fission process rests on the possibility of obtaining extremely low fuel cost, variously estimated at from less than one to several mills/kwhr of power produced. Even though it be granted that the fuel cost is extremely low, the margin of cost between it and conventional fuel must be wide enough to warrant any increased capital expenditure. Low fuel cost, be it one mill or two, is offset in part, if not in whole, if greater fixed charges are necessitated by the complications and dangers of the fission process.

Viewed from the economic standpoint, atomic power can be regarded at present only as a possible supplement to power resources in very high-cost, energy-deficient areas. Also, Canada could not seemingly derive any particular advantage over

other countries since, presumably, the cost of power from nuclear fission will be approximately the same regardless of plant location.

On the economic side, the following press statements attributed to power authorities are of interest:

(*A*) Mr. J. A. Fuller, President, Shawinigan Water and Power Company, *Financial Post*, March 21/55: "I think it can be said that atomic power will supplement but not supplant our conventional power sources, at least so long as our supply of fossil fuels (coal, oil, and gas) holds out. . .

"It will never displace presently developed hydro power nor in fact future hydro power which can be sold near the site of development or transmitted over feasible distances."

(*B*) Sir John Cockcroft, Director, Atomic Energy Research Establishment, Harwell, England, *Ottawa Citizen, C. P.*, April 2/56: "Sir John says he sees little likelihood of any widespread use of atomic power in countries like Canada where abundant hydro-electric resources exist. 'Hydro-electric resources can provide power much more cheaply than nuclear energy'. . ."

Thermal Electric Power Outlook

In Canada, when power comes to mind, one quite naturally thinks of hydroelectric power derived from the force of falling water. This is so because, with the single exception of Norway, the Canadian per capita production of electricity from water power leads the world. Hydro generation furnishes about 95% of the electricity produced in Canada. It also accounts for as much as 10% of Canada's present energy consumption for all purposes, a figure that is approached by few nations. Only three countries, United States, Russia, and United Kingdom, each with from 3 to 14 times Canada's population, produce more electric power on a volume basis, and this mostly from coal-fired steam plants.

In consequence, the average Canadian has become very "hydro-minded," and has certain fixed ideas, if not real prejudices in favor of the relative importance of hydro vs. thermal electric power. He is firmly convinced that hydro power is cheap and all thermal power must be dear. In his opinion steam-electric power is outmoded, and positively antiquated if it must be produced from coal. This average Canadian does not fully realize that his electrical requirements are rising faster than the ability of hydro to provide power on economic grounds. Neither does he realize that the total known hydro potential available for his use is very small, less than 1/10 of 1% in relation to Canada's potentially available reserves in coal, oil, and natural gas. Nor does he fully appreciate the insatiable world demand for the products of the vast Canadian stores of forest and mineral wealth, a demand created by two world wars, and the threat of a third, a demand which can be satisfied only by gigantic expenditures of energy fast outpacing any past rate of use. This gives rise to speculation, in no small degree, in regard to the relative importance of hydraulic energy and thermal energy in a future economy. While both are important, the latter for obvious reasons becomes increasingly so as load requirements develop.

Table I. Canada's available energy reserves from conventional sources. Estimated Dec. 31, 1955, in millions of net tons of equivalent coal (24 million Btu/ton)

Source	Type	Amount	% of Total
Coal	Expendable	98,816	98.3
Natural gas	Expendable	875	0.9
Crude oil*	Expendable	726	0.7
Water power	Renewable	58	0.1
	Total	100,475	100.0

* Exclusive of potential in tar sands and oil shales.

Canada's Energy Reserves

Canada's increasing population, its desire for ever-higher living standards, the changes in outlook and technology that have taken place during and since World War II are mainly responsible for the present great concern with energy reserves. Since 1950, that concern has been expressed widely in print. There have been several book-length surveys, literally hundreds of technical papers, and an untold number of popular articles and published discourses on every phase of energy assessment. Taken with the popular and vociferous outcry for atomic power, and the benefits it in particular is expected to bring, one must almost conclude that the world, and every country in it, is shortly to be faced with an energy crisis. Can this possibly be true for Canada?

First look at an estimate of Canada's reserves, as given in Table I.

It should be noted that in this and subsequent tables the estimates for coal and oil are calculated from somewhat different bases. Oil reserves are computed from recovery estimates of a high degree of reliability. Coal reserves, although subject to a recovery factor, still remain mostly reserves computed from geological evidence rather than from mining evidence.

Recoverable reserves of conventional energy at the end of 1955 were estimated to be of about the following order: 99 billion tons of mineable coal; 3 billion barrels of recoverable crude oil; 21 trillion ft^3 of natural gas; and 66 million hp of hydraulic power, truly a remarkable conglomeration of figures.

To assess these figures on a comparable basis, a common unit that is readily understood must be adopted. If stated in ordinary units of hp-hr, kwhr, or Btu's, the figures become so enormous as to be almost beyond understanding. Therefore, the author presents the reserves in terms of one million tons of equivalent coal with a heat content of 12,000 Btu/lb; first, because it is easier to visualize what a ton of coal looks like than a single Btu, kwhr, or hp-hr; second, because this large unit aids comparison and simplifies tabulation.

As an indication of the size of this unit, one million tons of such coal, used at the average 1954 operating efficiency of American steam-electric generating plants, would produce two billion kwhr of electricity. As few as 35 of these units would produce Canada's total 1954 electrical output.

Table II. Geographic distribution of Canada's energy reserves. Estimated as of Dec. 31, 1955, in millions of net tons of equivalent coal (24 million Btu/ton)

Region	Amount	% of Total	Percentage from Coal	Oil	Gas	Hydro
Alberta	49,201	49.0	97.3	1.3	1.4	*
Saskatchewan	24,246	24.1	99.5	0.3	0.2	*
British Columbia	18,988	18.9	99.2	*	0.8	*
Yukon & N. W. T.	4,521	4.5	99.8	0.2	—	*
Nova Scotia	3,115	3.1	100.0	—	—	*
Ontario	159	0.2	94.5	0.3	*	5.2
Manitoba	117	0.1	86.5	8.1	*	5.5
New Brunswick	102	0.1	99.6	*	*	0.4
Quebec	23	*	—	—	—	100.0
Newfoundland	3	*	—	—	—	100.0
Prince Edward Island	*	*	—	—	—	100.0
Canada	100,475	100.0	98.3	0.9	0.7	0.1

* Negligible amount of total.

Here it will be noted that, of the energy sources shown, coal is by far the most abundant. While water power is shown to be only a small fraction of the total, its importance in Canada's economy is much greater than this comparison suggests, because of its availability and its renewable characteristic in the otherwise energy-deficient area of the "St. Lawrence Lowlands." This relatively small area supports as much as 60% of Canada's total population and the bulk of the secondary industries, and requires, with minor exception, import of all its fuel energy either from distant points in Canada or the United States. On the other hand, proven oil and gas reserves in Canada, although not large in comparison with coal, are increasing at a phenomenal rate. One authority has recently estimated that in 1980 proven oil reserves will be about 5 times greater than they are today.

Table II shows the geographic distribution of reserves. Here it will be noted that over 96% of these reserves are located west of the Manitoba-Saskatchewan border, and of the remaining 4% at least 3 are in Nova Scotia. The table shows also that coal is preponderantly the greatest reserve in

Table III. 1954 Production of energy in Canada. In millions of net tons of equivalent coal (24 million Btu/ton)

Region	Amount	% of Total	Percentage from Coal	Oil	Gas	Hydro
Alberta	30.7	58.4	15.8	69.2	14.6	0.4
Nova Scotia	5.9	11.2	98.7	—	—	1.3
Quebec	4.9	9.3	—	—	—	100.0
Saskatchewan	3.7	7.0	58.0	35.9	3.9	2.2
Ontario	3.4	6.5	—	3.0	12.4	84.6
British Columbia	2.0	3.8	63.4	—	—	36.6
Manitoba	1.0	1.9	—	54.9	—	45.1
New Brunswick	0.9	1.7	88.2	0.3	0.9	10.6
Yukon & N. W. T.	0.1	0.2	13.7	85.2	1.1	*
Newfoundland	*	*	—	—	—	100.0
Prince Edward Island	*	*	—	—	—	100.0
Canada	52.6†	100.0	28.4	44.2	9.6	17.8

* Negligible amount of total.
† Approximately 1900 years supply at this rate and with present reserves.

Table IV. 1954 Total energy made available for use in Canada. In millions of net tons of equivalent coal (24 million Btu/ton)

Source	Amount	% of Total
Crude oil	50	50.5
Coal	34	34.3
Water power	10	10.1
Natural gas	5	5.1
Total	99*	100.0

* Approximately 1000 years supply at 1954 rate of use.

8 of the 11 specified regions, with hydraulic power the only energy source in the remaining three.

Table III shows the 1954 production from Canada's reserves. Here it is seen that as much as 71% of the 1954 production of primary energy was produced in Western Canada, with the province of Alberta contributing over 58% of the total. Nova Scotia was second with about 11% of the total. In only 4 of the 11 specified regions did coal lead. Oil led in 3 and hydraulic power in the remaining 4. It should be noted that, at the rate of production shown, Canada's present reserves are sufficient for a minimum of 1900 years.

Table IV gives an approximation of the energy consumed in 1954.

Remembering, as shown in Table III, that Canada's production is 52.6 units of energy and its consumption, as shown in Table IV, is approximately 99 units, it is apparent that Canada is dependent on import for about one-half of its energy requirements, mostly in the form of coal and oil. It is also apparent that oil leads coal by a considerable margin, a reversal of position which has developed very recently owing in no small measure to the phenomenal advance in production from indigenous oil reserves. It is further apparent that present Canadian energy reserves are sufficient to support the current rate of use for a minimum of 1000 years and, in the case of a fourfold increase, as has been forecast by some, for something in excess of 250 years. Consequently, there is no danger of an energy shortage from conventional sources for a long time. Some of the energy reserve may be badly placed, but at the least, it is available for use if, as, and when required. Moreover, there is every assurance that more energy, particularly in the form of oil and gas, will be found to supplement present reserves, and extend their life even beyond the times here forecast.

Development of Thermal-Electric Power

Fig. 1 and 2 and Table V give a view of the history and of the progress attained in using heat-activated motive force in the production of electricity.

Fig. 1 illustrates successive time stages in the method of converting fuel energy to power, and the corresponding practical efficiencies obtained from various types of prime mover. At present, the steam turbine outranks all other heat engines in size and performance for powering central generating plants. In the United States, station heat rates of well under 10,000 Btu/net kwhr have been reached, with efficiencies of 37-38%. New units under construc-

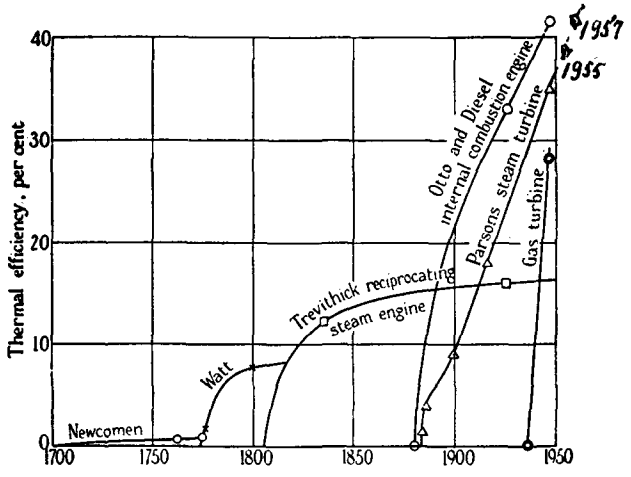

Fig. 1. Development of fuel energized prime movers and corresponding plant efficiencies, 1700-1950. From "Revolution in Fuel Technology," by M. W. Thring, Journal of the Institute of Fuel, Vol. XXVII, No. 163, Aug. 1954.

tion, employing advanced steam cycles with supercritical pressures as high as 5000 psi, temperatures to 1200°F, and double-stage reheat, are expected to raise efficiency for condensing plants by as much as 3-4%. Turbo-generator size has reached 250,000-kw capacity; 325,000-kw capacity machines are being built, and 400,000- to 500,000-kw sets are regarded as possible.

Fig. 2 illustrates the progressive improvement in the efficient use of fuel. One pound of coal, or its equivalent in oil or natural gas, now develops as much electricity as did 3 lb in 1920, and as did 10 lb when the Central Electric Station Industry came into being in the last quarter of the 19th Century.

Table V shows the present average conditions applying to steam-electric generating plants operating in Canada, and comparable conditions for the United States and the United Kingdom. These data speak for themselves and require little comment. However, it should be noted that the averages given in respect to performance and economy are far below the best attainable from the most advanced plants. Canada suffers in the comparison, largely because of the amount of capacity held in reserve, the preponderance of small generating units, and over-all

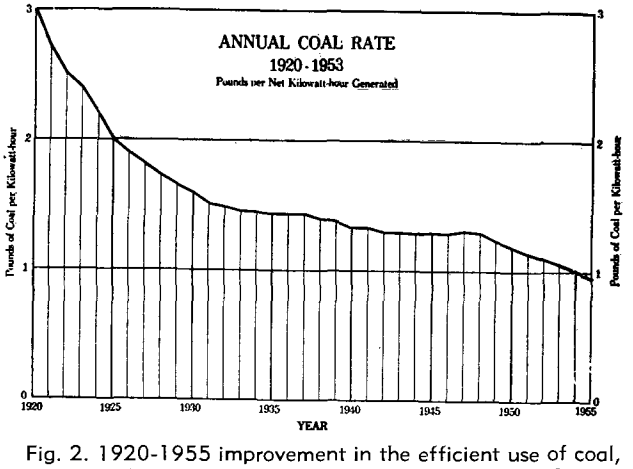

Fig. 2. 1920-1955 improvement in the efficient use of coal, or its equivalent in oil or natural gas, in American Steam-Electric Utility Plants. Adapted from 34th Annual Report 1954, U. S. Federal Power Commission.

Table V. 1954 Comparative data for steam-electric generating plant. Operated by The Central Electric Station Industry

	Canada	United States	B.E.A.* United Kingdom
Production, 10^6 kwhr	3,144	360,973	61,658
% (of thermal generation	93	99	100
(of total generation	5	77	99
Capacity, 10^3 kw	1,551	74,773	—
% (of thermal capacity	92	97	—
(of total capacity	12	75	—
Weighted Average	†		
Heat in coal used, Btu/lb	10,660	12,180	10,792
Heat rate, Btu/net kwhr	15,555	12,180	14,580
Coal rate, lb/net kwhr	1.459	1.000	1.352
Thermal efficiency, %	21.9	28.0	23.4
Price of coal/net ton, $	7.08	6.25	7.88
Cost of fuel/million Btu, ¢	33.2	25.7	36.6
Fuel cost/net kwhr, ¢	0.443	0.300	0.494

* British Electricity Authority, Sixth Annual Report, year ending March 31, 1954.

† Canadian averages are based on 24 of the largest steam-electric stations. In 1954, these 24 operations accounted for over 90% of the capacity and production from the 168 thermal plants controlled by the industry.

operation at very low load factor, all of which militate against the most efficient performance.

Table VI gives a projection of the amounts and types of electrical generating capacity that will be needed between 1951 and 1981. It has been said that "people would rather be misinformed about the future than correctly informed about the past." If this be true, a forecast of the power trend would seem to be in order at this point. This projection, the counterpart of several all showing similarity in regard to over-all amounts, has been selected because of its bold attempt to delineate the type as well as the amount of operating capacity at five-year intervals, a quarter of a century into the future. Here it is indicated that hydroelectric power will remain Canada's principal source of electrical energy for at least the next 25 years. At that time, it will possibly represent as much as 2/3 of the total. In the meantime, thermal capacity will have become increasingly important and will have risen from a quite minor position in 1951 to about 30% of the total by 1981.

Table VII, in another way, attempts to show the past and future growth trend of thermal vs. hydro-generating capacity. In the 10-yr period prior to the end of the war, thermal power had a growth rate and total capacity less than hydro power. In the

Table VI. Projected electrical capacity in Canada 1951-1981*. In millions of kilowatts

Year	Total	Hydro	Thermal		
			Total	Coal, oil, gas	Nuclear fuel
1951	11.1	10.0	1.1	1.1	nil
1956	16.0	14.0	2.0	2.0	nil
1961	22.5	20.0	2.5	2.4-2.3	0.1-0.2
1966	28.0	24.5	3.9	3.7-2.9	0.2-1.0
1971	34.0	27.4	6.6	6.0-4.9	0.6-1.7
1976	41.0	30.2	10.8	8.8-7.5	2.0-3.3
1981	48.0	33.0	15.0	11.0-8.0	4.0-7.0

* Source—Unclassified A.E.C.L. Paper No. 210 presented at Geneva, Switzerland, Aug. 1955 by Messrs. Davis and Lewis.

Table VII. Growth trend of thermal vs. hydro electric capacity. Expressed in annual (compound) percentage and by ratio

Interval	Period	Thermal	Hydro	Ratio thermal to hydro
10 years	1935-45	2%	3%	1:15
10 years	1945-55	14%	6%	1:7
Projected 30 years*	1951-81	9%	4%	1:2

* Calculated from data taken from unclassified A.E.C.L. paper No. 210 presented at Geneva, Switzerland, Aug. 1955 by Messrs. Davis and Lewis.

10-yr period after the war, the growth rate of thermal power was more than double that of hydro, and quantitatively had halved the former capacity ratio of 1:15. Projection in the 30-yr period 1951-1981 indicates that the accelerated growth rate for thermal capacity will continue at about the same differential, and that, quantitatively, the ratio between thermal and hydro capacity will narrow to a ratio of as little as 1:2.

Conclusion

From present indications it is evident that most progress in the use of thermally generated power is developing in three main regions, viz., the Maritimes, southern Ontario, and the Prairie Provinces. In these regions it is anticipated that the power demands within the next 25 years will far surpass the supply of economically available hydraulic energy. Therefore, from now on, it can be reasonably expected that thermal power will be called on to play an increasingly important role in the Canadian power picture.

Because of the location of existing fuel supplies, development will probably follow some fairly definable pattern. In Western Canada, where coal, oil, and gas reserves are most abundant, these fuels will likely continue to give the cheapest and most dependable thermal power. In fuel-deficient Central Canada, imported American coal would seem to be in the best position to provide the cheapest thermal power until nuclear fuel becomes a cheaper source. In Eastern Canada, where highest fuel costs apply at present, indigenous coal and imported oil have become increasingly competitive, and either one or the other, depending on circumstances, will produce the cheapest thermal power until nuclear fuel gains the hoped-for advantage at some time as yet unknown. Meanwhile, Canada is indeed fortunate in being endowed with such abundant fuel resources with which to meet the indicated growing demand for thermally generated electric power.

Manuscript received Oct. 2, 1956. This paper was prepared for delivery before the Ontario-Quebec Section of the Society, May 11, 1956.

Any discussion of this paper will appear in a Discussion Section to be published in the June 1958 JOURNAL.

Report of the Chlor-Alkali Committee of the Industrial Electrolytic Division for the Year 1956

Jeff C. Cole
Diamond Alkali Company, Cleveland, Ohio

and

R. B. MacMullin
R. B. MacMullin Associates, Niagara Falls, New York

For over a decade each succeeding year has marked a new production record for Cl and caustic soda. The year 1956 was no exception with Cl hitting an all-time high of 3.78 million tons, an increase of 11% over 1955. Caustic soda production likewise established a record in 1956 reaching 4.21 million tons, an 8% increase over 1955. Lime-soda caustic represented about 11% of the total, with the remainder being electrolytic caustic.

The chlor-alkali industry has grown so large that its power requirement in 1956 is estimated to have been over 12 billion kwhr. This is about 2% of the total electrical energy output of the nation.

Caustic potash is being looked upon with greater interest by the chlor-alkali producers. The production in 1956 was 92,000 tons on an 88-92% KOH basis. During the year Diamond Alkali started producing caustic potash at Muscle Shoals, as did Pennsalt Chemicals at Calvert City.

Sodium chlorate production in 1956 was 55,000 tons, up 11.8% over 1955.

The Cl growth rate averaged about 12% annually for many years. Although there are indications of a lower growth rate in the production figures for the last 5 or 6 years, the forecasters predict an impressive 10% increase in 1957. This new demand will be adequately met with new plants and expansion programs now under construction.

Caustic soda has experienced a steady growth rate of about 7% annually over many years, and this rate is expected to continue for at least 5-10 years. In 1955 Dow started producing soda ash from electrolytic caustic at its Freeport, Texas, plant. Other producers are known to be preparing themselves for this means of solving their excess caustic problem.

Markets and End-Use Patterns

There were no outstanding changes in the markets and end-use patterns for Cl and caustic during 1956. Chlorine requirements for $TiCl_4$ increased because the growing Ti metal industry doubled production in 1956. The pulp and paper industry required more of both Cl and caustic. Other Cl-consuming industries showing growth during 1956 were plastics, chlorinated solvents, agricultural chemicals, and textiles. Chlorine also continues to be a growing workhorse in its role as an intermediate in the production of chemicals.

Process changes do occur in which a Cl-consuming process may be modified or substituted for, and thus eliminate the need for Cl. For example, C_2H_4O is now made by direct oxidation in preference to the Cl-consuming chlorohydrin process, and some phenol is made by the cumene process instead of the long-practiced chlorobenzene route. No process changes of this type, however, occurred during 1956.

Caustic soda is enjoying its growth in (*a*) metal ore digestion, (*b*) development of cold caustic pulping in the paper industry, (*c*) petroleum, (*d*) textiles, and (*e*) chemical manufacture. The Al industry is expanding and the increased alumina production requires more alkali. A trend in this industry is the increasing use of electrolytic caustic instead of soda ash to supply alkali requirements.

The year 1956 found an increasing number of small chlor-alkali plants being built in foreign countries. Our caustic exports may decrease as these foreign plants are put into operation to supply local demands. Consequently, a decrease in caustic exports will make it more difficult for some companies to dispose of excess caustic.

Table I.[1]

Cl		Caustic soda	
	%		%
Pulp and paper	15.0	Chemicals	26.9
Chlorinated solvents	13.0	Rayon and film	17.8
Automotive fluids	11.0	Pulp and paper	6.6
Plastics and resins	11.0	Exports	5.9
Insecticides, herbicides	7.5	Petroleum refining	5.5
Refrigerants, propellants	5.0	Lye and cleansers	4.1
Water and sewage	3.5	Textiles	3.5
Others	34.0	Soap	2.1
		Others	27.6
	100.0		100.0

[1] Source, *Chemical Week*, May 26, 1956.

Table I shows the approximate end-use patterns for Cl and caustic soda.[1]

Announcements of New Plants and Expansions—Current to May 1957

Kaiser Aluminum & Chemical Corp.'s 36,000-ton/yr Cl—40,000-ton/yr caustic plant now under construction at Gramercy, La., will go into production this year. This marks the first entry of an U. S. aluminum company into the chlor-alkali field. The caustic will be used in the company's adjoining alumina plant. Diaphragm cells of the Hooker S3B type will be installed.

Dow Chemical is another chlor-alkali producer favoring Louisiana with a new facility. The company is building a plant at Plaquemine to produce Cl and caustic and a number of organic chemicals.

Wyandotte Chemical Corp. also selected Louisiana for a Cl and caustic plant to be built at Geismar. Contracts for design and construction of the diaphragm cell plant have already been awarded. This new 300-ton/day chlorine and 350-ton/day caustic plant increases Wyandotte's capacity by over 50% and represents their first move away from Michigan and into the South.

Jefferson Chemical Co., a large consumer of Cl, is in the planning stages of a new diaphragm cell plant to be located in Port Neches, Texas.

The Solvay Process Division of Allied Chemical & Dye Co. has built a new Hg cell plant at Brunswick, Ga. Before the plant was completed, the company announced plans to double the initially planned capacity. The additional capacity is expected to be in operation by this fall, making a total daily output of about 200 tons of Cl and 250 tons of caustic.

Weyerhaeuser Timber Co.'s new Cl plant at Longview, Wash., started operation December 1, 1956. Initial capacity is 80 tons/day, with provision for doubling in the near future. This is the largest captive Cl plant in the paper industry. It employs the new De Nora 14TGL cell.

Expansions of existing chlor-alkali plants are also very much in the news. Columbia Southern is expanding at Lake Charles, La. Frontier Chemical Division of Union Chemical & Materials Corp. announced expansion plans at both Denver City, Texas, and Wichita, Kan., to make a total production of about 225 tons/day of Cl. At Calvert City, Ky., Pennsalt Chemicals Corp. announced an expansion scheduled to go into operation during 1957 to increase Cl production from 50 to 150 tons/day.

Olin-Mathieson's subsidiary is expanding its McIntosh, Ala., plant to 250 tons/day of Cl; completion was scheduled for the early part of this year.

At Deer Park, Texas, Diamond Alkali is building a Hg cell plant to operate in combination with an existing diaphragm cell plant. The added facilities are scheduled to be in operation during the first half of 1958. The addition will increase daily production at Deer Park by approximately 40%, or 200 tons of Cl and 220 tons of caustic.

Westvaco Chemical Division of Food Machinery & Chemical Co. is in the middle of a complete overhaul of their 460-ton Cl plant at South Charleston, W. Va. The first circuit of Hooker S3B cells went on the line in March 1957.

Du Pont recently announced a multimillion dollar expansion at its Memphis, Tenn., plant to produce Cl and Na metal. The expansion will represent an increase of better than 50% in Du Pont's Na capacity.

Dow Chemical Co. of Canada, Ltd., announced an increase in facilities at Sarnia. Early in 1956 it was announced that Shawinigan Chemicals, Ltd., would build a new chlorine-caustic plant at Shawinigan Falls. In British Columbia, Hooker Chemicals of Vancouver, Ltd., has a large chlorine-caustic plant under construction, scheduled for completion in June 1957. This is the first plant of this type in Western Canada, and employs the S3B cell now rated at 30,000 amp instead of 25,000 amp.

The Oldbury Division of the Hooker Electrochemical Co. is expanding an existing $NaClO_3$ plant at Columbus, Miss., to bring total capacity to 22,000 tons/yr.

The American Potash & Chemical Corp. is coming East, having announced a new $NaClO_3$ plant to be constructed on a 586-acre site on the Tombigbee River about 8 miles south of Aberdeen, Miss. The plant, scheduled for completion in mid-1958, will have an initial capacity of 15,000 ton/yr.

Technical and Outstanding Commercial Developments

A pioneering step to convert a-c to d-c power for a chlor-alkali plant is being taken by Diamond Alkali in their multimillion dollar expansion program at Deer Park, Texas. The company plans to install the world's largest Ge rectifier system instead of the normally used Hg arc or mechanical rectifiers.

A new De Nora development is a high capacity Hg cell design on which the company has been working for several years. The cell, referred to as the SGL type, has a rated capacity of 120,000 amp, but is reported to be capable of operating at a still higher amperage. The first major application of this cell in this country will be Diamond Alkali's installation of 52 cells at Deer Park, Texas.

A patent has been granted to the Hooker Electrochemical Co. for the recovery of dilute Cl gas. The process is based on the preferential absorption of Cl into water at high pressure. The company offers to make the process available to the industry on a license basis.

Manuscript received May 22, 1957. This paper was prepared for delivery at the Washington Meeting, May 12 to 16, 1957.

Any discussion of this paper will appear in a Discussion Section to be published in the June 1958 JOURNAL.

An Investigation of the Discharge Characteristics of Groups Ib-Vb Oxides in an Alkaline Electrolyte

R. Glicksman and C. K. Morehouse

RCA Laboratories, Radio Corporation of America, Princeton, New Jersey

ABSTRACT

Experimental half-cell discharge data are given for a number of Groups Ib-Vb oxides in strongly alkaline NaOH solution, along with comparisons between these data and their theoretical potentials. The effect of cathode solubility on the half-cell discharge potential of a few sparingly soluble silver salts is also discussed.

Many of the desirable features of a battery cathode material, such as a high reversible electrode potential and coulombic capacity, stability, and compatability with other cell components, are found among the metallic oxides. In practice, cathodes operate at potentials lower than their reversible values, due to polarization effects encountered under load conditions, while their electrode efficiencies also vary with current drain. Thus, evaluation of these materials is best made under conditions of discharge. In this paper experimental half-cell discharge data for a number of Group Ib-Vb oxides in an alkaline NaOH electrolyte are given, along with comparisons between these data and thermodynamically calculated values of the reversible electrode potentials.

Experimental

Discharge data on the various oxides were obtained using a technique described by the authors (1). This technique involves discharging at constant current in a large volume of electrolyte a 0.5-g sample of the cathode material mixed with 10% Shawinigan acetylene black. The change in the operating cathode potential with time is measured with a L&N Type K potentiometer using a saturated calomel reference electrode. The discharge data were corrected for the *IR* drop associated with the apparatus and electrolyte by means of an oscillographic technique (2).

The half-cell potentials are all referred to the normal hydrogen scale, and represent the average of two or three runs, the reproducibility being ± 0.01-0.02 v when measured with a saturated calomel electrode (S.C.E.). The variation of the S.C.E. potential with temperature over the course of the measurements was less than 0.01 v, usually lower than 0.005 v, and no correction was made for this factor, i.e., all measured results were calculated using a value of 0.246 v for the S.C.E. potential.

In this study a zinc anode was employed with an alkaline electrolyte of 30% NaOH solution by weight which was saturated with ZnO, the solution being 10.7*M* prior to the addition of ZnO. The addition of ZnO decreases the molality of the solution in accordance with the following equation

$$ZnO + 2NaOH = Na_2ZnO_2 + H_2O \qquad (I)$$

the purpose of the ZnO being to reduce the corrosion of the Zn anode in the strongly alkaline electrolyte. During the course of the discharge, hydroxide ions are formed, but as the solution is strongly alkaline initially, the change in hydroxide ion activity of the solution is negligible.

Potential measurements of the HgO electrode in this electrolyte vs. a S.C.E. give a value of +0.043 v for the HgO half-cell referred to the normal hydrogen scale. The deviation from the standard potential of the HgO electrode ($E^\circ - E = +0.055$ v) is due to the greater hydroxide ion activity of the electrolyte, as well as to the existence of a liquid junction potential at the alkaline-saturated KCl interface. As these factors are constant for all measurements of the half-cell potentials, one can add +0.055 v to the experimentally determined discharge potentials of the various oxides in order to compare these values with their standard electrode potentials.

Group Ib Oxides

Presented in Table I are the standard potentials of the group Ib-Vb oxides in basic solution, the potentials being computed from the free energy data given by Latimer (3).

These potentials are referred to the normal hydrogen electrode, but in alkaline solutions this couple has the form

$$H_2 + 2OH^- = 2H_2O + 2e^- \qquad E^\circ = 0.828 \qquad (II)$$

so the E° values of the half reactions in alkaline solution will be designated as E°_B to indicate that this basic potential of the hydrogen couple must be used to obtain the completed reaction potential against hydrogen.

Early studies of the anodic oxidation of Ag in alkaline solution by Luther and Pokorny (4) and Zimmerman (5) show Ag to be oxidized quantitatively first to Ag_2O and then to AgO; when the AgO was made cathodic, the reverse reactions took place. This type of stepwise reduction would be expected from the standard potentials presented in Table I.

Typical discharge curves of commercial Zn-AgO cells (6) indicate a two-step reduction only at low

Table I. Standard potentials of the group Ib-Vb oxides in basic solution

Group		E^0_B
Ib	AgO-Ag	+0.458
	Ag_2O-Ag	+0.570
	AgO-Ag_2O	+0.345
	CuO-Cu	−0.258
	CuO-Cu_2O	−0.159
	Cu_2O-Cu	−0.357
IIb	HgO-Hg	+0.098
IIIb	$Tl(OH)_3$-Tl	−0.148
	$Tl(OH)_3$-TlOH	−0.050
	TlOH-Tl	−0.343
	Tl_2O-Tl	−0.304
	$In(OH)_3$-In	−1.00
	$H_2GaO_3^-$-Ga	−1.22
IVb	PbO_2-Pb	−0.166
	PbO_2-PbO	+0.247
	PbO-Pb	−0.580
	$HPbO_2^-$-Pb	−0.540
	$Sn(OH)_6^=$-$HSnO_2^-$	−0.93
	SnO-Sn	−0.93
	$HSnO_2^-$-Sn	−0.91
	$HGeO_3^-$-Ge	−1.0
Vb	Bi_2O_3-Bi	−0.457
	SbO_2^--Sb	−0.658
	AsO_2^--As	−0.675

current drains; at the higher current drains AgO discharge takes place in one step at a potential corresponding to Ag_2O. The latter finding is in agreement with the data shown in Fig. 1, where it is seen that both AgO [1] and Ag_2O [1] are discharged in one step, in 30% NaOH electrolyte, at a rate of 0.005 amp/g, at a potential of +0.25 v on the normal hydrogen scale, a value 0.04 v lower than the thermodynamically calculated value of the reversible potential of the Ag_2O electrode. The observed capacities of the AgO and Ag_2O cathodes to a −0.40 v cut off are 21.5 and 13.5 amp-min/g, respectively, which correspond to efficiencies of 83 and 97%, indicative of a 2 and 1 electron change per gram atom of silver, for the respective oxides.

According to the thermodynamic data, electrochemical reduction of CuO in basic solution also should take place in two steps.

$$2CuO + H_2O + 2e^- = Cu_2O + 2OH^- \quad (III)$$

$$Cu_2O + H_2O + 2e^- = 2Cu + 2OH^- \quad (IV)$$

Evidence to support this view is found in the work of Johnson (7) who studied the charge and discharge characteristics of CuO plates in alkaline solution. Johnson noted a two-step reduction of the CuO plates in 4.2*N* KOH solution, the first step, which was thought to be the reduction of CuO to Cu_2O, consisted of approximately 20% of the total discharge time, while the remaining 80% was attributed to the reduction of Cu_2O.

On the other hand, discharge curves of present day alkaline CuO cells show no breaks that would

[1] Chemically prepared by Merck & Company, Inc., Rahway, New Jersey.

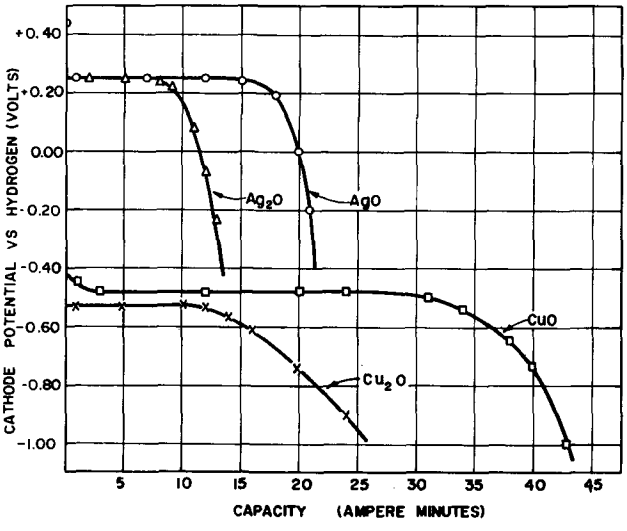

Fig. 1. Cathode potential of various group Ib oxides discharged in 30% NaOH −70% H_2O, sat'd with ZnO, electrolyte at a rate of 0.005 amp/g.

indicate a change in the reaction mechanisms. Schumacher and Heise (8) attribute this to the fact that CuO can react with Cu in accordance with the following equation:

$$CuO + Cu \rightarrow Cu_2O \quad (V)$$

and after the initial stages of discharge, Eq. (IV) is assumed to be the principal cathodic reaction.

The discharge data presented in Fig. 1 show CuO [2] to be reduced in one step at a potential of −0.48, while the discharge potential of Cu_2O [2] is −0.53 v. The fact that CuO operates at a higher potential level than Cu_2O indicates the reaction is not simply one of reduction of Cu_2O, but rather represents a more complex reduction.

Allmand and Ellingham (9) suggest that initially CuO is reduced to Cu_2O, but polarization lowers the potential to a point at which Cu_2O is reduced to Cu, this latter reaction being the chief process, although the further reduction of CuO to Cu_2O occurs simultaneously. This being the case, one would expect the discharge potential of CuO to be close to that of Cu_2O, but slightly higher; in addition, CuO should give about twice the ampere minute per gram capacity of Cu_2O on comparable tests. This is in agreement with the data presented here.

Group IIb and IIIb Oxides

Mercuric oxide, which has found use as a reference electrode in strongly alkaline solutions and for the measurement of hydroxyl ion concentration (10), constitutes the cathode of the alkaline HgO dry cell (11, 12).

Because of the instability of Hg_2O in aqueous solutions, HgO is reduced directly to Hg (3). This type of mechanism is evident from the flat voltage discharge curves of commercial HgO/KOH/Zn dry cells, as well as from the half-cell discharge data presented in Fig. 2. Under the latter conditions of discharge, the HgO cathode operated at 80% efficiency (assuming −0.40 v end point), and at a potential of +0.03 v which approximates the reversi-

[2] Fisher Scientific Company certified grades.

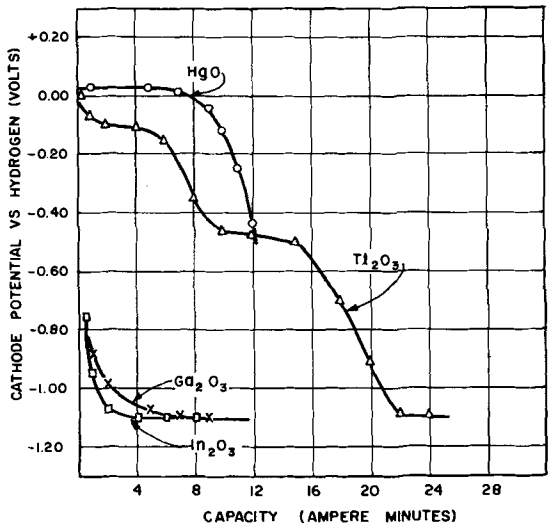

Fig. 2. Cathode potential of various group IIb and IIIb oxides discharged in 30% NaOH —70% H_2O, sat'd with ZnO, electrolyte at a rate of 0.005 amp/g.

ble electrode potential value given in Table I, after a correction of 0.055 v is made for the increased hydroxide ion activity of the electrolyte and the liquid junction potential.

Also shown in Table I and Fig. 2 are standard potentials and discharge curves for a few of the Group IIIb oxides. The reduction of Tl_2O_3 in alkaline solution takes place in two well-defined steps as expected from the chemical properties of this compound and its lower oxide, while Ga_2O_3 and In_2O_3 appear to have discharge potentials of —1.10 v or lower. However the —1.10 value is the potential characteristic of the discharge of hydrogen on the carbon electrode in this alkaline solution. This value was obtained by placing a 0.5-g sample of Shawinigan acetylene black in the cathode chamber in the absence of any other cathode material and discharging the experimental cell in the usual manner at a 0.0025 amp rate, the measured cathode potential of —1.10 v being due to the discharge of hydrogen on the carbon black.

The discharge data for Tl_2O_3 show an efficiency of 67% for the first step of reduction, and 94% for the complete reduction to the metal, assuming end points of —0.45 and —0.90 v, respectively.

Thallic oxide, because of its relatively high oxidation potential, has been considered as a cathode material for a storage cell, and in a primary fuel cell, but neither of these applications has met with any appreciable success (13).

Group IVb Oxides

It follows from the oxidation-reduction potentials for Pb that this metal is a fair reducing agent in acid solutions and a strong reducing agent in alkaline solutions, and that the dioxide is an extremely powerful oxidizing agent in acid solutions, but much weaker in alkaline solutions.

A Pb anode in an alkali hydroxide solution dissolves at first in the plumbous state, to form plumbite, but, when the solution in the vicinity of the anode becomes saturated, the dioxide is deposited. It has also been found that the oxidation of plumbite at a Pt anode yields lead dioxide (14).

Grube (15), who used both these methods to prepare alkali plumbates, made systematic measurements of the oxidation potentials of the processes. He found, at a temperature of 18°C, in 8.4*N* KOH, that the potential on the normal hydrogen scale of Pb against K_2PbO_2 was —0.613 v, while that of the plumbite-plumbate couple was +0.208. This latter potential appears to correspond to an E°_B of about +0.28 v (16), i.e., for a hydroxide ion activity of unity.

According to Glasstone (17), the reversible potential of the PbO-PbO_2 couple cannot be measured directly in alkaline solution because of the formation of the intermediate oxide, Pb_3O_4 and probably also Pb_2O_3. He estimates an E°_B value of +0.27 v on the basis of his experimental results, which is approximately the same as the E°_B value obtained from Grube's measurements. Reversible potential measurements of the Pb-PbO couple in alkaline solution have been made by Smith and Woods (18) who report a value of $E^\circ_B = -0.5785$ v for this system.

In Table I and Fig. 3 are presented the standard potentials and discharge curves for both the monoxide and dioxide of Pb, along with those of the other group IVb oxides. It is seen that PbO_2 is reduced in two steps in accordance with theory, and at potentials close to the thermodynamically calculated values of the reversible electrode potentials. The discharge potential of PbO corresponds almost exactly to the second step of the PbO_2 discharge, leaving no doubt as to the nature of the discharge.

The cathodic discharge curves of SnO, SnO_2, and GeO_2 in alkaline solution are also presented in Fig. 3, and it is seen that the SnO_2 and GeO_2 cathodes operate at too low a potential to be measured under the experimental conditions. The SnO cathode, however, operates at a potential close to its reversible value after corrections are made for the hydroxide ion activity and liquid junction potential, and is reduced with a 63% efficiency. This low cathode efficiency is probably due to the high solu-

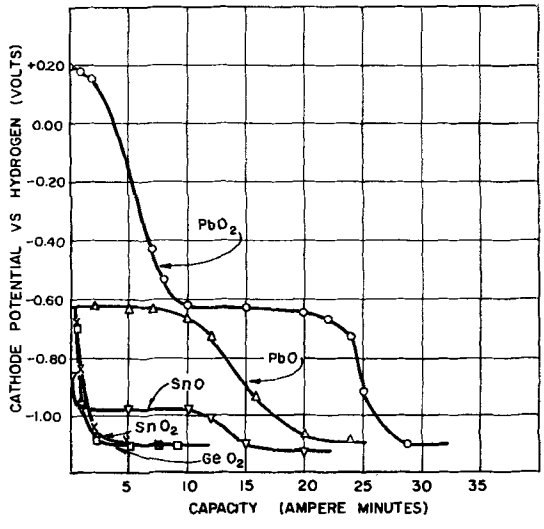

Fig. 3. Cathode potential of various group IVb oxides discharged in 30% NaOH —70% H_2O, sat'd with ZnO, electrolyte at a rate of 0.005 amp/g.

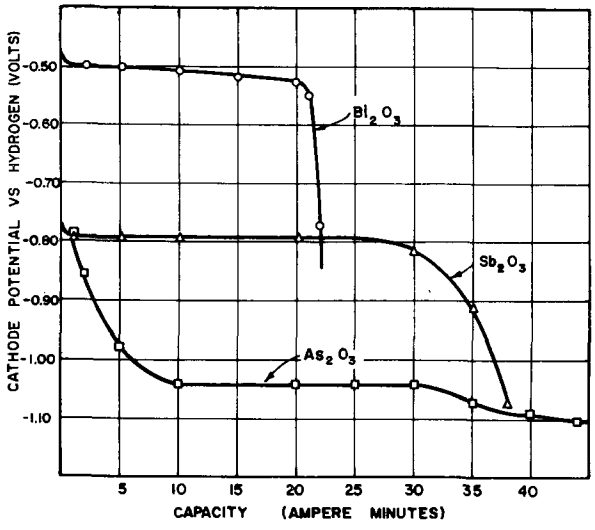

Fig. 4. Cathode potential of various group Vb oxides discharged in 30% NaOH —70% H_2O, sat'd with ZnO, electrolyte at a rate of 0.005 amp/g.

bility of the SnO with subsequent local discharge at the anode.

Group Vb Oxides

Presented in Fig. 4 are discharge curves of the +3 oxides of As, Sb, and Bi, the more metallic of the group Vb elements, when discharged in a 30% NaOH solution saturated with ZnO, at a current drain of 0.005 amp/g. It is seen from these curves and the standard potentials listed in Table I that the oxidizing power of the +3 oxides increases with increasing atomic weight of the metal.

Both the Bi_2O_3 and Sb_2O_3 cathodes display flat voltage discharge curves, corresponding to a 3-electron reduction step. This is in agreement with the work of Grube and Schweigardt (19) who found that both Bi and Sb dissolve anodically in alkaline solution in the form of tervalent ions, with the formation of alkali bismuthites and antimonites. The Bi_2O_3 electrode operates at a value close to the thermodynamically calculated value of its reversible potential, while the Sb_2O_3 cathode is seen to show a 0.07-v deviation from its reversible electrode potential. The reduction efficiencies of these materials are approximately 100%, giving the best efficiencies of all the cathodes studied.

Although the reversible electrode potential of As_2O_3 is close to that of Sb_2O_3, this electrode polarizes slowly to a potential of —1.04 v after 10 amp-min of discharge at the 0.005 amp/g rate, and remains at that potential for the remainder of its discharge.

Effect of Cathode Solubility on Discharge Potential

In the present study, only the oxides of the group I-Vb elements have been considered as cathode materials. However, compounds containing anions, such as the halides and sulfides, can also function as cathode materials. The oxides, because of their high theoretical capacity, stability, and availability are preferred as cathodes, and are used extensively in both dry and storage cells. However, there are some applications in which compounds containing other anions are used; for example in standard cells Hg_2SO_4 and Hg_2Cl_2 are used, while in reserve-type batteries, AgCl finds use as a cathode material.

The reduction of Hg_2Cl_2 is typical of these materials and is represented by the following equation

$$Hg_2Cl_2 + 2e^- \rightleftarrows 2Hg + 2Cl^- \qquad (VI)$$

Electrodes in which reactions such as the above occur and which involve a metal, M, a sparingly soluble salt of the metal, MX, and a solution of a soluble salt containing X, are termed "electrodes of the second kind". The potential of such sparingly soluble salts depends on the reversible electrode potential of the metal as well as its own solubility product (20).

Latimer (21) has listed E° values and solubility products for a number of Ag compounds; the data for a few of these materials are presented in Table II along with their coulombic capacities. It is evident that the capacity of the Ag salts increases with increasing anion valency and decreasing anion weight. It is also seen that the oxidizing potential of the Ag salt increases with increasing solubility of the salt.

In Fig. 5 discharge data are presented for these Ag salts, discharged at a rate of 0.030 amp/g in the 30% NaOH solution. It is seen that the AgI and Ag_2S cathodes operate at values close to their reversible electrode potentials, as does the Ag_2O electrode when its reversible potential is corrected for the activity of the hydroxide ion. The cathodes are reduced with an efficiency of 85-95% under these conditions of discharge. The reversible electrode potential and solubility data for Ag_2Se were not available, but from the discharge curves one would predict a lower solubility for this compound than for Ag_2S.

The use of this method in making approximate measurements of salt solubilities should apply to any couple containing a precipitate or a complex ion which is only a variation of the simple couple involving the free ions; then its potential may be

Table II. Half-cell reactions, capacity, and solubility products of various Ag Compounds

Cathode	Half-cell reaction	E°	Solubility product	Cathode capacity (amp-min/g)
Ag^+	$Ag^+ + e^- = Ag$	+0.7991	—	—
Ag_2O	$Ag_2O + H_2O + 2e^- = 2Ag + 2OH^-$	+0.344	2.0×10^{-8}	13.9
AgI	$AgI + e^- = Ag + I^-$	—0.151	8.5×10^{-17}	6.8
Ag_2S	$Ag_2S + 2e^- = 2Ag + S^=$	—0.69	5.5×10^{-51}	13.0
Ag_2Se	$Ag_2Se + 2e^- = 2Ag + Se^=$	—	—	10.9

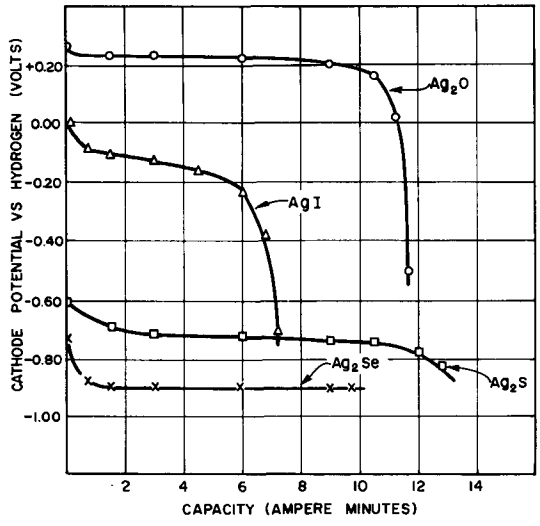

Fig. 5. Cathode potential of various Ag salts discharged in 30% NaOH —70% H_2O, sat'd with ZnO, electrolyte at a rate of 0.030 amp/g.

regarded as a corrected value based on the standard potential of the simple reaction.

Summary

1. The reduction of AgO and CuO in concentrated NaOH electrolyte takes place in one step (in disagreement with predictions based on available thermodynamic data). When cells with these cathodes undergo reduction, the AgO is reduced to Ag at the same potential as that found for the discharge of Ag_2O to Ag under similar conditions, while the reduction of CuO to Cu takes place at a potential 0.05 v higher than the corresponding reduction of Cu_2O to Cu.

2. Among the Group IIb and IIIb oxides, HgO is reduced directly to Hg in concentrated NaOH electrolyte, while Tl_2O_3 shows two well-defined reduction steps corresponding to the +3 and +1 oxidation states of Tl.

3. PbO_2 also shows a two-step reduction at potentials corresponding to the theoretical values of the PbO_2-PbO, and PbO-Pb couples, while SnO_2 and GeO_2 polarize under load to low potential levels.

4. Among the Group Vb oxides, Bi_2O_3 and Sb_2O_3 display flat voltage discharge curves corresponding to a 3-electron reduction step, the former operating close to its reversible potential level, while the latter shows a small deviation from its theoretical potential.

5. The electrode potential, under current drain, of a few sparingly soluble Ag salts has been found to be dependent on its solubility product, the oxidizing power of the Ag salt increasing with increasing solubility of the salt.

Manuscript received Nov. 1, 1956. This paper was prepared for delivery before the Cleveland Meeting, Sept. 30-Oct. 4, 1956.

Any discussion of this paper will appear in a Discussion Section to be published in the June 1958 JOURNAL.

REFERENCES

1. C. K. Morehouse and R. Glicksman, *This Journal*, **103**, 94 (1956).
2. R. Glicksman and C. K. Morehouse, *ibid.*, **102**, 273 (1955).
3. W. M. Latimer, "Oxidation Potentials," 2nd ed., Prentice Hall, Inc., New York (1952).
4. R. Luther and F. Pokorny, *Z. Anorg. Chem.*, **57**, 290 (1908).
5. J. G. Zimmerman, *Trans. Electrochem. Soc.*, **68**, 231 (1935).
6. G. W. Vinal, "Storage Batteries," 4th ed., p. 101, John Wiley & Sons, Inc., New York (1955).
7. W. M. Johnson, *Trans. Amer. Electrochem. Soc.*, **1**, 187 (1902).
8. E. A. Schumacher and G. W. Heise, *This Journal*, **99**, 191C (1952).
9. A. J. Allmand and H. J. T. Ellingham, "The Principles of Applied Electrochemistry," 2nd ed., p. 212, Edward Arnold & Co., London (1924).
10. D. A. MacInnes, "The Principles of Electrochemistry," p. 253, Rheinhold Publishing Corp., New York (1939).
11. S. Ruben, *Trans. Electrochem. Soc.*, **92**, 183 (1947).
12. M. Friedman and C. E. McCauley, *ibid.*, **92**, 195 (1947).
13. S. Glasstone and A. Hickling, "Electrolytic Oxidation and Reduction," p. 105, D. Van Nostrand Co., Inc., New York (1936).
14. Ref. (13), p. 111.
15. G. Grube, *Z. Elektrochem.*, **28**, 273 (1922).
16. Ref. (3), p. 156.
17. S. Glasstone, *J. Chem. Soc.*, **121**, 1469 (1922).
18. D. F. Smith and H. K. Woods, *J. Am. Chem. Soc.*, **45**, 2632 (1923).
19. G. Grube and F. Schweigardt, *Z. Elektrochem.*, **29**, 257 (1923).
20. Ref. (10), p. 255.
21. Ref. (3), p. 191.

Potential-pH Diagram of the Antimony-Water System

Its Applications to Properties of the Metal, Its Compounds, Its Corrosion, and Antimony Electrodes

Arthur L. Pitman

Naval Research Laboratory, Washington, D. C.

Marcel Pourbaix

University of Brussels, Brussels, Belgium, Belgian Center for Corrosion Study (CEBELCOR)

and

Nina de Zoubov

Belgian Center for Corrosion Study (CEBELCOR), Brussels, Belgium

ABSTRACT

Using methods and conventions described previously together with the available thermodynamic and electrochemical data, equations have been formulated and represented as a potential-pH equilibrium diagram of the antimony-water system for 25°C. Other diagrams are presented for the domains of solubility, predominance of ions, and for corrosion. The reason for the observed resistance of antimony coatings to hydrochloric and hydrofluoric acids is made clear. Applications are made to the antimony electrodes. The free energies of formation of the antimonate, $Sb(OH)_6^-$, and the SbO_2^+ ion have been calculated and are given.

The usefulness of potential-pH diagrams in research has been shown previously by one of the authors (1), by Delahay and Van Rysselberghe (2), and others too numerous to mention. If a reaction is thermodynamically impossible under given conditions, one can dismiss that reaction from further consideration, directing his attention instead to other closely related reactions. Consider the case of the resistance of Sb coatings on Fe to nonoxidizing acids such as HCl or HF (3). The electrode potential[1] of an isolated Sb-coated electrode in such acids and in an oxygen-free atmosphere will lie a little above the potential of the hydrogen electrode. This is to be assumed at present, but will be demonstrated later. It will be shown by thermodynamical data and methods that a perfect coating of Sb cannot be attacked under the stipulated conditions. Therefore if attack occurs, it must be due to an oxidizing agent such as air which elevates the potential into a zone where attack occurs, or from pinholes in the coating of Sb.

A further field of use for diagrams such as are in this paper is that of simplifying and explaining the study of metals and their compounds in aqueous solutions (1).

The previously unknown free energies of formation for antimonate, $Sb(OH)_6^-$, and SbO_2^+ ions have been computed and are used in the preparation of the potential-pH diagram.

The free energies of formation of compounds and ions given in Table I are those recommended by Latimer (7) unless otherwise mentioned.

There are two known polymorphs of antimony trioxide. The cubic form, $Sb_2O_3(c)$, existing in nature as the mineral senarmontite, and the orthorhombic form, existing as the mineral valentinite (8). As Table I shows, the free energy of formation of the cubic form is the more negative of the two at 25°C so that it is the inherently more stable of the two at this temperature. For this reason, it is the form which Latimer (7) tabulates, taking −149,000 cal as the value of free energy of formation from Table 21-2 of the U. S. Bureau of Standards' Tables

Table I. Free energies of formation used in calculating equilibrium equations

Solvent and dissolved substances	ΔFf° (cal)	Solid substances	ΔFf° (cal)
H_2O	−56,690	Sb_2O_3 (cubic)	−149,000
H^+	0	Sb_2O_3 (ortho) *	−147,000
OH^-	−37,595	Sb_2O_4	−165,900
SbO^+	−42,000	Sb_2O_5	−200,500
SbO_2^-	−82,500		
$HSbO_2$(aq)	−97,500	Gaseous substances	ΔFf° (cal)
$Sb(OH)_4^-$*	−195,880		
SbO_2^+*	−65,500	SbH_3	35,300
$Sb(OH)_6^-$*	−293,000		

* $\Delta Ff^\circ_{Sb(OH)_4^-} = \Delta Ff^\circ_{SbO_2^-} + 2\Delta Ff^\circ_{H_2O} = -195{,}880$ cal. The free energies of the other marked ions are derived by methods which are described later.

[1] The term "electrode potential" is the same as that recommended at the meeting of the International Union of Pure and Applied Chemistry at Stockholm, 1953, (4, 5); at the equilibrium it is equal to the emf of half-cells where electrons appear as reactants on the left side of the equations. When the algebraic sum of free energies in the reaction is positive, the sign of the electrode potential E° is positive. Thus, the manner of writing the equations and the signs for electrode potential are the same as in reference (6). The electrode potential is thus positive for oxidizing systems (F_2, F^-) and negative for reducing systems (Zn, Zn^{++}).

(9). The basis for the National Bureau of Standards' value was the work of Roberts and Fenwick (10) who found $\Delta Ff^\circ_{Sb_2O_3(c)}$ equal to $-149{,}690 \pm 200$ cal. Roberts and Fenwick determined the potentials of the cells: Pt,H_2 solution, Sb_2O_3(c) Sb and Pt,H_2 solution, Sb_2O_3(o) Sb, both with air excluded. From these measurements they computed the free energy for Sb_2O_3(ortho) → Sb_2O_3(cubic) as $\Delta F^\circ = -1{,}800$ cal. From the free energy of formation of Sb_2O_3(c) in Table I, the free energy of formation of Sb_2O_3(o) becomes −147,000 cal in round numbers.

A review of the researches cited herein shows that only in two of them have single allotropic forms of Sb_2O_3 been used (8, 10). The results of these two researches have been used to compute $\Delta Ff^\circ_{HSbO_2(aq)} = -96{,}510$ cal from the use of Sb_2O_3(c) and −96,440 cal from the use of Sb_2O_3(o). Latimer's value (7) of −97,500 cal was derived from Schulze's solubility data at 15°C on mixed crystal forms combined with $\Delta Ff^\circ Sb_2O_3(c) = -149{,}000$ cal.

The value of $\Delta Ff^\circ_{Sb_2O_3(s)}$ equals −148,640 cal was determined by Schuhmann (11). His method of precipitating and purifying Sb_2O_3 was followed by Roberts and Fenwick (10) who found that it resulted in a mixture which was chiefly in the orthorhombic form. Tourky and Mousa (12) used practically the same method of preparation. Bloom (8) could precipitate the orthorhombic form with HCl, or the cubic form with $HClO_4$, both at $pH = 2.2$. Thus most experiments behind free energy values for Sb use a mixture of Sb_2O_3 crystals possibly high in the orthorhombic form. Furthermore, the free energy of formation of this Sb_2O_3(s) mixture as found by Schuhmann was 400 cal lower than −149,000 cal which is the value selected for the (c) form by the Bureau of Standards and by Latimer (7) which the authors have placed in Table I for use when Sb_2O_3(s) participates in a reaction.

Furthermore the solubility at measured pH values is of use in determining the form of ion or molecule in which the solute exists. The most useful relation to present (1) is used in Fig. 1 for Sb_2O_3, namely, the log solubility plotted against the pH. Such curves normally consist of straight-line branches. The slope of each branch is directly related to the formulas for the principal reaction occurring upon solution in the corresponding range of pH. In the pH range from 0 to 1+ taken from Schuhmann (11), the slope is −1. This corresponds to the presence of the SbO^+ ion, as previously established (8). Two circles at pH about 2 represent Bloom's (8) results for valentinite and senarmontite at approximately

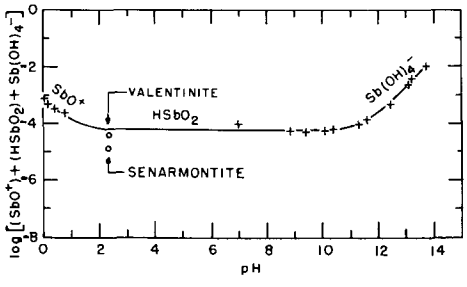

Fig. 1. Solubility of antimony trioxide (5, 8, 9)

25°C. Tourky and Mousa's (12) data at 35°C for the range of pH from 9 to 10.4 are essentially constant and nearly equal to Bloom's (8) data for senarmontite. Tourky and Mousa found some evidence for the Sb^{+++} ion just below $pH = 9.5$. The slope of log solubility with pH is zero from below $pH = 2$ to 10.4 indicating a nonionic solute. This solute has been regarded by Latimer (7) as meta-antimonious acid, $HSbO_2$, and is so treated in this paper. Finally the log solubility in the pH range of 11 to about 13.7 (12) forms a branch with a slope of 1. Latimer has regarded the corresponding ion to be SbO_2^-. His selected value for the free energy of formation are given in Table I, as is that for the $Sb(OH)_4^-$ ion. The latter form was identified by Brintzinger (13) in 2.5*N* KOH through dialysis experiments. The authors prefer the latter form of Brintzinger for the negative ion.

The antimonate ion was shown by Brintzinger (13) to be $Sb(OH)_6^-$ in 2.5*N* KOH. It is now possible to compute the previously unknown energy of formation for this ion both by the use of oxidation-reduction potentials and from measurements of the solubilities of Sb_2O_5. The oxidation-reduction potentials of the anions of trivalent and pentavalent Sb were measured in 1923 by Grube and Schweigardt (14) in 3*N*-10*N* KOH. They assumed that the couple was SbO_2^--SbO_3^- corresponding to a two hydroxyl, two electron reaction, but could not prove it so far as the hydroxyl relation was concerned because data was then lacking on the activity coefficients of the electrolyte in the solutions of KOH employed. Since then these coefficients have been published by Akerlof and Bender (15). Haight (16) studied the oxidation-reduction potentials by polarographic methods. He measured the half-wave potential, $E_{1/2}$, of trivalent Sb anodically polarized in 1*M*-10*M* KOH and found that the 0.060 slope of $E_{1/2}$ to pH corresponded to a reversible reaction of the two hydroxyl, two electron form just as Grube and Schweigardt had conjectured. Haight proposed tentatively that the reaction might be

$$2OH^- + Sb(OH)_4^- \rightleftarrows Sb(OH)_6^- + 2e^- \qquad (I)$$

The evidence of Brintzinger cited already by the authors confirms this equation of Haight.

The formula corresponding to the equilibrium of reaction (I) is

$$E_A = E^\circ_A - 0.0591 \log (a_{OH^-}) + 0.0295 \log \frac{[Sb(OH)_6^-]}{[Sb(OH)_4^-]}$$

where E_A is the equilibrium electrode potential of reaction (I) with reference to the standard hydrogen electrode; E°_A is the standard electrode potential (for $pH = 14.0$), coresponding to value 1 for the activity a_{OH^-} of the OH^- ion and for the ratio $[Sb(OH)_6^-]/[Sb(OH)_4^-]$ of the concentrations of the $Sb(OH)_4^-$ and $Sb(OH)_6^-$. If reaction (I) is written as follows:

$$Sb(OH)_6^- + 2H^+ + 2e^- = Sb(OH)_4^- + 2H_2O \qquad (II)$$

its equilibrium electrode potential may be written as follows:

$$E_B = E^\circ_B - 0.0591\ pH + 0.0295 \log [Sb(OH)_6^-]/[Sb(OH)_4^-]$$

Table II. Thermodynamic data on antimonite-antimonate potentials

N KOH	*E*	log (a_{OH^-})	E°_B	E°_A
1	2	3	4	5
9	—0.577	1.9097	—0.464	+0.364
8	—0.567	1.6589	—0.469	0.359
7.5	—0.561	1.5755	—0.469	0.359
7	—0.555	1.4478	—0.469	0.359
6	—0.540	1.2269	—0.467	0.361
5	—0.516	1.0390	—0.455	0.373
4	—0.484	0.8108	—0.436	0.393
3	—0.428	0.4952	—0.399	0.429

where E°_B is the standard electrode potential (for $pH = 0.0$) corresponding to value 1 for the activity a_{H^+} of the H^+ ion and for the ratio $[Sb(OH)_6^-]/[Sb(OH)_4^-]$. As is well known, $E^\circ_B = E^\circ_A + E^\circ_A + 0.828$ volt. Thermodynamic data on the antimonite-antimonate potentials are given in Table II. The normality of KOH used by Grube and Schweigardt (14) and the values of the electrode potential, found when the Sb^V to Sb^{III} ratio is unity, are in columns 1 and 2. Columns 3, 4, and 5 give the calculated values for log a_{OH^-} (15) (which is assumed to be equal to log $a\pm$) E°_B and E°_A.

The values of the mean activity coefficient, γ, are from Akerlof and Bender (15). The $a\pm = \gamma m\pm$, where $m\pm$, the mean concentration of K^+ and OH^- ions, is assumed equal to m_{KOH} in the solution. A representative value for E°_B is +0.363 volt, the average of the top six values in column 5. This leads to the following formula for the equilibrium potential of the reaction:

$$E = 0.363 - 0.0591\ pH + 0.0295 \log \frac{[Sb(OH)_6^-]}{[Sb(OH)_4^-]}$$

From $E^\circ_B = 0.363$ volt, $\Delta Ff^\circ_{H_2O} = -56{,}690$ cal, $\Delta Ff^\circ_{Sb(OH)_4^-} = -195{,}880$ cal, the calculations are $\Delta Ff^\circ_{Sb(OH)_6^-} = -292{,}500$ cal ±2000 cal.

The free energy of formation of $Sb(OH)_6^-$ may be derived with somewhat greater accuracy from the solubility of Sb_2O_5 as measured by Tourky and Mousa (12) in HCl of various concentrations. From their data and published data on the activity coefficients of HCl, a graph has been prepared which shows log Sb^V (gram atoms per 1000 g H_2O) vs. pH (Fig. 2). The two branches of the curve meet at $pH = -0.27$, the isoelectric point. The branch above this point is linear and, from Brintzinger's results already noted, the ion must be $Sb(OH)_6^-$ (13). The equation for one branch of the curve, then, is

$$2Sb(OH)_6^- + 2H^+ = Sb_2O_5 + 7H_2O \qquad (III)^2$$
$$2 \log [Sb(OH)_6^-] = \log K_c + 2pH$$

It follows from formula (III) and the data of Fig. 2 that at $pH = 0$ log $K_c = 2$ log $[Sb(OH)_6^-]$ or —8.31. Applying the conditions log $K_c = -8.31$, $\Delta Ff^\circ_{Sb_2O_5} = -200{,}500$ cal, and $\Delta Ff^\circ_{H_2O} = -56{,}690$ cal to the equilibrium formula for log K in terms of the free energies of formation, $\Delta Ff^\circ_{Sb(OH)_6^-} = -293{,}000$ cal. This value is within 500 cal of the value derived by the authors from Grube and Schweigardt's data

[2] The theoretical slope of formula (III) is +1 pH but the experimental slope shown in Fig. 2 is +0.25 pH. No likely equation known to the writers has a slope of +0.25 pH. The cause of this difference is not known.

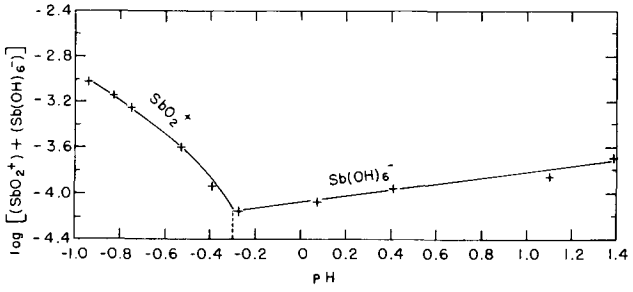

Fig. 2. Solubility of antimony pentoxide (9)

(14). This value is used in Table I since it is the more accurate of the two computed.

The pentavalent Sb cation, according to Tourky and Mousa (12) was probably SbO^{+3} but might be monovalent SbO_2^+ below the isoelectric point. The author's choice of SbO_2^+ is based on the theoretical slope of —1 for its formations in solutions saturated with Sb_2O_5 below the isoelectric point as indicated by Eq. [15] in the table of equations and formulas. Although the experimental slope shown in Fig. 2 varies from —1.2 to —2, one can hardly expect a constant slope in such acid solutions and the lowest theoretical slope is —1. On the other hand, the theoretical slope for the formation of SbO^{+++} is only —0.33. Of the two ions, therefore, SbO_2^+ is to be preferred since its theoretical slope is much nearer to the experimental one.

For the SbO_2^+ ion

$$SbO_2^+ + 4H_2O = Sb(OH)_6^- + 2H^+ \qquad (IV)$$
$$\log \frac{[Sb(OH)_6^-]}{(SbO_2^+)} = \log K_d + 2\ pH$$

In Fig. 2 at the isoelectric point of $pH = -0.27$, the left-hand member of the formula equals zero and log $K_d = -2\ pH$ or 0.54. Substituting this value and the free energies of formation for water and for $Sb(OH)_6^-$, —56,690 and —293,000 cal, respectively, in the equilibrium formula for log K_d the authors calculate that $\Delta Ff^\circ_{SbO_2^+}$ equals —65,500 cal.

Equilibrium Equations

The equilibrium equations which follow have been calculated by the use of the usual thermodynamic formulas which are given by Pourbaix (1) and others (2).

For Water

$$2H^+ + 2e^- = H_2 \qquad (a)$$
$$E = -0.0591\ pH - 0.0295 \log P_{H_2}$$

$$O_2 + 4H^+ + 4e^- = 2H_2O \qquad (b)$$
$$E = 1.229 - 0.0591\ pH + 0.0148 \log P_{O_2}$$

For Antimony and Its Compounds

A. *Homogeneous Reactions Without Oxidation*

$$HSbO_2 + H^+ = SbO^+ + H_2O \qquad [1]$$
$$\log \frac{(HSbO_2)}{(SbO^+)} = -0.87 + pH$$

$$Sb(OH)_4^- + H^+ = HSbO_2 + 2H_2O \qquad [2]$$
$$\log \frac{[Sb(OH)_4^-]}{(HSbO_2)} = -11.00 + pH$$

$$Sb(OH)_6^- + 2H^+ = SbO_2^+ + 4H_2O \quad [3]$$
$$\log \frac{[Sb(OH)_6^-]}{(SbO_2^+)} = 0.54 + 2\,pH$$

With Oxidation

$$SbO_2^+ + 2H^+ + 2e^- = SbO^+ + H_2O \quad [4]$$
$$E = 0.720 - 0.0591\,pH + 0.0295 \log \frac{(SbO_2^+)}{(SbO^+)}$$

$$Sb(OH)_6^- + 4H^+ + 2e^- = SbO^+ + 5H_2O \quad [5]$$
$$E = 0.704 - 0.1182\,pH + 0.0295 \log \frac{[Sb(OH)_6^-]}{(SbO^+)}$$

$$Sb(OH)_6^- + 3H^+ + 2e^- = HSbO_2 + 4H_2O \quad [6]$$
$$E = 0.678 - 0.0886\,pH + 0.0295 \log \frac{[Sb(OH)_6^-]}{(HSbO_2)}$$

$$Sb(OH)_6^- + 2H^+ + 2e^- = Sb(OH)_4^- + 2H_2O \quad [7]$$
$$E = 0.353 - 0.0591\,pH + 0.0295 \log \frac{[Sb(OH)_6^-]}{[Sb(OH)_4^-]}$$

B. *Heterogeneous Reactions Involving Two Sides*

With Oxidation

$$Sb_2O_3 + 6H^+ + 6e^- = 2Sb + 3H_2O \quad [8]$$
(cubic) $E = 0.152 - 0.0591\,pH$
(ortho) $= 0.167 - 0.0591\,pH$

$$Sb_2O_4 + 2H^+ + 2e^- = Sb_2O_3 + H_2O \quad [9]$$
(cubic) $E = 0.863 - 0.0591\,pH$
(ortho) $= 0.819 - 0.0591\,pH$

$$Sb_2O_5 + 2H^+ + 2e^- = Sb_2O_4 + H_2O \quad [10]$$
$$E = 0.479 - 0.0591\,pH$$

$$Sb_2O_5 + 4H^+ + 4e^- = Sb_2O_3 + 2H_2O \quad [11]$$
(cubic) $E = 0.671 - 0.0591\,pH$
(ortho) $= 0.649 - 0.0591\,pH$

C. *Heterogeneous Reactions Involving One Solid*

Without Oxidation

$$Sb_2O_3 + 2H^+ = 2SbO^+ + H_2O \quad [12]$$
(cubic) $\log (SbO^+) = -3.05 - pH$
(ortho) $= -2.32 - pH$

$$Sb_2O_3 + H_2O = 2HSbO_2 \quad [13]$$
(cubic) $\log (HSbO_2) = -3.92$
(ortho) $= -3.19$

$$2\,Sb(OH)_4^- + 2H^+ = Sb_2O_3 + 5H_2O \quad [14]$$
(cubic) $\log [Sb(OH)_4^-] = -14.91 + pH$
(ortho) $= -14.18 + pH$

$$Sb_2O_5 + 2H^+ = 2SbO_2^+ + H_2O \quad [15]$$
$$\log (SbO_2^+) = -4.70 - pH$$

$$2Sb(OH)_6^- + 2H^+ = Sb_2O_5 + 7H_2O \quad [16]$$
$$\log [Sb(OH)_6^-] = -4.16 + pH$$

With Oxidation

$$Sb + 3H^+ + 3e^- = SbH_{3\,gas} \quad [17]$$
$$E = -0.510 - 0.0591\,pH - 0.0197 \log P_{SbH_3}$$

$$SbO^+ + 2H^+ + 3e^- = Sb + H_2O \quad [18]$$
$$E = 0.212 - 0.0394\,pH + 0.0197 \log (SbO^+)$$

$$HSbO_2 + 3H^+ + 3e^- = Sb + 2H_2O \quad [19]$$
$$E = 0.230 - 0.0591\,pH + 0.0197 \log (HSbO_2)$$

$$Sb(OH)_4^- + 4H^+ + 3e^- = Sb + 4H_2O \quad [20]$$
$$E = 0.446 - 0.0788\,pH + 0.0197 \log [Sb(OH)_4^-]$$

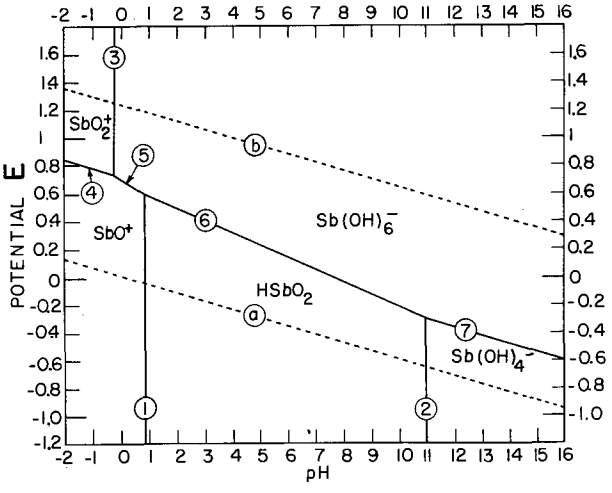

Fig. 3. Zones of predominance for ions containing Sb

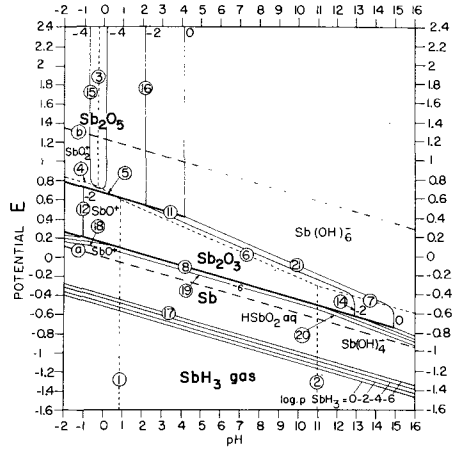

Fig. 4. Equilibria of antimony-water

$$2Sb(OH)_6^- + 6H^+ + 4e^- = Sb_2O_3 + 9H_2O \quad [21]$$
(cubic) $E = 0.794 - 0.0886\,pH + 0.0295 \log [Sb(OH)_6^-]$
(ortho) $= 0.722 - 0.0886\,pH + 0.0295 \log [Sb(OH)_6^-]$

$$Sb_2O_5 + 6H^+ + 4e^- = 2SbO^+ + 3H_2O \quad [22]$$
$$E = 0.581 - 0.0886\,pH - 0.0295 \log (SbO^+)$$

Stability of Antimony, Its Oxides, and Its Solutions

The zones of predominance of the solutes are shown in Fig. 3. The lines show the loci of points for which the activities (or the concentrations in ideal solutions) of two Sb ions, simultaneously present in the solution, are equal to one another.

SbO_2^+	:	Limited by lines 3 and 4.
$Sb(OH)_6^-$	:	Limited by lines 3, 5, 6, and 7.
SbO^+	:	Limited by lines 4, 5, and 1.
$HSbO_2$	:	Limited by lines 1, 6, and 2.
$Sb(OH)_4^-$	:	Limited by lines 2 and 7.

Figure 4 is a diagram for the thermodynamic equilibria of the system Sb-H_2O at 25°C as developed from Eq. (I), (II), and [2] through [22]. When one ion takes part in a reaction, the equilibrium is shown for values of concentration in dissolved Sb equal to 1, 10^{-2}, 10^{-4}, and 10^{-6} g at./l. For the reaction [17] of reduction of solid Sb to gaseous SbH_3, the equilibrium is shown for partial pressures of SbH_3 equal to 1, 10^{-2}, 10^{-4}, and 10^{-6}, the metal or

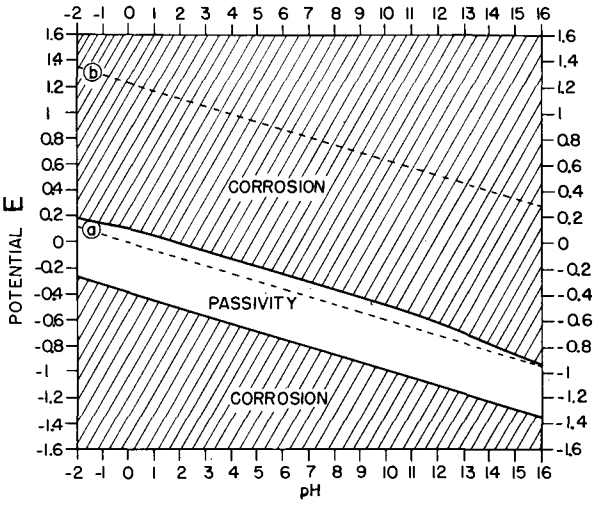

Fig. 5. Corrosion and passivity of Sb

oxide in contact with the solution is considered to be stable (1, 2).

Domains of stability of solid compounds shown in Fig. 4 are:

- Sb : Below line 8, and within the families of lines 18, 19, 20, and 17.
- Sb_2O_3 : Between lines 8 and 11, and between the families of lines 12 and 21.
- Sb_2O_5 : Possibly in a narrow zone above line 11 and between the families of lines 15 and 16.
- Sb_2O_4 : This oxide is never thermodynamically stable at 25°C in the presence of water.

Gaseous SbH_3 is stable below the family of line 17.

The great area of stability of the $Sb(OH)_6^-$ ion is responsible for a strong tendency of Sb_2O_3 to dissolve at potentials more positive than those of line 21. In this, the Sb diagram resembles that of Cr (1).

Antimony tetroxide Sb_2O_4 in the dry state is well defined and shows a distinctive x-ray diffraction pattern (17). Konopik and Zwiauer (18) found that when the dry oxide is dissolved in water, however, it behaved like a compound of trivalent and pentavalent oxides, giving rise to a mixture of Sb^{III} and Sb^{V} in solution. This is in accordance with the above-mentioned fact that Sb_2O_4 is thermodynamically unstable in the presence of aqueous solutions.

Figure 4 shows that SbH_3 may be prepared, together with hydrogen, by a sufficiently strong reductive action on Sb salt solutions or on metallic Sb in the presence of water, but that it is thermodynamically unstable and tends to decompose into Sb and H_2.

In fact, SbH_3 may be prepared by electrolysis of acid or alkaline solutions with a cathode of metallic Sb (19); yields of SbH_3 as high as 15% by volume in the gas evolved at the cathode have been reported. SbH_3 is usually prepared by acid treatment of an alloy of Sb with a reactive metal such as Zn or Mg.

SbH_3 is unstable in the presence of aqueous solutions, and tends then to decompose with formation of Sb and of H_2; but Salzberg and Andreatch (20) found that the velocity of this decomposition is negligible between the limits set by 0.1*N* acid and 0.1*N* alkali, i.e., approximately between a *p*H of 1 and 13.7. The decomposition is rapid in solutions which are strongly alkaline (20, 21) or strongly acid (21).

Applications of the Diagrams

A few applications are made here of the equilibrium diagrams to the study of electrochemical systems. Because the diagrams represent equilibrium conditions they can be used only to set limits within which practical, nonequilibrium systems operate.

Reduction of Corrosion by Antimony Coatings or by Its Compounds

Figure 5, which is derived from the equilibrium diagram (Fig. 4), represents the theoretical conditions of corrosion and of immunity (noncorrosion) of Sb, according to assumptions which have been made previously (1). Passivation is not considered in Fig. 5 because of the great solubility of the antimony oxides.

According to Burns and Bradley (3), nonporous coatings of Sb on steel resist attack by HCl and HF but are attacked by HNO_3. A study of the diagram as simplified in Fig. 5 would have led to the same general conclusions. From this diagram one would expect that *p*H = 0 in HCl or HF, Sb would be passive since the potential of the metal-metal ion couple would be about 0.1 volt more positive than the hydrogen potential at the same *p*H. Under such a condition hydrogen ions will not be displaced from solution by the metal ions. The above acids are nonoxidizing. On the other hand, when Burns and Bradley tested an Sb-coating against strong HNO_3 which is a powerful oxidizing agent, the metal was attacked. This is because the HNO_3 would cause the potential of the metal in it to be higher than 0.1 volt above line (a). Such a potential would be in the upper corrosion zone of Fig. 5.

Piontelli and Fagnani (22) have reviewed the theory of pickling inhibitors and have experimented with Sb_2O_3 in 3*M* to 10*M* HCl to restrain the corrosion of mild steel under treatment. It was concluded that metallic Sb displaces Fe in the stronger solutions and this action is in accordance with predictions which may be made from the thermodynamic emf of the process, a statement which is readily verified. They pointed out that because the overvoltage of hydrogen is higher on Sb than on Fe, corrosion is lessened as the deposited Sb film spreads. As discussed in the previous paragraph, Fig. 5 shows that, as the surface is covered progressively, with Sb, the potential of the isolated metallic surface will approach that of Sb. Such a potential is more positive than the hydrogen potential. Attack of the metal will lessen and can cease for this reason.

Figure 5 also shows that there is a possibility of cathodic corrosion of Sb under very reducing conditions, with formation of gaseous SbH_3. Salzberg and Andreatch (20) have formed gaseous SbH_3 in this manner.

Antimony Electrodes

The prevalent theory of the Sb electrodes (10) is not entirely accurate since the Sb^{+++} ion, assumed to take part in an intermediate electrode reaction, is now shown by the authors to be unproven in aqueous solutions. In the following, a mechanism is suggested which is consistent with the facts about the two general types of Sb electrode in use: the Sb-Sb_2O_3 electrode and the Sb rod electrode.

The Sb-Sb_2O_3 electrode contains a mixture of powdered Sb and of Sb_2O_3 in an electrode vessel with a side arm. Electrolyte moves slowly through the vessel and is saturated with respect to Sb_2O_3 before entering the side arm at the tip of which the liquid junction occurs. The cell is kept saturated with nitrogen. Under such conditions, Roberts and Fenwick (10) determined $\Delta F^{\circ}_{Sb_2O_3(c)}$ and $\Delta F^{\circ}_{Sb_2O_3(o)}$, and Schuhmann (11) determined ΔF_{SbO^+}.

At present, the accepted theory for the Sb-Sb_2O_3 electrode is that of Roberts and Fenwick (10). They proposed these intermediate reactions for the Sb-Sb_2O_3 couple:

$$2\,Sb \rightleftarrows 2\,Sb^{+++} + 6e^- \qquad (V)$$

$$2Sb^{+++} + 6\,OH^- \rightleftarrows Sb_2O_3 + 3H_2O \qquad (VI)$$

Conceivably, the Sb^{+++} ion could possibly be derived from orthoantimonious acid, $Sb(OH)_3$, solid salts of which are known. The above mechanism is considered to be unlikely since the Sb^{+++} ion has not been found to be present in any part of the *p*H range from 0 to 14. However, the SbO^+ ion has been shown to exist in solutions of low *p*H (11), *see* Eq. [12], and the $Sb(OH)_4^-$ ion has been shown to exist in solutions of high *p*H (Eq. [14]); for intermediate values of the *p*H, the dissolved Sb exists as undissociated $HSbO_2$ molecules.

According to Schuhmann (11) and Roberts and Fenwick (10), the value of the potential of Sb-$Sb_2O_{3\,cubic}$ electrodes is given by Eq. [8].

$$E = 0.152 - 0.0591\ pH \text{ (at 25°C)}$$

It may be seen on Fig. 4 and 1 that for *p*H approximately from 2 to 10, the Sb-Sb_2O_3 electrode can be represented by the Sb-$Sb_2O_{3\,cubic}$ couple, in the presence of a constant concentration in dissolved Sb $10^{-3.9}$ mole $HSbO_2$/l, or 10 mg Sb/l; for *p*H lower than 1-2, or higher than 10-11, the electrode potentials may correspond to the theoretical value given by Eq. [8] only if the solution has a higher content in dissolved Sb, respectively as SbO^+ or as $Sb(OH)_4^-$ ions.

The Sb rod electrode may be used under controlled conditions, preferably with mechanical agitation and in the absence of dissolved oxygen. Potential values given by Kolthoff and Hartong (23) for the temperature of 14°C are shown in Fig. 6. The two following equations are given for these values:

For *p*H 1-5

$E = -0.0415 - 0.0485\ pH$ (14°C) shown as line A

For *p*H 9-12

$E = -0.009 - 0.0536\ pH$ (14°C) shown as line B

Grube and Schweigardt (14) have reported that potential values may be appreciably lower for *p*H higher than 12.

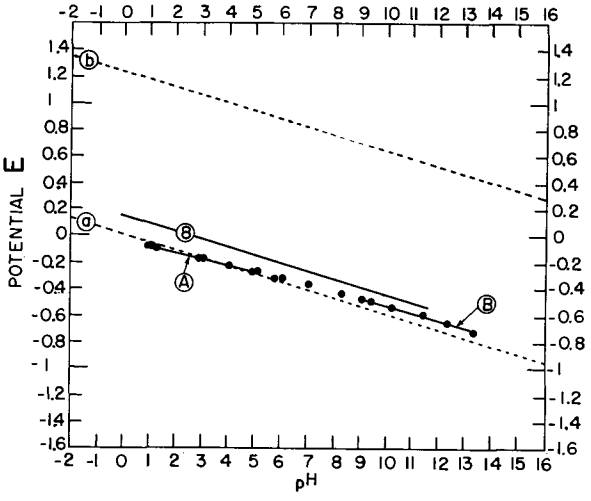

Fig. 6. Antimony electrodes. Line 8—powdered Sb-$Sb_2O_{3(cubic)}$ electrode data from reference (10). Dots and Lines A and B—results obtained by Kolthoff and Hartong (23) with cast electrodes of Sb-Sb_2O_3.

It may be seen on Fig. 6 that, if the values for 25°C are approximately the same as the values given by Kolthoff (23) for 14°, they do not correspond to a Sb-Sb_2O_3 equilibrium shown as line 8; they correspond approximately to a H_2-H^+ equilibrium under 0.01 to 1 atm hydrogen pressure.Thus, it seems that the Sb rod electrode behaves approximately as a hydrogen electrode, this hydrogen being formed at the surface of the Sb as a result of a very minute corrosion of the metal. As the equilibrium concentration of dissolved Sb at these potentials is extremely low (approximately 10^{-10}), the amount of dissolved Sb is usually not noticeable; care should be taken to avoid the formation of Sb_2O_3, which could increase the potential. Some more experimental investigations on this subject might be welcome.

Acknowledgment

Two of the authors, M. Pourbaix and N. de Zoubov, wish to thank the l'Union Minière du Haut Katanga and l'Institut pour l'Encouragement de la Recherche Scientifique dans l'Industrie et dans l'Agriculture, IRSIA (Brussels, Belgium) for their support in this work.

Manuscript received Sept. 24, 1956. This paper was prepared for delivery before the Cleveland Meeting, Sept. 30-Oct. 4, 1956.

Any discussion of this paper will appear in a Discussion Section to be published in the June 1958 JOURNAL.

REFERENCES

1. M. J. N. Pourbaix, "Thermodynamics of Dilute Aqueous Solutions," Edward Arnold and Co., London (1949).
2. P. Delahay, M. Pourbaix, and P. Van Rysselberghe, *This Journal*, **98**, 57 (1951); *J. Chem. Educ.*, **27**, 683 (1950).
3. R. M. Burns and W. W. Bradley, "Protective Coatings for Metals," 2nd Ed., p. 274, Reinhold Publishing Co., New York (1955).
4. J. A. Christiansen and M. Pourbaix, *Compt. rend. XVII Conf. inter. union pure and appl. chem.,*

Stockholm, (1953) p. 82-84, Maison de la Chimie, Paris (1954).
5. A. J. de Bethune, *This Journal*, **102**, 288C (1955).
6. Paul Delahay, Marcel Pourbaix, and Pierre Van Rysselberghe, *ibid.*, **98**, 57, 65 (1951).
7. W. M. Latimer, "The Oxidation States of the Elements and their Potentials in Aqueous Solutions," 2nd Ed., pp. 117-18, Prentice-Hall, Inc., New York (1952).
8. M. C. Bloom, *Am. Mineralogist*, **24**, 281 (1939).
9. F. D. Rossini, U. S. Bureau of Standards, "Selected Values of Chemical Thermodynamic Properties," (1949), Table 21-2, p. 90; Part IV, p. 823 ff.
10. E. J. Roberts and F. Fenwick, *J. Am. Chem. Soc.*, **50**, 2125 (1928).
11. R. Schuhmann, *ibid.*, **46**, 52 (1924).
12. A. R. Tourky and A. A. Mousa, *J. Chem. Soc. (London)*, **1948**, Part I, 759.
13. H. Brintzinger, *Z. Anorg. Chem.*, **256**, 98 (1948).
14. G. Grube and F. Schweigardt, *Z. Elektrochem.*, **29**, 257 (1923).
15. G. C. Akerlof and Paul Bender, *J. Am. Chem. Soc.*, **70**, 2366 (1948).
16. G. P. Haight, Jr., *ibid.*, **75**, 3848 (1953).
17. Alphabetical Index of X-Ray Diffraction Patterns, A.S.T.M., Philadelphia, Pa., June, August, 1945.
18. A. N. Konopik and J. Zwiauer, *Monatsheft*, **83**, 189 (1952).
19. D. T. Hurd, "Chemistry of the Hydrides," John Wiley & Sons, Inc., New York (1952).
20. H. W. Salzberg and A. J. Andreatch, *This Journal*, **101**, 528 (1954).
21. H. J. S. Sands, E. J. Weeks, and S. W. Worrell, *J. Chem. Soc. (London) TRANS.*, Part I, **123**, 456 (1923).
22. R. Piontelli and L. Fagnani, *Korr. und Metallsch.*, **19**, 259 (1943).
23. I. M. Kolthoff and B. D. Hartong, *Rec. Trav. Chim.*, **44**, 113 (1925).

The Relation between Pitting Corrosion and the Ferrous-Ferric Oxidation-Reduction Kinetics on Passive Surfaces

Milton Stern

Metals Research Laboratories, Electro Metallurgical Company,

A Division of Union Carbide Corporation, Niagara Falls, New York

ABSTRACT

Ferrous-ferric electrode kinetics have been studied on a variety of passive alloys. Activation polarization parameters are not markedly different for all the surfaces studied except for titanium where the exchange current is an order of magnitude smaller. The local anodic polarization curve for solution of metal under passive conditions was found to be extremely steep. This is suggested as typical behavior for the passive condition.

Pitting of a metal may be divided into two separate aspects, pit initiation and pit propagation.

Streicher (1) has developed an accelerated pit initiation test and has described several of the factors which are important in initiation of pitting on stainless steels. His discussion contains an excellent review of the literature in the field; this need not be repeated here.

Uhlig (2) and Liebhafsky (3) have contributed significantly to an understanding of the basic processes which occur during pit growth. At the base of the pit, which is the anode in a passive-active cell, metal goes into solution. A reduction reaction occurs on the cathode regions of the surface which correspond to the unattacked areas. In $FeCl_3$ solution, the primary cathodic reaction is reduction of ferric ions to form ferrous ions. It has also been shown that the pitting process is essentially under cathodic control. The anodic areas do not appear to polarize significantly, while the cathodic areas polarize markedly. Thus, the pitting rate is a direct function of the exposed cathode area.

The discussion presented here is limited to a consideration of the electrochemical factors entailed in the pit propagation process. Since the system is primarily under cathodic control, the overvoltage behavior for ferric ion reduction on the cathode surface should influence the rate of pit growth.

Ferric-ferrous activation overvoltage behavior was determined on a series of alloys with different inherent pitting resistance to evaluate the importance of this aspect of the corrosion process in determining the differences in resistance to pit propagation of the various compositions.

When a metal pits in $FeCl_3$, the corrosion potential is active to the equilibrium potential of the ferrous-ferric oxidation-reduction potential of the system. The cathodic overvoltage during corrosion may amount to more than 1 v. In addition, the corrosion current is often extremely high. Since currents greater than the corrosion current must be applied in order to polarize a pitting electrode (4), experimental difficulties arise in the determination of activation overvoltage due to interference from concentration polarization and resistance drop effects. It was found that this interference could be eliminated without significantly changing ferric-ferrous activation polarization parameters by inhibiting the pitting process with $NaNO_3$ additions to $FeCl_3$. Uhlig (2) and Gilman (5) have demonstrated the effec-

tiveness with which nitrate inhibits pitting. Addition of $NaNO_3$ to a ferrous-ferric solution does not affect the equilibrium ferrous-ferric potential measured with a Pt electrode. Nitrate additions also produce a steady-state potential for stainless steel which is very close to the potential of Pt in the same solution. That nitrate does not significantly affect activation overvoltage parameters (6) was demonstrated with overvoltage measurements on stainless steel in ferric sulfate solutions[1] with and without nitrate additions. Similar measurements on a Ti surface in $FeCl_3$ where pitting does not occur even in the presence of chloride also showed no significant effect of nitrate on ferric-ferrous activation overvoltage behavior.

Thus, activation polarization measurements on a variety of surfaces in $FeCl_3$ containing nitrate as a pitting inhibitor may be considered representative of that activation polarization behavior which exists during pitting without nitrate.

Procedure

The procedure and equipment used for potential and overvoltage measurements have been described previously (6). The analysis of the alloys used is presented in Table I. The Ti was vacuum arc-melted and contained 0.05% C, 0.12% O, and 0.004% H. Ferric-ferrous chloride solutions were prepared by the addition of 100 g of $FeCl_3 \cdot 6H_2O$ and 0.9 g of $FeCl_2 \cdot 4H_2O$ to 1000 g of distilled water.[2]

Results

Type 310 Stainless Steel

Type 310 stainless steel was placed in a ferric-ferrous chloride solution containing approximately 0.4*N* $NaNO_3$. The equilibrium ferric-ferrous potential of the solution measured with platinized Pt was 0.858 v on the standard hydrogen scale. After the sample had reached a steady-state potential of −13 mv vs. Pt in the same solution, polarization measurements were conducted. Fig. 1 shows the cathodic polarization data obtained. The curve shows the

[1] Pitting of stainless steel does not occur in ferric sulfate solutions without nitrate, whereas pitting in chloride solutions is extremely rapid.

[2] The equilibrium potential of a solution prepared in this manner and measured with a platinized Pt electrode is approximately 0.83 v on the standard hydrogen scale. The potential is not exactly reproducible from batch to batch because the ferrous salt contains varying amounts of ferric contamination. When a more active ferric-ferrous potential was required, ferrous chloride was added to the above solution until the desired potential was reached. The actual ferrous ion concentration was not determined.

Table I. Analysis of alloys

	% Cr	% Ni	% Mn	% Mo	% C	% Others
Type 304 stainless	18.36	9.06	0.94	—	0.05	bal. Fe
Type 316 stainless	17.25	13.02	1.66	2.54	0.04	bal. Fe
Type 310 stainless	24.66	19.68	1.27	—	0.05	bal. Fe
Hastelloy* alloy F	21.73	46.35	1.70	6.89	0.08	19.50 Fe
Hastelloy* alloy C	16.03	55.85	0.53	15.85	0.06	5.60 Fe 4.04 W

* A trade mark of the Haynes Stellite Company, Division of Union Carbide Corporation.

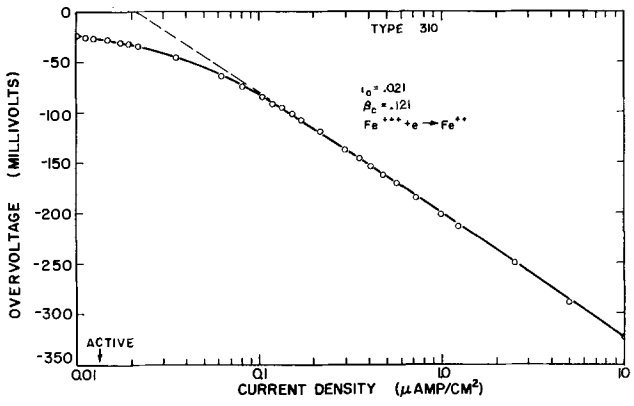

Fig. 1. Cathodic polarization of a nitrate-inhibited ferric-ferrous chloride solution with an equilibrium potential of 0.858 v on Type 310 stainless steel.

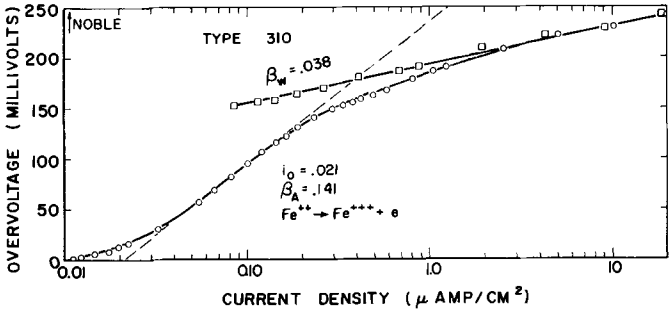

Fig. 2. Anodic polarization of a nitrate-inhibited ferric-ferrous chloride solution with an equilibrium potential of 0.858 v on Type 310 stainless steel.

normal expected shape for activation polarization (4) and represents the reduction rate of ferric ions on a Type 310 surface as a function of overvoltage. The exchange current is 0.021 μa/cm², and the measured Tafel slope, β_C, is 0.121 v. Fig. 2 illustrates the anodic polarization behavior. Two distinct Tafel lines are obtained. As illustrated previously (6), during anodic polarization, a potential region is reached where another oxidation proceeds at a rate comparable to the rate of oxidation of ferrous ions. This reaction is most likely oxygen-evolution produced by oxidation of water. Thus, at any potential, the experimental curve represents the sum of the rate of oxidation of ferrous ions, $\overleftarrow{i}_{Fe^{++}}$, and the rate of oxidation of water, $\overleftarrow{i}_w$. The low current Tafel region provides the quantitative expression for activation polarization for ferrous ion oxidation.

$$\eta = \beta_A \log \overleftarrow{i}_{Fe^{++}}/i_o \qquad (I)$$

where $\beta_A = 0.141$ and $i_o = 0.021$ μa/cm². Thus, in the region where the experimental curve bends from a slope of 0.141 to a lower value, $\overleftarrow{i}_w$ may be calculated at any potential by subtracting $\overleftarrow{i}_{Fe^{++}}$ from the applied anodic current, $\overleftarrow{i}_x$. At any potential in this region

$$\overleftarrow{i}_w = \overleftarrow{i}_x - \overleftarrow{i}_{Fe^{++}} \qquad (II)$$

The Tafel slope for oxygen evolution, β_w, is thus determined as 0.038 v. The exchange current for

this reaction cannot be calculated since the equilibrium potential is not known.

It has been shown previously (6) that, if the steady-state potential of an electrode is equal to the equilibrium ferrous-ferric potential, then the reverse current which exists during polarization may be calculated. That is, $\overleftarrow{i}_{Fe^{++}}$ as a function of overvoltage on the active side of the reversible potential may be calculated from a measurement of overvoltage as a function of applied cathodic current. Also, the current equivalent to the rate of reduction of ferric ions during anodic polarization may be calculated. The method used is explained briefly in the following discussion. When an electrode at equilibrium is polarized cathodically, the total rate of reduction of ferric ions is equal to the sum of the applied current, $\overrightarrow{i}_x$, and the rate of oxidation of ferrous ions (the reverse current).

$$\overrightarrow{i}_{Fe^{+++}} = \overrightarrow{i}_x + \overleftarrow{i}_{Fe^{++}} \qquad \text{(III)}$$

The Tafel equation describes $\overrightarrow{i}_{Fe^{+++}}$ as a function of overvoltage.

$$\eta = -\beta_C \log \overrightarrow{i}_{Fe^{+++}}/i_o \qquad \text{(IV)}$$

Thus, with a measurement of β_C and i_o, Eqs. (III) and (IV) permit calculation of $\overleftarrow{i}_{Fe^{++}}$ at overvoltage values more active than the equilibrium potential. The method is similar for anodic polarization.

The steady-state potential of 310 stainless steel is more active by 13 mv than the equilibrium potential of the ferrous-ferric solution. This is best explained by considering that the sample is corroding so that, at the corrosion potential, the rate of reduction of ferric ions is equal to the sum of the rate of oxidation of ferrous ions and the rate of solution (oxidation) of metal. Thus,

$$\overrightarrow{i}_{Fe^{+++}} = \overleftarrow{i}_{Fe^{++}} + \overleftarrow{i}_m \qquad \text{(V)}$$

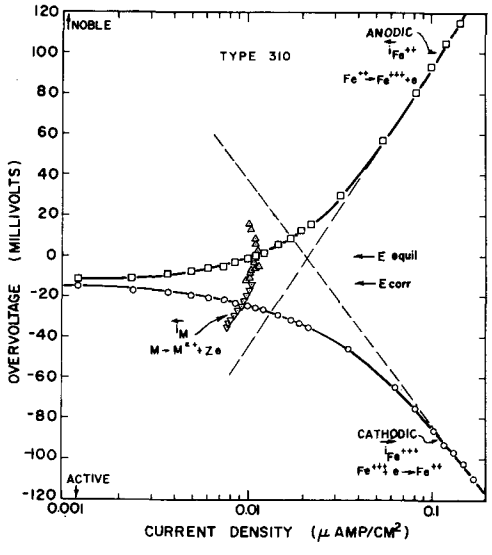

Fig. 3. Low current-density polarization data for Type 310 stainless steel showing corrosion current as a function of potential.

where $\overleftarrow{i}_m$ is that current which is equivalent to the rate of oxidation of metal. If the electrode is polarized cathodically with an external current, the total reduction rate of ferric ions is equal to that which is reduced by the applied current plus that amount of reduction which is equivalent to the rate of oxidation of both metal and ferrous ions. Thus, for cathodic polarization,

$$\overleftarrow{i}_m = \overrightarrow{i}_{Fe^{+++}} - \overleftarrow{i}_{Fe^{++}} - \overrightarrow{i}_x \qquad \text{(VI)}$$

The analogous equation for anodic polarization is

$$\overleftarrow{i}_m = \overrightarrow{i}_{Fe^{+++}} - \overleftarrow{i}_{Fe^{++}} + \overleftarrow{i}_x \qquad \text{(VII)}$$

Fig. 3 shows the low current data on Fig. 1 and 2 extended to lower currents and plotted on an expanded potential scale. The calculated values of $\overleftarrow{i}_m$ as a function of overvoltage are included. This is essentially a plot of the local anodic polarization curve of the metal. It is important to note the steep slope of $\overleftarrow{i}_m$ plotted as a function of overvoltage.

Type 316 Stainless Steel

Measurements were conducted on Type 316 stainless steel surfaces in two inhibited solutions with different ferrous-ferric potentials. The steady-state potential of Type 316 in a solution with an oxidation-reduction potential of 0.757 v on the standard hydrogen scale was the same as Pt to within 0.1 mv. This means that the ferrous-ferric system is at equilibrium on the stainless steel surface and that corrosion, $\overleftarrow{i}_m$, is negligible. The polarization curves are similar to those already illustrated for Type 310 and may be represented in terms of the Tafel constants. The exchange current is 0.49 μa/cm^2, $\beta_A = 0.185$ v, and $\beta_C = 0.095$ v. A value for β_w could not be obtained since the equilibrium ferric-ferrous potential of this solution is relatively active, and *IR* drop errors were introduced during anodic measurements in the potential region where oxygen is evolved.

In a solution with a ferrous-ferric potential of 0.832, the steady-state potential of Type 316 stain-

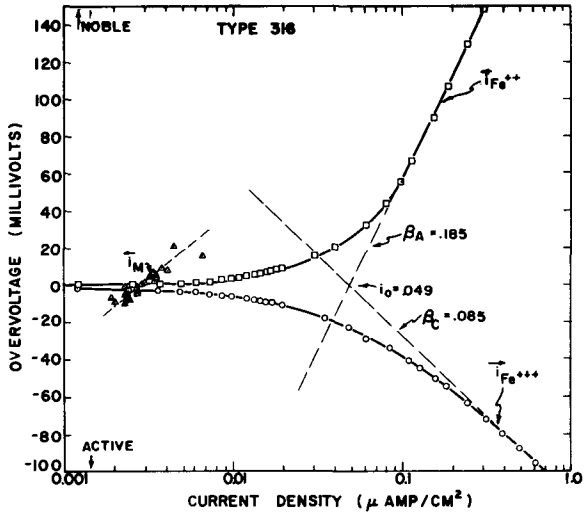

Fig. 4. Low current-density polarization data for Type 316 stainless steel, $E_{Fe^{+++}-Fe^{++}} = 0.832$ v.

less steel is 1 mv more active than Pt in the same solution. In this case, a slight corrosion current must exist which, though small in comparison to i_o, is sufficient to polarize the electrode by 1 mv. Fig. 4 shows the polarization curves only in the low current region to illustrate how $\overleftarrow{i_m}$ varies with potential. In this case, the corrosion current is of the order of 0.003 μa/cm^2, and $\overleftarrow{i_m}$ plotted as a function of overvoltage is not so steep as is found for Type 310 stainless steel. The Tafel constants obtained for this system are $i_o = 0.049$ μa/cm^2, $\beta_C = 0.085$ v, $\beta_A = 0.185$ v, $\beta_w = 0.032$ v.

In many discussions of the shape of electrochemical polarization curves, the question continually arises as to whether polarization should be a linear or logarithmic (Tafel) function of applied current. For example, Straumanis, Shih, and Schlechten (7,8) have observed Tafel behavior for hydrogen overvoltage on Ti in HCl, HBr, and H_2SO_4, but report a linear dependence of overvoltage on applied current in HF. In addition, these authors show that the linear relation is maintained if the Ti corrodes, while the Tafel relation holds if the Ti ceases to dissolve because of fluoride additions. Results of this type have been explained in terms of theory (4) which shows that an electrode whose potential is determined by two intersecting Tafel functions (whether corroding or at equilibrium) exhibits a linear dependence of overvoltage as a function of applied current values less than the exchange current or corrosion current. For an electrode at equilibrium, the slope of the linear polarization curve is given by Eq. (VIII).

$$\left(\frac{d\eta}{di_x}\right)_{\eta\to 0} = \frac{\beta_A\beta_C}{(2.3)\,(i_o)\,(\beta_A+\beta_C)} \qquad \text{(VIII)}$$

For a corroding electrode, the expression becomes

$$\left(\frac{d\epsilon}{di_x}\right)_{\epsilon\to 0} = \frac{\beta_A\beta_C}{(2.3)\,(i_{corr})\,(\beta_A+\beta_C)} \qquad \text{(IX)}$$

where ϵ is the difference in potential between the corrosion potential, E_{corr}, and the polarized potential.

Tafel behavior is not observed until applied current values become significantly larger than the exchange current or the corrosion current. The linear relation reported by Straumanis and coworkers is consistent with this picture since their applied currents were smaller than the very large corrosion current of Ti in HF. Thus, the extent of the linear dependence is determined by the magnitude of the exchange current or corrosion current, and the slope of the linear function is inversely proportional to i_o or i_{corr}.

This behavior can be illustrated quantitatively with the low current data obtained for the Type 316 electrode described above where two markedly different exchange currents were observed for the two ferric-ferrous solutions investigated. Fig. 5 shows the low current data plotted on a linear scale for Type 316 stainless steel in solutions with ferric-ferrous equilibrium potentials of 0.757 and 0.832 v. The slopes obtained are inversely proportional to the

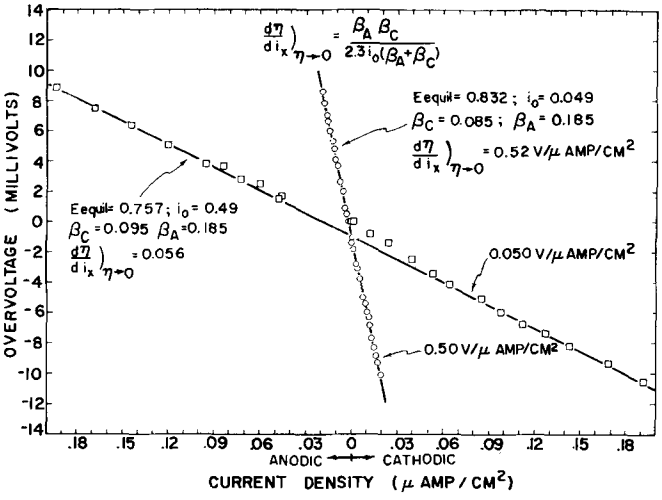

Fig. 5. Linear relationship between overvoltage and applied current density for two different ferric-ferrous solutions on Type 316 stainless steel.

exchange current, and the calculated value of $d\eta/di_x$ using Eq. (VIII) checks the experimental determination within experimental error.

Type 304 Stainless Steel

The polarization curves for Type 304 stainless steel are similar to those already illustrated and may be summarized in terms of the experimental electrochemical constants. In an inhibited ferric-ferrous chloride solution with a reversible potential of 0.824 v vs. the standard hydrogen electrode, the values obtained are: $\eta_{corr} = -0.006$ v, $\beta_C = 0.146$ v, $\beta_A = 0.165$ v, $i_o = 0.0634$ μa/cm^2, and $\left(\frac{d\eta}{di_x}\right)_{\eta\to 0} = 0.48$ v/μa/cm^2.

If sufficient ferrous chloride is added to the solution to bring the equilibrium ferrous-ferric potential down to a value of 0.744 v, then the measured constants become: $\eta_{corr} = -0.002$ v, $\beta_C = 0.139$ v, $\beta_A = 0.161$ v, $i_o = 0.172$ μa/cm^2, and $\left(\frac{d\eta}{di_x}\right)_{\eta\to 0} = 0.188$ v/μa/cm^2. Insufficient data were obtained in the low current region to calculate $\overleftarrow{i_m}$ as a function of potential. At the corrosion potential, however, the corrosion current was calculated as 0.013 μa/cm^2 in the former case and 0.014 μa/cm^2 in the latter experiment.

Hastelloy F

Hastelloy F is an alloy with good pit and corrosion resistance in oxidizing environments. Anodic and cathodic polarization measurements in a ferric-ferrous chloride solution with an equilibrium potential of 0.830 v are illustrated in Fig. 6. It is interesting to note in this case that $\beta_A = \beta_C = 0.148$ v. The exchange current is 0.063 μa/cm^2 while $\beta_w = 0.035$ v. Fig. 7 shows part of the same data plotted on an expanded potential scale and extended to lower values of applied current than that shown in Fig. 6. During these experiments, the steady-state potential of the alloy prior to anodic measurements was

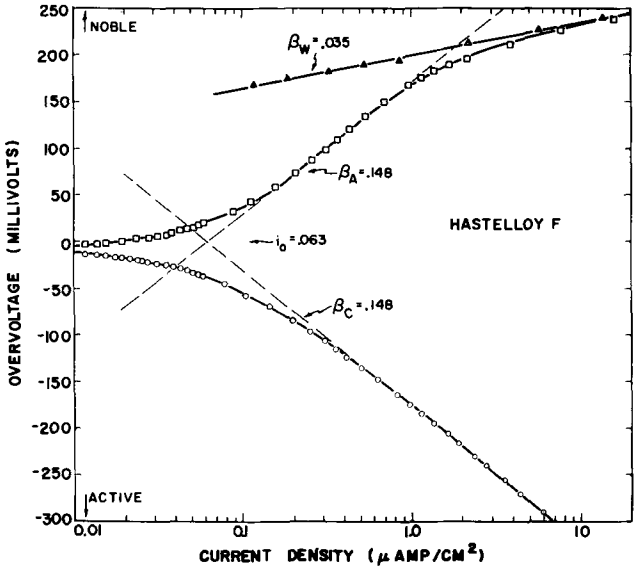

Fig. 6. Anodic and cathodic polarization of nitrate-inhibited ferric-ferrous chloride with an equilibrium potential of 0.830 v on Hastelloy alloy F.

9.5 mv more active than Pt in the same solution. However, prior to cathodic polarization, the potential had changed to 8.0 mv. This change is reflected in an abrupt change in $\overleftarrow{i_m}$ calculated from anodic data as compared to that calculated from cathodic measurements. The values of $\overleftarrow{i_m}$ as a function of potential are plotted on Fig. 7. The data calculated from both anodic and cathodic polarization show a remarkably steep slope. Thus, $\overleftarrow{i_m}$ is essentially independent of overvoltage. When the steady-state potential is —9.5 mv, $\overleftarrow{i_m}$ is 0.020 μa/cm², whereas $\overleftarrow{i_m}$ is 0.016 μa/cm² when the corrosion potential is —8.0 mv.

Further evidence that $\overleftarrow{i_m}$ is independent of potential may be found in application of Eq. (VIII) to the low current data. Eq. (VIII) is based on the assumption that the steady-state potential is determined by only two interesting Tafel functions. If the electrode is in a region where three potential-current

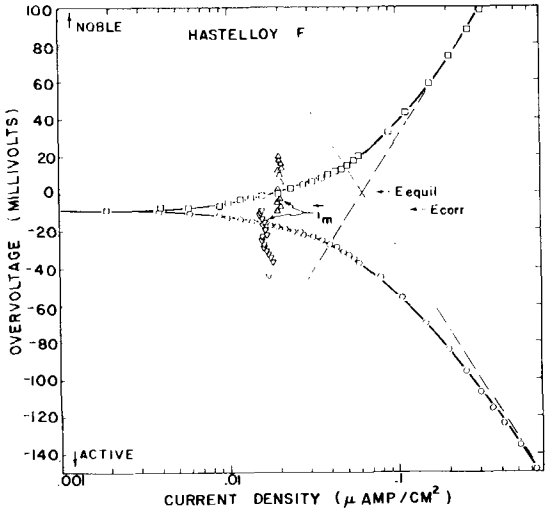

Fig. 7. Low current-density polarization data for Hastelloy alloy F showing corrosion current as a function of potential.

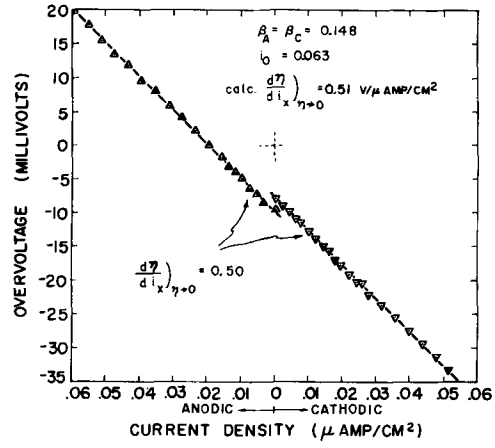

Fig. 8. Linear relationship between overvoltage and applied current density for Hastelloy alloy F.

functions are operative, Eq. (VIII) becomes more complex and cannot be expected to apply in its present form. This would be the case for an electrode 9 mv removed from the reversible ferric-ferrous potential. However, if one of the three polarization curves which determine the potential of the electrode shows an independence of current on potential, then it can be shown that Eq. (VIII) is still applicable.

Fig. 8 illustrates the low current data for Hastelloy F. Both the anodic and cathodic data are linear and yield the same value of $d\eta/di_x$, 0.50 v/μa/cm². The value of $d\eta/di_x$ calculated from Eq. (VIII) is 0.51 v/μa/cm². As stated above, this is further evidence that the local anodic polarization curve for Hastelloy F is practically vertical. This behavior undoubtedly explains, in part, the excellent corrosion resistance of this alloy.

Hastelloy C

Hastelloy alloy C is a Ni-Mo-Cr alloy with excellent corrosion resistance in a wide variety of oxidizing and reducing media. It shows no weight loss or pitting after a ten-year immersion in sea water, nor does it pit in the annealed condition in boiling 10% $FeCl_3$ (9).

The behavior of this alloy is similar to that already illustrated for Hastelloy alloy F. Thus, the results may be summarized in terms of the Tafel constants. In a ferric-ferrous system with an equilibrium potential of 0.758 v, the alloy exhibits a steady-state potential which is 27 mv more active than Pt in the same solution. The exchange current is 0.10 μa/cm² with β_C = 0.190 v and β_A = 0.167 v. As was the case with Hastelloy alloy F, calculated values of $\overleftarrow{i_m}$ for Hastelloy alloy C were relatively independent of potential, the average value in this solution being 0.07 μa/cm².

Results for a ferric-ferrous system with a reversible potential of 0.825 v are shown in Table II. The local action current in this case was 0.3 μa/cm².

Titanium

Titanium metal shows no pitting tendency in chloride solutions. Measurements were conducted

Table II. Summary of electrochemical constants for various alloys

Alloy	$Fe^{+++}-Fe^{++}$* potential, v	η_{corr}† v	β_C v	β_A v	β_w v	i_o‡
Type 304 stainless	0.824	−0.006	0.146	0.165	0.039	0.063
Type 304 stainless	0.744	−0.002	0.139	0.161	—	0.172
Type 316 stainless	0.832	−0.001	0.085	0.185	0.032	0.049
Type 316 stainless	0.757	0.000	0.095	0.185	—	0.49
Type 310 stainless	0.858	−0.013	0.121	0.141	0.038	0.021
Hastelloy alloy F	0.830	−0.009	0.148	0.148	0.035	0.063
Hastelloy alloy C	0.825	−0.070	0.228	0.222	0.030	0.20
Hastelloy alloy C	0.758	−0.027	0.190	0.167	0.039	0.10
Titanium	0.830	−0.016	0.104	—	—	0.0052
Titanium	0.789	−0.003	0.102	0.358	—	0.0110
Titanium	0.736	0.000	0.091	0.352	—	0.024

* Standard hydrogen scale.
† Potential alloy vs. Pt in same solution.
‡ Microampere/cm².

on the same sample in three different ferric-ferrous chloride solutions containing $NaNO_3$ with equilibrium potentials of 0.830 v (solution A), 0.789 v (solution B), and 0.736 v (solution C). Solutions B and C were prepared by addition of ferrous chloride to solution A. Subsequent experiments showed that the nitrate addition had no significant effect on the polarization characteristics. It was included here in order to compare the results with those obtained with alloys which require nitrate to inhibit pitting.

Fig. 9 illustrates the anodic and cathodic measurements obtained in the three environments. The results are quite different from those shown previously in that the anodic exchange current (determined by extrapolation from the Tafel region) is greater than the cathodic exchange current in solutions A and B. The electrochemical constants obtained for solution A are: $\beta_C = 0.104$ v, $\beta_A = 0.286$ v, $i_{oa} = 0.0085$ μa/cm², and $i_{oc} = 0.0052$ μa/cm². Also the intersection of the

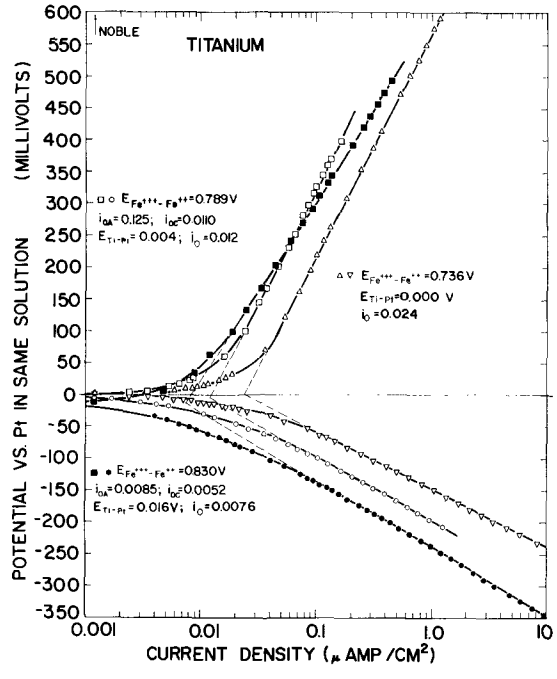

Fig. 9. Anodic and cathodic polarization of three different ferric-ferrous solutions on Ti.

anodic and cathodic Tafel curves occurs at a potential 15 mv more active than Pt in the same solution, while the steady-state potential was 16 mv more active than Pt.

These observations are best explained by considering that Ti is reacting in this environment and that during anodic polarization measurements the rate of oxidation of Ti metal is the same order of magnitude as the rate of oxidation of ferrous ions. Thus, the observed anodic data represent the summation of $\overleftarrow{i_m}$ and $\overleftarrow{i_{Fe^{++}}}$ at any potential. The sum of two Tafel lines can result in data which are Tafel-like in appearance. Thus, the value of β_A given above cannot be considered as representative of the oxidation of ferrous ions. The exchange current for the ferric-ferrous system, however, can be considered as equal to the value determined from the cathodic data, since the cathodic Tafel slope would not be influenced significantly by Ti solution. It is interesting to note that the corrosion current necessary to polarize the ferric-ferrous system to the steady-state electrode potential of 16 mv is only about 0.003 μa/cm². This corrosion rate is too low to measure by direct weight-loss techniques since a 1 cm² sample would lose only about 1 mg in 60 years. This extremely small corrosion rate affects the potential significantly because the exchange current in this environment is very small.

A situation similar to that described above exists for solution B where the electrochemical constants were found to be: $\beta_C = 0.102$ v, $\beta_A = 0.358$ v, $i_{oa} = 0.0125$ μa/cm², and $i_{oc} = 0.0110$ μa/cm².

The intersection of anodic and cathodic curves in this case occurs at a potential 4 mv more active than Pt in the same solution whereas the steady-state potential was 3 mv more active than Pt. In this case, β_A is probably not markedly affected by $\overleftarrow{i_m}$.

The potential of Ti in solution C is the same as Pt to within 0.1 mv. In this case, the anodic and cathodic exchange currents were equal. The electrochemical constants determined from the polarization curves are $\beta_C = 0.091$ v, $\beta_A = 0.352$ v, $i_o = 0.024$ μa/cm². Also, the cathodic polarization curve for reduction of ferric ions can be calculated from anodic data, and the anodic polarization curve for oxidation of ferrous ions can be calculated from cathodic measurements in the manner described previously (6).

It is interesting to note that no indication of oxygen evolution was observed in the anodic data of Fig. 9 even though potentials more noble than 1.2 v vs. the standard hydrogen electrode were reached. This must mean that the Tafel parameters for oxygen evolution are such that polarization is quite pronounced. The exchange current must be very small, and the β_w value may be higher than the values reported for the Fe- and Ni-base alloys investigated.

Discussion

One of the factors which affects the rate of propagation of pitting of an alloy in $FeCl_3$ is the degree of cathode polarization. This may be measured by the activation overvoltage parameters for the reduction of ferric ions. Polarization is more pronounced if β_C is greater or if i_o is smaller. The exchange cur-

rent is actually a function of the ferric and ferrous ion activity (10) and, thus, different alloys should be compared *in* solutions of similar composition. Table II gives a summary of electrochemical data for all the alloys investigated.

Exchange currents at similar ferric-ferrous potentials for all the materials except Ti are of similar magnitude. The exchange current on a Ti surface is consistently an order of magnitude smaller. The cathodic Tafel slope, β_c, does not vary in any uniform manner with regard to the general pitting resistance of the alloys. However, the largest values were obtained with Hastelloy alloy C.

Thus, only small differences in pit propagation rates among the various materials can be explained in terms of differences in local cathodic polarization. The major difference must, therefore, reside in variations in local anodic polarization during pitting and differences in pit initiation.

The calculated anodic polarization curve for solution of metal (potential vs. $\dot{i}_m$) should not be considered that which exists during pitting. Uhlig (2) has shown that a pit in stainless steel contains metallic ions in amounts proportional to the original alloy composition in their lower valent state. Thus, active Fe goes into solution as ferrous ions. However, when Fe is passive, the element apparently goes into solution directly as ferric ions (11).

O'Connor (12) has also shown that chromate is formed during anodic passivation of an Fe-Cr alloy in sodium sulfate and in nitric acid. Chromate was also detected during the corrosion of this material in concentrated nitric acid where the alloy is passive.

Thus, the data shown for the local anodic polarization of the alloys used here are best considered as solution of metal to directly form ions in a higher state of oxidation. Little is known about the kinetics of such processes, and, therefore, it is difficult to provide a reason for the very steep slope of the anodic polarization curve. However, this may well be a characteristic feature of passive surfaces. For example, Vetter (13) has shown that the corrosion rate of Fe passivated in nitric acid can be determined electrochemically by polarizing the surface anodically to the potential of Pt in the same solution. The current required to polarize to the Pt potential is equivalent to the corrosion rate. This can be true only if the local anodic polarization curve for passive Fe is practically vertical.

Since nitrate does not affect ferric-ferrous electrode kinetics significantly, it must be concluded that this pitting inhibitor affects either the local anodic polarization behavior of the metal or the pit initiation process. It is possible that nitrate competes with the chloride ion for adsorption surface sites, thus eliminating the tendency for local breakdown of passivity which chloride normally would create.

Acknowledgments

The author would like to acknowledge the skillful assistance of E. A. Tomes who carried out the extensive calculations and conducted many of the polarization measurements. R. C. Wilson conducted the measurements with Type 304 stainless steel, while R. M. Roth determined the effect of nitrate additions upon the polarization behavior of Ti.

Manuscript received Nov. 29, 1956. This paper was prepared for delivery before the Washington Meeting, May 12-16, 1957.

Any discussion of this paper will appear in a Discussion Section to be published in the June 1958 JOURNAL.

REFERENCES

1. M. A. Streicher, *This Journal*, **103**, 375 (1956).
2. H. H. Uhlig, *Trans. Am. Inst. Mining Met. Engrs.*, **140**, 442 (1940).
3. H. A. Liebhafsky and A. E. Newkirk, *Corrosion*, **9**, 432 (1953); *ibid.*, **12**, 48 (1956).
4. M. Stern and A. L. Geary, *This Journal*, **104**, 56 (1957).
5. J. R. Gilman, B. S. Thesis, Chemical Engrg. Dept., Massachusetts Institute of Technology (1940).
6. M. Stern, *This Journal*, **104**, 559 (1957).
7. M. E. Straumanis, S. T. Shih, and A. W. Schlechten, *ibid.*, **102**, 573 (1955).
8. M. E. Straumanis, S. T. Shih, and A. W. Schlechten, *J. Phys. Chem.*, **59**, 317 (1955).
9. E. D. Weisert, Submitted to *Corrosion*, June 1956.
10. J. E. B. Randles, *Trans. Faraday Soc.*, **48**, 828 (1952).
11. H. H. Uhlig and G. E. Woodside, *J. Phys. Chem.*, **57**, 280 (1953).
12. T. L. O'Connor and H. H. Uhlig, *This Journal*, **102**, 562 (1955).
13. K. J. Vetter, *Z. Elektrochem.*, **55**, 274 (1951).

Filamentary Growths on Copper Cathodes

T. C. J. Ovenston, C. A. Parker, and A. E. Robinson

Admiralty Materials Laboratory, Holton Heath, Poole, Dorset, England

ABSTRACT

An investigation has been made of the filamentary growths which are produced under certain conditions during copper plating at low current density. The conditions under which these growths occur have now been defined more clearly and the effect of various types of surface active agent in enhancing or preventing their occurrence has been demonstrated. Possible mechanisms for the formation of the filaments have been discussed.

The formation of polycrystalline filamentary growths of Cu during Cu plating at low current density was first reported from this laboratory by Gollop (1). At that time considerable data had already been accumulated about the conditions under which such growths would take place. The investigation was continued and it is now possible to define these conditions more clearly and to put forward a tentative theory to account for this phenomenon.

This investigation arose through the occurrence, during operation, of filamentary growths in electrolytic cells, made of Bakelite, and coated internally with a water-proof varnish, which were in extensive use. To elucidate the possible effect of the varnish coating, a large number of experiments were also carried out in glass cells. This paper reports the results of both series of experiments.

Since the original publication from this laboratory, and after the further work had been completed, van der Meulen and Lindstrom (2) reported the results of a similar investigation of filamentary growth in which the size of cell, composition of electrolyte, and current density used were all similar to those used in the present investigation. Some of the observations and certain details of procedure differed, however, and, in particular, the work of van der Meulen and Lindstrom also covered the effect of addition of chloride to the electrolyte (a study not covered at all by the present authors). To avoid confusion, therefore, references to and comparisons with this work have been made where appropriate.

Experimental

Electrolysis was carried out in sealed cylindrical cells having an internal diameter of 3.5 cm and a volume of about 30 ml. The electrodes were disks of pure Cu, the cathode having a diameter of about 2 cm. Separation between the electrode faces was 1.5 cm. In all experiments the main constituents of the electrolyte were $CuSO_4 \cdot 5H_2O$, 105; H_2SO_4, 65.5; hydroxylamine sulfate, 5.0 g/l. During electrolysis the current density on the cathode was kept constant (generally at 1 ma/cm^2) by means of a rheostat in series with the cell and 6 v storage battery. Throughout electrolysis the cells were kept entirely undisturbed with either the anode or the cathode face downward. Electrolysis was allowed to proceed for at least two weeks, but the first sign of filaments, when they were generated, usually appeared within one or two days.

Two types of plating cell were employed. The first was of Bakelite, coated internally with a bituminous varnish. The second was of glass, with polythene ends in which the electrodes were fixed. In certain experiments the glass sides of the cells were fitted with flat windows for visual and photographic observation. No attempt was made to deaerate the solutions before sealing the cells. A small air bubble (approx. 3 ml) was present in the sealed cells. In this respect, the procedure differed from that of van der Meulen and Lindstrom who flushed the electrolyte with N before electrolysis.

Some cells were fitted with an internal reference electrode of Cu through the side of the cell in a position approximately midway between the anode and cathode. Potential measurements between anode and cathode and between anode or cathode and the reference electrode were made with a d-c valve voltmeter.

The resistance of the electrolyte between anode and cathode was less than 5 ohms, giving rise to a potential drop of less than 5 mv. All potential values include the ohmic potential drop which, however, was negligible compared with the cathode overvoltages associated with filament formation.

Observations from trials in varnished cells suggested that filamentary growths were associated with some surface-active substance arising from the varnish coating, and in some experiments, therefore, commercial surface-active agents (1 g/l) were added to the electrolyte to determine their effect. The agents used were:

Anionic—Belloid: sodium salt of dinaphthylmethane disulfonic acid; Teepol: sodium salt of sulfonated secondary alcohol; Effesay L: sodium lauryl sulfate.

Nonionic—Lubrol: ethylene oxide condensed with alcohols.

Cationic—Fixanol C: cetyl pyridinium bromide.

It is understood that these are commercial products and the chemical description given is only a representation of their general character. They probably consist of a complex mixture of reacted or partly reacted substances and are likely to be

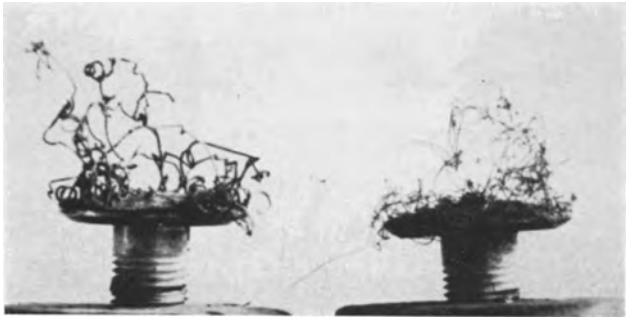

Fig. 1. Typical filamentary growth on Cu cathode

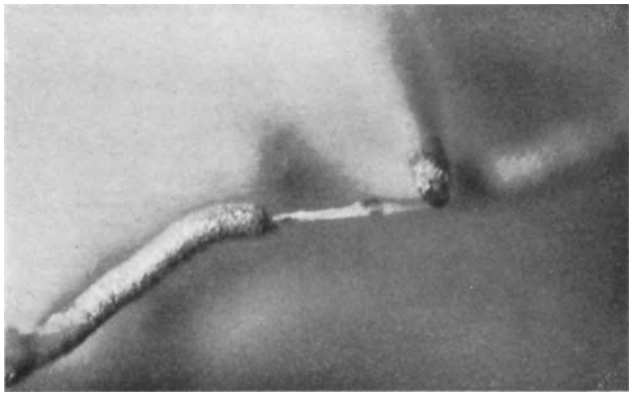

Fig. 2. Cotton fiber partly Cu plated

polymerized in varying degrees. Of the anionic agents, Effesay L was found most effective and was the one used after the first preliminary experiments.

Nature of the Filaments

The filaments were first observed in the varnished cells after plating for about two weeks. Fig. 1 shows two cathodes, selected from a large number of similar ones, which exhibit typical filamentary growths. The proportion of Cu deposited as filaments varied considerably and, in many cases such as these, it was found that an appreciable fraction of the total deposition on the cathode had occurred in the form of these filaments which were frequently several centimeters in length and of fairly uniform thickness up to 0.3 mm, depending on the duration of plating. A small proportion of the filaments were found to have a core of organic material, usually a cotton fiber. The fibers were adventitious impurity which had become electroplated. In certain cases the sheath of Cu had not extended along the whole length of the fiber. For example, Fig. 2 shows part of one such fiber, the two ends of which had been in contact with the cathode; plating had extended along the fiber from each end except for the short length in the center. It was clear, from a comparison of the thickness of Cu on the fiber with that deposited on the cathode proper, that in many cases plating had occurred on the fiber from an early stage in the electrolysis.

Although the occurrence of plating on an apparently nonconducting fiber was in itself remarkable, the nature of the majority of the filaments was even more so. Microscopic examination of sections through the latter failed to reveal any discrete core. Fig. 3 shows a section through the root of a typical filament at the point where it joins the main cathode. The core consists of fine-grain Cu similar to

Fig. 3. Section through root of a typical filament

that which was first deposited on the cathode. Subsequent plating consists of much larger oriented crystals, again similar to those subsequently deposited on the cathode. After examination of many such sections one is bound to postulate the existence of invisibly fine conducting paths leading from the cathode at an early stage in the plating process, notwithstanding the fact that such growths appeared even after filtration of the electrolyte through sintered glass filters and prewashing of the cells with distilled water.

Correlation of Filamentary Growths with Cathode Potential

When a number of varnished plating baths were run simultaneously under apparently identical conditions, filamentary growths did not necessarily appear in all cells. Over a period of time, a large number of apparently identical tests were run in which measurements of interelectrode potential were made. As might be expected it was found that the occurrence of the abnormal growths was associated with very high interelectrode potentials. Thus, in 155 such tests in varnished cells, 82 gave anode-cathode voltages between 100 and 250 mv, even after plating had proceeded for several days. Of these 82 cells, 59 produced filaments and the plating in the remainder was abnormal, being of nodular form. All cells showing an interelectrode potential greater than 150 mv produced filaments, while none which showed potentials less than 100 mv produced them. It was also observed that those cells which had stood for one or two weeks with the electrolyte in contact with the varnish before electrolysis gave higher potentials and showed a greater tendency to filamentary growth than those in which electrolysis had been started almost immediately after filling.

That the high potentials and growths were due to impurities leached from the varnish was demonstrated by experiments with the glass cells. With unadulterated electrolyte, low cell potentials were invariably obtained (30-50 mv) and no filamentary growths were formed. Electrolyte which had been in contact with the varnish produced high potentials and, frequently, filamentary growths. In the latter experiments it was demonstrated, by measurements

Table I. Some typical electrode potentials

Time	Cell (a) (plain electrolyte) Cathode	Cathode — anode	Cell (b) (electrolyte adulterated with varnish) Cathode	Cathode — anode	Cell (c) (electrolyte containing 0.1% "Fixanol C") Cathode	Cathode — anode
Start of electrolysis	20-30	40-50	160	240	300	420
After 10 min	20-30	40-50	175	220	300	360
After 2 weeks	20-30	40-50	150	170	290	350

against the third reference electrode, that the persistently high potentials originated at the cathode, the anodic potential always remaining low (20-30 mv) except during the very early stages of the electrolysis.

Experiments with Surface Active Agents

From the experiments just described it was clear that the cause of the abnormal growths was some impurity leached from the varnish by the action of the electrolyte. This impurity apparently became adsorbed on the cathode to produce the high overvoltages observed. Experiments were therefore carried out with various surface active agents in attempts either to produce filaments in the absence of varnish extract or to suppress their formation in its presence.

The following effects were observed using commercial products (*see* experimental section) as compared with control experiments without additions: (*a*) in the presence of varnish, anionic agents gave fair or good plating with no Cu filaments; nonionic and cationic agents led to greatly increased crops of filaments; (*b*) in the absence of varnish, anionic and nonionic additions gave normal plating, but cationic additions led to numerous growths.

This was the first occasion on which the effect of cationic agents in promoting these filamentary growths had been demonstrated unambiguously, and was described by one of the authors (A.E.R.) in a report from this laboratory in February 1954, and which was communicated to van der Meulen and Lindstrom, who have recently reported similar experiments with surface-active agents (2). The latter authors have acknowledged this source of information in an unpublished report from their laboratory.

Table I records some typical electrode potentials observed in the presence of a cationic agent ("Fixanol C") as compared with those obtained with unadulterated electrolyte and with electrolyte adulterated by the varnish.

There was a marked similarity between the potentials obtained when the cationic agent was added to the electrolyte in glass cells, those from varnish-adulterated electrolyte in glass cells, and those from the varnished Bakelite cells. This strongly suggested that the substance responsible for the filamentary growths in varnished cells was cationic in character. Experiments with anionic agents, on the other hand, showed that these were able to neutralize the effect of the cationic ones. The increase in growths in the presence together of varnish and nonionic surface active agent was probably due to more effective wetting of the varnish surface and leaching of the active impurity. The results in columns 6 and 7 of Table I suggest that the cationic agent adsorbed on the anode is capable of producing a high overvoltage here also at the start of the electrolysis but, as might be expected, this is largely destroyed after electrolysis proceeded for a short while.

Because the substances responsible for filamentary growth in the varnished cells were shown to be cationic in character, it would be expected that the addition of an anionic agent would neutralize their effect. To test this possibility, trials were carried out with the anionic agent Effesay L, in concentrations 0.02-0.5 g/l, in 20 varnished cells. No cell gave filaments and in all cases the final potential difference was less than 100 mv.

After the present investigation had been completed, van der Meulen and Lindstrom (2) reported that the addition of 0.03 g/l of Dupont Safranine T "125%" to the electrolyte prevented filament formation caused by the presence of Polysoap G.147. To determine the effect of this addition in the varnished cells, trials were carried out by the present authors using cells drawn from the same group as the twenty referred to in the previous paragraph, and which were known to be prone to filament formation. Eight cells containing Dupont Safranine T "125%" (at the recommended concentration) and four cells containing Safranine T from another source all produced filaments. The cell potentials in these tests were all in the range 140-150 mv and remained high throughout the 14-day trial. Therefore, it seems that, although the Safranine T in the experiments of van der Meulen and Lindstrom was able to reduce cathodic overvoltage and prevent filament formation arising from the presence of Polysoap G.147, it was unable to prevent the formation of filaments caused by the agent in the varnish, and is not therefore of general application for the inhibition of filamentary growth.

Direct Observation of Filamentary Growth

Some experiments were carried out in sealed glass cells with plane windows so that successive stages in the development of the filaments could be closely watched and photographed. In these experiments the end caps of these cells were varnished, and the electrolyte was allowed to stand in contact with the varnish for a week before electrolysis. Thus, the observed behavior is as would have been expected for varnished cells. Successive stages in the filamentary growth are shown in Fig. 4 *a*, *b*, and *c*. Within a few hours after the start of electrolysis some very fine short tendrils of Cu were observed (Fig. 4*a*). With the passage of time these thickened and lengthened as shown in Fig. 4*b* and *c*. In a similar manner the growth of Cu along textile fibers was observed in

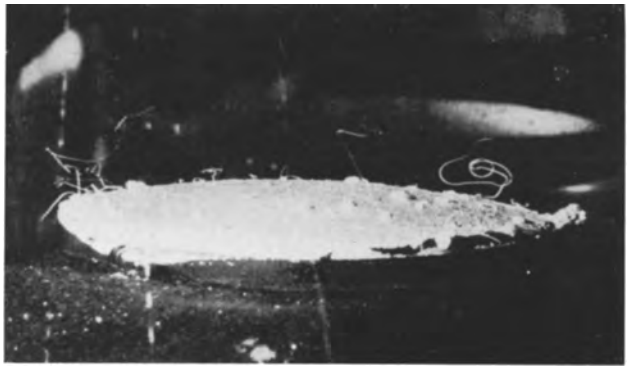

Fig. 4a. Stages in the growth of Cu filaments: after electrolysis for 7 hr.

Fig. 4b. Stoges in the growth of Cu filaments: after electrolysis for 27 hr.

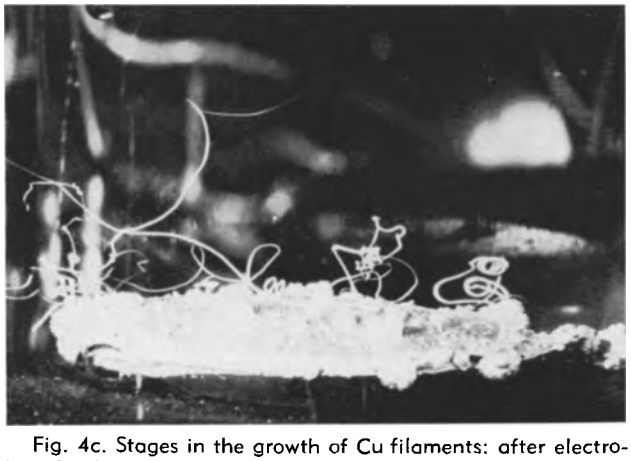

Fig. 4c. Stages in the growth of Cu filaments: after electrolysis for 6 days.

cells containing contaminated electrolyte (and showing a high cathodic overvoltage). For example, with a small bunch of untreated cotton wool in contact with the cathode, Cu plating was observed to extend along the fibers and ultimately thicken to produce filaments of the type already found in small numbers in the original experiments. Some cotton wool which has become partly Cu-plated by this process is shown in Fig. 5.

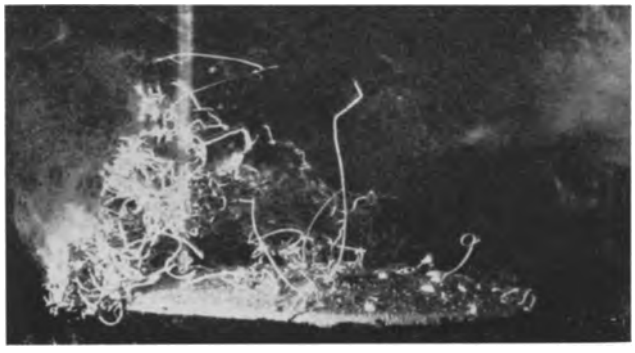

Fig. 5. Cotton wool plated by contact with cathode showing high overvoltage.

Mechanism of Filamentary Growth

From the results already described, it is evident that two types of filament have been observed in the present investigation. Both are of similar outward appearance but they differ in the fact that one contains an observable core of organic fibrous material on which the growth has taken place, while the other contains no such discrete core. It is possible, however, that the difference is only one of degree and before considering mechanisms for the formation of the second type of filament it is worth considering the first in more detail.

These two types of filaments should not be confused with the two types referred to by van der Meulen and Lindstrom (2), who have not reported the phenomenon of the plating of cotton fibers and other organic material, which plays a prominent part in the theory of filament formation discussed here. Van der Meulen and Lindstrom observed the convoluted type of filament associated with high cathodic overvoltage which corresponds to the second type described herein, and they also observed an unusual type of growth arising in the presence of chloride in the electrolyte. The chloride-produced filaments, which are apparently associated with lower cathodic overvoltages and have an entirely different structure, were not studied by the present authors, whose experiments were conducted throughout with chloride-free electrolyte (except in the later experiment in which Safranine T, which itself contained chloride, was used).

The observed requirement for the plating of certain organic material is, simply, contact with a cathode showing high and persistent overvoltage. In the absence of this high overvoltage, plating of such organic material never occurs, although all other conditions may be the same. It is suggested therefore that the cellulose fiber (for example) has the property of destroying locally the overvoltage at its point of contact with the cathode so that Cu is deposited rapidly at this point. Assuming that the newly deposited Cu itself rapidly adsorbs surface active agent (and thus effectively becomes a part of the main cathode), the only point at which plating can occur readily is at the newly formed interface between the deposited Cu and the fiber. It is postulated therefore that deposition continues to take place rapidly and preferentially at this point and that an exceedingly thin coating of Cu thus grows rapidly along the fiber from the cathode. In the early stages this coating might well be invisible and of comparatively high resistance per unit length of fiber. Forming part of the cathode, however, it subsequently plates in the normal manner but more rapidly at points close to the cathode than at more distant points owing to its very high resistance. Ultimately

the plating becomes thick enough to be visible, first near to the cathode and then at more distant points, as has actually been observed. The formation of Cu-coated fibers seems to be explained satisfactorily on this basis.

At first sight, the formation of filaments of the second type by a similar process seems likely. For example, the initial growth of Cu, i.e., to the point where the filament first becomes visible, certainly takes place from the main cathode outward (*see* Fig. 4). There is also evidence of the presence of a very fine conducting path on which the initial (fine grain) deposition of Cu takes place (*see* Fig. 3). However it is very difficult to account for the source of this conducting path in terms of a discrete thread of material on which the deposition could have taken place. Such threads would have to be up to an inch or more long and would surely have been removed by filtration. Therefore, if the filaments of the second type have indeed been formed in this way, the fine threads must have been built up in the solution from smaller units capable of passing the filter, e.g., the molecules of surface active agent. Unfortunately, no direct evidence of the formation of such long "polymer chains" in the solution is available.

Although the experimental evidence is at present insufficient to provide the basis for a complete explanation of the mechanism of the growth of the Cu filaments, it is worth mentioning one or two incidental observations which were made during the course of the experiments, and which have led to conjectures about the mechanism of their formation. In particular it was observed that soon after the start of electrolysis in the presence of the added cationic surface-active agent, a visible film of the coagulated surface-active agent was observed on the anode. This material subsequently broke away from the anode and fragments coming into contact with the cathode rapidly became Cu plated. It would seem, therefore, that the surface-active agent, which when adsorbed from solution causes a high overvoltage on the cathode, is capable, when coagulated, of breaking down this overvoltage locally. If a mechanism could be envisaged whereby the coagulated material formed long and extremely fine threads, then the formation of Cu filaments could be readily explained. One hypothesis which has been considered is that the organic thread is produced continuously at the tip of the growing filament (in the very early stages when the Cu coating is invisibly thin) by coagulation resulting from the rapid deposition of Cu occurring at an adjacent point on the tip. However, no theoretical basis for this mechanism can be produced.

Another unusual and possibly significant phenomenon was observed in solutions containing added cationic surface-active agent. After electrolysis had started and the film of coagulated surface-active agent on the anode was disrupted, fine particles were observed in the liquid; these occasionally appeared to form into fairly well defined streams between the anode and the cathode. It is perhaps tempting to connect these streams of particles with the filament formation, but again no reasonable mechanism has been formulated.

All these tentative theories for filamentary growth differ fundamentally from the theory advanced by van der Meulen and Lindstrom (2). Although these authors recognize the importance of the adsorbed layer on the cathode, they assume, apparently without experimental evidence, that the birth of a filament depends on the coincidence of a suspended particle meeting a break in this layer and, also, the propagation of the filament by the continuous displacement of this particle by the depositing Cu. The present authors prefer the mechanism in which the contact of the foreign matter itself causes the local breakdown of the high overvoltage and becomes Cu-plated, although whether the organic core of the resultant Cu filament is "pre-formed' in the solution or is built up simultaneously with the plating process has not been decided. This theory is strongly supported by the experimental evidence that (*a*) foreign matter in the form of filaments, e.g., cotton wool, does, in fact, become plated on contact with a cathode showing the high overvoltage, and (*b*) coagulated surface-active agent also becomes plated on contact with such a cathode.

Although the suggested mechanism of formation of filaments of the first type (having a discrete fibrous core) is a reasonable one, it has not yet been possible to show how this mechanism can be extended to explain in detail the formation of the second type of filament having no discrete organic core, and it must be admitted that this still remains largely a matter for conjecture and further experimental work.

Acknowledgment

This communication is published by permission of the Admiralty.

Manuscript received October 1, 1956. This paper was prepared for delivery before the Buffalo Meeting, Oct. 6-10, 1957.

Any discussion of this paper will appear in a Discussion Section to be published in the June 1958 JOURNAL.

REFERENCES

1. H. Gollop, *Bull. Inst. Metals*, **2** (1), 7 (1953).
2. P. A. van der Meulen and H. V. Lindstrom, *This Journal*, **103**, 390 (1956).

Cerium-Activated Halophosphate Phosphors

S. T. Henderson and P. W. Ranby

Thorn Electrical Industries Ltd., London, England

ABSTRACT

This paper describes the characteristics of a new group of alkaline earth halophosphate phosphors activated by cerium and manganese, and contrasts their behavior with that of halophosphates containing other primary activators. In their preparation these cerium-activated materials show marked differences from other previously known halophosphates, but the luminescent properties are similar to those of the tin-activated system. The behavior and possible uses of these phosphors in fluorescent lamps are described.

The use in fluorescent lamps of Sb-activated alkaline earth halophosphate phosphors of an apatite-like structure was first proposed in 1942; almost immediately it was found that the primary activator Sb could be replaced by other elements, As, Bi, Sn, or Pb (1). About eight years later a method of activating the matrix by Ag was developed (2). It has now been found that these materials can be activated by Ce; Mn can be incorporated as a secondary activator to modify the fluorescent emission in much the same way as with other primary activators (3). The discovery of new primary activators of this system has resulted from advances in the techniques of phosphor research, and also from a changing appreciation of the wide variations in formulation which can result in the formation of an apatite structure.

Preparation of Cerium-Activated Halophosphates

Essentially, these materials are prepared by the usual methods adopted for phosphate phosphors. For example, an intimate mixture of the matrix forming components and suitable compounds of the activators is heated to 1100°-1200°C in a mildly reducing atmosphere such as a mixture of H_2 and N_2.

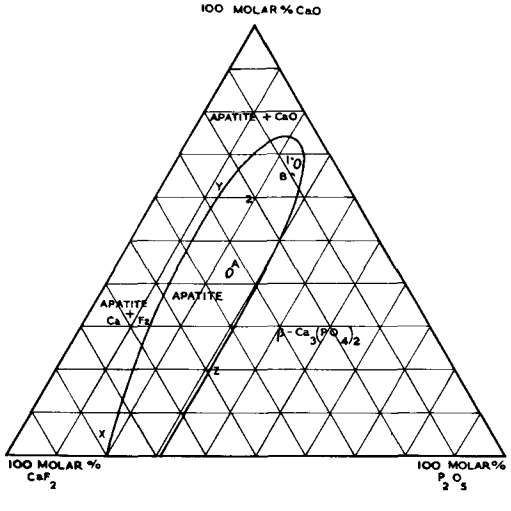

Fig. 1. XYZ: initial formulations (in molar percentages) of unfired mixtures which give products with the apatite crystal structure after firing. Points 1 and 2: theoretical apatite and wagnerite compositions, respectively. A, compositions for Ce-activated halophosphates; B, compositions for Sb-, As-, Sn-, Pb-, or Ag-activated halophosphates.

Formulation

The ratio of the matrix forming components in the initial mixture differs widely from that which would be expected to yield an apatite structure. However, x-ray analysis confirms the crystal structure of these Ce-activated phosphors to be essentially that of apatite. This wide divergence in initial formulation is shown in Fig. 1.

In Fig. 1 the ranges of formulations of starting components which will yield the apatite structure by heating to temperatures of the order of 1100°-1200°C are those within the continuous line XYZ. The formulations are expressed in terms of molar percentages of CaO added as $CaCO_3$, P_2O_5 added as diammonium hydrogen phosphate, and CaF_2 used in the initial mixtures. These were heated in silica crucibles, and reactions such as the following could account for the formation of apatite-like products from any mixtures initially free from $CaCO_3$, i.e., oxide.

$$25CaF_2 + 6P_2O_5 \rightarrow 5Ca_5(PO_4)_3F + 9PF_5$$
$$20CaF_2 + 6P_2O_5 + 9SiO_2 \rightarrow 4Ca_5(PO_4)_3F + 9SiF_4$$

Irrespective of the mechanism by which apatite results from initial mixtures widely differing from those which would be expected to yield apatite, it is found that the mixtures used to prepare bright Ce- or Ce- and Mn-activated phosphors lie within area A, whereas those for the preparation of Ag-, Sb-, Sn-, Pb-, and As-activated halophosphates (with or without Mn) lie within the area B. Area B is adjacent to point 1, which is the theoretical formulation of apatite $Ca_5(PO_4)_3F$; point 2 is theoretical wagnerite $Ca_2(PO_4)F$.

Analysis of Ce-activated fluorophosphate phosphors shows that, despite the high proportion of fluoride used in the preparation, they are readily soluble in acid without leaving any insoluble residue; the proportion of fluoride in the product is about 10% greater than in a normal fluoroapatite.

The formulations defining the areas A and B are empirical mixtures arrived at solely for the purpose of producing the optimum brightness of fluorescence,

using the normal type of phosphor preparation in silica ware. For the purposes of calculation all chloride in the initial mixtures, even when present as NH_4Cl, has been calculated as its equivalent in terms of CaF_2, all Mn and Sr compounds have been calculated as their equivalent of Ca compounds. Also, in practically all cases the formulations defining areas A and B utilized a precipitated phosphate such as $CaHPO_4$ as the source of phosphorus, and this has been calculated in terms of metal oxide and P_2O_5. In every case the primary activator has been ignored in the calculation. The outstanding feature shown by these calculations is that for calcium or calcium strontium fluoro- or fluorochloro-phosphates of an apatite structure, the initial compositions for the preparation of phosphors of the brightest luminescence are essentially the same irrespective of the primary activator, except when this is Ce.

Position of Activator

This effect, when the primary activator is Ce, is not explained by differences in the concentrations of the primary activators in the initial mixtures for the brightest luminescence (Table I), nor is it explained by differences in the volatility of the halides of the primary activators.

In view of the relatively low concentrations of activators present in a phosphor and the many assumptions which have to be made, it is felt that normal analytical methods give meaningless results for the valency of activators unless the system is a particularly simple one. It is therefore necessary to deduce the valency of Ce from the preparative conditions, which in this case indicate that the Ce is trivalent. The most likely position for the Ce in the apatite lattice is at alkaline earth metal sites especially as the ionic radius of the cerous ion is intermediate between those of Ca and Sr. This position for the trivalent Ce requires charge compensation satisfied by the incorporation of additional fluoride ions in the lattice. To achieve this increase in fluoride concentration in the matrix a relatively large excess of fluoride is required during the preparation.

Evidence in support of this explanation is provided by F estimations on calcium strontium fluorophosphate (Ce, Mn) phosphors. For a sample with a Ca to Sr ratio of 4:1 and containing known amounts of Ce and Mn, the calculated concentration of F would be 3.43% if present in only normal apatite proportions, and 3.95% if in addition 1 F atom/Ce atom is required for charge compensation. The amount of F actually found was 3.76%. In a similar fluoro-chloro-phosphor the total halogen was found to be equivalent to 3.70% F. These analyses would indicate that only about 60% of the Ce is charge-compensated by F if all the Ce is present in the trivalent form. It is interesting that in a study of the Ce- and Mn-activated calcium orthophosphates Froelich and Margolis (4) found that sufficient charge compensation of the (cerous) cerium activator was effected by 1 Na ion/2 cerous ions. It may be noted that in the present halophosphate materials there is some benefit from the incorporation during the preparation of an alkali metal (Li or Na) (3) which may complement the F as charge compensator.

Table I. Atoms of primary activator/atom of phosphorus used in initial mixtures for optimum fluorescence

Sb	4×10^{-2}
As	6×10^{-2}
Sn	6×10^{-2}
Pb	8×10^{-2}
Ag	6×10^{-3}
Ce	6×10^{-2}

In contrast to the behavior of these Ce-activated halophosphates, the Sb-activated materials generally contain less than the calculated concentration of halogen. For example, a Cool White type of halophosphate was found to contain 2.98% F and 0.61% Cl, giving a total equivalent of 3.30% of F compared with a theoretical value of 3.75% for apatite.

Except with Ag, the primary activators of the halophosphate matrix are all used in similar proportions (Table I). Some of these (Sn^{2+}, Pb^{2+}) are present in the matrix in the divalent form and require no excess of halide. The others (As, Sb) can occupy lattice sites other than those of the alkaline earth metals, for example the phosphorus positions, or they may be incorporated so that two alkaline earth atoms are replaced by two trivalent antimony atoms and one oxygen to maintain neutrality (5). The position of Ag is more difficult to explain unless pairs of ions replace a single alkaline earth metal, but the role of Ag is obviously different from that of any of the other primary activators as its smaller concentration shows.

Luminescence of Cerium-Activated Halophosphates

Like other halophosphate systems, these Ce-activated materials are strongly excited by short wave-length ultraviolet; long wave-length ultraviolet only excites a feeble luminescence associated with the secondary activator Mn. In general luminescent characteristics, these materials resemble those with Sn and Pb more closely than those with Sb.

In the absence of Mn, the Ce-activated phosphors emit strongly in the ultraviolet when excited by 2537Å radiation. For example, the relative values of the ultraviolet emission peaks, in energy per unit wave length, for calcium strontium halophosphate (Ce), calcium halophosphate (Sn), calcium halophosphate (Pb), and calcium silicate (Pb), are 75, 5, 2, and 20, respectively, whereas for barium disilicate (Pb), a system not capable of transforming its ultraviolet energy into the emission of another activator, the value is 100. Incorporation of Mn produces a strong emission in the visible and the posision of this band depends on the ratio of combined F to Cl in the matrix. Consequently a range of phosphors varying in color of fluorescence from yellow to orange-red can be obtained by variations in the concentration of Mn and ratio of F to Cl.

Replacement of Ca by Sr causes a slight shift of the emission to longer wave lengths and in addition products containing both Ca and Sr are brighter than the corresponding Ca material. An atomic ratio of Ca to Sr of 4:1 is desirable for maximum intensity of luminescence, and except where otherwise indi-

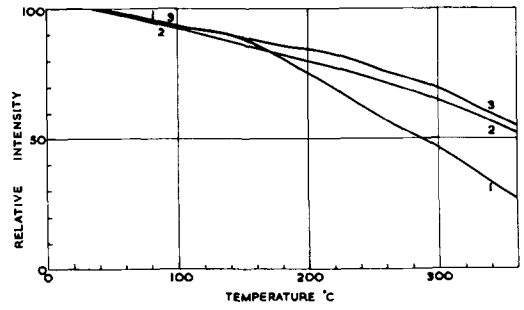

Fig. 2. Brightness vs. temperature curves of [1] calcium strontium fluorochlorophosphate (Ce, Mn); [2] calcium fluorochlorophosphate (Sn, Mn); [3] calcium fluorochlorophosphate (Sb, Mn).

cated this ratio has been used in all the materials described.

The fluorescence excited by 2537Å is slowly reduced in intensity as the temperature of the phosphor is raised (Fig. 2). The decline in intensity is of about the same order as that shown by other halophosphates and, as with these other materials, the color of the fluorescence is seen to become more green as the temperature is raised.

Use in lamps.—These materials can be used in conventional fluorescent discharge lamps but, as usual with phosphors whose preparation requires a reducing or partially reducing atmosphere, baking of coated tubes needs special care in order to minimize oxidation of the phosphor which would cause loss of brightness.

Although the initial intrinsic brightness of Ce-activated halophosphates is at least as high as that of similar Sb-activated materials, owing to the difficulties of lamp processing the brightest 48T12 40W lamps prepared by conventional suspension coating and baking techniques are only of the order of 55 lpw initially, with a maintenance of about 96% and 93% at 100 and 500 hr, respectively. However, binderless coating techniques may overcome the loss in brightness incurred by binder-removing processes; since these Ce-activated materials are not so susceptible to grinding as Sb-activated halophosphates they may prove very suitable for electrostatic coating.

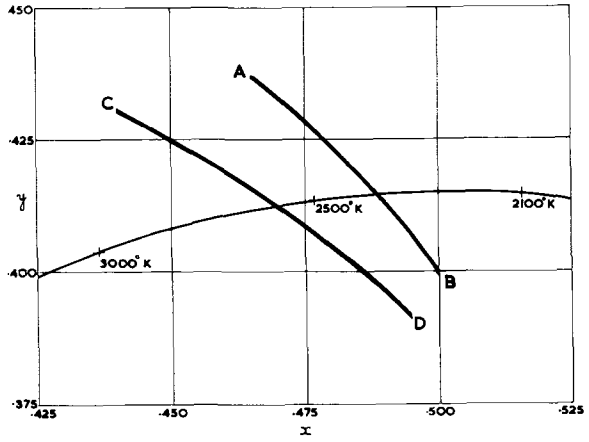

Fig. 3. Chromaticity plots of 48T12 40W lamps containing: (A-B) Ce- and Mn-activated halophosphates ond (C-D) Sn- and Mn-activated halophosphates.

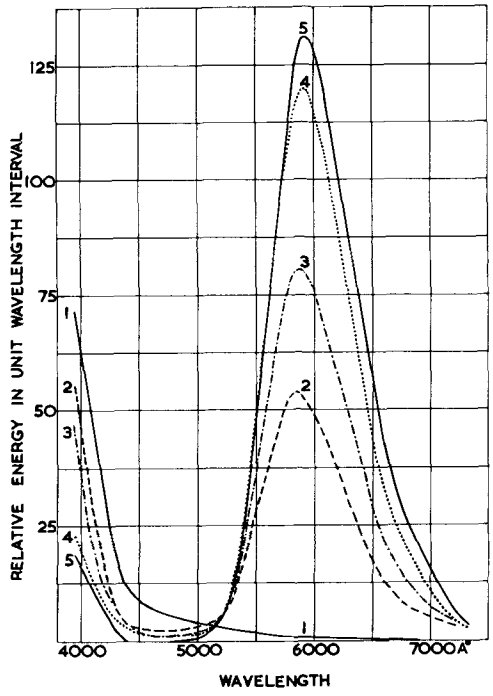

Fig. 4. Spectral energy distribution curves of calcium strontium fluorochlorophosphates activated by Ce and [1] 0, [2] 0.006, [3] 0.012, [4] 0.024, and [5] 0.036 atoms of Mn/atom of P, excited by 2537Å at room temperature. Phosphor composition: (Ca + Sr + Mn):Ce:P = 4.8:0.16:3. Ca:Sr = 4:1. F:Cl = 0.85:0.15. Fired at 1150°C for ½ hr in a closed crucible followed by ½ hr at 1150°C in N_2 + H_2.

Color measurements on 48T12 40W lamps show that the color changes obtained by variations in composition follow a narrow band about the line AB (Fig. 3) which cuts the black body locus at 2360°K. A similar series of lamps prepared using the Sn- and Mn-activated materials gives colors following a narrow band about the line CD which cuts the black body locus at 2580°K.

Cerium emission.—The fluorescent emission due to activation by Ce alone is a fairly broad band centered at about 3400Å when the phosphor is excited by 2537Å radiation. Activation of the halophosphate matrix by Sn or Pb produces similar emission bands in the ultraviolet centered at about 3900 and 4400Å, respectively.

Manganese emission.—Incorporation of Mn as a secondary activator produces emission in the visible of an intensity depending on the concentration of Mn. These changes are shown by the curves in Fig. 4. These materials differ only in concentration of Mn. As this concentration increases, the Mn emission increases in intensity to a maximum at about 0.036 atoms Mn/atom of P; the ultraviolet band due to Ce, of which only part is shown, decreases. This is obviously a case of sensitized luminescence similar to that of calcium orthophosphate (4), or calcium fluoride (6), similarly activated.

If these emission curves, converted to a frequency basis, are analyzed by the usual methods (7), it is found that the Mn emission consists of at least two bands, a major band in the yellow and a minor one in the red, and that both of these increase with Mn concentration. These results are tabulated in Table II.

Table II. Emission bands of Ce-activated halophosphates

Matrix	Mn content atoms Mn/ atom P	Relative intensity of maximum of Yellow band	Relative intensity of maximum of Red band	Position of yellow band maximum Å
Fluoro-phosphate	0	0	0	—
	0.006	33	3.5	5750
	0.012	51	5.5	5760
	0.024	87	16	5815
	0.036	100	14.5	5840
Fluoro-chloro-phosphate	0	0	0	—
	0.006	33	3.5	5840
	0.012	51	8	5870
	0.024	76	11	5915
	0.036	84	13	5930

In all cases the main yellow band is very close to a Gaussian distribution, but the red emission may consist of more than one band. This red emission extends from 6000 to 7000Å in the fluorophosphates and even further, to 7300Å, in fluorochlorophosphates of high Mn content.

As indicated earlier, the intensity of the Mn emission is at a maximum when the atomic ratio of Ca to Sr in the matrix is about 4:1, but the effect on the position of the emission band of partially replacing Ca of the matrix by Sr is relatively slight. For example, the peak of the Mn yellow band is displaced to shorter wave lengths by only about 40Å when the alkaline earth metal is all Ca instead of the 4:1 ratio more generally used.

Conclusion

In a previous paper (8) on magnesium fluorosilicate it was suggested that the efficiency of emission in sensitized phosphors was increased by proximity of the sensitizer and activator bands. The optimum relation of these bands appeared to occur in Sb-sensitized halophosphates, but the present Ce-sensitized materials have a luminous efficiency at least as high as the Sb phosphors, in spite of the location of the sensitizing band in the ultraviolet. The original hypothesis assumed that all sensitizing bands were excited with equal efficiency by 2537Å radiation. It is clear that this is not the case, for the Ce-activated halophosphates, in the absence of Mn, show an exceptionally high ultraviolet emission compared with other systems having sensitizer emission bands in this region. This high efficiency would clearly have a favorable effect on the amount of emission in the Mn band and might offset the energy loss due to the production of one activator quantum from one much larger sensitizer quantum. A continued study of the efficiency of excitation of these sensitizer bands and their conversion to visible emission bands by secondary activators is in progress.

Acknowledgment

The authors thank the Directors of Thorn Electrical Industries Ltd. for permission to publish.

Manuscript received March 22, 1957. This paper was prepared for delivery before the Washington Meeting, May 12-16, 1957.

Any discussion of this paper will appear in a Discussion Section to be published in the June 1958 JOURNAL.

REFERENCES

1. H. G. Jenkins, A. H. McKeag, and P. W. Ranby, *J. (and Trans.) Electrochem. Soc.*, **96**, 1 (1949).
2. P. W. Ranby, *This Journal*, **98**, 299 (1951).
3. P. W. Ranby, British Pat. 21348/55, July 22, 1955; 8893/56, Mar. 21, 1956.
4. H. C. Froelich and J. M. Margolis, *This Journal*, **98**, 400 (1951).
5. K. H. Butler and C. W. Jerome, *ibid.*, **97**, 265 (1950).
6. R. J. Ginther, *ibid.*, **101**, 248 (1954).
7. P. W. Ranby, D. H. Mash, and S. T. Henderson, *Brit. J. Appl. Phys.*, Suppl. 4, S18 (1955).
8. P. W. Ranby and S. T. Henderson, *This Journal*, **102**, 631 (1955).

The System Cadmium Oxide-Boric Oxide

II. Fluorescence

F. A. Hummel and E. C. Subbarao

Department of Ceramic Technology, College of Mineral Industries,
The Pennsylvania State University, University Park, Pennsylvania

ABSTRACT

The luminescence of the compounds $2CdO \cdot B_2O_3$, $3CdO \cdot 2B_2O_3$, and $2CdO \cdot 3B_2O_3$ has been investigated under 2537Å radiation and cathode ray excitation for a wide range of manganese concentrations. Under 2537Å radiation, each compound emits in the orange or orange-red with a peak intensity near 6200Å at room temperature. For each composition there is a broad maximum in the relative intensity between MnO concentrations of 0.1-1%. The 3:2 compound appears to yield the brightest phosphor, but the 2:1 compound is only slightly less intense for equivalent manganese additions. The 2:3 compound yields only half the relative brightness of the 3:2 compound for equivalent manganese concentrations.

Under cathode ray excitation, the 2:1 and 3:2 compounds fluoresce orange and the 2:3 compound fluoresces green for manganese concentrations between 0.01 and 2%.

In a recent paper (1) thermal, optical, and x-ray data were provided for four compounds in the system CdO-B_2O_3. Three of the compounds ($2CdO \cdot B_2O_3$, $3CdO \cdot 2B_2O_3$, $2CdO \cdot 3B_2O_3$) are fluorescent when activated with Mn and it is the purpose of this paper to provide some quantitative data on their emission under 2537Å and cathode ray excitation over a wide range of Mn concentrations.

Many references to cadmium borate phosphors have been made in the literature but the present data demonstrate that their compositions have been primarily in terms of technical formulations and did not necessarily denote the constitution of compounds. A review of some of the more recent papers will make manifest the significance of the data of this paper in clarifying the situation.

Kroger (2) has indicated green cathodoluminescence for the "matrices" $3CdO \cdot B_2O_3$, $CdO \cdot B_2O_3$, and $CdO \cdot 2B_2O_3$ and orange for the "matrix" $2CdO \cdot B_2O_3$.

Botden and Kroger (3) stated that $2CdO \cdot B_2O_3$ is excited by $\lambda < 3200$Å and cathode rays and then shows an orange luminescence, whereas $CdO \cdot B_2O_3$, $2CdO \cdot 3B_2O_3$, and $3CdO \cdot B_2O_3$ show a green cathodoluminescence only.

Leverenz (4) has presented emission curves for $3CdO \cdot 2B_2O_3$: 0.018 MnO and $2CdO \cdot B_2O_3$: 0.012 MnO, indicating a peak at 6260Å under 6-kv, 1μa cm^2 C. R. $CdO \cdot 2B_2O_3$: 0.006 peaked at 5380 while $CdO \cdot B_2O_3$ had both the 5380Å peak and another near 6200Å. In speaking about luminescence as a function of time, Leverenz states, "In some cadmium-borate:Mn phosphors having both a green and an orange emission band, the orange band predominates during phosphorescence".

Fonda (5), working with Mn concentrations of 0.02-1.00% by weight, 2537Å excitation, and temperatures of 80°, 300°, and 375°K, showed that above 0.50% Mn, the peak of the emission of $2CdO \cdot B_2O_3$ at 80°K lies at 6300Å and is reduced to 6200Å on sufficient increase in temperature. Below 0.1% Mn, the peak is altered only insignificantly by change in temperature and persists at the stable value of 6200Å.

Experimental Procedure

The phosphors were prepared from the fluorescent grade materials $CdCO_3$, boric acid, and $MnCO_3$. The most significant impurity present may have been sulfate, introduced through the $CdCO_3$ and ranging in amount from 0.3-1% on the basis of $CdCO_3$. The Mn concentrations (MnO) investigated for each compound were 0.01, 0.02, 0.03, 0.04, 0.06, 0.08, 0.10, 0.12, 0.15, 0.20, 0.25, 0.50, 1.00, and 2.00%.

The $3CdO \cdot 2B_2O_3$ and $2CdO \cdot 3B_2O_3$ compositions were fired in fused silica crucibles at 810° ±10°C for 2 hr. The $2CdO \cdot B_2O_3$ phosphors were fired at 850° ±15°C for 2 hr. The higher firing temperature for the 2:1 compound was necessary in order to insure complete conversion to this stoichiometric ratio, since it is known from the previous phase equilibrium studies that this compound has a lower limit of stability near 780°C.

Three additional mixtures were made with 0.1% MnO at CdO:B_2O_3 ratios of 1:1, 1:2, and 1:3.

Emission curves for 2537Å and cathode ray excitation were obtained on a General Electric recording spectrophotometer, standardized with a commercial sample of cadmium borate.

Reproducibility of results was checked by measurements on the same composition prepared at intervals of two months or more, by firing at several different temperatures other than those listed above,

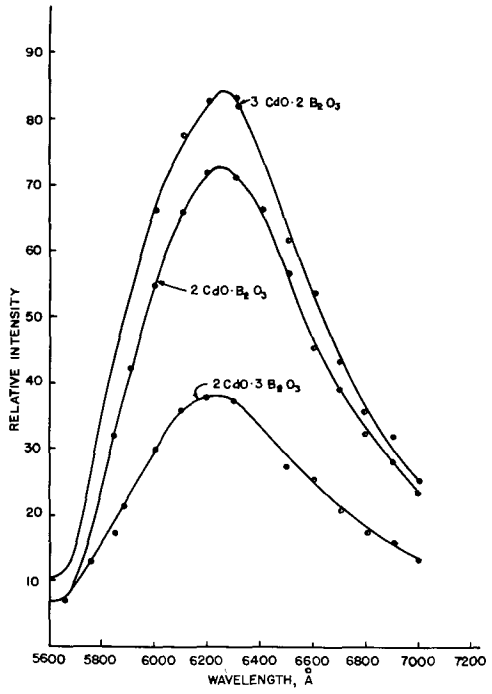

Fig. 1. Typical emission curves for three cadmium borate compounds activated with 0.25% MnO (2537Å excitation); intensity relative in terms of a commercial cadmium borate phosphor.

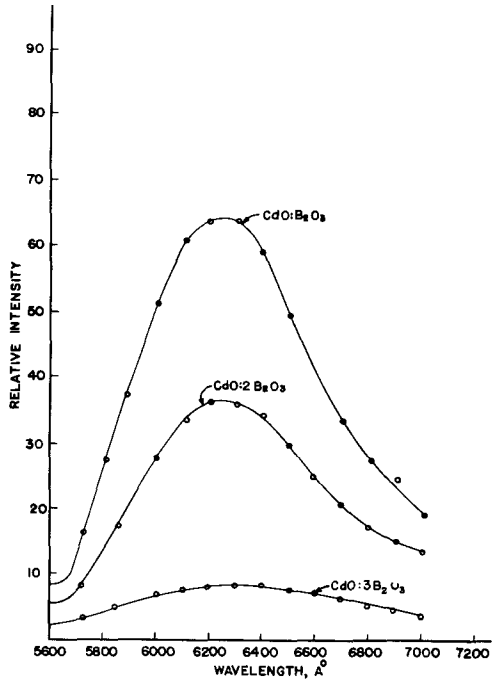

Fig. 2. Emission curves for $CdO:B_2O_3$ mixtures 1:1, 1:2, and 1:3 activated with 0.1% MnO (2537Å excitation); intensity relative in terms of a commercial cadmium borate phosphor.

and by comparing results from sintered samples with those which had been obtained on fused and recrystallized products.

Results and Discussion

2537Å Excitation.—The form of the emission curve which is typical for all three compounds for 2537Å excitation is shown in Fig. 1. The peak emission at room temperature occurred near 6200Å. It is interesting to note that, although the emission spectra for the 3:2 and 2:3 compounds are similar in form, the 2:3 preparation looks much "pinker" when made into lamps, relative to the 3:2 compound, due probably to the difference in brightness.

The emission curves for the 1:1, 1:2, and 1:3 mixtures for 2537Å excitation are shown in Fig. 2. It is noteworthy that the curve for 1:1 is intermediate between that for 3:2 and 2:3 as might be expected on the basis of a mechanical mixture. The peak intensity for the 1:2 mixture is comparable to that for the 2:3 compound, while the relative intensity falls off markedly for the 1:3 mixture.

The relative intensity vs. Mn concentration is shown for the three compounds in Fig. 3, using a log scale for the MnO content. There is a characteristically broad maximum between 0.1 and 1% MnO and a rapid drop above 2% MnO. In the previous paper on equilibrium relationships, it was estimated that the solid solubility of MnO in the 2:1 and 3:2 compounds was relatively low (possibly 1-3%) while perhaps 5-8% could be incorporated in the 2:3 lattice. In view of these figures it appears that the decrease in relative intensity above 1% MnO may not be related to the limit of solid solubility of MnO in these compounds.

Cathode ray excitation.—Under cathode ray excitation, for Mn concentrations ranging from 0.01-2%, the 2:1 and 3:2 compounds fluoresce orange (Fig. 4). The 2:3 compound ranges from a very pale green for low concentrations of MnO such as 0.01-0.1% to a stronger, but still not very intense green for MnO contents between 0.1 and 2%. These results are in total agreement with the data of Leverenz (6) who shows orange peaks at 6260Å for 2:1 and 3:2, green for 1:2, and both green and orange peaks for 1:1, indicating that the latter is actually a mixture of the two compounds, $3CdO \cdot 2B_2O_3$ and $2CdO \cdot 3B_2O_3$. He also indicates a much greater relative intensity (30 and 15) for the 2:1 and 3:2 compounds than for the matrices which yield the green band (5 for the 1:1 and 4 for the 1:2 mixture).

Activators other than Mn.—Brief experiments with 0.1% additions of other activators are sum-

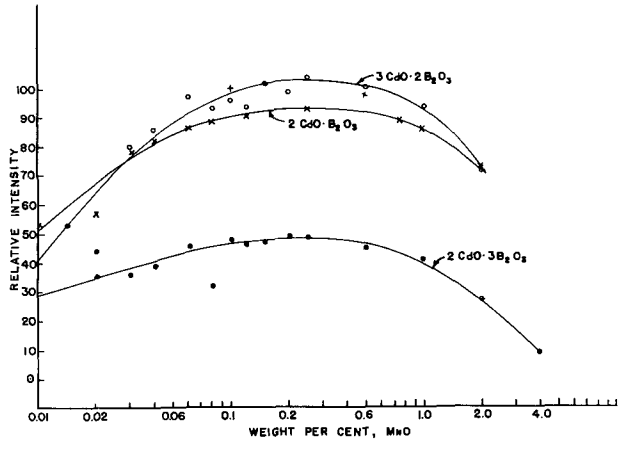

Fig. 3. Relative intensity vs. Mn concentration for the 2:1, 3:2, and 2:3 cadmium borate compounds (2537Å excitation).

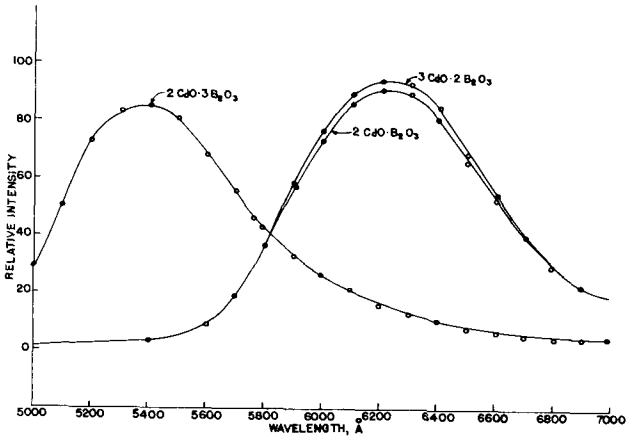

Fig. 4. Typical emission curves for three cadmium borate compounds (cathode ray excitation); [2:1 and 3:2 compounds activated with 0.15% MnO, 2:3 compound with 2.0% MnO]; intensity relative in terms of a commercial cadmium borate phosphor.

marized in Table I. Activators were added as C.P. compounds and each preparation was fired to 800°C for 2 hr in the case of the 3:2 and 2:3 compounds and at 850°C for 2 hr for the 2:1 compound.

Summary

Data are presented on the fluorescence of the three cadmium borate phosphors whose composition is that of specific compounds. It is now evident that previous data frequently have been in terms of technical formulations. It is now possible to associate characteristic emission color with a particular compound, and to describe the behavior of intermediate mixtures in terms of the 2:1, 3:2, and 2:3 compounds.

All three compounds are excited to orange emission by 2537Å radiation and the 2:1 and 3:2 compounds also emit in the orange region under cathode ray excitation. The 2:3 compound is distinct from the others in emitting in the green region under cathode ray excitation. Future work on the decay, temperature dependence, nature of the emitting centers, or other aspects of the luminescence of compositions in this system may be guided by these results for the pure compounds.

Acknowledgment

The authors wish to thank members of the Chemical Products Plant of the General Electric Company for their assistance in obtaining emission curves.

Manuscript received April 11, 1957. Contribution #56-28 from the Department of Ceramic Technology, College of Mineral Industries, Pennsylvania State University, University Park, Pennsylvania.

Any discussion of this paper will appear in a Discussion Section to be published in the June 1958 JOURNAL.

REFERENCES

1. E. C. Subbarao and F. A. Hummel, *This Journal*, **103**, 29 (1956).
2. F. A. Kroger, "Some Aspects of the Luminescence of Solids," pp. 60, 61, 270, Elsevier Publishing Co., New York (1948).
3. Th. P. J. Botden and F. A. Kroger, *Physica*, **13**, 216 (1947).
4. H. W. Leverenz, "An Introduction to Luminescence of Solids," pp. 233, 256, John Wiley & Sons, Inc., New York (1948).
5. G. R. Fonda, *J. Opt. Soc. Amer.*, **40**, 347 (1950).
6. Ref. (4), p. 234.

Table I. Fluorescence of cadmium borate compounds with various activators

Activator	2537	$2CdO \cdot B_2O_3$ 3650	C.R.	2537	$3CdO \cdot 2B_2O_3$ 3650	C.R.	2537	$2CdO \cdot 3B_2O_3$ 3650	C.R.
Sn	Weak blue	Weak orange	Weak orange	Dead	Weak orange	Weak orange	Dead	Dead	Weak blue
Sb	Weak blue	Weak orange	Weak orange	Dead	Weak orange	Weak orange	Dead	Dead	Weak blue
Ti	Weak blue	Weak orange	Weak orange	Dead	Weak orange	Weak orange	Dead	Dead	Weak blue
Hg	Weak blue	Weak orange	Weak orange	Dead	Weak orange	Weak orange	Dead	Weak orange	Weak blue
Sm	Weak blue	Weak blue	Grey	—	—	—	Dead	Dead	Weak blue
Bi	—	—	—	Dead	Weak blue	Weak orange	Dead	Dead	Weak blue
Ag	—	—	—	Dead	Weak blue	Weak orange	Dead	Weak orange	Brown(?)
Tl	—	—	—	Dead	Weak orange	Weak orange	Dead	Weak orange	Pale blue
Pb	—	—	—	Pale blue	Pale blue	Weak orange	Dead	Weak blue	Pale blue

Optical Measurement of Film Growth on Silicon and Germanium Surfaces in Room Air

R. J. Archer

Bell Telephone Laboratories, Incorporated, Murray Hill, New Jersey

ABSTRACT

The thickness and growth kinetics of oxide films on polished silicon and germanium exposed to room air after having been rinsed in hydrofluoric acid were obtained by measuring the ellipticity of reflected polarized light. Film growth obeys the Elovich equation. Plots of thickness vs. the logarithm of the time in air are linear after about 15000 sec with slopes of 6.8Å/decade (Si) and 8.1Å/decade (Ge). Immediately after the hydrofluoric acid rinses the films are 10-15Å thick and increase in thickness by about 11-12Å after one day in air. A small part of the films dissolves in certain organic liquids. Measurements of ellipticity at two angles of incidence during film growth gave an experimental check of the optical theory.

The rates of growth of films—presumably oxide films—on polished Si and Ge in room air following a rinse in HF were obtained by measuring the ellipticity of polarized light reflected from the surfaces. The measurements were undertaken because a simple experimental system was desired for evaluating the applicability of this optical technique for studying Si and Ge surfaces and because of interest in the system itself since the surfaces in these experiments are similar to etched surfaces in room air upon which the majority of physical measurements have been made and which are the most common device surfaces. Film thicknesses and growth rates have not been measured previously for such surfaces.

When plane polarized light, with the plane of oscillation of the electric field vector inclined at 45° to the plane of incidence, is reflected from a surface, the state of polarization, i.e., the ellipticity, of the reflected beam is characterized by the phase difference, Δ, and the amplitude ratio, $\tan \Psi$, between the two components of the electric field vector measured in and normal to the plane of incidence. The magnitudes of Δ and Ψ (expressed in degrees) depend on the angle of incidence, the optical constants of the reflecting substance, and the thickness and index of refraction of the surface film. For films thin compared to the wave length of the incident light, first order linear relationships between film thickness and the reflection parameters obtain. By expanding the exact equation and retaining only first order terms in thickness, the following equations, valid for films thinner than about 50Å, are derived (1)[1]

$$\Delta = \overline{\Delta} - \alpha L \qquad \text{(I)}$$

$$\Psi = \overline{\Psi} + \beta L \qquad \text{(II)}$$

[1] Reference (1a) gives simple derivation of exact equation, (1b) best expansion procedure. Above Eqs. (I) and (II) have same form as well-known Drude equations (1c). However, certain terms missing in Drude's equations are retained here which significantly affect the magnitude of the coefficients when evaluated for Si and Ge.

$$\alpha = \frac{720 \cos\phi \sin^2\phi \ (n_1^2 - 1) \ (1/n_1^2 - a)}{\lambda([\cos^2\phi - a + \sin^2\phi \ (a^2 - a'^2) \ ]^2 + a'^2)} \qquad \text{(III)}$$

$$\beta = \frac{720 \sin^2\overline{\Psi} \cos\phi \sin^2\phi \ (n_1^2 - 1) \ a' \ ((1/n_1^2 - a) \ (1 - 2a \sin^2\phi) - [\cos^2\phi - a + \sin^2\phi \ (a^2 - a'^2)\,])}{\lambda([\cos^2\phi - a + \sin^2\phi \ (a^2 - a'^2) \ ]^2 + a'^2)} \qquad \text{(IV)}$$

Film thicknesses are calculated from the experimental quantities Δ and Ψ using the relationships (I) and (II). The evaluation of the coefficients of these equations requires values for the optical constants of the film and subphase. $\overline{\Delta}$ and $\overline{\Psi}$ are calculated from standard formulas (2) and α and β from Eqs. (III) and (IV). Values for the optical constants are given in Table II along with the calculated coefficients for two angles of incidence.

Since $\alpha >> \beta$ and Δ and Ψ can be measured with about the same precision and accuracy, film thicknesses are obtained from measurements of Δ. n and κ were determined experimentally from measurements of Δ and Ψ using special techniques, and the problems attending the evaluation of these measurements—because of the unavoidable presence of surface films when high vacuum cleaning techniques

Table I. Glossary of symbols

ϕ —angle of incidence.
n_1—index of refraction of surface film.
L—film thickness expressed in Ångstrom units.
a —$(1-\kappa^2)/n^2(1+\kappa^2)^2$
a'—$2\kappa/n^2(1+\kappa^2)^2$
n —real part of complex index of refraction of reflecting substance
κ —absorption coefficient of reflecting substance. The complex index of refraction is written $\overline{n} = n(1-i\kappa)$.
$\overline{\Delta}$ —value of Δ for a film free surface.
$\overline{\psi}$ —value of ψ for a film free surface.
λ —vacuum wave length of light. In these experiments $\lambda = 5461$Å.

Table II. Optical constants (λ=5461Å) and values for α, β, $\bar{\Delta}$, and $\bar{\psi}$ at two angles of incidence

	n	κ	n_1
Si	4.13 ± 1%	0.01 ± 50%	1.55 ± 5%
Ge	5.01 ± 2%	0.387 ± 6%	1.9 ± 10%

	Si		Ge	
ϕ	61.26°	70°	61.26°	70°
α deg/Å	0.140 ± 6%	0.325 ± 5%	0.154 ± 6%	0.276 ± 6%
β deg/Å	0.00010	0.0033	0.005	0.014
$\bar{\Delta}$	179.43° ± 0.28°	178.70° ± 0.64°	166.28° ± 0.81°	154.73° ± 1.08°
$\bar{\psi}$	23.40°	12.10°	29.58°	21.54°

are not applied—make uncertain the errors in the values obtained. The uncertainties given in Table II are for the most part estimated but are believed to be realistic. The indices of refraction of the films were obtained from measurements of Δ as a function of the refractive index of the mirror's ambient medium using a series of organic liquids. The values agree with the bulk values for quartz (1.55) and insoluble germanium dioxide (1.99-2.10). All of the constants, n, κ, and n_1 are from preliminary measurements and are qualified as tentative. More refined experiments are underway and a complete report of the problems, techniques, and results of the reflection measurement of the optical constants of Si and Ge and their surface films is forthcoming. For present purposes it is sufficient to state that the maximum possible errors in the constants will not significantly affect the values for α, given in Table II, so that relative thicknesses and changes in thickness can be calculated accurately. $\bar{\Delta}$ is more sensitive to the values for the optical constants used in its evaluation. Consequently, calculated total or absolute thicknesses have relatively large uncertainties.

Technique

The instrument for measuring Δ and Ψ, the ellipsometer, is shown in Fig. 1. It consists of a spectrometer fitted with two nicol prisms and a mica quarter-wave plate, all mounted in divided circles. The procedure is to align the fast axis of the mica plate at 45° to the plane of incidence and to adjust the azimuths of the nicol prisms until the reflected beam is extinguished. Δ and Ψ are directly measured by the orientations of the nicols at extinction (3). A photomultiplier microphotometric technique is used to obtain extinction settings, and Δ and Ψ can be measured with a precision of ±0.04° and ±0.02°, respectively. Therefore, from the magnitude of α in Table II, changes in thickness can be measured to ±0.15Å (for Ge at ϕ = 70°).

The surfaces were polished mechanically using as a final abrasive Linde B in water and were judged adequately flat when straight parallel fringes were observed with an optical flat. After polishing, the mirrors were boiled in acetone and benzene, rinsed in hot tap water and deionized distilled water, refluxed over ethyl ether, and rinsed for several minutes in HF. The mirror to be studied was mounted and aligned at the spectrometer axis; Δ and Ψ were measured; while still aligned, the mirror was immersed for 1 min in CP quality concentrated HF and immediately rinsed in three separate portions of re-distilled acetone to remove the pendent HF. As soon as possible (about 200 sec) after this treatment, Δ and Ψ were again measured and followed as a function of time while the mirror was exposed to room air. A typical experiment lasted for two days.

The measurements were made in a closed room in which the relative humidity and temperature were maintained at 54% ±4% and 28°C ±2°. The Si mirror is 10 ohm-cm n-type, the Ge 6 ohm-cm p-type. The polished faces are of unknown orientation.

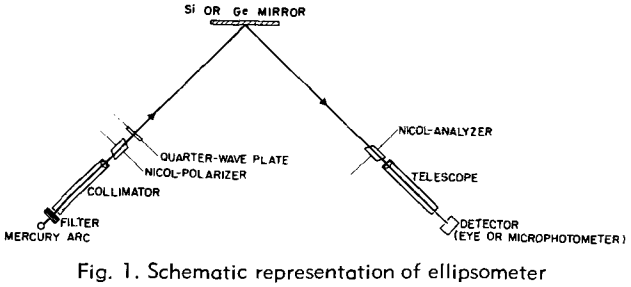

Fig. 1. Schematic representation of ellipsometer

Results

The results to be reported include film growth data, experimental verification of Eq. (I), and data demonstrating the partial solubility of the surface films in certain organic liquids.

Fig. 2 plots Δ, measured at ϕ = 61.26°, as a function of the logarithm of time following the HF rinse.

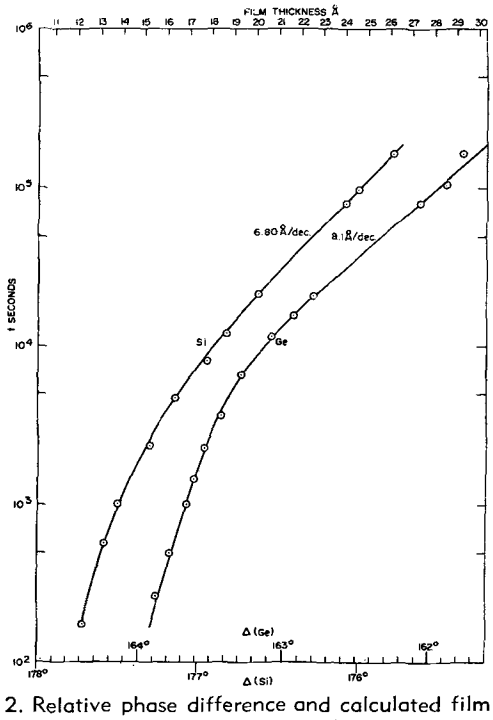

Fig. 2. Relative phase difference and calculated film thickness as o function of the time in air after an HF rinse. ϕ = 61.26°.

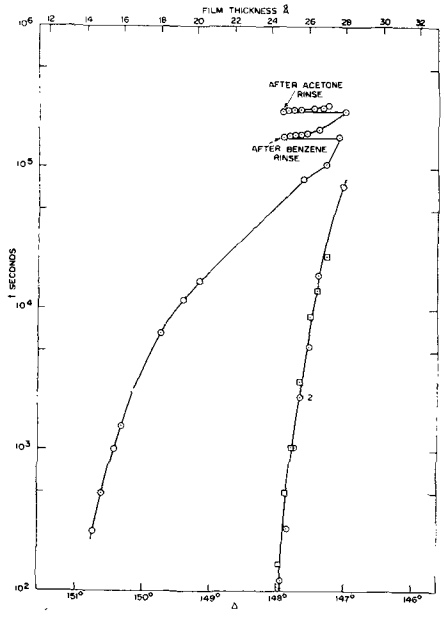

Fig. 3. Curve 1, film growth curve showing effects of 1-min benzene and acetone rinses; curve 2, Δ vs. log t for t = 0 instant of removal from organic liquid. Circle with dot = benzene, square with dot = acetone. Ge, $\phi = 70°$.

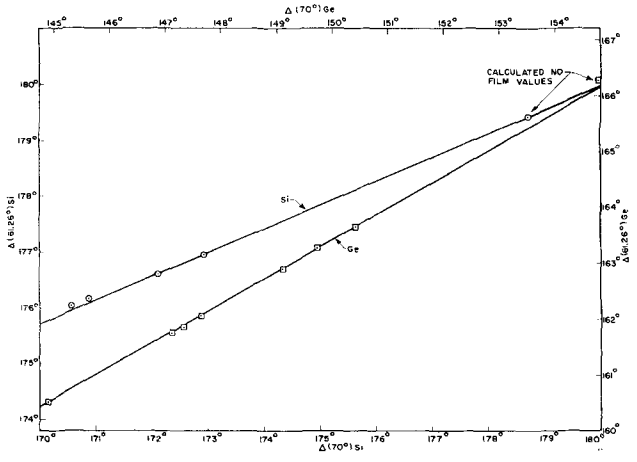

Fig. 4. Δ measured simultoneously at two angles of incidence during film growth. Fit of points to lines is degree to which experiment checks theory.

The zero of time is the instant of removal of the mirror from the HF. The two Δ axes are adjusted relative to each other so that the thickness axis at the top of the figure is for both the Si and Ge data. Thickness is obtained from Δ using Eq. (I) and the values of the coefficients given in Table II. Repeating the measurements several times on each mirror established their reproducibility, and the results of representative experiments are plotted. The linear parts of the curves (t>15000 sec) have slopes of 6.8Å/decade (Si) and 8.1Å/decade (Ge) which values were reproducible to about ±2% from experiment to experiment.

A reproducible decrease in the thickness of the regrown films on both Si and Ge accompanies rinsing in acetone, ether, benzene, hexane, and pentane. The latter two substances cause the smallest effect. Fig. 3 shows a film growth curve for Ge and the effect of rinses in acetone and benzene. The changes in Δ following the rinses are also plotted, taking as the zero

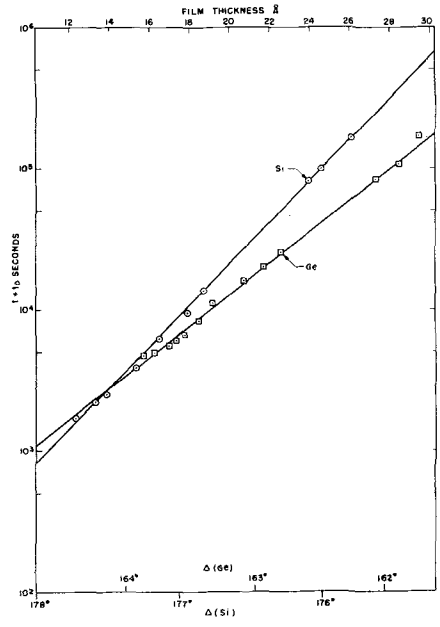

Fig. 5. Data of Fig. 2 plotted against t + t_0; t_0(Si) = 1500 sec, t_0(Ge) = 4500 sec.

of time the instant of removal from the organic liquid. The data following the benzene and acetone rinses are colinear and the slope decreases with time.

The measurement of each point on the film growth curve at two angles of incidence yielded the plots of Δ ($\phi = 61.26°$) vs. Δ ($\phi = 70°$), Fig. 4. Eq. (I) predicts the slope of these curves, $\alpha(61.26°)/\alpha(70°)$, so that comparison of experiment and theory serves to check the validity of Eq. (I). For Ge the data are fairly extensive and the agreement of theory and experiment is good. The slope of the Ge curve is 0.571 and, from Table II, the calculated value is 0.558. The best straight line through the Si points has a slope of 0.40 whereas the calculated slope is 0.430. There is not enough data to make this difference certain, and the line for Si is drawn to agree with theory. The fit is reasonably good. A further agreement with theory is obtained from the colinearity with the experimental data of the calculated clean surface points $\bar{\Delta}$ (61.26°), $\bar{\Delta}$ (70°). The displacement of this point from the experimental curve for Ge is within its limits of uncertainty.

The variation of Ψ is so small that no useful information was forthcoming from its measurement. However, the magnitudes of the changes observed are in agreement with that predicted by Eq. (II).

Discussion

The film growth data accord reasonably well with the Elovich (4) equation

$$dL/dt = A \exp(-BL) \qquad \text{(V)}$$

which, integrated, has the form

$$L = a + b \log(t + t_0) \qquad \text{(VI)}$$

Values for t_0 are estimated from Fig. 2 and the data are re-plotted in Fig. 5 as Δ vs. $(t + t_0)$. The equations for these curves are

$$\text{Si: } L = -9.74 + 6.86 \log (t + 1500) \quad \text{(VII)}$$

$$\text{Ge: } L = -17.2 + 9.05 \log (t + 4500) \quad \text{(VIII)}$$

From these relationships are obtained the values 12.1Å and 15.8Å for film thickness at zero time for Si and Ge, respectively. From the uncertainties given for the coefficients of Eq. (I) in Table II, the uncertainty in calculated absolute thickness values is ±2Å for Si and ±5Å for Ge, and the uncertainty in the relative values is ±6%.

The changes in thickness accompanying the organic liquid rinses may result from the removal of a slowly growing "grease" film. Depending on the refractive index of such a film, curve 2 of Fig. 3 gives a growth rate of 1-2Å/decade between 10^4 and 10^5 sec with a total thickness of 3-4Å after 24 hr in air. Other explanations of the effect are possible, and the grease film hypothesis will not be further discussed.

These results can be compared with those of Green and Kafalas (5) on the oxidation of atomically clean Si and Ge. They measured oxygen uptake at relatively low pressures and reported logarithmic rates about an order of magnitude smaller than obtained here. The difference in rates may be due to a difference in mechanism. In the present case, the phenomenon observed is probably the growth of a nucleated oxide film accelerated by the relatively high humidity, whereas the data of Green and Kafalas measure oxygen chemisorption. The differences should be resolved by future experiments with the ellipsometer under controlled surface and ambient conditions.

Manuscript received April 26, 1957. This paper was prepared for delivery before the Washington Meeting, May 12-16, 1957.

Any discussion of this paper will appear in a Discussion Section to be published in the June 1958 JOURNAL.

REFERENCES

1a. O. S. Heavens, "Optical Properties of Thin Solid Films," p. 55, Butterworths Scientific Publications, London (1955).
1b. C. E. Leberknight and B. Lustman, *J. Opt. Soc. Amer.*, **29**, 59 (1939).
1c. P. Drude, *Wied. Ann.*, **36**, 532, 865 (1889); *ibid.*, **39**, 481 (1890).
2. R. W. Ditchburn, *J. Opt. Soc. Amer.*, **45**, 743 (1955).
3. A. B. Winterbottom, *ibid.*, **38**, 1074 (1948).
4. S. Yu Elovich and G. M. Zhabrova, *Zhur. fiz. Khim. USSR*, **13**, 1761, 1775 (1939).
5. M. Green and J. A. Kafalas, *Phys. Rev.*, **98**, 1566 (1955).

Electrical Conductivity of Molten Fluorides

I. Apparatus and Method

Ernest W. Yim and Morris Feinleib

Chemical Research Department, Kaiser Aluminum & Chemical Corporation, Permanente, California

ABSTRACT

A method and apparatus have been developed for determining the electrical conductivity of cryolite-base melts and other fluorides. Hot-pressed boron nitride was used to fabricate high-resistance cells with constants ranging from 17 to 39 cm^{-1}. Such cells must be used under an inert atmosphere, and correction must be made for the conductance of the cell body proper. A furnace and apparatus for accomplishing these objectives are described. An a-c Wheatstone bridge is used for measurements. In spite of the fact that Inconel electrodes were employed, resistance values were found to be independent of frequency above 1000 cycles.

The many attempts to measure the conductivity of cryolite-base melts and the importance of these measurements have been summarized by Edwards, *et al.* (1). They point out the wide discrepancy in the conductance results coming out of various laboratories.

The major difficulty in determining conductivities of fused fluorides is to find a suitable conductance cell material. It should not be attacked by the melts, should be an electrical insulator at temperatures of the order of 1000°C, and should have dimensional stability at those temperatures. Until recently, no such material was available. Accordingly, most investigators sidestepped the problem by using Pt cells (1). Such cells have a very low resistance, and electrode polarization becomes a major problem. Other difficulties with this type of cell are the lack of dimensional stability at high temperatures, and the fact that the electrodes may no longer be strictly equipotential surfaces.

Cuthbertson and Waddington (2) attempted to get away from the limitations of the Pt cell by using a magnesia tube. However, magnesia is attacked by cryolite rather rapidly, and therefore reproducibility was limited. A similar attempt with a quartz cell was not successful (1).

Lately, electrolysis of fused fluorides has been applied to several new fields. Yet a recent exhaustive compilation of data on alkali halide systems (3) shows a conspicuous lack of data on fluorides due to the absence of a suitable measuring tool. While the present work is concerned primarily with systems of

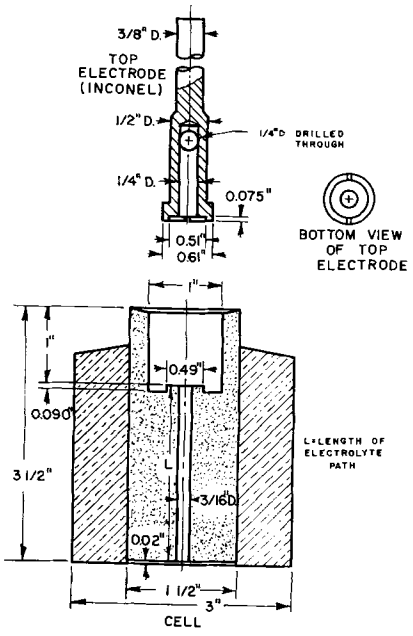

Fig. 1. Boron nitride conductivity cell with graphite jacket

interest to the aluminum industry, the method and apparatus described are applicable to measurements of electrical conductance in many fused fluorides.

Conductivity Cell and Electrodes

After examining a great number of standard and special materials, it was decided that hot-pressed BN was the most promising refractory for a conductance cell. Laboratory tests indicate that this material is not attacked by molten cryolite, and that it is readily drilled and machined.

The properties of hot-pressed BN have been described (4). Its electrical resistivity has been reported to be 3.1 x 10^4 ohm-cm at 1000°C. This value is sufficiently high so that the conductance of a BN cell could be neglected in comparison to that of most fused salts. However, even hot-pressed BN bodies have some porosity and, therefore, become impregnated with melts gradually. As a result, the conductance of the cell body becomes appreciable and needs to be taken into account. This was achieved by lowering the cell assembly into the melt under investigation and measuring the combined conductance of the electrolyte and cell body, then lifting the cell out of the melt and determining the "empty cell conductance".

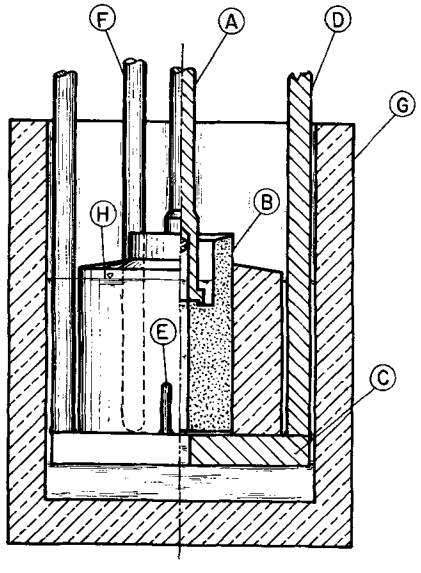

Fig. 2. Cell assembly in melt. A, top electrode; B, boron nitride cell; C, Inconel carriage and bottom electrode; D, bottom electrode leads, and supports; E, cell positioning studs; F, thermocouple tube; G, graphite crucible; H, melt level.

In the final design, the BN cell was surrounded by a graphite jacket. This jacket served a dual purpose: (*a*) it retarded the rate of melt penetration and, therefore, decreased the magnitude of the empty cell correction; and (*b*) in a graphite-jacketed cell, the paths of flow of current through impregnated cell walls are almost the same whether the cell is immersed in a melt or out of the melt, so that a representative empty cell correction can be measured.

Boron nitride is normally hot-pressed inside a graphite mold. Some of the cells were machined from 1 in. BN cylinders which had been left inside their original 3 in. mold. Boron nitride has a radial coefficient of expansion (perpendicular to pressing direction), which is much smaller than that of graphite (4); therefore, in a cold cell, the graphite is under considerable tensile stress, and the assembly must be machined carefully.

For pressing 1½ in. BN cylinders, a 5 in. graphite mold is needed. When attempting to machine this graphite down to 3 in., as required by furnace size limitations, it was impossible to avoid cracking the graphite. As an alternative, a graphite sleeve was machined separately and then slipped over an unjacketed BN cylinder to make a tight-fitting jacket.

A typical cell with matching top electrode is shown in Fig. 1. The reasons for its particular shape will become apparent during the discussion of the operating procedure. Alternate designs were also used successfully. Fig. 2 shows the cell and electrode assembly immersed in melt.

The top electrode was made of Inconel. The cell rested on an Inconel carriage which also constituted the bottom electrode (Fig. 2). Platinum electrodes were used initially, but it was soon found that BN reacts with Pt at about 1000°C; this embrittles the Pt and causes erosion of the BN; also the Pt sticks to the BN after prolonged contact. The use of Inconel was made possible by the fact that a relatively high-constant cell was available and that the polarization of Inconel was therefore of a tolerable order of magnitude. Inconel had the advantages of relatively good strength and dimensional stability at the temperatures of the experiments.

Most of the dimensions given in Fig. 1 are typical, but by no means critical. The electrolyte path consisted of a nominal 3/16 in. D. hole; its actual bore and length were carefully measured for each cell. The 3/16 in. dimension was a compromise; the smaller the bore, the higher the resistance of the electrolytic path and, therefore, the smaller the relative effect of electrode polarization. On the other hand, in smaller bores, gas bubbles tend to become trapped when the cell is lowered into a melt, and the effect of cell contamination by previously used melts may become serious. In this connection, the

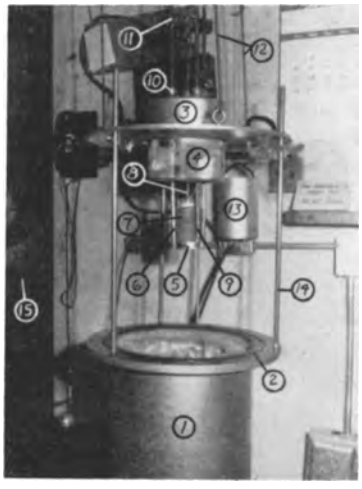

Fig. 3. Furnace and cell assembly ready for a conductivity determination. 1, Furnace shell; 2, O-ring (Neoprene); 3, furnace cover; 4, top insulator; 5, carriage and bottom electrode; 6, bottom electrode leads; 7, cell; 8, top electrode; 9, thermocouple protection tube; 10, Condulets; 11, clamping block; 12, lifting rig for furnace cover; 13, counterweight for furnace cover; 14, furnace cover guide rods; 15, fan.

holes through the bottom part of the top electrode are designed to facilitate the escape of gas bubbles from the cell bore as it is being immersed, and to hasten drainage as the carriage is being lifted out of the fused salt.

Precautions are needed against the tendency of melts to creep and thus provide an extra path between top electrode and graphite jacket. This is minimized by tapering both the graphite and the BN, and by designing the cell so that the melt level stays ¾ in. below the top of the BN.

Furnace

Boron nitride is oxidized at an excessive rate at about 1000°C, as is graphite. Therefore, it was necessary to make the conductivity measurements in an inert atmosphere.

A special furnace was built (Fig. 3) for taking resistance readings in or out of melts. It consists essentially of a flanged can, 1, and a matching cover, 3, built sufficiently strong to stand vacuum. Through the bottom, connections were made to a vacuum pump and to an argon tank. The furnace element consisted of heavy Nichrome V wire (#1 or #2 gauge): the ends of the wire were welded to ½ in. Inconel rods, which also came out through the bottom. To insure a vacuum-tight fit where the element is brought in, "Condulets" (waterproof electrical conduit fittings) were used in connection with specially fabricated Teflon compression grommets. The control thermocouple was also brought in through a Condulet provided with a rubber stopper. Since the heat generated in the furnace is normally sufficient to cause plastic deformation of the sealing grommets and stoppers (with resulting loss of vacuum), these connections were water-cooled through loops of Cu tubing soldered to the outside of the fittings.

The cover, 3, consisted of a central recessed portion and a machined flange to match that of the furnace. Thermal insulation, 4, filled the central portion and projected below the flange; it was supported by Inconel strips bolted to the underside of the cover and was therefore readily replaceable.

The conductivity cell electrode leads and an Inconel thermocouple protection tube were led in through the furnace cover; Condulets, 10, with rubber grommets were used to achieve a vacuum-tight seal and to permit vertical motion of the cell and electrode assembly. Again, there was the problem of keeping heat away from the rubber grommets. The use of Teflon grommets with movable rods was not satisfactory from the sealing standpoint. The difficulties were overcome by a combination of the following steps: (*a*) the cover was designed with the recessed central portion to remove the sealing fittings from the hot zone of the furnace; (*b*) the Inconel rods were kept down to ⅜ in. in order to decrease heat conduction along the metal; this is also the reason for reducing the diameter of the top electrode, as shown in Fig. 1; the ⅜ in. dimension was a compromise: with a smaller cross section, the electrical resistance of the Inconel would become appreciable in comparison to that of the cell, and the mechanical stability of the assembly at high temperatures would not be satisfactory; and (*c*) a fan, 15, cooled the furnace cover during runs.

Electrical Circuit

For many measurements, a self-contained conductivity bridge was used (Model RC-16, Industrial Instruments Inc.). This bridge is normally accurate to 1% of its reading, but its lower recommended limit of measurement is 0.2 ohm. In the case of highly conductive melts, cell resistances were of the order of 3 to 6 ohms and, therefore, this accuracy was no longer adequate. Accordingly, the circuit shown in Fig. 4 was used in such cases. Another reason for using the latter circuit was to determine the effects of a-c frequency on the readings. By using 4 precision resistors (General Radio, one 1Ω, two 10Ω, and one 100Ω), the scale factor for the decade box could be varied from 0.01 to 100. In this particular circuit, in view of other experimental limitations, the oscilloscope null detector was sufficiently sensitive (±0.5%) so that it was not necessary to use a variable capacitor in order to increase the sharpness of the null point. It was determined that resistance readings did not vary appreciably between 1,000 and 20,000 cycles; accordingly, a 2,000-cycle oscillator setting was normally used.

The total lead resistance, including the Inconel rods, was less than 0.04 ohm. A blanket value of 0.04Ω was subtracted from all resistance readings.

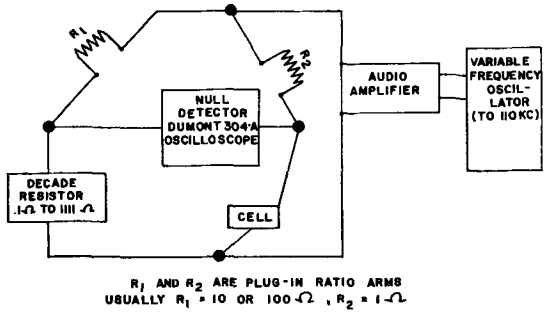

Fig. 4. Electrical circuit for conductivity measurements

This never amounted to more than a 1% correction; its variation with temperature is entirely negligible.

Care had to be taken to eliminate any unintentional grounding of the conductivity cell. This was especially true when using the RC-16 bridge, which already has an internal ground connection. A low-resistance path to the grounded furnace shell can exist at high temperatures by way of the crucible containing the melt and the insulation which becomes impregnated with fluorides. It becomes, therefore, necessary to change the insulation at times. Similarly, the top insulator (4, Fig. 3) may provide an electrical path between top and bottom electrode leads when it becomes impregnated with salt vapors. Finally, the a.c. going through the furnace element interferes with the balancing of the conductivity bridge; therefore, readings were normally taken during the off-cycle of the furnace controller.

Experimental Procedure

(*a*) *Setting up a determination.*—Fig. 2 and 3 show the way the cell and electrodes are assembled prior to making a determination. It is essential to press the top electrode down firmly against the cell, and to lock it to the carriage and bottom electrode leads by means of a Bakelite clamping block, 11, provided with thumbscrews. This prevents any motion of the top electrode relative to the cell when the assembly is raised or lowered inside the furnace. The Inconel thermocouple protection tube, 9 (which has been tested for tightness to vacuum) is lowered against the carriage and, therefore, the thermocouple indicates the temperature of the bottom electrode at all times.

After making sure that the graphite crucible containing the bath is properly centered under the carriage, the furnace cover is lowered, and the chamber is pumped down to approximately 200μ. The furnace is then flushed with argon and heated to 300°C, while again pumping to 200μ or less. After refilling the furnace with argon, the temperature is raised to 600°C; the furnace is pumped to 100 mm, and argon is again admitted until the pressure reaches about 600 mm. Finally the temperature is raised to the desired level. The argon pressure inside the furnace is kept slightly below atmospheric in order to make sure that the cover is properly seated at all times. The proper positioning of the top electrode is again tested by loosening the clamping block, 11, pushing the top electrode down, and retightening the thumbscrews.

(*b*) *Determination of cell resistance.*—When the bath inside the furnace is molten, the cell assembly is slowly lowered into the melt. An ohmmeter is connected across the electrode leads; a sharp jump of the ohmmeter pointer indicates that the top electrode has become immersed into the melt. It is important not to lower the cell too fast, since liquid may rise faster on the outside of the cell than in the small central hole and actually flow over the top of the BN. This will create a parallel path through a film of salt which drains only gradually and makes it extremely difficult to determine the true cell resistance.

After the cell has been lowered the first time, the ohmmeter is removed, and either the RC-16 conductivity bridge or the decade bridge and variable frequency source are connected to the electrode leads. A reading of resistance and temperature is taken. An adjustable pointer is lined up with a reference mark on the electrode lead rods to indicate how far the carriage should be lowered during subsequent immersions. The carriage is then raised, allowed to drain, and reimmersed. If the second resistance reading approximates the first one and is steady, it means that the assembly has been lowered to the correct level. It is necessary to lower and raise the cell two or three times (*a*) to make sure that no gas bubbles are trapped in the bore of the cell, and (*b*) to rinse off any residue of melt from a previous run. Such residues rarely amount to more than 0.1 g, and usually less than that. After about two immersions, the effect of such residues is entirely negligible.

At this point, initial cell resistance readings are taken for the record. Usually the immersed cell resistance shows very little variation at a given temperature. Normally, about 3-5 successive readings at a given temperature are taken over a period of 5-10 min.

The cell is then raised and the empty cell resistance is measured every minute for about 3-4 min. This resistance drifts for several reasons: [1] At first, the liquid film on the walls of the cell bore will be draining. [2] After a while, some liquid impregnating the cell body (and which, therefore, properly contributes to the empty cell resistance value) will also start to drain. [3] The cell is more responsive to temperature fluctuations when out of the bath since the thermal mass is smaller.

It is usually found that the rate of increase of empty cell resistance tapers off after about 2 min. Therefore, it is assumed that at that time any liquid remaining in the cell bore has drained, whereas the walls are still impregnated, and that the 2-min value of empty cell resistance is the most representative value.

It is important to secure a low and reproducible contact resistance between top electrode and cell body. This is no problem when the cell is immersed; the melt automatically makes for a low-resistance contact. In order to achieve a similar condition when the assembly is out of the melt, the cell in Fig. 1 was provided with an annular top groove to trap a small amount of melt. The matching top electrode seats in this groove when pressed against the cell body. The clamping block helps to maintain a good contact.

The contact between the bottom of the cell and the Inconel carriage is essentially made through the graphite jacket when the cell is empty, and is inherently low in resistance. However, the axial coefficient of thermal expansion of BN (i.e., parallel to the direction of pressing) is higher than that of graphite (4) unlike the radial expansion coefficient. Therefore, the bottom of the BN cylinder is 0.02 in. above the bottom of the graphite (Fig. 1), so that,

on heating, the BN expansion does not cause the graphite jacket to lift off the bottom electrode.

If a cell impregnated with one melt is used in a bath of a different composition, it takes considerable time for the original melt within the pores to be replaced by the new melt. The effect on the composition of the new melt is negligible, but the effect on the empty cell resistance is considerable. Thus, the empty cell resistance varies during the course of a run because of melt replacement as well as temperature variations. It is, therefore, necessary to determine the empty cell resistance after each reading of total resistance.

(c) *Measurement of cell constant.*—In most cases, the cell constant (length/cross sectional area) was calculated from the dimensions of the central bore which were accurately measured. From thermal expansion data (4), the constant increases by about 0.5% between room temperature and 1000°C.

In a few cases, cells were also standardized in molten KCl. Their constants were determined using published conductivity values for KCl (1, 5, 6). The values thus obtained checked with the values calculated from cell dimensions to better than 1%.

Cell constants ranged from about 17 to 39 cm^{-1}.

Reproducibility and Errors

In the absence of cracking in the cell, unintentional grounding, or parallel paths, the reproducibility between duplicate runs was usually 2% or better; in many cases, it was better than 1%. Typical standard deviations of the mean ranged from 0.3% to 1.4%. A good run was always characterized by steady, reproducible readings when the cell was immersed in melt. When the readings were erratic, one could usually ascribe this to a damaged cell body, or to stray electrical paths; such runs were discarded.

Most of the sources of error have been discussed. It is believed that the measurement of empty cell resistance contributes the most to errors. From the fact that readings did not vary with frequency between 1,000 and 20,000 cycles, polarization is not considered a major factor. Melt composition changes were found to be small in all systems investigated.

Acknowledgment

The authors wish to acknowledge the helpful suggestions of B. Porter and other members of the Chemical Research Department in designing the apparatus. Machining of the cells was performed by K. I. Booth and G. D. Wilson who also helped in the construction of the apparatus. The Carborundum Company, Niagara Falls, N. Y., and the Norton Company, Worcester, Mass., were most cooperative in supplying the BN cell bodies.

Manuscript received Jan. 8, 1957. This paper was prepared for delivery before the Washington Meeting, May 12-16, 1957.

Any discussion of this paper will appear in a Discussion Section to be published in the June 1958 JOURNAL.

REFERENCES

1. J. D. Edwards, C. S. Taylor, A. S. Russell, and F. Maranville, *This Journal*, **99**, 527 (1952).
2. J. W. Cuthbertson and J. Waddington, *Trans. Faraday Soc.*, **32**, 745 (1936).
3. E. R. Van Artsdalen and I. S. Yaffe, *J. Phys. Chem.*, **59**, 118 (1955); **60**, 1125 (1956).
4. K. M. Taylor, *Ind. Eng. Chem.*, **47**, 2506 (1955).
5. R. W. Huber, E. V. Potter, and H. W. St. Clair, *U. S. Bur. Mines Rept. Investig.* 4858.
6. E. K. Lee and E. P. Pearson, *Trans. Electrochem. Soc.*, **88**, 171 (1945).

Electrical Conductivity of Molten Fluorides

II. Conductance of Alkali Fluorides, Cryolites, and Cryolite-Base Melts

Ernest W. Yim and Morris Feinleib

Chemical Research Department, Kaiser Aluminum & Chemical Corporation, Permanente, California

ABSTRACT

The electrical conductivities of molten LiF, NaF, KF, Li_3AlF_6, Na_3AlF_6, and K_3AlF_6 have been determined. The effect of alumina, CaF_2, and NaF:AlF_3 ratio on the conductivity of cryolite-base melts has been studied. Molar and equivalent conductances have been calculated for several melts, and their significance is discussed.

A previous paper (1) described a new technique and apparatus for determining electrical conductivities of fused fluorides. The present work deals with the conductance of pure alkali fluorides and cryolites as well as cryolite-base melts of interest in the electrolytic production of aluminum.

A comprehensive investigation of the conductivity of sodium cryolite, with and without additives, was reported by Edwards, *et al.* (2, 3). For their determinations, these authors used a Pt dip cell, limitations of which have been discussed previously (1). Drossbach (4) reported values for the conductivity

of LiF, NaF, and KF, without indicating the source of the data. No conductivity values for lithium and potassium cryolites have been found in the literature.

Experimental

The apparatus and general procedure have been described in detail (1). The conductance cell was made of hot-pressed BN; all measurements were carried out in an inert atmosphere.

The usual practice was to make at least two runs for each melt composition. Furthermore, the temperature was lowered from maximum to minimum and then raised again; data were taken on both the descending and the ascending temperature cycles. In a typical run, data were usually taken over a span of 3 hr.

The following raw materials were used:

LiF, NaF, KF, CaF_2, KCl: Baker's reagent grade;

Alumina: Kaiser reduction grade;

Cryolite: natural hand-picked crystals, obtained from Pennsylvania Salt Mfg. Company, were further sorted in the laboratory, and the selected fraction was ground for use. This material has a melting point of 1005°C [cf. a mp of 1009° reported by Phillips, Singleton, and Hollingshead (5) for the purest available natural cryolite]. Analysis corresponds to the theoretical composition of pure cryolite within the limits of experimental error.

AlF_3: Alcoa X-2A grade powder containing approximately 97% AlF_3, about 1.2% NaF and 1.5% Al_2O_3. In view of the relatively large quantity of melt required for each run, and the number of experiments performed, it was not practical to use vacuum-sublimed AlF_3. The error introduced by the use of Alcoa X-2A grade AlF_3 was negligible except in the case of conductance determinations for Li_3AlF_6 and K_3AlF_6.

Melts whose main constituent was sodium cryolite were synthesized from this material and additives such as AlF_3, NaF, CaF_2, or Al_2O_3. Li_3AlF_6 and K_3AlF_6 were prepared starting from LiF or KF and AlF_3. In view of the relatively large proportions of impure AlF_3 required to prepare the cryolites of Li and K, conductance values reported for these two compounds are less reliable than for the rest of the fluoride melts.

In all cases, even with pure salts, melts were fused before each determination. A furnace was preheated to about 50°C above the melting point of the composition under investigation. The melt constituents were mixed in the dry state and placed in a graphite crucible, which was then placed inside the hot furnace. As soon as melting occurred, the crucible contents were stirred with a graphite rod to insure homogeneity and then chilled. This procedure was designed to cut down the time that the melts were at high temperatures; consequently composition changes due to volatilization or hydrolysis were kept to a minimum.

The chilled melt was pulverized, thoroughly mixed, and sampled. It was then placed in another graphite crucible which served as the container for conductance determinations. After one or more runs, the melt was again pulverized and sampled.

Table I. Comparison of alkali fluoride conductivities

	Conductivity in $ohm^{-1}cm^{-1}$		
	LiF at 900°C	NaF at 1020°C	KF at 900°C
This work	8.43	5.15	3.80
Drossbach (4)	19.8	3.32	4.32
Edwards, *et al.* (3)	—	5.63	—

Cryolite-base melts were analyzed by control methods used in the aluminum industry. The NaF: AlF_3 ratio was determined by pyrotitration (6), and the "free alumina" (7) was also determined. In all cases, little or no melt composition change was found, in spite of the fact that each run lasted several hours (it is important to remember here that the experiments were carried out in a closed furnace under an inert atmosphere). In the case of Li_3AlF_6 and K_3AlF_6, it was assumed that the composition did not change during runs.

Conductivity of alkali fluorides.—The specific conductances of LiF, NaF, and KF are plotted in Fig. 1. Table I shows wide differences between these values and Drossbach's (4). The conductivity of NaF reported by Edwards, *et al.* (3) is appreciably higher than that determined in the present study.

Specific conductance of cryolites without additives.—The conductivity of pure lithium, sodium, and potassium cryolites is shown in Fig. 2. Values for a mixture of 60% Li_3AlF_6 and 40% Na_3AlF_6 by weight have also been included in Fig. 2: this composition is close to the eutectic reported by Drossbach (8).

The conductance of sodium cryolite determined in this laboratory is in good agreement with that reported by Edwards, *et al.* (2).

It is interesting to note the high conductivity of lithium cryolite. The data for this compound have been extrapolated to 1010°C, at which temperature the conductivity of Li_3AlF_6 is almost 1.5 times that of Na_3AlF_6.

Effect of alumina on the conductivity of cryolite and cryolite-CaF_2 melts.—The conductivities of cryolite-alumina melts are plotted in Fig. 3, and for cryolite-alumina-8% CaF_2 melts in Fig. 4.

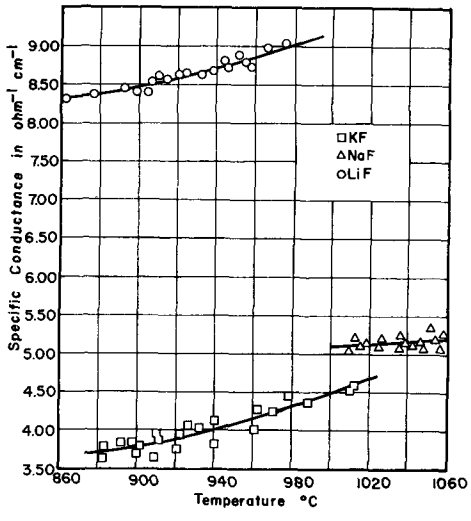

Fig. 1. Conductivity of alkali fluorides

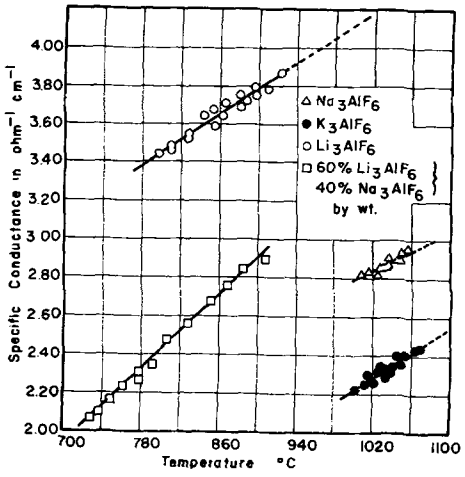

Fig. 2. Conductivity of cryolites

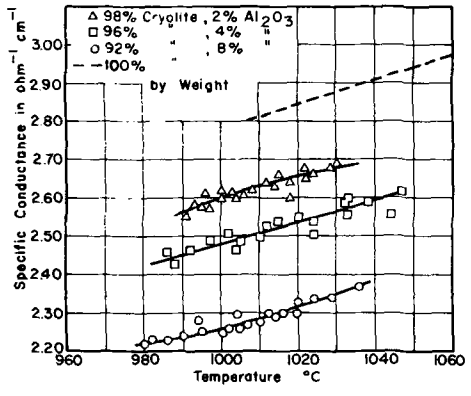

Fig. 3. Conductivity of cryolite-alumina melts (The line for 100% cryolite is taken from Fig. 2.)

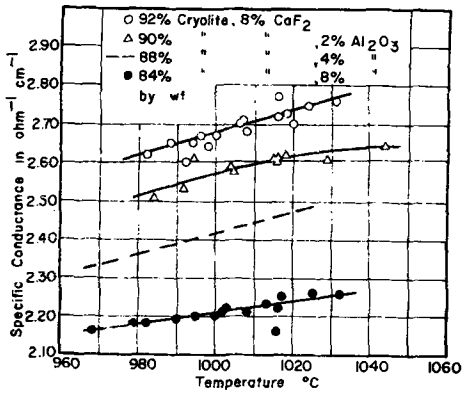

Fig. 4. Conductivity of cryolite-Al_2O_3-CaF_2 melts. (The line for 4% Al_2O_3 is taken from Fig. 7.)

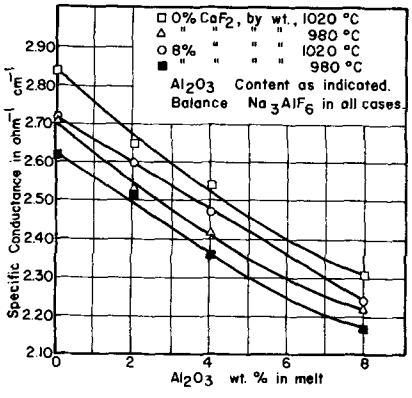

Fig. 5. Effect of alumina on the conductivity of Na_3AlF_6-CaF_2-Al_2O_3 melts.

These data are replotted in Fig. 5 to show the effect of alumina additions on the conductivity of cryolite and cryolite-8% CaF_2 melts. The conductivity of a typical aluminum reduction bath at 980°C decreases by 13% when the alumina concentration increases from 2% to 8%. This rate of decrease is somewhat greater than the one reported by Edwards, *et al.* (3).

Effect of NaF:AlF_3 *ratio on the conductivity of cryolite-base melts.*—The conductivity of NaF-AlF_3 melts without additives was determined at several NaF:AlF_3 ratios (Fig. 6).

The NaF:AlF_3 ratio was also varied in a typical aluminum reduction bath containing 8% CaF_2 and 4% Al_2O_3. Results have been plotted in Fig. 7.

The data of Fig. 6 and 7 have been rearranged in Fig. 8 to show the effect of NaF:AlF_3 ratio on the conductivity of cryolite-base melts. Comparing the conductivity of pure cryolite and that of a melt whose NaF:AlF_3 weight ratio is 1.22, the present study indicates that the effect of AlF_3 in decreasing the conductivity of cryolite is greater than reported by Edwards, *et al.* (3). On the other hand, the effect of NaF on conductivity, at a NaF:AlF_3 ratio of 1.76, appears to be smaller than shown by Edwards, *et al.* For the time being, no good explanation can be given for the shape of the curves shown in Fig. 8.

Molar and Equivalent Conductances

A. Definitions and calculations.—For a binary mixture of A and B, the molar conductance is

$$\mu = \frac{N_A \times MW_A + N_B \times MW_B}{d} \times K$$

where N_A and N_B are mole fractions, MW molecular weights, K the specific conductance, and d the melt density.

In terms of weight fractions W_A and W_B

$$\mu = \frac{1}{\left[\frac{W_A}{MW_A} + \frac{W_B}{MW_B}\right] \times d} \times K$$

Similarly, for equivalent conductance,

$$\Lambda = \frac{1}{\left[\frac{W_A}{EW_A} + \frac{W_B}{EW_B}\right] \times d} \times K$$

where EW_A and EW_B represent equivalent weights.

For more than two components

$$\Lambda = \frac{1}{\left[\frac{W_A}{EW_A} + \frac{W_B}{EW_B} + \frac{W_C}{EW_C} + \ldots.\right] \times d} \times K$$

and a similar expression can be obtained for μ

Density data were obtained from published values by Drossbach (4), Edwards, *et al.* (2, 3) and Vajna (9), as well as from unpublished work carried out in this laboratory.

B. Equivalent conductances of fluorides and cryolites.—Yaffe and Van Artsdalen (10) have proposed to compare melts at "corresponding tempera-

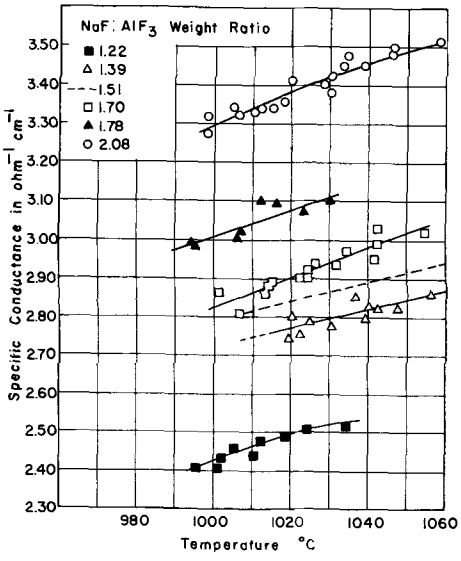

Fig. 6. Conductivity of AlF_3-NaF melts as a function of NaF:AlF_3 ratio (no additives). The line for a ratio of 1.51 is taken from Fig. 2.

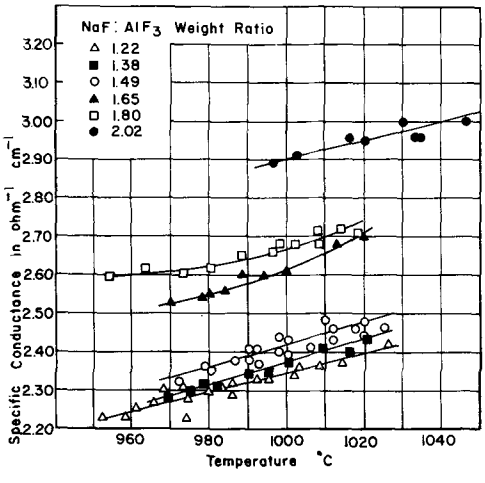

Fig. 7. Conductivity of a typical aluminum reduction bath as a function of NaF:AlF_3 ratio. Composition: 8% CaF_2, 4% Al_2O_3; balance AlF_3 + NaF by weight.

tures", i.e., at equal fractions above their melting point:

$$\theta = \frac{T°K}{T_m°K}$$

where T_m is the melting point. The equivalent conductances of the fluorides and cryolites of Li, Na, and K have been plotted in Fig. 9. It shows that, at a given temperature, the equivalent conductance of each cryolite is somewhat lower than that of the fluoride of the same cation. This relationship also holds true at "corresponding temperatures". A possible explanation is that the F^- ion is more mobile than a complex fluoaluminate ion (e.g., $AlF_6^{\equiv}$), and/or that the latter exerts more of an attractive force on the cations than the former.

Comparing the alkali fluorides, Table II shows that NaF has a smaller equivalent conductance than either LiF or KF, even at "corresponding temperatures". Equivalent conductances of other halides were taken from Yaffe and Van Artsdalen (10).

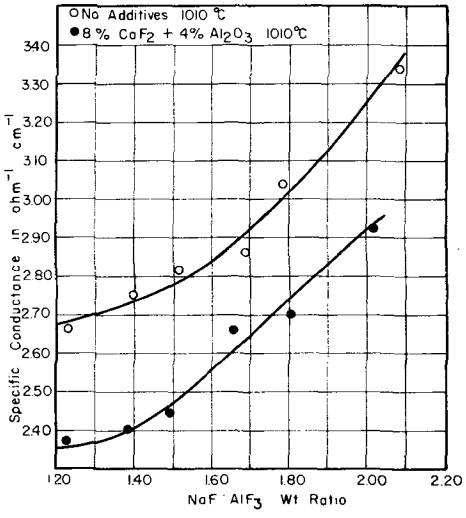

Fig. 8. Effect of NaF:AlF_3 rotio on the conductivity of cryolite-base melts.

Both LiF and NaF have a considerably lower equivalent conductance than the rest of the corresponding halides, even though one might expect the F^- ion to be more mobile than the other halide ions. It may be that the attractive forces between the small F^- ion and other small ions such as Li^+ and even Na^+ are the determining factor here. In the case of the larger K^+ ion, the interionic forces may be less important, and the greater mobility of the F^- ion may now become the dominant factor: this may account for the fact that the equivalent conductance of KF is higher than that of the other potassium halides.

C. Effect of alumina on molar conductance of cryolite.—The molar conductance of cryolite-alumina melts is shown in Fig. 10, as is the theoretical effect of an inert diluent. It is apparent that alumina depresses the molar conductance of cryolite considerably more than an inert diluent does. This effect is especially pronounced at low alumina concentrations; above a certain point, e.g. 8 mole % Al_2O_3, further additions of Al_2O_3 do not depress the conductance much more than an inert diluent would. Edwards, *et al.* (3) reported similar findings.

D. Effect of CaF_2 on molar conductance of cryolite.—The effect of CaF_2 on molar conductance of cryolite can be calculated from Fig. 2 and 4, as

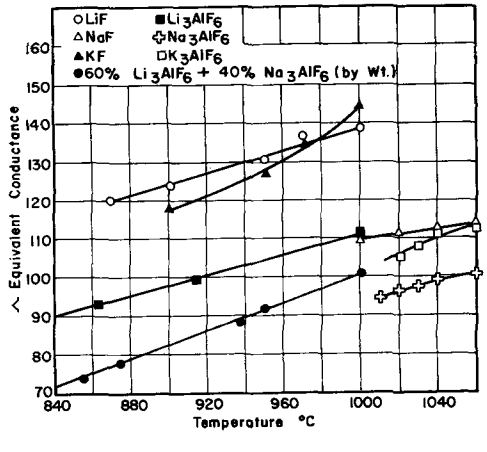

Fig. 9. Equivalent conductance of fluorides and cryolites

Table II.—Equivalent conductances of alkali halides at $\theta = T\ °K/T_m\ °K = 1.05$

LiF	**NaF**	**KF**
128	113	124
LiCl	**NaCl**	**KCl**
170	143	114
LiBr	**NaBr**	**KBr**
170	136	99
LiI	**NaI**	**KI**
163	132	94

shown in Table III. The values for 19% inert unionized diluent are obtained by taking 81% of the molar conductance of cryolite.

Within the limits of experimental error, it appears that CaF_2 acts as an inert diluent when added to neutral cryolite (NaF:AlF_3 mole ratio = 3:1). The situation is different in "acid baths", where the NaF:AlF_3 ratio is smaller than 3:1.

Table IV compares the conductances of two melts, both having a NaF:AlF_3 mole ratio of 2.57, but one of them containing CaF_2.

The conductivity of melt 1 can be taken from Fig. 8. The conductivity of melt 2 was determined separately but was not plotted in this paper. The effect of 17.7 mole % inert diluent on melt 1 would have been to lower the molar conductance to 206. Calculations at different temperatures, or in acid melts containing both CaF_2 and Al_2O_3, show a similar trend; at NaF:AlF_3 mole ratios lower than 3, CaF_2 decreases the molar conductance to a lesser extent than an inert diluent would.

To explain the behavior of CaF_2 in acid melts, the following hypothesis is offered.

The ionization of CaF_2 is repressed in neutral or alkaline cryolite-base melts, where sufficient F^- ions are present. In baths containing excess AlF_3, the activity of free F^- ions is low because of the complexing power of AlF_3 to form fluoaluminate ions (e.g., $AlF_6^{\equiv}$), and CaF_2 may ionize. This is equivalent to saying that CaF_2 may react with excess AlF_3 to form a calcium cryolite, which is partially ionized.

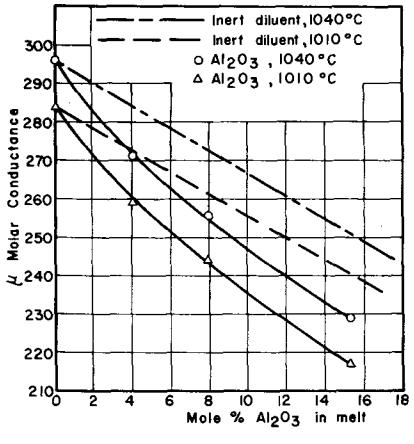

Fig. 10. Molar conductance of cryolite-alumina melts

Table III. Effect of CaF_2 on molar conductance of Na_3AlF_6

Mole % additive to cryolite	Molar conductance 1010°C	Molar conductance 1040°C
0	284	296
19% CaF_2	232	242
19% Inert diluent	230	240

Table IV. Effect of CaF_2 on "Acid" NaF:AlF_3 Melt

Melt No.	1	2
Composition	Na_3AlF_6 + AlF_3 NaF:AlF_3 mole ratio = 2.57 Mole % CaF_2 = 0	Na_3AlF_6 + AlF_3 + CaF_2 NaF:AlF_3 mole ratio = 2.57 Mole % CaF_2 = 17.7
K ohm^{-1}cm^{-1} at 1010°C	2.69	2.70
μ at 1010°C	250	218

Acknowledgment

The authors wish to acknowledge the assistance of R. Lum, M. Waggoner, and P. Robba in performing the analyses, and of B. Porter in carrying out the calculations. Some of the density data used in the calculations of molar and equivalent conductances were determined by W. M. Lafky and J. L. Henry.

Manuscript received Jan. 8, 1957. This paper was prepared for delivery before the Washington Meeting, May 12-16, 1957.

Any discussion of this paper will appear in a Discussion Section to be published in the June 1958 JOURNAL.

REFERENCES

1. E. W. Yim and M. Feinleib, *This Journal*, **104**, 622 (1957).
2. J. D. Edwards, C. S. Taylor, A. S. Russell, and F. Maranville, *ibid.*, **99**, 527 (1952).
3. J. D. Edwards, C. S. Taylor, L. A. Cosgrove, and A. S. Russell, *ibid.*, **100**, 508 (1953).
4. P. Drossbach, "Elektrochemie Geschmolzener Salze," Julius Springer, Berlin (1938).
5. N. W. F. Phillips, R. H. Singleton, and E. A. Hollingshead, *This Journal*, **102**, 648 (1955).
6. M. Feinleib and B. Porter, *ibid.*, **103**, 234 (1956).
7. J. L. Henry and W. M. Lafky, *Ind. Eng. Chem.*, **48**, 126 (1956).
8. P. Drossbach, *Z. Elektrochem.*, **42**, 65 (1936).
9. A. Vajna, *Alluminio*, **6**, 541 (1950).
10. I. S. Yaffe and E. R. Van Artsdalen, *J. Phys. Chem.*, **60**, 1125 (1956).

Contribution to the Theory of Cathodic Protection, II

Carl Wagner

Department of Metallurgy, Massachusetts Institute of Technology, Cambridge, Massachusetts

ABSTRACT

The distribution of the electrical potential inside an electrolytic solution has been calculated for typical cases of cathodic protection involving an impressed current. In particular, it is shown under which conditions the differences in the local single electrode potential are sufficiently low so that complete cathodic protection without significant hydrogen evolution can be accomplished by using an automatic control of the impressed current.

Corrosion of a metal in an electrolyte may be prevented by cathodic protection, i.e., by providing a sufficiently negative electrode potential. This may be accomplished by passing electrical current from an auxiliary anode through the electrolyte to the metal to be protected as cathode. The minimum current required for complete protection is determined by the condition that the local single electrode potential $E_1(X)$ of metal 1 to be protected must be more negative (less noble) at any point X than its equilibrium single electrode potential $E_{1(eq)}$ in the given electrolyte (1),

$$E_1(X) < E_{1(eq)} \qquad [1]$$

The local single electrode potential $E_1(X)$ is defined as the voltage of the cell

standard hydrogen electrode	salt bridge	electrolyte	metal 1

where the opening of the capillary leading from the electrolyte to the salt bridge is located next to point X at the surface of metal 1.

If the anodic dissolution rate of metal 1 rises rather slowly with increasing potential, virtually complete cathodic protection may be accomplished at a potential above $E_{1(eq)}$. Then Eq. [1] and likewise Eq. [2] below may be replaced by less rigorous conditions where $E_{1(eq)}$ is replaced by E_1' defined as the highest single electrode potential at which the anodic dissolution rate is negligibly small in the environment under consideration. It has been shown previously (1) how the values of $E_{1(eq)}$ and E_1' can be estimated.

The minimum current for complete cathodic protection can be calculated readily if the geometry is such that the current density and the single electrode potential are the same at all points of the cathode, e.g., when the inner side of a tube as cathode is protected by means of an anode located in the axis of the tube. In this case, the current required for complete cathodic protection is equal to the product of area and the sum of the current densities at potential $E_{1(eq)}$ for all possible reduction processes of oxidizers present in the electrolyte. If hydrogen evolution is negligible at this potential and oxygen dissolved in the electrolyte is the only oxidizer, the minimum current is equivalent to the diffusion rate of oxygen to the metal.

In general, conditions are more involved. In particular, when a local electrode potential $E_1(X) < E_{1(eq)}$ at points remote from the anode is maintained, the local potential at points close to the anode may be considerably more negative than $E_{1(eq)}$ and accordingly an appreciable portion of the current may be used for cathodic evolution of hydrogen. Since hydrogen evolution may cause undesirable effects such as blistering of paint and embrittlement of steel, it is of interest to know under which conditions complete cathodic protection can be accomplished without significant hydrogen evolution when the local electrode potential at points most remote from the anode is made equal to $E_{1(eq)}$. Under most conditions the rate of hydrogen evolution rises exponentially when the electrode potential is made more negative. For practical purposes an electrode potential E^* for the onset of significant hydrogen evolution may be introduced. For instance, E^* may be defined as the potential at which the current density used for hydrogen evolution is equal to the current density J_{ox} used for reduction of oxygen, or a certain fraction thereof. Then the first requirement is that the equilibrium potential $E_{1(eq)}$ is more positive (more noble) than E^*. In addition, the difference $E_{1(eq)} - E^*$ must be greater than the maximum variation of the local single electrode potential, ΔE_{max}, under conditions providing complete cathodic protection. Thus the condition for insignificant hydrogen evolution becomes

$$\Delta E_{max} < E_{1(eq)} - E^* \qquad [2]$$

The following cases are amenable to a theoretical treatment and may be considered as a basis for a qualitative discussion of more complex situations.

Wire Anodes in Front of the Metal to Be Protected

Oxygen reduction as the only cathodic process.— To protect the surface of an infinite plate of metal 1, equidistant auxiliary anodes in the form of wires parallel to the surface of metal 1 may be provided (*see* Fig. 1). It is assumed that the oxidizer, e.g., oxygen, is readily reduced if $E_1(X) \leqq E_{1(eq)}$, i.e., the

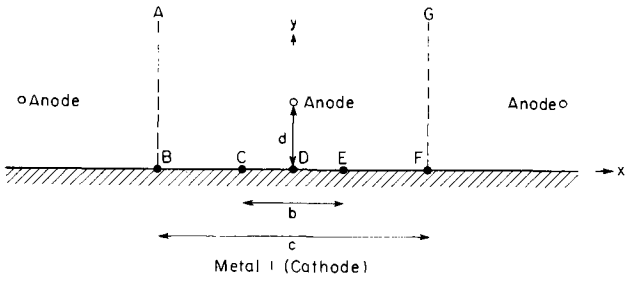

Fig. 1. Metal 1 protected by equidistant auxiliary wire anodes. Hydrogen evolution is supposed to take place between points C and E.

current density J_{ox} for the reduction of the oxidizer, is supposed to be determined by the maximum diffusion rate for zero concentration of the oxidizer at the surface of metal 1 and to be independent of the local electrode potential $E_1(X)$. Moreover, a virtually uniform effective thickness of the diffusion boundary layer is assumed so that the current density J_{ox} is the same at all points along the surface of metal 1. The surface may involve microscopic inhomogeneities, e.g., inclusions of a second phase, but the dimensions of inclusions are supposed to be less than the thickness of the hydrodynamic boundary layer. In this case, the local single electrode potential is not affected by the heterogeneity of the surface (2-4).

The potential ϕ in the electrolyte has to satisfy the Laplace differential equation

$$\partial^2\phi/\partial x^2 + \partial^2\phi/\partial y^2 = 0 \qquad [3]$$

where x and y are the coordinates shown in Fig. 1.

For negligible hydrogen evolution, the boundary conditions are

$$\partial\phi/\partial y = 0 \text{ at } y = \infty \qquad [4]$$

$$\partial\phi/\partial y = J_{ox}/\sigma \text{ at } y = 0 \qquad [5]$$

where σ is the electrical conductivity of the electrolyte and Eq. [5] is a consequence of Ohm's law. For equidistant auxiliary anodes as line sources shown in Fig. 1, the potential distribution in the electrolyte ($y > 0$) is found to be

$$\phi(x, y) = \text{constant} + J_{ox}\, y/\sigma - \frac{J_{ox}c}{2\pi\sigma} Re\left[\ln \sin \frac{\pi(z-id)}{c} + \ln \sin \frac{\pi(z+id)}{c}\right] \qquad [6]$$

where c is the distance between adjacent anodes, d is their distance from the metal to be protected, $z = x + iy$, $i = (-1)^{1/2}$, and $Re[..]$ denotes the real part of the complex function in brackets. The term $J_{ox}y/\sigma$ represents a uniform field which gives the potential gradient at the surface of metal 1 in accord with Eq. [5]. The following term represents the field resulting from an infinite series of positive line sources at $x = \pm nc$, $y = d$ where $n = 0, 1, 2$, etc., and their images at $\pm nc$, $y = -d$. The latter term does not give a contribution to the potential gradient at $y = 0$. The intensity of these line sources is chosen so that the potential gradient at infinite distance y vanishes in accord with Eq. [4].

From Eq. [5] the potential in the electrolyte at the surface of metal 1 is obtained as

$$\phi(x, y = 0) = \phi(x = 0, y = 0) - \frac{J_{ox}c}{2\pi\sigma} \ln\left[1 + \frac{\sin^2(\pi x/c)}{\sinh^2(\pi d/c)}\right] \qquad [7]$$

According to Eq. [7] the potential ϕ in the electrolyte along the surface of metal 1 is a periodic function of distance x. The maximum potential difference occurs between points opposite to auxiliary anodes (e.g., $x = 0$, $y = 0$) and points located half way between the anodes (e.g., $x = \frac{1}{2}c, y = 0$). Inside metal 1 a virtually constant potential is assumed. Hence the local single electrode potential $E_1(X)$ is equal to a constant value minus the local electrical potential in the electrolyte. The maximum difference ΔE_{max} of the local single electrode potential between different points of metal 1 is, therefore, found to be

$$\Delta E_{max} = E(x = \tfrac{1}{2}c) - E(x = 0)$$
$$= \phi(x = 0, y = 0) - \phi(x = \tfrac{1}{2}c, y = 0)$$
$$= (J_{ox}c/\pi\sigma) \ln \coth (\pi d/c) \qquad [8]$$

Upon introducing the dimensionless group

$$f_1 = \pi^{-1} \ln[\coth (\pi d/c)] \qquad [9]$$

the maximum difference of the local single electrode potentials may be calculated as

$$\Delta E_{max} = (J_{ox}c/\sigma) f_1 \qquad [10]$$

A graph for f_1 as a function of the distance ratio d/c is shown in Fig. 2.

If the ratio d/c is much less than unity, the hyperbolic cotangent in Eq. [9] may be replaced by the reciprocal of its argument as a close approximation. Thus

$$f_1 \cong (1/\pi) \ln (c/\pi d) \text{ if } d << c \qquad [11]$$

i.e., f_1 is of the order of unity if $d/c << 1$.

If the distance d of the auxiliary anodes from metal 1 is greater than half the distance c between neighboring anodes, the following approximation holds

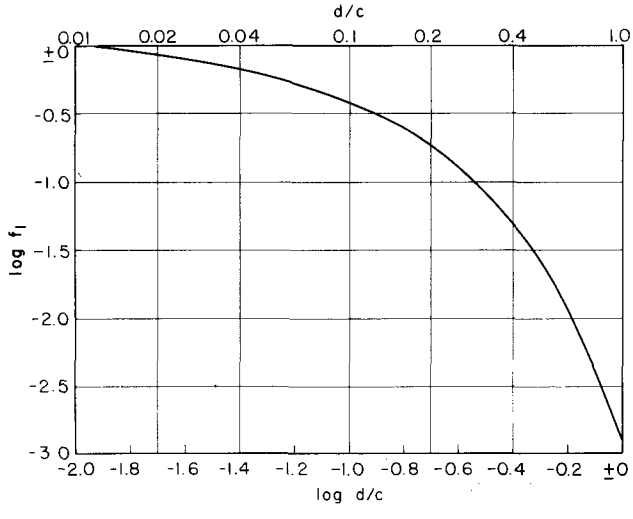

Fig. 2. Dimensionless group f_1 vs. ratio d/c according to Eq. [9].

$$\ln [\coth (\pi d/c)] = -\ln [\tanh (\pi d/c)] \cong -\ln [1 - 2 \exp (-2\pi d/c)] \cong 2 \exp (-2\pi d/c) \quad [12]$$

Upon substitution of Eq. [12] in Eq. [8], it follows that

$$\Delta E_{max} \cong (2J_{ox}c/\pi\sigma) \exp (-2\pi d/c) \text{ if } d/c > 0.5 \quad [13]$$

Hence ΔE_{max} may be decreased to very low values by increasing the anode-cathode distance d.

If the value of ΔE_{max} is less than the difference $E_{1(eq)} - E^*$ in Eq. [2], complete cathodic protection can be accomplished without significant hydrogen evolution. Upon combining Eqs. [2] and [10], the condition for the possibility of complete cathodic protection without significant hydrogen evolution becomes

$$E_{1(eq)} - E^* > (J_{ox}c/\sigma) f_1 \quad [14]$$

With the aid of Eq. [14] it is possible to calculate the minimum distance d for this condition. For instance, if $E_{1(eq)} - E^* = 0.2$ volt, $J_{ox} = 10^{-4}$ amp/cm^2, c = 200 cm, and the corroding solution is sea water having a specific electrical conductivity $\sigma = 0.1$ ohm^{-1}cm^{-1}, it follows from Eq. [14] that $f_1 \leqq 1$, or $d/c \geqq 0.01$ according to Fig. 2, and d $\geqq$ 2 cm. If, however, the corroding solution is fresh water having a low conductivity, e.g., $\sigma = 10^{-4}$ ohm^{-1}cm^{-1}, hydrogen evolution can be avoided only if $f_1 \leqq 0.001$, or d/c $\geqq$ 1 according to Fig. 2 and $d \geqq 200$ cm.

If the value of ΔE_{max} is below the limit stated in Eq. [2], cathodic protection without significant hydrogen evolution may be accomplished by making the current equal to the product of J_{ox} and the area of metal 1, e.g., by using an automatic control of the current so that at points most remote from the anodes, i.e., at $x = \frac{1}{2}$ c, $y = 0$, the local single electrode potential measured with the help of a probe is equal to or slightly lower than the equilibrium potential $E_{1(eq)}$. This may be accomplished with the help of a potentiostat as described by Hickling (5) and others (6-8). Use of a circuit involving a magnetic amplifier (9, 10) may be particularly appropriate. In spite of higher costs, an automatic control of the current may be economical because sufficient current for cathodic protection without significant hydrogen evolution is provided even under variable conditions which result, for instance, from different rates of oxygen diffusion toward the surface when a ship travels at different speeds, or is at rest.

Simultaneous reduction of oxygen and evolution of hydrogen.—If an automatic current control is not provided, it is necessary to apply a constant current which is greater than the product of the maximum value of J_{ox} expected under practical conditions and the area A of metal 1. Use of excess current necessarily results in evolution of hydrogen. Hydrogen evolution will be nearly uniform along the surface of metal 1 if the potential of the solution and accordingly the single electrode potential $E_1(X)$ varies only slightly, e.g., if $\Delta E_{max} < 0.02$ volt.

On the other hand, if $\Delta E_{max} > 0.1$ volt, hydrogen evolution will predominate in the vicinity of the anodes, whereas at points more remote from the anodes hydrogen evolution may be negligible. For regions with significant hydrogen evolution the single electrode potential of metal 1 is nearly equal to E^* irrespective of the local current density since a very steep rise of the current density-potential curve below E^* is assumed. Accordingly, for the sake of mathematical simplification, the potential in the electrolyte along sections of metal 1 where hydrogen is evolved may be considered to be constant, i.e., equal to $\phi(x = 0, y = 0)$ as a fair approximation. On the other hand, at points more remote from the auxiliary anodes, the potential gradient in the electrolyte is determined essentially by the current density used for cathodic reduction of oxygen.

For the strip ABCDEFG between $y = -\frac{1}{2}$c and $y = \frac{1}{2}$c with significant hydrogen evolution between $y = -\frac{1}{2}b$ and $y = \frac{1}{2}b$ (*see* Fig. 1), the boundary conditions are, therefore, assumed to be

$$\phi = \phi(x = 0, y = 0) \text{ at } |x| < \frac{1}{2}b, y = 0 \quad [15a]$$

$$\partial\phi/\partial y = J_{ox}/\sigma \text{ at } \frac{1}{2}b \leqq |x| \leqq \frac{1}{2}c \quad [15b]$$

which replace Eq. [5].

A solution for conditions stated in Eq. [15a] and [15b] but without a line source at $x = 0$, $y = d$ has already been obtained in Eq. (36) of a previous paper (1). On this solution, the solution for a line source at $x = 0$, $y = d$ satisfying the boundary conditions $\phi = 0$ along the line CDE and $\partial\phi/\partial y = 0$ along the lines BC and EF in Fig. 1 is superimposed. In the z'' plane of Fig. 6 of the previous paper the boundary conditions are satisfied by a line source at

$$x'' = 0, y'' = \sinh^{-1} (\sinh\alpha/\sin\beta) = v$$

and its negative image at

$$x'' = 0, y'' = -\sinh^{-1}(\sinh\alpha/\sin\beta) = -v$$

where

$$\alpha = \pi d/c \quad [16a]$$

$$\beta = \pi b/2c \quad [16b]$$

$$v = \sinh^{-1}(\sinh\alpha/\sinh\beta) \quad [17]$$

The corresponding solution in the z plane is obtained by using the pertinent relation between z and z''. Thus the complete solution is found to be

$$\phi(x,y) = \phi(x = 0, y = 0) + \frac{J_{ox}}{\sigma}\left\{y + \frac{c}{\pi} Re\left[i \sin^{-1}\left(\frac{\sin\zeta}{\sin\beta}\right)\right]\right\} - \frac{J_{ox}c}{2\pi\sigma} g\, Re\left\{\ln \sin\left[\sin^{-1}\left(\frac{\sin\zeta}{\sin\beta}\right) - iv\right] - \ln \sin\left[\sin^{-1}\left(\frac{\sin\zeta}{\sin\beta}\right) + iv\right]\right\} \quad [18]$$

where

$$\zeta = \pi z/c \quad [19]$$

The factor g in Eq. [18] is proportional to the strength of the line source at $x = 0$, $y = d$. Upon

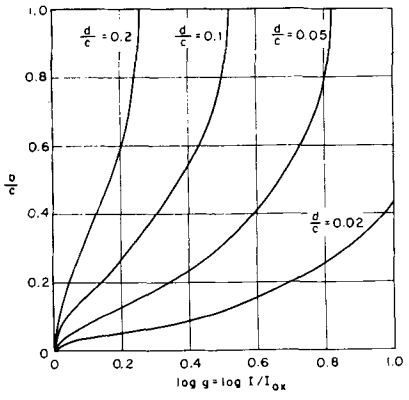

Fig. 3. Ratio b/c vs. log g = log I/I_{ox} according to Eq. [21]

using the condition that $\partial\phi/\partial y$ must be continuous at $x = b, y = 0$, it follows that

$$g = \coth v \qquad [20]$$

Since $g = 1$ for $b = 0$ according to Eqs. [17] and [20], it follows that g is equal to the ratio of the current I for conditions involving hydrogen evolution to the current I_{ox} for exclusive reduction of oxygen,

$$I/I_{ox} = g = \coth \{\sinh^{-1} [\sinh (\pi d/c)/\sin(\pi b/2c)]\} \qquad [21]$$

Eq. [21] has been used in order to draw graphs shown in Fig. 3 from which one may read the width b of the section of metal 1 at which hydrogen is evolved if the current ratio I/I_{ox} and the distance ratio d/c are given.

Inspection of Fig. 3 shows that a high increase of the current is required in order to obtain significant hydrogen evolution along the entire surface of metal 1 if the distance d of the auxiliary anodes is small as compared to the distance c between neighboring anodes. On the other hand, a moderate increase of the current leads to hydrogen evolution along the entire surface of metal 1 if the distances c and d are of the same order of magnitude.

For the section of metal 1 at which hydrogen is evolved, the single electrode potential $E_1(X)$ is assumed to be equal to E^*. The single electrode potential $E_1(X)$ at any point is equal to a constant value minus the local electrical potential in the electrolyte. Thus, $E_1(X)$ for the section of metal 1 at which cathodic reduction of oxygen prevails is obtained from Eq. [18] as

$$E(X) = E^* - [\phi(x, y = 0)^* - \phi(x = 0, y = 0)]$$
$$= E^* + (J_{ox}c/\pi\sigma)\{u - g \tanh^{-1}[(\tanh v)(\tanh u)]\}$$

$$\text{if } \frac{1}{2} b \leqq |x| \leqq \frac{1}{2} c \qquad [22]$$

where

$$u = \cosh^{-1}[\sin(\pi x/c)/\sin(\pi b/2c)] \qquad [23]$$

and v is defined by Eq. [17].

Upon substituting Eq. [21] in Eq. [22] and letting $x = \frac{1}{2} c$, the maximum difference of the local single electrode potential is found to be

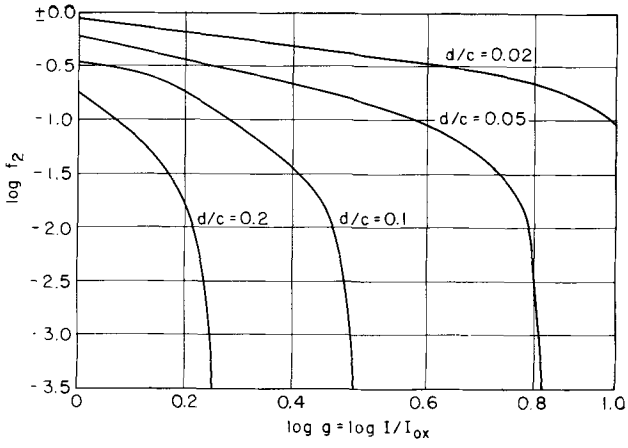

Fig. 4. Dimensionless group f_2 vs. log g = log I/I_{ox} according to Eq. [26].

$$\Delta E_{max} = E(x = \frac{1}{2} c) - E^*$$
$$= \frac{J_{ox}c}{\pi\sigma}\left[w - \frac{I}{I_{ox}} \tanh^{-1}\left(\frac{I_{ox}}{I} \tanh w\right)\right] \qquad [24]$$

where in view of Eq. [21]

$$w = u(x = \frac{1}{2} c) = \cosh^{-1}\left\{\frac{\sinh [\coth^{-1}(I/I_{ox})]}{\sinh (\pi d/c)}\right\} \qquad [25]$$

Upon introduction of the dimensionless group

$$f_2 = \frac{1}{\pi}\left[w - \frac{I}{I_{ox}} \tanh^{-1}\left(\frac{I_{ox}}{I} \tanh w\right)\right] \qquad [26]$$

the values of ΔE_{max} may be calculated as

$$\Delta E_{max} = (J_{ox}c/\sigma) f_2 \text{ if } I > I_{ox} \qquad [27]$$

Fig. 4 shows curves for f_2 as a function of the applied current according to Eq. [26]. Thus one may calculate ΔE_{max} with the help of Eq. [27]. Values of f_2 are equal to values of f_1 if $I = I_{ox}$, and decrease if $I > I_{ox}$, i.e., ΔE_{max} decreases with increasing current. Consequently, the necessary condition for complete cathodic protection in Eq. [2] may not be satisfied for $I = I_{ox}$ but may be satisfied by increasing the current. If $d/c << 1$, f_2 is of the order of unity, and a decrease of f_2 may be very desirable in order to satisfy Eq. [2], but for small d/c ratios f_2 decreases only slowly with increasing current. Unless the excess current is very high, hydrogen evolution is confined to the vicinity of the anodes and, therefore, the potential distribution along the cathode is changed only slightly. Only when hydrogen is evolved along most of the surface of metal 1, do the values of f_2 and ΔE_{max} drop markedly. Calculated values of ΔE_{max} and f_2 become zero according to Eqs. [24] and [26] if $b = c$, but this results only from the simplifying presupposition that the variation of the single electrode potential with current density used for hydrogen evolution is negligible.

On the other hand, if the anode-cathode distance d is of the same order of magnitude as the distance c between neighboring anodes, a relatively small increase of the current suffices to obtain significant hydrogen evolution along the entire surface of

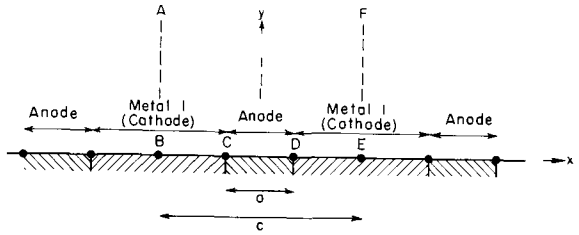

Fig. 5. Metal 1 as a cathode protected by auxiliary anodes at the surface of metal 1.

metal 1 and a considerable decrease of f_2 as shown in Fig. 3 and 4. Since the value of $f_1 = f_2 (I = I_{ox})$ for $d \sim c$ is small and, therefore, Eq. [2] is easy to satisfy, a decrease of f_3 and ΔE_{max} due to a current $I > I_{ox}$ is, in general, not of practical importance.

Anodes in the Plane of the Metal to Be Protected

A periodic array of strips of metal 1 and anodes lying in the same plane is shown in Fig. 5. Calculations are confined to the strip ABCDEF. Insulating sections between cathodes and anodes are assumed to be negligibly small. The width of the anodes is designated by a and the distance between the midlines of sections of metal 1 by c. At the cathodic areas of metal 1, only reduction of oxygen is supposed to occur. Thus, the boundary condition is analogous to that stated in Eq. [5]

$$\partial\phi/\partial y = J_{ox}/\sigma \text{ at } \frac{1}{2}a < |x| < \frac{1}{2}c,\ y = 0 \quad [28]$$

At the anodes either a constant electrode potential or a constant current density may be assumed. For a constant electrode potential, the solution obtained in Eqs. [38] and [39] of the previous paper (1) may be used. With the present notation, the maximum difference of the single electrode potential of metal 1 is found to be

$$\Delta E_{max} = (J_{ox}c/\sigma) f_3 \quad [29]$$

where

$$f_3 = \pi^{-1} \cosh^{-1}[1/\sin(\pi a/2c)] \quad [30]$$

On the other hand, there may be considered a uniform current density along the anode, which is $(c - a)/a$ times greater than the cathodic current density J_{ox} corresponding to the area ratio of anodes and cathodes. Thus

$$\partial\phi/\partial y = -(c-a) J_{ox}/a\sigma \text{ at } 0 < |x| < \frac{1}{2}a,\ y = 0 \quad [31]$$

A solution of the Laplace equation [3] for boundary conditions [28] and [31] may be obtained by a superposition of line sources at the surface of anodes and line sinks at the surface of cathodes.

$$\phi = \text{constant} + \frac{J_{ox}}{\sigma}\left[y - \frac{c}{\pi a} Re \int_{-\frac{1}{2}a}^{\frac{1}{2}a} \ln \sin \frac{\pi(z-\xi)}{c}\, d\xi\right] \quad [32]$$

where the variable of integration ξ is the distance of a line source from the origin.

To find the potential at the surface of cathodes and anodes, $\eta = \pi(x - \xi)/c$ is substituted as the variable of integration. Thus

$$\phi(x, y = 0) = \text{constant} - \frac{J_{ox}c}{\sigma}\frac{c}{\pi^2 a} \mathrm{Re} \int_{\pi(x - \frac{1}{2}a)/c}^{\pi(x + \frac{1}{2}a)/c} \ln \sin \eta\, d\eta \quad [33]$$

Hence the maximum difference of the single electrode potential at the surface of metal 1 is

$$\Delta E_{max} = \phi(x = \frac{1}{2}a, y = 0) - \phi(x = \frac{1}{2}c, y = 0) = (J_{ox}c/\sigma) f_4 \quad [34]$$

where

$$f_4 = \frac{c}{\pi^2 a}\left\{\int_{\frac{1}{2}\pi(1 - a/c)}^{\frac{1}{2}\pi(1 + a/c)} \ln \sin \eta\, d\eta - \int_0^{\pi a/c} \ln \sin \eta\, d\eta\right\} \quad [35]$$

The integrals in Eq. [35] can be evaluated readily by means of numerical methods.

Graphs of f_3 and f_4 vs. a/c are shown in Fig. 6. The difference between the curves for f_3 and f_4 is relatively small. It is, therefore, irrelevant whether a constant electrode potential or a constant current density at the anodes is assumed.

In the foregoing calculation the effect of insulating strips between cathodes and anodes has been neglected. The effect is of minor importance if the width of the anodes is much less than that of the cathodes. As a limiting case, wire anodes in the plane of metal 1 as shown in Fig. 7 are considered. The width of insulating sections between metal 1 and a wire anode is denoted by $\frac{1}{2}s$. Thus the boundary conditions for the strip ABCDEF are

$$\partial\phi/\partial y = J_{ox}/\sigma \text{ at } \frac{1}{2}s < |x| < \frac{1}{2}c,\ y = 0 \quad [36]$$

$$\partial\phi/\partial y = 0 \text{ at } 0 < x < \frac{1}{2}s,\ y = 0 \quad [37]$$

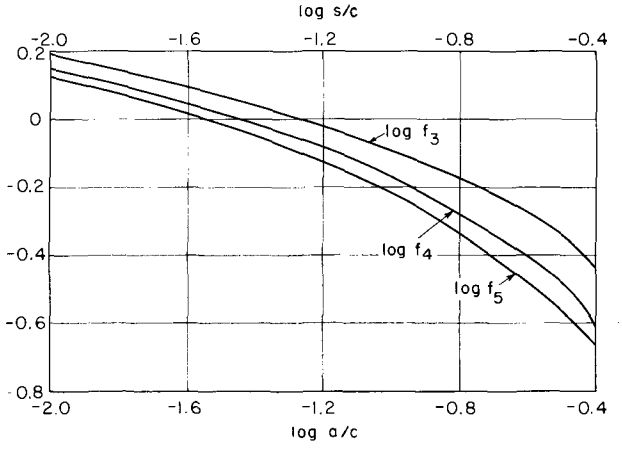

Fig. 6. Dimensionless groups f_3, f_4, and f_5 vs. log a/c and log s/c according to Eqs. [30], [35], and [41], respectively.

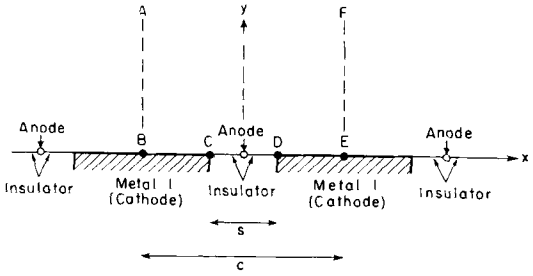

Fig. 7. Metal 1 as a cathode protected by wire anodes at the surface of metal 1.

Since all current lines originating from the anode are supposed to enter metal 1 as cathode, the potential gradient at infinite distance y must vanish,

$$\partial\phi/\partial y = 0 \text{ at } y = \infty \qquad [38]$$

The latter condition determines the strength of the line source at $x = 0$, $y = 0$ where the wire anode is located.

The Laplace equation [3] and the boundary conditions [36] to [38] are satisfied by

$$\phi = (J_{ox}/\sigma)\left\{ y - \pi^{-1} Re \int_{-\frac{1}{2}s}^{\frac{1}{2}s} \ln \sin\left[\pi(z-\xi)/c\right] d\xi - (c-s)\pi^{-1} Re \ln \sin(\pi z/c) \right\} + \text{constant} \qquad [39]$$

Hence the maximum difference of the local single electrode potential at the surface of metal 1 is found to be

$$\Delta E_{max} = \phi(x = \frac{1}{2}s,\ y = 0) - \phi(x = \frac{1}{2}c,\ y = 0) = (J_{ox}c/\sigma) f_5 \qquad [40]$$

$$f_5 = -\left[(c-s)/c\right]\pi^{-1} \ln \sin(\pi s/2c) + \pi^{-2} \int_{\frac{1}{2}\pi(1-s/c)}^{\frac{1}{2}\pi(1+s/c)} \ln \sin y \, dy - \pi^{-2} \int_0^{\pi s/c} \ln \sin y \, dy \qquad [41]$$

A graph for f_5 as a function of s/c is shown in Fig. 6. Since the curves for f_3, f_4, and f_5 lie relatively close together, it follows that the value of ΔE_{max} is determined mainly by the width of the section where metal 1 is not present, regardless of the width of the anodes.

Moreover, curves in Fig. 6 show that the factors f_3, f_4, and f_5 are of the order of unity except for very small values of a/c or s/c. For anodes located in or close to the surface plane of the metal to be protected, ΔE_{max} is, therefore, of the order of $J_{ox}c/\sigma$. Hence the distance c between neighboring anodes is the most important controllable factor in order to make ΔE_{max} sufficiently small as a necessary requirement for the possibility of complete cathodic protection without significant hydrogen evolution. In particular, a low conductivity of the electrolyte requires small distances between neighboring anodes.

If $E_{1(eq)} - E^* = 0.2$ volt, $J_{ox} = 10^{-4}$ amp/cm^2, and the corroding solution is sea water with a specific electrical conductivity $\sigma = 0.1$ ohm^{-1}cm^{-1}, the permissible maximum value of c is of the order of 200 cm. A low conductivity of the electrolyte, however, requires much smaller distances between neighboring anodes located in the plane of the metal to be protected. In fresh water with an electrical conductivity of 10^{-4} ohm^{-1} cm^{-1}, the permissible maximum value of c under the aforementioned conditions would be of the order of 0.2 cm. Under these conditions, anodes located in the plane of the metal to be protected are not helpful and anodes must be placed at a sufficient distance in front of the metal to be protected.

For the configurations shown in Fig. 5 and 7, the potential distribution for conditions involving hydrogen evolution has not been calculated. If only oxygen is reduced, values of f_3, f_4, and f_5 for small values of a/c or s/c are of the same order of magnitude as the values of f_1 for comparable values of d/c. Thus it may be concluded that conditions involving hydrogen evolution for configurations shown in Fig. 5 and 7 and small values of a/c or s/c are similar to those for wire anodes in front of the metal to be protected. By and large, a significant decrease in ΔE_{max} will require a current I much greater than I_{ox} with significant hydrogen evolution along most of the surface of metal 1.

Cathodic Protection of Bare Sections of a Painted Metal

In many cases, most of the metal is painted and there are only small bare sections for which cathodic protection is needed. In what follows it is shown that the potential distribution in the electrolyte and the value of ΔE_{max} are determined mainly by equations derived above if the current density in these equations is replaced by $J_{ox(av)}$, i.e., the current density for oxygen reduction averaged over painted and bare sections.

Fig. 8 shows a periodic array of bare and painted sections of metal 1 with wire anodes in front of metal 1. The distance between anodes is denoted by c, the width of bare sections by p, and the distance between the midlines of neighboring bare sections of metal 1 by q. Thus the boundary conditions for the strip ABCD in Fig. 8 are

$$\partial\phi/\partial y = J_{ox}/\sigma \text{ at } \mu q - \frac{1}{2}p < |x| < \mu q + \frac{1}{2}p \qquad [42]$$

$$\partial\phi/\partial y = 0 \text{ at } \mu q + \frac{1}{2}p < |x| < (\mu+1)q - \frac{1}{2}p \qquad [43]$$

$$\partial\phi/\partial y = 0 \text{ at } y = \infty \qquad [44]$$

where μ is 0, ±1, ±2, . . . , or $\pm m$ corresponding to $2m = c/q$ bare sections per length c.

The potential distribution may be represented by a superposition of line sources and line sinks,

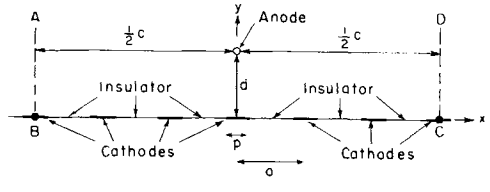

Fig. 8. Periodic array of bare and painted sections of metal 1 with wire anodes in front of metal 1.

$$\phi = \text{constant} + Re\{-(mp\,J_{ox}/\pi\sigma)\ln\sin[\pi(z-id)/c] - (mp\,J_{ox}/\pi\sigma)\ln\sin[\pi(z+id)/c] + \frac{J_{ox}}{\pi\sigma}\sum_{\mu=-m}^{\mu=+m} I_\mu(z) \quad [45]$$

where the integral $I_\mu(z)$ involving the serial number μ is

$$I_\mu(z) = \int_{\mu q-\frac{1}{2}p}^{\mu q+\frac{1}{2}p} \ln\sin\frac{\pi(z-\mu q-\xi)}{c}\,d\xi \quad [46]$$

In Eq. [45] the first two terms result from line sources located at the positions of the anodes at $x = \pm nc$, $y = d$ and their images at $x = \pm nc$, $y = -d$. The integrals result from line sinks located at bare sections of metal 1. The validity of Eq. [45] may be verified by substituting Eq. [45] in Eqs. [42] to [44].

Hence the difference ΔE in the single electrode potential between points at $x = \frac{1}{2}c$ and $x = 0$ is found to be

$$\Delta E = \phi(x=0, y=0) - \phi(x=\tfrac{1}{2}c, y=0) = (2mp\,J_{ox}/\pi\sigma)\ln\coth(\pi d/c) + \frac{J_{ox}}{\pi\sigma}\sum_{\mu=-m}^{\mu=+m}\left[I_\mu(z=0) - I_\mu(z=-\tfrac{1}{2}c)\right] \quad [47]$$

Shifting the origin of the coordinate system and substituting $\xi' = \xi - \frac{1}{2}c$ as the variable of integration in the integrals for $z = \frac{1}{2}c$, it can be shown that the two sums of integrals in Eq. [47] are equal and, therefore, cancel each other. Upon substituting

$$J_{ox(av)} = J_{ox}(2mp/c) = J_{ox}(p/q) \quad [48]$$

as the current density averaged over bare and painted sections, it follows that

$$\Delta E = (J_{ox(av)}\,c/\pi\sigma)\ln\coth(\pi d/c) \quad [49]$$

This is the same result that has been found above in Eq. [8] for a completely bare surface of metal 1.

In addition, it can be shown with the help of Eq. [45] that local differences of the single electrode potential along an individual section of metal, e.g., between $x = \frac{1}{2}p$, $y = 0$, and $x = 0$, $y = 0$ are insignificant in comparison to the value of ΔE calculated in Eq. [49].

Similar calculations can be made for the configurations shown in Fig. 5 and 7. By and large, the foregoing equations for ΔE_{max} remain valid for partly painted structural components if $J_{ox(av)}$ is substituted for J_{ox}.

Concluding Remarks

In the present paper, variations in the local single electrode potential of cathodes have been calculated (*a*) for anodes placed in front of the cathodes as shown in Fig. 1 and (*b*) for anodes and cathodes lying in the same plane as shown in Fig. 5 and 7. In both cases, the maximum variation in the local potential of the cathodes is found to be

$$\Delta E = J_{ox(av)}\,(c/\sigma)f \quad [50]$$

where the dimensionless factor f depends on length ratios characteristic of the geometries shown in Fig. 1, 5, and 7.

If anodes are placed in front of the cathodes, the value of $f = f_1$ shown in Fig. 2 can always be made sufficiently small by providing an anode-cathode distance d comparable to or greater than the distance c between neighboring anodes. Under these conditions, hydrogen evolution may be avoided easily by automatic adjustment of the impressed current so that a predetermined single electrode potential of the cathodes is maintained.

In contrast, if anodes and cathodes lie in the same plane, the value of the factor $f = f_3$, f_4, or f_5 shown in Fig. 6 is in general of the order of unity. Consequently, in order to keep ΔE_{max} within limits required for the suppression of hydrogen evolution, it is necessary to make the width c of the cathodic areas sufficiently small. A small width c is especially necessary if the conductivity σ of the electrolyte is low. Consequently, if anodes and cathodes lie in the same plane, cathodic protection is, in general, practical only in electrolytes which have a high electrical conductivity as, e.g., sea water, and the average current density for reduction of oxygen is relatively low owing to painting most of the metal which is to be protected.

Manuscript received Dec. 3, 1956.
Any discussion of this paper will appear in a Discussion Section to be published in the June 1958 JOURNAL.

REFERENCES

1. C. Wagner, *This Journal*, **99**, 1 (1952).
2. C. Wagner, "Chemische Reaktionen der Metalle," in "Handbuch der Metallphysik," edited by G. Masing, Vol. 1, Part 2, pp. 196-199, Akademische Verlagsgesellschaft Becker & Erler, Leipzig (1940).
3. A. Frumkin and B. Levich, *Acta Physicochim. U.R.S.S.*, **18**, 325 (1943).
4. J. T. Waber, *This Journal*, **101**, 271 (1954).
5. A. Hickling, *Trans. Faraday Soc.*, **38**, 27 (1942).
6. J. J. Lingane, "Electroanalytical Chemistry," pp. 214 ff, Interscience Publishers, Inc., New York (1953).
7. J. Schoen and K. E. Staubach, *Regeltechnik*, **2**, 7 (1954).
8. W. Vielstich and H. Gerischer, *Z. physik. Chem. N.F.*, **4**, 10 (1955).
9. C. J. Penther and D. J. Pompeo, *Anal. Chem.*, **21**, 178 (1948).
10. M. H. Aronson, *Instruments*, **25**, 608 (1952).

APPENDIX

Errata in Eqs. [29] and [36] of the previous paper (1) have occurred. The correct form of Eq. [29] is

$$z'' = \sin^{-1}\left\{\frac{z'}{\sin\left[\frac{1}{2}\pi b/(a+b)\right]}\right\} \quad [29]$$

In Eq. [36] x is to be replaced by z.

Technical Note

The Silver and Thallium Oxide Coulometer

W. T. Foley

Chemistry Department, St. Francis Xavier University, Antigonish, Nova Scotia

The standard instrument for measuring quantity of electricity is the silver coulometer, but the iodine coulometer is of equally high precision (1). The copper coulometer is subject to secondary chemical reactions at the electrode, and it suffers from the disadvantage of a low equivalent weight. The water coulometer is subject to a negative error which increases rapidly with decreasing current (2).

A simple and precise coulometer using Ag and Tl salts at *p*H 9.5 is described here. It possesses the advantage of adherent Ag deposits and the use of conventional Pt gauze electrodes. The cell reaction is as follows:

$$4Ag^+ + 2Tl^+ + 6OH^- = Tl_2O_3 + 3H_2O + 4Ag$$

The value of the normal potential for the reaction

$$2Tl^+ + 6OH^- = Tl_2O_3(s) + 3H_2O + 4e^-$$

is -0.23 ± 0.02 vs. S.C.E. (3). Hence, at unit activity of thallous ion the oxidation potential at *p*H 9.5 is $+0.40$ v. At the same *p*H and in the absence of overvoltage, which is usually high, the oxidation potential of hydroxide to oxygen is $+0.67$ v. Thus thallous ion is an excellent depolarizer to prevent the formation of oxygen at the anode. The potential for the reaction

$$Tl = Tl^+ + e^-$$

is -0.33 v. A solution containing 0.1M $AgNO_3$, 0.5M NH_4OH, and 0.2M NH_4NO_3 will have a Ag ion concentration of, say, 10^{-8}M. At this concentration the plating of Ag on the cathode will occur at a potential of about 0.3 v. If these solutions are stirred, there is no danger of plating Tl or H_2.

Apparatus.—Reagent grade $AgNO_3$, Tl_2SO_4, NH_4NO_3, and NH_4OH were used without further purification. Before the start of each of the first few runs the solution was scavenged electrolytically; this was later abandoned as unnecessary. The electrolyte was prepared by dissolving in 300 ml of water 4 g Tl_2SO_4, 4 g $AgNO_3$, 4 g NH_4NO_3, and 8 ml 15M NH_4OH. The Pt gauze cathode was 40 cm^2 and the anode was 23 cm^2; they were attached to the holder concentrically. A magnetic stirrer was used. Electrical energy was obtained from six 2-v storage batteries of 900 amp-hr capacity. The standard resistors[1] with conventional current and potential leads were 1 ohm and 10 ohms in nominal value. A Rubicon type B potentiometer was used for all measurements except one in which a L&N K2 was used. The limit of accuracy of calibration was $\pm 0.0001\%$. Two saturated Weston cells were used, one for preliminary adjustment of the potentiometer and the other for actual measurements. Time was measured by means of the WWV time signal.

Procedure.—The current through the electrolysis cell ran through the standard resistor across which the potential drop was measured. A DPDT switch in series with the resistor had across two of its terminals a dummy electrolysis cell with the same electrolyte and the same size electrodes as the working cell. Current was allowed to flow until all adjustments had been made and then at zero time the switch was made to the working coulometer. The potentiometer was read every 30 sec. The start and finish of the electrolysis was timed by the time signal from radio station WWV. At the conclusion of the electrolysis the electrodes were removed and washed with distilled water. The cathode, whose deposit was a beautiful silvery white, was dried at 110°C and weighed. If the deposit is not silvery white, the rate of stirring or the area of the cathode should be increased. The Tl_2O_3 is jet black except when very thin and it may be removed with H_2SO_3 or more conveniently with HCl.

Results.—The IR drop through the calibrated resistor enabled one to calculate the value of the current. The product of the average current and the time gave the quantity of electricity passed. The value of 107.88 was taken as the atomic weight of

Table I. Observed and calculated weights of Ag

Current, amp	Grams, Ag	Calculated Ag	Δ mg
1.0	1.0154	1.0153	+0.1
0.37	0.7496	0.7494	+0.2
0.28	1.0436	1.0429	+0.7
0.25	0.9235	0.9239	−0.4
0.22	1.1790	1.1794	−0.4
0.20	0.2550	0.2552	−0.2
0.19	0.3725	0.3725	0.0
0.18	0.2827	0.2827	0.0
0.16	0.2507	0.2505	+0.2
0.009	0.0958	0.0958	0.0

[1] Calibrated by the Applied Physics Division of the National Research Council of Canada.

Ag and 96,492 absolute coulombs (4) was taken as the value of the Faraday. Results are given in Table I.

Acknowledgment

This work was supported by the Defence Research Board of Canada Grant No. 7510-19, Project D-44-75-10-19.

Manuscript received July 27, 1956. This paper was prepared for delivery before the Washington Meeting, May 12-16, 1957.

Any discussion of this paper will appear in a Discussion Section to be published in the June 1958 JOURNAL.

REFERENCES

1. E. W. Washburn and S. J. Bates, *J. Am. Chem. Soc.*, **34**, 1341 (1912).
2. J. A. Page and J. J. Lingane, *Anal. Chim. Acta*, **16**, 175 (1957).
3. I. M. Kolthoff and J. Jordan, *J. Am. Chem. Soc.*, **74**, 382 (1952).
4. D. M. Craig and J. I. Hoffman, *Natl. Bur. Standards Circ.*,**524**, 13 (1953).

Technical Feature

The Past and Future of Silicon Carbide

G. M. Butler

Research and Development Division, The Carborundum Company, Niagara Falls, New York

When, in 1891, E. G. Acheson first found tiny, shining crystals on the electrode in his furnace made from a plumber's bowl, he did not know that the new compound was silicon carbide or that it was to prove the most versatile of all carbides. Within a few years, however, he himself found that his new crystals were not only very hard, but also possessed unique refractory, electrical, chemical, and metallurgical properties.

While calcium carbide and tungsten carbide, the two other really important carbides of commerce, have contributed greatly to the world's economy, each of them can do only one job well: calcium carbide is the basis of acetylene chemistry, and tungsten carbide yields hard, wear-resistant tools, dies, and similar parts.

Silicon carbide, on the other hand, can do many tasks well. Its attributes challenge the imagination:

Extreme hardness and resistance to wear and abrasion.

High strength and very slow oxidation rate at extremely high temperatures.

Chemical inertness to all acids and many other corrodants.

Chemical reactivity with chlorine and other halogens, and with several metal oxides.

Electrical semiconductive and rectifying properties.

Low absorption or "capture" of thermal neutrons.

High thermal conductivity.

High thermal emf when paired with graphite.

Low density and thermal expansibility.

Raw materials abundant and cheap.

Surely such a material is uniquely valuable to mankind! Even today its valuable characteristics are not fully exploited, although the demand for silicon carbide taxes every manufacturer.

Those who work with SiC believe that its future holds uses as yet only dimly foreseen. By outlining the extent to which its abilities are now utilized, and by showing wherein greater knowledge of it should lead to enhancement of these good properties, the author hopes to encourage workers in many fields to explore this unusual "man-made mineral."

Synthesis.—Although SiC has been manufactured for 65 years, the process of making it has changed little. Silica and carbon are still packed around a graphite resistor and heated to cause the reaction, $SiO_2 + 3C \rightarrow SiC + 2CO$. While some of the characteristics of the product, such as crystal size, purity, and resistivity, can be varied to a limited degree by furnacing practice and choice of raw materials, the manufacturer cannot yet persuade his furnaces to yield crystals of controlled size, density, shape, and other properties. He can select from the crude "ingot" various areas differing in character, but this is at best a compromise.

In the research laboratory many investigators have formed SiC crystals of higher purity than can be made easily commercially. They have used a variety of methods: heating mixtures of high purity SiO_2 and C in crucibles or packed around resistors; substituting Si for the SiO_2 to avoid the need for additional C; use of the "hot wire" process to reduce volatile Si halides in hydrogen; sublimation and recrystallization of previously formed SiC; adding C to a molten high-Si alloy; reacting molten or vaporized Si with C, etc.

No one has yet announced a method by which large, flawless single crystals of SiC can be synthesized, comparable to those grown from oxides by the flame-fusing process. This should be feasible, once a solution is found to the mechanical problem of providing a continuous, uniform flow of vapors containing Si and C, within which the crystal can grow as desired.

All evidence indicates that the commercial hexagonal crystal product is the result of a vapor-phase reaction in which Si unites with C. Some uncertainty exists as to the form in which C is present in the vapor, since the vapor pressure of elemental C at the reaction temperature range of 1800°-2400°C (3270°-4350°F) seems to be too low to provide the necessary concentration for crystal growth. Nevertheless, SiC crystals will grow whenever vapors carrying Si pass over C or when a mixture of C and SiO_2 is sufficiently hot.

Availability of large, ultrapure crystals would free the researcher from the vexing limitations imposed by the lack of high purity except in tiny crystals. Laboratory quantities of silicon carbide are available with moderately high purity, probably better than 99.9% SiC but only in particle sizes of about 80 mesh.

Of equal interest would be a way to grow large crystals of the low-temperature primary or cubic form of SiC. Apparently all SiC first forms as tiny cubic crystals, which transform at higher temperatures to the hexagonal or rhombohedral crystal forms. The largest cubic crystals seem to be less than 0.02 in. across, so they have little use at present.

These cubic crystals differ from the usual hexagonal product in electrical properties and perhaps also in chemical reactivity. Theoretically, large cubic crystals should make beautiful gem stones; DeMent (1) has presented arguments for this contention. Cubic crystals appear to grow from a liquid, such as molten Si or Si alloy, thus offering promise of growing large ones by techniques used to grow other crystals from molten baths.

Silicon carbide can be formed in high-Si alloys, both ferrous and nonferrous, in the presence of C. For many years after Moissan (2) first claimed to have found tiny crystals of SiC in meteoric iron, no other occurrence in nature was known. Later, Baumann (3) summarized the work of investigators who were able to produce SiC crystals in various Al-Si alloys, and also showed evidence for its formation in such alloys at temperatures as low as 525°C (977°F). Fulton and Chipman (4) recently showed that high-Si irons can contain small SiC crystals.

Loose grain.—One major division of SiC uses is as loose grits or "grain." Acheson first used his SiC crystals in loose form for the lapping and polishing of diamonds. Today substantial quantities of graded grits are sold for lapping, polishing, sawing, and similar operations using grits either loose or in a vehicle such as tallow, grease, or other lubricant and carrier. Rock sawing, stone and gem polishing, glass grinding, valve lapping, and other familiar operations make use of the hard, sharp crystals. Challenges to these uses of loose grain are coming from improved bonded abrasive materials and from new mechanical methods for grinding and polishing; but the low cost and convenience of loose grain methods will ensure them popularity for a long time to come.

Acheson also soon learned that his new product had interesting chemical properties. Before the turn of the century, he established that it would react with molten Fe with deoxidizing effect, and that numerous metal oxides, which might otherwise be lost in slags, could be reduced to metal by SiC additions. From this knowledge grew the widespread usage of specially processed SiC grain and briquettes in iron foundries and steel plants, and in certain nonferrous smelting processes, as a metallurgical additive, amounting to thousands of tons annually.

Another unusual chemical property, that of vigorous reaction with halogens such as chlorine at elevated temperatures, was utilized in World War I to produce $SiCl_4$, which was released into the air to produce smoke screens. Nowadays $SiCl_4$ is an industrial chemical of rapidly increasing importance, from which fine silica for rubber reinforcement, ethyl silicate for foundry sand binder, and silicon itself for transistor and rectifier use are made. Simply by "burning" SiC in Cl_2, $SiCl_4$ can be manufactured easily and cheaply. Recent developments in elemental Si technology, leading to huge potential use in solar batteries and rectifiers, offer promise of great expansion in this use of SiC.

Acheson knew that SiC was an electrical conductor, but he could hardly have foreseen that nearly every major high-voltage power distribution line in the world would be protected against lightning damage by arresters made with loose SiC grain, or with grain bonded with clays. SiC grains in contact with each other will conduct almost no current at low voltages, but the contact resistance decreases very rapidly with increasing voltage. When a voltage surge caused by lightning hits an arrester, current jumps across spark gaps in series with the grain column or stack of bonded disks, then through the grain, and harmlessly to ground. When the surge decreases, the grain column regains its high resistance and cuts off the current flow to ground, an action which it can perform many times without damage.

The important commercial uses of loose grain are summarized in Table I. There are, however, other potentially important uses. Older radio fans remember crystal sets, in many of which the sensitive detector was SiC, carefully selected and mounted with the "Cat's Whisker" permanently sealed in contact with an active spot on the crystal surface. With the passing of crystal sets, this rectification ability of SiC has been little utilized. Materials such as Si and Ge have been refined until they demonstrate dramatically valuable rectification properties, opening up the whole transistor development. When comparable progress is made in purifying SiC and controlling the introduction of certain trace impurities into its structure, a new transistor material, stable to higher temperatures, may result. The importance of high temperature transistors in high-speed aircraft and missiles could be enormous.

Such controlled-purity SiC, in the form of fine powder, may become an important source of illumination. Like certain other compounds, it has the property of electroluminescence, or glowing when subjected to a small electrical current. Recent developments promise large panels of electroluminescent material glowing over whole ceilings; perhaps SiC will prove suitable for this use.

Coated abrasives using SiC.—"Sandpaper" was once a properly descriptive name for coated abra-

Table I. Important uses of loose SiC grain

Abrasive:	Lapping and polishing Wire sawing of stone Abrasive blasting Non-slip additive for concrete
Metallurgical:	For deoxidation of steels and reducing agent in alloy steel and ferroalloy manufacture
Chemical:	For chlorination to produce silicon tetrachloride, made into silicones, silicon metal, ethyl silicate, and fine silica
Electrical:	Lightning arresters

sives. Sand or crushed flint was sprinkled on a paper coated with wet glue and then dried. Nowadays, coated abrasives include products whose backings may be paper, of a wide variety of types, but also cloths and vulcanized fiber, and the abrasive particles may be flint, garnet, fused alumina, SiC, or even diamond.

Silicon carbide coated abrasives find their greatest usefulness in grinding very hard or very soft materials. One of the important uses is for sanding hard undercoat primer paint of automobile bodies, which is done wet, by hand, with flexible papers coated with fine-grit SiC. On the other hand, the leather industry is a big user of SiC coated abrasives, especially in shoe manufacturing and repairing. Soft metals like aluminum, brass, and copper are best ground with this material, as is also cast iron.

Grinding the edges of plate glass, especially for automobile use, is done very effectively by belts coated with SiC, which are also used for grinding and finishing marble and other decorative stone. Power-driven floor sanders equipped with drums or disks coated with SiC, are familiar to do-it-yourself fans, who have seen how the coarse open-coat papers rip through old paint and warped wood floors. The advent of resins reinforced with glass fibers, for cars, boats and other uses, opens additional markets for SiC belts and disks, especially in fine finishing operations.

Coated abrasive uses in general are expected to grow moderately as novel materials are developed which need the sharp, brittle cutting action of SiC. The important present uses are listed in Table II.

Bonded SiC

Abrasives: Acheson soon incorporated his newly discovered SiC into grinding wheels. He used the techniques and bonding agents of the emery wheel industry. This practice was based on natural clays and other minerals mixed with the abrasive grain, formed into wheels, and fired to "mature" the bond and cause it to wet the grains and join them together. Even today most SiC articles are bonded with such materials. The abrasive applications listed in Table III are mostly carried out with vitrified wheels. Other bonding materials, such as resins and rubbers, are displacing some of the vitrified materials, especially where toughness is desired.

Table II. Principal coated abrasive SiC applications

Auto body undercoat sanding
Glass edging
Leather grinding and finishing
Floor sanding
Stone grinding and polishing
Grinding soft nonferrous metals and alloys; also cast iron
Finish-grinding glass-reinforced resins

Table III. Principal bonded SiC abrasive uses

Wheels:	Tungsten carbide rough-grinding
	Grinding and cutting glass, gems, marble, ceramics, stone
	Grinding cast iron and hard cast alloys
	Wood pulp grinding; leather, rubber and plastic grinding
	Aluminum, copper, brass, bronze grinding
Sticks and stones:	Cast iron cylinder honing
	Sharpening stones
Nonslip uses:	Stair treads and floor inserts

The properties of SiC fit it best for grinding either very hard and brittle materials such as cemented carbides, stone, glass, ceramics, cast iron, and hard alloys, or at the other extreme of the scale for very soft materials like resins, leather, rubber, and soft nonferrous metals. The consumption of SiC in bonded form as abrasives is apt to increase only in proportion to the general growth of business, without dramatic possibilities for rapid upswings.

Refractories.—The high temperature resistance and good heat conductivity of SiC were long ago put to service in the form of vitrified "super-refractory" wares. Today the possibilities for growth of this outlet for SiC are impressive. The super-refractories are formulated for resistance to deformation, corrosion, and other destructive effects of service at extremely high temperatures.

The standard products made by several companies are bonded with mixtures of minerals and clays which form silicates during firing. These wares have become widely accepted for good strength, oxidation resistance, heat conduction, and ability to withstand wear and corrosion. They go into kiln furniture, retorts, and condensers in zinc refining, linings for blast furnace dust cyclones, and a host of other specialized uses.

The softening temperature of the silicate bond imposes a definite limit on the temperature which these refractories can endure. New and more severe demands have pushed these materials to their limit. It was evident that the potentialities of SiC could be realized only by drastically improved bonding techniques.

Silicon nitride bonding.—The first major "breakthrough" came when it was proved that a new silicon carbide-silicon nitride material[1] made an outstandingly successful nozzle and combustion chamber liner for rockets. It can now be revealed that rocket nozzle production from this material has become "big business."

This new composition, in which silicon nitride is formed *in situ*, is itself a great advance over conventional SiC refractories bonded with silicates formed from clays. Whereas the older materials weaken seriously at temperatures of 2500°-2700°F (1480°-1590°C), the new silicon nitride bond does not melt up to its dissociation point of 3450°F (1900°C), and retains useful strength to much higher temperatures. Even more important, it will withstand the stresses of rapid heating and cooling, with much less tendency to crack than conventional bonds.

Once thoroughly proved in the inferno of rocket motors, modifications of this novel super-refractory began to find important roles in jobs formerly done only by metals (5). Jet engine makers used to bemoan the high cost of maintaining cast alloy jigs used for brazing together the halves of hollow

[1] Niafrax® silicon carbide, a trade mark of The Carborundum Company.

blades for the compressor. After a few trips through the brazing furnaces, the alloy jigs were so warped that they had to be recut to dimensions, and the blades came out so distorted they had to be coined to restore them to accurate shape. Now silicon nitride-bonded silicon carbide[2] jigs make hundreds of trips through the furnaces with no distortion, generating accurate blades which require no dimensional correction.

The new nitride-bonded material has unusual resistance to corrosion by molten aluminum and fluxes used with it. Now the aluminum industry is carrying on extensive tests which may result in many new applications for this product.

Other bonds.—SiC can be bonded with elemental Si. One such body[3] has been used for years as terminals for SiC heating elements and to a limited extent for igniters and heating elements, using its capacity to generate heat by resistance to electric current (6). This composition is now under investigation as a container for nuclear fuel, to make ceramic fuel elements for nuclear reactors (7).

Carbon also is used to bond SiC, especially for the familiar graphite-silicon carbide crucibles used for nonferrous metal melting.

Table IV summarizes these bonds and their major fields of usefulness. Efforts to use refractory metals to bond SiC have not yet yielded results of commercial importance.

Self-bonded silicon carbide.—Although silicon nitride-bonded SiC is a great advance over conventional refractories, it still is bonded with a material with less heat resistance than itself, and it cannot be made impermeable to gases and liquids. Self-bonded SiC recrystallized in such a way that the interstices are filled completely with more SiC should be a still more valuable material.

[2] Refrax® silicon carbide, a trade mark of The Carborundum Company.

[3] Durhy® silicon carbide, a trade mark of The Carborundum Company.

Table IV. Refractory uses for SiC wares

Silicate bond:	Kiln furniture (tiles, posts, saggers)
	Muffles, hearths, skid rails in furnaces
	Retorts and condensers for zinc distillation
	Heat recuperator tubes and core-busters
	Wear and erosion-resistant parts such as hot cyclones and downcomers for blast furnaces; acid domes
	Boiler settings
Silicon nitride bond:	Rocket motor nozzles and combustion chambers
	Brazing jigs
	Containers, pump parts, protection tubes and allied parts for molten aluminum and zinc
	Acid burner tips and spray nozzles
Silicon bond:	Heating elements
	Thermocouple protection tubes
	Nuclear fuel elements (possibility)
Carbon bond:	Graphite-silicon carbide crucibles

Tinklepaugh (8, 9), at Alfred University, was able to produce such a body by hot pressing fine SiC grains at very high temperatures and pressures. The limitations of this technique prevent production of pieces of large or complicated nature, but his work directly inspired the development of a practical method to produce a wholly dense, self-bonded SiC body.

This revolutionary new material, christened KT[4] (the initials of its inventor, Kenneth Taylor), consists of SiC with less than 5% of any other material. It is wholly impervious to gases and liquids, has great strength at high temperatures, better thermal conductivity at high temperatures than any other known ceramic and most metallic heat-resisting alloys, and other properties such as great resistance to abrasion and corrosion. It was first described publicly before the Electrochemical Society in May 1956, in San Francisco, and in an article recently published (10).

KT silicon carbide is the first commercial material utilizing to the fullest the valuable properties of SiC. One can confidently expect tremendously wide application of it, as its properties become better known and adequate capacity is installed for its production.

Some of the uses now being explored are shown in Table V.

Electrical uses of bonded silicon carbide.—Nonmetallic heating elements of SiC are widely used in furnaces operating above the useful temperature of metallic resistors. They are composed of grains recrystallized together at high temperatures into self-bonded, porous rods, which are usually equipped with terminal ends of lower electrical resistance made of siliconized SiC. Continued improvement in these elements is extending their useful life to temperatures approaching 3000°F (1650°C), and steady expansion of volume is to be expected.

Heating elements are formulated to have relatively small change in electrical resistance with temperature; at temperatures reached in service they resemble metallic elements in displaying increase of resistance as the temperature goes up.

Changes in manufacturing techniques, raw materials, or use of bonding agents can give drastically different resistance characteristics. At low voltages resistance can be very high but can drop rapidly as voltage is increased. An electrical "safety valve" such as this has many uses in electronic design, plus the very important use in lightning arresters.

The unusual electrical properties of SiC derive in part from the phenomena associated with surface contacts between semiconductive materials and in

[4] KT silicon carbide, a trade mark of The Carborundum Company.

Table V. Potential uses for dense, impervious SiC ware

Valves and piping for corrosive and erosive materials
Pumps and related parts for handling molten alumina
Sandblast nozzles
Rocket nozzles
Fuel elements and structural members in gas-cooled nuclear reactors
Thermocouple protection tubes
Heat exchangers

Table VI. Predicted areas for increased SiC consumption

Chemical:	Rapid growth as raw material for silicon tetrachloride production, ending up as silicon metal and as fine silica.
	Piping, valves, and other parts for corrosion and heat resistance, out of dense, self-bonded silicon carbide.
Metallurgical:	Marked upswing as addition to ferrosilicon furnaces to increase production.
	Continued growth in briquette use in iron foundry practice.
	Possible new source of silicon metal by thermal dissociation.
Electrical:	Transistor and rectifier use at elevated temperatures, if necessary purity can be achieved.
	Electroluminescent powder for low-intensity area lighting.
	Increased use of nonlinear resistors.
Nuclear Energy:	Fuel element sheaths or fuel carriers for high temperature gas-cooled reactors; also structural parts.

part from the basic properties of the material itself. Much can be done by control of purity of the crystals, with resistivity variable over several orders of magnitude.

Transistors have been made experimentally with selected SiC crystals, but their performance has not been good enough to compete with Si or Ge. Here again lack of ability to regulate what is in the crystal may be at fault. Theoretical considerations suggest great promise for this application when crystal growing becomes better controlled.

The ability of certain silicon carbide crystals to emit light when excited by a weak electric current has been long known but never used commercially. Since not all crystals can be so excited as to be electroluminescent, more must be learned about the effects of impurities and structure variations before such uses are perfected.

The Future

Those most familiar with this remarkable compound are confident that it will grow into new and even more valuable uses. Likewise, one can confidently predict continued growth in its nonabrasive uses. These are summarized in Table VI.

Acheson, imaginative scientist that he was, could hardly foresee all the possibilities for the compound he discovered. Emphasis on high temperature technology will present further new and important uses for this compound which will keep it at the front of modern man-made minerals.

Manuscript received April 5, 1957. This paper was prepared for delivery before the Cleveland Meeting, Sept. 30-Oct. 4, 1956.

Any discussion of this paper will appear in a Discussion Section to be published in the June 1958 JOURNAL.

REFERENCES

1. J. DeMent, *Mineralogist*, **16**, 211 (1948).
2. Henri Moissan, *Compt. rend.*, **140**, 405 (1905).
3. H. N. Baumann, Jr., *This Journal*, **99**, 109 (1952).
4. J. C. Fulton and J. Chipman, *J. Metals*, **6**, 356 (1954).
5. W. L. Wroten, *Materials & Methods*, **40**, 83 (1954).
6. C. G. Rose, *Brick & Clay Record*, **117**, 62 (1951).
7. J. R. Johnson, *J. Metals*, **8**, 660 (1956).
8. R. A. Alliegro and J. R. Tinklepaugh, *WADC Tech. Report 53-5*, Jan. 1953.
9. R. E. Wilson, L. B. Coffin, and J. R. Tinklepaugh, *WADC Tech. Report* 54-38, Part 2, Jan. 1955.
10. K. M. Taylor, *Materials & Methods*, **44**, 92 (1956).

Electrochemical Polarization

III. Further Aspects of the Shape of Polarization Curves

Milton Stern

Metals Research Laboratories, Electro Metallurgical Company,
A Division of Union Carbide Corporation, Niagara Falls, New York

ABSTRACT

The shape of electrochemical polarization curves is discussed for ideal systems containing more than two oxidation-reduction reactions. Situations are described where measured Tafel parameters have no direct relationship to the parameters of any of the oxidation-reduction reactions. The analysis, while containing several simplifying assumptions, shows the complexity of polarization measurements and indicates the care which must be taken if such measurements are to be interpreted quantitatively.

Polarization measurements have been used for many years in studies of corrosion, electrodeposition, and battery performance. In spite of the wide use of such measurements, considerable uncertainty in their interpretation still appears to exist.

Stern and Geary (1) have presented a theoretical analysis of the shape of polarization curves for both reversible electrodes and corroding electrodes and have described some of the reasons for observed deviations from Tafel behavior. They warned against the indiscriminate introduction of breaks in polarization measurements and listed several of the pitfalls which exist in the interpretation of such measurements. Experimental verification of the equations which they presented has been obtained (2). The methods described have proved useful in studies of pit propagation in stainless steels (3) and anodic polarization of iron (4).

This discussion is an extension of the analysis by Stern and Geary which describes more complex systems including those where three oxidation-reduction reactions are operative. Some examples are presented where concentration polarization plays a role in determining the steady-state electrode potential.

Basic Principle of the Method

The method which Stern and Geary (1) describe is based on the principle that the steady-state potential of an electrode is that potential at which the sum of the rates of all the oxidation reactions is equal to the sum of the rates of all the reduction reactions. This value of potential may be called the corrosion potential or the mixed potential and occurs when

$$\Sigma\ \overleftarrow{i}_m,\ \overleftarrow{i}_y,\ \overleftarrow{i}_z \ldots = \Sigma\ \overrightarrow{i}_m,\ \overrightarrow{i}_y,\ \overrightarrow{i}_z \ldots \qquad \text{(I)}$$

where $\overleftarrow{i}_m$, $\overleftarrow{i}_y$, $\overleftarrow{i}_z$ are the currents equivalent to the rates of oxidation of the M, Y, and Z oxidation-reduction systems, and $\overrightarrow{i}_m$, $\overrightarrow{i}_y$, and $\overrightarrow{i}_z$ are the currents equivalent to the rates of reduction for these systems. When current is applied from an external source, the applied current, $\overrightarrow{i}_x$, (cathodic current) is equal to the difference between the current equivalent to the total rate of all the reduction reactions and the current equivalent to the total rate of all the oxidation reactions.

$$\overrightarrow{i}_x = \Sigma\ \overrightarrow{i}_m,\ \overrightarrow{i}_y,\ \overrightarrow{i}_z \ldots - \Sigma\ \overleftarrow{i}_m,\ \overleftarrow{i}_y,\ \overleftarrow{i}_z \ldots \qquad \text{(II)}$$

Since a similar expression exists for anodic polarization, only cathodic polarization is discussed here. If equations are available which describe the relationships between potential and the individual oxidation and reduction currents, then an expression can be derived which describes the variation of the potential of a system as a function of applied current.

System with Two Oxidation-Reduction Reactions

Consider a system with two possible oxidation-reduction reactions Z and M, the rates of which are controlled by activation polarization so that at the reversible potential of the Z reaction the equilibrium $Z^+ + e \rightleftarrows Z$ exists, while at the reversible potential of the M reaction the equilibrium $M^+ + e \rightleftarrows M$ occurs. At equilibrium, the rate of the individual oxidation and reduction reactions is equal so that $\overrightarrow{i}_z = \overleftarrow{i}_z = i_{oz}$ and $\overrightarrow{i}_m = \overleftarrow{i}_m = i_{om}$ where i_{oz} and i_{om} are the exchange currents for the Z and M reaction, respectively. The current equivalent to the total rate of each of the individual oxidation or reduction reactions may be expressed in the following form (5), using $\overrightarrow{i}_z$ as an example.

$$\eta = -\beta_z \log \frac{\overrightarrow{i}_z}{i_{oz}} \qquad \text{(III)}$$

where β_z is a constant (the Tafel slope) and η is the overvoltage or the difference between the potential of an electrode at which z is being reduced and the equilibrium potential. Similar equations exist for the dependence of $\overleftarrow{i}_z$, $\overleftarrow{i}_m$, and $\overrightarrow{i}_m$ on potential. To aid in visualizing the shape of an experimental polar-

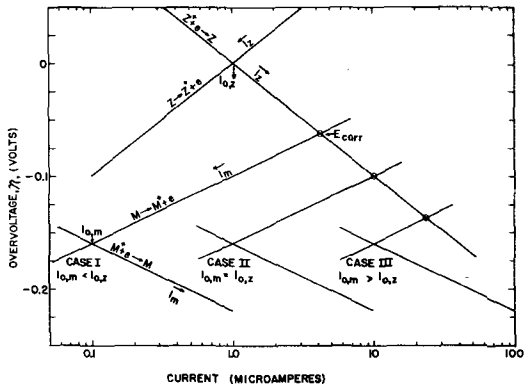

Fig. 1. Electrochemical system with two oxidation-reduction reactions. Illustration of Cases I, II, and III.

ization curve resulting from such a mixed electrode system, it is convenient to assign values to the Tafel constants for each oxidation-reduction system in order to show the effect of changes in these parameters. To express potentials of the various oxidation-reduction systems on the same scale, the equilibrium potential of the Z oxidation-reduction system will be used as a reference, and the equilibrium potential of the M oxidation-reduction system will be given a value of 0.160 v more active than the reversible potential of the Z oxidation-reduction potential.

Three cases will be considered: Case I where i_{om} is smaller than i_{oz}, Case II where i_{om} equals i_{oz}, and Case III where i_{om} is greater than i_{oz}. The following parameters will be held constant at their indicated values ($\beta_z = 0.100$ v, $\beta_m = 0.060$ v, $i_{oz} = 1.0$ μa) and i_{om} will be assigned values of 0.1 μa for Case I, 1.0 μa for Case II, and 10 μa for Case III. Fig. 1 illustrates the three cases described, the circles indicating the mixed or corrosion potential in each case. This is the potential at which $\vec{i}_z + \vec{i}_m = \overleftarrow{i}_z + \overleftarrow{i}_m$.

Case I.—This situation has already been described quantitatively using the same polarization parameters used here (1). The overvoltage as a function of applied cathodic current, $\vec{i}_z$, may be expressed by the following equation.

$$\eta = -\beta_z \log \frac{\vec{i}_z + \overleftarrow{i}_z + \overleftarrow{i}_m - \vec{i}_m}{i_{oz}} \qquad \text{(IV)}$$

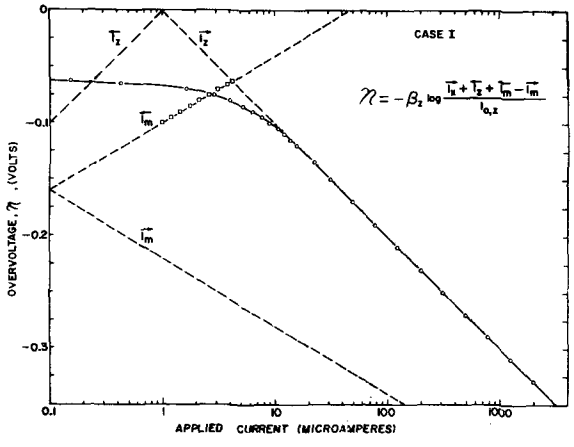

Fig. 2. Overvoltage as a function of applied cathodic current for Case I ($i_{om} < i_{oz}$) showing region where anodic curve can be calculated from cathodic data.

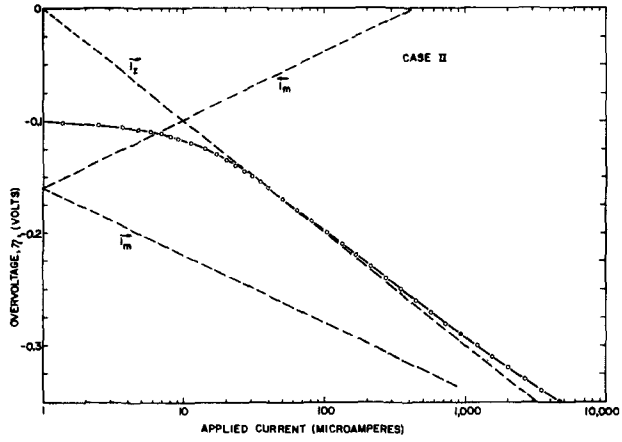

Fig. 3. Overvoltage as a function of applied cathodic current for Case II ($i_{om} = i_{oz}$).

This is derived by substituting Eq. (II) into Eq. (III). A plot of η vs. $\vec{i}_z$ yields a curve which shows deviation from Tafel behavior at low values of $\vec{i}_z$. At higher values of applied current, $\vec{i}_z$ approaches $\vec{i}_z$ and the resulting curve shows Tafel behavior with a β value equal to β_z and an extrapolated exchange current value equal to i_{oz}.

Under these conditions, it is possible to obtain experimental values for the Tafel constants of the Z reaction. It is important to note that a determination of β_z and i_{oz} permits calculation of $\overleftarrow{i}_m$ as a function of potential in the region close to the corrosion potential.[1] This is a measure of the local anodic polarization in a corroding system. Thus, cathodic polarization measurements under conditions indicated in Case I permit a determination of the local anodic polarization curve of the system in the potential region more active than the steady-state potential. This is illustrated in Fig. 2[2] which shows the expected shape of a cathodic polarization curve for the conditions defined in Case I. The region where Eq. (IV) can be used to calculate the local anodic polarization curve is also shown on Fig. 2.

Case II.—When i_{om} is increased so that polarized potentials are reached where $\vec{i}_m$ is significant in comparison to $\vec{i}_z$, the resulting measured polarization curve will not exhibit true Tafel behavior. This situation is illustrated in Fig. 3. Note that the curve of overvoltage vs. applied current follows $\vec{i}_z$ for a short potential interval but then deviates from straight line behavior. Experimental observations under conditions of Case II would yield data suffi-

[1] This calculation is possible since an experimental determination of η vs. $\vec{i}_z$ yields values for β_z and i_{oz}. From these constants $\vec{i}_z$ is known as a function of η. If the corrosion potential is sufficiently removed from the reversible potentials, the rate of metal plating, $\vec{i}_m$, and the rate of oxidation, $\overleftarrow{i}_z$, are negligible. Thus sufficient information is available to apply Eq. (IV) to calculate $\overleftarrow{i}_m$ as a function of η.

[2] Points shown on this curve and all subsequent figures are not experimental. They are calculated from the derived equations and are included to illustrate the need for considerable data to define accurately the shape of a polarization curve.

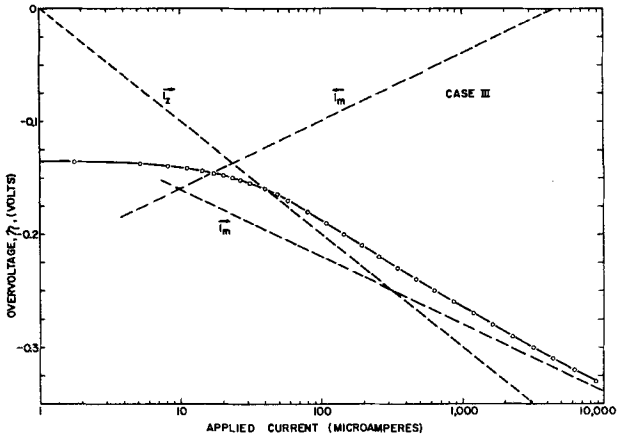

Fig. 4. Overvoltage as a function of applied cathodic current for Case III ($i_{om} > i_{oz}$).

ciently "Tafel-like" in behavior to generally be considered satisfactory. However, such data would yield inaccurate values for β_z and i_{oz}, both measured values being slightly low.

Case III.—When i_{om} is considerably larger than i_{oz}, the resulting curve of overvoltage vs. applied current shows some interesting characteristics. Fig. 4 shows that a "Tafel-like" region is still observed but Tafel constants determined from such data are completely inaccurate and have no direct connection with the Tafel constants of either oxidation-reduction system. Thus, cathodic polarization measurements alone do not permit direct measurement of β_z and i_{oz} under the conditions of Case III. However, three methods are available which yield values for these constants, but the techniques are more tedious and inaccurate than the direct method of measurement illustrated in Case I.

One may measure by chemical means the rate at which Z^+ is reduced at various potentials during cathodic polarization. For example, if reduction of Z^+ represents the rate at which hydrogen ions are reduced to form hydrogen gas, then measurement of the rate of hydrogen evolution as a function of overvoltage during cathodic polarization will yield data from which the Tafel constants can be calculated. The second method is also indirect. Under the conditions stipulated for Case III, anodic polarization measurements yield accurate values for β_m and i_{om}. These data can then be used in the anodic polarization analog to Eq. (IV) to calculate $\vec{i}_z$ as a function of overvoltage on the noble side of the corrosion potential. This is the reverse of what was done in Fig. 2 to calculate the local anodic polarization curve from cathodic polarization data.

The third method is based on polarization measurements at potentials close to the corrosion potential. It has been shown that such data show a linear dependence of overvoltage on applied current (1). The equation which relates the change in potential with applied current is

$$\left(\frac{d\epsilon}{di_z}\right)_{\epsilon \to 0} = \frac{\beta_z \beta_m}{(2.3)(i_{corr})(\beta_m + \beta_z)} \qquad (V)$$

where e is the difference between the polarized potential and the corrosion potential. Note that i_{corr} is

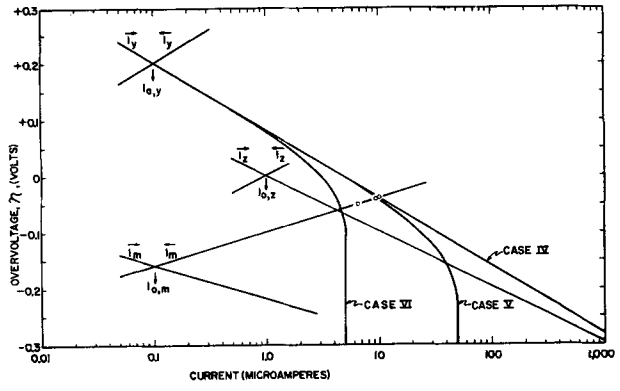

Fig. 5. Electrochemical system with three oxidation-reduction reactions. Illustration of Cases IV, V, and VI.

equivalent to $\overleftarrow{i}_m$ at the corrosion potential. The slope of the linear region, $d\epsilon/di_z$, is the same for both cathodic and anodic polarization. Thus, an anodic polarization measurement yields values for $d\epsilon/di_z$, β_m, and i_{corr}, and permits calculation of β_z using Eq. (V). The second and third methods described above have been used (4) to show that the anodic polarization curve for Fe in HCl is not remarkably steep as was postulated previously (6) from indirect observations.

System with Three Oxidation-Reduction Reactions

The method described above for determining potential as a function of applied current can be used also for a system with three redox reactions. Three examples will be shown for a system containing redox reactions M, Z, and Y where the Tafel parameters of all three are held constant and a limiting diffusion current for reduction of Y is introduced. The constants assigned for this situation are $\beta_m = 0.060$ v, $\beta_z = 0.100$ v, $\beta_y = 0.120$ v, $i_{om} = 0.1$ μa, $i_{oz} = 1.0$ μa, $i_{oy} = 0.1$ μa with the reversible potential of the M redox system more active by 0.160 v and the reversible potential of the Y redox system more noble by 0.200 v than the reversible potential of the Z redox system. The three situations to be considered for this system differ by introducing a limiting diffusion current for reduction of Y with values of I_{L_y} equal to infinity (Case IV), 50 μa (Case V), and 5 μa (Case VI).

Cases IV, V, and VI are illustrated graphically in Fig. 5. The circles indicate the corrosion potential and corrosion current for each set of conditions.

It is worth emphasizing here that Eq. (II) is used in conjunction with the Tafel constants assigned to each redox reaction to determine the relationship between overvoltage and applied current. Thus,

$$\vec{i}_a = \vec{i}_z + \vec{i}_y + \vec{i}_m - \overleftarrow{i}_z - \overleftarrow{i}_y - \overleftarrow{i}_m \qquad (VI)$$

Since the current equivalent to each of the individual oxidation or reduction reactions is known as a function of potential from the Tafel equation [Eq. (III)], $\vec{i}_z$ may be calculated as a function of potential.

For the cases where a limiting diffusion current exists, the value of $\vec{i}_y$ at any overvoltage value is determined from the relation

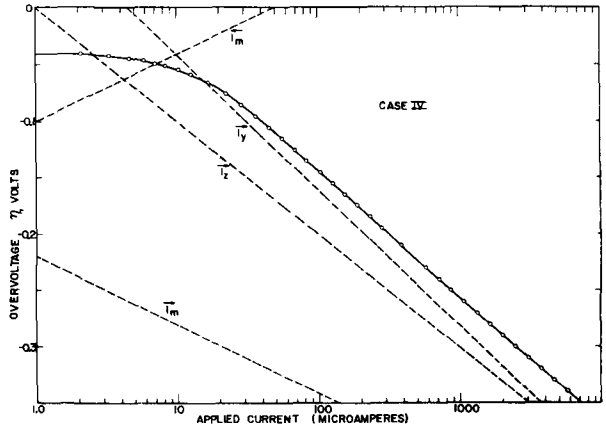

Fig. 6. Overvoltage as a function of applied cathodic current for Case IV.

$$\eta = 0.200 - \beta_y \log \frac{\vec{i}_y}{i_{oy}} + 0.059 \log \frac{I_{Ly} - \vec{i}_y}{I_{Ly}} \qquad \text{(VII)}$$

Case IV.—Potential as a function of applied current for Case IV is shown in Fig. 6. Here as in Case III, a "Tafel-like" relation is observed but β calculated from such a curve is a compromise between β_z and β_y. The exchange current obtained from such data would be markedly different from the real value of i_{oy}.

Case V.—When I_{Ly} equals 50 μa, the plot of potential vs. applied current (Fig. 7) does not show any recognizable diffusion wave. Instead two Tafel-like regions are observed. The first region, from −0.08 to −0.22 v, does not even approximate the Tafel parameters of any of the redox systems. The second Tafel-like region does, however, closely parallel the Tafel parameters of the *X* redox system.

Case VI.—An interesting situation arises when I_{Ly} equals 5 μa. Under these conditions, the mixed or corrosion potential does not approximate the intersection of any of the individual Tafel lines. The corrosion potential is determined by the condition set by Eq. (I) or when

$$\vec{i}_m + \vec{i}_z + \vec{i}_y = \overleftarrow{i}_m + \overleftarrow{i}_z + \overleftarrow{i}_y \qquad \text{(VIII)}$$

In the potential region of interest, $\vec{i}_m$, $\overleftarrow{i}_z$, and $\overleftarrow{i}_y$ are negligible so that $\vec{i}_z + \vec{i}_y = \overleftarrow{i}_m$ at the mixed potential.

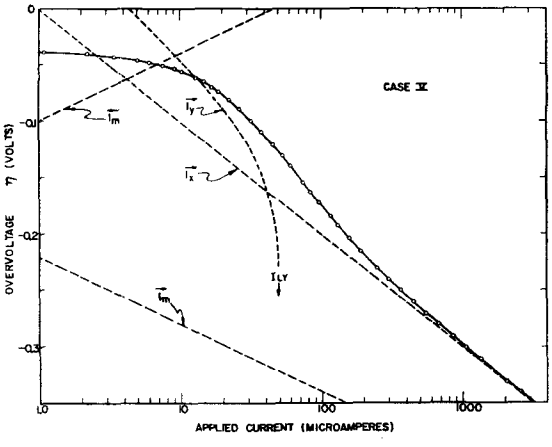

Fig. 7. Overvoltage as a function of applied cathodic current for Case V.

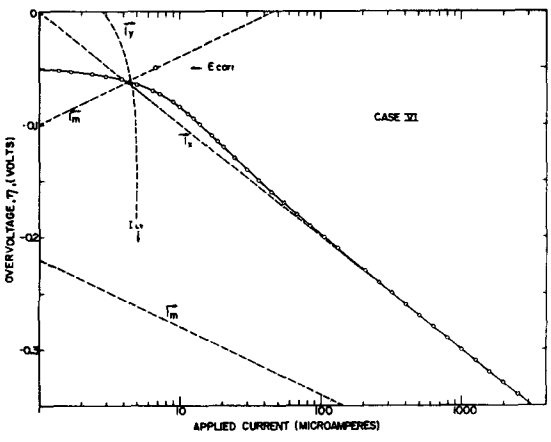

Fig. 8. Overvoltage as a function of applied cathodic current for Case VI.

In the examples illustrated previously, $\vec{i}_z$ was also negligible at the mixed potential so that this potential was approximated by the condition where $\vec{i}_y = \overleftarrow{i}_m$. This is the potential at which the overvoltage curves for $\vec{i}_y$ and $\overleftarrow{i}_m$ cross. Case VI also shows two Tafel-like regions, one of which is false and the other of which will yield valid parameters for the Z redox system.

It is interesting to note that no indication of a limiting diffusion current is obtained in Fig. 7 and 8. A limiting diffusion current will be evident, however, on a plot of overvoltage vs. applied current if I_{Ly} is increased further or if the reversible potential of the Y redox system is made more noble. This will be illustrated by changing the conditions indicated in Cases IV, V, and VI so that the reversible potential of the Y redox system is 0.45 v more noble than the Z redox system, and considering two cases where I_{Ly} equals 1000 μa and 80 μa. Cases VII and VIII are illustrated in Fig. 9, the circles indicating the corrosion potential in each case.

Case VII.—Fig. 10 illustrates the polarization curve which would be obtained for Case VII. No activation overvoltage parameters can be measured, and the curve represents the typical concentration polarization curve often observed.

Case VIII.—Under these conditions, the corrosion rate is determined by the limiting diffusion current,

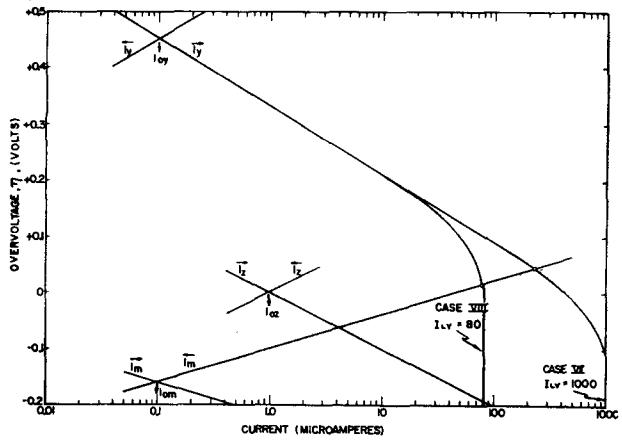

Fig. 9. Electrochemical system with three oxidation-reduction reactions. Illustration of Cases VII and VIII.

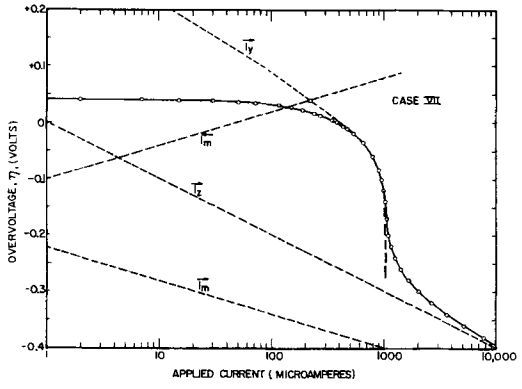

Fig. 10. Overvoltage as a function of applied cathodic current for Case VII.

I_{Ly}. This was not the situation in Case VII where the corrosion potential occurs in the activation polarization region of the Y reduction system. Thus, physical changes in the system which increase the limiting diffusion current, such as stirring effects, markedly affect the corrosion potential and corrosion rate in Case VIII but have no effect in Case VII except to move the position of the diffusion wave in Fig. 10 further to the right. Fig. 11 shows the polarization curve which is obtained for Case VIII.

Discussion

Even though several simplifying assumptions have been made, this analysis shows the complexity of polarization measurements and indicates the care which must be taken if such measurements are to be interpreted quantitatively. The chemistry of the system must be understood, and the number and magnitude of the rates of oxidation or reduction occurring during polarization should be known.

The primary assumption in this treatment considers that the Tafel parameters remain constant during polarization. This is undoubtedly the case in some real systems, since this is the basis on which all experimental observations of Tafel constants depend. It is important to remember, however, that many situations exist where such an assumption is not valid, certain passivity phenomena being typical. One obvious way to study and recognize systems where the Tafel parameters change is to realize first what the behavior would be if the parameters remain constant and then observe deviations from such behavior.

The treatment does not consider several other complicating factors which influence the shape of polarization curves. Such factors include systems where the electrode surface contains regions with different overvoltage parameters for the same reaction; where anode-cathode area ratios change as a function of potential; and where corrosion product films, which are formed during polarization, change the nature of the surface. Changes in anode-cathode area ratio or film formation appear to give rise to a time effect during polarization which also has not been considered here.

Since it has been shown that ideal systems can produce polarization data which may be difficult to interpret, complicating factors such as those described above would result in a system which is beyond quantitative description with the present knowledge of electrode processes. However, concepts obtained from this treatment of ideal systems provide a guide to an understanding of important practical systems. This can be illustrated in the following manner. Individuals working in the cathodic protection field are constantly concerned with minimum current requirements for complete protection; the potential necessary to achieve protection; and the correlation between "breaks" in polarization curves and the metal equilibrium potential. It has already been shown that "breaks" in polarization curves cannot be expected to have a direct connection to the equilibrium anode potential. If the anodic polarization of metal is activation controlled, the corrosion rate decreases logarithmically as the potential is made more active. Case VIII described above is analogous to the situation which exists when Fe corrodes in sea water under conditions of natural convection. In this case, the corrosion rate of Fe is determined by the limiting diffusion current of oxygen. Iron solution is represented by $\overleftarrow{i_m}$, hydrogen evolution by $\overrightarrow{i_z}$, and oxygen reduction by $\overrightarrow{i_y}$. The per cent change in corrosion rate as a function of potential and applied current for Case VIII is illustrated in Fig. 12. Note the rapid decrease in corrosion rate as the potential is made more cathodic. The rate of decrease of corrosion rate is actually a function of β_m. A larger value of β_m would require that the metal be polarized to a more ca-

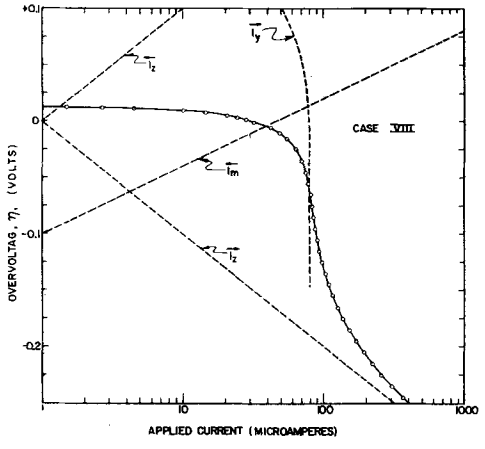

Fig. 11. Overvoltage as a function of applied cathodic current for Case VIII.

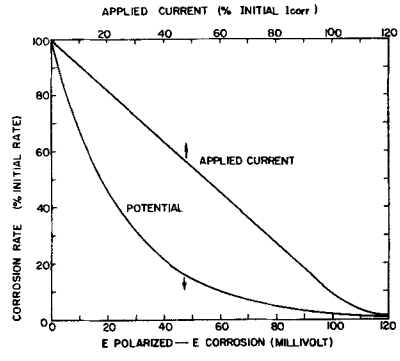

Fig. 12. Per cent change in corrosion rate as a function of potential and applied current for Case VIII.

thodic potential to achieve a corrosion rate of one tenth its steady-state value. It is also interesting to note that the decrease in corrosion rate is directly proportional to the applied cathodic current up to applied current values approximating the initial corrosion current. This situation occurs only for conditions where the corrosion rate is determined by a cathodic limiting diffusion current (Case VIII). This can be shown by considering the general Eq. (II) for these conditions.

$$\vec{i}_x = \vec{i}_y + \vec{i}_z + \vec{i}_m - \overleftarrow{i}_y - \overleftarrow{i}_z - \overleftarrow{i}_m \qquad \text{(IX)}$$

In the potential region of interest, $\vec{i}_z$, $\vec{i}_m$, $\overleftarrow{i}_y$, and $\overleftarrow{i}_z$ can be considered negligible and $\vec{i}_y$ approximates the constant I_{Ly}. Thus, $\vec{i}_x = K - \overleftarrow{i}_m$, and, therefore, the corrosion rate, $\overleftarrow{i}_m$, approximates a linear function of the applied cathodic current, $\vec{i}_x$.

Although this analysis contains calculated polarization curves, an effort was made to select conditions which parallel many found in practice in order to provide a clearer understanding of the effect which many variables have on electrode behavior.

Acknowledgment

The author would like to acknowledge the cooperation of A. L. Geary who carried out several of the calculations used here and supplied valuable discussion.

Manuscript received Dec. 26, 1956. This paper was prepared for delivery before the Buffalo Meeting, Oct. 6-10, 1957.

Any discussion of this paper will appear in a Discussion Section to be published in the June 1958 JOURNAL.

REFERENCES

1. M. Stern and A. L. Geary, *This Journal*, **104**, 56 (1957).
2. M. Stern, *ibid.*, **104**, 559 (1957).
3. M. Stern, *ibid.*, **104**, 600 (1957).
4. M. Stern and R. M. Roth, *ibid.*, **104**, 390 (1957).
5. J. O'M. Bockris, "Modern Aspects of Electrochemistry," Academic Press Inc., New York (1954).
6. M. Stern, *This Journal*, **102**, 609 (1955).

Some Testing Cells for the Study of Electroplating Devices

J. K. Skwirzynski and M. Huttly

Marconi's Wireless Telegraph Company Limited, Baddow Research Laboratories, West Hanningfield Road, Great Baddow, Chelmsford, Essex, England

ABSTRACT

The complete theoretical treatment is given for two kinds of cells, both of which are shown to yield a reasonably linear primary current density distribution along the cathode, calculated under the assumption of negligible polarization. The actual value of these current densities can be ascertained directly from the total current fed into the cell. The first cell is very similar to that proposed by Hull, i.e., trapezoidal in shape, the angle of the slanting side being 45°. The electrodes can be placed either along the parallel sides of the cell or, as first suggested by Hull, along the other two sides, when a singularity of the current density appears on the slanting electrode. In both cases the current density may be arranged to be very nearly linear over almost two thirds of the length of the cathode.

The second cell is triangular in shape; the cathode is placed along the base of a 45° isosceles triangle whereas the anode occupies a part of one of the other sides. The current density distribution along the cathode has almost a triangular shape with good linearity.

Both cells are easy to construct and normalized graphs of the current density allow for straightforward comparison with experimental results.

A plating test designed to detect sources of trouble, such as improper chemical concentrations, impurities, contaminations from the atmosphere, etc., should be designed so as to exhibit simultaneously the results of plating over a range of current densities. Furthermore such a display of the effects of varying and determinable current densities may be used to decide on optimum conditions for the operation of newly formulated baths (1).

A well-known testing device is the Hull cell (2). It consists of a small trapezoidal cell, whose plan view is shown in Fig. 1a and 1b. The parallel sides are insulators, the side, AB, perpendicular to these is the anode, and the fourth side, OC, inclined to the parallel sides is the cathode, on which the deposition is studied. Because of the inclination of the cathode with respect to the anode, the current density on the former varies uniformly and actually reaches a very high value (theoretically an infinity) at the end of the cathode nearest to the anode. The actual Hull cell (2) has fixed dimensions, holding 267 cc; the angle AOC (Fig. 1a and 1b) is about 38°40′.

Recently Gilmont and Walton (3) proposed another cell consisting of two plane walls inclined at 45° and two others shaped as hyperbolae. One of the plane sides is the cathode and one of the curved ones

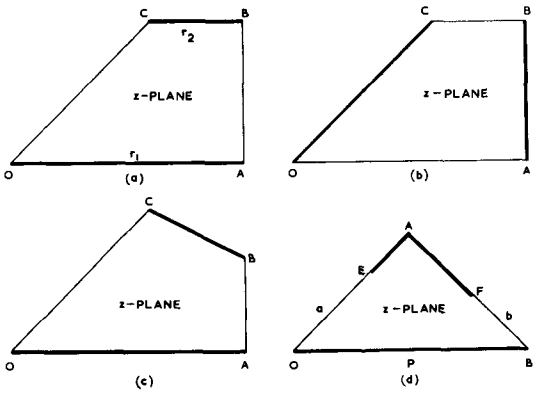

Fig. 1. Plan views of the cells in the z-plane

is the anode. The current density along the cathode is stated to vary linearly with the distance along it and therefore could be calculated exactly. The authors show that the hyperbolic shape of the anode is the necessary condition for a linear variation of the current density.

It would seem that the geometry of an ideal cell should have these properties: (*a*) be easy to construct; (*b*) be equally suitable for large and for small baths; (*c*) yield linear current density along the cathode which can be correlated with the total current fed into the baths; (*d*) have no "infinities" of current which will cause excessive polarization. (This last requirement is not always necessary as occasionally it may be required to observe the effects of very dense currents, e.g., when investigating the deposition on sharp corners.) The Hull and the Gilmont and Walton cells each satisfy some but not all of these requirements.

Thus it is proposed here to investigate a type of a versatile cell which it is hoped would satisfy the points mentioned above. A simple tank should be built of plane walls, typical shapes being shown in Fig. 1 where the electrodes are indicated by thick lines. Assuming uniform electrolyte and infinite extension in the direction perpendicular to the plane of the paper, the tanks shown can only be investigated analytically if the angles between individual walls are multiples of $\pi/6$ or $\pi/4$. Fig. 1a and 1b show two possible electrode positions for a tank of a Hull type. This case is investigated fully below for both electrode configurations; the ratio of the side lengths OA and BC is of course arbitrary, so that the side of the cell can be varied at will. Fig. 1c shows a different configuration whose analysis, although theoretically possible, presents great computational difficulties, e.g., computation of elliptic functions with complex moduli; this case is not considered here. Fig. 1d shows a triangular tank which is considered here for an isosceles case when angles BOA and ABO are both 45°. The second electrode EAF can be either as shown, with sides EA and AF of arbitrary length or it can consist of a single side, say AE. This case is also considered here, in particular when AE = ½AB.

The three cases 1a, b, and d yield almost linear portions of the current density distribution curves. Cases 1a and 1d have no current singularities when OA and OB are respectively cathodes. Case 1b yields a singularity at C on the cathode OC.

The two cases are considered separately, that of the trapezium and the triangle, pointing out only the more important and essential mathematical steps.

1. General Considerations

Assume that the electrolytic conduction in one of the cells shown in Fig. 1 is essentially a two-dimensional one, i.e., that the cell extends infinitely at right angles to its plane cross section shown. In practice, to obtain good agreement with the theoretical predictions, the height of the cell should be at least as big as its lateral dimensions and the investigations should be limited to the medium portion of the plated electrode [*see* Ref. (2), Fig. 3]. Assuming further that the electrolyte is homogeneous, obeys Ohm's Law, that the electrodes are at the same potential throughout this area, and that the polarization, if any, is the same over the electrode surface [*see* Ref. (3)], the current density on an electrode is given by:

$$\tilde{C} = \kappa \left.\frac{\partial V}{\partial n}\right|_s \qquad [1]$$

where n denotes direction normal to the electrode in question and the suffix s denotes the co-ordinates of that electrode in the two-dimensional representation in the complex $z = x + iy$ plane (Fig. 1a). Then $V = V(x,y)$ can be considered as the imaginary part of the complex function

$$w = U + iV = f(z) = f(x + iy) \qquad [2]$$

and

$$\tilde{C} = \kappa \left|\frac{\partial w}{\partial z}\right| \qquad [3]$$

anywhere in the complex z-plane (4).

In order to find the function w for the particular cell in Fig. 1 the z-plane is transformed conformally until the inside of the cell assumes the shape of a rectangle with two electrodes forming the two opposite sides of this rectangle (Fig. 2b) in the new w-plane. Then obviously w is the required function since the lines of current flow and the equipotentials now form the usual cartesian grid. The suitable transformation in this case, or several of them if necessary, is the well-known Schwarz-Christoffel transformation.

2. The Trapezoidal Cell Mathematical Analysis

Consider a trapezium OABC in the complex z-plane as shown in Fig. 1a, whose parallel sides are r_1 and r_2, respectively; the angle AOC is 45°; then:

$$z = \int_0^u \frac{du}{\sqrt{u(1-u^2)(1-k^2u^2)}} \qquad [4]$$

transforms the inside of the trapezium in the z-plane to the first quadrant of the u-plane (Fig. 2a), the corresponding points being

$$\begin{aligned} &O : z = 0 \rightarrow u = 0 \\ &A : z = r_1 \rightarrow u = 1 \\ &B : z = r_1 + i\,(r_1 - r_2) \rightarrow u = 1/k \\ &C : z = (1+i)\,(r_1 - r_2) \rightarrow u = \infty \text{ and } i\,\infty \end{aligned}$$

$k < 1$ is as yet an arbitrary real number. The quad-

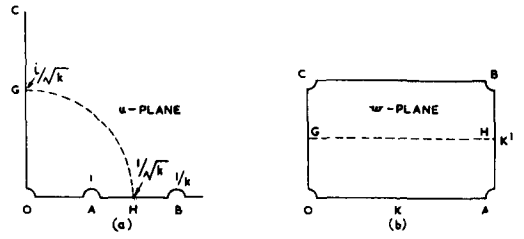

Fig. 2. (a) Trapeziums of Fig. 1a and 1b transformed to the u-plane; (b) the same in the w-plane.

rant in the u-plane can now be transformed to the inside of a rectangle in the w-plane by:

$$u = sn(w,k) \qquad [5]$$

where sn is the Jacobi's elliptic function of modulus k. Then, from [4] and the well-known properties of sn:

$$z = \int_0^w \frac{dw}{\sqrt{sn(w,k)}} \qquad [6]$$

The vertices of the trapezium are now transformed in the w-plane to:

$$O : w = 0$$
$$A : w = K$$
$$B : w = K + iK'$$
$$C : w = iK'$$

where K and K' are the complete elliptic integrals of the first kind with complimentary moduli k and $k' = \sqrt{1-k^2}$, respectively. The rectangle in the w-plane is shown in Fig. 2b. From [3] and [6], the current density becomes:

$$\tilde{C} = \kappa \left| \frac{dw}{dz} \right| = \kappa \left| sn(w,k) \right|^{1/2} = \kappa \left| u \right|^{1/2} \qquad [7]$$

One requires the current density in the z-plane, i.e., the plane of the trapezium, and this can be obtained only by expressing u as a function of z, i.e., by inverting the integral expression [4]. The integral [4] can be evaluated by using a substitution given by Cayley (5). Let:

$$\sqrt{u} = \frac{(\lambda + \lambda')\zeta}{\sqrt{1-\lambda^2\zeta^2} + \sqrt{1-\lambda'^2\zeta^2}} \qquad [8]$$

where

$$\lambda = (1 + \sqrt{k})/\sqrt{2(1+k)} \qquad [9]$$

and

$$\lambda' = \sqrt{1-\lambda^2} \qquad [10]$$

Then:

$$z = \frac{1}{\sqrt{2(1+k)}} \left[F(\sin^{-1}\zeta, \lambda) + F(\sin^{-1}\zeta, \lambda')\right] \qquad [11]$$

where F is the elliptic integral of the first kind of moduli λ and λ' respectively and ζ is the new variable which defines by means of [8] and [11] u as a function of z & vice versa. It is interesting to study the contour in the ζ-plane corresponding to the contours OABC in the z-plane (Fig. 1a) and the boundaries OABC of the first quadrant in the u-plane (Fig. 2a). This contour is shown in Fig. 3 [*see* also Ref. (6)]. The three sides of the trapezium and the real axis in the u-plane have been transformed to a

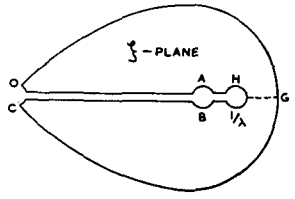

Fig. 3. Trapeziums in Fig. 1a and 1b transformed to the ζ-plane.

cut from the origin to a point H where $\zeta = 1/\lambda$. The boundary OC has become now a part of a lemniscate. Let any point on this lemniscate be denoted as $a + ib$ in the complex ζ-plane. It is easy to show then that:

$$(a^2 + b^2)^2 = 2(a^2 - b^2) \qquad [12]$$

In order to find the current density along any boundary of the trapezium, it is now necessary to evaluate z as a function of given ζ by [11] and then by means of [8] obtain the corresponding $\tilde{C}$ from [7]. Before proceeding with the construction of the current density curves, it is necessary to correlate the parameters λ and k with the actual dimensions of the cell.

In equation [11], let:

$$F(\sin^{-1}\zeta, \lambda) = v$$
$$F(\sin^{-1}\zeta, \lambda') = v' \qquad [13]$$

so that [11] becomes:

$$\sqrt{2(1+k)}\,z = v + v' \qquad [14]$$

Eq. [13] can be considered as defining a transformation from the ζ-plane to the v- and v'-planes, respectively. It can be shown easily that corresponding to lemniscate contour OABC in the ζ-plane; the contours in the v- and v'-planes are as shown in Fig. 4a and 4b. Here L and L' are the complete elliptic integrals of the first kind with moduli λ and λ', respectively. Consider the vertex B. Then in the z-plane (Fig. 1a)

$$z_B = r_1 + i(r_1 - r_2)$$

and in the v- and v'-planes:

$$v_B = L + 2iL'$$
$$v'_B = L'$$

Hence, from [14]

$$\sqrt{2(1+k)}\,[r_1 + i(r_1 - r_2)] = L + L' + 2iL'$$

Comparing the real and the imaginary parts and dividing:

$$\frac{r_1}{r_2} = \frac{L + L'}{L - L'} \qquad [15]$$

Thus, given the ratio of the parallel sides of the trapezium, one can determine the ratio L'/L, which in turn defines uniquely the modulus λ by means of the Jacobi's Nome:

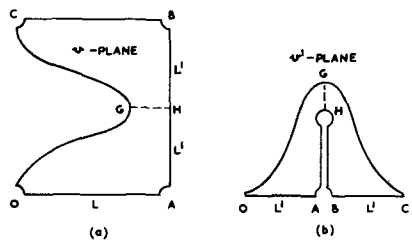

Fig. 4. Auxiliary v- and v'-planes

$$q(\lambda) = \exp\left(-\frac{\pi L'}{L}\right) \qquad [16]$$

The q-function is tabulated extensively (7,8). Having determined λ, the corresponding value of k can be evaluated from [9].

This completes the analysis of a trapezium cell. Now consider, in turn, two possible electrode configurations as depicted in Fig. 1a and 1b.

3. The Trapezoidal Cell First Electrode Position

Assume that the cell is constructed as in Fig. 1a while OA is the cathode. To evaluate the current density along this electrode it is observed that corresponding to the variation of z along OA in Fig. 1a:

$$O \leqq z \leqq r_1$$

the quantity ζ varies:

$$O \leqq \zeta \leqq 1 \quad (see\ Fig.\ 3)$$

Thus for a given ratio r_1/r_2 λ is evaluated by [15] and [16] and hence the values of z are correlated with those of ζ along OA in both planes, respectively. The values of ζ so obtained are then used to compute corresponding values of u from [8]. Then, from [7] current density values are obtained. In order to normalize these values with respect to the total current fed into the cell, it is observed that the total area under a current density curve is:

$$\int_o^{z_1} \sqrt{u}\, dz = \int_o^K dw = K(k)$$

where $z_1 = \max z$ obtained from [11]. In order to insure unit area under the current density curve over the normalized range of z $(O \leqq z \leqq 1)$, one multiplies all the ordinates by z_1/K and divides all the abscissas by z_1. If the height of the electrolyte in the cell is h and A amps are fed into the cell, then $CA/hr_1 = \tilde{C}$ gives the actual current density on the cathode in amp/cm^2. The curves of C are plotted in Fig. 5 for $S = r_1/r_2$ ranging from 1.1 to ∞. It will be observed that for $S = 2$ (i.e., $r_1 = 2r_2$) the current density is almost linear over two thirds of the cathode length. A useful feature of such a cell is that the primary current here does not reach excessively high values at it does in the Hull cell, where polarization errors may become serious; on the other hand this tank is simpler to construct than the hyperbolical Gilmont and Walton cell.

A sample cell was constructed with $S = 2$. The side OA was approximately 8 in. long and the depth of the electrolyte was approximately 1.5 in. The Cu

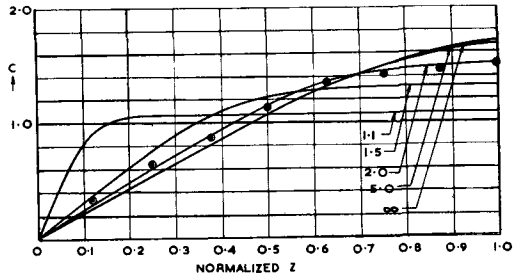

Fig. 5. Normalized current density curves for a cell shown in Fig. 1a. The numbers associated with the curves indicate the corresponding values of $S = r_1/r_2$. The points on the curve for $S = 2$ are experimental (see above).

was deposited from an acid Cu electrolyte, peeled off and its thickness at about 0.5 in. from the bottom of the bath was measured at eight equidistant points.[1] In Fig. 5 the suitably normalized micrometer readings are shown. The agreement between the predicted and the practical results seems to be good.

4. The Trapezoidal Cell Second Electrode Position

Now consider a cell with electrodes situated as in Fig. 1b while OC is the cathode. This arrangement is the same as in the Hull cell and a current density singularity at C is expected. It will be found that this singularity is integrable so as to yield a finite value for the total current, as required.

In this case the evaluation of z corresponding to a given ζ is more involved since the contour OC becomes a lemniscate in the ζ-plane so that

$$\zeta = a + ib \qquad [17]$$

is a complex number whose real and imaginary parts are related by [12].

For a complex angular argument, the elliptic integral of the first kind can be expressed as [*see* Ref. (8) p. 12, Eq. 115.01]

$$F(\theta + i\Psi, \lambda) = F(B, \lambda) + iF(A, \lambda') \qquad [18]$$

where both B and A are real and given by:

$$\cosh \Psi \sin \theta = \frac{\sin B \sqrt{1 - \lambda'^2 \sin^2 A}}{1 - \sin^2 A (1 - \lambda^2 \sin^2 B)}$$

$$\cos \theta \sinh \Psi = \frac{\cos B \cos A \sin A \sqrt{1 - \lambda^2 \sin^2 B}}{1 - \sin^2 A (1 - \lambda^2 \sin^2 B)} \qquad [19]$$

In the present case, from [11]

$$\sin^{-1} \zeta = \theta + i\Psi$$

so that

$$\zeta = a + ib = \sin \theta \cosh \Psi + i \cos \theta \sinh \Psi \qquad [20]$$

The quantities A and B in [19] cannot be found directly from this equation in terms of a and b which define the lemniscate; however using the Eq. [12] of the lemniscate and considering A and B corresponding to the modulus λ as well as A' and B' corresponding to λ', both of which are to be found for the same ζ in [11], one can find a simple relation between A and B:

$$\sin^2 B = \frac{\sin^2 A}{1 + (2\lambda^2 - 1) \sin^2 A} \qquad [21]$$

Furthermore, on the lemniscate:

$$A = B'$$
$$B = A' \qquad [22]$$

Thus [11] can be written:

$$z = \frac{(1 + i)}{\sqrt{2(1 + k)}} [F(B, \lambda) + F(A, \lambda')] \qquad [23]$$

which is of required form since OC is inclined at 45° in the z-plane. Changing A from O to π, one obtains B from [21] and hence z corresponding to

[1] The acid Cu bath was chosen ($CuSO_4$-150 g/l; H_2SO_4-25 g/l) because the polarization in such a bath is low. The total current fed into the cell during 26 hr was 2 amp.

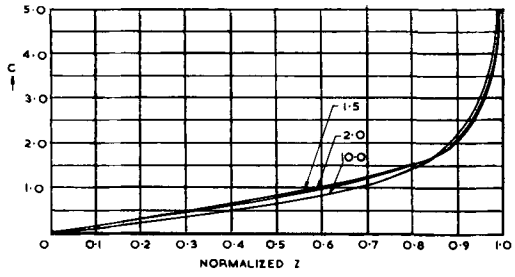

Fig. 6. Normalized current density curves for o cell shown in Fig. 1b. The numbers associated with the curves indicate the corresponding values of $S = r_1/r_2$.

given ζ on the lemniscate as defined by [19] and [20]. Hence the current density curves can be plotted as explained in the previous section. In this case, however, the total area under a curve for given S is equal to K', in analogy to K in the previous section.

The normalized current density curves are plotted in Fig. 6 for $S = 1.5$, 2, and 10. The curves are almost coincident and show reasonable linearity over about two thirds of the cathode length.

5. Triangular Cell

Mathematical Analysis

Consider a right angled isosceles triangle in the complex z-plane as shown in Fig. 1d. Then the inside of the triangle can be transformed into the upper half t-plane (Fig. 7a) by

$$z = z_o + \int_o^t \frac{dr}{2r^{1/2}(r^2-1)^{3/4}} \qquad [24]$$

The corresponding points are

$$O : z = 0 \rightarrow t = 1$$
$$A : z = \tfrac{1}{2} p (1+i) \rightarrow t = 0$$
$$B : z = p \rightarrow t = -1$$
$$E : z = z_E \rightarrow t = n$$
$$F : z = z_F \rightarrow t = -m$$

The half t-plane can now be transformed into the inside of a rectangle in the w-plane by

$$\sqrt{\frac{(1+m)(1+t)}{(1-m)(1-t)}} = sn(w,k) \qquad [25]$$

where

$$\sqrt{\frac{(1-m)(1-n)}{(1+m)(1+n)}} = k \qquad [26]$$

and where

$$z_o = \frac{(1+i)}{\sqrt{2}} K\left(\frac{1}{\sqrt{2}}\right)$$

The vertices of the rectangle (Fig. 7b) are

$$O : w = iK'$$
$$B : w = 0$$
$$E : w = K + iK'$$
$$F : w = K$$

K and K' are complete elliptic integrals of the first kind with moduli k and k', respectively. From [3], [24], and [25] the current density is given by:

$$\tilde{C} = \kappa \left| \frac{dw}{dz} \right| = \kappa \left| \frac{(1+m)(1+n)t(t^2-1)^{1/2}}{(t+m)(t-n)} \right|^{1/2} \qquad [27]$$

Since the current density is required in the z-plane using [24], t must be expressed as a function of z. The integral can be evaluated by using the substitution given in Ref. (9) (case IV), i.e.,

$$\zeta^2 = \frac{t^2}{t^2-1} \qquad [28]$$

Then ζ is given as a Weierstrassian elliptic function of z.

$$\zeta = \wp z \qquad [29]$$

defined by

$$\left(\frac{d}{dz}\wp z\right)^2 = 4(\wp z - e_1)(\wp z - e_2)(\wp z - e_3)$$

where

$$e_1 = 1,\ e_2 = 0,\ \text{and}\ e_3 = -1.$$

Since e_1, e_2, and e_3 are real, [29] can be expressed as a Jacobi elliptic function of real modulus

$$sn(\sqrt{2}\, z, \lambda) = \sqrt{\frac{2}{\zeta+1}} \qquad [30]$$

where

$$\lambda^2 = \frac{e_2 - e_3}{e_1 - e_3} = \frac{1}{2} \qquad [31]$$

Treating the other triangles given in Ref. (9) in a similar manner, the Jacobi elliptic functions arrived at have a complex moduli and, since Weierstrassian elliptic functions are not extensively tabulated, the problem becomes numerically intractable.

The contour in the ζ-plane which corresponds to the triangle in the z-plane is as shown in Fig. 8. The side OB of the triangle forms a cut in the ζ-plane from $\zeta = \infty$ to the branch point at $\zeta = 1$; the side OA is the negative imaginary axis and the side AB is the positive imaginary axis. In order to evaluate the current density along any boundary of the triangle, z can now be related to t through [28] and [30]. In [27] m and n still remain unknown and must be related to the positions of F and E, respectively. It can be shown that along OA

$$\zeta = -2i \frac{cn^2(|z|,\lambda)}{1 - cn^4(|z|,\lambda)} \qquad [32]$$

where $\lambda = \dfrac{1}{\sqrt{2}}$, as given in [31].

Since at the point E in the t-plane $t = n$, then using [28]

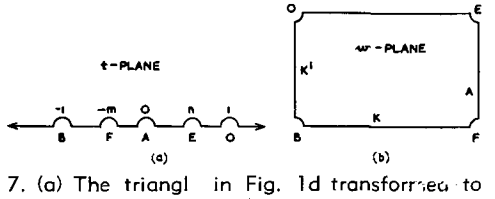

Fig. 7. (a) The triangl in Fig. 1d transformed to the t-plane; (b) the same in the w-plane.

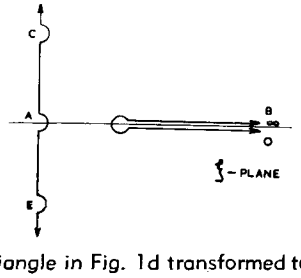

Fig. 8. The triangle in Fig. 1d transformed to the ζ-plane

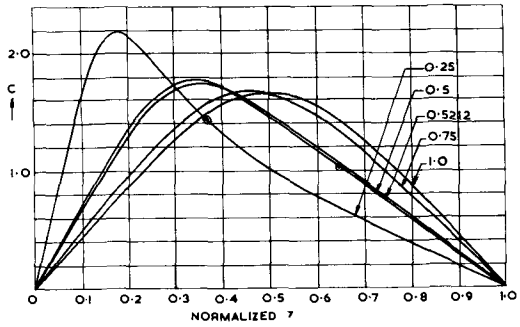

Fig. 9. Normalized current density curves for a cell shown in Fig. 1d when the cathode is along EA only. The numbers associated with the curves indicate the corresponding values of $\sqrt{2}a/p$. The points on the curves for $\sqrt{2}a/p = 0.25$ and 0.5 show the position of the points of inflection.

$$n = \frac{2cn^2\,(a,\lambda)}{1 + cn^4\,(a,\lambda)} \qquad [33]$$

where $a = OE$

Similarly,

$$m = \frac{2cn^2\,(b,\lambda)}{1 + cn^4\,(b,\lambda)} \qquad [34]$$

where $b = FB$

6. Triangular Cell Special Electrode Position

The current density curves shown in Fig. 9 are for a 45° triangular, isosceles cell discussed above when the anode is along OB in Fig. 1d and the cathode is along EA where E can be practically anywhere between O and A. The curves are normalized as before to unit area, the normalizing constant being again $K'(k)$, similarly as in section 4, where now k is given by [26], [33], and [34]. A current density singularity is observed at E, but this singularity is integrable giving a finite value for the total current. No singularity occurs on the cathode OB and the current density curves there are roughly triangular in shape with good linearity between their maximum $z = z_{max}$ and the normalized $z = 1$. When the anode occupies the whole of AO (i.e., $a = 0$ as defined in [33]), this maximum is at $z = 0$ and as E moves along OA toward A the maximum moves along the z-axis until for a point cathode at A (i.e., $a = p/\sqrt{2}$) it occurs at $z_{max} = 0.5$ and the current density curve is symmetrical as expected. For a less than some value, say a_i, the curves have a point of inflection between z_{max} and $z = 1$; such point of inflection destroys the linearity somewhat (*see* Fig. 9 for $a = 0.25$). It is therefore advisable in practice to construct a cell with an $a < a_i$ and in order to have large range of linearity at the same time, the best value is

$$a = a_i = 0.52120\,p/\sqrt{2} \qquad [35]$$

For the ease of construction, it is suggested to take:

$$a = p/2\sqrt{2} \qquad [36]$$

when good linearity is observed. Thus in the last case the slope between $z = 1$ and $z = 0.5$ does not vary by more than 8%. Moreover, the area under the current density curve in Fig. 9 for $\sqrt{2}\,a/p = \frac{1}{2}$ is 0.3695 between $z = 0.5$ and $z = 1$, whereas the area of the corresponding right-angled triangle, between the same limits (the slope of the hypotenuse of this triangle is equal to that of the curve at $z = 1$), is 0.3693.

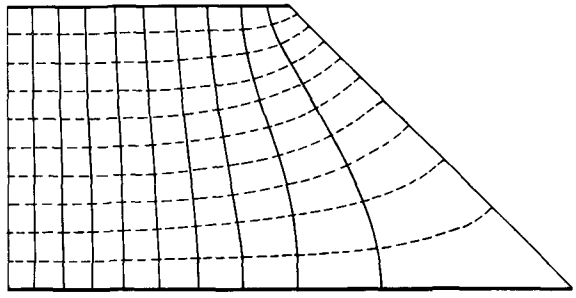

Fig. 10. Equipotentials (broken lines) and the current flow lines (full lines) of a cell shown in Fig. 1a.

Hence, if the total current fed into each cell is A, then 0.3695 A is distributed linearly over that half of the cathode which is further from the anode, while the length of the latter is $1/2\sqrt{2}$ of the total cathode length.

No experiments were made on the triangular cell, which is described here as an interesting alternative to the trapezium one. It seems however that it is more convenient to use practically, since (because of the triangular shape of the primary current distribution; *see* Fig. 9) there are two determinable points on the cathode where the current density is the same. This property could be profitably used for the experimental testing of the deposition, e.g., for deciding the level in the bath at which the actual deposition can be related proportionally to the primary current density.

7. Conclusion

Fig. 10 and 11 show the current flow lines (full lines) and the equipotentials (broken lines) of the two cells discussed in Sections 3 and 6. In both cases the electrodes are marked by thick lines. Reversing the positions of the electrodes and the insulators one interchanges the meaning of the equipotentials and the current lines, so that, in particular, Fig. 10 shows the conditions in one cell discussed in Section 4 (the Hull type cell) when the insulators are marked by thick segments, the current flow lines by broken lines, and the equipotentials by full lines.

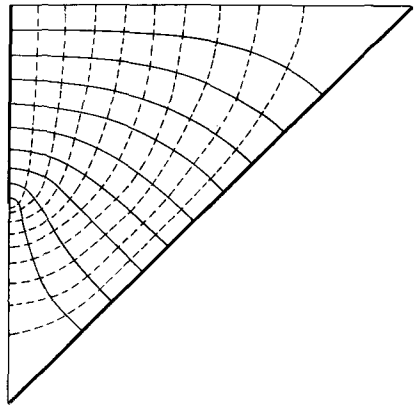

Fig. 11. Equipotentials (broken lines) and the current flow lines (full lines) of a cell shown in Fig. 1d when the cathode is along EA only.

The curves were obtained by the relaxation methods, since analytic computation is made difficult by the lack of appropriate mathematical tables.

Acknowledgments

The authors wish to thank L. E. Q. Walker and D. W. G. Ballentyne for proposing the problem and for many helpful discussions, Miss M. A. Millidge for computing some of the curves, also Miss E. Kowszynis for supplying experimental data for Fig. 5, and the Chief of Research of the Marconi's Wireless Telegraph Company for the permission to publish.

Manuscript received April 22, 1957.

Any discussion of this paper will appear in a Discussion Section to be published in the June 1958 JOURNAL.

REFERENCES

1. C. Kasper, *Trans. Am. Electrochem. Soc.*, **77**, 353 (1940).
2. R. O. Hull, "Control of Plating Baths by Plating Cells," "Metal Finishing" Guidebook-Directory, 18th annual ed., p. 367 (1949).
3. R. Gilmont and R. F. Walton, *This Journal*, **103**, 549 (1956).
4. W. R. Smythe, "Static and Dynamic Electricity," McGraw-Hill Book Co., Inc., p. 233 (1950).
5. A. Cayley, "Elliptic Functions," G. Bell & Sons, London or Deighton, Bell & Co., Cambridge, p. 360 (1895).
6. F. Bowman, *Proc. London Math. Soc.*, **39**, 211 (1939).
7. E. Jahnke and F. Emde, "Tables of Functions with Formulae and Curves," Dover Publications, New York (1945).
8. P. F. Byrd and M. D. Friedman, "Handbook of Elliptic Integrals for Engineers and Physicists," Springer Verlag-Berlin, New York (1954).
9. A. E. H. Love, *Am. J. Math.*, **2**, 158 (1889).

Transistor-Grade Silicon

I. The Preparation of Ultrapure Silicon Tetraiodide

Bernard Rubin, Guy H. Moates, and Joseph R. Weiner

Radiochemistry Section, Components and Techniques Laboratory, Electronics Research Directorate, Air Force Cambridge Research Center, Air Research and Development Command, Bedford, Massachusetts

ABSTRACT

A stepwise method of preparing and purifying SiI_4 has been found involving the direct combination of the elements, recrystallization of the product, followed by sublimation and zone purification steps. The values of the segregation coefficients of several impurity elements have been determined, and it is shown that under ideal conditions some of these elements can be removed to concentrations of less than one part impurity per billion parts of SiI_4 in sixty passes for a 50 cm length charge.

The requirements for transistors and other semiconductor devices that operate at temperatures higher than those at which Ge is effective have stimulated considerable research in the preparation of "transistor-grade silicon." This term refers to a Si matrix in which the impurity levels are at concentrations of one part in one hundred million and preferably as low as one part per one hundred billion of Si. Because the sources of this material in the United States are few, the Air Force has initiated a research program in Si chemistry in order to provide alternate methods of refinement.

Most Si in this country is made according to the reaction

$$2C + SiO_2 \rightarrow 2CO + Si$$

in electric arc furnaces. A typical product[1] has the following spectrographic analysis shown in Table I (1). Semiconductor devices made of Si with levels of impurities as shown in Table I would be of little practicality and transistor devices with acceptors, donors, and lifetime-killers at such high concentrations would not function. Two approaches are available for removing these impurities, a metallurgical and a physicochemical. The former involves the zone refining technique originated by Pfann (2). By this

[1] Obtained from Coleman and Bell Company, Norwood, Ohio.

Table I. Spectrographic analysis of reagent Si

Impurity element	Conc. in parts of impurity per million parts of Si
Al	6900
As	150
B	60
Ca	7100
Co	7
Cr	250
Cu	300
Fe	6700
Ga	<10
In	3
K	<10
Li	2.5
Mg	120
Mn	350
Na	18
Ni	80
P	80
Ta	140
Ti	1300
Tl	5
V	60
Zr	250

method, some elements, e.g., Al, may be removed effectively from Si. However, B, with a segregation coefficient of about 0.9 (3) cannot be separated efficiently from the matrix. In addition, because of the high melting point of Si (1420°C), contamination by leaching from the container material presents problems. For these reasons, the physicochemical approach which involves the synthesis of a convenient compound of Si, its purification to the desired levels of purity that are required ultimately for transistor-grade silicon and its decomposition into elemental Si, has been chosen by this laboratory. In order that this approach be effective, there were certain prerequisites. The compound had to be either easily synthesized or available, it had to be capable of being purified to the extent required by the final Si specification, and it had to be capable of being decomposed relatively easily into elemental Si which would not be contaminated in the decomposition process. Of the variety of Si compounds that suggested themselves, i.e., the silanes, siloxanes, silicates, and halides, the latter seemed to be best suited to fulfill the above requirements. They are stable substances, relatively easy to synthesize and handle, and are potentially decomposable or reducible to polycrystalline or single-crystal Si and the halogen or hydrogen halide. Of the four unmixed tetrahalides, SiF_4 is the most stable and decomposes only under extremes of temperature and pressure. Furthermore, it is a gas under normal conditions and, as such, is difficult to handle and purify. $SiBr_4$ and $SiCl_4$ are both liquids possessing the advantages of this state with respect to purification, but both are more difficult to decompose than the tetraiodide. Thermodynamic data indicate that the latter decomposes at about 1500°C at one atmosphere and can be reduced with hydrogen at about 600°C under these conditions. At 1000°C, the dissociation equilibrium constant (Kp) was calculated to be 1.86×10^{-12} from the free energy data. Assuming a partial pressure of 3 mm of SiI_4 in the reaction chamber, then the limiting partial pressure of I_2 is 0.236 mm. By lowering the partial pressure of I_2 below this value, decomposition of the SiI_4 occurs. Since it is a solid under normal conditions with a relatively low boiling point (290°C), it can be purified not only by the usual techniques of recrystallization and distillation, but it lends itself to zone purification. Since SiI_4 offers a different matrix than Si to impurities, it need not be expected that the segregation coefficients of these impurities be the same in both matrices. If the impurities that are not removed in the current technique of zone purification of Si can be removed in SiI_4, then a combination of the two zone purifications could lead to transistor-grade Si. It seemed for most intents and purposes that SiI_4 offered the greatest potentiality as an intermediate in the synthesis of transistor-grade Si.

A literature survey indicated that high purity Si has been prepared by methods utilizing the tetrachloride, the tetrabromide, and the tetraiodide of Si. The tetrachloride is reduced in a quartz apparatus at about 1000°C with Zn vapor as the reductant (4).

Sangster (5) has reduced the purified tetrabromide with H_2. Litton (6) investigated the thermal decomposition of fractionally distilled tetraiodide. More recently, Theuerer (7) reduced $SiCl_4$ with H_2.

Experimental

Preparation of silicon tetraiodide.—SiI_4 was prepared by the direct reaction of I_2 with Si in a horizontal reaction chamber (8). The iodine boiler, heated by a mantle to about 115°C, was a 500 ml round-bottomed Pyrex flask sealed at the top and equipped with a 28/15 ball joint at right angles to the neck. A side arm was present to permit the entry of the dried flushing gas, argon. The reagent was Baker and Adamson resublimed iodine. The reaction chamber was a 30-mm inner diameter Vycor furnace tube, 70 cm long, with 28/15 socket joints at each end. The connection of Pyrex to Vycor permitted easy removal of one joint from the other owing to the difference in coefficients of expansion. The furnace tube was heated by two electric multiple unit furnaces made by Hevi-Duty Electric Company, Milwaukee, Wisconsin, and the temperature monitored by using a chromel-alumel thermocouple adjacent to the furnace tube. The SiI_4 receiver was a 500-ml round-bottomed Pyrex flask similar to the iodine boiler.

In a typical run, reagent Si was ground into particles and then collected between No. 4 and No. 10 sieves to permit as close packing of the particles as was practicable in the furnace tube without channeling or back pressures of I_2. The charged I_2 flask, reaction chamber, and receiver were connected using a minimum of Dow Corning Silicone grease at the joints and a mercury pressure release valve was inserted in parallel with the system. The argon was flushed through the system at a flow rate of about 524 ml/min and the temperature of the Si was raised to 810°C. All exposed connecting sections between boiler, chamber, and receiver were maintained at suitable temperatures by means of heating tapes. When temperature equilibrium was attained, the I_2 was heated to 115°C and carried into contact with the Si. The product as it entered the receiver was a white mist and, after condensation, a pinkish white to red solid. The coloration was probably due to unreacted I_2 or some Si_2I_4 from the reaction:

$$Si + SiI_4 \rightleftarrows Si_2I_4$$

Gravimetric analysis. Calculated for SiI_4: Si, 5.2%; I, 94.8%. Found: Si, 5.6%; I, 91.0%. Emission spectrographic analysis of the crude SiI_4 gave the impurities as listed in Table II.

A comparison with Table I indicates that three elements have increased in concentration: Na, B, and V. An analysis of Pyrex glass showed that Na was present to the extent of about 8.5% and B about 10.8%. It was evident that leaching of these two impurities from the glass took place under the conditions of the SiI_4 synthesis. There was also the possibility of leaching from the Vycor. For this reason, an all-quartz apparatus will be substituted for Pyrex in the synthesis step. The daily production rate is about 450 g of SiI_4 and the apparatus may be scaled up for larger yields if necessary. There is about ≥ 95% conversion to SiI_4 based on I_2.

Table II. Emission spectrographic analyses

Impurity element	Crude SiI_4	Conc. of impurity in parts of impurity per million parts SiI_4 Recrystallized SiI_4	Sublimed SiI_4
Ag	1.0	0.1	N.D.
Al	28.0	6.5	0.2
As	<1	N.D.	N.D.
Au	N.D.*	N.D.	N.D.
B	16.0	N.D.	N.D.
Be	N.D.	N.D.	N.D.
Bi	N.D.	N.D.	N.D.
Ca	N.D.	N.D.	N.D.
Cd	<1	N.D.	N.D.
Co	N.D.	N.D.	N.D.
Cr	1.5	N.D.	N.D.
Cu	12.0	0.3	2.7
Fe	55.0	0.5	0.6
Ga	<0.1	N.D.	N.D.
Hg	<1	N.D.	N.D.
In	<0.1	0.5	N.D.
K	N.D.	N.D.	N.D.
Li	N.D.	N.D.	N.D.
Mg	1.6	0.4	0.1
Mn	4.5	2.0	0.1
Mo	N.D.	N.D.	N.D.
Na	2.0	N.D.	N.D.
Ni	1.0	N.D.	N.D.
P	<5	N.D.	N.D.
Pb	<0.5	N.D.	N.D.
Sb	<1	N.D.	N.D.
Sn	<0.5	N.D.	N.D.
Ti	21.0	16.5	1.3
V	12	N.D.	N.D.
Zn	N.D.	N.D.	N.D.
Zr	1.2	5.0	N.D.

* Not detected.

Analysis of silicon tetraiodide.—Analyses of SiI_4 were carried out[2] after hydrolyzing a sample with conductivity water in Pt crucibles and heating to 500°C until the reaction was complete. Commercially available mixed internal standards were then added to the silica. Thin-walled graphite electrodes were filled with adequate silica and ignited in a He atmosphere for 10 sec at 5 amp. Another silica sample was ignited in air for 50 sec at 10 amp and burned to completion. Those elements whose lines were masked by SiO, SiO_2, and CN bands in the atmospheric run were read from the spectrum obtained in the He run. The sensitivities of some of the impurity elements in SiO_2 are given in Table III.

Crystallization.—Of the various purification techniques that are available for solids, zone purification has the potentiality, if the segregation coefficients are favorable, of yielding a matrix in which the desired concentrations of impurities can be attained practicably. Although successful zone purification is not dependent on attaining low concentrations of impurity initially, the ultimate concentration can be minimized if the initial concentrations are low. For this reason, other methods of preliminary purification have been invoked. The first of these was crystallization of the crude SiI_4 from toluene. The solubility of SiI_4 in toluene was found to be 10.3% by weight at 110°C and 3.2% at 20°C indicating about an 82% recovery of SiI_4 in a single step crystallization.

[2] To be published by the Metal Hydrides Co., *Journal of Analytical Chemistry*.

Table III. Sensitivities of impurities by emission spectrographic analysis

Impurity elements	Sensitivity in parts of impurity per million parts SiO_2
Ag	0.25
Al	0.65
As	15
B	0.50
Be	0.25
Ca	0.50
Cd	1.0
Cr	2.5
Cu	0.25
Fe	0.65
Hg	5.0
Mg	0.25
Mn	0.75
P	25
Sb	3.0
Ti	1.0
Zn	10
Zr	5

In practice, the crude SiI_4 was transferred in the sealed receiver to a dry box, and sufficient fractionally distilled toluene, dried over Na, was added to make a 10% solution. The solution was heated to the boiling point, and the resulting solution was cooled slowly to 0°C. The liquor was decanted, and the remainder removed under vacuum at about 70°C. A spectrographic analysis of the crystallized product is given in Table II.

A comparison of the crystallized and crude product indicates that there is a considerable decrease in the over-all impurity concentrations of most of the elements. It can be postulated that the impurity elements are in a molecular form that is toluene-soluble, and, in all probability, this form is the iodide. It is possible that the efficiency of the crystallization step is the result, in part, of small amounts of silica introduced by the unavoidable hydrolysis of the SiI_4 during handling. Furthermore, since the extraction is a relatively low temperature step, there is little or no occasion for leaching as is indicated by the low concentrations of such constituents of glass as B and Fe. Gravimetric analytical methods on the crystallized SiI_4 yielded the following analysis: Si, 5.4%; I, 91.9%. These values are closer to theoretical than the crude SiI_4, and indicate that some of the I_2 or higher homologues have been removed by the crystallization step. The appearance of the more lightly colored material supports this assumption.

Sublimation.—Fractional distillation of the recrystallized SiI_4 was next considered as a possible purification technique. It was observed that sublimation occurred with use of a vacuum fractional distillation system. Sublimation had also been used as a transfer procedure (6) for SiI_4 and it was decided to utilize it as the second step in the purification. The sublimation apparatus consisted of a 30-cm long Pyrex cylinder 10 cm in diameter with 10-mm ground flanges on each end. Around the cylinder were wrapped two heating tapes individually controlled by Powerstats. A dome with a 4-mm stopcock was connected to one end of the cylinder, and, on the other end, a second dome

equipped with a 32-cm long cold finger. The latter dome was charged in a dry box with enough crystallized SiI_4 to fill it. The apparatus was assembled with the ends held temporarily in position by clamps; a partial vacuum was applied to complete the seals. The charged assembly was then removed from the dry box, connected to a vacuum system, and the charged end was heated by a mantle to about 100°C. When the sublimate appeared as large white crystals on the area adjacent to the heated charge, the sublimation was repeated by heating the first tape, then the second until ultimately the crystals appeared on the dome. The apparatus was disassembled and the product scraped off with Lucite rods. An emission spectrographic analysis of the sublimed product is given in Table II. It is obvious from comparison of the results in Table II that considerable purification is effected by sublimation of the crystallized product, particularly in the cases of Al, Mn, Ti, and Mg. The Cu concentration is seen to increase from 0.3 to 2.7 ppm and this is due to Cu impurities found in the Pt crucibles used in the hydrolysis of the SiI_4 prior to spectrographic analysis. The source of contamination has been eliminated by substituting quartz for Pt. Concentrations of all the impurities detected are now in or below the part per million range. Further purification may be effected by the zone-melting process in the case of impurities with favorable segregation coefficients.

Zone purification.—Determination of effective segregation coefficients, K_{eff}, under a given set of experimental conditions was undertaken. It is emphasized that the values reported are those of effective coefficients, and not equilibrium values. Because more subtle variables such as crystal orientation, convection, effective boundary layer, silica formation, and supercooling were not controlled, there exists some discrepancy in the values reported.

Silicon tetraiodide recrystallized from toluene was encapsulated in sealed Pyrex ampoules, densified, and leveled by repeated vertical reverse passage of a single zone (2). A single molten zone 2-cm long was passed through the 20-cm length of leveled charge. The zone-melted charge was then segmented into ten equal sections, each section hydrolyzed to silica in conductivity water, and finally each section was analyzed spectrographically as described above.

Profiles constructed from the results of these analyses depicted concentrations, C_s, of impurities retained in the solid after passage of one molten zone. The initial concentration, C_o, was taken as the average concentration of the ten segments. This average value is valid because the charge was leveled to assure an invariance of impurity concentrations along the longitudinal axis. By definition

$$C_s = KC_l \qquad \text{(I)}$$

where C_l is the concentration of an impurity in the liquid. At the point of the first freezing (i.e., at $X = 0$, if X is the distance along the charge), $C_l = C_o$. Therefore,

$$K = C_s/C_o \text{ at } X = 0 \qquad \text{(II)}$$

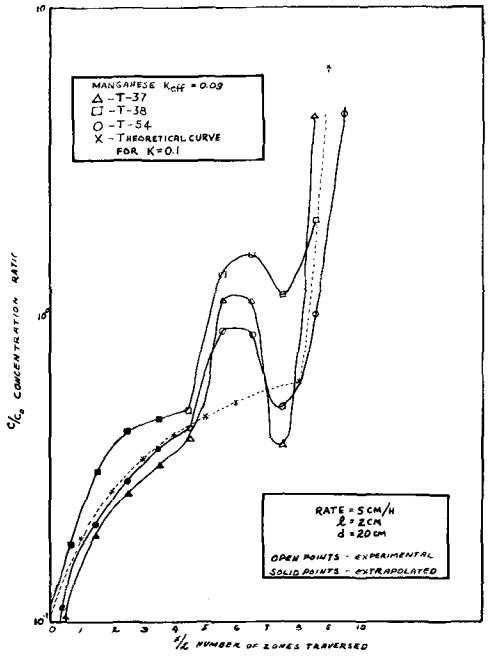

Fig. 1. Concentration profiles of Mn impurity species in a SiI_4 matrix.

By plotting the ratio C_s/C_o vs. X/l (l is the zone length) it was possible to determine K_{eff} from the intersection of the profile with the y-axis. Fig. 1 is a series of experimental profiles for the Mn species in the silicon tetraiodide matrix. Also depicted is the calculated curve for a solute having a K equal to 0.1.

These profiles are typical of those species which display segregation in accordance with K_{eff} of approximately 0.1. The preponderance of impurity solute in the end of the charge toward which the zones traveled is evidence that the segregation coefficient is less than unity. The sharp drops in concentration at the minima observed in the next to last zone are due to the growth of the last zone at the conclusion of the pass. It was necessary to stop the travel of the zone before it proceeded into an unleveled portion of the charge; at this time the final zone grew back into a large part of the preceding zone, and then solidified by normal freezing from both ends.

Although only a single molten zone was passed through the charge, the concentrations in the first half of the charge to be melted were below the limits of spectrographic detectability for about half of the impurities studied. Therefore, it was necessary to resort to a method of mathematical extrapolation in order to extend the profile to the y-axis. The expression

$$C_z = K_{eff}\left[C_o + \frac{C_{z-1}}{K_{eff}} - C_{z-1}\right] \qquad \text{(III)}$$

was employed. Here C_z is the solute concentration frozen out in any given zone (except the last), C_{z-1} is the solute concentration frozen out in the prior zone, and C_o is the initial invariant concentration. The equation is an expression of approximation and becomes less valid as the l/d ratio (zone length: charge length) increases. Values of K_{eff} are substituted until C_{z-1} at $X = 0$ is equal to $K_{eff}\,C_o$. Valid-

ity of these extrapolations is based on the reasonable degree of agreement between computed and experimental curves for impurities detectable in all segments.

Zones have been passed downward through the charge with similar results, thereby eliminating the possibility of any separation by flotation. Therefore, regardless of the anomalies in the profile, it may be assumed that a K of a certain value exists in order to relocate the impurities as depicted. This is so if one assumes that segregation is caused only by the differences in solubility in the solid and liquid phases.

Table IV summarizes the effective segregation coefficients of various impurity species in a SiI_4 matrix. Inasmuch as all values reported in Table IV are less than unity, purification can be effected by moving each of the solute impurities to the end of the charge toward which the molten zones travel.

Applying the value of K_{eff} as determined for boron triiodide (i.e., 0.4) to the family of equations given by Pfann (2), it can be shown that an ultimate concentration ratio of 1×10^{-12} can be attained for a charge having a d/l ratio of 20:1. Furthermore, 70% of this charge will have a concentration which has been reduced to one part in a billion or less if the initial concentration was one part in a million.

The number of passes required to attain this concentration is approximated by

$$K^n = C_{x=0} \qquad \text{(IV)}$$

where n is the number of passes. An efficiency factor (9) of 53% must be applied for a K equal to 0.4. With use of this factor in conjunction with Eq. (IV), 60 passes are required to attain this concentration profile.

Table IV. Effective segregation coefficients of various impurity species in a SiI_4 matrix

(Charge length, d = 20 cm; zone length, l = 2 cm; zone temperature = 135° ±4°C; rate of crystallization = 5 cm/hr)

Impurity species	K_{eff}
B*	0.16 ± 0.07‡
Al	0.70 ± 0.35
Na	0.10 (single run)
Mg*	0.16 ± 0.01
Cu	0.64 ± 0.17
Fe*	0.15 ± 0.08
Ti	0.91 ± 0.08
Mn*	0.09 ± 0.04
Boron triiodide†	0.42 ± 0.22

* Values obtained by extrapolation.
† Doped samples.
‡ Maximum variability of results.

The concentrations computed above indicate that SiI_4 can be purified to less than one part of impurity per billion parts of SiI_4 provided equilibrium conditions prevail to the extent demonstrated in these experiments. Furthermore, it must be assumed that impurities are not leached from container walls. Finally, it should be mentioned that the purity of a sample can be improved by: (*a*) decreasing the value of the effective segregation coefficient (for $K < 1$) by controlling conditions in order to more closely approximate equilibrium, (*b*) controlling the l/d ratio in order to make the ultimate concentration profile more favorable, and (*c*) choosing a smaller fraction of the zone-refined charge.

A more detailed treatment of the zone purification of SiI_4 is forthcoming in the second paper of this series.

Acknowledgments

The authors thank B. Manning of Technical Operations, Inc., Arlington, Massachusetts, for his advice on the design of the zone purification furnace; W. Jackson and R. Morrison of the Engineering Division, Air Force Cambridge Research Center, for the modifications and construction of this apparatus. Acknowledgment is also expressed to A. Kant, Watertown Arsenal, Watertown, Mass., for his helpful suggestions.

Manuscript received July 16, 1956. This paper was prepared for delivery before the Washington Meeting, May 12-16, 1957.

Any discussion of this paper will appear in a Discussion Section to be published in the June 1958 JOURNAL.

REFERENCES

1. Spectrographic Analyses by Metal Hydrides, Inc., Beverly, Mass.
2. W. G. Pfann, *J. Metals*, **194**, 747 (1952).
3. J. A. Burton, *Physica*, **20**, 845 (1954).
4. D. W. Lyon, C. M. Olson, and E. D. Lewis, *J. (and Trans.) Electrochem. Soc.*, **96**, 359 (1949).
5. Hughes Aircraft Co., Quarterly Technical Rpts., Signal Corps Contract No. DA-36-039-SC-42574 (1952-1953).
6. Foote Mineral Co., Quarterly Technical Rpts., Signal Corps Contract No. Da-36-039-SC-5550 and DA-36-039-SC-56993 (1951-1954).
7. H. C. Theuerer, *Bell Labs. Record*, **33**, No. 9, 327 (1955).
8. R. Schwarz and A. Pflugmacher, *Berichte*, **75B**, 1062 (1942).
9. R. J. Dunworth, "Some Theoretical Factors in the Zone Melting Process," ANL-5360, Metallurgy Division, Argonne National Laboratory, Lemont, Ill., (February 1956).

The Systems CaF_2-LiF and CaF_2-LiF-MgF_2

W. E. Roake

Ceramic Fuels Development Operation, Hanford Laboratories Operation,

General Electric Company, Richland, Washington

ABSTRACT

Temperature-composition relationships have been measured in the CaF_2-LiF and the CaF_2-LiF-MgF_2 systems in the areas of liquidus temperatures below 1000°C. A binary eutectic composition of 80.5 mole % LiF and 19.5 mole % CaF_2 was observed to melt at 769°C. A ternary eutectic composition of 59.0 mole % LiF, 2.9 mole % MgF_2, and 13.1 mole % CaF_2 was observed to melt at 672°C.

Current interest in fused salts as metallurgical process media has led to the examination of relatively low melting fluoride mixtures. Of primary interest are those fluorides of metals whose oxides and fluorides are thermodynamically compatible with metallic uranium. Ruff and Busch (1) published phase diagrams for both systems reported here. However, their diagram for the system CaF_2-LiF is somewhat incorrect and their diagram for the system CaF_2-LiF-MgF_2 was constructed from few known points and based on the erroneous assumption that the system MgF_2-LiF contains no solid solutions. More recently Bergman and Dergunov (2) and Counts, Roy, and Osborn (3) reported solid solutions in the system MgF_2-LiF. The third binary combination, CaF_2-MgF_2, was published by Beck (4). The work reported here has defined more accurately the subject systems in the areas of such mixtures melting at temperatures below 1000°C.

Experimental

Mixtures of reagent grade CaF_2 and LiF and Baker and Adamson "purified" MgF_2 were prepared by accurate weighing of components, mixing, and melting in Pt vessels. Spectrographic analysis of the MgF_2 showed only Ca as a major contaminant of the order of 0.1%. The mixtures of fused salts were subjected to continual mechanical agitation while in the molten state, and were so mixed for 30 min before measuring cooling curves from the melt. For each mixture a rough cooling curve was observed to locate the temperature points of interest. These temperatures then were located accurately by cooling from 100°C above each point. This was done by adjusting the power supply of the electric crucible furnace to that voltage which would maintain the furnace at an equilibrium temperature 100°C below the point of interest. At least two reproducible cooling curves were charted at each point of interest. Temperature measurements within the cooling mixtures were obtained by means of a chromel-alumel thermocouple situated in a thin submerged Pt thimble. A calibrated automatic recording potentiometer was used to chart the time-temperature relationships. The chart is easily readable with an accuracy of 1°C. Cooling curve breaks and thermal arrests are generally sharp and reproducible. In those cases in which a well-defined break or arrest was not easily obtained a best estimate of the true value was chosen from smoothed curve plots of temperature points vs. CaF_2 mole %, holding the mole ratio of LiF:MgF_2 constant. Intersections with the boundaries were determined in the same manner. During the time of each experiment no variation of fixed temperature points and no salt discoloration was observed to be caused by salt oxidation, volatilization, or by slight fluoride attack on Pt.

Results

System CaF_2-LiF.—Temperature-composition relationships were measured in the CaF_2-LiF system at compositions containing greater than 60 mole % LiF. An eutectic composition of 80.5 mole % LiF was observed melting at 769°C. No evidence of intermediate compounds or of solid solutions was observed. The experimental data are recorded in Table I and are plotted in Fig. 1.

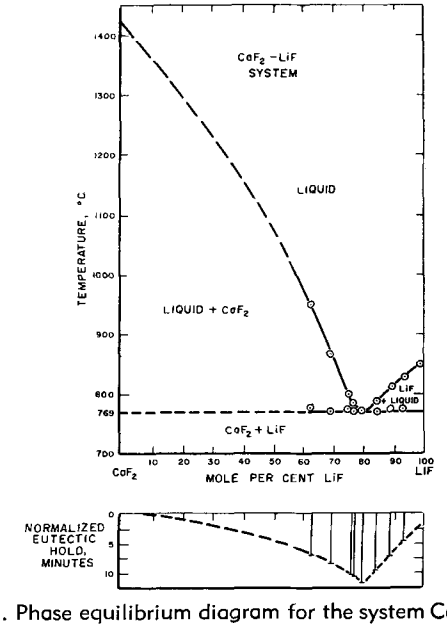

Fig. 1. Phase equilibrium diagram for the system CaF_2-LiF

Table I. Liquidus and eutectic temperatures of mixtures of calcium fluoride and lithium fluoride

CaF_2 g	LiF g	Mole % LiF	Temp of first solidification, °C	Temp of eutectic halt, °C	Time of eutectic halt, min
0	20	100	847	—	—
2.5411	13.3907	93.98	827	773	5.85
4.6596	13.3907	89.63	810	773	9.75
7.5376	13.3907	85.33	785	769	15.75
10.0830	13.3907	80.00	774	769	20.4
12.5098	13.3907	76.32	797	770	20.2
17.4064	13.3907	69.84	865	769	19.5
23.6571	13.3907	63.01	948	770	20.4
10.0800	13.3900	77.99	777	770	19.4

System CaF_2-LiF-MgF_2.—Temperature-composition relationships of the CaF_2-LiF-MgF_2 system were explored in the region of liquidus temperatures below 1000°C. A ternary eutectic composition was observed at 59.0 mole % LiF, 27.9 mole % MgF_2, and 13.1 mole % CaF_2. The melting point of the ternary eutectic is 672°C. Ternary solid solutions are formed except in the CaF_2 primary phase area (cf. Fig. 2). The melting points of CaF_2 and MgF_2 are from Rossini (5).The melting point of LiF is from Kelley (6) and was verified by measurement. Experimental data are recorded in Table II. The phase diagram showing liquidus isotherms, binary and ternary eutectic points, and the boundary curves is plotted in Fig. 2. The solid isotherms are based on experimental data, the dotted line isotherms are extrapolated. Due to the nature of the work and the time involved no attempts were made to determine the extent of binary and ternary solid solutions in the system or to locate three phase boundaries. Examination of Counts, Roy, and Osborne's MgF_2-LiF diagram coupled with the observation of the failure of some of the ternary compositions (cf. Table II) to reach the ternary eutectic discloses the expected complexity of the progress of equilibrium crystallization in the system.

Manuscript received May 18, 1956.

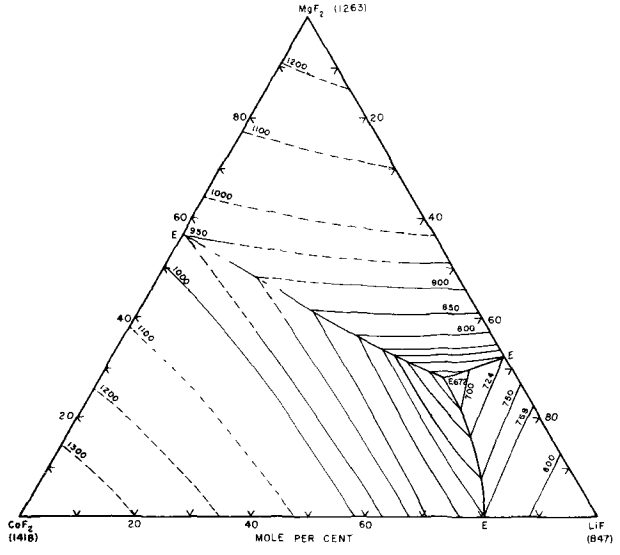

Fig. 2. The system CaF_2-LiF-MgF_2. Primary phase fields and liquidus isotherms. (Solid solutions are not shown.)

Table II. Temperature-composition data for system CaF_2-MgF_2-LiF

Composition, mole %			Fixed points on cooling curves		
CaF_2	MgF_2	LiF	Liquidus, °C	Boundary, °C	Eutectic, °C
22.9	35.0	42.1	790	—	675
9.1	30.9	60.0	728	686*	672
10.0	30.6	59.4	723	684	672
11.7	30.0	58.3	714	685	672
16.0	28.5	55.5	693*	685	672
17.8	28.0	54.2	715	685	672
20.0	27.2	52.8	740*	687	672
22.0	26.5	51.5	765*	687	672
24.5	25.7	49.8	796*	687	672
28.8	24.2	47.0	847	690	672
0	40	60	837	—	724 (binary)
7.0	37.2	55.8	812*	690	675
10	36	54	801	684	672
13	34.8	52.2	786	684	672
18.1	32.8	49.1	758	742	672
21.7	31.3	47.0	782*	755	—
26.0	29.6	44.4	825	755±3	672
28.5	28.6	42.9	849	755*	672
31.8	27.3	40.9	889	757	Not measured
0	50	50	940	—	724 (binary)
9.1	45.45	45.45	900	715	669
13.8	43.1	43.1	879	719	672
16.8	41.6	41.6	862	747	672
18.9	40.55	40.55	851	764	672
21.1	39.45	39.45	834	782	672
23.0	38.5	38.5	824	800	672
24.9	37.45	37.45	815	814	672
29.9	35.05	35.05	862	814	670
35.4	32.3	32.3	921	812	672
0	15	85	796	—	Not reached
3	14.5	82.5	788	675	Not reached
6.4	14.0	79.6	773	691	Not reached
8.7	13.7	77.6	766	701	Not reached
13.0	13.0	74.0	748	718	Not reached
17.8	12.3	69.9	748	736	Not reached
23.3	11.5	65.2	807*	735	Not reached
28.5	10.7	60.8	860*	735*	Not reached
32.5	10.1	57.4	900	727	Not reached
16.6	27.4	56.0	717	690	680
16.0	27.8	56.2	710	689	680
14.9	28.6	56.5	709	694	676
13.90	29.25	56.85	717	693	679
12.00	27.47	60.53	679	675	672
13.03	27.15	59.82	674	—	670
14.82	26.59	58.59	698	677	672
17.64	25.71	56.65	726	676	671
23.50	23.88	52.62	800	673	671
13.5	27.5	59.0	678	673	672
13.43	27.47	59.10	683	674	672
13.7	27.7	58.6	678	—	673
14.63	27.40	57.97	689	—	672
16.48	26.81	56.71	710	—	672

* Best estimate, *see* text.

Any discussion of this paper will appear in a Discussion Section to be published in the June 1958 JOURNAL.

REFERENCES

1. O. Ruff and W. Busch, *Z. Anorg. Chem.*, **144**, 87 (1925).
2. A. G. Bergman and E. P. Dergunov, *Compt. Rend. Acad. Sci. URSS*, **31**, 755 (1941).
3. W. E. Counts, R. Roy, and E. F. Osborn, *J. Am. Ceram. Soc.*, **36**, 12 (1953).
4. E. Beck, *Metallurgie*, **5**, 504 (1908).
5. F. D. Rossini, *et al.*, "Selected Values of Chemical Thermodynamic Properties," U. S. Department of Commerce, National Bureau of Standards (1952).
6. K. K. Kelley, "Contributions to the Data on Theoretical Metallurgy," U. S. Bureau of Mines Bulletin 393 (1936).

Preparation of Pure Silicon by the Hydrogen Reduction of Silicon Tetraiodide

Gustav Szekely

Chemistry Laboratory, Sylvania Electric Products Inc., Flushing, New York

ABSTRACT

The reduction of silicon tetraiodide by hydrogen to form pure silicon and hydrogen iodide has been investigated. The reaction is heterogeneous, taking place on a hot surface. Dense silicon layers as well as crystals can be deposited. The reaction gives a chemical yield as high as 96%, but the over-all best conditions found resulted in a rate of deposition of 4.4 g Si/dm²/hr at a chemical yield of 55%. Data on the purity of the silicon obtained are presented.

The reaction of silicon and iodine to form silicon tetraiodide and the fractional distillation of this compound are discussed. An apparatus is described which permits good control over the composition of a mixture consisting of two gaseous reactants, one of which is generated from the liquid state by vaporization at a uniform rate of flow.

At the inception of this work two processes for preparing pure Si were prominent. In one, Si crystals are deposited in a quartz tube, kept at 950°C, by passing Zn and $SiCl_4$ vapors through it at atmospheric pressure (1). This process is currently used to fill almost the entire demand for Si needed for semiconductor devices in this country. The second (2) permits deposition of solid Si layers on a hot Ta wire (980°C) by thermally decomposing SiI_4 vapor at a greatly reduced pressure.

The aim of this work was to find a means of combining the attractive features of both of these processes, namely convenient deposition of Si in a furnace tube at atmospheric pressure and high volatility of reactants and by-products to insure highest obtainable purity. For this purpose, the hitherto unreported reaction $2H_2(g) + SiI_4(g) = Si(s) + 4HI(g)$ was investigated.

Small-Scale Experiments

In a preliminary set of experiments H_2, purified with respect to O_2, was passed over liquid SiI_4 (mp about 120°C, bp about 300°C) and the vapor mixture then passed through graphite tubes maintained at temperatures between 900° and 1000°C. Small needles as well as more compact crystals were deposited, which by means of x-ray diffraction were unambiguously identified as elemental Si.[1] In these preliminary experiments a relatively low H_2 flow rate was used resulting in a correspondingly low deposition rate, but in one experiment the chemical yield was found to be 96%. This approaches the theoretical yield based on a calculated equilibrium constant. The SiI_4 was prepared by passing vapors of reagent grade I_2 over an inexpensive grade of Si at about 800°C.

[1] Tammann (3) showed that Si and graphite do not react until temperatures several hundred degrees above the temperatures of these experiments are reached. The absence of SiC formation at these temperatures has been confirmed by means of a chemical test, by means of x-ray diffraction, and by means of metallographic examinations.

Apparatus

Apparatus was built to study the reaction further and, incidentally, increase the rate of Si deposition. During operation, H_2 was passed through a catalytic oxygen removal unit, through a drying tower containing silica gel, through a flowmeter, and through a vessel containing liquid SiI_4. The relative amount of SiI_4 entrained in the H_2 stream depended on the vapor pressure of the liquid and thus on the temperature of this vessel. The gas mixture was passed into a graphite cylinder located inside of a quartz tube and maintained at the reaction temperature by means of high frequency induction heating. Silicon deposited in the hottest part of the graphite tube, while unreacted SiI_4 and the by-product HI could be collected in traps. In one experiment HI was frozen out and identified by its boiling point.

Results

Temperature dependence of reaction.—To study the dependence of the rate of deposition of Si on the reaction temperature a set of three runs was made. The apparatus described above was used but, in addition, a preheater was inserted which heated the gas mixture prior to entry into the reaction zone. The reaction temperature was measured with a calibrated thermocouple located at the center of the

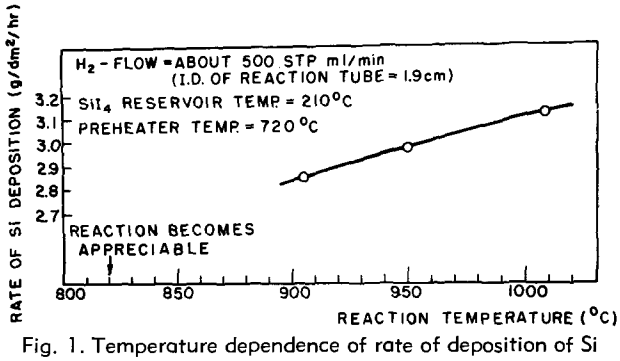

Fig. 1. Temperature dependence of rate of deposition of Si

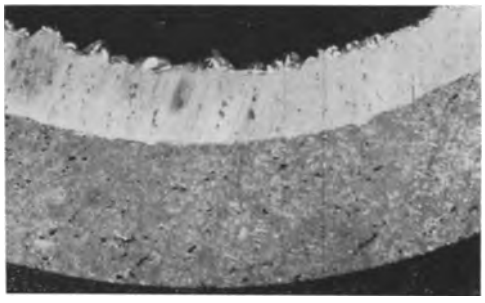

Fig. 2. Sawed through layer of Si on graphite (X8)

inner wall of the reaction tube and indicated the peak of the prevailing temperature distribution. Experimental conditions as well as the results are summarized in Fig. 1. A fourth run indicated qualitatively at which temperature the reaction begins to proceed at an appreciable rate. The low temperature coefficient of the deposition rate in the region studied together with the fact that Si deposited apparently exclusively on the hot wall of the reaction tube seemed to indicate the reaction to be a heterogeneous or surface reaction.

Packed reaction zone experiment.—To further bear on this point, the surface to volume ratio of the reaction zone was increased considerably by packing a graphite tube with small graphite cylinders. The experimental conditions were otherwise comparable to those of the above runs. By this means, it proved possible almost to double the deposition rate (in grams per hour), thus showing that the surface is involved to a considerable extent in this reaction. Presumably, the reactants are adsorbed at the surface, reaction proceeds resulting in the formation of crystalline Si and HI, the latter then being desorbed from the surface.

Deposition rate and chemical yield as functions of reactant gas composition and flow rate.—In order to obtain a further check on the reaction rates obtained so far and to observe whether these rates can be maintained over a longer period of time, a run lasting over 7 hr and at experimental conditions equivalent to those of Fig. 1 was undertaken. The resultant deposition rate turned out to be 2.8 g Si/dm²/hr, in good agreement with the previous shorter runs.

Fig. 2 shows a cross section of the Si thus obtained on its graphite substrate. On several spots of this sample, formation of crystals set in (Fig. 3). Under certain experimental conditions, it proved possible to grow crystals almost exclusively. Needles

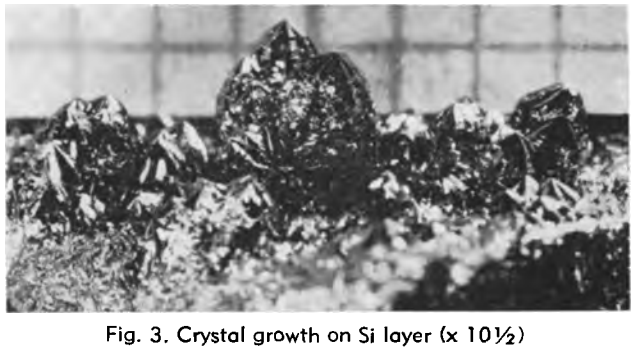

Fig. 3. Crystal growth on Si layer (x 10½)

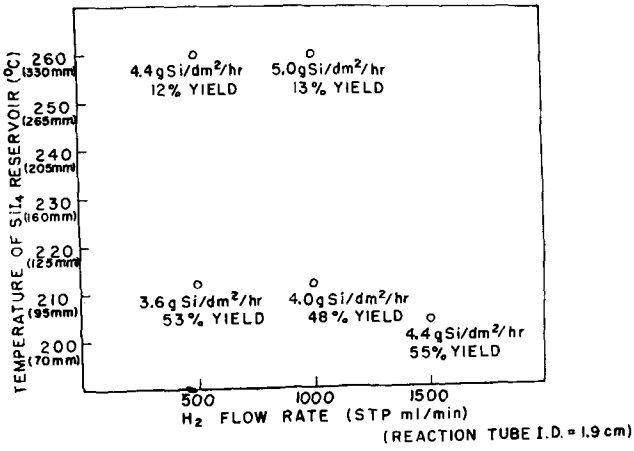

Fig. 4. Rate of deposition and chemical yield obtained in 5 runs at a reaction zone temperature of about 950°C.

as well as more compact types of crystals could be grown. Needles of regular hexagonal cross section were found, while the compact crystals frequently exhibited equilateral triangular faces, apparently (111) faces.

It was now of interest to study at least qualitatively the dependence of the rate of deposition and the chemical yield on the gas composition and velocity. The apparatus used was that described above, the preheater having been eliminated. The results of these experiments are listed in Fig. 4. Underneath

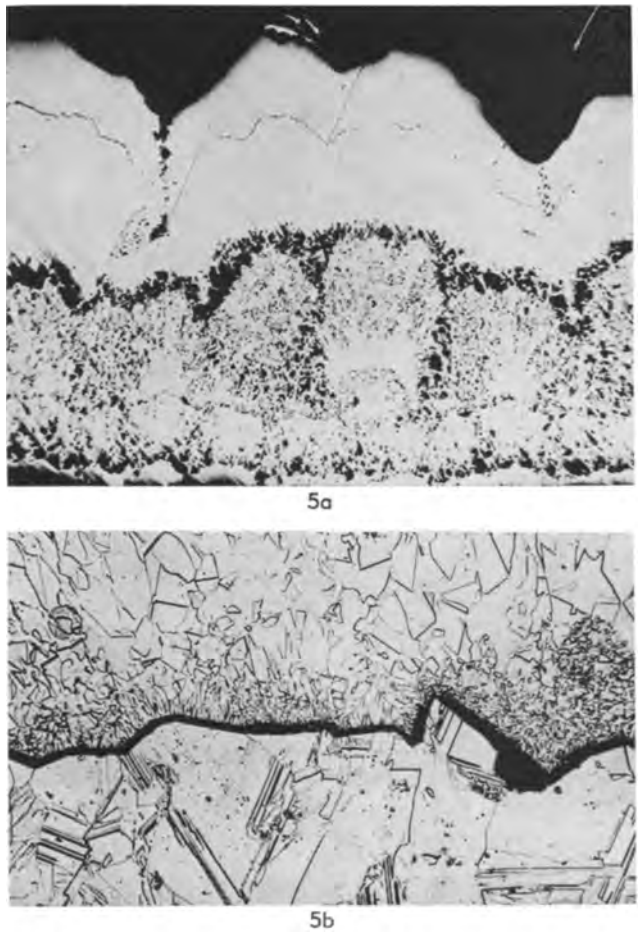

5a

5b

Fig. 5. Series of Si layers on graphite. a. (top) polished (75X before reduction for publication); b. (bottom) detail of outermost two layers; polished and etched (300X before reduction for publication).

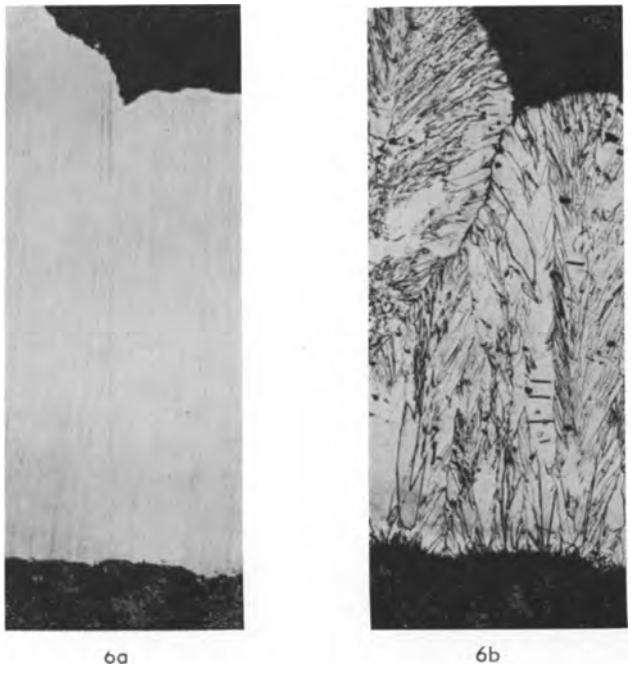

6a 6b

Fig. 6. Metallographic section of Si on graphite deposited by "best" conditions. a. left) polished (75X before reduction for publication); b. (right) polished and etched (75X before reduction for publication).

the iodide reservoir temperatures the corresponding vapor pressures of SiI_4 (4) are written in parentheses to serve as a qualitative guide to the gas composition. Deposition rates throughout this work were determined by weighing the reaction tube before and after the run. The weight thus obtained checked well with that of the Si after removal of the substrate. Chemical yields were determined by using the weight of Si deposited and the weight of the iodide vessel before and after each run.

A cross section of a successive series of Si layers deposited on graphite is seen in Fig. 5a. The outermost dense Si layer is due to the decomposition conditions on the lower right in Fig. 4. The structure of the dense layers is seen in Fig. 5b.

To substantiate these findings, another run was made at an iodide reservoir temperature of 204°C and a H_2 flow rate of about 1500 STP ml/min, but lasting more than 6 hr. The deposition rate found

Table I. Purity of starting Si (97%) and refined product (part Pyrex, part quartz apparatus)

	97% Si starting material	H_2 reduction product	
	Spectrographic analysis	Spectrographic analysis	Activation analysis
Al	$10^4 - 10^5$ ppm	$10 - 10^2$ ppm	
B	$10 - 10^2$ ppm	—	
Ba	$10 - 10^2$ ppm	—	—
Ca	$10^3 - 10^4$ ppm	—	
Cr	$10^2 - 10^3$ ppm	—	—
Cu	$10 - 10^2$ ppm	< 1 ppm	3 ppm
Fe	$10^3 - 10^4$ ppm	—	a trace
Mg	$10 - 10^2$ ppm	< 1 ppm	
Mn	$10^3 - 10^4$ ppm	—	—
Ni	$10 - 10^2$ ppm	—	—
Ti	$10^2 - 10^3$ ppm	—	
As	—	—	0.9 ppm
Na			0.03 ppm
K			0.3 ppm

Table II. Purity of starting Si (99.9%) and refined product (part Pyrex, part quartz apparatus)

	99.9% Si starting material	H_2 reduction product	
	Spectrographic analysis	Spectrographic analysis	Activation analysis
Al	$10^2 - 10^3$ ppm	—	
B	$10 - 10^2$ ppm	—	
Ba	—	—	—
Ca	$10^2 - 10^3$ ppm	—	—
Cr	$10 - 10^2$ ppm	—	—
Cu	$1 - 10$ ppm	< 1 ppm	—
Fe	$10 - 10^2$ ppm	—	—
Mg	$1 - 10$ ppm	—	
Mn	$10 - 10^2$ ppm	—	—
Ni	—	—	—
Ti	$10 - 10^2$ ppm	—	
As	—	—	—
Na			—
K			—
La			a trace

was 4.1g/dm²/hr, in fair agreement with the corresponding short run. Due to an experimental difficulty, the yield could not be confirmed. Fig. 6 shows a metallographic cross section of the deposit, again exhibiting the highly dense structure.

Analytical results.—In the preparation of SiI_4, which was used without further purification for H_2 reduction, two grades of starting material Si were used: a very inexpensive grade analyzing to be about 97% Si and a more expensive grade analyzed to be about 99.9% Si.[2] Typical analyses of these materials and the refined Si obtained from them are given in Table I and II. The spectrographic analyses are general qualitative ones. The activation analyses are described in more detail elsewhere (5). In brief, Si samples are activated by neutron bombardment. Some of the impurity atoms form radioisotopes emitting γ-radiation, the energy of which is measured and the impurity atoms are thereby identified. The γ-scintillation spectrometer permits measurement of these energies on the bombarded Si sample without carrying out any separations. It is seen that the two refining steps, formation of the iodide and reduction of this compound with H_2, resulted in considerable purification.

Substrate study.—As a substrate material for Si deposition, graphite has the advantage of being obtainable in a form of considerably higher purity than, for example, quartz. The porosity of graphite, however, causes the Si deposit to lock into the pores which makes separation of the two materials difficult. A study designed to find a substrate on which Si can be deposited, and subsequently removed readily, showed Ta to be such a material.[3] The reaction tube can be lined by a thin foil of this metal and at completion of a run, Si slides freely off the foil. The foil may require periodic replacement because of H_2 embrittlement. A sample of Si deposited in this way was analyzed by the scintillation spectrometer technique and found to contain 3.8 ppm Ta. After removing 2.8% of the sample weight by etching, the Ta content dropped below the limit of detection of the method, 2.7 ppm Ta. This, borne

[2] Both these materials are obtained from the Electro Metallurgical Company, Union Carbide and Carbon Corporation.

[3] Litton and Andersen (2) have used Ta as a substrate metal in their work with somewhat different chemical species present.

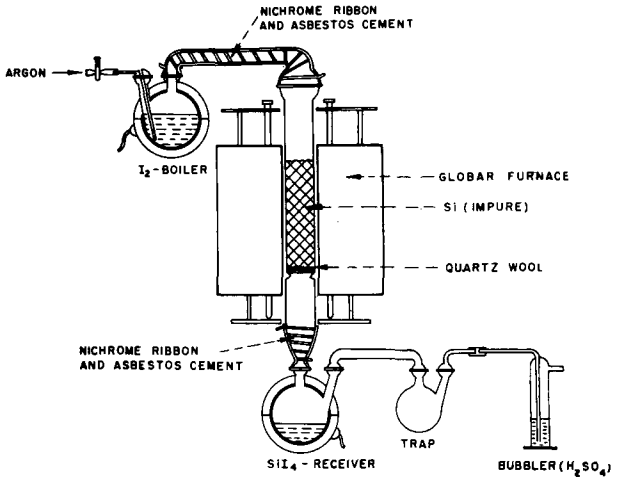

Fig. 7. Large iodination apparatus (fused quartz)

out by other similar experiments, shows the Ta contamination to be located mainly at the surface of the Si sample.

Large-Scale Experiments

It was of interest to experiment with larger equipment. All Pyrex parts in contact with SiI_4 or at elevated temperatures were eliminated and replaced by fused quartz. A fractional distillation apparatus was built to further purify the SiI_4 before its use in the H_2-reduction. The reduction apparatus was built according to a new design.

Iodination

The apparatus to carry out the reaction $Si(s) + 2I_2(g) = SiI_4(g)$ is shown in Fig. 7. Prior to operation, it is flushed with dry argon gas. The temperature of the iodine boiler is then brought up to the boiling point of I_2 (183°C) and the halogen is distilled onto a bed of raw material Si maintained at 750°-850°C (furnace tube ID = 6.2 cm). SiI_4 is collected as liquid at a rate of 1.3 kg/hr. The reaction yield is practically 100%. Frequently after about 7-9 kg of SiI_4 are collected, larger channels begin to form in the Si bed through which unreacted I_2 commences to flow. The apparatus is then opened up and a new charge of Si is placed into it. A particle size of 30-80 mesh is suitable. It has been found desirable, but not always necessary, to etch the Si raw material with HF (aq), rinse, and dry (methanol, ether) prior to insertion into the iodination apparatus.

At the end of a set of iodination runs, a wool-like residue remains in the reaction tube. Qualitative spectrographic analysis showed this Si-rich material to have a total detectable impurity content about six times that of the 99.9% Si starting material. Particularly noticeable is the enrichment of the residue in Al, B, Cr, Fe, and Mg but to a lesser extent also in other elements. These results are further confirmed by a spectrographic analysis of the oxide obtained by hydrolysis of the SiI_4. This material showed a reduction of detectable impurity content by about a factor of 30 below that in the starting Si.

Fractional Distillation

To purify the SiI_4 further, an all-quartz fractionation apparatus was built. The column (1.5 m long, 4 cm ID) was packed with small lengths of quartz tubing (about 5 x 5 mm) and kept adiabatic by the usual means of a compensating heat jacket. The still head was of the swinging funnel type and the fraction splitter also contained a pivoting funnel controlled by a magnet. The apparatus was operated at a throughput of 0.7 kg/hr, a reflux ratio of 9:1, and at atmospheric pressure. (A sample of SiI_4 was refluxed for 10 hr at atmospheric pressure without any decomposition occurring. Subsequently, most of the sample distilled between 300°-302°C.) The size of the fractions in these runs was approximately: 1st fraction = 1.8 kg, main fraction = 4.3 kg, residue in still pot = 1.8 kg.

Table III. Analytical results on fractional distillation of SiI_4 (fused quartz apparatus)

	Distillation residue	First fraction	Main fraction	
Al	$10 - 10^2$ ppm	1 – 10 ppm	1 – 10 ppm	Qualitative spectrographic analysis on hydrolyzed SiI_4 samples.
Cu	<1 ppm	——	——	
Mg	1 – 10 ppm	1 – 10 ppm	1 – 10 ppm	
B	>5 ppm	<0.1 ppm	<0.1 ppm	Spectrographic analysis on hydrolyzed SiI_4 samples (arced in inert atmosphere to suppress SiO bands).
As	15 ppm	11 ppm	1.6 ppm	Activation analysis on SiI_4 samples.
Na	1.4 ppm	1.3 ppm	0.16 ppm	
Fe	10 ppm	<10 ppm	<10 ppm	

An indication of the effectiveness of the fractional distillation apparatus in separating impurities from SiI_4 is obtained from Table III. On the basis of qualitative spectrographic analysis of hydrolyzates the impurity content of the distilled SiI_4 (main fraction) was reduced by a factor of about 6 below that of the iodide collected in the iodination procedure.

Hydrogen Reduction

In building a larger all-quartz H_2-reduction apparatus, it was desired to obtain improved control over the composition of the gas mixture entering the reaction chamber. Fig. 8 shows how this was accomplished. During operation of this equipment, H_2 is passed through a catalytic unit converting traces of O_2 to H_2O, through a silica gel drying tower, through a mechanical filter, into a flow meter, through a preheater maintained at about 720°C, and into a Venturi. Liquid SiI_4 is maintained in a reservoir from which at intervals it is transferred to a U-tube by the application of argon pressure. This U-tube is of special design. In one arm of the U, a cylindrical quartz felt wick is partly immersed in the liquid SiI_4. A heater surrounds the portion of the U-tube containing the unimmersed part of the wick. By capillary action SiI_4 is drawn up into the

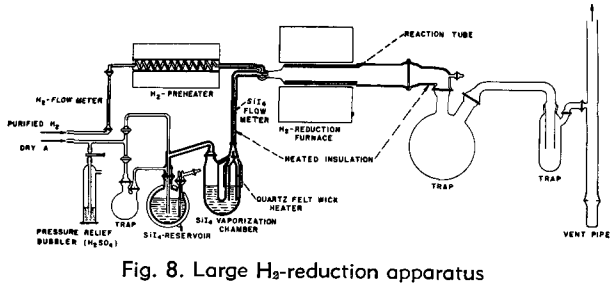

Fig. 8. Large H_2-reduction apparatus

wick and is smoothly vaporized off its surface. The rate of vaporization is controlled by the temperature of the heater. In this way a large range of uniform flow rates can be obtained through the SiI_4 flow meter and into the Venturi, where the two gaseous constituents are thoroughly mixed and passed into the reduction zone. The train is completed by a trap in which unreacted SiI_4 is collected, a second trap where HI can be frozen out, and finally a vent tube through which excess H_2 leaves the system.

At the present time a study is under way with this apparatus to determine the dependence of deposition rate and chemical yield upon the gas composition and velocity. It can be stated that deposition rates closely approaching those obtained with the small apparatus already have been obtained.

Acknowledgments

The contributions of the following are greatly appreciated: C. O. Creter, apparatus construction and experimental runs; K. D. Earley and V. C. DeMaria, glass and quartz apparatus construction; J. F. Cosgrove, scintillation spectrometric analyses; T. J. Veleker, spectrographic analyses; R. L. Rupp, boron determinations; H. Woods, metallographic examinations of Si samples; J. Pacher, x-ray diffraction work.

Much valued discussion is acknowledged with G. H. Morrison, D. J. Bracco, and D. H. Baird.

Manuscript received April 25, 1957. Part of this paper was presented before the Cincinnati Meeting, May 1-5, 1955.

Any discussion of this paper will appear in a Discussion Section to be published in the June 1958 JOURNAL.

REFERENCES

1. D. W. Lyon, C. M. Olson, and E. D. Lewis, *J. (and Trans.) Electrochem. Soc.*, **96**, 359 (1949).
2. F. B. Litton and H. C. Andersen, *This Journal*, **101**, 287 (1954.)
3. G. Tammann, *Z. anorg. u. allgem. Chem.*, **115**, 141 (1921).
4. H. C. Andersen and L. H. Belz, *J. Am. Chem. Soc.*, **75**, 4828 (1953).
5. G. H. Morrison and J. F. Cosgrove, *Anal. Chem.*, **27**, 810 (1955).

Electrolytic Reduction of 2-Amino-4-chloropyrimidine, 2-Amino-4-chloro-6-methylpyrimidine, and 2-Aminopyrimidine

Kiichiro Sugino, Kozo Shirai, Taro Sekine, and Keijiro Odo

Laboratory of Organic Electrochemistry, Department of Chemical Engineering, Tokyo Institute of Technology, Tokyo, Japan

ABSTRACT

2-Amino-4-chloropyrimidine and its 6-methyl derivative give two polarographic waves in the pH region of 7.4-8.9; 2-aminopyrimidine and 2-amino-6-methylpyrimidine yield but a single wave in this region. Macroscale electrolysis at lead or mercury cathodes in ammoniacal medium shows that the first wave of the chlorocompounds arises from reductive dehalogenation. The second wave of the chlorocompounds coincides with the single wave of their parent compounds, the 2-aminopyrimidines, and is ascribed to reduction of the pyrimidine nucleus in both cases. The macroreduction of 2-aminopyrimidine takes place easily at lead or mercury cathodes in ammoniacal medium to yield 2-aminodihydropyrimidine. The mechanism of reduction is tentatively identified as pure electrolytic reduction.

The reduction of 2-amino-4-chloropyrimidine to 2-aminopyrimidine at cathodes of lead and mercury in aqueous methanolic ammonium sulfate was found to be impractical on a preparative scale. On the other hand at spongy cadmium the reduction takes place in 90% yield. At spongy zinc the yield is poorer due to further reduction of the pyrimidine nucleus. However, for the reduction of 2-amino-4-chloro-6-methylpyrimidine zinc is superior to cadmium as a cathode.

2-Amino-4-chloropyrimidine and its 6-methyl derivative suspended in dilute aqueous ethanolic alkali are reduced at a lead cathode to 2-aminopyrimidine and 2-amino-6-methylpyrimidine, respectively, in 60% yield together with further reduced product (1). Further investigation resulted in a method for nearly quantitative production of 2-amino-6-methylpyrimidine (2). 2-Amino-4-chloro-6-methylpyrimidine suspended in an aqueous-methanolic solution of ammonia and ammonium sulfate is reduced at a spongy zinc cathode with greater than 90% yield and about 80% current efficiency. However, when the same procedure was applied to 2-amino-4-chloropyrimidine, 2-aminopyrimidine could not be obtained in greater than 60% yield due to further reduction of the pyrimidine nucleus. If cadmium is substituted for zinc, the yield approaches 90% with a current efficiency of 65% (3).

The anomalous behavior of these compounds prompted polarographic and macroelectrolytic studies which would throw some light on the mechanism

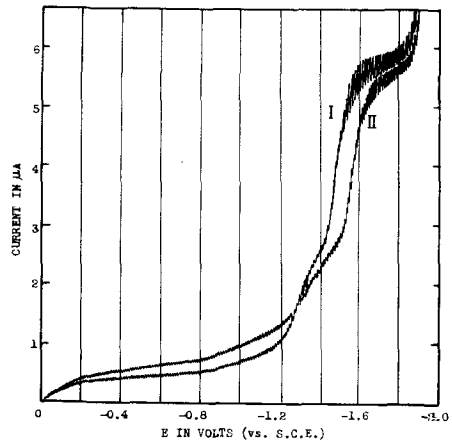

Fig. 1. Polarograms for 2-amino-4-chloropyrimidine and 2-amino-4-chloro-6-methylpyrimidine at pH 7.4. Curve I, 2-amino-4-chloropyrimidine, $E^{1/2}$: —1.35 v (1st wave) and —1.48 v (2nd wave); curve II, 2-amino-4-chloro-6-methylpyrimidine, $E^{1/2}$: —1.36 v (1st wave) and —1.56 v (2nd wave).

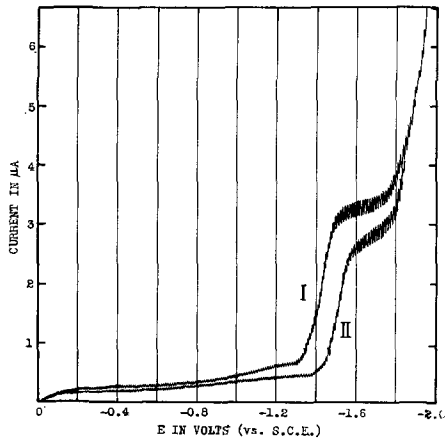

Fig. 2. Polarograms for 2-aminopyrimidine and 2-amino-6-methylpyrimidine at pH 7.4. Curve 1, 2-aminopyrimidine, $E^{1/2}$: —1.45v; Curve II, 2-amino-6-methylpyrimidine, $E^{1/2}$: —1.53 v.

of the reductions. The present paper reports the results of these studies and is also a summary of work on chloropyrimidines carried out in this laboratory.

No literature was found on the electrolytic reduction of these compounds.

Polarographic studies were carried out in the *p*H range of 4.7-10.3. In this paper, only the polarograms at *p*H 7.4 of each compound are shown for purposes of comparison. The polarograms at *p*H 8.9 are included, because this is the approximate *p*H of the macroscale electrolyses.

Experimental

An improved Heyrovsky-Shikata polarograph, Model 52-Type PS, made by Yanagimoto Company, Kyoto, Japan, was used with a galvanometer having an intrinsic sensitivity of 3.29×10^{-9} μa/mm. The sensitivity used at all times was 3.29×10^{-8}. A cell of conventional design having a saturated calomel electrode (S.C.E.) as reference electrode was used. The dropping mercury electrode had a drop time of 3.5 sec at 45 cm mercury height; the capillary constant, $m^{2/3}\,t^{1/6}$, was 1.37 $mg^{2/3}\,sec^{-1/2}$. A TOA DEMPAS type HM-3 *p*H meter and glass electrode was used for *p*H measurements. Stock solutions of the compounds were prepared by dissolving 1 millimole in 50 cc ethanol. 2-Amino-4-chloropyrimidine (mp 164°-165°C dec.[1]), 2-amino-4-chloro-6-methylpyrimidine (mp 182°-183°C), and 2-amino-6-methylpyrimidine (mp 158°-159°C) were prepared and purified according to previously published procedures (2,4). 2-Aminopyrimidine, obtained from Calco Chemical Division, American Cyanamid Company, Bound Brook, New Jersey, was recrystallized from hot benzene (mp 127°-128°C). The buffer solutions used were:

(*a*) CH_3COOH-CH_3COONa, *p*H 4.7-5.6
(*b*) Na_2HPO_4-KH_2PO_4, *p*H 6.8-7.4
(*c*) $Na_2B_4O_7$-H_3BO_3, *p*H 8.0
(*d*) $Na_2B_4O_7$-NaOH, *p*H 8.9-10.3

Test solutions were prepared from the proper volumes of stock and buffer solutions to produce a concentration of the pyrimidine of 6×10^{-4}M/l in all cases. The solutions were deoxygenated with hydrogen for 15 min before use.

[1] All melting points are uncorrected.

Polarographic Studies

Polarographic behavior at pH 7.4.—Polarograms obtained from solutions of the four pyrimidines buffered at *p*H 7.4 are shown in Fig. 1 and 2. Table I lists the values of the diffusion current, i_d, and the diffusion current constant, *I*, for each compound.

The half-wave potentials of the first waves are nearly identical, but the second wave for the 6-methyl compound occurs at a potential approximately 80 mv more negative than that of the parent 2-amino-4-chloropyrimidine.

2-Aminopyrimidine and 2-amino-6-methylpyrimidine each give a single well-defined wave at —1.45 and —1.53 v vs. S.C.E., respectively. Again the half-wave potential for the 6-methyl derivative is 80 mv more negative than that of its parent compound.

Comparison of the polarograms of Fig. 1 and 2 demonstrates the probability that the second waves of the chlorinated compounds correspond to the single waves of the parent compounds. The reduction wave of 2-aminopyrimidine was found to be due to the reduction of pyrimidine nucleus based on the result of macroelectrolysis to be described later. If the second waves of 2-amino-4-chloropyrimidine (and its 6-methyl derivative) are regarded as the reduction wave of the pyrimidine nucleus, the first waves may be due to reductive dehalogenation.

Table I.

	i_d (μa)		I ($i_d/C\ m^{2/3}\,t^{1/6}$)	
	Wave I	Wave II	Wave I	Wave II
2-amino-4-chloropyrimidine	1.02	2.04	1.23	2.48
2-amino-4-chloro-6-methylpyrimidine	0.86	2.17	1.04	2.64
2-aminopyrimidine	—	2.03	—	2.47
2-amino-6-methylpyrimidine	—	1.48	—	1.80

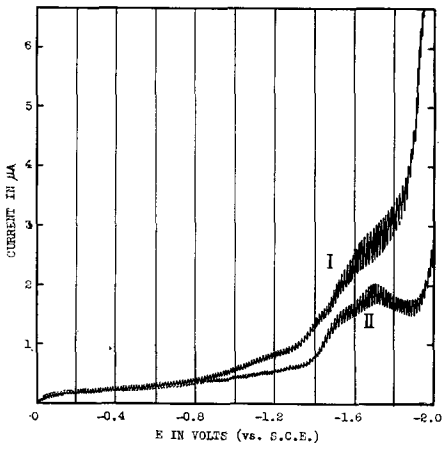

Fig. 3. Polarograms for 2-amino-4-chloropyrimidine and 2-amino-4-chloro-6-methylpyrimidine at pH 8.9. Curve I, 2-amino-4-chloropyrimidine, $E^{1/2}$: —1.40 v (1st wave) and —1.57 v (2nd wave); Curve II. 2-amino-4-chloro-6-methylpyrimidine, $E^{1/2}$: —1.46 v (1st wave) and —1.63 v (2nd wave).

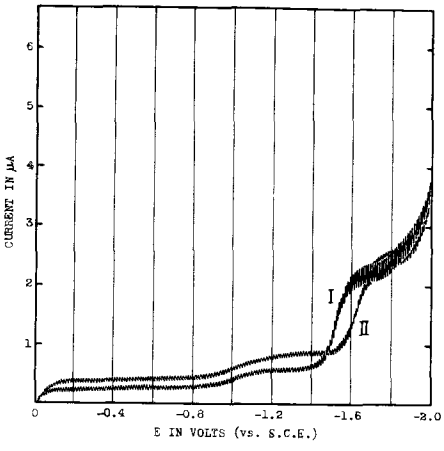

Fig. 4. Polarograms for 2-aminopyrimidine and 2-amino-6-methylpyrimidine at pH 8.9. Curve I, 2-aminopyrimidine, $E^{1/2}$: —1.52 v; Curve II, 2-amino-6-methylpyrimidine, $E^{1/2}$: —1.62 v.

Polarographic behavior at pH 8.9.—Polarograms of solutions of the four compounds buffered at *p*H 8.9 are shown in Fig. 3 and 4. The values of i_d and I are also given in Table II.

These polarograms are of similar shape to those at *p*H 7.4, but the wave heights are considerably lower. The half-wave potentials also shift to more negative values.

Polarographic behavior of hydrogenated pyrimidines.—Polarograms of buffered solutions of the hydrogenated pyrimidines in the *p*H region 4.7-8.9 showed no wave prior to the final current rise of hydrogen ion discharge.

Table II.

	i_d (μa) Wave I	i_d (μa) Wave II	I ($i_d/C\ m^{2/3}\ t^{1/6}$) Wave I	I ($i_d/C\ m^{2/3}\ t^{1/6}$) Wave II
2-amino-4-chloropyrimidine	0.66	0.59	0.80	0.72
2-amino-4-chloro-6-methylpyrimidine	0.92	0.33	1.12	0.40
2-aminopyrimidine	—	1.08	—	1.32
2-amino-6-methylpyrimidine	—	1.19	—	1.45

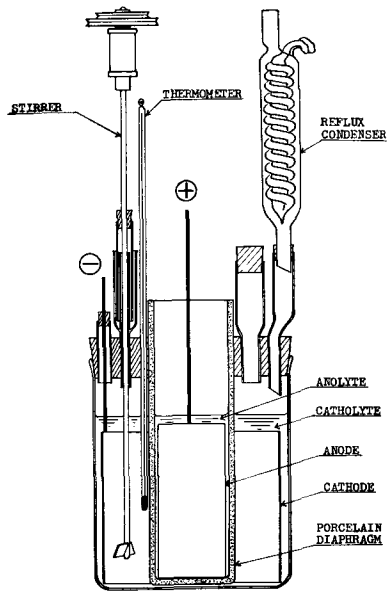

Fig. 5. Electrolytic cell

Macroelectrolysis

Apparatus.—The apparatus used is similar to that described in the preceding paper (5), but is of somewhat different design; details are shown in Fig. 5.

The catholyte (suspensions except for 2-aminopyrimidine) was thoroughly stirred by a glass stirrer rotated at 800 rpm. Anodes were chiefly of platinum in the small-scale electrolyses. In the anolyte containing both sulfate and chloride ions, the pure lead dioxide electrode previously reported by one of the authors could be used.[2]

Results and Conclusions

1. *Preliminary investigation of 2-amino-4-chloropyrimidine.*—Macroreduction of 2-amino-4-chloropyrimidine suspended in an aqueous methanolic solution of ammonium sulfate[3] was carried out at lead or mercury as cathode in order to confirm the postulated polarographic behavior. The electrolysis conditions were:

Anode: Pt, anolyte: 50 cc 0.2*N* H_2SO_4, catholyte: (*a*) 1.30 g, (*b*) 6.50 g 2-amino-4-chloropyrimidine, 6.6 g $(NH_4)_2SO_4$, 45 cc methanol, 45 cc water, a few cc of ammonia added to adjust the *p*H at 7.6, cathode area: Hg, 0.33 dm^2, Pb, 0.65 dm^2, cathodic current density: 1.5 amp/dm^2, temp: (*a*) 12°-18°C, (*b*) 60°-65°C.

It was found that even a small current density of 0.32 amp/dm^2 seemed to exceed the limit, due to the extremely low solubility of the compound in the catholyte. In case (*a*), therefore, 10-11 hr were needed to complete the reduction. At the higher temperature this rate was not increased. In case (*b*), after reduction for 4 hr, 4.8-4.9 g of starting material was recovered unchanged.

[2] This electrode is a thick sheet of pure lead dioxide of rectangular shape described in Method I in Ref. (6) and now being manufactured at Sanwa Pure Chemical Co., Dodobashi-cho, Ohta-ku, Tokyo, Japan.

[3] The reduction of 2-amino-4-chloropyrimidine cannot be carried out in acidic medium due to its instability. In alkaline medium at a lead cathode, some difficulty was experienced performing the reduction described above; at inefficient cathodes such as copper, 2-amino-4-alkoxypyrimidine is formed in the presence of alcohols.

After reduction a large amount of chloride ion was detected in the catholyte, indicating dechlorination by reduction. Then the catholyte was treated according to the procedure described later to isolate 2-aminopyrimidine. However, this did not succeed, suggesting the further reduction of 2-aminopyrimidine. In this procedure, upon evaporation of the ether extract, no material was recovered. The residue was again extracted with ethanol. The evaporation of this extract left a glutinous substance which would not crystallize.

In a separate run, 1.30 g 2-amino-4-chloropyrimidine suspended in the same catholyte was reduced at a lead cathode at a current density of 3 amp/dm^2 at 12°-18°C for 11 hr. After 5 hr of electrolysis an additional 6.6 g ammonium sulfate was added to decrease the cell resistance. After the reduction a saturated solution of ammonium picrate was added to the electrolyte without any prior treatment. A picrate melting at 192°C (recrystallized from ethanol) which differed from that of 2-aminopyrimidine was obtained. This was later identified as the derivative of 2-aminodihydropyrimidine.

From these results it was concluded that the polarographic reduction of 2-amino-4-chloropyrimidine on a macroscale was impractical due to its slowness. Moreover, the reduction yielded the further reduced 2-amino-dihydropyrimidine rather than the desired 2-aminopyrimidine. Therefore different solution compositions and cathode materials were investigated in an attempt to improve the yield of 2-aminopyrimidine.

When the reductions of 2-amino-4-chloropyrimidine and also its 6-methyl derivative in very dilute aqueous ethanolic sodium hydroxide were carried out at a lead cathode, 2-aminopyrimidine and its 6-methyl analog were obtained in 60% yield. If methanol is substituted for ethanol the corresponding 4-methoxy derivatives were obtained due to alkaline methanolysis being more rapid than the reductive dehalogenation.[4] The results are shown in Table III.

The reduction may take place through chemical dehalogenation by the lead cathode followed by reelectrodeposition of lead from the alkaline catholyte.[5] This observation led to the following improved method for the preparation of 2-aminopyrimidine and its 6-methyl derivative.

2. *Preparation of 2-aminopyrimidine and its 6-methyl derivative by the electrolytic reduction of 2-amino-4-chloropyrimidine and 2-amino-4-chloro-6-methylpyrimidine.*—A suspension of 2-amino-4-chloropyrimidine and also 2-amino-4-chloro-6-methylpyrimidine in an aqueous methanolic solution of ammonia and ammonium sulfate was reduced at a higher temperature using a spongy cadmium or zinc cathode respectively to give 2-aminopyrimidine and its 6-methyl derivative in nearly quantitative yields. The completeness of the reduction could be estimated by the disappearance of the crystals of the chloropyrimidines and the appearance of those of the corresponding 2-aminopyrimidines as shown by microscopic examination of the cooled catholyte. These crystals are easily differentiated by their characteristic form.

[4] When an inefficient electrode, such as copper, was used, the product consisted of 2-amino-4-ethoxypyrimidine in the concentrated ethanolic solution.

[5] Sodium hydroxide was useful to dissolve lead chloride formed on the electrode surface by chemical reaction. Ammoniacal catholyte was inefficient for the same purpose, because it could not dissolve lead chloride.

Table III.

Anode: Platinum; anolyte: 0.5% sodium hydroxide solution; catholyte: (1) 6.45 g 2-amino-4-chloropyrimidine, 75 cc 80% ethanol, 0.4 g NaOH, (2) 7.18 g 2-amino-4-chloro-6-methylpyrimidine, 85 cc 80% ethanol, 0.4 g NaOH; cathodic current density: 2.5-5.0 amp/dm^2; temp: 40-55°C; amount of current: 3.0-3.5 times the theoretical.

Run No.	2-amino (6-Me) pyrimidine* g	%	Others %
1	2.81	60	about 40
2	3.75	60	40

* mp 2-aminopyrimidine 118°C, 2-amino-6-methylpyrimidine 156-157°C.

After reduction, the catholyte was neutralized with acid and the insoluble matter filtered off. The solution was then evaporated to dryness under reduced pressure. The residue was treated with sodium bicarbonate to regenerate free 2-aminopyrimidine (or its 6-methyl compound) which was then extracted with hot benzene or ether. The extract was evaporated to dryness to give crystals of 2-aminopyrimidine (or its 6-methyl compound).

The results of the reduction of 2-amino-4-chloropyrimidine at a cadmium cathode are shown in Table IV; the yields are the optimum obtainable.

The results of the reduction of 2-amino-4-chloro-6-methylpyrimidine at zinc (2) are shown in Table V.

It was observed that the reduction at zinc and at cadmium began to occur when the temperature was raised sufficiently even though current was not passed. This observation suggested that the reaction might again be a purely chemical one of 2-amino-

Table IV. Reduction of 2-amino-4-chloropyrimidine at Cadmium

Anolyte: 40 cc 0.2*N* H_2SO_4; cathode: spongy cadmium deposited on iron from a catholyte containing 7.32 g $Cd(OH)_2$; catholyte: 6.50 g 2-amino-4-chloropyrimidine, 6.6 g $(NH_4)_2SO_4$, 3.3 cc 28% NH_4OH, 100 cc 1:1 methanol water, *p*H 7.2-7.4; current: 1 amp; current density: 2.0 amp/dm^2; temperature: 72°-73°C; current consumed: 3.38 amp-hr.; yield: 4.30 g (91%) 2-aminopyrimidine, mp 124°-125°C.

Table V. Reduction of 2-amino-4-chloro-6-methylpyrimidine at zinc

Anolyte: 50 cc 0.2*N* H_2SO_4; cathode: spongy zinc deposited on zinc from catholyte containing $ZnSO_4 \cdot 7H_2O$; starting catholyte: 14.36 g 2-amino-4-chloro-6-methylpyrimidine, 2.5 g $(NH_4)_2SO_4$, 90 cc 1:1 methanol water, a little NH_4OH added to adjust the *p*H to 7-9; catholyte of runs 2-4: the catholyte of the previous run after removal of the 2-amino-6-methylpyrimidine which crystallized out on cooling to −10°C addition of 14.36 g of starting material and readjustment of *p*H; current density: 2.5 amp/dm^2; temp. 60°-65°C.

Run	Current passed (amp-hr)	Yield (g)	%	Current efficiency %
1	6.50	10.02 (8.63) *	91	75
2	5.57	(9.62)	88	85
3	5.83	(10.10)	93	85
4	6.80	(10.21)	94	74

* Figures in parentheses are yields of product obtained on cooling the catholyte to −10°C.

chloropyrimidines with the cathode metal and that the current was being used simply to reduce the metal ion thus formed back to metal. However, little noticeable change occurred at the electrode surface.

3. *Electrolytic reduction of 2-aminopyrimidine at a lead cathode in ammoniacal medium.*—In an attempt to duplicate the reduction corresponding to the polarographic wave and to identify the product resulting from the reduction of the pyrimidine nucleus a run was made with 2-aminopyrimidine as starting material at a lead cathode.

Anode: platinum; anolyte: 60 cc 2*N* H_2SO_4; catholyte: 19.0 g of 2-aminopyrimidine, 6.6 g $(NH_4)_2SO_4$, 200 cc water, *p*H of 6.0-8.0 maintained by adding sulfuric acid during the electrolysis; amp: 3; cathodic current density: 3.0 amp/dm^2; temp: 10°-12°C. The theoretical amount of current for 4H was passed.

It was found that hydrogen began to be evolved vigorously at the cathode after an amount of electricity equivalent to 2H[6] had been passed. It was also found that the reduction product was stable only at low temperatures in aqueous medium so that cooling in an ice-bath was necessary to obtain reasonable yields.

The reduction product was obtained as the picrate only, by adding a saturated solution of ammonium picrate to the ice-cooled catholyte after reduction. (The yield was 54.1 g or 83% of theoretical for the dihydro compound.) The picrate melted at 192°C and decomposed on crystallization from hot water; it can be recrystallized from ethanol without change in melting point, indicating a single compound.

Anal. calcd for $C_{10}H_{10}O_7N_6$: C, 36.8; H, 3.09; N, 25.8
Found: C, 36.6; H, 3.08; N, 25.7

In order to convert this compound to a stable product for identification a catalytic hydrogenation of the catholyte was carried out by the following procedure.

Fifty cc of the catholyte was reduced by hydrogen at atmospheric pressure in the presence of 2 g Pd-$CaCO_3$ catalyst (Pd: 1.3%) at 15°C. After absorbing about 1 mole of hydrogen based on moles of picrate obtained (749 cc at 0°C and 760 mm) 10.9 g of a picrate was obtained. The picrate melted at 179°-180°C after recrystallization from ethanol. The monohydrochloride and carbonate derived from the picrate melted at 145°-146°C and 237°C (dec.), respectively.

Anal. Picrate:
calcd for $C_{10}H_{12}O_7N_6$: C, 36.6; H, 3.69; N, 25.6
Found: C, 36.5; H, 3.44; N, 25.4

Hydrochloride:
calcd for $C_4H_{10}N_3Cl$: C, 35.4; H, 7.43; Cl, 26.2
Found: C, 35.4; H, 7.17; Cl, 26.0

The picrate may be that of 2-amino-tetrahydropyrimidine[7] based on the quantity of hydrogen absorbed and the elemental analysis. Decomposition by alkali (a mixture of 2.5 g of the hydrochloride, 10 g NaOH in 150 cc water was heated) resulted in the formation of 1,3-diaminopropane (dihydrochloride; mp 243°C, calcd for $C_3H_{12}N_2Cl_2$; N, 19.05; found: N, 18.80), ammonia, and carbon dioxide. The absence of formic acid among these products eliminated the possibility that the compound was 2-aminohexahydropyrimidine or contained any of the latter as contaminant.[8] The decompositions in alkali are formulated as:

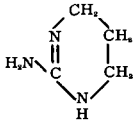

$+2\,H_2O = H_2N(CH_2)_3NH_2 + CO_2 + NH_3$

and:

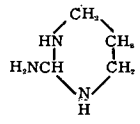

$+\,2H_2O \rightarrow NH_2(CH_2)_3NH_2 + HCOOH + NH_3$

Catalytic hydrogenation did not occur after the catholyte had been heated to decomposition.

From these results, the product of the electrolytic reduction of 2-aminopyrimidine was shown to be an unstable 2-amino-dihydropyrimidine.

The reduction of 2-aminopyrimidine at a mercury cathode was found to proceed in the same manner as that at a lead cathode and to the same product. The reduction of 2-amino-6-methylpyrimidine, will be reported later.

Nature of the reduction process.—By combining the results of the polarographic study and the macroelectrolysis, the nature of each reduction process is considered to be as follows:

1. It has been indicated by polarography that 2-amino-4-chloropyrimidine and its 6-methyl compound are reduced electrolytically not only to the dechlorination product, but also to a hydrogenation product of the pyrimidine nucleus. Results of preliminary macroelectrolysis at a lead or mercury cathode in ammoniacal solution substantiated these observations.

2. The reduction of 2-amino-4-chloropyrimidine and its 6-methyl compound at cadmium and zinc, respectively, in ammoniacal solution seems to be of a different nature from the polarographic reduction. This may be the chemical reaction of the starting material with the cathode surface in the presence of ammonia which dissolves the resulting metal chloride, the current being used mainly to redeposit metal on the cathode. In this case, the reduction may be carried out at the potential at which the deposition of metal occurs if the current density is less than the limiting one for the reduction of metal ion to metal. However, if a current greater than the limiting one is applied or the electrolysis is continued after all 2-amino-4-chloropyrimidine or its 6-methyl compound disappears, a hydrogenation product of the pyrimidine nucleus will be formed.

[6] The value of "n" obtained by the analysis of polarogram at *p*H 7.4 was about 1.3.

[7] Recently, Smith and Christensen (8) obtained 2-amino-dihydropyrimidine (?) and 2-amino-tetrahydropyrimidine by the catalytic hydrogenation of 2-aminopyrimidine and 2-amino-4,6-dichloropyrimidine, respectively. They reported that the dihydrochlorides melted at 231°C (2-amino-dihydro-) and 208°C (2-aminotetrahydro-). The reference to the patent of Sugino in their paper is incorrect.

[8] Kitani and Sodeoka (7) carried out the hydrogenation of 2-amino-4,6-dichloropyrimidine with a Pd catalyst. They reported 2-aminohexahydropyrimidine as the final product, the picrate and carbonate of which melt at 179°-180° and 237°C, respectively. They did not carry out the decomposition of this compound by alkali.

The reason for obtaining 2-aminopyrimidine and its 6-methyl compound quantitatively by a suitable combination of chloropyrimidine with the metal appears to depend entirely on the nature of the chemical reaction. 2-Aminopyrimidine and 2-amino-6-methylpyrimidine were not obtained quantitatively at both metals. Of the two metals, zinc is more active than cadmium. The parent 2-amino-4-chloropyrimidine was more reactive than its 6-methyl compound.

3. The reduction of 2-aminopyrimidine at lead cathode in ammoniacal solution seems to be essentially a pure electrochemical reduction corresponding to the polarographic wave. This gives a hydrogenation product of pyrimidine nucleus, the unstable 2-aminodihydropyrimidine.

Summary

1. 2-Amino-4-chloropyrimidine or its 6-methyl compound is reduced polarographically first to 2-aminopyrimidine or its 6-methyl compound and then to the hydrogenated pyrimidine. At cathodes of lead or mercury in an ammoniacal catholyte macroreduction proceeds in two successive rapid steps to a hydrogenation product of the pyrimidine nucleus. However, it is of dubious practical preparative value due to slowness necessitated by low solubility of the starting material. On the other hand, the macroreduction of 2-aminopyrimidine itself on account of its solubility proceeds very easily even at low temperature to the unstable 2-aminodihydropyrimidine in a pure state. This is the reaction corresponding to the polarographic wave.

2. At cathodes of cadmium or zinc at a higher temperature another reaction can occur. 2-Amino-4-chloropyrimidine or its 6-methyl compound is reduced to the corresponding 2-aminopyrimidine. Almost quantitative yields may be obtained by the selection of cathode metal suitable to each compound.

Manuscript received Nov. 3, 1955. This paper was prepared for delivery before the Pittsburgh Meeting, Oct. 9-13, 1955.

Any discussion of this paper will appear in a Discussion Section to be published in the June 1958 JOURNAL.

REFERENCES

1. K. Sugino and K. Shirai, *J. Chem. Soc. Japan, Pure Chemistry Section*, **70**, 111 (1949).
2. K. Sugino, K. Odo, and K. Shirai, *ibid.*, **71**, 396 (1950); K. Shirai, Y. Usui, and K. Odo, *J. Electrochem. Soc. Japan*, **20**, 28 (1952).
3. K. Shirai, *ibid.*, **21**, 387 (1953).
4. K. Sugino, K. Odo, K. Shirai, and Y. Sugito, *J. Chem. Soc. Japan, Industrial Chemistry Section*, **53**, 219 (1950).
5. M. Yamashita and K. Sugino, *This Journal*, **104**, 100 (1957).
6. K. Sugino, *Bull. Chem. Soc. Japan*, **23**, 115 (1950).
7. K. Kitani and H. Sodeoka, *J. Chem. Soc. Japan, Pure Chemistry Section*, **74**, 624 (1953).
8. V. H. Smith and B. D. Christensen, *J. Org. Chem.*, **20**, 829 (1955).

Preparation of Feed Materials for Electrolytic Production of Thorium Metal

Charles E. Fisher and James L. Wyatt

Horizons Incorporated, Cleveland, Ohio

ABSTRACT

A potentially economical method for production of thorium metal is the electrolysis of fused thorium tetrachloride in sodium chloride. Preparation of suitable feed constituents for the electrolyte is described. Thorium nitrate was converted to thorium tetrachloride by aqueous chemical and thermal decomposition techniques; intermediate steps include the formation of an ammonium complex which may be dehydrated.

During the past decade much emphasis has been placed on the development of processes for the production of fissionable materials, thorium as well as uranium. Because of the greater availability of Th, and probable lower cost, it seems almost a certainty that the civilian atomic energy program will utilize its potentialities to the fullest extent in the not too distant future.

Dunworth (1) has outlined the possible role of Th in nuclear energy and emphasized its potentiality. Carlson, *et al.* (2) discussed all phases of Th production from ore processing to finished metallurgical products, following techniques developed at Ames. This is the only method for producing Th that has been operated on a large scale. A brief description of the more promising methods of preparing Th is given by Hampel (3).

Driggs and Lilliendahl (4) produced Th electrolytically, and Kaplan (5) describes the preparation of Th by electrolysis of fused salt systems.

This paper describes the pilot and development programs which were carried out in order to produce Th-bearing cell feed materials suitable for conversion to metal. A companion paper (6) describes in part the metal production phase.

An exhaustive laboratory evaluation here (7) of the various methods for preparation of Th led to the conclusion that electrolysis of the fused chloride is

by far the most feasible method for metal production. Accordingly, this system has been established, and has been operated on a small tonnage basis to produce quantities of high quality metal.

Feed materials processing is not too dissimilar from the Ames procedures (8). Thorium nitrate is reacted with sodium carbonate to produce thorium oxycarbonate, which is dissolved in HCl, the chloride complexed with NH_4Cl, dried, and separated by thermal decomposition. The anhydrous thorium tetrachloride is utilized as cell feed for preparation of Th metal.

Deposits of metal produced by electrolysis, consisting of coarse, granular metal interspersed with salt, are removed from the cells periodically, crushed, and recovered by aqueous techniques. The process lends itself well to remote operation, is relatively economical to operate, and utilizes inexpensive reagents and standard chemical engineering equipment for all processing steps except electrolysis. Recognized engineering organizations have estimated that production costs of a different order of magnitude may be realized as compared with reported costs for the Ames process (7).

Feed Materials Preparation

Any metal production operation dealing with fuel materials for atomic power must of necessity encompass techniques which provide for utilization of materials from which fission products have been extracted. While many changes undoubtedly will occur during the coming years, at the present time a nitric acid solution step is contemplated; it therefore is a requirement of the process that the feed materials preparation end be able to process nitrates.

The development operations herein reported have been established with this requirement in mind, the starting raw material being crystalline form of hydrated thorium nitrate. The process is equally suitable for carbonates, oxalates, oxides, and other compounds.

Conversion Chemistry

The electrolytic process requires anhydrous chloride feed. Early experiments demonstrated that aqueous Th solutions evaporated to dryness decomposed to produce first a thorium oxychloride, then a thorium oxide, giving off hydrogen chloride gas. Even under conditions during which hydrogen chloride atmospheres under pressure were maintained, dewatering of thorium chloride without oxide formation proved to be a major problem.

Thorium tetrachloride forms a complex with NH_4Cl which can be dehydrated under atmospheric pressure with either an inert atmosphere or a partial HCl atmosphere to produce an anhydrous thorium complex. The complex may then be broken up by heating to an elevated temperature, driving off NH_4Cl, and leaving anhydrous thorium chloride.

Pilot Preparation of Feed Materials

Process

Figure 1 is a flow diagram of the procedure which was established for the aqueous preparation of anhydrous cell feed. The operation involves the following steps: preparation of thorium nitrate and sodium carbonate solutions; precipitation of thorium oxycarbonate; dissolution of thorium oxycarbonate in HCl; complexing with NH_4Cl; dehydration; sublimation; and fusion.

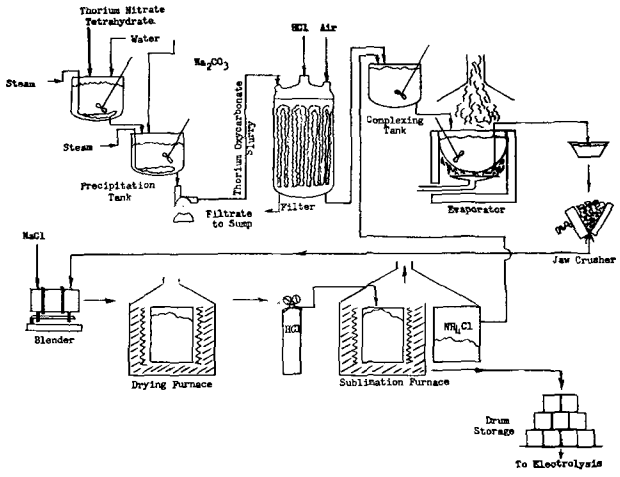

Fig. 1. Flow diagram for preparation of cell feed

Thorium nitrate was supplied by the Atomic Energy Commission in crystalline, hydrated form. It was dissolved in hot water and added directly into a solution of sodium carbonate, where the following reaction occurred:

$$Th(NO_3)_4 \cdot xH_2O + 2Na_2CO_3 \xrightarrow{H_2O} ThOCO_3 + 4NaNO_3 + CO_2 + xH_2O$$

The thorium oxycarbonate precipitation is quantitative.

Subsequent steps included settling the precipitate, decanting the nitrate solution, repulping in fresh water, repeating the decant step, and finally filtering on a vertical pressure-type Oliver filter. Filtrates were found to be completely free of radioactivity and hence could be directed to waste disposal without any unusual safeguards.

Then 37% HCl was pumped directly into the pressure filter, where it reacted with the thorium oxycarbonate to produce an aqueous thorium chloride solution. The enclosed pressure filter was ideally suited to the dissolution operation, since it confined all radioactive vapors.

The thorium chloride solution was pumped into a mixer vessel to which were added 2 moles of solid NH_4Cl per mole of contained Th. A slight excess over this amount was generally desirable. The aqueous chlorides were boiled down to a syrupy consistency, to a maximum temperature of approximately 126°C, and cast into a chill mold for solidification. The solidified cake was then crushed, mixed with NaCl, and fed into a dryer where the temperature was raised to 260°C. Dehydration of the solid complex was thus effected without going through a fused state again.

The dry chloride complex was placed into a denitrating vessel where NH_4Cl was sublimed off, at temperatures ranging from 600° to 800°C. In this manner a completely fused product, precisely the composition required for electrolysis, was obtained from the over-all processing. The fused product was

handled in a number of ways, including: solidification in the crucible, followed by mechanical removal; tapping into a cold wall receiver; removal in the molten state by siphon techniques.

In an integrated plant, in which cell feed would be manufactured adjacent to the electrolytic plant, the most logical procedure would be to pump or tap the molten salt directly into the electrolytic cells without going through intermediate stages of solidification, crushing, and feeding to the cells as a solid constituent.

Equipment

Specifications on the metal product limited contaminants to parts per million or less and corrosion of equipment had to be held to a minimum. Materials of construction and equipment designs were therefore governed to a large extent by the purity criteria. Wherever possible, rubber-lined equipment was used. This included dissolving tanks, filter, and pumps.

For dissolving thorium nitrate, sodium carbonate, and precipitating thorium oxycarbonate, two 1200-gal rubber-lined tanks were used. These vessels were provided with openings at the top for introduction of solids and for removal of gases such as CO_2 during the precipitation. Tanks were equipped with rubber-covered agitators and Monel immersion heaters. Outlets at the bottom of each tank provided for transfer either of liquid solution or of slurry to respective receivers. In some operations rubber diaphragm pumps were used for liquid transfer; in others an all-plastic pump was provided for this service. All piping was polyvinyl chloride.

Filtration of the thorium oxycarbonate solution was carried out in a vertical Oliver filter containing seven leaves of varying sizes. The shell of the filter was rubber coated, and filter leaves were constructed of polystyrene. The filter cloth was Vinyon. Pressure was applied by means of compressed air which was prefiltered.

On completion of a filtration cycle HCl was pumped into the filter, and liquor was drawn off into a rubber-lined holding vessel which fed a specially designed evaporator. Originally, glass-lined steel pots were selected for the evaporation cycle; but excessive breakage of the lining, contamination of the product by glass particles, and pickup of boron necessitated elimination of any form of glass in contact with the boiling liquor.

As an alternative, a semicylindrical vessel was constructed from stainless steel and lined with a graphite lining approximately ¾ in. thick. A thin layer, approximately ½ in. thick, of densely packed lampblack was placed between the graphite pot liner and the stainless steel shell itself. The entire unit was supported in a brick furnace and was underfired with gas burners. The evaporator was equipped with an agitator constructed of graphite and an exhaust system for ducting away vapors emanating from the evaporation process. The evaporator was operated on a batch basis, fresh liquor being added incrementally until the concentrated solution nearly filled the evaporating pot. This material was then cast into a stainless steel chill mold, where it solidified into pigs. The pigs were crushed to −¼ in., mixed with NaCl, and placed in a graphite furnace for dehydration.

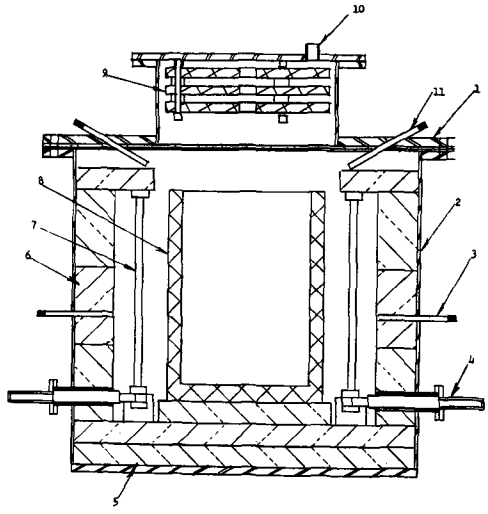

Fig. 2. Denitration furnace used to decompose ammonium-thorium complex.

The dehydrating apparatus consisted of a Glo-bar resistor heated furnace, insulated with firebrick and equipped with a graphite crucible concentrically positioned. Dimensions of the crucibles were approximately 18 in. in diameter and 26-30 in. high, with a capacity of between 200 and 300 lb of total feed material. Approximately 8 hr were required to bring the mass to a temperature of 260°C, and an additional 8 hr to complete the processing of each batch. The temperature was maintained at 260°C until all the water had been driven off, as indicated by a Carl Fischer analysis for moisture.

The graphite vessel containing the dehydrated salt was then placed in a totally enclosed sublimation unit heated by graphite resistors and capable of much higher temperatures. The graphite crucibles were interchangeable between the two types of furnaces, allowing for direct transfer from one to the other. The sublimation furnace was equipped with a side-arm condenser, a sparging system for maintaining HCl atmospheres, and a gas off-take to a scrubber system. The furnace shell was constructed of nickel, and all internal components other than insulation were made of graphite. Fig. 2 is a cross section of a typical furnace used for sublimation.

Operations

Operations were scaled on the basis of accommodating a precipitate batch containing 165 kg of Th. Thorium nitrate in crystalline form, the starting raw material, generally averaged between 41 and 43% Th by weight.

City water heated to 80°C was run into the oxycarbonate precipitation tank to a level of approximately 44 in. (equivalent to 510 gal). The tank agitator was started and an immersion heater used in order to maintain uniform temperature. While thermal equilibrium was being established at 80°C, 179.5 kg of light soda ash were weighed up and 157 kg dissolved in hot water. A hold-out of approximately 22½ kg was found desirable in practice,

since the free acidity of thorium nitrate was somewhat variable. The hold-out material was used to complete the chemical precipitation reaction when near-equilibrium was approached.

The soda ash solution was formulated for approximately 7.5% caustic by weight, a concentration which proved to be one of the determining factors for achieving the desired physical properties in the precipitated thorium oxycarbonate.

Simultaneously with preparation of the sodium carbonate solution, hot water was run into the thorium nitrate dissolver tank to a level of 50 in. (equivalent to 420 gal), and the immersion heater and agitator turned on. When thermal equilibrium was reached, 410 kg of thorium nitrate were added and completely dissolved. This represents a solution of approximately 10% Th by weight.

On completion of the dissolving steps, the thorium nitrate solution was pumped into the sodium carbonate tank at an initial rate of approximately 20 gal/min. Continuous agitation was maintained during the mixing step.

No noticeable reaction occurs until chemical equilibrium is approached. At this point a white precipitate begins to form, followed shortly thereafter by severe foaming. Careful regulation of the rate of introduction of thorium nitrate solution was required at that point; it generally was necessary to stop the thorium nitrate addition several times in order to permit the foam to subside, a factor attributable to limited tank volume.

Upon reaching equilibrium, the foaming subsided entirely; however, equilibrium was seldom reached until some or all of the additional 22.5 kg of soda ash was added incrementally. Completion of the reaction was determined by pH measurement, the final pH being adjusted to 7.6-8.0 with soda ash.

Thorium oxycarbonate when precipitated cold tends to be somewhat slimy and difficult to filter. Careful control of concentration, temperature of precipitation, and pH, however, results in a product which is granular and is relatively easy to filter.

The precipitated slurry, containing approximately 15% solids, was agitated for 5-10 min, allowed to settle for 6 hr, and the supernatant liquor decanted. Additional quantities of water were added, the slurry agitated, allowed to settle and again decanted. The decantation-wash cycle was repeated twice, followed by further additions of water in order to provide a suitable slurry for feed to the pressure filter.

The thorium oxycarbonate slurry served as a reserve for several filtration and hydrochlorination batches. The filter was limited in capacity to approximately 36 kg of contained Th per batch, this representing a buildup on the leaves of approximately 1¼ in. in thickness. Some three hours were required for each filtration cycle, followed by a washing cycle of from 1½ to 3 hr, using water heated to 120°F. Washing generally was continued until the wash water showed negative results when tested for nitrate ion, and specific gravity measurements indicated 1.0000 ±0.0001. The cake was then blown with filtered air, using pressures of approximately 25 psi, for a period of 2 hr in order to remove most of the contained moisture.

On completion of the partial dehydrating step, HCl (37%) was sprayed into the top of the filter through a pressure opening, a vigorous reaction occurring between the acid and the thorium oxycarbonate. Introduction of acid was intermittent, by-product gases being vented through a port in the lid into a scrubber system. Approximately 1 hr was required to complete the dissolution step, converting all of the Th values to $ThCl_4$ in aqueous solution. Sampling of the liquor provided analytical data from which the quantity of excess free HCl was determined. This was adjusted to a minimum of 5% HCl by volume.

The hydrochlorinated Th solution was then pumped into a rubber-lined storage tank, it serving as a reservoir for intermittent feed to the graphite-lined evaporator. Ammonium chloride in proportions of approximately 2.1 moles of NH_4Cl per mole of Th contained was added in the rubber-lined holding vessel prior to transfer of the complexed liquor into the evaporator.

Evaporation of the chloride complex was carried out semicontinuously, with additions of further solution as the volume increased. When the evaporator was nearly filled with concentrated liquor, the consistency being similar to syrup, the entire batch was cast into stainless steel molds and allowed to solidify in air. The casting operation took place generally between 135° and 145°C, this being partially dependent on the excess amount of HCl in the bath, the mole fraction of NH_4Cl, and certain other minor factors. Agitation was maintained throughout the evaporation cycle until increased viscosity discouraged the use of agitators.

Cast pigs of the NH_4Cl-Th complex were crushed and placed in a storage bin for feed to the next step in the operation. The cast and crushed materials contained 3-10% moisture.

To the crushed chloride complex was added enough NaCl to produce a product $ThCl_4$-NaCl analyzing approximately 35% Th by weight. After thorough blending, the mix was placed in graphite crucibles with a capacity of approximately 17 kg of contained Th, and loaded into Glo-bar heated furnaces for the dehydration step. Three furnaces of this type were required in order to process materials at the rate supplied by the evaporation cycle, each dehydration stage requiring approximately 8 hr after reaching a temperature of 260°C. The entire dehydration cycle required nearly 24 hr, including the heat-up, holding, and cooling stages. Throughout this operation a continuous bleed of HCl gas was maintained through the furnace, moisture and excess HCl being ducted to a scrubber system.

Thermocouples centered in the charge two-thirds of the way down from the uppermost layer were utilized in the determination of temperatures in the charge. Actual temperatures achieved near the perimeter of the crucible were somewhat higher than 260°, this being not too critical as long as the entire mass reached that temperature. It was found by experiment that the moisture content remaining

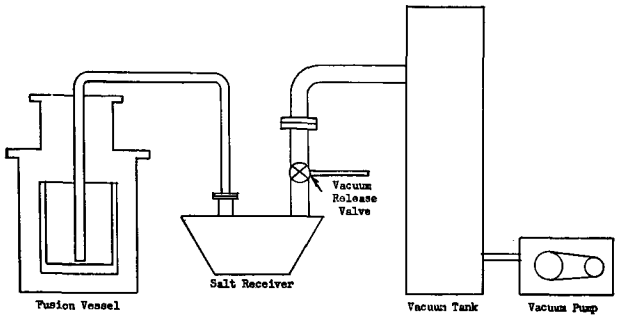

Fig. 3. System used to siphon molten salt from fusion vessel

after such treatment was always less than 1%, and generally less than 0.5%, as determined by the Carl Fischer method.

On completion of dehydration the charge was transferred to a graphite resistor-heated furnace, completely enclosed from the atmosphere. The unit was evacuated, flushed with argon, and heated under inert atmosphere to a temperature of 600°-860°C, during a cycle time of approximately 36 hr. Some 18 hr were required to reach the desired temperature; the vessel was held at temperature for 3 hr, and the remainder of the time was consumed in cooling. On completion of the cycle the graphite crucible was removed, the charge chipped out, jaw crushed, and stored as feed material for the electrolytic operation.

Alternatives to the sublimation process included the use of HCl as an atmosphere in preference to argon. Comparable results were obtained, it being a matter of economics to determine which system to use.

As a modification to the chipping operation, later aspects of the program incorporated heating the NaCl-$ThCl_4$ mix to a temperature somewhat above the fusion point, i. e., to 750°C, in order to achieve thorough homogenization of the charge and provide an easier method of removal from the crucible. The design of the equipment precluded tapping directly, but a system was devised wherein siphoning techniques were utilized to transfer the molten salt from the graphite crucible to a water-cooled nickel salt receiver. Figure 3 shows the siphoning system.

In operation a vacuum surge tank was preevacuated to a level of 100-500μ pressure. A quick-opening valve, positioned between the surge vessel and the tapping receiver, was then opened, causing the duplex system to equalize at a level of 4-6 psi of negative pressure. This pressure differential immediately effected a flow of molten salt through a connecting tube between the receiver and the graphite vessel containing the molten salts. Once established, flow continued until all molten salt had been transferred. In a typical salt-transfer operation of this type, some 250-300 lb could be transferred in less than 5 min through a ½ in. diameter nickel tube. By this technique the entire system could be maintained under a partial vacuum or inert atmosphere until the entire salt mass had been solidified without fear of moisture contamination. The Th salt cake resulting from the siphon operation was then chipped from the receiving vessel, crushed, and stored for use as cell feed to the electrolytic operations.

Table I. Typical analysis of thorium-sodium chloride cell feed

Constituent	Analysis, wt %
Thorium	33.2
Sodium	18.2
Chlorine	48.4
Insolubles*	0.06
Moisture	0.04
Total	99.9

* Insolubles determined by dissolving salt sample in water, treating residue with HCl. Insolubles represent ThO_2.

Cell feed materials were analyzed prior to acceptance for electrolysis and to provide a basis for Th accountability. Table I shows a typical analysis of the product.

Operational Efficiencies

The process as described was operated on a continuous basis for several months and supplied a small tonnage of cell feed for electrolytic operations which were carried out concurrently. Feed material preparation was operated on a 3-shift, 5-day week basis with a crew of two men per shift, operations being controlled and supervised by a single crew leader.

During full-scale production operations the normal yield was 100 kg of contained metal per week. The over-all metal recovery for the life of the campaign averaged 92.8% on the basis of total Th charged. During the last three months this average was increased to 95%, and probably could be improved upon with certain minor additions and modifications to equipment. The percentages indicated are recovered quantities, and do not include Th absorbed into crucible linings in the furnacing equipment.

Summary and Conclusions

This paper has presented a method for the production of Th cell feed which has been found suitable in quantity and quality for moderate-scale experimental electrolytic production of Th metal. In general, the equipment and materials of construction described have proven adequate.

Several hundred pounds of adequate quality Th metal for Atomic Energy Commission applications were produced from cell feed manufactured by the method described above. It is therefore concluded that the procedures are feasible and might be considered for commercial production operations should the need arise.

Acknowledgments

The pilot operation for preparation of Th cell feed was carried out under Atomic Energy Commission Contract AT(30-1)-1335. Permission to publish this paper is gratefully acknowledged.

The work was carried out under the general direction of Eugene Wainer, Director of Research of the laboratory, by personnel in the Department of Process Engineering. The efforts of these men led to a successful pilot operation in a minimum of time, and their commendable efforts are hereby acknowledged.

Manuscript received Jan. 23, 1957.

Any discussion of this paper will appear in a Discussion Section to be published in the June 1958 JOURNAL.

REFERENCES

1. "Proceedings of the International Conference on the Peaceful Uses of Atomic Energy," 16 vol., United Nations Press, New York (1956).
2. *Ibid.*, Vol. 1, pp. 335-336.
3. Hampel, "Rare Metals Handbook," Chap. 23, pp. 429-454, Reinhold Publishing Co., New York, (1954).
4. F. H. Driggs and W. C. Lilliendahl, *Ind. Eng. Chem.*, **22**, 1302 (1930).
5. Ref. 1, **9**, pp. 74-106.
6. E. L. Thellmann and J. L. Wyatt, *This Journal*, To be published.
7. B. C. Raynes, J. C. Bleweiss, M. E. Sibert, and M. A. Steinberg, "Electrolyte Preparation of Thorium Metal," To be published in *Journal of Metals*.
8. Ref. 1, **8**, pp. 184-187.

Stoichiometric Numbers and Hydrogen Overpotential

A. C. Makrides

Department of Chemistry, The University of Texas, Austin, Texas

ABSTRACT

An extended definition of the stoichiometric number of a mechanism is given and its use is demonstrated with a number of proposed hydrogen evolution reaction mechanisms.

Stoichiometric numbers were introduced in electrochemical kinetics in 1939 by Horiuti and Ikusima (1). A generalized treatment was recently given by Parsons (2).

Stoichiometric numbers provide an additional criterion for differentiating between possible reaction mechanisms. The expected stoichiometric number for a mechanism, commonly defined as the number of times the postulated rate-determining step is repeated when the over-all reaction occurs once, may be compared with a number computed from measured quantities. While the usefulness of this procedure is obvious, its employment is limited by difficulties in measuring overpotentials at current densities close to the exchange current. However, it is probable that, with recent techniques, stoichiometric numbers can be determined for an increasingly wider variety of systems.

The Parsons Derivation

In the theory of electrode processes given by Parsons (2), stoichiometric numbers are formally introduced by assuming that the completion of one over-all process, as represented by the stoichiometric equation, requires the formation and decomposition of ν activated complexes. The stoichiometric number, ν, is defined as some integer, equal to or greater than unity, with which the rate-determining equation must be multiplied to yield the stoichiometric equation.[1] Expressions for ν in terms of observable quantities are then derived by employing transition state theory to calculate specific reaction rate constants. Among other parameters, the Galvani potential difference, $\Delta\phi$, between metal and solution is used. Quantities p (and q), defined as the electrical part of the work of transferring the reactants (or products) from the original (or final) state to a state immediately preceding the energy barrier for the reaction, are also introduced.

[1] However, as shown below, even with this definition, ν can be less than unity.

Of the two expressions for ν derived by Parsons (2), one is applicable to states slightly removed from equilibrium and gives ν in terms of $(\partial\eta/\partial i)_{\eta\to 0}$, where η is the overpotential and i the current density. The other involves quantities $\left(\frac{\partial \ln i}{\partial \eta}\right)$ evaluated at large values of η for both the anodic and cathodic parts of the η vs. i curve. This paper deals with the former case.

Although Parsons' treatment is satisfactory on the whole, it is restricted to a certain extent by the assumptions involved in his derivation. The use of quantities $\Delta\phi$, p, and q, for example, implies a separation of the total work of transfer across an interface into electrical and chemical parts,[2] an operation which is not generally feasible (3). A more serious limitation of Parsons' derivation lies in his definition of stoichiometric numbers (2). As noted above, it rests essentially on the statement: let the rate determining reaction occur ν times when the over-all reaction occurs once. This definition apparently precludes their use in cases where two competing reaction mechanisms, both yielding the same over-all reaction but having different stoichiometric numbers, operate at comparable rates. An example of such a case is hydrogen evolution on a cathode where both discharge of hydrogen ions and electrochemical removal of adsorbed hydrogen atoms are slow.

An objection of a different nature may be raised on the following grounds. Parsons' treatment is based on absolute reaction rate theory and refers to the general case of an electrochemical reaction. Accordingly, the equilibrium postulate of absolute re-

[2] While for any given composition of the reaction system "the final expressions involve changes in the Galvani potential difference which can be measured" (2), difficulties still arise from the use of Galvani potentials. For example, to compare results obtained with a given electrode in solutions of different composition, a constant $\Delta\phi$ is specified. If the solutions are so concentrated that single ion activities cannot be calculated, the specification is of no practical value since it cannot be carried out. Similar difficulties are encountered in separating the dependence of p and q on $\Delta\phi$ and solution composition.

action rate theory is assumed for states far removed from thermoydnamic equilibrium. Although this assumption is probably satisfied for reactions slow enough to be measurable, proof of its validity is lacking (4-6). The postulate is rigorously applicable only to reversible reactions proceeding at dynamic equilibrium. Parsons' procedure, for the cases of interest here, is complicated thus unnecessarily: expressions are derived first for states far removed from equilibrium, and are then extrapolated to the equilibrium state for which the postulate is exact. The alternative procedure, i.e., extrapolation from the equilibrium state, is preferable.

It is shown below that an extended definition of the stoichiometric number of a mechanism can be formulated from the kinetic behavior of systems neighboring equilibrium without recourse to any particular model of reaction rate theory. While the extended definition coincides with that of Parsons for single reactions, it can also be used in the case of two or more competing reaction mechanisms.

Reaction Rates Close to Equilibrium

The conditions satisfied by rate laws at states close to equilibrium have been examined by Prigogine and co-workers (7,8), and by Manes, Hofer, and Weller (9), among others. Prigogine, Outer, and Herbo (8) have shown that for sufficiently small values of the affinity, A, the net reaction rate, v, is proportional to the affinity:

$$v = L\,(A/T) \qquad \text{(I)}$$

Here

$$A = -\sum_i a_i\,\mu_i$$

with a_i the coefficients in the corresponding stoichiometric equation, μ_i the chemical potentials, and T the temperature. Equation (I) follows from the fact that v and A vanish together at equilibrium. It assumes that there are no discontinuities in the region of equilibrium and that the forward and reverse reactions proceed at finite rates. Subject to these conditions, Eq. (I) has extreme generality, being independent of all hypotheses as to the reaction mechanism. The coefficient of proportionality, L, is however a function of both thermodynamic and nonthermodynamic variables, and its magnitude depends on the actual mechanism of the reaction.

A more detailed examination shows that for simple reactions L is equal to v^e/R, where v^e is the rate at equilibrium (in either direction), and R the gas constant. A demonstration is given by Prigogine (7). Consider the reaction

$$A + B \rightarrow C$$

with a net rate in the direction indicated

$$v = \vec{v} - \overleftarrow{v} = \vec{k}c_Ac_B - \overleftarrow{k}c_C = \vec{k}c_Ac_B\left(1 - \frac{\overleftarrow{k}}{\vec{k}}\frac{c_C}{c_Ac_B}\right)$$

where $\vec{k}/\overleftarrow{k} = K(T)$, the equilibrium constant. The chemical potentials, assuming an ideal system, are

$$\mu_i = \mu_i^\circ(T) + RT \ln c_i$$

and the affinity

$$A = -\sum_i a_i\,\mu_i^\circ(T) - RT\sum_i a_i \ln c_i = RT \ln \frac{K(T)}{c_A^{-1}c_B^{-1}c_C}$$

Substituting in the expression for the net rate

$$v = \vec{v}\,[1 - \exp(-A/RT)] \qquad \text{(II)}$$

For small values of A, i.e., $A/RT << 1$,

$$v = \frac{v^e}{R}\,(A/T) \qquad \text{(III)}$$

where v^e ($\vec{v}^e = \overleftarrow{v}^e$) is the value of $\vec{v}$ at equilibrium ($A = 0$).

Only rarely, however, does the stoichiometric equation coincide with the rate laws for the reaction. Generally, the over-all reaction is the sum of a series of simple reactions which frequently involve species not appearing in the stoichiometric equation. To treat this case, an analysis given by Manes, Hofer, and Weller (9) is used.

Let

$$aA + bB + \ldots \rightarrow mM + nN + \ldots$$

be the stoichiometric equation for the over-all reaction, written, for convenience, with the smallest possible integral coefficients $a, b, \ldots m, n, \ldots$. If v_f is the rate of the forward reaction and v_r that of the reverse,

$$v_f = V_f[(A), (B), \ldots (M), (N), \ldots (X), \ldots]$$
$$v_r = V_r[(A), (B), \ldots (M), (N), \ldots (X), \ldots]$$

where V_f and V_r are, in general, complex algebraic functions of the concentrations of reactants and products and are assumed to be the actual rate laws, independent of the arbitrary coefficients of the stoichiometric equation. Species not appearing in the over-all reaction, for example, catalysts, are denoted by (X). The dependence of V_f and V_r on (X) must be such that, at equilibrium, (X) does not appear in the ratio V_f/V_r.

The only restrictions imposed by classical thermodynamics on the rate laws are

$$\frac{v_f}{v_r} = 1 \text{ for } A = 0; \frac{v_f}{v_r} > 1 \text{ for } A > 0 \qquad \text{(IV)}$$

To fulfill conditions (IV) it is sufficient to assume

$$\frac{v_f}{v_r} = \frac{k_f}{k_r}\left[\frac{(A)^a\,(B)^b\ldots}{(M)^m\,(N)^n\ldots}\right]^z \text{ with } \frac{k_f}{k_r} = K^z \qquad \text{(V)}$$

where z is any constant, positive number, and K the equilibrium constant. An example of such functions V_f and V_r which includes the case of simultaneous reactions, is given by Manes, Hofer, and Weller (9).

From (V)

$$\ln\frac{v_f}{v_r} = z\left[\ln K - \ln\frac{(M)^m\,(N)^n\ldots}{(A)^a\,(B)^b\ldots}\right] = z\frac{A}{RT}$$

Expanding around $A = 0$ and neglecting higher order terms [$A << RT$]

$$v = v_f - v_r = z\frac{v^e}{R}\,(A/T) \qquad \text{(VI)}$$

where $v^e = v_f^e = v_r^e$, the rate in either direction at equilibrium. Equation (VI) is of the form (I) with $L = zv^e/R$.

Stoichiometric Numbers

The constant of proportionality appearing in Eq. (I) can be decomposed, as shown by Eq. (VI), into the rate at equilibrium and a constant z. The origin of this last factor can be demonstrated best by an example.

Consider the reaction

$$2A + 2B \rightarrow C_2$$

and assume for the mechanism

$$A + B \rightarrow C \qquad \text{(slow)} \qquad \text{(i)}$$

$$C + C \rightleftarrows C_2 \qquad \text{(fast)} \qquad \text{(ii)}$$

Provided we are sufficiently close to equilibrium, the net rate of (i) is

$$v_i = \frac{v_i^e}{R}(A_i/T)$$

where

$$A_i = \mu_A + \mu_B - \mu_C$$

Since the mechanism assumes step (i) to be rate determining, $v_i/v_i^e = v/v^e$. Substituting

$$v = \frac{v^e}{R}(A_i/T)$$

The affinity of the over-all reaction is[3]

$$A = 2A_i + A_{ii}$$

According to the assumed mechanism, $A_{ii} \cong 0$, and $A_i = (\frac{1}{2})A$.[4] Substituting

$$v = \frac{1}{2}\frac{v^e}{R}(A/T)$$

The factor z gives therefore the relation between the affinity for the over-all reaction and the affinity for the rate-determining step or steps. This relation is determined by the mechanism of the reaction. The value of z for any assumed mechanism may be obtained by an analysis similar to the above, or by comparing Eq. (V) with the expression for the ratio, at equilibrium, of the forward to the reverse reaction rates as given by the mechanism. Examination of the usual kinetic expressions for reactions with a single rate-determining step, including cases involving equilibria between reactants and/or products and intermediate species, and of mechanisms where a steady state is postulated (e. g., collision theory), shows that z gives the number of times the over-all reaction occurs when the rate-determining step occurs once. In these cases therefore one may identify z with the reciprocal of the stoichiometric number as defined by Parsons (2). In cases of reactions proceeding through more than one path, a value of z can again be calculated using the same procedure. This case is examined below.

Conditions (IV) allow z to take any constant, positive value. In view of the above, z is usually equal to the ratio of two small integers and is smaller than one in most cases. There are however reactions for which z is larger than one [the corresponding value of ν, as defined by Parsons (2), being less than one]. Thus for chain mechanisms (10), the slow step is often followed by a series of fast reactions involving additional molecules of the reactants so that the stoichiometric equation may be repeated several times for each occurrence of the slow step. This is also true for the mechanisms of certain photochemical reactions (10).

Competing reaction mechanisms.—A reaction proceeding through only two competing reaction mechanisms is considered. The argument can be extended easily to any number of competing reaction mechanisms.

Let the reaction

$$A_2 + B_2 \rightarrow 2C$$

proceed through the independent mechanisms

[1] $A_2 \rightleftarrows A + A$ (i)

$B_2 \rightleftarrows B + B$ (ii)

$A + B \rightarrow C$ (slow) (iii)

and

[2] $A_2 + B_2 \rightarrow 2C$ (slow)

The net rate of the reaction is $v = v_1 + v_2$ and similarly $v^e = v_1^e + v_2^e$, where the subscripts (1) and (2) refer to reaction mechanisms [1] and [2] respectively. If $A << RT$,

$$v_1 = \frac{v_1^e}{R}(A_{iii}/T) = \frac{1}{2}\frac{v_1^e}{R}(A/T)$$

$$v_2 = \frac{v_2^e}{R}(A/T)$$

Therefore

$$v = \frac{(\frac{1}{2}v_1^e + v_2^e)}{R}(A/T)$$

If $v_1^e >> v_2^e$, $v = (\frac{1}{2})\frac{v^e}{R}(A/T)$ and $z = \frac{1}{2}$, while for $v_2^e >> v_1^e$, $v = \frac{v^e}{R}(A/T)$ and $z = 1$. If $v_1^e = v_2^e$ then $v^e = 2v_1^e$ and

$$v = \frac{3}{4}\frac{v^e}{R}(A/T)$$

form which $z = \frac{3}{4}$. In general, $\frac{1}{2} \leqq z \leqq 1$, the value of z within this interval being determined by the relative rates of mechanisms [1] and [2].

Electrochemical Systems

Electrochemical systems involve phases which may be at different electrical potentials. With charged species the μ's used above depend on the electrical state of the phase as well as on its chemical composition. It is therefore convenient in these cases to speak of electrochemical potentials, $\tilde{\mu}_i$, and electrochemical affinities, $\tilde{A} = -\sum_i a_i \tilde{\mu}_i$ (11). With this change in notation, Eq. (VI) reads

$$v = z\frac{v^e}{R}(\tilde{A}/T)$$

[3] In general, $A = \sum_\rho \alpha_\rho A_\rho$, where A is the affinity for the over-all reaction, A_ρ the affinities of individual steps, and the α_ρ constants. Prigogine (7) writes $A = \sum_\rho A_\rho$ and similarly omits the factor z in the expression for L. It is clear, however, that in the cases examined by Prigogine the stoichiometric and rate equations coincide.

[4] To be exact, $A_{ii} = \frac{2v_i^e}{v_{ii}^e}A_i$. Since the mechanism postulates $v_{ii}^e >> v_i^e$, A_{ii} may be neglected in comparison to A_i and, therefore, $2A_i + A_{ii} \cong 2A_i \cong A$.

To express this relation in terms more familiar in electrochemical kinetics, consider a half-cell reaction occurring at an electrode immersed in a solution of constant composition. A current i is impressed on the electrode and the electrode potential is determined as a function of i. The affinity of the reaction taking place is

$$\tilde{A} = -\sum_i a_i \tilde{\mu}_i = -\sum_i a_i (\tilde{\mu}_i - \tilde{\mu}_{i_o})$$

where $\tilde{\mu}_{i_o}$ are the electrochemical potentials at equilibrium ($\sum_i a_i \tilde{\mu}_{i_o} = 0$). If η is the difference between the potentials with current i flowing and at equilibrium

$$\tilde{A} = -\sum_i a_i (\tilde{\mu}_i - \tilde{\mu}_{i_o}) = nF\eta$$

where n is the number of electrons involved in the half-reaction and F is Faraday's constant.[5] Here η is equal to the difference between the electrode-solution electric potential difference when current i is flowing and that at equilibrium, i.e., η is the overpotential [*see* Parsons (2)].

Noting that

$$v/v^e = i/i_o$$

where i is the net current and i_o the exchange current, Eq. (VI) may be written in the form

$$i = z\frac{nFi_o}{R}(\eta/T) \quad |\eta| << \frac{RT}{r}$$

or

$$\frac{1}{z} = \frac{nFi_o}{RT}\left(\frac{\partial\eta}{\partial i}\right)_{\eta\to 0} \qquad \text{(VII)}$$

which is the relation derived by Parsons (2) with $z = 1/\nu$.[6] Equation (VII) can be used to calculate z for any reaction for which the overpotential curve for $\eta \to 0$ and i_o are known. The exchange current can be measured with systems which are essentially at equilibrium (say, by use of tracers). Commonly however i_o is found by extrapolation from the region of large values of η, where the reverse reaction may be neglected, to $\eta = 0$. This procedure assumes that the reaction mechanism remains the same over the range of η values considered.

It should be noted that the actual numerical values of z, or ν, are trivial in the sense that they depend on the arbitrary formulation of the stoichiometric equation. This is reflected in Eq. (VII) which shows that z depends on n, the number of electrons involved in the half-reaction as written. However, relative values of z for different reaction mechanisms, which may be used as an additional criterion for the reaction mechanism, are independent of n.

Application to Hydrogen Overpotential

In this section expected stoichiometric numbers for various possible reaction mechanisms for the hydrogen evolution reaction, $2H^+ + 2e \to H_2$, are derived by using the procedure given above. Slow combination, slow discharge, slow electrochemical, and the case where both the rates of discharge and of electrochemical removal of adsorbed hydrogen atoms are slow, are considered. The first three cases demonstrate the procedure used here, the results being identical with counting the number of times the rate determining step occurs when the over-all reaction occurs once. The last case is an example of a mechanism involving two simultaneous reaction paths of comparable rates.

1. *Slow combination.*—The mechanism postulates (12),

$$H^+ + e \overset{\text{fast}}{\rightleftharpoons} H_{ads} \qquad \text{(i)}$$

$$H_{ads} + H_{ads} \overset{\text{slow}}{\to} H_{2(g)} \qquad \text{(ii)}$$

If $A << RT$

$$v = \frac{v^e}{R}(A_{ii}/T)$$

but

$$A = 2A_i + A_{ii} \cong A_{ii} \qquad \text{(VIII)}$$

from which

$$v = \frac{v^e}{R}(A/T)$$

Comparing to (VI), $z = 1$ (or $\nu = 1$).

Alternatively, the rates of the forward and reverse reactions are

$$i_c = k_f x^2$$
$$i_a = k_r P_{H_2}(1-x)^2$$

where x is the fraction of the surface covered by adsorbed hydrogen atoms. From (i) and at equilibrium

$$\frac{x}{1-x} = (\text{Const.})\, a_{H^+}$$

Therefore at equilibrium

$$\frac{v_f}{v_r} = 1 = \frac{k_f}{k_r}\frac{x^2}{P_{H_2}(1-x)^2} = \frac{k_f}{(\text{Const.})k_r}\left[\frac{a_{H^+}^2}{P_{H_2}}\right]$$

and by comparing to (V), $z = 1$.

2. *Slow discharge* (13).—(*a*) Slow discharge followed by fast combination: The mechanism postulates

$$H^+ + e \overset{\text{slow}}{\to} H_{ads} \qquad \text{(i)}$$

$$H_{ads} + H_{ads} \overset{\text{fast}}{\rightleftharpoons} H_2(g) \qquad \text{(ii)}$$

Sufficiently close to equilibrium,

$$v = \frac{v^e}{R}(A_i/T) \qquad \text{(IX)}$$

and from (VIII) with $A_{ii} \cong 0$, $A = \frac{1}{2}A$. Therefore

$$v = \frac{1}{2}\frac{v^e}{R}(A/T)$$

and $z = \frac{1}{2}$.

(*b*) Slow discharge followed by fast electrochemical: In this case (i) is followed by

$$H_{ads} + H^+ + e \overset{\text{fast}}{\rightleftharpoons} H_2(g) \qquad \text{(iii)}$$

The rate is again given by (VIII). Here, however,

[5] It is assumed that the chemical reaction is the only cause of irreversibility present in the system. In other words, the contribution of concentration and ohmic overvoltages to the measured potential difference is assumed to be negligible.

[6] Since the rate of entropy production, $nF\eta i$, is positive, η and i must have the same sign. On cathodic polarization η is negative and therefore i must be given a negative sign.

$$A = A_i + A_{iii}$$

and for $A_{iii} \cong 0$,

$$v = \frac{v^e}{R}(A/T)$$

from which $z = 1$.

3. *Slow electrochemical.*—The mechanism postulates (14)

$$H^+ + e \overset{\text{fast}}{\rightleftharpoons} H_{ads} \qquad \text{(i)}$$

$$H_{ads} + H^+ + e \overset{\text{slow}}{\rightarrow} H_2(g) \qquad \text{(iii)}$$

The rate is

$$v = \frac{v^e}{R}(A_{iii}/T)$$

and from (IX) with $A_i \cong 0$,

$$v = \frac{v^e}{R}(A/T)$$

so that $z = 1$.

4. *Slow discharge and slow electrochemical.*—There are two possible reaction schemes here

(a)

$$H^+ + e \overset{\text{slow}}{\rightarrow} H_{ads} \qquad \text{(i)}$$

$$H_{ads} + H_{ads} \overset{\text{fast}}{\rightleftharpoons} H_2(g) \qquad \text{(ii)}$$

$$H_{ads} + H^+ + e \overset{\text{slow}}{\rightarrow} H_2(g) \qquad \text{(iii)}$$

(b)

$$H^+ + e \overset{\text{slow}}{\rightarrow} H_{ads} \qquad \text{(i)}$$

$$H_{ads} + H^+ + e \overset{\text{slow}}{\rightarrow} H_2(g) \qquad \text{(iii)}$$

with the rate of (ii) negligible. This may be the case if there is strong localized adsorption of hydrogen with a negligible rate of surface migration, or, less likely, appreciable surface migration but a high energy of activation for surface combination of two adsorbed atoms.

For mechanism (a)

$$2A_i + A_{ii} = A$$

and

$$A_i + A_{iii} = A$$

so that with $A_{ii} \cong 0$ and $v^e = v_i{}^e + v^e{}_{iii}$,

$$v = \frac{1}{2}\frac{v^e}{R}(A/T)$$

from which $z = \frac{1}{2}$. Therefore, if (i) is slow and (ii) much faster than (iii), the occurrence of reaction (iii) does not change the value of the stoichiometric number (compare mechanism 2a).

For mechansism (b)

$$v_i = \frac{v_i{}^e}{R}(A_i/T)$$

$$v_{iii} = \frac{v^e{}_{iii}}{R}(A_{iii}/T)$$

with

$$A_i + A_{iii} = A$$

The steady-state condition, $d[H_{ads}]/dt = 0$, is $v_i = v_{iii}$. If $v^e{}_{iii} > v^e{}_i$, then the rate of the over-all reaction at equilibrium is $v^e = v^e{}_i$. If, say, $v^e{}_{iii} = 10v^e{}_i$, then

$$v = \frac{v^e}{R}(A_i/T)$$

From the steady-state condition, $v^e{}_i A_i = v^e{}_{iii} A_{iii}$, or $A_i = 10A_{iii}$. Therefore, $A_i = (10/11)A$ and substituting

$$v = \frac{10}{11}\frac{v^e}{R}(A/T)$$

from which $z = 10/11$. Thus, for $v^e{}_{iii} >> v^e{}_i$, $z \rightarrow 1$ (slow discharge followed by fast electrochemical). Similarly, if $v^e{}_i >> v^e{}_{iii}$, $z \rightarrow 1$ (slow electrochemical).

If $v^e{}_i = v^e{}_{iii}$, then $A_i = A_{iii}$, or $A_i = A/2$, and

$$v = \frac{v^e}{R}(A_i/T) = \frac{1}{2}\frac{v^e}{R}(A/T)$$

so that $z = \frac{1}{2}$. In general, z approaches 1 as either step becomes much faster than the other, and $\frac{1}{2}$ when $v^e{}_i \sim v^e{}_{iii}$.

The statement (15) that an experimental value of 0.116 v for the Tafel slope at 25°C coupled with $z = \frac{1}{2}$ ($\nu = 2$) uniquely determines 2a above as the mechanism of the hydrogen evolution reaction is incorrect. Mechanisms 4a and 4b (provided $v^e{}_i \sim v^e{}_{iii}$) yield the same values for these two quantities.

Manuscript received Oct. 11, 1956.

Any discussion of this paper will appear in a Discussion Section to be published in the June 1958 JOURNAL.

REFERENCES

1. J. Horiuti and M. Ikusima, *Proc. Imp. Acad. Tokyo*, **15**, 39 (1939); J. Horiuti, *J. Res. Inst. Catalysis*, **1**, 8, (1948).
2. Roger Parsons, *Trans. Faraday Soc.*, **47**, 1332 (1951).
3. E. A. Guggenheim, "Thermodynamics," Interscience Publishers, Inc., New York (1950).
4. E. A. Guggenheim and J. Weiss, *Trans. Faraday Soc.*, **34**, 57 (1938).
5. B. J. Zwolinski and H. Eyring, *J. Am. Chem. Soc.*, **69**, 2702 (1947).
6. H. M. Hulburt and J. O. Hirschfelder, *J. Chem. Phys.*, **17**, 964 (1949).
7. I. Prigogine, "Thermodynamics of Irreversible Processes," C. C. Thomas Publishers, Springfield, Ill. (1955).
8. I. Prigogine, P. Outer, and Cl. Herbo, *J. Phys. Chem.*, **52**, 321 (1948).
9. M. Manes, L. J. E. Hofer, and Sol Weller, *J. Chem. Phys.*, **18**, 1355 (1950).
10. K. J. Laidler, "Chemical Kinetics," McGraw-Hill Book Co., New York (1950).
11. P. Van Rysselberghe, "Electrochemical Affinity," Hermann and Co., Paris (1955).
12. J. Tafel, *Z. physik. Chem.*, **34**, 187 (1900).
13. *See*, for example, Ref. (2) above.
14. A. Frumkin, *Acta Physicochim.*, **7**, 475 (1937).
15. J. O'M. Bockris, "Modern Aspects of Electrochemistry," Academic Press Inc., New York (1954).

The Composition of Copper Complexes in Cuprocyanide Solutions

H. P. Rothbaum[1]

Department of Physical Chemistry, University of Liverpool, Liverpool, England

ABSTRACT

The static potential of copper in a range of cuprocyanide solutions was measured at 20° and at 80°C. The values agreed well with those calculated on the assumption that $Cu(CN)_4^{=}$, $Cu(Cn)_3^{=}$, and $Cu(CN)_2^{-}$ ions are present, and the association constants of these complexes were calculated. Addition of alkali does not affect any of the quantities measured materially. The ultraviolet absorption spectra of the solutions qualitatively confirmed the presence of $Cu(CN)_4^{=}$ ions.

There appears to have been some doubt in the literature as to the form in which Cu exists in cuprocyanide solutions.

Of early workers, Kunschert (1) concluded on the basis of potentiometric experiments that Cu was present as the $Cu(CN)_4^{=}$ ion in solutions containing excess cyanide. Grossman and Von der Forst (2) supported this conclusion from freezing point data, but Höing (3) claimed that $Cu(CN)_3^{=}$ was the highest complex possible. Glasstone (4) gravely criticized Höing's work, but from the variation of the static potential with the Cu to cyanide ratio he also concluded that $Cu(CN)_2^{-}$ and $Cu(CN)_3^{=}$ were the principal ions present. Britton and Dodd (5) partly repeated Glasstone's work and arrived at the same conclusion. But Brintzinger and Osswald (6) showed by dialysis that Cu ions in excess cyanide solutions had a molecular weight of 166 which corresponds closely to a formula of $Cu(CN)_4^{=}$. Thompson (7) in a review suggests that in most copper cyanide plating solutions, Cu is present principally as $Cu(CN)_3^{=}$ with minor amounts of $Cu(CN)_2^{-}$ and $Cu(CN)_4^{=}$, but stresses that some authors have used titration methods for estimating free cyanide in solutions and that these do not furnish evidence for any complexes present, as the equilibrium is disturbed during titration. Yet Gabrielson (8) in an extensive study solely by a titration method for free cyanide concluded that under all conditions $Cu(CN)_3^{=}$ is the main ion, with only a little $Cu(CN)_4^{=}$ present at high cyanide to Cu ratios. Calmar and Costa (9) recently claimed, on the basis of conductometric experiments, that $KCu(CN)_2$ and $K_2Cu(CN)_3$ are the only two compounds present in potassium cuprocyanide solutions.

Since the work for this paper was completed, Penneman and Jones (10), by using infrared ab-absorption spectroscopy, have proved conclusively that $Cu(CN)_4^{=}$ is the principal ion present at high cyanide to Cu ratios and have, for the first time, evaluated the dissociation constants for all cuprocyanide complexes.

In this paper the problem has been re-examined by measurement of the static potential of Cu in stronger cyanide solutions than have so far been used and by u.v. spectrophotometry. It was possible to calculate the static potentials; they are in very good agreement with experimental values for a wide range of conditions. The association constants for the cuprocyanide complexes have also been deduced; they are in good agreement with the values of Penneman and Jones (10) derived by an entirely different method.

It is concluded that substantially all the Cu is in the form of $Cu(CN)_4^{=}$ as long as sufficient cyanide is present, and only at higher Cu to cyanide ratios are lower complexes formed. Thus in most plating baths, where this ratio is about 0.32, $Cu(CN)_3^{=}$ is the principal ion present and at higher ratios $Cu(CN)_2^{-}$ begins to be formed.

Experimental

Cuprocyanide solutions were made from A. R. KCN (loss in weight after melting 0.5%, volumetric cyanide analysis corresponds to 99.5% KCN) and CuCN made from A. R. chemicals by the method of Barber (11) (loss in weight after melting 0.6%, electrolytic Cu analysis corresponds to 99.3% CuCN).

The absorption spectra of a number of cuprocyanide solutions were obtained on a Unicam spectrophotometer using KCN solutions of corresponding concentrations as blanks. All solutions were 4M in total cyanide, except the one highest in Cu which is saturated above 1M. Results are shown in Fig. 1 as density for a 1 cm cell (multiplied by 4 in the one case mentioned), as molecular extinction coefficients would involve exact knowledge of the complexes present.

The potential of a freshly cleaned Cu wire in a large number of cuprocyanide solutions against a calomel electrode was measured on a Vernier potentiometer. As noted by most previous authors (1, 3, 4, 5, 12, 13) potentials, especially in low Cu

[1] Present address: Dominion Laboratory, Department of Scientific and Industrial Research, Wellington, New Zealand.

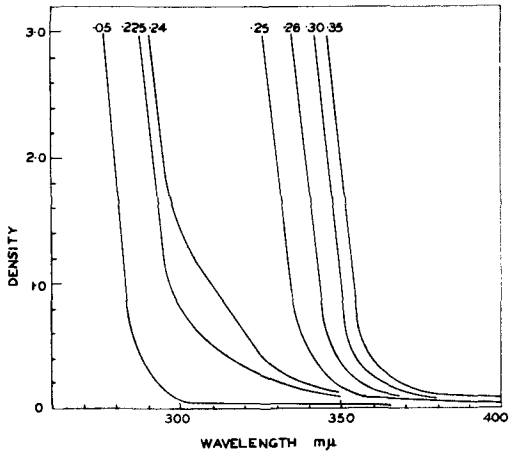

Fig. 1. Ultraviolet absorption spectra of cuprocyanide solutions at Cu:CN ratios indicated. Density is expressed for a 4M cyanide solution in a 1 cm cell.

solutions, fluctuated somewhat erratically initially, but settled to more steady values after some minutes. For each solution a number of readings were taken, covering about 3 hr, and it is estimated that the results quoted are accurate at least to ±0.02 v. Room temperature in all cases was between 18° and 20°C. No thermostating was employed as the accuracy of the results obtained did not warrant it and the temperature coefficient of the potentials was small.

A series of readings at a temperature of 79°-80°C was obtained in a boiling benzene (bp 80.1°C) thermostat.

Theoretical

The absorption spectra (Fig. 1) with a sharp break in character at a Cu:CN ratio of 0.25 suggest very strongly that in low Cu solutions the ion $Cu(CN)_4^{\equiv}$ is present. On the basis of this assumption one has the following equilibria:

$$Cu^+ + 2CN^- \overset{k_1}{\rightleftarrows} Cu(CN)_2^-$$

$$Cu(CN)_2^- + CN^- \overset{k_2}{\rightleftarrows} Cu(CN)_3^{\equiv}$$

$$Cu(CN)_3^{\equiv} + CN^- \overset{k_3}{\rightleftarrows} Cu(CN)_4^{\equiv}$$

All authors agree that k_1 is very large and therefore $[Cu^+]$ may be neglected in comparison with other species present.

Exact treatment of these equilibria gives equations that are too complicated to be easily solved, but on assuming that $1 << k_3 << k_2 << k_1$ (assumptions later verified) great simplifications result. These assumptions imply that the total Cu is always present in the most complex form compatible with the amount of cyanide present.

Let Cu be the total copper concentration and CN the total cyanide concentration in moles/liter. Thus

$$Cu = [Cu(CN)_2^-] + [Cu(CN)_3^{\equiv}] + [Cu(CN)_4^{\equiv}]$$

and

$$CN = [CN^-] + 2[Cu(CN)_2^-] + 3[Cu(CN_3^{\equiv}] + 4[Cu(CN)_4^{\equiv}]$$

On the basis of the above assumptions it can then be shown that

$$[Cu^+] = \frac{k_2^2\,(3Cu - CN)^3}{k_1\,(CN - 2Cu)^2} \quad \left(\text{if } \frac{CN}{2} > Cu > \frac{CN}{3}\right)$$

$$= \frac{k_3^3\,(4Cu - CN)^4}{k_1 k_2\,(CN - 3Cu)^3} \quad \left(\text{if } \frac{CN}{3} > Cu > \frac{CN}{4}\right)$$

$$= \frac{Cu}{k_1 k_2 k_3\,(CN - 4Cu)^4} \quad \left(\text{if } \frac{CN}{4} > Cu\right)$$

If the static potential of Cu in cuprocyanide solutions is dependent only on $[Cu^+]$, it should be possible to calculate it in any solution if total Cu and cyanide are estimated and k_1, k_2, and k_3 are known.

Alternatively, if one potential in each of the three regions has been determined experimentally, the three equilibrium constants can be calculated and from these the potentials at all other Cu:CN ratios and dilutions deduced. This has been done and the results compared with the full range of experimental values.

Results

A series of solutions having total cyanide contents (i.e., CuCN + KCN) of 4M, 2M, 1M, and 0.5M were

Table I. Experimental and calculated static potentials of Cu in cuprocyanide solutions at 20°C on the hydrogen scale

Ratio Cu:CN	Experimental 4M Cyanide	2M	1M	0.5M	Calculated 4M Cyanide	2M	1M	0.5M
0.00	−1.37	−1.31	−1.26	−1.17	—	—	—	—
0.025	—	—	—	—	−1.37	−1.32	−1.27	−1.21
0.05	−1.33	−1.26	−1.22	−1.13	−1.34	−1.29	−1.24	−1.18
0.10	−1.31	−1.25	−1.16	−1.12	−1.29	−1.24	−1.19	−1.13
0.15	−1.24	−1.20	−1.14	−1.09	−1.24	−1.19	−1.14	−1.08
0.20	−1.18	−1.14	−1.08	−1.02	−1.17	−1.12	−1.07	−1.01
0.225	−1.09	−1.03	−0.99	−0.93	−1.09	−1.04	−0.99	−0.93
0.24	—	—	—	—	−1.00	−0.95	−0.90	−0.84
0.25	−0.83	−0.86	−0.86	−0.85	—	—	—	—
0.26	—	—	—	—	−0.83	−0.85	−0.86	−0.88
0.275	−0.69	−0.72	−0.75	−0.76	−0.72	−0.74	−0.75	−0.77
0.30	−0.61	−0.64	−0.65	−0.67	−0.61	−0.63	−0.64	−0.66
0.325	−0.55	−0.56	−0.56	−0.54	−0.46	−0.48	−0.49	−0.51
0.35	sat.	sat.	−0.41	−0.39	−0.39	−0.41	−0.42	−0.44
0.375			sat.	−0.35	−0.30	−0.32	−0.33	−0.35
0.40				sat.	−0.24	−0.26	−0.27	−0.29
0.425					−0.21	−0.23	−0.24	−0.26

prepared. The potential was calculated from the formula

$$E = \pi o + \frac{2.30nRT}{F} \log [Cu^+]$$

by using as reference points the following three experimental values on the hydrogen scale:

Cu:CN 0.15 cyanide 4M −1.24 v
Cu:CN 0.30 cyanide 4M −0.61 v
Cu:CN 0.375 cyanide 0.5M −0.35 v

Experimental and calculated values at 20°C are shown in Table I. Saturation of the solutions has been ignored in the calculations, and these values, therefore, extend to higher concentrations than the experimental ones.

Bassett and Corbet (14) made a phase rule study of the system KCN:CuCN:H_2O at 25°C. Their values for the composition of saturated solutions are similar to the ones obtained here. Using the three reference points quoted, the formula derived above, and the most recent value of 0.48 v at 21°C for the standard cuprous potential (15) one has:

$$-1.24 = 0.48 + 0.058 \left[\log \frac{0.6}{(4-2.4)^4} - \log k_1 - \log k_2 - \log k_3 \right]$$

$$-0.61 = 0.48 + 0.058 \left[\log \frac{(4.8-4)^4}{(4-3.6)^3} + 3 \log k_3 - \log k_1 - \log k_2 \right]$$

$$-0.35 = 0.48 + 0.058 \left[\log \frac{(0.5625-0.5)^3}{(0.5-0.375)^2} + 2 \log k_2 - \log k_1 \right]$$

Allowing for the maximum uncertainty of ±0.02 v in the potential readings, at 20°C

$\log k_1 = 21.7 \pm 1.0$ $\quad 5 \times 10^{20} < k_1 < 5 \times 10^{22}$
$\log k_2 = 4.6 \pm 0.30$ $\quad 2 \times 10^4 < k_2 < 8 \times 10^4$
$\log k_3 = 2.3 \pm 0.15$ $\quad k_3 = (2 \pm 0.7) \times 10^2$

If the older, still generally accepted value of 0.52 v for the standard cuprous potential (16) is used, only k_1 is affected and it becomes 3×10^{21} to 3×10^{23}.

Kunschert (1) quotes a value for $K = 2 \times 10^{27}$ (corrected for a cuprous potential of 0.48 v this gives 7×10^{27}). His K corresponds to $k_1 \times k_2 \times k_3$ in this work which comes to 4×10^{28}. Latimer (16) quotes only $k_1 \times 10^{16}$, derived from early work (13) which ignores the existence of complexes higher than $Cu(CN)_2^-$.

Recently (12), k_1 has been redetermined in HCN where it was established that no complexes higher than $Cu(CN)_2^-$ exist in appreciable quantities. However, the square of the not accurately known dissociation constant of HCN enters the calculation. A value for k_1 of the order 5×10^{23} was obtained at 25°C.

k_2 and k_3 have been determined only very recently for the first time by infrared absorption spectroscopy (10). The following values, recalculated as association constants, were obtained:

29°C	25°C
k_2 $(4.1 \pm 0.6) \times 10^4$	approx. 7×10^4
k_3 $(1.4 \pm 0.1) \times 10^2$	approx. 1.8×10^2

The entire work at room temperature was repeated in solutions containing 0.7M KOH; substantially similar results were obtained. The absorption spectra were practically identical with those in Fig. 1 (KOH only absorbs appreciably below 260 mμ) and the values of the association constants were close to those without alkali.

The experiments (without alkali) were performed at 80°C and the potentials calculated as before by using as reference points

Cu:CN 0.15 cyanide 4M −1.23 v
Cu:CN 0.30 cyanide 4M −0.76 v
Cu:CN 0.375 cyanide 0.5M −0.37 v

Experimental and calculated values are shown in Table II.

No experimental value for πo at 80°C is available, but Tourky and Khairy (17) have calculated that the temperature coefficient of the standard cuprous potential is −0.8 mv/°C from 20° to 47°C. Extrapolating this temperature coefficient gives a value for πo at 80°C of 0.44 v. The accuracy of this value affects only the accuracy of k_1.

Using the three reference points quoted,

Table II. Experimental and calculated static potentials of Cu in cuprocyanide solutions at 80°C on the hydrogen scale

Ratio Cu:CN	Experimental 4M Cyanide	Experimental 2M	Experimental 1M	Experimental 0.5M	Calculated 4M Cyanide	Calculated 2M	Calculated 1M	Calculated 0.5M
0.00	−1.38	−1.33	−1.23	−1.21	—	—	—	—
0.025	—	—	—	—	−1.39	−1.33	−1.26	−1.20
0.05	−1.37	−1.28	−1.22	−1.17	−1.35	−1.29	−1.22	−1.16
0.10	−1.30	−1.25	−1.17	−1.13	−1.29	−1.23	−1.16	−1.10
0.15	−1.23	−1.17	−1.10	−1.07	−1.23	−1.17	−1.10	−1.04
0.20	−1.16	−1.11	−1.06	−1.00	−1.14	−1.08	−1.01	−0.95
0.225	−1.12	−1.08	−1.01	−0.99	−1.05	−0.99	−0.92	−0.86
0.24	—	—	—	—	−0.94	−0.88	−0.81	−0.75
0.25	−0.98	−1.00	−0.99	−0.95	—	—	—	—
0.26	—	—	—	—	−1.03	−1.05	−1.07	−1.09
0.275	−0.86	−0.89	−0.92	−0.91	−0.90	−0.92	−0.94	−0.96
0.30	−0.76	−0.80	−0.81	−0.83	−0.76	−0.78	−0.80	−0.82
0.325	−0.63	−0.65	−0.67	−0.64	−0.59	−0.61	−0.63	−0.65
0.35	−0.50	−0.47	−0.43	−0.42	−0.43	−0.45	−0.47	−0.49
0.375	−0.44	−0.40	−0.38	−0.37	−0.31	−0.33	−0.35	−0.37
0.40	−0.41	−0.37	−0.34	−0.33	−0.26	−0.28	−0.30	−0.32
0.425	sat.	sat.	sat.	sat.	−0.21	−0.23	−0.25	−0.27

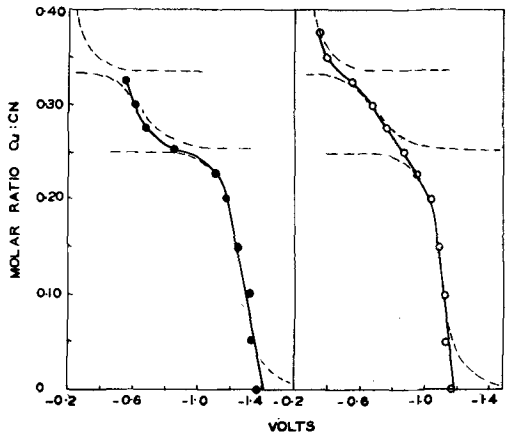

Fig. 2. Static potential of cuprocyanide solutions at 20°C on the hydrogen scale. ● Total cyanide 4M, ○ total cyanide 0.5M. The broken lines show the corresponding calculated values.

$$-1.23 = 0.44 + 0.070\ [-1.0 - \log k_1 - \log k_2 - \log k_3]$$
$$-0.76 = 0.44 + 0.070\ [0.8 + 3\log k_3 - \log k_1 - \log k_2]$$
$$-0.37 = 0.44 + 0.070\ [-1.8 + 2\log k_2 - \log k_1]$$

Allowing for the maximum uncertainty of ±0.02 v in the potential readings at 80°C

$$\log k_1 = 17.7 \pm 1.0 \quad 5 \times 10^{16} < k_1 < 5 \times 10^{18}$$
$$\log k_2 = 3.9 \pm 0.30 \quad 4 \times 10^3 < k_2 < 1.5 \times 10^4$$
$$\log k_3 = 1.23 \pm 0.14 \quad k_3 = 17 \pm 5$$

No values for these constants at an elevated temperature were found in the literature.

The work at 80°C was repeated with solutions of total cyanide content of 3.1M, containing 0.7M KOH, because solutions about 2.1M KCN, 1.0M CuCN, 0.7M KOH at about 80°C are commonly employed for high speed and periodic reverse copper cyanide electroplating.

The potentials obtained and the constants calculated were close to those observed without alkali.

Discussion

In general, agreement between the experimental and calculated values for the static potential in cyanide solutions is satisfactory. This is shown in Fig. 2 at 20°C for solutions of total cyanide 4M and 0.5M. Some deviation naturally occurs at the transition stages between the three regions, where the calculated values become infinite.

The calculations predict that, if CN/4 > Cu, a dilution to a half should increase the cuprous ion concentration eight times, while, if Cu > CN/4, a dilution to a half should halve the cuprous ion concentration. The experimental potential values in Table I and II confirm this prediction by the sudden reversal and change in magnitude of the effect of dilution on the potential at a Cu:CN ratio of 0.25.

Table III. Experimental static potentials of Cu in cuprocyanide solutions at 80°C

Ratio Cu:CN	4M Cyanide	2M	1M	0.5M	0.25M	0.125M	0.06M
0.35	—0.50	—0.47	—0.43	—0.42	—0.41	—0.42	—0.44
0.375	—0.44	—0.40	—0.38	—0.37	—0.37	—0.38	—0.39
0.40	—0.41	—0.37	—0.34	—0.33	—0.33	—0.35	—0.36

The calculation of the association constants also verifies the initial assumptions that $1 << k_3 << k_2 << k_1$. Agreement with other published values is satisfactory. At 80°C k_3 has dropped to 17 and, although still comparatively large, some small deviations from the calculated values might be expected.

The most serious deviations from the calculations occur at 80°C at a Cu:CN ratio of 0.35 and above, where dilution changes the potential in the opposite direction to that calculated. However, at lower concentrations it is again in the calculated direction as shown in Table III.

Because of this effect the reference point for the ratio Cu:CN 0.375 was chosen at a low total cyanide concentration. At this ratio at 20°C a low total cyanide concentration reference point was also employed, on account of the solubility limits shown in Table I.

The absorption spectra at room temperature (Fig. 1) confirm the assumption that k_3 is large, by the abrupt transition at a Cu:CN ratio of 0.25. k_3 could not actually be calculated, because even in very dilute solutions no absorption maximum could be obtained, as the spectra may be due to electron transfer.

The absorption spectra do not differentiate between the $Cu(CN)_3^=$ and $Cu(CN)_2^-$ ions, but good independent evidence that $k_3 << k_2$ is provided by titrating cuprocyanide solutions at room temperature with $AgNO_3$ using KI as indicator. Silver iodide is precipitated when sufficient argentocyanide has been formed to leave the Cu:CN ratio 0.33. While this titration cannot be used to study cuprocyanide equilibria in general, it suggests that at the end point $Cu(CN)_3^=$ is the principal ion, and not just a mixture of $Cu(CN)_2^-$ and $Cu(CN)_4^{\equiv}$ is present. A modification of this titration is used to estimate "free cyanide" in commercial plating baths.

Glasstone (4) argues that $Cu(CN)_2^-$ and $Cu(CN)_3^=$ are the only ions in cuprocyanide solution. Working in solutions from 0.1 to 0.5M cyanide he gets a clear inflexion on his potential curve at a Cu:CN ratio of 0.32 on which he bases his conclusion. Britton and Dodd (5) in similar work obtain an inflexion at a ratio of 0.28. However, taking all three complexes into account, Fig. 2 shows a very clear inflexion at a ratio of 0.25 at high concentrations, but at lower concentrations (more especially at high temperatures) this almost disappears and a pronounced inflexion at 0.33 becomes apparent.

Acknowledgments

The author wishes to thank Dr. A. Hickling for his encouragement and much helpful advice, and Dr. L. H. Sutcliffe for many useful comments. The work was carried out during the tenure of a New Zealand National Research Fellowship.

Manuscript received June 6, 1956.

Any discussion of this paper will appear in a Discussion Section to be published in the June 1958 JOURNAL.

REFERENCES

1. F. Kunschert, *Z. anorg. Chem.*, **41**, 359 (1904).
2. H. Grossmann and P. Von der Forst, *ibid.*, **43**, 94 (1905).

3. A. Höing, *Z. Elektrochem.*, **22**, 286 (1916).
4. S. Glasstone, *J. Chem. Soc.*, **1929**, 690.
5. H. T. S. Britton and E. N. Dodd, *ibid.*, **1935**, 100.
6. H. Brintzinger and H. Osswald, *Z. anorg. Chem.*, **220**, 177 (1934).
7. M. R. Thompson, *Trans. Electrochem. Soc.*, **79**, 417 (1941).
8. G. Gabrielson, *Metal Finishing*, **52**, 60 (1954).
9. C. Calmar and M. Costa, *Compt. rend.*, **243**, 56 (1956).
10. R. Penneman and L. H. Jones, *J. Chem. Phys.*, **24**, 293 (1956).
11. H. J. Barber, *J. Chem. Soc.*, **1943**, 79.
12. M. G. Vladimirova and I. A. Kakovskii, *J. Appl. Chem. U.S.S.R.*, **23**, 615 (1950). (English translation.)
13. F. Spitzer, *Z. Elektrochem.*, **11**, 345 (1905).
14. H. Bassett and A. S. Corbet, *J. Chem Soc.*, **125**, 1660 (1924).
15. S. E. S. El Wakkad, *ibid.*, **1950**, 3563.
16. W. M. Latimer, "The Oxidation States of the Elements and their Potentials in Aqueous Solutions," 2nd ed., pp. 185-6, Prentice Hall, Inc., New York (1952).
17. A. R. Tourky and E. M. Khairy, *J. Chem. Soc.*, **1952**, 2626.

Hydrogen Overpotential on Electrodeposited Ni in NaOH Solutions

I. A. Ammar and S. A. Awad

Chemistry Department, Faculty of Science, Cairo University, Cairo, Egypt

ABSTRACT

Hydrogen overpotential, η, is measured for electrodeposited Ni in 0.01-1.0*N* NaOH solutions. The effect of temperature on η is studied and the heat of activation, ΔHo^*, at the reversible potential is calculated. The *p*H effect $(\partial\eta/\partial p\mathrm{H})_i$ is calculated at 25°C and is equal to 26 mv per unit increase of *p*H. The electron number, λ, calculated from the overpotential results at very low current densities, is very near to unity. The Tafel line slope, *b*, increases with temperature. Results are compared with those obtained for Ni in the form of a wire.

Hydrogen overpotential on electrodeposited metals has not been studied extensively. A few studies are, however, recorded in the literature (1, 2). The uncertainty concerning the magnitude of the true surface area of an electrodeposited electrode, together with the possibility of contaminating the electrode surface during electrodeposition, hinder the progress in this field. Recent work on electrodeposited Ni in HCl solutions (3) has indicated that the parameters of cathodic hydrogen evolution on electrodeposited Ni are different from those observed for a Ni wire. Consequently the mechanism of hydrogen evolution is different for the two types of electrodes. Bockris and co-workers (4, 5) have formulated several criteria for distinguishing between the possible rate-determining mechanisms. The aim of the present work is to study the hydrogen overpotential on electrodeposited Ni in NaOH solutions, particularly at the very low current density range, with the hope of evaluating the number of electrons, λ, necessary to complete one act of the rate-determining mechanism (5).

Experimental

The experimental technique was essentially the same as that of Bockris, *et al.* (4, 6). The electrolytic cell was constructed of arsenic-free glass. All ground glass joints and taps were of the solution-sealed type. This helped to hinder the diffusion of atmospheric oxygen inside the cell. A platinized Pt electrode, in the same solution and at the same temperature as the test cathode, was used as a reference electrode. Electrical contact between the cathode and the reference electrode was made through a Luggin capillary. To avoid complications due to resistance overpotential, the test cathode was adjusted to touch the tip of the Luggin capillary.

Electrodeposition of Ni was carried out from the following bath: 30 g $NiSO_4$, 10 g $(NH_4)_2SO_4$, 150 cc conductance water, and 100 cc concentrated NH_4OH. "AnalaR" grade reagents were used. Electrodeposition was carried out for 2 hr at a current density of 1 ma/cm^2, on a Ni substrate sealed to glass. The apparent surface area of the electrode was 0.8 cm^2. The electrode was thoroughly washed with conductance water before use.

Pure NaOH solutions were prepared under an atmosphere of pure hydrogen. Conductance water ($K = 2.0 \times 10^{-7}$ ohm^{-1} cm^{-1}) was used for the solution preparation. The solution was then extensively purified by pre-electrolysis (7) at 1×10^{-2} amp/cm^2 for 20 hr. A Ni electrode, prepared in the same manner as the test electrode, was used for pre-electrolysis. Pure hydrogen was passed into the cell during pre-electrolysis. Hydrogen was purified from O_2 by Cu heated to 450°C, from CO_2 by soda lime and from CO by a mixture of MnO_2 and CuO, technically known as "Hopcalite" (8).

The direct method of measurements was used and the current density was calculated using the apparent surface area. The potential was measured with a valve potentiometer and the current with a sensitive micromilliammeter. At low currents the current was checked by measuring the potential drop across a standard resistance. The temperature was kept constant, to ±0.5°C, with the help of an air thermostat.

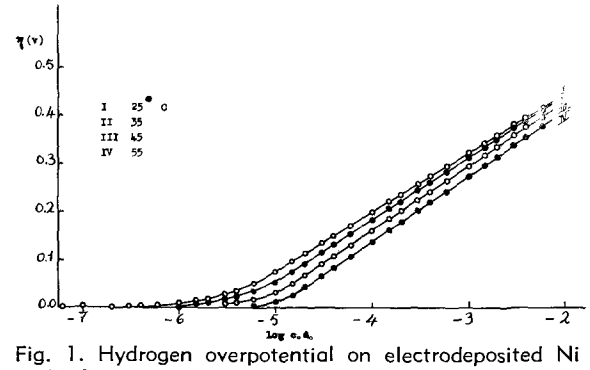

Fig. 1. Hydrogen overpotential on electrodeposited Ni in 0.1N NaOH.

Before each run, all glass parts of the apparatus were cleaned with a mixture of "AnalaR" HNO_3 and H_2SO_4. This was followed by washing with equilibrium water and then with conductance water. Care was also taken to free the previously cleaned cell from oxygen. This was done by filling the cell completely with conductance water (distilled under hydrogen), and then replacing this water by pure hydrogen before the NaOH solution was introduced. With the above precautions, the overpotential results obtained with different test electrodes agreed within ±10 mv at intermediate and high current densities, and ±3 mv at low current densities. For each test electrode, the overpotential results were in agreement within less than ±10 mv. For each concentration and temperature studied, at least six Tafel lines (a new electrode and a new solution for each Tafel line) were measured and the mean line was computed.

Results

The Tafel line slope, b, the transfer coefficient, α, and the exchange current, i_o, for the mean Tafel lines on electrodeposited Ni in 0.01, 0.05, 0.10, 0.50, and 1.0N aq NaOH solutions are given in Table I. Fig. 1 shows four mean Tafel lines on electrodeposited Ni in 0.1N NaOH solution at 25°, 35°, 45°, and 55°C. The transfer coefficient is calculated according to $b = 2.303\ RT/\alpha F$.

The electron number, λ, defined as the number of electrons necessary to complete one act of the rate-determining step (5), is calculated using:

Table I*

Conc. N	Temp, °C	b, mv	α	i_o, amp/cm²	$(\partial\eta/\partial i_c)\,\eta\to 0$‡	λ
0.01	25	122	0.48	1.6×10^{-6}	1.50×10^{4}	1.1
0.05	25	122	0.48	2.0×10^{-6}	1.25×10^{4}	1.0
	35	125	0.49	3.2×10^{-6}	7.50×10^{3}	1.1
	45	128	0.49	5.0×10^{-6}	5.00×10^{3}	1.1
	55	130	0.50	7.9×10^{-6}	2.70×10^{3}	1.3
0.10	25	122	0.48	2.5×10^{-6}	1.06×10^{4}	1.0
	35	130	0.47	4.0×10^{-6}	7.50×10^{3}	0.9
	45	135	0.47	6.6×10^{-6}	4.40×10^{3}	0.9
	55	137	0.47	1.0×10^{-5}	2.65×10^{3}	1.1
0.50	25	122	0.48	3.3×10^{-6}	8.12×10^{3}	1.0
	35	130	0.47	5.0×10^{-6}	5.25×10^{3}	1.0
	45	135	0.47	8.3×10^{-6}	3.50×10^{3}	1.1
	55	138	0.47	1.3×10^{-5}	2.65×10^{3}	0.8
1.00	25	125	0.47	4.5×10^{-6}	6.00×10^{3}	1.0

* Values of α are given to the nearest second decimal figure, and λ to the nearest first decimal figure.
‡ Reproducible within ±3%.

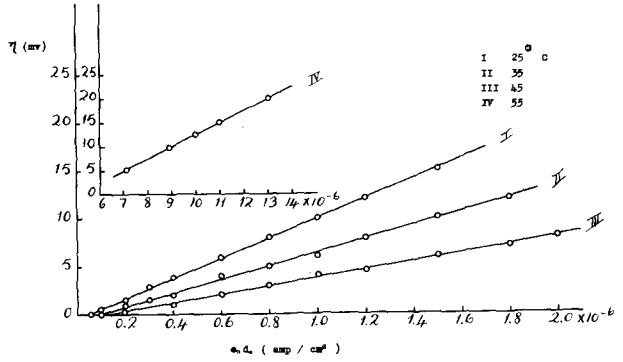

Fig. 2. Relation between overpotential and current density at very low cathodic polarization for electrodeposited Ni in 0.1N NaOH.

$$\lambda = \frac{RT}{i_o F}\,(\partial i_c/\partial\eta)\ \eta \to 0 \qquad \text{(I)}$$

and,

$$\exp\,(\lambda\eta_s F/RT) = 0.05 \qquad \text{(II)}$$

η_s is the overpotential at which the Tafel line departs from linearity owing to the appreciable rate of ionization of adsorbed atomic hydrogen. Eq. II gives approximate values for λ. The values of the electron number calculated according to Eq. (I) are included in Table (I). Values of λ calculated according to Eq. II are in substantial agreement with the values obtained from Eq. (I). The relation between η and the current density for small cathodic polarization (below 20 mv) is shown in Fig. 2 for the mean Tafel lines in 0.1N NaOH.

The effect of pH on hydrogen overpotential is studied at 25°C. The overpotential at three different current densities (10^{-3}, 10^{-4}, and 10^{-5} amp/cm²) is plotted against the pH; the result is shown in Fig. 3. From Fig. 3 it is clear that the value of $(\partial\eta/\partial\mathrm{pH})_i$ at the three different current densities is 26 ± 1 mv/unit increase of pH.

The relation between log i_o and the reciprocal of temperature is shown in Fig. 4 for 0.05, 0.10, and 0.50N aq. NaOH solutions. The heat of activation, ΔHo^*, at the reversible potential is calculated from the slope of log $i_o - 1/T$ relation according to (6,9):

$$i_o = B \exp\,(-\Delta Ho^*/RT) \qquad \text{(III)}$$

where B is the Eyring entropy factor (5, 6, 10). A mean value of 8.8 ± 0.1 kcal/mole is calculated for ΔHo^* from the results in 0.05, 0.10, and 0.50N NaOH according to Eq. (III). Using this mean value of

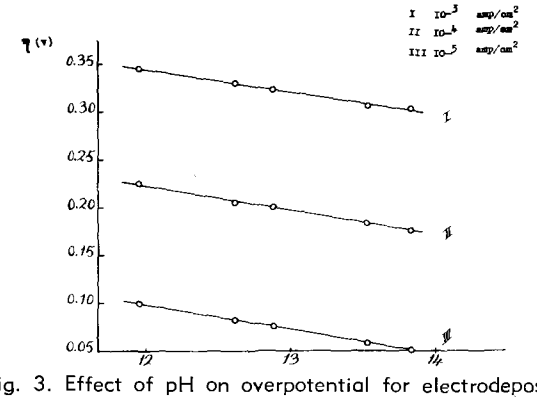

Fig. 3. Effect of pH on overpotential for electrodeposited Ni in NaOH solutions at 25°C.

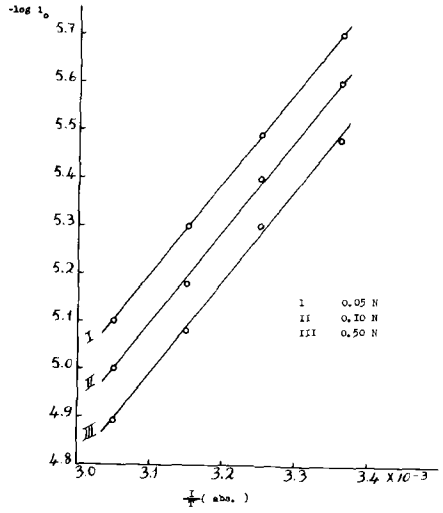

Fig. 4. Relation between the logarithm of the exchange current and the reciprocal of temperature for electrodeposited Ni in NaOH solutions.

ΔHo^* in Eq. (III), log B is calculated, at 25°C, for the various NaOH solutions studied. The relation between log B and log a_{NaOH} is linear with a slope of approximately 0.23. This relation is shown in Fig. 5.

The heat of activation, ΔHo^*, may also be calculated from the rate of change of η with temperature at a constant current density according to (5):

$$(\partial\eta/\partial T)_i = (\Delta Ho^* + \alpha\eta F)/\alpha FT \qquad \text{(IV)}$$

The results obtained by this method are less reproducible than those obtained from the slope of log $i_o - 1/T$ relation (3). ΔHo^* is calculated using the mean values of α, η, and T in the right hand side of Eq. (IV); the results are given in Table (II).

Discussion

The results for electrodeposited Ni are not concordant with the results on Ni in the form of a wire (6, 11, 12). Thus, the overpotential at a constant current density is numerically lower for electrodeposited Ni than that for Ni wire in the same solution and at the same temperature. The exchange currents for electrodeposited Ni are higher than the corresponding values for Ni wire. Thus, the value of i_o for electrodeposited Ni in 0.1N NaOH at 25°C is 2.5×10^{-6} amp/cm^2 (cf. Table I), whereas for Ni wire i_o in the same solution lies between 4×10^{-7} amp/cm^2 at 20°C, and 7.9×10^{-7} amp/cm^2 at 40°C [cf. Ref. (6)]. The difference between the i_o values for electrodeposited and bulk Ni (wire) may be partly attributed to a large true surface area for the former as compared to the latter. The apparent current density corresponds to a lower true current density in the case of electrodeposited Ni and consequently η is numerically smaller than in the case of bulk Ni. The i_o values for electrodeposited Ni are therefore greater than those of bulk Ni. Furthermore, it has been observed (6) that the Tafel line slope b for Ni wire does not vary with temperature, whereas for electrodeposited Ni it is clear from Table (I) that b increases with temperature. This also accounts for the difference between the i_o values obtained in the present investigation and those of Bockris and Potter (6). Since $b = 2.303\ RT/\alpha F$, α may therefore be taken as independent of temperature with a value lying between 0.47 and 0.50. The fact that b increases with temperature is in accordance with the results of others (13, 14). It is also to be noted that no effect of time on the overpotential on electrodeposited Ni is observed in the present investigation. In other words, η reaches a constant value in less than a minute. On the other hand, an appreciable time effect is observed for bulk Ni (11, 15). This is in agreement with the results of Bockris and Parsons (1) who observe that the attainment of the steady-state value of η is quicker for electrodeposited metals probably because of the co-deposition of hydrogen during electrodeposition.

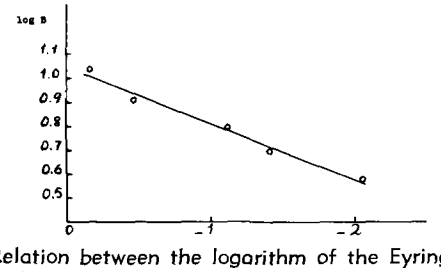

Fig. 5. Relation between the logarithm of the Eyring entropy factor and log a_{NaOH}.

Table II

Conc. N	Temp range, °C	$(\partial\eta/\partial T)_i$ mv/degree	Mean α	Mean η mv, at 10^{-4}amp/cm^2	ΔHo^*, kcal	Mean ΔHo^*
0.05	25-35	1.8	0.485	197	8.3	
	35-45	2.1	0.490	178	9.4	9.2
	45-55	2.2	0.495	156	9.9	
0.10	25-35	1.6	0.475	191	7.4	
	35-45	2.3	0.470	172	9.7	9.2
	45-55	2.5	0.470	148	10.4	
0.50	25-35	1.5	0.475	176	6.9	
	35-45	2.1	0.470	158	8.8	8.3
	45-55	2.2	0.470	136	9.2	

The activation overpotential associated with the cathodic evolution of hydrogen may be attributed to a rate-determining slow discharge process, electrochemical desorption, or catalytic combination (5). Other rate-determining mechanisms of less importance are cited in the literature (4). A rate-determining slow discharge is characterized by a Tafel line slope of 0.120 v at 30°C and by $\lambda = 1$. For a rate-determining electrochemical desorption, the Tafel line exhibits two slopes (21) of 0.040 v and 0.120 v at 30°C in the linear logarithmic section, and λ is 2. A rate-determining catalytic combination is distinguished by a Tafel line slope of 0.030 v at 30°C in the range of current densities used in the present investigation. For this mechanism λ is also 2. From this and the data given in Table I it is evident that the rate of hydrogen evolution on electrodeposited Ni in NaOH solutions is controlled by a slow discharge mechanism. This is supported by the fact that the values of the transfer coefficient, α, are very near to 0.5 (cf. Table I), the value usually observed for a slow discharge mechanism (16, 17). Owing to the diminishingly small concentration of H_3O^+ ions in alkaline solutions, it is possible that the discharge takes place from water molecules and not from H_3O^+ ions (18). This is supported by the positive values of $(\partial\eta/\partial p\mathrm{H})_i$ obtained

in the present investigation (cf. Fig. 3). The rate-determining step in the over-all reaction for hydrogen evolution on electrodeposited Ni in NaOH solutions is, therefore, represented by:

$$H_2O + e \rightarrow OH' + MH \qquad (V)$$

where M represents the electrode surface. This is followed either by a fast catalytic combination:

$$MH + MH \rightarrow H_2 \qquad (VI)$$

or by a fast electrochemical desorption:

$$H_2O + MH + e \rightarrow H_2 + OH' \qquad (VII)$$

There is, however, no evidence to favor either the catalytic combination or the electrochemical desorption.

Values theoretically deduced (6) for $(\partial\eta/\partial p\mathrm{H})_i$ in the case of the discharge from water molecules lie between 60 mv and 120 mv per unit increase of pH at 30°C for conditions near and far from the electrocapillary maximum, respectively. The experimentally observed value of $(\partial\eta/\partial p\mathrm{H})_i$ for electrodeposited Ni is 26 mv, thus indicating that the experimental pH effect is much smaller than the theoretical values. Similar observations have been made for Ag in NaOH solutions (20). For Ni wire the pH effect, observed by Bockris and Potter (6), lies between 10 and 25 mv per unit increase of pH whereas the work of Lukovstev and Lewina (12) indicates a pH effect of 40 mv per unit pH. The experimental pH effect cannot be accounted for by Bockris and Watson's mechanism (19), in which the hydrogen originates from Na atoms and water molecules, since this mechanism does not apply to Ni (6). For the discharge from water molecules, Bockris and Potter (6) have taken into consideration the effect of the orientation of water molecules in the double layer. The main postulate of this treatment is that the activity of water in the double layer increases faster than that in the bulk of solution owing to the effect of the high field strength near the electrode. Even with this treatment the theoretical values of $(\partial\eta/\partial p\mathrm{H})_i$ for the discharge from water molecules are still different from the experimental values. Bearing in mind that the discharge for H_2O molecules is rate determining for hydrogen evolution on electrodeposited Ni in NaOH solutions one may proceed to explain the experimental pH effect of 26 mv/unit increase of pH at 30°C.

The expression for the cathodic current density, taking $\alpha = 0.5$, is given by (5):

$$i = i_o \cdot \exp \cdot (-\eta F/2RT) \qquad (VIII)$$

It is clear from Eq. (VIII) and Fig. 3 that:

$$(\partial\eta/\partial p\mathrm{H})_i = 2\left(\frac{2.303\,RT}{F}\right)\left(\frac{\partial \log i_o}{\partial p\mathrm{H}}\right) = 0.026 \pm 0.001 \text{ v} \qquad (IX)$$

and from (IX) taking $\partial p\mathrm{H} = \partial \log a_{NaOH}$ one gets at 25°C:

$$i_o = K(a_{NaOH})^{0.23} \qquad (X)$$

where K is a constant at constant temperature. Equation (X) is based on the experimental pH effect observed in the present investigation. The dependence of i_o on a_{NaOH} may be attributed to the dependence of the activity of water, in the initial state of the reaction, on a_{NaOH}. Thus, the expression for i_o may be given by (5):

$$i_o = \lambda F X \frac{kT}{h}(a_{H_2O}) \cdot \exp \cdot (\Delta So^*/R) \exp \cdot (-\Delta Ho^*/RT) \qquad (XI)$$

where X is the transmission coefficient, a_{H_2O} is the activity of the reactant (water) in the initial state, ΔSo^* is the standard entropy of activation at the reversible potential, and (kT/h) has its usual significance as given by the theory of absolute reaction rates (10). From (III) and (XI) it follows that:

$$B = \lambda F X \frac{kT}{h}(a_{H_2O}) \cdot \exp \cdot (\Delta So^*/R) \qquad (XII)$$

It has been observed experimentally that ΔHo^*, for hydrogen evolution on electrodeposited Ni in NaOH solutions, is independent of a_{NaOH}. If the assumption is made that ΔSo^* is also independent of a_{NaOH} it follows from (X) and (XI) that :

$$a_{H_2O} \propto (a_{NaOH})^{0.23} \qquad (XIII)$$

and the experimental pH effect observed in the present investigation may, thus, be due to the dependence of the activity of water in the initial state on a_{NaOH} as given by (XIII). The linearity between log B and log a_{NaOH} (Fig. 5) follows, therefore, from Eqs. (XII) and (XIII). Combining (XII) and (XIII) one gets:

$$B = K'(a_{NaOH})^{0.23} \cdot \exp(\Delta So^*/R) \qquad (XIV)$$

ΔSo^* may be calculated according to (XIV) from the value of B corresponding to $a_{NaOH} = 1$ (Fig. 5). If the proportionality constant in (XIII) is assumed to be equal to unity, K' becomes:

$$K' = \lambda F X \frac{kT}{h} \qquad (XV)$$

where X is usually taken as unity (10), and the value of ΔSo^* (standard state $a_{NaOH} = 1$) calculated according to (XIV) and (XV) is −77 cal/degree/mole.

Variation of i_o with a_{NaOH} [Eq. (X)] may also be attributed to the change of the free energy of activation with a_{NaOH}. At present there is, however, no evidence to favor one of the above two possibilities and the solution to this problem will be dealt with in a later publication.

Acknowledgments

The authors wish to express their thanks to A. R. Tourky for his interest in this work, and to J. O'M. Bockris for helpful discussions.

Manuscript received Oct. 22, 1956.

Any discussion of this paper will appear in a Discussion Section to be published in the June 1958 JOURNAL.

REFERENCES

1. J. O'M. Bockris and R. Parsons, *Trans. Faraday Soc.*, **44**, 860 (1948).
2. W. Senett and C. Hiskey, *J. Am. Chem. Soc.*, **74**, 3754 (1952).

3. I. A. Ammar and S. Awad, *J. Phys. Chem.*, **60**, 837 (1956).
4. J. O'M. Bockris, *Chem. Rev.*, **43**, 525 (1948).
5. J. O'M. Bockris and E. C. Potter, *This Journal*, **99**, 169 (1952).
6. J. O'M. Bockris and E. C. Potter, *J. Chem. Phys.*, **20**, 614 (1952).
7. A. Azzam, J. O'M. Bockris, B. Conway, and H. Rosenberg, *Trans. Faraday Soc.*, **46**, 918 (1950).
8. G. Schwab and G. Drikos, *Z. Physik. Chem.*, **185A**, 405 (1940).
9. J. O'M. Bockris, *Ann. Rev. Phys. Chem.*, **5**, 477 (1954).
10. S. Glasstone, H. Eyring, and K. Laidler, *J. Chem. Phys.*, **7**, 1053 (1939); Theory of Rate Processes, p. 588, McGraw-Hill Co. (1941).
11. S. Lewina, P. Lukovstev, and A. Frumkin, *Acta Physicochim.*, **11**, 21 (1939).
12. P. Lukovstev and S. Lewina, *J. Phys. Chem., U.S.S.R.*, **21**, 599 (1947).
13. F. Bowden and J. Agar, *Ann. Report*, **35**, 90 (1938); F. Bowden, *Proc. Roy. Soc.*, **A126**, 107 (1929).
14. B. Post and C. Hiskey, *J. Am. Chem. Soc.*, **72**, 4203 (1950).
15. J. O'M. Bockris and B. Conway, *Trans. Faraday Soc.*, **45**, 989 (1949).
16. A. Frumkin, *Discussion Faraday Soc.*, **1**, 62 (1947).
17. Z. Jofa and A. Frumkin, *Acta Physicochim.*, **18**, 183 (1943).
18. J. O'M. Bockris and R. Parsons, *Trans. Faraday Soc.*, **47**, 914 (1951).
19. J. O'M. Bockris and R. G. Watson, *J. Chim. Phys.*, **49**, c70 (1952).
20. I. A. Ammar and S. Awad, *J. Phys. Chem.*, **60**, 1290 (1956).
21. I. A. Ammar and S. Awad, *This Journal*, **103**, 182 (1956).

Discussion of Papers

December 1957 Discussion Section—A Discussion Section, covering papers published in the January-June 1957 JOURNALS, is scheduled for publication in the December 1957 issue. Any discussion which did not reach the Editor in time for inclusion in the June 1957 Discussion Section will be included in the December 1957 issue.

June 1958 Discussion Section—A Discussion Section, covering papers published in the July-December 1957 JOURNALS, will appear in the June 1958 issue. Those who plan to contribute remarks for this Discussion Section should submit their comments or questions in triplicate to the Managing Editor of the JOURNAL, 1860 Broadway, New York 23, N. Y., *not later than March 1, 1958*. All discussion will be forwarded to the author, or authors, for reply before being printed in the JOURNAL.

Technical Note

The Value of the Electromotive Force of a Voltaic Cell; A Magnitude Without Sign

J. B. Ramsey

Department of Chemistry, University of California, Los Angeles, California

There exists considerable doubt among chemists and other physical scientists regarding the need of giving a sign to the value of the electromotive force of a voltaic cell.

It is the purpose of this paper to present justification for a nonalgebraic definition of the value of the emf of a voltaic cell, that is, for giving the emf of a cell a numerical value (a magnitude without sign) irrespective of the orientation of its two electrodes in its symbolic formulation.

The sign convention quite generally used in assigning an algebraic value to the emf of a voltaic cell is the one originally adopted by Lewis (1). According to this sign convention the value to be given to the electromotive force of a cell *as formulated* "shall represent the tendency of the negative current to pass spontaneously through the cell from right to left." This convention has been reaffirmed in the recommendations made by the Commission on Physico-Chemical Symbols and Terminology and the Commission on Electrochemistry (2), both of the International Union of Pure and Applied Chemistry, at their meeting in Stockholm in 1953. Recently deBethune (3) has given a clarifying discussion of the recommendations of these Commissions.

Proposed nonalgebraic definition of the emf of a voltaic cell.—We propose to define the value of the emf of a voltaic cell as the absolute value of the difference between the electrode potentials of the two electrodes of the cell, which is, therefore, independent of the way in which the cell may be formulated. This definition is expressed by the following relation,

$$\text{emf}_{\text{Cell}} = | V_1 - V_2 | = | \mathcal{E}_1 - \mathcal{E}_2 |$$

where V_1 represents the Gibbs-Stockholm (electrostatic) electrode potential of the ith electrode and $\mathcal{E}_i$, the electron chemical potential of the ith electrode as defined by Ramsey (4).

Consequence of this definition.—Consider the occurrence of an isothermal change in state requiring the passage of n faradays of electricity (positive or negative) in the direction required by the change in state considered. The numerical value (magnitude) of the maximum (isothermal) electrical work producible either in the surroundings or in the system (the voltaic cell) during this isothermal change in state is $nE_{\text{Cell}}F$. The sign given to $nE_{\text{Cell}}F$ is dependent on the thermodynamic definition of "work." Most American physical chemists define "work" in such a way that it is given a positive value if produced in the surroundings and a negative value if produced in the system ($Q = \Delta E + W$).

Now if the isothermal change in state being considered occurs spontaneously, then work will be produced in the surroundings during this change and $nE_{\text{Cell}}F$ will have a positive value. If, on the other hand, electrical work must be done on the system (the voltaic cell) in order to bring about the change considered, $nE_{\text{Cell}}F$ must be given a negative value.

The change in free energy, ΔF, accompanying the change in state considered, is then given by the relation.

$$\Delta F = -(nE_{\text{Cell}}F)$$

in which the sign to be given $nE_{\text{Cell}}F$ is determined as described in the preceding paragraph, viz., a positive sign if electrical work is produced in the surroundings (change will occur spontaneously) and a negative sign if electrical work must be done on the system to bring about the change considered (the change would occur spontaneously in the reverse direction to that being considered).

The definition of the electromotive force of a voltaic cell, conceived as a magnitude without sign, in terms of the potentials of its two electrodes depends on the definition of an electrode potential which is used. If the Gibbs-Stockholm electrode potential, V_i, is adopted [*see* Ref. (3)], (where the term "potential" is used in the electrostatic sense) then the emf of a cell is defined as the tendency of positive current to flow through the outer circuit from the electrode having the greater value of V to the one with the smaller value of V. It may be noted the potential, V, applies strictly to the piece of "external circuit" metal connected with each of the electrodes respectively. If, however, the "electron chemical potential," $\mathcal{E}$, of an electrode [*see* Ref. (4)] is adopted (where the term "potential" is used in its thermodynamic sense) then the emf of a cell is defined as the tendency of electrons to flow through the external circuit from the electrode hav-

ing the greater $\mathcal{E}$-value to the one having the smaller $\mathcal{E}$-value. It should be noted that nothing is said in these definitions of the emf regarding the orientation of the two electrodes of the cell *as it may be arbitrarily formulated.*

The justification for considering the value of the emf of a cell to have a magnitude without sign may be summarized as follows: when a sign convention has been adopted for the maximum (isothermal) electrical work, $W_{rev.el.}$, transferred during the isothermal change in state considered, namely (according to many thermodynamicists) that it, $W_{rev.el.}$, have a positive sign if work is produced in the surroundings and a negative sign if produced in the system (the voltaic cell in this case), the adoption of an additional sign convention for the electromotive force of a voltaic cell, as formulated, is redundant and serves no useful purpose.

Manuscript received July 9, 1957.

Any discussion of this paper will appear in a Discussion Section to be published in the June 1958 JOURNAL.

REFERENCES

1. G. N. Lewis and M. Randall, "Thermodynamics and the Free Energy of Chemical Substances," p. 390, McGraw-Hill Book Co., Inc., New York, New York (1923).
2. J. A. Christiansen and M. Pourbaix, Compt. rend. XVII. Conf. Inter. Union Pure and Appl. Chem., held in Stockholm in 1953, Maison de la Chemie, Paris (1954), pp. 82-84.
3. A. M. deBethune, *This Journal*, **102**, 288C (1955).
4. J. B. Ramsey, *ibid.*, **104**, 255 (1957).

Anodization of Lead and Lead Alloys in Sulfuric Acid

Jeanne Burbank

U. S. Naval Research Laboratory, Washington, D. C.

ABSTRACT

The anodic lead dioxide coatings formed on lead and selected alloys in sulfuric acid were examined by electron and x-ray diffraction and by electron and light microscopy; the self-discharge of the dioxide films on the metals was followed by time-potential curves; the relation between anodic attack, self-discharge characteristics, and the microstructures of the metals are reported.

Anodically formed dioxide coatings on lead and the alloys comprise a mixture of two polymorphic forms of PbO_2 at the metal-coating interface, and common tetragonal lead dioxide at the solution-coating interface. Discharge of these dioxide coatings indicates that βPbO_2 discharges more rapidly than αPbO_2. The potential of a discharging surface is determined by these relative rates as well as by the physical structure of the dioxide layers. This in turn is determined to some extent by the microstructure of the metal.

The metals were shown to be preferentially attacked at grain boundaries and in interdendritic areas depending on the nature of the segregated material and structural discontinuities. A discussion of some of the crystal chemistry of the lead compounds, potential-pH diagram, and the lead acid cell is included.

Corrosion of the positive grid in the lead acid cell is a limiting factor in useful cell life, and examination of such processes includes a study of the anodic coatings formed on grid metals under cell environments. This paper is a continuation of studies reported earlier (1, 2) concerning the anodic coatings formed on Pb and its alloys in H_2SO_4, and their electrochemical and physical characterization. The experimental work comprised (*a*) determination of the self-discharge characteristics of the coatings, (*b*) determination of the relation between anodic attack of the metals and their microstructures, (c) identification of the anodic products by electron and x-ray diffraction, and (*d*) the microscopic examination of the anodic coatings formed on Pb and its alloys. Where possible such studies have been related to the corrosion rates of the alloys reported by Lander (3). To eliminate the possibility that preparation for electron diffraction examination caused changes in the nature of the anodic products, several experiments are reported on electrochemical preparations of the oxides deposited on Pt, and on bulk oxides.

Two crystal forms of PbO_2 have been reported, the common tetragonal variety, and an orthorhombic form (4-6). For purposes of this report the alpha form of PbO_2 is accepted as a second polymorphic form of the dioxide; however, despite the crystallographic studies devoted to this material, only very incomplete information on its stoichiometry has been published (5).

Experimental

Time-potential studies.—Alloys having the nominal compositions shown in Table I were prepared by melting weighed quantities of the pure metals in Pyrex tubes, and casting in Al molds. Specimens of each of the alloys, prepared in the same manner as previously used for pure Pb (1), were anodized above the $PbO_2/PbSO_4$ potential to develop a coating of PbO_2, and then allowed to self-discharge. The electrolyte was 1.210 sp gr H_2SO_4. The polarization and open circuit self-discharge were followed with a Hg, Hg_2SO_4 reference electrode in the same cell

Table I. Relation of microstructure to corrosion topography and rate in Pb alloys

Alloy additions wt % Ca	Sb	Sn	Relation of corrosion topography to microstructure	Corrosion rate penetration (3) cm/year
0.05	—	—	Intergranular penetration with undercutting subgrain crystallographic pitting	4.6×10^{-3}
0.09	—	—	Intergranular penetration and secondary interdendritic attack	
0.15	—	—	Severe intergranular and interdendritic penetration	
—	12	—	Severe intergranular and interdendritic penetration	
—	0.5	—	Intergranular penetration and secondary interdendritic attack	
—	2	4½	Intergranular penetration and secondary interdendritic attack	2.3×10^{-3}
—	—	4½	Intergranular attack, V notch type	
0.05	—	4½	Intergranular penetration, V notch type	
0.09	—	4½	Intergranular penetration, V notch type	
0.15	—	4½	Primarily intergranular attack with secondary interdendritic penetration	
	0.01		The relation of microstructure and corrosion in the Pb-Sb alloys has been reported (2).	
	1			
	6			
	9½			

and in precisely the same fashion used in the previous work.

A freshly polished metal specimen was used in most instances, but several specimens were reused after stripping the anodic products in NH_4Ac (saturated ammonium acetate solution) and rinsing.

Microstructure and Corrosion.—Portions of each of the alloy castings used by Lander (3) for corrosion rate determinations in the 40-week cycling test were examined at the end of the test to show the relation of corrosion to their microstructures. The corrosion products were stripped by soaking in NH_4Ac followed by rinsing and drying. Faxfilm[1] replicas were made of the corroded surfaces. A portion of each specimen was milled, polished, and etched in acetic acid, hydrogen peroxide solution to develop the microstructure. Photomicrographs were made of the replicas and metallographic specimens.

Corrosion products and special preparations.—The anodic corrosion products formed on alloys used in this study were examined by reflection electron diffraction. Specimens were prepared by polishing, etching, rinsing in NH_4Ac, and distilled water. They were anodized in H_2SO_4 above the $PbO_2/PbSO_4$ potential for varying lengths of time up to 8 hr. Specimens were blotted dry with tissue, and electron diffraction patterns taken.

Rolled Pb sheet annealed at 100°C for six weeks was cleaned by etching, rinsing in NH_4Ac and distilled water. The sheet was then anodized above the $PbO_2/PbSO_4$ potential in H_2SO_4 for various periods of time up to 30 days. The surface was blotted dry. Similarly prepared specimens were allowed to self-discharge to near the $Pb/PbSO_4$ potential, and the surfaces blotted dry. These charged and discharged surfaces were examined by reflection electron and x-ray diffraction. Anodic products were freed from such surfaces by soaking in NH_4Ac and gently lowering the specimen through a water surface. The floating residues were picked up on film-coated specimen screens for electron microscope and diffraction examinations. A similar discharged specimen was mounted in casting plastic (7), sectioned, polished, and photomicrographs made under polarized light.

Similarly prepared specimens of pure Pb sheet were anodized at constant potentials below the $PbO_2/PbSO_4$ potential, at this potential, and at gassing. The electrode products were examined by electron and x-ray diffraction.

Chemical replicas of 1% and 9½% Sb-Pb alloys were prepared and photographed (8).

Lead dioxide was deposited on Pt foil electrodes from divalent lead solutions, under conditions described by Zaslavskii, *et al.* (6), to give deposits of known crystal form. The structures were verified by x-ray diffraction. Such electrodes were rinsed in distilled water and used in these subsequent studies: *(a)* soaked in 1.250 sp gr H_2SO_4 for three days; *(b)* anodized in 1.250 sp gr H_2SO_4 above the $PbO_2/PbSO_4$ potential up to one week against a Pt cathode; *(c)* discharged cathodically against a Pt cathode in 1.250 sp gr H_2SO_4 followed by anodization above the $PbO_2/PbSO_4$ potential to reform the dioxide; *(d)* anodized in 3N NaOH solution using a Pt cathode for as long as three days.

The anodic products from this series of tests were examined by x-ray and electron diffraction and electron microscopy. The microscope specimens were prepared by soaking in NH_4Ac, floating on water, and mounting on film-covered specimen screens.

Chemically prepared tetragonal PbO_2 (9) and reagent grade PbO_2 were pressed onto lead sheets and soaked or anodized above the $PbO_2/PbSO_4$ potential in 1.250 sp gr H_2SO_4 for varying periods up to one week. The materials were then examined by x-ray and electron diffraction. After treating with NH_4Ac and floating on water, the materials were mounted on screens for electron diffraction and microscope examination.

Electron diffraction patterns and micrographs were obtained with an RCA EMU 2, and the x-ray patterns were made with Phillips or General Electric direct recording spectrogoniometers. Free use was made of the optical microscope to examine sur-

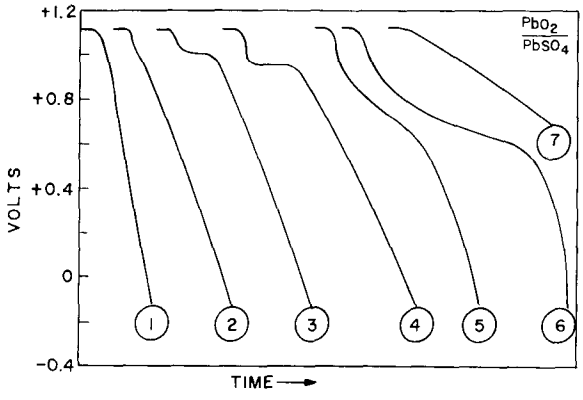

Fig. 1. Self-discharge of PbO_2 coatings on Pb alloys in H_2SO_4 vs. Hg_2SO_4/Hg electrode. The curves are numbered and were obtained with the following alloys (composition indicated is nominal weight per cent): curve 1, 4½ Sn 2 Sb; 4½ Sn; 0.15 Ca; 0.01 Sb; 12 Sb (first run); curve 2, 0.05 Ca; 9½ Sb; curve 3, 0.09 Ca; 0.05 Ca; 1 Sb; curve 4, 0.15 Ca 4½ Sn; 0.15 Ca; 12 Sb (second run); curve 5, 6 Sb; curve 6, 12 Sb (third run); curve 7, 0.09 Ca 4½ Sn; 0.05 Ca 4½ Sn.

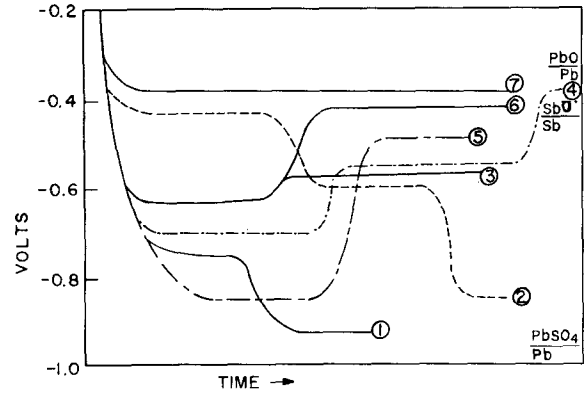

Fig. 2. Prolonged self-discharge of PbO_2 coatings on Pb alloys in H_2SO_4 vs. Hg_2SO_4/Hg electrode. The curves for the several alloys are numbered according to the following order: curve 1, 4½ Sn; 0.09 Ca 4½ Sn; curve 2, 0.09 Ca; 0.09 Ca 4½ Sn; 0.15 Ca 4½ Sn; curve 3, 4½ Sn 2 Sb; curve 4, 0.05 Ca; curve 5, 0.15 Ca; 6 Sb; curve 6, 0.09 Ca 4½ Sn; 0.01 Sb; curve 7, 12 Sb; 0.15 Ca; 0.05 Ca 4½ Sn; 1 Sb; 9½ Sb.

[1] The Faxfilm Co., 1220 W. Sixth St., Cleveland 13, Ohio.

faces during the electrochemical treatments and after removal from the electrolyte.

Results and Discussion

Time potential studies.—The self-discharge of thin coatings of anodically formed PbO_2 on the Pb alloys used in this study are shown in the schematic time-potential curves of Fig. 1 and 2. The general shape of the curves is considered, and this is not a comparison of the time intervals. It is seen that the slope of the discharge curves from the $PbO_2/PbSO_4$ potential arrest varies over wide limits and may exhibit well-defined arrests. These intermediate arrests are real in that cathodic or anodic pulses of current do not destroy them; however, they are not thought to correspond to thermodynamic equilibrium potentials, but rather to mixed potentials caused by physical changes of the anodic coatings. These physical changes are induced at least in part by the nature of the metal itself. Random metallographic cuts of a cast alloy may be expected to give rise to variation in discharge characteristics because the relative amount of segregated material exposed on a given small surface area will vary. For example, three types of discharge curve were observed for a specimen of 12% Pb-Sb alloy. These were developed by reusing the same specimen, stripping the corrosion product, rinsing, and anodizing, omitting the resurfacing or metallographic polishing between runs. Type curves numbered 1, 4, and 6 were obtained from a single specimen. The freshly prepared and polished specimen (curve 1) was found to discharge after barely pausing at the $PbO_2/PbSO_4$ potential by falling rapidly to an arrest near that of the Sb electrode. Reuse of the same area after cleaning and rinsing resulted in curve 4, and curve 6 was obtained on the third run. The change in the discharge curves is attributed to the relative amounts of segregated Sb present in the metal surface. Antimony is preferentially leached from the metal during anodization; thus reuse of a specimen causes a progressive depletion but not elimination of Sb from the surface, and produces a progressively less steep discharge curve. It is doubtful whether the Sb may be completely leached from the surface of alloys containing 1% or more, as the interdendritic canals of segregated Sb are continuous.

When clear-cut arrests appear near the $PbO_2/PbSO_4$ potential, it is believed that a fixed but limited pore area is induced in the anodic film by solution of the segregated metal phase. The potential of the surface will then be determined by simultaneous electrochemical processes, the resultant being a mutually polarized potential. This mixed potential of the surface gives rise to thermodynamically unexpected anodic products (1, 10) owing to depletion of hydrogen ion in the pore areas and polarization of the surface by PbO_2. When Pb is anodized to develop a coating of PbO_2 and allowed to stand on open circuit, it exhibits the reversible $PbO_2/PbSO_4$ potential. Scratching to expose bare metal causes a lowering of potential, but a rapid restoration occurs on termination of the disturbance. The scratch marks remain bright and clean. Such a phenomenon is considered to be healing of the anodic film by sulfation of the exposed metal. In those cases where the anodic films discharge with a steep slope, it is believed that a large pore area rapidly develops on the surface once the film becomes porous at all, and that the pores do not become sealed. When the discharge curve shows a lower slope it is thought that the pores develop continuously at a slow rate. In those instances where well-defined intermediate arrests occur, the film becomes porous, but the pores remain open and constant in area during the time of the arrest. A soluble alloy component acts as a pore generator and tends to keep the pores open. A similar effect would be expected when the specific volume of the anodic products of the alloying metal differs markedly from those of Pb. The positive plate discharge reactions take place simultaneously with the physical destruction of the coating. The ultimate materials present on a "discharged" surface depend on the relative rates of the processes. Thus it is possible to observe residual undischarged PbO_2 on the surface after complete apparent discharge (1). The tendency of the metal to develop and maintain porosity in the anodic film influences the apparent efficiency of the discharge process at the reversible $PbO_2/PbSO_4$ potential.

Prolonged self-discharge of the anodized surfaces of the several alloys shows the series of curves in Fig. 2. In some cases the discharge terminated at −0.38 v relative to the Hg, Hg_2SO_4 electrode, and others fell to the $Pb/PbSO_4$ potential only to rise again toward more positive values as sulfation was completed. These curves are similar to those reported for static passivation (11-13), and if sufficient time had elapsed, they would probably all have leveled off near the value −0.4 v. In these cases the porosity of the sulfate film is considered to be the controlling factor in the time required for total passivation as suggested by the several investigators. Here again thermodynamically unexpected materials occur because of acid depletion at the metal interface (1, 11).

Microstructure and corrosion.—The anodic corrosion of Pb alloys is related to their microstructures and usually proceeds by grain boundary attack, or a combination of grain boundary and interdendritic penetration (2). The alloys used in this study showed three types of corrosion topography. Examples of each of the categories are shown in Fig. 3, 4, and 5; results are summarized in Table I.

The relation of corrosion and microstructure in the Pb-Sb alloys has been described earlier (2). The cause of the preferential attack at the grain boundaries in the lower alloys is attributed to discontinuities in the segregated Sb at low concentrations. The higher alloys, however, have a greater degree of continuity between the material segregated at grain boundaries and in the interdendritic network as shown in Fig. 6. These microphotographs show chemical replicas (8) of two grain boundary areas of 1% and 9½% Pb-Sb alloys. The spheroidal segregation in the low alloys is less continuous than the eutectic segregation of the higher wherein the grain boundary area is not markedly different from the interdendritic.

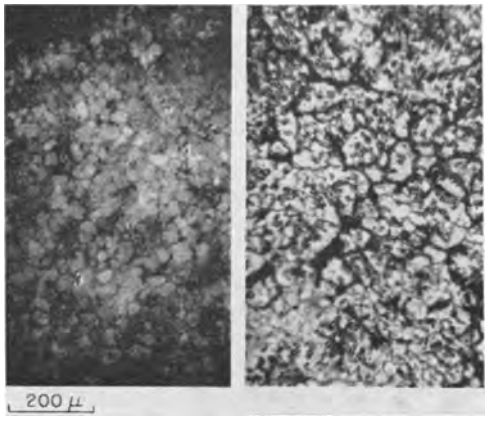

Fig. 3a. (left) 0.05 Ca-Pb binary alloy as-cast structure; Fig. 3b. (right) Replica of the corroded surface of 0.05 Ca-Pb binary alloy after removal of the corrosion products showing penetration at the grain boundaries, and areas where whole grains were undercut.

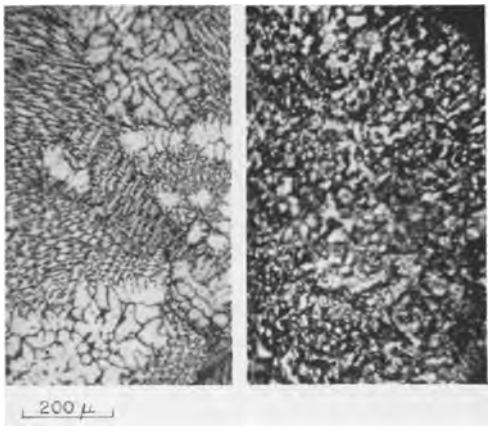

Fig. 4a. (left) 0.15 Ca-Pb binary alloy as-cast structure; Fig. 4b. (right) Replica of the corroded surface of 0.05 Ca-Pb binary alloy showing interdendritic and intergranular penetration.

The binary Pb-Ca alloys showed a behavior similar to that of the Pb-Sb system. The alloy containing 0.05% Ca corroded preferentially at the grain boundaries, and the sub-grain attack took the form of small crystallographic etch pits as seen in Fig. 3. In addition there are numerous areas where entire grains have been completely undercut. A metallographic specimen of the alloy is also shown in the photograph. In alloys of 0.09% Ca, the attack resulted in primary grain boundary penetration and secondary interdendritic attack. Fig. 4 shows the microstructure of 0.15% Ca alloy, typical of as-cast binary structures; and the corroded surface that shows deep penetration in both grain boundary and interdendritic areas.

The binary Pb-Sn alloy showed preferential attack of the V-notch type at the grain boundaries similar to that seen on pure Pb (2).

The ternary Sn, Ca, Pb alloys resembled the Pb-Sb series in their corrosion topography. Those with 0.05 and 0.09% Ca showed intergranular V-notch attack, and that with 0.15% Ca showed primarily intergranular with secondary interdendritic attack.

The microstructure of the ternary alloy with 2% Sb and 4½% Sn showed a mixture of large and small grains of different compositions (Fig. 5). The

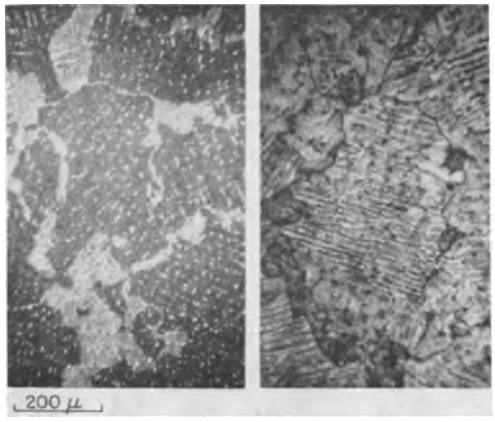

Fig. 5a (left) 2 Sb 4½ Sn-Pb ternary alloy as-cast structure showing pseudobinary structure; Fig. 5b. (right) Replica of the corroded surface showing preferential attack of the segregated eutectic material.

Fig. 6a. Chemical replica of 1% Sb-Pb alloy showing spheroidal Sb particles and discontinuity at the grain boundary region. The light areas are primary Pb dendrites, and the dark areas are segregated Sb.

smaller grains lie at the boundary areas of the larger, and it is apparent that this alloy is a pseudobinary structure, indicating that the liquidus attains the ternary eutectic composition during freezing (14). The anodic attack is primarily in the areas of the segregated ternary eutectic material as shown in the photograph of the corroded surface.

It is possible to correlate the corrosion rates with the physical pattern of the anodic attack. Lander's (3) corrosion rate determinations on these same alloys showed that the Sn binary and ternary alloys had lower rates than the alloys without Sn additions. The higher rates were associated with simultaneous attack at the grain boundaries and subgrain structures, and with deep intergranular attack, whereas the lower rates were associated with moderate grain boundary penetration and only secondary attack in the body of the grain.

Corrosion products.—The identification and characterization of the anodic corrosion products on Pb and the alloys was accomplished by electron and x-ray diffraction examination. Identification by diffraction techniques of the several anodic oxides on Pb has been effected by holding the specimens at

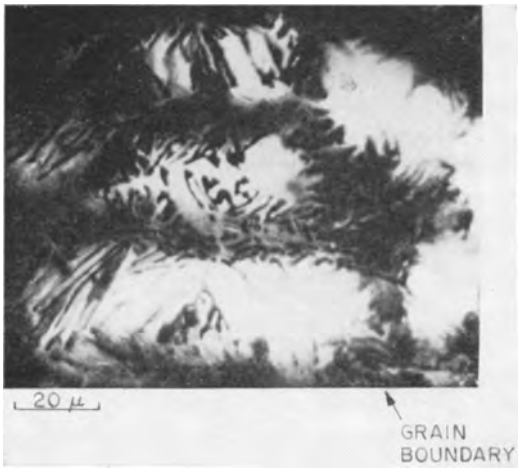

Fig. 6b. Chemical replica of 9½% Sb-Pb alloy showing typical as-cast structure with eutectic segregation continuous at the grain boundaries and interdendritic areas. Light areas are primary Pb dendrites and dark material is segregated Sb.

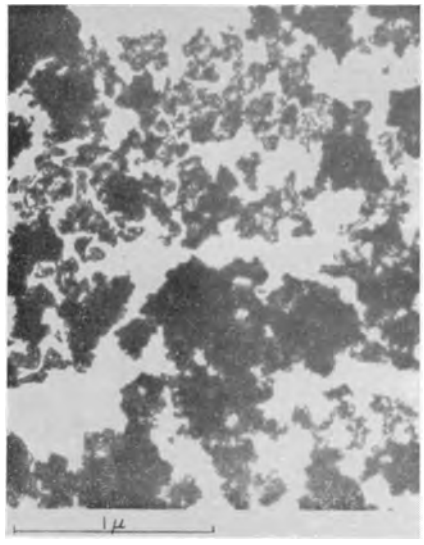

Fig. 7. Electron micrograph of αPbO_2 particles after isolation from the anodic surface.

selected potentials for sufficient time to produce coatings heavy enough to give strong clear patterns in the low theta region.

Earlier work (1) indicated the presence of an unidentified species on Pb anodes in H_2SO_4. This material has been identified as αPbO_2 in the present study. Fig. 7 is an electron micrograph of αPbO_2 after isolation from the other anodic products and the base metal. The particles exhibit no holohedral forms, and are approximately 0.1μ in diameter. This is the same size range reported by Feitknecht and Gaumann (15), and observed in this study for electrolytic tetragonal PbO_2.

Alpha PbO_2 is commonly prepared by anodic oxidation of plumbites, by extraction of plumbates, and it is the form of PbO_2 occurring on Pb in alkaline solutions at elevated potentials. The appearance of α and β PbO_2 as anodic corrosion products on Pb in acid solutions indicates that the oxidation proceeds by formation of tetravalent Pb in two ionic configurations—the so-called plumbic and plumbate.

Alpha PbO_2 has been observed in battery research in at least four independent investigations by Kameyama and Fukumoto (4), Bode and Voss (16), Ruetschi and Cahan (17), and at this Laboratory.

Anodization of Pb in acid at potentials immediately below the reversible $\beta PbO_2/PbSO_4$ potential produces a deposit of PbO_t (1, 10) that may exhibit a preferred orientation with (110) parallel to the substrate. This causes the d = 2.81 line to be the strongest in the pattern. The pattern for $PbSO_4$ is present at certain potentials but does not occur if the potential of anodization is sufficiently near that

Table II. Some typical diffraction patterns of anodic corrosion products on Pb

βPbO_2*		βPbO_2		PbO_t		$\alpha+\beta$ PbO_2		αPbO_2		αPbO_2		αPbO_2	
H_2SO_4** x-ray†		H_2SO_4 electron diffraction		H_2SO_4 x-ray		H_2SO_4 x-ray		H_2SO_4 x-ray		H_2SO_4 electron diffraction°		KOH x-ray	
d	I‡	d	I	d	I	d	I	d	I	d	I	d	I
3.50	vvs	3.50	s	3.12	s	3.83	w	3.82	mB	3.80	w	3.82	mB
2.79	s	2.80	vvs	2.81	vvs	3.50	w	3.12	vvvs	3.11	vvvs	3.12	vvs
2.46	vs	2.46	m	2.51	vw	3.14	vvs	2.97	w	2.74	m	2.97	w
1.85	m	1.86	s	1.87	m	2.79	s	2.73	mB	2.60	m	2.74	mB
1.75	m	1.69	s	1.68	mB	2.74	m	2.61	mB	2.23	vvwB	2.61	mB
1.68	m	1.56	mB	1.406	w	2.60	m	2.23	w	2.00	wB	2.21	w
1.556	w	1.48	mB	1.218	m	1.85	sBB	1.89	w	1.81	vsB	2.01	w
1.519	w	1.28	m	1.077	m	1.687	w	1.84	mB	1.64	m	1.84	mB
1.486	m	1.22	m			1.550	w	1.81	mB	1.53	s	1.81	mB
1.387	w	1.15	mB			1.520	m	1.80	mB	1.42	w	1.64	m
1.273	m	1.123	mB			1.510	m	1.64	w	1.22	wB	1.55	w
1.238	w	0.996	m			1.257	w	1.54	mB	1.205	wB	1.53	mB
1.214	w							1.27	wB	1.155	wB		
1.152	w							1.23	wB	1.087	wB		
								1.19	wB	1.038	mB		
								1.15	wB				

* Identification on the basis of pattern shown.
** Electrolyte in which anodization was carried out. H_2SO_4 signifies 1.250 sp gr H_2SO_4. KOH signifies 3N KOH.
† Diffraction technique used.
‡ Estimated intensities: v = very; s = strong; m = medium; w = weak; B = broad peak; BB = very broad.
° Residue from extracted film by transmission electron diffraction; all other patterns shown were obtained by reflection.

of $PbO_2/PbSO_4$. Upon subsequent anodization of the same specimen immediately above the reversible potential, the pattern of βPbO_2 appears, and the strong pattern for PbO_t persists. Only the pattern for βPbO_2 is observed by reflection electron diffraction from such a surface while that of PbO_t is the stronger in the x-ray pattern. If anodization is continued at the elevated potential, the diffraction pattern for PbO_t diminishes gradually; the pattern for βPbO_2 increases in intensity simultaneously. The length of anodic time required to observe these effects depends on the amounts of the several materials present on the surface, and if an initial layer of $PbSO_4$ is heavy enough, its pattern and subsequently that of βPbO_2 will be the only ones observed by electron or x-ray diffraction. Superficial coatings of $PbSO_4$ and βPbO_2 may be removed by wiping the surface vigorously with dry lens tissue. It must be emphasized that the detection of PbO_t and αPbO_2 depends on the presence of limited amounts of $PbSO_4$ or βPbO_2. This is one reason why work at this Laboratory has employed constant potential anodization, as the development of the electrode product is limited to a single material characteristic of the selected potential. Anodization of cleaned lead surfaces at potentials above the $PbO_2/PbSO_4$ potential (gassing O_2) produces a deposit of αPbO_2 having a strong clear x-ray pattern in the low theta region.

Table II shows some typical diffraction patterns observed for anodic coatings on Pb. Standard comparison patterns are available in the literature, although definitive readings are best made by comparison of standards recorded on the same equipment.

As on pure Pb, the alloys of this study developed PbO_2 coatings in H_2SO_4 that were shown by electron diffraction to be laminates of βPbO_2 at the solution interface, and a composite of α and βPbO_2 at the metal surface. The greatest attention was devoted to the anodic products on pure Pb owing to the fact that the alloying agents used in the study have diffraction patterns that introduce certain difficulties. For example, Sb gives an x-ray pattern resembling that of a mixture of lead oxides, and rather strong patterns are obtained for Sb in the Pb alloys. In addition it is likely that the oxides of certain alloying agents form mixed crystals with the lead oxides, and have similar structures. The possibilities of mixed oxide formations must rest with future investigation.

The PbO_2 deposits formed on the alloys listed in Table I were variable in appearance. All were dark brown to black in color, but their textures ranged from smooth, hard, brittle, glossy adherent coatings to flaky, porous, friable, lusterless, loose deposits. In general, the alloys exhibiting low corrosion rates (Table I) produced smoother deposits. These ultimately fracture and part from the metal in large brittle concave flakes suggesting that when attached to the metal the oxide is under compression. At the base of the fracture fissures shiny base metal was visible, and on occasion the oxide flakes pulled metal away from the surface. The loose scaly deposits came away from the metal as powder; however the porosity of the deposit appeared greater in areas corresponding to the segregated phase of the metal structure.

The earlier report (1) described an unidentified anodic product on pure Pb having a body-centered tetragonal lattice with the parameters a_0 3.54, c_0 5.86 kX units. The orientation determination and parameters were calculated from reflection cross grating electron diffraction patterns of anodized surfaces. These patterns may be of normal twinned crystals, or of distorted lattices caused by compression while in contact with the metal. As mentioned above there is evidence that the anodic deposit is under compression while attached to the metal surface. The c_0 value of 5.86 observed by electron diffraction is in reasonable agreement with b_0 reported for αPbO_2 of 5.93 from x-ray studies. The parameter $a_0 = 3.54$ would then correspond to that of 3.668 of the [101] of αPbO_2. This oxide appears to be deformed into this tetragonal lattice when attached to the metal, and to assume its normal parameters after separation from the influence of the Pb surface by fracture or by growing to sufficient depth. The stresses exerted by such a deformed lattice growing epitaxially on the Pb may be the primary cause of growth of pure Pb grids in cell use.

Special preparations.—Special preparations were undertaken to determine the nature and origin of αPbO_2 in the anodic corrosion product. It was suggested by Bode and Voss (16) that solid phase oxidation of PbO_t formed αPbO_2. Similarly it was possible that αPbO_2 had formed during some of the treatments applied to the corrosion products in this study. Alpha and beta PbO_2 could be expected to be different in their electrochemical behavior: would αPbO_2 discharge to $PbSO_4$? If so, would this sulfate anodize to αPbO_2? What significance could then be attached to the familiar $\beta PbO_2/PbSO_4$ electrode? These questions among others prompted a few special preparations and preliminary studies.

X-ray diffraction examinations showed that coatings of αPbO_2 on Pt discharged in H_2SO_4 to form $PbSO_4$. When reanodized in H_2SO_4 βPbO_2 was the solid product. Therefore, formation of αPbO_2 may be considered an irreversible electrode process when it occurs in the positive plate of the lead acid cell, and it is necessary to differentiate between studies of reversible systems such as reported by Beck, Lind, and Wynne-Jones (18) and of irreversible systems such as grid corrosion.

Chemically pure βPbO_2 was treated with solutions of H_2SO_4 and NH_4Ac in contact with metallic Pb and $PbSO_4$. The extracted residues showed only βPbO_2 by electron diffraction. Therefore αPbO_2 is not formed by chemical reaction nor during subsequent treatments of the corrosion products used in this study. The isolation of αPbO_2 from the other anodic products eliminated the possibility that x-ray patterns obtained by reflection from the anodic material *in situ* arise from oriented $PbSO_4$ and PbO_t.

Lead sheet anodized above the $PbO_2/PbSO_4$ potential in H_2SO_4 was allowed to self-discharge to

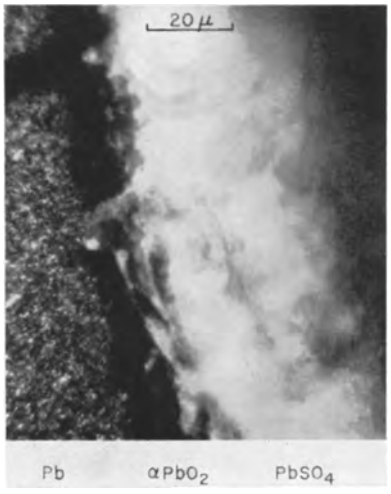

Fig. 8. Plastic mounted section of discharged PbO_2 coating on Pb showing $PbSO_4$ and heavy layer of αPbO_2. Magnification 1000x before reduction for publication.

near the $Pb/PbSO_4$ potential. The specimen appeared gray and totally discharged; x-ray diffraction examination of the surface showed only $PbSO_4$. Extraction with NH_4Ac removed the heavy sulfate coating leaving considerable residue of dark brown material. This residue was shown by electron diffraction to be αPbO_2 of very high purity. The two materials, $PbSO_4$ and αPbO_2, are visible in the micrograph of the cross section of the discharged sheet shown in Fig. 8.

The fact that discharged films are composed chiefly of these two materials indicates that the two forms of PbO_2 discharge at different rates. On the specimen, Fig. 8, the discharge has taken place at discontinuities in the αPbO_2 layer and across the surface, precisely where the βPbO_2 appears, indicating that βPbO_2 discharges more readily than αPbO_2.

It is clear that the efficiency of the discharge of PbO_2 coatings on Pb and its alloys in H_2SO_4 is governed by the physical nature of the films (porosity, stress, alloying metals); the morphology of the crystalline phases present; and the rates and mechanisms of discharge of the two forms of PbO_2.

Crystal Chemistry and Thermodynamics

The formation of the anodic corrosion products of Pb in H_2SO_4 is considered to take place by three crystallization mechanisms summarized succinctly by Feitknecht (19): (*a*) by way of the free solution; (*b*) by boundary nucleation and growth; and (*c*) by solid phase transformation. These three mechanisms may be applied equally well to the cycling processes of the active material, and interpreted in terms of the crystal chemistry of the lead oxides, and the thermodynamic equilibria of the system summarized by Delahay, Pourbaix, and Van Rysselberghe (20) in the potential-pH phase diagram. For convenience part of the diagram has been reprinted in Fig. 9, with the solid phases indicated. The reactions and numeration are retained from the original presentation.

Lead sulfate is in equilibrium under conditions defined by lines 51 and 52 with βPbO_2. During anodization of sulfate crystals they were observed by

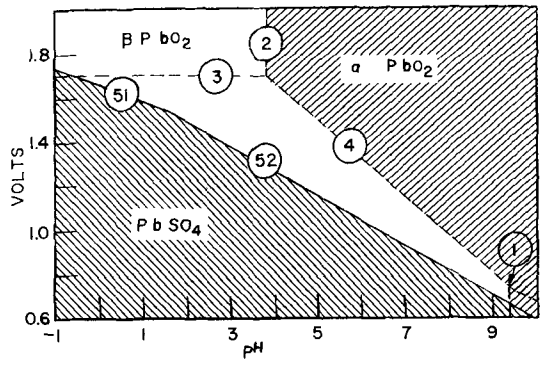

Fig. 9. Portion of the potential-pH diagram of Pb in H_2SO_4 with solid phases indicated. The reactions indicated by the original numerations are:

1. $HPbO_2^- + 3H^+ = Pb^{++} + 2H_2O$
2. $PbO_3^= + 6H^+ = Pb^{+4} + 3H_2O$
3. $Pb^{+4} + 2e^- = Pb^{++}$
4. $PbO_3^= + 6H^+ + 2e^- = Pb^{++} + 3H_2O$
51. $PbO_2 + HSO_4^- + 3H^+ + 2e^- = PbSO_4 + 2H_2O$
52. $PbO_2 + SO_4^= + 4H^+ + 2e^- = PbSO_4 + 2H_2O$

The equilibrium between the two forms of PbO_2 remains to be verified by experiment in the region of line 4. Potentials are shown vs. standard hydrogen electrode.

optical microscope to become colored dark brown. A single crystal of sulfate may be part clear sulfate, part opaque brown, and the conversion appears to take place as a solid phase transformation. The complete conversion to βPbO_2 of the sulfate crystal occurs because the transformation liberates H_2SO_4, and the interior of the crystal does not suffer a depletion of acid. The transformation is best described as a boundary nucleation and growth phenomenon, rather than a solid phase oxidation. The direction of growth is toward the Pb-rich interior of the crystal, and the holohedry of the sulfate crystal is sometimes maintained by the mass of small βPbO_2 crystals.

Microscopic observation of the discharge of a coating of βPbO_2 on Pb indicates that the sulfate forms by way of the free volume of solution as dendritic crystals grow out into the solution. However, they are anchored in the dioxide coating and probably originate from nuclei in the boundary layer and grow outward into the sulfate-rich solution. If such crystals are knocked off the surface, it may be seen that the hole in the PbO_2 coating is an intaglio of the base of the sulfate crystal. These dendritic sulfate crystals are smoothly reconverted to βPbO_2 upon anodization.

Prolonged discharge results in a heavy layer of congealed rhomboidal sulfate crystals in which the dendritic crystals are embedded. These larger crystals are reconverted to βPbO_2 with difficulty because they frequently lose contact with the anodic surface owing to gas formation in the interstices where βPbO_2 first forms in such coatings (15).

The diagram of Fig. 9 shows that in solutions of pH 9.4 and higher, βPbO_2 would not be expected to form reversibly at any potential, whereas below this pH, βPbO_2 can be expected as the dominant phase in certain potential ranges. The area where αPbO_2 would be expected approaches the $PbSO_4$ do-

main at pH 9.4 and higher; therefore, αPbO_2 and $PbSO_4$ may comprise a reversible system at this area unless compounds not shown on the diagram intervene.

In an area near lines 4 and 2 an eutectic of both phases of PbO_2 could occur, and may be expected to transform reversibly by proper choice of environment.[2] But this change is not rapid as coatings of αPbO_2 and βPbO_2 on Pt do not transform upon anodization in H_2SO_4 and NaOH, respectively, for as long as three days as shown by x-ray diffraction examination.

It is now evident why the anodic corrosion products formed on Pb above the $PbO_2/PbSO_4$ potential and the active material paste of a charged cell (16) exhibit the same lamellar formation: the solution interface shows only tetragonal PbO_2, the stable phase in acid of battery strength at positive plate potentials. At the anodic surface water and/or hydroxyl ions are being discharged. At the metal surface and inner layers of the active material, the potential and pH may lie within the domain of αPbO_2, or at least in the area where mixtures of the two phases are formed. At constant high potential, once the βPbO_2 coating forms, it may increase in thickness only by deposition of Pb ion in solution or by conversion of the underlying material. The heavy layer of αPbO_2 (Fig. 8) indicates that corrosion of the underlying metal at elevated potentials takes place to a considerable extent by migration of the oxygen species into the surface. The occurrence of the αPbO_2 growing epitaxially on the Pb and in a deformed lattice suggests that the oxidation takes place beneath the βPbO_2 surface coating as a solid phase oxidation of the base metal, and an oxide layer progressively richer in metal toward the center of the specimen would be expected. The rate of formation of the αPbO_2 as a corrosion product must be controlled by the rate of penetration of the oxygen species through the βPbO_2 layer.

The point of zero charge on a βPbO_2 electrode is approximately 0.1 v positive to the $PbO_2/PbSO_4$ electrode in battery electrolyte (21). Anodization of Pb coated with βPbO_2 at such a potential produces a positive surface charge. At the positive interface owing to charge orientation, hydrogen ion would not be the dominant species, nor would it be able to penetrate the coating, and an increase in pH would be expected at the metal-coating interface. Therefore the thermodynamically stable phase at elevated pH and potential is formed by grid corrosion beneath the original βPbO_2 coating. If the metal ion migrated out to form PbO_2 at the solution interface, βPbO_2 would become buried in the αPbO_2, and such is not the case, as a superficial coating of βPbO_2 was always observed by electron diffraction. It was suggested by Kabanov, Kiseleva, and Leikis (21) that oxygen does penetrate the βPbO_2 lattice, and cause recrystallization and a change in crystal structure of βPbO_2. The rate of penetration of the oxygen species through the lattice would control the rate of corrosion of the underlying Pb, and would be dependent on the effective oxygen concentration at the surface. Thus a high corrosion rate of grid metal would be expected under overcharge conditions, as is well known to be the case in actual practice.

On cycling a mixture of the two forms of PbO_2, both discharge to $PbSO_4$, but owing to the difference in rates some αPbO_2 remains in the discharged mixture. Upon reconverting the $PbSO_4$ to βPbO_2 H_2SO_4 is liberated in contact with the αPbO_2 and it tends to convert to $PbSO_4$ and βPbO_2. Thus, upon cycling, αPbO_2 will gradually be consumed, and Bode and Voss (16) reported that the amount of αPbO_2 in the interior of the active material of a cell does indeed diminish with cycling. However, αPbO_2 continues to be generated by the corrosion mechanism until complete exhaustion of the free metal.

It was observed in this study that initially a conversion to βPbO_2 takes place at the surface of PbO_t crystals on anodizing in acid.[3] Formation of PbO_2 from such crystals at elevated potentials must therefore occur beneath a superficial βPbO_2 coating which prevents ready access of acid. Therefore paste materials that contain lower oxides and sulfate deficient mixtures may be expected to give rise to αPbO_2 and very slow development of full capacity. Any treatment of a cell that would shift the conditions of the positive plate away from those pertaining near lines 51 and 52 in Fig. 9 toward lines 2 and 4 would be expected to form some αPbO_2 both by grid corrosion and from active material components.

Beneficial effects of gradients in acid concentration existing in the cross section of the plate may be inferred from the diagram. The high positive polarization of the plate is fixed by the βPbO_2 surface. Areas deficient in acid would be held above their discharge potentials. At the beginning of discharge the process would be confined to the high acid surface of the plate. As this area became deficient in acid the discharge would extend into the deeper layers, and ultimately all the βPbO_2 could be converted to $PbSO_4$ provided sufficient acid were present. If such a mechanism did not apply, little capacity would be obtainable as the material immediately adjacent to the grid would discharge simultaneously with the outer surface and undercut active material.

Manuscript received May 3, 1957.

Any discussion of this paper will appear in a Discussion Section to be published in the June 1958 JOURNAL.

REFERENCES

1. J. Burbank, *This Journal*, **103**, 87 (1956).
2. J. B. Burbank and A. C. Simon, *ibid.*, **100**, 11 (1953).
3. J. J. Lander, *ibid.*, **99**, 467 (1952).
4. N. Kameyama and T. Fukumoto, *J. Soc. Chem. Ind., Japan*, **49**, 154 (1946).
5. T. Katz, *Ann. de Chim.*, 12th Ser., **5**, 5 (1950).
6. A. I. Zaslavskii, Yu. D. Kondrashov, and S. S. Toklachev, *Doklady Akad. Nauk, SSSR*, **75**, 559 (1950).

[2] The precise location of the eutectic line separating the two solid phases of PbO_2 must be determined by future investigation.

[3] The conversion of the lead monoxides to sulfate is not rapid, and several days' soaking in acid is required to produce sufficient sulfate to be detectable by x-ray diffraction. In anodizing the PbO_t crystals in acid, a βPbO_2 coating was observed by electron diffraction during the period when x-ray diffraction showed only unconverted PbO_t. The open circuit potential of such a specimen was that of the $PbO_2/PbSO_4$ electrode.

7. A. C. Simon and E. L. Jones, *This Journal*, **102**, 279 (1955).
8. J. Burbank, *J. Metals*, **5**, 55 (1953).
9. M. P. Applebey and R. D. Reid, *J. Chem. Soc.*, **1922**, 2129.
10. J. J. Lander, *This Journal*, **98**, 213 (1951).
11. W. J. Muller and W. Machu, *Korr. u. Met.*, **16**, 187 (1940).
12. E. J. Casey and K. N. Campney, *This Journal*, **102**, 219 (1955).
13. H. E. Haring and U. B. Thomas, *Trans. Electrochem. Soc.*, **68**, 163 (1935).
14. W. Hofmann, "Blei und Bleilegierungen," p. 75 ff., Julius Springer, Berlin (1941).
15. W. Feitknecht and A. Gaumann, *J. Chim. Phys.*, **49**, 135 (1952).
16. H. Bode and E. Voss, *Z. Elektrochem.*, **60**, 1053 (1956).
17. P. Ruetschi and B. D. Cahan, *This Journal*, **104**, 406 (1957).
18. W. H. Beck, R. Lind, and W. F. K. Wynne-Jones, *Trans. Faraday Soc.*, **50**, 147 (1954).
19. W. Feitknecht, *Fortschr. chem. Forsch.*, **2**, 670 (1953).
20. P. Delahay, M. Pourbaix, and P. Van Rysselberghe, *This Journal*, **98**, 57 (1951).
21. B. N. Kabanov, I. G. Kiseleva, and D. I. Leikis, *Doklady Akad. Nauk, SSSR*, **99**, 805 (1954).

Disintegration of Lead Cathodes, II

L. W. Gastwirt[1] and H. W. Salzberg

Chemistry Department, City College, New York, New York

ABSTRACT

In continuation of previous work, the disintegration of lead cathodes at high current densities at 25°C was studied. The solutions were acid, basic, and neutral combinations of sulfuric and phosphoric acids and ammonium and alkali sulfates, chlorides, and phosphates. The results support the hydride mechanism and contradict the alkali alloy hypothesis. The data are interpreted to indicate that water molecules are reduced at current densities below those needed for visible disintegration and that the surface is saturated with adsorbed hydrogen atoms at the start of disintegration.

Bredig and Haber (1) reported disintegration of cathodes of Pb, As, Sb, Sn, and other metals and ascribed it to the formation of an alkali alloy which reacted with the solution and disintegrated. They were at a loss to explain disintegration in acid solutions. Salzberg (2) studied the disintegration of Pb cathodes at high current densities in alkaline, neutral, and slightly acidic solutions, and suggested that the phenomenon was due to the formation of an unstable volatile hydride of Pb with the empirical formula PbH_2. This hypothesis was confirmed qualitatively by Pourbaix and Van Muylder (3) who reported that the standard free energy of formation of the compound was $+69.5 \pm 4.5$ kcal/mole, which would explain its instability and the high cathodic voltage needed for its formation.

However, Angerstein (4) stated that he was not able to obtain disintegration in molar and tenth molar acids in the absence of alkali metal cations at current densities of 10-100 ma/cm^2 and that he was not able to reproduce the results in dilute acids reported previously (1, 2). He therefore reiterated the alkali-alloy hypothesis in preference to a hydride mechanism.

The purposes of the present work were to check the results Angerstein stated that he could not duplicate and to obtain data using solutions that did not contain alkali cations.

Apparatus, Method, and Materials

An apparatus described previously (5) was simplified to facilitate removal of the cathode between runs. The cathodes were replaceable lead washers, usually 7-8 mm in diameter and about 1 mm thick, held between polyethylene washers on an iron shaft with a teflon sleeve. All work was done at 25°C.

Cathodes were prepared as in previous work (2). The materials were C.P. grade except for CsCl and RbCl. All solutions were pre-electrolyzed before use and frequently between runs. Whenever results were low or erratic either the solution or the cathode or both were cleaned or replaced. Checks were run using samples from different lots of material and sometimes using solutions prepared by different methods from different starting materials.

In spite of these precautions, reproducibility was poor. Consequently data were considered reliable only when obtained using different washers in several samples of each solution and reproduced in successive runs. Whenever cleaning or replacing the cathode or solution increased the rate, the lower result was discarded when preparing the graph.

Results

The dissolution rates were independent of time and the graphs of rate vs. current density were straight lines intercepting the current density axis. The intercept, i_o, varied with the solution. The slopes were of the correct theoretical value if, starting at i_o, one equivalent of divalent Pb left the electrode with each Faraday of current. Disintegration was observed in neutral, acid, and alkaline solutions in the presence of alkali cations, ammonium ions, and hydronium ions, either separately or in combination. No differences were noted between results in chloride, sulfate, and phosphate solution, at the same ionic strengths. Impurities caused lower and more erratic results.

[1] Present address: Princeton University, Princeton, N. J.

Table I.

H_2SO_4 Molarity	Current density	Dissolution rate
0.001	94 ma/cm²	0.1 mg/cm²-min
0.01	535	0.2
0.1	630	0.1

Acid inhibits the reaction. Table I shows a lack of appreciable disintegration in acid solutions containing no salt. Fig. 1 shows that in the presence of salt there is disintegration but that it falls off with increasing acidity. Note that until the acid concentration is about 0.05M, the slopes of the curves are unchanged, although the i_0's are increased.

Fig. 2 shows the same type of inhibition in ammonium sulfate solution. Here, however, there is an anomaly. In the concentrated salt solution a small increment of acid increases the rate, although a large increment, as usual, decreases the rate. A comparison of Fig. 1 and Fig. 2 show that the rates in ammonium salt solution are much lower than in sodium sulfate solution.

Salt effect.—Fig. 3 shows that, in the absence of acid, in dilute solution the disintegration rate is the same in all of the alkali salt solutions, but in concentrated solutions differences do show up. In molar salt solution the rates were higher in sodium sulfate than in potassium sulfate. In all cases the rates in ammonium salt solutions were less than in alkali salt solutions. Obviously, there is some inhibition due to ammonium ions.

In the presence of acid the (ungraphed) results were somewhat uncertain. The curves for each separate alkali salt solution were within the experimental error of each other and conceivably all the points could fall on the same curve. However, there did seem to be a trend indicating that the rates in Li solution were the highest, the rates in Na, K, and Rb solutions were all about the same, and those in Cs solution were significantly lower. The rates in ammonium salt solution were the lowest of all.

Conclusions and Discussion

The results are in qualitative and quantitative agreement with those previously published (2). Angerstein failed to obtain disintegration in acid solutions because his current densities were too low.

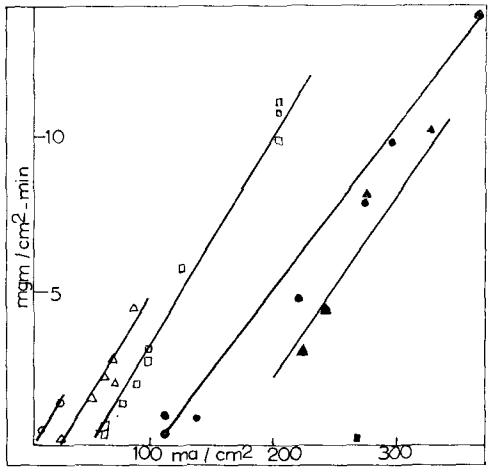

Fig. 2. Acid and NH_4^+ effects. Open circle, 0.01M $(NH_4)_2SO_4$ + 0.001M H_2SO_4; open triangle, 0.01M $(NH_4)_2SO_4$ + 0.01 H_2SO_4; closed square, 0.01M $(NH_4)_2SO_4$ + 0.1M H_2SO_4; closed circle, 0.1M $(NH_4)_2SO_4$ + 0 H_2SO_4; open square, 0.1M $(NH_4)_2SO_4$ + 0.01M H_2SO_4; closed triangle, 0.1M $(NH_4)_2SO_4$ + 0.1M H_2SO_4.

In 0.1-1M H_2SO_4 without added salt his maximum current density was 100 ma/cm², whereas Fig. 1 shows that even in 0.1M sodium sulfate it is necessary to go to at least 200 ma/cm² to get disintegration. In the absence of salt much higher current densities are needed.

The alkali-alloy hypothesis cannot be correct because: *(a)* as previously reported (2) the addition of alkali cations, in the absence of acid, decreased the disintegration rate instead of increasing it; *(b)* disintegration was observed when there was no alkali cation present (Table I, Fig. 2, 3); (c) this mechanism would require a positive temperature coefficient, whereas the temperature coefficient actually is negative (2); and *(d)* when alkali alloys do form, as at mercury cathodes, they are not volatile and, although they react with water, this reaction does not produce disintegration of the surface with formation of colloidal mercury.

Other than the work of Paneth (6), there is still no direct proof of the formation of volatile lead hydride, due to the instability of the hydride at room temperature. However, the indirect evidence seems to be rather conclusive. Work is now in prog-

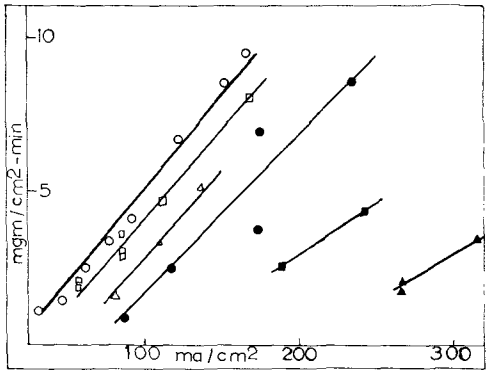

Fig. 1. Acid effect, 0.1M Na_2SO_4. Open circle, 0 H_2SO_4; open square, 0.01M H_2SO_4; open triangle, 0.02M H_2SO_4; closed circle, 0.05M H_2SO_4; closed square, 0.08M H_2SO_4; closed triangle, 0.1M H_2SO_4.

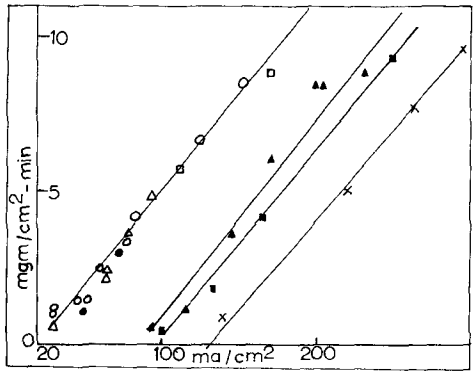

Fig. 3. Salt effect. Open circle, 0.1M Na_2SO_4; open triangle, 0.1M RuCl; open square, 0.1M CsCl; closed circle, 0.1M K_2SO_4; cross, 0.1M $(NH_4)_2SO_4$; closed triangle, M Na_2SO_4; closed square, M KCl.

ress at lower temperatures in an attempt to obtain lead hydride in the gases leaving the cell.

The surface hydronium ion concentration must be slight at and below the critical current density, i_0. The high free energy of formation of Pb would require a high potential. The reduction of hydronium ion obviously takes place at a much lower potential than that of the water molecule, and so only when the surface hydronium ion concentration is too low to support the current would water molecules be reduced. If the potential needed for hydride formation is greater than that needed for hydronium ion reduction, there would be no hydride formed until the surface hydronium ion concentration was depleted and water molecules were reduced, with an attendant rise in potential. Therefore, addition of acid would increase the current density required to start water reduction and hydride formation. Addition of alkali cations which would displace the hydronium ion from the surface would therefore decrease i_0.

Since the experimental data seem to support these ideas, it follows that, at and above i_0, water molecules are being reduced. However, the situation below i_0 is still not understood. Schuldiner's results (7) indicate that water reduction may commence at potentials of about 0.1-0.2 v, which is certainly below that needed for the formation of lead hydride. Also, even in alkaline solutions with practically no hydronium ion (2) there is a large i_0, showing that even after the start of water reduction there must be an appreciable increase of current to build up the potential to the required value. So, although the point at which water reduction commences is not yet known, it seems safe to say that, even in acid solutions, water discharge commences below the onset of cathode disintegration.

The surface is largely covered with hydrogen atoms, even below i_0. Since PbH_2 contains two hydrogen atoms, the mechanism of its formation must involve the production of two high energy atoms near enough to each other to produce a hydride molecule before the activation energy is dissipated to the electrode or the solution, i.e., they must be on the same or adjacent sites. This is true whether the rate-determining step is a chemical combination of adsorbed hydrogen atoms or an electrochemical reduction of a water molecule adjacent to an adsorbed atom. So, at i_0, there must be both a high potential and a high degree of surface coverage. Below i_0 either the potential factor or the surface coverage is insufficient.

If the surface is covered but the potential is too low, i_0 will coincide with the attainment of a critical potential and the disintegration will therefore be an exponential function of potential. Since the over-all current density is also an exponential function of potential, the disintegration rate and the over-all current density would be linear with each other. There should be a sharp intercept of the disintegration rate-current density curve. This is actually observed.

If, on the other hand, the potential is already sufficient, the rate of disintegration at i_0 would depend only on the concentration of adsorbed hydrogen atoms. Since below i_0 all hydrogen leaves the surface as H_2, the concentration of hydrogen would be proportional to the square root of the current density. This means that if the rate-controlling step is the electrochemical production of a hydrogen atom adjacent to another, the disintegration rate would be proportional to the concentration of hydrogen atoms and would be linear with the square root of current density. This is not the case on Pb although it is observed on Sn (8). If the rate-controlling step in hydride production is the chemical combination of adsorbed atoms, then under these irreversible conditions (at about 1 v overvoltage) the surface would have to be saturated with hydrogen atoms, anyhow.

The effect of ammonium ion is probably to inhibit the disintegration by being itself reduced at potentials below those needed for hydride formation. This opinion is based on the following:

The rates in ammonium salt solution are lower than in corresponding solutions of the alkali metal cations (Fig. 2, 3). Addition of ammonium ions to solutions of sodium salts decreases the rate markedly, indicating that there is a specific inhibition. Addition of small increments of acid to concentrated ammonium salt solutions increased the rate slightly, probably by decreasing the amount of ammonium ion migrating to the surface (hydronium ion has a higher transference number than ammonium ion). Finally, a lead cathode in ammonium salt solutions undergoes a change in appearance from a shiny brightness to a dull, almost velvet-like blackness. This black coating is a nonadherent deposit of lead characteristic of the decomposition of a surface compound analogous to the mercury ammonia compound forming at a mercury cathode. Further work is now in progress on this subject

Acknowledgment

This work was done under the sponsorship of the Office of Naval Research. The authors wish to thank J. C. White and Sigmund Schuldiner, both of the Naval Research Laboratory, for their advice and help with the theoretical end of the work and Saul Berman, of the Office of Naval Research, for his aid in administrative matters.

Manuscript received Nov. 13, 1956.

Any discussion of this paper will appear in a Discussion Section to be published in the June 1958 JOURNAL.

REFERENCES

1. G. Bredig and F. Haber, *Berichte*, **31**, 2741 (1898); F. Haber, *Trans. Electrochem. Soc.*, **2**, 190 (1904).
2. H. W. Salzberg, *This Journal*, **100**, 146 (1953).
3. M. Pourbaix and J. Van Muylder, Cebelcor Rept. #14 (1954).
4. H. Angerstein, *Bull. Acad. Polon Sci.*, **3**, 447 (1955).
5. A. Andreatch and H. Salzberg, *This Journal*, **101**, 528 (1954).
6. F. Paneth, *Z. Elektrochem.*, **24**, 298 (1918).
7. S. Schuldiner, *This Journal*, **99**, 488 (1952).
8. H. Salzberg and F. Mies, To be published.

Polarization Capacity at Solid Electrodes and True Surface Area Values

Ralph J. Brodd[1] and Norman Hackerman

Department of Chemistry, University of Texas, Austin, Texas

ABSTRACT

The polarization capacities of Pt, Ni, Cr, Fe, Ta, Al, Cu, and Pb in 1M Na_2SO_4 were evaluated from charging and decay curves obtained by imposing a 2 cps signal on a cell containing one of these metals and a large nonpolarizable electrode. These values are compared to surface areas for the metals determined by Kr adsorption at 78°K in a very small volume adsorption apparatus. For some of the metals the electrochemical method is suitable for routine surface measurements. The use of the parallel procedures provided some additional insight into electrical double layer phenomena at solid electrodes.

The need for a convenient method for measuring actual surface areas of solids often arises. For small areas, as with metals, the gas adsorption method is difficult and often not feasible. The use of charging curves for electrode area measurements was described by Bowden and Rideal (1) and a somewhat more satisfactory procedure was given by Wagner (2) more recently. These methods depend on the proposition that the electrical double layer (edl) capacity at any electrode at which the hydrogen reduction potential is being approached is about 20 $\mu F/cm^2$. However, the quantity in question is actually the differential capacity C, which is a function of the potential of the electrode (3). C is believed to be relatively insensitive to potential in the region considerably cathodic to the zero point of charge (zpc) but short of the hydrogen discharge potential (reversible hydrogen potential plus hydrogen overpotential under the experimental conditions employed), a range comprising probably no more than 200-300 mv at best. Thus, to use a constant C the measurement must be restricted to the range indicated. There is no comparable insensitive region on the anodic side of the zpc. In fact, such curves of C vs. E as are available for solid electrodes suggest that the insensitive region on the cathodic side is small or lacking, in contrast to the case for mercury.

Pegues (4), following Wagner's method, measured the areas of a number of metal electrodes. These depended on assessing the capacity of a mercury surface of known area and comparing to the capacity of a solid electrode of known projected area. The values obtained were satisfactorily reproducible but suffered from lack of suitable calibration because leakage of solution between the mercury pool and its glass container made the "known" mercury surface area uncertain.

For these reasons it was decided to obtain charging curves of each metal at whatever potential it exhibited in the solution used, and to use gas adsorption areas of the metals for comparison purposes. In other words, the electrode was not polarized by applied current except to the extent caused by the input signal, and the total capacity could be compared to the total area determined by an accepted standard procedure. Thus, if the ratio of capacity to area is constant for a variety of sample sizes of the same metal under the same conditions, the method provides reproducible information. Then it becomes necessary only to decide on a value for C in order to calculate surface areas from capacities thereafter. For this purpose the differential capacity curves for mercury [using largely the data of Grahame (3)] were used as guides.

The important assumptions required are: *(a)* the edl capacity can be measured by charging curves; *(b)* the area seen by solution species and by adsorbing gas does not differ by more than the errors inherent in either method—and differ by a constant amount under all conditions; and *(c)* the values of C for mercury are not markedly different from those for other metals under the same conditions. The last implies a lack of specific interaction between the metal and solution species.

Experimental

The charging curve method was used here because it is capable of measuring larger capacities than is the inherently more accurate bridge method. At constant current, I, the capacity, C, is given by

$$C = I(dt/dV) \qquad (I)$$

where (dt/dV) is the reciprocal of the slope of the charging curve. This assumes that I remains constant as the electrode interfaces become charged, and that the slope to be measured is unequivocally recognizable. If either or both of these assumptions do not hold, the method is of little use in so far as C is concerned. Nevertheless so long as conditions are reproduced it can be a useful, empirical area measuring procedure.

The circuit shown in Fig. 1 contained a Dumont model 304-H oscilloscope and a Hewlett-Packard model 202-A function generator. A large area plati-

[1] Present address: National Bureau of Standards, Washington 25, D. C.

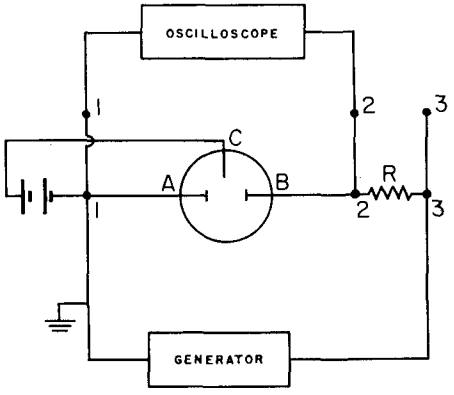

Fig. 1. Circuit diagram: A—lead to test electrode; B—lead to platinized platinum electrode; C—auxiliary electrode for polarizing purposes; R—standard resistor; 1, 2, 3—oscilloscope connections.

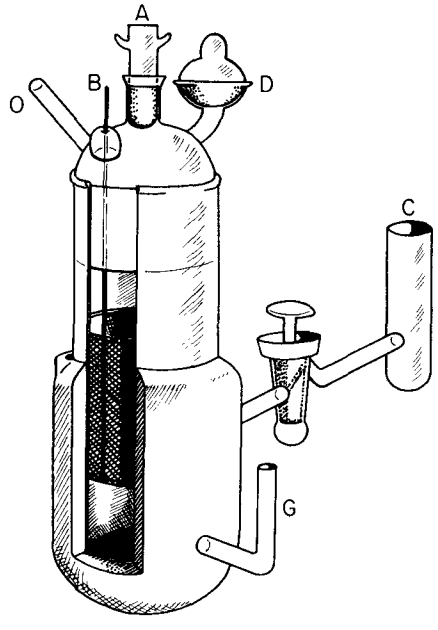

Fig. 2. Polarization cell: A, B, C as in Fig. 1; O—gas inlet; G—gas outlet.

nized platinum electrode, B, served as a nonpolarizable mate for the electrode under study and an auxiliary lead, C, was available for polarizing purposes. The current was determined with the aid of the standard resistor R.

The cell is shown diagramatically in Fig. 2. The solution could be boiled in place by means of a nichrome wire heater in the asbestos casing around the cell. Bureau of Mines grade A helium (their assay showed 99.997% purity with less than 10^{-6}% of either oxygen or water vapor) was bubbled through the cell during the boiling period and during a 20-hr pre-electrolysis treatment.

In all experiments the solution was 1M Na_2SO_4. This was prepared from analytical reagent grade material and doubly distilled water (specific conductance less than 1.5×10^{-6} mho/cm). Organic material was removed from the water by carrying out the second distillation from alkaline permanganate.

The test electrode was introduced through A, Fig. 2, and current from the generator was adjusted to give a total voltage increment on the test electrode

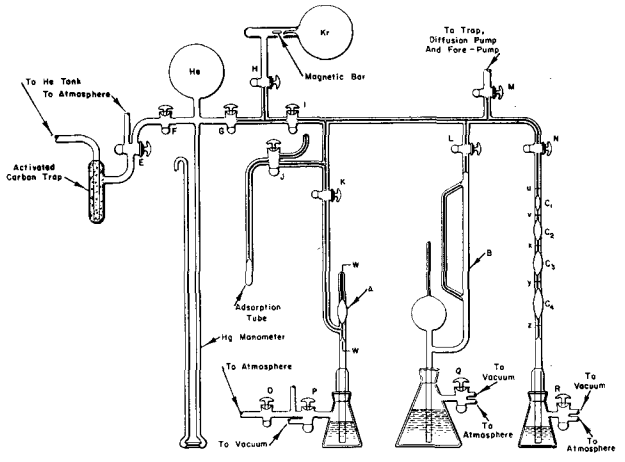

Fig. 3. Small surface area gas adsorption apparatus. E-R, vacuum stopcock; W, tungsten leads; A, high pressure McLeod gauge; B, low pressure McLeod gauge; C_1—C_4, calibrated bulbs; u, v, x, y, z, calibration marks.

of not more than 20 mv. The function used was a 2 cps [2] square wave and the current through the cell was adjusted by means of the auxiliary polarizing circuit so that the square wave current went equally on either side of zero. A picture was taken of the polarization and decay trace on the oscilloscope after allowing for equilibration between electrode and solution. The current was obtained from a picture of the trace of the potential drop across the standard resistor. The capacity was then calculated from an analysis of the photographs, using Eq. (I). It was independent of oscilloscope calibration. The temperature of the cell was maintained at 30°±1°C.

The small surface areas were measured by adsorption of Kr at 78°K (5). The low vapor pressure of Kr at this temperature minimizes dead space corrections. In addition the adsorption apparatus (Fig. 3) was made of 2 mm tubing throughout to reduce the total volume and the total glass area. The free volume was about 14 cc and the dead space about 0.8 cc, varying slightly each time the adsorption chamber was sealed onto the system. A modified McLeod gauge (6) of very small internal volume was used. Because of the small areas involved, it was necessary to correct for adsorption on the walls of the system. It was assumed that the roughness factor (ratio of B.E.T. surface area to projected geometric area) of the glass did not change with use of the system since the walls were subjected to treatment no more drastic than adsorption and desorption of krypton (and perhaps a little water vapor when the system was opened). More complete details of the krypton adsorption unit are given by Joncich (7).

Platinized Pt, Ni, and Cr electrodes were prepared by electrodeposition on Pt, Ni, and Cu, respectively, by standard plating procedures for each. The deposits ranged in thickness from a tenth up to several millimeters. Cu (from Malin & Company) Fe, Ta, Pb (from A. D. MacKay Company), and Al (from Alcoa) were used in the form of wire. The electrodeposited electrodes were washed thoroughly with 1M Na_2SO_4 before being placed in the cell. The

[2] Chosen so as to permit polarizing large area electrodes.

wire electrodes were degreased with benzene. In addition Cu was washed with 7M H_2SO_4 and 1M Na_2SO_4, while Fe, Pb, and Al were cleaned cathodically in 7M H_2SO_4 and washed with 1M Na_2SO_4.

Discussion of Results

Frumkin (8) suggested a useful relationship between the zpc of a metal and its work function. At the zpc the potential drop across the solution side of the interface is zero in the absence of adsorbed species on the electrode surface. If a cell is made up of two such "null" electrodes, the potential difference between them should be also the junction potential difference between the metals. This is the contact potential difference between the metals, which, in turn, equals the difference in work functions. Corroboration of this deduction is supplied by the fact that for Ag (9), Pb, Te, Cd (10), and Pt (11) differences in potential between their zpc and that of mercury (the electrocapillary maximum in this case) are approximately equal to the differences in work function.

By obtaining the zpc of each metal using the indirect method just described and knowing the potential of each electrode while it is being polarized it becomes possible to make comparisons with mercury at equivalent displacements from the zpc. Also, it is possible to suggest whether cations or anions predominate in the inner Helmholtz layer.

It should be remembered that accurate prediction is not possible because *(a)* a truly null electrode is unlikely on the basis of specific metal-solution species interaction and *(b)* the work function values in the literature for most metals show considerable variation. A recent discussion of the relationship is pertinent (12). Table I lists the work functions and the approximate zpc potentials relative to the saturated calomel electrode (SCE) for all of the metals used in this work, using Frumkin's relation between work function and zpc and based on the experimental zpc of mercury for Na_2SO_4 solutions (3).

In the following results the gas adsorption surface area of the actual electrode was determined wherever possible. Otherwise measurements were made on relatively long lengths of wire and the surface area of the electrode itself was calculated from the ratio of lengths. Potentials were determined relative to SCE and were also rationalized and are given also relative to the zpc of the metal.

Platinum.—Fig. 4a is a picture of a trace produced on imposing the 2 cps square wave on a cell containing a Pt test electrode and a nonpolarizable electrode. The capacity was measured on 6 separate samples and was found to be 20.1±0.7 $\mu F/cm^2$ (Table II).

Robertson (11) obtained 19±1 $\mu F/cm^2$ for smooth Pt in 1*N* HCl at the zpc. Other values reported (13, 14) are 25 and 30 $\mu F/cm^2$. Since the electrodes in this work were at 0.2 v relative to SCE, or about −0.2 v relative to the zpc, cations populated the Helmholtz layer. Robertson's comparable value was

Table I. Calculated zero point of charge

Metal	Work function* (ev.)	Estimated zpc (v on SCE scale)
Mercury	4.5	−0.45
Platinum	5.3	+0.4
Nickel	4.6	−0.4
Chromium	4.0	−1.0
Iron	4.4	−0.6
Tantalum	4.2	−0.8
Aluminum	4.2	−0.8
Copper	4.6	−0.4
Lead	4.0	−1.0

* C. J. Smithells, "Metals Reference Book," Vol. 2, p. 668, Interscience Publisher Inc., New York (1955).

Table II. Platinum electrodes*

Electrode	Surface area by Kr adsorption, cm^2	Capacity in μF by polarization	Capacity in $\mu F/cm^2$
1	56.7	1210	21.4
2	271	5900	21.8
3	615	10600	17.3
4	407	8750	21.5
5	80.3	1460	18.2
6	23.9	494	20.7
		Average	20.1 ± 0.7

* The surface area of each electrode was measured.

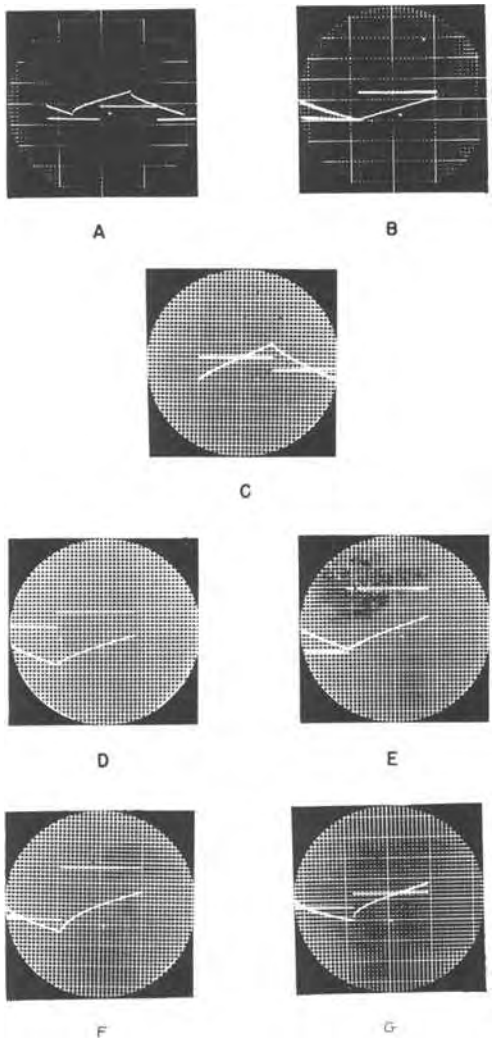

Fig. 4. Polarization traces: A—Pt; B—Ni; C—Cr; D—Fe; E—Ta; F—Cu; G—Pb. Horizontal traces, current input; angular traces, cell output or charging curves.

22 $\mu F/cm^2$. Incidentally, his measured zpc for Pt in 0.01*N* HCl was 0.35 v relative to SCE in satisfactory agreement with the estimated value here. Because of some doubt concerning the surface areas of the electrodes leading to the highest two values cited above, it may be concluded that there is reasonable agreement and that the most likely value is closer to 20 than 25 $\mu F/cm^2$.

There is no regular variation in polarization capacity per unit area with total area of the electrodes used. Thus it is possible to use this method as a means of determining the surface area of Pt or Pt black. The "roughness factors" of the electrodes used here varied from 3,900 to 20,000.

Nickel.—A typical polarization curve is given in Fig. 4b. The average value of the polarization capacity of 7 Ni electrodes was 28.8±0.5 $\mu F/cm^2$ (Table III).

The potential of the Ni electrodes was —0.4 v relative to SCE, or just about at zpc. This compares satisfactorily with values of 28 $\mu F/cm^2$ in 0.01*N* HCl, 37 $\mu F/cm^2$ in 0.1*N* HCl, 41 $\mu F/cm^2$ in 1*N* HCl, 22 $\mu F/cm^2$ in 0.006*N* NaOH, and 27 $\mu F/cm^2$ in 0.12*N* NaOH (15). Rakov, Borisova, and Ershler (16) reported 22-27 $\mu F/cm^2$ in 1*N* NaOH.

The potentials of the Ni electrodes lie near the zpc (see Table I) and applying Grahame's differential capacity curve (3) to Ni, the predicted capacity of the Ni electrode is about 27 $\mu F/cm^2$. This value and the experimental value agree satisfactorily.

There is no trend in polarization capacity with total area of the electrodes. This indicates that the polarization capacity may be used to estimate the surface area of a Ni electrode. The roughness factor of the plated Ni electrodes varied from 80 to 175.

Chromium.—A picture of a polarization curve for a Cr electrode is given in Fig. 4c. The average value of the polarization capacity of 6 Cr electrodes was 9.7±0.6 $\mu F/cm^2$ (Table IV).

The potential of the Cr electrodes was —0.1 v relative to SCE or 0.9 v relative to zpc. The experimental value of 9.7 $\mu F/cm^2$ may be compared to the value of 10 $\mu F/cm^2$ found by Powers (17) for Cr electrodes. However, the capacity expected from a consideration of the work function and the differential capacity curve of Grahame (3) is 39 $\mu F/cm^2$.

Most Cr plate has an elaborate crack network and is therefore quite porous. The outer surface projections probably shield the interior of the cracks and pores from any electrochemical reaction. Therefore, only a small fraction of the total surface as seen by gas adsorption may be expected to participate in a buildup of the edl. Thus, this method is not useful in studying the edl at a Cr surface unless the true area is known; it gives too low a capacity. It would be useful as an area measuring method only if the relation between the thickness and porosity of plate were constant for all samples. An alternate explanation of the experimental results could be based on the postulation of an oxide film on the electrodes.

Iron.—A typical polarization curve is shown in Fig. 4d. The average polarization capacity of the edl at 7 Fe electrodes was 35.9±0.8 $\mu F/cm^2$ (Table V). The potential of these electrodes was about —0.8 v relative to SCE or —0.2 v relative to zpc.

The polarization capacity predicted from a consideration of the work function and Grahame's differential capacity curves of Hg (3) is about 22 $\mu F/cm^2$. The polarization capacity of a Hg surface at which there is adsorption of anions is about 40 $\mu F/cm^2$ (3). It has been shown that sulfate ions adsorb irreversibly on Fe (18). It has also been shown that specific adsorption of iodide ions on Hg shifts the zpc as much as —0.4 v (3, 19). Thus, it is possible that sulfate ions adsorbed specifically on the Fe electrodes at the potential and caused the polarization capacity to be higher than would be predicted in the absence of specific adsorption.

The polarization capacity at Fe electrodes showed no definite trend with total surface area. Thus, it may be used to determine the extent of an Fe surface. The roughness factor of the Fe electrodes was 9.3, probably somewhat high.

Tantalum.—A typical polarization curve for a Ta electrode is shown in Fig. 4e. The average polarization capacity of the edl at 9 Ta electrodes was 4.61 ± 0.1 $\mu F/cm^2$ (Table VI). The potential of the

Table III. Nickel electrodes*

Electrode	Surface area by Kr adsorption, cm^2	Capacity in μF by polarization	Capacity in $\mu F/cm^2$
1	119	3350	28.0
2	134	3670	27.4
3	183	5400	29.4
4	118	2985	26.4
5	63	1930	30.5
6	100	3035	30.4
7	139	4075	29.3
			Average 28.8 ± 0.5

* The surface area of each electrode was measured.

Table IV. Chromium electrodes*

Electrode	Surface area by Kr adsorption, cm^2	Capacity in μF by polarization	Capacity in $\mu F/cm^2$
1	128	1390	10.9
2	36	412	11.1
3	56	640	11.5
4	116	1450	8.8
5	275	2150	7.8
6	225	1750	7.8
			Average 9.7 ± 0.6

* The surface area of each electrode was measured.

Table V. Iron electrodes*

Electrode	Surface area by Kr adsorption, cm^2	Capacity in μF by polarization	Capacity in $\mu F/cm^2$
1	23.1	785	34.0
2	20.2	795	39.4
3	17.9	575	37.9
4	16.7	525	31.4
5	14.6	510	35.0
6	10.7	392	37.6
7	10.2	369	36.2
			Average 35.9 ± 0.8

* The surface area was measured on 6 meters of wire. The surface area of each electrode is a proportionate part of the total area.

Table VI. Tantalum electrodes*

Electrode	Surface area by Kr adsorption, cm²	Capacity in μF by polarization	Capacity in μF/cm²
1	3.58	15.4	4.23
2	4.08	20.5	5.26
3	4.52	21.2	4.76
4	5.30	27.5	5.40
5	6.25	27.7	4.47
6	7.64	33.0	4.36
7	8.86	37.7	4.23
8	9.95	43.1	4.38
9	10.1	45.7	4.18
			Average 4.59 ± 0.11

* The surface area was measured on 6 meters of wire. The surface area of each electrode is a proportionate part of the total area.

Ta electrodes was —0.2 v relative to SCE, or 0.6 v relative to zpc. The polarization capacity expected from a consideration of the work function and the differential capacity curves of Hg (3) is about 40 μF/cm².

The low value of the polarization capacity is thought to be due to the oxide film on the surface of the electrodes. A similar low value of 7 μF/cm² for an oxide film on the surface of an electrode was found by Ershler *et al.* (16). The presence of the oxide film on the surface lowers the charge density on the surface of the electrode. This produces an increase in the thickness of the edl, and, as a result, decreases the capacity. The lower capacity may also be thought of as being caused by an increase in distance between plates of the condenser formed by the electrode and the solution.

It should be noted that the results, while low, are consistent, and may be used to determine the extent of the surface of oxide-coated Ta electrodes. The roughness factor of the Ta electrodes was 3.3.

Aluminum.—Problems wtih Al were manifold. The portion of the charging curve from which to take the slope was usually in doubt. Also there appeared to be a frequency dependence which resisted clarification. About all that can be said at this time is that "capacity" was not a function of the total (gas) surface area available. Therefore, the method is applicable to Al provided a firm value can be obtained for C. Work on this system is continuing.

Copper.—A typical polarization curve for Cu electrodes is given in Fig. 4f. The average polarization capacity of 10 Cu electrodes was 32.9 ± 0.8 μF/cm² (Table VII). This may be compared to 32 μF/cm² found by Bockris and Pentland (20) and to 23 μF/cm² obtained by Wiebe and Winkler (21) on cathodic charging. The potential of the Cu electrodes was —0.2 v relative to SCE, or 0.2 v relative to zpc. The capacity expected from a consideration of the work function and the differential capacity curves of Hg (3) is about 30 μF/cm². This is in fair agreement with the experimental value, but here again there was some question about choice of the applicable slope.

The polarization capacity of the Cu electrodes is fairly constant over the range of surface areas studied. The roughness factor of the Cu electrodes was 1.5.

Table VII. Copper electrodes*

Electrode	Surface area by Kr adsorption, cm²	Capacity in μF by polarization	Capacity in μF/cm²
1	4.54	125	28.5
2	5.0	155	31.0
3	5.12	159	31.1
4	5.6	195	34.8
5	6.59	243	36.9
6	6.8	246	36.2
7	7.57	265	35.0
8	8.3	240	28.9
9	9.1	315	34.6
10	10.7	344	32.2
			Average 32.9 ± 0.8

* The surface area was measured on 6 meters of wire. The surface area of each electrode is a proportionate part of the total area.

Table VIII. Lead electrodes*

Electrode	Surface area by Kr adsorption, cm²	Capacity in μF by polarization	Capacity in μF/cm²
1	14.1	690	47.7
2	12.3	650	52.7
3	9.81	527	62.1
4	8.3	460	55.4
5	6.54	326	50.0
6	4.65	221	47.5
			Average 52.6 ± 1.7

* The surface area was measured on 6 meters of wire. The surface area of each electrode is a proportionate part of the total area.

Lead.—A typical polarization curve for a Pb electrode is shown in Fig. 4g. The average polarization capacity at 6 Pb electrodes was 52.6 ± 1.7 μF/cm² (Table VIII). The potential of the Pb electrodes was —0.6 v relative to SCE, or 0.4 v relative to zpc.

The expected polarization capacity for Pb electrodes at this potential from a consideration of the work function and the differential capacity curves of Hg (3) is about 45 μF/cm², but the estimated capacity is not very accurate as the capacity curve of Hg rises rapidly at this potential. Kabanov and Jofa (22) found a polarization capacity of 30 μF/cm² at a potential of —0.70 v relative to SCE and the polarization capacity rose rapidly to about 40 μF/cm² as the potential was changed to —0.68 v relative to SCE. The high value of the polarization capacity suggests that sulfate ions are adsorbed on the surface. Subject to the indicated limitations the roughness factor of the Pb electrodes was 5.6.

Conclusions

The polarization capacity appears to be a satisfactory measure of the extent of the surface of an electrode (*a*) if the value of the polarization capacity is actually known, or (*b*) if a standardized procedure is worked out for each case. The measurement of the polarization capacity is fast, relatively accurate, and is made easily and quickly in contrast to the more tedious measurement of surface area by gas adsorption techniques. The method appears to be applicable to Pt, Ni, Fe, Ta; less so to Cr, Cu, and Pb for different reasons; and inapplicable to Al so far.

The relationship of the work function to the position of the zpc first noted by Frumkin (8) and the electrocapillary behavior of Hg may be used in the absence of specific interaction or reaction to predict with fair accuracy the polarization capacity of metal electrodes. The apparent failure of these relationships in the case of Al, Ta, Cr, Fe, and Pb are believed to be due to specific adsorption of ions on the electrode, the presence of oxide layers, or the passage of faradaic current. In comparing the capacity of metal electrodes the potential relative to the zpc is a very important factor. Comparisons made at nonequivalent potentials are meaningless.

Acknowledgment

The authors are pleased to take this opportunity to express their appreciation to the Office of Naval Research for its financial support of this work. They also acknowledge helpful discussions with J. J. McMullen of this laboratory.

Manuscript received Nov. 1, 1956. This paper was prepared for delivery before the San Francisco Meeting, April 29-May 3, 1956.

Any discussion of this paper will appear in a Discussion Section to be published in the June 1958 JOURNAL.

REFERENCES

1. F. P. Bowden and E. K. Rideal, *Proc. Roy. Soc. (London)*, **120A**, 59 (1928).
2. C. Wagner, *This Journal*, **97**, 72 (1950).
3. D. C. Grahame, *Chem. Rev.*, **41**, 441 (1947).
4. Betty Pegues, M.A. Thesis, University of Texas (1951).
5. R. A. Beebe, J. B. Beckwith, and J. M. Honig, *J. Am. Chem. Soc.*, **67**, 1554 (1945).
6. C. Kenty, *Rev. Sci. Instr.*, **22**, 217 (1951).
7. M. J. Joncich, Ph.D. Dissertation, University of Texas, p. 26 (1953).
8. A. Frumkin, *Colloid Symposium Annual*, **7**, 89 (1930).
9. T. Veslovsky, *Acta Physicochim, U.R.S.S.*, **11**, 815 (1939).
10. T. Borisova, B. Ershler, and A. Frumkin, *Zhur. Fiz. Khim.*, **22**, 925 (1948).
11. W. D. Robertson, *This Journal*, **100**, 194 (1953).
12. P. Ruetschi and P. Delahay, *J. Chem. Phys.*, **23**, 697 (1955).
13. B. Ershler and M. Proskurnin, *Acta Physicochim., U.R.S.S.*, **6**, 195 (1937).
14. P. Dolin and B. Ershler, *ibid.*, **13**, 747 (1940).
15. J. O'M. Bockris and E. C. Potter, *J. Chem. Phys.*, **20**, 614 (1952).
16. A. Rakov, T. Borisova, and B. Ershler, *Zhur. Fiz. Khim.*, **22**, 1390 (1948).
17. R. A. Powers, Ph.D. Dissertation, University of Texas, p. 29 (1952).
18. N. Hackerman and S. J. Stephens, *J. Phys. Chem.*, **58**, 904 (1954).
19. O. Essin and B. Markov, *Acta Physicochim., U.R.S.S.*, **10**, 353 (1939).
20. J. O'M. Bockris and N. Pentland, *Trans. Faraday Soc.*, **48**, 833 (1952).
21. A. K. Wiebe and C. A. Winkler, *Can. J. Chem.*, **31**, 1118 (1953).
22. B. Kabanov and S. Jofa, *Acta Physicochim. U.R.S.S.*, **10**, 617 (1939).

Reaction of Hydrogen with Preoxidized Zircaloy-2 at 300° to 400°C

Earl A. Gulbransen and Kenneth F. Andrew

Research Laboratories, Westinghouse Electric Corporation, Pittsburgh, Pennsylvania

ABSTRACT

The permeability of preformed oxide films to hydrogen at 300°-400°C was studied. Two types of reactions were observed. If the oxide film was permeable, a general reaction occurred with the formation of zirconium hydride phases on the surface. If the oxide film was relatively impermeable, reaction occurred at the edges of the sample where defects probably exist in the oxide. The reaction starts at localized areas and spreads through the metal with hydride and oxide film spalling from the metal continually.

Zirconium reacts with hydrogen at temperatures up to 550°C to form stable hydrides of the metal when the hydrogen concentration exceeds the terminal solubility (1,2). The formation of a hydride phase on the surface and in the metal causes major changes in the physical and chemical properties of the metal or alloy (3).

Hydride phases can form readily at 400°C since the terminal solubility is only 1.86 at. % or 200 ppm by weight of hydrogen. One of the effective barriers to reaction of Zr at 300°-400°C with hydrogen is a surface oxide film (4).

With the development of Zr-Sn alloys for use in nuclear power reactors, it is of interest to study the permeability of several types of oxide films to hydrogen at temperatures of 300°-400°C and the effects of the hydrogen reaction on the alloy.

The mechanism of the reaction of hydrogen with pure Zr was considered earlier (4). The permeability of several types and thicknesses of oxide films to hydrogen was determined at 150°C. The results showed that the oxide film formed at room temperature on abraded and cleaned metal samples offered more resistance to hydrogen permeation than thicker oxide films formed at 250°C and higher. Oxygen and nitrogen dissolved in the metal phase had no effect on the rate of permeation when compared to an oxide-free surface. Chemically polished surfaces of Zr were impermeable to hydrogen at 150°C.

Experimental

Apparatus.—The vacuum microbalance apparatus was used (5) for preparing the oxide films and for determining the reaction with hydrogen. Details of

Table I. Chemical and spectrographic analyses of Zircaloy-2

Element	Zircaloy-2 Foil Wt %	Element	Wt %
Zr	Major	Hf	0.0055
Sn	1.45*	Si	——
Fe	0.135*	N	0.0038
Ni	0.055*	H	0.0020
Cr	0.100*	O	0.1400
Al	0.0045		

* Chemical.

the apparatus and method have been described (5).

Pure hydrogen was prepared by diffusing a purified grade of hydrogen through a hot Pd tube.

Samples.—Thick strips of Zircaloy-2 were obtained from the Westinghouse Atomic Power Division and rolled to strips 5 and 10 mil thick. Table I shows the spectrographic and chemical analyses of the alloy.

Samples were abraded and cleaned (6). Some of the samples were given a chemical polishing treatment in a special acid bath having the composition: 45% HNO_3, 10% HF, and 45% H_2O.

Steam reacted samples.—These were reacted with steam at 399°C for three days to weight gains of 118 to 155 $\mu g/cm^2$. Although most of the oxygen forms an external oxide film, some oxygen may dissolve in the metal.

Results and Discussion

Comparison of Initial Pretreating Procedures

Abraded and chemically polished samples of Zircaloy-2 were reacted at 400°C with pure hydrogen at 5.0 cm Hg pressure. Since the vacuum was better than 10^{-6} mm Hg, the samples showed no evidence for a pick-up of oxygen on heating to the reaction temperature.

Fig. 1 shows the time course of the hydriding reaction for both samples. Here weight gain in micrograms per cm^2 was plotted against the time in minutes. Curve A shows the time course for the abraded sample containing the room temperature oxide film. A rapid sorption of hydrogen occurs with the composition $ZrH_{0.77}$ (43 at. % hydrogen) being formed in 2 min of reaction. Although the hydrogen was evacuated at the end of 2 min, the reaction continued during evacuation until the hydrogen pressure was reduced to a value corresponding to the decomposition pressure characteristic of the hydride phase (about 10^{-4} mm Hg) (2).

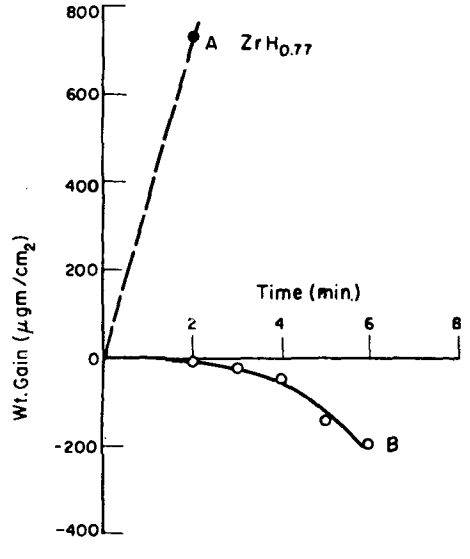

Fig. 1. Comparison of initial oxide film on hydriding Zircaloy-2, 400°C, 5.0 cm Hg of H_2. Curve A, abraded, room temperature oxide film; curve B, chemically polished oxide film.

On cooling to room temperature, the sample was found to be brittle and cracked readily into a number of pieces. Since the terminal solubility was only 1.86 at. % at 400°C, most of the hydrogen was in the hydride phase $ZrH_{1.5}$ and was concentrated in the surface layer. A rapid reaction occurred at 400°C although the room temperature oxide film limited the reaction with hydrogen at 150°C.

Curve B of Fig. 1 shows the results for the chemically polished sample. Although the chemical polishing solution removes metal from the sample, a passive type of oxide or corrosion film remains on the alloy. Curve B shows that the passive film protects the metal for 2 min of reaction time after which reaction occurs. However, as fast as hydride is formed, it spalls from the metal giving a weight loss instead of a weight gain. The rate of spalling increases steadily with time as more surface is exposed for reaction. An examination of the specimen after cooling shows that the sample edges were the only regions attacked by hydrogen.

It is concluded that chemical polishing the alloy forms a film which was nearly impermeable to hydrogen over the major portion of the surface. However, reaction occurred at the sample edges. Since the attack is highly localized, spalling of hydride occurred with a loss of weight. Curves A and B of Fig. 1 were reproducible.

Permeability of Preformed Oxide Films to Hydrogen

Zircaloy-2 samples were reacted with pure oxygen at 400°C to form oxide film thicknesses of 10, 24.5, and 73 $\mu g/cm^2$. These weight gains corresponded to 615, 1510, and 4480Å of oxide using the conversion factor of 61.5 (6) to relate Angstroms to weight gain in micrograms per cm^2.

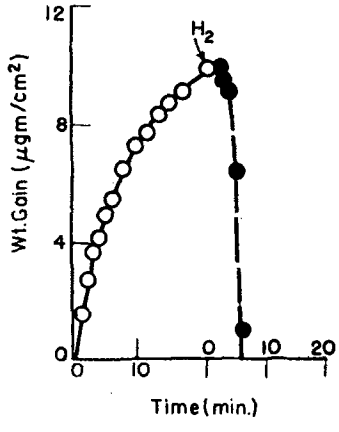

Fig. 2. Effect of thin oxide film (10 $\mu g/cm^2$) on hydriding Zircaloy-2, 400°C, 5.0 cm Hg of H_2.

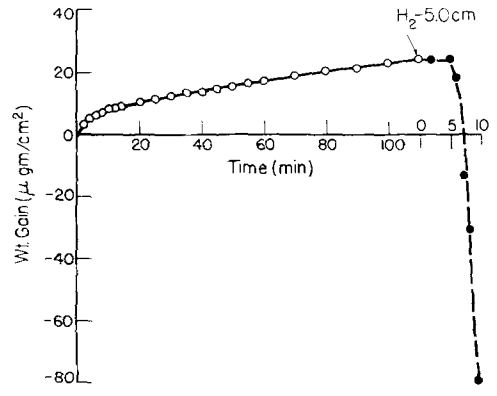

Fig. 3. Effect of thin oxide film (24.5 $\mu g/cm^2$) on hydriding Zircaloy-2, 400°C, 5 cm Hg of H_2.

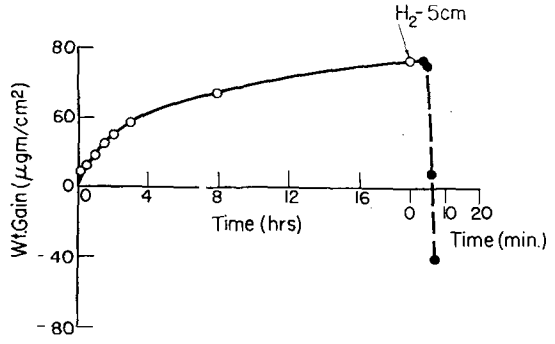

Fig. 4. Effect of thin oxide film (73 $\mu g/cm^2$) on hydriding Zircaloy-2, 400°C, 5.0 cm Hg of H_2.

These samples were reacted with hydrogen at 400°C and 5.0 cm Hg pressure. Fig. 2, 3, and 4 show the time courses for the oxidation and hydrogen reaction curves for three experiments. Hydrogen was added after removing the oxygen and evacuating to a pressure of 1×10^{-6} mm Hg.

The weight change-time curves for the hydrogen reaction were similar to Curve B of Fig. 1. After an induction period, reaction occurred with immediate spalling of hydride. This behavior was characteristic of a highly localized attack. On cooling, all of the samples showed a highly localized attack at the edges.

Table II summarizes the results on this series of experiments. It is concluded that the oxide films were nearly impermeable to hydrogen except at the edges where localized attack occurs with spalling of the hydride together with the oxide film.

Studies on Steam Formed Oxide Films

Six samples of Zircaloy-2 were reacted with steam at 399°C for three days to form oxide films of thicknesses between 119-155 $\mu g/cm^2$. These thicknesses were 33-44% of the 350 $\mu g/cm^2$ film thickness found by Thomas (7) for transition in the corrosion rate. The presence of hydride in the steam-reacted films before hydriding was not tested.

Samples were reacted in the as-received condition with hydrogen at pressures of 1, 2.4, and 5.0 cm Hg and at temperatures of 300°-400°C. Table III shows a summary of the oxide thicknesses, the hydrogen reaction conditions, and results.

At 300°C no reaction occurred in 20 hr for a hydrogen pressure of 2.4 cm Hg, while at 350°C reaction occurred after 62 hr for 1 cm Hg hydrogen pressure and after 12 min for 5.0 cm Hg hydrogen pressure. The 400°C experiments showed reaction in three of the four experiments. The fourth experiment would probably show reaction if the reaction time had been extended.

Fig. 5 shows a photograph of the 350°C-1 cm Hg pressure experiment. The course of the edge type of spalling is seen clearly. All of the samples which reacted with hydrogen in this group of experiments reacted at the edges as shown in Fig. 5.

To prove that the alloys having a steam-formed oxide film react with hydrogen at the edges, x-ray diffraction studies were made of the spalled material and the remaining metal phase. The steam-corroded Zircaloy-2 sample reacted with hydrogen at 400°C and 5.0 cm Hg of H_2 was studied (*see* Fig. 5).

The spalled reaction product gave an x-ray diffraction pattern characteristic of the delta-hydride phase having the composition $ZrH_{1.4-1.6}$ (1) with no evidence of a metal phase. The x-ray diffraction pattern of the remaining metal gave a pattern characteristic of Zr with no hydride reflections. Although oxide reflections may be expected, the amount was too small to detect by x-ray diffraction methods. It is concluded from these observations that spal-

Table II. Summary of results of hydrogen reaction of alloy and alloy with oxide film formed in oxygen atmospheres, hydrogen, 400°C, 5.0 cm Hg pressure

Oxide thickness $\mu g/cm^2$	Oxide thickness A ($\rho = 1$) *	Color of oxide	Results
Room temp oxide		None	Adsorbed hydrogen, no spalling. Fine cracks on surface.
Chem. polished		None	Reaction at edges with spalling.
10	615	Blue-green	Reaction at edges with spalling.
24.5	1510	Pink-green	Reaction at edges with spalling.
73	4480	Gray	Reaction at edges with spalling.

* ρ = surface roughness ratio.

Table III. Summary of results on hydrogen reaction of corrosion films on Zircaloy-2 Prepared (Lustman) H_2O—3 days at 400°C

Area cm^2	Wt gain, g	Thickness $\mu g/cm^2$	Thickness A°(ρ=1)*	Hydrogen conditions Temp, °C	Hydrogen conditions Pressure cm	Results
17.42	0.0027	155	9,510	300	2.4	No reaction in 20 hr.
17.42	0.0027	155	9,510	400	5.0	Edge reaction in 6 min, spalling.
17.96	0.0023	128	7,850	400	1.0	No failure in 3 hr.
17.96	0.0023	128	7,850	400	5.0	Edge reaction in 2 hr, spalling.
18 45	0.0022	119	7,300	400	1.0	Edge reaction in 3 min, spalling.
17.35	0.0023	133	8,150	350	5.0	Edge reaction in 12 min, spalling.
18.45	0.0025	135	8,310	350	1.0	Edge reaction after 62 hr, spalling.

* ρ = surface roughness ratio.

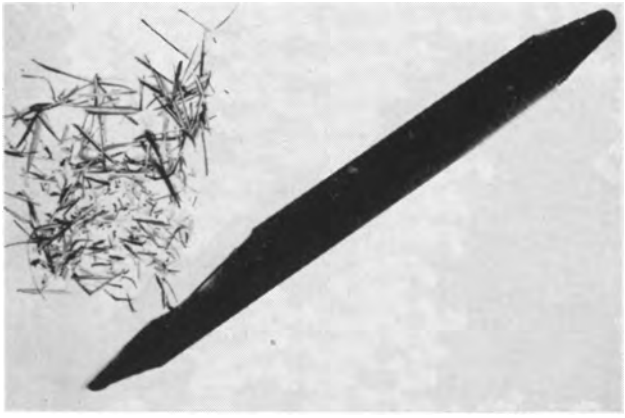

Fig. 5. Effect of hydrogen on steam-corroded Zircaloy-2; steam, 750°F, 3 days; hydrogen, 350°C, 1.0 cm Hg of H_2. Magnification, 2X before reduction for publication.

ling of the metal phase is due to the formation of the hydride phase at the sample edges and that no appreciable attack occurs through the oxide film on the flat surface.

Several additional facts can be drawn from Table III: (*A*) hydrogen reaction increases with pressure and temperature; (*B*) since the reaction occurs at the edges the results suggest a variation in reactivity due to defects in the metal at the edges such as cracks, strains, etc.

Conclusions

Two types of reaction were observed when Zircaloy-2 was exposed to hydrogen at temperatures of 400°C. If the oxide film was permeable to hydrogen, a general reaction occurred with the hydride $ZrH_{1.5}$ forming on the surface. This type of reaction was observed on abraded samples when the equilibrium room temperature film was present on the metal. If the oxide, on the other hand, was impermeable, reaction occurred at the edges where defects exist due to cracks in the metal or stresses set up in the metal during rolling, cutting, etc. The reaction starts at localized areas and spreads through the metal with the hydride continually spalling from the metal.

Manuscript received April 15, 1957. This paper was prepared for delivery before the Buffalo Meeting, Oct. 6-10, 1957.

Any discussion of this paper will appear in a Discussion Section to be published in the June 1958 JOURNAL.

REFERENCES

1. E. A. Gulbransen and K. F. Andrew, *This Journal*, **101**, 474 (1954).
2. E. A. Gulbransen and K. F. Andrew, *J. Metals*, **7**, 136 (1955).
3. W. L. Mudge, Jr., "Zirconium and Zirconium Alloys," p. 730, American Society for Metals, Cleveland (1953).
4. E. A. Gulbransen and K. F. Andrew, *This Journal*, **101**, 348 (1954).
5. E. A. Gulbransen, *Trans. Electrochem. Soc.*, **81**, 187 (1942).
6. E. A. Gulbransen and K. F. Andrew, *Trans. Am. Inst. Mining Met. Engrs.*, **185**, 515 (1949).
7. D. E. Thomas, "Metallurgy of Zirconium," by Lustman and Kerze, pp. 608-640, McGraw-Hill Book Co., New York (1953).

Effect of Current Drains on Cadmium Standard Cells

George D. Vincent

Standard Cell Department, The Eppley Laboratory, Inc., Newport, Rhode Island

ABSTRACT

Various sizes of unsaturated cadmium standard cells were subjected to current drains of from 0.5 to 12 μa (0.2 — 20 μa/cm^2). Voltages across the terminals of these cells were observed for several years. The relationship between change in voltage and time is not a linear one; an approximation of the decrease per unit area of electrode is 11 μv/coulomb cm^{-2}.

Although the use of standard cells has received considerable attention (1-3), the determination of conditions to maintain the highest accuracy and constancy has been the intent, with few exceptions (4), of previously published work. The statement appears on standard cell certificates that the maximum permissible current through a cell is 100 μa, but since it may be assumed that such current will flow for very short periods, a few seconds at most, and also that it will probably flow as often in the charging as in the discharging direction, the total effect of the current on the cell is negligible.

However, certain instruments now available, in addition to a very recently described potentiometer (5), use standard cells under conditions of current drain. The purpose of this paper is to make known the results of tests on standard cells made at intervals during the past nine years, which will be useful in estimating the error likely to arise from the use of a standard cell under conditions which draw a small current from it.

Apparatus and Procedure

The main body of observations were measurements of voltages between terminals of standard

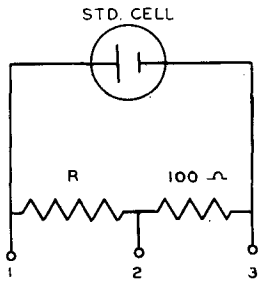

Fig. 1. Test circuit. R = 0.08—2 megohms

cells which were delivering from 0.5 to 12 μa. As indicated in Fig. 1, each cell was connected to a load resistor R of appropriate value (0.08-2 megohms) in series with a precision 100-ohm resistor, which was compared to within 0.01% against N.B.S. certified laboratory standards at the beginning and the end of the test. The voltage across points 1 and 3 is the closed circuit voltage of the cell, while the measurement of the voltage across 2 and 3 provides a means of determining the current.

Voltages were measured with a Feussner-type potentiometer (6), using as a standard a saturated cell from the working standards group of the Eppley Laboratory. This cell was maintained in an oil thermostat and was constant and accurate to within 2 ppm as determined by frequent comparison with the standards bank which is maintained at this Laboratory, and checked at six-month intervals at the National Bureau of Standards. The sum of all instrumental errors was within 0.01%. All test measurements were made at room temperature, 25° ± 3°C.

Three sizes of commercially available types of unsaturated cells were used, with cross-sectional areas of 5.5 cm², 1.43 cm², and 0.50 cm². All were taken from the regular production of this Laboratory. They all had 12½% cadmium amalgam as the negative electrode, purified mercury as the positive electrode, electrolytic mercurous sulfate as the depolarizer, and unsaturated cadmium sulfate solution, slightly acidified with sulfuric acid, as the electrolyte. They were hermetically sealed in H-shaped glass vessels, both limbs being the same size, and had plugs and septa (7) to hold the electrode materials in place. These plugs and septa, consisting of either cork or polystyrene (8) washers covered with linen, reduced the electrode area by the reduction of physical surface due to the area occupied by the materials comprising them, and in effect by the restriction which they imposed on free circulation of the components of the electrolyte.

Results

Four groups of cells were used in the principal test. In each of three groups were 3 cells from which no current was drawn, and 2 each from which currents of about ½, 1, 2, 5, and 10 μa were taken continuously for 52 months, or until the voltage became erratic, if that condition was reached in less than 52 months. One of the groups was composed of cells of 0.50 cm² electrode area, which had septa of linen held in place by polystyrene washers. The other two groups where composed of cells of 1.43 cm² electrode area, with linen septa held in place by treated cork washers. The fourth group, which also had linen septa and cork washers, consisted of 15 cells of 5.5 cm² area. In this group were 3 cells with no current drain; 2 with 1 μa; 1 with 2 μa; 1 each with 3.7, 4.2, and 4.7 μa, which are averaged together and reported as 4.2 μa; 1 each with 6.1 and 7.0 which are reported together as 6.5 μa; 1 each with 8.0, 8.7, and 8.9, reported together as 8.5 μa, and 1 with 12 μa current drain. The quotient of the current, as determined by the drop across the 100-ohm resistor (Fig. 1), divided by the electrode area is reported as the current density of the discharge currents. From the current density and the elapsed time of discharge the quantity of electricity withdrawn per unit area in coulombs/cm² is determined.

Throughout the discharge period, the closed circuit voltages of the cells were determined from time to time. Fig. 2, 3, and 4 show the decrease in closed circuit voltage against elapsed time.

The zero point of these curves is the closed circuit voltage at the beginning of the test, and differs from the open circuit emf of the cell by the *IR* drop due to the internal resistance. This is discussed further below. The general form of the discharge curves is similar to other battery curves, with a relatively rapid decrease in voltage at first, which becomes progressively slower until a "knee" is reached, beyond which the decrease again becomes more rapid. It appears that this knee is reached when the cell has decreased about 5 mv. The change in voltage beyond this point being sufficiently rapid and unpredictable to make the cell of little value as a standard, a decrease of 5 mv in the closed circuit voltage may be taken as the end point of the useful life of a standard cell under discharge.

The data on which Fig. 2, 3, and 4 were based then were calculated to the basis of quantity of electricity withdrawn in coulombs/cm², which permits the various rates of decrease in voltage in the three sizes of cells tested to be correlated. The results of this reduction of the data are listed in Table I and the average decrease in voltage as shown in

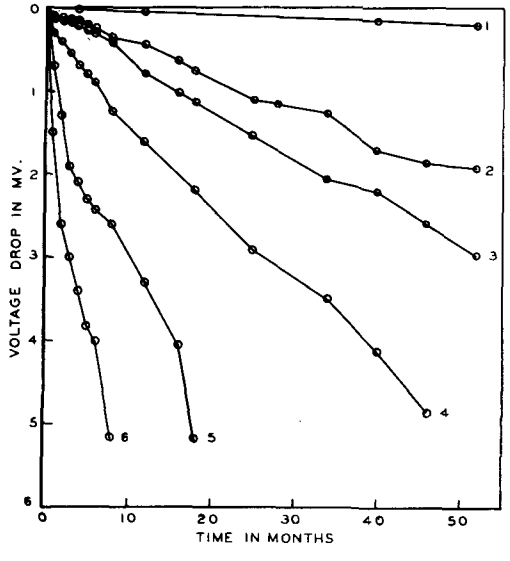

Fig. 2. Decrease in closed circuit voltage of cells with 0.5 cm² electrode area vs. time. 1, Controls, no current; 2, 0.5 μa; 3, 1 μa; 4, 2 μa; 5, 5 μa; 6, 10 μa.

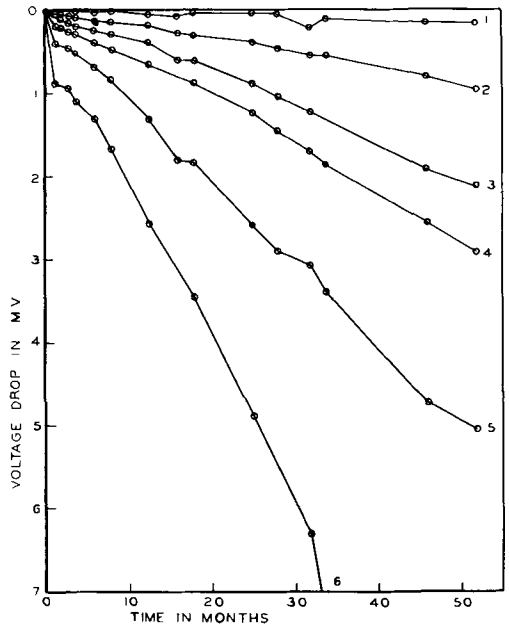

Fig. 3. Decrease in closed circuit voltage of cells with 1.43 cm^2 electrode area vs. time. 1, Control, no current; 2, 0.5 μa; 3, 1 μa; 4, 2μa; 5, 5μa; 6, 10 μa.

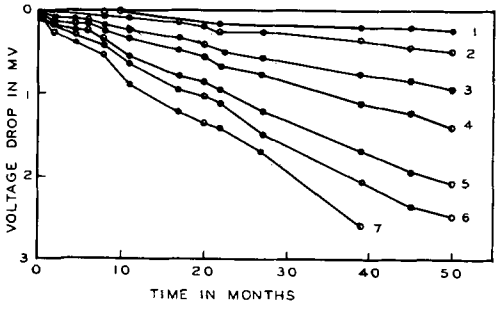

Fig. 4. Decrease in closed circuit voltage of cells with 5.5 cm^2 electrode area. 1, Controls, no current; 2, 1 μa; 3, 2 μa; 4, 4.2 μa; 5, 6.5 μa; 6, 8.5 μa; 7, 12 μa.

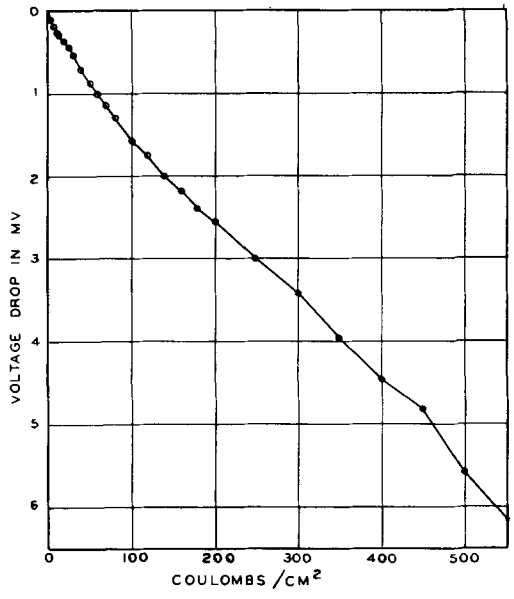

Fig. 5. Decrease in closed circuit voltage vs. total quantity of electricity withdrawn per unit area of electrode.

the last column is plotted in Fig. 5 against the total quantity of electricity per unit area.

From the data in Table I, the average rate of decrease in voltage over intervals of discharge can be calculated, as listed in Table II.

As confirmation of the above results, another separate test, similar to the above, was run with two groups, each consisting of three cells of 1.43 cm^2 electrode area. One group was discharged at a rate of 1 μa and the other at a rate of 5 μa. The decrease in voltage against time is displayed in Fig. 6.

The dashed lines in Fig. 6 represent a rate of decrease of 11 μv/coulomb cm^{-2} for the respective groups.

Table I

No. of cells:	2	4	1	4	3	2	2	4	3	2	1	4	2	4	2	2	
Area cm^2:	5.5	1.4	5.5	1.4	5.5	0.5	5.5	1.4	5.5	0.5	5.5	1.4	0.5	1.4	0.5	0.5	
$\mu a/cm^2$:	0.18	0.29	0.36	0.69	0.76	0.99	1.19	1.34	1.56	2.01	2.17	3.46	3.86	6.91	10.1	19.2	Average
Coul./cm^2									Closed circuit decrease, μv								
3		95	85	110	90	100	110	115	90	75	130	170	90	120	100	200	112
6	102	155	125	180	120	130	185	190	160	140	190	265	180	360	250	400	196
9	171	185	210	235	150	180	210	235	190	150	250	340	270	460	360	620	264
12	260	275	275	285	165	225	230	275	210	165	290	420	320	490	450	660	312
18	350	365	390	355	280	320	250	370	275	200	330	420	380	530	540	690	378
24	515	555	530	450	360	385	345	435	320	260	375	435	425	650	670	800	469
30		680	650	605	430	435	460	495	400	290	420	490	540	730	800	1000	562
40		980	810	780	575	620	615	615	570	400	505	595	680	845	1015	1280	726
50			1020	1040	740	820	745	735	720	587	645	670	800	930	1250	1500	872
60				1265	870	1030	840	855	850	750	845	750	900	1030	1480	1780	1019
70				1540	1015	1140	985	985	960	890	965	830	1120	1115	1710	1900	1166
80				1835	1150	1220	1150	1140	1035	980	1065	935	1240	1165	1910	2140	1305
100					1410	1640	1415	1510	1315	1125	1260	1160	1420	1280	2060	2600	1516
120						1860	1675	1900	1595	1430	1410	1400	1600	1440	2220	2780	1755
140						2410	1935	2230	1830	1645	1590	1625	1800	1650	2340	2950	2000
160							2130	2550	2070	1870	1800	1855	2000	1860	2440	3100	2168
180								2910	2330	2090	2065	2085	2190	2080	2500	3260	2390
200									2460	2310	2330	2320	2410	2300	2575	3710	2552
250										2715	2980	2900	2915	2820	2870	3840	3006
300												3195	3340	3335	3220	4010	3420
350												3950	3830	3845	3560	4625	3962
400												4570	4210	4365	3920	5220	4457
450												4950	4780	4875	4730		4834
500														5355	5800		5578
550														6150			6150

Table II. Rate of decrease in closed circuit voltage

Interval in coulombs/cm²	Rate of decrease in μv/coulomb cm⁻²
0-50	17.4
50-100	12.9
100-200	10.4
200-300	8.7
300-400	10.4
400-500	11.2

IR Drop

Fig. 6 was drawn to illustrate also the *IR* drop due to the internal resistance of the cell. This has been discussed by Hartshorn and Manning (4). They express the voltage of a cell which has been delivering current as

$$V = E_o - IR_o - \Delta V \qquad (I)$$

where "IR_o is the initial drop" and "ΔV is the slow change of voltage associated with chemical changes".

Some of the decrease in voltage of an unsaturated cell on closed circuit is no doubt due to formation of $CdSO_4$ and the consequent increase in the concentration of the electrolyte (9). However, it is unlikely that any gain in accuracy would result from the use of a saturated cell, because such a cell would immediately deposit solid $CdSO_4 \cdot 8/3\ H_2O$ as a result of the discharge current, which deposit would increase the internal resistance in an erratic manner, similarly increasing the *IR* drop.

Effect of Interrupted Currents

To determine whether the summed up effects of discontinuous current drains might be predicted from the continuous current drain data, 3 cells of 1.43 cm² area were discharged at 30.3 μa, one continuously, one for 16 hr continuously out of every 24, and the third for 8 hr continuously out of 24. At the end of 31 days, the closed circuit voltage of the cell on continuous discharge had decreased 740

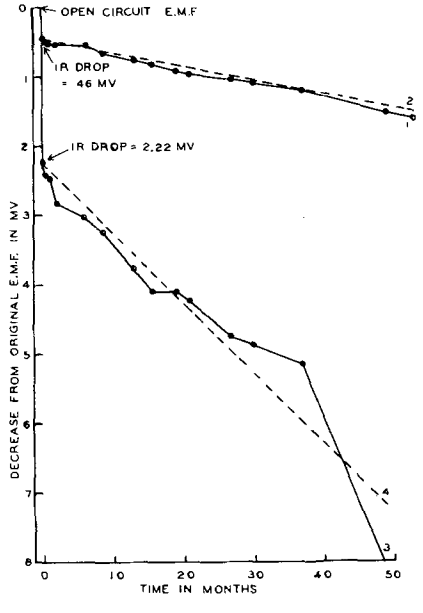

Fig. 6. Decrease in closed circuit voltage of cells with 1.43 cm² electrode area vs. time, showing IR drop immediately upon closing circuit. 1, Avg. 3 cells at 1 μa; 2, rate of 11 μv/coulomb cm² for 1 μa and 1.43 cm²; 3, avg. 3 cells at 5 μa; 4, rate of 11 μv/coulomb cm⁻² for 5 μa and 1.43 cm².

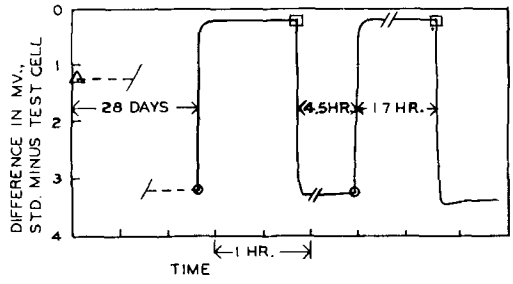

Fig. 7. Extracted from continuous strip chart recording, showing rate of return to closed circuit voltage after interruption of current. Open triangle, closed circuit voltage at beginning of discharge; open circle, circuit opened; open square, circuit reclosed.

μv, or 13.1 μv/coulomb cm⁻²; the cell on discharge 16 hr /day had decreased 600 μv, or 15.9 μv/coulomb cm⁻², and the cell on discharge 8 hr/day, 230 μv or 12.2 μv/coulomb cm⁻².

The same question was further investigated in another test, in which a cell was discharged by withdrawing about 180 coulomb/cm², and the drop in voltage continuously recorded. The cell under load was opposed by a saturated standard cell, and the difference in voltage continuously balanced and recorded by a 16 mv full scale L&N Speedomax recorder. At the beginning of the discharge period, the open circuit voltage was about 1.1 mv higher than the standard. At the end of the discharge period, when the closed circuit voltage had decreased about 2 mv, the load was removed from the cell under test for a period of 1 hr. The load was then reconnected for 4½ hr, when it was again removed, this time for 17 hr. When the load was removed, the voltage of the cell rose within 15 min to a value within 0.05% of the open circuit value to which it eventually recovered. Both times, upon reconnecting the load, the closed circuit voltage dropped immediately to the value it had when the load was disconnected. Fig. 7 is drawn from the chart curve obtained. This was repeated with two other cells, with the same results.

It appears, therefore, from the evidence in the two preceding paragraphs, that no large error is introduced by considering the effects of an interrupted current approximately the same as that of an equal quantity of electricity withdrawn in a continuous current.

Variations of Individual Cells

With the portable types of unsaturated cells such as those in this work, there is probably considerable variation in the effective electrode area, due to the effect of the septa. Although test cells made without septa would lead to better agreement in comparing the results on individual cells, the variations encountered in available types of cells must be considered in predicting the performance of instruments, and are therefore of interest.

The distribution of deviations from the average rate of closed circuit voltage decrease indicates that there is greater probability of encountering wide deviations for any individual cell on the side of higher-than-average rate. Table III lists the rate of de-

Table III. Decrease rates of 22 individual cells

Electrode area	Current	Rate of decrease at 200 coulomb/cm²
cm²	μa	μv/coulomb cm⁻²
5.5	8.0	12.7
5.5	8.9	12.6
5.5	8.9	13.4
5.5	12.0	10.4
1.43	4.8	9.3
1.43	5.0	13.8
1.43	5.0	12.4
1.43	5.0	14.6
1.43	5.0	14.2
1.43	5.1	11.0
1.43	9.5	11.7
1.43	9.6	9.9
1.43	9.9	11.2
1.43	10.6	12.8
0.5	0.9	10.4
0.5	1.0	13.1
0.5	1.9	11.3
0.5	1.9	12.2
0.5	5.0	14.8
0.5	5.1	10.6
0.5	9.4	16.2
0.5	9.8	18.0

crease in μv/coulomb cm^{-2} of 22 cells at 200 coulombs/cm², which is about the midpoint of the useful life of a discharging standard cell.

Of the 48 cells measured, the greatest rate of decrease observed after the initial rapid drop was 28.9 μv/coulomb cm^{-2} in a cell of 1.43 cm² electrode area discharging at 0.622 μa/cm², and the smallest was 9.7 μv/coulomb cm^{-2} in a cell of the same size discharging at 3.34 μa/cm².

Internal Resistance of Cells

The internal resistances of the cells used in this test were measured with a 60 cycle A. C. Bridge (L&N type 4960 Portable Electrolytic Resistance Indicator). The cells of 5.5 cm² area average about 75 ohms at 25°C; those of 1.43 cm² area, about 350 ohms, and those of 0.5 cm² area, about 750 ohms. No significant change in a-c resistance was observed throughout the test. A word of caution may be inserted here. Since the emf of a cell which has been discharging will drop quite rapidly by an amount equal to $IR_o + \Delta V$ (Eq. I), it is not possible to measure the internal resistance of such a cell by simple measurement of the voltage drop across its terminals under fixed load. A later paper will deal with this matter more completely.

Control Cells

The several cells under no current drain carried along as controls with each test group exhibited no abnormal behavior. They decreased in emf at a rate which varied for different cells from 30 to 60 μv/yr, with an average of about 45 μv/yr (10).

Summary

It is possible to use a standard cell under conditions which require the withdrawal of small currents, with the probability that it will decrease in closed circuit voltage by about 11 μv/coulomb cm^{-2}. The magnitude and duration of the current should be limited by the error which can be tolerated in the complete system. After about 450 coulombs/cm² have been withdrawn, the closed circuit voltage of the cell will have decreased about 5 mv at which point the cell becomes so unreliable that further use as a standard cell is not advisable.

Acknowledgment

The author is indebted to his colleagues at the Eppley Laboratory, where this work was performed, for valuable assistance, and especially to Marion Eppley, for guidance in many fruitful discussions.

Manuscript received May 27, 1957. This paper was prepared for delivery before the Washington Meeting, May 12-16, 1957.

Any discussion of this paper will appear in a Discussion Section to be published in the June 1958 JOURNAL.

REFERENCES

1. M. Eppley, *Elec. Eng.*, **51**, 341 (1932).
2. G. W. Vinal, "Primary Batteries," p. 212, John Wiley & Sons, Inc., New York (1950).
3. J. H. Park, *J. Research Nat. Bur. Standards*, **10**, 89 (1933).
4. L. Hartshorn and F. A. Manning, *J. Sci. Instr.*, **31**, 115 (1954).
5. W. H. Wood, *Rev. Sci. Instr.*, **28**, 202 (1957).
6. M. Eppley and W. R. Gray, *ibid.*, **2**, 242 (1931).
7. M. Eppley and G. Vincent, *Nat. Bur. Standards Circ 524*, 81 (1953).
8. M. Eppley (to The Eppley Laboratory, Inc.) U. S. Pat. 2613234, Oct. 7, 1952.
9. W. C. Vosburgh and M. Eppley, *J. Am. Chem. Soc.*, **45**, 2268 (1923).
10. W. C. Vosburgh, *J. Opt. Soc. Amer.*, **11**, 59 (1925).

Electroluminescence of Zinc Sulfoselenide Phosphors with Copper Activator and Halide Coactivators

I. J. Hegyi, S. Larach, and R. E. Shrader

RCA Laboratories, Radio Corporation of America, Princeton, New Jersey

ABSTRACT

The choice of halide coactivators in the synthesis of electroluminescent powder phosphors of the Zn(S:Se):Cu system markedly affects the spectral distribution and efficiency of the phosphors. Iodide coactivated ZnS:Cu can be prepared as a blue-emitting phosphor exhibiting no shift in spectral emission with field excitation from 20 to 50,000 cps. Several-fold increase in radiant output over the chloride coactivated ZnS:Cu phosphor is obtained by using iodide coactivator.

ZnSe:Cu phosphors, iodide coactivated, also show no shift in spectral distribution with frequency. However, the emission from Zn(S:Se):Cu materials, prepared with any of the halide coactivators, shifts to lower peak wave length with increasing frequency of excitation. A red-emitting electroluminescent phosphor can be synthesized from the (Zn:Cd):Se:Cu system by the use of bromide or iodide as a coactivator.

The role of the halide is extended from that of a randomly distributed donor to one of association with the activator, and consequences of such activator-coactivator association are discussed.

Although some references to the electroluminescence of a few particular Zn(S:Se):Cu phosphors have appeared in the literature (1-4), no systematic investigation of such materials has been published. Such an investigation has been carried out, and the following represents some of the results.

Experimental

The zinc sulfoselenide phosphors were prepared by the addition of Cu (0.1% by weight) activator (as the halide dissolved in NH_4OH) to the desired proportions of ZnS and ZnSe. Crystallizations were carried out in a nonflowing purified nitrogen atmosphere at 1075°C, with a large amount of ammonium halide (10% by weight). The amount of ammonium halide used was determined empirically for the maximum light output. As the halides sublime at temperatures under 551°C, only a small proportion is retained and incorporated into the phosphor. Deviation of lattice constants (as determined by x-ray analysis) from values to be expected from application of Vegard's law indicate that there is no significant loss of ZnSe.

The spectral emission and light intensity were examined in a capacitor-type electroluminescent (EL) cell with castor oil dielectric, using sinusoidal excitation up to 50 kc. Samples for these measurements were ground in a mortar and mixed in constant proportion with castor oil. No other treatment, such as washing, was given to the samples.

A few of the samples were analyzed for total Cu and Cu remaining after washing in KCN solution. It is assumed that Cu remaining after the cyanide wash is in solid solution in the ZnS·ZnSe host crystal, and the Cu dissolved in the cyanide is excess Cu forming a second phase of Cu_2S. This assumption is based on experimental observation that for a given composition subsequent cyanide washings failed to change the measured Cu concentration.

Chemical analysis for Cu of ZnS and 0.6ZnS:0.4ZnSe samples coactivated with the halides showed that no Cu is lost during synthesis. However, the proportion of Cu (in solid solution) remaining after KCN wash was dependent on the halide used. Table I lists the percentage of Cu in solid solution (remaining after cyanide wash) in the host crystals of ZnS and 0.6ZnS:0.4ZnSe originally containing 0.1% Cu.

The above analysis shows that the amount of Cu incorporated in the lattice is a function of both the host crystal and the halide coactivator. In general, the solubility of copper in the ZnS lattice decreases with increase in the size of the halide.

Chemical analysis for iodide content before and after cyanide wash was also made on ZnS:Cu(0.1) coactivated with iodide. The analysis for I and Cu for both unwashed and cyanide washed samples are shown in Table II.

The above data show that there are equal amounts of Cu and I by weight in solid solution in

Table I

	ZnS	0.6 ZnS:0.4 ZnSe
	%	%
Cl	88	62
Br	53	62
I	25	34

Table II

	Unwashed	Washed in Cyanide
	%	%
Cu	0.098	0.024
I	0.036	0.024

ZnS. The atomic weight ratio of I/Cu is about 2, consequently for each I there are 2 Cu atoms in solid solution.

X-ray diffraction examination of zinc sulfoselenide series synthesized at 1075°C showed that from ZnS to 0.6Zn:0.4ZnSe both cubic and hexagonal phases are present. With more than 0.4ZnSe only the cubic phase is present. The unit cell of the cubic phase expands linearly with increase in ZnSe; however, the hexagonal lattice showed no observable expansion with increase in ZnSe content. This indicates that in the two-phase region up to 0.6ZnS: 0.4ZnSe, one phase is a solid solution of ZnSe in ZnS, and the other phase, hexagonal ZnS. The amount of the hexagonal phase present is apparently not enough to give a significant deviation from Vegard's law for the cubic phase.

Results

The effect of frequency on the chloride coactivated ZnS:Cu is well known (6, 7) in that the blue-to-green ratio increases with increasing frequency. However, ZnS:Cu, coactivated with iodide, has essentially a single emission band with excitation frequencies of 20 cps to 50,000 cps. The Cu content can be varied from 0.02% to 0.2% Cu, (3×10^{-4} to 3×10^{-3} Cu/mole ZnS), with but small changes in spectral emission for all compositions.

In Fig. 1a, normalized spectral distribution curves of emission for ZnS:Cu are shown for the different halides as coactivators. The spectral distribution curve of ZnS:Cu:I shows a narrow band with peak wave length in the blue. The chloride and bromide coactivated spectral distribution curves show much broader bands whose apparent peak is at a longer wave length than the iodide curve. It is quite apparent that the spectral emission of ZnS:Cu(Cl,Br) consists of at least two emission bands of different relative intensity. The relative intensity of blue and green present in bromide coactivated materials appears to be more sensitive to amount of activator, coactivator, and processing than in chloride phosphors. The emissions of the bromide coactivated phosphors do not necessarily always peak at a longer wave length than the chloride coactivated samples, as shown in Fig. 1a. Phosphors have been prepared with almost identical spectral distribution for chloride and bromide coactivators. Curves are also shown, Fig. 1b, relating the integrated output (as observed with RCA 5217 Photomultiplier, S10 surface), and frequency of field excitation, at 280 v rms.[1] These curves show the superiority of iodide and bromide over chloride coactivated electroluminescent phosphors, for integrated output.

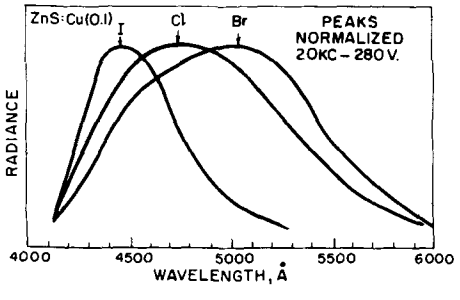

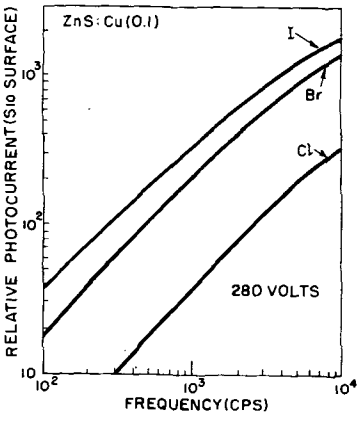

Fig. 1a. (Top) Spectral distribution curves of the electroluminescence of chloride, bromide, and iodide coactivated ZnS:Cu. Fig. 1b (Bottom) Relative radionce of chloride, bromide, and iodide coactivated ZnS:Cu El phosphors.

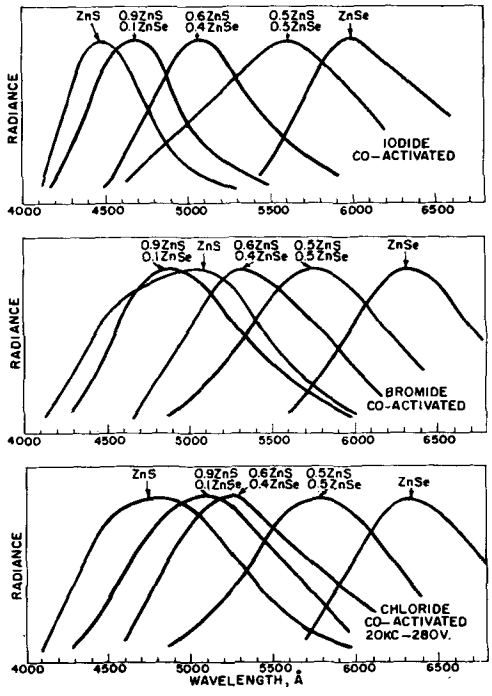

Fig. 2. Spectral distribution curves of the electroluminescence of Zn(S:Se):Cu with varying S:Se ratios, coactivated with chloride, bromide, or iodide. The S:Se ratios refer to compositions before firing.

In Fig. 2 spectral distribution curves are given for materials with varying amounts of S and Se. Curves for iodide coactivated materials peak at shorter wave length than corresponding bromide or chloride coactivated phosphors. For iodide-containing phosphors, the spectral shift with increasing Se content is monotonic and comparatively uniform with change in composition. With chloride, however, the first 10% Se produces a large color shift, which is not renewed until 20-25% Se is incorporated. The bromide coactivated phosphors with low Se content are centered at shorter wave length than corresponding chloride coactivated materials, while at increasing Se concentration the curves of chloride and bromide materials become more similar.

[1] Cell thickness was 0.002 in.

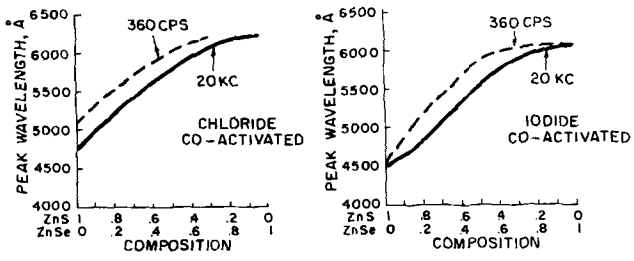

Fig. 3a. (Left) Peak wave length EL emission (at excitation frequency of 360 cps, and 20 kc) of Zn(S:Se):Cu:Cl with varying S:Se ratios. Fig. 3b. (Right) Peak wave length EL emission (at excitation frequency of 360 cps, and 20 kc) of Zn(S:Se):Cu:I with varying S:Se ratios.

In Fig. 3, peak wave length of spectral emission is plotted as a function of ZnS:ZnSe composition for copper activated iodide and chloride coactivated phosphors at two frequencies, 360 cps and 20,000 cps. With increase in frequency the iodide coactivated curve shows no change in peak wave length at the extremities (ZnS or ZnSe), but at intermediate compositions [Zn(S:Se)], the peak shifts to shorter wave lengths. The chloride coactivated materials show a shift to shorter wave length with increasing frequency for ZnS. This shift decreases in the Zn(S:Se) region, and appears to disappear for ZnSe.

In Fig. 4, curves are shown of spectral emission for the material 0.6ZnS:0.4ZnSe:Cu(0.1), iodide, bromide, and chloride coactivated, under EL excitation at 20 kc, 2 kc, and 0.2 kc. The spectral shift from 20 kc to 2 kc is largest for the chloride coactivated material, and smallest for the iodide. At frequencies of 2-0.2 kc the shift is largest for the iodide and smallest for the chloride. The bromide coactivated samples show a more linear spectral shift over the 20-0.2 kc frequency range. Relative peak intensity data are also shown. For comparison purposes, the dotted curves show the spectral distribution under excitation by 3650Å u.v. radiation.

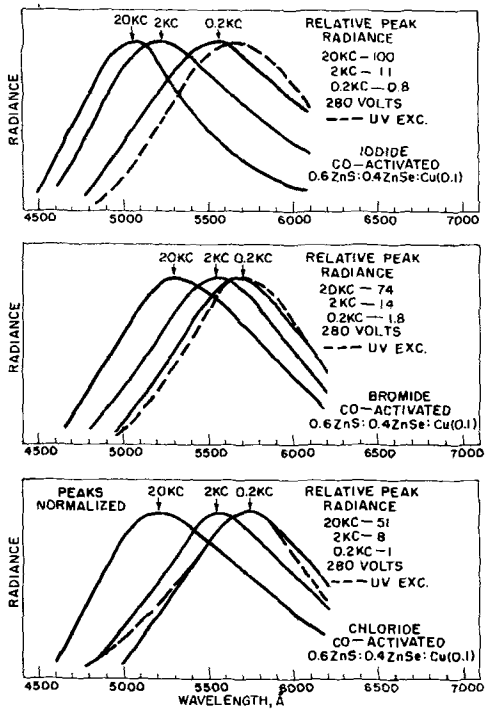

Fig. 4. Spectral distribution curves of the electroluminescence of 0.6ZnS:0.4ZnSe:Cu(0.1) coactivated with chloride, bromide, and iodide for the excitation frequencies of 20, 2, and 0.2 kc; also of the photoluminescence under excitation by 3650 Å u.v. radiation.

Fig. 5 shows the relative photoluminescent efficiencies of the three materials for Fig. 4 as a function of the exciting wave length.

The phosphor with the longest dominant wave length (ZnSe:Cu) is still subjectively red-orange. Using the same synthesis procedure but replacing some of the ZnSe with CdSe, and using either bromide or iodide as coactivator, a red-emitting phosphor can be obtained.

In Fig. 6, the peak wave length of EL from iodide coactivated (Zn:Cd) Se:Cu is plotted as a function of ZnSe/CdSe ratio. It is seen that a linear increase of peak wave length is obtained with increased amounts of CdSe.

Discussion

There are three features of this study that should be emphasized. These are: (a) the effects of the

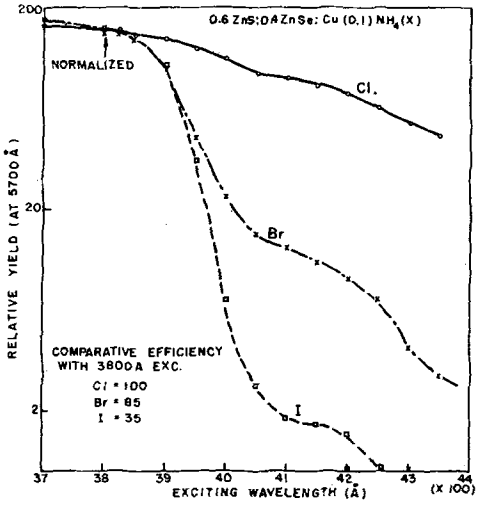

Fig. 5. Relative photoluminescent yield of the materials of Fig. 4 under excitation for radiation of various wave lengths.

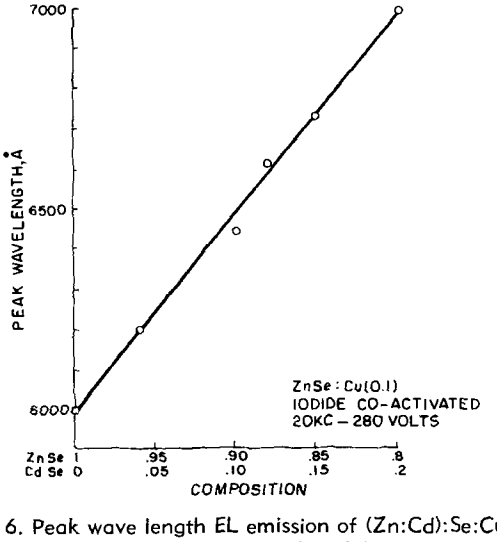

Fig. 6. Peak wave length EL emission of (Zn:Cd):Se:Cu with varying Zn:Cd ratios coactivated with iodide.

nature of the halide coactivator; (*b*) the effect of operating frequency on the emission; and (*c*) the effects of composition (S:Se ratio) on the emission under EL excitation. These aspects are interdependent, but also are complicated by the peculiar nature of EL excitation.

It is well known that ZnS phosphors with certain activators are prepared in the presence of halide. It was originally believed that the function of the halide was that of a "flux", i.e., a low melting phase to aid in recrystallization and particle growth. This view was modified when Smith (7) proposed that the halide actually was incorporated into the lattice. The function of the halide as a charge-compensating agent has been set forth by Kroger and his collaborators. The role of halide as a donor has recently been proposed (8-10). The cathodoluminescence of ZnS:Cu with chloride, bromide, or iodide coactivator, is predominantly in the blue region of the spectrum, with only traces of a green band for the materials prepared with chloride and bromide. These same materials, when excited by photons, show wide variations in their emission colors (blue/green), particularly as functions of excitation wave length and density, and operating temperature. Thus, in all three materials, emission centers giving rise either to blue or to green emissions are present, regardless of the nature of the coactivator halide. If more than one emission center exists, the observed emission of a crystallite is determined by the competitive process which exists between centers. In turn, the competitive situation is determined by the concentration distribution, temperature, excitation nature, etc. The Schon-Klasens hypothesis describes the simplest type of competitive process whereby a hole captured at one recombination level is transferred to another level of the type which accounts for the majority of the radiative recombinations. This explains qualitatively the green-to-blue shift of ZnS phosphors with low Cu content, with increasing u.v. irradiation density, in which the presence of two emission bands is easily demonstrated. Nevertheless, for photo-excitation and electroluminescence, Zn(S:Se):Cu phosphors prepared with different halide coactivators exhibit markedly different properties.

The role of the halide merely as a randomly distributed donor must, therefore, be modified or extended. One modification is to abandon the requirement that the coactivator is randomly distributed in the crystal, and to assume association exists between activator and coactivator. If activator-coactivator association exists in varying degrees, the diffusion differences of the various coupled complexes could make for distribution inhomogeneities. Further, the nature of the activator determines the density of each type of association and its distribution throughout a crystallite volume.

The phenomenon of color shift with frequency reported in this paper cannot be explained by a simple application of the Schon-Klasens hypothesis. A material excited at fixed voltage and two different frequencies may show a marked color shift. The same material operated at an intermediate frequency and at two voltages which produce the same brightness levels as previously obtained by the two different frequencies shows negligible color shift. Since the same change in over-all output results in both cases but with color shift in one case and not in the other, it must be assumed that the two cases involve a different distribution of absorbed (or, at least, emitted) energy throughout the bulk of the crystallite. If one reconsiders the hypothesis of activator-coactivator association and the probable effect on center distribution, it can be seen qualitatively how the halide effects on color shift may be explained. This is especially so if one makes the reasonable assumption that the complexes involving the large iodine ions have low volume solubility and, hence, are to be found in greater concentration near the surface. Iodine coactivated Zn(S:Se) in Fig. 4 was shown to be most frequency-sensitive.

What is still unknown is the exact nature of the complete emission center, either blue or green, and the closeness of coupling between the Cu atom or ion and the halide atom (or ion). Measurements cited show that the incorporated Cu content is definitely related to the particular halide and that the Cu-halide ratio is also affected. This further confirms the premise that not only do the different halides have different solubilities but that there are different solubilities (concentrations) of the Cu-halide complexes.

The concept of a Cu-halide complex is strengthened by the determination (11) that the blue emission band of ZnS:Cu(0.1):I is not the usual "host-crystal" blue band of ZnS:I, but is as associated with Cu as is the usual green band.

The predominance of the blue band in ZnS:Cu (0.1):I regardless of type of excitation, and in spite of the reduced amount of incorporated Cu, suggests that the Cu-I complex is closely coupled, and is the only such closely coupled complex of significant solubility in the ZnS lattice.

When the Se proportion is 40% or larger, the shape of the spectral distribution obtained for any one material and mode of excitation seemingly shows that only one emission band is significant. With this situation, an explanation of color shift with frequency is even more difficult to achieve than for the cases where interplay between two emission bands could be postulated. It is seen in Fig. 4 that u.v. excitation causes essentially identical emissions from 0.6ZnS:0.4ZnSe:Cu:X regardless of the nature of X. That there is still a marked effect of halide present is shown in Fig. 5 in which I is found to reduce the "impurity excitation band" drastically. Whether this effect is best explained by the absorption properties of the complex or by some feature of its distribution between surface and volume is not now known. It is significant that, although the relative photo-excitation efficiency of Cl-coactivation to I-coactivation is 3 to 1, the EL excitation at 20 kc is 1 to 2. The "sliding sidewise" type of color shift suggests that in the disorder present in a mixed lattice there is an effective continuum of levels separated spacewise by their distance from the EL surface barrier. Tests of this hypothesis us-

ing x-rays, C-R excitation, annealing, digestion, etc., are planned.

The first-order effects of S-to-Se ratio in the composition are, of course, expected since the band gap of the Zn:Se series shows a smooth monotonic variation from ZnS to ZnSe. What is of more interest is the way in which addition of Se to the ZnS:Cu:(x) lattice disturbs the blue-green competitive balance.

Manuscript received July 23, 1956. This paper was prepared for delivery before the San Francisco Meeting, April 29-May 3, 1956.

Any discussion of this paper will appear in a Discussion Section to be published in the June 1958 JOURNAL.

REFERENCES

1. S. Roberts, Jr., *J. Opt. Soc. Amer.*, **42**, 850 (1952).
2. U. S. Patent No. 716,159.
3. J. S. Prener, U. S. Patent No. 2,731,423.
4. A. Fisher, *Z. Naturf.*, **8a**, 756 (1953).
5. H. H. Homer, R. M. Rulon, and K. H. Butler, Jr., *This Journal*, **100**, 566 (1953).
6. P. Zalm, G. Diemer, and H. A. Klasens, *Philip Res. Repts.*, **9**, 81 (1954).
7. A. L. Smith, *This Journal*, **96**, 75 (1949).
8. F. A. Kroger, et al., *Z. Physik u. Chem.*, **203**, 1 (1954).
9. R. H. Bube and S. M. Thomsen, *J. Chem. Phys.*, **23**, 15 (1955).
10. J. S. Prener and F. E. Williams, *Phys. Rev.*, **101**, 1427 (1956).
11. R. E. Shrader and S. Larach, *ibid.*, **106**, 1899 (1956).

Heat Treatment of Silicon Using Zone Heating Techniques

H. C. Theuerer, J. M. Whelan, H. E. Bridgers, and E. Buehler

Bell Telephone Laboratories, Inc., Murray Hill, New Jersey

ABSTRACT

New insight into the mechanism for the changes in silicon with solid-state heat treatment has been obtained with the aid of the floating zone apparatus normally used to refine silicon. With this system, a liquid or solid hot zone may be caused to traverse the rod while the rest of the apparatus is kept relatively cool.

Through the use of this technique, it has been established that contaminants left on the silicon surface even after careful etching and washing procedures are a controlling factor in the observed heat treating effects. The impurities involved have high diffusivities, as is the case for copper and iron in silicon. That these impurities lower lifetime on heat treatment has been demonstrated by rubbing the silicon rod with copper or iron wires prior to zone heat treatment.

The heat treatment of Si at temperatures between 400° and 1200°C usually causes changes in carrier lifetime, resistivity (1), and in some cases conductivity type. Such changes are not, however, a necessary consequence of heating high purity Si. For example, Si has been prepared by the floating zone method (2) which can be heat treated without changes in properties if contamination is avoided. Residual impurities left on the surface after etching and cleaning procedures and the furnace environment during heat treatment are contamination sources capable of causing serious lifetime and resistivity changes. The impurities responsible for these changes must have a high diffusivity in Si, as is the case for Cu, Fe, and Au (3), since the time required to obtain the effects is short.

In heat treating studies furnace contamination can be avoided by using the floating zone apparatus in which the high purity Si is initially prepared. However, if the Si is handled prior to heat treatment, serious contamination is encountered; this is not eliminated by the usual etching and cleaning procedures. With the zone heating technique, lifetime changes may be used effectively to evaluate new etching procedures. Details of the method and results obtained in a number of experiments are given herein.

Apparatus

The apparatus used in the floating zone technique consists of a quartz tube 22 in. long and ¾ in. OD which is fitted to metal end heads. The end heads contain stainless steel chucks used to clamp quartz holders with which the Si under test is suspended axially in the apparatus. A single turn induction coil surrounds the quartz tube and is connected to a 5 MC generator for direct induction heating of the Si. Provision is made to cool the entire quartz envelope during the heating of the Si by means of a water curtain. The entire apparatus is mounted from a carriage, allowing the quartz tube to be moved through the induction coil at a controlled rate, usually 0.05 in./min in these experiments. By this means, the hot zone may be caused to traverse the entire rod. During zone treatment, the apparatus is flushed continually with pure dry hydrogen entering and leaving through ports provided in the metal heads.

Surface Contamination Studies with Liquid Zones

Extensive refining with the apparatus described above results in p-type Si with resistivities above 10,000 ohm-cm and carrier lifetimes above a millisecond. This establishes that this furnace is not a serious source of contamination and should, there-

fore, be suitable for heat treating studies. In an initial investigation to determine the effect of residual surface impurities on resistivity and lifetime, a Si rod was given four liquid zone treatments. A p-type rod with resistivities ranging between 25-60 ohm-cm and having carrier lifetimes between 200-250 μsec was obtained. The lifetime measurements were made by the photoconductivity decay method. The rod was then etched with the standard HF-HNO_3 mixture,[1] washed with deionized water, and dried. One additional zone pass through the rod degraded the lifetime to values of 30-40 μsec without a significant change in resistivity. A second experiment clearly established that the furnace environment was not the source of the contaminants responsible for this lifetime degradation. A rod was given 10 zone passes and was then removed from the apparatus without handling of the surface. The furnace tube, however, was cleaned in HF-HNO_3 and rinsed, as was done in the initial experiment. The Si was then remounted in the apparatus and one-half of the rod given an additional zone pass. No significant lifetime differences were observed. The control section with 10 zone passes had lifetimes between 600-300 μsec; the section with one additional pass had lifetimes between 480-330 μsec.

In addition to lifetime changes, etching a Si rod in HF-HNO_3 prior to a liquid zone pass also results in donor contamination, observed as a change in resistivity or conductivity type if the starting material is sufficiently pure. For example, after extensive zone refining, a p-type Si rod section had a resistivity of 3300 ohm-cm. An additional zone pass was put through the rod after sandblasting, etching in HF-HNO_3, and washing in deionized water. The Si obtained was p-type, and the resistivity in the previously measured section was now 6000 ohm-cm. Since the acceptor impurity in this Si was B, with a distribution coefficient of 0.8, the increase in resistivity could not have been due to refining by the single zone pass but must have been due to donor contamination. This was further substantiated by repeating the above surface treatment prior to a second zone pass. The rod section was now n-type with a resistivity of 1000 ohm-cm. From the resistivity data, the donor contamination was estimated to be about 3×10^{12} at./cm^3/treatment. Assuming that all of the contaminants were on the Si surface initially, the concentration calculated from the above value is $\approx 4 \times 10^{11}$ atoms/cm^2, which is equivalent to 0.001 of a monolayer.

[1] This mixture contains 1 part HF 48%, 3 parts HNO_3 71%.

Surface Contamination Effects in Solid Zone Studies

It is apparent from the liquid zone experiments that contaminants from the surface may degrade lifetime seriously. Similar results have been obtained in heat treating studies with solid Si. In such experiments, a hot zone at 1100°-1200°C is initiated at the end of the rod and is caused to traverse the rod by moving the system through the induction coil at a controlled rate. In this way a zone approximately ¼ in. long is maintained at 1200°C, and the material on either side of the zone for a distance of approximately 1 in. is visibly red. Using a zone velocity of 0.05 in./min the material is at 1200°C for approximately 5 min during each pass and cools to 650°C in approximately 20 min.

In initial experiments, using this method, the following questions were answered: (*a*) can Si be heat treated at 1200°C using the floating zone apparatus without deterioration of lifetime? (*b*) is water cooling of the quartz furnace tube essential to preservation of high lifetime during heat treatment? (c) is etching and washing the rod prior to heat treatment deleterious to lifetime?

In these experiments high lifetime Si crystals were prepared by passing 10 zones through each rod. The first 4 cm of the rods were then given three zone treatments at 1200°C leaving a 10 cm section at the end of these rods for control purposes. The experimental conditions and the results obtained are summarized in Table I. From the data of Table I, it is evident that Si can be heated in the range between 400°-1200°C without serious deterioration of lifetime, provided the quartz envelope is kept cool with an external water curtain during the heat treatment. If the furnace tube is allowed to heat by removing the water curtain, the lifetime of the Si drops drastically when heat treated in the range between approximately 400° and 1200°C. Etching and washing the Si prior to heat treatment results in serious changes in lifetime. The evidence is clear that contaminants which impair lifetime on heat treatment may be introduced from a hot quartz tube, even with the specimen freely suspended. Such contaminants may also be introduced as residual impurities left on the surface after etching and washing.

In a second group of experiments, attempts were made to establish what steps in the etching and

Table I. Variations in heat-treating procedures and their effect on the lifetime of Si

Procedure	Lifetime μsec, Distance along rod from lead end in cm						
	2	4	6	8	10	12	14
Rod grown and not removed from furnace, given three zone passes at 1200°C, quartz tube water cooled	300	150	500	600	840	700	500
Rod grown and not removed from furnace, given three zone passes at 1200°C, quartz tube not water cooled	<3	<3	<3	4	580	650	650
Rod grown and exposed to air 15 min, rod remounted, three zone passes at 1200°C, quartz tube water cooled	90	135	320	550	520	570	480
Rod etched in HF-HNO_3, washed three zone passes at 1100°C, quartz tube water cooled	5	3	10	3	7	150	180
	Section heated to 1200°C		Section heated above 400°C		Section heated <400°C		

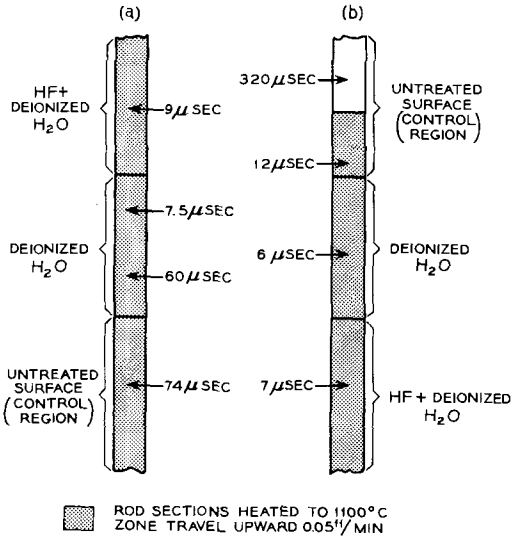

Fig. 1. Effect of surface preparation prior to heat treatment on the lifetime of Si.

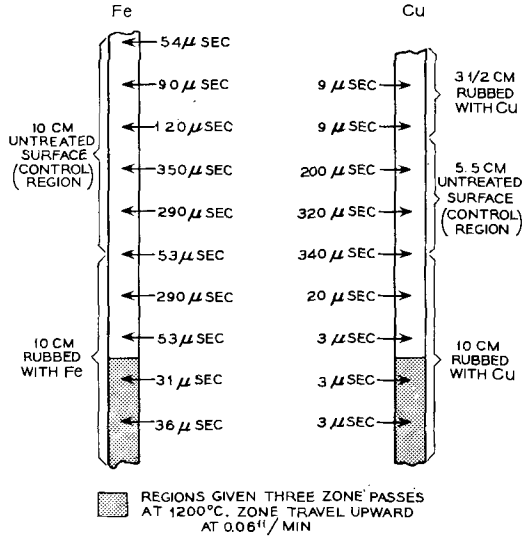

Fig. 2. Effect of surface deposits of Fe and Cu on the lifetime of Si after heat treatment.

washing technique were responsible for lifetime deterioration. In these experiments, two high lifetime crystals were prepared by passing 5 liquid zones through each rod. The rods were removed from the apparatus and given the surface treatments indicated in Fig. 1. After treatment, the rods were given a single zone pass at 1100°C using a zone velocity of 0.05 in./min. From the lifetime data of Fig. 1a, it is obvious that washing with HF followed by a deionized water rinse reduces the lifetime drastically. Although not as severe, some lifetime deterioration after heat treatment is indicated in the rod sections washed with deionized water or only exposed to air. Note also that the lifetime in the upper region of the rod section treated with deionized water had a lifetime of 7.5 μsec, whereas lower in this section the lifetime was 60 μsec. This is an indication that impurities introduced by the HF rinse diffuse into the deionized water-treated region during the zone heating process. That this occurs is shown more clearly by the results, given in Fig. 1b, for the second rod. In this case, the hot zone was passed from the section treated with HF through the section treated only with water and part way through the section which was exposed only to air. The lifetime was drastically reduced through the entire area which had been heat treated irrespective of the prior surface treatment; only in the unheated region was the lifetime preserved. This establishes that the impurities responsible for lifetime deterioration have a high diffusivity in Si.

Copper and iron, for example, are known to diffuse rapidly through Si and destroy the lifetime. This was confirmed by preparing two high lifetime rods using the floating zone method. Without other treatment, the rods were rubbed with Cu in one case and with Fe in the other at the locations indicated in Fig. 2. The lower 5 cm of the rubbed rods were then heat-treated at 1200°C by passing three zones at the rate of 0.06 in./min through these regions. As can be seen from the data, the lifetime was seriously impaired by both Cu and Fe, the damage in each case extending well beyond the 1200° hot zone. The lifetime deterioration was most severe with Cu, and surprisingly it was effective in the upper Cu-treated region of the rod which could not have been heated at temperatures much above 400°C.

Using the basic method discussed above, a number of etching and cleaning methods for the removal of surface contaminants have been investigated. Etching Si with Br_2 at elevated temperatures or with NaOH solutions is no more effective than the standard HF-HNO_3 treatment. Immersion in hot HNO_3, H_2SO_4, H_2O_2, and NaCN after etching has not led to improved lifetime after heat treatment.

Manuscript received May 23, 1957. This paper was prepared for delivery before the Washington Meeting, May 12-16, 1957.

Any discussion of this paper will appear in a Discussion Section to be published in the June 1958 JOURNAL.

REFERENCES

1. C. S. Fuller, J. A. Ditzenberger, N. B. Hannay, and E. Beuhler, *Acta Metallurgica*, **3**, 97 (1955).
2. P. H. Keck and M. J. E. Golay, *Phys. Rev.*, **89**, 1297 (1950); H. C. Theuerer, *J. Metals*, **8**, 1316 (1956).
3. C. S. Fuller, J. D. Struthers, J. A. Ditzenberger, and K. B. Wolfstein, *Phys. Rev.*, **93**, 1182 (1954); J. D. Struthers, *J. Appl. Phys.*, **27**, 1560 (1956).

Electrolytic Extraction of Thorium from Fused Salts

Lothar Abraham, Edward L. Thellmann, and James L. Wyatt[1]

Horizons Incorporated, Cleveland, Ohio

ABSTRACT

High purity thorium metal powder has been produced by fused salt electrolysis of thorium chloride by a process readily adaptable to continuous production techniques. An electrolytic cell design based on a frozen-salt crucible design concept has been evolved. Heating of the salt bath was accomplished by graphite resistance heaters immersed in the bath. Metal quality, current efficiency, and other operating characteristics of the internally heated electrolytic cell compare favorably with those experienced in smaller scale, externally heated cells.

Numerous processes for the preparation of thorium metal have been investigated, including thermal reduction of halides with Ca (1), thermal reduction of the oxide with Ca (2) or a metal hydride, and by fused salt electrolysis (3). The latter approach was considered promising and as such has merited intensive investigation.

Small-scale investigations of a chloride fused salt system, carried out by Raynes, *et al.* (4), have led to the successful development of an electrolytic process which readily lends itself to continuous operation. The process can be summarized as encompassing the electrolysis of fused anhydrous $ThCl_4$ in NaCl under an inert atmosphere. The Th is deposited as dendritic crystalline metal in a matrix of salts from which it can be separated readily by aqueous methods.

Anhydrous $ThCl_4$ is supplied to the electrolytic cell in the form of a $ThCl_4$-NaCl mixture and diluted with NaCl to obtain an electrolyte containing approximately 15% Th by weight.

A companion paper (5) describes one method for producing a suitable electrolyte.

Electrolytic Equipment

Early in the development program, fused salt electrolysis was carried out in externally heated cells which have been described previously (4). The basic design proved satisfactory for small-scale operations and served as prototype for larger capacity units.

Electrolytic Cell Scale-Up

The limitation of construction materials for the fused salt container imposed a severe problem in attempts to scale up operations, principally because of the porosity of commercial grade graphite and carbon crucibles. Crucibles up to 24 in. in diameter were evaluated, leakage invariably developing. The results of these operations clearly pointed to the necessity of developing an entirely different concept of cell design.

Prior research in a related field at this laboratory had investigated a concept of cell construction which utilized an internal graphite heater. While the work did not include Th, the principles appeared to be applicable to any fused salt system. Accordingly, a program was initiated to apply these approaches to the production of Th. This program was primarily an engineering development effort, and no particular efforts were made to produce high quality Th metal. For example, cells were opened frequently to allow observation of various cell components during operations; of necessity, therefore, the cell atmosphere at times was badly contaminated with air.

Briefly, the cell consisted of a rectangular Ni shell surrounded by mild steel air jackets for controlled cooling. The crucible was centrally located within the shell and constructed of graphite slabs. Carbon black was tamped to a density of approximately 40 lb/ft^3 in the 1-in. wide annular space between the graphite crucible and the shell to serve as an insulating medium. A 1½ in. layer of carbon black was also tamped into the shell bottom. This gave a crucible with inside dimensions of 8½ in. x 9½ in. x 17 in. deep. The graphite slabs forming the crucible needed only to fit reasonably close together since they were not required to form a leakproof, impervious vessel. To complete the assembly, a 2-in. thick piece of porous graphite was positioned across the top of the crucible to reduce radiated heat losses out the cell top. Fig. 1 is a schematic view of the frozen salt crucible cell.

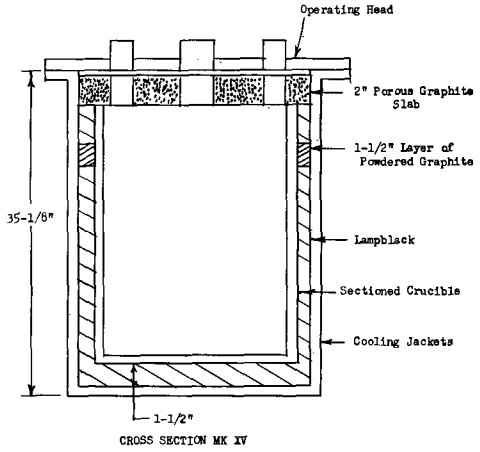

Fig. 1. Typical cross section of rectangular cell, showing major construction features.

[1] Present address: Booz, Allen and Hamilton, 380 Madison Ave., New York, N. Y.

For heating, two ¾ in. diameter graphite rods were press-fitted into the bottom of the crucible as shown in Fig. 2 and served as electrical resistors in an a-c power circuit.

In operation, it was found that the molten salt tends to leak through pores or discontinuities in the crucible walls and penetrates the carbon black slightly. Coolant flow through the air jackets was adjusted so that a portion of the liquid salt was frozen solid in the carbon black insulation; in this manner, the contents of the crucible remained molten and the entire crucible functioned as one electrode (anode) in the electrolysis.

Eleven runs were made in this unit without any major changes except for modifying the graphite heating elements. Several designs were tried, the one exhibiting the most desirable characteristics (highest resistance), consisting of a simple graphite "U" fabricated from ¾ in. diameter graphite rods. It was insulated from the crucible bottom with ½ in. thick porcelain slabs. Fig. 3 shows the graphite "U" heating element assembled. Typical circuit impedance under operating conditions at 750°C was 0.02 ohm. Total a-c heat input requirements ranged from 3 to 5 kw in order to maintain proper bath temperatures.

Cell Operation

Since the electrolytic deposition of Th was carried out in an all-chloride system, it was possible to place a thermocouple directly into the bath protected only by a quartz tube.

Prior to cell start-up, the electrolytic cell was hot-evacuated until outgassing ceased, then flushed with argon. The salt charge was melted under an argon atmosphere in approximately 7 hr. Fifty pounds of NaCl were melted first, followed by cell feed additions consisting of NaCl-$ThCl_4$. The total charge was 75 lb, initially containing approximately 15% Th by weight. The bath temperature was controlled at 790°-800°C.

A cathode consisting of a steel tip 1 in. in diameter and 5 in. long, attached to a ½-in. Ni shaft protected by graphite tubing, was immersed to a depth of 6 in. in the fused salt bath with a small d-c voltage impressed on it. When the cathode reached bath temperature (in 3-5 min), the voltage was increased to operating level (4-5 v) and current flow maintained thereafter at a cathode current density of 250 to 350 amp/dm², based on initial cathode area.

When a predetermined number of ampere hours had been passed through the electrolyte, the d-c voltage was lowered, and the cathode was raised to a position above the bath. It was maintained in this position in argon until the temperature of the entire unit was below 100°C, after which the deposit was removed. This procedure was necessary since no provisions for a removal chamber had been made. With a removal chamber, the bath could be maintained molten; theoretically, $ThCl_4$-NaCl additions could be made indefinitely without any detrimental effects on the electrolyte; thus, additional deposits could be produced with a minimal amount of down time.

The Th was deposited as dendritic crystalline metal in a matrix of salts from which it could be readily separated by water leaching. Fig. 4 shows a typical cathode and cathode deposit after removal from the cell. Fig. 5 shows the deposit broken open to reveal the characteristic internal appearance of Th metal deposits.

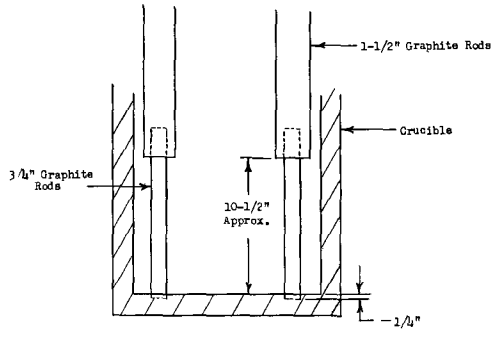

Fig. 2. View of rectangular cell, showing method of installing heating element rods.

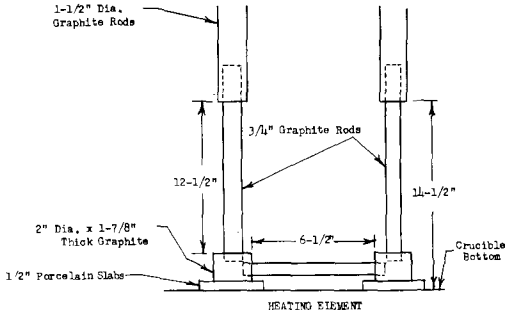

Fig. 3. Revised design of heating element for rectangular electrolytic cell.

Experimental Results

Cathode deposits produced in the electrolysis of anhydrous $ThCl_4$ in fused NaCl generally averaged 45-60% Th metal by weight. Current efficiencies averaged in excess of 75%. The Th metal produced in this campaign ranged from Rockwell B-30 to Rockwell B-58.5 in hardness. Hardness was determined on metal buttons produced by melting compacted metal powder in a water-cooled copper hearth arc furnace.

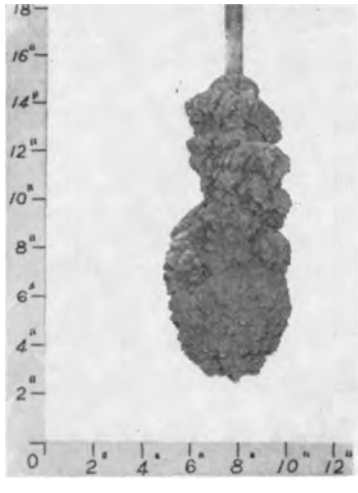

Fig. 4. Typical deposit of thorium metal produced in rectangular laboratory electrolytic cell.

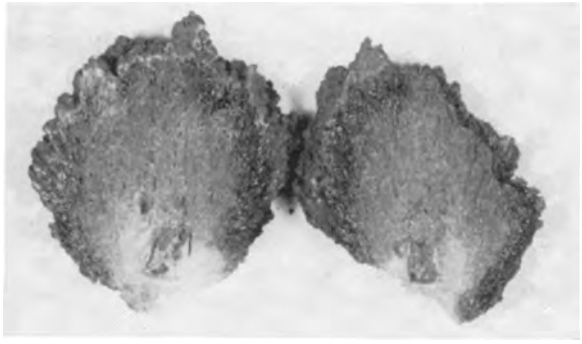

Fig. 5. Internal structure of thorium cathode deposit

The Th powder produced by fused salt electrolysis had a particle size distribution which made the metal readily amenable to powder metallurgy techniques. Generally, less than 10% of the powder was +20 mesh, and 70% was +70 mesh.

Table I presents a summary of data pertinent to the operation of the electrolytic cell.

Discussion and Conclusions

A program to evaluate fused salt electrolytic techniques for producing Th metal has been carried out in an attempt to devise a commercially feasible cell design concept. It has been demonstrated that satisfactory cell linings for Th production may be constructed of graphite slabs without regard for porosity and close tolerances, thereby eliminating problems attendant with size limitations on monolithic crucibles. The use of lampblack as an insulator, the establishment of a "frozen salt crucible" therein, and application of internal resistive heating have been incorporated experimentally in a device for the preparation of Th metal.

Observations of cell components showed no measurable deterioration, attrition, or chemical attack during the operational period, and, based on the extent of exposure time and extrapolation, it appears probable that cell linings will last at least one year. Heating element life probably will be shorter, perhaps 3-6 months. Designs, therefore, should provide for occasional replacement of the heater components.

Production of relatively good quality Th metal with high yield and acceptable current efficiency was demonstrated on a small scale, all results comparing favorably with previous work which has been carried out in monolithic cells.

Results on the small-scale program clearly demonstrated feasibility and warranted scale-up for pilot evaluation of equipment and processes on a semicontinuous basis.

Acknowledgments

The work described in this paper was carried out under the sponsorship of the Atomic Energy Commission, Contract No. AT(30-1)-1335, and grateful acknowledgment for permission to publish the data is made. Certain aspects of processes and equipment form the basis for patent applications pending at present.

The authors wish to make special acknowledgment to B. C. Raynes, J. C. Bleiweiss, J. A. DaMico, and R. Engle, present or former members of Horizons' staff, each of whom made major contributions to the program.

Permission to describe the crucible design, developed by Horizons Incorporated under contract with Horizons Titanium Corporation, is also gratefully acknowledged.

Manuscript received Jan. 23, 1957.

Any discussion of this paper will appear in a Discussion Section to be published in the June 1958 JOURNAL.

REFERENCES

1. C. A. Hampel, "Rare Metals Handbook," p. 435 Reinhold Publishing Co., New York (1954).
2. *Ibid.*, p. 433.
3. F. H. Driggs and W. C. Lilliendahl, *Ind. Eng. Chem.*, **22**, 1302 (1930).
4. B. C. Raynes, J. C. Bleiweiss, M. E. Sibert, and M. A. Steinberg, "Electrolytic Preparation of Thorium Metal," submitted to AIME for publication, 1956.
5. C. E. Fisher and J. L. Wyatt, *This Journal*, **104**, 672 (1957).

Table I. Summary of Mark-15 electrolytic runs

Run No.	Total charge wt lb	% Th in bath	Bath temp °C	D.C. current amp	D.C. v	Amp hr	Weight water washed metal g	Weight acid treat. metal g	Weight* recov. fines in overflow	% Current eff.†	Hardness R_B	% Th metal in dep.
1	80	16	800	270-335	4.4	3000	2211	2133	320	39.0	53	32.0
2	84	17	775-815	260-320	4.4	2350	3455	2814	73	69.5	50	—
3	88	15	800	280-300	4.9-4.2	2300	3191	2977	216	68.5	30-35	—
5	80	13	800	240-300	5.5-5.3	1480	2561	2534	176	85.5	35	57.5
6	75	13	810	260-280	5.6-5.3	1220	1893	1860	120	76.5	56	56.0
7	77	14	800	230-260	5.6-5.1	1655	2759	2708	140	81.0	49	54.5
8	80	10.6	785-800	170-290	5.5	1500	2773	2697	155	90.5	58	58.5
10	75	11.3	790-800	220-310	5.2-5.4	1200	2375	2298	69	94.0	43.5	55.0
11	70	12	790-800	220-275	5.8-5.5	1200	2130	1996	190	89.5	58.5	60.0

† Current efficiency has been calculated on the basis of total weight of metal recovered.
* "Fines" refers to powder metal less than 325 mesh in size that becomes suspended during washing and acid-treating operations; it is collected separately by settling or filtration.

Principles of Very Low Power Electrochemical Control Devices

Ray M. Hurd and R. N. Lane

Defense Research Laboratory, The University of Texas, Austin, Texas

ABSTRACT

A new technology utilizing electrochemical phenomena has been developed, from which it is possible to design detection and control devices requiring extremely low power consumption, in the order of 100-1000 times smaller than that of transistors. As an example, an electrochemical detector for acoustic energy operates on 10 μw in the quiescent state, delivering 300-500 μw when fully excited. Development work to date has been limited to low frequencies (0-200 cps). Reversible redox systems and working d-c electrodes are used in conjunction with such electrochemical phenomena as concentration polarization, electrokinetic effects, and the electrocapillary curve of mercury.

Use of Concentration Polarization for Flow Detection

The use of Pt wire micro-electrodes and the diffusion current for the analysis of electrolytically reducible or oxidizable substances is well known (1). A great deal of information on the effects of stirring (as, for example, with rotating Pt electrodes) has also been published in the chemical literature (2). That these phenomena can be used for detecting and measuring fluid flows will be immediately apparent to the reader. That the type of function obtainable from an electrochemical unit operating on this principle may be made to vary over a considerable range by changing the electrode design is not quite so obvious.

A typical flow detector is shown in Fig. 1. Electrodes may be of any metal which is inert to the electrolytic system used. In this particular example Pt electrodes are used in an electrolytic system of I_2 and KI in water. The cathodic reduction of I_2 is made the controlling reaction by using a low concentration of iodine ($10^{-2}N$) and a high KI (supporting electrolyte) concentration ($0.5N$). Other electrolyte systems may be used, as, for example, ferricyanide-ferrocyanide, bromine-bromide, ceric-cerous, ferric-ferrous, etc. It is only necessary that they be reversible redox systems.

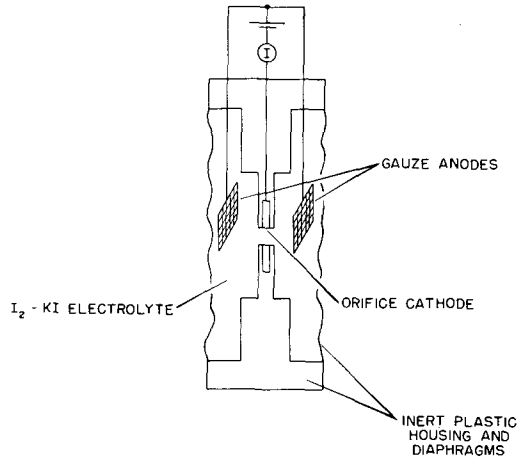

Fig. 1. Acoustic detector

Current-voltage curves for a cell of this type are shown in Fig. 2 for different values of low frequency acoustic energy incident on the diaphragms. A plot of the equilibrium current as a function of the incident pressure is given in Fig. 3. The relationship between current and pressure is expressed by equations of the type:

$$I = k P^n$$

or

$$I = k \log P$$

with the values of n and k dependent on the geometry of the cathode.

From an electrochemical standpoint, the proper operation of these units requires the following: (*a*) as nearly reversible electrode reactions as possible, so that no energy is consumed in overcoming activation polarization; (*b*) equal and opposite reactions occurring at the anode and cathode; i.e., a redox system, so that no net changes in concentration take place as current flows through the cell; it is also necessary to adjust the bias voltage to a value low enough that consecutive electrode reactions do not occur; (c) absence of reducible or oxi-

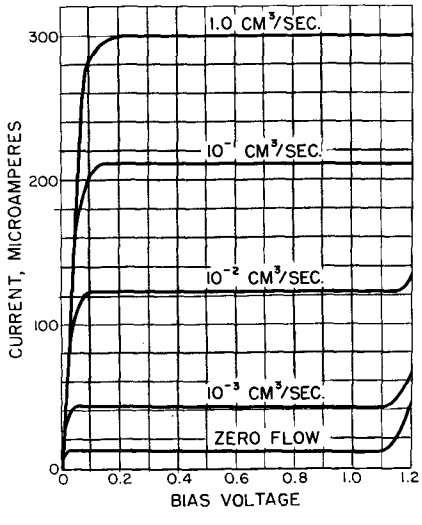

Fig. 2. Current-voltage curves for varying sinusoidal flows in acoustic detector.

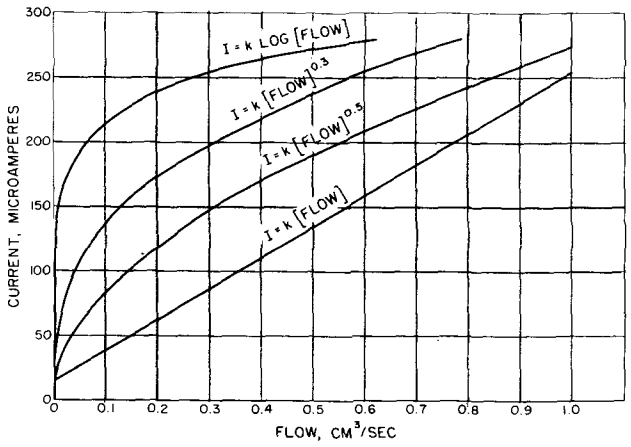

Fig. 3. Current-flow curves for acoustic detectors with different orifice designs.

dizable impurities. A reducible impurity not only yields a momentarily higher current, but builds up a permanent higher concentration of the primary reducible reactant (in this example, iodine) by the increased anodic oxidation.

Separated Detector for D-C Measurements

The cell described above was designed primarily for detection and metering of acoustic energy (a-c pressures). A more satisfactory design for d-c flows and pressures is shown in Fig. 4. In this cell an additional cathode is placed in the right-hand compartment so that the bias voltage transfers the I_2 from this side to the anode side, resulting in a final concentration of virtually zero in the cathode side. This transfer of I_2 is entirely analogous to that encountered in the simple I_2 coulometer as described by Washburn and Bates (2). In all such cells, the electrodes used primarily for separation of the I_2 are called the "main" cathode and the "main" anode.

The working cathode consists of a small piece of closely woven Pt gauze situated in an orifice between the two compartments. A small background current (of the order of 10 μa) flows continually in the detecting cathode circuit due to diffusion of I from the concentrated side. Fluid flow from left to right (concentrated to dilute) produces an electrical signal directly proportional to the magnitude of the flow. For a detector operating linearly, i. e., reducing all the I in the fluid flowing through the gauze, the current output is given by the equation:

$$I = 10^{-3} \mathbf{F} N \, dv/dt$$

where $\mathbf{F}$ = the Faraday, N = normality of the reducible substance on the anode side, dv/dt = flow rate in cm³/sec.

From this equation, assuming an I_2 normality of 10^{-1}, it can be seen that flow rates as low as 10^{-5} cm³/sec yield currents in the neighborhood of 100 μa, or some ten times the background current. Experiments have shown that, by suitable design of the detecting cathode, linear current outputs are obtainable over a range of four orders of magnitude in the flow rates.

Note that the unit shown in Fig. 4 is also a rectifier, in that fluid flow from right to left will not produce a current, since no I_2 is carried over the detector gauze. A full-wave detector may be constructed easily by using two anode compartments and two detector gauzes.

Conversion of Electrical Current to Fluid Flow

In order to perform various mathematical operations on the output currents of the devices described above, it is necessary to have a unit which carries out the reverse operation of converting these very low power electrical signals into fluid flows. In this manner, electrical and fluid flow signals may be fed from unit to unit in much the same manner that currents and voltages are fed through electronic networks. In addition to simple amplification, several mathematical operations may be carried out upon the original incident signal or signals in this manner; for example, products, ratios, derivatives, etc., may be obtained.

The simplest and most reliable method of carrying out this reverse effect is by the use of electro-osmosis, a phenomenon described in most standard textbooks on electrochemistry (4). An electro-osmotic cell (Fig. 5) consists of a fritted glass disk dividing a cell into two compartments, with electrodes on each face of the disk. The operating characteristics of such a cell can be made to vary over extremely wide ranges by control of such variables as disk porosity, thickness, and diameter, and choice of working liquid. The important point, however, is that the fluid flow produced by an applied voltage is linear with the value of voltage. If the flow is restrained, as, for example, by means of the plastic diaphragms of Fig. 5, then the electro-osmotic pressure developed is linear with the voltage. In Fig. 6 the equilibrium pressures for a typical "fine" porosity disk (about 4.0 μ pore diameter) is shown plotted as a function of applied voltage, using distilled water as the working fluid. Unrestrained fluid

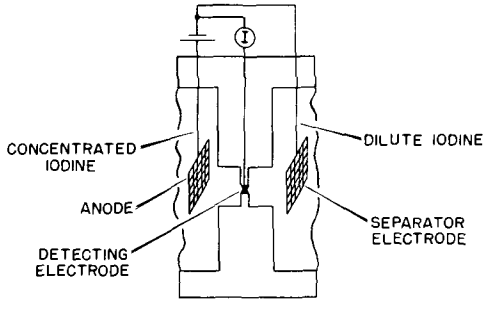

Fig. 4. Separated detector

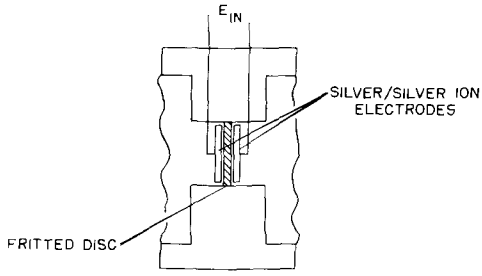

Fig. 5. Electro-osmotic cell

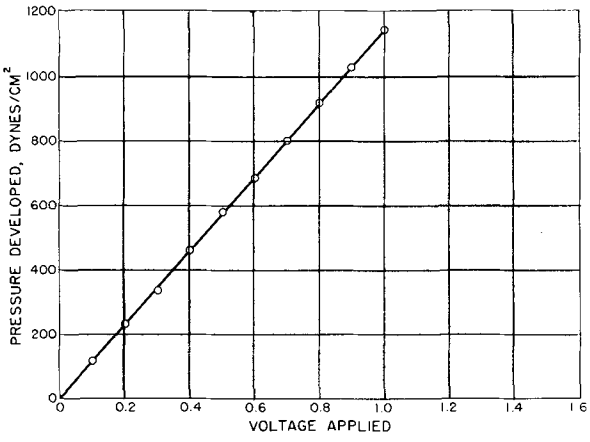

Fig. 6. Pressure-voltage curve for typical electro-osmotic cell.

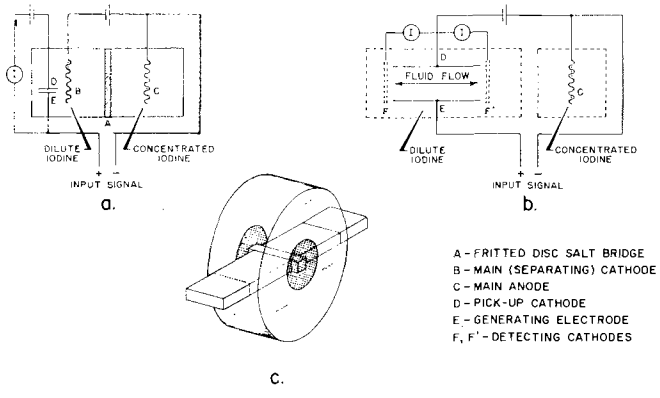

Fig. 7. Electrode arrangements for using anodically deposited iodine.

flow for a 30 mm diameter, 20 mm thick disk of this type is in the neighborhood of 10^{-3} cm³/sec at 1.0 v applied to the electrodes. It will be remembered that a flow rate of 10^{-5} cm³/sec through a separated detector will yield some 100 μa output, so that the values of flow rate produced by the electro-osmotic cell easily cover the working range of the other electrochemical units.

An idea of the power gains obtainable with these electrochemical units may be illustrated by combining the electro-osmotic cell with a linearly operating separated detector. The current drawn by the electro-osmotic cell at 1.0 v applied can be held to about 30 μa if the working fluid has a conductivity of some 10^{-6} ohm^{-1} cm^{-1}, giving a power input of 30 μw. The linear detector coupled to the cell can be designed to give an output of 10 ma dropped across a load resistor of 100 ohms, or a power output of 10 mw. This represents a power gain of some 330 fold; this could be increased easily by an additional order of magnitude.

One of the essential requirements of a properly operating electro-osmotic cell is that the working electrodes polarize as little as possible. For a-c signals this is no particular problem, but for continuous and unidirectional d-c signals, suitable electrodes are not so easily found. To date, the most satisfactory electrodes have been the simple metal/metal-ion type, particularly Ag/Ag$^+$ made by firing compressed tablets of Ag_2O.

Another method of obtaining the conversion of electrical energy into flow energy is through the use of the electrocapillary curve of Hg (5). This has not been studied as thoroughly as has the electro-osmotic cell, but its workability has been demonstrated. The most interesting aspect of the electrocapillary curve is the fact that the surface tension (and thus the fluid displacement) varies as the square of the voltage applied to the interface. Furthermore, because of the extremely low currents required to charge the Hg double layer, and the relatively large displacements obtainable by the changes in surface tension, the power gain through such a system can be higher even than the examples cited above.

Use of Anodically Deposited Iodine

The last aspect of these electrochemical devices to be described in this paper is the use of a reducible substance (I_2) formed in place by the passage of anodic current through the electrolyte solution. For example, Fig. 7a shows a small cell separated into two compartments by a fritted disk salt bridge, A. If the cell is filled with an iodine-iodide solution and electrodes B and C connected as shown, the I will be transferred to the anode side as described previously. Electrodes D and E are two closely spaced (<0.010 in.) Pt plates, insulated so that their inner faces only are exposed to the solution. Now if the battery and meter connections are made as shown, a very small (<1 μa) background current will flow in the meter circuit. However, if an input signal is applied to electrodes E and C such that iodine is generated at E and consumed at C, the iodine thus formed at E will diffuse across to D and be reduced, causing the meter current to increase. Note that the increased current is fed directly back to electrode E, so that iodine, once formed between the electrodes, cannot escape. By means of suitable relays and switches (not shown), it can be shunted back to electrode C, so that the space can be returned to its initial iodine-free condition. The current flowing in the meter circuit is proportional to the time integral of the input signal.

If electrodes D and E are made the opposite faces of a corridor through which the electrolyte solution can flow, the product of a generating current and a fluid flow may be obtained. A typical arrangement is shown schematically in Fig. 7b, and a cutaway of the corridor in Fig. 7c. In Fig. 7b, electrode E is again the generating electrode, D the pickup electrode, and C the main anode, while the two electrodes F and F^1 are the detecting electrodes. The separating cathode B and fritted disk A are not shown, but must be present to maintain the separated iodine condition (dilute throughout the corridor region, concentrated around C). Since there is no iodine initially inside the corridor, no current is obtained at the end electrodes, regardless of flow. If, however, an external current is applied across electrodes E and C, iodine will be formed inside the corridor, which will then either diffuse across to D, or may be forced to either of the detecting electrodes F and F^1. The current in the meter circuits

is proportional to the product of the generating current and the fluid flow.

By use of the principles just described, operations other than simple integration and multiplication can be carried out.

Summary

The method in which several common electrochemical phenomena have been combined to yield a new technology for very low power detection and control devices has been described. The operation of a few of the many possible units has been described also as well as some of the characteristics cited to show the operating ranges, low power requirements, and power gains obtainable. Some of the electrochemical requirements of properly operating cells have also been mentioned. Further details on the operation of the units and of the research which has been done to bring them to the present state of development will be revealed in subsequent papers.

Manuscript received June 26, 1957. This paper was prepared for delivery before the Cleveland Meeting, Sept. 30-Oct. 4, 1956.

Any discussion of this paper will appear in a Discussion Section to be published in the June 1958 JOURNAL.

REFERENCES

1. I. M. Kolthoff and J. J. Lingane, "Polarography," Vol. I, Chap. XIX, Interscience Publishers, Inc., New York (1952).
2. H. A. Laitinen and I. M. Kolthoff, *J. Phys. Chem.*, **45**, 1079 (1941).
3. E. W. Washburn and S. J. Bates, *J. Am. Chem. Soc.*, **34**, 1341 (1912).
4. For example, G. Kortüm and J. O'M. Bockris, "Electrochemistry," Vol. II, Chap. X, Elsevier Publishing Co., New York (1951).
5. G. Lippmann, *Ann. chim. et phys.*, **5**, 494 (1875).

Impedance and Polarization Measurements in Fused Lithium Chloride-Potassium Chloride

H. A. Laitinen and H. C. Gaur[1]

Department of Chemistry and Chemical Engineering, University of Illinois, Urbana, Illinois

ABSTRACT

Impedance measurements with a platinum microelectrode in fused eutectic mixture of potassium chloride (41 mole %) and lithium chloride (59 mole %) are described. The residual resistance and capacitance showed frequency dispersion; probable causes are discussed.

Most of the metal ions showed a tendency for "predeposition." The faradaic admittance in the reduction of Pb^{++}, Co^{++}, Ni^{++}, Zn^{++}, and Cd^{++} ions had a phase angle of the combination greater than 45°, which has been ascribed to the adsorption of metal ions on the electrode surface. After application of an empirical correction for this effect, the faradaic admittance became normal and was used to calculate the rate constants for the above processes.

The current-potential curves showing the polarization behavior in the vicinity of equilibrium potential are described. By a curve fitting method the values of α, the transfer coefficient for the cathodic process, and i_o, the exchange current, are computed. These values of i_o are, however, much lower than those calculated by using the rate constants obtained from impedance measurements.

In a previous communication (1) impedance measurements for solid microelectrodes in a fused eutectic mixture of LiCl (59 mole %) and KCl (41 mole %) at 450°C were reported. It was found that the residual capacity (apparent double layer capacity) of Pt showed a large frequency dispersion. In the presence of Ni(II) and Co(II), a pronounced increase of capacitance was found for a Pt microelectrode even at potentials considerably anodic to the reversible equilibrium potentials of Ni or Co in the solutions. This effect was attributed to "predeposition."

The present investigation was undertaken with several objectives: (*a*) to determine whether the frequency dispersion of residual capacity would be decreased by improved techniques of melt dehydration (2); (*b*) to ascertain whether the dispersion is sensitive to roughness of the electrode; (*c*) to find whether predeposition occurs quite generally with metals of high and low melting points; (*d*) to attempt a quantitative estimate of rate constants of electrode reactions from impedance data; and (*e*) to compare such values with those obtained from polarization data.

Experimental

The difficulties encountered in the preparation of a suitably dry melt, and the procedure now followed in these laboratories have been described elsewhere (2-4). Before carrying out an experiment, the purity of the melt was tested by measuring the polarographic residual current and the double layer capacity of the Pt electrode in the melt. With the microelectrodes as employed (vide infra), the resid-

[1] On leave of absence from Chemistry Department, University of Delhi, Delhi, India.

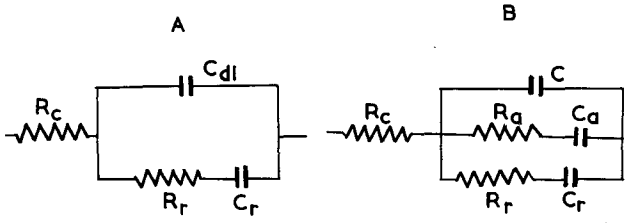

Fig. 1. The equivalent circuit (A) employed by Randles (5) and the modified circuit (B) used by Laitinen and Randles (18) to account for the adsorption of reactants at the electrode surface.

ual current up to a potential of —1.8 v vs. Pt. Ref. did not exceed 2-3 μa, and the double layer capacity at a frequency of 1000 cps of the a-c signal and at a potential of about —0.5 v vs. Pt. Ref. was of the order of 2.5-3 μF mm^{-2}.

The microelectrodes used in this investigation were prepared by sealing No. 26 B and S gauge Pt wire into Corning 0120 glass and flush grinding the tip with fine carborundum. This electrode had a rough surface (electrode A), which could be buffed with finest grade emery paper to a shiny smooth surface (electrode B). Unless otherwise stated, the electrode B has been used in this investigation. The projected area of the electrode was the cross-sectional area of the Pt wire, viz., 0.129 mm^2.

The reference electrode was a Pt foil ca. 8 x 6 mm^2 in contact with Pt(II) solution in the melt which has been shown (3, 4) to be reproducible and nonpolarizable. The concentration of Pt(II) was 0.1*M*.

For impedance measurement the conventional a-c bridge as used by Laitinen and Osteryoung (1) was employed. However, in view of the measurement with lower frequencies, a high inductance choke (3000 henries) was introduced in the d-c circuit to avoid the grounding of a.c. through this path.

By a potentiometric arrangement and employing a Pt working foil, the microelectrode was polarized, its potential with respect to Pt reference being meas-

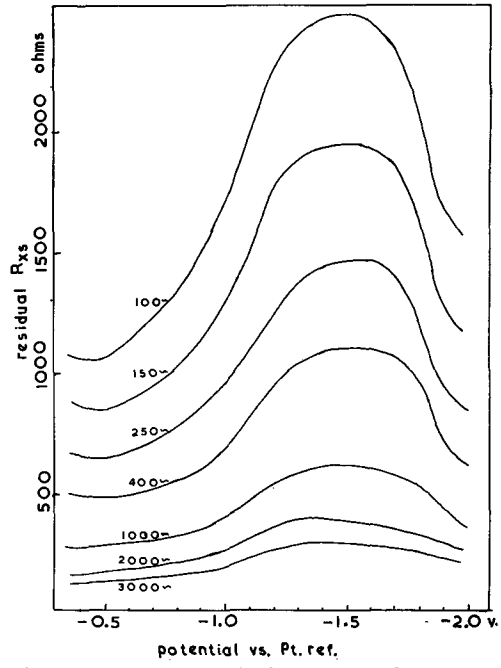

Fig. 2. Variation of residual R_{xs} with frequency of the a-c signal and at various potentials of the microelectrode. PME with smooth surface used.

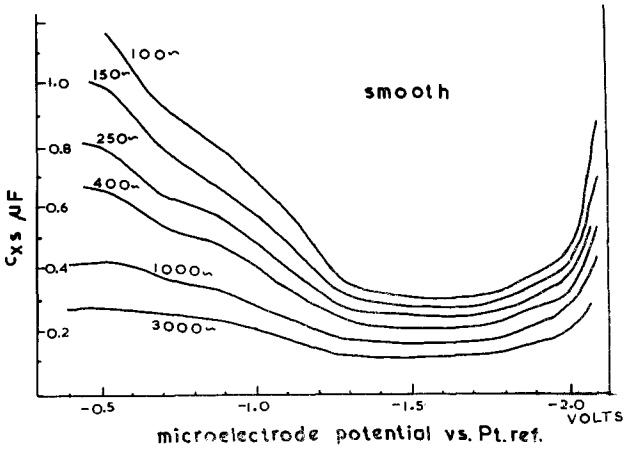

Fig. 3. Residual C_{xs} value at different frequencies of the applied signal and at various PME potentials for electrode with smooth and rough surfaces.

ured with a L&N students' potentiometer. At a given microelectrode potential the over-all impedance of the system was measured at frequencies ranging from 100 to 3,000 cps of the a-c signal applied to the bridge; the current passing through the cell was also measured. Measurements were repeated at various potentials, anodic as well as cathodic to the equilibrium potential; the latter being the open circuit potential of the metal coated electrode.

Results and Discussion

Residual C_{xs} and R_{xs}

The bridge measures the gross impedance of the system as a series combination of a resistance (R_{xs}) and a capacity (C_{xs}). If an electrochemical reaction is occurring at the electrode, the impedance will be composed of the double layer capacity at the Pt-melt interface (C_{dl}), the solution resistance (R_c) and the reaction impedance (R_r, C_r). Considering the network of Fig. 1A employed by Randles (5), in the (pure) melt, i.e., when no charge crosses the double layer, the residual C_{xs} and R_{xs} should correspond to C_{dl} and R_c, respectively, and the values of both should be independent of the frequency of the a-c signal applied to the bridge. However, both have been reported (1) and found in this study to be frequency dependent. Similar frequency dispersion in residual impedance has been observed with solid microelectrodes in aqueous systems also (6-11) and have been ascribed to roughness of the electrode surface or due to the presence of impurities in the solution. It is difficult to ascribe, at present, the cause(s) of this dispersion in the present case but the various possibilities are discussed.

The gross impedance for electrodes A and B was measured; only the observations for electrode B are shown in Fig. 2 and 3, since no substantial difference in R_{xs} or C_{xs} was observed between electrodes A and B in spite of the fact that electrode A appeared "rough" under the microscope and therefore appeared to have a larger true area than electrode B which appeared "shiny". Likewise the dispersion expressed as a ratio of the value of R_{xs} or C_{xs} at a given frequency to its value at 1000 cps is only slightly higher for the rough electrode than for the smooth electrode. This suggests that the smooth surface is not of smaller true area than the rough one.

Fig. 4. Rough (left); smooth, right. (Same length of cutting edge in both figures.)

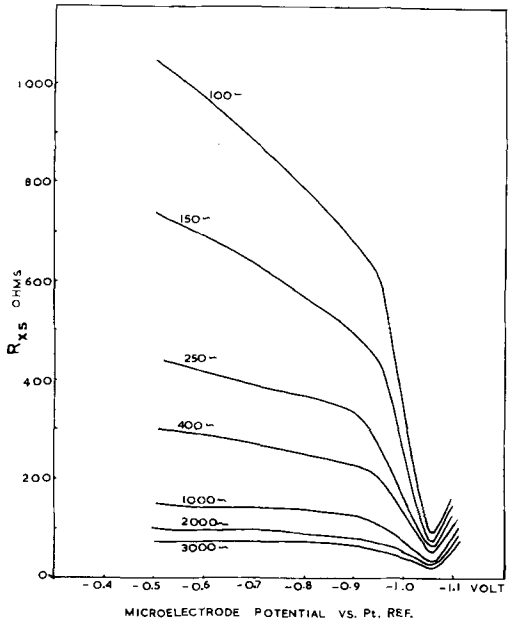

Fig. 5. The R_{xs} values in the reduction of 0.02604M Co^{++} in KCl-LiCl at 450°C at various a-c frequencies and microelectrode potentials.

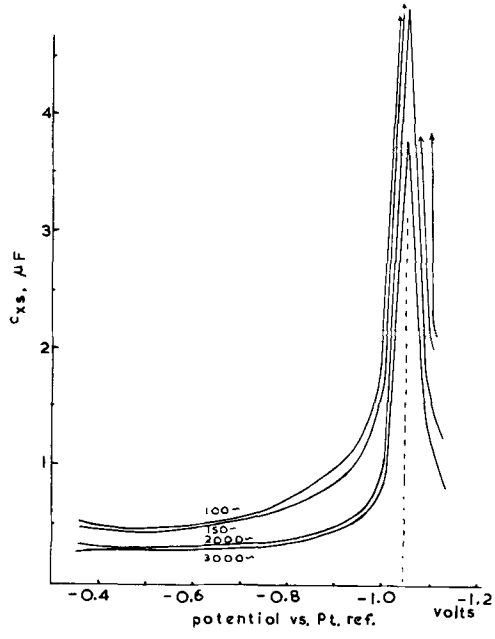

Fig. 6. The C_{xs} values in the reduction of 0.02604M Co^{++} in the melt at 450°C at various microelectrode potentials and at frequencies ranging from 100 to 3000 cps of the a-c signal.

This is clear from the following consideration.[2] If a saw tooth is made finer (Fig. 4) the actual length of the cutting edge is not thereby decreased. The same idea applies on a three dimensional surface. Only if the depth of the groove becomes comparable to or smaller than the thickness of the double layer does the smooth surface look smaller to an impedance measuring device. No very pronounced trends of dispersion with potential over the range —0.5 to —1.0 (vs. Pt. reference) were noted. In contrast, Osteryoung and Laitinen (1) reported that the residual capacity at low frequencies increased rapidly from —0.8 to —1.0 v, while at frequencies of 1000 or 2000 cps it remained sensibly constant in this range. This difference in behavior can no doubt be attributed to the fact that water was more completely removed by the technique used in the present study.

Recent work of Hillson (6) and Grahame (9) with a solid microelectrode in aqueous medium has shown that the impedance behavior of such electrodes is extremely sensitive to traces of surface active impurities. Although the most important category of surface contaminant, namely traces of organic matter, is presumably absent under our conditions, one cannot rule out the possible adsorption of impurities. Indeed, the detailed behavior of impedance in the presence of an electrode reaction is discussed below in terms of an adsorbed layer of metal atoms or ions. Traces of water, or more likely hydroxyl ions resulting from the hydrolytic decomposition of the melt, may be surface active, as may traces of various impurities present in reagent grade salts used for the solvent.

Several investigators (12, 13) have observed frequency dispersion with metal electrodes coated with oxide films. The formation of an oxide layer on a surface during abrasion of the surface in air, as employed at present, has been observed for some metals (14), and it is not unlikely that such a film is present on the electrode surface, and causes the observed dispersion, which has been interpreted (12) in terms of an equivalent circuit composed of a condenser with a relatively low parallel "leakage resistance" in series with the ordinary electrolytic resistance and the frequency independent double layer capacity. Such a model would account satisfactorily for the higher R_{xs} values at low frequencies in the present case also but would lead to C_{xs} values lower than the double layer capacity at high frequencies and increasing to that value at low frequencies. The true double layer capacity is probably actually approached at high frequencies. This concept therefore is inadequate to account for the high C_{xs} values experimentally observed.

A faradaic admittance (15, 16) properly accounts for high C_{xs} values but such a process should be highly dependent on the applied potential.

Recently Bockris, *et al.* (17) suggested that a dielectric loss could be associated with a firmly attached layer of solvent, which has a relaxation time comparable with the applied frequency. In a molten salt one may be dealing with a layer of adsorbed hydroxyl ions which operate in a similar way. This dispersion, however, is remarkably insensitive to refinements in the purification scheme, and may be characteristic of even a pure molten salt system.

Over the potential range of —0.5 to —1.5 v (vs. Pt. reference) the value of residual C_{xs}, extrapolated to infinite frequency, which would approximate closely to the double layer capacity, varied between 0.05 and 0.10 μF, and considering as an approximation the area of the electrode as equal to its projected area, the C_{dl} would correspond to 38-77 μF

[2] The authors are grateful to Dr. David C. Grahame who kindly suggested this idea.

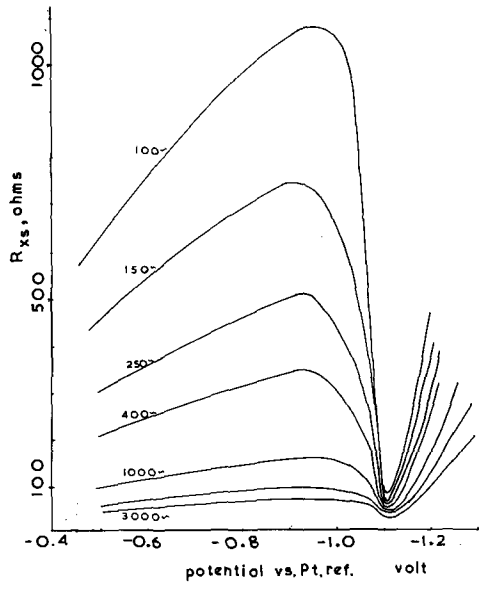

Fig. 7. Pb^{++} in KCl-LiCl at 450°C: the variation of R_{xs} at different frequencies and microelectrode potentials. The equilibrium potential for 0.0432M solution is —1.11 v vs. 0.1M Pt/Pt(II) reference.

cm^{-2}. It would appear that residual C_{xs} may be regarded as consisting of a relatively small frequency independent C_{dl} and a large frequency dependent value arising out of the cause(s) discussed above.

Impedance Measurements

Impedance measurements in the reduction of several metal ions as Co^{++}, Zn^{++}, Pb^{++}, Bi^{+++}, Ni^{++}, Cd^{++} were carried out. In the typical plots in Fig. 7-10, the gross C_{xs} and R_{xs} values are plotted against the electrode potential. Since the maximum change in impedance arises primarily from the electrode process involving the reduction of metal ion, the change in reaction impedance is reflected in these plots. The

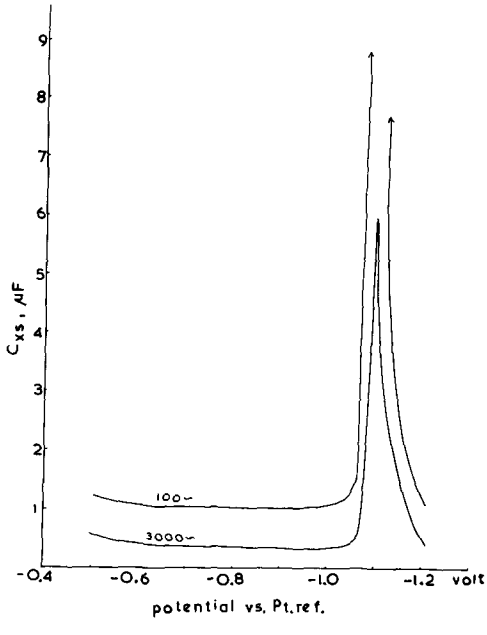

Fig. 8. Pb^{++} in KCl-LiCl at 450°C: the variation of C_{xs} at different frequencies and microelectrode potentials. Only curves for 100 ond 3000 cps are shown; for intermediate frequencies the curves lay between these two. The equilibrium potential is —1.11 v vs. 0.1M Pt/Pt(II) reference.

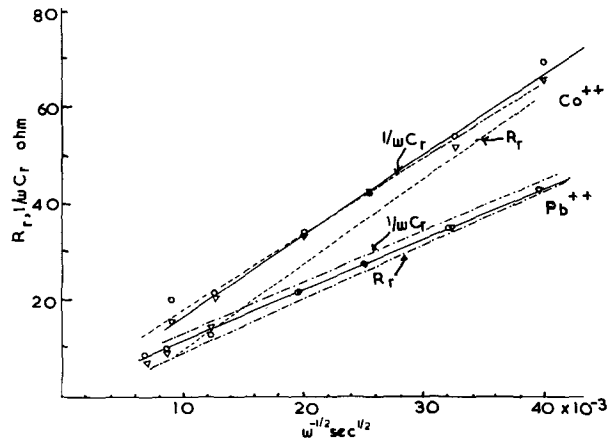

Fig. 9. The broken lines are uncorrected plots for R_r and $1/wC_r$ against $1/\sqrt{w}$. The solid line was obtained after correcting for the admittance due to adsorbed reactants; open circle for R_r and open triangle for $1/wC_r$ for the corrected plots. The concentration of Co and Pb solutions were 2.604 x 10^{-6} and 4.32 x 10^{-6} moles cm^{-3}, respectively.

plots are essentially similar: the C_{xs} passes through a maximum value (pseudo capacity) and R_{xs} through a minimum at the equilibrium potential; there is a tendency for predeposition in most of the cases. For example, in the reduction of Co(II) ion, there is an increasing tendency in C_{xs} from about —0.75 v vs. 0.1*M* Pt. Ref. which gradually develops into a maximum at the equilibrium potential (—1.05 v vs. Pt. Ref.). Since the pseudo capacity could only arise from the reduction of Co^{++} at the electrode, the gradually increasing maximum indicates the deposition and discharge of Co^{++} occurring at potentials at least 0.25 v anodic to the equilibrium potential. Such undervoltages were observed in all the cases studied and varied from 0.035 v for Pb^{++} to 0.45 v for Zn^{++}.

It may be pointed out that predeposition in dilute aqueous media has been observed by Rogers, *et al.* (19, 24), Haissinsky (25), and others (26, 27); it

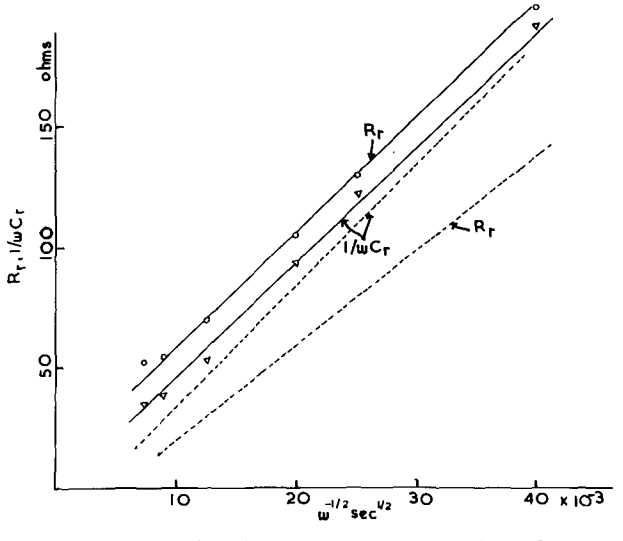

Fig. 10. The broken lines are uncorrected plots of R_r and $1/wC_r$ against $1/\sqrt{w}$ for the reduction of Zn^{++} in KCl-LiCl at 390°C; the solid lines represent the plots after a correction for admittance due to adsorbed ions was introduced. The Zn concentration was 7.16 x 10^{-6} moles cm^{-3}.

appears to be more common in fused salt media however and is shown even in relatively concentrated solutions.

Calculation of Rate Constants

From the observed R_{xs} and C_{xs} values in presence of metal ion at the equilibrium potential and the values of C_{dl} and R_c, the reaction impedance can be calculated by several series → parallel and parallel to series transformations as employed by Laitinen and Randles (18). To allow for the dispersion in residual C_{xs}, for the purpose of calculations of reaction impedance, at a given frequency, the C_{xs} as measured in the melt was employed instead of any value obtained by extrapolation to infinite frequency; the residual R_{xs} values are in general much higher and these could not be used; the solution resistance was obtained by extrapolating the observed R_{xs} values to infinite frequency.

For the deposition of a metal ion on an inert electrode the reaction impedance, in terms of the electrical analogy, a resistive (R_r) and capacitative (C_r) component in series is given by:

$$R_r = \frac{RT}{n^2\mathbf{F}^2AC}\left[\sqrt{\frac{2}{wD}} + \frac{1}{k}\right] \qquad \text{(I)}$$

$$\frac{1}{C_r} = \frac{RT}{n^2\mathbf{F}^2AC}\left[\frac{2}{wD}\right] \qquad \text{(II)}$$

so that

$$\Delta = R_r - \frac{1}{wC_r} = \frac{RT}{n^2\mathbf{F}^2AC} \cdot \frac{1}{k} \qquad \text{(III)}$$

where $w = 2\pi f$, f being the number of cycles per second of a-c signal fed to the bridge; n is the number of electrons involved in the rate-determining step; A is the area of the electrode in cm^2; C is the concentration of the reducible ion in moles cm^{-3}; k is the rate constant for the electrode process in cm sec^{-1}; R, T, and $\mathbf{F}$ have their usual significance.

It is seen that a plot of R_r and $1/wC_r$ against $1/\sqrt{w}$ should give two straight and parallel lines; the resistance plot lying over the reactance plot and the latter passing through the origin; their separation given by Eq. (III) being dependent, *inter alia*, on the rate of the electrochemical reaction. The phase angle of the combination ϕ given by $\tan\phi = 1/wC_rR_r$ would be less than $\pi/4$, this value being approached for an immeasurably fast reaction.

In the present study ϕ was always greater than $\pi/4$ so that the impedance plots were reversed and furthermore the reactance plot missed the origin. A similar situation was encountered by Laitinen and Randles (18) in the study of faradaic admittance to a. c. of a dropping mercury electrode in a solution containing *tris* (ethylenediamine) cobaltous and -cobaltic ions. The effect was ascribed to the adsorption of the reactant ions at the electrode. These authors considered the admittance due to the adsorbed reactants to be pure capacitance or a series combination of capacitance and resistance and as additional to that arising from the electrochemical reaction. After making an empirical correction for this effect, the faradaic admittance was used for calculating the rate constant for the electrode process.

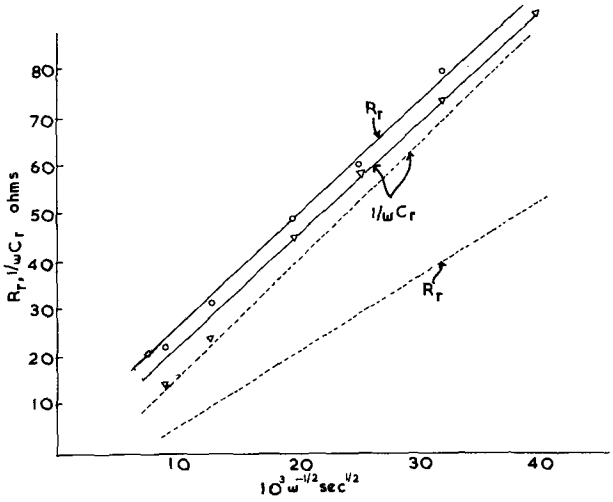

Fig. 11. The broken lines are the uncorrected reaction impedance plots for the reduction of $CdCl_2$ in KCl-LiCl at 450°C. The solid lines represent the plots obtained after correcting for the admittance due to the adsorbed ions. The Cd concentration was 5.95×10^{-5} moles cm^{-3}.

Corrections of similar nature were also applied in the present case, suitable values being found by several trials. The equivalent circuit for the process is given in Fig. 1(b).

In the reduction of Pb^{++}, Ni^{++}, and Co^{++} ions the uncorrected plots were very close to each other and only a capacitative correction of 1.1, 0.3, and 1.3 μF, respectively, was needed for the reactance plot to pass through the origin; this correction also shifted the resistance plot and the two overlapped, as would be the case for an immeasurably fast reaction. For the reduction of Cd^{++} and Zn^{++} the correction needed was a series combination of a resistance and capacitance, and furthermore the corrected plots were separated from each other (Fig. 11, 12, and 13).

The rate constants for the reduction of these ions were calculated by use of Eq. (III) and were found to be 0.686 and 1.27 cm sec^{-1}, corresponding to exchange currents of 172 and 31.8 amp at the hypothetical concentration of 1 mole cm^{-3}. Taking the value $\alpha = 0.5$ the exchange currents at a concentration of 0.1M are calculated to be 1.72 amp and 0.32 amp, respectively, for our electrode area.

The significance of the correction may be clarified by the following considerations. A frequency-independent admittance, such as that applied as an empirical correction, was shown by Laitinen and Randles (18) to correspond to a surface electron exchange reaction occurring without a diffusion step which introduces frequency dependence. An infinitely rapid electron exchange would give rise to a purely capacitative correction, whereas one of finite rate would add a resistive component.

Considering the heterogeneous nature of the electrode surface, it appears reasonable to postulate the adsorption of heavy metal ions on certain active sites at potentials anodic to the equilibrium potentials and the conversion of such adsorbed ions by electron exchange to adsorbed (predeposited) metal atoms. As the equilibrium potential is approached

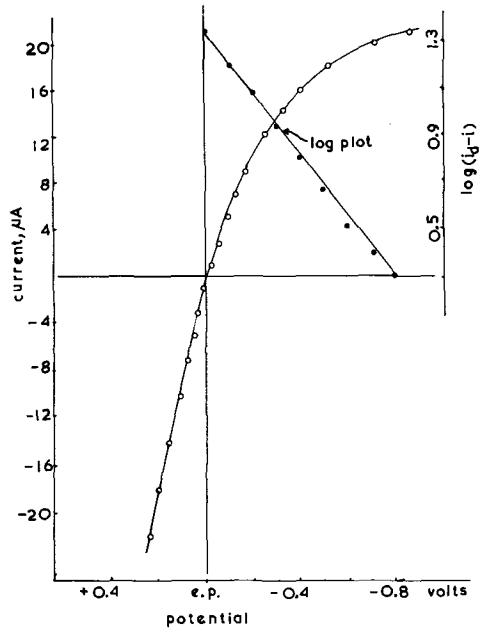

Fig. 12. The polarization curve for Pb^{++} in KCl-LiCl eutectic at 450°C. The Pb^{++} concentration was 4.32 x 10^{-5} moles cm^{-3}. The equilibrium potential at this concentration was —1.11 v vs. 0.1M Pt/Pt(II) reference. The potentials are referred to the equilibrium potential. The log plot has a slope of 0.077 v.

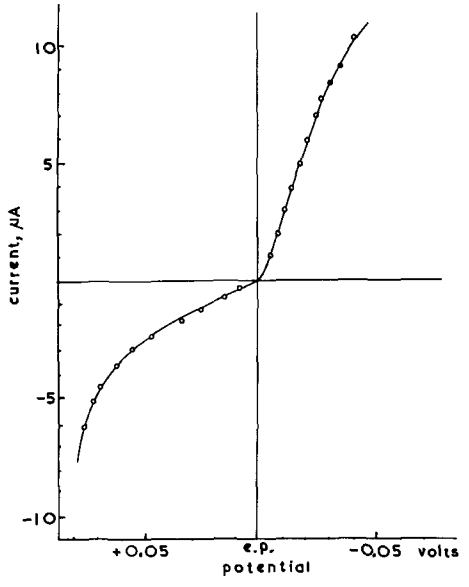

Fig. 13. The c.v. curve for Co^{++} in KCl-LiCl at 450°C. The concentration of Co was 2.604 x 10^{-5} moles cm^{-3} and the equilibrium potential —1.05 v vs. 0.1M Pt/Pt(II) reference. The potentials are referred to the equilibrium potential.

from the anodic direction, a greater fraction of the total area of Pt is called into play, so that a greater amount of electron exchange between adsorbed ions and atoms, and therefore a greater pseudocapacity, is observed. At cathodic potentials, the normal decrease due to concentration polarization occurs.

Polarization Studies

These studies describe the current-potential behavior on cathodic and anodic polarization of Pt microelectrode with respect to its equilibrium potential for several metal ions. The results are summarized in Fig. 12 to 16. In agreement with the polarographic practice the cathodic currents are regarded as positive and the cathodic potentials are plotted on the abscissa axis from left to right.

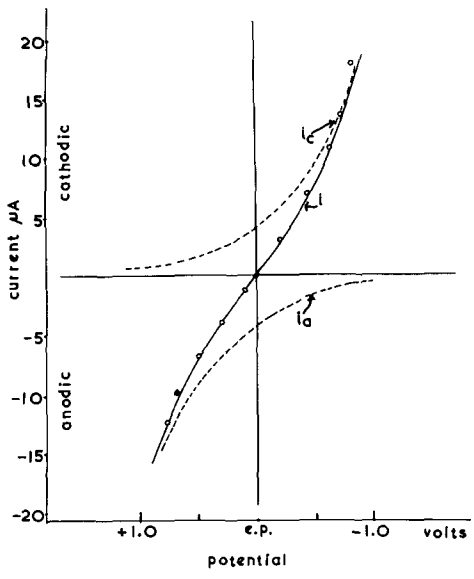

Fig. 14. The current-potential curve for the system Zn^{++} in KCl-LiCl at 390°C. The solid line is calculated curve for $\alpha = 0.53$ and $i_o = 4 \times 10^{-6}$ amp for the area of the electrode used (0.13 mm^2) and the dots are the experimental points. The potentials are referred to the equilibrium potential (—1.47 v vs. 0.1M Pt/Pt^{++}). Current (i) is the algebraic sum of the cathodic (i_c) and anodic (i_a) currents.

The current-potential curve for Pb^{++} is the nearest ideal case: a well-defined reduction wave with a diffusion current plateau is obtained at appreciable cathodic overpotentials; on reversing the polarization the current retraces the path, passes through zero value at equilibrium potential, and, at anodic potential, an anodic current is drawn due to the dissolution of metal from the electrode. Using the value of 22.6 μa for i_d, a plot of $-E_{me}$ vs. log $(i_d - i)$ for the small voltage span had a slope of 0.077 v as compared to 0.0717 v for a reversible two electron reduction. In the Ni curve the limiting cathodic current was not well defined and the value varied somewhat with time; this has been the experience in a majority of the cases where the metal deposits onto the electrode in the solid state. In both these cases, the electrode processes are very fast, a conclusion which is in accord with the one arrived at by the impedance technique. The anodic portion of the Co^{++} curve (Fig. 13) has an unusual shape. Instead of a sharp increase in anodic current with increase of anodic overvoltage, as would be expected of a process involving only the dissolution of the metal, there is a gradual increase at first which at appreciable anodic overpotentials increases rapidly. This part of the curve is reproducible although the actual current varied somewhat in different experiments. This anomalous shape could be explained due to the formation of a film of an insoluble material which introduces a slow step in the dissolution of the metal into the solution. At appreciable anodic overpotentials the film is partially or completely dissolved and then the normal shape of the curve follows. The passivity of the freshly

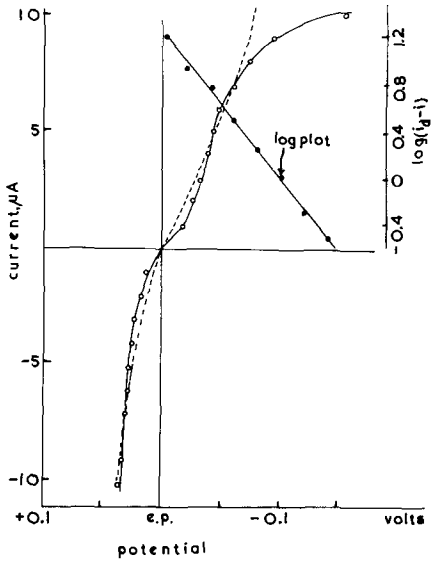

Fig. 15. The c.v. curve for the Bi^{+++} ion in KCl-LiCl at 450°C. The potentials are referred to the equilibrium potential. The broken line is calculated for $i_o = 3.5 \times 10^{-6}$ amp and $\alpha = 0.30$. The log plot has a slope of 0.0239 v. The details are in the text.

formed metal on the electrode surface could also be responsible for such an observation.

The Zn, Bi, and Cd polarization curves have definite inflections in the equilibrium potential region indicating that the electrochemical reaction proceeds with a measurable speed. For the deposition of a metal ion on an inert electrode and for a process involving a single rate-determining step, the current potential relationships are given by:

$$i = n\mathbf{F}Ak\left[C\exp\left\{\frac{-\alpha n\mathbf{F}\eta}{RT}\right\} - \exp\left\{(1-\alpha)\frac{n\mathbf{F}\eta}{RT}\right\}\right] \quad \text{(IV)}$$

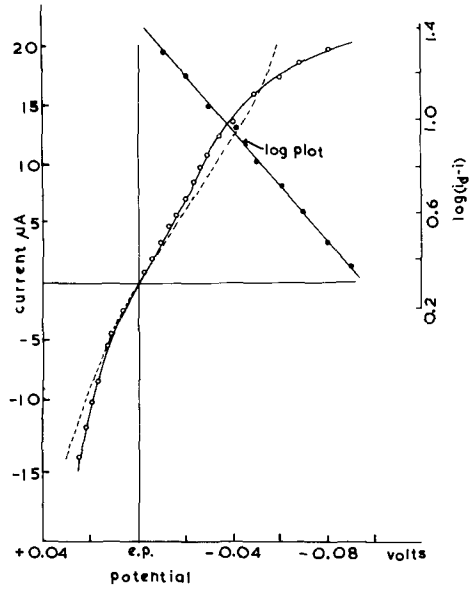

Fig. 16. The polarization curve (solid line) for Cd^{++} in KCl-LiCl at 450°C. The Cd concentration was 5.95×10^{-5} moles cm^{-3}, and the open circuit potential for the metal coated electrode (equilibrium potential) was −1.278 v vs. 0.1M Pt/Pt(II). The potentials are referred to the equilibrium potential. The dotted line is calculated for $i_o = 12 \times 10^{-6}$ amp and $\alpha = 0.30$. The slope of log plot is 0.0864 v.

$$i_o = n\mathbf{F}AkC^{1-\alpha} \quad \text{(V)}$$

and

$$i = i_o\left[\exp\left\{\frac{-\alpha n\mathbf{F}\eta}{RT}\right\} - \exp\left\{(1-\alpha)\frac{n\mathbf{F}\eta}{RT}\right\}\right] \quad \text{(VI)}$$

where i is the current in amperes for an overvoltage η; i_o is the exchange current, and α is the transfer coefficient for the cathodic process; n is the number of electrons in the rate-determining step; A is the area of the electron in cm^2; C is the concentration of the metal ion in moles cm^{-3} and $\mathbf{F}$, R, T have their usual significance.

Equation (VI) involves two experimentally controllable variables i and η and hence direct determination of the two unknown variables i_o and α by this is not possible since, over the narrow potential range, the current due to reverse process cannot be neglected. By several trials values of i_o and α were so chosen that for a given curve the values of i for different values of η calculated from (VI) corresponded as nearly as possible to the observed values of i. In Fig. 14 the dots are experimental points for the zinc curve while the curve is theoretical for $\alpha = 0.53$ and $i_o = 4\,\mu a$.

For the cadmium and bismuth curves (Fig. 15, 16) the dotted lines are for $\alpha = 0.30$, and i_o is equal to 12 and 3 μa, respectively.

An attempt was made to compare the exchange current from the polarization curve with those computed by use of Eq. (V) and employing the rate constants from the impedance measurements. Taking as an example the reduction of Cd^{++} and Zn^{++} ions for a concentration of 10^{-4} mole cm^{-3}, and $\alpha = 0.5$, the exchange current would be 1.72 and 0.318 amp, respectively, for our electrode area. These are of the order of 10^5 larger than those computed from the polarization curves. In calculating the values from impedance data it was necessary to apply an empirical correction for adsorption and a considerable uncertainty is thus introduced in the value of rate constant by the necessity of this correction. However, no adjustment of empirical parameters could possibly change the values more than a power of ten because the impedance plots would then have impossible shapes.

Alternatively a tenfold increase in the exchange current would completely remove the inflection from the region of origin of the polarization curves. Therefore, the two sets of values must be regarded as incompatible.

The weight of evidence appears to favor the impedance method because of the appearance of unexplained inflections in several of the polarization curves. The matter will not be completely settled, however, until independent methods of kinetic studies are carried out.

Acknowledgments

The authors are grateful to the Office of Ordnance Research and the Diamond Ordnance Fuse Laboratory for the financial support of this project and for the research associateship held by one of them (H. C. G.).

Manuscript received March 11, 1957. This paper is based on a Technical Report submitted to the Office of

Ordnance Research and Diamond Ordnance Fuse Laboratory, Jan. 15, 1957.

Any discussion of this paper will appear in a Discussion Section to be published in the June 1958 JOURNAL.

REFERENCES

1. H. A. Laitinen and R. A. Osteryoung, *This Journal*, **102**, 598 (1955).
2. H. A. Laitinen, W. S. Ferguson, and R. A. Osteryoung, **ibid., 104**, 516 (1957).
3. R. A. Osteryoung, Ph.D. Thesis, University of Illinois (1954).
4. W. S. Ferguson, Ph.D. Thesis, University of Illinois (1956).
5. J. E. B. Randles, *Disc. Faraday Soc.*, **1**, 11 (1947).
6. P. J. Hillson, *Trans. Faraday Soc.*, **50**, 385 (1954).
7. W. Lorenz, *Z. Elektrochem.*, **58**, 912 (1954).
8. W. D. Robertson, *This Journal*, **100**, 194 (1953).
9. D. C. Grahame, R. E. Ireland, and R. C. Peterson, ONR Tech. Rep. No. 22, Research Contract N8-ONR-66903 (March 1956).
10. J. J. Vetter, *Z. physik. chem.*, **199**, 300 (1952).
11. J. N. Sarmousakis and M. J. Prager, *This Journal*, **104**, 454 (1957).
12. J. E. Lillienfield and C. Miller, *ibid.*, **100**, 222 (1953).
13. L. Young, *Trans. Faraday Soc.*, **51**, 1250 (1955).
14. R. T. Foley, B. T. Stark, and C. J. Guare, *This Journal*, **103**, 534 (1956).
15. D. C. Grahame, *Chem. Rev.*, **41**, 441 (1947).
16. D. C. Grahame, *This Journal*, **99**, 370C (1952).
17. J. O'M. Bockris, W. Mehl, B. E. Conway, and L. Young, *J. Chem. Phys.*, **25**, 776 (1956).
18. H. A. Laitinen and J. E. B. Randles, *Trans. Faraday Soc.*, **51**, 54 (1955).
19. L. B. Rogers and A. F. Stehney, *J. (and Trans.) Electrochem. Soc.*, **95**, 25 (1949).
20. L. B. Rogers, D. P. Krause, J. C. Griess, and D. B. Ehrlinger, *ibid.*, **95**, 33 (1949).
21. J. C. Griess and L. B. Rogers, *ibid.*, **95**, 129 (1949).
22. J. C. Griess, Jr., J. T. Byrne, and L. B. Rogers, *ibid.*, **98**, 447 (1951).
23. J. T. Byrne and L. B. Rogers, *This Journal*, **98**, 457 (1951).
24. L. B. Rogers, *Rec. chem. Progress*, **16**, No. 3, 197 (1955).
25. M. Haissinsky, *J. Chim. Phys.*, **43**, 21 (1946).
26. T. Berzins and P. Delahay, *J. Am. Chem. Soc.*, **75**, 555 (1953).
27. M. M. Nicholson, *ibid.*, **79**, 7 (1957).

Technical Note

The Influence of Surface Pretreatment on the Atmospheric Oxidation of 2S (U. S. Alloy 1100) Aluminum

Philip M. Aziz and Hugh P. Godard

Aluminium Laboratories Limited, Kingston, Ontario, Canada

In the course of an experimental study of the room temperature atmospheric oxidation of aluminum and its alloys the influence of a variety of surface pretreatments on the oxidation rate was investigated. This work was carried out on 5 x 20 x 0.025 cm samples of Alcan 2S (U. S. 1100) aluminum in the H-18 temper. The oxidation process was followed by determining the change in weight of the sample with a Mettler constant load microbalance. All weighings were corrected for atmospheric buoyancy taking into account the influence of barometric pressure, temperature, and relative humidity. The samples were given the desired pretreatment, then immediately weighed and transferred to a desiccator containing a saturated sodium carbonate solution which maintained a relative humidity of 87% within the desiccator at ambient room temperature. Weighings were continued over a period of time providing a weight gain-time curve. The experimental results presented in Fig. 1 are representative of the large number of such curves obtained. Since the weight gains observed on duplicate samples were reproducible to ± 5 μg, the observed differences are not due to experimental error.

The chemically polished samples (phosphoric-nitric acid type bath) were subsequently washed, dipped into acetone, and air dried prior to weighing. The surfaces which had been scratch brushed under kerosene were washed with acetone and air dried before weighing, while the surfaces which had been abraded with emery were washed with fresh kerosene between changes of paper and finally washed with acetone. The initial weighing was completed within 10 min of the cessation of the surface treatment. Scratch brushing was carried out by hand using a steel wire brush.

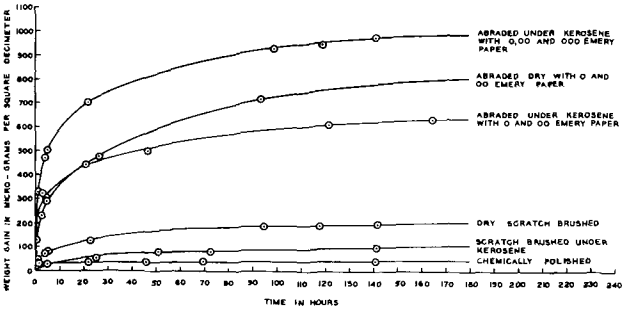

Fig. 1. Atmospheric oxidation of Alcan 2S alloy (US1100-H18) relative humidity of 87% as a function of surface treatment.

The difference in weight gains between the chemically polished and dry scratch brushed surfaces can probably be accounted for by the difference in true surface areas of the samples. The former surface has a roughness factor of about 1-2 whereas the latter is about 3-4. This can account for the observed difference within the limits of reproducibility from sample to sample for the same pretreatment.

The reason for the influence of the kerosene lubricant on the scratch brushed surface is not clear. It is possible that the presence of kerosene may influence the degree of surface roughness obtained or it may react with the surface producing an initial film influencing the subsequent reaction.

The large difference in weight gains as shown by the lower and upper three curves is more difficult to explain. It is hard to conceive of surface roughness having any major effect since it is very difficult to picture large differences in surface roughness between abraded and scratch brushed surfaces and in addition it is difficult to conceive of roughness factors greater than 3-4 on metal surfaces. Also both methods of surface treatment, abrasion and scratch brushing, should effectively remove the initial oxide film and leave a bare metal surface.

Microscopic examination of the abraded surfaces after gentle metallographic polishing has shown that they contain a great deal of embedded emery and that the degree of oxidation that they undergo increases with the quantity of emery in the surface. This then seems to be the cause of the enhanced oxidation of the emery abraded surfaces over the scratch brushed and chemically polished surfaces.

Vernon (1) has presented data on the atmospheric oxidation of commercially pure aluminum with a dry scratch brushed surface and his measured weight gains are in good agreement with those obtained during the course of this work. In view of the difference in relative humidity between the two sets of experiments, great significance should not be

attached to the close agreement, but it is nevertheless gratifying.

These results point up the importance of surface treatment in the study of the oxidation of metals especially in the case of soft metals where abrasive particles can become embedded in the surface. Chemical etching methods are suspect because of the ever present danger of preferential etching, as is chemical polishing since, especially in the case of alloys, it could lead to an enrichment of the alloying elements in the surface. Thus it is felt that for work where the use of evaporated films is not possible and alloys are to be studied, a mechanical method of removing the surface film such as dry scratch brushing, as first introduced by Vernon, is the most satisfactory.

Manuscript received Nov. 26, 1956.

Any discussion of this paper will appear in a Discussion Section to be published in the June 1958 JOURNAL.

REFERENCE

1. W. H. J. Vernon, *Trans. Faraday Soc.*, **23**, 113 (1927).

Technical Review

Electroluminescence and Field Effects in Phosphors

Henry F. Ivey

Research Department, Westinghouse Electric Corporation, Bloomfield, New Jersey

Today the word electroluminescence is used almost universally to indicate the generation of light in a solid material when it is excited solely by electric fields or currents, the light thus generated being in excess, in some spectral region, of the thermal radiation of the material. If other means of excitation, such a ultraviolet, x-rays, or cathode rays, for example, act simultaneously with the electric field or current, then some materials display more complicated phenomena which here for the moment are classified simply as "field effects". Today a wide variety of these phenomena are known and it is the main purpose here to differentiate these various effects, to explain them qualitatively, and to discuss something of their history.

It should be pointed out that the definition suggested above for electroluminescence is not one that has always been used consistently in the past by various workers in the field of luminescence. Thus, Leverenz writes (1) that "electroluminescence is obtained during electric discharges in gases", while on page 148 of the same book he indicates that electroluminescence is the same as cathodoluminescence, i. e., the light generated when a solid is bombarded with electrons or cathode rays.[1] These definitions would make both neon signs and television picture tubes examples of electroluminescence. It was because of such previous wide use of the word electroluminescence that Destriau in his early publications (2) used the word "electrophotoluminescence" to indicate what is now meant by the shorter word. "Electroluminescence" was first used in the modern sense by Payne, Mager, and Jerome in 1950 (3). Modern terminology completes the confusion by using the word electrophotoluminescence to describe a case in which the material is subjected simultaneously to the action of an electric field and to photoexcitation. With time, this distinction and the restriction of electroluminescence to the case of a solid excited only electrically, without external irradiation (either electromagnetic or corpuscular), seems to have become crystallized and is today the common usage.[2]

Although here electroluminescence is considered as restricted to purely solid systems, it is of interest that a similar effect in liquid systems has been known for a much longer time. The fact that electrodes immersed in electrolytes through which an electric current was passed often showed luminescence was known to Braun in 1898 (5) and may be of even more ancient vintage; the emission probably originates in an oxide layer on the electrode. This phenomenon is today called "galvanoluminescence", a name apparently first used by Sullivan and Dufford (6) in 1931.[3]

It should also be noted that modern usage is to confine the words "light" and "luminescence" to radiation in the visible region of the spectrum; this usage has been approved by the American Standards Association, the Illuminating Engineering Society, and the Optical Society of America. It is thus necessary to have a different word to describe the process which differs from electroluminescence only in that the emitted radiation lies outside the visible region. Since materials emitting in the ultraviolet and infrared regions are now known, one of the Task Groups of the AIEE-IRE Subcommittee on Dielectric Devices has tentatively suggested the name "electroradiescence" for this phenomenon. In this connection there comes to mind the old "Reboul effect".[4] In 1920 Reboul (9) found that, if a high electric field is applied to certain semiconductors by means of perforated electrodes, the air in the vicinity of the anode becomes ionized by some kind of radiation emitted by the solid. From latter experiments it seems that this radiation is composed of electrons, soft x-rays, and ultraviolet radiation and is thus, at least in part, electroradiescence.

Recombination Electroluminescence

The first observation of what would today be called electroluminescence was made in Russia in 1923 by Lossew (10). It seems unusual that the Russians have not emphasized this priority in their usual style; as a matter of fact, since this early work there has apparently been very little activity on

[1] It is also of interest that on page 392 of the same book Leverenz expresses doubts as to the existence of true electroluminescence as defined here!

[2] There are, however, still unfortunate exceptions to this terminology. Thus, for example, in a paper (4) published in March, 1957, the word "electrofluorescence" is used to describe the light emission of dynodes in a photomultiplier under electron impact.

[3] In an earlier paper Dufford (7) states, "The name electroluminescence naturally suggests itself for a luminescence produced in this way; but unfortunately this term, along with anodoluminescence and cathodoluminescence, has been appropriated for the description of the effects observed in the discharge through gases."

[4] The only reference to the Reboul effect known to the writer in the modern literature is the book by Zwikker (8). There seems to have been no work on this effect for the last twenty years.

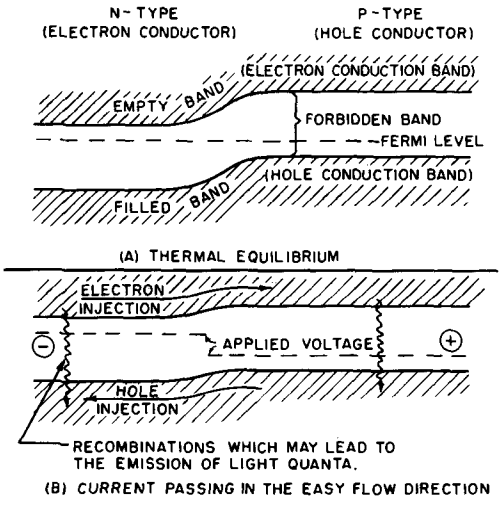

Fig. 1. Energy diagrams for a p-n barrier in the absence of an applied field (A) and for current flow in the forward direction with consequent injection of minority charge carriers (B). In addition to direct radiative recombination of holes and electrons as shown, recombination may also occur via luminescence activator centers or in a radiationless manner.

electroluminescence in Russia. Lossew found that when point contacts were applied to certain SiC crystals (used for radio detection at that time) and current passed through the crystal, light was often emitted.

In recent times this emission in SiC has been studied by Lehovec, Accardo, and Jamgochian (11), who also gave the currently accepted explanation, which was not possible before the advent of modern solid-state physics and semiconductor theory. In Fig. 1A is shown the energy level diagram for a p-n junction in the absence of an applied voltage. By definition, in the n-type region the density of negatively charged carriers (electrons in the "empty" conduction band) exceeds that of positively charged carriers (positive holes in the "filled" valence band); here electrons are the majority carriers and holes the minority carriers. In the p-type region the situation is reversed. In each region there is continual thermal production and subsequent recombination of electron-hole pairs. The system is thus in a state of dynamic equilibrium. Some of the recombinations occur with the emission of radiation; the emission generated in this way simply contributes to the normal thermal radiation characteristic of the material at the ambient temperature and is quite small.

If a voltage is applied to such a junction in the so-called forward direction or direction of easy flow (Fig. 1B), then electrons are injected into the p-type region and positive-holes into the n-type region; this then corresponds to minority carrier injection. The increased minority carrier concentration produced in this way obviously leads to an increased rate of recombination; if part of these recombinations are radiative, then one has electroluminescence. In principle this is the type of electroluminescence discovered by Lossew. In the case of SiC, where the emitted radiation is in the yellow region of the spectrum although the energy gap between conduction and valence bands corresponds to an energy in the blue region, the recombination does not occur directly band-to-band but indirectly through intermediate impurity or activator levels. A similar kind of emission has been observed in CdS, Ge, Si, diamond, and some of the so-called III-V compounds, particularly indium antimonide; in the case of Si and Ge the emission is in the infrared region of the spectrum and corresponds, at least in part, to band-to-band transitions. In this discussion the picture of a p-n junction has been used. From transistor experience it is known that point contacts can also produce minority carrier injection in much the same way as area junctions.

It is of value here to emphasize the characteristics of this kind of electroluminescence which distinguish it from another type to be discussed later. These are:

1. There is no high electric field required to excite the emission; the field in the junction is actually lower when the voltage is applied than in its absence.
2. The fundamental controlling quantity is the injected current, not the voltage producing this current.
3. The charge carriers of importance are minority carriers.
4. Once these carriers are injected, they are able immediately to recombine with carriers of the opposite sign to produce radiation without the necessity of gaining further energy from the field. Because of these characteristics this type of luminescence has been or might be called "recombination electroluminescence", "minority carrier injection electroluminescence", or "current-controlled electroluminescence". It has also been called "d-c electroluminescence", but since it can also be excited by a.c., at least on alternate half-cycles, this does not seem to be a good description.

Not all electron-hole recombinations following minority carrier injection are of the radiating variety. As a matter of fact at the present time, with perhaps the exception of the infrared-emitting indium antimonide, this is most often not the case. As a result, the efficiency of materials emitting in the visible due to recombination electroluminescence is comparatively low.

The Destriau Effect

In 1936 Destriau (12) observed a different kind of electroluminescence. Here the experimental arrangement consisted of a zinc sulfide phosphor powder suspended in a dielectric and subjected to an intense alternating electric field (of the order of 10^5 v/cm). The purpose of the dielectric is to exclude air, breakdown of which under the intense fields will produce u. v. radiation which can indirectly excite the phosphor to photoluminescence. For a time there was some doubt that such indirect excitation could be completely avoided and hence doubt as to the existence of true electroluminescence in the solid state. Today, however, there can be no question as to existence of this effect. Within the past ten years the Destriau effect has been investigated extensively. Limitation of space does not permit a discussion of the wide variety of experimental observations;

these have, however, been reviewed elsewhere (13-15). Today the brightnesses and efficiencies obtained with the Destriau effect far exceed those of recombination electroluminescence.

Consider the possible physical effects of such intense fields on a phosphor material. The energy-level diagram of such a material consists in general, in addition to the valence and conduction bands, of isolated, normally filled levels lying above the valence band (the activator or luminescence centers) and isolated, normally empty levels lying below the conduction band (electron trapping centers). Under conditions of excitation some of the normally filled luminescence centers are, of course, emptied and some of the normally empty traps filled. The various possibilities are:[5]

1. The field may induce the transfer of an electron from the valence band to the conduction band by quantum-mechanical tunneling, thus simultaneously producing a free electron and a free hole. Such a Zener effect (17) does indeed occur in some materials, but it is most unlikely in normal phosphors at the field strengths utilized in electroluminescence because of the wide energy gap (forbidden zone) in these materials.

2. The field may induce the transfer of an electron from a filled luminescence center to the conduction band by quantum-mechanical tunneling. This process has been studied theoretically by Franz (18), but again it is unlikely at normal field strengths in electroluminescence.

3. The field may cause the transfer of an electron from the valence band to an empty luminescence center. Since the energy difference in this case is comparatively small (a few tenths of an electron volt) this is much more likely than the effects discussed above. Since such transfer can in addition be produced thermally, the transition may also occur under the combined action of field and temperature; the field in this case serves to lower the thermal activation energy for the transition. Since this process fills empty luminescence centers, it is obviously a de-exciting rather than an exciting effect. Evidence that field filling of empty centers occurs will be discussed later.

4. The field may cause the release of an electron from a filled trap. Here again, as in the previous case, the effect may be due to field action alone (tunneling) or to lowering of the trap barrier by the field and subsequent thermal release.[6] The release of trapped electrons by an electric field has been directly observed by Böer and Kümmel (22) in their experiments on "electrical glow curves". Here the phosphor is excited at low temperatures and then the electric field is continually increased; the resultant release of carriers can be observed by conduction effects in a manner analogous to the usual thermoluminescence experiment where the temperature is continually increased and the emission observed.

5. Once electrons are introduced into the conduction band (by any conceivable method) they can be accelerated by the electric field. Such accelerated electrons may excite or ionize luminescence centers as well as cause emptying of filled traps or ionization of the lattice material itself. Avalanche formation and carrier multiplication may occur. Such an acceleration-collision process is well-known from the field of dielectric breakdown of solids.

6. Under the action of the field, free carriers of both signs are swept toward the surface of the phosphor particles. Recombination rates and the concentration of traps are normally quite different (higher) at surfaces than in the bulk, and this action therefore serves as a means of de-excitation.

It remains to be discussed which of these mechanisms are important in the Destriau effect and, in latter sections, in the other field effects related to electroluminescence.

Destriau in his early papers (2) made the suggestion that the observed dependence of electroluminescent brightness on applied field strength could be explained either on the basis of a field emission process or an acceleration collision process. Because of the extremely high fields necessary for field emission, it is now commonly agreed that the acceleration-collision model is the correct one. Garlick (23) was apparently the first to realize the importance of field emptying of traps in electroluminescence. In 1949 he wrote, "There are always a few electrons in traps in unexcited phosphors which can be freed by the field and accelerated to produce excitation of luminescence centers." The details of the theoretical treatment of this kind of electroluminescence have been presented by Curie (24), Piper and Williams (25, 26), Zalm (14), and Alfrey and Taylor (27), among others. The essential steps in the process are shown in Fig. 2.

One essential feature of the current explanation of the mechanism of the Destriau effect is the existence within the phosphor particles of localized regions within which the field strength is much higher than the average or applied field strength. In these special regions the field strengths may be as high

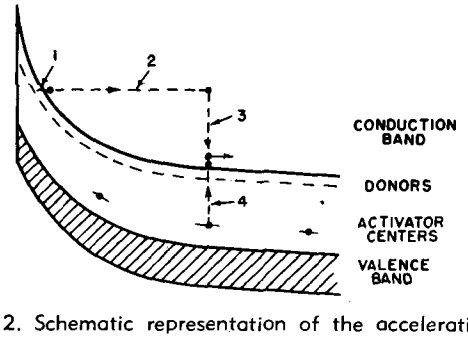

Fig. 2. Schematic representation of the acceleration-collision mechanism of electroluminescence. Electrons from traps in the localized high field region are liberated by the action of the high electric field and/or temperature [1], are then accelerated by the field [2] to acquire energies above the bottom of the conduction band, and collide with activator centers whereby they lose their energy [3] and the activator center is ionized [4] or excited. Emission usually occurs later in the cycle when the applied potential is reversing.

[5] Some of these possibilities were reviewed in the keynote speech of F. E. Williams at the Symposium on Luminescence held by this Society in Cincinnati two years ago and in a subsequent paper by Piper and Williams (16).

[6] Frenkel (19) has used this concept in a discussion of dielectric breakdown. The hydrogenic model for electron traps has, of course, been used extensively (20). Lanczos (21) has discussed the effect of electric fields on the hydrogen atom but this quantitative treatment does not seem to have been extended to the solid-state case.

as 10^6 or 10^7 v/cm. If such fields extended throughout the bulk of the particle, dielectric breakdown would probably occur as a result of avalanche formation. It is generally believed that in most normal electroluminescent phosphors, which are almost universally of the ZnS class, these regions of enhanced field arise from the presence of a second chemical phase, usually copper sulfide or ZnO. The exact location of these important regions inside or on the particles and the details of the mechanism of their operation is still, however, open to discussion (13, 28-30). Destriau's early phosphors contained large amounts of ZnO. Zalm, Diemer, and Klasens (29) showed that small amounts of copper sulfide deposited on the surface of ZnS made it electroluminescent. Lehmann (30) has found that a wide variety of normally nonelectroluminescent phosphors become electroluminescent if they are simply mechanically mixed with metal or semiconductor powders. The creation of these localized regions of high field is the key to the production of the relatively small number of known efficient electroluminescent phosphors compared to the comparatively large number of available photoluminescent systems.

In the presence of the applied field and the resultant excitation, the electroluminescent particles become polarized. The influence of this polarization on the details of the light emission has been investigated by various workers (14, 31-33). One important result is that the electroluminescent emission is "delayed emission"; the charges excited during one half-cycle of the applied voltage can recombine and emit only during the subsequent half-cycle (at least for ZnS:Cu phosphors). This has been shown strikingly by Zalm (14). During the charge separation trapping occurs and is responsible for many of the experimentally observed aspects of electroluminescence (14, 27, 34-36), including the dependence of average brightness on frequency and temperature, the nature of the variation of output during one cycle of the applied voltage ("brightness waves"), and the growth in output after application of the field and before equilibrium is reached ("buildup"). The emptying of electron traps by the combined action of field and temperature and the collision excitation of luminescent centers by accelerated electrons (processes 4 and 5 in the list given previously) are the predominant mechanisms in the Destriau effect; the statement of Garlick quoted earlier still contains the essence of the process as it is understood today. The role of traps has been recently reviewed by Haake (37).

Let us now summarize the characteristics of the Destriau effect which distinguish it from recombination electroluminescence as discussed earlier. These are:

1. The phenomenon is a field-dominated one, although thermal effects also play a role.

2. The charge carriers of importance are majority carriers.

3. After these carriers are introduced they must be accelerated by the field in order to obtain sufficient energy to excite luminescence centers by collision.

Because of these characteristics this type of luminescence has been or might be called "acceleration-collision electroluminescence", "majority-carrier injection electroluminescence", or "field-controlled electroluminescence". It has sometimes been called "a. c. electroluminescence" but since in the case of single crystals or thin phosphor films it can be excited by static fields, this does not seem to be a good description. The present writer (13) is responsible for the term "intrinsic electroluminescence". This was an attempt to specify the fact that the process is confined to the phosphor particles and does not depend on external carrier injection by means of electrodes. In view, however, of the present knowledge of the complexity of electroluminescent phosphors and the fact that the segregated second phase essentially corresponds to internal electrodes, this terminology should probably be abandoned.

If instead of a phosphor powder separated from electrodes by an insulator, a powder (38, 38a), a thin continuous film (39), or a single crystal (40-42) in contact with electrodes is employed, then sometimes there are observed additional experimental details which are due to carrier injection from the electrodes. As long as the carriers, however, correspond to majority carriers, acceleration will be necessary to achieve excitation and the process is similar in principle, although different in detail, to that observed in powders embedded in an insulator. Although it has been hoped that experiments on single crystals would clarify some of the results obtained with powders, this does not seem to be the case in reality because of the various difficulties or ambiguities involved.

In the previous section the recombination electroluminescence resulting when a p-n junction is biased in the forward direction was discussed. In the case of Si, for example, this radiation lies in the infrared region of the spectrum. If, however, such a junction is biased in the reverse or blocking direction so that high electric fields are produced in the junction, then a visible emission may be observed (43). An apparently similar emission was indeed observed by Lossew (10) in his earliest experiments on SiC and called by him Luminescence I in distinction to the other type which he called Luminescence II. Since this emission occurs when high fields are developed and when the polarity is such as to cause injection of majority carriers, it is believed that here also one has a process involving an acceleration-collision mechanism. Chynoweth and McKay (44) have also reported an emission in reverse-biased very narrow Si p-n junctions which is believed to result from internal field emission (Zener emission) rather than from an avalanche mechanism.

In concluding this section on the excitation of phosphors by electric fields alone, it is perhaps of interest to mention that Diemer (45) has observed what seems to be a third kind of electroluminescence in CdS crystals. His observation paralleled in many respects the characteristics of a gas discharge; it was also apparent that the local temperature of the specimen increased remarkably and played a role in the process. It has been suggested that this

type of excitation be called "breakdown electroluminescence". It should perhaps also be mentioned that Smith (46) has observed recombination electroluminescence in CdS crystals.

Electric Field Effects in Excited Phosphors

Now turn from a consideration of the effects produced by applying an electric field to a phosphor to the more complicated situation where the field is applied simultaneously with or subsequent to excitation by some other means.[7]

The Gudden-Pohl Effect (Transient Stimulation of Luminescence)

The earliest discovery of an electrophotoluminescent[8] effect was that of Gudden and Pohl (47) in 1920, even before the discovery of electroluminescence itself. Here the phosphor is first excited (by u. v. radiation, for example) and then an electric field (of the order of 10^3 v/cm) is applied during the afterglow or phosphorescence of the phosphor, or even after the emission has decayed below the limit of detection. A burst of emission is observed with some materials, even those which do not exhibit electroluminescence. During normal phosphorescence the electrons recombining with empty luminescence centers are provided by thermal emptying of electron traps. In the Gudden-Pohl effect the obvious effect of the field is to facilitate this trap emptying process. Curie (24) has also suggested that the field might accelerate electrons released from traps, either by the field alone (tunneling) or by the joint action of field and temperature, so that they acquire sufficient energy to cause emptying of additional filled traps by impact; the amount of energy required in this case is not very great. Although this effect may indeed occur, it is very difficult to distinguish experimentally from a direct action of the field on the traps.

When a static field is applied to a phosphor powder, polarization charges develop in the material and the effective internal field eventually becomes quite small. Under some cases this polarization may persist for very long times after the field has been removed; this subject has been studied extensively by Kallmann and Rosenberg (48). Because of these polarization effects the effective field in the Gudden-Pohl effect rapidly becomes zero if a static field is applied; this may, of course, be avoided by removing and applying the field periodically or by using an alternating field. Correspondingly, if a static field is applied to the phosphor during excitation and then removed during the afterglow, i. e., the reverse of the procedure for observing the normal Gudden-Pohl effect, a result similar to the normal effect is obtained (49). In this case, removal of the external field actually causes the effective internal field to increase, so that in reality there is no difference between the two methods of inducing the effect.

[7] The experimental details have been reviewed in a number of places (2, 13, 15).

[8] F. E. Williams in his keynote speech for the Luminescence Symposium of this Society in 1955 suggested that the terminology in these field effects gives the controlling agency as the first prefix and the source of power as the second prefix, although the two are difficult to unscramble in some cases. The terminology in this field has not always been consistent, however.

The Déchêne Effect (Field Quenching of Luminescence)

Many of the early experiments on electrophotoluminescence were, unfortunately, not carried out under very simple conditions and are often very difficult to interpret. For example, in 1934 Coustal (50) subjected a previously excited phosphor layer to an electrical glow discharge in air. Depending upon circumstances he obtained either quenching (presumably due to the field of the discharge) or enhancement (presumably due to u. v. radiation generated in the discharge) of the phosphorescence.

In 1935 Déchêne (51) performed an electrophotoluminescent experiment under slightly better conditions. He wet a sulfide phosphor powder with water and placed it between electrodes to which was applied a high direct voltage. Under these conditions the ionic conductivity of the water was sufficient to maintain a current of the order of microamperes per square centimeter, sufficient to counteract the polarization of the phosphor particles and maintain a field across them. Actually the field in Déchêne's experiments was strongest near the electrodes and the effects he observed were also greatest there. (It may be mentioned that this arrangement was also used by Déchêne to study the Reboul effect.) By the use of a slightly conducting medium for the phosphor Déchêne was able to observe field effects on phosphors with sustained fields and not simply during the short interval before polarization built up.

Déchêne made his observations both during the phosphorescence and with simultaneous u. v. excitation. At the moment of field application he observed a momentary increase in emission—the Gudden-Pohl effect. This, however, was followed, by a sustained quenching of the emission. This quenched emission in the afterglow might be only 24% of the normal value; for simultaneous excitation and field action, however, the quenching observed was fairly small (only to 82% of normal). Upon removal of the applied voltage a second Gudden-Pohl stimulation was observed. Fig. 3 shows the general results obtained by Déchêne for the case of continuous excitation. In 1943 Destriau (52) reported on field quench-

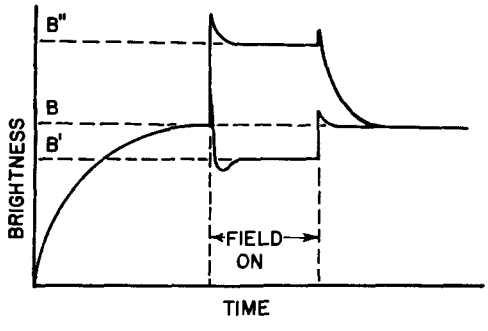

Fig. 3. Schematic representation of field quenching and enhancement effects on the brightness of an excited phosphor. Upon application of the field the brightness B may be either, depending on the material and on the experimental conditions, depressed to a new value B' or raised to a new value B". At the times the field is applied or removed there are also usually transient effects as shown; the short flashes of light observed at these times are due to the Gudden-Pohl effect and may not always be observed.

ing experiments on phosphors using powders imbedded in an insulator and alternating fields,[9] i. e., the arrangement used by him in electroluminescence. This method of avoiding polarization effects has obvious advantages over that used by Déchêne in that higher and uniform fields may be obtained. In this way the luminescence may be quenched almost to zero.

Two possible causes for the quenching effect suggest themselves: (*a*) the field may cause filling of empty luminescent centers from the valence band, or (*b*) the electrons are forced by the field to the surface of the crystals where nonradiating transitions are favored or they become deeply trapped. The fact that quenching occurs more readily in ZnS:Ag than in ZnS:Cu, as observed by Steinberger, Low, and Alexander (53, 54), gives some evidence for the former effect, but both may occur. It may be noted that Déchêne himself suggested the second explanation (although naturally not in modern parlance). He reported that thermoluminescence experiments on phosphors after quenching indicated a more intense emission persisting at higher temperatures (indicating the presence of electrons in deeper traps) but also a smaller total emission (fewer total number of filled traps, indicating that some nonradiating transitions had occurred). The kinetics of the quenching effect have been discussed by Matossi (55).

Field Effects on Infrared Stimulation or Quenching of Emission

In the preceding sections it is apparent that an electric field applied to a previously excited phosphor may empty filled traps, leading to stimulated emission, or fill empty luminescence centers, leading to emission quenching. Exactly similar effects may be induced by infrared radiation and have been known since the time of Lenard and even earlier. In 1937, one year after his discovery of acceleration-collision electroluminescence, Destriau (56) discovered that in some cases infrared quenching could be enhanced by the simultaneous application of an electric field. Correspondingly, in 1954, Low, Steinberger, and Braun (57) discovered that the response of some infrared stimulable phosphors could be enhanced by electric fields. In these cases the action of field and infrared radiation is combined.

Photoelectroluminescence and Cathodoelectroluminescence (Field Enhancement of Luminescence)

In 1954 Destriau and his son reported on a completely new effect (58-60). If certain phosphor powders, primarily ZnS:Mn, Cl and ZnCdS:Mn, Cl, are excited by x-rays and then an alternating electric field is applied, it is found that the luminescence intensity is increased (see Fig. 3). This has been called field enhancement of luminescence or the electroenhancement effect; according to Williams' nomenclature it is photoelectroluminescence. The materials showing this effect are only weakly electroluminescent and the enhancement effect can be observed at field strengths below those at which any detectable electroluminescent output is obtained.

Destriau found that the same phosphors which showed field enhancement of the x-ray excited luminescence showed, on the contrary, field quenching if excited by u. v. radiation. Recently Gobrecht and Gumlich (61) have shown, however, that although quenching is observed at low field frequencies and low u. v. intensity, at high frequencies and high exciting intensities enhancement is observed with the same materials.[10] Thus it appears that the enhancement effect and the quenching effect can occur simultaneously; depending on circumstances, one or the other may predominate. Cusano (62, 63) has also found that transparent films of ZnS:Mn, Cl show enhancement for either kind of excitation; in this case the effect may also be obtained with direct rather than alternating voltage since electrodes may be applied directly to the film. In photoelectroluminescence the energy emitted may exceed the controlling radiant energy so that radiation amplification is achieved.

Low (64) in 1955 suggested that field enhancement should also exist for luminescence excited by nuclear particles and suggested the effect as a radiation detector. The effect was actually first observed, for the case of alpha-particle excitation, in 1956 by Mattler (65) using the same phosphors used by Destriau for x-ray excitation.[11] Jaffe (67) reported that the same phosphors also show enhancement when bombarded with electrons.[12] The differences in the detailed performance of the same materials under the three types of excitation are presumably due to the differences in penetration depth and density of ionization in the three cases. Woods and Wright (69) also reported in 1955 that the cathodoluminescence of MgO could be enhanced by static electric fields. According to Williams' nomenclature, these last two effects are both examples of cathodoelectroluminescence, although in his abstract Jaffe called the effect electrocathodoluminescence.

Williams (70) in 1955 presented an explanation of all these field enhancement effects which today seem to be generally accepted. His picture is that enhancement of luminescence is really externally controlled electroluminescence as distinguished from normal electroluminescence which is self-sustained. Thus in the usual type of acceleration-collision elec-

[9] Déchêne also mentions the use of alternating fields and the electroluminescence experiments of Destriau. In an earlier paper (13) it was stated incorrectly that Déchêne worked only in the afterglow region. The correct picture of the situation was first given by Matossi (15).

[10] It has recently been brought to the writer's attention by C. H. Haake that Schmidt (49) in his 1923 paper (page 174) mentions the existance of an enhancement effect. Schmidt says, "It is a remarkable fact that phosphors excited while in an electric field sometimes luminesce noticeably brighter than during normal excitation. This can be easily demonstrated if one makes two cells of the same phosphor and applies to one a high voltage while both are irradiated with the 365 mμ Hg line and the brightness observed." There is no further information given in the paper. It may be that with the field applied, u.v. radiation generated in the powder provided the additional excitation. In any case, it was 22 years before anyone duplicated this observation despite the fact that many people studied field effects in phosphors in the interim.

[11] Earlier, in 1944, Destriau (66) looked for field enhancement of the scintillations produced by alpha particles, but was unable to find the effect in the materials then available.

[12] Note added May 24, 1957: Since the above was written it has been brought to the writer's attention that in a recent publication Cusano (68) mentions that he has obtained field enhancement of the luminescence of thin phosphor films of ZnS:Mn, Cl under cathode-ray excitation; no details of these experiments have been published, however.

troluminescence there are three steps in the excitation process (*see* Fig. 2):

1. Production of the initial free electrons by action of the field.
2. Acceleration of these electrons by the field.
3. Impact excitation of luminescence centers.

In photoelectroluminescence or cathodoelectroluminescence the initial electrons are supplied, either directly or indirectly, by the external radiation so that step [1] above is modified, but thereafter the process is essentially unchanged. In the opinion of the writer, this theory does not explain to complete satisfaction why sulfides containing Cu as an activator (which are very good materials for pure electroluminescence) do not show photoelectroluminescence, but only the quenching effect. Most phosphors which show photoelectroluminescence are activated by Mn, although Cusano (71) has recently reported the effect with As and P as activators. In addition, it should be noted that with alternating fields, the effect of frequency, field strength, and temperature is quite different in electroluminescence and in photoelectroluminescence. (See note on page 748.)

Thermoelectroluminescence and Electrothermoluminescence

In a normal thermoluminescence experiment, the phosphor is excited at low temperatures so that electron traps are filled. The excitation is then removed and the temperature allowed to increase; thermal detrapping results in emission of radiation. Reference has already been made to the experiments of Böer and Kümmel (22), who maintained the phosphor at the low temperature following excitation and applied a field of increasing magnitude. Trap emptying by the field was detected by changes in electrical conductivity.[13] It would appear that radiation resulting from the freed charges should also be detectable, but this apparently has not yet been observed.

Neumark (73) has studied the effects of applying an electric field to phosphor single crystals during a thermoluminescence experiment. She found, in the case of crystals which showed electroluminescence, that electrons released thermally from traps can be accelerated to give emission greater than the sum of the normal thermoluminescence and the electroluminescence at that temperature. The effect is thus quite similar to that of photoelectroluminescence discussed above; it is temperature-controlled electroluminescence or thermoelectroluminescence. Strangely, however, Neumark found no evidence for appreciable field release of trapped electrons in these crystals. This is in contradiction to the results of Johnson, Piper, and Williams (34) who also used single crystals in their experiments on the effect of temperature on electroluminescent brightness; these workers, however, did not study thermoluminescence with applied fields.

[13] Jensen and Cashman (72) have also observed what they called "electrical glow curves"; they, however, used increasing temperature rather than increasing field strength and measured the conductivity. Since there are two quantities which may be varied (the temperature and the field strength) and two which may be observed (luminescence and conductivity), there are obviously four possible experimental arrangements.

Prior to Neumark's work, Gobrecht, Hahn, and Gumlich (74), and later Hahn (75), observed effects on the temperature dependence of the brightness of electroluminescent powders which they interpreted in a manner similar to that given above for Neumark's experiments. On cooling the samples they obtained a smooth curve, but on heating they obtained a series of maxima and minima; this effect they called "electrothermoluminescence". Most good electroluminescent powders do not display this behavior, however, and even in those that do, Hahn reports that the nature of the embedding medium has a profound influence so that the effect may not be characteristic of the phosphor itself.

Other Field Effects in Phosphors

The use of photoelectroluminescence or the electroenhancement effect as a radiation amplifier has been described above. Halsted (76) recently described an amplification effect utilizing electrophotoluminescence. He makes use of the fact that in ZnS, for example, 2537Å radiation is very strongly absorbed compared to 3650Å radiation. Thus, for 2537Å excitation the excited luminescent centers are very nonuniformly distributed in the material and are concentrated near the side of the material on which the radiation impinged. If an alternating field is applied, carriers periodically will be swept out of and into the excitation region so that the luminescence output will be modulated at the field frequency.[14] Modulation levels of 50% may be achieved in this way with quite low fields (100 v/cm). Under proper conditions, the energy content of the modulated component of output may exceed the electrical input so that in this sense amplification is obtained. This effect differs from the photoelectroluminescent amplifier, however, in that the input and output are not both radiation.

Destriau (77) recently described a new storage or memory effect in conjunction with the field enhancement of x-ray excited luminescence. The material is first subjected simultaneously to x-ray excitation and to a field and then the x-rays are turned off before the field; this constitutes the sensitization. If now after an interval of time during which the phosphor is stored in the dark (experiments have been performed up to 17 hr) x-rays are again applied, without the field, the emission will rise to an enhanced value and then decay to an equilibrium. The effect of the sensitization by the field has thus been stored in the material. If the intensity of x-rays striking the phosphor during the sensitization period varies over its area, as is the case if an object is placed before the phosphor, then an image of this object will be obtained at the second irradiation even though the object has been removed and the second irradiation done with uniform excitation; the phosphor has stored a latent image of the object which is revealed by the subsequent irradiation. Under suitable conditions the contrast in the image may be enhanced in this way.

The explanation of this storage effect of Destriau seems to be the following. During the sensitization

[14] In the usual electrophotoluminescence experiment with more or less uniform excitation (penetrating radiation) the output is also modulated, but at a frequency twice that of the applied field (15).

period the degree of excitation is greater than that corresponding to the x-ray excitation alone since the material shows electroenhancement. During sensitization, the field draws off some of the electrons to the surfaces of the particles where they are held in deep traps.[15] In the dark these stored charges will be retained for long periods. When the x-ray beam is reapplied, without field, electrons are excited from these deep traps as well as from luminescence centers and the output rises to a transient value higher than the equilibrium value. As the traps are emptied, the emission decays to its normal value. As the x-ray intensity at the second irradiation may be made greater than that used for sensitization, the image may be displayed at high output levels; this may be of value if it is not desired to expose the object itself to intense x-irradiation.

Alburger (79) has also discussed materials which he calls "electroflors". These are liquids which show no luminescence under u. v. excitation in the absence of a voltage but which become luminescent when a voltage is applied. No information has been published on the composition of these substances, but B. Rosenberg has suggested to the writer that they involve organic materials whose luminescence is sensitive to pH value. This material is dissolved in a solvent containing an ionized salt and the local pH is controlled by polarization produced by the applied voltage. Since they are liquid, they bear no connection with normal inorganic phosphors, but their existence is at least of general interest.

Conclusion

As has been shown by the preceding discussion, the variety and the ramifications of the effects of electric fields on phosphors and the number of possible experimental arrangements are exceedingly great. It seems, however, that the observations may usually be explained by a combination of a few fairly simple basic physical processes. These are:

1. Field emptying of traps (Gudden-Pohl).

2. Field quenching of photoluminescence (Déchêne). This may occur either by field induced filling of empty luminescence centers from the valence band or by the action of the field in sweeping electrons away from the excitation region to regions where trapping and/or nonradiating recombination are favored.

3. Acceleration-collision electroluminscence (Destriau). Majority carriers may be accelerated by sufficiently high fields to excite luminescence centers by collision. The initial electrons may be supplied by the field itself (self-sustained electroluminescence) or by external action (photoelectroluminescence, etc.).

4. Recombination electroluminescence (Lossew). Minority carriers injected from contacts or over p-n barriers may immediately recombine, often with the emission of radiation.

From these basic processes there have come a wide variety of experimental effects. In the future many others will undoubtedly be discovered.

Acknowledgments

The writer is indebted for valuable discussion to Dr. Lehmann, Dr. Thornton, Dr. Rosenberg, and Mr. Jaffe, and especially to Dr. Haake, all of the Westinghouse Phosphor Research Section in Bloomfield, and to Professor Destriau and Dr. Mattler, our consultants, of the Faculty of Sciences in Paris.

Manuscript received June 14, 1957. This paper was prepared for delivery before the Washington Meeting, May 12-16, 1957.

Any discussion of this paper will appear in a Discussion Section to be published in the June 1958 JOURNAL.

REFERENCES

1. H. W. Leverenz, "An Introduction to Luminescence of Solids," p. 152, John Wiley & Sons, Inc., New York (1950).
2. G. Destriau, *Trans. Faraday Soc.*, **35**, 227 (1939); *Phil. Mag.*, **38**, 700, 774, 880, 885 (1947).
3. E. C. Payne, E. L. Mager, and C. W. Jerome, *Illum. Eng.*, **45**, 688 (1950).
4. R. Gerharz, *J. Electronics*, **2**, 409 (1957).
5. F. Braun, *Ann. der Phys.*, **65**, 361 (1898).
6. R. R. Sullivan and R. T. Dufford, *Phys. Rev.*, **37**, 1019 (1931).
7. R. T. Dufford, *J. Opt. Soc. Amer.*, **18**, 17 (1929).
8. C. Zwikker, "Physical Properties of Solid Materials," p. 279, Interscience Publishers Inc., New York (1954).
9. G. Reboul, *Compt. rend.*, **171**, 1052 (1920); **172**, 210 (1921); **173**, 222 (1921); *J. Phys. Rad.*, **2**, 86 (1931); **5**, 329 (1934).
10. O. W. Lossew, *Telegrafia i Telefonia*, No. 18, 61 (1923); No. 26, 403 (1924); *Wireless World*, **15**, 93 (1924); *Phil. Mag.*, **6**, 1024 (1928).
11. K. Lehovec, C. A. Accardo, and E. Jamgochian, *Phys. Rev.*, **83**, 603 (1951); **89**, 20 (1953).
12. G. Destriau, *J. Chim. Phys.*, **33**, 620 (1936); **34**, 117 (1937).
13. G. Destriau, and H. F. Ivey, *Proc. IRE*, **43**, 1911 (1955).
14. P. Zalm, *Philips Res. Repts.*, **11**, 353, 415 (1956).
15. F. Matossi, "Elektrolumineszenz und Elektrophotolumineszenz," Vieweg, Braunschweig (1957).
16. W. W. Piper and F. E. Williams, *Phys. Rev.*, **98**, 1809 (1955).
17. C. Zener, *Proc. Roy. Soc.*, **A145**, 523 (1934).
18. W. Franz, *Ann. der Phys.*, **11**, 17 (1952).
19. J. Frenkel, *Phys. Rev.*, **54**, 647 (1938); *Tech. Phys. USSR*, **5**, 685 (1938).
20. D. Curie, *J. Phys. radium*, **17**, 16 (1956).
21. C. Lanczos, *Z. Physik.*, **62**, 518 (1930); **65**, 413 (1930); **68**, 204 (1931).
22. K. W. Böer and U. Kümmel, *Z. Naturforsch.*, **9a**, 177 (1954).
23. G. F. J. Garlick, "Luminescent Materials," p. 150, Oxford Univ. Press (1949).
24. D. Curie, *J. Phys. Radium*, **14**, 510, 673 (1953).
25. F. E. Williams, in "Advances in Electronics," Vol. V, p. 137, Academic Press, New York (1953).
26. W. W. Piper and F. E. Williams, *Brit J. Appl. Phys.*, Suppl. No. 4, p. 39 (1955).
27. G. F. Alfrey and J. B. Taylor, *Proc. Phys. Soc. (London)*, **66B**, 775 (1955).
28. L. Burns, *This Journal*, **100**, 572 (1953).
29. P. Zalm, G. Diemer, and H. A. Klasens, *Philips Res. Repts.*, **9**, 81 (1954).
30. W. Lehmann, *This Journal*, **104**, 45 (1957).
31. J. F. Waymouth and F. Bitter, *Phys. Rev.*, **95**, 941 (1954); **102**, 686 (1956).

[15] Neumark (73) has presented experimental evidence for the filling of traps by electric fields and has shown that the effect is greater with alternating than with static fields. Kallmann and Mark (78) have discussed the de-exciting effects of electric fields on the photoconductivity of phosphors.

32. F. Matossi, *ibid.*, **98**, 434 (1955).
33. F. Matossi and S. Nudelman, *ibid.*, **99**, 1100 (1955); *This Journal*, **101**, 546 (1954).
34. P. D. Johnson, W. W. Piper, and F. E. Williams, *ibid.*, **103**, 221 (1956).
35. W. A. Thornton, Phys. Rev., **102**, 38 (1956).
36. C. H. Haake, *J. Appl. Phys.*, **28**, 117, 245 (1957); *This Journal*, **104**, 291 (1957).
37. C. H. Haake, *J. Opt. Soc. Amer.*, **47**, 881 (1957).
38. G. Destriau, *Illum. Eng.*, **51**, 197 (1956).
38a. D. Hahn and F. W. Seemann, *Z. Physik*, **146**, 644 (1956).
39. R. E. Halsted and L. R. Koller, *Phys. Rev.*, **93**, 349 (1954).
40. W. W. Piper and F. E. Williams, *ibid.*, **87**, 151 (1952).
41. D. R. Frankl, *ibid.*, **100**, 1105, 1790 (1955).
42. G. Diemer, *Philips Res. Repts.*, **10**, 194 (1955).
43. R. Newman, W. C. Dash, R. N. Hall, and W. E. Burch, *Phys. Rev.*, **98**, 1536 (1955).
44. A. G. Chynoweth and K. G. McKay, *ibid.*, **106** 418 (1957).
45. G. Diemer, *Philips Res. Repts.*, **9**, 109 (1954).
46. R. W. Smith, *Phys. Rev.*, **98**, 1169 (1955); **105**, 900 (1957).
47. B. Gudden and R. W. Pohl, *Z. Physik.*, **2**, 192 (1920).
48. H. Kallmann and B. Rosenberg, *Phys. Rev.*, **97**, 1596 (1955).
49. F. Schmidt, *Ann. Physik.*, **70**, 161 (1923).
50. R. Coustal, *Compt. rend.*, **198**, 1403, 1596 (1934).
51. G. Déchêne, *ibid.*, **201**, 139 (1935); *J. Phys. Radium*, **9**, 109 (1938).
52. G. Destriau, *ibid.*, **4**, 32 (1943).
53. I. T. Steinberger, W. Low, and E. Alexander, *Phys. Rev.*, **99**, 1213 (1955).
54. E. Alexander, W. Low, I. T. Steinberger, and S. Z. Weiss, *J. Phys. Radium*, **17**, 737 (1956).
55. F. Matossi, *Phys. Rev.*, **94**, 1151 (1955); *This Journal*, **103**, 662 (1956).
56. G. Destriau, *J. Chim. Phys.*, **34**, 327 (1937); *J. Phys. Radium*, **4**, 77 (1943).
57. W. Low, I. T. Steinberger, and E. A. Braun, *J. Opt. Soc. Amer.*, **44**, 504 (1954).
58. M. Destriau, *Compt. rend.*, **238**, 2298 (1954).
59. G. Destriau and M. Destriau, Paper presented at ECS Meeting, Chicago, 1954.
60. G. Destriau, J. Mattler, M. Destriau, and H. E. Gumlich, *This Journal*, **102**, 682 (1955).
61. H. Gobrecht and H. E. Gumlich, *J. Phys. Radium*, **17**, 754 (1956).
62. D. A. Cusano, *Phys. Rev.*, **98**, 546 (1955).
63. D. A. Cusano and F. E. Williams, *J. Phys. Radium*, **17**, 742 (1956).
64. W. Low, *Phys. Rev.*, **98**, 556 (1955).
65. J. Mattler, *J. Phys. Radium*, **17**, 758 (1956).
66. G. Destriau, *Comp. rend.*, **218**, 791 (1944).
67. P. M. Jaffe, Paper presented at ECS Meeting, Washington, 1957.
68. D. A. Cusano, *IRE Trans. Nuclear Sci.*, Vol. NS-3, No. 4, November (1956).
69. J. Woods and D. A. Wright, *Proc. Phys. Soc. (London)*, **68B**, 566 (1955).
70. F. E. Williams, *Phys. Rev.*, **98**, 547 (1955).
71. D. A. Cusano, *ibid.*, **106**, 604 (1957).
72. H. C. Jensen and R. J. Cashman, *ibid.*, **96**, 798 (1954).
73. G. Neumark, *ibid.*, **103**, 41 (1956); *Sylvania Technologist*, **10**, 29 (1957).
74. H. Gobrecht, D. Hahn, and H. E. Gumlich, *Z. Physik*, **136**, 623 (1954).
75. D. Hahn, *J. Phys. Radium*, **17**, 748 (1956).
76. R. E. Halsted, *Phys. Rev.*, **99**, 1897 (1955); *Bull. Am. Phys. Soc.*, **2**, 155 (1957).
77. G. Destriau, Meeting Physical Society, Berlin, March 15, 1957.
78. H. Kallmann and P. Mark, *Phys. Rev.*, **105**, 1445 (1957).
79. J. R. Alburger, *Electronic Indus. and Tele-Tech.*, p. 50, February, 1957.
80. D. Curie, "Progress in Semiconductors," Vol. 2, p. 249, John Wiley & Sons, Inc., New York (1957).
81. J. Mattler, Abstract 28, Washington Meeting, ECS, May 1957.

NOTE Added in Proof: In a recent article (80) Curie has concluded that the field-enhancement effect observed by Cusano does not have the same mechanism as that observed by Destriau. He comes to this conclusion because of the quite different effects of field strength and temperature in the two cases. In Destriau's experiments the output increases only slowly as the field strength is increased and approaches a limiting value; in Cusano's experiments, on the other hand, the output increases more or less exponentially with applied voltage above a threshold voltage. Mattler (81) has also shown that the enhancement ratio (with x-ray excitation) increases as the temperature is increased despite the fact that the electroluminescence of the same material (at higher field strengths) decreases with increasing temperature. Curie concludes that excitation by accelerated electrons does not occur in the enhancement experiments of Destriau.

Discussion Section

This Discussion Section includes discussion of papers appearing in the JOURNAL of The Electrochemical Society, **103**, No. 9 (September 1956), and **104**, No. 1-6 (January-June 1957). Discussion not available for this issue will appear in the Discussion Section of the June 1958 JOURNAL.

Oxidation of Copper to Cu_2O and CuO

D. W. Bridges, J. P. Baur, G. S. Baur, and W. M. Fassell, Jr.

(pp. 475-478, Vol. 103)

J. Paidassi[1]: We are studying the oxidation of OFHC copper in air under atmospheric pressure between 300° and 1050°C and thought that it might be interesting to summarize our results so that they could be compared with those obtained by the authors.

Our preparation of the specimens consisted of grinding on metallographic polishing papers to a fineness of 4/0, washing with toluene, and finally annealing in vacuum (10^{-4} mm Hg) at 900°C for 4 hr. The specimens were oxidized in a vertical, open furnace, where the atmosphere was renewed and finally quenched in air. The minimum duration of the oxidation varied between 1 and 60 min, the maximum between 4 and 200 hr, depending on the temperature. In each sample Δm, the increase of weight per cm^2 of the initial surface, and e, e_1, e_2, the total thickness of the scale, and the thickness of the CuO and Cu_2O layers, respectively, were determined. We restrict ourselves below to a summary of the results obtained between 600° and 1000°C.

At all the temperatures one obtains, with a good approximation, the following relations:

$$\Delta m = k_m \sqrt{t}\ (\mathrm{I});\ e = k \sqrt{t}\ (\mathrm{II});\ e_2 = k_2 \sqrt{t}\ (\mathrm{III})$$

where t is the time, and k_m, k, k_2 are constants.

The formulation of the law of growth of the thickness of the CuO layers is more complicated. In the 600°-800°C range and durations of oxidation up to 48 hr, it is of the following type:

$$e_1 = k_1 \sqrt{t} + k'_1 \qquad (\mathrm{IV})$$

where k_1 and k'_1 are two positive constants. Between 850°-1000°C the growth rate at first follows a law of type (IV), but subsequently its growth is retarded and the thickness e_1 finally reaches a limiting value for a time of oxidation, which varies between 16 and 2 hr depending on the temperature. (We believe that the above particularities of the law of growth of the CuO layer at temperatures exceeding 850°C may be explained by dissociation of the CuO in the course of oxidation.)

It follows that the relative thickness $e_{1/e}$ of the CuO layer in relation to the total thickness of the scale, strictly speaking, is not constant at any temperature. Nevertheless, because of the smallness of k'_1 of Eq. (IV) at any temperature throughout the 650°-800°C range, $e_{1/e}$, with the exception of the shortest times of oxidation, does not vary more than 20%, the limiting value being reached after from 16 to 32 hr, depending on the temperature. For temperatures higher than 800°C the diminution of the relative value of this ratio is of the same order of magnitude, although the absolute variations remain very small due to the low values of $e_{1/e}$ (from 0.3 to 3%) within the 800°-1000°C range. Fig. 1 shows the relative variations of the thickness of the CuO layer with the duration of oxidation at temperatures of 600°, 800°, and 1000°C, respectively, and Fig. 2 the variation with temperature of the limit of the $e_{1/e}$ ratio corresponding to "steady" rate of oxidation.

If we compare the above results with those of the authors it may be concluded that, on the whole, agreement is satisfactory. The observed differences may be due partly to the different surface preparation of the specimens. On the other hand, we believe that the considerable dispersion of results recorded

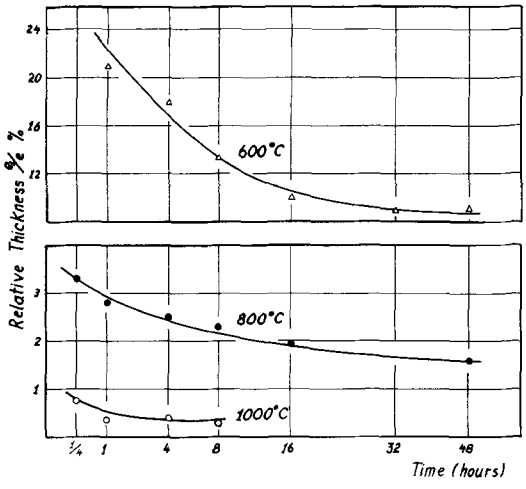

Fig. 1

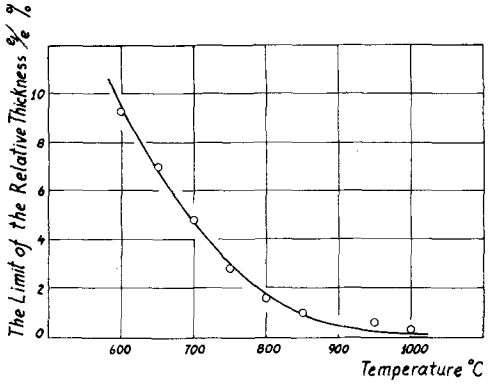

Fig. 2

[1] Dept. of Metallurgy, School of Chemical Engineering, University of Concepción, Concepción, Chile.

The partial results reported in this discussion are relative to the research corresponding to Contract No. 43 between the discussor and the "Consejo de Investigación Científica" of the "Universidad de Concepción," Chile.

by the authors may be due principally to the method used for the determination in the scales of the CuO/Cu_2O ratio, which was fundamentally a bulk x-ray analytical procedure and for this reason did not take into account the localized irregularities of the thickness of the scale. In any case, we would like to know if the authors checked the precision of the x-ray method proper through analyses of synthetic mixtures. For the determination of the layers in the scale we preferred a refined technique of the micrographic method, as used by us in the solution of a similar problem previously.[2]

D. W. Bridges, J. P. Baur, G. S. Baur, and W. M. Fassell, Jr.: We wish to thank Prof. Paidassi for his comments and interest in our work. In the last paragraph of his discussion, Professor Paidassi comments on the advisability of the use of quantitative x-ray diffraction techniques to determine the amounts of CuO and Cu_2O present, and whether or not such a method was checked through analysis of synthetic mixtures. The method as outlined in the paper consisted of mixing known weights of CuO (Baker & Adamson reagent grade) and Cu_2O (made by oxidation of OFHC copper at 1000°C and 20 mm-Hg oxygen pressure) with a known weight of high grade CaO. This technique, known as the "addition of an internal standard" has long been accepted as a most satisfactory method of quantitative analysis. Its relative merits as compared to the photomicrographic method described by Professor Paidassi and other methods[3,4] is at present speculative. However, the authors believe that the "localized irregularities of the thickness of the scale" would affect the photomicrographic method as much if not more than the x-ray method.

It is interesting to note the over-all agreement between the results of Professor Paidassi and those of the authors. These results with those of other investigators are summarized in Table I.

The authors' results can best be summarized by rephrasing a portion of the abstract. Quantitative x-ray diffraction analysis of the scale disclosed approximately 4% CuO at high and low pressures for temperatures above 800°C. Below 750°C, high pressure coatings contained 10% CuO while subatmospheric coatings continued to assay about 4% CuO. The effect of the relative amounts of the oxides present on the parabolic rate constant is shown in Fig. 1 [of the paper]. Average values of the parabolic rate constants at temperatures and oxygen pressures at which the relative amount of CuO is 4% can be connected with a "fair" straight line, while deviations occur for those points at temperatures and oxygen pressures where the amount of CuO present is greater. This evidence is believed to further the postulate that diffusion of cuprous ions through the Cu_2O layer is the rate-determining step.

Table I. Per cent CuO in the oxide layer formed at various temperatures and 1 atm air

	Temp, °C							
Investigation	600	650	700	750	800	850	900	950
Valensi[3]	60		30			7	5	
Tylecote[4]	30	20	15			10		
Paidassi	9	7	4.5		1.8	1.0		0.5
Bridges, *et al.*	3.6*		2.4*	6.6*	4.1*	3.7*	3.2*	
Average of 2-hr oxidation period experiments	10.0**		11.5**		7.3**			

* Average % CuO for samples oxidized at oxygen pressures less than 1 atm.
** Average % CuO for samples oxidized at oxygen pressures in excess of 1 atm.

[2] J. Paidassi, *Rev. mét.*, 52, 869 (1955).

[3] G. Valensi, Proceedings of the Pittsburgh International Conference on Surface Reactions, p. 156, Corrosion Publishing Co., Pittsburgh (1948).

[4] R. F. Tylecote, *Metallurgia*, 53, 191 (1956).

Cathode Ray Tube Screen Charging and Conditions Leading to Positive Ion Deterioration

A. B. Laponsky, M. J. Ozeroff, W. A. Thornton, and J. R. Young (pp. 498-507, Vol. 103)

A. B. McFarlane[5]: The authors give results showing that the sticking potential of the luminescent screen used in television tubes exceeds 25 kv. Early screens for this purpose were known to stick at various potentials up to 15 kv[6,7,8] but usually well below this value. Therefore, these latest results show a very great improvement. They apparently attribute this improvement to the "roughness" of the surface, but early screens also had rough surfaces. It is, therefore, difficult to explain the improvement merely in terms of "roughness" and I should like the authors' comments on this point.

I would add that the *British Journal of Applied Physics* has published a paper entitled "The Movement of the Second Crossover Potential of Insulators."[9] In it I give results showing that by suitable treatment[10] of luminescent screen the second crossover potential (about 7 kv for zero field) may be made very field dependent, so much so that negligible signs of sticking are apparent up to 20 kv and possibly beyond. I have not yet established the exact explanation of this phenomenon, and therefore I am particularly interested in the authors' comments.

Contact Electroluminescence

Willi Lehmann (pp. 45-50, Vol. 104)

W. Lehmann: In the paper I unfortunately omitted reference to the fact that Mr. Luke Thorington, formerly of this laboratory,[11] first reported at the 1952 Spring Meeting of The Electrochemical Society in Pittsburgh that "It has been observed that a purely mechanical mixture of certain phosphors in vacuum may be electroluminescent while the separate phosphors are not." The effect observed by

[5] Kingsmead Works, Electronic Tubes Ltd., High Wycombe, Bucks, England.

[6] H. Moss, "Advances in Electronics," Vol. II, p. 1, Academic Press, Inc., New York (1949).

[7] H. W. Leverenz, "Luminescence of Solids," p. 437, John Wiley & Sons, Inc., New York (1950).

[8] A. B. McFarlane, M.Sc. Thesis, Engineering, London University (1955).

[9] A. B. McFarlane, *Brit. J. App. Phys.*, 8, 248 (1957).

[10] (*a*) Coating the electron-bombarded side with a layer of MgO smoke; (b) settling screen in concentrated potassium silicate solutions.

[11] Lamp Div., Westinghouse Electric Corp., Bloomfield, N. J.

Thorington was restricted to high vacuum, however, and any admission of gases or of other embedding materials either greatly reduced or completely destroyed the effect.

Electrochemical Polarization, 1. A Theoretical Analysis of the Shape of Polarization Curves

M. Stern and A. L. Geary (pp. 56-63, Vol. 104)

E. W. Haycock[12]: The paper by Stern and Geary is a welcome and timely contribution to the theoretical study of polarization phenomena at electrode surfaces. Their reference to the recent paper by Logan, however, projects the authors into the realm of practical applications of the shape of polarization curves. In this regard, the following comments are offered. These comments are made for two reasons. First, to counteract the possible impression that the "current-potential break" criterion, as widely used in cathodic protection applications, has little or no theoretical basis; second, to clarify understanding of the conditions most usually encountered in the practical application of the "break" criterion.

The choice of the word "break" to describe a discontinuity or transition region in the polarization curves perhaps is unfortunate. However, the problem is one of semantics rather than science and in cathodic protection usage no real misunderstanding exists.

The drawing of a straight line through a few experimental points is usually recognized as being scientifically hazardous. In many cases it can be explained as being due to an optimism which arises from necessity rather than misunderstanding.

The requirement for the successful application of the "break" criterion to determine complete cathodic protection has been clearly stated by Mears and co-workers.[13] This is that the corrosion system be under cathodic control.

The widest application of cathodic protection at present is in the mitigation of soil corrosion. This corrosion system, in the majority of cases, is best described as a series of differential aeration cells in a nearly neutral environment. In low resistivity soils the corrosion is cathodically controlled by the availability of oxygen at the cathodic areas. As cathodic protection current is applied and the current is reached at which complete protection is achieved, the net anode reaction changes from the solution of iron to, most probably, the evolution of hydrogen. If the system is under complete cathodic control, this also will coincide with a change in the reaction at the cathode. The oxidizing capacity of the oxygen depolarizer at the cathode is being balanced by the electron flux from an external source, and any further increase in the protection current will result in the evolution of hydrogen. Since the anode and cathode reactions both change as the system is protected, a "break" or transition region in the polarization curves is expected at this point.

If the system is under anodic rather than cathodic control, it is doubtful if the transition due to the change in anode reaction could be detected experimentally in a practical case by measuring the corrosion potential as a function of the cathodic protection current applied. Similarly, the transition corresponding to protection would be masked if the system were under resistance control and to a lesser extent if an *IR* term were incorporated in the measurement of the corrosion potential due to the position of the reference electrode. In soil corrosion systems which are nearly neutral, the hydrogen ion concentration polarization effects referred to by Stern and Geary usually occur at a low current density compared to the corrosion and protection current densities involved and hence do not interfere with the shape of the polarization curve in the region of interest.

In reviewing Logan's comparison of the criteria of protection, it is interesting to note that the other criteria considered have much less scientific basis than the "break" criterion. The discrepancies reported by Logan are most probably due to reasons other than those suggested by the paper under discussion.

M. Stern: Mr. Haycock's comments provide a welcomed opportunity to discuss one of the practical applications of polarization measurements. The author believes that there is no theoretical basis for the "current-potential break" criterion, as widely used in cathodic protection applications, and is disappointed in his ability to make the reason for this view clear to Mr. Haycock in the text of the paper under discussion. An additional paper on this subject[14] illustrates the reasoning further. In particular, Case VIII, where the corrosion rate is determined by a limiting diffusion current, can be considered close to the condition existing during corrosion in some soils. A study of this will show that any break criterion is completely inaccurate.

The work of Mears and associates referred to by Mr. Haycock requires that a system be under *complete* cathodic control. More important, however, this work contains an assumption which is not often appreciated. This assumption requires that all anodes remain anodes during application of cathodic current and suddenly revert to cathodes at the equilibrium metal potential. Such a requirement has neither a theoretical basis nor (to the author's knowledge) experimental support. Theoretical and experimental work by many investigators shows that polarizing a redox system through the equilibrium potential does not necessarily result in a discontinuity.

Concerning the practical application of the "break criterion," it is doubtful that any real system has the requirements described above. Corroding iron in soils is not under complete cathodic control, but should be considered under mixed and resistance control. Also, in field measurements, *IR* terms are often the most important part of polarization observations, and obviously have a significant influence on curve shape. The recent contribution to N.A.C.E. Committee T-2C on Minimum Current Requirements by Sudrabin and Ringer[15] supports the au-

[12] Shell Development Co., Emeryville, Calif.

[13] *See*, for example, R. B. Mears and J. M. Bialosky, "Cathodic Protection," p. 37, National Association of Corrosion Engineers (1947).

[14] M. Stern, *This Journal*, **104**, 645 (1957).

[15] L. P. Sudrabin and F. W. Ringer, *Corrosion*, **13**, 351 (1957).

thor's contention that this method is not reliable. It is significant to note that this committee report actually refers to the method as the "apparent" break relation.

There are so many reported cases where the "apparent" break method does not work, and there are so many conditions where the method cannot work, that it is difficult to understand why it is used. Other criteria are available which are more accurate, have a sounder foundation in theory, and are easier to use.

Thermogalvanic Potentials and Currents at Aluminum Surfaces in Industrial Water

Edgar C. Pitzer (pp. 70-74, Vol. 104)

R. A. Hine[16]: This investigation is of great interest since we have made rather similar measurements of potentials in studying the formation of Boehmite films on Al immersed in distilled water at elevated temperatures. In this case the potential difference between the Al specimen and a Pt electrode also immersed in the water was measured directly. At 20°C the potential of the Al was of the order of −0.5 to −0.6 v, and slowly became more base with increasing temperature until at 80°-90°C a rapid change took place to a maximum of −1.25 v at boiling; on continued boiling, the potential became slightly less base, and after ½ hr remained fairly steady at about −0.95 v. The maximum current densities on the anode were about 3×10^{-6} amp/cm^2.

There obviously is some correspondence between these results and those of the author using supply water. The formation of Boehmite films on Al has been extensively studied by Altenpohl.[17] In distilled water, reaction visibly appears to start at about 80°-90°C and is accompanied by evolution of hydrogen. The corrosion product has been definitely established as Boehmite, $Al_2O_3 \cdot H_2O$ (or AlO·OH), by x-ray diffraction. It is formed as a continuous adherent film, and hence its growth rate is of an exponential type; after 1 hr's immersion at boiling, the thickness is usually of the order of 0.5 μ, and immersion for many hours is required to obtain a thickness of 2 μ, this being about the maximum thickness obtainable. It is also clear that the Boehmite film produced in distilled water is protective in nature, and Al utensils processed to produce such a film have markedly increased resistance to corrosion. In less pure water, such as supply waters, Boehmite films are also produced, but usually they are more porous and less protective than with distilled water and they may be discolored by the inclusion of small particles of unoxidized Al metal in the film; in tap water buffered to about pH 10, for example with ammonia, very much thicker Boehmite films are produced.

In view of these facts it is difficult in the case of distilled water to regard the phenomenon of the potential change to a value some 0.6 v more negative as an impairment of the protective film on the surface; on the contrary, in fact, it is known that the change is accompanied by the formation of a highly protective film. The formation of this film is probably indicated by the potential change from −1.25 v to −0.95 v during continued immersion at the boiling point observed in our results. Further, the potential of the Al after formation of the film, and after allowing to cool again to 20°C, was some 0.1 v more noble than at the commencement of the experiment. In the author's experiments the films produced in supply water were probably not protective since no potential change in the positive direction was noted on prolonged exposure. Altenpohl states that in such cases the Boehmite produced is more in the nature of a corrosion product than a protective film.

There are many questions unanswered about the mechanism of this reaction of Al with heated water, but it is generally assumed that Al^{+++} ions diffuse through the film to react with OH^- ions, and it is clear that the change of K_w with temperature may have an important bearing on this aspect of the matter.

[16] Aluminium Labs. Ltd., Banbury, Oscon, England.

[17] D. Altenpohl, *Aluminium*, 33, [2], 78 (1957).

Electrochemical Properties of a Cation-Transfer Membrane

N. W. Rosenberg, J. H. B. George, and W. D. Potter (pp. 111-115, Vol. 104)

Reinhard H. Beutner[18]: Drs. Rosenberg, George, and Potter explain the electromotive forces by ion transfer and ion mobilities in the hypothetical pores. They disregard the possibility that potential differences exist at the phase boundary (or contact) surface of the Nepton membrane on both sides where the membrane is in contact with aqueous solutions.

N. W. Rosenberg and J. H. B. George: Dr. Beutner has two reservations with respect to the membrane model suggested by the authors: namely, mass transfer through pores, and emf caused by such mass transfer.

A membrane of the type under discussion is formed from a cross-linked organic polymer, which, prior to sulfonation, has substantially no permeability to water or to ions. After sulfonation, which provides negative exchange sites on the polymer, the membrane will swell in aqueous systems, by absorption of water, to an extent determined by the cross-linking. Thus, previous workers in the field (and the authors) describe the resin as a network of hydrocarbon chains, "welded" at intervals of 10-20Å by cross chains, and permeable to water and to ions through the interstices of the network, defined as pores. The level of porosity in ion exchange resins has been reported by Kressman[19] and Partridge and Brimley[20] by measurement of capacity for a series of ions of increasing size, and noting a complete loss of capacity for ions of greater than 10-20Å diameter.

With respect to selective mass transfer as a source of emf, we have used the conventional Nernst equation for electrochemical potential of a cell with membrane transference, recently critically re-ex-

[18] Des Moines Still College of Osteopathy and Surgery, Des Moines 9, Iowa.

[19] T. R. E. Kressman, *J. Phys. Chem.*, 56, 118 (1952).

[20] S. M. Partridge and R. C. Brimley, *Biochem. J. (London)*, 51, 628 (1952).

amined by Scatchard[21] in view of water transport. Potential differences (other than those considered by the Nernst equation) may well exist at a single-phase boundary surface but cannot be measured since a membrane separating two solutions has two such surfaces and an equal and opposite potential will, of course, exist at the second surface, cancelling that at the first surface.

Current Distribution in Galvanic Cells Involving Natural Convection

Carl Wagner (pp. 129-131, Vol. 104)

E. M. Sparrow[22]: Professor Wagner's interesting paper is a clear demonstration of the advances which may be made by application of results which were initially derived in a rather different field of scientific research. By using the analogy between the transfer processes involved, results for free convection heat transfer were applied to the mass transfer problem.

It is the purpose of this discussion to present some additional results, initially found for heat transfer, which may be useful in extending Professor Wagner's analysis. Suppose that instead of treating the case where the rate of mass transfer of Cu ions (j) is uniform over the electrode, the more general situation where $j \sim x^r$ is considered. (The notation is identical to that of the discussed paper.) Then, the value of Δc at a distance x from the leading edge of the electrode is[23]

$$\Delta c = 1.31 \frac{jx}{D} \left[\frac{\left(\frac{35}{12} Sc + 1\right)(r+1) + \frac{4}{3}}{(r+1)\, Sc^2\, Gr_x^*} \right]^{1/5} \qquad \text{(I)}$$

When $r = 0$, this equation corresponds to Eq. (IV) in the discussed paper.[24] It is expected that Eq. (I) will be sufficiently accurate for most applications for $r > -0.5$.

Another situation of possible interest is that in which Δc is prescribed and it is desired to compute j. For the case where $\Delta c \sim x^n$, the variation of j with x is given by[23]

$$j = 0.715 \mid \Delta c \mid \frac{D}{x} \left[\frac{\left(\frac{5n+3}{4}\right)^2 Sc^2\, Gr_x}{\left(\frac{35}{12} Sc + 1\right)\left(\frac{5n+3}{4}\right) + \frac{4}{3}} \right]^{1/4} \qquad \text{(II)}$$

where

$$Gr_x = \frac{g\beta' \mid \Delta c \mid x^3}{\nu^2}$$

Eq. (II) is expected to be of adequate accuracy for $n > -0.2$.

[21] G. Scatchard, *J. Am. Chem. Soc.*, 75, 2883 (1953).

[22] NACA Lewis Lab., Cleveland 11, Ohio.

[23] M. Tribus, Discussion of A.S.M.E. paper 57-SA-3, "Similar Solutions for Free Convection from a Nonisothermal Vertical Plate" by E. M. Sparrow and J. L. Gregg, to be published in *Trans. A.S.M.E.*, **80** (1958).

[24] There is a printing error in Eq. (IV) of the discussed paper in that $(0.8 + Sc)/Sc^2\, Gr_x^*$ should be raised to the one-fifth power.

Notes on Hydrogen Overvoltage, I. Maximum Concentration of Atomic Hydrogen on the Surface of a Working Cathode

Hugh W. Salzberg and Sigmund Schuldiner (pp. 319-321, Vol. 104)

H. W. Salzberg and S. Schuldiner: The following corrections should be made to the equations on page 320 of the paper.

(*A*) Eq. (I): change $F^2{}_H$ to $f^2{}_H$.

(*B*) t in equations should be changed to T.

(*C*) Expressions on right-hand sides for r_{mobile} should be multiplied by 2.

(*D*) The term $H^2\ \sigma\ (kT/h)^{1/2}$ immediately following Eq. (II*a*) should be changed to read $2H^2\ \sigma\ (kT/m)^{1/2}$.

Preparation of Thorium Bismuth Dispersions from Electrolytic Thorium

M. E. Sibert and M. A. Steinberg (pp. 374-378, Vol. 104)

R. P. Marshall[25]: Reference is made to the conditions required for electrolysis to yield a fine particle size, viz., high current density, low temperature, and high Th content. In the next paragraph reference is made to the melt being exhausted of Th content. Therefore these two statements are incompatible because, even though a high starting Th content is used, ultimately this is to be nearly all removed, when the progressively lowering Th content should affect the particular size of the deposit.

The authors refer to a temperature of 550°-650°C. This probably is satisfactory in the presence of 10% of Th, but, when the melt has been stripped of $ThCl_4$, pure NaCl will be left which has a melting point of 801°C. It is therefore not clear from the authors' comments for how long they maintained the temperature of 550°-650°C to which they refer.

The term "high current density" is correlated to a cathode current density of 200-300 amp/dm^{-2}. In my opinion, the cathode current density can only effectively apply to the starting current density and is very rapidly altered as the dendritic deposit grows. Therefore the starting cathode current density cannot have a serious influence on the particular size of the deposit if any appreciable quantity of Th is being deposited. Incidentally, I was surprised that the authors consider a cathode current density of the above magnitude to be high, since from my practical experience cathode current densities of 1000 amp/dm^{-2} are normal and frequently current densities much in excess of this have been applied to fused alkali chloride electrolytes.

I shall be interested in the authors' comments on the mechanism of the purification of $ThCl_4$ melts by the passing of HCl gas through them.

M. E. Sibert: In reference to the statement concerning exhaustion of Th content of the bath during electrolysis at 550°-650°C, this was possible for the majority of runs where eutectic melts such as KCl-NaCl or NaCl-$CaCl_2$ were employed. Obviously, if NaCl were used alone as a solvent, the temperature

[25] T. A. Dept., Impregnated Diamond Products Ltd., Tuffley Crescent, Gloucester, England.

would rise to 801°C (mp of NaCl) when the Th content is exhausted as Mr. Marshall states. In most cases the melt was not exhausted of Th content; melts contained 110-225 g Th, and, in general, 55-165 g were deposited out.

Mr. Marshall is correct in his statement regarding cathode current density. All figures shown are starting cathode current densities based on initial cathode areas. The values of 200-300 amp/dm^2 are termed "high" only in comparison with the "low" range of <50 amp/dm^2 also employed in the work.

Starting cathode current density does have a marked effect on average particle size of the deposit. Raising the starting cathode current density from 50 to 250 amp/dm^2 will reduce the average particle size of the deposit by 50% or more.

The apparent mechanism of purification of $ThCl_4$-bearing melts by HCl sparging is a straightforward one although the actual mechanism is possibly quite complex. It appears that oxidic impurities in the melt (e.g., ThO_2, $ThOCl_2$, etc.) are chlorinated and moisture eliminated (at 800°-900°C)

$$\text{e.g., } ThOCl_2 + 2HCl \rightarrow ThCl_4 + \overline{H_2O}$$

This has been indicated by melt analyses plus analysis and dew point measurements on effluent gases from the cell during sparging.